Initial Reports of the Deep Sea Drilling Project

Volume LXXXII

Ponta Delgada, Azores to Balboa, Panama
September – November 1981

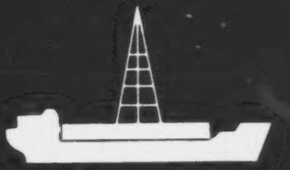

READEX
FICHE
best copy available

NATIONAL SCIENCE FOUNDATION
National Ocean Sediment Coring Program

NSFSP – 82

June 1985

82

Drilling locations

Leg	Location	Sites
Phase 1 1968–1970		
1	North Atlantic	1–7
2	North Atlantic	8–12
3	South Atlantic	13–22
4	Central Atlantic	23–31
5	North Pacific	32–43
6	North Pacific	44–60
7	Central Pacific	61–67
8	Central Pacific	68–75
9	Central Pacific	76–84
Phase 2 1970–1972		
10	Gulf of Mexico	85–97
11	North Atlantic	98–108
Re-entry trials		109–110
12	North Atlantic	111–119
13	Mediterranean	120–134
14	Central Atlantic	135–144
15	Caribbean	146–154
16	Central Pacific	155–163
17	Central Pacific	164–171
18	North Pacific	172–182
19	North Pacific	183–193
20	North Pacific	194–202
21	Coral Sea	203–210
22	Indian Ocean	211–218
23	Arabian Sea	219–230
24	Indian Ocean	231–238
25	Indian Ocean	239–249
Phase 3 1972–1975		
26	Indian Ocean	250–258
27	Indian Ocean	259–263
28	Antarctic	264–274
29	Tasman Sea	275–284
30	South Pacific	285–289
31	North Pacific	290–302
32	North Pacific	303–313
33	North Pacific	314–318
34	South Pacific	319–321
35	South Pacific	322–325
36	South Atlantic	326–331
37	North Atlantic	332–335
38	Arctic	336–352
39	Atlantic	353–359
40	South Atlantic	360–365
41	South Atlantic	366–370
42A	Mediterranean	371–378
42B	Black Sea	379–381
43	North Atlantic	382–387
44	North Atlantic	388–392
44A	North Atlantic	393–394
IPOD I 1975–present		
45	North Atlantic	395–396
46	North Atlantic	396A–396B
47	North Atlantic	397–398
48	North Atlantic	399–406
49	North Atlantic	407–414
50	North Atlantic	415–416
51A	North Atlantic	417–417A
51B	North Atlantic	417B–417D
52	North Atlantic	417D–418A
53	North Atlantic	418A–418B
54	Central Pacific	419–429
55	North Pacific	430–433
56	North Pacific	434–437
57	North Pacific	438–441
58	North Pacific	442–446
59	North Pacific	447–451
60	North Pacific	452–461
61	Central Pacific	462
62	North Pacific	463–466
63	North Pacific	467–473
64	Gulf of California	474–481
65	Gulf of California	482–485
66	Central Pacific	486–493
67	Central Pacific	494–500
68	Central Pacific	502–503
69	Central Pacific	504–505, 501
70	Central Pacific	506–510, 504B
71	South Atlantic	511–514
72	South Atlantic	515–518
73	South Atlantic	519–524
74	South Atlantic	525–529
75	South Atlantic	530–532
76	North Atlantic	533–534
77	Caribbean	535–540
78	North Atlantic	541–543, 395A, B
79	North Atlantic	544–547
80	North Atlantic	548–551
81	North Atlantic	552–555
82	North Atlantic	556–564

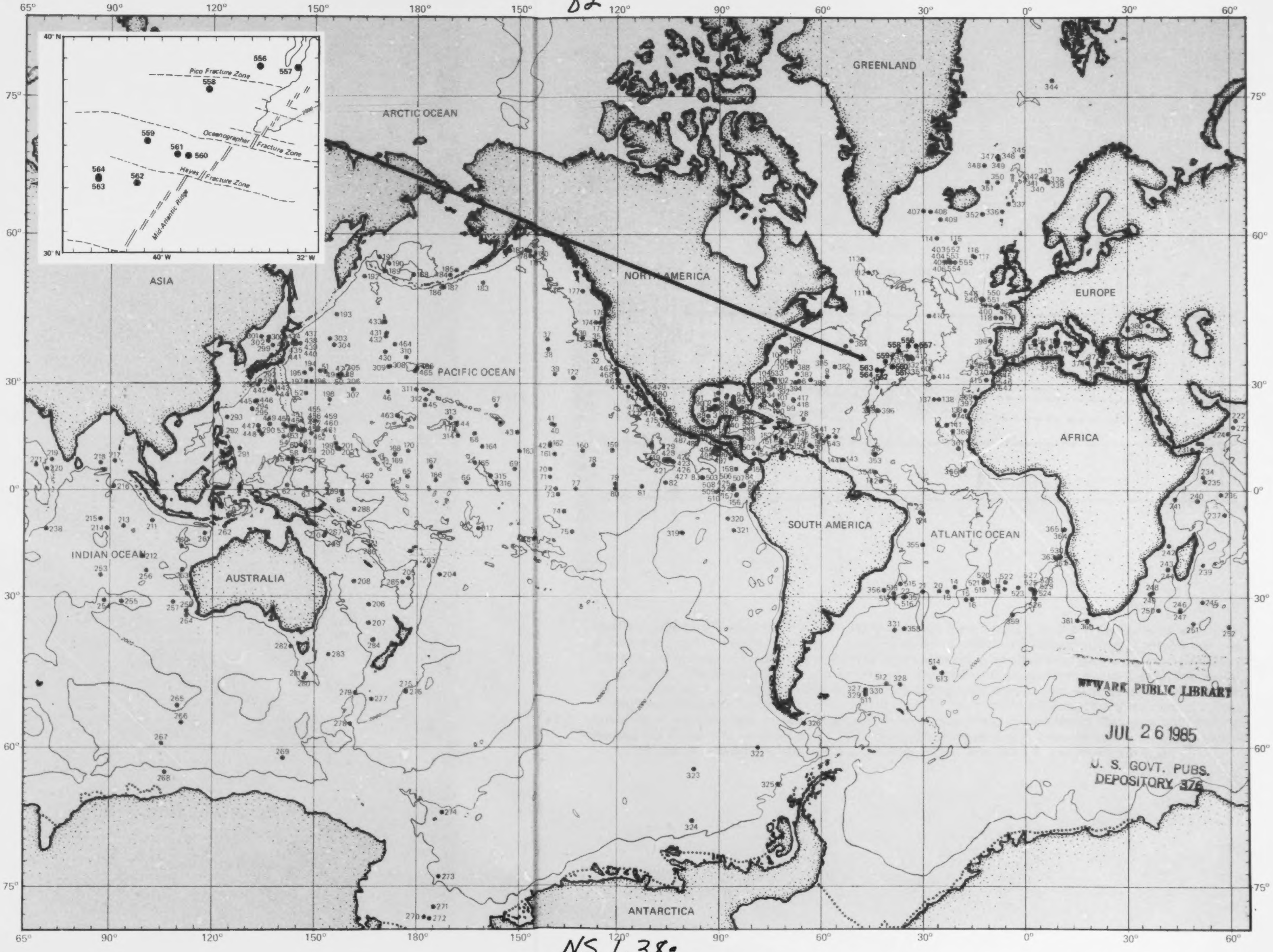
40° N
556
557
Pico Fracture Zone
558
559
Oceanographer Fracture Zone
561
560
564
563
562
Hayes Fracture Zone
Mid-Atlantic Ridge
30° N
40° W
32° W
ARCTIC OCEAN
GREENLAND
ASIA
NORTH AMERICA
EUROPE
PACIFIC OCEAN
AFRICA
INDIAN OCEAN
AUSTRALIA
SOUTH AMERICA
ATLANTIC OCEAN
ANTARCTICA
65°
90°
120°
150°
180°
150°
120°
90°
60°
30°
0°
30°
60°
75°
60°
30°
0°
30°
60°
75°

NEWARK PUBLIC LIBRARY
JUL 26 1985
U. S. GOVT. PUBS.
DEPOSITORY 376

NS 1.38:

DEEP SEA DRILLING PROJECT

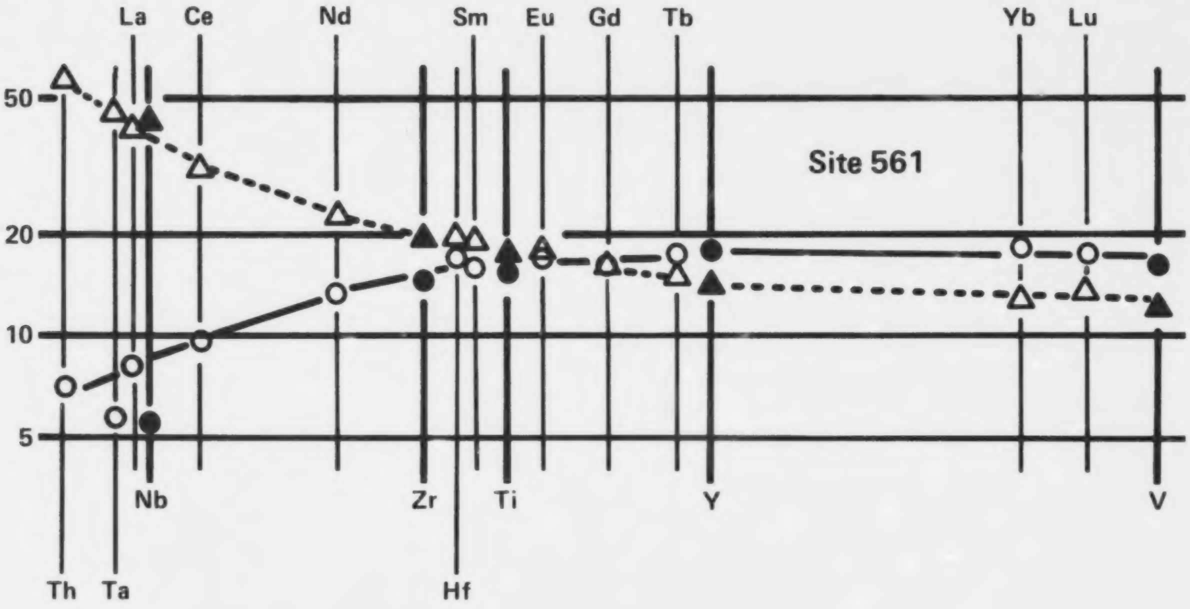

Crossing patterns of hygromagmaphile elements in basalts from Site 561. Such crossing patterns, also found at Site 558, reflect mantle heterogeneity and/or different extents of partial melting of mantle material. The ordinate corresponds to the concentrations of the elements in basalts normalized to their concentrations in chondrites. The rare earth elements are plotted versus their atomic numbers (upper part of the figure); the non–rare earth elements are plotted according to their similarity to rare earth elements with respect to magmatic processes (lower part of the figure). Nb, Zr, Ti, Y, and V (filled symbols) correspond to shipboard data (see Etoubleau et al., this volume, for analytical chemistry on board) that were used for conducting the cruise. The other elements (open symbols) correspond to onshore data from several references in this volume (Bougault et al., Rideout and Schilling, Weaver et al., Drake et al., Hertogen et al.).

Initial Reports
# of the
Deep Sea Drilling Project

A Project Planned by and Carried Out With the Advice of the
JOINT OCEANOGRAPHIC INSTITUTIONS FOR DEEP EARTH SAMPLING (JOIDES)

VOLUME LXXXII

covering Leg 82 of the cruises of the Drilling Vessel *Glomar Challenger*
Ponta Delgada, Azores, to Balboa, Panama
September–November 1981

PARTICIPATING SCIENTISTS

Henri Bougault, Steven C. Cande, Joyce C. Brannon, David M. Christie,
Murlene Clark, Doris M. Curtis, Natalie Drake, Dorothy Echols,
Ian Ashley Hill, Mohammad Javed Khan, William Mills,
Rolf Neuser, Marion L. Rideout, and Barry L. Weaver

SHIPBOARD SCIENCE REPRESENTATIVE

William Mills

EDITOR

Elizabeth Whalen

Prepared for the
NATIONAL SCIENCE FOUNDATION
National Ocean Sediment Coring Program
Under Contract C-482
By the
UNIVERSITY OF CALIFORNIA
Scripps Institution of Oceanography
Prime Contractor for the Project

This material is based upon research supported by the National Science Foundation under Contract No. C-482.

Any opinions, findings, and conclusions or recommendations expressed in this publication are those of the author(s) and do not necessarily reflect the views of the National Science Foundation.

It is recommended that reference to the whole or to part of this volume be made in one of the following forms, as appropriate:

Bougault, H., Cande, S. C., et al., 19__. *Init. Repts. DSDP*, 82: Washington (U.S. Govt. Printing Office).

Bukry, D., 19__. Mid-Atlantic Ridge coccolith and silicoflagellate biostratigraphy, Deep Sea Drilling Project Sites 558 and 563. *In* Bougault, H., Cande, S. C., et al., *Init. Repts. DSDP*, 82: Washington (U.S. Govt. Printing Office), 591-603.

Effective Publication Dates of DSDP *Initial Reports*

According to the International Code of Zoological Nomenclature, the date of publication of a work and of a contained name or statement affecting nomenclature is the date on which the publication was mailed to subscribers, placed on sale, or when the whole edition is distributed free of charge, mailed to institutions and individuals to whom free copies are distributed. The mailing date, *not the printed date*, is the correct one.

Mailing dates of the more recent *Initial Reports of the Deep Sea Drilling Project* are as follows:

Volume 75—June, 1984
Volume 76—November, 1983
Volume 77—September, 1984
Volume 78A,B—August, 1984
Volume 79—November, 1984
Volume 81—January, 1985

Printed June 1985

Library of Congress Catalog Card Number 74—603338

For sale by the Superintendent of Documents, U.S. Government Printing Office
Washington, D.C. 20402

Stock Number 038-000-00556-1

Foreword

The world's first major oceanographic expedition took place between 1872 and 1876. This expedition, aboard the H.M.S. *Challenger* covering nearly 70,000 nautical miles and gathering oceanographic data from 362 stations, expanded our knowledge of the ocean and provided a solid foundation for future studies in marine geology. A century later, another vessel also named *Challenger* continued to expand our knowledge of the world's ocean and helped revolutionize our concepts of how the seafloor and the continents form and change. The drilling vessel *Glomar Challenger* sailed the same waters as its historic counterpart, seeking answers to new questions concerning the history of our planet and the life it supports. The continued advancement of knowledge about the fundamental processes and dynamics of the earth is leading to a greater understanding of our planet and more intelligent use of its resources.

Since 1968, the Deep Sea Drilling Project (DSDP) has been supported by the National Science Foundation, primarily through a contract with the University of California which, in turn, subcontracted to Global Marine Incorporated for the services of the D/V *Glomar Challenger*.

Through contracts with Joint Oceanographic Institutions, Inc. (JOI, Inc.), the National Science Foundation supported the scientific advisory structure for the project and funded predrilling geophysical site surveys. Scientific planning was conducted under the auspices of the Joint Oceanographic Institutions for Deep Earth Sampling (JOIDES). The JOIDES advisory group consisted of over 250 members who made up 24 committees, panels, and working groups. The members were distinguished scientists from academic institutions, government agencies, and private industry all over the world.

In 1975, the International Phase of Ocean Drilling (IPOD) began. The IPOD member nations, Federal Republic of Germany, Japan, United Kingdom, Soviet Union, and France, partially supported the project. Each member nation actively participated in the scientific planning of the project through membership in JOIDES. Scientists from these countries also took part in the field work aboard the D/V *Glomar Challenger* and postcruise scientific studies.

The first ocean coring operations for the Deep Sea Drilling Project began on August 11, 1968. During the ensuing years of drilling operations in the Atlantic, Pacific, and Indian oceans, the Gulf of Mexico, Caribbean Sea, Mediterranean Sea, and Antarctic waters, the scientific objectives that had been proposed were successfully accomplished. Primarily, the age of the ocean basins and their processes of development were determined. The validity of the hypothesis of seafloor spreading was firmly demonstrated and its dynamics studied. Emphasis was placed on broad reconnaissance and testing the involvement of mid-oceanic ridge systems in the development of the ocean basin. Later legs of the *Challenger's* voyages concentrated on the nature of the oceanic crust, the sedimentary history of the passive ocean margins, sediment dynamics along active ocean margins, and other areas of interest. The accumulated results of this project have led to major new interpretations of the pattern of sedimentation and the physical and chemical characteristics of the ancient oceans.

Technological advances have provided new tools which in turn have opened new dimensions of scientific discovery. The introduction of the Hydraulic Piston Corer in 1979 permitted virtually undisturbed cores of soft sediment layers to be obtained. This technological advance has greatly enhanced the ability of scientists to study ancient ocean environments, as recorded by sediment characteristics and flora and fauna preserved in these deposits.

A second major advance has been the use of the hole after drilling. The project routinely logged holes and performed geophysical and geochemical studies before, during, and after drilling. Long-term downhole geophysical seismic monitoring devices have been implanted successfully in DSDP holes. These new listening devices and geophysical studies have provided valuable information about the origin and nature of the dynamic processes of plate tectonics.

These reports contain the results of the initial studies of the recovered core material and the associated geophysical information. All the world's people benefit either directly or indirectly from this fundamental research. Knowledge about past and present conditions and processes are the foundations for future predictions and developments. Both short- and long-term benefits are obtained by advances in drilling technology and instrumentation. Information is being obtained about the origin and geographic distribution of natural resources. Just as the H.M.S. *Challenger* had a profound impact on scientific thought for over a century, this second *Challenger* expedition has given a greater understanding of the oceans and the processes that form and shape the earth.

Erich Bloch,
Director

Washington, D.C.

Preface

Recognizing the need in the oceanographic community for scientific planning of a program to obtain deep sedimentary cores from the ocean bottoms, four of the major oceanographic institutions that had strong interests and programs in the fields of marine geology and geophysics formed, in May 1964, the Joint Oceanographic Institutions for Deep Earth Sampling (JOIDES). This group, Lamont-Doherty Geological Observatory; Rosenstiel School of Marine and Atmospheric Science, University of Miami; the Scripps Institution of Oceanography, University of California at San Diego; and the Woods Hole Oceanographic Institution, expressed an interest in undertaking scientific planning and guidance of the sedimentary drilling program. It was the purpose of this group to foster programs to investigate the sediments and rocks beneath the deep oceans by drilling and coring. The membership of this original group was later enlarged in 1968 when the University of Washington became a member, and again in 1975 when University of Hawaii Institute of Geophysics, the Oregon State University School of Oceanography, the University of Rhode Island Graduate School of Oceanography, and Texas A&M University Department of Oceanography became members. In accordance with international agreements, institutions of participating nations became members of JOIDES. Thus, during 1974 to 1976, the Bundesanstalt für Geowissenschaften und Rohstoffe of the Federal Republic of Germany, the Centre National pour l'Exploitation des Océans of France, the Natural Environment Research Council of the United Kingdom, the University of Tokyo of Japan, and Academy of Sciences of the USSR became JOIDES members.

Through discussions sponsored by the JOIDES organization, with support from the National Science Foundation, Columbia University's Lamont-Doherty Geological Observatory operated a drilling program in the summer of 1965, on the Blake Plateau region off Jacksonville, Florida.

With this success in hand, planning began for a more extensive deep sea effort. This resulted in the award of a contract by the National Science Foundation to the Scripps Institution of Oceanography, University of California at San Diego for an eighteen-month drilling program in the Atlantic and Pacific oceans, termed the Deep Sea Drilling Project (DSDP). Operations at sea began in August 1968, using the now-famous drilling vessel, the *Glomar Challenger*.

The goal of the Deep Sea Drilling Project is to gather scientific information that will help determine the age and processes of development of the ocean basins. The primary strategy is to drill deep holes into the ocean floor, relying largely on technology developed by the petroleum industry.

Through the efforts of the principal organizations and of the panel members, who were drawn from a large cross section of leading earth scientists and associates, a scientific program was developed.

Cores recovered from deep beneath the ocean floor provide reference material for a multitude of studies in fields such as biostratigraphy, physical stratigraphy, and paleomagnetism that afford a new scope for investigating the physical and chemical aspects of sediment provenance, transportation, deposition, and diagenesis. In-hole measurements, as feasible, provide petrophysical data to permit inference of lithology of intervals from which no cores were recovered.

A report, describing the core materials and information obtained both at sea and in laboratories onshore, is published after the completion of each cruise. These reports are a cooperative effort of shipboard and shore-based scientists and are intended primarily to be a compilation of results which, it is hoped, will be the starting point for many future new and exciting research programs. Preliminary interpretations of the data and observations taken at sea are also included.

Core materials and data collected on each cruise will be made available to qualified scientists through the Curator of the Deep Sea Drilling Project, following a Sample Distribution Policy (p. xvii) approved by the National Science Foundation.

The advent of *Glomar Challenger*, with its deep-water drilling capability, is exceedingly timely. It has come when geophysical investigation of the oceans has matured through 20 to 30 years of vigorous growth to the point where we have some knowledge about much of the formerly unknown oceanic areas of our planet. About one million miles of traverses have been made which tell us much about the global pattern of gravity, magnetic and thermal anomalies, and about the composition, thickness, and stratigraphy of the sedimentary cover of the deep sea and continental margin. The coverage with such data has enabled the site selection panels to pick choice locations for drilling. The knowledge gained from each hole can be extended into the surrounding area. Detailed geophysical surveys were made for most of the selected locations prior to drilling.

The earth sciences have recently matured from an empirical status to one in which substantial theories and hypotheses about major tectonic processes are flourishing. Theories about the origin of magnetic fields and magnetic reversals, about ocean floor spreading and continental drift, and about the thermal history of our planet have led to specific predictions that could be tested best by an enlightened program of sampling of deep sea and continental margin sediments and underlying rocks.

In October 1975, the International Phase of Ocean Drilling (IPOD) began. This international interest, and the true participation of both the scientists and governments of a number of nations, are eloquent testimony to the importance of the work being done by the Deep Sea Drilling Project.

The members of JOIDES and DSDP and the scientists from all interested organizations and nations who have served on the various advisory panels are proud to have been of service and believe that the information and core materials that have been obtained will be of value to students of earth sciences and to all humanity for many years to come.

Deep Sea Drilling Project

MEMBER ORGANIZATIONS OF THE JOINT OCEANOGRAPHIC INSTITUTIONS FOR DEEP EARTH SAMPLING (JOIDES):[1]

Bundesanstalt für Geowissenschaften und Rohstoffe, Federal Republic of Germany

University of California at San Diego, Scripps Institution of Oceanography

Centre National pour l'Exploitation des Océans, Paris

Columbia University, Lamont-Doherty Geological Observatory

University of Hawaii, Hawaii Institute of Geophysics

University of Miami, Rosenstiel School of Marine and Atmospheric Science

Natural Environment Research Council, London

Oregon State University, School of Oceanography

University of Rhode Island, Graduate School of Oceanography

Texas A&M University, Department of Oceanography

University of Tokyo, Ocean Research Institute

University of Washington, Department of Oceanography

U.S.S.R. Academy of Sciences[2]

Woods Hole Oceanographic Institution

OPERATING INSTITUTION

Scripps Institution of Oceanography
University of California at San Diego
La Jolla, California
W. A. Nierenberg, Director

DEEP SEA DRILLING PROJECT

Dr. M. N. A. Peterson
Principal Investigator
Project Manager

Mr. Robert S. Bower
Assistant Project Manager for
Administration and Contracts

Dr. Yves Lancelot
Chief Scientist

Mr. Ed Dean
Finance Administrator

Ms. Sue Strain
Personnel Officer

---

[1] Includes member organizations during time of cruise.

[2] This institution and its committees and panel members were noncontributing members of JOIDES at time of cruise.

blank page

Participants aboard GLOMAR CHALLENGER for Leg Eighty-two

Dr. Henri Bougault
Co-Chief Scientist
Centre Océanologique de Bretagne
Boite Postale 337
29273 Brest Cedex
France

Dr. Steven C. Cande
Co-Chief Scientist
Lamont-Doherty Geological Observatory
Columbia University
Palisades, New York 10964

Dr. Joyce C. Brannon
Igneous Petrologist/Geochemist
Department of Earth and
Planetary Sciences
Washington University
Box 1169
St. Louis, Missouri 63130

Mr. David M. Christie
Igneous Petrologist
Hawaii Institute of Geophysics
University of Hawaii
2525 Correa Road
Honolulu, Hawaii 96822

Dr. Marlene Clark
Paleontologist (nannofossils)
Department of Geology
Florida State University
Tallahassee, Florida 32306

Dr. Doris M. Curtis
Sedimentologist
Curtis & Echols
Geological Consultants
16730 Hedgecroft
Houston, Texas 77060

Dr. Natalie Drake
Igneous Petrologist/Geochemist
Department of Geology
University of Massachusetts
Amherst, Massachusetts 01003

Dr. Dorothy Echols
Paleontologist (foraminifers)
Department of Earth and Planetary Sciences
Washington University
St. Louis, Missouri 63130

Dr. Ian Ashley Hill
Physical Properties Specialist
Department of Geology
University of Leicester
University Road
Leicester LE1 7RH, England

Mr. Mohammad Javed Khan
Paleomagnetist
Lamont-Doherty Geological Observatory
Columbia University
Palisades, New York 10964

Mr. William Mills
Sedimentologist/Shipboard Science
Representative
Deep Sea Drilling Project, A-031
Scripps Institution of Oceanography
La Jolla, California 92093

Dr. Rolf Neuser
Igneous Petrologist
Institut für Geologie
Ruhr-Universität Bochum
Postfach 102148
4630 Bochum 1
Federal Republic of Germany

Dr. Marion L. Rideout
Igneous Petrologist
Graduate School of Oceanography
Narragansett Bay campus
University of Rhode Island
Kingston, Rhode Island 02881

Dr. Barry L. Weaver
Igneous Petrologist/Geochemist
Department of Geology
University of Leicester
University Road
Leicester LE1 7RH, England

Mr. Glen Foss
Cruise Operations Manager
Deep Sea Drilling Project, A-031
Scripps Institution of Oceanography
La Jolla, California 92093

Mr. Melvin Fields
Weatherman
Deep Sea Drilling Project, A-031
Scripps Institution of Oceanography
La Jolla, California 92093

Captain Joseph A. Clarke
Captain of the Drilling Vessel
Global Marine, Inc.
San Diego, California 92111

Mr. James A. Ruddell
Drilling Superintendent
Global Marine, Inc.
San Diego, California 92111

Mr. Burney Hamlin
Laboratory Officer
Deep Sea Drilling Project, A-031
Scripps Institution of Oceanography
La Jolla, California 92093

Ms. Leslie Reynolds
Curatorial Representative
Office of Marine Geology
U.S. Geological Survey
Woods Hole, Massachusetts 02543

Mr. Don Marsee
Chemist
Deep Sea Drilling Project, A-031
Scripps Institution of Oceanography
La Jolla, California 92093

Mr. Edward Moffatt
Logging Engineer
Schlumberger (Europe)
1, Kingsway
London WC2B 6XH
United Kingdom

Mr. Joel Etoubleau
XRF Technician
Centre Océanologique de Bretagne
Boite Postal 337
29273 Brest Cedex, France

Mr. Mark Aunchman
Electronics Technician
Deep Sea Drilling Project, A-031
Scripps Institution of Oceanography
La Jolla, California 92093

Mr. Bruce Blumer
Marine Technician
Deep Sea Drilling Project, A-031
Scripps Institution of Oceanography
La Jolla, California 92093

Mr. Dennis Graham
Marine Technician
Deep Sea Drilling Project, A-031
Scripps Institution of Oceanography
La Jolla, California 92093

Mr. Brad Julson
Marine Technician
Deep Sea Drilling Project, A-031
Scripps Institution of Oceanography
La Jolla, California 92093

Mr. William Meyer
Marine Technician
Deep Sea Drilling Project, A-031
Scripps Institution of Oceanography
La Jolla, California 92093

Mr. Kevin Reid
Photographer
Deep Sea Drilling Project, A-031
Scripps Institution of Oceanography
La Jolla, California 92093

Ms. Louise Henry
Yeoperson
Deep Sea Drilling Project, A-031
Scripps Institution of Oceanography
La Jolla, California 92093

Deep Sea Drilling Project Publications Staff

Publications Manager
Jan H. Blakeslee

Editors
Marian G. Bailey
Susan Orlofsky
Katie L. Turner
Elizabeth Whalen

Production Manager
Raymond F. Silk

Production Assistants
Elaine Bruer
Madeleine A. Mahnken

Production Coordinators
Carolina Bertling
Mary A. Young

Art-Photo Supervisor
Virginia L. Roman

Illustrators
Myrtali Anagnostopoulos
Aileen Bobryk
Vicki Cypherd (this volume)
Kathleen Sanderson
Alice N. Thompson

JOIDES Advisory Groups[1]

Executive Committee

Dr. James D. Baker, Jr.
University of Washington

Prof. Dr. Friedrich Bender
Bundesanstalt für Geowissenschaften und Rohstoffe

Dr. G. Ross Heath
Oregon State University

Dr. Charles E. Helsley
Hawaii Institute of Geophysics

Sir Peter Kent, F.R.S.
Natural Environment Research Council

Dr. John A. Knauss
University of Rhode Island

Dr. Noriyuki Nasu
University of Tokyo

Dr. William A. Nierenberg, Chairman
Scripps Institution of Oceanography

Dr. M. N. A. Peterson (ex-officio)
Scripps Institution of Oceanography

Monsieur Gerard Piketty
Centre National pour l'Exploitation des Océans

Dr. Barry Raleigh
Lamont-Doherty Geological Observatory

Prof. Robert D. Reid
Texas A&M University

Dr. Alexander V. Sidorenko
U.S.S.R. Academy of Sciences

Dr. John Steele
Woods Hole Oceanographic Institution

Dr. Warren Wisby
Rosenstiel School of Marine and Atmospheric Science

Planning Committee

Prof. Jean Aubouin
Université Pierre et Marie Curie

Dr. Helmut Beiersdorf
Bundesanstalt für Geowissenschaften und Rohstoffe

Dr. William R. Bryant
Texas A&M University

Dr. Joe R. Cann
University of Newcastle-upon-Tyne

Dr. John B. Corliss
Oregon State University

Dr. Joe S. Creager
University of Washington

Mr. John I. Ewing
Woods Hole Oceanographic Institution

Dr. Dennis E. Hayes
Lamont-Doherty Geological Observatory

Dr. James P. Kennett
University of Rhode Island

Dr. Kazuo Kobayashi
University of Tokyo

Dr. Yves Lancelot (ex-officio)
Scripps Institution of Oceanography

Dr. Ralph Moberly
Hawaii Institute of Geophysics

Dr. Lev Nikitin
U.S.S.R. Academy of Sciences

Dr. Wolfgang Schlager
University of Miami

Dr. Edward L. Winterer, Chairman
Scripps Institution of Oceanography

Advisory Panel on Sedimentary Petrology and Physical Properties

Dr. Michael A. Arthur
University of South Carolina, Columbia

Dr. Richard Bennett
National Oceanic and Atmospheric Administration

Dr. John W. Handin
Texas A&M University

Dr. George deVries Klein
University of Illinois, Urbana

Dr. Leland Kraft
McClelland Engineers, Inc.

Dr. I. Nick McCave
University of East Anglia

Dr. Frédéric Mélières
Université Pierre et Marie Curie

Dr. Ralph Moberly (ex-officio)
Hawaii Institute of Geophysics

Dr. Orrin H. Pilkey
Duke University

Dr. Adrian Richards, Chairman
Lehigh University

Dr. Peter Rothe
Universität Mannheim

Dr. Matthew H. Salisbury (ex-officio)
Scripps Institution of Oceanography

Prof. Peter P. Timofeev
U.S.S.R. Academy of Sciences

Advisory Panel on Organic Geochemistry

Dr. Earl W. Baker
Florida Atlantic University

Dr. John B. Corliss (ex-officio)
Oregon State University

---

[1] Membership at time of cruise.

Dr. William T. Coulbourn (ex-officio)
Scripps Institution of Oceanography

Prof. Geoffrey Eglinton
University of Bristol

Dr. Gordon Erdman
Phillips Petroleum Company

Dr. Eric M. Galimov
U.S.S.R. Academy of Sciences

Dr. John M. Hunt
Woods Hole Oceanographic Institution

Dr. Keith Kvenvolden
U.S. Geological Survey

Dr. Philip A. Meyers
University of Michigan

Dr. Bernd R. Simoneit, Chairman
Oregon State University

Dr. Colin P. Summerhayes
Exxon Production Research Company

Dr. Bernard Tissot
Institut Français du Pétrole

Dr. Dietrich Welte
Lehrstuhl für Geologie, Geochemie, und Lagerstätten des Erdöls und der Kohle

Advisory Panel on Information Handling

Dr. Daniel E. Appleman, Chairman
Smithsonian Institution

Dr. John C. Hathaway
U.S. Geological Survey

Dr. Alfred Loeblich, Jr.
University of California, Los Angeles

Dr. Michael S. Loughridge
National Oceanic and Atmospheric Administration

Dr. Marthe Melguen
Centre Océanologique de Bretagne (BNDO)

Mrs. Judit Nowak
Bundesanstalt für Geowissenschaften und Rohstoffe

Mr. Peter Woodbury (ex-officio)
Scripps Institution of Oceanography

Dr. Valery V. Zdorovenin
U.S.S.R. Academy of Sciences

Industrial Liaison Panel

Mr. R. L. Adams
Conoco Incorporated

Prof. Nikolai P. Budnikov
Ministry of Geology of the U.S.S.R.

Mr. Melvin J. Hill
Gulf Oil Exploration and Production Company

Dr. Ing. Guenter Peterson
Gewerkschaft Walter

Mr. W. A. Roberts, Chairman
Phillips Petroleum Company

Dr. Gilbert Rutman
Société Nationale des Pétroles d'Aquitaine

Mr. G. Williams
United Kingdom Offshore Operators Association, Ltd.

Advisory Panel on Ocean Crust

Dr. Roger N. Anderson
Lamont-Doherty Geological Observatory

Dr. Henri Bougault
Centre Océanologique de Bretagne (CNEXO)

Dr. John B. Corliss (ex-officio)
Oregon State University

Prof. Dr. Rolf Emmermann
Universität Karlsruhe

Dr. Paul J. Fox, Chairman
University of Rhode Island

Dr. Jose Honnorez
Rosenstiel School of Marine and Atmospheric Sciences

Dr. Paul Johnson
University of Washington

Dr. Ralph Moberly (ex-officio)
Hawaii Institute of Geophysics

Dr. James Natland (ex-officio)
Scripps Institution of Oceanography

Dr. Minoru Ozima
University of Tokyo

Dr. Paul Robinson
Dalhousie University

Dr. Hans Schouten
Woods Hole Oceanographic Institution

Dr. Ralph Stephen
Woods Hole Oceanographic Institution

Dr. John Tarney
The University of Leicester

Dr. Andrei A. Tsvetkov
U.S.S.R. Academy of Sciences

Advisory Panel on Ocean Margin (Active)

Dr. Peter F. Barker
The University of Birmingham

Dr. Jean-Paul Cadet
Université d'Orleans

Dr. Darrel Cowan
University of Washington

Dr. Joe S. Creager (ex-officio)
University of Washington

Dr. Yury I. Dmitriev
U.S.S.R. Academy of Sciences

Dr. Dennis E. Hayes (ex-officio)
Lamont-Doherty Geological Observatory

Dr. Donald M. Hussong, Chairman
Hawaii Institute of Geophysics

Dr. Daniel Karig
Cornell University

Dr. John W. Ladd
Lamont-Doherty Geological Observatory

Dr. Kazuaki Nakamura
University of Tokyo
Dr. Thomas Shipley (ex-officio)
Scripps Institution of Oceanography
Dr. Roland von Huene, Chairman
U.S. Geological Survey
Dr. Hansjust Walter
Bundesanstalt für Geowissenschaften und Rohstoffe

Advisory Panel on Ocean Margin (Passive)

Dr. Mikhail E. Artemiev
U.S.S.R. Academy of Sciences
Dr. Arnold H. Bouma
Gulf Science and Technology Company
Dr. William R. Bryant (ex-officio)
Texas A&M University
Mr. John A. Grow
U.S. Geological Survey
Dr. Karl Hinz
Bundesanstalt für Geowissenschaften und Rohstoffe
Dr. Hideo Kagami
University of Tokyo
Dr. Charlotte Keene
Geological Survey of Canada
Dr. Yves Lancelot (ex-officio)
Scripps Institution of Oceanography
Dr. Lucien Montadert
Institut Français du Pétrole
Dr. David G. Roberts, Chairman
Institute of Oceanographic Sciences, Surrey
Dr. William B. F. Ryan
Lamont-Doherty Geological Observatory
Dr. Robert Sheridan
University of Delaware
Dr. Sigmund Snelson
Shell Oil Company
Dr. Jørn Thiede
Universitetet I Oslo
Dr. Brian E. Tucholke
Woods Hole Oceanographic Institution
Dr. Peter R. Vail
Exxon Production Company
Dr. Jan E. van Hinte
Vrije Universiteit
Dr. Edward L. Winterer (ex-officio)
Scripps Institution of Oceanography

Advisory Panel on Pollution Prevention and Safety

Dr. N. I. Beliy
Ministry of Gas Industry, U.S.S.R.
Dr. Rustum J. Byramjee
Compagnie Français des Pétroles
Dr. George Claypool
U.S. Geological Survey
Mr. Brian E. Davies
Sohio Petroleum Company
Dr. Louis E. Garrison, Chairman
U.S. Geological Survey
Dr. Arthur E. Green
Exxon Production Research Laboratory
Prof. A. J. Horn
Atherton, California
Dr. Ernst Hotz
Deminex, Essen, Federal Republic of Germany
Dr. Yves Lancelot (ex-officio)
Scripps Institution of Oceanography
Dr. David B. MacKenzie
Marathon Oil Company
Dr. Geoffrey D. Taylor
British Petroleum Company, Ltd.
Dr. Edward L. Winterer (ex-officio)
Scripps Institution of Oceanography

Advisory Panel on Inorganic Geochemistry

Dr. Joe R. Cann (ex-officio)
The University of Newcastle-upon-Tyne
Dr. William T. Coulbourn (ex-officio)
Scripps Institution of Oceanography
Dr. Henry Elderfield
The University of Leeds
Dr. Joris M. Gieskes, Chairman
Scripps Institution of Oceanography
Dr. Miriam Kastner
Scripps Institution of Oceanography
Dr. Margaret Leinen
University of Rhode Island
Dr. Igor D. Ryabchikou
U.S.S.R. Academy of Sciences
Dr. Sam Savin
Case Western Reserve University
Dr. Fred L. Sayles
Woods Hole Oceanographic Institution
Dr. Yves Tardy
Laboratoire de Pédologie et Géochemie, Toulouse
Dr. Karl-Heinz Wedepohl
Universität Gottingen

Stratigraphic Correlations Panel

Dr. Ivan Basov
U.S.S.R. Academy of Sciences
Dr. Lloyd H. Burckle
Lamont-Doherty Geological Observatory
Dr. William Coulbourn (ex-officio)
Scripps Institution of Oceanography
Dr. Joe S. Creager (ex-officio)
University of Washington
Dr. D. Graham Jenkins
The Open University, Buckinghamshire

Prof. Erlend Martini
Universität Frankfurt

Dr. Catherine Nigrini
La Habra Heights, California

Dr. Richard Poore, Chairman
U.S. Geological Survey

Dr. John B. Saunders
Naturhistorisches Museum, Basel

Downhole Measurements Panel

Dr. Heinz Beckmann
Technische Universität Claustahl

Mr. Robert E. Boyce (ex-officio)
Scripps Institution of Oceanography

Dr. William R. Bryant (ex-officio)
Texas A&M University

Dr. Nikolas I. Christensen
University of Washington

Dr. Timothy J. G. Francis
Natural Environment Research Council

Dr. Roy Hyndman
Pacific Geoscience Centre, Sidney, BC

Mr. Alfred H. Jageler
Amoco Production Research Company

Dr. Hajimu Kinoshita
Chiba University

Dr. Mark Mathews
Los Alamos Scientific Laboratory

Dr. Yuri Neprochnov
U.S.S.R. Academy of Sciences

Dr. Lev Nikitin (ex-officio)
U.S.S.R. Academy of Sciences

Dr. Vincent Renard
Centre National pour l'Exploitation des Océans

Dr. Richard P. Von Herzen, Chairman
Woods Hole Oceanographic Institution

Advisory Panel on Ocean Paleoenvironment

Dr. Helmut Beiersdorf (ex-officio)
Bundesanstalt für Geowissenschaften und Rohstoffe

Dr. Hervé Chamley
Université des Sciences et Techniques de Lille

Dr. Robert G. Douglas, Chairman
University of Southern California

Dr. Dieter Futterer
Universität Kiel

Dr. Robert E. Garrison
University of California, Santa Cruz

Dr. James D. Hays
Lamont-Doherty Geological Observatory

Dr. Hugh C. Jenkyns
University of Oxford

Dr. Matthew Salisbury (ex-officio)
Scripps Institution of Oceanography

Dr. Seymour O. Schlanger
Hawaii Institute of Geophysics

Dr. Yokichi Takayanagi
Tohoku University

Dr. Fritz Theyer
Hawaii Institute of Geophysics

Dr. Peter P. Timofeev
U.S.S.R. Academy of Sciences

Advisory Panel on Site Surveying

Dr. Helmut Beiersdorf (ex-officio)
Bundesanstalt für Geowissenschaften und Rohstoffe

Dr. LeRoy M. Dorman
Scripps Institution of Oceanography

Dr. Dennis E. Hayes (ex-officio)
Lamont-Doherty Geological Observatory

Dr. E. John W. Jones, Chairman
University College London

Dr. Shozaburo Nagumo
University of Tokyo

Dr. Philip D. Rabinowitz (ex-officio)
Lamont-Doherty Geological Observatory

Dr. Roland Schlich
Institut Physique du Globe

Dr. Alexander A. Schreider
U.S.S.R. Academy of Sciences

Dr. Thomas Shipley (ex-officio)
Scripps Institution of Oceanography

Dr. Wilfried Weigel
Universität Hamburg

SAMPLE DISTRIBUTION POLICY*

Distribution of Ocean Drilling Program and of Deep Sea Drilling Project samples is undertaken in order to (1) provide support to shipboard scientists in achieving the scientific objectives of their cruise, and support shorebased investigators who are preparing contributions to DSDP and ODP reports; (2) provide individual investigators with materials to conduct detailed studies beyond the scope of ODP reports; (3) provide paleontological reference centers with samples for reference and comparison purposes; and (4) provide educators with samples for teaching purposes.

Funding for sample-related activities must be secured by the investigator independently of requesting the samples.

The Ocean Drilling Program Curator is responsible for distributing samples and for preserving and conserving core material. The Curator, who may accept advice from chairmen of the appropriate JOIDES advisory panels, is responsible for enforcing the provisions of this sample distribution policy. He is responsible for maintaining a record of all samples that have been distributed, both onboard ship and subsequently from the repositories, indicating the recipients and the nature of investigations proposed. This information is available to interested investigators on request.

Every sample distributed from the ship or from a repository is labeled with a standard identifier, which includes leg number, hole number, core and section numbers, and interval within the section from which the sample was removed. It is imperative that this standard identifier be associated with all data reported in the literature, and that residues of the sample remain labeled throughout their lives, so that later workers can relate the data to the cores.

Distribution of sample materials is made directly from the repositories (Lamont-Doherty Geological Observatory, Scripps Institution of Oceanography, or Texas A&M University) by the Curator or his designated representative.

1. *Distribution of Samples for Research Leading to Contributions to ODP Reports*

Any investigator who wishes to contribute to the reports of a scheduled cruise may write to the Curator, Ocean Drilling Program, Texas A&M University, College Station, Texas 77843-3469, U.S.A., in order to request samples from that cruise. Requests for a specific cruise must be received by the Curator at least TWO MONTHS in advance of the departure of that cruise, in order to allow time for the review of the request in conjunction with other requests, so that a suitable shipboard sampling program can be assembled. The request should include a statement of the nature of the proposed research, size and approximate number of samples required to complete the study, and any particular sampling technique or equipment which may be required. Requests will be reviewed by the staff representative and co-chief scientists of the cruise and by the Curator. Approval/disapproval will be based upon the scientific requirements of the cruise as determined by the appropriate JOIDES advisory panel(s). The scope of a request must be such that samples can be processed, that proposed research can be completed, and that the paper can be written in time for submission to the relevant ODP cruise report.

Except for rare, specific instances involving ephemeral properties, the total volume of samples removed during a cruise-related sampling program will not exceed one-quarter of the volume of core recovered, and no interval will be depleted. One-half of all recovered materials will be retained in the archives in as pristine a condition as is practicable. Investigators requesting shipboard samples of igneous materials may receive a maximum of 100 igneous samples per cruise.

Because many sample requests are received for shipboard work and because the time of the shipboard party is at a premium, co-chief scientists are strongly urged to limit shipboard sampling to the minimum necessary to accomplish the cruise objectives. Shore-based investigators whose requests for cruise-related samples are approved should expect that they will receive the samples after the cores are returned to the repository, and should schedule research activities accordingly.

Co-chief scientists may invite investigators who are not cruise participants to perform special studies of selected core samples in direct support of shipboard activities. If this occurs, the names and addresses of these investigators and details of all samples loaned or distributed to them must be forwarded to the Curator, via the ODP Staff Representative to that cruise, immediately after the cruise. These investigators are expected to contribute to the cruise reports as though they had been cruise participants. All requirements of the Sample Distribution Policy apply.

Any publication of results other than in ODP reports within twelve (12) months of completion of the cruise must be approved and authored by the whole shipboard party and, where appropriate, shorebased investigators. After twelve months, individual investigators may submit related papers for open publication provided they have already submitted their contributions to ODP reports. Investigations which are not completed in time for inclusion in ODP reports for a specific cruise may be published in a later edition of ODP reports; however, they may not appear in another journal until the ODP report for which they were intended has been published.

---

*Revised October 1984

2. *Distribution of Samples for Research Leading to Publication Outside of the DSDP and ODP Reports*

   A. Researchers who wish to use samples for studies beyond the scope of the DSDP or ODP reports should obtain sample request forms from the Curator, Ocean Drilling Program, Texas A&M University, College Station, Texas 77843-3469, U.S.A. Requestors are required to specify the quantities and intervals of core required, to make a clear statement of the nature of the proposed research, to state the time which will be required to complete the work and to submit results for publication, and to specify funding status and the availability of equipment and space for the research.

   Additionally, if the requestor has received samples from ODP or from DSDP previously, he/she will be required to account for the disposition of those samples by citing published works, six (6) copies of which must be sent to the Curator. If no report has been published, this requirement can be fulfilled by sending a brief (two or three page) report of the status of the research. Unused and residual samples should be returned and data should be sent to the Curator if the project has terminated. Paleontological materials may be returned either to the Curator at ODP or to one of the designated paleontological reference centers. If material is returned to a reference center, notify the Curator when it is sent.

   Requests for samples from researchers in industrial laboratories will be honored in the same manner as those from academic organizations. Industrial investigators have the same obligations as other investigators to publish all results promptly in the open literature and to provide the Curator with copies of all reports published and of all data acquired in their research.

   In order to ensure that all requests for highly desirable but limited samples can be considered together, approval of requests and distribution of samples will be delayed until twelve (12) months after completion of the cruise or two (2) months after official publication of the core descriptions, whichever occurs earlier. The only exceptions to this policy will be made for specific requests involving ephemeral properties. Requests for samples may be based on core descriptions published in ODP reports produced by the shipboard party, copies of which are on file at various institutions throughout the world. Copies of original core logs and data are kept on open file at ODP, and at the repositories at Lamont-Doherty Geological Observatory and at Scripps Institution of Oceanography.

   B. Most investigations can be accomplished handily with sample volumes of 10 ml or less. Investigators must provide explicit justification of requests for larger sample sizes or for frequent intervals within a core. Requests which exceed reasonable size or frequency limits will require explicit justifications and more time to process, and are unlikely to be granted in their entirety.

   Requests for samples from thin layers, from stratigraphically important boundaries, from sections which are badly depleted or in unusually high demand may be delayed in order to coordinate requests from several investigators or while the Curator seeks advice from the community. Investigators who submit such requests may expect to receive suggestions for alternative sampling programs or that they join a research consortium which will share the samples. In any event, such exceptional requests will require more time for processing than will more routine requests.

   Investigators who wish to study ephemeral properties may request a waiver of the waiting period; however, such requests will be referred automatically to the relevant co-chiefs. If approved, the investigator will join the shore-based contributors to the shipboard science effort, and will incur the obligations thereof (see section 1).

   C. Samples will not be provided until the requestor assures the Curator that funding for the proposed research is available or unnecessary. If a sample request is dependent in any way upon proposed funding, the Curator is prepared to provide the proposed funding organization with information on the availability (or potential availability) of suitable samples.

D. Investigators who receive samples incur the following obligations:

(1) To publish significant results promptly; however, no contribution may be submitted for publication prior to twelve (12) months following the termination of the relevant leg unless it is approved and authored by the entire shipboard party.

(2) To acknowledge in all publications that the samples were supplied through the assistance of the international Ocean Drilling Program and others as appropriate.

(3) To submit six (6) copies of reprints of all published works to the Curator, Ocean Drilling Program, Texas A&M University, College Station, Texas 77843-3469, U.S.A. These reprints will be distributed to the repositories, to the ship, to the National Science Foundation, and to the Curator's reprint file.

(4) To submit all final analytical data obtained from the samples to Data Base Manager, Ocean Drilling Program, Texas A&M University, College Station, Texas 77843-3469, U.S.A. Please consult recent issues of the JOIDES Journal or call (409-845-2673) for information on acceptable data formats. Investigators should be aware that they may have other data obligations under NSF's Ocean Science Data Policy or under relevant policies of other funding agencies which require submission of data to national data centers.

(5) To return all unused or residual samples, in good condition and with a detailed explanation of any processing they may have experienced, upon termination of the proposed research. In particular, all thin sections and smear slides manufactured onboard the vessel or in the repositories are to be returned to the Curator. Paleontological materials may be returned either to the Curator at ODP or to one of the designated paleontological reference centers.

Failure to honor these obligations will prejudice future applications for samples.

E. Cores are available for examination by interested parties at the repositories. Investigators are welcome to visit the repositories in order to inspect cores and to specify sample locations when that is required for their research; however, time and space in the workrooms are limited, so advance appointments are required. Occasionally, the space may be fully booked several weeks in advance, so investigators are urged to call for appointments well ahead in order to avoid disappointment. Only the Curator or his delegate may actually remove samples from the cores.

F. A reference library of thin sections, smear slides, and archive photographs is maintained in the repositories for the use of visting investigators. All thin sections and smear slides produced onboard the ship or in the repositories belong to this library.

3. *Distribution of Samples to Paleontological Reference Centers*

As a separate and special category of repository activity, selected samples are being distributed to paleontological reference centers, where the prepared material may be studied by visitors. As of this writing (mid-1984), Foraminifera and Calcareous Nannofossils can be viewed; Radiolaria and Diatoms will be prepared in the future. The present centers are Scripps Institution of Oceanography, California (W. R. Riedel, tel. 619-452-4386); Basel Natural History Museum, Switzerland (J. B. Saunders, tel. 061-25.82.82); and New Zealand Geological Survey, Lower Hutt, New Zealand (A. R. Edwards, tel. 699.059). Future centers are likely to include Texas A&M University, College Station, Texas (S. Gartner, tel. 409-845-8479); Smithsonian Institution, Washington, D.C.; Lamont-Doherty Geological Observatory, Palisades, New York; and an as yet undesignated center in Japan.

Further details concerning the paleontological reference centers are reported periodically in the JOIDES Journal.

4. *Distribution of Samples for Educational Purposes*

Samples may be available in limited quantities to college-level educators for teaching purposes. Interested educators should request application forms from the Curator, Ocean Drilling Program, Texas A&M University, College Station, Texas 77843-3469, U.S.A. Requestors are required to specify preferred sample size and location, to make a very clear statement of the nature of the coursework in which the samples will be used, to explain how the core samples will be prepared and how they will be used in the classroom, to explain in detail why they cannot use similar materials derived from outcrops or dredge hauls (it is NOT acceptable to argue that it requires less effort for the requestor to obtain samples from ODP than to assemble them from other sources), and to certify that funds are available to prepare the materials for classroom use. In general, only samples of materials which are abundant in the collection and which are in little demand for research purposes should be requested for educational purposes. The Curator will not ap-prove requests for materials which are limited in supply or for which demand (real or potential) is great, including most paleontological materials.

5. *Distribution of Data*

The Deep Sea Drilling Project and the Ocean Drilling Program routinely capture much of the data generated onboard ship and published in Program reports. Additionally, data supplied by investigators who have received samples are incorporated into the data bases, so data sets which are larger than can be published are available to investigators. Magnetics, downhole logging, seismic reflection, bathymetric data, and other data collected by the drilling vessel become available for distribution to investigators at the same time as core samples.

At least through mid-1986, DSDP data will continue to be distributed by the Data Base Manager, Deep Sea Drilling Project, A-031, University of California, San Diego, California 92093, U.S.A. A charge will be made to recover expenses in excess of $50.00 incurred in filling individual requests. If required, estimates of charges can be furnished before the work is performed. As DSDP phases down, DSDP data will be available primarily from the National Geophysical Data Center, Boulder, Colorado.

Requests for ODP data should be addressed to the Data Base Manager, Ocean Drilling Program, Texas A&M University, College Station, Texas 77843-3469, U.S.A. Many varieties of DSDP data will be included in ODP data bases. Information on sources of DSDP data will be available from the ODP Data Base Manager.

CONTENTS

Chapter Page

ACKNOWLEDGMENTS 1

PART I: INTRODUCTION AND REGIONAL GEOPHYSICS

1. BACKGROUND, OBJECTIVES, AND SUMMARY OF PRINCIPAL RESULTS: DEEP SEA DRILLING PROJECT SITES 556-564 5
H. Bougault and S. C. Cande

2. TECTONIC FABRIC OF THE SEAFLOOR NEAR NORTH CENTRAL ATLANTIC DRILL SITES 17
S. C. Cande, R. C. Searle, and I. A. Hill

3. ANALYSIS OF TRACE ELEMENTS IN BASALTS BY SHIPBOARD X-RAY FLUORESCENCE SPECTROMETRY: A DISCUSSION OF NIOBIUM 35
J. Etoubleau, H. Bougault, M. Rideout, J. Brannon, and B. Weaver

4. EXPLANATORY NOTES, DEEP SEA DRILLING PROJECT LEG 82 45
W. G. Mills

PART II: SITE CHAPTERS

5. SITE 556.................................... 61
Shipboard Scientific Party

6. SITE 557....................................115
Shipboard Scientific Party

7. SITE 558....................................127
Shipboard Scientific Party

8. SITE 559....................................215
Shipboard Scientific Party

9. SITE 560....................................233
Shipboard Scientific Party

10. SITE 561....................................245
Shipboard Scientific Party

11. SITE 562....................................255
Shipboard Scientific Party

12. SITE 563....................................279
Shipboard Scientific Party

13. SITE 564....................................325
Shipboard Scientific Party

Chapter Page

PART III: PHYSICAL PROPERTIES, PALEOMAGNETICS, AND ROCK MAGNETICS

14. DOWNHOLE LOGGING AND LABORATORY PHYSICAL PROPERTIES MEASUREMENTS..........................351
I. A. Hill and S. C. Cande

15. THERMAL MEASUREMENTS AND SEAWATER DOWNFLOW INTO 35-Ma-OLD OCEAN CRUST, CENTRAL NORTH ATLANTIC 361
I. A. Hill and S. C. Cande

16. MAGNETIC PROPERTIES OF BASALTS FROM THE CENTRAL NORTH ATLANTIC OCEAN 369
G. M. Smith and S. K. Banerjee

17. MAGNETIC PROPERTIES OF PLUTONIC ROCKS FROM THE CENTRAL NORTH ATLANTIC OCEAN 377
G. M. Smith and S. K. Banerjee

18. MAGNETOSTRATIGRAPHY OF OLIGOCENE TO PLEISTOCENE SEDIMENTS, SITES 558 AND 563........................385
M. J. Khan, D. V. Kent, and K. G. Miller

PART IV: PETROLOGY, MINERALOGY, AND GEOCHEMISTRY

19. GEOCHEMISTRY AND MINERALOGY OF BASALTS RECOVERED FROM THE CENTRAL NORTH ATLANTIC 395
B. L. Weaver, J. Tarney, and A. D. Saunders

20. GEOCHEMISTRY OF BASALTS FROM DEEP SEA DRILLING PROJECT HOLES 556-564 421
N. E. R. Drake, J. M. Rhodes, and L. K. Autio

21. THE DEGREE OF HETEROGENEITY IN BASALTS NEAR THE HAYES FRACTURE ZONE, MID-ATLANTIC RIDGE: HOLES 561, 562, AND 564 439
J. C. Brannon

22. TRACE ELEMENT GEOCHEMISTRY AND PETROGENESIS OF BASALTS FROM DEEP SEA DRILLING PROJECT SITES 556-559 AND 561-564 449
J. Hertogen, Th. Sachtleben, H.-U. Schmincke, and G. A. Jenner

Chapter Page

23. LOCAL VERSUS REGIONAL MANTLE HETEROGENEITIES: EVIDENCE FROM HYGROMAGMAPHILE ELEMENTS 459
H. Bougault, J. L. Joron, M. Treuil, and R. Maury

24. RARE-EARTH ELEMENTS, ^{87}Sr/^{86}Sr, AND ^{143}Nd/^{144}Nd MANTLE SOURCE VARIATIONS..............................483
M. L. Rideout and J.-G. Schilling

25. LEAD ISOTOPIC VARIATIONS IN OLD OCEAN CRUST NEAR THE AZORES........497
B. Dupré, C. Göpel, and H. Bougault

26. ISOTOPIC AND TRACE ELEMENT COMPOSITION OF BASALTS FROM SITES 556-559 AND 561-564: CONSTRAINTS ON SOME PROCESSES AFFECTING THEIR COMPOSITION 501
G. A. Jenner, J. Hertogen, Th. Sachtleben, and H.-U. Schmincke

27. ABYSSAL GLASSES, PETROLOGIC MAPPING OF THE OCEANIC FLOOR AND "GEOCHEMICAL LEG" 82 509
L. V. Dmitriev, A. V. Sobolev, N. M. Suschevskaya, and S. A. Zapunny

28. THE SULFUR CONTENT AND ISOTOPIC COMPOSITION IN BASALTS FROM HOLES 558, 559, 562, AND 564 519
H.-W. Hubberten and H. Puchelt

29. PETROLOGY OF ULTRAMAFIC ROCKS FROM SITES 556, 558, AND 560 IN THE NORTH ATLANTIC 523
P. J. Michael and E. Bonatti

PART V: SEDIMENTOLOGY AND PALEONTOLOGY

30. X-RAY MINERALOGY OF SITES 558 AND 563 531
C. Latouche and N. Maillet

31. INTERSTITIAL WATER STUDIES, CENTRAL NORTH ATLANTIC 539
J. M. Gieskes, K. Johnston, and M. Boehm

32. CROSS-LAMINATED AND GRADED INTERPILLOW LIMESTONES, SITE 562 543
L. A. Reynolds and B. K. Linsley

Chapter Page

33. LOWER OLIGOCENE THROUGH PLEISTOCENE PLANKTONIC FORAMINIFERAL BIOSTRATIGRAPHY, NORTH ATLANTIC SITES 558 AND 563 (MID-ATLANTIC RIDGE) 547
D. J. Echols

34. CALCAREOUS NANNOFOSSILS OF DEEP SEA DRILLING PROJECT SITES 558 AND 563, NORTH ATLANTIC OCEAN: BIOSTRATIGRAPHY AND THE DISTRIBUTION OF OLIGOCENE BRAARUDOSPHAERIDS 559
M. E. Parker, M. Clark, and S. W. Wise, Jr.

35. MID-ATLANTIC RIDGE COCCOLITH AND SILICOFLAGELLATE BIOSTRATIGRAPHY, DEEP SEA DRILLING PROJECT SITES 558 AND 563.........................591
D. Bukry

36. "*BOLBOFORMA*": A MIOCENE ALGAE(?) OF POSSIBLE BIOSTRATIGRAPHIC AND PALEOCLIMATIC VALUE 605
D. J. Echols

37. OLIGOCENE BENTHIC FORAMINIFERS FROM NORTH ATLANTIC SITES: BENTHIC FORAMINIFERS AS WATER-MASS INDEXES IN THE NORTH AND SOUTH ATLANTIC 611
A. Boersma

38. CARBONATE AND COARSE FRACTION RECORDS OF THE PLEISTOCENE INTERVAL IN THE NORTH ATLANTIC, HYDRAULIC PISTON CORER HOLE 558A 629
G. G. Start

PART VI: APPENDIX

APPENDIX: GEOCHEMICAL DATA FOR BASALTS 639
H. Bougault and D. Hawkins

BACKPOCKET FIGURES

CHAPTER 14: FIGURE 4. LOGGED CURVES FOR HOLES 558 (A), 556 (B), 564 (C), AND 417D (D).

CHAPTER 34: FIGURE 8. MID-TERTIARY *BRAARUDOSPHAERA* OOZES, CHALKS, AND *BRAARUDOSPHAERA*/HOLOCOCCOLITH ASSOCIATIONS.

ACKNOWLEDGMENTS

The scientists of DSDP Leg 82 wish to thank the many people who contributed to the success of this cruise. We acknowledge those who helped with the development of the theme of mantle heterogeneity and the identification of the objectives for Leg 82, particularly Jean-Guy Schilling, Michel Treuil, Jeff Fox, Hans Schouten, and members of the Ocean Crust Panel of IPOD. We express our appreciation to Captain Joe Clarke, the officers, the crew, and the drilling team of the *Glomar Challenger* for their sustained efforts, especially because the objectives of the leg required a large number of holes. Indicative of their exceptional skill was the acquisition of a small, but highly valued piece of ocean basement at Site 557 in the face of an approaching hurricane. We also thank the technical staff on board the *Challenger* for their considerable assistance in the laboratory, and, in particular, we thank Glen Foss, the cruise operations manager, for providing the liaison between the scientists and Global Marine personnel. We are grateful to Jacques Debyser at Centre National pour l'Exploitation des Océans for making it possible to have the X-ray fluorescence container on board the *Challenger* during Legs 82 and 83 and J. Vicariot at Centre de Océanologique des Bretagnes for helping in logistics and discussions with PIRO and DSDP.

We also wish to thank all the reviewers who reviewed manuscripts for this volume. A partial list includes:

Cyrus Field, Oregon State University; William P. Leeman, Rice University; John F. Bender, The University of North Carolina; John Longhi, Yale University; R. G. Miller, Cambridge University; Bruce M. Moskowitz, Princeton University; Suzanne Beske-Diehl, Michigan Technological University; Ronald T. Merrill, University of Washington; Matthew H. Salisbury, Scripps Institute of Oceanography; Keir Becker, Scripps Institute of Oceanography; Harry, P. McSween, Jr., University of Tennessee at Knoxville; Martin Lagoe, Arco Oil & Gas Company; James Ling, Northern Illinois University; Stan Hart, Massachusetts Institute of Technology; Martin Flower, University of Illinois at Chicago Circle; J. Michael Rhodes, University of Massachusetts; Fred A. Frey, Massachusetts Institute of Technology; John A. Philpotts, U.S. Geological Survey, Reston, VA; Bob Whitmarsh, National Institution of Oceanography, England; and Randy Korotev, Washington University.

Finally, the staff members at DSDP put a tremendous effort into the final production of this volume of the *Initial Reports*. Especially, we thank Elizabeth Whalen for her careful editing of a seemingly endless number of manuscripts and Vicki Cypherd for accurate drafting of the figures.

PART I: INTRODUCTION AND REGIONAL GEOPHYSICS

1. BACKGROUND, OBJECTIVES, AND SUMMARY OF PRINCIPAL RESULTS: DEEP SEA DRILLING PROJECT SITES 556–564[1]

H. Bougault, Institut Français pour la Recherche et l'Exploitation de la Mer
and
S. C. Cande, Lamont-Doherty Geological Observatory[2]

BACKGROUND

MORB Tholetiites, Transitional, and Alkalic Basalts

One of the most important geologic discoveries of the 1960s was the remarkable uniformity of the basalts produced at mid-ocean ridges. These basalts have a markedly different tholeiitic composition compared to the alkalic basalts from ocean islands (Engel et al., 1965). The major element compositions of ocean-floor basalts and the compositions of the phenocrysts when present (plagioclase, olivine, and, more rarely, clinopyroxene) were considered so similar in all of the oceans that the acronym MORB (mid-ocean ridge basalt) was used to characterize basalts formed at seafloor spreading ridges.

Just as remarkable, considering the homogeneity of mid-ocean ridge basalts, is the presence of sections of ridges where basalts of significantly different characteristics are found. For example, along the Mid-Atlantic Ridge at 45°N, alkalic basalts and basalts with "alkalic tendencies" are associated with more normal tholeiitic basalts (Aumento, 1968). Trace element and isotopic ratio studies conducted in the past 15 years have shown that basalts produced at the mid-ocean ridges have a much greater variation than researchers originally realized. MORB now appears to be simply one end member of a broad spectrum of basalts of which alkalic basalt is the other end member; basalts of intermediate composition are referred to as "transitional basalts."

The occurrence of alkalic and transitional basalts is not random. In the North Atlantic they are generally found along abnormally shallow sections of the mid-ocean ridge. Transitional basalts are found north of 60°N along the Reykjanes Ridge (Schilling, 1973) and along the Mid-Atlantic Ridge where it crosses the Azores Platform (Schilling, 1975). The occurrence of alkalic basalts at 45°N is also associated with a shallower than normal section of the Mid-Atlantic Ridge (Le Douaran and Francheteau, 1981). In addition, as already mentioned, alkalic basalts are characteristic of both ocean islands and seamounts. Furthermore, there is a gradient in the characteristics of transitional basalts from transitional to normal MORB away from the highest elevations of the Iceland and Azores platforms (Schilling, 1973; 1975).

Sr, Pb, and Nd Isotopic Ratios, Rare Earth Elements, and Mantle Sources

Studies of radiogenic isotopes (Sr, Nd, Pb) in ocean basalts have helped to classify the different basalt types and to interpret possible petrogenetic relationships (Gast, 1960; Gast et al., 1964; Tatsumoto et al., 1965). Variations in isotopic ratios of Sr (Tatsumoto et al., 1965; Hart et al., 1973; O'Nions and Pankhurst, 1974), Pb (Gast et al., 1964; Sun, 1973; Sun et al., 1975; Sun and Jahn, 1975; Tatsumoto, 1978), and Nd (DePaolo and Wasserburg, 1976; O'Nions et al., 1977; Richard et al., 1977) among MORB, transitional basalts, and alkalic basalts cannot be fully explained in terms of crystal fractionation and/or melting processes responsible for the formation of basalt from a mantle source. The differences in the isotopic compositions of these basalts can only be explained in terms of their derivation from different mantle sources.

Another important distinction between normal MORB and transitional and alkalic basalts lies in the relative abundances of those trace elements that have low mineral-liquid partition coefficients (Schneitzler and Philpotts, 1970). The best studied of these so called "magmaphile" elements (to indicate their affinity for the liquid phase) are the rare earth elements (Gast, 1968; Frey et al., 1968; Frey et al., 1974; Schilling, 1973, 1975; Sun et al., 1979; Bougault et al., 1980). MORB are typically "depleted" in the light rare earth elements (LREE) (relative to heavy rare earth elements [HREE]), whereas alkalic basalts are strongly enriched and transitional basalts are either "flat" or slightly enriched.

This relative enrichment or depletion of light rare earth elements is represented in a diagram proposed by Masuda (1962) and Coryell et al. (1963). The ratio of the concentration of each rare earth element in a given sample to its concentration in chondritic meteorites (the normalized concentration) is plotted against its atomic number. Normalized concentrations of the lightest rare earths (La, Ce) are higher than the normalized concentrations of the middle to heavy rare earths (from Sm to Lu) in enriched samples and vice versa. Flat patterns occur when all normalized concentrations are approximately equal. Examples of enriched (alkalic basalt from Site 410 at 45°N), flat (Site 332 at 36°N), and depleted (Site 395 at 22°N) patterns are given in Figure 1.

---

[1] Bougault, H., Cande, S. C., et al., *Init. Repts. DSDP*, 82: Washington (U.S. Govt. Printing Office).

[2] Addresses: (Bougault) Institut Français pour la Recherche et l'Exploitation de la Mer (formerly, Centre National pour l'Expolitation des Océans), Centre de Brest, B. P. 337, 29273 Brest Cedex, France; (Cande) Lamont-Doherty Geological Observatory, Columbia University, Palisades, New York 10964.

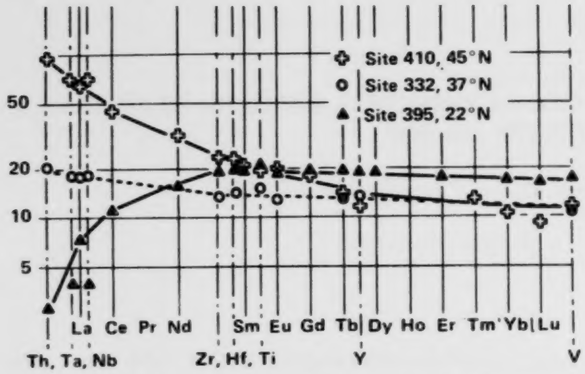

Figure 1. Coryell-Masuda diagram showing examples of Mid-Atlantic Ridge basalts that are enriched (Site 410), flat (Site 332), and depleted (Site 395). This is an "extended" Coryell-Masuda diagram because of inclusion of non-rare earth magmaphile elements, such as niobium and zirconium.

Theoretically, different relative light rare earth abundances in basalts may result from differences in mantle source composition, in extent of partial melting, or in the process by which melting occurs (Langmuir et al., 1977). However, variations in melting processes do not account for the known regional variation in patterns of enrichment or depletion of light rare earth elements in basalts. These regional patterns are assumed to reflect variations in the composition of mantle sources from which the basalts are derived. This inference is supported by correlations between the degree of light rare earth depletion or enrichment found in ocean basalts and variations in isotopic ratios of Sr, Pb, and Nd (White et al.,1976; White and Schilling, 1978; Dupré and Allègre, 1980; Zindler and Hart, 1978). Variations in relative abundances in the mantle of both isotopes and rare earth elements are attributed to fractionations of the primordial mantle early in the history of the Earth (O'Nions et al., 1978; Allègre et al., 1980).

The present-day geochemical properties of the upper mantle can be studied by dredging basalts from ridge crests. Upper mantle time variations can be studied by sampling older parts of the seafloor crust, which are found on the flanks of mid-ocean ridges. To obtain these older basalts, it is necessary to drill through the hundreds of meters of sediments that have been deposited since the basalts were formed at the ridge crest.

The topographic highs found along the axis of the mid-ocean ridge, with which transitional basalts and sometimes alkalic basalts are associated, are not explained by general plate tectonic theory (Menard, 1967; Morgan, 1968; Sclater et al., 1971). Plate tectonics allows only for small variations in elevation near ridge crests (for example, variations in spreading rate) but cannot explain the exceptional topographic highs in the North Atlantic represented by the Iceland and Azores platforms. These topographic highs, or hot spots may be the surface manifestations of mantle plumes that bring magma up from mantle levels deeper than the levels that normally feed mid-ocean ridges (Morgan, 1971). These mantle plumes may also contribute to the driving forces that move the lithospheric plates. The mantle plume concept (or variations on it such as mantle blobs) can explain the apparently distinct mantle source of the "abnormal" ridge basalts associated with hot spots (Schilling, 1973; 1975). The gradients observed in basalt composition away from the centers of hot spots have also been explained by mixing of plume and nonplume sources (Vogt, 1972; Sun et al., 1975; White et al., 1976; O'Nions et al., 1976; White and Schilling, 1978).

Our knowledge of the distribution of transitional or alkalic basalts relative to normal MORB is limited to samples dredged at the ridge crest or recovered from the relatively few drill holes that have penetrated basement rocks. The most complete coverage is in the North Atlantic, particularly along the Mid-Atlantic Ridge in the vicinity of the Azores Triple Junction (Bougault and Hekinian, 1974; Bryan and Moore, 1977; White and Bryan, 1977; Hekinian et al., 1976), and the results of drilling at Sites 332, 333, 334, 335, 441, 412, and 413 (Aumento, Melson, et al., 1977; Luyendyk, Cann, et al., 1979). Chemical analyses of basalts dredged along the ridge crest show that there is a boundary at the latitude of the Hayes Fracture Zone (33°N) between enriched basalts associated with the topographic high of the Azores and normal MORB associated with a deeper part of the Mid-Atlantic Ridge south of the Hayes Fracture Zone (White and Schilling, 1978; Bougault and Treuil, 1980).

Much less is known about the variations in time away from the ridge. The results of drilling along a flow line passing through the FAMOUS area (south of the Azores Triple Junction at 37°N) on Legs 37 and 49 showed that transitional basalts with flat to enriched light rare earth elements are found in crust up to 10 Ma old (Sites 332, 333, 334, 411, 412, and 413), but that basalts significantly depleted in light rare earth elements are found in crust 16.5 Ma old (Site 335) (Schilling et al., 1977). A transect along a flow line cutting across the Reykjanes Ridge south of Iceland recovered abnormal basalts at Sites 407 (35 Ma), 408 (20 Ma), and 409 (2.4 Ma). On the basis of magmaphile element abundances and Sr isotopic ratios, Site 409 is significantly different from Sites 407 and 408 (Wood et al., 1979a; 1979b). These results suggest that the composition of basalts formed at a particular section of a ridge crest within the zone influenced by topographic highs (hot spots) can change over a period of a few million years.

The results of drilling on a flow line south of the Kane Fracture Zone (24°N at its intersection with the rift axis), in an area where the ridge is much deeper and not influenced by abnormal topographic features, show that basalts were produced with uniform composition over a long period of time (Melson, Rabinowitz, et al., 1979; Donnelly, Francheteau, Bryan, Robinson, Flower, Salisbury, et al., 1980).

Samples recovered at the following places are all depleted: Anomaly Mo (110 Ma old; Sites 417, 418); Anomaly 5 (10 Ma old; Sites 395 [Melson, Rabinowitz, et al., 1979] and 396 [Dmitriev, Heirtzler, et al., 1979] almost symmetric with respect to the ridge); and samples recovered by dredging at the ridge crest. These results are consistent with a MORB mantle source that has remained uniform with time, but the gap of 100 Ma between Anomalies 5 and Mo will have to be sampled for confirmation.

OBJECTIVE

Trace Element Geochemistry

As stated in the foregoing discussion, very little is known about temporal variations in the composition of basalts derived from one or several mantle sources associated with both normal and anomalously shallow sections of the mid-ocean ridges. A more detailed knowledge of these variations is required if we are to better understand the relationship between mantle sources and anomalous topographic features.

The principal objective of Leg 82 of the *Glomar Challenger* was to try to relate regional variations in basalt chemistry to the geodynamics of an abnormal section of the mid-ocean ridge. Specifically, we planned to relate the chemical characteristics of basalts sampled on the flanks of the Mid-Atlantic Ridge to the functioning of the Azores Triple Junction topographic high or "Azores hot spot." The Azores area was chosen for this study because it is perhaps the best studied abnormal region of mid-ocean ridge. Dredging along the ridge is extensive, and drilling on crust up to 16 Ma old has already taken place on a flow line passing through the FAMOUS area (37°N).

Because so little was known about how depleted and enriched rocks were distributed in this area, a grid of sites planned ahead of time might have fallen completely within the bounds of either enriched or depleted material and would have revealed very little about the regional distribution of the various types of basalts. Consequently, we wanted to determine the nature of the basalts as they were recovered and to use this information to determine where to drill next. The composition of the basalts was determined by X-ray fluorescence (XRF) in a van specially provided by The Centre National pour l'Exploitation des Océans (CNEXO)[3] and placed on board the *Challenger*. The CNEXO XRF van was first used in 1974 (Leg 37; Bougault, 1977) and has been used successfully on several subsequent occasions. Although in the past the van had been used chiefly to determine major element abundances, on Leg 82 the priority was to determine the abundances of magmaphile trace elements that could be used to distinguished enriched and depleted basalts.

Strictly speaking, the enrichment or depletion of the LREE determines whether a basalt is abnormal or normal. Unfortunately, the rare earth element abundances are too low to be determined by XRF analysis and can only be studied in shore-based laboratories. However, several trace elements qualitatively show the same tendency as rare earth elements to remain in the silicate liquid phase rather than to enter into the mineral phase. These magmaphile elements have already been studied in ocean basalts (Cann, 1970; Erlank and Kable, 1976) and have been used for discriminant analysis (Pearce and Cann, 1971) and for tentative quantitative assessment of magmatic processes (Treuil and Varet, 1973; Treuil and Joron, 1975). For alkalic and tholeiitic basalts, some elements have chemical properties very similar to those of particular rare earths (e.g., yttrium versus HREEs) or have been shown to behave like rare earth elements (zirconium, hafnium, and titanium versus samarium; tantalum and niobium versus lanthanum) (Bougault et al., 1979). These elements can be used to deduce the shape of the Coryell-Masuda diagram, which represents the rare earth concentrations of a sample normalized to chondrites (Bougault, 1980; Bougault and Treuil, 1980). Figure 1 shows that the Coryell-Masuda diagram can be extended to other magmaphile elements. Thus, non–rare earth magmaphile elements define the same enriched or depleted patterns as the rare earths.

The abundances of the trace elements Nb, Z, Ti, Y, and V were determined by the XRF unit on board the *Glomar Challenger*. The most important element to be studied was Nb because its behavior closely mimics the lightest of the rare earth elements (e.g., La) and therefore fluctuates the most. The Nb/Zr ratio is a key indicator of enrichment or depletion, almost identical to the La/Sm ratio. The determination Nb concentration had not been done on board before and required an accuracy better than 1 ppm in the range of concentrations from 0 to 15 ppm (for a detailed discussion of this analysis, see Etoubleau et al., this volume).

The strategy for drilling on this cruise was to set up a broad grid encompassing all possible drilling sites west and southwest of the present Azores Triple Junction. On each flow line drilling started at an intermediate distance from the ridge and, depending on the XRF results, subsequent sites were drilled either closer to the ridge or further away. In this way, the boundary between normal and abnormal basalts along several flow lines could be quickly established.

The proposed drill sites for Leg 82 are shown in Figure 2. The sites situated along flow lines passing (1) through the Azores Triple Junction (MAR-1 to MAR-3), (2) through the FAMOUS area and the sites drilled on Leg 37 (MAR-4 and MAR-5), and (3) straddling the Hayes Fracture Zone (MAR-6 to MAR-11). The sites are located on magnetic Anomalies 6, 13, and 24 for the two northern transects and on magnetic Anomalies 5, 6, and 13 straddling the Hayes Fracture Zone. This network of sites provided information along both flow lines and isochrons over a wide area and provided valuable information, not only for the specific objectives of the cruise, but for other studies of the ocean crust.

Geophysical Logging and Sediment Studies

The principal objective of Leg 82 was to study mantle heterogeneity by sampling the ocean crust in the manner described above. Three other objectives were planned to take advantage of the opportunity to log basement holes and to collect pelagic sediments in the North Atlantic.

DSDP has accumulated a large and valuable data bank of physical property measurements on recovered cores. Borehole logging is a very desirable complement to these data; it can provide a continuous record of *in situ* physical properties, largely avoiding the deformation and systematic sampling bias inherent in core recovery. It was hoped that it would be possible to log several deep penetration holes to allow comparison of logs with physical property measurements on cores.

---

[3] Funded by CNEXO, Délegation Générale à la Recherche Scientifique et Technique, and Centre National de la Recherche Scientifique.

Within sediments, which may be expected in this area to be fairly uniform pelagic ooze, it would be interesting to compare physical properties measured on the cores to *in situ* values. Additionally, it may be possible to correlate between holes with sufficient downhole logs. Within the basalt basement, physical properties of core specimens changed little during the coring operation; however, core recovery averaged only 50% at best, so it is possible that a truly representative sample was not recovered.

Comparison between downhole logs and cored material can: (1) locate the accurate depth of lithologic unit boundaries, which are always indeterminate to some extent unless core recovery is 100%; (2) provide evidence of the degree to which the recovered core represents the total section and can locate and identify nonrecovered lithologic units; (3) facilitate quantitative estimation of *in situ* physical properties, such as secondary porosity, bulk-formation density, and seismic velocity.

It was hoped that logging of deep holes in medium-age ocean crust (15–30 Ma) could provide information about the aging processes of ocean crust when combined with results from previous legs (particularly 37, 51, and 52). Particular features that may be available from log data would be the changes in primary and secondary porosity. This would reflect mineral alteration, faulting, and fracture infilling processes.

Until now, complete section of Cenozoic pelagic sediments has been cored in the North Atlantic. Investigation of the sedimentation, stratigraphy, paleoenvironments, paleomagnetics, and geologic history of this area has been limited to spot cores and partial sections. At Site 334 (Leg 37) a thick section of upper Miocene calcareous pelagic ooze and chalk was cored. At Site 335, five spot cores were taken though 450 m of Pleistocene through middle Miocene sediments. A small number of spot cores were taken in Pleistocene to Eocene sections at Sites 10 and 11 (Leg 2). Other sites in the North Atlantic region recovered Cenozoic sections consisting principally of turbidites and hemipelagic sediments.

In order to fill a large gap in sampling and to provide data for study of the Cenozoic history, paleomagnetics, and paleoenvironment of the North Atlantic, continuous coring should be done at as many sites as possible within the constraints of time imposed by the principal objective of the leg. The sites chosen for continuous coring should be determined by several criteria including (1) age of the section to be recovered and (2) probability of recovering a complete section above the calcite compensation depth (CCD) for biostratigraphic zonation and magnetostratigraphic dating. A well-chosen site on Anomaly 13 should provide a complete section through the Neogene and most of the Oligocene. A site on Anomaly 24 would also penetrate most of the Eocene. Continuous coring at such sites would satisfy the sediment objectives of the leg by providing samples for biostratigraphic, paleoclimatic, paleoenvironmental, sedimentologic, and paleomagnetic studies in this area. Hydraulic piston coring should be a high priority of this sediment program.

Recent paleomagnetic studies on terrestrial and marine sediments have shown that magnetostratigraphy is very important and useful for absolute chronostratigraphic correlation. The use of the hydraulic piston corer (HPC) is important to get the least disturbed sediments essential for successful paleomagnetic studies. The increasing hardness of the sediments with depth limited the use of the HPC and required coring to be done by conventional rotary coring. The detailed magnetostratigraphic work done on sediments cored by the HPC and the conventional methods during Legs 68 and 73 has further emphasized the need to do more work in order to establish the absolute temporal correlation of sediments, which, in turn, is of great significance for paleoenvironmental studies and tectonic analysis of the various ocean basins.

PRINCIPAL RESULTS

As the cruise progressed, each site was selected from a grid of 11 potential locations (Fig. 2) on the basis of shipboard chemical determinations of abundances of key trace elements: niobium, zirconium, titanium, yttrium, and vanadium (Etoubleau et al., this volume). Specifically, the chondrite-normalized $(Nb/Zr)_{ch}$ ratio, was used to determine the enriched or depleted character of recovered basalts. On this basis, the first drilled site (556) at the location of MAR-2 on the Azores Triple Junction flow line (Figs. 2, 3) was found to be typical of depleted ocean crust without significant influence of the Azores Hot Spot plume, with $(Nb/Zr)_{ch}$ ratio ranging from 0.15 to 0.30 (Table 1). Considering this result, we drilled the next site (557) closer to the Azores Triple Junction at the location of MAR-1 (Figs. 2, 3). Site 557 is typical of the Azores area, with enrichment factors lying between 1.3 and 1.9 for $(Nb/Zr)_{ch}$ ratio (Table 1).

During Leg 82, there was not enough time to drill all potential locations (Fig. 2), so we decided to drill other holes close to Anomalies 6 and 13 in order to obtain a coherent picture along two isochrons. The drilled sites during Leg 82 are presented in Figure 3. The stratigraphy of Leg 82 sites is shown in Figure 4.

On board, 163 samples were selected and analyzed for both major elements (except Na_2O) and trace elements. The data that were later obtained on shore (Bougault et al., Rideout and Schilling, Weaver et al., Brannon, Hertogen et al., Drake et al., this volume)—including classic rare earth element data—confirmed all of the shipboard data. In addition, isotopic data were obtained after the cruise (Rideout and Schilling, Jenner et al., Dupré et al., this volume) and are reported in the Geochemistry part of this volume. Figures 5 and 6 (ϵNd versus Nb/Zr and ϵNd versus La/Ta) compare trace ele-

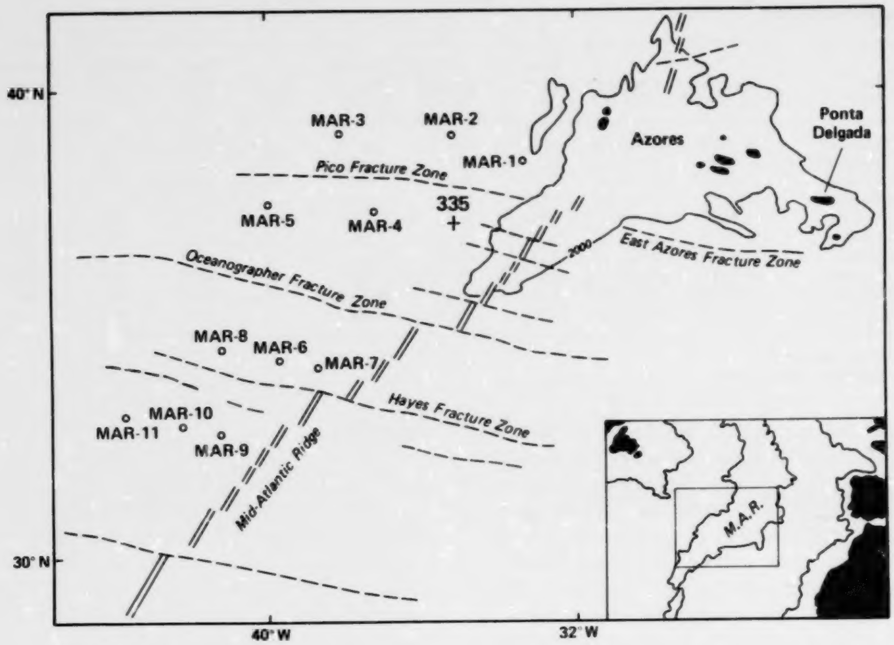
40° N
30° N
40° W
32° W
MAR-3
MAR-2
MAR-1
MAR-5
MAR-4
335
MAR-8
MAR-6
MAR-7
MAR-10
MAR-11
MAR-9
Azores
Ponta Delgada
Pico Fracture Zone
Oceanographer Fracture Zone
Hayes Fracture Zone
East Azores Fracture Zone
Mid-Atlantic Ridge
2000
M.A.R.

Figure 2. Proposed Leg 82 site locations.

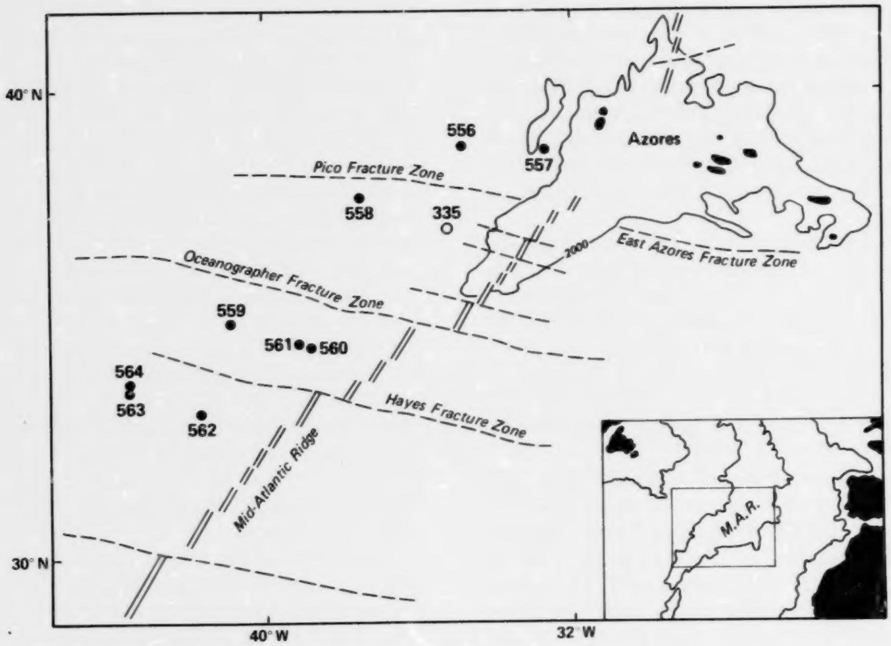
40° N
30° N
40° W
32° W
556
557
558
335
559
561
560
564
563
562
Azores
Pico Fracture Zone
Oceanographer Fracture Zone
Hayes Fracture Zone
East Azores Fracture Zone
Mid-Atlantic Ridge
2000
M.A.R.

Figure 3. Leg 82 drill sites.

ment and isotope abundances; Figure 7 shows the comparison between two isotopic ratios ($^{206}Pb/^{204}Pb$ versus ϵNd).

Site 556

Hole 556 was drilled on Anomaly 12 on the west flank of the Mid-Atlantic Ridge, about 50 miles north of the Pico Fracture Zone on a flow line passing through the Azores Triple Junction (Fig. 3). At 461 m sub-bottom, basalts occur as clasts in breccias, as pillow flows, and as massive flows. On the basis of macro- descriptions and microscopic descriptions of the samples, together with on-board chemical analyses, four chemically distinct basalt groups were defined within the different lith-

Table 1. Leg 82 coring summary.

Hole	Dates (1981)	Latitude (all north)	Longitude (all west)	Water depth (m)	Penetration (m)	Sediment thickness (m)	No. of cores	Total meters cored	Basement cored (m)	Basement recovery (%)	$(Nb/Zr)_{ch}$ range
556	22–29 September	38°56.38′	34°41.12′	3672	639.0	461.5	22	184.0	177.5	44.6	0.15–0.30
557	29–30 September	38°49.95′	32°33.58′	2143	463.5	460.0	1	3.0	3.0	40.0	1.30–1.90
558	3–11 October	37°46.24′	37°20.61′	3754	561.0	406.0	44	403.5	155.0	38.4	0.50–1.60
558A	11–12 October	37°46.24′	37°20.61′	3754	131.5	406.0	16	131.5[a]			
559	14–16 October	35°07.45′	40°55.00′	3754	301.0	238.0	8	63.0	63.0	37.0	1.5
560	16–18 October	34°43.33′	38°50.56′	3443	421.5	374.5	6	48.5	48.5[b]	16.0	0.8
561	18–20 October	34°47.10′	39°01.70′	3459	426.5	411.5	3	15.0	15.0	40.0	0.30–2.20
562	21–24 October	33°08.49′	41°40.76′	3172	331.0	240.0	11	90.0	90.0	44.9	0.30
563	24–28 October	33°38.53′	43°46.04′	3786	382.5	364.0	25	226.0	18.5	48.7	0.30
564	28 October–1 November	33°44.36′	43°46.03′	3820	365.0	284.0	9	81.0	81.0	43.0	0.37–0.54

[a] Percent recovery piston coring: 94.
[b] Only serpentinized gabbro and serpentine.

ologic units. Below 561 m sub-bottom, to the bottom of the hole (78 m) the core contained two units of partially to completely serpentinized gabbro breccia separated by a thin basalt layer. The depleted character [$(Nb/Zr)_{ch}$ = 0.15 to 0.3] of all basalts recovered at Site 556 is well correlated with normal topography of the ocean floor at this site. Nevertheless, although Figures 5 and 6 confirm that the basalts at Site 556 are typical of "normal" ocean crust, with ϵNd of about 10, Figure 7 shows that the $^{206}Pb/^{204}Pb$ values are much closer to values expected for "enriched" material. This result limits the understanding of mantle heterogeneities because it cannot be explained simply by mixing of two well-defined end-member-type mantle sources (e.g., depleted low-velocity-zone [LVZ]-type and enriched plume type). The combination in the same sample of depletion in magmaphile elements, of high ϵNd value, and also of high Pb isotopic ratios required that a particular mantle source was isolated a long time ago from either an Azores-plume-type or LVZ-type source.

The geothermal gradient is 36°C/km within the sediment above basement. A complete set of logs were run upon completion of the hole. These logs showed a constant temperature of about 2°C down to the sediment/basement interface, suggesting that seawater was flowing into the hole.

Site 557

Site 557 is located on Magnetic Anomaly 5D at the center of a broad elevated basin on the same flow line as Site 556 passing through the Azores Triple Junction (Fig. 3). After the discovery of depleted ocean crust at Site 556 (in contrast to the well-known enriched character of the ocean crust in the area of the triple junction), we deemed it important to verify the presence of enriched material closer to the ridge crest. In a duel with hurricane Irene, we had just enough time to core 3 m of basalt before being forced to abandon the hole. The high-Fe-Ti, coarse-grained aphyric basalts recovered there have the same typical enriched character [$(Nb/Zr)_{ch}$ = 1.3 to 1.9] found at the spreading center in the area of the Azores Triple Junction. This result has been confirmed by isotope data.

Site 558

Site 558 is located between Anomalies 13 and 15 on a flow line passing through the FAMOUS area (36°N) and through younger off-axis sites drilled during Legs 37 and 49 (Fig. 3). We decided on a complete program of coring (both sediment and basement) and logging to complement the large amount of data already available near and at the ridge crest.

The upper part of the basement of Site 558 consists of nine lithologic units of aphyric basalt—mostly pillow basalts with variable amounts of interpillow breccia and some basalt breccias (Fig. 4). Fresh glass is very common at pillow margins throughout the basalt layer. Calcite and/or limestone fills cracks and interpillow spaces. The deeper basement cores contain two lithologic units of serpentinized gabbro, fresh and altered serpentinite, serpentinite breccia, and mylonite.

On the basis of chemical analyses of 29 samples of the basalt layer, we identified six homogeneous chemical groups (Table 2 shows the average compositions). No cogenetic relationship exists between the different groups. The most striking result obtained at Site 558 is the occurrence, in the same hole, of depleted [$(Nb/Zr)_{ch}$ = 0.4], flat [$(Nb/Zr)_{ch}$ = 1], and enriched [$(Nb/Zr)_{ch}$ = 1.6] patterns of magmaphile element abundance (Fig. 8). After Sites 413 (Leg 49) and 504 (Legs 69 and 70), Site 558 is the third site presenting this feature.

Glass and bulk-rock samples show rather evolved Pb isotopic composition (Fig. 7) and extend the domain of the Atlantic Ocean basalts in lead-lead diagrams (Dupré et al., this volume).

In addition to the range of variation in isotopic ratios (Fig. 7), enriched and depleted (Nb/Zr or La/Ta ratio) values occur that correspond to the same ϵNd value (Fig. 5 and 6). Some basalts defined as "normal" mid-ocean ridge basalts (MORB) by magmaphile-element characteristics have ϵNd values typical of "enriched" MORB. This is a significant deviation to a general rule that would predict a perfect correlation between trace-element and isotopic ratios. Recent events can modify the trace-element characteristics from an "enriched" to a "depleted" signature without changing the "enriched" signature of isotopes (Langmuir et al., 1977; Bougault et al., 1979).

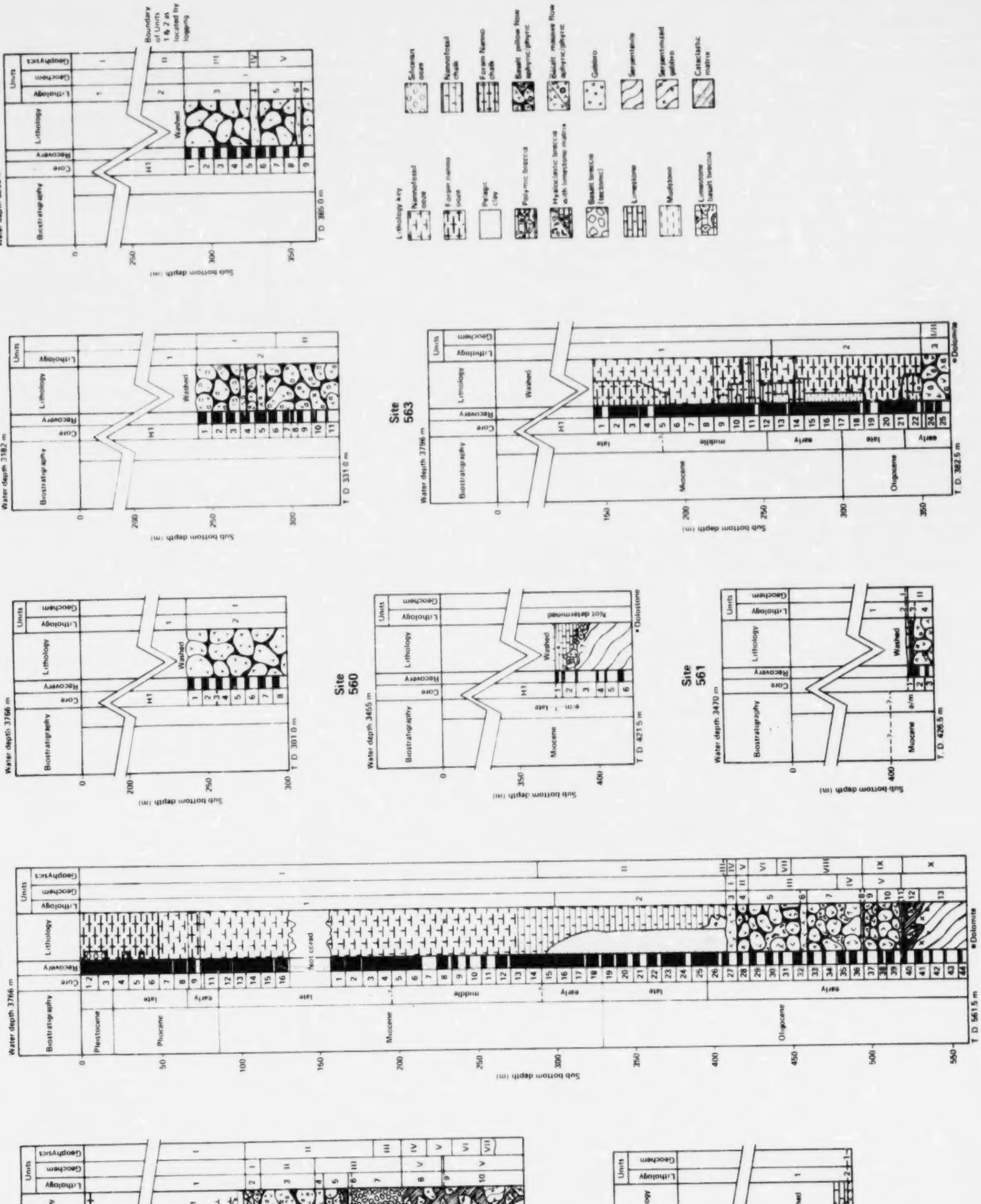
Site 556
Water depth 3690 m
T.D. 639.0 m
Site 557
Water depth 2150 m
T.D. 463.5 m
Site 558
Water depth 3766 m
T.D. 561.5 m
Site 559
Water depth 3766 m
T.D. 301.0 m
Site 560
Water depth 3455 m
T.D. 421.5 m
Site 561
Water depth 3470 m
T.D. 426.5 m
Site 562
Water depth 3182 m
T.D. 331.0 m
Site 563
Water depth 3796 m
T.D. 382.5 m
Site 564
Water depth 3830 m
T.D. 365.0 m
Biostratigraphy
Core
Recovery
Lithology
Units
Lithology
Geochem
Geophysics
Washed
Not cored
Sub bottom depth (m)
Pleistocene
Pliocene
Miocene
Oligocene
early
middle
late
Dolomite
Dolostone
Not determined
Boundary of Units 1 & 2 as located by logging
Lithology key
Nannofossil ooze
Foram-nanno ooze
Pelagic clay
Polymictic breccia
Phytoclastic breccia with limestone matrix
Basalt breccia (tectonic)
Limestone
Mudstone
Limestone basalt breccia
Siliceous ooze
Nannofossil chalk
Foram-Nanno chalk
Basalt pillow flow aphyric/phyric
Basalt massive flow aphyric/phyric
Gabbro
Serpentinite
Serpentinized gabbro
Cataclastic matrix

Figure 4. Stratigraphy of Leg 82 drill sites. T.D. = total depth.

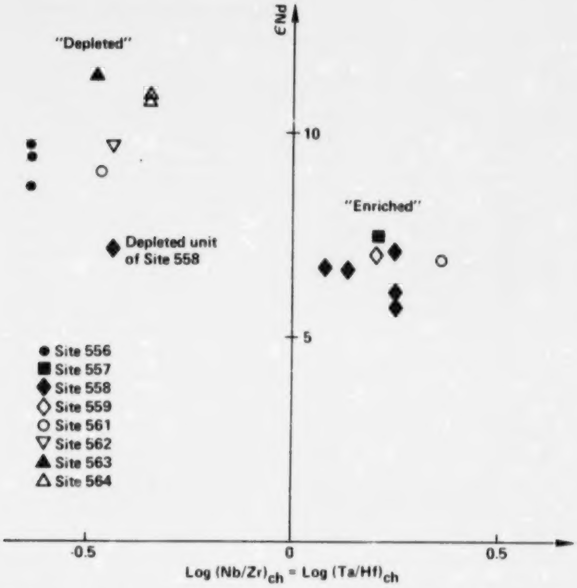

Figure 5. εNd versus Log (Nb/Zr). The logarithm of the normalized ratio of Nb/Zr on the *x* axis yields directly the enrichment or depletion factor observed from extended Coryell-Masuda plots (by definition, 0 corresponds to the flat distribution). (The normalized Nb/Zr ratio is equal to the normalized Ta/Hf ratio.)

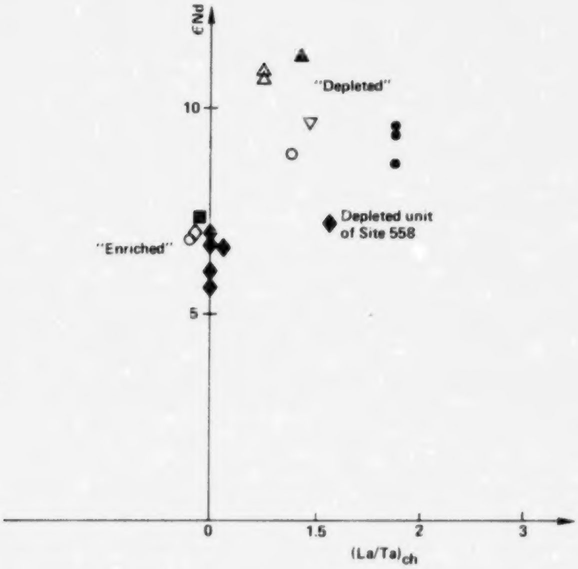

Figure 6. εNd versus normalized La/Ta ratio. This plot is chosen because of the well-known constant value of La/Ta in basalts that exhibit flat-to-enriched patterns (mantle-plume type). Symbols as in Figure 5.

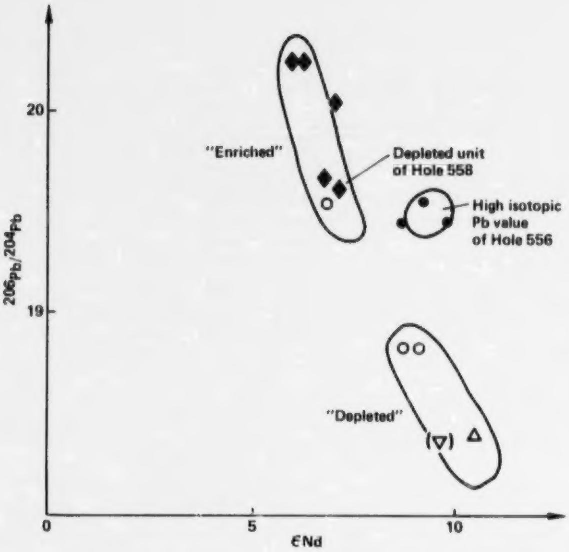

Figure 7. ^{206}Pb/^{204}Pb versus εNd. This plot shows possible anomalies in the correlation of isotopic ratios. Note the positions of samples from Hole 556, which are outside the two groups defined by Figures 5 and 6. They have a very high Pb radiogenic ratio for an εNd value of ~9.5. The parentheses around the Site 562 data point indicates that εNd and ^{206}Pb/^{204}Pb were determined on different units (Dupré et al., Jenner et al., Rideout and Schilling, this volume). Symbols as in Figure 5.

Table 2. Averages of major-element and trace-element concentrations of the different units at Site 558: on-board determinations.

Chemical group	I	II	III	IV	V	VI
n	1	3	13	5	6	1
SiO_2	50.67	50.86	50.70	50.19	49.37	48.71
TiO_2	1.22	1.12	1.38	1.22	0.96	0.92
Al_2O_3	14.10	15.11	14.82	14.65	15.49	15.81
Fe_2O_3	10.92	10.08	10.17	10.98	10.17	10.73
MnO	0.16	0.15	0.15	0.16	0.16	0.16
MgO	9.87	7.69	8.33	8.90	9.48	10.55
CaO	10.55	12.23	11.64	11.90	12.06	11.56
K_2O	0.18	0.18	0.30	0.30	0.20	0.10
P_2O_5	0.14	0.12	0.18	0.13	0.12	0.07
Ti	7320	6720	8280	7308	5780	5520
V	207	255	275	266	224	194
Sr	128	92	175	144	115	107
Y	27.7	29.7	28.7	28.1	22.9	23
Zr	83	66	88	80	61	51
Nb	8.6	3.2	14.8	10.5	7.3	2
$(Nb/Zr)_{ch}$	1.00	0.47	1.63	1.27	1.16	0.38

Note: n = number of samples on which mean is based.

Almost the entire sedimentary section (406 m) was recovered through a combination of piston coring (Hole 558A; 0–131.5 m) and rotary coring (Hole 558; 158–406 m) (Fig. 4). We have for the first time in the North Atlantic a continuously cored section of calcareous pelagic ooze and chalk that appears to be almost complete from the lower Oligocene through the lower Pleistocene. The age of the oldest sediment (34 to 37 Ma) obtained from nannofossils found in the basalt breccias at the top of basement is in agreement with the position of the hole between Magnetic Anomalies 13 and 15. A major change in the sediment lithology near the lower/middle Miocene boundary corresponds to a change in carbonate content (90% in the upper part, 50% below) and in the average sediment accumulation rate (20 m/Ma above and 8 m/Ma below).

Magnetostratigraphic studies of the lower part of the sedimentary section show a complete record of magnetic polarity reversals, correlating almost one to one with

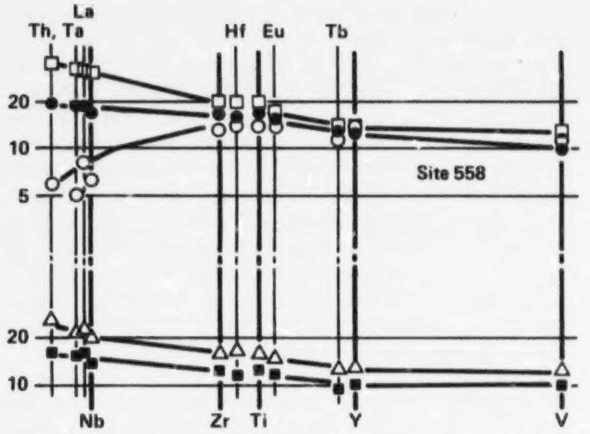

Figure 8. Hole 558: extended Coryell-Masuda plots. On the *x* axis, the elements indicated at the bottom of the figure (Nb, Zr, Ti, Y, V) were the objects of on-board measurements, whereas the concentrations of elements indicated at the top were determined on shore.

known reversals from Chron 16 to the lower part of Chron 12.

We attempted to run a complete set of geophysical logs, but owing to poor hole conditions, these were only partially successful. The major lithologic boundary in the sediments is clearly marked in the density, sonic, and resistivity logs and in shipboard physical properties measurements. We detected a similar change in the same logs at an equivalent depth at Site 556, implying that this lithologic change is probably a broad regional feature. Other minor changes within the sets of logs at Site 556 and 558 also appear to coincide.

Site 559

Hole 559, located between Anomalies 12 and 13 midway between the Oceanographer and Hayes fracture zones (Fig. 3), penetrated 63 m into basement, encountering uniform aphyric pillow basalts that belong to a single magmatic unit (Fig. 4). Low-temperature alteration effects are variable and randomly distributed, but fresh glass is common at pillow margins. Calcite is present in cracks and veins. The MgO concentration, about 8% in fresh samples, decreases to as little as 3% in badly altered samples. The Site 559 basalts are characterized by a typical enriched distribution of magmaphile elements $[(\mathrm{Nb/Zr})_{ch} = 1.65]$. Both magmaphile elements and isotopic data are characteristic of "enriched" MORB (Figs. 5, 6).

Sites 560 and 561

Hole 560 was drilled on Anomaly 5D midway between the Oceanographer and Hayes fracture zones (Fig. 3). At Site 560, serpentinized gabbro and serpentinite with chrysotile veinlets are present throughout the 49 m of basement cored (Fig. 4). Because the only basalt recovered was a single altered fragment within this serpentinized material, we decided to drill a second hole in the same area. This basalt fragment has a slightly depleted magmaphile element pattern $[(\mathrm{Nb/Zr})_{ch} = 0.8]$.

We drilled Site 561 on Anomaly 5E about 10 miles northwest of Site 560. We had cored the basement for only 15 m when the bit failed. Despite this low penetration, we sampled three different chemical groups of aphyric pillow basalts. As at Site 558, these groups include both depleted $[(\mathrm{Nb/Zr})_{ch} = 0.3]$ and enriched $[(\mathrm{Nb/Zr})_{ch} = 2.2]$ basalts (Fig. 9).

The isotopic signatures of the chemical groups at Site 561 are quite in agreement with the trace-element characteristics (Figs. 5, 6, 7). Hole 561 is a perfect example of local heterogeneities (in terms of mantle sources) and is a strong argument against the notion of long-term steady-state magma chambers.

Site 562

Hole 562 is located on Magnetic Anomaly 5D, 60 miles south of the Hayes Fracture Zone (Fig. 3). The basement, cored for 90 m, consists of sparsely plagioclase-phyric pillow basalts. Fresh glass is very common at the pillow margins. Despite some altered parts, the bulk of the crystalline basalts are fairly fresh, and we recognized two units on the basis of major-element and trace-element geochemistry (Fig. 4). The magmaphile elements show a typically depleted distribution with a $(\mathrm{Nb/Zr})_{ch}$ ratio of 0.3. Isotopic data are also typical of "normal" depleted MORB (Figs. 5, 6, 7).

Site 563

Hole 563 was drilled on Anomaly 13, on the same flow line as Hole 562 (Fig. 3). The lower part (156.5–364 m) of the sediment column was continuously cored and showed the same major change in the rate of sedimentation near the lower/middle Miocene boundary as we observed at Site 558, although the carbonate values, averaging 90%, changed only slightly. In addition, a good correlation exists between the sediments studied at Site 563 and the geophysical logs of Site 564 (6 mi. away), the logs and sediments at Site 558, and the logs at Site 556. The change in sedimentation rate near the lower/middle Miocene boundary can thus be considered a general event in this part of the Atlantic.

The basement was cored for only 18.5 m because of difficult drilling conditions and a premature bit release. It consists of one petrographic unit of sparsely plagioclase phyric pillow basalts. The on-board magmaphile

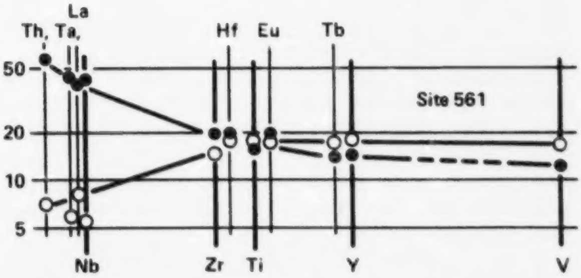

Figure 9. Hole 561: extended Coryell-Masuda plots. On the *x* axis, the elements indicated at the bottom of the figure (Nb, Zr, Ti, Y, V) were the objects of on-board measurements, whereas the concentrations of elements indicated at the top were determined on shore.

element analyses indicate a depleted character [$(Nb/Zr)_{ch}$ = 0.3]. Isotopic data are also characteristic of a "depleted" mantle source (Figs. 5, 6).

Site 564

The poor penetration into the basement at Site 563 (only a single petrographic unit was recovered) forced us to drill another site (6 mi. north) to document better the geochemistry of the basement south of the Hayes Fracture Zone.

At Site 564, we washed down through 284 m of sediment to the basement, which we then cored for 81 m. The recovered basement section consists of a single petrographic unit of aphyric pillow basalts interrupted by two massive flows (Fig. 4). Fresh glass occurred throughout the sequence. Chemically, the recovered samples form a single group, although forming a compositional gradient. CaO, for example, varies linearly from 12% at the top to 11.5% at the bottom with very little scatter. We also noted concentration gradients for the magmaphile elements; it appears that the Nb/Zr ratio is not constant downhole. This on-board observation, difficult to verify because of the Nb analytical precision, has been confirmed by onshore studies (Brannon, this volume). On the basis of the $(Nb/Zr)_{ch}$ ratio, which varies from 0.37 to 0.54, the basalts at this site are depleted. Isotopic data are also typical of "depleted" MORB's (Figs. 5, 6, 7).

We ran a complete set of geophysical logs in Hole 564, deriving the most significant conclusions from the temperature logs. We recorded two temperature profiles to test for thermal equilibrium. The first run was 18 hr. after circulation was stopped, and the second was 10 hr. later. The two profiles were identical down to below the sediment/basement interface, indicating a low gradient of about 5°C/km (which is only a fraction of the normal gradient). In the basement, between 45 and 60 m, the gradient increased to 250°C/km. This provides additional evidence at Anomaly 13 of downflow of seawater when the sedimentary layer is pierced.

Summary

Drilling operations during Leg 82 were very successful; we were able to achieve both the broad coverage necessary for the major objectives of the cruise and the detailed studies of individual sites required by our secondary objectives. Major results included:

1. There are very few examples of possible cogenetic relationships (i.e., related by shallow-level fractionation) between the basalt units identified at each site.
2. Basalts recovered at Site 556 (Anomaly 13 on the Azores Triple Junction flow line) show depleted magmaphile-element patterns compatible with low $^{87}Sr/^{86}Sr$ and high $^{143}Nd/^{144}Nd$ ratios. Nevertheless, the high Pb isotopic ratios require that a particular mantle source was isolated a long time ago, either from an Azores-type plume or from an LVZ-type source.
3. At two sites (558 and 561), we recovered both depleted and enriched material. Together with two previous occurrences at Site 413 (Leg 49) and Hole 504B (Leg 69-70), this finding demonstrates that the association of depleted and enriched magmaphile element patterns at the same site is more common than previously thought. It represents a strong argument in favor of discrete magma chambers.
4. At Site 558, two basalt groups, which have the same "enriched" signature of isotopes, display "enriched" and "depleted" magmaphile element characteristics. This can be explained by recent events that modify the trace-element pattern from "enriched" to "depleted" but do not change the "enriched" signature for isotopic ratios.
5. North of Hayes Fracture Zone, with the exception of the complexities of Hole 556 previously discussed, all sites show the evidence of a contribution of a "plume"-type source, even though a typical "depleted" basalt unit is also present at Site 561. South of Hayes Fracture Zone, all sites contain "depleted" MORB.
6. Serpentinites, serpentinized gabbros, and serpentinite breccias occurred at shallow depths at three sites (556, 558, and 560), suggesting that this material is common in the basement and probably related to normal faulting.
7. We recovered a nearly complete section of lower Oligocene to lower Pleistocene pelagic sediment from this part of the North Atlantic (Site 558 on Anomaly 13). This section will serve as a reference section for biostratigraphy and magnetostratigraphy in the area; of particular importance is the record of a regional increase in the sedimentation rate at about the lower/middle Miocene boundary.
8. *Bolboforma*—a tiny calcareous algae(?)—has to date only been recorded from five or six localities. Its discovery in Miocene sediments cored at Site 558 and 563 may provide a good stratigraphic marker and a climatic indicator of cooler temperatures.
9. We can deduce from downhole measurements taken above basement and within the basement that, at Site 556, seawater began to flow into the hole when the sedimentary layer was pierced. Other groups have observed this process on younger crust (at Sites 335, 395, and 504), and its occurrence on old crust places constraints on its interpretation closer to the ridge.

REFERENCES

Allègre, C. J., Brevart, O., Dupré, B., and Minster, J. R., 1980. Chemical effect produced in a continuously differentiating correcting earth mantle. *Phil. Trans. R. Soc. London, Ser. A*, 297:310-341.

Aumento, F., 1968. The Mid-Atlantic Ridge near 45°N II. Basalts from the area of Confederation Peak. *Can. J. Earth Sci.*, 5:1-21.

Aumento, F., Melson, W. G., et al., 1977. *Init. Repts. DSDP*, 37: Washington (U.S. Govt. Printing Office).

Bougault, H., 1977. Major elements: analytical chemistry on board and preliminary results. *In* Aumento, F., Melson, W., et al., *Init. Repts. DSDP*, 37: Washington (U.S. Govt. Printing Office), 643-652.

———, 1980. Contribution des éléments de transition à la compréhension de la genèse des basaltes océaniques. Analyse des éléments traces dans les roches par spectrométrie de fluorescence X [Thesis]. Université Paris VII.

Bougault, H., Cambon, P., Corre, O., Joron, J. L., and Treuil, M., 1979. Evidence for variability of magmatic processes and upper mantle heterogeneity in the axial region of the Mid-Atlantic Ridge near 22° and 36°N. *Tectonophysics*, 55:11-34.

Bougault, H., and Hekinian, R., 1974. Rift valley in the Atlantic Ocean near 36°N: petrology and geochemistry of basalt rocks. *Earth Planet. Sci. Lett.*, 24:249-261.

Bougault, H., Joron, J. L., and Treuil, M., 1979. Alteration, fractional crystallization, partial melting, mantle properties from trace elements in basalts recovered in the North Atlantic. *In* Talwani, M., Harrison, C. G., and Hayes, D. E. (Eds.): *Deep Drilling Results in the Atlantic Ocean: Ocean Crust*: Washington (Am. Geophys. Union), Maurice Ewing Series, 2:352–368.

________, 1980. The primordial chondritic nature and large scale heterogeneities in the mantle: evidence from high and low partition coefficient elements in ocean basalts. *Phil. Trans. R. Soc. London, Ser. A*, 297:203–213.

Bougault, H., and Treuil, M., 1980. Mid-Atlantic Ridge: zero age geochemical variations between Azores and 22°N, *Nature*, 986(5770): 209–212.

Bryan, W. B., and Moore, J. G., 1977. Compositional variations of young basalts in the Mid-Atlantic Ridge rift valley near lat. 36°49′N. *Geol. Soc. Am. Bull.*, 88:556–570.

Cann, J. R., 1970. Rb, Sr, Y, Zr, and Nb in some ocean floor basaltic rocks. *Earth Planet. Sci. Lett.*, 10:7–11.

Coryell, C. D., Chase, J. W., and Winchester, J. W., 1963. A procedure for geochemical interpretation of terrestrial rare earth abundance patterns. *J. Geophys. Res.*, 68:559.

DePaolo, D. J., and Wasserburg, G. J., 1976. Inferences about magma sources and mantle structure from variations of ^{143}Nd/^{144}Nd. *Geophys. Res. Lett.*, 3:743–746.

Dmitriev, L., Heirtzler, J. R., et al., 1979. *Init. Repts. DSDP*, 46: Washington (U.S. Govt. Printing Office).

Donnelly, T., Francheteau, J., Bryan, W., Robinson, P., Flower, M., Salisbury, M., et al., 1980. *Init. Repts. DSDP*, 51, 52, 53, Pts. 1, 2: Washington (U.S. Govt. Printing Office).

Dupré, B., and Allègre, C. J., 1980. Pb-Sr-Nd isotopic correlation and the chemistry of the North Atlantic mantle. *Nature*, 286(5768): 17–22.

Engle, A. E. J., Engle, C., and Havens, R. G., 1965. Chemical characteristics of oceanic basalts and the upper mantle. *Geol. Soc. Am. Bull.*, 76:719–734.

Erlank, A. J., and Kable, E. J. D., 1976. The significance of incompatible elements in Mid-Atlantic Ridge basalts from 45°N with particular reference to Zr/Nb. *Contrib, Mineral. Petrol.*, 54:281.

Frey, F. A., Bryan, W. B., and Thompson, G., 1974. Atlantic ocean floor: geochemistry and petrology of basalts from Legs 2 and 3 of the Deep Sea Drilling Project. *J. Geophys. Res.*, 79: 5507–5527.

Frey, F. A., Haskin. M. A., Poetz, J. A., and Haskin, L. A., 1968. Rare earth abundances in some basic rocks. *J. Geophys. Res.*, 73: 6085–6089.

Gast, P. W., 1960. Limitations on the composition of the upper mantle. *J. Geophys. Res.*, 65:1287–1293.

________, 1968. Trace element fractionation and the origin of tholeiitic and alkaline magma types. *Geochim. Cosmochim. Acta*, 32: 1057–1086.

Gast, P. W., Tilton, G. R., and Hedge, C. E., 1964. Isotopic composition of lead and strontium from Ascension and Gough Islands. *Science*, 145:1181–1185.

Hart, S. R., Schilling, J. -G., and Powell, J. L., 1973. Basalts from Iceland and along the Reykjanes Ridge: Sr-isotope geochemistry. *Nature, Phys. Sci.*, 268:707–725.

Hekinian, R., Moore, J. G., and Bryan, W. B., 1976. Volcanic rocks and processes of the Mid-Atlantic Ridge rift valley near 35°49N. *Contrib. Mineral. Petrol.*, 58:83–110.

Langmuir, C. H., Bender, J. F., Bence, A. E., Hanson, G. N., and Taylor, S. R., 1977. Petrogenesis of basalts from the FAMOUS area: Mid-Atlantic Ridge. *Earth Planet. Sci. Lett.*, 36:133–156.

LeDouaran, S., and Francheteau, S., 1981. Aerial depth anomalies from 10° to 50° north along the Mid-Atlantic Ridge: correlation with other mantle properties. *Earth Planet. Sci. Lett.*, 54:29–47.

Luyendyk, B. P., Cann, J. R., et al., 1979. *Init. Repts. DSDP*, 49: Washington (U.S. Govt. Printing Office).

Masuda, A., 1962. Regularities in variation of relative abundances of lanthanide elements and an attempt to analyze separation-index patterns of some minerals. *J. Earth Sci. Nagoya Univ.*, 10:173–187.

Melson, W. G., Rabinowitz, P. D., et al., 1979. *Init. Repts. DSDP*, 45: Washington (U.S. Govt. Printing Office).

Menard, H. W., 1967. Sea floor spreading, topography and the second layer. *Science*, 157:923–924.

Morgan, W. J., 1968. Rises, trenches, great faults and crustal blocks. *J. Geophys. Res.*, 73:1959–1982.

________, 1971. Convection plumes in the lower mantle. *Nature*, 230: 42–43.

O'Nions, R. K., Evensen, N. M., Hamilton, P. J., and Carter, S. R., 1978. Melting of the mantle past and present: isotope and trace element evidence. *Phil. Trans. R. Soc. London, Ser. A*, 258: 546–559.

O'Nions, R. K., Hamilton, P. J., and Evensen, N. M., 1977. Variations in ^{143}Nd/^{144}Nd and ^{87}Sr/^{86}Sr ratios in oceanic basalts. *Earth Planet. Sci. Lett.*, 34:13–22.

O'Nions, R.K., and Pankhurst, R. J., 1974. Petrogenetic significance of isotope and trace element variations in volcanic rocks from the Mid-Atlantic. *J. Petrol.*, 15:603–634.

O'Nions, R. K., Pankhurst, R. J., and Gronvold, K., 1976. Nature and development of basalt magma sources beneath Iceland and the Reykjanes Ridge. *J. Petrol.*, 17:315–338.

Pearce, J. A., and Cann, J. R., 1971. Ophiolite origin investigated by discriminant analysis using Ti, Zr, and Y. *Earth Planet. Sci. Lett.*, 12:339–349.

Richard, P., Shimizu, N., and Allègre, C. J., 1977. ^{143}Nd/^{146}Nd a natural tracer: an application to oceanic basalts. *Earth Planet. Sci. Lett.*, 31:269–278.

Schilling, J. -G., 1973. Iceland mantle plume: geochemical study of Reykjanes Ridge. *Nature London*, 242:565–575.

________, 1975. Azores mantle blob: rare earth evidence. *Earth Planet. Sci. Lett.*, 25:103–115.

Schilling, J. G., Kingsley, R., and Bergeron, M., 1977. Rare earth abundances in DSDP Sites 332, 334, and 335, and inferences on the Azores Mantle blob activity with time. *In* Aumento, F., Melson, W. G., et al., *Init. Repts. DSDP*, 37: Washington (U.S. Govt. Printing Office), 591–598.

Schneitzler, C. C., and Philpotts, J. A., 1970. Partition co-efficients of rare earth elements between igneous matrix material and rock forming mineral phenocryst. *Geochim. Cosmochim. Acta*, 34: 331–340.

Sclater, J. G., Anderson, R. N., and Bell, W. L., 1971. Elevation of ridges and evolution of the central eastern Pacific. *J. Geophys. Res.*, 76:7888–7915.

Sun, S. S., 1973. Lead isotope studies of young volcanic rocks from oceanic islands, mid-ocean ridges and island arcs [Ph. D. dissert.]. Columbia University, New York.

Sun, S. S., and Jahn, B., 1975. Lead and strontium isotopes in postglacial basalts from Iceland. *Nature*, 255:527–530.

Sun, S. S., Nesbitt, R. W., and Sharaskin, A. Y., 1979. Geochemical characteristics of mid-ocean ridge basalts. *Earth Planet. Sci. Lett.*, 44(1):119–138.

Sun, S. S., Tatsumoto, M., and Schilling, J. -G., 1975. Mantle-plume mixing along the Reykjanes Ridge Axis: lead isotopic evidence. *Science*, 190:143–147.

Tatsumoto, M., Hedge, C. E., and Engle, A. E. J., 1965. Potassium, rubidium, strontium-87 to strontium-86 in oceanic tholeiite basalts. *Science*, 150:886–888.

Tatsumoto, M., 1978. Isotopic composition of lead in oceanic basalt and its implication to mantle evolution. *Earth Planet Sci. Lett.*, 38:63–88.

Treuil, M., and Joron, J. L., 1975. Utilisation des elements hygromagmatophiles pour la simplification de la modelisation quantitative des processus magmatiques, exemples de l'Afar et de la dorsale medio-atlantique. *Soc. Ital. Mineral. Petrol, Milano*, XXXI:125–174.

Treuil, M., and Varet, J., 1973. Criteres volcanologiques, petrologiques de la genese et de la differenciation des magmas basaltiques: exemple de *l'Afar.Bull. Soc. Geol. France*, 7th series, XV:506–540.

Vogt, P. R., 1972. Evidence for global synchronism in mantle plume convection, and possible significance for geology. *Nature*, 240: 338–342.

White, W. M., and Bryan, W. B., 1977. Sr isotope, K, Rb, Cs, Sr, Ba, and rare earth geochemistry of basalts from the FAMOUS area. *Geol. Soc. Am. Bull.*, 88:571–576.

White, W. M., and Schilling, J. -G., 1978. The nature and origin of geochemical variation in Mid-Atlantic Ridge from central N. Atlantic. *Geochimica. Cosmochim. Acta*, 42:1501–1517.

White, W. M., Schilling, J. -G., and Hart, S. R., 1976. Evidence for the Azores mantle plume from strontium isotope geochemistry of the central N. Atlantic. *Nature*, 263:659–663.

Wood, D. A., Varet, J., Bougault, H., Corre, O., Joron, J. L., Treuil, M., Bizouard, H., Norry, M. J., Hawkesworth, C. J., and Roddick, J. G., 1979a. The petrology, geochemistry, and mineralogy of North Atlantic basalts: a discussion based on IPOD Leg 49. *In* Luyendyk, B. P., Cann, J. R., et al., *Init. Repts. DSDP*, 49: Washington (U.S. Govt. Printing Office), 597–655.

Wood, D. A., Tarney, J., Varet, J., Saunders, A. A., Bougault, H., Joron, J. L., Treuil, M., and Cann, J., 1979b. Geochemistry of basalts drilled in the North Atlantic by IPOD Leg 49: implications for mantle heterogeneity. *Earth Planet. Sci. Lett.*, 42:77–97.

Zindler, A., and Hart, S. R., 1978. Nd and Sr isotopic compositions and REE abundances in Reykjanes Peninsula basalts: evidence for mantle heterogeneity. *EOS, Trans. Am. Geophys. Union*, 59:410.

Date of Initial Receipt: 5 December 1983
Date of Acceptance: 13 February 1984

2. TECTONIC FABRIC OF THE SEAFLOOR NEAR NORTH CENTRAL ATLANTIC DRILL SITES[1]

S. C. Cande, Lamont-Doherty Geological Observatory
R. C. Searle, Institute of Oceanographic Sciences
and
I. Hill, University of Leicester[2]

INTRODUCTION

The nine sites drilled during Leg 82 are located along four flow lines that run perpendicular to the Mid-Atlantic Ridge (MAR). Together with Site 335 (Leg 37), these sites form a grid that samples the ocean basement along two isochrons, 17 and 35 Ma old, parallel to the ridge crest. The criteria used in selecting the sites was that the ocean basement should be "typical" of normal Mid-Atlantic Ridge terrain. "Typical" means that the basement has a lineated character, with the grain running parallel to the ridge (Atwater, 1979). This lineated character is best seen in side-scan images (e.g., Searle and Laughton, 1977; Laughton and Searle, 1979) or SEABEAM maps of the ocean floor. The only exception to the criteria of drilling on typical MAR terrain was made at Site 557, which was purposefully located on a flat-floored basin.

In this paper we present the geophysical data that exists in the region of each site drilled during Leg 82. These sites were not surveyed before drilling. Instead, the sites were selected based on the existing underway geophysical data in the Lamont-Doherty Geological Observatory and Woods Hole data libraries at the time of the cruise. Some of these data had been compiled before the cruise as part of the Ocean Margin Drilling (OMD) Area 11 data synthesis effort. Preliminary copies of the OMD bathymetric and magnetic maps for the region south of 38°N were used in selecting the sites. Following the cruise, Sites 556 through 562 were surveyed by R. C. Searle using the *Gloria* side-scan sonar system aboard the *Farnella*. In addition, copies of data collected near Site 558 by W. van der Linden on board the Canadian Research Vessel *Baffin* were made available to us after the cruise. We will combine all of these data in order to more fully describe the tectonic setting of the Leg 82 sites.

THE AZORES AND FAMOUS FLOW LINES

The two northern flow lines straddle the Pico Fracture Zone. An index map for the geophysical data on the northern flow lines is shown in Figure 1. Bathymetric and magnetics data for this region are shown in Figures 2 and 3, respectively. A seismic reflection profile available along the Azores flow line before the cruise is shown in Figure 4. Additional seismic reflection data available before the cruise consisted of a profile along the Knorr (*Kn*311) track in Figure 1 passing near Site 558. Seismic reflection data collected on the *Glomar Challenger* while moving between sites are shown in Figure 5. The interpretations of the *Gloria* sonographs presented below were made by R. C. Searle.

Technical details and principles of *Gloria* interpretation are given in Searle and Laughton (1977). In this paper, we interpret the brightest reflections on the *Gloria* sonographs as probably coming from basement outcrops; we believe that less bright, but still relatively strong, reflections arise from steeply sloping, possibly winnowed, pelagic sediments draping abyssal hills, although this interpretation is more tentative. During the surveys of Sites 556 through 558, the resolution of *Gloria* was degraded by a technical fault. The system was working normally for the other surveys.

Site 556

The drilling strategy decided upon before the cruise dictated that the first site would be drilled north of the Pico Fracture Zone near Anomaly 13. The seismic reflection data from *Vema* Cruise 32, shown in Figure 4, indicated that this was a region of typical Mid-Atlantic Ridge topography. The preliminary location of the site was based on the magnetics data from the *Atlantis II* (*A*II-49), *Bowditch* (*BD*63), and *Snellius* (*Sn*ll) cruises on which Anomaly 13 was identified striking north-south near 35°W. Although Anomaly 13 was poorly formed on the *Bowditch* profile, it was easily identified on the *Challenger* magnetometer data as the site was crossed.

The *Gloria* data (Fig. 6) confirm that the topography in this region is typical of normal MAR terrain, with strongly lineated north-south trending outcrops probably associated mainly with fault blocks. The nearest outcrops appear to be about 7 to 10 km south of the drill site and are quite small. There may be a few small, more rounded areas of outcrop in this region, but it is difficult to judge because of the degraded resolution in the sonar beam. The north-south striking basement outcrops observed about 25 km east of the drill site near 34°30′W correspond to the twin peaks observed at 0000 hr. on the *Vema* 32 profiler record. The north-south basement out-

---

[1] Bougault, H., Cande, S. C., et al., *Init. Repts. DSDP*, 82: Washington (U.S. Govt. Printing Office).

[2] Addresses: (Cande) Lamont-Doherty Geological Observatory, Palisades, New York 10964; (Searle) Institute of Oceanographic Sciences, Wormley, Surrey, United Kingdom; (Hill) Department of Geology, University of Leicester, Leicester, United Kingdom.

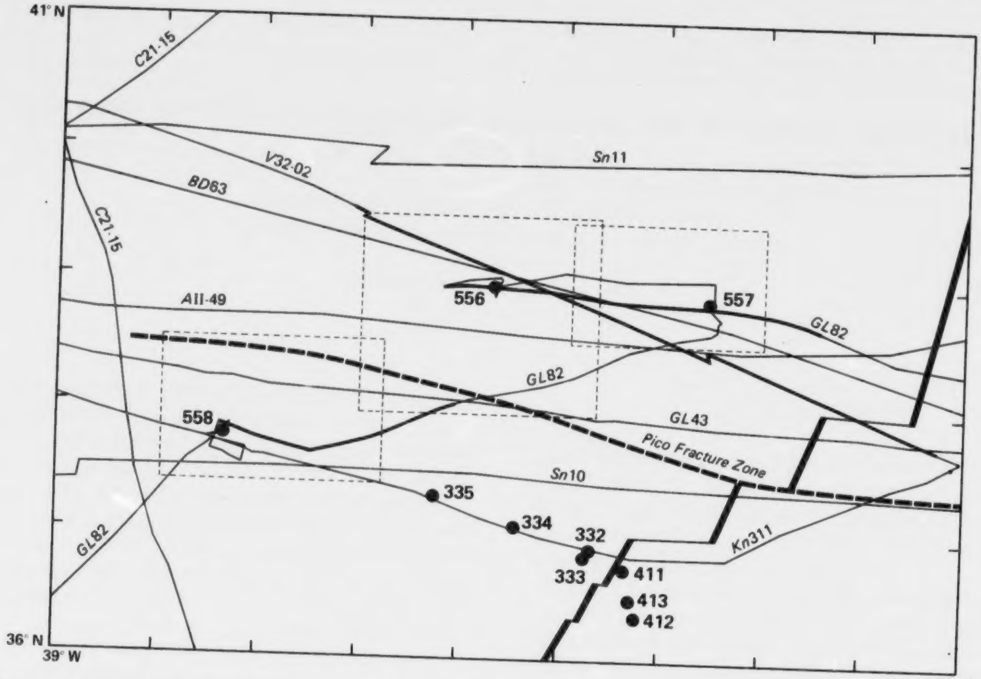
41° N
36° N
39° W
30° W
C21-15
C21-15
V32-02
BD63
Sn11
A11-49
GL82
GL82
GL82
GL43
Sn10
Kn311
Pico Fracture Zone
556
557
558
335
334
332
333
411
413
412

Figure 1. Identification of ships' tracks with geophysical data near Sites 556 through 558 (Azores and FAMOUS flow lines). Dashed boxes indicate location of Figures 6, 8, and 10 showing *Gloria* data. Heavy lines show portions of track with seismic profiler data displayed in Figures 4 and 5. Solid circles are DSDP sites. Ship identifications as follows: *C*21-15 = *Conrad* Cruise 21, Leg 15; *V*32-02 = *Vema* Cruise 32, Leg 02; *A*II-49 = *Atlantis* II, Leg 49; *GL*82 = *Challenger* Leg 82; *Sn*11 = *Snellius*; *BD*63 = *Bowditch*; *KN*311 = *Knorr*.

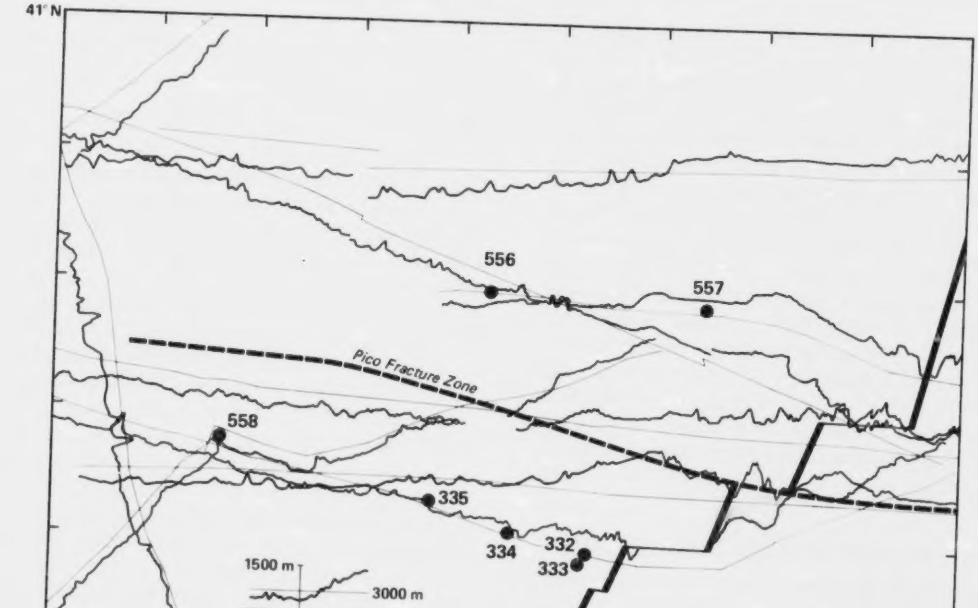
41° N
36° N
39° W
30° W
556
557
558
335
334
332
333
Pico Fracture Zone
1500 m
3000 m
4500 m

Figure 2. Bathymetry (Azores and FAMOUS flow lines) plotted as profiles perpendicular to the track. Solid circles are DSDP sites.

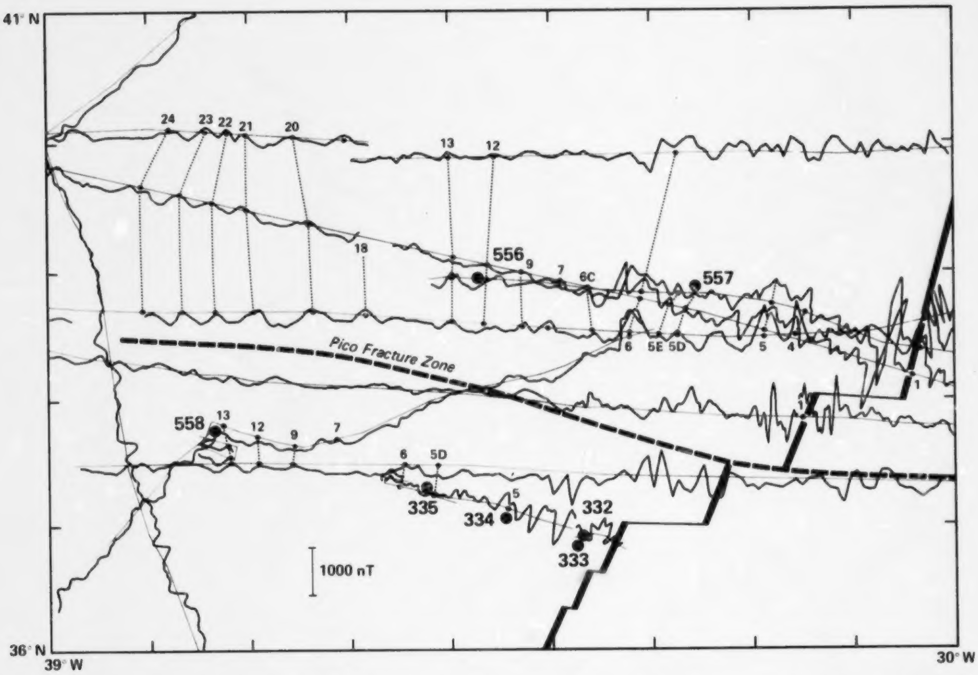

Figure 3. Residual magnetic anomaly field plotted perpendicular to the track. Solid circles are DSDP sites; other numbers are magnetic anomalies.

crops seen on the *Gloria* record near 34°00′W correspond to the peaks crossed at 0200 hr. on the *Vema* 32 profiler record (Fig. 4) and at 1900 hr. on the *Glomar Challenger* profile (top, Fig. 5).

Site 557

The preliminary planning for Site 557 was based on the *Vema* 32 seismic reflection line and the *Bowditch* (*BD*63) and *Atlantis II* (*A*II-49) magnetics data. These data showed that east of Anomaly 6 there was a 40-km-wide basin located on anomalously shallow and smooth basement. However, even through the basement structure is abnormal for the Mid-Atlantic Ridge, the magnetic anomalies (Fig. 3) are lineated and can be identified in the framework of magnetic reversal lineations. Site 557 was located on what was identified during the cruise as Anomaly 5D.

A model of the seafloor-spreading magnetic anomalies suggests that the initial anomaly identifications may be incorrect (Fig. 7). If the two prominent anomalies bordering the east and west side of the basin are identified as Anomalies 5 and 6, respectively, than a constant spreading rate shows that Site 557 may have been drilled on Anomaly 5B. Because the hole was washed to basement, and sediments were only recovered from a wash core, there is no reliable biostratigraphic constraint on the basement age. The oldest sediments in the wash core are dated as 13 Ma old, which is roughly the age of Anomaly 5B. Fortunately, a change (or uncertainty) in age of the site has little effect on the interpretation of the drilling results.

The *Gloria* sonographs (Fig. 8) showed that there are hills within 5 km to the northwest and northeast of Site 557. These and most other structures visible within about 65 km of the site are only poorly lineated. Generally, areas of outcrop are equidimensional suggesting volcanic construction rather than tectonic relief. Indeed, it may be possible to discern two craters associated with the hills just north of the drill site. The existence of this presumed volcanic terrain is strongly consistent with the association of this area with mantle blob or hot-spot activity, as inferred from the basalt chemistry. Normally lineated seafloor occurs west of 33°30′W (Fig. 8), which is where the smooth basement gives way to normal rugged basement (0500 hr. on the *Vema* 32 seismic profile, Fig. 4).

Site 558

The preliminary location of Site 558 was based on the *Snellius* (*Sn*10) magnetics and the *Knorr* (*Kn*311) seismic data (not shown). Although the basement around the site on the *Knorr* profile appeared to be representative of typical MAR topography, the data collected on the *Challenger* while surveying the site showed that the tectonic fabric was atypical. The most obvious complexity was that the magnetic anomalies in the immediate vicinity of the site strike about 350°, oblique to the ridge crest. Additional magnetic data made available to us by W. van der Linden (pers. comm., 1983) and shown in Figure 9 document the varying trends of the magnetic anomalies in this area. Near Site 558, Anomalies 12 and 13 strike slightly west of North. Near the Pico Fracture

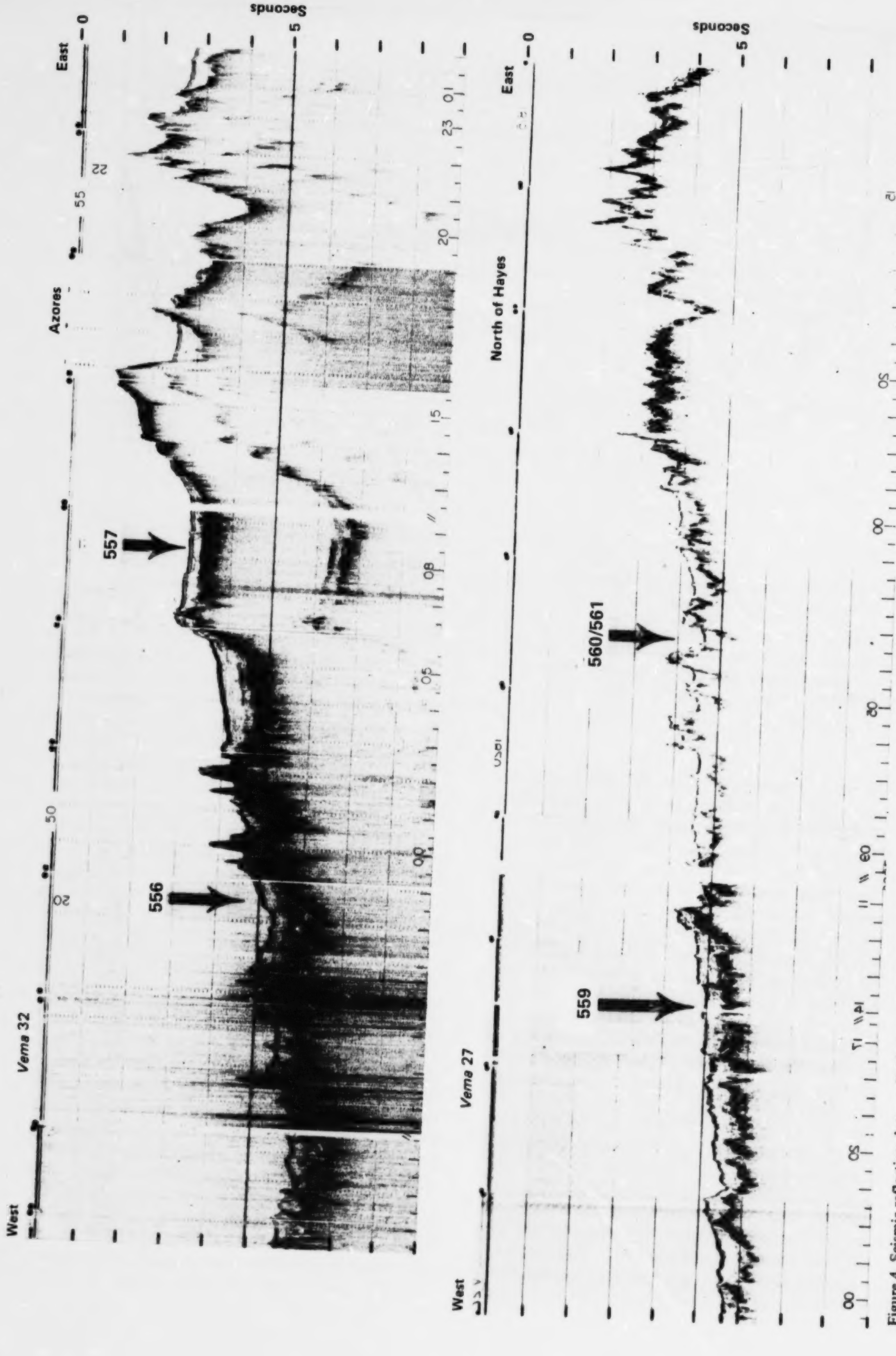

Figure 4. Seismic reflection data available from the library at Lamont-Doherty Geological observatory before Leg 82. The closest approach of the ship's tracks to the drilled sites are indicated by arrows.

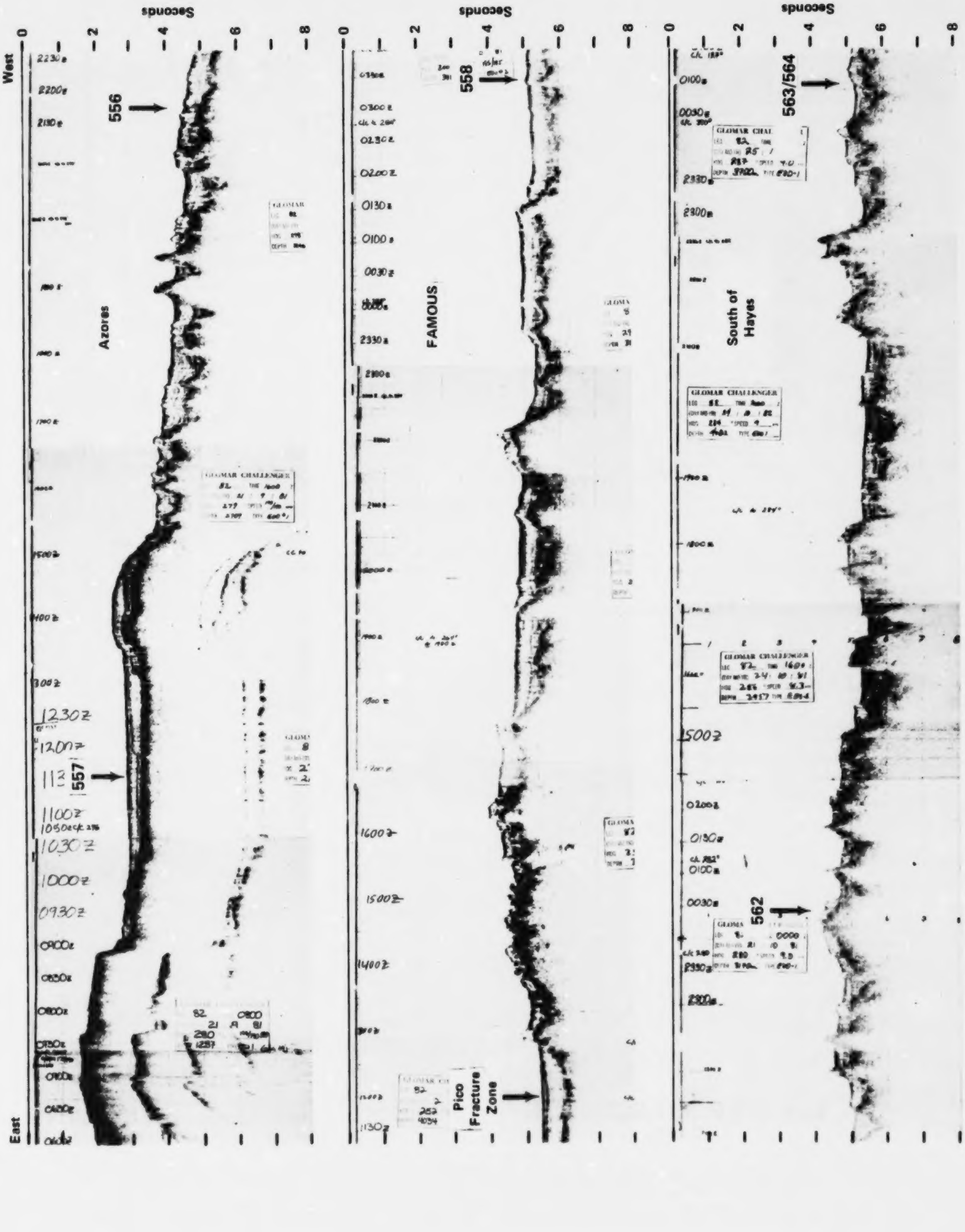

Figure 5. Seismic reflection data collected on the *Challenger* while moving between sites.

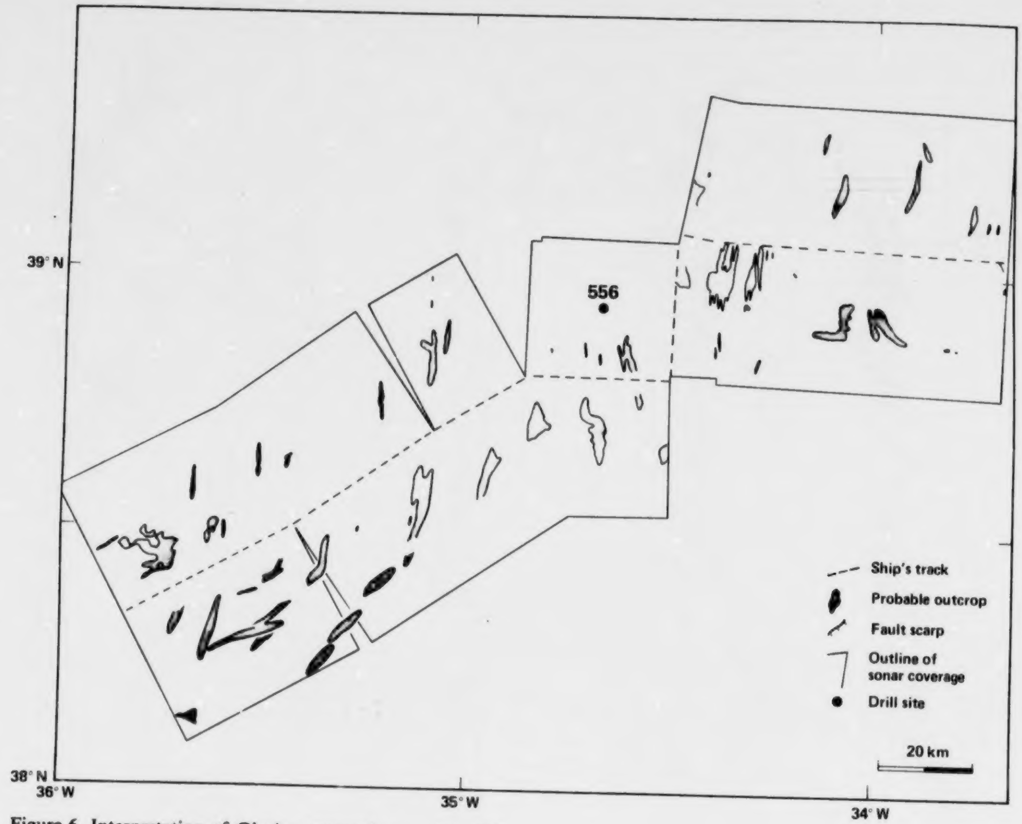
39° N
556
Ship's track
Probable outcrop
Fault scarp
Outline of sonar coverage
Drill site
20 km
38° N
36° W
35° W
34° W

Figure 6. Interpretation of *Gloria* sonographs near Site 556.

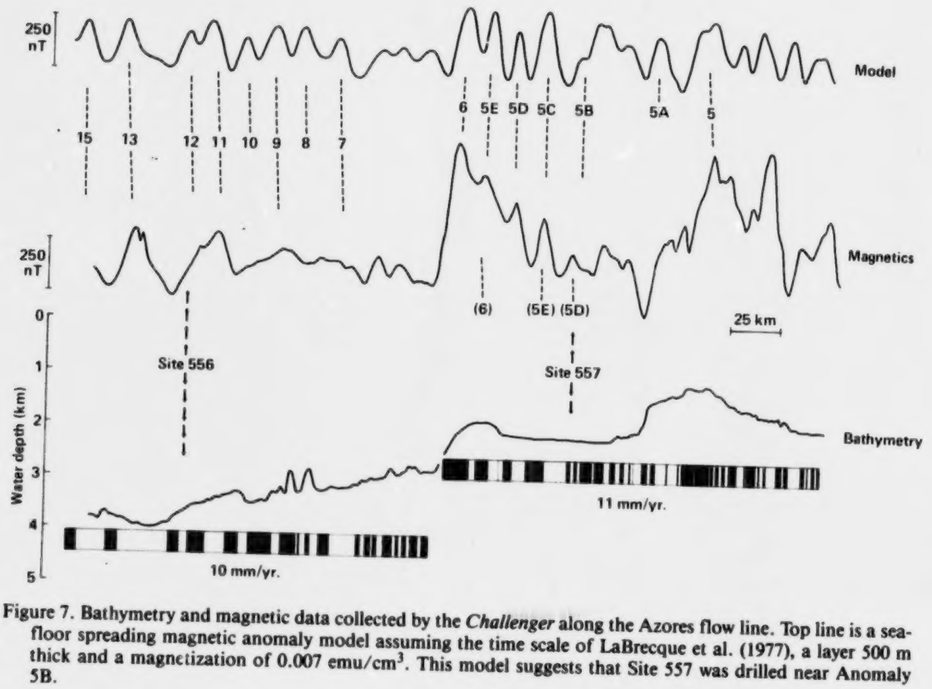

Figure 7. Bathymetry and magnetic data collected by the *Challenger* along the Azores flow line. Top line is a sea-floor spreading magnetic anomaly model assuming the time scale of LaBrecque et al. (1977), a layer 500 m thick and a magnetization of 0.007 emu/cm^3. This model suggests that Site 557 was drilled near Anomaly 5B.

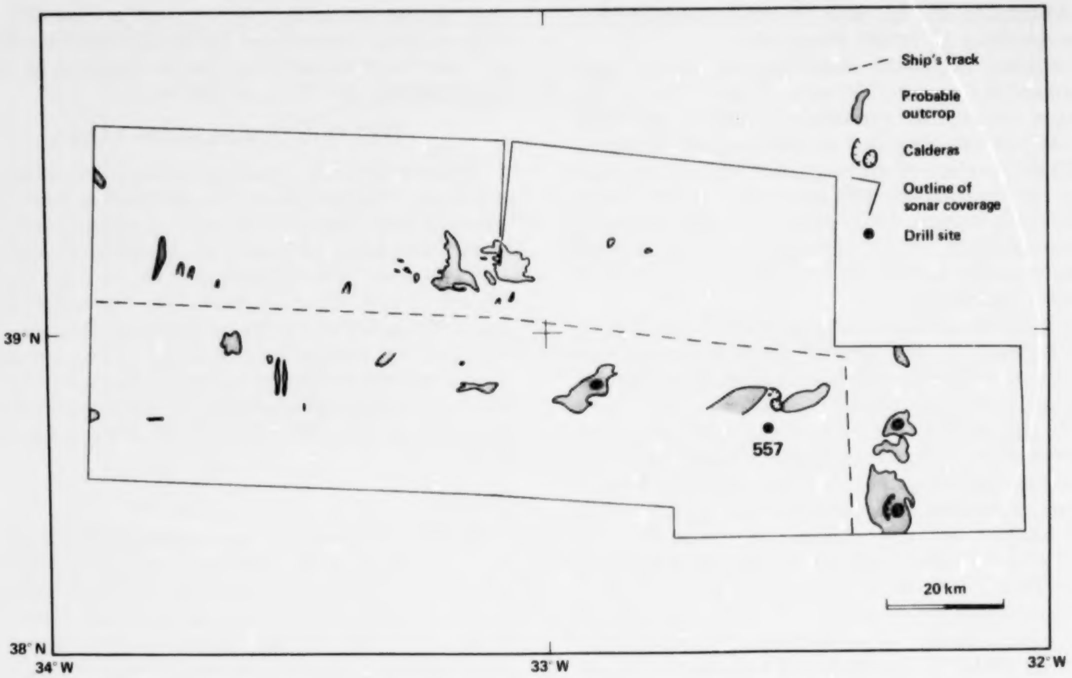
Ship's track
Probable outcrop
Calderas
Outline of sonar coverage
Drill site
557
20 km
39° N
38° N
34° W
33° W
32° W

Figure 8. Interpretation of *Gloria* sonographs near Site 557.

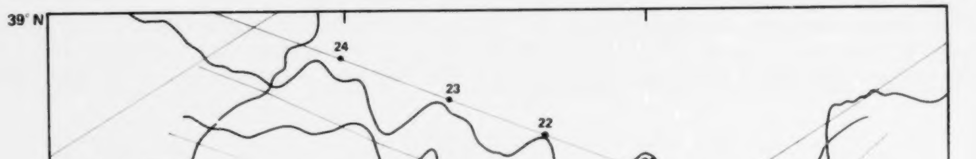

Figure 9. Magnetic anomaly data near Site 558 (with the exception of the *Challenger* data, these data were compiled by W. van der Linden).

Zone; Anomalies 13, 15, and 16 strike roughly 010° whereas Anomaly 12 strikes about 040°.

The original shipboard identifications of the magnetic anomalies near Site 558 were in error. During the *Challenger* cruise, the prominent magnetic anomaly east of the site was identified as Anomaly 12. However, based on the rotation of all anomalies west of the ridge back to the location of anomalies east of the ridge, Schouten (pers. comm., 1983) determined that the prominent anomaly east of the site was Anomaly 13. This new identification is supported by the large amount of data now available (Fig. 9).

The complexity of the basement trends is also seen in the *Gloria* data (Fig. 10). West of the drill site and east of it to about 37°20′W, outcrops indicating the general tectonic fabric strike about 004°. Between 37°20′W and 36°45′W, the trend is generally about 040°. Some of these northwest-southwest lineaments border the Pico Fracture Zone and may have had their origin in the dextral offset transform that produced it, because such oblique features are characteristic of fracture zones (Searle, 1979). However, such features are normally confined to within 20 km of the fracture zone axis, whereas here oblique structures are seen up to 70 km south of the fracture zone. Another or additional explanation may be that they represent the results of a phase of oblique spreading such as occurred near the Oceanographer Fracture Zone before Anomaly 6 and since Anomaly 4 (Phillips et al., 1975). If oblique spreading is more likely during times of high plume discharge, as suggested for the Reykjanes Ridge by Vogt and Johnson (1975), these observations may indicate that such a discharge was imminent during formation of the crust at Site 558. This might account for some of the basalt chemical variability. The Pico Fracture Zone can be discerned on the sonographs near 38°15′N, 36°00′W.

THE SOUTHERN FLOW LINES

The two southern flow lines straddle the Hayes Fracture Zone. The location of the geophysical lines used in selecting these sites and the location of the *Gloria* sonographs are shown in Figure 11. Bathymetric and magnetics data on tracks passing near the sites are shown in Figures 12 and 13, respectively. The *Challenger* seismic data from north of the Hayes Fracture Zone are shown in Figure 14. Interpretations of the *Gloria* sonographs from Sites 559–562 are presented in Figures 15, 17, and 19. The original montages of the *Gloria* records from these sites are shown in Figures 16, 18, and 20, respectively.

Site 559

Site 559 was located near Anomaly 13 on the flow line north of the Hayes Fracture Zone. The preliminary planning for the site was based on a *Vema* 27 seismic reflection profile (Fig. 4) that indicated that about 400 m of sediment cover normal-looking basement near Anomaly 13. Existing magnetic anomaly data consisted of the *Trident* (*T*152) profile and the *Vema* 27 profile. The identifications of Anomalies 12 and 13 were straightforward (Fig. 13).

The *Gloria* sonographs (Figs. 15 and 16) showed that Site 559 was located 2 km, northwest of a small abyssal hill. The hill is fault-bounded on its east-southeast side,

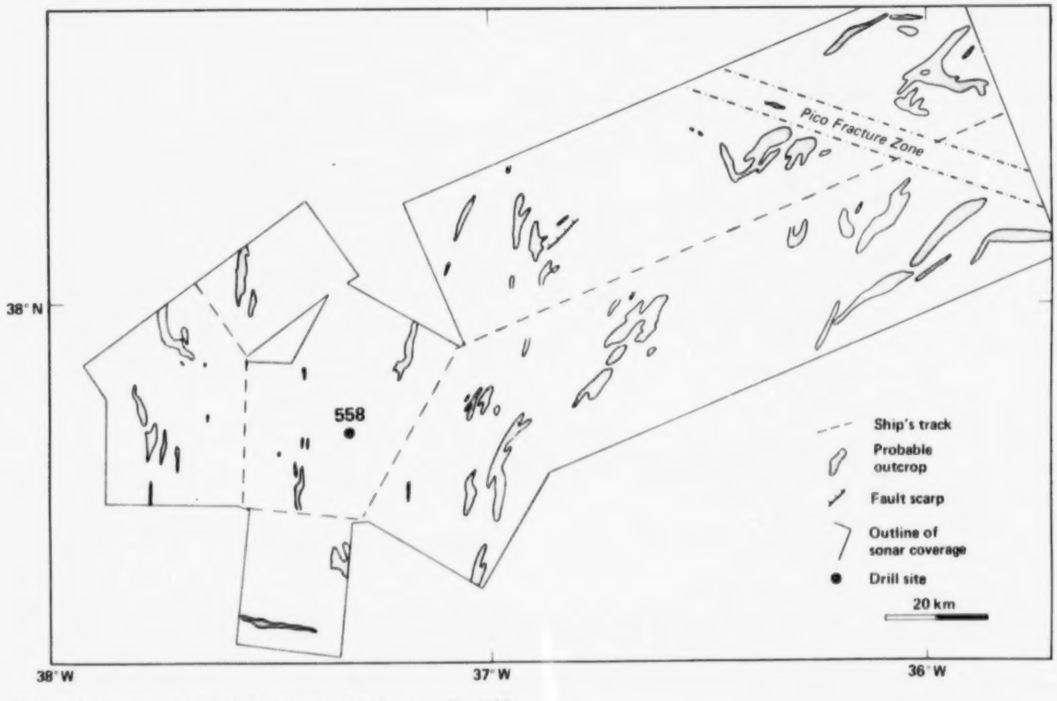

Figure 10. Interpretation of *Gloria* sonographs near Site 558.

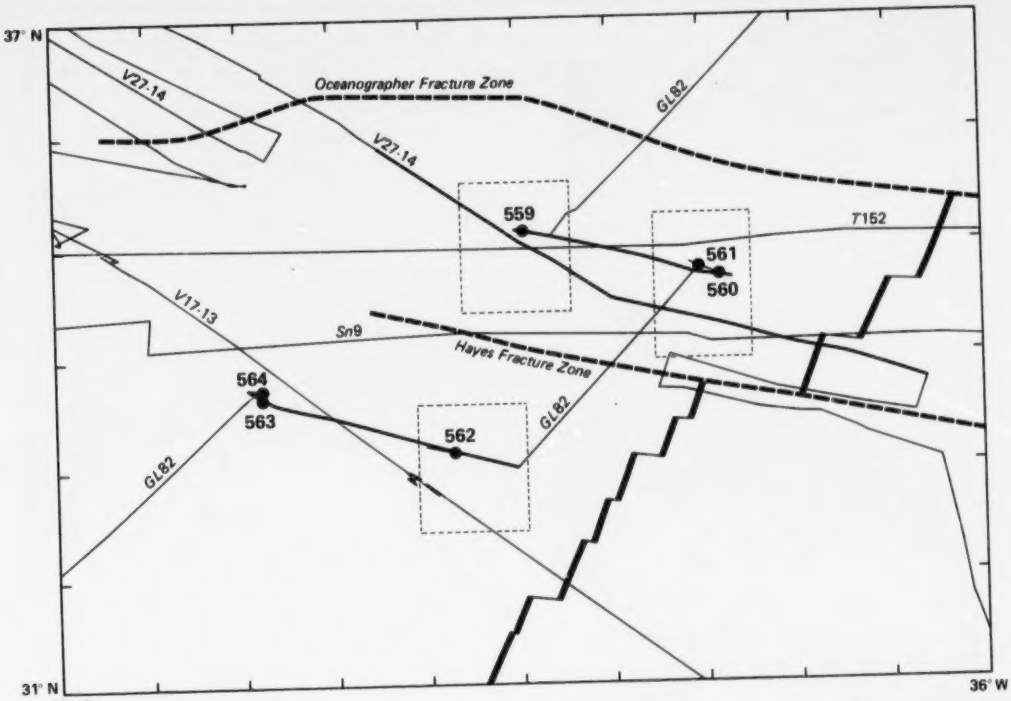
37° N
V27-14
Oceanographer Fracture Zone
GL82
V27-14
559
T152
561
560
V17-13
Sn9
Hayes Fracture Zone
564
563
562
GL82
GL82
31° N
46° W
36° W

Figure 11. Identification of ships' tracks near Sites 559 through 564. Dashed boxes show location of Figures 15–20 which contain *Gloria* data. Solid circles are DSDP sites. For ship identifications, see Fig. 1; also *T*152 = *Trident* Cruise 152.

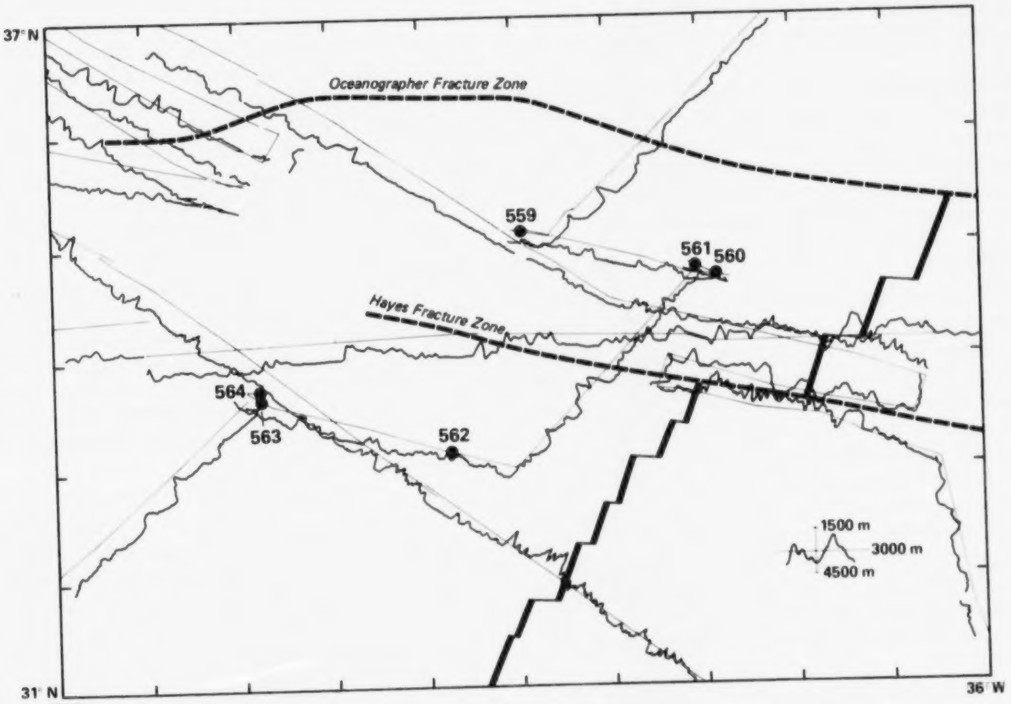
37° N
Oceanographer Fracture Zone
559
561
560
Hayes Fracture Zone
564
563
562
1500 m
3000 m
4500 m
31° N
46° W
36° W

Figure 12. Bathymetric data plotted as profiles perpendicular to the track. Solid circles are DSDP sites.

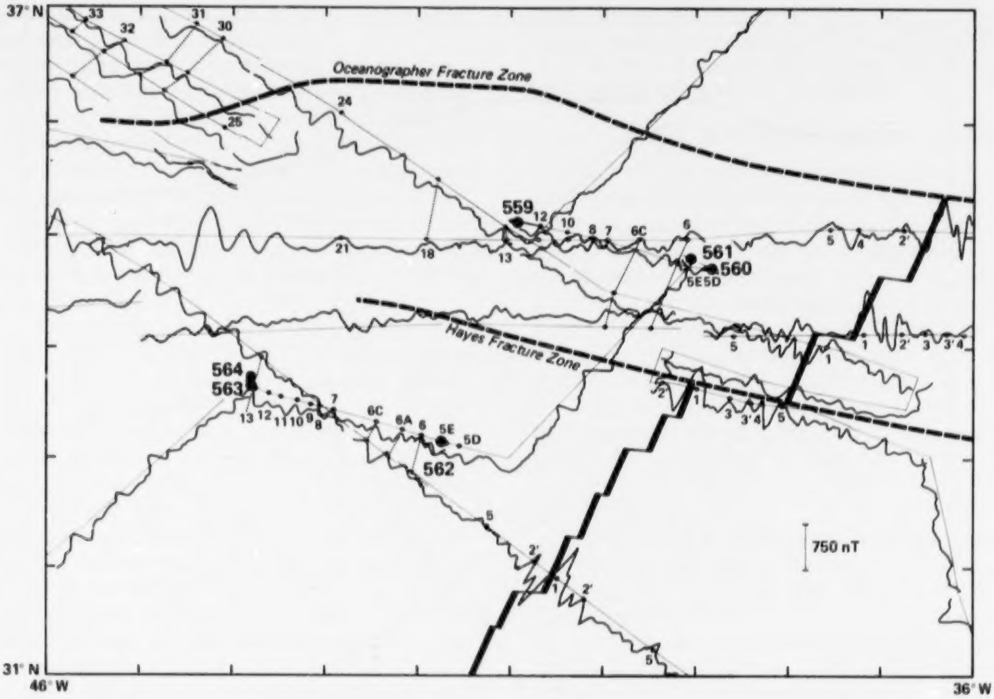

Figure 13. Residual magnetic anomaly data (Hayes Fracture Zone flow lines) plotted as profiles perpendicular to the track. Solid circles are DSDP sites; other numbers are anomalies.

but a dip slope faces the drill site. The hill displays several areas of probably thinly sedimented volcanic basement. Another small hill is situated 15 km northwest of the site.

The drill site appears to be situated in a region of normal tectonic fabric, exemplified by the tilted fault blocks striking north-northeast that make up the lineated abyssal hills. However, a small fracture zone, indicated by a 100-km-long series of outcrops trending east-west passes about 60 km to the south of the site.

Sites 560 and 561

Site 560 was located near Anomaly 5D along the same flow line as Site 559. The closest seismic profiler record was from *Vema* 27 (*V*27-14) (Fig. 4) and the nearest magnetic data were from *Trident* (*T*152). Anomaly 6 is easy to identify on both the *Vema* and *Trident* tracks. The seismic reflection data showed that the basement relief was typical of the Mid-Atlantic Ridge.

Very poor core recovery was achieved at Site 560, probably because the hole had been drilled through a talus slope facing the spreading axis. The *Gloria* data (Figs. 17 and 18) confirm this, showing that the site is situated less than 2 km to the east of an abyssal hill, which is bounded on its eastern side by an east-facing fault scarp. Basement appears to outcrop along this scarp.

Site 561 was drilled on Anomaly 5E, 10 miles northwest of Site 560. The *Gloria* data show that the site is situated in a 15 km-wide basin between abyssal hills. The nearest hill is about 4 km east-southeast of the site.

Both Sites 560 and 561 appear to be in region of normal MAR volcanic and tectonic fabric. The abyssal hills are strongly lineated and aligned north-northeast-south-southwest parallel to the magnetic isochrons. In a small *Gloria* survey carried out near the MAR axis on this same flow line (R. C. Searle, unpublished data), a relatively complicated tectonic fabric was found, with several short-offset fracture zones and some large volcanic massifs devoid of the normal lineated tectonic fabric (similar to those found at Site 557). There is no evidence of such massifs around Sites 560 and 561. However, the presence of two zones of outcrops trending east-northeast just 15 km north of Site 561, suggests a small fracture zone or zone of oblique spreading. Other outcrops trending east-northeast occur 60, 75, and 90 km south of Site 561, still north of Hayes Fracture Zone. It may be, therefore, as argued for Site 558, that the basalt variability is in some way related to a tendency to oblique spreading.

Site 562

Site 562 was located near Anomaly 5D south of the Hayes Fracture Zone. The only seismic data near the site before drilling was an early *Vema* 17 (*V*17-13) profile shot with explosives. Anomaly 6 was identified on the magnetic data from this cruise and was used to select the general location of the site. The seismic data collected on the *Challenger* (Fig. 5) showed that the basement in this area was normal in appearance.

Gloria is not very sensitive to small variations in seabed slope. The interpretation shown in Figure 19 was

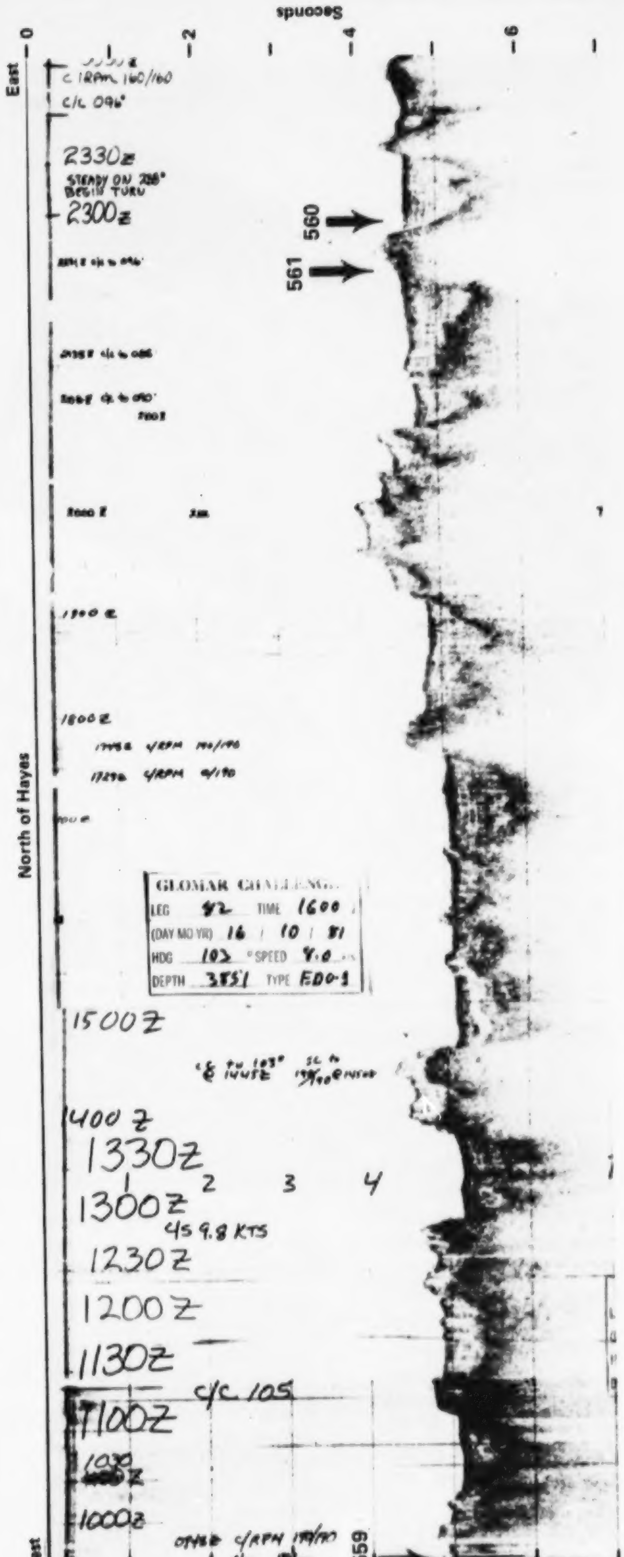

Figure 14. Seismic reflection data collected by the *Challenger* in transit between Sites 559 and 560.

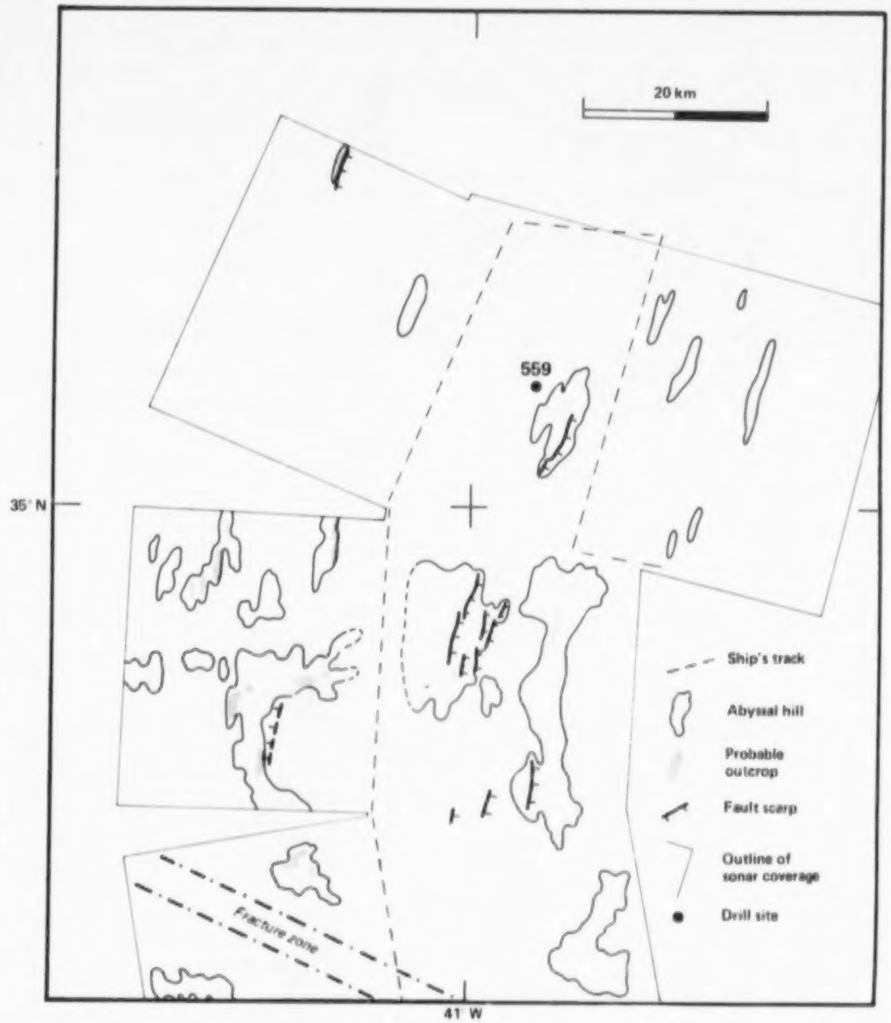

Figure 15. Interpretation of *Gloria* sonographs near Site 559.

done without benefit of the seismic profile (Fig. 5) and shows a number of small abyssal hills closely surrounding the site. The seismic profile indicates that the site is actually on a very broad hill, so the best interpretation of the *Gloria* data (Fig. 20) is that the bright areas seen there represent either small hills or ridges superimposed on the broad one (which is not seen because of its low slope).

The nearest of these ridges, less than 2 km away to the northeast of the site, is very small and covered with sediment. A much larger ridge (15 km long, 2 km wide) has its southern end 2 km northwest of the site. Basement outcrops along an east-facing fault scarp along the entire eastern edge of this ridge. As at Site 559, the whole area is characterized by hills trending east-northeast that were formed as fault blocks striking parallel to the magnetic lineations. However, once again some oblique outcrops trending east-northeast attest to the existence of oblique spreading or short-offset fracture zones in the area. The nearest of these oblique trending outcrops are 50 km northeast and 65 km southeast of Site 562. There is no evidence of nonlineated volcanic massifs in this region.

Sites 563/564

The preliminary location of Site 563 was based on the *Vema* (*V*17-13) seismic and magnetic data. The *Challenger* seismic data collected in transit from Sites 562 and 563 (Fig. 5) indicated a normal tectonic setting. The limited magnetic data in the area give a strike of about 10°, which is consistent with an orthogonal spreading system. These sites were not surveyed by *Gloria*.

CONCLUSIONS

With the exception of Site 557, which intentionally drilled on a smoothed-floor basin, most of the sites meet the criteria of being located on typical ocean basement. Site 558, which had the most complex chemical signature of any site during the cruise, also had the most complex tectonic fabric. In particular, the ocean base-

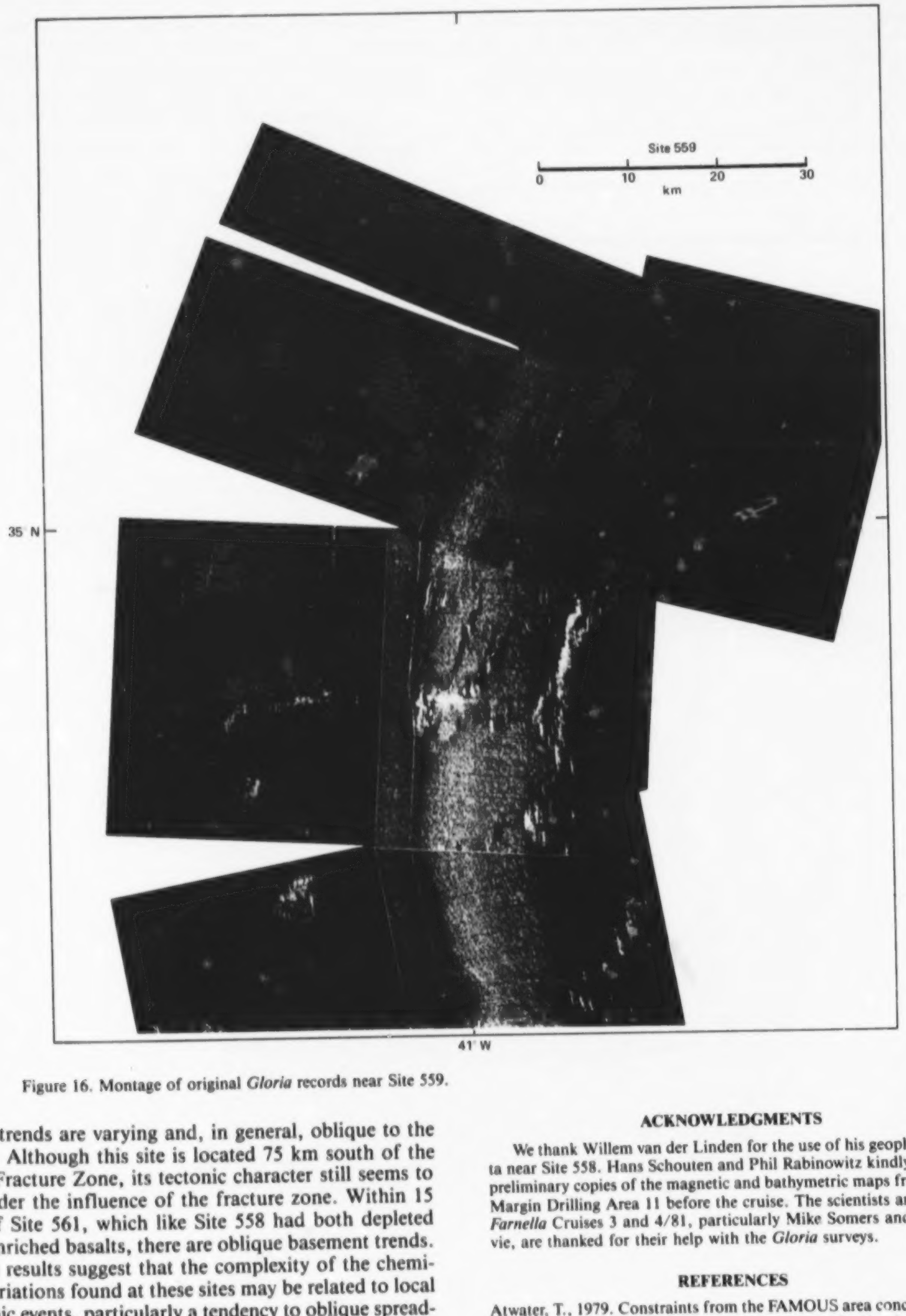

Figure 16. Montage of original *Gloria* records near Site 559.

ment trends are varying and, in general, oblique to the ridge. Although this site is located 75 km south of the Pico Fracture Zone, its tectonic character still seems to be under the influence of the fracture zone. Within 15 km of Site 561, which like Site 558 had both depleted and enriched basalts, there are oblique basement trends. These results suggest that the complexity of the chemical variations found at these sites may be related to local tectonic events, particularly a tendency to oblique spreading, rather than to a regional geochemical phenomenon.

ACKNOWLEDGMENTS

We thank Willem van der Linden for the use of his geophysical data near Site 558. Hans Schouten and Phil Rabinowitz kindly provided preliminary copies of the magnetic and bathymetric maps from Ocean Margin Drilling Area 11 before the cruise. The scientists and crew of *Farnella* Cruises 3 and 4/81, particularly Mike Somers and Jack Revie, are thanked for their help with the *Gloria* surveys.

REFERENCES

Atwater, T., 1979. Constraints from the FAMOUS area concerning the structure of the oceanic section. *In* Talwani, M., Harrison, C. G., and Hayes, D. E. (Eds.), *Deep Sea Drilling Results in the Atlantic Ocean: Ocean Crust:* Washington (Am. Geophys. Union), Maurice Ewing Series, 2: 33–42.

LaBrecque, J. L., Kent, D. V., and Cande, S. C., 1977. Revised magnetic polarity time scale for late Cretaceous and Cenozoic time. *Geology*, 5:330–335.

Laughton, A. S., and Searle, R. C., 1979. Tectonic processes on slow spreading ridges. *In* Talwani, M., Harrison, C. G., and Hayes, D. E. (Eds.), *Deep Drilling Results in the Atlantic Ocean: Ocean Crust*: Washington (Am. Geophys. Union), Maurice Ewing Series, 2:15–32.

Phillips, J. D., Fleming, H. S., Feden, R. H., King, W. E., Perry, R. K., 1975. Aeromagnetic survey of the Mid-Atlantic Ridge near the Oceanographer Fracture Zone. *Geol. Soc. Am. Bull.*, 86:1348–1357.

Searle, R. C., 1979. Side-scan sonar studies of North Atlantic fracture zones. *J. Geol. Soc., London*, 136:283–292.

Searle, R. C., and Laughton, A. S., 1977. Sonar studies of the Mid-Atlantic Ridge and Kurchatov Fracture Zone. *J. Geophys. Res.*, 82:5313–5328.

Vogt, P. R., and Johnson, G. L., 1975. Transform faults and longitudinal flow beneath the Midoceanic Ridge. *J. Geophys. Res.*, 80: 1399–1328.

Date of Initial Receipt: 27 February 1984
Date of Acceptance:13 June 1984

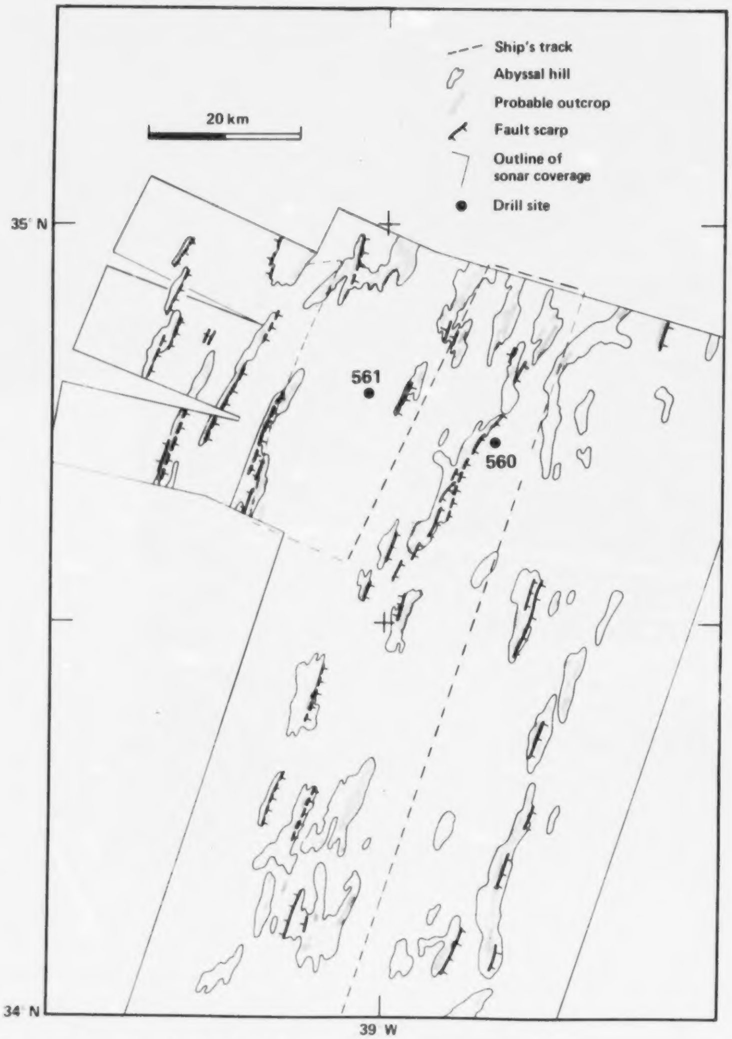

Figure 17. Interpretation of *Gloria* sonographs near Sites 560 and 561.

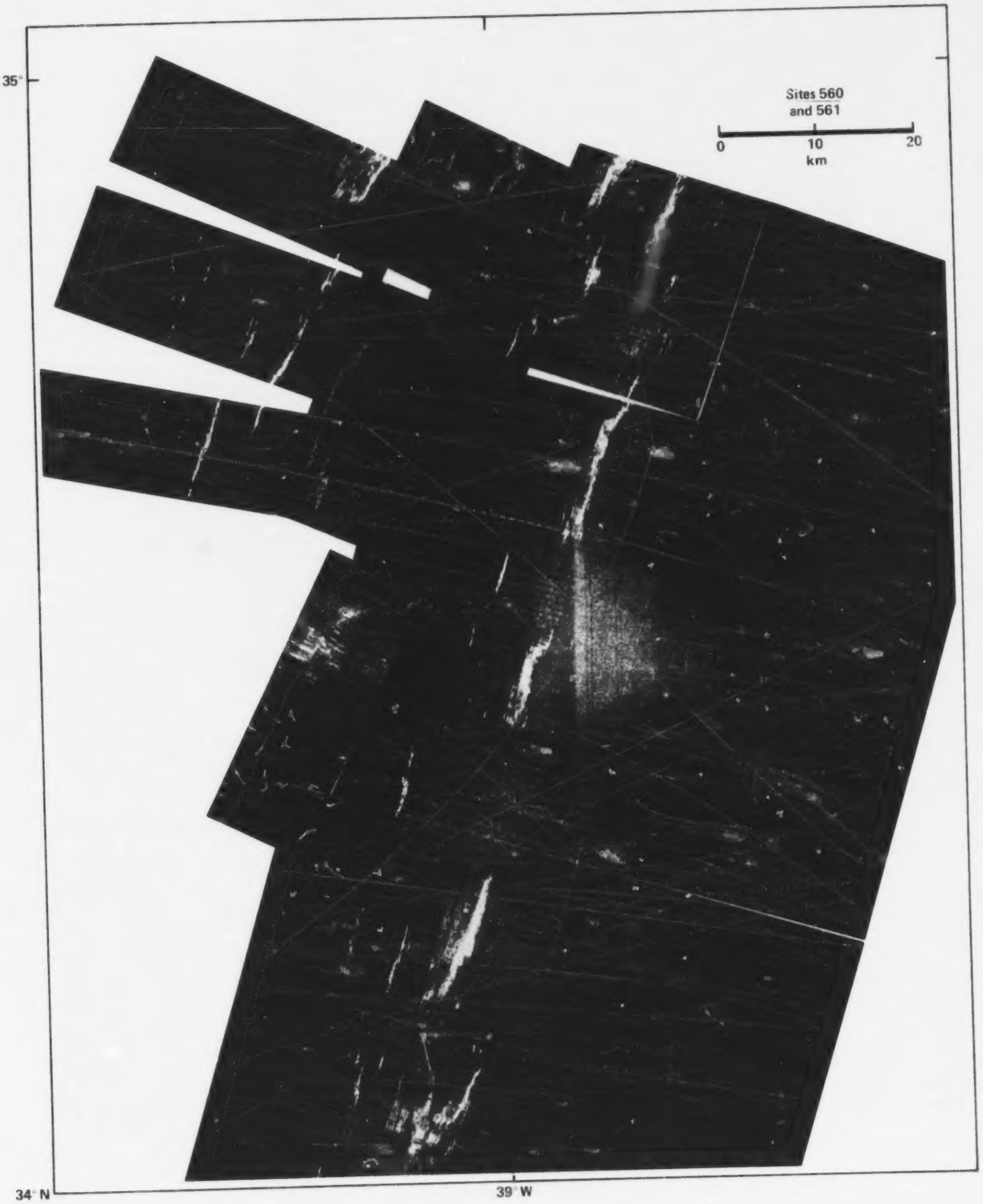
35°
Sites 560
and 561
0
10
20
km
34° N
39° W

Figure 18. Original *Gloria* records near Sites 560 and 561.

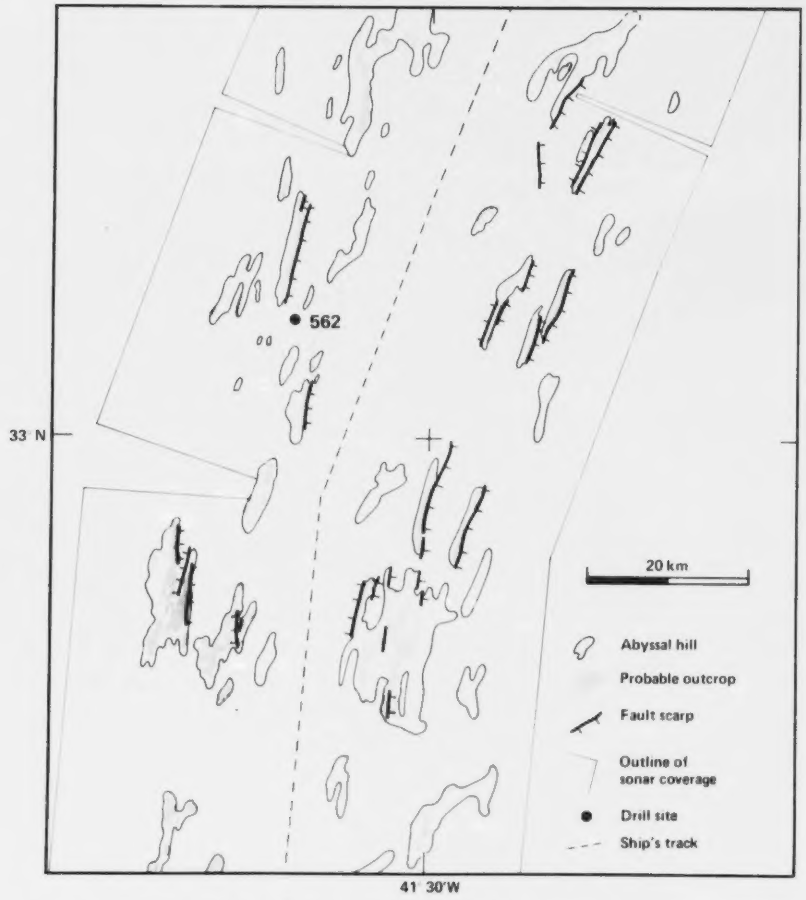
562
33°N
41°30'W
20 km
Abyssal hill
Probable outcrop
Fault scarp
Outline of sonar coverage
Drill site
Ship's track

Figure 19. Interpretation of *Gloria* sonographs near Site 562.

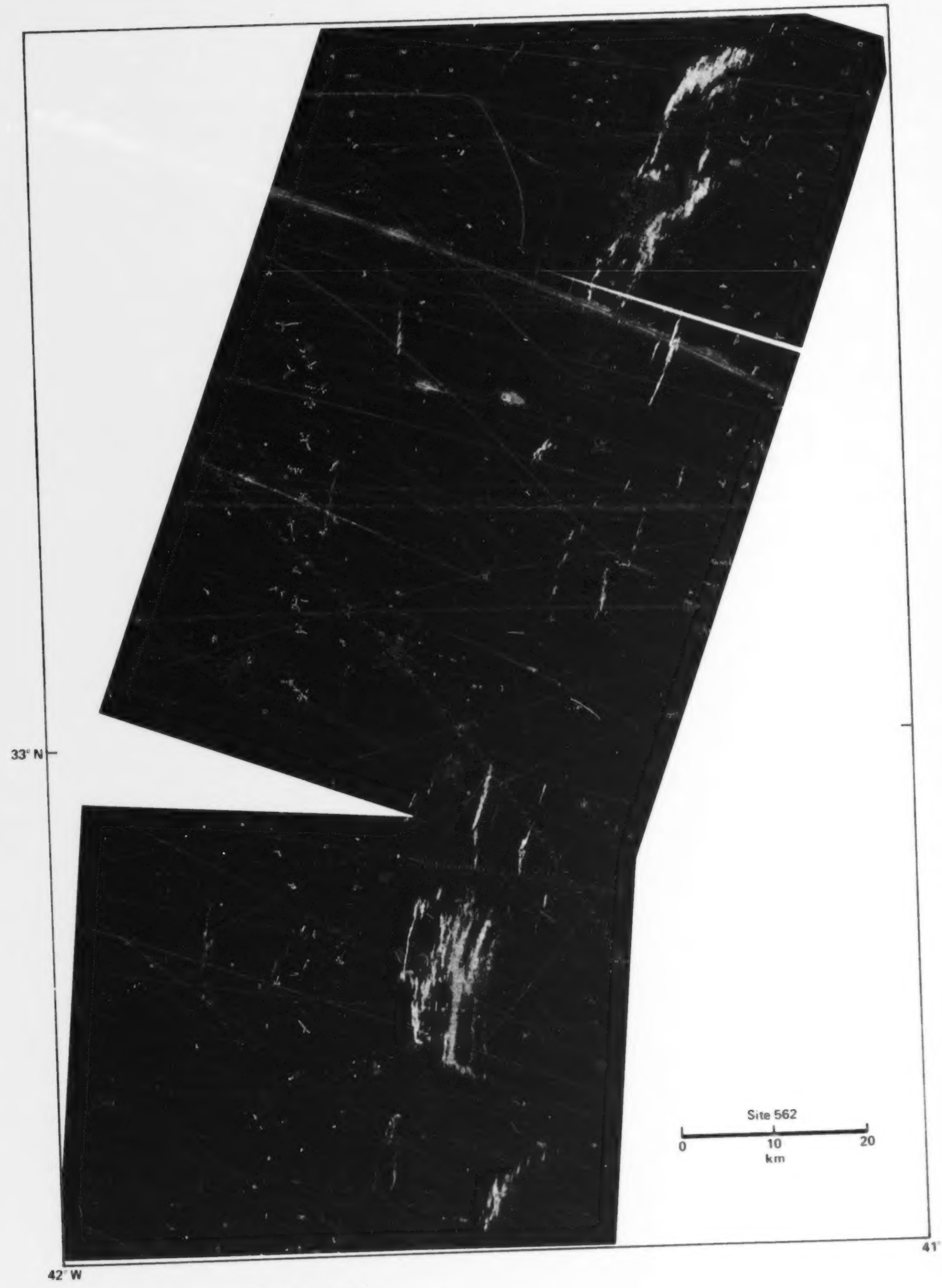
33° N
42° W
41°
Site 562
0
10
20
km

Figure 20. Original *Gloria* records near Site 562.

blank page

3. ANALYSIS OF TRACE ELEMENTS IN BASALTS BY SHIPBOARD X-RAY FLUORESCENCE SPECTROMETRY: A DISCUSSION OF NIOBIUM[1]

J. Etoubleau and H. Bougault, Centre National pour l'Exploitation des Océans, Centre Océanologique de Bretagne
M. Rideout, Graduate School of Oceanography, University of Rhode Island
J. Brannon, Department of Earth and Planetary Sciences, Washington University
and
B. Weaver, Department of Geology, University of Leicester[2]

ABSTRACT

X-ray fluorescence spectrometry was used on board the *Glomar Challenger* during Leg 82 for analysis of "hygromagmaphile" trace elements that are useful to identify so-called "depleted" or "enriched" basalts; the results were used in choosing the new sites to be drilled on the basis of the "enriched" or "depleted" character of previous sites. This chapter describes a hitherto unpublished method for deducing concentrations from intensity measurements; the method yielded the precision (better than 1 ppm for Nb) necessary for purposes of the cruise.

The procedure for the matrix-effect correction is described. The case of Nb is discussed in detail because Nb concentrations in basalts are the lowest among the elements investigated (Nb, Zr, Ti, Y, V) and because it is the key element for deducing the enriched or depleted character of the different basalt units. Ta neutron-activation measurements made on shore after the cruise demonstrate, on the basis of the well-known constant Nb/Ta ratio in basalts, that the accuracy of the shipboard measurements of Nb concentrations in basalt units is about 0.5 ppm.

INTRODUCTION

Nine years after the first experimental X-ray Fluorescence (XRF) chemical analysis of rocks on board a research vessel during the GIBRACO cruise of the *Jean Charcot* (Bougault and Cambon, 1973), the XRF van provided by CNEXO[3] was successfully used during DSDP Leg 82. Before that cruise, the XRF van had been used 12 times on board the *Glomar Challenger* since 1974 (Leg 37). On these earlier legs, the analyses were performed mainly to obtain the best descriptions of the different basalt units, based on major-element compositions and petrographic descriptions; these descriptions were then used as a guide in sampling for shore-based studies. The equipment, analytical procedures, and calculations used to derive major-element concentrations were described in *Initial Reports* Volumes 37 (Bougault, 1977); (Bougault, Treuil, et al., 1979; Natland et al., 1979); and 65 (Cambon et al., 1983). During some of these cruises (Legs 45, 55, 65, 69), the concentrations of some trace elements (Ni, Sr, Zr) were also measured to aid in describing the basalt units.

For Leg 82, as the cruise progressed, we had to select each site from a grid of 11 potential locations that were chosen ahead of time according to the objectives of the cruise: to examine mantle heterogeneity in the Azores Triple Junction area, away from the ridge axis, and along isochrons (see "Background and Objectives," this volume). The elements that can give information about mantle heterogeneity and that can be measured on board by X-ray fluorescence spectrometry are niobium, zirconium, titanium, yttrium, and vanadium. The behavior of each of these "hygromagmaphile" trace elements mimics that of a different rare earth element (REE). For example, Nb behaves like La (the lightest REE), and Zr behaves like Sm (an REE of medium atomic number); consequently, the ratio Nb/Zr can be used in place of La/Sm to determine the depleted or enriched character of the basalts (Schilling and Winchester, 1967; Bougault et al., this volume). Expressed in their most convenient form (normalized to chondrite), the ratios are nearly equal; that is, $(Nb/Zr)_{ch}$ is about equal to $(La/Sm)_{ch}$. Thus, in addition to providing data for the best descriptions of basalt units through major-element and some trace-element abundances, the main objective of on-board XRF analyses during Leg 82 was to determine concentrations of those "hygromagmaphile" trace elements, which could be used as a basis for site selection consistent with the objectives of the cruise.

The concentrations of the pertinent hygromagmaphile elements are of the following orders of magnitude: Nb, 0–50 ppm, with a critical range of values for geochemical interpretation between 0 and 15 ppm; Zr, 50–200 ppm); Ti, 3000–15,000 ppm (the abundance of this element is obtained from the major–minor analytical procedure); Y, 15–45 ppm; and V, 150–450 ppm. From these ranges of concentrations, it is clear that Nb is the most critical element. We will examine and determine the accuracy and limits of detection through the statistics of counting rates, possible interferences, the matrix-effect correction that we have used, and standard concentrations.

---

[1] Bougault, H., Cande, S. C., et al., *Init. Repts. DSDP*, 82: Washington (U.S. Govt. Printing Office).

[2] Addresses: (Etoubleau and Bougault, present address) IFREMER (formerly CNEXO), Centre de Brest, B. P. 337, 29273 Brest Cedex, France; (Rideout, present address) Department of Geology, Rice University, P.O. Box 1892, Houston, Texas 77251; (Brannon) Department of Earth and Planetary Sciences, Washington University, St. Louis, Missouri 63130; (Weaver, present address) School of Geology and Geophysics, University of Oklahoma, Norman, Oklahoma 73019.

[3] The XRF van was built with funds from a program sponsored by Centre National pour l'Exploitation des Océans (CNEXO), Centre National de la Recherche Scientifique, Délegation Générale à la Recherche Scientifique et Technique, and the "Ministère des Universités" to promote chemical analysis on board oceanographic research vessels.

MATRIX EFFECT

The relationship between the concentration c and the intensity I emitted by an element in a sample irradiated by X rays is

$$I = \frac{Ac}{M}, \tag{1}$$

where A is a constant and M the matrix effect. Usually, for a simple geometry of the spectrometer, the matrix effect M can be formulated by

$$M = \Sigma(\mu/\rho)_{pi}\, c_i + \Sigma(\mu/\rho)_{zi}\, c_i, \tag{2}$$

where c_i is the concentration of an element i, $(\mu/\rho)_{pi}$ the coefficient of absorption of the primary excitating beam by the element i, and $(\mu/\rho)_{zi}$ the coefficient of absorption of the emitted beam (wavelength λ_z) by the element i.

It is difficult in trace-element analysis to use a "buffer" glass disc, such as is used in major-element analysis; such a method would increase M (relative to the numerator in Eq. [1]) and thus diminish I, the sensitivity, and the limit of detection. As far as possible, for trace elements, the measurements have to be done on the rock powders themselves. The rocks are crushed in an agate mortar, and the powder is pressed into a pellet, using wax as a binder. This method of preparation, which is employed to obtain the best counting rate, limits the possibilities of contamination, and is simple and quick to use on board the ship. The same pellets can then be used on shore, either to verify on-board measurements or for additional determinations. But, because the matrix effect can vary by as much as a factor of 2, it is necessary to have a precise method of either calculating or measuring M, in order to calculate accurate concentrations of trace elements.

Among the three main methods that permit access to the value of the matrix effect are (1) use of standards that have the same major-element compositions as unknown samples; (2) measurement of the background or Compton peak (Anderman and Kemp, 1958; Champion et al., 1960; Clark and Mitchell, 1972; Cullen, 1962; DeLong and McCullough, 1973; Feather and Willis, 1976; Hower, 1959; Hutton and Norrish, 1977; Johnson and Stout, 1958; Kalman and Heller, 1962; Leoni and Saitta, 1977; Nesbitt et al., 1976; Price and Angell, 1968; Reynolds, 1963, 1967; Sherman, 1955; Verdumen, 1977; Walker, 1973; Weber and Newbury, 1971; Wilband, 1975; Wyrobish, 1977); and (3) calculation of M from the major-element composition of each sample.

We chose the third one, because the major-element compositions had to be determined on board to be useful in preparing the best descriptions of the different basalt units. Nevertheless, we still have to prove that this method is practicable and attains the necessary precision.

The matrix effect is the sum of two terms (Eq. [2]), one related to the primary excitating X-ray beam and the other to the beam emitted by the studied element in the sample, provided that the parameters accounting for the geometry of the instrument are integrated into the constant A in Equation (1).

When we know the wavelength of the beam absorbed by the sample, it is easy to find μ/ρ from a table of mass-absorption coefficients. This coefficient $(\mu/\rho)_{zi}$, is straightforward for the emitted beam, because by definition its wavelength, λ_z, is known. But finding $(\mu/\rho)_{pi}$, corresponding to the excitating beam is much more difficult, because that beam is polychromatic; this is the classic problem of finding the "equivalent" wavelength that would induce the same fluorescence intensity as the polychromatic beam from the X-ray tube. We want to show that, in general, knowledge of the equivalent wavelength is not necessary for calculating the matrix effect from the major-element concentrations.

λ_z is the wavelength of X rays emitted by the element of atomic number z. λ_{AE} is the absorption edge of this element. For rock samples, the trace elements can be classified into two groups according to the value of λ_z or λ_{AE} with respect to Fe K_{AE} (Hower, 1959; Quintin, 1970; Reynolds, 1963); Fe is the major element with the highest atomic number:

1. λ_{AE} is higher than Fe K_{AE}: The pertinent elements for silicate rock samples are Sc, V, Cr, and Co.
2. λ_z is shorter than Fe K_{AE}: This is the general case if a K line can be excited.

In the second general case, the range of wavelengths that permit excitation of an element is necessarily out of the range of absorption discontinuities of major elements (Fig. 1). A trace element whose atomic number z is higher than 27 has a K absorption edge lower than Fe K_{AE}: the photons able to excite this element have wavelengths shorter than λ_{AE}. Under these conditions, whatever the equivalent wavelength λ_p, the mass-absorption

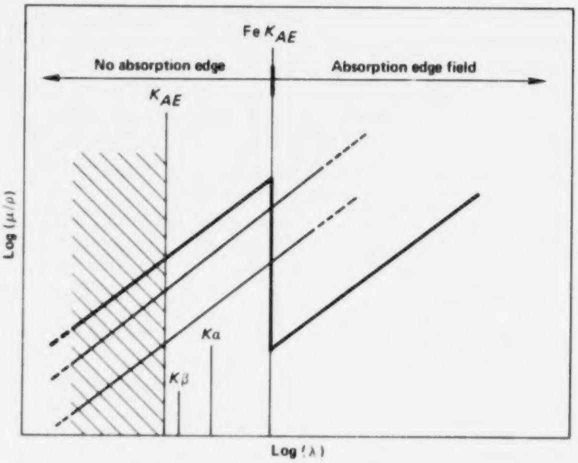

Figure 1. Range of absorption edges for trace elements, referred to Fe K_{AE} (Fe being the major element with the highest atomic number). See text for discussion.

coefficient of the major element i with respect to the primary excitating beam can be written as

$$(\mu/\rho)_{pi} = \delta_i(\lambda_z)^\gamma. \tag{3}$$

This is the classic equation that shows the relationship between mass-absorption and wavelength; δ_i is characteristic of the absorbing element and γ is a constant.

From Equation (2), the matrix effect M, which is a function of the primary beam (wavelength λ_p), the emitted X rays (wavelength λ_z), and the major elements (i) can be written as

$$M(\lambda_p, \lambda_z, i) = (\lambda_p)^\gamma \, \Sigma\delta_i c_i + (\lambda_z)^\gamma \, \Sigma\delta_i c_i, \text{ or}$$

$$M(\lambda_p, \lambda_z, i) = [(\lambda_p)^\gamma + (\lambda_z)^\gamma] \, \Sigma\delta_i c_i. \tag{4}$$

Whatever the value of the equivalent wavelength λ_p, we can write $(\lambda_p)^\gamma = K(\lambda_z)^\gamma$ and deduce that

$$M(\lambda_p, \lambda_z, i) = (1 + K)(\lambda_z)^\gamma \, \Sigma\delta_i c_i = M(\lambda_z, i). \tag{5}$$

This result can be expressed as follows: For a trace element whose emitted X rays are of a wavelength shorter than the absorption edge of the major element with the highest atomic number in the studied sample, the matrix effect is independent of the primary excitation X rays.

If a trace element z' meets the same requirement as z, it is also possible to write

$$(\lambda_{z'})^\gamma = K'(\lambda_z)^\gamma. \tag{6}$$

This observation permits us to deduce that

$$M(\lambda_{z'}, i) = K'(1 + K)(\lambda_z)^\gamma \Sigma\delta_i c_i. \tag{7}$$

This relationship can be expressed in the following way: For two trace elements z and z' whose emitted X rays are of a wavelength shorter than the absorption edge of the major element with the highest atomic number in the studied sample, the ratio of the matrix effect for z' to the matrix effect for z is a constant.

With the conditions that have been given here for a trace element, the calculation of the matrix effect is thus, except for a constant, independent of the wavelength of the studied trace element. We note that that constant need not be known, because the constant A in Equation (1) has to be determined anyway, and the constant $K'(1 + K)(\lambda_z)^\gamma$ can be implicitly included in A during the standardization procedure.

It is now possible to account for a second relationship between the mass-absorption coefficients and atomic numbers of the absorbing elements (the major elements in the sample):

$$(\mu/\rho)_i = \beta(z_i)^\alpha, \tag{8}$$

where z_i is the atomic number of the absorbing major element i and α and β are constants.

With this relationship, it is easy to deduce that

$$\mathrm{I} = \frac{\mathrm{A}c}{M} = \frac{\mathrm{A}c}{\Sigma\beta(\mathrm{z}_i)^\alpha \, c_i} = \frac{\mathrm{A}c}{\beta\Sigma(\mathrm{z}_i)^\alpha \, c_i} \, . \tag{9}$$

β is included in the constant A during standardization:

$$I = \frac{\mathrm{A}c}{\Sigma(z_i)^\alpha \, c_i} \, . \tag{10}$$

This is the simple general relationship that exists between the intensity of X rays emitted by a trace element under the conditions mentioned, its concentration, and the matrix effect of the sample. In particular, this relationship applies for K emissions of trace elements in rocks whose atomic numbers are higher than 27, such as Nb, Zr, and Y. The concentrations of these elements were calculated during Leg 82 by using Equation (10).

The value of the constant α can be determined from tables of mass-absorption coefficients (Leroux and Thin, 1977). Different values of α, given in different tables, do not produce significant differences in the results for a wide range of rock compositions. An example is given in Table 1, where Rb and Nb concentrations have been calculated using α values of 2.65 and 2.81.

SHIPBOARD TRACE-ELEMENT ANALYSIS DURING LEG 82: A SPECIFIC APPROACH FOR NIOBIUM

For K emissions, the theoretical precision of determinations of trace-element concentrations is about 1 ppm. Even if there are other parameters to account for in determinating concentrations, such as instrumental interferences (Bougault et al., 1977) and spectral interferences (e.g., Y and V), the precision obtained is not generally critical for geochemical interpretation if the concentrations are higher than 20 or 30 ppm. An example is provided by Y, where the Rb K_β line interferes with the Y K_α line. The results are given in Table 2. A general relationship accounting for instrumental and spectral interference (Rb K_β) has been used:

$$(I - I_0)M = \mathrm{A}c + \mathrm{A}'\,c' + B, \tag{11}$$

where

I = net intensity,
I_0 and B = two parameters for instrumental interferences,
A = sensitivity for the studied element,
A' = sensitivity for the interfering element,
c and c' = the concentrations of the studied element and the interfering element, respectively.

From Figure 2 and the calculated Y concentrations in Table 2, it appears that the precision of about 1 ppm is not critical for geochemical interpretations for concentrations in basalts that range between 20 and 50 ppm.

Table 1. Influence of the choice of the value of α on the calibration (concentrations in ppm).

	Rb concentration			Nb concentration		
		Calculated			Calculated	
Standard	Recommended	(α = 2.65)	(α = 2.81)	Proposed	(α = 2.65)	(α = 2.81)
AGV_1	67	67.2	67.9	15.0	14.6	14.7
BR	45	45.2	44.8	114	114	115
BCR_1	46	46.6	46.5	14.5	14.9	14.2
W1	21	21.8	20.9	8.5	9.0	8.3
DTS_1	0	−0.6	−1.2	0.0	0.0	0.3
G_2	169	170.0	171.0	11.0	10.1	10.7
GSP_1	254	253.0	255.0			
PCC_1	0	0.1	−0.4	0.0	0.8	1.4
DRN	75	73.2	74.2	9.0	8.2	7.9
GH	390	390.0	389.0	85.0	85.0	84.0
GA				11.0	11.1	11.6
r^2		0.99994	0.99993		0.99979	0.99963
σ		0.33	0.34		0.19	0.25

Note: Rb and Nb concentrations have been calculated using α values of 2.65 and 2.81 (see text). "Recommended" and "proposed" have the usual meanings as applied to concentrations for standards. A recommended value has a higher probability of being close to the true value than a proposed value. r^2 = the correlation coefficient and σ = the standard deviation in ppm.

Table 2. Niobium: net intensities, matrix-effect values (M), and recommended and calculated concentrations of standards.

Hole-Core-Section (interval in cm)	Intensity	M	Nb conc. = 16Ta (ppm)	Nb. conc. (calculated) (ppm)
Leg 55				
433C-10-4, 118–121	4160	122.08	6.9	5.9
433C-10-2, 58–60	8739	126.30	12.5	12.5
433C-14-3, 55–57	10,969	125.29	15.5	15.4
433C-32-1, 98–101	2914	117.69	4.3	4.1
Leg 69				
504B-19-2, 46–49	8091	112.93	9.9	10.4
504B-19-1, 73–77	10,664	114.47	13.6	13.8
504B-4-2, 52–58	116	115.40	0.3	0.5
Leg 70				
504B-56-1, 139–142	1825	118.50	2.6	2.7
Leg 65				
482D-10-3, 101–103	683	118.97	1.4	1.2
483-26-1, 128–130	2720	121.70	3.5	4.0

Note: $IM = Ac + B$; A = 90,954.29; B = −30,708.25. (See text for discussion.) Tube, Au; counter, NaI; crystal, LIF; collimator, 0°15; background counting time, 4 × 40 s; peak counting time, 4 × 40 s; peak, 21°34′; left background, 20°94′; right background, 21°72′.

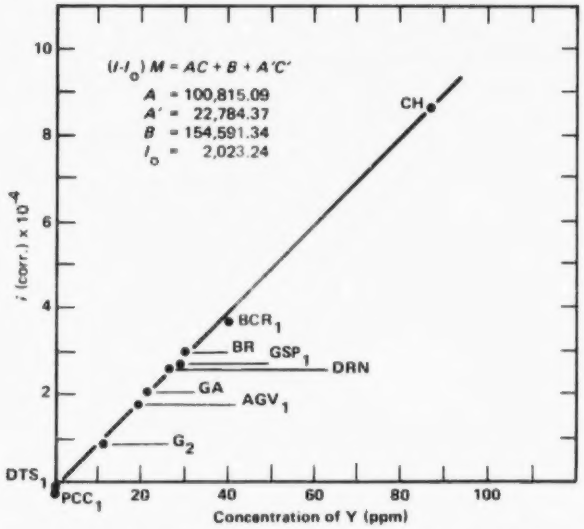

Figure 2. Y calibration curve. Intensities (corrected for matrix effects) versus concentrations. The parameters A, A', B, and I_0 are discussed in text. Data points correspond to geologic standards listed in Table 3. Corr. = corrected.

Another example is given by V. There is a spectral interference with the Ti K_β line, Ti being a minor element, and even if V does not meet the theoretical requirements previously mentioned as regards K absorption edge versus Fe K_{AE} (we will not discuss the specific method used), the precision obtained at the end is comparable to that obtained for Y (Table 3, Fig. 3).

The examples of Y and V show that even when spectral interferences exist it is possible to attain a convenient accuracy, if the concentrations of the elements are higher than about 20 ppm. In the case of Nb, a specific problem exists for a range of concentrations between 0 and 15 ppm. In this range of concentrations, two additional factors must be considered to avoid systematic errors that could be larger than the precision related to counting statistics. The first concerns the settings of the spectrometer (peak and background positions), and the second relates to knowledge of recommended concentrations of standards.

The setting of the spectrometer requires careful selection of peak and background positions to obtain a zero net intensity (peak minus background) for a blank (pure quartz, for instance). This zero intensity for zero concentration of Nb must then be checked in relation to the second factor (knowledge of standards) for a natural sample; this is to minimize possible interference with the tail of the Y K_β peak.

Table 3. Yttrium: net intensities, matrix-effect values (*M*), and recommended and calculated concentrations of standards.

Standard	Intensity	*M*	Recommended concentration (ppm) Y	Recommended concentration (ppm) Rb	Calculated concentration (ppm) Y
GH	23,5349	75.08	87	390	87.2
GA	76,369	81.94	21	176	22.2
PCC_1	−721	88.25	0	0	−0.9
DRN	41,542	109.3	26	75	27.4
BR	32,378	131.38	30	45	30.9
BCR_1	40,119	124.98	40	47	38.1
AGV_1	35,409	98.71	19	67	19.1
GSP_1	97,384	89.00	29	254	28.3
G_2	60,217	81.31	11	170	10.0
DTS_1	979	90.26	0	0	0.6

Note: $(I - I_0)M = AC + A'C' + B$. $A = 100{,}815.09$; $A' = 22{,}784.37$; $B = 154{,}591.34$; $I_0 = 2023.24$. (See text for discussion.) Tube, Au; counter, NaI; crystal, LIF; collimator, 0°15; background counting time, 100 s; peak counting time, 2 × 100 s; peak, 23°73′; left background, 23°42′; right background, 24°08′.

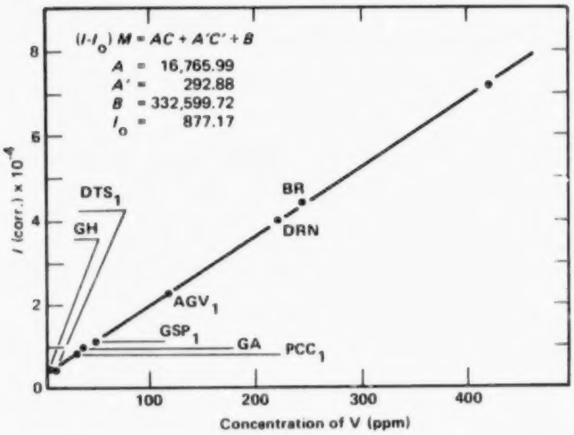

Figure 3. V calibration curve. Intensities (corrected for matrix effects) versus concentrations. The parameters A, A', B, and I_0 are discussed in text. Data points correspond to geologic standards listed in Table 4.

For Nb concentrations of standards, according to the last review of trace elements in rocks by Abbey (1980), no recommended Nb concentrations exist between 0 and 15 ppm, and there are none for higher concentrations, either; all values are "proposed" concentrations. The good fit in Table 1 between "proposed" concentrations and concentrations found with either $\alpha = 2.65$ or $\alpha = 2.81$ demonstrates the coherence of the analytical method between 0 and 115 ppm. For these international standards, one observes that two of them are close to zero concentration, five are between 8 and 15 ppm, and the last two are between 85 and 114 ppm. Such a distribution of Nb concentrations in standards does not preclude a constant error of between 0 and 15 ppm, particularly if we keep in mind that the values in Table 1 are only "proposed."

To overcome the absence of well-known certified standards for Nb between 0 and 15 ppm, we will use the geochemical properties of the pair of elements Nb and Ta. A large number of samples, many of them DSDP samples, have been studied for these two elements. Nb concentrations were determined by XRF spectrometry using the calibration corresponding to values proposed in Table 1 (Bougault, 1980). Ta concentrations were measured through instrumental neutron activation analysis (INAA), using cadmium vials (Jaffrezic et al., 1977). These results demonstrate that the Nb/Ta ratio is constant in mid-ocean ridge basalts, from "depleted" to "enriched" types according to the "rare earths" definition (Bougault, Joron, et al., 1979). Since that last-mentioned study, the Nb/Ta value of 16 has been confirmed by analysis of several other samples from different geologic environments: seamounts in the North Pacific (Leg 55: Cambon et al., 1980) and volcanoes of "la chaîne des Puys" (El Azzouzi, 1981; El Azzouzi et al., 1982). The accuracy of Ta measurements by INAA, especially for low values, is much better than the accuracy of Nb determinations by XRF spectrometry. From these observations (constant Nb/Ta ratio in basalts and accuracies of Nb and Ta measurements), we were able to detect a systematic Nb overestimate of about 1 ppm for the lowest concentrations (between 0 and about 6 ppm). Taking this into account, it was possible to demonstrate that the constant Nb/Ta ratio in the most "depleted" basalts (Leg 65 and Legs 69 and 70, Hole 504B) is preserved (Cambon et al., 1983; Etoubleau et al., 1983), as shown in Figure 4. For Leg 82, we thus selected our own standards, whose Nb and Ta concentrations are well distributed (0 to 15 ppm for Nb; 0 to 1 ppm for Ta). Because the Ta accuracy is better than the Nb accuracy and the Nb/Ta ratio is constant in basalt rocks, we chose the Nb concentrations of selected standards to be 16 times the Ta concentrations; this was a better approximation to the true Nb concentrations than could be obtained through Nb measurements themselves.

We thus come to a set of standards of basalts whose Nb concentrations are between 0 and 15 ppm. The determination of these concentrations is based both on the determination from international standards and on the

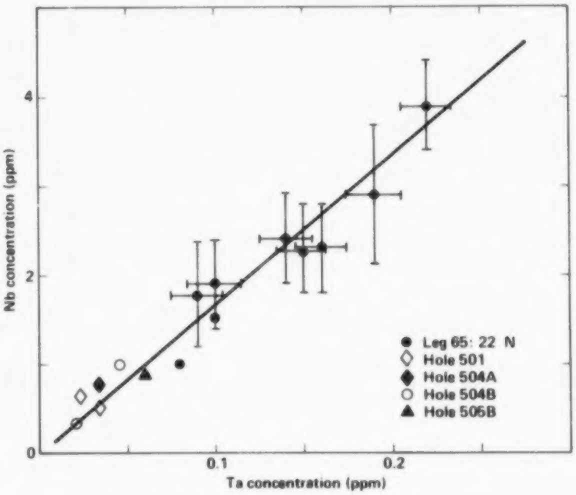

Figure 4. Nb versus Ta concentrations. Filled circles correspond to the different basalt units encountered at 22°N on the East Pacific Rise during Leg 65; other symbols identified in key to figure.

constant Nb/Ta ratio in basalts. Some uncertainties can remain for true concentrations, but because Ta is determined with better precision than Nb, we are sure to have a correct classification (concentrations relative to each other).

In addition to this approach to developing standards with well-known Nb concentrations, the proposed method presents the two following advantages:

1. Even if the matrix effect is well calculated, as demonstrated by Table 1 for Rb and Nb, this method uses known basalt standards, which reduce the range of variation of the matrix effect; it varies here by about 10%, whereas it varies by a factor of 2 for the usual standards mentioned in Table 1.

2. A possible spectral interference, like the Y K_β line, should not be critical in this method when the same rock types are considered for standardization.

The calibration curves obtained on board are presented in Figures 5 and 6: net intensity versus Nb concentrations and matrix-effect-corrected intensity versus concentration, respectively. The standard deviations, indicated on each figure, demonstrate the efficiency of matrix-effect correction even within a narrow range of rock compositions. Net intensities and Nb concentrations of standards found from the calibration are indicated in Table 4; they correspond to a single measurement run. Instrumental settings and conditions of measurements are also mentioned in the footnote to Table 4.

The standard BR, whose proposed Nb concentration is 114 ppm, was used to check to stability of the instrument during Leg 82. The calculated Nb concentration from the parameters obtained by the calibration in Figure 6 (whose range is 0–15 ppm) was found to be 115 ppm. This value is in agreement with the values presented in Table 1 and is a guarantee of self-consistency between high and low Nb concentrations.

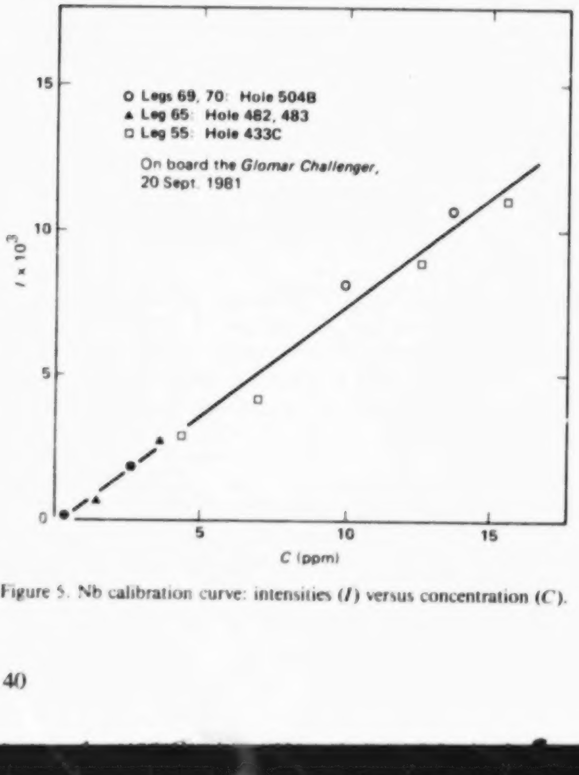

Figure 5. Nb calibration curve: intensities (I) versus concentration (C).

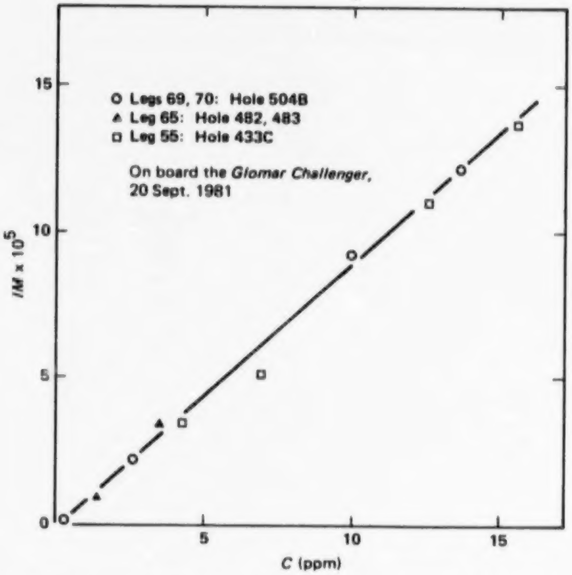

Figure 6. Nb calibration curve: intensities (IM) (corrected for matrix effects) versus concentration (C).

Table 4. Vanadium: net intensities, matrix-effect values (M), and recommended and calculated concentrations of standards.

Standard	Intensity	M	Recommended concentration (ppm) V	Interfering element: recommended concentration Ti	Calculated concentration (ppm) V
BCR_1	37,464	289.68	410	13,320	410
PCC_1	3109	226.28	31	60	33
DTS_1	1306	222.06	9.5	60	8
GSP_1	7141	284.71	49	3960	47
AGV_1	13,768	282.15	118	6300	117
GA	5105	278.11	36	2280	40
GH	1087	274.04	5	480	4
BR	26,943	324.30	244	15,660	245
DRN	19,864	287.66	221	6600	221

Note: $(I - I_0)M = AC + A'C' + B$. $A = 16{,}765.99$; $A' = 292.88$; $B = 332{,}599.72$; $I_0 = -877.17$. (See text for discussion.) Tube, Au; flow counter; collimator, 0°15; crystal, LIF; vacuum; background counting time, 40 s; peak counting time, 2 × 40 s; 2θ left background, 76°00′; 2θ right background, 78°20′; 2θ peak, 76°98′.

The stability of the instrument and the variation of calculated concentrations can also be evaluated in Figure 7. On this figure, the calculated Nb concentrations of the lowest (Leg 69: Sample 504B-4-2, 52–58 cm, 0.3 ppm) and the highest (Leg 55: Sample 433C-14-3, 55–57 cm, 15.3 ppm) standard are plotted versus time: 21 measurements for the highest standard and 25 measurements for the lowest, made on different days during Leg 82. The standard deviation calculated from both standards (≅0.7 ppm) is consistent with the standard deviation from the calibration curve itself in Figure 6. This standard deviation represents one determination; repeated measurements of the same sample or of samples belonging to the same magmatic unit improve the precision. During Leg 82, two to about ten samples were analyzed for a given basalt unit; this gives a better precision than the standard deviation mentioned above. We

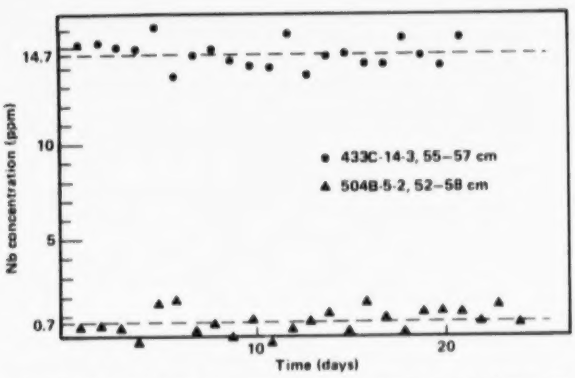

Figure 7. Calculated Nb concentration of the lowest standard (Leg 69, Sample 504B-4-2, 52–58 cm: 0.3 ppm) and the highest standard (Leg 55, Sample 433C-14-3, 55–57 cm: 15.3 ppm) versus time as the cruise progressed.

will consider that the Nb concentration of each basalt unit is known with an accuracy of between 0.8 and 0.3 ppm, according to the number of samples analyzed per unit.

Verification of the shipboard Nb measurements lies in the comparison to onshore INAA for Ta performed by J. L. Joron at "Laboratoire P. Sue du CNRS Saclay," because it has been well demonstrated that the Nb/Ta ratio is constant. Nb concentrations determined aboard ship are plotted versus these Ta concentrations in Figures 8 and 9. Figure 9 enlarges the area enclosed by dashed lines in Figure 8 (Nb varying between 0 and 10 ppm). The Nb/Ta ratio of 16 is well confirmed, and the dispersion of points around the straight lines of Figures 8 and 9 demonstrates that the Nb accuracy is better than the 0.8 ppm just mentioned.

Figure 10 is an example of interpreted data combining shipboard data (Nb, Zr, Ti, Y, and V) and onshore INAA data (Th, Ta, La, Hf, Tb). On the ordinate it represents the logarithm of the element concentration normalized to chondrites (Bougault et al., this volume) versus, on the abscissa, the (decreasing) values of hygromagmaphile character of the elements (Th to V). For Nb, the value 10 represents 5 ppm; because the objective of on-board analyses was to detect enriched and depleted samples, it is easy to understand why we had to be very cautious in measuring Nb concentrations.

CONCLUSION

The strategy for conducting Leg 82 was largely based on geochemical results that could be obtained on board the ship. The elements of interest, those that make possible identification of so-called "enriched" or "depleted" basalts, and whose concentrations could be measured by XRF spectrometry on board, are trace elements, with ranges of concentration between 0 and 300 ppm. A special case is represented by Nb, because its concentration is low in basalts (most of the values are between 0 and 15 ppm), and it can be considered a key element in deducing the "enrichment" or "depletion." Special care was taken in analyzing for this element, both to improve the statistics and to minimize the possible systematic errors.

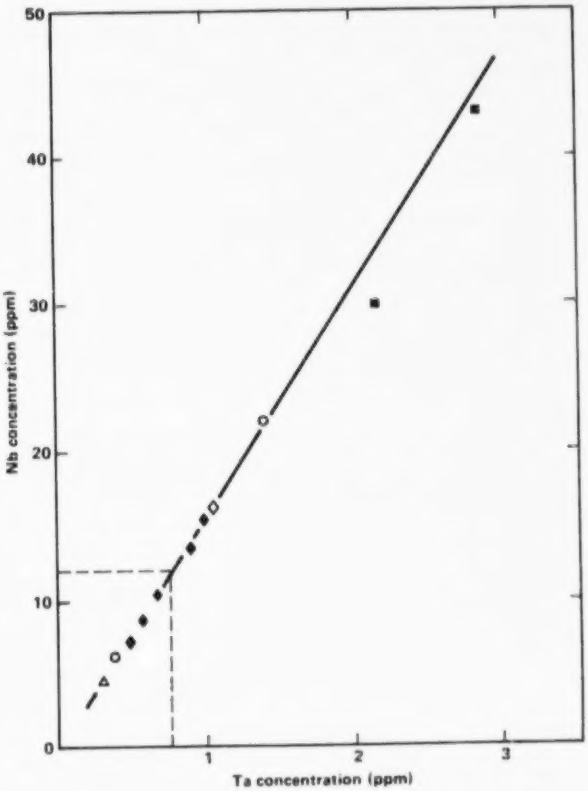

Figure 8. Nb concentration (shipboard determination) versus Ta concentrations (on-shore determination). The different symbols stand for the individual Leg 82 sites.

Shipboard Nb measurements have been verified on shore through Ta INAA, taking advantage of the constant Nb/Ta ratio in basalts. It has been proven that the accuracy of Nb concentration in each basalt unit as determined on board is better than 1 ppm. The accuracy depends upon the number of analyzed samples per basalt unit; a good estimate is 0.5 ppm.

ACKNOWLEDGMENTS

We are grateful to CNEXO, CNRS, and DGRST, the French agencies that funded the XRF van and that, together with DSDP, made use of it possible during Leg 82.

REFERENCES

Abbey, S., 1980. Studies in "standard samples" for use in the general analysis of silicate rocks and minerals. *Geostandards Newslett.*, 4(2):163–190.

Andermann, G., and Kemp, J. W., 1958. Scattered X-rays as internal standards in X-ray emission spectroscopy. *Anal. Chem.*, 30: 1306–1309.

Bougault, H., 1977. Major elements: analytical chemistry on board and preliminary results. *In* Aumento, F., Melson, W. G., et al., *Init. Repts. DSDP*, 37: Washington (U.S. Govt. Printing Office), 643–652.

________, 1980. Contribution des éléments de transition à la compréhension de la génèse des basaltes océaniques. Analyse des éléments traces dans les roches par spectrométrie de fluorescence X [thèse]. Université Paris.

Bougault, H., and Cambon, P., 1973. Dispersive X-ray fluorescence analysis on board oceanographic vessels. *Mar. Geol.*, 15:37–41..

Bougault, H., Cambon, P., and Toulhouat, H., 1977. X-ray spectrometric analysis of trace elements in rocks—correction for instrumental interferences. *X-Ray Spectrom.*, 6(2):66–72.

Bougault, H., Joron, J. L., and Treuil, M., 1979. Alteration, fractional crystallization, partial melting, mantle properties from trace elements in basalts recovered in the North Atlantic. *In* Talwani, M., Harrison, C. G., and Hayes, D. E. (Eds.), *Deep Drilling Results in the Atlantic Ocean: Ocean Crust:* Washington (Am. Geophys. Union), Maurice Ewing Series, 2:352–368.

Bougault, H., Treuil, M., and Joron, J. L., 1979. Trace elements in basalts from 23°N and 36°N in the Atlantic Ocean: fractional crystallization, partial melting, and heterogeneity of the upper mantle. *In* Melson, W. G., Rabinowitz, P. D., et al., *Init. Repts. DSDP*, 45: Washington (U.S. Govt. Printing Office), 493–506.

Cambon, P., Joron, J. L., Bougault, H., and Treuil, M., 1980. Emperor seamounts, trace elements in transitional tholeiites, alkali basalts and hawaiites: mantle homogeneity or heterogeneity and magmatic processes. *In* Jackson, E. D., Koizumi, I., et al., *Init. Repts. DSDP*, 55: Washington (U.S. Govt. Printing Office), 585–597.

————, 1983. Leg 65: East Pacific Rise—typical oceanic crust depleted in hydromagmaphile elements. *In* Lewis, B. T. R., Robinson, P., et al., *Init. Repts. DSDP*, 65: Washington (U.S. Govt. Printing Office), 623–634.

Champion, K. P., Taylor, J. C., and Wittem, R. N., 1960. Rapid X-ray fluorescence determination of traces of strontium in samples of biological and geologic origin. *Anal. Chem.*, 38(1):109–112.

Clark, N. H., and Mitchell, R. J., 1972. Scattered primary radiation as an internal standard in X-ray emission spectrometry use in the analysis of copper metallurgical products. *X-Ray Spectrom.*, 2: 47–55.

Cullen, T. J., 1962. Coherent scattered radiation: internal standardization in X-ray spectrometric analysis of solutions. *Anal. Chem.*, 34(7):812–814.

Delong, S. E., and McCullough, D., 1973. Compton scattered tungsten X-rays as a measure of mass absorption coefficients in rocks. *Am. Mineral.*, 58:1073–1075.

El Azzouzi, M., 1981. Géochimie comparée de quelques éléments hygromagmaphiles dans les roches volcaniques de contextes géodynamiques variés [thèse]. Université de Bretagne Occidentale, Bretagne, France.

El Azzouzi, M., Bougault, H., Maury, R., and Villemant, B., 1982. Application du diagramme de Coryell-Masuda "élargi" à l'étude du fractionnement du titane et du vanadium dans la série alcaline de la chaine des Puys. *C. R. Hebd. Acad. Sci. Paris*, Ser. 2, 295: 1117–1120.

Etoubleau, J., Corre, O., Joron, J. L., Bougault, H., and Treuil, M., 1983. Costa Rica Rift: Variably depleted basalts in the same hole. *In* Cann, J. R., Langseth, M. G., Honnorez, J., Von Herzen, R. P., White, S. M., *Init. Repts. DSDP*, 69: Washington (U.S. Govt. Printing Office), 765–773.

Feather, C. E., and Willis, J. P., 1976. A simple method for background and matrix correction of spectral peaks in trace element determination by X-ray fluorescence spectrometry. *X-Ray Spectrom.*, 5:41–48.

Hower, J., 1959. Matrix corrections in the X-ray spectrographic trace element analysis of rocks and minerals. *Am. Mineral.*, 44:19–32.

Hutton, J. T., and Norrish, K., 1977. Plant analyses by X-ray spectrometry. II. Elements of atomic number greater than 20. *X-Ray Spectrom.*, 6(1):12–17.

Jaffrezic, H., Joron, J. L., and Treuil, M., 1977. Trace element determination in rock powder. A study of the precision for a given analytical procedure: instrumental epithermal neutron activation. *J. Radioanal. Chem.*, 39:185–188.

Johnson, C. M., and Stout, P. R., 1958. Fluorescent X-ray spectrometry, interferences from Compton scattering from matrices of low atomic number. *Anal. Chem.*, 30:1921.

Kalman, Z. H., and Heller, L., 1962. Theoretical study of X-ray fluorescent determination of trace of heavy elements in light matrix. *Anal. Chem.*, 34:946–951.

Leoni, L., and Saitta, M., 1977. Matrix effect corrections by Ag Kα Compton scattered radiation in the analysis of rock sample for trace elements. *X-Ray Spectrom.*, 6:181–186.

Leroux, J., and Thinh, T. P., 1977. *Tables revisées des coefficients d'absorption massique des rayons X:* Quebec, Canada (Corporation Scientifique Claisse).

Natland, J., Bougault, H., Fujii, T., Graham, A. L., Melson, W. G. Prosser, E., Rhodes, J. M., and Zolotarev, B., 1979. Chemical data for Sites 395 and 396: analytical procedures and comparison of interlaboratory standards. *In* Melson, W. G., Rabinowitz, P. D., et al., *Init. Repts. DSDP*, 45: Washington (U.S. Govt. Printing Office), 681–705.

Nesbit, R. W., Haskins, H., Stolz, G. W., and Bruce, D. R., 1976. Matrix corrections in trace element analysis by X-ray fluorescence: an extension of the Compton scattering technique to long wavelengths. *Chem. Geol.*, 18:203–213.

Price, N. B., and Angell, G. R., 1968. Determination of minor elements in rocks by thin film X-ray fluorescence techniques. *Anal. Chem.*, 40(3):660–663.

Quintin, M., 1970. Utilisation de la fluorescence X pour l'analyse non destructive des éléments en traces de numéro atomique supérieur à 27 dans les roches silicatées, bauxites et carbonates. *Colloque Int. CNRS* (Nancy, 1968), 923:75–86.

Reynolds, R. C., 1963. Matrix correction in trace element analysis by X-ray fluorescence. Estimation of the mass absorption coefficient by Compton scattering. *Am. Mineral.*, 48:1133–1143.

————, 1967. Estimation of mass absorption coefficient by Compton scattering: improvements and extensions of the method. *Am. Mineral.*, 52:1493–1502.

Schilling, J.-G., and Winchester, J. W., 1967. Rare earth fractionation and magmatic processes. *In* Runcorn, S. K. (Ed.), *Mantles of the Earth and Terrestrial Planets*: New York (Interscience), pp. 267–283.

Sherman, J., 1955. Theoretical derivation of fluorescent X-ray intensities from mixtures. *Spectrochim. Acta*, 7:283.

Verdumen, E. A. T. H., 1977. Accuracy of X-ray fluorescence spectrometric determination of Rb and Sr concentrations in rock samples. *X-Ray Spectrom.*, 6(3):117–122.

Walker, D., 1973. Behavior of X-ray mass absorption coefficients near absorption edges: Reynold's method revisited. *Am. Mineral.*, 58: 1069–1072.

Weber, G. K., and Newbury, M. L., 1971. X-ray fluorescence determination of minor and trace elements in silicate rocks. *Can. Spectrosc.*, 90-91.

Wilband, J. T., 1975. Rapid method for background corrections in trace element analysis by X-ray fluorescence: an extension of Reynold's method. *Am. Mineral.*, 60:320–323.

Wyrobisch, W., 1977. Comparison of two background correction procedures for X-ray fluorescence trace element analysis of some standard samples. *Geostandards Newslett.*, 1:107–110.

Date of Initial Receipt: 1 August 1983
Date of Acceptance: 22 December 1983

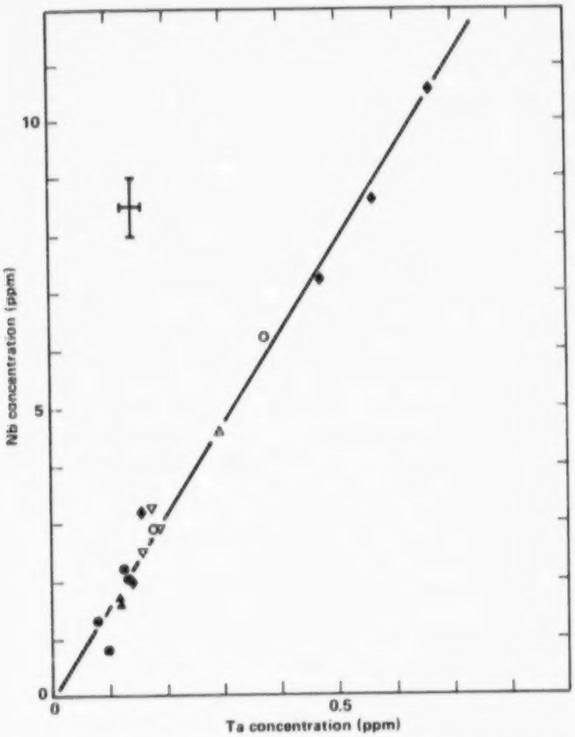

Figure 9. Nb versus Ta concentrations: enlargement of the area within the dashed lines on Figure 8. Symbols as in Figure 8; cross indicates theoretical precision.

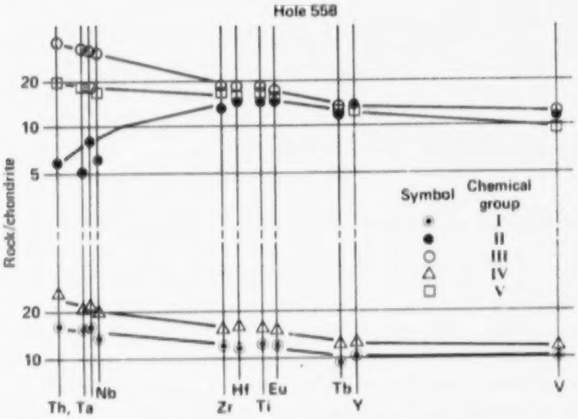

Figure 10. Extended Coryell-Masuda plot obtained for Site 558. On the *Y* axis is plotted the logarithm of the concentrations normalized to chondrite concentrations. On the *X* axis the elements are positioned according to their affinity for the liquid phase of the magma, on a scale defined by the continuous variation of this property of rare earth elements.

blank page

4. EXPLANATORY NOTES, DEEP SEA DRILLING PROJECT LEG 82[1]

William G. Mills, Scripps Institution of Oceanography, University of California at San Diego[2]

RESPONSIBILITY FOR AUTHORSHIP

Authorship of the site chapters includes the complete scientific party, with the ultimate responsibility lying with the two co-chiefs. Within the site chapters the assigned responsibilities are as follows: Site summary and Principal Results (Bougault and Cande); Operations (Cande, Hill, and Bougault); Sediment Lithology and Biostratigraphy (Clark, Curtis, Echols, and Mills); Igneous Petrology and Geochemistry (Bougault, Brannon, Christie, Drake, Neuser, Rideout; and Weaver); Magnetics (Khan); Physical Properties (Hill); Downhole Measurements (Hill and Cande); and Summary and Conclusions (Bougault and Cande).

We also acknowledge the help of Drs. Thomas Sachtleben and Russell Merrill in the final preparation of the site chapters at our postcruise meeting.

The interpretations of individual authors have been retained in the section for which they were responsible. Therefore, conflict between interpretations in a particular section and in the summary are sometimes apparent. Authors of special-topic chapters and the synthesis chapters are cited in the text.

SURVEY AND DRILLING DATA

The survey data used for specific site selections are given in each site-report chapter. Underway geophysical data can be found in Appendix I. On passage between sites, continuous observations were made of depth, magnetic field, and sub-bottom structure. Short surveys were made on *Glomar Challenger* before dropping the beacon, using a precision echo sounder, seismic profiles, and magnetometer.

Depths were continuously recorded underway on a EDO graphic recorder. The depths were read on the basis of an assumed 1500 m/s sounding velocity compensated for two-way traveltime. The sea depth (in meters) at each site was corrected (1) according to the tables of Matthews (1939), and (2) for the depth of the hull transducer (6 m) below sea level. In addition, any depths referred to the drilling platform have been calculated on the assumption that this level is 10 m above the water line.

The seismic-profiling system consisted of two Bolt air guns, a Scripps-designed hydrophone array, Bolt amplifiers, two bandpass filters, and two EDO recorders, usually recording at two different filter settings.

SHIPBOARD SCIENTIFIC PROCEDURES

Number of Sites, Holes, Cores, and Samples

DSDP drill sites are numbered consecutively from the first site drilled by *Glomar Challenger* in 1968. Site numbers are different from hole numbers. A site number refers to one or more holes drilled while the ship was positioned over one acoustic beacon. These holes could be within a radius as great as 900 m from the beacon. Several holes may be drilled at a single site by pulling the drill pipe above the seafloor (out of one hole), moving the ship away from the previous hole any distance within the 900 m radius of the beacon, and then drilling another hole.

The first (or only) hole drilled at a site takes the site number. A letter suffix distinguishes each additional hole at the same site. For example: the first hole takes only the site number; the second takes the site number with suffix A; the third takes the site number with suffix B, and so forth. It is important, for sampling purposes, to distinguish the holes drilled at a site, because recovered sediments or rocks from different holes usually do not come from equivalent positions in the stratigraphic column.

The cored interval is measured in meters below the seafloor. The depth interval of an individual core is the depth below seafloor that the coring operation began to the depth that the coring operation ended. Each coring interval is generally 9.5 m long, which is the nominal length of a core barrel; however, the coring interval may be shorter or longer (rare). "Cored intervals" are not necessarily adjacent to each other, but may be separated by "drilled intervals." In soft sediment, the drill string can be "washed ahead" with the core barrel in place, but not recovering sediment, by pumping water down the pipe at high pressure to wash the sediment out of the way of the bit and up the space between the drill pipe and wall of the hole; however, if thin, hard rock layers are present, it is possible to get "spotty" sampling of these resistant layers within the washed interval, and thus have a cored interval greater than 9.5 m.

Cores taken from a hole are numbered serially from the top of the hole downward. Core numbers and their associated cored interval in meters below the seafloor are normally unique for a hole; however, problems may arise if an interval is cored twice. When this occurs, the core number is assigned a suffix, such as "S" for supplementary. The designation "S" has been used in previous legs as a prefix to the core number for sidewall core samples.

---

[1] Bougault, H., Cande, S. C., et al., *Init. Repts. DSDP*, 82: Washington (U.S. Govt. Printing Office).

[2] Present address: Ocean Drilling Program, Texas A&M University, College Station, Texas 77843.

Full recovery for a single core is normally 9.28 m of sediment or rock, which is in a plastic liner (6.6 cm inside diameter), plus about a 0.2-m-long sample (without a plastic liner) in the core catcher. The core catcher is a device at the bottom of the core barrel; it prevents the core from sliding out when the barrel is being retrieved from the hole. The sediment core, which is in the plastic liner, is then cut into 1.5-m-long sections and numbered serially from the top of the sediment core (Fig. 1). When full recovery is obtained, the sections are numbered from 1 through 7, the last section possibly being shorter than 1.5 m. The core catcher sample is placed below the last section when the core is described, and labeled core-catcher (CC); it is treated as a separate section (for sediments only).

When recovery is less than 100%, and if the sediment is placed in the top of the cored interval, then 1.5-m-long sections are numbered serially, starting with Section 1 at the top. There will be as many sections as needed to accommodate the length of the core recovered (Fig. 1); for example, 3 m of core sample in plastic liners will be divided into two 1.5-m-long sections. Sections are cut

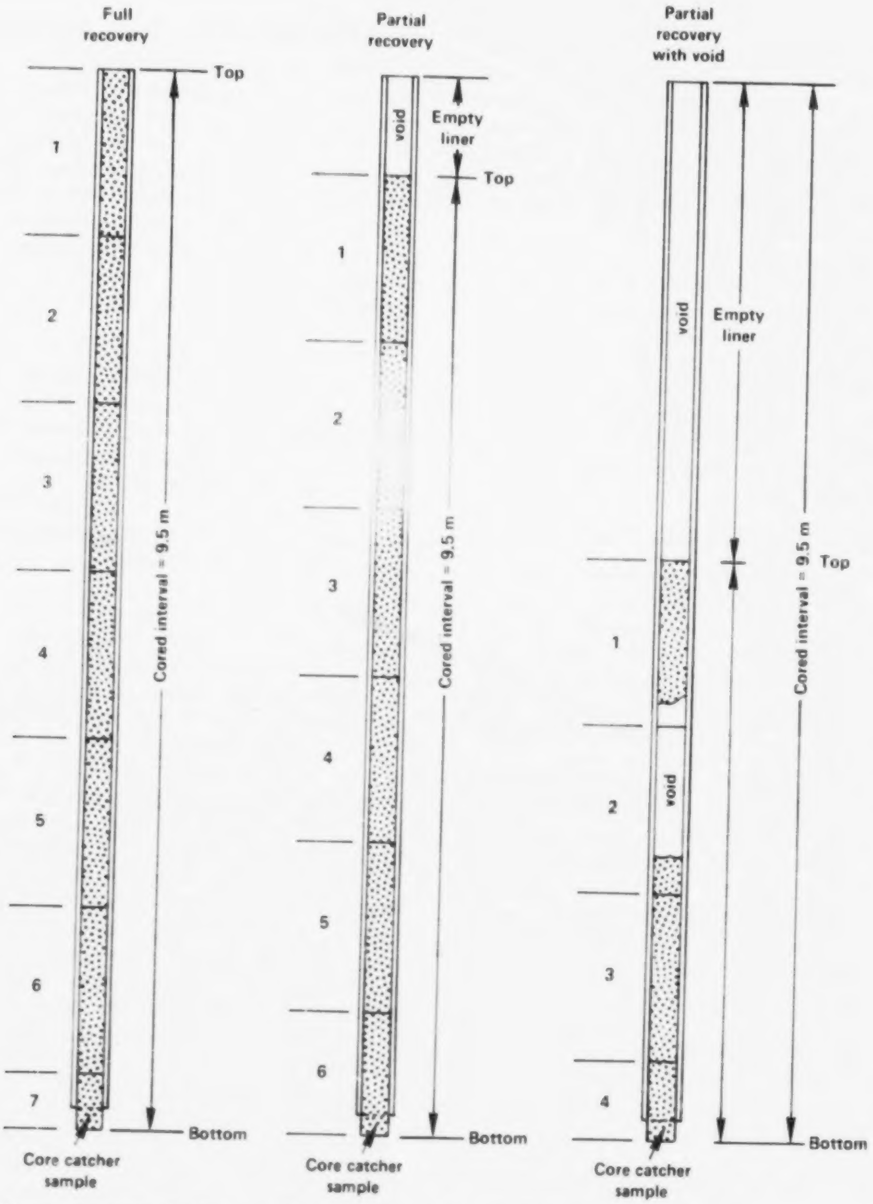
Full recovery
Top
1
2
3
4
5
6
7
Cored interval = 9.5 m
Bottom
Core catcher sample
Partial recovery
void
Empty liner
Top
1
2
3
4
5
6
Cored interval = 9.5 m
Bottom
Core catcher sample
Partial recovery with void
void
Empty liner
Top
1
void
2
3
4
Cored interval = 9.5 m
Bottom
Core catcher sample

Figure 1. Diagram showing procedure in cutting and labeling of core sections.

starting at the top of the recovered sediment, and the last section may be shorter than the normal 1.5-m length.

When recovery is less than 100%, the original stratigraphic position of the sediment in the cored interval is unknown; we conventionally attribute the top of the recovered sediment to the top of the cored interval. This is done for convenience in data handling and for consistency. If recovery is less than 100%, if the core is fragmented, the sections are still numbered serially and the intervening sections are noted as void, whether the fragments as found were contiguous or not.

Samples are designated by distances in centimeters from the top of each section to the top and bottom of the sample in that section. A full identification number for a sample consists of the following information: (1) leg, (2) site, (3) hole, (4) core number, (5) section number, and (6) interval in centimeters from the top of the section. For example, the sample identification number "82-558A-11-3, 98-100 cm" means that a sample was taken between 98 and 100 cm from the top of Section 3 of Core 11, from the second hole drilled at Site 558 during Leg 82. A sample from the core catcher of this core is designated 82-558A-1,CC (8-9 cm).

The depth below the seafloor for a sample numbered "82-558A-11-3, 98-100 cm" is the sum of the depth to the top of the cored interval for Core 11 (77.0 m) and the 3 m included in Sections 1 and 2 (each 1.5 m long) and the 98 cm below the top of Section 3. The sample in question is located at 80.98 m sub-bottom, which in principle is the sample depth below the seafloor. (Sample requests should refer to a specific interval within a core section, rather than the depth below seafloor.)

Conventions regarding the cataloging of the hydraulic piston cores are the same as those for the rotary cores.

Handling of Cores

A core was normally cut into 1.5-m sections, sealed, and labeled; the sections then were brought into the core laboratory for processing. The following determinations were normally made before the sections were split; gas analysis, thermal-conductivity analysis (soft sediment only), and continuous wet-bulk density determinations using the Gamma Ray Attenuation Porosity Evaluator (GRAPE).

The cores were then split longitudinally into "working" and "archive" halves, either by wire cutter, or by "super-saw." The contrast in appearance between cores cut by the two methods can be significant. Samples extracted from the "working" half included samples for the determination of mineralogy by X-ray diffraction, measurement of sonic velocity by the Hamilton Frame method, measurement of wet-bulk density by a GRAPE technique, measurement of water content by gravimetric analysis, measurement of calcium-carbonate percentage (carbonate bomb), geochemical analysis, paleontologic studies, and other studies.

Whenever the archive half was sufficiently firm, it was washed on the cut surface to emphasize the sedimentary features. The color, texture, structure, and composition of the various lithologically different parts of a section were described (Fig. 2) on standard visual core description sheets (one per section), and any unusual features were noted. A smear slide was made, usually at 75 cm if the core was uniform. However, two or more smear slides were often made for each area of distinct lithology in the core section. The smear slides were examined by petrographic microscope. The archive half of the core section was then photographed.

After the cores were sampled and described, they were maintained in cold storage aboard *Glomar Challenger* until transferred to the DSDP East Coast Repository (Lamont-Doherty Geological Observatory). Core sections that were removed for organic geochemistry studies were frozen immediately aboard ship and kept frozen. All Leg 82 frozen cores are presently stored at the DSDP West Coast Repository (Scripps Institution of Oceanography).

Rock and sediment obtained from core catchers and not used in the initial examination were retained in core liners for subsequent work.

Visual core descriptions, smear-slide descriptions, and carbonate bomb (%$CaCO_3$) determinations (all done aboard ship) provide the data for the core descriptions in this volume. This information is summarized and sample locations in the core are indicated on the core description sheets (Fig. 2).

SEDIMENTS AND SEDIMENTARY ROCKS

Core Description Forms

Drilling Disturbance

Recovered rocks, particularly soft sediments, may be extremely disturbed. This mechanical disturbance is a result of the coring technique, which uses a 25-cm-diameter bit with a 6-cm-diameter opening for the core sample. Symbols for the four disturbance categories used for soft and firm sediment are shown in Figure 2. These symbols are used on the core description sheets. The disturbance categories are defined as: (1) slightly deformed: bedding contacts are slightly bent; (2) moderately deformed: bedding contacts have undergone extreme bowing, firm sediment is fractured; (3) very deformed: bedding is completely disturbed or homogenized by drilling, sometimes showing symmetrical diapirlike structure; (4) soupy: water-saturated intervals that have lost all aspects of original bedding; (5) breccia: indurated sediments broken into angular fragments by the drilling process, perhaps along pre-existing fractures; and (6) biscuited: sediment firm and broken chunks about 5-10 cm in length. These categories are coded on the core description form in the column headed "Drilling Disturbance" (Fig. 2).

Sedimentary Structures

In the soft, and even in some harder, sedimentary cores, it may be extremely difficult to distinguish between natural structures and structures created by the coring process. Thus the description of sedimentary structures was optional. Locations and types of structures appear as

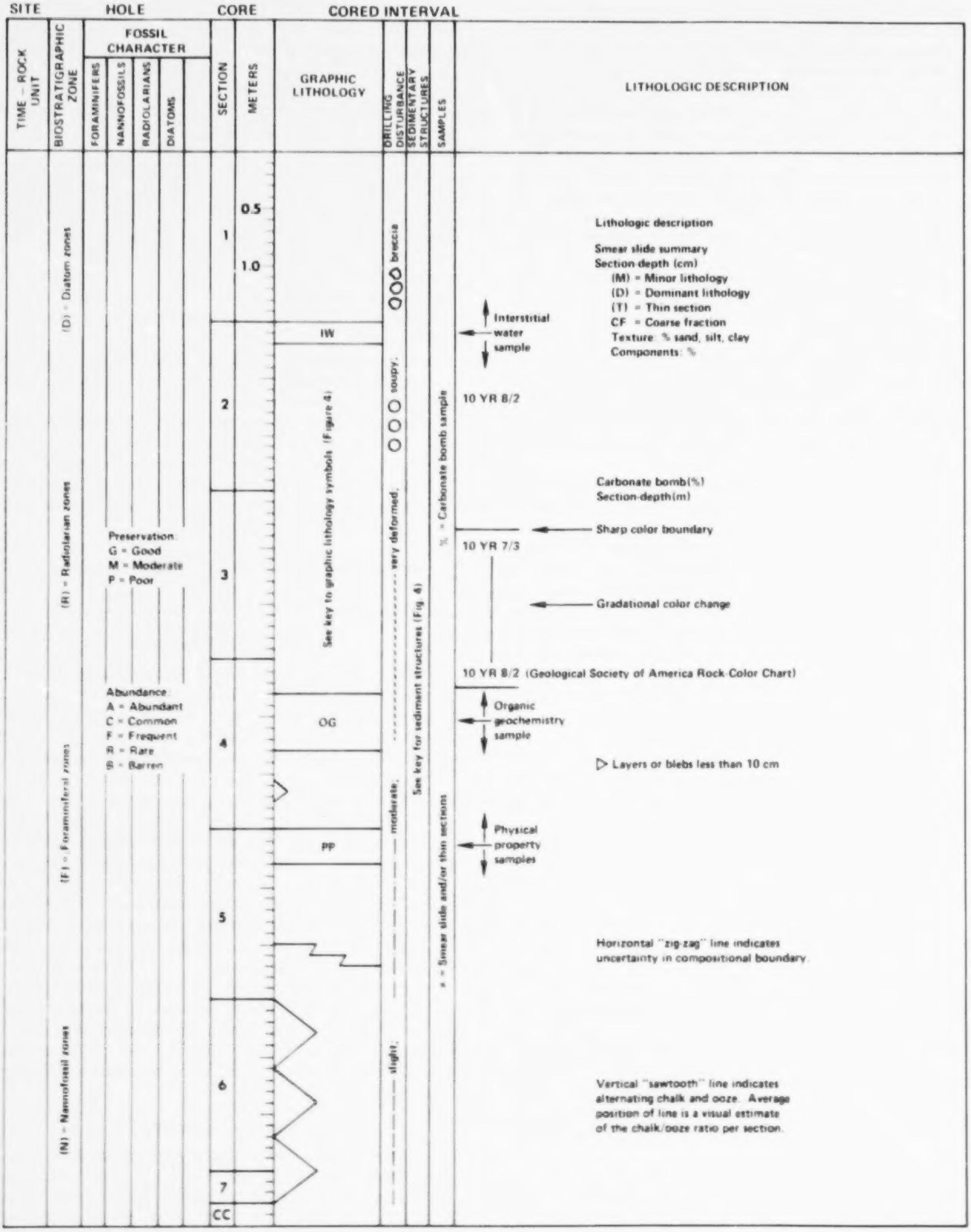
SITE
HOLE
CORE
CORED INTERVAL
TIME – ROCK UNIT
BIOSTRATIGRAPHIC ZONE
FOSSIL CHARACTER
FORAMINIFERS
NANNOFOSSILS
RADIOLARIANS
DIATOMS
SECTION
METERS
GRAPHIC LITHOLOGY
DRILLING DISTURBANCE
SEDIMENTARY STRUCTURES
SAMPLES
LITHOLOGIC DESCRIPTION
(D) = Diatom zones
(R) = Radiolarian zones
(F) = Foraminiferal zones
(N) = Nannofossil zones
Preservation:
G = Good
M = Moderate
P = Poor
Abundance:
A = Abundant
C = Common
F = Frequent
R = Rare
B = Barren
1
2
3
4
5
6
7
CC
0.5
1.0
IW
OG
PP
See key to graphic lithology symbols (Figure 4)
OOO breccia
soupy;
very deformed;
moderate;
slight;
See key for sediment structures (Fig. 4)
% = Carbonate bomb sample
x = Smear slide and/or thin sections
Interstitial water sample
Organic geochemistry sample
Physical property samples
10 YR 8/2
10 YR 7/3
10 YR 8/2 (Geological Society of America Rock-Color Chart)
Lithologic description
Smear slide summary
Section-depth (cm)
(M) = Minor lithology
(D) = Dominant lithology
(T) = Thin section
CF = Coarse fraction
Texture: % sand, silt, clay
Components: %
Carbonate bomb(%)
Section-depth(m)
Sharp color boundary
Gradational color change
▷ Layers or blebs less than 10 cm
Horizontal "zig-zag" line indicates uncertainty in compositional boundary.
Vertical "sawtooth" line indicates alternating chalk and ooze. Average position of line is a visual estimate of the chalk/ooze ratio per section.

Figure 2. Sample core description sheet (sediment).

graphic symbols in the column headed "Sedimentary Structures" on the core description form (Fig. 2). The keys to these symbols are shown in Figure 3.

Bioturbation is difficult to recognize in the monotonous hemipelagic muds but is noted, where distinguishable, on the graphic column.

Color

Colors of the core samples are determined with a Geological Society of America Rock-Color Chart. Colors are determined immediately after the cores are split and while wet color codes are placed to the right of the sample column on the core description forms (Fig. 2). Solid short horizontal lines between color codes indicate sharp contacts; dashed horizontal lines indicate vague color contacts; and vertical lines indicate intervals of gradational color change.

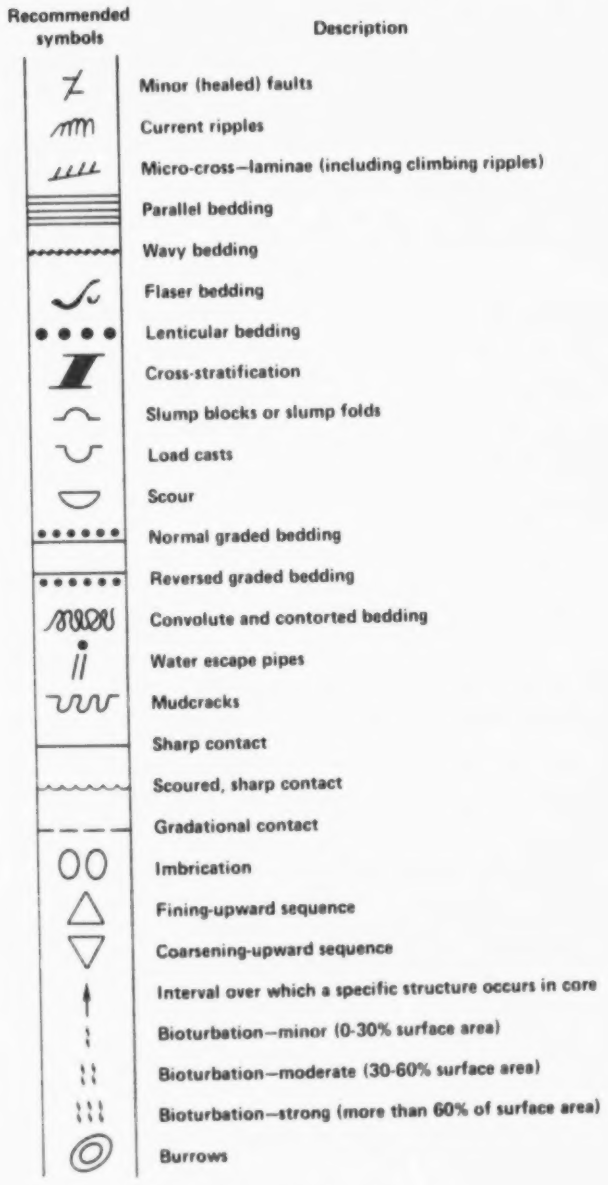
Recommended symbols
Description
Minor (healed) faults
Current ripples
Micro-cross–laminae (including climbing ripples)
Parallel bedding
Wavy bedding
Flaser bedding
Lenticular bedding
Cross-stratification
Slump blocks or slump folds
Load casts
Scour
Normal graded bedding
Reversed graded bedding
Convolute and contorted bedding
Water escape pipes
Mudcracks
Sharp contact
Scoured, sharp contact
Gradational contact
Imbrication
Fining-upward sequence
Coarsening-upward sequence
Interval over which a specific structure occurs in core
Bioturbation–minor (0-30% surface area)
Bioturbation–moderate (30-60% surface area)
Bioturbation–strong (more than 60% of surface area)
Burrows

Figure 3. Symbols for sedimentary structures.

Lithology

In the graphic column on the core description form, different lithologies are represented by a single pattern or by a grouping of two or more lithologic component symbols (Fig. 4). The abundance of any lithologic component approximately equals the percentage of the width of the graphic column its symbol occupies. For example, the left 20% of the column may have a diatom ooze symbol, whereas the right 80% may have a silt-clay symbol, indicating sediment composed of 80% mud and 20% diatoms.

Because of the difference in the length-to-width ratio between the actual sediment core and the graphic lithology column, it is not possible to reproduce structures as they appeared in the core; in the graphic representation they are highly flattened and distorted. The same is true for rock fragments or pebbles in the cores. As a result, the locations of pebbles are shown by a solid square and the depth of small "patches" of ash or other lithologic changes are given by triangular inset of the appropriate lithologic symbol on the left side of the lithologic column (Fig. 2). This convention applies also to beds thinner than 1 cm. Voids less than 10 cm are not shown.

Smear-slide (or thin-section) compositions and carbonate content (%$CaCO_3$) determined on board are listed below the core description; the two numbers separated by a hyphen refer to the section and centimeter interval, respectively, of the sample. The locations of these samples in the core and a key to the codes used to identify these samples are given in the column headed "Samples" (Fig. 2). Locations and intervals of organic geochemistry (OG), interstitial water (IW), and physical property (PP) samples are given in the lithology column.

Lithologic Classification of Sediments

The basic classification system used here was devised by the JOIDES Panel on Sedimentary Petrology and Physical Properties (SPPP) and adopted for use by the JOIDES Planning Committee in March 1974. This classification is descriptive rather than generic, and divisions between different types of sediment are somewhat arbitrary. We treat lithologic types not covered in this classification as a separate category termed Special Rock Types. A brief outline for the conventions and descriptive data used to construct this classification follows.

Conventions and Descriptive Data

Composition and Texture

In this classification, composition and texture are the only criteria used to define the type of sediment or sedimentary rock. Composition is more important for describing sediments deposited in the open ocean, and texture becomes significant for hemipelagic and nearshore sediments. These data come principally from the use of a petrographic microscope for visual estimates of smear slides. They are estimates of areal abundance and size components on the slide and may differ somewhat from

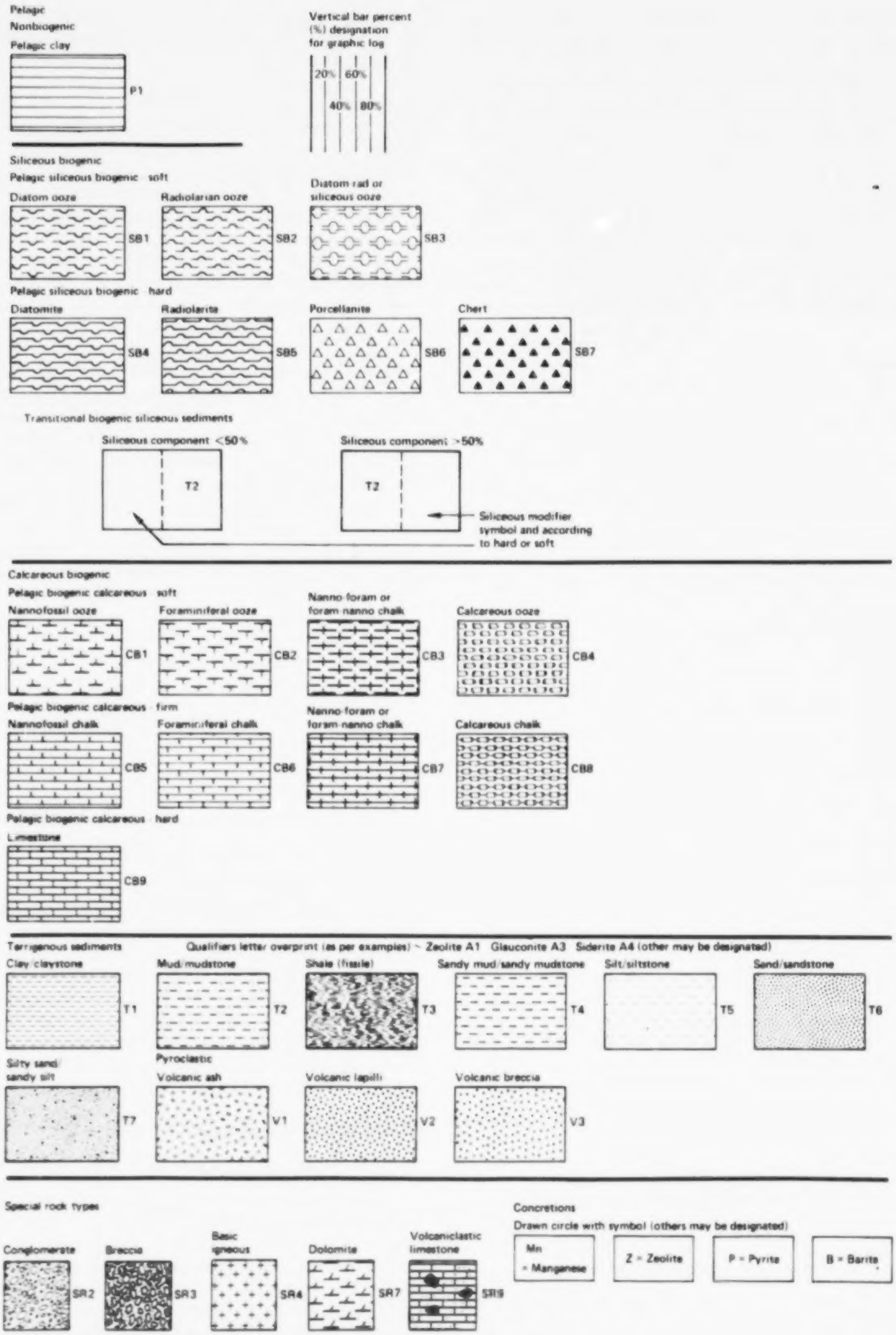
Pelagic
Nonbiogenic
Pelagic clay
P1
Vertical bar percent (%) designation for graphic log
20%
60%
40%
80%
Siliceous biogenic
Pelagic siliceous biogenic soft
Diatom ooze
SB1
Radiolarian ooze
SB2
Diatom rad or siliceous ooze
SB3
Pelagic siliceous biogenic hard
Diatomite
SB4
Radiolarite
SB5
Porcellanite
SB6
Chert
SB7
Transitional biogenic siliceous sediments
Siliceous component <50%
T2
Siliceous component >50%
T2
Siliceous modifier symbol and according to hard or soft
Calcareous biogenic
Pelagic biogenic calcareous soft
Nannofossil ooze
CB1
Foraminiferal ooze
CB2
Nanno-foram or foram-nanno chalk
CB3
Calcareous ooze
CB4
Pelagic biogenic calcareous firm
Nannofossil chalk
CB5
Foraminiferal chalk
CB6
Nanno-foram or foram-nanno chalk
CB7
Calcareous chalk
CB8
Pelagic biogenic calcareous hard
Limestone
CB9
Terrigenous sediments
Qualifiers letter overprint (as per examples) ~ Zeolite A1 Glauconite A3 Siderite A4 (other may be designated)
Clay/claystone
T1
Mud/mudstone
T2
Shale (fissile)
T3
Sandy mud/sandy mudstone
T4
Silt/siltstone
T5
Sand/sandstone
T6
Silty sand/ sandy silt
T7
Pyroclastic
Volcanic ash
V1
Volcanic lapilli
V2
Volcanic breccia
V3
Special rock types
Conglomerate
SR2
Breccia
SR3
Basic igneous
SR4
Dolomite
SR7
Volcaniclastic limestone
SR9
Concretions
Drawn circle with symbol (others may be designated)
Mn = Manganese
Z = Zeolite
P = Pyrite
B = Barite

Figure 4. Symbols used to identify lithology on sediment core description forms.

more accurate analyses of grain size, carbonate content, and mineralogy. From past experience, we find quantitative estimates of distinctive minor components to be accurate to within 1–2%, but for major constituents accuracy is poorer, ± 10%. All smear-slide estimates were done on board.

Induration of Sediments

We recognize three classes of induration or lithification for all sediments. In the next two paragraphs, these classes are defined for two types of sediments.

1. For calcareous sediments and sedimentary rocks, categories after Gealey and others (1971): soft = ooze, has little strength and is readily deformed under pressure of finger or broad blade of spatula; firm = chalk, partially lithified, readily scratched with fingernail or edge of spatula; hard = limestone, dolostone, well lithified and cemented, resistant or impossible to scratch with fingernail or edge of spatula.

2. For transitional carbonates, siliceous, pelagic, and terrigenous sediments: soft = sediment core that may be split with wire cutter; firm = partially lithified, but fingertip pressure leaves an indentation; hard = cannot be compressed with fingertip pressure.

Basic Sediment Types

Biogenic Siliceous Sediments

Biogenic siliceous sediments are those that contain more than 30% siliceous microfossils. Sediments containing between 10 and 30% siliceous microfossils should contain the name(s) of the microfossil(s) as qualifiers. The following terminology is used for siliceous biogenic sediments:

1. Soft: siliceous ooze (radiolarian ooze, diatom ooze, etc., depending on the dominant fossil component).

2. Hard: radiolarite, diatomite, chert, or porcellanite. The term "chert" in the past has been used in a very broad sense to designate almost any form of recrystallized silica. The term procellanite (which also had a very broad usage in the past) will be used here to refer to "low density, more or less porous and dull-lustered varieties of 'chert' made of opaline silica or cristobalite..." (Lancelot, 1973). "Chert," as used here, will have a narrower scope than that of past usage, and will refer to "hard nodules and sometimes beds that are largely quartz and (or) chalcedony, and show a conchoidal fracture and a bitreous luster..." (Lancelot, 1973).

3. Compositional qualifiers: diatoms and radiolarians may be the principle components; thus, one or two qualifiers may be used, for example: indeterminate siliceous fossils (siliceous ooze, chert, or porcellanite); radiolarians only (radiolarian ooze, or radiolarite); diatoms only (diatom ooze or diatomite); diatom < radiolarians (diatom radiolarian ooze or diatom radiolarite); diatom > radiolarians (radiolarian diatom ooze or radiolarian diatomite).

The order of the two modifiers in the terms is dependent on the dominant fossil type. The dominant component is listed last and the minor component is listed first. The terminology for mixtures of clay with diatom sediments is:

Biogenic siliceous fossil particles (%)	Nonbiogenic particles (example: clay) (%)	Lithologic type
< 10	90	Clay (soft) Claystone (hard)
30–10	70–90	Diatom clay (soft) Diatom claystone (hard)
60–30	40–70	Clayey diatom ooze (soft) Clayey diatomite (hard)
100–60	0–40	Diatom ooze (soft) Diatomite (hard)

If radiolarians are the dominant siliceous microfossil, the terms "radiolarian" and "radiolarite" are substituted for "diatom" and "diatomite", respectively. The term "siliceous" may be used if the fossil type is indeterminate. Likewise, other textural terms for the nonbiogenic components can be substituted for clay (e.g., silty diatom ooze, diatom silty clay, etc.).

Biogenic Calcareous Sediment

Calcareous biogenic sediments are distinguished by a $CaCO_3$ content in excess of 30%. There are two classes: (1) biogenic calcareous sediments, that contain 60–100% biogenic $CaCO_3$, and (2) transitional biogenic calcareous sediments, that contain 30–60% biogenic $CaCO_3$.

1. For biogenic calcareous sediment, with 60–100% biogenic $CaCO_3$, the following terminology is used: soft: calcareous ooze, firm: chalk, and hard and cemented: limestone.

If nannofossils and foraminifers are the principal components, then one or two qualifiers may be used, as in the following examples: indeterminate carbonate fossils: calcareous ooze, calcareous chalk, or calcareous limestone; foraminifers 0–10%, nannofossils 90–100%: nannofossil ooze, nannofossil chalk, or nannofossil limestone; foraminifers 10–30%, nannofossils 60–90%: foraminiferal-nannofossil ooze, foraminiferal-nannofossil chalk, or foraminiferal-nannofossil limestone; foraminifers 30–60%, nannofossils 40–70%: nannofossil-foraminiferal ooze, nannofossil-foraminiferal chalk, or nannofossil-foraminiferal limestone.

2. For transitional biogenic calcareous sediments, with 30 to 60% biogenic $CaCO_3$ the following terminology is used: marl or marlstone: 30–60% $CaCO_3$, nonbiogenic components greater than siliceous biogenic component; soft: calcareous marl, foraminifer marl, or nannofossil marl; hard: calcareous marlstone, foraminiferal marlstone, or nannofossil marlstone.

Note that the use of the terms "marl" or "marlstone" differ from the SPPP classification. The panel's classification used "marly" as an adjective modifying ooze, chalk, or limestone (e.g., "marly limestone"), to denote sediments that had 30–60% biogenic carbonate. Our terminology for mixtures of clay with nannofossil sediments is as follows:

Biogenic calcareous fossil particles (%)	Nonbiogenic particles (%)	Lithologic type
0–10	90–100	Clay (soft) Claystone (hard)
30–10	70–90	Nannofossil clay (soft) Nannofossil claystone (hard)
60–30	40–70	Nannofossil marl (soft) Marly nannofossil chalk (firm) Nannofossil marlstone (hard)
100–60	0–40	Nannofossil ooze (soft) Nannofossil chalk (firm) Nannofossil limestone (hard)

Other terms may be substituted for nannofossil, such as (1) "foraminiferal, nannofossil-foraminiferal," if foraminifers are present in the percentages as discussed, or (2) "calcareous," if the fossil type is indeterminate. Likewise, other textural terms for the nonbiogenic components can be substituted for clay (e.g., silty nannofossil ooze, foraminifer silty clay, etc.).

Biogenic ooze: 30–60% $CaCO_3$, siliceous biogenic components greater than nonbiogenic components.

Calcareous components greater than siliceous components (examples: radiolarian-nannofossil ooze [chalk], diatom-foraminiferal ooze, siliceous limestone).

Siliceous components greater than calcareous components (examples: nannofossil-diatom ooze [diatomite], foraminiferal-radiolarian ooze [radiolarite]).

Volcanogenic Sediments

Pyroclastic rocks are described according to the textural and compositional scheme of Wentworth and Williams (1932): The textural groups are: more than 32 mm, volcanic breccia; 4–32 mm, volcanic lapilli; less than 4, volcanic ash (tuff, if indurated). These pyroclastic rocks are described as vitric, crystal, or lithic.

IGNEOUS AND METAMORPHIC ROCK DESCRIPTION CONVENTIONS

Core Forms

Core description forms for igneous and metamorphic rocks are not the same as those used for sediments. The latter are essentially those published in previous *Initial Reports*. Igneous rock representation on such sheets, however, is too compressed to provide adequate information for rock sampling. Consequently, visual core description forms, modified from those used aboard ship, are used here for more complete graphic representation. Each of these forms covers one 1.5-m section. All shipboard chemical and physical-property data, as well as summary hand-specimen and thin-section descriptions, are presented for each section.

All basalts are split with a rock saw into archive and working halves. The latter is described and sampled aboard ship. In a typical basalt description form (Fig. 5), the left box is a visual representation of the working half. Lithologies are indicated in the graphic representation column using the symbols shown on Figure 6. Two closely spaced horizontal lines in this column indicate the location of styrofoam spacers taped between basalt pieces inside the liner. Each piece is numbered sequentially from the top of each section, beginning with the number 1. Pieces are labeled on the rounded, not the sawed surface. Pieces that could fit together before splitting are given the same number, but are lettered consecutively as "1a, 1b, 1c," etc. Spacers are placed between pieces with different numbers, but not between those with different letters and the same number. In general,

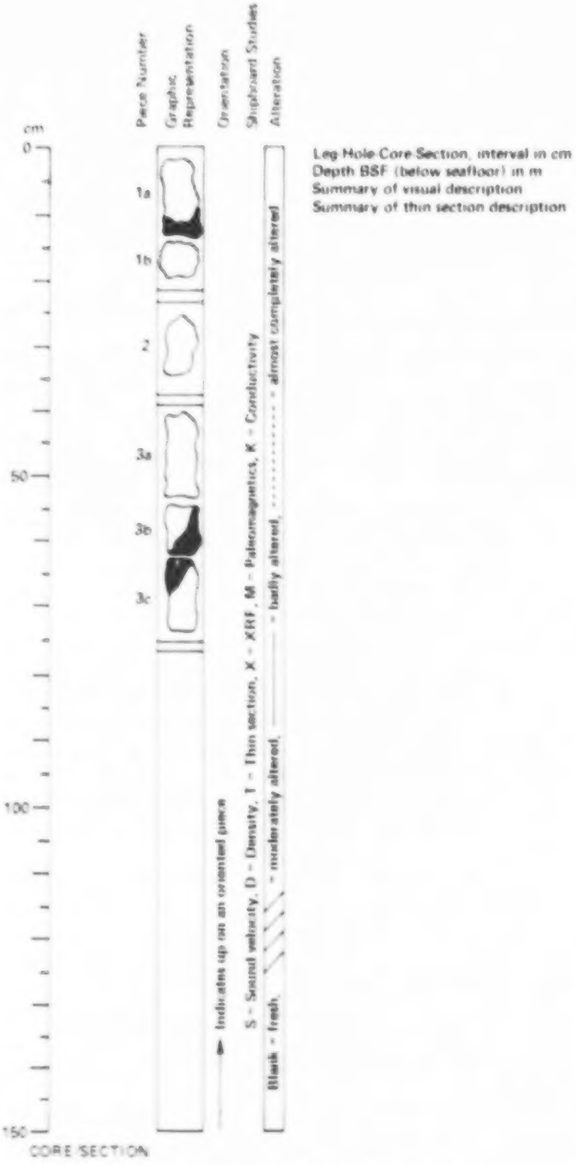

cm
0
50
100
150
CORE SECTION
Piece Number
Graphic Representation
Orientation
Shipboard Studies
Alteration
1a
1b
2
3a
3b
3c
Indicates up on an oriented piece
S – Sound velocity, D – Density, T – Thin section, X – XRF, M – Paleomagnetics, K – Conductivity
Blank – fresh, = moderately altered, —— = badly altered, - - - - - - - = almost completely altered
Leg-Hole-Core-Section, interval in cm
Depth BSF (below seafloor) in m
Summary of visual description
Summary of thin section description

Figure 5. Sample core description form (igneous rocks).

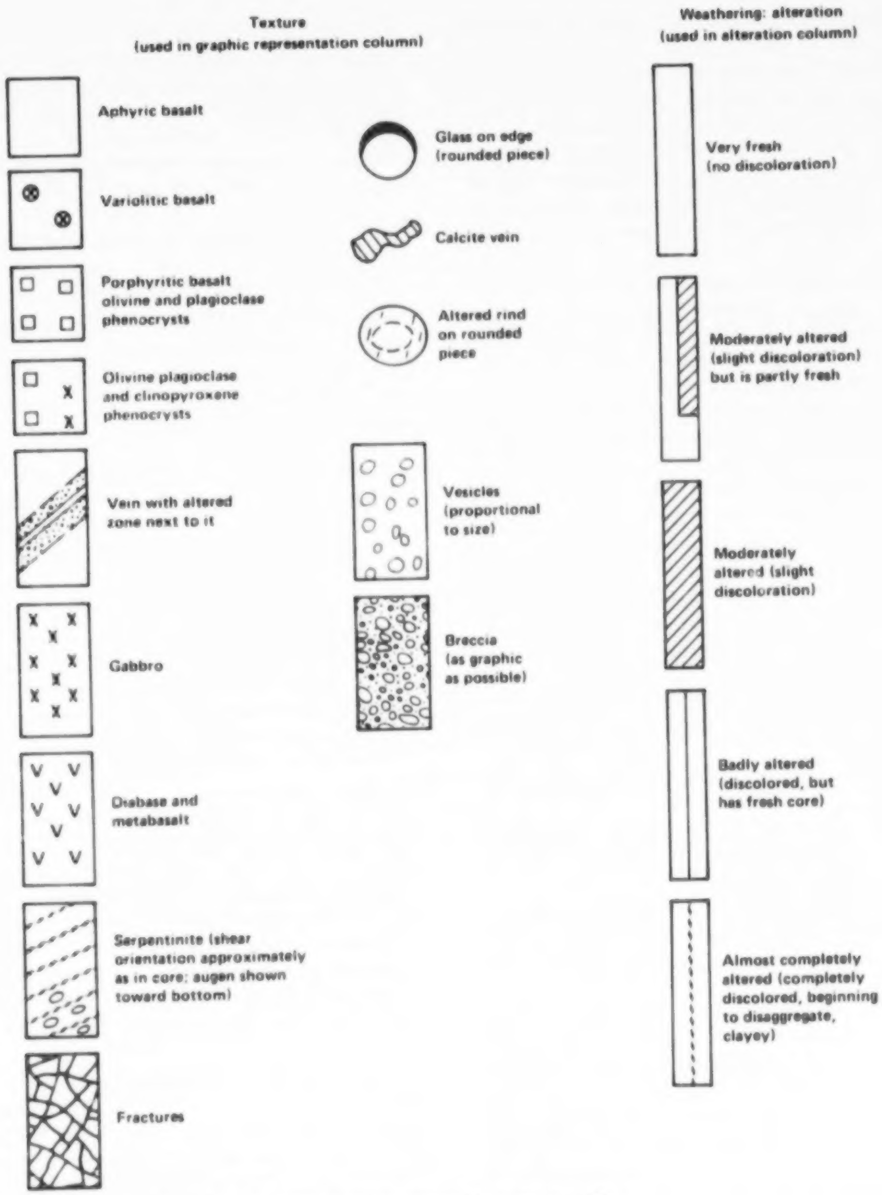
Texture
(used in graphic representation column)
Aphyric basalt
Variolitic basalt
Porphyritic basalt olivine and plagioclase phenocrysts
Olivine plagioclase and clinopyroxene phenocrysts
Vein with altered zone next to it
Gabbro
Diabase and metabasalt
Serpentinite (shear orientation approximately as in core; augen shown toward bottom)
Fractures
Glass on edge (rounded piece)
Calcite vein
Altered rind on rounded piece
Vesicles (proportional to size)
Breccia (as graphic as possible)
Weathering: alteration
(used in alteration column)
Very fresh (no discoloration)
Moderately altered (slight discoloration) but is partly fresh
Moderately altered (slight discoloration)
Badly altered (discolored, but has fresh core)
Almost completely altered (completely discolored, beginning to disaggregate, clayey)

Figure 6. List of symbols for igneous and metamorphic rocks, Leg 82.

addition of spacers represents a drilling gap (no recovery). All pieces that are cylindrical and longer than the liner diameter have orientation arrows pointing up, both on the archive and working halves. Special procedures are used to ensure that orientation is preserved through every step of the sawing and labeling process. All orientable pieces are indicated by upward-pointing arrows to the right of the graphic representation on the description forms. Because the pieces are rotated during drilling, it is not possible to sample for declination studies.

Samples are taken for various measurements aboard ship. The type of measurement and approximate location are indicated in the column headed "Shipboard Studies," using the following notation: X = X-ray fluorescence and CHN chemical analysis; M = magnetics measurement; S = sonic velocity measurement; T = thin section; D = density measurement; and P = porosity measurement.

The state of alteration (see Fig. 6 for symbols) is shown in the Alteration column.

Classification of Igneous Rocks

We informally classified igneous rocks recovered on Leg 82 according to mineralogy and texture determined from visual inspection of hand specimens and thin sections. We agreed upon the following conventions while we were at sea, and we realize that they are generalized.

It is possible that gradations may exist within and among textural groups in a single sample:

A. *Quench textures recognized and described*:

1. Glassy: matrix is amorphous, basaltic glass with no visible, incipient crystallization.

2. Variolitic: texture characterized by the presence of varioles, which are spherical bodies, usually consisting of radiating plagioclase and/or clinopyroxene microlites or crystals; individual crystals are indistinguishable with the microscope.

3. Subvariolitic: texture in which variolites coalesce.

4. Immature sheaf: a bundled arrangement of small crystals (which cannot be individually distinguished with the microscope) assuming a sheaflike appearance; a central axis of crystal growth often occurs.

5. Mature sheaf: same as above, but, discrete skeletal crystals can be distinguished with the microscope (usually greater than 0.005 mm wide).

6. Plumose: plumelike or featherlike arrangement of microlites or crystals; may grade from immature to mature (as in sheaf texture) because of crystal size.

B. *Major textural classification for basaltic samples*:

1. Phyric: a term describing igneous rocks in which larger crystals (phenocrysts) are set in a finer groundmass, which may be crystalline or glassy, or both. Aphric: no phenocrysts; sparsely phyric: 1-2% phenocrysts; moderately phyric: 2-10% phenocrysts; high phyric: more than 10% phenocrysts.

2. Glomerophyric: a term applied to phyric rocks containing clusters of equant crystals larger than the matrix crystals.

3. Ophitic: a term applied to a texture in which euhedral or subhedral crystals of plagioclase are embedded in a mesostasis of pyroxene crystals.

4. Subophitic: a term applied to the ophitic texture of an igneous rock in which the feldspar crystals are approximately the same size as the pyroxene and are only partially included by them.

5. Intergranular: a term applied to volcanic rocks in which there is an aggregation of grains of clinopyroxene, not in parallel optical continuity (as in subophitic texture), between a network of feldspar laths that may be diverse, subradial, or subparallel. It is distinguished from an intersertal texture by the absence of both interstitial glass and other quenched places that may fill the interstices between the feldspar laths.

6. Intersertal: a term applied to volcanic rocks wherein a base of mesostasis or glass and small crystals fill the interstices between unoriented feldspar laths, the base forming a relatively small proportion of the rock. When the amount of the base increases and feldspar laths decrease, the texture becomes hyalophitic, and with a still greater increase in the amount of the base, the texture becomes hyalopilitic.

Designation of Informal Lithologic Units and Petrographic or Chemical Groups

For Leg 82 arabic numerals (1, 2, 3...) are used to designate lithologic units. Lithologic units are numbered sequentially from the top to the bottom of the hole, including both sedimentary, igneous, and metamorphic rocks. Petrographic or chemical groups involve igneous rocks only and are designated with Roman numerals (I, II, III,...). The groups are numbered sequentially as each new group is identified from the first occurrence of igneous rocks to the bottom of the hole. This does not exclude a group from reoccurring further downhole from where it was first identified.

SHIPBOARD MEASUREMENTS

Physical Properties Procedures

A thorough discussion of physical properties is presented by Boyce (1976) with respect to equipment, methods, errors, correction factors, and problems related to coring disturbance. Only a brief review of methods employed on Leg 82 is given here.

Velocity

Compressional-wave velocity was measured on the Hamilton Frame Velocimeter by timing a 400-kHz pulse between two transducers and by measuring the distance across the sample with a dial gauge. Measurements were made at laboratory temperature and pressure. With consolidated sediments, a piece was removed from the core and trimmed carefully to form two parallel surfaces to ensure good contact with the transducer heads. Water was used to make good acoustical contact between the sample and the transducers.

Calibration of the velocimeter consisted of making numerous measurements through lucite, aluminum, and brass standards of varying thicknesses to obtain a calibration constant for each of three μs/cm settings on the DSDP Tektronix 485 oscilloscope used to make the travel-time measurements. This calibration constant reflects the position picked by the operator as representing the first break from horizontal of the sonic signal. Data from the calibrations remained constant throughout the duration of Leg 82.

GRAPE

The Gamma Ray Attenuation and Porosity Evaluator (GRAPE) was used to determine wet-bulk density based on the attenuation of gamma rays by the sample. Boyce (1976) discusses the theoretical aspects in detail. During Leg 82 the GRAPE was used in two modes: (1) continuous GRAPE, in which most sections of the core were irradiated; continuous "corrected" wet-bulk density (relative to quartz) was plotted on an analog graph: and (2) two-minute GRAPE, in which the gamma count through a small piece of the core was measured for two minutes, followed by a similar count through air and/or a quartz standard.

Continuous GRAPE

Before each core was run through the device, an aluminum standard was measured. A density of 2.60 Mg/m^3 was assigned to the 6.61-cm (diameter) aluminum standard analog record and a density of 1.0 Mg/m^3 to the 2.54-cm (diameter) aluminum standard analog record. Linear interpolation of the GRAPE analog data between these values yielded an "empirical" wet-bulk density of the sediment sample in the core (ρ_{bcz}). If the sample completely filled the core, then $\rho_{bc} = \rho_{bcz}$, where ρ_{bc} = "corrected" wet-bulk density (relative to quartz). Then:

$$\rho_b = \frac{(\rho_{bc}-\rho_{fc})(\rho_g-\rho_f)}{(\rho_{gc}-\rho_{fc})} + \rho_f,$$

where ρ_g = true grain density (≈ 2.7 Mg/m^3 for sediments), ρ_{gc} = corrected grain density (≈ 2.7 Mg/m$_3$ for sediment); ρ_f = true fluid density (≈ 1.025 Mg/m^3); ρ_{fc} = corrected fluid density (≈ 1.125 Mg/m^3); and ρ_b = true wet-bulk density.

Using the above values,

$$\rho_b = 1.066\,(\rho_{bc} - 1.125) + 1.025. \tag{1}$$

Shipboard reduction of analog GRAPE records involved the selection of high-density portions of each core section on the analog record, and the calculation of true wet-bulk density (ρ_b) by formula (1). The porosity ϕ is obtained by

$$\phi(\%) = \frac{\rho_g-\rho_b}{\rho_g-\rho_f} \times 100.$$

Two-Minute GRAPE

For two-minute GRAPE calculations,

$$\rho_{bc} = \frac{\ln (I_o/I)}{d\ \mu\text{qtz}},$$

where I_o = two-minute gamma count through air, I = two-minute gamma count through the sample, d = gamma ray path length through the sample, and μqtz = quartz attenuation coefficient determined daily by measuring through a quartz standard. Then as in the continuous GRAPE calculation (assuming a 2.7 grain density),

$$\rho_b = 1.066\,(\rho_{bc} - 1.125) + 1.025,$$

and

$$\phi(\%) = \frac{100(2.70-\rho_b)}{1.675}.$$

Boyce (1976) estimates ±5% accuracy for continuous GRAPE data and ±2% for two-minute GRAPE data. In practice, it was found that the error on Leg 82 seemed to be higher, because of the highly disturbed nature of many of the cores. However, good agreement exists between the GRAPE data and gravimetric methods.

Samples for the two-minute GRAPE counts were also used for gravimetric methods. One of three different sampling techniques was used depending on the stiffness and the fissility of the sediments and rocks. In soft sediments, Boyce cylinders were inserted and cut from the split cores to produce the most undisturbed sample possible. The upper and lower sample surfaces were gradually trimmed flush with the cylinder to minimize sediment remolding. The resulting disturbance was small enough to have a negligible effect either on the GRAPE counts or on the gravimetric analysis. In harder sediments, when cylinders could no longer be inserted without causing severe deformation or cracking, slices (10–20 cm^3) were removed using razor blades. Parallel surfaces were trimmed on four sides to allow GRAPE counts both perpendicular and parallel to bedding. When increased induration allowed, mini-cores were cut from the drilling biscuits and coherent sections. Again, the surfaces were carefully trimmed.

Gravimetric Technique: Boyce Cylinder, Chunk, and Mini-Core

After the two-minute GRAPE counts, the samples prepared as described above were used for water content and porosity determinations. No salt corrections were applied in any of these techniques. Drying and weighing equipment on board *Glomar Challenger* was used for these measurements.

Water content (% wet wt.) =

$$100 \times \frac{[(\text{wt. wet sediment}) - (\text{wt. dry sediment})]}{(\text{wt. wet sediment})}.$$

For porosity determinations, a grain density of 2.65 g/m^3 and a water density of 1.03 g/m^3 were assumed.

$$\text{Porosity } (\%) = 100 \times \frac{\text{vol. evaporated water}}{\text{vol. wet sediment}}$$

$$= 100 \times \frac{[(\text{wt. evaporated water})/(1.03\ \text{Mg/m}^3)]}{\left[\dfrac{(\text{wt. dry sediment})}{(2.65\ \text{mg/m}^3)} + \dfrac{(\text{wt. evaporated water})}{(1.03\ \text{mg/m}^3)}\right]}.$$

Shear Strength

A Soiltest Torvane was used on board to determine the undrained shear strength of clayey sediments. The Torvane was hand-rotated at a rate designed to reach failure in about 10 s with constant loading. Repeated determinations yielded results that were generally reproducible to ±15%. Measurements were made in the least disturbed sediments.

Conductivity is determined from the relation that applies for a line source in an infinite medium:

$$K = \frac{AI^2\ln(t_2/t_1)}{T_2 - T_1} - B,$$

where K = the thermal conductivity, I = the current flowing in the heater wire, t_1 and t_2 are two times in the measurement period, T_2 and T_1 are temperatures at times t_2 and t_1, and A and B are constants. For the needle probe device, B = 0 and A is determined directly from probe parameters.

Geochemical Procedures

Carbonate Bomb

Percent $CaCO_3$ was also determined on board ship by the "Karbonate Bombe" technique (Müller and Gastner, 1971). In this simple procedure, a sample is powdered and treated with HC1 in a closed cylinder. Any resulting CO_2 pressure is proportional to the $CaCO_3$ content of the sample. Application of the calibration factor to the manometer reaching (× 100) yields $\%CaCO_3$. Percent error can be as low as 1% for sediments high in $CaCO_3$, and in general an accuracy of about 2 to 5% can be obtained.

These data are presented on the core-description sheets. The sample interval is designated by two numbers: the section number, followed by the top of the sample interval. For example, a sample from Section 558-9-2, 11 to 12 cm, with 90% calcium carbonate will be represented on the core description sheet for Core 558-9 as "2-11 (90%)."

On-board analyses for pH, alkalinity, salinity, calcium, magnesium, and chlorinity are conducted routinely. Interstitial waters are routinely analyzed for pH, alkalinity, salinity, calcium, magnesium, and chlorinity. Sediments are squeezed using a stainless steel press; the water collects in plastic syringes and is then filtered through 0.45-μm, 1-in. millipore filters. Interstitial waters collected with the *in situ* Water Sampler are filtered through 0.4-μm, 13-mm filters before analysis.

A Corning Model 130 pH meter and a Markson combination electrode were used to determine pH. The pH meter is calibrated with 4.01 and 7.42 buffer standards, all readings are originally in millivolts and later are converted to pH. All pH measurements are made in conjunction with alkalinity.

Alkalinites are determined potentiometrically. Five to ten ml samples are first tested for pH then titrated with 0.1 N HCL. Near the endpoint acid is added in 0.01-ml and 0.005-ml increments, and the millivolt readings noted for each increment. The exact endpoint is then calculated using the Gran Factor method (Gieskes and Rogers, 1973).

Salinity (‰) is calculated from the fluid refractive index, as measured by a Goldberg optical refractometer, using this expression:

$$\text{Salinity (‰)} = 0.55 \times \Delta N,$$

where ΔN is the refractive index multiplied by 10^4. The refractometer's calibration is checked periodically using IAPSO seawater standard and deionized water.

Calcium is determined by titrating a 0.5-ml sample with EGTA (a complexing agent), using GHA as an indicator. To sharpen the endpoint, the calcium-GHA complex is extracted into a layer of butanol. No correction is made for strontium, which is also included in the result.

Magnesium is determined by titrating a buffered 0.5-ml sample to an Ereochrome Black-T endpoint, using EDTA (sodium salt) as a titrant. This method analyzes all alkaline earths, including calcium, strontium, and magnesium; concentrations are obtained by subtracting the calcium (which includes strontium) from this analysis.

Chlorinity is determined by titrating a 0.1-ml sample (diluted with 1 ml of deionized water) with silver nitrate to a potassium chromate endpoint.

Methods and equipment are checked and standardized at each site using IAPSO standard seawater. As a further check, a surface seawater sample is also analyzed and archived. This sample is also used to test for possible drill water contamination of the interstitial water samples.

Paleomagnetic Techniques

Remanent magnetization of sediment and rock samples is measured with a Digico balanced fluxgate rock magnetometer, calibrated frequently with a shipboard standard. Error direction of remanent magnetization is less than 4°. The noise level is $2.3 \pm (1.1 \times 10^{-7})$ emv/cm^3.

A Schonstedt A. C. geophysical specimen demagnetizer (Model GSD-1) is used for alternating field (AF) demagnetization of the samples. With this single-axis system demagnetizer, every sample was demagnetized three times, about each of the three orthogonal axes.

Samples for paleomagnetic analysis are taken from unconsolidated and semiconsolidated sediments in the upper parts of the cores by inserting plastic 2.5-cm cubes into the split sections. In more lithified samples from deeper levels, cylindrical samples (2.5 cm in diameter) are taken from the split core sections with a diamond corer ("mini-core drill"). An orientation is marked with an arrow in the uphole direction on every sample before removal from the split core section.

Photography

Sets of color and black-and-white negatives of whole cores are available for consultation. In addition, negatives in black and white for closeup documentation of special structures are archived at DSDP.

Obtaining Samples

Potential investigators who desire to obtain samples should refer to the DSDP-NSF Sample Distribution Policy. Sample request forms may be obtained from The Curator, Ocean Drilling Program, Texas A&M University, College Station, Texas 77843. Requests must be as specific as possible; include site, core, section, interval within a section, and volume of sample required.

BIOSTRATIGRAPHY-MAGNETIC STRATIGRAPHY CORRELATION CHART

Biostratigraphic zonations are placed under the column heading "Biostratigraphic Zone" on the core description form. Under the column heading "Fossil Character," the following letters are used to indicate fossil abundance: A = abundant (flood, many species and specimens); C = common (many species, easy to make age assignment); R = rare (enough for age assignment); T = trace (few species and specimens, not enough for age assignment); and B = barren.

Letters used to designate fossil preservation are: E = excellent (no dissolution or abrasion); G = good (very little dissolution or abrasion); M = moderate (dissolution and/or abrasion and/or recrystallization very noticeable); and P = poor (substantial or very strong evidence of dissolution and/or abrasion, and/or recrystallization).

Figure 7 shows the zonation used on board ship for nannofossils, foraminifers, and magnetostratigraphic correlations.

REFERENCES

Berggren, W. A., and Amdurer, M., 1973. Late Paleogene (Oligocene) and Neogene planktonic foraminiferal biostratigraphy of the Atlantic Ocean (lat. 30°N to lat. 30°S). *Rev. Ital. Paleontol. Strat.*, 79:337-391.

Blow, W. H., 1969. Late middle Eocene to Recent planktonic foraminiferal biostratigraphy. *In* Brönnimann, P., and Renz, H. H. (Eds.), *Proc. First Int. Conf. Plankt. Microfossils*: Leiden (E. J. Brill), 1: 199-422.

Boyce, R. E., 1976. Definitions and laboratory techniques of compressional sound velocity parameters and wet-water content, wet-bulk density, and porosity parameters by gravimetric and gamma ray attenuation techniques. *In* Schlanger, S. O., Jackson, E. D., et al., *Init. Repts. DSDP*, 33: Washington (U.S. Govt. Printing Office), 931-958.

Gealy, E. L., Winterer, E. L., and Moberly, R. M., Jr., 1971. Methods conventions, and general observation. *In* Winterer, E. L., Riedel, W. R., et al., *Init. Repts. DSDP*, 7, Pt. 1: Washington (U.S. Govt. Printing Office), 9-26.

LaBrecque, J. L., Kent, D. V., and Cande, S. C., 1977. Revised magnetic polarity time scale for Late Cretaceous and Cenozoic time. *Geology*, 5(6):330-335.

Lancelot, Y., 1973. Chert and silica diagenesis in sediments from the central Pacific. *In* Winterer, E. L., Ewing, J. I., et al., *Init. Repts. DSDP*, 17: Washington (U.S. Govt. Printing Office). 377-405.

Martini, E., 1971. Standard Tertiary and Quaternary calcareous nannoplankton zonations. *In* Farinacci, A. (Ed.), *Proc. II Plankt. Conf. Roma*: Rome (Edizioni Tecnoscienza), pp. 739-785.

Matthews, D. J., 1939. *Tables of the Velocity of Sound in Pore Water and in Seawater*: London (Admiralty, Hydrographic Department).

Müller, G., and Gastner, M., 1971. The "Karbonate-Bombe", a simple device for determination of the carbonate content in sediments, soils and other materials. *Neues Jahrb. Mineral. Monatshi*, 10: 466-469.

Okada, H., and Bukry, D., 1980. Supplementary modification and introduction of code numbers to the low latitude coccolith biostratigraphy zonation (Bukry, 1973, 1975). *Mar. Micropaleont.*, 5: 321-325.

Wentworth, C. K., and Williams, H., 1932. The classification and terminology of the pyroclastic rocks: report of the Committee on Sedimentation, *Bull. Nat. Res. Counc. U.S.*, 80:10-53.

Date of Initial Receipt: September 30, 1983
Date of Acceptance: January 20, 1984

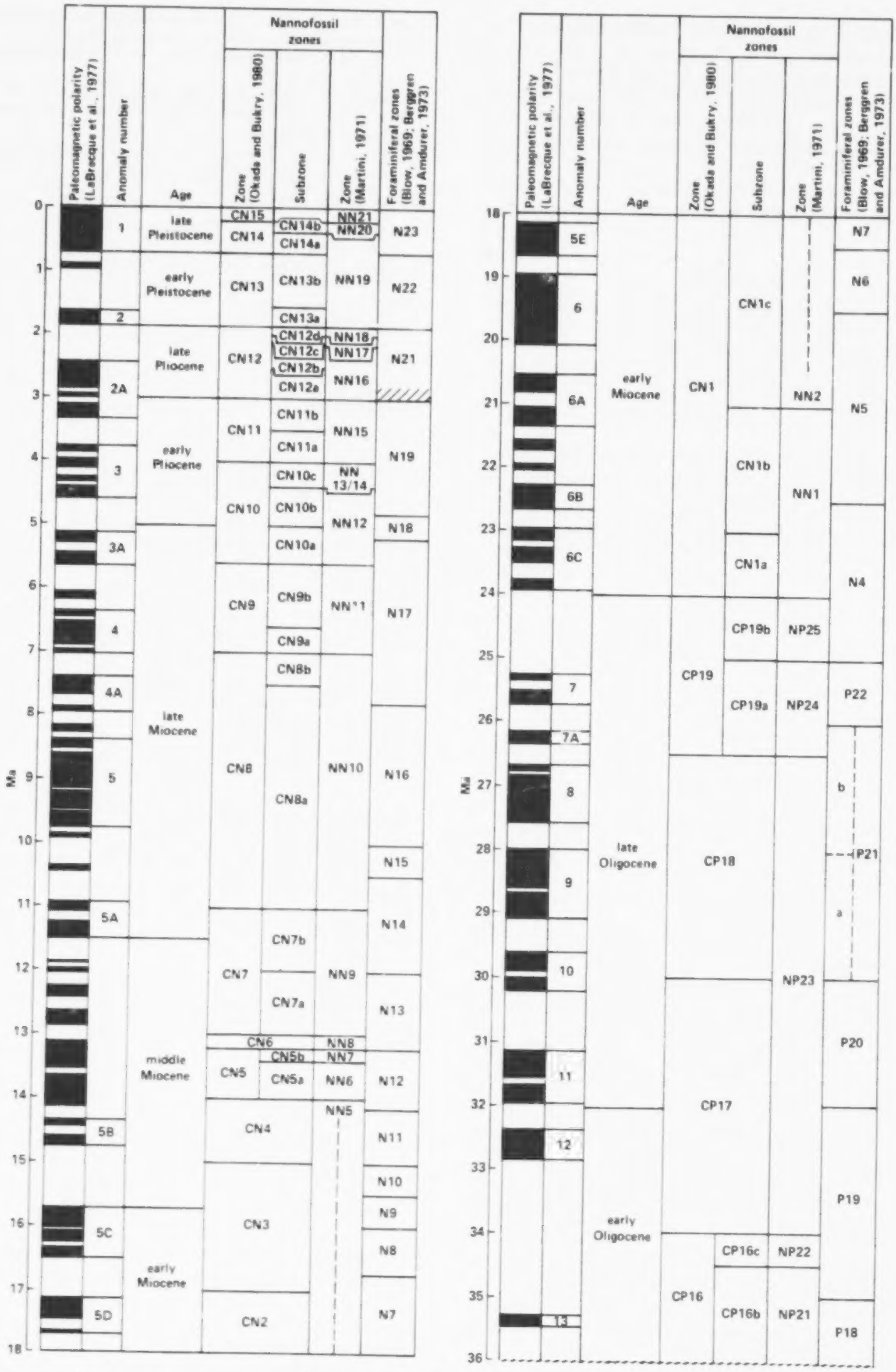

Figure 7. Biostratigraphy and magnetostratigraphy correlation chart, Leg 82. Black is normal polarity; white is reversed.

PART II: SITE CHAPTERS

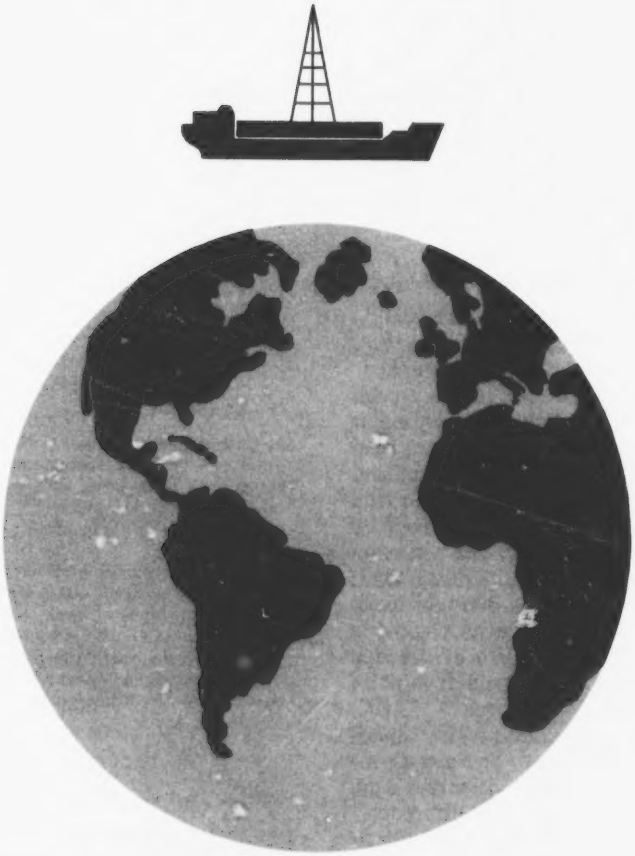

blank page

5. SITE 556[1]

Shipboard Scientific Party[2]

HOLE 556

Date occupied: 22 September 1981

Date departed: 29 September 1981

Time on hole: 172.9 hr.

Position (latitude; longitude): 38°56.38′N; 34°41.12′W

Water depth (sea level; corrected m, echo-sounding): 3672

Water depth (rig floor; corrected m, echo-sounding): 3682

Bottom felt (m, drill pipe): 3690

Penetration (m): 639.0

Number of cores: 22

Total length of cored section (m): 184

Total core recovered (m): 85.21

Core recovery (%): 46

Oldest sediment cored:
  Depth sub-bottom (m): 471.0
  Nature: Basalt limestone breccia
  Age: latest early Oligocene
  Measured velocity (km/s): 5.61

Basement:
  Depth sub-bottom (m): 461.5
  Nature: Basalt, basalt breccias, gabbro, and gabbro breccias

Principal results: Hole 556 (Site MAR-2) was drilled on Anomaly 12 on the west flank of the Mid-Atlantic Ridge, about 50 miles north of the Pico Fracture Zone, on a flow line passing through the Azores Triple Junction (Fig. 1). The seismic profile collected on the way to the site indicated approximately 500 m of sediment overlying basement.

After washing down through 461 m of sediment, we cored 177 m into the basement until bit destruction. Three different basaltic and basalt breccia units were cored down to 96 m sub-basement. Below, gabbro and gabbro breccias were recovered down to the bottom of the hole (177 m sub-basement) interrupted by a thin basaltic layer. Nannofossils found in the basalt breccias at 10 m sub-basement are dated at 30 to 34 Ma in agreement with the magnetic anomaly age.

The concentrations of the magmaphile trace elements in the 33 basaltic samples analyzed on board with the X-ray fluorescence (XRF) unit are representative of depleted Mid-Oceanic Ridge Basalts. Typical concentrations in these basalts are: Nb = 1.5 ppm, Zr = 85 ppm, Ti = 8400 ppm, Y = 36 ppm, V = 270 ppm. This unexpected result demonstrates that if an Azores Mantle Plume exists, it either has been active for a shorter period of time than previously thought or is an intermittent process.

The average core remanent magnetization inclinations within the upper part of the pillow and massive basaltic units are closely grouped (−25 to −30°), whereas the lower basaltic units have more scattered inclinations (−12 to −46°).

Three temperature measurements were made at different depths when washing down to the basement; they showed a geothermal gradient of 36°C/km. A successful suite of logs were run after bit destruction. A constant temperature of about 2°C was observed down to the sediment-basement interface, suggesting seawater flow into the hole.

OPERATIONS

Approach to the Site

The exact location of Site 556 was required to fulfill three criteria. It should be at the latitude of the Azores Triple Junction, near Magnetic Anomaly 13, contain sediments as thin as possible, and avoid basement peaks or ridges and fracture zones. No previous site survey had been performed; the closest useful data was a reflection profile record along an east-west track some 15 miles north of the tentative site location.

A westward course was set just south of 39°N, and magnetic and seismic profiler records were monitored (Figs. 2 and 3). Magnetic Anomalies 11 and 12 were situated over sediment thicknesses of about 0.5 s overlying a strongly reflecting acoustic basement (2230Z, 21 September). In places, the reflector became weak and was difficult to distinguish. Continuing west to Anomaly 13 (0015Z, 22 September), the basement topography became rough, with a prominent peak at 0030Z. This correlated with a peak on the profiler record to the north, indicating a prominent basement ridge underlying Anomaly 13.

To avoid this ridge, we decide to return to the area of strong basement reflectors previously noted underlying Anomaly 12. An eastward course was set diverging to the north from the westward track, to determine the linearity of features seen on that track. A pass across the site was made to the south to check for basement peaks, and the beacon dropped at 0351 hr., 22 September on a final northward pass. The correlation of magnetic anomalies along these tracks with previous data tracks in the area precludes the possibility of any significant offset fracture zones close to this site.

On-Site Operations

At Site 556 (MAR-2), we decide that, in addition to the basic program of drilling the basement until bit de-

---

[1] Bougault, H., Cande, S. C., et al., *Init. Repts. DSDP*, 82: Washington (U.S. Govt. Printing Office).

[2] Henri Bougault (Co-Chief Scientist), IFREMER (formerly CNEXO), Centre de Brest, B. P. 337, 29273 Brest Cedex, France; Steven C. Cande (Co-Chief Scientist), Lamont-Doherty Geological Observatory, Columbia University, Palisades, New York; Joyce Brannon, Department of Earth and Planetary Sciences, Washington University, St. Louis, Missouri; David M. Christie, Hawaii Institute of Geophysics, University of Hawaii at Manoa, Honolulu, Hawaii; Murlene Clark, Department of Geology, Florida State University, Tallahassee, Florida; Doris M. Curtis, Curtis and Echols, Geological Consultants, Houston, Texas; Natalie Drake, Department of Geology, University of Massachusetts, Amherst, Massachusetts; Dorothy Echols, Department of Earth and Planetary Sciences, Washington University, St. Louis, Missouri (present address: Curtis and Echols, Geological Consultants, 300 Anderson, Houston, Texas 77401); Ian Ashley Hill, Department of Geology, University of Leicester, Leicester LE1 7RH, United Kingdom; M. Javed Khan, Lamont-Doherty Geological Observatory, Columbia University, Palisades, New York (present address: Department of Geology, Peshawar University, Peshawar, Pakistan); William Mills, Deep Sea Drilling Project, Scripps Institution of Oceanography, La Jolla, California (present address: Ocean Drilling Program, Texas A&M University, College Station, Texas 77843); Rolf Neuser, Institut für Geologie, Ruhr Universität Bochum, 4630 Bochum 1, Federal Republic of Germany; Marion Rideout, Graduate School of Oceanography, University of Rhode Island, Kingston, Rhode Island (present address: Department of Geology, Rice University, P.O. Box 1892, Houston, Texas 77251); and Barry L. Weaver, Department of Geology, University of Leicester, Leicester, LE1 7RH, United Kingdom (present address: School of Geology and Geophysics, University of Oklahoma, Norman, Oklahoma 73019).

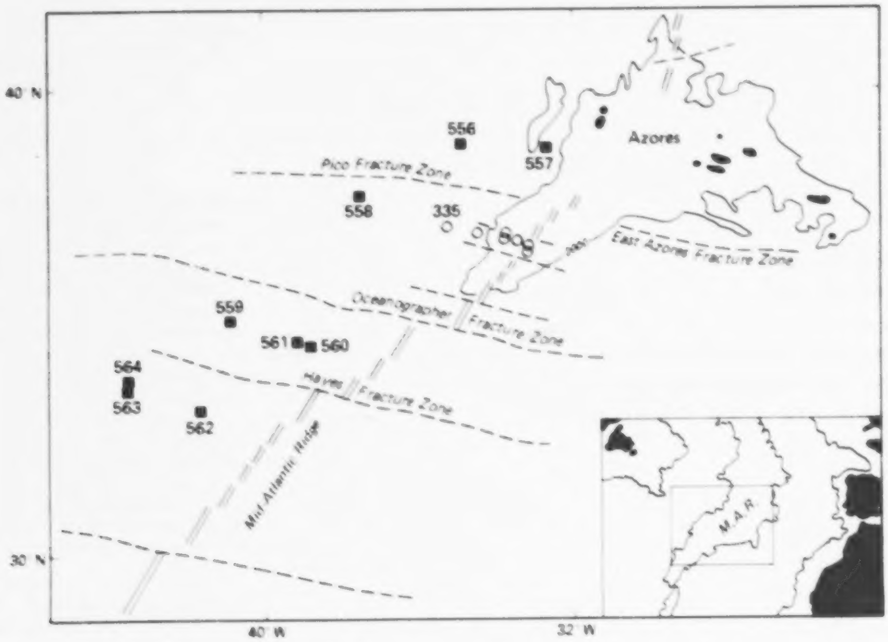

Figure 1. Site location map, Leg 82. M.A.R. = Mid-Atlantic Ridge.

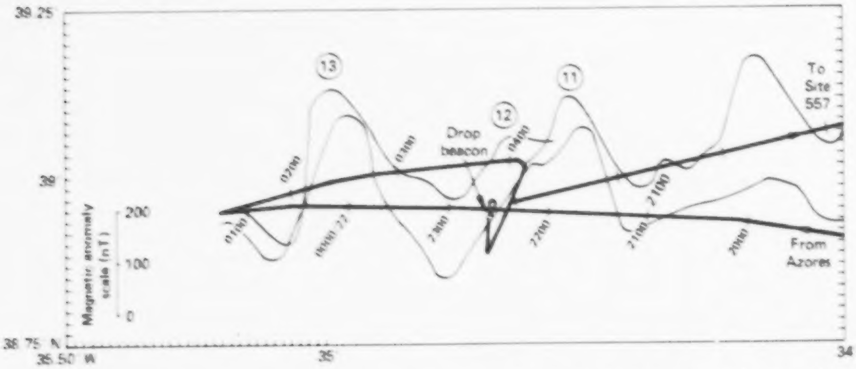

Figure 2. Approach and site survey tracks for Site 556. Heavy line is the ship's track with hour marks in GMT. Faint line is magnetic anomaly line projected perpendicularly from the ship's track. Circled numbers are magnetic anomalies based on work at Lamont-Doherty Geological Observatory. Beacon position is 38°56.38′N, 34°41.12′W.

struction, we would also make heat flow measurements. A logging option was included in the program in the event of basement penetration exceeding 100 m.

The mudline core was recovered at 1805 hr. on 22 September, establishing the correct depth at 3690 m below the drill floor. Sediments were washed down to a depth of 97.5 m below mudline, where the first heat-flow station was taken. Additional temperature measurements were made at 145.0 and 192.5 m below the mudline. Wash cores were recovered at each of these stations. Basement was felt at 461.5 m (below mudline), and a wash core containing the first basaltic pieces was recovered at 1930 hr., 23 September. We then continuously cored basalts, breccias, gabbros, and gabbro breccias down to 639 m below mudline, for a total basement penetration of 177.5 m. The bit failed during the drilling of Core 22. The last core was recovered at 1925 hr. on 27 September. In the upper part of the hole (basalt and basalt breccia), the average recovery was fairly good (65%), but it decreased in the lower part (gabbro, serpentinized gabbro breccia) to approximately 20%. The good basement penetration was probably the result of several factors, including the good condition of the drilling equipment, the good weather, and the consolidation of the basement rocks. Table 1 contains the coring summary for Site 556.

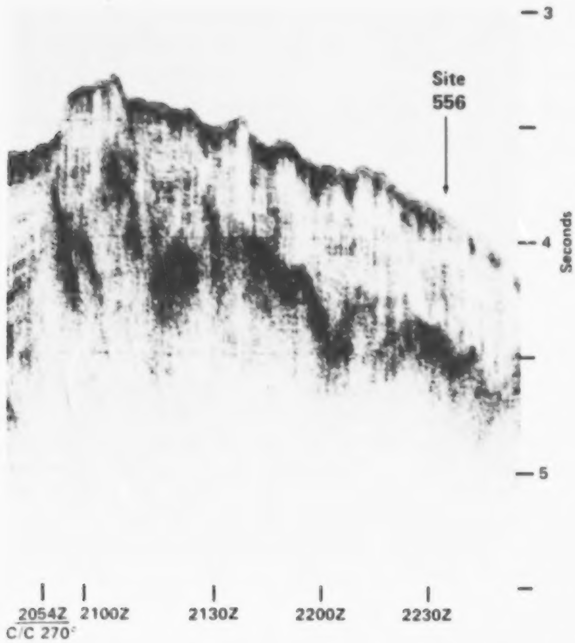

Figure 3. *Glomar Challenger* seismic profile approaching Site 556. See Figure 2 for location of profile. C/C = course change.

A suite of logs was run on 28 September:

Tools	Time at the bottom of the hole (hr.)
The sonic, caliper, and natural gamma ray	0200
Dual laterolog, S.P., and natural gamma ray	0900
Formation density and neutron porosity, caliper and natural gamma ray	1500
Temperature log	2130

The first three logs were run the total depth of the hole; the temperature log could only be lowered to 20 m below the sediment/basement interface because of blockage at that level.

SEDIMENTOLOGY

A single bit hole was drilled at Site 556; 639 m were penetrated, including 461 m of sediment (lower Pleistocene to upper lower Oligocene) above the first major basalt unit. Of these sediments, a mudline punch core, four wash cores, and a single rotary core at the base of the sedimentary section (see coring summary) were taken. These recovered sediments were divided into two major units (see Table 2) based on lithology and depositional style. These are Unit 1, calcareous biogenic ooze and chalk, and Unit 2, limestone basalt breccia. We have also included in this section a description of interpillow sediments and Unit 7, a basalt breccia, and a discussion of its probable tectonic origin.

Table 1. Coring summary, Hole 556.

Core	Date (Sept 1981)	Time (Z)	Depth from drill floor (m)	Depth below seafloor (m)	Length cored (m)	Length recovered (m)	Percent recovered
1	22	1805	3690.0-3696.5	0.0-6.5	6.5	6.09	94
H1	22	2128	3696.5-3787.5	6.5-97.5	0.0	0.00	0
H2	23	0135	3787.5-3835.0	97.5-145.0	0.0	0.00	0
H3	23	0600	3835.0-3882.5	145.0-192.5	0.0	0.00	0
H4	23	1930	3882.5-4151.5	192.5-461.5	0.0	0.00	0
2	24	0148	4151.5-4161.0	461.5-471.0	9.5	6.24	66
3	24	0810	4161.0-4170.0	471.0-480.0	9.0	2.91	32
4	24	1250	4170.0-4179.0	480.0-489.0	9.0	8.40	93
5	24	2022	4179.0-4188.0	489.0-498.0	9.0	7.06	78
6	25	0203	4188.0-4197.0	498.0-507.0	9.0	7.23	80
7	25	0638	4197.0-4206.0	507.0-516.0	9.0	4.22	47
8	25	1134	4206.0-4215.0	516.0-525.0	9.0	5.17	57
9	25	1632	4215.0-4224.0	525.0-534.0	9.0	5.83	65
10	25	2117	4224.0-4233.0	534.0-543.0	9.0	5.80	64
11	26	0051	4233.0-4242.0	543.0-552.0	9.0	2.65	29
12	26	0507	4242.0-4251.0	552.0-561.0	9.0	4.45	49
13	26	0900	4251.0-4255.5	561.0-565.5	4.5	0.77	17
14	26	1227	4255.5-4264.5	565.5-574.5	9.0	3.01	33
15	26	1731	4264.5-4273.5	574.5-583.5	9.0	4.03	45
16	26	2255	4273.5-4282.5	583.5-592.5	9.0	2.40	27
17	27	0217	4282.5-4291.5	592.5-601.5	9.0	2.06	23
18	27	0514	4291.5-4300.5	601.5-610.5	9.0	1.30	14
19	27	0713	4300.5-4309.5	610.5-619.5	9.0	1.28	14
20	27	1056	4309.5-4318.5	619.5-628.5	9.0	1.74	19
21	27	1450	4318.5-4327.5	628.5-637.5	9.0	1.98	22
22	27	1925	4327.5-4329.0	637.5-639.0	1.5	0.59	39
					184.0	85.21	46

Unit 1

One-half meter (556-H4-4, 90–143 cm) of pinkish white (5Y 8/2) nannofossil chalk (upper Oligocene to lower Miocene) overlies Unit 2. Although the chalk of this unit is similar to the matrix and limestone clasts of Unit 2, it contains no clasts of basalt or of reworked limestone and has no apparent transport structures. The sediment components are nannofossils (93–95%), foraminifers (1–3%) and traces of quartz, feldspar, heavy minerals, volcanic glass, palagonite, and sponge spicules. No distinct bioturbation or bedding is observed.

In the remaining upper portion of Core 556-H4, the lithology is a white (2.5YN8-5Y 8/1), firm nannofossil ooze with interbedded Miocene chalk. The color change with the underlying sediment is sharp. The sediment components are nannofossils (95%) and unspecified carbonate (5%). No distinct bioturbation is observed, but rare, faint black streaks were observed. Bedding is indistinct.

Starting at the bottom of Section 556-1 up to 556-1-4, 105 cm the lithology is a light yellowish brown (10YR 6/4), firm foraminiferal-nannofossil to nannofossil ooze dated early Pleistocene and older(?). The sediment components include nannofossils (85–90%), foraminifers (5–15%), and traces of clay, volcanic glass, and palagonite. No distinct bedding, bioturbation, or black streaks were observed.

In the remaining upper portion of Core 556-1, the lithology is a light gray (2.5RN7), soft to firm nannofossil to foraminiferal-nannofossil ooze (lower Pleistocene). The contact with the underlying sediment is sharp. The sediment components include nannofossils (82–95%), foraminifers (3–14%), and traces of clay minerals, feldspar, volcanic glass, palagonite, pyrite, diatoms, radiolarians, sponge spicules, and silicoflagellates. Interbedded are layers of greenish gray (5GY 6/1) firm siliceous

Table 2. Sediment lithology summary, Hole 556.

Interval	Unit designation	Depth and thickness (m)	Main colors	Main lithology	Main components	Structure	Age
556-1-1, 0 cm washed to 556-H4-2, 143 cm	1	0–461.0 (461.0)	White, light gray, light yellowish brown, and pinkish white	Nannofossil ooze, foraminiferal-nannofossil ooze, nannofossil chalk	Nannofossil, foraminifers, and siliceous fossils	Homogeneous with slight mottling	early Pleistocene to middle Miocene
556-H4-2, 143 cm to 556-3-1, 5 cm	2	461.0–471.1 (10 m)	Pinkish white to gray matrix with pinkish gray to gray clasts	Limestone basalt breccia	Volcaniclasts, limestone clasts, limestone matrix	Crudely graded	late Oligocene

nannofossil ooze. There appears to be a direct relationship between the color changes and the higher percentage of siliceous microfossils in these greenish gray layers. The sediment components of these layers are: nannofossils (80%), foraminifers (3–5%), diatoms (10%), radiolarians (3–5%), sponge spicules (2%), and traces of silicoflagellates, feldspar, volcanic glass, palagonite, and pyrite. No distinct bedding or bioturbation was present, although rare, faint black streaks (pyrite?) and mottling were observed.

Unit 2

This unit consists of approximately 10 m (Core 556-H4-2, 143–150 cm; all of Core 556-2 and 556-3-1, 0–5 cm) of a limestone basalt breccia (uppermost lower Oligocene) (see Fig. 4). The basalt clasts (moderately plagioclase phyric) range in size from boulders to silt-size particles, with sand and finer particles considered as part of the matrix. The basalt clasts are poorly sorted, although three crudely fining-upward sequences can be recognized: (1) from Core 556-H4-2, 143 cm to 556-2-2, 150 cm; (2) 556-2-3, 0 cm to 556-2-5, 30 cm, and (3) 556-2-5, 32 cm to 556-3-1, 5 cm. The basalt clasts are subrounded to angular, gray (7.5YR N5) to pinkish gray (7.5YR N6/2) in color, fresh and altered respectively. Also included with the basalts are angular clasts of grayish green (5G 4/2) to dark brown (7.5YR 3/2) volcanic glass.

The limestone clasts are subrounded, 5 mm to 5+ cm in diameter and are occasionally attached to basalt to form a composite clast. The limestone clasts are similar in color to the calcareous matrix, pinkish white (5YR 8/2) to light gray (10YR 7/1), but are easily distinguished from the matrix in both thin section and hand specimen. In thin section, the limestone clasts are microcrystalline (biomicrite), similar to the chalks of Subunit 1d, but much more indurated.

The matrix is also a microcrystalline (biomicrite) limestone that contains minor amounts of volcanic material similar to the basalt clasts. In hand specimen, the matrix often appears to have flowed around clasts and to infill cracks in the basalt clasts assumed to have formed during deposition. The matrix also appears as light-colored halos around some of the basalt clasts. Thin-section examination showed that this halo effect is the result of the finer crystal size of the microcrystalline matrix adjacent to the basalt clasts. Also in thin section we observed discontinuous recrystallization, as irregular patches of both matrix and limestone clasts, to sparry calcite. Often these veins are rimmed by dendritic manganese oxide (see Fig. 5). In parts of this unit, both matrix and limestone clasts were completely recrystallized to sparry calcite by fluids subsequent to deposition, which left occasional solution vugs lines with yellow-stained, "dog tooth" calcite.

Intrapillow Sediments

In the basalt of Core 556-5, pinkish white (5YR 8/2) micritic limestone occurs between flow margins. In Core 556-4, pale yellow (5Y 7/3) chalk with small rounded (1 to 5 mm) intraclasts have infilled cracks in basalts. These infilling sediments show well-preserved geopetal structures (see Fig. 6).

Unit 7

This unit consists of 28.8 m (556-9-3, 30 cm to 556-12-4, 63 cm) of predominantly basalt breccia. The basalts are mostly very angular to occasionally subrounded and range in size from boulder to clay, with the sand-size and finer fraction considered as matrix. From 556-9-3 cm to 556-12-1, 135 cm, the clasts are all uniformly medium gray (5Y 5/1), aphyric to moderately plagioclase phyric basalt (see Fig. 7). The matrix, except for minor amounts of microcrystalline calcite, is predominantly basalt-derived, clay-size to sand-size particles clearly derived from the adjacent basalt clasts. X-ray diffraction (XRD) analysis shows that no clay minerals are present in the matrix in this section of the breccia, and thin-section examination shows no obvious alteration of clasts or matrix.

Beginning in 556-12-1, 135 cm, the compositions of both clasts and matrix change to include more basaltic glass rims, light brownish gray (10YR 6/1) to reddish brown (2.5YR 4/4) altered basalt and rare, pale red (10R 6/3) chalk clasts (see Fig. 8). The matrix also reflects this change in the clasts composition by mimicking, as a finer-grain equivalent, the neighboring clasts.

The boundary between Units 7 and 8 occurs in the bottom of Section 556-12-4 and is recognized as a transitional change from basaltic clasts to gabbroic clasts.

Discussion

The basalt breccias observed at Site 556 are quite dissimilar in character and origin. The first one, cored im-

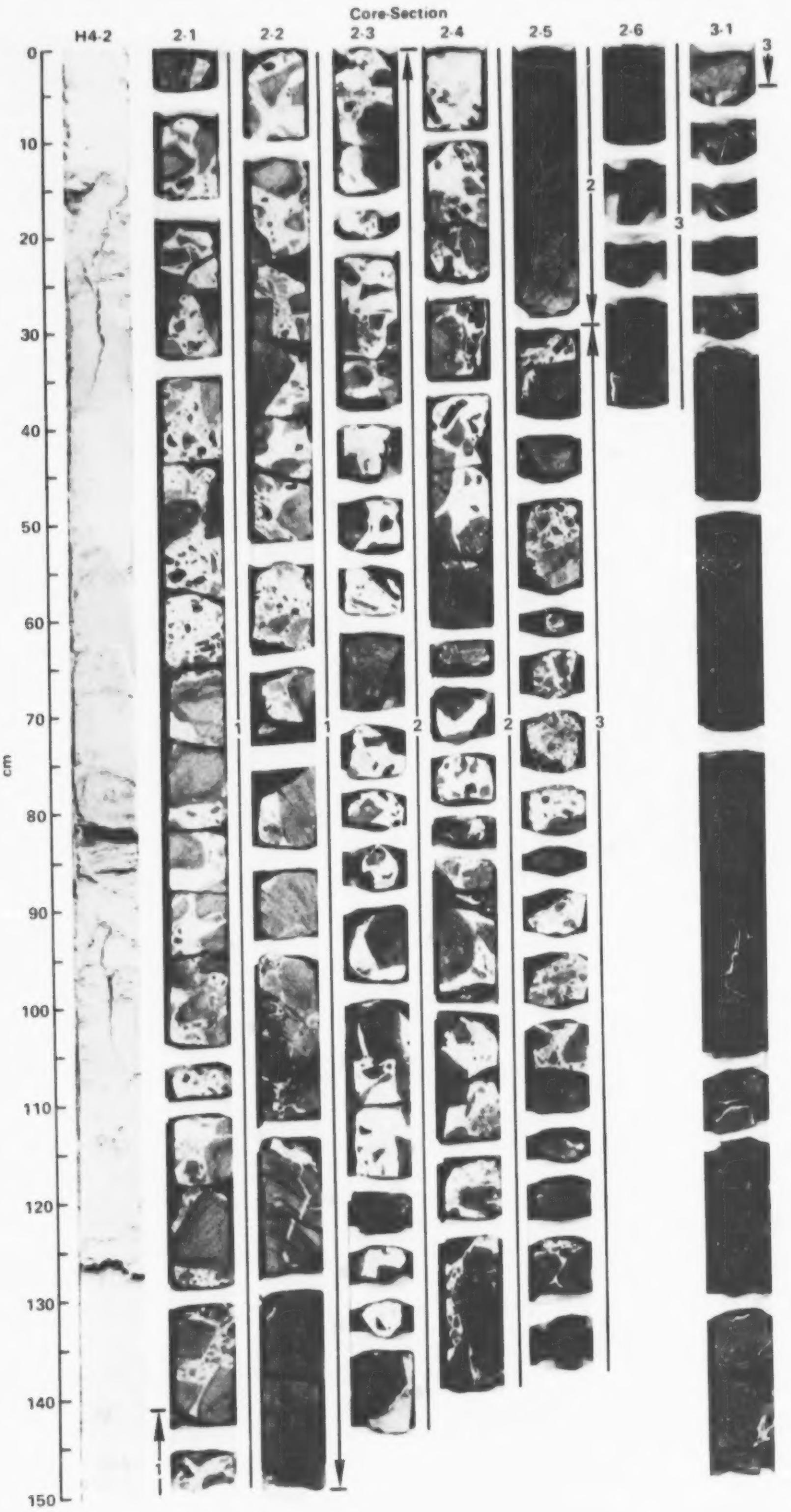
Core-Section
H4-2
2-1
2-2
2-3
2-4
2-5
2-6
3-1
0
10
20
30
40
50
60
70
80
90
100
110
120
130
140
150
cm
1
2
3

Figure 4. Limestone basalt breccia of Unit 2 (Core 556-2), showing positions of the three crudely fining upward sequences.

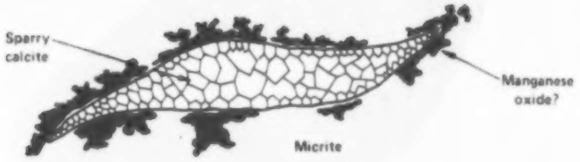

Figure 5. Sketch of sparite patches in limestone, rimmed by dendritic manganese oxide(?).

mediately below the nannofossil oozes and chalks of Unit 1, is a limestone basalt breccia, designated as Unit 2. The second breccia, cored between a basalt flow and a gabbroic or polymict breccia, is a basalt breccia, designated as Unit 7. Table 3 is a summary of the contrasting characteristics of each breccia.

On the basis of the comparison listed in Table 3, we believe that Unit 7 (basalt breccia) did not originate as a slump or debris flow as in the case of Unit 2 (limestone basalt breccia), nor do we believe that Unit 7 is an autoclastic breccia as described from DSDP Sites 407, 408, and 410 (Luyendyk, Cann, et al., 1979) and discussed by Varet and Demange (1978).

With only preliminary data it is impossible to give a specific origin for Unit 7, but we do believe that it is related to local tectonics and to the emplacement of the serpentinized gabbros of Units 8 and 10.

BIOSTRATIGRAPHY

One rotary core and four wash cores were obtained at Site 556. Zonation of wash core catchers was attempted to permit tentative correlation between age and depth at several points. Sediments ranged in age from early Pleistocene (±1.6 to 1.8 Ma) to late early Oligocene (30 to 34 Ma). In both fossil groups, preservation is moderate to good, and assemblages are characteristic of temperate to warm-temperate regions. Figure 7 in the Explanatory Notes chapter (this volume), shows the zonations for nannofossils and foraminifers as well as the magnetostratigraphy correlation used for all site chapters, the numerical time scale, and the European stages.

Nannofossils

Core 556-1 is early Pleistocene in age based on the presence of *Calcidiscus macintyrei* and *Helicopontosphaera sellii* above the last appearance datum (LAD) of *Discoaster brouweri*. Core 556-1 is placed in the *C. macintyrei* Zone (bottom of NN19) (Gartner, 1977). The presence of *Gephyrocapsa caribbeanica* in the top of Core 556-1 indicates that a younger age for the upper sediment is possible if reworking of *C. macintyrei* has occurred.

The Pliocene/Pleistocene boundary is located between 556-1,CC and 556-H1-1, 70 cm. An abundance of *D. brouweri* and *C. macintyrei* is contained in 556-H1-1, 70 cm; it is late Pliocene in age, NN18 or CN12D (Okada and Bukry, 1980). The core catcher of 556-H1 contains *Reticulofenestra pseudoumbilica, Discoaster tamalis, D. brouweri, D. asymmetricus*, and *C. macintyrei*. Because *R. pseudoumbilica* is rare, 556-H1,CC is placed within either the *D. asymmetricus* Subzone 11b (Okada and Bukry, 1980) (upper NN15) or the *D. tamalis* Subzone 12a (Okada and Bukry, 1980) (lower NN16).

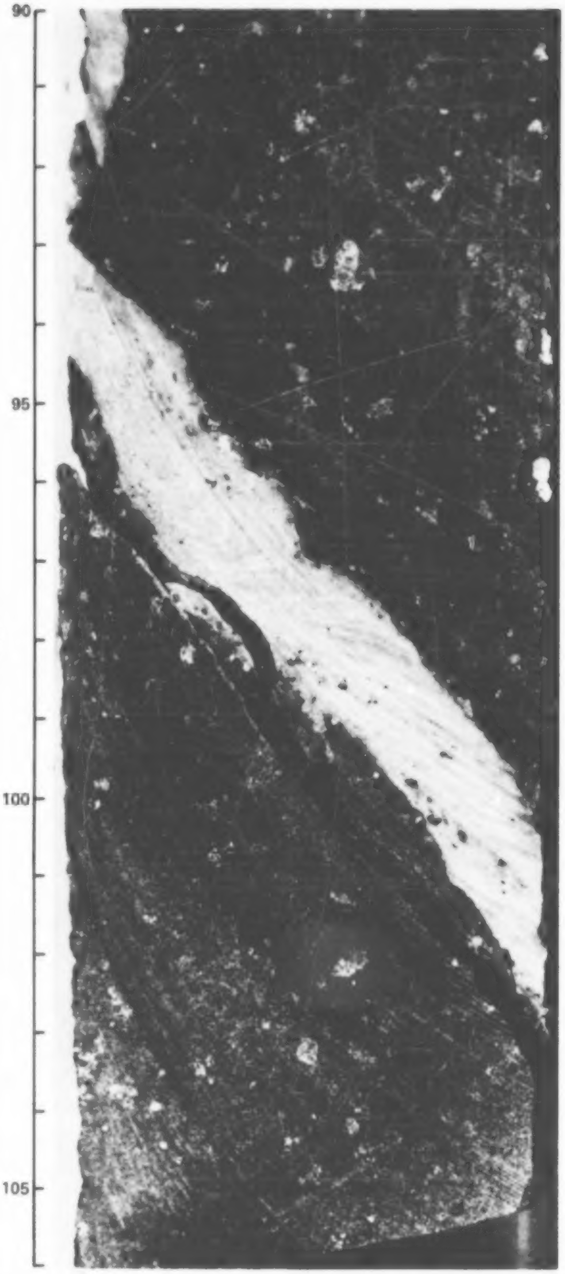

Figure 6. 556-4-1, 90–106 cm; nannofossil chalk infilling cracks in basalt flow. Note the geopetal structures.

The core catcher of Core 556-H2 is assigned to the *Discoaster neohamatus* Zone CN8–NN10, upper Miocene, because of an abundance of *D. neohamatus* in an assemblage composed of *Triquetrorhabdulus rugosus, Discoaster variabilis, D. pentaradiatus*, and possibly a

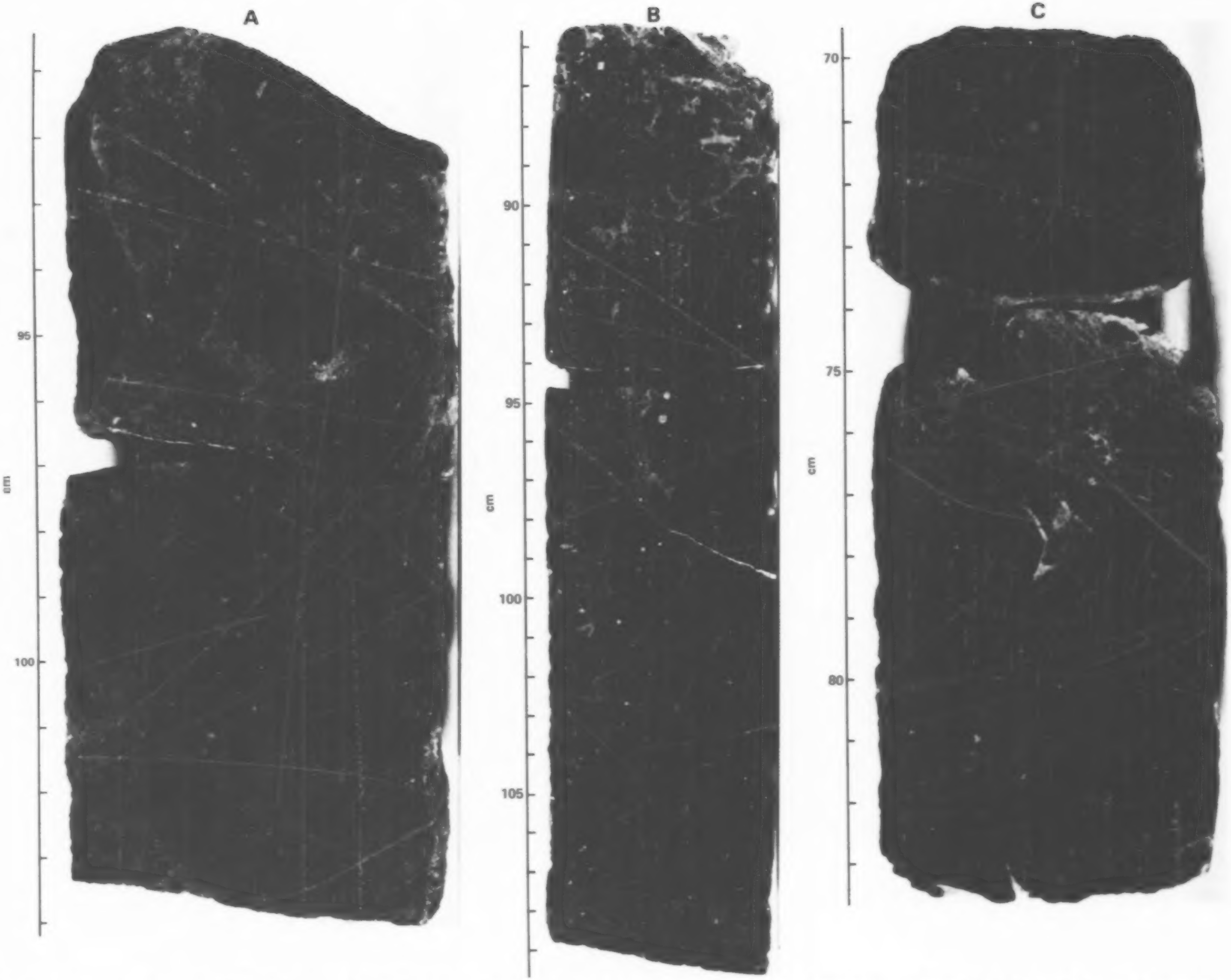
A
B
C
95
100
cm
90
95
100
105
cm
70
75
80
cm

Figure 7. Three examples of the upper position of the basalt breccia (Unit 7). A, 556-9-3, 91–103 cm; B, 556-10-2, 86–110 cm; C, 556-10-4, 70–83 cm. In Figure 7C, note the replacement of original matrix by calcite (lighter-colored area between 74 and 78 cm) and the formation of vugs by fluids subsequent to the breccia's development.

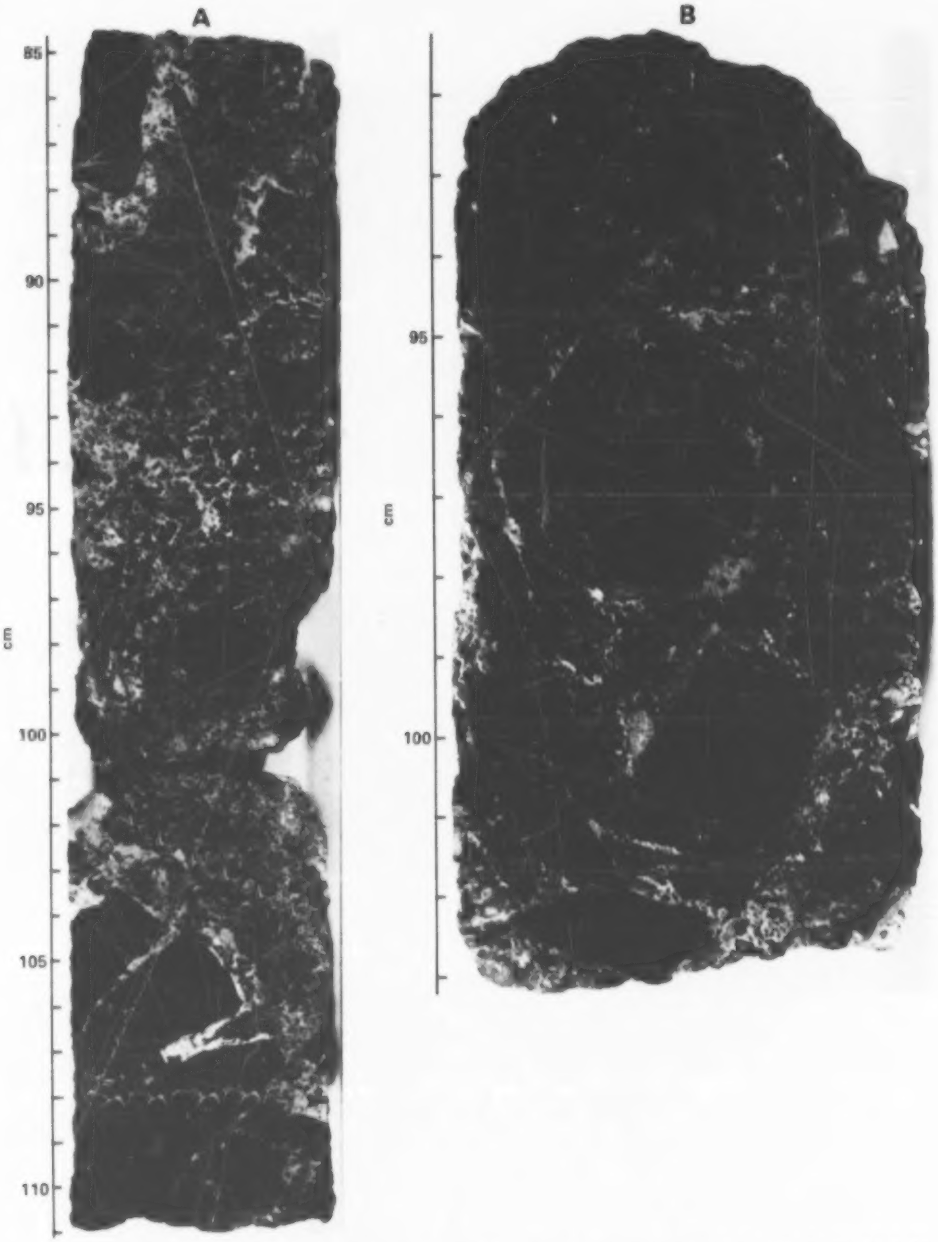

Figure 8. Two examples of the lower position of the basalt breccia (Unit 7). A, 556-12-2, 85-111; B, 556-12-2, 91-103 cm. Compare to Figure 7 and notice the change in both clasts and matrix.

few *D. berggrenii*. The tentative presence of *D. berggrenii* may extend the zonation into CN9a (lower NN11)

The rare occurrence *hamatus* in 556-H3,CC indicates the upper middle Miocene or lower upper Miocene *D. hamatus* Zone CN7–NN9.

Two samples taken within 556-H4, 556-H4-2, 72 cm and 556-H4-2, 92 cm contain *D. exilis*. The deeper sample also contains *Sphenolithus heteromorphus*. The upper sample falls into the *D. exilis* Zone CN5 (NN6–7) and the lower one is within the *S. heteromorphus* Zone CN4 (NN5). Both samples are middle Miocene.

The base of the sediment column, 556-H4,CC, contains *S. ciperoensis*, *S. distentus*, and *S. predistentus*. The presence of these species indicates an age of 30–24 Ma (late Oligocene) (NP23–24) (CP18/19). Core 556-3, which is composed primarily of basalt, contains a pocket of nannofossil chalk at the top of the section that can be assigned to the *S. predistentus* Zone CP17 (N23), dat-

Table 3. Comparison between basalt breccias of Unit 2 and Unit 7 of Site 556.

Unit 2: limestone basalt breccia	Unit 7: basalt breccia
Clasts	
Predominantly basalt, with minor limestone and volcanic glass; glass appears to be randomly distributed throughout the unit.	Almost entirely basalt, with rare limestone; glass in lower part (556-12, 4 cm).
Clast subrounded to angular.	Clasts mostly angular to subangular; some subrounded.
Altered basalt common, but mixture of altered and fresh basalt occurs throughout the unit; both fresh and altered glass present.	Altered basalt is common in the lower part of the unit, associated with altered glass rinds, pillows, and sedimentary clasts; fresh basalt predominates above 556-12-4.
Clasts range from boulders to silt and clay size. Particles smaller than sand size are considered part of the matrix. The boulders to sand-size clasts occur in crudely graded sequences with boulders at the base of each fining-upward sequence. Part of the nannofossil chalk overlying the breccia (Subunit 1d) could be the youngest fining-upward sequence.	Clasts range from boulders to clay size. Silt-size and clay-size fragments make up the matrix. The boulders to sand-size clasts show no apparent grading; size of clasts and clast: matrix ratio appears to increase downward from Section 556-9-3 through Core 556-11.
Matrix	
Matrix predominantly microcrystalline limestone of biogenic origin; silt-size and clay-size particles of basalt-derived material are a very minor constituent.	Matrix predominantly basalt-derived clay-size lithic and mineral fragments; no biogenic limestone except in rare clasts, as in 556-12-4.
Calcite also occurs in vugs and as veins and fracture fillings; microcrystalline calcite commonly forms light-colored rims around the basalt clasts.	Calcite is a very minor constituent of the matrix, probably secondary; calcite also occurs in veins and veinlets.
Matrix has flow lines.	Matrix does not have flow lines.
XRD analysis shows small amount of clay.	XRD analysis shows no clay.

Note: XRD = X-ray diffraction.

ed 30–34 Ma (latest early Oligocene). This date matches the proposed basement age for Anomaly 12.

Foraminifers

Core 556-1 recovered a Pleistocene nannofossil–foraminiferal ooze. The core catcher sediments examined for foraminifers contain an assemblage of lower Pleistocene planktonic and benthic species, which characterize Zone N22. This correlates, in the present study, with nannofossil Zones CN13–NN19.

The planktonic fauna is made up of abundant *Globorotalia truncatulinoides*, *G. menardii* s.l. complex, *G. inflata*, *G. scitula; Globigerina bulloides*, *G. aequilateralis*, *G. falconensis*, *G. calida* and *G. rubescens; Globigerinoides conglobatus*, *G. ruber*, and *G. sacculifer; Orbulina universa; Pulleniatina obliquiloculata;* and *Sphaeroidinella dehiscens*. The assemblage is dominated by species characteristic of temperate to warm-temperate regions.

The benthics are not common but are represented by a fairly diverse group of deep-water forms. Ostracodes, diatoms, silicoflagellates, and radiolarians are also present.

The core catcher of Core 556-H1 contains a lower Pliocene planktonic foraminiferal fauna and is assigned to the upper part of foraminiferal Zone N19 *(Globoratalia margaritae)* within the PL2, *G. margaritae–G. prehirsuta* in the subdivision of the Pliocene (Fig. 9). This assignment is based on abundant *G. margaritae* and the absence of *Globigerina nepenthes*, which was extinct by 3.7 Ma. Well-preserved ostracodes and a few benthic foraminifers are present.

Preservation in general is good but with some indication of crystalline overgrowth on the globorotalid forms. The fauna is considered characteristic of temperate to warm-temperate regions.

The core catcher of Core 556-H2 is a white chalky nannofossil marl that contains Miocene planktonic and benthic foraminifers. In this sample there is a high benthic-to-planktonic ratio, and the thin-walled planktonic forms show dissolution. *G. nepenthes, S. subdehiscens*, and *S. seminulina* and the accompanying fauna indicate an upper Miocene assignment.

The core catcher of Core 556-H3 is a nannofossil ooze with common to abundant planktonic and few benthic foraminifers. The sediment is lower upper Miocene, foraminiferal Zone N14 *(G. nepenthes–Globorotalia siakensis)*. This agrees well with the nannofossil determination (CN7–NN9).

On the basis of the planktonic foraminifers, the core catcher of Core 556-H4 is upper Oligocene and falls in the upper portion of foraminiferal Zone P21 *(Globoratalia opima opima)*. The planktonic foraminifers are common, and preservation is moderate to good.

IGNEOUS PETROLOGY AND GEOCHEMISTRY

Basalt occurs as clasts in breccias, as pillowed flows, and as massive flows throughout the basement section. Gabbro, in both fresh and serpentinized forms, occurs as clasts in breccia. We have recognized ten lithologic units (Table 4) and five chemical groups. Lithologic units are indicated by Arabic numbers (1, 2, 3 . . .) and petrographic or chemical groups by Roman numerals (I, II, III . . .) throughout this volume.

Lithologic Units

Unit 2. Basalt-Carbonate Breccia (462–469.5 m)

The breccia of Unit 2 is composed of angular basalt clasts set in a matrix of biogenic limestone (as described in the Sedimentary and Biostratigraphy section). Clasts range downwards in size from a maximum of about 10

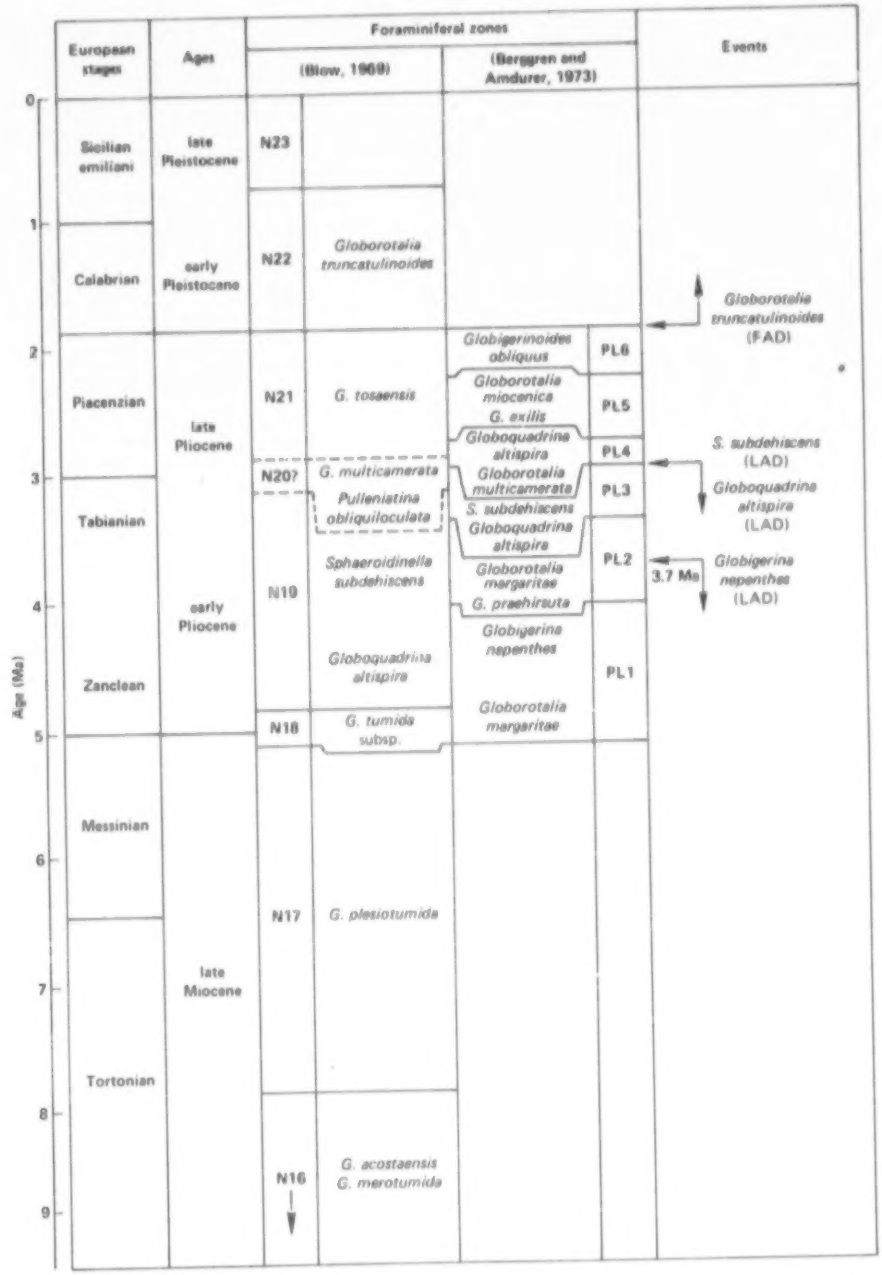

Figure 9. Foraminiferal biostratigraphic zonation, Site 556. FAD = first appearance datum; LAD = last appearance datum.

cm to a few millimeters or less. Glass rims and isolated glass fragments are occasionally present. A majority of clasts have light brown weathered rims, up to 2 cm thick, and relatively fresh cores. Within the breccia, there is a downward transition from aphyric basalt (Petrographic Group I) to moderately plagioclase phyric basalt (Petrographic Group II); the latter is chemically identical with that of the underlying unit.

Unit 3. Upper Pillow Basalts (469.5-505 m)

Basalts of Unit 3 are plagioclase phyric, ranging from 2-5% phenocrysts with occasional patches of higher or lower concentration. Within this section of the core, 30 recognized pillows or flow lobes are separated by narrow bands of glass. This glass, generally only 2 to 3 cm thick, is moderately palagonitized and may be veined

Table 4. Site 556 lithologic units and petrographic and chemical groups.

Sub-bottom depth (m)	Lithologic unit	Lithology	Petrographic and chemical groups
461.0	1	Nannofossil ooze	
465.0	2	Basalt carbonate breccia	I
469.5			
	3	Upper pillow basalts	II
505.0			
	4	Massive aphyric basalts	
512.0			
	5	Small pillow basalts and pillow breccia	III
526.5			
	6	Massive aphyric basalt	
528.5			
543.0	7	Basalt breccia	
546.0			IV
			III
561.0			
	8	Gabbro breccia (serpentinized)	V
586.0			
	9	Aphyric basalt	IV
587.0			
	10	Talc serpentinized gabbro breccia	V
693.0			

Note: Sub-bottom depth column not to scale.

with calcite, or have glassy rinds separated by calcite veins. Pillow thicknesses range from 30 to 170 cm and average 73.5 cm; a basalt(?) flow 300 cm thick is also present. No interpillow sedimentary material was recovered; calcite cement filling in fractures, however, is common in the upper third of the unit and rare in the lower part of the unit.

The unit is chemically and petrographically homogeneous. The plagioclase phyric clasts of the overlying breccia and Unit 3 compose Petrographic Group II.

Unit 4. Massive Aphyric Basalt (505–512 m)

This unit appears to be composed of two massive flows, separated at 507.2 m by a narrow glass band with associated calcite veining and palagonitization. Calcite-filled fractures are also common near the upper and lower boundaries of the unit. The basalt is fine-grained and light gray in color, with approximately 1% plagioclase phenocrysts in the upper 1.5 m and scattered equant plagioclase phenocrysts in the remainder of the unit. The basalts of Unit 4 belong to the Petrographic Group III.

Unit 5. Pillow Basalts and Pillow Breccia (512–526.5 m)

Unit 5 consists of approximately 4 m of small basalt pillows grading down the core into pillow breccia. Pillow diameters appear to be a few tens of centimeters. Glass margins are strongly palagonitized, although fresh glass is still present in very small quantities. Interpillow spaces are filled by angular glass fragments and calcite cement. Pillow centers are aphyric basalt identical to that of the overlying massive Unit 4. Well-formed pillows give way downwards to pillow breccia, composed of angular basalt and glass fragments in a matrix of smaller glass fragments and calcite cement. The basalts of this unit are classified as Petrographic Group III.

Unit 6. Massive Aphyric Basalt (526.5–528.5 m)

This unit is a single flow of strongly fractured and weathered aphyric fine-grained basalt, similar to that of Unit 4 and also classified as Petrographic Group III.

Unit 7. Basalt Breccia (528.5–561 m)

This breccia is texturally very similar to that of Unit 2, yet significantly different in its matrix composition. Matrix material is gray green in color and appears to be composed of a mixture of carbonate and finely comminuted basaltic material (per description of matrix in the Sedimentology and Biostratigraphy sections). Basalt clasts are predominantly aphyric with scattered plagioclase phenocrysts; occasionally, phenocrysts range up to 5% of the basalt content. The olivene occurs as microphenocrysts (1 mm in diameter) and composes up to 5% of the basalt content. Petrographic and chemical studies demonstrate that clasts of both Petrographic Groups III and IV occur throughout most of this unit.

Unit 8. Serpentinized Gabbro Breccia (561–586 m)

This unit consists of a largely serpentinized gabbro breccia, the matrix of which appears to be composed of finely comminuted serpentinized material. Clast size varies from a few millimeters to about half a meter in diameter. Serpentinization is virtually complete in the upper half of the unit, but some fresh gabbro clasts are present further down the core.

Serpentinized gabbro clasts are composed of up to 15% brown, prismatic, altered orthopyroxene phenocrysts up to 10 mm long. These phenocrysts are set in a dark green black foliated matrix, composed almost entirely of serpentine. The dominant serpentine mineral is antigorite as determined by XRD.

Fresh gabbro clasts are coarse grained (3–10 mm in diameter), equigranular, dark gray to black aggregates of (in order of decreasing abundance) plagioclase, orthopyroxene, clinopyroxene, and minor olivine. The clasts show varied stages of alteration, ranging from completely fresh to completely altered.

Also present as smaller (1–2 cm in diameter) clasts within this unit are pieces of anorthosite (plagioclase-clinopyroxene–composed rock), some of which appear to have formed as small veins within the gabbro. Occasionally, prismatic clinopyroxene crystals up to 1 cm long are also present in the breccia. This unit (along with Unit 10) is classified as Petrographic Group V.

Unit 9. Aphyric Basalt (586–587 m)

This light gray, aphyric basalt occupies slightly less than 1 m of core separating two units of gabbro breccia. It is not clear whether this is an unusually large clast or a flow of a narrow intrusive body. However, the presence of small, petrographically and/or chemically identical clasts (Petrographic Group IV) within Unit 7 may suggest that this is simply a large clast.

Unit 10. Talc-Serpentinized Gabbro Breccia (587–639 m)

This lowermost unit of Hole 556 differs from Unit 8 only by the presence of blue green talc as an alteration mineral in addition to serpentine. No fresh gabbro was recovered in this interval. Petrographic Group V comprises the gabbroic breccia units (8 and 10).

Petrographic Groups

The samples recovered at Site 556 have been classified into five groups, based upon macroscopic and microscopic descriptions and chemical analyses (see Fig. 10 and Table 5).

Group I

This group coincides with the upper part of Lithologic Unit 2, consisting of basalt carbonate breccia. The aphyric basaltic clasts are reasonably fresh, although weathering occurs around the rims and along fractures. Rare equant plagioclase phenocrysts (3-5 mm) are present in a dominantly intergranular groundmass. Group I basalt clasts have a distinctive groundmass: lath-shaped to acicular-shaped plagioclase that comprises 30-35% of the groundmass ranges in size from 0.6 to 0.1 mm in length; clinopyroxene (about 40%) occurs mostly as fine-grained (0.1 mm) aggregates interstitial to plagioclase with scattered larger (0.5 mm) granules; altered granular olivine (5%, 0.1-0.2 mm), granular magnetite (3%), and up to 15% dark brown mesostasis are distributed throughout the groundmass.

The two samples analyzed (556-2-1, 78-82 cm; 556-2-2, 145-150 cm) are very similar in both major and trace element composition. Noteworthy are the relatively high CaO (~13%) and Al_2O_3 (~16%) concentrations.

Group II

The lower part of Lithologic Unit 2 and all of Unit 3 compose Group II. The recovered samples are fresh to moderately altered. These basalts are moderately to sparsely plagioclase phyric, containing 2-5% equant to prismatic plagioclase phenocrysts, some of which form glomerocrysts. The plagioclase is unzoned or normally zoned. Optically determined compositions cluster around AN_{70}, occasionally ranging to An_{60} at the rims. Some prismatic olivine phenocrysts (2-3 mm), altered to a variable extent to green or brown clay, are also present[3].

The groundmass texture varies from hyalophitic to intergranular and slightly subophitic. This variation corresponds to position within the pillow relative to the cooling margin. In all cases skeletal, swallowtail to narrow lath-shaped plagioclase make up 35 to 40% of the groundmass. Fine granular magnetite is relatively abundant (5%). Interstitial clinopyroxene varies from extremely fine intergranular branches of sheaf aggregates in hyalophitic and intersertal textures to coarser (0.2 mm) granules forming aggregates up to 1 mm in coarser-grained textures. Olivine (about 5%) occurs both as diamond-shaped microphenocrysts (up to 1 mm) and scattered small granules altered to clay. Clay contents, mainly after olivine and mesostasis, vary from 5-10% in the freshest samples to 20-30% in moderately weathered samples.

Sixteen samples were analyzed for trace elements and seven for major elements. The chemical composition of this group is fairly homogeneous. This composition is typical of oceanic tholeiite with TiO_2 concentrations (1.46%) falling in the upper range of values for oceanic tholeiites.

Group III

Lithologic Units 4, 5, 6, and the majority of Unit 7 form Group III. The extent of weathering is quite variable.

Although lithologically, petrographically, and chemically heterogeneous as a basalt type, the petrology and major and trace element characteristics of samples from this group are distinctive from the other identified groups. Most of the basalts composing this group are aphyric, but concentrations of up to 5% of plagioclase phenocrysts may occur, and scattered phenocrysts are common. Within the group, intersertal textures are common with 15-20% altered mesostasis in most samples. Some varieties are more granular and richer in glass. Plagioclase laths frequently radiate from a single nucleus with interstitial granular clinopyroxene. Interstitial plagioclase and relatively large prismatic pyroxene grains are also common. The amount of plagioclase present (about 30%) is always subordinate to clinopyroxene (about 40%). Olivine is only present as microphenocrysts (about 5%) and is completely altered to green brown clays.

The chemical heterogeneity of Group II is reflected by the greater variation of TiO_2 (0.82-1.06%), Al_2O_3 (14.9-17.6%), and CaO (12.5-14.5%) abundances. Al_2O_3 and CaO have been plotted versus TiO_2 in Figure 11; it is clear from this figure that it is difficult to find more than two samples that could define separate subgroups. A notable feature for some samples is the high CaO content (~14%), as noted in Group I, but not necessarily related to high Al_2O_3 content. This high CaO content cannot be accounted for by calcite contamination alone. The average values given in Table 6 are uninformative because of the heterogeneity in this group.

Group IV

This group is represented by two samples, one of which occurs in Unit 7 and the other in Unit 9. They are aphyric basalts characterized by a greater abundance of plagioclase in the groundmass than in the other groups, and by an almost complete lack of olivine. Plagioclase laths frequently radiate from a single nucleus and are surrounded by granular clinopyroxene forming rounded patches of subophitic texture. The patches are separated by irregularly shaped areas of mesostasis, largely altered to green brown clay, and contain up to 5% granular magnetite. The SiO_2 content (~52%) is the highest encountered among the four basaltic groups.

Group V

Gabbros of Site 556 are fairly uniform in grain size (3-5 mm) but variable in mineralogy and in degree of alteration. Primary minerals are plagioclase (An_{60}), clinopyroxene, orthopyroxene, and minor amphibole and magnetite. Relative proportions of orthopyroxene and clinopyroxene vary widely from orthopyroxene less than 5% (clinopyroxene 35%) to orthopyroxene 20% (clinopyroxene 15%). Clinopyroxene occurs in large (3–7 mm) prismatic grains showing extensive twinning, evolution, and alteration. Orthopyroxene is generally less altered and occurs as slightly smaller prismatic or subhedral grains. Occasional unaltered, pleochroic (dark to light brown) amphibole grains may also be primary. Magnetite(?) is present in trace amounts only. Olivine has not been identified.

---

[3] Preliminary shore-based microprobe studies suggest phenocryst core compositions of AN_{87} and rim compositions of An_{70}.

Both pyroxenes are altered to masses of green or colorless fibrous amphibole and to chlorite. Plagioclase is altered to prehnite. The degree of alteration varies from almost none to as much as 30–40%.

Serpentinized gabbros generally display very little relict structure. Isolated prismatic grains of pyroxene and rare plagioclase are surrounded by weakly foliated serpentine (antigorite by XRD).

Small (1–2 cm diameter) fragments of anorthosite (80% plagioclase, 20% clinopyroxene), are strongly altered to prehnite; talc(?), amphibole, and chlorite also occur within the breccia. They appear to have formed as small veins within the gabbro.

Geochemistry

At Site 556, 33 samples were analyzed for trace and major elements. The data are presented in Table 5 and plotted in Figure 10 (Zr, Ti, Al_2O_3, CaO, Fe_2O_3, MgO); they contribute to the definition of petrographic groups together with lithology and the description of the samples. Groups I and IV are represented by only two samples each. Group I samples are chemically similar to those of Group III, whereas Group IV samples are chemically similar to those of Group II. Inspection of Table 5 and Figure 10 shows that samples of Group II are homogeneous compared to Group III samples, except for K_2O concentrations. The first standard deviation of K_2O for 16 Group II samples is 0.12 wt.% or 54 relative percent of the mean value (0.22 wt.%), which is far larger than the analytical uncertainty (0.02 wt.% or 9 relative percent). This effect is attributable to low-temperature weathering rather than magmatic processes. The distinction between Group II and Group III is obvious when one considers the wide range of variation of certain plotted elements in Group III, which do not overlap with the narrow range of variation in Group II (Zr, Ti).

All of the compositions found are characteristic of mid-ocean ridge basalt (MORB). A peculiar feature is the high CaO content in some of the analyzed samples (up to 14%) in Group III; there is no covariation of CaO and Al_2O_3 concentrations (Fig. 11), excluding the possibility of plagioclase accumulation (an exclusion that is supported by the macro and micro descriptions of the rocks). Part of the CaO content could be accounted for by calcite contamination, but such contamination is no more pervasive in Group III than in the other petrographic groups. This hypothesis of calcite contamination is also discounted by the variations of other elements in Group III.

None of the samples can be considered as primary liquids in view of phenocryst assemblages and chemical composition. In general, it is difficult to relate basalt groups by fractional crystallization; Group II could possibly be related to Groups I or III by such a process, but that would require an extensive degree of fractionation (from Zr and Ti values), which in detail is incompatible with the major and trace element variations. The chemistry of gabbros composing petrographic Group V clearly indicates that they are cumulates (low Zr, Ti concentrations and high Mg′-numbers).

Magmaphile elements (Nb, Zr, Ti, and V) are plotted in Figure 12 normalized to chondritic values, in an extended Coryell-Masuda plot (see Introduction, this volume). Error bars for a single determination are shown for the Nb values. The proportion of Nb-normalized values relative to that of Zr, Ti, and Y defines a depleted character for all samples recovered at Site 556. Compared to similar results obtained at various sites (e.g., 22°N, Leg 45; Melson, Rabinowitz, et al., 1979), the La-normalized values are inferred to be twice the Nb-normalized values; dashed lines have been drawn through these hypothetical points to suggest the probable rare earth element patterns.

The probability of finding depleted basalts at Site 556 (MAR-2 of scientific prospectus) was thought to be low according to extrapolation of zero-age data and assuming the influence of Azores mantle plume at the time of formation of this crust. The only previous evidence of depleted character between 33°N and the Azores Triple Junction area was the slightly depleted signature at Site 335 (on the FAMOUS flow line at 16 Ma; Aumento, Melson, et al., 1977). The results of Site 556 together with the previous Site 335 results suggest that the present enriched character of the Azores Triple Junction has not been constant with time. We drilled at MAR-1 to obtain a better resolution of the temporal evolution of the enriched or depleted character of the inferred mantle source(s).

MAGNETICS

Basalt Paleomagnetism

The major aim at Site 556 was to get the maximum basalt from the basement before the destruction of the drilling bit. One hundred seventy-seven meters of basalt were cored with 44% recovery. Four different units were identified based on petrographic studies done onboard. These units are described in detail in the Igneous Petrology and Geochemistry section. Phyric and aphyric basalts were studied for present paleomagnetic studies. One sample from each core was taken for detailed studies of the general paleomagnetic properties of these rocks. Natural remanent magnetization (NRM) of these samples varies between 10^{-4} and $\sim 10^{-2}$ emu/cm^3 Oe (Table 7). After the NRM was measured, each sample was subjected to alternating field (AF) demagnetization at various steps from 25 to 600 Oe, and in some cases up to 900 Oe. Plots of natural remanent magnetization versus AF demagnetizing field (Fig. 13) suggest the presence of

READEX FICHE best copy available

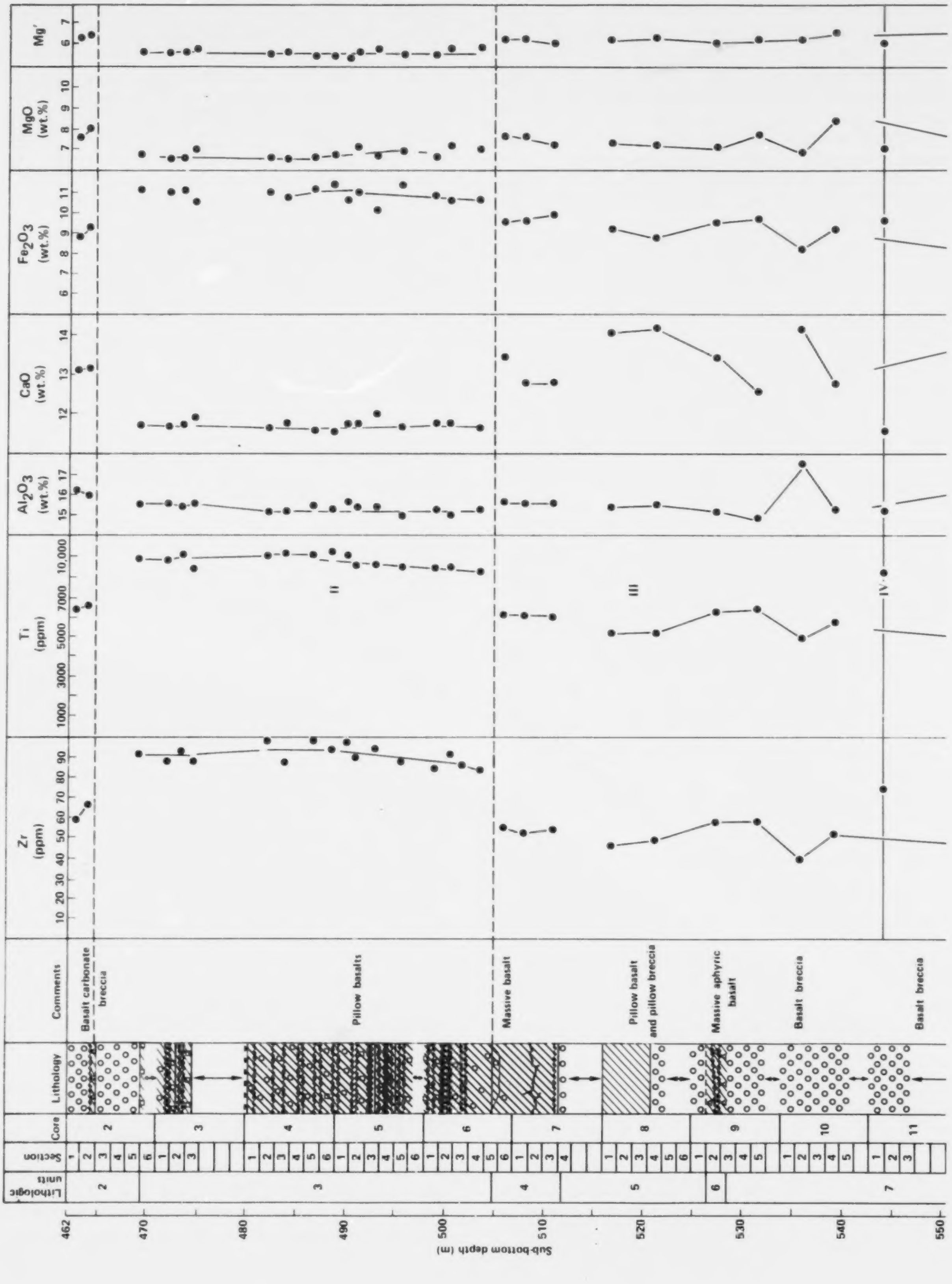
Sub-bottom depth (m)
462
470
480
490
500
510
520
530
540
550
Lithologic units
Section
Core
Lithology
Comments
Basalt carbonate breccia
Pillow basalts
Massive basalt
Pillow basalt and pillow breccia
Massive aphyric basalt
Basalt breccia
Basalt breccia
Zr (ppm)
Ti (ppm)
Al$_2$O$_3$ (wt.%)
CaO (wt.%)
Fe$_2$O$_3$ (wt.%)
MgO (wt.%)
Mg'
II
III
IV

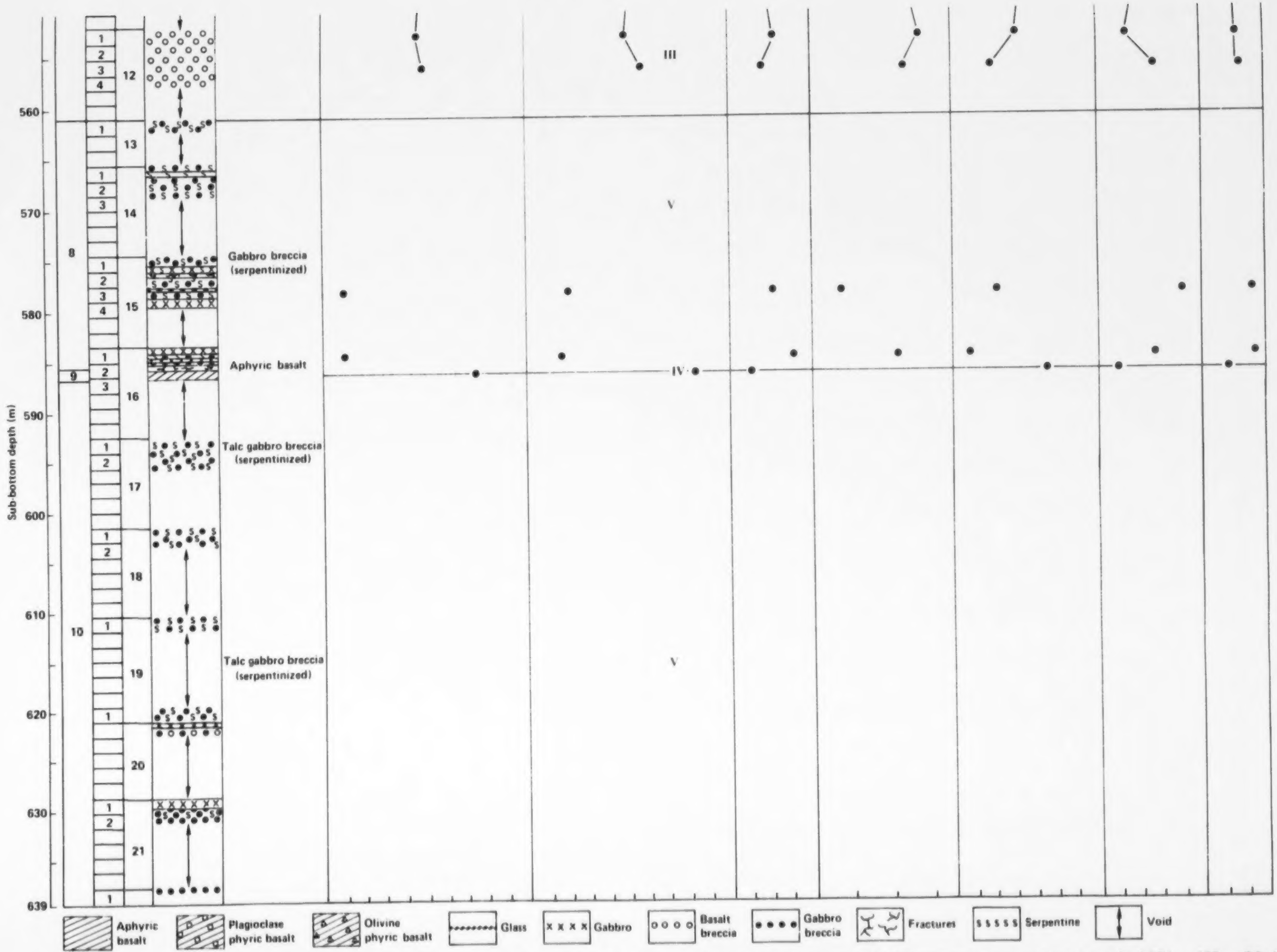

Figure 10. Lithology column and downhole plot of chemical abundances, Hole 556 basalts. Roman numerals are chemical groups. Zr and Ti expressed in ppm; others in wt.%. MG′ = 100 × (Mg/[Mg + Fe^{2+}]), calculated using an assumed Fe$_2$O$_3$ ratio of 0.15.

Table 5. Major (in wt. %) and trace (ppm) element analysis of basalts and gabbros from Hole 556.[a]

Core-Section, interval in cm (piece number)	Depth (m)	Chemical group	SiO_2	TiO_2	Al_2O_3	Fe_2O_3[b]	MnO	MgO	CaO	K_2O	P_2O_5	Total	Mg′[c]	Ti	V	Sr	Y	Zr	Nb
2-1, 78-82 (4E)	462.8	I	50.92	1.05	16.17	8.71	0.16	7.55	13.09	0.16	0.11	97.92	66	6300	277	106	28.0	59	0.8
2-2, 145-150 (9B)	464.5		50.54	1.07	15.97	9.27	0.16	7.92	13.10	0.17	0.12	98.32	66	6420	279	98	27.7	66	0.9
2-5, 12-16 (1A)	468.2	II	50.58	1.46	15.59	11.06	0.18	6.71	11.71	0.33	0.15	97.77	58	8760	280	98	38.3	91	0.9
3-1, 60-70 (7)	471.5		50.42	1.46	15.60	11.06	0.17	6.50	11.71	0.27	0.15	96.34	57	8760	292	97	39.3	88	2.2
3-2, 52-56 (4B)	473.0		49.83	1.50	15.46	11.14	0.18	6.52	11.74	0.30	0.16	96.83	57	9000	299	96	40.3	93	1.5
3-3, 70-74 (7)	474.6		50.44	1.41	15.58	10.62	0.17	6.92	11.94	0.14	0.15	97.37	59	8460	270	97	37.0	88	2.9
4-2, 77-84 (2C)	482.3		49.68	1.51	15.24	11.08	0.19	6.66	11.69	0.20	0.15	96.40	57	9052	293	93	40.2	98	3.2
4-3, 132-136 (1L)	483.9		50.37	1.53	15.09	10.89	0.20	6.56	11.78	0.09	0.16	96.67	58	9172	307	91	39.4	88	2.8
4-5, 31-33 (2B)	486.4		50.14	1.51	15.47	11.20	0.18	6.65	11.60	0.18	0.15	97.08	57	9060	286	92	38.7	99	1.8
4-6, 61-63 (2A)	488.1		50.25	1.53	15.36	11.46	0.17	6.62	11.58	0.40	0.18	97.55	57	9180	300	95	41.2	94	2.4
5-1, 73-75 (3E)	489.7		50.72	1.51	15.78	10.86	0.17	6.10	11.78	0.36	0.16	97.44	56	9060	297	96	40.5	98	1.5
5-2, 65-73 (1D)	491.0		50.07	1.42	15.44	11.15	0.18	7.18	11.79	0.29	0.14	97.66	59	8520	283	96	38.6	90	1.7
5-3, 75-80 (4)	492.8		50.62	1.42	15.45	10.22	0.16	6.72	12.05	0.32	0.14	97.10	60	8520	279	103	38.9	95	1.9
5-5, 145-150 (7)	497.3		50.46	1.40	14.98	11.43	0.17	6.99	11.71	0.07	0.14	97.35	58	8393	268	94	36.0	88	2.8
6-1, 66-70 (3A)	498.7		50.11	1.41	15.43	10.93	0.15	6.74	11.85	0.26	0.13	97.01	58	8460	269	110	36.0	85	1.9
6-2, 30-34 (2A)	499.9		50.87	1.41	15.11	10.73	0.17	7.28	11.77	0.19	0.16	97.69	60	8460	273	93	36.0	92	1.9
6-3, 82-86 (1D)	501.9		50.67	1.42	15.10	11.06	0.16	7.33	11.53	0.05	0.14	97.46	60	8540	274	92	35.1	86	0.7
6-4, 121-126 (5B)	503.7		50.08	1.36	15.35	10.78	0.16	7.18	11.70	0.02	0.14	96.77	60	8160	257	94	35.3	84	1.7
6-6, 44-48 (2A)	505.9	III	49.89	1.02	15.75	9.68	0.16	7.82	13.50	0.16	0.09	98.07	64	6120	249	94	26.1	56	2.0
7-1, 123-126 (5A)	508.1		50.56	1.01	15.67	9.68	0.17	7.78	12.81	0.14	0.10	97.92	64	6055	241	98	25.7	53	0.1
7-3, 12-15 (1B)	510.3		50.57	1.01	15.74	10.03	0.16	7.34	12.71	0.15	0.11	97.82	62	6055	245	98	26.9	55	0.9
8-1, 107-111 (7)	517.1		50.01	0.87	15.50	9.32	0.15	7.41	14.04	0.37	0.11	97.78	64	5220	257	96	24.7	47	1.1
8-4, 60-63 (3B)	521.1		50.03	0.87	15.60	8.86	0.16	7.24	14.46	0.35	0.12	97.69	65	5216	248	97	24.3	50	0.6
9-2, 82-84 (4B)	527.4		50.53	1.05	15.33	9.52	0.17	7.12	13.42	0.24	0.12	97.50	63	6295	275	97	26.1	59	2.1
9-5,64-68 (8A)	531.8		51.22	1.06	14.94	9.71	0.17	7.75	12.54	0.22	0.09	97.70	64	6360	282	101	28.7	59	1.3
10-2, 137-141 (3B)	536.8		49.87	0.82	17.58	8.17	0.14	6.86	14.13	0.26	0.10	97.93	65	4920	250	94	23.0	41	2.4
10-4, 50-54 (4)	538.9		50.37	0.95	15.38	9.22	C.16	8.49	12.73	0.21	0.09	97.60	67	5700	247	85	24.8	53	1.2
11-1, 105-115 (13)	544.1	IV	51.84	1.38	15.23	9.73	0.19	7.06	11.63	0.12	0.15	97.33	62	8273	333	107	37.7	77	2.5
12-1, 55-59 (4B)	552.6	III	49.81	0.83	17.24	8.16	0.13	7.41	13.69	0.24	0.09	97.60	67	4976	247	94	21.8	48	1.5
12-3, 118-122 (5B)	556.1		50.85	0.96	15.64	8.74	0.15	8.83	12.49	0.17	0.09	97.92	69	5755	243	87	24.6	51	0.7
15-3, 33-35 (2B)	577.9	V	52.51	0.32	15.98	7.17	0.14	10.16	11.85	0.00	0.03	98.16	76	1918	163	84	8.7	10	<0.1
16-1, 21-27 (3B)	583.8		52.61	0.28	17.21	5.92	0.12	8.82	13.21	0.00	0.03	98.20	77	1680	164	90	9.9	10	<0.1
16-2, 137-140 (15)	586.3	IV	52.46	1.38	15.06	9.66	0.14	6.86	11.06	0.29	0.15	97.06	63	8273	326	108	36.2	77	1.8

[a] On-board measurements were made on ignited samples. Onshore analyses of loss on ignition are less than 1% in most cases. Compiled data tables in Appendix at the end of the volume include volatile components.

[b] Total Fe as Fe_2O_3.

[c] Mg′ is the atomic ratio of 100 × Mg/(Mg + Fe^{2+}); calculated using an assumed Fe_2O_3/FeO ratio of 0.15.

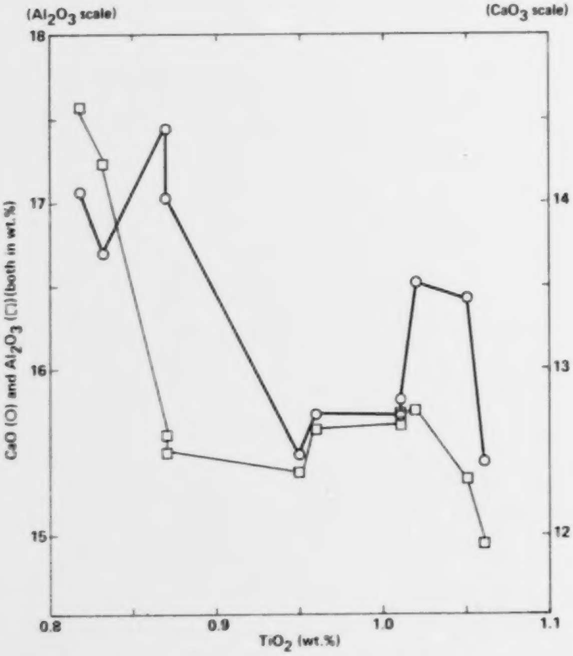

Figure 11. Variation of TiO_2 with CaO and Al_2O_3 for heterogeneous Chemical Group III, Hole 556.

Table 6. Average analyses for the five chemical groups from Hole 556.

Chemical group	I	II	III[a]	IV	V
N[b]	2	16	11	2	2
SiO_2 (wt.%)	50.73	50.31	50.34	52.15	52.55
TiO_2	1.06	1.46	0.95	1.38	0.30
Al_2O_3	16.07	15.40	15.85	15.15	16.60
Fe_2O_3[c]	. 8.99	10.97	9.19	9.70	6.54
MnO	0.16	0.17	0.16	0.17	0.13
MgO	7.74	6.76	7.64	6.96	9.49
CaO	13.10	11.76	13.32	11.35	12.53
K_2O	0.17	0.23	0.23	0.21	
P_2O_5	0.12	0.15	0.10	0.15	0.03
Ti (ppm)	6360	8722	5697	8273	1800
V	278	283	253	330	164
Sr	102	96	95	108	87
Y	27.9	38.0	25.2	37.0	9.3
Zr	63	91	52	77	10
Nb	0.9	2.0	1.3	2.2	<0.1
Mg′[d]	66	58	65	63	77
Al_2O_3/TiO_2	15.2	10.5	16.9	11.0	56
Ti/Zr	102	96	110	107	(180)

[a] A heterogeneous chemical group.

[b] Number of samples on which the mean is based.

[c] Total Fe as Fe_2O_3.

[d] Mg′ is the atomic ratio of 100 × Mg/(Mg + Fe^{2+}); calculated using an assumed Fe_2O_3/FeO ratio of 0.15.

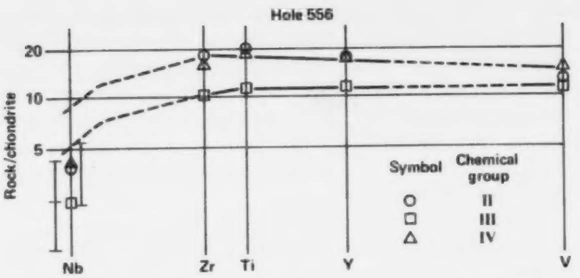

Figure 12. Extended Coryell-Masuda diagram for averages of Chemical Groups II, III, and IV. Error bars for Nb are shown at the left.

Table 7. Paleomagnetic properties, Hole 556.

Core-Section (interval in cm)	J_{NRM} ($\times 10^{-3}$ emu/cm^3)	NRM inc.	Stable inc.	($\times 10^{-6}$ g/cm^{-3} Oe)	Q ($= J_{NRM}/0.45\ \chi$)
3-1, 42-44	2.07	−36.4	−32.0	52	89
3-1, 102-105	3.22	−31.5	−30.8	40	179
3-2, 116-119	2.77	−42.5	−39.6	43	143
4-1, 118-120	6.97	−38.7	−33.9	100	155
4-2, 62-65	5.32	−35.5	−35.8	45	263
4-3, 63-66	1.64	−31.8	−31.9	198	184
4-4, 95-98	5.84	−33.7	−29.9	65	200
4-5, 71-74	7.75	−22.4	−34.4	355	49
4-6, 23-26	1.92	−36.3	−36.9	57	75
5-1, 38-41	1.72	−25.7	−26.5	45	85
5-3, 139-142	1.71	−40.4	−38.9	65	59
5-4, 102-105	3.38	−30.0	−26.7	58	130
5-5, 126-129	1.13	−27.7	−31.3	56	45
6-1, 112-115	0.64	−25.4	−24.5	64	22
6-2, 125-128	2.94	−20.8	−25.6	91	67
6-3, 103-106	5.15	−13.4	−28.9	383	30
6-4, 75-78	9.5	−25.0	−23.3	94	225
6-5, 73-76	4.32	−25.3	−31.1	70	137
7-1, 12-15	1.46	−10.1	−17.1	80	41
7-2, 95-98	0.33	− 2.1	−20.5	76	10
7-3, 97-100	0.73	−23.2	−27.0	85	19
8-2, 105-108	2.67	−49.4	−49.9	104	57
8-3, 96-99	3.35	−42.5	−43.6	85	88

Note: J_{NRM} = natural remanent magnetization; inc. = inclination; χ = susceptibility; Q = Königsberger ratio.

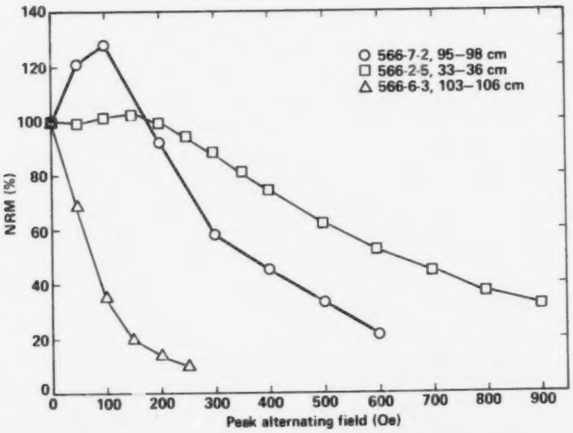

Figure 13. Plots of natural remanent magnetization (NRM) versus alternating field demagnetization, Hole 556.

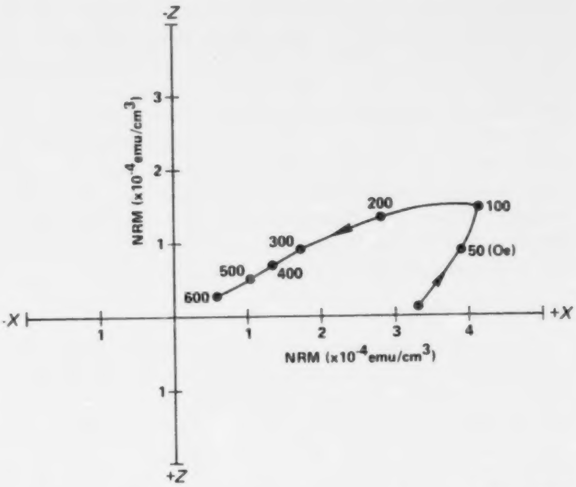

Figure 14. Vertical versus horizontal component of magnetization, Hole 556 (556-7-2, 95–98 cm).

a weak secondary component of magnetization that is removed after demagnetization at 150 Oe. To observe this secondary component, vertical component of magnetization z was plotted against horizontal component of magnetization x (Fig. 14). This orthogonal plot clearly indicates the secondary component of magnetization, which in some cases has antiparallel orientation with respect to the main component of magnetization.

Inclination values of individual samples are given in Table 8. Inclination values observed are shallower than expected and may be the result of tectonic rotation of the oceanic crust since the acquisition of remanent magnetization.

Susceptibility of the samples was measured using Bison's Magnetic Susceptibility System, Model 3101. The susceptibility values are given in Table 7.

PHYSICAL PROPERTIES

The drill string was washed down through the sediments, but some sediment was recovered in the mudline core and in wash cores taken at points of temperature

Table 8. Magnetic inclinations, Hole 556.

Core-Section (interval in cm)	Inclination after AF demag. (°)[a]	Core mean inclination (°)[b]
3-1, 42–44	−33.6	−34.6
3-1, 102–105	−30.8	
3-2, 116–119	−39.6	
4-1, 118–120	−34.8	−34.0
4-2, 62–65	−35.8	
4-3, 63–66	−31.9	
4-4, 95–98	−30.2	
4-5, 71–74	−34.4	
4-6, 23–26	−36.9	
5-1, 38–41	−26.5	−30.8
5-3, 139–142	−38.9	
5-4, 102–105	−26.7	
5-5, 126–125	−31.3	
6-1, 12–15	−24.5	−26.6
6-2, 125–128	−25.6	
6-3, 103–106	−28.9	
6-4, 75–78	−23.3	
6-5, 73–76	−31.1	
7-1, 12–15	−17.1	−21.5
7-2, 95–98	−20.5	
7-3, 97–100	−27.0	
8-2, 105–108	−49.9	−46.7
8-3, 96–99	−43.6	

[a] AF demag. = alternating - field demagnetization.
[b] Core mean inclination was calculated by assuming same declination for all samples.

measurements for heat flow calculations. Because all of these sediment samples were highly disturbed and their depth of origin unknown, no physical properties measurements were made. The basement was continuously cored to bit destruction through pillow basalts, breccia, and gabbros with high core recovery. Measurements were made of seismic velocity, density, and thermal conductivity. Details of basement physical properties measurements are described in the following paragraphs, and the downhole temperature data are included in the discussion of wireline logging.

Basement Section

The drilled sequence of pillow basalts, basalt, and gabbro was sampled to determine typical values for fresh rocks. Altered specimens were difficult to sample but did indicate the range of values with alteration. All measured values are shown in Table 9, and plotted in Figure 15.

Seismic velocities were measured in the Hamilton frame velocimeter on seawater-saturated samples to an estimated accuracy of 0.02 km/s. Densities were determined by 2-minute GRAPE and gravimetric methods to an accuracy of about 0.02 g/cm^3. Thermal conductivities were measured on saturated specimens in a water bath to an accuracy of about 5%. Values in Table 9 are in units of mcal·cm^{-1}·deg^{-1}·s^{-1} under laboratory conditions. The correction to *in situ* conditions is small compared to the measurement error.

The values in Table 9 should be compared with bulk *in situ* values determined by the downhole measurements (see Downhole Measurements section) to estimate the degree of alteration of the rock units for which there was no core recovery.

Densities determined by GRAPE and gravimetric methods agree quite well; discrepancies are mainly due to the fact that each measurement was made on separate but adjacent samples, and in altered rocks there is variability over this small distance. Seismic velocities vary systematically with density as would be expected. The thermal conductivity values give mean values for basalt and gabbro, which are very similar to those determined on Leg 37 (FAMOUS area; Aumento, Melson, et al., 1977) for similar lithologies.

Comparison with the downhole geophysical log records shows excellent agreement; the bulk downhole values for density and velocity are lower than the laboratory values by an amount that reflects the degree of jointing and fracturing of the rock.

DOWNHOLE MEASUREMENTS

Heat Flow Measurements

Measurements were made at depths of 97.5, 145.0 and 192.5 m sub-bottom using the downhole thermal probe. This is inserted above the drill bit in place of the core barrel, with the thermistor probe protruding about 1 m through the center of the drill bit. The bit is then lowered to the base of the hole so that the probe is inserted into "undisturbed" sediment. The first measurement was not taken until 97.5 m sub-bottom because the sediment above this depth would not support the weight of the bit.

For each measurement, the probe was lowered to seabed depth and left to equilibrate for 20 minutes, then lowered to the drill bit, inserted in the sediments, and again left to equilibrate for 20 minutes. Resulting temperatures are accurate to better then ±0.1°C.

The three measurements (Fig. 16) yield four points on a temperature-depth plot (Fig. 17). This gives a linear gradient of 36°C/km over the interval from 97.5 to 192.5 m. The sea-bottom temperature lies below this

Table 9. Physical property measurements for Hole 556.

Core-Section (interval in cm)	Sub-bottom depth (m)	Sonic velocity (km/s)		T(°C)	Thermal conductivity	GRAPE density (g/cm^3)		Gravimetric data			Acoustic impedance	Lithology and remarks
		V.	H.		(mcal · cm^{-1} · deg^{-1} · s^{-1})	V.	H.	Wet-bulk density (g/cm^3)	Water content (%)	Porosity (%)	(× 10^5 g · cm^{-1} · s^{-1})	
2-5, 33-36	467.8	5.61		21.5	4.06	2.80		2.82	2	4	15.76	Basalt
3-1, 42-44	471.4		5.75	21.8	3.76			2.86	1	4	16.45	Basalt
4-1, 118-120	481.2	5.69		23.0	4.12	2.77		2.81	2	6	15.88	Basalt
4-4, 95-98	485.5	5.58		23.0	4.12	2.77		2.85	2	5	15.68	Basalt
6-3, 115-118	502.2	5.84		21.4	4.26	2.85		2.84	2	6	16.61	Basalt
7-2, 95-98	509.5	5.77		21.5	3.99	2.88		2.85	2	6	16.53	Basalt
8-3, 139-142	520.4	5.29		22.0	3.99			2.78	4	10	14.71	Altered basalt
9-3, 8-21	528.1	5.52	5.53	22.0	4.12	2.83		2.88	2	6	15.77	Basalt
10-1, 5-17	534.1	4.97		22.0	3.87	2.71		2.64	5	14	13.29	Basalt breccia
11-1, 40-50	543.5	4.16	4.11	22.5		2.48					10.32	Basalt breccia
12-1,121-124	553.2	4.76		22.5	4.12	2.67					12.66	Basalt breccia
13-1, 39-44	561.4			22.0			2.48					Very altered breccia
13-1, 62-65	561.6							2.53	5	12		Serpentinized gabbro
13-1, 65-70	561.7		4.91	22.0	7.10		2.87				14.09	Serpentinized gabbro
14-1, 37-43	565.9		3.99	22.0	6.39		2.56	2.53	4	11	10.15	Serpentinized gabbro
15-1, 74-83	575.3	6.32		22.0	5.55	2.90					18.33	Gabbro
15-3, 120-132	578.2		6.34	22.0			2.99				18.96	Fresh gabbro
16-1, 110-120	584.6		5.88	22.0								Gabbro with calcite veins
18-1, 16-24	601.7		6.06	23.0			2.89	2.85	2	5	17.51	Gabbro
19-1, 119-133	611.7		3.60	23.0				2.59	7	17		Altered gabbro with calcite veins
20-1, 138-139	620.9							2.86	3	9		Gabbro
21-2, 63-65	630.1							2.55	4	11		Gabbro

Note: All values measured at laboratory temperature and pressure. For details of methods, see Explanatory Notes chapter, this volume. V. = vertical; H. = horizontal; T = temperature; water content is corrected.

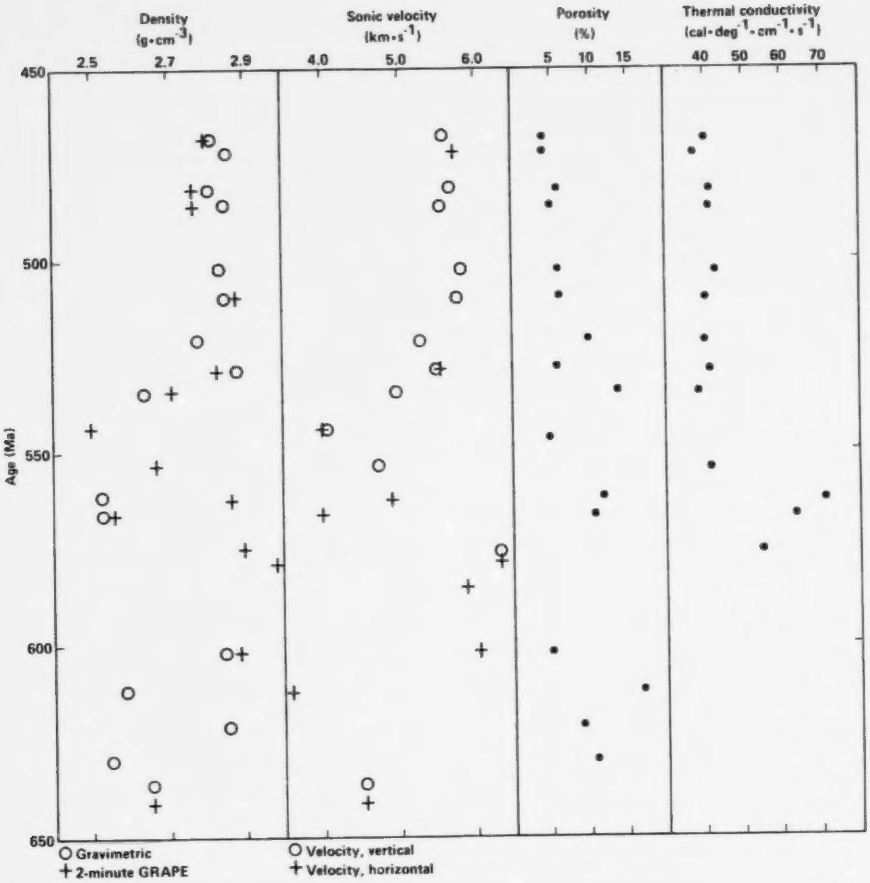

Figure 15. Downhole variation in laboratory measured physical properties, Hole 556.

trend, perhaps showing an effect of secular bottom-water temperature variation and/or a possibility of a higher thermal conductivity in the uppermost sediments.

After continuous coring at Site 558 (MAR-4), thermal conductivity measurements were made on the sedimentary sequence that was similar in age and lithology to that of Site 556. The data show a rise in thermal conductivity as a function of depth and compaction, displaying a similar trend to that determined by Hyndman and others (1977), but with slightly higher values. A mean conductivity for the depth range over which the thermal gradient was determined can thus be estimated as 2.85 (Hyndman) or 3.10 (this study) mcal·cm^{-1} sec^{-1} °C^{-1}.

Using a value of 3.0, which is within the error limits of both data sets, and the thermal gradient of 36°C km^{-1}, the heat flow is calculated as 1.08 μcal cm^{-2} sec^{-1}. This is below average for 33-Ma-old crust, but within the range of variation commonly found.

Logging

Operations

After completion of the hole, we decided to run a complete suite of logs, because the basement penetration exceeded 150 m and the lithologies encountered were unusual and complex. The bit was dropped and drill pipe withdrawn until the end of the drill string was 113 m below the mudline. Four logging runs were made using various combinations of tools as given in Table 10.

Within the sediments the caliper logs show that the hole was washed out to more than 16-in. diameter, whereas the diameter in basement was generally of bit size, approximately 10 in. There was a washout within the basement between 561 and 578 m sub-bottom to a diameter of approximately 12 in. Two constrictions were found, one just above basement between 453 and 456 m sub-bottom and the second 40 m below the sediment/basement interface (503–508 m sub-bottom).

There were no serious technical problems with the logging equipment, and complete logs were obtained for all tools. The large-hole diameter in the sediments was greater than the excentralizer extension of the density log (FDC) and the neutron porosity log (CNL), hence these logs were not in continuous contact with the sidewall and resulting data are of doubtful value. Noise on the sonic log is caused by the tool contacting constrictions in the hole and results in localized noisy sections. "Spikes" on the caliper log attached to the sonic tool result from modifications made to allow it to pass down the drill string, but these are easily removed by eye. All

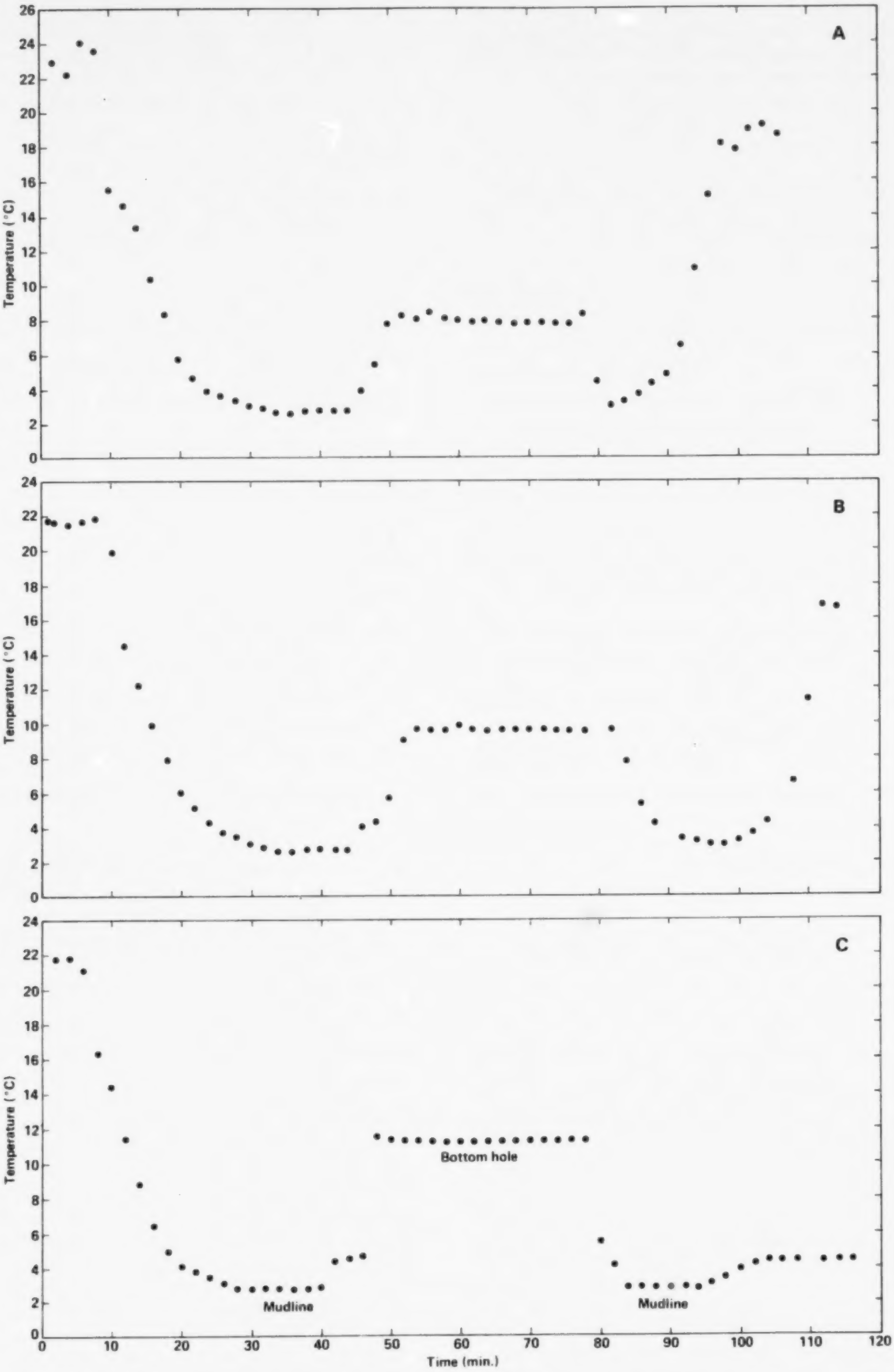

Figure 16. Heat probe measurements in Hole 556. Sub-bottom depths are: A, 97.5 m; B, 145.0 m; C, 192.5 m.

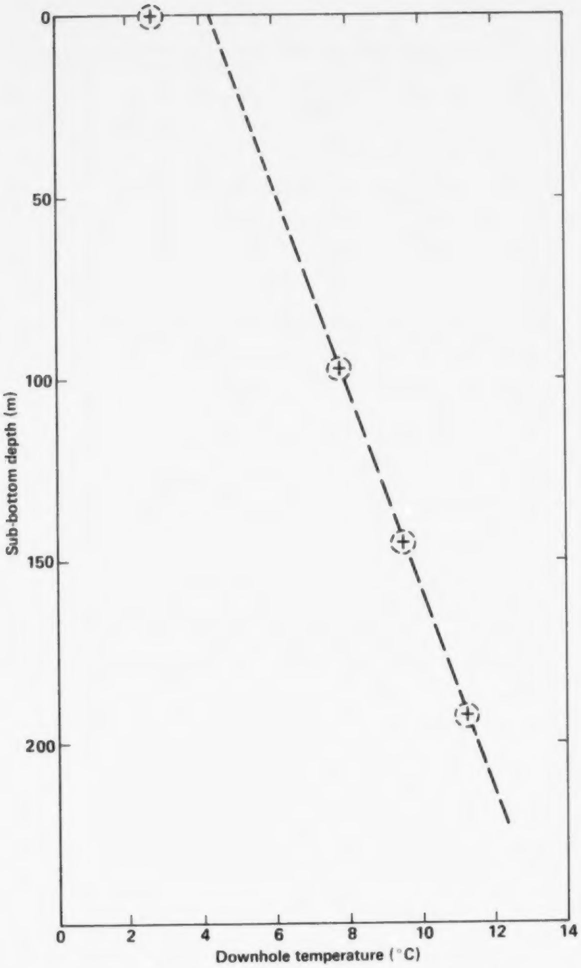

Figure 17. Thermal gradient within sediments at Hole 556.

Table 10. Schedule of logging runs.

Run 1:	Sonic velocity (DDBHC), natural gamma ray (GR), and caliper (CAL) Logger on bottom 02.00 9/28 Pass 1. Sonic velocity. Pass 2. Waveform recording.
Run 2:	Dual laterlog, GR, and self potential (SP) Logger on bottom 06.45 9/28
Run 3:	Gamma ray density (FDC), neutron porosity (CNL), GR, and CAL Logger on bottom 15.00 9/28
Run 4:	High resolution temperature (HRT) Logger on bottom 21.30 9/28 Tool pumped to bottom of drill pipe

three physical property logging runs were started within 20 m of the bottom of the hole.

Sedimentary and Basement Sections

The hole is divided into seven geophysical (log) units (Fig. 18 and Table 11), based on characteristic combinations of physical properties. The boundaries of the units correspond to abrupt simultaneous changes in at least two log curves and generally in three or more. Several excursions (i.e., brief simultaneous changes in several logs that occur within the previously defined units) are noted in Figure 18 (as shown by dashed horizontal lines). Comparison of the boundaries of the geophysical units to the lithologic record from the cores reveals the expected close correlation.

The sedimentary section, Unit 1, is very uniform and both sonic and resistivity logs show gradual changes caused by compaction (Fig. 19). There is a sharp rise in sonic velocity at about 330 m sub-bottom, which may reflect a change in sediment lithology or diagenesis. The curves contain some short-wavelength variations that are difficult to interpret. The density curve is drawn dashed because the curve has many noise spikes and has been filtered by eye. Within the basement, the highest sonic velocities, resistivities, and densities and the lowest porosities correspond to the pillows, massive basalts, and gabbro units. Changes from these values reflect alteration, fracturing and brecciation. A detailed description of the units is given in Table 11. Physical parameter values derived from the logs correlate very well with laboratory sample measurements (see Physical Properties section).

Only one gamma-ray anomaly was noted, at 529 m sub-bottom, corresponding to a low-velocity, low-density, and high-porosity excursion. This may be caused by a localized zone of high clay mineral content within the upper part of the lower basaltic breccia.

Because there is such a close correlation between the log records and lithologic units derived from core description, it is deduced that units are homogeneous and that cored material is probably quite representative of the entire cored section. Where both the lithology and the logs change rapidly within a single core, the logs provide the means of precisely locating the position of the lithology changes.

Downhole Temperatures

The temperature log (high resolution temperature or HRT) was the last log run, giving the hole a period of 24.5 hours to equilibrate. Unfortunately, the hole had closed within the basement section, and the tool could not be lowered more than 20 m below the basement interface; however, the temperature profile above this level is interesting. From the mudline to just above the basement interface, the temperature was nearly uniform at the bottom-water temperature, whereas within the 20 m of basement section, the temperature rose rapidly by 3°C. The absolute calibration of the thermistor used is uncertain within ±2°C, but this does not affect the conclusion that the hole is at bottom-water temperature down to the level of the basement interface. The preexisting temperature was established during drilling (see Heat Flow Measurements section). The logged temperature profile suggests downward flow of bottom water into porous formations just below the sediment/basement interface.

Seawater Drawdown

The geothermal gradient at Site 556 was determined to be 36°C per km. The thickness of sediment was 461

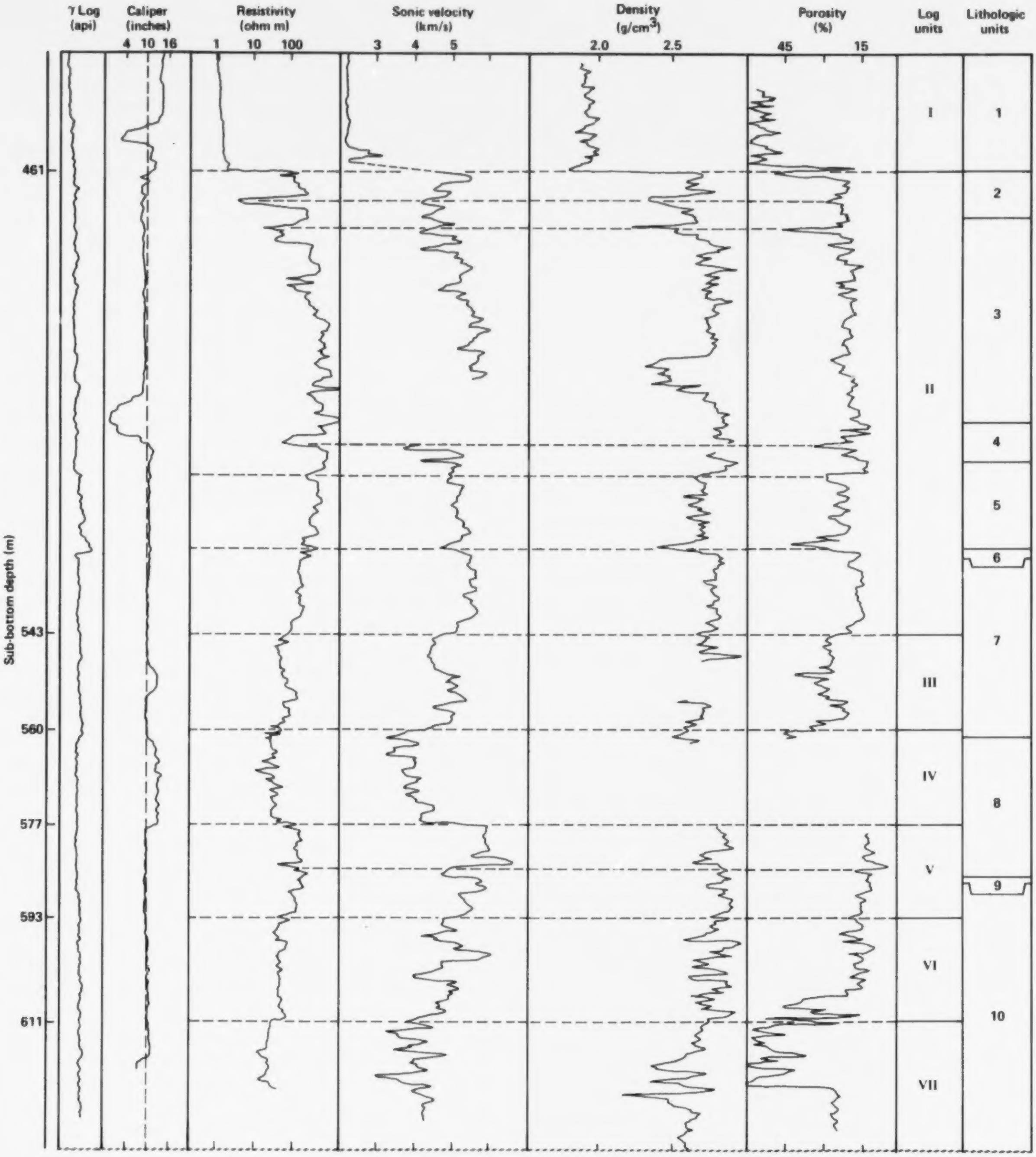

Figure 18. Wireline log curves for the basement section of Hole 556. Curves have been redrawn omitting noise spikes; gaps indicate intervals where noise obscured data.

m, hence a linear gradient would imply a temperature at basement interface of 21°C. If we allow for an increase in conductivity with depth, this value may decrease to about 18°C.

As drilling proceeds, the hole is flushed with seawater pumped from the surface. As it travels down the drill string (about 30 min.), this water cools to equilibrate with ocean water so that it enters the hole at bottom-water temperature. At the cessation of drilling, the hole is uniformly chilled to ocean bottom-water temperature. Because forced-water circulation has now ceased, the hole will tend to return to its equlibrium tempera-

Table 11. Description of geophysical (log) units, Hole 556.

Unit	Sub-bottom depth range (m)	Resistivity (ohm m)	Sonic velocity (km/s)	Density (g/cm^{-3})	Porosity (%)	Lithology	Remarks
I	113–461	1	up to 2.1	up to 1.9	up to 55%	Nannofossil ooze	Only logged from base of drill string.
II	461–543	500	5.4	2.75	20	Basalt breccia, pillow basalts, massive basalts	These values are for the interval 483-500 m.
III	543–560	50	4.6	2.65	27	Lower basalt breccia	
IV	560–577	20	3.8	2.50	50	Serpentinized gabbroic breccia	
V	577–593	100	5.5	2.80	15	Gabbro	Lower sonic velocity occurs in lower half of unit.
VI	593–611	30	4.6	2.70	18	Serpentinized gabbroic breccia	
VII	611–620	15	4.0	2.50	54	Serpentinized gabbroic breccia	

ture at a rate dependent on the duration of chilling (drilling) and the thermal diffusivity of the drilled rock. The return to thermal equilibrium of DSDP holes has been discussed in detail by Hyndman and others (1977). For this study, the simplest treatment has been used, modeling the drilling as a line heat source in an infinite medium. For this model, the temperature disturbance decays approximately as derived by Jaeger (1975):

$$\frac{T}{T_0} = \frac{\ln\left(1 + \frac{t_0}{t}\right)}{\ln\,(4kt_0/a^2 - 0.577)},$$

where T/T_0 is the ratio of temperature at time t to equilibrium value T_0; t_0 is duration of disturbance (drilling) (122.5 hr.); t is time since the disturbance ceased (25 hr.); k is the diffusivity of the medium (0.003 cm^2/hr.); a is the radius of the hole (12.5 cm).

This equation has been applied to the sedimentary section of Hole 556 where the predrilling temperature was measured by Uyeda heat probe, and the postdrilling temperature was determined by Schlumberger HRT log. The solution predicts a T/T_0 value of 0.5 (i.e., temperatures should have returned to half their equilibrium value by the time of the Schlumberger logging). Because the HRT log showed constant bottom-water temperature throughout the sediment section, continuing cooling of the hole by natural drawdown must be assumed.

If we assume that the drill hole acts as a cooling line element within the sedimentary section, we can calculate approximately the quantity of heat that must be removed to prevent reequilibration. For a rise in water temperature of less than 1°C this requires a water flow rate of about 70 m per hour down the hole. This volume of water must flow away from the hole through fractures and joints in the basement.

SUMMARY AND CONCLUSIONS

The principal objective of Leg 82 is to study the evidence for mantle heterogeneity in the vicinity of the Azores Triple Junction. From data collected along the axis of the Mid-Atlantic Ridge (zero age), it appears that the Azores Triple Junction corresponds to the center of a major mantle anomaly in respect to the well-known "depleted" character in the magmaphile elements of typical mid-oceanic crust and mantle. This anomaly is also documented by Sr, Pb, and Nd isotopic ratios. The location of the proposed drill sites forms a grid that makes it possible to sample the oceanic crust between the latitudes of 40 and 32° over a broad span of time.

Site 556 is located on a flow line passing through the Azores Triple Junction, where it is thought that the geochemical anomaly is the highest and should have persisted for the longest period of time. The first site on this flow line was chosen to be on Anomaly 13, which was thought to be a good compromise between the distance from the axis of the ridge, the thickness of sediments, and the location of other proposed sites in the grid. To summarize, the principal objective of drilling at Site 556 was to answer the question: "Was the Azores Mantle Plume producing abnormal (enriched in magmaphile elements) crust at the axis of the ridge 35 Ma?"

The exact position of Site MAR-2 had not been surveyed ahead of time. Although we had intended to drill on Anomaly 13 because of its prominence, a suitable locality could not be found on our approach to the site, because of the rough nature of the basement and the extreme sediment thicknesses. Because smoother basement had been observed in the area of Anomaly 12 and because the sediment thickness there was less than 500 m, the site was moved to Anomaly 12. More precisely, Site 556 is located close to the transition between the positive Anomaly 12 and the negative anomaly between 12 and 13 (about 34 Ma old). The water depth is 3680 m.

The sediments were washed down until basement was felt at a level of 461 m sub-bottom. The last sediment was recovered several meters below in a basaltic breccia. Nannofossils identified within the sediment matrix of the basaltic breccia give an age of 30 to 34 Ma, in agreement with the age of Magnetic Anomaly 12.

Drilling within basement penetrated 177 m before bit destruction. Basalt breccias, pillows, and massive basalts

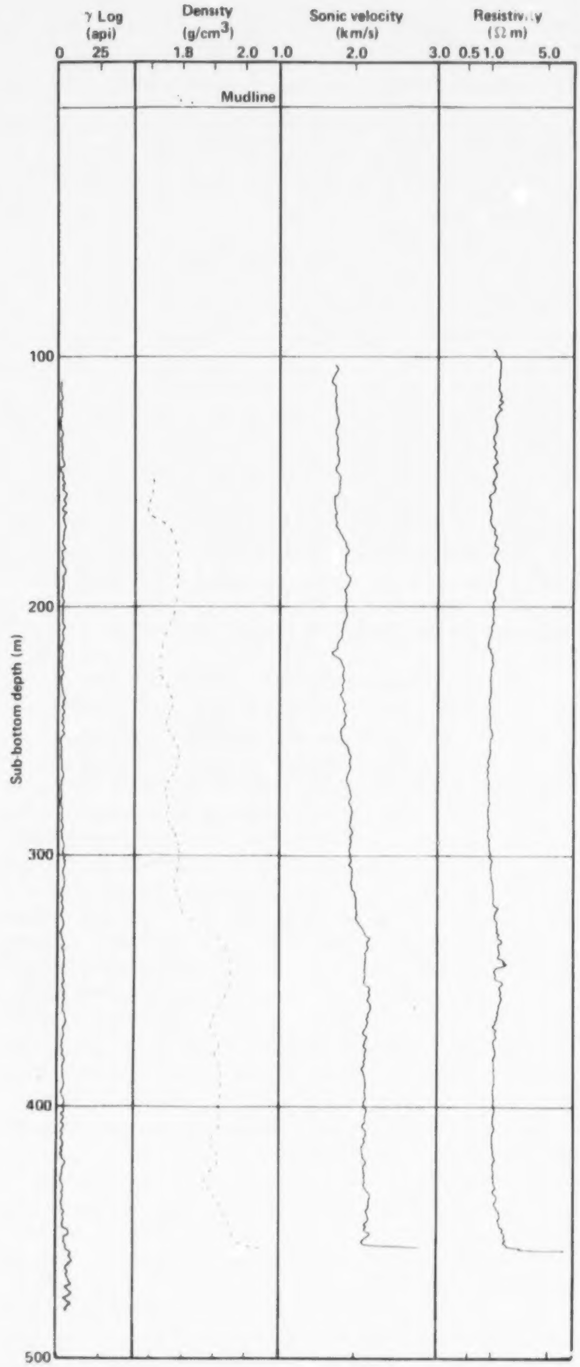

Figure 19. Wireline log curves for the sedimentary section of Hole 556. Density curve is dashed to indicate the low quality of the data. Numbers on the horizontal lines are sub-bottom depth (in m).

were recovered in the upper 99 m of basement, and gabbros and highly altered gabbroic breccias were encountered in the lower part of the basement. The average recovery in the upper basaltic layer was about 64%, whereas recovery in the lower gabbroic unit was only about 20%. Nine lithologic units have been identified within the basement. The macro and micro descriptions of the samples together with the shipboard geochemical analyses make it possible to define five petrographic groups (four basaltic groups and one gabbroic group) within the different lithologic units.

The shipboard geochemical analyses were focused on determining the concentrations of certain key magmaphile trace elements that are critical in determining the depleted or enriched geochemical character of the basalt: Nb, Zr, Ti, Y, and V. Figure 12 shows the concentrations of the elements normalized to chondrites.

The results obtained at Hole 556 show that the geochemical character of the oceanic crust produced at this latitude on the Mid-Atlantic Ridge 34 Ma is typical of normal depleted mid-oceanic basalts. The results demonstrate that the Azores Triple Junction has not been continuously associated with a mantle plume insofar as there is a correlation between mantle plumes and enriched oceanic basalts.

The remanent magnetization inclinations found in the pillow and massive basalt units are negative and consistent with the location of the site near the transition zone between positive and negative anomalies. A narrow range of core average values are found in the upper units (−30 to −35°), and more widely scattered values are found in the lower basaltic units (−21 to −47°).

A complete set of logs were conducted following completion of the hole. Variations in the sonic velocity, resistivity, density, and porosity logs closely follow changes in the lithology within the basement. The temperature profile recorded by the high resolution thermometer showed a nearly uniform bottom-water temperature (about 2°C) all the way down to the sediment/basement interface. This observation contrasts with the thermal gradient of 36°C per km measured at three levels within the sediment when washing down to the basement. This result suggests that a downward flow of deep water was initiated by drilling the basement.

REFERENCES

Aumento, F., Melson, W. G., et al., 1977. *Init. Repts. DSDP*, 37: Washington (U.S. Govt. Printing Office).

Berggren, W. A., and Amdurer, M., 1973. Late Paleogene (Oligocene) and Neogene planktonic foraminiferal biostratigraphy of the Atlantic Ocean (Lat. 30°N to Lat. 30°S). *Rev. Ital. Paleontol. Strati.*, 79:337–391.

Blow, W. H., 1969. Late middle Eocene to Recent planktonic foraminiferal biostratigraphy. *In* Brönnimann, P., and Renz, H. H. (Eds.), *Proc. First Planktonic Conf.*: Leiden (E. J. Brill), pp. 199–422.

Gartner, S., 1977. Calcareous nannofossil biostratigraphy and revised zonation of the Pleistocene. *Mar. Micropaleontol.*, 2:1–25.

Hyndman, R., Von Herzen, R. P., Erickson, A. J., and Jolivet, J., 1977. Heat flow measurements DSDP Leg 37. *In* Aumento, F., Melson, W. G., et al., *Init. Repts. DSDP*, 37: Washington (U.S. Govt. Printing Office), 347–362.

Luyendyk, B. P., Cann, J. R., et al., 1979. *Init. Repts. DSDP*, 49: Washington (U.S. Govt. Printing Office).

Melson, W. G., Rabinowitz, P. D., et al., 1979. *Init. Repts. DSDP*, 45: Washington (U.S. Govt. Printing Office).

Okada, H., and Bukry, D., 1980. Supplementary modification and introduction of code numbers to the low-latitude coccolith biostigraphy zonation (Bukry, 1973:1975). *Mar. Micropaleontol.*, 5: 321–325.

Varet, J., and Demange, J., 1979. Autoclastic submarine breccias in Hole 410, Leg 49, and other DSDP sites. *In* Luyendyk, B. P., Cann, J. R., et al., *Init. Repts. DSDP*, 49: Washington (U.S. Govt. Printing Office), 749–760.

SITE 556 HOLE CORE 1 CORED INTERVAL 0.0–6.5 m

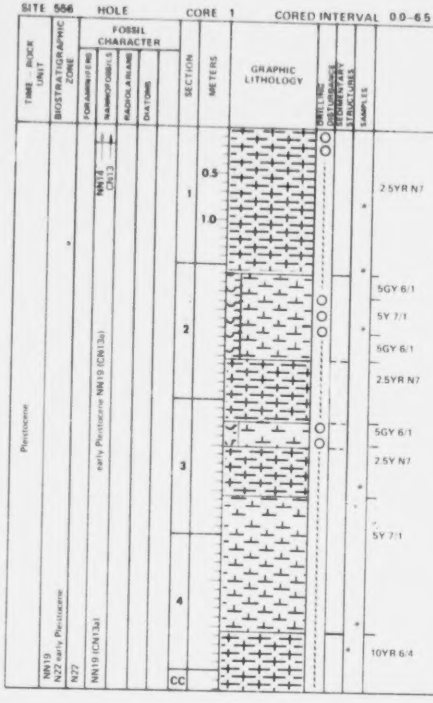
TIME – ROCK UNIT
BIOSTRATIGRAPHIC ZONE
FOSSIL CHARACTER
FORAMINIFERS
NANNOFOSSILS
RADIOLARIANS
DIATOMS
SECTION
METERS
GRAPHIC LITHOLOGY
DRILLING DISTURBANCE
SEDIMENTARY STRUCTURES
SAMPLES
Pleistocene
NN19
N22 early Pleistocene
N22
NN14
CN13
early Pleistocene NN19 (CN13a)
NN19 (CN13a)
1
2
3
4
CC
0.5
1.0
2.5YR N7
5GY 6/1
5Y 7/1
5GY 6/1
2.5YR N7
5GY 6/1
2.5Y N7
5Y 7/1
10YR 6/4

LITHOLOGIC DESCRIPTION

DOMINANT LITHOLOGIES

(1) NANNOFOSSIL OOZE TO FORAM NANNOFOSSIL OOZE

Light gray (2.5YR N7) with rare black streaks (pyrite?)
Massive bedding slightly mottled

(2) FORAM NANNOFOSSIL OOZE TO NANNOFOSSIL OOZE, in sharp contact with dominant lithology (1)

Light yellowish brown (10YR 6/4)
Massive bedding

Minor lithology:
Siliceous nannofossil ooze, interbedded with dominant lithology (1), possibly gradational

Greenish gray (5GY 6/1) with rare black streaks

SMEAR SLIDE SUMMARY (%):

	1, 88	2, 6	2, 70	3, 94	4, 99	4, 124	CC
	D	D	D	D	D	D	D
Composition							
Feldspar	Tr	Tr	—	—	—	—	
Clay	—	—	—	—	—	Tr	2
Volcanic glass	—	Tr	—	Tr		—	—
Palagonite	Tr	—	Tr	Tr	Tr	Tr	Tr
Pyrite	—	Tr	Tr	—		—	—
Carbonte unspec	—	—	—	—	—	—	3
Foraminifers	10	5	3	14	5	15	5
Calc. nannofossils	82	80	80	85	93	85	90
Diatoms	3	10	10	Tr	2	—	—
Radiolarians	5	3	5	Tr	Tr	—	—
Sponge spicules	Tr	2	2	Tr	Tr	—	—
Silicoflagellates	Tr	—	Tr	Tr	Tr	—	—

SITE 556 HOLE CORE H1 CORED INTERVAL 6.5–97.5 m

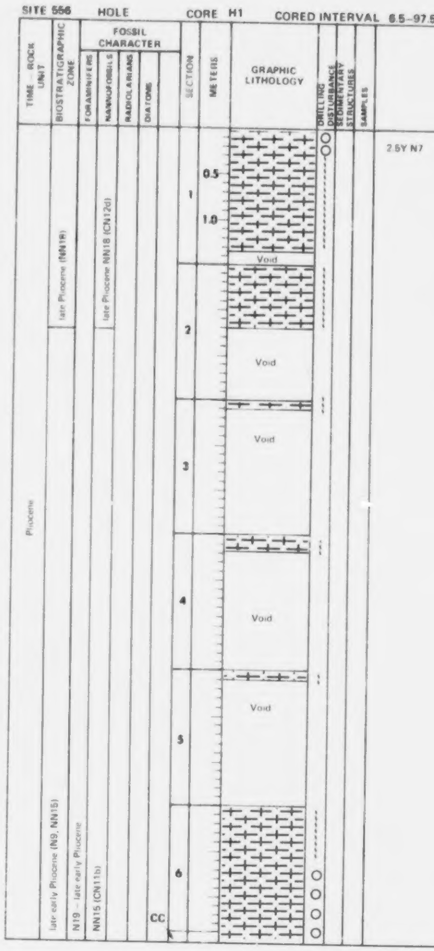
TIME – ROCK UNIT
BIOSTRATIGRAPHIC ZONE
FOSSIL CHARACTER
FORAMINIFERS
NANNOFOSSILS
RADIOLARIANS
DIATOMS
SECTION
METERS
GRAPHIC LITHOLOGY
DRILLING DISTURBANCE
SEDIMENTARY STRUCTURES
SAMPLES
Pliocene
late Pliocene (NN18)
late Pliocene NN18 (CN12d)
late early Pliocene (N9, NN15)
N19 – late early Pliocene
NN15 (CN11b)
1
2
3
4
5
6
CC
0.5
1.0
Void
Void
Void
Void
Void
2.5Y N7

LITHOLOGIC DESCRIPTION

DOMINANT LITHOLOGY FORAM NANNOFOSSIL OOZE

Light gray (2.5Y N7) with green streak (Section 1) possibly altered ash

Massive bedding

Warning! – wash core, stratigraphic position is questionable

SMEAR SLIDE SUMMARY (%):

	CC
	D
Composition:	
Feldspar	Tr
Palagonite	Tr
Foraminifers	15
Calc. nannofossils	80
Discoasters	5

SITE 556 HOLE CORE H2 CORED INTERVAL 97.5–145.0 m

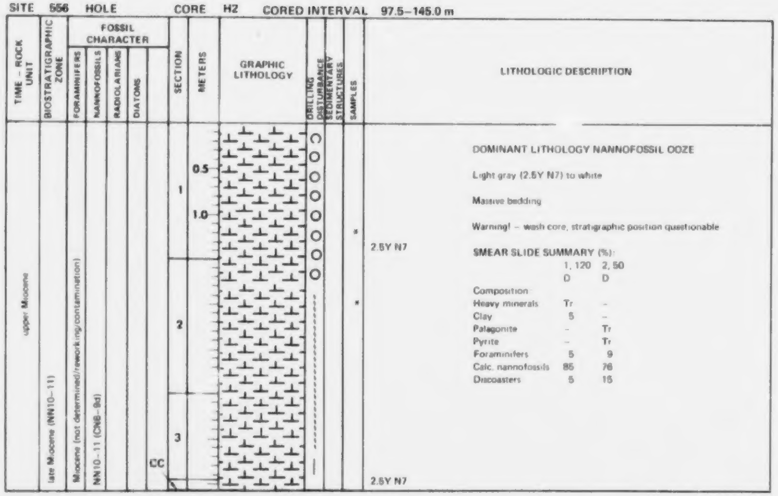
TIME – ROCK UNIT
BIOSTRATIGRAPHIC ZONE
FOSSIL CHARACTER
FORAMINIFERS
NANNOFOSSILS
RADIOLARIANS
DIATOMS
SECTION
METERS
GRAPHIC LITHOLOGY
DRILLING DISTURBANCE
SEDIMENTARY STRUCTURES
SAMPLES
LITHOLOGIC DESCRIPTION
upper Miocene
late Miocene (NN10–11)
Miocene (not determined/reworking/contamination)
NN10–11 (CN8–9d)
1
2
3
CC
0.5
1.0
2.5Y N7
2.5Y N7

DOMINANT LITHOLOGY NANNOFOSSIL OOZE

Light gray (2.5Y N7) to white

Massive bedding

Warning! – wash core, stratigraphic position questionable

SMEAR SLIDE SUMMARY (%):

	1, 120	2, 50
	D	D
Composition:		
Heavy minerals	Tr	–
Clay	5	–
Palagonite	–	Tr
Pyrite	–	Tr
Foraminifers	5	9
Calc. nannofossils	85	76
Discoasters	5	15

SITE 556 HOLE CORE H3 CORED INTERVAL 145.0–192.5 m

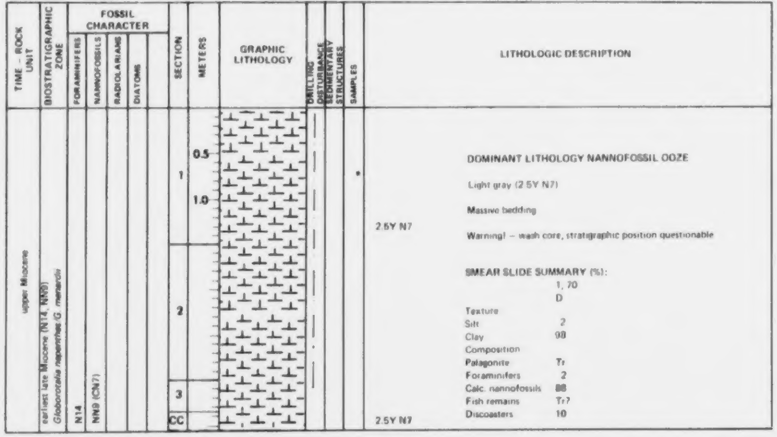
TIME – ROCK UNIT
BIOSTRATIGRAPHIC ZONE
FOSSIL CHARACTER
FORAMINIFERS
NANNOFOSSILS
RADIOLARIANS
DIATOMS
SECTION
METERS
GRAPHIC LITHOLOGY
DRILLING DISTURBANCE
SEDIMENTARY STRUCTURES
SAMPLES
LITHOLOGIC DESCRIPTION
upper Miocene
earliest late Miocene (N14, NN9)
Globorotalia nepenthes/G. menardii
N14
NN9 (CN7)
1
2
3
CC
0.5
1.0
2.5Y N7
2.5Y N7

DOMINANT LITHOLOGY NANNOFOSSIL OOZE

Light gray (2.5Y N7)

Massive bedding

Warning! – wash core, stratigraphic position questionable

SMEAR SLIDE SUMMARY (%):

	1, 70
	D
Texture	
Silt	2
Clay	98
Composition	
Palagonite	Tr
Foraminifers	2
Calc. nannofossils	88
Fish remains	Tr?
Discoasters	10

SITE 556 HOLE CORE H4 CORED INTERVAL 192.5–461.5 m

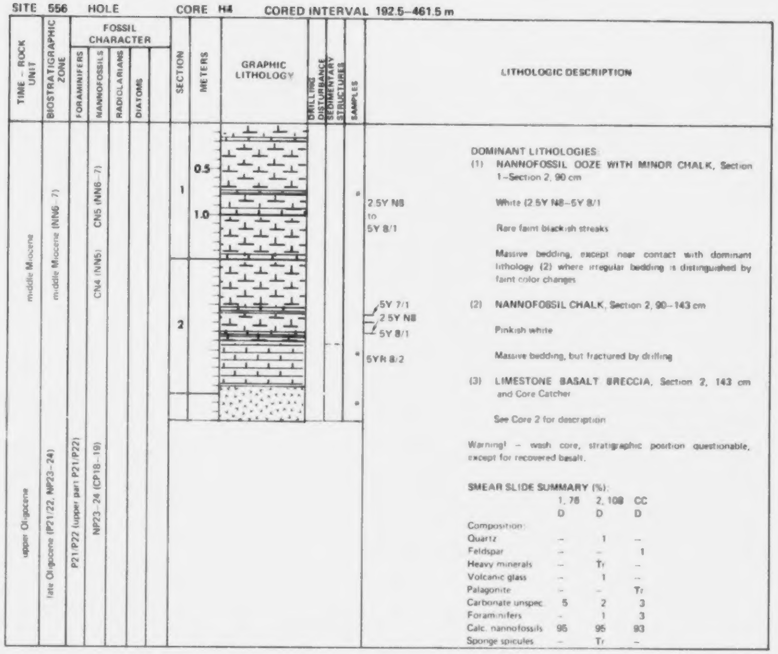
TIME – ROCK UNIT
BIOSTRATIGRAPHIC ZONE
FOSSIL CHARACTER
FORAMINIFERS
NANNOFOSSILS
RADIOLARIANS
DIATOMS
SECTION
METERS
GRAPHIC LITHOLOGY
DRILLING DISTURBANCE
SEDIMENTARY STRUCTURES
SAMPLES
LITHOLOGIC DESCRIPTION
middle Miocene
middle Miocene (NN6–7)
CN4 (NN5) CN5 (NN6–7)
upper Oligocene
late Oligocene (P21/22, NP23–24)
P21/P22 (upper part P21/P22)
NP23–24 (CP18–19)
1
2
0.5
1.0
2.5Y N8
to
5Y 8/1
5Y 7/1
2.5Y N8
5Y 8/1
5YR 8/2

DOMINANT LITHOLOGIES:

(1) NANNOFOSSIL OOZE WITH MINOR CHALK, Section 1–Section 2, 90 cm

White (2.5Y N8–5Y 8/1

Rare faint blackish streaks

Massive bedding, except near contact with dominant lithology (2) where irregular bedding is distinguished by faint color changes

(2) NANNOFOSSIL CHALK, Section 2, 90–143 cm

Pinkish white

Massive bedding, but fractured by drilling

(3) LIMESTONE BASALT BRECCIA, Section 2, 143 cm and Core Catcher

See Core 2 for description

Warning! – wash core, stratigraphic position questionable, except for recovered basalt.

SMEAR SLIDE SUMMARY (%):

	1, 78	2, 108	CC
	D	D	D
Composition:			
Quartz	–	1	–
Feldspar	–	–	1
Heavy minerals	–	Tr	–
Volcanic glass	–	1	–
Palagonite	–	–	Tr
Carbonate unspec.	5	2	3
Foraminifers	–	1	3
Calc. nannofossils	95	95	93
Sponge spicules	–	Tr	–

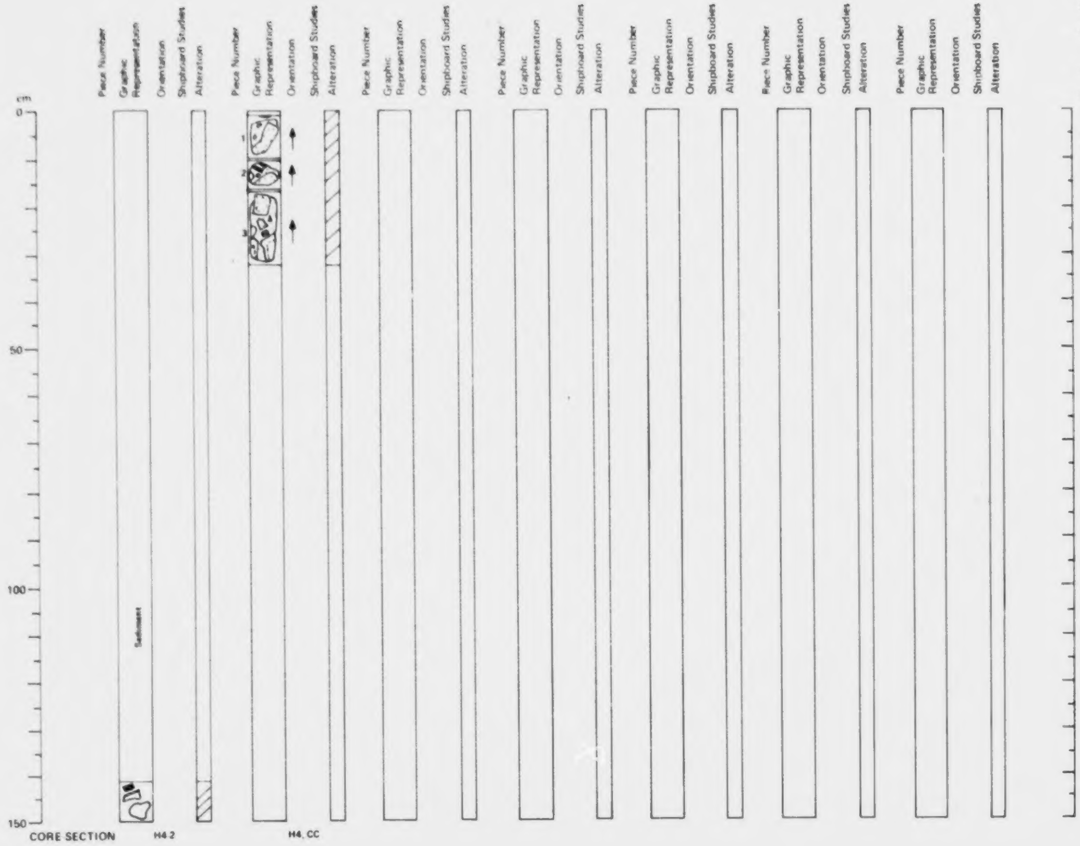
cm
0
50
100
150
CORE SECTION
Piece Number
Graphic Representation
Orientation
Shipboard Studies
Alteration
Sediment
H4.2
1
2
3
H4, CC

SITE 556, CORE H4 Depth 192.5–461.5 m

SECTION 2

Chalk — a clear calcite cemented breccia. 2 clasts moderately altered, fine grained aphyric basalt. Glass fragment weathered to dark brown palagonite. Minor fresh glass at center.

SECTION CC

Basalt breccia. Basalt is medium gray–gray (7.5YR N5), moderately altered and aphyric. Fine grained plagioclase and olivine (plagioclase ~0.5 mm, olivine up to 2 mm). Olivine is completely replaced by smectite. Vesicles are very rare and not filled.

Some of the basalt pieces show a vitric rim, which is mostly altered (in Piece 2 it looks like fresh glass).

The breccia is indurated by a calcite cement.

The cement, which fills up nearly all space between the basalt pieces, sometimes shows drusy cavities.

SITE 556 HOLE CORE 2 CORED INTERVAL 461.5–471.0 m

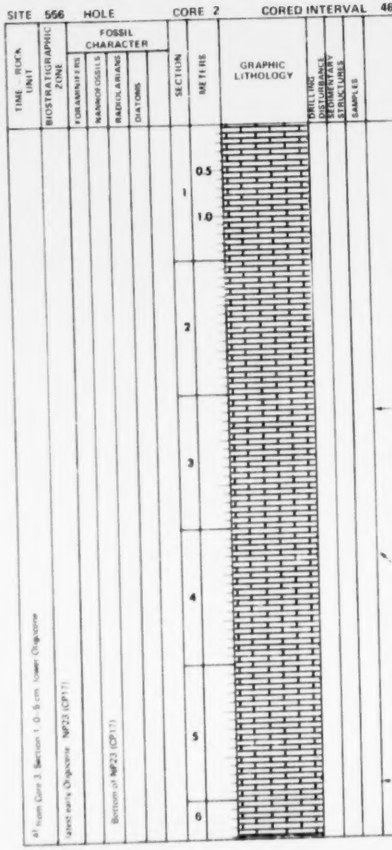
TIME – ROCK UNIT
BIOSTRATIGRAPHIC ZONE
FOSSIL CHARACTER
FORAMINIFERS
NANNOFOSSILS
RADIOLARIANS
DIATOMS
SECTION
METERS
GRAPHIC LITHOLOGY
DRILLING DISTURBANCE
SEDIMENTARY STRUCTURES
SAMPLES
a) from Core 3, Section 1, 0–6 cm: lower Oligocene
latest early Oligocene: NP23 (CP17)
Bottom of NP23 (CP17)
1
2
3
4
5
6
0.5
1.0
vug
vug
vug

LITHOLOGIC DESCRIPTION

DOMINANT LITHOLOGY LIMESTONE BASALT BRECCIA

Poorly sorted, with clast size ranging from boulders to coarse sand. Boulder size clasts are prominent at three intervals in the core (Section 6, base of Section 4, and base of Section 2).

Volcaniclasts are dominated by fresh, gray (7.5YR N5) to weathered, pinkish gray (7.5YR 6/2) basalt (moderately plagioclase-phyric) along with both fresh and altered, grayish green (5G 4/2) to dark brown (7.5YR 3/2) volcanic glass.

Biogenic limestone (nannofossil limestone and chalk) pinkish white (5YR 8/2) to light gray (10YR 7/1) not only makes up the matrix of the breccia but also provides subrounded intraclasts and fracture filling in the basalt clasts. Both limestone clasts and matrix are recrystallized discontinuously, as veins, to sparite and in places the entire limestone matrix and clasts have been recrystallized to sparite with solution vugs. Also, basalt clasts are rimmed by very fine microcrystalline calcite.

Please note that the original recovered interval has been expanded by spacers separating broken sections of core.

a) Note: base of this lithology is nanno chalk in Core 3, Section 1, 0–5 cm in contact with basalt flow.

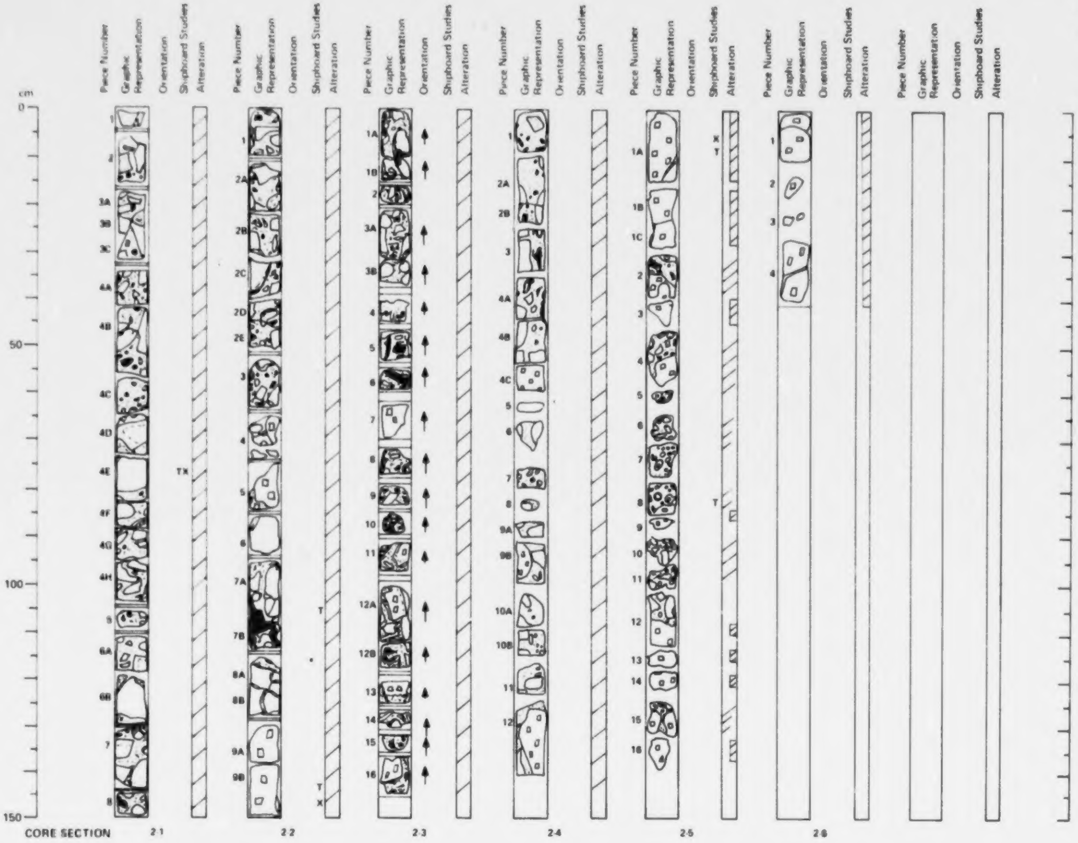

SITE 556, CORE 2 Depth 461.5–471.0 m

SECTION 1

Basalt breccia – indurated calcareous chalk matrix with ~5% drusy clear calcite

Clasts

1 – Fine grained, medium gray (7.5YR N5) aphyric to sparsely phyric basalt. Dark brown (7.5YR 4/4) altered olivine? (to 1 mm) varying 0–2% rarely to ~ 5%. Light brown–pinkish gray (7.5YR 6/2) weathered margins to 1 cm thick on some clasts.

2 – Dark brown altered glass fragments and occasional glass rims. Some unaltered glass in centers of larger pieces.

Thin Section: Intergranular aphyric basalt, round vesicles (0.5–1%) filled with calcite.

SECTION 2

Basalt breccia as in Section 1

Clasts as in Section 1 with addition of sparsely plagioclase phyric basalts at 66–70, 75–86, and 130–150 cm. Equant plagioclase phenocrysts to 5 mm increasing downhole to ~3%.

95–115 cm: Strong development of dark green–grayish green (5G 4/2) pumpellyite(?) in glass fragments and glass rim. Chalk matrix stained pink.

110 cm: Fresh glass fragment.

Thin Section: Intersertal, sparsely plagioclase phyric (<2%) basalt. Olivine in groundmass (~8%) is altered to clay. Other groundmass minerals: plag (30%), cpx (40%), magnetite (3%), mesostasis (15%).

SECTION 3

0–5 cm: Drusy calcite vein

Basalt breccia as in Sections 1 and 2

Clasts: Basalt and glass as in Sections 1 and 2 becoming moderately plagioclase phyric downhole

56–57 cm: Fresh glass fragment.

SECTION 4

Basalt breccia – matrix as in Sections 1–3

Clasts

1 – Few reworked chalk fragments

2 – Sparsely to moderately plagioclase phyric basalt as in Sections 2–3

3 – Altered glass as in Sections 1–3 becoming larger with larger fresh centers

45 cm: Fresh glass

130 cm: Drusy calcite vein

SECTION 5

0–70 cm: Basalt breccia – chalk matrix. Large clasts all fresh to moderately weathered, moderately plagioclase phyric basalt as in Sections 2–4. Smaller angular fragments of weathered glass with fresh cores as in Sections 1–4.

32 cm: Fresh glass

70–130 cm: Calcite cemented polymict breccia. Basalt clasts as above, however generally weathered light brown–pinkish gray (7.5YR 6/2) and more rounded. Few well rounded weathered glass fragments. Tabular to well rounded reworked chalk clasts abundant in parts. Cement is white, finely crystalline calcite with numerous drusy vug linings. Solution channel(?) – above basement

130 cm: Probable start of basalt pillows

Thin Section: Intergranular, moderately plagioclase phyric (2–3%) basalt. Glomerophyric clusters of plagioclase, which often have many liquid inclusions. Groundmass: ol (20%), pl (30%), cpx (40%), vesicles are rare and filled with clay.

SECTION 6

Moderately plagioclase phyric basalt as in Sections 2–5. No matrix present – probably first flow material

35 cm: 2 mm clear drusy calcite vein

SITE 556 HOLE CORE 3 CORED INTERVAL 471.0–480.0 m

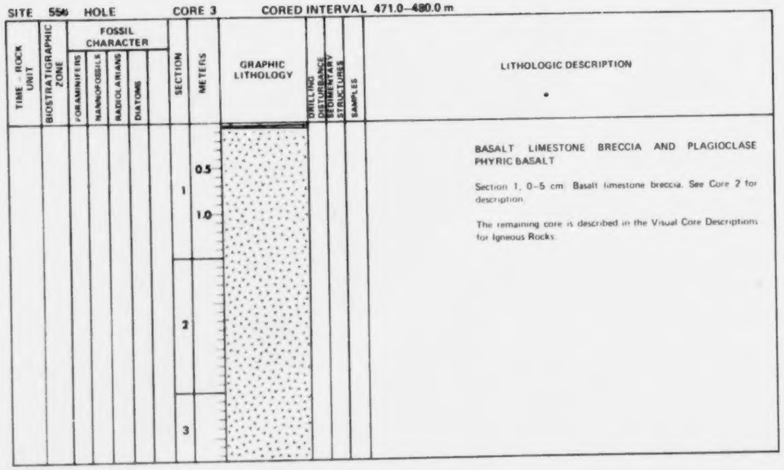
TIME - ROCK UNIT
BIOSTRATIGRAPHIC ZONE
FOSSIL CHARACTER
FORAMINIFERS
NANNOFOSSILS
RADIOLARIANS
DIATOMS
SECTION
METERS
GRAPHIC LITHOLOGY
DRILLING DISTURBANCE
SEDIMENTARY STRUCTURES
SAMPLES
LITHOLOGIC DESCRIPTION
0.5
1.0
1
2
3

BASALT LIMESTONE BRECCIA AND PLAGIOCLASE PHYRIC BASALT

Section 1, 0–5 cm Basalt limestone breccia. See Core 2 for description.

The remaining core is described in the Visual Core Descriptions for Igneous Rocks.

SITE 556, CORE 3 Depth 471.0–480.0 m

SECTION 1

LIMESTONE BASALT BRECCIA AND PLAGIOCLASE PHYRIC BASALT

0–5 cm: Limestone basalt breccia, see description of Core 2.

5–150 cm: Fine grained, moderately phyric basalt, dark gray (2.5YR N4). Equant plagioclase phenocrysts (~5 mm) up to 5%. Minor olivine (~1 mm) that is weathered dark grayish brown (2.5Y 4/2). Minor calcite veins are present.

138 cm: ~1 cm, thick glass band (wedge shaped) about 50% weathered to dark brown (7.5YR 3/2).

Thin Section at 63–65 cm: Moderately plagioclase phyric (5–7%), hyalophitic basalt; traces of olivine phenocryts (mostly altered). Mesostasis (20–23%) devitrified and partially altered (1–3%) to clay; groundmass: ol (5%), plag (35%), cpx (35%). Vesicles (~1%) are filled with clay.

SECTION 2

PLAGIOCLASE PHYRIC BASALT

Same as in Section 1 although slightly more weathered with ~1% round amygdules (1 mm) filled with dark clay minerals. Calcite veins (1–2 mm wide) are common.

61 and 115 cm: Intervals of fresh glass, heavily veined by carbonate.

Thin Section at 30–33 cm: Sparsely plagioclase phyric (~2%), hyalophitic basalt; groundmass: ol (3%), plag (30%), cpx (30%); mesostasis (~23%) is devitrified glass, partly altered to clay (chlorite?). Rare vesicles (<1%) filled with clay; fractures and veins filled with calcite.

SECTION 3

PLAGIOCLASE PHYRIC BASALT

Similar to Sections 1 and 2, medium gray (2.5Y N5) with prismatic plagioclase phenocrysts (up to 7 mm), 2%. Calcite veins are common.

Thin Section at 65–67 cm: Plagioclase phyric (~5%) hyalopilitic basalt, olivine phenos also present (~2%), groundmass: pl (30%), cpx (<10%), ol (<1%), opaques (< 1%); mesostasis (~50%) devitrified glass.

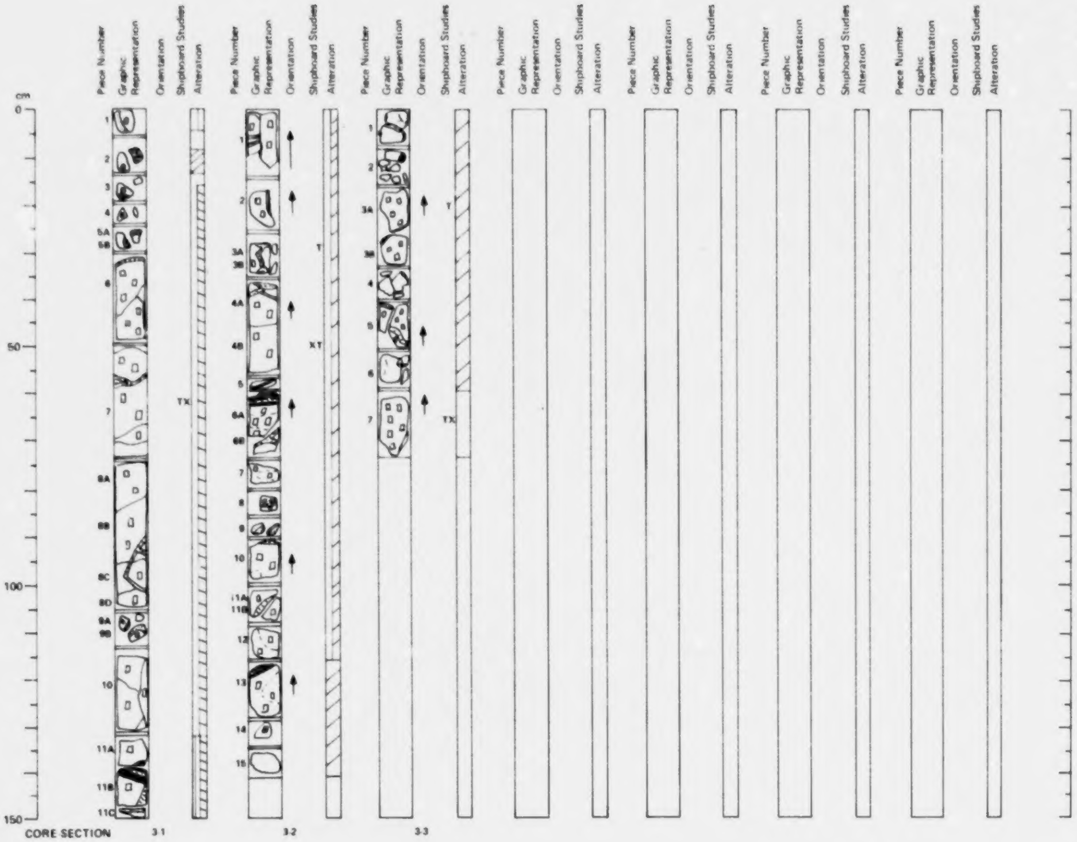

cm
0
50
100
150
CORE SECTION
Piece Number
Graphic Representation
Orientation
Shipboard Studies
Alteration
3-1
3-2
3-3
1
2
3
4
5A
5B
6
7
8A
8B
8C
8D
9A
9B
10
11A
11B
11C
1
2
3A
3B
4A
4B
5
6A
6B
7
8
9
10
11A
11B
12
13
14
15
1
2
3A
3B
4
5
6
7
TX
T
XT
T
TX

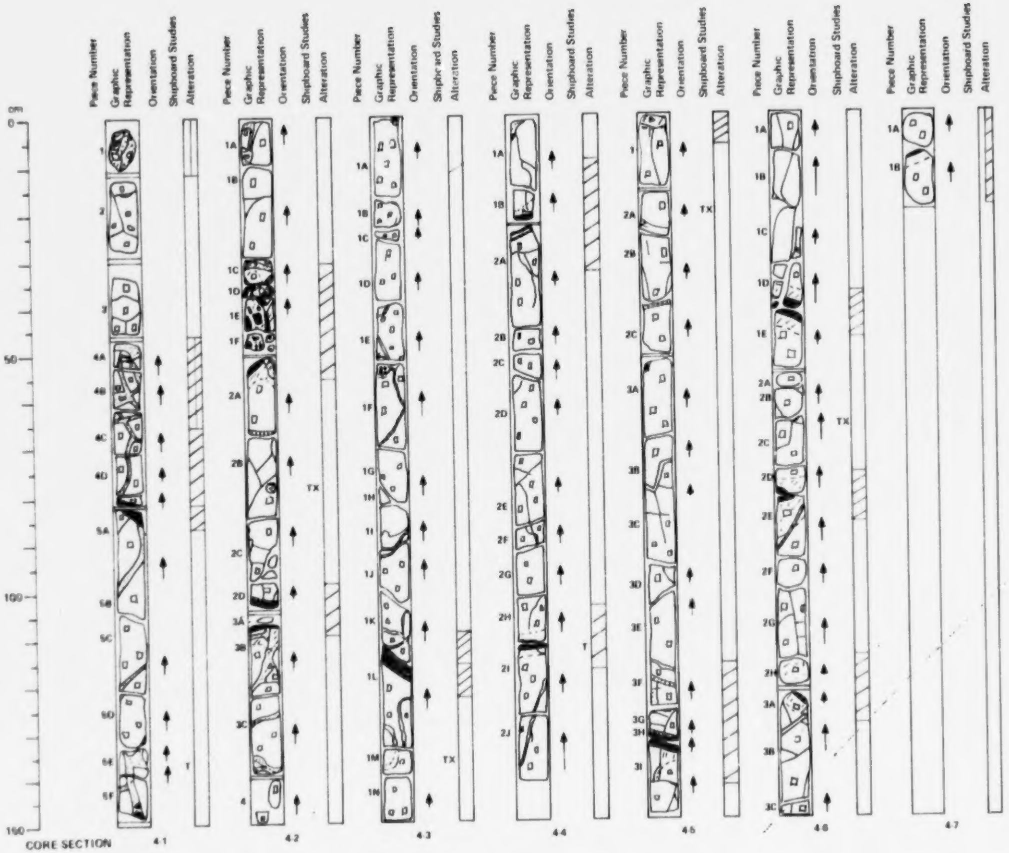

SITE 556 CORE 4 Depth 480.0–489.0 m

SECTION 1

PLAGIOCLASE PHYRIC BASALT (BRECCIA)

0–10 cm: Fine grained, phyric basalt breccia, grayish brown (2.5Y 5/2) with plagioclase phenocrysts (4 mm). Finer matrix cemented by calcite.

10–150 cm: Fine grained, phyric basalt, dark gray (7.5YR N4). Plagioclase phenocrysts are common (5–10% and often partially reabsorbed, size is <10 mm. Olivine (1%) is mostly altered to smectite.

79–84 cm: Vitric rims separating two pillows?

Infilling the fractures is pale yellow (5Y 7/3) nannofossil chalk. Geopetal structures are common, showing that the sediment has filtered into the basalt after its emplacement. In some places this sediment has been completely recrystallized to calcite.

Thin Section at 45–47 cm: Volcanic intraclastic chalk is composed of the following: volcaniclastics (< 2 mm) 10%, foraminifers 5%, intraclasts (micrite) 30% and with a micrite matrix 55%. Clasts are poorly sorted, angular to subrounded, but do show stratification (geopetal).

SECTION 2

PLAGIOCLASE PHYRIC BASALT

Plagioclase phenocrysts (<10 mm to 15 mm) and fine- to medium-grained, dark gray (7.5YR N4/0) phyric basalt make up 5–10%. Fresh olivine (~2–3 mm in diameter) is rare. Olivine is usually altered to smectite. Vesicles are either filled with smectite or with calcite.

33–54 and 101–108 cm: Vitric rims occurring between different pillows. Close to the glass the basalt is moderately altered. Fractures that occur in fresh regions are filled with pale yellow (5Y 7/3) nannofossil chalk.

Thin Section at 80–88 cm: Plagioclase-phyric (~10%), vitrophyric basalt, olivine-phenocrysts up to 1%, groundmass: plag (40%), ol (2%), devitrified glass (45%), segregation vesicles are rare and filled with smectite(?)

SECTION 3

PLAGIOCLASE PHYRIC BASALT

0–110 cm: Same unit as Section 2.

51–56 cm: Sediment-dendritic pattern, penetrating the basalt from a fracture.

110–150 cm: Fine grained gray (2.5Y N5) plagioclase phyric (<5%) basalt. Plagioclase phenocrysts are rounded (partial resorbed), upper portion has glass rim.

120–134 cm: has 'chlorite?' filled amygules (2–4%) and fewer phenocrysts.

128–137 cm: Alteration zone.

SECTION 4

APHYRIC AND PLAGIOCLASE PHYRIC BASALT

0–22 cm: Fine to medium grained aphyric basalt. Color medium gray (2.5YR N5/0). Fractures filled with carbonate. Vitric rim at the bottom.

22–140 cm: Medium grained phyric basalt. Color dark gray (2.5YR N4/0). Vitric rims at top and bottom with moderately altered zones beside them. Fractures filled with carbonate. Plagioclase phenocrysts (< 10 mm). Percentage of phenocrysts increases from top to bottom (5–15%).

112 cm: Vitric rim with fractures filled by smectite and carbonate.

Thin Section at 110–113 cm: Plagioclase-glomerophyric (3–5%), vitrophyric to tachylitic basalt, groundmass: plag (35%), cpx (~2%), glass of groundmass is mostly devitrified (55%) and shows dots of ore minerals (magnetite?)

SECTION 5

PLAGIOCLASE PHYRIC BASALT

Medium grained phyric basalt. Color dark gray (2.5YR N4/0). Plagioclase phenocrysts (< 15 mm) 5–10%. Vesicles partly round and partly irregular shaped. Fractures partly filled with carbonate.

130–135 cm: Vitric bottom of upper and vitric top of lower unit.

Thin Section at 32–34 cm: Plagioclase-glomerophyric (3–5%), vitrophyric to tachylitic basalt, groundmass: plag (35%), cpx (2%), glass is devitrified (~55%) and shows dots of ore, vesicles (< 1%) are filled with clay.

SECTION 6

PLAGIOCLASE PHYRIC BASALT

0–42 cm: Same as bottom of Section 5. Vitric rim at bottom.

42–150 cm: Fine grained gray (2.5Y N5/0) basalt with vitric rim at top and bottom. Plagioclase phyric (~5–10%, <14 mm). Fractures are filled with carbonate.

82–122 cm: Vitric rims.

SECTION 7

PLAGIOCLASE PHYRIC BASALT

Moderately plagioclase-phyric basalt as in Section 6.

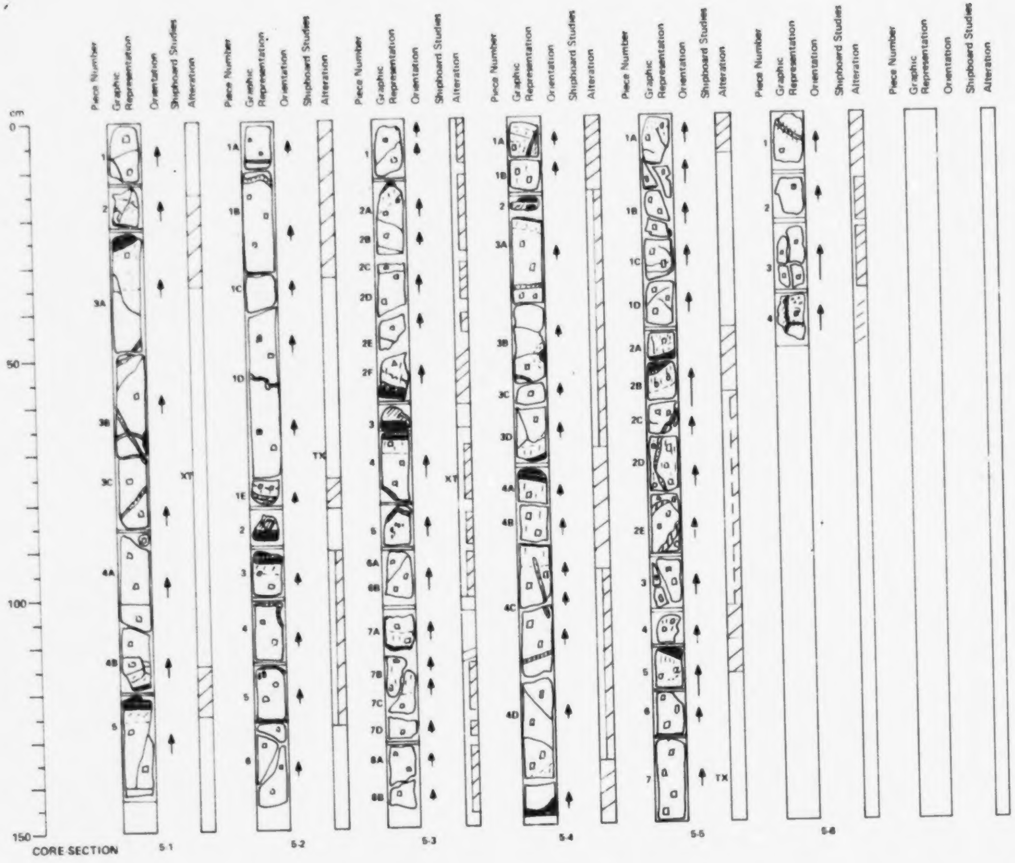

SITE 556, CORE 5 Depth 489.0–498.0 m

SECTION 1

PLAGIOCLASE PHYRIC BASALT

Medium grained, plagioclase-phyric basalt. Color medium gray (7.5YR N5/0). Plagioclase about 5 mm to 8 mm (~5%) and mostly anhedral (resorbed). Round amygdules filled with smectite. At 55 cm patchy vesicles filled with (smectite?) clay minerals occur. At the top of Pieces 3 and 5 there are multiple vitric cooling rims. Calcitic and clayey fracture fillings are common.

0–23 cm: Lower part of pillow.

23–118 cm: Separate pillow.

118–143 cm: Upper part of pillow.

Thin Section at 75–78 cm: Interserta! to intergranular plagioclase-phyric basalt; plagioclase occurs in glomerophyric clusters and is often resorbed; groundmass: plag (50%), cpx (40%), mesostasis (10%) looks like devitrified glass.

SECTION 2

PLAGIOCLASE PHYRIC BASALT

Moderately plagioclase phyric basalt throughout as in Section 1 and above. Minor carbonate veins (shown with hatched | = | pattern). Color gray (7.5YR N5).

1–32 cm: Vesicular. < 5% rounded vesicles filled with moderate green (5G 5/6) clays(?) and/or white calcite.

Thin Section at 70–73 cm: Hyalophitic, plagioclase-phyric (~5%) basalt, olivine phenocrysts are present (~1%) but altered or corroded (skeletons). Groundmass: plag (35%), cpx (4%), ol (1%), glass (devitrified) (55%) with opaques, like the olivine, cpx is often replaced by clay minerals.

83–87 cm: Fresh glass and carbonate.

SECTION 3

PLAGIOCLASE PHYRIC BASALT

Moderately plagioclase phyric basalt throughout the core section as in Sections 1 and 2. Minor carbonate veins (shown by hatched | ⊂⊃ | pattern). (Gradational alteration indicated by | ⁍ |, as per legend.) Color gray (7.5YR N6).

82–90 cm: Note the calcite veins within the top of the sample. Irregular vesicles (denoted by ⁂) filled with dark greenish clays.

SECTION 4

PLAGIOCLASE PHYRIC BASALT

Sparsely to moderately plagioclase phyric basalt as in Sections 1–3. Phenocryst abundance gradually decreasing downhole.

SECTION 5

PLAGIOCLASE PHYRIC BASALT

0–5 cm: < 5% small vesicles mostly empty, some with calcite. Sparsely to moderately plagioclase phyric basalts as in Sections 1–4, dark gray (7.5YR N4).

50 cm: Fresh to moderately altered glass with calcite vein (bottom of upper pillow).

54 cm: Fresh to moderately altered glass (top of pillow).

65–70 cm: Moderate sized calcite vein.

85–90 cm: Pinkish gray (7.5YR 7/2) vein of carbonate cement with small pieces of basalt and altered glass.

100 cm: Larger (12 mm) equant plagioclase phenocryst.

113–115 cm: Glass with calcite vein containing angular pieces of fresh glass with altered rims; top of pillow.

Thin Section at 140–143 cm: Moderately plagioclase-phyric (~3%), intergranular to intersertal basalt, plagioclase phenocrysts often show liquid inclusions. Groundmass: plag (50%), cpx (30%), ol (~1%), mesostasis (15%) is devitrified glass, containing opaques (magnetite?).

SECTION 6

PLAGIOCLASE PHYRIC BASALT

Slightly to moderately plagioclase phyric basalts, as in Sections 1–5.

38–46 cm: Irregular vesicles filled with calcite.

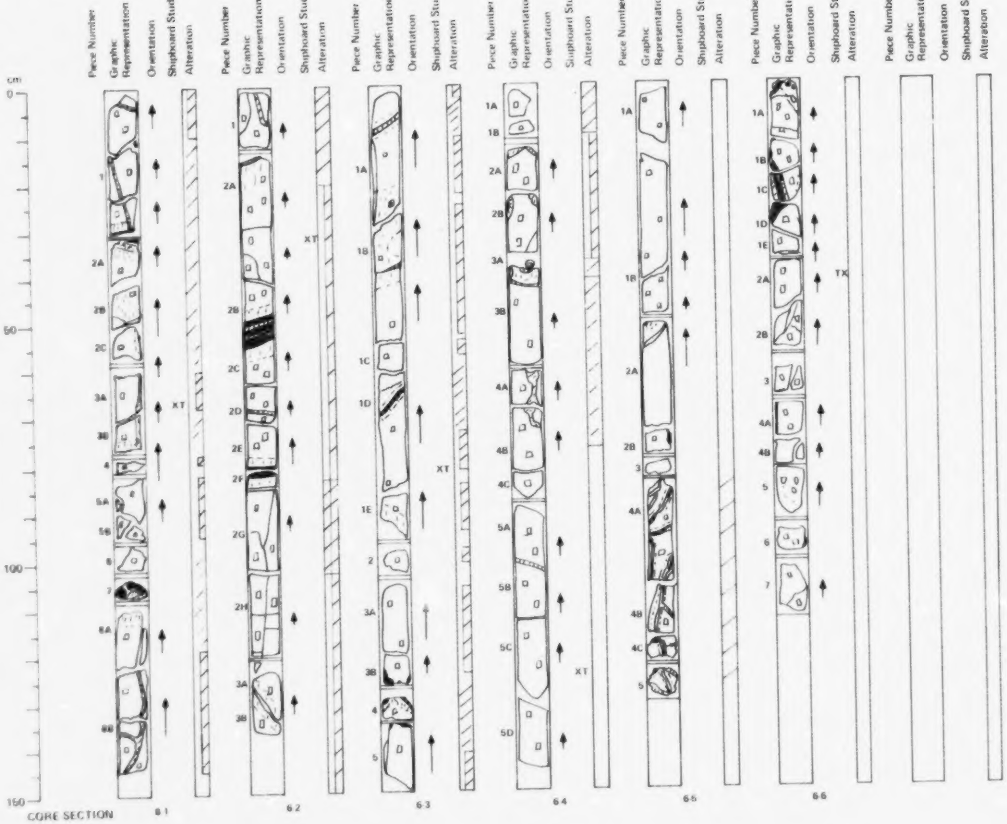

SITE 556, CORE 6 Depth 498.0–507.0 m

SECTION 1

PLAGIOCLASE PHYRIC BASALT

Slightly to moderately plagioclase phyric basalt decreasing in frequency and becoming more rounded down the core. Irregular vesicles found throughout, often with greenish clay or calcite included. Color 7.5YR N6/0.

33–40 cm, Piece 2A: Altered multiple glass rinds separated by calcite veins. Small unaltered pieces of glass remain. Irregular vesicles throughout entire unit 2.

101–107 cm, Piece 7: Altered glass and calcite, dark brown to black glass, white calcite, ruddy orange zone between the two (color 5YR N6/6).

Thin Section at 65–68 cm: Sparsely plagioclase-phyric (~2%) intergranular basalt, groundmass: cpx (45%), plag (30%), ol (20%), magnetite (5%); olivine is mostly altered to clay minerals.

SECTION 2

PLAGIOCLASE PHYRIC BASALT

Sparsely plagioclase phyric basalt as in Section 1. Phenocrysts (~3%) prismatic to rounded, up to ~4 mm maximum dimension. Minor calcite veins to ~1 mm. Light brown weathering along many cracks.

many cracks.

Thin Section at 32–36 cm: Moderately plagioclase-phyric (~5%) basalt, minor ol phenocrysts are present (<1%), groundmass: plag (45%), cpx (45%), ol (5%), magnetite (5%), vesicles occur up to 1% and are filled with clay, olivine and partly cpx are replaced by clay minerals.

SECTION 3

PLAGIOCLASE PHYRIC BASALT

Sparsely plagioclase phyric basalt as in Sections 1 and 2.

0–60 cm: 2–3% vesicles to 1 mm. Most filled with dark green (5G 5/2) clay(?) or chlorite.

0–45 and 90–96 cm: Weathered zones greenish brown (2.5Y 5/4) in color in contrast to normal light brown (7.5YR 6/4).

Thin Section at 80–83 cm: Moderately plagioclase-phyric (~3%) intergranular to intersertal basalt containing traces of olivine phenocrysts, the normally zoned plagioclase phenocrysts show liquid inclusions; groundmass: cpx (45%), plag (35%), ol (0.5%), magnetite (5%), mesostasis (~5%) is altered to clay, olivine is replaced by clay minerals, too.

SECTION 4

PLAGIOCLASE PHYRIC BASALT

Sparsely plagioclase phyric basalt as in Sections 1–3. Calcite veins open in several places to drusy cavities.

25 cm: Dark green chlorite(?) in cavity in calcite vein (XRD – chlorite and montmorillonite [dioctahedral]).

SECTION 5

PLAGIOCLASE PHYRIC BASALT

Moderately plagioclase phyric basalts to sparsely plagioclase phyric down core. Color dark gray (7.5YR N4).

80 cm: Major(?) break – increase in occurrence and complexity of calcite vein pattern. Noticeable small (<0.1 mm) orange brown patches in irregular vesicles: iddingsite? (probably clay alteration product). Alteration along calcite veins. (Steroscopic examination further suggests highly weathered olivines: iddingsite?.) Gradient in color most noticeable from 80 cm down, gray (7.5YR N6). Less crystalline, more massive character.

SECTION 6

PLAGIOCLASE PHYRIC TO APHYRIC BASALT

Fine grained, sparsely plagioclase phyric to aphyric basalt with small plagioclase laths and 1–2% equant plagioclase phenocrysts (similar to 85–130 cm in Section 5).

Color medium gray (7.5YR N6), red brown altered olivines.

17–30 cm: Large calcite vein to fresh altered glass.

Thin Section at 44–47 cm: Aphyric, intergranular basalt; microphenocrysts: plag (2–3%); groundmass: cpx (50%), plag (25%), ol (10%), clay minerals (5–10%).

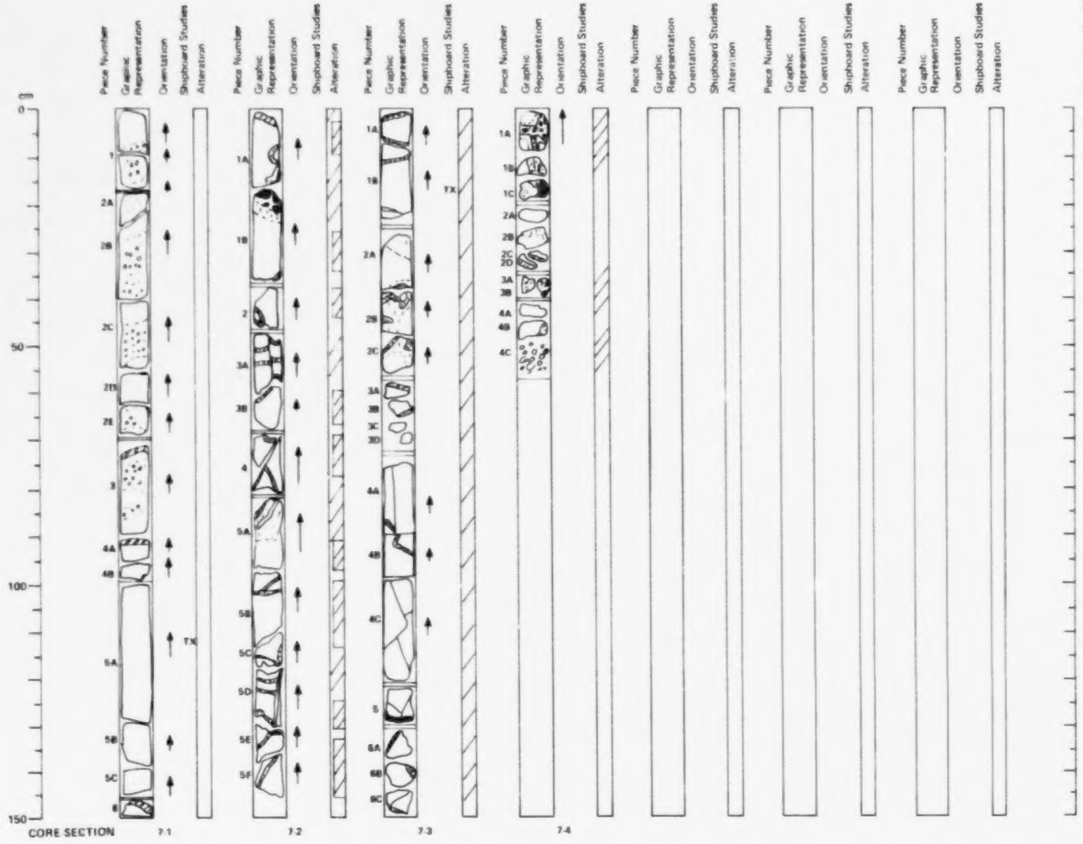
cm
0
50
100
150
CORE SECTION
7-1
7-2
7-3
7-4
Piece Number
Graphic Representation
Orientation
Shipboard Studies
Alteration
TX
1
2A
2B
2C
2D
2E
3
4A
4B
5A
5B
5C
6
1A
1B
2
3A
3B
4
5A
5B
5C
5D
5E
5F
1A
1B
2A
2B
2C
3A
3B
3C
3D
4A
4B
4C
5
6A
6B
6C
1A
1B
1C
2A
2B
2C
2D
3A
3B
4A
4B
4C

SITE 556 CORE 7 Depth 507.0–516.0 m

SECTION 1

APHYRIC BASALT

Fine grained, light gray (7.5YR N6) aphyric basalt to sparse equant plagioclase phenocrysts up to 3 mm. Varying amounts (up to 3–4%) of vesicles [illegible] up to 1 mm, most are empty, but some are filled with calcite. Sparse altered red brown (7.5YR 6/8) olivine(?) phenocrysts up to 1 mm.

Thin Section at 113–115 cm: Intergranular to subophitic sparsely plagioclase phyric (1–3%) basalt. Plagioclase phenocrysts show liquid inclusions, their approximate composition is An_{68}. Groundmass: plag (40%), cpx (35%), ol (10%), magnetite (5%). Olivine and mesostasis are partly replaced by clay.

SECTION 2

APHYRIC BASALT

Aphyric, fine grained basalt with patches of slightly plagioclase phyric basalt mainly in the top 35 cm. Color light gray (7.5YR N6).

13–20 cm: Glass fragments imbedded in and reacted with calcite.

Irregular vesicles throughout, extensive about the calcite veins. Vesicles empty, or containing green clay or calcite. Altered olivine crystals (<1.5 mm) to iddingsite product.

SECTION 3

APHYRIC BASALT

Aphyric fine grained basalt with scattered equant plagioclase phenocrysts as in Section 2. Vesicles scarce.

Thin Section at 17–19 cm: Aphyric to sparsely plagioclase phyric (< 1%) intergranular to intersertal basalt, plagioclase laths are resorbed. Groundmass: plag (36%), cpx (36%), ol (10%), magnetite (5%). Round vesicles (<1%) are filled with clay. Parts of olivine and mesostasis are replaced by clay.

SECTION 4

APHYRIC BASALT

Vesicular aphyric basalt, light gray (7.5YR N6). High degree of calcite vein intrusion, causing distinct alteration about veins, light brown (10YR N6/2) in color. Glass fragments in Pieces 1A and C.

35–38 cm, Pieces 3A and B: Calcareous sediment(?) positive acid test.

48–57 cm, Piece 4C: Gravel, mixture of small aphyric basalt and calcite chips.

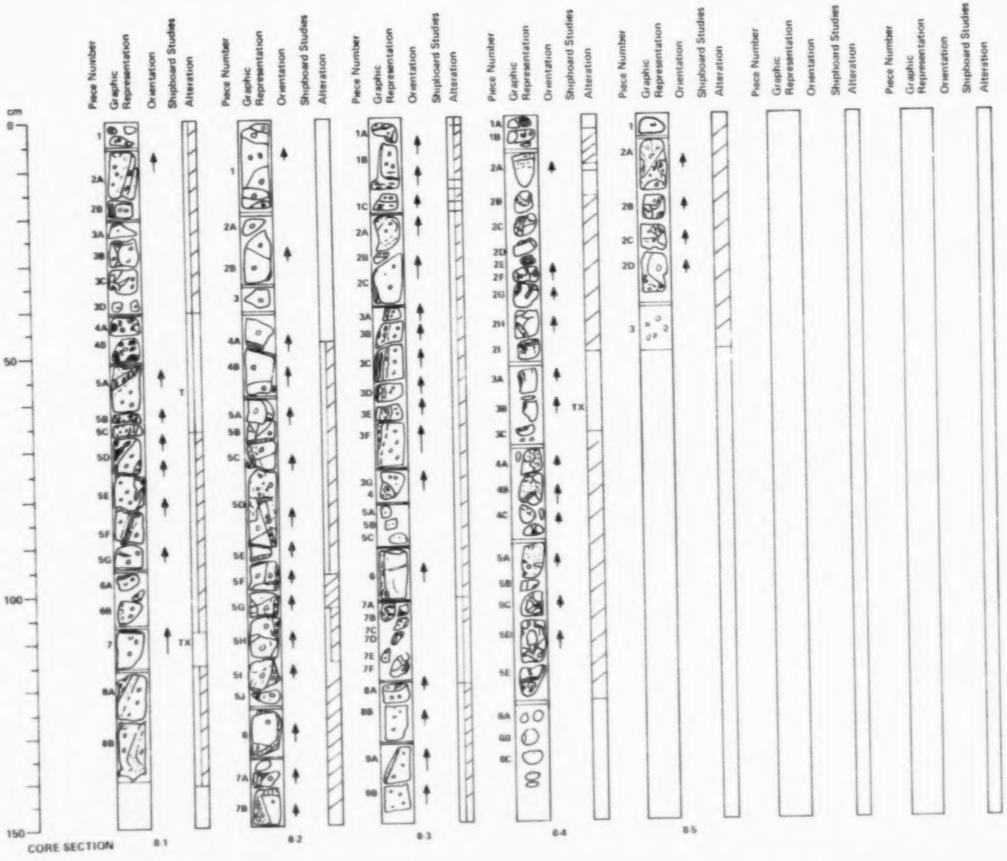

SITE 556, CORE 8 Depth 516.0–525.0 m

SECTION 1

OLIVINE MICRO PHYRIC BASALT

0–5 cm. Moderately plagioclase and olivine micro-phyric basalt, plagioclase ~5% anhedral and partially resorbed, olivine 5–7% altered.

5–140 cm. New unit — moderately olivine micro-phyric basalt, color gray (7.5YR N6/0), fine grained. Olivines are altered, 5% rounded vesicles.

40–50 and 60–68 cm. Broken pieces of glass and/or basalt which have altered to palagonite. Some pieces of palagonite have basalt cores. All pieces are cemented with micrite and then spary calcite cement.

Thin Section taken to compare altered and fresh basalt, and cemented palagonite pieces.

Thin Section at 110–113 cm: Sparsely phyric to aphyric intersertal to intergranular basalt. Microphenos: ol (3%), plag (1%), cpx (1%); groundmass: cpx (45%), plag (30–35%), magnetite (3%); segregation vesicles (1%) filled with devitrified glass and carbonate; olivine is completely altered to clay.

SECTION 2

OLIVINE MICRO PHYRIC BASALT

Moderately olivine micro-phyric, gray (7.5YR N6/0) basalt. Olivine is mostly altered into smectite. Olivine ~5–7%, size ≥1 mm. There are some large equant (some >5 mm), light colored phenocrysts in the upper 38 cm of this section (plagioclase?). Vesicles are common and empty. The whole section is highly fractured. Some fractures are filled with sparry calcite cement (see Pieces 4, 6, and 7). From 68 to 120 cm a fracture occurs which is filled with highly palagonitized basalt breccia. The same occurs in Piece 7. These brecciated fractures have palagonite edges.

Piece 5C, 68–74 cm

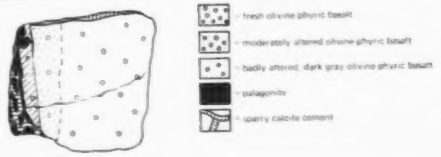
= fresh olivine-phyric basalt
= moderately altered olivine-phyric basalt
= badly altered, dark gray olivine-phyric basalt
= palagonite
= sparry calcite cement

SECTION 3

OLIVINE MICRO PHYRIC BASALT

See Section 2 description for details of this moderately olivine micro-phyric basalt (≈10% olivine).

Rare (2 mm) partially resorbed plagioclase phenocrysts are found in Pieces 1B, 8–10 cm; 1C, 23–24 cm; and 3E, 62 cm.

SECTION 4

OLIVINE MICRO PHYRIC BASALT

Moderately olivine micro-phyric basalt, color light brownish gray to gray (2.5Y 6/2–2.5Y 6/0). Olivine (up to 10%), mostly altered (diameter 0.8–1 mm). Almost whole section is brecciated and shows palagonitization and calcite cementation in and close to the fractures and veins.

Thin Section at 63–66 cm: Hyalophitic basalt; groundmass: cpx (40%), plag (25–30%), ol (<5%), magnetite (3%); rest: devitrified glass (25–30%); vesicles (3%) are round and filled with calcite; some of them show segregation. Olivine is replaced by clay.

SECTION 5

OLIVINE MICRO PHYRIC BASALT (BRECCIA)

Larger basalt pieces: light brownish gray (2.5Y 6/2) olivine micro-phyric basalt, moderately altered, with mostly empty round vesicles. Pieces are fairly rounded. Smaller pieces: basalt as above and palagonite pieces. The breccia is cemented by calcite.

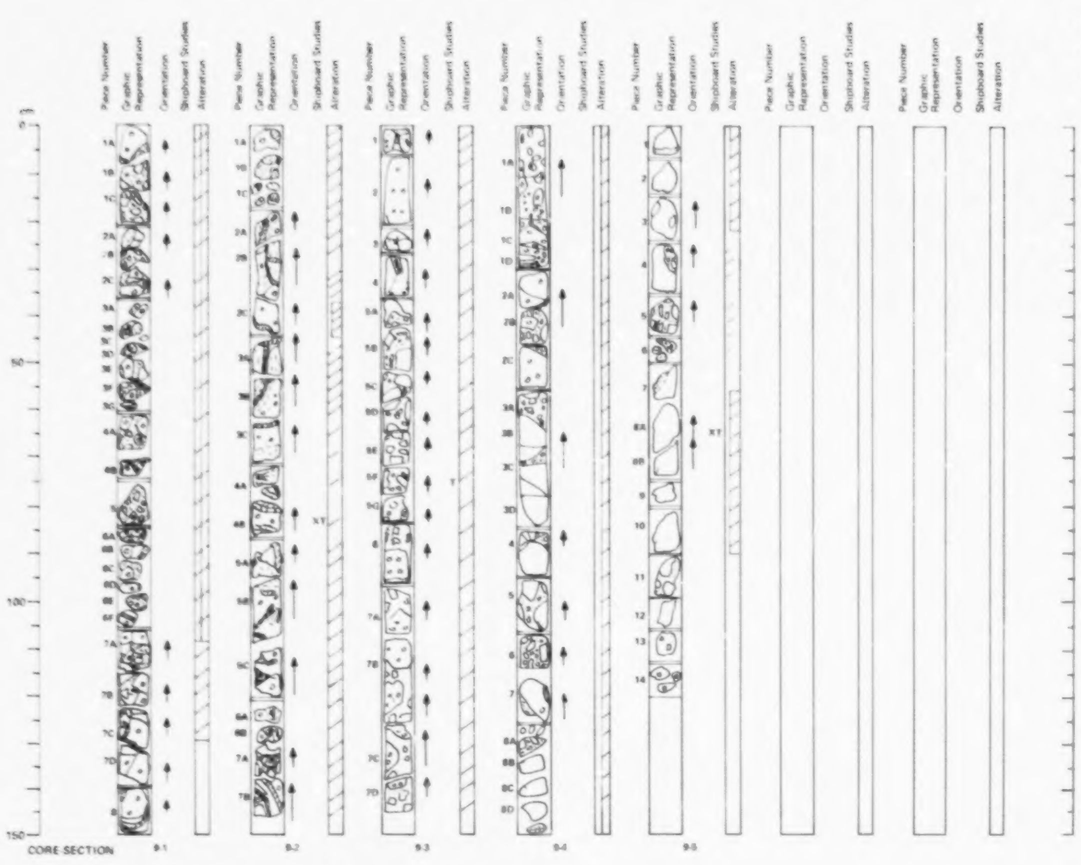

SITE 556 CORE 9 Depth 525.0–534.0 m

SECTION 1

OLIVINE MICRO PHYRIC BASALT

0–105 cm: Moderately to badly altered, vesicular, olivine micro phyric, medium grained basalt breccia. Olivine (5–10%) diameter >1 mm and altered to smectite.

From 0– ~50 cm: "Matrix" consists of angular – rounded palagonite pieces.

From 50– ~110 cm: Calcite cementation increases.

From ~110 cm–bottom of section: The basalt is fairly fresh. Here the narrow fractures are filled by carbonate cement. Color gray (2.5Y N5/0). Most of the vesicles in the basalt throughout the whole section are not filled.

SECTION 2

OLIVINE MICRO PHYRIC BASALT

Olivine microphenocrystic basalt light gray (7.5YR N/6) in color. Calcite veins infiltrate the basalt, pattern quite complex and frequent down core. Alteration of basalt about calcite veins yield clay basalt mixture, light brown (10YR N6/2) in color. General alteration to brown throughout, very noticeable in Pieces 3A, B, and C and 5A, B, and C. Interpreted as brecciated basalt transition zone: just fractured, slightly moved to stationary.

Irregular vesicles throughout, size ranging up to 1 mm in diameter. Often empty, some filled with calcite or clay alteration product.

107–118 cm, Piece 5C: Glass altered to palagonite surrounded by calcite alteration rim. Subsequent product is ruddy orange (7.5YR N7/6) in color.

120–145 cm: Calcite rim with palagonitized glass.

SECTION 3

OLIVINE MICRO PHYRIC BASALT AND BASALT BRECCIA

0–30 cm: Moderately olivine (5–7%) micro phyric gray (7.5YR N5) fine grained basalt. Olivines are altered to smectite (~0.5 mm) 5% round vesicles.

27–143 cm: Breccia – made up of angular and subrounded pieces of moderately olivine microphyric gray fine grained basalt. These pieces range in sizes from 10 cm to a few mm. The degree of alterations is not a function of size (i.e. smaller pieces are fresher then larger pieces). The matrix contains carbonate.

Thin Section, 72–75 cm: Basalt breccia matrix, basalt lithic and glass fragments, subangular to subrounded, no sorting or stratification noticed, size range coarse sand to clay size. XRD shows no clay minerals. Micritic calcite is common.

SECTION 4

BASALT BRECCIA (OLIVINE MICRO PHYRIC)

Fresh to moderately altered basalt breccia. Upper half is olivine micro phyric (<5%, <1 mm). From ~98 cm to the bottom basalt is aphyric. Vesicles occur anywhere, partly empty, partly filled with smectite. Color of basalt is gray to light brownish gray (2.5Y N6–2.5Y 6/2). Color of "matrix" is light yellowish gray (2.5Y 7/2).

SECTION 5

BASALT BRECCIA (APHYRIC)

Aphyric basalt, exceptions as noted. Color 10YR N6/1. Hints of central phases of brecciated basalt zone.

35–42 cm: Brecciated basalt, carbonate cement.

44–50 cm: Brecciated basalt pieces, carbonate cement.

91–92 cm, Piece 11: Hazy brecciated basalt transition zone. Calcite cement light brown gray (10YR 6/2).

106–110 cm, Piece 13: Plagioclase phyric basalt, clasts up to 3.5 mm in diameter.

111–116 cm: Pieces of slightly plagiophyric basalt.

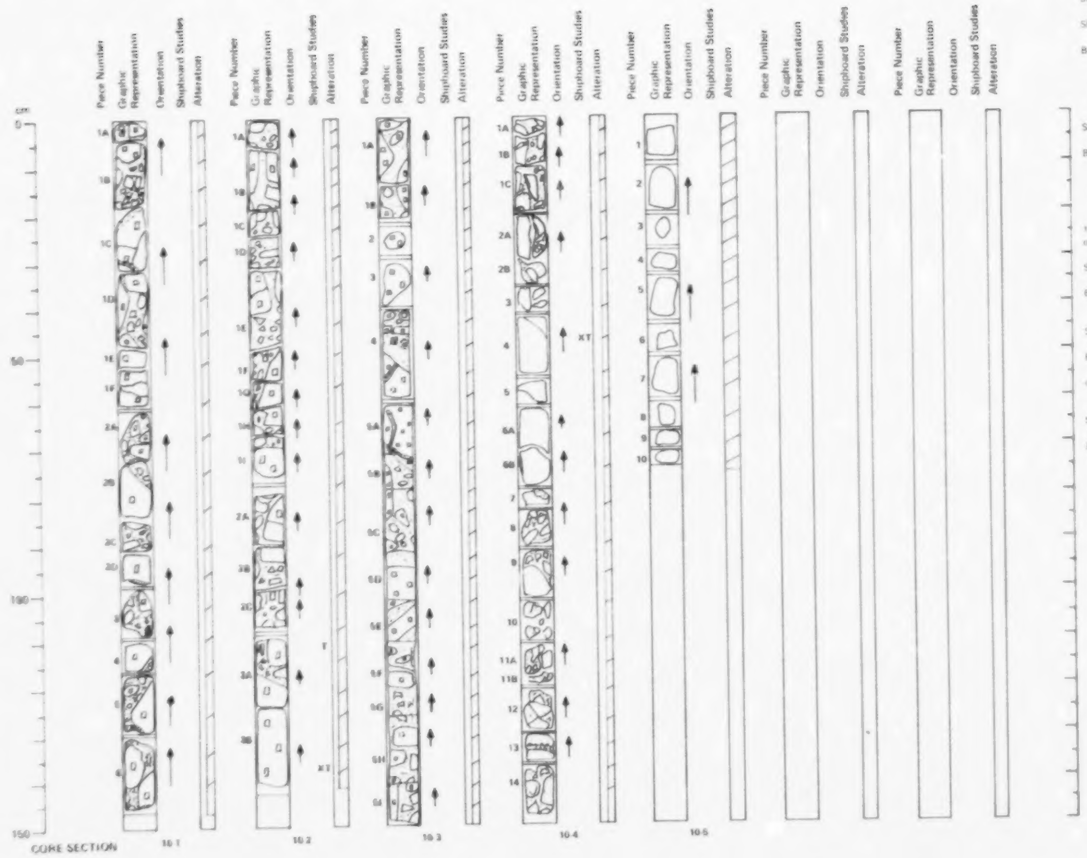

SITE 556, CORE 10 Depth 534.0–543.0 m

SECTION 1

BASALT BRECCIA (PLAGIOCLASE PHYRIC)

Basalt: Moderately plagioclase-phyric, gray (2.5Y N5/0). Vesicles are common and mostly filled with smectite.

At 30 cm: Narrow calcitic vein.

"Matrix": Olive (5Y 5/3) with many angular pieces of basalt.

115–128 cm: Partly calcite-cemented with some open cavities.

SECTION 2

BASALT BRECCIA (PLAGIOCLASE PHYRIC)

Basalt breccia.

Angular clasts of moderately plagioclase phyric light gray (2.5Y N5/0) basalt.

~5% equant plagioclase phenocrysts to about 2 mm.

Matrix: Indurated light gray-green (5Y 5/3) calcareous(?) ooze.

Thin Section, 36–39 cm: Moderately plagioclase-phyric (5%) intersertal basalt; plagioclase-phenocryst composition An_{60}; groundmass: cpx (40%), plag (30%), ol (5–10%), magnetite (3–5%), mesostasis (15–20%) is altered; olivine is replaced by clay.

SECTION 3

BASALT BRECCIA (PLAGIOCLASE PHYRIC)

Becoming less plagioclase phyric downwards, but otherwise exactly as Section 2.

SECTION 4

BASALT BRECCIA (like Sections 2 and 3)

Clasts: Angular, fine grained, medium gray (5Y 5/1) aphyric to very sparse small olivine and plagioclase phenocrysts.

Matrix: Indurated light gray green (5Y 5/3) calcareous(?) ooze.

SECTION 5

BASALT BRECCIA (APHYRIC TO PLAGIOCLASE PHYRIC)

Medium gray aphyric fine grained basalt with occasional plagioclase phenocrysts to 2 mm.

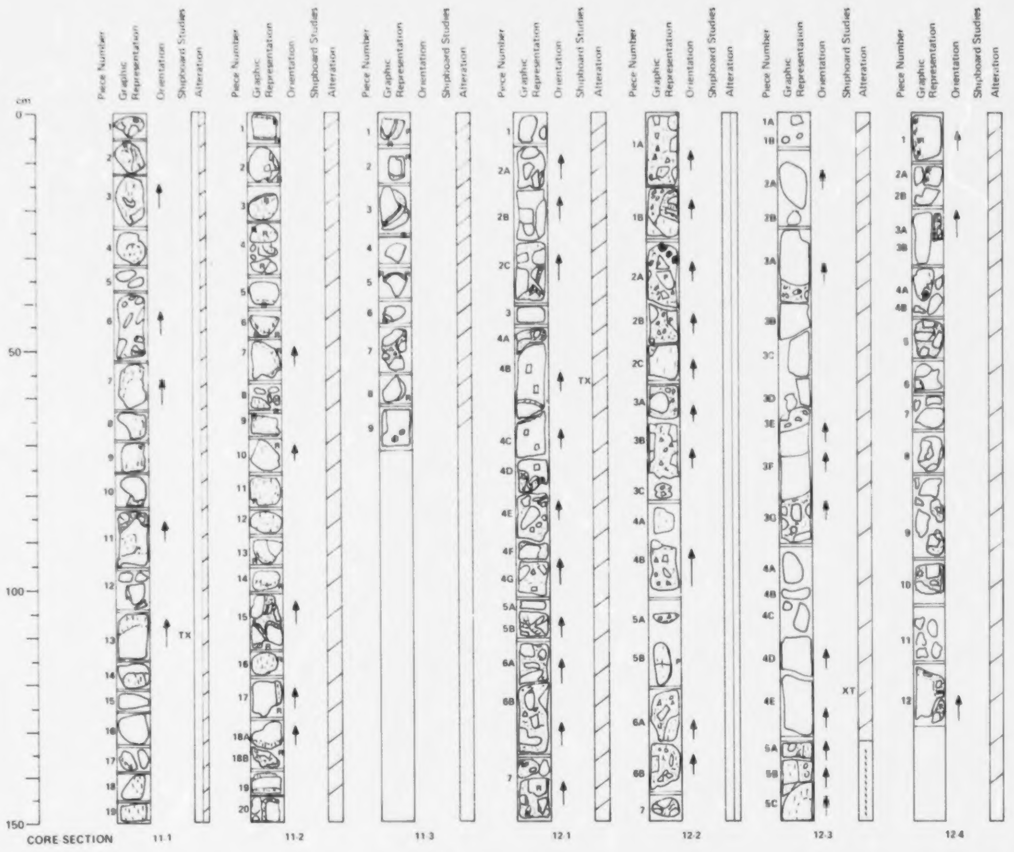
cm
0
50
100
150
CORE SECTION
Piece Number
Graphic Representation
Orientation
Shipboard Studies
Alteration
11-1
11-2
11-3
12-1
12-2
12-3
12-4
TX
TX
XT
1 2 3 4 5 6 7 8 9 10 11 12 13 14 15 16 17 18 19
1 2 3 4 5 6 7 8 9 10 11 12 13 14 15 16 17 18A 18B 19 20
1 2 3 4 5 6 7 8 9
1 2A 2B 2C 3 4A 4B 4C 4D 4E 4F 4G 5A 5B 6A 6B 7
1A 1B 2A 2B 2C 3A 3B 3C 4A 4B 5A 5B 6A 6B 7
1A 1B 2A 2B 3A 3B 3C 3D 3E 3F 3G 4A 4B 4C 4D 4E 5A 5B 5C
1 2A 2B 3A 3B 4A 4B 5 6 7 8 9 10 11 12
R
P

SITE 556, CORE 11 Depth 543.0–552.0 m

SECTION 1

BASALT BRECCIA (APHYRIC)

Clasts: Angular, fine grained, medium gray (2.5Y N6) aphyric with very sparse plagioclase phenocrysts and altered olivine. Sparse vesicles throughout (up to 1 mm), some empty, some filled with calcite and/or green clays. Slight to moderate weathering ([illegible]).

17 cm: Larger (1 cm) cavity filled with calcite and dark green clays(?).

Matrix: Indurated, dark olive gray (5Y 4/3).

Thin Section at 110–112 cm: Aphyric to sparsely plagioclase-phyric (1–2%) intersertal to subophitic basalt. Groundmass: plag (40%), cpx (30%), magnetite (5%), mesostasis (20–25%) partly altered to clay, segregation vesicles (1%) filled with carbonate, olivine is also altered to clay.

140–150 cm: Medium red (5YR 5/3) alteration (oxidation?) and dark red (5YR 3/3) alteration.

SECTION 2

BASALT BRECCIA (APHYRIC)

Mostly single pieces of basalt, but at 25–35 cm, 103–113 cm and 130–136 cm there are angular to subrounded basalt clasts in dark gray green (5GY 3/2) chlorite(?) carbonate matrix.

Basalt itself is fine grained, aphyric medium gray (2.5Y N5).

Extensive red (5R 4/6) alteration in bands or on surface (indicated by R).

SECTION 3

BASALT BRECCIA (APHYRIC)

Light gray (2.5Y N5) aphyric basalt subrounded clasts in dark green (5GY 3/2) chlorite(?) matrix.

Red (5R 4/6) alteration bands in many pieces (indicated by R).

44–52 cm: Chlorite(?) – carbonate matrix.

52–70 cm: No matrix present.

SITE 556, CORE 12 Depth 552.0–561.0 m

SECTION 1

BASALT BRECCIA (APHYRIC TO PLAGIOCLASE PHYRIC)

0–133 cm: Basalt breccia.

Clasts: Medium to fine grained, medium gray (5Y 4/1) aphyric to sparsely plagioclase phyric basalt.

Matrix: greenish gray (5Y 5/3) silt, fine sand size sedimentary matrix (non-carbonate) with ~5% fine carbonate veins.

Thin Section at 55–57 cm: Identical to Core 10, Section 2, Piece 3B.

135–137 cm: See Core 12, Section 2.

SECTION 2

BASALT BRECCIA (APHYRIC)

Section 1, 137–150 cm and Section 2, 0–150 cm: Altered basalt breccia (hyaloclastic).

Clasts

1 – Angular fine grained aphyric basalt clasts to ~ 8 cm maximum dimension. Almost entirely altered light brownish gray (10YR 6/1) to red (2.5YR 4/4).

2 – Black devitrified pillow fragments (marked P) grading to light brown (10YR 6/1) interiors.

3 – Rounded to angular glass fragments. Some fresh, most altered rusty brown or green (10GY 3/2).

Matrix: White to light green (10Y 4/2).

SECTION 3

BASALT BRECCIA (APHYRIC)

0–130 cm: Basalt breccia as in Section 2.

130–150 cm: Altered basalt breccia. Aphyric basalt clasts with red (2.5YR 4/4) altered rims in reddish matrix of comminuted basalt fragments. Chlorite along fracture surfaces in matrix.

SECTION 4

CHALK BASALT BRECCIA (APHYRIC)

More basalt breccias as in Section 3.

More red (5R 5/4) alteration rims.

33–40 cm and 52–57 cm: Reddish (5R 5/4) micritic chalk.

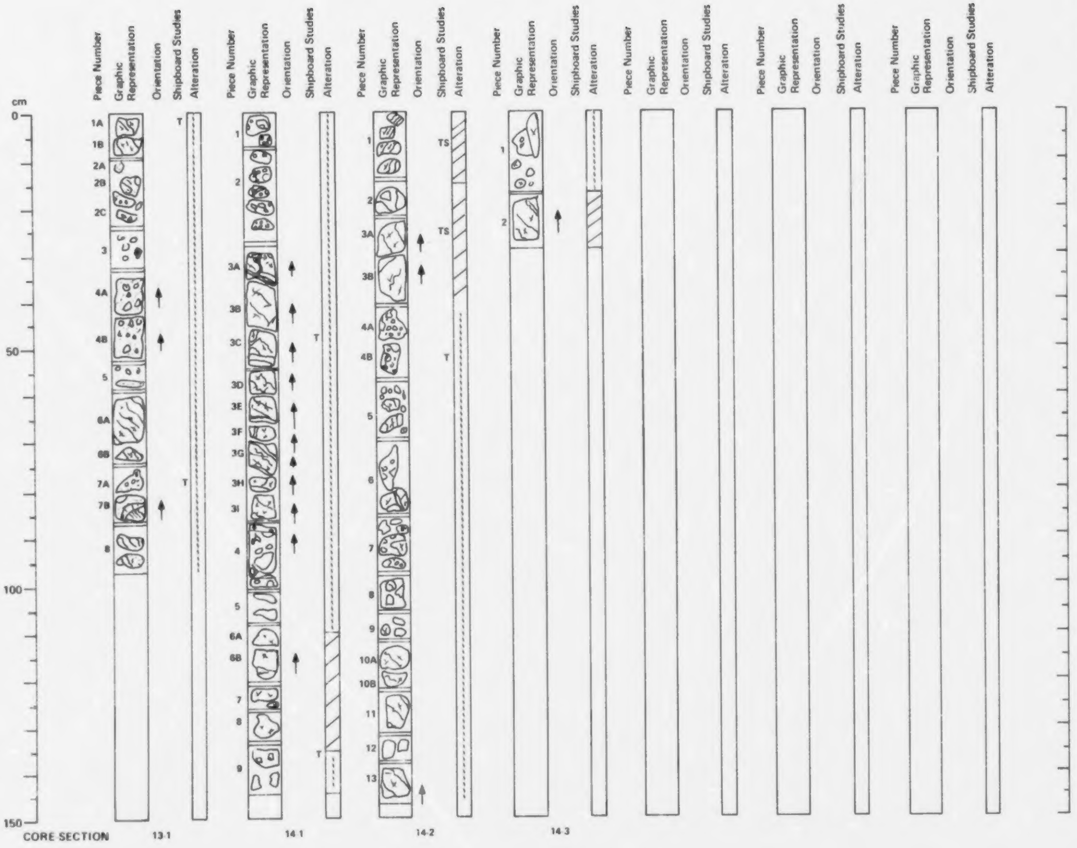

cm
0
50
100
150
CORE SECTION
Piece Number
Graphic Representation
Orientation
Shipboard Studies
Alteration
1A
1B
2A
2B
2C
3
4A
4B
5
6A
6B
7A
7B
8
T
T
13-1
1
2
3A
3B
3C
3D
3E
3F
3G
3H
3I
4
5
6A
6B
7
8
9
T
T
14-1
1
2
3A
3B
4A
4B
5
6
7
8
9
10A
10B
11
12
13
TS
TS
T
14-2
1
2
14-3

SITE 556, CORE 13 Depth 561.0–570.0 m

SECTION 1

SERPENTINIZED GABBRO BRECCIA

Clasts:

1 – Serpentinized gabbro greenish black (BY 2/2) weathering greenish brown (5Y 5/3). Weakly foliated 10–15% altered pyroxene (opx?), brown (10YR 6/4 to 10YR 5/4) in color.

Minor angular clasts of:

Black clinopyroxene

White plagioclase

Gabbro

Matrix: Nondescript brownish green (2.5Y 5/4) fine grained material.

Thin Section at 6–9 cm: Serpentinite (serpentinized noritic?), holocrystalline, phenocrysts: opx (10%), plag (~1%), groundmass: serpentine (80%), magnetite (5%), hematite (3%) – probably after magnetite.

SITE 556, CORE 14 Depth 565.5–574.5 m

SECTION 1

SERPENTINIZED GABBRO BRECCIA

0–30 cm Clasts – large plagioclase crystal (3 cm) black clinopyroxene. See Core 13, Section 1 description.

30–86 cm Serpentinized gabbro with calcite veins.

86–107 cm Polymict breccia with carbonate cement.

107–134 cm Moderately altered gabbro with ≈10% pyroxene.

134–144 cm Polymict breccia with plagioclase clasts.

SECTION 2

SERPENTINIZED GABBRO BRECCIA

0–15 cm Moderately altered serpentinized gabbro. Pyroxene is brown (altered).

15–23 cm Polymict breccia with clasts of gabbro.

23–40 cm Serpentinized gabbro with ≥ 15% opx.

40–56 cm Polymict breccia with gabbro clasts 3 cm–3 mm in size.

56–70 cm Serpentinized gabbro.

70–111 cm Polymict breccia.

111–145 cm Serpentinized gabbro.

Thin Section at 8–11 cm: Clast of holocrystalline (granitic) gabbro, bearing plag (60%), cpx (40%) and traces of magnetite. Plagioclase has approximate composition of An_{60}. Adjacent to cpx occurs light brown amphibole (~10% of cpx) and chlorite (5% of cpx). White prehnite occurs in scattered patches (~15%), serpentine and carbonate are found in small veinlets.

SECTION 3

SERPENTINIZED GABBRO BRECCIA

0–17 cm Polymict breccia – matrix is not carbonate. The rock is so friable that the clasts of serpentinized gabbro and matrix are disassociating.

17–29 cm Moderately altered gabbro.

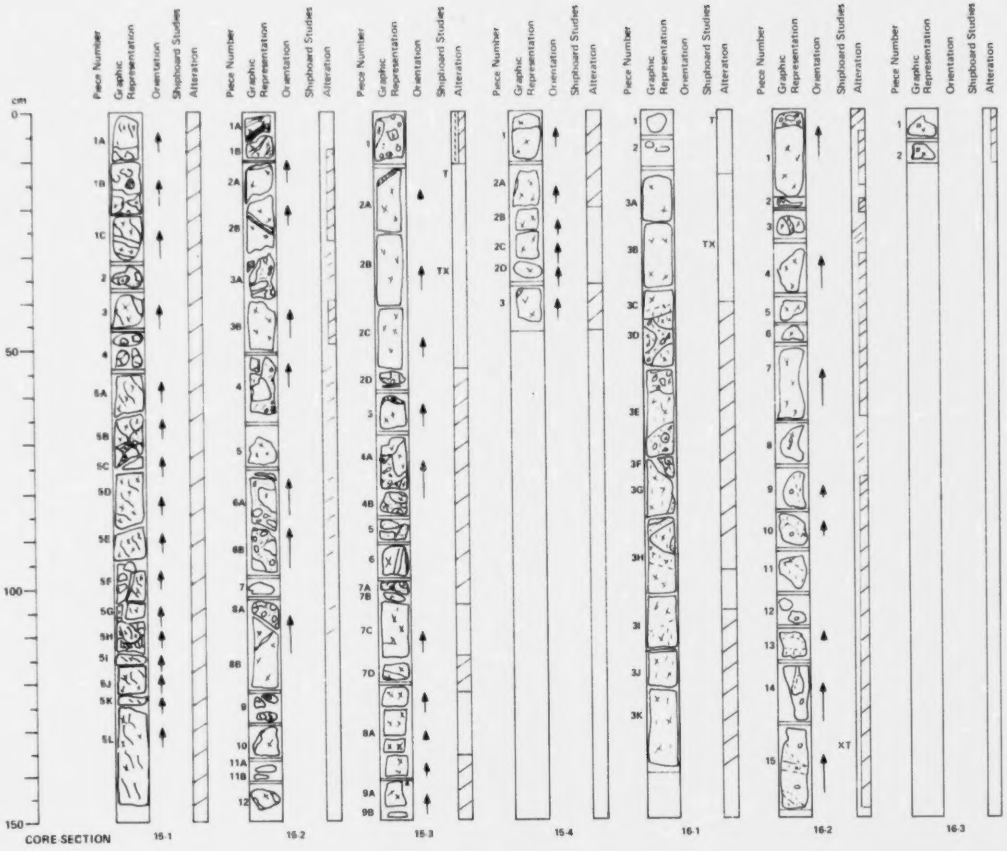

SITE 556, CORE 15 Depth 574.5–583.5 m

SECTION 1

SERPENTINIZED GABBRO BRECCIA

Similar to Core 14, Sections 2 and 3 with clasts of gabbro

Medium brown (4.5YR 5/6) pyroxene (10%), size 1–5 mm and plagioclase plus <1% dark green cpx(?)

0–15 cm Polymict breccia.

15–30 cm Moderately altered gabbro

30–53 cm Polymict breccia.

53–90 cm Moderately altered gabbro with some breccia

90–140 cm Moderately altered gabbro

SECTION 2

SERPENTINIZED GABBRO BRECCIA

Slightly serpentinized gabbro with altered brown pyroxenes infiltrated by calcite veins

30–38 cm, Piece 3A Polymict breccia of clasts of gabbro (serpentinized) containing altered brown pyroxene

53–64 cm, Piece 4 Polymict breccia with clasts of gabbro slightly serpentinized with brown pyroxenes

67–74 cm, Piece 5 Gabbro of brown slightly altered pyroxenes

76–107 cm, Pieces 6A–8A Polymict breccia with clasts of serpentinized gabbros (serpentine obvious) with brown pyroxenes

104–119 cm, Piece 8B Same as for 0–30 cm, except amount of serpentine is increasing.

120–124 cm Piece 9 Polymict breccia with clasts (small) of serpentinized gabbro

126–133 cm, Piece 10 Same as for 0–30 cm except highly serpentinized rim

134–139 cm, Piece 11 Polymict breccia with clast of gabbro

141–145 cm, Piece 12 Same as for 0–30 cm

SECTION 3

SERPENTINIZED GABBRO BRECCIA

Piece 1 Polymict gabbro breccia, gray gabbro clasts contain large pyroxene which is partly altered Some clasts are serpentinized (dark green color) Matrix of breccia is serpentine, too.

Piece 2 Gabbro as above, but very fresh and masive

60–103 cm Polymict gabbro breccia as in Piece 1 but all are altered and brown colored

103–150 cm Gabbro, mostly fresh Pyroxene is altered in some pieces (7A, 7B, top of 7C, 7D, top and bottom of 8A, and 9A, and B)

Thin Section at 15–17 cm Holocrystalline (granitic) gabbro with plag (45%), cpx (35%) opx (5%), magnetite (3%), amphibole (5%) Carbonate, hematite and rutile (1–2%) probably pseudomorphs after olivine

Thin Section at 34–37 cm Holocrystalline (granitic) gabbro with plag (60%) opx (20%), cpx (15%), amph (~1%), 10% of pyroxene replaced by green brown amph

SECTION 4

SERPENTINIZED GABBRO BRECCIA

Fresh to moderately altered dark gray gabbro containing large opx (<1 cm) At upper edge of Piece 3A occurs yellow greenish brecciated gabbro with serpentine matrix

SITE 556, CORE 16 Depth 583.5–592.5 m

SECTION 1

SERPENTINIZED GABBRO BRECCIA

0–10 cm Anorthosite(?) vein Coarse white plagioclase with minor opx(?)

15–40 cm Fresh gabbro becoming altered (opx turns brown) at lower end

40–95 cm Gabbro breccia Angular gabbro and minor gabbro (~1 cm) clasts in nondescript greenish brown (5Y 6/3) matrix

Thin Section, Piece 1 Holocrystalline (granitic), partly altered anorthosite, contains plag (80%), cpx (20%) Amphibole (2%) and chlorite (5–10%) are replacing cpx (around cpx), prehnite occurs up to 20% in veinlets and patches replacing plagioclase

92–136 cm Moderately altered gabbro

Thin Section at 3–6 cm Holocrystalline (granitic) gabbro with plag (60%), opx (20%), cpx (20%) and traces of magnetite Plagioclase approximately An_{80} Pyroxene (10%) is replaced by amphibole

SECTION 2

SERPENTINIZED GABBRO BRECCIA WITH APHYRIC BASALT (CLAST?)

0–3 cm Polymite breccia, clasts are altered gabbro (serpentinized) with brown pyroxenes

30–75 cm Moderately altered gabbro with large phenocrysts of brown (altered?) pyroxene diameter ≳4.0 mm Dark red clay alteration product

68–75 cm, Piece 8 Highly(?) altered gabbro with altered brown pyroxene surface is impregnated with dark red with altered brown clay alteration product

75 cm Major unit break

75–145 cm Slightly olivine micro-phyric basalt, somewhat altered in places and light gray (10YR N6/2) in color Alteration light gray brown (10YRN 6/4) in color Transition is rather sharp and sudden, occurring immediately after Piece 8 Alteration shown to light brown gray by

Thin Section at 138–141 cm Aphyric intergranular to intersertal basalt, groundmass plag (50%), cpx (20%), magnetite (5%), mesostasis (20%) is devitrified glass Vesicles are filled with clay

SECTION 3

APHYRIC BASALT (CLAST?)

Slightly olivine micro-phyric basalt, olivines altered and discolored Smaller phenocrysts of plagioclase are also present Diameter < 1 mm Color basalt 10YR N6/2

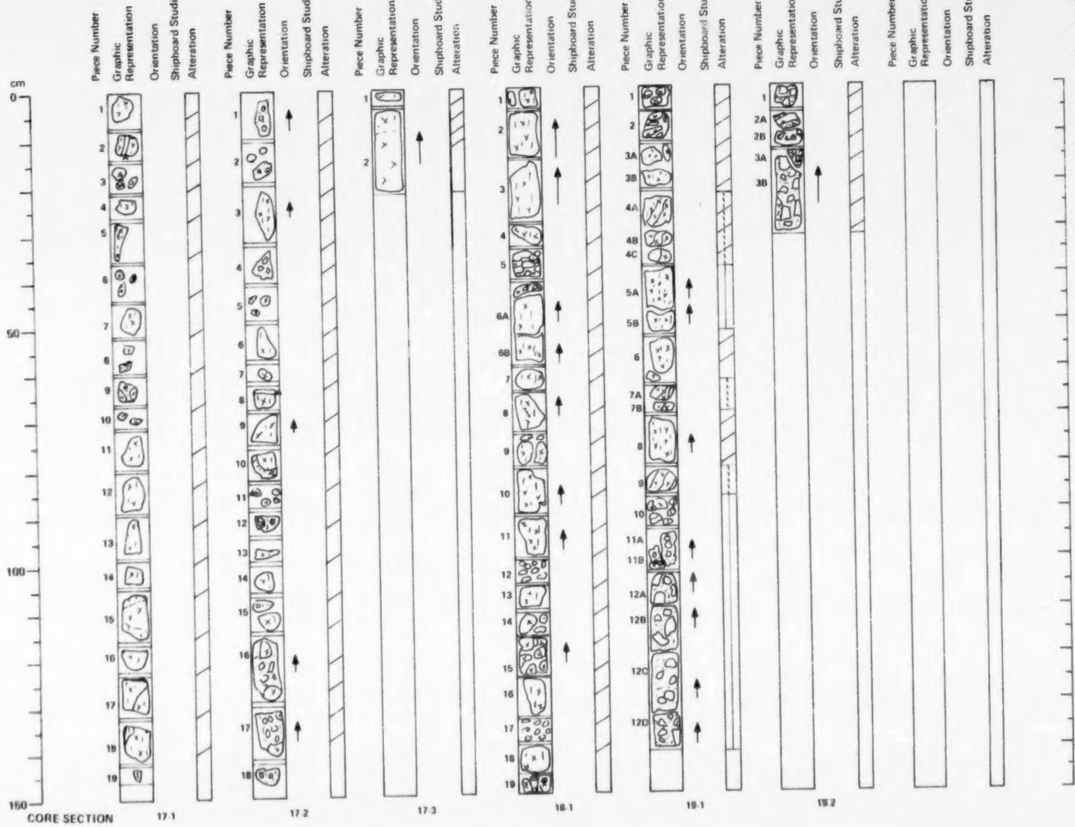
cm
0
50
100
150
CORE SECTION
Piece Number
Graphic Representation
Orientation
Shipboard Studies
Alteration
17-1
17-2
17-3
18-1
19-1
19-2
1
2
2A
2B
3
3A
3B
4
4A
4B
4C
5
5A
5B
6
6A
6B
7
7A
7B
8
9
10
11
11A
11B
12
12A
12B
12C
12D
13
14
15
16
17
18
19

SITE 556, CORE 17 Depth 592.5–601.5 m

SECTION 1

TALC SERPENTINE GABBRO BRECCIA
Moderately altered gabbro as in Core 16. Anorthosite veins (A) at 10–20 cm. Breccia matrix in Pieces 6, 8, and 9 – same as Core 16.

SECTION 2

TALC SERPENTINE GABBRO BRECCIA
Gabbro breccia as in Section 1.

SECTION 3

TALC SERPENTINE GABBRO BRECCIA
Gabbro (clast) as in Section 1.

SITE 556, CORE 18 Depth 601.5–610.5 m

SECTION 1

TALC SERPENTINE GABBRO BRECCIA
Gabbro breccia as in Sections 1–3.
36–40 cm: Chlorite (talc) rich matrix.
100–105 cm: Rubble.
118–125 cm: Matrix.
134–139 cm: Rubble.

SITE 556, CORE 19 Depth 610.5–619.5 m

SECTION 1

TALC SERPENTINE GABBRO BRECCIA
0–15 cm: Breccia with gabbro clasts.
15–23 cm: Serpentinized gabbro (breccia).
23–38 cm: Serpentinized gabbro.
38–53 cm: Breccia in gabbro clasts.
53–62 cm: Serpentinized gabbro breccia.
62–69 cm: Serpentinized gabbro.
69–79 cm: Moderately altered gabbro.
79–86 cm: Serpentinized gabbro.
86–93 cm: Highly altered (dark red brown – 10R 3/4) gabbro and breccia rubble.
93–138 cm: Breccia to predominantely anorthorite clasts and dark green (5G 3/2) chlorite(?) rich matrix with dark red brown (10R 3/4) alteration.

SECTION 2

TALC SERPENTINE GABBRO BRECCIA
As in Section 1, 93–138 cm.

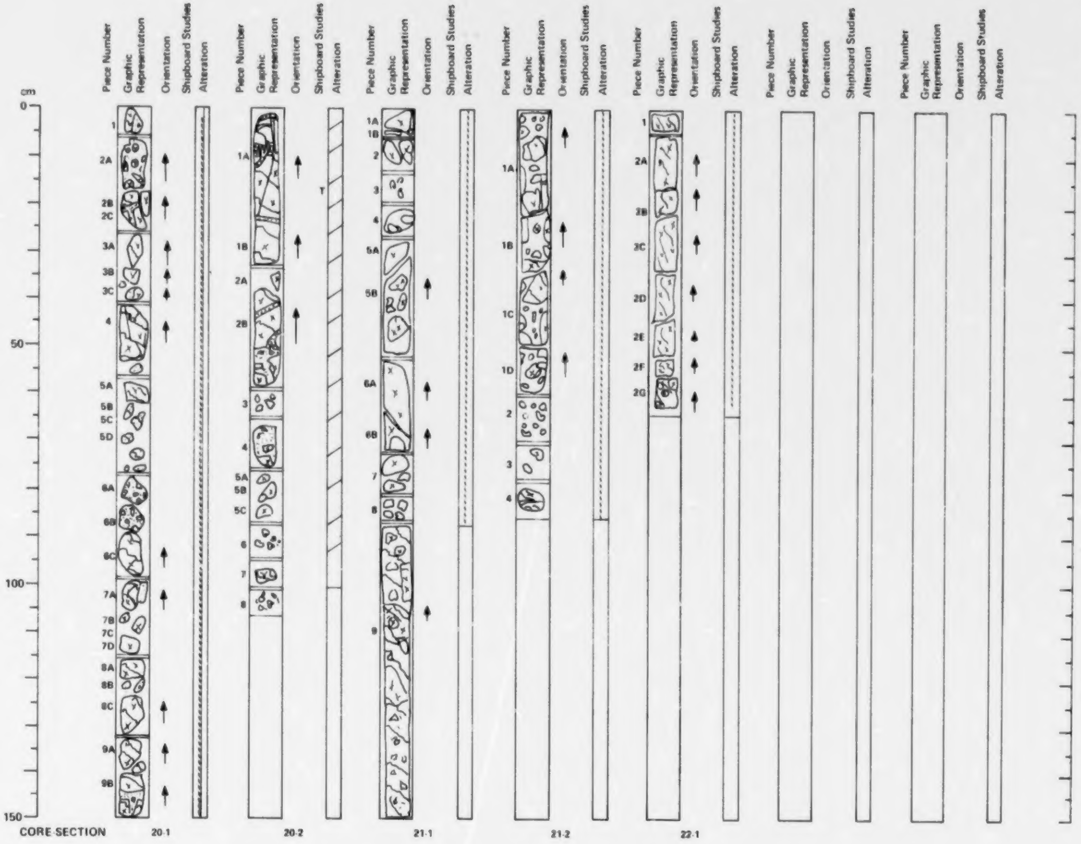
cm
0
50
100
150
CORE SECTION
Piece Number
Graphic Representation
Orientation
Shipboard Studies
Alteration
1
2A
2B
2C
3A
3B
3C
4
5A
5B
5C
5D
6A
6B
6C
7A
7B
7C
7D
8A
8B
8C
9A
9B
20-1
1A
1B
2A
2B
3
4
5A
5B
5C
6
7
8
T
20-2
1A
1B
2
3
4
5A
5B
6A
6B
7
8
9
21-1
1A
1B
1C
1D
2
3
4
21-2
1
2A
2B
2C
2D
2E
2F
2G
22-1

SITE 556, CORE 20 Depth 619.5–628.5 m

SECTION 1

TALC SERPENTINE GABBRO BRECCIA

Highly altered predominately serpentinized gabbro breccia. A high amount of the "matrix" is green talc. Orthopyroxene is very common (~15–20%). In Piece 9 the talc is dark green and predominant.

SECTION 2

TALC SERPENTINE GABBRO BRECCIA

0–56 cm: Massive dark gray greenish serpentinized gabbro with large opx (size up to 13 mm). Upper and lower parts are highly fractured, veins filled with calcite. At the bottom between 50 and 56 cm brecciation occurs.

56–105 cm: Continuation of brecciation. Breccia is cemented by calcite.

CC = Calcite cement.

SITE 556, CORE 21 Depth 628.5–637.5 m

SECTION 1

TALC-SERPENTINE GABBRO BRECCIA

0–20 cm: Serpentinized gabbro.

20–87 cm: Breccia. Serpentinized gabbro, gabbro and anorthosite (talc rims) clasts in talc-rich matrix.

87–150 cm: Foliated, serpentinized breccia. Clasts of dark green black serpentinized (5Y 2.5/2) gabbro in serpentinized matrix of small angular gabbro fragments and nondescript light gray green (5G 5/2) material.

SECTION 2

TALC SERPENTINE GABBRO BRECCIA

Serpentinized breccia with clasts of gabbro. Veins of calcite run between the clasts. Serpentinization appears to have taken place before formation of the breccia, since the clasts fabric is different.

Gabbro contains orthopyroxene and plagioclase.

70–80 cm: Talc present.

SITE 556, CORE 22 Depth 637.5–639.0 m

SECTION 1

TALC SERPENTINE GABBRO BRECCIA

Foliated serpentinized gabbro, partly brecciated (similar to Core 21, Section 1, 87–150 cm).

Piece 2G: Clasts of dark green black (5G 2/1). Serpentinized gabbro in serpentinized matrix of small angular clasts of gabbro and nondescript light gray green (5G 6/1) material.

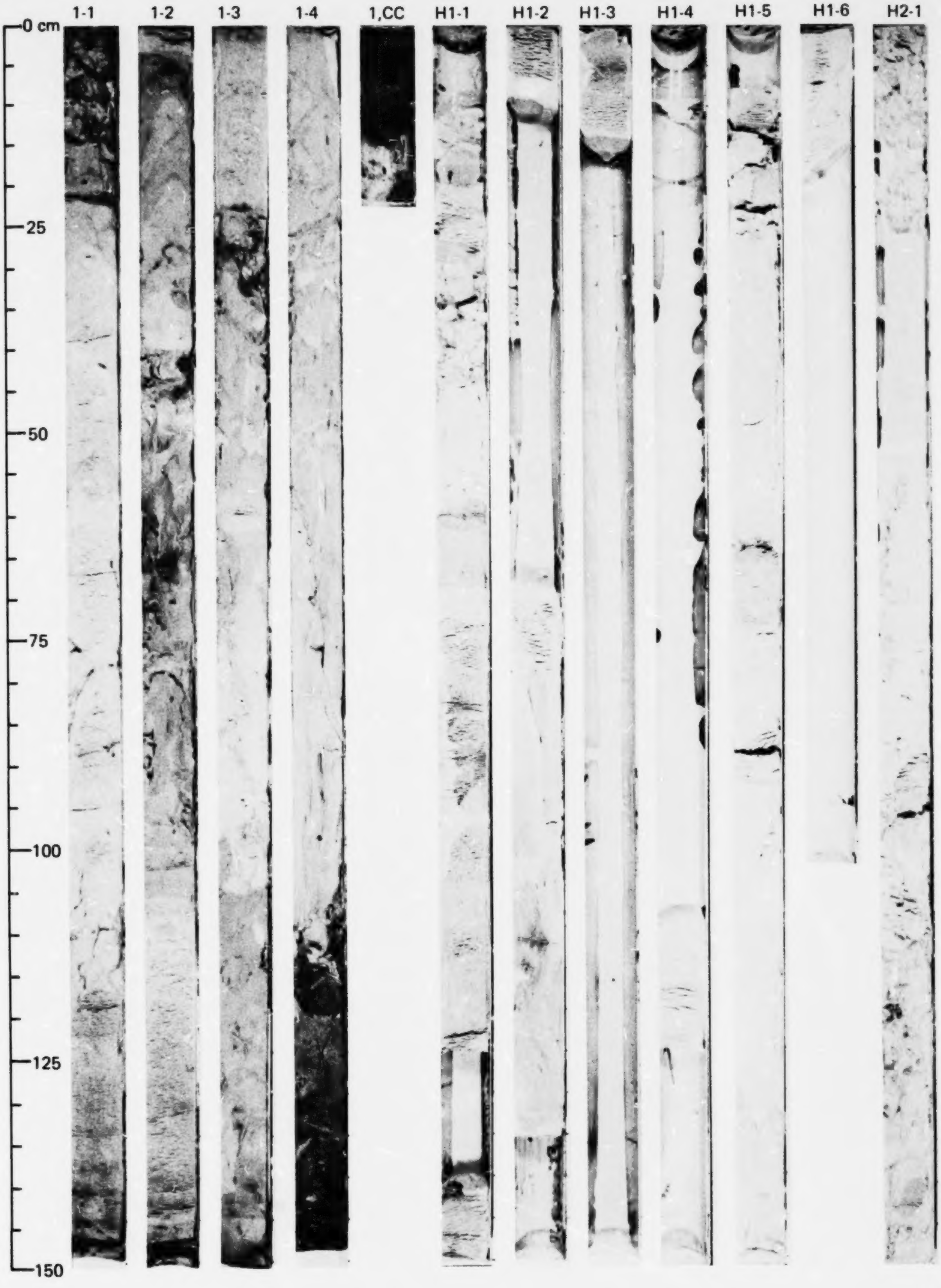
1-1
1-2
1-3
1-4
1,CC
H1-1
H1-2
H1-3
H1-4
H1-5
H1-6
H2-1
0 cm
25
50
75
100
125
150

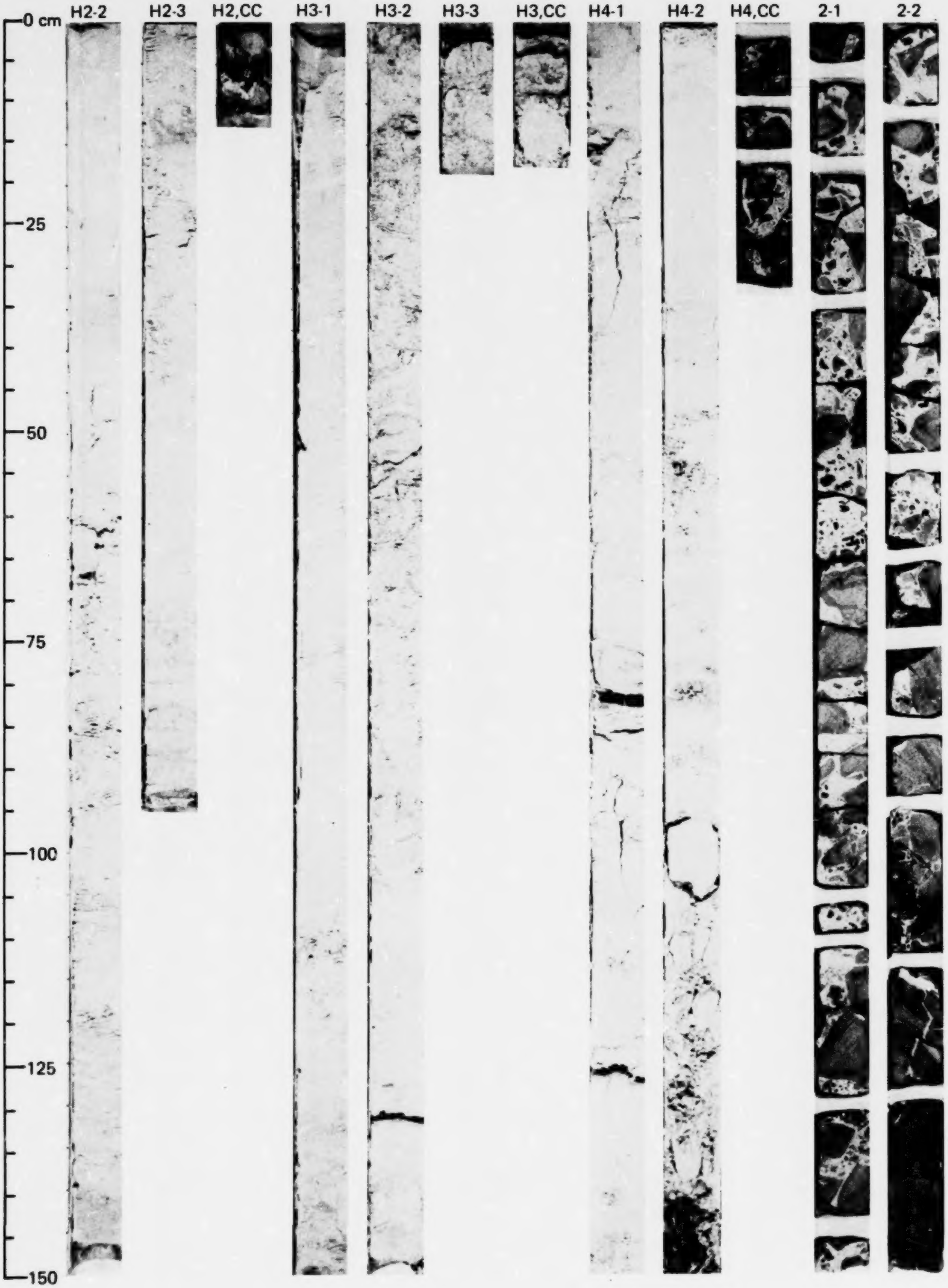
H2-2
H2-3
H2,CC
H3-1
H3-2
H3-3
H3,CC
H4-1
H4-2
H4,CC
2-1
2-2
0 cm
25
50
75
100
125
150

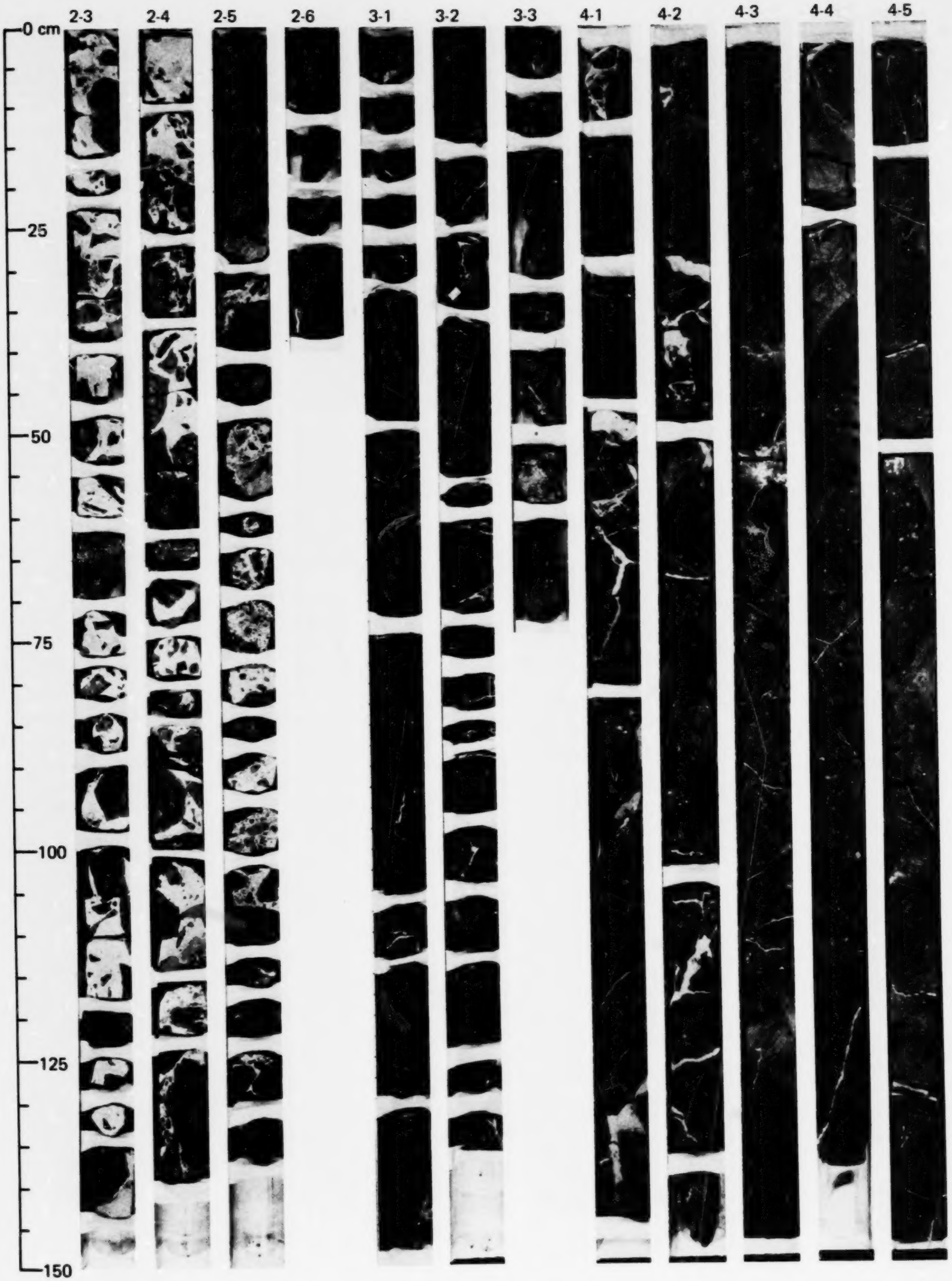
2-3
2-4
2-5
2-6
3-1
3-2
3-3
4-1
4-2
4-3
4-4
4-5
0 cm
25
50
75
100
125
150

0 cm
25
50
75
100
125
150
4-6
4-7
5-1
5-2
5-3
5-4
5-5
5-6
6-1
6-2
6-3
6-4

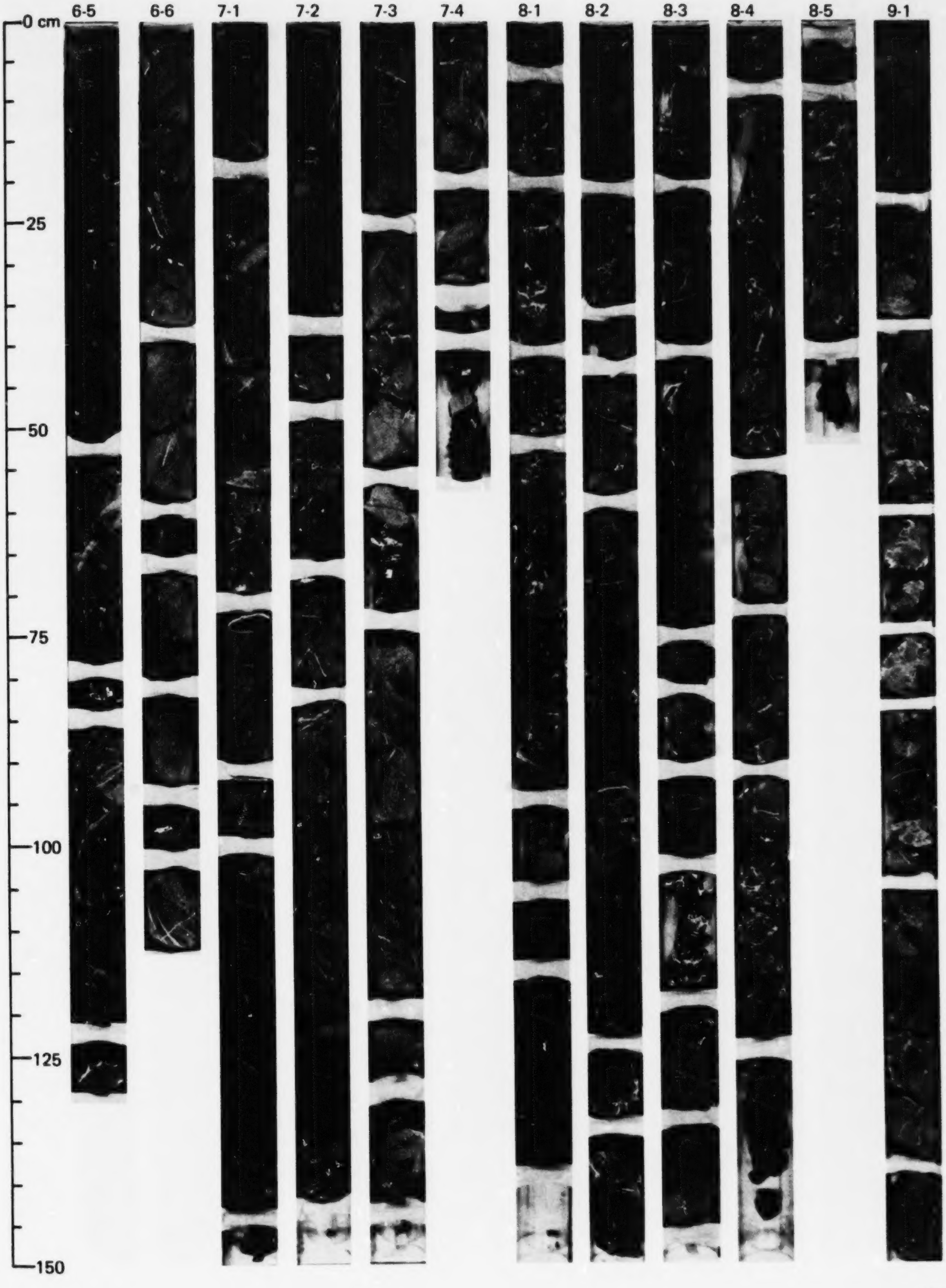

6-5
6-6
7-1
7-2
7-3
7-4
8-1
8-2
8-3
8-4
8-5
9-1
0 cm
25
50
75
100
125
150

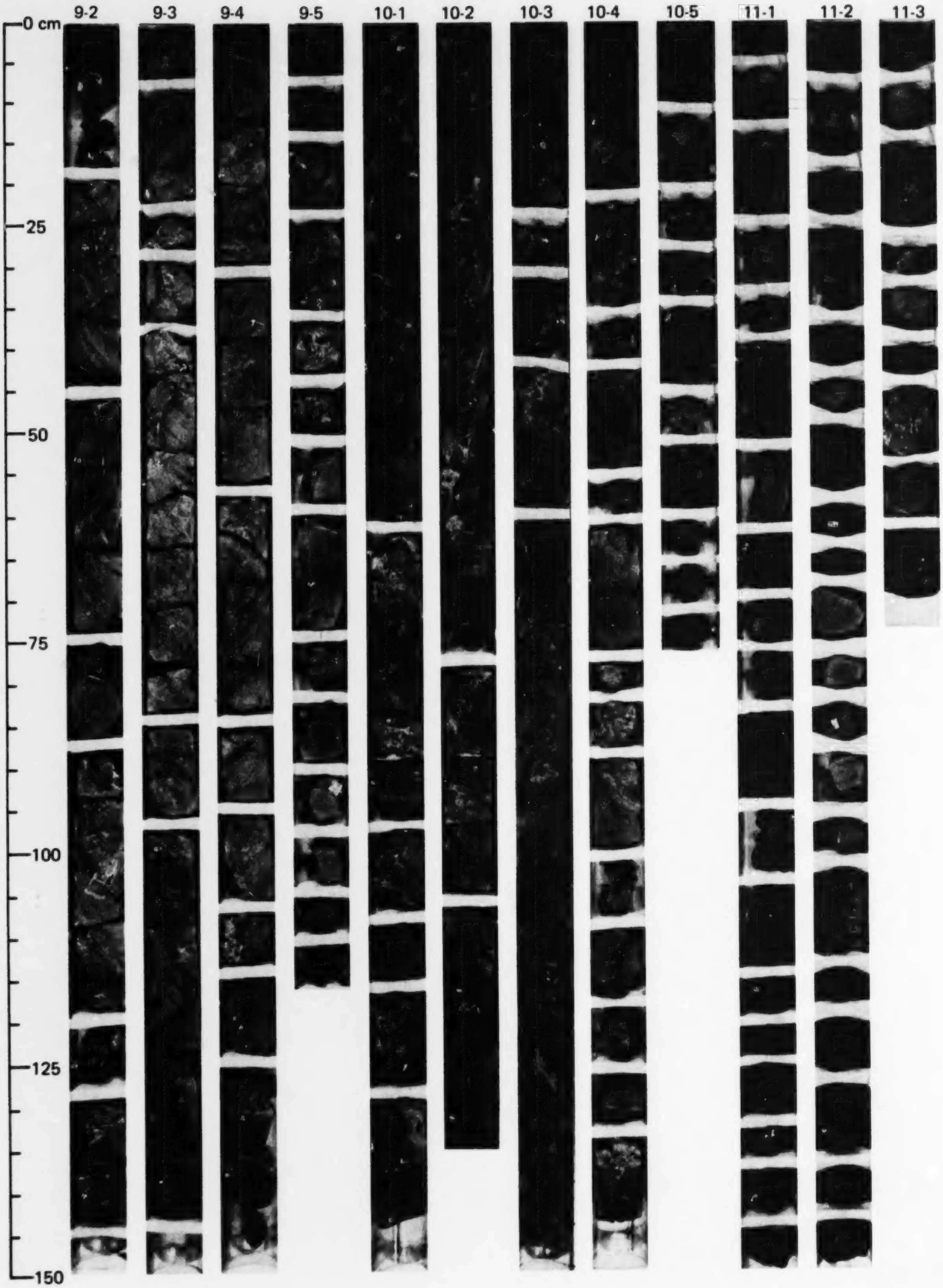
9-2
9-3
9-4
9-5
10-1
10-2
10-3
10-4
10-5
11-1
11-2
11-3
0 cm
25
50
75
100
125
150

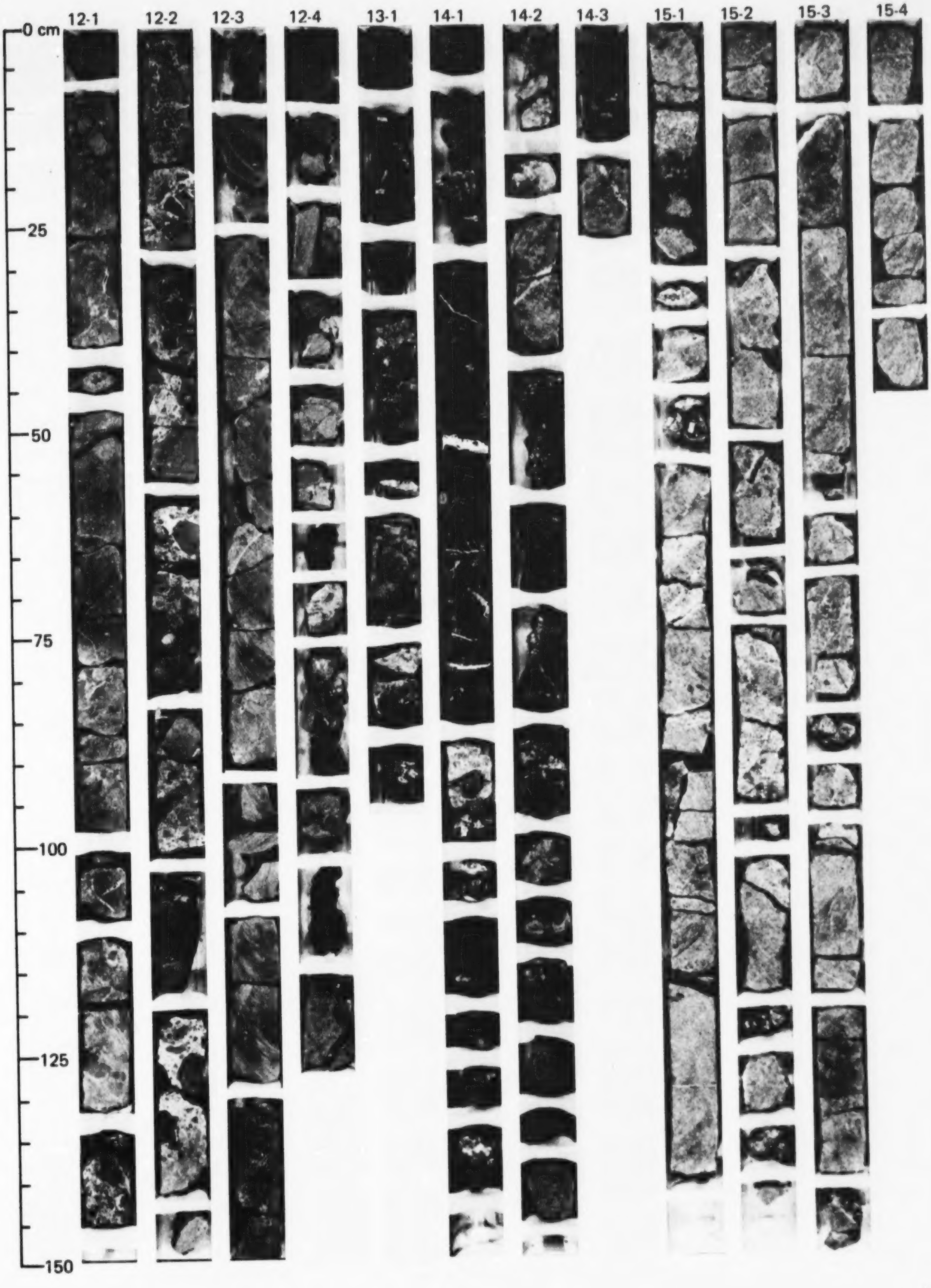
12-1
12-2
12-3
12-4
13-1
14-1
14-2
14-3
15-1
15-2
15-3
15-4
0 cm
25
50
75
100
125
150

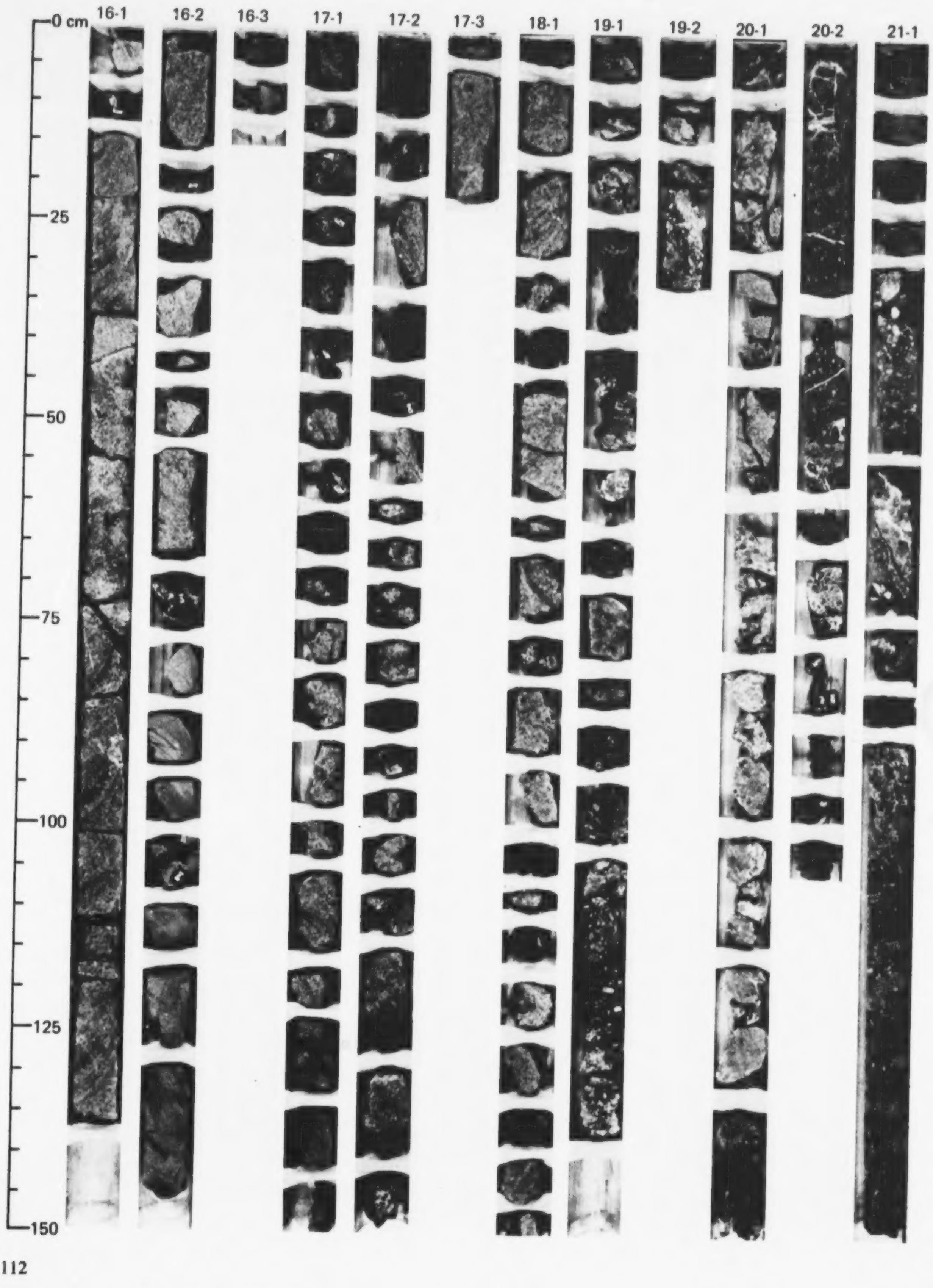
0 cm
25
50
75
100
125
150
16-1
16-2
16-3
17-1
17-2
17-3
18-1
19-1
19-2
20-1
20-2
21-1

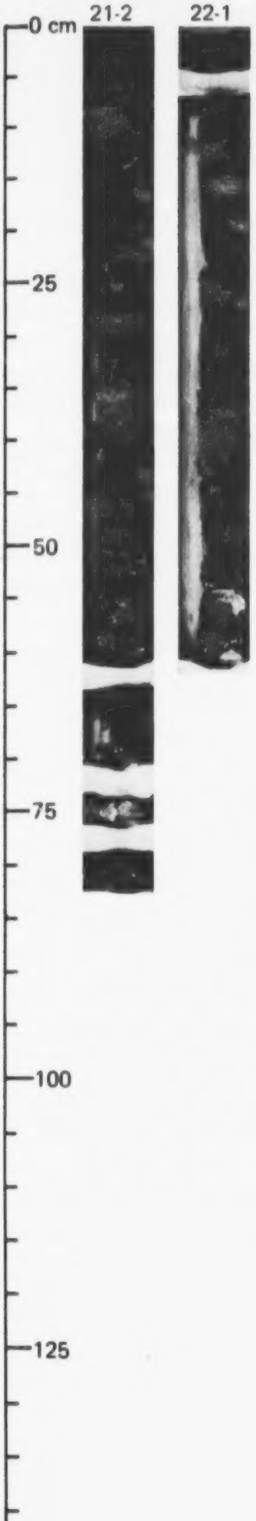
0 cm
25
50
75
100
125
150
21-2
22-1

blank page

6. SITE 557[1]

Shipboard Scientific Party[2]

HOLE 557

Date occupied: 29 September, 2119 hr.

Date departed: 30 September, 2300 hr.

Time on hole: 25.7 hr.

Position (latitude; longitude): 38°49.95′N; 32°33.58′W

Water depth (sea level; corrected m, echo-sounding): 2143

Water depth (rig floor; corrected m, echo-sounding): 2153

Bottom felt (m, drill pipe): 2155

Penetration (m): 463.5

Number of cores: 1

Total length of cored section (m): 3

Total core recovered (m): 1.2

Core recovery (%): 40

Oldest sediment cored:
  Depth sub-bottom (m): 460.5
  Nature: Volcaniclastic nannofossil chalk
  Age: late Miocene
  Measured velocity (km/s): 1.76

Basement:
  Depth sub-bottom (m): 460.5
  Nature: Basalt

Principal results: Because of the depleted character of the oceanic crust found unexpectedly at Site 556 (MAR-2), we decided to drill at least one additional hole closer to the ridge on the same flow line passing through the Azores Triple Junction (Fig. 1). Hole 557 (MAR-1) is located on Magnetic Anomaly 5D (18 Ma) in the center of a broad (40-km wide) elevated basin. This site is roughly on the same isochron as Site 335 drilled during Leg 37 on a flow line passing through the FAMOUS area (Aumento, Nelson, et al., 1977).

After washing down through 460.5 m of sediments and coring 3 m of basalts, we abandoned the hole because of an approaching storm. The recovered samples are fresh and are characterized by high iron and titanium contents and low magnesium content; the concentrations of magmaphile elements (Nb = 30 ppm, Zr = 220 ppm, Ti = 21,100 ppm, V = 420 ppm) display an "enriched" normalized diagram typical of the basalts associated with the present-day Azores Mantle Plume. In conjunction with the new results at Site 556, the present findings demonstrate that the effect of the mantle plume at the Azores Triple Junction changed radically between 34 and 18 Ma.

For this site, the following analyses were not done: sediment accumulation rates, pore water chemistry, and downhole measurements.

OPERATIONS

Approach to Site

The criteria for selecting Site 557 were that it should be on roughly the same isochron as Site 335 (i.e., 16 Ma) and on the same flow line as Site 556 (i.e., north of the Pico Fracture Zone). A tentative location was determined from the magnetic and seismic profiler records made on the *Glomar Challenger* enroute to Site 556 (Fig. 2). The site chosen was on Anomaly 5D, with a water depth of about 2150 m, in the center of a broad (40-km wide) elevated basin that is bounded by ridges to the west and east. The seismic profile indicated 0.4 s of sediments above a strong acoustic basement reflector (Fig. 3).

The site was approached by steaming eastward from Site 556 along a track 10 n. mi. north of the earlier *Glomar Challenger* track. At the estimated longitude of the site, we changed course to 180° in order to make a perpendicular crossing of the site. A satellite fix along this southward course indicated that we were slightly east of the site, and a final course correction to 240° was made that brought us across the site at 2119Z 29 September, at which time the beacon was dropped. Seismic data were collected for an additional 3 n. mi. on a course of 180° to check for unexpected basement features south of the site. The underway geophysical gear was then retrieved and the site was occupied at 2300Z.

On-Site Operations

Our only objective at this site was to recover representative basement samples. With this limited objective in mind, it was decided to proceed with drilling operations despite the fact that Hurricane Irene was on a track that would take her close to the site in roughly 30 hr. No mudline core was taken, and sediments were washed down to a depth of 425 m sub-button, at which time wash Core H1 was taken to replace the core barrel. Basement was felt at a sub-bottom depth of 460 m and was cored for approximately 1 hr. At 1730Z, drilling operations were stopped in the face of deteriorating weather conditions and the drill string was recovered (Table 1). Wash Core H2 and Core 1 were removed from the core barrel when the last section of pipe was brought aboard at 2216Z.

---

[1] Bougault, H., Cande, S. C., et al., *Init. Repts. DSDP*, 82: Washington (U.S. Govt. Printing Office).

[2] Henri Bougault (Co-Chief Scientist), IFREMER (formerly CNEXO), Centre de Brest, B. P. 337, 29273 Brest Cedex, France; Steven C. Cande (Co-Chief Scientist), Lamont-Doherty Geological Observatory, Columbia University, Palisades, New York; Joyce Brannon, Department of Earth and Planetary Sciences, Washington University, St. Louis, Missouri; David M. Christie, Hawaii Institute of Geophysics, University of Hawaii at Manoa, Honolulu, Hawaii; Marlene Clark, Department of Geology, Florida State University, Tallahassee, Florida; Doris M. Curtis, Curtis and Echols, Geological Consultants, Houston, Texas; Natalie Drake, Department of Geology, University of Massachusetts, Amherst, Massachusetts; Dorothy Echols, Department of Earth and Planetary Sciences, Washington University, St. Louis, Missouri (present address: Curtis and Echols, Geological Consultants, 800 Anderson, Houston, Texas 77401); Ian Ashley Hill, Department of Geology, University of Leicester, Leicester LEI 7RH, United Kingdom; M. Javed Khan, Lamont-Doherty Geological Observatory, Columbia University, Palisades, New York (present address: Department of Geology, Peshawar University, Peshawar, Pakistan); William Mills, Deep Sea Drilling Project, Scripps Institution of Oceanography, La Jolla, California (present address: Ocean Drilling Program, Texas A&M University, College Station, Texas 77843); Rolf Neuser, Institut für Geologie, Ruhr Universität Bochum, 4630 Bochum 1, Federal Republic of Germany; Marion Rideout, Graduate School of Oceanography, University of Rhode Island, Kingston, Rhode Island (present address: Department of Geology, Rice University, P. O. Box 1892, Houston, Texas 77251); and Barry L. Weaver, Department of Geology, University of Leicester, Leicester, LEI 7RH, United Kingdom (present address: School of Geology and Geophysics, University of Oklahoma, Norman, Oklahoma 73019).

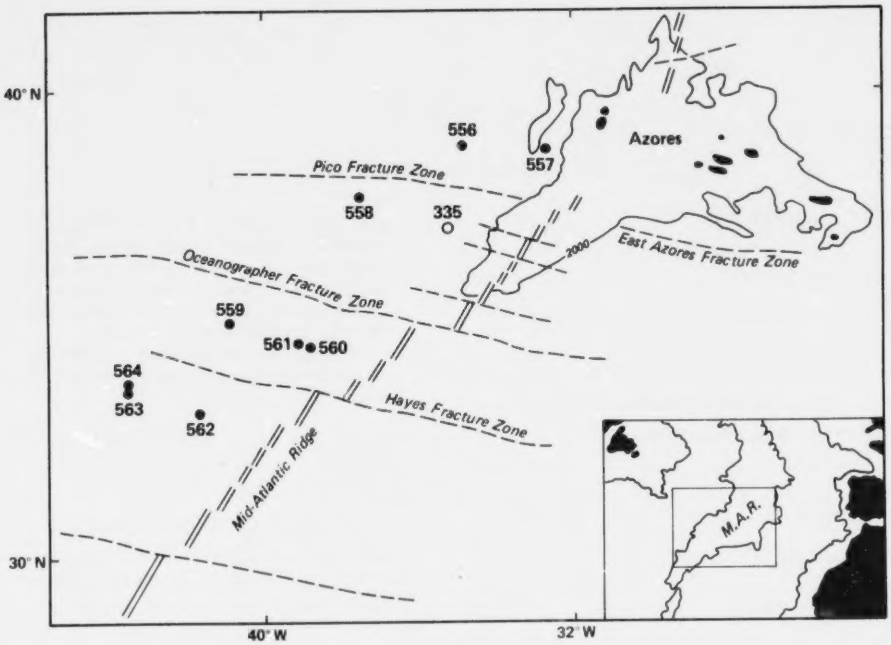

Figure 1. Site location map, Leg 82.

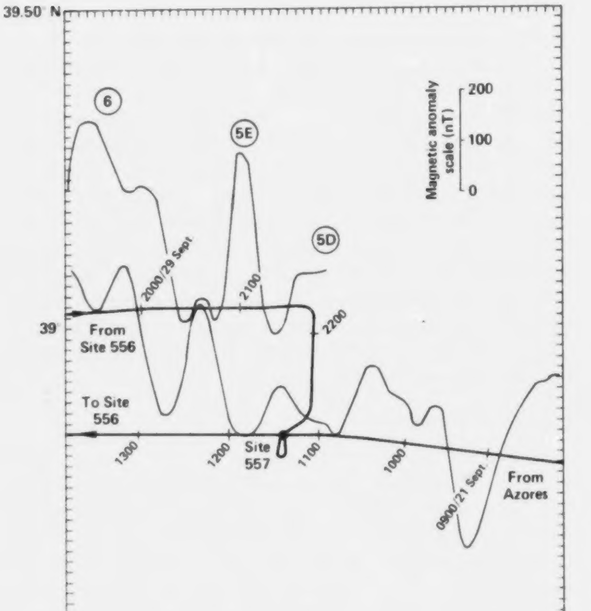

Figure 2. Approach and site survey tracks for Site 557. Heavy line is the ship's track with hours marked in GMT. Faint line is the magnetic anomaly line, projected perpendicularly from ship's track. Circled numbers are anomalies based on work at Lamont-Doherty Geological Observatory.

SEDIMENT LITHOLOGY

Hole 557 was washed from a sub-bottom depth of about 2150 m down through 460.5 m of sediments where the drill encountered basalt. Two wash cores were recovered. Because of the nature of the wash core (Core H1), we cannot assign an upper limit to the age range of the sediments at this site, nor can we evaluate the significance of several interesting details observed in the recovered sediments. The oldest sediments in Core H2 are dated at 10 to 12 Ma by foraminifers.

On visual description, the recovered material in Core H1 is nannofossil to foraminiferal-nannofossil chalk and limestone, whereas the sedimentary rock in Core H2 consists of alternating dark to light mudstones to limestones in distal turbidite cycles. However, the presence of microlaminae and grading in Core H1 suggest that the limestones and chalks are a distal, dwindling continuation of the deposition represented by Core H2. Therefore we recognize in the recovered cores only one sediment unit divided into "a" and "b" subunits (see Table 2).

Subunit 1a

Subunit 1a (0–425.5 m) (Section 557-H1-1 through 557-H1-2, 35 cm and H1, CC) includes 220 cm of white to greenish gray (2.5YN 7 to 2.5YN 4, 5YN 8, and 5G 7/1) nannofossil chalk to limestone and foraminiferal-nannofossil chalk of the late Miocene (5.2 to 10 Ma). Although much of the core is brecciated by drilling, enough undisturbed material remains to preserve the sedimentary structures. These include parallel and wavy laminae and occasional micro-crosslaminae, alternating with unbedded, bioturbated layers. Thin-section examination shows that the laminated layers represent "mi-

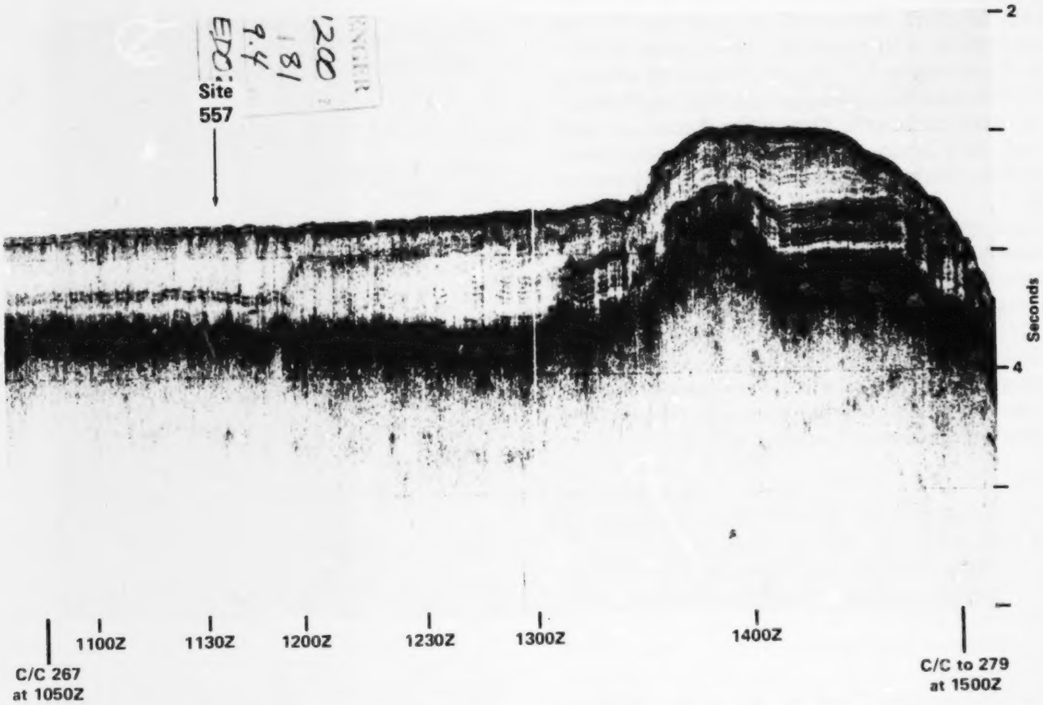

Figure 3. *Glomar Challenger* seismic record crossing to Site 557 made on route to Site 556. C/C is course change. For location of profile, see Figure 2.

Table 1. Coring summary, Hole 557.

Core	Date (Sept. 1981)	Time	Depth from drill floor (m)	Depth below seafloor (m)	Length cored (m)	Length recovered (m)	Percent recovered
H1	30	1442	2155.0–2580.5	0.0–425.5	0.0	0.00	0
H2	30	2216	2580.5–2615.5	425.5–460.5	0.0	0.00	0
1	30	2216	2615.5–2618.5	460.5–463.5	3.0	1.20	40
					3.0	1.20	40

cro-turbidite" sequences a few millimeters thick, grading upward from chalk with less abundant small foraminifers to chalk with more abundant, smaller foraminifers, forming a foraminiferal ooze at the bedding plane contact with the overlying lamina. The bioturbated portions contain a greater proportion of nannofossils. The slightly darker layers appear to be more siliceous than the lighter ones.

Several interesting details appear in this unit but, because of the possible displacement by washing, we cannot make a meaningful interpretation of their significance.

1. A cobble-size fragment of fresh vesicular basalt, about 6 mm in diameter, was embedded in the sediment in C H1,CC. It looks like a volcanic bomb, but there is little evidence of pyroclastic material elsewhere in the unit, except for a small quantity of fresh ash in 557-H1-1, 104 cm. The sediment layers immediately adjacent to the basalt fragment are chertified and appear to be de-

Table 2. Sediment lithology summary, Hole 557.

Core	Lithologic unit	Depth and thickness (m)	Main colors	Main lithology	Main components	Structure	Age
H1	1a	0 m washed to 425.5 m	Light gray to greenish gray	Nannofossil chalk, foraminiferal-nannofossil chalk, and limestone	Nannofossils foraminifers, and siliceous fossils	Parallel, wavy, and crosslaminae cyclic with bioturbated intervals	late Miocene
H2	1b	425.5–460.5	Alternating dark to light greenish gray	Cyclic foraminiferal-nannofossil limestone with calcareous volcaniclastic mudstone	Nannofossils foraminifers, and volcaniclastic mud	Graded cycles, parallel, wavy laminae and crosslaminae	early late Miocene

Note: Core 557-1 is not included in this table because it consisted of only basalt.

formed parallel with the fragment outline, but we do not know the true orientation of the fragment in the core.

2. Pieces of chert, about 4-5 cm wide and 2-3 cm thick, interbedded with limestone, were found in 557-H1-1, 28-32 cm and in 557-H1,CC. The chert contains abundant silicified foraminifers and includes small patches of unreplaced carbonate. One of the pieces has faint parallel and wavy laminations and micro-crosslaminae. The other has contorted swirls of interlayered limestone and chert.

3. A hard, encrusting, nodular "celestone," composed predominantly of foraminiferal chalk, calcite, and celestite, was found in 557-H1-1, 0-8 cm, in association with drill-brecciated foraminiferal-nannofossil chalk. We verified the optical identification of the celestite by X-ray diffraction (XRD) and X-ray fluorescence (XRF) (for strontium) analyses. The celestite is crystallized in optically continuous patches so that the entire thin section, in polarized light, presents a mosaic effect.

Subunit 1b

Subunit 1b (425.5-460.5 m) (557-H2-1 through 557-H2-7) includes 9.5 m of light greenish gray and light gray (5G 4/1 to 5GY 7/1) to dark greenish gray (5G 2/1) and black limestone and nannofossil limestone, volcaniclastic nannofossil limestone, and calcareous volcaniclastic mudstone of the early late Miocene (10 to 12 Ma). There appears to be almost no drilling disturbance in this relatively well-lithified unit. The dark and light sediments occur in cyclic pairs, beginning with dark mudstone at the base of each cycle (see Fig. 4), in sharp contact with the underlying limestone, and grading upward into lighter-colored volcaniclastic nannofossil limestone and limestone. Not all cycles are complete, and some include only the mudstone and volcaniclastic nannofossil limestone. The incomplete cycles, however, appear to be subcycles within larger cycles. The larger cycles are 1-1.5 m thick; the smaller subcycles are 10-30 cm thick. We interpret these sediments as distal turbidites derived from a volcanic ridge or island.

The darker portions of the sequence exhibit graded bedding, in fining-upward cycles from mudstone with 25-40% silt-size components to limestone with 10-20% silt-size components, then to almost pure biogenic limestone. Parallel and wavy laminations occur in the darkest portion of the turbidite cycles. Bioturbation occurs only in the light-colored portion. In many cases, borings are truncated by the sharp contact with the overlying black sediment.

Carbonate content is distinctly different in each of the three dominant lithologic categories making up the turbidite cycles. In the sections in which carbonate bomb measurements were made, the lowest carbonate percentages are in the darkest lithology, where the carbonate percentage range is 10-14%. The major components of these samples are volcaniclastic material, including ash and lithic fragments, clay derived from alteration of such material, foraminifers, and nannofossils. Opaque minerals are also prominent.

In the medium-colored, greenish gray parts of the cycles, or in laminae or beds within the lighter or darker por-

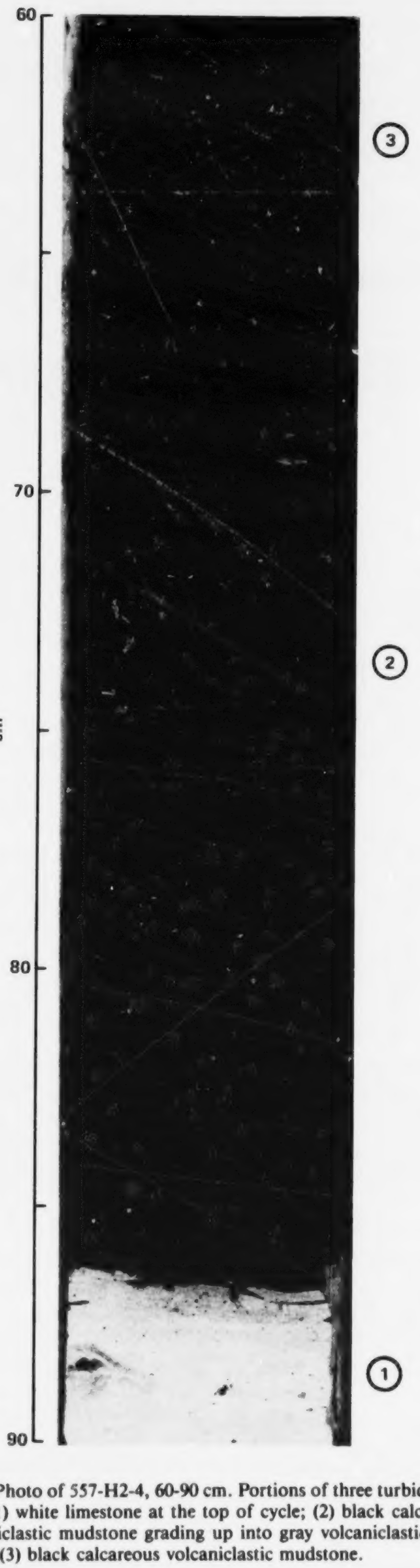

Figure 4. Photo of 557-H2-4, 60-90 cm. Portions of three turbidite cycles: (1) white limestone at the top of cycle; (2) black calcareous volcaniclastic mudstone grading up into gray volcaniclastic limestone; (3) black calcareous volcaniclastic mudstone.

tions, the carbonate content ranges up to 45%. In these layers, the dominant components are nannofossils, foraminifers, volcaniclastic material, and clay.

The light-colored limestone portions of the cycles are composed of 78–88% carbonate. The dominant components are nannofossils and foraminifers.

BIOSTRATIGRAPHY

Material recovered from the two sediment cores drilled at Site 557 is from the late Miocene (5.2–12 Ma). The dates are tentatively based on foraminifers. Nannofossils are poorly preserved and not definitive in this interval.

Nannofossils

Because of poor preservation of calcareous nannofossils, the sediments at Site 557 cannot be precisely zoned using this fossil group. In 557-H1,CC *Calcidiscus macintyrei* and *Reticulofenestra pseudoumbilica* are abundant. Discoasters from these two samples are rare and cannot be identified to the species level. The assemblage suggests an assignment of middle Miocene to lower Pliocene.

Rare *Discoaster variabilis* (in addition to *C. macintyrei, R. pseudoumbilica*, and *Sphenolithus abies*) are contained in 557-H2-3, 77 cm and 557-H2-6, 53 cm. A possible *berggrenii* is found in 557-H2-3, 77 cm. Because of poor preservation, a middle Miocene to lower Pliocene is the best assignment that can be made from these samples.

The middle Miocene to lower Pliocene assignment suggested by the calcareous nannofossils for these sediments is contrary to the upper Miocene assignment indicated by the planktonic foraminifers.

Foraminifers

The core catcher of Core H1, drilled to 425.5 m at Site 557, contains an upper Miocene, white chalkly marl. Foraminifers are common to abundant, and preservation is moderate to good. The assemblage consists of abundant *Globorotalia conoidea, Globigerina nepenthes* and an accompanying fauna of *Globorotalia plesiotumida, G. conomiozea, Globigerinoides quadrilobatus triloba, Sphaeroidinellopsis subdehiscens*, and *Orbulina universa*. Well-preserved benthic forms are present and the environment is interpreted as warm temperate. Figure 5 shows the tentative placement within the numeric time scale of this sample and the other samples examined from this hole.

Foraminifers recovered from 557-H1-1, 13–15 cm are characteristic of the uppermost upper Miocene foraminiferal Zone N17 (5.2–7.8 Ma).

The washed residue from a piece of chert in 557-H1-1, 33–35 cm, which was in contact with a pale green-gray carbonate, contained many tiny foraminifers and a normal-size upper Miocene fauna.

An upper Miocene foraminiferal fauna (probably Zone N17) is contained in 557-H1-1, 103–105 cm. Sections 557-H2-1 and 557-H2-3 are also Miocene; the fauna in samples from Sections 557-H2-6 and 557-H2-7 indicate a lower upper Miocene assignment (10.5–12 Ma; Zones N15–N14) (see Fig. 5).

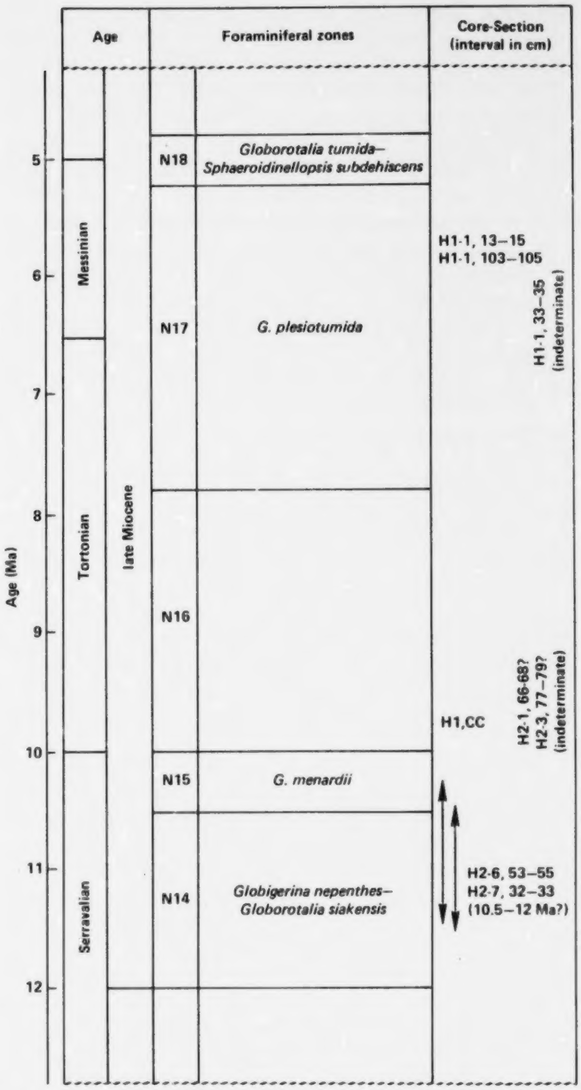

Figure 5. Biostratigraphic zonation of foraminifer samples, Hole 557.

IGNEOUS PETROLOGY AND GEOCHEMISTRY

The first basaltic sample that was incorporated in sediment was retrieved from wash Core H1. The pebble (6 cm in diameter) is a highly vesicular dark gray aphyric basalt.

Only the uppermost 3 m of the basement were drilled from 460.5–463.5 m sub-bottom with 50% recovery. The samples appear to be homogeneous and to form a single lithologic unit. It consists of massive, relatively coarse-grained aphyric basalt, which appears very fresh. The uniformly dark gray color of this basalt may be due to a high content of mafic minerals. Plagioclase laths 2 mm in length are common, and irregular dark patches up to 1 mm can be observed. Vesicules are scattered throughout the section, varying in size from 1 to 3 mm. At 461 m, some large eye-shaped (greater than 1.5 cm) vesicles showing fine-grained geopetal segregation occur. The walls of the vesicles are coated by a black botryoidal mineral. Some of the smaller vesicles are completely filled with glassy segregation material. Clay and calcitic filling of some of the vesicles is due to alteration.

The pebble in the wash Core H1 displays microlithic areas composed of plagioclase and clinopyroxene; these minerals surround the unfilled vesicles (30%) in a halo. Sparse plagioclase microphenocrysts (0.8–1.7 mm) of composition An_{54} (optically determined) are surrounded by plagioclase laths (25%; 0.2–0.6 mm), prismatic clinopyroxene (20%; 0.2–0.6 mm), equant magnetite (5%; 0.1–0.2 mm), and acicular to skeletal ilmenite (4%; 0.2–0.6 mm). Mesostasis (15%) fills the crystal interstices.

The petrographic unit recovered in the uppermost part of the basement (Section 557-1-1) consists of a fresh medium-grained aphyric basalt with intersertal to intergranular texture. Clinopyroxene (35%; 0.1–0.6 mm) occurs as single granules and aggregates up to 1 mm, and, along with devitrified glass[3] (occasionally fresh) (17%), fills the interstices in a random network of larger plagioclase laths (0.4–1.9 mm) with an optically determined composition of An_{56}[4]. Equant magnetite (9%, 0.1–0.5 mm) crystals occur throughout the rock. A series of elongated segregation vesicules filled with devitrified glass lie within a band of small plagioclase (0.1–0.6 mm) and clinopyroxene (0.1–0.6 mm) laths. Devitrified glass, apatite, and magnetite fill the interstices of the laths in this band.

Four samples have been analyzed for major and trace elements, one from the pebble found within the wash Core H1 and three from the basement. The data are reported in Table 3. The composition of the pebble from H1 is very similar in composition to the basement samples. Characteristics of these samples are the high TiO_2 (about 3.5%) and Fe_2O_3 (about 16%) contents and the low MgO value (about 5%), which lead to a very low Mg′ number (about 42%). These features are representative of evolved samples in terms of low-pressure fractional crystallization of olivine and plagioclase and allow the classification of these rocks as ferro basalts.

Chondrite-normalized values of elements Nb, Zr, Ti, Y, and V, which yield plots similar to chondrite-normalized rare earth element (REE) diagrams, show an enriched composition (Fig. 6). The three basement samples analyzed are identical, but the pebble recovered in the sediment is somewhat different, slightly more enriched in the most magmaphile element (Nb). These patterns are similar to those encountered in or near the triple junction area. The absence of a negative Ti anomaly suggests that no removal of titanomagnetite has occurred during the petrogenesis of these basalts.

MAGNETICS

Basalt Paleomagnetism

The intensity of NRM was measured for three basalt samples. These samples are more strongly magnetized than those of Site 556. The NRM and susceptibility values are given in Table 4. The high values of susceptibility were believed to be caused by the higher amounts of titanomagnetite in these basalts. This conclusion is supported by the geochemical analyses (see Igneous Petrology and Geochemistry section), which showed higher amounts of titanium in these basalts.

The inclinations are shallower than the expected value of 58° for the dipole magnetic field at the latitude of this site. This may be the result of tectonic rotation.

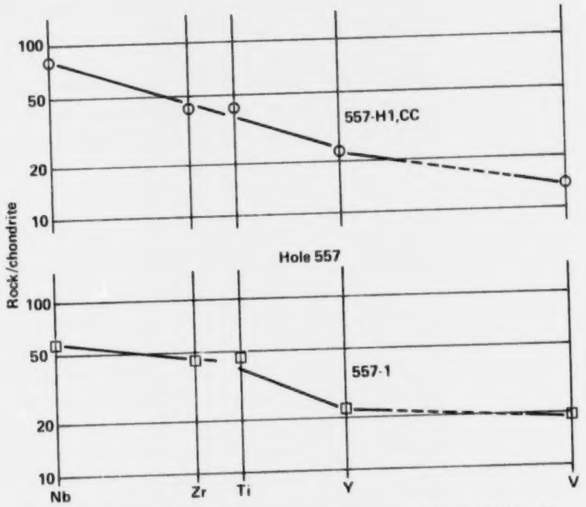

Figure 6. Extended Coryell-Masuda diagrams for Hole 557 basalts.

Table 3. Analyses of major elements (in wt.%) and trace elements (in ppm) for Hole 557 basalts.[a]

Core-Section (interval in cm; piece number)	Depth (m)	Chemical group	SiO_2	TiO_2	Al_2O_3	Fe_2O_3[b]	MnO	MgO	CaO	K_2O	P_2O_5	Total	Mg′[c]	Ti	V	Sr	Y	Zr	Nb
H1,CC		I	49.07	3.28	13.42	15.42	0.18	4.71	9.51	0.61	0.46	96.66	41	19,680	313	344	49.2	219	42.9
1-1, 0–3 (1)	460.5		48.69	3.52	12.53	16.00	0.19	5.92	9.07	0.40	0.38	96.70	45	21,120	415	311	46.7	219	30.2
1-1, 25–28 (3)	460.8		48.22	3.53	12.35	16.79	0.20	5.62	9.73	0.46	0.40	97.30	43	21,180	459	315	48.7	222	29.9
1-1, 40–43 (4)	460.9		48.30	3.49	12.33	16.50	0.23	5.21	10.09	0.45	0.42	97.02	42	20,940	422	300	48.9	220	29.9

[a] On-board measurements were made on ignited samples. Onshore analyses of loss of ignition are less than 1% in most cases. Compiled data tables in Appendix at the end of this volume include volatile components.
[b] Total Fe as Fe_2O_3.
[c] Mg′ is the atomic ratio of 100 × Mg/(Mg + Fe^{2+}); calculated using an assumed Fe_2O_3/FeO ratio of 0.15.

---

[3] Onshore microprobe analyses indicate a smectite composition.

[4] Onshore microprobe analyses indicate plagioclase core compositions of An_{59} and rim compositions of An_{48}.

Table 4. Magnetic measurements, Hole 557.

Measurement	Core-Section (interval in cm)		
	1-1, 35–37	1-1, 63–65	1-1, 131–133
NRM intensity ($\times 10^{-3}$ emu/cm^3)	3.06	7.02	8.39
χ ($\times 10^{-6}$ emu/cm^3 Oe)	940	700	1110
NRM inclination (°)	44.7	32.7	46.1
Q (= NRM/0.45 χ)	7.23	22.28	16.80

Note: NRM = natural remanent magnetization; Q = Königsberger ratio; χ = susceptibility.

PHYSICAL PROPERTIES

Because of the operational constraints on this hole, only two wash cores were recovered from the sedimentary section. The first contained little undisturbed sediment and was not sampled. The second (from the interval 425.5–460.5 m sub-bottom depth) contained well-lithified sediments from which samples were taken for seismic velocity and density measurements as shown in Table 5.

The sediments recovered are a cyclic sequence, and the base of each cycle is a dark green black color grading to pale gray. In general, the dark bases of cycles are less dense and of lower sonic velocity than the tops, although there does seem to be considerable variability. The very low density and velocity measured on Sample 557-H2-4, 53–61 cm may be due to the presence of burrows within the sample. There seems to be a slight seismic anisotropy within the sediments; *p*-wave velocities parallel to bedding are about 5% greater than vertical velocities.

The high seismic velocity of these sediments contrasts strongly with the sediments encountered at Site 556, where the sediments had a smooth increase in velocity with depth to values of 2.1 km/s at the basement interface. From the reflection profile, the sediment two-way time at Site 557 is 0.38 s, with a prominent reflector at 0.27 s. The total drilled thickness of sediments was 460 m giving a mean velocity of 2.42 km/s. Even if we assume that the strong reflector marks an increase in velocity to 2.60 km/s, the upper sediments would still require a mean velocity of 2.30 km/s. This shows that the whole sedimentary sequence at Site 577 is of higher velocity than that at Site 556 and suggests that the lithologies are correspondingly different.

The quantity of basalt rock recovered in Core 1 was small and no physical properties measurements were made.

SUMMARY AND CONCLUSIONS

Site 557 is located on Magnetic Anomaly 5D (18 Ma old) in the center of a broad (40-km wide) elevated basin (Fig. 7) on the same flow line as Site 556 (34 Ma old) passing through the Azores Triple Junction area. Site 557 is roughly on the same isochron as Site 335, drilled during Leg 37, on a flow line passing through the FAMOUS area (Fig. 7).

Site 557 was located in the center of this basin to avoid elevated ridges and seamounts whose material is generally enriched in the most magmaphile elements. If we had chosen the site on one of the anomalously high features in the area, the finding of "enriched" material could have been attributed to a local event rather than to an event affecting the entire area.

After the sediment was washed down, basement was reached at a sub-bottom depth of 460.5 m. Only the uppermost 3 m of basement were cored because of the rapid approach of a hurricane. A total of 1.2 m of basalt was recovered. An additional basaltic fragment was also collected in a wash core (at 425 m depth). All of the samples recovered are fresh and are characterized by high Fe_2O_3 (16%) and TiO_2 (3.5%) content. The normalized concentrations of magmaphile elements are typical of "light rare earth" enriched material; the normalized concentrations of Nb (same behavior as La) are up to 80 times the chondrite value.

The geochemical data from Sites 556 and 557, together with those of dredged material in the area of the Azores Triple Junction, provide for the first time temporal limits on the behavior of a mantle plume associated with a triple junction. The extended Coryell Masuda plots (using Nb, Zr, Ti, Y and V) shown in Figures 6, 8, and 9 document a clear boundary between the typically de-

Table 5. Physical property measurements, Hole 557.

Core-Section (interval in cm)	Sonic velocity (km/s)		T(°C)	GRAPE density (g/cm^3)		Acoustic impedance ($\times 10^5$) (g/[cm·s])	Lithology
	Vertical	Horizontal		Vertical	Horizontal		
H2-1, 10–13	2.69		21.5	2.20		5.92	Pale gray turbidite
H2-1, 29–33	2.30		21.0	1.94		4.46	Dark gray, basal turbidite
H2-1, 113–119	2.69	2.59	21.0	2.17	2.20	5.70	Pale gray, well-laminated turbidite
H2-2, 54–60	2.59	2.50	21.0	1.91	1.91	4.78	Black massive basal turbidite
H2-4, 53–61	1.88	1.76	21.0	1.80	1.79	3.24	Black burrowed basal turbidite

Note: Sub-bottom depth interval for these samples is 425.5–460.5 m. T = temperature. All values are measured at laboratory temperature and pressure. For details of techniques see Explanatory Notes chapter, this volume.

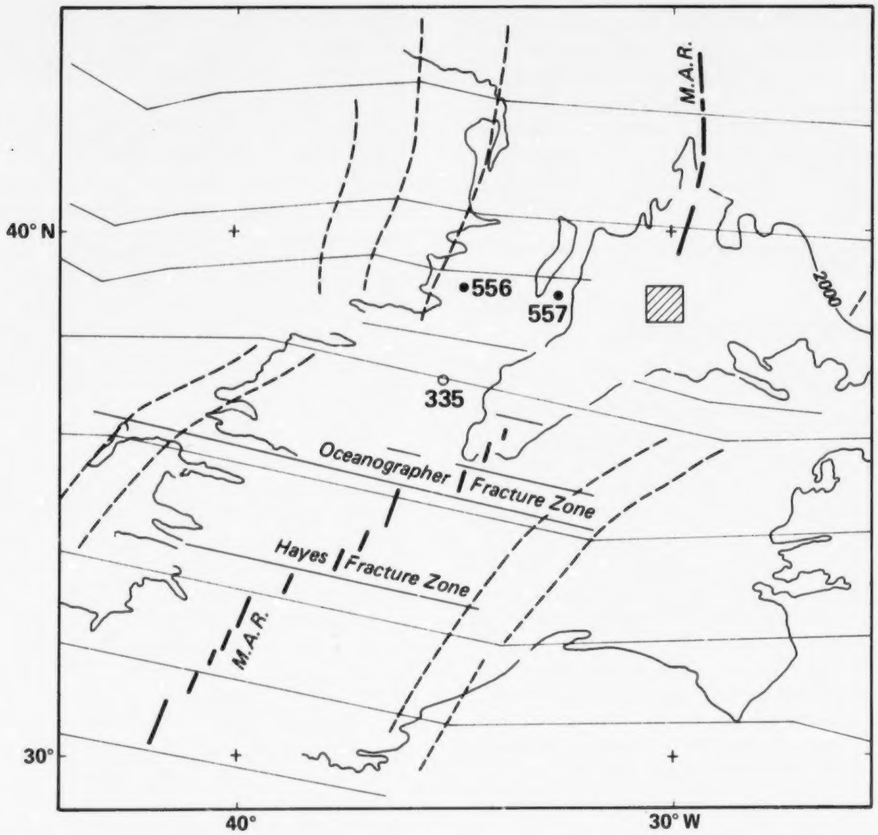

Figure 7. Sketch map of the ocean floor in the vicinity of the Azores Triple Junction. The hachured area marks the location of dredge sites for samples plotted in Figure 9. Contours in meters; straight lines: flow lines; dashed lines: isochrons; circle labeled 335: reference point for Leg 37 (Hole 335); MAR: Mid-Atlantic Ridge.

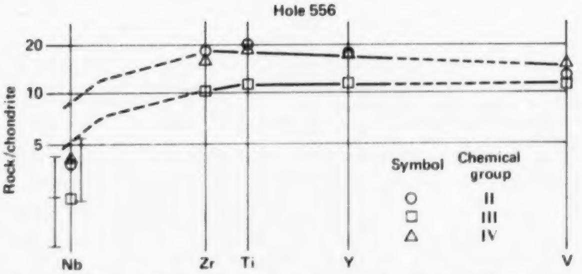

Figure 8. Extended Coryell-Masuda diagram for basalts of chemical Groups II, III, and IV, Hole 556, indicating the depleted character of these rocks. Also shown are error bars for Nb.

pleted oceanic crust at Site 556 (Fig. 8) and the enriched oceanic crust observed both at Site 557 (Fig. 6) and at the triple junction today (Fig. 9).

The geochemical data available do not permit us to locate the actual boundary between basalts with depleted chemical character at Hole 556 (34 Ma old) and basalts with enriched chemical character at Hole 557 (18 Ma old). However, a sharp discontinuity is observed on the seismic profile records in the character of the basement (Fig. 3). The boundary is slightly older than Anomaly 6 (20 Ma) and corresponds to a transition from smooth elevated basement to the east to a more irregular and a more "typical-looking" oceanic basement to the west. We speculate that this topographic boundary corresponds to the geochemical boundary between enriched and depleted oceanic crust.

REFERENCES

Aumento, F., Melson, M. G., et al., 1977. *Init. Repts. DSDP*, 37: Washington (U.S. Govt. Printing Office).

Bougault, H., and Treuil, M., 1980. Mid-Atlantic Ridge: zero age geochemical variations between Azores and 22°N. *Nature*, 986:209–212.

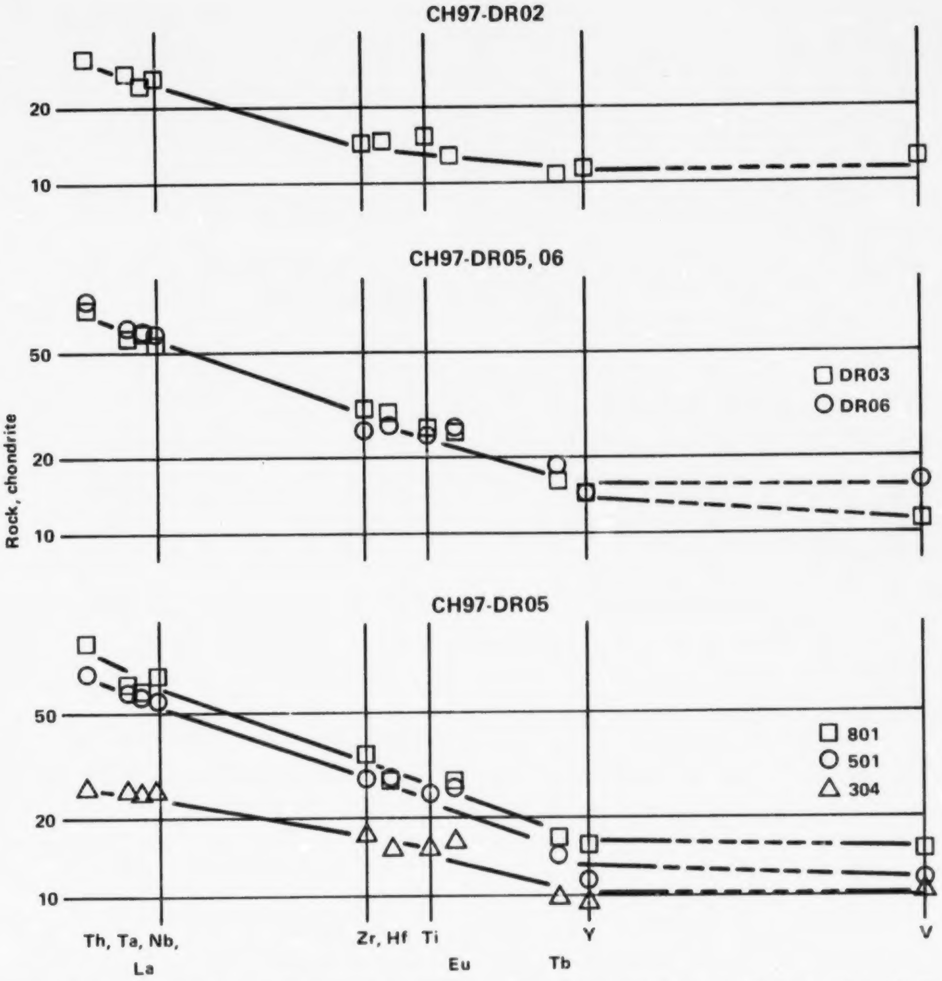

Figure 9. Extended Coryell-Masuda diagrams for samples collected at dredge sites indicated by hachured area in Figure 7. For details, see Bougault and Treuil, 1980.

SITE 557 HOLE CORE H1 CORED INTERVAL 0.0–425.5 m

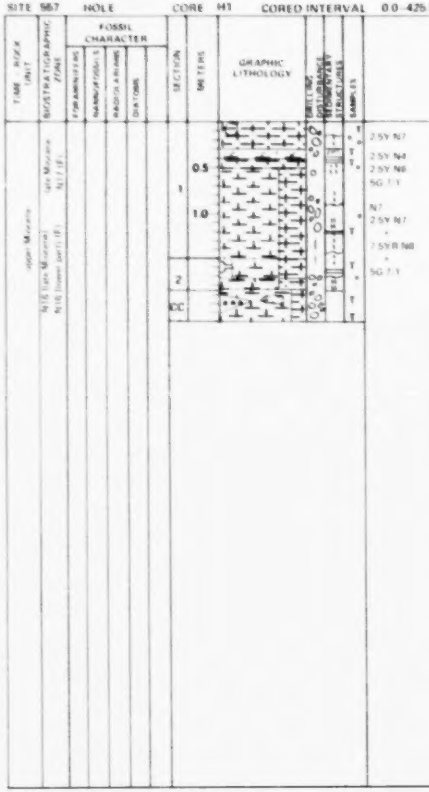
TIME – ROCK UNIT
BIOSTRATIGRAPHIC ZONE
FOSSIL CHARACTER
FORAMINIFERS
NANNOFOSSILS
RADIOLARIANS
DIATOMS
SECTION
METERS
GRAPHIC LITHOLOGY
DRILLING DISTURBANCE
SEDIMENTARY STRUCTURES
SAMPLES
upper Miocene
late Miocene N17 (F)
N16 (late Miocene) N16 (lower part) (F)
0.5
1.0
1
2
CC
2.5Y N7
2.5Y N4
2.5Y N6
5G 7/1
N7
2.5Y N7
7.5YR N6
5G 7/1

LITHOLOGIC DESCRIPTION

DOMINANT LITHOLOGY NANNOFOSSIL CHALK TO LIMESTONE AND FORAM NANNOFOSSIL CHALK

(Wash core)

Light gray to greenish gray with darker shades in more siliceous bands.

Parallel and wavy microlaminae, possible cross-laminae, much bioturbation.

Foram content and size varies to indicate possible micro- or mini-grading, forams in layers grading from larger to smaller, and from less abundant to more abundant, with some layers a foram ooze. Foram content 10–50% (thin section), nannos to 75%.

Minor lithologies

(1) Basalt: "volcanic bomb(?)" clast of fresh vesicular basalt embedded in sediment in CC; has caused deformation and chertification of underlying sediment layers.

(2) Chert: fragment, dark gray, faint parallel bedding and ripples, abundant silicified forams and minor CO_3 content and (argillaceous limestone on edges).

(3) Nodular limestone: light gray with wavy black streaks and hard lumpy nodules, encrusting. Has high strontium content by XRF analysis.

(4) Siliceous nanno chalk

SMEAR SLIDE SUMMARY (%)

	1-21	1-28	1-50	1-104	2-25
	D	M	D	M	D
Composition:					
Feldspar	1	1	Tr	1	Tr
Heavy minerals	Tr	Tr	Tr	Tr	–
Volcanic glass	–	10	Tr	–	–
lith. frag.					
Pyrite	1	Tr	Tr	1	Tr
opaques					
Carbonate unspec.	–	Tr	–	–	–
Foraminifers	4	79	25	5	40
Calc. nannofossils	25	–	5	1	5
Diatoms	70	10	70	75	55
Radiolarians	–	–	–	10	–
Sponge spicules	–	–	–	5	–

SITE 557 HOLE CORE H2 CORED INTERVAL 425.5–460.5 m

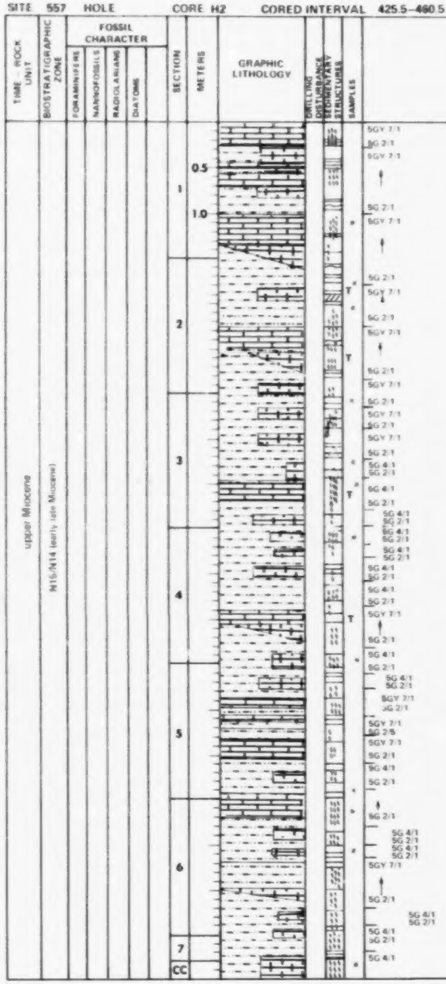
TIME – ROCK UNIT
BIOSTRATIGRAPHIC ZONE
FOSSIL CHARACTER
FORAMINIFERS
NANNOFOSSILS
RADIOLARIANS
DIATOMS
SECTION
METERS
GRAPHIC LITHOLOGY
DRILLING DISTURBANCE
SEDIMENTARY STRUCTURES
SAMPLES
upper Miocene
N15/N14 (early late Miocene)
0.5
1.0
1
2
3
4
5
6
7
CC
5GY 7/1
5G 2/1
5GY 7/1
5G 2/1
5GY 7/1
5G 2/1
5GY 7/1
5G 2/1
5GY 7/1
5G 2/1
5GY 7/1
5G 2/1
5GY 7/1
5G 2/1
5GY 7/1
5G 2/1
5G 4/1
5G 2/1
5G 4/1
5G 2/1
5G 4/1
5G 2/1
5G 4/1
5G 2/1
5G 4/1
5G 2/1
5G 4/1
5G 2/1
5G 4/1
5G 2/1
5GY 7/1
5G 2/1
5G 4/1
5G 2/1
5G 4/1
5G 2/1
5GY 7/1
5G 2/1
5GY 7/1
5G 2/5
5GY 7/1
5G 2/1
5G 4/1
5G 2/1
5G 2/1
5G 4/1
5G 2/1
5G 4/1
5G 2/1
5GY 7/1
5G 2/1
5G 4/1
5G 2/1
5G 4/1
5G 2/1
5G 4/1

LITHOLOGIC DESCRIPTION

DOMINANT LITHOLOGIES (wash core):

(1) LIMESTONE TO NANNOFOSSIL LIMESTONE TO NANNO-FORAM OR FORAM-NANNO LIMESTONE

Light gray to light greenish gray, grading downward to greenish gray; sharp contacts with overlying black beds.

Intensely bioturbated; bioturbation increasing upward and sometimes abruptly truncated at top at contact with black bed. Few bedding planes.

Nannofossils abundant, forams appear to be more common in more greenish portions; 50–75% of the carbonate may be micrite. Minor constituents are volcaniclastic rock and mineral particles to 2%.

(2) VOLCANICLASTIC NANNOFOSSIL CHALK

Greenish gray, grading upward to light-colored limestone downward to dark-colored mudstone.

Intense bioturbation and burrowing; some parallel and wavy bedding, and color-banding.

Silt-size particles 10–20%, nannofossils 30–60%, forams 5–10%, volcaniclastic (glass and lithic fragments and clay) 10–25%, and CO_3 20–40%.

(3) CALCAREOUS VOLCANICLASTIC MUDSTONE

Dark greenish gray to black, grading downward from lighter to darker. Sharp contact at base of dark with light gray limestone beneath.

Parallel and wavy bedding, lamination, microcross-laminae; graded beds in fining-upward sequence. Bioturbation intense in darker portions, increasing upward into lighter portions.

Silt-size particles 20–40%, nannofossils 10–15%, forams 3–10%, unspecified carbonate 1–15%, and volcaniclastic (glass, lithic fragments and clay) 40–60%.

SMEAR SLIDE SUMMARY (%):

Lithology type	(1)	(2)	(3)
Composition:			
Feldspar	Tr–1	0–1	Tr–1
Heavy minerals	Tr–1	1–3	1–2
Clay	–	3–6	6–25
Volcanic glass	Tr–2	5–20	40–60
Palagonite	Tr–1	–	Tr–5
Glauconite	–	–	Tr–1
Opaques	Tr–2	Tr	5–15
Micronodules	0–3	1–2	0–2
Zeolite	–	Tr	0–2
Carbonate	50–75	20–40	1–15
Foraminifers	3–8	5–10	3–10
Calc. nannofossils	15–40	30–60	10–15

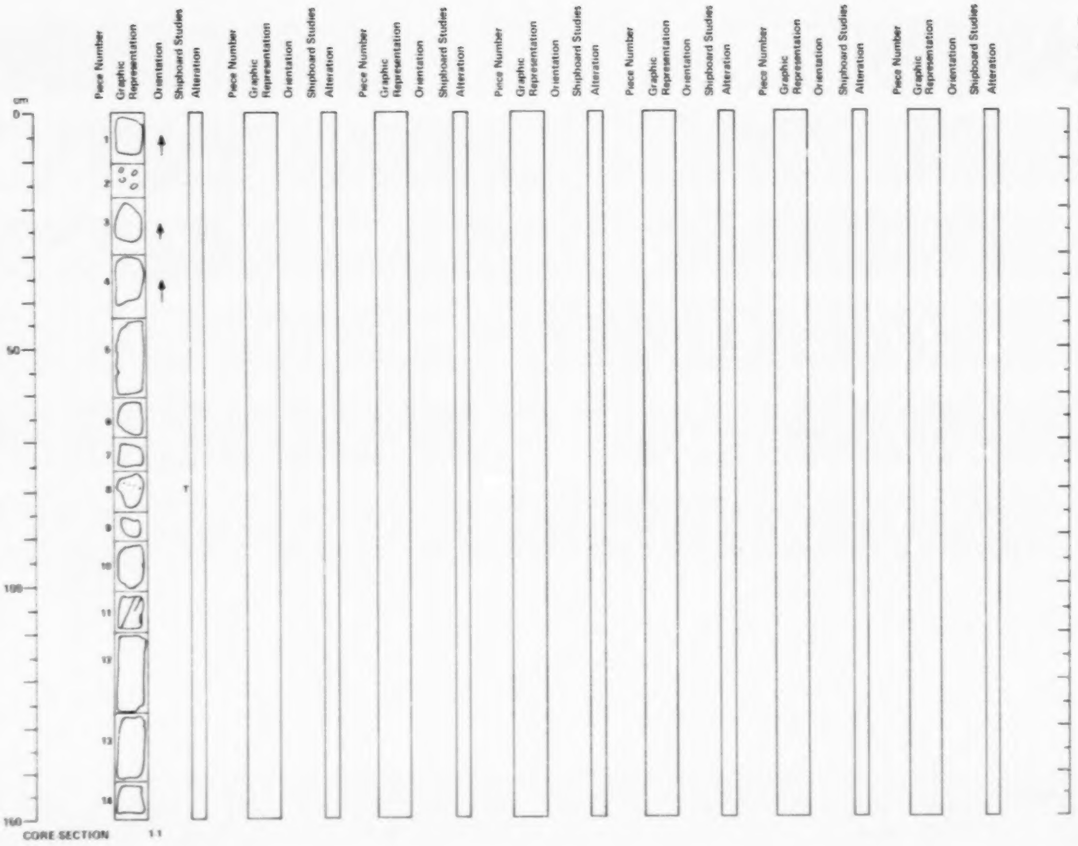
cm
0
50
100
150
CORE SECTION
1-1
Piece Number
Graphic Representation
Orientation
Shipboard Studies
Alteration
1
2
3
4
5
6
7
8
9
10
11
12
13
14
T

SITE 557, CORE 1 Depth 460.5–463.5 m

SECTION 1

APHYRIC BASALT

Medium-grained aphyric basalt, color dark gray (7.5YR N3/0), appears very fresh except some clay filled vesicles. Vesicles are mostly round. Their size in the upper third (Pieces 1–5) is between 1 and 3 mm. In Piece 5 some very large segregation vesicles (>1.5 cm) occur. From Piece 6 to the bottom of the section size of vesicles generally decreases to a maximum of ~1.5 mm. Piece 8 shows a group of large vesicles aligned on a plane (shown ● ∘ ∘).

Thin Section at 22–25 cm: Medium grained aphyric basalt with intersertal to intergranular texture. Clinopyroxene (35%), and devitrified glass (17%) fill the interstices of randomly placed plagioclase laths (40%). An_{56}. A band of segregation vesicles filled with devitrified glass lie in smaller plagioclase and pyroxene laths.

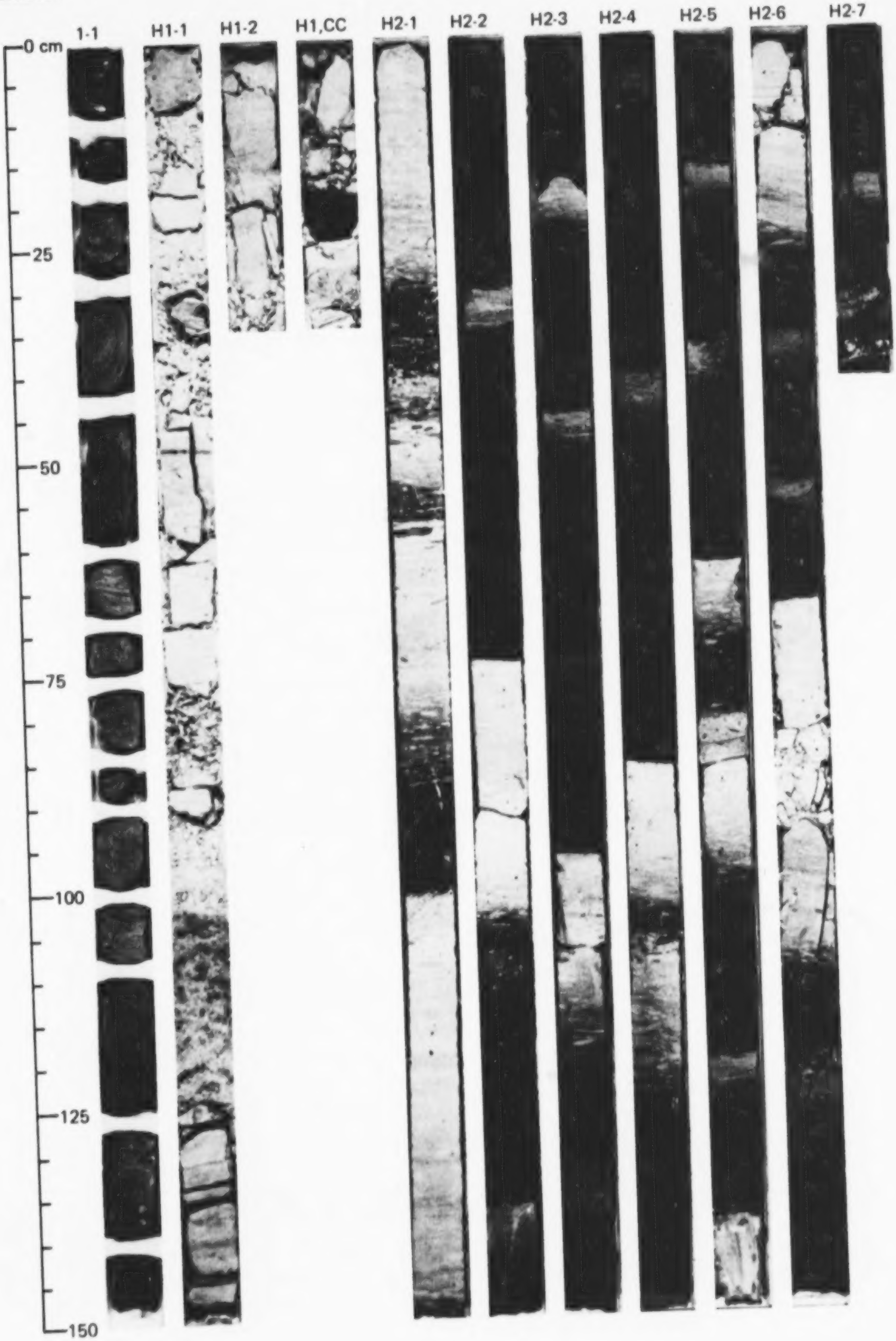
1-1
H1-1
H1-2
H1,CC
H2-1
H2-2
H2-3
H2-4
H2-5
H2-6
H2-7
0 cm
25
50
75
100
125
150

7. SITE 558[1]

Shipboard Scientific Party[2]

HOLE 558

Date occupied: 3 October 1981

Date departed: 11 October 1981

Time on hole: 196 hr.

Position (latitude; longitude): 37°46.2′N; 37°20.61′W

Water depth (sea level; corrected m, echo-sounding): 3754

Water depth (rig floor; corrected m, echo-sounding): 3764

Bottom felt (m, drill pipe): 3766

Penetration (m): 561

Number of cores: 44

Total length of cored section (m): 403.5

Total core recovered (m): 239.16

Core recovery (%): 59

Oldest sediment cored:
Depth sub-bottom (m): 408
Nature: Nannofossil chalk
Age: lower Oligocene

Basement:
Depth sub-bottom (m); 408
Nature: Basalt and serpentinized gabbro

HOLE 558A

Date occupied: 11 October 1981

Date departed: 12 October 1981

Time on hole: 28 hr.

Position (latitude; longitude): 37°46.2′N; 37°20.61′W

Water depth (sea level; corrected m, echo-sounding): 3754

Water depth (rig floor; corrected m, echo-sounding): 3764

Bottom felt (m, drill pipe): 3777

Penetration (m): 131.5

Number of cores: 16

Total length of cored section (m): 131.5

Total core recovered (m): 123.69

Core recovery (%): 94

Oldest sediment cored:
Depth sub-bottom (m): 131.5
Nature: Nannofossil ooze
Age: late Miocene

Principal results: Hole 558 (Site MAR-4) was drilled between Anomalies 13 and 15 on the west flank of the Mid-Atlantic Ridge about 30 miles south of the Pico Fracture Zone on a flow line passing through the FAMOUS area and the Leg 37 drilled sites (Fig. 1). The total penetration depth is 561 m, comprising 408 m of sediments and 153 m of basement.

In order to optimize the limited sediment program on this ocean crust leg, the shipboard scientists agreed that Site 558 would be suitable for continuous coring through the entire Neogene section and most of the Oligocene. The sediments recovered from the two holes cored at this site (558 and 558A) provide the first section of lower Oligocene through Pleistocene calcareous pelagic sediments from the North Atlantic.

The entire sediment layer (408 m) has been cored through a combination of piston coring and rotary coring; except for a 26-m gap where Holes 558 and 558A do not overlap. The recovered section provides an almost complete stratigraphic sequence from the Oligocene through the Pleistocene, with a minor hiatus in the lower Pliocene. There is a major change in the sediment lithology in the lower middle Miocene. The lower part of the section is characterized by a lower accumulation rate and a lower carbonate content. Nannofossils found within basalt breccias at the top of the basement are dated between 34 and 37 Ma, which is in agreement with the magnetic anomaly age. The magnetic reversal stratigraphy obtained from the lower part of the sedimentary section is very distinct and will provide strict limits for dating.

The upper 110 m of basement consisted almost entirely of aphyric pillow basalts and pillow breccias. Below this level, 43 m of serpentinized gabbros, serpentinite, and serpentinite mylonite were cored down to the bottom of the hole (561 m sub-bottom).

Six chemical units are distinguished within the pile of aphyric pillow basalts. Depleted (Nb = 3 ppm, Zr = 65 ppm), flat (Nb = 8.5 ppm, Zr = 83 ppm), and enriched (Nb = 15 ppm, Zr = 90 ppm) basalts are all represented. Interpretation of these results in terms of mantle plume and geodynamics will be very complex and will necessarily require isotopic and Ta/La data. These samples will be very valuable on the basis of fundamental and comparative geochemistry.

A complete set of logs was attempted. Because of poor hole conditions the logging runs were only partially successful.

OPERATIONS

Approach to Site 558

The criteria for Site 558 (MAR-4) were that it be on or near Anomaly 13 and on a flow line passing through the FAMOUS area and Site 335 of Leg 37 (Aumento, Melson, et al, 1977). The optimum sediment thickness was about 400 or 500 m, which we planned to continu-

---

[1] Bougault, H., Cande, S. C., et al., *Init. Repts. DSDP*, 82: Washington (U.S. Govt. Printing Office).

[2] Henri Bougault (Co-Chief Scientist), IFREMER (formerly CNEXO), Centre de Brest, 29273 Brest Cedex, France; Steven C. Cande (Co-Chief Scientist), Lamont-Doherty Geological Observatory, Columbia University, Palisades, New York; Joyce Brannon, Department of Earth and Planetary Sciences, Washington University, St. Louis, Missouri; David M. Christie, Hawaii Institute of Geophysics, University of Hawaii at Manoa, Honolulu, Hawaii; Murlene Clark, Department of Geology, Florida State University, Tallahassee, Florida; Doris M. Curtis, Curtis and Echols, Geological Consultants, Houston, Texas; Natalie Drake, Department of Geology, University of Massachusetts, Amherst, Massachusetts; Dorothy Echols, Department of Earth and Planetary Sciences, Washington University, St. Louis, Missouri (present address: Curtis and Echols, Geological Consultants, 800 Anderson, Houston, Texas 77401); Ian Ashley Hill, Department of Geology, University of Leicester, Leicester LE1 7RH, United Kingdom; M. Javed Khan, Lamont-Doherty Geological Observatory, Columbia University, Palisades, New York (present address: Department of Geology, Peshawar University, Peshawar, Pakistan); William Mills, Deep Sea Drilling Project, Scripps Institution of Oceanography, La Jolla, California (present address: Ocean Drilling Program, Texas A&M University, College Station, Texas 77843); Rolf Neuser, Institut für Geologie, Ruhr Universität Bochum, 4630 Bochum 1, Federal Republic of Germany; Marion Rideout, Graduate School of Oceanography, University of Rhode Island, Kingston, Rhode Island (present address: Department of Geology, Rice University, P.O. Box 1892, Houston, Texas 77251); and Barry L. Weaver, Department of Geology, University of Leicester, Leicester, LE1 7RH, United Kingdom (present address: School of Geology and Geophysics, University of Oklahoma, Norman, Oklahoma 73019).

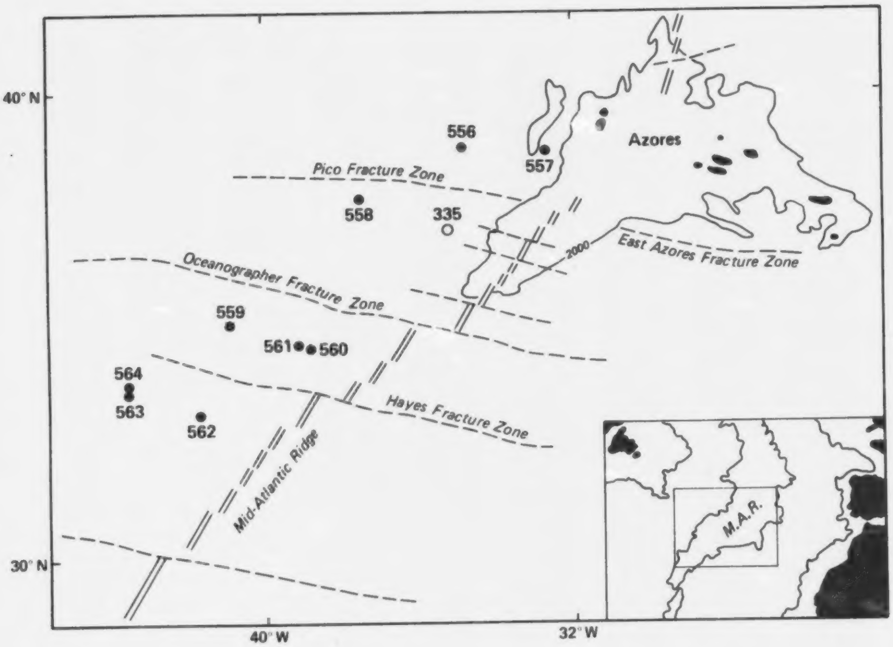

Figure 1. Site location map for Leg 82.

ously core. As at Sites 556 and 557, we wanted to avoid drilling on any irregular basement features that could not be considered typical oceanic crust.

The only existing geophysical data in the area were three magnetic lines (on which Anomalies 12 and 13 could be tentatively identified) and a poor quality seismic profiler record that showed an undulating basement with widely variable sediment thicknesses. Based on these data, we made a tentative site selection at 37°41′N, 37°19′W and laid out a track to survey it on the *Challenger* (Fig. 2). We were concerned that the site might be on one of the many fracture zones that offset the Mid-Atlantic Ridge near the FAMOUS area.

The survey on the approach to the site demonstrated that Anomaly 13 trended 12° *west* of north, which was unexpected because the trend of Magnetic Anomalies 12 and 13 further south near the Kane Fracture Zone is about 15° *east* of north. Basement relief is very irregular, and it is not clear whether the basement relief follows the same trend as the magnetic lineations. The reason for the anomalous trend of the magnetic lineations and the irregular basement relief is not known and requires more detailed surveying. It might reflect either oblique spreading at the ridge crest or possibly a series of small left lateral fracture zones that cannot be resolved at the spacing of our survey. We prefer the former interpretation of oblique spreading, because the peaks of Magnetic Anomaly 13 line up perfectly on all of the tracks with no hint of small, discrete offsets.

It was difficult to find a site within the survey area that met the requirements of a nominal 500 m of sediments underlain by a typical piece of oceanic basement. In general, the basement relief was quite irregular and the sediment cover was too thick to be continuously cored in a reasonable length of time. After completing the original planned survey of three east-west tracks parallel to the flow line, we found ourselves leaving the survey area without a prime site selected. At 1045Z, 3 October, we doubled back and headed for a site crossed at 0430Z on the north-south leg of the survey. However, we could not relocate this exact site and instead found a promising site about 5 miles north of our original tentative site selection (made before the survey was run). The beacon was dropped at 1146Z, 3 October, on a rolling basement hill covered with about 0.5 s of sediment (Fig. 3). Profiling was continued for a mile beyond the site and showed that the beacon had been dropped on a moderately steep slope. The actual site was offset 2500 ft. east of the beacon to a more level location in 3741 m of water.

The site is located on the negative anomaly between Anomalies 13 and 15 and has a theoretical age of 37 Ma based on the Lowrie and Alvarez (1981) time scale.

On-Site Operations

Hole 558 was spudded at 2122 hr. 3 October. No mudline core was taken and, in anticipation of hydraulic piston coring at the end of drilling operations, sediments were washed down to a depth of 158 m sub-bottom. Continuous coring was then started; the first core was on deck at 0220 hr. 4 October. Basement was reached around 1600 hr. 5 October at a depth of 406 m sub-bottom during cutting of Core 558-27. Coring within basement continued until 0754 hr. 9 October when, at a depth of 561 m sub-bottom, coring was halted because of a slow drilling rate and low recovery within thick serpentinite (Table 1). Total basement penetration was 155.5 m. After two attempts, the drill bit was dropped.

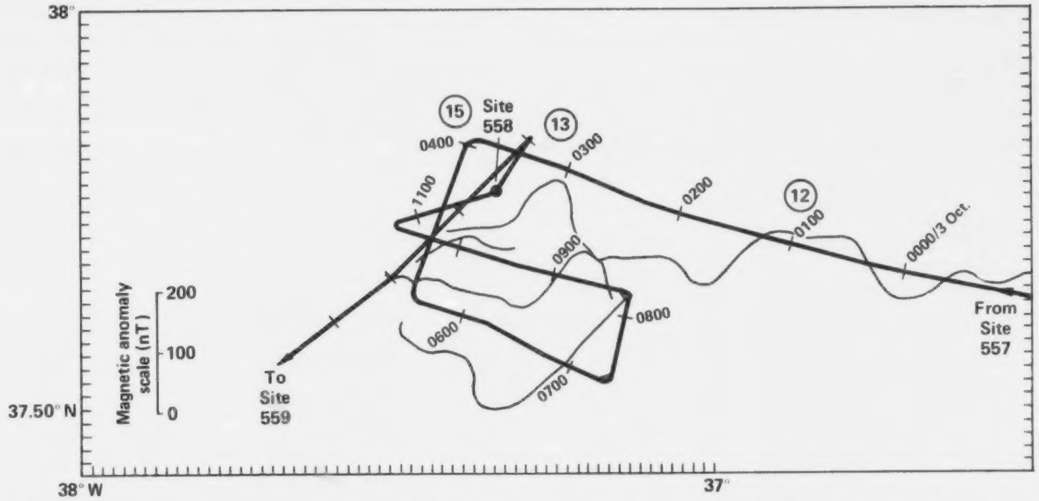

Figure 2. Approach and site survey tracks for Site 558. Heavy line is ship track with hour marks in GMT. Faint line is magnetic anomaly projected perpendicularly from the ship's track. Circled numbers are magnetic anomalies based on work at Lamont-Doherty Geological Observatory.

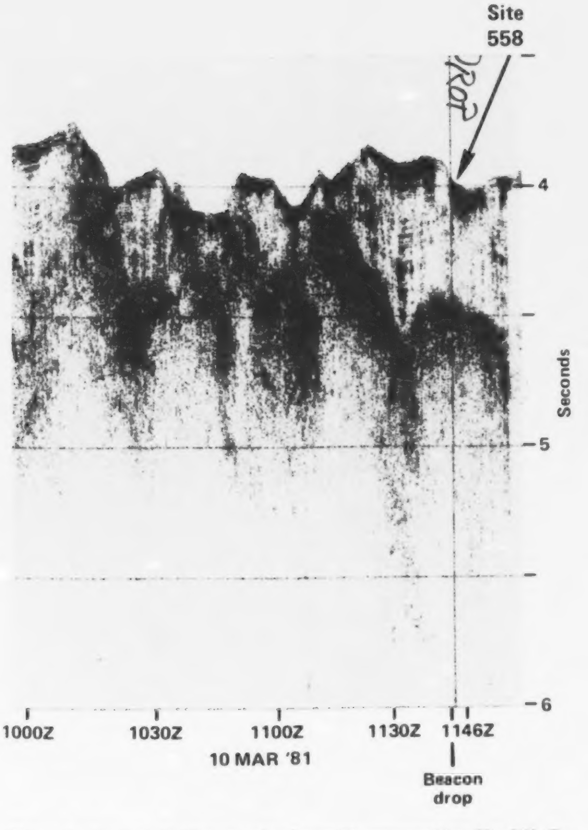

Figure 3. *Glomar Challenger* seismic profile approaching Site 558. For location of profile, see Figure 2.

Circulation was stopped at 1430 hr. 9 October and the end of the drill string pulled up to a depth of about 110 m sub-bottom. Logging operations were carried out between 1600 hr. 9 October and 0330 hr. 11 October. These operations are described in detail in the Downhole Measurements section. After logging was completed, preparations were made for hydraulic piston coring, which commenced at 1350 hr. 11 October and continued until 0930 hr. 12 October. A total of 132 m was piston cored (Table 1). Piston coring was halted before complete overlap of the sedimentary section when the pins holding the inner core barrel sheared and the core barrel became lodged in the hole, which forced us to abandon the hole. Piston coring operations were plagued repeatedly with the premature firing of the core barrel. However, this did not appear to affect the recovery of sediments, which was generally 100%. The *Challenger* was under way to Site 559 (MAR-8) by 1700 hr. 12 October. During the drilling of Holes 558 and 558A, operations were repeatedly hampered by a bad combination of current and swell that occasionally required a halt in operations for periods as long as 5 hr.

SEDIMENT LITHOLOGY

Two holes were cored at Site 558 in order to recover the upper portion of the sediment by hydraulic piston coring.

The first hole (558) was washed to 158 m before continuous rotary coring was begun. In this first hole a total of 561 m (measured from mudline) were penetrated, of which 408 m consisted of calcareous pelagic sediments.

After the first hole was successfully logged, Hole 558A was piston-cored to a depth of 131 m. Unfortunately, we were forced to stop operation at this depth before overlapping with the top of the cored interval from Hole 558. This left a gap of 26.5 m, which represents approxi-

Table 1. Coring summary, Site 558.

Core	Date (Oct. 1981)	Time (Z)	Depth from drill floor (m)	Depth below seafloor (m)	Length cored (m)	Length recovered (m)	Percent recovered
Hole 558							
H1	4	0039	3766.0-3924.0	0.0-158.0	0.0	0.00	0
1	4	0220	3924.0-3933.5	158.0-167.5	9.5	9.15	96
2	4	0353	3933.5-3943.0	167.5-177.0	9.5	8.78	92
3	4	0515	3943.0-3952.5	177.0-186.5	9.5	9.48	99
4	4	0652	3952.5-3962.0	186.5-196.0	9.5	9.65	100 +
5	4	0800	3962.5-3971.5	196.0-205.5	9.5	9.40	99
6	4	0954	3971.5-3981.0	205.5-215.0	9.5	9.05	95
7	4	1120	3981.0-3990.5	215.0-224.5	9.5	0.89	9
8	4	1300	3990.5-4000.0	224.5-234.0	9.5	5.65	59
9	4	1450	4000.0-4009.5	234.0-243.5	9.5	3.28	35
10	4	1610	4009.5-4019.0	243.5-253.0	9.5	1.54	16
11	4	1740	4019.0-4028.5	253.0-262.5	9.5	2.74	29
12	4	1910	4028.5-4038.0	262.5-272.0	9.5	7.05	74
13	4	2055	4038.0-4047.5	272.0-281.5	9.5	9.00	96
14	4	2159	4047.5-4057.0	281.5-291.0	9.5	9.59	100 +
15	4	2325	4057.0-4066.5	291.0-300.5	9.5	9.09	96
16	5	0057	4066.5-4076.0	300.5-310.0	9.5	9.70	100 +
17	5	0236	4076.0-4085.5	310.0-319.5	9.5	7.43	78
18	5	0354	4085.5-4095.0	319.5-329.0	9.5	6.86	72
19	5	0525	4095.0-4104.5	329.0-338.5	9.5	7.60	80
20	5	0651	4104.5-4114.0	338.5-348.0	9.5	6.47	68
21	5	0805	4114.0-4123.5	348.0-357.5	9.5	3.64	38
22	5	0925	4123.5-4133.0	357.5-367.0	9.5	5.42	57
23	5	1045	4133.0-4142.5	367.0-376.5	9.5	9.36	99
24	5	1210	4142.5-4152.0	376.5-386.0	9.5	5.98	63
25	5	1340	4152.0-4161.5	386.0-395.5	9.5	8.97	94
26	5	1500	4161.5-4171.0	395.5-405.0	9.5	6.94	73
27	5	1801	4171.0-4180.5	405.0-414.5	9.5	3.78	40
28	5	2354	4180.5-4189.5	414.5-423.5	9.0	3.09	34
29	6	0553	4189.5-4198.5	423.5-432.5	9.0	3.29	37
30	6	1038	4198.5-4207.5	432.5-441.5	9.0	4.08	45
31	6	1538	4207.5-4216.5	441.5-450.5	9.0	2.20	24
32	6	2050	4216.5-4225.5	450.5-459.5	9.0	5.00	56
33	7	0435	4225.5-4234.5	459.5-468.5	9.0	3.79	42
34	7	0801	4234.5-4243.5	468.5-477.5	9.0	1.50	17
35	7	1110	4243.5-4252.5	477.5-486.5	9.0	4.12	46
36	7	1445	4252.5-4261.5	486.5-495.5	9.0	3.09	34
37	7	1928	4261.5-4270.5	495.5-504.5	9.0	1.29	14
38	8	0110	4270.5-4275.0	504.5-509.0	4.5	2.45	54
39	8	0605	4275.0-4284.0	509.0-518.0	9.0	4.83	54
40	8	0858	4284.0-4293.0	518.0-527.0	9.0	3.37	37
41	8	1350	4293.0-4302.0	527.0-536.0	9.0	4.10	46
42	8	1955	4302.0-4311.0	536.0-545.0	9.0	1.78	20
43	9	0224	4311.0-4320.0	545.0-554.0	9.0	1.30	14
44	9	0754	4320.0-4327.5	554.0-561.5	7.5	3.39	45
					403.5	239.16	59
Hole 558A							
1	11	1415	3777.0-3777.5	0.0-0.5	0.5	0.47	94
2	11	1523	3777.5-3787.0	0.5-10.0	9.5	9.36	99
3	11	1639	3787.0-3796.5	10.0-19.5	9.5	9.51	100 +
4	11	1752	3796.5-3806.0	19.5-29.0	9.5	9.32	98
5	11	1920	3806.0-3815.5	29.0-38.5	9.5	9.71	100 +
6	11	2040	3815.5-3825.0	38.5-48.0	9.5	9.70	100 +
7	11	2145	3825.0-3834.5	48.0-57.5	9.5	8.22	87
8	11	2255	3834.5-3844.0	57.5-67.0	9.5	7.78	82
9	12	0025	3844.0-3851.0	67.0-74.0	7.0	4.76	68
10	12	0147	3851.0-3854.0	74.0-77.0	3.0	3.24	100 +
11	12	0305	3854.0-3863.5	77.0-86.5	9.5	9.63	100 +
12	12	0425	3863.5-3873.0	86.5-96.0	9.5	8.47	89
13	12	0546	3873.0-3880.0	96.0-103.0	7.0	6.98	100 +
14	12	0652	3880.0-3889.5	103.0-112.5	9.5	9.65	100 +
15	12	0810	3889.5-3899.0	112.5-122.0	9.5	8.11	85
16	12	0910	3899.0-3908.5	122.0-131.5	9.5	8.78	92
					131.5	123.69	94

mately 1–3 Ma of sedimentation. Because this gap represents such a short time span, and logging results through the same section in Hole 558 indicate that the lithology remains unchanged, we believe that we are justified in extrapolating sedimentation rates and lithology through this interval. Also for this discussion we have treated the cored sediment from both holes as one continuous section (see Fig. 4).

Based on carbonate and clay content (see Fig. 5) and the consequent color change, we have divided the sediment section into two major units. The lithologic unit descriptions are discussed in order of their deposition,

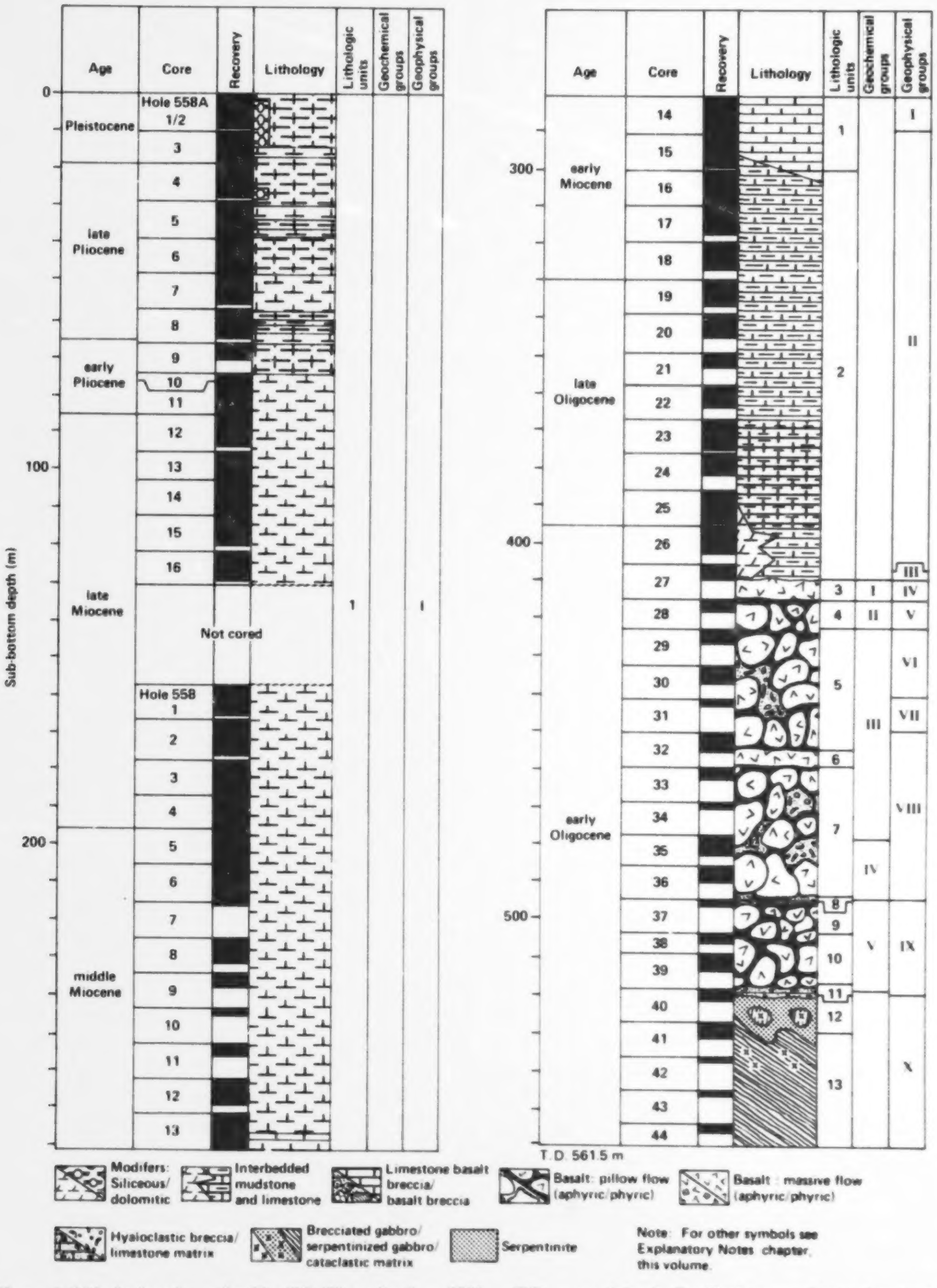
Age
Core
Recovery
Lithology
Lithologic units
Geochemical groups
Geophysical groups
Sub-bottom depth (m)
0
100
200
300
400
500
Pleistocene
late Pliocene
early Pliocene
late Miocene
middle Miocene
early Miocene
late Oligocene
early Oligocene
Hole 558A
1/2
Hole 558
Not cored
T.D. 561.5 m
I
II
III
IV
V
VI
VII
VIII
IX
X
Modifers: Siliceous/dolomitic
Interbedded mudstone and limestone
Limestone basalt breccia/basalt breccia
Basalt: pillow flow (aphyric/phyric)
Basalt: massive flow (aphyric/phyric)
Hyaloclastic breccia/limestone matrix
Brecciated gabbro/serpentinized gabbro/cataclastic matrix
Serpentinite
Note: For other symbols see Explanatory Notes chapter, this volume.

Figure 4. Lithologic column for Site 558. Water depth = 3766 m. T.D. = total depth. See Explanatory Notes chapter (this volume) for lithologic symbols.

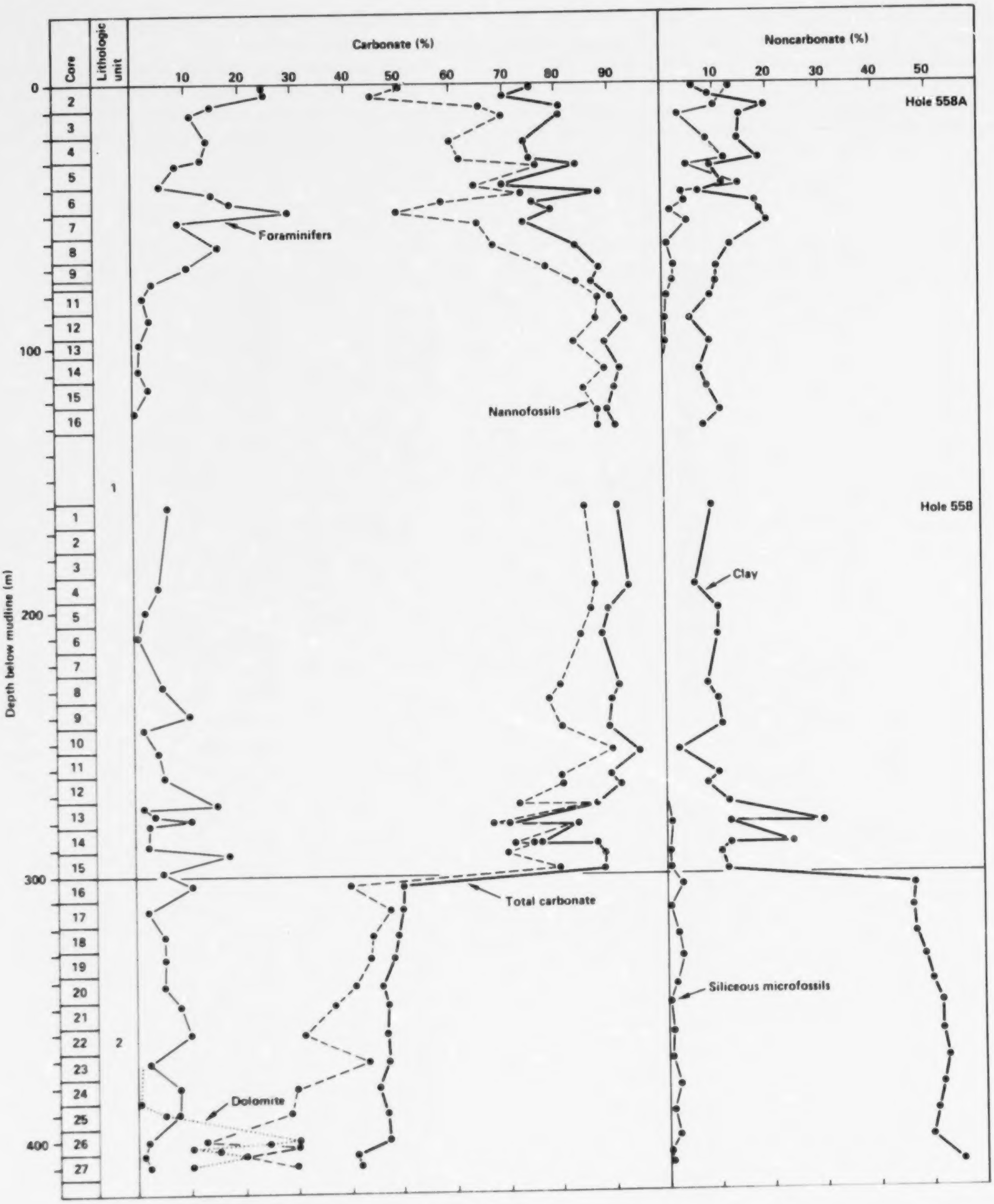

Figure 5. Percentage plot of major sediment components for Site 558.

beginning at the base of the sediment section with Unit 2 (summarized in Table 2).

Unit 2

This unit consists of 108 m (558-16-3, 40 cm through 558-27-2, 130 cm) of marly nannofossil chalk and limestone, marly foraminiferal nannofossil chalk, and dolomitic marly nannofossil chalk of the early Oligocene to early Miocene time (from 17–19 to 34–37 Ma). Colors of the chalks and limestones vary from brown (10YR 5/3) and yellowish brown (10YR 5/4) to pale brown (10YR 6/3). The color changes are usually gradational

Table 2. Sedimentary lithologic units at Site 558.

Interval	Lithologic unit	Sub-bottom depth (thickness) (m)	Main colors	Main lithology	Main components	Structure	Age
All of Hole 558A and 558-H1 to 558-16-3, 40 cm	1	0–300.0 (300)	Shades of white to pale brown	Nannofossil ooze; siliceous foraminiferal-nannofossil ooze; foraminiferal-nannofossil ooze	Nannofossils, foraminifers	Uniform with moderate mottling	late Pleistocene to early Miocene
558-16-3, 40 cm to 558-27-2, 130 cm	2	300.0–408.0 (108)	Yellowish brown to brown	Marly nannofossil chalk and limestone; marly foraminiferal-nannofossil chalk; dolomitic marly nannofossil chalk/limestone	Nannofossils, foraminifers, clay, dolomite	Uniform with moderate to intense mottling	early Miocene to early Oligocene

with few sharp contacts. These color changes reflect the change in carbonate versus clay content, although in Cores 26 and 27 the presence of dolomite may be the cause of darker shades of brown.

We observed no sediment transport textures or structures. Bedding is massive. Bioturbation/mottling is moderate to intense. Burrows (2–3 cm in diameter) have white halos around darker cores and are somewhat ellipsoid. Open ocean pelagic sedimentation began at this site in the early Oligocene and has continued to the present. But the deposition of sediments characterized by low carbonate values (40–50%) and high clay content (45–55%) ended in the late early Miocene. The presence of clay minerals is confirmed by X-ray diffraction analysis. Clay percentages were calculated by subtracting the percentage of carbonate (determined by carbonate bomb analysis), siliceous microfossils, feldspar, and other components (estimated from smear-slide examination) from 100 (Fig. 5).

Throughout this unit, siliceous microfossils and volcanic-derived debris (i.e., volcanic glass, feldspar, palagonite, and heavy minerals) occur in only trace amounts to a few percent. Manganese micronodules are also present in trace quantities in all the cores, although in Cores 558-17 through 558-15, larger nodules (1–3 cm in diameter) do occur. The presence of these manganese nodules suggests a low sediment deposition rate. This observation is supported by an average sedimentation rate of about 8 m/Ma calculated from biostratigraphic data (Fig. 7).

Carbonate values change very little within Unit 2 with a slight increase from 41% at the bottom of the unit to 50% at the top (see Fig. 5). Discussion of the carbonate component in terms of foraminifer-nannofossil ratios is complicated by the presence of authigenic dolomite rhombs in Cores 27 through 23. In the chalks and limestones of Core 27, the dolomite content is between 15 and 20%, then increases rapidly to 30% in Core 26. From Cores 26 to 23, the dolomite decreases to trace amounts and is absent from the rest of the sediment section. The constant carbonate composition through this section and the decrease in foraminiferal and nannofossil components with increase in dolomite would suggest that the dolomite is forming at the expense of the original carbonate constituents. Dolomite was observed encrusting (and possibly replacing) tests of washed foraminifers. In smear-slide examination, the majority of the dolomite rhombs are euhedral, although some show textures of previous resorption and recrystallization. Occurrence of the dolomite is discussed further in the Pore Water Chemistry section of this report.

The foraminiferal content changes from 5% or less in the zone of maximum dolomitization to an estimated 10% at the top of the dolomitized section in Core 25 and continues through Core 21 at 8–10%, with lower values in some samples (Fig. 5). Between Cores 21 and 16, the foraminiferal content is less than 5%, but increases erratically upward from the upper part of Unit 2 in Core 558-17 through the transition zone into Unit 1, reaching a maximum of 15% in Core 558-13.

The nannofossil abundance curve is essentially a mirror-image of the foraminifers, except in the dolomitized portion where both are in reduced abundance. Again beginning in the top of the dolomitized zone, nannofossils increase from an estimated 35% in Core 558-25 to 55% just below Core 558-16 and maintain values averaging 40–50% until the top of the unit in Core 558-16. Nannofossil percentages in the transition zone between Unit 1 and Unit 2 average between 60 and 70%.

Unit 1

This unit consists of 300 m (Hole 558A to 558-16-1, 0 cm) of nannofossil ooze and chalk, foraminiferal-nannofossil ooze and siliceous foraminiferal-nannofossil ooze. Unit 1 represents a period of deposition from the late early Miocene to the late Pleistocene (0 to 17–19 Ma) and is a continuation of the open ocean pelagic sedimentation from Unit 2, but with less clay deposition and higher sedimentation rates averaging 16 m/Ma.

We observed no sediment transport textures or structures. Bedding is massive. Bioturbation/mottling is moderate, when observed, although the lack of color contrast may have resulted in underestimating the degree of intensity or in overlooking these structures.

The lower portion of Unit 1 is transitional from Unit 2. In fact the first signs of the transition begin within Unit 2 at 558-18-4, 90 cm with the first minor occurrences of white (10YR 8/1) to light brownish gray (10YR 6/2) nannofossil chalk. These interbeds of nannofossil chalk (10–20 cm thick) continue irregularly uphole until

558-15-5, 40 cm, where they become the dominant lithology. The pale brown (10YR 6/3) to very pale brown (10YR 8/3) clayey interbeds persist uphole to 558-13-4, 60 cm, becoming less frequent, thinner, and less clayey (less than 10%). The change in lithification from chalk to ooze also takes place here.

Within the transition zone the nannofossil content (60–70%) varies inversely with the clay content (see Fig. 5). The foraminifers vary erratically from 1 to 15%. Because the total carbonate values are calculated from carbonate bomb data, a more reliable method than smear slide estimates, the variation shown by its curve (range 70 to 90%) demonstrates best the transitional nature of the lower portion of Unit 1.

Most of Unit 1 above the transition zone, through Core 558A-8 is very uniform in composition and this is reflected in coloration that varies only in shades of white (2.5YN 8 to 10YR 8/1). The total carbonate curve (Fig. 5) maintains a rather uniform average value of 90% with a range of 83 to 97%. Through this interval, nannofossil abundances range between 70 and 90% and foraminiferal abundances range from trace amounts to less than 10%. Clay, like the total carbonate curve, remains rather consistent at 10% with a range of 2 to 17%. Siliceous microfossils along with volcanic-derived material are absent or occur in trace amounts only. Micronodules of either pyrite or manganese minerals are present in trace or small amounts and may produce black streaks on the cut surface of the cores as a result of the core-splitting process.

Above Core 558A-8, the sediment color is white (5YR 8/1) up to 558A-1, which is pale brown (10YR 6/3), and sediment constituents depart from their uniform nature as previously described. Although overall clay content departs very little from its previous average value of 10%, except for a tendency to decrease near the top of the sediment section, a noticeable difference in the clay abundance curve is the increased variation in the range of values (2–20%).

This increase in range and variation is common to all the sediment constituents, although noticeable trends are observed with sedimentation (uphole). The total carbonate range is from 70 to 88%, with a decreasing trend with younger sedimentation. Nannofossils, while still the dominant sediment component, have a range of 80 to 45% with a decreasing trend with younger sedimentation. Foraminifers have a range of 2 to 29% with an increasing trend with younger sedimentation. Siliceous microfossils like the foraminifers also increase with younger sedimentation and have a range of trace amounts to 20%.

The relative increase of ratio of foraminifers and siliceous microfossils to nannofossil abundances may reflect an increase of productivity of the surface water. The higher variability may be due to cyclic environmental changes that cannot be resolved by our sampling density.

Miscellaneous Sediments

Intrapillow-basalt (volcaniclastic) limestone is common throughout the basalt units. It occurs either between pillow margins or as fillings in basalt cracks. Colors vary from light brownish yellow (10YR 6/4) to white (10YR 8/2). The volcaniclasts are mostly derived from the adjacent vitric rims of basalt pillows. Along with these volcaniclasts, foraminifers and micronodules are roughly stratified (geopetal texture?).

The degree of recrystallization of the former pelagic ooze is variable. The present limestone is mostly composed of micritic calcite, along with some rare unrecrystallized nannofossils, although irregular patches of sparite are common. These limestones have been heavily mineralized by dendritic manganese oxides.

BIOSTRATIGRAPHY

At Site 558, located near Anomaly 13, two holes were drilled; Hole 558 and Hole 558A. Hole 558 was washed down to a depth of 158 m and then sediments were continuously cored to a total penetration above basement of 408 m. The sediments recovered range from late Miocene to early Oligocene. The age of the oldest sediment, based on the microfossils, is in agreement with the estimated age of basement at the site.

Hole 558A had been piston-cored to a total depth of 132 m when mechanical problems in the inner core barrel forced termination before biostratigraphic overlap was accomplished. Sediments recovered from Hole 558A are Pleistocene to upper Miocene.

The combined section recovered from Holes 558 and 558A as dated by calcareous nannofossils ranges from Pleistocene to lower Oligocene. All major zones of Okada and Bukry (1980) are represented except CN11a and b, CN10b and c, and CN8. Nannofossil preservation is generally good in Hole 558A and remains so down to Core 558-5, which is middle Miocene. Preservation is only moderate from Core 558-5 down to the base of the sediment column.

Figure 6 shows the cored intervals, approximate ages based on foraminifers and position of the biostratigraphic gap. Foraminiferal ages are in general agreement with the nannofossil dates. Planktonic foraminifers are common to abundant and preservation moderate to good throughout most of the section (except for the middle and upper Miocene sections where there is evidence of dissolution and in the Oligocene section above the basalt where there is evidence of destruction of foraminifers by the growth of dolomite crystals in and on the tests).

Benthic foraminifers are fairly common and diversified and are indicative of deep water.

Other elements of the fauna such as well-preserved diverse ostracodes, radiolarians, sponge spicules, fish teeth, echinoid spines and *Bolboforma* (calcareous algae?) are significant (see Echols, this volume, for discussion of *Bolboforma*).

Calcareous Nannofossils

Hole 558

Hole 558 was washed down to a depth of 158 m where Core 558-1 was taken. Core 558-H1,CC contains an upper Miocene assemblage that includes *Discoaster neoha-*

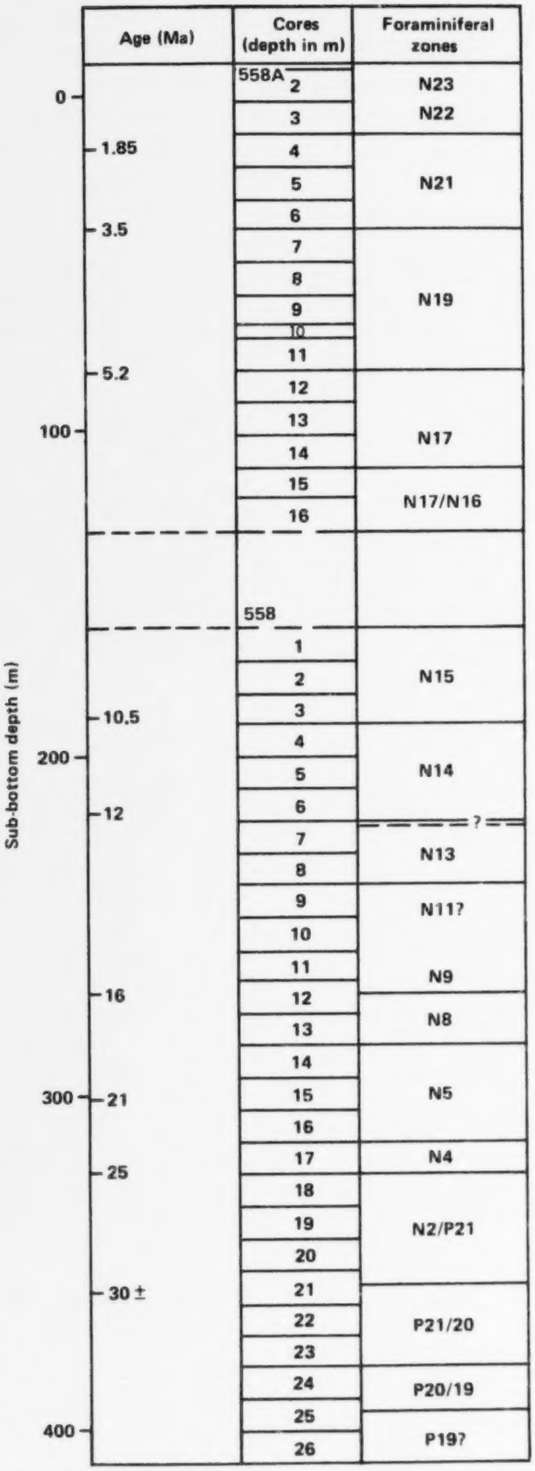

Figure 6. Preliminary zonation of Holes 558 and 558A.

matus, Calcidiscus macintyrei, D. bellus, and *Triquetrorhabdulus rugosus* and is characteristic of the *D. neohamatus* Zone CN8 of Okada and Bukry (1980) NN10. Because of the common occurrence of *D. bellus*, it is possible that Core 558-H1 corresponds to the lower part of the *D. neohamatus* Zone.

Cores 1 to 3 were recovered by rotary methods and are assigned to the upper middle Miocene to lower upper Miocene based on the occurrence of *D. hamatus* and *Catinaster calyculus. D. hamatus* is the index species for CN7 (NN9) and according to Okada and Bukry (1980), the base of *C. calyculus* is the marker for Subzone CN7b.

The core catcher of Core 558-4 contains *C. coalitus* without *D. hamatus* and is placed within the *C. coalitus* Zone CN6 (NN8), which is middle Miocene.

Cores 5 to 11 occur between the first appearance of *C. coalitus* and the last appearance of *Sphenolithus heteromorphus*. This interval is assigned to the *D. exilis* Zone CN5 (NN6–NN7) and indicates an accelerated accumulation rate for the middle Miocene. *D. exilis* is abundant and occurs with *D. variabilis, D. bollii, Calcidiscus macintyrei, Coccolithus pelagicus*, and *T. rugosus*.

Cores 12 to 14 are assigned to the middle Miocene because of the presence of *S. heteromorphus* with the common occurrence of long-armed discoasters. Core 15 contains *S. heteromorphus* but the long-armed discoasters are absent, creating an overall change in the appearance of the assemblage. This suggests that Core 15 probably should be attributed to the *Helicosphaera ampliaperta* Zone CN3 (NN4–NN3). *H. ampliaperta* is absent in Cores 12 to 15, so the first appearance of the long-armed discoasters is used to separate Zones CN3 and CN4.

The core catcher of Core 16 is lower Miocene, based on the presence of *S. belemnos* CN2 (NN3-2).

The Oligocene/Miocene boundary occurs within Cores 17 and 18, which are placed into the *T. carinatus* Zone CN1 (NN1–NP25). The assemblage is characterized by *T. carinatus, D. deflandrei*, and *Cyclicargolithus floridanus*.

The interval 558-19,CC through 558-22,CC contains *S. ciperoensis and is assigned to the upper Oligocene S. ciperoensis* Zone CP19 (NP24–NP25). *S. distentus*, whose last appearance datum marks the boundary between Subzones 19b *Dictyococcites bisectus* and 19a *C. floridanus*, is not present until 558-21,CC. The interval 558-19,CC through 558-21,CC is assigned to Subzone 19b, and 558-22,CC is assigned to Subzone 19a.

The core catcher of Core 23 is assigned to the lower upper Oligocene *S. distentus* Zone CP18 (NP23) because of the occurrence of *S. distentus* without *S. ciperoensis*. A lower upper Oligocene CP17 (NP23) assignment is inferred for 558-24,CC because of the presence of *S. predistentus* in the absence of *S. distentus* or *Reticulofenestra umbilica*.

The presence of rare *R. umbilica* in 558-25,CC indicates that this sample occurs within CP16c (NP22) *H. reticulata* Zone, *R. hillae* Subzone. The core catcher of Core 26 and 558-27-2, 42 cm contain *R. umbilica* and *Coccolithus formosus*, which indicate that this interval belongs to the *H. reticulata* Zone, *C. formosus* Subzone CP16b (NP21). Cores 25 to 27 are lower Oligocene.

Hole 558A

Hole 558A was cored by the hydraulic piston corer (HPC), and 123.69 m of sediment were recovered. Core 1 contains abundant *Gephyrocapsa caribbeanica* and *G. oceanica*, indicating the upper Pleistocene. The presence of *Emiliania huxleyi* is indefinite because of the difficulty in recognizing this species with the light microscope. Core 1 contains common and well-preserved *Ceratolithus telesmus* and *C. cristatus*. Although 558A-2,CC is Pleistocene, assignment to a particular zone is questionable because of the small size of the nannofossils present: exceptions are *Cycloccolithus leptoporus* and *Helicopontosphaera sellii*. *Calcidiscus macintyrei* is encountered in Core 3 above the extinction of *Discoaster brouweri*. This sample corresponds to the lower Pleistocene *C. macintyrei* Zone of Gartner (1977) (NN19).

Cores 4 to 7 are upper Pliocene and are assigned to the *D. brouweri* Zone CN12 of Okada and Bukry (1980) (NN16, NN17, NN18) on the basis of the occurrence of *D. brouweri* above the last appearance of *Reticulofenestra pseudoumbilica*. The core catcher of Core 4 contains *C. macintyrei* and *D. brouweri* without *D. pentaradiatus*. This indicates the uppermost Subzone CN12d of the *D. brouweri* Zone of Okada and Bukry (1980). Cores 5 and 6 contain *D. pentaradiatus* and possibly *D. surculus* and are placed within the Subzones CN12b–c. *D. tamalis* is first encountered in 558A-7,CC, and the sample is therefore assigned to Subzone CN12a.

Very rare *R. pseudoumbilica* are found in 558A-8,CC, as well as *D. tamalis* and *Ceratolithus rugosus*. Because specimens of *R. pseudoumbilica* are so rare and *Sphenolithus abies* is absent, this sample is assigned to the *D. brouweri* Zone, *D. tamalis* Subzone CN12a (NN16).

The core catcher of Core 9 contains a color change that marks the position of a lower Pliocene hiatus. The top of the core catcher contains *R. pseudoumbilica, D. asymmetricus*, and *D. tamalis* and is assigned to the *D. asymmetricus* Subzone of the *R. pseudoumbilica* Zone CN11b (NN15). The lower part of the core catcher contains *Amaurolithus primus, A. delicatus*, and a possible *C. acutus*. Two specimens of *Triquetrorhabdulus rugosus* are also present but may be reworked. This places the lower part of 558A-9,CC in either the *C. acutus* or *T. rugosus* Subzone of the *A. tricorniculatus* Zone CN10a,b (NN12). Subzone CN11a and CN10c of the lower Pliocene are absent, signaling a hiatus during this interval.

The interval from 558A-10,CC to 558A-12,CC contains *T. rugosus* with *A. primus, A. delicatus*, and *A. tricorniculatus*. This indicates that this interval is uppermost Miocene. Because the presence of *D, quinqueramus* could not be clearly established, Cores 10 and 11 are thought to occur within the *A. tricorniculatus* Zone, *T. rugosus* Subzone CN10a (NN12).

The interval from 558A-13,CC to 558A-14,CC is attributed to the upper Miocene *D. quinqueramus* Zone, *A. primus* Subzone CN9b (NN11). *D. quinqueramus* is observed in these samples as well as *A. amplificus* and *A. primus*. The core catcher samples from Cores 15 and 16 also belong to the *D. quinqueramus* zone. The absence of *A. primus* and the presence of *D. berggrenii* place this interval within the *D. berggrenii* Subzone CN9a (NN11).

Foraminifers

Hole 558

Miocene (upper)

Hole 558 was washed down to a depth of 158 m. The first rotary core taken recovered a white nannofossil-foraminiferal ooze with an abundant and well-preserved middle-upper-Miocene fauna. Although placement is tentative, abundant specimens of the *Globorotalia menardii-(cultrata)* s.l. lineage and the presence of *Globigerina nepenthes, Globoquadrina altispira, G. dehiscens, Sphaeroidinellopsis subdehiscens* and *S. seminulina* seem to be indicative of foraminiferal Zone N15 (10–10.5 Ma). The core catchers of Cores 2 and 3 contain a similar fauna, but the planktonic foraminifers in 558-3,CC show signs of fragmentation. The core catcher of Core 4, which also shows fragmentation and/or dissolution, is assigned to lower Zone N15/upper N14 because of the presence of very abundant *Globigerina nepenthes*,which makes its first appearance at approximately 12 Ma.

Miocene (middle)

The core catcher of Core 5, Zone N14, is significant in the marked increase in numbers of *Globoquadrina dehiscens* and *G. advena* and for the interesting tiny spherical to flattened spherical calcareous forms found in the finest fractions. These forms probably belong to the *incertae sedis Bolboforma*, originally described from the Oligocene and Miocene of northwestern Germany by Daniels and Spiegler in 1974. Since then the forms have been recorded from Miocene sediments drilled during DSDP Legs 35, 48, and 80 (Rögl and Hochuli, 1976; Murray, 1979; and Graciansky, Poag, et al., in press, respectively). In these reports they have been referred to as cysts or reproductive bodies of an unknown algae, and it has been suggested, because the species described have distinct stratigraphic ranges, that they may be regional markers in deep-sea sediments (see Echols, this volume).

The core catcher of Core 6, which is older than 12 Ma, shows considerable fragmentation of the planktonic forms and, because of the selective dissolution, a high proportion of large, well-preserved diverse benthic foraminifers. The rare specimens of *Globigerina nepenthes* present are attributed to uphole contamination. In 558-7,CC, planktonic forms are common and moderately well preserved. *Sphaeroidinellopsis seminulina* and *S. subdehiscens* are the dominant forms in the assemblage. This sample is assigned to the middle Miocene Zone N13. The fauna in 558-8,CC shows some fragmentation and overgrowths on the globorotalid forms. The core catcher of Core 9 has a fairly abundant but fragmented fauna. *Globorotalia peripheroronda*, which becomes extinct around 14+ Ma, is first encountered in this sample. *Orbulina universa* and *O. suturalis* are also present in fair numbers, indicating an age older than 14 Ma and less than 16 Ma. This sample is assigned to Zone N11. The core catchers of Cores 10 and 11 are also middle Miocene but are heavily contaminated with Pleistocene and Pliocene material. In 558-12,CC, foraminifers are common but fractured. *G. peripheroronda, S. subdehiscens*, and *S. seminulina* are common, and *Globigerinoides sicanus* is rare.

Miocene (lower)

The core catcher of Core 13 is assigned to the foraminiferal Zone N8, upper part of the lower Miocene. In this sample *Globigerinoides sicanus, Globoquadrina dehiscens*, and *Globigerinoides trilobus* are common and *Orbulina* species are absent. In this sample the siliceous element is apparent; radiolarians, diatoms, and sponge spicules are very abundant and diverse. The core catcher of Core 14, lower Miocene, contains abundant and well-preserved *Globoquadrina dehiscens* and globorotalid forms, such as *Globorotalia praemenardii* and *G. praescitula*.

The core catcher of Cores 15 and 16 are also lower Miocene. In the larger fraction these samples contain very abundant *Globoquadrina dehiscens*, and in the finer fractions abundant *Catapsydrax* and *Globigerinoides*. The core catcher of Core 17 is assigned to Zone N4 based on the assemblage of *Catapsydrax dissimilis, Globorotalia kugleri, Globoquadrina dehiscens*, and *Globigerina tripartita*.

Oligocene (upper)

The core catchers of Cores 18 and 19 are considered uppermost Oligocene. The core catcher of Core 18, although contaminated with Pliocene-Pleistocene material, does contain abundant *Globigerina tripartita, G. venezuelana*, and *Catapsydrax dissimilis*. The core catcher of Core 19 also contains these forms in abundance along with *Globoquadrina baroemoenensis* (= *dehiscens* of some authors), *Globigerina gortanii* (*Catapsydrax* of some authors), and rare *Globorotalia opima*. Very large specimens of *C. dissimilis* have been used, where other markers are missing, for the Oligocene assignment (the *Globorotalia opima opima* Zone). The core catcher of Core 19 is assigned to N2/P21 *G. opima opima* Zone.

The core catchers of Cores 20 and 21 have essentially the same abundant well-preserved fauna, whereas 558-22,CC and 558-23,CC have in addition abundant well-developed *Chiloguembelina cubensis, Globorotaloides suteri, Globigerina praebulloides*, and *Globorotalia opima nana*. This assemblage is assigned to the lower part of P21, or upper part of P20.

Oligocene (lower)

The core catchers of Cores 24 and 25 have a similar fauna with abundant *Chiloguembelina cubensis* and in addition, abundant *Pseudohastigerina* sp. These samples are assigned to the zonal interval P20/P19.

The core catcher of Core 26 contains abundant *Pseudohastigerina* sp., planispirally coiled specimens common in the lower Oligocene, and a similar fauna to that found in the preceding cores. Although this sample is not particularly diagnostic, it is tentatively assigned to P19.

Of interest in this sample is the fact that the foraminifers show some destruction, and dolomite rhombs are growing in and on the foraminiferal tests. The pan fraction of this sample consists of dolomite crystals and tiny corroded foraminifers.

Basalt was reached in 558-27,CC at approximately 408 m. The washed residue of a sample 1 m above the basalt contains nothing but dolomite rhombs, rare fragments of foraminifer shells, and manganese(?) nodules.

Age of basement based on the foraminifers is estimated at 32–35 Ma.

Hole 558A

Pleistocene

Sixteen HPC cores, to a total depth of 131.5 m, were drilled into Hole 558A. Core 558A-1,CC, a white nannofossil-foraminiferal ooze at 5 m, recovered Pleistocene sediments. Dominant elements of the foraminiferal fauna that are characteristic of Zones N22/N23 are *Globorotalia truncatulinoides, G. inflata, G. scitula, Globigerina bulloides, Globigerinoides ruber, G. obliquus, Neogloboquadrina pachyderma*, and *Orbulina universa*. Benthic foraminifers, ostracodes, and abundant beautiful diverse radiolarians are well preserved.

Sample 558A-2,CC (which is also Pleistocene) contains essentially the same fauna with an increase in the abundance of *Globorotalia truncatulinoides* and the addition of abundant *G. tumida, G. flexuosa*, and *G. crassaformis*.

Pliocene-Pleistocene

Core 558A-3,CC at 19.5 m is lower Pleistocene–uppermost Pliocene. Besides the fauna found above it contains abundant *Pulleniatina obliquiloculata*. Core 558A-4,CC is considered uppermost Pliocene (N21) and is characterized by a reduction in numbers of Pleistocene species and by the appearance of the gradational forms in the *Globorotalia truncatulinoides* lineage (i.e., *G. ronda* and *G. tosaensis*). The core catchers of Cores 5 and 6 are also upper Pliocene (N21). *G. truncatulinoides* is very rare in 558A-5,CC and absent from 558A-6,CC.

Pliocene (lower)

The core catchers of Cores 7 and 8 contain foraminifers indicative of the lower Pliocene (N19). (Zone N20 of Blow, 1969, if it exists, was not recognized in this hole.) Both samples have very abundant, well-preserved foraminifers in a white nannofossil-foraminiferal ooze. The core catcher of Core 7 has very abundant and large *Orbulina* species, abundant *Globorotalia crassaformis* (*crassula*), *G. ronda, Globigerinoides conglobata, G. sacculifer*, and pink *G. ruber*. The core catcher of Core 8 contains essentially the same fauna in different proportions and in addition large well-preserved *Globorotalia pertenuis*. The fauna indicates a warm-temperate climate.

Samples from 558A-9,CC are also assigned to Zone N19; but the fauna indicates a slightly older age. As a matter of fact, reexamination of the core catcher seems to indicate that the Miocene/Pliocene boundary may have been penetrated in this section between 558A-9,CC and 558A-10-1.

Therefore, until detailed zonation is complete, 558A-10,CC and 558A-11,CC are tentatively assigned to the lowermost Pliocene-uppermost Miocene.

Miocene (upper)

The core catchers of Cores 12 through 15 are upper Miocene and are assigned to the N17 foraminiferal zone. Zone N18 is either missing from the section or just not apparent in the core catcher material. Further study of the sections may resolve this question. The planktonic fauna in the core catchers of Cores 12 through 14 show fracturing and/or dissolution in all size fractions, and the forms are considerably smaller in size than the preceding sample. This may be more apparent than real and due to the fact that the larger forms are fractured. The core catcher of Core 15 contains very abundant *Globigerina nepenthes* and may be representative of the lower part of N17.

The core catcher of Core 16 at 131.5 m, the last HPC core recovered from Hole 558A, contains a well-preserved, diverse, robust fauna of abundant *G. nepenthes, Sphaeroidinellopsis seminulina, S. subdehiscens*, large *G. bulloides* (*praebulloides*?), *G. atlantica*, and *Orbulina*. This sample is assigned to N16 and may be dated at approximately 8 Ma+.

Biostratigraphic overlap with Hole 558 was not accomplished (Fig. 6).

SEDIMENT ACCUMULATION RATES

Sediment accumulation rates are plotted from foraminiferal and nannofossil biostratigraphic zone determinations from core catcher samples. Because preliminary age designations show some differences between nannofossil and foraminiferal dates, we have plotted the age ranges at each core catcher depth (Fig. 7) and have calculated an average sediment accumulation rate for each stratigraphic interval, based on the boundaries determined from nannofossils and foraminifers respectively (Fig. 7; Table 3).

The changes in sediment accumulation rates correspond approximately with stratigraphic boundaries. The most obvious change in sediment accumulation rate (from 16.6-26.2 m/Ma to 4.7-5.8 m/Ma) near the top of the lower Miocene corresponds to the boundary of Lithologic Units 1 and 2. This boundary is defined by a downhole decrease in carbonate content and an increase in the clay content. In the transition zone between the two lithologic units (approximately 277 to 304 m), we calculated a sediment accumulation rate of 7 to 9 m/Ma.

The causes of the quite abrupt decrease in sediment accumulation rate and carbonate content (to less than 50%) were discussed extensively on board ship but no conclusions were reached. The following are possible factors that were considered. (1) Dissolution may account for only part of the reduction. Preservation of the nannofossils is only moderate throughout the interval from the top of the lower Miocene to the base of the sediment section, although the site has probably been above the calcite compensation depth (CCD) throughout its history. (Backtrack curves for this area in the vicinity of the Azores Triple Junction have greater uncertainty.) Dissolution resulting from characteristics of the Oligocene to early Miocene water mass is also a possibility. (2) Changes in carbonate productivity may have some affect. (3) Possibly, the carbonate underwent some dissolution and some proportion of the nannofossils may have been "winnowed" away by bottom water movement, reworking, and bioturbation, leaving reduced nannofossil percentages and increasing clay and foraminiferal percentages. The irregular basement topography and the fact that the site is situated on a basement high could well be the key cause. Similar problems have been discussed by Berger and von Rad (1972).

In the upper portion of the hole, above the lower Pliocene hiatus, the upper Pliocene has an extremely high sediment accumulation rate (40.8 m/Ma). This high rate may correspond to increased productivity of the surface waters. As shown in Figure 5, this same interval shows an increase in siliceous microfossils content. The presence of siliceous microfossils is used as an indicator of surface water productivity.

PORE WATER CHEMISTRY

The results of the interstitial water chemistry analysis for Hole 558 and Hole 558A are shown in Figure 8 and tabulated in Table 4.

The values of pH, alkalinity, and chlorinity remain fairly constant with depth. The salinity values, on the other hand, are very erratic, which may reflect contamination by surface seawater (seawater is used as a drilling fluid in rotary coring).

Except for the sample taken immediately above the basalt, the calcium and magnesium concentration gradients are typical for calcareous pelagic sediments overlying basalt; that is, the pore waters are enriched in calcium and depleted in magnesium. However, the pore waters sampled immediately above the basalts are just the opposite, being depleted in calcium and enriched in magnesium. The possible cause for these anomalous values could be the result of seawater contamination, but note that this pore water sample was taken from dolomitic (authigenic, 20%) nannofossil chalk.

IGNEOUS PETROLOGY AND GEOCHEMISTRY

Igneous rocks, consisting mainly of pillow basalts and varying amounts of interpillow breccia (hyaloclastite limestone breccia) occur below 408 m sub-bottom depth throughout the drilled basement section. Two thin, massive basalt flows were encountered within and above the pillow layers. Serpentinite rocks, initially moderately altered grading down through fresh serpentinite to highly sheared serpentinite mylonite, were drilled from 520 m

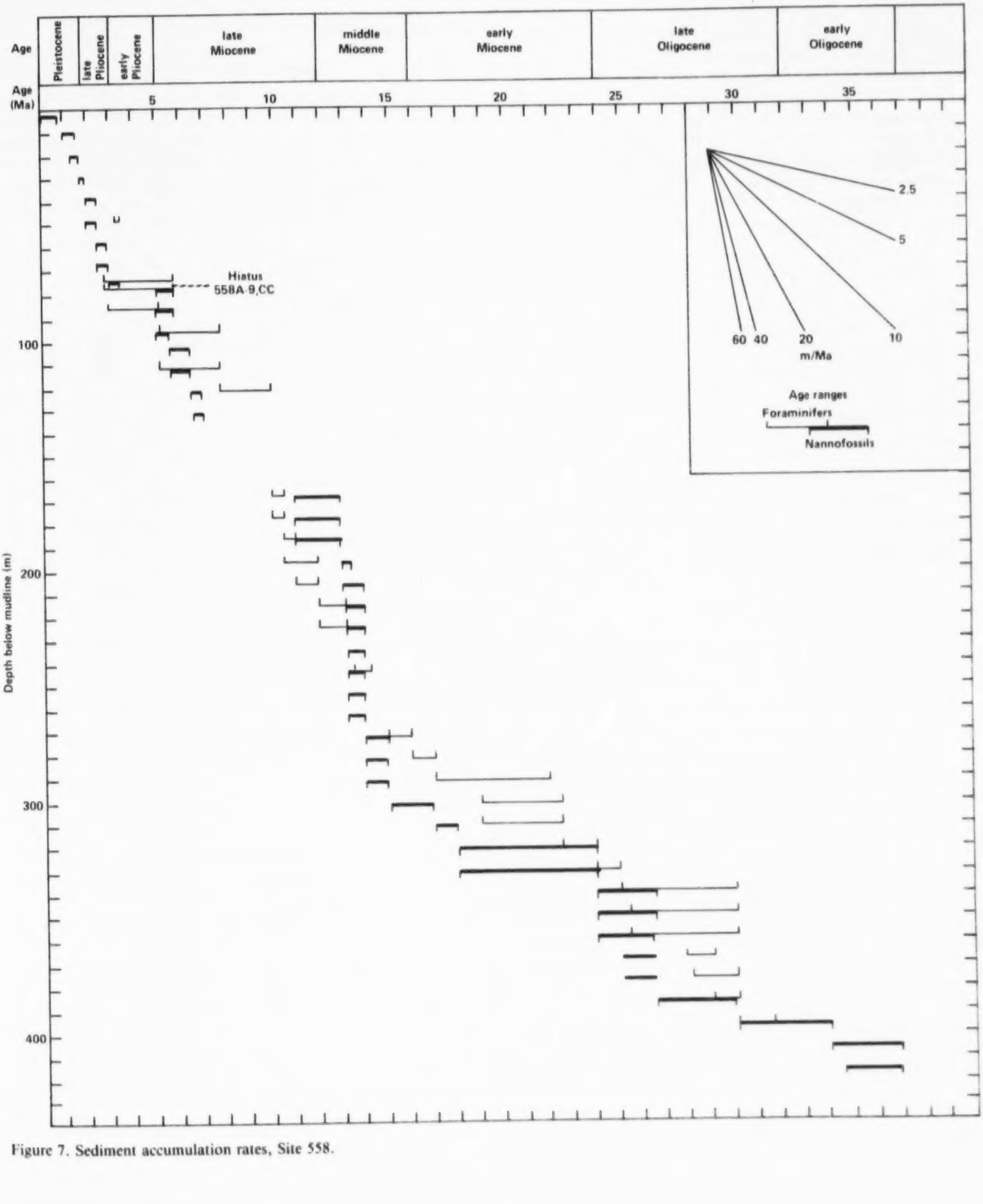

Figure 7. Sediment accumulation rates, Site 558.

Table 3. Sediment accumulation rates.

Stratigraphic unit	Age (Ma)	Nannofossils Depth (m)	Nannofossils Rate (m/Ma)	Foraminifers Depth (m)	Foraminifers Rate (m/Ma)
Pleistocene	1.8	0–18	10.0		
upper Pliocene	1.8–3	18–67	40.8		
lower Pliocene	3–5	67–74			
		Hiatus			
upper Miocene	5–12	74–186	16	86–205	17
middle Miocene	12–16	186–291	26.2	205–272	16.7
lower Miocene	16–24	291–329	4.7	272–319	5.8
upper Oligocene	24–32	329–386	7.1	319–395	9.5
lower Oligocene	32–37	386–414	5.6		

to the end of drilling at 561.5 m. Eleven lithologic units and six chemical groups have been identified in the basement at Site 558 (Units 3–13, Figs. 9 and 10).

Lithologic Units

Unit 3 (408–414.9 m)

The first igneous rock unit, occurring below sedimentary Units 1 and 2 is a moderately altered, weathered, fine-grained aphyric massive basalt flow. Unit 3 has been interpreted as a massive flow because it lacks glass or other evidence of internal cooling margins. Variolitic basalt is observed in the upper 40 cm of this unit. The size

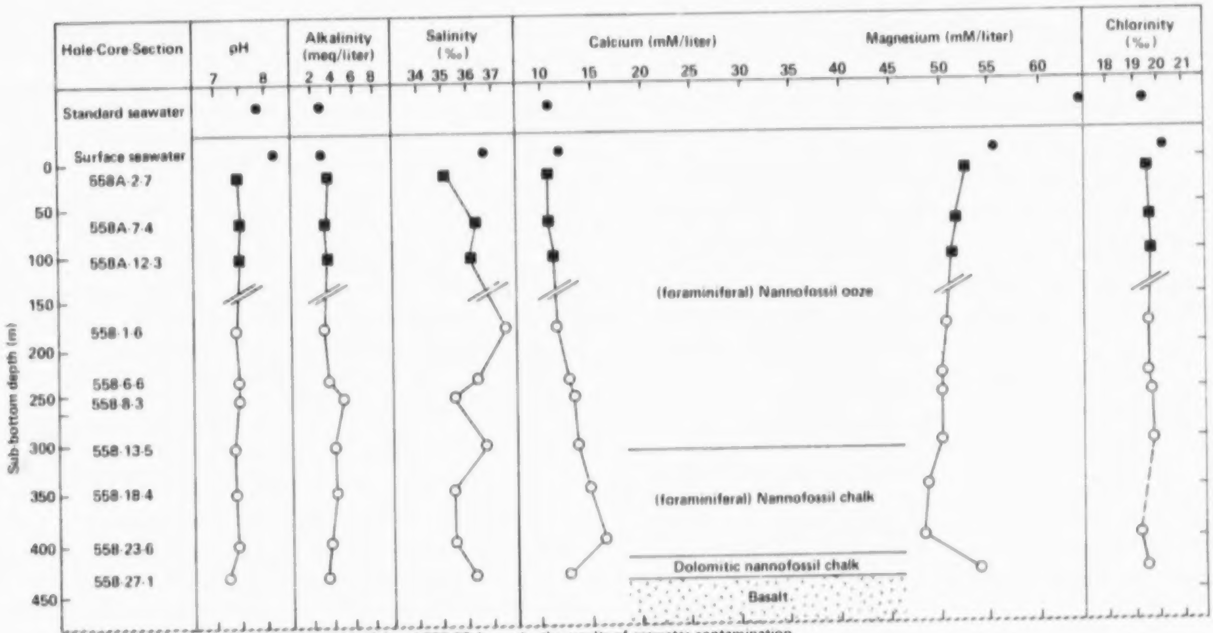

Note: Anomalous values from Sections 558-23-6 and 558-27-1 may be the results of seawater contamination.

Figure 8. Pore water chemistry water profile, Site 558. Hole 558 results are open circles; Hole 558A, squares.

Table 4. Pore water chemistry results, Site 558.

Core-Section (interval in cm)	Sub-bottom depth (m)	pH	Alkalinity (meq/liter)	Salinity (‰)	Calcium (mM/liter)	Magnesium (mM/liter)	Chlorinity (‰)
Hole 588A							
2-7, 12-19	10.0	7.43	3.47	35.1	10.67	52.16	19.55
7-4, 144-150	56.0	7.44	3.19	36.3	10.67	51.40	19.62
12-3, 143-150	92.0	7.42	3.20	36.1	11.02	51.05	19.65
Hole 558							
1-6, 144-150	167.5	7.36	2.99	37.6	11.00	50.71	19.48
6-6, 140-150	215.0	7.43	3.50	36.4	12.13	49.99	19.41
8-3, 110-120	230.0	7.42	4.79	35.3	12.60	50.05	19.58
13-5, 144-150	280.0	7.31	3.92	36.8	13.39	50.15	19.62
18-4, 110-120	325.0	7.34	4.03	35.3	14.08	48.28	
23-6, 140-150	376.5	7.39	3.27	35.3	15.20	47.81	19.04
27-1, 140-150	411.0	7.13	3.00	36.2	12.09	53.27	19.31

Note: The anomalous values from Sections 558-23-6 and 558-27-1 may be the results of seawater contamination.

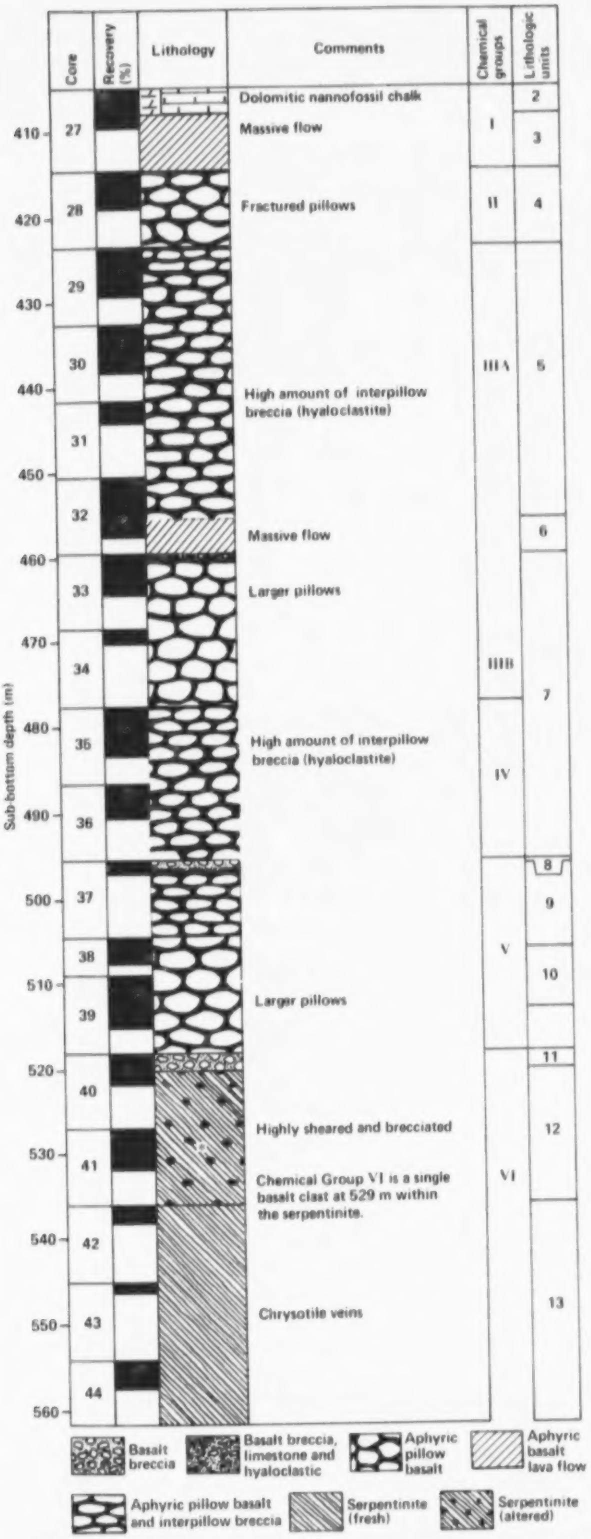
Core
Recovery (%)
Lithology
Comments
Chemical groups
Lithologic units
Sub-bottom depth (m)
410
420
430
440
450
460
470
480
490
500
510
520
530
540
550
560
27
28
29
30
31
32
33
34
35
36
37
38
39
40
41
42
43
44
Dolomitic nannofossil chalk
Massive flow
Fractured pillows
High amount of interpillow breccia (hyaloclastite)
Massive flow
Larger pillows
High amount of interpillow breccia (hyaloclastite)
Larger pillows
Highly sheared and brecciated
Chemical Group VI is a single basalt clast at 529 m within the serpentinite.
Chrysotile veins
I
II
IIIA
IIIB
IV
V
VI
2
3
4
5
6
7
8
9
10
11
12
13
Basalt breccia
Basalt breccia, limestone and hyaloclastic
Aphyric pillow basalt
Aphyric basalt lava flow
Aphyric pillow basalt and interpillow breccia
Serpentinite (fresh)
Serpentinite (altered)

Figure 9. Basement lithology column, Hole 558. See Explanatory Notes (this volume) for lithology symbols.

of the varioles increases downward, ranging from 1 to 6 mm in diameter.

Unit 4 (414.9–423.5 m)

This unit consists of fine-grained aphyric basalt pillows, which are sometimes separated by multiple chilled glass margins. It is overlain by a thin hyaloclastite layer containing flat, angular pieces of glass altered to palagonite at their rims and aligned parallel to one another within a limestone matrix. The whole pillow sequence is highly fractured and contains strongly weathered zones close to the fractures. The remainder of the rock appears fresh to slightly weathered. Pillow thickness, about 60 cm in the upper part of the unit, increases slightly towards the bottom.

Unit 5 (423.5–455.5 m)

This unit consists of approximately 32 m of aphyric basalt pillows with abundant interpillow breccia. The fine-grained pillow interiors appear to be fresh to moderately altered and grade outwards through an altered variolitic zone to fresh aphanitic basalt close to cooling margins. Basalt glass usually occurs as a rind around the pillows. Interpillow hyaloclastite breccias consist of glass pieces with minor basalt clasts in a limestone matrix or calcite cement. Glass clasts smaller than 5 mm are mostly completely altered to palagonite, whereas the larger clasts are only rimmed by alteration products. Roughly 30 pillows were recovered in this unit, ranging in drilled thickness from about 30 cm to approximately 1 m.

Unit 6 (455.5–459.5 m)

Unit 6 consists of fine-grained aphyric massive basalt. A vertical fracture filled with calcite extends along the length of the cored section. Weathered areas extend 0.5 cm on either side of the fracture. Vesicles are rare; they are small (less than 2 mm), round, and clay filled.

Unit 7 (459.5–495.5 m)

This unit strongly resembles Unit 5. It consists of about 36 m of fine-grained aphyric basalt pillows, nearly all of which are separated by fresh glass margins. The amount of interpillow breccia, although less than in Unit 5, increases down the unit. Altered variolitic transition zones commonly separate fresh or moderately altered, fine-grained pillow interiors from fresh aphanitic to glassy outer zones. Calcite-filled veinlets and fractures occur throughout this unit.

Unit 8 (495.5–496.2 m)

This 70-cm-thick unit consists mainly of limestone with interbedded altered basalt breccia and hyaloclastite layers. Smaller clasts (less than 1 cm) are mostly altered to palagonite, whereas the larger clasts are fresh with narrow palagonite rims. The limestone contains a dendritic pattern of black oxides. In places, cavities are filled with calcite cement.

Unit 9 (496.2–505.0 m)

Unit 9 consists of fresh to moderately altered fine-grained aphyric basalt, occurring as pillows and interpil-

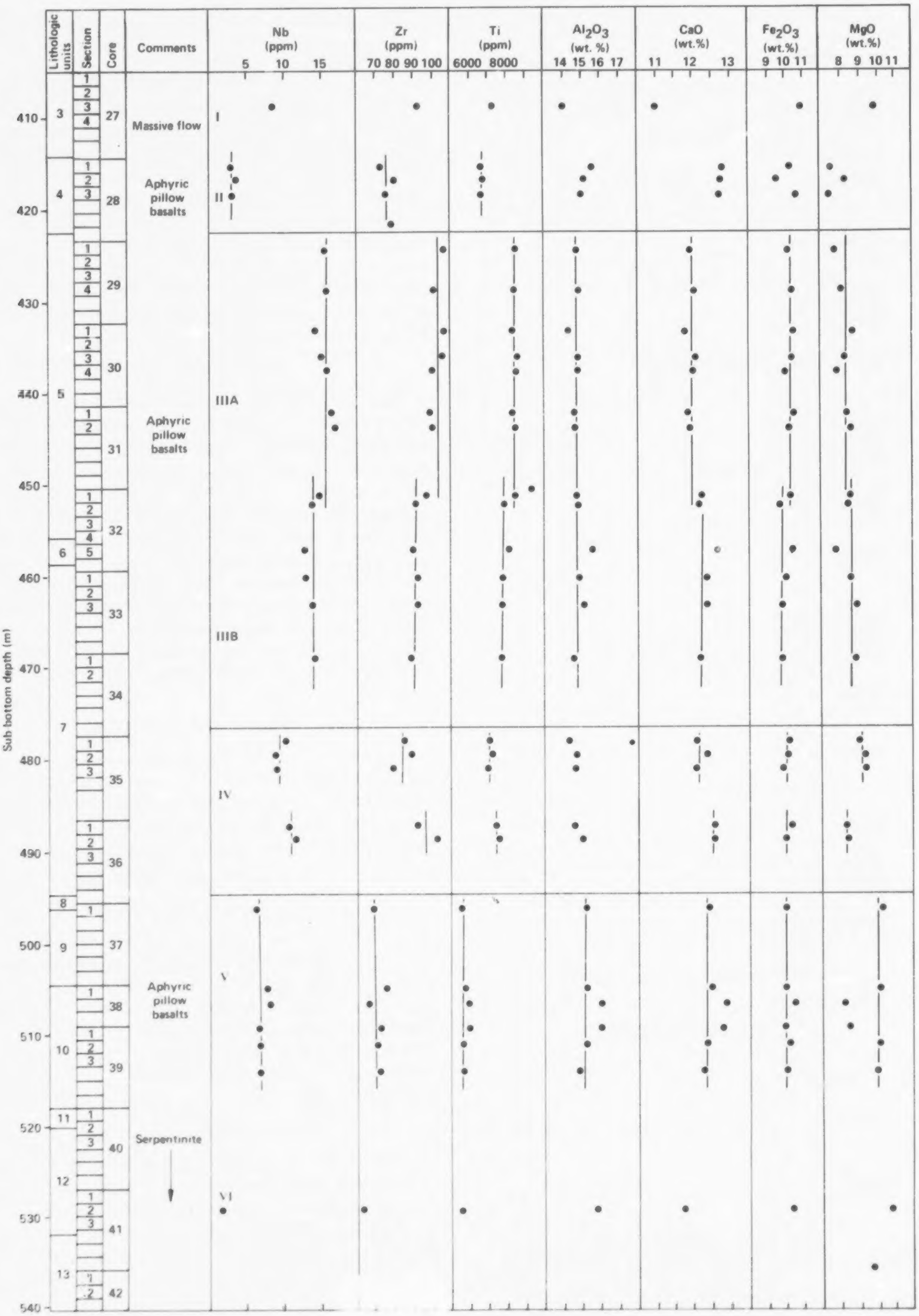

Figure 10. Downhole variations in chemical abundances, Hole 558. Chemical groups are designated by Roman numerals.

low breccia. Clasts of glass derived from pillow margins, aphanitic basalt, and variolitic basalt are common in the breccia. The majority of glass shards are approximately 2 to 10 mm long and are slightly altered to palagonite.

Unit 10 (505.0–518.0 m)

Unit 10 consists of moderately altered fine-grained aphyric basalt forming large pillows. Pillow rims are marked by a gradation from fine-grained aphyric basalt through variolitic basalt to aphanitic basalt. The drilled thickness of the pillows ranges from a few tens of centimeters to about 1.5 m; most pillows are less than 80 cm. Clay-filled or calcite-filled fractures and calcite veinlets are common throughout the section.

Unit 11 (518.0–520.0 m)

This unit is a basalt breccia composed of angular to subrounded aphyric, fine-grained to aphanitic basalt clasts. Clast size ranges from a few millimeters to a few centimeters. The matrix is mainly limestone accompanied by some sparry calcite cement.

Unit 12 (520.0–531.5 m)

Unit 12 consists of brown altered serpentinite and serpentinite breccia (often described as sheared gabbro in visual core descriptions) and mylonite with minor, less strongly serpentinized, anorthosite veins. The serpentinite is highly altered gabbro with rare relict pyroxenes 1–5 mm in size. The serpentinite breccia consists of clasts of serpentinite in a matrix of clay minerals, talc, and additional serpentine. The clasts range in size from approximately 1 mm to several centimeters. Two meters above the bottom of Unit 12, the mylonite zone contains angular, moderately altered basalt clasts, including one large basalt clast at 529.9 m.

Unit 13 (531.5–561.5 m)

Unit 13 is composed of strongly sheared blue green serpentinite mylonite containing clasts of serpentinite up to 1 m in drilled thickness. Serpentinite clasts are dark green to black, and weakly to moderately sheared, with sinuous, white, chrysotile veinlets varying in abundance from 2–20% and ranging from 0.1 to 20 mm in thickness.

Petrographic and Chemical Groups

Basalts from Site 558 can be divided into six groups on the basis of chemical analysis (Tables 5 and 6). Chemical group boundaries do not always coincide with lithologic unit boundaries described in the previous section. Samples from each chemical group are also petrographically similar regardless of lithologic unit, but not all groups are petrographically distinct (Groups I, IV, and V are very similar).

All basalts from this site are aphyric and few are holocrystalline; the majority of samples examined display intersertal textures, with more glass-rich textures occurring closer to pillow margins. Weathering is pervasive throughout Site 558; most samples show at least some brownish discoloration in hand specimen, and orange brown iron hydroxides are present in varying amounts in virtually all thin sections. Brown discoloration is strongly developed in variolitic zones throughout the hole.

Table 5. Average analyses for the six chemical groups from Hole 558.

Chemical group	I	II	III	IV	V	VI
N	1	3	13	5	6	1
Major elements (wt.%)						
SiO_2	50.67	50.86	50.70	50.19	49.37	48.71
TiO_2	1.22	1.12	1.38	1.22	0.96	0.92
Al_2O_3	14.10	15.11	14.82	14.65	15.49	15.81
Fe_2O_3	10.92	10.08	10.17	10.98	10.17	10.73
MnO	0.16	0.15	0.15	0.16	0.16	0.16
MgO	9.87	7.69	8.33	8.90	9.48	10.55
CaO	10.55	12.23	11.64	11.90	12.06	11.56
K_2O	0.18	0.18	0.30	0.30	0.20	0.10
P_2O_5	0.14	0.12	0.18	0.13	0.12	0.07
Trace elements (ppm)						
Ti	7320	6720	8280	7308	5780	5520
V	207	255	275	266	224	194
Sr	128	92	175	144	115	107
Y	27.0	29.7	28.7	28.1	22.9	23.0
Zr	83	66	88	80	61	51
Nb	8.6	3.2	14.8	10.5	7.3	2.0
Mg′	67	63	65	65	68	69
Al_2O_3/TiO_2	11.6	13.5	10.8	12.0	16.1	17.2
Ti/Zr	88	102	94	92	96	108

Note: N is the number of samples on which the mean is based. Mg′ is the atomic ratio of 100 × Mg/(Mg + Fe^{2+}), calculated using an assumed Fe_2O_3/FeO ratio of 0.15. Averages are calculated from data listed in Table 6.

Twenty-eight samples from Site 558 were analyzed for major and trace elements. The data are shown in Tables 5 and 6, and in Figure 10, depth is plotted versus each of the following elements: Zr, TiO_2, Al_2O_3, CaO, Fe_2O_3, and MgO.

Chemical Group I is defined by a single sample from Section 558-27-3. It is clear from Table 5 and Figure 10 that this sample has a unique chemistry compared to the other chemical groups. The CaO content of this sample (10.7 wt.%) is very low compared to that of the other groups.

Chemical Group IV consists of five samples from Cores 558-35 and 558-36. There may be a minor subdivision in this group between the samples from Cores 558-35 and 558-36. The two samples from Core 558-36 have lower MgO and Mg-numbers than Core 558-35 samples, and higher concentrations of TiO_2, Zr, and Nb. As a group, however, the Zr/Nb ratio is consistent at values of 7–8.3. This is greater than the Zr/Nb ratio value exhibited by chemical Group III but less than for Groups I and II, reflecting the slightly enriched nature of this group, which shows up on the extended Coryell-Masuda diagram (Fig. 11).

Chemical Group V consists of six analyzed samples from Cores 558-37 to 558-39. In terms of most of the major and trace elements, this group is chemically homogeneous with the apparent exception of the two samples from Sections 558-38-2, and 558-39-1, which have low MgO contents (8.2–8.4%) and Mg numbers (63–65) compared to the other basalts in this group (MgO, 10%; Mg-number, 69). Basalts of this group display relatively enriched Coryell-Masuda patterns, similar to those of Groups I and IV (Fig. 11), but with somewhat lower ab-

Table 6. Analyses of major elements (wt.%) and trace elements (ppm) from Hole 558 basalts.

Core-Section (interval in cm) (piece number)	Sub-bottom depth (m)	Chemical group	SiO_2	TiO_2	Al_2O_3	Fe_2O_3	MnO	MgO	CaO	K_2O	P_2O_5	Total	Mg′	Ti	V	Sr	Y	Zr	Nb
27-3, 74-77 (8)	408.9	I	50.67	1.22	14.10	10.92	0.16	9.87	10.55	0.18	0.14	97.81	67	7320	207	128	27.0	83	8.6
28-1, 91-94 (9)	415.4	II	50.95	1.12	15.14	10.22	0.15	7.51	12.28	0.21	0.12	97.70	62	6720	256	93	29.3	63	2.8
28-2, 121-125 (15)	417.3		51.00	1.13	15.15	9.48	0.16	8.22	12.24	0.11	0.13	97.62	66	6780	257	96	29.7	69	3.5
28-3, 60-64 (7)	418.2		50.62	1.11	15.03	10.55	0.15	7.35	12.18	0.21	0.10	97.30	61	6660	253	88	30.2	65	3.2
29-1, 120-125 (7D)	424.8	III	52.17	1.43	14.76	10.12	0.14	7.68	11.42	0.43	0.19	98.34	63	8580	277	176	30.2	97	15.3
29-4, 71-76 (6)	428.7		50.88	1.41	14.83	10.37	0.15	8.08	11.53	0.39	0.21	97.85	64	8460	273	171	29.6	91	15.7
30-1, 60-64 (8A)	433.1		50.30	1.39	14.34	10.47	0.18	8.66	11.30	0.26	0.18	97.08	65	8340	281	165	29.8	97	14.3
30-3, 99-103 (10B)	436.5		50.28	1.43	14.84	10.35	0.15	8.31	11.60	0.34	0.19	97.49	64	8580	278	173	30.2	96	15.2
30-4, 55-59 (4C)	437.5		51.57	1.42	14.77	10.07	0.14	7.78	11.50	0.23	0.20	97.68	63	8520	268	172	28.8	90	16.0
31-1, 62-64 (5C)	442.2		51.07	1.39	14.61	10.44	0.15	8.32	11.37	0.29	0.19	97.83	64	8340	277	174	31.1	89	16.4
31-2, 128-130 (9)	444.3		51.27	1.41	14.64	10.21	0.15	8.52	11.44	0.28	0.19	98.11	65	8460	280	172	28.9	90	17.2
32-1, 106-110 (8A)	451.5		50.33	1.42	14.76	10.28	0.15	8.49	11.74	0.35	0.19	97.71	65	8520	280	171	30.5	87	15.0
32-3, 63-67 (4C)	454.1		50.09	1.32	14.89	9.64	0.13	8.44	11.68	0.26	0.18	96.63	66	7920	274	173	26.2	81	13.9
32-5, 66-70 (2B)	456.2		49.73	1.36	15.68	10.39	0.15	7.81	12.31	0.30	0.19	97.92	63	8160	291	187	27.3	80	12.9
33-1, 77-80 (9A)	460.2		50.05	1.31	14.88	10.09	0.14	8.49	11.80	0.24	0.16	97.16	65	7860	267	180	28.0	82	13.0
33-3, 142-145 (9D)	463.9		50.70	1.30	15.12	9.87	0.14	8.94	11.90	0.28	0.17	98.42	67	7800	274	183	25.7	83	13.9
34-1, 34-38 (3B)	468.8		50.62	1.29	14.62	9.92	0.14	8.77	11.72	0.21	0.17	97.46	67	7740	255	177	26.5	79	14.2
35-1, 128-131 (11C)	478.8	IV	50.24	1.19	14.37	10.29	0.16	9.06	11.65	0.33	0.16	97.45	66	7140	261	146	27.7	75	10.4
35-2, 97-102 (6A)	480.0		50.08	1.21	14.75	10.22	0.15	9.28	11.92	0.25	0.15	98.01	67	7260	273	146	26.5	79	9.3
35-3, 100-102 (8B)	481.6		50.25	1.18	14.38	9.98	0.15	9.41	11.61	0.30	0.13	97.39	68	7080	250	141	26.6	69	9.4
36-1, 62-65 (5)	487.2		49.94	1.24	14.69	10.36	0.16	8.30	12.09	0.28	0.16	97.22	64	7440	284	139	29.9	83	11.5
36-2, 107-110 (5E)	489.1		50.45	1.27	15.06	10.07	0.16	8.43	12.21	0.33	0.17	98.15	65	7620	265	149	30.0	93	12.1
37-1, 137-141 (19A)	496.9	V	49.18	0.94	15.35	10.12	0.15	10.19	11.95	0.21	0.09	98.18	69	5640	243	113	22.7	58	6.4
38-1, 126-130 (16)	505.8		48.82	0.96	15.33	10.02	0.16	10.01	12.02	0.15	0.11	97.58	69	5760	222	113	22.5	65	7.8
38-2, 84-88 (5B)	506.8		49.85	1.00	16.02	10.55	0.16	8.17	12.42	0.20	0.13	98.50	63	6000	235	117	23.2	56	8.4
39-1, 83-87 (5G)	509.8		49.64	1.00	16.01	9.99	0.17	8.43	12.29	0.19	0.13	97.85	65	6000	223	115	23.7	62	6.9
39-2, 35-38 (3A)	510.9		49.77	0.94	15.27	10.21	0.17	10.10	11.87	0.22	0.12	98.67	69	5640	218	112	23.1	61	6.9
39-4, 131-135 (6)	514.8		48.97	0.94	14.93	10.11	0.15	9.95	11.79	0.20	0.11	97.15	69	5640	204	121	22.4	62	7.1
41-2, 143-146 (6F)	529.9	VI	48.71	0.92	15.81	10.73	0.16	10.55	11.56	0.10	0.07	98.61	69	5520	194	107	23.0	51	2.0

Note: Measurements were made on board using ignited samples. On-shore analyses have shown the loss on ignition to be less than 1%. The concentrations listed in the tables of compiled data (Appendix at the end of this volume) include volatile contents. Mg′ is the atomic ratio of 100 × $Mg/(Mg + Fe^{2+})$, calculated using an assumed Fe_2O_3/FeO ratio of 0.15.

solute abundances. The variation of chemical composition between the higher and lower MgO members of Group V could possibly be explained by subtraction of a small proportion (few percent) of olivine.

Basalts of Groups I, IV, and V are composed of 30–40% hollow, elongate plagioclase laths up to 0.5 mm long, often arranged in parallel or slightly radiating bundles; different bundles have random orientations. Euhedral-shaped, diamond-shaped, lantern-shaped, or prism-shaped olivine (5–10%) ranges from completely altered (to green brown clay) to less than 50% altered with fresh, clear cores. The remainder of each rock is made up of about 20% granular clinopyroxene and 30–40% dark mesostasis. Depending on the degree to which each sample has crystallized, this mesostasis may be composed of fine granular of sheaflike clinopyroxene and dark brown devitrified glass in almost any proportion. Associated with the mesostasis is about 5% fine granular or skeletal magnetite. An unusual feature of some of the rocks in these groups is the presence, in plagioclase, of numerous, tiny dark brown octahedra of spinel.

Chemical Group II comprises the three analyzed samples from Core 558-28. In terms of both major and trace elements, this group is homogeneous, except for a higher MgO content (and consequently higher Mg-number) in the sample from Section 558-28-2. In comparison to Group I, the aphyric basalts of Group II are notably lower in TiO_2, MgO, Fe_2O_3, Sr, Zr, and Nb but have greater abundances of Al_2O_3 (Table 5 and Fig. 10). Although both Zr and Nb are lower in Group II basalts with respect to Group I, Nb is more strongly depleted than Zr, as is shown by the extended Coryell-Masuda plot for the Group II average in Figure 11.

Group II basalts are almost olivine free, containing at most 2–3% small diamond-shaped olivine euhedra. They contain 30–40% randomly oriented hollow plagioclase laths, 30–40% granular clinopyroxene, and 20–30% dark brown devitrified glass with approximately 5% skeletal magnetite.

Chemical Group III encompasses Lithologic Units 5, 6, and part of 7. Thirteen analyzed samples from Cores 558-28 to 558-34 compose chemical Group III, which has been subdivided into two homogeneous subgroups denoted IIIA and IIIB, encompassing, respectively, samples above and below Section 558-32-2 (Fig. 9).

Although there is no obvious lithologic or petrographic break between these subgroups, the chemical distinction is quite clear (Table 6 and Fig. 10): IIIB has lower TiO_2, Zr, and Nb and slightly greater Sr, Al_2O_3, and CaO. Both groups have similar Fe_2O_3, MgO, and, hence, Mg-numbers. Section 558-32-5 is slightly different from Group IIIB; there is a marked change in CaO, TiO_2, and MgO. The general chemical coherency of this group is demonstrated by the constant Zr/Nb ratio, which reflects the enriched nature of this group when plotted on an extended Coryell-Masuda diagram (Fig. 11). This contrasts markedly with the patterns exhibited by chemical Groups I and II.

Group III basalts contain unusually large amounts of olivine. Glassy rocks adjacent to pillow rims are characterized by up to 10% diamond-shaped and lantern-shaped microphenocrysts as well as abundant chains, branching aggregates, and other skeletal forms of olivine. Plagioclase is present in such samples only in variolites. More-crystalline members of this group contain as much as 20% olivine as small (less than 0.3 mm) diamond-shaped or prism-shaped euhedra, largely altered to clay or, in some cases, to colorless high birefringent aggregates of talc. In these rocks, plagioclase (25–30%) is subordinate to clinopyroxene (30–40%). Granular to skeletal magnetite is unusually abundant (about 10%).

Because these rocks contain twice the amount of olivine usually observed, a high Mg-number is predicted; this, however, is not the case here. The absolute amount of olivine is offset by a larger absolute amount of opaque minerals. This relative abundance of magnetite explains the small difference in MgO content between this and other less olivine-rich groups.

Finally, chemical Group VI consists of a single basalt clast from the serpentinite breccia of Unit 12 (Section 558-41-2). This sample is depleted on an extended Coryell-Masuda diagram (Fig. 11). It is quite different in nature and chemical composition from the depleted samples of chemical Group II (Table 6, Fig. 10).

Geochemistry

The normalized magmaphile element concentrations for the five chemical groups recognized in Site 558 are plotted in Figure 11. Depleted (Nb with respect to Zr), flat, and significantly enriched distributions in the most magmaphile elements within the same hole compose the major results and striking characteristics of Site 558.

Interpreting the Nb/Zr ratio, of the five chemical groups, in respect to the mantle source characteristics, leads to the conclusion that the basalts recovered from Site 558 have a complex origin. At least three different sources appear to have contributed to the basaltic layer. However, the relative enrichment or depletion of the most magmaphile elements (e.g., Nb) with respect to the least magmaphile elements (e.g., Zr) is a function of both the chemical "fingerprint" of the mantle source and of the extent and method of melting. Thus, onshore measurements of rare earth elements, Ta/La (or Nb/La) ratios and Pb, Sr, and Nd isotopic ratios are necessary before distinct mantle sources can be confirmed.

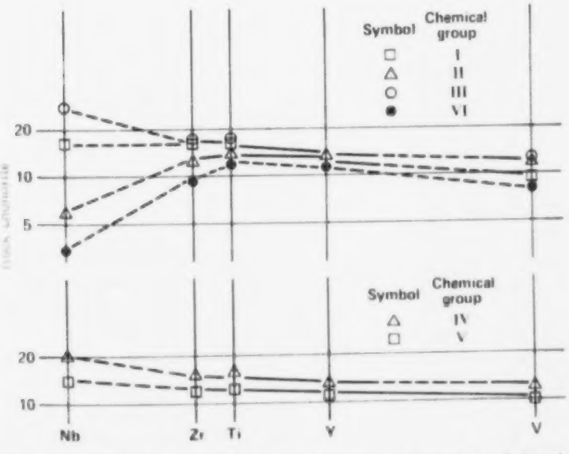

Figure 11. Extended Coryell-Masuda diagram for averages of chemical Groups I–VI, Hole 558.

In Figure 12 normalized Ta concentrations (which are the same as normalized Nb concentrations) are plotted against normalized La for basalts from a variety of localities. All analyses are from the laboratory of P. Sue of CNRS (Treuil et al., 1973).

In general, all samples presenting flat to enriched Coryell-Masuda diagrams have a chondritic $(Ta/La)_{ch}$ ratio (1, by definition) (e.g., Mid-Atlantic Ridge from Azores Triple Junction to Hayes Fracture Zone; Leg 37 and 49 samples from near the FAMOUS area; continental alkali basalt [El Azzouzi, 1981]; basalt from seamounts [Cambon et al, 1980]).

Samples with depleted patterns such as basalts from Site 395 at 22°N on the Mid-Atlantic Ridge and Site 483 on the East Pacific Rise have $(Ta/La)_{Ch}$ ratios close to 0.5. Exceptions to both generalizations do occur. Basalt from Site 409 on the Reykjanes Ridge have $(Ta/La)_{Ch}$ of 1 and slightly depleted patterns (Figs. 12 and 13), whereas basalts from Walvis Ridge (Fig. 12) and dolerite from Morocco (Figs. 12 and 14) have enriched patterns with $(Ta/La)_{Ch}$ of 0.5.

Chondritic $(Ta/La)_{Ch}$ ratios (1.0 by definition) are thought to reflect an initial property of the mantle and are characteristic of most alkalic and transitional basalts (Bougault, 1980). $(Ta/La)_{Ch}$ values of 0.5 may be characteristic of depleted mantle or they may be attributable to fractionation of Ta and La (Nb and La) despite the similarity of their physico-chemical properties (reflected by the constancy of these element ratios over a wide concentration range). Such fractionation could only result from very high degrees of partial melting or from specific melting processes such as dynamic melting (Langmuir et al., 1977) or step melting (Bougault et al., 1979).

In either case, it is clear that the range of extended Coryell-Masuda plots observed at Site 558 will be better understood when isotopic data are available; both extended Coryell-Masuda plots and isotopic data will contribute to the understanding of the variations of the Ta/La ratios and the cause of these variations.

Independently of the geodynamic-geochemical target of Leg 82 (to try to obtain a perspective in space and time of mantle heterogeneities), the results obtained at Site 558 are interesting from the purely fundamental point of view of geochemistry. Using these results in conjunction with isotopic data, we may be able to answer questions such as the following: (1) what are the relative contribution(s) of the "fingerprint" of mantle source(s), and (2) what is the effect of melting on the distribution of magmaphile elements, according to an extended Coryell-Masuda plot?

The relative contributions of mantle source and melting effects could not be resolved on board, but the extent of fractional crystallization and magma chamber processes can be determined. Within chemical Group V, low MgO samples from Sections 558-38-2, and 558-39-1, may be derived from the subgroup of the four remaining samples by removal of 5% olivine. However, major and minor element contents suggest that it is not possible for the different chemical units to be derived from one an-

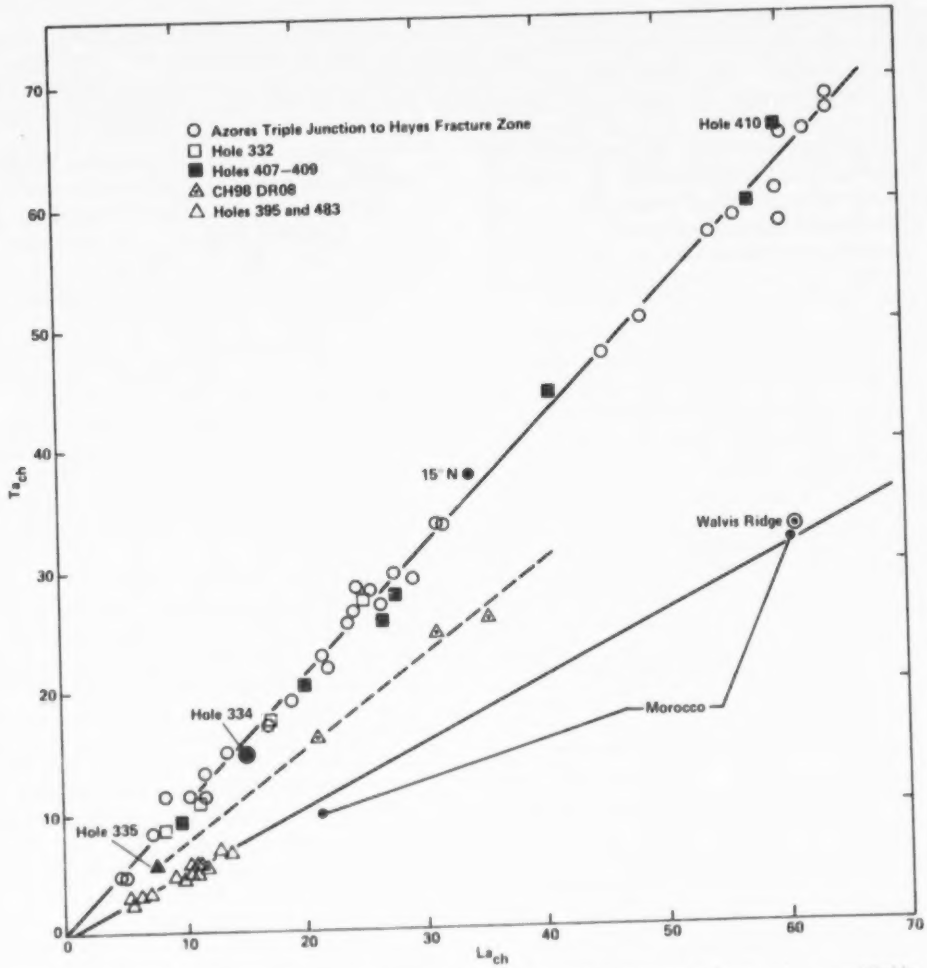

Figure 12. Plot of Ta versus La concentrations normalized to chondrites for basalts from various, worldwide locations.

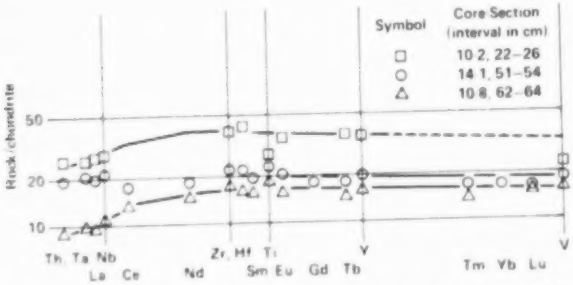

Figure 13. Extended Coryell-Masuda diagram for basalts from Hole 409.

other, solely by fractional crystallization. In addition, the large differences in their extended Coryell-Masuda plots make it highly unlikely that the parental liquids of the different units could have resided in the same magma chamber, or that magma mixing could account for the observed geochemistry. The results obtained at Site 558 fit much more easily with the hypothesis of magma batches from different short-lived magma reservoirs.

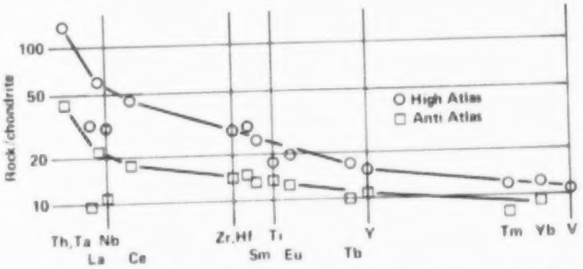

Figure 14. Extended Coryell-Masuda diagram for Moroccan dolerites (Bertrand et al., 1981).

MAGNETICS

Basalt Paleomagnetism

After 158 m of sediments were washed down and 256.5 m of sediments were cored, 114 m of basalts were cored. Twenty-six minicores were collected from basalts in Cores 558-28 through 558-39. The intensity of natural remanent magnetization (NRM) and other paleomagnetic properties are given in Table 7. Samples from Sections 558-28-1, 558-28-3 and 558-29-2 are weakly magnetized compared to the samples from the rest of the cores. This may be the result of alteration of titanomagnetite or a different grain size of the same mineral. Demagnetization was not done on board so that additional properties could be studied on shore.

Based on NRM inclination values, two groups were identified. The samples with negative inclination are dominant and suggest that the site is located between Anomalies 13 and 15, whereas the samples with positive inclination suggest either a later time of intrusion or acquisition of secondary magnetization caused by the present magnetic field of the earth. However, some of the samples with positive inclination may not be *in situ;* they were collected between brecciated layers.

Inclination values are much shallower than the expected dipole inclination for the latitude of this site (37°46′); this suggests tectonic rotation since the acquisition of remanence.

Sediment Paleomagnetism-Magnetostratigraphy

We cored 256.5 m of sediments before hitting the basement basalts. Using small plastic cubes, we collected oriented samples at intervals of 25 cm. However, because of the varying degree of compactness of the sediments, some of the samples were collected at 40–50 cm intervals, and other samples were taken at intervals of 10–15 cm.

The samples from Cores 558-1 through 558-14 were very weakly magnetized (0.001–0.01 μG). Their intensity was very close to or even below the noise level (0.01 μG) of the Digico spinner magnetometer and the measurements were not reliable. Therefore, the samples from Cores 558-1 through 558-14 were collected for onshore studies at Lamont-Doherty Geological Observatory, where a cryogenic magnetometer is available.

The intensity and directions of NRM for samples from Core 558-15 through Section 558-27-2 were measured on board. Only 7 of 191 samples had reversed polarity. A few samples were selected for progressive alternating-field (AF) demagnetization to see if the remanence directions were stable or not. A typical result of AF demagnetization is shown in Figure 15. Most of the samples had a secondary component of magnetization caused by the present-day earth's magnetic field, but the secondary component is removed after AF demagnetization at 50–75 Oe. An AF of 100 Oe was selected as an optimum field to remove this secondary component of magnetization. Therefore, all samples from Core 558-15 through Section 558-27-2 were demagnetized at a single step of 100 Oe. The stable directions of inclination and corresponding polarities are plotted in Figure 16.

A brief look at the paleontologic ages assigned to sediments from these cores suggested that (1) the Oligocene/Miocene boundary was in Core 558-18, (2) Core 558-15 was older than 15 Ma, and (3) Section 558-25-2 was 34–35 Ma old (for details, see Sedimentology and Biostratigraphy section). Based on these observations, we compared the correlation of the observed magnetic polarity reversal sequence with the Magnetic Polarity Time Scale (MPTS) of Lowrie and Alvarez (1981). The long normal in Core 558-16 is correlated with Anomaly 6, the long reversal in the upper part of Core 558-19 with the reversal between Anomalies 6C and 7, the long normal at the top of Core 558-15 with Anomaly 5C, and the long reversal in Cores 558-25 and 558-26 with the long reversal between Anomalies 12 and 13. After this,

Table 7. Paleomagnetic properties, Hole 558.

Core-Section (interval in cm)	J_{NRM} ($\times 10^{-3}$ emu/cm^3)	Dec. NRM (°)	Inc. NRM (°)	χ ($\times 10^{-6}$ emu/cm^3 Oe)	Q ($= J_{NRM}/0.45\chi$)
28-1, 52–54	0.29	101.0	−10.2	53	12.07
28-3, 2–4	0.25	130.7	3.3	95	5.74
29-1, 126–128	2.65	240.0	−21.7	84	70.21
29-2, 124–126	0.76	325.9	52.4	71	23.70
29-3, 7–9	2.76	91.7	57.0	147	41.79
29-3, 101–103	2.74	72.6	−1.3	93	65.55
29-4, 3–5	4.17	355.1	−33.8	112	82.75
30-1, 72–79	3.80	357.3	−39.1	110	76.70
30-2, 12–14	1.22	81.1	−46.0	100	16.06
30-3, 81–83	2.25	189.7	−41.8	84	59.65
30-4, 65–67	2.96	206.2	−30.5	81	81.31
31-1, 56–58	3.26	270.8	−35.7	66	109.75
31-2, 97–99	4.87	271.2	38.9	76	141.83
32-1, 15–17	1.55	5.7	−35.3	65	52.81
32-3, 4–6	5.04	355.9	−40.1	105	106.76
32-4, 120–122	2.41	207.0	−24.5	90	59.40
32-5, 36–38	1.85	104.2	−43.3	80	51.32
33-1, 46–48	4.31	314.0	−32.0	84	113.93
33-2, 2–4	4.99	231.8	−28.2	95	116.70
33-3, 120–122	6.59	27.3	−34.4	126	116.27
34-1, 23–25	7.01	325.2	−28.7	266	58.58
38-2, 28–30	3.71	264.7	37.5	68	121.29
39-1, 127–129	2.28	14.9	−27.2	77	65.70
39-2, 15–17	4.28	278.1	−16.5	100	95.15

Note: J_{NRM} is the intensity of the natural remanent magnetization; Dec. is declination; Inc. = inclination; χ = susceptibility; Q = Königsberger ratio.

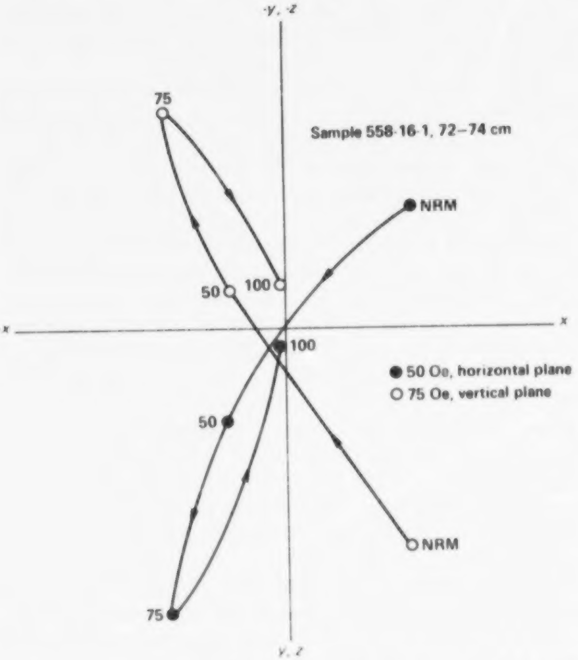

Figure 15. Vector diagram showing the results of alternating field demagnetization. NRM = natural remanent magnetization.

the rest of the correlation is checked and compared with the standard MPTS. The correlation chart given in Figure 16 suggests that an almost complete sequence of magnetic polarity reversals is recorded in these sediments and that a precise age can be assigned to the sedimentary sequence using magnetostratigraphic studies. See Khan and others (this volume) for the results of magnetostratigraphic studies for Cores 558-1 through 558-14 and for Hole 558A cores.

After the observed magnetic polarity reversal sequence was correlated with the standard MPTS, the sediment accumulation rate was calculated by plotting age versus sediment depth (Fig. 17). A very steady sediment accumulation rate of 0.47 cm/ky was calculated for Core 558-15 through Section 558-22-2, whereas a higher rate of 1.0 cm/ky was calculated for Sections 558-22-3 through 558-27-2. Although no drastic change is observed at this break, it does correspond to a slight change in lithology from CB5 (nannofossil chalk) to CB7 (nannofossil-foraminiferal chalk). For details, see Sedimentology and Biostratigraphy section. Based on the depth versus age curve of Figure 17, an age of 36 Ma is calculated for the basement basalt, which agrees with the location of this site between Magnetic Anomalies 13 and 15 (close to 13).

In conclusion, the sediments in Core 558-15 through 558-27-2 range in age from 16.2 to 36 Ma and record an almost complete sequence of magnetic polarity reversal of earth's magnetic field for this span of time. The sediment accumulation rate calculated for Sections 558-22-3 through 558-27-2 is twice the rate calculated for Core 558-15 through Section 558-22-2.

PHYSICAL PROPERTIES

Sediments

Combination of the cores from Holes 558 and 558A gives an almost continuously cored section with good recovery. Measurement of seismic velocity, density, and thermal conductivity was made systematically with all core sections being run through the continuous GRAPE system. The preliminary results are shown in Table 8 and Figure 18.

The density data are rather sparse in this report because of the difficulty of taking discrete undeformed samples from the soft sediments. When the continuous GRAPE data are processed, a complete record will be available. Data shown in Figure 18 are a combination of 2-minute GRAPE on rock chunks and cylinder samples, as well as some points from the continuous GRAPE analog records.

Velocity data above 330 m sub-bottom were measured on core halves in liners and are hence measured horizontally, parallel to any bedding traces. Below this depth, the rock was sufficiently lithified to be cut into discrete samples and measurements were made parallel to the core axis, normal to bedding. Because sediments of this type typically show velocity anisotropy of around 5%, we would expect values for sediments below 330 m to be systematically lower by this percentage. Such an offset is apparent in Figure 18. All measured velocities are low compared to those recorded by the Schlumberger sonic log (see Downhole Measurements section). This could be due either to drying of the cores to undersaturation by pore water before measurement, or to the removal of the cores from their *in situ* confining pressures. Because care was taken to sample core material as soon as possible after splitting, and the data are consistently lower than the downhole values, we deduce that the major factor in reducing sample velocity is release of confining pressure.

The thermal conductivity data were measured by the routine needle-probe technique and show an increase in conductivity with depth. Units used in Table 8 and Figure 18 are in mcal $\mathrm{cm^{-1}\ s^{-1}\ {}^{\circ}C^{-1}}$. Accuracy of values is about ± 8%. One surprising feature of the conductivity measurements is their lack of dependence on the degree of deformation of the core. Because measurements were made on unsplit cores, occasionally, when the core was split, the measured volume was shown to be significantly deformed. Such positions are noted in the righthand column of Table 8. The data from these points are included in Figure 18 and do not show values significantly different from those of undeformed core, so are not separately identified on Figure 18.

Vane shear strength measurements were made on all sediments sampled down to 270 m sub-bottom, after which the state of lithification precluded measurements. Apart from showing an increase in shear strength with depth, and a high dependence on the state of deformation of the core, the data are unremarkable and are not plotted in Figure 18.

The variation of physical properties with depth shown in Figure 18 reveals only one major feature. There is a

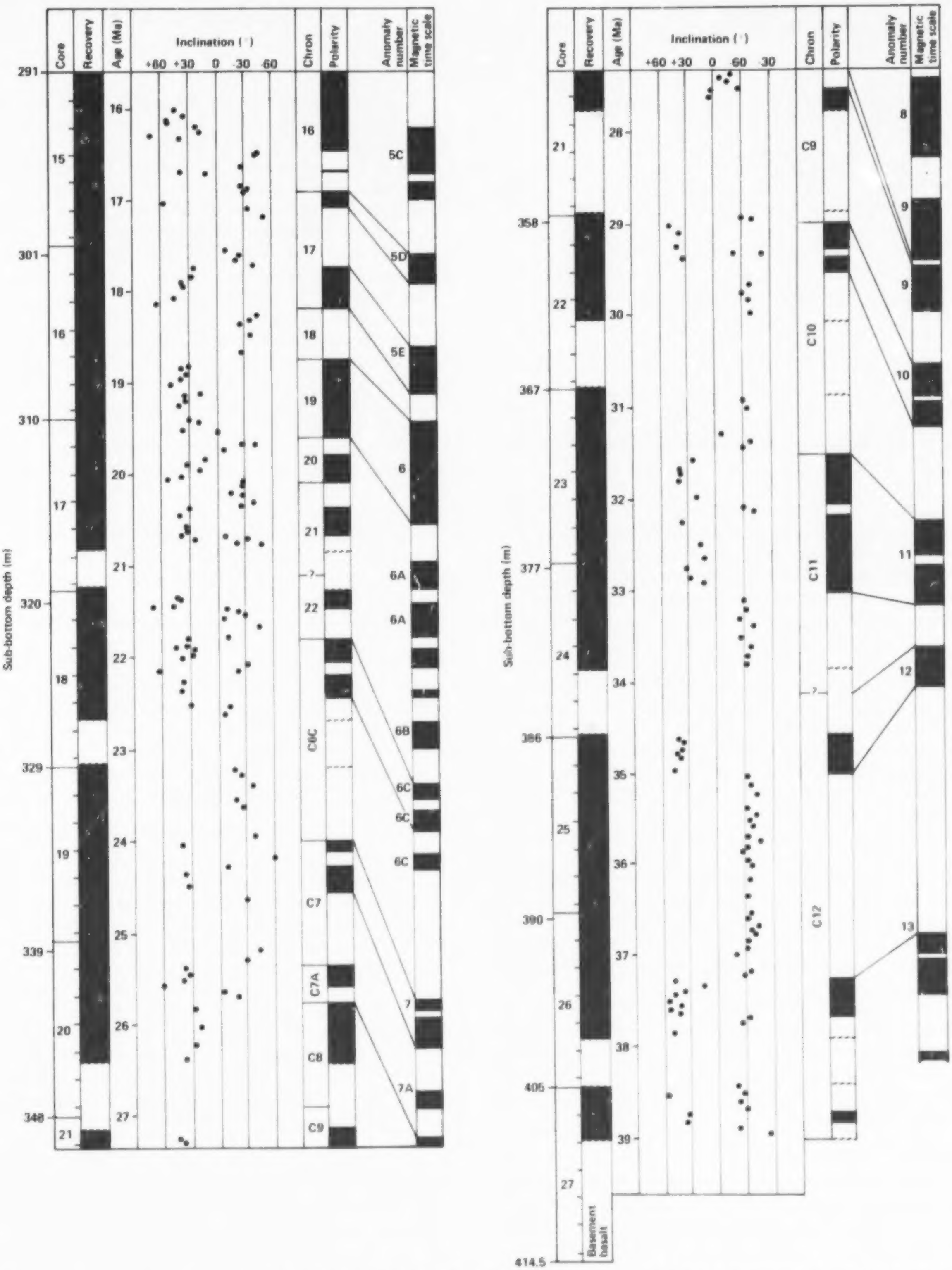

Figure 16. Downhole plot of magnetic inclinations and polarities, Hole 558. All polarity reversals are based on at least two samples. Black = normal polarity; white = reversed.

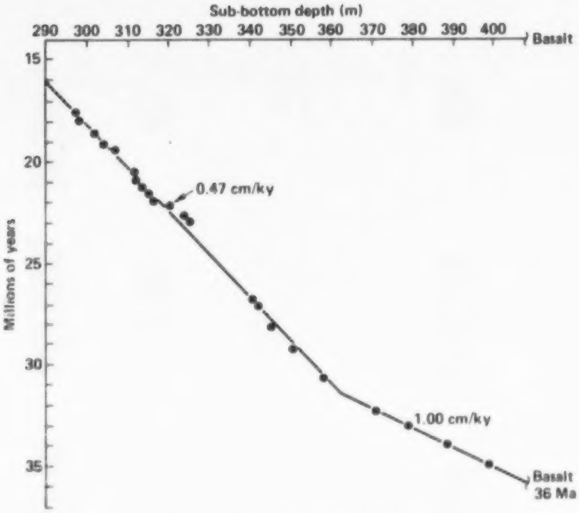

Figure 17. Sediment accumulation rates based on paleomagnetic data, Site 558.

gradational but fairly rapid increase in density and seismic velocity, and a rather poorly defined increase in thermal conductivity between 280 and 300 m sub-bottom, centered on 290 m sub-bottom. This feature is far greater in amplitude than progressive compaction effects and must represent a change in the composition of the sediment or a sudden increase in age (disconformity). This feature correlates with a change in accumulation rate detected by nannofossils and foraminifers and with a decrease in carbonate content of the sediment.

The change in density and sonic velocity at 290 m sub-bottom results in a marked change in acoustic impedance, which is gradational over a depth interval of 30 m and correlates with the similar features seen in the log curves for Site 556.

The underway profiling data near both Site 556 and Site 558 show no continuous reflector, which presumably indicates that the transition in physical properties is a gradation as shown by the physical property measurements and the downhole logs, rather than a sharp boundary. This would in turn suggest that the boundary represents a compositional change in the sediment rather than a disconformity.

At the base of the sedimentary section, the two last velocity measurements show a rise in velocity, then a sharp decrease. The feature is due to a dolomitized horizon in the sediments and the velocity change is clearly seen in the sonic downhole log (Fig. 21) just above the basement interface.

Basement Section

Within the basement section of the hole, sampling for physical property measurement was difficult because of the friable nature of the altered basalts and gabbros. Measurements are hence strongly biased towards fresh specimens of each lithology. The values measured are unremarkable and are mainly of use as a control on the wireline log data.

DOWNHOLE MEASUREMENTS

Logging

Operations

Logging of Hole 558 was made difficult by extremely bad hole conditions. After the bit was dropped, the drill string was pulled to a sub-bottom depth of 127 m by 1600 hr. 9 October, and the sonic log was run first. On the first run (recording velocity), it reached a depth of 546 m, but on the second run (for waveform recording), the hole was blocked at 452 m sub-bottom. The recorded data are very noisy, and the depth scale is distorted by repeated jamming of the tool in the hole, which had closed in places to a diameter of 4 in. These runs were completed at 2300 hr.

An attempt was made to run a temperature log (small diameter tool) that only reached 189 m sub-bottom. We decided to wash down the hole to total depth, then flush with 100 barrels of gel mud. This operation was performed between 0400 and 0915 hr. 10 October.

The laterolog was run to nearly total depth, 544 m sub-bottom, but during the attempt to repeat the section, the tool hit a blockage at 444 m sub-bottom, indicating very rapid deterioration of the hole. This operation was completed at 1500 hr. Density and porosity logs were lowered with great difficulty to 445 m and the caliper was broken in spudding the tool during attempts to penetrate further.

A second attempt to run the temperature log was started at 2045 hr. Because of the low tool weight and large heave motion of the ship, the tool was overrun and the cable became knotted. Fortunately, the cable and tool were successfully recovered through the drill pipe. Total depth reached by the tool is uncertain but probably about 200 m sub-bottom. Logging operations were concluded at 0300 hr. 11 October. Total logging operations required 37 hr. The operations are summarized in Table 9.

Sediment Section

Figure 19 shows the density, sonic velocity, and resistivity, and natural gamma-ray logs for Hole 558. The data generally are of good quality. An exception to this is the density log (shown dashed) and the porosity log (which is not shown). Throughout the sediment section, the hole is washed to a diameter greater than the span of the excentralizer on the density and porosity tools. The result of this is that the tools make poor wall contact and read erroneously low density and high porosity.

The logs show that the sediments below the drill pipe can be divided into two units with a gradational boundary at about 290 m sub-bottom. The density increases from 1.8 to 1.95 $g \cdot cm^{-3}$, the sonic velocity from 1.9 to 2.1 $km \cdot s^{-1}$, and the resistivity from 0.9 ohm-m to 1.3 ohm-m. These changes are also apparent in the physical properties measurements (Fig. 18). The boundary at 290 m separates geophysical Units I and II. These correlate with Lithologic Units 1 and 2, and the boundary is a change of carbonate content from 90 to 50%. Within each unit, the logs show small-scale variability that is above the noise level of the logs, but the interpretation of which is uncertain.

Table 8. Physical properties measurements, Site 558.

Core-Section (interval or depth in section in cm)	Sub-bottom depth (m)	Sonic velocity (km/s)		Temperature (°C)	Thermal conductivity (mcal/[cm·deg·s])	GRAPE density (g/cm^3)		Gravimetric density			Acoustic impedance (g/[cm·s])	Vane shear strength (g/cm^2)	Lithology or remarks
		V.	H.			V.	H.	Wet-bulk density (g/cm^3)	Water content (%)	φ (%)			
Hole 558													
1-2, 30	159.8	2.05*		21.0								2300	Nannofossil ooze *Sample deformed during velocity measurements
1-2, 57	160.1	2.18*		21.0								1400	
1-2, 115	160.6	2.22*		20.0					31			900	
1-6, 84	166.3	2.10*		21.0								1400	
2-2, 66	169.7	1.59		21.0	3.38				35			1000	
2-2, 135	170.4	1.57		21.0								700	
2-4, 138	173.4	1.67		21.0								1200	
3-3, 16	180.2	1.59		21.0								800	
3-3, 85	180.9	1.59		21.0								700	
3-5, 12	183.1	1.57		21.0								500	
4-2, 76	188.8	1.57		21.0	3.38							2000	
4-2, 138	189.4	1.56		21.0								1700	
4-5, 57	193.1	1.54		21.0					34			700	
4-5, 141	193.9	1.58		21.0								800	
5-2, 79	198.3	1.58		21.0	3.80							1100	
5-2, 139	198.9	1.58		21.0								1100	
5-5, 37	202.4	1.58		21.0					33			1500	Nannofossil ooze
5-5, 130	203.3	1.60		21.0								750	
6-2, 12	207.1	1.56		22.0								1700	
6-2, 131	208.3	1.56		22.0	3.52							1200	
8-1, 14	224.6	1.58		22.0								1900	
8-1, 120	225.7	1.59		22.0								1500	
8-2, 111	227.1				3.60								
9-2, 15	235.7	1.54		22.0								2300	Slight green color
9-2, 119	236.7	1.56		22.0								2400	
11-2, 15	254.6	1.57		22.0								1000	Shear strength underestimated
11-2, 44	254.9	1.67		22.0								1500	
12-2, 18	264.2	1.59		22.0								1600	
12-2, 135	265.4	1.62		22.0	3.82							2000	
12-4, 14	267.1	1.59		22.0								2200	
12-4, 98	268.0	1.65		22.0								1800	
13-2, 15	273.6	1.62		22.0									Nonlithified sediment crumbles, does not shear.
13-2, 98	274.5	1.58		22.0	3.59								Nannofossil ooze
13-4, 12	276.6	1.60		22.0									
13-4, 132	277.8	1.63		22.0									
15-2, 12	292.6	1.74		22.0									
15-2, 86	293.4	1.75		22.0	4.62								
16-2, 22	302.2	1.67		21.0									Velocity low because of poor condition (deformed)
16-2, 146	303.5	1.73		21.0									
17-2, 14	311.6	1.80		21.0									
17-2, 81	312.3	1.72		21.0	4.44								
18-2, 35	321.4			22.0	4.12								
18-2, 136-139	322.4	1.71		22.0			1.94				3.3		
19-2, 29-33	330.7		1.66	22.0	4.10		2.00				3.3		
19-2, 80-84	331.3		1.67	22.0			1.99				3.3		
20-2, 28-31	340.3		1.67	22.0			1.96				3.3		
20-2, 107	341.1				3.92								
21-2, 89-92	350.4		1.64	22.0			1.94				3.2		
21-2, 137	350.9				4.20								Nannofossil ooze
22-2, 26-31	359.3		1.67	22.0			1.93				3.2		
22-2, 132	360.3				4.0								
23-2, 8-12	368.6		1.65	22.0			1.81				3.0		
23-2, 103	369.5				4.02								
24-2, 65-69	378.7		1.63	22.0			1.97				3.2		
25-2, 57-61	388.1		1.66	22.0			1.92				3.2		
25-2, 133	388.8				4.22								
26-2, 46-50	397.5		1.66	22.0			2.02				3.3		
27-1, 16-20	405.2		1.74	22.0			2.11	2.0	21.2	42.5	3.6		
27-2, 113-118	407.7		1.64	22.0			2.08				3.4		Dolomite rich
28-3, 4-14	417.6		5.39	22.0									Basalt
29-4, 15-25	428.2	4.45		22.0		2.63					11.7		Glassy margin of pillow basalt
30-3, 19-30	435.7		5.36	22.0	3.99		2.79				15.0		Basalt
33-1, 86-96	460.4	4.90		22.0		2.71					13.3		Slightly altered basalt
34-1, 20-34	468.8		5.45	22.0	3.99		2.79				15.2		Basalt
35-3, 122-127	481.7		4.91	22.0									Altered basalt
36-1, 5-20	486.6		4.75	22.0			2.70				12.8		Basalt
38-2, 71-78	506.7	5.30		22.0		2.82					14.9		Basalt
39-4, 114-115	508.7							2.7	5.0	13.2			
40-1, 123-129	519.3	3.79		22.0	2.78	2.20					8.3		Breccia
40-3, 109-110	520.6							2.4	7.6	18.4			

Table 8. (Continued).

Core-Section (interval or depth in section in cm)	Sub-bottom depth (m)	Sonic velocity (km/s)		Temperature (°C)	Thermal conductivity (mcal/[cm·deg·s])	GRAPE density (g/cm^3)		Gravimetric density			Acoustic impedance (g/[cm·s])	Vane shear strength (g/cm^2)	Lithology or remarks
		V.	H.			V.	H.	Wet-bulk density (g/cm^3)	Water content (%)	φ (%)			
Hole 558 (Cont.)													
41-1, 60-63	527.6	3.58		22.0		2.44					8.7		Serpentinized gabbro
41-3, 8-9	528.6							2.8	1.8	5.0			
43-1, 40-50	545.4	3.26		22.0		2.35					7.7		Altered gabbro
44-1, 22-31	554.3	3.55		22.0	6.08	2.49					8.8		Altered gabbro
Hole 558A													
2-2, 35	2.3	1.58		23.0								600	Nannofossil ooze
2-2, 113-115	3.1	1.56		23.0	2.43	1.63					2.5	400	
2-5, 77	7.3	1.57		23.0					42			600	
2-5, 136	7.9	1.57		23.0								700	
3-2, 19	11.7	1.54		23.0								600	
3-2, 114	12.6	1.55		23.0	2.79	1.81					2.8	1000	
3-5, 14-16	16.2	1.55		23.0					44			2000	
3-5, 140-142	17.4	1.56		23.0								1700	
4-2, 23	21.2	1.59		23.0								1000	
4-2, 123	22.2	1.59		23.0	2.71	1.77					2.8	800	
4-5, 35	25.8	1.59		23.0								2000	
4-5, 134	26.8	1.59		23.0								1200	
5-2, 17	30.7	1.61		23.0								1400	
5-2, 133	31.8	1.58		23.0	3.11	1.82					2.9	1300	
5-5, 17	35.2	1.58		23.0								2300	
5-5, 137	36.4	1.60		23.0					37			2400	
6-2, 35	40.3	1.61		23.0								1600	Nannofossil ooze
6-2, 131	41.3	1.60		23.0	3.15	1.84					2.9	1900	
6-5, 20-23	44.7	1.60		23.0								1800	
6-5, 132-135	45.8	1.62		23.0								2600	
7-2, 66	50.2	1.60		23.0								1500	Very deformed
7-2, 130	50.8	1.58		23.0	3.28							1400	Very deformed
7-5, 18-20	54.2	1.61		23.0					36		3.1	2000	
7-5, 135-137	55.4	1.61		23.0								1900	
8-3, 18-20	60.7	1.59		23.0								2000	
8-3, 130	61.8	1.59		23.0	3.37	1.91					3.0	2200	
8-5, 20-22	63.7	1.59		23.0					37			1800	
8-5, 124-126	64.8	1.62		23.0								1300	
9-2, 132	69.8				3.36								Very deformed
9-3, 104-106	71.0	1.61		23.0		1.93			36		3.1	1500	
10-2, 15-17	75.7	1.58		23.0					33			1000	
10-2, 116-120	76.7	1.60		23.0								750	
11-2, 131	79.8	1.59		23.0	3.62							700	Very deformed
11-5, 21-23	83.2	1.62		23.0					33			1600	
11-5, 135-137	84.4	1.62		23.0		2.07					3.4	2750	
12-2, 26-28	88.3	1.57		23.0								700	Deformed
12-2, 128	89.3	1.57		23.0	3.75							1300	Deformed
12-5, 20-22	92.7	1.58		23.0		1.94			33		3.1	1300	
12-5, 140-143	93.9	1.59		23.0								1600	
13-2, 15-17	97.7	1.58		23.0								1100	
13-2, 129	98.8	1.58		23.0	3.66	1.97					3.1	2700	
13-5, 27-29	102.3	1.60		23.0					31			2200	
14-5, 24-26	109.2	1.58		23.0					33			2100	
14-5, 130	110.3	1.59		23.0	3.75	1.92					3.0	2500	
15-2, 14-16	114.2	1.58		23.0								2500	
15-2, 129	115.3	1.57		23.0		1.96					3.1	2400	
15-5, 13-15	118.6	1.58		23.0					32			2500	
15-5, 134-137	119.9	1.59		23.0								2900	
16-2, 10-12	123.6	1.56		23.0								1500	Nannofossil ooze
16-2, 136-138	124.9	1.58		23.0	3.62							3000	
16-5, 15-17	128.2	1.56		23.0	3.62				33			2600	
16-5, 137-140	129.4	1.58		23.0		1.94					3.1	3800	

Note: V. = vertical, H. = horizontal; water content is corrected; φ = porosity. All values measured at laboratory temperature and pressure. For details of techniques, see Explanatory Notes, this volume.

Figure 20 shows the equivalent logs from Hole 556 where no sediment cores were taken. The correspondence between the logs is remarkable; not only does a major change in physical properties occur in Hole 556 at a proportional depth in the sediment section, but minor variations in the logs are correlatable from Site 556 to Site 558. It is inferred that the sediment lithology and depositional history of the two sites, which are on the same isochron and at similar water depths, were the same.

The change in density and sonic velocity between chemical Units I and II generates the only appreciable acoustic impedance contrast within the sediments. It may be expected that this horizon could be traced through the area between the sites on seismic profiler records. Initial study of underway data shows several weak reflectors, which are geographically discontinuous within the lower part of the sediments. The quality of reflection at the Unit I/Unit II boundary will be strongly related to the

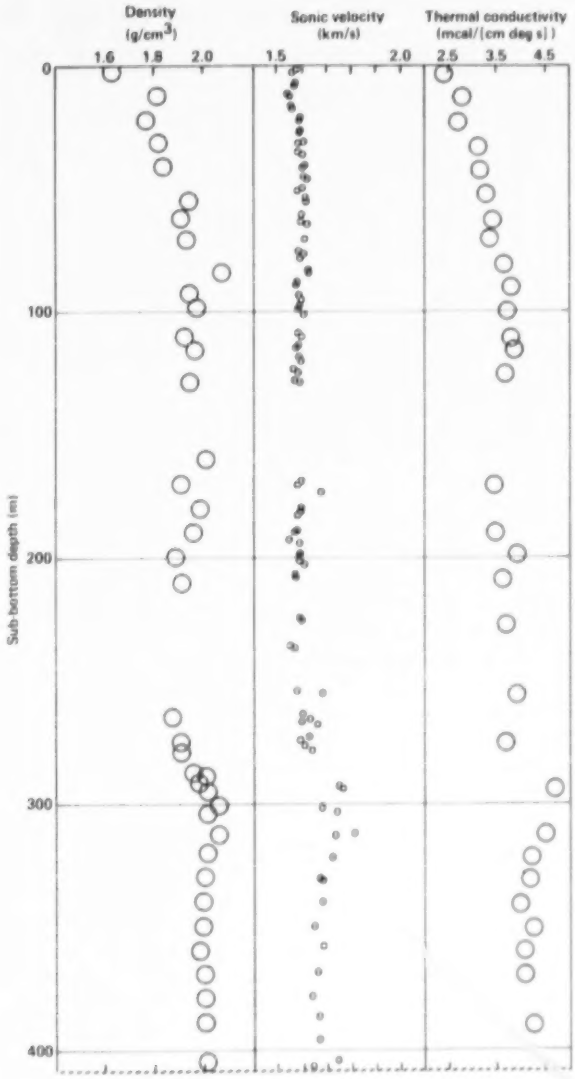

Figure 18. Physical property variations in the sediment section of Holes 558 and 588A. Symbol diameter shows the measurement error of that physical property. Density values above 320 m sub-bottom depth are taken from analog GRAPE records and do not appear in Table 8.

sharpness of that boundary, and this may well vary geographically.

Basement Section

The poor hole condition resulted in data that were generally poor in quality. The laterolog was the only tool that reached the bottom of the hole and provided good data, although this tool had a broken caliper. The sonic log also reached near-bottom on the velocity run, but the data are very noisy, probably because of wall contact. The sonic caliper log contained spikes because of tool malfunction (which also occurred during the logging of Hole 556). Both sonic and resistivity logs have distorted depth scales because the tools became jammed in the lower part of the hole, but these can be recognized by steps in the tension log that are part of the original records. The porosity and density logs appear to be of good quality but only extend to 37 m below the basement interface.

Table 9. Schedule of logging runs.

Run 1. Sonic velocity (DDBHC), natural gamma ray (GR) caliper (CAL)
    Pass 1: sonic velocity
        Logger on bottom 1830 10/9; maximum sub-bottom depth = 546 m
    Pass 2: waveform recording
        Logger on bottom 2030 10/9; maximum sub-bottom depth = 452 m
Run 2. High resolution temperature (HRT)
    Logger on bottom 0300 10/10; maximum sub-bottom depth = 189 m
0400-0915 10/10:
    Wash to total depth; flush hole with mud
    Circulation stopped 0815 10/10
Run 3. Dual laterolog, GR, self potential (SP)
    Logger on bottom 1130 10/10; maximum sub-bottom depth = 544 m
Run 4. Gamma ray density (FDC), neutron porosity (CNL), GR
    Logger on bottom 1800 10/10; maximum sub-bottom depth = 445 m
Run 5. HRT
    Logger on bottom 2300 10/10; maximum sub-bottom depth = 200 m

Note: Circulation stopped: 1400 hr. 9 October.

As at Site 556, the basement section has been divided into geophysical units in the lower part of the hole based primarily on the resistivity log. These units are shown in Figure 21 and Table 10. Comparison with the lithologic column shows that the pillow basalt units and altered gabbros give a similar log response to that seen at Hole 556. However, the interpretation of the interval from 405 to 425 m reveals complexity that is not apparent in the lithologic column.

The density log shows a progressive increase in density down through the dolomitic nannofossil ooze, with a sharp decrease just above the basalt at 408 m sub-bottom. These changes can also been seen in physical property measurements (Fig. 18) and are reflected in the sonic and porosity logs. The basalt, Lithologic Unit 3, can be clearly identified by its high velocity, resistivity, density, and low porosity and is shown to be only 2 m thick. Below this is a unit of variable density around 2.2 g/cm³, low porosity, high resistivity, and high but variable sonic velocity (about 4.7 km/s). This is interpreted as a sedimentary unit; however, it is difficult to reconcile the low density with the high sonic velocity. Using a Schlumberger sonic-density crossplot diagram, we can see that the porosity and velocity are appropriate for a limestone, but the low density requires a lower grain density such as that of gypsum. No material was recovered from this unit, possibly because of a blockage of the drill bit as indicated by the slow drilling rate. This unit is 6 m thick.

Below this, pillow basalts occur in the lithologic column and are shown by high resistivity and high, variable sonic velocity as was detected at Hole 556. Within the pillow basalts, a lower unit from 497 to 522 m sub-bottom is distinguished by a high and relatively constant resistivity of 250 ohm-m. This unit corresponds to Lithologic Units 9 and 10 and Chemical Unit V. Although the sonic velocity is also high and steady at 5.2 km/s in this unit above 514 m sub-bottom, the sonic log is extremely noisy below this depth.

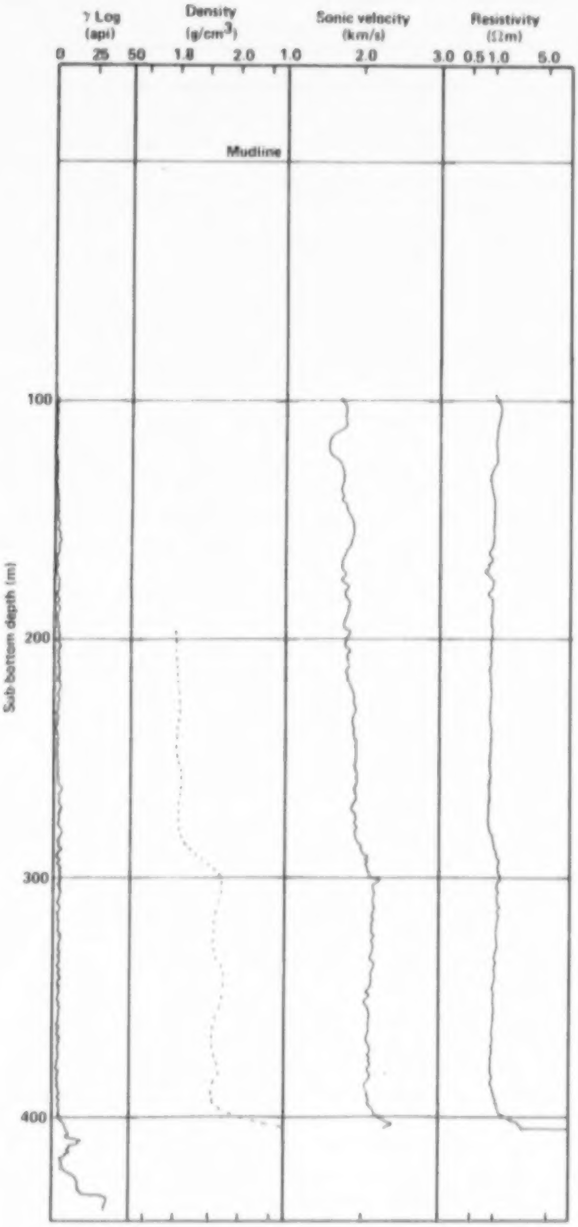

Figure 19. Wireline log curves for sedimentary section of Hole 558. Density curve drawn with dashed line to indicate the poor quality of the data.

Below 522 m, the resistivity and sonic velocity fall to lower values in the serpentinite, Lithologic Units 12 and 13. It is not clear whether the basalt breccia, Lithologic Unit 11, occurs above or below the logging boundary at 522 m.

Downhole Temperatures

Because of the poor hole conditions, no temperature measurements were made in the basement section of the hole or in the lower sedimentary unit (Unit 2). The available data from the mudline to a depth of 234 m sub-bottom are shown in Figure 22. Two depth profiles are available from the two attempts to run a temperature log. For a depth of some 100 m below the mudline, the logs

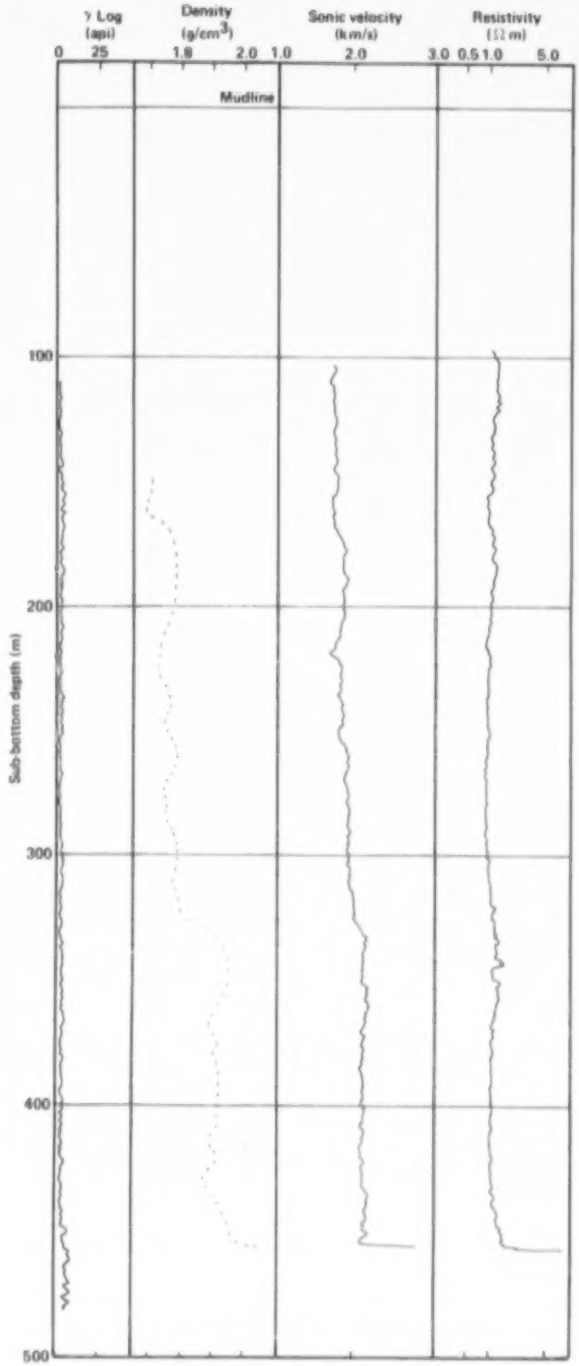

Figure 20. Wireline log curves for the sedimentary section of Hole 556. Density curve drawn with dashed line to indicate the poor quality of the data.

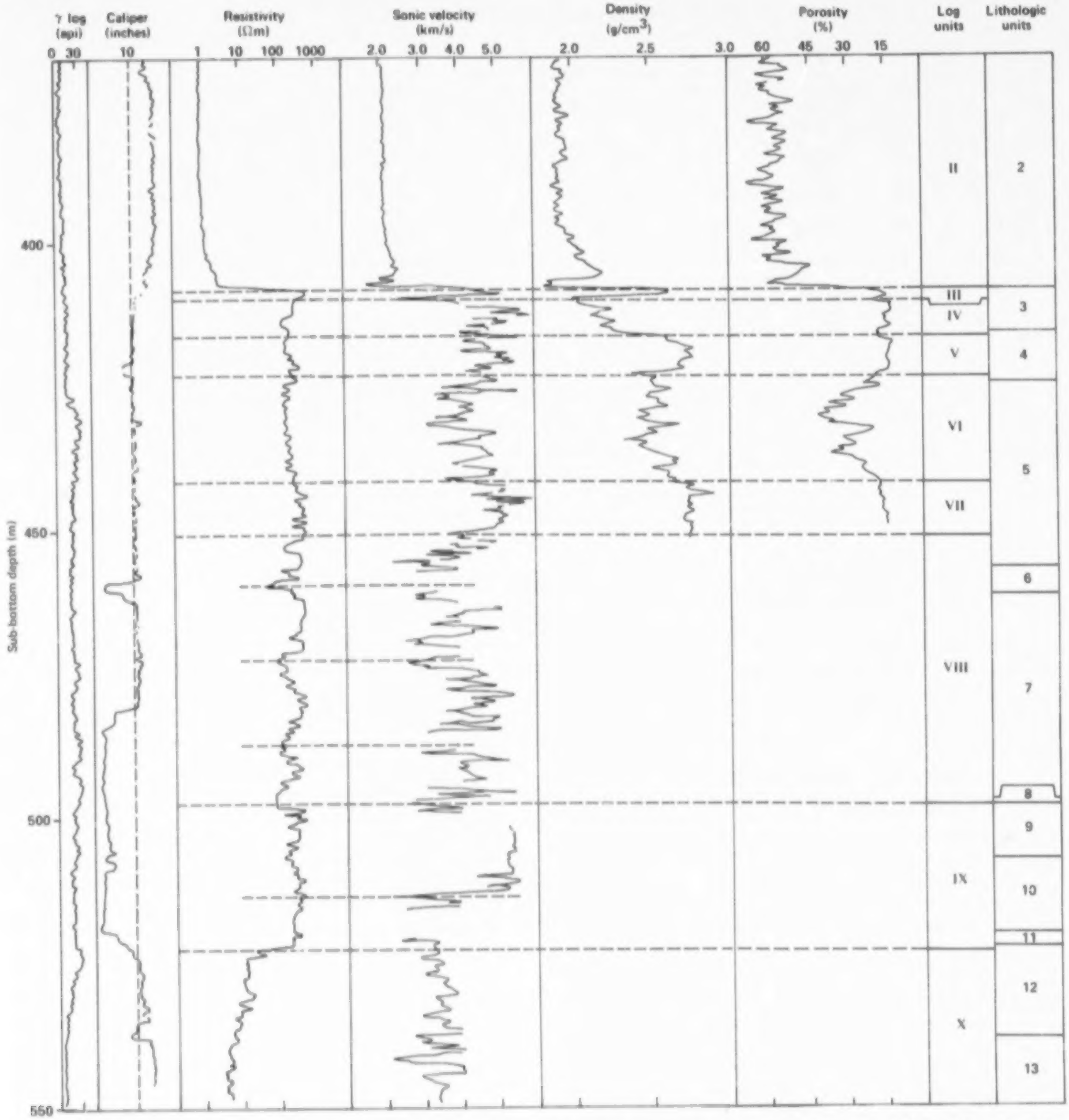

Figure 21. Wireline log curves for basement section of Hole 558. Curves have been redrawn omitting noise spikes. Gaps indicates intervals where noise obscures data.

were run inside the drill pipe, and the minor rise in temperature at 3820 m below rig floor may be a feature of the drill string or of contact between the drill string and the sidewall of the hole.

The rise in temperature with depth over the short interval logged is taken as evidence that there is no large-scale water flow in the hole and that the hole is reequilibrating. Because the hole was blocked below the logged depth, this result is not totally unexpected. The lower temperature gradient in the upper part of the hole may be due to the pumping action of the drill string caused by the heave of the ship.

The mudline temperature of 0.5°C is lower than expected, and a temperature log was made of the ocean water as the log was raised through the drill string after pass 2. The results are shown in Figure 23. The temperature tool was accurately calibrated in the interval between logging Hole 556 and 558, and temperatures at

Table 10. Geophysical units identified by logging measurements, Hole 558.

Unit	Depth range (m sub-bottom)	Resistivity (ohm m)	Sonic velocity (km/s)	Density (g/cm^3)	Porosity (%)	Lithology	Remarks
I	0–290	0.9	1.9	1.8	[a]	Nannofossil ooze	Carbonate content = 90% 0–17 Ma
II	290–408	1.3	2.1	1.95	[a]	Nannofossil ooze	Carbonate content = 50% 17–34 Ma
III	408–410	500	4.5	2.6	15	Massive pillow basalt	Tight constraint on layer thickness
IV	410–416	200	4.7	2.2	15	Unknown: limestone?	Inferred sedimentary layer
V	416–423	200	4.7	2.7	15	Fractured pillow basalt	Very uniform properties
VI	423–441	150	4.4	2.5	30	Pillow basalt and interpillow breccia	High gamma-ray value
VII	441–450	400	5.1	2.75	17		Very uniform properties
VIII	450–497	100–400	3.7–4.6				Broad (15-m wavelength) variations in sonic velocity and resistivity; X-ray peaks at 474, 488, and 494 m
IX	497–522	250	5.1				Very uniform resistivity throughout; uniform sonic velocity above 514 m; poor sonic return below
X	522–581	3–10	3.4			Fresh and altered serpentinite	Resistivity decreases toward bottom; gamma-ray peak at 524 m

Note: Top of basement taken to be 4170 m on resistivity log and 4172 m on sonic velocity and porosity/density logs.
[a] Data unreliable because of poor sidewall contact.

558 should be accurate to ±0.2°C. It is hoped that the information in Figure 23 may be useful to physical oceanographers; depth profiles such as this are simple to obtain and incur neither financial nor time cost at any hole that is logged.

SUMMARY AND CONCLUSIONS

Site 558 is located between Anomalies 13 and 15 on a flow line passing through the FAMOUS area and sites drilled during Legs 37 (332, 333, 334, 335) and 49 (411, 412, 413). We decided to have a complete program of coring basement and sediment and logging because of the large amount of data already available near and at the ridge crest.

The upper part of the basement drilled at Site 558 comprises nine lithologic units of aphyric basalt. Most of these units are composed of pillow basalt with variable amounts of interpillow breccia or of basaltic breccia. Fresh glass is very common at the margin of the pillows throughout the basaltic layer and is usually embedded in neoformed calcite filling cracks and interpillow spaces. The lower part of the basement comprises two lithologic units of altered serpentinite, serpentinite breccia, and mylonite. A basalt clast was found in one of these units.

The chemical analyses of 29 samples of the basaltic layer define six homogeneous chemical groups whose average major and trace element concentrations are given in Table 6. Five percent of olivine fractionation can account for the small compositional variations observed in Unit V. There is no cogenetic relationship between the different homogeneous groups. The most striking result obtained at Site 558 is the occurrence of depleted ($[\mathrm{Nb}/\mathrm{Zr}]_{\mathrm{Ch}} = 0.4$), flat ($[\mathrm{Nb}/\mathrm{Zr}]_{\mathrm{Ch}} = 1$), and enriched ($[\mathrm{Nb}/\mathrm{Zr}]_{\mathrm{Ch}} = 1.6$) patterns of magmaphile elements presented in Figure 11. After Holes 413 (Leg 49) and 504B (Leg 69–70), Site 558 is the third site presenting this feature. Isotope data and other trace elements are necessary to go further in interpretation in terms of mantle sources and petrogenetic processes.

The entire sedimentary layer (408 m) was cored through a combination of piston coring (Hole 558A) (0 to 131.5 m) and rotary coring (158 to 408 m). The recovered lower Oligocene through Pleistocene pelagic calcareous sediments provide a more complete stratigraphic section than has yet been obtained from the North Atlantic. The age of oldest sediment (34–37 Ma—as determined from the nannofossils found in basalt breccia at the top of basement—and 36 Ma—as determined by magnetostratigraphic studies) is in agreement with the position of the hole between Magnetic Anomalies 13 and 15. A major change in the sediment lithology at a depth of 300 m (approximately at the boundary between lower and middle Miocene) corresponds to a change of carbonate content (90% in the upper part, 50% below) and in the accumulation rate (16 m/Ma in the upper part and 8 m/Ma in the lower part). The well-defined magnetic polarity stratigraphy in the lower part of the section should provide reliable limits on the ages of biostratigraphic zones.

A complete set of logs was attempted; because of poor hole conditions, the attempt was not entirely successful. However, the major lithologic boundary in the sediment is clearly evident within density, sonic, and resistivity logs. A similar change in these logs was noted at an equivalent depth at Site 556, implying that this li-

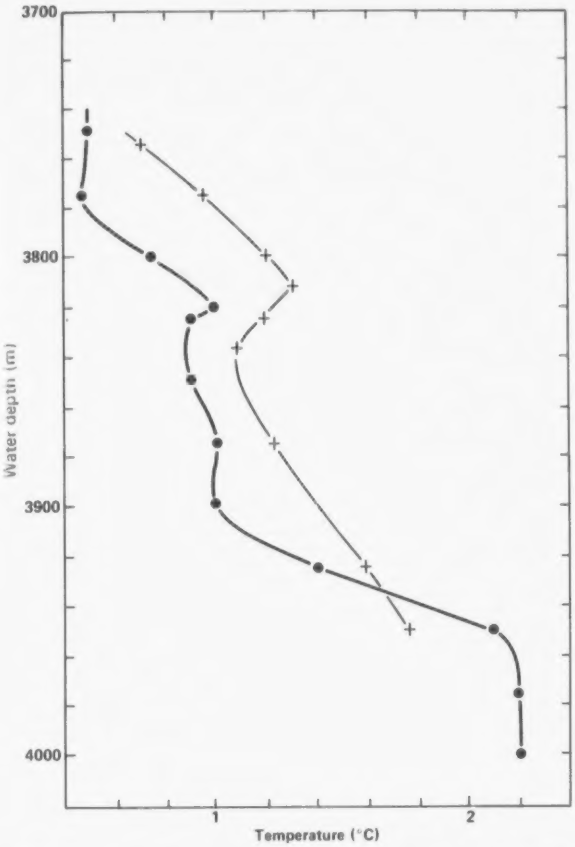

Figure 22. High-resolution temperature (HRT) log curves for Hole 558. The curve joining X data points represents HRT Run 1 (circulation stopped: 1400 Oct. 9; log on bottom: 0130 Oct. 10; elapsed time: 11.5 hr.). The curve joining ● data points represents HRT Run 2 (circulation stopped; 0815 Oct. 10; log on bottom: 2300 Oct. 10; elapsed time: 14.75 hr.). Mudline depth = 3766 m; Units 1/2 boundary = 4056 m; sediment/basement boundary = 4171 m.

thology change is probably a broad regional feature. Other minor changes within the sets of logs at Sites 556 and 558 also appear to coincide.

REFERENCES

Aumento, F., Melson, W. G., et al., 1977. *Init. Repts. DSDP*, 37: Washington (U.S. Govt. Printing Office).

Berger, W. H, and von Rad, U., 1972. Cretaceous and Cenozoic sediments from the Atlantic ocean. *In* Hayes, D. E., Pimm, A. C., et al., *Init. Repts. DSDP*, 14: Washington (U.S. Govt. Printing Office), 787–954.

Bertrand, H., Dostal, J., and Dupuy, C., 1982. Geochemistry of early Mesozoic tholeiites from Morocco. *Earth Planet. Sci. Lett.*, 58: 225–239.

Blow, W. H., 1969. Late middle Eocene to Recent planktonic foraminiferal biostratigraphy. *In* Brönnimann, P., and Renz, H. H. (Eds.), *Proc. First Int. conf. Plankt. Microfossils:* Leiden (E. J. Brill), 1: 199–422.

Bougault, H., 1980. Contribution des éléments de transition à la compréhension de la genèse des basaltes océaniques. Analyse des éléments traces dans les roche par spectrométrie de fluorescence X [Thèse]. Université Paris VII, Paris, France.

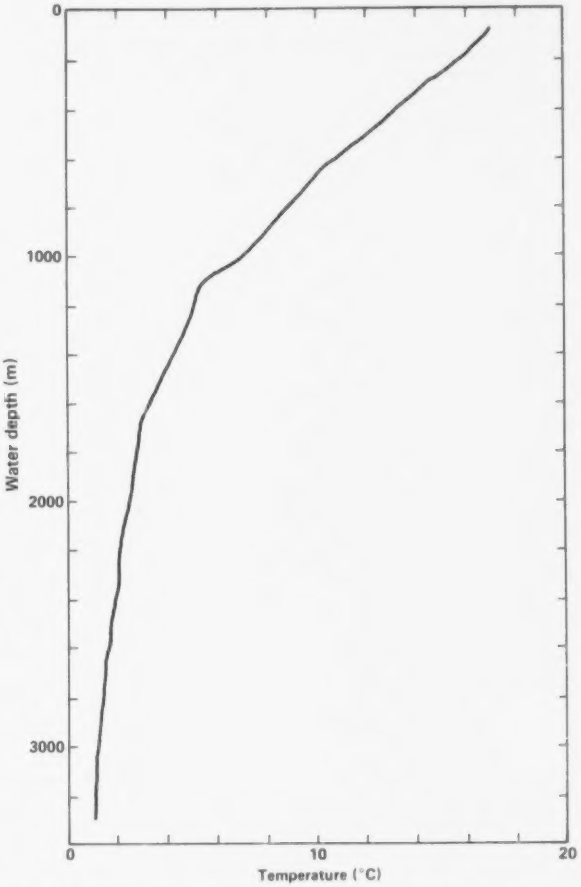

Figure 23. Ocean temperature profile recorded by high-resolution temperature log within drill pipe.

Bougault, H., Cambon, P., Corre, O., Joron, J. L., and Treuil, M., 1979. Evidence for variability of magmatic processes and upper mantle heterogeneity in the axial region of the Mid-Atlantic Ridge near 22° and 36°N. *Tectonophysics* 55:11–34.

Cambon, P., Joron, J. L., Bougault, H., and Treuil, M., 1980. Leg 55 Emperor Seamounts: trace elements in transitional tholeiites, alkali basalts and hawaiites—mantle homogeneity or heterogeneity and magmatic processes. *In* Jackson, E. D., Koizumi, I., et al., *Init. Repts. DSDP*, 55: Washington (U.S. Govt. Printing Office), 585–598.

El Azzouzi, M., 1981. Géochimie comparee de quelques éléments hygromagmaphiles dans des roches volcaniques de contextes geódynamiques variés [Thèse de 3$^{\text{eme}}$ cycle]. Université de Bretagne Occidentale, Brest, France.

Gartner, S., 1977. Calcareous nannofossil biostratigraphy and revised zonation of the Pleistocene. *Mar. Micropaleontol.*, 2:1–25.

Graciansky, P. C. de, Poag, C. W., and Shipboard Scientific Party, in press. Site 550. *In* Graciansky, P. C. de, Poag, C. W., et al., *Init. Repts. DSDP*, 80: Washington (U.S. Govt. Printing Office).

Langmuir, C. H., Bender, J. F., Bence, A. E., Hanson, G. N., and Taylor, S. R., 1977. Petrogenesis of basalts from the FAMOUS area: Mid-Atlantic Ridge. *Earth Planet. Sci. Lett.* 36:133–156.

Lowrie, W., and Alvarez, W., 1981. One hundred million years of geomagnetic polarity history. *Geology*, 9:392–397.

Murray, J. W., 1979. Cenozoic biostratigraphy and paleoecology of Sites 403 to 406 based on the foraminifers. *In* Montadert, L., Roberts, D. G., et al., *Init. Repts. DSDP*, 48: Washington (U.S. Govt. Printing Office), 415–430.

Okada, H., and Bukry, D., 1980. Supplementary modification and introduction of code numbers to the low-latitude coccolith biostratigraphic zonation. *Mar. Micropaleontol.*, 5(3):321–325.

Rögl, F., and Hochuli, P., 1976. The occurrence of *Bolboforma*, a probable algal cyst, in the Antarctic Miocene of DSDP Leg 35. *In* Hollister, C. D., Craddock, C., et al., *Init. Repts. DSDP*, 35: Washington (U.S. Govt. Printing Office), 713–720.

Treuil, M., Jaffrezic, H., Deschamps, N., Derrec, G. F., Joron, J. L., Pelletier, B., Novotny, S., and Courtois, C., 1973. Analyse des lanthanides, du hafnium, du scandium, du chrome, du manganese du cobalt, du cuivre dans les minéraux et les roches par activatio neutronique. *J. Radioanal. Chem.*, 18:55–68.

von Daniels, C. H, and Spiegler, D., 1974. *Bolboforma* n. gen. (Protozoa?) eine neue stratigraphisch wichtige Gattung aus dem Oligozän/Miozän Nordwestdeutschlands. *Palaontol. Z.*, 48:57–76.

SITE 558 HOLE CORE 1 CORED INTERVAL 158.0–167.5 m

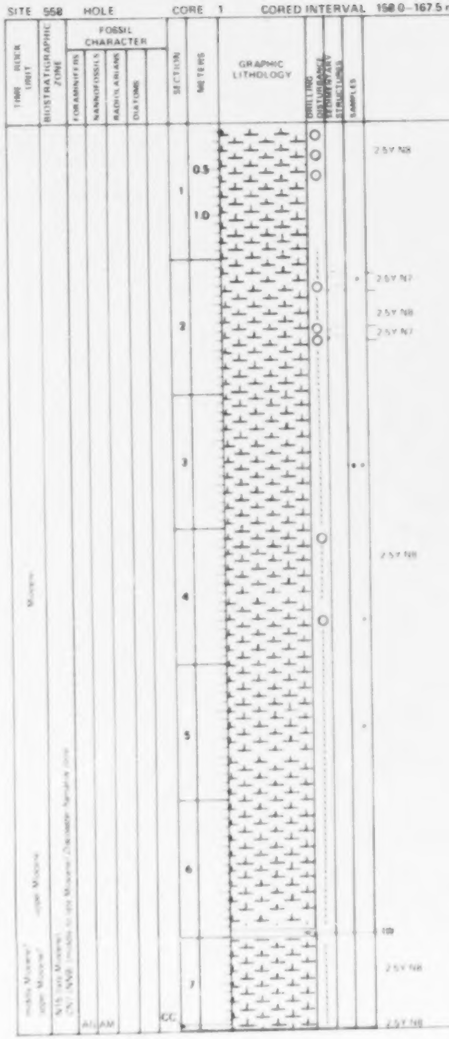
TIME-ROCK UNIT
BIOSTRATIGRAPHIC ZONE
FOSSIL CHARACTER
FORAMINIFERS
NANNOFOSSILS
RADIOLARIANS
DIATOMS
SECTION
METERS
GRAPHIC LITHOLOGY
DRILLING DISTURBANCE
SEDIMENTARY STRUCTURES
SAMPLES
Miocene
middle Miocene?
upper Miocene?
N15 (late Miocene)
CN7 (NN9) (middle to late Miocene) Discoaster hamatus zone
AG AM
0.5
1.0
1
2
3
4
5
6
7
CC
2.5Y N8
2.5Y N7
2.5Y N8
2.5Y N7
2.5Y N8
IW
2.5Y N8
2.5Y N8

LITHOLOGIC DESCRIPTION

DOMINANT LITHOLOGY NANNOFOSSIL OOZE

White (2.5Y N8)

Firm

Uniform with no obvious bedding or bioturbation.

In Section 2 two faint interbeds of light gray nannofossil ooze slightly firmer but no change in sediment components can be seen in smear slide examination.

SMEAR SLIDE SUMMARY (%):

	2, 24 M	3, 80	4, 100 D	5, 70
Composition:				
Feldspar	Tr	Tr	Tr	Tr
Clay	6	9	9	9
Pyrite	Tr	—	—	—
Carbonate unspec.	1	1	3	—
Foraminifers	3	10	8	6
Calc. nannofossils	90	80	80	85
Radiolarians	Tr	—	—	—

Carbonate Bomb (%):
3, 80 = 91

SITE 558 HOLE CORE 2 CORED INTERVAL 167.5–177.0 m

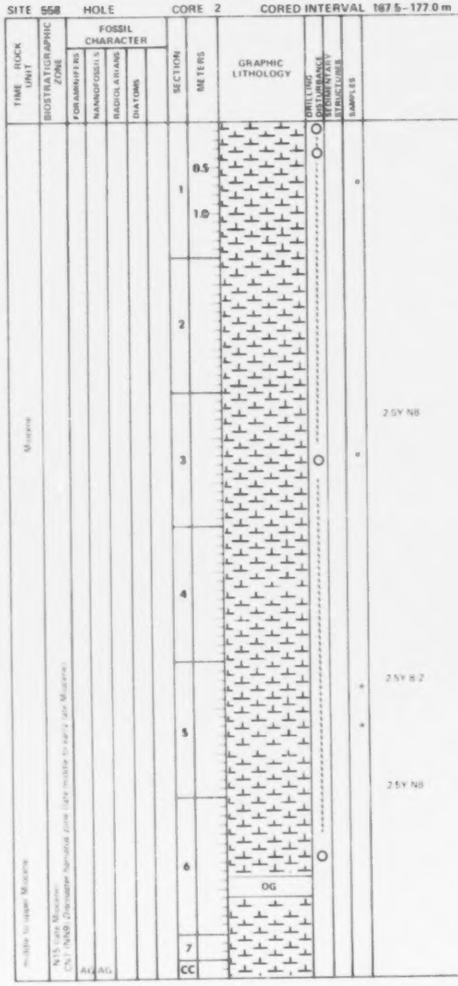
TIME-ROCK UNIT
BIOSTRATIGRAPHIC ZONE
FOSSIL CHARACTER
FORAMINIFERS
NANNOFOSSILS
RADIOLARIANS
DIATOMS
SECTION
METERS
GRAPHIC LITHOLOGY
DRILLING DISTURBANCE
SEDIMENTARY STRUCTURES
SAMPLES
Miocene
middle to upper Miocene
N15 (late Miocene)
CN7 (NN9) Discoaster hamatus zone (late middle to early late Miocene)
AG AG
0.5
1.0
1
2
3
4
5
6
7
CC
OG
2.5Y N8
2.5Y 8/2
2.5Y N8

LITHOLOGIC DESCRIPTION

DOMINANT LITHOLOGY NANNOFOSSIL OOZE

White (2.5Y N8 to 2.5Y 8/2)

Firm

Uniform with no obvious bedding or bioturbation.

SMEAR SLIDE SUMMARY (%):

	1, 70 D	3, 70 D	5, 30 M	5, 70 D
Composition:				
Feldspar	Tr	Tr	—	—
Clay	9	9	9	9
Palagonite				Tr
Pyrite	—	—	Tr	
Carbonate unspec.	1	2	Tr	2
Foraminifers	8	3	5	3
Calc. nannofossils	82	86	85	86

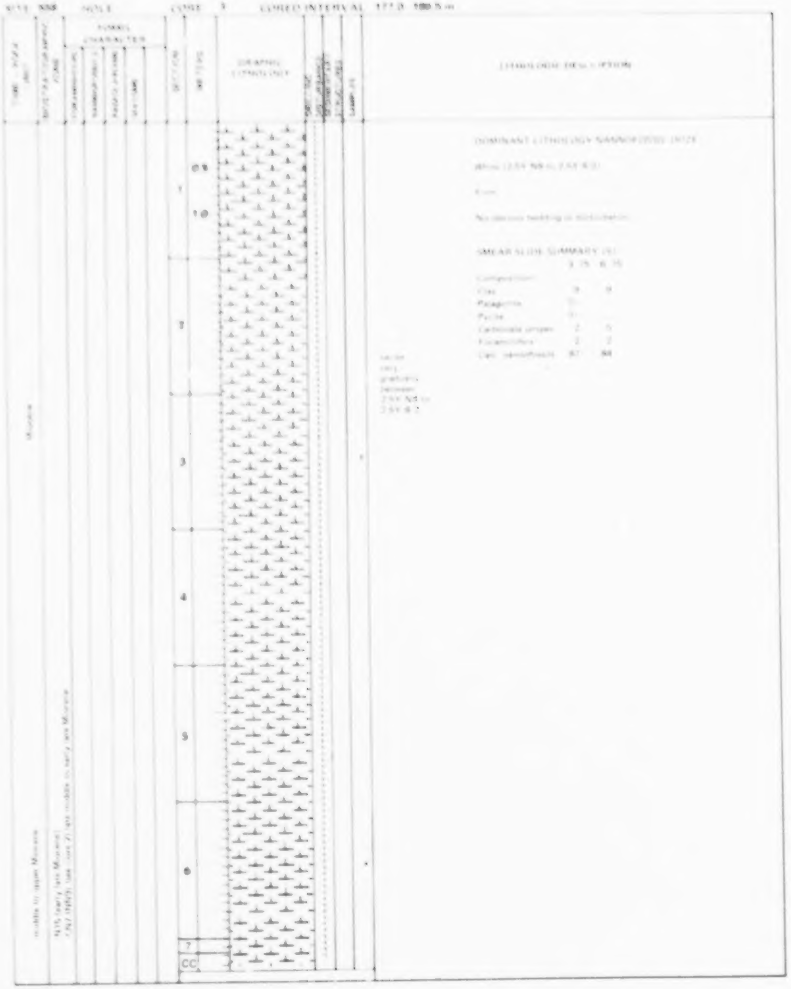
SITE 558 HOLE CORE 3 CORED INTERVAL 177.0–186.5 m
TIME-ROCK UNIT
BIOSTRATIGRAPHIC ZONE
FOSSIL CHARACTER
FORAMINIFERS
NANNOFOSSILS
RADIOLARIANS
DIATOMS
SECTION
METERS
GRAPHIC LITHOLOGY
DRILLING DISTURBANCE
SEDIMENTARY STRUCTURES
SAMPLES
LITHOLOGIC DESCRIPTION
Miocene
middle to upper Miocene
N15 (early late Miocene)
CN7 (NN9) (see core 2) late middle to early late Miocene
0.5
1.0
1
2
3
4
5
6
7
CC

DOMINANT LITHOLOGY NANNOFOSSIL OOZE

White (2.5Y N8 to 2.5Y 8/2)

Firm

No obvious bedding or bioturbation

SMEAR SLIDE SUMMARY (%)

	3, 75	6, 75
Composition:		
Clay	9	9
Palagonite	Tr	—
Pyrite	Tr	—
Carbonate unspec.	2	5
Foraminifers	2	2
Calc. nannofossils	87	84

color
very
gradually
between
2.5Y N8 to
2.5Y 8/2

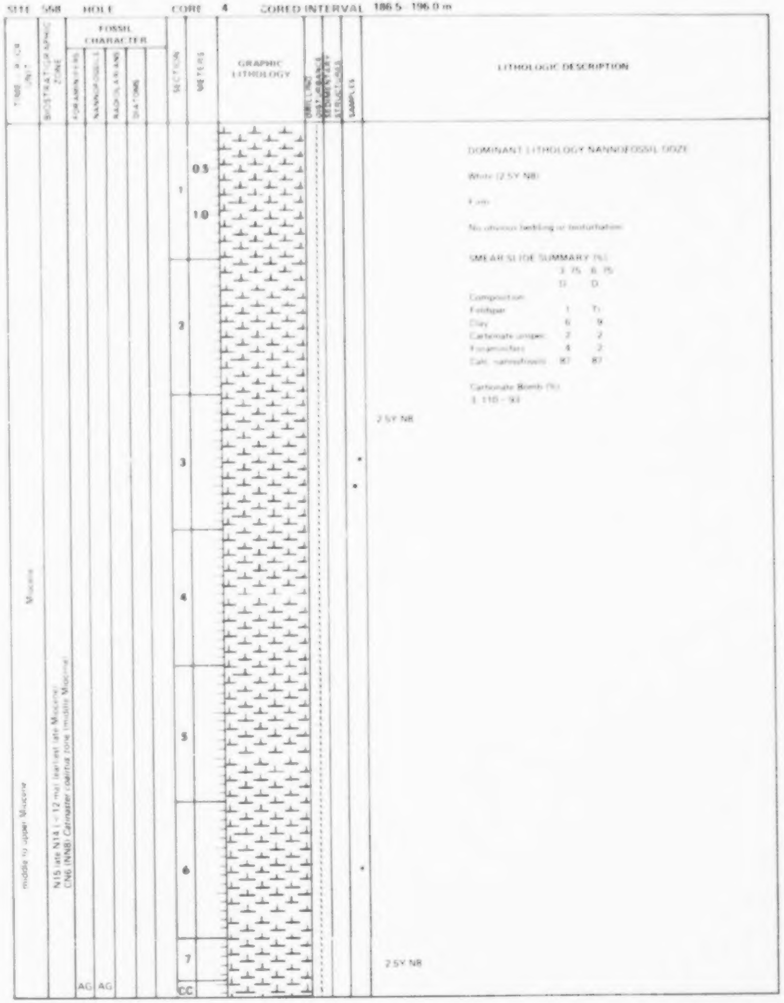
SITE 558 HOLE CORE 4 CORED INTERVAL 186.5–196.0 m
TIME-ROCK UNIT
BIOSTRATIGRAPHIC ZONE
FOSSIL CHARACTER
FORAMINIFERS
NANNOFOSSILS
RADIOLARIANS
DIATOMS
SECTION
METERS
GRAPHIC LITHOLOGY
DRILLING DISTURBANCE
SEDIMENTARY STRUCTURES
SAMPLES
LITHOLOGIC DESCRIPTION
Miocene
middle to upper Miocene
N15 late N14 (~12 ma) (earliest late Miocene)
CN6 (NN8) Catinaster coalitus zone (middle Miocene)
AG
AG
0.5
1.0
1
2
3
4
5
6
7
CC

DOMINANT LITHOLOGY NANNOFOSSIL OOZE

White (2.5Y N8)

Firm

No obvious bedding or bioturbation

SMEAR SLIDE SUMMARY (%)

	3, 75	6, 75
	D	D
Composition:		
Feldspar	1	Tr
Clay	6	9
Carbonate unspec.	2	2
Foraminifers	4	2
Calc. nannofossils	87	87

Carbonate Bomb (%)
3, 110 – 93

2.5Y N8

2.5Y N8

SITE 558 HOLE CORE 5 CORED INTERVAL 196.0–205.5 m

TIME–ROCK UNIT	BIOSTRATIGRAPHIC ZONE	FORAMINIFERS	NANNOFOSSILS	RADIOLARIANS	DIATOMS	SECTION	METERS
Miocene middle Miocene	N.9–N.12 (late middle Miocene) CN5 (NN6–8) Discoaster exilis–Catinaster coalitus zone (middle Miocene)	AG	CM			1 2 3 4 5 6 7 CC	0.5 1.0

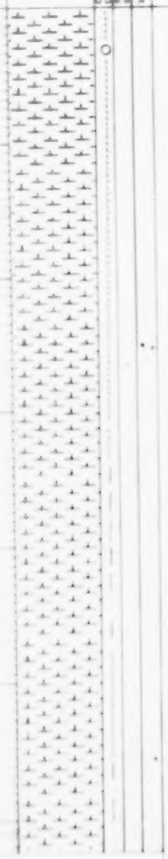

GRAPHIC LITHOLOGY
DRILLING DISTURBANCE
SEDIMENTARY STRUCTURES
SAMPLES

LITHOLOGIC DESCRIPTION

2.5Y N8

DOMINANT LITHOLOGY NANNOFOSSIL OOZE

White (2.5Y N8)

Firm

No obvious bioturbation or bedding

Occasional faint gray streaks

SMEAR SLIDE SUMMARY (%)

	3, 80	6, 80
	D	D
Composition:		
Feldspar	—	1
Clay	10	10
Palagonite	Tr	Tr
Carbonate unspec.	2	3
Foraminifers	2	Tr
Calc. nannofossils	86	86

Carbonate Bomb (%)
3, 80 = 89

SITE 558 HOLE CORE 6 CORED INTERVAL 205.5–215.0 m

TIME–ROCK UNIT	BIOSTRATIGRAPHIC ZONE	FORAMINIFERS	NANNOFOSSILS	RADIOLARIANS	DIATOMS	SECTION	METERS
Miocene	N? (middle Miocene) CN5 NN6 ? Discoaster exilis zone (middle Miocene)	CM	CM			1 2 3 4 5 6 CC	0.5 1.0

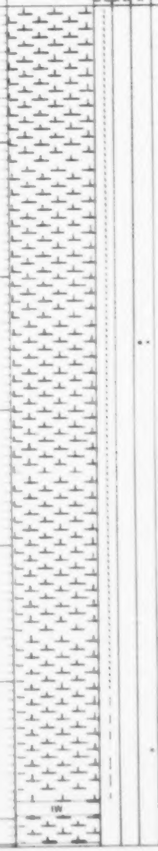

GRAPHIC LITHOLOGY
DRILLING DISTURBANCE
SEDIMENTARY STRUCTURES
SAMPLES
IW

LITHOLOGIC DESCRIPTION

2.5Y N8

DOMINANT LITHOLOGY NANNOFOSSIL OOZE

White (2.5Y N8)

Firm

No obvious bedding or bioturbation

SMEAR SLIDE SUMMARY (%)

	3, 80	6, 80
Composition:		
Feldspar	Tr	Tr
Mica	Tr?	Tr?
Heavy minerals		Tr
Clay	10	10
Volcanic glass	Tr	—
Palagonite	Tr	—
Carbonate unspec.	4	3
Calc. nannofossils	84	86
Radiolarians	Tr?	—

Carbonate Bomb (%)
3, 80 = 88

SITE 558 HOLE CORE 7 CORED INTERVAL 215.0–224.5 m

TIME-ROCK UNIT: Miocene

BIOSTRATIGRAPHIC ZONE: N12 middle Miocene; CN5 (NN6 ?) Discoaster exilis zone (middle Miocene)

FOSSIL CHARACTER: FORAMINIFERS CM; NANNOFOSSILS CM; RADIOLARIANS; DIATOMS

SECTION: 1, CC METERS: 0.5, 1.0

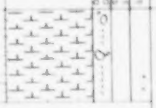

LITHOLOGIC DESCRIPTION

5Y 8/1

2.5Y N8

DOMINANT LITHOLOGY NANNOFOSSIL OOZE

White (5Y 8/1 to 2.5Y N8)

Firm to soft

No obvious bedding or bioturbation

SMEAR SLIDE SUMMARY (%):

	1, 80	CC
		D
Composition:		
Feldspar	Tr	Tr
Clay	90	10
Opaques	Tr	Tr
Carbonate unspec.	1	3
Foraminifers	1	1
Calc. nannofossils	88	85
Other		Tr

SITE 558 HOLE CORE 8 CORED INTERVAL 224.5–234.0 m

TIME-ROCK UNIT: Miocene; middle Miocene

BIOSTRATIGRAPHIC ZONE: CN5 (NN6 ?) D. exilis zone

FOSSIL CHARACTER: FORAMINIFERS CM; NANNOFOSSILS AM; RADIOLARIANS; DIATOMS

SECTION: 1, 2, 3, 4, CC METERS: 0.5, 1.0

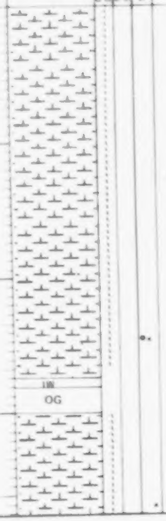

LITHOLOGIC DESCRIPTION

7.5YR 8

7.5YR 8

DOMINANT LITHOLOGY NANNOFOSSIL OOZE

White (7.5YR 8)

Firm

No obvious bedding

Possibly very faint white mottling but no obvious bioturbation

SMEAR SLIDE SUMMARY (%):

	3, 75	CC
	D	M
Composition:		
Feldspar	Tr	Tr
Heavy minerals		2
Clay	8	10
Palagonite		Tr
Opaques	Tr	2
Carbonate unspec.	5	5
Foraminifers	5	10
Calc. nannofossils	80	70
Other	Tr	

Carbonate Bomb (%):
3, 70 = 91

SITE 558 HOLE CORE 9 CORED INTERVAL 234.0–243.5 m

TIME-ROCK UNIT: middle Miocene

BIOSTRATIGRAPHIC ZONE: N11–N9 (early middle Miocene); CN5 (NN6 ?) D. exilis zone

FOSSIL CHARACTER: FORAMINIFERS CM; NANNOFOSSILS; RADIOLARIANS; DIATOMS

SECTION: 1, 2, 3, CC METERS: 0.5, 1.0

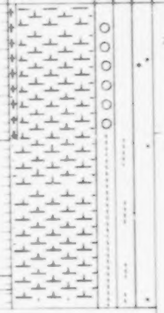

LITHOLOGIC DESCRIPTION

2.5Y N8

7.5YR N8

DOMINANT LITHOLOGY NANNOFOSSIL OOZE

Soupy to firm; very firm at Section 2, 10 cm

White (2.5Y N8 to 7.5YR N8)

No obvious bedding or bioturbation; faint mottling, 0.2 cm thick layer.
At Section 2, 10–12 cm — more firm than rest of Sections 2 and 3.

Possible burrow in Section 3 and CC.

Minor lithologies:
(1) Foram nanno ooze in Section 1

Soupy, white.

(2) Nanno ooze with micronodules

Same as dominant litho. but has darker streaks and mottles.

SMEAR SLIDE SUMMARY (%):

	1, 68	2, 10	CC
	M	D	M
Composition:			
Feldspar	Tr	Tr	Tr
Heavy minerals			Tr
Clay	10	10	8
Opaques		Tr	
Micronodules			1
Carbonate unspec.	2	3	3
Foraminifers	10	1	1
Calc. nannofossils	78	85	85
Fish remains		Tr	
Other		Tr	

Carbonate Bomb (%):
1, 70 = 90

SITE 558 HOLE CORE 10 CORED INTERVAL 243.5–253.0 m

TIME – ROCK UNIT	BIOSTRATIGRAPHIC ZONE	FORAMINIFERS	NANNOFOSSILS	RADIOLARIANS	DIATOMS	SECTION	METERS
middle Miocene	N? (middle Miocene) CN5 (NN6–7) ? zone (middle Miocene)	AG	AG			1 CC	0.5 1.0

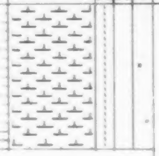
GRAPHIC LITHOLOGY
DRILLING DISTURBANCE
SEDIMENTARY STRUCTURES
SAMPLES

LITHOLOGIC DESCRIPTION

2.5Y N8
to
7.5YR N8

DOMINANT LITHOLOGY NANNOFOSSIL OOZE

Soft to firm.

White (2.5Y N8–7.5YR N8).

No bedding or bioturbation obvious, faint mottling in bottom of Section 1.

SMEAR SLIDE SUMMARY (%)

	1, 135
	D
Composition:	
Feldspar	Tr
Clay	10
Carbonate unspec.	8
Foraminifers	1
Calc. nannofossils	80
Sponge spicules	Tr
Other	Tr

Carbonate Bomb (%)
1, 70 = 89

SITE 558 HOLE CORE 11 CORED INTERVAL 253.0–262.5 m

TIME – ROCK UNIT	BIOSTRATIGRAPHIC ZONE	FORAMINIFERS	NANNOFOSSILS	RADIOLARIANS	DIATOMS	SECTION	METERS
middle Miocene	N? (middle Miocene) CN5 (NN6–7) (lower middle Miocene) ? zone	CM	AG			1 2 3 CC	0.5 1.0

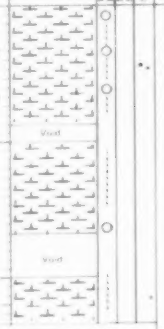

GRAPHIC LITHOLOGY
DRILLING DISTURBANCE
SEDIMENTARY STRUCTURES
SAMPLES

LITHOLOGIC DESCRIPTION

7.5YR N8
to
2.5Y N8

DOMINANT LITHOLOGY NANNOFOSSIL OOZE

White (7.5YR N8–2.5Y N8).

Soft to soupy to firm.

No obvious bedding or any bioturbation.

SMEAR SLIDE SUMMARY (%)

	1, 74	3, 75
Composition:		
Feldspar	1	Tr
Clay	1	9
Volcanic glass	Tr	—
Zeolite	Tr	Tr?
Carbonate unspec.	3	5
Foraminifers	2	1
Calc. nannofossils	90	84

Carbonate Bomb (%)
1, 70 = 95

SITE 558 HOLE CORE 12 CORED INTERVAL 262.5–272.0 m

TIME – ROCK UNIT	BIOSTRATIGRAPHIC ZONE	FORAMINIFERS	NANNOFOSSILS	RADIOLARIANS	DIATOMS	SECTION	METERS
Miocene lower(-middle) Miocene	N9–N8 (base of middle Miocene) CN4 (NN5) *Sphenolithus heteromorphus* zone (middle Miocene)	CM	AG			1 2 3 4 5 6 CC	0.5 1.0

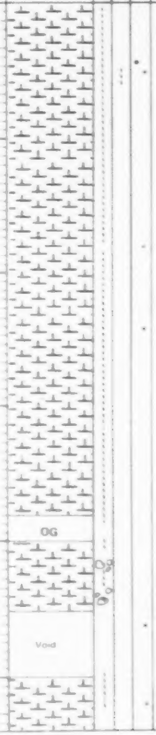

GRAPHIC LITHOLOGY
DRILLING DISTURBANCE
SEDIMENTARY STRUCTURES
SAMPLES

LITHOLOGIC DESCRIPTION

2.5Y N8
to
7.5YR N8

DOMINANT LITHOLOGY NANNOFOSSIL OOZE

White (2.5Y N8)

Firm, except soupy in Section 5.

No obvious bedding or bioturbation except faint mottling at Section 1, 80 cm and possible faint color mottling randomly distributed. Dark streak at Section 2, 120 cm.

SMEAR SLIDE SUMMARY (%)

	1, 80	2, 120	3, 63	3, 90	6, 30
	M	M	D	D	D
Composition:					
Feldspar	Tr	Tr	Tr	Tr	Tr
Heavy minerals	—	—	—	—	Tr
Clay	9	8	7	6	8
Palagonite	—	Tr	—	—	—
Opaques	Tr	Tr	Tr		
Micronodules	Tr–1	1	—	—	
Carbonate unspec.	5	3	2	2	
Foraminifers	5	5	10	1	1
Calc. nannofossils	80	80	80	90	90
Diatoms	Tr	Tr	—	—	—
Sponge spicules	Tr	Tr	Tr	Tr	Tr
Other	Tr	Tr	Tr	Tr	

Carbonate Bomb (%)
1, 70 = 90

SITE 558 HOLE CORE 13 CORED INTERVAL 272.0–281.5 m

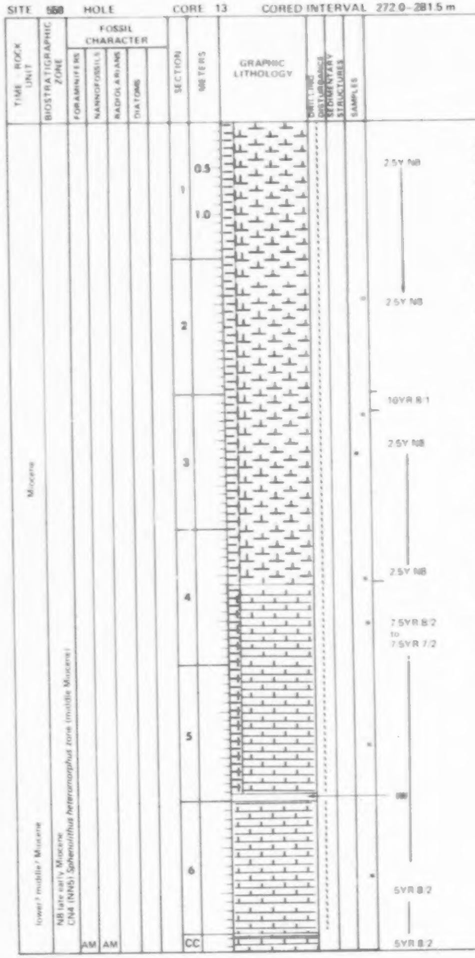
TIME – ROCK UNIT
BIOSTRATIGRAPHIC ZONE
FOSSIL CHARACTER
FORAMINIFERS
NANNOFOSSILS
RADIOLARIANS
DIATOMS
SECTION
METERS
GRAPHIC LITHOLOGY
DRILLING DISTURBANCE
SEDIMENTARY STRUCTURES
SAMPLES
Miocene
lower? middle? Miocene
N8 late early Miocene
CN4 (NN5) Sphenolithus heteromorphus zone (middle Miocene)
AM
AM
0.5
1.0
1
2
3
4
5
6
CC
2.5Y N8
2.5Y N8
10YR 8/1
2.5Y N8
2.5Y N8
7.5YR 8/2 to 7.5YR 7/2
5YR 8/2
5YR 8/2

LITHOLOGIC DESCRIPTION

DOMINANT LITHOLOGY NANNOFOSSIL OOZE TO NANNOFOSSIL CHALK

White (2.5Y N8) to pinkish white (10YR N8 and 7.5YR 8/2) to pinkish gray (7.5YR 7/2) to pinkish white (5YR 8/2)

Firm to very firm

No obvious bedding or bioturbation

Minor lithology
Foram-nanno ooze, similar to above with >10% forams

At top of Section 3 – slight color change pinkish chalk ooze

At 60 cm of Section 4 – marked color change to pinkish white chalk

SMEAR SLIDE SUMMARY (%)

	2, 45	3, 25	4, 55	4, 105	5, 90	6, 85
	M	D	D	D	M	D
Composition:						
Feldspar	Tr	Tr	Tr	Tr	1	Tr
Heavy minerals	Tr	Tr	Tr	1	Tr	—
Clay	10	12	20	10	10	10
Volcanic glass	—	Tr	—	—	—	—
Opaques	—	Tr	—	—	—	—
Carbonate unspec.	5	5	16	15	17	16
Foraminifers	15	2	3	1	10	2
Calc. nannofossils	70	80	60	70	60	70
Diatoms	—	—	Tr	—	1	Tr
Radiolarians	Tr	Tr	Tr	Tr	—	Tr
Sponge spicules	Tr	Tr	Tr	1	Tr	Tr
Silicoflagellates	Tr	—	Tr	1	—	Tr
Other	—	—	—	Tr	—	—

Carbonate Bomb (%):
3, 70 – 87

SITE 558 HOLE CORE 14 CORED INTERVAL 281.5–291.0 m

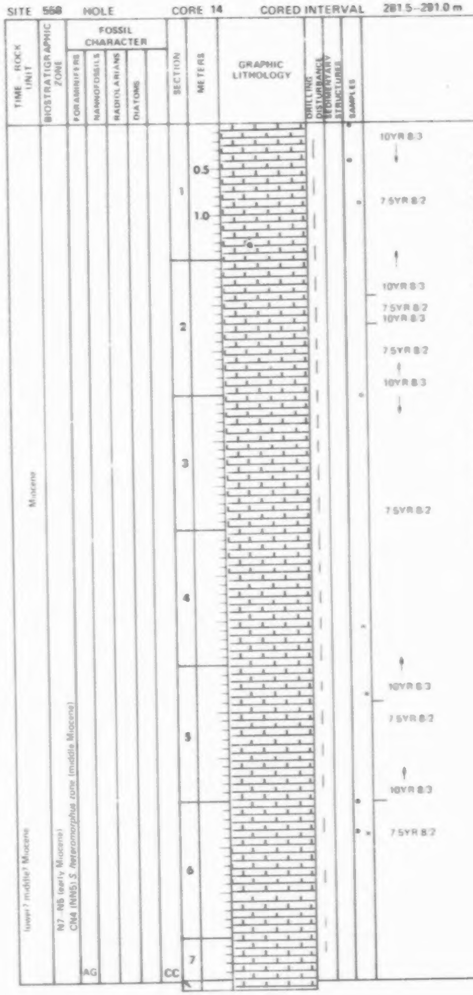
TIME – ROCK UNIT
BIOSTRATIGRAPHIC ZONE
FOSSIL CHARACTER
FORAMINIFERS
NANNOFOSSILS
RADIOLARIANS
DIATOMS
SECTION
METERS
GRAPHIC LITHOLOGY
DRILLING DISTURBANCE
SEDIMENTARY STRUCTURES
SAMPLES
Miocene
lower? middle? Miocene
N7–N8 (early Miocene)
CN4 (NN5) S. heteromorphus zone (middle Miocene)
AG
0.5
1.0
1
2
3
4
5
6
7
CC
10YR 8/3
7.5YR 8/2
10YR 8/3
7.5YR 8/2
10YR 8/3
7.5YR 8/2
10YR 8/3
7.5YR 8/2
10YR 8/3
7.5YR 8/2
10YR 8/3
7.5YR 8/2

LITHOLOGIC DESCRIPTION

DOMINANT LITHOLOGY NANNOFOSSIL CHALK

Very pale brown (10YR 8/3) grades to the dominant color of pinkish white (7.5YR 8/2)

Occasional black streaks (nodules?)

Chalk are usually fractured by drilling with occasionally soupy zones

No obvious bedding

SMEAR SLIDE SUMMARY (%)

	1, 95	3, 5	4, 110	5, 35	6, 40
	D	M			
Composition					
Feldspar	Tr	Tr	Tr	Tr	Tr
Clay	15	15	10	14	10
Micronodules	Tr	1	Tr	Tr	Tr
Carbonate unspec.	1	1	8	1	10
Foraminifers	3	2	10	5	3
Calc. nannofossils	80	80	70	80	75
Diatoms	Tr	—	Tr	Tr	Tr
Radiolarians	Tr	Tr	Tr	Tr	Tr
Sponge spicules	Tr	Tr	Tr	Tr	Tr
Silicoflagellates	Tr	Tr	Tr	Tr	—

Carbonate Bomb (%)
1, 5 – 70
1, 42 – 88
6, 2 – 74
6, 38 – 88

SITE 558 HOLE CORE 15 CORED INTERVAL 291.0–300.5 m

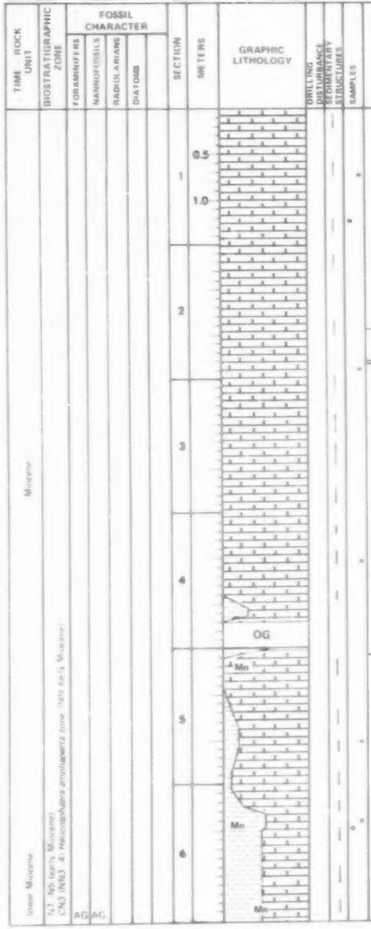
TIME – ROCK UNIT
BIOSTRATIGRAPHIC ZONE
FOSSIL CHARACTER
FORAMINIFERS
NANNOFOSSILS
RADIOLARIANS
DIATOMS
SECTION
METERS
GRAPHIC LITHOLOGY
DRILLING DISTURBANCE
SEDIMENTARY STRUCTURES
SAMPLES
Miocene
lower Miocene
N7 - N6 (early Miocene)
CN3 (NN3 - 4) Helicosphaera ampliaperta zone (late early Miocene)
AG AG
0.5
1.0
1
2
3
4
5
6
OG
Mn
Mn
Mn

LITHOLOGIC DESCRIPTION

7.5YR 8/2
10YR 8/1
10YR 8/2
10YR 8/1
10YR 8/2
2.5Y N7
10YR 8/2
10YR 6/2
10YR 8/2
10YR 6/2
10YR 5/2
10YR 8/2
10YR 6/2
10YR 8/2
10YR 6/3
10YR 6/2

DOMINANT LITHOLOGIES
(1) NANNOFOSSIL CHALK

The dominant color changes from pinkish white (7.5 YR 8/2) to light brownish gray (10YR 6/2), these colors grade to white (10YR 8/1–10YR 8/2) and occasionally to grayish brown (10YR 5/2) and light gray (2.5Y N7)

Fractured by drilling

Mottled by bioturbation to lighter color than surrounding sediment

No obvious bedding

(2) MARLY NANNOFOSSIL CHALK

Section 4, 105–112 cm and Section 6 : light brownish gray (10YR 6/2) to pale brown (10YR 6/3)

Occasional nodules (manganese?) are scattered throughout Sections 5 and 6

SMEAR SLIDE SUMMARY (%)

	1, 75	2, 140	4, 57	5, 100	6, 40
	D	M	D	D	M
Composition					
Feldspar	Tr	5	Tr	Tr	Tr
Heavy minerals	Tr	—	Tr	Tr	Tr
Clay	10	60	15	10	12
Volcanic glass	Tr	Tr	Tr	—	Tr
Micronodules	Tr	—	Tr	1	Tr
Carbonate unspec.	16	10	8	7	5
Foraminifers	2	—	5	2	1
Calc. nannofossils	70	25	70	79	82
Diatoms	Tr	—	Tr	—	Tr
Radiolarians	Tr	—	Tr	Tr	Tr
Sponge spicules	Tr	—	Tr	Tr	Tr
Silicoflagellates	Tr	—	Tr	Tr	Tr

Carbonate Bomb (%)
1, 122 = 86
6, 50 = 86

SITE 558 HOLE CORE 16 CORED INTERVAL 300.5–310.0 m

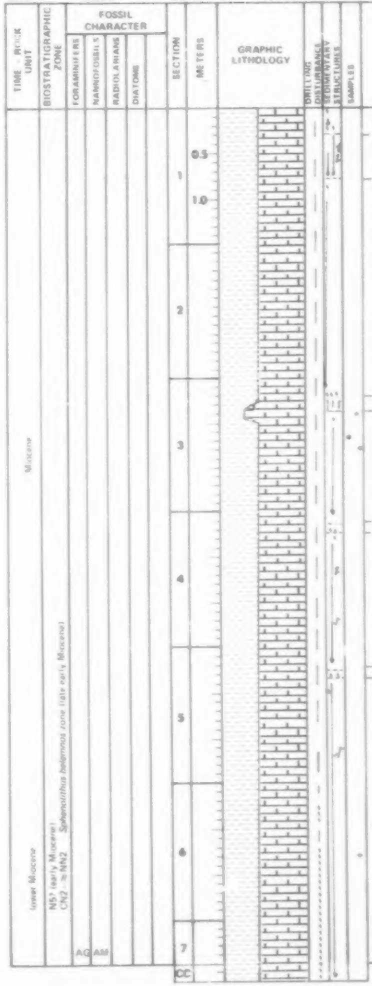
TIME – ROCK UNIT
BIOSTRATIGRAPHIC ZONE
FOSSIL CHARACTER
FORAMINIFERS
NANNOFOSSILS
RADIOLARIANS
DIATOMS
SECTION
METERS
GRAPHIC LITHOLOGY
DRILLING DISTURBANCE
SEDIMENTARY STRUCTURES
SAMPLES
Miocene
lower Miocene
N5? (early Miocene)
CN2 = NN2 Sphenolithus belemnos zone (late early Miocene)
AG AM
0.5
1.0
1
2
3
4
5
6
7
CC

LITHOLOGIC DESCRIPTION

10YR 6/2
10YR 6/4
10YR 6/2
10YR 6/4
10YR 6/2
10YR N8
10YR 6/3
10YR 6/4
10YR 6/3
10YR 6/4
10YR 6/3

DOMINANT LITHOLOGY: MARLY NANNOFOSSIL OOZE

Light brownish gray to light yellowish brown in alternating vague cycles; some dark micronodules.

This color change is associated with reduction of carbonate to 50% (see below).

Firm to hard, very slightly deformed, friable.

Bioturbated to highly bioturbated; halo burrows common; nodules. Massive bedding with vague color changes. Small fractures or slickensided faults with very minor offset (penecontemporaneous deformation).

SMEAR SLIDE SUMMARY (%)

	3, 40	3, 80	6, 80
Composition			
Feldspar	Tr	Tr	Tr
Heavy minerals	Tr	Tr	Tr
Clay	18	45	45
Volcanic glass	—	Tr	—
Micronodules	1	1	—
Zeolite	—	—	1?
Carbonate unspec.	2	1	7
Foraminifers	1	9	8
Calc. nannofossils	78	40	42
Diatoms	Tr	1	Tr
Radiolarians	Tr	2	Tr
Sponge spicules	—	Tr	2
Silicoflagellates	—	Tr	Tr

Carbonate Bomb (%)
3, 70 = 50

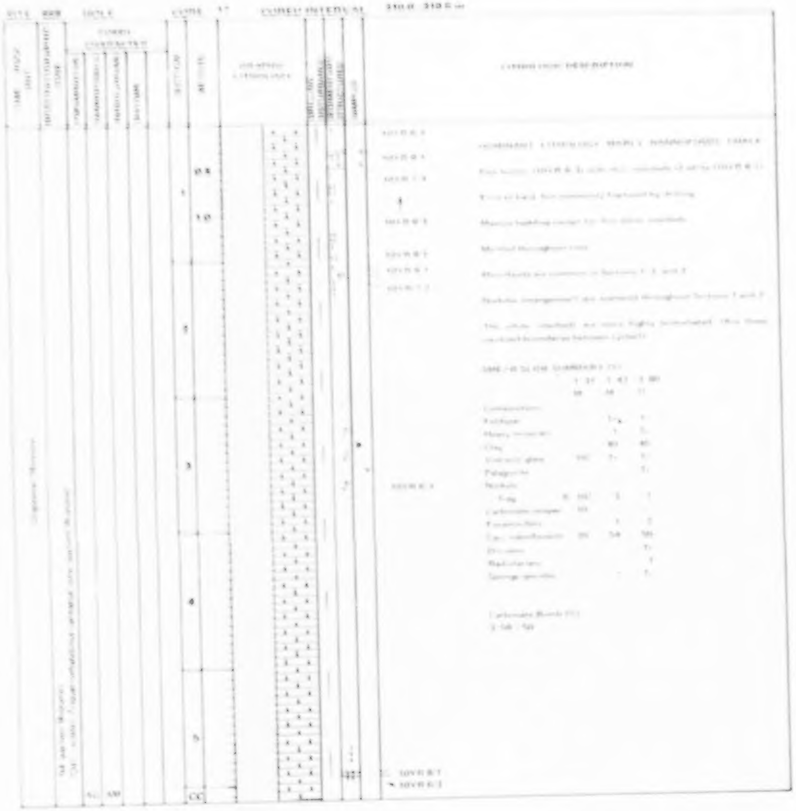
SITE 558 HOLE CORE 17 CORED INTERVAL 310.0–319.5 m
TIME-ROCK UNIT
BIOSTRATIGRAPHIC ZONE
FOSSIL CHARACTER
SECTION
METERS
GRAPHIC LITHOLOGY
DRILLING DISTURBANCE
SEDIMENTARY STRUCTURES
SAMPLES
Oligocene / Miocene
0.5
1.0
1
2
3
4
5
CC
RG
AM

LITHOLOGIC DESCRIPTION

10YR 8.2
10YR 8.4
10YR 7.4
10YR 8.2
10YR 8.2
10YR 8.2
10YR 7.2
10YR 8.4
10YR 8.1
10YR 6.3

DOMINANT LITHOLOGY: MARLY NANNOFOSSIL CHALK

Pale brown (10YR 6.3) with rare mottles of white (10YR 8.2).

Firm to hard, but commonly fractured by drilling.

Massive bedding except for thin black laminae.

Mottled throughout core.

Microfaults are common in Sections 1, 2, and 3.

Nodules (manganese?) are scattered throughout Sections 1 and 2.

The colour (marked) are more highly bioturbated. [illegible] boundaries between [illegible]

SMEAR SLIDE SUMMARY (%):

	1, 37	1, 42	3, 80
	M	M	D
Composition:			
Feldspar		Tr	Tr
Heavy minerals		1	Tr
Clay		80	40
Volcanic glass	100	Tr	Tr
Palagonite			Tr
Nodule			
Fe-Mg	100	3	1
Carbonate unspec.	10		
Foraminifers		1	2
Calc. nannofossils	20	14	50
Diatoms			Tr
Radiolarians			1
Sponge spicules			Tr

Carbonate Bomb (%):
3, 58 = 50

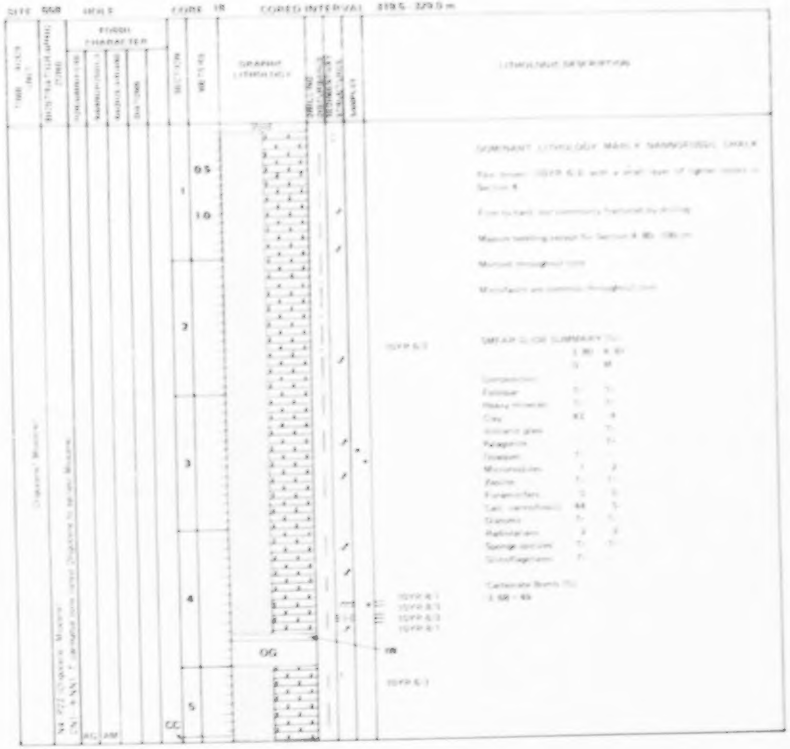
SITE 558 HOLE CORE 18 CORED INTERVAL 319.5–329.0 m
TIME-ROCK UNIT
BIOSTRATIGRAPHIC ZONE
FOSSIL CHARACTER
SECTION
METERS
GRAPHIC LITHOLOGY
DRILLING DISTURBANCE
SEDIMENTARY STRUCTURES
SAMPLES
Oligocene / Miocene
0.5
1.0
1
2
3
4
5
CC
OG
RG
AM

LITHOLOGIC DESCRIPTION

10YR 6.3
10YR 8.1
10YR 8.3
10YR 6.3
10YR 8.1
10YR 6.3

DOMINANT LITHOLOGY: MARLY NANNOFOSSIL CHALK

Pale brown (10YR 6.3) with a small layer of lighter color in Section 4.

Firm to hard, but commonly fractured by drilling.

Massive bedding except for Section 4, 80–106 cm.

Mottled throughout core.

Microfaults are common throughout core.

SMEAR SLIDE SUMMARY (%):

	1, 80	4, 81
	D	M
Composition:		
Feldspar	Tr	Tr
Heavy minerals	Tr	Tr
Clay	42	4
Volcanic glass		Tr
Palagonite		Tr
Dolomite	1	
Micronodules	1	2
Zeolite	Tr	Tr
Foraminifers	2	3
Calc. nannofossils	44	5
Diatoms	Tr	Tr
Radiolarians	3	3
Sponge spicules	Tr	Tr
Silicoflagellates	Tr	

Carbonate Bomb (%):
3, 68 = 45

SITE 558 HOLE CORE 19 CORED INTERVAL 329.0–338.5 m

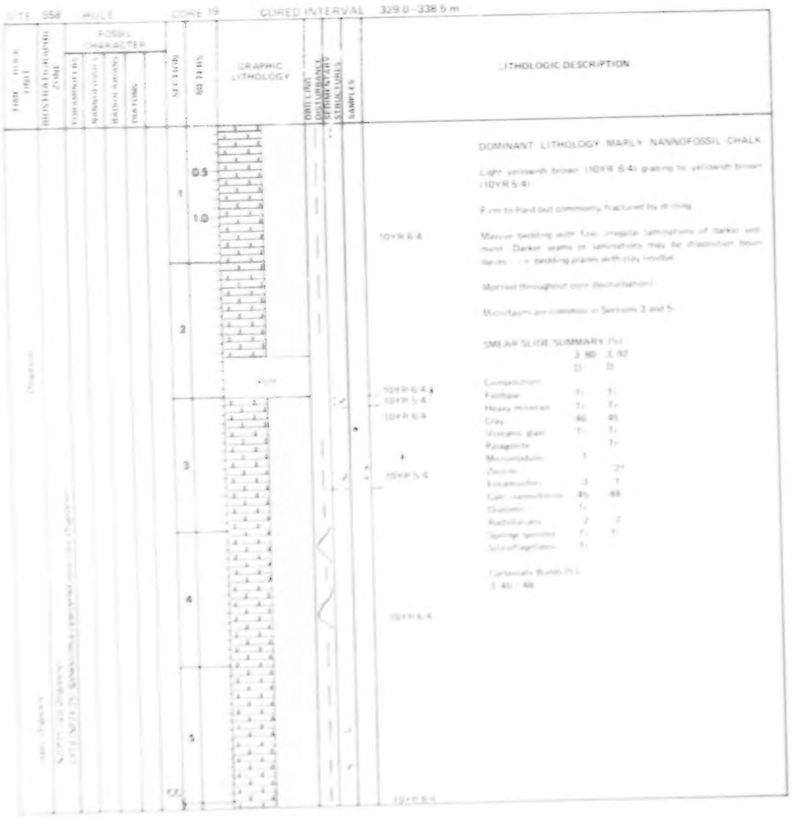
TIME-ROCK UNIT
BIOSTRATIGRAPHIC ZONE
FOSSIL CHARACTER
FORAMINIFERS
NANNOFOSSILS
RADIOLARIANS
DIATOMS
SECTION
METERS
GRAPHIC LITHOLOGY
DRILLING DISTURBANCE
SEDIMENTARY STRUCTURES
SAMPLES
Oligocene
upper Oligocene
0.5
1.0
1
2
3
4
5
CC
Void
10YR 6/4
10YR 6/4
10YR 5/4
10YR 6/4
10YR 5/4
10YR 6/4
10YR 6/4

LITHOLOGIC DESCRIPTION

DOMINANT LITHOLOGY: MARLY NANNOFOSSIL CHALK

Light yellowish brown (10YR 6/4) grading to yellowish brown (10YR 5/4).

Firm to hard but commonly fractured by drilling.

Massive bedding with fine, irregular laminations of darker sediment. Darker seams or laminations may be dissolution faces (i.e., bedding planes with clay residue).

Mottled throughout core (bioturbation).

Microfaults are common in Sections 3 and 5.

SMEAR SLIDE SUMMARY (%)

	3, 80 D	3, 97 D
Composition:		
Feldspar	Tr	Tr
Heavy minerals	Tr	Tr
Clay	46	45
Volcanic glass	Tr	Tr
Palagonite		Tr
Micronodules	1	
Zeolite		2?
Foraminifers	3	1
Calc. nannofossils	45	48
Diatoms	Tr	
Radiolarians	2	2
Sponge spicules	Tr	Tr
Silicoflagellates	Tr	

Carbonate Bomb (%):
3, 40 = 48

SITE 558 HOLE CORE 20 CORED INTERVAL 338.5–348.0 m

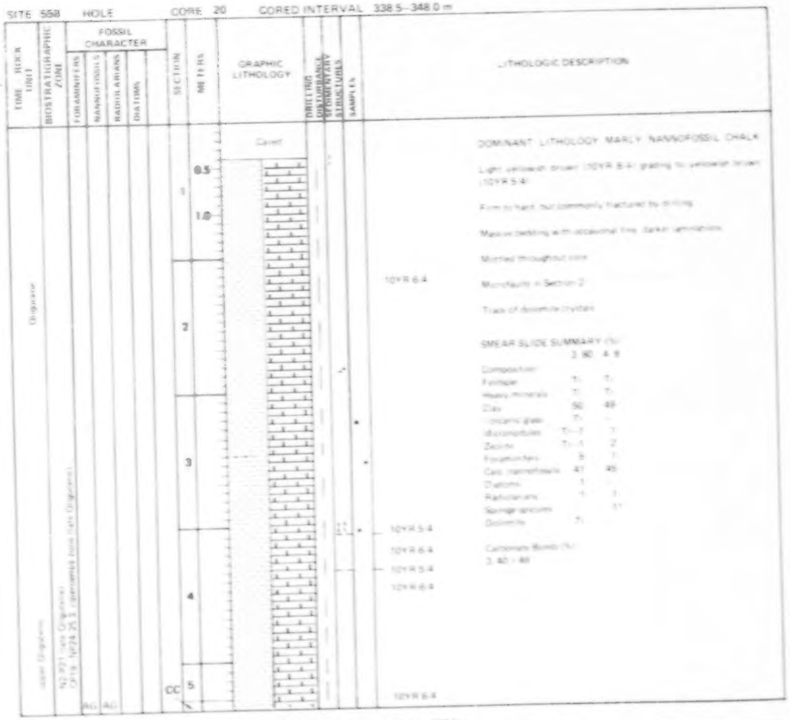
TIME-ROCK UNIT
BIOSTRATIGRAPHIC ZONE
FOSSIL CHARACTER
FORAMINIFERS
NANNOFOSSILS
RADIOLARIANS
DIATOMS
SECTION
METERS
GRAPHIC LITHOLOGY
DRILLING DISTURBANCE
SEDIMENTARY STRUCTURES
SAMPLES
Oligocene
upper Oligocene
N2-P21 (late Oligocene)
CP19 (NP24-25.3 (late Oligocene)
AG
AG
Caved
0.5
1.0
1
2
3
4
5
CC
10YR 6/4
10YR 5/4
10YR 6/4
10YR 5/4
10YR 6/4
10YR 6/4

LITHOLOGIC DESCRIPTION

DOMINANT LITHOLOGY: MARLY NANNOFOSSIL CHALK

Light yellowish brown (10YR 6/4) grading to yellowish brown (10YR 5/4).

Firm to hard, but commonly fractured by drilling.

Massive bedding with occasional fine, darker laminations.

Mottled throughout core.

Microfaults in Section 2.

Trace of dolomite crystals.

SMEAR SLIDE SUMMARY (%)

	3, 80	4, 9
Composition:		
Feldspar	Tr	Tr
Heavy minerals	Tr	Tr
Clay	50	49
Volcanic glass	Tr	—
Micronodules	Tr–1	1
Zeolite	Tr–1	2
Foraminifers	3	1
Calc. nannofossils	41	45
Diatoms	1	—
Radiolarians	1	1
Sponge spicules		1?
Dolomite	Tr	

Carbonate Bomb (%):
3, 40 = 48

SITE 558 HOLE CORE 21 CORED INTERVAL 348.0–357.5 m

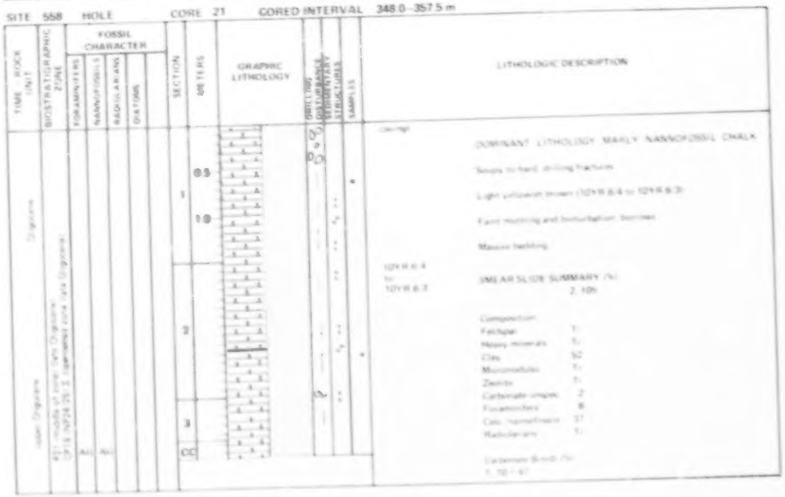
TIME-ROCK UNIT
BIOSTRATIGRAPHIC ZONE
FOSSIL CHARACTER
FORAMINIFERS
NANNOFOSSILS
RADIOLARIANS
DIATOMS
SECTION
METERS
GRAPHIC LITHOLOGY
DRILLING DISTURBANCE
SEDIMENTARY STRUCTURES
SAMPLES
Oligocene
upper Oligocene
P21 (middle of zone) (late Oligocene)
CP19 (NP24-25.3 (late Oligocene)
AG
AG
0.5
1.0
1
2
3
CC
10YR 6/4
to
10YR 6/3

LITHOLOGIC DESCRIPTION

DOMINANT LITHOLOGY: MARLY NANNOFOSSIL CHALK

Stiff to hard, drilling fractures.

Light yellowish brown (10YR 6/4 to 10YR 6/3).

Faint mottling and bioturbation burrows.

Massive bedding.

SMEAR SLIDE SUMMARY (%)

	2, 105
Composition:	
Feldspar	Tr
Heavy minerals	Tr
Clay	52
Micronodules	Tr
Zeolite	Tr
Carbonate unspec.	2
Foraminifers	8
Calc. nannofossils	37
Radiolarians	Tr

Carbonate Bomb (%):
1, 70 = 47

SITE 558 HOLE CORE 22 CORED INTERVAL 357.5–367.0 m

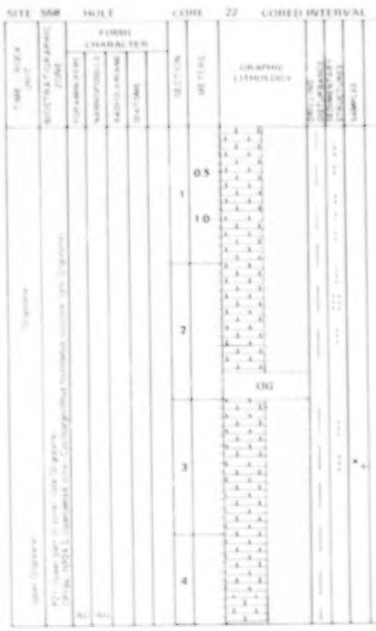
TIME-ROCK UNIT
BIOSTRATIGRAPHIC ZONE
FOSSIL CHARACTER
FORAMINIFERS
NANNOFOSSILS
RADIOLARIANS
DIATOMS
SECTION
METERS
GRAPHIC LITHOLOGY
DRILLING DISTURBANCE
SEDIMENTARY STRUCTURES
SAMPLES
Oligocene
upper Oligocene
AG
AG
1
2
3
4
0.5
1.0
OG

LITHOLOGIC DESCRIPTION

10YR 6/4

DOMINANT LITHOLOGY: MARLY NANNOFOSSIL CHALK

Soft to hard, fractured by drilling.

Light yellowish brown (10YR 6/4).

Burrows: 10YR 8/4

Massive bedding with faint mottling and bioturbation.

SMEAR SLIDE SUMMARY (%):

	3, 80
Composition:	
Feldspar	Tr
Heavy minerals	Tr
Clay	52
Zeolite	Tr
Carbonate unspec.	7
Foraminifers	8
Calc. nannofossils	36
Radiolarians	1

Carbonate Bomb (%):
3, 30 – 46

10YR 6/4

SITE 558 HOLE CORE 23 CORED INTERVAL 367.0–376.5 m

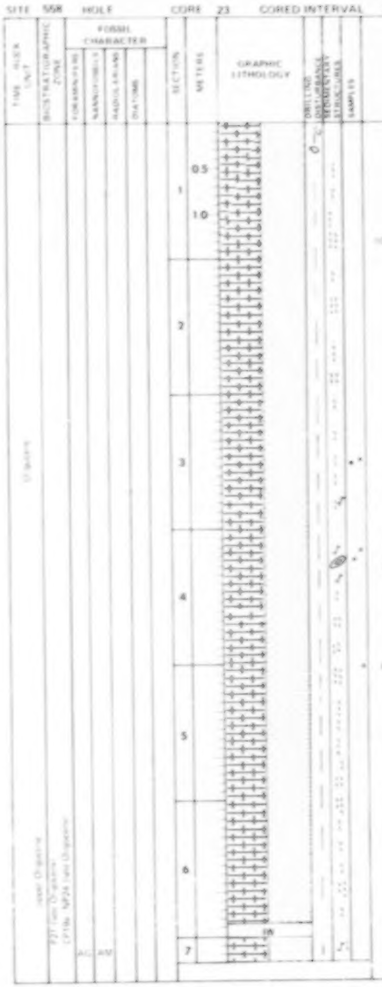
TIME-ROCK UNIT
BIOSTRATIGRAPHIC ZONE
FOSSIL CHARACTER
FORAMINIFERS
NANNOFOSSILS
RADIOLARIANS
DIATOMS
SECTION
METERS
GRAPHIC LITHOLOGY
DRILLING DISTURBANCE
SEDIMENTARY STRUCTURES
SAMPLES
Oligocene
upper Oligocene
P21 (late Oligocene)
CP19a; NP24 (late Oligocene)
AG
AM
1
2
3
4
5
6
7
0.5
1.0

LITHOLOGIC DESCRIPTION

10YR 6/4

DOMINANT LITHOLOGY: MARLY FORAM NANNOFOSSIL CHALK

Light yellowish brown (10YR 6/4).

Fractured by drilling, firm to hard.

Faint mottling, bioturbation and burrows of very pale brown (10YR 8/3) material; otherwise massive bedding.

Faint darker streaks and darker brown (10YR 5/4) mottling at Section 5, 5 cm.

smear slide in burrow

burrow

SMEAR SLIDE SUMMARY (%):

	3, 80 D	4, 28 M	4, 33 M	5, 5 M
Composition:				
Feldspar	Tr	Tr	Tr	Tr
Heavy minerals	Tr	Tr	Tr	Tr
Clay	51	46	40	48
Volcanic glass	—	—	Tr	Tr
Palagonite	—	—	Tr	—
Micronodules	Tr	1	Tr	Tr
Zeolite	Tr	1	2	Tr
Carbonate unspec.	—	—	—	3
Foraminifers	2	10	10	2
Calc. nannofossils	43	40	40	44
Radiolarians	Tr	1	Tr	Tr
Sponge spicules	—	—	—	1
Silicoflagellates	Tr	Tr	—	—
Dolomite	—	Tr	—	Tr

Carbonate Bomb (%):
3, 80 – 47

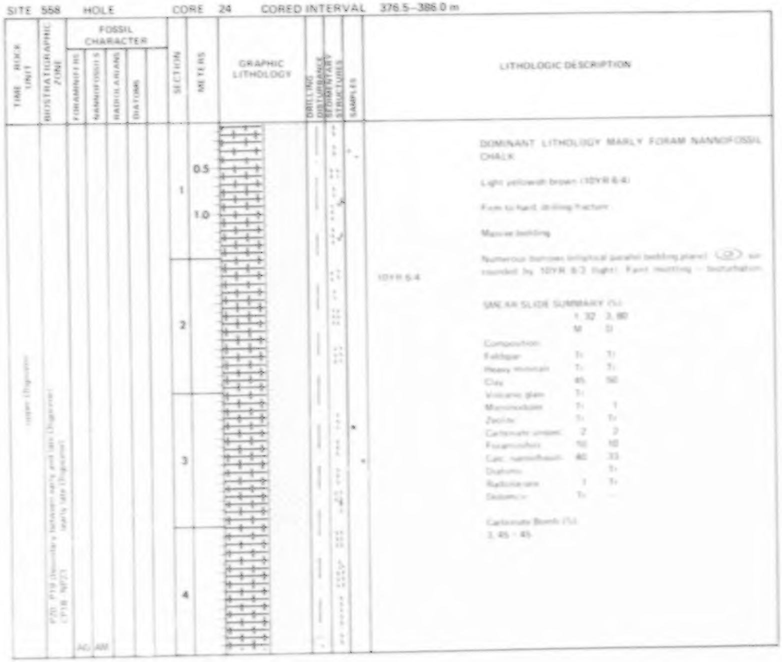
SITE 558 HOLE CORE 24 CORED INTERVAL 376.5–386.0 m
TIME - ROCK UNIT
BIOSTRATIGRAPHIC ZONE
FOSSIL CHARACTER
FORAMINIFERS
NANNOFOSSILS
RADIOLARIANS
DIATOMS
SECTION
METERS
GRAPHIC LITHOLOGY
DRILLING DISTURBANCE
SEDIMENTARY STRUCTURES
SAMPLES
LITHOLOGIC DESCRIPTION
upper Oligocene
P20 - P19 (boundary between early and late Oligocene)
CP18 - NP23 early late Oligocene)
AG AM
1
2
3
4
0.5
1.0
10YR 6/4

DOMINANT LITHOLOGY MARLY FORAM NANNOFOSSIL CHALK

Light yellowish brown (10YR 6/4)

Firm to hard, drilling fracture

Massive bedding

Numerous burrows (elliptical parallel bedding plane) ⊂⊃ surrounded by 10YR 8/3 (light). Faint mottling – bioturbation

SMEAR SLIDE SUMMARY (%):

	1, 32	3, 80
	M	D
Composition:		
Feldspar	Tr	Tr
Heavy minerals	Tr	Tr
Clay	45	50
Volcanic glass	Tr	–
Micronodules	Tr	1
Zeolite	Tr	Tr
Carbonate unspec.	2	2
Foraminifers	10	10
Calc. nannofossils	40	33
Diatoms		Tr
Radiolarians	1	Tr
Dolomite	Tr	–

Carbonate Bomb (%):
3, 45 = 45

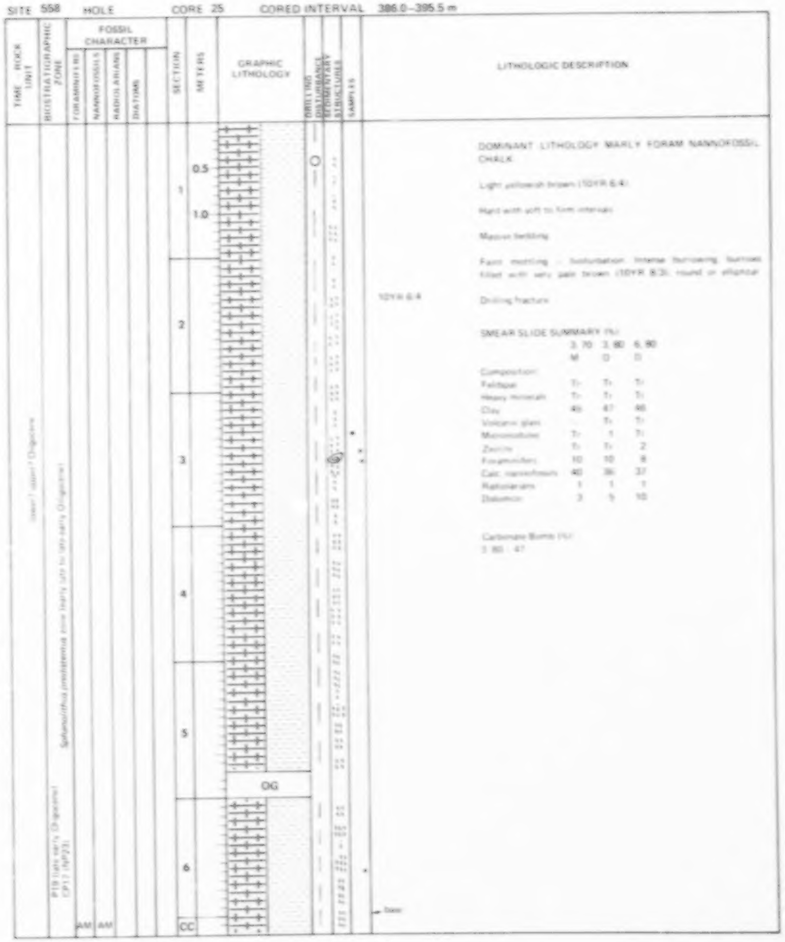
SITE 558 HOLE CORE 25 CORED INTERVAL 386.0–395.5 m
TIME - ROCK UNIT
BIOSTRATIGRAPHIC ZONE
FOSSIL CHARACTER
FORAMINIFERS
NANNOFOSSILS
RADIOLARIANS
DIATOMS
SECTION
METERS
GRAPHIC LITHOLOGY
DRILLING DISTURBANCE
SEDIMENTARY STRUCTURES
SAMPLES
LITHOLOGIC DESCRIPTION
lower? upper? Oligocene
Sphenolithus predistentus zone (early late to late early Oligocene)
P19 (late early Oligocene)
CP17 (NP23)
AM AM
1
2
3
4
5
6
CC
0.5
1.0
OG
10YR 6/4
Slate

DOMINANT LITHOLOGY MARLY FORAM NANNOFOSSIL CHALK

Light yellowish brown (10YR 6/4)

Hard with soft to firm intervals

Massive bedding

Faint mottling – bioturbation. Intense burrowing, burrows filled with very pale brown (10YR 8/3), round or elliptical

Drilling fracture

SMEAR SLIDE SUMMARY (%):

	3, 70	3, 80	6, 80
	M	D	D
Composition:			
Feldspar	Tr	Tr	Tr
Heavy minerals	Tr	Tr	Tr
Clay	45	47	46
Volcanic glass	–	Tr	Tr
Micronodules	Tr	1	Tr
Zeolite	Tr	Tr	2
Foraminifers	10	10	8
Calc. nannofossils	40	36	37
Radiolarians	1	1	1
Dolomite	3	5	10

Carbonate Bomb (%):
3, 80 = 47

SITE 558 HOLE CORE 26 CORED INTERVAL 395.5–405.0 m

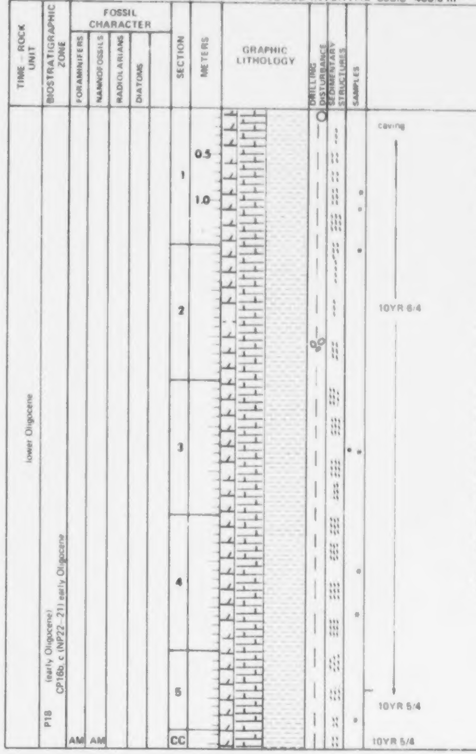
TIME – ROCK UNIT
BIOSTRATIGRAPHIC ZONE
FOSSIL CHARACTER
FORAMINIFERS
NANNOFOSSILS
RADIOLARIANS
DIATOMS
SECTION
METERS
GRAPHIC LITHOLOGY
DRILLING DISTURBANCE
SEDIMENTARY STRUCTURES
SAMPLES
lower Oligocene
P18
(early Oligocene)
CP16b, c (NP22–21) early Oligocene
AM
AM
1
2
3
4
5
CC
0.5
1.0
caving
10YR 6/4
10YR 5/4
10YR 5/4

LITHOLOGIC DESCRIPTION

DOMINANT LITHOLOGY MARLY DOLOMITIC NANNO CHALK

Brown (10YR 6/4 to 10YR 5/4) becoming darker towards base of core

Darker (10YR 5/4) at bottom of Section 5

Firm to hard

Intense bioturbation, massive bedding

Drilling fracture

The presence of authigenic dolomite rhombs increases in this core from the small percentages seen in Core 25

SMEAR SLIDE SUMMARY (%)

	1, 100 D	2, 5 D	3, 80 D	4, 60 D	4, 110	5, 75
Composition:						
Feldspar	Tr	Tr	Tr	Tr	Tr?	Tr
Heavy minerals	Tr	Tr	Tr	Tr	Tr	–
Clay	50	51	49	50	50	51
Volcanic glass	Tr	Tr	Tr	–	–	Tr
Palagonite	–	–	Tr	–	–	–
Micronodules	1	Tr	Tr	1	1	Tr
Carbonate unspec	1	1	1	2	1	–
Foraminifers	2	5	2	2	3	2
Calc. nannofossils	20	20	15	20	0	7
Radiolarians	?	2	2	Tr	Tr	1
Silicoflagellates	–	–	–	Tr	Tr	–
Dolomite	25	20	30	25	25	10

Carbonate Bomb (%)
3, 79 = 47

SITE 558 HOLE CORE 27 CORED INTERVAL 405.0–414.5 m

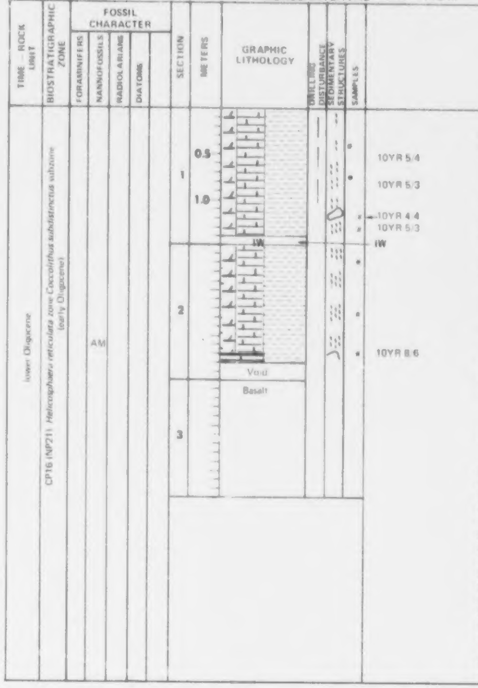
TIME – ROCK UNIT
BIOSTRATIGRAPHIC ZONE
FOSSIL CHARACTER
FORAMINIFERS
NANNOFOSSILS
RADIOLARIANS
DIATOMS
SECTION
METERS
GRAPHIC LITHOLOGY
DRILLING DISTURBANCE
SEDIMENTARY STRUCTURES
SAMPLES
lower Oligocene
CP16 (NP21) Helicosphaera reticulata zone Coccolithus subdistinctus subzone (early Oligocene)
AM
1
2
3
0.5
1.0
IW
Void
Basalt
10YR 5/4
10YR 5/3
10YR 4/4
10YR 5/3
IW
10YR 8/6

LITHOLOGIC DESCRIPTION

DOMINANT LITHOLOGY MARLY DOLOMITIC NANNO CHALK

Firm to hard

Brown (10YR 5/4) to yellowish brown (10YR 5/3)

Mottled and bioturbated throughout, with dark specks in bioturbated sections

Bioturbation increases downward and color also darkens from 10YR 5/4 to 10YR 5/6

Intense bioturbation in Section 2

Authigenic dolomite rhombs present throughout (15–20%)

Minor lithology
Marly nannofossil limestone

Pale yellowish brown, as broken pieces just above basalt. It is altered limestone

SMEAR SLIDE SUMMARY (%)

	1, 40 D	1, 120 M	1, 135 D	2, 20	2, 80	2, 120 D
Composition:						
Feldspar	Tr	Tr	Tr	Tr	Tr	Tr
Heavy minerals	Tr	Tr	Tr	Tr	Tr	Tr
Clay	48	57	56	56	56	56
Volcanic glass	–	Tr	–	–	Tr	–
Palagonite	–	Tr	Tr	Tr	–	1
Micronodules	1	1	1	Tr	Tr	Tr
Zeolite	Tr	–	–	Tr	–	Tr
Foraminifers	1	1	1	2	2	2
Calc. nannofossils	25	20	20	20	20	30
Radiolarians	–	–	1	1	1	Tr
Sponge spicules	–	Tr	–	–	–	–
Silicoflagellates	–	–	–	–	Tr	–
Dolomite	15	20	20	20	20	10

Carbonate Bomb (%):
1, 78 = 41

READEX FICHE best copy available

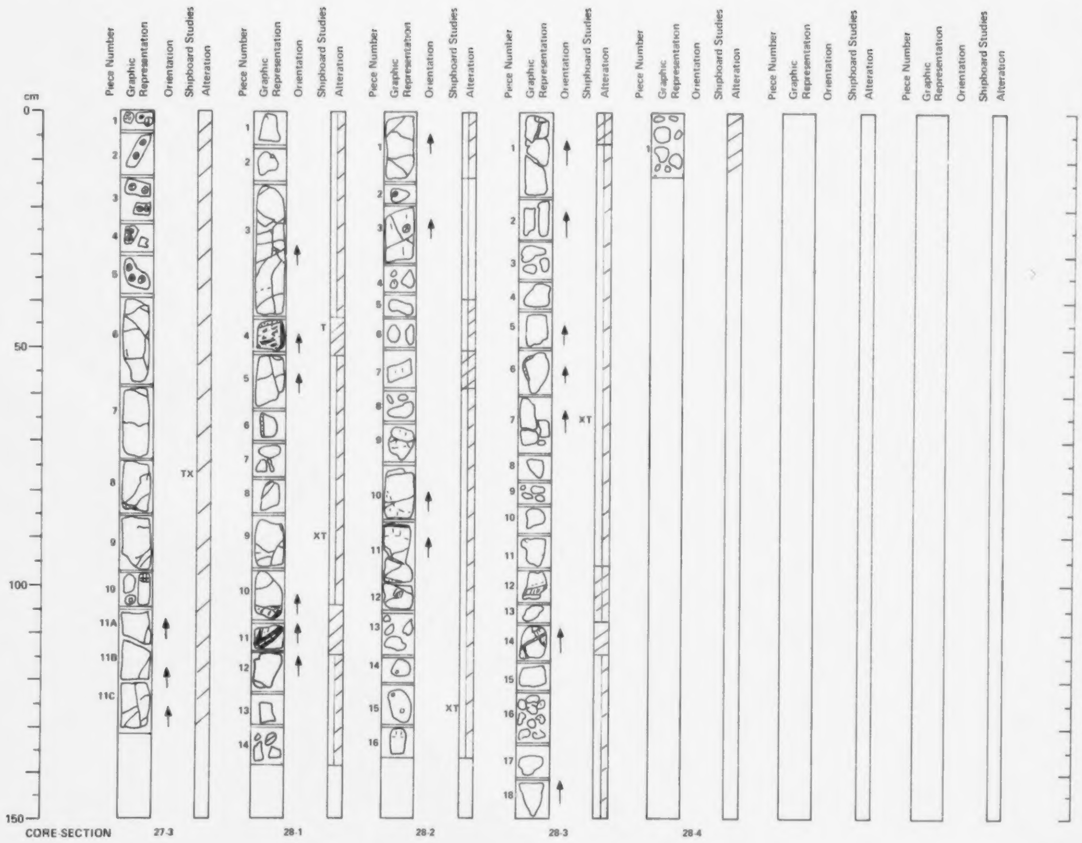

SITE 558, CORE 27 Depth 405.0–414.5 m

SECTION 3

0–105 cm: The pieces in the interval are of questionable order.

Pieces 1–5: Variolitic texture. The varioles range from 1–6 mm in diameter. The varioles range from dark brown in the center to light brown at the edges. Some pockets of devitrified glass (gray) lie between the varioles.

Piece 6–9: Fine grained dark gray (2.5YR N4/0) aphyric basalt. There are many irregular and undulating fractures filled with calcite. Alteration is more extensive in the basalt along the fractures. Vesicles (< 1 mm) are rare and filled.

Piece 10: Badly altered aphyric basalt with calcite filled fractures. One edge has zoned calcite sedimentation: 1) brick red fine grained calcite with mixed layer clay mineral (XRD determinates), 2) transparent sparry calcite, and 3) fine grained white calcite.

Piece 11: Has the same description as Pieces 6–9 of this section (3).

SITE 558, CORE 28 Depth 414.5–423.5 m

SECTION 1

HIGHLY FRACTURED APHYRIC PILLOW BASALTS

Pieces 1–3: Fine grained aphyric basalt; color ranges from dark gray (7.5YR N4/0) in Pieces 1 and 2 to gray (7.5YR N5/0) in Piece 3. Piece 3 appears strongly fractured — some small veins are filled with calcite cement. Vesicles are rare; in Piece 2 are some round vesicles filled with clay (size ~ 2.0–2.5 mm) some are empty (size <0.5 mm).

Piece 4: Hyaloclastite interpillow breccia (basalt-glass breccia). Elongated glass pieces (size 1–30 mm) are aligned horizontally and are fresh. Only their rims and some very small breccia pieces are altered to brown clay. One vertical oriented glass piece shows multiple glass rinds separated from one another by clay. At the top of this piece occurs transparent calcite cement. Matrix of breccia is limestone.

Pieces 5–14: Fine-grained aphyric basalt, color gray (7.5YR N5/0). Fractures are common. Vesicles are very rare and sometimes filled with clay. Piece 9 shows transition from vitric basalt at the top to tachylitic(?) devitrified basalt. At the bottom of Pieces 10 and 11 occur pillow rinds of fresh glass – the rind of Piece 11 is a multiple one, the glass is separated by clay and calcite.

SECTION 2

FRACTURED APHYRIC PILLOW BASALTS

Light gray (7.5YR 6/0), mottled brown alteration along some broken and fractured surfaces. Scattered vesicles partially filled by white or gray(?) zeolites.

16–36 and 82–88 cm: mottled gray–light brown (10YR 6/4) variolitic basalt (close to pillow margins).

Thin Section at 122–124 cm: Aphyric basalt, intersertal texture, fine grained, 35% plagioclase (0.1–0.4 mm) skeletal to accicular, 20% granular clinopyroxene (0.01–0.05 mm), 3% granular magnetite (0.01–0.04 mm), 5% devitrified glass, 36% mesostasis, 1% vesicles.

SECTION 3

FRACTURED APHYRIC BASALT (PILLOWS?)

Light gray (7.5YR N6/0). Calcite veins occasionally found; slight alteration to light gray brown (7.5YR N6/2).

51–59 cm: Slightly altered basalt, slightly brown–gray in color. Small plagioclase crystals 1–2 mm diameter visible (7.5YR N6/2). Some dark patches noted, identification uncertain.

Pieces 3, 9, and 16: Actually collections of small pebble-sized basalt fragments (Similar to Sections 1 and 2).

Thin Section at 61–63 cm: Aphyric to sparsely phyric hyalopilitic, tachylitic basalt.

SECTION 4

FRACTURED APHYRIC BASALT

Weathered brown along fractures.

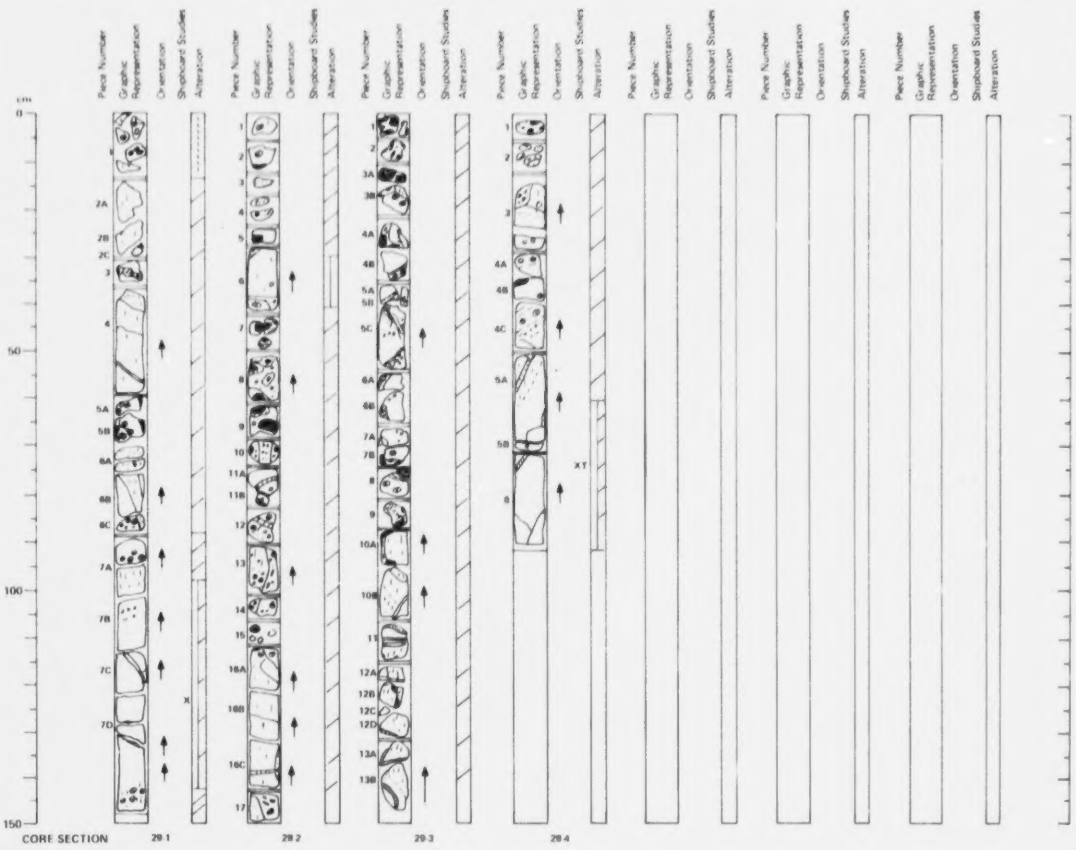
cm
0
50
100
150
CORE SECTION
Piece Number
Graphic Representation
Orientation
Shipboard Studies
Alteration
1
2A
2B
2C
3
4
5A
5B
6A
6B
6C
7A
7B
7C
7D
X
1
2
3
4
5
6
7
8
9
10
11A
11B
12
13
14
15
16A
16B
16C
17
1
2
3A
3B
4A
4B
5A
5B
5C
6A
6B
7A
7B
8
9
10A
10B
11
12A
12B
12C
12D
13A
13B
1
2
3
4A
4B
4C
5A
5B
6
XT
29-1
29-2
29-3
29-4

SITE 558, CORE 29 Depth 423.5–432.5 m

SECTION 1

APHYRIC PILLOW BASALT

0–13 cm: Strongly altered variolitic basalt.

13–87 cm: Moderately altered variolitic basalt with limestone fillings in fractures (▬). Fine grained brownish gray (2.5Y 5/2).

87–146 cm: Single pillow with gray brown (10YR 5/2) variolitic edges (top 89–92 cm, bottom 140–148 cm); fine grained, gray (1.5Y N5).

94–96 cm: ~5% vesicles filled with black clay.

SECTION 2

APHYRIC PILLOW BASALT AND INTERPILLOW BRECCIA

0–110 and 143–149 cm: Interpillow breccia.

1) Aphanitic, aphyric black basalt clasts: sparsely vesicular, altered gray green at edges. Sometimes grading into 2) (unshaded).

2) Fine grained aphyric basalt – medium gray (2.5Y 5/0) (pillow interior), generally altered mottled gray and light brown (10YR 6/2) (shown by vertical dashes).

3) Smaller (<2 cm) angular glass fragments, largely palagonitized, but most with fresh centers.

4) Limestone matrix (dotted), buff colored (7.5YR 7/2) lithified limestone with small calcite veins (diagonally hatched).

110–140 cm: Pillow of dark gray (5Y 4/0) aphyric basalt with black aphanitic upper margin (minor glass) and narrow (4 cm) gray brown (10YR 4/2) variolitic zone.

SECTION 3

PILLOW BASALT FLOW WITH INTERSPERSED LIMESTONE CEMENTED INTERPILLOW BRECCIA

As in Sections 1 and 2 (full description Section 2).

42–51 cm: Piece 5C: Aphyric basalt with green (10G N8/2) discolored limestones matrix, glass fragments set within. Vesicles filled with calcite, irregular black patches interspersed.

54–63 cm: Aphyric basalt with a lighter shade of green than above.

SECTION 4

0–32 cm: Interpillow breccia with sparry calcite cement.

33–88 cm: Single aphyric fine grained basalt pillow as in Section 2.

20–27 cm: Occasional large (5–10 mm) calcite filled vesicles.

43–48 cm: Vesicular (~5%) zone inside variolitic zone. Vesicles (1–2 mm) either unfilled or calcite filled.

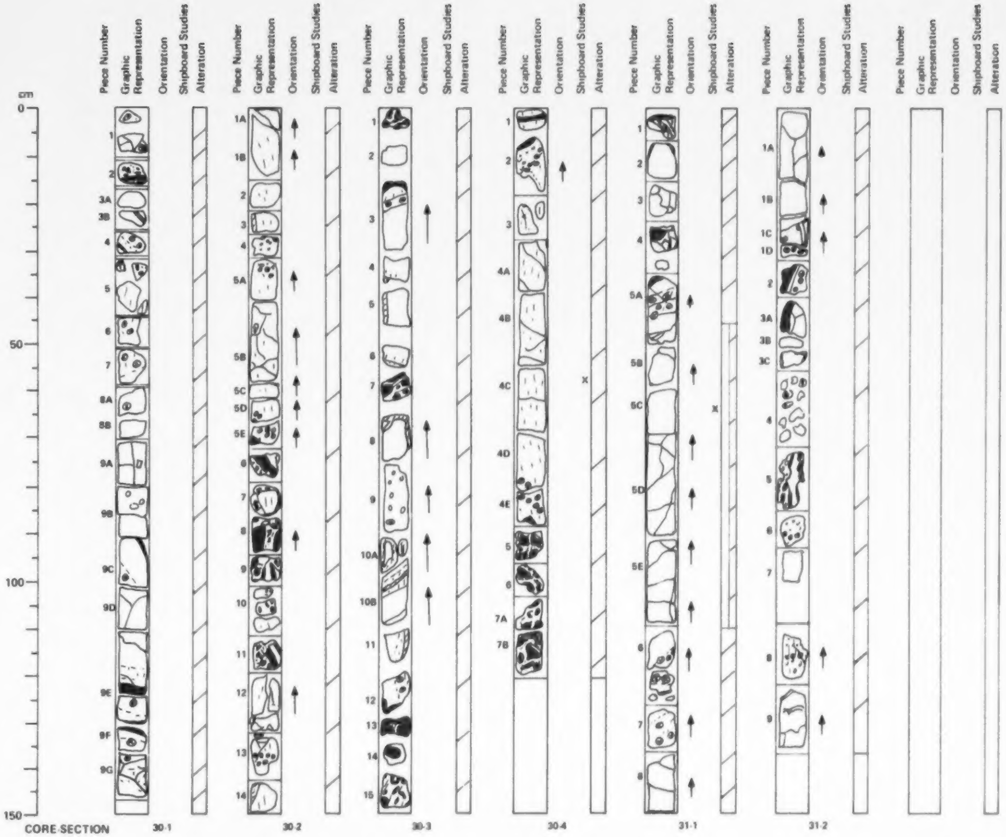

SITE 558, CORE 30 Depth 432.5–441.5 m

SECTION 1

APHYRIC PILLOW BASALT AND INTERPILLOW BRECCIA

0–64 cm: Black aphyric aphanitic basalt grading to grayish brown (10YR 6/2) variolitic basalt forming broken pillow fragments. Matrix of smaller (<2 cm) angular glass fragments largely palagonitized cemented by clear sparry calcite.

64–145 cm: Fine grained aphyric basalt, dark gray (2.5Y 4/0) altered to gray brown (10YR 5/2) along fractures. Pillow margins grade through variolitic, and aphanitic zones to glass where shown. Irregular, calcite filled(?, vesicles form ~5% of rock from 75–86 cm, scattered elsewhere. Needles of zeolite(?) in calcite.

Note slight darkening (2.5Y 5/0–2.5Y 4/0) of fine grained basalt from Core 29 to Core 30.

SECTION 2

APHYRIC PILLOW BASALT

0–25 cm: Medium gray (7.5YR N5), fine grained basalt with calcite in fractures.

33–77 cm: Medium brownish gray (2.5Y N6) single pillow with yellow brown (2.5Y 6/2) variolitic edges (top 33–38 cm, bottom 66–70 cm) and 5% round empty vesicles (up to 2 mm) at top and calcite in fractures and irregular calcite and green clay filled vesicles (up to 8 mm).

72–79 cm: Interpillow breccia in calcite matrix. Many glass angular clasts, some altered to yellow brown and green clays.

79–146 cm: Fine grained grading down through variolitic zone (136–138 cm) into black aphanitic zone (138–146 cm) with calcite in fractures.

SECTION 3

APHYRIC PILLOW BASALTS AND INTERPILLOW GLASS/CALCITE BRECCIA

As in Sections 1 and 2. Pillows dark gray (2.5Y N4) in color, grading to gray brown (10YR 5/2) along fractures to black aphanitic aphyric basalt rimmed with glass.

0–20 cm: Glass/calcite breccia (sparry calcite matrix) 2 mm to 1 cm diameter glass fragments.

20–55 cm (pillow unit): glass to variolitic aphanitic aphyric black basalt to variolitic, dark gray brown to gray aphyric basalt, inverse sequence on bottom.

64–122 cm: Single pillow unit: sequence same as for 20–55 cm pillow.

64–88 cm: Irregular vesicles, majority of which appear empty near top of segment to mostly calcite and/or clay filled.

90–120 cm: Calcite rinds on aphyric basalts get thicker and more involved.

120–125 cm: Aphyric basalt grades through variolitic texture to glassy bottom.

125–150 cm: Glass/calcite breccia as in 0–20 cm, fragments are larger, some up to ~4 cm in length.

SECTION 4

APHYRIC PILLOW BASALT

0–5 cm: Glass rim with calcite followed by aphanitic black basalt.

5–30 cm: Glass rim to aphanitic black basalt grading into fine grained medium gray (2.5Y N6) with empty vesicles in aphanitic zone and calcite filled vesicles in fine grained zone.

30–106 cm: Single pillow with no top and variolitic lower edge (79–86 cm).

106–120 cm: Interpillow breccia — fresh glass clasts in calcite matrix with rims altered to yellow brown clay.

SITE 558, CORE 31 Depth 441.5–450.5 m

SECTION 1

Section comprises aphyric basalt, color dark gray (2.5Y N4), thin mostly calcite filled fractures are common.

Fresh glass in Pieces 1, 2, 4, 5A, and 6 partly altered to palagonite.

Variolitic texture in Pieces 2, 3, 5A, and 6. Variolites are < 2 mm. Empty round vesicles occur scattered throughout Pieces 2–4 (size < 2 mm). Round vesicles in Pieces 7 and 8 are filled with calcite and clay (size < 2 mm). One large elongated vesicle occurs at the bottom of Piece 8, filled half with green clay and half with calcite (size ~20 × 3 mm). Piece 5–6 is a separated pillow with chilled rinds at the top and bottom. The amount of vesicles decreases downward.

SECTION 2

APHYRIC PILLOW BASALT

0–30 cm: Bottom part of single pillow, medium gray (2.5Y N6), fine grained with medium yellow brown (10YR 6/2) very variolitic lower edge (26–28 cm) and calcite in fractures and in irregular vesicles (1%).

30–73 cm: Isolated pieces of pillow basalt. Piece 2 with variolitic edge (36–37 cm) and Piece 3A with glass rim in calcite matrix.

73–85 cm: Interpillow breccia fresh glass clasts (with yellow/orange rims) in calcite matrix and one large (2 cm) cavity with drusy calcite.

85–133 cm: More isolated pieces of pillow basalt as in 30–73 cm. Piece 6 has variolitic edge at 88–90 cm. Piece 8 has variolitic edge at 111–116 cm, plus empty vesicles (up to 4 mm) below variolitic edge and calcite filled vesicles in interior of pillow.

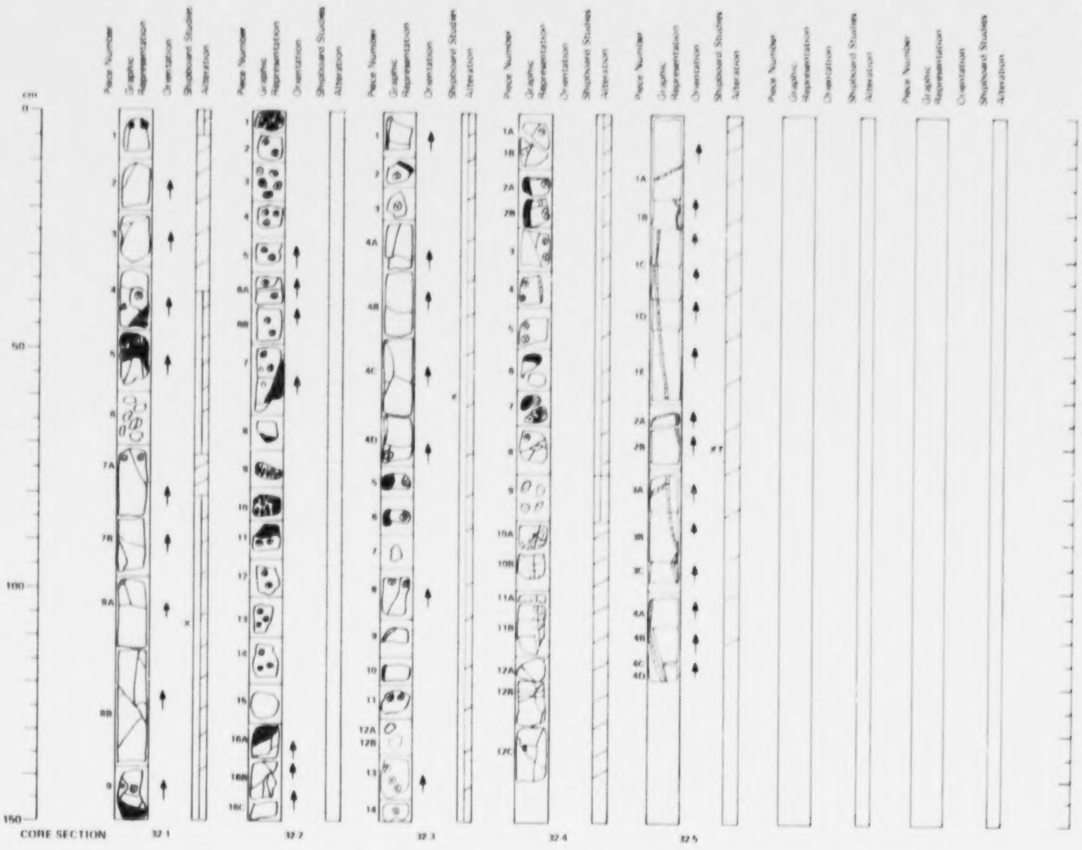

SITE 558 CORE 32 Depth 450.5–459.5 m

SECTION 1

Fresh to moderately altered aphyric pillow basalt; color dark gray (2.5Y N4/0); chilled glass rinds occur in Pieces 4, 5, and 9; close to these rinds to the interior of pillows occurs variolitic transition from vitric to fine grained crystallized basalt.

Vesicles are common and partly round (size <2 mm), partly irregular shaped (size <8 mm). In the interior of pillow (Piece 7B to upper part of Piece 8B) vesicles are rare. Vesicle filled with calcite and clay.

Fractures and veins are filled with calcite.

SECTION 2

Piece 1 is part of a chill margin with calcite veins.

Pieces 2–15 are variolitic basalt, dark gray (2.5Y N4/0). Varioles are brown.

Pieces 1, 7, 8, 9, 10, and 16A has chilled margins.

Pieces 9 and 10 have calcite between broken pieces of glass.

Pieces 16A, B, and C are fine-grained aphyric gray basalt with many calcite filled fractures.

<1 mm calcite filled round vesicles (2%) occur in Pieces 6, 7, and 12.

<1 mm unfilled round vesicles (2%) occur in Pieces 2, 3, 4, 5, 8, 12, 14, and 15.

SECTION 3

Fine grained aphyric gray (7.5YR N5/0) basalt. Round vesicles up to 3.5 mm; irregular vesicles are rare (<5 mm).

Fresh glass (chilled pillow margins) in Pieces 2, 5, and 6 always accompanied by variolitic transition zone.

The whole section is strongly fractured; veins are filled with calcite ([illegible]).

SECTION 4

0–58 cm and 65–75 cm: Pieces 1–8: Aphyric, variolitic pillow basalt with chilled rinds in Pieces 2 and 6; color dark gray (2.5YR N4/0); vesicles are common and round and empty (size <1.5 mm).

58–64 cm: Piece 7: Hyaloclastite (calcite cemented glass breccia).

75–140 cm: Pieces 9–12: Fine grained aphyric basalt, color gray (2.5YR N5/0); vesicles are rare, round, and filled (with clay?). This basalt is more altered than the upper one (in Pieces 1–8). Fractures are cemented with calcite and show partly altered zone beside them.

At 75 cm: Break? – end pillow lava.

SECTION 5

Single flow (continues from Section 4).

Massive fine grained aphyric basalt, color gray (2.5YR N5/0); shows no vesicles; fractures and veins are filled with calcite ([illegible]).

Frequent fine traces (healed fractures?) altered brown and fine mottled brown alteration of mesostasis(?).

Thin Section at 66–70 cm: Hyaloclastic aphyric basalt.

120 cm: End of flow.

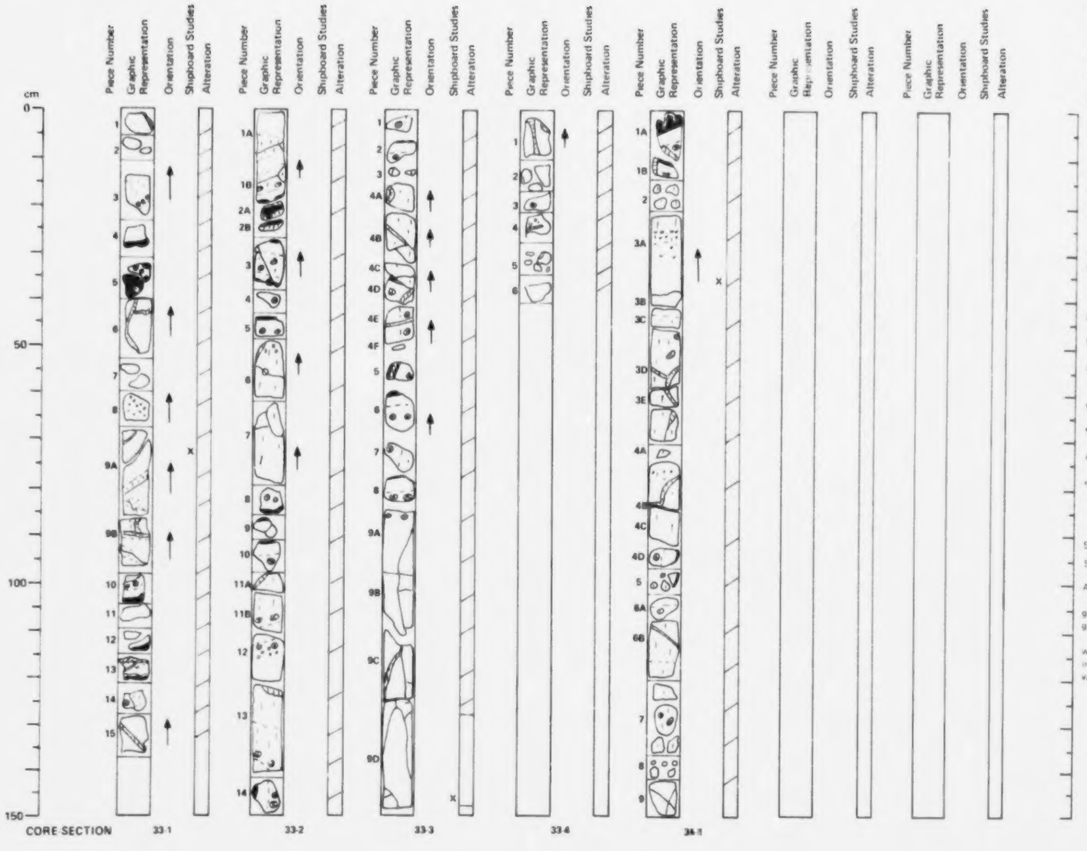

SITE 558, CORE 33 Depth 459.5–468.5 m

SECTION 1

APHYRIC PILLOW BASALT

0–32 cm: Light gray brown (10YR 6/2) aphyric basalt grading through variolitic basalt to black aphanitic aphyric basalt rimmed with glass (25–29 cm).

32–38 cm: Large glass fragments (3 mm to 4 cm long) in calcite matrix = breccia. Less cement (10 volume %) lots of glass.

59–103 cm: Pillow unit, glass at top, grading into black aphanitic aphyric basalt, then dark gray (2.5Y 4/0) aphyric basalt; bottom inverse sequence of top. Irregular vesicles throughout unit, mainly empty above variolitic zone, calcite filled below this zone through aphyric basalt.

104–113 cm: Pieces of dark gray aphyric basalt. One piece within Piece 12 has a glass rind (devitrified).

115–135 cm: Pillow unit, only top half, down through sequence to aphyric basalt.

SECTION 2

APHYRIC PILLOW BASALT

Sequence consisting of:

1) Fine grained aphyric basalt (pillow interiors), generally weathered dark grayish brown (10YR 4/2) with occasional large (5 mm), irregular calcite filled vesicles. Small (1 mm) vesicles up to 5% may be concentrated adjacent to variolitic zones. These are filled by calcite or part filled by dark bluish gray clay (shown by vertical dashes).

2) Variolitic pale brown (10YR 6/3) basalt (crosses in circles).

3) Black aphanitic basalt adjacent to pillow rims (white).

4) Fresh basalt glass (black) generally veined by, or forming angular fragments within white calcite. Moderately palagonitized around edges (calcite diagonally hatched).

SECTION 3

APHYRIC PILLOW BASALT SEQUENCE CONTINUED

0–76 cm: Lithology and symbols as for Section 2.

76–147 cm: Single aphyric pillow. Calcite veins as shown (diagonal hatch). Calcite present also along all fractures. Lithologies as for Section 2 except fresh fine grained aphyric dark gray (7.5YR N4) basalt from 118–147 cm.

SECTION 4

APHYRIC PILLOW BASALT

Dark gray (2.5Y 4/0). Calcite rims edges of most pieces, several are veined. Vesicles scattered, <1 mm in diameter.

16–20 cm: Piece of large (diameter ~8 mm) vesicle, calcite filled.

30–34 cm: Multiple pieces of dark gray aphyric basalt.

SITE 558, CORE 34 Depth 468.5–477.5 m

SECTION 1

APHYRIC PILLOW BASALT SEQUENCE

0–13 cm, Pieces 1A, B; 91–94 cm, Piece 4D; 103–106 cm, Piece 6A: Aphyric basalt, black, aphanitic with glass rims as shown. Grading to: Variolitic basalt, light brownish gray (10YR 6/2), moving inwards from pillow margins.

15–89 and 106–150 cm: Aphyric basalt, fine grained, dark gray (7.5YR N4) grading to brown (7.5YR 4/4) with alteration, especially adjacent to fractures. This rock type represents pillow interiors. Vesicles: scattered, irregular ~5 mm calcite filled. Small (<1 mm) bluish gray or green clay filled concentrated (up to 5%) just inside variolitic zones.

0–10, 52–70, and 107–115 cm: Calcite veinlets (diagonal hatched).

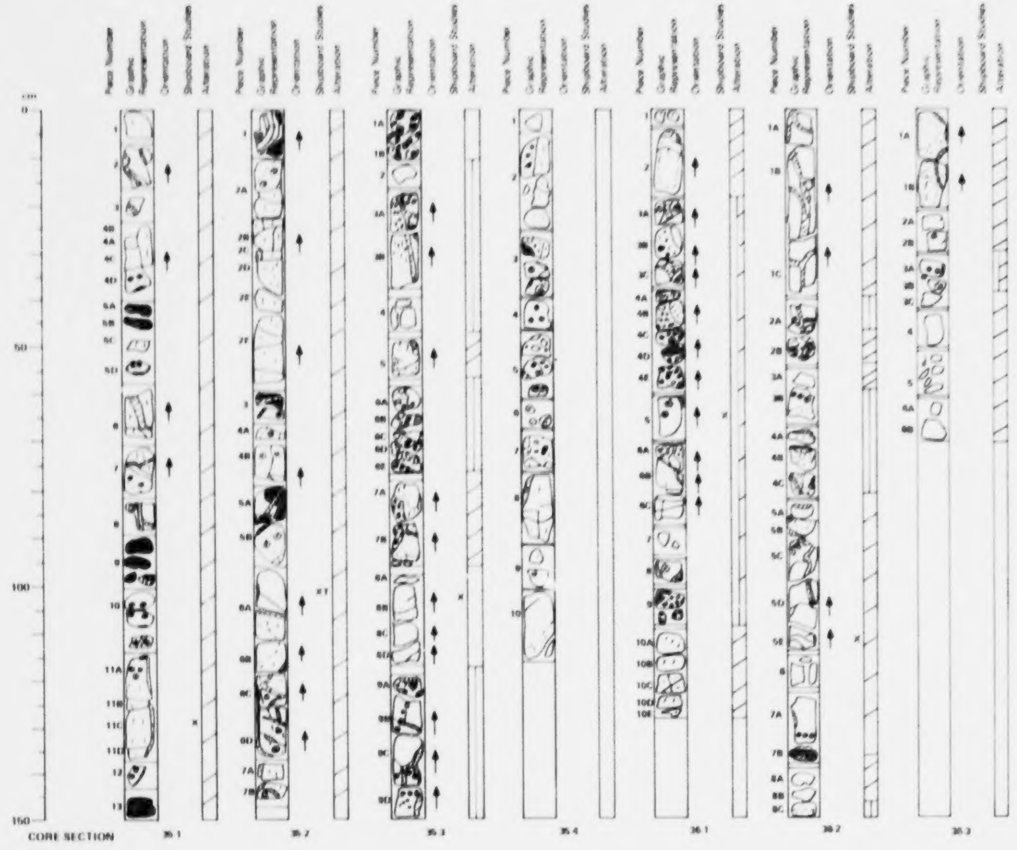

SITE 558 CORE 35 Depth 477.5–486.5 m

SECTION 1

APHYRIC PILLOW BASALT SEQUENCE

Lithologies and symbols as in Core 34, Section 1.

0–33, 58–76, and 119–135 cm: Aphyric basalt, fine-grained, altered grayish brown (10YR 5/2).

33–38, 54–57, 77–87, 100–111, and 137–147 cm: Aphyric basalt, black, aphanitic grading to variolitic basalt.

41–46, 82–98, and 144–148 cm: Aphyric black basalt glass, moderately palagonitized and veined by calcite.

Calcite veins throughout as shown and abundance is greater than in previous cores.

SECTION 2

APHYRIC PILLOW BASALT SEQUENCE

Lithology and symbols as for Core 34, Section 1.

8–58 and 94–122 cm: Fine grained basalt as in Section 1. Fresh(?) only at 33–37 and 107–115 cm.

0–20, 62–66, and 120–145 cm: Aphanitic and variolitic basalt as in Section 1.

5–10, 60–64, 80–88, and 125–130 cm: Basalt glass moderately altered to palagonite and veined by calcite.

SECTION 3

APHYRIC PILLOW BASALT SEQUENCE

5–10 cm (Pieces 1A and B): Interpillow breccia of fresh glass.

80–90 cm (Pieces 7A and B): Clasts in calcite matrix.

58–77 cm (Pieces 6A–E): Interpillow breccia of altered light brownish gray (10YR 6/2) basalt clasts and black aphanitic basalt clasts in calcite matrix, some with fine bits of glass and basalt ground up in it (Pieces 6A–C).

17–58 cm (Pieces 2–5) and 77–117 cm (Pieces 7–8): Pieces of fine grained pillows with no variolitic edges (except at 18–25 cm) and 2% (<3 mm) rounded vesicles, some filled with clay, some with calcite. Fresher parts are gray (7.5YR N5) and more altered parts ([illegible]) are light brownish gray (10YR 6/2).

117–125 cm (Piece 9A): Clasts of fresh and altered glass with calcite between.

126–140 cm: Single pillow of fine grained highly altered grayish brown (10YR 5/2) basalt with variolitic edge top (122–129 cm) and bottom (139–140 cm) grading into black aphanitic basalt.

140–150 cm: Top of second pillow with black aphanitic basalt grading through variolitic edge to same altered basalt interior. Both pillows have calcite in fractures and Piece 9D has 1% (<2 mm) rounded and irregular vesicles filled with calcite.

SECTION 4

PILLOW(?) BRECCIA, HYALOCLASTITE MATRIX

Basalt lithologies as in Core 34, Section 1 and Core 35, Section 1.

0–24, 40–45, and 77–113 cm: Aphyric basalt, fine grained dark gray (7.5YR N4) grading to brown (7.5YR 4/4) with alteration (fresh only from 102–108 cm).

5–12 and 26–82 cm: Hyaloclastite breccia. Angular to subrounded clasts of variably altered aphanitic to variolitic basalt (< 5 cm) and generally completely palagonitized glass (< 1 cm). Matrix dominated by finely ground basaltic material with subordinate calcite.

SITE 558 CORE 36 Depth 486.5–495.5 m

SECTION 1

PILLOW BRECCIA, HYALOCLASTITE MATRIX

Basalt lithologies as in Core 34, Section 1 and Core 35, Section 1.

0–18 cm: Aphyric, fine grained basalt, color gray (2.5Y N5/0) to light brownish gray (2.5Y N6/2) in altered parts.

20–108 cm: Hyaloclastite breccia, consisting of angular to subrounded clasts of mostly palagonitized glass (< 30 mm) and aphanitic to variolitic basalt (< 15 cm). Breccia is mostly cemented by calcite, but fine grained matrix of basalt alteration products is also present.

109–127 cm: Aphyric fine grained basalt as in Pieces 1 and 2 (0–18 cm).

SECTION 2

APHYRIC PILLOW BASALT SEQUENCE

Series of isolated pillow pieces as in Section 1.

89–92 cm: 10% large (< 7 mm) irregular vesicles filled with calcite and some (< 1%) light yellowish brown (10YR 6/4) clay. Heavy calcite veining throughout.

SECTION 3

BASALT

1–70 cm: Aphyric, fine grained basalt, color gray (2.5Y N5.0) to light brownish gray (2.5Y N6.2) in altered zones along fractures and veins. Shows no vesicles.

25–38 cm: Aphanitic to variolitic textured basalt, varioles up to 5 mm. Veinlets are filled with calcite cement.

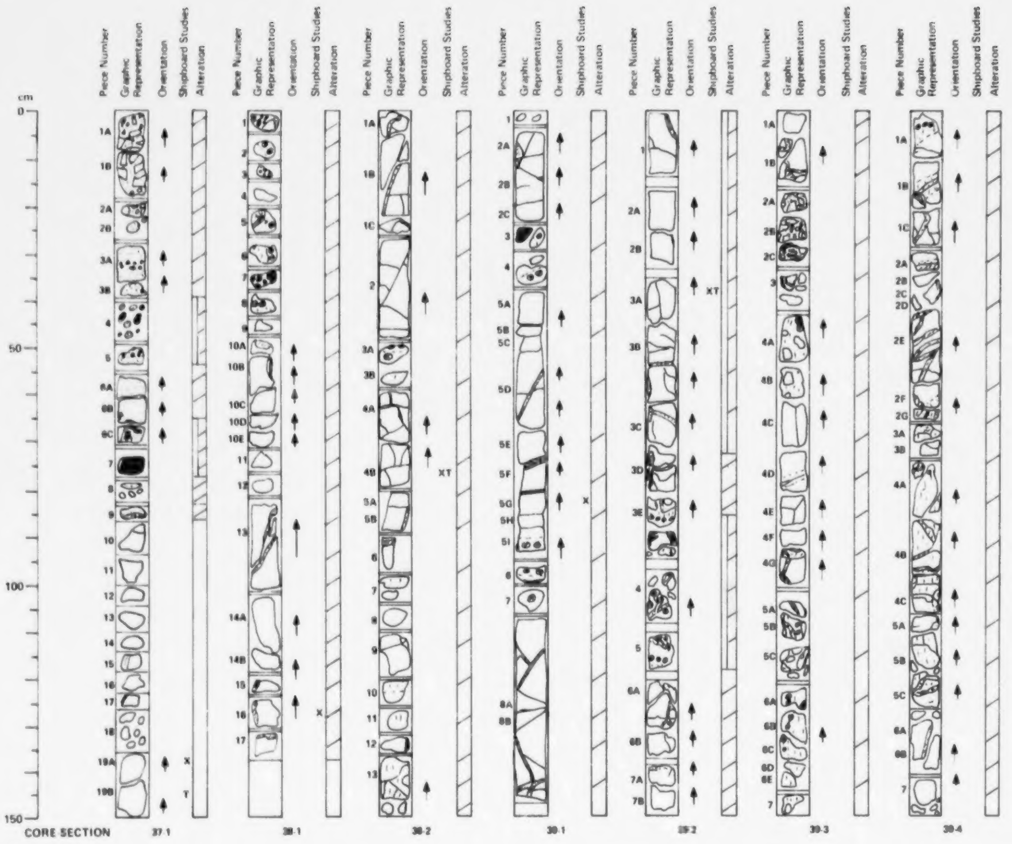

SITE 558, CORE 37 Depth 496.5–504.5 m

SECTION 1

0–82 c Basalt breccia, hyaloclastite and limestone
82–150 cm Basalt

0–18 cm Basalt breccia. Clasts of moderately to badly altered aphyric basalt (size <4 cm), the angular clasts "swim" within a limestone matrix – some cavities are cemented with calcite, color of clasts grayish brown (10YR 5/2)

19–82 cm Limestone, color brownish white (10YR 8/2). Black MnO – dendrites are scattered throughout the sediment, which is partly interlayered by brecciated volcanic glass (hyaloclastite) (See Pieces 3A, 4, 5, 6B, and 6C). The glass is mostly altered to brown clay. Piece 7 (73–76 cm): Clast of drilled basalt glass with clayey alteration along fractures.

83–150 cm Aphyric, fine grained fresh basalt color gray (7.5YR N5/0), vesicles are rare and filled with clay (size <1 mm).

SITE 558, CORE 38 Depth 504.5–509.0 m

SECTION 1

0–48 cm Basalt breccia and pieces of aphanitic basalt/aphyric basalt
48–134 cm Aphyric basalt

0–4, 11–13, and 34–37 cm Basalt breccia. Clasts of aphanitic black (10YR 2.5/1) basalt and glass fragments set in calcite matrix. Aphanitic clasts ~1–2 cm in diameter. Vesicles irregularly scattered, some containing clay. Glass 2 mm–1 cm in diameter, majority of fragments slightly altered to palagonite. Clays observed along glass fractures.

4–11, 13–34, and 37–48 cm Pieces of aphanitic basalt, dark gray (2.5Y N4/0) grading through variolitic texture to light brownish gray (10YR 6/2) altered aphyric basalt to aphyric basalt, gray (10YR 6/1).

48–134 cm Aphyric basalt, gray (2.5Y N5/0). Some pieces are fractured, with calcite in/along the fractures. Calcite rims are observed on some pieces. Vesicles are variable in frequency, some are empty, most are calcite-filled (< 1 mm). Slight weathering to a different gray (10YR 5/1) is patchy and seen along the borders of most pieces.

Boundary of larger pillow unit at 56 cm?

SECTION 2

APHYRIC PILLOW BASALT

New Unit? – large pillows, narrower margins, no breccia, slightly coarser grained

0–150 cm Aphyric basalt, gray (5Y 5/1), fine grained (slightly coarser than overlying unit). Plagioclase laths (~0.5 mm) randomly altered or in radiating clusters altered deep green (~chlorite?). Weathered grayish brown (2.5Y 5/2 to 10YR 5/2) adjacent to fractures. Vesicles 1–2% scattered throughout (<0.5 mm filled mainly with grayish green chlorite(?)).

50–53 and 132–136 cm Pillow rims – glass to black aphanitic basalt to grayish brown variolitic basalt

0–70 cm Minor veinlets and fracture fillings of calcite

SITE 558, CORE 39 Depth 509.0–518.0 m

SECTION 1

PILLOW BASALT

Large pillow unit
0–147 cm Aphyric basalt as in Core 38, Section 2
23–37 and 90–105 cm Pillow margins as in Core 38, Section 2
26 cm Glass altered to dark green clay/chlorite(?) (grayish olive green – 5GY 3/2)
Calcite veinlets as shown, some with pale green (5G 7/2) clay

SECTION 2

PILLOW BASALT

Large pillow units
Aphyric basalt as in Core 38, Section 2 with small plagioclase laths randomly oriented
84–86, 103–106, and 115–117 cm Variolitic pillow margins as in Core 38, Section 2 and Core 39, Section 1
Minor veinlets and fracture fillings of calcite and pale green (5G 7/2) clay
86–88 cm Minor glass clasts
111–114 cm Glass rim of pillow

SECTION 3

APHYRIC PILLOW BASALT

18–43, 107–120, and 143–150 cm Aphanitic black basalt and altered aphyric basalt, interspersed with calcite veins (very small) and greenish alteration product, especially noticeable on surface. Colors same as in Core 38, Section 2 – aphyric basalt gray (5Y 5/1). Weathered and altered grayish brown (2.5Y 5/2 to 10YR 5/2) adjacent to aphanitic regions. Altered product possibly chlorite or smectite. Could imply hydrothermal processes in the region.

0–18, 43–107, and 120–143 cm Aphyric basalt (5Y 5/1) relatively fine grained. Calcite fractures interspersed throughout section; weathered grayish brown (2.5Y 5/2 to 10YR 5/2) along fractures. Patches of pillow rims: black (10YR 2.5/1) aphanitic basalt to grayish brown variolitic basalt. Aphyric basalt pieces set within grayish brown "massive" region (as opposed to variolitic region). Minor veins of calcite, also present in fractures and some rim edges.

107–120 cm olive green (5Y 5/3) alteration product referred to in above description especially evident. Same conclusion reached.

SECTION 4

APHYRIC PILLOW BASALT

Larger unit. Plagioclase laths are finer (~0.1–0.2 mm), aphyric gray (2.5Y N5) basalt with grayish brown (2.5Y N5/2) alteration (indicated ⁚⁚.).

0–3 and 77–79 cm Narrow variolitic edges, zoning to black aphanitic basalt, pillows are larger with narrower edges.

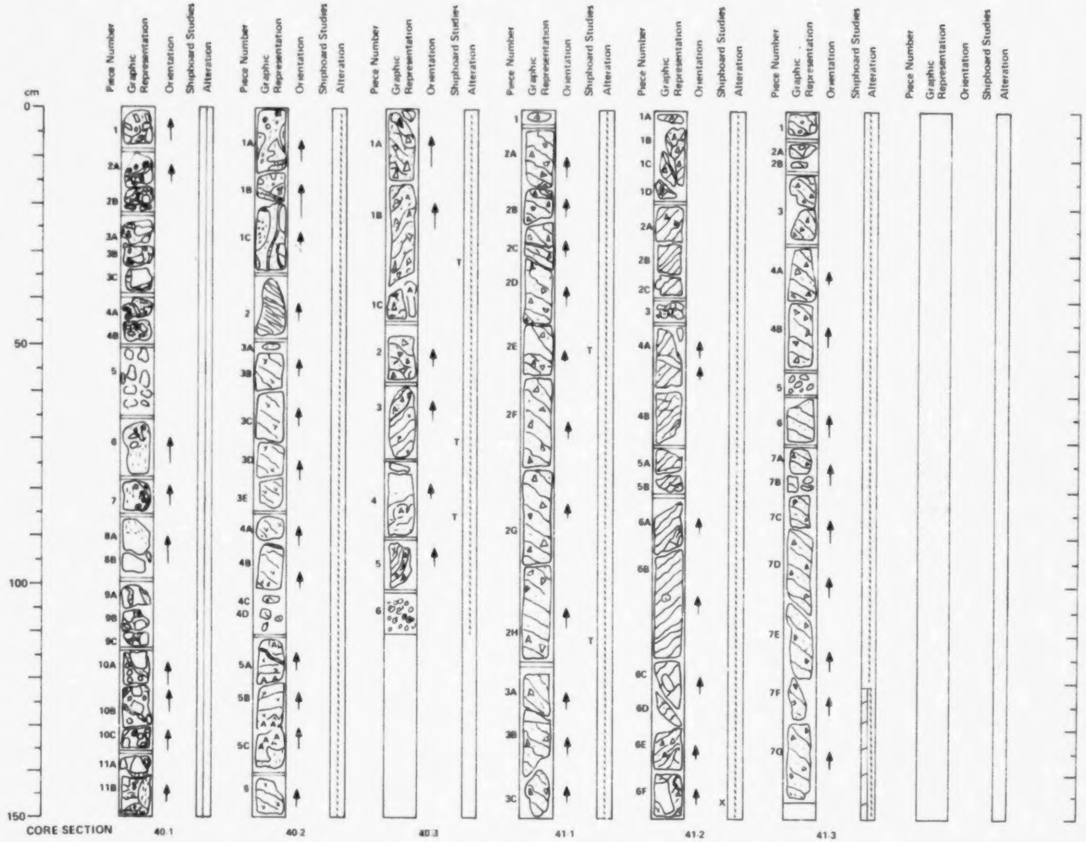

SITE 558 CORE 40 Depth 518.0–527.0 m

SECTION 1

BASALT BRECCIA

0–150 cm Aphyric, grayish brown (10YR 5/2) altered, angular to subrounded basalt clasts.

0–88 cm Matrix is combination of calcite (white) and limestone. Clasts (<10%) are rounded with black aphanitic cores and altered rims.

88–150 cm Matrix is very fine basalt fragments with calcite in fractures. Smaller (<1 cm) clasts generally more altered including 20% reddish yellow (7.5YR 7/8) basalt clasts.

11–14 and 79–86 cm Rounded clasts with variolitic texture (= pillow fragment?)

SECTION 2

0–34 cm Basalt breccia. Aphyric, angular to subrounded basalt clasts of similar lithology to basalts higher in hole. Some have ~5% vesicles, often iron oxide filled. Matrix mainly comminuted basaltic material, lesser calcite.

36–47 cm Mylonite. Soft, clay-rich mylonite. Strongly sheared with alternating, 1–2 cm, irregular bands of yellowish brown (10YR 5/8) and mottled greenish gray (5BG 5/1) with pale green (5G 6/2).

49–150 cm Sheared gabbro. Weakly sheared, altered gabbro, overall dark grayish brown (10YR 4/2). Bronze reddish brown (5YR 5/4) relict pyroxene (5–10%).

126–136 cm Sheared anorthosite vein. Relict coarse grains (1–2 cm) of plagioclase and pale green pyroxene separated by interlaced zones of white finely sheared material. Designated (A). Vein margins are highly irregular. Generally abuts fine grained dark reddish brown (5YR 3/3) material.

SECTION 3

0–66 cm Sheared fault breccia. Polymict breccia composed of recognizable gabbro chunks and basalt clasts. Entire breccia is sheared, rendering individual boundaries undefinable. "Matrix" is brown (10YR 4/3) to yellowish brown (10YR 5/6). Basalt clast are gray (2.5Y N5/0) and range in size from 1 mm to < 1 cm in diameter. Gabbro chunks range from olive (5Y 5/3) to olive gray (5Y 5/2). Clays abound.

37–43 and 82–89 cm Sheared anorthosite. Anorthosite pieces roughly cemented together in a clay (calcite?) matrix then completely sheared. Anorthosite piece at 37–43 cm is more massive and less "fragmented" then at 82–89 cm. They are light gray/gray (2.5Y N6/0).

66–82 and 89–113 cm Sheared gabbro. Gabbro, strongly altered and sheared pyroxenes and relict pyroxenes are observed, 1 mm– < 5 mm diameter. Gabbro ranges from dark grayish brown (10YR 4/2) to reddish brown (5YR 5/4) relict pyroxene patches (5–10% in places) to light reddish brown (5YR 6/5) pyroxenes (5–10%). Clays worked into fabric throughout.

107–113 cm Sheared gabbro rubble. Very small pieces (5 mm–1.5 cm) of sheared gabbro debris, with a large volume % of clays.

SITE 558 CORE 41 Depth 527.0–536.0 m

SECTION 1

0–150 cm Sheared gabbro (breccia). The gabbro clasts are strongly altered to clay minerals and serpentine, which makes up the matrix, too. Altered opx occurs throughout the section (color light to dark brown, size < 5 mm). The clasts (size from ~1 mm up to several centimeters) are colored from light brownish gray (2.5Y 6/2) to brown (10YR 5/3).

43–52 and 125–128 cm Calcite veins, the lower one looks like sheared and shows some greenish clay beside it.

SECTION 2

SHEARED GABBRO (BRECCIA)

Similar to Section 1 but more altered and brecciated as it nears shear zone at 115–150 cm.

0–83 cm Sheared gabbro, more altered and sheared than Core 40, Section 1.

83–150 cm Gabbro breccia grading into shear zone of soft clay rich mylonite with multiple irregular colored bands very dark grayish brown (10YR 3/2), brown (10YR 4/3), gray (10YR 5/1) grading into pale green (5G 6/2) with angular clasts (< 5 mm) of same green. Mylonite zone also contains angular, moderately altered clasts of basalt with gray (7.5YR N/0) cores and narrow brownish yellow (10YR 6/8) altered rims.

143–148 cm Note single larger (7 cm) basalt clast in Piece 6F.

SECTION 3

0–12 cm Polymict breccia. Clasts: Serpentinized, olive (5Y 5/3) colored gabbro (size < 5 mm) and aphyric basalt, fine-grained, color gray (10YR 6/1). Center is fresh, rim is altered to brown clay. One clast shows fresh black glass. Matrix: serpentine and other clays, greenish.

14–60 cm Sheared fault breccia. Parallel textured multicolor layers of different clays (color ranges from dark brown over pale brown to dark green). Calcite within thin fissures is common. Subrounded clasts of serpentinized gabbro are scattered (size < 8 mm).

61–70 cm Larger clast of serpentinized gabbro. Dunite? (no visible opx). Color greenish gray (5GY 5/1).

71–145 cm Sheared gabbro (breccia). Clasts of serpentinized gabbro (size < 1 cm) are separated by fissures and veins, which are usually filled with calcite. In the lower part veinlets are filled with clay and chrysolite (asbestos). Color of rock dark green to dark brown. Orthopyroxene (~5 volume %) is moderately altered (size < 6 mm).

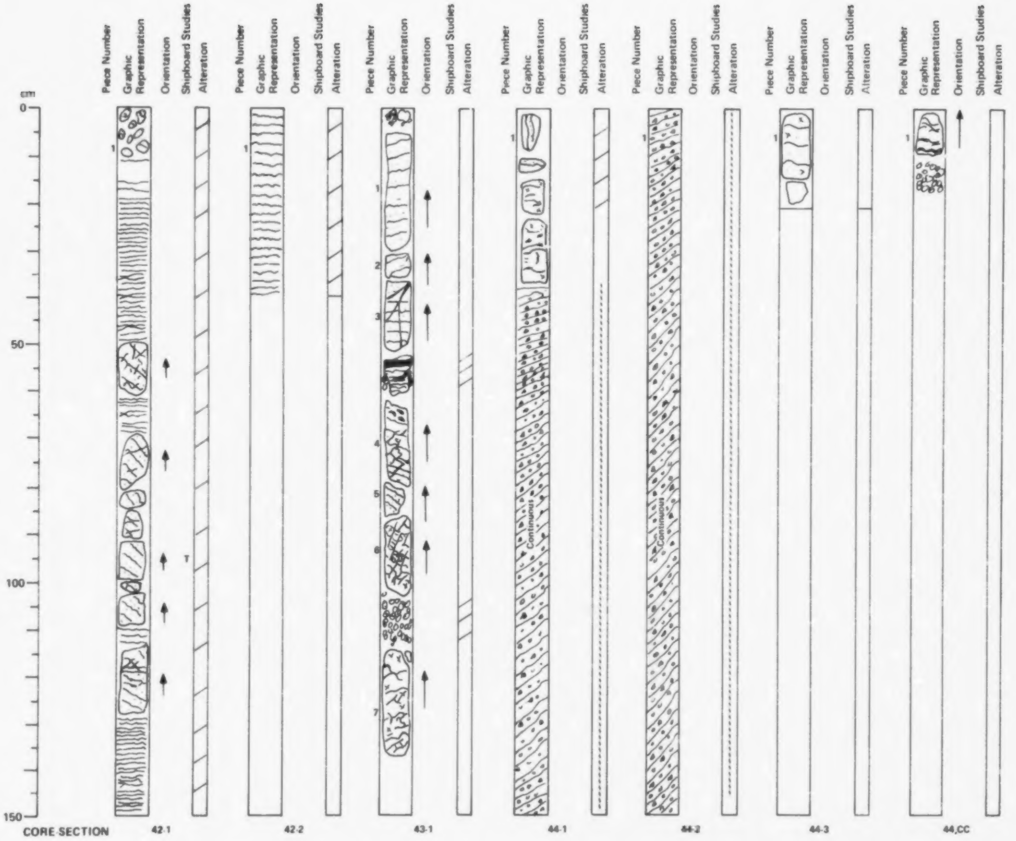

SITE 558, CORE 42 Depth 536.0–545.0 m

SECTION 1

0–150 cm: Serpentinized gabbro (dunite?). Rock: black serpentinized gabbro (dunite?); serpentine is fresh to moderately altered. Small veinlets in the serpentinite are filled with white chrysotile (shown diagramatically as heavy black wavy lines). Clay (marked ≋): these parts of the section probably consist of highly sheared serpentinite (ground by drilling?). Abundant chrysotile fibers may be an indicator of the occurrence of thicker chrysotile veins; color varies from white to dark gray.

SECTION 2

0–39 cm: Sheared serpentinite. Ground clayey serpentinite as described in Section 1.

SITE 558, CORE 43 Depth 545.0–554.0 m

SECTION 1

SERPENTINITE

0–139 cm: Black (5Y 2.5/1) serpentinite, weakly–moderately sheared with varying abundance of sinuous veinlets of white chrysotile (represented by heavy black wavy lines).

0–5 cm: Several small aphyric basalt pebbles (fallen downhole?).

56–67 and 106–118 cm: Highly fractured (by drilling) serpentinite.

56–68 cm: 2 cm chrysotile vein.

70–149 cm: 10–30% large (< 1 cm), pale green (close to 5GY 7/2, grayish yellow green) crystals of antigorite(?).

SITE 558, CORE 44 Depth 554.0–563.0 m

SECTION 1

SERPENTINITE AND SERPENTINITE FAULT BRECCIA

0–38 cm: Serpentinite as in Core 43, Section 1.

38–150 cm: Serpentinite fragments (< 1 cm) in shear-layered, soft, clay matrix.

SECTION 2

SERPENTINITE FAULT BRECCIA

As in Section 1.

SECTION 3

SERPENTINITE

0–20 cm: Serpentinite with large (<1 cm) antigorite(?) crystals as in Core 43, Section 1.

CORE CATCHER

SERPENTINITE

0–9 cm: Serpentinite as in Core 43, Section 1; large augens (≤ 1 cm) of antigorite crystals. Chrysotile veins represented by heavy wavy lines.

10–16 cm: Serpentinite rubble.

SITE 558 HOLE A CORE 1 CORED INTERVAL 0.0–0.5 m

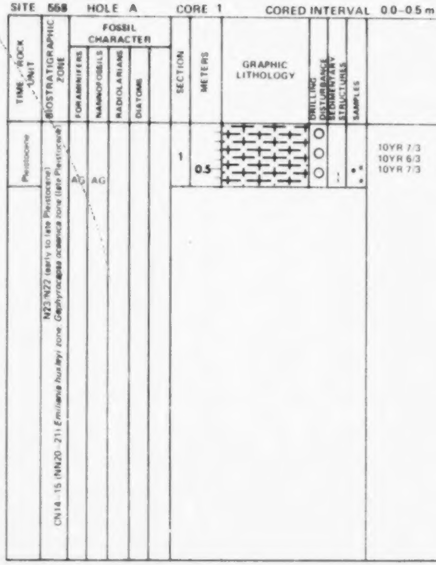
TIME – ROCK UNIT
BIOSTRATIGRAPHIC ZONE
FOSSIL CHARACTER
FORAMINIFERS
NANNOFOSSILS
RADIOLARIANS
DIATOMS
SECTION
METERS
GRAPHIC LITHOLOGY
DRILLING DISTURBANCE
SEDIMENTARY STRUCTURES
SAMPLES
Pleistocene
N23/N22 (early to late Pleistocene)
CN14–15 (NN20–21) Emiliania huxleyi zone, Gephyrocapsa oceanica zone (late Pleistocene)
AG
AG
1
0.5
10YR 7/3
10YR 6/3
10YR 7/3

LITHOLOGIC DESCRIPTION

DOMINANT LITHOLOGY SILICEOUS FORAM NANNOFOSSIL OOZE

Pale brown (10YR 6/3) to very pale brown (10YR 7/3)

Soft and soupy, but with some "gelatinous" cohesiveness. No bedding or bioturbation observable, but faint lighter pale brown mottling may be bioturbation

Principal constituents: nannos, forams, volcanic glass, siliceous organisms

SMEAR SLIDE SUMMARY (%)

	1, 50	1, 55
	D	D
Composition		
Feldspar	Tr	Tr
Heavy minerals	–	1
Clay	?	6
Volcanic glass (incl. clay size)	10	5
Carbonate unspec	–	1
Foraminifers	20	25
Calc. nannofossils	60	50
Diatoms Radiolarians Sponge spicules Silicoflagellates	10	12

Carbonate Bomb (%)
1, 55–56 = 75

SITE 558 HOLE A CORE 2 CORED INTERVAL 0.5–10.0 m

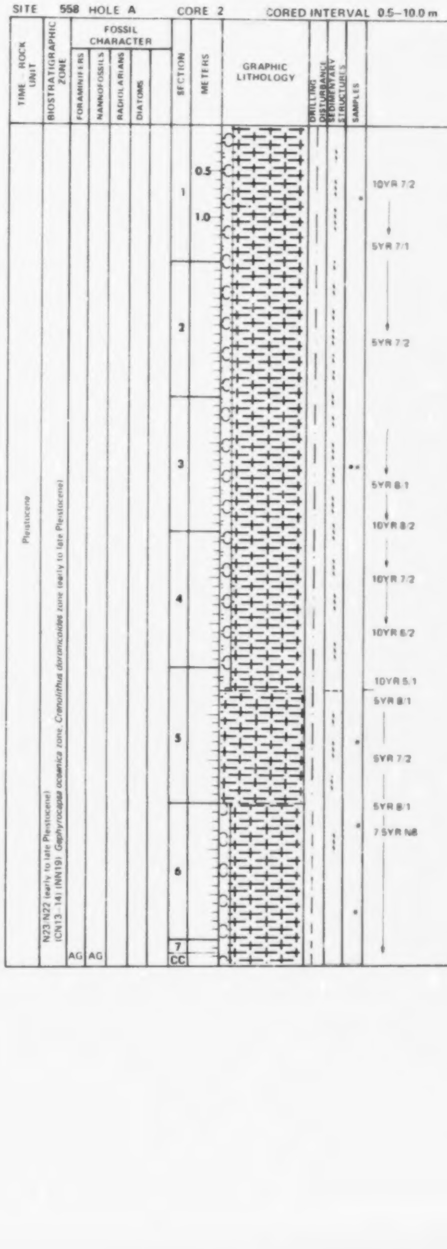
TIME – ROCK UNIT
BIOSTRATIGRAPHIC ZONE
FOSSIL CHARACTER
FORAMINIFERS
NANNOFOSSILS
RADIOLARIANS
DIATOMS
SECTION
METERS
GRAPHIC LITHOLOGY
DRILLING DISTURBANCE
SEDIMENTARY STRUCTURES
SAMPLES
Pleistocene
N23/N22 (early to late Pleistocene)
(CN13–14) (NN19) Gephyrocapsa oceanica zone, Crenolithus doronicoides zone (early to late Pleistocene)
AG
AG
1
0.5
1.0
2
3
4
5
6
7
CC
10YR 7/2
5YR 7/1
5YR 7/2
5YR 8/1
10YR 8/2
10YR 7/2
10YR 6/2
10YR 5/1
5YR 8/1
5YR 7/2
5YR 8/1
7.5YR N8

LITHOLOGIC DESCRIPTION

DOMINANT LITHOLOGY SILICEOUS FORAM NANNOFOSSIL OOZE

Light gray to pinkish gray to white to light brownish gray with occasional gray streaks, dark streaks in Section 4

Soft to firm, disturbed

Faintly mottled and indistinctly bioturbated, no evidence of bedding or other structures

Dominant components are calcareous nannofossils and forams. Siliceous biogenic content variable

SMEAR SLIDE SUMMARY (%)

	1, 80	3, 80	5, 80	6, 25	6, 120
	D	D	D	D	D
Composition:					
Feldspar	2	1	Tr	Tr	Tr
Heavy minerals	–	–	Tr	Tr	Tr
Clay	5	9	5	2	2
Volcanic glass	2	Tr	1	Tr	Tr
Opaques	–	1	1	1	–
Carbonate unspec	3	–	–	1	2
Foraminifers	20	25	10	10	10
Calc. nannofossils	50	45	75	65	75
Diatoms	3	1	1	2	1
Radiolarians	3	8	5	5	2
Sponge spicules	7	8	Tr	10	6
Silicoflagellates	5	1	2	3	1

Carbonate Bomb (%)
3, 80–81 = 70

SITE 558 HOLE A CORE 3 CORED INTERVAL 10.0–19.5 m

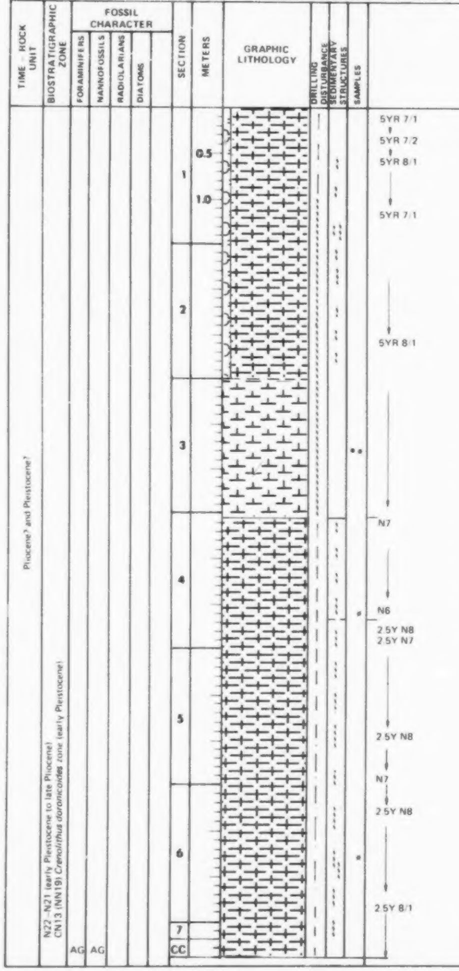
TIME – ROCK UNIT
BIOSTRATIGRAPHIC ZONE
FOSSIL CHARACTER
FORAMINIFERS
NANNOFOSSILS
RADIOLARIANS
DIATOMS
SECTION
METERS
GRAPHIC LITHOLOGY
DRILLING DISTURBANCE
SEDIMENTARY STRUCTURES
SAMPLES
Pliocene? and Pleistocene?
N22–N21 (early Pleistocene to late Pliocene)
CN13 (NN19) Crenolithus doronicoides zone (early Pleistocene)
AG
AG
1
2
3
4
5
6
7
CC
0.5
1.0
5YR 7/1
5YR 7/2
5YR 8/1
5YR 7/1
5YR 8/1
N7
N6
2.5Y N8
2.5Y N7
2.5Y N8
N7
2.5Y N8
2.5Y 8/1

LITHOLOGIC DESCRIPTION

DOMINANT LITHOLOGIES

(1) FORAM-NANNOFOSSIL OOZE TO NANNOFOSSIL OOZE

White to light gray with faint gradual color changes

Soft to firm; disturbed

Moderately to mildly bioturbated, massive bedding; distinct contact at Section 4, 5 cm, between nanno ooze (white) and foram-nanno ooze (light gray).

The nanno oooze may contain more clay, the foram-nanno ooze is more siliceous and has >25% forams.

(2) SILICEOUS FORAM-NANNOFOSSIL OOZE

Continues from Core 2, with gradual decrease in siliceous material and increase in carbonate.

SMEAR SLIDE SUMMARY (%)

	3, 80	4, 110	6, 80
	D	D	D
Composition			
Feldspar	1	Tr	Tr
Heavy minerals	–	Tr	–
Clay	15	8	9
Volcanic glass	–	Tr	Tr
Opaques	Tr	–	–
Micronodules	–	–	1
Carbonate unspec.	2	–	–
Foraminifers	9	25	25
Calc. nannofossils	70	64	60
Diatoms	1	3	5
Radiolarians	1		
Sponge spicules	1		
Silicoflagellates	Tr		

Carbonate Bomb (%)
3, 80 = 81

SITE 558 HOLE A CORE 4 CORED INTERVAL 19.5–29.0 m

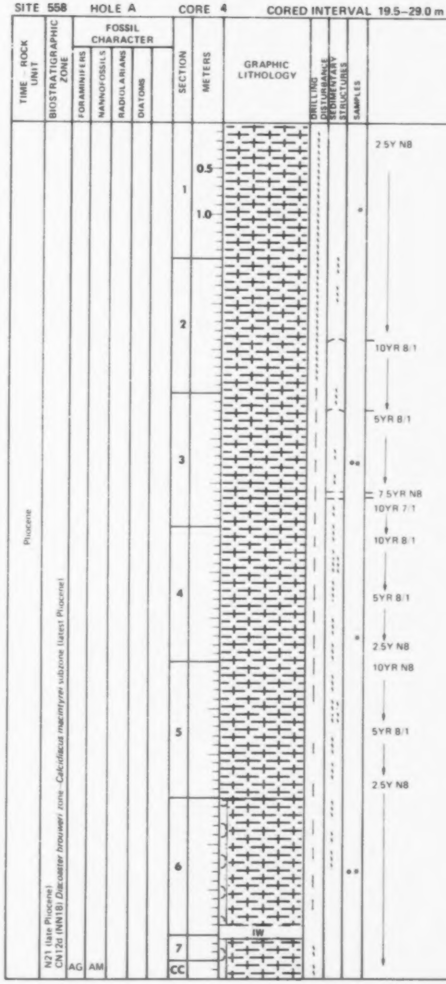
TIME – ROCK UNIT
BIOSTRATIGRAPHIC ZONE
FOSSIL CHARACTER
FORAMINIFERS
NANNOFOSSILS
RADIOLARIANS
DIATOMS
SECTION
METERS
GRAPHIC LITHOLOGY
DRILLING DISTURBANCE
SEDIMENTARY STRUCTURES
SAMPLES
Pliocene
N21 (late Pliocene)
CN12d (NN18) Discoaster brouweri zone–Calcidiscus macintyrei subzone (latest Pliocene)
AG
AM
1
2
3
4
5
6
7
CC
0.5
1.0
IW
2.5Y N8
10YR 8/1
5YR 8/1
7.5YR N8
10YR 7/1
10YR 8/1
5YR 8/1
2.5Y N8
10YR N8
5YR 8/1
2.5Y N8

LITHOLOGIC DESCRIPTION

DOMINANT LITHOLOGIES

(1) FORAM-NANNOFOSSIL OOZE

White, with subtle color variations to other shades of white, light gray to gray bed in Section 3, indistinct contact with white. Black (MnO_2?) streaks and spots in Sections 1 and 6.

Soft to firm, disturbed

Mottled and mildly bioturbated, massive bedding, and indistinct bed contacts marked by subtle color changes.

Principal constituents are nannofossils and forams, with variable quantities of siliceous components and clay.

(2) SILICEOUS FORAM-NANNOFOSSIL OOZE

As in Core 2.

SMEAR SLIDE SUMMARY (%)

	1, 45	3, 80	4, 120	6, 80
	D	D	D	D
Composition				
Feldspar	1	1	1	1
Heavy minerals	Tr	–	–	–
Clay	9	14	9	13
Volcanic glass	2	2	1	1
Opaques	3	1	–	–
Micronodules	Tr?	–	–	–
Carbonate unspec.	–	–	3	–
Foraminifers	15	14	10	13
Calc. nannofossils	65	60	70	62
Diatoms Radiolarians Sponge spicules Silicoflagellates	4	8	6	12

Carbonate Bomb (%)
3, 80 = 74
6, 80 = 75

SITE 558 HOLE A CORE 5 CORED INTERVAL 29.0–38.5 m

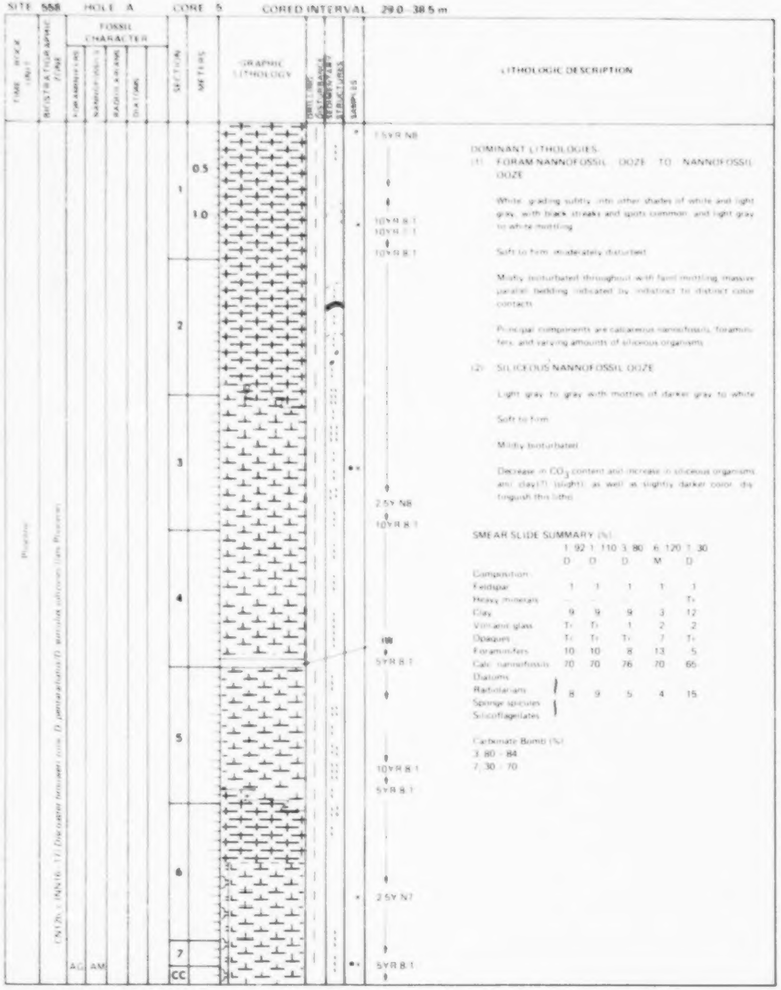
TIME-ROCK UNIT
BIOSTRATIGRAPHIC ZONE
FOSSIL CHARACTER
FORAMINIFERS
NANNOFOSSILS
RADIOLARIANS
DIATOMS
SECTION
METERS
GRAPHIC LITHOLOGY
DRILLING DISTURBANCE
SEDIMENTARY STRUCTURES
SAMPLES
Pliocene
CN12b, c (NN16–17) Discoaster brouweri zone, D. pentaradiatus/D. surculus subzones (late Pliocene)
AG
AM
1
2
3
4
5
6
7
CC
0.5
1.0
7.5YR N8
10YR 8/1
10YR 7/1
10YR 8/1
2.5Y N8
10YR 8/1
5YR 8/1
10YR 8/1
5YR 8/1
2.5Y N7
5YR 8/1

LITHOLOGIC DESCRIPTION

DOMINANT LITHOLOGIES:

(1) FORAM-NANNOFOSSIL OOZE TO NANNOFOSSIL OOZE

White, grading subtly into other shades of white and light gray, with black streaks and spots common, and light gray to white mottling

Soft to firm, moderately disturbed

Mildly bioturbated throughout with faint mottling, massive parallel bedding indicated by indistinct to distinct color contacts

Principal components are calcareous nannofossils, foraminifers, and varying amounts of siliceous organisms

(2) SILICEOUS NANNOFOSSIL OOZE

Light gray to gray with mottles of darker gray to white

Soft to firm

Mildly bioturbated

Decrease in CO_3 content and increase in siliceous organisms and clay(?) (slight), as well as slightly darker color, distinguish this litho

SMEAR SLIDE SUMMARY (%):

	1, 92 D	1, 110 D	3, 80 D	6, 120 M	7, 30 D
Composition:					
Feldspar	1	1	1	1	1
Heavy minerals	–	–	–		Tr
Clay	9	9	9	3	12
Volcanic glass	Tr	Tr	1	2	2
Opaques	Tr	Tr	Tr	7	Tr
Foraminifers	10	10	8	13	5
Calc. nannofossils	70	70	76	70	65
Diatoms Radiolarians Sponge spicules Silicoflagellates	8	9	5	4	15

Carbonate Bomb (%):
3, 80 = 84
7, 30 = 70

SITE 558 HOLE A CORE 6 CORED INTERVAL 38.5–48.0 m

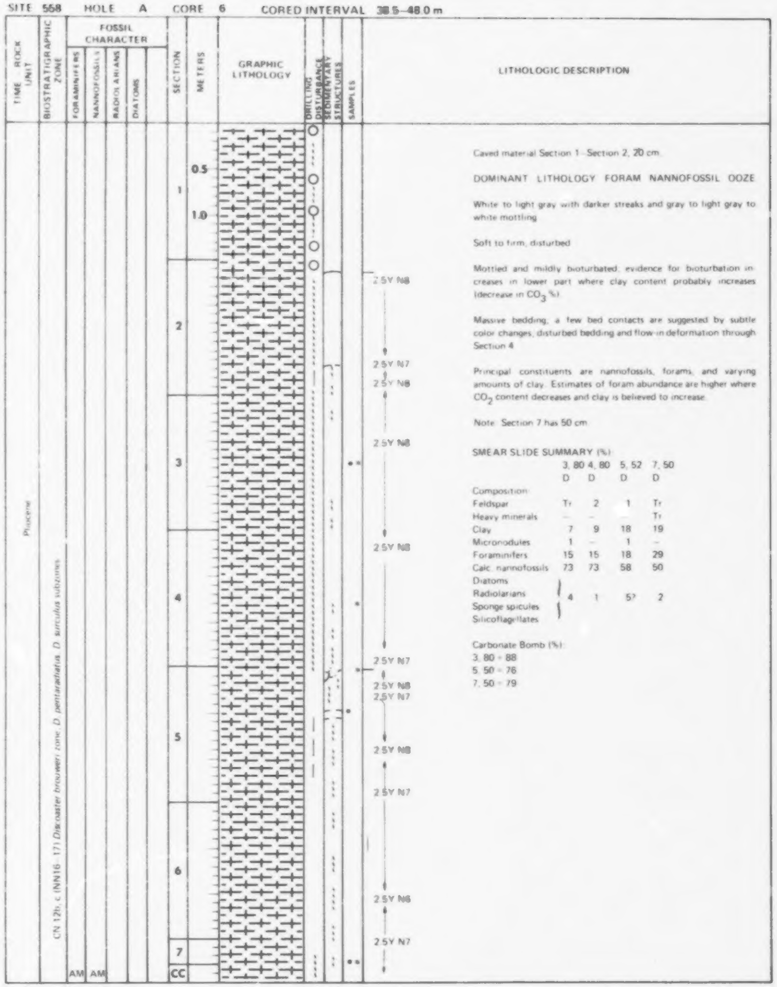
TIME-ROCK UNIT
BIOSTRATIGRAPHIC ZONE
FOSSIL CHARACTER
FORAMINIFERS
NANNOFOSSILS
RADIOLARIANS
DIATOMS
SECTION
METERS
GRAPHIC LITHOLOGY
DRILLING DISTURBANCE
SEDIMENTARY STRUCTURES
SAMPLES
Pliocene
CN 12b, c (NN16–17) Discoaster brouweri zone, D. pentaradiatus, D. surculus subzones
AM
AM
1
2
3
4
5
6
7
CC
0.5
1.0
2.5Y N8
2.5Y N7
2.5Y N8
2.5Y N8
2.5Y N8
2.5Y N7
2.5Y N8
2.5Y N7
2.5Y N8
2.5Y N7
2.5Y N6
2.5Y N7

LITHOLOGIC DESCRIPTION

Caved material Section 1–Section 2, 20 cm

DOMINANT LITHOLOGY FORAM NANNOFOSSIL OOZE

White to light gray with darker streaks and gray to light gray to white mottling

Soft to firm, disturbed

Mottled and mildly bioturbated; evidence for bioturbation increases in lower part where clay content probably increases (decrease in CO_3 %)

Massive bedding; a few bed contacts are suggested by subtle color changes; disturbed bedding and flow-in deformation through Section 4

Principal constituents are nannofossils, forams, and varying amounts of clay. Estimates of foram abundance are higher where CO_2 content decreases and clay is believed to increase

Note: Section 7 has 50 cm

SMEAR SLIDE SUMMARY (%):

	3, 80 D	4, 80 D	5, 52 D	7, 50 D
Composition:				
Feldspar	Tr	2	1	Tr
Heavy minerals	–	–	–	Tr
Clay	7	9	18	19
Micronodules	1	–	1	–
Foraminifers	15	15	18	29
Calc. nannofossils	73	73	58	50
Diatoms Radiolarians Sponge spicules Silicoflagellates	4	1	5?	2

Carbonate Bomb (%):
3, 80 = 88
5, 50 = 76
7, 50 = 79

SITE 558 HOLE A CORE 7 CORED INTERVAL 48.0–57.5 m

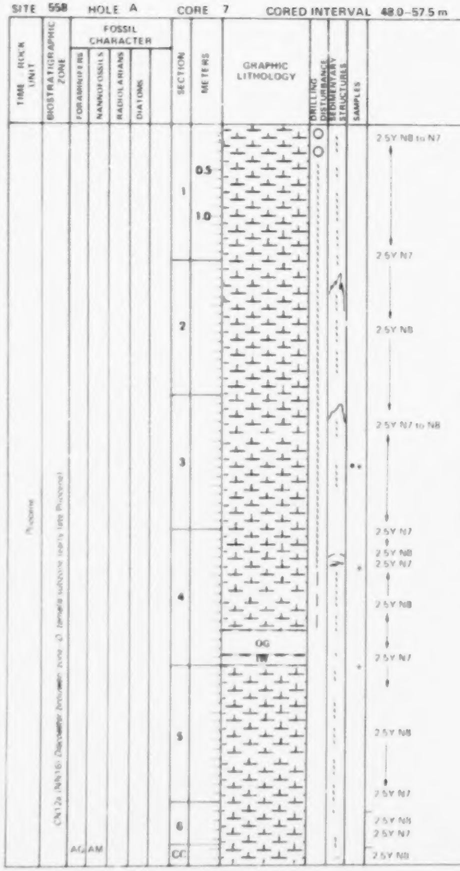
TIME - ROCK UNIT
BIOSTRATIGRAPHIC ZONE
FOSSIL CHARACTER
FORAMINIFERS
NANNOFOSSILS
RADIOLARIANS
DIATOMS
SECTION
METERS
GRAPHIC LITHOLOGY
DRILLING DISTURBANCE
SEDIMENTARY STRUCTURES
SAMPLES
Pliocene
CN12a (NN16) Discoaster brouweri zone - D. tamalis subzone (early late Pliocene)
AG AM
1
2
3
4
5
6
CC
0.5
1.0
OG
IW
2.5Y N8 to N7
2.5Y N7
2.5Y N8
2.5Y N7 to N8
2.5Y N7
2.5Y N8
2.5Y N7
2.5Y N8
2.5Y N7
2.5Y N8
2.5Y N7
2.5Y N8
2.5Y N7
2.5Y N8

LITHOLOGIC DESCRIPTION

DOMINANT LITHOLOGY NANNOFOSSIL OOZE

White to light gray to gray with faint mottling, black streaks, and indistinct color banding

Soft to firm, disturbed to Section 4

Mildly bioturbated and mottled throughout, intense flow-in deformation through Section 4, 37 cm.

Massive bedding with faint color banding

Principal constituents are calcareous nannofossils, quantity of clay appears to be variable

SMEAR SLIDE SUMMARY (%)

	3, 80	4, 43	5, 3
	D	M	D
Composition			
Feldspar	Tr	Tr	Tr
Heavy minerals	Tr	–	–
Clay	20	10	10
Micronodules	Tr	–	2
Carbonate unspec	1	5	Tr
Foraminifers	8	5	7
Calc. nannofossils	65	75	80
Diatoms Radiolarians Sponge spicules Silicoflagellates	5	5?	Tr?

Carbonate Bomb (%)
3, 80 = 74

SITE 558 HOLE A CORE 8 CORED INTERVAL 57.5–67.0 m

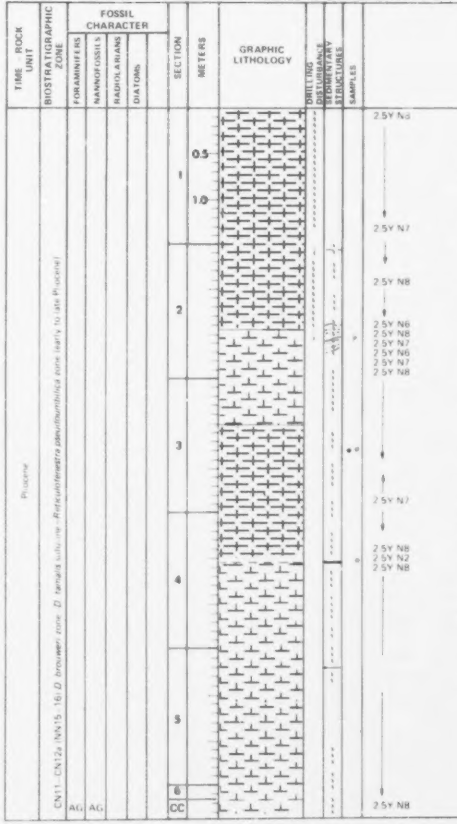
TIME - ROCK UNIT
BIOSTRATIGRAPHIC ZONE
FOSSIL CHARACTER
FORAMINIFERS
NANNOFOSSILS
RADIOLARIANS
DIATOMS
SECTION
METERS
GRAPHIC LITHOLOGY
DRILLING DISTURBANCE
SEDIMENTARY STRUCTURES
SAMPLES
Pliocene
CN11–CN12a (NN15–16) D. brouweri zone: D. tamalis subzone – Reticulofenestra pseudoumbilica zone (early to late Pliocene)
AG AG
1
2
3
4
5
6
CC
0.5
1.0
2.5Y N8
2.5Y N7
2.5Y N8
2.5Y N6
2.5Y N8
2.5Y N7
2.5Y N6
2.5Y N7
2.5Y N8
2.5Y N7
2.5Y N8
2.5Y N2
2.5Y N8
2.5Y N8

LITHOLOGIC DESCRIPTION

DOMINANT LITHOLOGY FORAM-NANNOFOSSIL OOZE TO NANNOFOSSIL OOZE

White to light gray, subtly grading, except where color bands define color changes, black streaks common throughout

Soft to firm, disturbed through Section 2, 95 cm

Bioturbation and mottling probably throughout, though very indistinct in some portions, bands 1–2 cm wide in Section 2 indicate more rapid alternation of lithologic character and suggest parallel bedding

Principal constituents are nannofossils and varying amounts of forams and clay

Minor lithology
Manganiferous(?) nanno ooze

Black streaks, as in Sections 4, 5, and 6 are concentrations of opaque minerals possibly marking bedding planes or depositional discontinuities.

SMEAR SLIDE SUMMARY (%)

	2, 103	3, 80	4, 52
	D	D	M
Composition			
Feldspar	Tr	1	1
Heavy minerals	Tr	–	–
Clay	10	13	8
Palagonite	Tr	–	–
Opaques	–		15
Micronodules	1	1	–
Carbonate unspec	–	1	–
Foraminifers	5	15	1
Calc. nannofossils	80	68	75
Diatoms Radiolarians Sponge spicules Silicoflagellates	3?	1?	–

Carbonate Bomb (%)
3, 80 = 84

SITE 558 HOLE A CORE 9 CORED INTERVAL 67.0–74.0 m

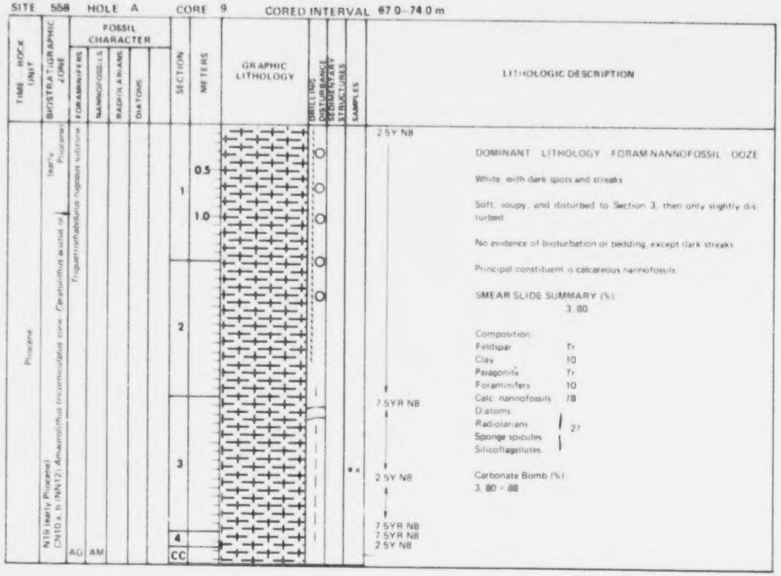
TIME – ROCK UNIT
BIOSTRATIGRAPHIC ZONE
FOSSIL CHARACTER
FORAMINIFERS
NANNOFOSSILS
RADIOLARIANS
DIATOMS
SECTION
METERS
GRAPHIC LITHOLOGY
DRILLING DISTURBANCE
SEDIMENTARY STRUCTURES
SAMPLES
LITHOLOGIC DESCRIPTION
Pliocene
N19 (early Pliocene)
CN10 a, b (NN12) Amaurolithus tricorniculatus zone – Ceratolithus acutus or Triquetrorhabdulus rugosus subzone
(early Pliocene)
AG
AM
1
2
3
4
CC
0.5
1.0
2.5Y N8
7.5YR N8
2.5Y N8
7.5YR N8
7.5YR N8
2.5Y N8

DOMINANT LITHOLOGY FORAM-NANNOFOSSIL OOZE

White, with dark spots and streaks

Soft, soupy, and disturbed to Section 3, then only slightly disturbed

No evidence of bioturbation or bedding, except dark streaks

Principal constituent is calcareous nannofossils

SMEAR SLIDE SUMMARY (%)

Composition:	3, 80
Feldspar	Tr
Clay	10
Palagonite	Tr
Foraminifers	10
Calc. nannofossils	78
Diatoms Radiolarians Sponge spicules Silicoflagellates	2?

Carbonate Bomb (%)
3, 80 – 88

SITE 558 HOLE A CORE 10 CORED INTERVAL 74.0–77.0 m

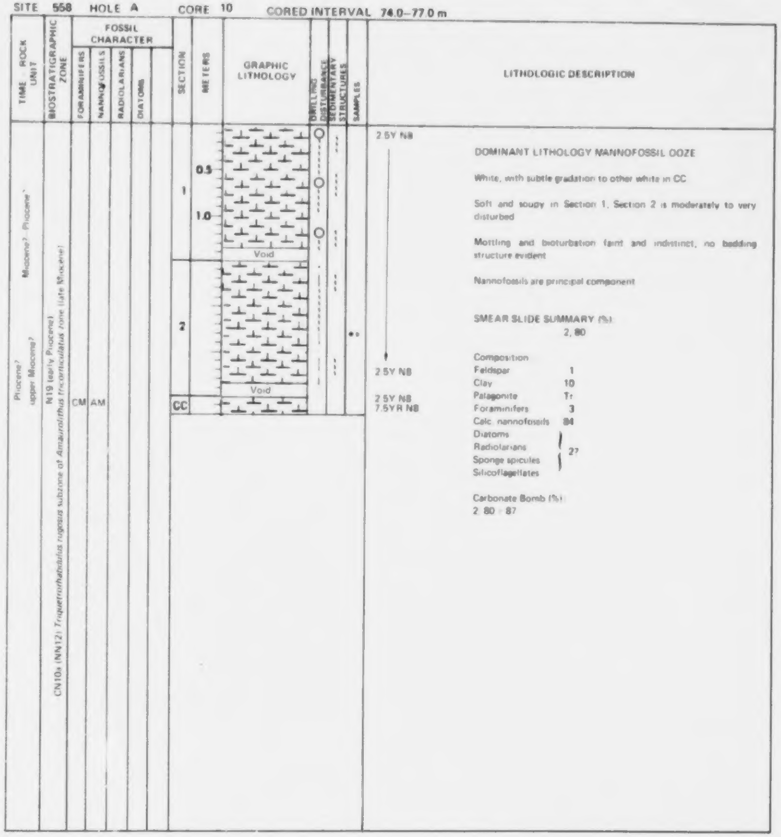
TIME – ROCK UNIT
BIOSTRATIGRAPHIC ZONE
FOSSIL CHARACTER
FORAMINIFERS
NANNOFOSSILS
RADIOLARIANS
DIATOMS
SECTION
METERS
GRAPHIC LITHOLOGY
DRILLING DISTURBANCE
SEDIMENTARY STRUCTURES
SAMPLES
LITHOLOGIC DESCRIPTION
Pliocene?
upper Miocene?
Miocene? – Pliocene?
N19 (early Pliocene)
CN10a (NN12) Triquetrorhabdulus rugosus subzone of Amaurolithus tricorniculatus zone (late Miocene)
CM
AM
1
2
CC
0.5
1.0
Void
Void
2.5Y N8
2.5Y N8
2.5Y N8
7.5YR N8

DOMINANT LITHOLOGY NANNOFOSSIL OOZE

White, with subtle gradation to other white in CC

Soft and soupy in Section 1, Section 2 is moderately to very disturbed

Mottling and bioturbation faint and indistinct, no bedding structure evident

Nannofossils are principal component

SMEAR SLIDE SUMMARY (%)

Composition	2, 80
Feldspar	1
Clay	10
Palagonite	Tr
Foraminifers	3
Calc. nannofossils	84
Diatoms Radiolarians Sponge spicules Silicoflagellates	2?

Carbonate Bomb (%)
2, 80 – 87

SITE 558 HOLE A CORE 11 CORED INTERVAL 77.0–86.5 m

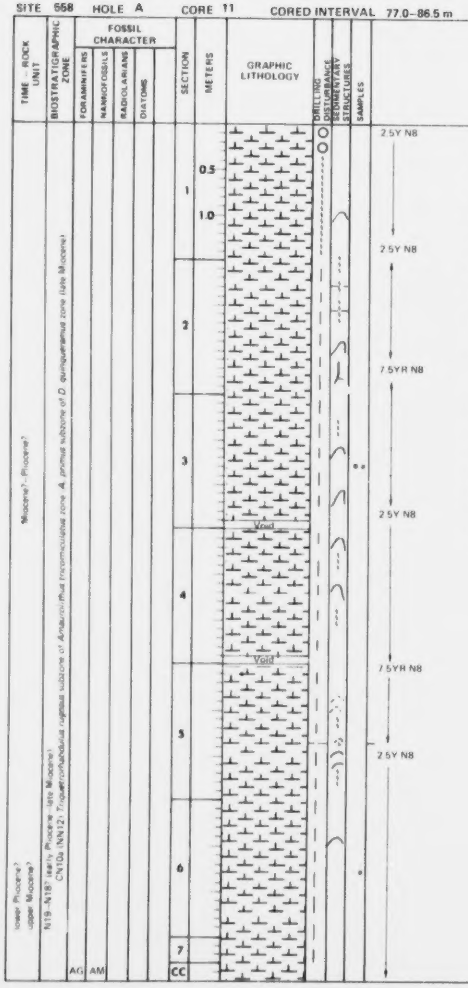
TIME – ROCK UNIT
BIOSTRATIGRAPHIC ZONE
FOSSIL CHARACTER
FORAMINIFERS
NANNOFOSSILS
RADIOLARIANS
DIATOMS
SECTION
METERS
GRAPHIC LITHOLOGY
DRILLING DISTURBANCE
SEDIMENTARY STRUCTURES
SAMPLES
Miocene?–Pliocene?
lower Pliocene?
upper Miocene?
N19–N18? (early Pliocene–late Miocene)
CN10a (NN12) Triquetrorhabdulus rugosus subzone of Amaurolithus tricorniculatus zone A. primus subzone of D. quinqueramus zone (late Miocene)
AG
AM
1
2
3
4
5
6
7
CC
0.5
1.0
Void
Void
2.5Y N8
2.5Y N8
7.5YR N8
2.5Y N8
7.5YR N8
2.5Y N8

LITHOLOGIC DESCRIPTION

DOMINANT LITHOLOGY NANNOFOSSIL OOZE

White, grading subtly to other shades of white, dark streaks present in every section

Soft to firm, moderately to severely disturbed

Very mildly bioturbated and faint mottling, dark patches may represent bioturbation. Dark streaks may be parallel with bedding surfaces but are deformed vertically by drilling disturbance

Principal constituent is calcareous nannofossils

Note: Section 7 has 50 cm

SMEAR SLIDE SUMMARY (%)

Composition:	3, 80	6, 80
Feldspar	Tr	—
Clay	9	10
Carbonate unspec	3	5
Foraminifers	2	—
Calc. nannofossils	85	85
Diatoms Radiolarians Sponge spicules Silicoflagellates	1?	—

Carbonate Bomb (%)
3, 80 = 90

SITE 558 HOLE A CORE 12 CORED INTERVAL 86.5–96.0 m

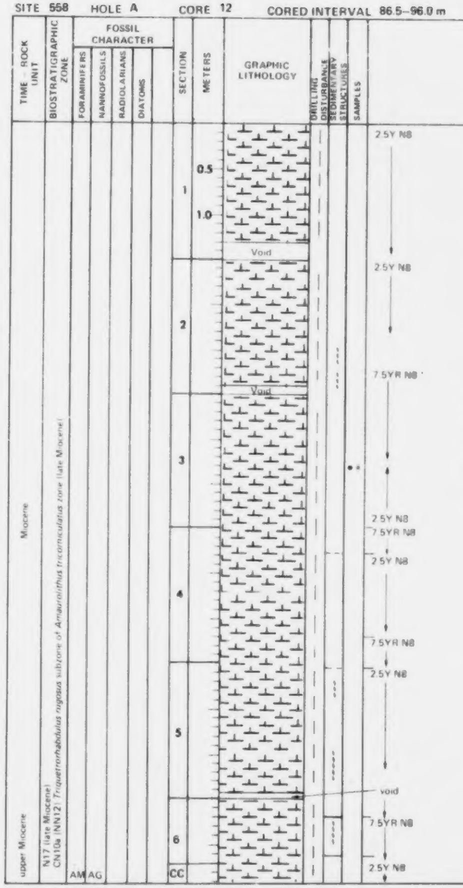
TIME – ROCK UNIT
BIOSTRATIGRAPHIC ZONE
FOSSIL CHARACTER
FORAMINIFERS
NANNOFOSSILS
RADIOLARIANS
DIATOMS
SECTION
METERS
GRAPHIC LITHOLOGY
DRILLING DISTURBANCE
SEDIMENTARY STRUCTURES
SAMPLES
Miocene
upper Miocene
N17 (late Miocene)
CN10a (NN12) Triquetrorhabdulus rugosus subzone of Amaurolithus tricorniculatus zone (late Miocene)
AM
AG
1
2
3
4
5
6
CC
0.5
1.0
Void
Void
2.5Y N8
2.5Y N8
7.5YR N8
2.5Y N8
7.5YR N8
2.5Y N8
7.5YR N8
2.5Y N8
void
7.5YR N8
2.5Y N8

LITHOLOGIC DESCRIPTION

DOMINANT LITHOLOGY NANNOFOSSIL OOZE

White, grading subtly within various shades of white, dark streaks and patches soft to firm

Moderately deformed to slightly deformed

Bioturbation not prominent but may be indicated by streaks and dark patches in Sections 2, 5, and 6. Dark spots and streaks throughout. Massive bedding with indistinct color contacts

Principal constituents are nannofossils

SMEAR SLIDE SUMMARY (%)

Composition:	3, 80
Feldspar	1
Clay	5
Carbonate unspec	2
Foraminifers	3
Calc. nannofossils	88
Diatoms Radiolarians Sponge spicules Silicoflagellates	1

Carbonate Bomb (%)
3, 80 = 93

SITE 558 HOLE A CORE 13 CORED INTERVAL 96.0–103.0 m

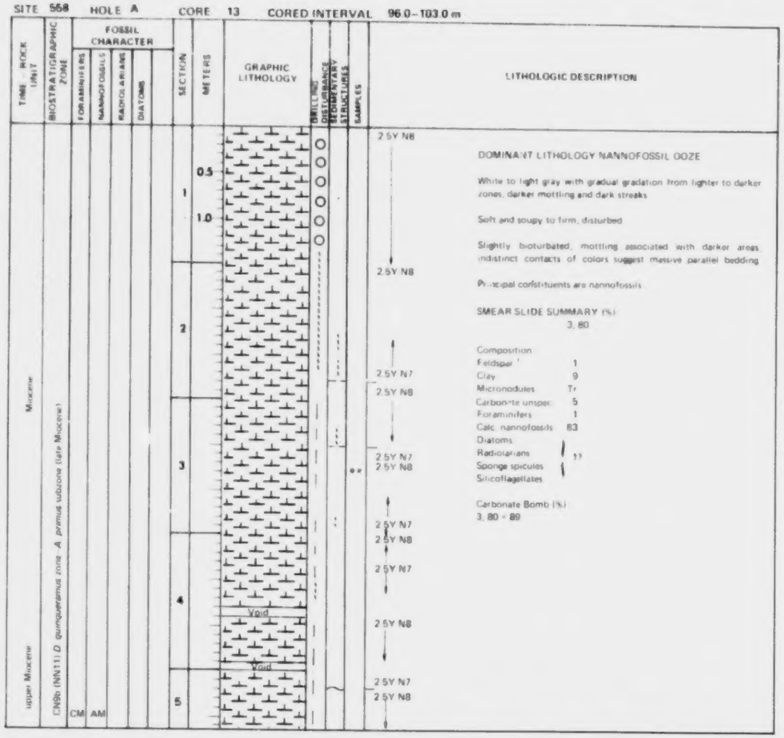
TIME-ROCK UNIT
BIOSTRATIGRAPHIC ZONE
FOSSIL CHARACTER
FORAMINIFERS
NANNOFOSSILS
RADIOLARIANS
DIATOMS
SECTION
METERS
GRAPHIC LITHOLOGY
DRILLING DISTURBANCE
SEDIMENTARY STRUCTURES
SAMPLES
LITHOLOGIC DESCRIPTION
Miocene
upper Miocene
CN9b (NN11) D. quinqueramus zone - A. primus subzone (late Miocene)
CM
AM
1
2
3
4
5
0.5
1.0
Void
Void
2.5Y N8
2.5Y N8
2.5Y N7
2.5Y N8
2.5Y N7
2.5Y N8
2.5Y N7
2.5Y N8
2.5Y N7
2.5Y N8
2.5Y N7
2.5Y N8

DOMINANT LITHOLOGY NANNOFOSSIL OOZE

White to light gray with gradual gradation from lighter to darker zones, darker mottling and dark streaks

Soft and soupy to firm, disturbed

Slightly bioturbated, mottling associated with darker areas indistinct contacts of colors suggest massive parallel bedding

Principal constituents are nannofossils

SMEAR SLIDE SUMMARY (%)

	3, 80
Composition	
Feldspar	1
Clay	9
Micronodules	Tr
Carbonate unspec.	5
Foraminifers	1
Calc. nannofossils	83
Diatoms	
Radiolarians	??
Sponge spicules	
Silicoflagellates	

Carbonate Bomb (%)
3, 80 = 89

SITE 558 HOLE A CORE 14 CORED INTERVAL 103.0–112.5 m

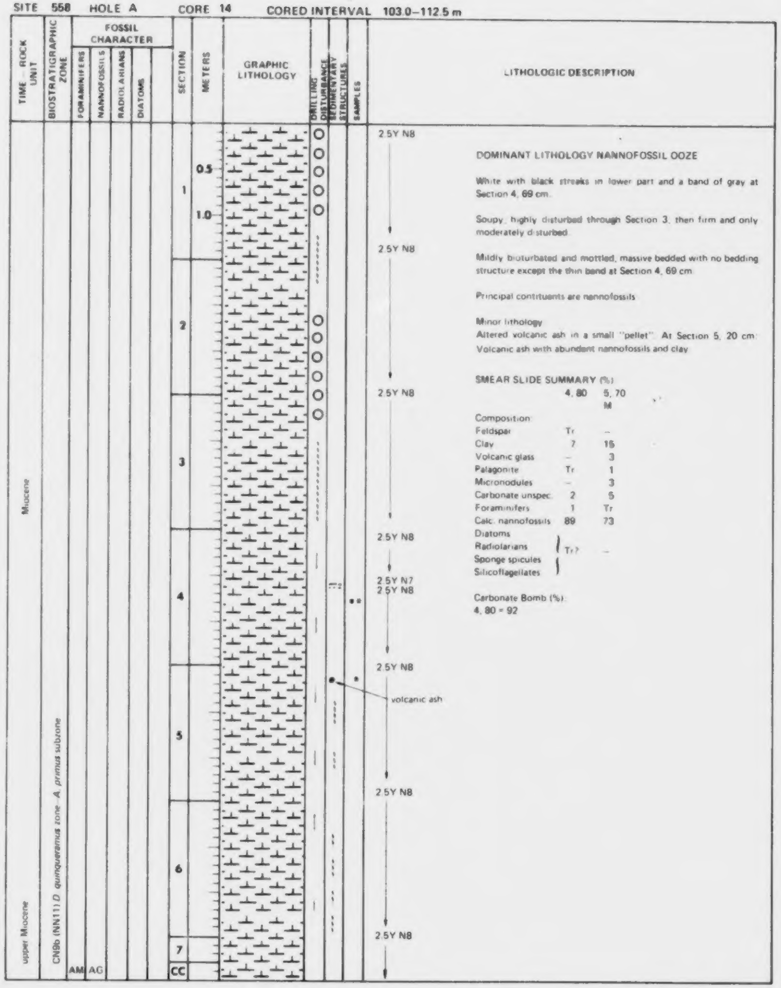
TIME-ROCK UNIT
BIOSTRATIGRAPHIC ZONE
FOSSIL CHARACTER
FORAMINIFERS
NANNOFOSSILS
RADIOLARIANS
DIATOMS
SECTION
METERS
GRAPHIC LITHOLOGY
DRILLING DISTURBANCE
SEDIMENTARY STRUCTURES
SAMPLES
LITHOLOGIC DESCRIPTION
Miocene
upper Miocene
CN9b (NN11) D. quinqueramus zone - A. primus subzone
AM
AG
1
2
3
4
5
6
7
CC
0.5
1.0
2.5Y N8
2.5Y N8
2.5Y N8
2.5Y N8
2.5Y N7
2.5Y N8
2.5Y N8
volcanic ash
2.5Y N8
2.5Y N8

DOMINANT LITHOLOGY NANNOFOSSIL OOZE

White with black streaks in lower part and a band of gray at Section 4, 69 cm.

Soupy, highly disturbed through Section 3, then firm and only moderately disturbed

Mildly bioturbated and mottled, massive bedded with no bedding structure except the thin band at Section 4, 69 cm

Principal contituents are nannofossils

Minor lithology
Altered volcanic ash in a small "pellet". At Section 5, 20 cm:
Volcanic ash with abundant nannofossils and clay

SMEAR SLIDE SUMMARY (%)

	4, 80	5, 70 M
Composition:		
Feldspar	Tr	–
Clay	7	15
Volcanic glass	–	3
Palagonite	Tr	1
Micronodules	–	3
Carbonate unspec.	2	5
Foraminifers	1	Tr
Calc. nannofossils	89	73
Diatoms		
Radiolarians	Tr?	–
Sponge spicules		
Silicoflagellates		

Carbonate Bomb (%):
4, 80 = 92

SITE 558 HOLE A CORE 15 CORED INTERVAL 112.5–122.0 m

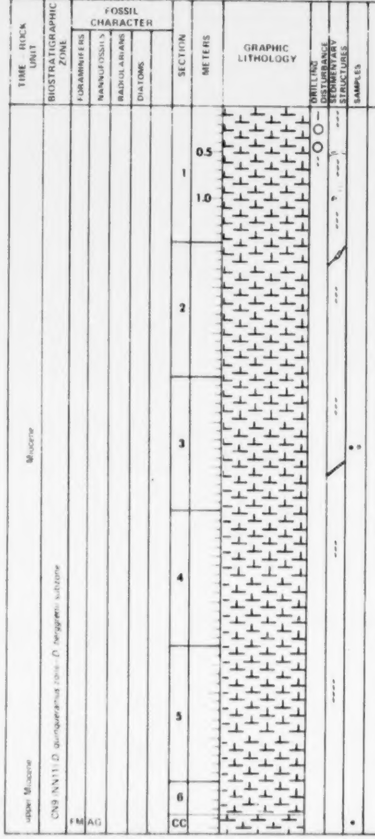
TIME-ROCK UNIT
BIOSTRATIGRAPHIC ZONE
FOSSIL CHARACTER
FORAMINIFERS
NANNOFOSSILS
RADIOLARIANS
DIATOMS
SECTION
METERS
GRAPHIC LITHOLOGY
DRILLING DISTURBANCE
SEDIMENTARY STRUCTURES
SAMPLES
Miocene
upper Miocene
CN9 (NN11) D. quinqueramus zone–D. berggrenii subzone
FM
AG
1
2
3
4
5
6
CC
0.5
1.0
2.5Y N8
2.5Y N7
2.5Y N8
2.5Y N8
2.5Y N8
2.5Y N2
2.5Y N8
2.5Y N8
2.5Y N8

LITHOLOGIC DESCRIPTION

DOMINANT LITHOLOGY NANNOFOSSIL OOZE

White with slight mottling and occasional dark thin (2 mm) streaks in Sections 2 and 3.

Soft to firm, apparently no deformation except at top of Section 1.

Mildly bioturbated at sporadic intervals. Massive bedding, inclined dark streaks suggest (inclined) parallel bedding (probably deformation by coring?).

Principal constituents are nannofossils.

SMEAR SLIDE SUMMARY (%)

Composition	3, 80
Feldspar	1
Clay	8
Carbonate unspec.	3
Foraminifers	3
Calc. nannofossils	85

Carbonate Bomb (%)
3, 80 = 91
CC = 89

SITE 558 HOLE A CORE 16 CORED INTERVAL 122.0–131.5 m

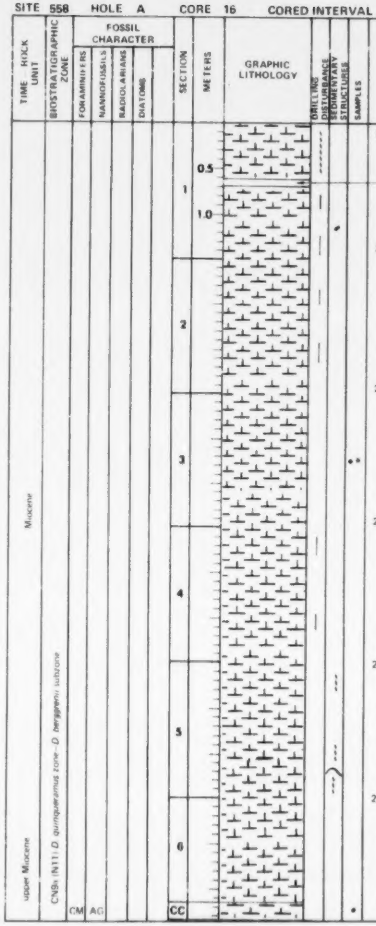
TIME-ROCK UNIT
BIOSTRATIGRAPHIC ZONE
FOSSIL CHARACTER
FORAMINIFERS
NANNOFOSSILS
RADIOLARIANS
DIATOMS
SECTION
METERS
GRAPHIC LITHOLOGY
DRILLING DISTURBANCE
SEDIMENTARY STRUCTURES
SAMPLES
Miocene
upper Miocene
CN9a (NN11) D. quinqueramus zone–D. berggrenii subzone
CM
AG
1
2
3
4
5
6
CC
0.5
1.0
2.5Y N8
void
2.5Y N8
2.5Y N8
2.5Y N8
2.5Y N8
2.5Y N8

LITHOLOGIC DESCRIPTION

DOMINANT LITHOLOGY NANNOFOSSIL OOZE

White with black streaks in Section 3 and an irregular 3 mm dark layer in Section 5, a black nodule in Section 1.

Soft to firm, relatively undisturbed.

Very slightly bioturbated and faintly mottled in lower part of core. No bedding structure apparent except for the irregular dark lamina in Section 5.

Principal constituents are nannofossils. The carbonate content is 84% (as compared with 91% in Core 15), but there is no apparent increase in siliceous components.

SMEAR SLIDE SUMMARY (%)

Composition:	3, 80
Feldspar	1
Clay	13
Palagonite	Tr
Micronodules	Tr
Carbonate unspec.	5
Foraminifers	Tr
Calc. nannofossils	80
Diatoms Radiolarians Sponge spicules Silicoflagellates	Tr?

Carbonate Bomb (%)
3, 80 = 84
CC = 91

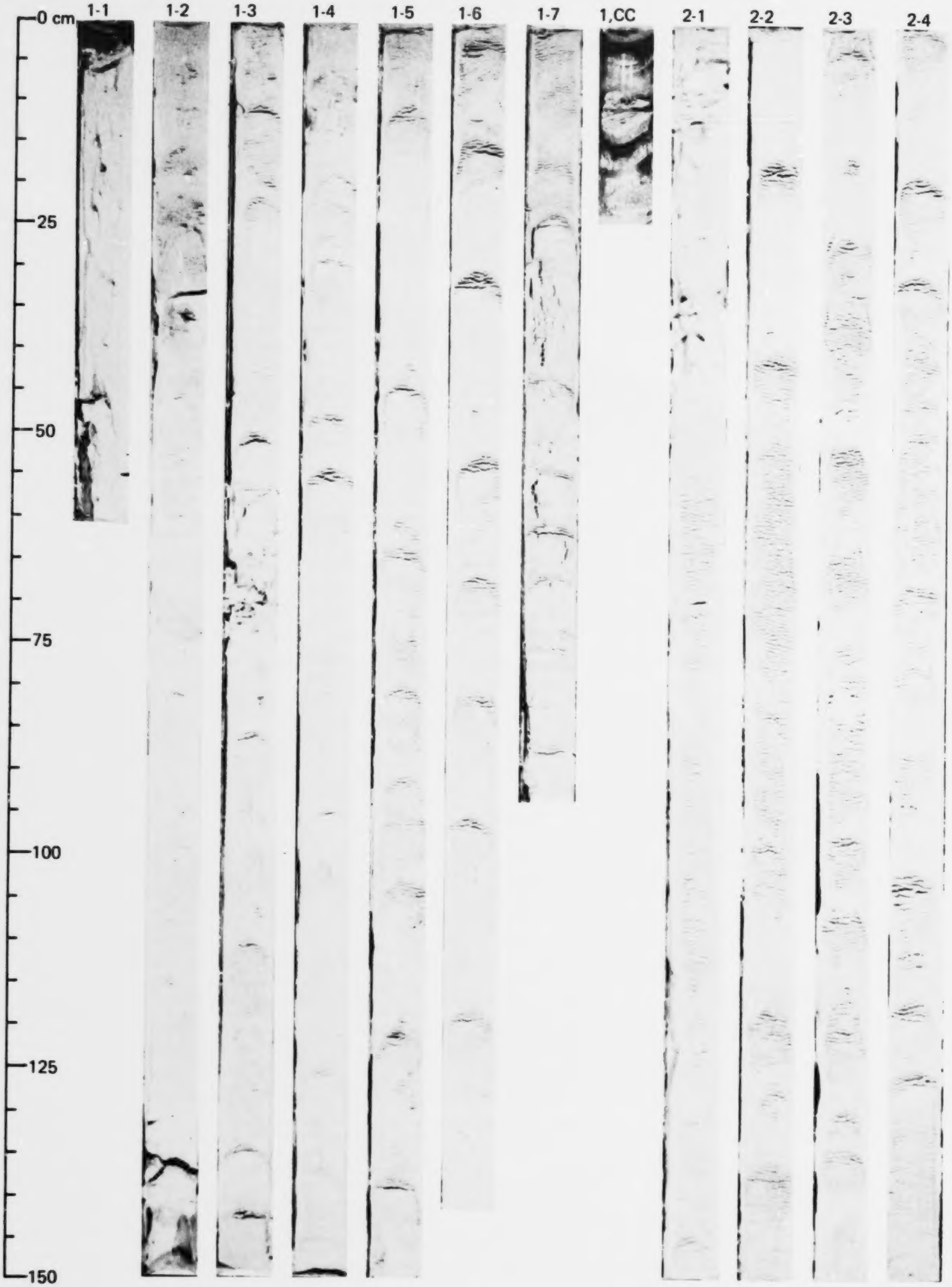
0 cm
25
50
75
100
125
150
1-1
1-2
1-3
1-4
1-5
1-6
1-7
1,CC
2-1
2-2
2-3
2-4

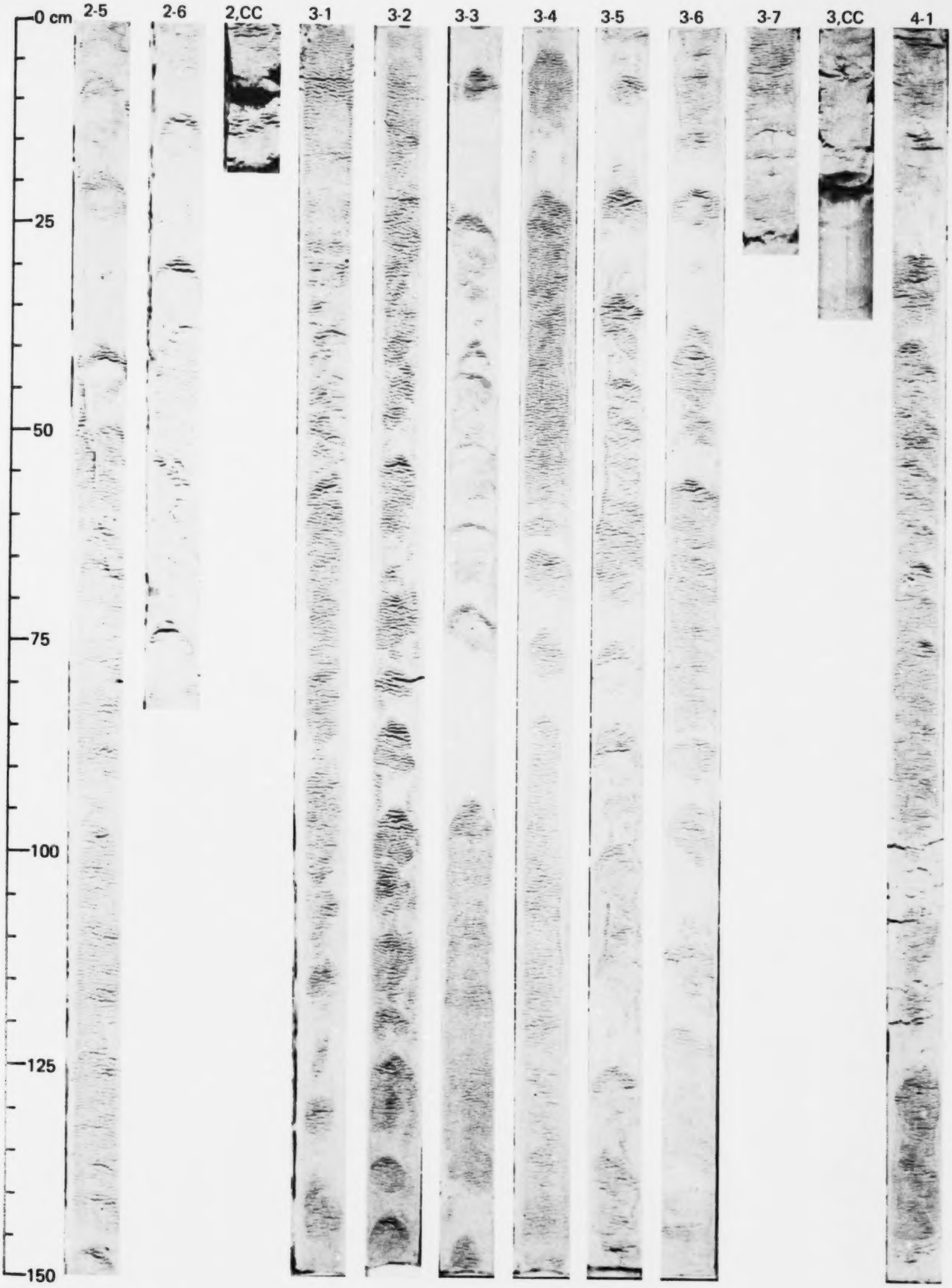
0 cm
25
50
75
100
125
150
2-5
2-6
2,CC
3-1
3-2
3-3
3-4
3-5
3-6
3-7
3,CC
4-1

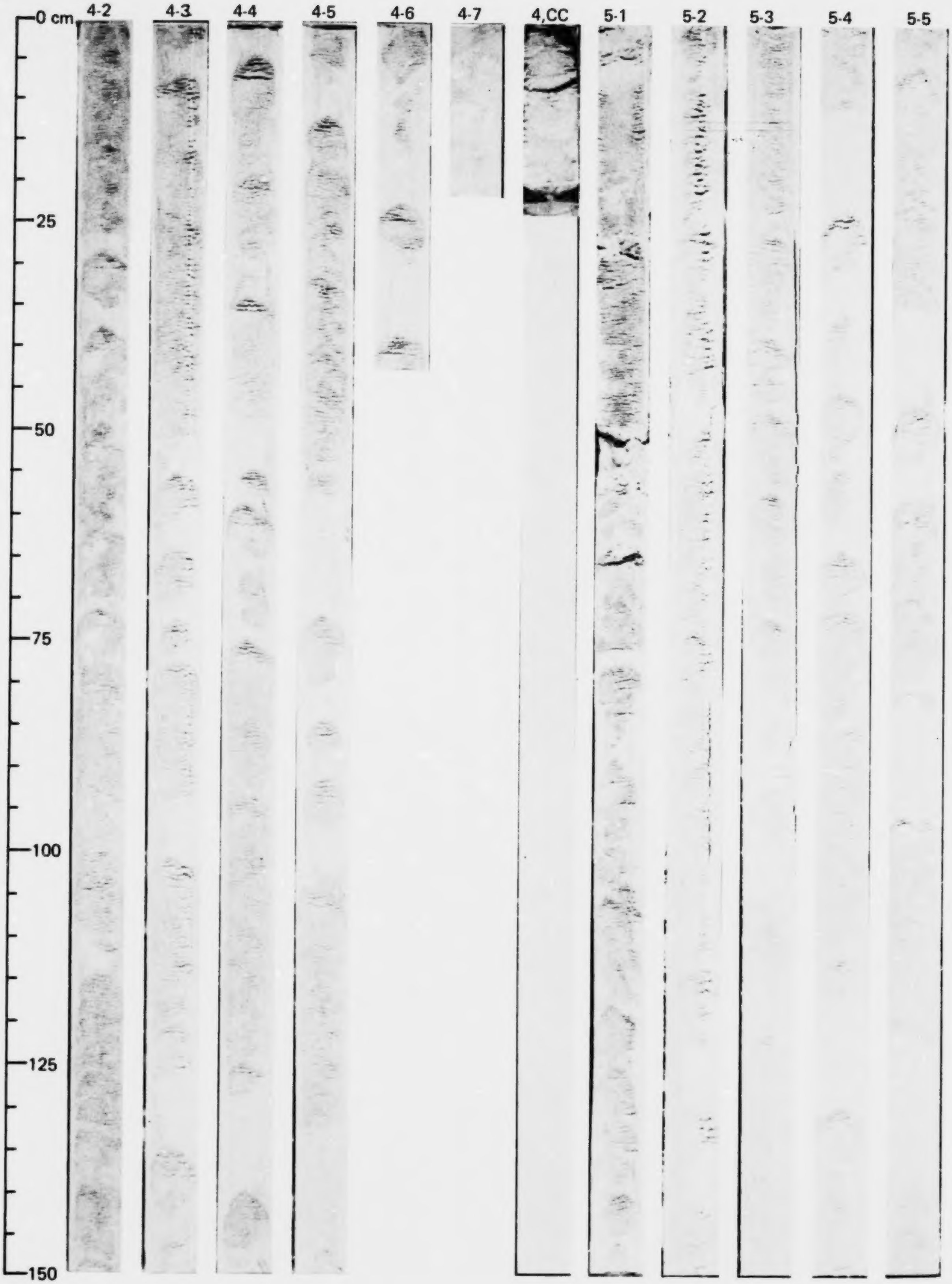
0 cm
25
50
75
100
125
150
4-2
4-3
4-4
4-5
4-6
4-7
4,CC
5-1
5-2
5-3
5-4
5-5

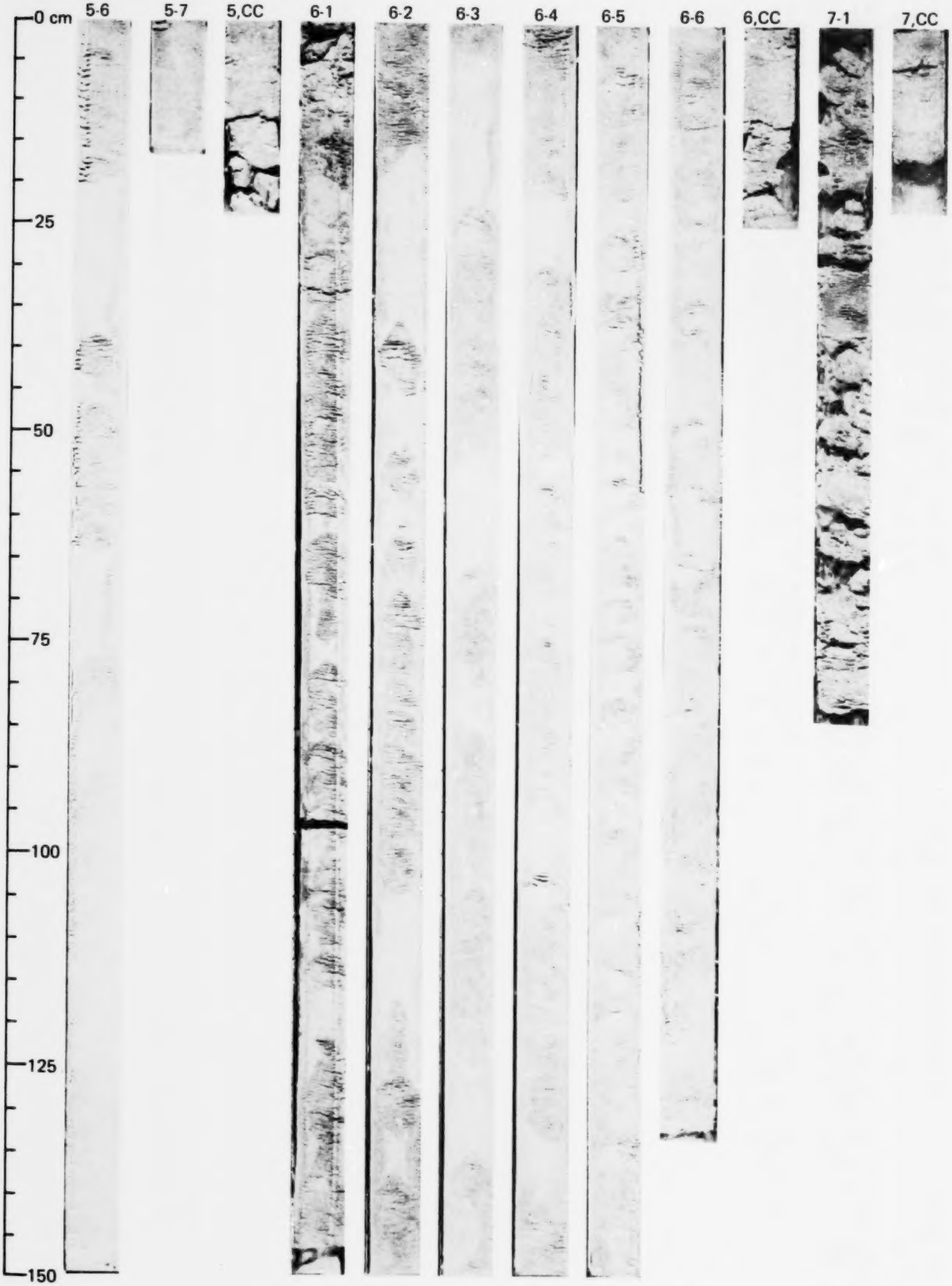
0 cm
25
50
75
100
125
150
5-6
5-7
5,CC
6-1
6-2
6-3
6-4
6-5
6-6
6,CC
7-1
7,CC

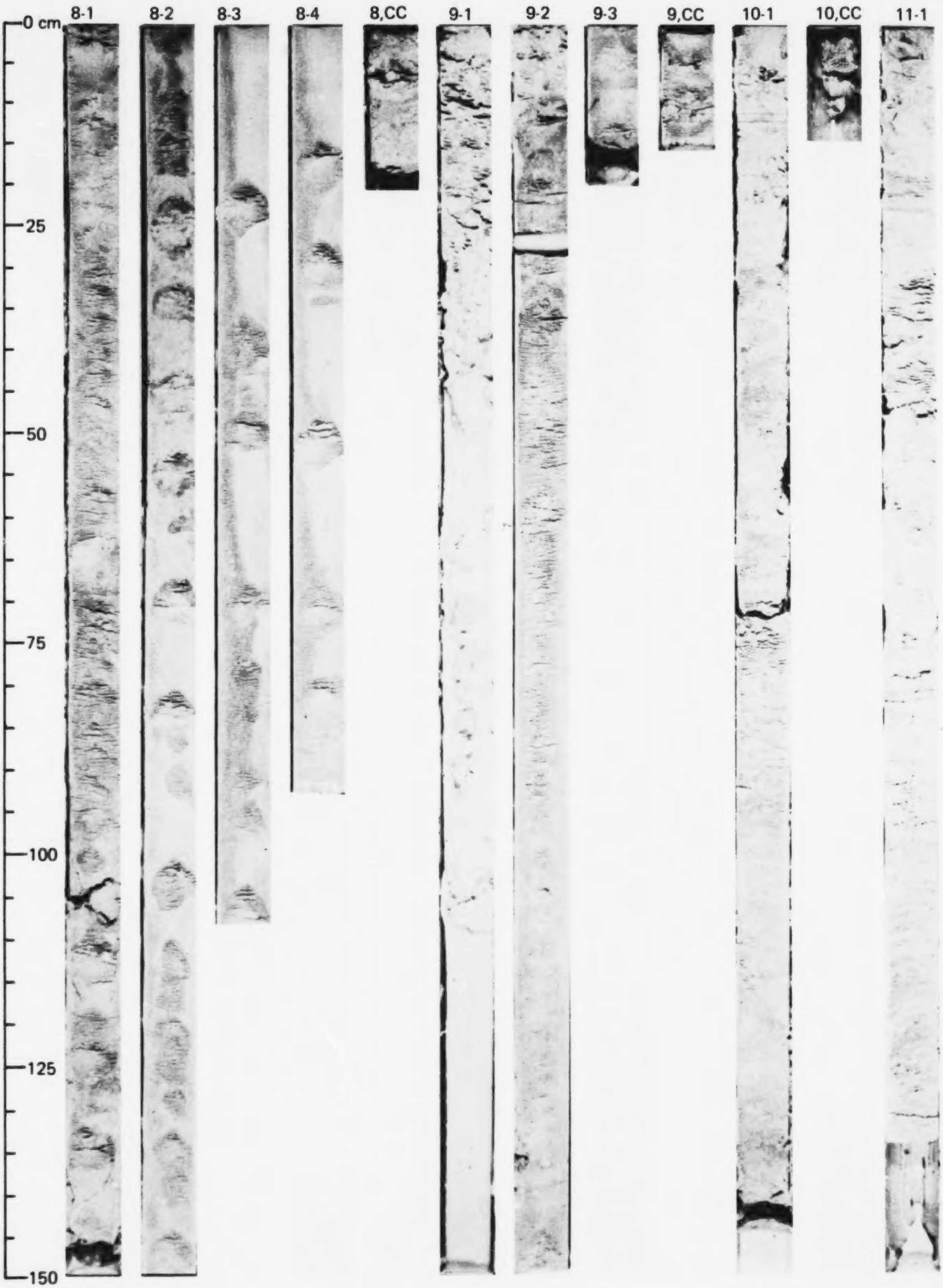
8-1
8-2
8-3
8-4
8,CC
9-1
9-2
9-3
9,CC
10-1
10,CC
11-1
0 cm
25
50
75
100
125
150

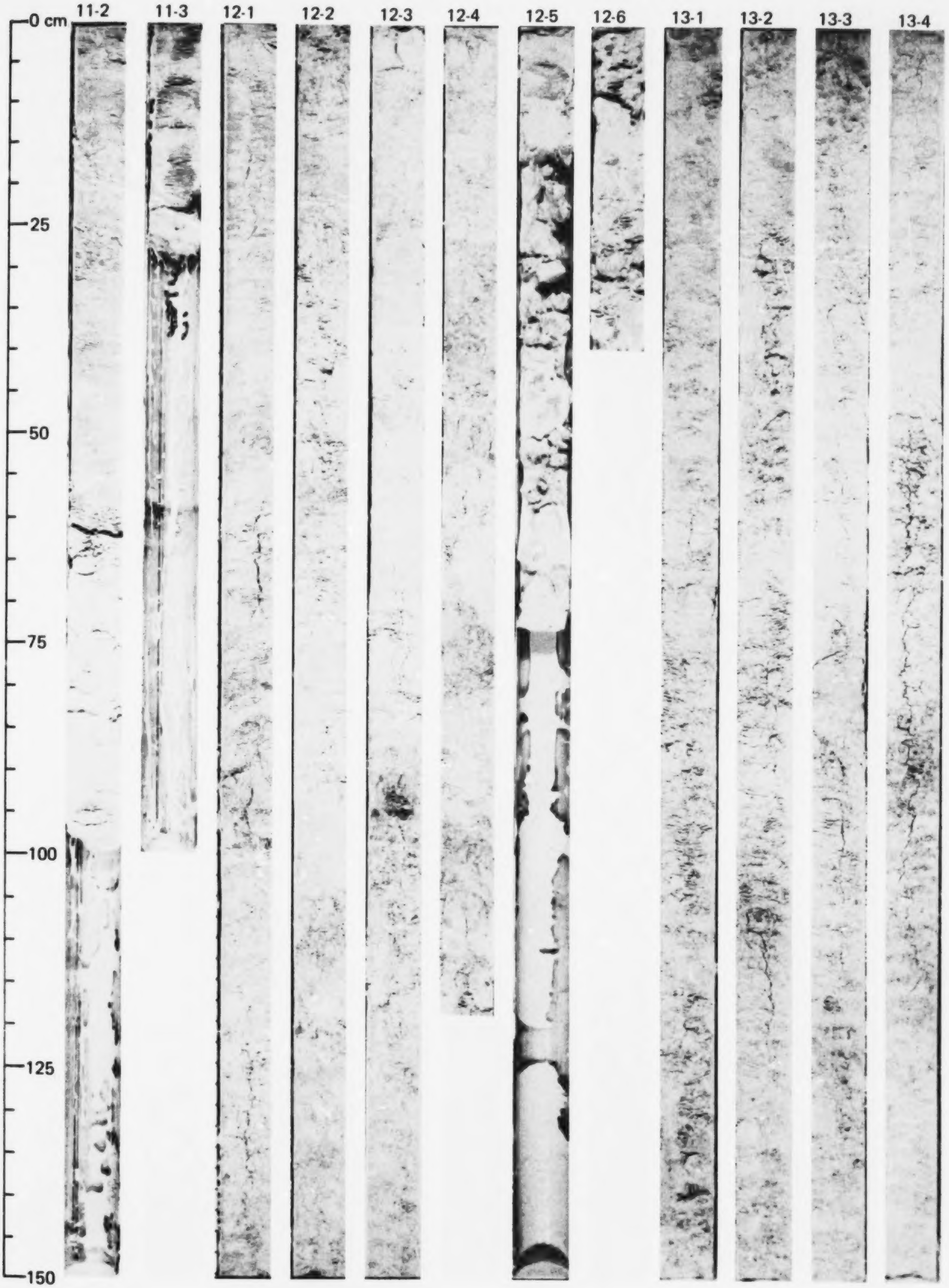
0 cm
25
50
75
100
125
150
11-2
11-3
12-1
12-2
12-3
12-4
12-5
12-6
13-1
13-2
13-3
13-4

0 cm
25
50
75
100
125
150
13-5
13-6
13,CC
14-1
14-2
14-3
14-4
14-5
14-6
14-7
14,CC
15-1

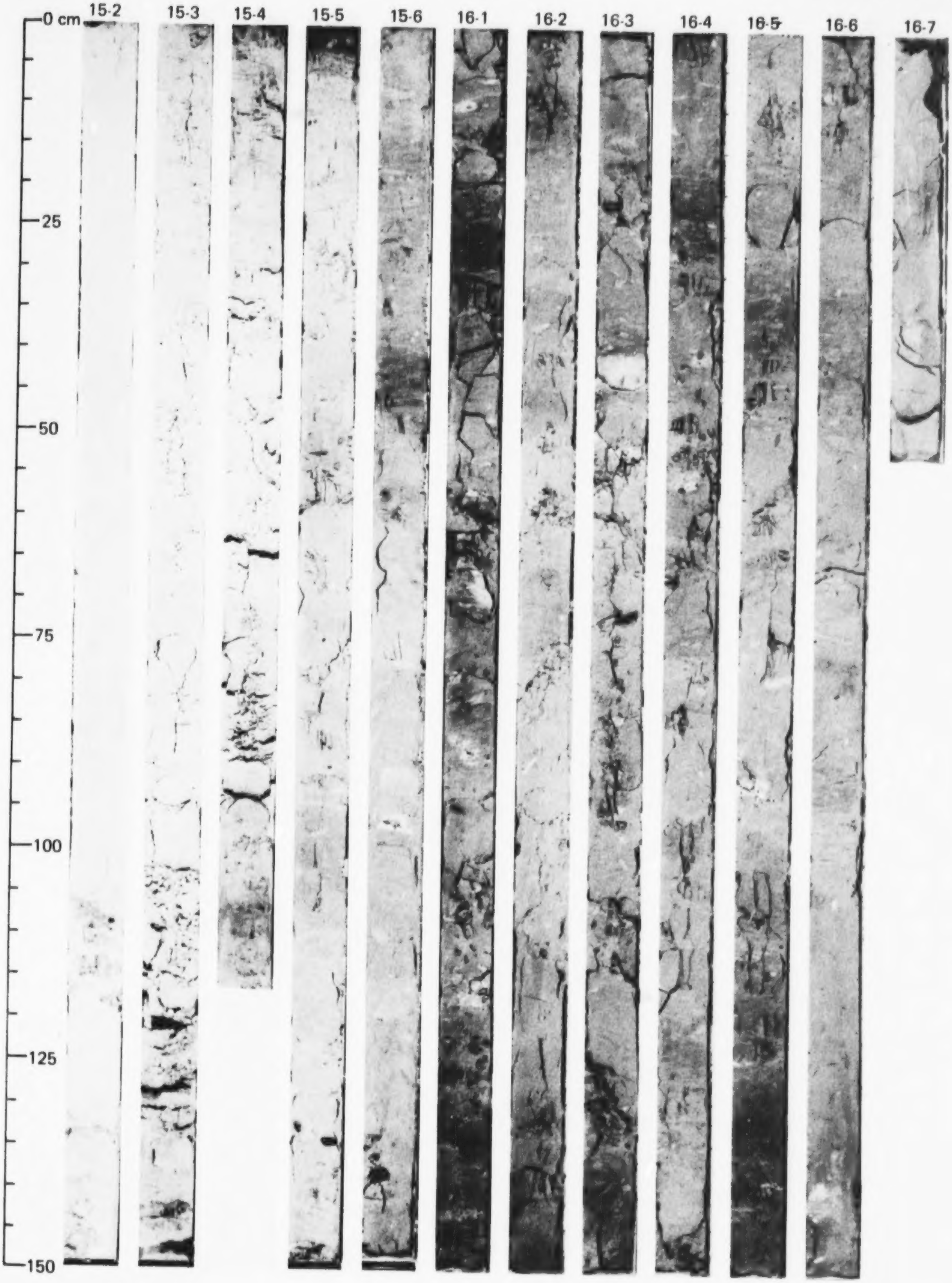
0 cm
25
50
75
100
125
150
15-2
15-3
15-4
15-5
15-6
16-1
16-2
16-3
16-4
16-5
16-6
16-7

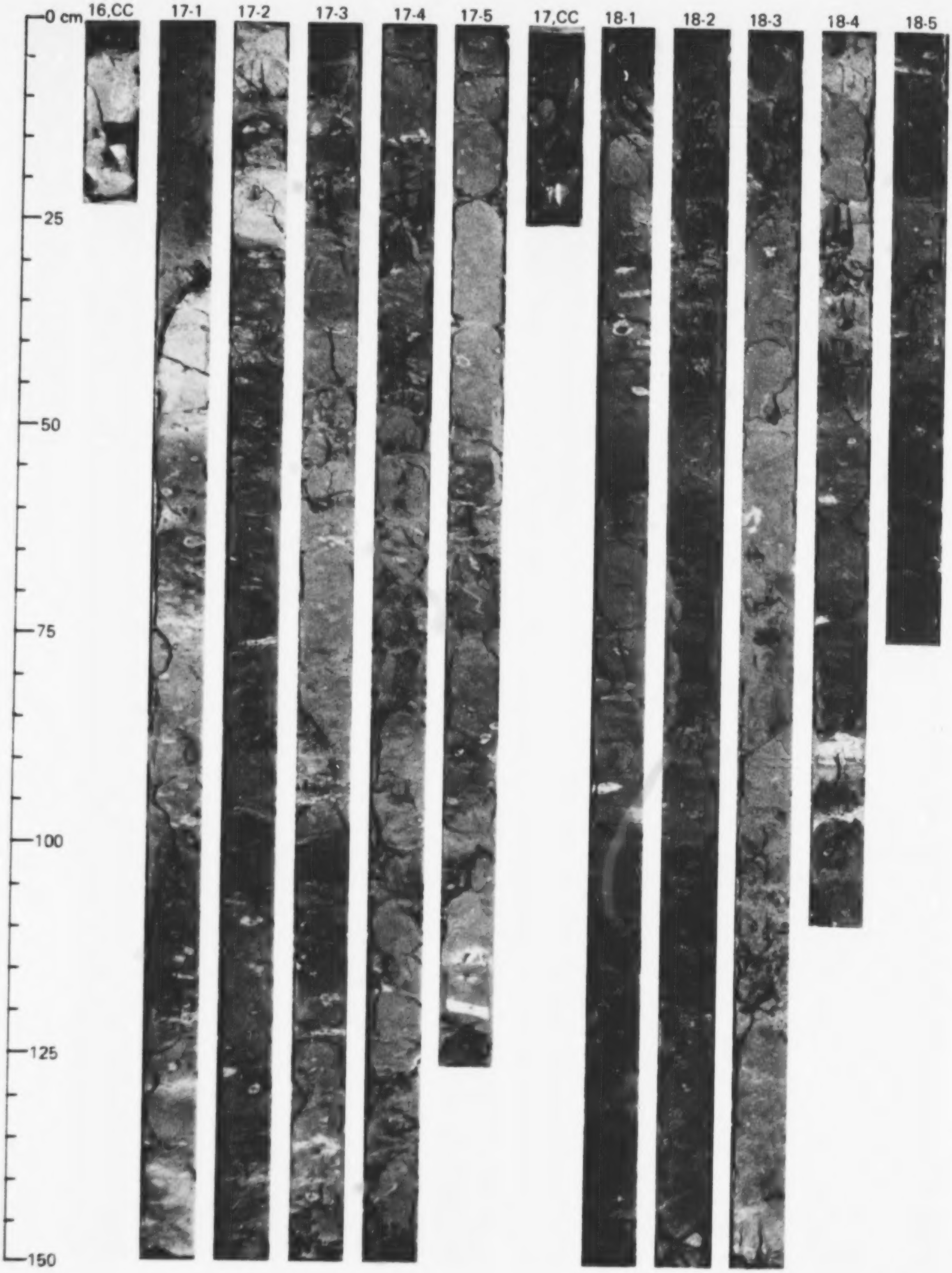
0 cm
25
50
75
100
125
150
16,CC
17-1
17-2
17-3
17-4
17-5
17,CC
18-1
18-2
18-3
18-4
18-5

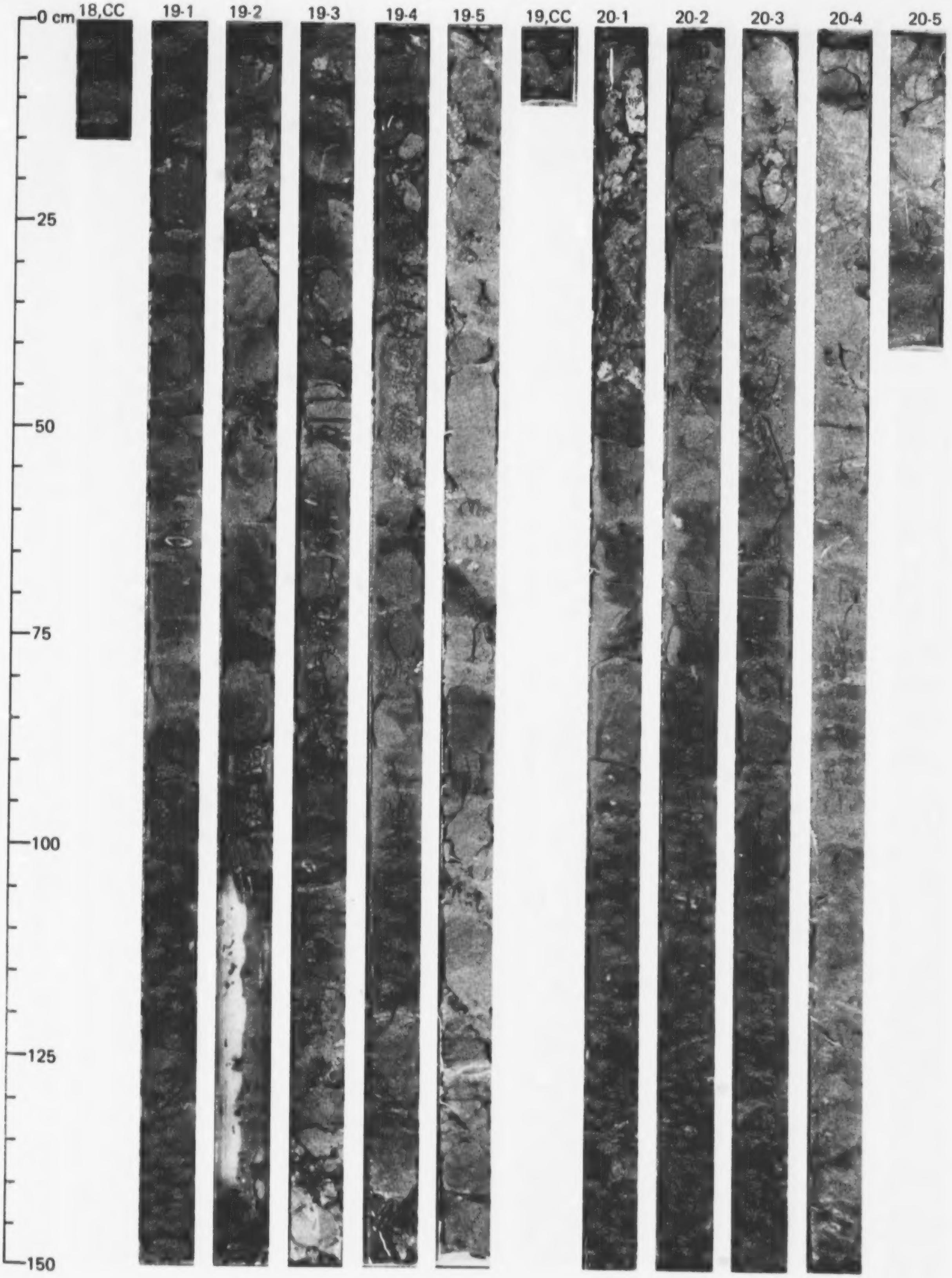
0 cm
25
50
75
100
125
150
18,CC
19-1
19-2
19-3
19-4
19-5
19,CC
20-1
20-2
20-3
20-4
20-5

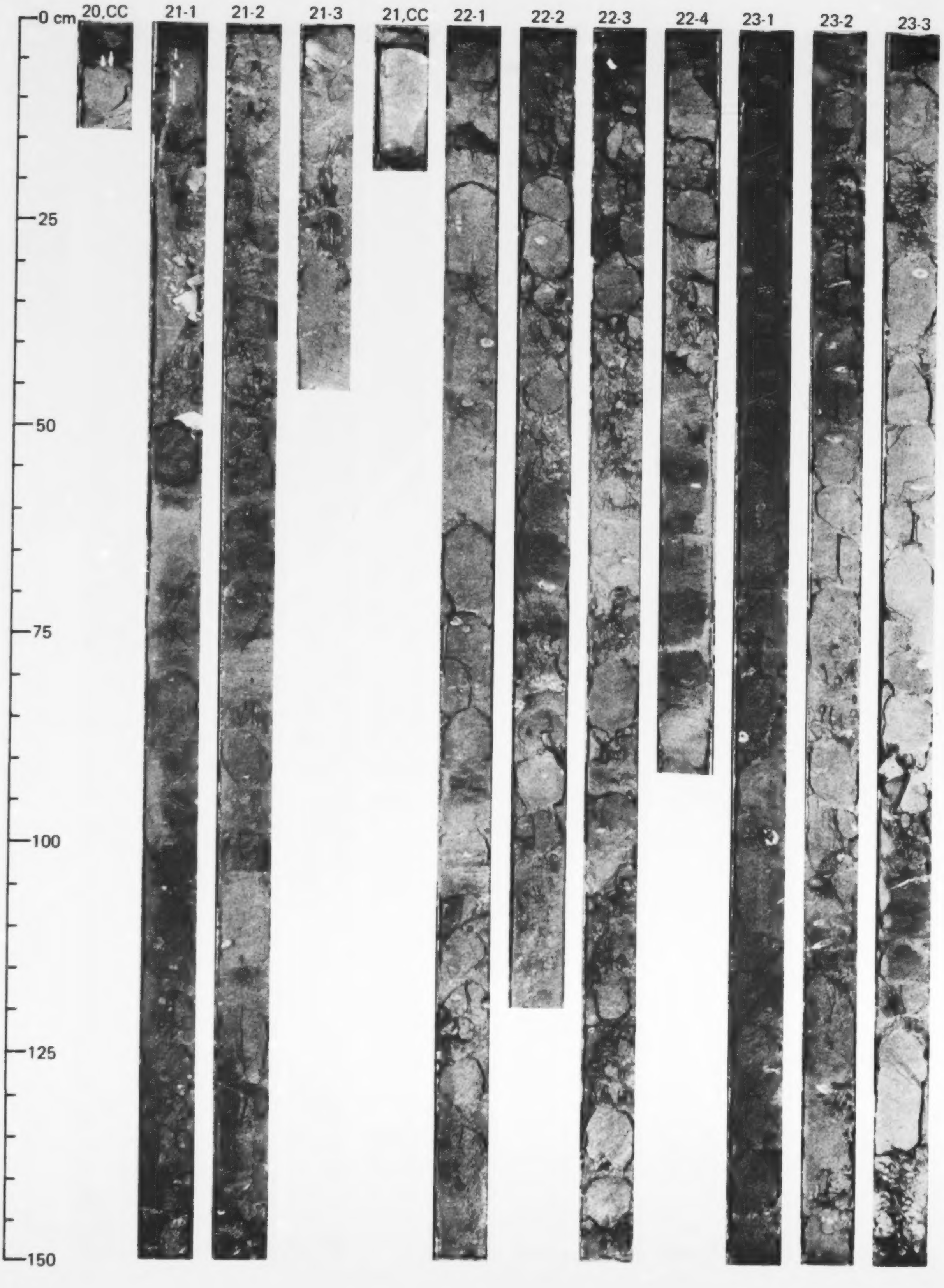
0 cm
25
50
75
100
125
150
20,CC
21-1
21-2
21-3
21,CC
22-1
22-2
22-3
22-4
23-1
23-2
23-3

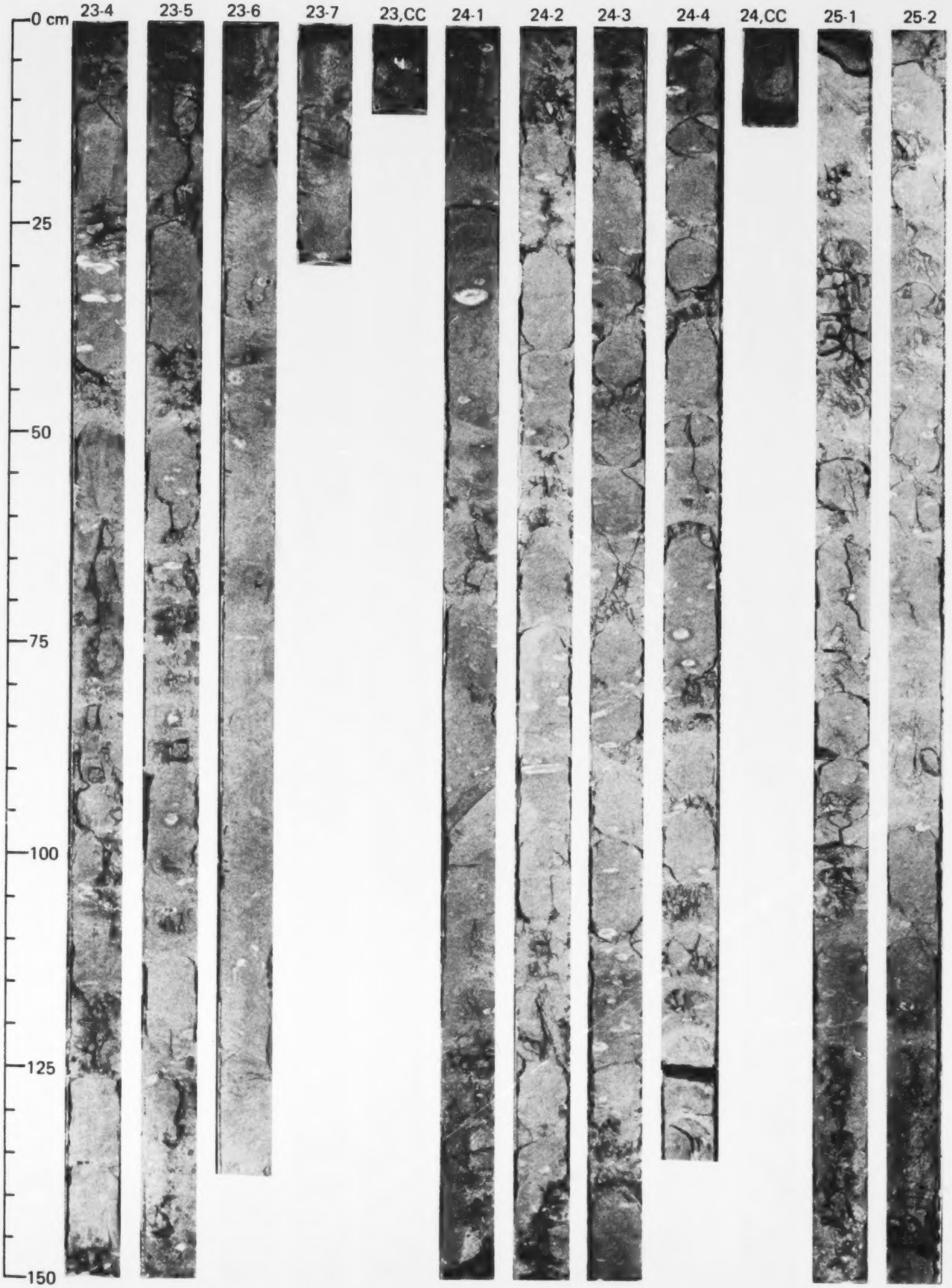
0 cm
25
50
75
100
125
150
23-4
23-5
23-6
23-7
23,CC
24-1
24-2
24-3
24-4
24,CC
25-1
25-2

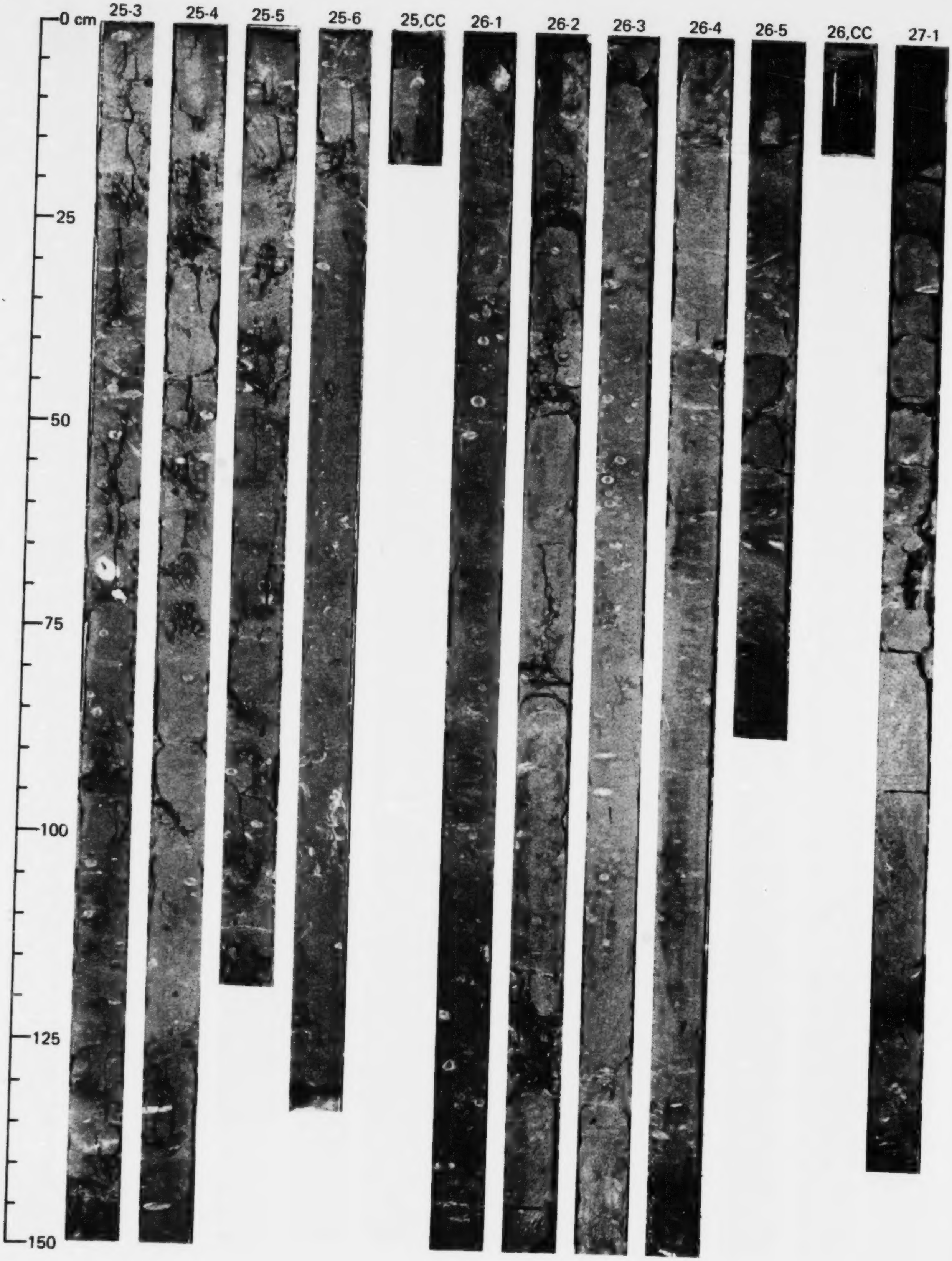
0 cm
25
50
75
100
125
150
25-3
25-4
25-5
25-6
25,CC
26-1
26-2
26-3
26-4
26-5
26,CC
27-1

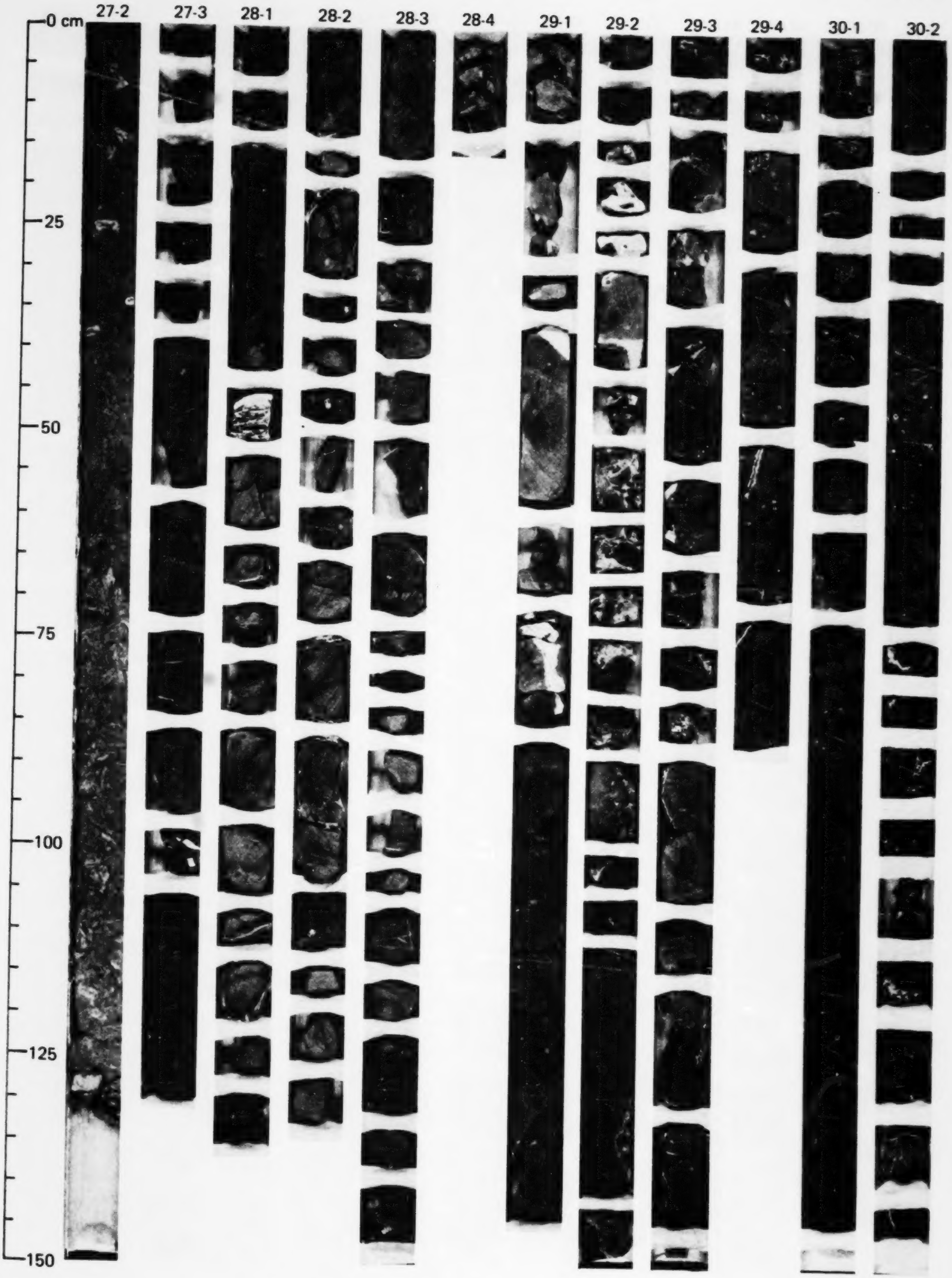
0 cm
25
50
75
100
125
150
27-2
27-3
28-1
28-2
28-3
28-4
29-1
29-2
29-3
29-4
30-1
30-2

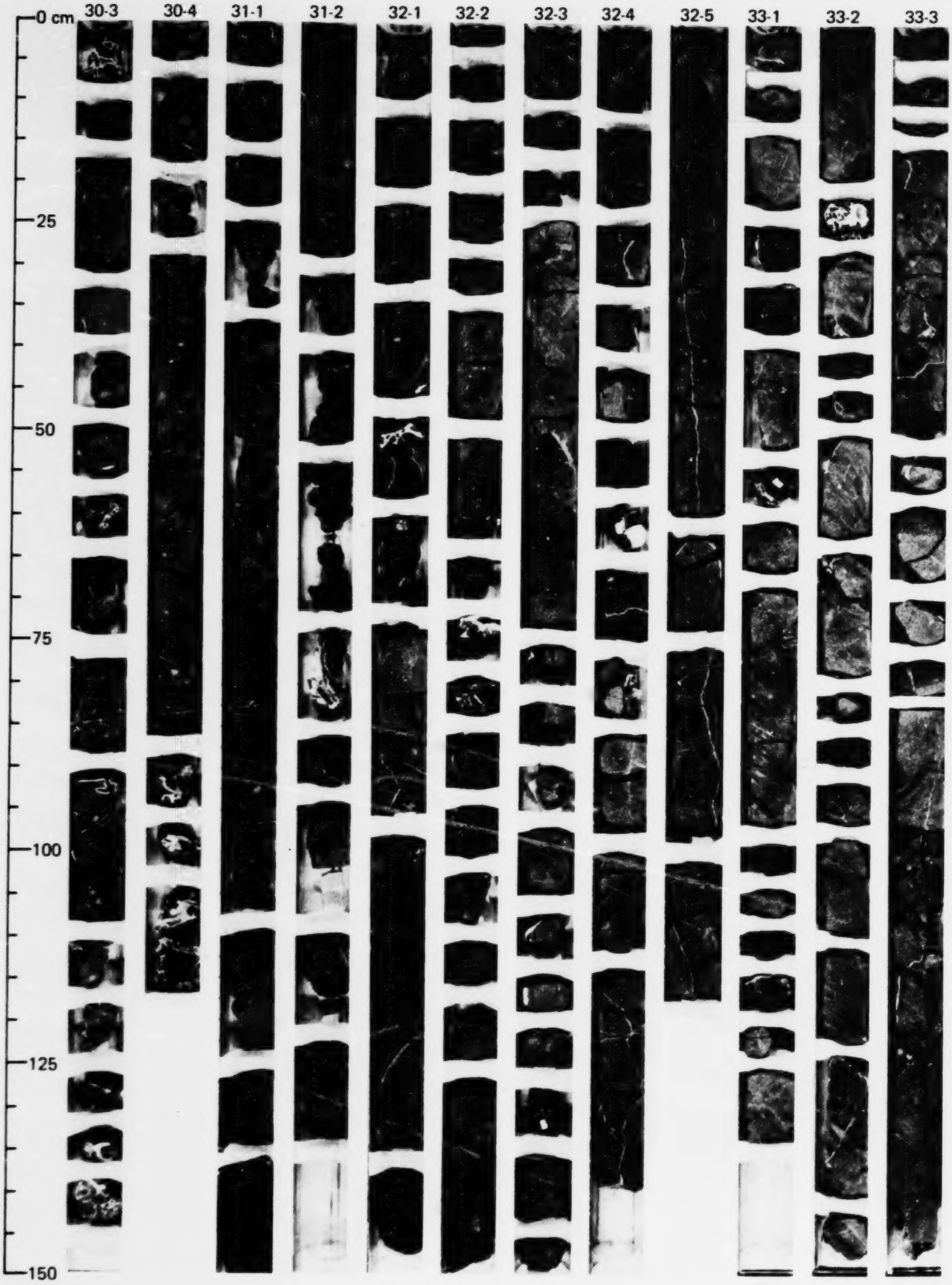
0 cm
25
50
75
100
125
150
30-3
30-4
31-1
31-2
32-1
32-2
32-3
32-4
32-5
33-1
33-2
33-3

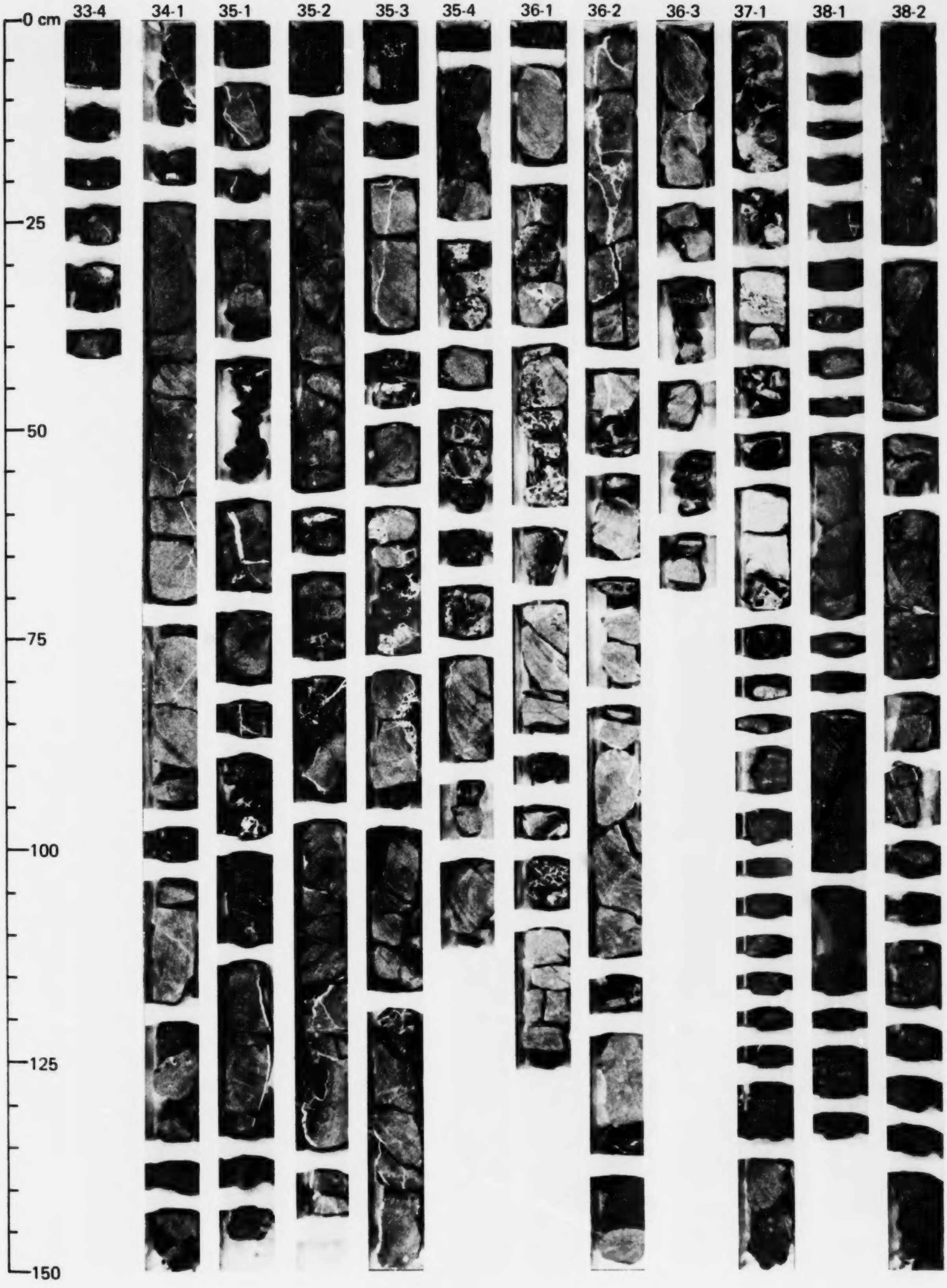
0 cm
25
50
75
100
125
150
33-4
34-1
35-1
35-2
35-3
35-4
36-1
36-2
36-3
37-1
38-1
38-2

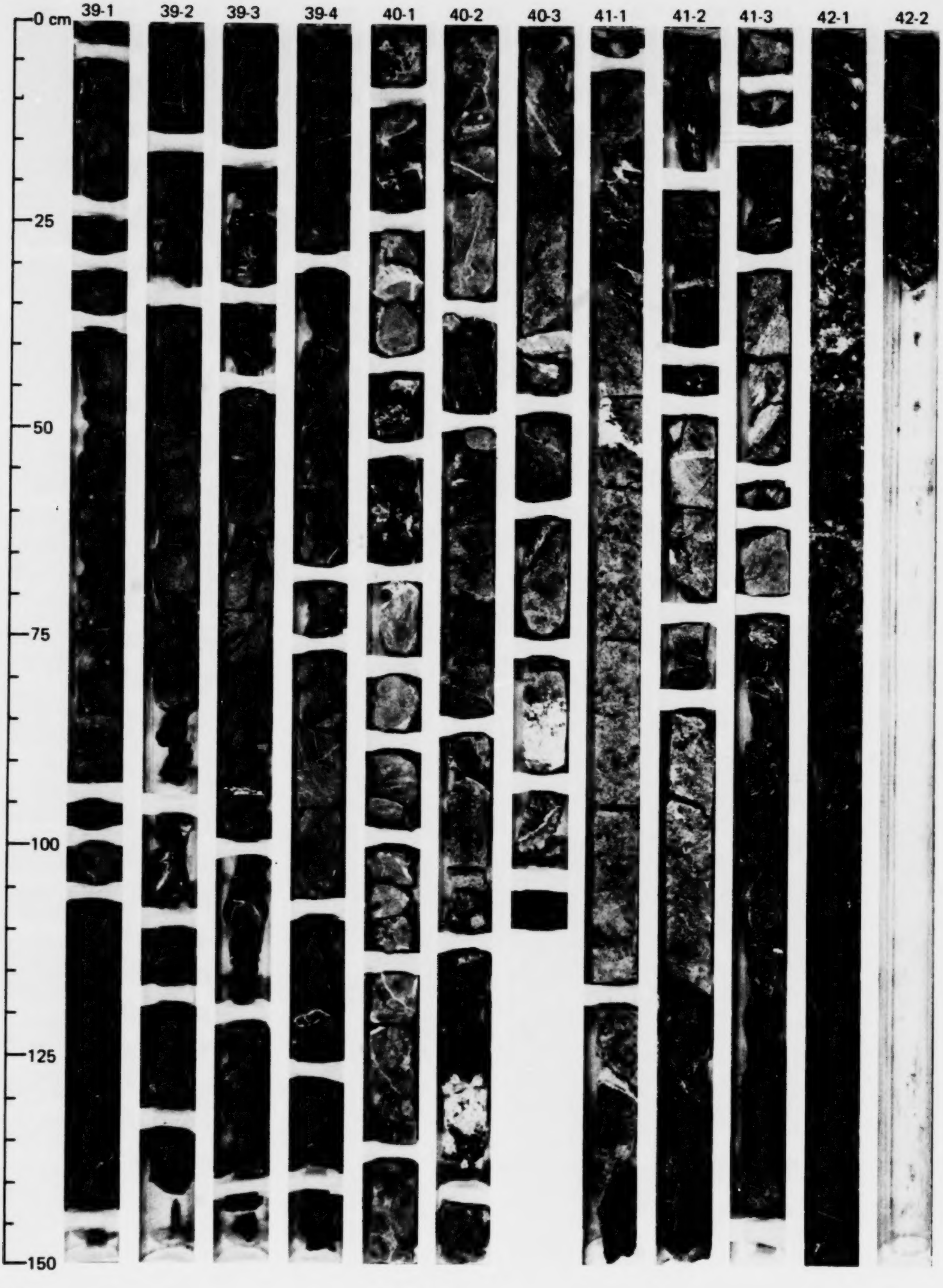
0 cm
25
50
75
100
125
150
39-1
39-2
39-3
39-4
40-1
40-2
40-3
41-1
41-2
41-3
42-1
42-2

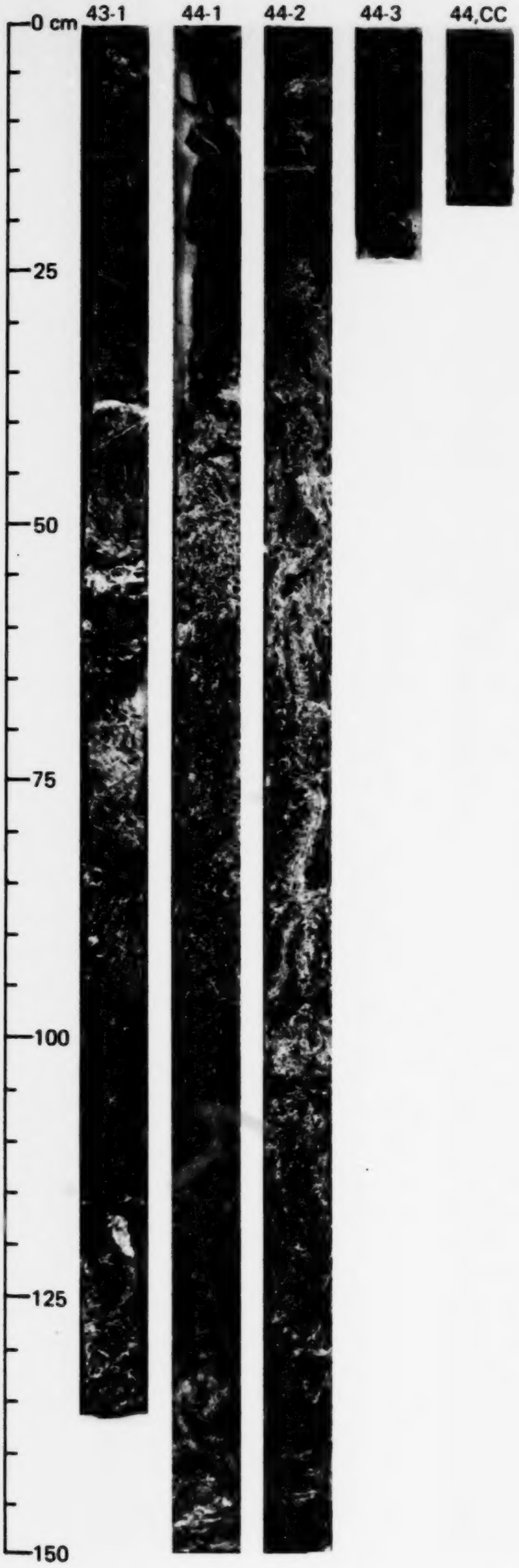
0 cm
25
50
75
100
125
150
43-1
44-1
44-2
44-3
44,CC

SITE 558 (HOLE 558A)

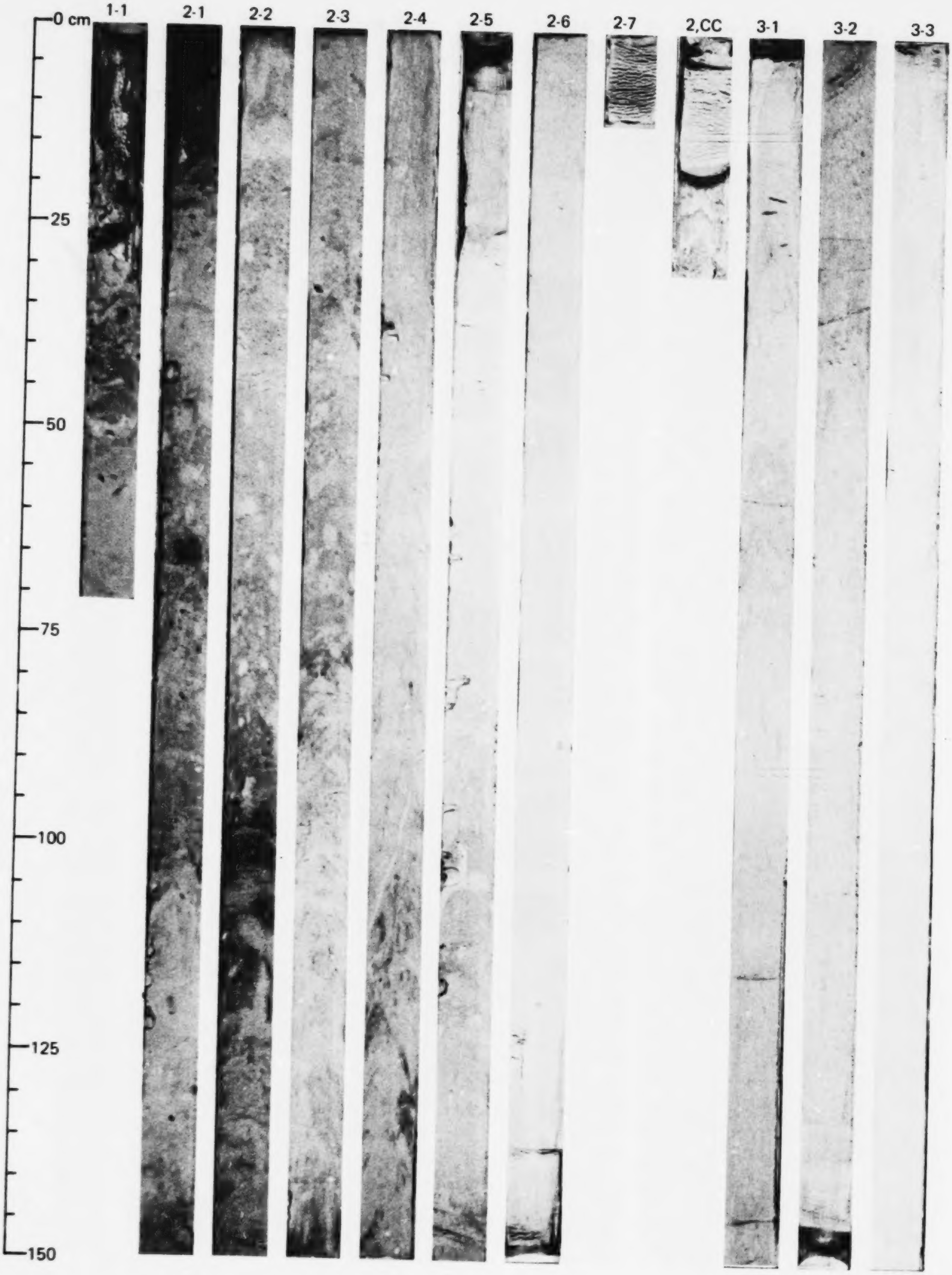
0 cm
25
50
75
100
125
150
1-1
2-1
2-2
2-3
2-4
2-5
2-6
2-7
2,CC
3-1
3-2
3-3

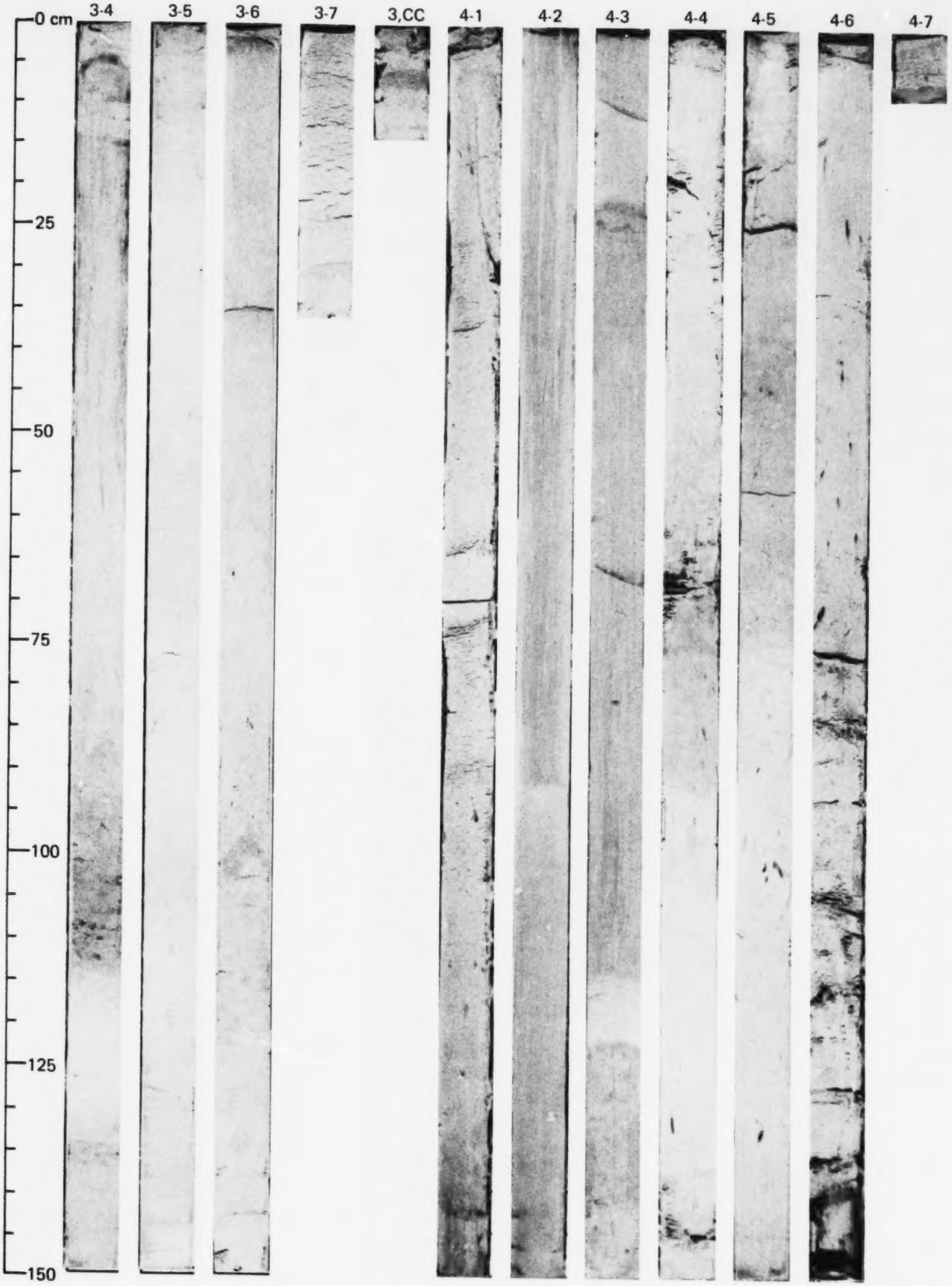
0 cm
25
50
75
100
125
150
3-4
3-5
3-6
3-7
3,CC
4-1
4-2
4-3
4-4
4-5
4-6
4-7

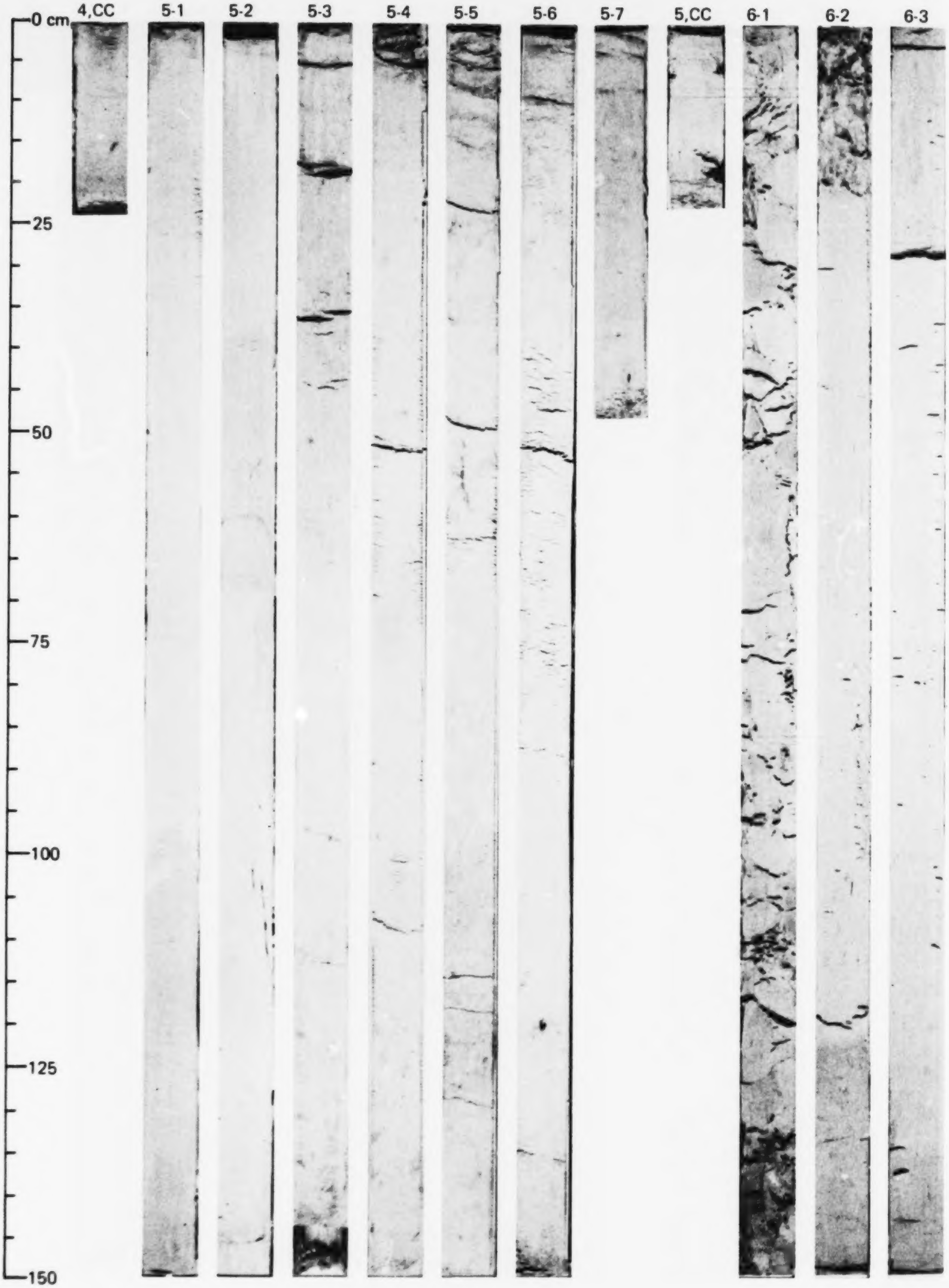
4,CC
5-1
5-2
5-3
5-4
5-5
5-6
5-7
5,CC
6-1
6-2
6-3
0 cm
25
50
75
100
125
150

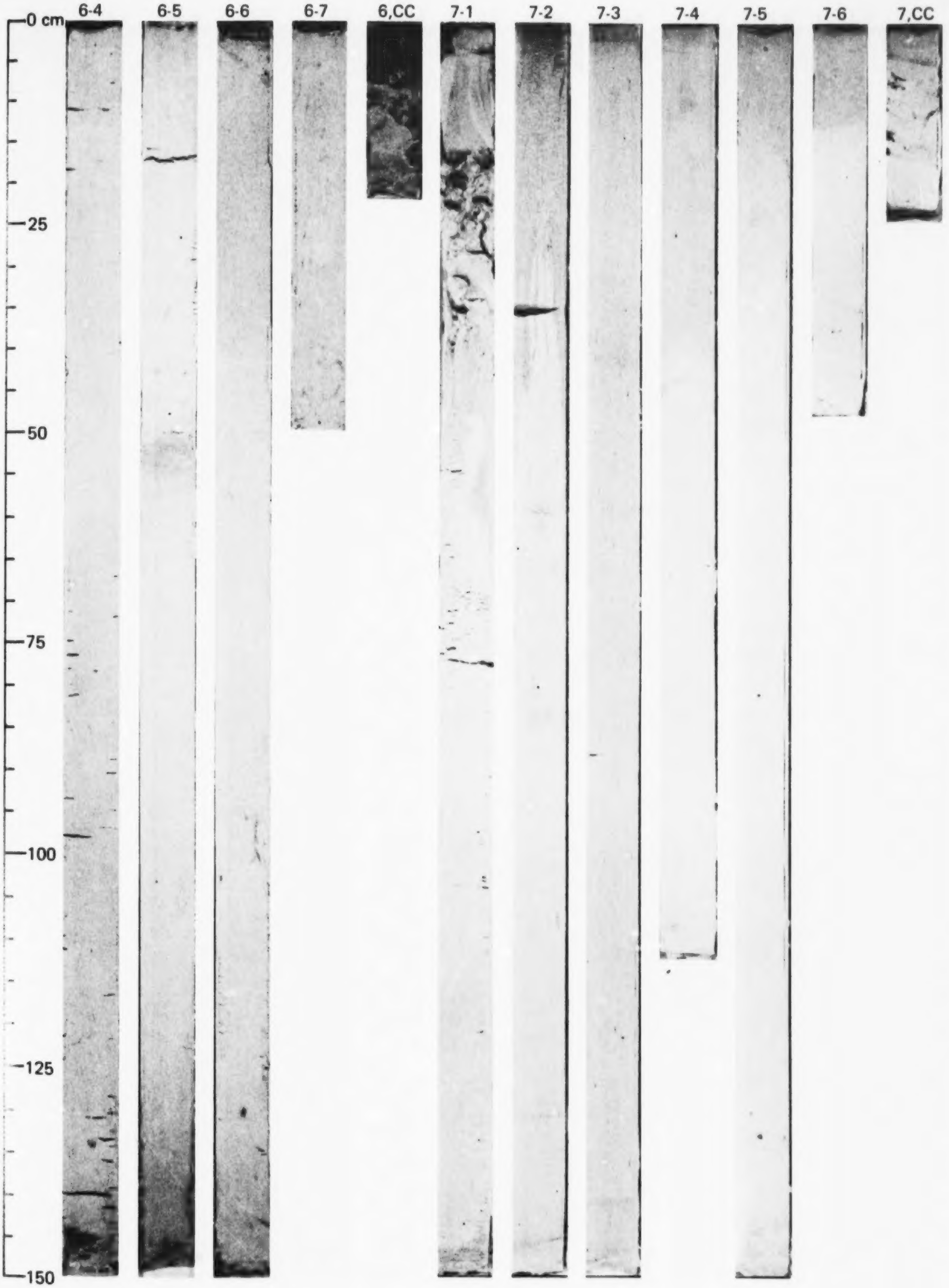
0 cm
25
50
75
100
125
150
6-4
6-5
6-6
6-7
6,CC
7-1
7-2
7-3
7-4
7-5
7-6
7,CC

0 cm
25
50
75
100
125
150
8-1
8-2
8-3
8-4
8-5
8-6
8,CC
9-1
9-2
9-3
9-4
9,CC

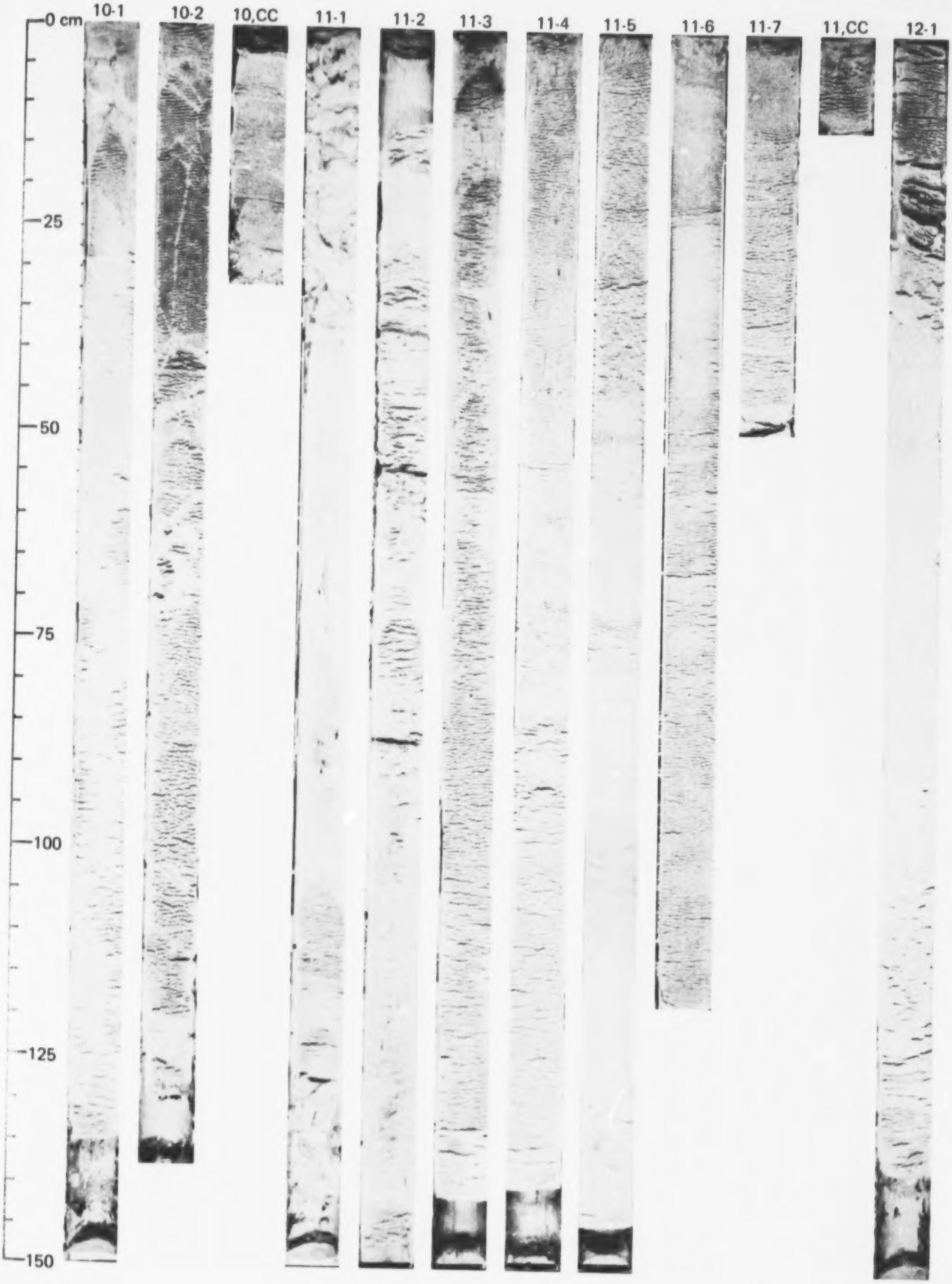
0 cm
25
50
75
100
125
150
10-1
10-2
10,CC
11-1
11-2
11-3
11-4
11-5
11-6
11-7
11,CC
12-1

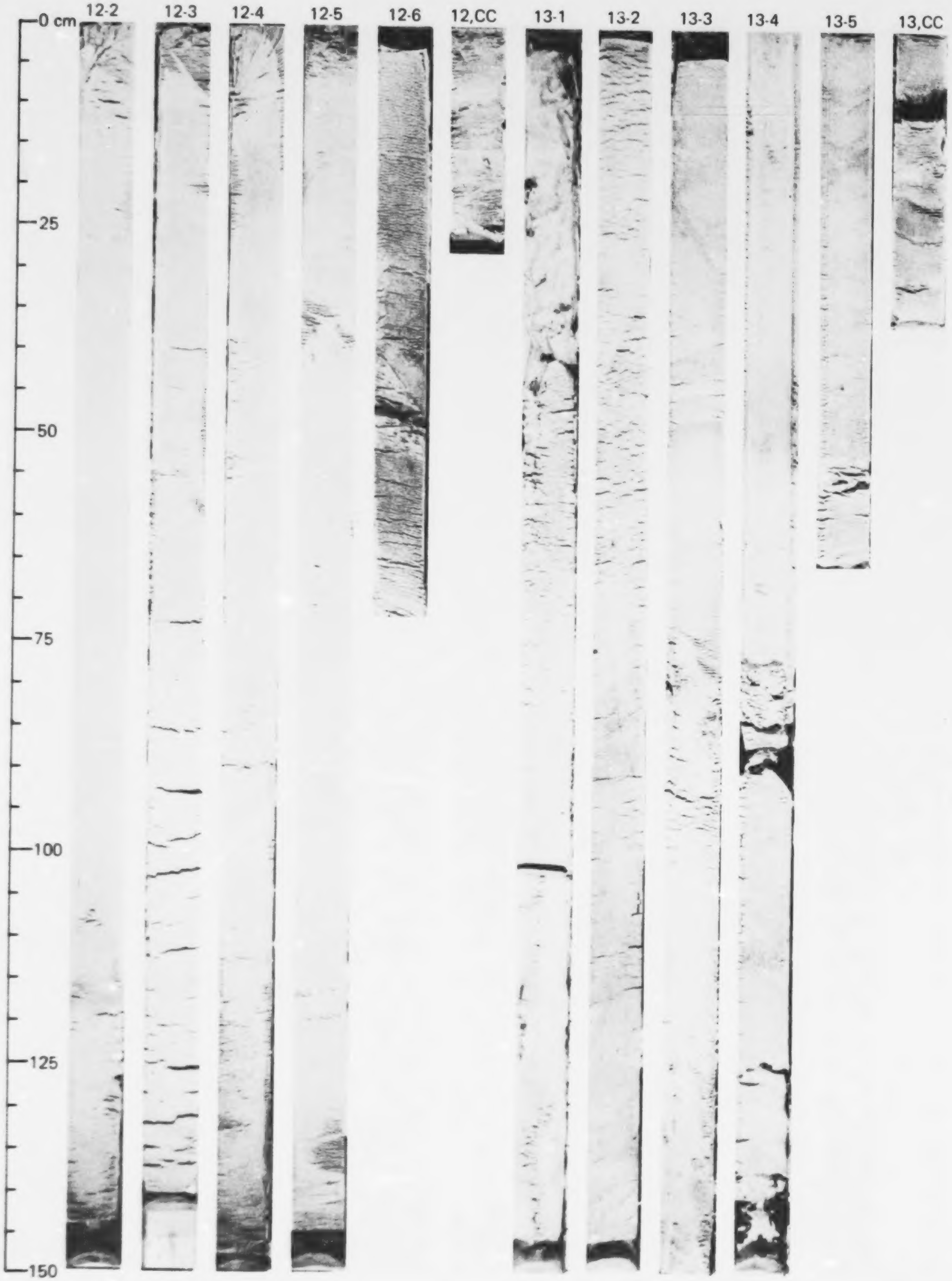
12-2
12-3
12-4
12-5
12-6
12,CC
13-1
13-2
13-3
13-4
13-5
13,CC
0 cm
25
50
75
100
125
150

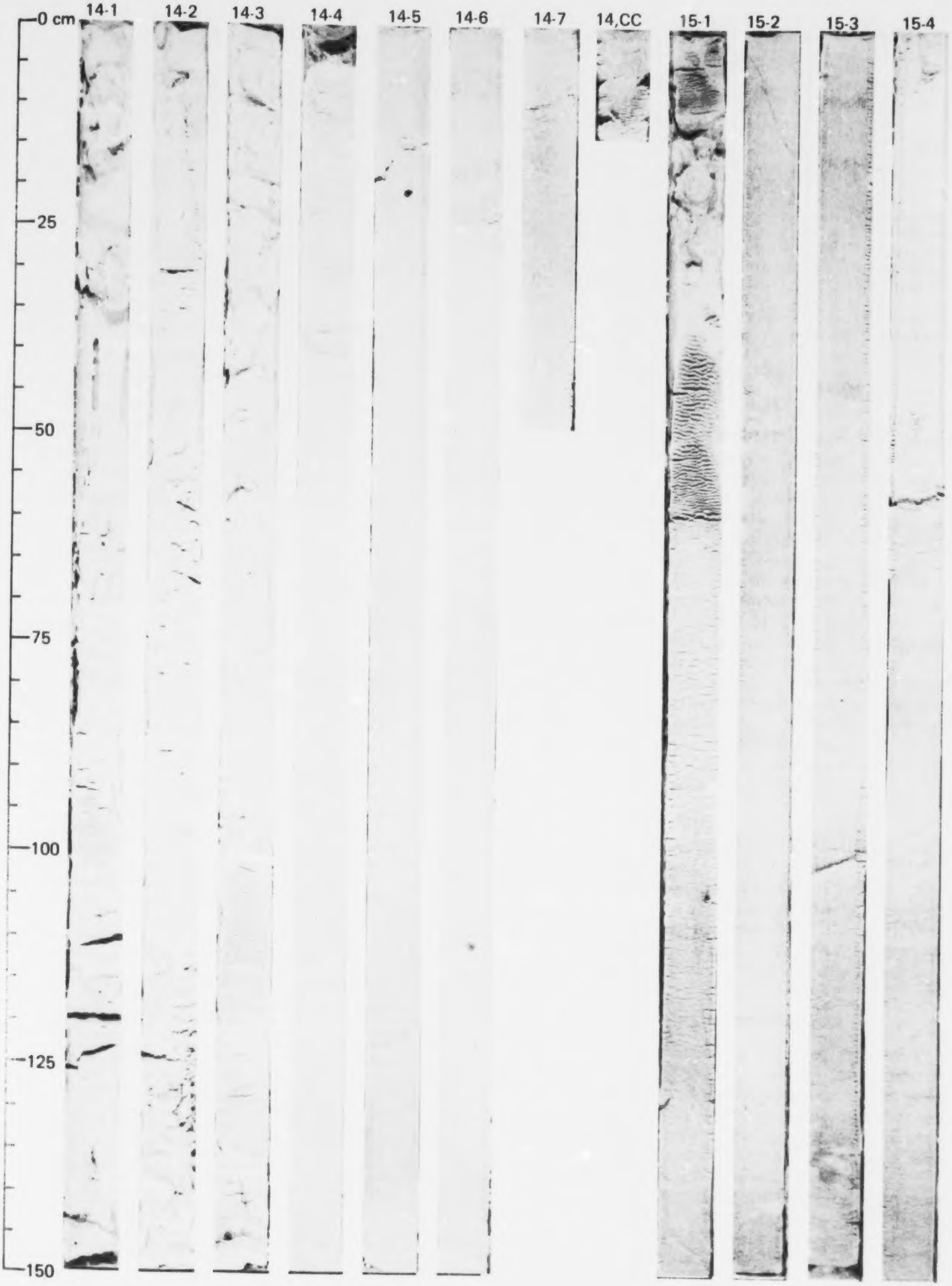
0 cm
25
50
75
100
125
150
14-1
14-2
14-3
14-4
14-5
14-6
14-7
14,CC
15-1
15-2
15-3
15-4

SITE 558 (HOLE 558A)

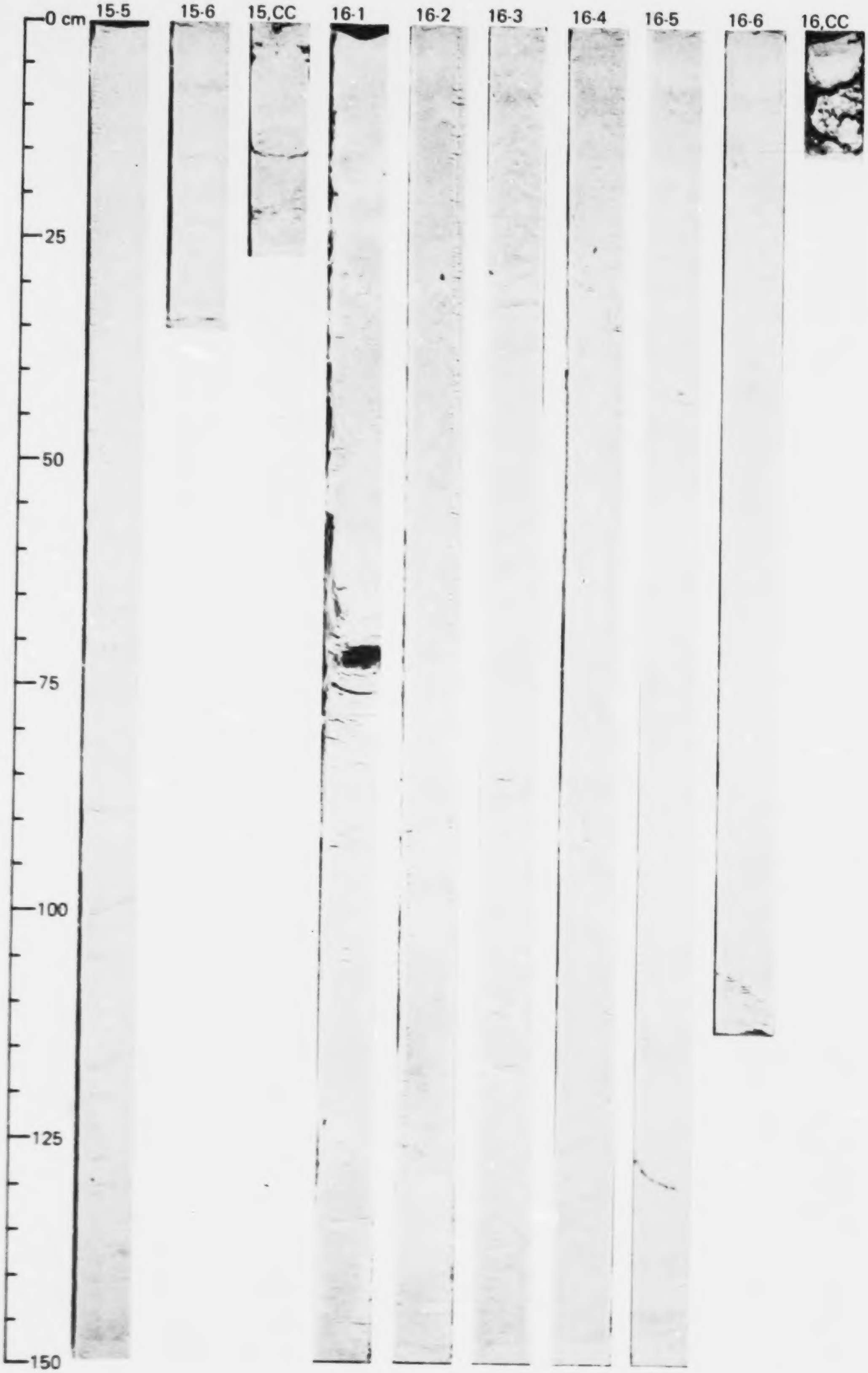
0 cm
25
50
75
100
125
150
15-5
15-6
15,CC
16-1
16-2
16-3
16-4
16-5
16-6
16,CC

8. SITE 559[1]

Shipboard Scientific Party[2]

HOLE 559

Date occupied: 14 October 1981

Date departed: 16 October 1981

Time on hole: 52 hr.

Position (latitude; longitude): 35°07.45′N; 40°55.00′W

Water depth (sea level; corrected m, echo-sounding): 3754

Water depth (rig floor; corrected m, echo-sounding): 3764

Bottom felt (m, drill pipe): 3766

Penetration (m): 301

Number of cores: 8

Total length of cored section (m): 63.0

Total core recovered (m): 23.5

Core recovery (%): 37.3

Oldest sediment cored:
Depth sub-bottom (m): 249
Nature: Limestone
Age: middle Miocene

Basement:
Depth sub-bottom (m): 238
Nature: Basalt

Principal results: Hole 559 (Site MAR-8) was drilled between Anomalies 12 and 13 on the west flank of the Mid-Atlantic Ridge midway between Oceanographer and Hayes fracture zones (Fig. 1). The sediments were washed down to basement, which was felt at 238 m sub-bottom.

Aphyric pillow basalts were cored through the entire 63-m basement section. The principal macroscopic features are the variability in degree of alteration and the large amount of fresh glass recovered. These basalts belong to a single petrographic chemical group. The effects of alteration are clearly shown by chemical data. The observed variations in Sr are due in part to contamination induced by alteration. These variations can be used for choosing samples whose inferred Sr contamination is less than 5 ppm for Sr isotopic studies. The Sr concentration in fresh glass is 157 ppm.

Magmaphile element concentrations are enriched relative to chondrites (Nb = 16, Zr = 100, Ti = 9000, Y = 35, and V = 300 ppm). Although this result agrees with the hypothesis of a boundary at the latitude of Hayes Fracture Zone, no definite conclusion can be made because of the complexities revealed at Sites 558 and 556 on the same isochron.

The following analyses were not done for Site 559: sediment accumulation rates, pore water chemistry, and downhole measurements.

OPERATIONS

Approach to Site

After analyzing the results of drilling at Site 558, we decided to drill Site 559 near the original location of MAR-8 between Anomalies 12 and 13 south of the Oceanographer Fracture Zone. A tentative site was located, based on existing magnetics data, halfway between two smaller fracture zones that are themselves sandwiched by the Hayes and Oceanographer fracture zones.

The initial approach to the site began at 0220Z on 14 October (Fig. 2) on a track parallel to the fracture zones and crossing the prime target area. Although in general the basement relief was quite variable and the sediment cover was greater than 0.5 s, a location was observed at 0353Z (Fig. 3) where the sediment cover thinned to less than 0.25 s on the flank of a small basement high. Profiling was continued for 4 miles beyond this point until the location of Anomaly 13 was confirmed. The ship's course was then reversed and the site relocated. The beacon was dropped on Site 559 at 0518Z.

On-Site Operations

Site 559 was spudded at 1238Z 14 October in 3766 m of water. Sediments were washed to a depth of 238 m sub-bottom where basement was reached. Between 1930Z 14 October and 2230Z 15 October, 63 m of basement were cored without any major problems (Table 1). Drilling was then discontinued because of time considerations. The *Challenger* was under way to Site 560 at 0730Z 16 October.

SEDIMENT LITHOLOGY

At Site 559 the sediments were washed to basement at 238 m. At that time a wash core was retrieved that contained 2 m of disturbed marly nannofossil ooze (white 2.5YN 8 and 10YR 8/2) and marly nannofossil ooze with volcanic glass. The core includes upper Pliocene to upper middle Miocene sediments. No bioturbation or bedding was observed, except for faint color changes.

The sediment components are calcareous nannofossils (20–40%), clay (35–55%), foraminifers (3–15%), unspecified carbonate (5–10%), trace amounts to 10% of volcanic-derived material, and micronodules. In 559-

---

[1] Bougault, H., Cande, S. C., et al., *Init. Repts. DSDP*, 82: Washington (U.S. Govt. Printing Office).

[2] Henri Bougault (Co-Chief Scientist), IFREMER (formerly CNEXO), Centre de Brest, B. P. 337 29273 Brest Cedex, France; Steven C. Cande (Co-Chief Scientist), Lamont-Doherty Geological Observatory, Columbia University, Palisades, New York; Joyce Brannon, Department of Earth and Planetary Sciences, Washington University, St. Louis, Missouri, David M. Christie, Hawaii Institute of Geophysics, University of Hawaii at Manoa, Honolulu, Hawaii; Murlene Clark, Department of Geology, Florida State University, Tallahassee, Florida; Doris M. Curtis, Curtis and Echols, Geological Consultants, Houston, Texas; Natalie Drake, Department of Geology, University of Massachusetts, Amherst, Massachusetts; Dorothy Echols, Department of Earth and Planetary Sciences, Washington University, St. Louis, Missouri (present address: Curtis and Echols, Geological Consultants, 800 Anderson, Houston, Texas 77401); Ian Ashley Hill, Department of Geology, University of Leicester, Leicester LEI 7RH, United Kingdom; M. Javed Khan, Lamont-Doherty Geological Observatory, Columbia University, Palisades, New York (present address: Department of Geology, Peshawar University, Peshawar, Pakistan); William Mills, Deep Sea Drilling Project, Scripps Institution of Oceanography, La Jolla, California (present address: Ocean Drilling Program, Texas A&M University, College Station, Texas 77843); Rolf Neuser, Institut für Geologie, Ruhr Universität Bochum, 4630 Bochum 1, Federal Republic of Germany; Marion Rideout, Graduate School of Oceanography, University of Rhode Island, Kingston, Rhode Island (present address: Department of Geology, Rice University, P.O. Box 1892, Houston, Texas 77251); and Barry L. Weaver, Department of Geology, University of Leicester, Leicester, LEI 7RH, United Kingdom (present address: School of Geology and Geophysics, University of Oklahoma, Norman, Oklahoma 73019).

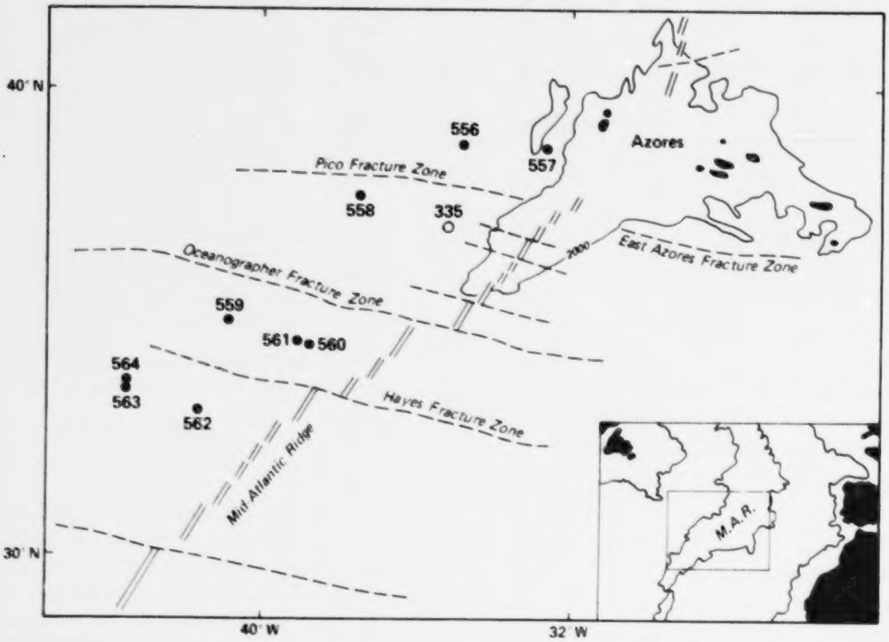
40° N
30° N
40° W
32° W
556
557
Azores
Pico Fracture Zone
558
335
2000
East Azores Fracture Zone
Oceanographer Fracture Zone
559
561
560
564
563
562
Hayes Fracture Zone
Mid Atlantic Ridge
M.A.R.

Figure 1. Site location map for Leg 82.

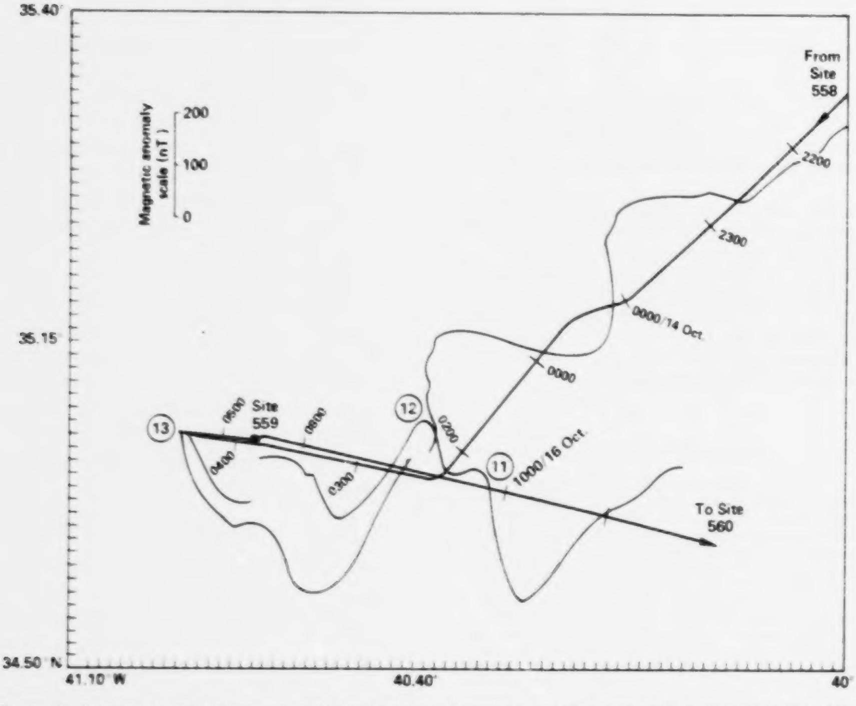

Figure 2. Approach and site survey track for Site 559. Heavy line is ship track with hour marks in GMT. Thin line is magnetic anomaly projected perpendicularly from the ship's track. Circled numbers are magnetic anomalies based on work at Lamont-Doherty Geological Observatory.

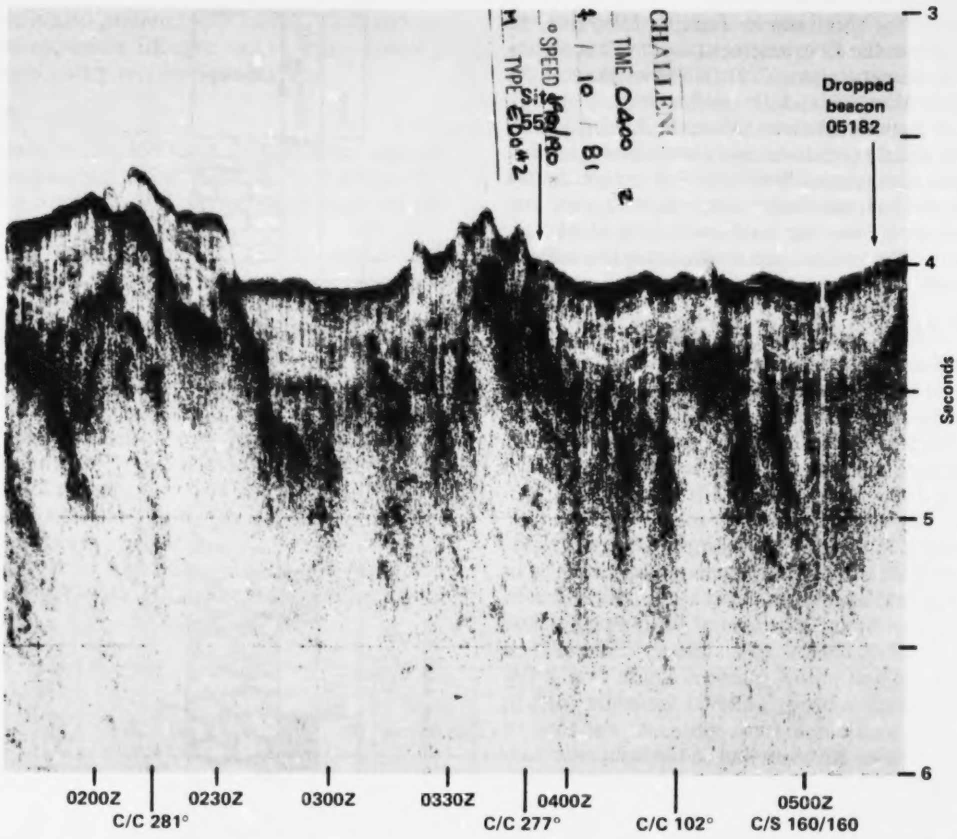

Figure 3. *Glomar Challenger* seismic profile over Site 559. For location of profile, see Figure 2. C/C = course change.

Table 1. Coring summary, Hole 559.

Core	Date (Oct. 1981)	Time (z)	Depth from drill floor (m)	Depth below seafloor (m)	Length cored (m)	Length recovered (m)	Percent recovered
H1	14	1605	3766.0–4004.0	0.0–238.0	0.0	0.00	0
1	14	2225	4004.0–4013.0	238.0–247.0	9.0	3.99	44
2	15	0310	4013.0–4022.0	247.0–256.0	9.0	3.82	42
3	15	0510	4022.0–4022.5	256.0–256.5	0.5	0.25	50
4	15	0920	4022.5–4031.0	256.5–265.0	8.5	2.72	32
5	15	1220	4031.0–4040.0	265.0–274.0	9.0	3.39	38
6	15	1550	4040.0–4049.0	274.0–283.0	9.0	2.60	29
7	15	1930	4049.0–4058.0	283.0–292.0	9.0	3.47	39
8	15	2230	4058.0–4067.0	292.0–301.0	9.0	3.27	36
					63.0	23.51	37

I1-2, 20 cm there is a thin layer of volcanic glass (moder- tely disturbed). As in Hole 558, traces of authigenic do- omite rhombs are present. The sediments retrieved at this ite represent Neogene ocean pelagic sedimentation be- inning in middle Miocene time.

Throughout the basalt units, intrapillow basalt (volca- iclastic) limestone is common. It occurs either between illow margins or as fillings in basalt cracks and vesicles. eopetal structures were observed in some vesicles. The imestones are moderately bioturbated and occasionally how inclined bedding contacts. Colors vary from very pale brown (10YR 8/3) to pale brown (10YR 6/3) and ight gray (5YR 7/1) to pinkish white (5YR 8/2).

Volcaniclasts are derived from adjacent vitric rims of pillow basalts. The original calcareous pelagic ooze has been recrystallized to micritic calcite, although ghosts of foraminifers still persist. The limestones in places are intensely mineralized by manganese oxide (usually dendritic) and are commonly veined by sparry calcite.

BIOSTRATIGRAPHY

Summary

Sediments for microfossil study from Hole 559 are wash cores. Based on the calcareous nannofossils, the age of the sediment ranges from middle Miocene to late Pliocene. One tentative determination based on poorly preserved nannofossils in Core 2 from a sediment streak below basement may be Oligocene.

Foraminifers in the wash core are from the latest Miocene to earliest Pliocene times. Although well preserved, they are not considered reliable age determinants.

Calcareous Nannofossils

Hole 559 was washed down to a depth of 238 m where basement material was encountered. Core H1 contains abundant and well-preserved nannofossils. *Discoaster brouweri* and *D. surculus* without *Reticulofenestra pseudoumbilica* occur in 559-H1-1, 14 cm. This suggests the upper Pliocene *D. brouweri* Zone, *D. surculus* Subzone

CN12b (NN16) for this sample. Sample 559-H1-2, 50 cm (slightly above the first basement material) is attributed to the *D. hamatus* Zone CN7 (NN9) because of the presence of *D. hamatus* and *D. neohamatus*.

A layer of sediment below basement level (Core 2) contains very poorly preserved nannofossils. A possible *Dictyococcites bisectus* and *Sphenolithus predistentus* are contained in this interval. Because they are so poorly preserved, these specimens are only tentatively identified. If these species do in fact occur, the sample could be lower Oligocene.

IGNEOUS PETROLOGY AND GEOCHEMISTRY

Hole 559 encountered basement at 238 m sub-bottom and penetrated 63 m of a single aphyric pillow basalt unit (Fig. 4). Basalts of this unit appear to belong to only one chemical group; a single, distinctive glass analysis may, however, indicate the existence of a second group.

Lithology

Pillow basalts of Site 559 are fine-grained, gray, aphyric basalts with localized small increases in grain size in the upper part and an overall grain-size increase downhole characterized by the presence of visible plagioclase needles (1-3 mm long) below about 286 m. Close to their margins, fine-grained pillow interiors grade over a few centimeters through a brown, altered variolitic zone to black aphanitic basalt and fresh glass. At the tops of most pillows, vesicles are abundant in the aphanitic zone and the outer few centimeters of the fine-grained zone. Two different types (generations?) of vesicles are present. Round vesicles up to 2 mm in diameter are commonly unfilled but may be calcite filled in altered zones. Larger, irregular vesicles up to 10 mm are calcite filled.

Fine-grained pillow interiors are largely weathered brown to brownish gray, particularly along fractures and calcite veinlets. Variolitic zones are generally altered light brown, but the outermost aphanitic basalt zones appear black and unaltered. Glass rims are generally fresh with only narrow palagonite rims along cracks and outer surfaces. Fractures and calcite-filled or limestone-filled veinlets are common throughout. Interpillow limestone is present above 266 m (Fig. 4).

Petrography

We examined seven thin sections of basalt from pillow interiors throughout the section. All are identical in primary mineralogy with only minor variations in grain size and texture. All contain interstitial zeolite (probably heulandite), replacing interstitial glass.

Site 559 basalts are composed of approximately 40% randomly oriented, elongate, hollow plagioclase laths (about An_{60}). Some anhedral, interstitial plagioclase is also present. Clinopyroxene occurs as relatively large prismatic grains (up to 0.5 mm), as parallel aggregates of smaller prisms and occasionally as sheaves or branching aggregates. Fresh olivine is present in only one sample, but relict outlines of small (1 mm) prismatic olivine grains, now completely altered to zeolite and brown clay, are always present (about 5%). Interstitial glass (about 25%) has been partially (one sample) or completely replaced by colorless to light brown zeolite. This mineral occurs as aggregates of very fine, irregular, sometimes radiating grains with complex, sutured boundaries. Its low relief, moderately low birefringence (cf. quartz), straight or near-straight extinction, and length-slow character tentatively identify it as heulandite. Heulandite peaks are also present in the whole-rock X-ray diffraction pattern.

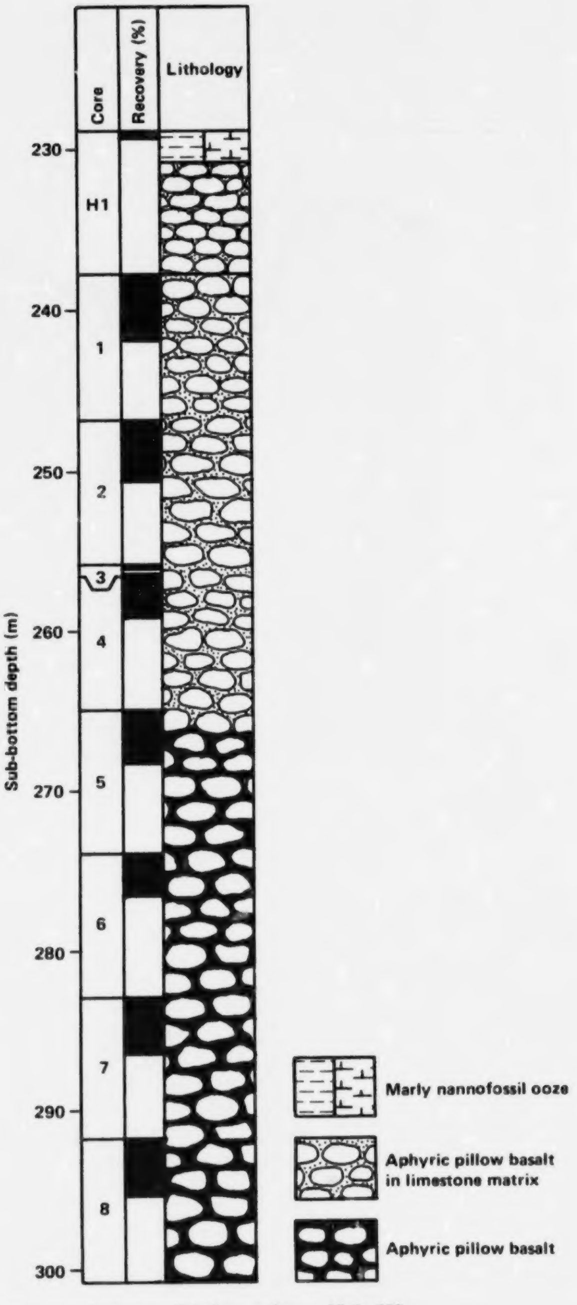

Figure 4. Basement lithology column, Hole 559.

Heulandite is also present, with calcite, clay, and devitrified glass as vesicle fillings, and in some places it appears to have partly replaced plagioclase.

Geochemistry

Pillow basalts of Site 559 form a single lithologic unit as well as a single chemical group (Fig. 5). Analyses for glasses, pillow interiors, and altered outer zones of pillows are shown in Table 2.

In some cases, it was necessary to analyze altered outer zones of pillows (as evidenced by brown discoloration) because of a lack of fresh basalt in the core. In order to observe chemical changes resulting from this alteration, a pillow interior (559-1-2, 56–59 cm, [Piece 5C]) and an altered variolitic zone (559-1-2, 36–39 cm [Piece 5B]) of a single pillow were analyzed.

Changes in major element concentration (mole%), normalized to constant TiO_2 between the pillow interior and the altered variolitic zone are shown in Table 3. Relative to the assumed chemical immobility of such elements as Ti and Zr, significant chemical changes induced by alteration appear to be a decrease in SiO_2 and MgO and an increase in MnO, K_2O, P_2O_5, Sr, and V content. With the exception of the increase in P_2O_5, these changes are consistent with those observed in other comparative studies of alteration occurring at a low temperature (Mattey et al., 1981; Rice et al., 1979). These changes are comparable to those between the average of fresh pillow interiors and the average of altered basalts (shown in Table 4). Again, SiO_2 and MgO contents decrease, whereas MnO, K_2O, P_2O_5 and V increase. Because these visibly altered outer pillow areas are not representative of the fresher pillow interiors, we caution against the use of the altered outer pillow areas as representative samples of this chemical unit.

The chemical uniformity of fresh basalts at Site 559 is demonstrated by average statistical analysis of 15 pillow interiors, which are only slightly to moderately altered (Table 5). Average statistical analysis of seven visibly altered basalts is also given in Table 5.

Glassy pillow rims are abundant. Two distinct glass compositions are shown in Table 5. The average composition of three glasses is virtually identical to that of the average basalt. One glass (559-1-4, 20–22 cm [Piece 2]) is quite distinct in composition from all other samples at Site 559 (Fig. 5). It contains significantly less CaO, V,

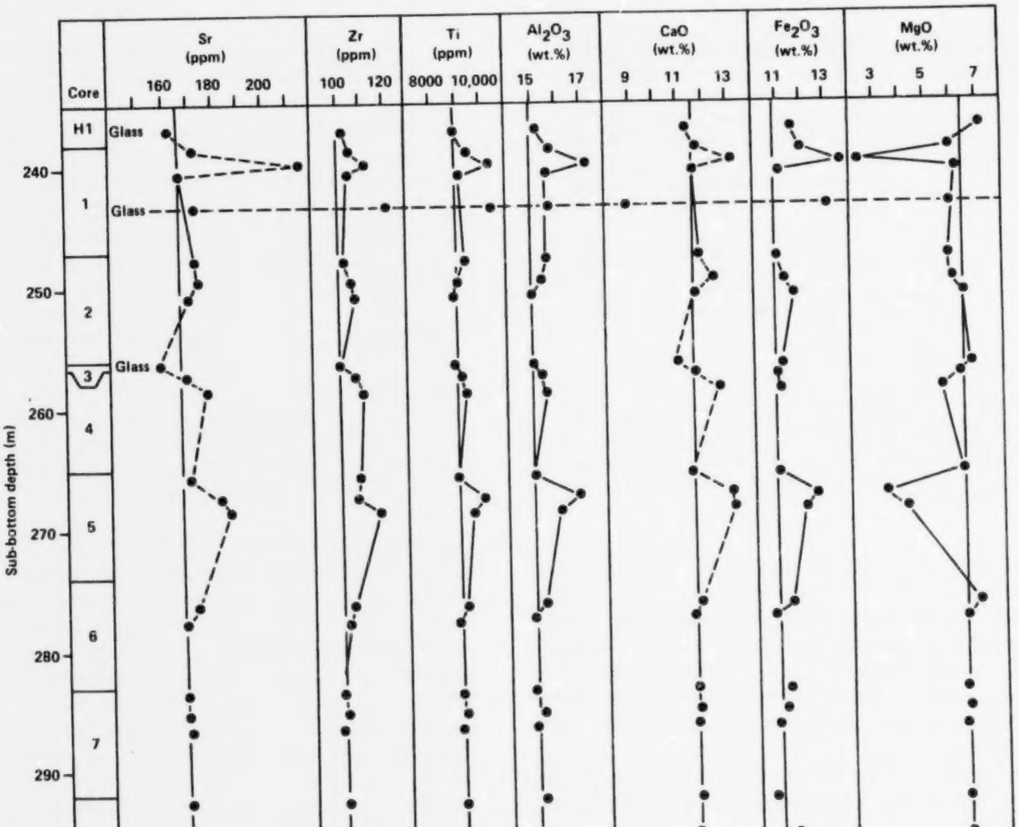

Figure 5. Downhole variations in chemical abundances, Hole 559. Some data appearing in Table 2 was not included in this figure because of the high degree of alteration.

Table 2. Analyses of major elements (in wt.%) and trace elements (in ppm) for Hole 559 basalts.

Core-Section (interval in cm) (piece number)	Depth (m)	Type of group	SiO_2	TiO_2	Al_2O_3	Fe_2O_3	MnO	Mg'	CaO	K_2O	P_2O_5	Total	Mg	Ti	V	Sr	Y	Zr	Nb
H1, CC (1)		G	50.62	1.49	15.20	11.70	0.18	8.29	11.32	0.30	0.19	99.29	61	8940	318	162	36.8	102	14.8
1-1, 120-123 (9B)	239.2	B	50.03	1.57	15.80	12.05	0.15	6.95	11.76	0.49	0.23	99.03	56	9420	317	172	37.3	105	17.5
1-2, 36-39 (5B)	239.8	AB	46.52	1.72	17.26	13.61	0.21	3.28	13.26	0.74	0.43	97.03	35	10,320	409	215	43.7	111	17.1
1-2, 56-59 (5C)	240.1	B	49.54	1.52	15.60	11.17	0.14	7.24	11.65	0.40	0.20	97.46	59	9120	305	166	36.4	104	15.2
1-3, 0-3 (1A)	241.0	AB	47.34	1.69	17.31	12.81	0.21	4.38	11.23	0.89	0.37	96.23	43	10,140	341	181	37.6	108	15.7
1-3, 44-47 (3B)	241.5	AB	46.70	1.60	16.59	12.31	0.16	3.97	14.15	0.64	0.29	96.41	42	9600	374	199	37.0	108	17.3
1-3, 76-79 (5A)	241.8	AB	48.16	1.58	15.94	11.83	0.18	5.22	13.19	0.38	0.26	96.74	50	9480	404	200	45.8	110	17.4
1-3, 129-132 (8C)	242.3	AB	47.82	1.69	16.93	12.79	0.23	5.91	12.97	0.50	0.29	97.13	41	10,140	404	187	39.2	108	14.9
1-3, 148-150 (9)	242.5	G	49.86	1.49	14.63	11.40	0.18	7.94	10.88	0.37	0.19	96.94	61	8940	301	157	33.4	101	16.0
1-4, 20-22 (2)	242.7	G	48.96	1.74	15.65	13.12	0.18	7.00	8.89	0.97	0.16	96.67	55	10,440	243	172	32.5	119	18.4
2-1, 1-3 (1A)	247.0	B	49.93	1.55	15.62	11.06	0.14	6.93	11.88	0.38	0.20	97.69	58	9300	304	172	35.9	102	16.9
2-2 24-28 (1B)	248.8	B	48.90	1.50	15.31	11.36	0.16	7.08	12.45	0.40	0.17	97.33	58	9000	248	173	33.6	105	16.1
2-3, 75-79 (4C)	250.8	B	49.80	1.47	14.91	11.78	0.17	7.55	11.78	0.49	0.18	98.13	59	8820	288	169	36.3	106	16.6
3-1, 13-14 (2)	256.1	G	50.35	1.48	15.02	11.25	0.18	7.81	10.92	0.40	0.18	97.19	61	8880	301	157	33.9	100	16.5
4-1, 125-129 (9B)	257.7	B	50.35	1.52	15.33	11.02	0.14	7.36	11.63	0.34	0.21	97.90	60	9120	300	168	35.3	106	16.0
4-2, 92-96 (5D)	258.9	B	49.42	1.54	15.47	11.15	0.15	6.67	12.76	0.43	0.20	97.79	57	9240	302	176	37.9	109	16.7
5-1, 45-48 (3B)	265.5	B	49.59	1.49	14.98	11.05	0.14	7.44	11.45	0.36	0.19	96.69	60	8940	283	169	35.4	97	15.5
5-2, 35-39 (4A)	266.8	AB	47.86	1.66	16.76	12.59	0.16	4.38	13.09	0.34	0.26	97.10	44	9960	369	181	37.3	106	16.7
5-3, 25-29 (2)	268.3	AB	48.72	1.58	16.01	12.11	0.15	5.10	13.19	0.44	0.23	97.53	49	9480	352	185	39.1	115	17.6
6-2, 25-29 (1B)	275.8	B	50.02	1.52	15.33	11.51	0.16	8.01	11.73	0.39	0.20	98.87	61	9120	314	171	36.0	104	15.3
6-3, 27-31 (1)	277.3	B	50.00	1.47	14.87	10.86	0.14	7.58	11.47	0.38	0.19	96.96	61	8820	298	167	35.9	102	16.3
7-1, 137-140 (12D)	284.4	B	49.67	1.49	14.81	11.33	0.17	7.46	11.55	0.42	0.19	97.09	60	8940	290	166	35.1	99	16.1
7-2, 143-146 (8C)	286.0	B	49.66	1.51	15.14	11.20	0.16	7.49	11.61	0.35	0.19	97.31	60	9060	307	166	35.3	100	15.8
7-3, 110-113 (7B)	287.1	B	50.06	1.48	14.84	10.90	0.14	7.34	11.54	0.34	0.18	96.82	60	8880	297	167	34.6	98	14.0
8-1, 48-51 (1B)	292.5	B	50.22	1.50	15.10	10.66	0.14	7.39	11.60	0.31	0.18	97.10	61	9000	304	167	34.0	100	16.1
8-3, 19-21 (1A)	295.2	B	49.96	1.49	14.80	11.51	0.15	7.46	11.44	0.41	0.20	97.42	59	8940	284	168	34.5	96	15.6

Note: Group types: G = glass, B = basalt, AB = altered basalt. Mg' is the atomic ratio of 100 × $(Mg/[Mg + Fe^{2+}])$ calculated using an assumed Fe_2O_3/FeO of 0.15. Measurements were made on board using ignited samples. Onshore analyses show loss on ignition to be less than 1%. The concentrations listed in the tables of compiled data (Appendix at end of volume) include volatile contents. Total Fe as Fe_2O_3.

Table 3. Assessment of chemical change during alteration of a pillow rim.

Element	Pillow interior (mole%)	Altered rim (mole%)	Normalized rim (mole%)	Relative change (%)
SiO_2	56.4	56.0	45.8	−19
TiO_2	1.30	1.59	1.30	0
Al_2O_3	10.5	12.2	10.0	−5
Fe_2O_3	4.8	6.2	5.0	+4
MnO	0.13	0.21	0.17	+31
MgO	12.3	5.9	4.8	−61
CaO	14.2	17.1	14.0	−1
K_2O	0.29	0.57	0.47	+62
P_2O_5	0.10	0.22	0.18	+80
Total	100.01	99.93	81.7	−18

Note: Pillow interior sample is 559-1-2, 56-59 cm (Piece 5C); altered variolitic rim from same pillow is 559-1-2, 36-39 cm (Piece 5B); "normalized rim" composition is normalized to 1.3 mole% TiO_2 (interior value); "relative change" is the change between normalized rim and pillow interior (normalized rim-pillow interior)/pillow interior. Analyses assume TiO_2 immobility.

Table 4. Chemical changes during alteration based on average Site 559 compositions.

Element	Fresh (mole%)	Altered (mole%)	Normalized altered (mole%)	Relative change (%)
SiO_2	56.5	56.3	49.4	−12
TiO_2	1.29	1.47	1.29	0
Al_2O_3	10.2	11.7	10.3	−1
Fe_2O_3	4.8	5.6	4.9	+21
MnO	0.12	0.19	0.17	+42
MgO	12.4	7.6	6.7	−46
CaO	14.3	16.5	14.5	+1
K_2O	0.28	0.45	0.39	+39
P_2O_5	0.09	0.15	0.13	+44
Total	99.98	100.01	87.78	−12

Note: "Fresh" is average fresh pillow interior; "altered" is average altered basalt; "normalized altered" is average altered basalt normalized to 1.2 mole% TiO_2; "relative change" is change between normalized altered basalt and fresh.

and Y and more Fe_2O_3, K_2O, Zr, and Nb than the average basalt. This sample may be the only representative of a second, distinct chemical unit. Pillow interiors adjacent both above and below this 6 cm-diameter glass piece have compositions close to the average of Site 559. No crystalline basalt analyzed at Site 559 has this unique glass composition. Further investigation of this sample is certainly required.

The relatively fresh sample (559-1-2, 56-59 cm [Piece 5C]) of the interior of a pillow and the strongly altered sample of the variolitic zone of the same section (559-1-2, 36-39 cm [Piece 5B]) were chosen to study the effect of alteration on the major element composition. These two samples were also chosen to study the effect of alteration on the abundances of the trace elements that have been chosen to describe the enrichment or depletion of magmaphile elements in terms of mantle heterogeneity: Nb, Zr, Ti, Y, and V. Rare earth elements have already been shown to be immobile in slightly to moderately altered basalts during low-temperature alteration (Rice et al., 1979), as have non-rare-earth magmaphile elements (Joron et al., 1979). However, because of the importance of measuring these elements on board in order to test for mantle heterogeneity, it was absolutely necessary to demonstrate on samples of this hole that low-temperature alteration has not modified the relative abundances of these elements. In the altered sample (559-1-2, 36-39 cm [Piece 5B]), the concentrations are increased by a factor of 1.15 ± 0.05 relative to the fresh

Table 5. Average analyses of Site 559 basalts. Major elements expressed in wt.%; trace elements in ppm.

Element	Fresh basalt (15)		Altered basalt[a] (7)		Glass[b] (3)		Glass[c] (1)
	$\overline{X}$	S	$\overline{X}$	S	$\overline{X}$	S	
SiO_2	49.8	0.4	47.6	0.8	50.3	0.4	48.96
TiO_2	1.51	0.03	1.65	0.06	1.49	0.01	1.74
Al_2O_3	15.2	0.3	16.7	0.6	15.0	0.3	15.65
Fe_2O_3	11.2	0.4	12.6	0.6	11.5	0.2	13.12
MnO	0.15	0.07	0.19	0.03	0.18	0	0.18
Mg'	7.3	0.3	4.3	0.7	8.0	0.2	7.00
CaO	11.8	0.4	13.0	0.9	11.0	0.2	8.89
K_2O	0.39	0.05	0.6	0.2	0.36	0.05	0.97
P_2O_5	0.19	0.07	0.30	0.07	0.19	0.01	0.16
Ti	9000	200	9900	300	8920	30	10,440
V	300	20	380	30	310	10	243
Sr	169	3	190	10	159	3	172
Y	36	1	40	3	35	2	32.5
Zr	102	4	109	3	101	1	119
Nb	16.0	0.8	17	1	15.8	0.9	18.4
Mg	59	1	43	5	61	0	55

Note: Numbers in parentheses are number of analyses. $\overline{X}$ = mean; S = standard deviation (1σ). Mg' is the atomic ratio of $100 \times (Mg/[Mg + Fe^{2+}])$ calculated using an assumed Fe_2O_3/FeO of 0.15. Averages are calculated from data listed in Table 2 and are rounded.

[a] Samples 559-1-2, 36–39 cm (Piece 5B); 559-5-2, 35–39 cm (Piece 4A); 559-5-3, 25–29 cm (Piece 2); 559-1-3, 0–3 cm (Piece 1A); 559-1-3, 44–47 cm (Piece 3B); 559-1-3, 76–79 cm (Piece 5A); and 559-1-3, 129–132 cm (Piece 8C).

[b] Samples 559-H1, CC (Piece 1); 559-3-1, 13–14 cm (Piece 2); and 559-1-3, 148–150 cm (Piece 9).

[c] Sample 559-1-4, 20–22 cm (Piece 2).

sample (559-1-2, 56–59 cm [Piece 5C]), except for V (for which the increase is somewhat higher). The factor 1.15 accounts for the leaching out of major elements (MgO, SiO_2), and its accuracy (0.05) relative to the different magmaphile trace elements agrees with the precision of the concentration measurements. Thus, the relative abundances of magmaphile elements investigated on board are not affected by low-temperature alteration. Their relative abundances can be interpreted in terms of mantle heterogeneity and/or melting processes.

Figure 6 illustrates the effects of low-temperature seawater alteration on strontium and calcium concentrations. As the degree of alteration increases, strontium concentration increases. The less-altered samples of Site 559 located at the bottom of the hole are grouped in the vicinity of 165 ppm Sr and 11.6 wt%. CaO. Altered samples, denoted by squares, show increasing Sr and CaO concentrations. Glass samples have the lowest Sr and CaO content; glass from Section 559-1-4 (the triangle) is again unique. The two glass samples collected within the basalt section (559-1-3 [Piece 9] and 559-3-1) have exactly the same CaO and Sr contents (10.9 wt.% and 157 ppm, respectively), whereas Core H1 collected at the sediment/basement interface shows slightly higher concentrations (11.3 wt.% and 162 ppm). "Fresh" glasses showing the lowest Ca-Sr concentration are a good indication of the lowest contamination in Sr for $^{87}Sr/^{86}Sr$ ratio measurements.

The following table shows calculated Sr isotopic ratios for various degrees of seawater contamination of a basalt that has an initial Sr concentration of 160 ppm and Sr isotopic ratio of 0.7020.

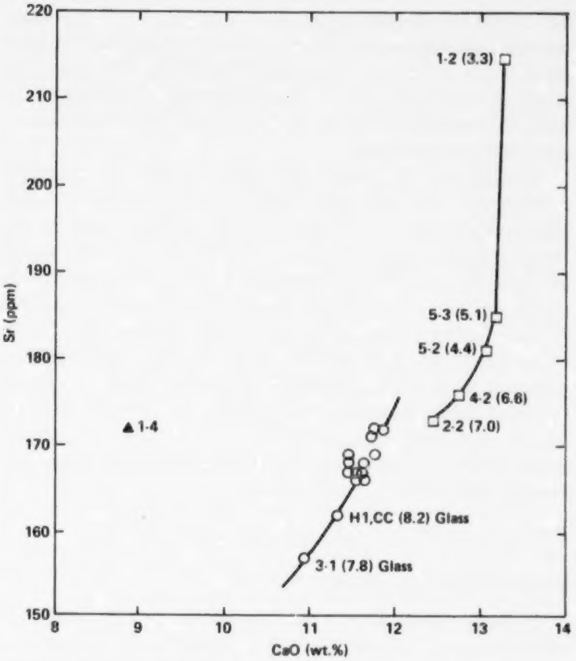

Figure 6. Sr versus CaO for altered and slightly altered basalts (squares) to unaltered basalts (circles). The triangle represents the unique glass sample (559-1-4, 20–22 cm [Piece 2]). Hyphenated numbers next to symbols represent Core-Section (in Hole 559); numbers in parentheses are Mg'-values (rounded to the nearest tenth) for these samples. Mg' is the atomic ratio of $100 \times (Mg/[Mg + Fe^{2+}])$ calculated using an assumed Fe_2O_3/FeO of 0.15. Overly altered data in Table 2 has been excluded from this figure.

Seawater Sr added (ppm)	$^{87}Sr/^{86}Sr$
0	0.7020
1	0.7020
5	0.7022
10	0.7024
15	0.7026
20	0.7028
25	0.7029
30	0.7031

The Sr isotopic ratio can only be reliably interpreted as reflecting the mantle source composition if the amount of Sr added from seawater is lower than 5 ppm. To the extent that there is no Sr exchange between glass and seawater (which is a possibility mentioned by Rice et al., 1979), the lowest Sr concentrations (157 ppm) found in two glasses compared to 165 ppm in relatively fresh basalts allows us to postulate that the true concentration in Sr—and thus the true $^{87}Sr/^{86}Sr$ ratio—could be reached with a precision better than 5 ppm. In addition, care has to be taken in separating clean fragments of glass (1 mm size) and then leaching the powder with HCl or HNO_3 solution several times: the Sr concentration of the powder could be checked after each leaching by X-ray fluorescence measurements on the powder itself, until a constant value is found. The true Sr and $^{87}Sr/^{86}Sr$ could be reached this way only if glass-seawater exchange of Sr had occurred without other detectable modifications of the glass composition.

The extended Coryell-Masuda diagram is presented in Figure 7. The enriched pattern (Nb in respect to other elements) is typical of transitional basalts found in the Azores Triple Junction area. This result *by itself* would agree with a boundary between an Azores-type source north of Hayes Fracture Zone and a depleted source south of Hayes Fracture Zone. Nevertheless, the results obtained at Site 558 (where depleted, flat, and enriched patterns were found) force us to be cautious in any attempted interpretation of geochemistry and geodynamics. A confident interpretation of this type can only be made when we know why such different patterns are found at Site 558.

MAGNETICS

Basalt Paleomagnetism

Eight samples of basalt were taken for the study of paleomagnetic properties. The intensity of natural remanent magnetization and initial susceptibility were measured and Koenigsberger ratio (Q) calculated. The results are given in Table 6. Six samples have low intensity (0.1–0.8 × 10^{-3} emu/cm^3), whereas only two samples have high intensity values (1.0–1.3 × 10^{-3} emu/cm^3). Two samples from Sections 559-6-1 and 559-7-2 have the lowest intensities and also low Q values, but susceptibility values are moderate to high. Demagnetization was not done on board so that further properties could be studied onshore.

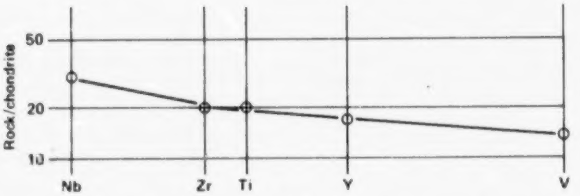

Figure 7. Extended Coryell-Masuda diagram for an average basalt composition, Hole 559.

The inclination values are shallower than the expected dipole inclination for the latitude of this site, which suggests tectonic rotation of the ocean crust since the acquisition of remanance. The negative values of inclination are in agreement with the location of this site between Anomalies 12 and 13.

PHYSICAL PROPERTIES

No sediment samples have been measured because no undisturbed sediment was recovered in the wash core. Samples from the basement cores were measured routinely for sonic velocity, density, and water content. The data are presented in Table 7.

Alteration of basalt specimens produces a wide range of densities and sonic velocities. Densities measured by the 2-minute GRAPE technique are systematically lower than those determined by the gravimetric technique. This is due to the core condition, which only allowed rather short minicores to be prepared. These were rather shorter than the minimum length (2.5 cm) required for an accurate determination by the GRAPE method. The limestone sediment with glass fragments measured from Section 559-1-4 has little acoustic impedance compared to the altered basalts, mainly because of its high sonic velocity of 3.84 km/s.

The data show no systematic variation down the hole.

SUMMARY AND CONCLUSIONS

Hole 559 is located between Anomalies 12 and 13 midway between the Oceanographer and Hayes fracture zones. The upper 63 m of the basement were cored and consist of aphyric pillow basalts belonging to a single magmatic unit. The effects of low-temperature alteration are variable and randomly distributed in the recovered samples. Fresh glasses are very common at the pillow margins; calcite is present in cracks and veins. MgO concentration (about 8% in fresh samples) decreases to 3% in badly altered samples. The loss of MgO and SiO_2 induces higher concentrations of other major elements and of magmaphile trace elements (e.g., Nb, Zr) in altered samples. We think that fresh glasses—which have a lower Sr concentration (157 ppm) than the freshest basalts (165 ppm)—should be suitable, after leaching processes, for Sr isotopic ratio measurements. A fresh glass sample with a different and unusual composition has been found (SiO_2 = 48.96, TiO_2 = 1.74, Al_2O_3 = 15.65, Fe_2O_3 = 13.12, Mg′ = 7.0, CaO = 8.89, and K_2O =

Table 6. Paleomagnetic properties, Hole 559.

Core-Section (interval in cm)	J_{NRM} (× 10^{-3} emu/cm^3)	NRM dec. (°)	NRM inc. (°)	χ (× 10^{-6} emu/cm^3 Oe)	Q (= $J_{NRM}/0.45\chi$)
1-2, 134-136	0.75	216.3	−32.7	72	23.15
2-1, 113-115	0.33	186.9	−22.9	65	11.28
4-2, 82-84	1.00	325.0	−29.5	76	29.24
6-1, 76-78	0.21	277.1	−22.2	84	5.56
7-2, 60-62	0.15	183.4	−27.0	64	5.21
7-3, 145-147	0.77	180.9	−26.9	94	18.20
8-1, 37-39	0.76	80.3	−7.0	58	29.12
8-3, 15-17	1.28	270.9	−22.9	64	44.44

Note: J_{NRM} = intensity of natural remanent magnetization (NRM); dec. = declination; inc. = inclination; χ = susceptibility; Q = Königsberger ratio.

Table 7. Physical properties, Hole 559.

Core-Section (interval in cm)	Sub-bottom depth (m)	Sonic velocity (km/s)		Temperature (°C)	Thermal conductivity (mcal/[cm · deg · s])	GRAPE density (g/cm^3)		Gravimetric density			Acoustic impedance (× 10^5 g/[cm·s])	Lithology or remarks
		V.	H.			V.	H.	Wet-bulk density (g/cm^3)	Water content (%)	ϕ (%)		
1-1, 93-107	239.0	4.73		22.0		2.55		2.7	5	14	12.8	Basalt
1-4, 0-7	242.5	3.84		22.0		2.24		2.4	8	20	9.2	Interpillow sediment
2-3, 93-107	251.0	4.52		22.0		2.55		2.6	7	17	11.8	Basalt
4-1, 35-37	256.9							2.8	<1	<1		Pillow basalt
5-3, 35-36	269.4							2.8	2	7		Basalt
6-1, 76-78	274.8	4.47		22.0		2.25(?)					10.1	Heavily altered basalt
6-2, 15-17	275.7							2.8	4	10	—	Basalt
7-2, 58-61	285.1	4.46		22.0		2.55					11.4	Altered basalt
7-2, 70-72	285.2							2.6	6	16	—	Altered basalt
8-3, 13-17	295.2	4.71		22.0		2.70		2.8	4	12	13.2	Basalt

Note: V. = vertical, H. = horizontal; water content is corrected; ϕ = porosity. All values measured at laboratory temperature and pressure. For details of techniques, see Explanatory Notes chapter (this volume).

0.97, all in wt.%). Site 559 is characterized by a typical enriched abundance pattern for magmaphile elements ($[\mathrm{Nb/Zr}]_{\mathrm{ch}}$ = 1.65).

This result would agree with a geochemical boundary between an Azores-type source north of Hayes Fracture Zone and a depleted source south of Hayes Fracture Zone. Nevertheless, the results obtained at Site 558 (where enriched, flat, and depleted materials were found) necessitate further analyses before a definite interpretation can be made.

REFERENCES

Joron, J. L., Bollinger, C., Quisefit, J. P., Bougault, H., and Treuil, M., 1980. Trace elements in Cretaceous basalts at 25°N in the Atlantic Ocean: Alteration, mantle composition, and magmatic processes. *In* Donnelly, T. W., Francheteau, J., Bryan, W., Robinson, P., Flower, M., Salisbury, M., et al., *Init. Repts. DSDP*, 51, 52, 53, Pt. 2: Washington (U.S. Govt. Printing Office), 1087-1098.

Mattey, D. P., Marsh, N. G., and Tarney, J., 1981. The geochemistry, mineralogy, and petrology of basalts from the West Philippine and Parece Vela Basins and from the Palau-Kyushu and West Mariana Ridges, Deep Sea Drilling Project, Leg 59. *In* Kroenke, L., Scott, R., et al., *Init. Repts. DSDP*, 59: Washington (U.S. Govt. Printing Office), 753-800.

Rice, S., Langmuir, C. H., Bender, J. F., Hanson, G. N., Bence, A. E., and Taylor, S. R., 1980. Basalts from Deep Sea Drilling Project Holes 417A and 417D, fractionated melts and a light rare-earth depleted source. *In* Donnelly, T. W., Francheteau, J., Bryan, W., Robinson, P., Flower, M., Salisbury, M., et al., *Init. Repts. DSDP*, 51, 52, 53, Pt. 2: Washington (U.S. Govt. Printing Office), 1099-1112.

SITE 559 HOLE CORE H1 CORED INTERVAL 0.0–238.0 m

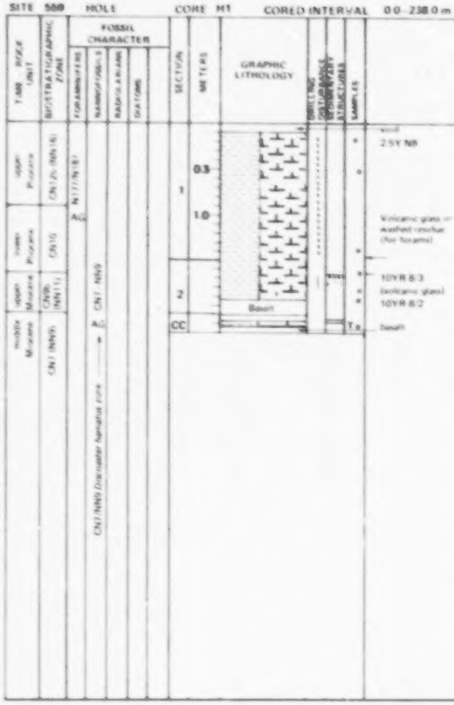
TIME - ROCK UNIT
BIOSTRATIGRAPHIC ZONE
FOSSIL CHARACTER
FORAMINIFERS
NANNOFOSSILS
RADIOLARIANS
DIATOMS
SECTION
METERS
GRAPHIC LITHOLOGY
DRILLING DISTURBANCE
SEDIMENTARY STRUCTURES
SAMPLES
upper Pliocene
lower Pliocene
upper Miocene
middle Miocene
CN12c (NN16)
CN10
CN9b (NN11)
CN7 (NN9)
N17/(N18)
AG
CN7 - NN9
AG
CN7 NN9 Discoaster hamatus zone
1
2
CC
0.5
1.0
Basalt
T
void
2.5Y N8
Volcanic glass = washed residue (for forams)
10YR 8/3
(volcanic glass)
10YR 8/2
basalt

LITHOLOGIC DESCRIPTION

Section 1, 10–60 cm: MARLY NANNO OOZE

Section 1, 60 cm–Section 2, 20 cm: MARLY NANNO OOZE with volcanic glass.

DOMINANT LITHOLOGY MARLY NANNOFOSSIL OOZE

White (2.5Y N8), 10YR 8/2 in Section 2, 32–42 cm
Soft or soupy to firm
No bioturbation or bedding except sharp color change at Section 2, 20 cm, and faint color change at Section 2, 32 cm.
Volcanic glass (black) and zeolites at contact Section 2, 20 cm.

Minor lithology:
Marly nanno ooze with volcanic glass.
Marly limestone (CC), white (10YR 8/2) with slightly darker laminae.

Note: glass makes up about 5–10% of the material from Section 1, 60 cm to Section 2, 20 cm, but fragments are large and do not appear in smear slide analysis.

SMEAR SLIDE SUMMARY (%):

	1, 20	1, 55	1, 140	2, 20	2, 31	2, 40	CC
Composition:							
Feldspar	Tr	Tr	Tr	Tr	Tr	Tr	Tr
Heavy minerals	Tr	Tr	Tr	Tr	Tr	Tr	Tr
Clay	50	40	49	50	43	50	35–55
Volcanic glass	1	Tr	—	3	Tr	—	—
Palagonite	—	—	—	2	—	—	—
Micronodules	2	1	3	Tr	Tr	Tr	1–2
Zeolite	—	—	—	5	—	—	—
Carbonate unspec.	5	8	7	10	5	5	22–35
Foraminifers	5	9	8	8	15	3	—
Calc. nannofossils	35	40	30	20	35	40	20–28
Diatoms	1	Tr	1	Tr	—	Tr	Tr
Radiolarians	1	Tr	1	Tr	Tr	Tr	—
Sponge spicules	—	—	—	—	—	Tr	—
Dolomite	—	Tr	Tr–1	—	Tr?	Tr	Tr

SITE 559 HOLE CORE 1 CORED INTERVAL 238.0–247.0 m

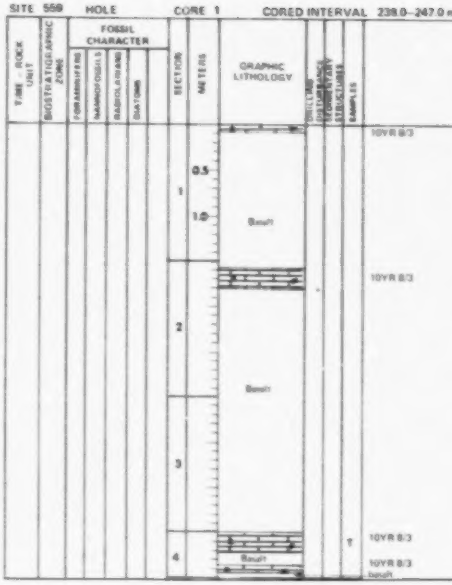
TIME - ROCK UNIT
BIOSTRATIGRAPHIC ZONE
FOSSIL CHARACTER
FORAMINIFERS
NANNOFOSSILS
RADIOLARIANS
DIATOMS
SECTION
METERS
GRAPHIC LITHOLOGY
DRILLING DISTURBANCE
SEDIMENTARY STRUCTURES
SAMPLES
1
2
3
4
0.5
1.0
Basalt
Basalt
Basalt
T
10YR 8/3
10YR 8/3
10YR 8/3
10YR 8/3
basalt

LITHOLOGIC DESCRIPTION

INTRAPILLOW BASALT (VOLCANICLASTIC) LIMESTONE

Very pale brown (10YR 8/3). The volcaniclastic component increase towards the margin of the pillow basalts.

Manganese mineralization occurs throughout the limestones as micronodules or dendrites.

The micritic limestone has been recrystallized to irregular patches of microspar.

Throughout the pillow basalts sediment (now limestone) has infiltrated cracks and vesicle with the latter often showing geopetal structures.

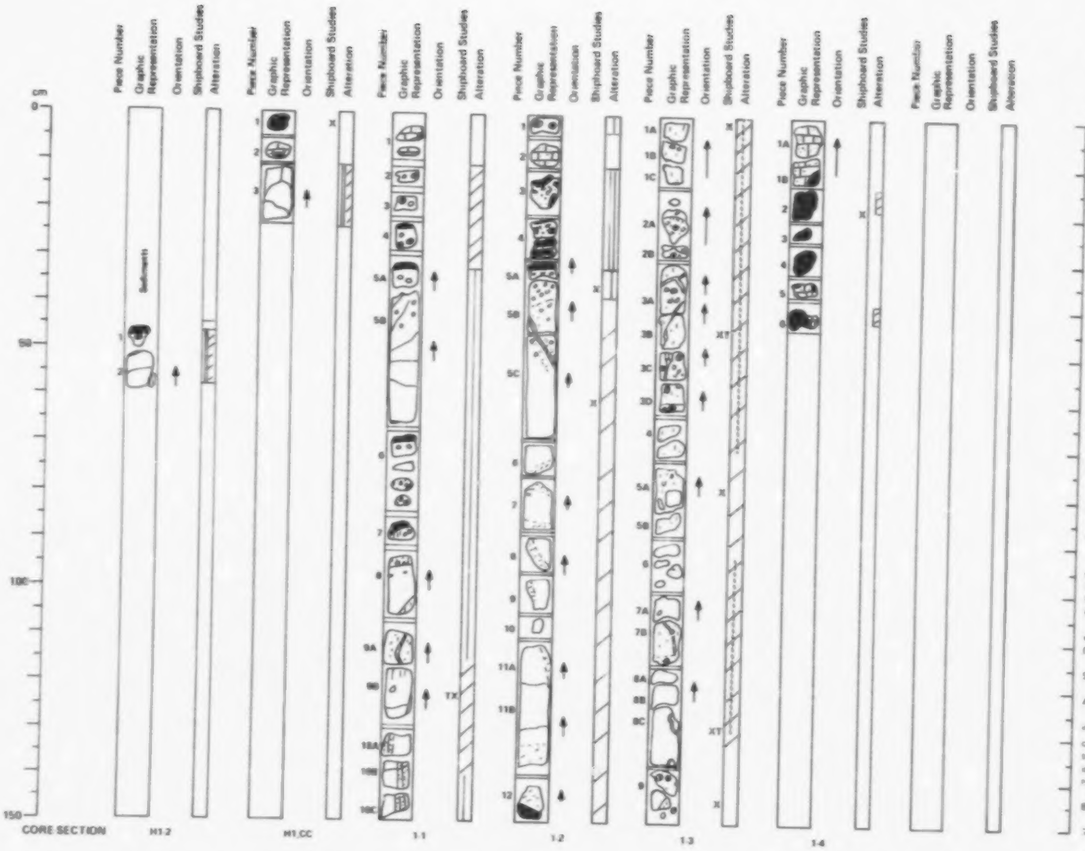

SITE 559, CORE H1 Depth 0.0–238.0 m

SECTION 2

APHYRIC PILLOW BASALT FRAGMENTS

Color dark brown (10YR 3/3) to brown (10YR 4/3), moderately to badly altered. Fresh black aphanitic to glassy basalt in Piece 1 with variolitic zone grading to altered basalt (size of varioles <1 mm). Vesicles are scattered throughout the rock (size <1 mm, few <3 mm) and often filled with calcite.

CORE-CATCHER

APHYRIC PILLOW BASALT FRAGMENTS

Pieces 1 and 3

1–4 cm: Black vesicular basalt glass. Vesicles (<1.5 mm) are round and empty.

7–10 cm: Limestone. One half is laminated.

13–23 cm: Moderately to badly altered aphyric basalt. Color brown to dark brown (10YR 4/3–10YR 3/3). Round vesicles (<1.5) and irregular shaped vesicles (<10 mm) are empty or calcite-filled. Some small veinlets are cemented by calcite, too.

SITE 559, CORE 1 Depth 238.0–267.0 m

SECTION 1

APHYRIC PILLOW BASALT SEQUENCE

0–10 cm: Limestone, very pale brown (10YR 8/3), dendrites throughout the limestone (MnO).

10–38 cm: Variolitic basalt, dark gray (2.5Y N4/0).

10–22 cm, Pieces 2 and 3: 30–40% vesicles, unfilled.

22–30 cm, Piece 4: Glass rim, 10% unfilled vesicles.

38–84 cm: Aphyric basalt, grayish brown (10YR 5/2), fine grained, highly altered, thin calcite filled fractures, round vesicles concentrated to 30% in Pieces 5A, 6 and the upper cm of Piece 5B.

84–150 cm: Aphyric basalt, dark gray (5Y 4/1), fine grained, alteration as noted at top of Pieces 7, 8, and 9B and along fractures. Vertical fractures are filled with limestone sediment, horizontal fractures are filled with calcite. Unfilled round vesicles (≥1 mm) in Piece 7 and upper 2 cm of Piece 8. Weathered areas are brown (10YR 5/3). Pieces 5B, 6, and 8 contain irregular shaped vesicles (2–8 mm) filled with calcite.

Thin Section at 120–123 cm.

SECTION 2

APHYRIC PILLOW BASALTS

1–4 cm: Strongly altered variolitic aphyric basalt, color brown (10YR 5/3). Size of varioles <4 mm.

6–11 cm: Limestone, color pale brown (10YR 6/3). Black dendrites of Mn-Oxide are grown throughout the sediment.

14–29 cm: Basalt glass breccia (hyaloclastite), angular clasts (size ranges between 1 mm and several cm) of vesicular (round, <2 mm) sideromelane, fresh (black) in the center, altered (brown) at the rims. Matrix is limestone as above (Piece 2).

31–140 cm: Separate pillow of fine-grained aphyric basalt, color dark gray (10YR 4/1). High amount of round vesicles in upper part (Piece 5A and B), size <2 mm. From 41–52 cm vein filled with lithified limestone from above. Pieces 5A and 12: Fresh glass rim on aphanitic, black basalt.

SECTION 3

APHYRIC PILLOW BASALTS

Moderately to highly altered aphyric basalt (highly altered brown (10YR 5/3), moderately grading to dark grayish brown (10YR 4/2)). Two generations of vesicles suggested, esp. in 0–60 cm interval. Large vesicles 2–5 mm, calcite filled*, smaller empty ones <1 mm–2 mm in diameter. Pieces 2A, 3D, 7B, and 9 are dark gray (7.5YR N4/0) to very dark gray (7.5YR N3/0) aphanitic, aphyric basalt grading to altered variolitic brown basalt. Calcite veining is frequent and dominantly longitudinal. Absence of consolidated glass relative to Sections 1 and 4 is striking relative to Sections 1 and 4 is striking.

*Some larger cavities are present with the longitudinal calcite veining, calcite lined, in Pieces 1A–C, 3C, 7B, and 8C)

SECTION 4

BASALT GLASS AND LIMESTONE

7–13.5, 36–38, and 43–46 cm, Pieces 1A and B, 5, and 6: Limestone with glass clasts (1–3 cm in diameter). Limestone shows dark "dendritic" pattern (MnO or Mn(OH)n). Glass clasts are slightly altered to very pale brown (10YR 8/4) palagonite around the rims and within the cracks.

15–33 and 40–43 cm, Pieces 2, 3, 4, and 6): Black (10YR 2.5/1) glass, relatively fresh and uncracked; some fractures, however, are observed and subsequent palagonitization has occurred. Vesicles are found throughout (1–3 mm in diameter).

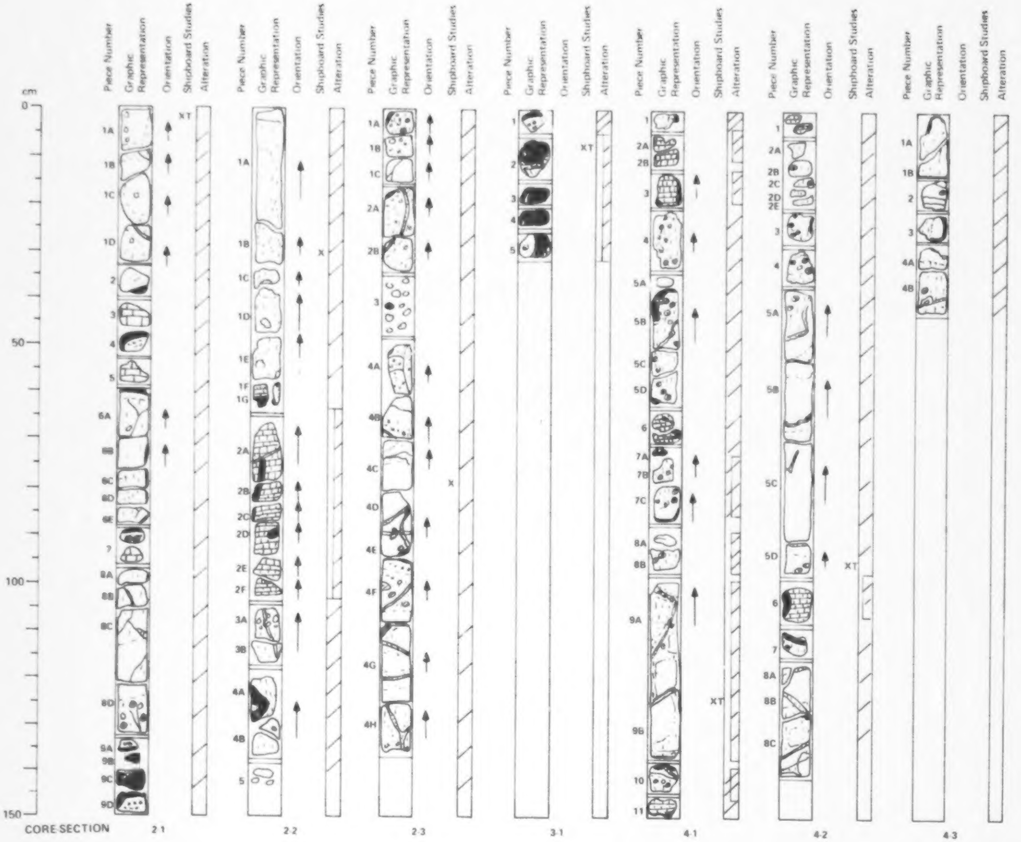
cm
0
50
100
150
CORE-SECTION
Piece Number
Graphic Representation
Orientation
Shipboard Studies
Alteration
2-1
1A 1B 1C 1D 2 3 4 5 6A 6B 6C 6D 6E 7 8A 8B 8C 8D 9A 9B 9C 9D
XT
2-2
1A 1B 1C 1D 1E 1F 1G 2A 2B 2C 2D 2E 2F 3A 3B 4A 4B 5
X
2-3
1A 1B 1C 2A 2B 3 4A 4B 4C 4D 4E 4F 4G 4H
X
3-1
1 2 3 4 5
XT
4-1
1 2A 2B 3 4 5A 5B 5C 5D 6 7A 7B 7C 8A 8B 9A 9B 10 11
XT
4-2
1 2A 2B 2C 2D 2E 3 4 5A 5B 5C 5D 6 7 8A 8B 8C
XT
4-3
1A 1B 2 3 4A 4B

SITE 559, CORE 2 Depth 247.0–256.0 m

SECTION 1

APHYRIC PILLOW BASALT

0–147 cm: Dominantly aphyric dark gray (10YR 4/1) basalt. Fine grained. Grading through variolitic to black aphanitic basalt approaching glassy pillow margins. Largely altered dark grayish brown (10YR 4/2) to brown (10YR 5/3). Sparsely vesicular with small, round, unfilled vesicles (1–2%) concentrated (~5%) near pillow margins. Scattered irregular larger vesicles (~5 mm) generally calcite filled.

Limestone (46, 54–58, and 93–95 cm): Interpillow sediment: very pale brown (10YR 7/3) limestone generally with black MnO dendrites.

Basalt glass (135–145 cm): Thick rinds black, sparsely vesicular glass with black aphanitic basalt. Only weakly palagonitized.

SECTION 2

APHYRIC PILLOW BASALT AND LIMESTONE

0–64 and 104–140 cm: Aphyric pillow basalt, moderately/highly altered. Altered to brown (10YR 5/3) (highly altered) grading to dark grayish brown (10YR 4/2) (moderately altered). In 0–64 cm cores of less altered aphyric aphanitic basalt pillows, dark gray (7.5YR N4/0) to very dark gray (7.5YR N5/0). Vesicles throughout section, two generations possible: large, calcite filled (3–7 mm) and small, empty (<1–2 mm). Larger vesicles are concentrated in the highly altered upper sections of Pieces 1A and 3A, and a few in 4B; smaller vesicles are scattered.

60–102 cm: Limestone with glass clasts, 1–3 cm in length. Bioturbation is faint but present in majority of limestone pieces. Piece 1G is limestone with glass fragment 63.0–64.5 cm. Glass is black (10YR 2.5/1). Limestone grades from very pale brown (10YR 8/3) to light gray (10YR 7/2).

SECTION 3

APHYRIC PILLOW BASALTS

Aphyric, fine grained basalt as in Section 1. No interpillow limestone recovered. Calcite veining present as shown (diagonal hatched). Vesicle abundance increasing downhole. Small (< 2 mm) round, generally unfilled vesicles sparsely distributed throughout concentrated to 5–10% near upper pillow margins (shown by small dots and circles). Large, irregular, calcite filled vesicles (up to 5%), concentrated near upper pillow margins. Shown thus: ✱ or ●

SITE 559, CORE 3 Depth 256.0–256.5 m

SECTION 1

BASALTIC PILLOW RIM PIECES

0–5 cm: Aphyric fine grained basalt altered grayish brown (10YR 6/2).

5–30 cm: Black basalt glass grading through black, aphanitic, sparsely vesicular basalt to grayish brown (10YR 6/2) variolitic basalt. Palagonite rims on exterior and fractured surfaces range from 1–4 mm thick.

Limestone (11–13 and 28–30 cm): brown (7.5YR 5/2) limestone filling interpillow voids.

SITE 559, CORE 4 Depth 256.5–265.0 m

SECTION 1

APHYRIC PILLOW BASALT, INTERPILLOW LIMESTONE

0–4, 24–62, and 70–144 cm: Aphyric pillow basalt sequence: black glass rims (10YR 2.5/1) grading into black aphanitic, aphyric basalt (same color). Aphanitic basalt grades into variolitic basalt. Small, empty vesicles (< 1 mm–1 mm in diameter) are present through this zone (aphanitic/variolitic), demarcating pillow interfaces. Variolitic to aphyric altered basalt ranges in color from yellowish brown (10YR 5/6) to grayish brown (10YR 5/8). Within this brown altered basalt are found larger vesicles (2–7 mm in length) filled with calcite; some cavities within calcite veins are lined with sparry calcite. In some pieces, unaltered dark gray (10YR 4/1) cores of unaltered aphanitic aphyric basalt are observed set within the brown altered basalt.

5–22, 64–69, and 146–150 cm: Limestone with glass clasts. Limestone ranges in color from brownish yellow (10YR 6/8) at 5–8 cm to very pale brown (10YR 8/4) at 8–12 cm to white (10YR 8/2) at 12–22 cm to very pale brown (10YR 8/3) at 64–69 cm to light gray (10YR 7/1) at 146–150 cm. Dendritic patterns (of Mn-Oxides or hydroxides?)
are present in all pieces. Glass is palagonitized along cracks and edges.

SECTION 2

APHYRIC PILLOW BASALT, INTERPILLOW LIMESTONE

0–5 and 99–106 cm: Limestone as in Section 1. Piece 6 contains a large glass fragment. Palagonitized along fracture joints and edges.

6–96 and 108–139 cm: Aphyric pillow basalt sequence as in Section 1. (Less total glass on aphyric basalt as compared to Section 1.) Vesicles pattern the same, all but fewer large vesicles about calcite veins. Gradation of brown altered basalt to cores of unaltered basalt is less clear than in Section 1, much more subtle and fuzzy.

SECTION 3

APHYRIC PILLOW BASALT

0–42 cm: Aphyric pillow basalt sequence as in Section 1. Aphanitic basalt borders are very clear as compared to Section 2.

SITE 559 HOLE CORE 2 CORED INTERVAL 247.0–256.0 m

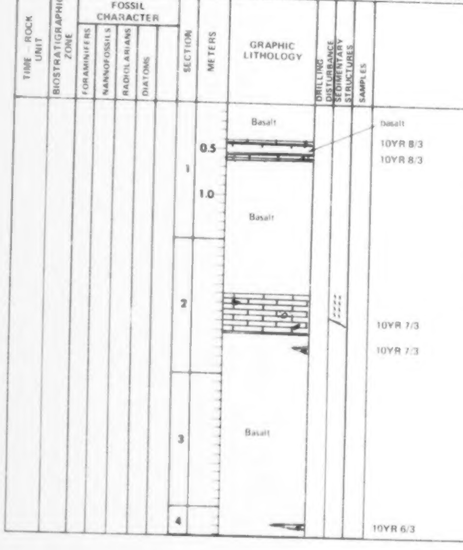
TIME – ROCK UNIT
BIOSTRATIGRAPHIC ZONE
FOSSIL CHARACTER
FORAMINIFERS
NANNOFOSSILS
RADIOLARIANS
DIATOMS
SECTION
METERS
GRAPHIC LITHOLOGY
DRILLING DISTURBANCE
SEDIMENTARY STRUCTURES
SAMPLES
1
2
3
4
0.5
1.0
Basalt
Basalt
Basalt
basalt
10YR 8/3
10YR 8/3
10YR 7/3
10YR 7/3
10YR 6/3

LITHOLOGIC DESCRIPTION

INTRAPILLOW-BASALT (VOLCANICLASTIC) LIMESTONE

Very pale brown (10YR 8/3) to pale brown (10YR 6/3)

Volcaniclasts are rare

Manganese mineralization occurs throughout the limestone as micronodules and dendrites

Limestones are veined by sparry calcite.

Section 2, 60–102 cm: Moderately bioturbated limestone is in scoured contact (dip ~30) lighter colored limestone

SITE 559 HOLE CORE 4 CORED INTERVAL 256.5–265.0 m

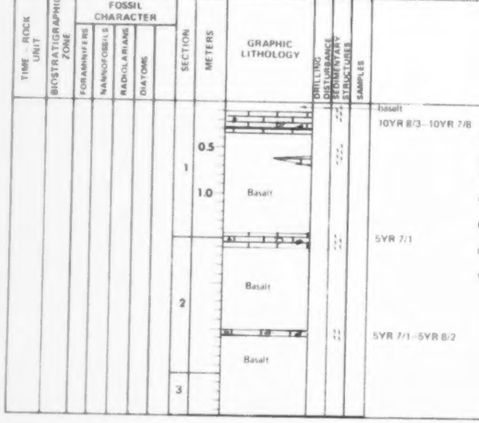
TIME – ROCK UNIT
BIOSTRATIGRAPHIC ZONE
FOSSIL CHARACTER
FORAMINIFERS
NANNOFOSSILS
RADIOLARIANS
DIATOMS
SECTION
METERS
GRAPHIC LITHOLOGY
DRILLING DISTURBANCE
SEDIMENTARY STRUCTURES
SAMPLES
1
2
3
0.5
1.0
Basalt
Basalt
Basalt
basalt
10YR 8/3–10YR 7/8
5YR 7/1
5YR 7/1–5YR 8/2

LITHOLOGIC DESCRIPTION

INTRAPILLOW BASALT (VOLCANICLASTIC) LIMESTONE

Colors vary from yellow (10YR 7/8), very pale brown (10YR 8/3) to light gray (5YR 7/1) and pinkish white (5YR 8/2)

Moderately bioturbated

Manganese mineralization occurs as dendrites and veins

Calcite veining common

Volcaniclasts are more common near pillow margins

SITE 559 HOLE CORE 5 CORED INTERVAL 265.0–274.0 m

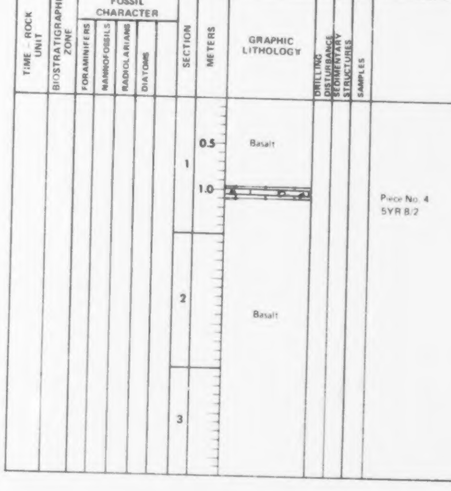
TIME – ROCK UNIT
BIOSTRATIGRAPHIC ZONE
FOSSIL CHARACTER
FORAMINIFERS
NANNOFOSSILS
RADIOLARIANS
DIATOMS
SECTION
METERS
GRAPHIC LITHOLOGY
DRILLING DISTURBANCE
SEDIMENTARY STRUCTURES
SAMPLES
1
2
3
0.5
1.0
Basalt
Basalt
Piece No. 4
5YR 8/2

LITHOLOGIC DESCRIPTION

INTRAPILLOW BASALT (VOLCANICLASTIC) LIMESTONE

Pinkish white (5YR 8/2) with manganese mineralisation as black flecks possibly (doubtful) bioturbated.

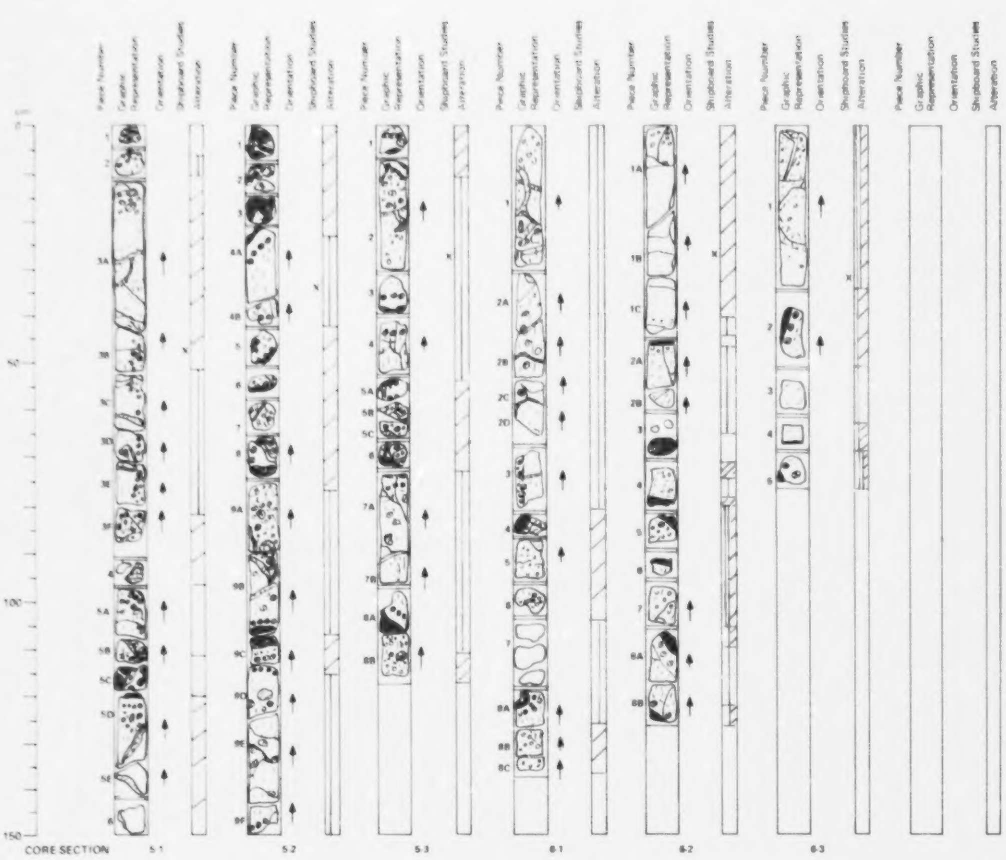

SITE 559 CORE 5 Depth 265.0–274.0 m

SECTION 1

APHYRIC PILLOW BASALT

4–90, 98–112, and 118–145 cm: Aphyric basalt pillows ranging from moderately altered (gray – 10YR 5/1) to highly altered (pale brown – 10YR 6/3). Variolitic texture grading to black aphanitic basalt grading to glass rims in some cases (black on diagram). In aphanitic basalt, rounded empty vesicles (1–2 mm).

14–20 and 119–128 cm: Rounded and irregular calcite filled vesicles (1–2 mm, some up to 1 cm) in the variolitic part. Minor calcite veining throughout.

1–4 and 112–118 cm: Mostly fresh glass clasts (with palagonitized rims) in pinkish gray (7.5YR 6/2) limestone matrix.

90–98 cm: One piece of pinkish gray (7.5YR 7/2) limestone with fine dendritic black pattern (MnO?) and mostly altered glass clast.

SECTION 2

APHYRIC PILLOW BASALT

23–150 cm: Aphyric pillow basalts as in Section 1. Round, empty vesicles (1–2 mm) in black aphanitic basalt.

78–88 cm: Round and irregular vesicles (1–2 mm up to 1 cm).

113–124 cm: Filled with calcite in the more altered cores of the pillows and top variolitic edges.

56–58, 71–72, 76–78, and 104–110 cm: Mostly fresh black glass rims with calcite veining and some alteration to clays grading into black aphanitic basalts (filled with rounded empty vesicles).

0–20 cm: Fresh and moderately altered glass in minor limestone matrix with minor calcite veining.

SECTION 3

APHYRIC PILLOW BASALT

As in Sections 1 and 2.

5–12 cm, 39–40, 70–77, and 101–104 cm: Glass rims grading to black aphanitic basalt (some with rounded, empty (1–3 mm) vesicles as in Sections 1 and 2) and variolites.

111–119, 46–47, 80–89, and 106–115 cm: Rounded to irregular calcite vesicles (1–2 mm up to 1.2 cm) in more altered upper variolitic edges of pillows.

SITE 559 CORE 6 Depth 274.0–283.0 m

APHYRIC PILLOW BASALT

Similar to Core 5. Moderately–heavily altered aphyric basalt ranging from dark gray (10YR 4/1) through grayish brown (10YR 5/2) to brown (10YR 5/3). Several areas grading from altered core through variolitic texture through black aphanitic basalt and some glass rims rounded to irregular calcite filled (1–2 mm up to 1 cm) vesicles in altered parts. Rounded empty (1–3 mm) vesicles in black aphanitic basalt. Minor calcite veining in fractures throughout section.

SECTION 2

APHYRIC PILLOW BASALT

Moderately to badly altered, fine grained aphyric basalt, color dark gray (10YR 4/1) to brown (10YR 5/3). Vitric cooling margins occur at 46–47, 65–70, 78–84, 90–92, 105–110, and 122–124 cm. Some pieces show variolitic transition to interior of pillows. Two kinds of vesicles are occurring: a) round shaped (size < 2 mm.), and b) irregular shaped (size < 10 mm); if vesicles are located in fresher parts of the basalt, they are mostly empty, otherwise filled with calcite. Fractures and veinlets are usually filled with calcite, too.

SECTION 3

APHYRIC PILLOW BASALT

Same description as Section 2.

Moderately to badly altered aphyric, fine grained basalt with some glass margins (Pieces 2, 4, and 5). Variolites in Pieces 2 and 5.

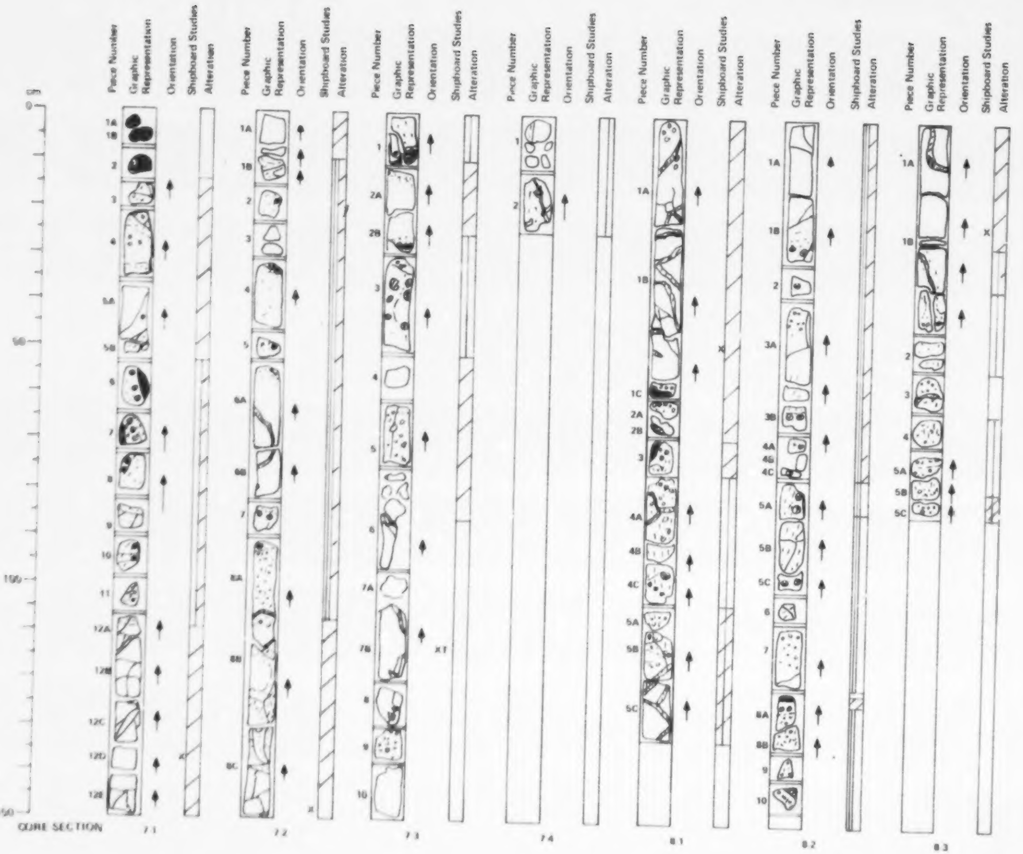

SITE 559, CORE 7 Depth 283.0–292.0 m

SECTION 1

APHYRIC PILLOW BASALT

0–14 cm Black glass and aphanitic basalt. Vesicles are common and mostly empty. Veinlets are filled with calcite. Piece 2 shows some varioles. (Size of vesicles < 1.5 mm, size of varioles < 2 mm.)

16–150 cm Fine grained, aphyric basalt, color dark gray (2.5Y N4/0) to dark grayish brown (2.5Y 4/2) in altered regions close to fractures and (calcite filled) veinlets. Two different kinds of vesicles occur: a) round, < 1.5 mm and b) irregular, < 1.2 cm. They are mostly filled with calcite.

54–80 cm Pieces show variolitic transition from fine grained to aphanitic basalt.

SECTION 2

1–150 cm Aphyric pillow basalt. Fine grained, moderately to badly altered. Color dark gray (2.5Y N4/0) to dark grayish brown (2.5Y 4/2). Variolitic texture in Pieces 2, 4, 5, 6, 7, and 8.

91–106 cm Basalt is highly vesicular: a) round vesicles < 2 mm are filled with calcite in altered part of rock, in aphanitic part empty, and b) irregular vesicles <8 mm are filled with calcite.

SECTION 3

APHYRIC PILLOW BASALT

0–12 cm Moderately altered, gray (2.5Y N5) aphyric fine grained basalt with glass chill margin of 10 cm (as in Sections 1 and 2).

New Unit

120–150 cm Coarser grained (but still fine) yellowish gray (5Y 5/1), aphyric basalt with very fine (≤3 mm) visible plagioclase needles and very small (< 0.5 mm) equant grains that are olive brown to reddish brown = olivine(?). Upper part (10–85 cm) is moderately altered, lower part (85–150 cm) is fresher.

33–42 and 63–74 cm 5% round and irregular calcite filled vesicles (≤3 mm) in altered part, and 2% round empty vesicles in aphanitic basalt margin and also in altered part near margin.

131–136 cm 5% round (≤ 2 mm) calcite filled vesicles and < 1% round (≤2 mm) empty vesicles on edge of rock.

SECTION 4

APHYRIC PILLOW BASALT

Highly altered continuation of fine grained, aphyric basalt starting at Section 3, 12 cm.

SITE 559, CORE 8 Depth 292.0–301.0 m

SECTION 1

APHYRIC PILLOW BASALT

0–54 and 69–132 cm Fine grained (coarser grained than previous unit), slightly to moderately to heavily (79–103 cm) altered, aphyric basalt as in Section 3, 12 cm and Section 4.

54–79 cm Black aphanitic basalt with glass chill margins and 2% round, empty (< 2 mm) vesicles. There is more fracturing (calcite filled) in Core 8, Section 1 than Core 7, Sections 3 and 4.

79–88 and 106–113 cm 5% round and irregular (≤ 3 mm) calcite filled vesicles in altered parts of pillows.

SECTION 2

0–146 cm Aphyric pillow basalt. Moderately to badly altered, fine grained. Partly variolitic transition from altered inner part to fresher aphanitic part (rim) of pillow. Glass occurs at 77–83 and 121–123 cm. Round vesicles (filled with calcite in altered regions of rock) are common at 38– ~ 45 and 107–146 cm (size < 3.5 mm). Color of basalt dark gray to dark grayish brown (2.5Y N4/0 to 2.5Y 4/2).

SECTION 3

APHYRIC PILLOW BASALT

Same unit and characteristics as in Sections 1 and 2 with usual calcite filled vesicles in altered part of rock (63–67 and 75–82 cm).

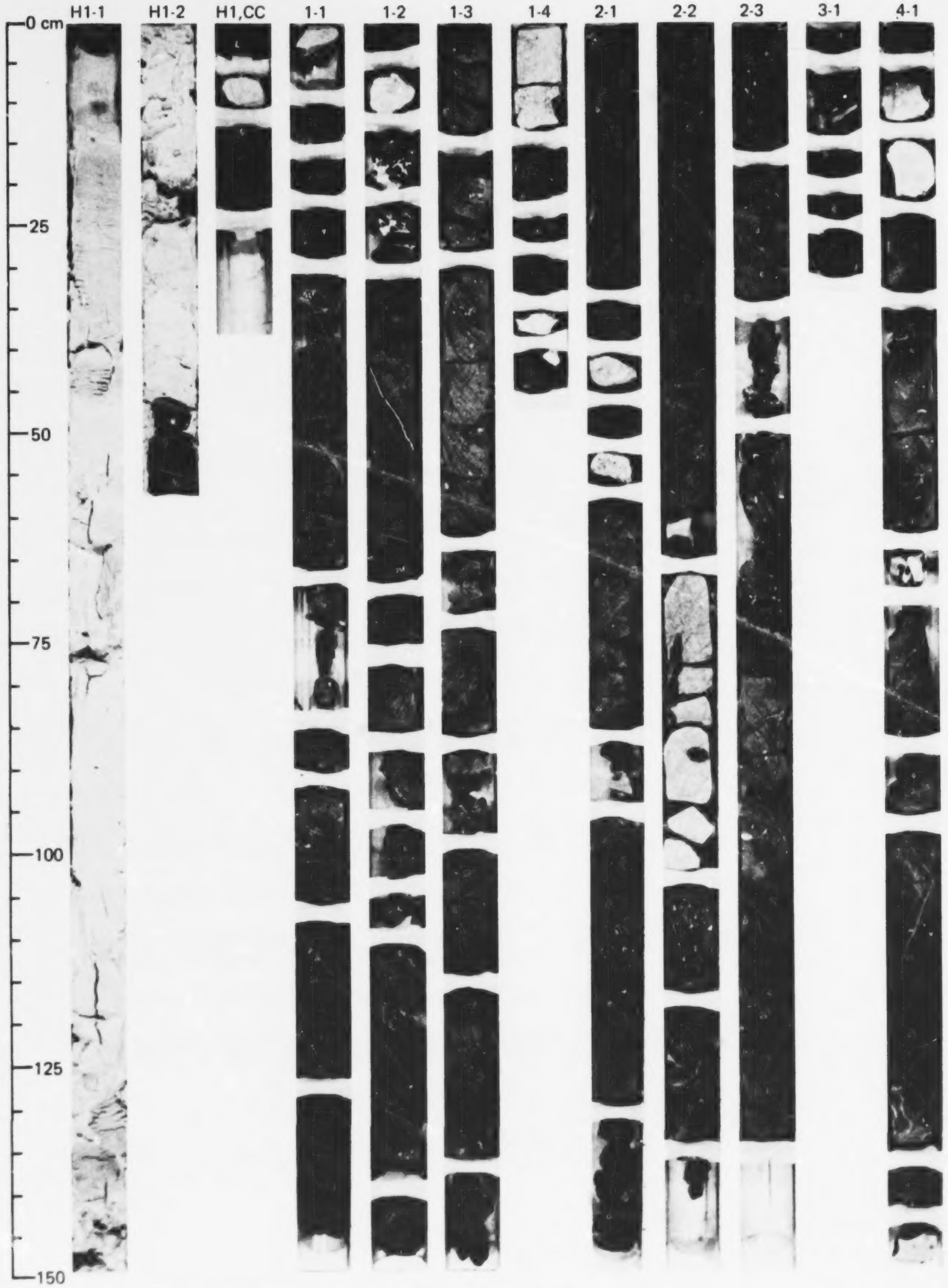
0 cm
25
50
75
100
125
150
H1-1
H1-2
H1,CC
1-1
1-2
1-3
1-4
2-1
2-2
2-3
3-1
4-1

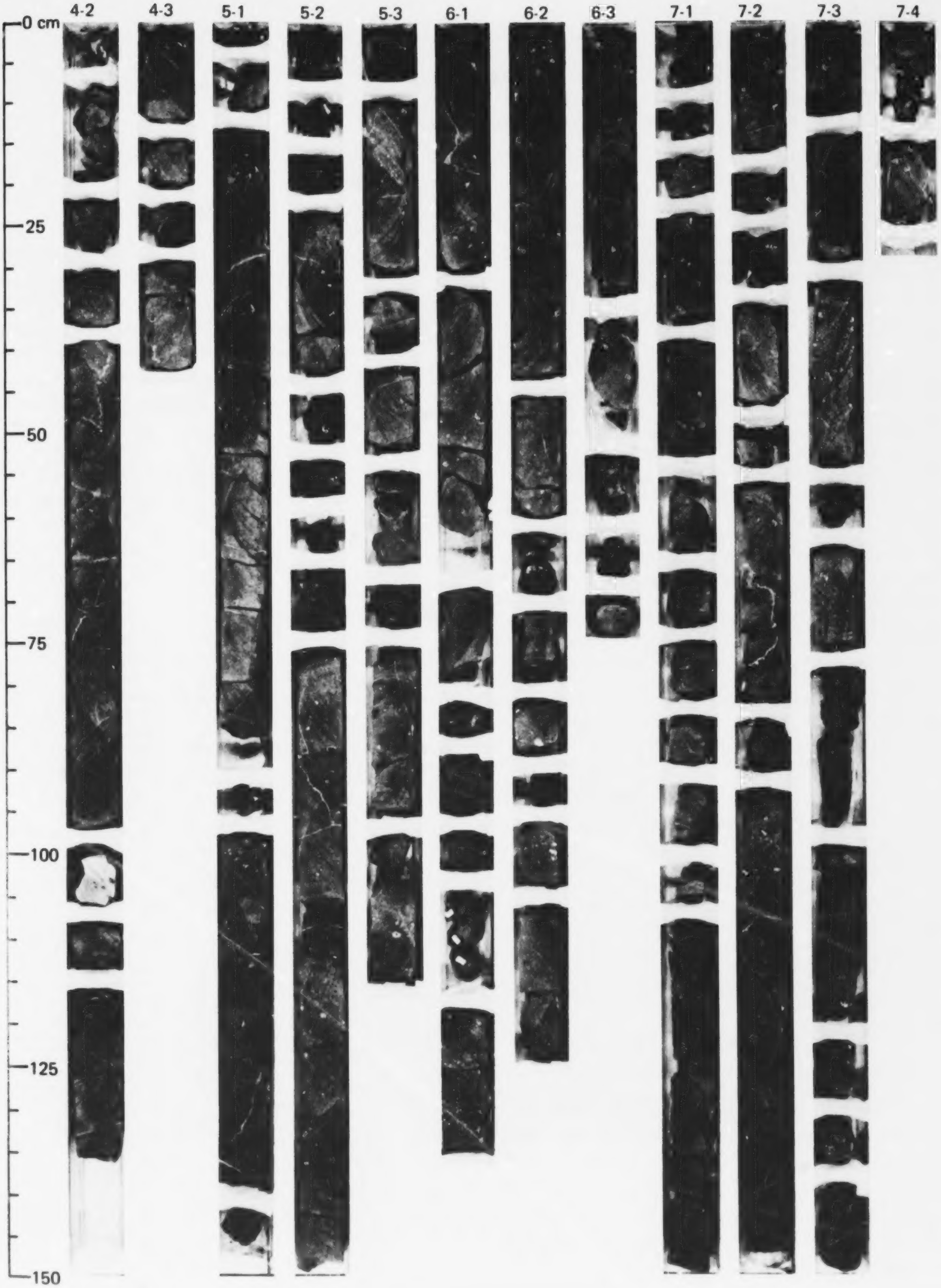
0 cm
25
50
75
100
125
150
4-2
4-3
5-1
5-2
5-3
6-1
6-2
6-3
7-1
7-2
7-3
7-4

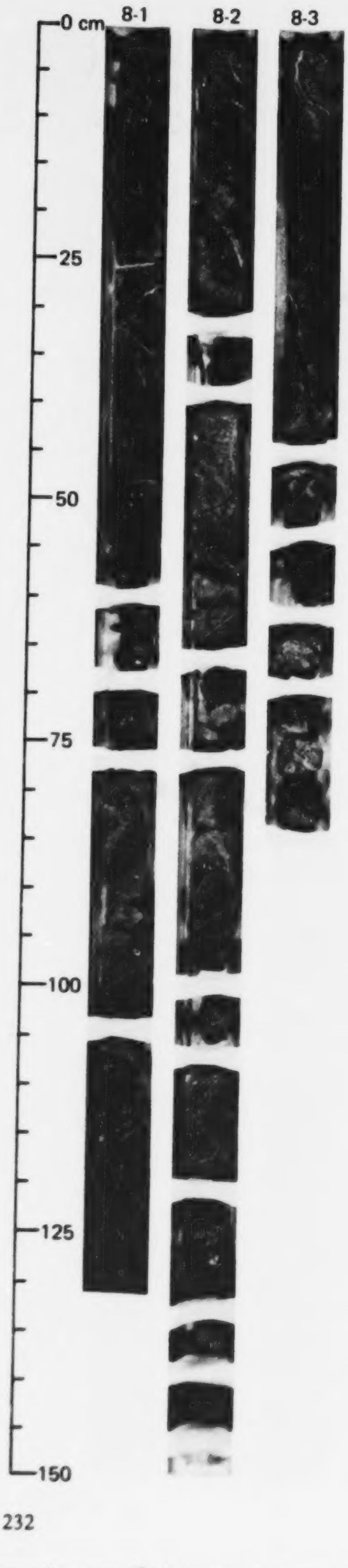
0 cm
25
50
75
100
125
150
8-1
8-2
8-3

9. SITE 560[1]

Shipboard Scientific Party[2]

HOLE 560

Date occupied: 16 October 1981

Date departed: 18 October 1981

Time on hole: 38 hr.

Position (latitude; longitude): 34°43.33′N; 38°50.56′W

Water depth (sea level; corrected m, echo-sounding): 3443

Water depth (rig floor; corrected m, echo-sounding): 3453

Bottom felt (m, drill pipe): 3455

Penetration (m): 421.5

Number of cores: 6

Total length of cored section (m): 48.5

Total core recovered (m): 7.81

Core recovery (%): 16

Oldest sediment cored:
Depth sub-bottom (m): 373
Nature: Dolomite
Age: Miocene

Basement:
Depth sub-bottom (m): 374.5
Nature: Serpentinized gabbros

Principal results: Hole 560 (MAR-7) was drilled on Anomaly 5D on the west flank of the Mid-Atlantic Ridge midway between the Oceanographer and Hayes fracture zones (Fig. 1). Sediments were washed down to the basement at a depth of 374.5 m sub-bottom.

Only serpentinized gabbros and serpentine with the presence of chrysotile were found with very poor recovery down to the bottom of the hole at 421.5 m sub-bottom. Failure to recover basalt can be attributed to drilling through a talus slope facing the spreading axis.

Repeated occurrence of shallow-level serpentinized gabbros (Holes 556, 558, and 560), as supported by previous drilling results at Holes 334 (Aumento, Melson, et al., 1977) and 395 (Melson, Rabinowitz, et al., 1979), seems to be a general characteristic connected with the high frequency of faulting.

Because we did not recover basalt, it was necessary to drill again in the same area.

At Site 560, no samples were taken for interstitial water analyses or for paleomagnetic measurements. No downhole measurements were taken at this site, and sediment accumulation rates could not be calculated.

OPERATIONS

Approach to Site

After completing operations at Site 559, we decided to drill on Anomaly 5D, which lies along the same flow line as Site 559 between the Oceanographer and Hayes Fracture Zones. The track of the *Challenger* followed the flow line toward the Mid-Atlantic Ridge and arrived in the general vicinity of the site on the evening of 16 October (Fig. 2). Potential drill sites were noted on a broad elevated ridge on Anomaly 6 (about 2000Z) and on a buried ridge on Anomaly 5E (about 2130Z). Both of these sites were characterized by rough basement and an irregular, fuzzy basement reflector. In the immediate vicinity of Anomaly 5D, a strong basement return was observed on the east flank of a structural high at 2250Z (Fig. 3). After profiling beyond this feature, we decided to drill on this site. Even though the slope was steeper here than on previous sites, we thought that the strong basement return indicated solid basement material. The course of the *Challenger* was reversed and the beacon dropped on Site 560 at 0039Z 17 October.

On-Site Operations

Site 560 was spudded at 0852Z 17 October, in an estimated 3443 m of water. No mudline core was taken, and sediments were washed down until basement was hit at a sub-bottom depth of 374.5 m. The first basement core was recovered at 1515Z and contained serpentinized gabbros mixed with sediments. At 0445Z, 18 October, after six cores penetrating 48.5 m failed to recover any basalt, we decided to abandon the hole (Table 1). The drill string was pulled and the *Challenger* was under way to Site 561 at 1244Z.

SEDIMENT LITHOLOGY

Site 560 was selected for basalt recovery only, to be washed to basement without coring. Because of the very steep basement topography, the site proved to be one at which apparently only a submarine talus or debris-flow deposit (as well as some of the overlying carbonate sediments) was penetrated.

Core H1, a wash core representing the sedimentary section from 0 to 373 m sub-bottom, consists of nannofossil ooze and chalk, and foraminiferal-nannofossil ooze and chalk. Core 1 (373.0–376.5 m) recovered 140 cm of

---

[1] Bougault, H., Cande, S. C., et al., *Init. Repts. DSDP*, 82: Washington (U.S. Govt. nting Office).

[2] Henri Bougault (Co-Chief Scientist), IFREMER (CNEXO), Centre de Brest, B. P. 337, 273 Brest Cedex, France; Steven C. Cande (Co-Chief Scientist), Lamont-Doherty Geologi- Observatory, Columbia University, Palisades, New York; Joyce Brannon, Department of rth and Planetary Sciences, Washington University, St. Louis, Missouri; David M. Chris- Hawaii Institute of Geophysics, University of Hawaii at Manoa, Honolulu, Hawaii; Murlene rk, Department of Geology, Florida State University, Tallahassee, Florida; Doris M. Cur- Curtis and Echols, Geological Consultants, Houston, Texas; Natalie Drake, Department Geology, University of Massachusetts, Amherst, Massachusetts; Dorothy Echols, Depart- nt of Earth and Planetary Sciences, Washington University, St. Louis, Missouri (present dress: Curtis and Echols, Geological Consultants, 800 Anderson, Houston, Texas 77401); Ashley Hill, Department of Geology, University of Leicester, Leicester LE1 7RH, United ngdom; M. Javed Khan, Lamont-Doherty Geological Observatory, Columbia University, lisades, New York (present address: Department of Geology, Peshawar University, Pesha- r, Pakistan); William Mills, Deep Sea Drilling Project, Scripps Institution of Oceanogra- ly, La Jolla, California (present address: Ocean Drilling Program, Texas A&M University, llege Station, Texas 77843); Rolf Neuser, Institut für Geologie, Ruhr Universität Bochum, 630 Bochum 1, Federal Republic of Germany; Marion Rideout, Graduate School of Ocean- graphy, University of Rhode Island, Kingston, Rhode Island (present address: Department Geology, Rice University, P. O. Box 1892, Houston, Texas 77251); and Barry L. Weaver, epartment of Geology, University of Leicester, Leicester, LE1 7RH, United Kingdom (present address: School of Geology and Geophysics, University of Oklahoma, Norman, Oklahoma 3019).

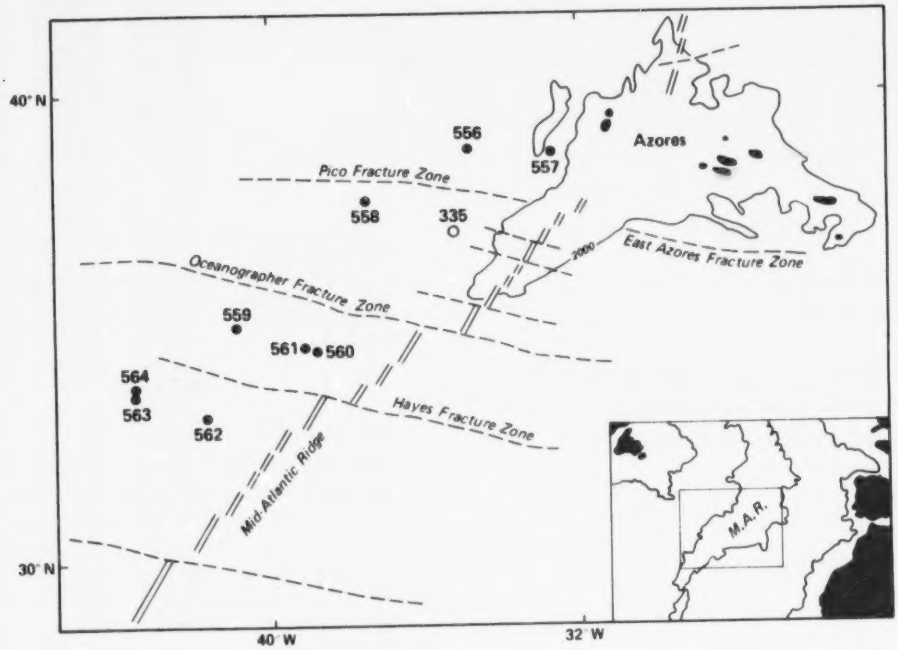
40° N
30° N
40° W
32° W
556
557
558
335
559
561
560
564
563
562
Azores
Pico Fracture Zone
Oceanographer Fracture Zone
East Azores Fracture Zone
Hayes Fracture Zone
Mid-Atlantic Ridge
2000
M.A.R.

Figure 1. Site location map for Leg 82.

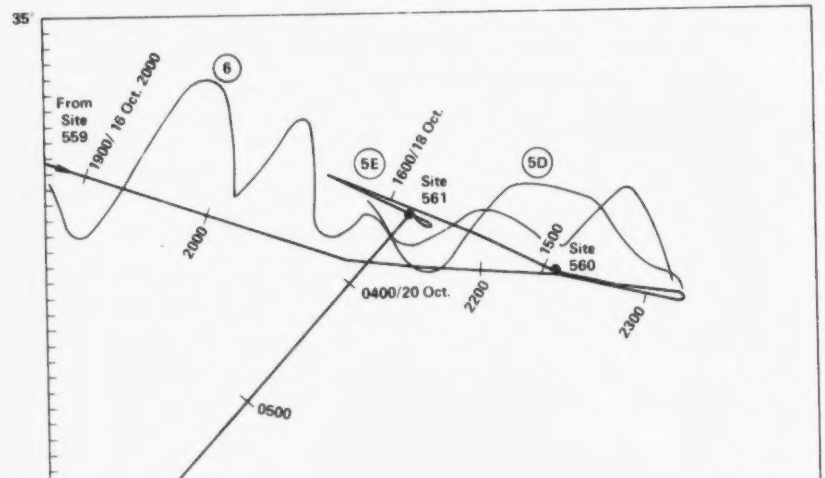

Figure 2. Approach and site survey track for Sites 560 and 561. Heavy line is the ship's track with hour marks in GMT. Thin line is magnetic anomaly line projected perpendicularly from the ship's track. Circled numbers are magnetic anomalies based on work at Lamont-Doherty Geological Observatory.

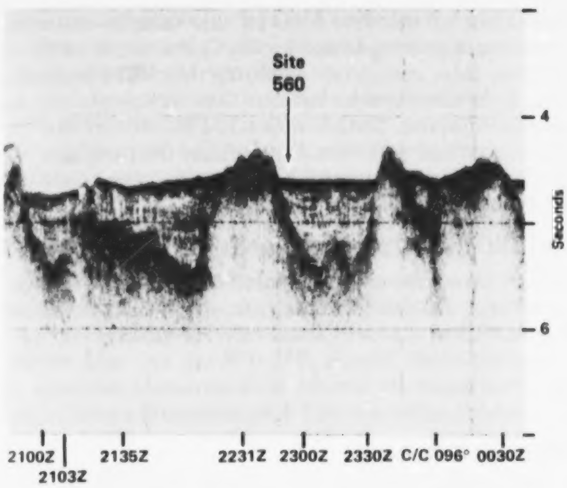

Figure 3. *Glomar Challenger* seismic profile over Site 560. For location of profile, see Figure 2. C/C = course change.

Table 1. Coring summary, Hole 560.

Core	Date (Oct. 1981)	Time (Z)	Depth from drill floor (m)	Depth below seafloor (m)	Length cored (m)	Length recovered (m)	Percent recovered
H1	17	1415	3455.0-3828.0	0.0-373.0	0.0	0.00	0
1	17	1515	3828.0-3831.5	373.0-376.5	3.5	1.55	44
2	17	1645	3831.5-3840.5	376.5-385.5	9.0	1.07	12
3	17	1920	3840.5-3853.5	385.5-398.5	13.0	0.63	5
4	17	2125	3853.5-3858.5	398.5-403.3	5.0	0.73	15
5	18	0042	3858.5-3867.5	403.5-412.5	9.0	1.13	13
6	18	0455	3867.5-3876.5	412.5-421.5	9.0	2.70	30
					48.5	7.81	16

nannofossil chalk, dolomitic nannofossil chalk, and marly dolomitic limestone, of the late early Miocene to early middle Miocene times (14 to 17 Ma), in contact with rubble or talus of serpentinized basement. Core 2 (376.5 to 385.5 m) recovered 140 cm of a mixture of limestone, polymict limestone breccia, and brecciated serpentinized basalt and gabbro, overlying a series of serpentinites and other tectonically altered basic igneous rocks.

If we had cored the sedimentary section at this site, we probably would have recognized three units: nanno-ossil to foraminiferal-nannofossil ooze and chalk; do-omitic nannofossil chalk to limestone; and redeposited olymict breccia.

The nannofossil and foraminiferal-nannofossil ooze nd chalk (Core H1) is white (7.5YRN 8, 2.5YN 8) to inkish white (7.5YR 8/2) to pink (2.5YR 8/4 and 5YR /3), with black streaks of ash (pumice). Two light brown 7.5YR 6/4) beds 10 to 20 cm thick in the lower part of Section 560-H1-6 indicate the transition upward from the dolomite and nannofossil chalk in the next core. The chalk s very mildly bioturbated, and only faint mottling is discernible. Bedding is massive. Calcareous nannofossils are the principal component of these sediments, and the carbonate content averages more than 90% (Fig. 4).

The dolomitic nannofossil chalk to limestone begins in the lower part of Section 560-H1-6 and continues through 560-1-1, 107 cm, where the base of the 12-cm-thick dolostone (85% dolomite) is in distinct contact with an underlying marly dolomitic limestone (107–115 cm). The dolostone is reddish brown (5YR 4/4 to 5YR 5/4), and the marly limestone below it is yellowish brown to brownish yellow. The chalk that occurs above the dolostone grades from very pale brown (10YR 7/4) to reddish yellow (7.5YR 6/6), light yellowish brown (10YR 6/4) to brownish yellow (10YR 6/6). The chalk is mildly to considerably bioturbated. The burrows and mottlings are a darker color than the unchurned material. Bedding is faint and parallel, and it appears to be inclined because of possible post-depositional slumping. At 560-1-1, 78–90 cm, there are indistinct microripples or flaser bedding. At 560-1-1, 107–115 cm, there is a graded, fining-upward turbidite sequence of silt-size to clay-size parti-

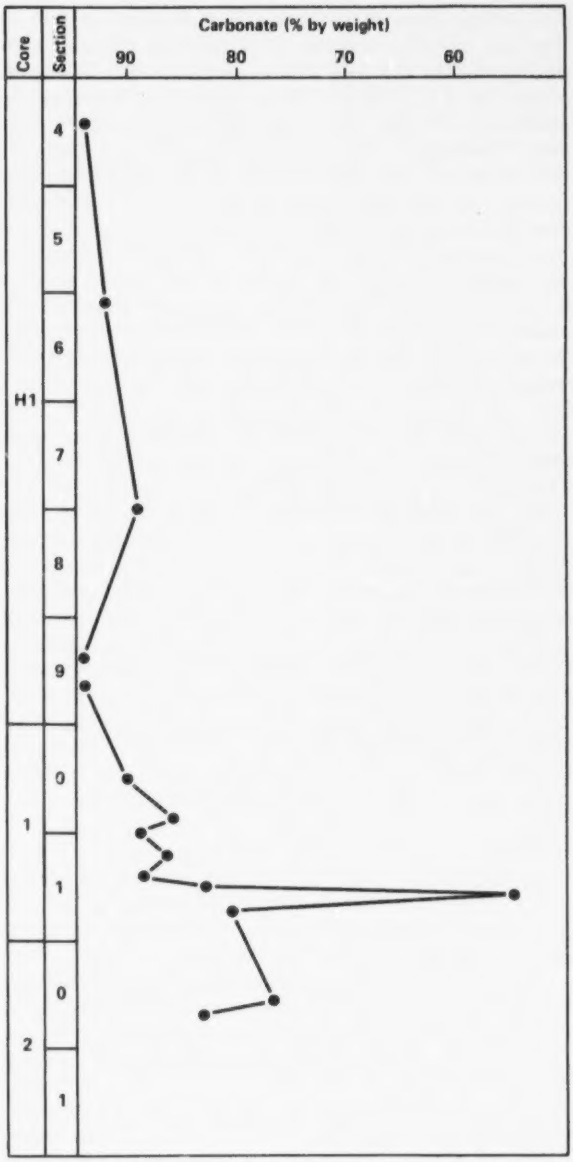

Figure 4. Carbonate curve, Hole 560.

cles, with a scour at the base. The carbonate content in this bed is 55%, whereas it is between 80 and 90% throughout the rest of the core. Dolomite increases from 3% at 560-1-1, 5 cm to 85% at 560-1-1, 100 cm, and it makes up 70% just above the sediment/basement contact. "Basement" was encountered at 374.2 m (560-1-1, 120 cm) in the form of serpentinite. This material (continuing through Core 2 and below) is part of a submarine talus or slump deposit (or debris flow), in which limestone, polymict limestone breccia, serpentinized gabbro and gabbroic breccia, and basalt are all present (probably as boulders). The turbidite described from Core 1 could be the end stage of the debris flow. The limestone (560-2-1, 8–60 cm) is a dolomitic clayey nannofossil limestone, reddish yellow (7.5YR 7/6 and 7.5YR 7/8) and light yellowish brown to olive yellow (2.5YR 6/6, 2.5Y 6/8) in color. Bedding is massive, with no obvious mottling. This micritic limestone contains more clay (15–25%), more nannofossils (40%), and less dolomite (10–15%) than that described from Core 1.

The polymict limestone breccia (560-2-1, 0–8 cm; 560-2-1, 75–90 cm; 560-2-1, 100-105 cm; and 560-2-1, 130–140 cm) consists of clasts (silt size to 15 mm) of basalt, glass, igneous lithic fragments (such as gabbro and gabbroic breccia), limestone, and volcaniclastic limestone breccia, in a pale brown to reddish brown microcrystalline limestone matrix.

The remainder of the core contains serpentinite, talc, basalt, and gabbroic breccia.

BIOSTRATIGRAPHY

Summary

Sediments recovered from 560-1-1, 20 cm are, based on the calcareous nannofossils, from the late early Miocene to early middle Miocene times. The faune is abundant and moderately well preserved.

On the other hand, the foraminifers from this part of the section, although abundant, are partially obliterated by dolomite crystals growing in and on the tests. The genera and species that could be identified indicate a middle Miocene assignment.

Calcareous Nannofossils

Hole 560 was washed down to 373.0 m and Core H1 was recovered. H1, CC contains *Discoaster neohamatus* without *D. quinqueramus* or *D. hamatus* and is placed within the *D. neohamatus* Zone CN8 (NN10) of the lower upper Miocene. Core 1, which contains the first basement material, was sampled at 560-1-1, 20 cm and 560-1-1, 117 cm. This interval is assigned to either the *Sphenolithus heteromorphus* Zone CN4 (NN5) or the *Helicosphaera ampliaperta* Zone CN3 (NN3-4) based on the occurrence of *Sphenolithus heteromorphus*. These two samples, the second of which is positioned just above basement, indicate the lower middle Miocene to upper lower Miocene.

Foraminifers

Foraminifers in Section 560-H1-6 are well preserved and from the Miocene time. Sample 560-1-1, 22–24 cm must have been a nannofossil-foraminiferal ooze before crystallization of the dolomite. In this sample, dolomite rhombs are growing in and on the foraminiferal tests and in some cases completely enclosing them. The recognizable genera and species indicate that the sample may be middle Miocene. Sample 560-1-1, 128–130 cm is a basalt rubble and rock flow. In the finest fraction, tiny microforaminifers or juveniles are present. Age could not be determined.

IGNEOUS PETROLOGY AND GEOCHEMISTRY

The cored sequence at Hole 560 passed from limestone and dolomite into serpentinite breccia at about 374 m. Below a short second interval of limestone and limestone-basalt breccia (376–378 m), the hole continued in serpentinite breccia, with increasing amounts of serpentinite mylonite until hole termination at 421.5 m.

Basement Lithologies

Basalt rocks were present as clasts in the basalt-limestone breccia. Only three clasts were sufficiently large to be of interest, each of a different lithology: zeolitized basalt ash, zeolitized variolitic basalt, and partially zeolotized fine-grained basalt. This last clast was the only rock analyzed from this hole.

Serpentinite breccias consist of serpentinite clasts in a bluish gray clayey matrix. The clasts are weathered brown in the upper serpentinite section and at the top of the lower section. Further downhole all clasts appear fresh. Prismatic, dark brown grains of relict pyroxene up to 5 mm long are present in all clasts in the upper part of the section, but they do not persist downhole where the serpentinization is more pervasive. Fresh serpentinite is dark greenish to black with varying degrees of foliation. Occasional large crystals of lighter green(?) antigorite are present. White crysotile veinlets increase in abundance downhole.

Below 398 m sub-bottom, bluish gray mylonite becomes the dominant lithology. This soft, highly cohesive clayey material shows a rough, near-horizontal parting when broken. It is not clear, however, whether this is a primary structure or a drilling-induced structure. In places minor compositional layering may also be present. Within the mylonite are numerous angular fragments (up to 2 cm) of dark green serpentinite and emerald green talc. Occasional large serpentinite pieces occur throughout.

Petrography

The fine-grained basalt fragment (560-2-1, 92–100 cm) has typical intersertal texture and consists of 40% randomly oriented plagioclase laths with 25% granular clinopyroxene and 25% mesostasis with up to 5% olivine and 5% magnetite. Both olivine and mesostasis are completely altered to light brown or colorless aggregates of zeolite.

Two zeolite minerals appear to be present. One occurs as relatively coarse-grained (about 0.02 mm) aggregates, especially after olivine, and is identified optically as gmelinite. The second is finer grained, but appears identical to the heulandite identified in basalts from Site 559.

The variolitic basalt fragment (560-2-1, 125–130 cm) is composed mainly of altered, devitrified glass with skeletal needles of plagioclase and altered skeletal chains of olivine. Veinlets of zeolite, probably gmelinite, occur between some of the variolites.

Only one serpentinite sample was examined. It consists almost entirely of serpentine with some fresh, relict clinopyroxene and altered orthopyroxene within the brown prismatic grains described above.

Geochemistry

Results from Sample 560-2-1, 93–96 cm are listed below.[3] The rather peculiar major element chemistry, notably with high SiO_2 and Al_2O_3, but low Fe_2O_3 relative to MgO concentrations, results in a very high Mg-value (75).

Major element	Concentration (wt. %)	Trace element	Concentration (ppm)
SiO_2	52.60	Ti	7260
TiO_2	1.21	V	268
Al_2O_3	17.26	Sr	121
Fe_2O_3	6.55	Y	29.0
MnO	0.11	Zr	73
MgO	8.51	Nb	6.2
CaO	10.59		
K_2O	0.06		
P_2O_5	0.12		
Total	97.01	Mg′-value = 75	

Qualitatively, these major element patterns may be accounted for by the zeolitization of olivine and mesostasis in this sample. The immobile trace elements, plotted on a modified Coryell-Masuda diagram, indicate a slightly depleted pattern for this sample (Fig. 5; $(Nb/Zr)_{ch} = 0.8$).

PHYSICAL PROPERTIES

During the attempt to wash down to basement, coring was started when the drilling rate slowed at 373 m sub-bottom. Through a cored depth of 48 m, recovery was very poor, and it was inferred that the hole was passing through a talus formation. Some pieces of lithified sediment were recovered, particularly in Cores 1 and 2. Velocity and density measurements were made on three samples from these cores and show variable but generally high velocity and density (Table 2). These values are high for calcareous sediments of this age and depth of burial, and the density of 2.46 g/cm³ is compatible with the effect of dolomitization reported by the sedimentologists.

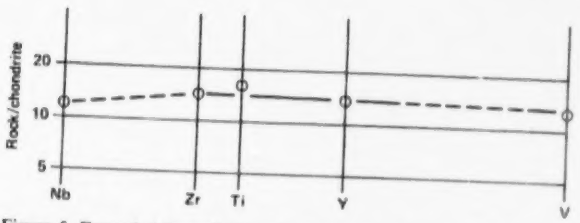

Figure 5. Extended Coryell-Masuda diagram for Sample 560-2-1, 93–96 cm.

Table 2. Physical properties measurements, Hole 560.

Core-Section (interval in cm)	Sub-bottom depth (m)	Sonic velocity (km/s)		Temperature (°C)	GRAPE density (g/cm³)		Gravimetric density			Acoustic impedance (× 10⁵ g/[cm · s])	Lithology or remarks
		V.	H.		V.	H.	Wet-bulk density (g/cm³)	Water content (%)	φ (%)		
1-1, 33-38	373.4		2.01	22.0		2.19	2.14	17	36	4.4	Marly limestone
1-1, 99-103	374.0		3.20	22.0		2.46	2.47	8	20	7.9	Siltstone (?)
2-1, 27-31	376.8		1.99	22.0		2.13	2.09	18	37	4.2	Marly limestone

Note: V. = vertical, H. = horizontal; water content is corrected; φ = porosity. All values measured at laboratory temperature and pressure. For details of techniques, see Explanatory Notes chapter (this volume).

SUMMARY AND CONCLUSIONS

Hole 560 was drilled on Anomaly 5D midway between the Oceanographer and Hayes fracture zones. Sediments were washed down to the basement at 374.5 m sub-bottom. The cored sequence passed from limestone and dolomite into serpentinite breccia at about 374 m. A second interval of limestone and limestone basalt breccia (376–378 m) was found, and then the serpentinite breccia continued. Because of the steep basement topography, this finding was interpreted as a submarine talus or debris-flow deposit. To obtain basalt samples at this site we had to choose between continuous drilling, which might get through this talus (as at Site 395), or abandoning the site immediately and drilling a short distance away. Because the necessary time for a round trip of the drill string and a short survey would result in cancellation of a planned future site, we decided to continue drilling at Site 560. Unfortunately only serpentinite breccias and serpentinite clasts in a bluish clayey matrix were recovered down to 47 m into the basement when it was estimated that future drilling would cancel another site of the program, so Hole 560 was terminated.

Only three basalt clasts were large enough to be of interest. A zeolitized fine-grained basalt was analyzed and, to the extent that the zeolitization process had not fractionated the magmaphile element abundances, this sample shows a flat or slightly depleted magmaphile element pattern.

REFERENCES

Aumento, F., Melson, W. G., et al., 1977. *Init. Repts. DSDP*, 37: Washington (U.S. Govt. Printing Office).

Melson, W. G., Rabinowitz, P. D., et al., 1979. *Init. Repts. DSDP*, 45: Washington (U.S. Govt. Printing Office).

---

[3] On-board measurements were made on ignited samples. Onshore analyses showed loss on ignition to be less than 1% in most cases. Compiled data tables at the end of this volume (Appendix) include volatile components. Total Fe as Fe_2O_3. Mg′ is the atomic ratio of $100 \times Mg/(Mg + Fe^{2+})$ (calculated using an assumed Fe_2O_3/FeO ratio of 0.15).

SITE 560 HOLE CORE H1 CORED INTERVAL 0.0–373.0 m

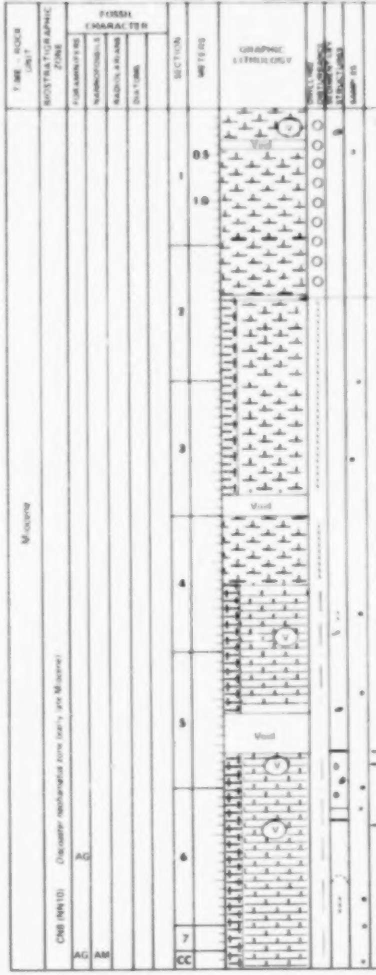
TIME—ROCK UNIT
BIOSTRATIGRAPHIC ZONE
FOSSIL CHARACTER
FORAMINIFERS
NANNOFOSSILS
RADIOLARIANS
DIATOMS
SECTION
METERS
GRAPHIC LITHOLOGY
DRILLING DISTURBANCE
SEDIMENTARY STRUCTURES
SAMPLES
Miocene
CN8 (NN10) Discoaster neohamatus zone (early late Miocene)
AG
AG AM
1
2
3
4
5
6
7
CC
0.5
1.0
Void
Void
Void
7.5YR N8
void
7.5YR 8/4
7.5YR 8/2
mixed pink and white
2.5Y N8
pumice streak
black streak
7.5YR 8/2
5G 7/1
7.5YR 8/4
black streak
5YR 8/3
7.5YR 6/4
7.5YR 8/4
7.5YR 6/4
7.5YR 8/4

LITHOLOGIC DESCRIPTION

DOMINANT LITHOLOGY

(1) NANNOFOSSIL OOZE/CHALK TO FORAM NANNO OOZE

White (7.5YR N8–2.5Y N8) to gray (5G 7/1) in Section 6 with black 1–2 m pellet of glass (pumice)

Soft to firm: soupy, brecciated, and badly disturbed

Very mildly bioturbated, slightly mottled; massive bedding; distinct to indistinct contacts between white and pink layers

In Section 6, clasts of pink chalk (drilling breccia?) are incorporated in gray (5G 7/1) ooze.

(2) FORAM NANNOFOSSIL CHALK/OOZE

Pinkish white to pink to light brown (intervals in Section 6), with black (pumice) streak (as at Section 6, 35 cm)

Soft to firm to hard, very to moderately disturbed

Very mildly bioturbated, slightly mottled (very faint); massive bedding, distinct to indistinct contacts with white layers

Minor lithology:
Volcanic glass (pumice) Section 6, 25 cm, dark particles

V = volcanic glass

SMEAR SLIDE SUMMARY (%):

	1,50	3,36	5,46	6,25	CC
	D	D	D	M	D
Composition:					
Feldspar	Tr	Tr	Tr	15	Tr
Clay	—	6	8	—	5
Volcanic glass	—	—	—	80	—
Palagonite	—	—	Tr	—	—
Opaques	1	—	—	—	Tr
Carbonate unspec.	1	12	—	—	10
Foraminifers	5	11	10	—	11
Calc. nannofossils	93	71	81	3	74

Carbonate Bomb (%):
3, 90–91 = 94
4, 110–111 = 92
6, 5–6 = 89
6, 125–126 = 94
7, 5–6 = 94

SITE 560 HOLE CORE 1 CORED INTERVAL 373.0–378.5 m

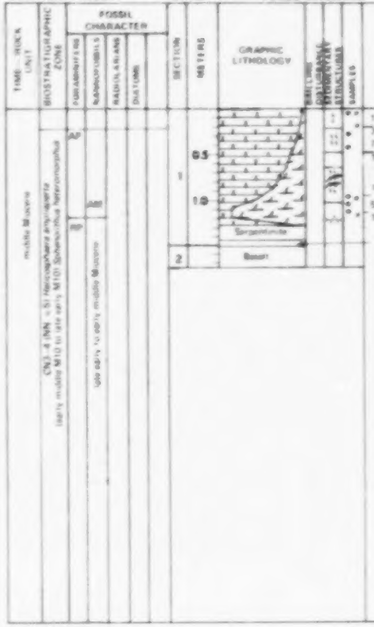
TIME—ROCK UNIT
BIOSTRATIGRAPHIC ZONE
FOSSIL CHARACTER
FORAMINIFERS
NANNOFOSSILS
RADIOLARIANS
DIATOMS
SECTION
METERS
GRAPHIC LITHOLOGY
DRILLING DISTURBANCE
SEDIMENTARY STRUCTURES
SAMPLES
middle Miocene
CN3–4 (NN4–5) Helicosphaera ampliaperta (early middle M10 to late early M10) Sphenolithus heteromorphus
late early to early middle Miocene
AP
AM
RP
1
2
0.5
1.0
Serpentinite
Basalt
10YR 8/4
7.5YR 6/6
7.5YR 6/8
10YR 7/4
10YR 6/4
5YR 4/4
10YR 5/6
void

LITHOLOGIC DESCRIPTION

DOMINANT LITHOLOGIES:

(1) NANNOFOSSIL CHALK TO DOLOMITIC NANNOFOSSIL CHALK (0–95 cm and 107–118 cm)

Very pale brown (10YR 8/4), light yellowish brown (10YR 6/4) and reddish yellow (7.5YR 6/6 to 6/8)

Firm to hard

Highly bioturbated, current or flaser bedding at 78 cm and possibly extending to 90 cm

Probable graded bedding with scoured base from 107–118 cm

(2) MARLY DOLOSTONE

Reddish brown (5YR 4/4)

SMEAR SLIDE SUMMARY (%):

	1,5	1,12	1,100	1,118
	D	D	D	D
Composition:				
Feldspar	2	Tr	1	Tr
Clay	8	12	12	15
Volcanic glass	—	—	—	2
Palagonite	Tr	2	2	Tr
Pyrite	—	—	—	2
Carbonate unspec.	5	5	—	—
Foraminifers	2	5	—	—
Calc. nannofossils	80	66	—	10
Dolomite	3	10	85	73

Carbonate Bomb (%):
1, 5–6 = 90
1, 30–31 = 87
1, 42 = 88
1, 100 = 80
1, 110 = 56
1, 118 = 81

SITE 560 HOLE CORE 2 CORED INTERVAL 376.5–385.5 m

TIME - ROCK UNIT	BIOSTRATIGRAPHIC ZONE	FOSSIL CHARACTER: FORAMINIFERS	NANNOFOSSILS	RADIOLARIANS	DIATOMS	SECTION	METERS	GRAPHIC LITHOLOGY	DRILLING DISTURBANCE	SEDIMENTARY STRUCTURES	SAMPLES
						1	0.5 1.0				
						2		brecciated igneous rock, serpentinite talc, etc.			
						3					
						4					
						5					

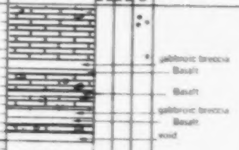

LITHOLOGIC DESCRIPTION

DOMINANT LITHOLOGIES

(1) **LIMESTONE** (dolomitic clayey nannofossil limestone to clayey dolomitic nannofossil limestone)

Reddish yellow (7.5YR 7/6, 7.5YR 7/8) and light yellowish brown (2.5Y 6/4) and olive yellow (2.5Y 6/8)

Massive bedding, no visible bioturbation or mottling

Contains 25% clay, 40% nannofossils, 10–15% dolomite

(2) **POLYMICT LIMESTONE BRECCIA**

Pale brown to reddish brown (10YR 6/3–5YR 4/4) limestone with dark brown to light gray clasts

Clasts include basalt, glass, igneous lithic fragments, also volcaniclastic limestone clasts enclosing clasts of volcaniclastic limestone breccia

Clasts range from silt size to 15 mm

(3) **GABBROIC BRECCIA** (autoclastic)

Brown to dark brown (7.5YR 5/2–7.5YR 4/2) with dark clasts of basic igneous rock with bronzy pyroxene

In Piece 10, approximately 112–122 cm the two types of breccia are "welded" into one fragment.

Note: Entire sequence may be a debris flow or submarine talus, in which the basalt and gabbro etc. are boulders as well.

SMEAR SLIDE SUMMARY (%):

Composition:	1, 20	1, 55
Feldspar	Tr	1
Heavy minerals	Tr	1
Clay	25	25
Volcanic glass	—	Tr
Palagonite	—	Tr
Micronodules	1	—
Carbonate unspec.	10	20
Foraminifers	8	2
Calc. nannofossils	40	40
Dolomite	15	10

Carbonate Bomb (%):

1, 11–20 = 77 1, 25–26 = 83

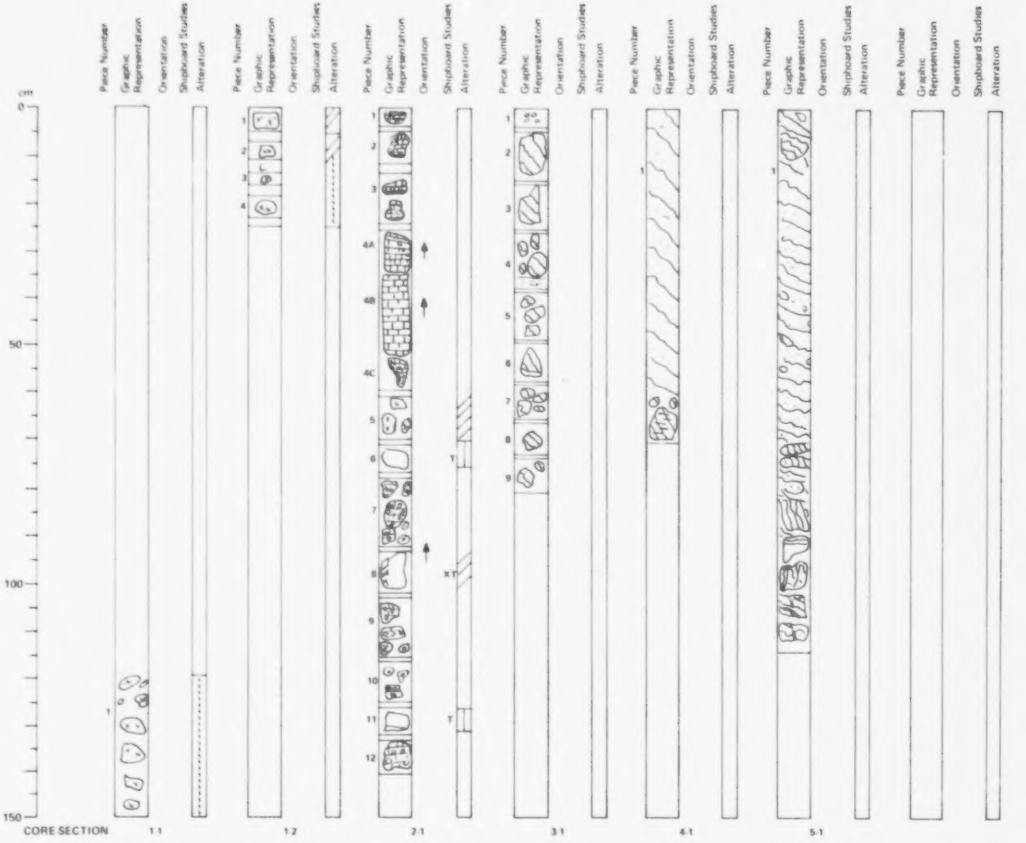

SITE 560, CORE 1 Depth 373.0–376.5 m

SECTION 1

CALCAREOUS BIOGENIC SEDIMENT AND BRECCIA

0–118 cm: Calcareous biogenic sediment.

118–143 cm: Serpentinized gabbro breccia, dusky blue (5PB 3/2) clayey matrix. Clasts are serpentinite showing relict pyroxene as dark brown prisms.

SECTION 2

SERPENTINITE (GABBRO)

0–23 cm: Serpentinized gabbro, very dark gray (7.5YR N3/0) with 2–5 cm orthopyroxene, brown (7.5YR 5/4), 30%.

SITE 560, CORE 2 Depth 376.5–385.5 m

SECTION 1

CLAYEY DOLOMITIC NANNOFOSSIL LIMESTONE, BRECCIA, GABBRO

0–58, 78–92, 103–124, and 133–139 cm: Clay dolomitic nannofossil limestone with breccia clasts in all pieces except 4B (33–50 cm). Clast range from 1 mm to 1 cm and are angular.

At 121–122 cm there is a sharp contact in the breccia.

60–70 cm: Gabbro, very dark gray (7.5YR N3/0) with orthopyroxene, 30%, brown (7.5YR 5/4) 2–5 cm.

70–75 cm: Ash. Indurated and zeolitized, grayish green (10GY 5/2).

92–100 cm: Fine grained aphyric basalt.

126–130 cm: Variolitic basalt altered grayish blue green (5BG 5/2).

SITE 560, CORE 3 Depth 385.5–398.5 m

SECTION 1

SERPENTINITE (BRECCIA) FRAGMENTS

Rock looks rather fresh, color from very dark gray (2.5Y N3/0) to dark green (5G 4/1).

5–14 cm: Rock appears to be very coarse-grained (<3 cm).

27–45 cm: Some very fine grained, light gray (2.5Y N2/0) rock occurs.

Pieces 3, 6, 7, 8, and 9 are brecciated: size of clasts < 6 mm. Clasts and matrix are both serpentine?

SITE 560, CORE 4 Depth 398.5–403.5 m

SECTION 1

SERPENTINITE AND BRECCIA (MYLONITE)

0–60 cm: Clayey, very deformed gray (2.5Y N6/0) to white (2.5Y N8/0) serpentinite. Some clasts of black to dark green (5G 4/1) serpentinite occur.

60–70 cm: Clasts of serpentinite with narrow veins, filled with white chrysotile.

SITE 560, CORE 5 Depth 403.5–412.5 m

SECTION 1

SERPENTINITE BRECCIA

0–81 cm: Mylonite clayey, very deformed gray (2.5Y N6/0) to white (2.5Y N8/0) serpentine. Some clasts of black to dark green (5G 4/1) serpentine occur. Size of clast ranges from 1–5 cm in diameter; some chrysotile veins.

81–111 cm: Clasts of serpentine occur, contain narrow veins of white chrysotile. Clasts are up to 6 cm in length.

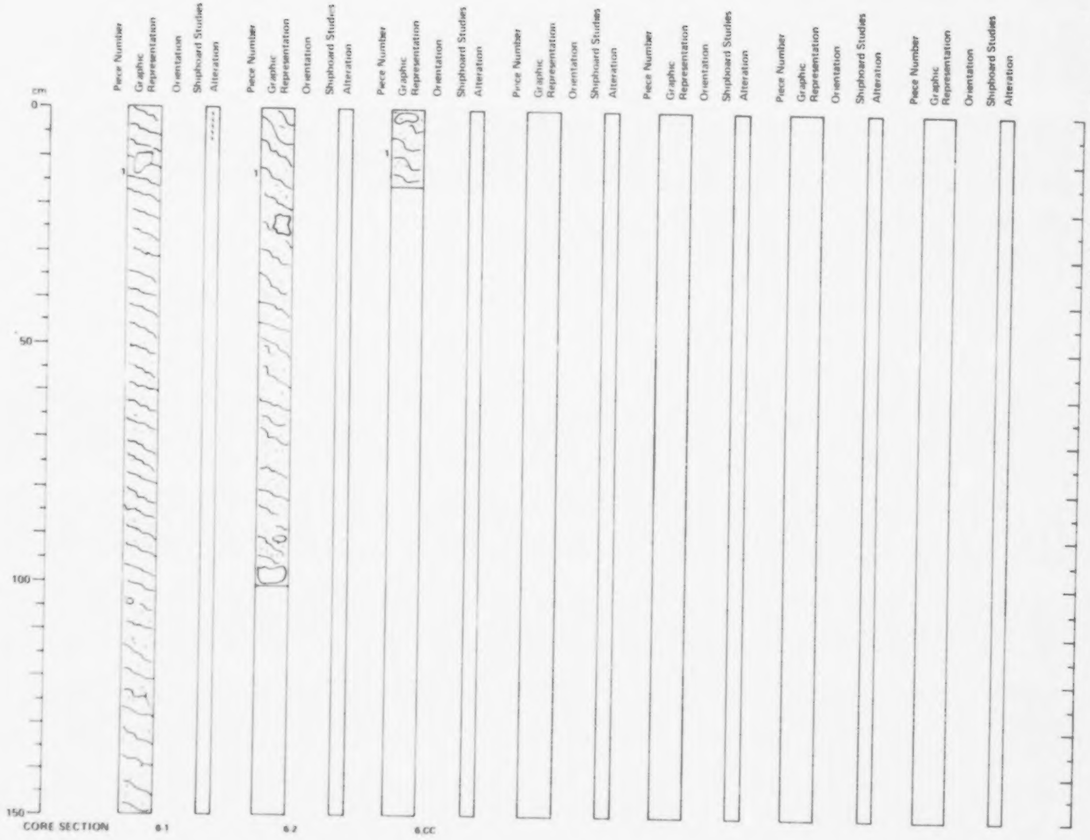
Piece Number
Graphic Representation
Orientation
Shipboard Studies
Alteration
cm
0
50
100
150
CORE SECTION
1
6-1
6-2
6,CC

SITE 560, CORE 6 Depth 412.5–421.5 m

SECTION 1

SERPENTINITE (BRECCIA)

Highly altered, sheared serpentinite breccia. Color of serpentine ranging from gray green (5GY 6/1 to lighter green (5G 5/2). A few clasts are present, ranging in size from 1–5 cm in diameter. Matrix is clayey and very deformed.

SECTION 2

SERPENTINITE BRECCIA (MYLONITE)

0–87 cm: Sheared serpentinite breccia as in Section 1. Color ranges from gray green (5G 6/1) to lighter green (5G 6/2). Highly deformed clayey matrix.

87–101 cm: Distinct change in color of matrix, more of an olive gray green (5G 5/2). Breccia as in above unit. Large clast 4 cm in diameter on bottom. Clays appear more consolidated and packed, fewer microclasts in the matrix.

CORE CATCHER

SERPENTINITE BRECCIA (MYLONITE)

Highly deformed and clayey as in Sections 1 and 2, more consolidation of clays as in lower centimeters of Section 2. Colors tend to be more of an olive green, roughly 5G 5/2 on chart, ranging down to 5G 7/2. Small veins of chrysotile can be observed in bottom of this section.

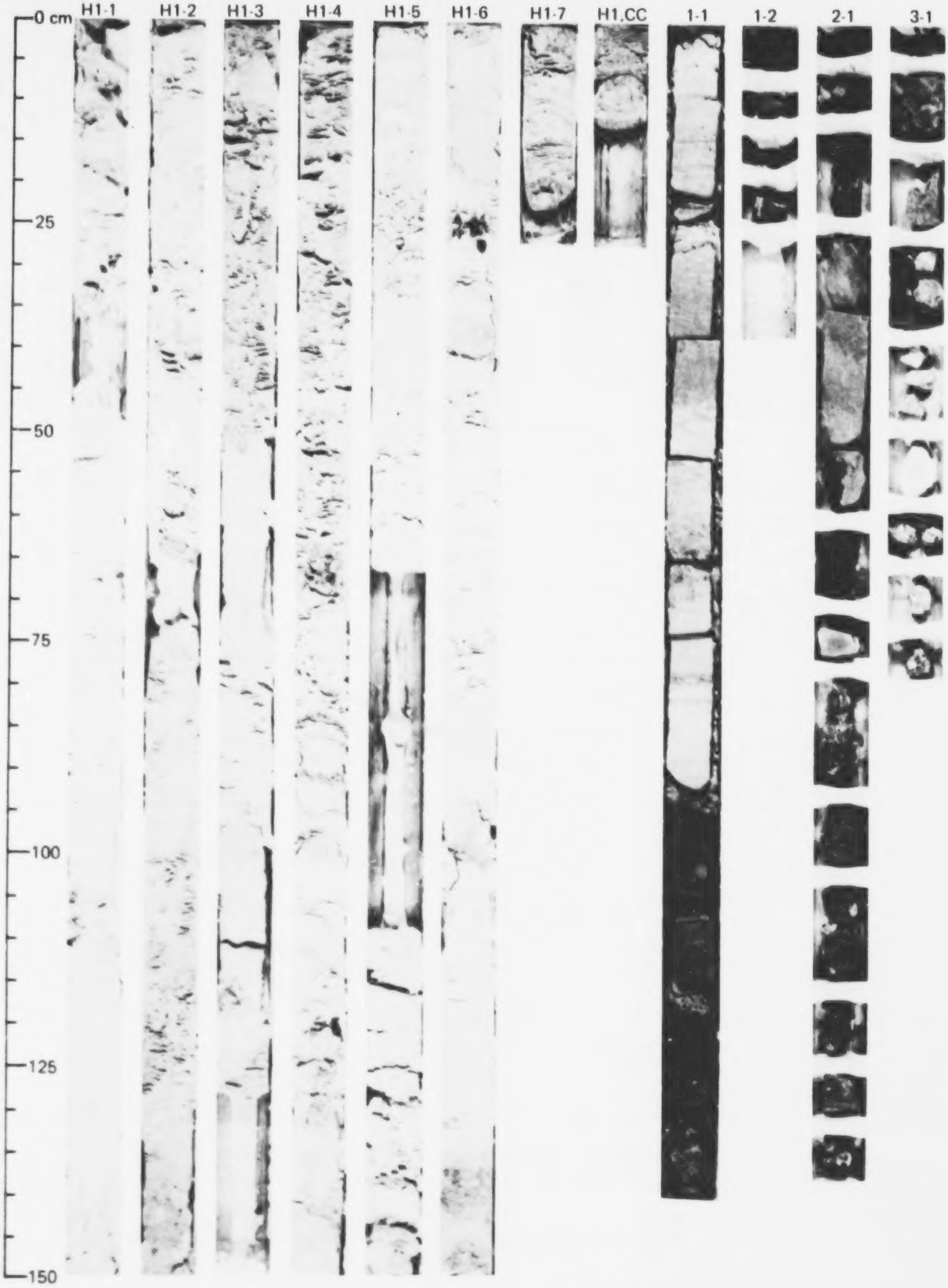
H1-1
H1-2
H1-3
H1-4
H1-5
H1-6
H1-7
H1,CC
1-1
1-2
2-1
3-1
0 cm
25
50
75
100
125
150

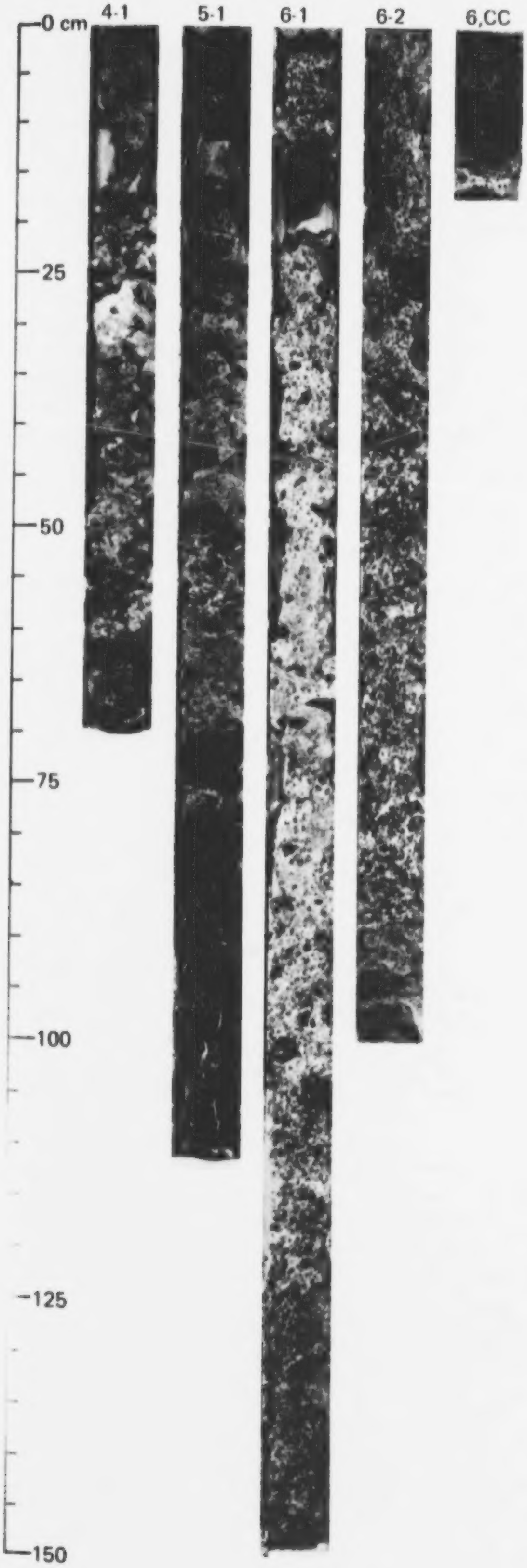
0 cm
4-1
5-1
6-1
6-2
6,CC
25
50
75
100
125
150

blank page

10. SITE 561[1]

Shipboard Scientific Party[2]

HOLE 561

Date occupied: 18 October 1981

Date departed: 20 October 1981

Time on hole: 35.7 hr.

Position (latitude; longitude): 34°47.10′N; 39°01.70′W

Water depth (sea level; corrected m, echo-sounding): 3459

Water depth (rig floor; corrected m, echo-sounding): 3469

Bottom felt (m, drill pipe): 3470

Penetration (m): 426.5

Number of cores: 3

Total length of cored section (m): 15

Total core recovered (m): 5.96

Core recovery (%): 40

Oldest sediment cored:
Depth sub-bottom (m): 411.5
Nature: Nannofossil ooze
Age: earliest middle Miocene

Basement:
Depth sub-bottom (m): 411.5
Nature: Basalt

Principal results: Hole 561 was drilled on Anomaly 5E on the west flank of the Mid-Atlantic Ridge midway between the Oceanographer and Hayes fracture zones (Fig. 1). It is located 10 miles northwest of Site 560 (it had not been possible to recover basalts at Site 560). Sediments were washed down to the basement at a depth of 411.5 m sub-bottom. The total penetration in the basement was only 15 m when the bit failed.

The recovered basement material consists of aphyric pillow basalts. At least three different groups are identified on the basis of geochemistry. Both depleted (Nb = 3 ppm, Zr = 75 ppm, $[Nb/Zr]_{Ch} \sim 0.4$) and enriched (Nb = 22 ppm, Zr = 98 ppm, $[Nb/Zr]_{Ch} \sim 2.2$) basalts are represented by these groups. Hole 561 is the second hole drilled on this leg from which both enriched and depleted basalts were recovered. Considered together with previous occurrences at Holes 413 (Luyendyk, Cann, et al., 1979) and 504B (Cann, Langseth, Honnorez, Von Herzen, White, et al., 1983), this wide range of abundance ratios (such as Nb/Zr) at a single spot of the ocean crust appears to be a more common feature than previously thought. The combination of isotopic data and trace element studies will help us to understand the relative contribution of mantle sources and melting processes.

Even though only 15 m of basalts were cored before bit failure, a wide variation in Nb/Zr ratio had already been found. It was, therefore, decided that additional recovery was not necessary, and the remaining time could be spent drilling on the same isochrons south of the Hayes Fracture Zone.

At Site 561, no downhole measurements were taken. No sediment accumulation rate could be calculated, and no samples were analyzed for pore-water chemistry.

OPERATIONS

Approach to Site

After we failed to recover basalt at Site 560, we decided to drill a second site in the same general area. The course of the *Challenger* was set in a north-northwest direction along a track that would cross approximately 3 miles north of a basement high observed at 2130Z 16 October on the approach to Site 560. Upon crossing this feature between 1530Z and 1600Z on 18 October, a good basement reflector was noted on the flank of a small peak (Fig. 2). After profiling 4 miles beyond this point, we reversed course. The beacon was dropped when the *Challenger* crossed the site for a second time at 1722Z (see Fig. 2, site chapter Site 560, this volume). Site 561 is located on Anomaly 5E and is roughly 10 miles northwest of Site 560.

On-Site Operations

The hole was spudded at 0100Z 19 October and sediments were washed to basement, which was reached at a depth of 411.5 m sub-bottom at 0400Z (Table 1). After the recovery of Core 2 at 1220Z, we found that a piece of rock had become lodged in the drill pipe and we pumped the center bit down to dislodge the rock. When drilling was resumed, the drill bit did not function properly, perhaps because of the impact of the center bit. After several more hours of attempted drilling, the bit failed completely, and we abandoned the hole. The drill string was pulled and the *Challenger* was under way to Site 562 at 0312Z 20 October.

SEDIMENT LITHOLOGY

The sedimentary section drilled at Site 561 consists of 411.5 m of calcareous pelagic deposits. One wash core (Core H1) recovered 8.5 m of siliceous foraminiferal nan-

---

[1] Bougault, H., Cande, S. C., et al., *Init. Repts. DSDP*, 82: Washington (U.S. Govt. nting Office).

[2] Henri Bougault (Co-Chief Scientist), IFREMER (formerly CNEXO), Centre de Brest, P. 337, 29273 Brest Cedex, France; Steven C. Cande (Co-Chief Scientist), Lamont-Doherty ological Observatory, Columbia University, Palisades, New York; Joyce Brannon, Depart ent of Earth and Planetary Sciences, Washington University, St. Louis, Missouri; David M. ristie, Hawaii Institute of Geophysics, University of Hawaii at Manoa, Honolulu, Hawaii; rlene Clark, Department of Geology, Florida State University, Tallahassee, Florida; Doris Curtis, Curtis and Echols, Geological Consultants, Houston, Texas; Natalie Drake, De rtment of Geology, University of Massachusetts, Amherst, Massachusetts; Dorothy Ech , Department of Earth and Planetary Sciences, Washington University, St. Louis, Missouri resent address: Curtis and Echols, Geological Consultants, 800 Anderson, Houston, Texas 401); Ian Ashley Hill, Department of Geology, University of Leicester, Leicester LE1 7RH, nited Kingdom; M. Javed Khan, Lamont-Doherty Geological Observatory, Columbia Uni rsity, Palisades, New York (present address: Department of Geology, Peshawar University, shawar, Pakistan); William Mills, Deep Sea Drilling Project, Scripps Institution of Ocean raphy, La Jolla, California (present address: Ocean Drilling Program, Texas A&M Univer ty, College Station, Texas 77843); Rolf Neuser, Institut für Geologie, Ruhr Universität Bo hum, 4630 Bochum 1, Federal Republic of Germany; Marion Rideout, Graduate School of ceanography, University of Rhode Island, Kingston, Rhode Island (present address: Depart ment of Geology, Rice University, P.O. Box 1892, Houston, Texas 77251); and Barry L. Weav er, Department of Geology, University of Leicester, Leicester, LE1 7RH, United Kingdom (present address: School of Geology and Geophysics, University of Oklahoma, Norman, Oklahoma 73019).

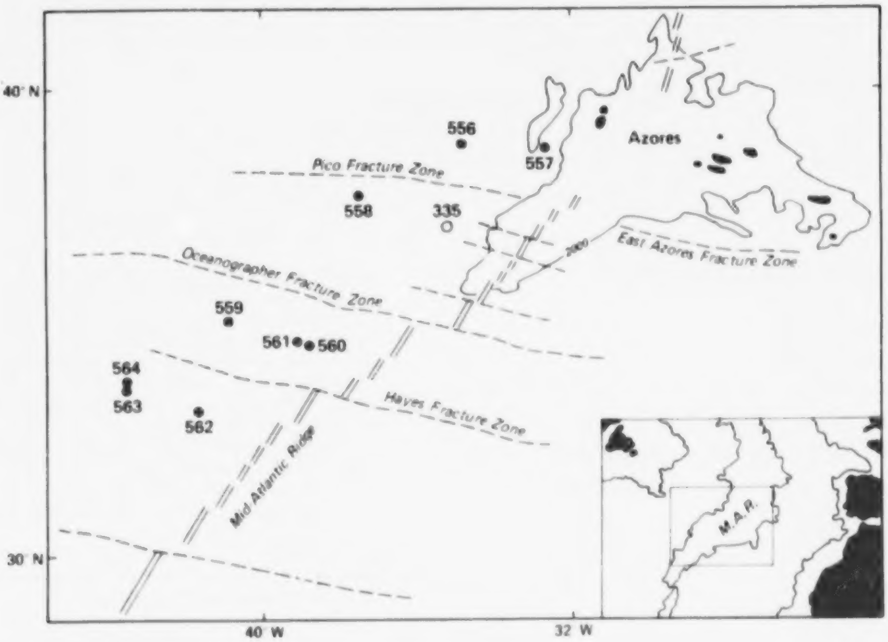
40° N
30° N
40° W
32° W
556
557
Azores
Pico Fracture Zone
558
335
East Azores Fracture Zone
2000
Oceanographer Fracture Zone
559
561
560
564
563
562
Hayes Fracture Zone
Mid-Atlantic Ridge
M.A.R.

Figure 1. Site location map, Leg 82.

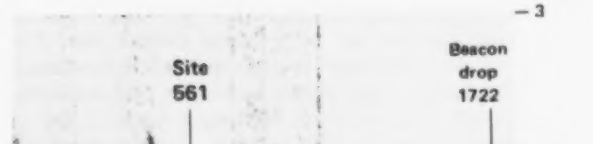

Figure 2. *Glomar Challenger* seismic profile over Site 561. For location of profile see Figure 2, site chapter, Site 560. C/C = course change.

Table 1. Coring summary, Hole 561.

Core	Date (Oct. 1981)	Time (Z)	Depth from drill floor (m)	Depth below seafloor (m)	Length cored (m)	Length recovered (m)	Percent recovered
H1	19	0618	3470.0-3881.5	0.0-411.5	0.0	0.0	0
1	19	0833	3881.5-3884.5	411.5-414.5	3.0	1.46	49
2	19	1220	3884.5-3893.5	414.5-423.5	9.0	2.99	33
3	19	2002	3893.5-3896.5	423.5-426.5	3.0	1.51	50
					15.0	5.96	40

nofossil ooze and nannofossil ooze/chalk. The age range included in the recovered material is Pleistocene to earliest middle Miocene (14-16 or 15-17 Ma). The age of the oldest sediments agrees with the expected basement age at this site.

The siliceous foraminiferal-nannofossil ooze is pal brown (10YR 6/3) with occasional moderate mottling Indistinct color contact (with 10YR 5/3) may represen massive parallel bedding. A contact with white nannofossil ooze below is disturbed but distinct. Smear-slid estimates of major components include 30% nannofossils, 29% siliceous fossils, 20% foraminifers, and 20% clay.

Most of the material recovered in Sections 561-H1- through 561-H1-6 is a mixture of nannofossil chalk and ooze, various shades of white in color (2.5Y 7/2 to 7. YRN 8). We observed no evidence of bioturbation. Fain parallel bedding is present in the chalk. Smear-slide esti mates of major components include 66-72% nannofossils, 8-9% foraminifers, 10-15% unspecified carbonate and 10% clay.

The recovered sediments are similar to the section in the same age range at Site 558.

BIOSTRATIGRAPHY

Sediments recovered from Section 561-H1-1 and from 561-H1,CC at Site 561 are from the late Pleistocene to middle Miocene time. These dates are based on the calcareous nannofossils, which are abundant and preserved well to moderately well.

The core-catcher sample examined for foraminifers contains an abundant and well-preserved suite of Neogene (middle Miocene–Pleistocene) markers. The oldest forms identified are middle Miocene with a possible range in age of 14–16 Ma.

Calcareous Nannofossils

One washed sediment core was retrieved from Hole 561 before basement was reached. Sample 561-H1-1, 10 cm is upper Pleistocene on the basis of an assemblage characterized by *Ceratolithus telesmus, Gephyrocapsa oceanica, G. caribbeanica*, and possibly *Emiliania huxyleyi*. This sample is placed in either the *E. huxyleyi* Zone (CN15 or NN21) or the *G. oceanica* Zone (CN14 or NN19–NN20) because of the questionable identification of *E. huxyleyi*. The core catcher of Core H1 occurs just above basement and is middle Miocene. This sample contains *Sphenolithus heteromorphus* and is assigned to either the *S. heteromorphus* Zone (CN4 or NN5) or the *Helicosphaera ampliaperta* Zone (CN3 or NN3–NN4).

IGNEOUS PETROLOGY AND GEOCHEMISTRY

At Site 561, basement was encountered below a 411.5-m-thick sequence of sediments. Three lithologic units and two chemical groups were identified.

Lithologic Units (Fig. 3)

Unit 1 (411.5–412.1 m) Aphyric Basalt

The fresh to moderately altered aphyric basalt of Unit 1 shows some minor, barely visible, plagioclase laths and a few olivine phenocrysts that are altered to brown clay. Round vesicles ≤ 1 mm in diameter and filled with green clay are randomly scattered and compose 2–5 vol.% of the unit. The basalt is weakly fractured; some narrow veins are filled with calcite.

This unit is only about 70 cm thick, and cooling margins are absent. It may be part of a pillow or single flow.

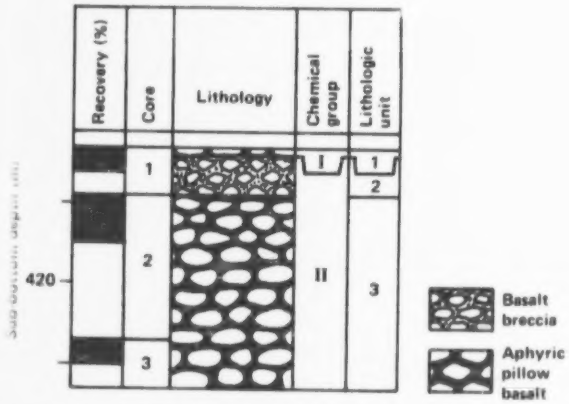

Figure 3. Basement lithology column, Hole 561.

Unit 2 (412.1–414.5 m) Basalt Breccia

This unit is composed of basalt breccia, with large (> 5 cm) angular clasts of fairly fresh, fine-grained aphyric basalt and occasional small (< 1 cm) palagonitized brown glass fragments within a pale brown limestone matrix. Similar to the basalts of Unit 1, the clasts of Unit 2 contain minor visible lath-shaped plagioclase and minor altered olivine phenocrysts. Round vesicles up to 2 mm in diameter are sometimes filled with clay. Some boundaries between basalt and limestone are very irregular, with numerous small lobes of limestones projecting into the basalt clasts. These may have developed from zones of very strong vesiculation within pillows.

Unit 3 (414.5–426.5 m) Aphyric Pillow Basalt

A sequence of aphyric basalt pillows makes up Unit 3. We drilled through about 10 pillows, ranging in thickness from a few tens of centimeters to 1 m; they are all separated by glass rinds.

The fairly fresh, fine-grained basalts of this unit are almost identical to those of Units 1 and 2. In places, local concentrations of larger plagioclase laths (less than 3 mm) form glomerophyric clusters. A few rounded, possibly partially resorbed, plagioclase phenocrysts (2–3 mm) occur. Olivine phenocrysts (< 3 mm) are rare and always altered to green or brown clay. Small round vesicles (mean diameter ~0.5 mm) filled with green clay are common throughout the section. Glass pillow margins are only a few millimeters thick. The glass appears fresh, although it is sometimes highly fractured. A variolitic transition to pillow interiors is common.

Limestone-filled fractures occur throughout the section and often display irregular lobe-shaped boundaries as in Unit 2.

Petrography

Site 561 basalts are characterized by the presence of plagioclase-olivine glomerocrysts (1–3 mm in diameter), which are surrounded by a halo of devitrified glass. The basalts are sparsely phyric, with 2–3% plagioclase phenocrysts (0.5–2 mm in length) occurring either singly or in glomerophyric aggregates with olivine. Most have an optically determined composition of about An_{65}, but two isolated determinations of An_{75} and An_{85} suggest a more complex assemblage. Most of the phenocrysts are either unzoned or display only a single zone boundary, although oscillatory zoning is also reasonably common. In no case, however, was the range of compositions in one zoned crystal observed to be more than about 5% anorthite.[3] Olivine phenocrysts and microphenocrysts (about 5%) are prismatic or diamond shaped and range from about 0.1 to 0.5 mm in size, but occasional grains are as large as 1 mm, especially in association with plagioclase. Fresh olivine is rare; most grains are completely altered to light brown clay.

---

[3] Preliminary shore-based microprobe studies suggest that plagioclase phenocryst compositions are close to An_{75} with little zoning, whereas the groundmass has a composition of An_{65}.

The groundmass of the basalts consists of about 35% randomly oriented, elongate plagioclase laths with abundant (45%) interstitial clinopyroxene. Most clinopyroxene occurs as aggregates of very fine (<0.2 mm) granules. Occasionally 5-10% large prismatic grains to about 0.1 mm, 5% granular magnetite, and 10-15% interstitial devitrified glass complete the assemblages.

Vesicles (1-2%) are well rounded and may be unfilled, partially filled by devitrified glass, or filled by emerald green clay or calcite.

Geochemistry

Eight basalt samples were analyzed from Site 561; the analyses are given in Table 2 and plotted versus depth in Figure 4.

The two samples from the wash Core H1 and the upper part of Section 561-1-1 compose Chemical Group I (Table 2, Fig. 4), which is identified with Lithologic Unit 1. Both samples have a very similar chemistry (Table 2) with quite high Mg′-numbers (65 and 67). However, the sample from Core 1 is notably enriched in Sr compared to the wash core sample. The high $(Nb/Zr)_{ch}$ ratio (~2.2) of these samples reflects the quite strongly enriched character that shows up on a modified Coryell-Masuda diagram (Fig. 5).

The six analyzed basalts forming Chemical Group II encompass samples from both Lithologic Units 2 and 3, and are somewhat heterogeneous in major elements if not in trace elements (Table 2). The four basalts in this group from Sample 561-1-1, 128-130 cm to Section 561-2-2 have a rather consistent major element chemistry (Table 2). In comparison to these samples, the sample from Section 561-2-3 has high Fe_2O_3 and low MgO, CaO, and Al_2O_3 abundances (Table 2; Fig. 4), whereas the sample from Section 561-3-1 has a somewhat high CaO content. These minor differences in major element chemistry are, however, not sufficient to warrant the designation of separate chemical groups for these samples. In marked contrast to Chemical Group I samples, Group II basalts display a quite strongly depleted pattern—$(Nb/Zr)_{ch}$ ~0.4—when plotted on a modified Coryell-Masuda diagram (Fig. 5).

Hole 561 is the second location of this leg (Hole 558 is the first) in which enriched and depleted basalts are

Table 2. Analyses of major elements (in wt.%) and trace elements (in ppm) for Hole 561 basalts.[a]

Core-Section (interval in cm) (piece number)	Sub-bottom depth (m)	Chemical group	SiO_2	TiO_2	Al_2O_3	Fe_2O_3[b]	MnO	MgO	CaO	K_2O	P_2O_5	Total	Mg′[c]	Ti	V	Sr	Y	Zr	Nb
H1-CC, 10-14		I	50.54	1.21	15.03	9.84	0.15	8.83	12.33	0.24	0.23	98.40	67	7260	263	225	31.0	100	22.4
1-1, 28-31 (C)	411.8		49.56	1.19	14.89	10.24	0.15	8.46	12.19	0.27	0.20	97.15	65	7140	267	457	29.8	96	21.8
1-1, 128-131 (9B)	412.8	II	50.43	1.34	14.85	11.10	0.17	7.43	12.50	0.18	0.13	98.13	60	8040	356	98	38.4	80	4.3
1-2, 17-20 (2A)	413.2		50.34	1.38	15.14	10.87	0.18	7.56	12.00	0.12	0.12	97.71	61	8280	359	97	39.3	76	2.5
2-1, 52-55 (4A)	415.0		50.18	1.35	14.59	11.48	0.18	7.65	11.90	0.12	0.13	97.58	60	8100	347	90	38.4	72	2.6
2-2, 122-126 (4C)	417.3		50.48	1.33	14.88	11.31	0.18	7.66	11.90	0.18	0.11	98.03	60	7980	349	92	39.2	76	3.3
2-3, 71-73 (6A)	418.2		50.46	1.35	14.27	13.33	0.19	6.75	11.40	0.49	0.12	98.36	53	8100	359	86	42.5	75	1.5
3-1, 114-118 (9F)	424.7		49.89	1.31	14.61	11.40	0.17	7.19	12.74	0.27	0.12	97.70	59	7860	345	90	37.2	73	3.3

[a] Measurements were made on board from ignited samples. Onshore analyses have shown the loss upon ignition to be less than 1%. The concentrations presented in the compilation tables at the end of this volume (Appendix) include volatile contents.

[b] Total Fe as Fe_2O_3.

[c] Mg′ is the atomic ratio of $100 \times (Mg/[Mg + Fe^{2+}])$; calculated using an assumed Fe_2O_3/FeO ratio of 0.15.

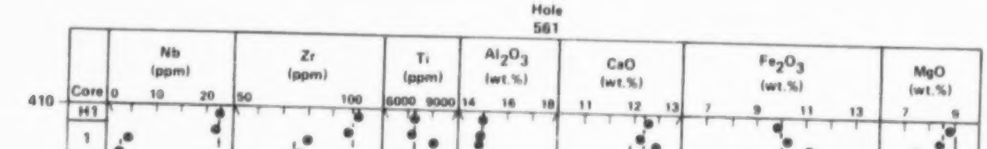

Figure 4. Downhole variations in chemical abundances, including samples from both Holes 561 (top) and 560 (bottom).

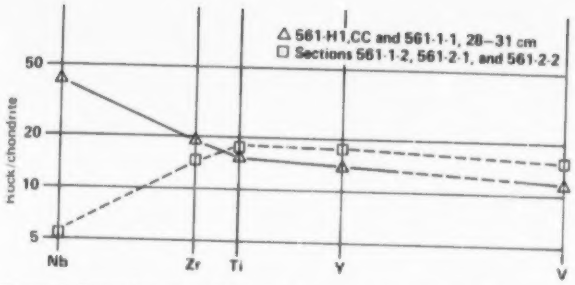

Figure 5. Extended Coryell-Masuda diagram of Chemical Groups I and II, Hole 561.

found. Together with the previous results obtained at Site 413 (Luyendyk, Cann, et al., 1979) and Hole 504B (Cann, Langseth, Honnorez, Von Herzen, White, et al., 1983), these findings tend to show that the occurrence of depleted and enriched material in the same place may be more common than previously thought.

The comments made for Site 558 apply for Site 561; additional data (isotopes, other trace elements, La/Ta) are needed for further interpretation in terms of mantle source and geodynamics.

MAGNETICS

Basalt Paleomagnetism

Three basalt samples were collected for paleomagnetic studies. Because of the few samples available, only natural remanent magnetization (NRM) and susceptibility were measured. Demagnetization was not done in order to allow further studies in shore-based labs. The range of NRM intensities of these basalt samples is 1.5-4.9 × 10^{-3} emu/cm^3. The susceptibility range is 45–95 × 10^{-6} emu/cm^3 Oe.

The NRM inclination is variable and ranges from -26.7 to $-60.8°$. We could not determine whether any of the samples is representative of a dominant inclination value.

The NRM intensity directions and susceptibilities are given in Table 3.

PHYSICAL PROPERTIES

The hole was washed down to basement with the recovery of one wash core. The sediment recovered was too deformed to allow useful measurements. A program of routine measurements of seismic velocity and density was begun. The premature failure of the bit caused abandonment of the hole with only three cores recovered, so that the physical properties measurements were not completed.

SUMMARY AND CONCLUSIONS

Because only three weathered pieces of basalt were recovered at Site 560, we decided to drill a second hole in the area to get a reasonable sampling at each chosen site on Anomalies 6 and 13.

Hole 561 was drilled on Anomaly 5E about 10 miles northwest of Site 560 (midway between the Oceanographer and Hayes fracture zones). Sediments were washed down to the basement felt at 411.5 m sub-bottom.

The total penetration in the basement was only 15 m when the bit failed, but at least three chemically distinct basalt groups were found within the aphyric pillow basalts that were recovered. Both depleted (Nb = 3 ppm, Zr = 75 ppm, $[\mathrm{Nb/Zr}]_{ch} \sim 0.4$) and enriched (Nb = 22 ppm, Zr = 98 ppm, $[\mathrm{Nb/Zr}_{ch} \sim 2.2]$ basalts are present in these groups. Of all the DSDP sites drilled before Leg 82 where basement was penetrated and detailed trace element data were available, only two (Site 413 and Hole 504B) recovered both enriched and depleted basalts. Sites 558 and 561 of Leg 82 represent the third and fourth occurrences of such a mixture. These samples will have to be studied in detail for other trace elements and for isotopic ratios. Fundamental petrogenetic processes, and fundamental and comparative geochemistry will have to be discussed before any interpretation of the mantle sources and geodynamics can be proposed.

REFERENCES

Cann, J. R., Langseth, M. G., Honnorez, J., Von Herzen, R. P., White, S. M., et al., 1983. *Init. Repts. DSDP*, 69: Washington (U.S. Govt. Printing Office).

Luyendyk, B. P., Cann J. R., et al., 1979. *Init. Repts. DSDP*, 49: Washington (U.S. Govt. Printing Office).

Table 3. Paleomagnetic properties of basalts from Hole 561.

Core-Section (interval in cm)	J_{NRM} (× 10^{-3} emu/cm^3)	NRM dec. (°)	NRM inc. (°)	χ (× 10^{-6} emu/cm^3 Oe)
2-1, 35-37	2.34	252.2	−60.8	45
2-1, 64	4.89	140.9	−44.3	65
2-3, 5-7	1.52	80.5	−26.7	95

Note: J_{NRM} = intensity of natural remanent magnetization (NRM); dec. = declination; inc. = inclination; χ = susceptibility.

SITE 561 HOLE CORE H1 CORED INTERVAL 0.0–411.5 m

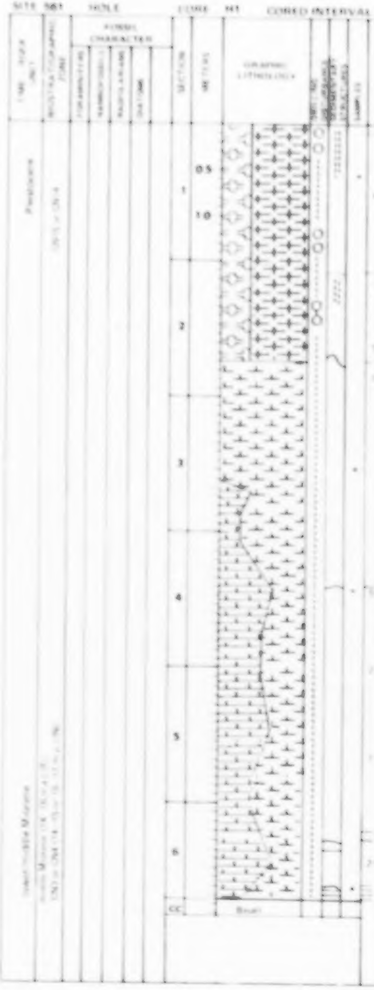
TIME-ROCK UNIT
BIOSTRATIGRAPHIC ZONE
FOSSIL CHARACTER
FORAMINIFERS
NANNOFOSSILS
RADIOLARIANS
DIATOMS
SECTION
METERS
GRAPHIC LITHOLOGY
DRILLING DISTURBANCE
SEDIMENTARY STRUCTURES
SAMPLES
Pleistocene
0.5
1.0
1
2
3
4
5
6
CC
Basalt

LITHOLOGIC DESCRIPTION

Void	
10YR 8/3	DOMINANT LITHOLOGY: SILICEOUS FORAMINIFER NANNOFOSSIL OOZE Pale brown Soft ooze Occasional moderate mottling NANNOFOSSIL OOZE/CHALK
10YR 5/3	Various shades white Faint bedding in pieces of chalk Mixture of chalk and ooze from Section 2, 80 cm to bottom of core Occasional black streaks
10YR 8/3 contact disturbed 7.5YR N8	SMEAR SLIDE SUMMARY (%):
5Y 8/1	
2.5Y N8	
7.5YR N8	
5Y 7/1	
2.5Y N8	
2.5Y N8	
2.5Y 7/2	

	1-58	3-80	4-60	6-56
Composition:				
Feldspar	Tr	Tr	Tr	Tr
Clay	20	15	10	10
Volcanic glass	Tr	—	—	—
Palagonite	Tr	—	—	—
Micronodules	—	Tr	—	—
Carbonate unspec.	1	15	10	10
Foraminifers	20	9	8	8
Calc. nannofossils	30	66	72	72
Diatoms	12	—	—	—
Radiolarians	4			
Sponge spicules	10			
Silicoflagellates	3			

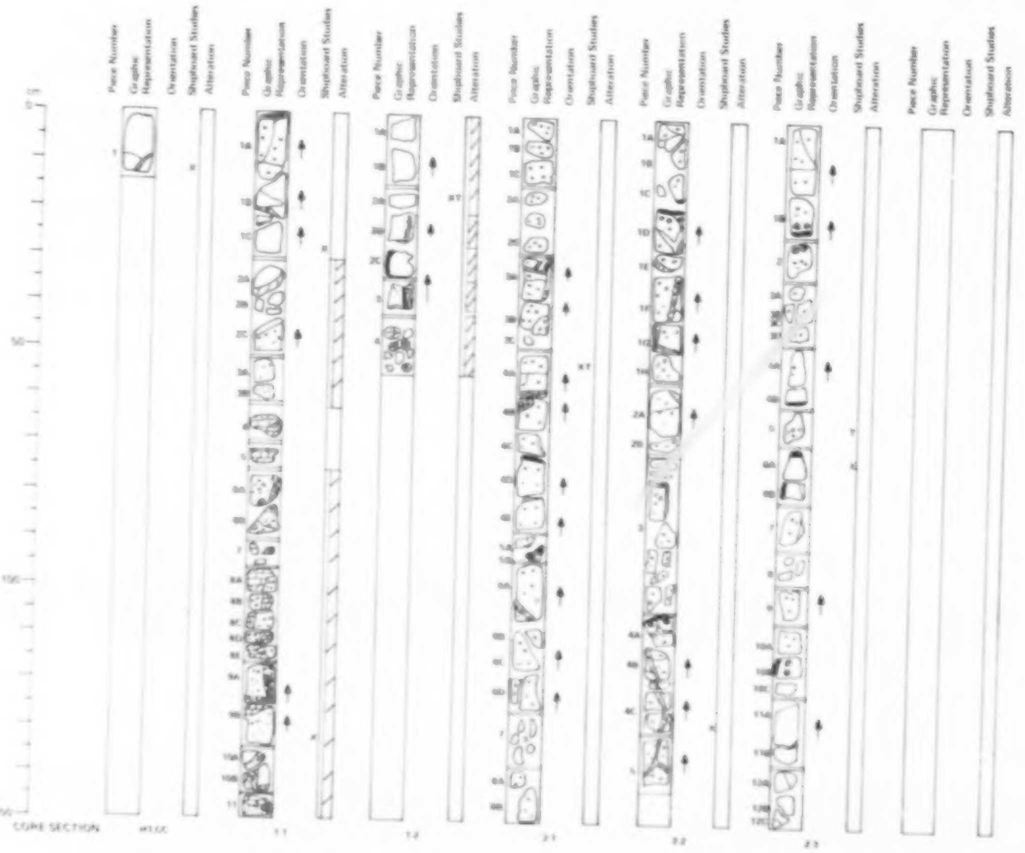

SITE 561, CORE H1 Depth 0.0–411.5 m

CORE CATCHER

APHYRIC BASALT

Aphyric basalt, gray (7.5YR N5.1) fine grained. Slightly altered grayish brown (10YR 5/2) along fractures. Vesicles scattered, clay filled (<1 mm). Calcite veined as shown.

SITE 561, CORE 1 Depth 411.5–414.5 m

SECTION 1

APHYRIC BASALT AND BASALT BRECCIA

0–64 cm: Aphyric basalt gray (7.5YR N6) fine grained with barely visible plagioclase laths and 2–3% round dark brown altered(?) olivine. Only slightly altered grayish brown–brown (10YR 5/2–10YR 5/3) adjacent to fractures. Sparsely to moderately vesicular (2–5%). Vesicles generally round, <1 mm filled by dark green clay (approx. grayish green ~10G 4/2). Minor calcite veining and fractures lined with dark green (~10G 4/2) clay.

64–150 cm: Basalt breccia, limestone matrix. Large (>8 cm) angular clasts of fine grained basalt (as above) in matrix of light gray (10YR 7/2) limestone. Some limestone-basalt contacts are highly irregular — appear corrosive. Others are sharp.

118–123 cm: Occasional small (<1 cm) palagonitized glass fragments.

SECTION 2

APHYRIC FINE GRAINED BASALT

0–55 cm: Fine grained basalt aphyric with plagioclase crystals just visible. Color is gray (7.5YR N6/0). Vesicles are scattered, fairly round (<1–2 mm in diameter), some are clay filled. Clays also present in fractures.

34–55 cm: Fine grained aphyric gray (7.5YR N6/0) basalt. Limestone is present as a rim to one-half of rock. Limestone is massive, very pale brown (10YR 8/4); cracks with dark clays and oxides are present. Vesicles and fractures as in above description. Rim grades in color from basalt gray (7.5YR N6/0) to very dark gray (10YR 3/1) devitrified glass to limestone 10YR 8/4.

28–34 cm: Glassy rim only slightly altered to clay.

34–41 cm: Devitrified(?) glass rim adjacent to limestone matrix.

SITE 561, CORE 2 Depth 414.5–423.5 m

SECTION 1

APHYRIC BASALT

0–150 cm: Aphyric basalt, gray (7.5YR N5) fine grained. Visible plagioclase laths, some to 3 mm. Plagioclase (as 1–7%) scattered equant microphenocrysts 1–3 mm. Scattered dark green pseudomorphs(?) after olivine (<1 mm). Alteration minor along fractures only. Vesicles uniformly scattered, round, most <1 mm, some to 3 mm filled by dark green clay. Minor irregular vesicles to 3 mm. Veinlets filled with limestone(?) (calcite + clay?) (greenish gray (7.5YR 7/2) to light yellowish brown (2.5Y 6/4)).

72–73 cm: Narrow glass rim. Transition to fine grained basalt over less than 2 cm.

90–93 cm: Angular glass fragments in limestone.

54–58 cm: Drusy calcite and green clay(?) vein.

SECTION 2

APHYRIC BASALT (LARGE PILLOWS?)

0–150 cm: Aphyric basalt as in Section 1 with occasional olivine (altered to green clay) up to 3 mm, but approximately 1–2% dark green clay in irregular vesicle-like patches may be pseudomorph olivine. Limestone(?) veins as in Section 1 where shown. Vein boundaries very irregularly shaped. Small (1–3 mm) patches of limestone occur within basalt.

16–19 and 104–107 cm: Pillow margins. Thin veneer of glass to 2 cm variolitic zone to normal fine grained basalt.

83–95 cm: Highly fractured. Fractures coated with light olive brown (2.5Y 5/4) calcite (+ clay?).

SECTION 3

APHYRIC BASALT (PILLOWS)

0–150 cm: Aphyric, fine grained fairly fresh basalt, olive gray (2.5YR N5/0). Olivine(?) pseudomorphs up to 3 mm filled with green clay (some olivine is fresh?). Vesicles are common, shape: round, size <1 mm. Few plagioclase phenocrysts occur, size <1.3 mm.

18–24 and 112–117 cm: Pillow margin with fine grained basalt through variolitic zone to [illegible] glass rind.

58, 60, 69–71, and 76–78 cm: Fresh glass rinds. Some smaller vesicles are filled with calcite.

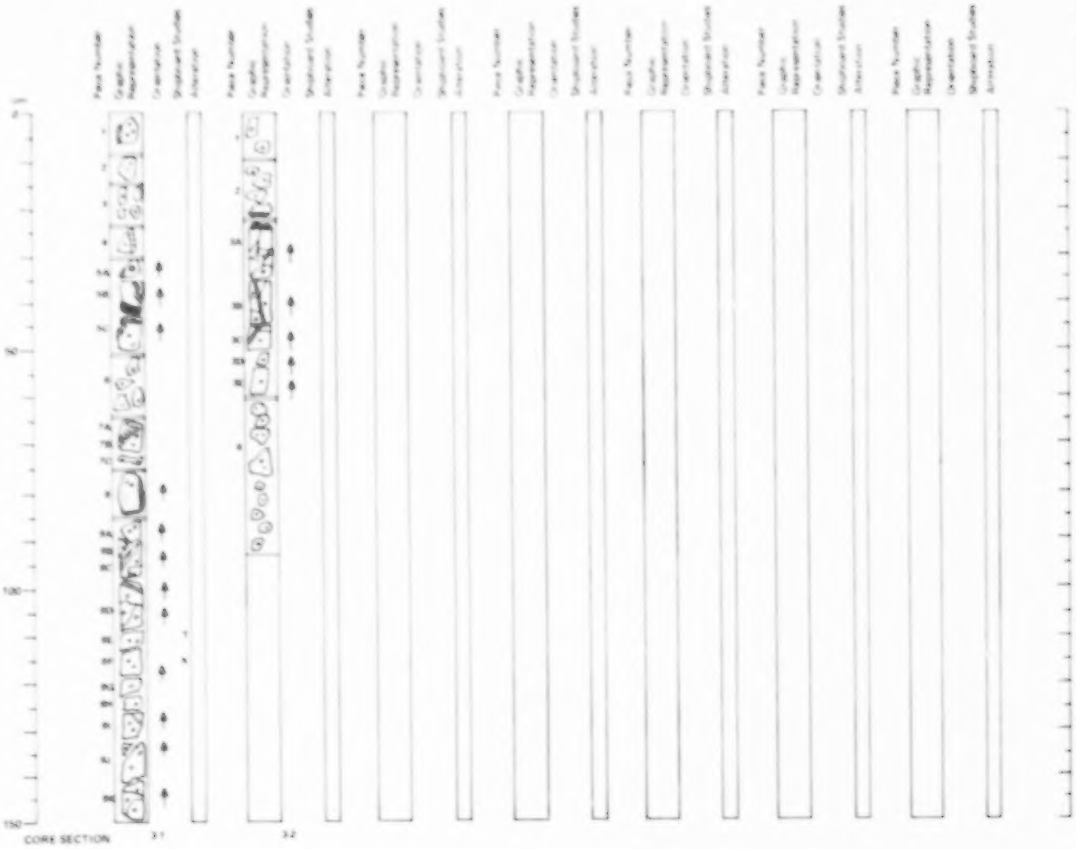
Piece Number
Graphic Representation
Orientation
Shipboard Studies
Alteration
0
50
100
150
CORE SECTION
3-1
3-2

SITE 561 CORE 3 Depth 423.5–428.5 m

SECTION 1

APHYRIC PILLOW BASALT

0–150 cm: Same rock as above. Fine-grained aphyric basalt; color gray (2.5YR N5/0). Some olivine(?) (<3 mm) [illegible] is mostly replaced by green clay. Few plagioclase phenocrysts (<3 mm) are scattered, rounded to resorbed(?). Vesicles are common (<1 mm) and mostly filled with green clay. Fractures are filled with pinkish gray (2.5YR 7/2) limestone and contain also angular, brecciated basalt fragments (size <1 cm). (Fractures signed [illegible])

40–42, 43–44, and 83–84 cm: Chilled yellow margins (fresh glass), accompanied by variolitic transition to fine grained basalt.

SECTION 2

APHYRIC PILLOW BASALT FRAGMENTS

0–98 cm: Fine-grained aphyric basalt, fairly fresh. Description see Section 1.

21–22 and 23–25 cm: Fresh glass.

40–48 cm: Very irregular bounded limestone filled vein (thickness: 1–3 mm).

H1-1
H1-2
H1-3
H1-4
H1-5
H1-6
H1,CC
1-1
1-2
2-1
2-2
2-3
0 cm
25
50
75
100
125
150

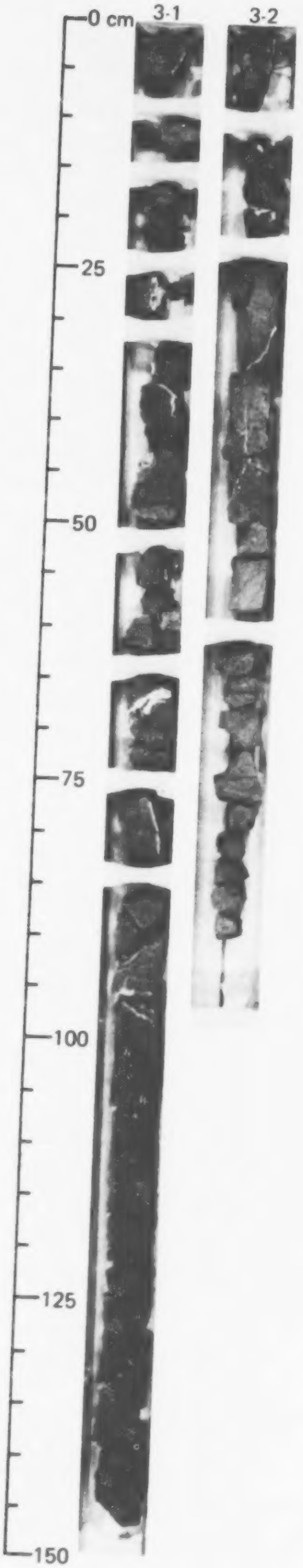
0 cm
3-1
3-2
25
50
75
100
125
150

11. SITE 562[1]

Shipboard Scientific Party[2]

HOLE 562

Date occupied: 21 October 1981

Date departed: 24 October 1981

Time on hole: 80 hr.

Position (latitude; longitude): 33°08.49′N, 41°40.76′W

Water depth (sea level; corrected m, echo-sounding): 3172

Water depth (rig floor; corrected m, echo-sounding): 3182

Bottom felt (m, drill pipe): 3182

Penetration (m): 331

Number of cores: 11

Total length of cored section (m): 90

Total core recovered (m): 44.9

Core recovery (%): 50

Oldest sediment cored:
Depth sub-bottom (m): 268
Nature: Limestone–interpillow breccia
Age: middle Miocene

Basement:
Depth sub-bottom (m): 240
Nature: Basalt

Principal results: Hole 562 was drilled on the west flank of the Mid-Atlantic Ridge south of the Hayes Fracture Zone on Magnetic Anomaly 5D (Fig. 1). The sediments were washed down to the basement, which was felt at 240 m sub-bottom depth.

The basement, cored for 90 m, consisted of sparsely plagioclase phyric pillow basalts. Two chemical groups have been recognized on the basis of major and trace elements. Fresh glasses at the margins of pillows are very common. Despite some altered parts, the bulk of the crystalline basalts is fairly fresh. The magmaphile elements show a typically depleted distribution with the following average figures: Nb = 3 ppm, Zr = 95 ppm, Ti = 9300 ppm, Y = 41 ppm, V = 325 ppm, and $(Nb/Zr)_{ch} \sim 0.3$. This result is consistent with the precruise hypothesis of a depleted mantle source south of the Hayes Fracture Zone.

No samples were taken for pore-water chemistry analysis, and no downhole measurements were taken at this site.

OPERATIONS

Approach to Site

It was decided to drill Site 562 (MAR-10) near Anomaly 5D and south of the Hayes Fracture Zone. The available geophysical data in the area, including a recent SEABEAM survey by Centre National pour l'Exploitation des Océans (now IFREMER) of the area near Anomaly 5 (MAR-9), indicated that there were several small fracture zones that had to be avoided. A tentative site was located midway between two small fracture zones about 50 and 75 miles respectively, south of the Hayes Fracture Zone. From Site 561, the track of the *Challenger* headed southwest and intersected a flow line passing through the proposed site about 40 miles east of the site. The track then followed the flow line in a northwesterly direction, crossing Anomalies 5B to 6 (Fig. 2). The identification of Anomaly 5B is not clear, and this anomaly could also be either Anomaly 5A or even Anomaly 5. Between 2330Z, 20 October and 0030Z, 21 October (Fig. 3), a low ridge was crossed with several potential drill sites. After steaming for two hours past this feature, no better sites were observed and we decided to drill on the site crossed at 0030Z. The course of the *Challenger* was reversed and the beacon was dropped on the site at 0412Z. The seismic profiler record indicated approximately 0.3 s of sediments above a strong basement reflector. The site is probably on Magnetic Anomaly 5D.

On-Site Operations

Hole 562 was spudded at 1053Z, 21 October and washed to basement. No mudline core was taken. Hard rock was hit at 240 m sub-bottom depth. Between 1400Z, 21 October and 2200Z, 23 October, 11 cores were cut penetrating 90 m of basement with 50% recovery without major incident (Table 1). Drilling was halted for time considerations; also, the diameter of the final cores was diminishing, indicating that bit failure was near. The drill string was pulled and the *Challenger* was under way to Site 563 at 1018Z, 24 October.

SEDIMENT LITHOLOGY

The sedimentary section drilled at Site 562 consists of 241 m of calcareous pelagic deposits, represented by one wash core (Core H1), in which 3.1 m of siliceous foraminiferal-nannofossil ooze and foraminiferal-nannofos-

---

[1] Bougalt, H., Cande, S. C., et al., *Init. Repts. DSDP*, 82: Washington (U.S. Govt. Print-
g Office).

[2] Henri Bougalt (Co-Chief Scientist), IFREMER (formerly CNEXO), Centre de Brest,
P. 337, 29273 Brest Cedex, France; Steven C. Cande (Co-Chief Scientist), Lamont-Doherty
eological Observatory, Columbia University, Palisades, New York; Joyce Brannon, Depart-
nent of Earth and Planetary Sciences, Washington University, St. Louis, Missouri; David M.
hristie, Hawaii Institute of Geophysics, University of Hawaii at Manoa, Honolulu, Hawaii;
urlene Clark, Department of Geology, Florida State University, Tallahassee, Florida; Doris
Curtis, Curtis and Echols, Geological Consultants, Houston, Texas; Natalie Drake, De-
artment of Geology, University of Massachusetts, Amherst, Massachesetts; Dorothy Echols,
epartment of Earth and Planetary Sciences, Washington University, St. Louis, Missouri (pres-
nt address: Curtis and Echols, Geological Consultants, 800 Anderson, Houston, Texas 77401);
n Ashley Hill, Department of Geology, University of Leicester, Leicester LEI 7RH, United
ingdom; M. Javed Khan, Lamont-Doherty Geological Observatory, Columbia University,
alisades, New York (present address: Department of Geology, Peshawar University, Pesha-
ar, Pakistan); William Mills, Deep Sea Drilling Project, Scripps Institution of Oceanogra-
hy, La Jolla, California (present address: Ocean Drilling Program, Texas A&M University,
ollege Station, Texas 77843); Rolf Neuser, Institut für Geologie, Ruhr Universität Bochum,
630 Bochum 1, Federal Republic of Germany; Marion Rideout, Graduate School of Ocean-
graphy, University of Rhode Island, Kingston, Rhode Island (present address: Department
f Geology, Rice University, P. O. Box 1892, Houston, Texas 77251); and Barry L. Weaver,
epartment of Geology, University of Leicester, Leicester, LEI 7RH, United Kingdom
present address: School of Geology and Geophysics, University of Oklahoma, Norman,
klahoma 73019).

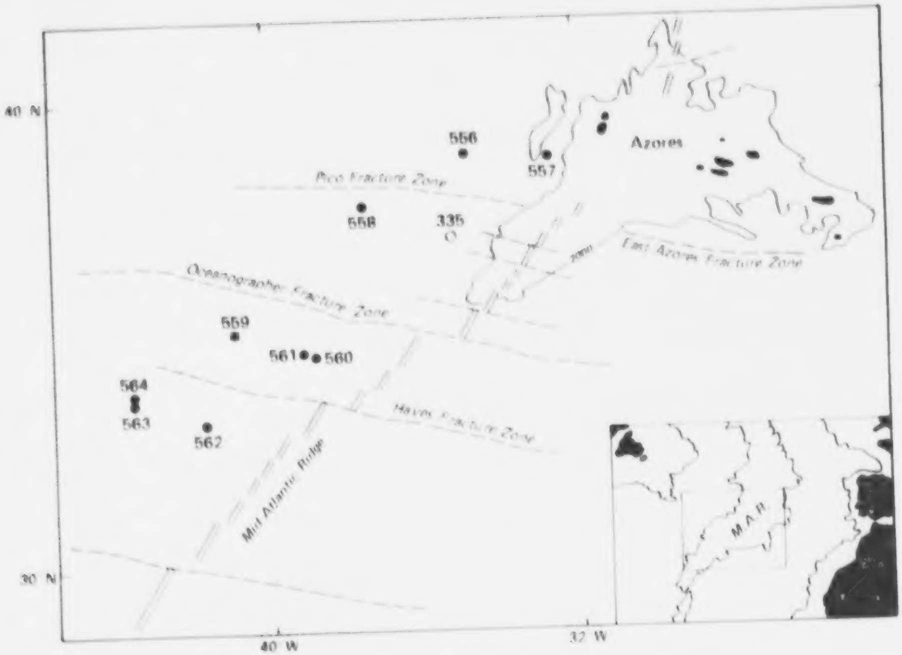
40 N
30 N
40 W
32 W
556
557
Azores
Pico Fracture Zone
558
335
East Azores Fracture Zone
Oceanographer Fracture Zone
559
561
560
564
563
562
Hayes Fracture Zone
Mid-Atlantic Ridge
M.A.R.

Figure 1. Site location map, Leg 82.

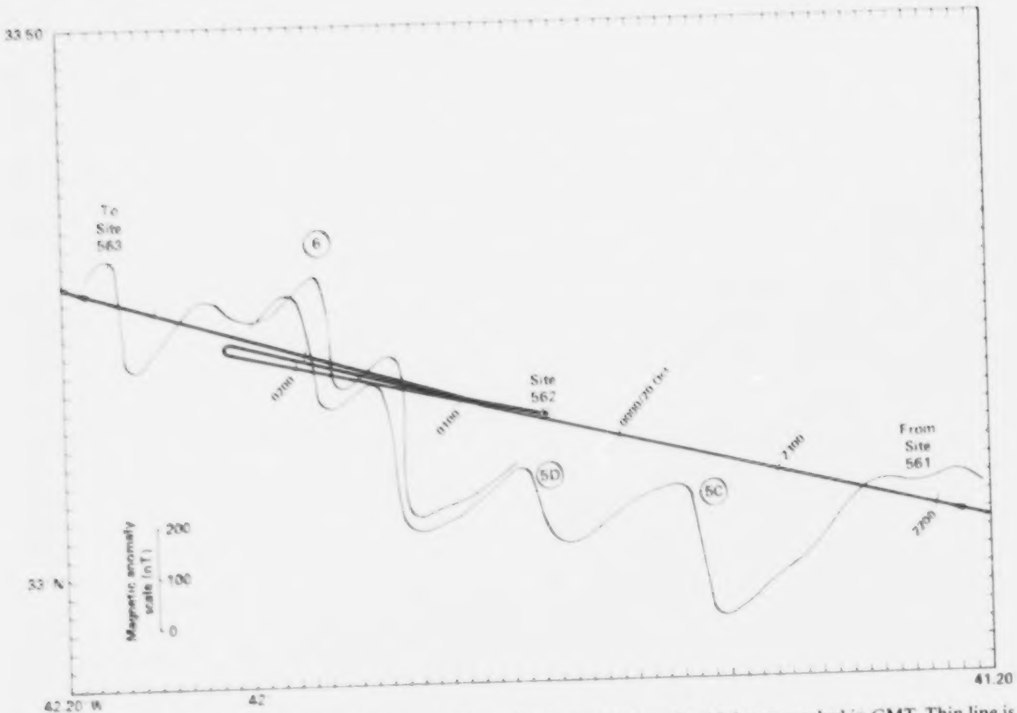

Figure 2. Approach and site survey track for Site 562. Heavy line is the ship's track with hours marked in GMT. Thin line is magnetic anomaly projected perpendicularly from the ship's track. Circled numbers are magnetic anomalies based on work at Lamont-Doherty Geological Observatory.

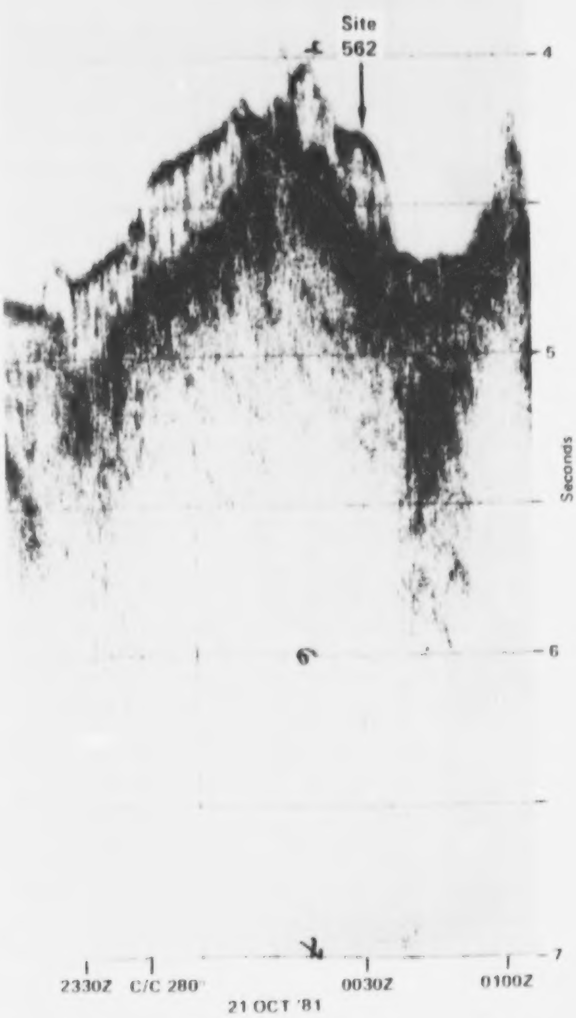

Figure 3. *Glomar Challenger* seismic profile over Site 562. For location of profile, see Figure 2. C/C = course change.

Table 1. Coring summary, Hole 562.

re	Date (Oct. 1981)	Time (Z)	Depth from drill floor (m)	Depth below seafloor (m)	Length cored (m)	Length recovered (m)	Percent recovered
H1	21	1402	3182.0-3423.0	0.0-241.0	0.0	0.00	0
1	21	1930	3423.0-3432.0	241.0-250.0	9.0	3.60	40
2	22	0240	3432.0-3441.0	250.0-259.0	9.0	5.68	63
3	22	0745	3441.0-3450.0	259.0-268.0	9.0	5.27	59
4	22	1155	3450.0-3459.0	268.0-277.0	9.0	5.61	62
5	22	1700	3459.0-3468.0	277.0-286.0	9.0	6.90	77
6	22	2053	3468.0-3477.0	286.0-295.0	9.0	4.82	54
7	23	0130	3477.0-3482.0	295.0-300.0	5.0	3.30	66
8	23	0510	3482.0-3486.0	300.0-304.0	4.0	2.13	53
9	23	1040	3486.0-3495.0	304.0-313.0	9.0	3.23	36
10	23	1630	3495.0-3504.0	313.0-322.0	9.0	3.08	34
11	23	2200	3504.0-3513.0	322.0-331.0	9.0	1.31	15
					90.0	44.93	50

sil ooze were recovered. Below the top of basalt at 241 m, intrapillow limestone breccias and limestones are present at several intervals in Cores 1 and 2. A foraminiferal-nannofossil limestone, from 562-1-3, 112-120 cm between two pillows, is dated at 15 to 17 Ma, which agrees with the basement age at this site.

The siliceous foraminiferal-nannofossil ooze is very pale brown (10YR 7/3) with rare mottling. The core is highly disturbed, so no sedimentary structures are evident. The bedding is massive. A smear-slide estimate indicates that this lithology contains about 15% clay and 13% siliceous fossils in addition to the principal calcareous components. The age range represented by the 2 m of this sediment lithology is late Pliocene to Pleistocene.

The foraminiferal-nannofossil ooze (represented by 1 m of sediment) is white (2.5Y 8/2 to 2.5YN 8), with possible faint massive bedding. We observed no mottling or bioturbation in this highly disturbed core. The principal component of this lithology is calcareous nannofossils. The oldest fauna in the core is from the early middle Miocene or late early Miocene.

The intrapillow limestone is white to pale grayish tan micrite. At 562-1-3, 112-120 cm (245 m sub-bottom) the limestone is cross laminated and contains abundant foraminifers. A slightly lower occurrence appears to be bioturbated. A similar limestone at 562-2-3, 80-88 cm (254 m sub-bottom), which fills a space between pillow margins, appears to have graded bedding (geopetal texture?).

The intrapillow limestone breccias are pinkish white to white, with either rounded or angular clasts of black basalt and/or glass.

BIOSTRATIGRAPHY

Hole 562 was washed down to 241 m. Lower Pleistocene to lower middle-upper lower Miocene sediments were retrieved. At this site both the calcareous nannofossils and the foraminifers agree on this age for basement.

Calcareous Nannofossils

On the basis of *Discoaster quinqueramus, Amaurolithus primus, S. amplificus, A. delicatus,* and *Triquetrorhabdulus rugosus*, 562-H1,CC is assigned to the upper Miocene *D. quinqueramus* Zone (NN11). Sediment contained within the first piece of basalt indicates a middle Miocene basement at this site. The included sediment contains *Sphenolithus heteromorphus*, which indicates either the *S. heteromorphus* Zone CN4 (NN5) or the *Helicosphaera ampliaperta* Zone CN3 (NN3-NN4). Because of poor nannofossil preservation, a more refined zonation of this interval was not possible.

Foraminifers

The core catcher of Core H1 is a white nannofossil-foraminiferal ooze with well-preserved, diverse foraminifers. Although Pliocene elements are present in the section, the oldest fauna in the core is Miocene. The sample is assigned to lower middle or possibly upper lower Miocene.

Sample 562-H1-2, 31-33 cm contains a lower Pleistocene fauna and 562-H1-3, 2-4 cm is upper(?) Miocene. A piece of bedded limestone found between two basalt flows in Section 562-1-3 (241-250 m) has abundant planktonic foraminifers that indicate a lower-middle or possibly upper-lower Miocene assignment.

SEDIMENT ACCUMULATION RATES

Although we cannot calculate detailed sedimentation rates at this site, an overall average sediment accumulation rate of 15 m/Ma (241 m in 16 Ma) seems consistent with those calculated for calcareous pelagic sedimentation during similar time periods at other sites.

IGNEOUS PETROLOGY AND GEOCHEMISTRY

Hole 562 reached basement at 241 m sub-bottom and penetrated 90 m into a sequence of plagioclase phyric pillow basalts interrupted by two massive flows of very similar lithology (Fig. 4). Two chemical groups have been recognized within this sequence.

Lithology (Fig. 4)

Basalts of Site 562 are for the most part sparsely to moderately plagioclase phyric with fine-grained groundmass. They range from fresh to moderately altered. Pillow diameters vary from a few tens of centimeters to about 1.5 m. Most pillows have fresh glass rinds less than 15 mm thick separated from fine-grained pillow cores by variolitic zones only a few millimeters thick. Varioles range from about 0.5 to 1 mm in diameter. Thicker glass rinds, up to 5 cm thick, are also present in several places, but generally detached from pillows (by drilling?). Glass clasts are also common in interpillow breccias, usually cemented with a fine-grained limestone matrix.

Plagioclase phenocrysts (2–5%) are mostly scattered uniformly throughout the rock, but in some places—mainly in the lower drilled portion—abundances may locally increase to as much as 15% or decrease to zero. Plagioclase phenocrysts range in size from about 1 to 10 mm and in shape from subhedral to rounded, possibly as a result of resorption. Glomerophyric clusters of plagioclase (about 15 mm in diameter) occur throughout the section.

Olivine microphenocrysts are sometimes observable, generally replaced by brown clay materials.

Vesicles are rare to absent (less than 1%), and commonly rounded, although some irregular ones do occur; they range from less than 1 mm to 2 mm in diameter. In the more altered parts of the basalt, vesicles are mainly clay filled, but calcite filling is also common. In fresh material close to pillow margins, most vesicles remain unfilled.

Massive lava flows were encountered at 268 m (3.7 m thick) and at 279 m (5.1 m thick). They are lithologically, petrographycally and chemically very similar to the pillow basalts, although slightly coarser grained. The upper flow is almost nonvesicular. It has an aphyric upper margin about 50 cm thick becoming sparsely phyric to moderately phyric downhole. Plagioclase phenocrysts increase in abundance from 0 to 10% and in size from 2 to 10 mm. An aphyric basalt margin about 25 cm thick with a narrow glass selvage marks the base of this flow. The lower flow has a narrow glass rim underlain by a narrow variolitic zone at its upper margin. It is sparsely to moderately plagioclase phyric (2–5%) throughout with no apparent systematic variation in phenocryst size or abundance. The lower boundary is not clearly defined and may not have been recovered. Vesicles are abundant

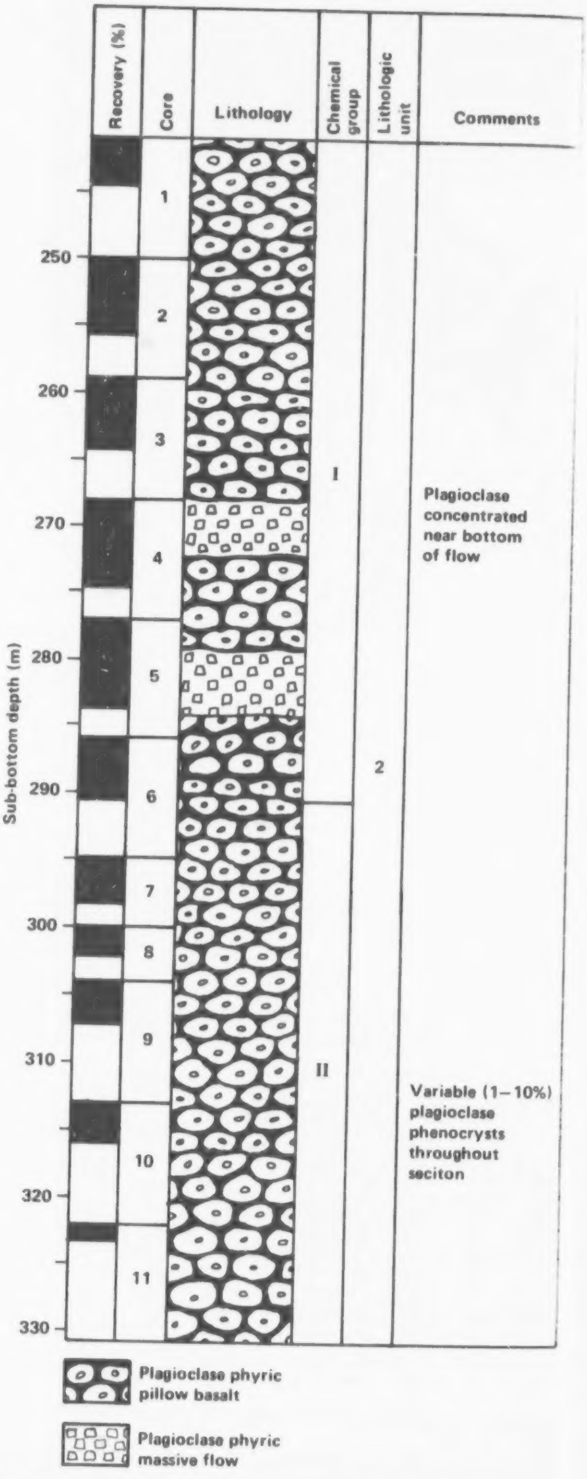
Recovery (%)
Core
Lithology
Chemical group
Lithologic unit
Comments
Sub-bottom depth (m)
250
260
270
280
290
300
310
320
330
1
2
3
4
5
6
7
8
9
10
11
I
II
2
Plagioclase concentrated near bottom of flow
Variable (1–10%) plagioclase phenocrysts throughout seciton
Plagioclase phyric pillow basalt
Plagioclase phyric massive flow

Figure 4. Basement lithology column, Hole 562.

(up to 5%) in the uppermost 20 cm of this lower flow, but are rare downwards.

Calcite-filled and/or limestone-filled veins and fractures occur throughput the drilled section. Minor basalt breccias and basalt-glass breccias with limestone matrix and sparry calcite are also present.

Petrography

The two chemical groups of Site 562 cannot be distinguished petrographically—all pillow basalts are very similar, with only minor variations in texture and grain size. The two massive flows differ from flows in other sections only in their slightly larger grain size and their almost complete lack of interstitial glass.

Site 562 basalts are characterized by the presence of three distinct generations of plagioclase. They also differ from basalts of previous sites in the rounded, possibly resorbed appearance of olivine. In their mineralogy, Site 562 basalts are remarkably uniform throughout the hole, with approximately 45% plagioclase, 35% clinopyroxene, 2–3% olivine, 5–10% magnetite, and 10–15% mesostasis. Plagioclase occurs in three distinct generations which are, in order of crystallization, as follows.

1. Large prismatic phenocryst are generally 2–3 mm, rarely up to 10 mm. They are typically subhedral (resorbed) and complex in internal structure, frequently with corroded cores. Small glass inclusions are also common. Few grains suitable for optical determination were observed; most yielded compositions close to AN_{60} with a few higher, but this figure may not be reliable.[3]

2. Elongate, hollow laths, generally about 1 mm long, but ranging up to 3 mm, form radiating clusters, generally centered on olivine, or parallel growths from the ends of prismatic, Type 1 phenocrysts. Compositions of laths and overgrowths appear to be 5–10 wt.% lower in An content than Type 1. Type 2 generally makes up 10 to 20% of all plagioclase.

3. Plagioclase in the form of fine laths less than 0.2 mm long and of anhedral intergrowths with fine, prismatic clinopyroxene makes up about 50% of the groundmass of most samples.

Clinopyroxene occurs mainly as small (less than 0.5 mm, generally less than 0.2 mm) prismatic or granular grains intergrown with Type 3 plagioclase and interstitial to Type 2 plagioclase. In samples close to pillow margins, this intergrowth has the appearance of devitrified glass, giving rise to a hyalophitic or hyalophilitic texture when viewed at low magnification. Such samples are, however, almost holocyrstalline, with only about 10% of interstitial glass remaining. Fine granular magnetite (about 0.05 mm) is associated with clinopyroxene and glass.

Olivine, as small (0.1–0.6 mm), rounded, anhedral microphenocrysts, forms 2–3% of these basalts. In one sample (562-3-3, 103–106 cm) from close to a pillow margin, quench chains of olivine are present along with sheaves of skeletal plagioclase (Type 2). Individual olivine crystallites in the chains appear corroded, suggesting resorption of olivine by liquid or during subsequent, plagioclase-dominated crystallization. The rounded shapes of olivine phenocrysts at this site contrast with the euhedral, prism-shaped, diamond-shaped, and lantern-shaped microphenocrysts of previous sites. These, too, may suggest that olivine is unstable relative to the liquids that formed these rocks.

In these rocks, plagioclase has begun to crystallize earlier in the cooling history, and has persisted longer throughout that history than at any previous Leg 82 site. Type 1 plagioclase phenocrysts clearly formed before eruption and were subsequently corroded. Olivine appears to be later that Type 1 plagioclase, but is earlier than Type 2, and may have been resorbed during crystallization of Type 2.

Finally, with the entry of clinopyroxene as a crystallizing phase, crystallization became more rapid. Type 3 plagioclase precipitated together with clinopyroxene, whereas magnetite crystallized at grain boundaries and within the small remaining amounts of interstitial liquid (glass).

Geochemistry

Twenty-six basalts samples were analyzed for major and trace elements at Site 562. Two distinct chemical groups can be recognized (Fig. 5), although the lithology and petrology are relatively homogeneous. On an extended Coryell-Masuda plot (Fig. 6), all samples analyzed display a depleted magmaphile element signature. Within Chemical Group II, a small subgroup occurs as a consequence of sampling within an aphyric region of the otherwise slightly to moderately plagioclase phyric pillow sequence.

Chemical Group I is represented by 19 samples from Sections 562-1-1 through 562-6-3 (Table 2). Samples from Sections 562-4-1 and 562-4-3 are the only visibly altered samples analyzed, but an examination of Sr and K_2O abundances suggests that the majority of samples have undergone some degree of alteration. Figure 7 shows the very scattered relationship of Sr values to CaO content. In an attempt to further assess the effects of alteration, we can assume that in a suite of fresh samples Sr and CaO should show a reasonably coherent, positive correlation and that seawater addition increases Sr content with little effect of CaO. The lower bound of the field of values in Figure 7 is a straight line passing through samples from Sections 562-2-1, 562-2-2, 562-2-3, 562-2-4, and 562-5-2. The slope of this line is the same as that derived in the same way for samples from Site 559. It seems reasonable to assume that these five samples are unaltered and that all other samples have undergone some Sr addition. When these samples are plotted on Figure 8 (K_2O versus Sr) they occupy a separate field at low K_2O and Sr values (along with other samples lying close to the Sr versus CaO line). Those samples that appear to have had Sr added have also had K_2O added.

In order to assess the effects of alteration on other elements, we take the average composition of the five unaltered samples (562-2-1 to 562-2-4 and 562-5-2), express it in mole %, and compare it to the compositions of vis-

---

[3] Preliminary shore-based microprobe studies suggests a plagioclase phenocryst core composition close to about An_{90}, zoned to a marginal composition of about An_{75}. Type 2 plagioclase compositions are An_{70}.

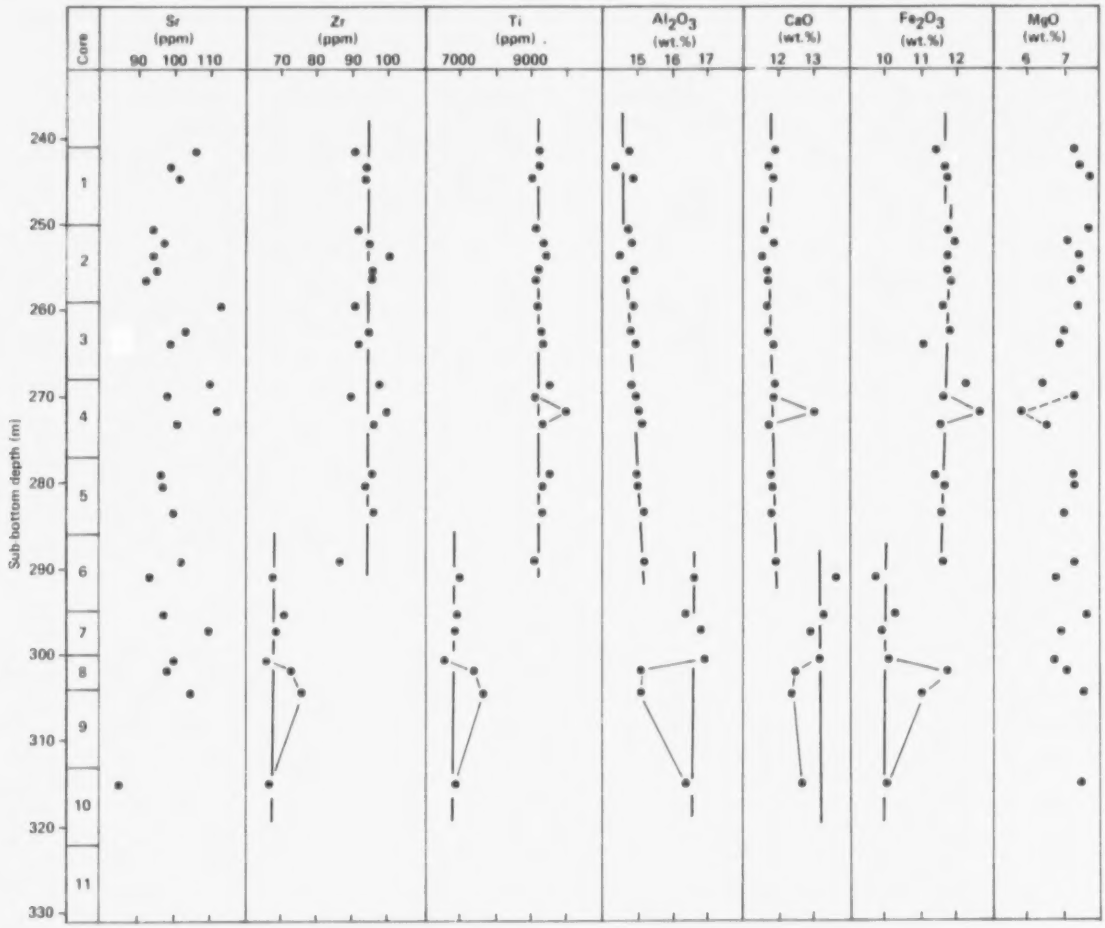

Figure 5. Downhole variations in chemical abundances, Hole 562.

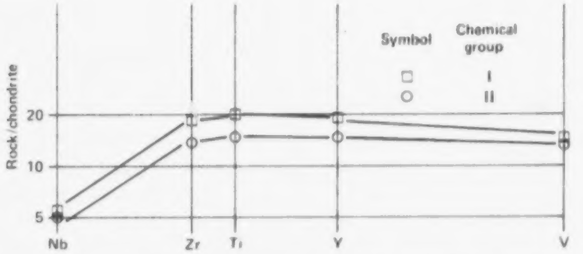

Figure 6. Extended Coryell-Masuda diagram for averages of chemical Groups I and II Hole 562 basalts.

ibly altered Samples 562-4-1, 9–12 cm and 562-4-3, 83–85 cm normalized to the unaltered TiO_2 value (Table 3). Relative to TiO_2, alteration has produced significant decreases in SiO_2 (Section 562-4-3 only) and MgO, with increases in K_2O and Sr. Apparent increases in V (562-4-3) and decreases in Nb (both samples) require further evaluation, preferably on single pillows. Nb variations, however, are within X-ray fluorescence analytical precision.

Chemical Group II is composed of the remaining samples from Site 562. Relative to Chemical Group I, Group II is lower in TiO_2, Fe_2O_3 (total iron), P_2O_5, V, Y, and Zr and higher in Al_2O_3 and CaO. Samples from Sections 562-8-2 and 562-9-1 form a separate subgroup; higher in TiO_2, Fe_2O_3 (total iron), V, Y, and Zr and lower in Al_2O and CaO relative to the remainder of Chemical Grou II. However, the two samples of this subgroup are aphyri whereas the remainder of Group II samples are sparsely t moderately plagioclase phyric. The geochemical differ ences between the subgroups are readily explained by thi difference in plagioclase phenocryst content. Calcula tions presented in Table 4 are for a mixture of one par liquid having a chemical composition equal to the aver age of samples from Sections 562-8-2 and 562-9-1 wit 8% added plagioclase phenocryst. Two plagioclase com positions were used, An_{60} and An_{75} (Deer et al., 1976) The composition resulting from An_{60} addition is remark ably similar to that of Section 562-7-2; the addition o An_{75} to the average liquid results in a composition al most exactly that of Sections 562-7-2 and 562-8-1. Thi calculated composition also approximates Sections 562

Table 2. Analyses of major elements (in wt.%) and trace elements (in ppm) of Hole 562 basalts.[a]

Core-Section (interval in cm) (piece number)	Sub-bottom depth (m)	Chemical group	SiO_2	TiO_2	Al_2O_3	Fe_2O_3[b]	MnO	MgO	CaO	K_2O	P_2O_5	Total	Mg'[c]	Ti	V	Sr	Y	Zr	Nb
1-1, 104-107 (6D)	242.1	I	50.06	1.54	14.79	11.42	0.18	7.20	11.87	0.17	0.14	97.37	59	9240	321	106	40.8	91	2.9
1-2, 34-37 (2C)	242.9		49.99	1.54	14.38	11.67	0.18	7.33	11.69	0.07	0.15	97.00	59	9240	311	99	41.3	94	2.3
1-3, 92-95 (3C)	244.9		49.47	1.51	14.87	11.73	0.18	7.65	11.81	0.20	0.14	97.56	59	9060	328	103	41.3	94	2.1
2-1, 55-59 (3B)	250.6		49.72	1.52	14.75	11.73	0.18	7.63	11.57	0.09	0.14	97.33	59	9120	319	94	40.5	92	2.2
2-2, 54-59 (8A)	252.1		49.19	1.56	14.86	11.93	0.18	7.01	11.87	0.33	0.14	97.07	57	9360	328	97	43.2	95	3.0
2-3, 61-65 (4C)	253.6		50.40	1.57	14.54	11.75	0.18	7.38	11.53	0.17	0.14	97.66	59	9420	326	94	41.6	101	3.1
2-4, 33-38 (2C)	254.9		50.37	1.54	14.92	11.73	0.18	7.41	11.67	0.04	0.14	98.00	59	9240	322	95	40.5	96	3.5
2-5, 73-76 (4B)	256.6		50.35	1.53	14.67	11.83	0.18	7.20	11.70	0.00	0.15	97.61	58	9180	317	92	41.3	96	2.9
3-1, 85-88 (3B)	259.9		50.39	1.54	14.91	11.62	0.18	7.35	11.68	0.11	0.16	97.94	59	9240	330	113	41.6	91	2.6
3-3, 103-106 (6D)	263.1		49.33	1.55	14.85	11.81	0.18	6.95	11.68	0.31	0.14	96.80	57	9300	327	103	41.9	95	3.7
3-4, 120-123 (7)	264.7		50.08	1.56	14.98	11.05	0.17	6.83	11.85	0.02	0.14	96.68	58	9360	322	99	40.6	92	2.2
4-1, 9-12 (1B)	268.1		49.40	1.59	14.83	12.28	0.18	6.34	11.89	0.22	0.15	96.88	58	9540	330	110	42.4	98	2.5
4-2, 0-3 (1A)	269.3		49.74	1.53	14.98	11.66	0.18	7.26	11.84	0.05	0.14	97.38	58	9180	316	98	40.3	90	3.4
4-3, 83-85 (2H)	271.7		48.23	1.67	15.06	12.64	0.21	5.80	13.02	0.24	0.18	97.05	51	10020	368	112	46.7	100	2.0
4-4, 100-103 (7B)	273.4		49.54	1.56	15.13	11.54	0.17	6.46	11.71	0.32	0.15	96.58	56	9360	316	101	43.0	96	4.1
5-2, 76-79 (4B)	279.3		50.16	1.59	15.00	11.37	0.17	7.20	11.75	0.13	0.15	97.52	59	9540	342	96	41.6	96	3.3
5-3, 104-107 (1G)	281.0		49.89	1.56	15.07	11.62	0.18	7.22	11.79	0.10	0.15	97.58	53	9360	319	97	40.5	94	2.2
5-5, 75-79 (3D)	283.6		49.79	1.56	15.21	11.56	0.18	6.93	11.77	0.27	0.15	97.42	57	9360	320	100	41.2	96	4.1
6-3, 74-77 (3A)	289.8		49.77	1.52	15.23	11.57	0.18	7.23	11.90	0.33	0.14	97.87	58	9120	334	102	40.2	87	2.9
6-4, 74-78 (2F)	291.3	II	48.94	1.17	16.63	9.78	0.15	6.74	13.61	0.16	0.12	97.30	61	7020	302	93	31.5	68	3.7
7-1, 29-33 (4B)	295.3		49.10	1.16	16.41	10.28	0.16	7.57	13.29	0.15	0.13	98.25	62	6960	299	97	31.5	71	2.3
7-2, 44-47 (2C)	297.0		50.00	1.15	16.82	9.95	0.14	6.86	12.92	0.14	0.12	98.10	61	6900	287	110	32.2	69	2.6
8-1, 95-98 (7A)	301.0		49.60	1.10	16.90	10.13	0.17	6.70	13.14	0.24	0.11	98.09	60	6600	277	100	31.1	66	2.2
8-2, 26-29 (4A)	301.8		49.59	1.24	15.12	11.71	0.18	7.03	12.48	0.39	0.13	97.87	57	7440	316	98	33.0	73	2.4
9-1, 140-142 (7)	305.4		50.36	1.28	15.13	11.01	0.17	7.48	12.40	0.38	0.16	98.37	60	7680	359	105	36.6	76	4.2
10-2, 125-128	315.8		49.89	1.16	16.40	10.07	0.14	7.43	12.66	0.04	0.10	97.89	62	6960	290	85	29.9	67	1.8

[a] On-board measurements were made on ignited samples. Onshore analyses of loss on ignition are less than 1% in most cases. Compiled data tables at the end of this volume (Appendix) include volatile components.

[b] Total Fe as Fe_2O_3.

[c] Mg' is the atomic ratio of $100 \times (Mg/[Mg + Fe^{2+}])$, calculated using an assumed Fe_2O_3/FeO ratio of 0.15.

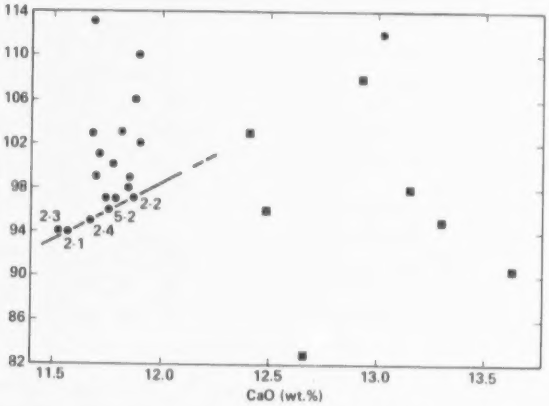

gure 7. Chemical alteration effects: Sr versus CaO, Chemical Groups I (circles) and II (squares). Numbers indicate core and section for certain samples.

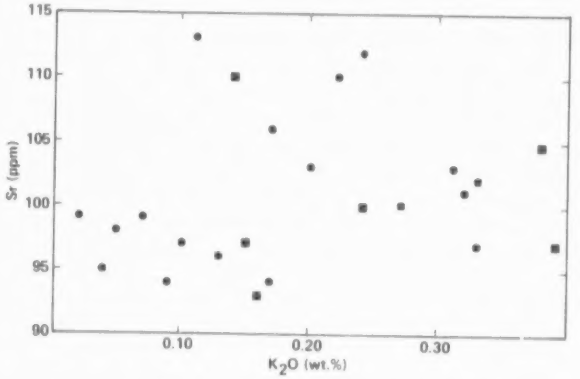

Figure 8. Chemical alteration effects: Sr versus K_2O, Chemical Groups I (circles) and II (squares).

4, 562-7-1, and 562-10-2, except that CaO and/or MgO ncentrations are higher than calculated. Hence, this emical subgroup is an artifact of sampling in a non-iiform sequence and not of petrogenetic significance.

K_2O and Sr abundances of Group II rocks also show wide scatter indicating widespread alteration with this oup (Figs. 7 and 8).

MAGNETICS

asalt Paleomagnetism

At this site, 90 m of basalt were cored and 33 orient-d minicores were taken for on-board study of paleomag-etic properties. The normal remanent magnetization (NRM) and susceptability were routinely measured, and then each sample was subjected to alternating field (AF) demagnetization at various steps until the remanent magnetization value was 50% of the NRM intensity. The NRM, susceptibility, median demagnetizing field (MDF), and the results of AF demagnetization are given in Table 5. The typical results of demagnetization (Figs. 9, 10) separated two types of basalt.

Type A basalt has high susceptibility (more than 200 × 10^{-6} emu/cm³, and mostly around 600 × 10^{-6} emu/cm³) and low MDF (less than 200 Oe, and mostly less than 100 Oe). This suggests that the magnetic mineral in the basalt is of low coercivity, which might be the result of the larger grain size of titanomagnetite or the presence of magnetite.

Type B basalt has low susceptibility (less than 200 × 10^{-6} emu/cm³, and mostly less than 100 × 10^{-6} emu/

Table 3. Effects of alteration on chemical composition Group I, Hole 562.

Element	Average	562-4-1, 9-12 cm Measured	562-4-1, 9-12 cm T	562-4-1, 9-12 cm Change (%)	562-4-3, 83-85 cm Measured	562-4-3, 83-85 cm T	562-4-3, 83-85 cm Change (%)
Major elements (mole %)							
SiO_2	56.51	57.20	55.10	-2	56.00	51.00	-10
TiO_2	1.33	1.38	1.33	0	1.46	1.33	0
Al_2O_3	9.97	10.10	9.73	-2	10.30	9.38	6
Fe_2O_3	5.05	5.35	5.16	+2	5.52	5.03	0
MnO	0.17	0.17	0.16	-5	0.21	0.19	+12
MgO	12.50	10.90	10.5	-16	10.00	9.11	-27
CaO	14.30	14.70	14.2	-1	16.20	14.80	+1
Na_2O	—	—	—	—	—	—	—
K_2O	0.11	0.16	0.15	+36	0.18	0.16	+45
P_2O_5	0.07	0.07	0.07	0	0.09	0.08	+14
	100.01	100.03	96.40		96.26	91.08	
Trace elements (ppm)							
Ti	9336	9540		+2	10020		+7
V	327	330		+1	368		+13
Sr	95	110		+16	112		+18
Y	14.5	42.40		+2	46.7		+13
Zr	96	98		+2	100		+4
Nb	3.0	2.50		-7	2.0		-33

Note: Average is average composition of the five least altered basalts from Group I; T is normalized composition with respect to TiO_2 = 1.33 wt.%; change (%) is change relative to average basalt composition. Total Fe as Fe_2O_3. Mg' is the atomic ratio of 100 × (Mg/[Mg + Fe^{2+}]); calculated using an assumed Fe_2O_3 ratio of 0.15.

cm³) and high MDF (more than 200 Oe; mostly more than 400 Oe). This suggests that these basalts have titanomagnetite of single-domain grain size of coercivity higher than those of Type A basalts.

The plot of susceptibility and MDF versus depth (Fig. 11) clearly indicates the two different types of basalts, and the two different units of basalts. Unit 1 is the upper unit of basalt from 240 m to a depth of about 286 m, and is identified by the presence of both Type A basalt and Type B basalt. Unit 2 is the lower unit of basalt from 286 m to last cored depth of 331 m, and is identified by the presence of only Type B basalt.

At this time, the reason for these two different types of basalts is not known, but they may be the results of two different magma sources or just different cooling histories.

The inclination values are much smaller than the expected dipole inclination for the latitude of this site, which may be due to a tectonic rotation of crust since the basalts were erupted.

PHYSICAL PROPERTIES

The hole was washed to basement with no recovery of undeformed sediment. Velocity and density measurements were made on basalt cores as shown in Table 6.

The results are remarkable only for densities and velocities that are generally higher than for average basalts from this leg. The specimen from Core 3 with a velocity of 5.98 km/s and density of 2.91 Mg/m³ is the highest of these, and well above a mean value for ocean basalts at laboratory temperature and pressure. The basalts recovered are from a massive flow unit, in contrast to the predominance of pillow basalts in the previous holes of this leg. The variation in properties downhole does not reveal any systematic pattern.

SUMMARY AND CONCLUSIONS

Hole 562 was drilled on Anomaly 5D about 60 miles south of the Hayes Fracture Zone, the first site on the southernmost flow line. The sediments were washed down and the bottom felt at 240 m.

The basement, cored for 90 m, consisted of sparsely plagioclase phyric pillow basalts. Fresh glasses at the margins of the pillows are very common. Despite some altered parts, the bulk of the crystalline basalts are fairly fresh. The macro-description and micro-description of recovered samples show one petrographic unit, but both major and trace element data show two different chemical groups. The first chemical group in the basement is fairly homogeneous even though a downhole gradient is observed for Al_2O_3 (from 14.6 at the top to 15.2 in the lower region). The second chemical group is less homogeneous, because of variable plagioclase phenocryst distribution. The two chemical groups show a depleted character for magmaphile elements, with $(Nb/Zr)_{ch}$ of ~ 0.3.

It would have been ideal to drill a second hole in the area to obtain a more extensive sampling of basalt material, but we decided to save time for the last hole at Anomaly 13, where logging and piston coring were planned.

REFERENCE

Deer, W. A., Howie, R. A., and Zussmann, J., 1976. *An Introduction to the Rock Forming Minerals*: London (Longmans).

Table 4. Effect of plagioclase phenocryst addition on chemical composition, Group II, Hole 562.

Element	Liquid (average composition of samples from Sections 562-8-2 and 562-9-1)	Composition of plagioclase An_{60}	1 part liquid + 0.08 plagioclase	Composition of plagioclase An_{75}	1 part liquid + 0.08 plagioclase
SiO_2	49.98	52.96	50.20	49.06	49.91
TiO_2	1.26		1.17		1.17
Al_2O_3	15.13	29.72	16.21	32.14	16.39
Fe_2O_3	11.36	0.84	10.58	0.27	10.54
MnO	0.18		0.17		0.17
MgO	7.26		6.72	0.20	6.74
CaO	12.44	12.28	12.43	15.38	12.66
K_2O	0.38	0.13	0.36	0.17	0.36
P_2O_5	0.16		0.15		0.15

Note: Plagioclase An_{60} and An_{75} compositions from Deer et al., 1976.

Table 5. Paleomagnetics properties of Site 562 basalts.

Core-Section (interval in cm)	JNRM (× 10−3 emu/cm³)	NRM inc. (°)	Stable inc. (°)	χ (× 10−6 emu/cm³ Oe)	MDF (Oe)
1-2, 28-30	16.77	− 27.4	− 34.3	410	90
2-1, 64-71	3.71	− 12.7	− 30.8	490	65
2-2, 142-144	1.95	− 27.7	− 29.4	110	370
2-3, 41-43	2.53	− 39.3	− 40.0	60	490
2-4, 7-9	3.95	− 18.8	− 39.1	600	85
2-5, 9-11	3.46	− 25.9	− 35.0	250	75
3-1, 46-48	1.66	− 21.8	− 38.0	145	360
3-2, 141-143	4.39	− 13.1	− 24.8	216	150
3-3, 86-88	0.77	− 29.2	− 45.6	108	365
3-4, 110-112	4.02	27.0	31.6	290	77
4-1, 75-77	4.01	− 21.5	− 28.0	746	200
4-2, 46-48	4.26	− 27.6	− 34.4	224	185
4-3, 26-28	4.31	− 17.1	− 38.7	682	75
4-4, 117-119	3.28	− 38.1	− 40.2	138	355
5-1, 64-66	2.34	− 31.2	− 40.9	82	325
5-2, 89-91	1.81	− 11.1	− 32.8	540	115
5-3, 40-42	3.59	− 2.2	− 19.1	652	170
5-3, 79-81	2.90	− 6.9	− 31.9	820	157
5-4, 29-31	3.41	− 14.6	− 27.3	610	75
5-4, 122-124	2.39	− 10.5	− 27.4	804	75
5-5, 47-49	2.21	− 10.3	− 24.6	135	280
6-3, 85-87	1.43	− 41.5	− 42.1	85	450
6-4, 94-96	2.85	− 43.9	− 49.8	85	465
7-1, 26-28	2.33	− 21.8	− 23.9	85	567
7-2, 56-58	3.02	− 25.7	− 28.1	105	375
7-1, 126-128	1.89	− 33.5	− 35.3	98	475
7-3, 64-66	1.42	− 28.4	− 29.7	80	625
8-1, 144-146	3.94	− 30.0	− 31.8	112	470
8-2, 7-9	4.01	− 36.5	− 36.2	132	410
9-1, 82-84	3.02	− 29.7	− 31.2	95	400
9-2, 23-25	2.18	− 30.4	− 33.3	92	450
9-2, 81-83	3.20	− 35.6	− 36.4	93	450
11-1, 115-117	1.48	− 33.5	− 33.9	94	550

Note: JNRM = intensity of natural remanent magnetization (NRM); inc. = inclination; χ = susceptibility; MDF = median demagnetizing field.

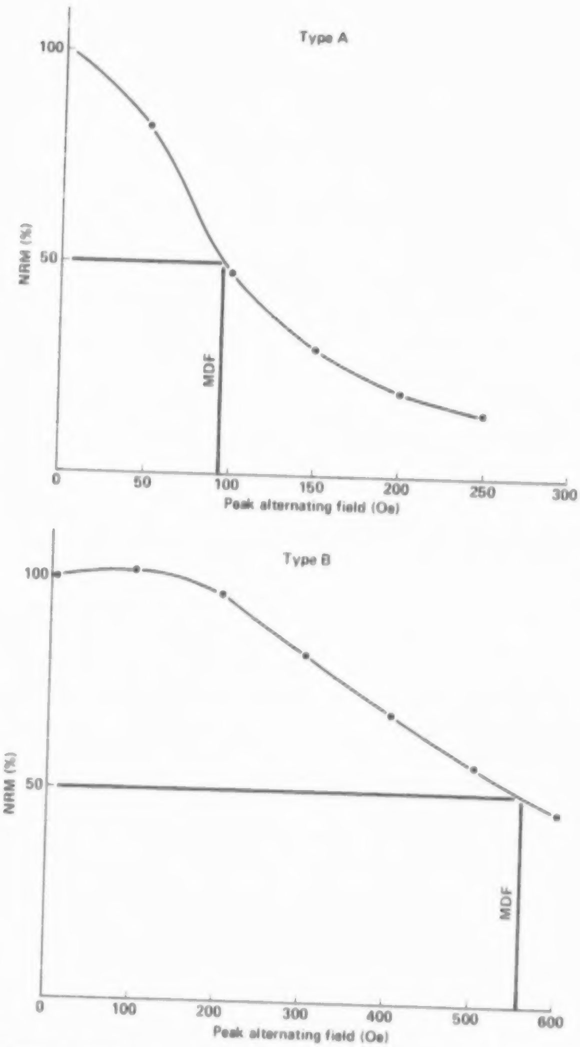

Figure 9. Percent natural remanent magnetization (NRM) versus peak alternating field curves for Type A basalt (562-5-4, 29-31 cm) and Type B basalt (562-7-1, 26-28 cm). MDF = median demagnetizing field.

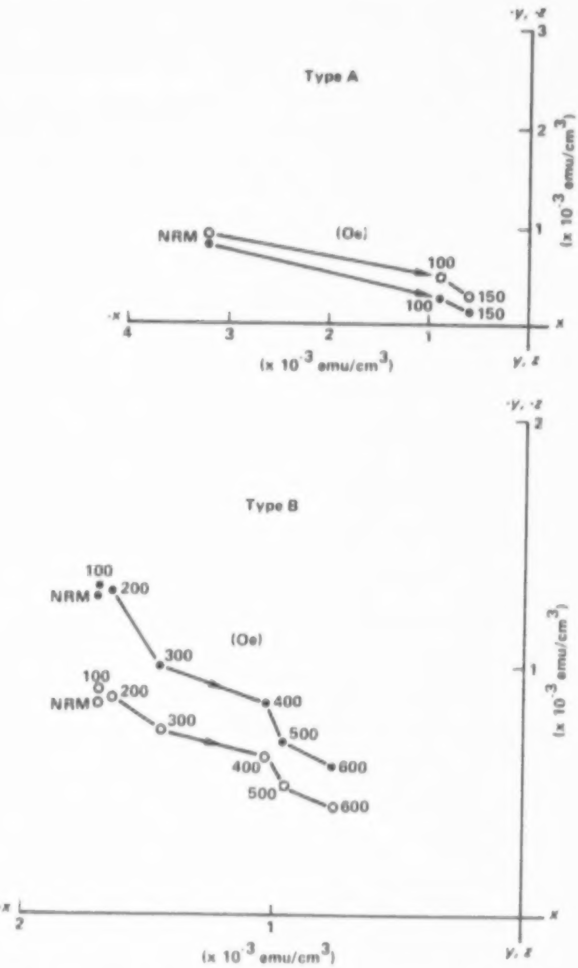

Figure 10. Vector diagrams showing the change of NRM after alternating field demagnetization for Type A basalt (562-5-4, 29-31 cm) and Type B basalt (562-7-1, 26-28 cm). Solid circles are plotted on the horizontal plane and open circles are plotted on the vertical plane. NRM = natural remanent magnetization.

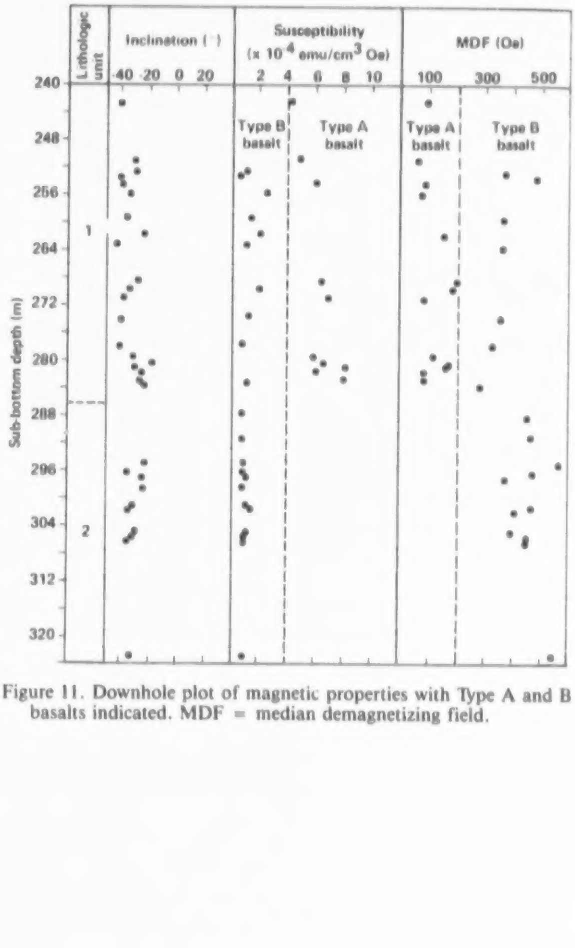

Figure 11. Downhole plot of magnetic properties with Type A and B basalts indicated. MDF = median demagnetizing field.

Table 6. Physical properties, Hole 562.

Core-Section (interval in cm)	Sub-bottom depth (m)	Sonic velocity (km/s) (horizontal)	Temperature (°C)	GRAPE density (g/cm³) (horizontal)	Gravimetric density			Lithology or remarks
					Wet-bulk density (g/cm³)	Water content (%)	ϕ (%)	
1-1, 94-104	242.0	5.70	22.0	2.88	2.86	1	3	Plag. phyric basalt
2-3, 113-117	254.2	5.63	22.0	2.80	2.87	1	4	Basalt
3-1, 31-36	259.3	5.98	22.0	2.91	2.91	1	3	Basalt
4-1, 52-57	268.5	5.42	22.0	2.83	2.85	2	6	Plag. phyric basalt
5-1, 20-25	277.2	5.15	22.0	2.77	2.82	3	8	Vesicular basalt
5-5, 54-59	283.6	5.82	22.0	2.88	2.90	1	3	Plag. phyric basalt
6-2, 100-112	287.0	5.44	22.0	2.78	2.84	2	7	Basalt
7-2, 134-138	297.2	5.32	22.0	2.76	2.82	2	7	Basalt

Note: Water content is corrected; ϕ = porosity; Plag. = plagioclase. All values measured at laboratory temperature and pressure. For details of techniques, see Explanatory Notes chapter (this volume).

SITE 562 HOLE CORE H1 CORED INTERVAL 0.0–241.0 m

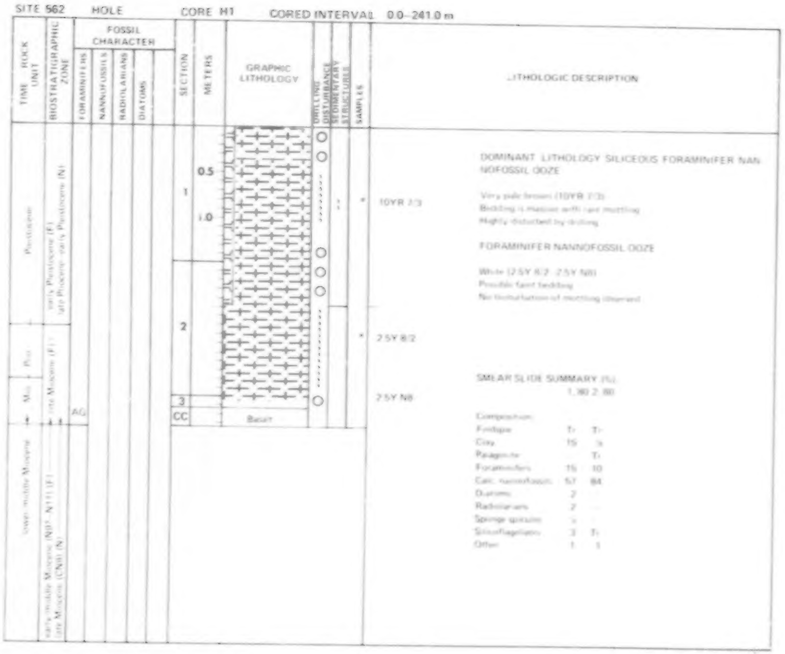
TIME-ROCK UNIT
BIOSTRATIGRAPHIC ZONE
FOSSIL CHARACTER
FORAMINIFERS
NANNOFOSSILS
RADIOLARIANS
DIATOMS
SECTION
METERS
GRAPHIC LITHOLOGY
DRILLING DISTURBANCE
SEDIMENTARY STRUCTURES
SAMPLES
Pleistocene
Plio
Mio
lower middle Miocene
early Pleistocene (F)
late Pliocene–early Pleistocene (N)
late Miocene (F)
early middle Miocene (N9?–N11) (F)
late Miocene (CN8) (N)
AG
0.5
1.0
1
2
3
CC
Basalt
10YR 7/3
2.5Y 8/2
2.5Y N8

LITHOLOGIC DESCRIPTION

DOMINANT LITHOLOGY SILICEOUS FORAMINIFER NANNOFOSSIL OOZE

Very pale brown (10YR 7/3)
Bedding is massive with rare mottling
Highly disturbed by drilling

FORAMINIFER NANNOFOSSIL OOZE

White (2.5Y 8/2, 2.5Y N8)
Possible faint bedding
No bioturbation or mottling observed

SMEAR SLIDE SUMMARY (%):

	1, 80	2, 80
Composition:		
Feldspar	Tr	Tr
Clay	15	5
Palagonite		Tr
Foraminifers	15	10
Calc. nannofossils	57	84
Diatoms	2	—
Radiolarians	2	—
Sponge spicules	5	—
Silicoflagellates	3	Tr
Other	1	1

SITE 562 HOLE CORE 1 CORED INTERVAL 241.0–250.0 m

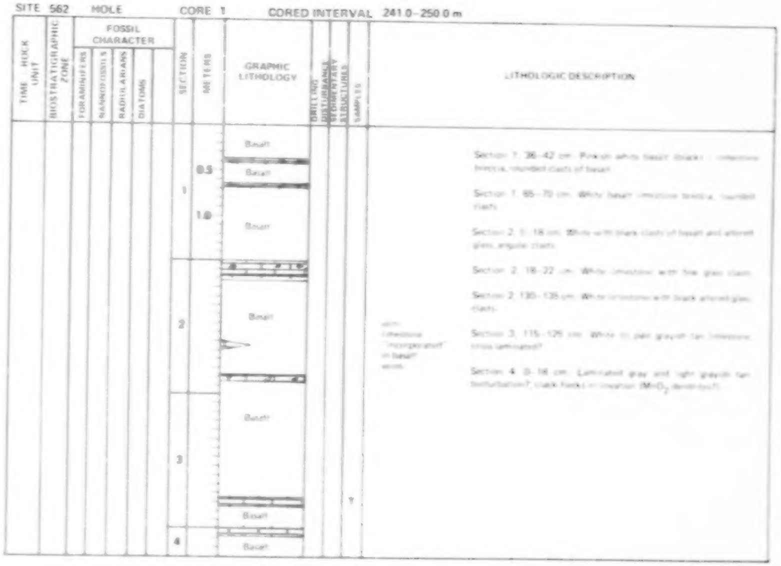
TIME-ROCK UNIT
BIOSTRATIGRAPHIC ZONE
FOSSIL CHARACTER
FORAMINIFERS
NANNOFOSSILS
RADIOLARIANS
DIATOMS
SECTION
METERS
GRAPHIC LITHOLOGY
DRILLING DISTURBANCE
SEDIMENTARY STRUCTURES
SAMPLES
0.5
1.0
1
2
3
4
Basalt
Basalt
Basalt
Basalt
Basalt
Basalt
Basalt
with
limestone
"incorporated"
in basalt
veins

LITHOLOGIC DESCRIPTION

Section 1, 36–42 cm: Pinkish white basalt (black) – limestone breccia, rounded clasts of basalt.

Section 1, 65–70 cm: White basalt limestone breccia, rounded clasts.

Section 2, 0–18 cm: White with black clasts of basalt and altered glass, angular clasts.

Section 2, 18–22 cm: White limestone with fine glass clasts.

Section 2, 130–135 cm: White limestone with black altered glass clasts.

Section 3, 115–125 cm: White to pale grayish tan limestone (cross laminated?)

Section 4, 0–18 cm: Laminated gray and light grayish tan (bioturbation?), black flecks in creation (MnO_2 dendrites?).

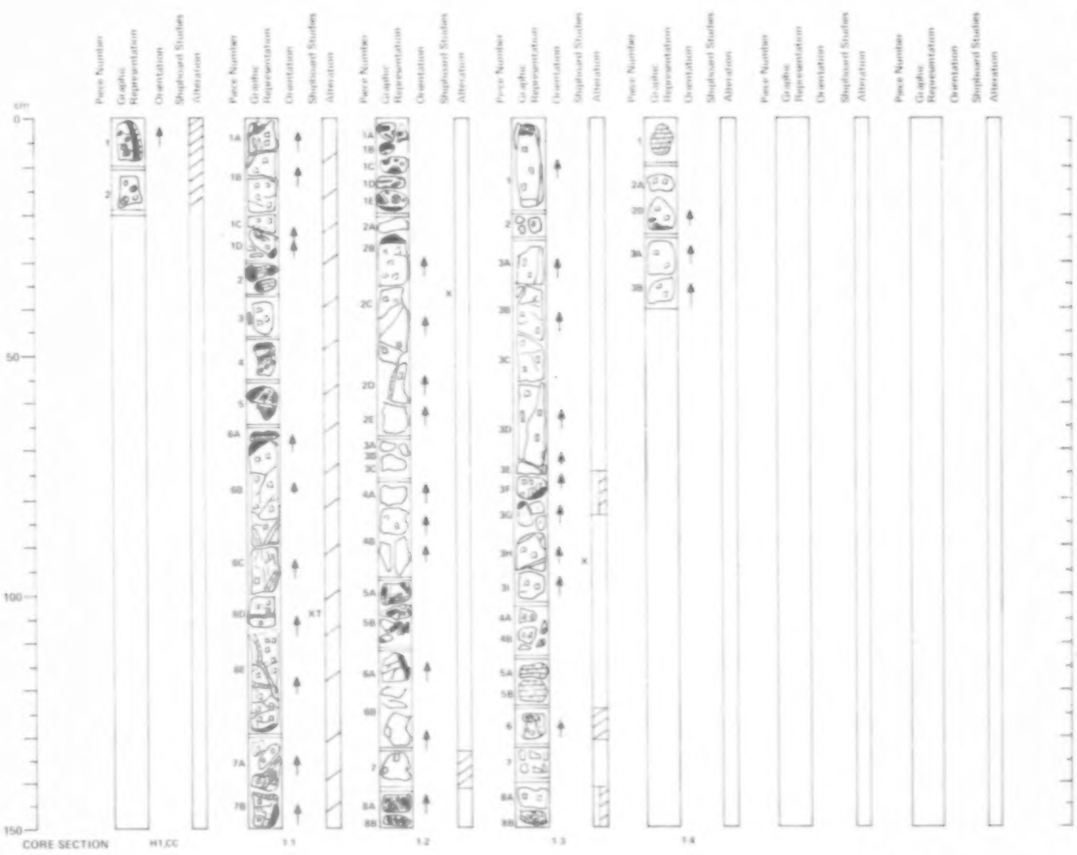

SITE 562 CORE H1 Depth 0.0–241.0 m

CORE CATCHER

VARIOLITIC BASALT

0–18 cm: Aphyric variolitic basalt with <1% scattered plagioclase phenocrysts and sericite/olivine microphenocrysts; dark gray (7.5YR N4/0); fine grained; plagioclase <1%; vesicles 2–10 mm; [illegible] <1 mm; moderately altered; varioles are brown (10YR 5/3). Volume percentage 10% in unfilled areas only.

0–10 cm: Piece 1: There is a rind (2 cm width) of fresh black basalt glass which grades into a variolitic zone. There is a crust of sediment on the glass rind which contains 1–2 mm devitrified glass shards.

SITE 562 CORE 1 Depth 241.0–250.0 m

SECTION 1

PLAGIOCLASE PHYRIC PILLOW BASALT

0–30, 38–42, and 65–150 cm: Plagioclase moderately phyric basalt: dark gray (2.5Y N4) in fresh parts and grayish brown (2.5Y 5/2) in altered parts; fine grained. Plagioclase phenocrysts (2–3%), 3 mm. 1 cm moderately altered to gray brown (2.5Y 5/2). <1% rounded and irregular vesicles (<1 mm) filled with light green clay(?). Veins filled with clay(?) or limestone.

30–38 and 42–65 cm: Glass clasts (black) in limestone matrix, mostly fresh with alteration to dark brown (7.5YR 4/4) clay(?) around edges of clasts.

SECTION 2

PLAGIOCLASE PHYRIC PILLOW BASALT

22–95 and 113–125 cm: Plagioclase moderately phyric pillow basalt gray (2.5Y N6), fresh to slightly altered; <1% rounded and irregular vesicles filled with dark to light green clay(?); 1–2% plagioclase phenocrysts (0.5 mm). Looks like less phyric than in Section 1.

0–22 and 97–110 cm: Glass clasts (black) in limestone matrix, mostly fresh with alteration as in Section 1.

125–140 cm: Limestone with heavily altered glass clasts (2–7 cm).

SECTION 3

PLAGIOCLASE PHYRIC PILLOW BASALT

0–113 and 125–150 cm: Moderately plagioclase phyric basalt: dark gray (7.5YR N4/0); fine to medium grained; plagioclase phenocrysts, 2–3%; anhedral (rounded), 1–10 mm.

Fresh interiors to moderately altered along fractures and variolitic zones: brown (10YR 5/3). 1% vesicles, <1 mm; white, talc, and green minerals.

0–1, 76–77, and 150 cm: Fresh black glass.

113–121 cm: Graded fossiliferous limestone, white (5YR 8/1) graded unindurated foram beds; sedimentary clasts (consolidated limestone); dendritic MnO.

SECTION 4

PLAGIOCLASE PHYRIC PILLOW BASALT

0–10 cm: Limestone white (5YR 8/1). Dendritic MnO.

10–40 cm: Same as Section 1 basalt description.

SITE 562 HOLE CORE 2 CORED INTERVAL 250.0–259.0 m

TIME – ROCK UNIT	BIOSTRATIGRAPHIC ZONE	FOSSIL CHARACTER FORAMINIFERS	FOSSIL CHARACTER NANNOFOSSILS	FOSSIL CHARACTER RADIOLARIANS	FOSSIL CHARACTER DIATOMS	SECTION	METERS	GRAPHIC LITHOLOGY	DRILLING DISTURBANCE	SEDIMENTARY STRUCTURES	SAMPLES	LITHOLOGIC DESCRIPTION
						1	0.5 1.0	Basalt with veins				Section 2, 20–40 cm: Intrapillow – basalt limestone (which infiltrated into broken pillow clast (glass). Between Section 2, 40 cm–Section 3, 80 cm: Small areas of intrapillow limestone. Section 3, 80–90 cm: Basalt (glass) and intrapillow limestone filling space between pillow margins; limestone appears to have graded bedding (geopetal, for skyward?).
						2		Basalt				
						3						
						4		Basalt				
						5						

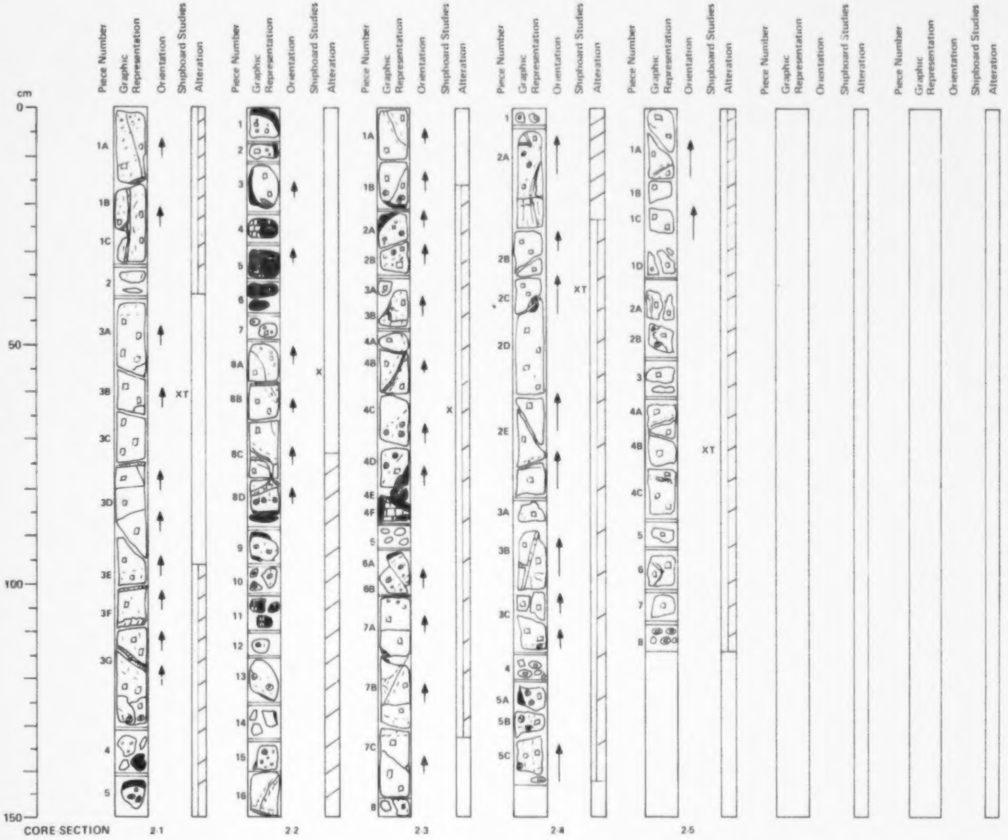

SITE 562 CORE 2 Depth 250.0–259.0 m

SECTION 1

PLAGIOCLASE PHYRIC PILLOW BASALT

0–129 cm: Sparsely to moderately plagioclase-phyric basalt. Plagioclase 1–5%, generally 2–3%. Prisms and rounded(?) glomerocrysts to 10 mm, generally 2–5 mm. Rare olivine to 2 mm, altered greenish clay. Matrix fine grained dark gray (7.5YR N4) with visible plagioclase laths to 1 mm weathered brown (7.5YR 5/4) close to fractures.

0–10 cm: Sparsely vesicular decreasing downhole. Vesicles round, generally < 1 mm dark clay filled.

15–80 cm: Minor calcite veinlets as shown (diagonal hatched).

95–120 cm: Limestone veins as shown. Irregular margins light gray (5Y 7/1) (greenish tint).

126–146 cm: Pillow margins dark gray aphanitic and variolitic, aphyric sparsely vesicular. Fresh glass, highly fractured but only slightly altered to palagonite along cracks.

SECTION 2

SPARSELY PLAGIOCLASE PHYRIC PILLOW BASALT

0–43 cm: Pillow margin material. Sparsely plagioclase phyric aphanitic basalt (very dark gray – 7.5YR N3) and fresh black glass. Plagioclase phenocrysts 2–3%, mainly 2–5 mm some to 10 mm rounded(?) glomerocrysts and prisms. Glass altered dark olive gray (5Y 3/2) along fractures.

43–140 cm: Sparsely phyric to aphyric (still with scattered phenocrysts) mainly aphanitic pillow basalt, dark gray (7.5YR N4). Variolitic where shown (). Altered brown (10YR 5/3) mottled gray along fractures. Sparse vesicles near tops of some pillows (~5 cm, 50 cm, and 135 cm). Vesicles round, < 1 mm filled with dark clay, sometimes bluish green (no number).

22–40, 70–80, and 102–109 cm: Limestone veins and interpillow breccia matrix. Fine grained limestone white (5YR 8/1) to pink (5YR 7/3).

SECTION 3

SPARSELY PLAGIOCLASE PHYRIC PILLOW BASALTS

0–15 and 105–145 cm: Sparsely phyric, fine grained basalt as in Section 1 – pillow interiors.

15–105 cm: Sparsely phyric, mainly aphanitic basalt and glass of pillow margins as in Section 2. Variolitic zones somewhat thicker (~5 cm) and more altered to light yellowish brown (10YR 6/4).

78–86 cm: Limestone. Pinkish gray (5YR 6/2) fine grained limestone with some laminae containing sand-sized, angular basalt grains.

22–35 and 95–103 cm: Sparsely vesicular near pillow tops. Small (< 1 mm) round vesicles unfilled or filled by white expanding clay.

SECTION 4

SPARSELY PLAGIOCLASE PHYRIC PILLOW BASALT

0–110 cm

Sparsely plagiolcase phyric pillow basalt (gray – 7.5YR N5/0)

Plagioclase phenocrysts, generally 2–4 mm long and needle-like aggregates visible with hand lens. Some 3–7 mm rounded prisms and/or glomerocrysts.

Altered along fractures within rock and adjacent to calcite veins. Tinged with yellowish brown hue (10YR 5/6). Zones few mm to few cm wide.

Variolitic where shown; gradation in gray, but no real color change in transition zone.

Vesicles sparsely scattered throughout, rounded < 1 mm–1.5 mm in diameter filled with dark clay, bluish green (no color since it changes with hydration).

110–140 cm

Sparsely plagioclase phyric pillow basalt gray (7.5YR N5/0) as above, exceptions as follows:

Variolitic zone as noted, grades from glass through aphanitic basalt (very dark gray – 7.5YR N3/0) through variolitic zone (brownish yellow – 10YR 6/6) to sparsely plagioclase phyric basalt (dark gray – 7.5YR N5/0).

114–120 cm, Piece 4: Rock pieces in Piece 4 show glass and variolitic transition, surfaces not cut.

Some glass, as indicated.

SECTION 5

SPARSELY PLAGIOCLASE PHYRIC PILLOW BASALT

8–113 cm

Sparsely plagioclase phyric pillow basalt gray (7.5YR N5/0).

Plagioclase phenocrysts, 2–4 mm long. Some 3–7 mm rounded prisms and/or glomerocrysts.

Alteration present along fractures and adjacent to calcite veinlets. Tinged with yellowish brown (10YR 5/6) hue. Zones narrow, only few mm wide.

Vesicles sparsely scattered throughout, rounded < 1 mm–1.5 mm diameter, filled with dark clay, some bluish green (no color code) or yellowish brown (10YR 5/6) as in alteration.

Variolitic where shown: grades in color with brownish yellow (10YR 6/6) in variolite zone grading to gray slightly plagioclase phyric basalt gray (7.5YR N5/0).

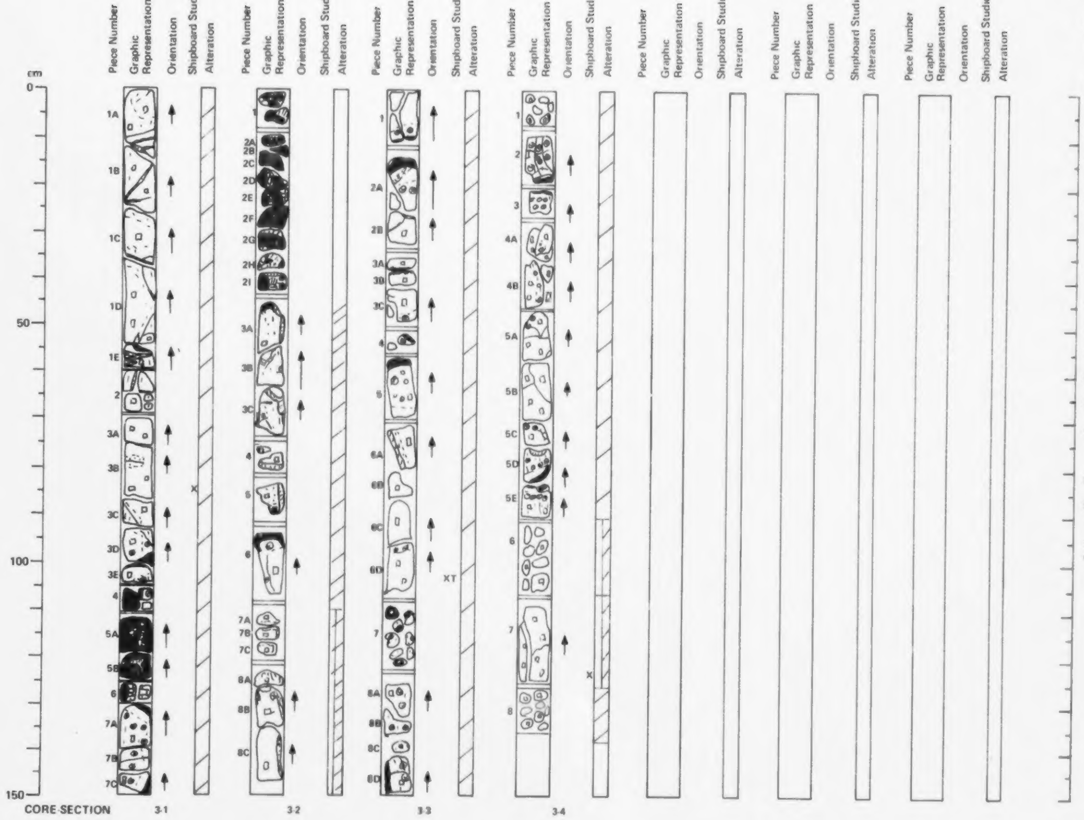

SITE 562, CORE 3

Depth 259.0–268.0 m

SECTION 1

SPARSELY PLAGIOCLASE PHYRIC PILLOW BASALT

0–40 and 70–85 cm. Sparsely phyric, fine grained basalt – pillow interiors as in Core 2, Section 1.

40–70 and 80–85 cm. Sparsely phyric aphanitic and variolitic basalt and glass – pillow margin material as in Core 2, Sections 2–5.

53–57 and 113–123 cm. Calcite veinlets, with cavities in lower interval.

125–128 cm. Limestone fine grained, light yellowish brown (10YR 6/4).

SECTION 2

GLASS AND SPARSELY PLAGIOCLASE PHYRIC PILLOW BASALT

0–44 cm. Black (10YR 2/1) glass in a calcite cement. May be broadly classified as a breccia, but some pieces are entirely glass without calcite, while other pieces have calcite and limestone. Calcite is sparry in cavities, and limestone and calcite are slightly off-white. Rims of glass pieces (those within limestone) slightly altered to palagonite. Vesicles are present and rounded < 1–2 mm in diameter.

47–147 cm.

Sparsely plagioclase phyric pillow basalt, gray (7.5YR N5/0).

Plagioclase phenocrysts, 3–5 mm long. Some 5–9 mm rounded prisms and/or glomerocrysts.

Alteration present along fractures within rock and adjacent to calcite rims. Color modified with yellowish brown (10YR 5/6) hue. Zones wide, few cm thick.

Variolitic sequence where shown. Glassy rim grades into black (10YR 2/1) aphanitic aphyric basalt, through variolitic zone (10YR 6/6) grading down to gray (7.5YR N5/0) slightly plagioclase phyric basalt.

Vesicles sparsely scattered, especially concentrated in altered basalt, aphanitic basalt and glass, and variolitic zone. May/may not be present in plagioclase phyric basalt adjacent to the variolite zone.

SECTION 3

SPARSELY PLAGIOCLASE PHYRIC PILLOW BASALT

43–49 and 65–105 cm. Sparsely phyric, fine grained basalt – pillow interiors as in Core 2, Section 1 and Core 3, Section 1.

0–43, 50–65, and 124–150 cm. Sparsely phyric aphanitic and variolitic basalt and basalt glass – pillow margins as in Core 2, Section 2 and Core 3, Section 1.

101–121 cm. Fragments include all above rock types plus angular glass fragments in calcite matrix.

Scattered calcite veinlets where shown.

SECTION 4

SPARSELY PLAGIOCLASE PHYRIC PILLOW BASALT

90–125 cm. Sparsely phyric, fine grained basalt – pillow interiors as in Core 2, Section 1 and Core 3, Section 1.

10–90 cm. Sparsely phyric aphanitic and variolitic pillow basalts as in Core 2, Section 2 and Core 3, Section 1. 1–2% rounded empty vesicles (<1 mm) in aphanitic and variolitic margins. 1–2% calcite filled rounded and irregular vesicles (1–2 mm) in pillow interiors and variolitic zone. Little calcite veining. Not much glass here.

0–10 and 125–135 cm. Basalt chips.

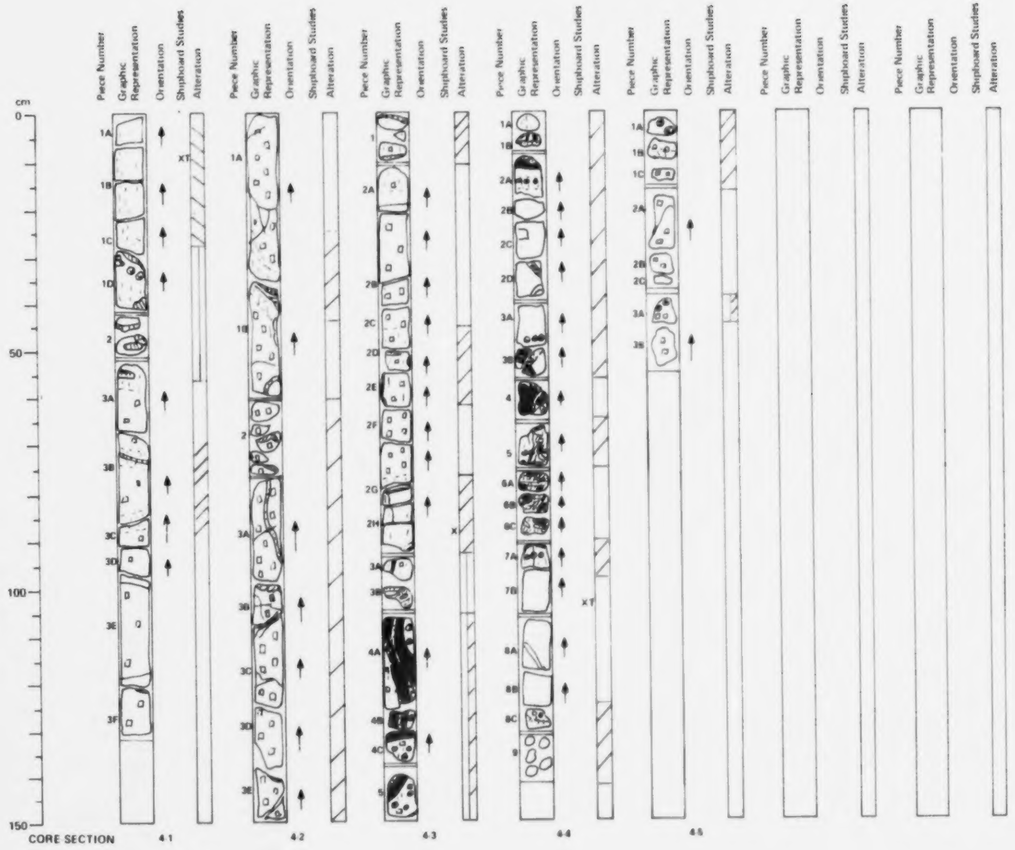

SITE 562, CORE 4

Depth 268.0–277.0 m

SECTION 1

APHYRIC TO SPARSELY PLAGIOCLASE PHYRIC BASALT (MASSIVE FLOW)

0–130 cm. Aphyric, fine grained basalt becoming sparsely plagioclase phyric downhole. Fine grained basalt gray (7.5YR N5) with abundant (30–40%?) unusually long plagioclase needles (to 3 mm) randomly oriented. Fine (< 0.5 mm) round, brown weathered? olivine (5–10%?) in weathered zones. Plagioclase phenocrysts, both prisms and rounded glomerocrysts(?) generally 2–5 mm, some to 10 mm. Abundance reaches 2–3% below 70 cm.

30–56 cm. Brick red, fine grained limestone as veins and irregular patches within basalt (yellowish red – 5YR 5/6) shown thus

Calcite veins where shown

SECTION 2

SPARSELY TO MODERATELY PLAGIOCLASE PHYRIC BASALT (MASSIVE FLOW)

0–150 cm

Fine grained, massive basalt becoming more plagioclase phyric downhole

30–40% elongate (3–4 mm) plagioclase needles randomly oriented

Fine, round, brown weathered olivine(?) (5–10%) in weathered zones

Plagioclase phenocrysts, prisms and rounded glomerocrysts (2–5 mm up to 10 mm)

Some calcite filled veins, moderately altered

SECTION 3

PLAGIOCLASE PHYRIC BASALT (MASSIVE FLOW)
PLAGIOCLASE PHYRIC PILLOW BASALT

0–77 cm

Moderately plagioclase phyric basalt, gray (7.5YR N5), fine grained as in Section 1

Plagioclase phenocrysts larger (to 10 mm) and more abundant (~5%, locally to 10%?)

Olivine phenocrysts to 2 mm, rare

Apparently gravity accumulation near base of flow

77–90 cm

Aphyric basalt with only scattered, smaller (≤5 mm) plagioclase phenocrysts. Similar to above, but finer grained. Mostly weathered light gray (10YR 6/1) to light brownish gray (10YR 6/2)

Apparently the lower margin of flow. Note small glass rind at 91 cm

93 cm: Base of flow

94–150 cm

Sparsely phyric aphanitic and variolitic basalt and basalt glass – pillow margins

Variolitic zones altered light olive gray (5Y 6/2)

Veinlets of calcite and larger veins of limestone, fine grained, light reddish brown (5YR 6/3)

Glass only slightly palagonitized

SECTION 4

SPARSELY PLAGIOCLASE PHYRIC PILLOW BASALT AND GLASS CLASTS IN LIMESTONE – CALCITE MATRIX

10–56, 66–75, and 90–130 cm. Basalt pillows with variolitic zone grading into aphanitic black basalt with glass rims. As in Section 3, 94–150 cm. Fairly fresh to moderately altered. ≤1% rounded and irregular vesicles (≤1 mm) calcite filled at pillow margins.

0–10, 58–66, and 77–90 cm. Fresh to moderately altered (black) glass clasts in limestone (pinkish gray – 7.5YR 6/2) or calcite (white) or both together (82–89 cm).

58–63 cm. Drusy calcite and glass clast with rounded, empty vesicles (1–2 mm).

SECTION 5

PLAGIOCLASE PHYRIC BASALT PILLOW

0–53 cm. Moderately plagioclase phyric basalt, dark gray (7.5YR N4/0), fine grained, plagioclase phenocrysts 3–5%, anhedral (resorbed), 3–15 mm, fresh to moderately altered. <1% unfilled vesicles in variolitic zones. <1 mm.

0–3 and 40–42 cm. Variolitic zones.

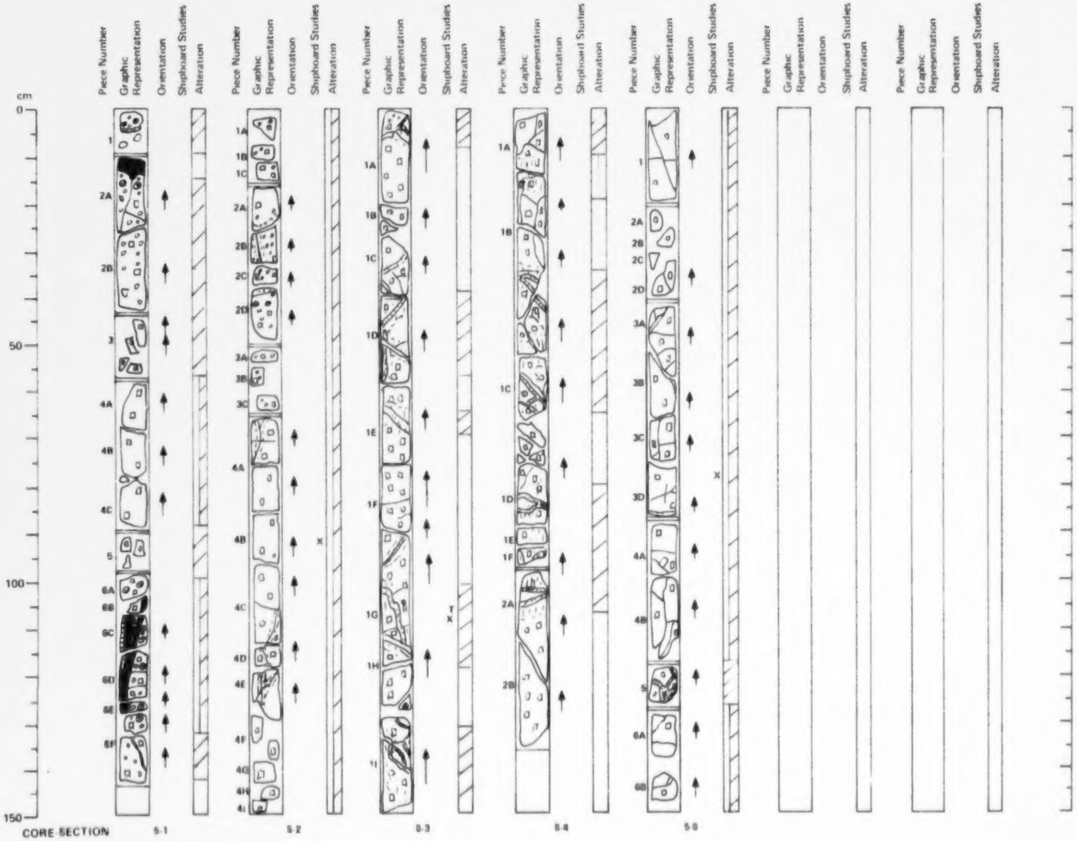

SITE 562 CORE 5 Depth 277.0–286.0 m

SECTION 1

PLAGIOCLASE PHYRIC PILLOW BASALT

0–142 cm: Moderately plagioclase-phyric fine grained basalt; color dark gray (7.5YR N4/0). Subhedral to round, resorbed plagioclase (~2–5 vol. %), (size up to 1 cm). Rock is fresh to moderately altered. Vesicles are abundant in upper parts of pillows (10–40 and 107–142 cm), shape: round, size <1.5 mm, filling: calcite or clay, some empty.

10–14 and 104–127 cm: Fresh black glass rinds of pillows, only weakly palagonitized along fractures. Variolitic zones occur close to glass and are moderately altered (color brown — 10YR 5/3). Few calcite-filled veins occur in Pieces 1, 6C and D.

SECTION 2

0–38 cm: PLAGIOCLASE PHYRIC (PILLOW?) BASALT. Moderately plagioclase-phyric basalt, color dark gray (7.5YR 5/3); contains subhedral to rounded plagioclase phenocrysts (size: <1 cm, abundance ~3 vol. %). Calcite filled vesicles increase at bottom (Pieces 2B and C). Piece 2C shows also irregular vesicles (<1 cm), partly calcite coated.

grained; color dark gray (7.5YR N4/0). Subhedral to rounded, resorbed plagioclase phenocrysts (~2–5 vol. %) (size: <1 cm). Basalt is fairly fresh except a small zone parallel to fractures. Vesicles are common in the upper part (39 to 65 cm) and decrease to bottom. They are mostly empty or just coated with some clay mineral.

39–40 cm: At the top of Piece 2D occurs thin (1 cm) layer of pinkish gray (7.5YR N6/2) limestone with angular palagonite fragments (size 1 to 6 mm). The basalt of Piece 2D shows variolitic transition from aphanitic to fine grained basalt downward. From 39 cm downward basalt looks more massive than above.

SECTION 3

MODERATELY PLAGIOCLASE PHYRIC MASSIVE BASALT

0–142 cm: Gray (7.5YR N5); fine grained plagioclase phyric basalt fairly fresh to moderately altered to grayish brown (2.5Y 5/2) along fractures. Some larger fractures are filled with pinkish gray (7.5YR 7/2) or light brown (7.5YR 6/4) limestone.

Some smaller fractures filled with calcite, particularly at 120–136 cm.

2–3% plagioclase phenocryts (3–7 mm, up to 10 mm) prisms or equant in shape.

30–40% plagioclase needles (2–3 mm) randomly oriented.

<1% round and irregular vesicles (1–2 mm) filled with greenish clay(?).

SECTION 4

MODERATELY PLAGIOCLASE PHYRIC MASSIVE BASALT

Similar to Section 3. Generally more altered than Section 3, but otherwise similar.

78–81 cm: Veins filled with pinkish gray (5YR 7/2) limestone.

Minor calcite veinlets.

SECTION 5

0–117 cm: PLAGIOCLASE PHYRIC BASALT. Moderately plagioclase-phyric fine grained basalt. Description as above. Few plagioclase phenocrysts coarser than 1 cm (<1.5 cm). No visible vesicles at 85 cm occurs pinkish gray limestone between sparry calcite and basalt.

At 117 cm: end of massive basalt.

118–126 cm: BASALT BRECCIA PIECE. Highly fractured and calcite cemented plagioclase-phyric basalt and palagonite. Variolites in basalt clasts <1 mm. Few vesicles occur: empty or calcite or clay filling.

128–150 cm: PLAGIOCLASE PHYRIC BASALT. Moderately plagioclase-phyric basalt, fine grained, dark gray (7.5YR N5/0) ~5% plagioclase phenocrysts. They are subhedral to rounded, resorbed. No vesicles.

READEX FICHE
best copy available

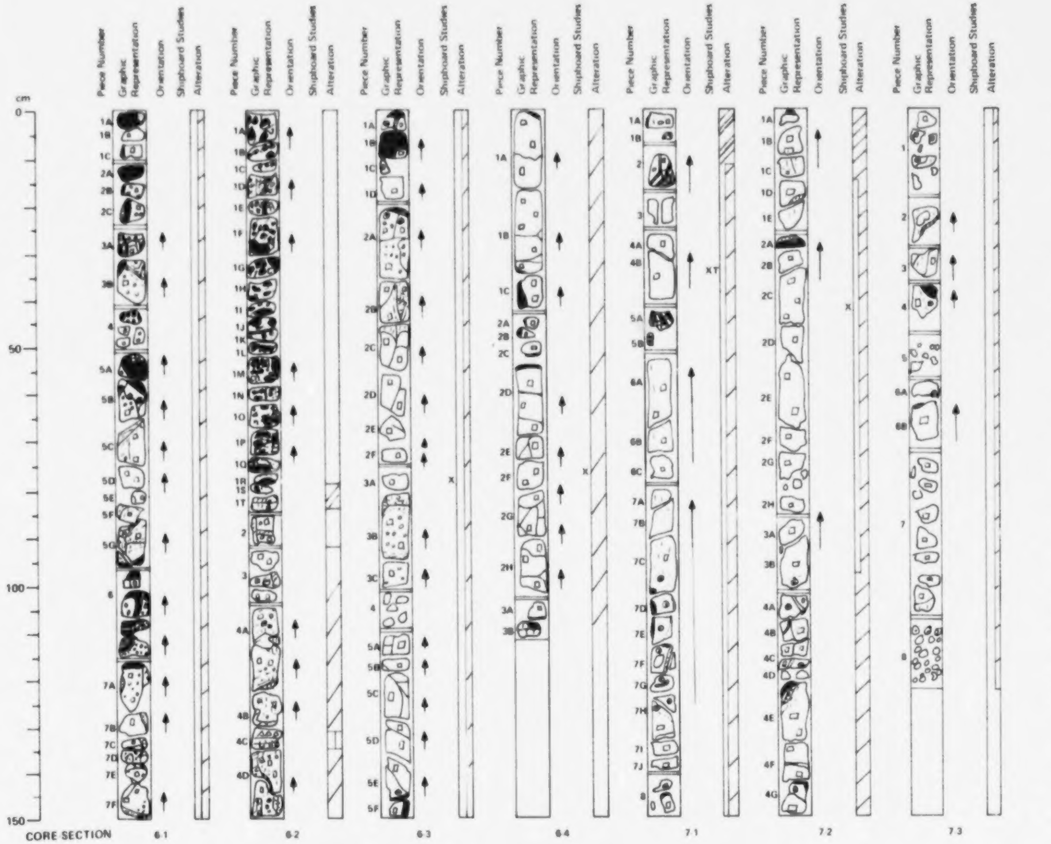

SITE 562, CORE 6 Depth 286.0–295.0 m

SECTION 1

PLAGIOCLASE PHYRIC PILLOW BASALT AND BASALT BRECCIA (+ HYALOCLASTITE?)

0–50 cm: Fragments of moderately plagioclase phyric basalt, fine grained. All pieces are from black aphanitic zone close to chilled glass rind and from glass rind. Vesicles are common, round (≤1.5 mm in diameter) and mostly empty. The glass shows some minor palagonitization along fractures.

Piece 3A: Shows basalt breccia with some altered glass clasts. Shape: rounded and angular, size: 15 mm to a few mm. Matrix is very pale brown (10YR 8/3) limestone and calcite.

52–95 cm: Separate pillow of moderately plagioclase-phyric, fine grained basalt, color: dark gray (2.5Y N4/0) to grayish brown (2.5YN 5/2) in altered zones close to calcite filled fractures. Plagioclase (2–3 vol. %) subhedral to rounded, resorbed, size < 8 mm. Vesicles are mostly empty.

97–150 cm: Pillow basalt fragments and interpillow breccia (hyaloclastite). Basalt is plagioclase phyric (see above description). Breccia contains angular glass and some aphanitic basalt clasts (< 1 cm). Some limestone matrix and finally calcite cement.

SECTION 2

SPARSELY PLAGIOCLASE PHYRIC PILLOW BASALT AND GLASS CLASTS AND BRECCIA

0–13 and 22–73 cm: Black glass clasts and breccia in calcite cement ( ) with limestone ( ) in some places (51–56 cm). Mostly fresh or altered to yellow (10YR 7/6) to reddish yellow (7.5YR 6/8) dark reddish brown (5YR 3/2) clays around edges or along fractures. 2–3% plagioclase glomerocrysts (2–5 mm) in the glass. 2–3% rounded empty vesicles (1–2 mm) in glass.

130–132 cm: Highly altered glass clasts in limestone matrix.

12–20 cm: Variolitic pillow edges with glass clast rims in calcite.

75–130 and 133–147 cm: Sparsely plagioclase phyric pillow basalts with brown (10YR 5/3) variolitic zones grading through black aphanitic basalt. Calcite and limestone in fractures. Plagioclase phenocrysts as in glass. Vesicles as in glass with some calcite filled in pillow interiors.

SECTION 3

PLAGIOCLASE PHYRIC PILLOW BASALT

0–19 cm: Fragments of moderately to sparsely plagioclase phyric basalt. Pieces 1C and D fine grained, gray (2.5Y N6/0). Pieces 1A and B aphanitic and chilled rind (glass). Plagioclase subhedral to rounded, resorbed (size < 5 mm). Minor palagonitization along fractures.

21–150 cm: Pillow basalt, moderately plagioclase phyric, color gray (2.5Y N6/0). Plagioclase up to 4 vol. %, size < 7 mm. Vesicles are abundant between 22–35 and 80–100 cm, filled with clay and calcite. Basalt is fairly fresh except narrow zones along fractures. Fresh glass at top and bottom.

SECTION 4

PLAGIOCLASE PHYRIC PILLOW BASALT

0–110 cm: Strongly plagioclase phyric, fine grained basalt, color gray (2.5Y N5/0) to grayish brown in altered parts. Plagioclase phenocrysts are abundant (10–15 vol. %), size: < 8 mm, shape: subhedral to rounded, resorbed. Vesicles are rare to absent. Some narrow veinlets are filled with calcite cement or limestone. Fresh glass at 0–2, 33–55, and 107–109 cm. Lowermost piece (3B) mainly consists of pinkish gray (7.5YR 7/2) limestone and shows fresh glass, too.

SITE 562, CORE 7 Depth 295.0–300.0 m

SECTION 1

MODERATE–STRONGLY PLAGIOCLASE PHYRIC PILLOW BASALT

0–150 cm

Moderate to strongly plagioclase phyric pillow basalt gray (2.5Y N5/0) altered* to brownish yellow (10YR 6/6) in fractures, pillow edges near calcite veins and vesicular zones.

Plagioclase phenocrysts are abundant grading from moderately to strongly phyric down core (5–10%) 4–9 mm in diameter, glomerocrysts and/or rounded prisms.

Alteration present as noted above.*

Variolitic sequence where shown. Glassy rims grade into black (10YR 2/1) aphanitic plagioclase phyric basalt through variolite zone (10YR 6/6) grading down to gray plagioclase-phyric basalt. Plagioclase phenosrysts are observed in all phases cited except glass.

Vesicles sparsely scattered, rounded < 1–2 mm in diameter. Filled with calcite predominantly, some clays noted. Few immediately adjacent to glass are empty.

Glass concentrated in Pieces 1A, 2, 5A, 7C–E and rim of a piece in 8.

SECTION 2

MODERATELY–STRONGLY PLAGIOCLASE PHYRIC PILLOW BASALT

0–150 cm: Same as for Section 1, exceptions as noted.

35–70 cm: Dark brownish green patches of material. Possibly alteration of olivine. May be remnants of olivine visible in thin section.

SECTION 3

MODERATELY PLAGIOCLASE PHYRIC PILLOW BASALT

0–121 cm

Same as for Section 1, with exceptions as noted.

Plagioclase phenocrysts larger 4–8 mm in larger pieces of basalt. Smaller (2–4 mm) in smaller rock fragments.

Alteration of basalt from gray (2.5Y N5/0) to brownish yellow (10YR 6/6 + gray 2.5Y N5/0) hued basalt. Not as pronounced due to smaller size of rocks. Still present at fractures and pillow edges.

Variolitic sequence (outlined in Section 1) present as noted.

Vesicles sparsely scattered round, < 1–2 mm in diameter. Calcite or clay lined, some empty.

Basalts are smaller pieces and clast fragments than previously cited in Sections 1 and 2. "Pieces" 1, 7, and 8 are good examples of this.

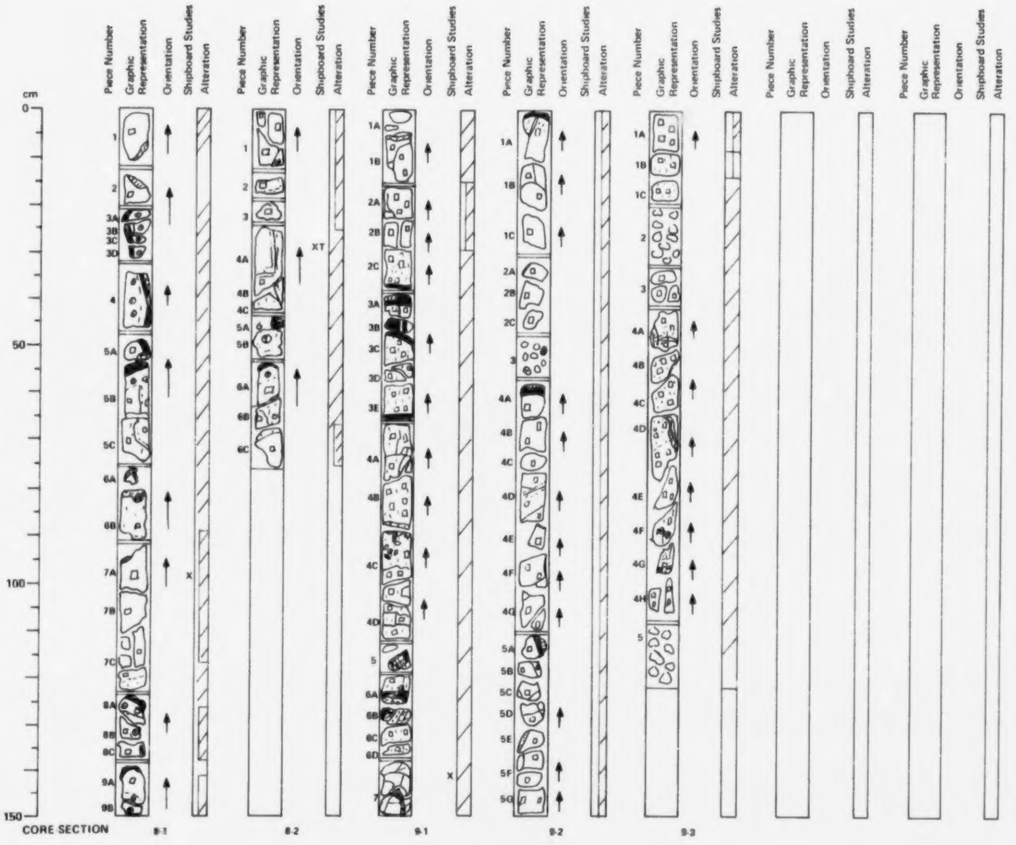

SITE 562, CORE 8 Depth 300.0–304.0 m

SECTION 1

SPARSELY PLAGIOCLASE PHYRIC PILLOW BASALT SEQUENCE

0–150 cm

Sparsely plagioclase phyric pillow basalt in sequence with glass – aphanitic plagioclase phyric – variolitic – plagioclase-phyric basalt. Generally gray (2.5YR N5/0); alteration present adjacent to fractures and pillow rims.

Plagioclase phenocrysts are present in various degrees of frequency, from nearly absent (Pieces 2, 8B and C, and 9A) to sparsely (Pieces 7A–C and 5B–C) to moderate (Pieces 1, 3, 4, and 5A). Overall, core is sparsely phyric: 2–9 mm diameter rounded prisms and/or glomerocrysts.

Alteration present as noted adjacent to calcite rinds, veins, and to rock fractures and pillow edges. Variolitic alteration as designated.

Variolitic sequence where shown. Interpillow glass – black aphanitic plagioclase-phyric basalt (10YR 2/1) – variolitic basalt, yellow brown "hued gray" (10YR 6/6) – 2.5Y N5/0 zone – gray (2.5Y N6/0) plagioclase phyric basalt. Plagioclase phenocrysts noted in all phases up to intersecting glasses.

Vesicles sparsely scattered throughout rock, mainly concentrated near pillow margins (variolitic sequence). Vesicles rounded <1–2 mm in diameter. Filled with calcite, clays are empty.

Glass concentrated in Pieces 3, 4, 5A and B, 8A, and 9A. Centimeters and/or volume.

SECTION 2

SPARSELY PLAGIOCLASE PHYRIC PILLOW BASALT

Sparsely plagioclase phyric pillow basalt sequence gray (2.5Y N5/0). Same as in Section 1. Exceptions noted.

Plagioclase phenocrysts 1–5 mm in diameter, nearly absent in Pieces 1, 2, and 6C and sections of others, all others are sparsely plagioclase phyric.

Alteration as in Section 1 to yellowish brown hued gray (10YR 6/6) plagioclase phyric.

Variolitic sequence as noted in Section 1 and indicated left.

Vesicles sparsely scattered, rounded <1–1 mm in diameter one-half empty, one-half clay and/or calcite filled.

Glass as indicated (Pieces 5A and 6A strong glass rims).

SITE 562, CORE 9 Depth 304.0–313.0 m

SECTION 1

SPARSELY TO MODERATELY PLAGIOCLASE PHYRIC BASALT PILLOWS

0–113 cm

Moderately plagioclase phyric pillow basalt gray (2.5Y N5), fine grained.

Glass margins almost right next to fine grained basalt with very narrow (1–2 mm) zones of black aphanitic basalt and/or very tiny (<1 mm) variolites (or no aphanitic basalt or variolities are visible at all).

3–5% plagioclase glomerocrysts (3–10 mm) in pillow interiors and glass rims.

Basalt fairly fresh gray (as above) to moderately altered (grayish brown – 2.5Y 5/2) especially along pillow edges next to glass rims or along fractures.

< 1% rounded empty vesicles (<1 mm) scattered.

85–92 cm: <1% irregular calcite-filled vesicles (1–6 mm). Calcite and reddish brown (5YR 5/4) and light reddish brown (5YR 6/3) limestone in fractures.

120–150 cm: Aphyric pillow basalt, finer grained, colors as above. Calcite and limestone in fractures. < 1% irregular, calcite filled vesicles (2–5 mm), black.

115–118 cm: One piece of fresh to moderately altered (yellowish red (5YR 4/6) palagonite) glass clasts in pinkish gray (5YR 7/2) limestone matrix.

0–150 cm: Plagioclase-phyric pillow basalt: fine grained, color: gray (2.5Y N5/0). Plagioclase phenocrysts up to 8%: shape: subangular to round, resorbed: size: < 8 mm. Vesicles are rare and mostly empty (a few filled with calcite).

0–2, 57–60, and 111–116 cm: Chilled glass rinds accompanied by very narrow variolitic zone (variolites < 0.5 mm).

Some pieces show calcite cemented veins (shown ▨).

SECTION 3

MODERATELY PLAGIOCLASE PHYRIC PILLOW BASALT

0–150 cm: Plagioclase phyric basalt gray (2.5Y N5), fine grained like Section 2.

3–5% plagioclase glomerocrysts (1–10 mm), fairly fresh (gray as above) to moderately altered (grayish brown – 5/2).

9–11 cm: One piece very strongly altered groundmass completely light grayish brown (2.5Y 6/2) in color with plagioclase phenocrysts.

< 1% rounded, empty vesicles (1–2 mm) scattered.

< 1% irregular and rounded vesicles (1–3 mm). Calcite and limestone in veins.

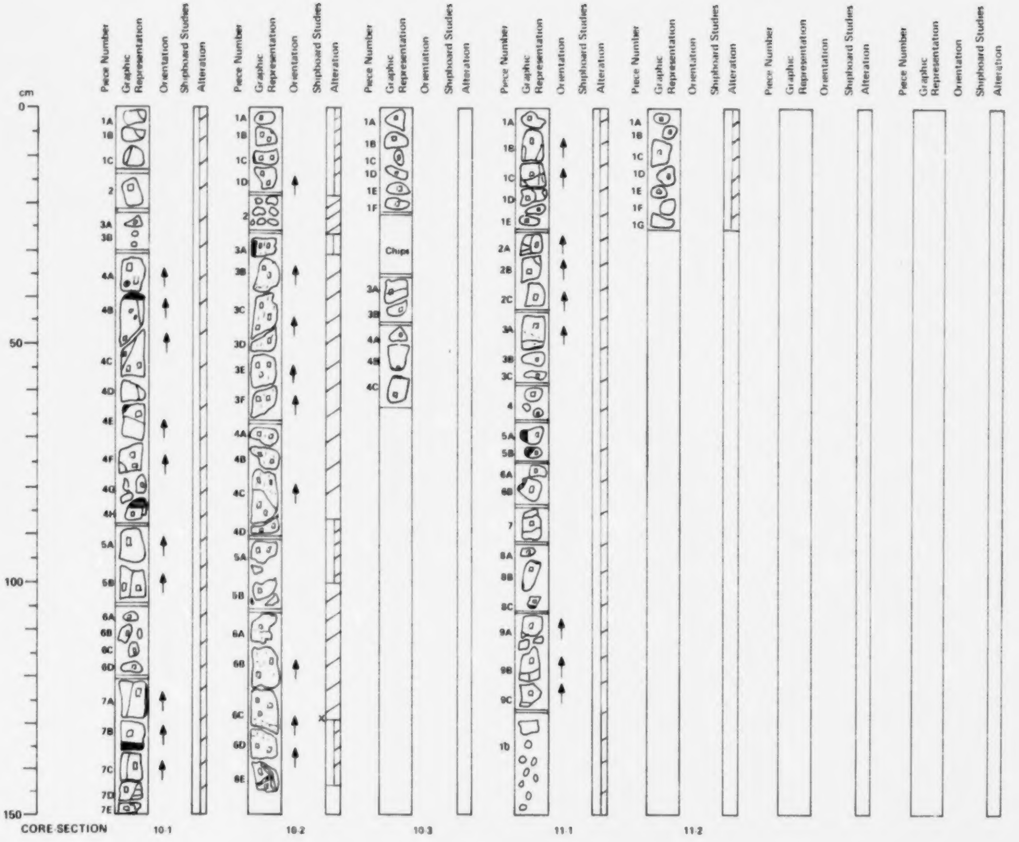
cm
0
50
100
150
CORE SECTION
Piece Number
Graphic Representation
Orientation
Shipboard Studies
Alteration
10-1
10-2
10-3
11-1
11-2
1A 1B 1C 2 3A 3B 4A 4B 4C 4D 4E 4F 4G 4H 5A 5B 6A 6B 6C 6D 7A 7B 7C 7D 7E
1A 1B 1C 1D 2 3A 3B 3C 3D 3E 3F 4A 4B 4C 4D 5A 5B 6A 6B 6C 6D 6E
1A 1B 1C 1D 1E 1F Chips 3A 3B 4A 4B 4C
1A 1B 1C 1D 1E 2A 2B 2C 3A 3B 3C 4 5A 5B 6A 6B 7 8A 8B 8C 9A 9B 9C 10
1A 1B 1C 1D 1E 1F 1G

SITE 562 CORE 10 Depth 313.0–322.0 m

SECTION 1

PLAGIOCLASE PHYRIC PILLOW BASALT

0–150 cm Moderately plagioclase phyric to aphyric, fine grained basalt, color gray (7.5YR N5/0); plagioclase phenocrysts up to 1 cm, subhedral to rounded to resorbed.

The following intervals of this section are aphyric to sparsely plagioclase phyric: 0–13, 40–50, and 57–62 cm. Vesicles only occur between 40–55 cm, rare, calcite filled, and <1 mm.

Fresh glass at 38–39, 39–41, 63–65, 82–84, and 133–135 cm.

SECTION 2

MODERATELY PLAGIOCLASE PHYRIC PILLOW BASALT

0–150 cm Fine grained, gray (2.5Y N5) moderately plagioclase phyric pillow basalt.

~ 5% plagioclase phenocrysts (2–10 mm), fairly fresh (gray as above) basalt to moderately altered (light olive brown – 2.5Y 5/5) along edges or fractures and some pillow interiors.

Calcite and pink (5YR 7/4) limestone in veins.

30–33 cm Fresh black glass rims.

SECTION 3

PLAGIOCLASE PHYRIC BASALT

0–62 cm Moderately to sparsely plagioclase phyric basalt, fine grained, color gray (7.5YR N5/0).

Plagioclase phenocrysts (3–5 vol. %) but rare to absent in Piece 4B.

Fresh glass at 55–58 cm.

SITE 562, CORE 11 Depth 322.0–331.0 m

SECTION 1

PLAGIOCLASE PHYRIC PILLOW BASALT

0–150 cm Sparsely to moderately plagioclase phyric, fine grained basalt, color gray (7.5YR N5/0). Plagioclase phenocrysts (2–4%) up to 7 mm.

Fresh glass rinds at 50–51, 66–74, and 104–105 cm.

SECTION 2

0–25 cm PLAGIOCLASE PHYRIC BASALT. See above descriptions.

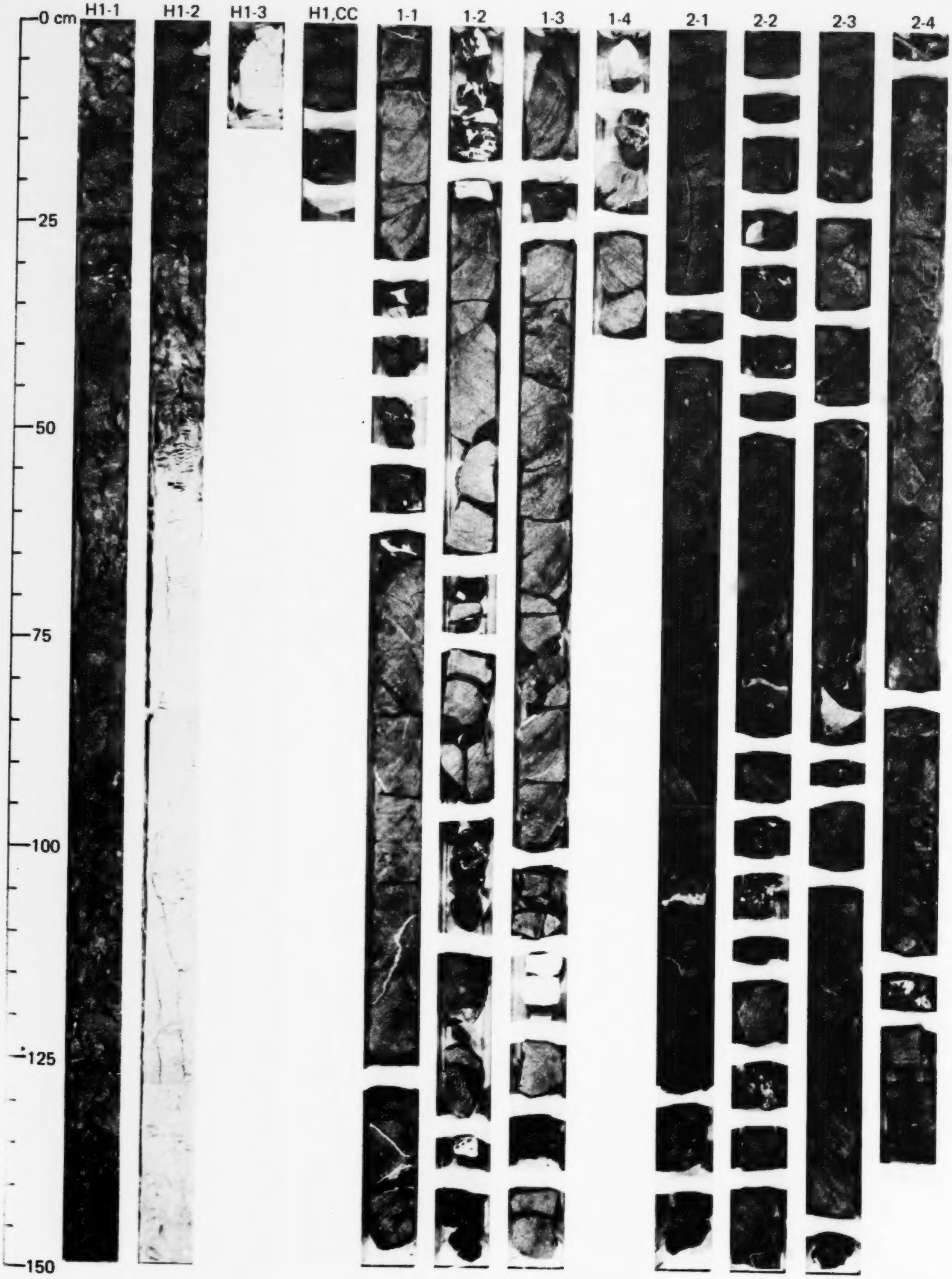
0 cm
25
50
75
100
125
150
H1-1
H1-2
H1-3
H1,CC
1-1
1-2
1-3
1-4
2-1
2-2
2-3
2-4

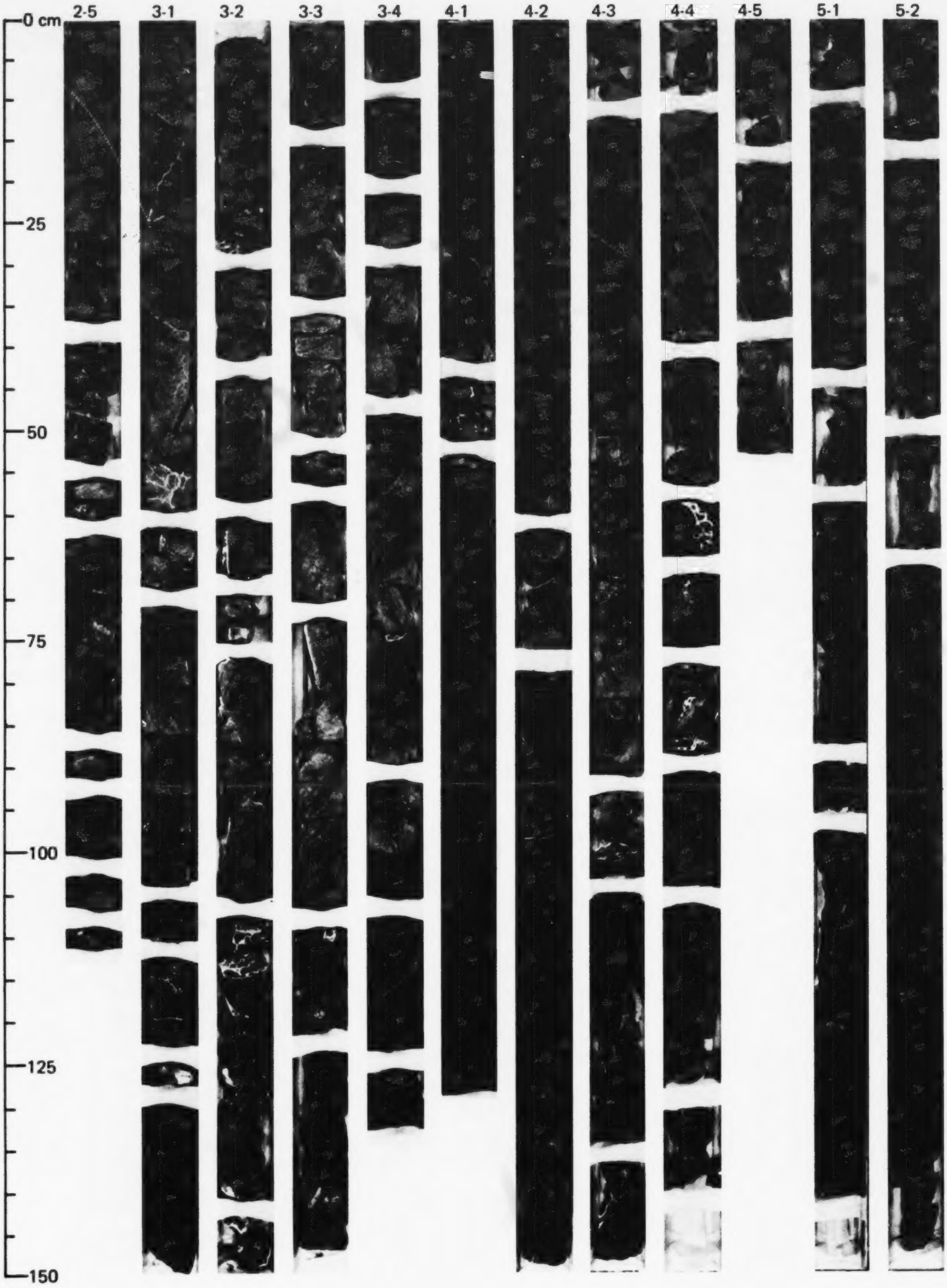
0 cm
25
50
75
100
125
150
2-5
3-1
3-2
3-3
3-4
4-1
4-2
4-3
4-4
4-5
5-1
5-2

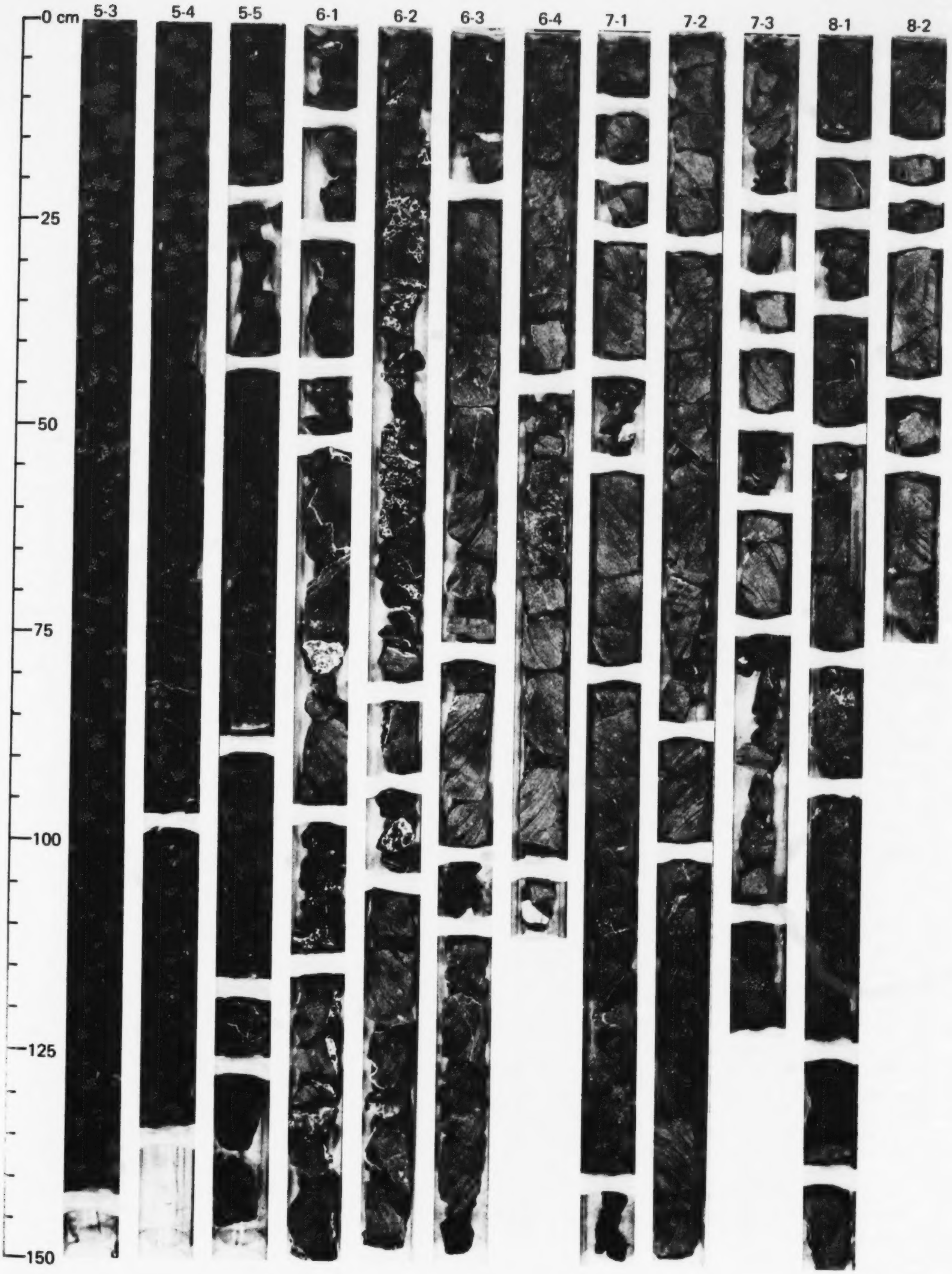
0 cm
25
50
75
100
125
150
5-3
5-4
5-5
6-1
6-2
6-3
6-4
7-1
7-2
7-3
8-1
8-2

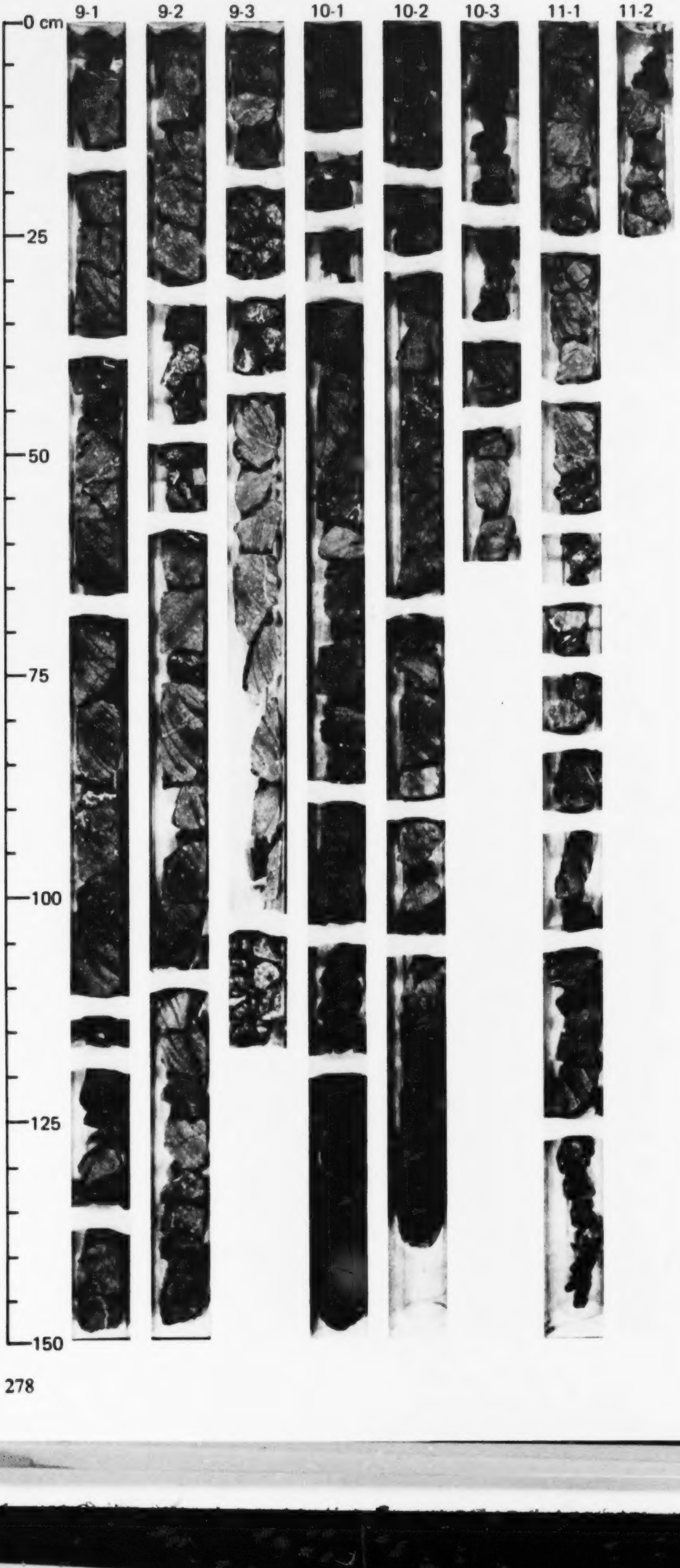
9-1
9-2
9-3
10-1
10-2
10-3
11-1
11-2
0 cm
25
50
75
100
125
150

12. SITE 563[1]

Shipboard Scientific Party[2]

HOLE 563

Date occupied: 24 October 1981

Date departed: 28 October 1981

Time on hole: 77 hr.

Position (latitude; longitude): 33°38.53′N; 43°46.04′W

Water depth (sea level; corrected m, echo-sounding): 3786

Water depth (rig floor; corrected m, echo-sounding): 3796

Bottom felt (m, drill pipe): 3796

Penetration (m): 382.5

Number of cores: 25

Total length of cored section (m): 226

Total core recovered (m): 190.6

Core recovery (%): 84

Oldest sediment cored:
Depth sub-bottom (m): 364.5
Nature: Limestone
Age: early Oligocene

Basement:
Depth sub-bottom (m): 364.5
Nature: Basalt

Principal results: Hole 563 (MAR-11) was drilled on Anomaly 13 on the west flank of the Mid-Atlantic Ridge about 60 mi. south of Hayes Fracture Zone (Fig. 1).

The sediments were washed down to 156.5 m and then rotary cored down to 364 m where the basement was felt. The entire recovered section of sediment consists of calcareous pelagic ooze. Two sediment units, similar to those at Site 558, are recognized and their boundary occurs roughly at the same age level as at Site 558. The sediment accumulation rates of each unit are similar to those of Site 558. However, the lithologic differences between the two units are more distinct at Site 558 than at Site 563.

The basement was only cored for 18.5 m because of difficult drilling conditions and premature bit failure. The recovered samples consist of one petrographic unit of sparsely plagioclase phyric basalts presenting a depleted character (Nb = 1.7 ppm, Zr = 55 ppm, $(Nb/Zr)_{ch} \sim 0.3$).

No downhole measurements were taken at this site.

OPERATIONS

Approach to Site

From Site 562, the *Challenger* headed northwest along a flow line toward Site MAR-11 located on Anomaly 13 south of the Hayes Fracture Zone. Around 0100Z, 25 October (Fig. 2), the *Challenger* crossed a buried basement ridge that had several potential sites. In particular, a site crossed at 0108Z (Fig. 3) had the right combination of relatively smooth basement and less than 0.4 s of sediments. At 0122Z the *Challenger* reversed course and the beacon was dropped on Site 563 at 0152Z.

On-Site Operations

Hole 563 was spudded at 1000Z, 25 October, in 3796 m of water. The sediments were washed to a depth of 156.5 m sub-bottom, where continuous rotary coring was started. Between 1330Z, 25 October and 1852Z, 26 October, 22 sediment cores were recovered (Table 1). Hard rock was hit at a depth of 364 m sub-bottom. Drilling within basement was extremely slow; it took 10 hr. to cut Core 25. While we were trying to retrieve Core 25, the drill string became stuck, the drill bit released prematurely, and the core barrel fell out. The core barrel was eventually recovered, but the hole had to be abandoned. We decided to continue drilling at Site MAR-11 at a site approximately 5 or 10 mi. away. The drill string was pulled, and the *Challenger* was underway to Site 564 at 0530Z, 28 October.

LITHOLOGY

Rotary coring in Hole 563 (water depth 3630 m) was begun after 156.5 m were washed down and one wash core was retrieved. The stratigraphic position of Core 563-1 is very close to that of Core 588-1 (lower upper Miocene). The sedimentary section was cored continuously from 156.5 m down to lower Oligocene basement at 364.5 m, so that a section very similar to that in Hole 558 was recovered (Fig. 4). Plans to recover the younger section from 0 to 156.5 m with the hydraulic piston corer had to be aborted when the bit and core barrel were lost in the hole during the cutting of the third basalt core. We then decided to move to another site and wash down to basement.

Based on differences in color, small differences in carbonate content, and changes in lithification and sediment accumulation rates (Fig. 5), we could recognize

---

[1] Bougault, H., Cande, S. C., et al., *Init. Repts. DSDP*, 82: Washington (U.S. Govt. Printing Office).

[2] Henri Bougault (Co-Chief Scientist), IFREMER (formerly CNEXO), Centre de Brest, B.P. 337, 29273 Brest Cedex, France; Steven C. Cande (Co-Chief Scientist), Lamont-Doherty eological Observatory, Columbia University, Palisades, New York; Joyce Brannon, Department of Earth and Planetary Sciences, Washington University, St. Louis, Missouri; David M. hristie, Hawaii Institute of Geophysics, University of Hawaii at Manoa, Honolulu, Hawaii; urlene Clark, Department of Geology, Florida State University, Tallahassee, Florida; Doris . Curtis, Curtis and Echols, Geological Consultants, Houston, Texas; Natalie Drake, Deartment of Geology, University of Massachusetts, Amherst, Massachusetts; Dorothy Echs, Department of Earth and Planetary Sciences, Washington University, St. Louis, Missouri resent address: Curtis and Echols, Geological Consultants, 800 Anderson, Houston, Texas 401); Ian Ashley Hill, Department of Geology, University of Leicester, Leicester LE1 7RH, nited Kingdom; M. Javed Khan, Lamont-Doherty Geological Observatory, Columbia Unirsity, Palisades, New York (present address: Department of Geology, Peshawar University, shawar, Pakistan); William Mills, Deep Sea Drilling Project, Scripps Institution of Oceanraphy, La Jolla, California (present address: Ocean Drilling Program, Texas A&M Univery, College Station, Texas 77843); Rolf Neuser, Institut für Geologie, Ruhr UniversitätBoum, 4630 Bochum 1, Federal Republic of Germany; Marion Rideout, Graduate School of ceanography, University of Rhode Island, Kingston, Rhode Island (present address: Department of Geology, Rice University, P.O. Box 1892, Houston, Texas 77251); and Barry L. Weavr, Department of Geology, University of Leicester, Leicester, LE1 7RH, United Kingdom resent address: School of Geology and Geophysics, University of Oklahoma, Norman, klahoma 73019).

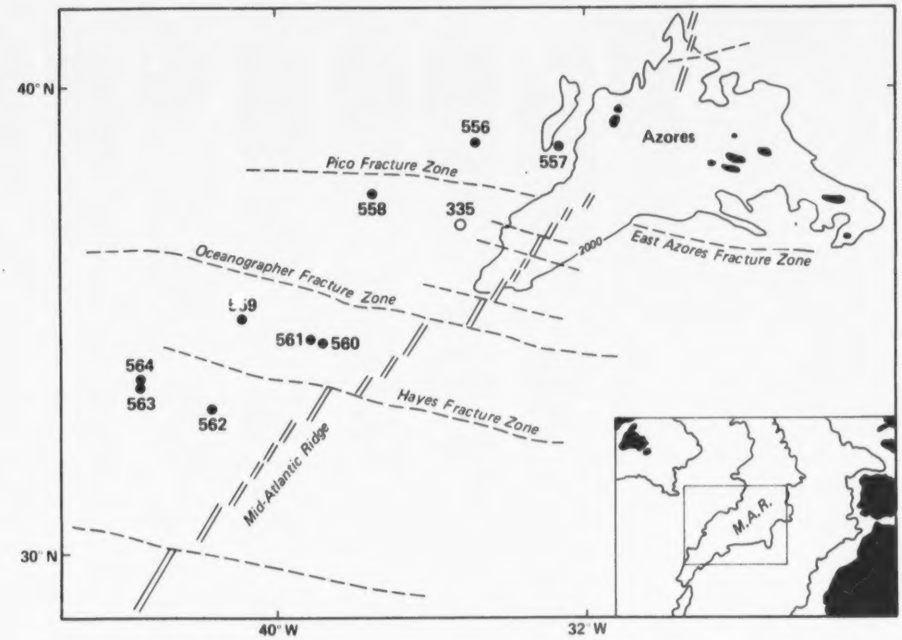
40° N
30° N
40° W
32° W
556
557
558
335
559
561
560
564
563
562
Azores
Pico Fracture Zone
Oceanographer Fracture Zone
Hayes Fracture Zone
East Azores Fracture Zone
Mid-Atlantic Ridge
2000
M.A.R.

Figure 1. Site location map, Leg 82.

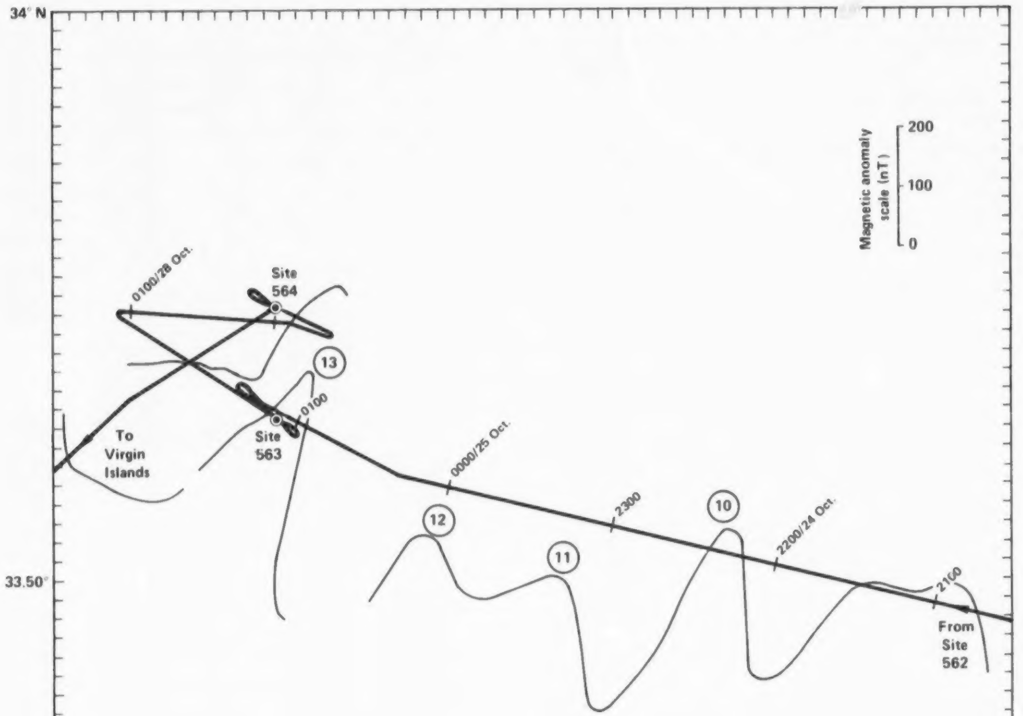

Figure 2. Approach and site survey tracks for Sites 563 and 564. Heavy line is the ship's track with hours marked in GMT. Thin line is the magnetic anomaly projected perpendicularly from ship's track. Circled numbers are anomalies based on work at Lamont-Doherty Geological Observatory.

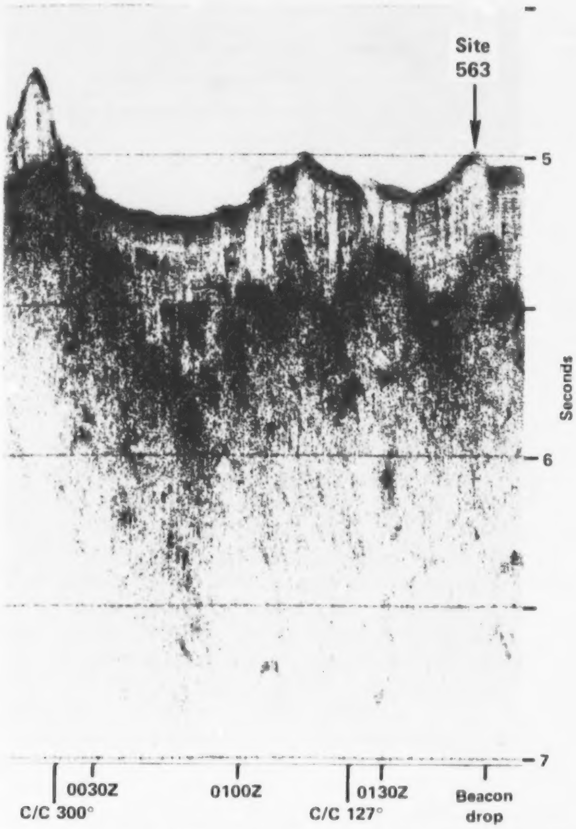

Figure 3. *Glomar Challenger* seismic profile of the approach to Site 563. C/C = course change. For location of profile, see Figure 2.

Table 1. Coring summary, Hole 563.

Core	Date (Oct. 1981)	Time (Z)	Depth from drill floor (m)	Depth below seafloor (m)	Length cored (m)	Length recovered (m)	Percent recovered
H1	25	1330	3796.0-3952.5	0.0-156.5	0.0	0.00	0
1	25	1508	3952.5-3962.0	156.5-166.0	9.5	4.52	48
2	25	1607	3962.0-3971.5	166.0-175.5	9.5	9.62	100+
3	25	1730	3971.5-3981.0	175.5-185.0	9.5	9.02	95
4	25	1845	3981.0-3990.5	185.0-194.5	9.5	5.01	53
5	25	2030	3990.5-4000.0	194.5-204.0	9.5	9.70	100+
6	25	2140	4000.0-4009.5	204.0-213.5	9.5	9.51	100+
7	25	2310	4009.5-4019.0	213.5-223.0	9.5	9.63	100+
8	26	0025	4019.0-4028.5	223.0-232.5	9.5	9.31	98
9	26	0150	4028.5-4038.0	232.5-242.0	9.5	9.58	100+
10	26	0300	4038.0-4047.5	242.0-251.5	9.5	9.63	100+
11	26	0405	4047.5-4057.0	251.5-261.0	9.5	6.31	66
12	26	0522	4057.0-4066.5	261.0-270.5	9.5	9.50	100
13	26	0714	4066.5-4076.0	270.5-280.0	9.5	7.47	79
14	26	0830	4076.0-4085.5	280.0-289.5	9.5	9.50	100
15	26	0942	4085.5-4095.0	289.5-299.0	9.5	9.48	99
16	26	1107	4095.0-4104.5	299.0-308.5	9.5	9.60	100+
17	26	1215	4104.5-4114.0	308.5-318.0	9.5	9.56	100+
18	26	1330	4114.0-4123.5	318.0-327.5	9.5	6.85	72
19	26	1450	4123.5-4133.0	327.5-337.0	9.5	3.66	39
20	26	1610	4133.0-4142.5	337.0-346.5	9.5	9.66	100+
21	26	1731	4142.5-4151.5	346.5-355.5	9.0	9.63	100+
22	26	1852	4151.5-4160.5	355.5-364.5	9.0	4.79	53
23	26	2318	4160.5-4162.5	364.5-366.5	2.0	1.20	60
24	27	0623	4162.5-4169.5	366.5-373.5	7.0	4.87	70
25	27	2115	4169.5-4178.5	373.5-382.5	9.0	2.95	33
					226.0	190.56	84

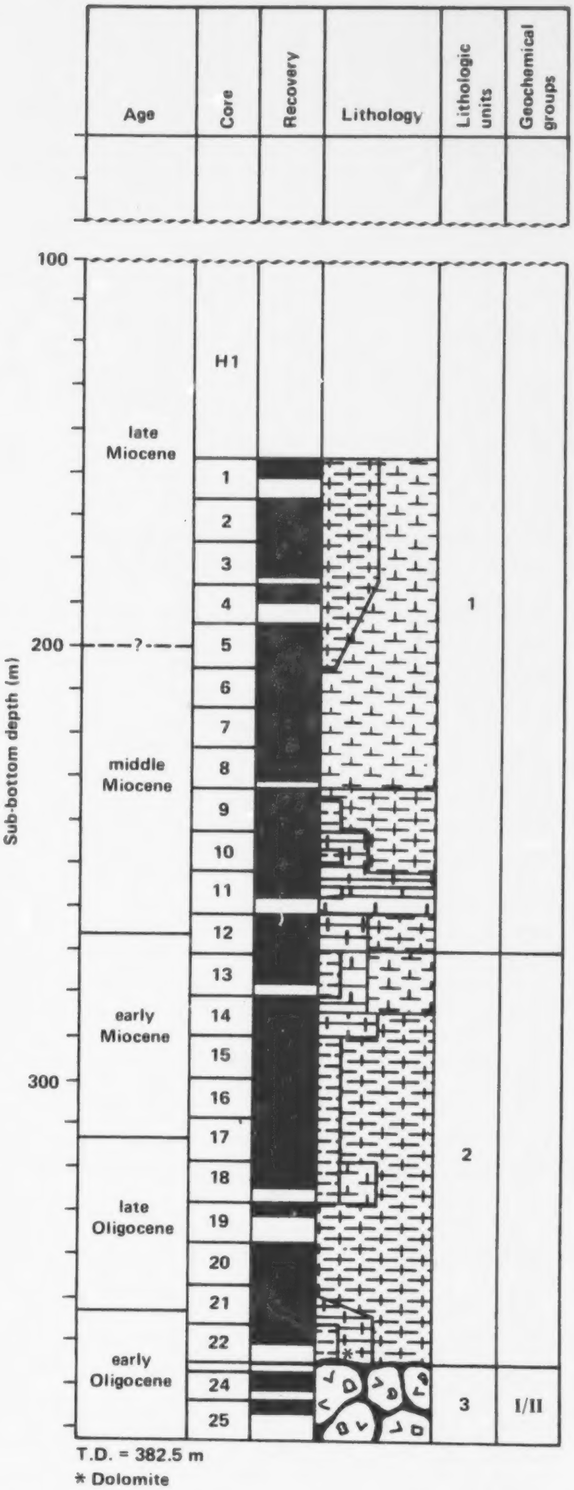
Age
Core
Recovery
Lithology
Lithologic units
Geochemical groups
100
200
300
Sub-bottom depth (m)
H1
late Miocene
?
middle Miocene
early Miocene
late Oligocene
early Oligocene
1
2
3
4
5
6
7
8
9
10
11
12
13
14
15
16
17
18
19
20
21
22
24
25
1
2
3
I/II
T.D. = 382.5 m
* Dolomite

Figure 4. Lithology column, Hole 563. Water depth is 3796.0 m. T.D. is total depth. Asterisk indicates dolomite. For lithologic symbols, see Explanatory Notes chapter, this volume.

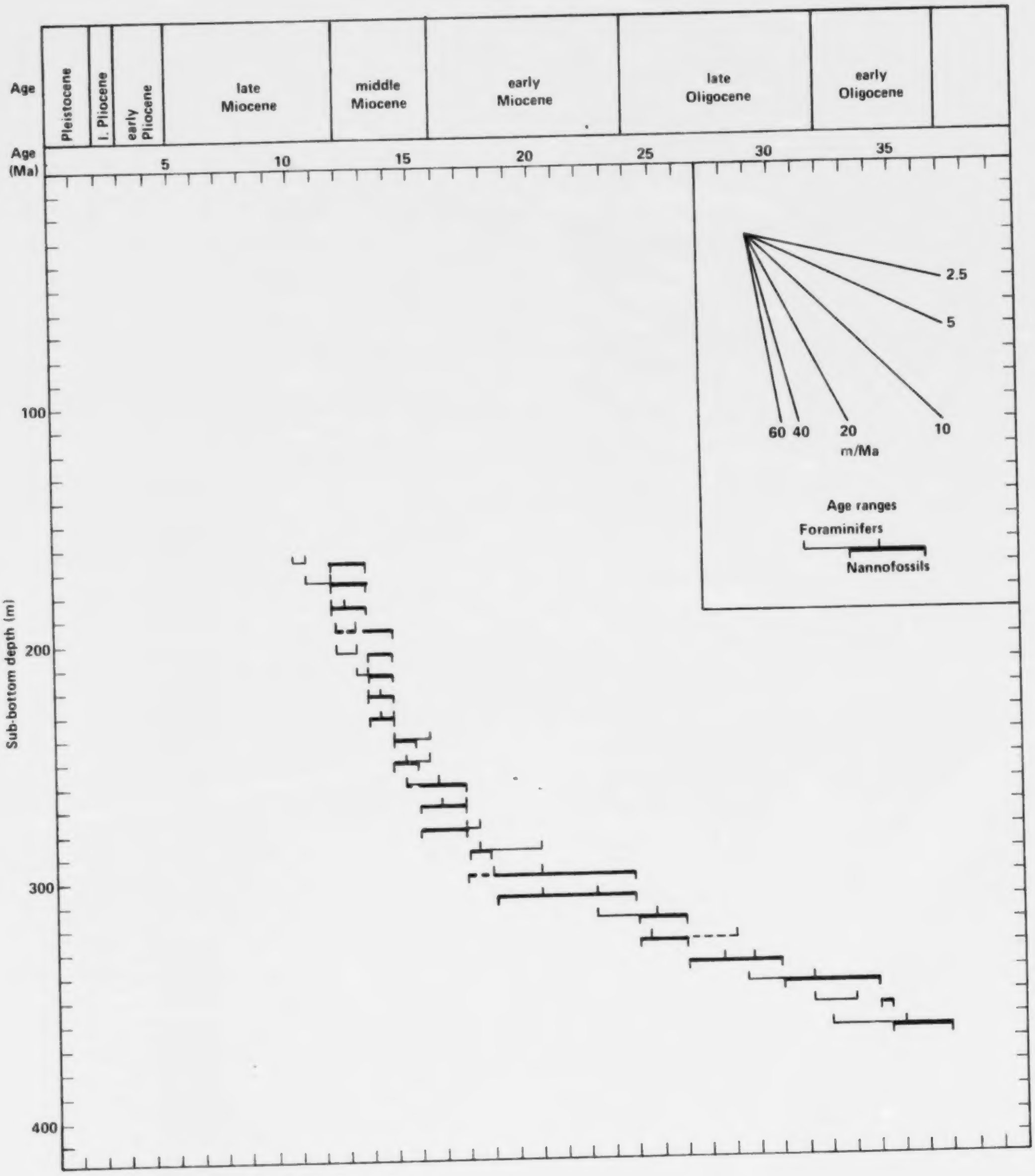

Figure 5. Sediment accumulation rates, Hole 563.

two units at this site. Unit 1 is a white to pale brown to yellowish brown ooze and chalk, of the middle to late Miocene, with an average sediment accumulation rate of 20 m/Ma. Unit 2 is a darker, pale brown to brown to yellowish brown, more-or-less clayey calcareous pelagic chalk and ooze of the early Miocene and Oligocene, with an average sediment accumulation rate of 5 m/Ma. We have summarized the sediment lithology of these two units in Table 2 and have described them in order of their depositional sequence beginning with Unit 2.

Unit 2

Open-ocean calcareous pelagic sedimentation began at this site immediately after the formation of the early Oligocene (34–37 Ma) ocean crust and continued throughout the Cenozoic. Lithologic Unit 2 of Hole 563 consists of 94 m of pelagic ooze and chalk deposited during the interval from the early Oligocene (34–37 Ma) through early Miocene (15–17 Ma). This unit extends from Core 22 (plus a 3-cm piece of limestone at the top of Core 23) up through Core 13. Throughout the unit, lithification alternates between chalk and ooze. Chalk is a dominant component only in Cores 21 and 22.

At the base of the sediment section is approximately 18 m (Core 563-22 and Sections 563-21-2 to 563-21-7) of dolomitic clayey chalk/ooze (Core 22) and dolomite-bearing chalk/ooze (Core 21), containing varying proportions of foraminifers and nannofossils. These lower

Table 2. Sediment lithology summary, Hole 563.

Interval	Unit designation	Depth interval (thickness) (m)	Main colors	Main lithology	Main components	Structure	Age
563-1-1 to 563-12, CC	1	156.5–270.5 (114.0)	White to pale brown	Foraminiferal-nannofossil ooze and chalk; nannofossil ooze	Nannofossils, foraminifers	Uniform with minor to moderate mottling	late/middle Miocene to middle/early Miocene
563-13-1 to 563-23-1, 3 cm	2	270.5–364.5 (94.0)	Pale brown to brown	Foraminiferal-nannofossil ooze and chalk; nannofossil ooze and chalk; clayey foraminiferal-nannofossil chalk and ooze	Nannofossils, foraminifers, clay	Uniform with minor mottling	middle/early Miocene to early Oligocene

Oligocene sediments are brown (10YR 5/3), massively bedded, and only very mildly bioturbated. They contain 87–92% carbonate (see Fig. 6), and their primary constituents are nannofossils (56–69%), foraminifers (5–24%), clay (7–15%), and authigenic dolomite rhombs (2–10%). The dolomite rhombs decrease from Core 563-22 up to Section 563-21-2, and then occur in trace quantities in Cores 20, 19, 14, 11, and 10. Zeolites are present in trace quantities except where we have estimated 1–5% (in Sections 563-21-3 and 563-21-4). Micronodules are present in trace quantities.

The greater part (80 m) of the sediments in Unit 2 (Section 563-21-1 up through Core 563-13; upper Oligocene through lower Miocene) consists of calcareous ooze/chalk and clayey calcareous ooze/chalk, with varying proportions of foraminifers and nannofossils. These beds are generally yellowish brown (10YR 5/4) and pale brown (10YR 6/3). Color changes are gradational and indistinct; hard layers are generally darker. The sediments are massively bedded. Bioturbation is minor to absent in Cores 21 through 17 and increases in Cores 16 through 13. Halo burrows are present in Cores 15 through 13. Average carbonate content is between 80 and 90%. The dominant sediment components are nannofossils (54–84%, but generally in the 60–70% range) and foraminifers, whose abundance is highly variable (5–25%, but generally more than 10%). Estimated clay content varies between 5 and 17%, but amounts less than 10% are found only in Cores 14 and 20. Zeolites occur in Cores 15 through 20 in quantities estimated between 1 and 5%. Micronodules are present in trace quantities, except for an estimated 2% in Core 18. Lithification alternates between ooze and chalk, but ooze is dominant in this interval.

The sediments in Cores 12 through 10, which we have assigned to Unit 1, have similar lithology but are transitional in composition, color, and lithification. Because of the similarity of their position in the lithologic sequence and their age, when compared to the sediments of Hole 558, we have placed these cores in Lithologic Unit 1.

Unit 1

Open-ocean calcareous pelagic sedimentation continued during the deposition of Unit 1 at Hole 563. The cored portion of the unit consists of 114 m (Cores 12 through 1) of pelagic ooze and chalk deposited during middle Miocene and early late Miocene times (10–13 to 15–17 Ma). Deposition of the unit began with a sequence transitional from Unit 2 that crosses the boundary between the lower and middle Miocene sections. This transitional sequence consists of 28.5 m of nannofossil and foraminiferal-nannofossil chalk/ooze, with a few clayey intervals. Colors alternate from very pale brown (10YR 7/3) to pale brown (10YR 6/3) to yellowish brown (10YR 5/4) with indistinct gradational contacts between the colors. Bedding is massive, and bioturbation is moderate; large halo burrows are common. Carbonate content is between 86 and 96%. The dominant sediment component (see Fig. 6) in the transitional sequence is nannofossils (66–84%), followed by foraminifers (2–25%, but mostly more than 10%), and clay (5–14%, but generally less than 10%). Manganese nodules 1 to 4 mm in diameter are present, as well as micronodules in trace amounts. Lithification alternates between ooze and chalk, but chalk predominates.

Above the transition zone, in Cores 9 through 1, the section consists of foraminiferal-nannofossil ooze and nannofossil ooze, with a few intervals of slightly clayey ooze. The dominant color is white grading with subtle color changes from mostly white (10YR 8/1–8/2) to light gray (10YR 7/1) and very pale brown (10YR 7/4 and 10YR 8/3), with the darker shades toward the bottom of Core 9. Mottling and bioturbation are minor to moderate, with more bioturbation in the darker intervals, especially in Core 9. Bedding is massive, but indistinct color banding may be related to bedding. Carbonate content is 87–97%; most values in the sediments above Core 9 are more than 90%. The principal sediment components are nannofossils, which vary in abundance between 69 and 93%. Foraminiferal abundances range between 1 and 15%; foraminifers appear to be more abun-

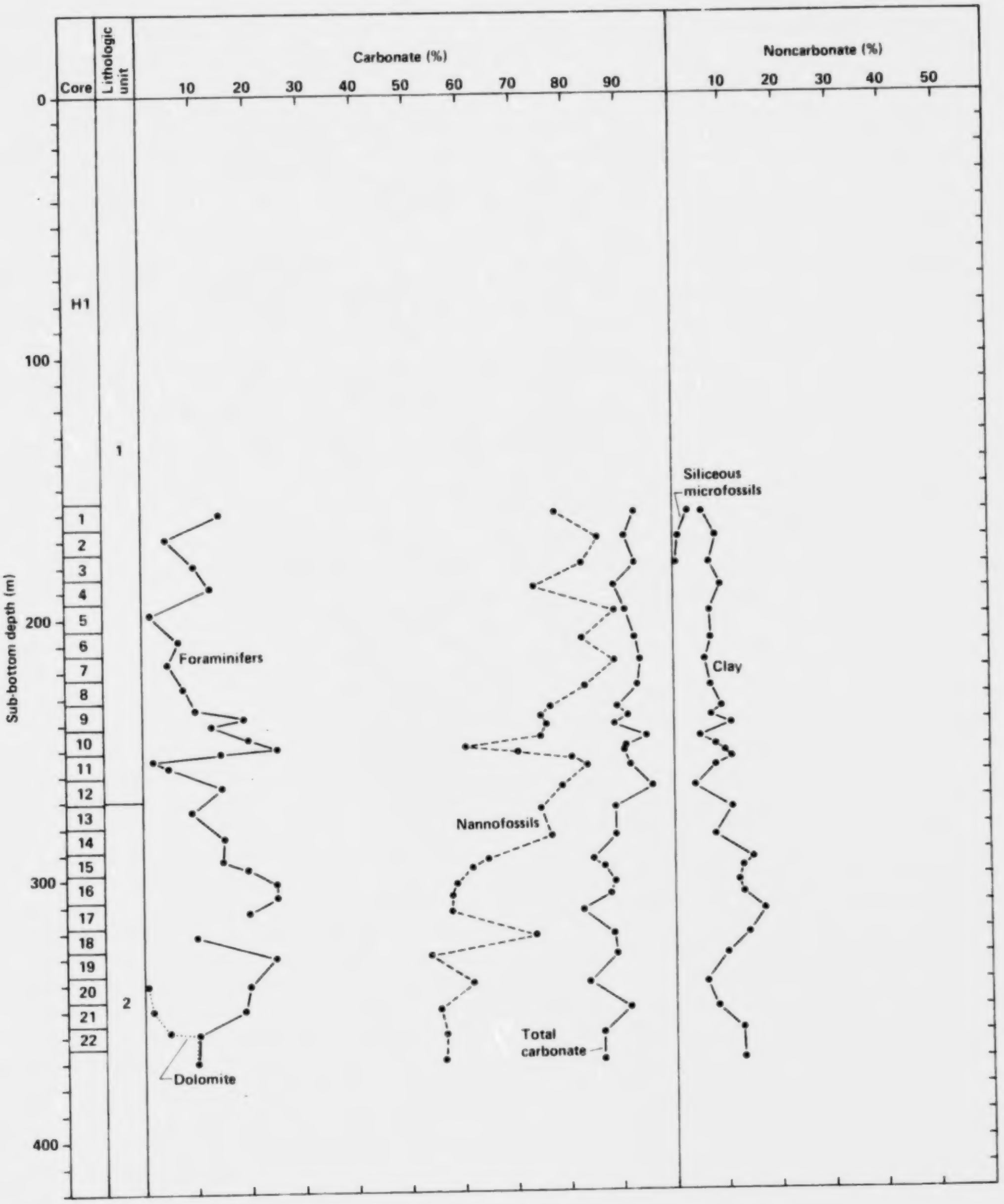

Figure 6. Percentage plot of major sediment components, Hole 563.

dant in Cores 1 through 5. Clay content is generally below 10%, except in short intervals in Core 4.

BIOSTRATIGRAPHY

Hole 563 was washed down to 156.5 m where 22 rotary sediment cores were taken above basement. Sediment was not obtained from Core 23, which reached basalt; consequently, the oldest part of the section was not recovered. Although hydraulic piston coring program was scheduled for this site to retrieve sediment from the top 156.5 m of the section, this part of the program was cancelled because of drilling problems.

Sediment recovered at this site is assigned to the lower upper Miocene to lower Oligocene based on data from calcareous nannofossils. Assignments based on planktonic foraminifers are upper Miocene to lower Oligocene. No hiatuses in the cored section are apparent; all major nannofossil zones of Okada and Bukry (1980) for this interval are recognized.

Calcareous nannofossils are abundant, and planktonic foraminifers are common to abundant throughout the section. Preservation in both microfossil groups ranges from good to moderate. Increased planktonic foraminiferal fragmentation is noted in the Miocene sections, which seems to indicate that increased dissolution occurred during the Miocene. Nannofossils are less well preserved in the lower Miocene and Oligocene sections.

Benthic foraminifers and ostracodes are diverse and well preserved throughout the section. Benthic foraminifers range in abundance from common to few.

Figure 7 shows the correlation of the foraminiferal and nannofossil zones encountered on Leg 82 (Holes 558, 558A, and 563) with Hole 334 drilled on Leg 37 (Aumento, Melson, et al., 1977). The lower upper Miocene section retrieved in Hole 334 approximates the intervals missing from sections cored on Leg 82; therefore we have a more complete sedimentary section than has previously been recovered from the Cenozoic of the mid-Atlantic between 20 and 40°N latitude.

Calcareous Nannofossils

Cores 1 through 3 contain *Discoaster hamatus* and are assigned to the *D. hamatus* Zone CN7 (NN9), which is upper middle to lower upper Miocene. Cores 2 and 3 contain common *Catinaster calyculus*, which may indicate the upper portion of the *Discoaster hamatus* Zone (Okada and Bukry, 1980).

The top of Core 4 (563-4-1, 80 cm) contains *C. coalitus* without *D. hamatus* and represents the rather short *C. coalitus* Zone CN6 (NN8), which is middle Miocene.

The interval from 563-4,CC through 563-8,CC is placed in the middle Miocene *D. exilis* Zone CN5 (NN6–NN7). This zone represents the interval between the first appearance of *D. hamatus* and the last appearance of *Sphenolithus heteromorphus.*

A lower middle Miocene CN4 (NN5) assignment is indicated for Cores 9 and 10 by the coexistence of *S. heteromorphus* and long-armed discoasters. Cores 11 through 12 contain *S. heteromorphus*, but the long-armed discoasters are rare to absent, suggesting that this interval belongs to the *Helicosphaera ampliaperta* Zone CN3 (NN3–NN4). *H. ampliaperta*, whose last occurrence marks the boundary between the *Sphenolithus heteromorphus* Zone and the *Helicosphaera ampliaperta* Zone, was not found at this site. The first appearance of long-armed discoasters must therefore be used to distinguish the two zones.

Because of the presence of *Sphenolithus belemnos* and *S. heteromorphus*, 563-12,CC is placed in the *S. be- mnos* Zone CN2 (NN2–NN3) and is lower Miocene. he core catcher of Core 14 is also assigned to this zone.

The Oligocene/Miocene boundary is located within e *Triquetrorhabdulus carinatus* Zone CN1 (NN1–NP25) presented by Cores 15 and 16. The characteristic spe- es for this interval are *T. carinatus, Cyclicargolithus oridanus*, and *Discoaster deflandrei.*

An upper Oligocene assignment is suggested for Cores 7 and 18 by the presence of *Sphenolithus ciperoensis.* *ciperoensis* is the index species for the *S. ciperoensis* one CP19 (NP24–NP25). Core 19 contains *S. disten- s* without *S. ciperoensis* and is placed in the upper Oli- ocene *S. distentus* Zone CP18 (NP23).

The core catcher of Core 20 represents the interval etween the last appearance of *Reticulofenestra umbilica* and the first appearance of *Sphenolithus distentus.* This sample is assigned to the *S. predistentus* Zone CP17 (NP23) and is lower Oligocene.

The core catcher of Core 21 contains *Reticulofenestra umbilica* without *Coccolithus formosus* and is placed in the *Helicosphaera reticulata* Zone, *Reticulofenestra hillae* Subzone CP16c (NP22). *R. umbilica* occurs with *Coccolithus formosus* in 563-22,CC, indicating that this sample should be assigned to the lower Oligocene *Coccolithus formosus* Subzone CN16b (NP21) of the *Helicosphaera ampliaperta* Zone.

Braarudosphaera rosa commonly occurs in Cores 20 through 22. The Oligocene presence of these species in the North Atlantic may in some way be environmentally related to the middle-Oligocene *Braarudosphaera* chalks in the South Atlantic.

Foraminifers

Miocene (upper)

Upper Miocene sediments were recovered in the core catcher of the Hole 563 wash core. The core catcher of Core 1 (the first rotary core) contained a white nannofossil-foraminiferal ooze with abundant *Globorotalia menardii* (*cultrata*) s.l., common *G. plesiotumida, Globoquadrina dehiscens, Orbulina universa, Sphaeroidinellopsis seminulina, S. subdehiscens*, and *Globigerina nepenthes*, which are indicative of foraminiferal Zone N15. Preservation is in general good, but there is a little fragmentation of the foraminiferal tests and some crystalline overgrowth on the globorotaliid forms. The core catchers of Cores 2 and 3 are lower upper Miocene. The composition of the faunas differ from 563-1,CC only in the proportional abundances of the species. *Globigerina nepenthes* is common in these samples, and, because the first appearance datum (FAD) of this species is 12 Ma, the samples are assigned to foraminiferal Zones N15–N14 (10–12 Ma). Fracturing and/or dissolution and overgrowth on many of the globorotaliid fauna are obvious. Sample 563-4,CC is assigned to N14; on the basis of the rare occurrence of *G. nepenthes* it is believed that this sample is close to the upper/middle Miocene boundary and is approximately 12 Ma old. The sample shows considerable dissolution and contains free manganese nodules and manganese infilling of the foraminifers.

Miocene (middle)

Sample 563-5,CC at 204 m is either lower N14 or upper N13. This sample contains abundant *Globoquadrina dehiscens*, and common *Sphaeroidinellopsis seminulina, S. subdehiscens*, and *Orbulina universa.* It is of particular interest because it contains the tiny spherical calcareous bodies reported from Zone N14 (558-5,CC at 205.5 m). These forms are recognized as *Bolboforma* and described as cysts or reproductive bodies of an unknown Miocene algae. Finding these little bodies in two Leg 82 holes 375 miles apart at the same depth and within the same stratigraphic horizon supports the theory that they may be regional markers in deep-sea sediments. The abundance and preservation of the forami-

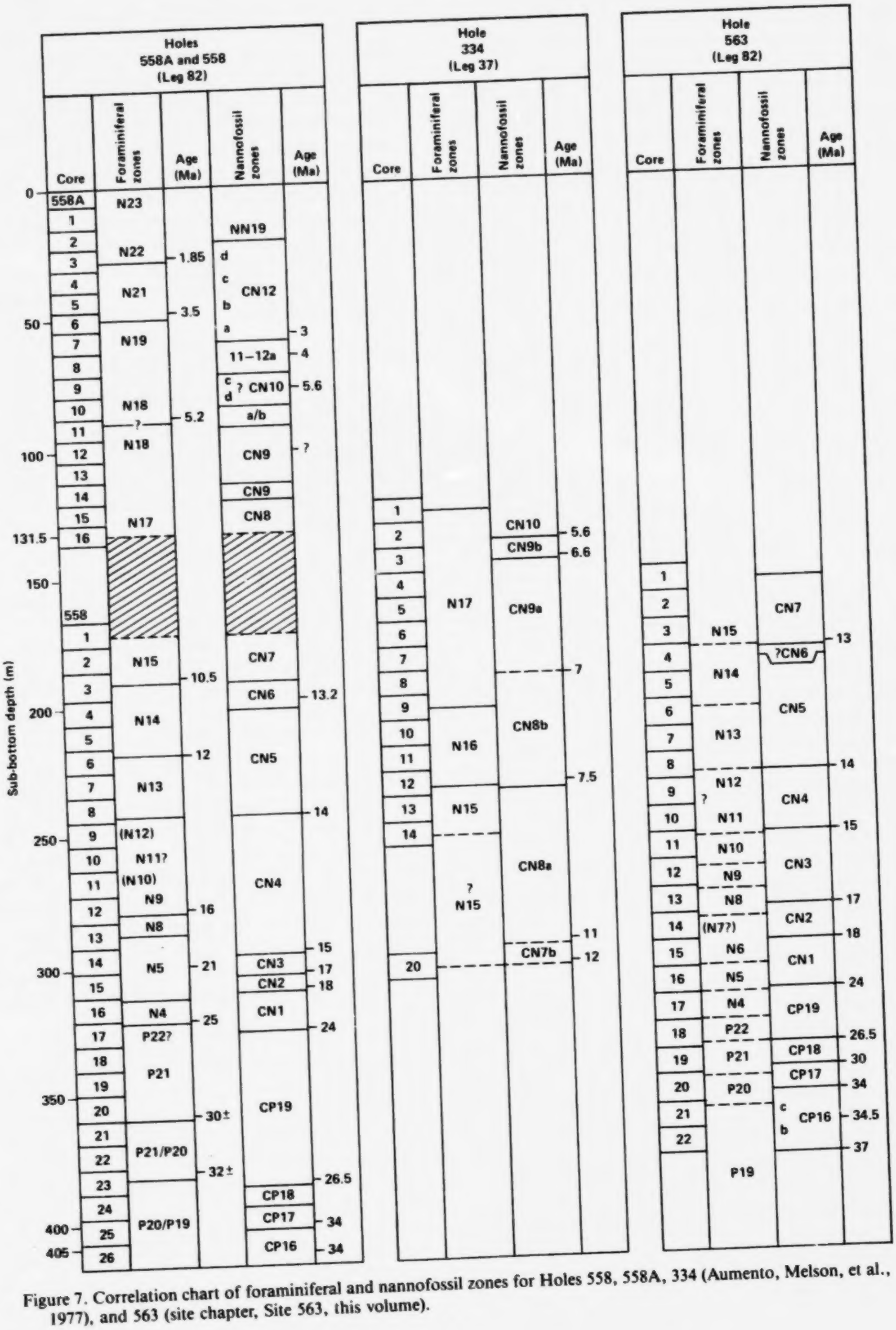

Figure 7. Correlation chart of foraminiferal and nannofossil zones for Holes 558, 558A, 334 (Aumento, Melson, et al., 1977), and 563 (site chapter, Site 563, this volume).

niferal fauna at both sites are similar: in both places there is a marked increase in numbers of *Globoquadrina dehiscens*, and both samples show similar dissolution.

The core catcher of Core 6 is assigned to the lower part of Zone N13 based on the common occurrence of *Globorotalia siakensis* (*mayeri* of some authors) and the associated fauna. The absence of *Globigerina nepenthes* specimens indicates an age older than 12 Ma. Dissolution and fragmentation of the specimens are apparent. Sample 563-7,CC is tentatively assigned to the same zone; in this sample, foraminifers are better preserved and more abundant than the preceding core. It must be pointed out that the zones and ranges assigned in this report are based solely on core catcher samples and that shore-based study of the sections will provide more accurate determinations and better resolution. The core catcher of Core 8 seems to be close to the top of the middle Miocene sequential series of *Globorotalia fohsi, G. lobata, G. robusta, G. fohsi, G. peripheroacuta*, and *G. peripheroronda*. In temperate regions large carinate end forms of the *fohsi* lineage are not well developed and that seems to be the case at this site. It is therefore necessary to use other indicators. The *fohsi* lineage and interval zones of the middle Miocene are, in increasing age, N12 (13.2–14.2 Ma), N11 (14.2–15 Ma), N10 (15–15.5 Ma), and N9 (15.5–16 Ma). Lacking the *fohsi* markers to separate these zones, other criteria relied upon indicate that the core catchers of Cores 9 through 11 span these intervals. The core catcher of Core 9 contains abundant *Globorotalia mayeri, Sphaerodinellopsis seminulina*, and *S. subdehiscens;* the core catcher of Core 10 has abundant *G. scitula* and other middle Miocene species; and the core catcher of Core 11 has abundant *G. praemenardii*. More precise zonation will be possible after the sections are studied. The core catcher of Core 12 is tentatively assigned to the lower part of N9 or topmost N8. The sample consists of abundant *S. subdehiscens* and *S. seminulina;* common *Globoquadrina dehiscens, G. altispira, Globorotalia scitula;* and floods of globigerinids in the finest fraction.

Miocene (lower)

The core catcher of Core 13 is in the lower Miocene Zone N8, based on the presence of abundant *Globoquadrina dehiscens, G. predehiscens*(?), *Catapsydrax dissimilis, C. unicavus*, and *Sphaerodinellopsis subdehiscens* and the absence of *Orbulina*. The core catchers of Cores 14 and 15 are also lower Miocene and tentatively assigned to N6. The core catchers of Cores 16 and 17 are assigned to N5/N4 based on the assemblage of *G. dehiscens, G. venezuelana, Catapsydrax dissimilis*, and rare *Globorotalia kugleri*. Rare *G. kugleri* was first observed in 563-16,CC. The last appearance datum (LAD) of this species is approximately 21 Ma old, so this core might be assigned to middle-lower N5, and 563-17,CC may be assigned to Zone N4. Both of these samples have abundant globigerinids.

Oligocene

The core catcher of Core 18 is upper Oligocene; the fauna consists of large *Globoquadrina venezuelana, G. advena, G. tripartita, Catapsydrax dissimilis*, and abundant small globigerinids. Tentative assignment is lowermost N4/P22 (24.5–26 Ma) or upper P21 (26 Ma). The core catcher of Core 19 is middle P21. Sample 563-20,CC at 346.5 m contains a large robust group of foraminifers plus abundant *Chiloguembelina* that may be assigned to the lower part of P21 or upper P20. The core catcher of Core 21 seems to be transitional between lower and upper Oligocene. The fauna shows considerable fragmentation, which may be an artifact of the violent reaction with hydrogen peroxide that was noted during washing. Manganese nodules are common. The core catcher of Core 22 is lower Oligocene and assigned to foraminiferal Zone P19 (or to a slightly older zone) based on the presence of *Pseudohastigerina* sp. and the extinction datum of *Globorotalia increbescens*.

SEDIMENT ACCUMULATION RATES

Because the upper 156 m of sediment were not recovered, sediment accumulation rates could only be calculated for the upper portion of the lower Oligocene through the middle Miocene. Preliminary age designations show some differences between nannofossil and foraminiferal dates, so we have plotted the age ranges at each core catcher depth and have calculated an average sediment accumulation rate for each stratigraphic interval, based on the boundaries determined from nannofossil and foraminifers respectively (see Fig. 5 and Table 3).

The sediment accumulation rates for the same stratigraphic intervals at Sites 563 and 558, are very similar. In general, the rates are lower in Site 563, which is expected because the sediment section is 42.5 m shorter than at Site 558.

Again, as at Site 558, the most obvious and marked change in sediment accumulation rates occurs near the top of the lower Miocene (from 21.3 to 6.1 m/Ma). This change also corresponds to the lithologic transition between Units 1 and 2.

PORE-WATER CHEMISTRY

The results of the interstitial water chemistry analysis for Hole 563 are shown in Figure 8 and tabulated in Table 4.

The values of pH, alkalinity, and chlorinity remain fairly constant with depth. The salinity values, on the other hand, show a sharp increase after crossing the boundary between Lithologic Units 1 and 2 and then decrease with depth. The calcium and magnesium concentration gradients are typical for calcareous pelagic sediments overlying basalt; that is, the pore waters are

Table 3. Sediment accumulation rates, Hole 563.

Stratigraphic unit	Age (Ma)	Nannofossils Depth (m)	Nannofossils Rate (m/Ma)	Foraminifers Depth (m)	Foraminifers Rate (m/Ma)
middle Miocene	12–16	183–280	24.3	195–280	21.3
lower Miocene	16–24	280–320	5.0	280–320	5.0
upper Oligocene	24–32	320–345	3.1	320–355	4.4
lower Oligocene	32–36	345–365	5.0		

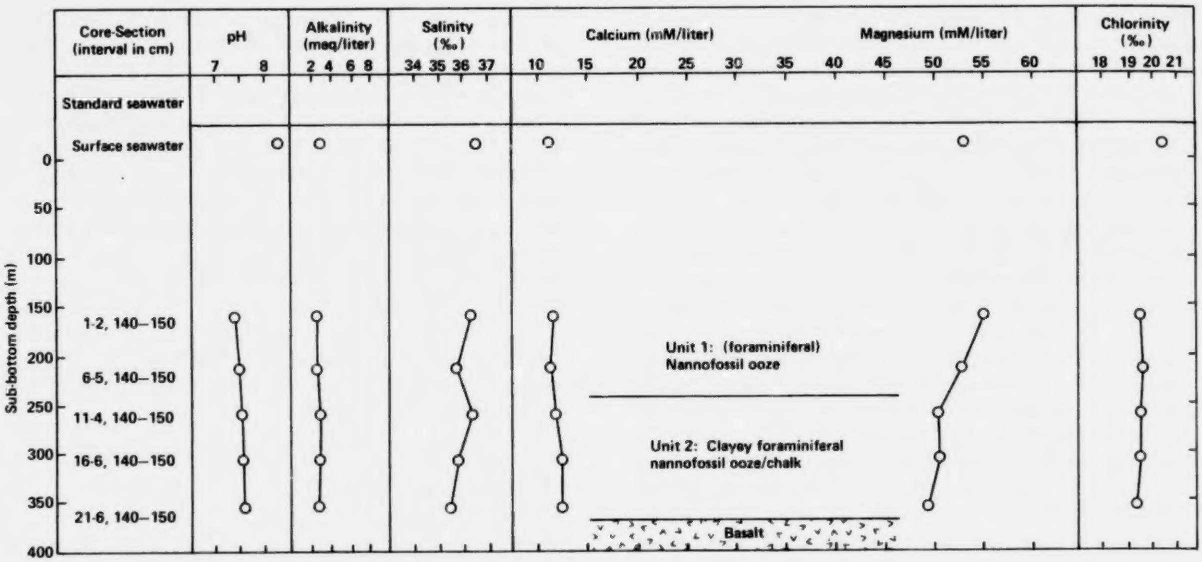

Figure 8. Downhole variations in interstitial water chemistry, Hole 563.

Table 4. Interstitial water chemistry, Hole 563.

Core-Section (interval in cm)	Sub-bottom depth (m)	pH	Alkalinity (meq/liter)	Salinity (‰)	Calcium (mmoles/liter)	Magnesium (mmoles/liter)	Chlorinity (‰)
1-2, 140–150	162	7.43	2.632	36.2	11.59	54.91	19.51
6-5, 140–150	212	7.47	2.541	35.7	11.55	53.29	19.71
11-4, 140–150	260	7.52	2.768	36.4	12.02	50.57	19.61
16-1, 140–150	308	7.48	2.621	35.8	12.51	50.73	19.54
21-6, 140–150	355	7.51	2.402	35.5	12.43	49.39	19.31

enriched in calcium and depleted in magnesium. We note also that rate of change for the concentrations of calcium and magnesium decreases after crossing the boundary between Lithologic Units 1 and 2.

As in Hole 558, we found authigenic dolomite rhombs in the lowermost 10 m of sediment in contact with the basalt, but with much lower concentrations (only 10% by visual estimate as compared to an estimated 30% in Hole 558). However, the calcium and magnesium values did not show anomalous concentrations for the pore-water sample taken in these dolomitic sediments as they did in Hole 558. We can speculate that the abundance of dolomite and the degree of change in the concentration curves of calcium and magnesium are directly related.

IGNEOUS PETROLOGY AND GEOCHEMISTRY

Basement rocks were first recovered at 364.5 m sub-bottom depth. We drilled only 18 m into a sequence of homogeneous, fresh to moderately altered pillow basalts, which represent two chemical groups.

Lithology (Fig. 9)

The pillows of Site 563 are between 30 and 70 cm thick and are usually rimmed by black glass. Interpillow breccias (hyaloclastites), composed of angular glass clasts ranging in size from a few millimeters to a few centimeters, occur in many places. The clasts are surrounded by

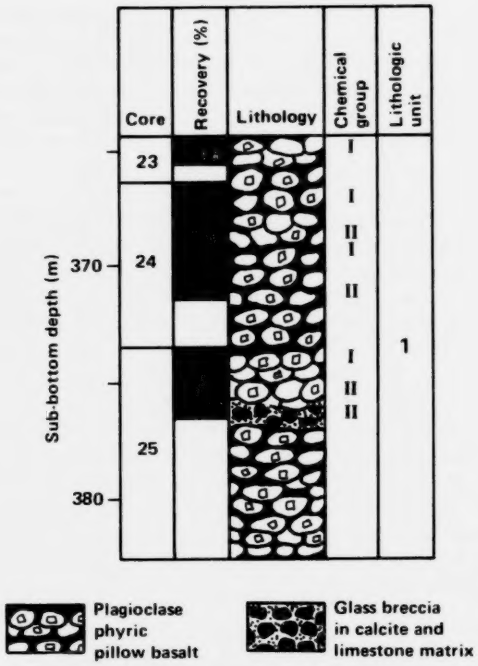

Figure 9. Basement lithology column, Hole 563.

limestone or sparry calcite, which has also filled remaining cavities. Along fractures and at carbonate contacts the glass is altered to thin brown palagonite rinds.

Site 563 basalts are sparsely plagioclase phyric. The plagioclase phenocrysts are randomly scattered (2–3%), most forming elongate to rounded, slightly resorbed glomerocrysts, ranging from 2 to 5 mm in diameter. Minor euhedral to anhedral olivine (less than 2 mm), now completely altered to brown clay, is also present (less than 1%).

Small round vesicles (less than 0.5 mm in diameter) are rare. A few irregular shaped vesicles (less than 7 mm) also occur; these are lined by calcite.

Fractures and veins, filled by either pinkish brown limestone or white sparry calcite, are present throughout the section. In some places vein boundaries are very irregular, with lobe-shaped embayments of limestone into the surrounding basalt.

Petrography

All pillow basalts examined from Site 563 have the same mineral proportions, with only a variation in grain size and texture of the groundmass. The texture ranges from glomerophyric intergranular to glomerophyric plumose.

Large lath-shaped to prism-shaped plagioclase phenocrysts (0.5–5 mm) with a composition of An_{60} (optically determined) make up 5% of the basalt. These glomerophyric phenocrysts are zoned and slightly resorbed, and they contain glass inclusions. Minor amounts of subhedral olivine phenocrysts (0.5–0.8 mm) are partially to fully replaced by brown clay.

The majority of the groundmass consists of equal proportions of randomly oriented, acicular-shaped to lath-shaped plagioclase (40%) and anhedral clinopyroxene (40%), plus 3% equant to granular opaques and 1% granular altered olivine. The last stage of crystallization is represented by either fine-grained intergranular or featherlike arrangements of plagioclase and clinopyroxene. Round to irregular shaped vesicles (0.1–0.8 mm) range from 1 to 10% in volume and usually contain calcite; clay-filled vesicles are rare or absent.

The sample from Core 563-24-2, 123 cm has a hyalophitic plumose texture. It contains only trace amounts of plagioclase phenocrysts, compared to the other samples.

Geochemistry

Ten pillow basalts were analyzed from Site 563, forming two chemical groups. Full analyses are presented in Table 5, and results are plotted against sub-bottom depth in Figure 10. Average analyses for the two chemical groups are given in Table 6. Group I and Group II have distinct Fe_2O_3 contents (10.7 and 9.7%, respectively) and K_2O contents (0.26 ± 0.06 and 0.12 ± 0.05%, respectively), but otherwise are chemically indistinguishable. These differences in Fe_2O_3 and K_2O concentrations between the two groups cannot be easily explained by phenocryst dilution, crystal fractionation, or varying degrees of alteration.

The chemical variation within Group I may, however, be explained by plagioclase addition (Table 7). Dilution of the Group I aphyric sample with 5% plagioclase of composition An_{60} (as observed in thin section) yields the average composition of Group I phyric samples (Table 7). The observed CaO concentration is somewhat higher than the calculated concentration, but this could well be due to calcite contamination (see Table 7).

Figure 11 is an extended Coryell-Masuda plot, which illustrates the depleted nature of Site 563 basalts.

MAGNETICS

Basalt Paleomagnetism

The very hard basalt and drilling problems forced us to stop coring after 18 m. Twelve oriented minicores were taken for on-board paleomagnetic studies. The intensity of natural remanent magnetization (NRM) ranges from 0.8 to 3.8 × 10^{-3} emu/cm^3, and susceptibility varies from 124 to 200 × 10^{-6} emu/cm^3 Oe. The values of NRM and susceptibility for each sample are given in Table 8. Each sample was then subjected to alternating field (AF) demagnetization at various steps until 50% or more of the NRM was randomized. The results are given in Table 8; typical results of AF demagnetization are plotted in Figure 12. The linear decay of orthogonal vectors of magnetization in Figure 12 suggest the presence of univectorial directions of magnetization. Medi-

Table 5. Analyses of major elements (in wt. %) and trace elements (in ppm) of Hole 563 basalts.[a]

Core-Section (interval in cm) (piece number)	Sub-bottom depth (m)	Chemical group	SiO_2	TiO_2	Al_2O_3	Fe_2O_3[b]	MnO	MgO	CaO	K_2O	P_2O_5	Total	Mg'	Ti	V	Sr	Y	Zr	Nb
23-1, 32-35	(2B) 364.8	I	49.87	1.01	15.32	10.48	0.17	7.70	13.46	0.22	0.10	98.33	62	6060	341	86	29.2	58	0.6
24-1, 80-83	(5B) 367.3		49.95	0.99	15.24	10.50	0.15	7.70	13.58	0.22	0.09	98.42	62	5940	332	87	27.9	54	1.9
24-2, 88-91	(3D) 368.9	II	49.95	0.97	15.87	9.56	0.15	7.94	13.58	0.07	0.08	98.17	65	5820	319	84	27.6	55	2.5
24-2, 121-124	(5A) 369.2	I	50.17	1.03	14.43	11.28	0.17	7.88	12.70	0.32	0.09	98.07	61	6180	336	83	29.8	55	2.0
24-4, 38-41	(1C) 371.4	II	50.08	0.99	15.31	9.77	0.16	8.05	13.27	0.09	0.09	97.81	65	5940	321	86	28.2	52	1.7
25-1, 43-46	(1F) 374.0		49.79	0.97	15.77	9.54	0.16	7.75	13.69	0.13	0.09	97.89	65	5820	315	82	27.6	52	1.8
25-2, 39-41	(2A) 375.4		49.66	0.97	15.46	9.53	0.16	7.88	14.28	0.12	0.09	98.15	65	5820	315	85	26.9	60	2.0
25-2, 71-74	(3A) 375.7		49.60	0.96	15.54	10.09	0.16	7.52	13.52	0.20	0.08	97.67	63	5760	314	84	27.7	50	0.6
25-2, 79-81	(3B) 375.8	I	49.68	0.95	15.30	10.96	0.17	7.37	13.38	0.33	0.08	98.22	60	5700	310	84	28.7	54	1.8
25-2, 101-103	(3B) 376.0	II	50.17	0.99	15.49	9.81	0.16	7.68	13.71	0.11	0.11	98.23	64	5940	317	84	27.9	52	1.5

[a] On-board measurements were made on ignited samples. Onshore analyses of loss on ignition are less than 1% in most cases. Compiled data tables at the end of this volume (Appendix) include volatile components.

[b] Total Fe as Fe_2O_3.

[c] Mg' is the atomic ratio of 100 × (Mg/[Mg + Fe^{2+}]) calculated using an assumed Fe_2O_3/FeO ratio of 0.15.

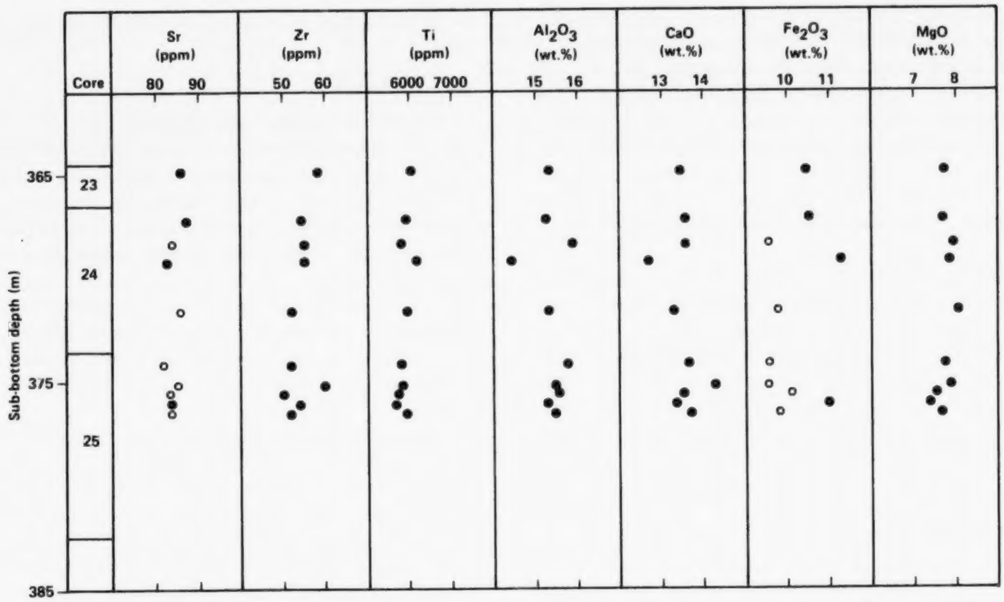

Figure 10. Downhole variations in chemical abundances, Hole 563. In Sr and Fe_2O_3 columns, closed circles are Chemical Group I and open circles are Chemical Group II.

Table 6. Average analyses of basalt chemical groups from Hole 563.

Element	Aphyric Group I (1)[a]	Phyric Group I (3) $\overline{X}$	Phyric Group I (3) σ	Phyric Group II (6) $\overline{X}$	Phyric Group II (6) σ
Major element (wt.%)					
SiO_2	50.17	49.83	0.14	49.90	0.20
TiO_2	1.03	0.98	0.03	0.98	0.51
Al_2O_3	14.43	15.29	0.04	15.60	0.20
Fe_2O_3	11.28	10.70	0.30	9.70	0.20
MnO	0.17	0.16	0.01	0.16	0.01
MgO	7.88	7.60	0.20	7.80	0.20
CaO	12.70	13.47	0.10	13.70	0.30
K_2O	0.32	0.26	0.06	0.12	0.05
P_2O_5	0.09	0.09	0.01	0.09	0.01
Mg′	61	62	1	64	1
Trace element (ppm)					
Ti	6180	5900	180	5850	70
V	336	330	20	317	3
Sr	83	86	2	84	1
Y	29.8	28.7	0.7	27.7	0.4
Zr	55	55	1	54	4
Nb	2.0	1.4	0.7	1.7	0.6

Note: Averages are calculated from the data presented in Table 5. Numbers in parentheses are number of samples analyzed. $\overline{X}$ is median and σ is standard deviation

[a] Sample 563-24-2, 121–124 cm.

Table 7. Major element modeling of plagioclase dilution in Group I basalts, Hole 563.

Element	Liquid[a]	An_{60}	Liquid + 5% An_{60}	Observed[b]
SiO_2	50.17	52.96	50.30	49.83
TiO_2	1.03		0.98	0.98
Al_2O_3	14.43	29.72	15.16	15.29
Fe_2O_3	11.28	0.84	10.78	10.65
MnO	0.17		0.16	0.16
MgO	7.88		7.50	7.59
CaO	12.70	12.28	12.68	13.47
K_2O	0.32	0.13	0.31	0.26
P_2O_5	0.09		0.09	0.09

Note: Concentrations are in wt.%.

[a] Liquid is the aphyric Group I sample from Table 6.

[b] Observed composition is the average phyric Group I from Table 6.

an demagnetizing field (MDF) for each sample was calculated by plotting the quick plot of NRM percentages at corresponding alternating field used for demagnetization (e.g., Fig. 12). The MDF of most samples is in the range of 150–250 Oe.

The plot of MDF and susceptibility versus depth does not show different units as observed at Site 562. However, based on inclination values (see Fig. 13) two units are recognized as follows. *Unit 1.* This is the upper part of basalt extending from 364.5 to about 375 m; it has positive inclination values. *Unit 2.* This is the lower part of the basalt extending from 375 m to the last cored depth of 377 m; it has negative inclination values.

At this stage, two more samples were collected from Section 563-25-2 to see if the negative inclination values were true or just the result of sample inversion. Then two more samples were taken from core specimens long enough so that there is no doubt of sample inversion. The results from these samples confirmed that the negative inclinations obtained previously from Section 563-25-2 are valid. There is no difference in MDF and susceptibility, so it is most likely that these two units represent two time units rather than two geochemical units. The positive inclinations are in agreement with the location of this site on Magnetic Anomaly 13, whereas nega-

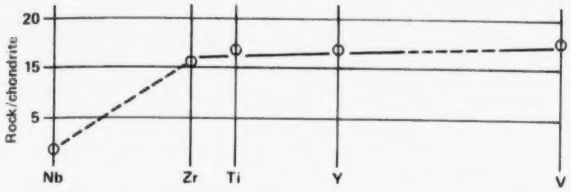

Figure 11. Extended Coryell-Masuda diagram for Hole 563 basalts.

Table 8. Basalt paleomagnetics, Hole 563.

Core-Section (nterval in cm)	J_{NRM} ($\times 10^{-3}$ emu/cm^3)	NRM inc. (°)	Stable inc. (°)	χ ($\times 10^{-6}$ emu/cm^3 Oe)	MDF (Oe)
3-1, 104-106	1.70	53.5	52.0	128	210
3-2, 2-4	2.82	45.1	40.8	125	238
4-1, 2-10	3.79	44.9	41.6	190	190
4-1, 74-76	6.21	36.8	45.4	200	195
4-2, 93-95	2.71	41.1	50.5	124	240
4-3, 112-114	2.83	47.7	43.3	133	285
4-4, 28-30	1.50	34.8	33.9	132	315
5-1, 36-38	2.30	51.3	48.4	130	218
5-2, 39-41	1.48	−52.9	−48.1	153	225
5-2, 101-103	0.99	−54.8	−65.1	145	160
5-2, 79-81	0.80	−30.7	−33.3	150	234
5-2, 115-117	1.20	−52.7	−49.7	144	232

ote: J_{NRM} = intensity of natural remanent magnetization (NRM); inc. = inclination; χ = susceptibility; MDF = median demagnetizing field.

tive inclinations may represent a short reversed subpolarity zone within Anomaly 13.

The fact that the inclination values are (as at most of the earlier Leg 82 holes) shallower than the expected dipole inclination value for the latitude of this site may be explained by tectonic rotation of the crust since the eruption of these basalts.

Sediment Paleomagnetism–Magnetostratigraphy

Two hundred eight meters of sediments were cored after drilling 156.5 m from the top. The sediment recovered was 85%. As at Hole 558, oriented samples were collected at 25-cm intervals depending on lithology. The lithologic similarity between sediments of this hole and the sediments of Hole 558 suggested that remanence in these samples would be of very low intensity and not measurable on the shipboard Digico spinner magnetometer. After measuring the NRM, we observed that remanent magnetization of samples from Core 563-1 though Section 563-10-4 was below or just above the noise level of the magnetometer. However, as the color of sediments changed from various shades of white in Core 9 o very light brown in Core 10, the remanent magnetizaon was measurable but still not reliable. However, samles from Section 563-10-5 to Core 18 had remanence easurable on the shipboard magnetometer with reliable results. The samples from Core 18 downhole were ain very weakly magnetized and the remanence could ot be measured. After measuring NRM, we realized at only 9 of 225 samples had reversed polarity. Two amples were selected for AF demagnetization to check e stability of the directions of magnetization. The reults are plotted in Figures 14 and 15. Sample 563-10-5, -11 cm shows the presence of an antiparallel compoent of magnetization (Fig. 14), which is removed at 75–100 Oe AF demagnetization. MDF of 120 Oe is calculated as shown in Figure 14. The second sample (563-12-2, 91–93 cm) shows a single component of magnetization, and the orthogonal components of magnetization gradually decay to the origin (Fig. 15). This sample has very low MDF (see Fig. 15). These results of AF demagnetization indicate that many of the samples with normal magnetic polarity have a secondary component of magnetization caused by the present magnetic field of the Earth and that this component can be removed by AF demagnetization at 100 Oe. Therefore all samples from Sections 563-10-5 through 563-18-5 were subjected to a single-step AF demagnetization at 100 Oe. The stable inclination values obtained after AF demagnetization are plotted in Figure 16. Negative inclination implies reversed magnetic polarity, and positive inclination means normal magnetic polarity. The sequence of mag-

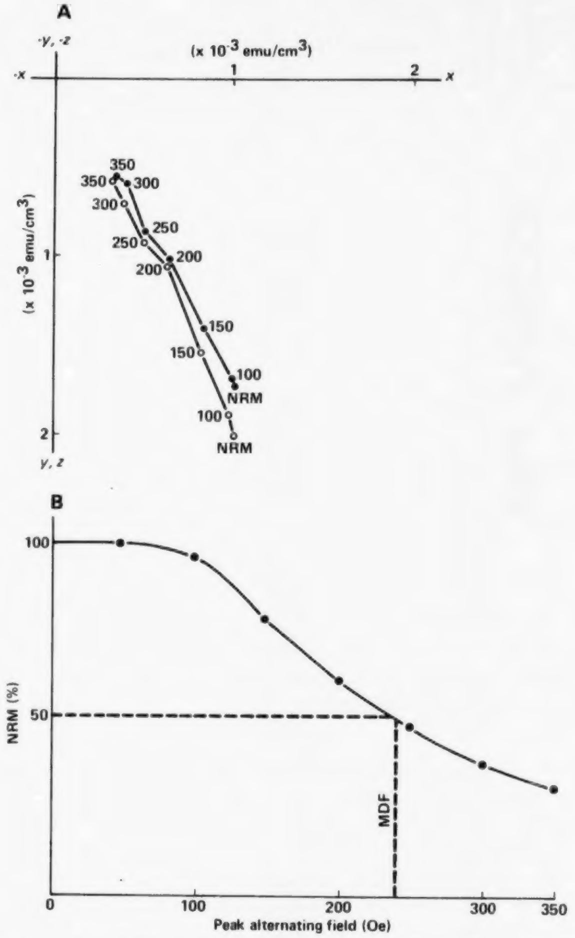

Figure 12. Basalt Sample 563-23-2, 2–4 cm. A. Vector diagram showing the change in NRM after alternating field demagnetization; solid circles are plotted on the horizontal plane and open circles are plotted on the vertical plane. B. Plot of percent natural remanent magnetization (NRM) versus peak alternating field for the determination of the median demagnetizing field (MDF).

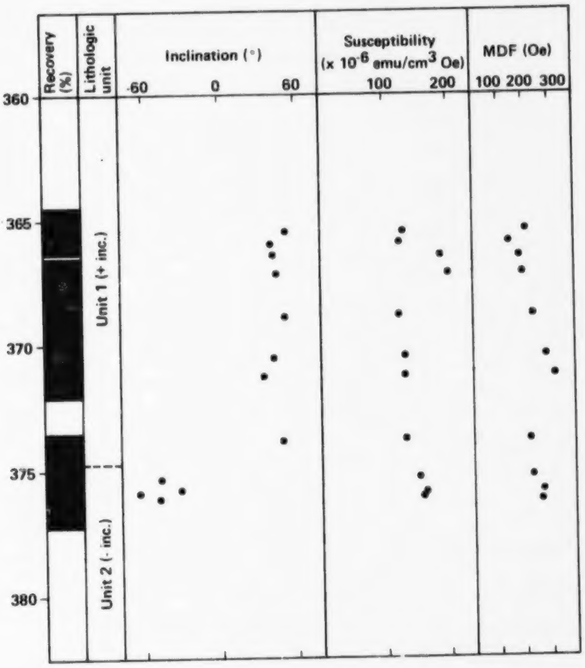

Figure 13. Downhole plot of paleomagnetic properties, Hole 563. MDF = median demagnetizing field.

netic polarity reversals in Figure 16 is based on these data. Single-sample polarity reversals are indicated by an arrow on the left side of the observed polarity sequence.

Using the nannofossil age assignments based on samples from the core catchers and comparing the results of this hole to those of Hole 558, we made the following observations:

1. The Paleogene/Neogene boundary (based on CN zones of Okada and Bukry, 1980) in sediments of Hole 558 occurs between 558-17-3 and 558-19-3, which corresponds to a long zone of reversed magnetic polarity. The same boundary occurs between Cores 563-15 and 563-17 from Hole 563, and there is a long zone of reversed magnetic polarity in Core 563-16. Based on this, the long zone of reversed polarity is correlated with Subchron C6CR (reversed polarity zone between Magnetic Anomalies 6C and 7).

2. Zone CP19 occurs in Core 558-20 and the same core has a long zone of normal magnetic polarity. The Zone CP19 also occurs in Core 563-18, and there is a long zone of normal polarity in 563-18 and the lower part of 563-17. This implies that the two long normal polarity zones can be correlated to each other. Knowing that the magnetostratigraphy is more elaborate for Hole 558 and having correlated this polarity zone with Subchron C8N (Magnetic Anomaly 8), we also correlated the long normal polarity zone in Core 563-18 and the lower part of 563-17 to the Subchron C8N.

The long normal polarity zone in Core 558-16 is correlated to magnetostratigraphic Chron 19 and the core catcher sample from the same core shows Zone CN2. The same Zone CN2 is recorded in the core catcher sam-

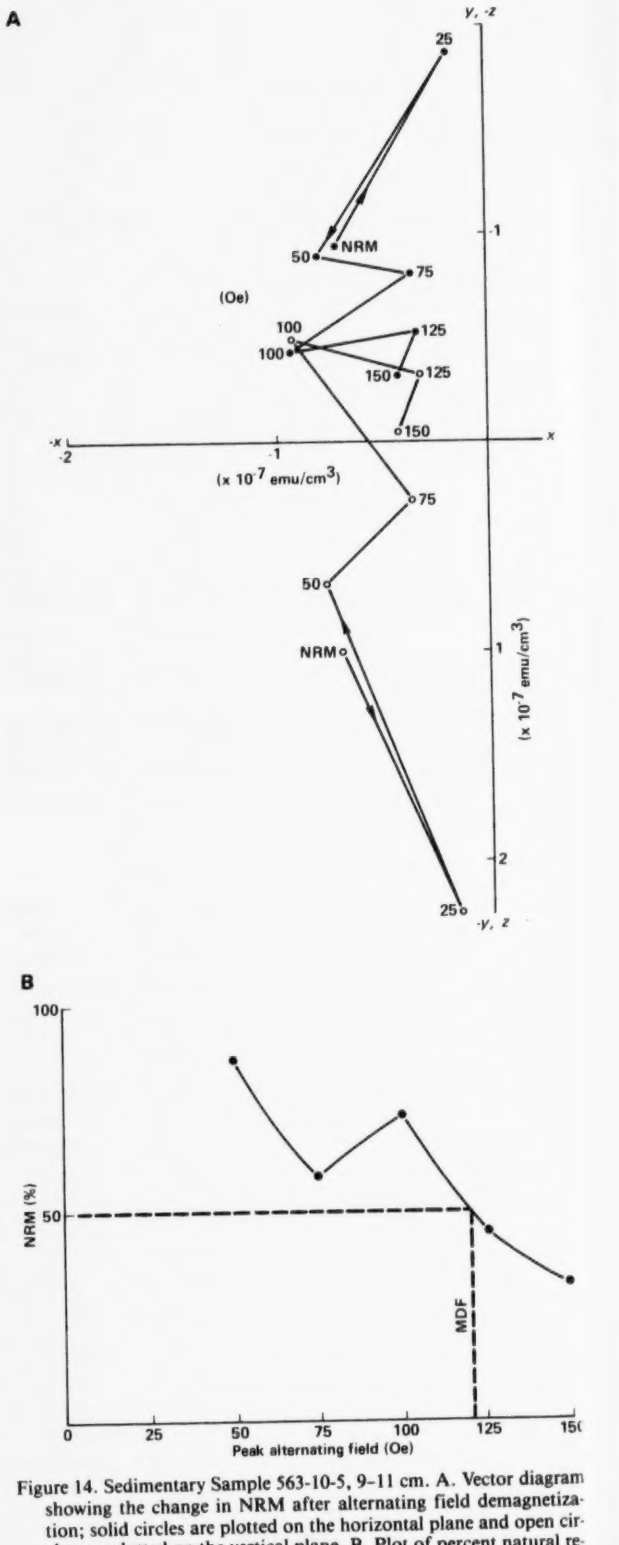

Figure 14. Sedimentary Sample 563-10-5, 9–11 cm. A. Vector diagram showing the change in NRM after alternating field demagnetization; solid circles are plotted on the horizontal plane and open circles are plotted on the vertical plane. B. Plot of percent natural remanent magnetization (NRM) versus peak alternating field for the determination of the median demagnetizing field (MDF).

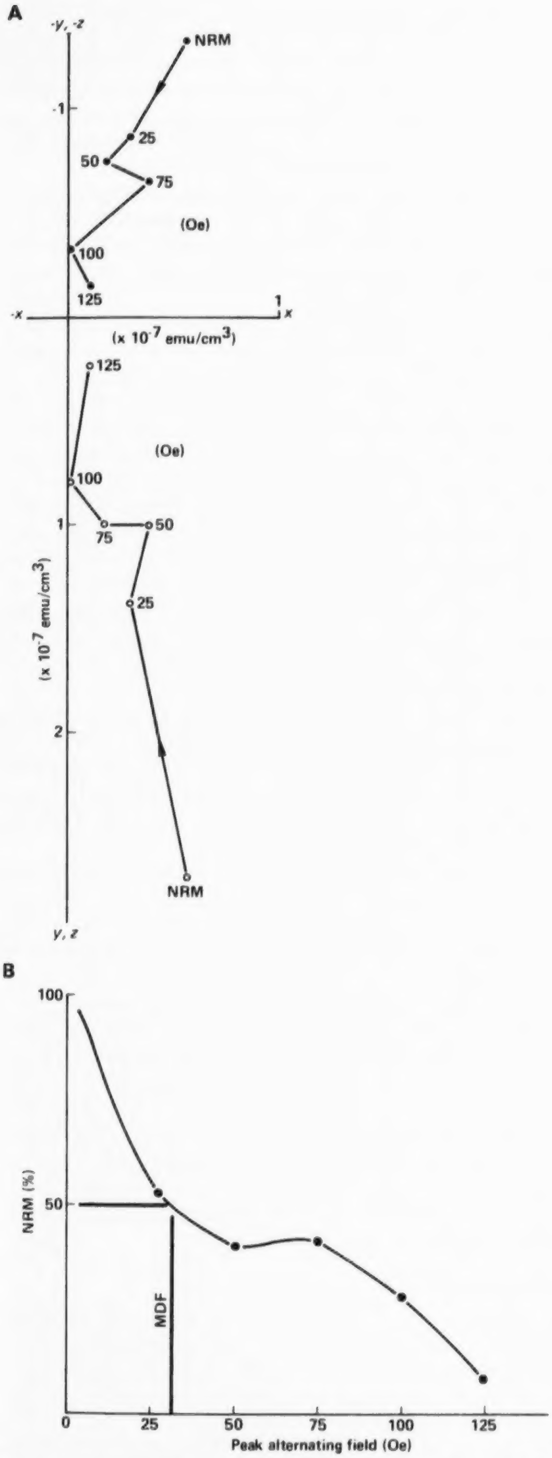

Figure 15. Sedimentary Sample 563-12-2, 91–93 cm. A. Vector diagram showing the change in NRM after alternating field demagnetization; solid circles are plotted on the horizontal plane and open circles are plotted on the vertical plane. B. Plot of percent natural remanent magnetization (NRM) versus peak alternating field for the determination of the median demagnetizing field (MDF).

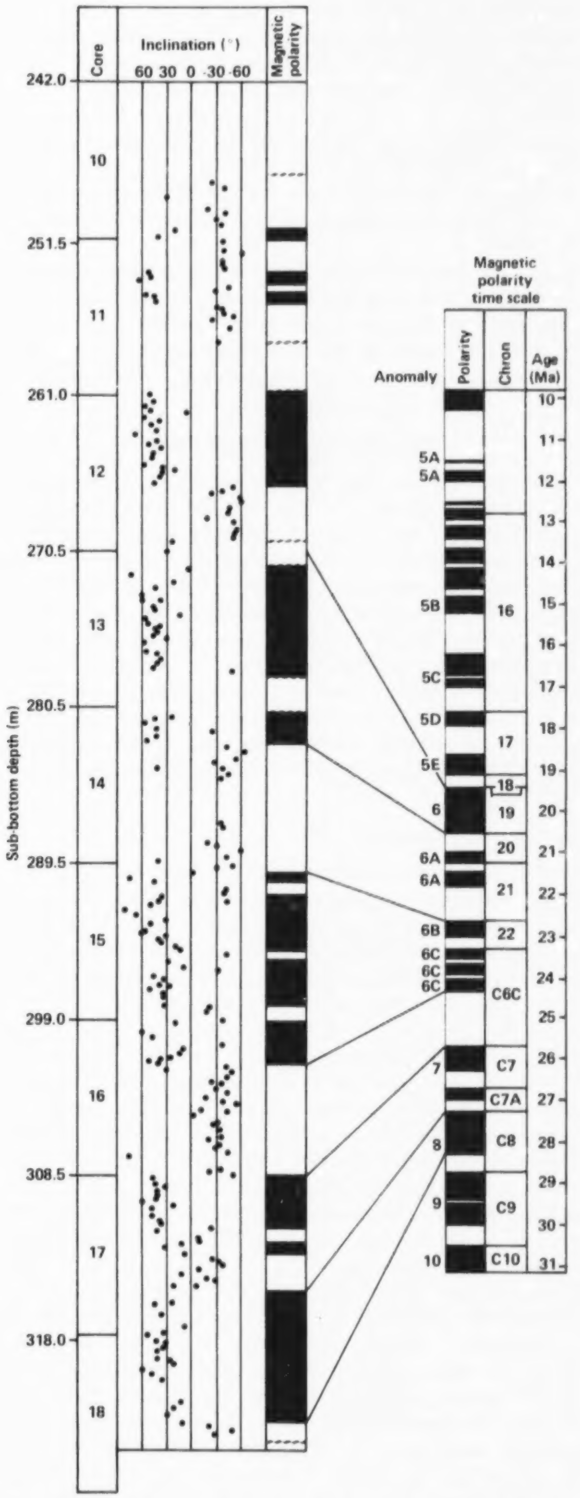

Figure 16. Correlation chart of magnetic inclinations and polarities with the magnetic polarity time scale of Lowrie and Alvarez (1981) for Hole 563.

ple from Core 563-14, but there is no long normal polarity zone. However, there is a long normal polarity zone in Core 563-13. If this is correlated to Chron 19, it implies a higher sedimentation rate for sediments of this age in Hole 563. This is also suggested by the preliminary work done (see Sedimentology and Biostratigraphy section), which shows Zone CN3 in Cores 11 through 13. Keeping this in mind, we correlated the long normal polarity zone of Core 563-13 to the magnetostratigraphic Chron 19.

On the basis of the evidence discussed here, the observed magnetic polarity reversal sequence is tentatively correlated to the standard magnetic polarity time scale, as shown in Figure 16. For a complete discussion of magnetostratigraphic results see Khan et al., this volume.

PHYSICAL PROPERTIES

It was intended that this site would be continuously cored and a full suite of logs run and would thus provide a second opportunity (after Site 558) to compare the physical property values obtained by laboratory and downhole measurements. Because of the premature operation of the bit-release mechanism after only a very shallow penetration of basement, the hole was abandoned without logging. A systematic pattern of measurements of density, porosity, seismic velocity, and thermal conductivity was made and will be discussed below in separate sections for sediment and basalt basement data. All measured physical property values are shown in Table 9.

Sedimentary Section

The sediments consisted of a sequence of calcareous oozes showing progressive compaction down the hole. The effect of the disturbance of rotary coring on these soft sediments was extensive, as is described in the Sedimentology and Biostratigraphy section. Determining useful physical property values from such cores is made difficult not only by the drilling disturbance, but also by the problem of sampling soft core material.

Density was measured by the continuous GRAPE technique on all core sections. Although the data from this method are affected by the degree of drilling disturbance, they should detect density variations in a qualitative manner. Comparison to downhole density logs should allow estimation of the error in continuous GRAPE data caused by drilling effects. Such a study will await shore-based processing of the GRAPE data.

For discrete sampling, the cylinder technique was used. Despite the difficulty of obtaining the sample without deformation, this is probably the best technique available. Two-minute GRAPE measurements were made on all samples; and gravimetric density, porosity, and grain density measurements will be made onshore. Additional samples were taken for shipboard bulk-density determination by cutting cubes of firm sediment and wrapping them in plastic film. This was unsuccessful because of the friability of the sediment.

Seismic velocities were measured on the working half of core sections while they were still in their liners. Despite the inherent inaccuracy of this method, the plotted data (Fig. 17) show a low degree of scatter. There is a suggestion of a cyclical pattern of changes in velocity in the central part of the section that may correspond to cyclical variation in sediment lithology. The wavelength of these cycles is 10 to 15 m. No clear correlation with the lithology has been established.

Thermal conductivity was measured once per core by the needle-probe technique on core sections that had been allowed to equilibrate to laboratory temperature for several hours. The data are plotted against sub-bottom depth in Figure 18, with the data for Site 558 for comparison. The measurements have not been corrected to *in situ* values; this correction would produce a lowering of all values by less than 5%. The error in determined values is estimated at less than 10%. The rotary-cored sections of Holes 558 and 563 produce a scatter of points in Figure 18 that form one population and indicate increasing conductivity with depth. This is a feature explained by increasing compaction. Points determined from the piston-cored section of Hole 558A also show increasing conductivity with depth, but with a nonlinear trend that is not continuous with that found for the rotary-cored sequences. The discontinuity in the values may be a product of the increased disturbance of rotary cores, which has the effect of destroying some of the *in situ* compaction effect.

On Figure 18 is shown the mean trend of thermal conductivity values with depth determined by Hyndman and others (1974) for carbonate sediments in the Indian Ocean. Values found in this study are markedly higher than Hyndman's, but the cause of this difference has not yet been established.

Shear-strength measurements were made on the first few cores recovered, but because of the great variability caused by deformation of the cores, the testing was discontinued. The Torvane instrument was used for all measurements.

The variation of physical properties shown in Figure 17 correlates with the lithology. The transitional boundary between Lithologic Units 1 and 2 occurs over the depth range from 230 to 270 m; this is reflected in an increase in density and thermal conductivity, although there is no clear increase in seismic velocity. The velocity increases steadily down the core with a possible cyclic trend visible over the depth range 270 to 320 m. This may well be due to the alternation of lithification between ooze and chalk within the upper part of Unit 2.

Basement Section

The two cores recovered from basement contained dominantly basalt rock, which was sampled for velocity and density measurements. Velocity was measured on minicore samples for horizontal velocity and on slices from the working half core for vertical velocity. The same samples were used for 2-minute GRAPE measurements; then the minicore was used as a paleomagnetic sample, and the rock slice was used for bulk density determination. Values of velocity and density show no trend within the small depth range sampled and are within a typical range for ocean basalts.

Table 9. Physical properties measurements for Hole 563.

Core-section (interval in cm)	Sub-bottom depth (m)	Sonic velocity (km/s)		T (°C)	Thermal conductivity (mcal/[cm·deg·s])	GRAPE density (g/cm^3)		Gravimetric density			Vane shear strength (g/cm^2)	Lithology or remarks
		V.	H.			V.	H.	Wet-bulk density (g/cm^3)	Water content (%)	φ (%)		
1-1, 27-31	158.8	1.60		22		1.78		1.65	32	53	2300	Pale ooze mod. deformed
1-1, 137-139	157.9	1.62		22							2000	Mod. deformed
1-2, 7-9	158.1	1.66		22								Very deformed
1-2, 96-98	159.0	1.63		22	3.53							Very deformed
2-2, 21-23	167.7	1.66		22							2300	Mod. deformed
2-2, 139-141	168.9	1.58		22							1000	
2-4, 10-12	170.6	1.59		22					33			Very deformed
2-4, 126-128	171.8	1.60		22	3.49							
3-2, 12-14	177.1	1.59		22							1200	
3-2, 135-137	178.4	1.59		22		1.87					1100	Cylinder sample
3-4, 8-10	180.9	1.60		22					34		1200	
3-4, 127-129	181.3	1.59		22	3.73						1200	
4-2, 9-11	186.6	1.60		22							1700	Moderately-very deformed
4-2, 110-112	187.6	1.59		22	3.59						1500	
5-2, 10-12	196.1	1.58		22							1300	Very deformed
5-2, 143-145	197.4	1.60		22							1500	
5-4, 10-12	199.1	1.60		22		1.82			33			Cylinder sample
5-4, 127-129	200.3	1.58		22	3.55							
5-6, 10-12	202.1	1.59		22								
5-6, 140-142	203.4	1.61		22								
6-2, 15-17	205.6	1.61		22								Moderately disturbed
6-2, 133-135	206.8	1.61		22	3.57							
6-4, 140-142	209.9	1.62		22					32			
6-6, 135-137	212.8	1.64		22								
7-2, 122-124	216.2	1.59		22								
7-4, 10-12	218.1	1.60		22					33			
7-4, 127-129	219.3	1.61		22	3.82	1.91						
7-6, 132-134	222.3	1.63		22								
8-2, 68-70	225.2	1.61		22								Cylinder sample
8-4, 6-9	227.6	1.60		22					33			
8-4, 126-128	228.8	1.62		22	3.80							
8-6, 138-140	231.9	1.67		22								
9-2, 123-125	235.2	1.64		22								
9-3, 65-68	236.2			22		1.82		1.54	32	49		Bulk density
9-4, 48-50	237.5	1.62		22		1.85			31			Cylinder sample
9-4, 115-123	238.2	1.64		22	3.75							
9-6, 16-18	240.2	1.62		22								
9-6, 118-120	241.2	1.66		22								
9-7, 35-37	241.9	1.65		22								Brown coloration
10-2, 100-102	244.5	1.65		22								
10-4, 19-21	246.7	1.65		22					32			
10-4, 129-131	247.8	1.65		22	3.64							
10-4, 145-147	248.0					1.83		1.02	34	56		Bulk density
10-6, 12-14	249.6	1.69		22								Light yellowish brown
10-6, 137-139	250.9	1.69		22								
11-1, 11-13	251.6	1.65		22								Pale brown
11-1, 141-143	252.9	1.65		22								Pale brown
11-2, 18-20	253.2	1.67		22								Color darkens
11-2, 127-129	254.3	1.62		22								
11-4, 29-31	256.3	1.66		22					31			
11-4, 125-127	257.3	1.68		22	4.43	1.91						Cylinder sample
12-2, 104-106	263.6	1.64		22								
12-4, 65-67	266.2	1.66		22					29			
12-4, 101-105	266.5					1.82		1.67	27	45		Bulk density
12-4, 127-129	266.8	1.63		22	4.00							
12-6, 133-135	269.8	1.70		22								
13-2, 133-135	273.3	1.64		22								
13-4, 99-101	276.0	1.67		22	4.10							
13-5, 106-110	277.5					1.93						Cylinder sample
13-5, 120-122	277.7	1.69		22								
14-2, 37-39	281.9	1.66		22								Core 14 very deformed
14-3, 131-133	284.3	1.65		22								
15-2, 21-23	291.2	1.66		22								
15-4, 16-18	294.2	1.64		22					31			
15-4, 117-119	295.2	1.66		22	3.97							
15-5, 136-139	296.9					1.90						Cylinder sample
15-6, 132-134	298.3	1.67		22								
16-2, 122-124	301.7	1.69		22								
16-4, 122-124	304.7	1.66		22	3.92				28			
16-6, 43-45	306.9	1.63		22								
17-2, 125-127	311.3	1.65		22								Core 17 very disturbed
17-4, 15-17	313.2	1.70		22					29			
17-4, 129-131	314.3			22	4.08							
18-2, 114-116	320.7	1.66		22								
18-4, 37-39	322.9	1.64		22								
18-4, 129-131	323.8	1.70		22	3.92							
19-2, 15-17	329.2	1.65		22		1.88						Cylinder sample
19-2, 114-116	330.2	1.65		22	4.10				28			
20-2, 18-20	338.7	1.65		22								
20-5, 111-113	344.1	1.67		22					29			
21-2, 144-146	349.5	1.69		22								
21-3, 73-75	350.2					1.95						Cylinder sample
21-4, 23-25	351.2	1.69		22					28			
21-4, 121-126	352.2	1.67		22	4.40							
21-6, 124-126	355.3	1.69		22								
22-2, 65-67	357.7	1.73		22								
22-2, 98-100	358.0					1.92		1.68	28	46		Bulk density
22-2, 126-130	358.3	1.75		22	4.71							
22-3, 135-137	359.9	1.70		22								
23-1, 105-107	365.6	5.71		22		2.87		2.86	3	7		
23-1, 116-122	365.7		5.56	22			2.84					
24-1, 8-10	366.6	5.42		22		2.78						
24-1, 86-90	367.4		5.57	22			2.86	2.84	3	8		
24-3, 136-138	370.9	5.43		22		2.79						
24-3, 140-144	370.9							2.87	2	6		

Note: V. = vertical, H. = horizontal; water content is corrected; φ = porosity. All values measured at laboratory temperature and pressure. For details of techniques, see Explanatory Notes chapter (this volume).

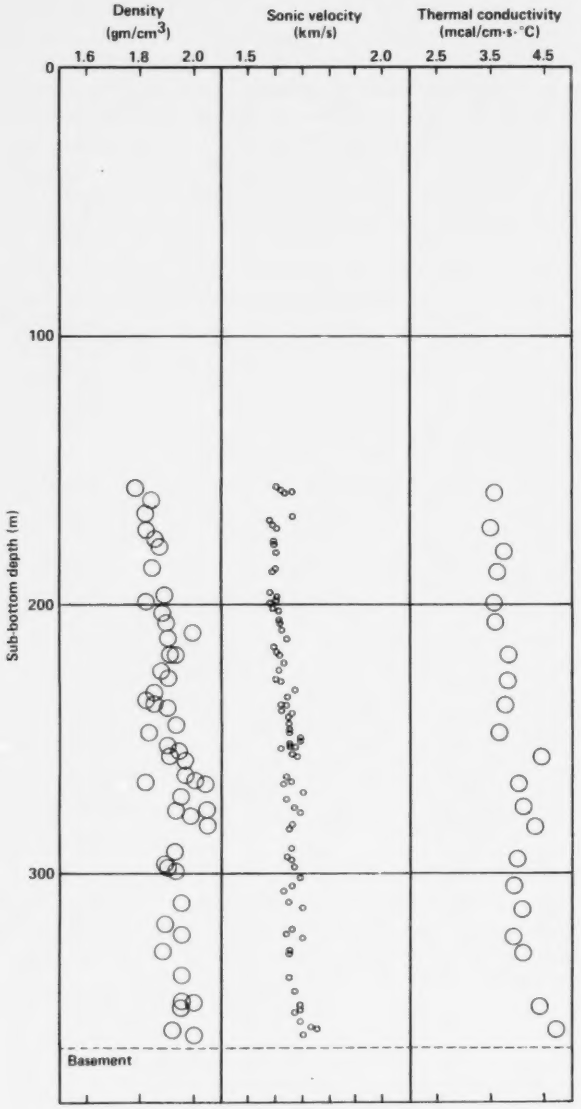

Figure 17. Physical property variations in the sediment section of Hole 563. Size of symbols is proportional to the measured errors.

SUMMARY AND CONCLUSIONS

Hole 563 was drilled on Anomaly 13 on the same flow line as Hole 562. The lower part (156.5-364 m) of the sediment column, which was continuously cored, showed the same major change in the rate of sedimentation near the lower/middle Miocene boundary as was observed at Site 558. From here, the correlation can be extended to Sites 556 and 558, which are also on Anomaly 13. This change in sediment accumulation rate occurring near to the time of the early/middle Miocene boundary can then be considered as a general event in this part of the Atlantic.

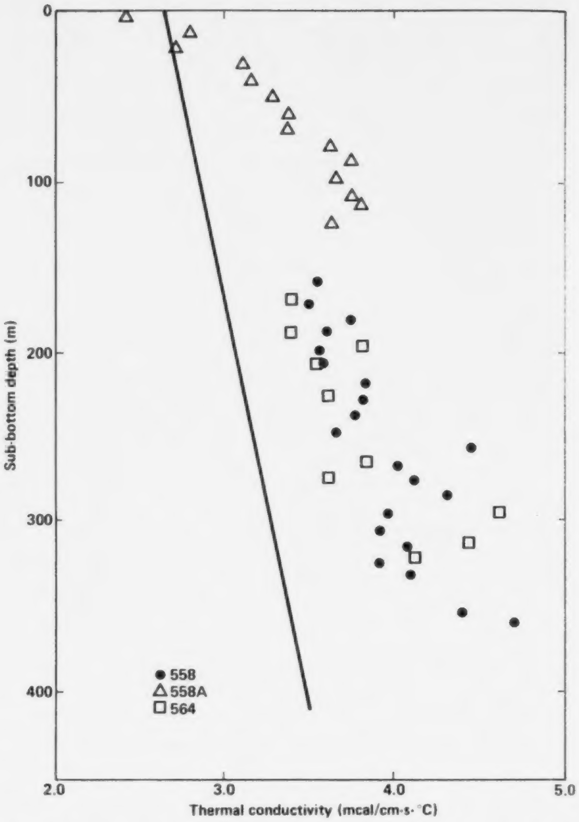

Figure 18. Thermal conductivity plotted against sub-bottom depth for Holes 558, 558A, and 564. Line represents Indian Ocean data from Hyndman et al., 1974. The equation for the line is $2.65 + 0.002d$, where d is sub-bottom depth.

The basement was only cored for 18.5 m because of difficult drilling conditions and premature bit release. The basement consists of one petrographic unit of sparsely plagioclase phyric basalts, in which two chemical groups are identified. The magmaphile element results indicate a depleted character, $(\mathrm{Nb/Zr})_{ch} = 0.3$.

REFERENCES

Aumento, F., Melson, W. G., et al., 1977. *Init. Repts. DSDP*, 37: Washington (U.S. Govt. Printing Office).

Hyndman, R. D., Erickson, A. J., and Von Herzen, R. P., 1974. Geothermal measurements on DSDP Leg 26. *In* Davies, T. A., Luyendyk, B. P., et al., *Init. Repts. DSDP*, 26: Washington (U.S. Govt. Printing Office), 451-464.

Lowrie, W., and Alvarez, W., 1981. One hundred million years of geomagnetic polarity history. *Geology*, 9:392-397.

Okada, H. and Bukry, D., 1980. Supplementary modification and introduction of code numbers to the low latitude coccolith biostratigraphic zonation. *Mar. Micropaleontol.*, 5(3):321-325.

SITE 563 HOLE CORE 1 CORED INTERVAL 156.5–166.0 m

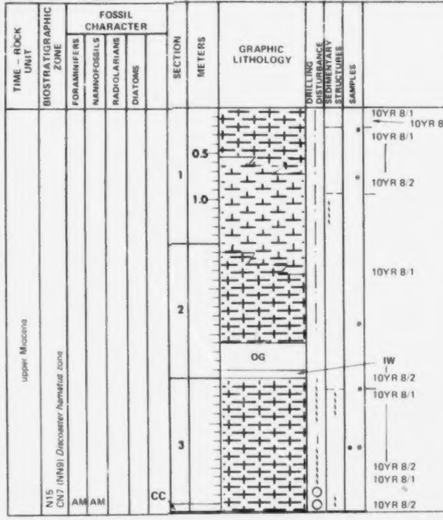
TIME – ROCK UNIT
BIOSTRATIGRAPHIC ZONE
FOSSIL CHARACTER
FORAMINIFERS
NANNOFOSSILS
RADIOLARIANS
DIATOMS
SECTION
METERS
GRAPHIC LITHOLOGY
DRILLING DISTURBANCE
SEDIMENTARY STRUCTURES
SAMPLES
upper Miocene
N15
CN7 (NN9) Discoaster hamatus zone
AM
AM
CC
1
2
3
0.5
1.0
OG
IW
10YR 8/1
10YR 8/3
10YR 8/1
10YR 8/2
10YR 8/1
10YR 8/2
10YR 8/1
10YR 8/2
10YR 8/1
10YR 8/2

LITHOLOGIC DESCRIPTION

DOMINANT LITHOLOGY FORAMINIFER NANNOFOSSIL TO NANNOFOSSIL OOZE

Mostly white (10YR 8/1) grading to very pale brown (10YR 8/3)

Bedding is massive

Bioturbation is very minor

Sediments are firmer and more cohesive in the darker layers

SMEAR SLIDE SUMMARY (%)

	1, 25	1, 80	2, 90	3, 20	3, 80
	D	D	D	D	D
Composition:					
Feldspar	Tr	Tr	Tr	Tr	Tr
Heavy minerals	–	Tr	–	Tr	Tr
Clay	2	4	5	4	6
Pyrite	Tr	–	–	–	–
Zeolites	–	1	–	Tr	?
Foraminifers	10	3	15	10	15
Calc. nannofossils	83	90	80	83	78
Diatoms	2	1	–	2	1
Radiolarians	3	1	Tr	1	Tr

Carbonate Bomb (%)
3, 80 = 93

SITE 563 HOLE CORE 2 CORED INTERVAL 166.0–175.5 m

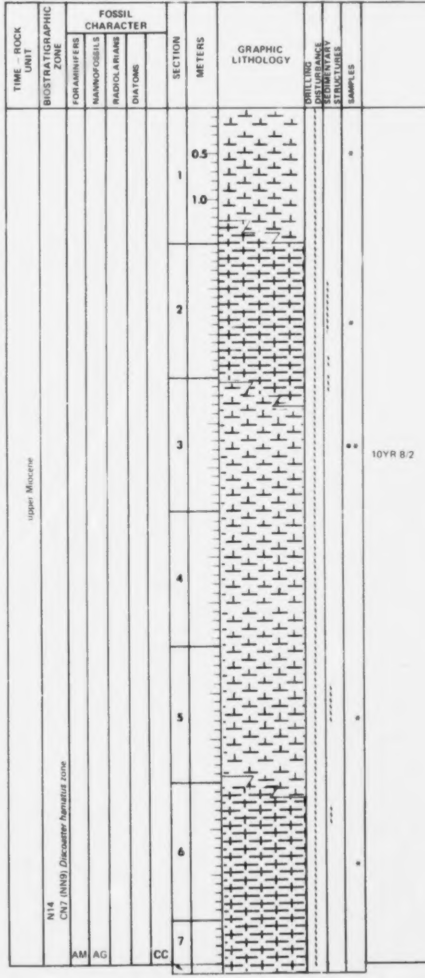
TIME – ROCK UNIT
BIOSTRATIGRAPHIC ZONE
FOSSIL CHARACTER
FORAMINIFERS
NANNOFOSSILS
RADIOLARIANS
DIATOMS
SECTION
METERS
GRAPHIC LITHOLOGY
DRILLING DISTURBANCE
SEDIMENTARY STRUCTURES
SAMPLES
upper Miocene
N14
CN7 (NN9) Discoaster hamatus zone
AM
AG
CC
1
2
3
4
5
6
7
0.5
1.0
10YR 8/2

LITHOLOGIC DESCRIPTION

DOMINANT LITHOLOGY NANNOFOSSIL TO FORAMINIFER NANNOFOSSIL OOZE

White (10YR 8/2)
No obvious bedding
Bioturbation is very minor
Occasional black streaks

SMEAR SLIDE SUMMARY (%)

	1, 50	2, 90	3, 80	5, 80	6, 90
	D	D	D	D	D
Composition:					
Feldspar	Tr	Tr	Tr	Tr	Tr
Heavy minerals	Tr	Tr	Tr	Tr	Tr
Clay	5	9	8	9	9
Volcanic glass	–	–	Tr	–	–
Opaques	–	–	–	Tr	–
Micronodules	–	–	–	–	Tr
Zeolite	–	–	–	Tr	?
Foraminifers	2	10	5	5	11
Calc. nannofossils	93	80	86	86	79
Diatoms	–	Tr	1	Tr	–

Carbonate Bomb (%)
3, 80 = 91

SITE 563 HOLE CORE 3 CORED INTERVAL 175.5–180.0 m

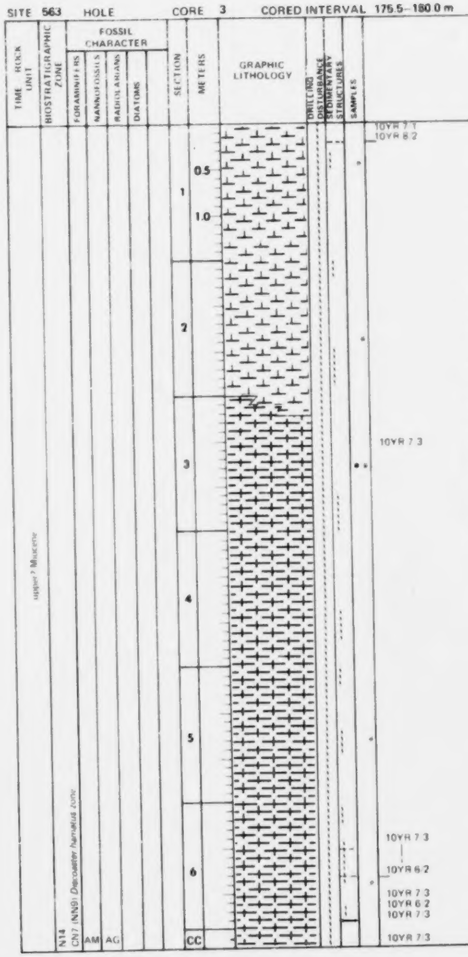
TIME ROCK UNIT
BIOSTRATIGRAPHIC ZONE
FOSSIL CHARACTER
FORAMINIFERS
NANNOFOSSILS
RADIOLARIANS
DIATOMS
SECTION
METERS
GRAPHIC LITHOLOGY
DRILLING DISTURBANCE
SEDIMENTARY STRUCTURES
SAMPLES
upper? Miocene
N14
CN7 (NN9) Discoaster hamatus zone
AM
AG
0.5
1.0
1
2
3
4
5
6
CC
10YR 7/1
10YR 8/2
10YR 7/3
10YR 7/3
10YR 6/2
10YR 7/3
10YR 6/2
10YR 7/3
10YR 7/3

LITHOLOGIC DESCRIPTION

DOMINANT LITHOLOGY FORAMINIFER NANNOFOSSIL TO NANNOFOSSIL OOZE

Dominant color is very pale brown (10YR 7/3) which grades from light gray (10YR 7/1) in Section 1 and grades to light brownish gray (10YR 6/2) in Section 6

Bedding is massive

Bioturbation is minor

Occasional black streaks

SMEAR SLIDE SUMMARY (%)

	1, 50	2, 90	3, 80	5, 80	6, 90
	D	D	D	D	D
Composition:					
Feldspar	Tr	Tr	Tr	Tr	Tr
Heavy minerals	Tr	Tr	?	–	–
Clay	9	9	7	7	8
Volcanic glass	Tr	Tr	–	–	–
Palagonite	–	–	–	Tr	–
Micronodules	1	–	1	–	Tr
Zeolite	Tr	Tr	Tr	–	–
Carbonte unspec	–	–	–	1	1
Foraminifers	5	8	10	15	12
Calc. nannofossils	84	82	83	77	79
Diatoms	–	Tr	–	–	Tr

Carbonate Bomb (%):
3, 80 = 93

SITE 563 HOLE CORE 4 CORED INTERVAL 185.0–194.5 m

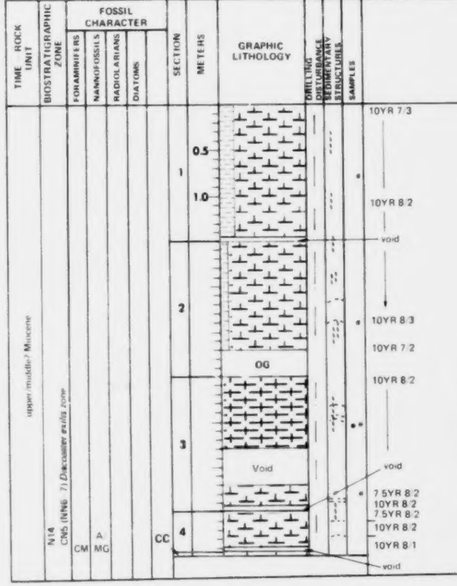
TIME ROCK UNIT
BIOSTRATIGRAPHIC ZONE
FOSSIL CHARACTER
FORAMINIFERS
NANNOFOSSILS
RADIOLARIANS
DIATOMS
SECTION
METERS
GRAPHIC LITHOLOGY
DRILLING DISTURBANCE
SEDIMENTARY STRUCTURES
SAMPLES
upper/middle? Miocene
N14
CN5 (NN6–7) Discoaster exilis zone
CM
A
MG
CC
0.5
1.0
1
2
3
4
OG
Void
10YR 7/3
10YR 8/2
void
10YR 8/3
10YR 7/2
10YR 8/2
void
7.5YR 8/2
10YR 8/2
7.5YR 8/2
10YR 8/2
10YR 8/1
void

LITHOLOGIC DESCRIPTION

DOMINANT LITHOLOGY CLAYEY NANNOFOSSIL, NANNOFOSSIL TO FORAMINIFER NANNOFOSSIL OOZE

Dominant color alternates in shades of white (10YR 8/2–10YR 8/1) which grade from very pale brown (10YR 7/3) in Section 1 and to pinkish white (7.5YR 8/2) in Sections 3 and 4.

Bedding is massive

Bioturbation is minor to moderate

Occasional black streaks

Sediments are generally stiff

SMEAR SLIDE SUMMARY (%)

	1, 80	2, 80	3, 54	3, 129
	D	D	D	D
Composition:				
Mica	–	–	Tr	–
Clay	15	11	9	8
Palagonite	Tr	Tr	Tr	Tr
Micronodules	1	Tr	1	Tr
Zeolite	Tr	Tr	–	–
Carbonate unspec.	2	1	2	–
Foraminifers	8	7	13	5
Calc. nannofossils	74	80	74	85
Fish remains	–	–	–	20
Dolomite	–	–	Tr	–

Carbonate Bomb (%):
3, 54 = 89

SITE 563 HOLE CORE 5 CORED INTERVAL 194.5–204.0 m

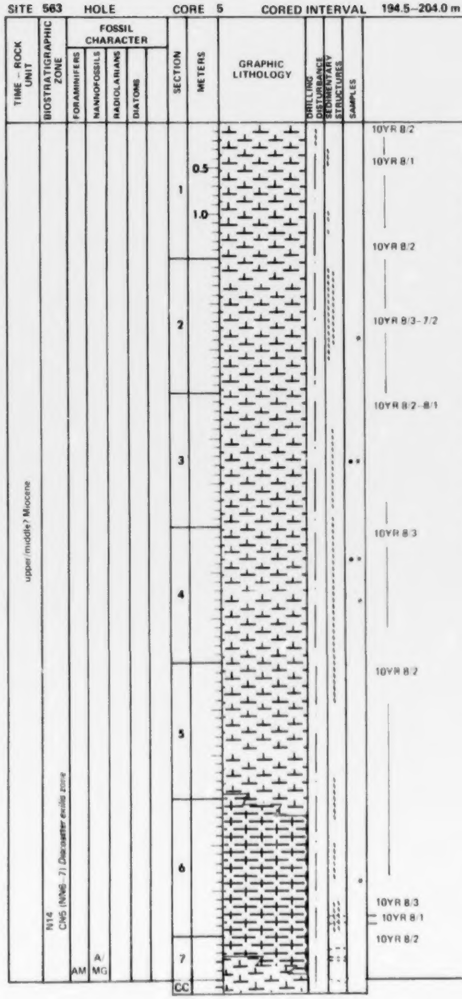
TIME – ROCK UNIT
BIOSTRATIGRAPHIC ZONE
FOSSIL CHARACTER
FORAMINIFERS
NANNOFOSSILS
RADIOLARIANS
DIATOMS
SECTION
METERS
GRAPHIC LITHOLOGY
DRILLING DISTURBANCE
SEDIMENTARY STRUCTURES
SAMPLES
upper/middle? Miocene
N14
CN5 (NN6–7) Discoaster exilis zone
AM
A/MG
1
2
3
4
5
6
7
CC
0.5
1.0
10YR 8/2
10YR 8/1
10YR 8/2
10YR 8/3–7/2
10YR 8/2–8/1
10YR 8/3
10YR 8/2
10YR 8/3
10YR 8/1
10YR 8/2

LITHOLOGIC DESCRIPTION

DOMINANT LITHOLOGY NANNOFOSSIL TO FORAMINIFER NANNOFOSSIL OOZE

Color varies in shades of white (10YR 8/2–10YR 8/1) with occasional light gray (10YR 7/2) mottling grading to very pale brown (10YR 8/3)

Bedding is massive

Bioturbation is minor to moderate

Occasional to common black streaks

Sediments are stiff to firm, and become firm and crumbly in CC

SMEAR SLIDE SUMMARY (%)

	2, 90	3, 80	4, 40	4, 80	6, 90
	D	D	D	D	D
Composition:					
Feldspar	Tr	Tr	Tr	Tr	Tr
Heavy minerals	–	–	Tr	Tr	Tr
Clay	8	8	10	10	8
Volcanic glass	–	–	Tr	–	–
Micronodules	Tr	Tr	Tr	Tr	Tr
Zeolite	–	–	–	–	Tr
Foraminifers	1	1	2	5	10
Calc. nannofossils	91	91	88	84	82

Carbonate Bomb (%)
3, 80 = 92
4, 40 = 90

SITE 563 HOLE CORE 6 CORED INTERVAL 204.0–213.5 m

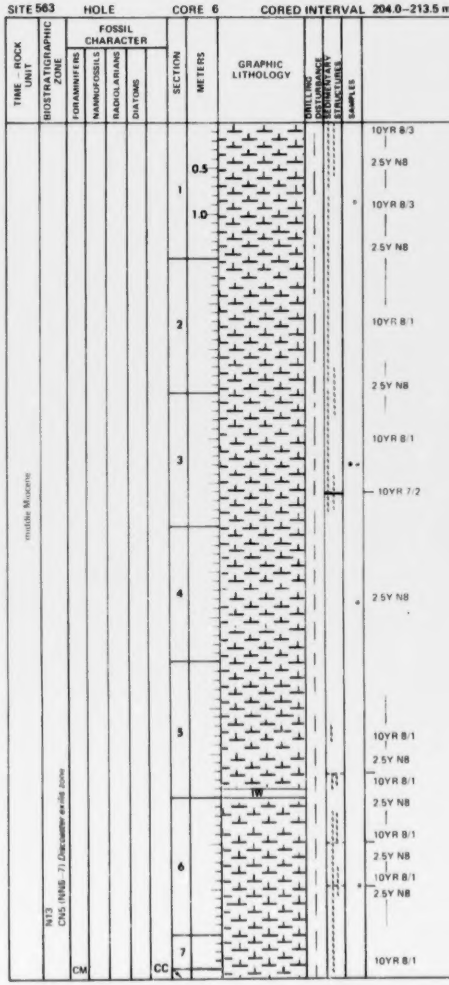
TIME – ROCK UNIT
BIOSTRATIGRAPHIC ZONE
FOSSIL CHARACTER
FORAMINIFERS
NANNOFOSSILS
RADIOLARIANS
DIATOMS
SECTION
METERS
GRAPHIC LITHOLOGY
DRILLING DISTURBANCE
SEDIMENTARY STRUCTURES
SAMPLES
middle Miocene
N13
CN5 (NN6–7) Discoaster exilis zone
CM
1
2
3
4
5
6
7
CC
0.5
1.0
IW
10YR 8/3
2.5Y N8
10YR 8/3
2.5Y N8
10YR 8/1
2.5Y N8
10YR 8/1
10YR 7/2
2.5Y N8
10YR 8/1
2.5Y N8
10YR 8/1
2.5Y N8
10YR 8/1
2.5Y N8
10YR 8/1
2.5Y N8
10YR 8/1

LITHOLOGIC DESCRIPTION

DOMINANT LITHOLOGY NANNOFOSSIL OOZE

Color varies in shades of white (2.5Y N8 to 10YR 8/1) grading to very pale brown (10YR 8/3), and a streak of light gray (10YR 7/2)

Bedding is massive

Bioturbation is minor to moderate (in darker zones)

Sediments are firm to stiff

SMEAR SLIDE SUMMARY (%)

	2, 90	3, 80	4, 90	6, 90
Composition:				
Feldspar	–	Tr	1	Tr
Clay	7	7	7	5
Palagonite	Tr	–	–	Tr
Micronodules	–	–	–	Tr
Zeolite	Tr	–	–	Tr
Carbonate unspec.	2	3	3	4
Foraminifers	3	7	5	1
Calc. nannofossils	88	83	84	90

Carbonate Bomb (%)
3, 80 = 93

SITE 563 HOLE CORE 7 CORED INTERVAL 213.5–223.0 m

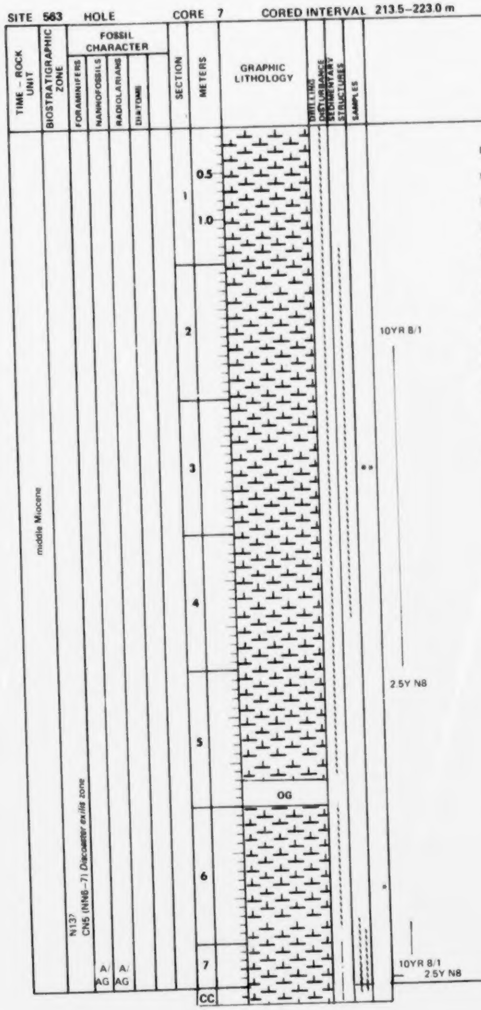
TIME – ROCK UNIT
BIOSTRATIGRAPHIC ZONE
FOSSIL CHARACTER
FORAMINIFERS
NANNOFOSSILS
RADIOLARIANS
DIATOMS
SECTION
METERS
GRAPHIC LITHOLOGY
DRILLING DISTURBANCE
SEDIMENTARY STRUCTURES
SAMPLES
middle Miocene
N13?
CN5 (NN6–7) Discoaster exilis zone
A/AG
A/AG
1
2
3
4
5
6
7
CC
0.5
1.0
OG
10YR 8/1
2.5Y N8
10YR 8/1
2.5Y N8

LITHOLOGIC DESCRIPTION

DOMINANT LITHOLOGY NANNOFOSSIL OOZE

White (10YR 8/1–2.5Y N8)

Bedding is massive

Bioturbation varies from absent to moderate

Core is badly disturbed by drilling

SMEAR SLIDE SUMMARY (%)

	3, 80 D	6, 90 D
Composition:		
Feldspar	Tr	Tr
Clay	6	9
Micronodules	Tr	1
Zeolite	Tr	–
Carbonate unspec.	–	5
Foraminifers	5	7
Calc. nannofossils	89	78

Carbonate Bomb (%):
3, 80 = 94

SITE 563 HOLE CORE 8 CORED INTERVAL 223.0–232.5 m

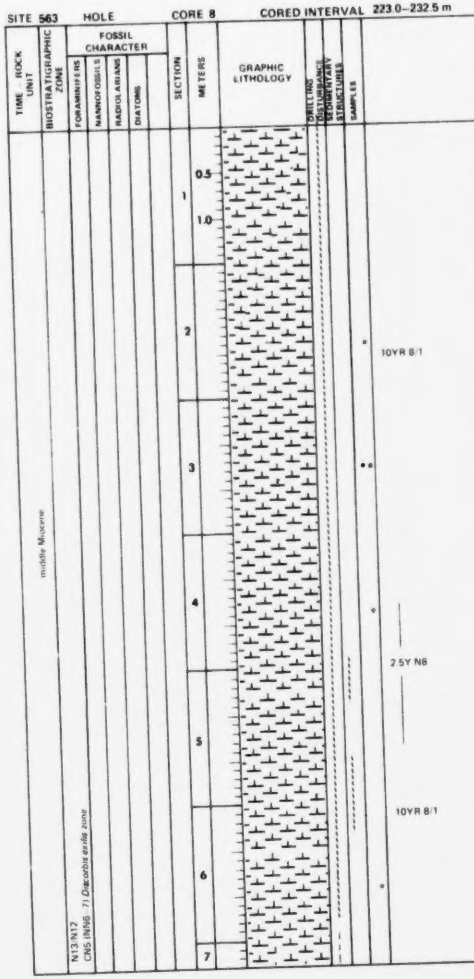
TIME – ROCK UNIT
BIOSTRATIGRAPHIC ZONE
FOSSIL CHARACTER
FORAMINIFERS
NANNOFOSSILS
RADIOLARIANS
DIATOMS
SECTION
METERS
GRAPHIC LITHOLOGY
DRILLING DISTURBANCE
SEDIMENTARY STRUCTURES
SAMPLES
middle Miocene
N13/N12
CN5 (NN6–7) Discorbis exilis zone
1
2
3
4
5
6
7
0.5
1.0
10YR 8/1
2.5Y N8
10YR 8/1

LITHOLOGIC DESCRIPTION

DOMINANT LITHOLOGY NANNOFOSSIL OOZE

White (10YR 8/1–2.5Y N8)

Bedding is massive

Bioturbation varies from absent to very minor

Core is badly disturbed by drilling

SMEAR SLIDE SUMMARY (%)

	2, 80 D	3, 80 D	4, 90 D	6, 90 D
Composition:				
Feldspar	–	Tr	Tr	Tr
Clay	8	7	7	7
Palagonite	–	–	–	Tr
Micronodules	Tr	Tr	Tr	Tr
Carbonate unspec.	3	2	3	3
Foraminifers	8	8	9	3
Calc. nannofossils	81	83	81	87

Carbonate Bomb (%)
3, 80 = 93

SITE 563 HOLE CORE 9 CORED INTERVAL 232.5–242.0 m

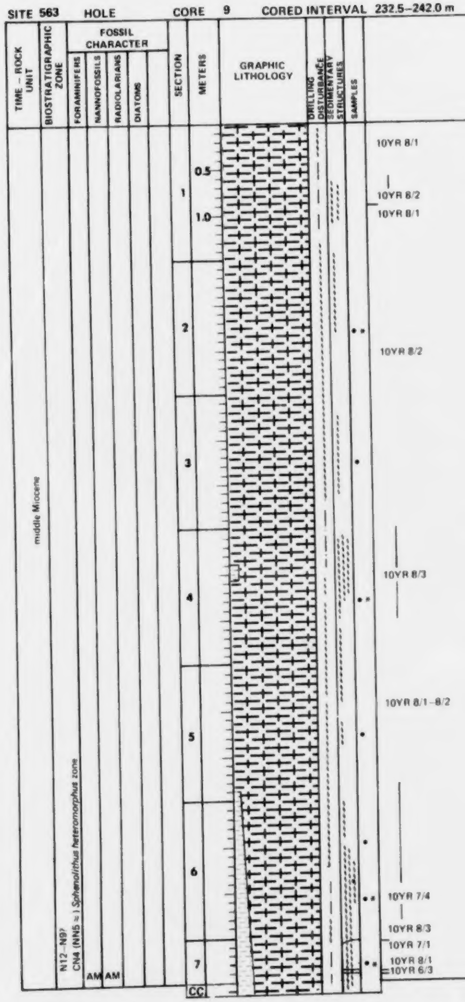
TIME – ROCK UNIT
BIOSTRATIGRAPHIC ZONE
FOSSIL CHARACTER
FORAMINIFERS
NANNOFOSSILS
RADIOLARIANS
DIATOMS
SECTION
METERS
GRAPHIC LITHOLOGY
DRILLING DISTURBANCE
SEDIMENTARY STRUCTURES
SAMPLES
middle Miocene
N12–N9?
CN4 (NN5 ≈) *Sphenolithus heteromorphus* zone
AM
AM
0.5
1.0
1
2
3
4
5
6
7
CC
10YR 8/1
10YR 8/2
10YR 8/1
10YR 8/2
10YR 8/3
10YR 8/1–8/2
10YR 7/4
10YR 8/3
10YR 7/1
10YR 8/1
10YR 6/3

LITHOLOGIC DESCRIPTION

DOMINANT LITHOLOGY FORAMINIFER NANNOFOSSIL OOZE TO CLAYEY FORAMINIFER NANNOFOSSIL OOZE in Section 4, 35–55 cm and Section 6, 140 cm to the bottom of the cored interval.

Colors alternate in shades of white (10YR 8/1–10YR 8/2). In the portions of the core with slightly higher clay content colors gradually darken to very pale brown (10YR 8/3), light gray (10YR 7/1) and pale brown (10YR 6/3). Except for the last meter the core is very deformed from drilling. Darker zones less deformed. Bioturbation is minor to intense. In Section 7 the first occurance of halo burrows is noted. Bedding is massive.

SMEAR SLIDE SUMMARY (%):

	2, 80 D	4, 80 D	6, 110 D	7, 40 M
Composition:				
Feldspar	Tr	1	Tr	Tr
Clay	9	7	11	11
Palagonite	–	Tr	Tr	Tr
Micronodules	1	Tr	Tr	Tr
Zeolites	Tr	–	–	Tr
Carbonate unspec.	2	3	5	6
Foraminifers	10	18	13	5
Calc. nannofossils	77	70	71	78
Fish remains	–	–	Tr	–
Dolomite	Tr	–	–	–

Carbonate Bomb (%):

1, 80 = 94
2, 80 = 89
3, 80 = 97
4, 42 = 86
4, 80 = 92
5, 80 = 90
6, 50 = 87
6, 110 = 89
7, 36 = 90

SITE 563 HOLE CORE 10 CORED INTERVAL 242.0–251.5 m

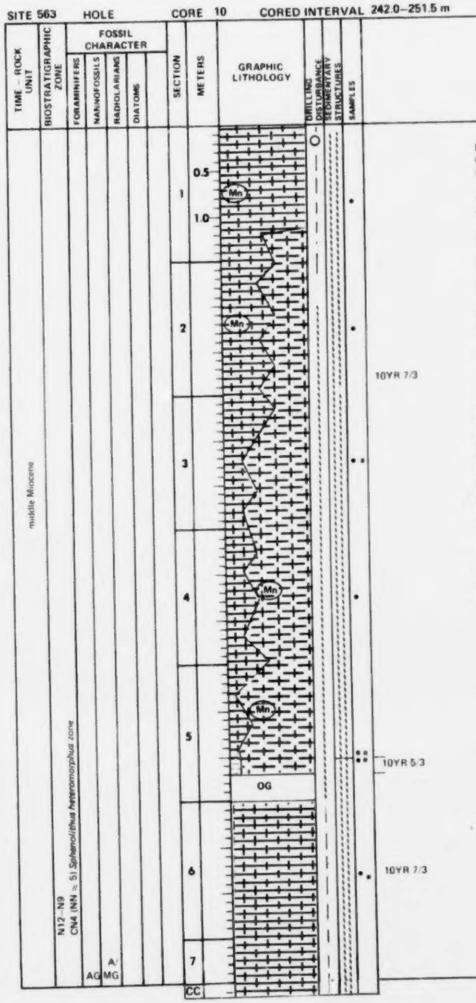
TIME – ROCK UNIT
BIOSTRATIGRAPHIC ZONE
FOSSIL CHARACTER
FORAMINIFERS
NANNOFOSSILS
RADIOLARIANS
DIATOMS
SECTION
METERS
GRAPHIC LITHOLOGY
DRILLING DISTURBANCE
SEDIMENTARY STRUCTURES
SAMPLES
middle Miocene
N12–N9
CN4 (NN ≈ 5) *Sphenolithus heteromorphus* zone
AG
A/MG
0.5
1.0
1
2
3
4
5
6
7
CC
Mn
OG
10YR 7/3
10YR 5/3
10YR 7/3

LITHOLOGIC DESCRIPTION

DOMINANT LITHOLOGY FORAMINIFER NANNOFOSSIL OOZE AND CHALK WITH CLAYEY FORAMINIFER NANNOFOSSIL OOZE at Section 5, 105–120 cm.

Very pale brown (10YR 7/3) to brown (10YR 5/3) at clayey interval.

Bedding is massive.

Bioturbation is moderate, large halo burrows are common.

Rare manganese nodules throughout core (2–4 mm in diameter).

Lithification alternates between chalk and ooze. Section 6 is all chalk.

SMEAR SLIDE SUMMARY (%):

	3, 80 D	5, 102 D	5, 105 D	6, 90 D
Composition:				
Feldspar	Tr	Tr	Tr	Tr
Heavy minerals	Tr	–	–	–
Clay	5	9	14	7
Palagonite	–	Tr	–	–
Micronodules	Tr	–	Tr	Tr
Zeolite	–	Tr	–	–
Carbonate unspec.	5	5	5	5
Foraminifers	20	25	15	20
Calc. nannofossils	70	61	66	68
Dolomite	Tr	–	–	Tr

Carbonate Bomb (%):

1, 85 = 93
2, 80 = 92
3, 80 = 95
4, 80 = 91
5, 104 = 91
5, 106 = 86
6, 80 = 93

SITE 563 HOLE CORE 11 CORED INTERVAL 251.5–261.0 m

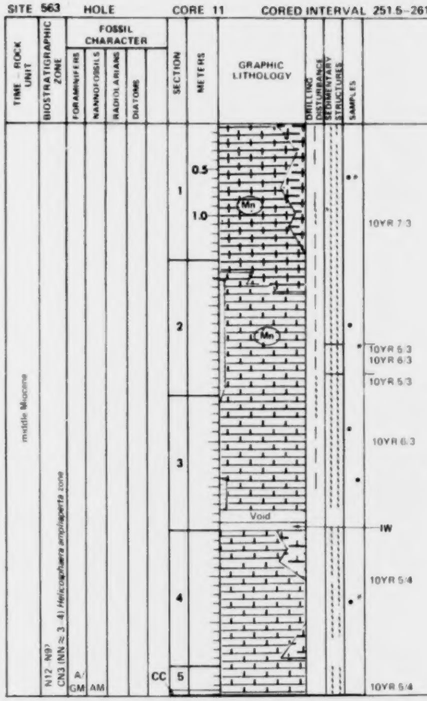
TIME – ROCK UNIT
BIOSTRATIGRAPHIC ZONE
FOSSIL CHARACTER
FORAMINIFERS
NANNOFOSSILS
RADIOLARIANS
DIATOMS
SECTION
METERS
GRAPHIC LITHOLOGY
DRILLING DISTURBANCE
SEDIMENTARY STRUCTURES
SAMPLES
middle Miocene
N12–N9?
CN3 (NN ≈ 3–4) Helicosphaera ampliaperta zone
A/GM
AM
CC
1
2
3
4
5
0.5
1.0
Mn
Mn
Void
IW
10YR 7/3
10YR 5/3
10YR 6/3
10YR 5/3
10YR 6/3
10YR 5/4
10YR 5/4

LITHOLOGIC DESCRIPTION

DOMINANT LITHOLOGY FORAMINIFER NANNOFOSSIL OOZE AND CHALK NANNOFOSSIL CHALK WITH CLAYEY INTERVALS AND NANNOFOSSIL OOZE AND CHALK

From very pale brown (10YR 7/3) at the top of the core, the colors darken to pale brown (10YR 6/3) and yellowish brown (10YR 5/4)

Bedding is massive

Bioturbation is moderate, large halo burrows are common

Sections 1 and 2 have rare manganese nodules (1–2 mm in diameter)

Alternating lithification from ooze to chalk in Section 1, becoming chalk in Section 2

SMEAR SLIDE SUMMARY (%)

	1, 60	2, 96	4, 79
	D	D	
Composition:			
Feldspar	Tr	Tr	Tr
Clay	9	11	8
Palagonite	Tr	Tr	Tr
Micronodules	Tr	1	Tr
Carbonate unspec.	5	5	3
Foraminifers	15	2	5
Calc. nannofossils	71	81	84
Sponge spicules	Tr	–	–
Dolomite	–	Tr	–

Carbonate Bomb (%):

1, 60 = 91	3, 96 = 89
2, 73 = 87	4, 80 = 92
3, 42 = 94	

SITE 563 HOLE CORE 12 CORED INTERVAL 261.0–270.5 m

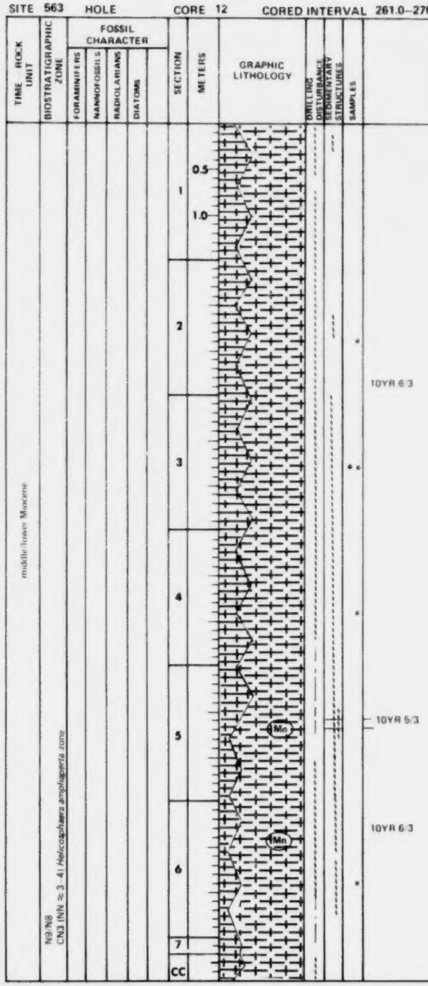
TIME – ROCK UNIT
BIOSTRATIGRAPHIC ZONE
FOSSIL CHARACTER
FORAMINIFERS
NANNOFOSSILS
RADIOLARIANS
DIATOMS
SECTION
METERS
GRAPHIC LITHOLOGY
DRILLING DISTURBANCE
SEDIMENTARY STRUCTURES
SAMPLES
middle/lower Miocene
N9/N8
CN3 (NN ≈ 3–4) Helicosphaera ampliaperta zone
1
2
3
4
5
6
7
CC
0.5
1.0
Mn
Mn
10YR 6/3
10YR 5/3
10YR 6/3

LITHOLOGIC DESCRIPTION

DOMINANT LITHOLOGY FORAMINIFER NANNOFOSSIL OOZE AND CHALK

Pale brown (10YR 6/3)

Massive bedding

Minor to moderate bioturbation, large halo burrows are common

Manganese nodules (1–2 mm in diameter) are rare in Sections 5 and 6

Alternating ooze and chalk

SMEAR SLIDE SUMMARY (%)

	2, 90	3, 80	4, 90	6, 90
	D	D	D	D
Composition:				
Feldspar	Tr	Tr	Tr	Tr
Clay	5	4	5	5
Palagonite	Tr	Tr	Tr	Tr
Micronodules	1	Tr	Tr	Tr
Carbonate unspec.	5	3	5	5
Foraminifers	10	15	15	10
Calc. nannofossils	79	78	75	80

Carbonate Bomb (%)
3, 80 = 96

SITE 563 HOLE CORE 13 CORED INTERVAL 270.5–280.0 m

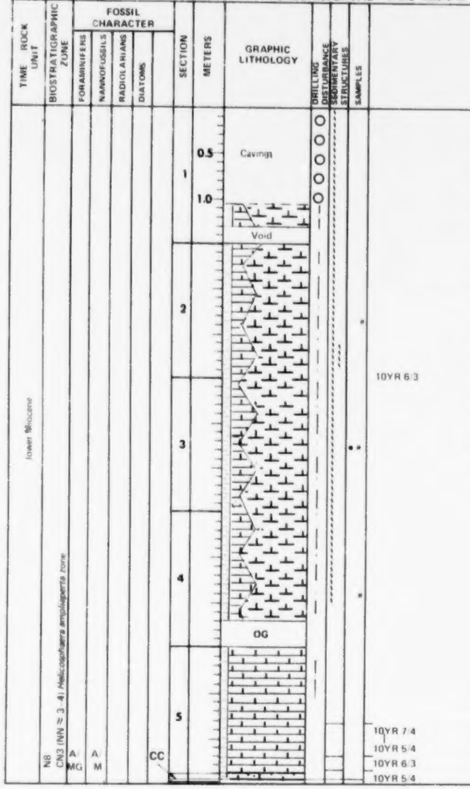
TIME ROCK UNIT
BIOSTRATIGRAPHIC ZONE
FOSSIL CHARACTER
FORAMINIFERS
NANNOFOSSILS
RADIOLARIANS
DIATOMS
SECTION
METERS
GRAPHIC LITHOLOGY
DRILLING DISTURBANCE
SEDIMENTARY STRUCTURES
SAMPLES
lower Miocene
N8
CN3 (NN ≈ 3–4) Helicosphaera ampliaperta zone
A
MG
A
M
CC
1
2
3
4
5
0.5
1.0
Cavings
Void
OG
10YR 6/3
10YR 7/4
10YR 5/4
10YR 6/3
10YR 5/4

LITHOLOGIC DESCRIPTION

DOMINANT LITHOLOGY CLAYEY NANNOFOSSIL OOZE AND CHALK

Pale borwn (10YR 6/3) with very pale brown (10YR 7/4) grading to yellowish brown (10YR 5/4) layers in the bottom of Section 5

Massive bedding

Minor bioturbation with rare halo burrows

Alternating chalk and ooze; more chalky in lower part

SMEAR SLIDE SUMMARY (%)

	2, 90 D	3, 80 D	4, 90 D
Composition:			
Feldspar	–	Tr	Tr
Heavy minerals	Tr	Tr	–
Clay	12	11	10
Volcanic glass	Tr	Tr	Tr
Palagonite	Tr	–	–
Micronodules	Tr	Tr	Tr
Carbonate unspec.	3	5	6
Foraminifers	8	9	8
Calc. nannofossils	77	75	76

Carbonate Bomb (%):
3, 80 = 89

SITE 563 HOLE CORE 14 CORED INTERVAL 280.0–289.5 m

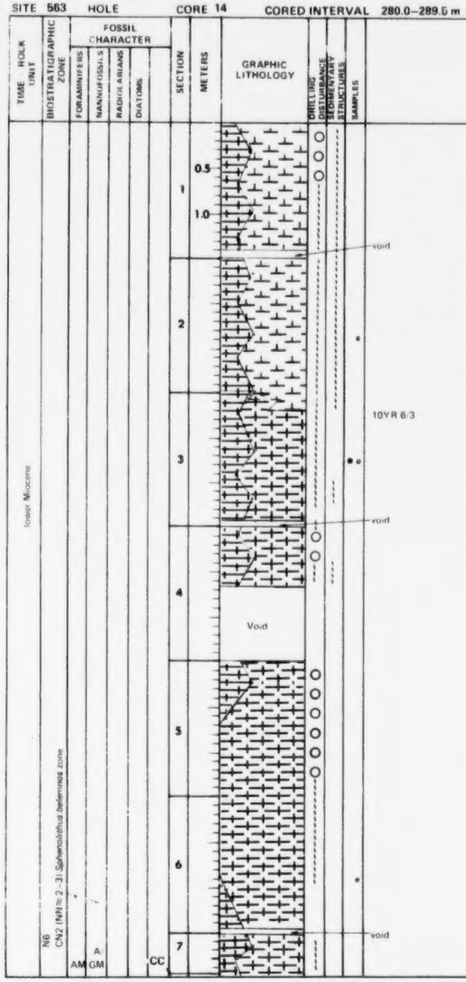
TIME ROCK UNIT
BIOSTRATIGRAPHIC ZONE
FOSSIL CHARACTER
FORAMINIFERS
NANNOFOSSILS
RADIOLARIANS
DIATOMS
SECTION
METERS
GRAPHIC LITHOLOGY
DRILLING DISTURBANCE
SEDIMENTARY STRUCTURES
SAMPLES
lower Miocene
N6
CN2 (NN ≈ 2–3) Sphenolithus belemnos zone
AM
A
GM
CC
1
2
3
4
5
6
7
0.5
1.0
Void
void
10YR 6/3
void
void

LITHOLOGIC DESCRIPTION

DOMINANT LITHOLOGY NANNOFOSSIL CHALK AND OOZE AND FORAMINIFER-NANNOFOSSIL CHALK AND OOZE

Pale brown (10YR 6/3)

Massive bedding

Bioturbation is absent to minor, although the intense drilling disturbance may have obscured these and any other sedimentary structures

Note: alternating soft and firm ooze or chalk and ooze. (Lithification probably not all the way to chalk.)

SMEAR SLIDE SUMMARY (%)

	2, 90 D	3, 80 D	6, 90 D
Composition:			
Feldspar	Tr	Tr	Tr
Heavy minerals	–	–	Tr
Clay	6	8	8
Volcanic glass	Tr	–	–
Palagonite	–	–	Tr
Micronodules	Tr	Tr	Tr
Zeolite	–	Tr	–
Carbonate unspec.	5	5	10
Foraminifers	5	15	20
Calc. nannofossils	84	72	62
Dolomite	Tr	–	–

Carbonate Bomb (%):
3, 80 = 92

SITE 563 HOLE CORE 15 CORED INTERVAL 289.5–299.0 m

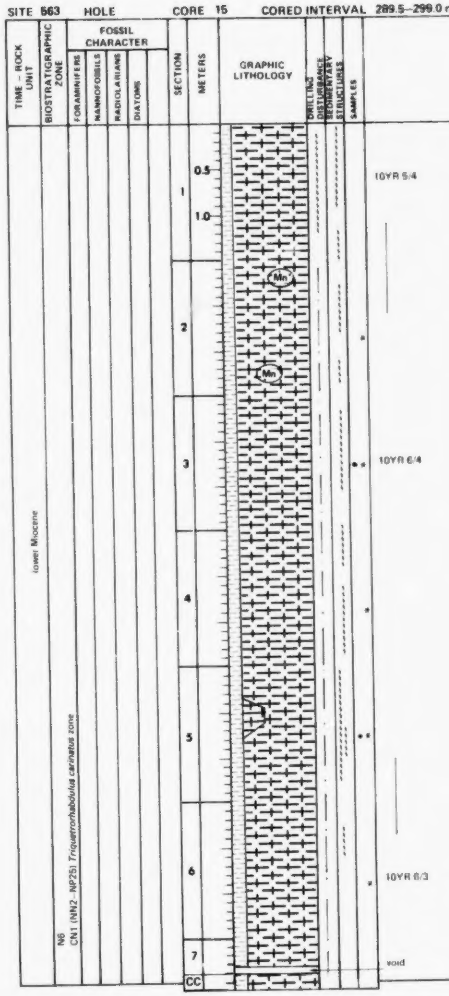
TIME – ROCK UNIT
BIOSTRATIGRAPHIC ZONE
FOSSIL CHARACTER
FORAMINIFERS
NANNOFOSSILS
RADIOLARIANS
DIATOMS
SECTION
METERS
GRAPHIC LITHOLOGY
DRILLING DISTURBANCE
SEDIMENTARY STRUCTURES
SAMPLES
lower Miocene
N6
CN1 (NN2–NP25) Triquetrorhabdulus carinatus zone
0.5
1.0
1
2
3
4
5
6
7
CC
Mn
Mn
10YR 5/4
10YR 6/4
10YR 6/3
void

LITHOLOGIC DESCRIPTION

DOMINANT LITHOLOGY CLAYEY FORAMINIFER-NANNOFOSSIL OOZE WITH MINOR CHALK

Colors lighten down core, beginning at the top with yellowish brown (10YR 5/4) to light yellowish brown (10YR 6/4) and ending in pale brown (10YR 6/3)

Massive bedding

Bioturbation is minor to moderate

Halo burrows occasionally contain very small manganese nodules

Sediments are soft to firm; chalky layer is crumbly

SMEAR SLIDE SUMMARY (%)

	2, 90 D	3, 80 D	4, 90 D	5, 80 D	6, 90 D
Composition:					
Feldspar	Tr	Tr	Tr	Tr	Tr
Heavy minerals	Tr	–	–	Tr	Tr
Clay	17	15	13	11	11
Volcanic glass	Tr	–	–	–	–
Palagonite	–	Tr	Tr	Tr	Tr
Micronodules	Tr	Tr	Tr	Tr	Tr
Zeolite	1	Tr	2	2	3
Carbonate unspec	10	5	5	5	5
Foraminifers	10	15	15	20	20
Calc. nannofossils	62	65	65	62	61

Carbonate Bomb (%):
3, 80 = 85 5, 80 = 87

SITE 563 HOLE CORE 16 CORED INTERVAL 299.0–308.5 m

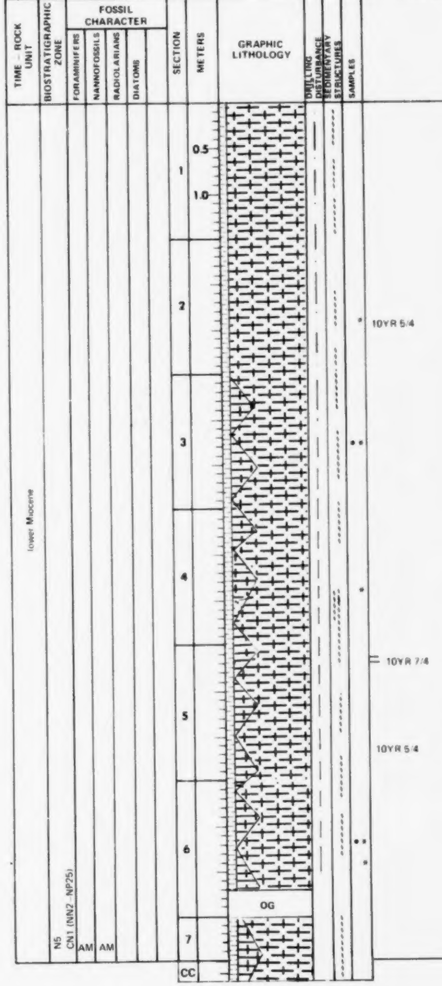
TIME – ROCK UNIT
BIOSTRATIGRAPHIC ZONE
FOSSIL CHARACTER
FORAMINIFERS
NANNOFOSSILS
RADIOLARIANS
DIATOMS
SECTION
METERS
GRAPHIC LITHOLOGY
DRILLING DISTURBANCE
SEDIMENTARY STRUCTURES
SAMPLES
lower Miocene
N5
CN1 (NN2–NP25)
AM
AM
0.5
1.0
1
2
3
4
5
6
7
CC
OG
10YR 5/4
10YR 7/4
10YR 5/4

LITHOLOGIC DESCRIPTION

DOMINANT LITHOLOGY CLAYEY FORAMINIFER-NANNOFOSSIL OOZE AND CHALK

Yellowish brown (10YR 5/4)

Massive bedding

Bioturbation is minor

Soft to firm sediments in Sections 1 and 2 have increasing frequency of chalky hard streaks downward into Section 3. Remainder of core is soft to firm with hard streaks. Chalk is minor constituent of all sections.

SMEAR SLIDE SUMMARY (%)

	2, 90 D	3, 80 D	4, 90 D	6, 70 M	6, 90 D
Composition:					
Feldspar	Tr	Tr	Tr	–	Tr
Clay	10	11	12	12	12
Palagonite	Tr	–	–	–	Tr
Micronodules	Tr	Tr	Tr	Tr	1
Zeolite	Tr	Tr	Tr	Tr	2
Carbonate unspec	5	5	5	5	5
Foraminifers	20	25	15	25	15
Calc. nannofossils	65	59	68	58	65

Carbonate Bomb (%):
3, 80 = 89 6, 70 = 88

SITE 563 HOLE CORE 17 CORED INTERVAL 308.5–318.0 m

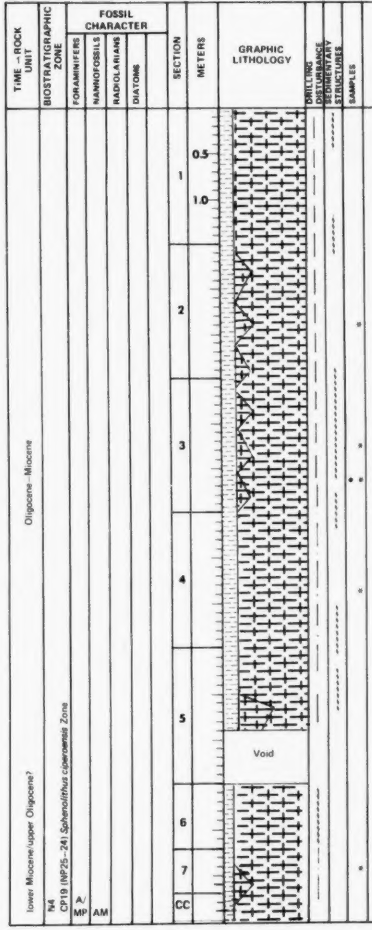
TIME – ROCK UNIT
BIOSTRATIGRAPHIC ZONE
FOSSIL CHARACTER
FORAMINIFERS
NANNOFOSSILS
RADIOLARIANS
DIATOMS
SECTION
METERS
GRAPHIC LITHOLOGY
DRILLING DISTURBANCE
SEDIMENTARY STRUCTURES
SAMPLES
Oligocene–Miocene
lower Miocene/upper Oligocene?
N4
CP19 (NP25–24) Sphenolithus ciperoensis Zone
A/MP
AM
0.5
1.0
1
2
3
4
5
6
7
CC
Void

10YR 5/4

LITHOLOGIC DESCRIPTION

DOMINANT LITHOLOGY CLAYEY FORAMINIFER-NANNOFOSSIL OOZE AND CHALK

Yellowish brown (10YR 5/4)

Massive bedding

Bioturbation is absent to minor

Alternating soft to firm ooze, with hard streaks. Chalk is minor constituent of all sections

SMEAR SLIDE SUMMARY (%):

	2, 90 D	3, 80 D	3, 118 D	4, 90 D	7, 25 D
Composition:					
Feldspar	Tr	Tr	Tr	Tr	Tr
Heavy minerals	–	–	–	Tr	–
Clay	15	10	16	13	16
Palagonite	Tr	Tr	Tr	Tr	Tr
Micronodules	Tr	Tr	Tr	1	Tr
Zeolite	1	2	1	3	2
Carbonate unspec.	5	5	5	5	5
Foraminifers	15	15	20	10	15
Calc. nannofossils	64	68	58	69	62

Carbonate Bomb (%):
3, 118 = 83

SITE 563 HOLE CORE 18 CORED INTERVAL 318.0–327.5 m

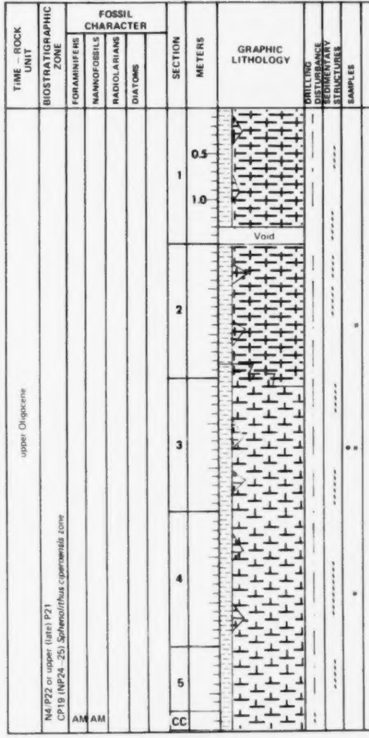
TIME – ROCK UNIT
BIOSTRATIGRAPHIC ZONE
FOSSIL CHARACTER
FORAMINIFERS
NANNOFOSSILS
RADIOLARIANS
DIATOMS
SECTION
METERS
GRAPHIC LITHOLOGY
DRILLING DISTURBANCE
SEDIMENTARY STRUCTURES
SAMPLES
upper Oligocene
N4/P22 or upper (late) P21
CP19 (NP24–25) Sphenolithus ciperoensis zone
AM
AM
0.5
1.0
1
2
3
4
5
CC
Void

10YR 5/4

LITHOLOGIC DESCRIPTION

DOMINANT LITHOLOGY CLAYEY FORAMINIFER-NANNOFOSSIL OOZE CLAYEY AND NANNOFOSSIL OOZE

Yellowish brown (10YR 5/4)

Massive bedding

Bioturbation is absent to minor

Sediments are soft to firm ooze with several hard streaks. Chalk is a minor constituent of all sections.

SMEAR SLIDE SUMMARY (%):

	2, 90 D	3, 80 D	4, 90 D
Composition:			
Feldspar	Tr	Tr	Tr
Clay	12	8	11
Palagonite	Tr	Tr	–
Micronodules	2	Tr	Tr
Zeolite	2	3	5
Carbonate unspec.	5	10	10
Foraminifers	15	5	5
Calc. nannofossils	64	74	69

Carbonate Bomb (%)
3, 80 = 89

SITE 563 HOLE CORE 19 CORED INTERVAL 327.5–337.0 m

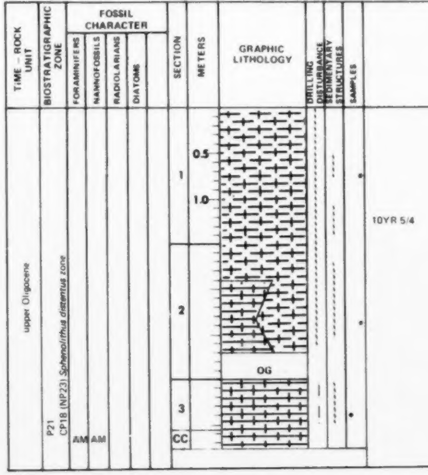
TIME – ROCK UNIT
BIOSTRATIGRAPHIC ZONE
FOSSIL CHARACTER
FORAMINIFERS
NANNOFOSSILS
RADIOLARIANS
DIATOMS
SECTION
METERS
GRAPHIC LITHOLOGY
DRILLING DISTURBANCE
SEDIMENTARY STRUCTURES
SAMPLES
upper Oligocene
P21
CP18 (NP23) Sphenolithus distentus zone
AM
AM
1
2
3
CC
0.5
1.0
OG
10YR 5/4

LITHOLOGIC DESCRIPTION

DOMINANT LITHOLOGY FORAMINIFER NANNOFOSSIL OOZE AND CHALK

Yellowish brown (10YR 5/4)

Massive bedding

Bioturbation is absent to minor

Distinct light-colored burrows in Section 3.

SMEAR SLIDE SUMMARY (%)

	1, 80	2, 90
	D	D
Composition		
Feldspar	Tr	Tr
Clay	,10	10
Micronodules	Tr	Tr
Zeolite	5	1
Carbonate unspec.	10	10
Foraminifers	20	25
Calc. nannofosils	35	54
Dolomite	Tr	–

Carbonate Bomb (%)
3, 41 = 89

SITE 563 HOLE CORE 20 CORED INTERVAL 337.0–346.5 m

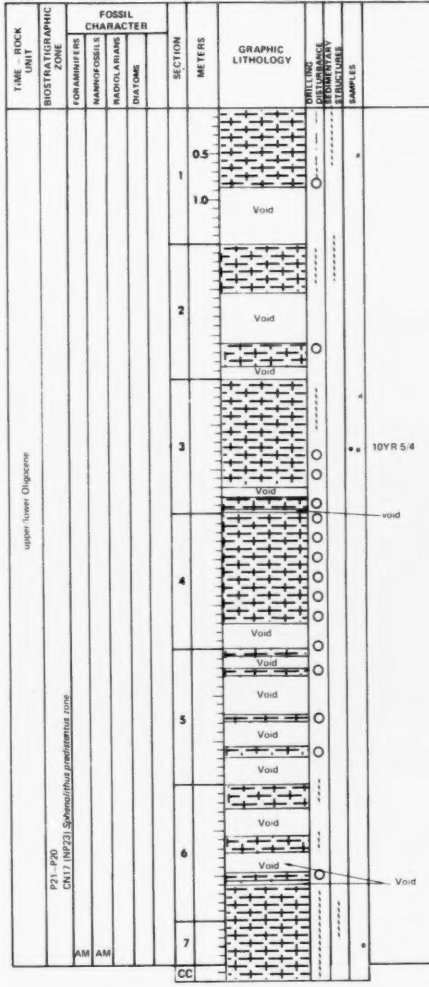
TIME – ROCK UNIT
BIOSTRATIGRAPHIC ZONE
FOSSIL CHARACTER
FORAMINIFERS
NANNOFOSSILS
RADIOLARIANS
DIATOMS
SECTION
METERS
GRAPHIC LITHOLOGY
DRILLING DISTURBANCE
SEDIMENTARY STRUCTURES
SAMPLES
upper/lower Oligocene
P21–P20
CN17 (NP23) Sphenolithus predistentus zone
AM
AM
1
2
3
4
5
6
7
CC
0.5
1.0
Void
Void
Void
Void
Void
Void
Void
Void
Void
Void
Void
10YR 5/4
void
Void

LITHOLOGIC DESCRIPTION

DOMINANT LITHOLOGY FORAMINIFER NANNOFOSSIL OOZE

Yellowish brown (10YR 5/4)

The entire core is extremely disturbed by drilling. Only very minor bioturbation is occasionally distinguishable.

Poor recovery and soupy condition of sediments are probably related to mechanical causes.

SMEAR SLIDE SUMMARY (%):

	1, 55	3, 20	3, 80	7, 30
	D	M	D	D
Composition:				
Feldspar	Tr	Tr	Tr	Tr
Clay	5	8	5	5
Micronodules	Tr	Tr	Tr	Tr
Zeolite	3	3	Tr	3
Carbonate unspec.	8	5	10	10
Foraminifers	15	10	20	10
Calc. nannofossils	69	73	65	72
Dolomite	–	Tr	–	–

Carbonate Bomb (%):
3, 80 = [illegible]

SITE 563 HOLE CORE 21 CORED INTERVAL 346.5–355.5 m

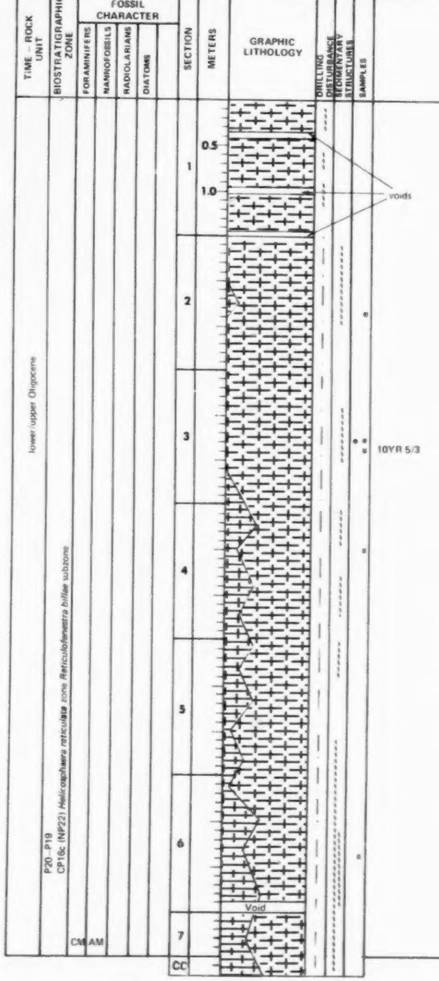
TIME – ROCK UNIT
BIOSTRATIGRAPHIC ZONE
FOSSIL CHARACTER
FORAMINIFERS
NANNOFOSSILS
RADIOLARIANS
DIATOMS
SECTION
METERS
GRAPHIC LITHOLOGY
DRILLING DISTURBANCE
SEDIMENTARY STRUCTURES
SAMPLES
lower/upper Oligocene
P20–P19
CP16c (NP22) Helicosphaera reticulata zone Reticulofenestra billae subzone
CM AM
1
2
3
4
5
6
7
CC
0.5
1.0
voids
Void
10YR 5/3

LITHOLOGIC DESCRIPTION

DOMINANT LITHOLOGY FORAMINIFER-NANNOFOSSIL OOZE AND CHALK

Brown (10YR 5/3)

Bedding is massive

Bioturbation is absent to minor

Alternating firm to hard (ooze to chalk). Chalk layers more common and thicker downward

SMEAR SLIDE SUMMARY (%):

	2, 90	3, 80	3, 90	4, 50	6, 90
	D	D	D	M	D
Composition:					
Feldspar	Tr	Tr	Tr	Tr	Tr
Clay	8	8	9	7	8
Micronodules	Tr	Tr	Tr	Tr	Tr
Zeolite	Tr	Tr	1	5	Tr
Carbonate unspec.	10	10	10	10	10
Foraminifers	20	24	20	10	18
Calc. nannofossils	62	56	58	68	69
Dolomite	–	2	2	Tr	3

Carbonate Bomb (%):
3, 80 = 92

SITE 563 HOLE CORE 22 CORED INTERVAL 355.5–364.5 m

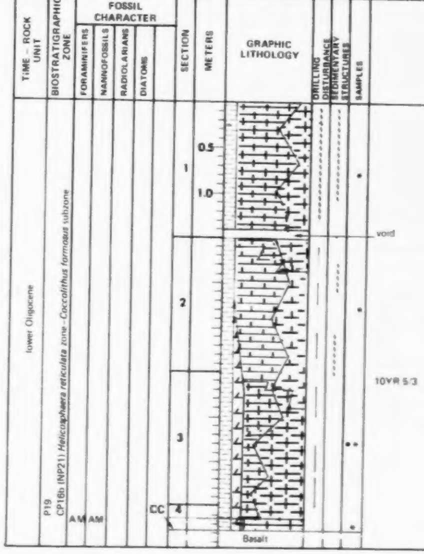
TIME – ROCK UNIT
BIOSTRATIGRAPHIC ZONE
FOSSIL CHARACTER
FORAMINIFERS
NANNOFOSSILS
RADIOLARIANS
DIATOMS
SECTION
METERS
GRAPHIC LITHOLOGY
DRILLING DISTURBANCE
SEDIMENTARY STRUCTURES
SAMPLES
lower Oligocene
P19
CP16b (NP21) Helicosphaera reticulata zone - Coccolithus formosus subzone
AM AM
1
2
3
4
CC
0.5
1.0
void
10YR 5/3
Basalt

LITHOLOGIC DESCRIPTION

DOMINANT LITHOLOGY CLAYEY FORMAINIFER-NANNOFOSSIL CHALK AND OOZE AND CLAYEY DOLOMITIC NANNOFOSSIL TO FORAMINIFER-NANNOFOSSIL CHALK AND OOZE

Brown (10YR 5/3)

Bedding is massive

Bioturbation is absent to minor

Chalk more dominant than in overlying cores

SMEAR SLIDE SUMMARY (%):

	1, 80	2, 90	3, 80	CC
	D	D	D	D
Composition:				
Feldspar	Tr	Tr	Tr	Tr
Clay	13	15	13	13
Palagonite	–	Tr	–	–
Micronodules	2	Tr	Tr	Tr
Zeolite	Tr	Tr	–	Tr
Carbonte unspec.	10	10	10	10
Foraminifers	15	5	10	10
Calc. nannofossils	60	65	57	57
Dolomite	Tr	5	10	10

Carbonate Bomb (%):
3, 80 = 87

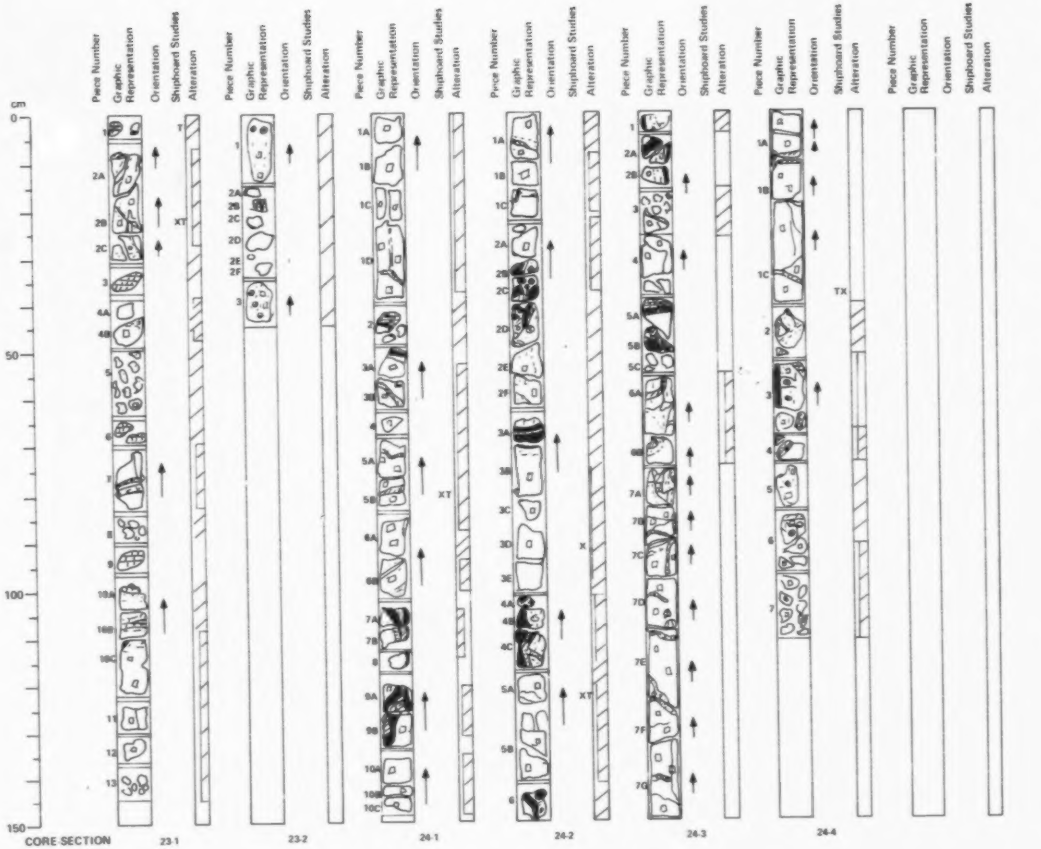

SITE 563, CORE 23 — Depth 384.5–386.5 m

SECTION 1

SPARSELY PLAGIOCLASE PHYRIC PILLOW BASALT

Sparsely plagioclase phyric (2–3%˚) pillow basalt gray (2.5Y N6/0). Microphenocrysts of olivine and/or alteration products thereof are visible. Frequency of olivine is variable, < 1–5% in places. Alteration variable as well.

Plagioclase phenocrysts are randomly oriented 2–4 mm long and/or rounded 2–5 mm glomerocrysts or laths.

Olivine is present < 1–2 mm in diameter. Dark orange brown alteration residue is present in most localities rather than fresh olivine itself. Frequency of occurrence is variable.

Sedimentary material (limestone) occurs as interpillow or irregularly shaped veins as indicated. Dendritic pattern of MnO or other oxides is visible in places. Alteration frequently occurs in the basalt adjacent to limestone units.

Alteration is moderate overall, higher in places. Highest adjacent to calcite veins and/or limestone units, gray (2.5Y N6/0) to pale brown (10YR 6/3).

Vesicles are scarce, rounded < 1–2 mm in diameter and often clay filled.

Glass is scarce. Piece 7 has a glassy rind grading into a black (10YR 2/1) aphanitic basalt grading into a very dark gray (10YR 3/1) aphyric to slightly phyric gray (2.5Y N6/0) pillow basalt.

SECTION 2

SPARSELY PLAGIOCLASE PHYRIC PILLOW BASALT

0–43 cm. Sparsely plagioclase phyric aphanitic basalt (close to pillow margins). Gray (10YR 5/1) to grayish brown (10YR 5/2) where shown. Plagioclase phenocrysts, prismatic to 1 mm (~1%).

17–19 cm. Limestone as in Section 1 with glass fragment.

SITE 563, CORE 24 — Depth 386.5–373.5 m

SECTION 1

SPARSELY PLAGIOCLASE PHYRIC PILLOW BASALT

0–50 cm

Sparsely plaioclase phyric pillow basalt with (micro) phenocrysts of olivine also present 85–150 cm increasing in frequency and size. Gray (1.5YN 5/0) basalt slightly altered along calcite veins and irregular veinlets.

Plagioclase crystals 1–5 mm in length and also as rounded laths and/or glomerocrysts 2–4 mm in diameter. Sparsely scattered throughout. No particular concentration anywhere in pillow.

Olivine phenocrysts become visible in hand sample 85–150 cm, in addition to plagioclase. Generally altered to dark orange brown clays (<1–1 mm).

Limestone as well as calcite is present in fractures and on rims of rocks.

Alteration is present in rock fractures, adjacent to calcite and limestone veins, slight color change to basalt by yellowish brown (10YR 5/8) hue to gray (2.5Y N5/0) basalt. Also see alteration in gradation to pillow margins (slight increase in gray intensity).

Glass present as rims and interpillow zones. Calcite veins, seem to co-occur with glass (could be incidental, but is noticeable). Slightly reactive with calcite/and or limestone to a palagonite – color calcite.

Sequence of glass to very dark gray (10YR 3/1) aphanitic zone to slightly plagioclase phyric gray (2.5Y N5/0) pillow basalt.

SECTION 2

SPARSELY PLAGIOCLASE PHYRIC PILLOW BASALT SEQUENCE AND MINOR GLASS BRECCIA

0–150 cm

Sparsely plagioclase phyric gray (2.5Y N5/0) basalt with (micro) phenocrysts of olivine as in Section 1.

Plagioclase crystals as in Section 1.

Olivine occurrence as in Section 1. Extends throughout core, size increasing to < 1–2 mm.

Alteration as in Section 1. In addition, alteration concurrent with variolitic basalt sequence.

Variolitic basalt, sequence where noted: glass to black (10YR 2/1) aphanitic basalt to variolite zone of yellow brown (10YR 5/8–10YR 5/6) to gray (2.5Y N5/0) slightly plagioclase phyric.

Glass present where indicated. Co-occurrence with calcite/limestone is enhanced in breccia zone, yet still occurs in whole rock samples.

33–45, 65–67, 100–102, and 143–148 cm. Breccia of glass clasts in a calcite (predominantly) and limestone matrix. Clasts are angular, few mm–few cm in diameter. Slightly palagonite tinted calcite product rims glass fragments. Some palagonitization of smaller clasts occurs.

SECTION 3

SPARSELY PLAGIOCLASE PHYRIC PILLOW BASALT

11–150 cm. Sparsely plagioclase phyric pillow basalt. Fine grained, gray (7.5YR N5). Fairly fresh to moderately altered (light grayish brown – 10YR 6/2) near pillow margins or along fractures. 1–2% plagioclase phenocrysts (2–5 mm), prisms, equant, some with rounded edges (resorbed?). 1–2% plagioclase needles (1–4 mm) randomly oriented. <1% olivine (1–2 mm) mostly altered to red brown clay(?).

0–4 cm. One piece of finer grained aphyric basalt (almost aphanitic) at pillow margin.

6–8 cm. Fresh, black glass clasts with rims altered to reddish yellow (7.5YR 7/8) (generally next to fresher glass) and dark brown (7.5YR 4/4) usually rimming the palagonite, but sometimes also next to glass in calcite limestone (pinkish gray – 7.5YR 7/2) matrix.

Fractures filled with calcite (▨) or pink (7.5YR 8/4) limestone or both mixed together(?) (pinkish gray – 7.5YR 7/2).

SECTION 4

SPARSELY PLAGIOCLASE PHYRIC PILLOW BASALT

0–40 cm. Same as Section 3.

40–150 cm. Very sparse plagioclase phyric to aphyric.

85–86 cm. Basalt with rim of limestone matrix with angular basalt breccia and altered glass clasts (2–4 mm) with outside 4 mm rim of white calcite.

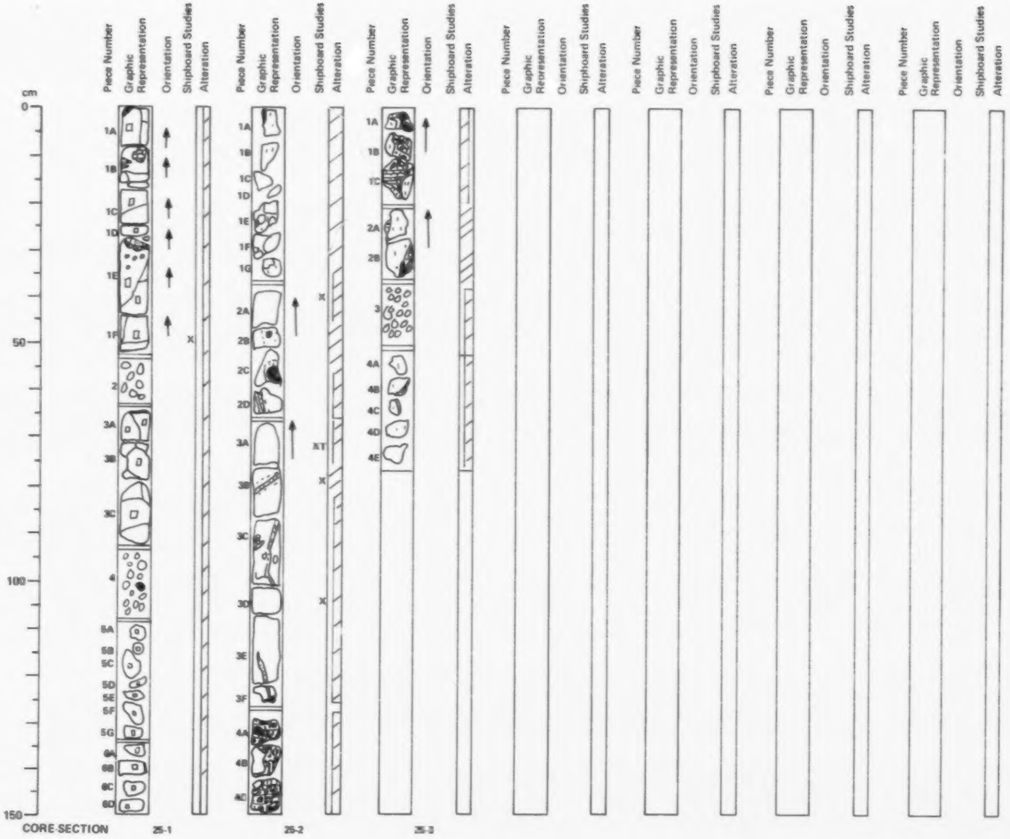

SITE 563, CORE 25 Depth 373.5–382.5 m

SECTION 1

SPARSELY PLAGIOCLASE PHYRIC PILLOW BASALT

0–150 cm

Fine grained, gray (2.5Y N6/0)

<2% plagioclase phenocrysts (1–7 mm), subhedral (slightly resorbed?), partly equant, partly needle shaped

<1% olivine phenocrysts (<2 mm), eu- and anhedral residues filled with brown clay

No visible round vesicles

A few irregular vesicles occur in Piece 1E (30–37 cm). They are coated with calcite cement.

At 0–2, 64–65, 100–102, and 138–142 cm occur fresh black glass rinds.

Limestone occurs at 8–13 cm, yellowish red (5YR 4/6) and at 28–40 cm, pink (5YR 7/3), partly as vein filling.

The boundary between basalt and limestone is often very irregular (lobes).

SECTION 2

SPARSELY PLAGIOCLASE PHYRIC PILLOW BASALT

Fine grained gray (2.5Y N6/0) sparsely plagioclase phyric pillow basalt with (micro) phenocrysts of dark orange brown alteration product of olivine

1–2% plagioclase phenocrysts 1–6 mm needle form or 2–5 mm diameter rounded aggregates and/or glomerocrysts

~1% olivine phenocrysts <2 mm in diameter euhedral to anhedral residual alteration residue dark orange brown in color. Sparsely scattered as well

Vesicles rare to absent, only present near glass and only visible with hand lens

Alteration to light gray (10YR 6/0) in patches with fresh "cores" of gray (2.5Y N6/0) basalt. Mainly occurs in Pieces 1A–G. Alteration present adjacent to rock fractures, calcite veins and limestone patches, to light gray (10YR 6/0) through light brownish gray (10YR 6/2).

Variolitic zone where noted. Slight color change with addition of yellowish brown (10YR 5/8) hue to gray basalt. Slight change in gray intensity. Glass present as indicated

127–150 cm: Glass breccia in a calcite and limestone matrix. Clasts are angular, few mm to few cm in diameter. Some palagonitization of glass clasts occurs, as well as a palagonite-tinted sedimentary product between clasts and matrix

SECTION 3

SPARSELY PLAGIOCLASE PHYRIC PILLOW BASALT AND GLASS BRECCIA

Fine grained gray (2.5Y N6/0) to light gray (10YR 6/0) sparsely plagioclase phyric pillow basalt as in Sections 1 and 2. Slightly more altered in glassy zones than in Section 2. Gravel pieces (Piece 3) more of a light brownish gray (10YR 6/2), possible indicating a higher degree of alteration than in above sections. (Micro) phenocrysts of dark orange brown alteration residue of olivine

Plagioclase phenocrysts as in Section 2, rounded 1–3⁺ mm in diameter

Olivine as in Section 2

Vesicles absent

Alteration as in Section 2 and as indicated. Light gray (10YR 6/0) to light brownish gray (10YR 6/2) alteration of basalts

Glass as indicated

0–18 cm: Glass breccia with calcite and limestone matrix. Angular clasts, edges palagonitized. Few large (few cm) fine grained basalt clasts, light brownish gray (10YR 6/2) and altered as indicated. Palagonite

1-1
1-2
1-3
1,CC
2-1
2-2
2-3
2-4
2-5
2-6
2-7
2,CC
0 cm
25
50
75
100
125
150

0 cm
25
50
75
100
125
150
3-1
3-2
3-3
3-4
3-5
3-6
3,CC
4-1
4-2
4-3
4-4
4,CC

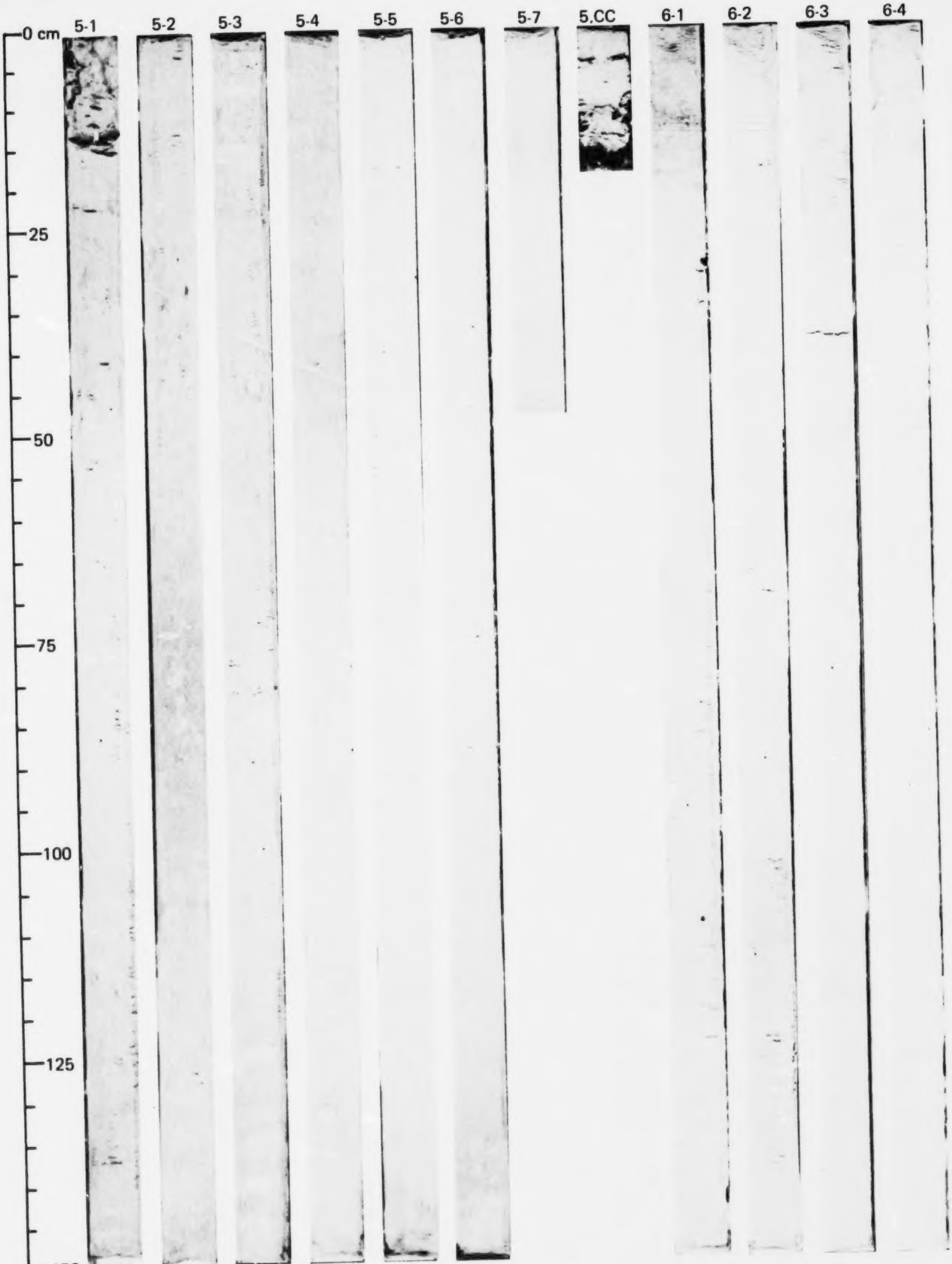
0 cm
25
50
75
100
125
150
5-1
5-2
5-3
5-4
5-5
5-6
5-7
5,CC
6-1
6-2
6-3
6-4

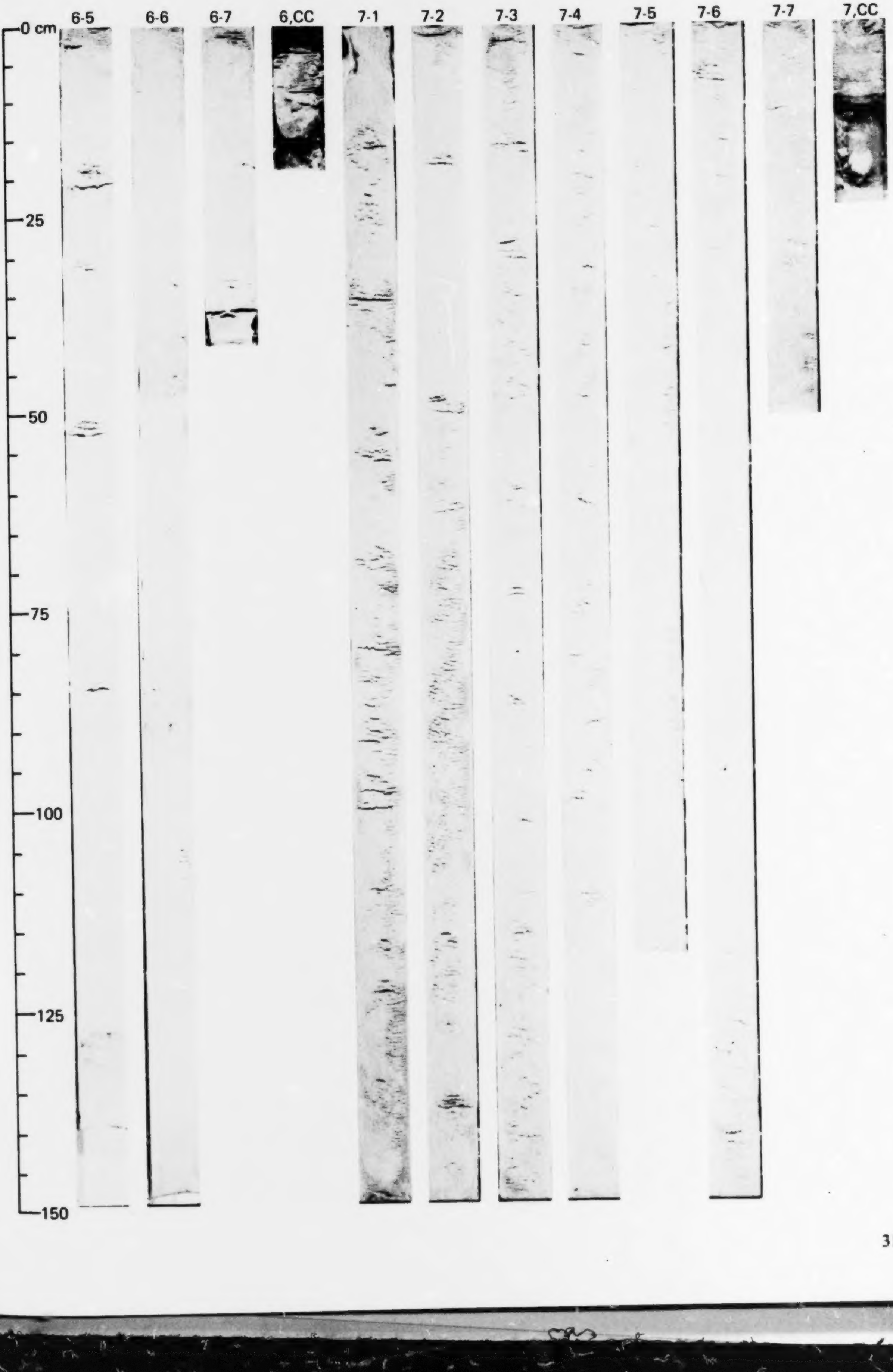
6-5
6-6
6-7
6,CC
7-1
7-2
7-3
7-4
7-5
7-6
7-7
7,CC
0 cm
25
50
75
100
125
150

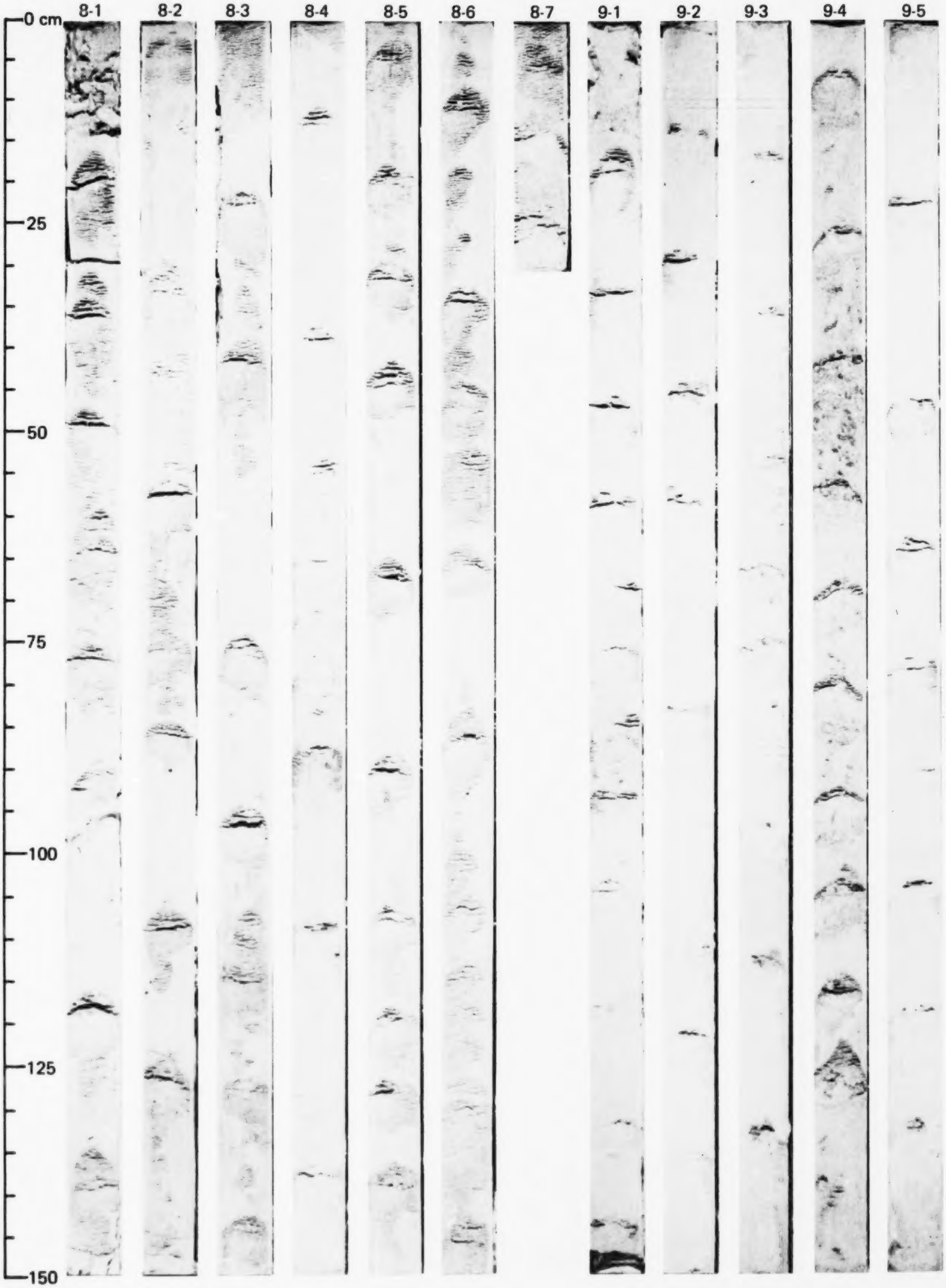
8-1
8-2
8-3
8-4
8-5
8-6
8-7
9-1
9-2
9-3
9-4
9-5
0 cm
25
50
75
100
125
150

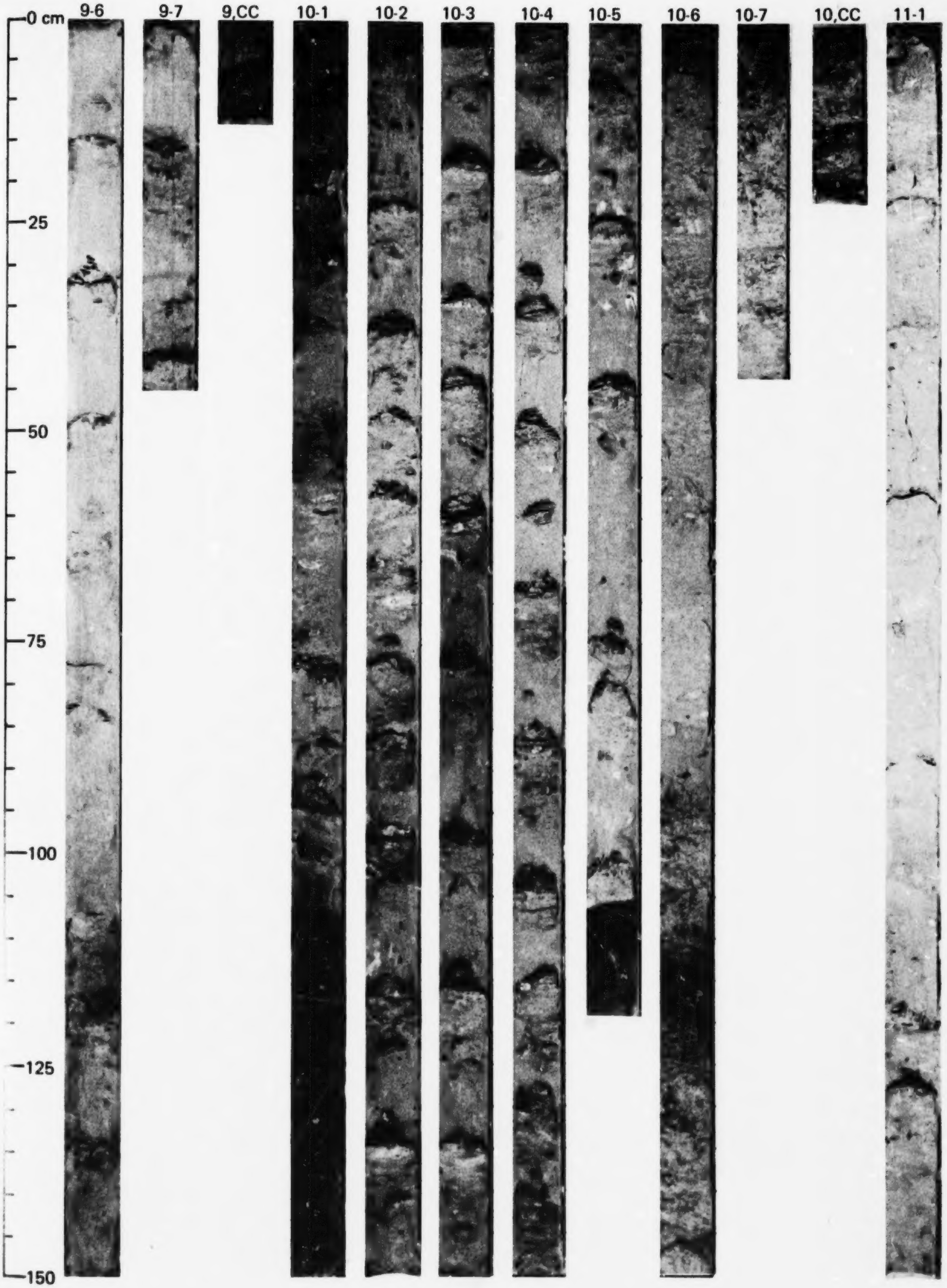
0 cm
25
50
75
100
125
150
9-6
9-7
9,CC
10-1
10-2
10-3
10-4
10-5
10-6
10-7
10,CC
11-1

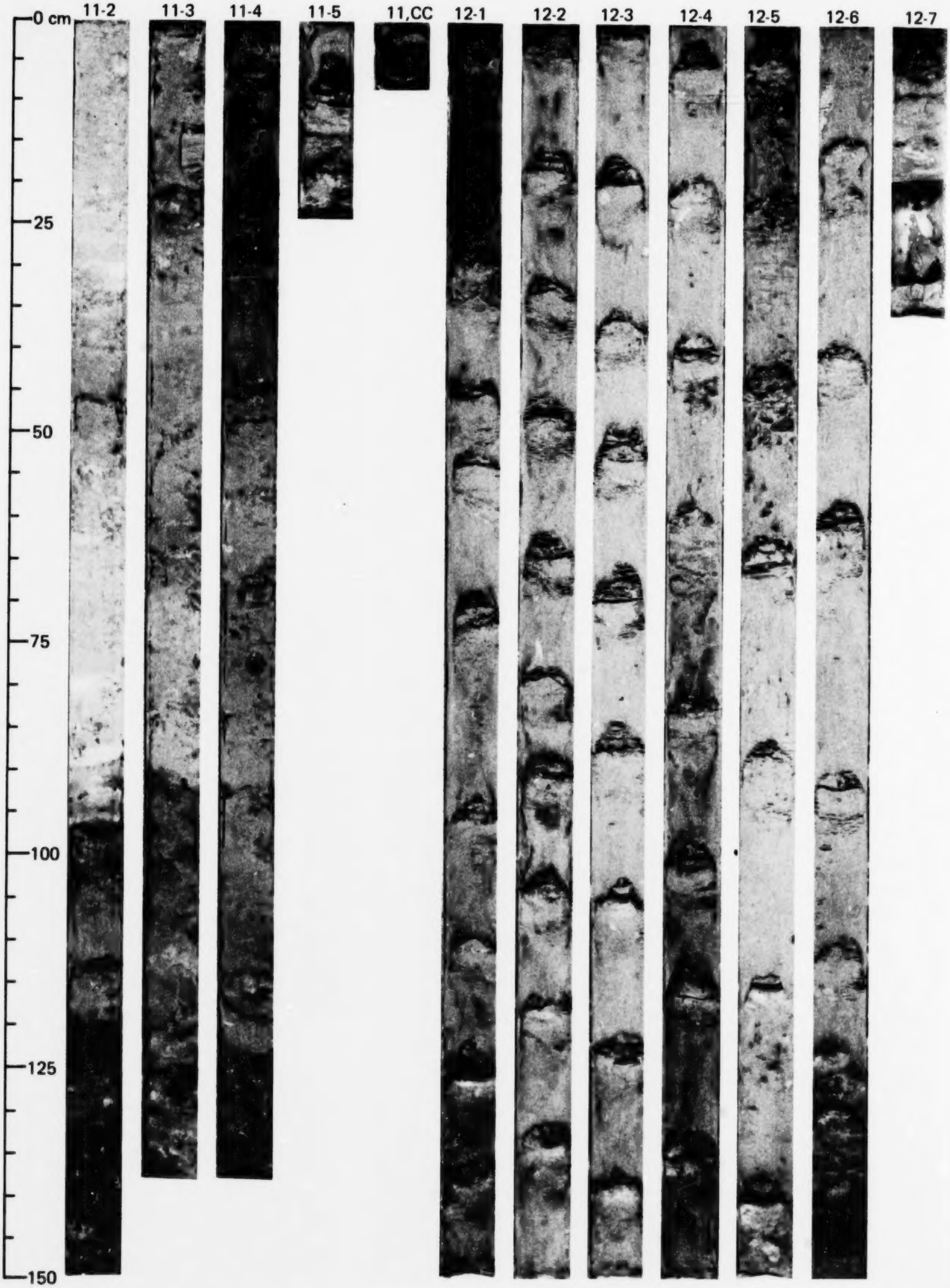
0 cm
25
50
75
100
125
150
11-2
11-3
11-4
11-5
11,CC
12-1
12-2
12-3
12-4
12-5
12-6
12-7

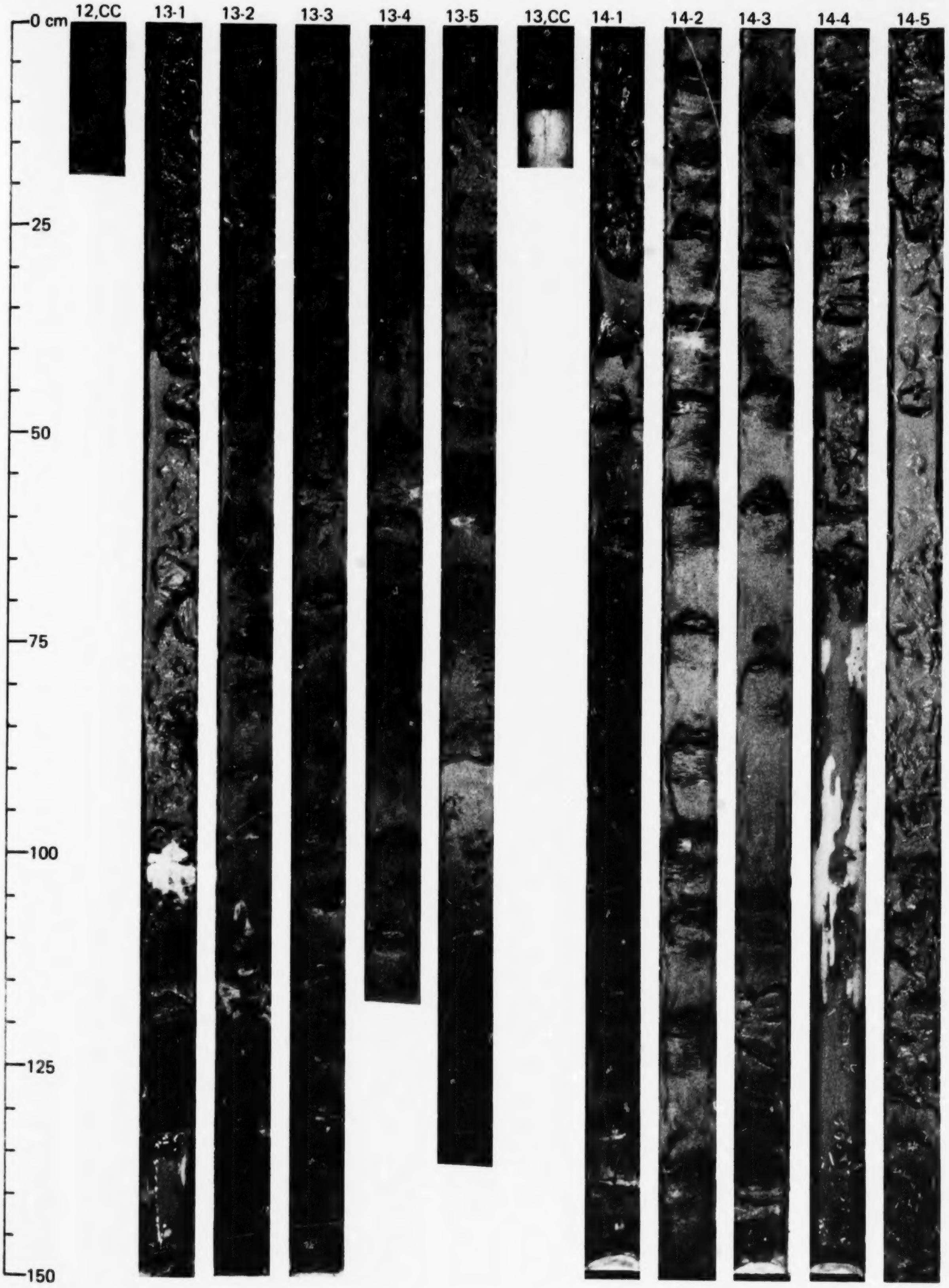
0 cm
25
50
75
100
125
150
12,CC
13-1
13-2
13-3
13-4
13-5
13,CC
14-1
14-2
14-3
14-4
14-5

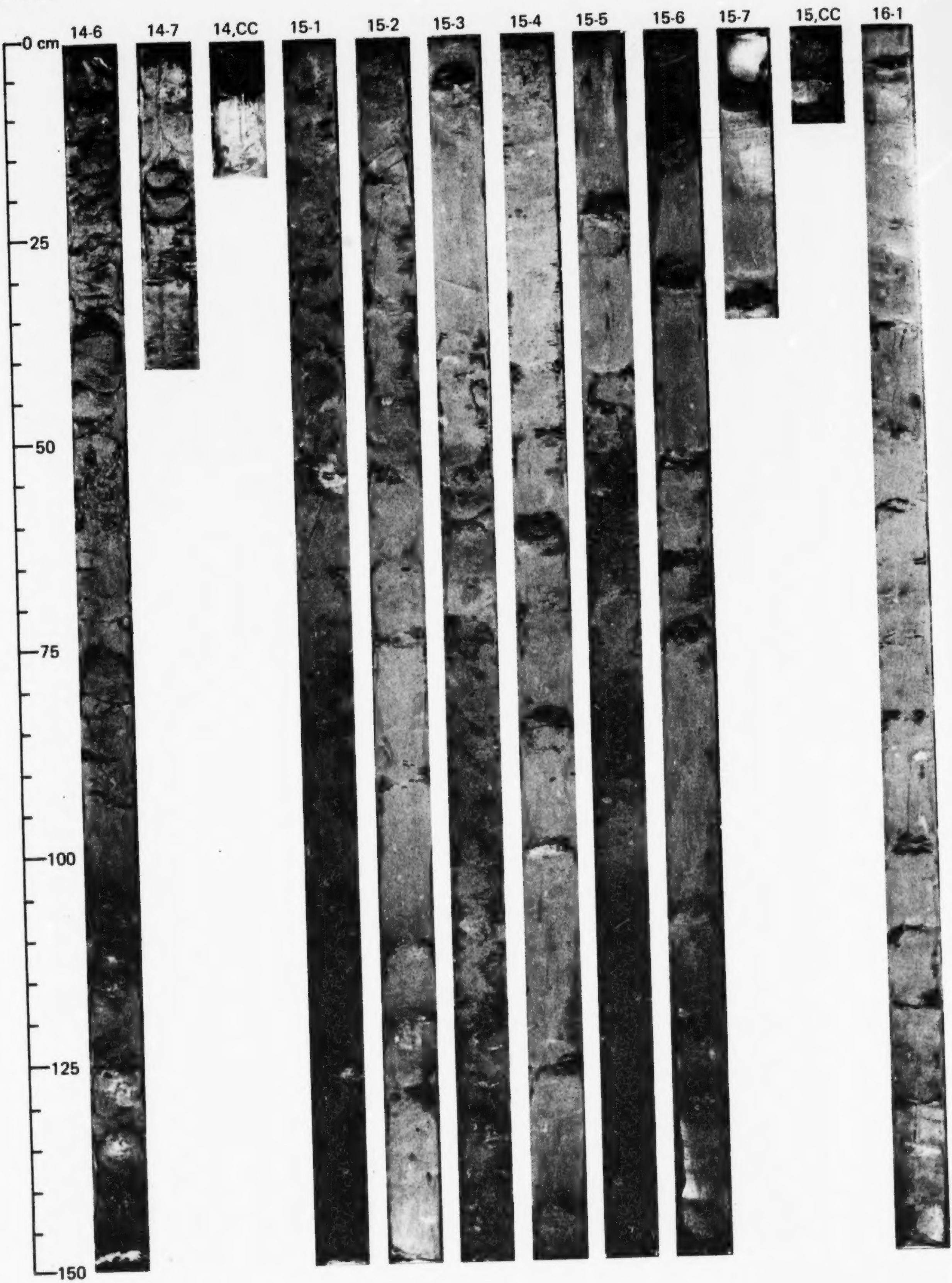
14-6
14-7
14,CC
15-1
15-2
15-3
15-4
15-5
15-6
15-7
15,CC
16-1
0 cm
25
50
75
100
125
150

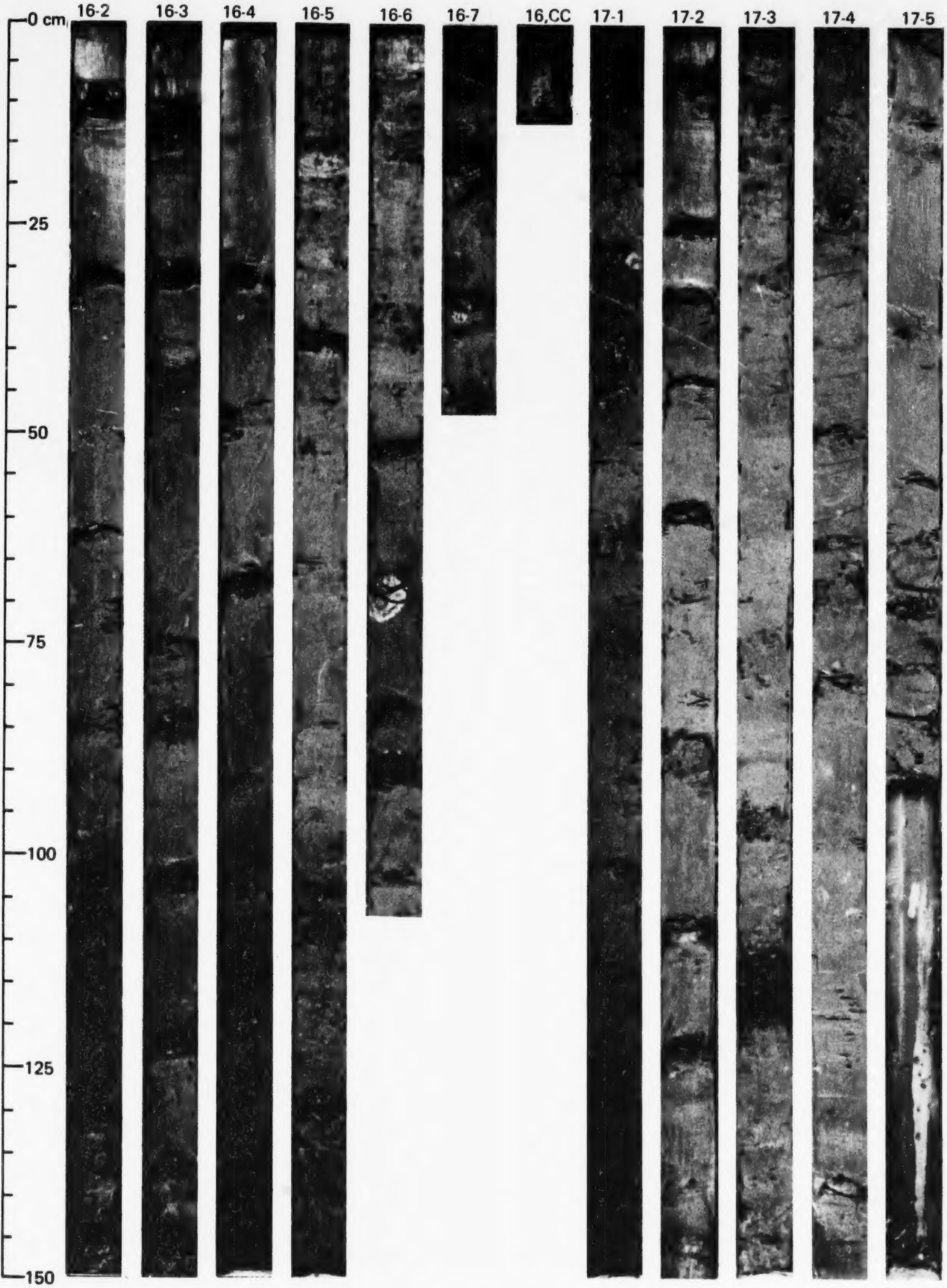
0 cm
25
50
75
100
125
150
16-2
16-3
16-4
16-5
16-6
16-7
16,CC
17-1
17-2
17-3
17-4
17-5

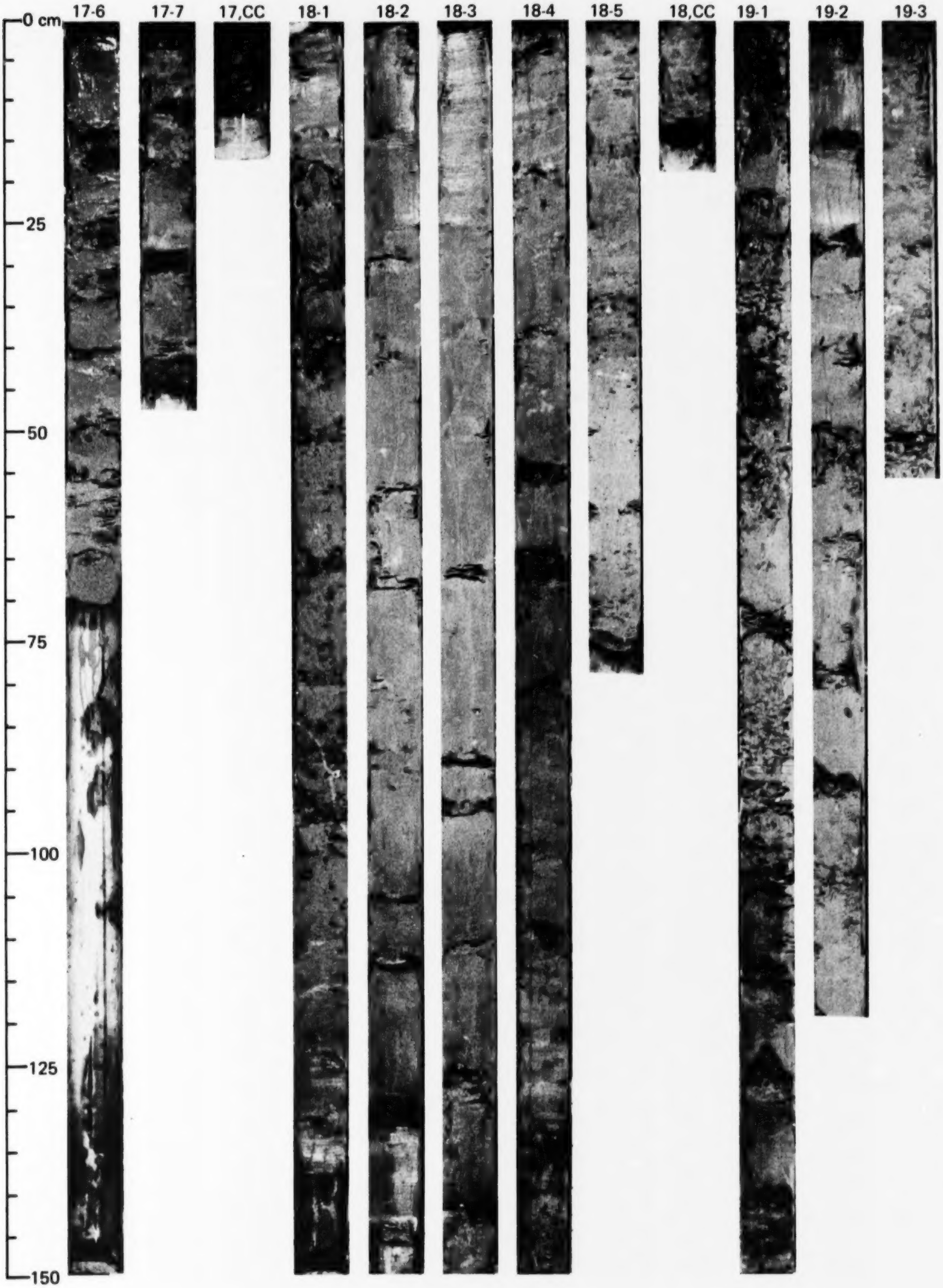
0 cm
25
50
75
100
125
150
17-6
17-7
17,CC
18-1
18-2
18-3
18-4
18-5
18,CC
19-1
19-2
19-3

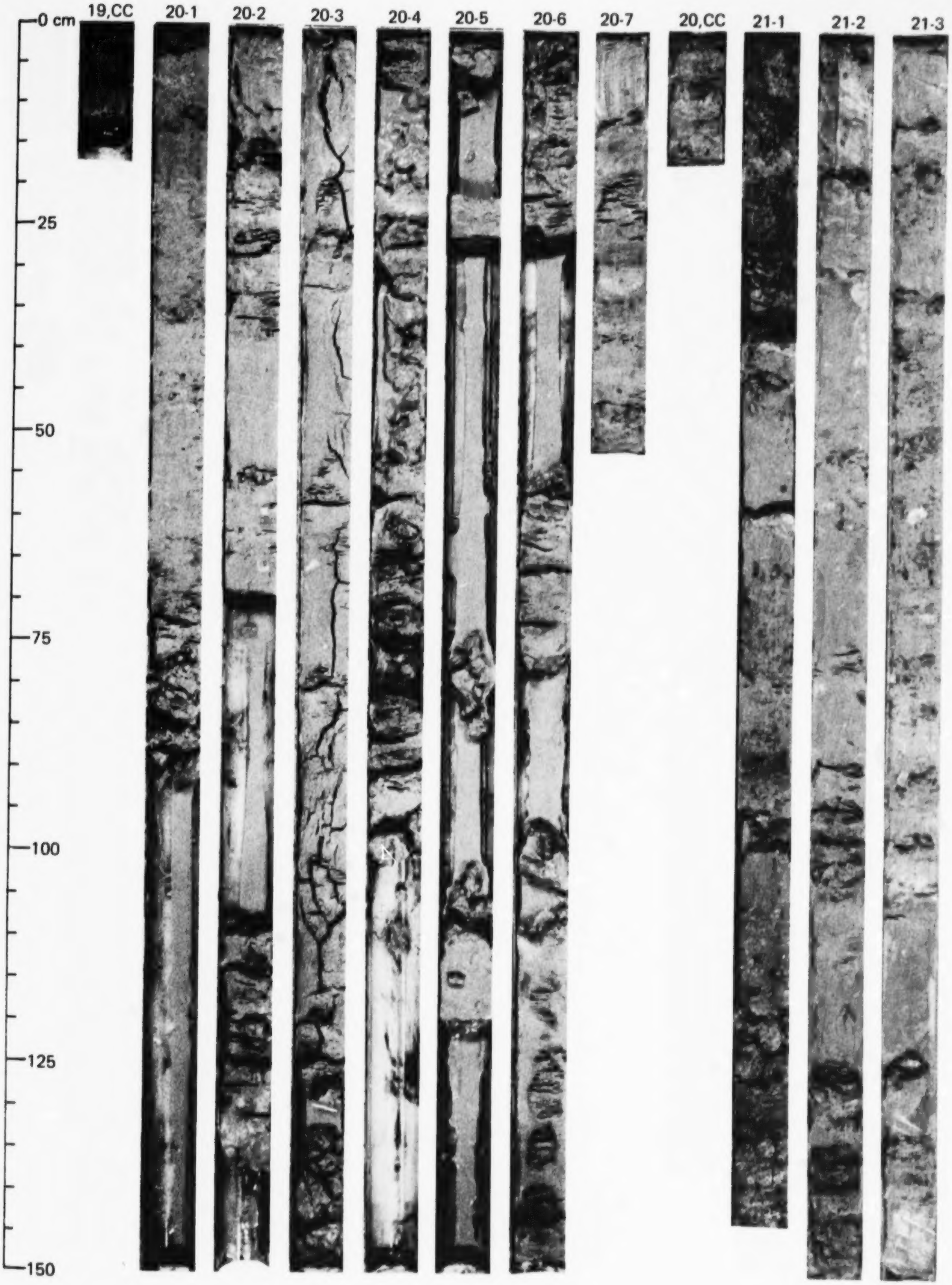

0 cm
25
50
75
100
125
150
19,CC
20-1
20-2
20-3
20-4
20-5
20-6
20-7
20,CC
21-1
21-2
21-3

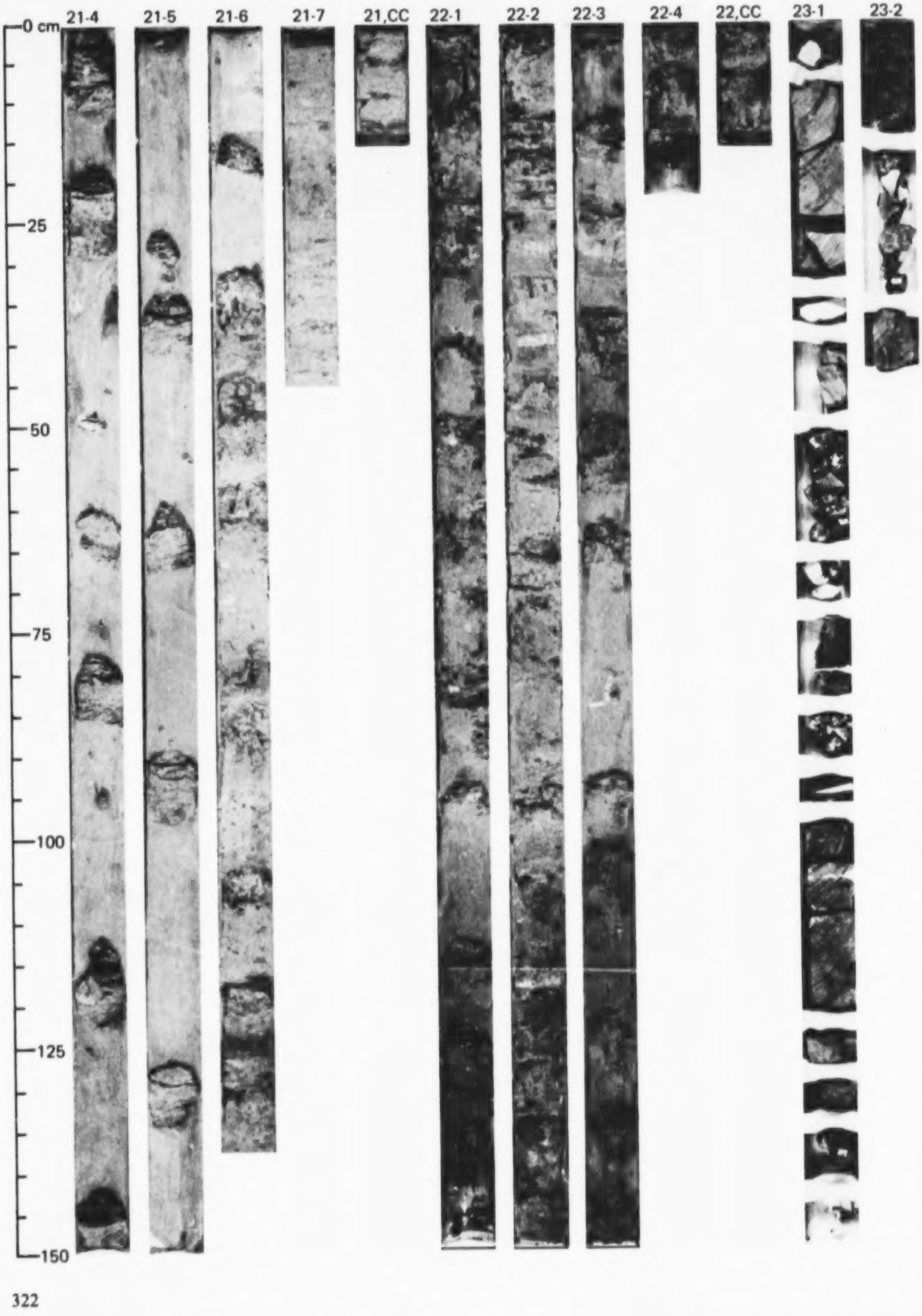
0 cm
25
50
75
100
125
150
21-4
21-5
21-6
21-7
21,CC
22-1
22-2
22-3
22-4
22,CC
23-1
23-2

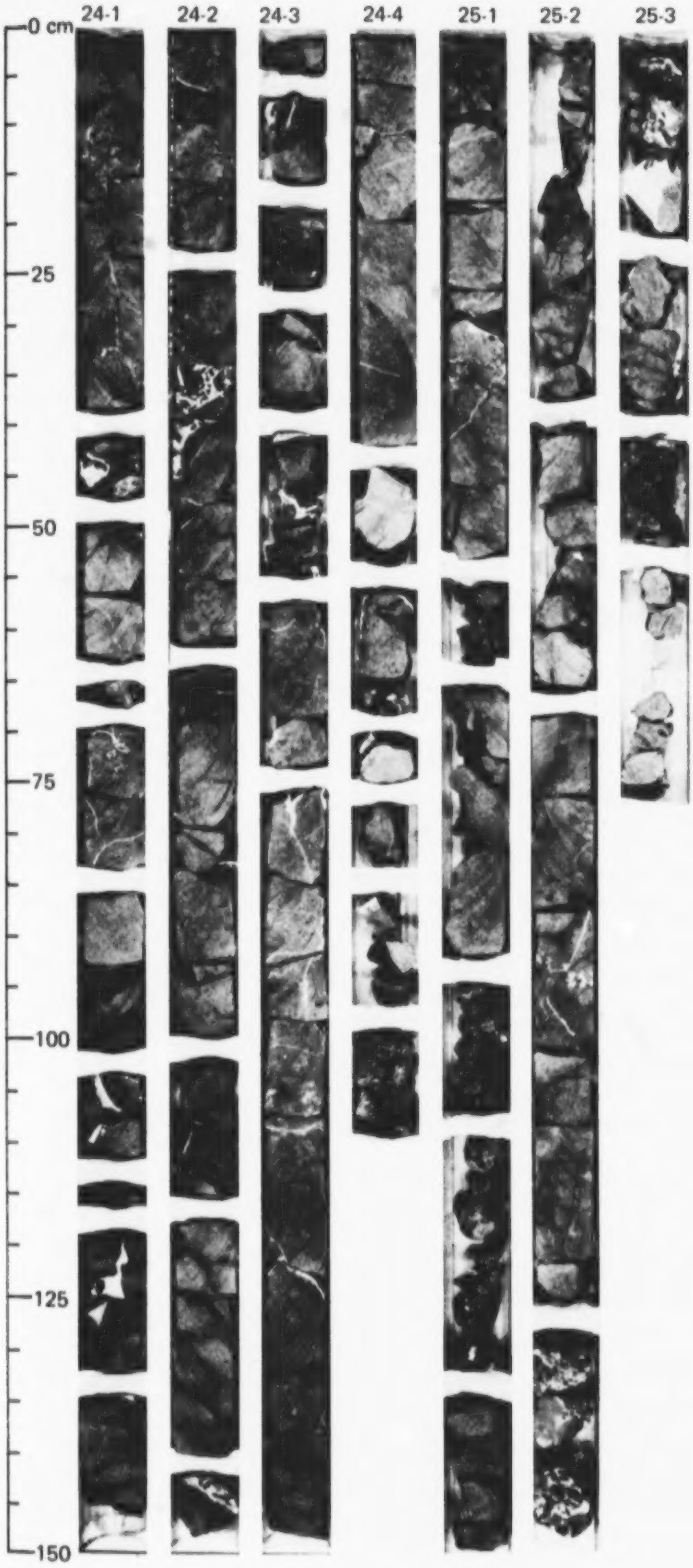
24-1
24-2
24-3
24-4
25-1
25-2
25-3
0 cm
25
50
75
100
125
150

13. SITE 564[1]

Shipboard Scientific Party[2]

HOLE 564

Date occupied: 28 October 1981

Date departed: 1 November 1981

Time on hole: 96 hr.

Position (latitude; longitude): 33°44.36′N; 43°46.03′W

Water depth (sea level; corrected m, echo-sounding): 3820

Water depth (rig floor; corrected m, echo-sounding): 3830

Bottom felt (m, drill pipe): 3830

Penetration (m): 365

Number of cores: 9

Total length of cored section (m): 81

Total core recovered (m): 34.75

Core recovery (%): 43

Oldest sediment cored:
Depth sub-bottom (m): 284+ (in the basement)
Nature: Limestone
Age: lower Oligocene

Basement:
Depth sub-bottom (m): 284

Nature: Basalt

Principal results: Hole 564 (Site MAR-11) was drilled on Anomaly 13 on the west flank of the Mid-Atlantic Ridge about 60 miles south of the Hayes Fracture Zone (Fig. 1). Site 564 is located about 6 miles north of Site 563.

The sediments were washed down to the basement, which was felt at a depth of 284 m sub-bottom. The basement was cored for 81 m. It is composed of aphyric basalts (both pillows and massive units) belonging to a single petrographic chemical group, even though some small variations close to the limit of precision of concentration measurements are observed. Nb varies from 2.8 to 6.1, Zr from 86 to 100, Ti from 8250 to 9000, Y from 38 to 42, and V from 345 to 463 (all measured in ppm). This range of variation is consistent with either depleted ($[Nb/Zr]_{ch} \sim 0.38$) or flat ($[Nb/Zr]_{ch} \sim 0.54$) rare earth patterns, but additional onshore measurements are needed to confirm this downhole variation.

A complete set of logs was run. As at Sites 556 and 558, two distinct sedimentary units are evident. Two temperature profiles were recorded; the first was run 18 hr. after circulation was stopped and the second 10 hr. later. The two profiles were identical down to below the sediment basement interface, showing a low gradient of about 6°C/km. Between 45 and 60 m in the basement, an increase of 2.5°C was observed. This is additional evidence at Anomaly 13 of downflow of seawater when the sedimentary layer is pierced.

No sediment accumulation rates could be calculated at this site, and no samples were taken for pore-water analysis.

OPERATIONS

Approach to Site

After drilling at Hole 563 ended, we decided to drill a second hole at MAR-11 but located about 5 or 10 miles away from Site 563. The *Challenger* got under way at 0730Z, 28 October, and headed in a northwesterly direction. Within two miles, basement became buried by a thick blanket of sediments. By 0850Z it was apparent that a suitable drill site might not be crossed for a long distance along this track. The course of the *Challenger* was altered to 090°, on a track that would pass about 6 miles north of Site 563 and that might cross the same basement ridge (Fig. 2, site chapter, Site 563, this volume). Upon crossing the ridge, we noted a location at 1005Z that fulfilled the requirements of thin sediments (less than 350 m) and smooth basement (Fig. 2). The course of the *Challenger* was reversed at 1022Z, and the beacon was dropped on Site 564 at 1047Z.

On-Site Operations

Hole 564 was spudded in at 1743Z, 28 October. Sediments were washed to a depth of 284 m sub-bottom where basement was hit. Coring within basement proceeded at a much faster rate than at Site 563 and without any major difficulties. Between 0305Z, 29 October and 1520Z, 30 October, nine cores were recovered, a total basement penetration of 81 m (Table 1). After Core 9 was recovered and we found out that a tropical storm might pass close by within 24 hr., we decided to begin logging operations three hours earlier than originally planned. The logging operations, which are described in detail in the Downhole Measurements section, proceeded smoothly and the tropical storm did not appear. Logging was completed at 2355Z, 31 October, and the drill string was pulled for the final time on Leg 82. The *Challenger* started on course to the Virgin Islands at 0847Z, 1 November.

---

[1] Bougault, H., Cande, S. C., et al., *Init. Repts. DSDP*, 82: Washington (U.S. Govt. Printing Office).

[2] Henri Bougault (Co-Chief Scientist), IFREMER (formerly CNEXO), Centre de Brest, B.P. 337, 29273 Brest Cedex, France; Steven C. Cande (Co-Chief Scientist), Lamont-Doherty Geological Observatory, Columbia University, Palisades, New York; Joyce Brannon, Department of Earth and Planetary Sciences, Washington University, St. Louis, Missouri; David M. Christie, Hawaii Institute of Geophysics, University of Hawaii at Manoa, Honolulu, Hawaii; Marlene Clark, Department of Geology, Florida State University, Tallahassee, Florida; Doris M. Curtis, Curtis and Echols, Geological Consultants, Houston, Texas; Natalie Drake, Department of Geology, University of Massachusetts, Amherst, Massachusetts; Dorothy Echols, Department of Earth and Planetary Sciences, Washington University, St. Louis, Missouri (present address: Curtis and Echols, Geological Consultants, 800 Anderson, Houston, Texas 77401); Ian Ashley Hill, Department of Geology, University of Leicester, Leicester LE1 7RH, United Kingdom; M. Javed Khan, Lamont-Doherty Geological Observatory, Columbia University, Palisades, New York (present address: Department of Geology, Peshawar University, Peshawar, Pakistan); William Mills, Deep Sea Drilling Project, Scripps Institution of Oceanography, La Jolla, California (present address: Ocean Drilling Program, Texas A&M University, College Station, Texas 77843); Rolf Neuser, Institut für Geologie, Ruhr Universität Bochum, 4630 Bochum 1, Federal Republic of Germany; Marion Rideout, Graduate School of Oceanography, University of Rhode Island, Kingston, Rhode Island (present address: Department of Geology, Rice University, P.O. Box 1892, Houston, Texas 77251); and Barry L. Weaver, Department of Geology, University of Leicester, Leicester, LE1 7RH, United Kingdom (present address: School of Geology and Geophysics, University of Oklahoma, Norman, Oklahoma 73019).

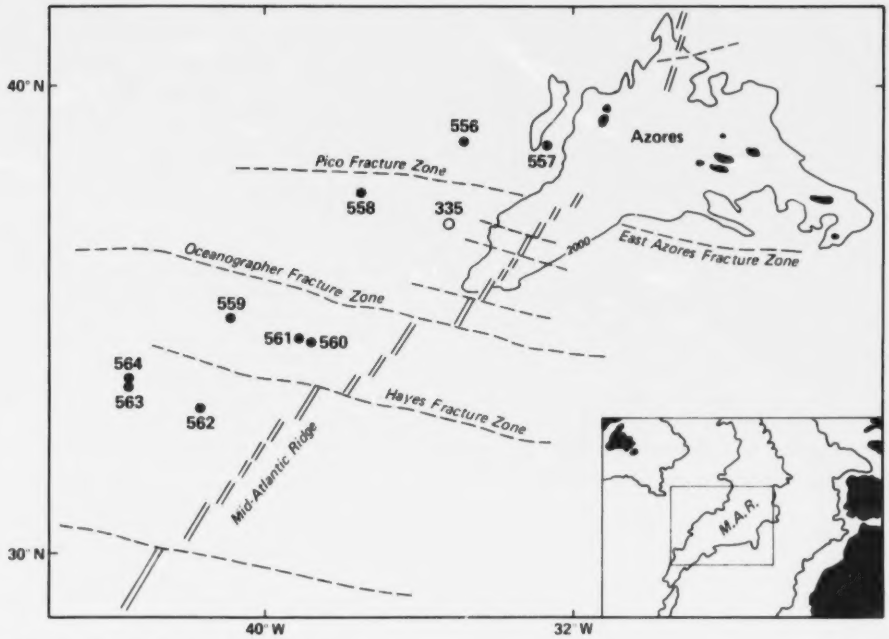

Figure 1. Site location map, Leg 82.

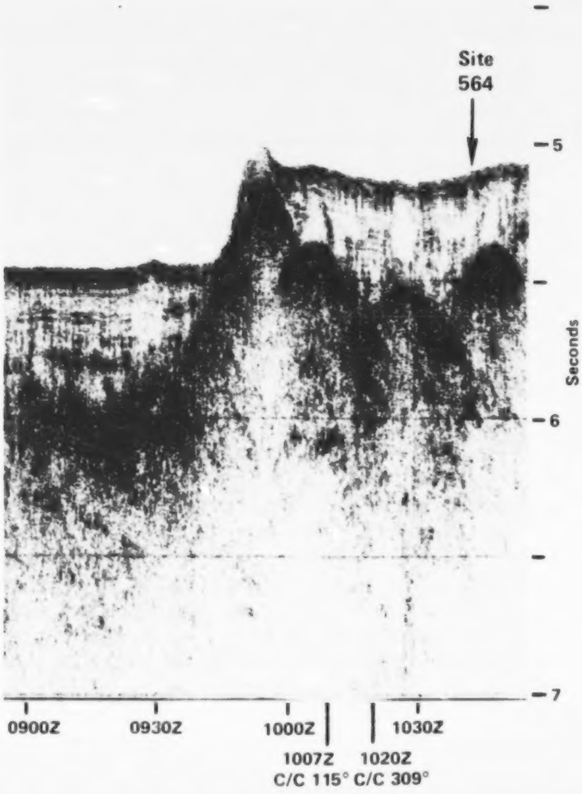

Figure 2. *Glomar Challenger* seismic records of the approach to Site 564. For location of profile see Figure 2, site chapter, Site 563, this volume. C/C = course change.

Table 1. Coring summary, Hole 564.

Core	Date (Oct. 1981)	Time (Z)	Depth from drill floor (m)	Depth below seafloor (m)	Length cored (m)	Length recovered (m)	Percent recovered
H1	28	2122	3830.0-4114.0	0.0-284.0	0.0	0.00	0
1	29	0305	4114.0-4123.0	284.0-293.0	9.0	3.40	38
2	29	0805	4123.0-4132.0	293.0-302.0	9.0	3.44	38
3	29	1240	4132.0-4141.0	302.0-311.0	9.0	4.10	46
4	29	1735	4141.0-4150.0	311.0-320.0	9.0	4.87	54
5	29	2202	4150.0-4159.0	320.0-329.0	9.0	5.19	58
6	30	0312	4159.0-4168.0	329.0-338.0	9.0	5.72	64
7	30	0740	4168.0-4177.0	338.0-347.0	9.0	3.31	37
8	30	1049	4177.0-4186.0	347.0-356.0	9.0	1.98	22
9	30	1520	4186.0-4195.0	356.0-365.0	9.0	2.74	30
					81.0	34.75	43

SEDIMENT LITHOLOGY

At Site 564 a single bit hole was drilled and washed down to basement at 284 m, and 9.6 m (564-H1-1 to 564-H1-7 and 564-H1,CC) of sediment were recovered. The site is located approximately 10 km north of Site 563 on Anomaly 13, in water depth of 3830 m. Although the sediment directly overlying the basalt was not recovered, the core catcher was dated as early Oligocene (34–34.5 Ma).

The 9.6 m of sediment recovered in Core H1 are predominantly foraminiferal nannofossil ooze, with chalk intervals increasing from Section 564-H1-4 downward and an interval of clayey ooze in Sections 564-H1-3 and 564-H1-4. Section 564-H1-7 and 564-H1,CC contain dolomitic nannofossil chalk and ooze. The sediment colors change from predominantly white and light gray (10YR 8/1–8/2, 5YR 8/1–7/1, 7/2) in Sections 564-H1-1 and 564-H1-2 to brown and yellowish brown (10YR 6/3, 6/4, 5/4, 4/4) in Sections 564-H1-3 to 564-H1-7. Bedding is massive; bioturbation/mottling and burrows are present throughout, increasing from mild in Sections 564-H1-1 to 564-H1-3 to moderate in Sections 564-H1-4 and 564-H1-5, but almost absent in Sections 564-H1-6 and 564-H1-7. Carbonate content, measured by carbonate bomb, is over 90% (up to 98%) in all sections except in 564-H1-3 and 564-H1-4 (83–89%). This repeats the results at Site 563. Principal sediment components are nannofossils (60–90%, except for 47% in the dolomitic chalk) and foraminifers (3–25%). Clay content is equal to or less than 10%. Dolomite rhombs are present in Sections 564-H1-6 and 564-H1-7 (2–10%) and 564-H1,CC (15%). Micronodules are present in trace amounts in most samples and are estimated at 3–5% in 564-H1-4 and 564-H1,CC.

We have given this detailed description of the lithologies found in the wash core because it shows the strong similarities to the lithologies at Site 563. Although condensed by discontinuous recovery in wash Core H1, Site 564 contains the same two sediment units with similar lithologic characteristics and similar stratigraphy. Even the transition zone between the units can be recognized in Sections 564-H1-3 and 564-H1-4 where the color changes, the carbonate content decreases slightly, and the samples contain lower middle Miocene to upper lower Miocene nannofossil zones.

BIOSTRATIGRAPHY

Summary

One washed core was retrieved above basement at Site 564. The sediment recovered ranges from lower Oligocene to upper middle Miocene based on calcareous nannofossils. Planktonic foraminifers from 564-H1,CC indicate that the base of the section is Oligocene and belongs to the *Chiloguembelina* Zone (lower NP21).

Calcareous Nannofossils

One washed core (H1) was obtained above basement in Hole 564. The top of 564-H1-1 is upper middle to lower upper Miocene and on the basis of *Discoaster hamatus* is placed in the *D. hamatus* Zone CN7 (NN9). Section 564-H1-7 is assigned to the lower Oligocene *S. predistentus* Zone on the basis of the absence of *S. ciperoensis* and *S. distentus*. The core catcher of Core H1 contains *Reticulofenestra umbilica* without *Coccolithus formosus* and belongs to the *Helicosphaera reticulata* Zone, *Reticulofenestra hillae* Subzone CN16c (NP22), which is lower Oligocene.

Both 564-H1-7 and 564-H1,CC contain *Braarudosphaera rosa*. This species is also found in the same stratigraphic range at Site 563 and may be related to the environmental events in the South Atlantic that produced the *Braarudosphaera* chalk.

IGENOUS PETROLOGY AND GEOCHEMISTRY

At Site 564, basement rocks occur below 284 m subbottom depth. We drilled 81 m through a pillow basalt sequence cut by two minor massive lava flows. We recognized five lithologic units, which appear to belong to a single chemical group.

Lithology (Fig. 3)

Unit 3 (284.0–332.5 m)

Unit 3 consists of aphyric pillow basalts. We penetrated about 37 pillows, ranging from 20 to 150 cm in diameter with a mean thickness of about 75 cm. The pillows are separated from each other by black glass margins up to 3 cm thick. Aphanitic basalt close to the glass grades through a variolitic zone into fresh, fine-grained basalt pillow interiors. Up to 2% of clay-filled, subhedral-to-anhedral pseudomorphs of olivine microphenocrysts, ranging up to 2 mm in diameter, are present. Plagioclase laths, forming glomerophyric clusters up to 2 mm in diameter, are sparsely and randomly scattered.

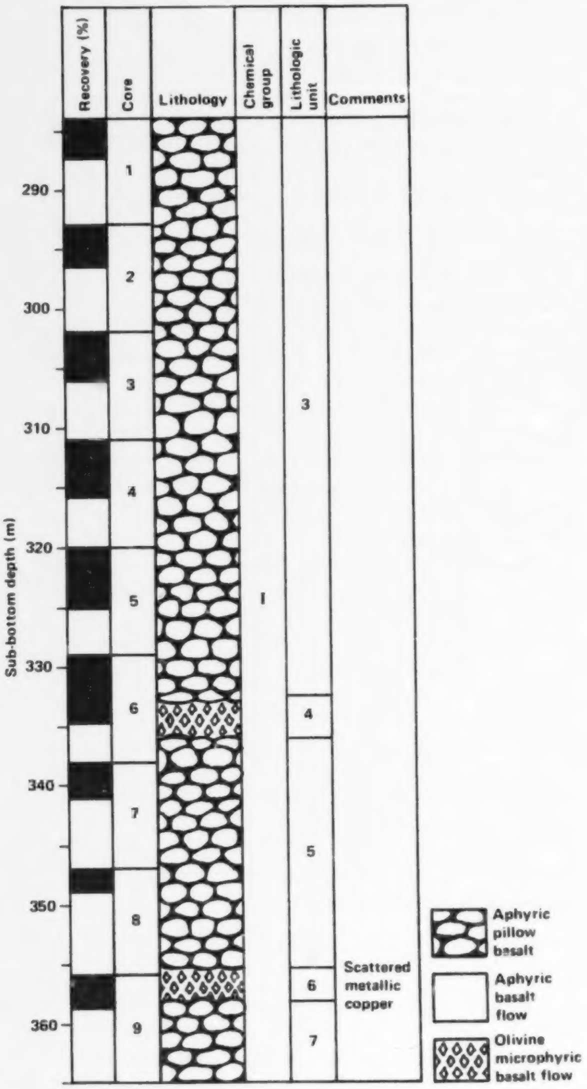

Figure 3. Basement lithology column, Hole 564.

Round and irregular vesicles are usually rare throughout the unit (less than 1%), but often show an increase in abundance close to upper pillow margins (2–3%). Most vesicles are empty, but if they are filled, calcite exceeds clay.

Interpillow breccia (hyaloclastite) was recovered in a few places. Black, angular-to-subrounded glass clasts occur either in a very pale brown limestone matrix or within a sparry calcite cement. Thin palagonite rinds on the glass are common throughout the section.

Unit 4 (332.5–336.5 m)

This unit (~4 m thick) consists of a massive aphyric basalt flow, containing a large amount of acicular plagioclase, ranging between 1 and 4 mm in length. Anhedral olivine microphenocrysts are replaced by dark brown clay. The base of the flow is marked by variolitic basalt with a narrow rim of weathered glass.

Unit 5 (336.5–355.5 m)

This unit is composed of fine-grained aphyric pillow basalts with pillow sizes ranging between 40 and 70 cm. Black glassy pillow margins are often slightly altered to palagonite. Black brecciated basalt glass, embedded in limestone and/or calcite, occurs between many pillows.

Unit 6 (355.5 to 358.0 m)

Unit 6 is a massive, olivine microphyric basalt. The occurrence of a few chilled black glass pieces in the upper half suggests that it may consist of two separate flows. At the bottom, a chilled glass margin is present. The minimum thickness of Unit 6 is about 2.5 m.

Plagioclase laths up to 5mm long are abundant in most parts of Unit 6, but they seem to decrease in size downhole. Olivine phenocrysts, ranging in size between 0.5 and 1 mm, are mostly replaced by brown clay. Their abundance decreases from about 5% at the top to about 1% at the bottom.

Fractures and veins, usually horizontally oriented, are common. They are mostly cemented by calcite, but light green chlorite occurs on fracture planes in some places. In Unit 6 (Section 564-9-1) we found native copper, forming small needles and plates (0.5–4 mm in size).

Unit 7 (358.0–365.0 m)

We only recovered fragments of this lowermost unit, which consists of fine-grained, aphyric pillow basalts, topped by a basalt glass breccia. In the upper portion, two pieces are highly vesicular with round-to-oval vesicles up to 5 mm in diameter; these vesicles are either empty or filled with clay or calcite. Pieces with black glass rinds are also present.

Petrography

Ten thin sections were examined from this site. All are aphyric and all are similar in mineralogy, although there is some variation in olivine abundance. None of the lithologic units appears petrographically distinct, except that Unit 6 (Sample 564-9-1, 45–47 cm) appears more altered. Noteworthy is the occurrence of small amounts of native copper in Sections 564-6-4 and 564-9-1.

Basalts of Site 564 are characterized by the presence, in varying proportions, of domains of contrasting grain size and texture. Both fine-grained and relatively coarse-grained domains are present, regardless of mean grain size or proximity to pillow or flow cooling surfaces. The relative abundance of coarse-grained domains appears to increase with increasing mean grain size.

Coarse domains range from isolated radiating clusters (10–15% of rock) surrounded by fine material, to continuous domains (60–70% of rock) surrounding circular or irregular, isolated fine-grained domains. Coarse domains are characterized by radiating clusters of hollow plagioclase laths (up to a maximum of 3 mm long) grading to randomly oriented aggregates in larger domains. Radiating clusters are frequently centered on one or more grains of olivine; relatively coarse, granular clinopyroxene fills the remaining interstices. Within these domains textures are intergranular or subophitic. Olivine, generally about 5% but ranging from 1 to 10% in abundance, is largely confined to these domains. It occurs as diamond-shaped, pseudohexagonal, or anhedral microphenocrysts and is seldom fresh, being altered to aggregates to pleochroic green montmorillonite (e.g., Section 564-6-4), green brown clay or, in some cases (e.g., Sample 564-5-3, 119–122 cm), to light brown zeolite similar to (?)heulandite of Site 559.

Fine domains are dominated by sheaflike or branching aggregates of clinopyroxene with an equal proportion of plagioclase occurring as interstitial patches, small laths, or (less commonly) plumose aggregates. Interstitial glass, colorless when fresh, crowded with extremely fine opaques and skeletal magnetite, and frequently altered to clay or zeolite, forms up to 15% of these domains. Granular magnetite (5–8% of rock) is largely confined to fine domains.

The precise cooling history of these unusual rocks is difficult to interpret in detail. However, it is clear that olivine and plagioclase were crystallizing together at an early, probably preeruptive, stage. Plagioclase continued to crystallize without further olivine after eruption-forming coarse domains. Final crystallization of clinopyroxene, plagioclase, and magnetite together formed the fine domains.

Alteration has had varying effects throughout the hole. Most samples show small amounts of brown or orange clay attributable to weathering. Zeolite, similar to heulandite identified at Site 559, has replaced olivine and glass in most samples. Montmorillonite, pleochroic from green to pale green or yellow, with $2V_x$ approximately 10° and occurring as relatively large (up to about 0.2 mm) single grains or optically continuous aggregates is also present replacing olivine in several samples. Traces of pyrrhotite and native copper occur in Sample 564-6-4, 44–46 cm. In Section 564-9-1 visible native copper occurs as scattered small granules within about 1 cm of small calcite-filled and chlorite-filled veinlets. A thin section from one such occurrence (Sample 564-9-1, 45–47 cm) contains up to 20% altered material; glass has been altered to a mixture of green and brown clays and possibly chlorite. Olivine has been altered to near-opaque to dark brown hematite and (?)goethite along with brown clay and calcite. Pyrrhotite is also present in trace amounts in this specimen.

Geochemistry

Twenty-six samples have been analyzed from Hole 564; the analyses are presented in Table 2, and selected elements are plotted against sub-bottom depth in Figure 4.

The analyzed basalts appear to compose a single chemical group, although there is apparent chemical variation downhole for some elements within this group. Table 3 contains the average analysis of 20 fresh basalts from Hole 564, together with average analyses for the six uppermost and six lowermost basalts in the hole. The average analysis for all fresh basalts suggests that much of the chemical variation may lie within analytical precision. However, the average analyses for uppermost and lowermost fresh basalts in Table 3 do indicate some significant differences, notably an increase in Fe_2O_3, TiO_2, Zr, Nb, and perhaps MgO abundances, and a decrease in Al_2O_3 and CaO abundances and Zr/Nb ratio downhole. The reported Nb values all lie within a factor of three times the analytical precision. For all elements, the downhole chemical gradient is continuous, making it impossible to define chemical subgroups.

In comparison to the fresh basalts, the altered basalts analyzed (Table 3) display chemical changes consistent with those described for altered basalts from Sites 559 and 562. The abundances of, particularly, Zr and Nb, and the value of the Nb/Zr ratio, do not change upon alteration (Table 3). Thus, the apparent increase in Zr and Nb content and in Nb/Zr ratio downhole cannot be correlated with secondary processes (such as degree of alteration) or with simple primary processes (such as variation in phenocryst content). At this stage, the significance of the downhole chemical gradient is uncertain.

Plotted on a modified Coryell-Masuda diagram (Fig. 5), all of the basalts from Hole 564 have depleted trace element characteristics. However, Figure 5 also illustrates the less depleted nature of the basalts from the deepest levels of the hole ($[Nb/Zr]_{ch} \sim 0.54$).

MAGNETICS

Oriented minicores were taken for on-board study of paleomagnetic properties. After measuring the natural remanent magnetization (NRM) and initial susceptibility, a few samples were subjected to alternating field (AF) demagnetization. Typical results of AF demagnetization are plotted in Figure 6. An orthogonal plot of the components of magnetization (Fig. 6) suggests the presence of univectorial direction, with shallow downward inclination value. Median demagnetizing field (MDF) is calculated using Figure 6. The detailed results of AF demagnetization, NRM, and susceptibility are given in Table 4.

The stable inclination and susceptibility values are plotted versus depth on Figure 7. All samples have shallower inclination values compared to the samples from previous holes, and the values are more shallow than the

Table 2. Analyses of major elements (in wt.%) and trace elements (in ppm) of Hole 564 basalts.

Core-Section (interval in cm) (piece number)	Sub-bottom depth (m)	SiO_2	TiO_2	Al_2O_3	Fe_2O_3	MnO	MgO	CaO	K_2O	P_2O_5	Total	Mg′	Ti	V	Sr	Y	Zr	Nb
1-1, 108–111 (10A)	285.1	50.48	1.42	14.68	11.05	0.16	7.16	12.09	0.27	0.17	97.48	59	8250	385	112	39.0	89	3.4
1-1, 140–143 (12A)	285.4	50.77	1.44	14.53	11.05	0.17	7.26	12.10	0.34	0.15	97.81	60	8640	413	108	42.0	91	3.3
1-2, 74–78 (5D)	286.3	49.85	1.43	14.89	11.99	0.18	7.06	12.13	0.26	0.14	97.93	57	8580	397	106	39.0	89	3.6
1-3, 103–105 (8B)	288.0	49.37	1.45	15.02	12.33	0.16	5.98	12.48	0.29	0.14	97.22	52	8700	403	104	39.6	92	4.0
-1, 53–55 (4B)	293.6	48.81	1.46	15.28	12.50	0.18	6.13	12.47	0.19	0.15	97.17	52	8760	426	107	37.3	90	3.4
-2, 46–49 (3B)	295.0	49.49	1.42	14.62	11.80	0.17	6.93	12.05	0.31	0.14	96.93	57	8520	378	102	38.2	88	3.2
-3, 60–63 (5)	296.6	49.67	1.41	14.45	11.87	0.17	7.75	11.98	0.24	0.14	97.68	60	8460	380	106	38.4	94	4.3
-1, 25–28 (2B)	302.3	50.09	1.42	14.42	11.69	0.17	7.09	12.00	0.28	0.15	97.31	58	8520	372	105	39.7	89	2.8
-2, 70–73 (5C)	304.3	48.75	1.45	14.76	12.14	0.18	6.46	12.43	0.26	0.15	96.58	55	8700	396	106	40.0	88	3.9
-3, 138–141 (8B)	306.4	50.65	1.42	14.46	11.67	0.16	6.84	11.86	0.15	0.14	97.35	57	8520	377	107	38.6	92	4.6
-1, 61–65 (4C)	311.6	50.14	1.41	14.26	11.57	0.17	7.54	11.80	0.26	0.15	97.30	59	8460	376	106	38.6	85	5.6
-2, 102–106 (6A)	313.5	49.67	1.43	14.61	11.81	0.18	7.14	11.94	0.28	0.15	97.21	58	8580	394	106	40.4	89	3.9
-4, 81–85 (3C)	316.4	50.33	1.43	14.53	11.78	0.17	7.07	11.81	0.34	0.15	97.61	57	8580	345	104	41.6	86	4.6
-1, 17–19 (1E)	320.2	49.26	1.47	14.99	12.08	0.18	6.42	12.16	0.25	0.15	96.96	54	8820	405	105	40.3	90	5.4
-2, 98–100 (4B)	322.5	50.67	1.44	14.44	11.85	0.18	7.56	11.79	0.13	0.16	98.22	59	8640	383	98	39.2	95	4.8
-3, 119–122 (5G)	324.2	50.44	1.45	14.47	11.03	0.19	7.81	11.84	0.20	0.15	97.58	61	8700	424	118	40.2	97	4.5
-1, 33–36 (1B)	329.4	50.33	1.45	14.32	12.11	0.17	7.55	11.72	0.06	0.15	97.86	58	8700	392	101	40.3	97	5.6
-3, 63–66 (5A)	332.6	49.81	1.45	14.24	12.18	0.18	7.41	11.52	0.37	0.14	97.30	58	8700	388	102	40.7	87	5.5
-4, 44–47 (2D)	334.0	49.56	1.42	14.25	11.88	0.18	8.25	11.54	0.18	0.15	97.41	61	8520	383	99	38.4	93	4.5
-5, 43–46 (1J)	335.5	50.61	1.49	14.40	11.55	0.18	7.20	11.74	0.22	0.15	97.54	58	8940	385	103	40.3	98	6.0
-2, 20–23 (1D)	339.7	49.63	1.49	14.41	12.31	0.18	7.15	11.75	0.31	0.16	97.39	57	8940	398	104	42.3	98	5.4
-3, 58–61 (4C)	341.6	50.21	1.47	14.03	12.11	0.18	7.62	11.60	0.18	0.15	97.55	59	8820	378	108	41.6	96	5.5
-2, 0–3 (1A)	348.5	50.12	1.47	14.24	12.21	0.17	7.38	11.60	0.35	0.13	97.67	58	8820	378	108	40.9	96	6.0
8-2, 75–77 (7)	349.3	48.66	1.50	14.94	12.92	0.18	5.94	11.98	0.24	0.17	96.53	51	9000	463	109	42.4	96	6.1
9-1, 43–45 (1D)	356.5	49.29	1.47	14.61	12.61	0.18	6.59	11.96	0.31	0.15	97.17	54	8820	463	108	42.5	99	5.4
9-3, 72–75 (4B)	358.3	49.75	1.46	14.05	12.25	0.19	7.40	11.49	0.16	0.15	96.90	58	8760	375	102	40.8	100	4.6

[a] On-board measurements were made on ignited samples. Onshore analyses of loss on ignition are less than 1% in most cases. Compiled data tables at the end of this volume (Appendix) include volatile components.

[b] Total Fe as Fe_2O_3.

[c] Mg′ is the atomic ratio of 100 × ($Mg/[Mg + Fe^{2+}]$); calculated using an assumed Fe_2O_3/FeO ratio of 0.15.

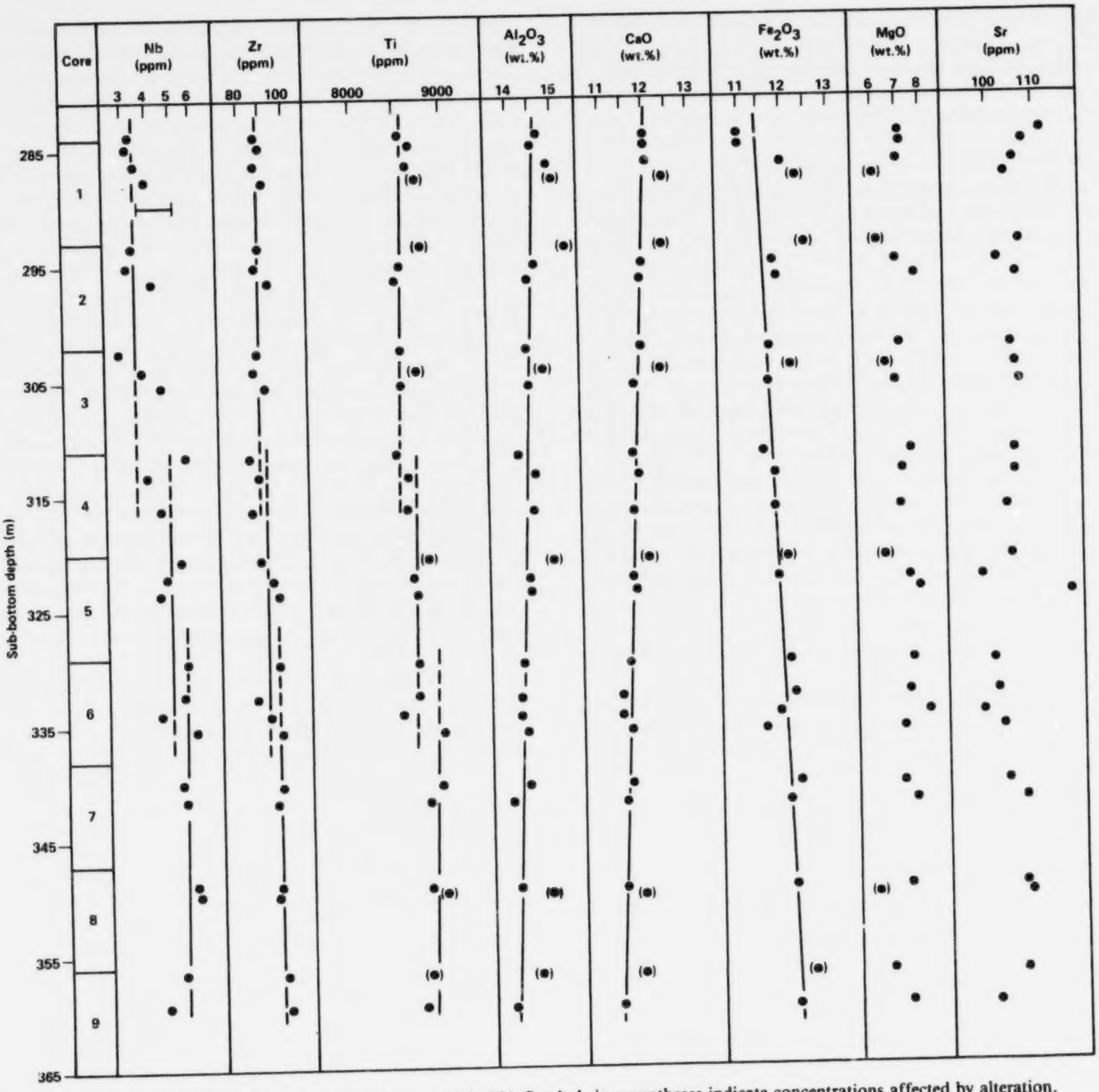

Figure 4. Downhole variations in chemical abundances, Hole 564. Symbols in parentheses indicate concentrations affected by alteration.

expected dipole inclination value for the latitude of this site. This may be due to tectonic rotation of the crust since the acquisition of magnetization by these basalts.

PHYSICAL PROPERTIES

A section of 81 m was cored through basalt basement. Lithologies include massive, glassy, and vesicular basalts and hyaloclastic breccias. Physical measurements could not be obtained for the breccias because the clasts were commonly 10 mm across, and a representative bulk sample of a suitably small size for laboratory measurements was not available.

All the samples measured were basalts, which make up the vast majority of the recovered material. Sonic velocities, bulk densities, and porosities were determined by the standard DSDP methods (see Explanatory Notes, this volume), and the results are presented in Table 5 and Figure 8. The data have a scattered distribution, shown on the expanded plot scales of Figure 8. There is an apparent variation of properties downhole with a peak in velocity at about 295 m followed by a gradual decrease to 315 m. This is almost certainly an artifact of the sampling, because much greater variability is seen where the sampling density is higher between 320 and 340 m subbottom. In this section, samples taken from within a few centimeters of each other for the separate determination of vertical and horizontal velocities show large differences that are not attributable to systematic seismic anisotropy down the section.

Table 3. Average analyses of basalts from Hole 564.

Element	Fresh basalts $\overline{X}$	Fresh basalts σ	Altered basalts $\overline{X}$	Altered basalts σ	Uppermost 6 fresh basalts $\overline{X}$	Uppermost 6 fresh basalts σ	Lowermost 6 fresh basalts $\overline{X}$	Lowermost 6 fresh basalts σ
Major elements (wt.%)								
SiO_2	50.11	0.40	49.02	0.29	50.06	0.45	49.98	0.37
TiO_2	1.44	0.02	1.47	0.02	1.42	0.01	1.47	0.02
Al_2O_3	14.42	0.20	14.93	0.21	14.60	0.16	14.23	0.15
Fe_2O_3	11.79	0.38	12.43	0.29	11.58	0.38	12.05	0.26
MnO	0.18	0.01	0.18	0.01	0.17	0.01	0.18	0.01
MgO	7.36	0.33	6.25	0.25	7.21	0.26	7.50	0.37
CaO	11.82	0.20	12.25	0.22	12.06	0.05	11.62	0.10
K_2O	0.24	0.08	0.26	0.04	0.28	0.03	0.23	0.07
P_2O_5	0.15	0.01	0.15	0.01	0.15	0.01	0.15	0.01
Mg′	58	1	53	1	58	1	59	1
Trace elements (ppm)								
V	385	16	426	28	388	14	383	8
Sr	105	4	107	2	107	3	104	3
Y	40.00	1.30	40.40	1.80	39.40	1.20	40.70	1.20
Zr	92	4	93	4	90	2	97	2
Nb	4.60	1.00	4.70	1.00	3.40	0.50	5.30	0.60
$(Nb/Zr)_{ch}$	0.46	0.11	0.46	0.09	0.36	0.04	0.54	0.06

Note: Averages of 20 fresh basalts and 6 altered basalts are calculated from data presented in Table 2. The altered basalts are samples from Sections 564-1-3, 564-2-1, 564-3-2, 564-5-1, and 564-9-1 and from Sample 564-8-2, 75–77 cm. $\overline{X}$ is mean; σ is standard deviation; Mg′ is the atomic ratio of 100 × $(Mg/[Mg + Fe^{2+}])$, calculated assuming an Fe_2O_3 ratio of 0.15.

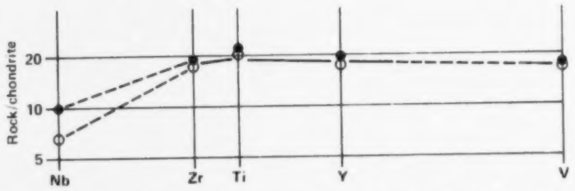

Figure 5. Extended Coryell-Masuda diagrams for basalts of Hole 564. Solid circles are average of lowermost six fresh basalts: $(Nb/Zr)_{ch}$ ~0.36. Open circles are average of uppermost six fresh basalts: $(Nb/Zr)_{ch}$ ~0.54.

Also apparent in Figure 8 is a negative correlation between density and seismic velocity, which is the inverse of the usual relationship. The bulk densities were determined while the ship was in moderately heavy seas, and weighing errors account for this unusual negative correlation.

DOWNHOLE MEASUREMENTS

Logging

Operations

Logging operations were started at 1530Z, 30 October with the intention of making as many logs as possible before the arrival of a predicted tropical storm. Because it seemed likely that bad weather would necessitate an early termination of operations, the order of the logging runs was changed so that the resistivity log, which has consistently given the best results, was first. We originally planned to run the porosity/density logs second, the sonic third and, if weather permitted, the high resolution temperature sonde (HRT) last. However, after the resistivity and porosity/density logs had been run, the predicted storm had not developed. Because there was not enough time to carry out a piston coring program, we decided to make two runs with the temperature probe.

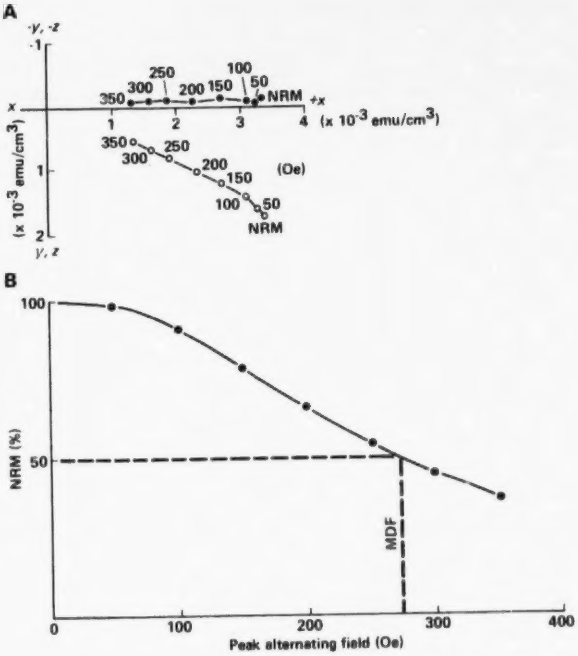

Figure 6. A. Vector diagram showing change in NRM after alternating field demagnetization (Sample 564-3-1, 39–41 cm). Solid circles are plotted on the horizontal plane and open circles are plotted on the vertical plane. B. Percent natural remanent magnetization (NRM) versus peak alternating field with the determination of median demagnetizing field (MDF).

Hole conditions were generally good. The amount of heave was the lowest of all three holes logged during this leg. High quality records were obtained for all logging runs despite minor problems with the caliper log and the porosity/density tool, which consumed about 1 1/2 additional hours. Because of problems at the previous two logged holes in lowering the HRT down the hole, the tool was weighted by being placed inside a perforated core barrel. This modification is described in detail in the Downhole Temperatures section. A schedule of logging runs is given in Table 6.

Sedimentary Section

All tools were logged continuously from the basement interface to the drill pipe at 100 m sub-bottom. The data quality is regarded as good because of the low sea state and good hole condition. In particular, the hole was not washed out beyond the limits of the sonic caliper (16 in.) and a full caliper log was recorded. Below 130 m sub-bottom, the maximum diameter is only 14 in., and although this is slightly greater than the reach of the density/porosity excentralizer (13 in.) this tool was very close to the hole wall, if not in contact with it, for most of the logged section. The density log contains more detail and less random noise than in Holes 556 or 558, but because

Table 4. Hole 564 basalt paleomagnetics.

Core-Section (interval in cm)	J_{NRM} ($\times 10^{-3}$ emu/cm^3)	NRM inc. (°)	Stable inc. (°)	χ ($\times 10^{-6}$ emu/cm^3 Oe)
3-1, 39-41	3.75	26.8	22.6	180
3-2, 35-37	3.47	19.3	17.0	76
3-2, 90-92	4.13	20.5	18.5	85
3-2, 129-131	2.39	36.0	27.1	70
3-3, 36-38	4.63	17.0	15.8	90
4-1, 7-9	3.13	28.2	21.8	115
4-2, 37-41	3.40	13.2	11.9	115
4-2, 49-51	2.30	36.9	30.5	105
4-3, 4-6	2.82	10.7	7.3	125
4-3, 137-139	2.16	9.6	9.4	117
4-4, 3-5	4.01	14.1	12.5	134
4-4, 78-80	2.38	24.0	19.9	115
4-4, 140-142	2.80	15.3	11.8	130
5-1, 6-8	4.04	26.4	20.7	160
5-1, 81-83	4.26	26.4	25.6	113
5-2, 31-33	2.88	16.1	11.7	120
5-3, 95-97	2.41	29.8	25.6	160
5-4, 144-146	1.55	17.8	17.1	161
5-5, 27-29	4.18	7.2	7.2	135
6-1, 26-28	5.71	28.3	15.6	234
6-2, 48-50	2.92	45.3	33.3	160
6-3, 145-147	2.31	50.4	31.0	166
6-4, 123-125	5.87	36.8	14.6	318
6-5, 32-34	3.18	20.9	12.3	124
7-2, 11-13	3.45	27.3	23.7	127
7-3, 102-104	1.89	24.5	13.1	167
8-1, 41-43	3.31	23.6	21.2	128
9-1, 8-10	4.36	31.1	21.7	384
9-2, 128-130	2.69	26.1	19.7	204
9-2, 142-144	0.59	44.1	25.1	142

Note: J_{NRM} = intensity of natural remanent magnetization (NRM); inc. = inclination; χ = susceptibility.

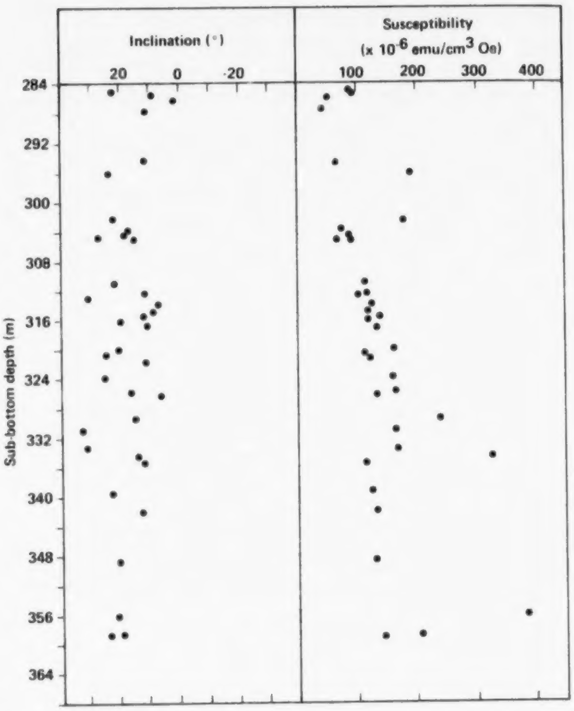

Figure 7. Downhole plot of stable inclinations and susceptibility of Site 564 basalts. (Values between 284 and 300 m sub-bottom are not listed in Table 4.)

it contains obvious noise spikes, it is drawn dashed in Figure 9, which compares density, velocity, resistivity, and natural gamma logs.

As was noted in the physical property measurements, there is no boundary within the sediments as clearly defined as the boundaries at Holes 556 and 558, although a gradational rise in velocity and density superimposed on the background compaction gradient can be seen over the depth range 160-200 m. Over this range the sedimentology changes character as described in the Sedimentology and Biostratigraphy section. Density, sonic velocity, natural gamma, and resistivity values all increase from 270-285 m sub-bottom towards the base-

Table 5. Physical properties measurements, Hole 564.

Core-Section (interval in cm)	Sub-bottom depth (m)	Sonic velocity (km/s) V.	Sonic velocity (km/s) H.	Temperature (°C)	Gravimetric density: Wet-bulk density (g/cm^3)	Gravimetric density: Water content (%)	Gravimetric density: ϕ (%)	Lithology or remarks
1-1, 35-40	284.4		5.28	23				All samples basalt
1-1, 112-114	285.1	5.12		23				
1-3, 18-20	287.2	5.52		23	2.88	2	6	
1-3, 23-27	287.2		5.43	23				
2-2, 16-21	294.7	5.92		23	2.81	3	9	
3-2, 121-131	304.8	5.56	5.26	23	2.82	3	9	
4-2, 37-41	312.9	5.27		23	2.87	2	5	
5-2, 44-56	322.0	5.05		24				
5-2, 51-57	322.0		5.39	24	2.87	2	5	
5-3, 68-75	323.7		5.25	24	2.86	2	7	
5-3, 82-84	323.8	5.77		24				
6-1, 11-13	329.1	5.73		24				
6-1, 80-90	329.8		4.88	24	2.76	4	12	Vesicular basalt
6-4, 48-52	334.0	5.31		24				All samples basalt
7-1, 139-143	339.4	5.68		24				
7-3, 13-15	341.1	6.17		24				
7-3, 51-55	341.5		5.62	24	2.88	1	4	
8-2, 76-85	349.3	4.83	4.74	24	2.80	5	13	
9-1, 25-35	356.3	5.07	4.87	24	2.84	3	10	

Note: V. = vertical, H. = horizontal; water content is corrected; ϕ = porosity. Weighing accuracy below average because of rough seas.

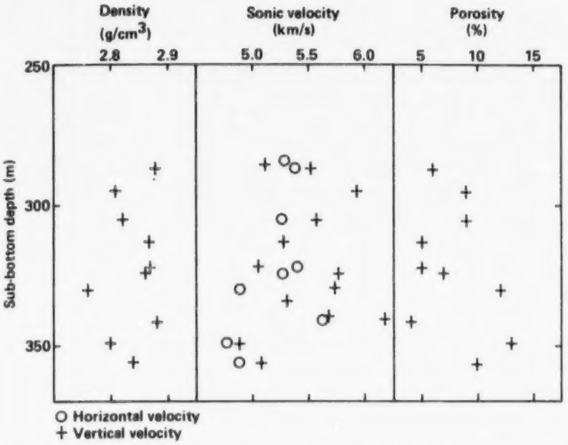

Figure 8. Selected physical property variations in the basement rocks of Hole 564.

Table 6. Schedule of logging runs.

Run 1. Dual laterolog (DLT), gamma ray (GR), caliper (CAL)
Logger on bottom 2045 10/30
Run 2. Formation density compensated (FGT), neutron porosity (CNT), GR, CAL
Logger on bottom 0330 10/31
Remarks: Three repeat sections made to observe variations caused by heave.
Run 3. High resolution temperature (HRT) #1
Logger on bottom 1000 10/31
Remarks: Sonde mounted inside modified core barrel to provide extra weight. Tool stood up at 4115 m, 4158 m, 4172 m; stationary measurements at 4135 m, 4178 m, 3830 m.
Run 4. Sonic velocity (DDBHC), GR, CAL
Logger on bottom 1500 10/31
Remarks: Transit time and waveform recordings both repeated.
Waveform in basement only.
Run 5. HRT #2
Logger on bottom: 2030 10/31
Remarks: Sonde mounted inside modified core barrel. Tool stood up at 4158 m, 4172 m; stationary measurements at 3815 m, 4158 m, 4170 m.

Note: Circulation stopped: 1600 hr. 30 October.

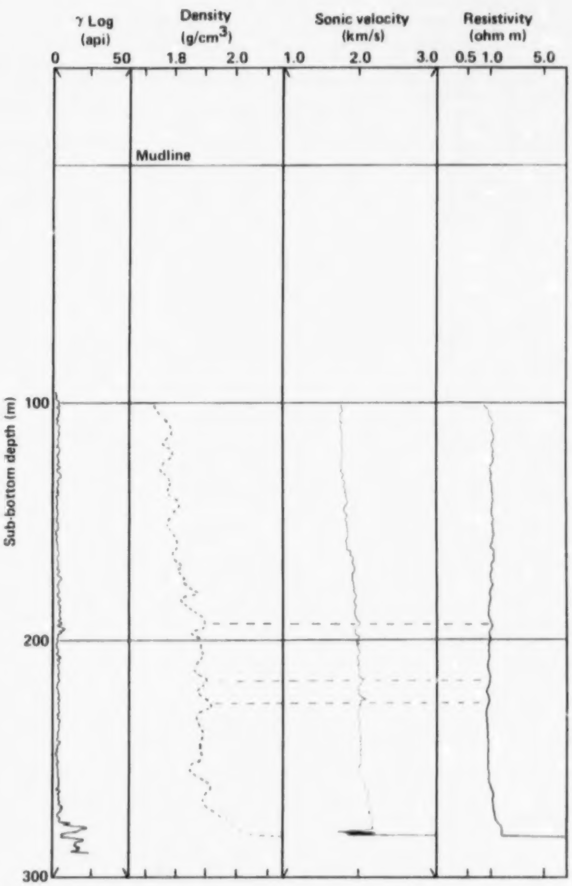

Figure 9. Wireline log curves for sedimentary section of Hole 564. Dashed density curve indicates low quality data. Dashed horizontal lines mark cyclical peaks discussed in text.

ment interface, probably because of a dolomitized layer as seen at Sites 558 and 563.

The most interesting feature of the logs is a cyclic variation in values with a wavelength of about 10 m within the depth range 180–230 m. Three prominent peaks in these cycles are shown by dashed lines in Figure 9. This variation was tentatively identified by physical property measurements at Site 563 and probably correlates with alternations of chalk and ooze as described in the sedimentology of the core section of Site 563. This cyclic variation makes the identification of a distinct sedimentologic boundary problematic. The best limits are those defined above (the depth range 160–200 m).

Basement Section

The results of logging within basement are shown in Figure 10. Each of the four major logs represents the average, by eye, of two or more passes through the basement.

The general character of the logs recorded in the basement is more uniform than that of the logs of the previous two logged holes. This is particularly true of the resistivity log, which is remarkably uniform from the sediment/basement interface down to a depth of 320 m sub-bottom. This relatively uniform character correlates with the thick layer of pillow basalts, Unit 3, at the top of the basement. A narrow interval between 330 and 336 m sub-bottom of high sonic velocity, high density, low porosity, and high resistivity corresponds to the massive basalt flow, Unit 4. This unit is shown by a vertical bar in Figure 10.

The porosity and density logs show several zones 2 to 4 m wide of high porosity and low density indicated by the speckled bands in Figure 10. To a lesser extent, these intervals correspond to anomalies in the resistivity and sonic velocity profiles. These low porosity zones reflect interpillow sediments and/or gaps and crevices that cannot be detected by drilling. The deepest of these high porosity zones, between 328 and 332 m sub-bottom, may correspond to the "thief zone" that has been inferred from the downhole temperature measurements. This high porosity zone also corresponds to the largest low-resistivity anomaly recorded within basement.

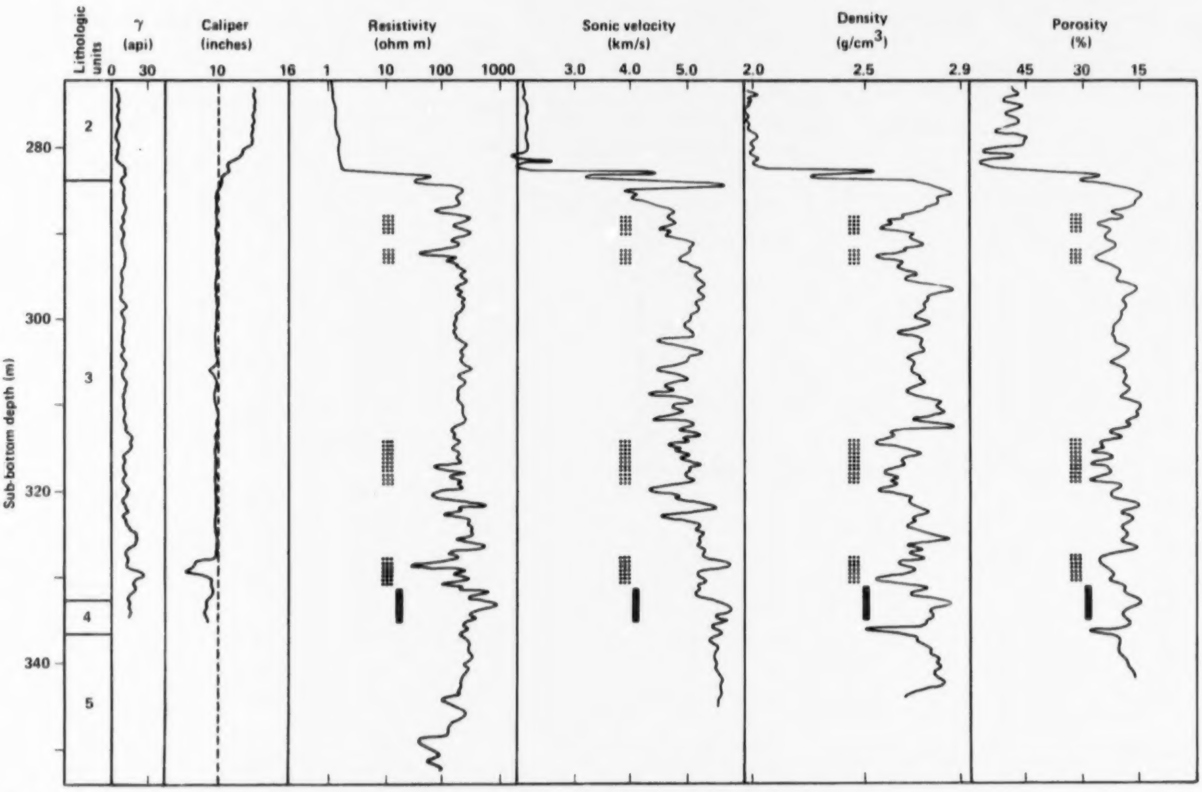

Figure 10. Wireline log curves for basement section of Hole 564. Curves have been redrawn omitting noise spikes. Gaps indicate intervals where noise obscures data. Speckled bands mark zones of high porosity and low density discussed in text. Vertical bar between 330 and 336 m sub-bottom depth marks the zone of high sonic velocity discussed in text.

It is not clear whether or not the high-amplitude, short-wavelength (about 1 m) variations observed in all four logs at the sediment/basement interface are real. These short-wavelength variations show up consistently on nearly every pass of the tools and also correspond to short-period variations in the drilling rate, suggesting that there is a very thin sedimentary layer just below the top of basement. However, the width of this feature is so small that the variation might also be due to the effect of heave on the tool as it crosses the sediment/basement interface. The wavelength of the heave is identical to the wavelength of the observed variation.

Downhole Temperatures

The data from the two HRT runs, recorded logging down the hole, are shown in Figure 11. The HRT tool was modified by encasing it in a modified core barrel as shown in Figure 12. The increased tool weight was sufficient to allow detection of setdown by the logging winch tension meter. On both runs it was necessary to spud the tool through blockages within the basement, and both times, after this the response of the tool was very slow, apparently because of mud packed around the thermistor, so that no useful data were obtained by logging back up the hole. However, by the time the tool was back up at the mudline, its response had returned to

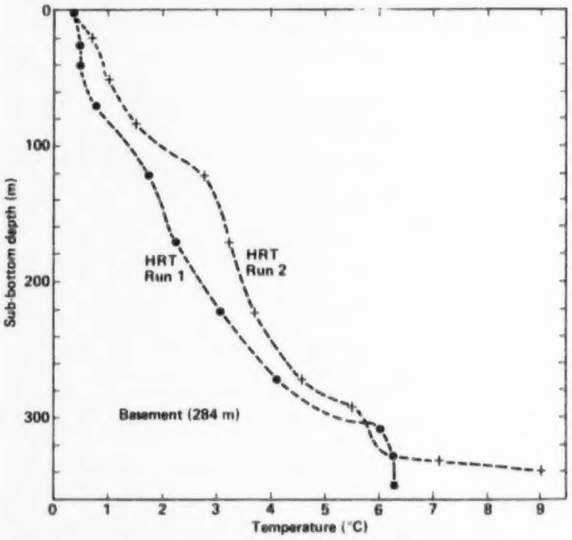

Figure 11. High resolution temperature (HRT) log curves for Hole 564. For explanation see text.

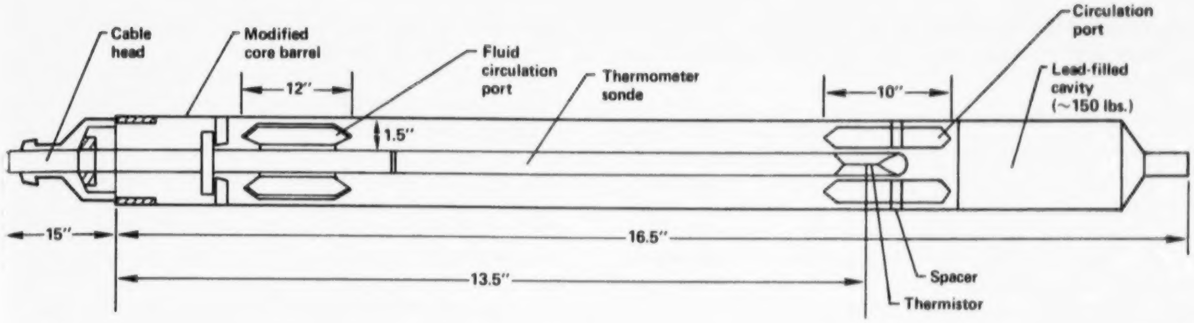

igure 12. Schematic diagram of high resolution temperature sonde with weight-adapter modification. Diameter = 3 5/8 in.; total weight = 300 lbs.

ormal. The important result of the two runs is the discovery of an equilibrated temperature profile with a very low gradient (4° C/km) in the range of 190 to 300 m sub-bottom as shown by the identical profiles on the two runs.

During logging the bottom of the drill pipe was moved between the depths of 3960 and 3930 m (100 and 130 m sub-bottom). The disparity in the two profiles centers on fluctuations at these depths and it is concluded that these are due to the interaction of the end of the drill pipe and the sidewall of the hole.

Within the basement, the temperature gradient is higher and more variable. Below 328 m sub-bottom, temperature measurement was difficult because of mud covering the thermistor, and temperatures were determined by allowing the tool to equilibrate at constant depth. The values thus determined define a very high temperature gradient of 250°C/km between 328 and 340 m sub-bottom. These data can be explained by downflow of seawater to below the sediment/basement interface producing the steady, low-temperature gradient within the sediments. The water must escape from the hole through a "thief zone" above the section with the high temperature gradient, and it probably does so through one or more of the high porosity zones identified in the well ogs in Figure 10.

The rate of waterflow must be less than that at Site 56, where the temperature gradient within the sediments as immeasurably low (less than 1°C/km). The impor-nce of temperature measurements at Sites 556 and this ole is the demonstration that the drawdown of seawa-r is a common, if not essential, feature of the ocean ust when the overlying sediment blanket is pierced.

cean-Water Profile

The ocean-water temperature profile (Fig. 13) was gged through the drill pipe as the HRT tool was being covered after the first run.

Below 1700 m, the profile is nearly identical to that t Site 558, slowly decreasing from 2.5°C to a similar ather cold bottom temperature of 0.4°C. Above 1700 m he temperature gradient is higher, the temperature ris-ng in a linear manner to 18°C at 80 m depth. Above this there is a very sharp rise in temperature within the surface water layer to 23°C.

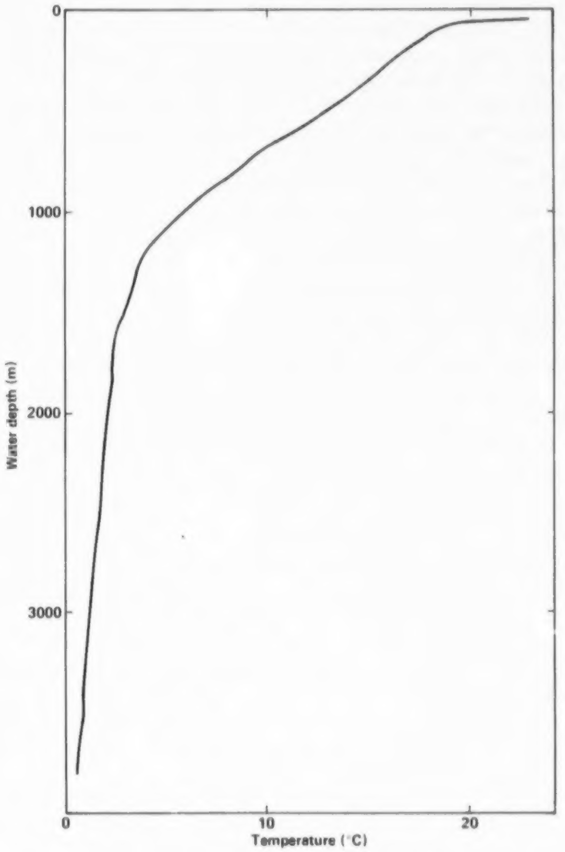

Figure 13. Ocean temperature profile recorded by high resolution temperature log within drill pipe.

This profile clearly defines three distinct layers within the ocean water and contains a detailed record of their boundaries. The drill string is regarded as being in equilibrium with the water at any depth because, although its conductivity is high, the temperature gradients along it are low. Also because of the low gradient, the temperature can be logged at the normal tool speed in drill string of 10,000 ft./hr. Thus good oceanographic data are obtained for no cost, and we suggest that ocean temperature logs be made for all future DSDP logged holes.

SUMMARY AND CONCLUSIONS

The poor penetration into the basement and the single petrographic unit recovered at Site 563 necessitated the drilling of another site nearby to document better this area south of the Hayes Fracture Zone. After the results obtained north of the Hayes Fracture Zone where depleted and enriched basalts were found at two sites (558 and 561), it was important to have the most extensive sampling program possible south of the Hayes Fracture Zone.

The sediments were washed down to the basement, which was cored for 81 m. The basement consists of a single petrographic unit of aphyric basalts forming pillows (fresh glass were recovered from the top to the bottom of the hole); two massive flows about 2 m thick were also identified. Chemically, the recovered samples form one single group even though a gradient is observed from the top to the bottom. CaO, for example, varies in a continuous way from 12% at the top to 11.5% at the bottom with very little scattering. Concentration gradients are also observed for the magmaphile elements; it may be that the Nb/Zr ratio is not constant from the top to the bottom but such a possible variation will have to be confirmed onshore by measurements of La and Ta concentrations, because the variations recorded in Nb are less than three times the estimated precision.

In terms of $(Nb/Zr)_{ch}$ ratio, varying from 0.36 to 0.54, the basalts at this site are depleted. In terms of rare earths, the patterns may range from depleted to flat according to the value of Nb/La ratio; onshore measurements are necessary.

Considering the enrichment or depletion of the most magmaphile elements compared to the less magmaphile elements, previous researchers had shown that, at zero age, a boundary exists at the latitude of the Hayes Fracture Zone between "Azores" abnormal basalts and typical MORB (see Background and Objectives section). With respect to such a boundary, only depleted material was recovered from the drilled holes on Anomalies [illegible] and 13 south of the Hayes Fracture Zone, whereas both enriched and depleted materials were recovered from the holes north of the Hayes Fracture Zone; it was also found that depleted and enriched basalts may occur at a single site. Because these results do not fulfill entirely the hypotheses made before the cruise and because more fundamental geochemical problems have been encountered, additional data—isotopic ratios and other magmaphile element determinations—are necessary before any further geochemical mantle sources-geodynamical interpretations are possible.

A complete set of logs was run at Site 564. The most important result probably concerns the temperature logs. Two temperature profiles were recorded, the first one 18 hr. after circulation was stopped and the second 10 hr. later to see if the hole had achieved equilibrium. The two profiles were identical down to below the sediment/basement interface showing a low gradient of about 4°C/km, which is only a fraction of the normal gradient. Between 45 and 60 m in the basement, an increase of 2.5°C was observed. This provides additional evidence at Anomaly 13 of downflow of seawater when the sedimentary layer is pierced.

SITE 564 HOLE CORE H1 CORED INTERVAL 0.0–284.0 m

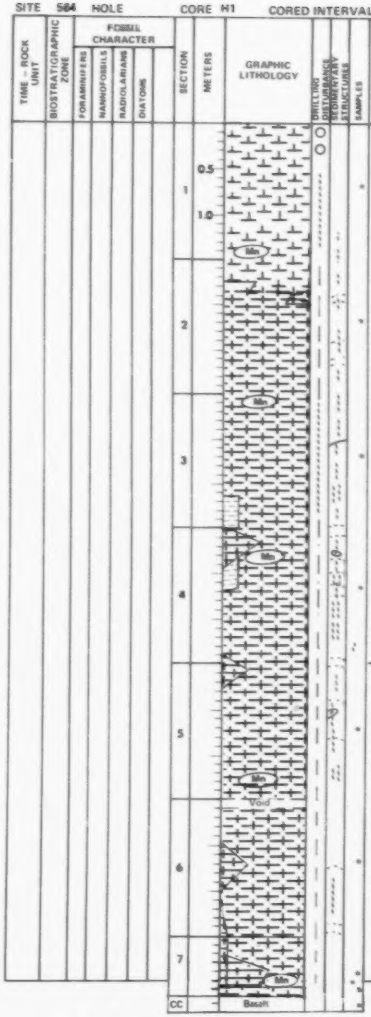
TIME – ROCK UNIT
BIOSTRATIGRAPHIC ZONE
FOSSIL CHARACTER
FORAMINIFERS
NANNOFOSSILS
RADIOLARIANS
DIATOMS
SECTION
METERS
GRAPHIC LITHOLOGY
DRILLING DISTURBANCE
SEDIMENTARY STRUCTURES
SAMPLES
0.5
1.0
1
2
3
4
5
6
7
CC
Mn
Mn
Mn
Mn
Mn
Void
Basalt

10YR 8/2 soft
10YR 7/1
10YR 8/1 soft to firm
5YR 8/1
very white
5YR 7/1
5YR 8/1
5YR 7/2
10YR 8/3
10YR 6/4
10YR 5/4
chalk (5 cm)
firm to very firm
to hard, halo
burrow
10YR 4/4
10YR 6/3
10YR 4/4
10YR 5/4
10YR 6/4
chalk firm to
very frim to
hard
7.5YR 5/4
10YR 6/4
firm to very firm
to hard
10YR 5/4
10YR 6/4
chalk
very firm to hard

LITHOLOGIC DESCRIPTION

DOMINANT LITHOLOGY FORAMINIFER-NANNOFOSSIL OOZE AND CHALK

White to light gray in Sections 1, 2, and top half of 3, pale brown to brown to yellowish brown from middle of Section 3–CC.

Soft in a few places, generally firm, stiff, to hard.

Several chalky beds, contacts indistinct.

Bedding massive except for chalk layers. Bioturbation mid to moderate. Burrows in Sections 4 and 5.

Dominant sediment components nannofossils, then forams.

Dolomite in Section 7 and CC 15%, 2% in Section 6. Mn 2–5% scattered in Sections 1, 3, 4, 5, and CC. Carbonate 98–83%, clay >10% only in Section 3, 100 cm – to Section 4, 75 cm.

SMEAR SLIDE SUMMARY (%):

	1-70	2-70	3-70	4-70	5-70	6-70	7-70	CC
	D	D	D	D	D	D	D	
Composition:								
Feldspar	–	Tr	Tr	Tr	Tr	5	Tr	Tr
Clay	5	2	12	10	8	8	6	8
Volcanic glass	–	–	–	–	–	–	Tr	–
Palagonite	–	–	Tr	–	Tr	–	–	–
Micronodules	1	Tr	1	3	2	Tr	Tr	5
Zeolite	–	–	–	Tr	–	Tr	Tr	–
Carbonate unspec.	–	4	2	–	–	–	4	–
Foraminifers	3	18	20	25	20	25	20	25
Calc. nannofossils	90	76	65	62	70	65	60	47
Sponge spicules	1	–	–	–	–	–	–	–
Dolomite	–	–	–	–	–	2	10	15

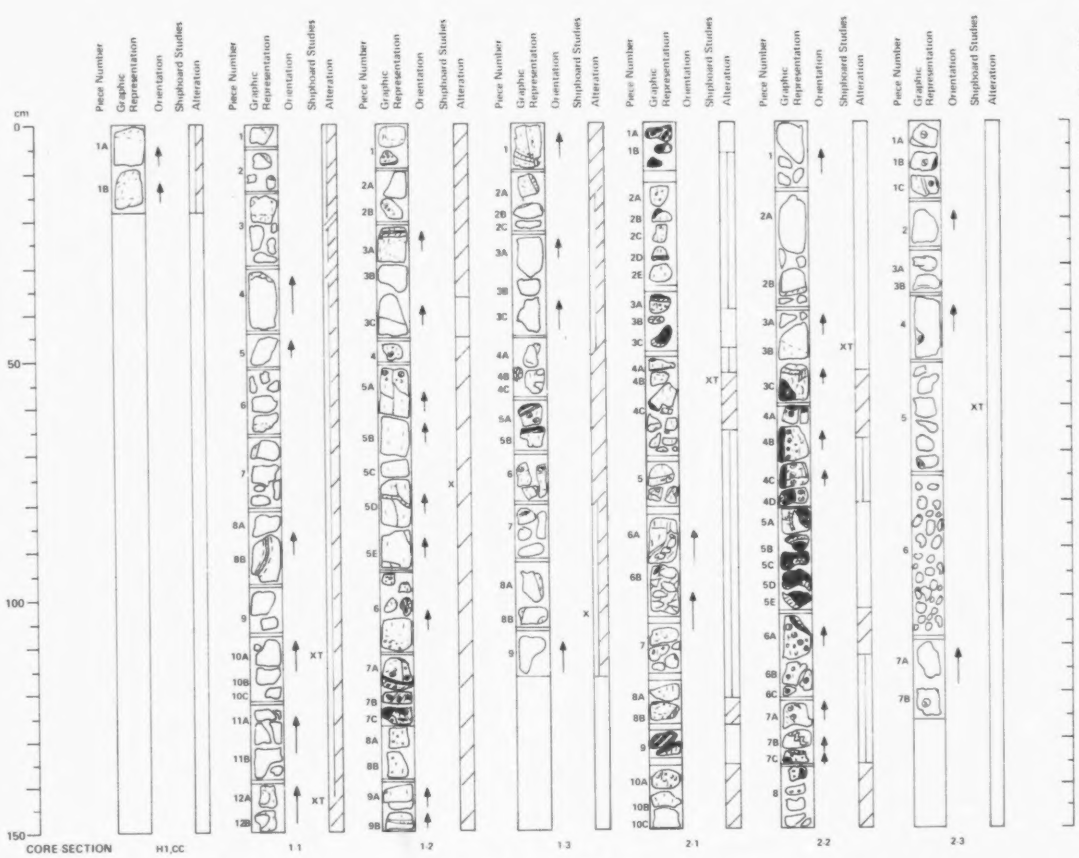

SITE 564, CORE H1 Depth 0.0–284.0 m

CORE CATCHER

APHYRIC TO SPARSELY PLAGIOCLASE (OLIVINE) PHYRIC BASALT

0–17 cm: Basalt appears fine grained, gray (7.5YR N5/0). Plagioclase forms glomerophyric clusters (<2 mm in diameter), abundance < 2%. Olivine phenocryst residues are filled with brown clay, shape: euhedral to angular, size: <1.5 mm, abundance < 1%. Both pieces are partly altered (as marked), color grayish brown (2.5Y N5/2). Vesicles (round) are rare (<1%) and clay-filled. Diameter: <1 mm.

SITE 564, CORE 1 Depth 284.0–293.0 m

SECTION 1

APHYRIC PILLOW BASALT

Fine grained slightly–moderately altered gray (7.5YR N5/0) aphyric pillow basalt with (micro) phenocrysts of dark orange brown clay alteration product, probably residue of olivine.

Olivine may be present as a dark orange brown clay residue, 1–1.5 mm in diameter an subhedral patches which are sparsely scattered.

Alteration ranges from slight to moderate slight causing only minor changes in the gray intensity to moderate, light brownish gray (10YR 6/2). Alteration appears at piece edges adjacent to calcite veins, and along rock fractures. Often it appears as an alteration zone rimming a fresher aphyric core. Excellent example in Pieces 12A and B, 140–150 cm.

Vesicles are sparsely scattered, rounded, < 1–< 2 mm in diameter, often calcite filled, sometimes clay filled.

No glass present.

65 cm: Pillow margin — brownish gray aphanitic margins.

140–150 cm: Aphanitic, light gray (7.5YR N6) pillow margin.

SECTION 2

APHYRIC PILLOW BASALT

0–5 cm: Aphanitic light gray basalt (near pillow margin) light gray (7.5YR N6) altered darker gray (7.5YR N5) 1 cm in from edge.

5–8, 95–117, and 128–130 cm: Aphanitic pillow margins with narrow (1–2 mm) glass rim where shown. Sometimes variolitic. Altered pale brown (10YR 6/3). Up to 5% irregular, unfilled vesicles.

10–95 and 130–150 cm: Fine grained aphyric basalt. Fresh gray (7.5YR N6) only from 35–45 cm. Slightly to moderately altered (brownish cast) gray (10YR 6/1) elsewhere. Olivine microphenocrysts 0.5–1 mm altered brown clay very firm 0–2%.

22–25 cm: Limestone-calcite vein. Lower part of calcite containing abundant, sand sized dark pieces of basalt(?). Limestone fine grained reddish yellow (7.5YR 6/6).

117–127 cm: Interpillow glass breccia, calcite cement. Glass fresh with narrow (< 0.5 mm) palagonite rims to hyaloclastite.

SECTION 3

APHYRIC PILLOW BASALT SEQUENCE

Fine grained, slightly–moderately altered gray (7.5YR N5/0) to brownish (10YR 5/1) pillow basalt. Microphenocrysts of olivine altered to dark orange brown residue are visible. Alteration as zones about fresher core as well as adjacent to calcite veins and fractures.

Olivine occurs as 1 mm microphenocrysts altered to form as a dark orange brown residue <1–2 mm in diameter. Anhedral in form. Abundance varies up to 2%.

Alteration occurs adjacent to rock fractures, calcite veins and pillow margins. Within pillows, alteration may also appear as brownish yellow (10YR 6/6) to yellow (10YR 7/6) zones about fresher cores of pillow grading into gray (7.5YR N5/0) aphyric basalt. Alteration also present in variolitic zone.

Variolitic pillow basalt present as indicated. Glassy margins grading into a thin zone of very dark gray (7.5YR N3/1) aphanitic basalt to variolite zone, yellowish brown (10YR 5/6 to 10YR 5/8) hue grading into gray (7.5YR N5/0) pillow basalt.

Vesicles are sparsely scattered, and rounded, some lined with clays, others filled, or irregular and concentrated in pillow margin from 58–78 cm, majority in this zone are empty.

Glass is present at pillow margin. Slight palagonitization of glass occurs within cracks and fractures of rind. Palagonite-tinted calcite product present on 5A and B as well.

SITE 564, CORE 2 Depth 293.0–302.0 m

SECTION 1

APHYRIC PILLOW BASALT

4–41, 50–73, 104–126, and 130–150 cm: Fine grained, light brownish gray (2.5Y 6/2) moderately to strongly altered pillow basalt, 1–2% rounded and irregular empty vesicles (<1–2 mm) especially near pillow margins. Some calcite in fractures.

0–4, 41–48, and 128–130 cm: Fresh, black glass clasts in calcite matrix.

76–102 cm: Altered basalt breccia and altered glass calcite matrix pieces angular to subrounded ranging in size from barely visible through 5 mm (mostly altered glass clasts), 1.5–2 cm (mostly basalt pieces and some partly altered glass clasts) to large (7 cm) basalt fragment at 85–89 cm. Glass fragments altered brownish yellow (10YR 6/6). This color also stains the calcite matrix.

SECTION 2

APHYRIC PILLOW BASALT

0–58 cm: Fine grained, gray (2.5Y N5) mostly fresh aphyric pillow basalt.

48–58 cm: Some alteration to light grayish brown (2.5Y 6/2) along pillow margins. No vesicles except < 1% on pillow margin (with glass) at 55–57 cm.

60–83 and 106–150 cm: Aphyric basalt like above but moderately to strongly altered (light olive brown – 2.5Y 5/4). 3–5% rounded empty vesicles (<1–2 mm) near pillow margins (glass rims) <1% rounded calcite filled vesicles (~1 mm).

86–104 cm: Black fresh glass clasts, some with sparry calcite and limestone calcite.

SECTION 3

APHYRIC PILLOW BASALT SEQUENCE

Fine grained gray (7.5YR N5/0) pillow basalt with variolite zones tinted brownish yellow (7.5YR 6/6). Mottled in appearance. Contains dark orange brown patches of clay residue altered olivine.

Olivine is present as a 1 mm microphenocryst altered to form dark orange brown residue <1–2 mm in diameter, anhedral in form. Abundance varies up to 2%.

Alteration occurs adjacent to calcite vein, rock fractures and in variolite zones of pillow margins. Within pillows alteration appears as mottling of intensity of grays (7.5YR N5/0–7.5YR N6/0).

Variolitic pillow basalt present as indicated. Glassy margins grading into a zone of very dark gray (7.5YR N5/1) aphanitic basalt to variolitic zone, yellowish brown (10YR 5/6) to brownish yellow (7.5YR 6/6) grading into gray (7.5YR N6/0) pillow basalt.

Vesicles are rounded or irregular, clay lined and/or calcite filled, with calcite present as well. Concentrated in pillow margins, 0–18, 75–107, and 120–127 cm in the pillow contact zone (aphanitic to variolitic). Most of the vesicles are empty.

Glass is present at pillow margin. No palagonitization is visible but glass is not extensive.

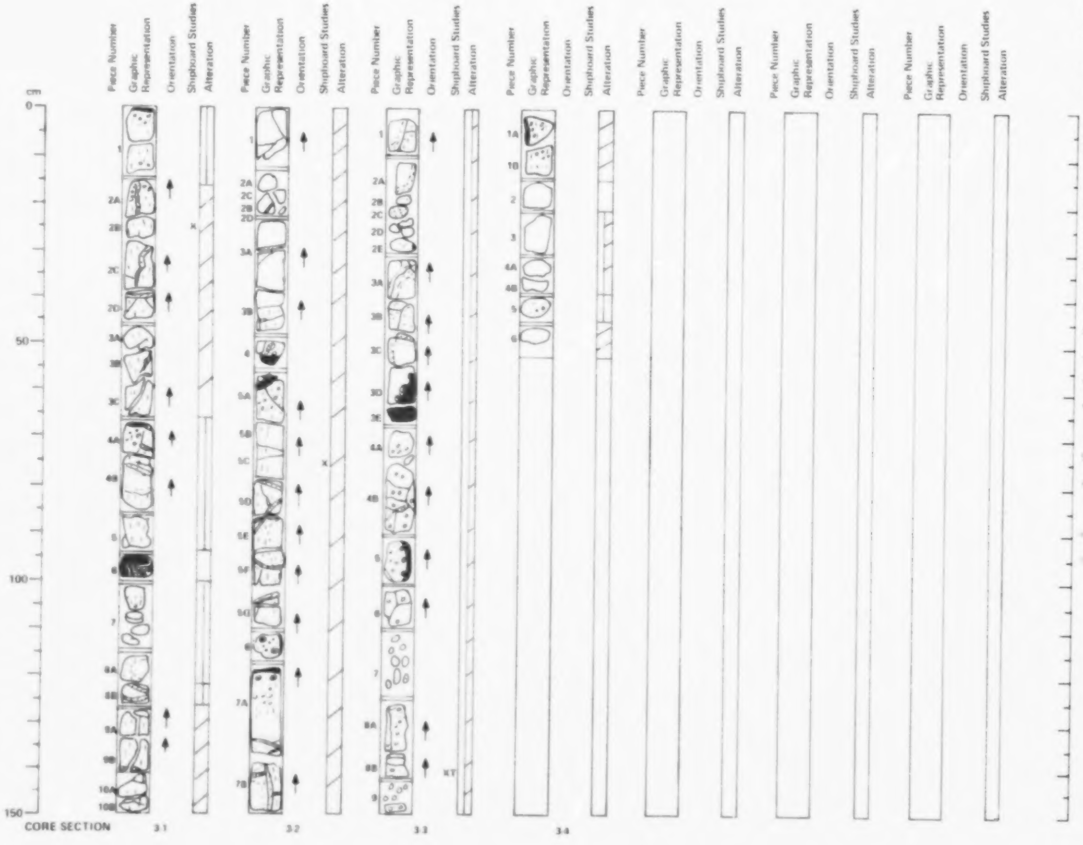

SITE 564 CORE 3 Depth 302.0–311.0 m

SECTION 1

APHYRIC PILLOW BASALT

16–66, 101–121, and 129–150 cm: Fine grained, gray (2.5Y N5) aphyric pillow basalt moderately altered to light yellowish brown (2.5Y 6/4) along pillow margins.

16–20 cm: ~1% round calcite filled vesicles at altered pillow margins (1–2 mm diameter).

35–40 cm: ≤1% irregular vesicles (1–3 mm) filled with dark green clay(?). Calcite in fractures.

0–15, 70–94, and 122–126 cm: Aphyric basalt as above but more highly altered to light yellowish brown (2.5Y 6/4) throughout. 2–3% round and irregular empty vesicles (1–2 mm), especially near pillow margins. Calcite in fractures.

0–1, 68 and 68–69 cm: Glass rims with calcite.

96–99 cm: Black fresh glass with yellow (2.5Y 7/6) limestone/calcite veins.

SECTION 2

APHYRIC PILLOW BASALT

Aphyric basalt: fine grained gray (7.5YR N5) ranging to pale brown (10YR 6/3) where altered.

Glass rims where shown grade into narrow (<1 cm) black aphanitic and variolitic rims (pale brown – 10YR 6/3) and then to fine grained basalt.

Minor calcite veins where shown.

Vesicles up to 1.5 mm generally round, some irregular concentrate up to ~5% within a few cm of upper pillow margin. Most are empty, a few are clay filled.

SECTION 3

APHYRIC PILLOW BASALT

0–150 cm: Fine grained, aphyric basalt, color gray (2.5Y N5/0) to grayish brown (2.5Y N5/2) in altered parts mainly close to fractures and veins (calcite filled).

28–30, 56–67, and 91–94 cm: Fresh black glass margins, up to 3 cm thick, beginning palagonitization from fractures; variolitic zone is very narrow (a few mm); variolites are <1.5 mm in diameter.

From 0–67 cm: No visible vesicles.

From 68–150 cm: ~2% round vesicles (<1.5 mm in diameter), half empty, half calcite filled.

SECTION 4

APHYRIC PILLOW BASALT

0–13, 41–50, and 33–39 cm: Fine grained aphyric pillow basalt as in Sections 1–3 — moderately altered.

0–10 cm: 2–7% rounded empty vesicles (1–2 mm) in pillow margin.

40–44 cm: Strongly altered (light brownish gray — 2.5Y 6/2) aphyric basalt as in Sections 1–3. 1–2% rounded empty vesicles (1–3 mm) and 1 rounded calcite-filled vesicle (2 mm).

22–38 cm: Fresher gray (7.5YR N4) aphyric basalt that is slightly to moderately altered. 1–2% tiny (1–2 mm) vesicles(?) altered to brown (7.5YR 5/4) clay(?).

16–20 cm: One piece of fresh gray (7.5YR N6) aphyric basalt.

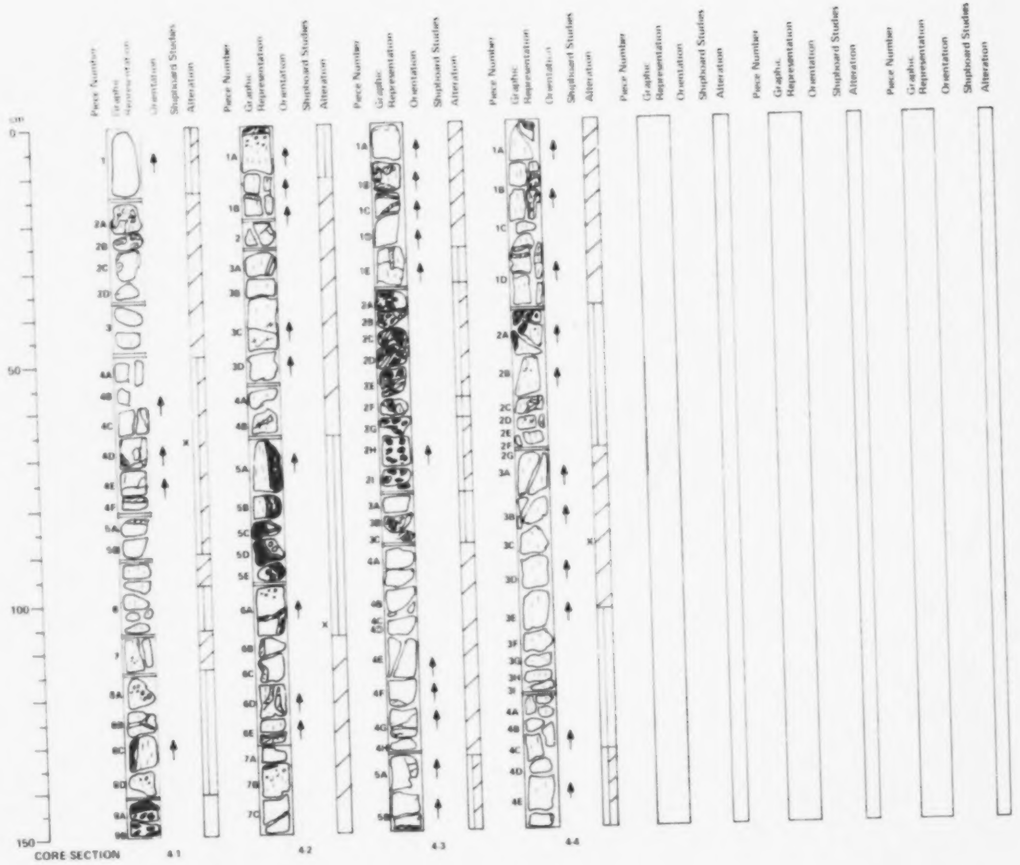
cm
0
50
100
150
CORE SECTION
Piece Number
Graphic Representation
Orientation
Shipboard Studies
Alteration
4-1
4-2
4-3
4-4
1
2A
2B
2C
2D
3
4A
4B
4C
4D
4E
4F
5A
5B
6
7
8A
8B
8C
8D
9A
9B
1A
1B
1C
1D
1E
2A
2B
2C
2D
2E
2F
2G
2H
2I
3A
3B
3C
3D
3E
3F
3G
3H
3I
4A
4B
4C
4D
4E
4F
4G
4H
5A
5B
5C
5D
5E
6A
6B
6C
6D
6E
7A
7B
7C
X

SITE 564 CORE 4 Depth 311.0–320.0 m

SECTION 1

APHYRIC PILLOW BASALT

0–15 and 23–80 cm: Fine grained gray (2.5Y N5) aphyric basalt, moderately altered, and coarser grained than previous cores. 5–10% plagioclase needles (1–4 mm) randomly oriented ore same in radiating clusters. 1–2% small (1–2 mm) olivines(?) altered to brown (7.5YR 5/4) clay(?). No vesicles and calcite in fractures.

108–139 cm: Fine grained, gray (2.5Y N6) pillow basalt moderately to highly altered to light brownish gray (2.5Y 6/2), finer grained than basalt above. 1–2% round and irregular empty vesicles (1–2 mm) especially in altered pillow rims. <1% irregular calcite-filled vesicles (1–2 mm) calcite in fractures.

128–132 cm: Glass rim.

18–21 cm (Piece 2A): Basalt breccia in calcite matrix.

130–148 cm: Fresh black glass clasts in calcite matrix.

SECTION 2

APHYRIC PILLOW BASALT

0–150 cm: Fine grained, gray (2.5Y N5) aphyric basalt, moderately to more strongly altered to light yellowish brown (2.5Y 6/4) especially near pillow margins and fractures. 1–2% round and irregular vesicles (1–2 mm) empty or filled with calcite especially near pillow margins. Calcite in fractures.

88–94 cm: Black glass pillow chill margins some altered to yellow (10YR 7/8) and strong brown (7.5YR 5/6) clays.

SECTION 3

APHYRIC PILLOW BASALT

0–33 cm: Fine grained, gray (7.5YR N5) aphyric basalt. Some moderate alteration to light grayish brown (2.5Y 6/2). 2–3% olivines(?) (1–2 mm) altered to strong brown (7.5YR 5/6) clays(?).

9–13 cm (Piece 1B): ~15% of the basalt consists of large (5–15 mm) irregular calcite-filled interconnecting cavities.

34–77 cm: Black glass clasts (angular to subrounded) in calcite matrix with very pale brown (10YR 8/3) limestone in places.

55–58 cm (Piece 2F): Glass more altered (strong brown – 7.5YR 5/8) and limestone/calcite matrix is yellow (2.5Y 8/6).

78–150 cm (Piece 3B): Finer grained aphyric pillow basalt, moderately altered – <1% visible olivines and vesicles.

82–85 cm: Basalt clast in calcite matrix with pale yellow (2.5Y 8/4) limestone band, more basalt glass in bands.

SECTION 4

APHYRIC PILLOW BASALT

0–150 cm: Fine grained, gray (2.5Y N5) aphyric pillow basalt, moderately to highly altered to light brownish gray (2.5Y 6/2) especially along fractures and pillow margins. <1% rounded, empty vesicles (1–2 mm) mostly in highly altered parts, extensive calcite filled fracturing.

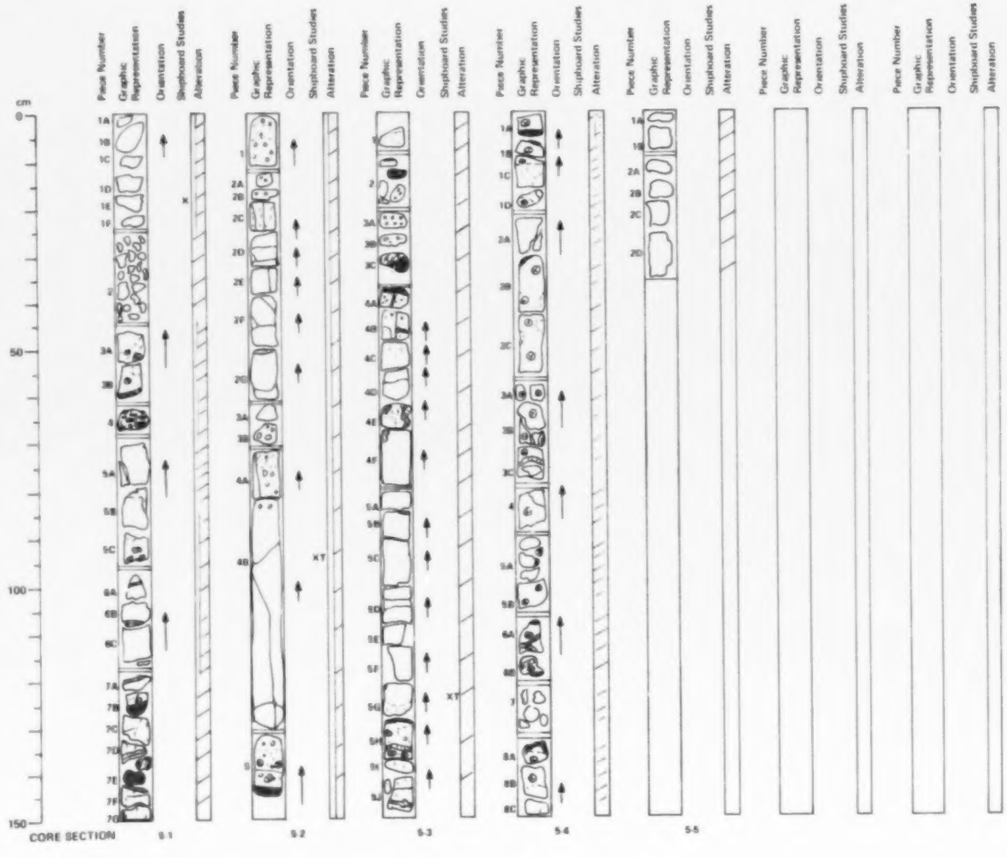

SITE 564 CORE 5 Depth 320.0–329.0 m

SECTION 1

APHYRIC PILLOW BASALT

Fine grained moderately–highly altered gray (7.5YR N5/0) to light yellowish brown (7.5YR 6/4) and brownish yellow (10YR 6/6) in altered and variolitic zones. Olivine is present as highly altered dark orange brown residues.

Olivine is present as ~1 mm microphenocrysts, scattered about pieces, highly altered to dark orange brown residue.

Calcite patches are present in some pieces, veins in others.

Variolitic basalt zones are present where indicated. Sequence of glass – black (7.5YR N2.5/0) aphanitic basalt – variolitic zone, few cm thick, light yellowish brown (10YR 6/4) to brownish yellow (10YR 6/6) grading to grayish brown (10YR 5/2) into fresher gray (7.5YR N5/0).

Alteration present where indicated, adjacent to calcite veins, rock fractures and variolitic zones. Maximum color change in highly altered regions to brownish yellow (10YR 6/6).

Vesicles sparsely scattered, some irregular and others rounded, ~1 mm–2+ mm in diameter concentrated in variolitic zones. Some clay lined, others calcite filled. Glass present where indicated.

62–68 and 134–138 cm: Glass clasts (few mm–few cm diameter) in a calcite matrix. Palagonitization of smaller clasts evident.

SECTION 2

APHYRIC PILLOW BASALT

0–150 cm: Fine grained aphyric basalt, color gray (7.5YR 5/0) to grayish brown (10YR 5/2) in altered parts (as signed). Small olivine (<1.5 mm) are sparsely scattered (< 1%) throughout the section. It is mostly replaced by a reddish brown clay mineral.

0–18 and 130–142 cm: Round vesicles occur at 0–18 cm and 130–142 cm; they are either unfilled or half or completely filled by calcite (<2 mm, <4%).

65–82 cm: Occur very irregular vesicles (< 1.3 mm, ~ 5%) which are calcite coated or cemented or clay filled (light green colored clay).

142–144 cm: Fresh black glass (~1.5 cm thick) with variolitic zone above it (~6 cm thick).

SECTION 3

APHYRIC PILLOW BASALTS

0–47 and 122–147 cm: Aphyric pillow margin material. Fresh black glass pieces < 1 cm thick and rinds 1–2 mm. Minor palagonite and carbonate. Grading through <1 cm black aphanitic basalt to gray (10YR N5) aphanitic, generally altered pale brown (10YR 6/3). Variolitic where shown. Vesicles round and irregular (< 2 mm) concentrated up to ~5% within a few cm of pillow margins. Minor calcite veinlets as shown.

47–122 cm: Aphyric basalt (pillow interior). Gray to dark gray (7.5YR N5 to N6) mottled with yellowish brown (10YR 5/6) patches – none completely fresh.

61–67 cm: Irregular calcite vein or cavity (vesicle train?) filling.

SECTION 4

APHYRIC PILLOW BASALT

0–21 and 30–144 cm: Aphyric pillow material at margin as in Section 3.

21–30 and 144–150 cm: Aphyric basalt pillow interior gray to dark gray (7.5YR N5/0 to 7.5YR N6/0) mottled with yellow brown (10YR 5/6) patches none entirely fresh as in Section 3.

SECTION 5

APHYRIC PILLOW BASALT

0–37 cm

Fine grained pillow basalt gray (7.5YR N5/0) with microphenocrysts of plagioclase and of olivine present as dark orange brown patches of altered residue.

Olivine is present as a dark orange brown alteration product, <1–2 mm in diameter, anhedral. Scattered in this section.

Plagioclase is present as 1–3 mm long microphenocrysts, needle-form in shape. Localized concentration of plagioclase.

Altered moderately, more so about calcite patches.

Vesicles rare, calcite filled.

20–27 cm: Irregular patches of calcite set into pillow basalt, 2–5 mm in diameter.

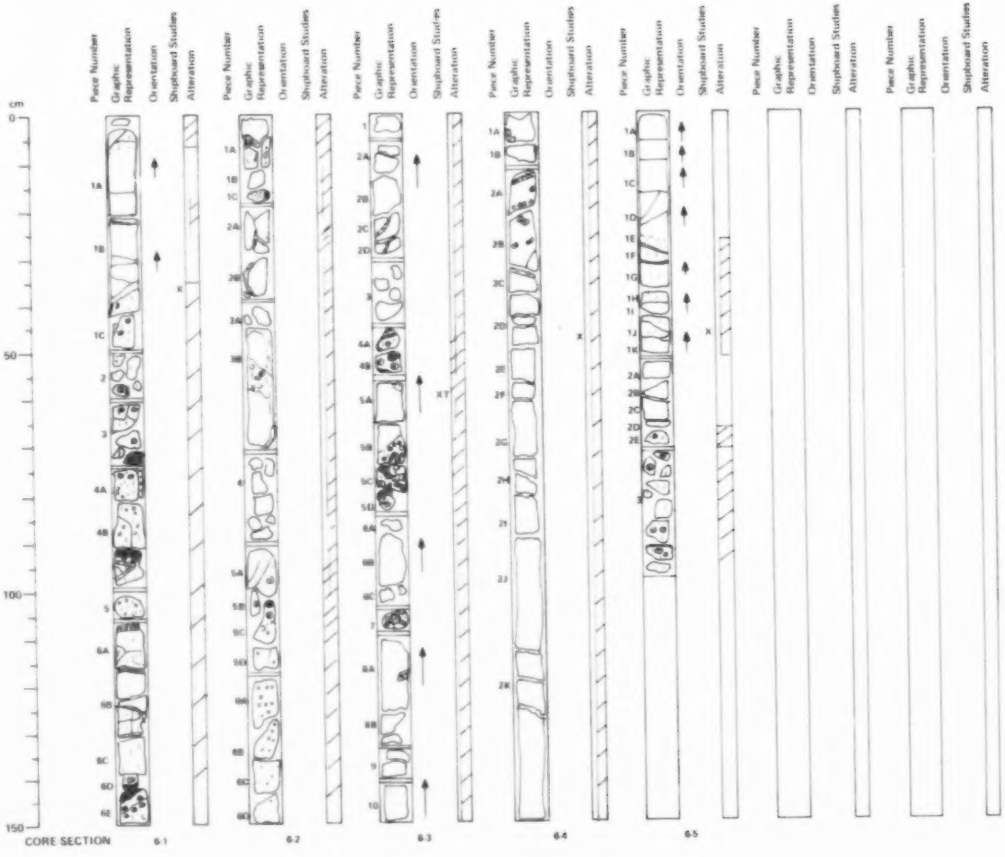

SITE 564 CORE 6 Depth 329.0–338.0 m

SECTION 1

APHYRIC PILLOW BASALT

0–42 cm: Pillow interior. Aphyric basalt, fine grained dark gray (7.5YR N7). Slightly altered towards brown (10YR 5/1) close to fractures, otherwise fresh. Abundant acicular plagioclase to 3 mm and 2–3% round ~0.5 mm olivine microphenocrysts completely altered brown or dark green.

41–150 cm: Pillow marginal zones. Aphanitic basalt, gray (7.5YR N5) where fresh. Generally altered, light brownish gray to pale brown (10YR 6/2–6/3). Variolitic where shown. Fresh glass where shown, black aphanitic basalt 1–2 cm thick beneath glass then variolitic zone up to several cm thick.

SECTION 2

APHYRIC PILLOW BASALTS

0–30 and 90–115 cm: Pillow margins – aphanitic basalt and glass as in Section 1.

30–90 and 118–150 cm: Fine grained basalt (pillow interior) as in Section 1.

55–62 cm: Irregular, calcite filled vesicles.

115–140 cm: Vesicles, round carbonate filled. Abundance increases downwards from 1–2% to ~8%. Size increases from ~1 mm to 2–3 mm.

SECTION 3

APHYRIC PILLOW BASALT AND MASSIVE FLOW

0–44, 60–70, 86–104, and 112–150 cm: Pillow interior as in Section 1. Probably still part of massive flow begun at 100 cm, Section 2. Altered to a mottled combination of fine grained dark gray (7.5YR N4) towards brown (10YR 5/1). Plagioclase and olivine as in Section 1.

46–59 and 105–109 cm: Highly altered basalt with calcite limestone blebs. Indications of Mn – calcite – basalt altered light brownish gray to pale brown. Pillow margin? Variolitic as indicated.

70–80 cm: Irregular calcite patches. Sparry calcite intergrown into basalt cavities.

50 cm: New massive flow? Variolitic top.

SECTION 4

APHYRIC BASALT

0–150 cm

Fine grained dark(?) gray (7.5YR N4/0) massive flow interior. Pillow flow continued from Section 3. Calcite patches 1–6 cm as indicated. Large amounts of acicular plagioclase 1–4 mm in length.

Olivine microphenocrysts present as dark orange brown altered residue anhedral.

Alteration is moderate. Observed in massive section as mottled gray appearance.

SECTION 5

APHYRIC BASALT

0–64 cm: Fine grained massive basalt flow as in Section 4.

70–95 cm: Aphanitic and variolitic basalt pillow margin (base of flow?) material as in Section 1.

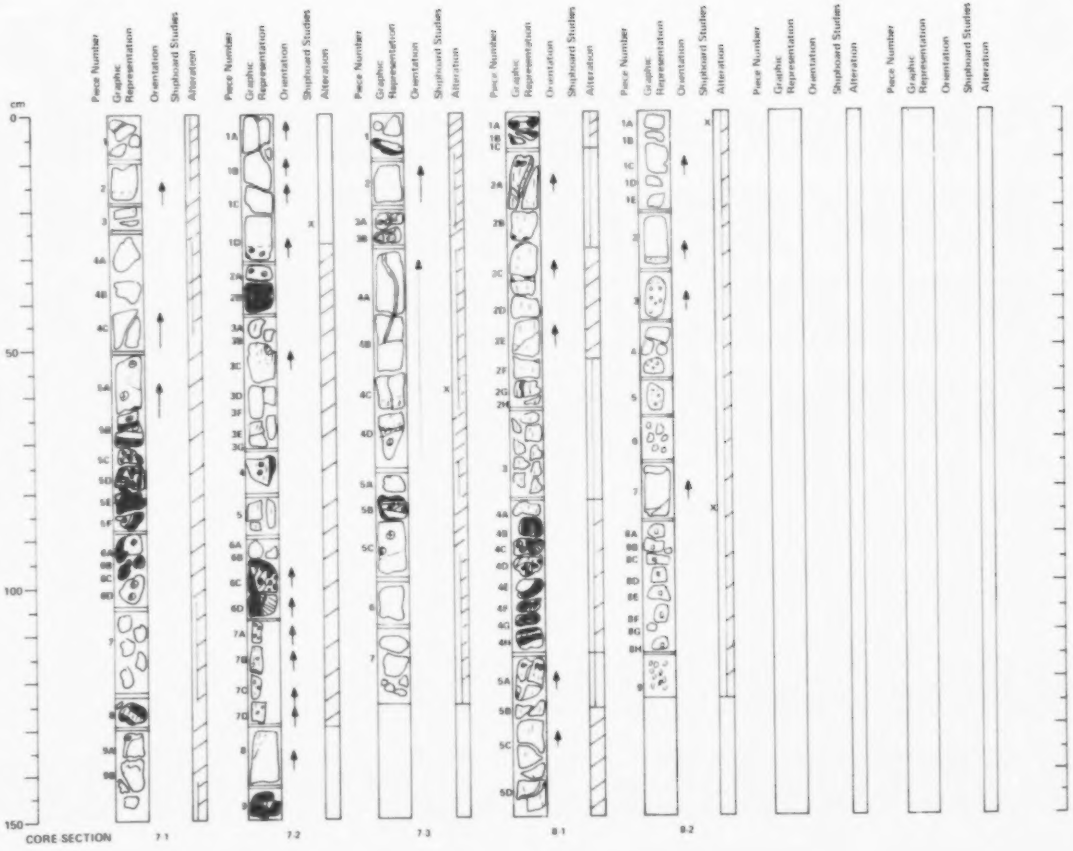

SITE 564 CORE 7 Depth 338.0–347.0

SECTION 1

APHYRIC PILLOW BASALT AND GLASS BRECCIA

0–49 and 134–150 cm: Fine grained dark gray (7.5YR N4/0) pillow basalt interior, slightly altered to a mottled gray (7.5YR N5/0), or a light yellowish brown (10YR 6/4).

49–134 cm:

Pillow margin sequence. Interpillow glass grading into variolitic zone (10YR 5/6–10YR 5/8) yellowish brown grading back into gray (7.5YR N 4/0) aphyric basalt. Alteration in variolitic zone to colors described.

Variolitic zone as indicated. Few cm thick aphanitic zone, few cm zone variolitic zone grading into aphyric zone.

Glass as indicated.

63–97 cm: Glass breccia with clasts cemented into a calcite/limestone matrix. Clasts are angular and aligned parallel to each other within a piece. Calcite/limestone may be tinted slight palagonite color, and also a light pink zone is seen.

SECTION 2

APHYRIC PILLOW BASALT

0–28 and 130–140 cm: Fine grained aphyric pillow interior as in Core 6, Section 1, and Core 7, Section 1

28–128 cm: Aphanitic basalt and glass pillow margin material as in Core 6, Section 1 and Core 7, Section 1

95–105 cm: Interpillow glass breccia. Matrix part white calcite, part light gray (10YR 7/1) fine grained limestone.

SECTION 3

APHYRIC PILLOW BASALT

0–127 cm: Fine grained dark gray (7.5YR N4/0) pillow basalt interior grading into an interpillow zone consisting of glass – aphanitic black (10YR N2/0) basalt – variolitic zone. Colors, alteration vesicles, etc. same as Section 1.

SITE 564 CORE 8 Depth 347.0–356.0 m

SECTION 1

APHYRIC PILLOW BASALT

10–84 and 116–150 cm: Fine grained, gray (2.5Y N5) aphyric basalt moderately to highly altered to pale brown (10YR 6/3). Variolitic texture grading through black aphanitic basalt to black glass rims <1% round empty and calcite filled vesicles (1–2 mm) especially in altered pillow margins. Calcite in fractures.

0–5 and 95–97 cm: Fresh to moderately altered glass clasts (reddish yellow – 7.5YR 6/8 nearest glass to brown 7.5YR 4/4 further out from glass core) in calcite matrix.

5–8, 86–93, and 99–113 cm: Mostly fresh black glass chill margins with calcite in fractures.

95–97 cm: Sparry calcite rim.

SECTION 2

APHYRIC PILLOW BASALT AND OLIVINE MICRO-PHYRIC BASALT (FLOW?)

0–65 cm: Aphyric, fine grained basalt, color gray (2.5Y N6/0) to light brownish gray (2.5Y N6/2) in altered parts. Mostly non-vesicular, but at:

35–44 and 52–64 cm: Highly vesicular, round, 0.5 to 2 mm in diameter, 5–10%, calcite filled except Piece 5 (empty).

Break at 65 cm.

65–123 cm: Moderately olivine micro-phyric basalt (~5% olivine), fine grained but coarser than upper pillow basalt. Visible plagioclase laths up to 4 mm. Olivine phenocrysts are randomly scattered, size <1 mm. Replaced by brown and green clay. No visible vesicles.

120 cm: Among the chips occur a few black glass splinters.

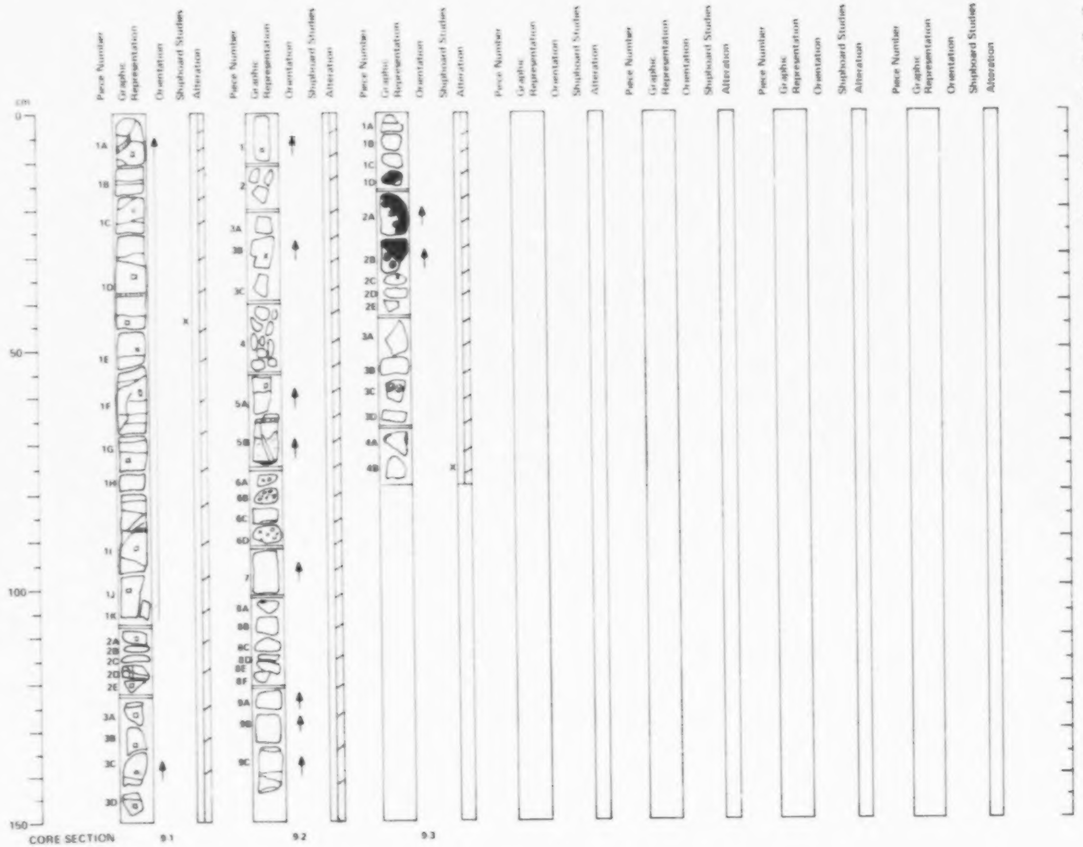

SITE 564 CORE 9 Depth 356.0–365.0 m

SECTION 1

MODERATELY TO SPARSELY OLIVINE MICROPHYRIC BASALT FLOW

0–150 cm: Fine-grained olivine micro-phyric basalt, color dark gray (5Y 4/1). Olivine phenocrysts are mostly replaced by clay (brown color), size <1 mm, abundance <5%. Acicular plagioclase up to 5 mm occurs throughout the section.

1–5 and 128–133 cm: A few scattered lath-shaped or round minerals occur (which look like metallic copper (size: 2 mm to <0.5 mm). Fractures are common and mostly oriented horizontal. They show calcite filling and – in some places – a soft dark to light green mineral on the fracture plane.

SECTION 2

SPARSELY OLIVINE MICROPHYRIC TO APHYRIC BASALT FLOW AND APHYRIC BASALT (PILLOW?)

0–75 cm: Sparsely olivine micro-phyric to aphyric basalt, fine-grained, color dark gray (5Y 4/1). Less olivine than in Section 1 (<2%). Plagioclase <1 mm.

73–74 cm: Black glass margin with altered basalt zone about it; color dark grayish brown (10YR 4/2).

Break – end of flow at 75 cm.

76–90 cm: Fragments of

Pieces A and D: Highly vesicular basalt, round to oval vesicles (<5 mm in diameter) are empty, light green clay filled or coated or calcite filled. Color of basalt: gray (5Y 5/1).

Piece B: Basalt glass breccia. Palagonitized glass clasts <6 mm; calcite cement.

Piece C: Fine-grained, sparsely olivine phyric basalt, color dark gray (2.5Y N4/0).

91–143 cm: Fine grained aphyric pillow(?) basalt; color gray (5Y 5/1). No visible vesicles.

SECTION 3

FRAGMENTS OF APHYRIC PILLOW BASALT

0–12 cm: Fine grained, aphyric basalt, colour gray (5Y 5/1). Green clay(?) mineral on fracture planes.

13–33 cm: Pieces of chilled pillow margins. Black, highly fractured, calcite-cemented and sometimes palagonitized glass is grading through variolitic zone (varioles <2 mm) into very fine grained, very dark gray (2.5YN 3/0) aphyric basalt.

34–77 cm: Fine grained aphyric basalt, color gray (5Y 6/1) with visible plagioclase laths (<3 mm). Irregular vesicles are sparsely scattered (<2%) and calcite filled.

56–61 cm: Piece 3C shows variolites <7 mm.

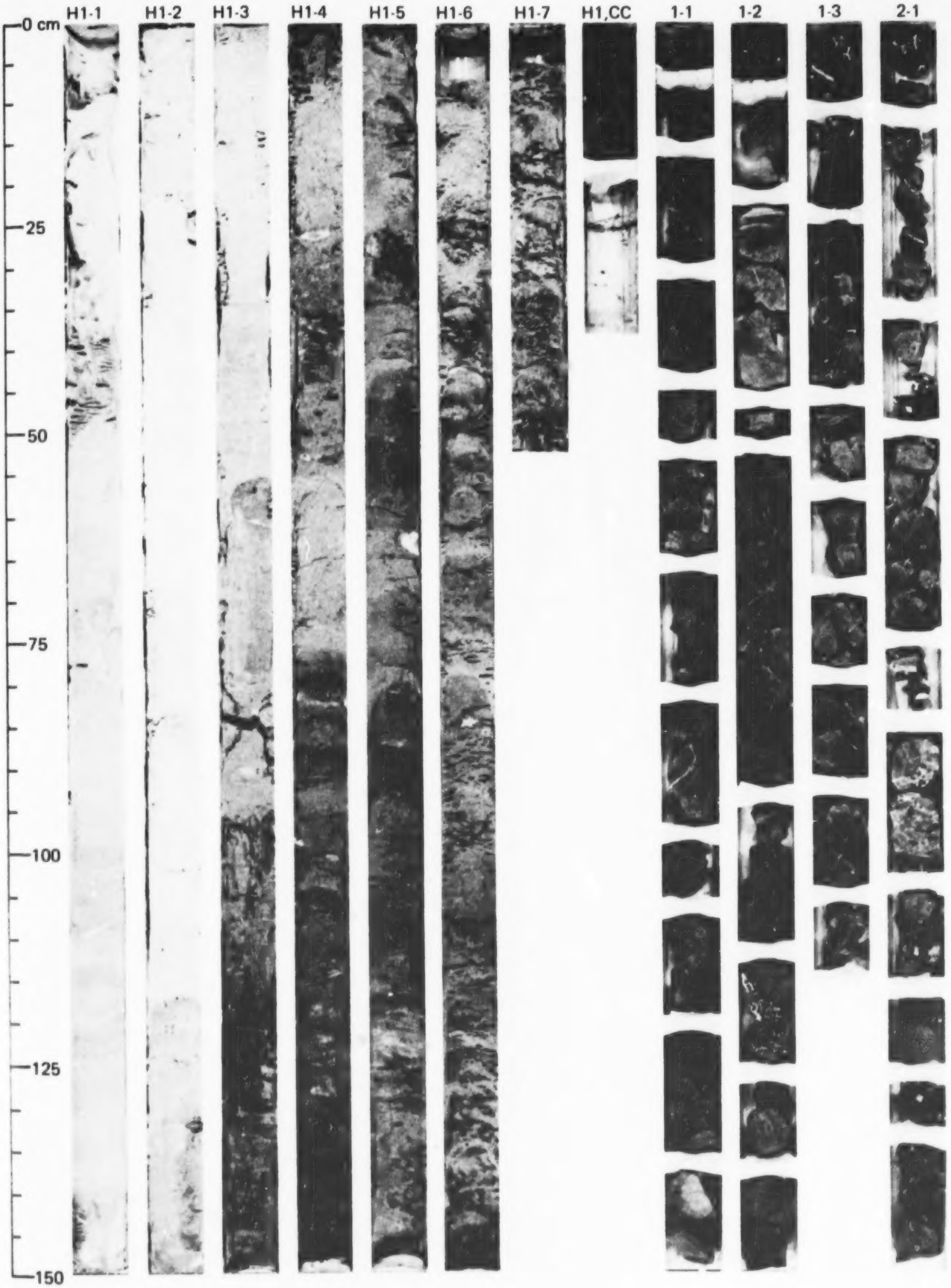
H1-1
H1-2
H1-3
H1-4
H1-5
H1-6
H1-7
H1,CC
1-1
1-2
1-3
2-1
0 cm
25
50
75
100
125
150

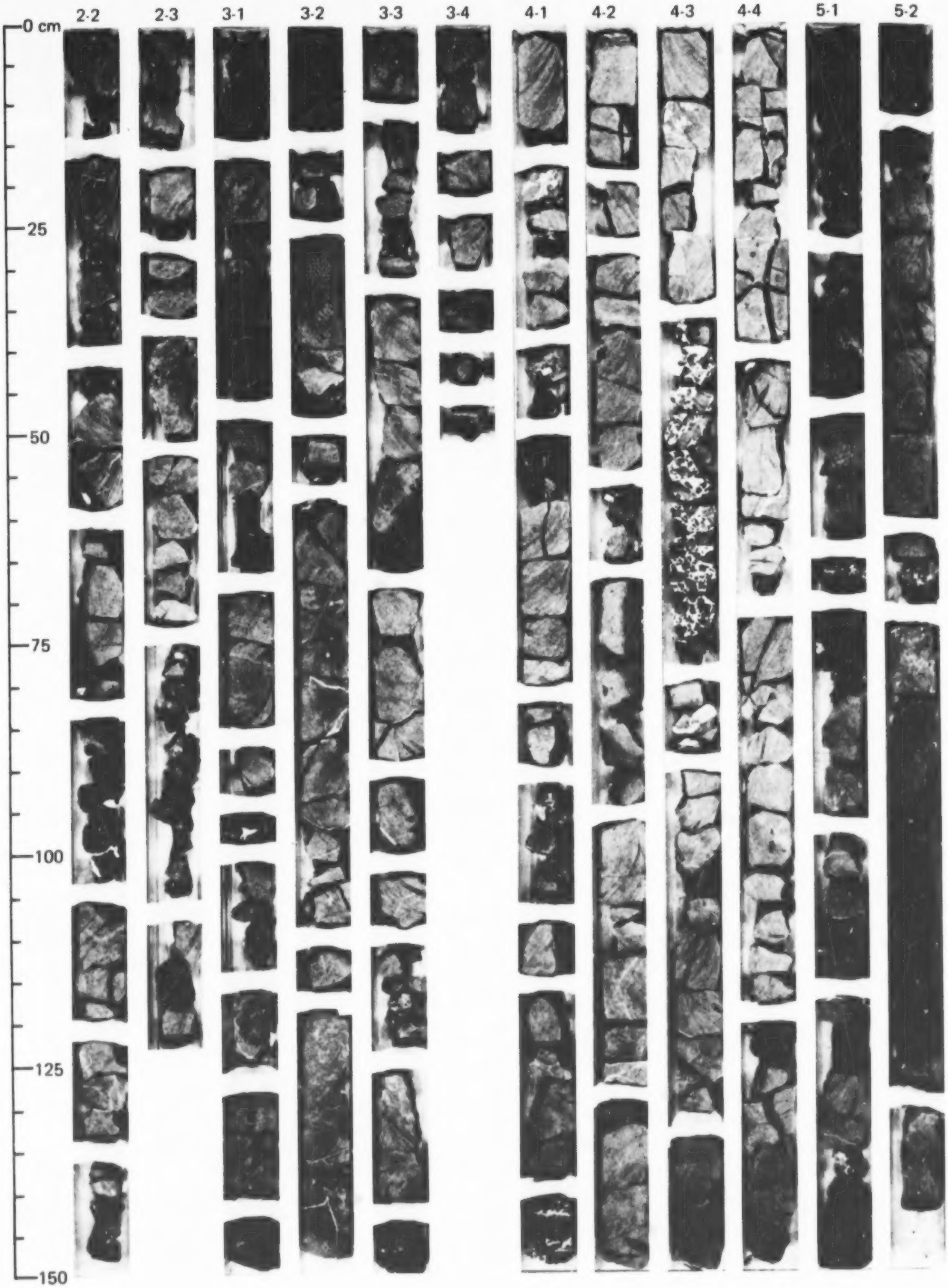
2-2
2-3
3-1
3-2
3-3
3-4
4-1
4-2
4-3
4-4
5-1
5-2
0 cm
25
50
75
100
125
150

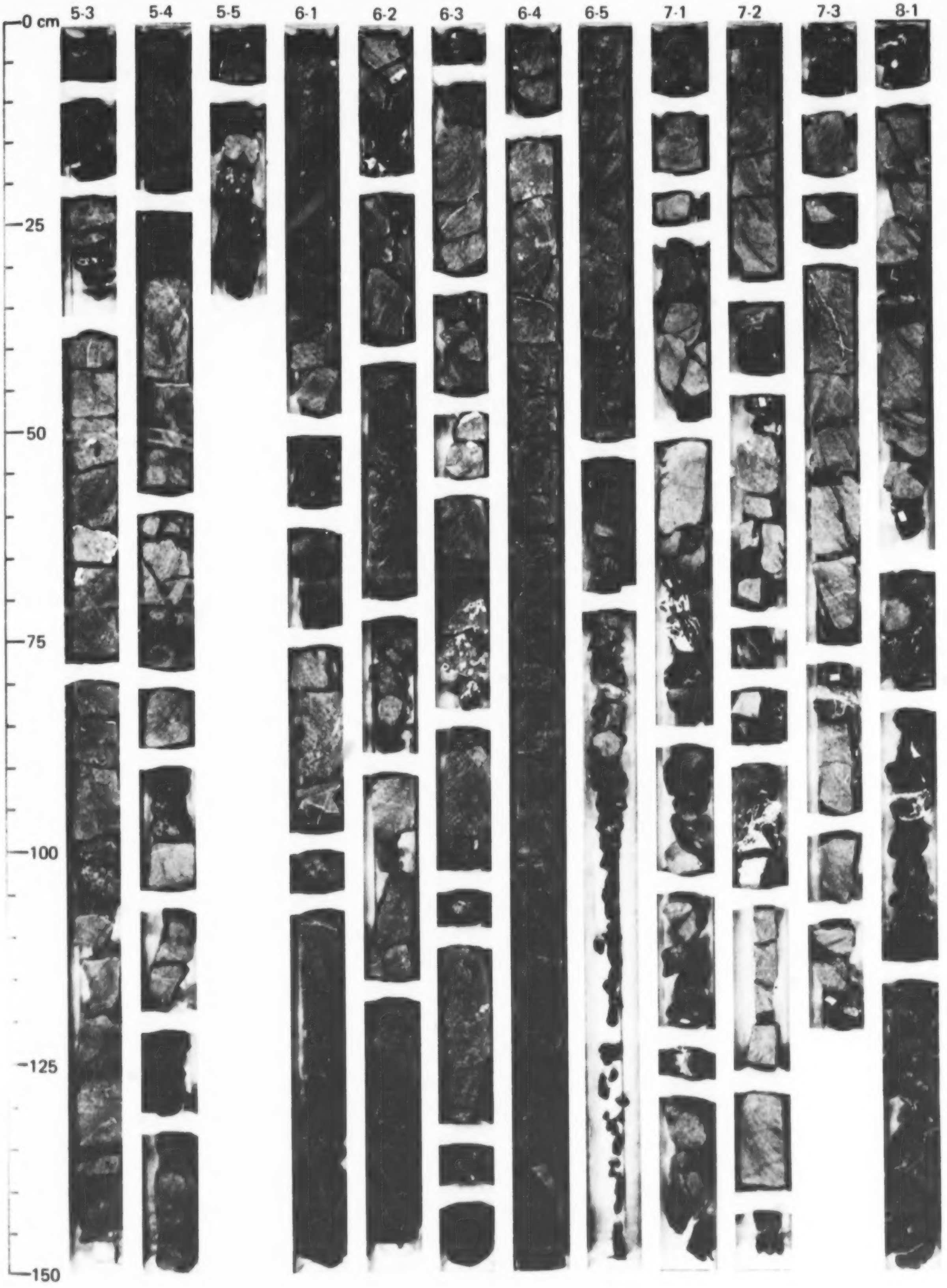
0 cm
25
50
75
100
125
150
5-3
5-4
5-5
6-1
6-2
6-3
6-4
6-5
7-1
7-2
7-3
8-1

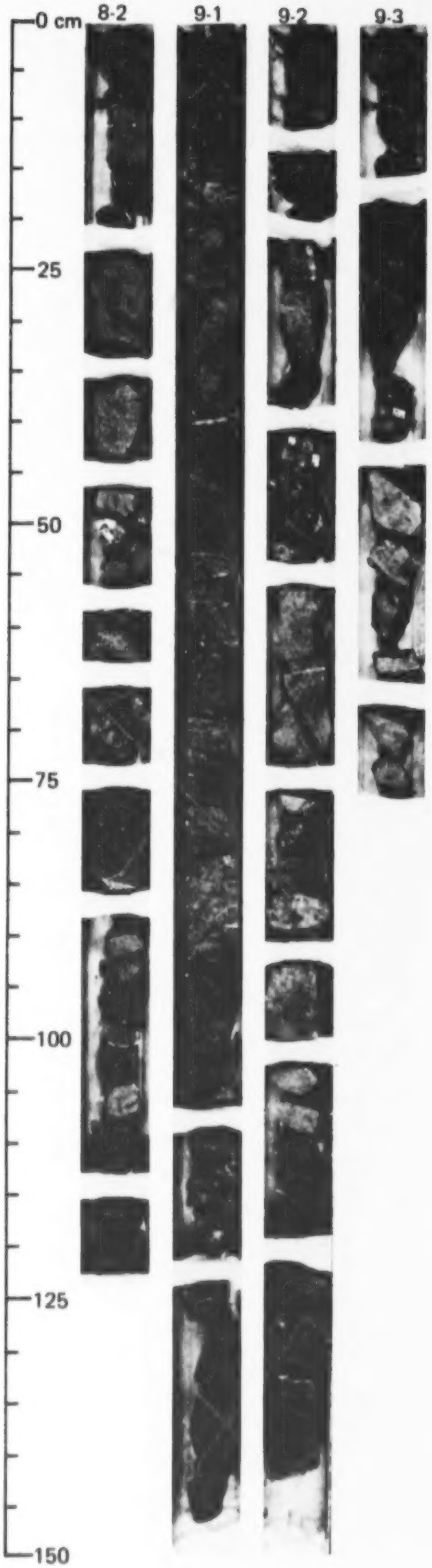
0 cm
8-2
9-1
9-2
9-3
25
50
75
100
125
150

PART III: PHYSICAL PROPERTIES, PALEOMAGNETICS, AND ROCK MAGNETICS

14. DOWNHOLE LOGGING AND LABORATORY PHYSICAL PROPERTIES MEASUREMENTS[1]

I. A. Hill, Department of Geology, Leicester University
and
S. C. Cande, Lamont-Doherty Geological Observatory[2]

ABSTRACT

During DSDP Leg 82 downhole logging experiments, the very poor hole conditions and technical failures that have affected earlier legs were absent. As a result, Holes 556, 558, and 564 were logged with a full suite of tools. In addition, nearly complete continuously cored sections were obtained at Sites 558 and 563, and these sections have been subjected to laboratory physical property measurements. The resulting data set allows a comparison of logged and laboratory measured values and correlation between holes.

The sediments encountered in all holes were calcareous oozes and chalks. Despite the lack of distinctive lithologies, changes in density and seismic velocity can be seen in both the laboratory and logged data and identified with sedimentologic features in the cores; the logged curves can be correlated between holes. Within basement rocks the logged curves provide information on the part of the formations not recovered by coring (about 55%) and allow comparison between bulk properties and the sample properties measured in the laboratory. Comparison of the logged data with that from Site 417 shows systematic differences, perhaps related to crustal aging.

INTRODUCTION

The primary objective of DSDP Leg 82 was the sampling of igneous basement in a systematic pattern to the southwest of the Azores in order to look for geochemical anomalies. This resulted in a strategy of drilling many holes into basement as quickly as possible and washing through sediments as necessary. Downhole logging was to be used on any deep-penetration basement holes to provide information about the material not recovered by continuous coring. When holes are logged, the sediments are logged as well and it was hoped to partially compensate for the lack of sediment coring in this way.

Figure 1 shows actual pattern of the drill sites lying along flow lines and isochrons to the west of the spreading ridge. Partly fortuitously and perhaps partly a reflection of the physical state of the crust, all the deep-penetration holes lie on the oldest isochron, Magnetic Anomaly 13, aged 35 Ma. The exact depths of these holes and the depths of sediment and basement penetrated at each are shown in Figure 2. Holes 556, 558, and 564 were logged, whereas Holes 558 and 563 were cored through sediments as well as basement. The logging was remarkably successful by DSDP standards with a suite of logs including density, neutron, sonic, caliper, gamma-ray, and resistivity being run at each of the three holes and recording good quality data. Temperature logs were also run; the results are reported elsewhere (Hill and Cande, this volume). Basement core samples from the remaining holes were also used for laboratory measurements.

These measurements constitute one of the most complete sets of physical property data collected by a single DSDP leg for both sediments and igneous crust of an extended region. This not only allows a reliable statement to be made about the formation of physical properties but allows comparison to be made between the log curves, the laboratory measurements, and the core descriptions. The high quality of the logging results also allows an examination of some of the problems of the unusual hole environment and its effect on the logging tool performance. Comparison can also be made with the results of previous logging in the Atlantic. The only data available at present is from Hole 417D, Legs 51, 52, 53, which has been fully reported by Salisbury et al. (1980). Because of operational difficulties, the Hole 417D data set was restricted to gamma-ray, resistivity, and sonic logs except for very restricted sections of the hole, but it does provide a useful comparative study with the present data. Hole 369B, Leg 46, was also logged successfully (Kirkpatrick, 1978) penetrating some 200 m into igneous basement. In the Pacific Ocean, logging data were obtained in the Gulf of California (Salisbury, 1983) where the crustal structure is very anomalous because of high sedimentation and in the Nauru Basin (Boyce, 1981) where 500 m of igneous basement were penetrated. The benchmark for DSDP logging experiments is Hole 504B, which has now been drilled and logged to over 1 km below the basement surface (Cann and Von Herzen, 1983; Anderson et al., 1982).

DATA QUALITY

The errors and inaccuracy in each data set must be checked before data interpretation can proceed. The laboratory measurements are relatively easy to check for error and accuracy, but their relevance to the actual physical conditions below the seabed before drilling disturbance and selective sampling are sometimes questionable. The logging tools measure properties *in situ* and are accurate within their design specifications, which may not include the particular hole conditions and li-

---

[1] Bougault, H., Cande, S. C., et al., *Init. Repts. DSDP*, 82: Washington (U.S. Govt. Printing Office).

[2] Addresses: (Hill) Department of Geology, Leicester University, Leicester LE1 7RH, England; (Cande) Lamont-Doherty Geological Observatory, Palisades, NY 10964.

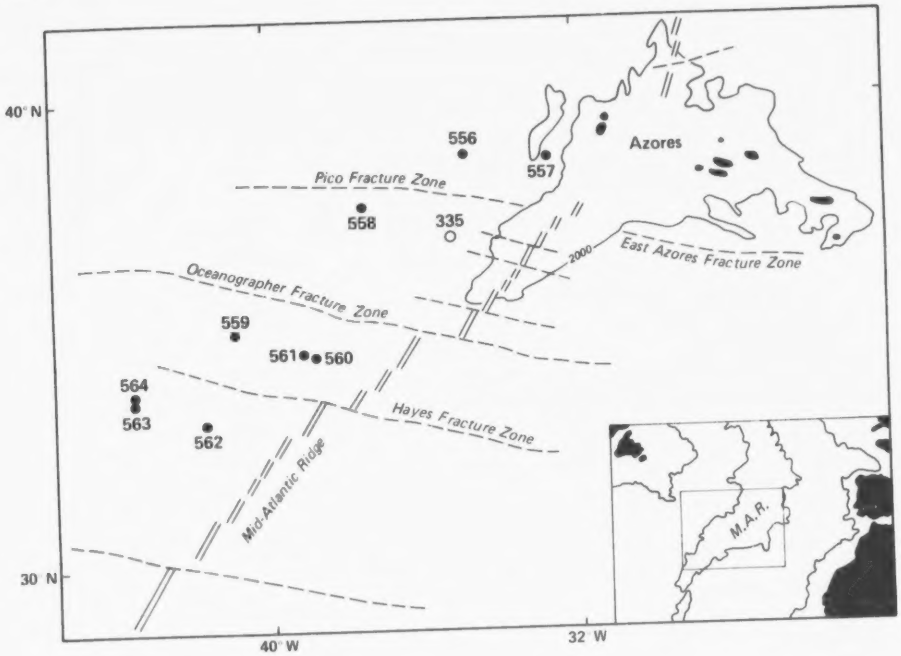

Figure 1. Location of Leg 82 drill sites.

thologies encountered in DSDP drilling. These problems will be reviewed below.

Downhole Measurements

All logging tools used during Leg 82 were of standard Schlumberger designs, optimized for use in mud-filled holes drilled through flat-lying, lithified, sedimentary strata. The contrasting conditions in DSDP holes is shown in Figure 3. The necessity to use the drill string as a casing into the top of the hole means that all tools must pass down the 4-in. diameter drill string cavity. This causes problems with sonic and caliper tools. Rubber pads designed to cushion impacts with the hole sidewall have to be removed to reduce the overall diameter of the tool. This results in more mechanical shock for the tool downhole and vibrations from these impacts add noise to sonic records. The drill string is safely located in the hole by extending it to 100 m sub-bottom depth. Few of the logging tools produce useful results when within the drillpipe and bottom hole assembly, hence the top part of any hole is inaccessible to logging.

Once within the open hole, soft sedimentary formations can become washed out by the circulating drilling water until the hole diameter exceeds the design limits of the tools. All the tools are designed and calibrated either to be operated along the axial centerline of the hole or to be held against the sidewall. Each of these modes of operation require the tool to possess arms that bear on the sidewall and physically locate the tool in the correct position. The maximum extension of the arms on different tools varies but is generally about 0.5 m. When the hole diameter exceeds this limit, the tool swings freely in the hole and recorded data contains uncorrectable errors. Most of the arms make a potentiometric measurement of their extension as a caliper log, hence washed out hole conditions produce a maximum caliper reading with spurious irregular data values on the log curves. These features are well illustrated by the logged curves for Hole 558 (Fig. 4, back pocket). The drill pipe extends to about 96 m sub-bottom for sonic, resistivity, caliper, and gamma-ray measurements but was extended to 145 m sub-bottom while density and neutron porosity measurements were made. Above the end of the drill pipe there are no useful data from any tool. From 100 to about 185 m sub-bottom, the hole diameter is greater than the caliper extension, and the caliper reading is maximum, with noise spikes caused by bumping on the sidewall. The hole diameter is so large that the density and neutron porosity tools cannot be kept in contact with the sidewall and all values above 185 m sub-bottom from these particular tools are erroneous. The sonic and resistivity tools are less affected by the hole diameter, but the random noise on the dual laterolog (LLD) curve becomes much less when the hole diameter decreases so that the tool can be positively located along the centerline of the hole where it is designed to operate.

Confirmation of the absolute calibration of data val ues is also problematic. If individual tools are calibrate for a known response in specifically chosen test rock li thologies, corrections may then be necessary for amb ent hole conditions of temperature and pressure, for th properties of the hole fluid and hole diameter, and fo the differing physical response of the sidewall rock l thology compared to that calibration. Corrections fo these effects are largely empirical but are fairly well de termined. All data shown in this paper has been cor rected for hole conditions assuming the hole is filled wit seawater, the hole diameter is as measured by the cali

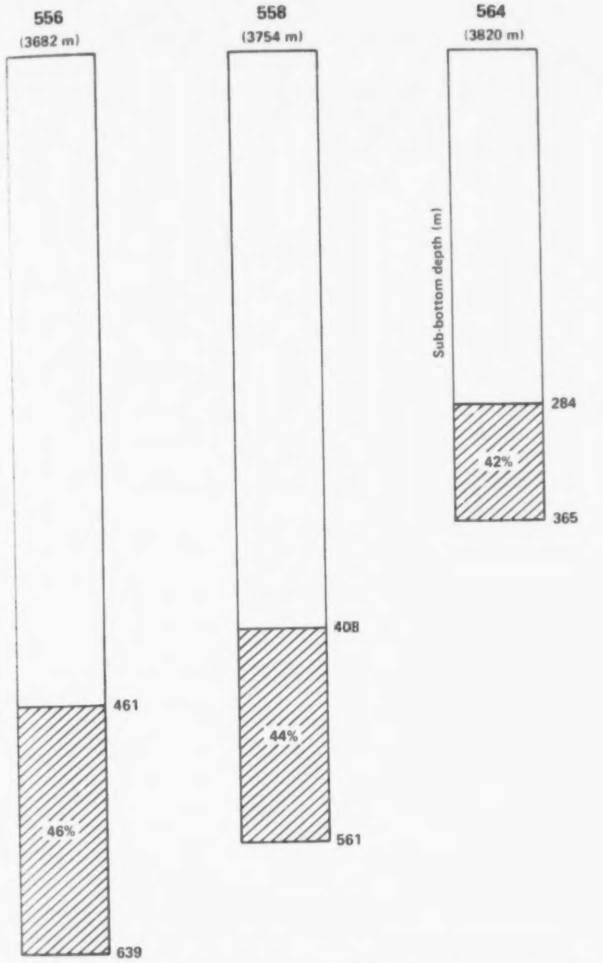

Figure 2. Sketch section of the formations drilled and logged at Holes 556, 558, and 564. Water depth shown in parentheses. Sedimentary section blank, basement hatched. Basement interface and total depth shown in m sub-bottom. Percentage recovery of basement holes shown.

er, and the temperature is as measured by the tempera- ure log (temperature variations are almost negligible) Hill and Cande, this volume). Surface seawater proper- es were measured at each hole and applied to that hole, ith all values similar (i.e., density, 1.06 g/cm^{-3}; resis- vity, 0.21 ohm m at 20°C, corrected to 0.30 ohm m at ole temperatures).

A ship-mounted rig presents the peculiar problem of eave. The drill string has a heave compensation mecha- ism to prevent the vertical motion of the ship from be- ng transmitted to the drill bit. There was, however, no milar mechanism on board *Glomar Challenger* to de- ouple the logging wire from ship motion. In average eep-sea conditions, the vertical motion of the ship is lightly faster than the speed at which logging wire is eaved in during measurements. The tool therefore moves up the hole in an irregular manner. The logging tools are deliberately made to be heavy, several hundred pounds each, and the wire has very low elasticity. The tension in

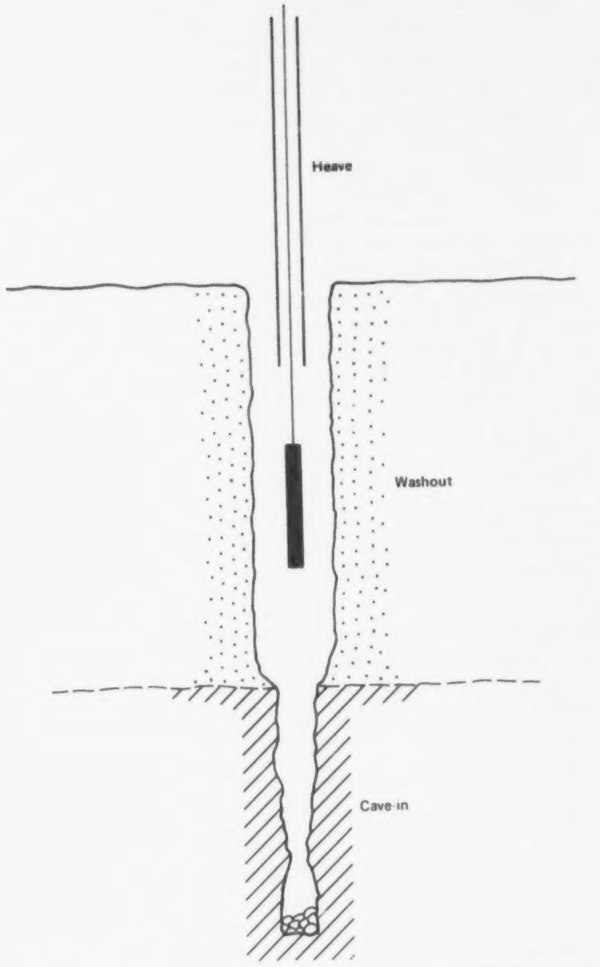

Figure 3. Diagrammatic section of a drilled hole showing conditions adversely affecting wireline logging. For discussion, see text.

the logging wire is continuously monitored and from the variations recorded, it appears that nearly all of the heave motion of the ship is transferred to the tool. Tests were conducted at Hole 564 where the resistivity tool was stopped at the basement/sediment interface and the heave motion in the wire moved the tool across the boundary so that the recorded values varied widely. This effect during normal logging inevitably results in uncertainty about the depth of any particular measurement. In addition, the tool may be in motion across any one lithologic boundary three times as it oscillates on its way up the hole. The Schlumberger Cyber Service Unit (CSU) logs data values at 6-in. intervals of logging wire on recovery. For all interpretations and discussions in this report, the data values have been subject to a weighted averaging over 2-ft. data intervals, after spurious noise values were deleted.

The suite of different logs is obtained by a sequence of three or four separate logging runs. On each of these a natural gamma-ray log is taken and used for depth correlation between different runs. The effect of the averaging procedure was monitored using this duplicate data and was found to improve correlation. Although differences can still arise, they do not inhibit correlation of the curves. Because the sediments have a uniformly low gamma-ray response, these differences are generally only evident in the basement section of the hole and may reflect more irregular motion of the tools against the rough (rugose) sidewalls.

For each hole the data from all log runs have been similarly treated and combined into one data file. This was done by using computer programs to read and edit the digitally recorded field data. Where duplicated log curves are available for gamma-ray and caliper measurements, the most complete and noise-free record was used in the final file. The complete suite of data thus comprises gamma-ray, caliper, density, neutron porosity, sonic transit time (inverse velocity), and deep and shallow laterolog resistivity. The principles and operation of the tools are well documented (Schlumberger, 1972) and will not be reviewed here. A summary of the particular tool types used in this work is given in Table 1.

Laboratory Measurements

The recovered cores were systematically sampled for measurement of sonic velocity, density, porosity, and thermal conductivity. All measurements were made using the standard equipment and techniques available on board *Glomar Challenger* and recommended by DSDP (Boyce, 1976). Details of individual sampling and measurement are included in the site chapters (this volume). Throughout the pelagic oozes and chalks, drilling disturbance was evident in the recovered cores, even in the cores recovered by hydraulic piston coring (HPC) although less disturbance was present than would have been expected from rotary coring. Because these least disturbed areas were selected, sampling for sonic velocity and density determination should have been as representative of undisturbed sediment as possible. Velocities for most of the oozes were measured through the plastic core liner, which adds considerably to the experimental error but cannot be avoided for very soft lithologies. Density and porosity were determined by 2-minute GRAPE and by gravimetric weighing, wherever possible on the same samples. The agreement of the two methods was good. Thermal conductivity measurements on soft lithologies were found to be little affected by drilling disturbance in the cores.

Cores from the sedimentary formations were measured with the continuous GRAPE method (Boyce, 1976) to provide a complete record of density variation with depth. Again, the data are subject to errors caused by drilling disturbance and void spaces within the core liner.

Comparison of Downhole and Laboratory Data

Site 558 provides an interesting comparison of the wireline density log, the continuous GRAPE measurements, and sampled density measurements for the sedimentary formations (Fig. 5). All three methods record the same major features with a marked gradational increase in density at around 300 m sub-bottom and another increase at the very base of the sediment column. The density data from both laboratory sampling and continuous GRAPE also show values similar to those of the wireline log curve.

The comparison of laboratory and logged velocity measurements is not as good. Again both show the same gross features, but the laboratory values are systematically lower than the logged curves by up to 0.4 km/s. The seismic profile shows a two-way time for the basement reflector of 0.45 ± 0.05 s. A mean velocity of 1.8 ± 0.2 km/s is required for the known depth of sediment. The error in this mean velocity is large because of the lack of definition of the basement reflector on the seismic profiler records. Although inconclusive, this mean velocity is more consistent with the logged *in situ* values than the laboratory values, which have no correction for the release of confining pressure and disturbance caused by core recovery. In these circumstances, there is no reason to doubt the accuracy of the logged curve values.

The thermal conductivity values, although not comparable to any logged data, do show a depth correlation with the other physical properties. The above consistency of the several data sets is a proof of the reliability and accuracy of the logging measurements in this particular application and lends confidence to the correlations of features between the logged curves for Holes 558, 556, and 564 and the sample measurements for Holes 55 and 563.

Table 1. The tool types used for measurements on Leg 82, the mnemonics for the data types recorded, and the approximate depth of investigation of the tool.

Measured quantity	Tool type	Curve mnemonic (units)	Depth of investigation (m)
Diameter of hole	Caliper	CALI (in.)	0.0
Natural gamma	Formation gamma tool	GR (api)	<1.0
Sonic velocity	Depth derived borehole compensated (DDBHC)	DT (μs/ft.)	<0.3
Bulk density	Formation density compensated log (FDC)	RHOB (g/cm^3)	<1.0
Neutron porosity	Compensated neutron tool (CNT)	NPHI (0–1.0)	<1.0
Formation resistivity	Laterolog dual spacing, termed deep and shallow, only values from deep log are used here (DLL).	LLD (ohm m)	4.0

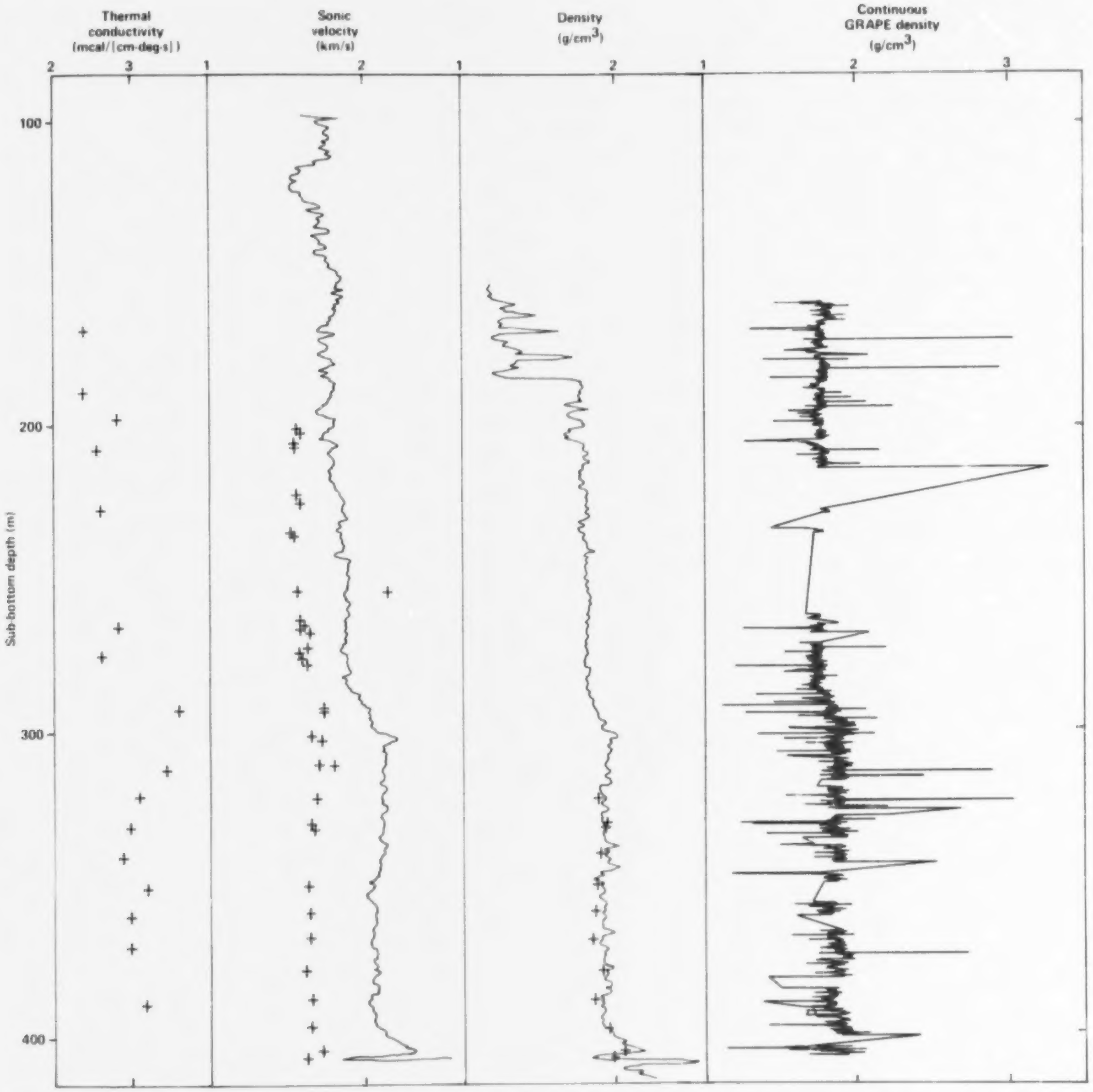

Figure 5. Comparison of laboratory and downhole physical property measurements for Hole 558. Thermal conductivity from sample measurement; sonic velocity from wireline logged curve (solid) and laboratory samples (crosses); density from wireline logged curve (solid), and individual sample measurements (crosses); density measurements from the continuous GRAPE.

For measurements within the basement formations, there is no such simple assessment of accuracy and reliability. The recovered core comprises the more physically resistant 44% of the drilled formation and the logging tools sample a more complete section, so that laboratory measurements probably represent the maximum likely values for the bulk properties of density, velocity, and resistivity, and the minimum value for porosity. The degree to which the log curves approach these values depends on the relative scales of the measured volume sampled by the logging tool and the wavelength of property variations within the formations. The sidewall penetration of the tools is shown in Table 1, but the effect of the tool motion because of ship's heave and the subsequent averaging in the data processing increases the effective sample volume. Thus, it is difficult to compare the laboratory and logged data sets and assess the accuracy of the logged curves independently. This problem is particularly acute for resistivity measurements where the bulk property is highly dependent on fracturing, which can never be represented in a laboratory sample. In the absence of such comparisons, the logged values will be assumed reliable, but the question of accuracy will be reassessed after the discussion of the data set below.

CORRELATION OF THE SEDIMENT MEASUREMENTS AND GEOLOGIC INTERPRETATION

The results from Hole 558 allow correlation between geologic observations on core material and logged curves. Figure 6 shows the sonic velocity curves through sediment formations and their correlation between holes, with core descriptions from Holes 558 and 563. The data can be examined on a larger scale in Figure 4 (back pocket).

The most prominent correlation from all the holes is the marked change in lithology and physical properties a little below the center of the stratigraphic column. This can be seen on all logged curves for density, velocity, and rather less prominently, resistivity. It is apparent on the laboratory physical properties at Holes 558 and 563 site chapters, Sites 558 and 563, this volume) and also in the sedimentologic core logs for these holes. The change is primarily due to a sharp increase in the clay content of the sediments below the boundary, which is placed at 300 m sub-bottom in Hole 558 from the sediment analysis. Although the sediment composition changes sharply at this depth (site chapter, Site 558, this volume), the physical property change is more gradual. The wireline logs are almost constant below 300 m sub-bottom, whereas above this level, there is a steady gradient in properties presumably because of compaction. In the 20 m immediately above the boundary, the gradient in physical properties is more marked but still relatively smooth, whereas the sediment composition appears to show sharp variations in the clay content within this region. It is quite likely that the sediment composition variations are on such a sufficiently short depth scale that the effects are averaged by the logging tools to produce the overall gradient. The sediment analyses are not closely enough spaced to accurately define the wavelength of these compositional variations. At 303 m sub-bottom, there is a prominent increase in seismic velocity, increase in resistivity, and increase in density over an interval of 4 m. This is, however, an artifact of the logging tools produced by the washout in the hole walls at that depth revealed by the caliper log. Most of the minor variations in logged values superimposed on the trends noted above probably are noise created by the irregular sidewalls and have no geologic significance.

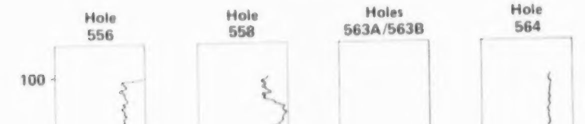

Figure 6. Correlation of logged sonic velocity curves for sediments at each hole with core descriptions for Holes 556, 558, 563A/563B, and 564 (velocity plotted as sonic transit time scaled as 0–200 μs/ft. from left to right, i.e., velocity increases to left of plots). Dashed lines are correlations based on the log curves. Units shown are lithologic units.

The logged curves for Hole 556 show a very clear correlation with those for Hole 558. All the major features described above can be easily identified at Hole 556 with the major lithologic change occurring at 336 m sub-bottom, 125 m above basement compared with the 103 m above basement at Hole 558. The data from Hole 556 also has the same sources of noise as that discussed above for Hole 558. In particular, the density and neutron porosity values are very noisy because of intermittent sidewall contact. The reason for this is not obvious because the longer-reach sonic log caliper shows that the mean diameter of the sedimentary section of Hole 556 is less than that of Hole 558, leading to an expectation of poorer sidewall contact for the nuclear logs in Hole 558. Despite this unexplained anomaly, the modal values for the densities over depth intervals correlated from the sonic logs are the same for both holes, lending confidence to the correlation. It is a reasonable inference that the lithologies within the sediment column at Hole 556 are very similar to those at Hole 558, implying similar depositional histories throughout the duration of sedimentation.

The situation at Hole 564 is slightly less clear because of the shorter length of the logged interval and the lower gradients in physical property changes. The sonic velocity curve shows four separate depth intervals. For the lowest, 30 m above basement, there is a marked gradient of increasing velocity. Above this for 60 m the velocity is constant, whereas above 195 m sub-bottom the velocity decreases again, then levels off to a lower gradient above 130 m sub-bottom. This pattern is shown weakly by the resistivity curve with two intervals of almost constant value, a low gradient between them, and a more marked increase towards basement. The density curve also shows these features. The depth intervals so defined and the relative changes in properties can be correlated with those for Hole 558, and the geologic interpretation of that hole extended to the area of Hole 564. The confidence in this correlation is greatly increased by the knowledge of the core logging from Hole 563, very close to Hole 564. At Hole 563, the sedimentary column was divided into two units that correlate with those at Hole 558 (the lower unit is about 90 m thick). From the sediment analysis at Hole 563, the lower unit again has an increase in clay content, but only to 15% rather than the 50% clay content at Hole 558.

The recognition of these two distinct lithologic units at each hole from the logged curves can be shown by the crossplots in Figure 7. Here the value at each depth interval is plotted in a field where position depends on the values of two of the logged values at that depth. The two curves with the most variations are the sonic velocity and density, and the crossplots of these values clearly show the division of the sedimentary sequence into two units for each hole.

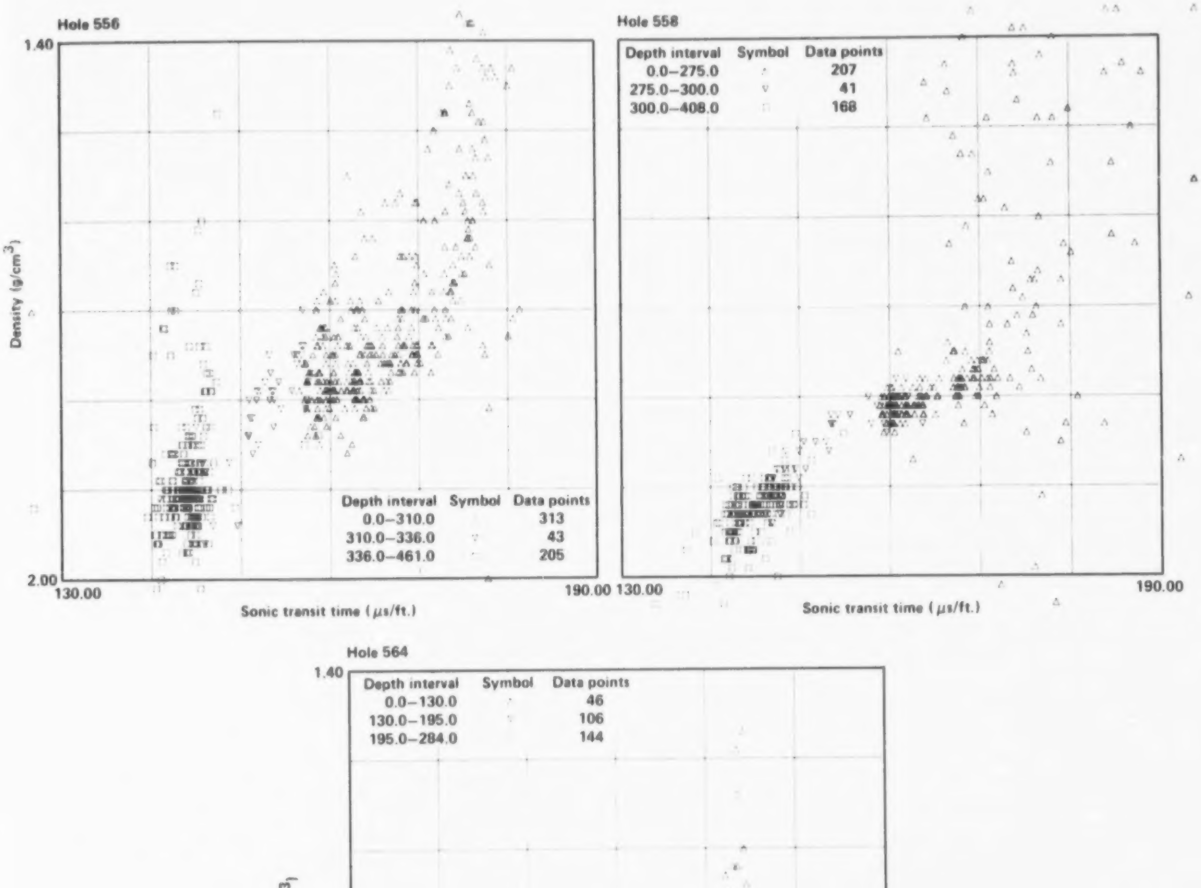

Figure 7. Density-sonic cross plots for the sedimentary formations of Holes 556, 558, and 564. Vertical data interval is 2.00 ft.

The logging results from the sedimentary columns in Holes 556, 558, and 564 thus allow correlation of sedimentary units between all holes. This has an important bearing on the interpretation of the depositional history at Hole 558 as found in detail from the core logging because it can now be seen as truly representative of a large geographic area and not a result of local effects.

LOGGING MEASUREMENTS IN IGNEOUS BASEMENT

The ocean basement constitutes a difficult environment for wireline logging because of the lateral and vertical inhomogeneity of the formations. Because this inhomogeneity often occurs on scales smaller than the sampling volume of the logging tool, the log curves often show a smoothed record of the variations in the formation. Nevertheless, continuous logged curves from this region are highly desirable because of the incomplete and biased nature of the recovered core. The problems of assessing the accuracy of the logged curve values has been discussed above. This report will consider the interpretation of the curves: first, with respect to the identification of major lithologic features and, second, with regard to the variation of properties of the igneous rocks.

Lithologic Units

The log curves were initially interpreted on board ship and the basement divided into a number of units as described in the site reports (this volume). This initial division was performed purely on the appearance of the curves from each individual hole. This process can now be repeated within the perspective of the curves for all holes and the units defined by core description and chemical analyses. The curves filtered as described above are shown in Figures 4A, 4B, and 4C (back pocket). The data for each hole will be described in turn.

Hole 556 had the most successful logging operations and hence has the most complete data set within the basement. The basement surface is prominently shown at 461 m sub-bottom by sharp deflections of all curves. Below this, the curve variations are more complex. Between 461 and 560 m sub-bottom, there is a gradual rise and then fall of resistivity values with a series of much shorter wavelength variations superimposed. On the lithologic log, this interval appears to be mainly pillow basalts. Such a response is to be expected with short wavelength variations because of the location of pillow margins and brecciated zones, which are somewhat smoothed out by the averaging effect of the resistivity tool. The longer wavelength variation must be due to more systematic processes. The upper surface of this unit must have had prolonged exposure to seabed weathering effects before being buried by sediment. Such alteration could produce the observed change in resistivity, but this simple explanation is unlikely to be true because recovered core material shows no systematic variation in alteration throughout this interval nor a change in percentage core recovery that might imply the same effect. The decreasing resistivity towards the surface may reflect increasing fracturing. The decrease towards the base of this unit may have a similar origin.

Below 560 m sub-bottom, the major lithology changes to altered gabbro. Between 560 and 577 m sub-bottom, there is a zone of particularly low resistivity that correlates with a high apparent porosity shown by the neutron porosity curve. The major serpentinization of recovered cores reveals that a great deal of seawater alteration has occurred at this level, and this alteration may have also affected the pillow lava unit, contributing to the long wavelength decrease in resistivity noted above. At 577 m sub-bottom there is a marked increase in resistivity, and density, but, because this is not revealed as a major change in the lithologic log, it can be attributed to a decrease in the alteration or, more probably, a decrease in the fracturing of the gabbros. Resistivity changes sharply downwards at 611 m sub-bottom to values of about 10 ohm m, which may again be interpreted as an increase in alteration and/or fracturing. The major boundaries noted above can be seen to correlate to features on other curves in Figure 4B (back pocket) as well as to the resistivity. The resistivity curve has been used as a basis of discussion because of the large volumetric averaging of this tool that smooths out the small-scale heterogeneity of the basement formations on a scale of less than 1 m and shows the systematic trends more clearly. More detailed resistivity investigations in Hole 504B (Becker, Von Herzen, et al., 1982) have demonstrated the usefulness of resistivity measurements in differentiating major lithologic units and support the correlation of resistivity variations primarily with fracturing. It is interesting that the Hole 504B data have mean resistivity values in the pillow lavas of Layer 2 of only 10 ohm m. The values from the Leg 82 data are higher by up to a factor of 10 and are also higher than equivalent data from Hole 417D. As discussed below, absolute calibration of resistivity tools is hard to verify and it remains to be determined whether differences are due to calibration errors, the variations in the effective volumes sampled by the different tools used for each set of measurements, or the true variations in the bulk properties of the wall rocks.

The curves for Hole 558 are less complete with the loss of density and neutron porosity data for much of the basement section because of hole cave-in. The basement surface is clearly seen at 408 m sub-bottom, but the sharp increase in resistivity occurs at 405 m sub-bottom. Possibly this effect originates from a depth error on the resistivity curve, but this is unlikely because all curves were depth correlated using the gamma-ray curves as was done for all other holes, and the change in resistivity and sonic velocity at 520 m sub-bottom shows no similar depth error. Therefore, the resistivity increase between 405 and 408 m sub-bottom is real and, as such, can be explained by an increase in cementation. This would increase resistivity while leaving density and sonic velocity relatively unaffected. This is likely because a marked increase in dolomitization was noted in the bottom few meters of sediments from the recovered cores. Apart from the boundaries noted above, there are no other major interfaces revealed by logging. This is not surprising because the lithologic log shows a continuous pillow basalt sequence to 520 m sub-bottom, underlain by altered gabbros.

Shorter wavelength variations are superimposed on these major units as was noted for Hole 556. In particular, there are a number of zones of lower resistivity and related lower seismic velocity within the pillow lava unit. The most prominent of these zones is that between 423 and 440 m sub-bottom, which is also defined by the density and neutron porosity curves. The logged values would suggest a region of increased porosity and, possibly, fracturing.

Hole 564 presented the same difficulties to logging as Hole 558 did, and the data are similarly incomplete. Once again the basement surface is apparent, but no other major features are seen. Yet porosity and density variations within the pillow lava sequence close below the basement surface coincide with a zone where water inflow is inferred by thermal data (Hill and Cande, this volume). The increase in neutron porosity and decrease in density with little effect on the sonic velocity could imply that the formation is vesicular or subject to microfractures rather than uniformly porous, with seismic ray paths available that can avoid small voids or fractures and hence leave the sonic velocity unaffected.

ACCURACY OF PHYSICAL PROPERTIES

The local heterogeneity of the basement formations is averaged to some extent by all logging tools. The bulk properties data recorded in the curves cannot be verified because there is no independent measures of similar quantities. Recovered cores will preferentially sample the harder lithologies, which withstand the drilling and recovery process better. The only check is to verify that the range of bulk properties is compatible with an average of the measured sample properties, taken in the correct proportions by volume.

Resistivity values can be subject to many effects of the hole diameter and borehole fluid salinity. The laterolog tool used here has electrode arrays to make resistivity measurements at two depths of penetration of the borehole walls, typically on the order of 1 and 4 m. Both values are corrected for estimated effects of hole diameter and fluid salinity, and the results have been compared. The deeper measurement gives values that are systematically higher than the shallow measurement by up to a factor of ten within basement lithologies. The shallow measurement is more affected by the hole fluid and the deep measurement has been taken as the more accurate value. These values are an average of about 300 ohm m for pillow basalt formations with variations between 1000 and 100 ohm m, whereas gabbros give lower values of about 10 ohm m, but up to 100 ohm m in one section of Hole 556. These maximum values are quite reasonable for igneous rocks with very low porosity; cored basalt samples have porosity as low as 2%. The lower values are due to averaging with interpillow breccia and void spaces. The altered gabbros would be expected to be systematically lower because of their increased porosity on alteration and the conductive nature of some of the alteration products. It is concluded that the measured values are quite plausible, if not strictly calibrated.

The consideration of sonic velocities follows a very similar line to that for resistivities. The logged curves have maximum values that agree quite well with the values measured on laboratory samples. Variations in the logged curves are generally smoother because of the considerable depth interval sampled by the tool, about 3 m. Intermittent spurious values are generated by physical shocks to the tool that are detected as spurious arrivals of sonic waves.

The density and neutron porosity tools have particular problems because of their use in sidewall contact measurements. Rugosity of the sidewall on a short wavelength prevents good sidewall contact and causes anomalously low density and high porosity values. In many cases there is a correlation between short-wavelength, high-amplitude variations on these logs and wall rugosity detected by the caliper log. Despite these problems, the maximum densities are similar to those determined from the samples. Neutron porosity values are systematically higher than porosities determined by sample measurements. The major cause of this is the highly fractured and jointed nature of the formations with these fractures contributing to the bulk porosity. Within the gabbro formations, and to a lesser extent in the altered basalts, the alteration products contain bound water that will be detected by the neutron log as a component of the total porosity.

The caliper log is not susceptible to errors such as those described above and is undoubtedly accurate. The gamma-ray curves can only be assessed by their repeatability because a separate curve is obtained with each logging run. The repeatability was found to be very good within the limitations set by tool heave as described earlier. There is no discernible correlation between the very low-level gamma radiation levels of the basement formations and lithologies.

COMPARISON WITH HOLE 417D RESULTS

The only other data for similar logging experiments available for identical analysis at the present are from Hole 417D. This hole in Atlantic crust (aged 108 Ma) was logged with partial success after many technical failures to give the data curves shown in Figure 4D (back pocket) and previously described by Salisbury et al. (1980). The basement surface is seen at a depth below sea level of 5823 m, and below this curve values for a formation of pillow lavas are broadly comparable to those of Leg 82. Particularly different features are the smoother nature of the curves and the generally lower values of resistivity. Whereas the former effect is likely to be a feature of the geology, the latter could well be an effect of the different type of resistivity tool used for the 417D measurements, the Laterolog 8. Resolution of this problem requires detailed investigation of the response of each tool in this environment and has not been completed. The sonic velocities are broadly comparable, but those for Hole 417D are more uniform in nature, which may well reflect infilling of fractures and void spaces by alteration products with age.

No density or neutron porosity data are available for Hole 417D except over the interval between 343 and 369 m sub-bottom. This limited sampling makes difficult any meaningful comparison with the results from Leg 82 on younger crust. The large range of logging experiments now completed in Hole 504B establish it as a reference for comparison of all other data, and such comparison has been made where relevant within the text.

CONCLUSIONS

Logging operations were particularly successful on Leg 82 and yielded good quality data. The sedimentary column contains little lithologic variation, but those minor variations present and identifiable by the downhole measurements can be reliably correlated between holes using the logged curves. The basement logging has clearly differentiated between pillow lavas and gabbros and reveals the presence of distinct zones of high degrees of alteration and high porosity and fracturing. Thin zones with poor core recovery can be assigned a more accurate depth extent from the logged curves than from the recovered core.

It is clear that logging operations are a very useful addition to the DSDP capability, but require more extensive use in drilled holes of greater depth before the data can be reliably interpreted in terms of the aging structure of ocean crust.

ACKNOWLEDGMENTS

We would like to thank the Captain and crew of the *Glomar Challenger* and especially Glen Foss and the Schlumberger engineer, Ed Moffat, for their work in collecting this data.

REFERENCES

Anderson, R. L., Honnorez, J., Becker, K., Adamson, A. C., Alt, J. C., Emmerman, R., Kempton, P. D., Kinoshita, H., Laverne, C., Mottl, M. J., and Newark, R. L., 1982. DSDP Hole 504, the first reference section over 1 km through Layer 2 of the oceanic crust. *Nature*, 300:589-594.

Becker, K., Von Herzen, R. P., Francis, T. J. G., Anderson, R. N., Honnorez, J., Adamson, A. C., Alt, J. C., Emmerman, R., Kempton, P. D., Kinoshita, H., Laverne, C., Mottl, M. J., and Newark, R. L., 1982. *In situ* electrical resistivity and bulk porosity of the oceanic crust, Costa Rica Rift. *Nature*, 300:594-598.

Boyce, R. E., 1976. Definitions and laboratory techniques of compressional sound velocity parameters and wet-water content, wet-bulk density, and porosity parameters by gravimetric and gamma ray attenuation techniques. *In* Schlanger, S. O., Jackson, E. D., et al., *Init. Repts. DSDP*, 33: Washington (U.S. Govt. Printing Office), 931-956.

________, 1981. Electrical resistivity, sound velocity, thermal conductivity, density-porosity, and temperature, obtained by laboratory techniques and well logs: Site 462 in the Nauru Basin of the Pacific Ocean. *In* Larson, R. L., Schlanger, S. O., et al., *Init. Repts. DSDP*, 61: Washington (U.S. Govt. Printing Office), 743-762.

Cann, J. R., and Von Herzen, R. P., 1983. Downhole logging at Deep Sea Drilling Project Sites 501, 504, and 505, near the Costa Rica Rift. *In* Cann, J. R., Langseth, M. G. Honnorez, J., Von Herzen, R. P., White, S. M., et al., *Init. Repts. DSDP*, 69: Washington (U.S. Govt. Printing Office), 281-300.

Kirkpatrick, R. J., 1978. Results of downhole geophysical logging Hole 396B, DSDP Leg 46. *In* Dmietriev, L., Heirtzler, J., et al., *Init. Repts. DSDP*, 46: Washington (U.S. Govt. Printing Office), 401-407.

Salisbury, M. H., 1983. Basement logs from the mouth of the Gulf of California, Deep Sea Drilling Project Leg 65. *In* Lewis, B. T. R., Robinson, P., et al., *Init. Repts. DSDP*, 65: Washington (U.S. Govt. Printing Office), 329-342.

Salisbury, M. H., Donnelly, T. W., and Francheteau, J., 1980. Geophysical logging in Deep Sea Drilling Project Hole 417D. *In* Donnelly, T., Francheteau, J., Bryan, W., Robinson, P., Flower, M., Salisbury, M. H., et al., *Init. Repts. DSDP*, 51, 52, 53, Pt. 1: Washington (U.S. Govt. Printing Office), 705-714.

Schlumberger, 1974. *Schlumberger Log Interpretation. Vol I: Principles*: New York (Schlumberger Ltd.)

Date of Initial Receipt: 2 December 1983
Date of Acceptance: 12 January 1984

15. THERMAL MEASUREMENTS AND SEAWATER DOWNFLOW INTO 35-Ma-OLD OCEAN CRUST, CENTRAL NORTH ATLANTIC[1]

Ian A. Hill, Department of Geology, Leicester University
and
Steven C. Cande, Lamont-Doherty Geological Observatory[2]

ABSTRACT

Measurements of temperature gradients in sediments, thermal conductivity and drill-hole temperatures (by wireline logging) were made in three holes drilled into basement in 35-Ma-old crust in the central North Atlantic during DSDP Leg 82. The temperature gradient and thermal conductivity values make a reliable estimate of the ambient heat flow value possible. Downhole temperatures measured by wireline logging after drilling indicate cooling of the hole in excess of that expected from the drilling process. This excess cooling effect is interpreted as a result of a substantial downflow of ocean water; a lower limit to the necessary volume of flow is derived from the data.

If the downflow is a secondary effect of hydrothermal circulation within oceanic crust, these data support the increasing body of evidence that hydrothermal circulation continues within ocean crust to considerable ages covered by a blanket of sediment allowing only conductive heat flow.

INTRODUCTION

DSDP Leg 82 was designed to drill a grid of holes along isochrons and flow lines from the Mid-Atlantic Ridge crest to the southwest of the Azores Triple Junction and to locate geochemical anomalies in the igneous rocks recovered. The holes actually drilled (Fig. 1) all lie on the western flank of the ridge. Although the objective was to find relationships with the Azores hot spot, all holes are sufficiently distant from this feature so that its thermal anomaly was not detectable in the elevation of the ocean crust. The sites were not surveyed in detail before Leg 82 but all underway profiling and bathymetry (Cande et al., this volume) show that the thermal evolution of the ocean crust has followed the expected age-depth relationship (Parsons and Sclater, 1977). In a regional context it is reasonable to view thermal measurements from this area as representative of crust produced from a slow-spreading ridge free from major subcrustal thermal perturbations.

Deep penetration into volcanic basement was only achieved at three sites (556, 558, and 564). These were all drilled within the width of Magnetic Reversal Anomaly 13 or in troughs to either side of it, indicating an age range of 35 ± 2 Ma. Palaeontologic dates from recovered sediments are compatible with this age range. Given the similar ages, the thermal evolution of ocean crust at these three sites should be very closely comparable. At each site the location was chosen to avoid basement topographic highs, and depths to basement are quite consistent. Also, at each site, the basement was overlain by between 280 and 460 m. of calcareous pelagic ooze and chalk (Fig. 2). Physical property measurements of the sediments show little significant variation between sites (Hill and Cande, this volume).

Over recent years the importance of hydrothermal circulation of seawater as a heat-transfer mechanism in young ocean crust has been well demonstrated (e.g., Fyfe and Lonsdale, 1981; Hyndman et al., 1977; Becker et al., 1983). As the crust becomes older, the effectiveness of such hydrothermal circulation may be reduced by two different processes. Firstly, the convective pathways within the volcanic crust may become restricted or blocked by such processes as growth of authigenic minerals or physical compression by increasing hydrostatic load. Secondly, the convective regime is blanketed by a layer of effectively impermeable sediment that allows only conductive heat transfer to the ocean water. When the sediment blanket becomes several hundred meters thick, surface heat flow measurements do not clearly resolve the effects of any hydrothermal circulation within the ocean layer. Hence, the age to which such circulation can persist is poorly known. The data discussed below allow some indirect inferences to be made concerning this question.

THERMAL MEASUREMENTS

A determination of the ambient geothermal gradient and heat flow was only made at Site 556. A temperature probe protruding ahead of the drill bit was used here to measure temperatures of undisturbed sediments at the mudline and at three depths well distributed in the 460 m sedimentary column. Measurements were made with the DSDP digital thermal instrument and are described in detail elsewhere (Site 556 report, this volume). Figure 3 shows a typical data record from these measurements, and Figure 4A shows the linearity of the thermal gradient determined, with a value of 0.036°C/m. Coring of the sediment was not carried out at Site 556, but was performed at Sites 558 and 563. Comparison of wireline logging data between Sites 558 and 556 reveals little dif-

---

[1] Bougault, H., Cande, S. C., et al., *Init. Repts. DSDP*, 82: Washington (U.S. Govt. Printing Office).

[2] Addresses: (Hill) Department of Geology, Leicester University, University Road, Leicester LE1 7RH, United Kingdom; (Cande) Lamont-Doherty Geological Observatory of Columbia University, Palisades, New York 10964.

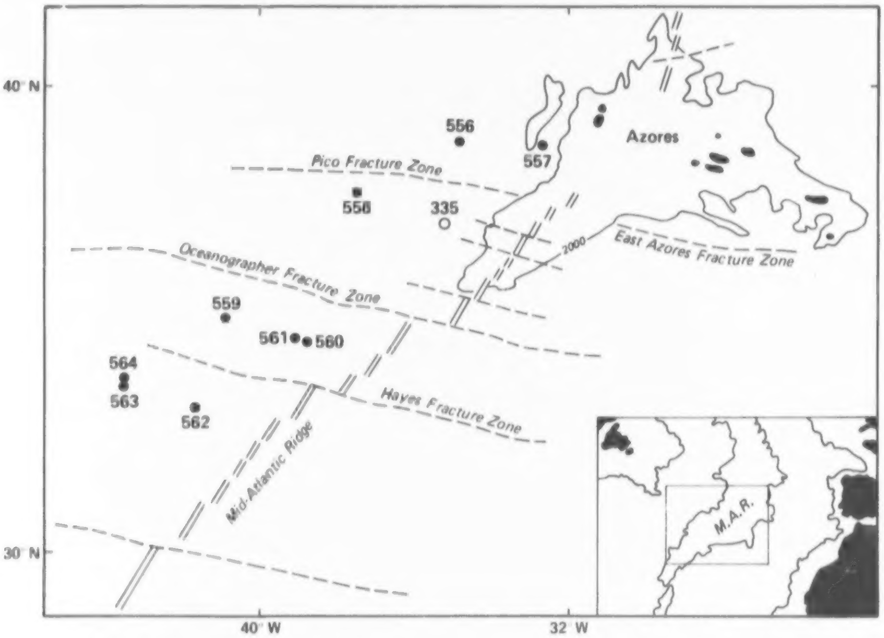

Figure 1. Location of DSDP Leg 82 drill holes.

ference in physical properties, with very good correlation between even fine details of the log curves (Hill and Cande, this volume). This correlation, the geographical proximity, and the similar depositional environments justify the use of thermal conductivity values measured at Site 558 to derive a heat flow value for Site 556. This leads to a value of 45 mW/m^2 with a likely error of ± 10% deriving mainly from the errors in determination of thermal conductivity values (Site 558 report, this volume).

The remaining thermal measurements were made as part of the downhole logging program after drilling had been completed. We used the standard Schlumberger High Resolution Thermister probe (HRT), a small-diameter tool normally used in the oil industry for logging cased holes. During Leg 82, this tool was modified to improve its ease of use in uncased holes with poor sidewall stability (typical of DSDP conditions) by mounting it inside a modified core barrel (Site 564 report, this volume). This increased the tool weight and protected the thermister probe from a mud coating, which considerably affects the time constant of the probe. These modifications were purely mechanical and did not affect the accuracy or precision of the tool. The precision is better than 0.01°C but absolute calibration was considerably poorer. The thermister was recalibrated during the cruise against mercury in glass thermometers at 0 and about 20°C, and the calibration derived was used throughout Leg 82. The calibration of the DSDP probe was believed reliable but was similarly checked at 0°C and found to be accurate. The only direct comparison of the data from both instruments is the mudline temperature determined by both at Site 556. Although these determinations were separated by a time interval of about 150 hours, it is likely that the bottom water would remain at constant temperature over this period. Comparison of Figures 3 and 4A shows the mudline temperatures to be 2.1 and 2.4°C, respectively. From these data it is concluded that the accuracy of the HRT is on the order of ±0.5°C, although there is no reason to dispute the specification sensitivity of 0.01°C. The difference in bottom water temperatures at Sites 556, 558, and 564 is shown in Figure 4. The variation between 2.1°C at Site 556 and 0.5°C at Sites 558 and 564 is regarded as outside the measurement error, but its cause is uncertain. It is probably not related to any drilling circulation effects because it was first measured after only a few hours of drilling disturbance, when penetration was only about 100 m.

During drilling, the hole is flushed with seawater pumped down the drill string from the surface to the bit, then vented from the hole at the sea bed. The water cools to within a degree or so of bottom water temperature as it travels down the drill string. Thus the hole is flushed and cooled by water at the temperature of ocean bottom water. Once drilling and the associated water circulation have finished and in the absence of other complicating factors, the hole will begin to reequilibrate with the preexisting geothermal gradient. Because measurements with the HRT took place at intervals on the order of one day after circulation ceased, the temperature in the holes will still be reequilibrating.

Figure 4 shows that none of the measurements show a temperature gradient similar to the undisturbed one measured in Hole 556. Indeed the thermal gradients are all very low. Hole 556 shows constant temperature with depth to 360 m sub-bottom. Below this, the temperature rises slightly until just below the basement interface where there is a sharp rise of temperature of 2°C. It would

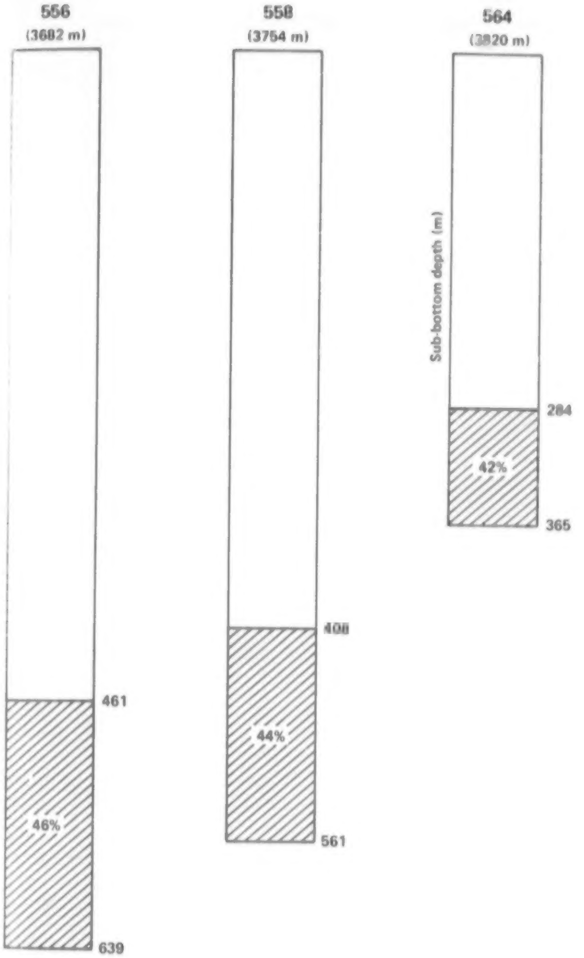

igure 2. Depths drilled in holes in 35-Ma-old crust. Sedimentary section blank, basement hatched. Basement interface and total depth shown in m sub-bottom. Percentage recovery of basement core shown.

eem that there is little or no thermal recovery in the
dimentary section, whereas the basement section ei-
er recovered relatively quickly or was less chilled. Hole
8 shows two curves of fairly similar shape. Between
easurements, the hole was flushed with water and mud
d this disturbance may explain the difference in the
orded curves. On both HRT runs, the tool could not
lowered below 220 m sub-bottom because of hole cave
The curves suggest the hole is slowly undergoing
ermal reequilibration. Hole 564 was not subject to
e in or flushing between the two HRT runs and showed
ree interesting features. Firstly, the temperatures mea-
red through the sediments between 200 and 280 m
b-bottom are identical on both runs. Secondly, the
mperatures within 50 m depth of 100 m sub-bottom
e substantially different. Thirdly, the basement temper-
ures on Run 2 are lower than those measured on Run
. The second feature can be related to motion of the
end of the drill string within the hole. The level was
changed between the two runs as shown in Figure 4C, and it is highly likely that the heave motion on the drill string may have heated the hole or caused some local water circulation. A similar, but much less marked, effect can be discerned in the data for Hole 556, where the sea conditions during logging were much calmer than at Site 564. The other two effects suggest that the hole did not recover thermally within the lower sedimentary section and had cooled within the basement.

Given these effects in Hole 564 coupled with the zero temperature gradient recorded in Hole 556, it is possible that the holes may be experiencing continued cooling and that this could be due to continued downflow of bottom water.

THERMAL MODELS OF BOREHOLES

A simple summary of the thermal effects of drilling has been given above during the consideration of the HRT results. Because the effect of drilling and the recovery after drilling ceases are time dependent, the best way to study these phenomena quantitatively is to make repeated thermal measurements over a long period of time. The length of time required depends on the drilling history and the thermal properties of the surrounding rock, but for DSDP holes, periods of 20 days or more are generally required for fairly complete thermal recovery. Because of operational constraints, such measurement intervals are impractical in most cases, and the discussion of thermal state must be conducted with reference to physical models. In the present case, the only initial requirement is to establish whether the data are compatible with a model in which there is no cooling of the hole after circulation associated with drilling is terminated. If, however, the data show further cooling, then we may consider the effects of likely cooling mechanisms.

We will assume that the sedimentary sequence is impermeable. This is reasonable in the light of previous studies of similar pelagic oozes and chalks (Bryant et al., 1981). Some interstitial water movement is likely due to compaction and should result in the slow upward migration of pore water from the depths at which major compaction is occurring, but this is a very slow process and may be neglected for the present purpose. The thermal conductivity and density of sediments were measured from recovered core at Hole 558. Bulk values for permeability, density, and thermal conductivity for the basement have not been determined. The thermal model can, however, be restricted to a consideration of the sedimentary section of the hole, with the assumption that there is no water flow into or out of basement formations and no thermal convection within the hole. The problem thus simplifies into a consideration of the thermal perturbation in the sediments.

Because the hole is drilled downward from the top, there is normally a considerable difference in the duration of cooling in the lower parts of the hole compared to the top. The time sequence of drilling operations in the three holes is shown in Table 1. It can be seen here that this is not a major effect. Hole 556 is the best documented example for thermal modeling. The hole was washed down through sediments in 25.5 hr. In fact, the washing and associated water circulation were suspend-

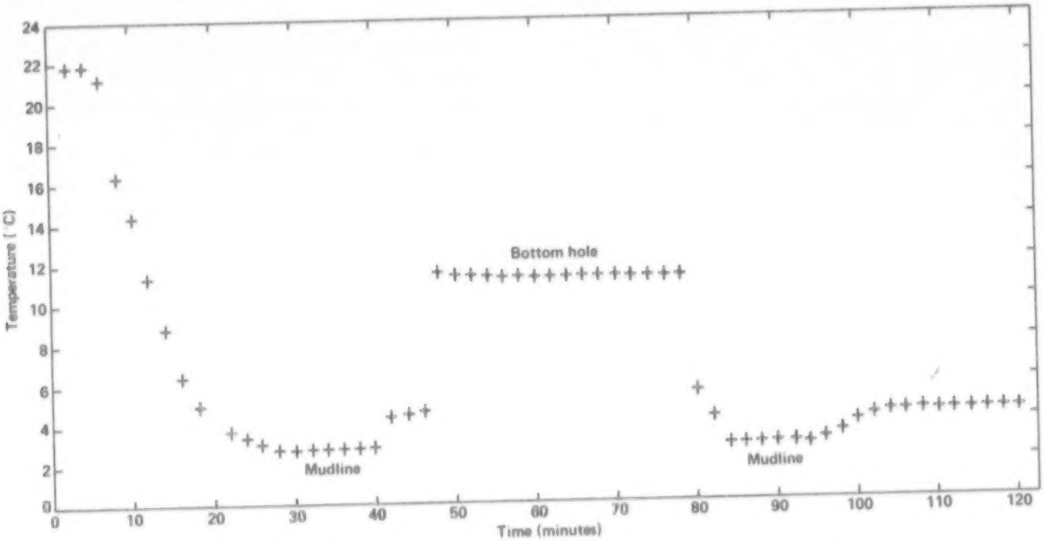

Figure 3. Typical record of DSDP downhole thermal probe (for measurement at 192 m sub-bottom, Hole 556). Note mudline temperatures as well as bottom-hole temperature measured over 15-minute equilibration period.

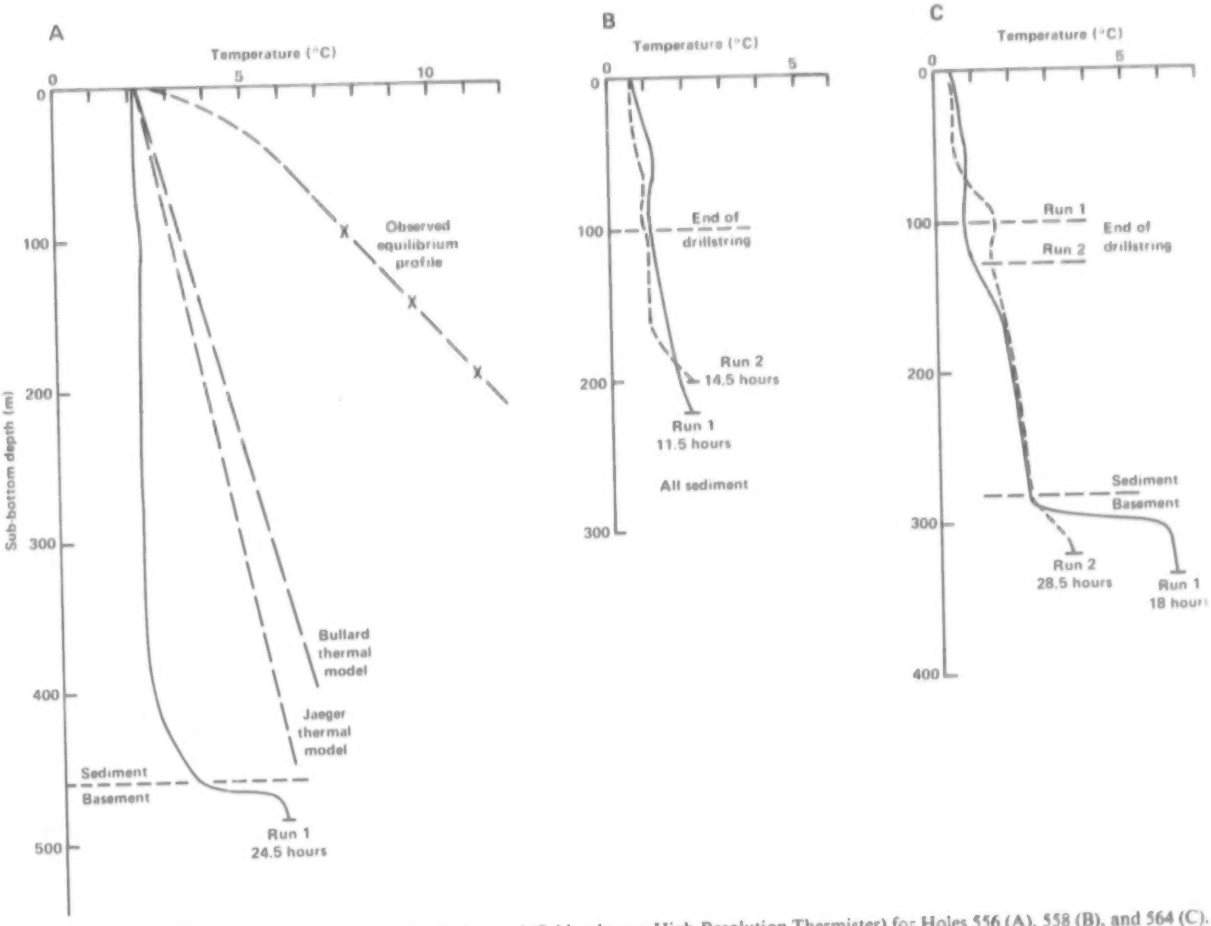

Figure 4. Thermal profiles obtained with downhole logging tool (Schlumberger High-Resolution Thermister) for Holes 556 (A), 558 (B), and 564 (C). Each tool run is annotated with elapsed time since last circulation in the hole. Thermal gradient determined for undisturbed sediment shown in A. Dashed lines show calculated thermal profiles from models of Bullard (1947) and Jaeger (1956) as noted.

Table 1. Time scale of drilling and logging operations at Holes 556, 558, and 564.

Hole	Time/Date	Operation	Elapsed time (hours)
556	1800/22 Sep	Spud in	0
	1930/23 Sep	Basement reached	25.5
	1925/27 Sep	Last Core	121.5
	2100/27 Sep	Pipe drawn to 100 m sub-bottom, circulation ceased	123
	0200/28 Sep	Logging started	128
	2130/28 Sep	HRT run	147.5
558	2122/03 Oct	Spud in	0
	1600/05 Oct	Basement reached	42.5
	0745/09 Oct	Coring ended	130.5
	1430/09 Oct	Circulation ceased	136.5
	1600/09 Oct	Logging started	138.5
	0130/10 Oct	HRT Run 1	148
	0400/10 Oct	Wash to base of hole flush with mud	150.5
	0815/10 Oct	Circulation stopped	155
	1130/10 Oct	Logging started	158
	2300/10 Oct	HRT Run 2	169.5
564	1743/28 Oct	Spud in	0
	0305/28 Oct	Basement reached	9.5
	1600/30 Oct	Circulation stopped	46.5
	1800/30 Oct	Logging started	48.5
	1000/31 Oct	HRT Run 1	64.5
	2030/31 Oct	HRT Run 2	75

Note: HRT = high resolution thermister probe.

ed for approximately 8 hours during this period while the sediment temperature measurements were made. Circulation then proceeded for 97.5 hr. during coring of the basement. The assumption will be made that the time of cooling was constant for the complete sedimentary section. The rate of heat loss will depend on the temperature of the circulating water and the flow rate as well as the properties of the formation and dimensions of the hole. Jaeger (1961) conducted a detailed study of the cooling effect of circulating fluids during drilling. If circulation rates are low, the drill string can act as an annular heat exchanger between the cool down-flowing water and the heated return flow. For usual pumping rates with rotary drilling, however, the flow rate is sufficient if the circulating water does not heat up appreciably and the heat exchange is negligible. There was no attempt to re- trict water circulation during drilling of any of the holes onsidered here, and we will assume that circulation was ufficient to keep the holes cooled to near bottom water emperature. The very low temperature gradients measured in the sedimentary sections of all three holes show hat the circulating water must have a temperature very lose to that of bottom water.

The model required is, thus, one that will predict the ooling effect of a borehole held at constant temperature or a known time period within a uniform impermeable ayer through which there is a known initial temperature gradient. In addition, the temperature must be known at any time after cooling is stopped and thermal equilibrium is allowed to return. The simplest treatment of this is to consider the drillhole as a line source of heat that acts in a homogeneous medium for time t_1 and calculate the remaining thermal perturbation at time t after t_1. The approximate solution for this case was derived by Bullard (1947) to give the expression:

$$\frac{T}{T_o} = \frac{[\ln(1 + t_1/t)]}{[\ln(4\kappa t_1/a^2) - 0.577]},$$

where

T = temperature disturbance at time t after t_1;
T_o = temperature disturbance at time t_1, end of drilling;
a = radius of drillhole; and
κ = thermal diffusivity of the medium.

The mean diameter of the borehole is known from wireline caliper logs to be.0.2 m, the conductivity is taken to be that measured at Hole 558 (1.6 W/m K) and the diffusivity is calculated as 6.3×10^{-7} m²/s (Hyndman et al., 1979). Using these values and the times from Table 1, we get a value for T/T_o of 0.75. Applying this ratio to the deepest point in the hole at which the undisturbed temperature gradient was measured (192 m sub-bottom, we get a predicted temperature at time of logging of 4.4°C. This is over 2°C above the measured value.

A fuller treatment of the same problem has been given by Jaeger (1956). In this study, the exact expression for the temperature distribution in a medium of uniform diffusivity caused by a cooling borehole of finite radius is derived. This is evaluated numerically and the results tabulated in terms of the dimensionless parameters;

$\tau_o = \kappa t/a^2$
$R = r/a$ (r is distance from axis of hole).

Using the values as above, we get a value for τ_o of about 7. These values lead to a prediction that considerable chilling of the wall rocks occurs to distances of the order of 1.2 m from the hole. The reequilibration of the borehole after disturbance is a similar case of conduction but with initial conditions determined by the thermal state determined as above for a perturbation time t_1. To calculate this it is assumed that the hole $r<a$ is filled by conducting material at the perturbed temperature. The temperature perturbation for this reequilibration case has been tabulated by Jaeger in terms of τ_o and n, where the reequilibration time is nt_o (see Table 2). Applying the data from Hole 556 with $\tau_o = 7$ and $n = 0.2$ gives a per-

Table 2. Values of thermal perturbation in a borehole after time $n\tau_O$, tabulated for parameters τ_O and n (from Jaeger, 1956). See text for explanation.

	n			
τ_O	0.1	1	10	100
1	0.988	0.543	0.095	0.010
10	0.722	0.252	0.038	0.004
100	0.477	0.143	0.020	0.002
1000	0.324	0.098	0.014	0.001

turbation of about 0.8 and a temperature of 3.9°C for the documented point at 192 m sub-bottom. However, this calculation assumes the material within the borehole is a perfect conductor and makes no allowance for the thermal capacity of this material. When the borehole is filled with water, the temperature rise will be affected by the requirement to heat the contained volume of water. This effect is only appreciable when the product $n\tau_0$ is less than 100; in this particular case, the value is about 1.5. In physical terms, the effect of the thermal capacity of the borehole fluid is only negligible when the rates of heating or cooling are low.

The heat flux into a borehole that has been cooled by being filled with fluid at a constant perturbing temperature for a known time period can be calculated from a result derived by Carslaw and Jaeger (1959, Section 13.5 [8]) to be

$$[4K(T_1 - T_0)/a^2]\ \mathrm{I}\ (\kappa t/a^2),$$

where K is thermal conductivity and I is an integral involving Bessel functions. It is this heat flux into the borehole that must heat the borehole fluid, and if this flux is large compared with the thermal capacity of the fluid, then appreciable heating will occur. Using the values previously given, and the tabulated values of I from Jaeger and Clark, (1942) results in a heat flux of 45 W at 192 m sub-bottom. This heat flow is easily adequate to heat the contained water at a rate of many degrees per hour. This, of course, will not happen because as soon as the water starts to heat, the temperature structure of the cooled rock will also have to adjust, but at least the thermal capacity of the water will not have a great delaying effect upon the heating.

Considerably more elegant models of the thermal effects surrounding boreholes have been advanced. Lachenbruch and Brewer (1959) extend the treatment of Jaeger (1956) and include a detailed assessment of the likely errors introduced by the departures of real formations and hole conditions from the idealized models studied. Hyndmann et al. (1977) review the relative merits of particular models for DSDP holes, and Burch and Langseth (1981) extend the treatments above to calculate corrections for thermal gradients measured in unequilibrated holes. Unfortunately, none of these methods is directly applicable to the present data set because they either require measurements at greater durations after drilling or detailed recording and control of parameters such as fluid circulation rate during drilling. The aim of the more complex models is to derive the equilibrium thermal gradient from measurements taken during the thermal recovery period. For the present data set, the equilibrium thermal gradient is known, and all that is required is to determine whether cooling in excess of that provided by drilling process is necessary to account for the observed thermal profiles.

Having established the errors involved in applying the theoretical models for borehole temperature recovery to this case, we can compare the calculated temperature profiles to the observed data in Figure 4A. Allowing for the lag caused by the thermal effect of the borehole fluid, there should be a temperature gradient down the hole reaching values of at least several tenths of a degree at the 192 m depth. The foremost feature of the Hole 556 data is the lack of any gradient to depths below 350 m. This measurement is independent of any calibration error of the HRT discussed earlier. There must be some mechanism to remove the heat that is entering the hole above these depths. Comparison with results from Hole 558 (Fig. 4B) emphasizes this point. The drilling and cooling history of Holes 556 and 558 are similar (Table 1); Hole 558 was cooled for a slightly longer period than Hole 556. On logging after a shorter equilibration period, we measured a thermal gradient. If we compare this gradient to computed gradients as described above, the two can be seen to be compatible, with the real data still showing a slower reequilibration than the models because of the thermal capacity of the hole fluid. The situation for Hole 564 is more complex: the thermal gradient measured is broadly compatible with the models, but shows no change in the depth interval between 190 and 280 m sub-bottom 18–28.5 hours after circulation. Above this range the temperatures are clearly affected by the end of the drill string. In the basement section of the hole, the decrease in temperature between the two runs is interesting. Great efforts were made to ensure that the tool was at the indicated cable depth and not hung up on the rough basement sidewalls. However, this would be the simplest explanation of the apparent temperature decrease.

SEAWATER DOWNFLOW

The differences between the measurements in Holes 556 and 558 could be explained by continued downflow of seawater at bottom water temperature after drilling had ceased. At Hole 558, the hole rapidly caved in and was blocked to logging tools at about 200 m depth. The flushing of the hole, which interrupts logging operations, was accompanied by lowering of the drill string in attempts to clear the hole. Despite these disturbances the hole was blocked again at the time of the second HRT run. Thermal recovery was taking place in this hole. In Hole 556, the hole remained open throughout the logging operations and no thermal recovery took place.

It could be argued that the basic model is wrong and that the flow rate of drill fluid is insufficient to chill the formations to its own temperature; and therefore, the thermal recovery is much slower than calculated, so little change is seen in Hole 564. This is quite possible but makes the explanation of the lack of a thermal gradient in Hole 556 more important because the hole will have to have been actively cooled after cessation of drilling rather than prevented from reheating. The argument hinges on the assumption of physical similarity of the sediment formation at the two holes, which is shown by logging results to be reasonable (Hill and Cande, this volume). Whereas the data set for any one hole can be explained in a variety of ways, the only consistent explanation of all the data presented above requires the existence of some cooling mechanism for at least Hole 556 and

READEX FICHE best copy available

possibly Hole 564. The simplest mechanism is the seawater downflow that has been observed in many holes in young ocean crust.

This inference is supported by the temperature gradients in the basement at Site 556. The temperature rose very sharply immediately below a zone identified by the logging as being of high porosity and low seismic velocity. This also correlates with a zone of carbonate breccia associated with pillow basalts identified in the recovered core. It is likely that such a zone could provide a highly permeable pathway where downflowing water could flow out of the hole into the surrounding formation. Below this zone a more normal temperature gradient existed that could be explained by a much lower or zero flow rate of water in this section of hole after drilling ceased. It may be significant that the high temperature gradient in the basement of Hole 564 is similarly identified with a zone of high porosity and low velocity on log curves and pillow basalts in recovered core material.

Accepting seawater downflow as a model for cooling, we can make a crude calculation of the minimum rate of flow required to produce the uniform temperature in Hole 556. This can be calculated as the volume throughput of water necessary to carry away the heat flux through the hole walls in this zone without measurable heating of the water. The heat flux can be calculated with the equation given above. Because this relationship between heat flux and temperature perturbation ($T_1 - T_0$) is linear, as is the initial temperature gradient, the mean heat flux for the top 350 m of Hole 556 can be calculated, and thus the total flux. Using a mean perturbation of 8.5°C and other values as above, we get a total heat flux of 14 kW. This value will, of course, rapidly decay as the sediments become progressively chilled. To remove this flux with a temperature rise of less than 0.2°C would require a flow rate of at least 3.5 liters/s. The heat flux into the hole at any level will increase linearly with depth. The slight rise in water temperature in the hole below 350 m sub-bottom may indicate that here the heat flux is sufficiently high to appreciably warm the water flowing past and to suggest that the flow rate is unlikely to be much larger than the minimum value required by the upper portion of the hole.

CONCLUSION

The data set of thermal measurements presented above s far from an ideal one for a clear interpretation of the hermal regime in each borehole. However, if the uniormity of the sedimentary layer and its thermal properies within and between holes is accepted, it is possible o seek a single consistent model that will fit all the daa. This model is one that involves substantial water downlow a Hole 556 and possibly a lower flow rate at Hole 64.

Because such flow is not forced by the drilling proess, it can only exist if the pressure at the base of the ole is less than the hydrostatic pressure of the water columnn in the borehole. Such underpressure in oceanic basement has been directly observed at Hole 504B (Anderson and Zoback, 1982), at which hole downflow of seawater is very well documented (Becker et al., 1983). The origin of this underpressure, which drives the downhole flow, is not clearly understood. Becker et al. (1983) consider the ability of the sediment layer at Hole 504B to allow "pressure diffusion" through the pore waters and concluded that the observed basement underpressure, about 8 bars, would dissipate in approximately 1000 years unless dynamically maintained. Both of the above analyses lend support to the idea that the pressure is a secondary effect of hydrothermal convection occurring within ocean basement under an impermeable seal of sediment through which the heat is transmitted by convection. The length of time for which convection may continue in this way is not known, but Embley et al. (1983) suggest that this may occur to ages of 80 Ma.

The data reported here documenting downflow of water demonstrate the existence of basement underpressure. This can be used to infer the presence of hydrothermal convection in 35-Ma-old crust under the assumptions above. However, definitive proof of this convection would require a suite of considerably more sophisticated experiments, such as those conducted at Hole 504B. The importance of establishing the existence of this convection, and the extent of its interchange with the oceans as inferred by Embley et al. (1982), lies in the implication of thermal and chemical exchange with ocean water. This data adds to the body of evidence suggesting that detailed study of convective systems should be conducted in older ocean crust as well as in flanks of active ridges.

ACKNOWLEDGMENTS

We wish to thank the ship's company of *Glomar Challenger* for their assistance during the data collection and Ed Moffat of Schlumberger Ltd. for operating the logging equipment. We also wish to thank Kier Becker for the careful review and discussion that considerably improved the manuscript.

REFERENCES

Anderson, R. N., and Zoback, M. D., 1982. Permeability, underpressures and convection in the oceanic crust near the Costa Rica Rift, eastern equatorial Pacific. *J. Geophys. Res.*, 87:2860–2868.

Becker, K., Langseth, M. G., Von Herzen, R. P., and Anderson, R. N., 1983. Deep crustal geothermal measurements, Hole 504B, Costa Rica Rift. *J. Geophys. Res.*, 88:3447–3457.

Burch, T. K., and Langseth, M. G., 1981. Heat-flow determination in three DSDP boreholes near the Japan Trench. *J. Geophys. Res.*, 86:9411–9419.

Bryant, W. R., Bennett, R. H., and Katherman, C. E., 1981. Shear strength, consolidation, porosity and permeability of oceanic sediments. *In* Emiliani, C. (Ed.), *The Sea* (Vol. 7): New York (John Wiley and Sons), 1555–1616.

Bullard, E. C., 1947. The time necessary for a borehole to attain temperature equilibrium. *Monthly Notices, R. Astron. Soc., Geophys. Suppl.*, 5:127–130.

Carslaw, H. S., and Jaeger, J. C., 1959. *Conduction of Heat in Solids, 2nd. Ed.:* London (Oxford University Press).

Embley, R. W., Hobart, M. A., Anderson, R. N., and Abbott, D., 1983. Anomalous heat-flow in the North Atlantic: a case for continued hydrothermal circulation in 80 Ma crust. *J. Geophys. Res.*, 88:1067–1074.

Fyfe, W. S., and Lonsdale, P., 1981. Ocean floor hydrothermal activity. *In* Emiliani, C. (Ed.), *The Sea* (Vol. 7): New York (John Wiley and Sons), 589–638.

Hyndman, R. D., Davis, E. E., and Wright, J. A., 1979. The measurement of marine geothermal heat flow by a multipenetration probe with digital acoustic telemetry and in situ thermal conductivity. *Mar. Geophys. Res.*, 4:181–205.

Hyndman, R. D., Von Herzen, R. P., Erickson, R. J., Jolivet, J., 1977. Heat flow measurements, DSDP Leg 37. *In* Aumento, F., Melson W. G., et al., *Init. Repts. DSDP*, 37: Washington (U.S. Govt. Printing Office), 347–362.

Jaeger, J. C., 1956. Numerical values for the temperature in radial heat flow. *J. Math. Phys.*, 34:316–321.

________, 1961. The effect of the drilling fluid on the temperature measured in boreholes. *J. Geophys. Res.*, 66:563–569.

Jaeger, J. C., and Clarke, M. E., 1942. A short table of I (0, 1; x). *Proc. R. Soc. Edinburgh, Sec. A*, 61:229–230.

Lachenbruch, A. H., and Brewer, M. C., 1959. Dissipation of the temperature effect of drilling a well in arctic Alaska. *Geol. Surv. Bull.*, 1083-C.

Parsons, B., and Sclater, J. G., 1977. An analysis of variation of ocean floor bathymetry and heat flow with age. *J. Geophys. Res.*, 82:803–827.

Date of Initial Receipt: 22 September 1983
Date of Acceptance: 16 November 1983

16. MAGNETIC PROPERTIES OF BASALTS FROM THE CENTRAL NORTH ATLANTIC OCEAN[1]

Guy M. Smith and Subir K. Banerjee, Department of Geology and Geophysics, University of Minnesota[2]

ABSTRACT

The magnetic properties of 56 samples of basalt from DSDP Leg 82 were studied in order to examine regional variations as well as the general question of the origin or remanence. Magnetization was carried, for the most part, by typical low temperature oxidized titanomagnetites, although two samples did show anomalous thermomagnetic curves. The natural remanence is distinctly different from an anhysteretic remanent magnetization and is hypothesized (by inference) to also be different from a thermoremanent magnetization (TRM) also. This suggests that alteration not only reduces the initial TRM but also changes it to chemical remanent magnetization with a significantly different magnetic character. An examination of thermomagnetic data tentatively suggests that the ulvospinel content of the titanomagnetites may be more variable than is commonly assumed. With the exception of a slight increase in saturation magnetization with decreasing latitude, no significant regional variations were evident.

INTRODUCTION

This paper reports on the magnetic properties of 56 samples of basalt from eight of the nine sites drilled on DSDP Leg 82 (no significant amount of basalt was recovered from Site 560). These sites were distributed over a fairly broad area and thus offer an opportunity to study the extent to which magnetic properties of the upper basement vary horizontally.

We measured a number of magnetic parameters including:

1. intensity, direction, and stability of natural remanent magnetization (NRM);
2. weak field susceptibility (χ_0).
3. hysteresis loop parameters, i.e., saturation magnetization, J_s; saturation remanence, J_{rs}; coercivity, H_c; remanent coercivity, H_{cr}; and paramagnetic susceptibility, χ_p.
4. Curie temperature, T_c, and thermomagnetic curve analysis; and
5. intensity and stability of anhysteretic remanent magnetization (ARM).

METHODS

Magnetic remanence measurements were made on a Schonstedt spinner magnetometer. Alternating field (AF) demagnetization was performed on a single axis Schonstedt demagnetizer. Each step was repeated for three orthogonal directions to ensure complete demagnetization. For ARM induction, we also used this instrument with a 0.5 Oe static bias field and a peak AF field (coaxial) of 1000 Oe.

Hysteresis loops were obtained with a Princeton Applied Research vibrating sample magnetometer coupled to an x-y recorder. Thermomagnetic measurements were also made on this instrument with an automatically controlled heating rate (20°C/minute) in a vacuum of better than 10^{-6} torr. Temperature calibration is based on measurements of pure Ni ($T_c = 358°C$) and pure Fe_3O_4 ($T_c = 580°C$). Values are obtained with the graphical method (Moskowitz, 1981).

Weak field susceptibility was measured with a Conservation Instruments ("Bartington") bridge.

RESULTS

Natural Remanent Magnetization

NRM intensities vary from 7.74×10^{-3} to 1.77×10^{-4} emu·cm^{-3}. Average values for each site and rock type are given in Table 1 (details are in Appendix A at the end of this chapter). With the exceptions of Sites 557 and 559, the site-averaged values are fairly close. Site 557 is slightly high but this is based on only two samples, which may not be representative. Site 559 is quite low but, again, the data represent only four samples and may be misleading. The first six sites have higher NRM intensities for pillow interiors than margins but the reverse is true for Sites 563 and 564. Flow interiors are also more strongly magnetized than margins with the exception of Site 562. Although these may be trends in these data, their validity seems questionable and no attempt to discover possible trends will be made here.

Median demagnetizing fields (MDF_N) run quite high generally with many in excess of 400 Oe and several above 1000 Oe. The notable exception is Site 559 with MDF's of 99 and 113 Oe. Hole 558 flow and pillow margins tend to have a somewhat higher MDF than their respective interiors, but otherwise no pattern is apparent.

Samples frequently have a small (<10%) low coercivity component (<100 Oe), which is generally steep and positive. Much of this is probably the result of relatively recent viscous remanence. Some have nearly vertical inclinations, but this may be an artifact of drilling. As these components are generally small and easily demagnetized, they represent no significant problem.

A few samples show multicomponent behavior persisting to such large fields that a stable secondary remanence is probable (see Appendix A). The difference in inclination is large enough so that magnetization must have been acquired in two or more episodes separated by tectonic rotation and/or a sufficient time lapse for

---

[1] Bougault, H., Cande, S. C., et al., *Init. Repts. DSDP*, 82: Washington (U.S. Govt. Printing Office).

[2] Address: Department of Geology and Geophysics, University of Minnesota, Minneapolis, Minnesota 55455.

Table 1. Natural remanent magnetization (NRM) values (in emu/cm^3).

Hole	Pillows		Flows		Average
	Margin	Interior	Margin	Interior	
556	1.27×10^{-3}	3.53×10^{-3}	2.20×10^{-3}	3.94×10^{-3}	3.04×10^{-3}
557					7.59×10^{-3}
558	8.84×10^{-4}	2.66×10^{-3}	8.88×10^{-4}	5.30×10^{-3}	2.20×10^{-3}
559	4.32×10^{-4}	5.87×10^{-4}			5.10×10^{-4}
561	2.35×10^{-3}	3.31×10^{-3}		2.22×10^{-3}	2.53×10^{-3}
562	1.32×10^{-3}	2.34×10^{-3}	2.00×10^{-3}	1.40×10^{-3}	1.85×10^{-3}
563	4.96×10^{-3}	1.95×10^{-3}			3.46×10^{-3}
564	4.46×10^{-3}	2.12×10^{-3}	1.68×10^{-3}	2.91×10^{-3}	2.78×10^{-3}
Average	2.79×10^{-3}	2.36×10^{-3}	1.65×10^{-3}	3.15×10^{-3}	3.00×10^{-3}

Note: Samples that could not be assigned to a particular rock type were included in the final averages.

the field to change significantly (1000 yr. or so). This phenomenon seems a local one; nearby samples with otherwise similar characteristics show no such behavior. Multicomponent remanence does not seem to be associated with any particular rock type.

Koenigsberger ratios were generally large, usually in excess of 10 and often much higher.

Hysteresis Loop Parameters

Hysteresis loop parameters provide a measure of the intrinsic magnetic properties of the samples and are useful in studying the origin of remanence. They are given in Appendix B at the end of this chapter.

Saturation magnetization, J_s, is a measure of the total amount of magnetic material present (if the composition is known, it is an exact measure). Average values of J_s are given in Table 2. With the exception of Sites 562 and 563, the variation of J_s between rock types is similar to that of J_N and suggests that the primary cause of variation in remanence is simply the amount of magnetic carrier present. There appears to be an increase in J_s as the latitude decreases, although the small number of sites precludes any meaningful statistical test.

Coercivity, H_c, is similar, though not identical, to the MDF as a measure of magnetic stability. Figure 1A shows a comparison of H_c and MDF_N and Figure 1B shows H_c and MDF_A. As can be seen, there is substantially less scatter for H_c-MDF_A graph. This is one piece of evidence (to be discussed later) that ARM and NRM are significantly different in these samples.

The two ratios, J_{rs}/J_s and H_{cr}/H_c, are commonly interpreted as indicators of domain state (Day et al., 1977). The values for these samples suggest that they contain predominantly single-domain or small pseudo-single domain grains with sizes of a few microns at most. An alternate possibility is that the sample contains larger (10–20 μm) grains that are in a metastable single-domain state (Halgedahl and Fuller, 1983). Future polished section work should help clarify this issue.

Curie Temperature

The Curie temperature, T_c, is the temperature below which a magnetic material becomes magnetically ordered. The value for titanomagnetites is very sensitive to both Ti content (usually expressed as the proportion of ulvospinel to magnetite) and degree of low temperature oxidation (Syono, 1965; Readman and O'Reilly, 1972; Moskowitz and Banerjee, 1981). Generally, T_c decreases with increasing Ti content and increases with oxidation. When a low temperature oxidized titanomagnetite (titanomaghemite) is heated, it produces the characteristic thermomagnetic curve seen in Figure 2A. The second maximum is due to the fact that titanomaghemite is metastable and inverts upon heating to a two-phase mixture with compositions close to magnetite and ilmenite. This causes a large difference in T_c measured from the heating and cooling curves, as well as a marked increase in magnetization.

There were only a few exceptions to the above pattern. Two samples had an initial T_c greater than 450°C

Table 2. Saturation magnetization (J_S) values (in emu·g^{-1}).

Hole	Pillows		Flows		Average
	Margin	Interior	Margin	Interior	
556	5.86×10^{-2}	1.19×10^{-1}	6.13×10^{-2}	1.05×10^{-1}	8.78×10^{-2}
557					1.48×10^{-1}
558	8.43×10^{-2}	1.48×10^{-1}	7.82×10^{-2}	1.44×10^{-1}	1.11×10^{-1}
559	7.18×10^{-2}	9.66×10^{-2}			8.41×10^{-2}
561	2.80×10^{-1}	3.16×10^{-1}		3.00×10^{-1}	2.99×10^{-1}
562	2.57×10^{-1}	1.67×10^{-1}	3.83×10^{-1}	2.77×10^{-1}	2.45×10^{-1}
563	2.66×10^{-1}	3.24×10^{-1}			2.95×10^{-1}
564	3.17×10^{-1}	2.00×10^{-1}	1.05×10^{-1}	3.72×10^{-1}	2.56×10^{-1}
Average	1.91×10^{-1}	1.96×10^{-1}	1.57×10^{-1}	2.40×10^{-1}	1.99×10^{-1}

Note: Samples that could not be assigned to a particular rock type were included in the final averages.

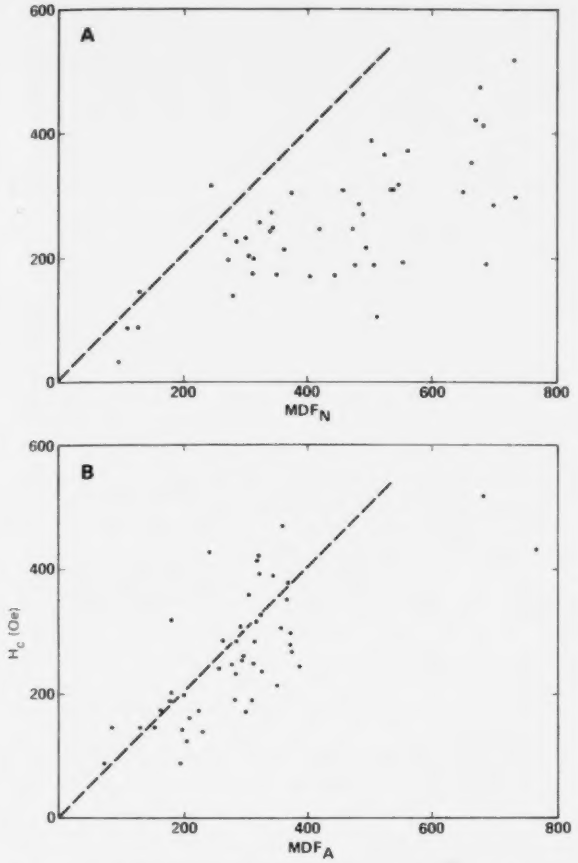

Figure 1. A. Coercivity (H_c) versus mean demagnetizing field for natural remanent magnetization (MDF_N). B. Coercivity (H_c) versus mean demagnetizing field for anhysteretic remanent magnetization (MDF_A).

(556-8-2, 80–83 cm and 564-6-2, 104–107 cm). Both were pillow margins and may have been partially deuterically altered at high temperature. Two other samples (561-3-1, 67–70 cm and 562-5-2, 104–107 cm) have somewhat unusual curves (Fig. 2B) with normal heating portions but apparently very low T_c cooling curves. We have, as yet, no explanation for this odd behavior, although reduction caused by presence of sulfides is a possibility. Two samples (557-1-1, 46–49 cm and 562-1-2, 27–30 cm) had very low T_c values and appear to be relatively unaltered.

Averages for the remaining more or less normal samples are given in Table 3. Pillow margins have consistently higher T_c suggesting that they are more altered than their interiors. The same is true for flows, with the exception of Site 562. There seems to be a general trend towards higher T_c's for older rocks but it is not very well defined.

It has been commonly accepted that the ulvospinel content of marine titanomagnetites is relatively constant (Johnson, 1979), although Steiner (1982) suggests that more variability may exist. Unfortunately, this is a difficult question to approach experimentally because the grains that carry much of the remanence are too small for direct measurement of their composition (e.g., by electron microprobe). Curie points are governed by both composition and oxidation state and hence are ambiguous. One way to circumvent this problem is suggested by O'Reilly (1983) who shows that for his synthetic x = 0.6 titanomaghemites, there is a definite relationship between oxidation state (or T_c) and the ratio of J_s before inversion to that after inversion (J_f/J_i). All of our samples were heated well beyond the inversion temperature (~350°C, O'Reilly, 1983) in the process of measuring T_c (maximum temperature was about 620°C). Although the heating runs were relatively rapid (20°C/min), reruns of several samples showed little or no additional change in J_s, indicating that the bulk of the inversion process was com-

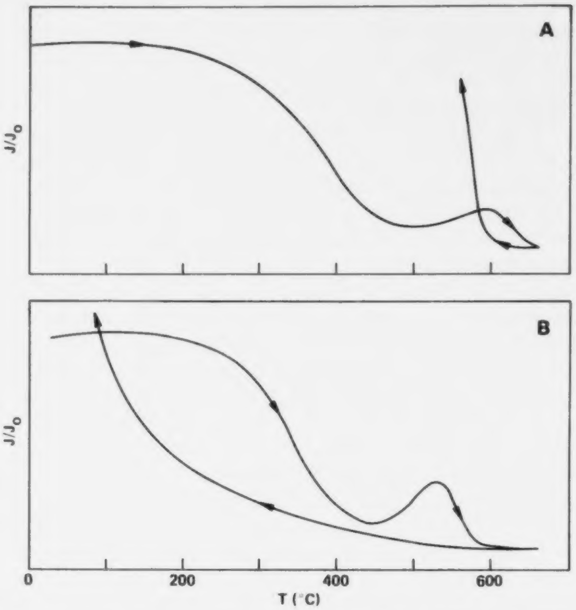

Figure 2. A. Thermomagnetic curve for a typical low temperature oxidized basalt (Sample 556-8-2, 6-9 cm). B. Atypical thermomagnetic curve (Sample 571-3-1, 67-70 cm) shown by two samples. Vertical axis is the relative magnetization (J/J_o) in arbitrary units. Horizontal axis (temperature) is uncorrected for instrumental offset (actual values are somewhat lower).

Table 3. Initial Curie temperatures (T_C) in °C.

	Pillows		Flows		
Hole	Margin	Interior	Margin	Interior	Average
556	405	325	365	340	357
557					273
558	353	297	328	313	325
559	355	338			346
561	375	335		323	339
562	260	275	265	338	284
563	414				415
564	423	335	365	285	321
Average	369	318	331	320	333

Note: Samples that could not be assigned to a particular rock type were included in the final averages.

plete after the first heating. Figure 3 shows our data along with the trend from O'Reilly (1983). Two things are immediately obvious; (1) there is no trend and (2) most of our values exceed those of O'Reilly, some by a substantial amount.

It is possible that there are some differences in the way in which the samples were inverted but this seems unlikely. Maximum temperatures were close to those of O'Reilly, and variations in vacuum and the possible presence of reducing agents do not seem sufficient to produce large discrepancies, although this matter needs further study. One factor that may contribute to the scatter of the data is variability in oxidation state among the various titanomaghemite grains in a sample; T_c tends to reflect the most oxidized grains, whereas J_f/J_i includes the whole assemblage. This mechanism does not, however, explain the large values of J_f/J_i relative to O'Reilly's results. We can find two possible explanations (not mutually exclusive) that could account for this discrepancy. One is that the seafloor oxidation process differed significantly from that to which O'Reilly's samples were exposed. The other is that the compositions of oceanic titanomagnetites are not as constant as has been commonly assumed. In all probability, two, or even all three, of these possible factors are present along with others that are less obvious. Further work is clearly necessary to resolve this issue.

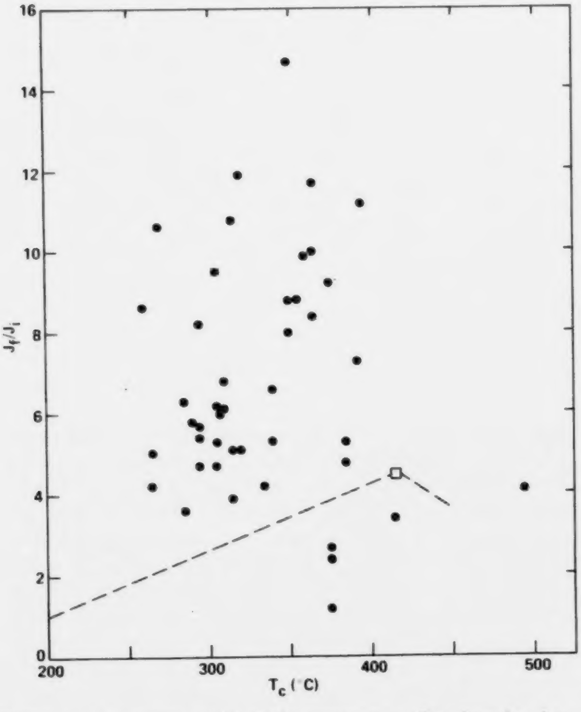

Figure 3. J_f/J_i versus initial Curie temperature (T_c). Samples that showed no sign of inversion were not included. J_f is saturation magnetization after inversion; J_i is saturation magnetization before inversion. The dashed line shows the trend of data from O'Reilly (1983).

Anhysteretic Remanent Magnetization

ARM is often used as a model for thermoremanent magnetization (TRM) because it does not require heating and consequent alteration of the sample. Levi and Merrill (1976) found that ARM intensity is usually less than TRM by a factor that varies but is generally greater than two (the exceptions were two large single crystals of magnetite that are not comparable to these samples). They also found that ARM and TRM had very similar AF demagnetization curves. In order to study the effect of low temperature oxidation on the original TRM, all samples were given an ARM, which was subsequently AF demagnetized. If the remanence is still essentially the original TRM, one would expect that the ARM intensity (J_A) would be less than half of the NRM value (J_N), and the median demagnetizing fields (MDF_A and MDF_N, respectively) should be about equal. This is generally not the case with our samples. J_A/J_N is greater than 0.5 in most cases, sometimes much greater (e.g., 559-6-2, 50–53 cm), and MDF_A/MDF_N generally is significantly less than 1.0 (Appendix A).

There are several sources of uncertainty in this comparison that should be considered in interpreting these data. J_A is a function of the inducing field and hence may be different from the actual field in which magnetization took place. However, it should be within, at most, ±50%. The MDF is not very sensitive to inducing field, and that comparison is probably reasonably accurate. Multicomponent remanence tends to produce an apparently harder demagnetization curve (i.e., greater MDF) than a comparable single component (this is a result of the geometry of vector demagnetization curves and has nothing to do with intrinsic magnetic properties). This effect is generally small and is not found in all samples in any case. Often a significant portion of the NRM is left at 1000 Oe (the limit of our machine). MDF_A would then only reflect the portion of the grains that can be affected by 1000-Oe fields and would be somewhat lower than MDF_N. This difference is easily corrected for, however, and is not sufficient to eliminate the disparity in MDF in many, if not most, samples. The comparison of results with those of Levi and Merrill (1976) may not be valid. They worked with pure magnetite, and only one of their samples was in the single-domain size range found for most (though not all) of the Leg 82 rocks (note that this sample had $J_A/J_N = 0.24$ and $MDF_A/MDF_N = 1.2$). Although further work is necessary, the consistency of their results suggests that more directly comparable samples would show similar behavior.

All factors taken into consideration, many, if not most of the samples still seem to show distinctly different behaviors for NRM and ARM (and presumably TRM). It is well known that oxidation tends to decrease remanence and increase stability relative to their original values (e.g., Johnson, 1979). We tentatively conclude from these data that oxidation also causes these same changes relative to intrinsic (oxidized) magnetic parameters. This behavior suggests that we are not simply seeing a reduction in TRM but, in fact, its replacement by a chemical remanence with entirely different character, as in fact suggested by Hall (1977) on somewhat different grounds. Unfortunately, these data tell us nothing about possible effects on the direction of remanence.

SUMMARY

In general, these basalts are very similar to other such ocks recovered by DSDP. The most notable distinction as that they were unusually stable magnetically. Although they span a broad area of seafloor, they show no ubstantial trends either with latitude or age; however, here appears to be a small increase in J_s with decreasing atitude. The remanence appears to be dominated by a hemical remanent magnetization produced by low temperature alteration of the original TRM-bearing titanomagnetites. This remanence seems to be distinctly different from what would exist if the samples could be given a TRM in their oxidized state, having a lesser remanence and a greater stability. Nevertheless, the validity of the ARM-TRM analogy remains to be confirmed. There is also some evidence that the Ti content of the titanomagnetites may be more variable than often supposed. This too will require further study.

ACKNOWLEDGMENTS

We would like to thank Wendy Tormanen and Yvonne Meeks for their assistance with some of the measurements. Valuable assistance was also rendered on many occasions by Jim Marvin. We would also like to thank our reviewers, S. Beske-Diehl, B. Moskowitz, and R. Merrill, for many helpful comments and criticisms. This work was performed under NSF Grants OCE-8018692 and OCE-8214652.

REFERENCES

Day, R., Fuller, M.D., and Schmidt, V. A., 1977. Hysteresis properties of titanomagnetites: grain size and composition dependence. *Phys. Earth Planet. Inter.*, 13:260.

Halgedahl, S., and Fuller, M. D., 1983. The dependence of magnetic domain structure upon magnetization state with emphasis upon nucleation as a mechanism for pseudo-single-domain behavior. *J. Geophys. Res.*, 88:6505–6522.

Hall, J. M., 1977. Does TRM occur in oceanic layer 2 basalts? *J. Geomagn. Geoelectr.*, 29:411–420.

Johnson, H.P., 1979. Magnetization of the oceanic crust. *Rev. Geophys. Space Phys.*, 17:215–226.

Levi, S., and Merrill, R. T., 1976. A comparison of ARM and TRM in magnetite. *Earth Planet. Sci. Lett.*, 32:171–184.

Moskowitz, B. M., 1981. Methods for estimating Curie temperatures of titanomagnetites from experimental J_s-T data. *Earth Planet. Sci. Lett.*, 53:84–88.

Moskowitz, B. M., and Banerjee, S. K., 1981. Magnetic properties of synthetic titanomaghemites and some oceanic basalts. *J. Geophys. Res.*, 86:11869–11882.

O'Reilly, W., 1983. The identification of titanomaghemites: model mechanisms for the maghemitization and inversion processes and their magnetic consequences. *Phys. Earth Planet. Sci.*, 31:65–76.

Readman, P. W., and O"Reilly, W. O., 1972. Magnetic properties of oxidized (cation deficient) titanomagnetites $(Fe,Ti,\square)_3O_4$. *J. Geomagn. Geoelectr.*, 24:69–90.

Steiner, M., 1982. An investigation of ulvospinel composition and cation migration during maghemitization in Deep Sea Drilling Project Leg 61 titanomagnetites. *J. Geophys. Res.*, 87:5361–5374.

Syono, Y., 1965. Magnetocrystalline anisotropy and magnetostriction of Fe_3O_4-Fe_2TiO_4 series, with special application to rock magnetization. *Jpn. J. Geophys.*, 4:71–142.

Date of Initial Receipt: 31 May 1983
Date of Acceptance: 16 November 1983

APPENDIX A
Remanent Properties

Core-Section (interval in cm)	J_N (emu·cm^{-3})	I (°)	MDF$_N$ (Oe)[a]	J_A (emu/cm^3)	MDF$_A$ (Oe)	J_A/J_N	MDF$_A$/MDF$_N$	χ_0 (emu·cm^{-3}·Oe^{-1})	Q	Description
Hole 556										
5-1, 78-80	4.01×10^{-3}	−31	562	2.04×10^{-3}	371	0.51	0.66	8.29×10^{-5}	96.7	Pillow interior
5-1, 111-113	1.27×10^{-3}	−35[b]	675	1.96×10^{-3}	323	1.54	0.48	9.98×10^{-5}	25.5	Pillow margin
7-1, 47-49	2.02×10^{-3}	−25	274	2.42×10^{-3}	200	1.20	0.73	1.41×10^{-4}	28.7	Flow margin
7-3, 18-21	6.36×10^{-4}	−30	315	2.30×10^{-3}	200	3.59	0.63	1.11×10^{-4}	11.5	Flow interior
8-2, 6-9	3.05×10^{-3}	−38	481	2.02×10^{-3}	374	0.66	0.78	1.50×10^{-4}	40.7	Pillow interior
9-1, 143-146	7.24×10^{-4}	−6[b]	540	1.26×10^{-3}	297	1.73	0.55	1.04×10^{-4}	13.9	Flow interior
Average	1.95×10^{-3}	−28	475	1.96×10^{-3}	294	1.54	0.64	1.15×10^{-4}	36.2	
Hole 557										
1-1, 46-49	4.38×10^{-3}	−55	99	7.34×10^{-3}	34	1.68	0.34	2.76×10^{-3}	3.2	Basalt
1-1, 120-123	1.08×10^{-2}	−46	113	5.96×10^{-3}	74	0.55	0.65	1.05×10^{-3}	20.6	Basalt
Average	7.59×10^{-3}	−51	106	6.52×10^{-3}	54	1.12	0.50	1.19×10^{-3}	11.9	
Hole 558										
27-3, 51-54	3.70×10^{-4}	−51[b]	690	1.51×10^{-3}	282	4.08	0.41	8.98×10^{-5}	8.2	Pillow margin
27-3, 123-126	1.81×10^{-3}	−45	405	3.00×10^{-3}	165	1.66	0.41	1.24×10^{-4}	29.2	Pillow interior
28-3, 9-12	4.19×10^{-4}	−20[b]	739	2.18×10^{-3}	372	5.20	0.50	1.13×10^{-4}	7.4	Pillow margin
28-3, 43-47	2.05×10^{-3}	−23	248	4.44×10^{-3}	181	2.17	0.73	2.25×10^{-4}	18.2	Pillow interior
29-2, 138-141	3.63×10^{-3}	+34[b]	541	2.33×10^{-3}	369	0.64	0.68	1.73×10^{-4}	42.0	Pillow interior
29-2, 100-103	1.11×10^{-3}	+29	61%	4.23×10^{-4}	769	0.38		7.08×10^{-5}	31.4	Pillow margin
32-5, 30-33	2.85×10^{-3}	−39	475	2.37×10^{-3}	277	0.83	0.58	1.08×10^{-4}	52.8	Flow interior
32-5, 106-109	1.32×10^{-3}	−42	652	2.04×10^{-3}	359	1.55	0.55	8.32×10^{-5}	31.7	Flow margin
35-2, 71-74	1.82×10^{-4}	−72	80%	3.49×10^{-4}	244	1.92		6.89×10^{-5}	5.3	Pillow margin
35-2, 98-101	2.18×10^{-3}	−54	681	1.53×10^{-3}	362	0.70	0.53	6.08×10^{-5}	71.7	Pillow interior
36-2, 130-133	4.55×10^{-4}	−44	667	1.66×10^{-3}	367	3.65	0.55	8.22×10^{-5}	11.1	Flow margin
36-3, 18-21	7.74×10^{-3}	−51[b]	685	1.52×10^{-3}	321	0.20	0.47	9.00×10^{-5}	172.0	Flow interior
38-1, 56-59	2.34×10^{-3}	−33	444	3.48×10^{-3}	226	1.49	0.51	1.25×10^{-4}	37.4	Pillow margin
38-2, 42-45	3.65×10^{-3}	+32	258	2.71×10^{-3}	182	0.74	0.71	1.70×10^{-4}	42.9	Pillow interior
39-4, 4-7	3.31×10^{-3}	−26	421	2.43×10^{-3}	388	0.73	0.92	1.04×10^{-4}	63.7	Possible flow
39-4, 55-57	1.82×10^{-3}	−26	485	1.40×10^{-3}	285	0.77	0.59	8.40×10^{-5}	43.3	Possible flow
Average	2.20×10^{-3}	−40[c]	528	2.09×10^{-3}	322	1.67	0.58	1.11×10^{-4}	32.1	
Hole 559										
4-1, 115-118	6.40×10^{-4}	−31	651	1.54×10^{-3}	315	2.41	0.48	1.20×10^{-4}	10.7	Pillow interior
4-1, 133-136	6.87×10^{-4}	−37	460	1.82×10^{-3}	292	2.64	0.63	1.34×10^{-4}	10.3	Pillow margin
6-2, 20-23	5.34×10^{-4}	−30[b]	804	1.27×10^{-3}	323	2.40	0.40	1.10×10^{-4}	9.7	Pillow interior
6-2, 50-53	1.77×10^{-4}	+27[b]	55%	2.73×10^{-3}	267	15.4		1.08×10^{-4}	3.3	Pillow margin
Average	5.10×10^{-4}	33[c]	638[d]	1.84×10^{-3}	299	5.64	0.50	1.18×10^{-4}	8.5	
Hole 561										
2-2, 15-18	2.35×10^{-3}	−62	303	4.09×10^{-3}	283	1.74	0.93	3.39×10^{-4}	13.9	Pillow margin
2-2, 45-48	3.31×10^{-3}	−59	345	3.61×10^{-3}	299	1.09	0.87	3.50×10^{-4}	18.9	Pillow interior
3-1, 67-70	3.07×10^{-3}	−53	346	3.86×10^{-3}	312	1.26	0.90	3.19×10^{-4}	19.2	Massive flow
3-2, 42-45	1.37×10^{-3}	−44[b]	341	3.53×10^{-3}	257	2.58	0.75	2.7×10^{-4}	10.1	Massive flow
Average	2.53×10^{-3}	−55	334	3.77×10^{-3}	288	1.67	0.86	3.20×10^{-4}	15.5	
Hole 562										
1-2, 27-30	8.81×10^{-4}	−33	513	7.81×10^{-3}	100	8.90	0.19	8.49×10^{-4}	2.1	Pillow margin
1-2, 61-64	2.43×10^{-3}	−50	363	3.78×10^{-3}	210	1.56	0.58	2.00×10^{-4}	24.3	Pillow interior
4-2, 38-41	1.67×10^{-3}	−36	353	4.44×10^{-3}	131	2.66	0.37	2.94×10^{-4}	11.4	Massive flow
4-3, 72-75	1.85×10^{-3}	−35	132	3.83×10^{-3}	86	2.07	0.65	3.47×10^{-4}	10.7	Flow margin
4-3, 129-132	6.90×10^{-4}	−30	478	3.20×10^{-3}	309	4.64	0.65	1.77×10^{-4}	7.8	Pillow margin
4-4, 30-33	2.19×10^{-3}	−31	526	2.71×10^{-3}	357	1.24	0.68	8.39×10^{-5}	52.0	Pillow interior
5-2, 78-81	2.14×10^{-3}	−33	414	5.03×10^{-3}	154	2.35	0.37	4.51×10^{-4}	9.5	Flow margin
5-2, 104-107	1.13×10^{-3}	−26	282	3.61×10^{-3}	232	3.19	0.82	3.28×10^{-4}	6.9	Flow interior
6-3, 19-22	3.13×10^{-3}	−31	736	3.20×10^{-3}	685	1.02	0.93	9.27×10^{-5}	67.5	Pillow margin
6-3, 61-64	2.39×10^{-3}	−29	505	2.85×10^{-3}	346	1.19	0.69	9.33×10^{-5}	51.2	Pillow interior
Average	1.85×10^{-3}	−33	430	4.05×10^{-3}	261	2.88	0.59	2.92×10^{-4}	24.3	
Hole 563										
24-1, 3-6	1.96×10^{-3}	+42	315	4.94×10^{-3}	207	2.52	0.66	4.27×10^{-4}	9.2	Pillow interior
24-1, 33-36	4.96×10^{-3}	+47	271	4.86×10^{-3}	327	0.98	1.21	3.43×10^{-4}	28.9	Pillow margin
Average	3.46×10^{-3}	+45	293	4.90×10^{-3}	267	1.75	0.94	3.85×10^{-4}	19.1	
Hole 564										
1-3, 4-7	1.94×10^{-3}	+10	549	1.29×10^{-3}	319	0.66	0.58	1.33×10^{-4}	29.2	Pillow interior
1-1, 46-47	3.77×10^{-3}	−5	379	4.34×10^{-3}	296	1.15	0.78	1.82×10^{-4}	41.4	Pillow margin
5-3, 93-96	1.93×10^{-3}	+26	457	6.01×10^{-3}	182	3.11	0.40	1.95×10^{-4}	19.8	Flow interior
5-3, 44-47	1.52×10^{-3}	+14	444	3.37×10^{-3}	351	2.22	0.79	1.82×10^{-4}	16.7	Flow margin
6-2, 104-107	5.15×10^{-3}	+9	129	8.11×10^{-3}	195	1.57	1.51	1.04×10^{-3}	10.6	Pillow margin
6-2, 50-53	2.30×10^{-3}	+28	554	4.72×10^{-3}	199	2.05	0.36	1.88×10^{-4}	24.5	Pillow interior
8-2, 75-78	3.88×10^{-3}	−20	240	4.94×10^{-3}	154	1.27	0.64	2.88×10^{-4}	26.9	Flow interior
9-2, 71-74	1.84×10^{-3}	+15	326	5.94×10^{-3}	326	3.23	1.0	1.63×10^{-4}	22.6	Flow margin
Average	2.78×10^{-3}	+17[c]	385	4.84×10^{-3}	253	1.91	0.76	2.94×10^{-4}	24.0	

Note: J_N is the natural remanent magnetization; I is the inclination; MDF$_N$ is median demagnetizing field for NRM; J_A is the anysteretic remanent magnetization (ARM) value; MDF$_A$ is the median demagnetizing field for ARM: χ_0 is weak field susceptibility; and Q is the Koenigsberger ratio ($J_N/0.5X_O$).

[a] % in this column indicates the remanence remaining at 1000 Oe.

[b] Multicomponent magnetization.

[c] Excludes values with different polarity than the majority of samples.

[d] Excludes samples wih MDF > 1000 Oe.

APPENDIX B
Intrinsic Properties

Core-Section (interval in cm)	J_s (emu·g^{-1})	J_r (emu·g^{-1})	H_c (Oe)	H_{cr} (Oe)	$\frac{J_r}{J_s}$	$\frac{H_{cr}}{H_c}$	χ_p (emu·g^{-1}·Oe^{-1} ·10^{-5})	T_c (°C)		$\frac{J_f}{J_A}$
								Heating	Cooling	
Hole 556										
5-1, 78-80	1.27×10^{-1}	8.25×10^{-2}	372	463	0.65	1.2	1.59	270	545	10.6
5-1, 111-113	8.95×10^{-2}	6.04×10^{-2}	419	581	0.67	1.4	1.54	315	535	
7-1, 47-49	1.26×10^{-1}	5.79×10^{-2}	198	269	0.46	1.4	1 13	355	590	8.8
7-3, 18-21	1.49×10^{-1}	8.10×10^{-2}	198	238	0.54	1.2	1.36	310	560	6.1
8-2, 6-9	1.11×10^{-1}	5.67×10^{-2}	269	363	0.51	1.35	1.08	380	610	7.3
8-2, 80-83	2.77×10^{-2}	1.26×10^{-2}	175	388	0.45	2.2	1.42	495	560	4.1
9-1, 143-146	1.15×10^{-1}	5.59×10^{-2}	259	363	0.49	1.4	1.32	365	575	8.4
9-1, 127-130	7.86×10^{-2}	4.35×10^{-2}	364	561	0.55	1.5	1.22	365	590	11.7
Average	1.03×10^{-1}	5.63×10^{-2}	282	403	0.54	1.5	1.33	357	571	8.1
Hole 557										
1-1, 46-49	1.47	1.89×10^{-1}	39	91	0.13	2.3	1.45	195		1.0
1-1, 120-123	1.48	2.80×10^{-1}	88	139	0.19	1.6	3.14	350	445	0.3
Average	1.48	2.35×10^{-1}	64	115	0.16	2.0	2.30	273	445	0.7
Hole 558										
27-3, 51-54	1.22×10^{-1}	5.01×10^{-2}	189	297	0.41	1.6	1.16	340	570	6 6
27-3, 123-126	1.83×10^{-1}	9.17×10^{-2}	173	247	0.50	1.4	1.55	265	445	5.0
28-3, 9-12	7.32×10^{-2}	3.66×10^{-2}	298	456	0.50	1.5	1.29	350	565	8.0
28-3, 43-47	1.16×10^{-1}	6.93×10^{-2}	317	398	0.60	1.3	1.45	295	545	5.6
29-2, 138-141	1.11×10^{-1}	6.46×10^{-2}	278	311	0.58	1.1	1.57	320	540	5.1
29-2, 100-103	4.05×10^{-2}	2.02×10^{-2}	431		0.50		1.48	375	570	2.4
32-5, 30-33	1.44×10^{-1}	6.66×10^{-2}	247	399	0.46	1.4	1.38	305	560	7.6
32-5, 106-109	1.03×10^{-1}	5.66×10^{-2}	306	427	0.55	1.4	1.36	295	560	8.2
35-2, 71-74	2.66×10^{-2}	1.51×10^{-2}	428		0.57		1.33	385	580	4.8
35-2, 98-101	1.14×10^{-1}	7.03×10^{-2}	472	636	0.62	1.4	1.46	310	570	6.8
36-2, 130-133	5.33×10^{-2}	3.24×10^{-2}	353	541	0.61	1.5	1.04	360	550	9.9
36-3, 18-21	1.43×10^{-1}	8.76×10^{-2}	411	542	0.61	1.3	1.46	320	580	6.0
38-1, 56-59	1.59×10^{-1}	7.41×10^{-2}	172	238	0.47	1.4	1.41	315	555	5.1
38-2, 42-45	2.15×10^{-1}	9.95×10^{-2}	202	275	0.46	1.4	1.41	295	530	4.7
39-4, 4-7	9.64×10^{-2}	4.92×10^{-2}	244	339	0.51	1.4	1.10	350	555	8.8
39-4, 55-57	8.35×10^{-2}	4.76×10^{-2}	284	398	0.57	1.4	1.20	320	580	11.9
Average	1.11×10^{-1}	5.82×10^{-2}	300	389	0.53	1.4	1.35	325	553	6.3
Hole 559										
4-1, 115-118	1.15×10^{-1}	5.97×10^{-2}	283	413	0.52	1.5	1.42	310	580	9.5
4-1, 133-136	8.44×10^{-2}	4.62×10^{-2}	309	463	0.55	1.5	0.93	315	560	10.8
6-2, 20-23	7.82×10^{-2}	4.86×10^{-2}	391	594	0.62	1.5	1.34	365	590	10.0
6-2, 50-53	5.92×10^{-2}	3.33×10^{-2}	281	466	0.56	1.7	1.16	395	580	11.2
Average	8.42×10^{-2}	4.70×10^{-2}	316	484	0.56	1.6	1.21	346	578	10.4
Hole 561										
2-2, 15-18	2.80×10^{-1}	1.33×10^{-1}	230	278	0.48	1.2	1.65	375	545	2.7
2-2, 45-48	3.16×10^{-1}	1.37×10^{-1}	272	384	0.43	1.4	1.62	335	570	4.2
3-1, 67-70	2.93×10^{-1}	1.40×10^{-1}	248	330	0.48	1.3	1.49	340	(a)	
3-2, 42-45	3.06×10^{-1}	1.37×10^{-1}	242	338	0.45	1.4	1.70	305	575	4.7
Average	2.99×10^{-1}	1.37×10^{-1}	248	333	0.46	1.3	1.62	339	563	3.9
Hole 562										
1-2, 27-30	5.80×10^{-1}	1.70×10^{-1}	106	194	0.29	1.8	2.07	205	(a)	1.1
1-2, 61-64	2.55×10^{-1}	1.20×10^{-1}	211	278	0.47	1.3	1.83	290	565	5.8
4-2, 38-41	2.54×10^{-1}	1.04×10^{-1}	172	230	0.41	1.3	1.49	305	520	
4-3, 72-75	3.83×10^{-1}	1.30×10^{-1}	145	217	0.34	1.5	1.96	270	550	4.2
4-3, 129-132	6.03×10^{-2}	2.49×10^{-2}	188	413	0.41	2.2	1.43	525	570	4.5
4-4, 30-33	1.31×10^{-1}	8.62×10^{-2}	304	467	0.66	1.3	1.50	260	545	8.6
5-2, 78-81	5.03×10^{-1}	1.16×10^{-1}	89	169	0.23	1.9	1.93	260		
5-2, 104-107	2.99×10^{-1}	8.80×10^{-2}	139	217	0.29	1.6	1.47	370	(a)	1.4
6-3, 19-22	1.32×10^{-1}	8.90×10^{-2}	517	728	0.67	1.4	1.71	315	550	3.9
6-3, 61-64	1.15×10^{-1}	7.53×10^{-2}	388	513	0.66	1.3	1.49	285	530	6.3
Average	2.71×10^{-1}	1.00×10^{-1}	226	343	0.44	1.6	1.69	309	547	4.5
Hole 563										
24-1, 3-6	3.24×10^{-1}	1.32×10^{-1}	173	238	0.41	1.4	1.35	415	575	3.4
24-1, 33-36	2.66×10^{-1}	1.05×10^{-1}	236	331	0.40	1.4	1.38	415		3.3
Average	2.95×10^{-1}	1.19×10^{-1}	205	285	0.41	1.4	1.37	415	575	3.4
Hole 564										
1-3, 4-7	1.38×10^{-1}	7.41×10^{-2}	313	472	0.54	1.5	1.43	375	580	9.2
1-1, 46-49	2.80×10^{-1}	1.42×10^{-1}	255	334	0.51	1.3	1.66	340	555	5.3
5-3, 93-96	2.68×10^{-1}	1.35×10^{-1}	188	233	0.51	1.2	1.68	305	560	6.2
5-3, 44-47	1.78×10^{-1}	7.52×10^{-2}	214	336	0.42	1.6	1.39	380	575	5.3
6-2, 104-107	4.79×10^{-1}	1.05×10^{-1}	88	159	0.22	1.8	1.38	505	575	1.3
6-2, 50-53	2.61×10^{-1}	1.24×10^{-1}	191	259	0.48	1.4	1.75	295	550	5.4
8-2, 75-78	4.76×10^{-1}	1.99×10^{-1}	145	191	0.42	1.3	2.21	285	560	3.6
9-2, 71-74	3.11×10^{-2}	1.48×10^{-2}	227	373	0.48	1.6	0.54	350	560	14.7
9-3, 18-21	1.92×10^{-1}	6.81×10^{-2}	231	473	0.36	2.1	1.72	575	555	1.2
Average	2.56×10^{-1}	1.04×10^{-1}	206	314	0.44	1.5	1.53	357	563	5.8

Note: J_s is saturation magnetization; J_r is saturation remanence; H_c is coercivity; H_{cr} is remanent coercivity; χ_p is paramagnetic susceptibility; T_c is Curie temperature; J_f is J_s after inversion; J_i is J_s before inversion. The heating value of T_c is that before inversion; the cooling value follows heating to about 620°.

[a] T_c too low to be measured accurately.

17. MAGNETIC PROPERTIES OF PLUTONIC ROCKS FROM THE CENTRAL NORTH ATLANTIC OCEAN[1]

Guy M. Smith and Subir K. Banerjee, Department of Geology and Geophysics, University of Minnesota[2]

ABSTRACT

Ten samples of gabbro and peridotite, with varying degrees of serpentinization, were studied by magnetic techniques and reflected light microscopy. Evidence from these methods suggests that the natural remanent magnetization is primarily of chemical origin. It is generally weak for the gabbros and much stronger for the peridotites. This difference is offset by the fact that the peridotites have generally lower magnetic stability and Koenigsberger ratios. There is a considerable variation in both magnetic parameters and petrology even among closely spaced samples, which suggests that some combination of source heterogeneity and tectonic mixing was involved in the production of these rocks. However, the small number of samples makes this conclusion tentative. There may also have been significant postemplacement alteration involved. All samples show a significant anisotropy of weak field susceptibility that appears to be related to deformation. This anisotropy may be useful in defining petrofabrics.

INTRODUCTION

In addition to the expected extrusive basalts, plutonic rocks (principally peridotites and gabbros) were recovered from Holes 556, 558, and 560. This paper reports on the magnetic characteristics of these plutonic rocks. These samples represent one of only a few suites recovered from normal crust (see Dunlop and Prevót, 1982), but may provide some interesting information, however murky, about the magnetic properties of the deeper parts of the oceanic crust. In addition, they may offer some insight into the nature of tectonic activity associated with the Mid-Atlantic Ridge.

We measured a number of standard magnetic parameters including:

1. intensity, direction, and stability of natural remanent magnetization (NRM);
2. intensity and stability of anhysteretic remanent magnetization (ARM);
3. hysteresis loop parameters; saturation magnetization, J_s; saturation remanence, J_{rs}; coercivity, H_c; remanent coercivity, H_{cr}; and paramagnetic susceptibility, χ_p;
4. weak field susceptibility, χ_0; and
5. Curie temperature, T_c, ratio of the magnetization before heating to the magnetization after heating, J_f/J_i, and thermomagnetic curve analysis.

We also did some preliminary analysis of polished thin sections using both reflected and transmitted light.

METHODS

Except as noted, the techniques used here are the same as described in the previous paper (Smith and Banerjee, this volume).

A modified sample holder was constructed for the susceptibility bridge in order to measure anisotropy. This permitted rotation of disk-shaped samples about an axis perpendicular to the measurement axis. Readings were taken every 20° for a complete rotation. Microscopy was done on a Zeiss microscope with oil immersion lenses and a Polaroid camera.

RESULTS

Natural Remanence

There are basically two types of rock discussed in this report, peridotites and gabbros, which both have varying degrees of serpentinization. NRM intensities of peridotites (J_N) tend to be somewhat higher than gabbros, although there is some overlap (Table 1). Median demagnetizing fields (MDF_N) are substantially larger for gabbros than peridotites. The directional data are not summarized so readily. The two gabbros from Site 556 were not consistent with each other or with the overlying basalts. Two of the serpentinites from Hole 558 had normal inclinations and the other two had the same value but reversed inclination. Comparison with the overlying basalts is uncertain, because they also show both normal and reversed directions.

The Site 560 samples show a fair amount of consistency and are reasonably close to the axial dipole value for the site (about 55°). Most of the samples have fairly straight univectorial demagnetization curves after about 100–150 Oe (Fig. 1A). The low coercivity component is probably viscous, as it is generally close to the current inclination at the site. Only one sample definitely shows multicomponent behavior (560-3-1, 9–12 cm) (Fig. 1B). This would suggest acquisition of remanence in two episodes separated by a significant time lapse (~1000 yr.) and/or tectonic activity. Curiously, the low coercivity "secondary" component is low inclination, whereas it is the "primary" component that is close to the present field.

Koenigsberger ratios (Q) varied from 0.02 to 19.5 (Table 1). They were generally higher for the gabbros than the peridotites.

---

[1] Bougault, H., Cande, S. C., et al., *Init. Repts. DSDP*, 82: Washington (U.S. Govt. Printing Office).

[2] Address: Department of Geology and Geophysics, University of Minnesota, Minneapolis, Minnesota 55455.

Table 1. Remanent properties.

Core-Section (interval in cm)	J_N (emu · cm^{-3})	I (°)	MDF_N (Oe)	J_A (emu · cm^{-3})	MDF_A (Oe)^a	$\frac{J_A}{J_N}$	$\frac{MDF_A}{MDF_N}$	χ_0 (emu · cm^{-3} · Oe^{-1})	Q	Description
Hole 556										
14-2, 29-32	3.51×10^{-4}	+51	400	1.17×10^{-2}	100%	33	>2.5	9.85×10^{-5}	7.1	Gabbro
14-2, 140-143	1.53×10^{-4}	+12	390	3.64×10^{-3}	88%	24	>2.6	9.27×10^{-5}	3.3	Gabbro
Hole 558										
41-2, 61-64	2.30×10^{-4}	−41	211	2.22×10^{-3}	165	9.65	0.78	1.13×10^{-3}	0.4	Peridotite
41-2, 54-57	4.20×10^{-4}	−41	161	3.71×10^{-3}	150	8.83	0.93	9.10×10^{-4}	0.9	Peridotite
41-2, 109-112	5.39×10^{-3}	+41	129	9.54×10^{-3}	150	1.77	1.16	4.72×10^{-3}	2.3	Peridotite
43-1, 8-11	2.62×10^{-3}	+42	74	2.62×10^{-3}	110	1.00	1.49	5.44×10^{-3}	1.0	Peridotite
Hole 560										
3-1, 9-12	5.00×10^{-4}	−45	350	4.67×10^{-4}	500	0.93	1.43	5.12×10^{-5}	19.5	Gabbro
3-1, 21-24	1.53×10^{-5}	−38	611	2.85×10^{-4}	500	19.0	0.82	3.08×10^{-5}	0.99	Gabbro
5-1, 98-101	3.12×10^{-4}	−65	154	1.30×10^{-1}	160	417.0	2.46	2.68×10^{-2}	0.02	Peridotite
5-1, 109-112	1.10×10^{-3}	−64	144	1.26×10^{-2}	150	11.0	1.04	5.50×10^{-3}	0.40	Peridotite
Averages										
Gabbro	2.55×10^{-4}	—	438	4.02×10^{-3}	>750	19.2	>1.84	6.83×10^{-5}	7.7	
Peridotite	1.68×10^{-3}	—	146	2.68×10^{-2}	148	75.0	1.31	7.42×10^{-3}	0.8	

Note: J_N is intensity of natural remanent magnetization (NRM); I is inclination; MDF_N is mean demagnetizing field for NRM; J_A is intensity of anhysteretic remanent magnetization (ARM); MDF_A is mean demagnetizing field for ARM; χ_0 is weak field susceptibility; and Q is Koenigsberger ratio ($J_N/0.5\chi_0$). Averages for gabbros and peridotites are given for selected measurements.

[a] % indicates the amount of remanence remaining at 1000 Oe.

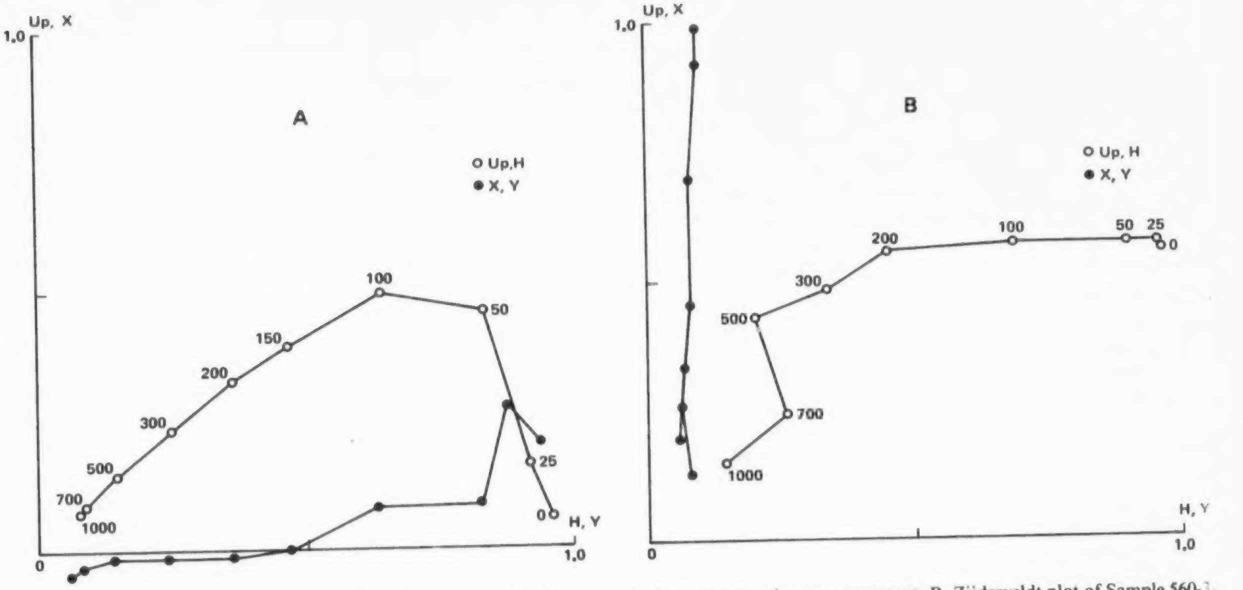

Figure 1. A. Zijderveldt plot of Sample 558-41-2, 61-64 cm showing removal of an apparent viscous component. B. Zijderveldt plot of Sample 560-3-1, 9-12 cm showing multicomponent behavior. Closed circles represent the x-y component; open circles, the z-horizontal component. Demagnetizing fields are in Oe.

Anhysteretic Remanent Magnetization

ARM intensities (J_A, Table 1) were generally much higher than J_N (as much as two orders of magnitude). The two exceptions were somewhat atypical: 560-3-1, 9-12 cm, a gabbro with multicomponent behavior, and 558-43-1, 8-11 cm, a peridotite with a very low MDF_N.

The MDF's (MDF_A, Table 1) were higher than MDF_N for most of the peridotite samples; the two exceptions were 558-41-2, 54-57 cm and 558-41-2, 61-64 cm. Three of the four gabbros had MDF_A/MDF_N larger than 1. the exception was 560-3-1, 21-24 cm. The exact ratio fo the samples from Site 556 cannot be determined becaus the MDF_A exceeds 1000 Oe (apparently by a substanti amount), but it must be in excess of 2.5.

Hysteresis Loop Parameters

The peridotites generally had substantially larger va ues of saturation magnetization (J_s) than the gabbros (Ta ble 2). The gabbro values were fairly consistent (2-3 ×

Table 2. Intrinsic properties.

Core-Section (interval in cm)	J_s (emu/cm^3)	J_r (emu/cm^3)	H_c (Oe)	H_{cr} (Oe)	$\frac{J_r}{J_s}$	$\frac{H_{cr}}{H_c}$	χ_p	T_c		$\frac{J_f}{J_i}$	Comments
								Heating	Cooling		
Hole 556											
14-2, 29–32	3.84×10^{-2}	1.30×10^{-2}	309	641	0.34	2.1	0.66	—	—	—	Bulk sample
	9.65×10^{-2}	2.99×10^{-2}	172	353	0.31	2.1	1.18	375	590	2.3	Pyroxene separate
	1.06×10^{-2}	—	—	—	—	—	0.03	—	—	—	Plagioclase separate
14-2, 140–143	3.33×10^{-2}	7.75×10^{-3}	163	391	0.23	2.4	0.61	560	565	2.5	
Hole 558											
41-2, 61–64	9.28×10^{-1}	1.35×10^{-1}	134	320	0.15	2.4	0.81	—	—	—	
41-2, 54–57	9.75×10^{-1}	1.86×10^{-1}	117	197	0.19	1.7	0.85	550	565	0.73	Sulfides?
42-1, 109–112	3.10	4.80×10^{-1}	113	165	0.16	1.7	1.4	560	580	0.95	
43-1, 8–11	4.03	5.40×10^{-1}	92	188	0.13	2.0	1.7	565	580	0.97	
Hole 560											
3-1, 9–12	3.30×10^{-2}	5.70×10^{-3}	116	266	0.17	2.3	0.81	555	580	1.1	
3-1, 21–24	2.30×10^{-2}	4.40×10^{-3}	84	250	0.19	3.0	0.83	550	580	2.0	
5-1, 98–101	3.71	8.03×10^{-1}	139	203	0.22	1.5	1.05	560	590	0.95	
5-1, 109–112	2.30	5.20×10^{-1}	136	188	0.23	1.4	0.96	—	—	—	
Averages											
Gabbro	3.19×10^{-2}	7.71×10^{-3}	168	387	0.23	2.5	0.73				
Peridotite	2.51	4.44×10^{-1}	122	210	0.18	1.8	1.1				

Note: J_s is saturation magnetization; J_r is saturation remanent magnetization; H_c is coercivity; H_{cr} is coercivity of remanence; χ_p is the paramagnetic susceptibility in emu · g^{-1} · Oe^{-1} · 10^{-5}; T_c is Curie temperature; J_f/J_i is the ratio of final to initial magnetization. Averages for gabbros and peridotites are given for selected measurements. Dashes indicate that measurements could not be performed.

10^{-2} emu/g). The peridotites fell into two groups. Four had values of about 2 emu/g and two from Hole 558 were slightly less than 1 emu/g. Coercivities seemed low compared to the MDF and often showed little relation to it. Sample 560-3-1, 21–24 cm had the lowest coercivity of either peridotite or gabbro samples, but it had one of the highest MDF's.

The ratios J_r/J_s and H_{cr}/H_c of all samples indicated a pseudo-single domain to small multidomain state. The Site 556 gabbros had relatively high J_r/J_s values but those for the other two gabbros were close to peridotite values.

The paramagnetic susceptibilities (χ_p) were interesting. Gabbro values were uniformly low (0.6–0.8 × 10^{-5} emu · g^{-1} · Oe^{-1}) compared to the peridotites and most basalts (typically, 1.2–1.5 × 10^{-5} emu · g^{-1} · Oe^{-1}). This is probably due to the presence of plagioclase, as the separate from 556-14-2, 29–32 cm had very low values of χ_p (Table 2). Peridotites split into the same two groups as defined by J_s, with the two low J_s samples also having low χ_p.

Thermomagnetic Measurements

The Curie temperature, T_c, of the peridotites is somewhat below that of pure magnetite (580°C) for the heating curve and essentially equal to 580°C for the cooling curve. It is uncertain just what this represents, because conversion of a nonstoichiometric phase to magnetite normally results in an increase in magnetization rather than the observed decrease. One sample showed an inflection in the heating curve at 350°C that may be caused by the breakdown of pyrrhotite.

The gabbros from Site 560 had T_c values similar to the peridotites, but the ratio of magnetization before heating to the magnetization after heating (J_f/J_i) was greater than 1.0 for both samples. There are a variety of possible explanations. One is the inversion of a titanomaghemite. The high heating T_c could be due to low Ti concentration or a pre-existing partial inversion. Another explanation is the reduction of hemoilmenite caused by heating, probably the result of a combination of a fairly hard vacuum with either backstreaming pump oil or some local reducing agent. There may also be other cations such as Mg or Mn involved. Microprobe work is clearly necessary to resolve this question.

One of the Hole 558 samples (558-14-2, 140–143 cm) behaved similarly to samples from Site 560. The other showed a T_c value typical of basaltic titanomaghemites followed by an apparent inversion to a mixed phase. This behavior suggests that at least some gabbros contain high Ti titanomagnetites that have been altered at low temperatures.

Susceptibility

One unexpected result of the weak field susceptibility measurements was the fortuitous discovery of a substantial anisotropy (as much as 15%). This was true not only for the peridotites, which often had an obvious fabric, but also for the gabbros, which appeared quite homogeneous. Ideally, one would measure the entire susceptibility tensor, but unfortunately this is beyond the capability of our instrument. However, we were able to measure the variation in the vertical plane. An example of the variation of χ_o with inclination is given in Figure 2. Table 3 summarizes the results for each sample.

With one exception (560-3-1, 9–12 cm), all samples had either essentially vertical or horizontal orientations of maximum susceptibility (χ_{max}). The two samples from Site 556 have mutually perpendicular χ_{max} orientations, although they are from the same core and only have a 40° difference in inclination. The other two sites had

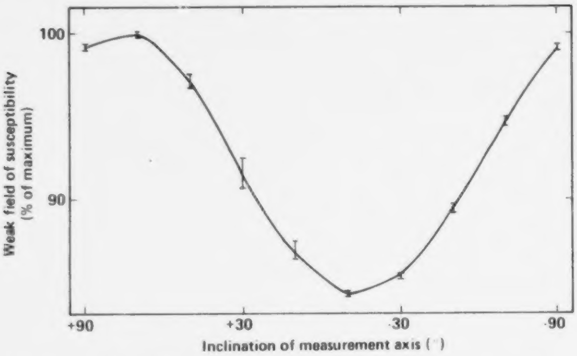

Figure 2. Weak field susceptibility versus sample orientation.

Table 3. Susceptibility anisotropy.

Sample (interval in cm)	χ_{min} (emu · cm^{-3} · Oe^{-1})	χ_{max} (emu · cm^{-3} · Oe^{-1})	Inclination (°)
Hole 556			
14-2, 29-32	8.75×10^{-5}	9.10×10^{-5}	90
14-2, 140-143	9.01×10^{-5}	1.03×10^{-4}	0
Hole 558			
41-2, 61-64	1.17×10^{-3}	1.24×10^{-3}	80
41-2, 54-57	9.54×10^{-4}	9.36×10^{-4}	90
42-1, 109-112	5.32×10^{-3}	6.34×10^{-3}	20
43-1, 8-11	4.71×10^{-3}	5.21×10^{-3}	90
Hole 560			
3-1, 9-12	4.73×10^{-5}	5.51×10^{-5}	50
3-1, 21-24	3.01×10^{-5}	3.14×10^{-5}	0
5-1, 98-101	4.19×10^{-2}	5.32×10^{-2}	20
5-1, 109-112	5.07×10^{-3}	5.92×10^{-3}	20

three samples with similar orientations and one odd one. Hole 558 had 90° as the dominant direction whereas the direction for Site 560 was close to horizontal.

Microscopy

In addition to magnetic measurements, polished thin sections of all samples were studied in both transmitted and reflected light. The results reported here are based on a relatively brief examination of the sections and should be regarded as preliminary and tentative.

Sample 556-14-2, 29-32 cm was a partially serpentinized gabbro with homogeneous magnetite or titanomagnetite as the dominant phase with little or no hematite present. It was found in two locations in the sample. Most had acicular (or tabular) habit and occurred along the twin (or cleavage) planes of partially serpentinized pyroxenes (Fig. 3). The rest was found as acicular inclusions in plagioclase grains (Fig. 4).

Sample 556-14-2, 140-143 cm was somewhat different, proximity to the previous sample notwithstanding. Little or no magnetite was present in the plagioclase even though it was common in the preceding sample. Magnetite was found in partially serpentinized pyroxenes, as before, but it also contained lamellar hematite (Fig. 5).

The serpentinites from Hole 558 could be grouped into two pairs on optical as well as magnetic grounds. The two samples from Core 558-41 were generally tan. Magnetite was found in two locations, along twin planes in relict pyroxenes (often not fully serpentinized) and as granular masses along grain boundaries (Fig. 6). Small amounts of what appeared to be hematite were also present as small (10–15 μm) discrete grains and perhaps as pigment.

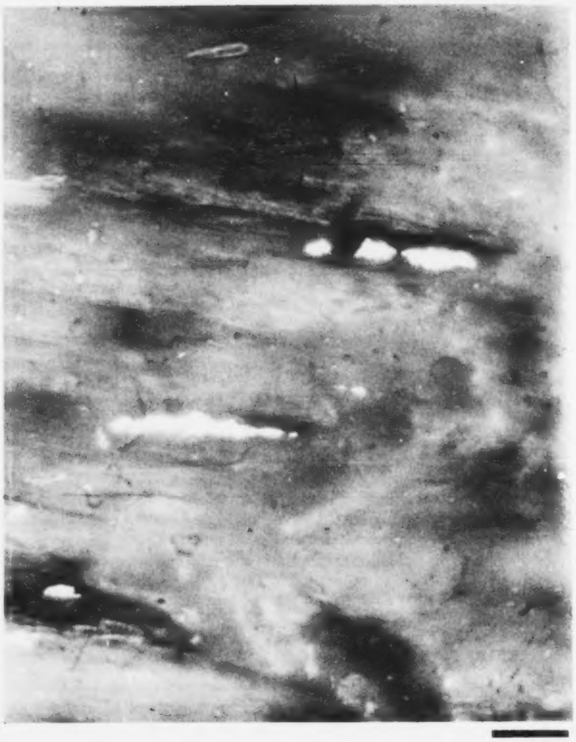

Figure 3. Elongated magnetite grains in altered pyroxene. Reflected light. Scale bar = 100 microns.

The second pair of samples, 558-42-1, 109–112 cm and 558-43-1, 8–11 cm, were dark green and looked like conventional serpentinite. Under the microscope, the only remnants of the original minerals were pseudomorphs of pyroxene. Magnetite was found as abundant granular clusters along grain boundaries. What magnetite was found in the relict pyroxenes was in the form of clusters of grains rather than the discrete elongated grains seen in the partially serpentinized samples.

Site 560 had two gabbros and two serpentinites within a few tens of meters. The upper two samples were gabbros (560-3-1, 9–12 cm and 560-3-1, 21–24 cm) that were significantly different in appearance than those from Site 556, being a fairly homogeneous dark green, whereas the Site 556 gabbros were gray with 2–3 mm brown pyroxenes. The plagioclase was extensively altered to sericite and showed little evidence of magnetite inclusions. Magnetite was located largely along twin planes of partially serpentinized pyroxene as seen in the previous sample. There appeared to be little or no hematite, and both samples contained minor sulfides. There was a substantial difference in silicate grain size, however; 560-

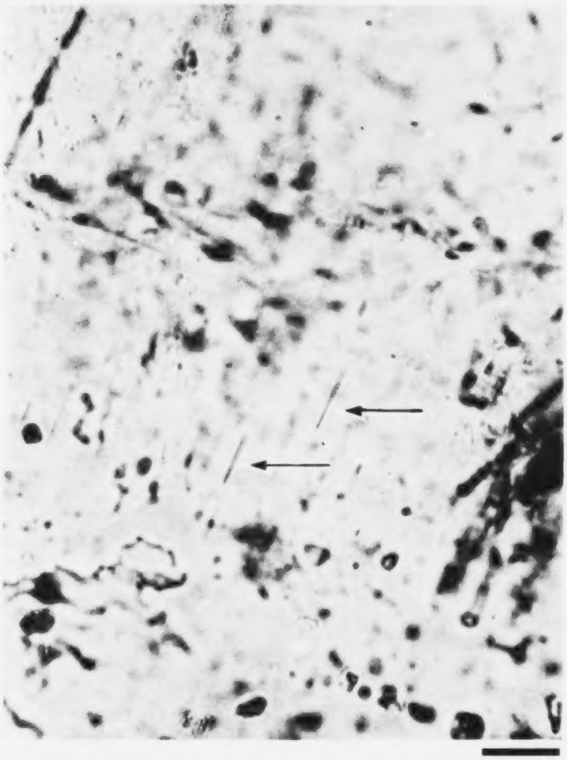

Figure 4. Magnetite needles in plagioclase (arrows). Transmitted light; scale bar = 100 μm.

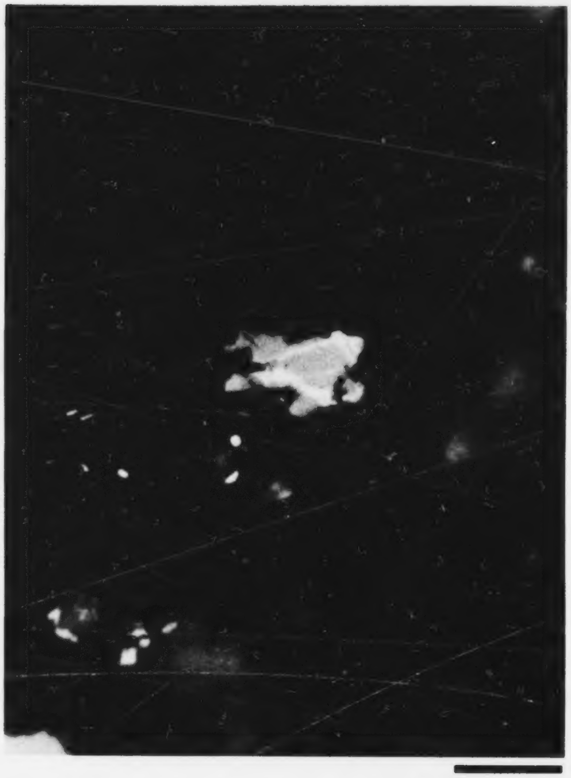

Figure 5. Lamellar hematite in magnetite matrix. Reflected light; scale bar = 50 μm.

3-1, 9–12 cm had relatively large ($\leq$ 5 mm) grains, whereas 560-3-1, 21–24 cm had much smaller ($\leq$ 1–2 mm) grains.

The peridotites were similar to the latter two samples from Site 558. Magnetite occurred as granular masses along grain boundaries and as a few large (~1 mm) grains. Some hematite was present, generally in contact with magnetite. Sulfides were also present, sometimes in contact with magnetite.

Low temperature alteration did not appear to be present in any of the samples, although thermomagnetic measurements suggest that a more thorough examination of better quality slides may change this conclusion.

Some of the serpentinites had an obvious fabric in thin section defined by the grain boundary magnetite that generally had the same orientation as χ_{max} (Fig. 7). Visual inspection of the cores suggests that a foliation rather than a lineation is defined by this fabric. This correspondence implies that χ_{max} is related to the stress regime these samples have been subjected to and might be useful in defining petrofabrics.

DISCUSSION

Probably the most notable thing about these samples is their lack of homogeneity, even on the scale of 1 m. This raises some questions as to how well these rocks represent their deep crustal counterparts and the tectonic and chemical processes involved in bringing them to the surface. Unfortunately, the small number of samples makes any conclusion tentative.

The Site 556 gabbros are from the same core and have similar NRM and silicate mineralogy. However, their opaque mineralogy (in particular, the presence or absence of hematitte and of magnetite inclusions in plagioclase and intrinsic magnetic parameters were significantly different. Virtually the converse was true for the two gabbros from Site 560. Intrinsic magnetic parameters and opaque mineralogy were similar, but NRM values differed by more than an order of magnitude. The grain sizes of the silicate phases were also significantly different.

The ultramafics from Hole 558 broke down into two pairs of similar samples. There were significant differences between the pairs, however, both in petrology and magnetic character. They appear to have been similar originally, but the Core 558-41 samples have been altered to a lesser degree. The opaque mineralogy suggests that this difference in alteration is also responsible to a large extent for the magnetic differences, in particular, the fact that NRM values differ by more than can be explained by intrinsic parameters. However, the difference in NRM values for the Site 560 ultramafics, which are otherwise very similar, indicates that other factors must also be operating.

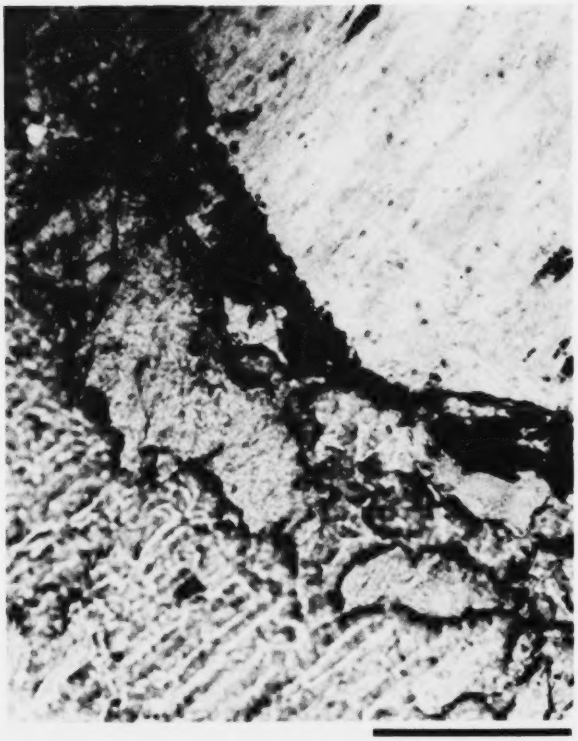

Figure 6. Granular magnetite along grain boundaries. Transmitted light; scale bar = 100 μm.

There seems to be three possible origins of this heterogeneity, not necessarily mutually exclusive; an initially homogeneous source that suffered varying degrees of alteration during and/or after emplacement, a somewhat heterogeneous source that was tectonically mixed by the emplacement process, and a source that was essentially similar to the samples recovered.

Some degree of source heterogeneity seems necessary to explain the abundance of magnetite in plagioclase in one of the Site 556 gabbros and its absence in the other, as it is presumably a primary phase. The difference in both NRM and χ_{max} inclination suggests that tectonic disruption did occur on a fine scale but says nothing about the possibilities of large-scale mixing versus fine-scale inhomogeneities in the source area.

The opposite inclinations of the two pairs of Hole 558 serpentinites may simply be a fortuitous tectonic (or shipboard) occurrence or they may reflect a field reversal. They may also represent self-reversal, although the magnetic mineralogy makes this unlikely. The fact that normal and reversed inclinations are seen in the overlying basalts indicates that a field reversal is at least plausible. The similarity of χ_{max} inclinations for three of the four samples suggests that they may not have been tectonically rotated relative to each other, although a 180° rotation is possible. If these samples do represent different geomagnetic polarities, then the similarity of inclination indicates that remanence was probably acquired after emplacement and that the samples were magnetized at least 2000–3000 yr. apart. As the remanence appears to be chemical in origin, it would also indicate significant alteration after emplacement. If this is the case, it is difficult to ascertain what relation these samples bear to their counterparts at depth.

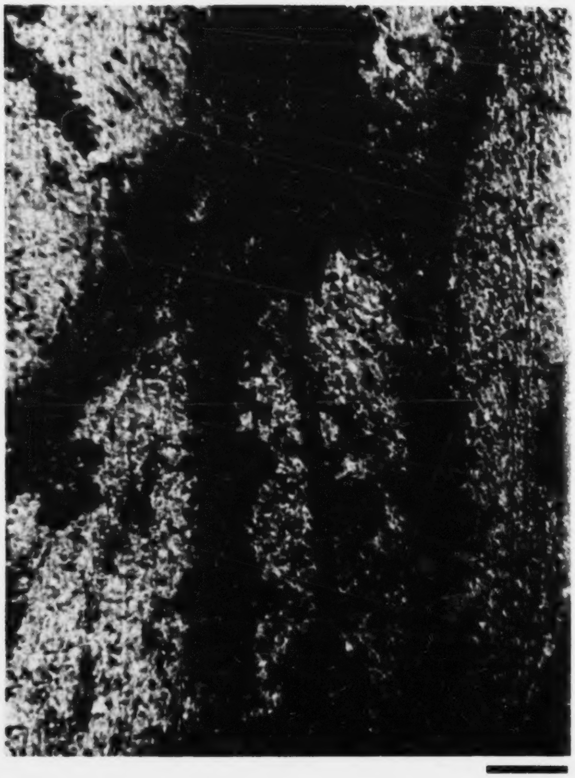

Figure 7. Aligned clusters of granular magnetite. Transmitted light; scale bar = 1 mm.

Given the difference in both petrology and alteration state for the Site 560 samples, some tectonic mixing seems probable, although variable alteration during or after emplacement may also have occurred. The similarity in NRM and three of the four χ_{max} inclinations may be a tectonic accident but, more likely, may also be related to remanence acquisition that postdates emplacement. As with Hole 558, this would imply significant postemplacement alteration.

It seems likely that the bulk of the remanence in these samples is of chemical rather than thermal origin. Most of the magnetic minerals seem to have been produced as a result of serpentinization, which takes place at relatively low temperatures (<400°C). As discussed in the previous paper (Smith and Banerjee, this volume), marked differences between J_A and J_N and MDF_A and MDF_N also suggest a chemical remanent magnetization. It is difficult to determine just when this alteration occurred, so that the relation of the magnetic properties of these samples to their sources is unclear at best.

The origin of susceptibility anisotropy is an interesting question. In the peridotite, it seems to be controlled by the orientation of the elongated clusters of magnetite grains, which are in turn controlled by the orientation of serpentine crystals. Thus, this orientation should be a reasonably accurate reflection of the deformation of the sample, at least qualitatively.

The gabbros hold few or no grain boundary magnetite clusters, but rather occur as elongated inclusions in pyroxene grains, and their orientation is crystallographically controlled. One possible connection between this orientation and deformation is suggested by Kolle and Blacic (1982), who show that clinopyroxene can respond to stress by mechanical twinning on (100) planes. If serpentinization occurs initially along these deformationally defined planes, it would then lead to a magnetic fabric defined by the magnetite precipitated along the planes.

The results of these studies are consistent with those of plutonic rocks recovered on DSDP Legs 37 and 45 (e.g., Dunlop and Prevót, 1982). We do not see any highly magnetized gabbros, but this may well be a sampling artifact. The peridotites are also generally similar. No weakly magnetized samples were found but, again, this may be due to insufficient sampling. Davis (1981) suggested magnetite inclusions in plagioclase as a major contributor to gabbro remanence. These were seen in only one of the our Leg 82 gabbros, indicating that other factors must also be important.

As the magnetic properties of these samples are controlled by alteration, what we see may simply reflect the peculiarities of the tectonic and chemical environment that placed them so close to the surface, making comparison to ophiolite studies questionable (e.g., Banerjee, 1980). With that caveat, the magnetic properties of the gabbros are comparable to the high level gabbros of the Samail ophiolite (Luyendyk and Day, 1982) and the greenschist facies gabbros of the Bay of Islands ophiolite (Swift and Johnson, 1984). The peridotites are comparable with the more strongly magnetized ophiolite samples.

To the extent that these samples may be representative of the deep crust, neither type would probably contribute much to magnetic anomalies. The gabbros are simply too weakly magnetized. The peridotites are strongly magnetized but their low stability and small Q make them marginal candidates at best.

SUMMARY

1. The NRM of these samples seems to be primarily chemical in origin and controlled by the degree to which the samples are serpentinized. Generally, gabbros have lower J_N than ultramafics but there is some overlap.

2. There is considerable variation in both magnetic properties and mineralogy/petrology, even for closely spaced samples. This suggests some combination of source heterogeneity, tectonics, and alteration during and after emplacement. The relation of these rocks to those of the deep crust is thus problematic.

3. The samples show a significant susceptibility anisotropy, at least in a vertical plane, which appears to be related to the deformation of the rocks.

4. The samples generally are comparable both to previous DSDP studies and to ophiolite studies. However, the uncertain relation of the samples to their source makes such comparisons somewhat speculative.

ACKNOWLEDGMENTS

We would like to thank Wendy Tormanen and Yvonne Meeks for their assistance with some of the measurements. Valuable assistance was also rendered on many occasions by Jim Marvin. We would also like to thank our reviewers, S. Beske-Diehl, B. Moskowitz, and R. Merrill, for many helpful comments and criticisms. This work was performed under NSF Grants OCE-8018692 and OCE-8214652; it is publication Number 1064 of the School of Earth Science, Department of Geology and Geophysics, University of Minnesota.

REFERENCES

Banerjee, S. K., 1980. Magnetism of the ocean crust—evidence from ophiolite complexes. *J. Geophys. Res.*, 85:3557–3566.

Davis, K. E., 1981. Magnetic rods in plagioclase as the primary carrier of stable NRM in ocean floor gabbros. *Earth Planet. Sci. Lett.*, 55:190–198.

Dunlop, D. J., and Prevót, M., 1982. Magnetic properties and opaque mineralogy of drilled submarine intrusive rocks. *Geophys. J. R. Astron. Soc.*, 69:763–802.

Kolle, J. J., and Blacic, J. D., 1982. Deformation of single crystal clinopyroxene, 1, Mechanical twinning of diopside and hedenbergite. *J. Geophys. Res.*, 87:4019–4034.

Luyendyk, B. P., and Day, R., 1982. Paleomagnetism of the Samail ophiolite, Oman, 2, The Wadi Kadir gabbro section. *J. Geophys. Res.*, 84:10,903–10,917.

Swift, B. A., and Johnson, H. P., 1984. Magnetic properties of the Bay of Islands ophiolite suite and implications for the magnetization of the ocean crust. *J. Geophys. Res.*, 89:3291–3308.

Date of Initial Receipt: 28 October 1983
Date of Acceptance: 31 January 1984

18. MAGNETOSTRATIGRAPHY OF OLIGOCENE TO PLEISTOCENE SEDIMENTS, SITES 558 AND 563[1]

M. Javed Khan, D. V. Kent, and K. G. Miller, Lamont-Doherty Geological Observatory[2]

ABSTRACT

Integrated magnetostratigraphic and biostratigraphic studies of DSDP Sites 563 and 558 (western North Atlantic) show that, except for a short (~2 Ma) early Miocene hiatus, deposition was continuous from time of seafloor formation (Site 563, between Anomalies 12 and 13; Site 558, between Anomalies 13 and 15) through the Miocene at both sites. Several biostratigraphic datum levels, which have been correlated firmly with magnetic polarity chrons elsewhere, allow correlation of the magnetostratigraphy with the geomagnetic polarity time scale. Based upon that calibration, sediment accumulation rates were low to moderate (< 10 m/Ma) in the Oligocene-early Miocene and higher (> 10 m/Ma) in the middle-late Miocene after a short hiatus (Chron C5E is missing at both sites).

The established magnetochronology is used to make direct magnetobiostratigraphic correlations. For the Oligocene-lower Miocene samples, these correlations agree well with previously published first-order correlations. However, our correlations differ from the earlier indirect middle to upper Miocene correlations. In particular, indirect methods were previously used to correlate magnetostratigraphic Chron 11 (= Zone NN9) with marine Anomaly 5A (Chron C5AN). However, Zone NN9 (= Chron 11) and associated Zone N16 occur in a long normal interval at Sites 563 and 558 that best correlates with marine magnetic Anomaly 5. This reassignment (Chron 11 = Anomaly 5 = Chron C5N) requires an approximately 1.5-2 Ma upward shift in nannofossil zonal boundaries NN7/NN8 through NN10/NN11. The stratotype lower upper Miocene (Tortonian) is biostratigraphically linked with Zones NN9-NN11. Because Zone NN9 occurs in magnetic Anomaly 5 correlative (Chron C5N), the middle-upper Miocene boundary (basal Tortonian) is probably near the base of Chron C5N, with an estimated magnetochronologic age of 10.4 Ma.

INTRODUCTION

Recent magnetostratigraphic studies of deep-sea sediments recovered by DSDP (e.g., Kent and Spariosu, 1983; Tauxe et al., 1983; Ogg, 1983) have demonstrated the potential of paleomagnetic techniques for precise stratigraphic control, encouraging further efforts. Such studies greatly improve chronostratigraphic correlation of deep-sea sediments. Biostratigraphy may be correlated with magnetostratigraphy and therefore related to the polarity time scale, providing numerical age limits for biozonal boundaries. A complete stratigraphic sequence suitable for magnetostratigraphic studies has not been recovered often by DSDP because of the problems associated with rotary drilling of soft sediments and the punctuation of the stratigraphic record by numerous hiatuses. Since the advent of hydraulic piston coring (HPC) techniques, most of the stratigraphic sequence can be cored without much sediment disturbance even though HPC has its own limitations and cannot penetrate the deeper and more compact sediments. With this in mind, we attempted to core the sediments of the western North Atlantic on Leg 82 using HPC to the maximum possible extent, and then to core the more consolidated sediments to basement using conventional rotary drilling techniques. Unfortunately, because of time constraints, HPC techniques were used to core only one hole, 558A, and rotary drilling was used to core the sequence of sediments at Holes 558 and 563, after the holes were washed through approximately the upper 150 m of soft sediment.

On-board paleomagnetic studies of these sediments are based on samples collected at 25 to 40 cm intervals and are also confined to the stratigraphic sequence where remanent magnetization was above the noise level of the shipboard Digico spinner magnetometer. More extensive sampling, with intervals of 10 to 40 cm, was done for shore-based studies. Because various degrees of drilling disturbance of the sediment are indicated in the coring logs, sampling was restricted to those portions of the cores that appeared to be more cohesive and less likely to have been adversely affected by the drilling procedures. Even with this attempt to obtain the best material for study, it is difficult to avoid completely the effects of drilling disturbance in the rotary cored sections, and they undoubtedly contribute to the overall scatter of the measured remanent inclinations. Combined with coring gaps and the absence of reliable paleomagnetic data in severely disturbed intervals, these problems add an undesirable but unavoidable element of uncertainty to the interpretation of the magnetic polarity record, particularly in the Miocene where the reversal frequency is high. Nevertheless, we found it possible to construct a provisional magnetobiostratigraphic framework of reasonable resolution at Sites 558 and 563 that is consistent within and between the sites; the more tentative correlations caused by poor or ambiguous data are indicated in the description of the sites below.

---

[1] Bougault, H., Cande, S. C., et al., *Init. Repts. DSDP*, 82: Washington (U.S. Govt. Printing Office).

[2] Addresses: (Khan, present address) Department of Geology, Peshawar University, Peshawar, Pakistan; (Kent and Miller) Lamont-Doherty Geological Observatory, Columbia University, Palisades, New York 10964.

METHODS

Natural remanent magnetization (NRM) of all samples was measured using a Digico spinner magnetometer for on-board studies and a ScT two-axis cryogenic magnetometer for shore-based studies. After measuring the NRM, a few samples were selected for progressive alternating field (AF) demagnetization to observe the stability of remanent magnetization. These samples were subjected to AF treatment generally to 30 mT in intervals of 2.5 to 5 mT; selected samples were subjected to AF treatment up to 80 mT. Remanent magnetization was measured after each step of demagnetization.

Typical results of these progressive AF demagnetizations are shown in Figure 1. These results suggest that the remanent magnetization of many of these samples is a composite of a low coercivity component of magnetization that, in most of the samples, is removed by AF treatment of 5 to 10 mT, and a more stable component of magnetization that is isolated after 10-mT treatment. The low coercivity component usually has a downward inclination and may represent a viscous remanence acquired in the present-day magnetic field. Removal of this secondary magnetization reveals a more stable component of magnetization that only decreases in intensity with further AF treatment. This higher coercivity component is considered to represent the original remanent magnetization acquired during the process of deposition of these sediments. All remaining samples were therefore subject to blanket demagnetization at 10 mT, although in some cases they were further subjected to 15-to-20-mT treatments to isolate this more stable component of magnetization. After AF demagnetization, the magnetic polarity of many samples became reversed; magnetostratigraphic study of the sediment sections without demagnetization would have resulted in predominantly normal polarity because of overprinting by secondary magnetization.

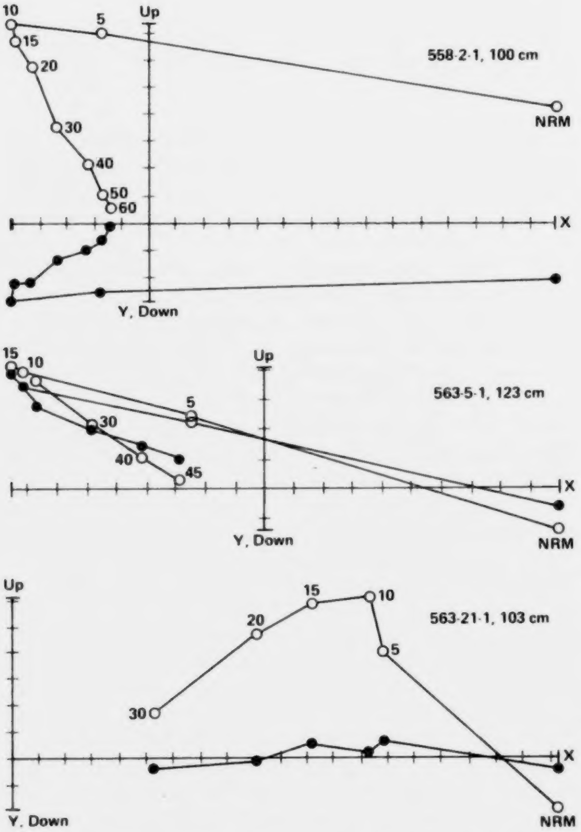

Figure 1. Orthogonal projection diagrams of alternating field demagnetization of the natural remanent magnetization of some representative samples from Holes 558 and 563. Open circles depict projection of remanence vector endpoints on vertical planes; closed circles depict projection of remanence vector endpoints on azimuthally unoriented horizontal planes. Magnetization units on axis in 5 × 10^{-4} A/m; demagnetization levels indicated in m/T.

Cores are nonoriented in the horizontal, and declinations are consequently not generally useful in determining polarity. Therefore, the values of remanent magnetization inclination after magnetic cleaning are used to establish magnetic polarity stratigraphy. Because all of the drilled holes are located in the northern hemisphere, positive (negative) inclination values are assigned normal (reversed) magnetic polarity. Because of the relatively small amount of apparent polar wander since the early Tertiary documented for the North America plate (Irving and Irving, 1982) on which Sites 558 and 563 are located, the Oligocene to Recent sediments are expected to record inclinations comparable to modern dipole field inclinations of 57° (Site 558) and 53° (Site 563). The stable inclination values are plotted stratigraphically, and a magnetic polarity reversal sequence is established (Figs. 2–4). Based on various age constraints, an attempt is made to correlate the observed normal and reversed magnetozones with the age-calibrated geomagnetic polarity time scale (Fig. 2) of Berggren, Kent, and, Flynn (in press) and Berggren, Kent, and Van Couvering (in press) as described below for each hole.

HOLE 558

The geophysical survey (see site chapter, this volume) showed that Site 558 is located between marine magnetic Anomalies 13 and 15, but is closer to magnetic Anomaly 13. According to the geomagnetic polarity time scale of Berggren, Kent, and Flynn (in press), the younger end of Anomaly 15 is assigned an age of 37.24 Ma. Based upon the position of the site relative to identified Anomalies 13 and 15, Site 558 is estimated to be located on ocean crust not older than 36.5 Ma, providing a maximum age for the overlying sediments. Preliminary biostratigraphic work suggests assignment of basal sediments to nannofossil Zone CP16a/b (Parker et al., this volume) and planktonic foraminiferal Zone P18 (Echols, this volume). According to numerical age estimates for these biostratigraphic zones (Berggren, Kent, and Flynn, in press), these data suggest that deposition began shortly (approximately <1 Ma) after seafloor formation. Based upon this corroborated bottom-hole age, the observed magnetic polarity reversal sequence is correlated with the geomagnetic polarity time scale (Fig. 3). The validity of the magnetostratigraphic correlation is indicated by the ease with which the observed magnetic polarity reversal sequence can be correlated with the standard geomagnetic polarity sequence (Fig. 2) and is further strengthened by the following biostratigraphic data.

1. The last occurrence (= LO) of *Pseudohastigerina* spp. occurs between 558-26-1, 93 cm and 558-25-4, 85 cm within a reversed magnetozone correlated with marine magnetic Anomaly 12 (= Magnetochron C12R, chron terminology of LaBrecque et al., 1983; Berggren, Kent, and Flynn, in press) in agreement with magnetobiostratigraphic correlations elsewhere (Berggren et al., 1983).
2. The LO of *Chiloguembelina* spp. occurs within a normal interval correlated with magnetochron C10N (Core 558-22), in close agreement with the results from Legs 72 (Pujol, 1983) and 73 (Poore et al., 1983). The last occurrence of this taxon can be used to recognize the lower/upper Oligocene boundary (Berggren, Kent, and Flynn, in press). Together with the bottom-hole age estimate,

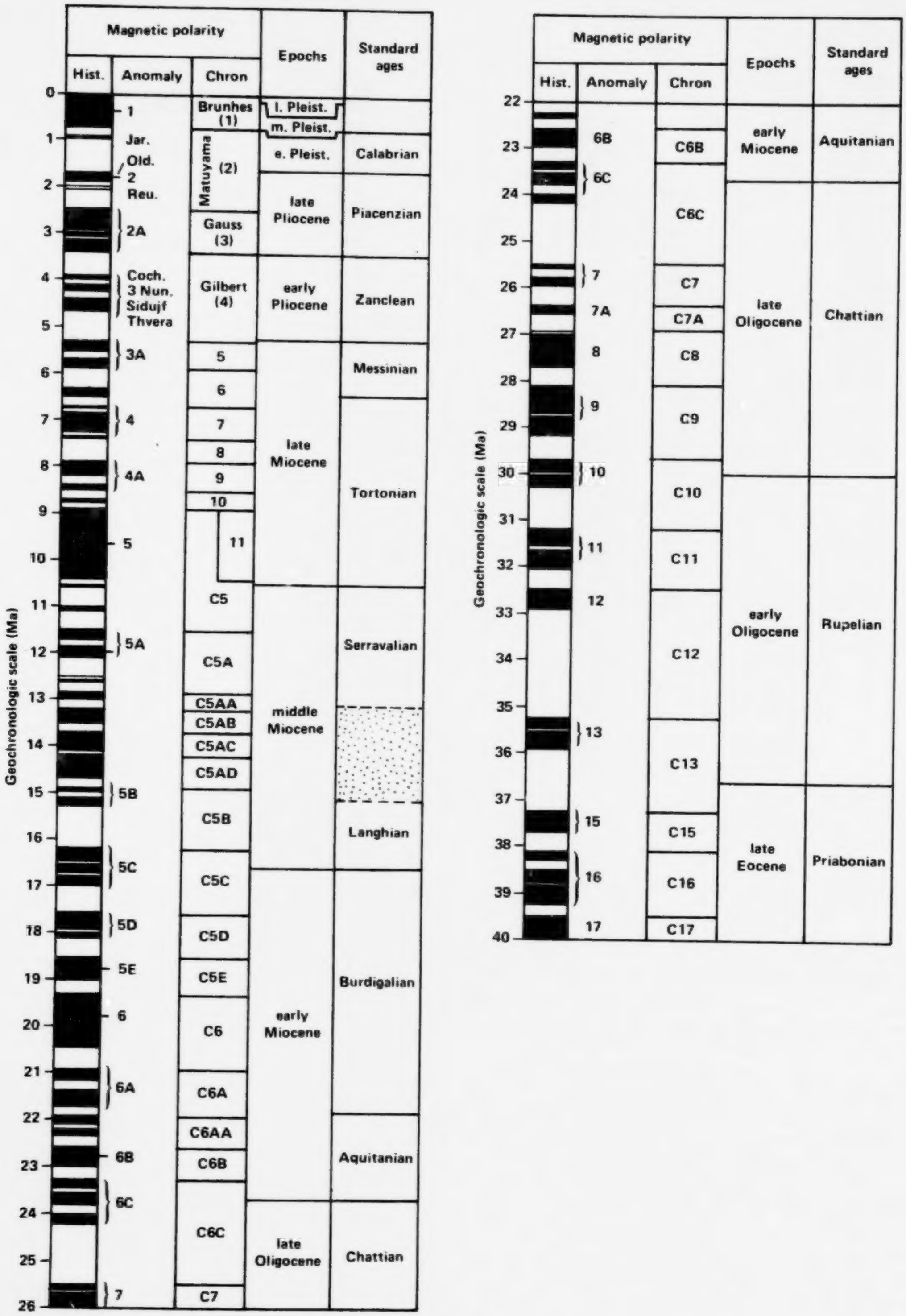

Figure 2. Geomagnetic polarity and geologic time scale from Berggren, Kent, and Flynn, in press; and Berggren, Kent, and Van Couvering, in press. In History (Hist.) column, normal is indicated by black, reversed by white. Jar. = Jaramillo; Old. = Olduvai; Reu. = Reunion; Coch. = Cochiti; Nun. = Nunivak.

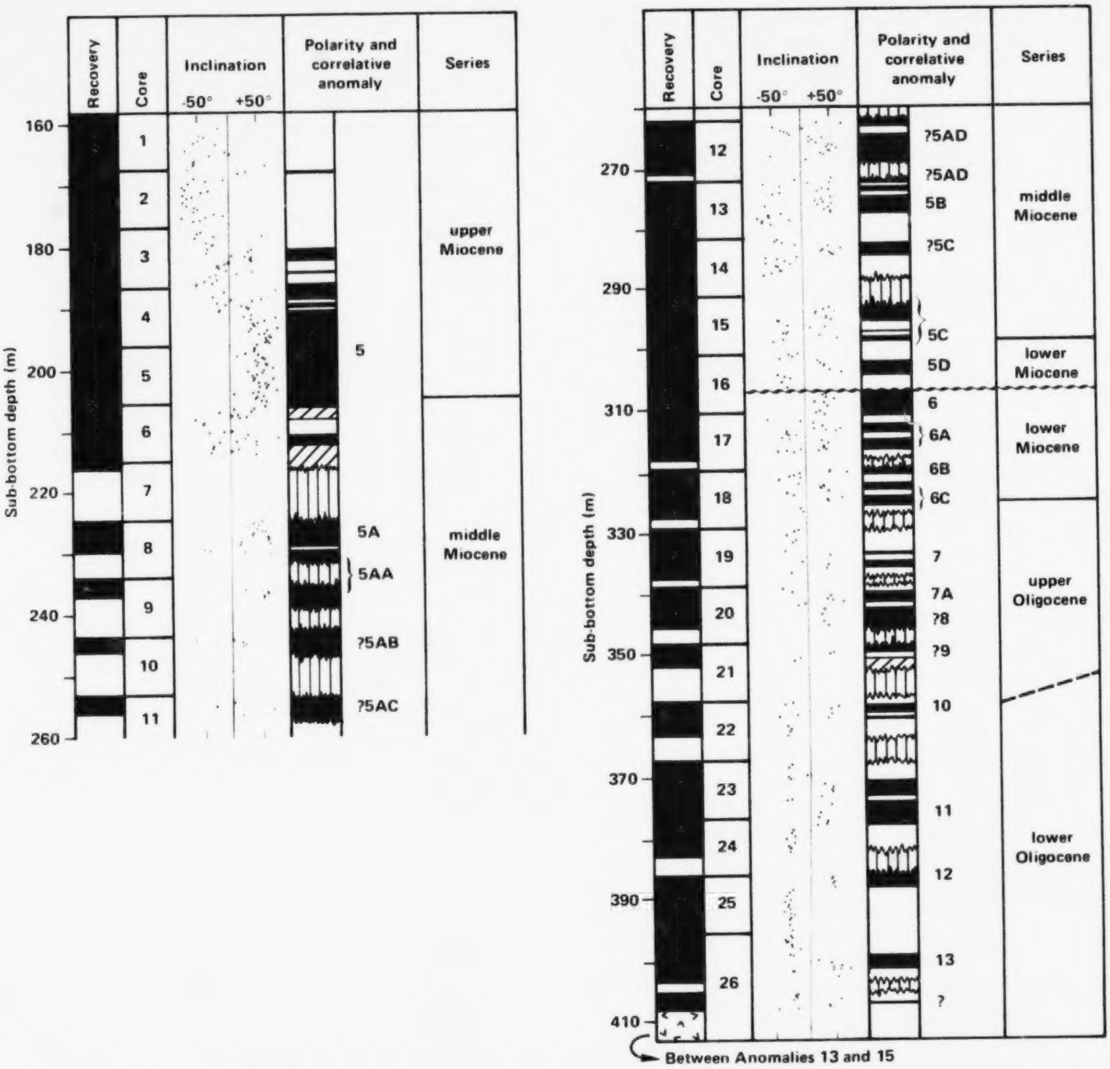

Figure 3. Interpretation of magnetic polarity stratigraphy for Hole 558. Columns from left to right show: portions of cores recovered (black); the sample remanent inclinations after partial alternating field demagnetization; and polarity magnetozones: normal (black), reversed (white), indeterminate (hatched), and broken (where no samples were available). Correlation of magnetozone to geomagnetic polarity time scale (using marine magnetic anomaly nomenclature, see Fig. 2) and to geologic subdivisions according to biostratigraphic constraints discussed in text. Note hiatus inferred in Core 558-16 and shown by wavy line. Vertical lines in polarity column indicate no data.

this consistency lends credence to the lower Oligocene (Core 558-22 to base of hole) magnetostratigraphic correlations made here.

3. Definite *Globorotalia kugleri* is observed in the lower part of Core 558-18 in association with the lower of two normals correlated with marine magnetic Anomaly 6C (Chron 6CN). This first occurrence (= FO) is quite consistent with correlations compiled by Berggren, Kent, and Flynn (in press) and supports the magnetostratigraphic correlations of the upper Oligocene (lower Core 558-18 to upper Core 558-22).

4. Nannofossils indicate the absence of Zone NN3 and most of Zone NN2 (M.-P. Aubry, pers. comm., 1984). A hiatus is therefore inferred for the time interval of Chrons C5E and possibly C5D; C5D or C5C (upper Core 558-169) therefore appears to be immediately above Chron C6 (lower Core 558-16). We suggest that Chron C5D is represented above Chron C6; this is supported by the LO of *Catapsydrax dissimilis* and the FO of *Globoratalia praescitula* in Sections 558-16-3 and 558-16-5, respectively; these datum levels have been reported as occurring in Chron C5D by Berggren, Kent, and Van Couvering (in press).

5. The FO of *Orbulina* spp. in Core 558-14 is associated with the lower part of a normal interval interpreted as C5BN; this is in excellent agreement with the correlations at Site 563 (this study) and Site 521 (Poore et al., 1983).

6. *Globigerina nepenthes* first appears in Core 558-7 above a level of poor recovery (Cores 558-7 through 558-11) and therefore of questionable magnetostratigraphic value. This poorly recovered section may, however, be correlated with the interval of Chrons C5AN to C5ADN. A long normal polarity magnetozone noted in Cores 558-4 to 558-6 (approximately 190 to 205 m sub-bottom) should therefore correspond to the prominent long interval of normal geomagnetic polarity represented by marine magnetic Anomaly 5. Here and at Site 563 (see below), this Anomaly 5 correlative is found to be associated with Zone NN9 (M.-P. Aubry, pers. comm., 1984), whereas the FO of *Neogloboquadrina acostaensis* occurs at the base of this normal magnetozone (Sample 558-5-5, 110–115 cm). These correlations at Sites 558 and 563 suggest that Anomaly 5 is equivalent to the magnetostratigraphic Chron 11 of Foster and Opdyke (1970) and is not equivalent to Chron 9 as suggested by Theyer and Hammond (1974) and Ryan et al. (1974) (see further discussion in Hole 563 section and in Miller et al., in press; Berggren, Kent, and Van Couvering, in press).

HOLE 558A

Hole 558A was piston cored to recover the upper part of the sediment section because Hole 558 was washed to 158 m sub-bottom. However, because of technical problems, Hole 558A was cored only to a depth of 132 m and an overlapping stratigraphic sequence was not cored. The observed magnetic polarity reversal sequence of Hole 558A is shown in Figure 4. The magnetostratigraphic correlation is limited by preliminary shipboard biostratigraphic data (site report, Site 558; Parker et al.; and Echols, all this volume).

The downcore normal-to-reversed polarity change at 14 m can be correlated to the Brunhes/Matuyama boundary and the normal polarity interval between 16.2 and 19.8 m to the Jaramillo Subchron. A short magnetozone present below the Jaramillo (at ~22.5 m) has also been detected elsewhere—for example, in the Siwalik group rocks of Pakistan (Khan and Opdyke, 1981); Site 502 (Kent and Spariosu, 1983); and Hole 552A (Shackleton et al., 1984). This magnetozone is correlated with the 1.1 Ma Cobb Mt. Subchron reported by Mankinen et al. (1978). Where recovered, the sediment sequence form 22.5 to 61.7 m has dominantly reversed polarity and probably represents the Matuyama Chron. An exception is the upper two sections of Core 558A-5 (29 to 32 m) with positive but scattered inclinations that may either represent the Olduvai Normal Subchron or, more likely, secondary magnetic overprints associated with core disturbance. If the latter is accepted, the Olduvai is not detected in this hole. The normal polarity intervals between 61.5 and 65 m and between 70 and 71.5 m presumably record part of the Gauss Normal Chron. Complicating magnetostratigraphic correlation below Core 558A-9 is the presence of an apparent hiatus within the lower Pliocene indicated by the calcareous nannoplankton stratigraphy (Parker et al., this volume). Most, if not all, of the Gilbert Chron may therefore be missing; Core 558A-10 contains Miocene (pre-Gilbert) sediments. The magnetic polarity zonation below Core 558A-9 cannot be interpreted until further biostratigraphic studies are finished.

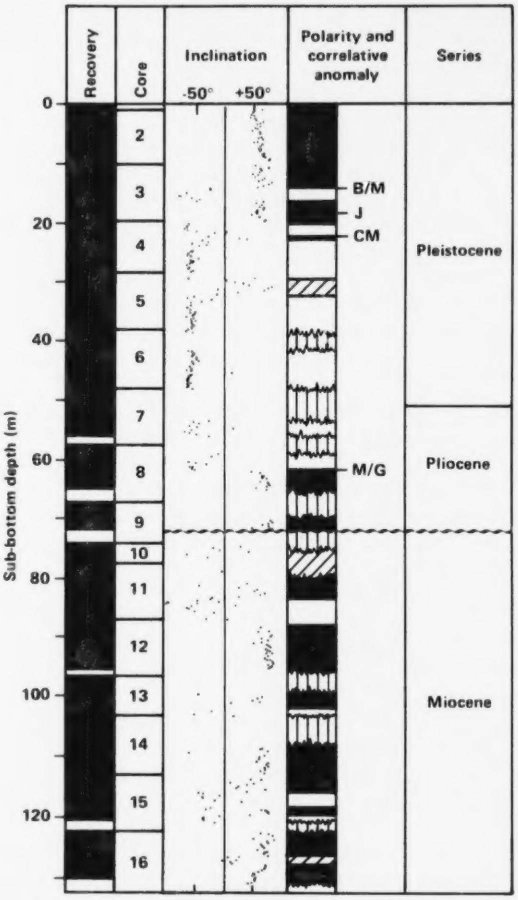

Figure 4. Magnetic polarity stratigraphy for Hole 558A. See Fig. 3 for explanation of columns, except for magnetozone correlation (B/M = Brunhes/Matuyama, J = Jaramillo, CM = Cobb Mt., and M/G = Matuyama/Gauss chrons, boundaries, or subchrons). Geologic subdivisions from preliminary biostratigraphy (Parker et al., this volume); note hiatus inferred near base of Core 558A-9. Vertical lines in polarity column indicate no data.

HOLE 563

According to the geophysical survey (site report, Site 563; Cande et al., both this volume), Site 563 is located between magnetic Anomalies 12 and 13, very close to magnetic Anomaly 13. The geomagnetic polarity time scale of Berggren, Kent, and Flynn et al. (in press) suggests that the younger end of magnetic Anomaly 13 is 35.29 Ma old, which provides a maximum age for the ocean crust and overlying sediments cored at Hole 563. Therefore, the long reversed polarity magnetozone observed in the basal part of the magnetic polarity reversal sequence established for this hole is correlated with Chron C12R. This interpretation agrees closely with biostratigraphic studies showing that the basal part of the sediments from this hole belongs to Zone NP21 and to Zone P18 (Parker et al., this volume, Echols, this volume; Miller and Fairbanks, 1983; Miller et al., in press). Extrapolation of sediment accumulation rates between biostratigraphic datums (Miller and Fairbanks, 1983), together with the assignment to Zone NP21, suggests that basal sediment ages should be older than 34.5 Ma. Sedimentation apparently began a short time (estimated as less than 0.8 Ma) after crustal formation, suggesting that bottom-hole ages are good indicators of crust age.

When the basal magnetostratigraphy has been established, the rest of the observed magnetic polarity reversal sequence can be correlated with the magnetic polarity time scale shown in Figure 5. These magnetostratigraphic assignments are supported by the following biostratigraphic correlations (see also Miller and Fairbanks, 1983; Miller et al., in press).

1. The LO of *Pseudohastigerina* spp. occurs in the base of Core 563-21, in a reversed polarity interval interpreted as Chron C12R. This observation is consistent with the fact that the last appearance datum (= LAD) of *Pseudohastigerina* spp. occurs between the correlatives of magnetic Anomalies 12 and 13 at other locations (Berggren, Kent, and Flynn, in press).

2. The LO of *Chiloguembelina* spp. occurs between 563-19-1, 12 cm and 563-18-5, 23 cm and should coincide with the middle of Chron C10N (Berggren et al., 1983). Chrons C10 and C11 are not observed at Site 563 because of poor recovery and the lack of suitable paleomagnetic samples from Core 563-19 and part of Core 563-18. Nevertheless, this LO can be used to indicate that the normal polarity interval found in Core 563-18 and the lower part of Core 563-17 is younger than Chron C10.

3. The LO of *Globorotalia opima opima*, associated with the younger part of Chron C9 (Berggren et al., 1983), occurs in Section 563-18-1. This supports the interpretation of the normal polarity interval in Cores 563-17 and 563-18 as formed by the concatenation of Chrons C8N and C9N, because Section 563-18-1 forms the middle part of this normal polarity interval.

4. The FO of *Globorotalia kugleri*, correlated elsewhere with Chron C6C (Berggren et al., 1983; Site 558 section of this chapter), occurs in the uppermost part of Core 563-16 in association with the lower of two normal intervals indentified here as correlative with Anomaly 6C. This assignment is also supported by the observation that the FO of *Globoquadrina dehiscens* occurs between 563-15-5, 117 cm and 563-15-2, 117 cm (the stratigraphic interval correlated with Chron C6BR). This agrees with the observation that the FO of *G. dehiscens* occurs in the older part of Chron 6B (Berggren et al., 1983). A similar correlation of *G. dehiscens* and Chron C6BR occurs at Sites 558 (this study), 522 (Poore et al., 1983), and 516 (Berggren et al., 1983). The correlation of the Oligocene/Miocene boundary, as recognized by the FO of *Globorotalia kugleri* (Berggren, Kent, and Flynn, in press; Berggren, Kent, and Van Couvering, in press) or the FO of *Globoquadrina dehiscens* (Kennett and Srinivasan, 1983) can thus be very closely associated with marine magnetic Anomaly 6C, which is equivalent at both Sites 563 and 558.

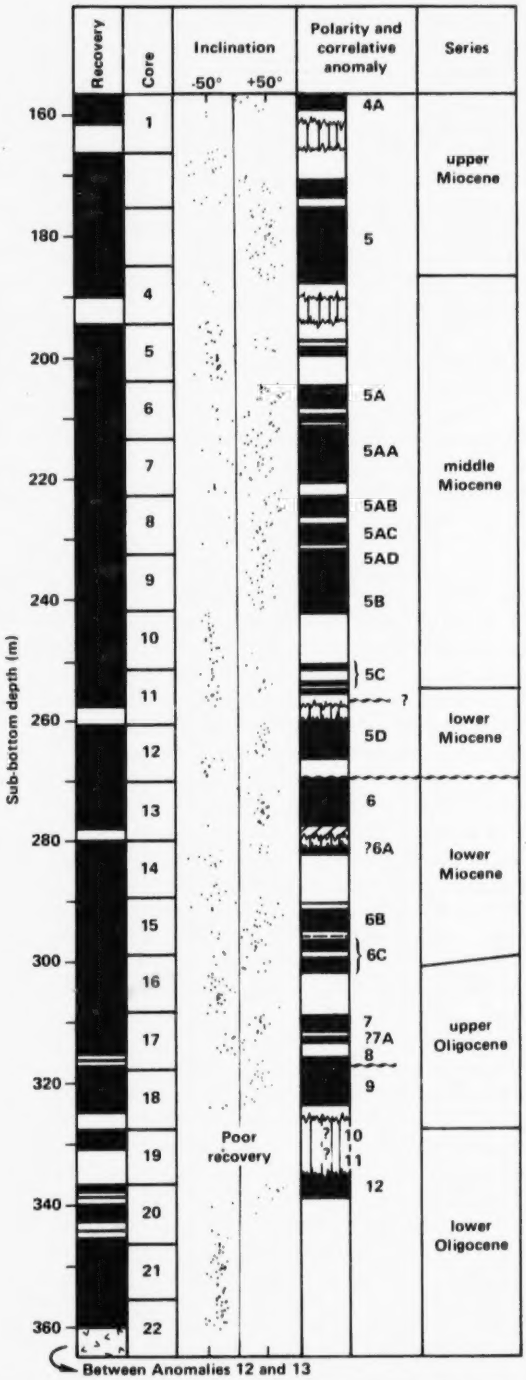

Figure 5. Interpretation of magnetic polarity stratigraphy for Hole 563. See Fig. 3 for explanation for columns. Note hiatus (wavy line) inferred near base of Core 563-12. Vertical lines in polarity column indicate no data.

5. As at Site 558, some section or sections are missing in the lower Miocene. The unconformity is difficult to place (either between Cores 563-12 and 563-13 or near the base of Core 563-11 or possibly at both levels), and the magnetostratigraphy in this interval is therefore uncertain. However, nannofossil Zone NN3 is apparently absent between Cores 563-12 and 563-13 (M.-P. Aubry, pers. comm., 1984), resulting in an unconformity at this level. This suggests that the hiatus represents the time between Chrons C6N and C5D to possibly C5CR (at least C5E was removed (approximately 1 Ma; age range, 18-19 Ma). This interpretation results in similar hiatuses at both Sites 558 and 563 and also is supported by the similarity in magnetic pattern and biostratigraphy above and below the unconformity at both sites. Chron C5D may be represented in Core 563-12 above Chron 6. This is supported by the LO of *Catapsydrax dissimilis* in the reversed interval at the base of Core 563-11 and the FO of *Globorotolia praescitula* in the reversed interval at the base of Core 563-12; these datums have been associated with Chron C5DN at Site 516 (Berggren, Kent, and Van Couvering, in press). From the planktonic foraminiferal data, we deduce a short hiatus or condensed interval occurring between Chrons C5CN and C5DN (i.e., part of C5CR may be missing), because Zone N7 is very short or absent. (There is virtually no section between the LO of *C. dissimilis* and the FO of *Praeorbulina* spp.; A. Melillo, pers. comm. 1984).

6. The FO of *Orbulina* spp. (base of Core 563-9) occurs at the base of a normal magnetozone correlated with Anomaly 5B, in precise agreement with Sites 521 (Poore et al., 1983) and 558 (this study).

7. The FO *Globigerina nepenthes* occurs at the base of Core 563-5 just above a normal magnetozone that we correlate with Anomaly 5A. This is considered to be the first reliable first-order magnetobiostratigraphic correlation of this taxon.

8. The middle/upper Miocene boundary, based on the FO of *Neogloboquadrina acostaensis*, occurs at the top of Core 563-4 at the base of a long normal polarity magnetozone. This normal magnetozone most likely correlates with the long marine magnetic Anomaly 5 that Ryan et al. (1974) correlated with magnetostratigraphic Chron 9 at RC12-65. Nannofossil studies (M.-P. Aubry, pers. comm., 1984; Miller et al., in press) show that Zone NN9 occurs in the upper part of this long normal polarity magnetozone at Site 563. Yet, Zone NN9 has been found with Chron 11 at RC12-65 (Ryan et al., 1974). This suggests that Chron 11 is equivalent to marine magnetic Anomaly 5 or Chron C5N (Khan et al., 1984; Miller et al., in press; Berggren, Kent, and Van Couvering, in press).

CONCLUSIONS

Oligocene and lower Miocene direct magnetobiostratigraphic correlations at Sites 558 and 563 are in good agreement with those made elsewhere as noted above. Despite the various uncertainties in the interpretation of the magnetobiostratigraphic sequence (most importantly, those uncertainties caused by coring gaps and degradation of magnetic data by drilling disturbance), the records at Sites 558 and 563 are of special importance for refining previous indirect correlations in the middle and upper Miocene. Of particular significance is the documentation that magnetostratigraphic Chron 11 (= Zone NN9), rather than Chron 9, should be correlated with the normal polarity equivalent of marine magnetic Anomaly 5 or Chron C5N. According to magnetochronology, this reassignment necessitates an approximately 1.5-2 Ma upward shift in nannofossil zonal boundaries NN7/NN8 through NN10/NN11 (Khan et al., 1984; Miller et al., in press; Berggren, Kent, and Van Couvering, in press). The stratotype lower upper Miocene (Tortonian) is biostratigraphically linked with Zones NN9-NN11 (Martini, 1971). Because Zone NN9 occurs in the magnetic Anomaly 5 correlative (Chron C5N) at Site 563 and Hole 558 (M.-P. Aubry, pers. comm., 1984), the middle/upper Miocene boundary (basal Tortonian) will be above that previously estimated (Ryan et al., 1974). We estimate that the middle/upper Miocene boundary is associated with the base of Chron C5N, with a magnetochronologic age of about 10.4 Ma (see discussion in Berggren, Kent, and Van Couvering, in press).

We expect that these proposed realignments of magnetobiostratigraphic correlations will be corroborated in other Miocene sections. However, to avoid further confusion in magnetostratigraphic polarity nomenclature, we suggest that the chron terminology adapted from marine magnetic anomaly identification (Cox, 1982; LaBrecque et al., 1983) be used in future magnetostratigraphic work and that the magnetostratigraphic numbering scheme of Hays and Opdyke (1967), Theyer and Hammond (1974), and Opdyke et al. (1974) be avoided, at least for correlations older than Chron 11 (= Chron C5N).

ACKNOWLEDGMENTS

We thank M.-P. Aubry, W. A. Berggren, M. Clark, B. Clement, D. Echols, A. J. Melillo, R. K. Olsson, M. E. Parker, L. Tauxe, and S. S. Wise for discussions of the magnetobiostratigraphy of Sites 563 and 558; J. Ogg and S. Cande for comments on the manuscript; and A. Dragonovic for drafting the figures. This study was supported by NSF grant OCE83-10086 (KGM) and OCE83-00356 (DVK); it is LDGO Contribution No. 3657.

REFERENCES

Berggren, W. A., Aubry, M.-P., and Hamilton, N., 1983. Neogene magnetobiostratigraphy of Deep Sea Drilling Project Site 516 (Rio Grande Rise, South Atlantic). *In* Barker, P. F., Carlson, R. L., Johnson, D. A., et al., *Init. Repts. DSDP*, 72: Washington (U.S. Govt. Printing Office), 675-713.

Berggren, W. A., Kent, D. V., and Flynn, J. J., in press. Paleogene chronology and chronostratigraphy. *In* Snelling, N. J. (Ed.), *Geochronology and the Geologic Time Scale*: London (Geol. Soc. London Spec. Pap.).

Berggren, W. A., Kent, D. V., and Van Couvering, J. A., in press. Neogene chronology and chronostratigraphy. *In* Snelling, N. J. (Ed.), *Geochronology and the Geologic Time Scale*: London (Geol. Soc. London Spec. Pap.).

Cox, A., 1982. Magnetostratigraphic time scale. *In* Harland, W. B., Cox, A. V., Llewellyn, P. G., Pickton, C. A. G., Smith, A. G., and Walters, R. (Eds.), *A Geologic Time Scale*: New York (Cambridge University Press), pp. 63-84.

Foster, J. H., and Opdyke, N. D., 1970. Upper Miocene to Recent magnetic stratigraphy in deep-sea sediments. *J. Geophys. Res.*, 75: 4465-4473.

Hays, J. D., and Opdyke, N. D., 1967. Antarctic radiolaria, magnetic reversals and climatic change. *Science*, 158:1001–1011.

Irving, E., and Irving, G. A., 1982. Apparent polar wander paths, Carboniferous through Cenozoic and the assembly of Gondwana. *Geophys. Surv.*, 5:141–188.

Kennett, J. P., and Srinivasan, M. S., 1983. *Neogene Planktonic Foraminifera: A Phylogenetic Atlas*: Stroudsburg, Pennsylvania (Hutchinson and Ross).

Kent, D. V., and Spariosu, D. J., 1983. High resolution magnetostratigraphy of Caribbean Plio-Pleistocene deep-sea sediments. *Palaeogeogr., Palaeoclimatol., Palaeoecol.*, 42:47–64.

Khan, M. J., Miller, K. G., Kent, D. V., Aubry, M.-P., and Berggren, W. A., 1984. Oligocene-Miocene magnetobiostratigraphy of the Western North Atlantic: age of the middle/late Miocene boundary. *EOS, Trans. Am. Geophys. Union*, 65:199.

Khan, M. J., and Opdyke, N. D., 1981. The magnetic polarity stratigraphy and correlation of the upper Siwalik sediments from the Bhittani Range, North West Frontier Province, Pakistan. *Phys. Earth Planet. Inter.*, 24:133–141.

LaBrecque, J. L., Hsü, K. J., Carman, M. F., Jr., Karpoff. A.-M., McKenzie, J. A., Percival, S. F., Jr., Petersen, N. P., Pisciotto, K. A., Schreiber, E., Tauxe, L., Tucker, P., Weissert, H. J., and Wright, R., 1983. DSDP Leg 73: contributions to Paleogene stratigraphy in nomenclature, chronology and sedimentation rates. *Palaeogeogr., Palaeoclimatol., Palaeoecol.*, 42:42–125.

Mankinen, E. A., Donnelly, J. M., and Gromme, C. S., 1978. Geomagnetic polarity event recorded at 1.1 my BP on Cobb Mountain, Clear Lake volcanic field, California. *Geology*, 6:653–656.

Martini, E., 1971. Standard Tertiary and Quaternary calcareous nannoplankton zonation. *In* Farinacci, A. (Ed.), *Proc. II Plankt. Conf. Roma*: Rome (Edizioni Tecnoscienza), pp. 739–785

Miller, K. G., Aubry, M.-P., Khan, M. J., Melillo, A. J., Kent, D. V., and Berggren, W. A., in press. Oligocene-Miocene magneto-, bio-, and isotope stratigraphy of the western North Atlantic. *Geology*.

Miller, K. G., and Fairbanks, R. G., 1983. Evidence for Oligocene-middle Miocene abyssal circulation changes in the western North Atlantic. *Nature*, 306:250–253.

Ogg, J. G., 1983. Magnetostratigraphy of Upper Jurassic and Lowest Cretaceous sediments, Deep Sea Drilling Project Site 534, western North Atlantic. *In* Sheridan, R. E., Gradstein, F. M., et al., *Init. Repts. DSDP*, 76: Washington (U.S. Govt. Printing Office), 685–697.

Opdyke, N. D., Burckle, L. H., and Todd, A., 1974. The extension of the magnetic time scale in sediments of the Central Pacific Ocean. *Earth Planet. Sci. Lett.*, 22:300–306.

Poore, R. Z., Tauxe, L., Percival, S. F., Jr., LaBrecque, J. L., Wright, R., Petersen, N. P., Smith, C. C., Tucker, P., and Hsü, K. J., 1983. Late Cretaceous-Cenozoic magnetostratigraphic and biostratigraphic correlations of the South Atlantic Ocean: DSDP Leg 73. *Palaeogeogr., Palaeoclimatol., Palaeoecol.*, 42:127–149.

Pujol, C., 1983. Cenozoic planktonic foraminiferal biostratigraphy of the southwestern Atlantic (Rio Grande Rise): Deep Sea Drilling Project Leg 72. *In* Barker, P. F., Carlson, R. L., Johnson, D. A., et al., *Init. Repts. DSDP*, 72: Washington (U.S. Govt. Printing Office), 623–673.

Ryan, W. B. F., Cita, M. B., Rawson, M. D., Burckle, L. H., and Saito, T., 1974. A paleomagnetic assignment of Neogene stage boundaries and the development of the isochronous datum planes between the Mediterranean, the Pacific and Indian Oceans in order to investigate the response of the World Ocean to the Mediterranean "salinity crisis." *Riv. Ital. Paleont.*, 80:631–688.

Shackleton, N. J., Backman, J., Zimmerman, H., Kent, D. V., Hall, M. A., Roberts, D. G., Schnitker, D., Baldauf, J. G., Desprairies, A., Homrighausen, R., Huddlestun, P., Keene, J. B., Kaltenback, A .J., Drumsiek, K. A. O., Morton, A. C., Murray J. W., and Westberg-Smith, J., 1984. Oxygen isotope calibration of the onset of icerafting in DSDP Site 552A: history of glaciation in the North Atlantic Region. *Nature*, 307:p620–623.

Tauxe, L., Tucker, P., Petersen, N. P., and LaBrecque, J. L., 1983. The magnetostratigraphy of Leg 73 sediments. *Palaeogeogr., Palaeoclimatol., Palaeoecol.*, 42:65–90.

Theyer, F., and Hammond, S. R., 1974. Paleomagnetic polarity sequence and radiolarian zones, Brunhes to Polarity Epoch 20. *Earth Planet. Sci. Lett.*, 22:307–319

Date of Initial Receipt: 7 May 1984
Date of Acceptance: 28 June 1984

PART IV: PETROLOGY, MINERALOGY, AND GEOCHEMISTRY

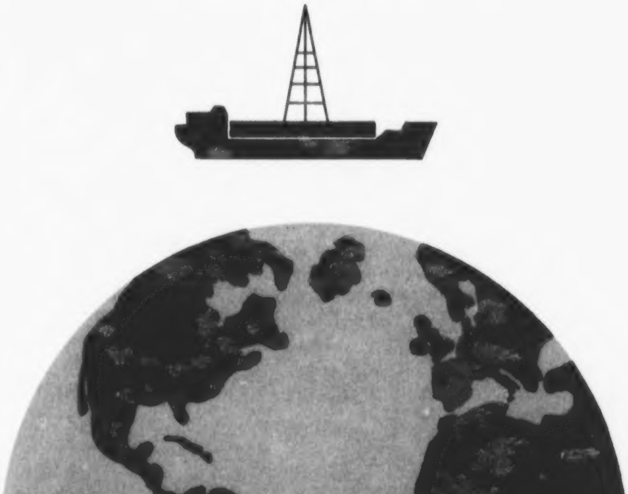

19. GEOCHEMISTRY AND MINERALOGY OF BASALTS RECOVERED FROM THE CENTRAL NORTH ATLANTIC[1]

Barry L. Weaver, John Tarney, Department of Geology, University of Leicester,
and
Andrew D. Saunders, Department of Geology, Bedford College[2]

ABSTRACT

DSDP Leg 82 drilled nine sites to the southwest of the Azores Islands on the west flank of the Mid-Atlantic Ridge (MAR) in an attempt to determine the temporal and spatial evolution of the Azores "hot-spot" activity. The chemistry of the basalts recovered during Leg 82 is extremely varied: in Holes 558 and 561, both enriched (E-type: Ce_N/Yb_N = 1.5 to 2.7; Zr/Nb = 4.5 to 9.6) and depleted (or normal-N-type: Ce_N/Yb_N = 0.6 to 0.8; Zr/Nb > 20) mid-ocean ridge basalts (MORB) occur as intercalated lava flows. To the north of the Hayes Fracture Zone, there is little apparent systematic relationship between basalt chemistry and geographic position. However, to the south of the Hayes Fracture Zone, the chemical character of the basalts (N-type MORB) is more uniform.

The coexistence of both E-type and N-type MORB in one hole may be explicable in terms of either complex melting/fractionation processes during basalt genesis or chemically heterogeneous mantle sources. Significant variation in the ratios of strongly incompatible trace elements (e.g., La/Ta; Th/Ta) in the basalts of Holes 558 and 561 are not easily explicable by processes such as dynamic partial melting or open system crystal fractionation. Rather, the trace element data require that the basalts are ultimately derived from at least two chemically distinct mantle sources.

The results from Leg 82 are equivocal in terms of the evolution of the Azores "hot spot," but would appear not to be compatible with a simple model of E-type MORB magmatism associated with upwelling mantle "blobs." Models that invoke a locally chemically heterogeneous mantle are best able to account for the small-scale variation in basalt chemistry.

INTRODUCTION

The nature of basaltic volcanism at mid-ocean ridges has been well studied in the North Atlantic. Extensive dredging along the axis of the Mid-Atlantic Ridge (MAR) (e.g., Schilling, 1973; White and Schilling, 1978; Bougault and Treuil, 1980; Sigurdsson, 1981) and drilling both near and off the ridge axis (accomplished during many previous DSDP legs) have demonstrated the chemical diversity of basalts that may be erupted at the MAR. Although much of the local variation may be attributable to the effects of physical processes operating during, or subsequent to, magma generation (Langmuir et al., 1977), critical chemical and isotopic features of erupted basalts require regionally heterogeneous mantle sources (White and Schilling, 1978; Wood, Joron, et al., 1979; Wood, Tarney, et al., 1979; Bougault et al., 1980). In the North Atlantic, basalts erupted at normal ridge segments typically display depletion in the light rare earth elements (LREE) and have low $^{87}Sr/^{86}Sr$ ratios (Hart, 1971; Schilling, 1971). These have been called normal (or N-type) mid-ocean ridge basalts (Tarney et al., 1980). At anomalous ridge segments, which have high heat flow and elevated topography, the erupted basalts are typically enriched in the LREE and have high $^{87}Sr/^{86}Sr$ ratios (Hart et al., 1973; White et al., 1976); these have been called enriched (E-type) MORB (Tarney et al., 1980). Examples of the former kind of ridge segment occur at 20–34°N and 49–59°N, whereas intervening ridge segments at 34–49°N (centered on the Azores platform) and north of 59°N (centered on Iceland) are examples of the latter type. The existence of geochemical gradients away from the topographic highs of Iceland and the Azores platform and towards normal ridge segments has been suggested by Schilling (1973; 1975) and White and Schilling (1978). Along these "transitional" ridge segments, the basalts appear to display progressively decreasing La/Sm and $^{87}Sr/^{86}Sr$ ratios away from the hot spots, often interpreted as a large-scale mixing feature between enriched and depleted mantle sources (White and Schilling, 1978; Schilling et al., 1980). However, an alternative model (Wood, Joron, et al., 1979; Tarney et al., 1980) ascribes the chemical variation in MORB to local heterogeneity of mantle source produced by veining of the mantle source of N-type MORB by an enriched component, which may be either an undersaturated melt or a metasomatic fluid.

In attempting to resolve the problem of the scale and causes of mantle heterogeneity in the North Atlantic, the nature of the basalts erupted at "transitional" ridge segments is of great importance. The MAR to the south of the Azores has been extensively studied, particularly in the vicinity of the FAMOUS area at 36°N, and a considerable data base now exists for basaltic basement recovered by dredging and submersibles (Arcyana, 1977) as well as drilling (DSDP Legs 37 and 49) operations in this region. Additionally, dredging of zero-age basalts from the ridge axis to the south of the Azores has indicated that the Hayes Fracture Zone (Fig. 1) appears to delineate an N-type MORB province to the south from

---

[1] Bougault, H., Cande, S. C., et al., *Init. Repts. DSDP*, 82: Washington (U.S. Govt. Printing Office).

[2] Addresses: (Weaver, present address) School of Geology and Geophysics, University of Oklahoma, Norman, Oklahoma 73019; (Tarney and Saunders, present address) Department of Geology, University of Leicester, Leicester LE1 7RH, England.

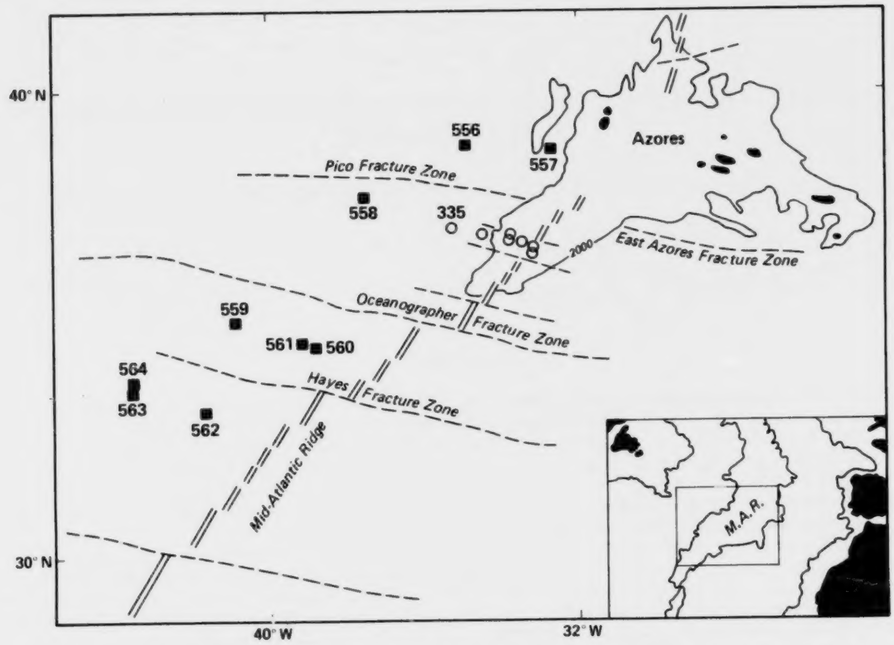

Figure 1. Map of part of the Central North Atlantic showing the location of DSDP Sites 556–564 drilled during Leg 82. Also shown is the location of Site 335 (Leg 37) and the sites drilled near the FAMOUS area during Legs 37 and 49 (open circles).

an E-type MORB province to the north (Bougault and Treuil, 1980). The objective of DSDP Leg 82 was to systematically sample basaltic basement from the west flank of the MAR to the south of the Azores, with the aim of defining the spatial and temporal development and influence of the Azores hot-spot activity. This was achieved by drilling at sites on crust of a particular age (~18 and 35 Ma) on the same mantle flow line and at a number of latitudes (Fig. 1). The most northerly pair of sites are on a flow line through the Azores Triple Junction, and the most southerly to the south of the Hayes Fracture Zone (Fig. 1). In all, Leg 82 drilled at nine sites in this portion of the North Atlantic; Site 335, drilled during Leg 37 on a flow line through the FAMOUS area, was used to complete the grid pattern of sites (Fig. 1).

ANALYTICAL TECHNIQUES

Seventy-two samples have been analyzed in the present study. The samples were selected on the basis of the chemical groups identified in each hole by the shipboard party. Thus the sampling density is greater in those holes that contain a number of chemical groups. Our new analyses largely confirm the chemical groups identified on board.

The samples were washed in distilled water and dried to remove surface contamination before crushing. The original minicores were then fly-pressed to produce small chips, and this material was ground to a fine powder (<240 mesh) in an agate Tema swing mill. Any obviously weathered or contaminated (e.g., calcite-filled fractures) material was removed before final crushing. However, in some cases, contamination from calcite-filled vesicles was unavoidable.

For trace element analysis, approximately 15 g of rock powder was mixed with a binder (an aqueous solution of polyvinyl alcohol) and pressed into 46 mm powder briquettes. For major element analysis, fusion beads were produced for all samples. The rock powders were heated at approximately 900°C for 1 hour and weight losses upon ignition were determined. Thus, the reported loss on ignition (LOI) also includes H_2O^-, of which no independent estimate was made. The ignited powder (0.9 g) was mixed with a lithium metaborate/lithium tetraborate flux (4.5 g) and fused in a vertical tube furnace at 1250°C. The glass melts were pressed into 46 mm diameter beads and then stored.

Major and trace element analyses were performed using a Philips PW1400 automatic X-ray fluorescence (XRF) spectrometer at the University of Leicester. The general XRF analytical technique employed has been detailed by Tarney et al. (1979), Marsh et al. (1980), and Weaver et al. (1983). These papers include data for international and internal reference standards by which the high accuracy and precision of the technique can be judged. The trace elements, Ni, Zn, Ga, Rb, Sr, Zr, Nb, and Y, were analyzed using a rhodium anode X-ray tube. Mass absorption corrections were applied using the intensity of the Rh K_α compton scatter line, and calibrations were compared to available international standard rocks. The remaining trace elements, Cr, V, Ba, La, Ce, and Nd, were analyzed using a tungsten anode X-ray tube. Calibrations were measured against basaltic international standards and other well-analyzed basalts. Major element abundances were determined using a rhodium anode X-ray tube calibrated against available international standards. Particular care was taken in the analysis of those petrogenetically important trace elements often present at low abundance levels in basalts. Specifically, very long count times were adopted in order to improve the precision and detection limits for the elements Nb, La, Ce, Nd, and Rb, for which the theoretical 3σ lower limits of detection are 0.7, 2, 4, 2, and 1 ppm, respectively.

In addition to the XRF analyses, the freshest sample from each chemical group was selected for analysis for the elements La, Ce, Nd, Sm, Eu, Gd, Tb, Tm, Yb, Lu, Th, Ta, and Hf by instrumental neutron activation analysis (INAA) techniques at Bedford College, London. Full details of the analytical procedure have been given by Saunders (1983). Only samples from Holes 556, 557, 558, and 561 were analyzed by INAA.

Selected mineral analyses were performed using the Cambridge Instruments Microscan V electron microscope, fitted with a Link Systems energy dispersive spectrometer, at the University of Leicester. Standard analytical procedure and full ZAF corrections were applied.

In general, one thin section from each chemical group was examined, and particular attention was paid to phenocryst compositions as a possible constraint upon crystallization processes.

In the following tables of whole-rock analyses, CIPW norms and Mg-values (100 Mg/[Mg + Fe^{2+}]) have been calculated using an assumed Fe_2O_3/FeO ratio of 0.15.

SITE 556

Site 556 (38°56.38′N; 34°41.12′W, 3672 m water depth) lies on Magnetic Anomaly 12 (34 Ma old) on the west flank of the Mid-Atlantic Ridge and is approximately 50 miles north of the Pico Fracture Zone on a flow line passing through the Azores Triple Junction (Fig. 1). A single hole was drilled at this site, and 178 m of basement (encountered at 461.5 m sub-bottom depth) was cored before bit failure. A total of nine lithologic units comprising five chemical groups were identified by the shipboard party. The upper 100 m of basement consists of basalt breccia, pillow basalts, and massive aphyric basalts. The lower 78 m of basement consists of mylonitized gabbro breccia, which includes a 1 m interval of aphyric basalt.

Group I basalts make up most of Lithologic Unit 2. The basalts of this group are aphyric but contain rare equant plagioclase phenocrysts (3–5 mm). These phenocrysts are zoned from core compositions of An_{88} to rim compositions of An_{75} (Table 1) and contain inclusions of magnesiochromite (Mg/[Mg + Fe^{2+}] = 0.66, Cr/Cr + Al = 0.49; Table 2) and melt (Mg-value ~68). Microphenocrysts of clinopyroxene (~0.5 mm) occur as scattered crystals and have high Mg-values (87) and Cr_2O_3 contents (0.64%) (Table 3). The groundmass has an intergranular texture and consists of 30–35 vol.% lath to acicular plagioclase (An_{72}; Table 1), approximately 40 vol.% fine-grained (0.1 mm) aggregates of clinopyroxene (Mg_{82}; Table 2) interstitial to the plagioclase, and approximately 5 vol.% olivine, 3 vol.% opaques, and 15 vol.% mesostasis.

Two samples were analyzed from this group (556-2-1, 77–79 cm and 556-2-2, 132–135 cm), and the data are presented in Table 4. In terms of the normative components Di-Ol-Hy (Fig. 2), the basalts are low in Ol and fall quite close to the Di-Hy join. The two analyses are very similar (Table 4), have notably high Mg-values (68–69), and very low levels of incompatible trace elements (e.g., TiO_2, Zr; Table 4), implying that these magmas are quite primitive. However, abundances of Ni and Cr are lower than anticipated in truly primitive melts, and these basalts must have undergone limited low-pressure crystal fractionation. The basalts of this group are depleted in the more-incompatible trace elements, as illustrated by the high Zr/Nb ratios (36–39; Table 4) and low Ce_N/Y_N ratios (0.4–0.5; Table 4), and are thus typical of rather unfractionated N-type MORB. Rare earth element (REE) data (Table 5) for one of these samples confirms the inferences from trace element data; this sample is strongly depleted in the LREE (Ce_N/Yb_N = 0.6; La_N/Sm_N = 0.4; Fig. 3), and has rather low abundances of the REE (Fig. 3).

Group II basalts make up the remainder of Lithologic Unit 2 and all of Unit 3. These basalts are sparsely to moderately plagioclase phyric, with approximately 2–5 vol.% of equant to prismatic plagioclase phenocrysts often occurring in glomerophyric clusters. The phenocrysts are zoned from core compositions of An_{87} to marginal compositions of An_{68} (Table 1) and contain melt inclusions. Euhedral olivine microphenocrysts (~5 vol.%) have a composition of Fo_{84} (Table 6). The intergranular to almost subophitic textured groundmass consists of approximately subequal (35–40 vol.%) amounts of swallowtail to narrow lath plagioclase (An_{70}; Table 1) and interstitial clinopyroxene. The mesostasis (~5–10 vol.%) is altered to clay.

Four samples were analyzed from this group (556-3-1, 57–60 cm; 556-3-2, 49–51 cm; 556-4-2, 65–68 cm; 556-6-4, 115–120 cm), and the data are presented in Table 4. Normatively, the basalts have small amounts of Ol, as in Group I, but a generally higher Hy/Di ratio (Fig. 2). The trend of increase in Ol and Di relative to Hy (Fig. 2) can be attributed to alteration; the two samples with high LOI and low Mg-values (Table 4) have higher Ol and lower Hy than the fresher material. These basalts are chemically more evolved than Group I basalts, having lower Mg-values (~60) and higher TiO_2 and Zr abundances (Figs. 4, 5), as well as somewhat lower Cr and much lower Ni (Table 4). There is some chemical heterogeneity within this group that cannot easily be a result of phenocryst dilution; for example, TiO_2 and Zr vary by approximately 0.1% and 8 ppm, respectively, and yet are not correlated with variation in Al_2O_3 or CaO, which would indicate dilution by plagioclase phenocrysts. Basalts of this group display a similar depletion in more incompatible trace elements (Zr/Nb, 28–40 (Fig. 3); Ce_N/Y_N, 0.5 to 0.6; Table 4) to basalts of Group I. This is illustrated by the REE data for the sample from this group (Table 5), which has a Ce_N/Yb_N ratio of 0.6 and a La_N/Sm_N ratio of 0.5 comparable to Group I but with greater abundances of the REE (Fig. 3).

Group III comprises Lithologic Units 4, 5, and 6. Much of this sequence is phyric, but some basalts are sparsely to moderately aphyric and scattered plagioclase phenocrysts are common. The phenocrysts range in composition from An_{84} (core) to An_{65} (rim) (Table 1) and contain melt inclusions with Mg-values of approximately 70. Olivine microphenocrysts (~5 vol.%) are completely altered to clay. The groundmass has an intersertal texture, comprising approximately 30 vol.% plagioclase laths, with 40 vol.% interstitial granular clinopyroxene and 15–20 vol.% altered mesostasis.

Five samples were analyzed from this group (556-7-1, 115–119 cm; 556-8-1, 118–110 cm; 556-9-2, 83–85 cm; 556-10-2, 130–133 cm; 556-12-1, 68–72 cm), and the analyses are presented in Table 4. These basalts display marked scatter on a normative Di-Ol-Hy diagram (Fig. 2), with very variable Hy; one sample is slightly Ne normative. This variation may be largely due to the effects of alteration or calcite contamination (calcite is common as vesicle and fracture fillings) but may also be partially due to the chemical heterogeneity within this group recognized by the shipboard party. This heterogeneity is apparent in the wide abundance ranges of the incompatible elements (e.g., TiO_2, 0.77–1.02%; Zr, 45–59 ppm;

Table 1. Analyses of plagioclase in Leg 82 basalts.

Hole	556									557		561			562						563		
Core-Section (interval in cm)	2-2, 132-135			4-2, 65-68			10-2, 130-133		16-1, 22-25	1-1, 38-41		2-1, 111-116			3-2, 141-143			8-1, 68-71			24-4, 0-7		
Chemical group	I			II			III		V			II			I			II					
Type	Pc	Pr	G	Pc	Pr	G	Pc	Pr				Pc	Pr	G	Pc	Pr	G	Pc	Pr	G	Pc	Pr	G
Major element (wt.%)																							
SiO_2	46.51	49.95	51.00	46.65	52.33	51.50	47.56	52.38	52.66	53.50	65.79	50.34	50.92	52.97	46.86	52.13	51.78	45.17	49.73	50.90	45.88	48.89	50.81
Al_2O_3	33.38	30.76	30.38	33.40	29.40	30.02	33.15	29.25	29.75	28.39	26.79	30.64	30.32	28.67	33.29	29.72	29.74	34.34	31.04	30.26	33.85	31.60	30.05
FeO	0.29	0.53	0.59	0.38	0.71	0.67		1.00	0.24	0.81	0.71	0.46	0.54	1.08	0.38	0.74	0.83		0.64	0.72	0.27	0.70	0.83
CaO	18.08	15.30	14.95	17.94	13.84	14.53	17.39	13.22	12.66	12.07	9.44	15.01	14.53	13.10	17.44	13.68	13.66	18.85	15.54	14.89	18.43	16.17	14.66
Na_2O	1.40	2.87	3.21	1.51	3.65	3.37	1.77	3.94	4.38	4.55	5.75	3.03	3.30	4.00	1.70	3.67	3.81	1.08	2.71	3.17	1.13	2.23	3.31
K_2O										0.14	0.21												
Total	99.66	99.41	100.13	99.88	99.93	100.09	99.87	99.79	99.69	99.46	99.69	99.48	99.61	99.82	99.77	99.94	99.82	99.44	99.66	99.94	99.56	99.59	99.66
Formula on the basis of 8 oxygens																							
Si	2.150	2.298	2.327	2.153	2.384	2.348	2.185	2.390	2.394	2.441	2.561	2.311	2.332	2.415	2.162	2.374	2.365	2.097	2.284	2.238	2.215	2.251	2.331
Al	1.820	1.668	1.643	1.817	1.579	1.613	1.796	1.574	1.595	1.527	1.424	1.658	1.637	1.541	1.816	1.596	1.601	1.880	1.681	1.631	1.849	1.715	1.625
Fe	0.011	0.020	0.023	0.015	0.027	0.026		0.038	0.009	0.031	0.027	0.018	0.021	0.041	0.015	0.028	0.032		0.024	0.028	0.011	0.027	0.032
Ca	0.896	0.754	0.731	0.887	0.675	0.710	0.856	0.647	0.617	0.590	0.456	0.738	0.713	0.640	0.862	0.667	0.668	0.938	0.765	0.730	0.915	0.798	0.721
Na	0.126	0.256	0.284	0.1325	0.322	0.298	0.158	0.349	0.386	0.403	0.503	0.270	0.293	0.354	0.152	0.324	0.337	0.097	0.242	0.281	0.101	0.200	0.295
K																							
An	88	75	72	87	68	70	84	65	62	59	48	73	71	64	85	67	66	91	76	72	90	80	71

Note: Pc = phenocryst core; Pr = phenocryst rim; G = groundmass.

Table 2. Analyses of magnesiochromite from Holes 556 and 562.

Hole	556		562		
Core-Section (interval in cm)	2-2, 132–135 (I) (1)	(2)	3-2, 141–143 (I) (1)	(2)	8-1, 68–71 (II)
Major element (wt.%)					
SiO_2	0.70	0.43	0.45	0.44	0.79
TiO_2	0.32	0.48	0.43	0.31	0.31
Al_2O_3	26.89	28.35	29.75	28.86	32.20
Cr_2O_3	38.74	39.00	36.56	37.77	34.66
Fe_2O_3	4.78	4.08	5.17	4.74	5.15
FeO	14.04	12.33	12.63	13.36	9.68
MgO	14.20	15.65	15.68	15.31	17.73
Total	99.67	100.32	100.85	100.79	100.52
Formula on the basis of 4 oxygens					
Si	0.021	0.013	0.013	0.013	0.023
Ri	0.007	0.011	0.010	0.007	0.007
Al	0.962	0.993	1.035	1.010	1.096
Cr	0.929	0.916	0.853	0.887	0.791
Fe^{3+}	0.109	0.091	0.115	0.106	0.112
Fe^{2+}	0.356	0.306	0.312	0.332	0.234
Mg	0.642	0.693	0.697	0.677	0.763
$Mg/(Mg + Fe^{2+})$	0.643	0.694	0.691	0.671	0.765
$Cr/(Cr + Al)$	0.491	0.480	0.452	0.468	0.419
$Fe^{3+}/(Fe^{3+} + Cr + Al)$	0.055	0.046	0.057	0.053	0.056
Host plag.	An_{88}	An_{85}	An_{87}	An_{85}	An_{90}

Note: Roman numerals in parentheses are chemical group numbers. Arabic numbers in parentheses are lithologic unit numbers; plag. = plagioclase.

Table 4). To a certain extent this variation can be modeled by phenocryst dilution, as the model in Table 7 illustrates, but such models cannot be applied successfully to all basalts of this group, because many are aphyric. Compositionally, the aphyric samples of this group are similar to basalts of Group I, at least in terms of the abundances of incompatible elements (e.g., Zr, Nb, TiO_2; Table 4; Figs. 4, 5). However, Mg-values are lower, as are Ni abundances (Table 4), whereas the Ti/Zr ratio of this group is lower (Fig. 5). Zr/Nb ratios (25–41; Table 4) are high and Ce_N/Y_N ratios low (0.4–0.7; Table 4), indicating that Group III basalts are as depleted in the more incompatible trace elements as Groups I and II.

Group IV comprises part of Lithologic Unit 7 and all of Lithologic Unit 9; the two parts of this group are separated by an interval of Group III basalts and Group IV gabbro. These basalts are aphyric and lack olivine. The texture is subophitic with subequal proportions of plagioclase laths and interstitial granular clinopyroxene, plus mesostasis.

Two samples were analyzed (556-12-1, 68–72 cm and 556-16-2, 128–131 cm) and the data are given in Table 4. Sample 556-12-1, 68–72 cm is normatively similar to the basalt of Groups I and II (Fig. 2), with a low proportion of normative Ol. Sample 556-16-2, 128–131 cm, however, has higher normative Ol and lower Hy and is somewhat more altered than 556-12-1, 68–72 cm, with a higher LOI and lower Mg-value (Table 4). The levels of the incompatible elements are quite high (Table 4), though slightly lower than in Group II (Figs. 4, 5). The Mg-values are rather low (~58, Table 4) and similar to those in Group II. However, a striking feature of these basalts is the very low abundances of Ni (~40 ppm) and Cr (~50 ppm) (Table 4) indicative of a rather evolved na-

Table 3. Analyses of clinopyroxene from Holes 556, 557, and 563 and clinopyroxene and orthopyroxene from the gabbro of Hole 556.

Hole	556		563		557	556		
Core-Section (interval in cm)	2-2, 132–135 (I)		24-4, 0–7		1-1, 38–41	16-1, 22–25 (V)		
Type	Mp	G	Mp	G		Cpx	Opx	Opx
Major elements (wt.%)								
SiO_2	52.84	51.57	50.99	50.65	49.05	52.01	53.91	51.40
TiO_2	0.41	0.71	0.57	0.71	1.74	0.44	0.34	0.25
Al_2O_3	2.58	3.76	4.10	4.55	3.13	2.27	1.16	0.68
FeO	4.93	7.47	5.86	6.72	11.15	8.43	15.78	25.21
MnO		0.25		0.21	0.29		0.28	0.82
MgO	18.19	18.47	17.03	16.86	14.18	15.41	26.33	19.67
CaO	20.42	17.84	20.45	19.77	19.38	20.80	2.10	1.68
Na_2O				0.39	0.56	0.55		
Cr_2O_3	0.64		0.77					
Total	100.01	100.07	99.77	99.86	99.48	99.91	99.90	99.71
Formula on the basis of 6 oxygens								
Si	1.925	1.887	1.875	1.866	1.860	1.932	1.957	1.961
Ti	0.011	0.020	0.016	0.020	0.050	0.012	0.009	0.007
Al	0.011	0.162	0.178	0.197	0.140	0.100	0.050	0.031
Fe	0.150	0.229	0.180	0.207	0.354	0.262	0.479	0.804
Mn		0.008		0.007	0.009		0.009	0.026
Mg	0.987	1.007	0.933	0.926	0.801	0.853	1.424	1.118
Ca	0.797	0.700	0.806	0.780	0.787	0.828	0.082	0.069
Na				0.028	0.041	0.039		
Cr	0.018		0.022					
Mg/(Mg + Fe)	0.87	0.81	0.84	0.82	0.69	0.77	0.75	0.58
Wo	39.2	33.9	39.4	39.8	41.5	43.5	2.9	2.7
En	52.8	55.2	52.1	53.1	45.1	46.5	73.4	57.3
Fs	2.0	10.9	8.5	7.1	13.4	10.0	23.7	40.0

Note: Mp = microphenocryst; G = groundmass; Cpx = clinopyroxene; Opx = orthopyroxene. Roman numerals in parentheses are chemical group numbers.

Table 4. Major and trace element analyses of basalts and gabbro from Hole 556.

Chemical group	I		II				III				IV	III	V	IV
Core-Section	2-1	2-2	3-1	3-2	4-2	6-4	7-1	8-1	9-2	10-2	11-1	12-1	16-1	16-2
(interval in cm)	77–79	132–135	57–60	49–51	65–68	115–120	115–119	118–120	83–85	130–133	106–109	68–72	14–18	128–13
Piece number	4e	9a	7	4b	2a	5b	5a	8a	4b	3b	13	4c	3a	15
Major elements (wt.%)														
SiO_2	50.56	50.02	49.02	49.66	48.62	49.73	48.46	49.25	49.78	47.95	50.35	49.01	52.10	49.08
TiO_2	1.04	1.02	1.46	1.41	1.45	1.37	0.99	0.83	1.02	0.77	1.31	0.84	0.26	1.33
Al_2O_3	15.96	15.65	15.61	15.76	15.93	15.26	15.21	15.44	15.43	17.09	15.00	16.44	18.14	14.35
Fe_2O_3	7.83	8.44	10.55	10.37	10.36	10.75	9.74	8.81	9.55	8.08	10.42	8.44	5.73	11.32
MnO	0.15	0.15	0.17	0.18	0.17	0.16	0.16	0.15	0.16	0.15	0.18	0.15	0.11	0.17
MgO	7.89	8.04	6.53	6.84	6.02	7.20	7.62	7.62	7.04	7.15	6.44	8.18	8.89	6.49
CaO	12.74	12.42	11.39	11.34	11.51	11.35	12.65	13.27	12.63	13.73	10.86	12.39	11.92	10.61
Na_2O	2.44	2.49	2.70	2.65	1.76	2.67	2.56	2.33	2.52	2.41	2.96	2.31	2.62	3.11
K_2O	0.16	0.17	0.28	0.28	0.28	0.10	0.22	0.36	0.35	0.21	0.45	0.20	0.07	0.48
P_2O_5	0.11	0.12	0.15	0.14	0.14	0.13	0.09	0.10	0.11	0.08	0.13	0.08	0.02	0.13
LOI	1.65	1.74	2.27	1.55	3.07	1.54	1.94	2.35	1.63	2.01	1.97	2.28	0.71	2.61
Total	100.53	100.26	100.13	100.18	100.31	100.26	99.64	100.51	100.22	99.63	100.07	100.32	100.57	99.68
Trace elements (ppm)														
Cr	326	336	284	287	300	277	379	298	127	439	48	400	84	47
Ni	140	153	70	72	69	71	92	96	68	106	40	97	80	41
V	267	268	292	280	304	274	239	260	286	218	320	225	148	306
Zn	74	72	87	85	89	78	71	68	73	58	90	60	39	84
Ga	16	16	17	17	17	18	16	14	17	15	17	15	14	19
Rb	2	2	6	4	5	2	4	6	6	4	9	3	<1	8
Sr	112	107	102	100	101	97	103	99	102	98	110	95	94	114
Ba	30	29	24	24	15	25	16	27	18	19	31	17	9	45
Zr	62	61	92	90	93	85	55	48	59	45	79	49	9	79
Nb	1.6	1.7	3.3	2.8	2.8	2.1	1.5	1.6	2.4	1.1	2.6	1.6	<1	1.9
La	2	2	2	3	3	3	2	2	2	<2	3	<2	<2	3
Ce	6	5	8	9	8	8	6	5	5	4	10	6	<4	9
Nd	7	7	9	9	9	9	6	6	7	5	9	7	2	8
Y	26	26	36	34	36	34	25	22	26	19	33	21	9	32
Selected element ratios														
Mg-value	69	68	58	60	57	60	64	66	62	66	58	69	78	56
Ti/Zr	101	100	95	94	93	97	108	104	104	103	99	103	172	101
Zr/Nb	39	36	28	32	33	40	37	30	25	41	30	31		42
Ce_N/Y_N	0.5	0.4	0.5	0.6	0.5	0.5	0.6	0.5	0.4	0.5	0.7	0.7		0.7
Zr/Ce	11	13	12	10	12	11	10	10	12	12	8.2	8.5		9.1
Zr/Y	2.5	2.5	2.7	2.8	2.7	2.6	2.3	2.3	2.3	2.5	2.5	2.4	1.0	2.6
CIPW norms														
Or	1.0	1.0	1.7	1.7	1.7	0.6	1.4	2.2	2.1	1.3	2.7	1.2	0.4	2.9
Ab	20.9	21.4	23.4	22.8	24.0	22.9	22.2	20.1	21.7	20.5	25.6	20.0	22.2	27.1
An	32.5	31.5	30.3	30.7	31.1	29.8	30.1	31.2	30.2	36.1	26.8	34.6	37.6	24.5
Ne										0.2				
Di	24.7	24.5	21.7	20.8	21.9	21.6	27.4	28.5	26.7	26.9	22.3	22.3	17.2	23.7
Hy	14.9	13.0	12.9	15.4	10.8	16.8	3.8	6.6	9.7		14.4	11.0	18.1	7.5
Ol	1.7	4.1	4.1	2.8	4.6	2.6	10.5	7.2	5.0	11.2	2.6	6.9	2.4	8.4
Mt	1.4	1.5	1.9	1.8	1.8	1.9	1.7	1.6	1.7	1.4	1.8	1.5	1.0	2.0
Il	2.0	2.0	2.8	2.7	2.8	2.6	1.9	1.6	2.0	1.5	2.5	1.6	0.5	2.6
Ap	0.3	0.3	0.4	0.3	0.4	0.3	0.2	0.3	0.3	0.2	0.3	0.2	0.1	0.3

Note: LOI is loss on ignition. Total iron is expressed as Fe_2O_3. CIPW norms and Mg-values (100 Mg/[Mg + Fe^{2+}]) are calculated using an assumed Fe_2O_3/FeO ratio of 0.15. Ce_N/ Y_N expresses the chondrite-normalized ratio of Ce to Y.

ture for this group. The depletion in more incompatible elements (Zr/Nb 30–42, Ce_N/Y_N 0.7; Table 4) is comparable to that in the other chemical groups of this hole.

Group V comprises Lithologic Units 8 and 10. The gabbros of this group have a uniform grain size but variable mineralogy; orthopyroxene contents range from 5–20 vol.% and clinopyroxene from 35–15 vol.%. In little deformed and fresh gabbros the plagioclase is up to 4 mm in size, though more commonly 1–2 mm, and is unzoned, with a uniform composition of An_{62} (Table 1). Clinopyroxene occurs as large (commonly 3–7 mm) prismatic grains that show extensive exsolution and twinning and have a composition of $Wo_{44}En_{47}Fs_{10}$ (Table 3). Orthopyroxene occurs as slightly smaller (commonly 2–4 mm) subhedral or prismatic grains and displays a range of variation from magnesian ($Wo_3En_{73}Fs_{24}$; Table 3 to more iron-rich ($Wo_3En_{57}Fs_{40}$; Table 3) composition. Occasional unaltered pleochroic amphibole grains als occur. Upon shearing, the plagioclase becomes granu lated, often very finely, whereas the pyroxenes retai their original size but become strained, granulation onl occurring in the presence of intensive shearing. Upon al teration, the pyroxenes change to a colorless-to-green fi brous amphibole and chlorite.

Only one sample was analyzed from this group, an the analysis is given in Table 4. Normatively this sampl has a high plagioclase content (60%; the normative com position (An_{63}) is very close to the observed composi tion) and 35% total pyroxene. The Mg-value is very hig (78; Table 4) and similar to that of the pyroxenes (Table 3)

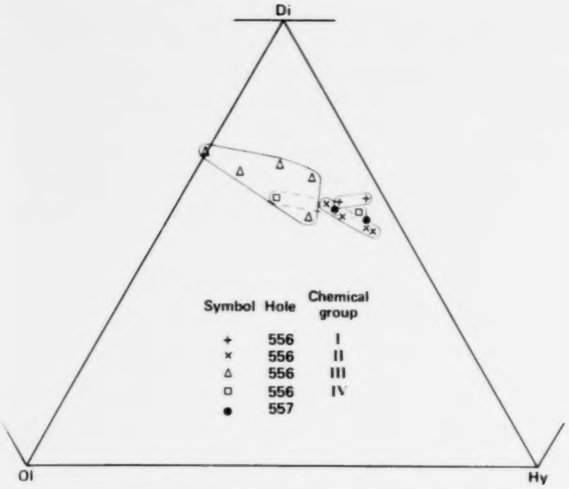

Figure 2. Plot of normative components Ol-Di-Hy for basalts from Holes 556 and 557. Norms are calculated using an Fe_2O_3/FeO ratio of 0.15.

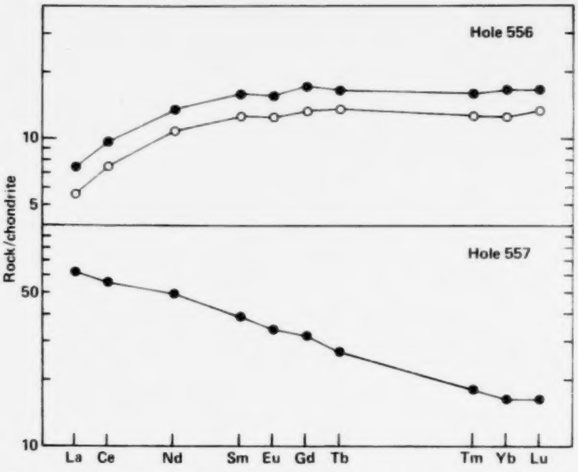

Figure 3. Abundances of the rare earth elements in basalts of Holes 556 and 557 normalized to the average chondrite values of Nakamura (1974). Closed circle = Group I, Hole 556; open circle = Group II, Hole 556.

This, combined with the high Al_2O_3 and CaO contents and low abundances of incompatible elements Ti and Zr (Table 4) clearly indicates the cumulate nature of this gabbro. The very high Ti/Zr ratio (172; Table 4) reflects the control of TiO_2 abundance in the whole rock by cumulus pyroxene, and the high Sr/Zr ratio (10 compared to 1-2.1 in basalt of Groups I to IV) reflects the control of Sr abundance by cumulus plagioclase.

This gabbro unit is very different from the gabbros recovered from Hole 334, which contain very calcic plagioclase (An_{80}) and magnesian pyroxenes (Mg_{87}) (Clarke and Loubat, 1977; Symes et al., 1977). They are, however, comparable to gabbroic rocks recovered from the Mathematician Ridge in the East Pacific (Vanko and Batiza, 1982). The mineral chemistry indicates that the Hole 556 gabbros must have been derived from rather evolved basalts. Applying Fe-Mg distribution coefficients between clinopyroxene and liquid derived for FAMOUS basalts (Bryan, 1979), the Mg-value of the liquid precipitating the clinopyroxene of Table 3 is 49 (all Fe in clino-

Table 5. INAA results for Leg 82 basalts.

Hole	556		557	558					561	
Core-Section	2-1	6-4	1-1	27-3	28-3	31-1	35-1	39-2	1-1	1-2
(interval in cm)	77–79	115–120	144–147	92–95	36–38	86–89	120–122	69–71	44–47	22–24
Chemical group	I	II		I	II	III	IV	V	I	II
Elements (ppm)										
La	1.84	2.44	20.0	6.05	2.68	10.6	6.62	5.24	14.1	3.04
Ce	6.45	8.38	47.3	15.2	8.52	22.9	16.3	12.7	30.1	8.88
Nd	6.88	8.55	31.0	9.39	7.54	13.7	10.1	8.32	16.3	9.22
Sm	2.59	3.25	7.83	3.04	2.63	3.76	2.99	2.53	4.14	3.32
Eu	0.98	1.20	2.57	1.06	0.97	1.29	1.05	0.87	1.40	1.28
Gd	3.66	4.75	8.70	3.46	3.59	4.05	3.44	2.69	4.86	4.66
Tb	0.71	0.86	1.39	0.63	0.70	0.74	0.67	0.57	0.82	1.03
Tm	0.43	0.54	0.61	0.35	0.48	0.47	0.44	0.30	0.44	0.66
Yb	2.77	3.68	3.60	2.26	2.73	2.68	2.39	2.12	2.88	4.01
Lu	0.45	0.57	0.55	0.38	0.45	0.43	0.38	0.32	0.47	0.62
Th	0.14	0.16	1.85	0.67	0.24	1.12	0.75	0.56	1.92	0.31
Ta	0.09	0.10	1.86	0.52	0.14	0.90	0.58	0.44	1.39	0.18
Hf	1.80	2.44	5.36	2.05	1.87	2.53	1.99	1.57	2.68	2.34
Element ratios										
Ce_N/Yb_N	0.59	0.58	3.3	1.71	0.79	2.17	1.73	1.52	2.7	0.56
La_N/Sm_N	0.44	0.47	1.58	1.23	0.63	1.75	1.37	1.28	2.11	0.57
Tb_N/Yb_N	1.09	0.99	1.63	1.17	1.09	1.17	1.18	1.14	1.21	1.09
La/Ta	20.4	24.4	10.8	11.6	19.1	11.8	11.4	11.9	10.1	16.9
Th/Ta	1.56	1.60	0.99	1.29	1.71	1.24	1.29	1.27	1.38	1.72

Note: Ce_N/Yb_N, La_N/Sm_N, and Tb_N/Yb_N express the ratios of chondrite-normalized (Nakamura, 1974) rare earth elements.

Table 6. Analyses of olivine microphenocrysts from Leg 82 holes.

Hole	556	558			561	562		563	564
Core-Section	4-2	27-3	30-3	35-1	H1-CC	3-2	8-1	24-4	5-2
(interval in cm)	65-68	92-95	12-14	120-122	9-13	14-143	68-71	0-7	115-118
Chemical group	II	I	III	IV	I	I	II		
Major elements (wt.%)									
SiO_2	39.29	39.69	39.86	40.26	40.05	38.93	39.35	39.80	39.14
FeO	15.61	14.70	13.97	12.28	12.92	17.72	14.98	14.35	16.43
MnO						0.34	0.26		
MgO	44.50	45.14	45.67	47.36	46.70	42.01	44.97	45.52	43.73
CaO	0.33	0.26	0.36	0.30	0.34	0.40	0.32	0.35	0.33
Total	99.73	99.79	99.86	100.20	100.01	99.40	99.88	100.02	99.63
Formula on the basis of 4 oxygens									
Si	0.993	0.997	0.997	0.996	0.996	0.998	0.991	0.996	0.994
Fe	0.330	0.309	0.292	0.254	0.269	0.380	0.316	0.300	0.349
Mn						0.007	0.006		
Mg	1.676	1.690	1.703	1.746	1.731	1.605	1.688	1.698	1.655
Ca	0.009	0.007	0.010	0.008	0.009	0.011	0.009	0.009	0.009
Fo	84	85	85	87	87	81	84	85	83

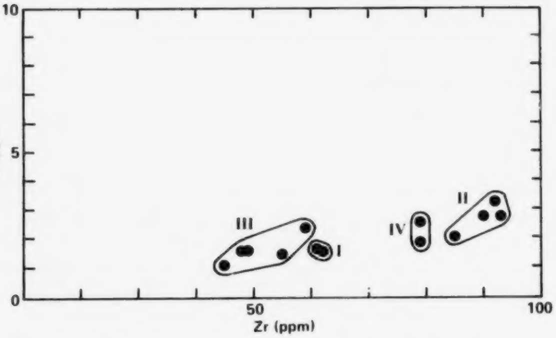

Figure 4. Plot of Nb versus Zr for Hole 556 basalts. Roman numerals show chemical groups.

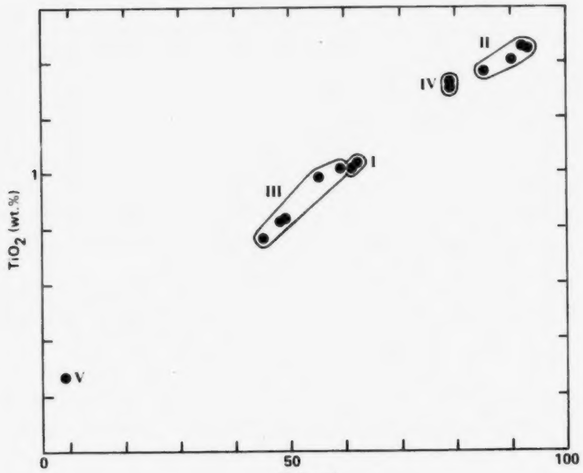

Figure 5. Plot of TiO_2 versus Zr for Hole 556 basalts. Roman numerals show chemical groups.

Table 7. Mixing calculations for the derivation of phyric basalts from aphyric basalts in Chemical Groups III, Hole 556, and II, Hole 562.

Section containing phenocryst-enriched magma (chemical group)	SiO_2	TiO_2	Al_2O_3	FeO*	MnO	MgO	Na_2O	P_2O_5
556-10-2 (III)								
Observed	49.12	0.79	17.51	7.45	0.15	7.32	2.47	0.09
Calculated	49.04	0.81	17.62	7.65	0.12	7.32	2.58	0.07
Mix (wt.%)	556-7-1 (80.1) + An_{75}(16.7) + Fo_{84}(2.4): $\Sigma R^2 = 0.0724$							
562-6-4 (II)								
Observed	49.09	1.09	18.01	8.59	0.14	6.76	2.16	0.11
Calculated	49.04	1.13	18.07	8.51	0.14	6.98	2.34	0.11
Mix (wt.%)	562-8-1 (93.9) + An_{91}(7.9): $\Sigma R^2 = 0.0934$							

Note: ΣR^2 is the sum of squares of residuals (obs. concentration-calc. concentration). FeO* is total iron expressed as FeO. CaO omitted from the calculation due to calcite contamination. For the least-squares approximations, the method of Bryan et al. (1969) has been used.

pyroxene as FeO) or 58 (Fe_2O_3 in clinopyroxene determined by charge balance). This latter composition corresponds to the basalts of Groups II or IV in Hole 556.

SITE 557

Site 557 (38°49.95′N; 32°33.58′W, 2143 m water depth) lies on Magnetic Anomaly 5D (18 Ma) on the west flank of the Mid-Atlantic Ridge on the same flow line through the Azores Triple Junction as Site 556. A single hole was drilled and only 3 m of basement (encountered at 460.5 m sub-bottom depth) was cored before enforced abandonment of the hole. A single lithologic unit composing one chemical group was recognized by the shipboard party, consisting of very fresh aphyric basalt.

The aphyric basalt from Hole 557 is medium grained with an intersertal to intergranular texture. Plagioclase (An_{59}–An_{48}; Table 1) and clinopyroxene ($Wo_{42}En_{45}Fs_{13}$; Table 3) occur in subequal proportions, the clinopyroxene and patches of devitrified glass (15–20 vol.% with the composition of smectite) filling the interstices in the random network of plagioclase laths, together with equant titanomagnetite (~10 vol.%).

Analyses of two samples from the top and bottom of Core 557-1, Section 1 (557-1-1, 38–41 cm and 557-1-1, 144–147 cm) are given in Table 8. Shipboard analyses indicated the chemical homogeneity of the basalt from this section, although a sample from a pebble in the wash-core is of a slightly different composition (see site chapter, Site 557, this volume). In terms of the normative components Di-Ol-Hy (Fig. 2), Hole 557 basalts are not dissimilar to the basalts from Chemical Units I and II of Hole 556, containing only small amounts of normative Ol. However, the basalt from Hole 557 is chemically highly evolved, having high contents of incompatible trace elements (e.g., Zr, Nb, Ba, LREE; Table 8; Fig. 6), total iron (as Fe_2O_3), and a low Mg-value (Table 8); it is clearly a ferrobasalt. In marked contrast to the basalts from Hole 556, the ferrobasalt from Hole 557 is enriched in the more-incompatible elements, as indicated by the high Ce_N/Y_N (2.7) and low Zr/Nb (7.6–7.9) ratios (Table 8; Fig. 6). The major and trace element chemistry is comparable to that of other ferrobasalts from the North Atlantic (Chemical Unit I, Hole 407; Wood, Tarney, et al., 1979), ferrobasalts from East Iceland (Wood, 1978), as well as ferrobasalts from the southwest

Table 8. Major and trace element analyses for Hole 557 basalts.

Core-Section (interval in cm) Piece number	1-1 38–41 4	1-1 144–147 14
Major elements (wt.%)		
SiO_2	47.18	46.40
TiO_2	3.42	3.43
Al_2O_3	12.73	12.38
Fe_2O_3	16.10	16.17
MnO	0.21	0.20
MgO	5.04	5.11
CaO	9.79	9.85
Na_2O	2.82	2.85
K_2O	0.55	0.48
P_2O_5	0.33	0.34
LOI	2.28	2.45
Total	100.45	99.66
Trace elements (ppm)		
Cr	32	30
Ni	36	37
V	384	384
Zn	131	130
Ga	23	24
Rb	14	10
Sr	298	304
Ba	133	123
Zr	225	218
Nb	30	28
La	21	21
Ce	52	52
Nd	30	30
Y	44	44
Selected element ratios		
Mg-value	41.0	42.0
Ti/Zr	91.0	94.0
Zr/Nb	7.6	7.9
Ce_N/Y_N	2.7	2.7
Zr/Ce	4.5	4.3
Zr/Y	5.3	5.1
CIPW norms		
Or	3.3	2.9
Ab	24.3	24.8
An	20.9	20.1
Di	22.0	23.2
Hy	15.4	12.6
Ol	2.5	4.5
Mt	2.8	2.9
Il	6.6	6.7
Ap	0.8	0.8

Note: LOI is loss on ignition. Total iron is expressed as Fe_2O_3. CIPW norms and Mg-values (100 Mg/[Mg + Fe^{2+}]) are calculated using an assumed Fe_2O_3/FeO ratio of 0.15. Ce_N/Y_N expresses the chondrite-normalized ratio of Ce to Y.

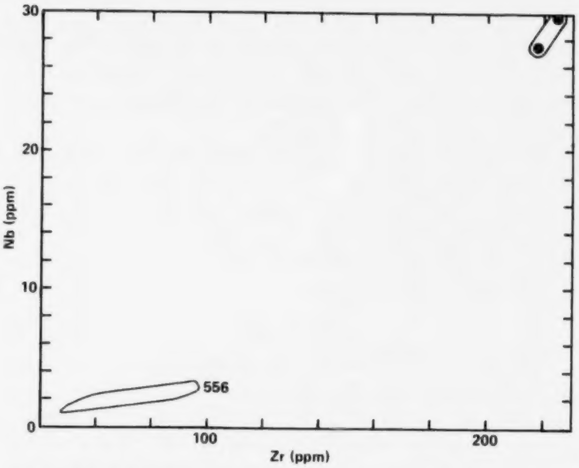

Figure 6. Plot of Nb versus Zr for Hole 557 basalts. Also shown is the field for Hole 556 basalts from Figure 4.

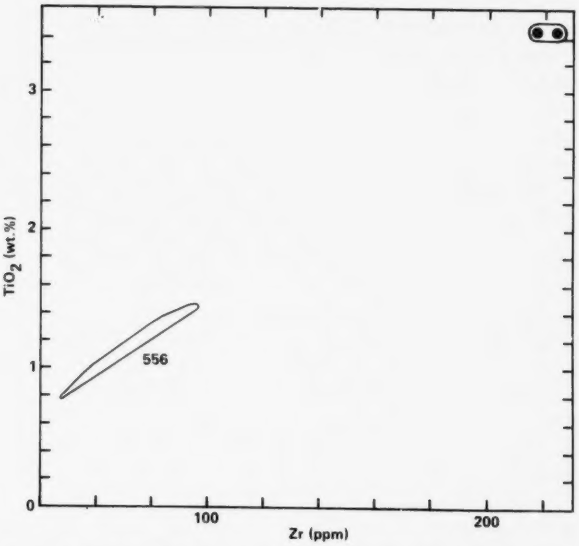

Figure 7. Plot of TiO_2 versus Zr for Hole 557 basalts. Also shown is the field for Hole 556 basalts from Figure 5.

Indian Ocean (Speiss Ridge; Le Roex et al., 1982) and the East Pacific (Galapagos spreading center, Clague et al., 1976). In each of these cases, the ferrobasalts have been modeled as the products of advanced degrees (70–80%) of fractional crystallization of primary liquid compositions, the crystal extract being dominated by subequal proportions of plagioclase and augite with minor olivine and titanomagnetite (Clague et al., 1976; Wood, Tarney, et al., 1979: Le Roex et al., 1982). Such a model is equally applicable to the ferrobasalts of Hole 557. However, although Hole 557 ferrobasalts may be the product of large degrees of crystal fractionation, ratios between more-incompatible and less-incompatible elements will not have been greatly modified. Adopting K_d data from Le Roex and others (1981; 1982) for Zr, Nb, Ce, and Y and assuming that a primary basalt undergoes 70% Rayleigh fractionation of equal proportions of plagioclase and augite, the Zr/Nb and Ce_N/Y_N ratios of the residual liquid change by only 10% (decrease) and 28% (increase), respectively, over those of the parent liquid. Thus the parent liquid would have Zr/Nb ~8.6 and Ce_N/Y_N ~ 2.1.

REE data are given in Table 5 and plotted in Figure 3. This sample has a high Ce_N/Yb_N ratio (3.3) with approximately 60 times the chondrite levels of the LREE. A significant Eu anomaly is absent. The marked contrast with the LREE-depleted basalts of Hole 556 (Fig. 3) is apparent.

SITE 558

Site 558 (37°46.20′N; 37°20.61′W, 3754 m water depth) lies between Magnetic Anomalies 12 and 13 (35 Ma old) on the west flank of the Mid-Atlantic Ridge. It is approximately 30 miles south of the Pico Fracture Zone on a flow line passing through the FAMOUS area, the four sites drilled by Leg 37, and the three sites drilled by Leg 49. Two holes were drilled, of which only the first (Hole 558) penetrated basement. In Hole 558, 153 m of basement (encountered at 408 m sub-bottom depth) were cored before the hole was abandoned. A total of 11 lithologic units comprising 6 chemical groups were identified by the shipboard party. The upper 110 m of basement consists of aphyric pillow basalts and pillow basalt breccias. Beneath this, 43 m of mylonitized gabbro was cored to the bottom of the hole.

Petrographically the basalts from Chemical Groups I, IV, and V are all similar, composed of euhedral olivine microphenocrysts (5–10 vol.%, composition Fo_{85} Group I, Fo_{87} Group IV; Table 6) that are generally altered to clay (completely so in the case of Group V). The groundmass comprises 30–40 vol.% swallowtail plagioclase laths (up to 0.5 mm), approximately 20 vol.% granular clinopyroxene, and 30–40 vol.% mesostasis. Chemical Group II basalts have only approximately 2 vol.% olivine microphenocrysts and contain subequal (30–40 vol.%) proportions of swallowtail plagioclase laths and granular clinopyroxene and 20–30 vol.% devitrified glass. Chemical Group II basalts have an unusually high proportion (up to 20 vol.%) of olivine micro-phenocrysts (Fo_{85}, Table 6), with groundmass plagioclase (25–30 vol.%) subordinate to clinopyroxene (30–40 vol.%) and quite a high proportion (~10 vol.%) of skeletal magnetite.

Group I comprises the massive aphyric basalt of Lithologic Unit 3. Only one sample was analyzed from this group (558-27-3, 92–95 cm) and the data are presented in Table 9. This sample has a moderate amount of normative Ol, but a rather high Hy/Di ratio, especially compared to the remainder of Hole 558 basalts (Fig. 8). This sample has a high Mg-value (67, Table 9) and N and Cr contents (Table 9; Figs. 9, 10) and has the characteristics of near primitive mantle melts in the FAMOUS area suggested by Fujii and Bougault (1983). In terms o incompatible trace elements, this group is enriched i the more-incompatible elements; Zr/Nb ratios are low (~10; Table 9) and Ce_N/Y_N is high (~1.3; Table 9). I also has a chemistry typical of E-type MORB, confirmed by the REE data (Table 5, Fig. 11) that demonstrates the LREE-enriched nature of the basalt of this group (Ce_N/Yb_N = 1.7, La_N/Sm_N = 1.2; Table 5).

Group II comprises basalts from Lithologic Unit 4. Four samples were analyzed from this group, and the data are given in Table 9. Normatively these basalts have low Ol and straddle the Di-Hy join (Fig. 8). In marked contrast to the basalt of Group I, this group displays depletion in the more-incompatible elements. Zr/Nb ratios are high (20–27, Table 9, Fig. 12); Ce_N/Y_N ratios are low (0.7–0.9; Table 9, Fig. 13) and comparable to the depleted basalts of Hole 556, although they have more Cr and a lower Mg-value than the basalts of Group I, Hole 556, to which they have the greatest similarity in terms of incompatible element abundances. The basalts of this group are, however, less depleted in the more-incompatible elements than any of the Hole 556 basalts.

The N-type MORB nature of this group is indicated by the REE data (Table 5, Fig. 11). Ce_N/Yb_N and La_N/Sm_N ratios are low (0.8 and 0.6, respectively), but the ratios of these elements are higher than in the N-MORB of Hole 556.

Group III comprises basalts from Lithological Units 5, 6, and part of 7. Eight samples were analyzed from this group (from Cores 558-29 to 558-34), and the data are presented in Table 9. The shipboard party divided this group into two subgroups, A and B, a division that is followed in this report. We have analyzed four basalts from each subgroup, and the chemical distinction is clear in terms of the normative mineralogy. Group IIIA basalts have low normative Ol and straddle the Di-Hy join, but contain relatively more Hy than Group II basalts (Fig. 8). Compared to Group IIIA basalts, Grou IIIB basalts are more Ol-rich and have a slightly highe Di/Hy ratio (Fig. 8). The coherence of these basalts a one chemical group is indicated by the similar Zr/Nb Ce/Y, Zr/P, and Zr/Y ratios (Figs. 12–15). Howeve the distinction of subgroups is clear from the differenc in abundance levels of particularly P, Ti, Zr, Nb, an the REE (Group IIIA is enriched in these element (Table 9; Figs. 12–16). The low Zr/Nb ratios (6–6. Table 9) and high Ce_N/Y_N ratios (1.7–2.1; Table 9) indicate enrichment of more incompatible elements in this group, the degree of enrichment being greater than that displayed by Group I (Figs. 12–17). It may be that the

Table 9. Major and trace element analyses for Hole 558 basalts.

Chemical group	I	II				IIIA				IIIB				IVA			IVB			V				
Core-Section	27-3	28-1	28-1	28-2	28-3	29-1	30-3	31-1	32-1	32-3	32-5	33-3	34-1	35-1	35-2	35-3	35-4	36-1	36-2	37-1	38-1	39-1	39-2	39-4
(interval in cm)	92-95	38-41	79-81	52-55	36-38	99-101	12-14	86-89	115-117	38-40	88-90	135-138	63-65	120-122	112-114	89-91	102-104	82-84	100-102	143-148	104-108	55-57	69-71	98-100
Piece number	9	3	8	7	4	7b	2	5d	8b	4b	3b	9d	3f	11a	6b	7b	10	6c	5d	19b	14a	5c	3c	4c
Major elements (wt.%)																								
SiO_2	49.58	49.86	49.49	49.60	50.20	49.58	49.21	50.10	48.41	48.36	49.08	48.47	48.39	49.13	48.50	48.45	48.99	48.65	49.04	48.34	47.34	48.19	48.21	47.96
TiO_2	1.22	1.08	1.08	1.09	1.08	1.37	1.38	1.38	1.38	1.26	1.27	1.26	1.26	1.18	1.20	1.20	1.22	1.22	1.23	0.93	0.95	0.96	0.94	0.94
Al_2O_3	14.43	15.01	15.14	15.14	15.05	14.63	14.65	14.75	14.78	14.82	14.86	14.69	15.12	14.56	14.88	14.82	14.77	14.73	14.92	15.26	15.82	15.85	15.59	15.57
Fe_2O_3	10.41	10.10	9.85	10.42	9.52	9.40	9.94	9.33	9.74	9.52	9.46	9.64	9.40	9.65	10.02	10.03	9.80	9.82	9.66	9.66	9.76	9.32	9.44	9.66
MnO	0.15	0.15	0.15	0.16	0.15	0.13	0.14	0.14	0.14	0.14	0.14	0.15	0.13	0.15	0.16	0.15	0.15	0.15	0.15	0.15	0.15	0.16	0.17	0.15
MgO	9.38	8.01	7.51	7.91	7.43	7.78	7.90	7.78	7.85	8.73	8.56	8.99	7.68	9.16	8.30	8.79	8.92	8.40	8.48	10.02	8.59	8.44	9.30	8.47
CaO	10.35	11.85	12.03	12.16	11.76	10.97	10.94	11.11	11.30	11.33	11.24	11.23	11.61	11.31	11.71	11.62	11.17	11.40	11.23	11.33	11.47	11.67	11.38	11.90
Na_2O	2.27	2.15	2.24	2.15	2.21	2.39	2.35	2.36	2.35	2.32	2.26	2.23	2.36	2.17	2.26	2.14	2.28	2.19	2.30	2.01	2.07	2.14	2.09	2.14
K_2O	0.39	0.31	0.29	0.25	0.24	0.47	0.49	0.29	0.39	0.32	0.41	0.36	0.36	0.33	0.35	0.32	0.35	0.38	0.39	0.29	0.29	0.24	0.23	0.25
P_2O_5	0.13	0.11	0.10	0.11	0.10	0.19	0.19	0.19	0.20	0.18	0.17	0.17	0.17	0.14	0.16	0.15	0.17	0.17	0.17	0.11	0.13	0.12	0.12	0.12
LOI	2.11	1.60	2.39	1.49	2.35	3.64	3.14	3.02	3.60	3.56	2.87	3.07	3.88	2.40	2.98	2.74	2.62	2.98	2.94	2.23	3.82	3.19	2.70	3.15
Total	100.42	100.23	100.27	100.48	100.09	100.55	100.33	100.14	100.14	100.54	100.32	100.26	100.36	100.18	100.52	100.41	100.44	100.09	100.51	100.33	100.39	100.28	100.17	100.31
Trace elements (ppm)																								
Cr	544	448	445	462	430	380	383	387	386	412	403	392	420	416	433	431	374	355	353	488	509	513	514	505
Ni	265	140	136	116	138	170	151	152	156	153	154	155	134	181	168	174	169	166	167	218	223	203	216	202
V	239	270	268	280	259	282	280	284	286	269	267	258	278	270	280	280	268	263	264	221	230	234	228	227
Zn	84	84	82	81	80	82	85	84	85	84	77	79	84	80	83	80	78	81	81	73	73	75	73	74
Ga	16	15	17	17	16	17	17	17	17	17	16	16	17	16	15	16	16	17	17	14	15	16	16	15
Rb	7	8	6	5	4	7	9	5	7	6	6	6	5	5	5	6	4	7	7	6	7	4	3	3
Sr	137	88	88	91	89	175	169	174	172	177	181	177	182	145	147	148	144	147	144	111	112	113	110	121
Ba	55	11	9	13	12	57	49	56	48	42	46	41	42	38	36	33	40	42	44	23	18	22	21	21
Zr	75	66	64	63	66	90	89	91	91	78	80	80	79	74	75	76	81	82	81	57	57	61	60	59
Nb	7.8	2.8	2.4	3.2	2.7	14.3	14.0	14.8	14.5	13.0	13.3	13.2	12.9	9.2	9.2	9.8	10.8	11.6	11.5	7.2	7.3	7.7	7.4	7.6
La	6	<2	2	<2	2	10	9	9	10	9	8	9	7	6	6	7	7	8	8	5	5	4	4	5
Ce	13	9	8	10	9	23	24	23	21	22	19	21	19	16	16	15	19	19	20	13	12	12	13	11
Nd	9	9	8	8	8	13	13	14	13	12	11	12	11	9	11	9	11	11	11	9	8	8	8	8
Y	24	28	25	27	27	26	25	25	28	24	24	23	23	25	25	25	25	25	26	20	21	21	22	21
Selected element ratios																								
Mg-value	67	64	63	63	64	65	64	65	64	67	67	68	65	68	65	66	67	66	66	70	66	67	69	66
Ti/Zr	98	98	101	103	98	91	93	91	91	96	95	94	96	96	96	95	90	89	91	98	99	94	93	95
Zr/Nb	9.6	24	27	20	24	6.3	6.4	6.1	6.3	6.1	6.0	6.1	6.1	8.0	8.2	7.8	7.5	7.1	7.0	7.9	7.8	7.9	8.1	7.8
Ce_N/Y_N	1.3	0.7	0.7	0.9	0.8	2.0	2.2	2.1	1.7	2.1	1.8	2.1	1.9	1.5	1.5	1.4	1.8	1.8	1.8	1.5	1.3	1.3	1.4	1.2
Zr/Ce	6.2	7.3	8.0	6.3	7.3	4.2	4.0	4.3	4.7	3.9	4.6	4.1	4.5	5.0	5.1	5.5	4.6	4.6	4.4	4.4	4.8	5.1	4.6	5.4
Zr/Y	3.3	2.4	2.6	2.3	2.4	3.7	3.8	3.9	3.5	3.6	3.6	3.8	3.7	3.2	3.2	3.3	3.5	3.5	3.3	2.9	2.7	2.9	2.7	2.8
CIPW norms																								
Q					1.2			1.0																
Or	2.4	1.8	1.8	1.5	1.5	2.8	3.0	1.8	2.4	2.0	2.5	2.2	2.2	2.0	2.1	2.0	2.1	2.3	2.4	1.8	1.8	1.5	1.4	1.5
Ab	19.6	18.5	19.4	18.4	19.1	20.9	20.5	20.5	20.3	20.2	19.6	19.4	20.7	18.8	19.6	18.5	19.7	19.1	20.0	17.4	18.1	18.6	18.1	18.6
An	28.5	30.8	31.0	31.3	31.2	28.7	28.8	29.6	29.8	30.0	30.0	29.9	30.7	29.7	30.1	30.6	29.7	30.1	30.0	32.4	34.2	34.0	33.4	33.1
Di	18.5	22.9	23.9	23.6	22.6	21.2	20.9	20.8	21.9	21.7	21.1	21.3	22.7	21.6	23.0	22.2	20.9	21.9	21.1	19.5	19.3	20.1	19.3	21.8
Hy	21.0	19.8	17.3	17.5	19.5	20.4	18.7	20.7	15.8	13.6	17.2	15.1	13.5	17;8	12.9	14.6	16.2	16.5	16.5	14.6	12.7	14.7	15.1	12.0
Ol	4.6	1.2	1.6	2.7		0.3	2.3		3.9	7.0	4.1	6.7	4.8	4.9	6.8	6.6	5.9	4.5	4.8	9;8	9.0	6.4	8.1	8.2
Mt	1.8	1.8	1.7	1.8	1.7	1.7	1.8	1.7	1.7	1.7	1.7	1.7	1.7	1.7	1.8	1.8	1.7	1.8	1.7	1.7	1.8	1.7	1.7	1.7
Il	2.4	2.1	2.1	2.1	2.1	2.7	2.7	2.7	2.7	2.5	2.5	2.5	2.5	2.3	2.3	2.3	2.4	2.4	2.4	1.8	1.9	1.9	1.8	1.8
Ap	0.3	0.3	0.2	0.3	0.3	0.5	0.5	0.5	0.5	0.4	0.4	0.4	0.4	0.4	0.4	0.4	0.4	0.4	0.4	0.3	0.3	0.3	0.3	0.3

Note: LOI is loss on ignition. Total iron is expressed as Fe_2O_3. CIPW norms and Mg-values (100 Mg/[Mg + Fe^{2+}]) are calculated using an assumed Fe_2O_3/FeO ratio of 0.15. Ce_N/Y_N expresses the chondrite-normalized ratio of Ce to Y.

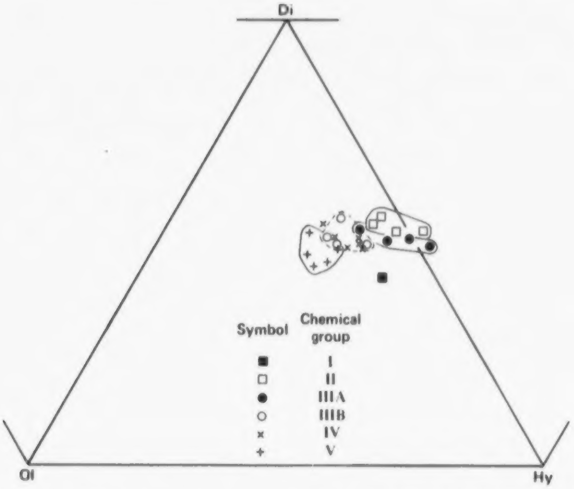

Figure 8. Plot of normative components Ol-Di-Hy for Hole 558 basalts. Norms are calculated using an Fe_2O_3/FeO ratio of 0.15.

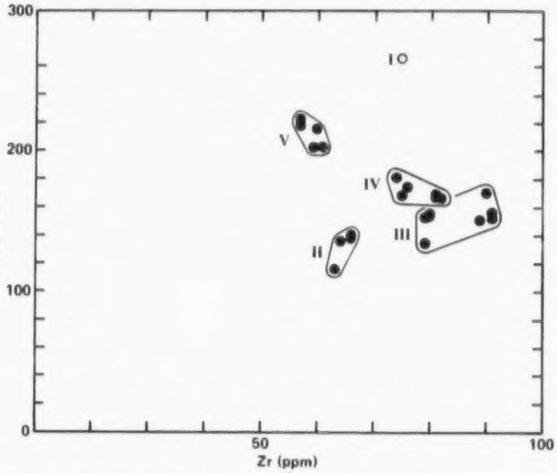

Figure 9. Plot of Ni versus Zr for Hole 558 basalts. Roman numerals indicate chemical groups.

two subgroups are related by crystal fractionation processes; certainly, ratios such as Zr/Nb and Ce/Y are not fractionated between the subgroups. However, the most successful least-squares models for the major elements require an olivine-plagioclase-clinopyroxene extract and even then, the sums of squares of residuals are unacceptably high.

REE data for Group IIIA basalt are given in Table 5 and plotted in Figure 11. This chemical group is the most evolved of the Hole 558 E-MORB units, with the highest Ce_N/Yb_N (2.2) and La_N/Sm_N (1.8) ratios and levels of the REE.

Group IV comprises basalts from the remaining part of Lithologic Unit 7. Six samples were analyzed from this group (from Cores 558-35 and 558-36), and the data are presented in Table 9. The shipboard party considered this to be a homogeneous chemical group. However, evidence from the trace element chemistry indicates that two subgroups may be present. In terms of normative mineralogy, the basalts of this group are indistinguishable from those of Group IIIB, and they behave as a coherent group (Fig. 8). Although there are only small differences in the levels of incompatible elements between the Subgroups IVA and IVB (i.e., TiO_2, 1.18–1.20% in IVA, 1.22–1.23% in IVB; Zr, 74–76 ppm in IVA, 81–82 ppm in IVB), there are significant differences in incompatible element ratios, particularly Zr/Nb (7.8–8.2 in IVA, 7.0–7.5 in IVB) and Ce_N/Y_N (1.4–1.5 in IVA, 1.8 in IVB) (Figs. 12, 13). It is apparent

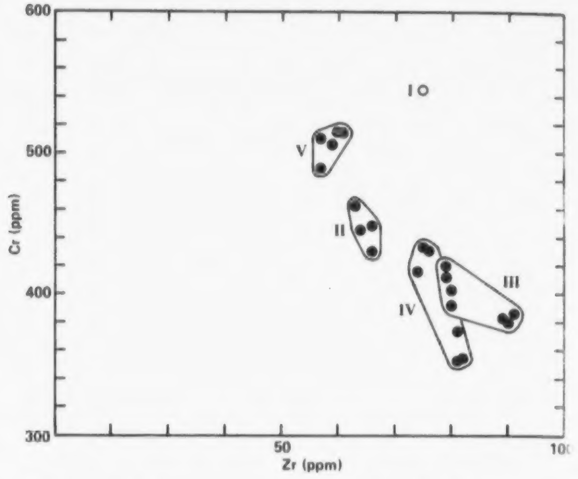

Figure 10. Plot of Cr versus Zr for Hole 558 basalts. Roman numerals indicate chemical groups.

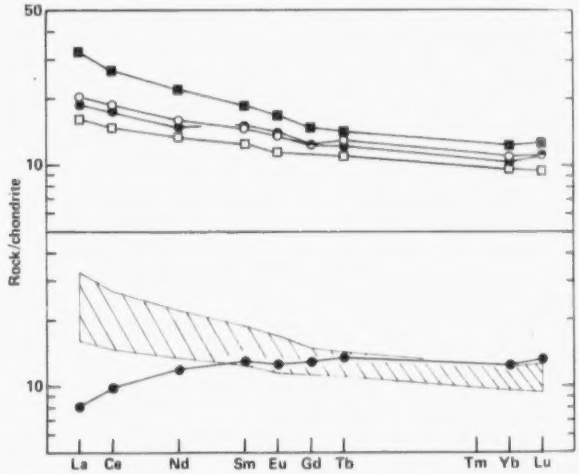

Figure 11. Abundances of the rare earth elements in Hole 558 basalts normalized to the average chondrite values of Nakumara (1974). In top diagram: closed circle = Group I; closed square = Group III; open circle = Group IV; open square = Group V. In bottom diagram: closed circle = Group II. Cross-hatched field is for E-type mid-ocean ridge basalts from top diagram.

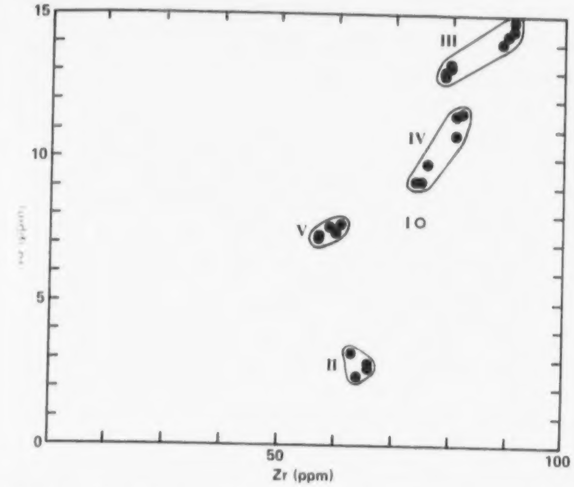

Figure 12. Plot of Nb versus Zr for Hole 558 basalts. Roman numerals indicate chemical groups.

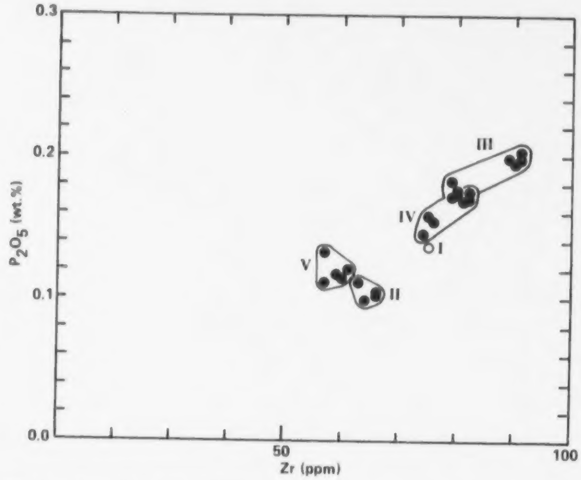

Figure 14. Plot of P_2O_5 versus Zr for Hole 558 basalts. Roman numerals indicate chemical groups.

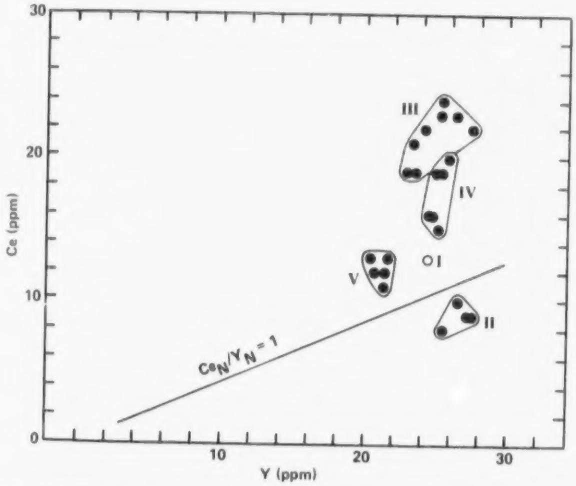

igure 13. Plot of Ce versus Y for Hole 558 basalts. Roman numerals indicate chemical groups.

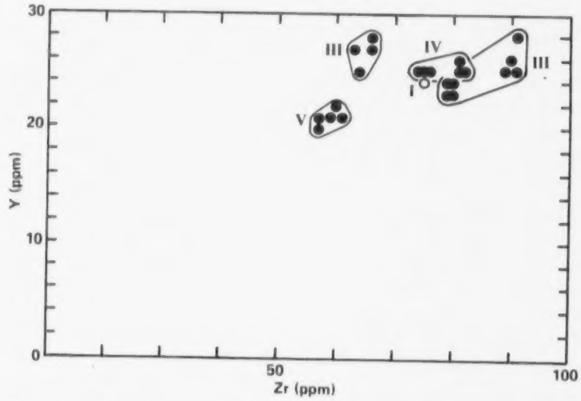

Figure 15. Plot of Y versus Zr for Hole 558 basalts. Roman numerals indicate chemical groups.

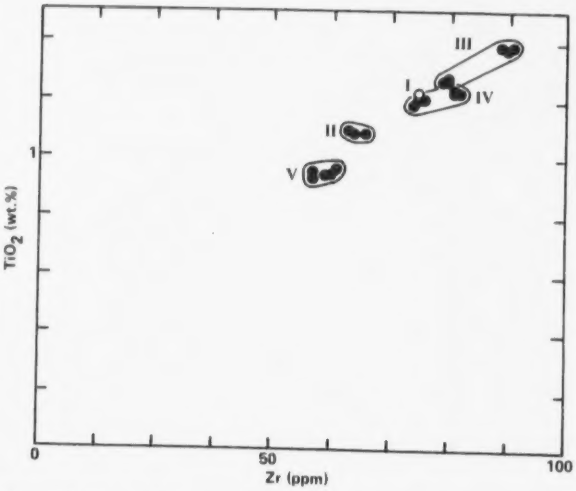

Figure 16. Plot of TiO_2 versus Zr for Hole 558 basalts. Roman numerals indicate chemical groups.

om the values for these ratios that the basalts of this oup are enriched in more-incompatible trace elements, hough not as enriched as the basalts of Group III igs. 12–17). Unlike the chemical variation between the bgroups in Group III, which might be attributable to ystal fractionation processes, the differences in Zr/Nb d Ce/Y ratios between IVA and IVB basalts prohibit imple relationship by crystal fractionation, especially only a small fractionation interval would be involved amely, a small difference in Zr abundance between the o subgroups; Table 9, Figs. 12–17). Rather, the differences might be related to degree, or type, or partial melting.

REE data for Group IVA basalt are given in Table 5 and plotted in Figure 11. The levels of REE and degree of LREE enrichment are comparable to the basalt of Chemical Group I.

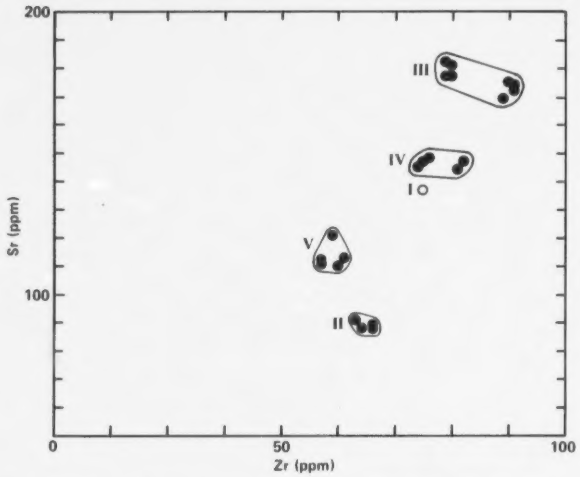

Figure 17. Plot of Sr versus Zr for Hole 558 basalts. Roman numerals indicate chemical groups.

Group V comprises basalts from Lithologic Units 8 to 10. Five samples have been analyzed from this group (from Cores 558-37 through 558-39), and the data are presented in Table 9. Normatively these basalts are more Ol rich than the other basalts from Hole 558 (Fig. 8). They are similar to basalts from Groups I, III, and IV because they are enriched in the more-incompatible (e.g., Nb, Ce) relative to the less-incompatible (e.g., Zr, Y) trace elements (Zr/Nb 7.8–8.1; Ce_N/Y_N 1.2–1.5; Table 9, Figs. 12, 13); the degree of enrichment is similar to Groups I and IVA for Ce/Y (Fig. 13) and similar to IVB for Zr/Nb (Fig. 12). These basalts are significantly less enriched than Group III, however (Figs. 12, 13). Basalts of Group V have the lowest absolute abundances of incompatible trace elements among Hole 558 basalts (Figs. 12–17), high Mg-values (66–70; Table 9), and also high Ni and Cr contents (Figs. 9, 10). The slight chemical variation within Group V (Table 9) can be successfully modeled on the basis of a small proportion of olivine fractionation or microphenocryst distribution (Table 10).

The basalts of this group have the lowest levels of REE among the E-MORB units of Hole 558 (Table 5, Fig. 11) with the least LREE enrichment (Ce_N/Yb_N = 1.5, La_N/Sm_N = 1.3).

Table 10. Least squares approximation relating the basalts of Chemical Group V, Hole 558, by olivine fractionation.

	Derivative (558-39-1, 55–57 cm)	Ol	Parent (558-37-1, 143–148 cm)	Calculated parent	Residuals
SiO_2	49.64	40.26	49.28	49.25	−0.03
TiO_2	0.99		0.95	0.95	0.00
Al_2O_3	16.33		15.56	15.66	0.10
FeO*	8.64	12.28	8.87	8.79	−0.08
MnO	0.16		0.15	0.15	0.00
MgO	8.69	47.36	10.22	10.27	0.05
CaO	12.02	0.30	11.55	11.54	−0.01
Na_2O	2.20		2.05	2.11	0.06
P_2O_5	0.13		0.12	0.12	0.00
Mix	95.9	4.1			$\Sigma R^2 = 0.0239$

Note: ΣR^2 is the sum of the squares of residuals (calculated parent − parent). FeO* is total iron expressed as FeO. For the least-squares approximations, the method of Bryan et al. (1969) has been used.

SITE 559

Site 559 (35°07.45′N; 40°55.00′W, 3754 m water depth) lies between Magnetic Anomalies 12 and 1 (35 Ma old) on the west flank of the Mid-Atlantic Ridg and is approximately midway between the Oceanogra pher and Hayes fracture zones. A single hole was drille and 63 m of basement (encountered at 238 m sub-bo tom depth) were cored before the hole was abandone A single lithologic unit comprising one chemical grou (consisting of variably, but quite heavily altered, aphyr pillow basalts) was identified.

The aphyric basalts from this hole contain subequ amounts (35–40 vol.%) of plagioclase and clinopyro ene. The plagioclase occurs as randomly oriented swa lowtail laths, and the clinopyroxene as relatively lar prismatic grains, parallel aggregates of smaller prism sheaves, or branching aggregates. Olivine (~5 vol.%) altered to clay and zeolite as is interstitial glass (~2 vol.%). A microprobe study of the mineral chemistry o basalts from this hole was not made.

Analyses of seven samples from Hole 559 are presented in Table 11. Shipboard analyses of basalts from this hole stressed the significance of chemical changes associated with alteration (site chapter, Site 559, this volume). Extensive alteration was found to produce pronounced depletion in SiO_2 and MgO (and thus a lowering of the Mg-value) and pronounced enrichment of MnO, K_2O, P_2O_5, Sr, and V. Of the other elements analyzed on board, the major elements TiO_2, Al_2O_3, Fe_2O_3, and CaO and the trace elements Zr, Nb, and Y were not significantly affected by even extreme degrees of alteration. These observations are largely in accord with previous studies of the chemical effects of low-temperature basalt-seawater interaction (Hart, 1970; Hart et al., 1974; Thompson and Humphris, 1977). However, the mobility of P is not generally recognized, although it has been noted by Marsh et al. (1980) and Weaver and others (1983). The shipboard study indicates that fresh basalts from Hole 559 have an Mg-value of 59, K_2O ~ 0.4%, P_2O_5 ~ 0.19%, and Sr ~ 169 ppm. Of the analyzed samples from this hole, all have rather high weight losses upon ignition (~2.9%, commonly 4%; Table 10), but only the Sample 559-1-2, 118–120 cm (Table 11) has a chemistry indicative of heavy alteration. In addition to the elements identified as mobile in the shipboard stud , the trace elements Ni and Zn appear to be respective y depleted and enriched in this altered sample, and the e is some suggestion that the LREE La and Ce may be e riched over the average abundance in the other sampl (Table 11). This again is largely in accord with previo studies of low-temperature basalt alteration.

Hole 559 basalts display some scatter on a plot of t normative components Di-Ol-Hy (Fig. 18), which is larg ly due to alteration that causes a decrease in the propo tion of Hy and an increase in the proportion of Ol rel tive to Di. The fresher basalts have moderate amour s of normative Ol and are similar to the basalts of Chem cal Groups IIIB and IV in Hole 558. In terms of tra e element chemistry, Hole 559 basalts are enriched in t

Table 11. Major and trace element analyses for Hole 559 basalts.

Core-Section (interval in cm) Piece number	1-2 118-120 11a	2-2 18-20 1a	4-1 118-121 9a	5-1 38-40 3a	6-2 12-14 1a	7-2 3-6 1a	8-1 18-20 1a
Major elements (wt.%)							
SiO_2	46.40	47.30	47.59	47.72	48.14	47.23	48.00
TiO_2	1.46	1.46	1.45	1.44	1.46	1.45	1.46
Al_2O_3	15.36	15.48	14.82	14.88	15.11	14.38	14.79
Fe_2O_3	10.98	10.77	10.34	10.30	9.92	10.65	10.34
MnO	0.15	0.16	0.13	0.13	0.13	0.15	0.14
MgO	6.50	7.16	7.37	6.99	7.20	8.05	7.22
CaO	11.38	12.14	11.14	11.11	11.12	11.03	10.89
Na_2O	2.68	2.49	2.65	2.58	2.55	2.58	2.50
K_2O	0.48	0.42	0.38	0.39	0.39	0.47	0.41
P_2O_5	0.23	0.20	0.19	0.19	0.20	0.18	0.19
LOI	4.61	2.93	4.29	4.38	4.21	3.53	4.23
Total	100.23	100.51	100.35	100.11	100.43	99.70	100.17
Trace elements (ppm)							
Cr	299	306	290	295	306	290	281
Ni	90	127	130	121	161	134	117
V	328	306	291	298	301	289	291
Zn	118	88	86	85	85	84	87
Ga	18	18	18	17	17	16	17
Rb	8	7	7	7	7	9	8
Sr	171	173	164	168	169	164	171
Ba	44	53	42	40	39	49	48
Zr	102	103	101	100	102	100	103
Nb	14.5	14.7	14.6	14.1	14.9	14.6	16.1
La	10	9	9	9	9	8	9
Ce	24	20	24	21	21	21	21
Nd	13	13	13	13	13	12	12
Y	31	31	31	30	31	30	31
Selected element ratios							
Mg-value	57	60	62	60	62	63	61
Ti/Zr	86	85	86	86	86	87	85
Zr/Nb	7.0	7.0	6.9	7.1	6.8	6.8	6.4
Ce_N/Y_N	1.8	1.5	1.8	1.6	1.6	1.6	1.6
Zr/Ce	4.6	5.6	4.5	5.1	5.2	5.1	5.3
Zr/Y	3.5	3.6	3.5	3.6	3.5	3.6	3.6
CIPW norms							
Or	3.0	2.5	2.4	2.4	2.4	2.9	2.5
Ab	23.7	21.6	23.4	22.8	22.4	22.7	22.1
An	29.8	30.6	28.5	29.1	29.7	27.3	29.1
Di	22.7	24.4	22.6	22.2	21.3	23.1	21.2
Hy	5.2	2.7	7.8	11.0	12.7	5.5	14.1
Ol	10.2	12.0	9.2	6.4	5.3	12.4	4.9
Mt	2.0	1.9	1.9	1.9	1.8	1.9	1.9
Il	2.9	2.9	2.9	2.9	2.9	2.9	2.9
Ap	0.6	0.5	0.5	0.4	0.5	0.4	0.5

Note: LOI is loss on ignition. Total iron is expressed as Fe_2O_3. CIPW norms and Mg-values (100 Mg/[Mg + Fe^{2+}]) are calculated using an assumed Fe_2O_3/FeO ratio of 0.15. Ce_N/Y_N expresses the chondrite-normalized ratio of Ce to Y.

more-incompatible (compared to less-incompatible) elements, with a low Zr/Nb ratio (~7; Table 11) and a high Ce_N/Y_N ratio (~1.6; Table 11). These ratios are most comparable to those in basalts from Chemical Group IVA and IVB, Hole 558 (Fig. 10). However, the Ti/Zr ratio (~86; Table 11) is rather low and less than the value for this ratio in any of the chemical groups from Hole 558 (Fig. 19). Additionally, the low Mg-value (~61), as well as the Cr (~300 ppm) and Ni (~130 ppm) abundances, do not approximate those expected in primary liquids; the Hole 559 basalts must have undergone significant crystal fractionation. In these terms, they are more evolved than any of the Hole 558 basalts, as also indicated by the greater absolute abundances of Zr, Nb, and TiO_2 (Figs. 19, 20) in the Hole 559 basalts.

SITE 560

Site 560 (34°43.33′N; 38°50.56′W, 3443 m water depth) lies on Magnetic Anomaly 5D (18 Ma old) on the west flank of the Mid-Atlantic Ridge and is midway between the Oceanographer and Hayes fracture zones on a flow line passing through Site 559. A single hole was drilled at this site, and 47.5 m of basement (encountered at 374.5 m sub-bottom depth) were cored before the hole was abandoned. Only mylonitized gabbro breccia, with two short intervals of limestone and limestone-basalt breccia, was recovered from the basement in Hole

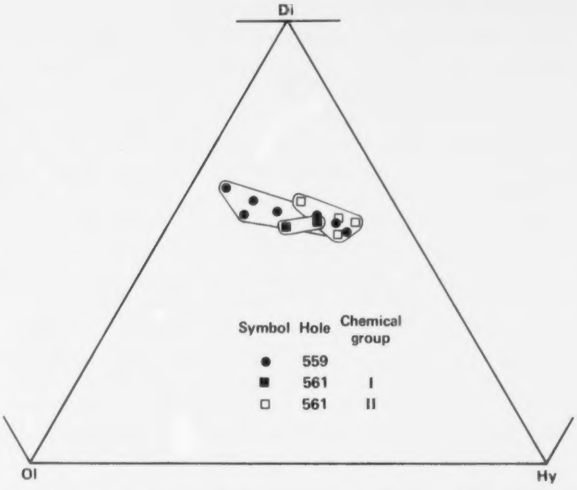

Figure 18. Plot of normative components Ol-Di-Hy for basalts from Holes 559 and 561. Norms are calculated using an Fe_2O_3/FeO ratio of 0.15.

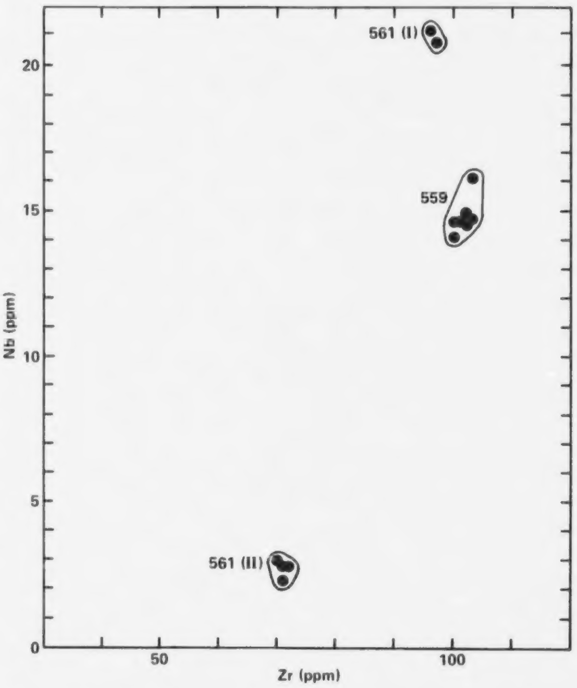

Figure 19. Plot of Nb versus Zr for basalts from Holes 559 and 561. Roman numerals indicate chemical groups.

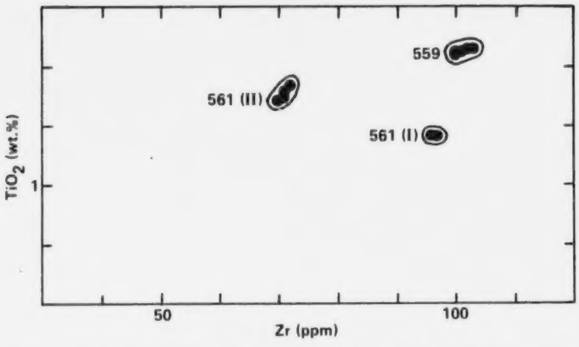

Figure 20. Plot of TiO_2 versus Zr for basalts from Holes 559 and 561. Roman numerals indicate chemical groups.

560. The basalt clasts from the limestone-basalt breccia are strongly zeolitized.

Because of the extremely limited recovery and the heavily altered nature of the basalt in Hole 560, no sample was taken. Indeed, only one sample was analyzed on board (site chapter, Site 560, this volume), and the major element chemistry appears to be controlled by the strong zeolitization. However, assuming that the relative abundances of the trace elements Zr, Nb, and Y have not been modified by zeolitization, original Zr/Nb and Zr/Y ratios of 11.8 and 2.5, respectively, are indicated for this sample, suggesting considerably less enrichment of more-incompatible (compared to less-incompatible) elements than in Hole 559 basalts.

SITE 561

Site 561 (34°47.10′N; 39°01.70′W, 3459 m water depth) lies on Magnetic Anomaly 5E (19 Ma old) on the west flank of the Mid-Atlantic Ridge 10 miles to the northwest of Site 560 and close to the flow line passing through Site 559. We needed to drill at another site in this area because of the failure to recover significant basaltic basement at Site 560. A single hole was drilled at Site 561 and 15 m of basement (encountered at 411.5 m sub-bottom depth) were cored before bit failure. The shipboard party identified three lithologic units comprising two chemical groups, which consisted of basalt-limestone breccia and two units of aphyric pillow basalt.

Group I basalts compose Lithologic Unit 1. The basalts of this group are aphyric, containing only small amounts (~2–3 vol.%) of rather magnesian olivine microphenocrysts (Fo_{87}; Table 6). The ground mass contains subequal (~35–40 vol.%) proportions of elongate (up to 1.5 mm) hollow plagioclase laths with interstitial granular clinopyroxene. The remainder of the groundmass consists largely of altered mesostasis.

Two samples were analyzed from this group (from the wash-core and the upper part of Core 561-1), and the analyses are given in Table 12. Normatively these basalts have moderate amounts of olivine and plot within the field defined by Hole 559 basalts on the Ol-Di-Hy diagram (Fig. 18). The two samples analyzed from this group are very similar chemically (Table 12), with the notable exception of Sr and Ba, which are enriched by factors of 2 and 3, respectively, in the sample from Core 561-1. The basalts of this group are quite strongly enriched in more-incompatible compared to less-incompatible trace elements, with very low Zr/Nb (4.5–4.7; Table 12, Fig. 19) and high Ce_N/Y_N (2.2–2.3; Table 12) ratios. These basalt are more enriched than any of the E-type MORB of Holes 558 and 559. They are, however, rather primitive; Mg-values are high (~67; Table 12) as are Cr and Ni abundances (Table 12). A feature of this group is the lo Ti/Zr (Table 12, Fig. 20) and high Zr/Y (Table 12) ratios, a feature also evident in the E-type MORB of Holes 558 and 559, but more pronounced in this chemical group.

The REE data (Table 5) for Sample 561-1-1, 44–47 cm demonstrate the strong enrichment in more-incompat

Table 12. Major and trace element analyses for Hole 561 basalts.

Chemical group	I		II			
Core-Section (interval in cm) Piece number	H1-CC 9–13 1	1-1 44–47 2c	1-2 22–24 2b	2-1 111–116 6c	2-3 127–130 11a	3-1 138–140 9j
Major elements (wt.%)						
SiO_2	48.53	48.30	48.76	48.98	48.42	48.7
TiO_2	1.16	1.16	1.34	1.32	1.30	1.2
Al_2O_3	15.13	14.84	14.91	14.88	14.61	14.6
Fe_2O_3	9.47	9.67	10.93	11.43	10.89	11.5
MnO	0.15	0.15	0.18	0.18	0.18	0.1
MgO	8.18	9.05	8.02	7.25	7.68	7.1
CaO	11.72	11.76	11.49	11.56	11.93	11.4
Na_2O	2.36	2.30	2.41	2.38	2.46	2.3
K_2O	0.37	0.35	0.15	0.40	0.22	0.4
P_2O_5	0.22	0.22	0.11	0.11	0.11	
LOI	2.79	2.63	1.53	1.84	2.08	2.1
Total	100.08	100.43	99.83	100.33	99.88	100.0
Trace elements (ppm)						
Cr	445	459	260	249	256	256
Ni	191	197	144	137	135	126
V	258	264	343	338	336	332
Zn	81	77	93	96	93	91
Ga	16	17	19	20	19	19
Rb	7	5	2	9	5	12
Sr	221	636	91	91	91	88
Ba	55	125	12	10	9	10
Zr	97	96	72	71	71	70
Nb	21	21	2.8	2.3	2.8	3.0
La	12	13	3	2	2	2
Ce	26	27	9	10	10	10
Nd	13	13	8	8	9	8
Y	27	27	34	35	35	34
Selected element ratios						
Mg-value	66	68	62	59	61	58
Ti/Zr	72	72	112	111	110	110
Zr/Nb	4.7	4.5	26	31	25	23
Ce_N/Y_N	2.2	2.3	0.6	0.7	0.7	0.7
Zr/Ce	4.1	4.3	8.3	7.4	7.4	7.3
Zr/Y	4.0	4.3	2.2	2.1	2.1	2.1
CIPW norms						
Or	2.3	2.1	0.9	2.4	1.4	2.6
Ab	20.6	19.9	20.7	20.5	21.2	19.9
An	30.4	29.8	30.0	29.2	28.8	29.0
Di	22.6	22.9	22.2	23.2	25.3	23.2
Hy	11.8	9.9	14.4	13.6	9.8	15.3
Ol	7.0	10.0	6.0	5.3	7.7	4.2
Mt	1.7	1.7	1.9	2.0	1.9	2.0
Il	2.3	2.3	2.6	2.5	2 5	2.5
Ap	0.5	0.5	0.3	0.3	0.3	0.3

Note: LOI is loss on ignition. Total iron is expressed as Fe_2O_3. CIPW norms and Mg-values (100 Mg/[Mg + Fe^{2+}]) are calculated using an assumed Fe_2O_3/FeO ratio of 0.15. Ce_N/Y_N expresses the chondrite-normalized ratio of Ce to Y.

ble elements in this group (Fig. 21). The Ce_N/Yb_N (2.7) and La_N/Sm_N (2.11) ratios are both high and higher than the values for these ratios in Hole 558 E-type MORB. The REE pattern (Fig. 21) appears to be somewhat concave downward.

Group II basalts compose Lithologic Units 2 and 3. The basalts of this group are characterized by the occurrence of variable proportions (2-3 vol.%) of plagioclase-olivine glomerocrysts ranging in diameter from 1-3 mm and surrounded by a halo of devitrified glass. The plagioclase phenocrysts are 0.5-2 mm in length, occur either singly or in glomerophyric aggregates with olivine, and are essentially unzoned, having core compositions of An_{73} and rim compositions of An_{71} (Table 1). Olivine phenocrysts (occurring in glomerophyric aggregates with plagioclase) and microphenocrysts range from 0.1 to 0.5 mm in size and are completely altered to brown clay. The groundmass consists of approximately 35 vol.% random plagioclase laths (composition An_{64}; Table 1) with approximately 45 vol.% interstitial prismatic to granular clinopyroxene, plus approximately 5 vol.% magnetite and 10-15 vol.% devitrified glass.

Four samples were analyzed from this group and the data are given in Table 12. In terms of normative components, the samples from this group generally have less normative Ol than Group I and are similar to the fresher basalts from Hole 559 (Fig. 18). In marked contrast to the E-type MORB of Group I, the basalts of this group are depleted in more-incompatible trace elements; Zr/Nb ratios are high (23-31; Table 12, Fig. 19) and Ce_N/Y_N ratios low (0.6-0.7; Table 12); they are similar to the N-type MORB of Holes 556 and 558. The Cr and Ni contents and Mg-values are much lower than in Group I basalts (Table 12), whereas the Ti/Zr ratio is considerably higher (Table 12, Fig. 20).

REE data for this group are given in Table 5 and plotted in Figure 21. The depletion in the LREE ($Ce_N/Yb_N = 0.6$, $La_N/Sm_N = 0.6$) is similar to that of the Hole 556 N-type MORB.

SITE 562

Site 562 (33°08.49′N; 41°40.76′W, 3172 m water depth) lies on Magnetic Anomaly 5D (18 Ma old) on the west flank of the Mid-Atlantic Ridge and is approximately 60 miles south of the Hayes Fracture Zone. A single hole was drilled at this site, and 91 m of basement (encountered at 240 m sub-bottom depth) were cored before the hole was abandoned. A single lithologic unit comprising two chemical groups was recognized by the shipboard party, consisting of slightly to moderately plagioclase phyric pillow basalts and massive basalt flows. The degree of alteration is variable.

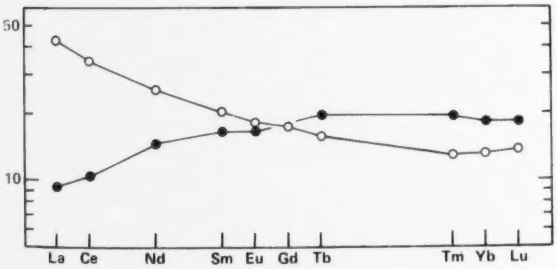

Figure 21. Abundances of the rare earth elements for Hole 561 basalts normalized to the average chondrite values of Nakamura (1974). Open circle = Chemical Group I; closed circle = Chemical Group II.

The basalts from Hole 562 contain approximately 5 vol.% plagioclase phenocrysts (generally 1-10 mm in size) that often occur as glomerophyric clusters. The phenocrysts are often subhedral to rounded in outline, are strongly zoned at the margins, and contain inclusions of melt and magnesiochromite. The phenocrysts are zoned from core compositions of An_{85} to rim compositions of An_{67} in the Chemical Group I sample (Table 1) and from An_{91} to An_{76} in the Chemical Group II sample (Table 1). The melt inclusions have Mg-values of approximately 71 in the Group I sample as opposed to Mg-values of 66 to 67 in the Group II sample. Magnesiochromite inclusions in Group I plagioclase phenocrysts are less magnesian ($Mg/[Mg + Fe^{2+}] = 0.67$) and more Cr-rich ($Cr/[Cr + Al] = 0.47$) than the inclusions in Group II plagioclase phenocrysts ($Mg/[Mg + Fe^{2+}] = 0.77$; $Cr/[Cr + Al] = 0.42$) (Table 2). Olivine (2-3 vol.%) occurs as small (0.1-0.6 mm) rounded anhedral microphenocrysts, which are less magnesian in the Group I (Fo_{81}; Table 6) as compared to the Group II (Fo_{84}; Table 6) sample. The fine-grained groundmass comprises subequal (35-40 vol.%) proportions of plagioclase and clinopyroxene with approximately 5-10 vol.% opaques and 10-15 vol.% mesostasis. The groundmass plagioclase occurs as two distinct generations: as elongate hollow laths (generally 1 mm, but up to 3 mm long) in radiating clusters originating from olivine microphenocrysts, or as parallel growths from the ends of prismatic plagioclase phenocrysts, and as fine laths (~0.2 mm) intergrown with prismatic clinopyroxene of a similar size. The composition of these two types of groundmass plagioclase is similar, An_{66} in Chemical Group I and An_{72} in Chemical Group II (Table 1).

Eleven samples were analyzed from Hole 562; five from Chemical Group I and six from Chemical Group II. The analyses are given in Table 13.

Group I basalts plot close to the Di-Hy join in the normative Di-Ol-Hy diagram (Fig. 22); they have only small amounts of normative Ol. The exception to this is Sample 562-2-4, 74-76 cm (Table 13), which is altered (high LOI, K_2O, Rb) and so displaced from the main group by the development of a high Ol/Hy ratio in the norm. Sample 562-1-2, 82-84 cm (Table 13) is also somewhat different chemically from the other samples; it has higher levels of incompatible elements (e.g., Ti, Zr), as well as higher Ni and Cr, than the other basalts in Group I (Table 13). This sample also has a higher Di/Hy ratio (Fig. 22), which cannot be attributed to the effects of alteration. Although significant chemical differences are apparent between this sample and the remainder of Group I, the identification of one aberrant sample is not sufficient to warrant the designation of a separate chemical group, thus this sample will be considered as part of Group I. The basalts of this group are depleted

Table 13. Major and trace element analyses of Hole 562 basalts.

Chemical group	I					II					
Core-Section	1-2	2-4	3-2	4-2	5-3	6-4	7-2	8-1	8-2	9-2	10-2
(interval in cm)	82–84	74–76	141–143	45–47	79–81	18–21	138–142	68–71	55–58	81–83	86–88
Piece number	4b	2e	8c	1b	1f	1b	4f	5c	6a	4d	4d
SiO_2	49.77	48.78	49.42	49.64	49.11	48.08	47.80	47.24	47.41	48.18	45.47
TiO_2	1.62	1.52	1.51	1.49	1.53	1.07	1.13	1.17	1.17	1.12	1.00
Al_2O_3	15.58	15.42	15.51	15.63	14.95	17.64	16.97	15.96	15.14	16.36	16.08
Fe_2O_3	9.92	11.08	11.09	10.71	11.52	9.34	10.04	9.82	10.23	9.84	10.09
MnO	0.17	0.18	0.17	0.17	0.18	0.14	0.16	0.15	0.16	0.16	0.15
MgO	6.16	6.75	7.08	6.69	7.47	6.62	6.80	7.25	7.14	7.50	6.18
CaO	12.34	11.56	11.46	11.49	11.23	12.54	12.87	13.22	13.06	12.48	14.41
Na_2O	2.72	2.62	2.44	2.49	2.42	2.12	2.20	2.34	2.22	2.23	2.06
K_2O	0.29	0.29	0.20	0.22	0.14	0.28	0.15	0.27	0.33	0.24	0.41
P_2O_5	0.15	0.14	0.14	0.14	0.14	0.11	0.12	0.12	0.12	0.11	0.11
LoI	0.87	2.09	1.30	1.51	1.58	2.58	1.99	2.13	3.39	1.85	4.48
Total	99.59	100.43	100.32	100.18	100.27	100.52	100.23	99.67	100.37	100.07	100.44
Trace elements in ppm											
Cr	275	248	249	230	236	266	280	271	276	279	248
Ni	138	96	90	103	90	79	83	117	94	93	86
V	359	319	316	307	311	260	290	281	296	277	259
Zn	107	88	89	89	87	75	80	81	82	79	73
Ga	19	16	16	18	18	17	18	16	17	17	16
Rb	6	5	4	4	2	6	2	5	8	3	11
Sr	107	100	98	100	100	96	97	91	98	99	105
Ba	13	10	11	10	12	12	12	7	12	10	9
Zr	98	89	92	91	92	63	65	66	67	65	69
Nb	3.0	2.9	2.9	3.0	3.1	2.4	2.4	2.8	3.2	2.4	2.6
La	3	3	3	3	3	2	<2	2	2	2	2
Ce	10	10	9	9	10	7	6	7	6	7	7
Nd	9	9	9	9	8	8	8	8	8	8	7
Y	40	36	36	36	36	26	29	29	30	28	25
Selected element ratios											
Mg-value	58	58	59	58	59	61	60	62	61	63	58
Ti/Zr	99	102	98	98	100	102	104	106	105	103	102
Zr/Nb	33	31	32	30	30	26	27	24	21	27	23
Ce_N/Y_N	0.6	0.6	0.6	0.6	0.6	0.6	0.5	0.6	0.5	0.6	0.6
Zr/Ce	10	10	11	10	10	9.3	11	9.7	12	10	8.7
Zr/Y	2.5	2.6	2.6	2.6	2.6	2.5	2.3	2.3	2.3	2.4	2.4
CIPW norms											
Or	1.7	1.7	1.2	1.3	0.8	1.7	0.9	1.7	2.0	1.4	2.5
Ab	23.4	22.5	20.8	21.3	20.7	18.3	19.0	20.3	19.4	19.2	13.5
An	29.8	30.0	31.1	31.3	29.9	38.6	36.7	33.1	31.3	34.6	34.8
Ne											2.5
Di	25.5	22.4	20.8	21.0	20.9	19.7	22.5	27.2	28.3	22.6	31.9
Hy	11.3	11.6	18.1	18.9	18.7	12.1	8.7	0.1	4.2	9.4	
Ol	2.2	5.5	1.8	0.2	2.6	4.8	7.2	12.4	9.4	7.7	9.7
Mt	1.7	2.0	1.9	1.9	2.0	1.7	1.8	1.7	1.8	1.7	1.8
Il	3.1	2.9	2.9	2.9	2.9	2.1	2.2	2.3	2.3	2.2	2.0
Ap	0.4	0.4	0.3	0.3	0.4	0.3	0.3	0.3	0.3	0.3	0.3

Note: LOI is loss on ignition. Total iron is expressed as Fe_2O_3. CIPW norms and Mg-values (100 Mg/[Mg + Fe^{2+}]) are calculated using an assumed Fe_2O_3/FeO ratio of 0.15. Ce_N/Y_N expresses the chondrite-normalized ratio of Ce to Y.

in trace elements and have high Zr/Nb ratios (30–33; Table 13; Fig. 23) and low Ce_N/Y_N ratios (0.6; Table 13). Mg-values (~58) and Cr and Ni abundances are relatively low, and abundances of the incompatible elements Ti and Zr are quite high (Table 13), indicating the relatively evolved nature of these basalts compared to depleted basalts from Chemical Groups I and III, Hole 556; Chemical Group II, Hole 558; and Chemical Group II, Hole 561 (see Figs. 5, 16, 20, 24).

Group II basalts plot in an elongated field in Figure 22 and show a wide variation in the proportion of normative Hy, but an approximately constant Ol/Di ratio. Some of this dispersion is due to chemical effects associated with alteration; Samples 562-8-2, 55–58 cm and 562-10-2, 86–88 cm both have high weight losses on ignition and K_2O and Rb contents (Table 13). In addition the Sample 562-10-2, 86–88 cm has a low Mg-valu (Table 13). The former sample is slightly Ne normative whereas the latter sample has low normative Hy (Fig. 22 Table 13). An additional problem with samples fro this group is the presence of a significant proportion o calcite-filled vesicles: Sample 562-8-1, 68–71 cm contains approximately 10% of these vesicles. The resultin CaO contamination of the whole-rock analysis will produce a decrease in Hy in the norm and even the development of normative Ne, although maintaining an approximately constant Di/Ol ratio. The basalts of this grou are less evolved than those of Group I and have highe

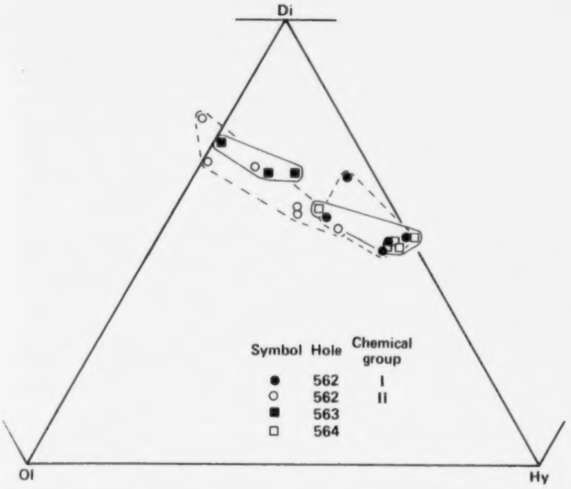

Figure 22. Plot of normative components Ol-Di-Hy in basalts from Holes 562, 563, and 564.

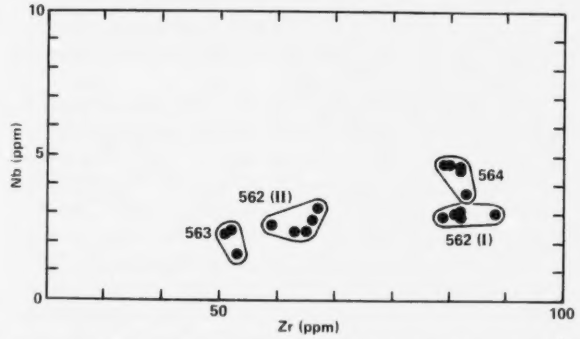

Figure 23. Plot of Nb versus Zr for basalts from Holes 562, 563, and 564. Roman numerals indicate chemical groups.

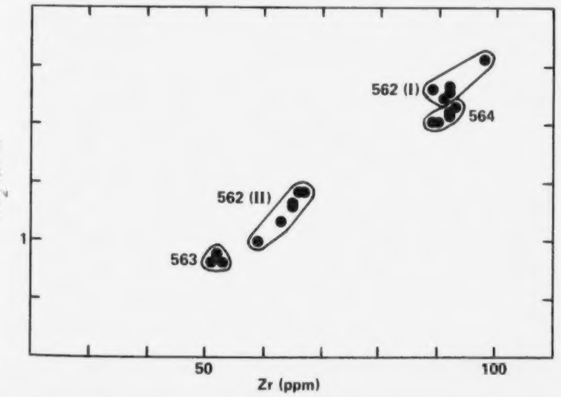

Figure 24. Plot of TiO_2 versus Zr for basalts from Holes 562, 563, and 564. Roman numerals indicate chemical groups.

Mg-numbers, somewhat higher Cr abundances, and lower Ti and Zr abundances (Table 13; Fig. 24). This is in accord with the mineralogic evidence; the Group II basalts have more anorthitic phenocryst and groundmass plagioclase and more forsteritic olivine microphenocrysts (Tables 1, 4) than the Group I basalts. However, Group II basalts are similar to Group I in displaying depletion in the more-incompatible elements; Ce_N/Y_N ratios are low (0.5–0.6; Table 13), and Zr/Nb ratios high (21–27; Table 13), although the latter ratios are lower than in Group I (Fig. 23). The rather wide chemical variation within the Group II basalts (Table 13) can be attributed to dilution by plagioclase phenocrysts (Table 7).

SITE 563

Site 563 (33°38.53′N; 43°46.04′W, 3786 m water depth) lies on Magnetic Anomaly 13 (37 Ma old) on the west flank of the Mid-Atlantic Ridge and is approximately 60 miles south of the Hayes Fracture Zone on the flow line through Site 562. A single hole was drilled at this site, and only 18 m of basement (encountered at 364.5 m sub-bottom depth) were cored before bit failure. The shipboard party identified a single lithologic unit comprising two chemical groups, consisting of sparsely plagioclase phyric pillow basalts.

Plagioclase phenocrysts (0.5–5 mm) compose approximately 5% of the basalt and generally occur in glomerophyric clusters. The phenocrysts are lath-shaped to prism-shaped and slightly resorbed; they contain melt inclusions (with Mg-values ranging from 66 to 70) and are strongly marginally zoned from core compositions of An_{90} to rim compositions of An_{80} (Table 1). Subhedral olivine microphenocrysts have a composition of Fo_{85} (Table 6). Rare clinopyroxene microphenocrysts (0.3–0.5 mm) occur that are quite magnesian ($Mg/[Mg + Fe^{2+}] = 0.84$) and have high Cr_2O_3 contents (0.77 wt.%) (Table 3). The groundmass comprises subequal proportions (~40%) of randomly oriented, acicular to lath-shaped plagioclase of composition An_{71} (Table 1) and anhedral clinopyroxene ($Mg/[Mg + Fe^{2+}] = 0.82$; Table 3). The remainder of the groundmass is composed of approximately 3% equant to granular opaque and approximately 1% altered granular olivine. The final stage of crystallization is represented by either fine-grained or featherlike arrangements of plagioclase and clinopyroxene. Up to 10 vol.% calcite-filled vesicles are present.

Only three samples were analyzed from Hole 563, and the data are presented in Table 14. Normatively the basalts have moderate amounts of Ol relative to Hy (Fig. 22) and, in this respect, are similar to the basalts of Chemical Group II, Hole 562 (Fig. 22). However, Ol/Hy ratios may be enhanced by both alteration and calcite contamination, as in Group II, Hole 562. The shipboard party recognized two chemical groups among Hole 563 basalts, although the sole apparent difference is in the abundances of Fe_2O_3 and K_2O. Basalts of these two groups occur as interdigitated pillow flows. Our limited number of samples do not conform to this pattern; Sample 563-25-2, 37–39 cm (Piece 2A) (Table 14) has Fe_2O_3 and K_2O abundances similar to Chemical Group I (identified by the shipboard party), although shipboard

Table 14. Major and trace element analyses for Hole 563 basalts.

Core-Section (interval in cm) Piece number	23-1 104–106 10b	24-4 0–7 1a	25-2 37–39 2a
Major elements (wt.%)			
SiO_2	48.50	48.04	47.69
TiO_2	0.93	0.93	0.96
Al_2O_3	16.23	15.58	14.96
Fe_2O_3	9.81	9.37	10.06
MnO	0.16	0.16	0.17
MgO	6.98	7.53	7.67
CaO	13.59	13.22	14.00
Na_2O	2.06	2.23	2.11
K_2O	0.30	0.23	0.31
P_2O_5	0.08	0.10	0.09
LOI	1.94	2.28	2.26
Total	100.58	99.67	100.28
Trace elements (ppm)			
Cr	347	344	352
Ni	98	114	102
V	318	315	316
Zn	73	74	76
Ga	15	16	16
Rb	5	5	7
Sr	92	86	87
Ba	8	7	10
Zr	51	53	53
Nb	2.3	1.6	2.4
La	2	2	2
Ce	6	6	6
Nd	6	7	6
Y	25	25	25
Selected element ratios			
Mg-value	62	64	63
Ti/Zr	109	105	111
Zr/Nb	22	33	22
Ce_N/Y_N	0.6	0.6	0.6
Zr/Ce	8.8	9.2	9.0
Zr/Y	2.1	2.2	2.2
CIPW norms			
Or	1.8	1.4	1.9
Ab	17.7	19.4	18.2
An	34.6	32.7	31.1
Di	27.1	27.6	32.0
Hy	7.8	5.6	0.4
Ol	6.5	8.7	11.8
Mt	1.7	1.7	1.8
Il	1.8	1.8	1.9
Ap	0.2	0.3	0.2

Note: LOI is loss on ignition. Total iron is expressed as Fe_2O_3. CIPW norms and Mg-values (100 Mg/[Mg + Fe^{2+}]) are calculated using an assumed Fe_2O_3/FeO ratio of 0.15. Ce_N/Y_N expresses the chondrite-normalized ratio of Ce to Y.

analysis of the same piece (site chapter, Site 563, this volume) has lower Fe_2O_3 and K_2O typical of Chemical Group II (identified by the shipboard party). We consider only one chemical group to be present in Hole 563 particularly because abundances and abundance ratios of incompatible trace elements do not vary significantly in this hole (Table 14; site chapter, Site 563, this volume). The rather small degree of chemical variation that is present in the basalts of Hole 563 can be attributed to phenocryst dilution. As was the case for Hole 562, the basalts from Hole 563 are depleted in the more-incompatible elements (Zr/Nb 22–33, Ce_N/Y_N 0.6; Table 14), but are more primitive than any of the Hole 562 basalts, having somewhat higher Mg-values and Cr contents (see Tables 13, 14) and lower abundances of incompatible elements (e.g., Ti, Zr; Figs. 23, 24).

SITE 564

Site 564 (33°44.36′N; 43°46.03′W, 3820 m water depth) lies on Magnetic Anomaly 13 (37 Ma) on the west flank of the Mid-Atlantic Ridge and is approximately 6 miles north of Site 563. Drilling at another site in this area was necessitated by the limited penetration of basaltic basement at Site 563. A single hole was drilled at Site 564 and 81 m of basement (encountered at 284 m sub-bottom depth) were cored before the hole was abandoned. A total of five lithologic units composing one chemical group was recognized by the shipboard party, consisting of aphyric pillow basalts and massive basalt flows. The degree of alteration is rather variable.

Although five lithologic units are recognized in this hole, there is little petrographic distinction between units, other than some variation in the proportion of olivine microphenocrysts (Fo_{83}; Table 4). The rather peculiar occurrence of domains of contrasting grain size and texture is fully described in the site chapter, Site 564 (this volume).

Analyses for five samples from Hole 564 are given in Table 15. Normatively they are similar to the basalts of Chemical Group I, Hole 562, and straddle the Di-Hy join (Fig. 22). The analyzed sample (564-3-2, 5–8 cm) is rather altered, having high LOI and K_2O and a low Mg-values. This sample contains appreciably more normative Ol, and less Hy, than the remaining samples (Table 15). The shipboard study indicated an apparent downhole chemical variation in the abundances, and abundance ratios, of some elements (see site chapter, Site 564, this volume). The density of sampling in this study is not sufficient to confirm this. The basalts from this hole are all depleted in the more-incompatible elements (Zr/Nb 19–25, Ce_N/Y_N 0.6–0.8; Table 15), as are the basalts from Holes 562 and 563, south of the Hayes Fracture Zone. However, there is some indication that the basalts of this hole are rather less depleted than those of Holes 562 and 563, which generally have lower Ce_N/Y_N ratios (0.5–0.6) and higher average Zr/Nb ratios (Fig. 23). This is particularly the case in comparison to basalts from Chemical Group I, Hole 562, which have equivalent Mg-values and Ti and Zr abundances (Fig. 24), but Zr/Nb ratio of 30–33 (Table 13; Fig. 23). The Ti/Zr ratio is also lower in Hole 564 basalts than in Hole 562 and 563 basalts (Fig. 24).

CONTROLS ON MORB CHEMISTRY

Before the chemical characteristics of the mantle sources of erupted basalts can be assessed, the degree of chemical fractionation that can be achieved during partial melting and crystal fractionation processes has to be defined. Any residual fractionation effects that cannot

Table 15. Major and trace element analyses for Hole 564 basalts.

Core-Section (interval in cm) Piece number	3-2 5-8 1	5-2 115-118 4b	6-1 26-28 1b	6-4 54-57 2e	7-3 60-63 4c
Major elements (wt.%)					
SiO_2	47.90	49.42	49.76	49.48	49.47
TiO_2	1.41	1.41	1.46	1.43	1.44
Al_2O_3	14.88	14.38	14.67	14.48	14.41
Fe_2O_3	11.97	11.73	11.27	11.81	11.60
MnO	0.18	0.18	0.17	0.18	0.17
MgO	6.70	7.76	7.27	7.62	7.56
CaO	11.82	11.28	11.32	11.25	11.19
Na_2O	2.32	2.26	2.35	2.36	2.38
K_2O	0.35	0.20	0.20	0.22	0.22
P_2O_5	0.14	0.14	0.15	0.15	0.15
LOI	2.71	1.29	1.67	1.48	1.64
Total	100.38	100.05	100.29	100.46	100.23
Trace elements in ppm					
Cr	267	254	249	241	252
Ni	104	118	114	121	119
V	396	380	387	376	382
Zn	95	89	91	88	92
Ga	18	17	19	19	18
Rb	6	3	4	4	3
Sr	109	102	102	103	107
Ba	16	18	23	22	24
Zr	89	90	93	92	92
Nb	4.7	4.7	3.7	4.5	4.6
La	4	4	5	4	5
Ce	10	12	10	12	12
Nd	9	10	9	10	10
Y	36	36	36	35	36
Selected element ratios					
Mg-value	56	60	59	59	59
Ti/Zr	95	94	94	93	94
Zr/Nb	19	19	25	20	20
Ce_N/Y_N	0.6	0.8	0.6	0.8	0.8
Zr/Ce	9.3	7.8	9.7	8.0	8.0
Zr/Y	2.6	2.6	2.7	2.7	2.7
CIPW norms					
Q			0.3		
Or	2.1	1.2	1.2	1.3	1.3
Ab	20.1	19.4	20.1	20.1	20.4
An	29.8	28.9	29.3	28.6	28.4
Di	24.0	22.0	21.8	22.0	22.0
Hy	11.4	21.2	21.0	19.7	20.2
Ol	6.2	1.3		2.1	1.4
Mt	2.1	2.1	2.0	2.1	2.0
Il	2.7	2.7	2.8	2.8	2.8
Ap	0.4	0.3	0.4	0.4	0.4

Note: LOI is loss on ignition. Total iron is expressed as Fe_2O_3. CIPW norms and Mg-values ($100\ Mg/[Mg + Fe^{2+}]$) are calculated using an assumed Fe_2O_3/FeO ratio of 0.15. Ce_N/Y_N expresses the chondrite-normalized ratio of Ce to Y.

e attributed to these processes can be assigned as source haracteristics. Of particular significance in this context re ratios between incompatible trace elements.

rystal Fractionation

For the incompatible trace elements, crystal fractionation is an inefficient mechanism for producing large variations in element ratios. This can be demonstrated by considering the variation that can be produced in ratios between elements with D = 0.1 and D = 0.01. Such bulk distribution coefficients might be appropriate for the elements Zr and Nb, respectively (Le Roex et al., 1981). Closed-system Rayleigh crystal fractionation could only produce a decrease in Zr/Nb ratio by approximately 20% after as much as 80% fractional crystallization. On the other hand, open system crystal fractionation (which is a more realistic process for generating the compositional variation in MORB, if we consider mineralogic and chemical evidence for magma mixing) is more capable of fractionating more-incompatible (e.g., Nb) from less-incompatible (e.g., Zr) trace elements (O'Hara and Mathews, 1981). The crucial parameter in open-system fractionation is the ratio of the fraction of melt removed (Y) to the fraction of melt crystallized (X) in each cycle. Large fractionation between Zr and Nb can only be achieved for very small Y (~1%) and large X (~60%), in which case a decrease in the Zr/Nb ratio by a factor of 3.5 can be produced in the steady-state magma relative to the parent magma (from equation 15 in O'Hara and Mathews, 1981). However, in this case, the absolute abundance of the less-incompatible element (Zr) in the steady-state liquid will have increased by a factor of 13 over that in the parent liquid, which is unacceptable for analyses of MORB. Basalts that can be considered as primary mantle-derived magmas parental to most MORB (e.g., Fujii and Bougault, 1983) have approximately 50 ppm Zr, and evolved MORB commonly have approximately 100 ppm Zr (e.g., evolved basalts from Holes 556 and 558). Hence the absolute enrichment of incompatible elements during fractional crystallization in most MORB is only by a factor of two. This imposes rather severe limits on permissible values of X and Y in open-system behavior, so that it is difficult to achieve more than approximately 20% variation in Zr/Nb ratios. It is clearly not possible to generate the extreme range in Zr/Nb ratios in the basalts of Holes 558 and 561 by fractional crystallization in either open or closed systems.

The inadequacy of fractional crystallization mechanisms in generating within-hole variations is well illustrated by the basalts from Hole 558. If we consider only the E-type chemical groups (I, III, IV, V) from this hole, it is very difficult to relate one to another by crystal fractionation. For example, the least-fractionated basalts in Hole 558 are those of Chemical Group V (Fig. 16). However, basalts of Group I (the most primitive in terms of Ni and Cr abundances; Figs. 9, 10) have higher concentrations of both incompatible (Zr) and compatible (Ni, Cr) trace elements than Group V basalts (Figs. 9, 10), precluding a simple relationship by crystal fractionation. A similar argument can be made on the basis of the variation of Sr with Zr (Fig. 17). In the N-type MORB of Holes 556, 558, 561, 562, 563, and 564, the Sr content is constant at 100–110 ppm irrespective of Zr abundance. This is a reflection of dominant plagioclase crystallization during the production of evolved N-type MORB. Successful major element models (Table 16) require that plagioclase comprises approximately 50% of the crystal extract. As $K_{Sr}^{plag/liq} = 1.8$ (Le Roex et al., 1981), then D_{Sr} approximates 1, resulting in buffering of Sr abundances. However, in the E-type MORB of Holes 557, 558, 559, and 561, Sr abundances are higher than in the N-type MORB and covary in a general way with Zr content (Fig. 17). Major element models that attempt to relate, for example, Group V basalts to those of Group

Table 16. Least squares approximations relating basalt groups within Hole 556.

Chemical Groups I to II

	Derivative (556-3-2, 49–51 cm)	Ol.	Plag.	Cpx.	Parent (556-2-2, 132–135 cm)	Calculated parent	Residuals
SiO_2	56.34	39.14	52.33	52.84	50.78	50.73	−0.05
TiO_2	1.43			0.41	1.04	1.06	0.02
Al_2O_3	15.98		29.40	2.58	15.89	15.95	0.06
FeO*	9.46	16.43	0.71	4.93	7.71	7.78	0.07
Mno	0.18				0.15	0.13	−0.02
MgO	6.93	43.73		18.19	8.16	8.18	0.02
CaO	11.50	0.33	13.84	20.42	12.61	12.70	0.09
Na_2O	2.69		3.65		2.53	2.44	−0.09
P_2O_5	0.14				0.12	0.10	−0.02
Mix	70.6	2.4	14.8	12.4		ΣR^2 0.0281	

Chemical Groups I to IV

	Derivative (556-11-1, 106–109 cm)	Ol.	Plag.	Cpx.	Parent (556-2-2, 132–135 cm)	Calculated parent	Residuals
SiO_2	51.32	39.14	50.90	50.99	50.78	50.77	−0.01
TiO_2	1.34			0.57	1.04	0.95	−0.09
Al_2O_3	15.29		30.26	4.10	15.89	15.89	0.00
FeO*	9.56	16.43	0.72	5.86	7.71	7.74	0.03
MnO	0.18				0.15	0.12	−0.03
MgO	6.56	43.73		17.03	8.16	8.15	−0.01
CaO	11.07	0.33	14.89	20.45	12.61	12.63	0.02
Na_2O	3.02		3.17		2.53	2.53	0.00
P_2O_5	0.14				0.12	0.09	−0.03
Mix	65.2	3.6	17.8	13.5		ΣR^2 0.0114	

Note: Ol. = olivine, Plag. = plagioclase; Cpx. = clinopyroxene. FeO* is total iron expressed as FeO. ΣR^2 is the sum of the squares of residuals (calculated parent − parent). For the least-squares approximations, the method of Bryan et al. (1969) has been used.

III require dominant plagioclase in the crystal extract, which would buffer Sr contents. This and other aspects of the chemistry of Hole 558 basalts strongly suggests that crystal fractionation is not the mechanism responsible for the large chemical variability of basalts in this hole. Nevertheless, it should be noted that some intra-group chemical variation may be related to crystal fractionation, as in the case of Group IIIA and IIIB basalts that do display buffering of Sr.

If extensive subaxial magma chambers through which all MORB were cycled were a feature of the MAR, a strong uniformity of basalt compositions would be expected. It is clear from the data for Hole 558 alone that this is not the case. Although most MORB have undergone some crystal fractionation, and many show evidence for magma mixing, this must occur in small, isolated, and short-lived magma chambers in order for chemical variability such as that observed in Hole 558 to be maintained. This is in accord with geophysical evidence that does not support the concept of a single, large subaxial magma chamber in this region (Nisbet and Fowler, 1978).

Partial Melting

In contrast to fractional crystallization processes, partial melting is more readily able to produce appreciable variation in ratios of less-incompatible to more-incompatible trace elements. Again, considering elements with D = 0.1 (Zr) and D = 0.01 (Nb), a variation in the degree of equilibrium batch melting from 5 to 20% can cause an increase in the Zr/Nb ratio by a factor of 2 in the derived liquids. A dynamic melting mechanism (as proposed by Langmuir et al., 1977) for FAMOUS basalts, whereby the source melts incrementally with a fraction of the partial melt retained in the residue at each increment of melting, can cause an increase by a factor of 3 in the Zr/Nb ratio from the 5% to the 20% melt (with 5% melt increments and 2% retained melt). In fact, these figures are probably overestimates of the degree of fractionation that can be attained, because consideration of realistic residual mineralogies coupled with the K_d data for Zr of Le Roex and others (1981) suggests that D_{Zr} = 0.04 is more reasonable during partial melting. However, there is little indication, in the form of crossing REE patterns, for the operation of dynamic melting as an important process in generating the chemical variability, particularly within-hole, of Leg 82 basalts. Such a model may be applicable to basalts of the FAMOUS area, where LREE-depleted and LREE-enriched basalts have similar ratios of more-incompatible trace elements (e.g., La/Ce; Langmuir et al., 1977), because dynamic melting allows constant ratios of more-incompatible elements while producing decoupling between the abundances of more-incompatible (e.g., LREE) and less-incompatible (e.g., heavy rare earth elements [HREE]) trace elements. However, in Holes 558 and 561, the depleted and enriched groups have different ratios of La/Ce, La/Ta, etc., which cannot be produced by any partial melting process.

In the case of Zr/Nb and Ce/Y (or Ce/Yb) ratios, consideration of residual garnet in the mantle source allows more marked fractionation of less-incompatible (Zr, HREE) from more-incompatible (Nb, LREE) trace elements because of the strong preferential concentration f the less-incompatible elements in garnet (Frey et al., 978; Le Roex et al., 1981). Indeed, in order to explain he variation in Zr/Nb ratios in FAMOUS basalts (range to 9.4), Le Roex et al. (1981) proposed that picritic ba- alts with high Zr/Nb ratios equilibrated with garnet- ree residues, whereas plagioclase-pyroxene basalts with ow Zr/Nb ratios were derived by melting of the same ource, but at higher pressure and with 8% residual gar- et. It is, however, questionable to what extent garnet an be considered as a realistic residual phase. Fujii and Bougault (1983) have shown that primitive basalts from the FAMOUS area can be derived by partial melting of lherzolite at approximately 10 kb, well above the stability limit for garnet lherzolite. Additionally, partial melts equilibrated with residues containing even quite small amounts (~2%) of garnet will show significant depletion in the HREE; melts from sources with as much as 8% residual garnet would display very strong HREE depletion. There is no evidence from FAMOUS basalts, or any of the Leg 82 basalts, for high Tb_N/Yb_N or Gd_N/Yb_N ratios (Langmuir et al., 1977; Wood, Tarney, et al., 1979). Some estimate of the degree of melting likely in the production of Hole 558 basalts can be obtained from Zr abundances. If we accept a primordial mantle abundance for Zr of 11 ppm (Wood, Joron, et al., 1979) and assume $D_{Zr} = 0.04$, the degree of partial melting required to generate the range of Zr abundances in Hole 558 basalts varies from 16 to 8%. However, most of these basalts have undergone significant crystal fractionation that will result in an underestimate of the degree of melting. Even allowing for a degree of melting varying from 20 to 10% and extreme values for D_{Zr} (0.1) and D_{Nb} (0.01), the Zr/Nb ratio can only vary by a factor of 1.3 during equilibrium partial melting. This contrasts with an observed variation by a factor of 1.6 among the E-type basalts, and by a factor of 3.9 among ll of the basalts of Hole 588. If only the E-type basalts were the product of different degrees of batch melting of the same source, the Zr/Nb ratio should increase with degree of melting. In fact, the least evolved chemi- al group (Group V), which has the highest Mg-values nd normative olivine content, has a Zr/Nb ratio of 7.9 Table 9), lower than in Groups I and III. Similar arguments could, for example, be applied to the behavior of a and Sm, and hence the production of variable LREE nrichment/depletion, during partial melting. Although ractionation of elements during partial melting can account for some of the variability in, for example, Zr/Nb nd La/Sm ratios, the wide observed range of these raios in MORB does require some source heterogeneity or these elements.

DISCUSSION

Many of the foregoing arguments have demonstrated the inadequacy of partial melting and fractional crystallization processes in producing large differences in incompatible element ratios. Even among those trace elements with quite large differences in D (e.g., Zr and Nb; La and Sm) the variation of element ratios within one hole (i.e., Holes 558 or 561) can only be partially attributed to melting processes. On the other hand, ratios among the more-incompatible trace elements closely reflect those of the mantle source, except at very low degrees of partial melting (which are inappropriate when considering MORB genesis). La, Ta, and Nb all have very similar bulk distribution coefficients and cannot be fractionated from each other during partial melting (Bougault, Joron, et al., 1979). Similarly, Th is more incompatible than La or Ta, but ratios between these elements are not modified during partial melting. Thus, ratios using La, Ta, and Th abundances in MORB should directly represent those of the mantle source and are indicators of heterogeneity/homogeneity within that source. They do not suffer from the ambiguity inherent in the use of Zr/Nb and La/Sm ratios.

Previous work in the North Atlantic has suggested that two distinct values for the La/Ta ratio exist in MORB (Wood, Tarney, et al., 1979; Bougault et al., 1980; Fig. 25). N-type MORB from the vicinity of the ridge axis at 22–29°N and from 110-Ma-old ocean crust at 25°N (Holes 417, 418; Legs 51 to 53) have La/Ta ratios close to 17.5 (Wood, Tarney, et al., 1979; Bougault et al., 1980; Bryan et al., 1981). On the other hand, E-type MORB from 63, 45, and 36°N all have low La/Ta ratios of ~9.25 (Wood, Tarney, et al., 1979; Bougault et al., 1980), a characteristic considered to be related to basalts erupted at anomalous ridge segments and representing large-scale mantle heterogeneity. Even LREE-depleted basalts erupted at these anomalous ridge segments have low La/Ta and Zr/Nb ratios (e.g., Hole 409, 63°N; Hole

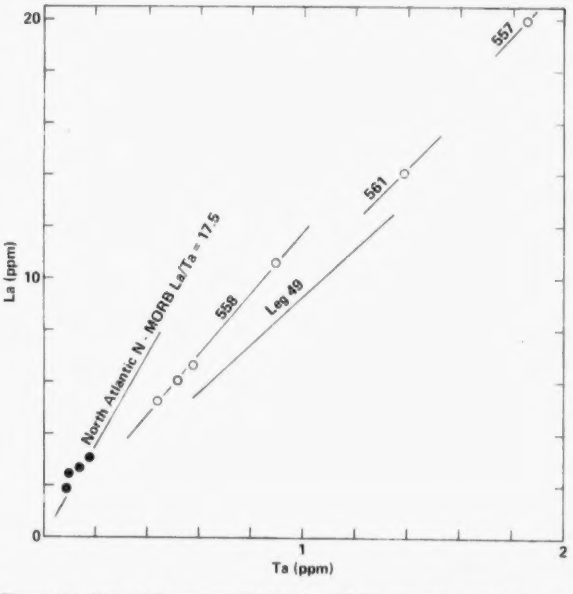

Figure 25. Plot of La versus Ta for Leg 82 basalts (closed circles = N-type MORB from Holes 556, 558, and 561; open circles = E-type MORB from Holes 557, 558, and 561). Also indicated are La/Ta ratios for N-MORB from the North Atlantic and for basalts recovered during Leg 49 (Bougault et al., 1980).

413, 36°N [Wood, Tarney, et al., 1979; Bougault et al., 1980]; FAMOUS area [Langmuir et al., 1977]). In contrast, the Th/Ta ratio gives a finer resolution of mantle heterogeneities, and for a single La/Ta ratio (e.g., E-type MORB from 63, 45, and 36°N), a number of different Th/Ta ratios are defined (Bougault et al., 1980; Fig. 26). The apparent consistency of more-incompatible element ratios in basalts erupted at a given ridge segment led Wood, Tarney, et al., (1979) to conclude that it was unlikely that basalts with the major and trace element characteristics of N-type MORB could ever be erupted at the 36°N segment of the MAR.

The data from Leg 82 add an extra degree of complexity to the concept of mantle heterogeneity in the North Atlantic. Clearly, the occurrence of E-type and N-type MORB with distinct La/Ta ratios is not a regional feature: the data from Holes 558 and 561 (Table 6) demonstrate that E-type MORB with La/Ta ratios of 11-12 and N-type MORB with La/Ta ratios of 19-20 can occur within the same hole. Thus the scale of heterogeneity is localized rather than regional, and mantle sources with both high La/Ta and low La/Ta ratios can be tapped penecontemporaneously at one small segment of the MAR. This observation also denies that given ridge segments necessarily erupt basalts with a uniform trace element composition over long periods of time. N-type MORB can be erupted from the 36°N segment of the MAR and indeed has been erupted from the ridge axis in this region in the recent past (35 Ma at Site 558 and 19 Ma at Site 561).

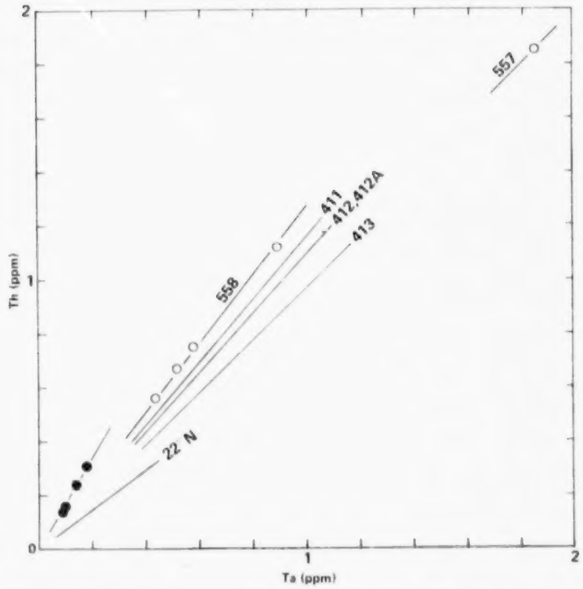

Figure 26. Plot of Th versus Ta for Leg 82 basalts (closed circles = N-type MORB from Holes 556, 558, and 561; open circles = E-Type MORB from Holes 557 and 558). Also indicated are Th/Ta ratios for basalts from Holes 411, 412, 412A, and 413 from the FAMOUS area (Bougault et al., 1980) and for N-type MORB from 22°N (Bougault, Cambon, et al., 1979).

The demonstration of the very localized nature of the chemical heterogeneities in the suboceanic mantle has considerable implications for models for the production of these heterogeneities. The mantle plume model developed by Schilling and coworkers (Schilling, 1973, 1975; White and Schilling, 1978; Schilling et al., 1980) was erected to explain the large scale heterogeneity in th composition of basalts erupted at the MAR. In this mode upwelling mantle plumes, centered under hot spots suc as the Azores and Iceland, are the source for E-typ MORB. Mixing of this enriched source with deplete upper mantle (the source for N-type MORB) produce basalts with a transitional chemistry dependent upo the proportions of end members. This model relies upo the occurrence of supposed large-scale geochemical gradients away from the hot spots, which reflect the diminishing influence of, and decreasing component from the plume. However, increasingly detailed drilling in th North Atlantic, and especially the results of Leg 82, cas doubts upon the existence of well-defined chemical gradients away from hot spots. For example, the wide range in La/Sm and Zr/Nb ratios on a very small scale, i.e., within-hole, is not easily explained by the plume model, particularly as the differences in La/Ta ratios precludes production of the variation by dynamic partial melting of a homogeneous mantle source.

Similarly, the chemistry of basalts recovered from systematic sampling of the ocean floor by Leg 82 is not easily explicable in terms of a migrating plume or waxing/waning plume activity. The eruption of N-type MORB at Site 556 would indicate that the Azores plume was not active at 34 Ma, and yet E-type MORB was being erupted at Sites 558 and 559 further to the south. However, the occurrence of E-type MORB at Site 557 would suggest that the Azores plume was active by 18-19 Ma and E-type MORB was also being produced at Site 335 (where the basalts are LREE depleted but have low [E-type] Zr/Nb and La/Ta ratios) and Site 561 to the south. This temporal and spatial variation might be interpreted in terms of a northward-propagating, expanding plume. However, the evidence for very localized mantle heterogeneity is inconsistent with this model. Rather, a model such as that developed by Wood, Joron, and others (1979) and Tarney and others (1980), whereby the depleted suboceanic upper mantle is variably veined by an enriched component, is more capable of explaining th development of local chemical heterogeneities in th mantle.

The results from Leg 82 also indicate the importanc of transform faults in delineating mantle domains. Th evidence from the sites to the south of the Hayes Fracture Zone (Sites 562 to 564) shows that typical N-typ MORB has been erupted in this region since approximately 37 Ma, whereas E-type MORB has been erupte at the sites (559 to 561) to the north of the fracture zone Similarly, evidence from the 24°N region of the MA demonstrates fine-scale isotopic heterogeneity in N-typ MORB erupted to the north and south of the Kane Fracture Zone (Machado et al., 1982). It is difficult to envisage how fracture zones could influence the activity o mantle plumes. It is perhaps more probable that the fracture zones are delineating regions of oceanic upper mantle that are inherently chemically and isotopically heterogeneous, perhaps because of the veining of the mantle.

REFERENCES

Arcyana, 1977. Rocks collected by bathyscaph and diving saucer in the FAMOUS area of the Mid-Atlantic Rift valley: petrological diversity and structural setting. *Deep-Sea Res.*, 24:565–589.

Bougault, H., Cambon, P., Corre, O., Joron, J.-L., and Treuil, M., 1979. Evidence for variability of magmatic processes and upper mantle heterogeneity in the axial region of the Mid-Atlantic Ridge near 22 and 36°N. *Tectonophysics*, 55:11–34.

Bougault, H., Joron, J.-L., and Treuil, M., 1979. Alteration, fractional crystallisation, partial melting, mantle properties from trace elements in basalts recovered in the North Atlantic. *In* Talwani, M. (Ed.), *Deep Drilling Results in the Atlantic Ocean: Ocean Crust:* Washington (American Geophysical Union), pp. 352–368.

_______, 1980. The primordial chondritic nature and large scale heterogeneities in the mantle: evidence from high and low partition coefficient elements in oceanic basalts. *Phils. Trans. R. soc. London, Ser. A*, 297:203–213.

Bougault, H., and Treuil, M., 1980. Mid-Atlantic Ridge: zero-age geochemical variations between Azores and 22°N. *Nature*, 286: 209–212.

Bryan, W. B., 1979. Regional variation and petrogenesis of basalt glasses from the FAMOUS area, Mid-Atlantic Ridge. *J. Petrol.*, 20:293–325.

Bryan, W. B., Finger, L. H., and Chayes, F., 1969. Estimating proportions in petrologic mixing equations by least squares approximation. *Science*, 163:926–927.

Bryan, W. B., Thompson, G., and Ludden, J. N., 1981. Compositional variation in normal MORB from 22°–25°N: Mid-Atlantic Ridge and Kane Fracture Zone. *J. Geophys. Res.*, 86:11815–11836.

Clague, D. A., Frey, F. A., Thompson, G., and Rindge, S., 1981. Minor and trace element geochemistry of volcanic rocks dredged from the Galapagos spreading centre: role of crystal fractionation and mantle heterogeneity. *J. Geophys. Res.*, 86:9469–9482.

Clarke, D. B., and Loubat, H., 1977. Mineral analysis from the peridotite-gabbro-basalt complex at Site 334, DSDP Leg 37. *In* Aumento, F., Melson, W. G., et al., *Init. Repts. DSDP*, 37: Washington (U.S. Govt. Printing Office), 847–855.

Frey, F. A., Green, D. H., and Roy, S. D., 1978. Integrated models of basalt petrogenesis: A study of quartz tholeiites to olivine melilites from South Eastern Australia utilizing geochemical and experimental petrological data. *J. Petrol.*, 19:463–513.

Fujii, T., and Bougault, H., 1983. Melting relations of a magnesian abyssal tholeiite and the origin of MORB's. *Earth Planet. Sci. Lett.*, 62:283–295.

Hart, R. A., 1970. Chemical exchange between seawater and deep ocean basalts. *Earth Planet. Sci. Lett.*, 9:269–279.

Hart, S. R., 1971. K, Rb, Cs, Sr and Ba and Sr isotope ratios of ocean floor basalts. *Phils. Trans. R. Soc. London Ser. A*, 268:573–588.

Hart, S. R., Erlank, A. J., and Kable, E. D. J., 1974. Sea floor basalt alteration: some chemical and Sr isotopic effects. *Contrib. Mineral. Petrol.*, 44:219–230.

Hart, S. R., Schilling, J.-G., and Powell, J. L., 1973. Basalts from Iceland and along the Reykjanes Ridge: Sr isotope geochemistry. *Nature*, 246:104–107.

Langmuir, C. H., Bender, J. F., Bence, A. E., Hanson, G. N., and Taylor, S. R., 1977. Petrogenesis of basalts from the FAMOUS area: Mid-Atlantic Ridge. *Earth Planet. Sci. Lett.*, 36:133–156.

Le Roex, A. P., Dick, H. J. B., Reid, A. M., and Erlank, A. J., 1982. Ferrobasalts from the Speiss Ridge segment of the Southwest Indian Ridge. *Earth Planet. Sci. Lett.*, 60:437–451.

Le Roex, A. P., Erlank, A. J., and Needham, H. D., 1981. Geochemical and mineralogical evidence for the occurrence of at least three distinct magma types in the 'FAMOUS' region. *Contrib. Mineral. Petrol.*, 77:24–37.

Machado, N., Ludden, J. N., Brooks, C., and Thompson, G., 1982. Fine-scale isotopic heterogeneity in the sub-Atlantic mantle. *Nature*, 295:226–228.

Marsh, N. G., Saunders, A. D., Tarney, J., and Dick, H. J. B., 1980. Geochemistry of basalts from the Shikoku and Daito basins, Deep Sea Drilling Project Leg 58. *In* Klein, G., de V., Kobayashi, K., et al., *Init. Repts. DSDP*, 58: Washington (U.S. Govt. Printing Office), 805–842.

Nakamura, N., 1974. Determination of REE, Ba, Fe, Mg, Na and K in carbonaceous and ordinary chondrites. *Geochim. Cosmochim. Acta*, 38:757–775.

Nisbet, E. G., and Fowler, C. M. R., 1978. The Mid-Atlantic Ridge at 37° and 45°N: some geophysical and petrological constraints. *Geophys. J. R. Astron. Soc.*, 54:631–660.

O'Hara, M. J., and Mathews, R. E., 1981. Geochemical evolution in an advancing, periodically replenished, periodically tapped, continuously fractionated magma chamber. *J. Geol. Soc. London*, 138:237–277.

Saunders, A. D., 1983. Geochemistry of basalts recovered from the Gulf of California during Leg 65 of the Deep Sea Drilling Project. *In* Lewis, B. T. R., Robinson, P., et al., *Init. Repts. DSDP*, 65: Washington (U.S. Govt. Printing Office), 591–621.

Schilling, J.-G., 1971. Sea-floor evolution: rare earth evidence. *Phils. Trans. R. Soc. London, Ser. A*, 286:663–706.

_______, 1973. Iceland mantle plume: geochemical study of the Reykjanes Ridge. *Nature*, 242:565–571.

_______, 1975. Azores mantle blob: rare-earth evidence. *Earth Planet. Sci. Lett.*, 25:103–115.

Schilling, J.-G., Bergeron M. B., and Evans, R., 1980. Halogens in the mantle beneath the North Atlantic. *Phils. Trans. R. Soc. London, Ser. A*, 297:147–178.

Sigurdsson., H. 1981. First-order major element variation in basalt glasses from the Mid-Atlantic Ridge: 29°N to 73°N. *J. Geophys. Res.*, 9483–9502.

Symes, R. F., Bevan, J. C., and Hutchison, R., 1977. Phase chemistry studies on gabbro and peridotite rocks from Site 334, DSDP Leg 37, *In* Aumento, F., Melson, W. G., et al., *Init. Repts. DSDP*, 37: Washington (U.S. Govt. Printing Office), 841–845.

Tarney, J. Saunders, A. D., Weaver, S. D., Donnellan, N. C. B., and Hendry, G. L., 1979. Minor-element geochemistry of basalts from Leg 49, North Atlantic Ocean. *In* Luyendyk, B. P., Cann, J. R., et al., *Init. Repts. DSDP*, 49: Washington (U.S. Govt. Printing Office), 657–691.

Tarney, J., Wood, D. A., Saunders, A. D., Conn, J. R., and Varet, J., 1980. Nature of mantle heterogeneity in the North Atlantic: evidence from Deep Sea Drilling. *Phils. Trans. R. Soc. London, Ser. A*, 297:179–202.

Thompson, G. and Humphris, S., 1977. Seawater-rock interactions in the oceanic basement. *Proc. 2nd Inter. Symp. Water-Rock Interaction* (Vol. III), 3–8.

Vanko, D. A., and Batiza, R., 1982. Gabbroic rocks from the Mathematician Ridge failed rift. *Nature*, 300:742–744.

Weaver, B. L., Marsh, N. G., and Tarney, J., 1983. Trace element geochemistry of basaltic rocks recovered at Site 516, Rio Grande Rise, Deep Sea Drilling Project Leg 72. *In* Barker, P. F., Carlson, R. L., Johnson, D. A., et al., *Init. Repts. DSDP*, 72: Washington (U.S. Govt. Printing Office), 451–466.

White, W. M., and Schilling, J.-G., 1978. The nature and origin of geochemical variation in Mid-Atlantic Ridge basalts from the central North Atlantic. *Geochim. Cosmochim. Acta*, 42:1501–1516.

White, W. M., Schilling, J.-G., and Hart, S. R., 1976. Evidence for the Azores mantle plume from strontium isotope geochemistry of the Central North atlantic. *Nature*, 263:659–663.

Wood, D. A., 1978. Major and trace element variations in the Tertiary lavas of East Iceland and their significance with respect to the Iceland geochemical anomaly. *J. Petrol.*, 19:393–436.

Wood, D. A., Joron, J.-L., Treuil, M., Norry, N., and Tarney, J. 1979. Elemental and Sr isotope variations in basic lavas from Iceland and the surrounding ocean floor. *Contrib. Mineral. Petrol.*, 70: 319–339.

Wood, D. A., Tarney, J., Varet., J., Saunders, A. D., Bougault, H., Joron, J.-L., Treuil, M., and Cann, J. R., 1979. Geochemistry of basalts drilled in the North Atlantic by IPOD Leg 49: implications for mantle heterogeneity. *Earth Planet. Sci. Lett.*, 42:77–97.

Date of Initial Receipt: 19 April 1983
Date of Acceptance: 11 November 1983

20. GEOCHEMISTRY OF BASALTS FROM DEEP SEA DRILLING PROJECT HOLES 556–564[1]

N. E. R. Drake, J. M. Rhodes, and L. K. Autio, Department of Geology and Geography,
University of Massachusetts[2]

ABSTRACT

The nine holes (556–564) drilled during DSDP Leg 82 in a region west and southwest of the Azores Platform (Fig. 1) exhibit a wide variety of chemical compositions that indicate a complex petrogenetic history involving crystal fractionation, magma mixing, complex melting, and mantle heterogeneity. The major element chemistry of each hole except Hole 557 is typical of mid-ocean ridge basalts (MORBs), whereas the trace element and rare earth element (REE) abundances and ratios are more variable, and show that both depleted Type I and enriched Type II basalts have been erupted in the region.

Hole 556 (30–34 Ma), located near a flow line through the Azores Triple Junction, contains typically depleted basalts, whereas Hole 557 (18 Ma), located near the same flow line but closer to the Azores Platform, is a highly enriched FeTi basalt, indicating that the Azores hot-spot anomaly has existed in its present configuration for at least 18 Ma, but less than 30–34 Ma.

Hole 558 (34–37 Ma), located near a flow line through the FAMOUS and Leg 37 sites, includes both Type I and II basalts. Although the differences in Zr/Nb and light REE/heavy REE ratios imply different mantle sources, the $(La/Ce)_{ch}$ (>1) and Nd isotopic ratios are almost the same, suggesting that the complex melting and pervasive, small-scale mantle heterogeneity may account for the variations in trace element and REE ratios observed in Hole 558 (and FAMOUS sites).

Farther south, Hole 559 (34–37 Ma), contains enriched Type II basalts, whereas Hole 561 (14–17 Ma), located further east near the same flow line, contains Type I and II basalts. In this case, the $(La/Ce)_{ch}$ and Nd isotopic ratios are different, indicating two distinct mantle sources. Again, the existence along the same flow line of two holes exhibiting such different chemistry suggests that mantle heterogeneity may exist on a more pervasive and transient smaller scale. (Hole 560 was not sampled for this study because the single basalt clast recovered was used for shipboard analysis.)

All of the remaining three holes (562, 563, 564), located along a flow line about 100 km south of the Hayes Fracture Zone (33°N), contain only depleted Type I basalts.

The contrast in chemical compositions suggests that the Hayes Fracture Zone may act as a "domain" boundary between an area of fairly homogeneous, depleted Type I basalts to the south (Holes 562–564) and a region of complex, highly variable basalts to the north near the Azores hot-spot anomaly (Holes 556–561).

INTRODUCTION

During DSDP Leg 82, nine holes (556–564) were drilled near several spreading flow lines perpendicular to the Mid-Atlantic Ridge in a region west and southwest of the Azores Platform (Fig. 1). The northern flow lines are on either side of the Pico Fracture Zone and pass through the Azores Triple Junction (Holes 556 and 557) and the FAMOUS and Leg 37 sites (Hole 558). The southern flow lines straddle the Hayes Fracture Zone (Holes 559–561 and 562–564) 650 km south of the Azores Triple Junction. Drilling perpendicular to the ridge axis in crust aged 14–18 Ma (Anomalies 5–6) and 30–37 Ma (Anomalies 12–13) provided an opportunity to examine geochemical changes with time at a particular ridge segment. Figure 1 shows the position of the drill sites and summarizes the geochemical characteristics of the basalts from each hole. No analyses from Hole 560 are included because only one basalt clast was recovered, which was used for shipboard analysis. Further details on locations and recovery are given in the site chapters of this volume.

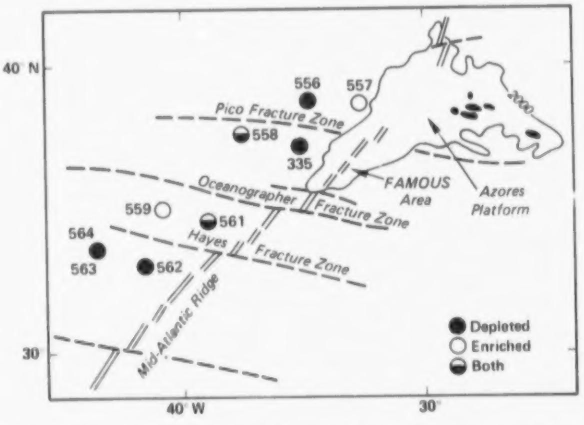

Figure 1. Location and chemical characteristics of basalts sampled on DSDP Leg 82.

The task of this study was to examine geochemical variations over the past 35 Ma in order to evaluate the roles played by crystal fractionation, magma mixing, complex melting, and large-scale or small-scale mantle heterogeneity in the petrogenesis of Leg 82 basaltic magmas. Such information is fundamental to a broader understanding of the composition and evolution of the oceanic mantle and crust.

---

[1] Bougault, H., Cande, S. C., et al., *Init. Repts. DSDP*, 82: Washington (U.S. Govt. Printing Office).

[2] Address: Department of Geology and Geography, University of Massachusetts, Amherst, Massachusetts 01003.

The 96 samples collected for this study were analyzed for major and trace elemental abundances by X-ray fluorescence (XRF) techniques (Appendixes A and B). Seven samples were selected for rare earth element (REE) analysis by instrumental neutron activation analysis (INAA) (Table 1). The chemical abundances and ratios were used to determine the chemical groups that in turn were used to evaluate the complex processes involved in basalt petrogenesis in the Leg 82 area. The geochemical data were also used to examine the important question of whether the Azores hot-spot anomaly consists of a single mantle plume (Schilling, 1975) or represents sampling of pervasive, small-scale mantle veining (Hanson, 1977; Zindler et al., 1979). The role of fracture zones (in this case, the Hayes Fracture Zone at 33°N) as possible domain boundaries between regions of mantle with different chemical signatures was also considered (Melson and O'Hearn, 1979; Bougault and Treuil, 1980).

Throughout the text, tables, figures, and appendixes we have used our own simplified sample numbering system. The first part of the number refers to the hole number (556–564) and the second part represents the samples in order of increasing depth within basement (i.e., the number 1 refers to the sample nearest the top of each hole). The DSDP designation for each sample can be found in the second to fourth rows at the top of Appendix A, Tables 1–7, which list all of the major and trace element abundances for each sample by hole number in order of increasing depth within basement.

METHODS

Samples were crushed in a tungsten carbide shatterbox at the Ronald B. Gilmore X-Ray Facility in the Department of Geology and Geography at the University of Massachusetts in Amherst. The major element data were obtained by XRF on fused glass disks, prepared by fusing the sample with a lanthanum-bearing lithium tetraborate flux (Norrish and Hutton, 1969). The trace elements (Rb, Sr, Y, Ga, Zr, Nb, Zn, Ni, Cr, and V) were determined by XRF analysis on pressed powder pellets. Corrections were made for nonlinear backgrounds, tube contamination, and interelement interferences (Norrish and Chappell, 1967). Corrections for matrix effects were based on a modification of the Compton scattering method (Reynolds, 1967). Additional trace element and REE data (La, Ce, Nd, Sm, Eu, Yb, Lu, Hf, Sc) (Table 1) were obtained by INAA in Fred Frey's laboratory at the Center for Geoalchemy in the Department of Earth and Planetary sciences at the Massachusetts Institute of Technology, by the methods of Jacobs and others (1977).

Average values for BCR-1 analyzed as an unknown by XRF are given in Table 2 with one standard deviation. Each element was analyzed twice for each sample. Error values labeled Leg 82 in Table 2 are based on these replicate analyses and apply directly to the Leg 82 basalts under the given operating conditions. The values were calculated using the formula:

$$s = \sqrt{\Sigma(x - \bar{x})^2/(n - 1)},$$

where x and $\bar{x}$ are observation and mean for replicate analyses of the same element in a single sample and n is the number of samples analyzed.

Mg′-values were calculated as molecular $Mg/(Mg + Fe^{2+})$, where molecular Fe has been proportioned as $Fe^{3+}/(Fe^{2+} + Fe^{3+}) = 0.$ (Basaltic Volcanism Study Project, 1981). Fe_2O_3* and FeO* refer to total Fe expressed as Fe^{3+} or Fe^{2+}, respectively. Major elements are expressed as weight percent (wt.%) and trace elements in parts per million (ppm).

BASALT CHEMISTRY

Hole 556

Hole 556 is located near Anomaly 12 (30–34 Ma) about 80 km north of the Pico Fracture Zone on a flow line extending through the Azores Triple Junction (Fig. 1). The 16 basalt samples analyzed from 177 m of basement may be classified as two distinct, but stratigraphically interlayered basalt types. Group I is the more primitive of the two, with moderately high MgO (7.4 wt.%) and CaO (13.3 wt.%) contents, Mg′-values (0.66), and CaO/Al_2O_3 ratios (0.83) (Appendix A, Table 1; Appendix B, Table 1; Figs. 2–4). Ni (100 ppm) and Cr (340 ppm) contents are the lowest of all Leg 82 basalts and the Sr (99 ppm) contents are relatively low also (Figs. 5, 6). Incompatible element abundances, TiO_2 (1 wt.%), Zr (48 ppm), Y (22 ppm), and Nb (1.8 ppm) as well as Zr/Y ratios (2.5) (Fig. 7), are low relative to other ocean-floor basalts (Melson et al., 1977; Basaltic Volcanism Study Project, 1981).

Within Group I, two subgroups can be recognized; IA (556-1, 2, 7, 8, 9, 11, 13–16) and IB (556-10, 12, 17). Subgroup IA has lower Ni (99 versus 110 ppm) contents, Mg′-values (0.64 versus 0.67), and CaO/Al_2O_3 ratios

Table 1. Rare earth element and trace element abundances (ppm) in selected Leg 82 basalts.

Univ. Mass. sample number	558-1	558-2	558-7	558-13	561-2	561-6	563-2	ML-76	NB-STD	N
Hole	558	558	558	558	561					
Core-Section	27-3	28-1	33-2	38-1	1-1	2-2	24-1			
(interval in cm)	112–114	55–58	144–147	97–99	4–9	82–84	22–25			
Sub-bottom depth (m)	409.13	415.07	462.46	505.48	411.57	416.83	366.24			
La	6.42	3.06	9.79	5.33	13.99	2.87	1.93	9.67	10.73	0.33
Ce	14.7	7.5	19.4	13.0	26.8	8.2	5.6	23.2	27.7	0.88
Nd	12.0	9.7	17.1	10.7	20.0	9.8	7.8	26.8	16.8	0.60
Sm	2.81	2.63	3.09	2.12	3.68	3.02	2.08	4.79	3.72	0.181
Eu	1.01	0.96	1.10	0.79	1.22	1.41	0.82	1.70	1.21	0.069
Yb	2.42	3.06	2.36	2.12	2.88	3.78	2.67	2.15	2.32	0.20
Lu	0.38	0.43	0.34	0.34	0.44	0.55	0.41	0.30	0.48	0.034
Sc	34.1	40.1	36.1	35.9	36.9	42.5	41.4	30.5	9.9	
Hf	1.97	1.70	2.01	1.50	2.20	2.10	1.37	3.43	5.76	
$(La/Ce)_{ch}$	1.16	1.09	1.35	1.09	1.39	0.93	0.92	1.11	1.02	
$(La/Sm)_{ch}$	1.25	0.63	1.74	1.38	2.09	0.52	0.51	1.11	1.58	
$(La/Yb)_{ch}$	1.61	0.61	2.51	1.52	2.94	0.46	0.49	2.73	2.80	

Note: ch = chondrite-normalized ratios. ML-76 = Mauna Loa sample used as University of Massachusetts internal standard. NB-STD = M.I.T. internal standard. N refers to values used to normalize REE abundances to chondrites.

Table 2. Precision of whole-rock basalt chemistry analyses.

Elements	BCR-1	Leg 82 error
Major element (wt.%)		
SiO_2	54.51 (0.17)	(0.07)
TiO_2	2.25 (0.01)	(0.03)
Al_2O_3	13.52 (0.10)	(0.05)
Fe_2O_3*	13.36 (0.04)	(0.04)
MnO	0.19 (0.01)	(0.01)
MgO	3.33 (0.04)	(0.04)
CaO	6.93 (0.03)	(0.19)
Na_2O	3.30 (0.28)	(0.18)
K_2O	1.70 (0.01)	(0.01)
P_2O_5	0.38 (0.01)	(0.001)
Trace element (ppm)		
Rb	46.4 (0.3)	(0.20)
Sr	326 (1)	(0.58)
Y	33.5 (0.3)	(0.28)
Ga	22.2 (0.6)	(1.49)
Zr	194.5 (1.8)	(0.55)
Nb	12.5 (0.4)	(0.46)
Zn	128 (2)	(0.56)
Ni	22.8 (9.7)	(6.60)
Cr	5.7 (1.4)	(1.28)
V	360 (4)	(2.39)

Note: BCR-1 is a U.S.G.S. standard analyzed with every X-ray fluorescence run. Mean and 1 standard deviation (expressed in wt.% or ppm) are given. The column labeled Leg 82 error refers to the precision of analysis at the Leg 82 concentrations (see text) and is given as 1 standard deviation.

(0.83 versus 0.87), along with higher incompatible element abundances, TiO_2 (1.02 versus 0.86 wt.%), Zr (58 versus 48 ppm), and Y (23 versus 20 ppm), than Subgroup IB. However, the Sr (99 versus 100 ppm) content is the same for both subgroups (Fig. 6). The three samples from Subgroup IB and one sample from Subgroup IA (556-7) are unusually high in CaO (14 wt.%) (Fig. 3) for ocean-floor basalts (Melson et al., 1977; Basaltic Volcanism Study Project, 1981). These samples have few or no phenocrysts and no obvious carbonate veining or alteration.

Group II, consisting of four samples (556-3 through 556-6) has lower MgO (6.75 wt.%), CaO (11.7 wt.%), Ni (89 ppm), and Cr (250 ppm) contents, Mg′-values (0.58), and CaO/Al_2O_3 ratios (0.70), along with greater Zr/Y ratios (2.9) and incompatible element abundances—TiO_2 (1.45 wt.%), Zr (90 ppm), Nb (2.5 ppm), and Y (30 ppm)—than Group I. Group II also contains 100 ppm of Sr, the same amount as in Group I (Fig. 6).

Both groups have high Zr/Nb ratios (≥ 30) (Fig. 8) and are typical depleted Type I ocean-floor basalts according to the classification scheme of Bryan and others (1976). The compositional differences between the two groups coupled with a constant Zr/Nb ratio (Fig. 8) are qualitatively consistent with a comagmatic relationship between the two groups. Approximately 50% crystal fractionation involving olivine, plagioclase, and clinopyroxene is required to generate Group II basalts from Group I basalts.

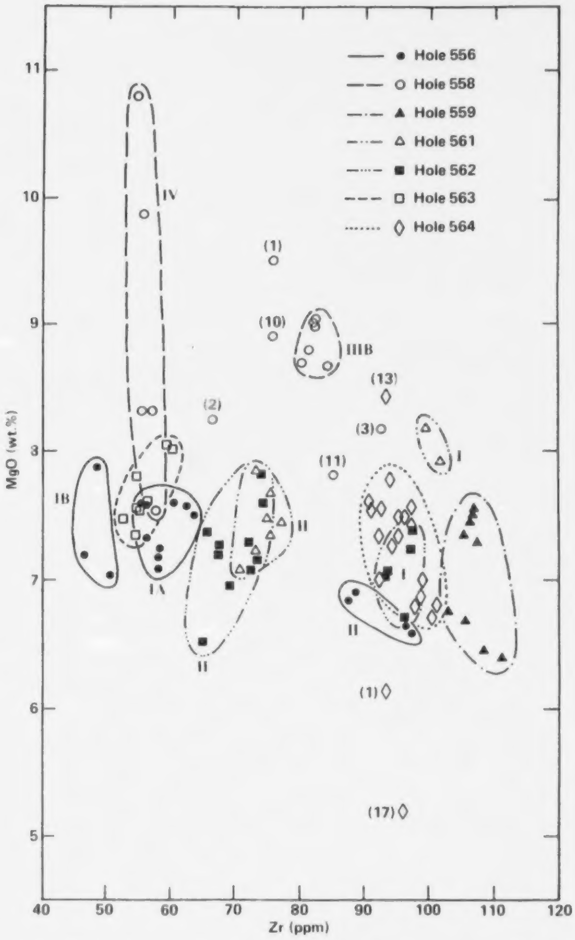

Figure 2. MgO versus Zr. Enclosures and Roman numerals refer to chemical groups within each hole. (All of the samples from Holes 559, 563, and 564 belong to Chemical Group I.) Arabic numbers in parentheses refer to the University of Massachusetts sample numbers (hole is indicated by shape of data point; see Appendix A tables for the DSDP sample designations for the samples).

It is unlikely, however, that this process is one of simple crystal fractionation. First, the observed phenocryst assemblages of only plagioclase ± olivine are not consistent with fractionation dominated by clinopyroxene (as is suggested by chemical considerations). Second, the fact that Ni and Cr abundances are approximately the same for the two groups, each with different amounts of incompatible elements (Fig. 5), is consistent with the evolution of both groups from a common parental magma. Such inconsistencies may be explained by a combination of fractional crystallization and mixing of consanguineous magmas (Rhodes et al., 1979). This interpretation receives support from the repetitive interlayering of Groups I and II. It is also possible to interpret the geochemical differences in terms of variable degrees of partial melting of a common source (Langmuir et al., 1977; Wood, 1979). In this case, the more enriched

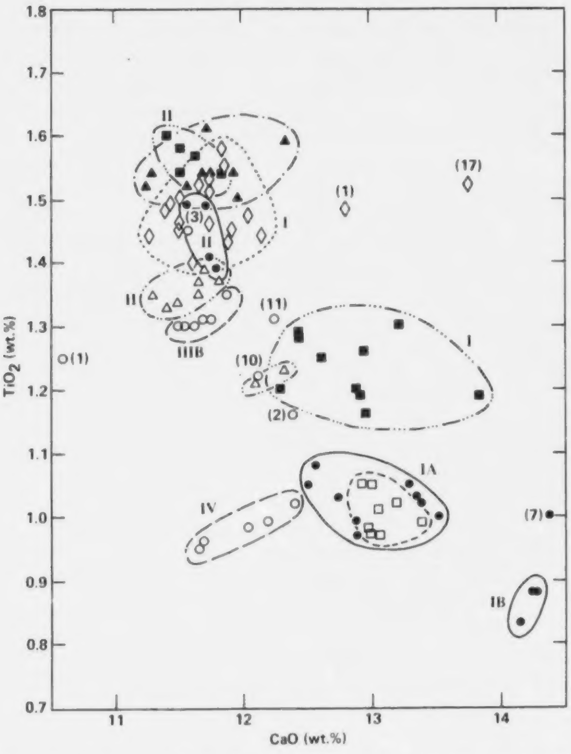

Figure 3. TiO_2 versus CaO. Symbols and enclosures are the same as in Figure 2.

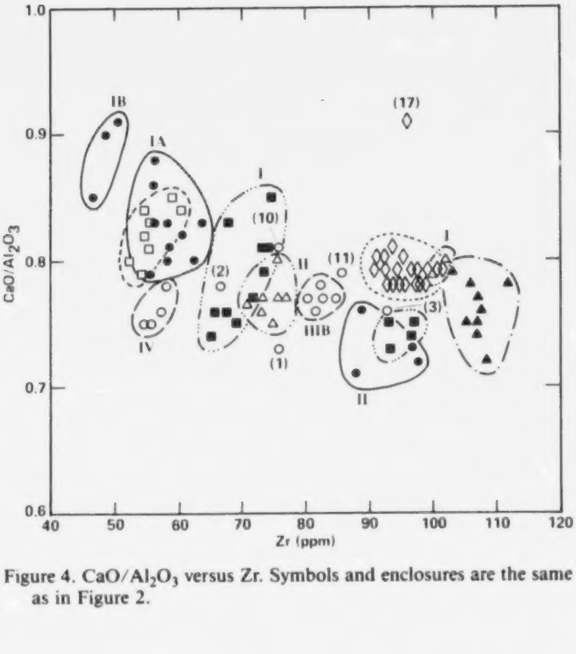

Figure 4. CaO/Al_2O_3 versus Zr. Symbols and enclosures are the same as in Figure 2.

Group II would have been produced by a lesser degree of melting. However, a plot of Sr versus Zr (Fig. 6) shows that both groups have about the same concentration of Sr (100 ppm) for very different concentrations of Zr. This relationship cannot be produced by different degrees of partial melting, but can be the result of fractionation/mixing processes.

Hole 557

Hole 557 is located near the same flow line as Hole 556, but near Anomaly 5D (18 Ma) closer to the Azores Triple Junction (Fig. 1). Only 3 m of basement were penetrated before the hole was abandoned because of inclement weather. Our one sample of this core, 557-1, falls into Group II of the shipboard studies (Site 557 chapter, this vol.). It has extremely high incompatible element abundances, TiO_2 (3.67 wt.%), Zr (216 ppm), Y (41 ppm), Nb (26 ppm) as well as high $Fe_2O_3^*$ (16.5 wt.%) and Sr (299 ppm), but very low MgO (5 wt.%), Ni (38 ppm), and Cr (19 ppm) abundances and a low Mg′-value (0.41) (Appendix A, Table 1). Thus, 557-1 is one of the more highly evolved or enriched basalts described to date from the ocean floor (Melson et al., 1977; Basaltic Volcanism Study Project, 1981). TiO_2 and FeO* abundances in 557-1 are similar to those of the enriched FeTi basalts of the Galapagos Spreading Center (Anderson et al., 1975; Schilling et al., 1976; Melson et al., 1977). Because of its extremely different abundances and ratios, Hole 557 data are not plotted on Figures 2–8.

The Zr/Nb ratio (8) and Zr/Y ratio (5) indicate that 557-1 is a Type II ocean-floor basalt (Bryan et al., 1976). The Zr/Y ratio is similar to that observed in Holes 407, 408, 410A, and 413 of DSDP Leg 49 (Tarney et al., 1979), but is higher than the Zr/Y ratios (2–4) observed in the other Leg 82 basalts (Fig. 7). It is likely that this basalt was derived from an unusually enriched source. If these basalts were derived from primitive Type II basalts similar to Group IV in Hole 558 (Appendix A, Table 2), the observed increase in incompatible element abundances would suggest as much as 70% crystal fractionation of olivine, plagioclase, and clinopyroxene. However, the lack of clinopyroxene phenocrysts and the close correlation of TiO_2 and Y abundances to other incompatible element abundances (indicating that clinopyroxene has not been a major fractionating phase) suggest that 557-1 is enriched by derivation from an enriched source rather than by evolution from a more typical ocean-floor basalt. CIPW norm calculations also indicate a more moderate state of evolution (557-1 is only slightly quartz normative).

Hole 558

Hole 558 is located between Anomalies 12 and 13 (34–37 Ma) about 50 km south of the Pico Fracture Zone on a flow line passing through DSDP Leg 37, Hole 335 (approximately 16.5 Ma), and the FAMOUS area (Recent) (Fig. 1). The 16 samples collected from 153.5 m of basement are compositionally the most complex of the Leg 82 basalts. The data indicate that four distinct basalt groups and two subgroups have been sampled (Appendix A, Table 2 and Appendix B, Table 2).

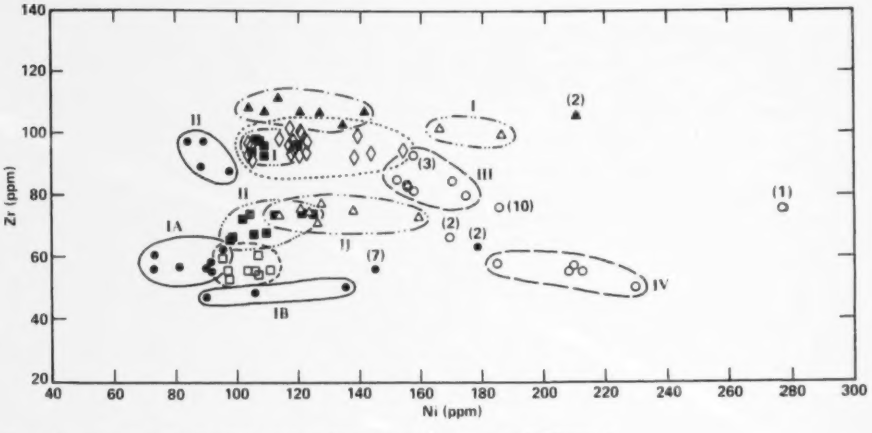

Figure 5. Zr versus Ni. Symbols and enclosures are the same as in Figure 2.

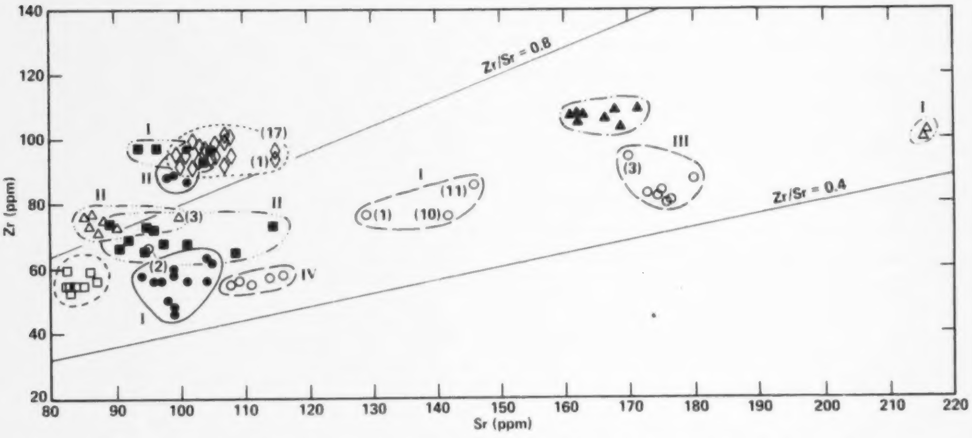

Figure 6. Zr versus Sr. Symbols and enclosures are the same as in Figure 2. Lines represent Zr/Sr ratios.

All of the chemical groups in this study correspond to shipboard groups except that three samples (558-1, 558-10, and 558-11) are included together in Group I because, although not stratigraphically contiguous, they have similar incompatible element abundances and ratios (Appendix A, Table 2; Figs. 7, 8).

Group I has moderate abundances of MgO (8.8 wt.%), CaO (11.7 wt.%), Sr (139 ppm), Ni (169 ppm) and Cr (344 ppm), Mg′-values (0.65), and CaO/Al_2O_3 ratios (0.77) (Appendix B, Table 2; Figs. 2–6). The abundances of incompatible elements are moderate as well, TiO_2 (1.26 wt.%), Zr (79 ppm), Nb (9.8 ppm), Y (23 ppm), as are the Zr/Y ratios (3.5) (Appendix B, Table 2; Fig. 7). Sample 558-1 has the highest MgO (9.5 wt.%), Ni (277 ppm), and Cr (510 ppm) abundances in Group I and the lowest CaO (10.6 wt.%) contents and CaO/Al_2O_3 ratio (0.73) (Appendix A, Table 2; Figs. 2–5), which could be due to olivine accumulation.

Group II, consisting of one sample, 558-2, also contains moderate abundances of major and trace elements; MgO (8.3 wt.%), CaO (12.4 wt.%), Ni (170 ppm), Cr (400 ppm), and CaO/Al_2O_3 ratio (0.78) (Appendix A, Table 2; Figs. 2–5). The Mg′-value is high (0.67), whereas the Sr content (95 ppm) is the lowest of all Hole 558 basalts (Fig. 6). Incompatible element abundances are somewhat low: TiO_2 (1.2 wt.%), Zr (66 ppm), Nb (2.3 ppm), and Y (26 ppm). The fact that Group II has the highest Y content and lowest Zr/Y ratio (2.6) for this hole (Fig. 7) precludes the possibility that Group II evolved from any of the other samples in Hole 558 by fractionation of clinopyroxene.

Group III consists of seven samples (558-3 through 558-9). It has the lowest CaO (11.6 wt.%), Ni (160 ppm), and Cr (368 ppm) and highest Sr (173 ppm), TiO_2 (1.35 wt.%), and Zr (88 ppm) abundances of all samples in Hole 558 (Appendix B, Table 2; Figs. 3, 5, 6). Yet the Ni and Cr contents are still fairly high, as are MgO contents (8.7 wt.%) and Mg′-values (0.66) (Figs. 2, 5). This suggests that the samples from Hole 558 are among the most primitive of Leg 82 basalts, even though Group III is the most evolved group at this site.

Within Group III are two subgroups. The single sample (558-3) in Subgroup IIIA differs from the other six samples in Subgroup IIIB; it has lower MgO (8.2 versus

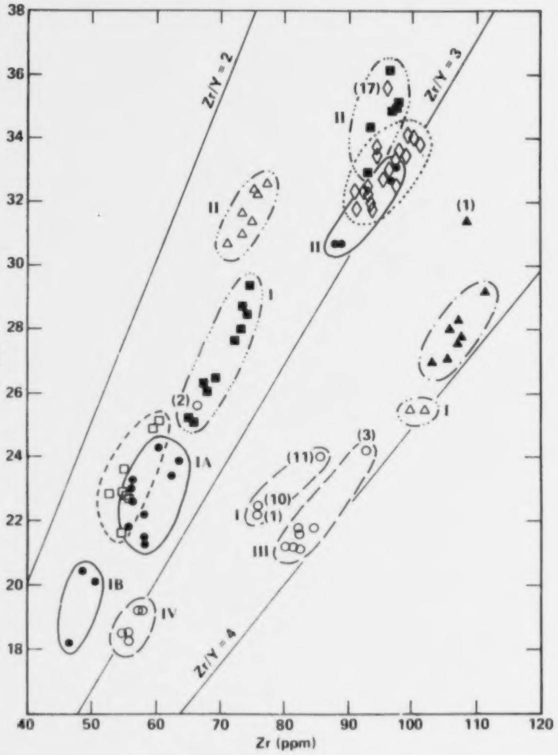

Figure 7. Y versus Zr. Symbols and enclosures are the same as in Figure 2. Lines represent constant Zr/Y ratios.

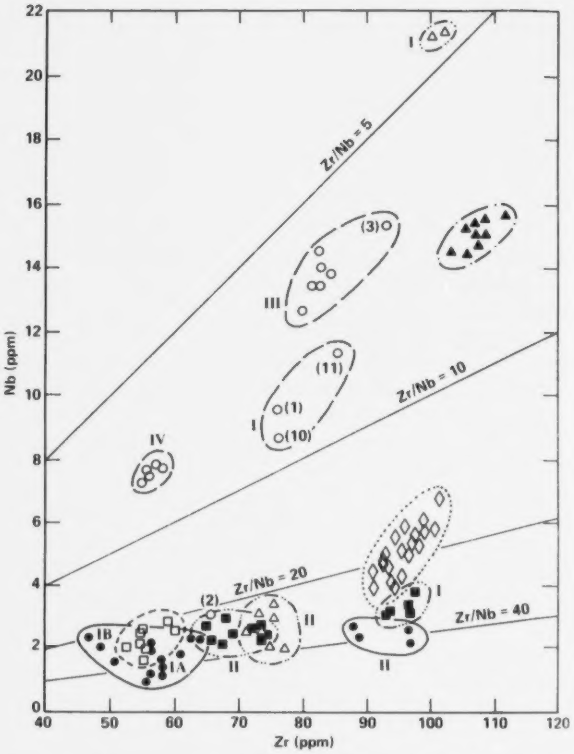

Figure 8. Nb versus Zr. Symbols and enclosures are the same as in Figure 2. Lines represent constant Zr/Nb ratios.

8.9 wt.%) contents and Mg′-values (0.64 versus 0.67) and greater abundances of incompatible elements, TiO_2 (1.45 versus 1.31 wt.%), Zr (93 versus 82 ppm), Nb (15.3 versus 13.6 ppm), and Y (24 versus 21 ppm) (Appendix B, Table 2). The similar CaO/Al_2O_3 ratios (0.77) and Ni (157 versus 162 ppm) and Cr (356 versus 379 ppm) contents for both subgroups (Figs. 4, 5) imply that Subgroups IIIA and IIIB may have either fractionated along closely parallel trends from slightly different parental magmas or undergone mixing during the fractionation process. Because IIIA contains about the same amount of Sr (170 versus 176 ppm) and more Zr than IIIB (Fig. 6), a melting trend is not possible, whereas mixing during fractionation is possible. Although the Zr/Y ratios are the same for both subgroups (3.8) (Fig. 7), the abundance of Y is higher for IIIA than IIIB, also supporting a more complex relationship than simple crystallization dominated by clinopyroxene fractionation.

Group IV, with five samples (558-12 through 558-16) has high MgO (7.5–10.8 wt.%), Ni (185–230 ppm) and Cr (442–482 ppm) contents, and Mg′-values (0.62–0.71), with moderate CaO (12.1 wt.%) and Sr (112 ppm) contents and CaO/Al_2O_3 ratios (0.76) (Appendix B, Table 2; Figs. 2–6). These basalts exhibit low incompatible element abundances; TiO_2 (<1 wt.%), Zr (55 ppm), Nb (7.6 ppm), and Y (19 ppm) and Zr/Y ratios (3.0) (Fig. 7). These abundances and ratios make Group IV the most primitive of the Leg 82 basalts. The primitive nature of Group IV basalts is also shown by the trends seen in Figures 2, 3, and 5 of Zr versus MgO, CaO, and Ni, respectively, which indicate olivine-controlled fractionation.

Within Group IV, Samples 558-13 and 558-16 are possible candidates for primary ocean-floor basalts. They have the highest abundances of MgO (10.8 and 9.9 wt.%), Ni (230 and 214 ppm) and Cr (449 and 441 ppm), and Mg′-values (0.71 and 0.69) of all Leg 82 basalts (except 558-1 for Ni) and low incompatible element abundances (Appendix A, Table 2). They are chemically similar to other proposed primary ocean-floor basalts such as those from DSDP Leg 3 (Frey et al., 1974), the FAMOUS area (Langmuir et al., 1977; White and Bryan, 1977), and the Mid-Atlantic Ridge at 45°N (Melson et al., 1977; Rhodes et al., 1979; Basaltic Volcanism Study Project, 1981).

It seems unlikely that the basalts from these four groups are comagmatic. Basalt samples from all four groups, which have comparable MgO and Ni abundances, Mg′-values, and CaO/Al_2O_3 ratios, have markedly different abundances of Zr and other incompatible elements (Figs. 2, 4, 5). In addition, these four chemical groups all have different Zr/Nb ratios (Fig. 8): Groups I, III, and IV have low values (8, 6, and 7.5, respectively), typical of Type II basalts (Bryan et al., 1976), but Group II is somewhat anomalous with a Zr/Nb ratio of about 20 (Fig. 8), similar to many basalts sampled on the Juan de Fuca Ridge (Liias and Rhodes, 1982).

REE data were obtained for four representative samples, one from each group (Table 1; Fig. 9A). Samples 558-1, 558-7, and 558-13 (Groups I, III, IV, respective-

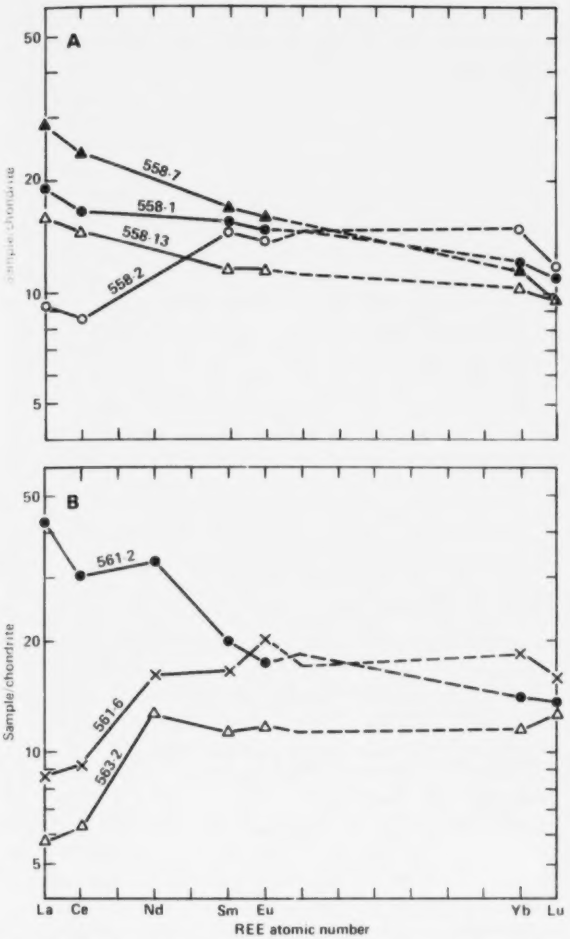

Figure 9. A. Chondrite-normalized rare earth element (REE) abundances for selected basalts in Hole 558. Sample numbers are the simplified numbers used in this study. Complete DSDP designations are located at the top of Appendix A, Table 2. B. Chondrite-normalized REE abundances for selected basalts in Holes 561 and 563. Sample numbers are the simplified numbers used for this study. Complete DSDP designations are located at the top of Appendix A, Tables 4 and 6.

y) all show LREE-enriched patterns with chondrite-normalized (ch) ratios: $(La/Sm)_{ch} > 1$ (1.25-1.8) and $(La/Yb)_{ch} > 1$ (1.5-2.5) (Table 1). In marked contrast, Sample 558-2 (Group II) has a LREE-depleted pattern with $La/Sm)_{ch} < 1$ (0.63) and $(La/Yb)_{ch} < 1$ (0.61). Although the $(La/Sm)_{ch}$ ratios are variable, the $(La/Ce)_{ch}$ ratios are >1 (1.09-1.35) for all four groups, similar to other basalts along this flow line, such as those from DSDP Leg 37 (Blanchard et al., 1976) and the FAMOUS area (Langmuir et al., 1977; White and Bryan, 1977).

Hole 559

Hole 559 is located between Anomalies 12 and 13 (34-37 Ma) midway between the Oceanographer and Hayes fracture zones (Fig. 1). All nine samples from the 63 m of basement are similar in composition (Appendix A, Table 3; Appendix B, Table 3) and compose a single chemical group consisting of enriched Type II basalts (Bryan et al., 1976) with typical Zr/Nb ratios (7-7.5) (Fig. 8). These basalts have some of the lowest CaO (11.7 wt.%) contents and CaO/Al_2O_3 ratios (0.76) and highest incompatible element abundances—TiO_2 (1.54 wt.%), Zr (107 ppm), Y (28 ppm), and Nb (15 ppm)—of all Leg 82 samples except 557-1 (Appendix A, Tables 1, 3; Appendix B, Table 3; Figs. 3, 4, 7, 8). However, the MgO (7.1 wt.%) and Ni (135 ppm) contents and the Mg′-value (0.59) are higher than expected relative to the concentration of incompatible elements (Figs. 2, 5).

The basalts from Hole 559 show stratigraphically interlayered variations in MgO, FeO*, and Mg′-values. Samples 559-2, 559-3, 559-5, 559-7, and 559-8 have lower MgO abundances (6.5 versus 7.5 wt.%) and Mg′-values (0.56 versus 0.62) and higher Fe_2O_3* (11.6 versus 10.5 wt.%) abundances than Samples 559-1, 559-4, 559-6, and 559-9 (Appendix B, Table 3; Fig. 2). This interlayering involving only the elements Mg and Fe could be the result of periodic replenishment of a multiply saturated magma by a more-primitive, olivine-rich melt (Rhodes et al., 1979). The relatively high Ni values (Fig. 5) also suggest that these basalts are enriched in olivine relative to other similarly evolved basalts (Basaltic Volcanism Study Project, 1981).

The incompatible element abundances (Appendix B, Table 3) are consistent with approximately 50% crystal fractionation from a more primitive Type II magma similar to the Group IV basalts sampled at Hole 558 (Appendix B, Table 2). Low CaO/Al_2O_3 ratios (0.76) (Fig. 4) coupled with high Zr/Y ratios (3.8) (Fig. 7) point towards clinopyroxene involvement in the fractionation process. However, clinopyroxene is notably absent from the observed phenocryst assemblage. The discrepancy between the chemistry and petrography, already encountered in Holes 556, 557, and 558, is a common problem for MORB (Dungan and Rhodes, 1978; Basaltic Volcanism Study Project, 1981) and points to a complex petrogenesis involving fractionation and mixing processes.

Sample 559-1 has the highest Y (31.6 ppm) abundance and the lowest Zr/Y ratio (3.43) of Hole 559 basalts (Fig. 7) and therefore could not have fractionated from compositions similar to the other samples in Hole 559. Possibly the observed anomalous behavior of 559-1 is a result of mantle heterogeneity or complex melting processes.

Hole 561

Hole 561 is located near Anomaly 5E (14-17 Ma) east of Hole 559 and along the same flow line (Fig. 1). The 15.1 m of basement is represented by nine samples that fall into two stratigraphically distinct groups. Group I is represented by two samples in the upper 0.7 m of the core, and Group II by seven samples in the lower 14.4 m. (Appendix A, Table 4; Appendix B, Table 4).

The upper basalts (Group I) have greater MgO (8.1 versus 7.4 wt.%), CaO (12.2 versus 11.6 wt.%), Sr (215 versus 89 ppm), and Ni (176 versus 130 ppm) abundances and Mg′-values (0.64 versus 0.59), but lower Fe_2O_3* contents (9.9 versus 11.5 wt.%) than the lower basalts (Group II).

Zr/Nb ratios are strikingly different for the two groups (Fig. 8). Group I, with low Zr/Nb ratios (<5), is a Type II basalt (Bryan et al., 1976), whereas Group II, which has higher Zr/Nb ratios (>25), is a Type I basalt. Two representative samples, 561-2 of Group I and 561-6 of Group II, were analyzed for REE (Table 1; Fig. 9B). Sample 561-2 is LREE enriched with chondrite-normalized ratios >1: $(La/Ce)_{ch} = 1.39$, $(La/Sm)_{ch} = 2.09$, and $(La/Yb)_{ch} = 2.94$, all typical of LREE-enriched Type II ocean-floor basalts (Bryan et al., 1976). Sample 561-6, however, is a typical LREE-depleted Type I ocean-floor basalt, with chondrite-normalized ratios <1: $(La/Ce)_{ch} = 0.93$, $(La/Sm)_{ch} = 0.52$, and $(La/Yb)_{ch} = 0.46$. This is in marked contrast to Hole 558 where the $(La/Ce)_{ch}$ ratio is fairly constant (>1) even though variations in the $(La/Sm)_{ch}$ ratios occur between Groups I and II (Table 1; Figs. 9A and 9B).

Group I has greater Zr/Y (4 versus 2.5) (Fig. 7) and Zr/TiO_2 (90 versus 55) ratios and Zr abundances (100 versus 75 ppm) than Group II, but lower Y (25 versus 30 ppm) and TiO_2 (1.2 versus 1.4 wt.%) contents (Appendix B, Table 4). These features, combined with the different Zr/Nb and $(La/Ce)_{ch}$ ratios, suggest that two distinct parental magmas are required, which is further supported by the two trends of decreasing Ni abundances at different Zr concentrations (Fig. 5). The Nd isotopic ratios (Jenner et al., this vol.) are distinctly different for the two groups and also indicate two distinct sources.

Hole 562

Hole 562 is located in 14–17 Ma crust near Anomaly 5D along a flow line about 100 km south of the Hayes Fracture Zone (Fig. 1). Sixteen samples from 90.1 m of basement fall into two stratigraphically separated chemical groups (Appendix A, Table 5; Appendix B, Table 5). Group I is represented by six samples in the upper 49.5 m of core and Group II by ten samples in the lower 40.6 m. Both groups have Zr/Nb ratios >20 (Fig. 8) and are depleted Type I MORB (Bryan et al., 1976).

Group I, which is higher stratigraphically and therefore more recently erupted, is the more evolved of the two groups. It has lower CaO (11.6 versus 12.9 wt.%) and MgO (7.0 versus 7.2 wt.%) abundances, CaO/Al_2O_3 ratios (0.74 versus 0.79), and Mg′-values (0.57 versus 0.61) (Figs. 2–4). Abundances of incompatible elements, TiO_2 (1.6 versus 1.2 wt.%), Zr (96 versus 70 ppm), and Y (35 versus 27 ppm), and Zr/Y ratios (2.8 versus 2.6) (Fig. 7), are correspondingly higher in Group I than Group II. However, Ni (109 versus 108 ppm), Cr (231 versus 257 ppm), and Sr (100 versus 98 ppm) abundances are similar for the two groups (Figs. 5, 6).

Within Group II, Al_2O_3 increases and CaO/Al_2O_3 ratios decrease with decreasing Zr (Fig. 4) as a consequence of plagioclase accumulation. The most plagioclase phyric samples occur at the high Al_2O_3–low Zr end of the trend.

The above-noted increase in incompatible elements is consistent with about 22–25% crystal fractionation. The small increase in Zr/Y ratios from Group II to Group I and the fact that TiO_2 and Y are behaving less incompatibly than Zr and Nb indicate clinopyroxene on the liquidus. Based on these relations and the trends shown in Figure 7, the two groups could be comagmatic, with Group I basalts having evolved from a magma with Grou II composition.

However, as in Hole 556, the Ni abundances for th two groups are approximately the same, although abundances of ZR (and other incompatible elements) are di ferent (Appendix B, Table 5; Fig. 5). These Ni-Zr relationships for the two basalt groups may be the result o the mixing of consanguineous magmas (Rhodes et al. 1979), or alternatively, fractionation of distinct parenta magmas produced by slightly different amounts of melting of a similar source. Once again, the two chemica groups have the same Sr concentrations with different Z concentrations (Fig. 6). This precludes partial melting an supports the idea of fractionation and magma mixing a proposed for Holes 556 and 558 in this study.

Hole 563

Hole 563 is located near Anomaly 13 (34–37 Ma) west of Hole 562 and near the same flow line south of the Hayes Fracture Zone (Fig. 1). The eight samples taken from 18 m of basement compose a single chemical group. These samples have the following major and trace element abundances: MgO (7.7 wt.%), CaO (13 wt.%), Fe_2O_3* (10.1 wt.%), Ni (103 ppm), and Cr (239 ppm), Mg′-values (0.63), and CaO/Al_2O_3 ratios (0.8) (Appendix A, Table 6; Appendix B, Table 6). Abundances of Sr (84 ppm) and incompatible elements, TiO_2 (1 wt.%), Zr (50 ppm), Y (23 ppm), and Nb (2.3 ppm), and Zr/Y ratios (<2.5) are low.

As in Hole 559, the samples in Hole 563 show similar stratigraphically interlayered variations in MgO and Fe_2O_3* abundances and Mg′-values (Appendix A, Table 6; Fig. 2). Samples 563-1, 563-2, 563-4, 563-6, and 563-8 have lower MgO (7.5 versus 8 wt.%) abundances and Mg′-values (0.62 versus 0.64) and greater Fe_2O_3* (10.3 versus 9.9 wt.%) abundances than Samples 563-3, 563-5, and 563-7. The interlayered fluctuations in these elements could imply periodic replenishment of an evolving magma reservoir by more primitive melts (Rhodes et al., 1979).

As in Hole 562, plagioclase accumulation is indicate both petrographically and chemically. In samples with such accumulations, MgO and Zr abundances and CaO Al_2O_3 ratios decrease whereas Al_2O_3 increases with increasing amounts of plagioclase (Figs. 2, 4).

The compositional data (Appendix A, Table 6) indicate that Hole 563 contains some of the more primitiv of the Leg 82 samples. Unlike most Leg 82 basalts, however, clinopyroxene fractionation does not appear to b important in the petrogenesis of Hole 563 basalts, a observation further supported by the Zr/Y ratios, which remain roughly constant (≤ 2.5) or decrease slightly with increasing Zr (Fig. 7).

One sample, 563-2, was analyzed for REE. It yielde chondrite-normalized ratios <1: $(La/Ce)_{ch} = 0.92$, $(La/Sm)_{ch} = 0.51$, and $(La/Yb)_{ch} = 0.49$ (Table 1; Fig. 9B)

The resulting LREE-depleted pattern, along with Zr/Nb ratios >20 (Fig. 8), mark Hole 563 samples as depleted Type I basalts (Bryan et al., 1976). Similar results were obtained for other basalts collected south of the Hayes Fracture Zone.

Hole 564

Hole 564 is located near Anomaly 13 (34–37 Ma) south of the Hayes Fracture Zone, about 10 km north of Hole 563 (Fig. 1). Twenty samples were taken from 1 m of basement. These basalts exhibit high incompatible element abundances, TiO_2 (1.5 wt.%), Zr (96 ppm), Y (33 ppm), and Nb (5 ppm); low abundances of CaO (11.8 wt.%) and Fe_2O_3* (11.9 wt.%); and moderate MgO (7.2 wt.%) and Sr (105 ppm) contents, Mg′-values (0.57), and CaO/Al_2O_3 ratios (0.80) (Appendix A, Table 7; Appendix B, Table 7). These compositional characteristics suggest that Hole 564 basalts are fairly evolved, possibly with clinopyroxene on the liquidus.

Sample 564-17 deviates from the compositional relationships exhibited by the other basalts from this hole and may constitute a separate group or subgroup. Its distinctly lower MgO content (5.2 wt.%) and Mg′-value (0.47) and higher Fe_2O_3* content (13.1 wt.%) suggest that 564-17 is much more evolved than the other samples. Yet the greater CaO content (13.8 wt.%) and CaO/Al_2O_3 ratio (0.90) and much lower SiO_2 content (47 wt.%) of this basalt are characteristic of more primitive basalts (Basaltic Volcanism Study Project, 1981). The higher K_2O (0.62 versus 0.33 wt.%), Rb (15 versus 6 ppm), and Sr (115 versus 105 ppm), coupled with the other major element characteristics, may indicate that extreme seawater alteration has occurred.

In the plot of Ni versus Zr (Fig. 5), the Ni content decreases markedly with almost constant Zr in all Hole 564 samples, suggesting that olivine is the only liquidus phase. However, the Ni values (117 ppm) appear to be too high relative to the low CaO contents and CaO/Al_2O_3 ratios and high incompatible element abundances normally associated with a more evolved magma. As in the other holes, this discrepancy in the chemistry implies a complex petrogenesis.

There is a pronounced and systematic change in basalt composition with depth. MgO, Ni, and Cr abundances and Mg′-values all decrease downhole, whereas Fe_2O_3* and incompatible element (Nb, Zr, Y, and TiO_2) abundances increase (Appendix A, Table 7). The gradual changes of concentration with depth suggest that the earlier erupted magma was more evolved than the more recently erupted magma. Such changes are commensurate with the gradual emptying of a zoned magma chamber or the relatively rapid replenishment of a slowly evolving magma by more primitive melt.

The most striking aspect of chemical variation with depth is the change in Zr/Nb ratio, which is greater (>20) near the top of the hole, but gradually decreases downhole to <15 (Appendix A, Table 7; Fig. 8). However, this appears to be mostly the result of changing Nb. On the other hand, Zr/Y ratios remain essentially constant (2.8–3.0) with the downhole increase in Zr and Y (Fig. 7). Zr/Nb ratios are unlikely to change during crystal fractionation or more complex processes involving both fractionation and mixing of consanguineous magmas. Therefore, it seems probable that changes in the Zr/Nb ratio result from the progressive mixing of a primitive but Nb-enriched melt with one that was evolved but had lower Zr/Nb ratios.

Again, Sample 564-17 is different from the others; it has a lower Zr/Y ratio (2.7) and greater Y content (36 ppm) (Fig. 7). This inverse relationship is similar to that exhibited by Sample 559-1. There is no obvious explanation for this anomalous behavior, and further investigation is warranted. Two representative samples, one from the top and one from the bottom of Hole 564, will be analyzed for REE and isotopes.

DISCUSSION

Numerous isotopic and chemical studies have been made of basalts along the Mid-Atlantic Ridge from the Azores Triple Junction to south of the Hayes Fracture Zone (Fig. 1) (Schilling, 1975; White et al., 1976; O'Nions et al., 1977; Tarney et al., 1979; White and Schilling, 1978; Zindler et al., 1979; Dupré and Allègre, 1980; White and Hoffman, 1982). These studies have shown that the basalts from this area exhibit compositional diversity ranging from primitive to highly evolved and LREE-depleted to LREE-enriched (Types I and II of Bryan et al., 1976).

The holes sampled during Leg 82 (Fig. 1) contain several types of basalts that exhibit a variety of chemical characteristics and may occur together within a given hole (Table 1; Appendix A, Tables 1-7; Appendix B, Tables 1-7). Most of these chemical groups are uniform in composition, and, in general, simple crystal fractionation cannot be readily documented by chemical variation within groups. The exceptions are the olivine fractionation trend observed in Hole 558 (Group IV) (Figs. 2, 3, 5) and the plagioclase accumulation trends observed in Hole 562 (Group II) and Hole 563 (Figs. 2, 4).

Chemical variation, however, does exist between groups within a given hole. In Holes 556, 558, and 562 (Fig. 1), the decreasing CaO/Al_2O_3 ratios and increasing Zr/Y ratios (Figs. 4 and 7) seem to indicate that one group may have evolved from another by multiply saturated crystal fractionation. However, several lines of evidence indicate that the chemical variation between groups is not compatible with simple crystal fractionation. First, in these same three holes there is a discrepancy between estimates of the state of magmatic evolution based on major and compatible trace elements (e.g., MgO, CaO, Ni, Cr contents, Mg′-value, CaO/Al_2O_3 ratios) and that based on incompatible elements (TiO_2, Zr, Nb, Y) (Appendix A, Tables 2, 3, 5; Figs. 2–5). This discrepancy is clearly evident in Zr versus MgO and Ni (Figs. 2, 5), where associated groups in Holes 556, 558, and 562 have similar MgO and Ni abundances, but markedly different Zr contents. This phenomenon may imply that (1) each of the groups evolved from slightly different parental magmas or (2) the groups within each hole are related to a common parental magma by interplay of mixing and fractionation (Rhodes et al., 1979). The latter hypothesis receives further support from the existence within Holes 556, 558, and 562 of different chemical groups with the same Sr but different Zr contents (Fig. 6). This cannot be explained by partial melting.

The stratigraphic interlayering of different chemical groups within the same hole (Holes 556 and 558) (Appendix A, Tables 1 and 2) indicates that similar magma compositions were episodically erupted. This supports the involvement of complex fractionation-mixing processes in the petrogenesis of these basalts. Further support comes from interlayered variations in Mg′-values in Holes 559 and 563 (Fig. 2), which could be due to repeated influxes of a more primitive melt into a more evolved magma (Rhodes et al., 1979). Further evidence for fractionation-mixing is the commonly observed discrepancy between the chemical criteria that appear to require clinopyroxene fractionation and the absence of clinopyroxene phenocrysts in any of the Leg 82 samples. This is a common problem in ocean-floor basalt petrogenesis (Dungan and Rhodes, 1978; Basaltic Volcanism Study Project, 1981) and is probably indicative of mixing between more-primitive and more fractionated magmas (Rhodes et al., 1979).

The systematic downhole trends in major and trace element abundances in Hole 564 (Appendix A, Table 7; Fig. 8) from relatively primitive to more evolved basalts is compatible with mixing of distinct magmas rather than simple crystal fractionation (Rhodes et al., 1979; Batiza and Johnson, 1980).

To gain a better understanding of Leg 82 basalt petrogenesis, it is important to assess the roles of mantle heterogeneity, complex melting, and melt segregation in the generation of the chemical diversity observed both within and between holes, especially Holes 558 and 561 (Table 1; Figs. 1–9; Appendix A, Tables 2, 4). For example, basalts with distinctly incompatible trace element ratios Zr/Y, Zr/Nb, and LREE/HREE (Figs. 7–9B) sampled within a single drill hole (Holes 558 and 561) have been cited as evidence for large-scale mantle heterogeneity involving a "depleted" upper mantle with mantle plumes upwelling from a more "fertile" deeper mantle layer (Schilling, 1973; Schilling et al., 1976; White and Schilling, 1978). Alternatively, mantle heterogeneity models involving mantle "blobs" (Schilling, 1975; Schilling et al., 1982), or pervasive small-scale veining or metasomatism of the upper mantle (Hanson, 1977; Zindler et al., 1979) have also been proposed. Complex melting and melt segregation in an otherwise homogeneous mantle (Langmuir et al., 1977; Wood, 1979) may cause similar differences in incompatible element and REE abundances, but not in ratios of highly incompatible elements $(La/Ce)_{ch}$ or Nd isotopes.

To evaluate these models it is necessary to develop a concept of the scale of heterogeneity with respect to both time and distance. The studies referenced above suggest the possibility of mantle "domains." For example, it appears that there is a boundary at about 33°N in the vicinity of the Hayes Fracture Zone separating depleted (Type I) MORBs (Bryan et al., 1976) to the south from enriched (Type II) basalts associated with the topographic high of the Azores Platform (White and Schilling, 1978; Bougault and Treuil, 1980).

In this study, basalts from holes drilled south of the Hayes Fracture Zone (Holes 562, 563, 564) (Fig. 1) are depleted in incompatible trace elements as expected. However, north of the Hayes Fracture Zone, basalts are both enriched (Holes 557 and 559) and depleted (Hole 556) in incompatible elements. At two sites (Holes 558 and 561), both types occur within the same hole (Figs. 1, 8, 9A, 9B). As other studies have shown (Blanchard et al., 1976; Langmuir et al., 1977; Tarney et al., 1979; Wood, 1979; Wood et al., 1979; Zindler et al., 1979), this close spatial association of enriched and depleted basalts is not uncommon. The occurrence of depleted basalts in older Hole 556 (30–34 Ma) and enriched basalts in younger Hole 557 (18 Ma) along a flow line from the Azore hot spot (Fig. 1) suggests that mantle anomalies are transient features, perhaps adding support to the mantle blob hypothesis (Schilling, 1975; Schilling et al., 1982 or small-scale mantle veining (Hanson, 1977; Zindler e al., 1979). In Hole 561, Groups I and II are not stratigraphically interlayered and have distinctly different ratios for the highly incompatible elements, Zr/Nb and $(La/Ce)_{ch}$, in addition to differences in Zr/Y, $(La/Sm)_{ch}$, and $(La/Yb)_{ch}$ ratios (Table 1; Figs. 7, 8, 9B). These traits suggest that Hole 561 basalts are derived from two distinct sources. Nd isotopic data (Jenner et al., this vol.) and geochemical data point to an LREE-enriched source for Group I and an LREE-depleted source for Group II (Table 1; Fig. 9B). The scale of the source heterogeneity cannot be pinpointed, although the presence within a single hole of magmas from two different sources may imply pervasive, small-scale heterogeneity such as mantle veining (Hanson, 1977; Zindler et al., 1979). The occurrence of only enriched basalts in older Hole 559 (34–37 Ma) along the same flow line as younger Hole 561 (14–17 Ma) (Fig. 1) could also be the result of a more transient mantle anomaly.

As noted above, variable incompatible and REE ratios within the same hole (such as Holes 558 and 561) may indicate either mantle heterogeneity or complex melting of a single source. If complex melting is involved, the ratios of the very highly incompatible elements, such as Zr/Nb and especially $(La/Ce)_{ch}$, should remain the same, whereas other ratios such as Zr/Y, $(La/Sm)_{ch}$, and $(La/Yb)_{ch}$ may vary (Langmuir et al., 1977; Wood, 1979). This is seen in Hole 558 where the $(La/Ce)_{ch}$ ratios are about the same (1.09–1.35) for all four groups (Table 1; Fig. 9A). In contrast, other incompatible and REE ratios vary from LREE enriched (Groups I, III, and IV) to LREE depleted (Group II) (Table 1; Figs. 7, 8, 9A; Appendix B, Table 2).

The data are not compatible with a petrogenesis involving only complex melting because Zr/Nb ratios vary considerably between Groups I, III, and IV (approximately 6–9) and Group II (20) (Fig. 8). Therefore, mantle heterogeneity may be indicated as well. The Nd isotopic ratios for Hole 558 basalts are almost identical for all four groups (Jenner et al., this vol.), so large-scale plume-related mantle heterogeneity involving two different sources does not seem likely.

A more plausible possibility is smaller-scale mantle veining and/or metasomatism (Hanson, 1977; Zindler et al., 1979) that may generate the highly variable incompatible element ratios and crossing REE pattern observed in Hole 558, along with the constant $(La/Ce)_{ch}$ and Nd isotopic ratios. Similarly, the repetitive interlayering of diverse magmas within the same hole does not support large-scale mantle heterogeneity. Variation in trace element ratios and crossing REE patterns appear to be restricted to regions of high volcanic activity along elevated ridge segments in hot-spot areas. Other examples are the Juan de Fuca Ridge (Liias and Rhodes, 1982); Iceland (Wood, 1979; Zindler et al., 1979; Schilling et al., 1982); FAMOUS (Langmuir et al., 1977; White and Bryan, 1977); and Hole 558 (site chapter, Site 558, this vol.). The observation that such highly variable basalt types appear to be confined to hot-spot areas suggests small-scale heterogeneity as well as complex melting.

Basalts in Hole 556 have a drastically different chemical signature from the basalts in Hole 557 (Appendix A, Table 1) even though both holes were drilled on the same flow line through the Azores Triple Junction (Fig. 1). This chemical difference, along with the abrupt changes in the Zr/Nb ratios and REE patterns between chemical groups within Holes 558 and 561 (Figs. 8, 9A, 9B), is counter to the more gradual transitions expected between Type I and II basalts in plume or mantle blob situations (Schilling, 1975). The basalts from Leg 82 appear to have undergone a complex petrogenesis involving small-scale mantle heterogeneity (veining or metasomatism), complex melting, and mixing-fractionation processes.

CONCLUSIONS

1. There is no evidence for simple crystal fractionation within or between chemical groups, except for Hole 558 (Group IV), Hole 562 (Group II), and Hole 563 as discussed above.

2. The concept of widespread, complex fractionation-mixing processes is supported by several lines of evidence: (1) similar MgO, Ni, and Sr abundances with different amounts of incompatible elements in different chemical groups within the same hole; (2) episodic eruptions of similar magmas within the same hole; (3) stratigraphic interlayering of basalts with changing Mg′-values in Holes 559 and 563, suggesting that multiply saturated magmas were periodically replenished by more primitive melt; and (4) discrepancy between chemical composition requiring clinopyroxene fractionation and the lack of clinopyroxene phenocrysts in the samples, a widely observed problem in ocean-floor basalt petrogenesis.

3. The Hayes Fracture Zone appears to be a "domain" boundary between the depleted Type I basalts in the south and the highly variable basalts in the area between the Hayes Fracture Zone and the Azores Triple Junction (Fig. 1).

4. Hole 557 is one of the most highly enriched and/or evolved basalts sampled in the Atlantic Ocean (or anywhere else) (Melson et al., 1977; Basalt Volcanism Study Project, 1981). The composition of Sample 557-1 most closely resembles the FeTi basalts at the Galapagos Spreading Center (Schilling et al., 1976; Melson et al., 1977).

5. Although incompatible and REE ratios vary from depleted to enriched in Hole 558, $(La/Ce)_{ch}$ ratios (1.09–1.35) (Table 1; Fig. 9A) and Nd isotopic ratios (Jenner et al., this vol.) are nearly the same for all four groups in Hole 558. These constant ratios suggest that complex melting of a single source is probably the main process generating the observed compositional variations, although the varying Zr/Nb ratios (Fig. 8) may imply source variability on a small scale.

6. Variations in trace element ratios and crossing REE patterns appear to be restricted to the region of high volcanic activity along elevated ridge segments in a hot-spot area (in this case, the Azores Platform) (Fig. 1).

7. Two distinct sources are indicated for Hole 561 because the two (noninterlayered) chemical groups have distinctly different, highly incompatible element ratios, including $(La/Ce)_{ch}$ (Table 1; Fig. 9B) and $143_{Nd}/144_{Nd}$ (Jenner et al., this vol.).

8. The concept of more pervasive, small-scale mantle heterogeneity such as veining and/or metasomatism rather than a large-scale mantle plume or mantle blobs receives support from several lines of evidence: (1) restriction of high variability in trace element and REE ratios to hot-spot areas (Holes 556–561); (2) abrupt changes in Zr/Nb ratios (Fig. 8), REE patterns (Table 1; Figs. 9A and 9B), and Nd isotopic ratios (Jenner et al., this vol.) between different groups within the same hole (Holes 558 and 561); (3) drastic differences in composition and incompatible element ratios between the older, depleted basalts in Hole 556 (30–34 Ma) and the younger, highly enriched FeTi basalt in Hole 557 (18 Ma) (Appendix A, Table 1), which are about 22 Ma apart along the flow line passing through the Azores Triple Junction (Fig. 1); and (4) the existence of enriched basalts in older Hole 559 (34–37 Ma) and of both enriched and depleted basalts in younger Hole 561 (14–17 Ma) along the same flow line between the Oceanographer and Hayes fracture zones (Fig. 1).

9. The Azores hot-spot anomaly has existed in its present configuration for at least 18 Ma (Hole 557), but less than 30–34 Ma (Hole 556) (Fig. 1).

ACKNOWLEDGMENTS

We wish to thank the following people for their help in completing this study: F. Frey for use of the MIT INAA laboratory and P. Ila for sample preparation and instruction in using the lab; Marie Litterer for drafting the figures; Gerda Kunkel for typing the tables; and Karen Thatcher of Words-Worth for typing the manuscript and additional tables.

We also wish to express our appreciation to John F. Bender and John Longhi for their many helpful suggestions and meticulous care in reviewing this paper.

This research was funded by NSF Grant #7826330.

REFERENCES

Anderson, R. N., Clague, D. A., Klitgord, K. D., Marshall, M., and Nishimori, R. K,. 1975. Magnetic and petrologic variations along the Galapagos Spreading Center and their relation to the Galapagos melting anomaly. *Geol. Soc. Am. Bull.*, 86:683–694.

Basaltic Volcanism Study Project, 1981. *Basaltic Volcanism on the Terrestrial Planets:* New York (Pergamon Press), pp. 132–160.

Batiza, R., and Johnson, J. R., 1980. Trace element and isotopic evidence for magma mixing in alkalic and transitional basalts near the East Pacific Rise at 8°N. *In* Rosendahl, B.R., Hekinian, R., et al., *Init. Repts. DSDP*, 54: Washington (U.S. Govt. Printing Office), 63–69.

Blanchard, D. P., Rhodes, J. M., Dungan, M. A., Rodgers, K. V., Donaldson, C. H., Brannon, J. C., Jacobs, J. W., and Gibson, E. K., 1976. Chemistry and petrology of basalts from Leg 37 of the Deep Sea Drilling Project. *J. Geophys. Res.*, 81:4231–4246.

Bougault, H., and Treuil, M., 1980. Mid-Atlantic Ridge: zero age geochemical variations between Azores and 22°N. *Nature*, 286: 209–212.

Bryan, W. B, Thompson, G., Frey, F. A., and Dickey, J. J., 1976. Inferred settings and differentiation in basalts from the Deep Sea Drilling Project. *J. Geophys. Res.*, 81:4285–4304.

Dungan, M. A., and Rhodes, J. M., 1978. Residual glasses and melt inclusions in basalts from DSDP Legs 45 and 46: evidence for magma mixing. *Contrib. Mineral. Petrol.*, 67:417–431.

Dupré, B., and Allègre, C. J,. 1980. Pb-Sr-Nd isotopic correlation and the chemistry of the North Atlantic mantle. *Nature*, 286:17–22.

Frey, F. A., Bryan, W. B., and Thompson, G., 1974. Atlantic Ocean floor: geochemistry and petrology of basalts from Legs 2 and 3 of the Deep Sea Drilling Project. *J. Geophys. Res.*, 79:5507–5527.

Hanson, G. N., 1977. Geochemical evolution of the sub-oceanic mantle. *J. Geol. Soc. London*, 134:235–253.

Jacobs, J. W., Korotev, R. L., Blanchard, D. P., and Haskin, L. A., 1977. A well-tested procedure for instrumental neutron activation analysis of silicate rocks and minerals. *J. Radioanal. Chem.*, 40: 93–114.

Langmuir, C. H., Bender, J. F., Bence, A. E., Hanson, G. N., and Taylor, S. R., 1977. Petrogenesis of basalts from the FAMOUS area: Mid-Atlantic Ridge. *Earth Plant. Sci. Lett.*, 36:133–156.

Liias, R. A., and Rhodes, J. M., 1982. Does a mantle plume influence basalt composition along the Juan de Fuca Ridge? *EOS, Trans. Am. Geophys. Union*, 63:1153–1154. (Abstract)

Melson, W. G., Byerly, G. R., Nelen, J. A., O'Hearn, T., Wright, T. L., and Vallier, T. L., 1977. A catalog of the major element chemistry of abyssal volcanic glasses. *Smithson. Contrib. Earth Sci.*, 19:31–60.

Melson, W. G., and O'Hearn, T., 1979. Basaltic glass erupted along the Mid-Atlantic Ridge between 0–37°N; relationships between composition and latitude. *In* Talwani, M., Harrison, C. G., and Hayes, D. E. (Eds.), *Deep Drilling Results in the Atlantic Ocean: Ocean Crust:* Washington (Am. Geophys. Union), pp. 249–261.

Norrish, K., and Chappell, B. W., 1967. X-ray fluorescence spectrometry. *In* Zussman, J. (Ed.), *Physical Methods in Determinative Mineralogy:* New York (Academic Press), pp. 161–214.

Norrish, K., and Hutton, J. T., 1969. An accurate X-ray spectrographic method for the analysis of a wide range of geological samples. *Geochim. Cosmochim. Acta*, 33:431–453.

O'Nions, R. K., Hamilton, P. J., and Evensen, N. M., 1977. Variation in ^{143}Nd/^{144}Nd and ^{87}Sr/^{86}Sr ratios in oceanic basalts. *Earth Planet Sci. Lett.*, 34:13–22.

Reynolds, R. C., 1967. Matrix corrections in trace element analysis by X-ray fluorescence: estimation of the mass absorption coefficient by Compton scattering. *Am. Mineral.*, 48:1133–1143.

Rhodes, J. M., Dungan, M. A., Blanchard, D. P., and Long, P. E., 1979. Magma mixing at mid-ocean ridges: evidence from basalts drilled near 22°N on the Mid-Atlantic ridge. *Tectonophysics*, 55: 36–61.

Schilling, J.-G., 1973. Iceland mantle plume: geochemical study of Reykjanes Ridge. *Nature*, 242:565–575.

_______, 1975. Azores mantle blob: Rare earth evidence. *Earth Planet. Sci. Lett.*, 25:103–115.

Schilling, J.-G., Anderson, R. N., and Vogt, P., 1976. Rare earth, Fe and Ti variations along the Galapagos spreading centre, and their relationship to the Galapagos mantle plume. *Nature*, 261:108–113

Schilling, J.-G., Meyer, P. S., and Kingsley, R. H., 1982. Evolution of the Iceland hot spot. *Nature*, 296:313–320.

Tarney, J., Wood, D. A., Varet, J., Saunders, A. D., and Cann, J. R. 1979. Nature of mantle heterogeneity in the North Atlantic: evidence from Leg 49 basalts. *Proc. Second M. Ewing Symp.* pp. 285–301.

White, W. M., and Bryan, W. B., 1977. Sr-isotope, K, Rb, Cs, Sr, Ba and rare-earth geochemistry of basalts from the FAMOUS area *Geol. Soc. Am. Bull.*, 88:571–576.

White, W. M., and Hofmann, A. W., 1982. Sr and Nd isotope geochemistry of oceanic basalts and mantle evolution. *Nature*, 296: 821–825.

White, W. M., and Schilling, J.-G., 1978. The nature and origin of geochemical variation in Mid-Atlantic Ridge basalts from central North Atlantic. *Geochim. Cosmochim. Acta*, 42:1501–1516.

White, W. M., Schilling, J.-G., and Hart, S. R., 1976. Evidence for the Azores mantle plume from strontium isotope geochemistry of the central North Atlantic. *Nature*, 263:659–663.

Wood, D. A., 1979. Dynamic partial melting: its application to the petrogenesis of basalts erupted in Iceland, the Faeroe Islands, the Isle of Skye (Scotland) and the Troodos Massif (Cypress). *Geochim. Cosmochim. Acta*, 43:1031–1046.

Wood, D. A., Tarney, J., Varet, J., Saunders, A. A., Bougault, H., Joron, J. L., Treuil, M., and Cann, J., 1979. Geochemistry of basalts drilled in the North Atlantic by IPOD Leg 49: implications for mantle heterogeneity. *Earth Planet. Sci. Lett.*, 42:77–97.

Zindler, A., Hart, S. R., Frey, F. A., and Jakobsson, S. P., 1979. Nd and Sr isotope ratios and rare earth element abundances in Reykjanes Peninsula basalts: evidence for mantle heterogeneity beneath Iceland. *Earth Planet. Sci. Lett.*, 45:249–262.

Date of Initial Receipt: 18 November 1983
Date of Acceptance: 4 April 1984

APPENDIX A

Chemical Compositions of Basalts from Leg 82

Note to Appendix A tables: Chemical group refers to chemical groups discussed in text. $Fe_2O_3^*$ and FeO^+ refer to total Fe expressed as Fe^{3+} and Fe^{2+}, respectively. Calculation of Mg′-value discussed in text (Mg/[Mg + Fe^2]). Small discrepancies in totals may be attributed to rounding.

Table 1. Holes 556 and 557.

Univ. Mass. sample no.	556-1	556-2	556-3	556-4	556-5	556-6	556-7	556-8	556-9	556-10	556-11	556-12	556-13	556-14	556-15	556-16	556-17	557-1
	Hole 556	Hole 556	Hole 556	Hole 556	Hole 556	Hole 556	Hole 556	Hole 556	Hole 556	Hole 556	Hole 556	Hole 556	Hole 556	Hole 556	Hole 556	Hole 556	Hole 556	Hole 557
Core-Section	2-1	2-2	2-5	3-3	5-1	6-5	6-6	7-1	7-3	8-2	9-4	10-3	10-4	11-2	12-3	12-4	16-2	1-1
(interval in cm)	74-76	141-144	26-28	66-69	99-102	64-67	108-111	128-132	83-86	13-16	64-67	63-66	72-75	121-124	54-57	27-30	110-113	50-53
Sub-bottom depth (m)	462.25	464.43	467.77	474.77	490.01	504.66	506.60	508.30	510.85	517.65	530.16	537.65	539.24	545.73	555.56	556.78	586.1	461.02
Chemical group	IA	IA	II	II	II	II	IA	IA	IA	IB	IA	IB	IA	IA	IA	IA	IB	II
Major elements (wt.%)																		
SiO_2	50.55	50.22	50.04	50.03	50.21	50.69	49.50	50.12	50.02	50.37	50.85	49.71	50.26	50.41	50.33	50.46	50.10	47.87
TiO_2	1.05	1.05	1.49	1.41	1.49	1.39	1.00	1.03	1.03	0.88	1.08	0.83	0.99	1.02	0.97	0.99	0.88	3.67
Al_2O_3	15.63	15.96	16.05	15.46	15.97	16.33	16.28	15.89	16.11	15.85	15.38	17.79	16.38	15.49	16.28	16.00	15.64	12.73
$Fe_2O_3^*$	9.54	8.72	10.91	11.42	10.83	9.75	8.43	10.08	8.98	8.33	9.49	7.55	8.72	9.19	8.91	9.11	8.59	16.51
MnO	0.15	0.15	0.17	0.18	0.17	0.17	0.15	0.16	0.17	0.14	0.15	0.12	0.15	0.16	0.14	0.15	0.16	0.22
MgO	7.58	7.51	6.64	6.92	6.58	6.84	7.59	7.17	7.33	7.87	7.60	7.19	7.09	7.57	7.58	7.26	7.54	5.01
CaO	12.52	13.31	11.72	11.74	11.57	11.80	14.39	12.74	13.36	14.25	12.57	14.16	13.53	13.38	12.90	12.88	14.27	10.00
Na_2O	2.01	2.02	2.83	2.58	2.46	3.09	2.59	2.60	2.51	2.38	2.76	2.54	2.33	2.26	2.21	2.30	2.09	2.66
K_2O	0.35	0.20	0.31	0.37	0.27	0.14	0.24	0.29	0.35	0.27	0.33	0.25	0.38	0.38	0.33	0.53	0.24	0.52
P_2O_5	0.12	0.12	0.15	0.16	0.16	0.14	0.11	0.11	0.11	0.11	0.11	0.10	0.12	0.10	0.11	0.11	0.11	0.41
Total	99.50	99.28	100.31	100.27	99.71	100.34	100.26	100.20	99.98	100.44	100.32	100.24	99.94	99.96	99.75	99.78	99.61	99.59
Trace elements (ppm)																		
Rb	7.1	2.4	5.5	7.1	4.3	1.8	2.3	6.3	4.1	3.2	10.7	3.8	10.7	9.4	5.7	14.4	2.8	10.8
Sr	105	104	101	99	101	98	101	99	97	99	99.3	99.1	97.2	103.6	95.7	94.1	98.5	299.0
Y	23.4	23.9	32.7	30.7	33.1	30.7	22.6	22.2	23.3	20.4	24.3	18.2	21.5	23.0	21.8	21.3	20.1	41.0
Ga	15.7	15.2	16.7	16.1	16.4	17.0	14.7	15.4	15.0	14.0	15.2	16.1	15.4	15.5	14.7	15.0	14.3	22.6
Zr	62	64	97	89	87	88	56	58	56	48	60.4	46.4	58.1	56.0	55.6	58.2	50.4	216.2
Nb	2.3	2.3	2.2	2.4	2.6	2.7	2.2	1.2	2.0	2.1	1.9	2.4	1.7	1.2	1.0	1.5	1.6	26.2
Zn	77	75	92	84	87	97	73	68	74	68	80.1	76.1	77.3	69.0	71.0	65.4	69.4	113.3
Ni	95	178	84	88	88	97	145	91	81	106	73.3	90.0	90.2	73.0	91.6	91.2	135.7	38.3
Cr	311	277	235	251	251	280	366	331	373	284	93.8	381.2	404.6	239.6	387.7	395.4	291.6	18.7
V	241	238	55	238	238	250	215	208	218	221	253.2	201.9	229.4	228.0	222.9	224.7	231.5	300.0
Mg′-value	0.64	0.65	0.57	0.57	0.57	0.61	0.66	0.61	0.64	0.68	0.64	0.68	0.64	0.64	0.65	0.64	0.66	0.40
FeO^*	8.58	7.85	9.82	10.28	9.75	8.77	7.59	9.07	8.08	7.50	8.54	6.79	7.85	8.27	8.02	8.20	7.73	14.86
CaO/Al_2O_3	0.80	0.83	0.73	0.76	0.72	0.72	0.88	0.80	0.83	0.90	0.82	0.80	0.83	0.86	0.79	0.81	0.91	0.61
Zr/Nb	27.2	27.7	43.9	37.0	37.5	32.6	25.5	48.4	28.2	23.1	31.8	19.3	34.2	46.7	55.6	38.8	31.5	8.3
Zr/Y	2.67	2.67	2.96	2.89	2.95	2.86	2.49	2.62	2.42	2.38	2.49	2.55	2.70	2.43	2.55	2.73	2.51	5.27

Note: See note at beginning of Appendix A.

Table 2. Hole 558.

Univ. Mass. sample no.	558-1	558-2	558-3	558-4	558-5	558-6	558-7	558-8	558-9	558-10	558-11	558-12	558-13	558-14	558-15	558-1
Core-Section	27-3	28-1	30-1	32-2	32-4	32-5	33-2	33-3	33-3	35-3	36-1	37-1	38-1	38-2	39-1	39-2
(interval in cm)	112-114	55-58	115-118	130-132	73-75	101-103	144-147	61-64	139-141	107-109	74-78	89-92	97-99	116-118	111-113	11-1
Sub-bottom depth (m)	409.13	415.07	433.67	453.31	455.74	457.51	462.46	463.13	463.90	481.58	487.26	496.41	505.48	507.17	510.12	510.6
Chemical group	IA	II	IIIA	IIIB	IIIB	IIIB	IIIB	IIIB	IIIB	IA	IB	IV	IV	IV	IV	IV
Major elements (wt.%)																
SiO_2	50.60	51.09	50.32	50.33	50.42	49.94	50.38	50.29	49.93	49.43	49.22	49.35	49.12	49.45	48.89	49.6
TiO_2	1.25	1.16	1.45	1.35	1.30	1.30	1.31	1.30	1.31	1.22	1.31	0.98	0.95	0.99	1.02	0.9
Al_2O_3	14.64	15.82	15.16	15.40	14.86	15.30	14.85	14.92	15.34	15.03	15.54	16.15	15.70	16.15	16.61	15.6
Fe_2O_3*	10.32	8.80	10.46	9.36	9.83	9.91	9.83	9.86	9.72	10.14	10.43	9.90	9.87	10.10	10.48	9.8
MnO	0.15	0.16	0.15	0.14	0.17	0.14	0.17	0.16	0.15	0.17	0.18	0.14	0.17	0.16	0.17	0.1
MgO	9.53	8.26	8.17	8.67	8.97	8.78	9.01	9.05	8.70	8.92	7.82	8.33	10.80	8.33	7.54	9.
CaO	10.62	12.40	11.58	11.89	11.63	11.70	11.55	11.51	11.74	12.13	12.26	12.04	11.71	12.21	12.92	11.7
Na_2O	2.21	2.15	2.30	2.24	2.13	2.35	1.84	1.88	2.36	2.52	2.28	2.16	2.09	2.12	2.32	2.1
K_2O	0.26	0.17	0.46	0.40	0.31	0.41	0.30	0.30	0.38	0.35	0.41	0.29	0.22	0.23	0.30	0.2
P_2O_5	0.15	0.12	0.21	0.19	0.17	0.19	0.18	0.18	0.18	0.16	0.20	0.14	0.13	0.13	0.14	0.1
Total	99.72	100.14	100.27	99.97	99.80	100.04	99.40	99.45	99.81	100.06	99.63	99.48	100.76	99.87	100.38	100.4
Trace elements (ppm)																
Rb	3.6	2.5	9.7	2.5	6.6	6.8	5.4	6.8	6.9	6	7.7	7	3.7	3.9	4.9	5
Sr	128.9	94.7	170	179.5	174.8	176.4	174.5	173	175.2	142.2	145.9	111.2	108.2	114.1	116.2	109.1
Y	22.2	25.6	24.2	21.8	21.6	21.2	21.8	21.1	21.2	22.5	24	18.5	18.5	19.2	19.2	18.2
Ga	15.7	16	15.6	15.1	15.4	14	15.4	14.8	16.2	14.8	15.3	14.7	15.2	14.3	15.4	14.3
Zr	75.87	66.53	92.80	84.62	82.60	81.50	82.19	82.79	80.24	75.99	85.64	55.40	54.76	57.29	57.86	55.7
Nb	8.64	3.10	15.25	13.75	14.49	13.39	13.41	13.98	12.65	9.53	11.34	7.57	7.24	7.75	7.74	7.44
Zn	83	90.33	89.45	85.61	83.87	81.33	87.74	98.53	84.74	87.02	87.44	78.63	73.14	82.6	88.65	72.26
Ni	277.4	169.8	157.5	170.6	156.2	157.9	156.1	155.9	175.0	185.8	152.5	208.3	230.1	219.6	184.88	213.6
Cr	509.7	400.5	356.3	367.0	388.9	371.6	384.8	398.3	362.8	380.5	308.5	458.4	449.4	481.5	476.6	441.5
V	195.6	238.3	257.9	242.8	249.8	233.9	243.7	252.0	233.4	239.9	246.4	197.6	190.5	211.5	224.4	191.6
Mg′-value	0.67	0.67	0.63	0.67	0.67	0.66	0.67	0.67	0.66	0.66	0.62	0.65	0.71	0.65	0.62	0.69
FeO*	9.29	7.92	9.41	8.42	8.85	8.92	8.85	8.87	8.75	9.12	9.39	8.90	8.88	9.09	9.43	8.88
CaO/Al_2O_3	0.73	0.78	0.76	0.77	0.78	0.76	0.78	0.77	0.77	0.81	0.79	0.75	0.75	0.76	0.78	0.75
Zr/Nb	8.78	21.46	6.09	6.15	5.70	6.09	6.13	5.92	6.34	7.97	7.55	7.32	7.56	7.39	7.48	7.49
Zr/Y	3.42	2.60	3.83	3.88	3.82	3.84	3.77	3.92	3.78	3.38	3.57	2.99	2.96	2.98	3.01	3.06

Note: See note at beginning of Appendix A.

Table 3. Hole 559.

Univ. Mass. sample no.	559-1	559-2	559-3	559-4	559-5	559-6	559-7	559-8	559-9
Core-Section	1-1	2-3	4-1	5-1	6-2	7-1	7-3	7-3	8-3
(interval in cm)	117-119	111-113	121-124	50-53	14-16	111-114	18-20	103-106	6-10
Sub-bottom depth (m)	239.18	251.12	257.72	265.51	275.65	284.12	286.19	287.19	295.08
Major elements (wt.%)									
SiO_2	49.23	50.62	49.90	49.50	49.67	48.48	49.68	49.97	48.65
TiO_2	1.61	1.52	1.54	1.54	1.54	1.59	1.54	1.52	1.50
Al_2O_3	16.19	15.49	15.35	15.40	15.39	15.86	15.31	14.97	15.14
Fe_2O_3*	11.30	9.93	10.44	11.21	10.59	11.71	10.77	10.80	12.02
MnO	0.17	0.12	0.16	0.19	0.15	0.19	0.15	0.16	0.24
MgO	6.45	7.84	7.56	6.69	7.28	6.38	7.46	7.52	6.77
CaO	11.73	11.57	11.78	11.94	11.69	12.35	11.35	11.24	11.98
Na_2O	2.76	2.70	2.64	2.77	2.39	2.47	2.54	2.59	2.33
K_2O	0.62	0.35	0.38	0.44	0.44	0.42	0.51	0.39	0.69
P_2O_5	0.25	0.20	0.21	0.21	0.20	0.24	0.20	0.21	0.20
Total	100.30	100.34	99.96	99.89	99.35	99.69	99.51	99.38	99.52
Trace elements (ppm)									
Rb	9.9	5.9	5.2	6.5	7.4	6.9	7.0	7.0	17.0
Sr	167.9	162.5	162.8	166.6	161.8	171.4	161.8	161.1	169.0
Y	31.6	27.1	28.3	28.0	27.8	29.2	28.2	27.6	27.1
Ga	13.3	15.7	15.8	16.0	17.2	16.9	16.5	15.7	17.2
Zr	108.4	105.4	107.0	105.7	107.5	111.6	106.8	107.0	103.1
Nb	15.5	14.4	15.0	15.2	14.7	15.6	15.4	15.0	14.5
Zn	176.0	90.4	98.3	102.7	91.0	96.6	96.5	88.3	83.6
Ni	103.9	211.2	142.0	126.9	127.3	113.2	121.0	108.9	134.4
Cr	163.8	254.7	267.3	260.9	277.1	276.1	247.3	245.5	253.6
V	291.9	246.5	266.8	276.9	267.1	291.9	253.8	252.7	253.6
Mg′-value	0.56	0.63	0.61	0.57	0.60	0.55	0.60	0.61	0.55
FeO*	10.17	8.94	9.39	10.09	9.53	10.54	9.69	9.72	10.82
CaO/Al_2O_3	0.72	0.75	0.77	0.78	0.76	0.78	0.74	0.75	0.79
Zr/Nb	6.99	7.32	7.13	6.95	7.31	7.15	6.94	7.13	7.11
Zr/Y	3.43	3.89	3.78	3.78	3.87	3.82	3.79	3.88	3.80

Note: See note at beginning of Appendix A. All samples belong to Chemical Group I.

Table 4. Hole 561.

Univ. Mass. sample no.	561-1	561-2	561-3	561-4	561-5	561-6	561-7	561-8	561-9
Core-Section	HI-CC	1-1	1-1	1-2	2-1	2-2	3-1	3-1	3-2
(interval in cm)	3-5	4-9	84-87	24-26	100-103	82-84	9-13	76-79	77-80
Sub-bottom depth (m)	8.60	411.57	412.36	413.25	415.52	416.83	417.61	424.28	425.79
Chemical group	I	I	II	II	II	II	II	II	II
Major elements (wt.%)									
SiO_2	49.71	49.75	50.45	50.13	50.25	49.99	50.11	50.09	50.05
TiO_2	1.23	1.21	1.37	1.35	1.33	1.35	1.34	1.39	1.37
Al_2O_3	15.49	15.26	15.29	15.05	14.96	15.28	14.88	15.10	14.79
Fe_2O_3*	9.97	9.87	11.08	11.61	11.82	10.94	1.89	11.39	11.41
MnO	0.16	0.15	0.18	0.18	0.18	0.20	0.18	0.17	0.18
MgO	7.93	8.18	7.34	7.48	7.08	7.85	7.22	7.44	7.67
CaO	12.33	12.10	11.66	11.31	11.42	11.66	11.49	11.69	11.83
Na_2O	2.48	2.51	2.72	2.57	2.58	2.55	2.59	2.53	2.24
K_2O	0.37	0.36	0.34	0.30	054	0.28	0.50	0.29	0.26
P_2O_5	0.23	0.23	0.13	0.14	0.13	0.13	0.13	0.13	0.13
Total	99.89	99.62	100.47	100.12	100.28	100.23	100.33	100.22	99.91
Trace elements (ppm)									
Rb	5.4	5.5	6.8	6.9	13.8	6.5	12.1	6.6	5.2
Sr	216	215	100	88	87	90	86	86	85
Y	25.5	25.5	32.3	31.4	30.7	31.7	31.0	32.6	32.4
Ga	15.6	14.8	18.1	17.6	17.4	17.4	16.8	17.0	17.7
Zr	102	100	76	75	71	73	73	77	76
Nb	21.9	21.6	3.5	2.1	2.6	2.6	3.1	2.0	3.0
Zn	85	93	104	109	96	106	96	101	101
Ni	166	186	120	123	126	159	114	128	138
Cr	416	413	228	245	222	237	217	236	238
V	240	236	297	305	292	302	290	313	311
Mg'-value	0.62	0.65	0.59	0.59	0.57	0.61	0.57	0.59	0.60
FeO*	0.97	8.88	9.97	10.45	10.64	9.84	10.70	10.25	10.27
CaO/Al_2O_3	0.80	0.79	0.77	0.75	0.76	0.76	0.77	0.77	0.80
Zr/Nb	4.7	4.6	21.8	35.2	26.9	28.0	23.7	38.6	25.2
Zr/Y	3.99	3.92	2.34	2.38	2.31	2.32	2.36	2.37	2.33

Note: See note at beginning of Appendix A.

Table 5. Hole 562.

Univ. Mass. sample no.	562-1	562-2	562-3	562-4	562-5	562-6	562-7	562-8	562-9	562-10	562-11	562-12	562-13	562-14	562-15	562-16
Core-Section	H1-CC	2-3	4-1	5-1	5-4	6-3	6-4	7-2	8-1	8-1	8-2	9-1	9-1	10-1	10-3	11-1
(interval in cm)	16-19	8-10	75-77	64-66	29-31	135-138	6-10	56-58	132-134	144-146	25-29	82-84	145-147	90-93	52-55	115-117
Sub-bottom depth (m)	243.23	253.09	268.76	277.65	281.80	290.37	290.58	297.07	301.33	301.45	306.77	304.77	305.46	313.92	316.54	323.16
Chemical group	I	I	I	I	I	I	I	I	I	I	II	II	II	II	II	II
Major elements (wt.%)																
SiO_2	49.23	49.91	49.83	50.32	49.52	49.32	50.19	49.98	49.67	49.43	48.90	48.33	49.78	49.12	49.72	49.18
TiO_2	1.57	1.58	1.60	1.58	1.54	1.54	1.20	1.20	1.25	1.30	1.16	1.19	1.28	1.26	1.29	1.15
Al_2O_3	15.71	15.31	15.21	15.97	15.82	15.69	17.27	16.22	16.38	15.50	17.11	16.73	15.75	16.01	15.38	17.43
Fe_2O_3*	11.90	11.79	11.75	10.70	11.25	11.54	8.95	10.34	9.89	10.17	9.91	9.89	10.57	11.07	10.60	9.81
MnO	0.18	0.18	0.19	0.16	0.17	0.20	0.13	0.16	0.16	0.17	0.15	0.18	0.17	0.18	0.17	0.16
MgO	6.71	7.24	7.41	6.73	7.05	7.03	6.94	7.19	7.28	7.61	7.37	7.28	7.16	7.09	7.82	6.52
CaO	11.64	11.53	11.42	11.85	11.53	11.84	12.90	12.31	12.63	13.23	12.97	13.85	12.44	12.96	12.45	12.92
Na_2O	2.29	2.42	2.55	2.52	2.70	2.63	2.14	2.01	2.17	2.20	1.97	2.04	2.04	2.1	2.02	1.91
K_2O	0.25	0.31	0.13	0.21	0.10	0.35	0.18	0.22	0.21	0.25	0.21	0.22	0.38	0.32	0.26	0.25
P_2O_5	0.15	0.14	0.17	0.16	0.15	0.16	0.13	0.12	0.13	0.13	0.13	0.13	0.14	0.14	0.13	0.12
Total	99.63	100.41	100.26	100.19	99.83	100.30	100.02	99.75	99.79	99.98	99.88	99.84	99.69	100.24	99.84	99.46
Trace elements (ppm)																
Rb	2.6	5.6	1.9	2.3	1.2	6.7	3.1	3.5	3.9	4.5	3.3	4.1	8.2	6.1	4.6	4.7
Sr	105	96.6	94.4	99.5	102.1	103.6	91.9	97.5	96.4	108.4	90.4	101.3	114.4	95.1	89.6	94.5
Y	36.1	35.1	35	34.9	34.4	32.9	26.5	26.3	27.7	29.4	25.1	26	28.7	28	28.5	25.2
Ga	17.5	17.3	17.8	17.3	17.1	17.9	16.1	16.3	16.5	16.1	15.5	16.1	16.9	16.6	16.5	15.9
Zr	96.5	97.3	92.4	96.4	93.4	93	69	67.5	72.1	74.3	65.7	67.8	73.4	73.3	74	65
Nb	3.1	3.9	3.8	3.4	3.2	3.1	2.5	2.2	2.7	2.5	2.3	3.0	2.3	2.7	2.5	2.8
Zn	103.9	95.6	90.1	95.8	86.6	106.2	83	80.1	88.1	93.1	81.2	83.6	93.9	99.3	95.2	81.1
Ni	109.2	107.6	106	119.5	105.1	109.2	169.5	105.7	102	121.6	98.7	109.6	112.5	104.2	124.4	98.2
Cr	241.8	236.5	211.1	235.4	215.3	246.6	244.9	242.8	262	267.8	248.6	251.2	265.1	264.2	268.1	250.6
V	313.8	298.9	284.1	286.7	274	286.1	250	243.3	267	278.4	243.4	254.6	282.7	277.3	279.9	244.2
Mg'-value	0.55	0.57	0.58	0.58	0.58	0.57	0.63	0.60	0.62	0.62	0.62	0.62	0.60	0.58	0.62	0.59
FeO*	10.71	10.61	10.57	9.63	10.12	10.38	8.05	9.30	8.90	9.15	8.92	8.90	9.51	9.96	9.54	8.83
CaO/Al_2O_3	0.74	0.75	0.75	0.74	0.73	0.75	0.75	0.76	0.77	0.85	0.76	0.83	0.79	0.81	0.81	0.74
Zr/Nb	31.1	24.9	25.6	28.4	29.2	30.0	27.6	30.7	26.7	29.7	28.6	22.6	31.9	27.1	29.6	23.2
Zr/Y	2.67	2.77	2.78	2.76	2.72	2.83	2.60	2.55	2.60	2.53	2.62	2.61	2.56	2.62	2.60	2.58

Note: See note at beginning of Appendix A.

Table 6. Hole 563.

Univ. Mass sample no. Core-Section (interval in cm) Sub-bottom depth (m)	563-1 23-1 115–117 365.66	563-2 24-1 22–25 366.74	563-3 24-1 57–60 367.09	563-4 24-2 93–95 368.94	563-5 24-2 123–127 369.94	563-6 24-4 7–10 371.09	563-7 25-1 36–38 373.87	563-8 25-2 115–117 376.16
Major elements (wt.%)								
SiO_2	49.73	49.47	49.76	49.23	49.98	49.58	49.79	49.96
TiO_2	1.02	0.97	1.05	0.97	1.05	0.99	0.98	1.01
Al_2O_3	15.78	16.40	15.26	16.09	15.40	16.02	16.37	15.85
Fe_2O_3	10.18	10.26	9.98	10.43	9.89	10.07	9.72	10.35
MnO	0.17	0.15	0.15	0.17	0.16	0.17	0.16	0.17
MgO	7.61	7.47	8.04	7.54	8.03	7.35	7.80	7.55
CaO	13.20	13.07	12.94	13.00	13.01	13.41	12.97	13.06
Na_2O	1.96	1.88	1.97	2.29	2.21	1.93	2.20	2.20
K_2O	0.26	0.32	0.26	0.29	0.25	0.31	0.20	0.27
P_2O_5	0.09	0.10	0.10	0.09	0.09	0.10	0.09	0.11
Total	99.99	100.11	99.52	100.09	100.06	99.93	100.27	100.53
Trace elements (ppm)								
Rb	5.5	7.4	5.2	6.8	5	6.8	2.5	5.7
Sr	86.7	83.3	86	82.1	82.5	82.3	82.6	83.7
Y	23.7	22.8	24.9	22.8	25.1	22.9	21.6	23.6
Ga	15.1	15.9	15.6	15.7	15.4	14.9	15.4	15.5
Zr	55.9	52.5	59.2	55.3	60.02	54.7	54.5	54.9
Nb	2.6	2.11	2.9	1.7	2.6	2.5	2.2	2.6
Zn	81.3	78.0	81.1	78.0	96.2	78.9	77.8	79.1
Ni	110.3	97.97	95.3	103.8	106.9	106.8	106.9	96.7
Cr	330.2	322.8	338.1	326.1	350.9	318.7	322.6	324.9
V	293.4	279.8	306.4	285.5	310.7	286.1	272.9	298.0
Mg'-value	0.63	0.62	0.64	0.61	0.64	0.62	0.64	0.62
FeO*	9.16	9.20	8.98	9.39	8.90	9.06	8.75	9.51
CaO/Al_2O_3	0.84	0.80	0.85	0.81	0.84	0.84	0.79	0.82
Zr/Nb	27.95	24.89	20.41	32.53	23.15	21.88	24.77	21.12
Zr/Y	2.36	2.30	2.38	2.43	2.40	2.39	2.52	2.33

Note: See note at beginning of Appendix A. All samples belong to Chemical Group I.

Table 7. Hole 564.

Univ Mass. sample no. Core-Section (interval in cm) Sub-bottom depth (m)	564-1 H1-CC 11–15 282.61	564-2 1-1 129–131 285.30	564-3 1-3 38–40 287.39	564-4 2-2 3–5 294.54	564-5 2-3 18–20 296.19	564-6 3-2 35–37 303.86	564-7 4-2 37–41 312.89	564-8 4-4 140–142 316.91	564-9 5-2 89–91 322.40	564-10 5-4 24–27 324.76	564-11 6-1 15–18 329.17	564-12 6-4 48–52 334.00	564-13 6-5 32–34 335.33	564-14 7-1 12–15 338.14	564-15 7-3 13–15 341.14	564-16 8-2 7–10 348.59	564-17 9-1 18–20 356.19	564-18 9-1 140–143 357.42	564-19 9-2 128–130 358.79	564-20 9-3 68–71 359.70
Major elements (wt.%)																				
SiO_2	49.35	50.21	49.86	49.57	50.58	49.62	49.87	49.88	50.39	49.44	50.54	49.42	50.17	49.77	50.63	49.67	47.24	49.11	48.99	[illegible]
TiO_2	1.48	1.43	1.40	1.44	1.47	1.45	1.46	1.45	1.46	1.51	1.48	1.44	1.50	1.49	1.52	1.48	1.52	1.53	1.58	[illegible]
Al_2O_3	15.77	14.94	14.71	15.22	15.17	14.92	14.89	14.76	14.69	14.99	14.64	14.38	14.64	14.5	14.73	14.56	15.16	15.08	15.04	[illegible]
Fe_2O_3*	11.55	11.29	11.58	11.60	10.11	11.71	11.92	11.82	11.82	12.37	11.86	12.31	11.95	11.96	11.56	11.90	13.07	12.01	12.53	[illegible]
MnO	0.19	0.18	0.17	0.18	0.17	0.20	0.20	0.16	0.17	0.19	0.17	0.19	0.18	0.17	0.18	0.17	0.19	0.18	0.18	[illegible]
MgO	6.13	7.52	7.39	7.00	7.77	7.32	7.32	7.54	7.48	6.78	7.24	8.43	7.48	7.42	6.99	7.54	5.20	6.86	6.70	[illegible]
CaO	12.82	11.89	11.63	12.15	12.05	11.92	11.76	11.52	11.52	11.76	11.42	11.28	11.53	11.45	11.67	11.40	13.83	11.76	11.86	[illegible]
Na_2O	2.51	2.47	2.76	2.39	2.26	2.82	2.31	2.56	2.48	2.58	2.12	2.05	2.08	2.10	2.15	2.22	2.26	2.66	2.28	[illegible]
K_2O	0.44	0.35	0.36	0.39	0.20	0.38	0.36	0.36	0.19	0.40	0.19	0.24	0.33	0.41	0.23	0.42	0.62	0.36	0.35	[illegible]
P_2O_5	0.16	0.14	0.15	0.16	0.15	0.14	0.15	0.17	0.16	0.17	0.16	0.16	0.17	0.16	0.16	0.16	0.21	0.17	0.17	[illegible]
Total	100.40	100.42	100.22	100.10	99.93	100.47	100.26	100.22	100.34	100.19	99.83	99.92	100.03	99.42	99.82	99.73	99.31	99.73	99.67	[illegible]
Trace elements (ppm)																				
Rb	7.5	6.4	6.0	5.8	2.7	6.3	5.8	7.2	2.6	7.0	2.3	4.9	5.7	7.2	2.6	7.5	14.7	6.9	6.2	[illegible]
Sr	115.1	106.8	101.8	103.6	108.1	105.5	103.0	99.9	99.5	105.6	100.9	104.8	101.2	103.6	102.1	103.2	114.6	106.9	107.9	[illegible]
Y	31.7	32.2	31.8	32.3	33.7	32.8	32.5	32.2	32.7	33.6	33.4	31.9	33.0	33.3	34.2	32.5	35.6	33.4	34.1	[illegible]
Ga	17.4	16.1	16.4	17.2	18.0	17.2	16.6	16.4	17.2	17.2	16.6	16.4	17.0	17.2	17.1	16.2	19.3	17.7	17.1	[illegible]
Zr	93.7	91.3	90.9	92.4	94.3	95.4	92.8	92.9	95.5	98.1	94.6	93.6	96.6	97.3	99.1	97.4	96.1	98.9	100.5	[illegible]
Nb	4.1	3.9	4.4	4.7	3.9	5.0	4.6	4.9	4.2	5.2	5.4	4.5	4.9	5.2	5.6	5.5	5.8	6.0	5.7	[illegible]
Zn	101.3	95.3	94.2	101.4	98.1	110.1	95.2	98.2	107.5	102.1	91.8	92.2	94.3	98.4	96.7	97.6	85.3	111.2	109.7	[illegible]
Ni	122.7	138.5	112.8	121.1	154.4	104.5	104.1	117.8	117.5	113.7	118.6	144.2	123.0	119.8	121.0	118.6	103.9	139.7	121.2	[illegible]
Cr	277.4	261.5	258.2	258.3	242.0	256.1	233.6	240.9	238.6	240.9	221.4	214.1	222.3	236.2	235.3	232.3	217.2	222.8	215.1	[illegible]
V	352.0	346.6	339.1	348.9	339.1	349.2	340.8	338.4	339.1	360.2	335.2	325.9	360.2	349.4	346.7	346.0	383.7	362.1	371.3	[illegible]
Mg'-value	0.54	0.59	0.59	0.57	0.63	0.58	0.58	0.58	0.58	0.55	0.57	0.60	0.58	0.58	0.57	0.58	0.47	0.56	0.54	[illegible]
FeO*	10.39	10.16	10.42	10.44	9.10	10.54	10.73	10.64	11.13	10.67	10.67	11.08	10.75	10.76	10.40	10.71	11.76	10.81	11.28	[illegible]
CaO/Al_2O_3	0.81	0.80	0.79	0.80	0.79	0.80	0.79	0.78	0.78	0.78	0.78	0.78	0.79	0.79	0.79	0.78	0.91	0.78	0.79	[illegible]
Zr/Nb	22.9	23.4	20.7	19.7	24.2	19.1	20.2	19.0	22.7	18.9	17.5	20.8	19.7	18.7	17.7	17.7	16.6	16.5	17.6	[illegible]
Zr/Y	2.96	2.83	2.86	2.86	2.80	2.91	2.86	2.88	2.92	2.92	2.83	2.93	2.93	2.92	2.90	3.00	2.70	2.96	2.95	[illegible]

Note: See note at beginning of Appendix A. All samples belong to Chemical Group I.

APPENDIX B
Average Compositions of Basalts from Leg 82

Note to Appendix B tables: N refers to number of samples in each chemical group. Fe_2O_3* and FeO* refer to total Fe expressed as Fe^{3+} or Fe^{2+}. Calculation of Mg′-value is discussed in the text (Mg/[Mg + Fe^2]). Small discrepancies in totals may be attributed to rounding.

Table 1. Hole 556.

Chemical group N	I 12	IA 9	IB 3	II 4
Major elements (wt.%)				
SiO_2	50.11	50.27	50.06	50.23
TiO_2	0.90	1.02	0.86	1.45
Al_2O_3	15.99	15.94	16.49	15.95
Fe_2O_3*	8.40	9.12	8.16	10.73
MnO	0.15	0.15	0.14	0.17
MgO	7.44	7.43	7.53	6.75
CaO	13.26	13.16	14.23	11.71
Na_2O	2.35	2.36	2.34	2.74
K_2O	0.33	0.34	0.25	0.27
P_2O_5	0.11	0.11	0.11	0.15
Total	99.04	99.90	100.17	100.16
Trace elements (ppm)				
Rb	6.4	7.3	3.3	4.7
Sr	99	99	100	100
Y	22.4	22.7	19.6	31.8
Ga	15.1	15.2	14.3	16.6
Zr	48.4	58.5	48.4	92.8
Nb	1.8	1.7	2	2.5
Zn	73	73	71	90
Ni	100	99	111	89
Cr	340	342	319	250
V	229	230	218	248
Mg′-value	0.66	0.64	0.67	0.58
FeO*	8.17	8.25	7.34	9.66
CaO/Al_2O_3	0.83	0.83	0.87	0.73
Zr/Nb	33.7	36.4	24.6	37.8
Zr/Y	2.57	2.58	2.57	2.92

Note: See note at beginning of Appendix B.

Table 2. Hole 558.

Chemical group N	I 3	II 1	III 7	IIIA 1	IIIB 6	IV 5
Major elements (wt.%)						
SiO_2	49.75	51.09	50.27	50.32	50.22	49.28
TiO_2	1.26	1.16	1.35	1.45	1.31	0.99
Al_2O_3	15.07	15.82	15.14	15.16	15.11	16.05
Fe_2O_3*	10.30	8.80	10.11	10.46	9.75	10.06
MnO	0.17	0.16	0.16	0.15	0.16	0.16
MgO	8.76	8.26	8.52	8.17	8.86	8.90
CaO	11.67	12.40	11.63	11.58	11.67	12.11
Na_2O	2.34	2.15	2.22	2.30	2.13	2.12
K_2O	0.36	0.17	0.41	0.46	0.35	0.26
P_2O_5	0.17	0.12	0.20	0.21	0.18	0.13
Total	99.85	100.14	100.01	100.27	99.75	100.06
Trace elements (ppm)						
Rb	5.8	2.5	8.20	9.7	6.7	4.9
Sr	139	95	173	170	176	112
Y	22.9	25.6	22.8	24.2	21.45	18.7
Ga	15.3	16.0	15.4	15.6	15.2	14.8
Zr	79.2	66.5	87.6	92.8	82.3	56.2
Nb	9.8	3.1	14.4	15.2	13.6	7.5
Zn	87.2	90	88	89	87	79
Ni	169	170	160	157	162	205
Cr	344	400	368	356	379	461
V	243	238	250	259	243	203
Mg′-value	0.65	0.68	0.66	0.64	0.67	0.66
FeO*	9.27	7.92	9.10	9.41	8.79	9.05
CaO/Al_2O_3	0.78	0.78	0.77	0.77	0.77	0.76
Zr/Nb	8.10	21.46	6.08	6.09	6.06	7.45
Zr/Y	3.46	2.60	3.83	3.83	3.83	3.00

Note: See note at beginning of Appendix B.

Table 3. Hole 559.

Chemical group	I
N	9
Major elements (wt.%)	
SiO_2	49.52
TiO_2	1.54
Al_2O_2	15.46
Fe_2O_3*	10.97
MnO	0.17
MgO	7.11
CaO	11.73
Na_2O	2.58
K_2O	0.47
P_2O_5	0.21
Total	99.77
Trace elements (ppm)	
Rb	8.1
Sr	165
Y	28.3
Ga	16.0
Zr	106.9
Nb	15.0
Zn	103
Ni	135
Cr	258
V	267
Mg′-value	0.59
FeO*	9.88
CaO/Al_2O_3	0.76
Zr/Nb	7.09
Zr/Y	3.78

Note: See note at beginning of Appendix B.

Table 4. Hole 561.

Chemical group	I	II
N	2	7
Major elements (wt.%)		
SiO_2	49.73	50.15
TiO_2	1.22	1.36
Al_2O_3	15.38	14.99
Fe_2O_3*	9.92	11.45
MnO	0.16	0.18
MgO	8.06	7.44
CaO	12.21	11.58
Na_2O	2.50	2.54
K_2O	0.36	0.36
P_2O_5	0.23	0.13
Total	99.75	100.18
Trace elements (ppm)		
Rb	5.5	8.3
Sr	215	89
Y	25.5	31.7
Ga	15.2	17.4
Zr	100.9	74.4
Nb	21.7	2.7
Zn	69	102
Ni	176	130
Cr	414	232
V	238	301
Mg′-value	0.64	0.59
FeO*	8.92	10.30
CaO/Al_2O_3	0.80	0.77
Zr/Nb	4.65	28.5
Zr/Y	3.95	2.34

Note: See note at beginning of Appendix B.

Table 5. Hole 562.

Chemical group	I	II
N	6	10
Major elements (wt.%)		
SiO_2	49.69	49.43
TiO_2	1.57	1.23
Al_2O_3	15.59	16.38
Fe_2O_3*	11.49	10.21
MnO	0.18	0.16
MgO	7.03	7.23
CaO	11.64	12.87
Na_2O	2.52	2.06
K_2O	0.23	0.25
P_2O_5	0.16	0.13
Total	100.10	99.95
Trace elements (ppm)		
Rb	3.9	4.6
Sr	100	98
Y	34.2	27.1
Ga	17.5	16.2
Zr	95.7	70.2
Nb	3.4	2.6
Zn	96	88
Ni	109	108
Cr	231	256
V	291	262
Mg′-value	0.57	0.61
FeO*	10.34	9.11
CaO/Al_2O_3	0.74	0.79
Zr/Nb	28.2	27.8
Zr/Y	2.76	2.59

Note: See note at beginning of Appendix B.

Table 6. Hole 563.

Chemical group	I
N	8
Major elements (wt.%)	
SiO_2	49.69
TiO_2	1.00
Al_2O_3	15.90
Fe_2O_3*	10.11
MnO	0.16
MgO	7.67
CaO	13.08
Na_2O	2.08
K_2O	0.27
P_2O_5	0.10
Total	100.06
Trace elements (ppm)	
Rb	5.6
Sr	84
Y	23.4
Ga	15.4
Zr	55.9
Nb	2.3
Zn	81
Ni	103
Cr	329
V	292
Mg′-value	0.63
FeO*	9.16
CaO/Al_2O_3	0.82
Zr/Nb	24.6
Zr/Y	2.39

Note: See note at beginning of Appendix B.

Table 7. Hole 564.

Chemical group	I
N	
Major elements (wt.%)	
SiO_2	49.69
TiO_2	1.48
Al_2O_3	14.89
Fe_2O_3	11.87
MnO	0.18
MgO	7.16
CaO	11.85
Na_2O	2.38
K_2O	0.35
P_2O_5	0.16
Total	100.01
Trace elements (ppm)	
Rb	6.1
Sr	105
Y	33.0
Ga	17.1
Zr	95.6
Nb	5.0
Zn	99
Ni	117
Cr	238
V	349
Mg′-value	0.57
FeO*	10.69
CaO/Al_2O_3	0.80
Zr/Nb	19.4
Zr/Y	2.90

Note: See note at beginning of Appendix B.

21. THE DEGREE OF HETEROGENEITY IN BASALTS NEAR THE HAYES FRACTURE ZONE, MID-ATLANTIC RIDGE: HOLES 561, 562, AND 564[1]

Joyce C. Brannon, Department of Earth and Planetary Sciences and McDonnell Center for the Space Sciences, Washington University[2]

ABSTRACT

Analyses of samples from Chemical Group II, Hole 561; Chemical Group I, Hole 562; and two pillows and a flow from Hole 564 show that the chemical groups and the individual structures are compositionally homogeneous for the data presented here except for the alkalies, Na_2O and Cs, and transition metals, FeO^* and Co, and sometimes Sc and Cr. The scatter in the alkalies is attributed to alteration and the scatter in the transition metals is attributed to a short-range segregation model. Although the pillows and flow from Hole 564 are each compositionally homogeneous, their compositions are distinct from one another. These results cannot support the preliminary interpretation by shipboard scientists that the basalts from Hole 564 comprise a single chemical group.

INTRODUCTION

Geologists often assume that a single sample is petrographically and chemically representative of an entire rock body, especially if there are no visible textural heterogeneities. It is also commonly assumed that such a sample is homogeneous to within the limits of analytical uncertainty. These assumptions have been accepted by generations of geologists who could easily obtain large samples from the field. With the advent of lunar science and drill core studies where sample availability, sample size, and the knowledge of field relations are restricted, it is prudent to shed these assumptions.

Quantitative petrogenetic modeling is used in an effort to describe compositional differences among related basalts and their mantle sources. One factor that affects accuracy of model predictions is the degree of heterogeneity of a basalt flow. This study was undertaken to determine the degree of compositional heterogeneity in three proposed chemical groups of Leg 82 basalts.

METHODS

Samples were obtained as either one-fourth core segments of the rking half of the core or as 1-inch paleomagnetic cores that were red from the original core, investigated, and then returned to the rking half of the core. Calcite veins and fractures were avoided dur- sampling. The external surfaces that were in contact with the drill- equipment were ground off with silicon carbide grinding paper. samples were placed in an ultrasonic cleaner in distilled water to ove any loose particles and then dried at 90°C. Each sample was shed in a Plattner steel mortar to pea-sized particles and then pow- d and homogenized in an alumina canister with a Shatterbox EX Industries, Inc., Metuchen, N J). The total masses of the sam- range from 2.9–11.8 g for Hole 561, 6.2–25.0 g for Hole 562, and 0–26.1 g for Hole 564.

Instrumental neutron activation analysis (INAA) was used to ana- 100-mg splits of the powder that had been weighed and sealed in- clean ultrapure silica tubing (T21 Suprasil, Heraeus-Amersil, Say- lle, New Jersey, outside diameter = 5 mm). Samples from Holes 562 and 564 were analyzed in the first experiment and samples from Hole 561 plus another split of the powdered sample from Hole 564 (564-6-4, 38–40 cm [Piece 2D]) were analyzed in a second experiment. In both experiments, samples and standards were irradiated for 20 hrs. with a thermal neutron flux of 4.0×10^{13} $cm^{-2} s^{-1}$ in the University of Missouri (Columbia) research reactor. Samples were each radioassayed twice, once between 6–12 days and again between 27–32 days after the irradiation. Gamma-ray spectral data were reduced with the TEABAGS programs of Lindstrom and Korotev (1982).

The following comparator standards were used. The concentration value used is listed in parentheses (same units as Table 1). USGS basalt BCR-1: FeO^* (total Fe as FeO, 12.1), Na_2O (3.27), Sc (31.6), Co (36.0), Cs (0.94), La (24.6), Ce (53.7), Sm (6.80), Eu (1.92), Tb (1.10), Yb (3.37), Lu (0.526), Hf (5.2), and Th (6.0). Knippa basalt (in-house standard): Cr (485), Ni (360), and Ta (6.3). For Br, no standard was used. Concentration values were estimated from the 554.4 keV photopeak of ^{82}Br using the pertinent nuclear and detector efficiency parameters. Because of the uncertainties in these parameters, particularly the flux and neutron capture cross section, all Br concentrations may be systematically high or low, but the values are known relative to one another within each experiment.

A separate split of powdered sample from 564-6-4, 38–40 cm (Piece 2D) was analyzed in each of the two experiments. These results (Columns 1 and 2) and the difference between them (Column Δ) along with the estimate of analytical precision (Column σ) are listed in Table 1. The estimate of precision is one standard deviation (1σ) based on the counting statistics and other factors associated with a single analysis (Lindstrom and Korotev, 1982). Tests in this laboratory involving multiple analyses of the same sample have shown this to be a good approximation to the true sample standard deviations. The ratio s/σ, where s is the sample standard deviation, averages unity over all elements and ranges from 0.3–3.0 (R. Korotev, pers. comm., 1983). Column Δ in Table 1 reflects both typical analytical precision and sample heterogeneity for the samples analyzed here. For only FeO^*, Cr, and Hf, does Δ exceed σ by more than a factor of 2. The estimate of relative analytical precision at these concentration levels for the elements listed in Table 1 ($100\,[\sigma/\bar{x}]$) is listed in the last column and is applicable to the data listed in all other tables.

The discrepancies found in FeO^*, Cr, and Hf concentrations between two splits of the same powder could be explained as (1) an underestimate of analytical precision for those elements at those concentration levels or (2) by heterogeneity within the powdered portion of the sample. Sample 1 listed in Table 1 was radioassayed twice in the same experiment. The differences between the concentrations for each element including FeO^*, Cr, and Hf are less than or equal to σ, except for Co, Yb, and Hf, which are less than 2σ. This suggests that the discrepancies found in FeO^*, Cr, and Hf concentrations can be attributed to small-scale heterogeneity in splits from the same sample powder ($100\,[\Delta/\bar{x}]$ = relative heterogeneity; 2.3% for FeO^*, 5.5% for Cr, and 7.1% for Hf).

---

[1] Bougault, H., Cande, S. C., et al., *Init. Repts. DSDP*, 82: Washington (U.S. Govt. Printing Office).

[2] Address: Box 1169, Washington University, St. Louis, MO 63130.

Table 1. Precision of replicate analyses of Sample 564-6-4, 38–40 cm (Piece 2D).

	1	2	$\bar{x}$	Δ	σ	A.U. (%)
FeO^*	11.02	10.77	10.90	0.25	0.11	1.0
Na_2O	2.31	2.31	2.31	0	0.03	1.3
Sc	41.9	41.8	41.85	0.1	0.4	1.0
Cr	228	241	234.5	13	3	1.3
Co	44.8	44.4	44.6	0.4	0.4	0.9
Ni	97	134	106	18	26	25
Cs	0.34	0.31	0.325	0.03	0.05	15
La	3.85	3.91	3.88	0.06	0.06	1.5
Ce	11.3	10.8	11.05	0.5	0.3	2.7
Sm	3.47	3.42	3.445	0.05	0.06	1.7
Eu	1.21	1.21	1.21	0	0.03	2.5
Tb	0.94	0.98	0.96	0.04	0.04	4.2
Yb	3.72	3.69	3.705	0.03	0.08	2.2
Lu	0.579	0.58	0.58	0.001	0.015	2.6
Hf	2.78	2.59	2.685	0.19	0.09	3.4
Ta	0.37	0.41	0.39	0.04	0.04	10
Th	0.30	0.22	0.26	0.08	0.05	19

Note: 1, 2 = two separate splits of 564-6-4, 38–40 cm (Piece 2D); $\bar{x}$ = mean; Δ = the difference in concentrations of 1 and 2; σ = one standard deviation uncertainty estimate of a single analysis based principally on counting statistics; A.U. (%) = % analytical uncertainty = $(\sigma/\bar{x})$ 100; and FeO^* = total Fe as FeO. FeO^* and Na_2O concentrations are weight percent (wt.%), all others are parts per million (ppm).

CHEMICAL GROUPS I AND II, HOLE 561

Only 6 m of basalts and basalt breccias from a 15-m cored section of the basement at Site 561 were recovered. Three lithologic units from the basement-sediment interface to the bottom of the core were identified (aphyric basalt, basalt breccia, and aphyric pillow basalt). On the basis of shipboard XRF (X-ray fluorescence) analyses, two compositionally distinct chemical groups were identified; Chemical Group I is LREE (light rare earth element) enriched and Chemical Group II is LREE depleted relative to chondrites. Chemical Group I correlates with Lithologic Unit 1 and Chemical Group II correlates with Lithologic Units 2 and 3. Subsequent analyses of samples from this site confirm the shipboard results. Analyses for 1 sample from Chemical Group I (a split of powder from a shipboard sample) and 15 samples from Chemical Group II are listed in Table 2.

The LREE-enriched nature of basalts from Chemical Group I relative to a chondritic REE (rare earth element) distribution and the LREE-depleted nature of basalts from Chemical Group II are illustrated in Figure 1 (chondrite values from Haskin et al., 1968). Mixed occurrence of both LREE-enriched and LREE-depleted basalts at DSDP sites is uncommon. Site 561 is the second hole drilled during Leg 82 where both types of basalts were recovered. This mixed occurrence was found before at Holes 413 (Leg 49) and 504B (Legs 69–70). The significance of finding both enriched and depleted basalts at the same site is discussed by Bougault et al., Drake et al., Weaver et al., Hertogen et al., Jenner et al., Rideout and Schilling, Dupré et al., all this volume.

The basalts identified on the basis of similar composition to Chemical Group II are fine-grained vesicular aphyric pillow basalts or basalt breccias. The vesicles (2 mm in size), some of which are clay filled, are dispersed throughout the basalts and are impractical if not impossible to avoid in a sample. Both Lithologic Units 2 and 3 contain fractures and calcite veins. Minor alteration, which manifests itself as brown coloration as opposed to the gray color of the fresh portions of the rocks, occurs along these fractures. This type of alteration appears to be related to the ease of access of seawater along cracks, joints, and generally more permeable areas. Litholog Unit 2 has undergone brecciation of the basalt, sed mentation, and consolidation of that sediment. Only fre portions of the basalt were collected as samples.

In addition to the analyses of samples from Hole 56 Table 2 lists the mean ($\bar{x}$) and sample standard devi tion (s) for Chemical Group II, and one sigma (σ) unce tainty estimate of a single analysis. Specimens fro Samples 561-2-3, 52–54 cm (Piece 4A) and 561-3-2, 5 60 cm (Piece 3E) are not included in the mean or sta dard deviation because they contain higher Br conce tration (by a factor of 3) than the average sample fro Hole 561. Presumably increased Br concentration corr sponds to increased seawater-rock interactions. For on FeO^*, Co, and Cs, does s exceed σ by more than a fact of 2.

Hart (1976) lists the average MORB (mid-ocean ridge basalts) Cs concentration as 0.013 ppm. This low abundance element provides a sensitive indicator for alteration in the abyssal tholeiites. Very often Cs concentrations are high in samples that show no other chemical effects of alteration processes (Hart, 1969). Clays, which fill the vesicles of this basalt, display marked cation exchange properties. Usually Ca^{2+} and Na^+ are the exchangeable cations, but K^+, Cs^+, Sr^{2+}, and Mg^{2+} are exchangeable to varying degrees (Deer et al., 1966; Hart, 1969). The range in Cs concentrations in Chemical Group II of Hole 561 (0.06–0.33 ppm) yields a higher sample standard deviation than analytical uncertainty and can be attributed to addition of Cs during alteration.

Br and Cs concentrations are not well correlated in these samples. Cs concentrations probably vary directly with the amount of clay present in the sample, and Br concentrations are probably higher in samples that are closer to cracks and joints that seawater can permeate more easily. A plausible explanation for the lack of correlation between Br and Cs is that clay-filled vesicles are found throughout the basalts at this site, rather than just near cracks and fractures.

Two samples each were cut from two different pieces of basalt from Sections 561-2-1 and 561-2-2 (Sampl s 561-2-1, 71–73 cm [Piece 4D]; 561-2-1, 78–80 cm [Pie e 4D]; 561-2-2, 18–21 cm [Piece 1D]; and 561-2-2, 25- 8 cm [Piece 1D]). The specimens from 561-2-2 (Piece 1) have essentially identical concentrations for all elemer s listed in Table 2 to within 1σ analytical uncertainty. Su n is not the case for the specimens from 561-2-1 (Pie e 4D). Co, Th, and FeO^* concentrations are outside 2σ a alytical uncertainty of each other, but all other eleme t concentrations are identical within 1σ analytical unc tainty. These differences found in samples 5 cm apart n a single hand-specimen are approximately the same ord r of magnitude as small-scale sample heterogeneity anal

Table 2. Elemental abundances of basalts from Chemical Groups I and II, Hole 561.

Core-Section Interval (in cm) Piece	1-1 28-31 1C	1-1 119-122 9A	1-2 3-6 1A	1-2 36-38 3	2-1 6-8 1B	2-1 71-73 4D	2-1 78-80 4D	2-1 86-88 4E	2-2 18-21 1D	2-2 25-28 1D	2-2 61-63 2A	2-2 80-82 3	2-3 28-30 2	2-3[a] 52-54 4A	3-1 140-142 9J	3-2[a] 56-60 3E	σ	x̄	s
FeO*	9.02	10.15	9.90	11.21	10.38	11.06	10.00	10.72	10.57	10.45	10.12	10.65	10.60	8.91	10.40	9.01	0.11	10.48	0.39
Na_2O	2.37	2.40	2.34	2.45	2.46	2.39	2.42	2.39	2.48	2.48	2.43	2.34	2.52	2.55	2.43	2.34	0.03	2.42	0.05
Sc	35.6	42.0	41.8	41.7	42.1	40.7	40.9	41.3	42.4	42.0	41.7	41.2	42.7	46.0	41.8	43.4	0.4	41.7	0.6
Cr	399	231	226	228	235	222	228	228	226	223	230	226	229	240	224	232	3	227	3
Co	44.9	51.0	52.0	54.2	49.1	44.8	48.0	42.8	49.2	48.7	48.6	51.4	46.5	56.1	49.4	48.3	0.5	48.9	3
Ni	165	180	160	130	180	130	140	110	110	130	160	150	120	130	120	160	25	140	24
Br[b]	0.21	0.26	0.33	0.37	0.27		0.09			0.15	0.16	0.19	0.36	0.69	0.15	0.65	0.12	0.23	0.10
Cs	0.08	0.09	0.15	0.20	0.10	0.18	0.12	0.35	0.08	0.10	0.24	0.33	0.17	0.06	0.10	0.17	0.04	0.17	0.09
La	12.5	2.61	2.65	2.65	2.65	2.49	2.59	2.54	2.64	2.62	2.60	2.60	2.71	3.13	2.58	2.69	0.05	2.61	0.06
Ce	26.9	8.2	8.3	8.1	8.5	7.8	8.4	8.1	8.1	8.3	8.5	8.4	8.7	10.0	8.1	8.6	0.3	8.3	0.2
Sm	3.71	3.18	3.24	3.16	3.20	3.04	3.08	3.05	3.22	3.20	3.14	3.10	3.25	3.73	3.15	3.22	0.06	3.15	0.07
Eu	1.21	1.10	1.10	1.13	1.12	1.09	1.06	1.10	1.14	1.16	1.15	1.11	1.14	1.33	1.14	1.16	0.03	1.12	0.03
Tb	0.78	0.91	0.91	0.89	0.93	0.87	0.84	0.86	0.88	0.91	0.85	0.86	0.91	1.00	0.83	0.89	0.03	0.88	0.03
Yb	2.54	3.52	3.65	3.52	3.50	3.38	3.46	3.45	3.79	3.73	3.70	3.64	3.73	4.41	3.72	3.78	0.07	3.60	0.13
Lu	0.425	0.589	0.576	0.561	0.572	0.548	0.566	0.557	0.572	0.570	0.573	0.561	0.595	0.696	0.576	0.575	0.014	0.570	0.013
Hf	2.47	2.30	2.24	2.30	2.23	2.25	2.18	2.22	2.45	2.41	2.36	2.38	2.43	2.58	2.36	2.42	0.08	2.32	0.09
Ta	1.43	0.20	0.21	0.24	0.18	0.16	0.18	0.09	0.22	0.20	0.21	0.17	0.20	0.20	0.10	0.17	0.03	0.18	0.04
Th	1.58	0.08	0.15	0.25	0.17	0.21	0.11	0.19	0.11	0.16	0.16	0.13	0.14	0.12	0.17	0.15	0.04	0.16	0.04
Chemical group	I	II	II	II	II	II	II	II	II	II	II	II	II	II	II	II	II	II	II

Note: Instrumental neutron activation analysis (INAA) was the method of analysis. σ = one standard deviation uncertainty estimate of a single analysis based principally on counting statistics, x̄ = mean, ans s = sample standard deviation. FeO* = total Fe as FeO. FeO* and Na_2O concentrations expressed in wt.%, all others expressed in ppm.

[a] These samples contain >0.6 ppm Br, which indicates interaction with seawater. They were not used to calculate the mean.

[b] This is an estimated value, no standard was used.

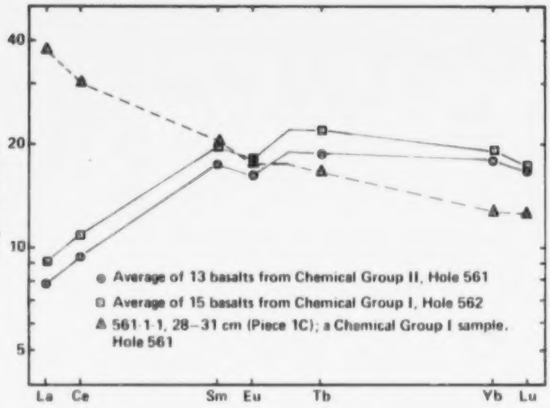

Figure 1. Rare earth element abundance patterns normalized to chondrites for basalts from Holes 561 and 562.

gous to those found in an Icelandic tholeiitic basalt by Lindstrom and Haskin (1981). Similarly, the discrepancies between analytical uncertainty and sample standard deviation for FeO* and Co in the 15 basalts from Chemical Group II are on the same order of magnitude as small-scale heterogeneity between separate hand-specimens of this mass range (2.9–11.8 g) (100 [s/x̄] = relative heterogeneity; 3.8% for FeO* and 6.1% for Co).

The composition of basalts from Chemical Group II is homogeneous for all elements listed in Table 2 to within 2σ analytical uncertainty except for FeO*, Co, and Cs. Any quantitative petrogenetic model used to describe the relationship of basalts from Chemical Group II to other basalts or its mantle source is limited by the analytical uncertainty for those elements found to be homogeneous and by the relative heterogeneity of FeO*, Co, and Cs.

CHEMICAL GROUP I, HOLE 562

Basalts from Hole 562 are sparsely to moderately plagioclase phyric. Most were extruded as pillows up to 1.5 m thick, but two thicker flows (3.7 and 5.1 m) occur. These are minimum thicknesses because recovery was only 62 and 77% for Cores 562-4 and 562-5, where these occur. The basalts are fresh to moderately altered with the alteration occurring primarily adjacent to fractures, veins, or glassy margins. Although no lithologic changes are apparent, two distinct chemical groups were proposed on the basis of shipboard XRF analyses. Chemical Group I is higher in TiO_2, Fe_2O_3 (total iron as Fe_2O_3), P_2O_5, V, Y, and Zr are lower in Al_2O_3 and CaO, relative to Chemical Group II.

Analyses of 16 basalts from Chemical Group I are tabulated in Table 3. The LREE-depleted nature relative to chondrites of these basalts is illustrated in Figure 1. Samples collected from Sections 562-4-1 through 562-4-3 are part of the 3.7-m thick flow and those from Sections 562-5-2 through 562-5-5 are part of the 5.1-m thick flow. Sample 562-4-3, 86–88 cm (Piece 2H) (collected 5 cm above the basal chilled glass rim) was not included in the mean or standard deviation because its Cs concentration (0.85 ppm) is higher—by at least a factor of 3—than any other analyzed sample from this group, which indicates a greater uptake of Cs from seawater (Bougault et al., 1979). The mean and standard deviation for each thick flow were calculated, but they are not tabulated here because they are essentially identical (to within analytical uncertainty) to the mean and standard deviation of all 15 samples. For only FeO*, Na_2O, Sc, and Co, does s exceed σ by more than a factor of 2. The scatter in the Na_2O data could be attributed to the increase of alkali metals with increased alteration (Bougault et al., 1979). The scatter in FeO*, Sc, and Co is on the same order of magnitude as small-scale heterogeneity from one hand-specimen to the next for this mass range (6.[illegible]–25.0 g) (100 [s/x̄] = relative heterogeneity; 2.8% for FeO*, 3.0% for Sc, and 2.1% for Co).

The composition of basalts from Chemical Group I is homogeneous for all elements listed in Table 3 to within 2σ analytical uncertainty except for FeO*, Na_2O, Sc, and Co. Comparing those elements (FeO* and Co) that are heterogeneous beyond analytical uncertainty in both Chemical Group II (Hole 561) and Chemical Group I (Hole 562), the basalts from Hole 561 are slightly more heterogeneous in those elements than the basalts from Hole 562 (3.8% relative heterogeneity as opposed to 2.8% for FeO* and 6.1% relative heterogeneity as opposed to 2.1% for Co).

HOLE 564

At Site 564, 35 m of basalts were recovered from an 81-m cored section of the basement. Five lithologic units from the basement-sediment interface to the bottom of the core were proposed aboard ship (Unit 3, aphyric pillow basalts; Unit 4, a 4-m thick (minimum thickness) aphyric basalt flow; Unit 5, aphyric pillow basalts; Unit 6, a 2.5-m thick olivine microphyric basalt; and Unit 7, aphyric pillow basalts).

Even though a chemical gradient was apparent in the XRF shipboard analyses as a function of depth (Fig. 2), the basalts from Hole 564 were defined as a single chemical group and much of the chemical variation was attributed to analytical precision. It was noted, however, that this apparent chemical gradient with depth should be investigated onshore.

Analyses for 19 basalts from Hole 564 are listed in Table 4. Samples from 564-2-1 through 564-5-2 correspond to Lithologic Unit 3. Four samples were collected from a single pillow (A) within this lithologic unit (samples from 564-2-1 through 564-2-2). Six samples from 564-6-3 through 564-6-5 were collected from Lithologic Unit 4 (Flow B), a 4-m thick flow. Samples from Sections 564-8-1 through 564-8-2 correspond to Lithologic Unit 5. Four samples from 564-8-1 were collected from a single pillow (C) in this pillow sequence. Sample 564-9-[illegible], 142–144 cm (Piece 9C) is the only sample from Lithologic Unit 7. An increase in the concentrations of REE, Ta, and Th and a decrease in Cr are readily apparent as Table 4 is read from left to right (top to bottom of the core). This same type of trend of increasing incompatible trace element concentrations and decreasing Cr con-

Table 3. Elemental abundances of basalts from Chemical Group I, Hole 562.

Core-Section	3-1	4-1	4-1	4-1	4-2	4-3	4-3	4-3[a]	4-4	4-5	5-2	5-3	5-3	5-4	5-5	5-5			
Interval (in cm)	46–48	14–16	58–60	78–80	22–25	27–29	64–67	86–88	117–119	26–28	89–91	9–11	58–60	106–108	69–71	95–97			
Piece	1D	1B	3A	3B	1A	2B	2F	2H	8B	2A	4B	1A	1E	2A	3C	4A	σ	x̄	s
FeO*	10.10	10.89	10.54	10.19	10.22	10.25	10.69	10.88	9.70	10.02	10.60	10.34	10.22	10.05	10.28	10.33	0.11	10.29	0.29
Na_2O	2.51	2.71	2.52	2.62	2.51	2.48	2.54	2.69	2.34	2.50	2.47	2.56	2.47	2.64	2.50	2.52	0.03	2.53	0.08
Sc	40.8	42.0	41.6	42.3	39.8	39.1	40.2	42.1	37.7	40.1	40.3	40.5	39.2	40.1	40.2	39.2	0.4	40.2	1.2
Cr	235	240	239	245	234	231	237	239	226	241	243	240	234	238	238	237	3	237	4.8
Co	42.1	42.8	42.1	43.5	41.5	41.6	41.6	38.8	39.7	42.2	42.4	42.7	41.0	41.8	42.1	41.3	0.4	41.9	0.9
Ni	120	30	100	110	120	150	110	100	110	100	100	110	100	70	70	90	27	100	27
Br[b]			0.08										0.14						
Cs	0.05	0.27	0.03	0.04	0.03	0.02	0.30	0.85	0.01	0.06	0.04	0.05	0.04	0.07	0.01	0.20	0.05	0.08	0.10
La	2.70	3.03	3.07	2.94	2.90	2.85	2.91	3.08	2.94	3.06	3.14	3.17	2.99	3.12	3.10	3.01	0.06	3.00	0.12
Ce	9.0	9.8	9.4	9.6	9.0	9.0	9.4	9.6	9.2	9.8	9.9	10.0	9.4	9.8	9.6	9.0	0.3	9.5	0.4
Sm	3.49	3.69	3.68	3.59	3.51	3.46	3.45	3.73	3.43	3.68	3.64	3.71	3.56	3.65	3.66	3.57	0.06	3.58	0.10
Eu	1.22	1.29	1.29	1.27	1.22	1.20	1.26	1.30	1.19	1.24	1.27	1.25	1.22	1.23	1.22	1.19	0.03	1.24	0.03
Tb	1.02	1.06	1.07	1.06	1.03	1.02	1.05	1.12	1.00	1.04	1.06	1.05	1.01	1.03	1.04	1.04	0.06	1.04	0.02
Yb	3.72	3.86	3.88	3.88	3.64	3.62	3.69	3.91	3.61	3.88	3.80	3.93	3.74	3.91	3.97	3.79	0.11	3.79	0.12
Lu	0.570	0.59	0.598	0.58	0.566	0.542	0.55	0.60	0.56	0.59	0.59	0.60	0.59	0.59	0.61	0.58	0.02	0.582	0.019
Hf	2.73	2.74	2.75	2.73	2.54	2.57	2.63	2.81	2.56	2.68	2.74	2.69	2.58	2.60	2.66	2.57	0.12	2.65	0.08
Ta	0.16	0.18	0.20	0.19	0.19	0.21	0.19	0.18	0.19	0.19	0.23	0.21	0.22	0.22	0.19	0.22	0.03	0.20	0.02
Th	0.12	0.29	0.05	0.10	0.20	0.03	0.09	0.08	0.14	0.10	0.21	0.21	0.10	0.17	0.07	0.10	0.04	0.13	0.07

Note: Instrumental neutron activation analysis (INAA) was the method of analysis. σ = one standard deviation uncertainty estimate of a single analysis based principally on counting statistics, x̄ = mean, and s = sample standard deviation. FeO* = total Fe as FeO. FeO* and Na_2O concentrations expressed in wt.%, all others expressed in ppm.

[a] This sample contains at least three times as much Cs than all the other samples, which indicates alteration. It was not used to calculate the mean.

[b] This is an estimated value, no standard was used.

Table 4. Elemental abundances of basalts from Hole 564.

	Pillow A							Flow B						Pillow C						
Core-Section	2-1	2-2	2-2	2-2	3-2	4-2	5-2	6-3	6-4	6-4	6-4	6-5	6-5	8-1	8-1	8-1	8-1	8-2	9-2	
Interval (in cm)	145–150	1–4	15–22	65–67	127–129	49–51	26–28	141–143	15–17	38–40	139–142	22–24	58–61	10–14	25–27	44–47	76–79	22–25	142–144	
Piece	10C	1	2A	4B	7A	3D	2D	10	2A	2D	2K	1E	2C	2A	2C	2E	3	2	9C	σ
FeO*	10.73	10.73	10.67	10.82	10.46	10.66	10.26	10.98	10.33	10.41	10.75	10.44	10.77	11.30	10.88	11.46	11.74	11.14	10.84	0.11
Na_2O	2.33	2.38	2.36	2.42	2.30	2.30	2.31	2.34	2.36	2.32	2.41	2.31	2.34	2.51	2.40	2.48	2.54	2.42	2.38	0.03
Sc	42.4	42.8	42.1	42.2	42.0	41.6	42.0	42.6	41.6	41.8	42.6	42.2	41.5	43.0	42.7	43.2	44.6	42.6	42.5	0.4
Cr	259	267	262	245	255	248	247	244	240	235	242	239	235	220	239	240	243	239	238	3
Co	43.1	41.0	43.7	34.8	46.6	43.4	48.0	43.5	43.8	44.5	44.8	45.1	44.3	45.2	44.5	43.5	31.5	40.1	52.2	0.4
Ni	70	110	120	110	130	120	160	70	130	115	130	120	120	140	110	130	70	100	90	28
Br[a]	0.16		0.12	0.6										0.6						
Cs	0.14	0.36	0.30	0.12	0.46	0.35	0.37	0.27	0.31	0.31	0.05	0.08	0.44	0.16	0.43	0.37	0.08	0.37	0.33	0.06
La	3.38	3.45	3.34	3.51	3.49	3.48	3.75	3.89	3.93	3.89	3.84	3.95	4.00	4.42	4.11	4.26	4.49	4.19	4.24	0.06
Ce	10.1	10.0	10.1	10.5	10.6	10.5	10.8	11.2	11.1	11.1	11.1	11.0	11.2	11.5	11.9	12.1	12.5	11.7	11.7	0.3
Sm	3.35	3.39	3.31	3.33	3.33	3.30	3.41	3.47	3.46	3.45	3.44	3.49	3.45	3.58	3.54	3.65	3.82	3.59	3.47	0.05
Eu	1.15	1.20	1.18	1.19	1.19	1.19	1.20	1.22	1.20	1.21	1.21	1.21	1.20	1.27	1.25	1.29	1.32	1.23	1.22	0.03
Tb	0.93	0.90	0.94	0.93	0.90	0.97	0.97	0.99	0.95	0.96	0.98	0.99	0.99	1.06	1.03	1.03	1.05	0.99	1.00	0.06
Yb	3.58	3.63	3.59	3.58	3.64	3.60	3.72	3.72	3.64	3.67	3.63	3.60	3.57	3.79	3.75	3.76	3.93	3.71	3.62	0.09
Lu	0.57	0.58	0.57	0.57	0.56	0.56	0.58	0.58	0.58	0.58	0.575	0.579	0.575	0.593	0.578	0.603	0.640	0.581	0.567	0.018
Hf	2.45	2.69	2.48	2.46	2.58	2.56	2.73	2.66	2.67	2.65	2.84	2.78	2.73	2.83	2.81	2.87	2.91	2.80	2.67	0.11
Ta	0.22	0.28	0.28	0.37	0.33	0.32	0.34	0.37	0.37	0.38	0.36	0.32	0.33	0.37	0.39	0.36	0.38	0.35	0.35	0.03
Th	0.20	0.22	0.19	0.20	0.20	0.22	0.25	0.23	0.25	0.26	0.26	0.30	0.26	0.34	0.33	0.31	0.32	0.31	0.32	0.05
Zone	I	I	I	V	I	I	I	I	I	I	I	I	I	V	I	I	I	I	V	

Note: Instrumental neutron activation analysis (INAA) was the method of analysis. I = interior portion of pillow, V = variolitic portion of pillow or flow. σ = one standard deviation uncertainty estimate of a single analysis based principally on counting statistics. FeO* = total Fe as FeO. FeO* and Na_2O concentrations in wt.%, all others in ppm.

[a] This is an estimated value, no standard was used.

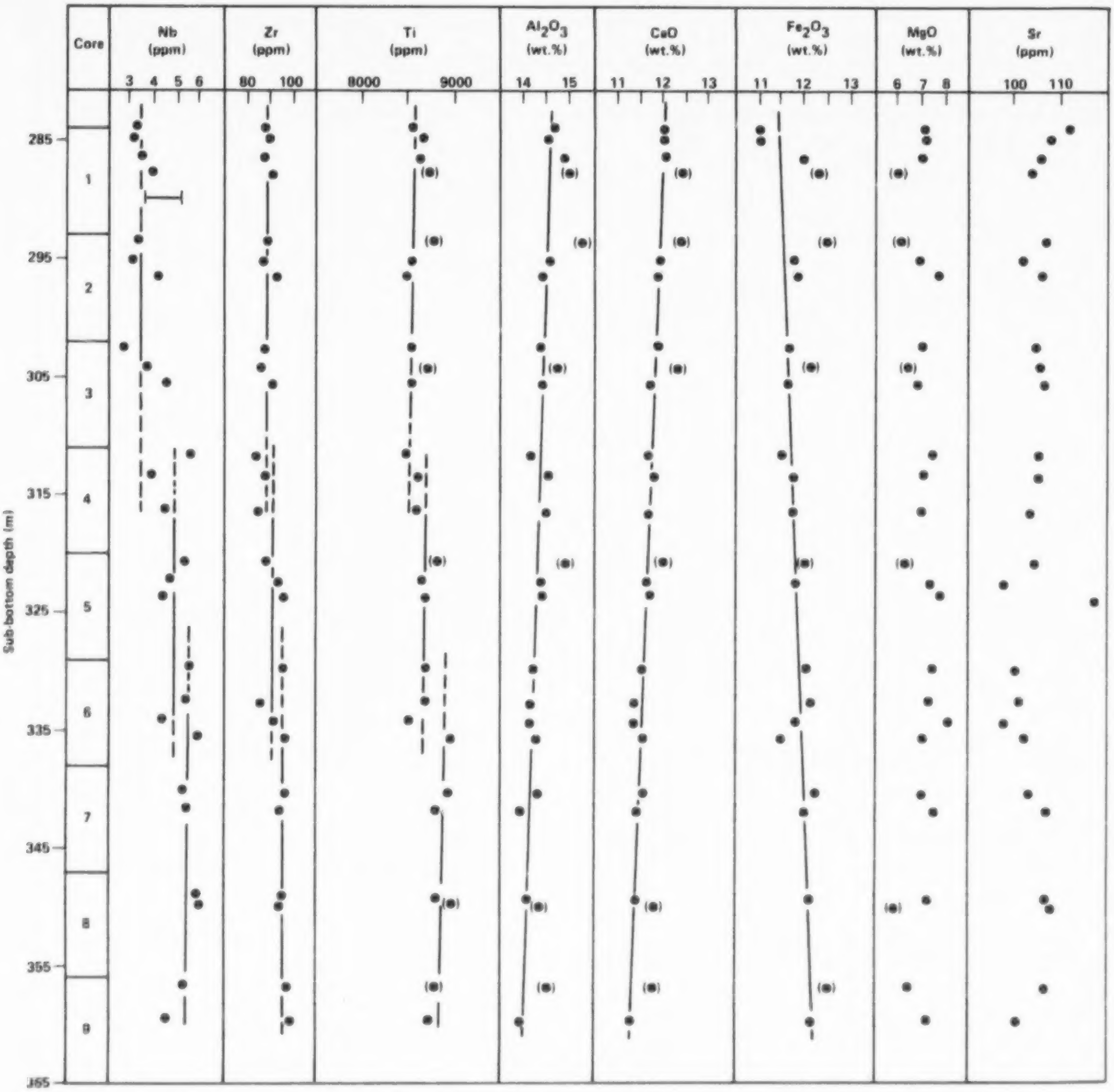

Figure 2. Downhole variations in chemical abundance of basalts from Hole 564, oxide concentrations are weight percent (wt.%), element concentrations are parts per million (ppm).

centrations with depth in the hole was observed in a sequence of sheet flows and submarine pahoehoe units at Site 462 of Leg 61 by Batiza (1981).

The mean and sample standard deviation for three recognizable structures from Hole 564 (Pillow A, Flow B, and Pillow C) are listed in Table 5. Samples from variolitic zones from Pillows A and C that appear altered (brown coloration rather than the gray color of the unaltered basalt) are not included in the mean or standard deviation calculation. They will be discussed later in detail. Only the sample standard deviation for Co exceeds its analytical uncertainty by a factor of 2 in Pillow A. The standard deviations of FeO* and Cs exceed their analytical uncertainties by a factor of 2 in Flow B. Th standard deviations of FeO*, Na_2O, Sc, Co, Cs, La, an Sm exceed their analytical uncertainties by a factor of in Pillow C.

Analyses of multiple samples from separate structur in this core gives us an idea of the intrastructure chemical variations. Pillow A is homogeneous to within 2 analytical uncertainty for all elements listed in Table except Co. This can be attributed to small-scale heterogeneity within the pillow with a relative heterogeneity o 3.3%. Flow B is homogeneous to within 2σ analytica uncertainty except for FeO* and Cs. Variations in Cs concentrations are again more easily explained by uptake of

Table 5. Average elemental abundances and standard deviation for Pillows A and C and Flow B for the basalts from Hole 564.

	Pillow A		Flow B		Pillow C		
n	3		6		3		
	$\bar{x}$	s	$\bar{x}$	s	$\bar{x}$	s	σ
eO^*	10.71	0.03	10.70	0.26	11.36	0.44	0.11
a_2O	2.36	0.02	2.35	0.04	2.47	0.07	0.03
c	42.4	0.3	42.1	0.5	43.5	1.0	0.4
r	263	4	239	4	241	2	3
o	42.6	1.4	44.3	0.6	40	7	0.4
i	100	26	114	22	103	31	28
s	0.27	0.11	0.24	0.15	0.29	0.19	0.06
a	3.39	0.06	3.92	0.06	4.29	0.19	0.06
e	10.07	0.06	11.12	0.08	12.2	0.3	0.3
m	3.35	0.04	3.46	0.018	3.67	0.14	0.05
u	1.18	0.03	1.208	0.008	1.27	0.02	0.03
b	0.92	0.02	0.977	0.018	1.037	0.012	0.06
Yb	3.60	0.03	3.64	0.05	3.81	0.10	0.09
u	0.573	0.006	0.578	0.002	0.591	0.013	0.018
Hf	2.54	0.13	2.72	0.08	2.86	0.05	0.11
Ta	0.26	0.03	0.36	0.02	0.377	0.015	0.03
Th	0.20	0.015	0.26	0.02	0.320	0.010	0.05

Note: n = number of samples analyzed. σ = one standard deviation uncertainty estimate of a single analysis based principally on counting statistics, $\bar{x}$ = mean, and s = sample standard deviation. FeO^* = total Fe as FeO. FeO^* and Na_2O concentrations expressed in wt.%, all others expressed in ppm.

Cs from seawater, and small-scale intrastructure sample heterogeneity can account for the variability of FeO^* (2.4% relative heterogeneity).

Pillow C is homogeneous to within 2σ analytical uncertainty except for FeO^*, Na_2O, Sc, Co, Cs, La, and Sm. The section (564-8-1) that contains this pillow is described as moderately to highly altered in the core description of the site chapter for Site 564 (this volume). Even though only the freshest portions of the pillow were sampled, the general degree of alteration is greater than that found in Pillow A and Flow B. This increased alteration may account for much of the scatter in the data for all these elements, certainly it does for Na_2O and Cs. The scatter found in the data of FeO^*, Sc, Co, La, and Sm may be analogous to the short-range segregation model in which the proportions of phenocrysts, groundmass minerals, and residual liquid vary randomly among ifferent samples of an Icelandic tholeiitic flow (Lindtrom and Haskin, 1981). There is some petrographic vidence for this process. These basalts are characterzed by varying proportions of domains with contrasting rain size and texture. Coarse-grained domains range rom 10–15% to 60–70% of the rock. For a more deiled description, see the site chapter, Site 564, this volme. The relative heterogeneities for these elements are eO^* = 3.9%, Sc = 2.3%, Co = 17.5%, La = 4.4%, nd Sm = 3.8%.

The intrastructure chemical variations have been es-ablished for the two pillows and the 4-m thick flow. Pil-ow A and Flow B are quite homogeneous and Pillow C s less so.

Are these three structures, which are each in a differ-nt lithologic unit, chemically alike or different? A t-test an be used to answer this question (Till, 1974). The ra-ios of the means of the elements for each structure to he other two structures and the composite sample standard deviations illustrate the results of the t-test graphically (Fig. 3). The means of Pillow A and Flow B are statistically different for Cr, La, Ce, Sm, Tb, Ta, and Th. The means of Pillow A and Pillow C are statistically different for Cr, La, Ce, Eu, Tb, Hf, Ta, and Th. The variance (s^2) for FeO^*, Sm, and Yb is statistically different for Pillows A and C, thus the t-test cannot be used. The positions of their ratio on Figure 3 are comparable to those ratios of means that are found to be statistically different. Although this observation is not a statistical test, by analogy FeO^*, Sm, and Yb appear to be different in Pillows A and C. The means of Flow B and Pillow C are statistically different for FeO^*, Na_2O, Sc, Eu, Tb, Yb, Hf, and Th. The t-test cannot be used to determine the differences of the means for elements La, Ce, or Sm for these two structures. Again the means of these elements appear to be different in Flow B and Pillow C. These results do not support the idea that all the basalts from Hole 564 comprise a single chemical group.

There are also other observations that do not support the single chemical group idea. The ratios of the means of Pillows A and C and their respective variolitic zones

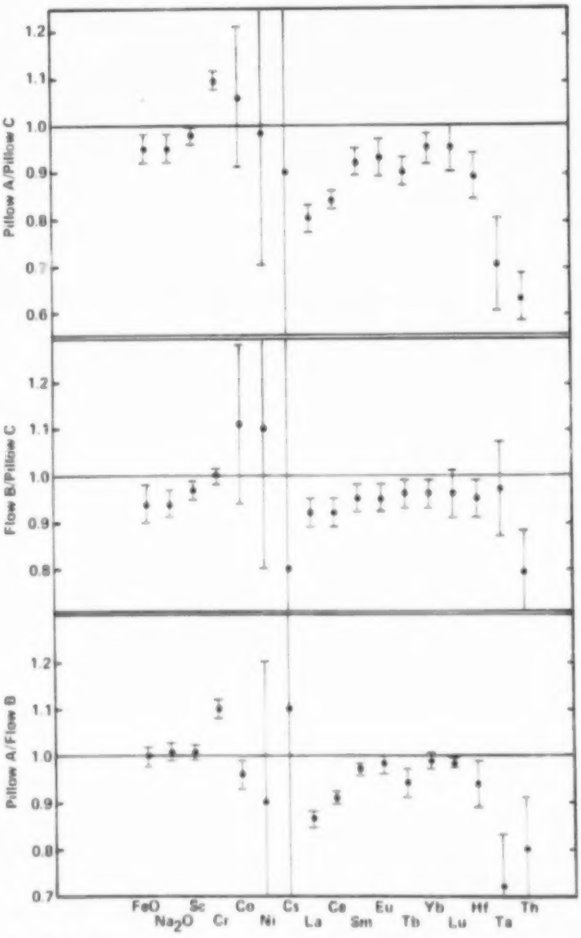

Figure 3. The ratios of average element abundances in three separate structures from Hole 564.

are shown in Figure 4. The variolitic zone of Pillow A appears to be depleted in Co and enriched in Ta compared to the mean. All other elements in these two portions of the pillow are identical to each other with the composite error of Pillow A sample standard deviation (s) and σ for the variolitic zone ($[s^2 + \sigma^2]^{1/2}$). The variolitic zone of Pillow C appears to be depleted only in Cr compared to the mean. Similar observations have been made. Frey et al. (1974) found that (compared to fresh basalt) altered glass samples are depleted in Cr, Ni, and V, but Co, Y, Zr, Hf, and Sc show little change. Staudigel et al. (1980) found that (relative to fresh glass), palagonite samples are depleted in Cr, Hf, and Sc. These variolitic zones that appear to be altered are compositionally closer to their respective pillow interiors than Pillow A, Flow B, and Pillow C are to each other. Also, the relative differences in compositions of basalts defined as distinct chemical groups at a single site (e.g., Site 562, Fig. 5) are less than the differences between these three structures at Site 564 (Fig. 6).

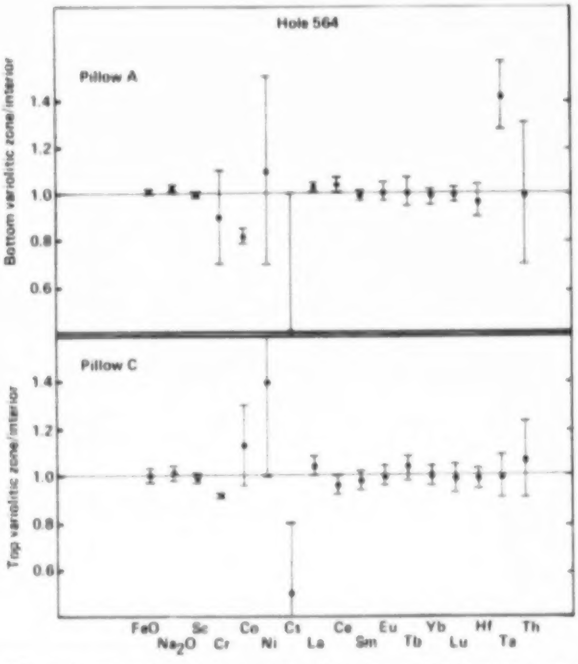

Figure 4. The ratios of element abundances in variolitic zones to the average interior abundances of two pillows.

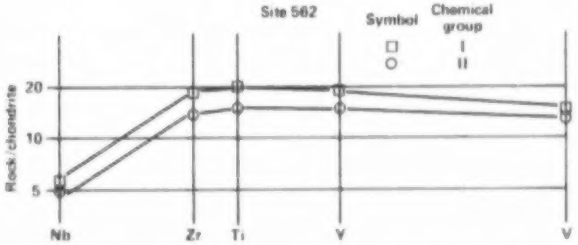

Figure 5. Extended Coryell-Masuda diagram for averages of basalts from Chemical Groups I and II.

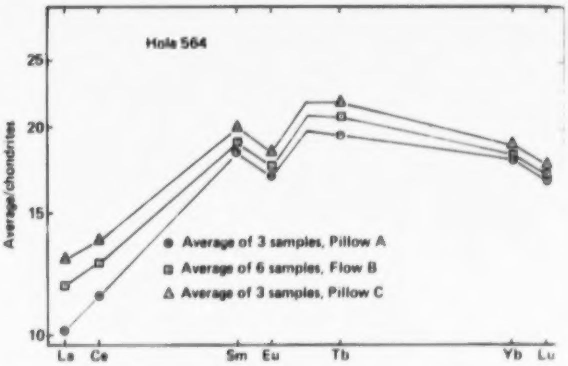

Figure 6. Rare earth element abundances normalized to chondrites f Hole 564 basalts.

SUMMARY

The composition of basalts from Chemical Group I (Hole 561) are homogeneous to within 2σ analytical un certainty from those elements listed in this paper excep for FeO*, Co, and Cs. The basalts of Chemical Group I (Hole 562) are homogeneous except for FeO*, Na$_2$O, Sc, and Co. Individual pillows and a 4-m thick flow from Hole 564 are homogeneous except for Co in Pillow A, FeO*, and Cs in Flow B, and FeO*, Na$_2$O, Sc, Co, Cs, La, and Sm in Pillow C.

The scatter in the alkalies is attributed to the addition of these elements during alteration. Often, no other chemical indication of alteration is detectable in otherwise fresh samples. Much of the scatter found in Pillow C may be attributed to alteration, because it is noted to be moderately to highly altered in the core description.

Transition elements Fe, Sc, and Co repeatedly have sample standard deviations that exceed 2σ analytical uncertainty. This scatter is on the same order of magnitude as the short-range segregation model of Lindstrom and Haskin (1981).

The basalts from Hole 564 were previously defined as a single chemical group even though downhole chemical gradients were found (Site 564 chapter, this vol.). Three individual homogeneous structures that are in separate lithologic units were found to be compositionally dis tinct to the same degree as the separate chemical group found in Hole 562. These results do not support the ide that all the basalts from Hole 564 comprise a single chem ical group. Obviously, a single sample in this core is on ly representative of its own structural unit (pillow o flow).

ACKNOWLEDGMENTS

I thank Randy Korotev, Marilyn and David Lindstrom, and Lar Haskin for constructive readings of the manuscript. Fred A. Frey ar John A. Philpotts reviewed the manuscript and suggested changes th improved the final version. This work was supported in part by th National Science Foundation through the DSDP/IPOD grant.

REFERENCES

Batiza, R., 1981. Trace-element characteristics of Leg 61 basalts. *I* Larson, R. L., Schlanger, S. O., et al., *Init. Repts. DSDP*, 6 Washington (U.S. Govt. Printing Office), 689–695.

Bougault, H., Jordan, J., and Treuil, M., 1979. Alteration, fractiona crystallization, partial melting, mantle properties from trace el ments in basalts recovered in North Atlantic. *In* Talwani, M., Harrison, C. G., and Hays, D. E. (Eds.), *Deep Drilling Results in the Atlantic Ocean: Ocean Crust*: Washington (Am. Geophys. Union), pp. 352–368.

Deer, W. A., Howie, R. A., and Zussman, J., 1966. *An Introduction to the Rock Forming Minerals*: London (Logman Group Limited).

Frey, F. A., Bryan, W. B., and Thompson, G., 1974. Atlantic Ocean floor: geochemistry and petrology of basalts from Legs 2 and 3 of the Deep-Sea Drilling Project. *J. Geophys. Res.*, 79:5507–5527.

Hart, S. R., 1969. K, Rb, Cs contents and K/Rb, K/Cs ratios of fresh and altered submarine basalts. *Earth Planet. Sci. Lett.*, 6:295–303.

______, 1976. LIL-element geochemistry, Leg 34 basalts. *In* Yeats, R. S., Hart, S. R., et al., *Init. Repts. DSDP*, 34: Washington (U.S. Govt. Printing Office), 283–288.

Haskin, L. A., Haskin, M. A., Frey, F. A., and Wildeman, T. R., 1968. Relative and absolute abundances of the rare earths. *In* Ahrens, L. H. (Ed.), *Origin and Distribution of the Elements*: New York (Pergamon Press), pp. 889–912.

Lindstrom, D. J., and Korotev, R. L., 1982. TEABAGS: Computer programs for instrumental neutron activation analysis. *J. Radioanal. Chem.*, 70:439–458.

Lindstrom, M. M., and Haskin, L. A., 1981. Compositional inhomogeneities in a single Icelandic tholeiitic flow. *Geochim. Cosmochim. Acta*, 45:15–31.

Staudigel, H., Frey, F. A., and Hart, S. R., 1980. Incompatible trace-element geochemistry and $^{87/86}$Sr in basalts and corresponding glasses and palagonites. *In* Donnelly, T., Francheteau, J., Bryan, W., Robinson, P., Flower, M., Salisbury, M., et al., *Init. Repts. DSDP*, 51,52,53, Pt. 2: Washington (U.S. Govt. Printing Office), 1137–1144.

Till, R., 1974. *Statistical Methods for the Earth Scientist*: New York (John Wiley and Sons).

Date of Initial Receipt: 18 April 1983
Date of Acceptance: 5 August 1983

22. TRACE ELEMENT GEOCHEMISTRY AND PETROGENESIS OF BASALTS FROM DEEP SEA DRILLING PROJECT SITES 556-559 AND 561-564[1]

J. Hertogen, Universiteit Leuven, Fysico-chemische geologie
Th. Sachtleben and H.-U. Schmincke, Ruhruniversität Bochum, Mineralogisches Institut
and
G. A. Jenner, Max-Planck-Institut für Chemie, Mainz[2]

ABSTRACT

Forty-three samples from DSDP Holes 556-559 and 561-564 were analyzed for rare earth elements (REE), Sc, Cr, Co, Hf, Ta, and Th by instrumental neutron activation analysis.

The recovered basalts range from those depleted in light REE (LREE) to those enriched in LREE. The two types of basalts occur together in Holes 558 and 561. The depleted basalts have remarkably constant La/Yb, La/Sm, and La/Ti ratios and apparently derive from a large, homogeneous, mantle source underneath a segment (1200 km long) of the Mid-Atlantic Ridge. The almost twofold variation in the concentrations of incompatible trace elements in the depleted basalts is primarily due to different degrees of batch partial melting.

The variation of highly to moderately incompatible elements in the Leg 82 enriched basalts can be successfully explained in terms of source mixing between depleted mantle sources and alkaline or nephelinitic magmas similar to Azores Islands magmas. However, the correlation of LREE enrichment with distance from the Azores Triple Junction is tenuous at best, and the enriched alkaline component is probably not directly related to the Azores volcanism.

INTRODUCTION

The geochemical studies of mid-ocean ridge basalts (MORB) from different regions in the northern Atlantic Ocean have revealed regionally marked differences in isotopic and trace element composition that are thought to be related to heterogeneities in the mantle source regions. One of these geochemically anomalous regions in the northern Atlantic is the Azores Triple Junction. Various hypotheses about the nature and origin of such anomalies have been developed based on one of two assumptions: either a mantle plume, enriched with large ion lithophile (LIL) elements rising beneath the Azores (White and Schilling, 1978), or the presence of separate magma reservoirs with different chemistries resulting from a complex melting history in the upper mantle (Wood, 1979).

One objective of Leg 82 was to relate regional variations of basalt geochemistry to geodynamic processes in an anomalous segment of the Mid-Atlantic Ridge, the Azores Triple Junction. *Glomar Challenger* drilled at nine sites southwest of the Azores (Fig. 1) during Leg 82. The recovered basalts span a wide range in age and trace element composition, varying from 14 to 37 Ma and from samples enriched in LREE to samples depleted in LREE. In this paper we present rare earth element (REE) and other trace element (Sc, Cr, Co, Hf, Ta, Th) data from 43 selected samples. The trace elements have been determined by instrumental neutron activation analysis (INAA). Two companion papers (Sachtleben et al. and Jenner et al., this volume) deal with the petrology, chemistry (major elements and Cr, Ni, Rb, Sr, Y, Zr, Nb, Ba), and Nd and Sr isotopic composition of the same samples.

ANALYTICAL TECHNIQUES

Samples for this study were selected (1) to be representative of the chemical units (magma groups) as defined by the shipboard party and by onshore analyses (Sachtleben et al., this volume), and (2) to be as fresh as possible. These criteria were checked by major element analyses taking into account only samples with low H_2O and/or CO_2 whenever possible. In addition, thin sections were examined for alteration.

Samples were coarsely crushed in an iron mortar and ground in an agate mill to 60 μm. Aliquots containing 800 mg of sample were irradiated for 7 hours in a thermal neutron flux of about 2×10^{12} neutrons cm^{-2} sec^{-1} in the Thetis reactor at Gent University, Belgium. The gamma-ray intensities were measured at Leuven University with a large volume Ge(Li)-detector and a hyperpure Ge "Low Energy Photon Detector" at intervals of 7 and 20-30 days after irradiation. Concentrations were determined relative to a secondary "in-house" alkali basalt standard, which has been repeatedly calibrated against USGS BCR-1 reference rock. For details of the analytical technique, see Hertogen and Gijbels (1971). Analytical precision for the different elements can be judged from the errors (2 × standard error of the mean) reported for Sample 564-9-1, 1-4 cm (Table 1). The errors were calculated from counting statistics and the observed dispersion of results from different countings and/or different gamma rays. The precision is generally better than 2% for Sc, Cr, Co, Sm, and Eu; 6% for La, Tb, and Yb; and 12% for Ce and Lu. The errors for Nd, Ta, and Th rapidly increase with decreasing concentration and may be as high as 15-20% for the most LIL-depleted samples.

RESULTS

The trace element data obtained by INAA are presented in Table 1. Chemical unit assignments listed in Table 1 are taken from Sachtleben et al. (this volume).

---

[1] Bougault, H., Cande, S. C., et al., *Init. Repts. DSDP*, 82: Washington (U.S. Govt. Printing Office).

[2] Addresses: (Hertogen) Universiteit Leuven, Fysico-chemische geologie, B-3030 Leuven, Belgium; (Sachtleben and Schmincke) Ruhruniversität Bochum, Mineralogisches Institut, D-4630 Bochum, West Germany; (Jenner, present address) Department of Earth Sciences, Memorial University of Newfoundland, St. John's, Newfoundland A1B 3X5, Canada.

Table 1. Trace element concentrations (ppm) in Leg 82 basalts.

Hole-Core-Section (interval in cm)	Chemical unit	Sc	Cr	Co	La	Ce	Nd	Sm	Eu	Gd	Tb	Yb	Lu	Hf	Ta	Th
556-2-1, 83-85	I	38.8	306	51.3	1.8	6.1	5.9	2.28	0.69	3.2	0.61	2.68	0.45	1.56	0.09	0.15
556-2-5, 5-7	II	36.0	243	40.3	2.6	9.2	8.8	3.23	1.18		0.85	3.53	0.63	2.35	0.13	≤0.15
556-3-2, 19-21	II	38.8	261	44.8	2.8	9.6	9.4	3.44	1.28	4.7	0.94	3.74	0.69	2.55	0.14	0.20
556-6-5, 68-70	II	37.6	275	47.1	2.4	8.3	8.1	3.02	1.12	4.0	0.80	3.25	0.57	2.14	0.11	0.22
556-7-1, 85-87	III	38.7	364	44.6	1.5	5.0	5.2	2.09	0.88	3.1	0.57	2.44	0.42	1.42	0.07	≤0.2
556-8-2, 27-29	III	40.8	281	43.6	1.45	4.8	5.0	1.88	0.79	2.7	0.51	2.20	0.39	1.29	0.07	≤0.15
556-12-3, 78-80	III	38.4	394	42.8	1.7	5.9	5.8	2.11	0.87		0.57	2.35	0.42	1.45	0.07	≤0.15
556-16-2, 131-133	V	40.6	47	42.9	2.3	7.9	6.9	3.01	1.18		0.80	3.22	0.59	2.13	0.13	≤0.4
557-1-1, 105-108		33.9	33	48.9	19.4	47.1	28.6	7.13	2.42	7.8	1.29	3.5	0.62	4.96	1.95	1.81
558-27-3, 69-72	I	32.3	478	48.1	5.7	14.4	9.3	2.72	1.02	3.5	0.63	2.34	0.42	1.84	0.53	0.63
558-27-3, 116-118	I	32.3	488	50.1	5.9	14.2	9.0	2.69	1.01	3.4	0.61	2.25	0.41	1.83	0.53	0.65
558-28-3, 118-120	II	38.5	402	40.2	2.7	8.4	7.3	2.49	0.94	3.7	0.65	2.63	0.47	1.70	0.15	0.31
558-29-1, 63-65	III	35.2	342	44.2	9.8	22.6	13.4	3.37	1.19		0.72	2.45	0.42	2.19	0.96	1.12
558-29-4, 83-85	III	33.9	321	40.3	9.4	21.3	13.2	3.28	1.15	3.7	0.64	2.35	0.41	2.10	0.90	1.00
558-31-1, 79-82	III	34.8	335	43.5	9.7	23.0	13.2	3.36	1.21		0.69	2.50	0.47	2.17	0.97	1.08
558-32-1, 123-125	III	35.6	337	47.7	10.0	22.9	13.8	3.42	1.22	3.6	0.68	2.45	0.43	2.24	0.98	1.11
558-33-2, 71-73	IVA	35.7	370	37.9	8.9	20.2	11.6	3.07	1.12	3.7	0.64	2.15	0.43	1.97	0.86	0.97
558-34-1, 30-32	IVA	35.5	366	44.1	8.7	20.5	12.2	3.03	1.09	3.3	0.60	2.18	0.38	1.94	0.86	0.94
558-35-3, 110-113	IVB	37.3	368	50.2	6.8	16.6	10.8	2.89	1.05	3.4	0.65	2.48	0.47	1.89	0.62	0.65
558-35-4, 106-108	IVB	36.3	362	42.8	6.6	15.8	9.9	2.79	1.01		0.60	2.35	0.41	1.77	0.59	0.69
558-38-1, 34-36	V	35.2	446	49.7	4.8	11.8	7.1	2.13	0.81	2.6	0.51	2.02	0.36	1.32	0.46	0.52
558-38-2, 61-63	IVA	37.1	342	44.0	7.8	18.5	11.5	3.05	1.10	3.6	0.65	2.53	0.45	2.07	0.71	0.83
558-40-1, 92-94	VI	36.5	462	50.2	5.0	11.8	6.7	2.18	0.83	2.8	0.50	2.06	0.39	1.40	0.47	0.55
558-40-2, 7-9	VI	36.0	500	41.5	13.5	27.6	17.8	3.69	1.33		0.62	1.85	0.31	2.18	1.32	1.45
559-1-1, 25-29	I	39.0	271	45.4	9.2	20.5	10.8	3.45	1.26		0.77	3.00	0.50	2.42	0.96	1.09
559-1-2, 52-56	I	37.9	260	42.5	8.5	19.7	11.8	3.36	1.20		0.76	2.93	0.58	2.37	0.91	0.94
559-8-1, 127-129	I	39.0	265	47.4	9.4	21.5	12.3	3.56	1.28	4.5	0.81	3.06	0.59	2.52	0.99	1.07
561-1-1, 33-38	I	34.8	391	50.5	12.3	25.9	13.5	3.4	1.2	3.7	0.69	2.51	0.46	2.16	1.29	1.52
561-2-1, 143-146	II	43.6	239	47.8	2.7	9.0	8.9	3.12	1.22	4.3	0.88	3.72	0.69	2.11	0.17	0.34
561-2-2, 138-141	II	41.4	232	66.5	2.6	8.3	8.3	2.95	1.13	4.0	0.79	3.48	0.62	2.00	0.16	0.26
561-3-2, 47-53	II	39.1	232	42.9	2.4	7.8	7.3	2.77	1.06	3.9	0.76	3.29	0.58	1.85	0.14	0.19
562-1-1, 110-112	I	39.6	228	44.3	2.6	9.0	9.3	3.28	1.25	4.8	0.89	3.61	0.64	2.30	0.14	≤0.15
562-4-1, 91-93	I	39.1	228	44.4	2.7	9.3	8.1	3.29	1.23	4.5	0.87	3.58	0.66	2.33	0.17	0.20
562-6-3, 120-123	I	41.0	244	48.5	3.1	10.0	9.5	3.41	1.31	5.0	0.93	3.69	0.70	2.47	0.21	0.25
562-6-4, 1-5	II	36.4	247	42.4	2.5	6.8	6.7	2.55	0.98	3.7	0.70	2.79	0.50	1.72	0.16	≤0.2
562-8-2, 6-9	II	38.5	254	43.5	2.4	7.8	7.7	2.70	1.03		0.73	3.10	0.56	1.82	0.16	0.19
563-23-1, 30-34	I	44.7	334	44.6	2.0	6.4	5.9	2.20	0.91		0.65	2.78	0.54	1.51	0.12	0.17
563-25-1, 19-22	I	41.1	321	45.2	1.85	5.7	5.3	2.06	0.83	3.0	0.57	2.51	0.43	1.41	0.11	0.24
563-25-2, 21-24	II	43.9	257	52.0	3.6	11.0	9.5	3.30	1.26		0.88	3.74	0.70	2.34	0.25	0.29
564-1-2, 21-25	I	43.7	333	46.3	1.9	5.6	5.6	2.14	0.89	3.1	0.61	2.64	0.48	1.47	0.11	0.21
564-1-2, 38-40	II	42.4	259		3.3	10.3	9.9	3.13	1.20		0.84	3.40	0.61	2.25		≤0.6
564-6-4, 71-74	II	39.9	227	50.7	3.8	10.6	8.7	3.13	1.17	4.2	0.81	3.40	0.59	2.25	0.28	0.35
564-9-1, 1-4	II	40.0	219	42.5	4.3	11.2	9.5	3.28	1.20	4.3	0.84	3.53	0.64	2.25	0.32	0.38
		±0.5[a]	±5	±0.8	±0.2	±0.7	±0.8	±0.06	±0.03	±0.4	±0.03	±0.15	±0.07	±0.08	±0.02	±0.07

[a] 2 times standard error of the mean.

Compatible Trace Elements (Sc, Cr, Co)

Sc, Cr, and Co concentrations are within the ranges typical of MORB from the North Atlantic (Bougault et al., 1979; Wood et al., 1979).

Sc and (to a lesser extent) Co contents are rather constant, which is in keeping with the scarcity of highly fractionated basalts in the Leg 82 holes. Neither systematic hole-to-hole differences nor clear-cut correlations with magma groups have been observed for Sc and Co.

Cr contents correlate with MgO values; for more details, see Sachtleben et al. (this volume), who report Cr data for a larger number of samples.

Incompatible Trace Elements (REE, Hf, Ta, Th)

Ta and Th strongly correlate with La, whereas Hf correlates with Sm. The following discussion is, therefore, largely restricted to the REE data.

Hole 556. The eight analyzed samples represent four magma groups and are all "normal" LREE-depleted basalts (N-MORBs) (Fig. 1). Absolute REE abundances span a rather large range, but the relative patterns are markedly similar (i.e., virtually constant La/Yb ratios; see Fig. 8 for details). Magma Groups II and V have consistently higher TiO_2 contents (Fig. 9) and lower Mg-numbers (58 ± 2 versus approximately 67 ± 2; Sachtleben et al., this volume) than Groups I and III. The same dichotomy shows up in the absolute REE abundances (Fig. 1).

Hole 557. Basalts from this site are unique among Leg 82 samples; they are highly fractionated (Mg-value of 44) and rich in Fe and Ti (15% FeO_{tot}, 3.6% TiO_2) (Sachtleben et al., this volume). The single sample analyzed for trace elements (557-1-1, 105-108 cm) is strongly enriched in LREE (Fig. 1), Hf, Ta, and Th.

Basalts of similar major and trace element compositions are known from Hole 407 in the Reykjanes Ridge at 63°N (Wood et al., 1979). However, the strongly LREE-enriched basalts from Holes 410 and 410A (Mid-Atlantic Ridge, 45°N) have a distinctly different major element chemistry; most are much less fractionated (Mg-values up to 66), and all have lower TiO_2 (1.4-1.5%) and FeO_{tot} (7-9%) contents (Wood et al., 1979). The Hole 557 basalts also differ from the Fe-rich and Ti-rich basalts from the Galapagos spreading center, which are typically depleted in LREE (Clague et al., 1981).

Hole 558. The 15 analyzed samples represent 6 magma groups, and all but one (558-28-3, 118-120 cm; Group

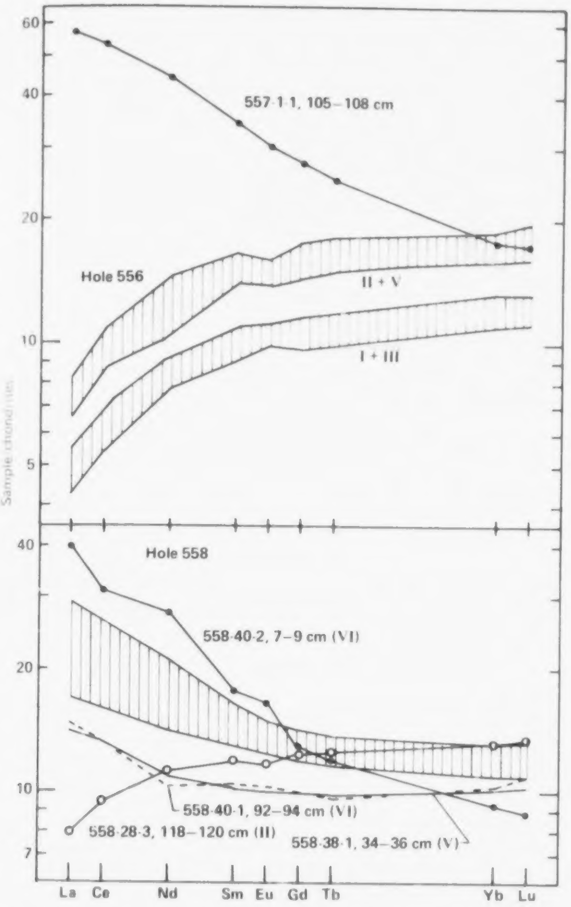

Figure 1. Rare earth element (REE) patterns of basalts normalized to chondrites from Holes 556 (8 samples), 557 (1 sample), and 558 (15 samples). Samples from different magma groups (chemical units in Roman numerals) generally have different REE contents. The samples from Hole 558 show the greatest diversity of REE patterns, ranging from LREE-enriched to LREE-depleted. The hatched field for Hole 558 covers the closely spaced patterns of 11 E-MORB samples from Groups I, III, and IV. The irregular REE distribution of Sample 558-40-2, 7-9 cm could be due to alteration.

I) are LREE-enriched basalts (Fig. 1). For the LREE-enriched basalts, a correlation between magma group and LREE enrichment is observed: V < I < IVA < IVB < III. Group VI is apparently a special case, because the two samples show grossly different REE patterns (558-40-1, 92–94 cm and 558-40-2, 7–9 cm). The Group VI samples belong lithologically to a breccia unit, but do not seem to form a single chemical unit (Sachtleben et al., this volume). The irregular REE pattern of 558-40-2, 7–9 cm could be due to alteration; the CO_2 content (0.94%) of this sample is among the highest measured in our sample suite.

The LREE-depleted basalt (558-28-3, 118–120 cm) also has the high La/Ta and Hf/Ta ratios typical of N-MORB (Fig. 5). However, this sample is unusual among the Leg 82 N-MORBs, because its $^{143}Nd/^{144}Nd$ isotopic ratio is virtually indistinguishable from that of the E-MORBs (enriched MORB) from Hole 558 (Jenner et al., this volume).

Hole 559. The basalts from this hole form a single magma group. The three analyzed samples are LREE enriched (Fig. 2) and show only limited variations of trace element abundances.

Hole 561. The two magma groups have distinctly different trace element (Fig. 2) and Nd isotopic (Jenner et al., this volume) characteristics. The occurrence of both E-MORBs and N-MORBs in a single hole underscores the small scale of mantle heterogeneities or the localized nature of mixing processes.

Hole 562. The five analyzed samples are all LREE depleted (Fig. 3). Basalts from magma Group I have consistently higher REE abundances than those from magma Group II.

Hole 563. The two magma groups are LREE depleted but are clearly separated by absolute REE abundances, which are much lower in Group I than in Group II (Fig. 3). Note the similarities between Groups I and II from Holes 563 and 564.

Hole 564. The sample from magma Group I (564-1-2, 21–25 cm) is a typical, depleted N-MORB (Fig. 3). The Group II basalts from Holes 563 and 564, though LREE depleted, have a more transitional character; the La/Yb ratios are higher (Fig. 8) and the Hf/Ta and La/Ta ratios (Fig. 5) are lower than in depleted basalts from the other Leg 82 holes. They are also clearly separated from the

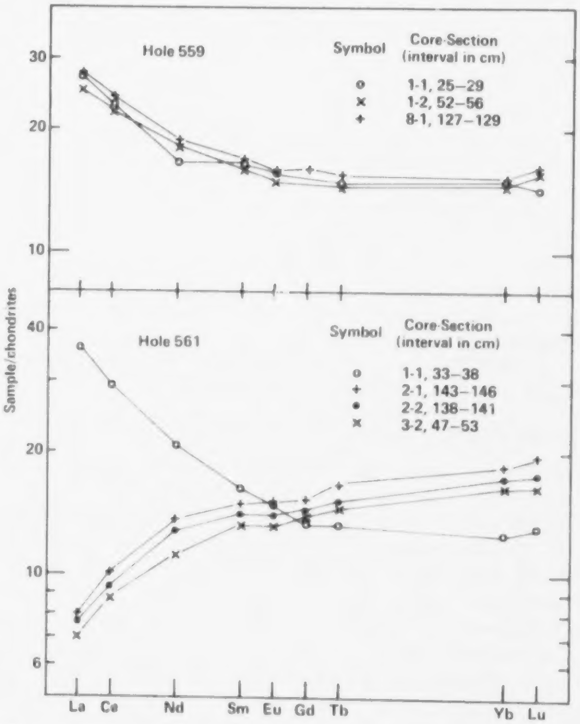

Figure 2. Rare earth element patterns of basalts normalized to chondrites from Holes 559 and 561. The Hole 559 basalts form a single, very homogeneous, magma group. Enriched (Group I) and depleted (Group II) basalts occur together in Hole 561.

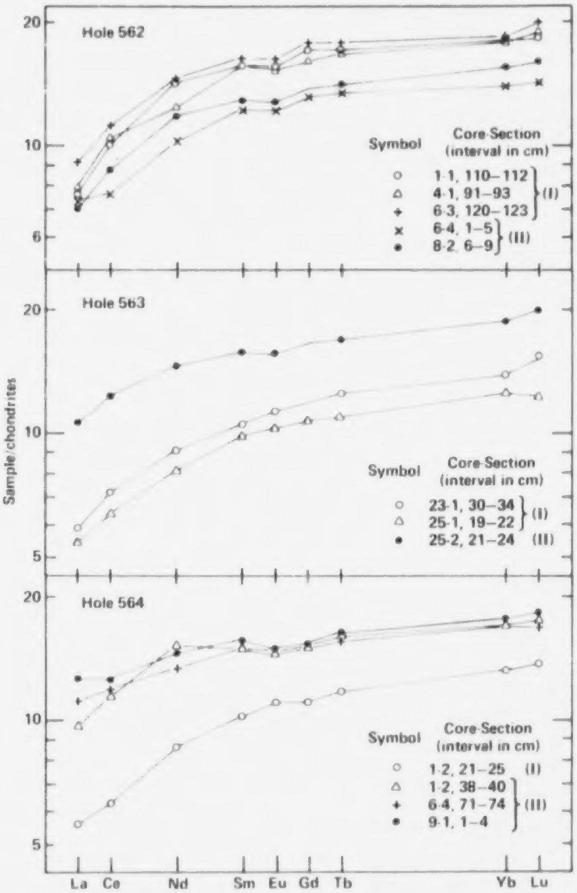

Figure 3. Rare earth element (REE) patterns of basalts normalized to chondrites from Holes 562, 563, and 564. Note the similarity of REE patterns of Group I and II samples from Holes 563 and 564. The Group II basalts from these two holes have somewhat higher La/Sm and La/Yb (see also Figs. 6 and 8) ratios than the LREE-depleted MORBs from the other Leg 82 holes.

common depleted basalts in the TiO_2 versus La variation diagram (Fig. 9).

DISCUSSION

Trace Element Variations in the Leg 82 N-MORBs

For the present discussion N-MORBs are defined as those samples that have a La/Yb ratio (normalized to chondrites) less than 0.5 and a La/Ta ratio greater than 15 (Figs. 5 and 8). The transitional Group II basalts from Holes 563 and 564 (Fig. 3) will be discussed together with the E-MORBs.

The Leg 82 N-MORBs have remarkably constant La/Yb, La/Sm, and La/Ti ratios, in spite of the almost twofold variation of absolute REE abundances (Figs. 6, 8, 9). This large variation of REE and other incompatible elements may be due to either substantial (40–50%) crystal fractionation or different degrees of partial melting. To determine which of these two processes is the most important or the most plausible, we will consider the variation of some critical major and trace elements in the Hole 556 N-MORBs that encompass the whole range of chemical variation in the Leg 82 N-MORBs (see also Sachtleben et al., this volume). Data for some key elements have been summarized in Table 2 to facilitate the discussion.

The chemical variation within the Hole 556 sequence cannot be explained by high-pressure clinopyroxene fractionation (above 10 kbar; Bender et al., 1978; Fujii and Bougault, 1983). This would lead to a noticeable increase in the La/Yb and La/Ti ratios and a significant decrease of Sc content with increasing La content. These trends are not observed (Figs. 8 and 9; Table 2). Low-pressure fractionation of olivine alone can also be dismissed because it would rapidly deplete the magmas in MgO (Fig. 4) and Ni. The depletion in MgO and Ni could be largely offset by simultaneous plagioclase crystallization. However, extensive plagioclase fractionation is definitely ruled out by the absence of large negative Eu-anomalies and by the increase of the Al_2O_3/CaO ratio in the Hole 556 N-MORBs (Table 2). Fractionation of plagioclase with Al_2O_3/CaO around 1.8—as observed in the cores of phenocrysts—would produce an opposite Al_2O_3/CaO variation trend. The Ca/Al fractionation by plagioclase could in turn be offset by cocrystallization of clinopyroxene. Least-squares mass balance calculations, using high-pressure (7–10 kbar) olivine, clinopyroxene, and plagioclase compositions from Fujii and Bougault (1983), suggest that Sample 556-3-2, 19–21 cm could be related to Sample 556-8-2, 27–29 cm by 21% clinopyroxene plus 12% plagioclase fractionation. This result conflicts with the constancy of Sc concentrations and La/Yb and La/Ti ratios. Moreover, clinopyroxene plus plagioclase without olivine does not appear to be a liquidus phase assemblage within the 1 atm to 15 kbar pressure range (Bender et al., 1978; Fujii and Bougault, 1983). Therefore, if the major and trace element variation in the Leg 82 N-MORBs are to be explained by crystal fractionation, complex mechanisms have to be invoked, such as the fractionation of a continuously replenished magma chamber (O'Hara, 1977). It is, however, beyond the scope of this paper to test the plausibility of this class of models.

Different degrees of batch partial melting of a lherzolite mantle source readily account for the twofold variation of incompatible elements and for the constant La/Yb and La/Ti ratios of the Leg 82 N-MORBs. A calculated partial melting path has been superimposed on Figure 8 to illustrate this point. The melting model assumed a depleted source consisting of 65% olivine (OL), 25% orthopyroxene (OPX), 10% clinopyroxene (CPX) with 0.26 ppm La (0.76 × chondrites), and 0.4 ppm Yb (2 × chondrites). The melting proportions were $OL_0OPX_{0.2}CPX_{0.8}$ from 0 to 12.5% melting and $OL_{0.2}OPX_{0.8}$ above 12.5% melting. Crystal/liquid partition coefficients for OL, OPX, and CPX were 0.0[illegible], 0.001, and 0.03 for La and 0.001, 0.05, and 0.3 for Yb. The outcome of calculations for a garnet-bearing mantle source is virtually identical provided that the garnet is exhausted from the source at 8 to 10% melting. The systematic decrease of the La/Sr ratio with decreasing

Table 2. Selected data for Hole 556 samples.

Measured value	Core-Section (interval in cm) 8-2 27-29	7-1 85-87	12-3 78-80	2-1 83-85	16-2 131-133	6-5 68-70	2-5 5-7	3-2 19-21
MgO (%)	8.09	6.74	7.99	7.80	6.57	6.94	6.18	6.10
Mg-number	68.8	64.6	67.2	67.2	56.4	61.6	56.4	57.6
Al_2O_3/CaO	1.11	1.03	1.23	1.23	1.37	1.34	1.34	1.37
Ni (ppm)	136	128	112	121	55	109	79	72
Sc (ppm)	40.8	38.7	38.4	38.8	40.6	37.6	36.0	38.8
La (ppm)	1.45	1.5	1.7	1.8	2.3	2.4	2.6	2.8
Sr (ppm)	98	106	95	114	120	103	108	108
$(La/Sr) \times 10^4$	148	142	179	158	192	233	241	260

Note: From this work and Sachtleben et al. (unpublished data).

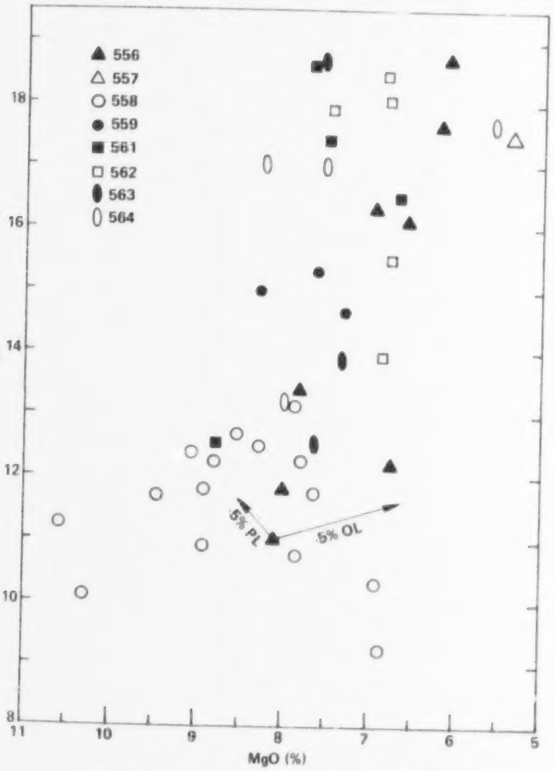

ure 4. Ytterbium (Yb_N) content normalized to chondrites versus MgO content for Leg 82 basalts. In order to produce the twofold increase of heavy rare earth element (REE) abundances in the N-MORBs (e.g., from Hole 556), low-pressure olivine (OL) + plagioclase (PL) fractionation should be dominated by plagioclase, as shown by the two fractionation vectors. Because extensive plagioclase fractionation is ruled out by the lack of large negative Eu-anomalies and the variation of the Al/Ca ratios, the large variation of REE abundances appears to be the result of different degrees of partial melting (see also Fig. 8).

a content (Table 2) and the small negative Eu-anomaes in some N-MORBs (Figs. 1-3) could imply that plagioclase was a residual source mineral throughout most of the melting range. This would be consistent with the model proposed by Fujii and Bougault (1983).

However, all Leg 82 N-MORBs have MgO contents and Mg-numbers that are too low to qualify the N-MORBs as primary or near-primary mantle melts (Rhodes and Dungan, 1979; Frey et al., 1980). So, even if the twofold variation of incompatible trace elements was primarily established by partial melting, the parental magmas of all N-MORBs most likely went through a stage of olivine fractionation before eruption (Stolper and Walker, 1980). Figure 4 suggests that the N-MORBs could have evolved from a parallel sequence of high-Mg magmas (≥ 10% MgO) by 5 to 15% olivine fractionation.

Although the constant La/Yb and La/Ti ratios of the Leg 82 N-MORBs require a very homogeneous mantle source, the substantial variation of the La/Ta, Hf/Ta, and La/Hf ratios (Fig. 5) nevertheless suggests some source heterogeneity or mixing. Indeed, it is generally assumed that basalts inherit the Hf/Ta and La/Ta ratios of their source region, because these incompatible elements are not substantially fractionated from each other by partial melting and fractional crystallization (Bougault et al., 1979; Wood et al., 1979; Langmuir et al., 1978).

The linear array of the Leg 82 N-MORBs in the Hf/Ta versus La/Ta diagram (Fig. 5) could be interpreted as a mixing line between N-MORB magmas (or sources) and E-MORB magmas or alkaline magmas similar to Azores alkali basalts. Mixing relations are further explored in Figure 7. The mixing curve was calculated for mixing between Sample 556-8-2, 27-29 cm and the alkali basalt F33 from Faial Island, Azores Island (White et al., 1979). This particular Faial sample (42.2 ppm La, 4.2 ppm Ta) has been chosen as being representative of relatively primitive (Mg-number > 65), enriched mantle magmas. The La/Ta ratios of the N-MORBs (La/Ta > 15) are very poorly correlated with La content, which is consistent with the tenet that La/Ta and La/Hf ratios are not systematically fractionated by moderate degrees of melting or crystallization. Figure 7 offers one explanation for the La/Ta variations in the Leg 82 N-MORBs, i.e., mixing of N-MORB magmas with less than 2% of an enriched alkaline component. This small amount of mixing will have a minor effect on absolute LREE contents but will not significantly alter La/Yb, La/Ti, and La/Sm ratios (Figs. 6, 8, 9). Actually, the E-MORB magmas also qualify as enriched end-members, but the re-

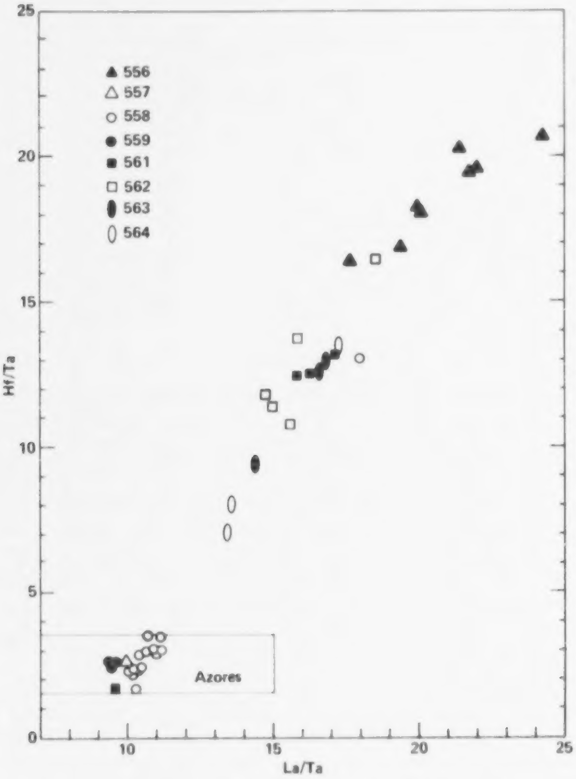

Figure 5. Hf/Ta versus La/Ta for Leg 82 basalts. The linear data array suggests that the variation is due to mixing involving an enriched alkaline end-member similar to Azores alkali basalt magmas (White et al., 1979). See Figure 7 for details of the mixing model.

quired amount of enriched component would then be five to ten times larger. The discussion in the next section will show that interpretation of the La/Ta variations in terms of magma mixing is not unique. The variable La/Ta ratios might equally well reflect source mixing (less than 0.1% enriched component) or local source heterogeneities that are too small to affect the ratios of other incompatible elements.

Mixing Relations in the Leg 82 E-MORBs

Two models have been proposed to explain the occurrence of E-MORBs along the Mid-Atlantic Ridge between 30 and 40°N. The first one invokes binary mixing between "normal" depleted MORB (or their source regions) and Azores Mantle Plume magmas enriched in incompatible trace elements and radiogenic Sr, Nd, and Pb isotopes (Schilling, 1975; White and Schilling, 1978). The second model postulates the existence of regional chemical and isotopic heterogeneities in the subocean mantle, whose origins might be unrelated to the Azores volcanism (O'Nions et al., 1978; Wood et al., 1979; Davies, 1981). Because of its conceptual simplicity, the Azores Mantle Plume mixing hypothesis can be tested quite rigorously. To do so we will investigate whether or not the trace element variations in the E-MORBs are consistent with magma or source mixing and whether or not the Azores magma are plausible enriched end-members.

Before proceeding with the discussion of mixing relations, we would like to call attention to two chemical aspects of the Leg 82 E-MORBs. Firstly, the MgO (Fig. 4), Cr (Table 1), and Ni (Sachtleben et al,. this volume) contents are generally higher than in the Leg 82 N-MORBs. This precludes crystal fractionation being of any importance in establishing the trace element characteristics of the Leg 82 E-MORBs. (The fractionated basalts from Hole 557 are an exception). Secondly, there is no correlation between LREE enrichment and HREE abundance in the Leg 82 E-MORBs. Crossing REE patterns, as observed in the Hole 558 E-MORBs, are the hallmark of the "dynamic melting" model proposed by Langmuir et al. (1977) for basalts from the FAMOUS area. However, no indication for dynamic melting could be found in the REE systematics of the Leg 82 N-MORBs. Because there is no obvious reason why dynamic melting should be restricted to particular areas along a ridge, or to enriched sources for that matter, we cannot accept dynamic melting as the preferred model.

Two mixing models will be explored: (1) mixing between N-MORB magmas and alkaline magmas; and (2) mixing of depleted N-MORB mantle sources with alkaline magmas. For the sake of clarity, the alkali basalt F33 from Faial Island, Azores, (White et al., 1979) has been chosen to represent alkaline magmas for both models.

We will first consider the mixing relations in the chondrite-normalized La/Yb versus La/Sm diagram (Fig. 6). With the exception of the basalts from Holes 557 and 561, the Leg 82 E-MORBs fit reasonably well to the mixing curve between N-MORB magmas and the alkali basalt F33. The magma mixing model predicts 8 to 40% alkaline component for the Hole 558 E-MORBs, 13 to 14% for the Hole 559 E-MORBs, and less than 3% for the transitional MORBs from Holes 562, 563, and 564. If we consider the magma mixing curve, crystal fractionation after magma mixing does not appear to be a plausible explanation for the deviation of the E-MORBs from Holes 557 and 561, because crystallization of moderate amounts of olivine, plagioclase, and clinopyroxene does not significantly change the La/Sm and La/Yb ratios. So, if the REE geochemistry of these samples is due to mixing, the enriched end-members must have been different. The alignment of the Leg 82 E-MORBs along a mixing line can also be explained in terms of source mixing. The heavy arrows in Figure 6 indicate the calculated La/Sm and La/Yb ratios of magmas generated by 20% partial melting of N-MORB sources "contaminated" with 1.5, 3, and 5% F33 alkaline component. The following assumptions were made for Sm: a concentration of 0.32 ppm (1.5 × chondrites) in the N-MORB source and partition coefficients of 0.001, 0.01, and 0.15 for olivine, orthopyroxene, and clinopyroxene. The other input parameters of the melting model were the same as used in the preceding section for modeling the La/Yb variation in the N-MORBs. Results of this source mixing/partial melting model will be discussed more in detail in subsequent paragraphs.

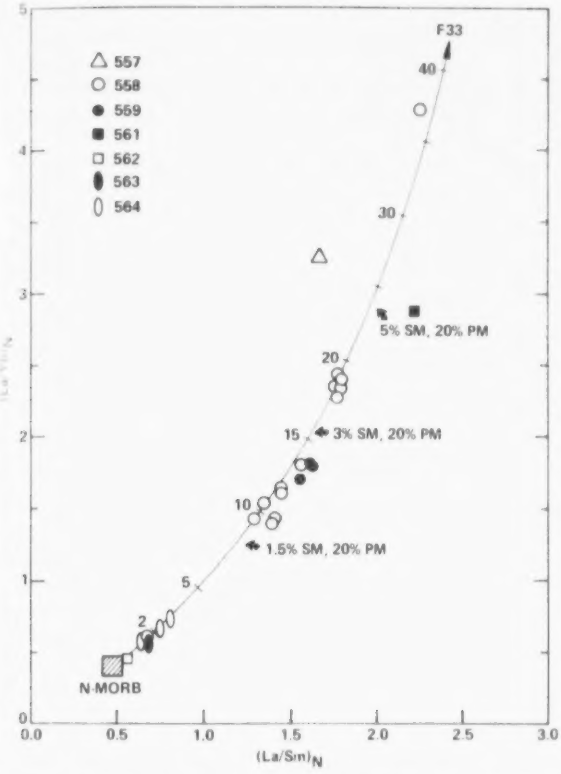

Figure 6. La/Yb versus La/Sm for Leg 82 basalts; both ratios are normalized to chondrites. The N-MORBs fall within a very narrow field (hatched square). The position of the E-MORBs (except for Holes 557 and 561) is consistent with either magma or source mixing. The mixing curve is calculated for magma mixing between Sample 556-8-2, 27–29 cm and alkali basalt F33 from Faial Island, Azores (White et al., 1979); numbers along the mixing curve refer to percentage of F33 component. The three heavy arrows indicate the calculated position of magmas derived by 20% partial melting (PM) of N-MORB sources mixed with 1.5, 3, and 5% of F33 component.

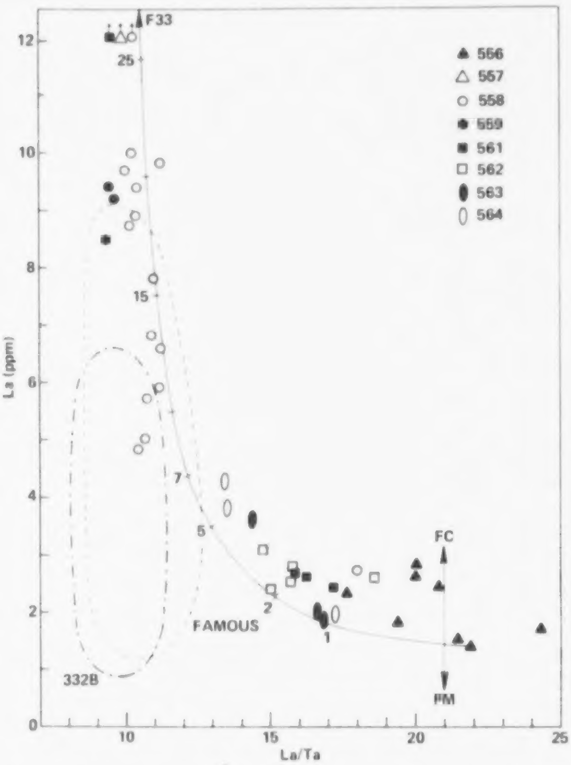

Figure 7. La versus La/Ta for Leg 82 basalts. As the La/Ta ratio is not changed by fractional crystallization (FC) or partial melting (PM), the variation of the La/Ta ratio must be ascribed to mixing or source heterogeneity. End-members of the mixing curve are the same as in Figure 6. The moderately enriched MORBs from Hole 332B (Bougault, 1980) and the FAMOUS area (Bougault et al., 1979) fall well off magma mixing curves between Azores alkaline magmas and N-MORBs. This suggests that the trace element chemistry of the E-MORBs is controlled by source mixing rather than by magma mixing.

Plots involving ratios of incompatible and slightly compatible elements, such as Figures 5 and 6, do not distinguish between magma or source mixing for the Leg 82 E-MORBs. It might, therefore, be instructive to consider mixing plots involving absolute concentrations, such as Figures 7–9.

The percentages of magma mixing indicated by the La versus La/Ta plot (Fig. 7) are not inconsistent with the amounts predicted by Figure 6, if allowance is made for minor variations in the composition of the depleted and enriched end-members and for changes in the La contents by moderate degrees of crystal fractionation after magma mixing. However, when the E-MORBs from the FAMOUS area (Bougault et al., 1979) and Hole 332B (Bougault, 1980) are considered, it appears that the chemistry of the E-MORBs has been controlled by source mixing rather than magma mixing. Indeed, the majority of the Hole 332B and FAMOUS MORBs plot well off magma mixing curves between common N-MORB and alkaline magmas. The near-vertical array of the Hole 332B, FAMOUS, and Leg 82 E-MORBs in Figure 7 is more readily explained by different degrees of partial melting of N-MORB sources contaminated with ≥1.5% alkaline magma.

To further explore mixing relations, magma mixing curves have been superimposed on the Yb versus La/Yb and TiO_2 versus La plots (Figs. 8 and 9). It is immediately apparent that the REE systematics and La/Ti variation of the Leg 82 E-MORBs are not consistent with magma mixing involving a unique depleted end-member. The whole array of N-MORB magmas must be considered as depleted end-members, and the magma mixing curves shown in Figures 8 and 9 are examples from a whole family of mixing curves converging towards the composition of basalt F33. Here again, source mixing offers an explanation that is at least as viable. The dashed, near-vertical lines in Figures 8 and 9 are batch partial melting paths calculated for depleted N-MORB sources contaminated with 1.5% (line A) and 3% (line B) F33 alkaline component. The numbers along the melting curves refer to the percentage of batch melting. (The melt-

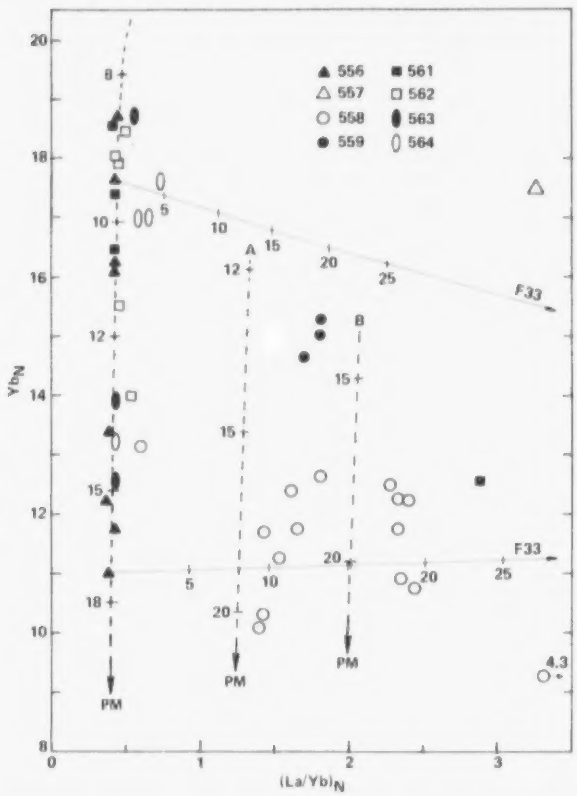

Figure 8. Yb versus La/Yb ratio normalized to chondrites for Leg 82 basalts. The twofold variation of rare earth element (REE) content in the Leg 82 N-MORBs (La/Yb ≤ 0.5) is primarily due to different degrees (8 to 18%) of partial melting (PM). The dashed curve passing through the N-MORBs is a calculated batch partial melting path; see text for input parameters of the melting model. The REE systematics of the Leg 82 E-MORBs can be interpreted in terms of magma or source mixing. The full lines are two examples from a whole family of magma mixing curves between N-MORB magmas and Azores alkali basalt F33; numbers along mixing curves refer to percentage of F33 component. The dashed lines marked A and B are calculated partial melting paths for N-MORB mantle sources mixed with 1.5% (line A) and 3% (line B) F33 magma; numbers refer to percentage of partial melting.

ing paths from Figure 9 are based on the reasonable assumptions that the La/Ti ratio of the N-MORB source was identical to the La/Ti ratio of the N-MORBs and that Ti behaved as an incompatible element after exhaustion of clinopyroxene from the mantle sources.) Our analysis of the data shows that the geochemistry of the transitional and enriched Leg 82 MORBs is consistent with ≥0.5 to 5% admixture of alkaline component.

Whereas the trace element characteristics of the Leg 82 E-MORBs can be used to promote both the magma and source mixing models, there is some evidence to definitely favor the source mixing model:

1. The Nd isotopic data are not easily reconciled with magma mixing, even if allowance is made for variability in the isotopic and trace element composition of the end-members (Jenner et al., this volume).

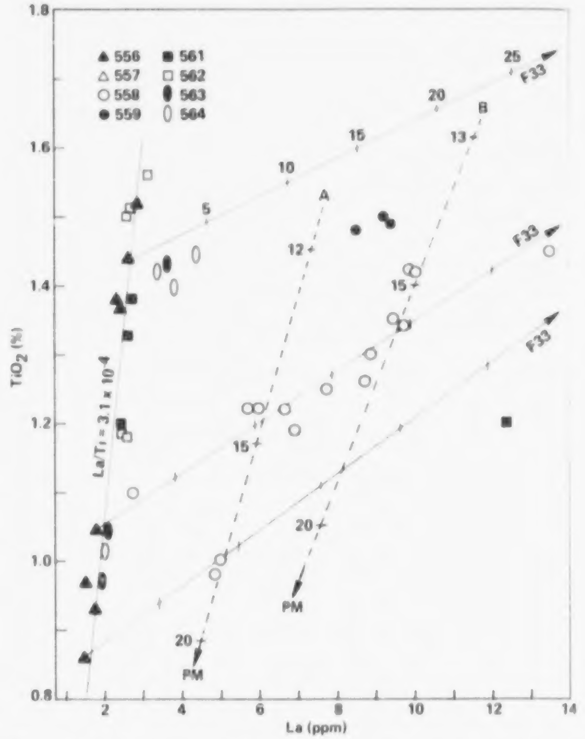

Figure 9. TiO_2 versus La for Leg 82 basalts. Note the constant La/Ti ratio of the N-MORBs. The full lines marked F33 are magma mixing curves, the dashed lines marked A and B are partial melting paths; see Figure 8 caption for further explanations.

2. Magma mixing does not appear to be a viable model for the moderately enriched FAMOUS and Hole 332B MORBs (Fig. 7), and there is no obvious reason to invoke special circumstances for either the Leg 82 or the FAMOUS and Hole 332B basalts.

3. The LREE-depleted basalt from Hole 558 (Sample 558-28-3, 118–120 cm) might provide an importan clue. Its $^{143}Nd/^{144}Nd$ ratio is within the range of E-MORBs (Jenner et al., this volume), although source o magma mixing calculations point to a much smaller admixture of enriched component. This sample apparentl derives from an enriched source that lost a small fraction of melt before the main melting event. In contrast it is not so easy to imagine a simple process that can deplete a melt in incompatible trace elements.

We are still left with the question of whether the sourc mixing process is directly related to the Azores Mantl Plume magmatism. The Azores magmas indeed appea to be suitable enriched end-members, but any alkalin or nephelinitic melt generated in the subocean mantle i probably quite similar to the Azores magmas with respect to trace element geochemistry. It seems reasonabl to attribute the occurrence of E-MORBs in Hole 557 t Azores plume input, but the correlation of light REI enrichment with distance from the Azores Triple Junc tion is tenuous at best for the other Leg 82 holes. Thi observation favors alternative models, such as episodic source mixing with "fracture zone-derived" enriched magmas (Flower, 1981).

Finally, there is the problem of recent mixing versus long-lived mantle heterogeneities (O'Nions et al., 1978; Wood et al., 1979; Davies, 1981). Although trace element concentrations do not provide information on the timing of the enrichment event, the data for the Leg 82 basalts may indirectly have a bearing on this question. Indeed, N-MORBs with amazingly constant La/Sm (Fig. 6), La/Yb (Fig. 8), and La/Ti (Fig. 9) ratios have been derived from a large, homogeneous mantle source over a distance of 1200 km along the Mid-Atlantic Ridge during a period of approximately 20 Ma (37-15 Ma). These data seem to be at variance with the recent emphasis on small-scale mantle heterogeneity in the area under study.

CONCLUSIONS

The almost twofold variation of absolute concentrations of incompatible trace elements in the Leg 82 N-MORBs is primarily due to different degrees (8 to 18%) of batch partial melting. The Leg 82 N-MORBs have MgO and Ni contents that are too low to qualify the MORBs as primary mantle melts; they most likely evolved from a sequence of more primitive magmas by 5 to 15% olivine fractionation before eruption. The remarkably constant La/Yb, La/Sm, and La/Ti ratios of the Leg 82 N-MORBs apparently require a large, homogeneous mantle source underneath a segment (1200 km long) of the Mid-Atlantic Ridge.

The variation of highly to moderately incompatible elements (REE, HF, Ta, Ti) in the Leg 82 E-MORBs is consistent with magma or source mixing between N-MORB magmas or sources and an enriched component similar to Azores alkali basalts. However, the combined trace element and Nd isotopic data (Jenner et al., this volume) strongly favor source mixing (≥ 0.5 to 5% enriched component). The association of depleted MORBs with transitional and enriched MORBs in Holes 561, 563, and 564 underscores the episodic and localized nature of mixing processes.

The absence of a regular spatial distribution of Leg 82 E-MORBs as a function of distance from the Azores Triple Junction casts serious doubts on the validity of Azores Mantle Plume mixing models advocated by Schilling (1975) and White and Schilling (1978). The enriched alkaline magmas involved in the source mixing are probably not directly related to the Azores magmatism.

ACKNOWLEDGMENTS

This paper has greatly benefited from constructive reviews by J. W. Delano and A. J. Irving. We thank G. Van Den Eynde for technical assistance with the analyses. This work was supported in part by the Belgian Inter-University Institute for Nuclear Sciences (I.I.K.W.) and the Deutsche Forschungsgemeinschaft (Grants Schm 250-28, 29).

REFERENCES

Bender, J. F., Hodges, F. N., and Bence, A. E., 1978. Petrogenesis of basalts from the project FAMOUS area: experimental study from 0 to 15 kbars. *Earth Planet. Sci. Lett.*, 41:277-302.

Bougault, H., 1980. Contribution des éléments de transition à la genèse des basaltes océaniques [Ph.D. dissert.]. Université de Paris VII, Paris.

Bougault, H., Cambon, P., Corré, O., Joron, J. L., and Treuil, M., 1979. Evidence for variability of magmatic processes and upper mantle heterogeneity in the axial region of the Mid-Atlantic Ridge near 22° and 36°N. *Tectonophysics*, 55:11-34.

Clague, D. A., Frey, F. A., Thompson, G., and Rindge, S., 1981. Minor and trace element geochemistry of volcanic rocks dredged from the Galapagos Spreading Centre: role of crystal fractionation and mantle heterogeneity. *J. Geophys. Res.*, 86:9469-9482.

Davies, G. F., 1981. The earth's neodymium budget and structure and evolution of the mantle. *Nature*, 290:208-213.

Flower, M. F. J., 1981. Binary mixing in ocean-ridge spreading segments. *Nature*, 292:45-47.

Frey, F. A., Dickey, J. S., Thompson, G., Bryan, W. B., and Davies, H. L., 1980. Evidence for heterogeneous primary MORB and mantle sources, NW Indian Ocean. *Contrib. Mineral. Petrol.*, 74: 387-402.

Fujii, T., and Bougault, H., 1983. Melting relations of a magnesian abyssal tholeiite and the origin of MORBs. *Earth Planet. Sci. Lett.*, 62:283-295.

Hertogen, J., and Gijbels, R., 1971. Instrumental neutron activation analysis of rocks with a Low-Energy Photon Detector. *Anal. Chim. Acta*, 56:61-82.

Langmuir, C. H., Bender, J. F., Bence, A. E., Hanson, G. N., and Taylor, S. R., 1977. Petrogenesis of basalts from the FAMOUS area: Mid-Atlantic Ridge. *Earth Planet. Sci. Lett.*, 36:133-156.

Langmuir, C. H., Vocke, R. D., Hanson, G. N., and Hart, S. R., 1978. A general mixing equation with applications to Icelandic basalts. *Earth Planet. Sci. Lett.*, 37:380-392.

O'Hara, M. J., 1977. Geochemical evolution during fractional crystallisation of a periodically refilled magma chamber. *Nature*, 266: 503-507.

O'Nions, R. K., Evensen, N. M., Hamilton, P. J., and Carter, S. R., 1978. Melting of the mantle past and present: isotope and trace element evidence. *Phil. Trans. R. Soc. London, Ser. A*, 258:547-559.

Rhodes, J. M., and Dungan, M. A., 1979. The evolution of ocean floor basalts. *In* Talwani, M., Harrison, C. G., and Hayes, D. E. (Eds.), *Deep drilling results in the Atlantic Ocean: ocean crust:* Washington (Am. Geophys. Union), Maurice Ewing Series, 2: 262-272.

Schilling, J.-G., 1975. Azores mantle blob: rare earth evidence. *Earth Planet. Sci. Lett.*, 25:103-115.

Stolper, E., and Walker, D., 1980. Melt density and the average composition of basalt. *Contrib. Mineral. Petrol.*, 74:7-12.

White, W. M., and Schilling, J.-G., 1978. The nature and origin of geochemical variation in Mid-Atlantic Ridge basalts from the Central North Atlantic. *Geochim. Cosmochim. Acta*, 42:1501-1516.

White, W. M., Tapia, M. D. M., and Schilling, J.-G., 1979. The petrology and geochemistry of the Azores Islands. *Contrib. Mineral. Petrol.*, 69:201-213.

Wood, D. A., 1979. A variably veined suboceanic upper mantle—genetic significance for mid-ocean ridge basalts from geochemical evidence. *Geology*, 7:499-503.

Wood, D. A., Tarney, J., Varet, J., Saunders, A. D., Bougault, H., Joron, J. L., Treuil, M., and Cann, J. R., 1979. Geochemistry of basalts drilled in the North Atlantic by IPOD Leg 49: implications for mantle heterogeneity. *Earth Planet. Sci. Lett.*, 42:77-97.

Date of Initial Receipt: 22 June 1983
Date of Acceptance: 31 January 1984

23. LOCAL VERSUS REGIONAL MANTLE HETEROGENEITIES: EVIDENCE FROM HYGROMAGMAPHILE ELEMENTS[1]

H. Bougault, Institut Français pour la Recherche et l'Exploitation de la Mer, Centre de Brest
J. L. Joron, Centre National de la Recherche Scientifique, Laboratoire Pierre Sue
M. Treuil, Laboratoire Géochimie, Université Pierre et Marie Curie
and
R. Maury, Université de Bretagne Occidentale[2]

ABSTRACT

The main objective of Leg 82 of the *Glomar Challenger* was to document mantle heterogeneity in the vicinity of, and away from, a so-called hot spot: the Azores Triple Junction. One of the geochemical tools that permits, at least in part, the recognition of mantle heterogeneities uses hygromagmaphile elements, those elements that have an affinity for the liquid. This tool is presented in terms of an extended Coryell-Masuda plot, which incorporates within the rare earth elements the hygromagmaphile transition elements Th, Ta, Zr, Hf, Ti, Y, and V. The extended Coryell-Masuda plot is used to summarize our knowledge of mantle heterogeneity along the ridge axis at zero-age. It is also used by choosing those hygromagmaphile elements that can be analyzed on board by X-ray fluorescence spectrometry to give preliminary information on the enriched or depleted character of recovered samples. Shore-based results, which include analyses of most of the hygromagmaphile elements measured either by X-ray spectrometry or neutron activation analysis, confirm the shipboard data.

From the point of view of comparative geochemistry, the variety of basalts recovered during Leg 82 provides a good opportunity to test and verify the classification of the hygromagmaphile elements. Analyses from Leg 82 provide new data about the relationship between extended rare earth patterns (enriched or depleted) that can be estimated either by La/Sm ratio or Nb/Zr (or Ta/Hf) ratios: samples from Hole 556 are depleted (low Nb/Zr ratio) but have a high ^{206}Pb/^{204}Pb (19.5) ratio; in Hole 558 a moderately enriched basalt unit with a La/Sm (= Nb/Zr) ratio (chondrite normalized) of 2 has a high ^{206}Pb/^{204}Pb (20) ratio. One of the most interesting results of Leg 82 lies in the crossing patterns of extended Coryell-Masuda plots for basalts from the same hole. This result enhances the notion of local mantle heterogeneity versus regional mantle heterogeneity and is confirmed by isotope data; it also favors a model of short-lived, discrete magma chambers. The data tend to confirm the Hayes Fracture Zone as a southern limit for the influence of Azores-type mantle. Nevertheless, north of the Hayes Fracture Zone, the influence of a plumelike mantle source is not simple and probably requires an explanation more complex than a contribution from a single fixed hot spot.

INTRODUCTION

The basalts of the ocean floor formed at spreading centers (mid-ocean ridge basalts: MORB) were considered to have a tholeiitic composition very similar in all of the oceans. This composition is markedly different from the composition of basalts from ocean islands (Engel et al., 1965). The most important differences between the two types are represented by radiogenic Sr, Pb, and Nd ratios (Gast et al., 1964; Tatsumoto et al., 1965; Hart et al., 1973; Sun, 1973; Richard et al., 1976; O'Nions et al., 1977), and their relative light to heavy rare earth element (REE) fractionation (Frey and Haskin, 1964; Gast, 1968; Sun et al., 1979). Ocean island basalts (both alkali and tholeiitic) are characterized by higher ^{87}Sr/^{86}Sr, ^{206}Pb/^{204}Pb, ^{207}Pb/^{204}Pb, ^{208}Pb/^{204}Pb, lower ^{143}Nd/^{144}Nd, and higher La/Sm ratios than MORB. Typical mid-ocean ridge basalts are also called depleted MORB because they are depleted in the most hygromagmaphile elements (i.e., those elements that have low bulk crystal-liquid partition coefficients).

Theoretically, different ratios of hygromagmaphile elements such as La/Sm can be explained as characteristic of different mantle sources *and* by fractionation during magmatic processes, mainly partial melting (Langmuir et al., 1977; Bougault, Cambon, et al., 1979). Theoretically, different isotopic ratios of Sr, Pb, and Nd can only be interpreted in terms of different mantle sources. One type of mantle source is associated with the notion of a mantle plume or hot spot (Wilson, 1963; Morgan, 1971; Schilling, 1973) and is related to intraplate volcanism (e.g., Hawaiian Seamount Chain). Another type of mantle source is associated with the generation of MORBs and the notion of a low velocity layer in the oceanic mantle (Schilling, 1971). However, limiting the number of types of oceanic basalts to two is an oversimplification. The acronym MORB was corrected by using typical MORB or depleted MORB. The usage of the expression "normal ridge segment" started at the same time. Some parts of ridges at zero-age have geochemical characteristics (isotopic ratios, rare earth concentrations) that tend to resemble intraplate volcanism; these locations are cha-

---

[1] Bougault, H., Cande, S. C., et al., *Init. Repts. DSDP*, 82: Washington (U.S. Govt. Printing Office).

[2] Addresses: (Bougault) Institut de Français pour la Recherche et l'Exploitation de la Mer (formerly Centre National pour l'Exploitation des Océans), Centre de Brest, B. P. 337, 29273 Brest Cedex, France; (Joron) Centre National de la Recherche Scientifique, Laboratoire Pierre Sue, Centre d'Etude Nucléaire Saclay, B. P. No. 2, 91191 Gif-Sur-Yvette, France; (Treuil) Laboratoire Géochimie, Université Pierre et Marie Curie, 4 place Jussieu, 75230 Paris Cedex 05, France; (Maury) Université de Bretagne Occidentale, 6 avenue Le Gorgeu, 29283 Brest Cedex, France.

racterized by "anomalous topographic highs." Three areas of this type have been intensively studied in the North Atlantic: Iceland, 45°N, and the Azores Triple Junction. However, there are not simply "normal" segments and "abnormal" ridge segments at zero-age, but a gradation along the ridge axis even if it is not a smooth continuous variation (Schilling, 1973; Hart et al., 1973; Sun et al., 1975; Schilling, 1975; White and Schilling, 1978; Tarney et al., 1980; Bougault and Treuil, 1980). This feature has been interpreted as a mixing of two mantle sources. One of them has its origin in the deep mantle and forms a mantle plume or blob that is responsible for the formation of thicker ocean crust with a morphology different from that of normal ridge segments; this mantle plume has more primordial characteristics than the normal ridge. The source that feeds normal ridge segments at the accreting plate boundaries has been depleted in hygromagmaphile elements a long time ago; this depletion, as a consequence of the fractionation of Rb-Sr, U and Th-Pb, Sm-Nd, leads to radiogenic isotope ratios (Sr, Pb, Nd) that are different from those of mantle plume material.

The variation of concentrations of light and heavy REEs (La/Sm ratio) and isotopic ratios (e.g., Sr) along the axis of the Mid-Atlantic Ridge, specifically from the Azores hot spot to the Atlantis Fracture Zone, have been well documented by Schilling (1975) and White and others (1976). Even if the variations observed along the axis are not smoothly continuous, a gradation does exist from enriched basalts at the Azores Triple Junction to depleted basalts south of 33°N. These variations were confirmed in 1979 by the MAPCO cruise (Bougault and Treuil, 1980). For zero-age basalts, the limit of the influence of the Azores mantle plume was found to be at the latitude of the Hayes Fracture Zone. But, as already pointed out by Schilling (1975), these results do not give any information about the time of the first appearance of a blob beneath the Azores. In other words, to get information about the contribution of the mantle plume versus time, we needed to drill away from the axis of the ridge. We realized that we might have to consider several possible variations versus time (such as the presence and the influence of other hot spots at a given time or discontinuous functioning of mantle blobs). First, however, we asked whether or not there were gradations versus time (away from the axis of the ridge) and along isochrons (away from a supposed fixed hot spot), and whether or not these gradations were similar to what is observed today for zero-age basalts.

In this paper, we present information about the geochemical tool represented by hygromagmaphile elements to trace mantle heterogeneities. Hygromagmaphile elements other than REEs that can be integrated in an extended Coryell-Masuda plot permitted us to obtain useful information on board for conducting the cruise. In order to complete the data set and facilitate comparisons, we include data for zero-age samples. Leg 82 data are presented in terms of comparative geochemistry and petrology; finally, we discuss the main discoveries and conclusions of Leg 82 of the *Glomar Challenger.*

EXTENDED CORYELL-MASUDA PLOT AND CLASSIFICATION OF HYGROMAGMAPHILE ELEMENTS

The term "hygromagmaphile" was initially proposed by Treuil (1973) to introduce the notion of affinity of some elements for the liquid phase of a magma. Treuil (1973) proposed that the behavior of such elements—often referred to as large ion lithophile elements (LIL)—be considered the result of both their difficulty entering a crystal structure and their ability to form complexes in the liquid phase of the magma.

Many of these elements, especially the REEs, have been the subject of several investigations: elements of the first transition series (Sc, Ti, V); the second transition series (Y, Zr, Nb); the third transition series (Lanthanides, Hf, Ta); and also heavy elements like Th and U. The elements of the two first columns of the classification of the elements have also been the matter of discussion and interpretation in terms of LIL elements. Nevertheless, very few studies (if any) were concerned with the study of all of these elements on the *same* samples. The "Groupe des Sciences de la Terre du Laboratoire P. Sue du Centre National de la Recherche Scientifique" for neutron activation analysis (NAA), and the "Groupe de Géochimie du Centre Océanologique de Bretagne" for X-ray fluorescence analysis (XRF) have, since 1973–1974, obtained a large set of data on the same basalt samples. Before using certain elements or groups of elements to deduce information about magmatic processes or mantle heterogeneity, we will use this data set to establish a classification of these elements with respect to their affinity for the liquid phase. In a first step, we will use the continuous variation of the properties of rare earth elements; considering the well-known Coryell-Masuda plot (Masuda, 1962; Coryell et al., 1963), we will see to what extent hygromagmaphile elements can be plotted in such a diagram, and to what extent it is possible to establish a classification of hygromagmaphile elements versus their affinity for the liquid. In a second step, this classification, which has been obtained through comparative geochemistry, will be compared to a classification deduced from a more theoretical approach, involving both crystal structural and complexing considerations.

The hygromagmaphile character of the elements Ti, V, Y, Zr, Nb, Lanthanides, Hf, Ta, and Th is well established. Yttrium, whose physicochemical properties are very close to the properties of heavy REEs, has already been included in a Coryell-Masuda plot (Frey et al., 1968). A triangular diagram has been proposed by Pearce and Cann (1971) for Zr, Ti, and Y. The relative behavior of Zr and Nb was studied by Erlank and Kable (1976). A correlation between Ti and Dy was shown by Bougault (1977) for ocean basalts and ophiolite suites. Hf, Ta, and Th were studied by Treuil (1973) and Treuil and others (1979). The absence of fractionation between elements of the second and third transition series that belong to the same column of the classification of the elements (namely the pairs Y-heavy REEs, Zr-Hf, and Nb-Ta) was shown by Bougault, Joron, and others (1979).

All these transition elements have a common property: they tend to have ions whose external electronic structure corresponds to the external electronic structure of rare gases. Also, all these elements are nonvolatile in respect to accretion processes and they are all lithophile. All these properties are common to the REEs, and it should be possible to normalize their concentrations in basalts to chondrite concentrations and to incorporate them in an extended Coryell-Masuda plot.

The observed abundances of REEs and other hygromagmaphile elements in chondrites vary by more than a factor of 20. The normalization values used for REEs are generally average concentrations obtained from different chondrites (Frey et al., 1968). Other authors prefer normalization values obtained from the concentrations of a reference chondrite, but accounting for the ratio "bulk rare earth content of the composite chondrite/bulk rare earth content of the reference chondrite" (Sun and Hanson, 1975). None of these methods can be used at the present time for Th, Ta, Nb, Hf, Zr, Ti, and V. The average concentrations of these elements from the *same* chondrites as for REEs are not available; in addition, a large dispersion of values exists between different authors for the same element in the same chondrite. Because of the difficulties in obtaining normalization values from chondrites, we propose to compute normalization values as follows.

We make the hypothesis that non-rare-earth hygromagmaphile elements behave similarly to the REEs. First, we choose a basalt sample A whose Coryell-Masuda plot is flat (i.e., a sample whose normalized concentrations of REEs all have the same value of R_A). If this hypothesis is valid, other hygromagmaphile elements will have the same normalized concentrations R_A. For an element i, it is possible to compute its normalization value Ch_i from R_A and the concentration of element i in Sample A, C_{Ai}:

$$Ch_i = \frac{C_{Ai}}{R_A}.$$

Second, we verify that these normalization values Ch_i produce constant normalized concentrations R_B, R_C, ... for all hygromagmaphile elements of samples B, C, ..., whose rare earth Coryell-Masuda plots are also flat, but have different R_B, R_C ... To be significant, this verification requires that samples B, C, ... are chosen from different locations of the Earth. It is somewhat difficult to find samples whose rare earth patterns are absolutely flat. Figures 1 and 2 show some examples obtained during Leg 37 (Mid-Atlantic Ridge, 36° N) and Leg 49 (Reykjanes Ridge). The normalization values that have been found and used to construct Figures 1 and 2 are shown in the following list. Except for V, all values lie in the range of published concentrations for chondrites and often seem to represent correct averages.

This list contains the normalization values of hygromagmaphile elements. Underlined elements correspond to elements whose normalization values have been calculated by the proposed method.

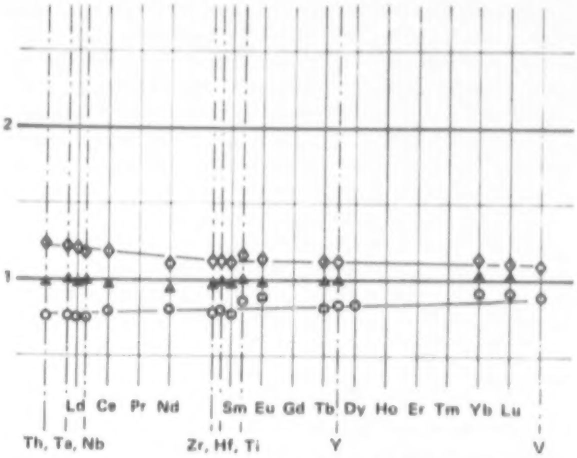

Figure 1. Flat or almost flat "extended" Coryell-Masuda plots: samples from Hole 332B (36°N): ◇ 332B-3-4; △ 332B-25-3; ○ 332B-36-3 and 332B-37-1. For data, see Bougault, 1980. On the *y* axis is the logarithm of the normalized concentrations.

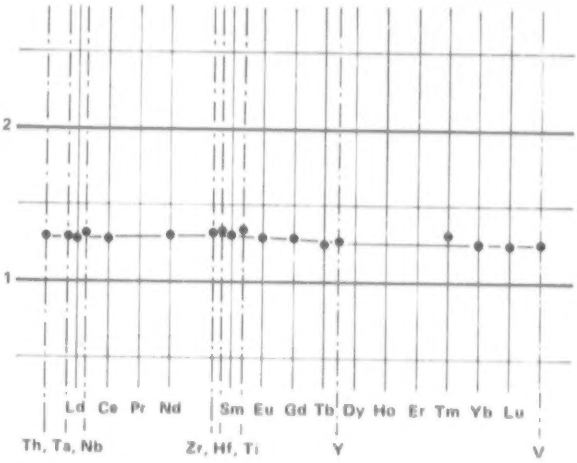

Figure 2. Flat "extended" Coryell-Masuda plot: samples from Hole 409 (Reykjanes Ridge, 63°N), 409-13-3 to 409-31-1. For data, see Bougault, 1980 and Woods, Varet, et al., 1979. On the *y* axis is the logarithm of the normalized concentrations.

Th	0.028	Eu	0.07
La	0.32	Gd	0.25
Ta	0.031	Tb	0.047
Nb	0.53	Y	2.16
Ce	0.85	Dy	0.32
Pr	0.112	Ho	0.07
Nd	0.60	Er	0.21
Zr	5.13	Tm	0.03
Hf	0.128	Yb	0.20
Sm	0.19	Lu	0.033
Ti	460	V	22

If the non-rare-earth hygromagmaphile elements plot in an extended Coryell-Masuda diagram, it is necessary to find the location of these elements within the rare earth atomic numbers (x axis). The normalized concentrations of non–rare-earth elements must then plot on the REE normalized pattern. In other words, the Coryell-Masuda plot extended to non–rare-earth elements allows us to obtain a classification of hygromagmaphile elements. Because of the continuous variation of their properties (versus atomic number), the REEs are used as a calibration scale for the hygromagmaphile character of the elements. This classification is obtained in two steps. We choose a sample whose REE pattern is very different from flat (enriched, for instance). The position of the elements within the REEs on the x axis is determined from their normalized concentrations (using normalization values obtained above) in the sample (Fig. 3). In a second step, with these positions of the elements and normalization values, we verify that continuous extended REE patterns are obtained for samples having different shapes of REE patterns. Typical examples are given in Figure 4. The discrepancy observed for Nb and Ta in the depleted samples will be discussed later. The classification of hygromagmaphile elements can be read on these diagrams (x axis) from Th to V (representing decreasing affinity for the liquid).

The basic property of hygromagmaphile elements—their affinity for the liquid phase of a magma—is the consequence of two effects: difficulty entering crystal structures (because of large ionic size), and complexing in the liquid (for ions that have high charge and small ionic radii) (Ringwood, 1955; Treuil, 1973). For a first approximation, the difficulty in entering a crystal structure can be estimated to be proportional to the difference between the ionic radius of the hygromagmaphile element and the radius of the major element that it is supposed to replace it in the crystal. The facility to form a complex in the liquid can be estimated to be proportional to the ionic potential of the element (charge/ionic radius).

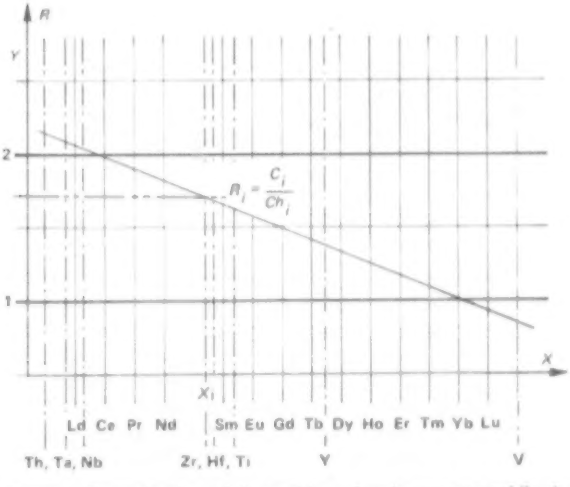

Figure 3. Determination of the position of an hygromagmaphile element (*x* axis) in respect to rare earth elements, from its normalized concentration in an "enriched" sample. On the *y* axis is the logarithm of the normalized concentrations (R).

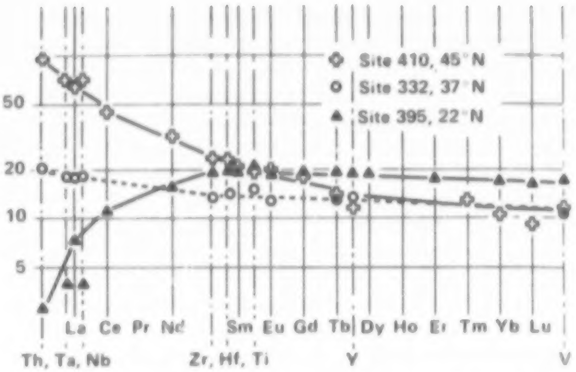

Figure 4. Typical examples showing "extended" Coryell-Masuda plot for enriched, flat, and depleted patterns.

We define thus the hygromagmaphile degree Ø by the following relationship:

$$Ø = a\,(\Delta R_i^2 + 1)\; n/R_i,$$

where ΔR_i corresponds to the difference of radii between the hygromagmaphile element and the substituted major element. The square of this difference is used to keep Ø positive and to indicate that the difficulty of entering into a crystal structure increases probably much more quickly than linearly. n/R_i is the ionic potential; n is the charge and R_i the ionic radius of the hygromagmaphile element.

In the case of identity of ionic radii between hygromagmaphile elements and major elements ($\Delta R_i = 0$), the relationship must indicate possible variations with ionic potentials. This observation requires an equation such as that above. The parameter a is calculated from two elements that have, for example, the same behavior, but different n and R_i. The results (Table 1) show that the hygromagmaphile degree Ø allows classification of the elements in almost the same order as obtained through comparative geochemistry. This table shows that the oxidation state for V is probably not +5, because this assumption would make it the most hygromagmaphile element.

This classification of hygromagmaphile elements and the extended Coryell-Masuda plot will not be valid for all types of rocks. For example, because of possible differences in oxidation states and valencies of some elements, some fractionation would be expected during magmatic processes that would induce anomalies in the diagrams, similar to Eu anomalies (El Azzouzi et al., 1982). For tholeiites and Alkali basalts, this classification and the related extended Coryell-Masuda plot avoids misinterpretations caused by ignorance of comparative properties of the elements. In this respect, for instance, the distinction between Ti-rich and Ti-poor basalts should be disregarded; as is generally the case, a classification of rock types cannot be made on a single absolute value of one element. Ti is one of the hygromagmaphile elements. Because of the possibility of crossing patterns of REEs and the position of Ti (close to Sm), one can find

Table 1. Ionic radii (R), charges (n), and calculated parameter ϕ (hygromagmaphile degree) for hygromagmaphile transition elements whose external shells of ions are the same as rare gas.

Element	R (Å)	n	ϕ
Th	0.99	4	8.34
La	1.06	3	7.35
Ta	0.68	5	7.25
Nb	0.69	5	7.35
Ce	1.03	3	6.90
Pr			
Nd	0.99	3	6.33
Zr	0.79	4	5.74
HF	0.79	4	5.74
Sm	0.96	3	5.89
Ti	0.68	4	5.88
Eu	0.95	3	5.71
Gd	0.94	3	5.56
Tb	0.92	3	5.37
Y	0.92	3	5.34
Dy	0.90	3	5.16
Ho		3	
Er	0.88	3	4.93
Tm		3	
Yb	0.86	3	4.72
Lu	0.85	3	4.64
V	0.59	5	9.23

Note: Pr row is blank because it is not a natural element. Other blanks indicate that analytical data were not available.

Ti-rich basalts depleted in light REEs and Ti-poor basalts rich in light REEs. No more importance should be credited to absolute concentrations of Ti than to absolute concentrations of Sm. This classification and the extended Coryell-Masuda plots will help us to find the anomalies of some elements (i.e., Ti and V when opaques start to crystallize; El Azzouzi et al., 1982) and to choose elements other than REEs for the identification of enriched and depleted material. This approach was used during the MAPCO cruise of *Jean Charcot* in 1979 (Bougault and Treuil, 1980) and during Leg 82 of the *Glomar Challenger* for analyses of Nb, Zr, Ti, Y, and V on board by X-ray fluorescence spectrometry. Details of the analytical procedures appear in another article (Etoubleau et al., this volume).

HYGROMAGMAPHILE ELEMENTS: ZERO-AGE VARIATION BETWEEN AZORES TRIPLE JUNCTION AND 10°N

On the basis of theoretical considerations and models of magmatic processes (such as partial melting and fractional crystallization), we concluded that the basalts produced in the FAMOUS area (36°N) (including samples recovered at Site 332 during Leg 37 [Aumento, Melson, et al., 1977] and the basalts produced at 22°N [Sites 395 and 396 of Legs 45 and 46 and zero-age samples]) were from two different mantle sources (Bougault, Cambon, et al., 1978; Bougault, Treuil, et al., 1978; Bougault, Joron, et al., 1979). The La/Ta ratio (2 very hygromagmaphile elements) defines distinct values in these two areas: La/Ta = 9 at 36°N, La/Ta = 18 at 22°N. This interpretation was supported by isotopic data (Dupré and Allègre, 1980). These values of the La/Ta ratio were thought to be characteristic of two mantle sources because one or the other value is found in several other places. For example, the value 9 (or 1 for the chondrite-normalized ratio) was found for the Reykjanes Ridge (Sites 407–409, Wood, Tarney, et al., 1979; Wood, Varet, et al., 1979), at 45°N on the Mid-Atlantic Ridge, and on the Emperor Seamount Chain (Leg 55; Cambon et al., 1980); the value 18 (2 for the normalized ratio) was found at 25°N for 110-Ma-old crust (Megaleg 51–53; Joron et al., 1980) and on the East Pacific Rise (Sites 482, 483 of Leg 65 at 21°N; Cambon et al., 1983). This observation is illustrated in Figure 5. The value 1 for the normalized La/Ta ratio is observed for normalized concentrations of La and Ta varying between 10 to more than 60, whereas the value 2 for this ratio (or 0.5 for Ta/La as plotted in Fig. 5) occurs mainly at low normalized concentrations of these elements (generally lower than 10). The La/Ta ratio for some dolerites of Morocco (Bertrand et al., 1982) and basalts from the Walvis Ridge (Bougault, 1980), which have high normalized concentrations, is also 2 (0.5 for Ta/La). This also supports the interpretation of La/Ta ratios as indicative of mantle source characteristics, because values do not depend on the absolute concentration of the elements. Samples from dredge CH98 DR08 (Bougault and Treuil, 1980), whose La/Ta ratio lies between the two values discussed above, could be interpreted as a result of a contribution from two mantle sources.

According to these observations and the data using the Coryell-Masuda diagrams defined in the previous paragraph, two types of pattern are observed for mid-ocean

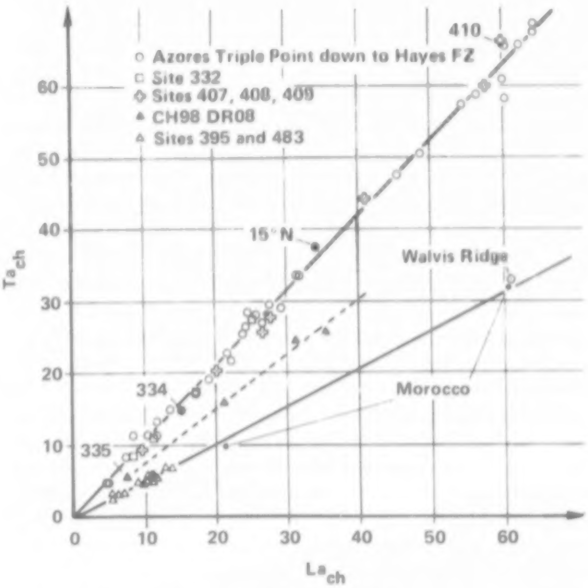

Figure 5. Normalized concentrations of tantalum versus normalized concentrations of lathanum. FZ = fracture zone. CH98 DR08 is a MAPCO station.

ridge basalts (Fig. 4): for flat to enriched patterns, Ta and Nb plot at the same ordinate position as La, but plot at a lower position than La (the factor two mentioned above for La/Ta ratio) for depleted samples. We thus come to the notion of enrichment and depletion in light rare earth elements (LREE); in addition, a Nb-Ta anomaly is evident with respect to La. Because Nb-Ta and La are not fractionated for large variations in concentrations (Fig. 4), the two different La/Ta values (and the correlative Ta-Nb anomaly) are thought to be representative of different mantle sources.

Schilling (1975) postulated his Azores mantle blob model from a large set of data obtained from samples dredged along the ridge axis between the Azores Triple Junction and 30°N. Based on La/Sm ratios, and confirmed by Sr isotope data (White et al., 1976; White and Schilling, 1978), the influence of the Azores mantle blob along the ridge axis at zero-age was shown to extend as far south as 33°N. Detailed study of the ridge axis at 36°N during the FAMOUS expedition and after Leg 37 at 36°N and Legs 45 and 46 at 22°N indicated that this area of the North Atlantic was a good region to study the influence of a mantle plume or blob both along strike and also versus time. In 1977, on the VEMA cruise of the *Jean Charcot*, we obtained dredge material in this area and designed a cruise specifically devoted to dredging zero-age basalts in 1979 (the MAPCO cruise by the same research vessel). The objectives of that cruise were (1) to improve the sampling density between the Azores Triple Junction and 30°N (Schilling, 1975) and (2) to complete sampling south of 30°N in order to see to what extent the depleted character was constant south of 33°N (Bougault and Treuil, 1980).

Using the XRF analytical facilities on board (Bougault and Cambon, 1973), Nb, Zr, Ti, and Y abundances were determined during the cruise to ascertain the enriched or depleted character of dredged materials (Bougault and Treuil, 1980). Onshore data obtained subsequent to the cruise confirmed the on-board results. The trace element data obtained both by XRF and NAA are given in (Appendix A at the end of this chapter). All Schilling's data are confirmed between the Azores Triple Junction and 30°N. As examples, Figure 6 shows enriched basalts from the Triple Junction and Figure 7 shows depleted material from south of 30°N. The ratios of hygromagmaphile element concentrations normalized to chondrites and including Schilling's data (Schilling, 1975) are shown in Appendix B (at the end of this chapter). La/Sm ratios are given for our data because Sm is not measured on a routine basis (Jaffrezic et al., 1977). Instead of the normalized La/Sm ratio, the normalized La/Ti ratio is presented for our data in Appendix B. From our study of the classification of hygromagmaphile elements, these two ratios should be about identical if no opaque minerals have been removed from the liquid). This condition is easily verified; in an extended Coryell-Masuda plot the normalized concentration of Ti must lie on the continuous REE pattern, including Zr and Hf (which plot close to Sm). In Appendix B we have also indicated the chondrite-normalized ratios of Ta/Hf (which is about identical to Nb/Zr) and of La/Ta. The logarithms of La/Sm,

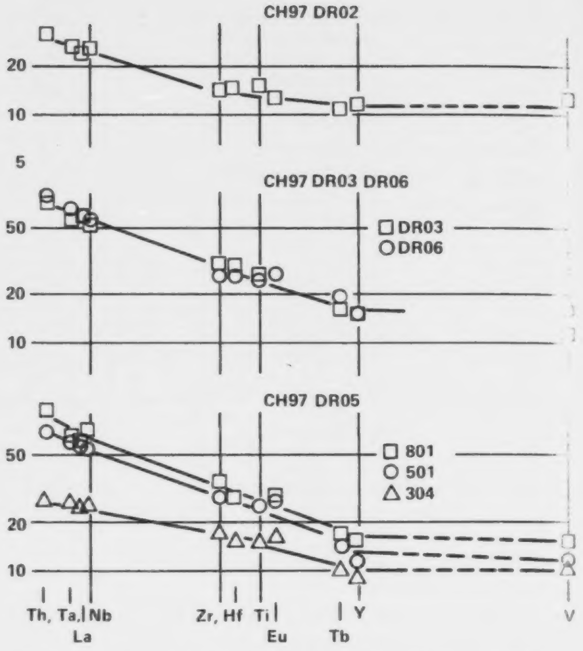

Figure 6. MAPCO cruise (Bougault and Treuil, 1980): extended Coryell-Masuda plot. Examples of typical enriched patterns in the Azores Triple Junction Area.

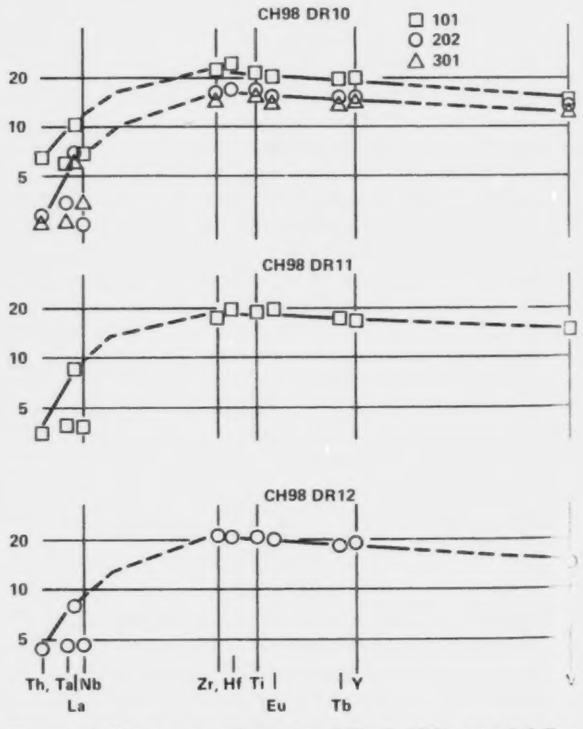

Figure 7. MAPCO cruise (Bougault and Treuil, 1980): extended Coryell-Masuda plot. Examples of typical depleted patterns south of 30°N, zero-age Mid-Atlantic Ridge. Note the Ta-Nb "anomaly" compared to Azores Triple Junction area in Figure 6. See text for further discussion.

READEX FICHE
best copy available

La/Ti, and Ta/Hf (Nb/Zr) are plotted in Figure 8. There are two reasons for plotting the logarithm instead of the ratio itself: the figure (1) preserves the importance of the ratios independently of their order of magnitude and (2) shows the differences observed for two elements in a Coryell-Masuda plot. Appendix B and Figure 8 clearly show the same results, confirming both a clear boundary at the level of Hayes Fracture Zone and the similarity of La/Sm (Schilling's data) and La/Ti (our data). Ta/Hf (≅ Nb/Zr) ratios also give the same information. Looking in more detail at Figure 8, one can make the following observations:

1. A range of variation of the ratios can be observed in a single dredge haul.
2. The differences in Ta/Hf (Nb/Zr) north and south of the Hayes Fracture Zone are larger than the differences in La/Sm or La/Ti ratios. This can easily be explained by the behavior of Ta (Nb) compared to La.
3. South of the Hayes Fracture Zone, the values of MAPCO CH98 DR08 resemble values to the north, confirming the results obtained on board (Bougault and Treuil, 1980).
4. The correlation between hygromagmaphile element ratios and the filtered bathymetry (Le Douaran and Francheteau, 1981) is obvious and confirms the observations of Schilling (1975).
5. Farther to the south, values characteristic of the Azores area are observed for a topographic high at zero-age at 14°N.

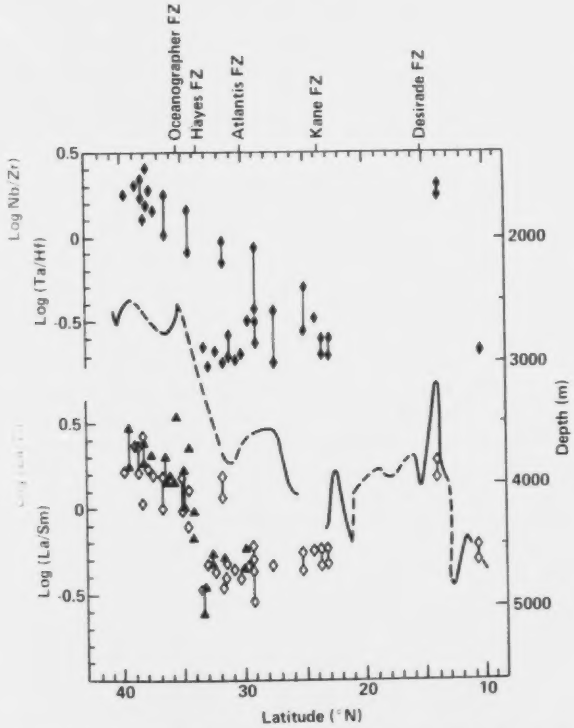

Figure 8. Logarithms of hygromagmaphile element ratios plotted versus latitude from the Azores Triple Junction to 10°N. The zero-age filtered depth indicated is from Le Douaran and Francheteau (1981). Filled diamonds correspond to the upper parameters (either log[Nb/Zr] or log[Ta/Hf]); open diamonds correspond to log(La/Ti) (author's data); filled triangles correspond to log(La/Sm) (data from Schilling, 1975). FZ = fracture zone.

The normalized La/Ta ratios (Appendix B) are close to 1 for the Azores Triple Junction to the Hayes Fracture Zone. South of the Hayes Fracture Zone, many of the values for this ratio are around 2, corresponding to the value typical of depleted MORB, but several values for this ratio are between 1 and 2. This is shown in Figure 9; samples recovered south of the Hayes Fracture Zone lie between the lines whose slopes are 1 and 0.5 (for Ta/La). Samples from CH98 DR08 also clearly lie between the two lines; the two types of samples in this dredge are confirmed by Pb isotope data (Dupré, 1982, pers. comm.). The variation in La/Ta ratio could then be tentatively interpreted in terms of mixing of two end members characterized by normalized La/Ta ratios of 1 and 2. An alternative interpretation could be continuous fractionation of La and Ta (or Nb), similar to La and Ce (Ta has a behavior closer to La than Ce). For clearer understanding of this "Nb-Ta" anomaly with respect to La, we need more data obtained from different geologic settings (i.e. Dupuy et al., 1982; Briqueu et al., in press).

LEG 82 COMPARATIVE GEOCHEMISTRY: ANALYTICAL RESULTS AND EXTENDED CORYELL-MASUDA PLOTS

To document mantle heterogeneity away from the present Azores Triple Junction versus time and along isochrons, a grid composed of 11 potential sites was prepared ahead of time. The sites were chosen to lie along flow lines (1) passing through the Azores Triple Junction, (2) passing through the FAMOUS area and the sites drilled

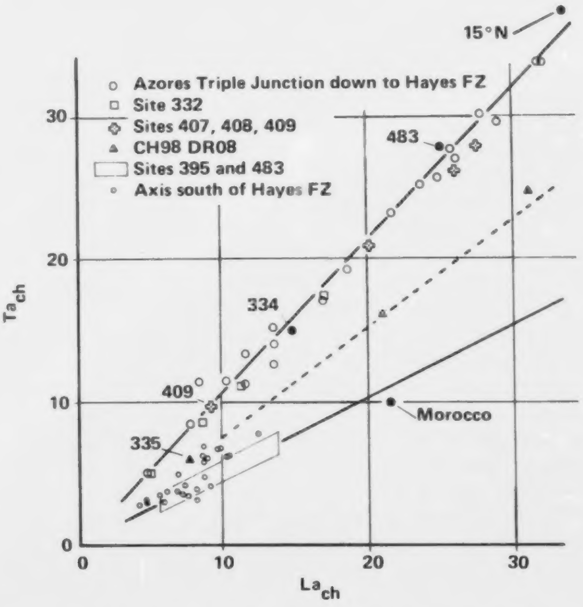

Figure 9. Normalized concentrations of tantalum versus normalized concentrations of lanthanum (as in Figure 5). Details for low values, specifically for dredged samples at zero age south of Hayes Fracture Zone. FZ = fracture zone.

on Leg 37 (Sites 332, 334, 335), and (3) straddling the Hayes Fracture Zone; they were located on Magnetic Anomalies 6, 13, and 24. The selection of these sites had to be made on board on the basis of the concentrations of hygromagmaphile elements measured by XRF analysis (Nb, Zr, Ti, Y, and V) (Etoubleau et al., this volume). We wanted to be somewhat consistent in the number of sites along isochrons and flow lines in order to obtain a representative regional picture. Actually, the selection was critical for the first two or three sites, because then the other sites had to be selected for consistency with both isochrons and flow lines. So, after we found depleted material at Site 556 (Azores flow line, Anomaly 5), we had to choose the other sites along other flow lines on the same isochrons (Anomalies 5 and 13) to produce a coherent distribution of sites. The final picture of the drilled sites during Leg 82 is presented in Figure 10. Before interpreting the results in terms of magmatic processes and mantle heterogeneity, we will discuss the classification of hygromagmaphile elements and the correlative extended Coryell-Masuda plot.

Trace element data obtained by XRF (either on board or on shore) and by NAA are presented in Appendix C as average concentrations for each chemical group. Data, sample by sample, are given in the Appendix at the end of this volume. As far as chemical data can be used as discriminant parameters to distinguish the different basaltic units encountered in each hole, onshore results have confirmed shipboard data. The classification into different chemical groups proposed in the site chapters is not modified. A standard deviation related to each average concentration (Appendix C) is given when the chemical group is defined by more than two samples. The significance of these standard deviations depends on the behavior of the element itself and on the analytical procedure. For example, alteration processes are not taken into consideration for the definition of a chemical group. As a consequence the standard deviation includes both the alteration effect and the analytical precision (e.g., Rb, Cs). Elements that are not affected by alteration have standard deviations for each chemical group that reflect the analytical precision. The standard deviations of Nb are less than one, except for 1.2 for Chemical Group IV of Hole 558; this result confirms the precision expected from the analytical work (Etoubleau et al., this volume).

Figure 11 is an example of an extended REE plot that was made on board during Leg 82. Figure 12 summarizes all results obtained during Leg 82, including onshore data. These figures will be used for the discussion of the results of Leg 82.

1. *Elements of first and second column of the classification of the elements*. These elements should not be included in an extended REE plot because of their sensitivity to alteration processes. The best example of the effect of low temperature alteration on alkali elements was obtained during Legs 51 and 52 at Sites 417 and 418 (Joron et al., 1979; Bougault, Joron, et al., 1979). The Rb concentration, which is lower than 1 ppm in unaltered samples, reaches 60 ppm in altered samples. Even in fresh samples or samples that appear fresh based on thin-section observations, the effect of contamination of alkali elements by low-temperature alteration is also apparent. An example was given during Leg 45 at Site 395 (Bougault, Joron, et al., 1979), where Rb concentration varies from values lower than 1 ppm up to 5 ppm and Cs

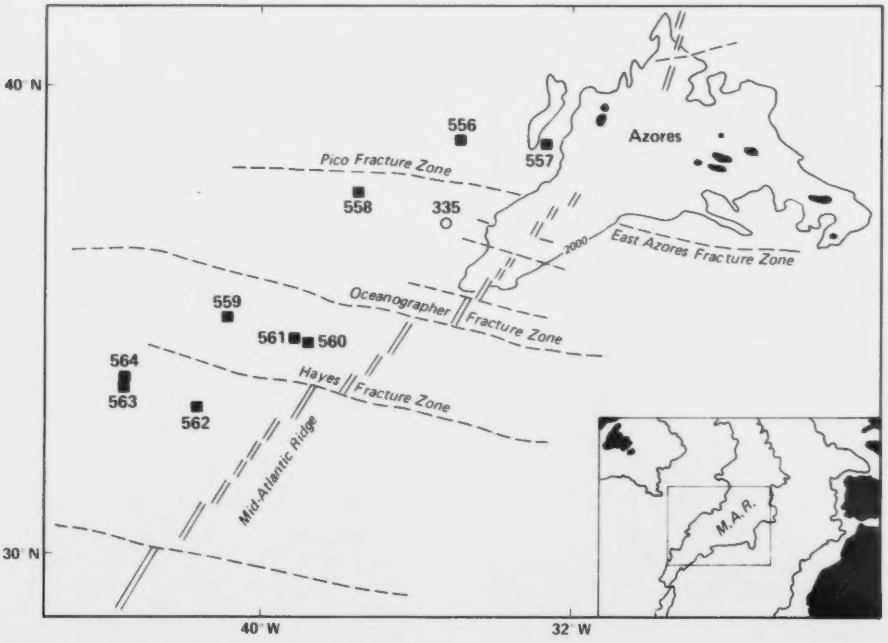

Figure 10. Locations of sites drilled during Leg 82.

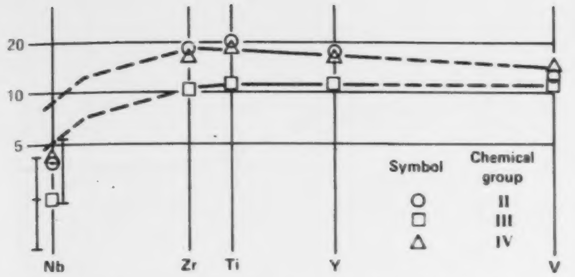

Figure 11. Extended Coryell-Masuda plot obtained on board for Hole 556. Between Zr and Nb, the line was tentatively drawn by assuming a factor two between normalized La and Nb concentrations. This assumption, deduced from previous studies, was shown to be correct (see Fig. 12).

from values lower than 0.02 ppm up to 0.2 ppm. Data obtained during Leg 82 provide additional information. Figure 13 shows the variations of K, Cs, and Sr versus Rb in hole 562. The correlation between alkali elements shows coherent behavior of these elements during alteration, as expected from their chemical properties; but it is almost impossible to deduce the values for unaltered basalts from these plots. Sr concentrations vary between 85 and 115 ppm: the absence of correlation with Rb tends to confirm the difference of behavior of Sr and alkali elements that was observed at Sites 417–418 (Legs 51–52; Bougault, Joron et al., 1979). The contamination in Sr is also shown by Sr isotopic data (Rideout and Schilling, this volume); when samples are suitably treated, the alteration effect can be removed.

2. *The pairs of elements that do not fractionate: Nb/Ta, Zr/Hf, Y/Tb—the relative positions of Zr, Hf, Ti.* Leg 82 provides an interesting regional set of data that covers almost the entire spectrum of enrichment and depletion in LREEs (Fig. 12). Some hygromagmaphile elements behave in such identical ways that they should be located at the same position (x axis) in an extended Coryell-Masuda plot. Because of the range of variation that is shown by Leg 82 results, we can test the nonfractionation of some elements. Figure 14 shows that the Nb/Ta ratio remains constant (Nb/Ta = 16) for a factor-30 variation in concentration. This is confirmation that Nb/Ta is constant in all basalts at the surface of the earth, and it probably represents the best value for the Earth's mantle and chondrites (Bougault, Joron, et al., 1979). Very little fractionation is observed for Zr/Hf and Y/Tb ratios (Fig. 15). For Zr/Hf, we note that the ratio Zr/Hf tends to increase somewhat from the most depleted samples to enriched samples: this observation confirms that Zr is probably a little more hygromagmaphile than Hf and has to be plotted on the left of Hf. The depleted samples (Site 556) tend to have Zr/Hf ratios (35) closer to the chondritic ratio (Shima, 1979) than flat to enriched samples, which have a Zr/Hf ratio close to 40. For Y and Tb, the Y/Tb ratio is constant for all samples except those of Hole 557. In Figure 16, the normalized concentrations of Hf are plotted versus normalized concentrations of Ti. This confirms the very similar behavior of Hf (and Zr) and Ti and their position close to each other in an extended Coryell-Masuda plot. The Hf/Ti ratio increases somewhat with concentration (except at Site 557), suggesting that Hf (and Zr) are more hygromagmaphile than Ti. One sample from Hole 561 lies off the normal trend; this low value of Ti compared to Hf (and Zr) is probably explained by some opaque phase removal (El Azzouzi et al., 1982).

3. *The La/Ta ratio*. The normalized concentrations of La are plotted versus normalized concentrations of Ta in Figure 17. The La/Ta normalized ratio is 1 for all chemical groups whose normalized concentrations are higher than 10. This is confirmation that Ta (and Nb) have to be plotted at the same position as, or very close to, the La position in an extended Coryell-Masuda plot. All chemical groups of Site 556 (depleted character) have the ratio that has been found in many other areas, $(La/Ta)_{ch} = 2$. On board the ship, the extended Coryell-Masuda plots were drawn when only Nb, Zr, Ti, Y, and V analyses were available. It was assumed at Site 556 that the normalized La/Nb (equivalent to La/Ta) ratio is equal to 2 to make the curve of the diagram pass through the predicted La position (Fig. 11). Onshore results show that this assumption was true (Fig. 12).

As is the case for many samples from south of the Hayes Fracture Zone (zero age), the other groups plot between the lines whose slopes are 1 and 2 (Fig. 17). For Sites 558 and 561 where both depleted and enriched material were found, the normalized La/Ta ratio is 1 for enriched material and lies between 1 and 2 for depleted material. We do not know at the moment if such a variation of the La/Ta ratio can be interpreted as continuous fractionation of two elements whose behavior is very similar but not identical, or if the intermediate ratios can be considered the result of mixing of two end-members characterized by normalized La/Ta ratio of 1 and 2. Hole 564 provides interesting data. The range of variation of La and Ta are indicated in Figure 17. Only one chemical group was defined at that site, but whereas elements like Ni or Cr (which are very sensitive to crystallization processes) do not show any significant variation, a regular increase of Zr and Nb abundances downhole was noted on board (see site chapter, Site 564, this volume). Downhole, Zr and Hf increase by about 10%. La increases by about 30%, Nb and Ta by 50%, and Th by 70%. These variations define a range of extended Coryell-Masuda plots for which the largest variation corresponds to the most hygromagmaphile element (Th; Fig. 12). The relative variations of La and Ta (or Nb) are not the same, so the normalized La/Ta ratio varies from about 1.1 to 1.6. These data cannot be explained by fractional crystallization; it is also difficult to see how, downhole, the different basalt samples could be derived by different degrees of partial melting of the same source. One possible explanation would be the mixing in different proportions of two liquids derived from two mantle sources. This interpretation could apply for samples other than those of Hole 564, whose normalized La/Ta ratios lie between 1 and 2.

The hypothesis that mixing of two mantle sources relates to observed variations of La/Ta is not immediately apparent from Figure 18, in which the logarithm of ra-

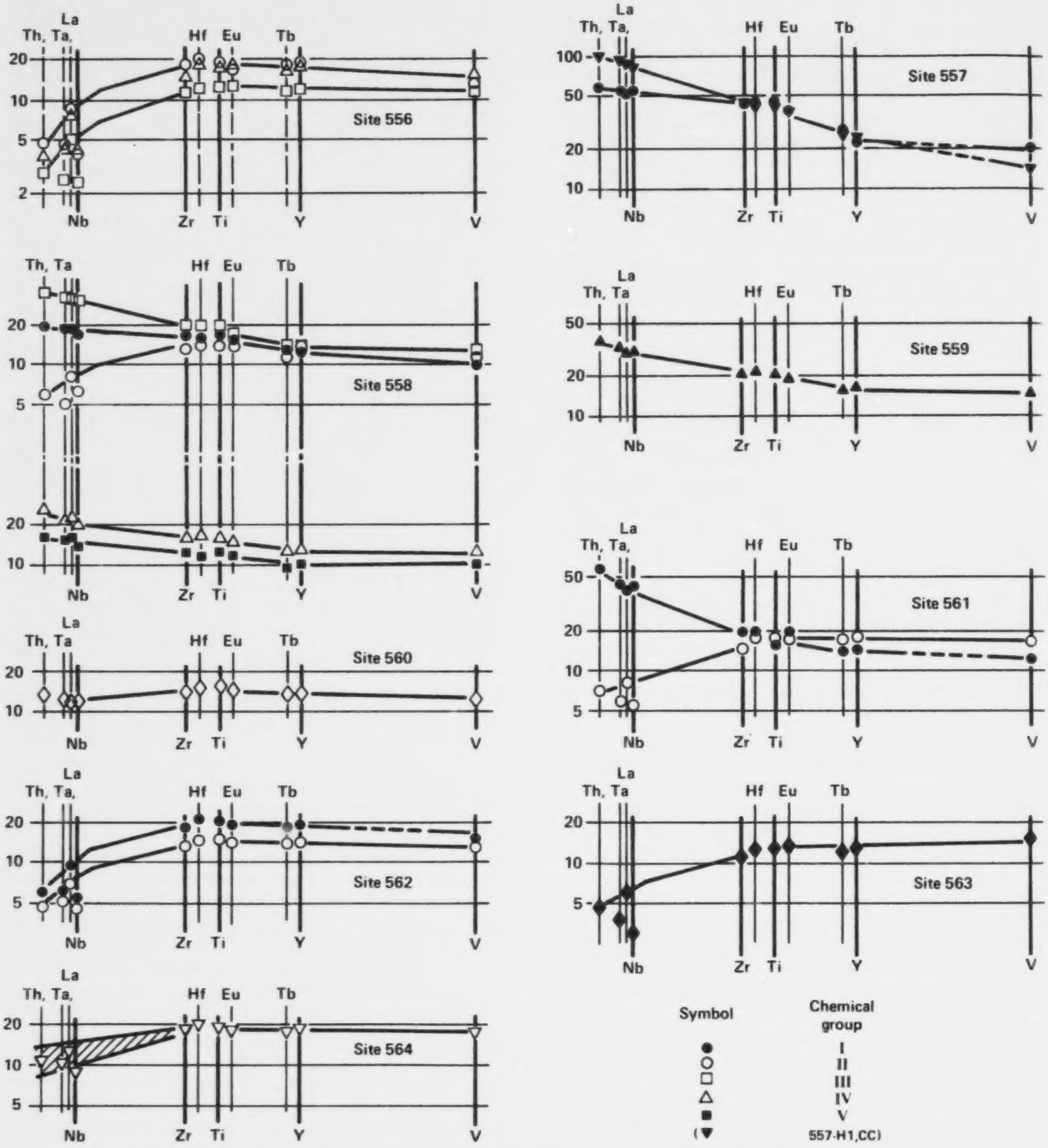

Figure 12. Extended Coryell-Masuda plots obtained for all Leg 82 sites, including on-board and onshore data.

tios involving the elements Th, Ta, La, and Hf are plotted. For both plots on this figure we used the same element in the denominator of the ratios (La for the upper plot, Th for the lower plot). The similar continuity on both diagrams does not indicate that we should make a special case of Ta/La, compared to other ratios (e.g., La/Th). There are however, two reasons for keeping in mind the hypothesis of two mantle sources: (1) for enriched samples, the La/Ta ratio remains constant (bu La/Th ratios are fractionated) and equal to the chondritic ratio (Log $(Ta/La)_{ch} \cong 0$); magmatic processes should thus have very little effect upon this ratio; and

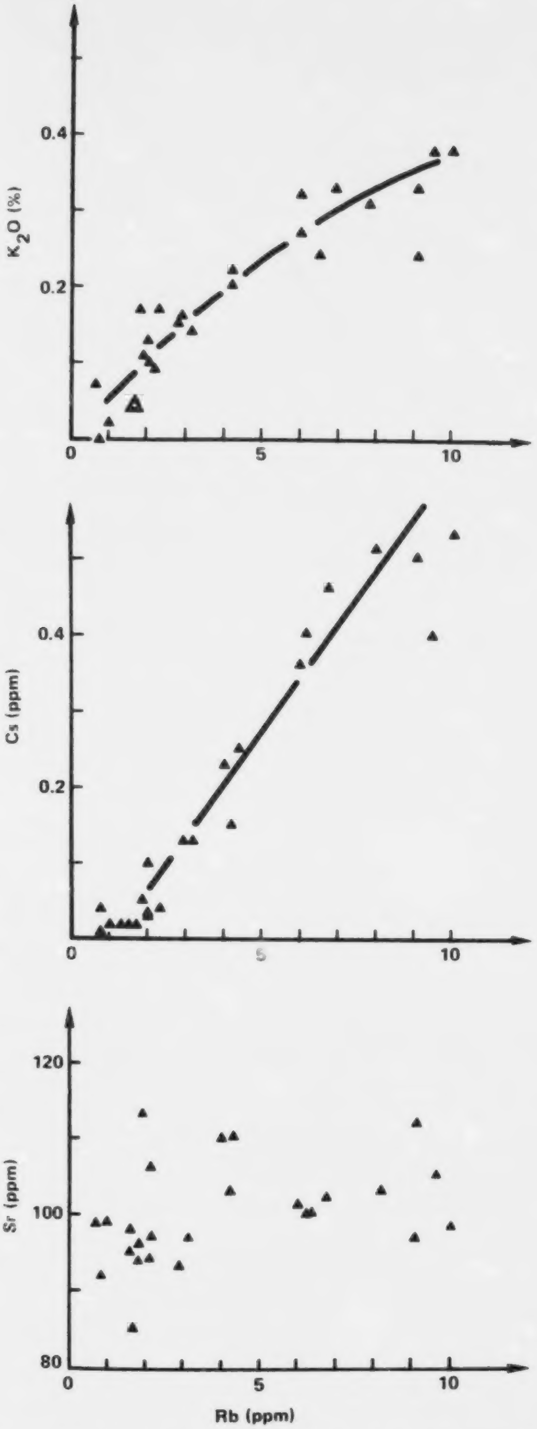

Figure 13. Site 562: potassium, cesium, and strontium versus rubidium.

(2) some samples (e.g., dolerites from Morocco and the Walvis Ridge (Fig. 5)) are enriched, have a Log $(Ta/La)_{ch}$ equal to −0.3 (like Hole 556), and do not plot on the trend of the upper diagram of Fig. 18, whereas they

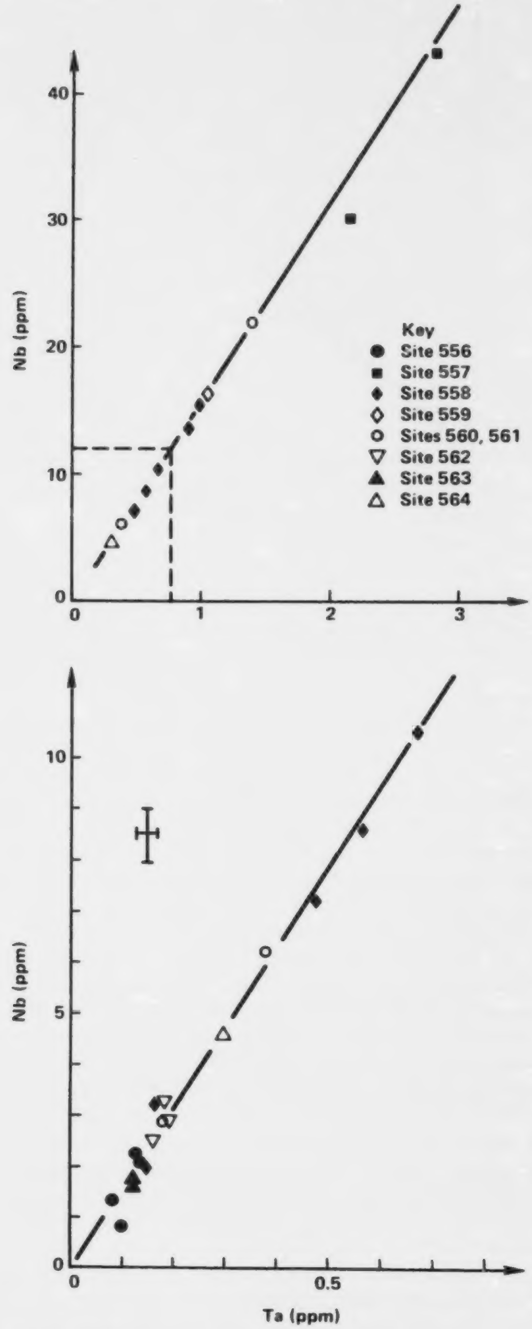

Figure 14. Niobium versus tantalum for Leg 82 sites.

plot on the continuous line in the lower diagram. In addition, basalts from subduction zones lying in the enriched field have Log $(La/Ta)_{ch}$ that can be much lower (−0.7 to −1) (Briqueu et al., in press; Dupuy et al., 1982).

These two reasons make it likely that La/Ta ratios reflect in part a mantle property, either chemical or mineralogic.

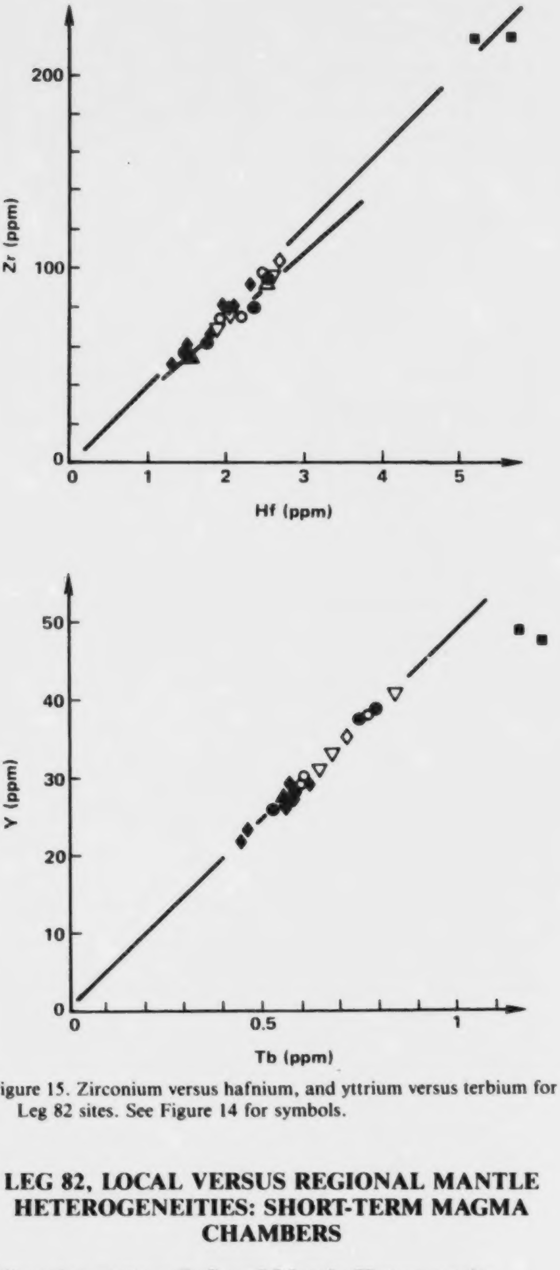

Figure 15. Zirconium versus hafnium, and yttrium versus terbium for Leg 82 sites. See Figure 14 for symbols.

LEG 82, LOCAL VERSUS REGIONAL MANTLE HETEROGENEITIES: SHORT-TERM MAGMA CHAMBERS

"Crossing patterns": Local Mantle Heterogeneity and Short-term Magma Chambers

Interesting "crossing patterns" of the REE plots and extended REE plots have been found at two Leg 82 sites, 558 and 561. These crossing patterns are related to two types of extended Coryell-Masuda plots found at the same location: one of them is enriched in the most hygromagmaphile elements, the other is depleted. In addition, the normalized concentrations of the less hygromagmaphile elements of the enriched samples are somewhat lower than the normalized concentrations of the depleted samples. A typical example is given in Figure 12 for Site 561; the two extended REE plots cover almost the entire spectrum of mid-ocean ridge basalts. Such crossing patterns found in the FAMOUS area, (presenting a narrower range than at Site 561) were discussed by Langmuir and others (1977) and were used as examples of possible results of dynamic melting. Such dynamic melting and other multistage melting models (Langmuir et al., 1977; Bougault, Cambon, et al., 1979; Bougault, 1980; Duncan and Green, 1980), when combined with crystallization effects (which increase all concentrations of hygromagmaphile elements in about the same proportion), can explain such distributions. However, without any real constraints on the degree of melting, it is always possible to find a model that fits the data, starting from a unique mantle source. Another feature presented by these crossing pattern is the Ta-Nb anomaly with respect to La, which has been tentatively interpreted as reflecting different mantle sources. For enriched samples, the Ta, Nb, and La normalized concentrations are about equal; for depleted samples Ta and Nb normalized concentrations are much lower than the La normalized concentration. Isotopic data provide limits for these interpretations.

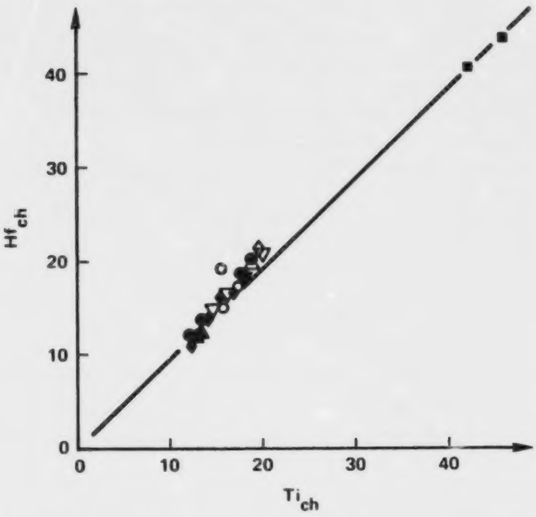

Figure 16. Normalized concentrations of hafnium versus normalized concentrations of titanium for Leg 82 sites. Symbols as in Figure 14.

At Site 561, isotopic ratios of Nd and Pb are very distinctive (Jenner et al., Dupré et al., Rideout and Schilling, all this volume): high Pb isotopic ratios ($^{206}Pb/^{204}Pb$ = 19.53; $^{207}Pb/^{204}Pb$ = 15.59; $^{208}Pb/^{204}Pb$ = 39.25) and low $^{143}Nd/^{144}Nd$ ratio (0.51298) correspond to the unit enriched in the most hygromagmaphile elements; low Pb isotopic ratios ($^{206}Pb/^{204}Pb$ = 18.83; $^{207}Pb/^{204}Pb$ = 15.53; $^{208}Pb/^{204}Pb$ = 38.35) and high $^{143}Nd/^{144}Nd$ ratios (0.51310) correspond to samples depleted in the most hygromagmaphile elements. This result has three important implications:

1. Two distinct mantle sources can contribute locally to the formation of the second layer of the oceanic crust.
2. Different extended Coryell-Masuda plots and Ta-Nb anomalies observed in liquids can reflect different mantle sources.

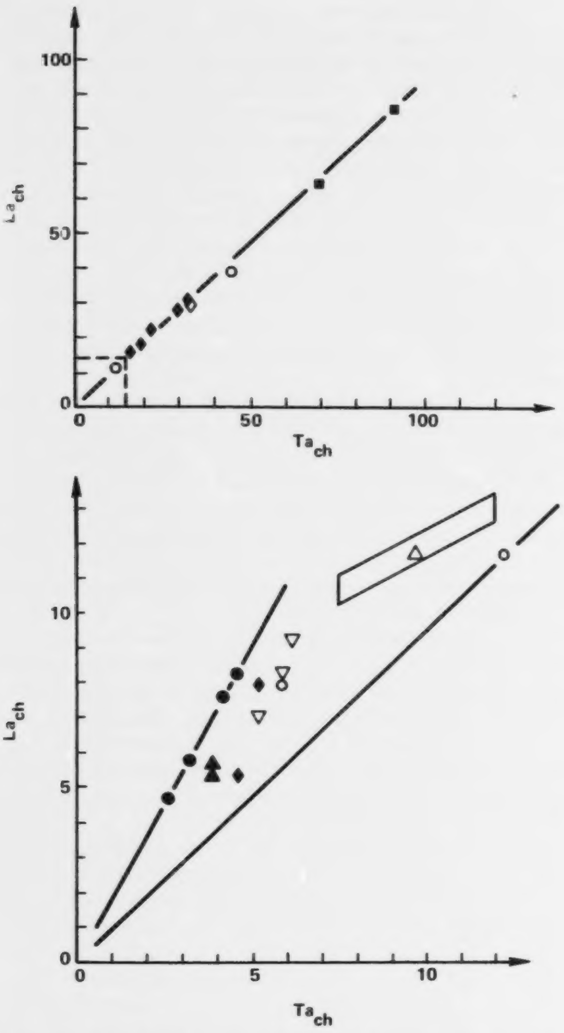

Figure 17. Normalized concentrations of lanthanum versus normalized concentrations of tantalum for Leg 82 sites. Symbols as in Figure 14. Parallelogram shows range of variation for Hole 564.

3. Samples with such different trace element and isotopic characteristics in a single hole can only be generated in the context of small, isolated, short-term magma chambers.

At Site 558, differences in isotopic ratios are also observed between enriched and depleted samples. Chemical Group III (the most enriched in Th, Ta, La, and Nb) has the highest Pb isotopic ratios ($^{206}Pb/^{204}Pb = 20.25$; $^{207}Pb/^{204}Pb = 15.63$; $^{208}Pb/^{204}Pb = 39.64$) and the lowest $^{143}Nd/^{144}Nd$ ratio (0.51291), whereas Chemical Group II, (the most "depleted" in this hole) has the lowest Pb isotopic ratios ($^{206}Pb/^{204}Pb = 19.61$; $^{207}Pb/^{204}Pb = 15.60$; $^{208}Pb/^{206}Pb = 39.17$) and the highest $^{143}Nd/^{144}Nd$ ratio (0.51296). The implications of Site 561 data (previously discussed) are confirmed by Site 558 data.

On the East Pacific Rise at about 22°N, all samples are depleted MORB and have a normalized La/Ta ratio of 2 (Cambon et al., 1983). On the Costa Rica Rift (Hole 504B, Legs 69, and 70) [Etoubleau et al., 1983] and Leg 83 [Anderson, Honnorez, Becker, et al., in press]), almost all basalt samples recovered are extremely depleted in the most hygromagmaphile elements; the normalized La/Ta ratio would be higher than 2, which could indicate some fractionation of La-Ta (Nb) for depleted samples, but the concentrations are so low that we have to be careful in such interpretations. However, in Hole 504B, two units show significant differences: one is less depleted than the majority of the samples and its normalized La/Ta ratio is equal to 2; the other is slightly enriched and its normalized La/Ta ratio is equal to 1 (Etoubleau et al., 1983; Tual et al., 1983). Significant variations in Nd isotopic ratios are also observed (E. Tual, personal communication, 1983).

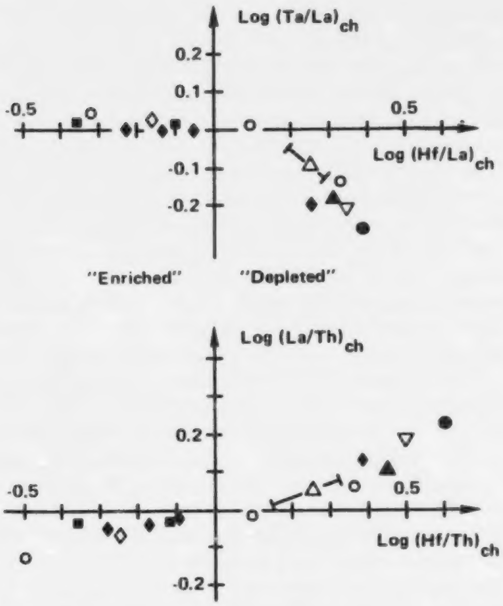

Figure 18. Leg 82 sites: logarithm of Ta/La normalized ratio versus logarithm of Hf/La normalized ratio and logarithm of La/Th normalized ratio versus logarithm of Hf/Th normalized ratio. Symbols as in Figure 14.

When the program of drilling ocean crust started in 1974, scientists attempted to sample different basalt units at one location and to relate them to one another through fractional crystallization processes. The results have shown that such cogenetic relationships are very difficult to find. This difficulty was interpreted in terms of magma mixing, whereby part of the basalt liquid is erupted on the seafloor and new primary liquid is injected in the magma chamber and is mixed with liquid that has already suffered some effects of fractional crystallization processes (Rhodes et al., 1979). This interpretation accounts for some of the complexity of the chemical compositions of lavas but cannot explain the different enriched and depleted extended Coryell-Masuda plots that have now been found in several locations. Some authors have also proposed the notion of permanent steady-state zoned magma chambers to account for some of the variation of the basalt samples that were collected in the FAMOUS area (Bryan and Moore, 1977; Bryan et al., 1979). Again, DSDP results since 1974 (based on mineralogic descriptions, major element compositions of lavas, and abundances of high partition coefficient elements and of hygromagmaphile elements) do not support this hypothesis. The absence of a negative correlation between high partition coefficient elements and hygromagmaphile elements can be interpreted by the proposition of Rhodes and others (1979); but, even if magma mixing is a likely process, it has a very strong limitation in terms of the duration of magma chambers. Such a process would imply high concentrations of all hygromagmaphile elements in the liquid phase; long-life steady-state magma chambers, even if zoned, would be factories for hygromagmaphile element enrichment (Cambon et al., 1983). More recently, it was proposed, for samples recovered between 22 and 25°N on the Mid-Atlantic Ridge, that simple low-pressure equilibrium crystallization during ascent in shallow vents or flow in seafloor lava tubes can account for a large part of the major and trace element variation within discrete data sets (Bryan et al., 1981).

The fact that we have now found, in the same hole, samples that present different extended Coryell-Masuda plots and crossing patterns—both on the Mid-Atlantic Ridge and on the East Pacific Rise—is a strong argument against the notion of long-term steady-state magma chambers. In addition, because the samples also have different isotopic ratios, the lavas were derived from different mantle sources. Extended Coryell-Masuda plots, La/Ta (or La/Nb) ratios and isotopic ratios confirm the difficulty of finding cogenetic basalt units on the basis of major and high-partition-coefficient trace elements (Cr, Ni). These results constitute important constraints for any physical model of the construction of the ocean crust. Magma cycles (a concept initially proposed by Flower and Robinson [1979]), along with basalt liquids that can be produced from different mantle sources at a single location (via small individual magma chambers whose average lifetime and number could be a function of the spreading rate) and mixing and fractional crystallization in these chambers and vents, make up a complex process that accounts for the geochemical data in hand at the moment.

Mineralogic Data: Lack of Compositional Variations Related to Mantle Heterogeneity

A comparative microprobe study of some LREE-enriched and depleted basalts from Leg 82 sites has been conducted in order to test hypothetical mineralogic differences between the two groups. Six samples have been investigated: two of them enriched in hygromagmaphile elements (557-1-1, 57–58 cm; 561-1-1, 8–10 cm), the other four depleted (561-1-1, 123–124 cm; 561-1-2, 32–40 cm; 561-2-5, 130–132 cm; 562-4-1, 104–106 cm). The major element and transition element compositions of the four samples from Hole 561 are fairly constant. Sample 557-1-1, 57–58 cm is noticeably enriched in TiO_2 and total iron and depleted in Al_2O_3, MgO, and CaO compared to the other samples.

A Camebax Microbeam automated electron microprobe "Microsonde Ouest" in Brest has been used for mineral analyses. Most of the elements have been analyzed in the following conditions: 15 kV, 10 nA, and counting time = 6 s. Special attention was paid to the analysis of elements, the concentration levels of which are of some thousands of ppm (Ni, Mn, and Ca in olivines; Ti, Mn, and Cr in clinopyroxene; Cr and V in titanomagnetites; Fe, Mg, and K, in plagioclases); they have been analyzed using 40 s counting time. Under these conditions, concentrations of 1000 and 5000 ppm are thought to be determined with precisions of 10 and 3%, respectively. Additionally, the plagioclases have been analyzed for Sr, which has never been found in significant amounts.

Mean compositions of the major minerals from Leg 82 basalts are given in Tables 2 to 5. The mineral compositions from LREE-enriched and LREE-depleted basalts, respectively, are systematically overlapping. The compositional variations encountered are like those classically described in ocean-floor tholeiites, and we have not found any indication of systematic differences in the physical or chemical conditions of crystallization of enriched and depleted basalts.

Olivines (Table 2) range in composition from Fo_{87} to Fo_{81}, according to the Fe/Fe + Mg ratios of their host lavas. A significant iron-enrichment is found from the cores of phenocrysts to their rims and to the groundmass. Their Ni contents show a positive correlation with Mg; their calcium contents, which are dependent on silica activity and total pressure (Stormer, 1973), are identical for enriched and depleted samples.

Calcic clinopyroxenes (Table 3), the compositions of which are considered to be strongly dependent on physical and chemical conditions of crystallization (Cameron and Papike, 1981; Leterrier et al., 1982) do not show systematic differences between the two groups. Their position in the Ca-Mg-(Fe + Mn) diagram is almost identical for pyroxenes from enriched and depleted tholeiites, and the groundmass pyroxenes show the iron-enrichment and Ca-depletion and Mg-depletion so often described in ocean basalts. The concentrations of Ca, Ti, Al, and Na in clinopyroxenes, which are thought to increase with the alkalinity of host basalts (Schweitzer et al., 1979), do not form independent fields that can be related to each group.

Groundmass Titanomagnetites (Table 4) from enriched and depleted samples show identical composition ranges, even for minor elements (Si, Cr, Mn, Ca, V).

Plagioclases (Table 5) show wide variations in composition, from An_{92} to An_{50} for the cores of the phenocrysts and An_{85} to An_{15} for groundmass plagioclases. These variations are primarily related to the more or less evolved character of their host magma: among the studied basalts, Sample 557-1-1, 57–58 cm contains plagioclase phenocrysts and groundmass crystals clearly more sodic than those from the other Leg 82 basalts; additionally, their analyses show significant amounts of K_2O, increasing from the cores of the phenocrysts to their rims and to the groundmass crystals. Enriched and depleted

Table 2. Mean compositions of olivines.

Sample	561-1-1, 8–10 (LREE enriched)				561-2-5, 120–132 (LREE depleted)			
Position	Cores (5)		Groundmass (5)		Cores (5)		Groundmass (5)	
	m	S	m	S	m	S	m	S
SiO_2	39.53	0.53	39.58	0.32	38.81	0.54	38.78	0.37
FeO^*	12.37	0.52	13.59	0.82	16.05	0.26	16.95	0.35
MnO	0.19	0.05	0.23	0.05	0.26	0.01	0.25	0.03
MgO	47.88	0.89	46.64	0.76	46.76	0.48	46.14	0.62
NiO	0.24	0.04	0.19	0.03	0.15	0.01	0.15	0.01

Note: LREE = light rare earth elements; m = mean value; S = standard deviation. The number of analyses is indicated in parentheses. FeO^* = total iron as FeO. Sample numbers are expressed as Hole-Core-Section (interval in cm).

Table 3. Mean compositions of clinopyroxenes.

LREE	LREE enriched						LREE depleted					
Sample	557-1-1, 57–58				561-1-1, 8–10		561-1-1, 123–124		561-1-1, 32–40		561-2-5, 130–132	
Position	Cores (4)		Groundmass (6)		Groundmass (6)		Groundmass (6)		Groundmass (6)		Groundmass (6)	
	m	S	m	S	m	S	m	S	m	S	m	S
SiO_2	50.34	0.31	48.51	0.85	47.80	0.94	49.46	1.87	48.94	1.48	49.20	0.77
TiO_2	1.23	0.21	0.80	0.28	1.55	0.19	1.20	0.50	1.23	0.36	1.13	0.25
Al_2O_3	2.40	0.38	1.05	0.33	5.07	1.32	4.64	1.23	5.57	0.75	4.60	0.67
Cr_2O_3	0.00	0.00	0.00	0.00	0.14	0.11	0.19	0.17	0.22	0.15	0.16	0.10
FeO	12.56	1.88	26.57	3.14	10.81	2.03	11.99	4.67	10.21	3.35	9.15	0.76
MnO	0.33	0.10	0.69	0.13	0.23	0.10	0.27	0.10	0.25	0.08	0.22	0.03
MgO	15.51	0.69	6.42	3.00	14.19	0.79	17.61	4.14	17.66	2.58	19.08	0.90
CaO	18.15	1.11	16.38	2.40	19.76	1.13	15.02	1.72	16.36	1.62	17.25	0.83
Na_2O	0.27	0.10	0.35	0.10	0.41	0.05	0.30	0.09	0.33	0.10	0.28	0.12

Note: Conventions as in Table 2.

Table 4. Representative analyses of groundmass titanomagnetites.

	LREE enriched				LREE depleted		
Sample	557-1-1, 57–58		561-1-1, 8–10		561-2-5, 130–132		562-4-1, 104–106
SiO_2	0.13	0.18	0.15	0.30	0.18	0.26	0.14
TiO_2	21.20	20.35	14.83	14.81	17.20	16.85	22.77
Al_2O_3	0.60	0.65	3.14	3.29	2.36	2.17	2.07
Cr_2O_3	0.00	0.00	0.05	0.05	0.00	0.01	0.00
Fe_2O_3	27.51	28.44	37.12	35.86	32.49	33.06	22.84
FeO	50.35	49.12	42.77	42.70	45.04	44.71	50.87
MnO	0.51	0.53	0.41	0.49	0.36	0.32	0.63
MgO	0.03	0.11	1.35	1.07	1.02	0.95	0.65
CaO	0.01	0.28	0.20	0.33	0.20	0.24	0.09
V_2O_5	0.00	0.00	0.60	0.67	0.64	0.74	0.56
Total	100.34	99.66	100.62	99.57	99.49	99.31	100.62

Note: Iron contents distributed as FeO and Fe_2O_3 according to R_3O_4 stoichiometry. Other conventions as in Table 2.

Table 5. Mean compositions of plagioclases.

	LREE enriched								LREE depleted							
Sample	557-1-1, 57–58				561-1-1, 8–10				561-1-1, 123–124				562-4-1, 104–106			
Position	Cores (6)		Groundmass (5)		Cores (5)		Groundmass (5)		Cores (6)		Groundmass (5)		Cores (6)		Groundmass (6)	
	m	S	m	S	m	S	m	S	m	S	m	S	m	S	m	S
SiO_2	54.37	1.09	60.56	3.51	52.27	0.65	52.01	0.81	49.80	1.54	51.28	0.75	45.67	0.93	53.12	1.25
Al_2O_3	29.10	0.38	24.99	2.40	30.21	0.84	30.57	0.53	32.67	1.00	31.67	0.85	35.11	0.63	29.28	1.06
$Fe_2O_3^*$	0.61	0.12	0.47	0.23	0.87	0.26	0.81	0.17	0.46	0.16	0.65	0.16	0.32	0.08	0.82	0.24
MgO	0.13	0.02	0.03	0.03	0.46	0.06	0.40	0.08	0.29	0.03	0.31	0.07	0.25	0.05	0.29	0.10
CaO	11.21	0.70	6.13	2.70	13.86	0.52	13.96	0.51	15.47	1.05	14.37	0.61	18.06	0.58	12.13	1.00
Na_2O	5.48	0.32	8.25	1.35	3.86	0.46	3.85	0.42	2.88	0.57	3.48	0.49	1.46	0.43	4.93	0.80
K_2O	0.19	0.03	0.51	0.22	0.06	0.02	0.05	0.02	0.00	0.00	0.01	0.01	0.00	0.00	0.04	0.01

Note: $Fe_2O_3^*$: total iron as Fe_2O_3. Other conventions as in Table 2.

basalts of fairly equivalent major element chemistry (e.g., Samples 561-1-1, 8–10 cm and 561-1-1, 123–124 cm) contain similar plagioclases, the compositions of which do not differ in any way from one another, even for Mg minor elements (Fe, Mg, K). The occurrence of significant amounts of Mg in plagioclases from ocean tholeiites (Hawkins, 1977) is confirmed by our data.

Pb, Sr, Nd Isotopic Ratios and Hygromagmaphile Element Ratios: New Constraints for Mantle Heterogeneities and Partial Melting Processes

Sites other than 558 and 561 drilled during Leg 82 are homogeneous in enrichment or depletion in hygromagmaphile elements. The related isotopic ratios (Jenner et al.; Dupré et al.; Rideout et al., all this volume) also show homogeneous data. Nevertheless, regular trends are *not* observed between isotopic ratios and hygromagmaphile element ratios. For example, Site 556 is the most depleted in LREEs and Th, Ta, and Nb, but the corresponding Pb isotopic ratios are by far not the lowest among the sites drilled during Leg 82, as shown in Figure 19 (Dupré et al., this volume). This figure shows that high isotopic ratios correspond to enriched material, but both low and somewhat high Pb isotopic ratios correspond to depleted material. In other words, the trends that would associate radiogenic ratios to hygromagmaphile ratios in a continuous regular variation, as proposed by Allègre and others (1980) and Dupré and Allègre (1980), are more complicated.

Different Pb, Sr, and Nd isotopic ratios in basalts indicate different histories of the mantle sources, different events that induced fractionation of hygromagmaphile elements, and different amounts of time are necessary to produce different isotopic ratios. The ratios of hygromagmaphile elements in basalts depend only on fractionation during these events but do not depend on time. Because we do not know how to evaluate the extent of the last melting event, it is theoretically not possible to distinguish between a basalt that was the product of a large degree of melting of a primordial mantle source and a basalt that would be the result of a smaller degree of melting of an already depleted mantle source. Another way of presenting this proposition is to consider a basalt as the result of a multistage melting process of primordial mantle without any reference to the time when these stages or events occurred; without isotopic data it is not possible to know when some of these stages occurred. If most of the episodes of melting occurred in a recent period, we can consider that the mantle is close to primordial in respect to isotopes. Basalt liquids will have high radiogenic Sr, Pb, and Nd contents, whatever the extent of melting and the number of melting stages. According to the extent and the methods of melting, theoretically either enriched or depleted liquids can be produced. If some episodes occurred a long time ago, the present basalt liquids necessarily derived from a depleted mantle source with low Pb and Sr and high Nd isotopic ratios; correlatively, because they were formed from a depleted source, basalt liquids tend to be depleted (Fig. 9). Even if mixing of mantle plume material with depleted mantle material involves differing extent or methods of melting, it is not possible to have samples with high Ta/Hf and low $^{206}Pb/^{204}Pb$. According to this interpretation, the main result would be that starting from a plumelike mantle material, it is possible to have extents and methods of melting that can produce LREE-depleted basalts. A quantitative approach would need to account for recycling part of the ocean crust and sediments through subduction zones (Cohen and O'Nions, 1982) and other processes that would tend to erase heterogeneities (by diffusion and advection, as discussed by Allègre and others (1980). The new information from Leg 82 is that basalt samples with high Pb isotopic ratios can have low hygromagmaphile ratios (such as La/Sm or Ta/Hf).

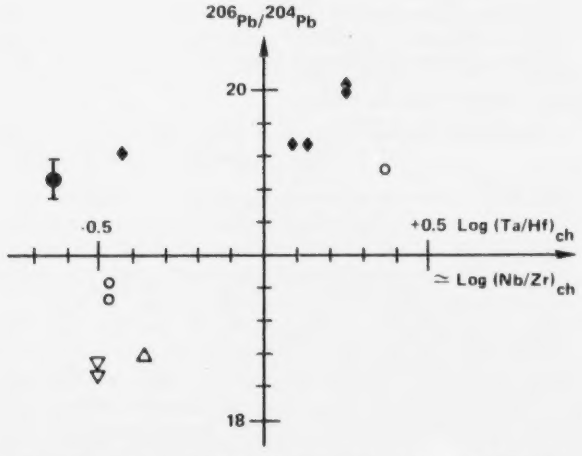

Figure 19. Leg 82 sites: $^{206}Pb/^{204}Pb$ versus logarithm of Ta/Hf normalized to chondrites. Ta/Hf is equivalent to Nb/Zr. Subscript ch indicates normalized to chondrites. From Dupré et al., this volume. Symbols as in Figure 14.

Regional Mantle Heterogeneity

So far, we have been discussing the data in terms of comparative geochemistry and processes; we have come to the conclusion that different mantle sources can contribute in forming layer two in a restricted area. What about the regional variation versus time and along isochrons? Is there any clear relationship with zero-age variations along the ridge axis from the Azores Triple Junction to south of Hayes Fracture Zone?

First, almost the entire range of possible variation of La/Sm ratio occurs in a single hole, which makes it somewhat difficult to produce a regional picture unless data are available for many sites. In this respect, drilling a hole down to some tens of meters is about the equivalent of a dredge haul at the axis. Producing a regional picture is then difficult both because of large variations that are observed within a single hole and because of the limited number of drilled sites when compared to the number of dredge sites along the axis.

South of the Hayes Fracture Zone, the samples recovered at three sites (562 on Anomaly 5, 563 and 564 on Anomaly 13) are depleted MORB with low Pb isotopic ratios and high Nd isotopic ratios. Nevertheless, we note that normalized La/Ta ratios do not reach the value 2 as observed at several locations for zero-age samples. In addition, a range of variation of this ratio and Ta/Hf, Nb/Zr, or La/Sm ratios is observed at Site 564. We thus conclude that south of the Hayes Fracture Zone the depleted character of the basalts is a general feature; but, the variations observed in the concentrations and ratios of hygromagmaphile elements preclude "typical depleted MORB's" being identical or being generated from identical mantle sources through identical extent of melting.

North of the Hayes Fracture Zone, the picture is more complicated. When compared to sites situated south of the Hayes Fracture Zone, the only common characteristic of the northern sites is a tendency to have higher Pb and lower Nd isotopic ratios and to be enriched in hygromagmaphile elements. Comparing the trace element and isotopic ratios of the northern sites, we cannot find relationships either away from the axis of the ridge or along isochrons that could be accounted for by the regular influence of a mantle plume at the present Azores Triple Junction. First, the interpretation needs to account for the reconstruction of the North Atlantic at the time of Anomalies 5 and 13, the possible variation of the Azores hot spot during the last 35 Ma (Cande et al., 1983), and the possible influence of other hot spots, such as defined by the New England Seamount Chain. Second, even with a hypothesis of a fixed hot spot (or a hot spot fixed for a period of time), we have to consider that the effect of a plume away from the hot spot is discontinuous and involves separated parts of the plume or blobs; if we add that mixing with a normal MORB source is far from ideal, we can explain, at least in part, the heterogeneity of the results. Third, a better understanding of this region and related mantle processes would need better documentation of the hygromagmaphile data *and* isotopes of this area. The density of holes drilled during Leg 82 (off the ridge axis) compared to the density of dredge hauls (at the axis) between the Hayes Fracture Zone and the Azores Triple Junction is obviously very low. We know that different enrichment factors can be observed within a single dredge and also that the deepest sample investigated in Hole 413 (Leg 49; Wood, Varet, et al., 1979), from close to the ridge axis in the FAMOUS area, has a depleted REE pattern (Wood, Tarney et al., 1979), which is opposite to all other samples of this hole; unfortunately, no isotope data are available.

CONCLUSIONS

Geochemistry of hygromagmaphile elements. We have been trying to incorporate both the REEs and other hygromagmaphile elements in a comprehensive picture, the so-called extended Coryell-Masuda plot, which is both a classification of the elements versus their bulk hygromagmaphile character and a tool for the characterization and the interpretation of the genesis of basalts. We have shown that this concept can be used practically; we were able on board to characterize the different groups of basalts recovered by using only Nb, Zr, Ti, Y, and V to deduce exactly the same information that can be obtained from the REEs themselves.

The nonfractionation of La and (Nb, Ta) over a large range of variation in concentration of these elements (from about 10 to 90 for normalized concentrations) is confirmed. The variation of the normalized La/(Ta, Nb) ratio for normalized concentrations lower than 10 (e.g., Hole 564) is interpreted either as the effect of mixing of different mantle sources or of fractionation of these elements in depleted mantle sources.

"Crossing patterns" in a single drill hole. Crossing patterns of extended Coryell-Masuda plots have been found in the same hole; these crossing patterns cover almost the entire spectrum of extended Coryell-Masuda plots; At site 561, they are associated with different isotopic ratios. This obviously demonstrates the contribution of at least two mantle sources at the same location in building the ocean crust. In addition, this result has implications for physical models that can account for the construction of the ocean crust; it favors a model of small, discrete, short-time magma chambers rather than a permanent steady-state magma chamber at the ridge axis. A mineralogic study did not find any indication of systematic differences in the physical or chemical conditions of crystallization for enriched and depleted basalts.

Hygromagmaphile ratios and isotopic ratios. Leg 82 provides new data on hygromagmaphile ratios and isotopic ratios; in particular, it shows that a sample can be characterized by high Pb isotopic ratios with a depleted hygromagmaphile element signature. This result indicates that a depleted basalt can be produced from plumelike mantle material in a short period of time, in contrast to other basalts that have a depleted character and low Pb isotopic ratios that by definition, need fractionations that occurred a long time ago. This casts new light on mantle source characteristics and partial melting processes.

Local versus regional mantle heterogeneity. We have already reported that Leg 82 has documented local mantle heterogeneity (crossing patterns of extended Coryell-Masuda plots and different isotopic ratios). South of the Hayes Fracture Zone, all sites yielded basalts with a depleted character and low Pb and Sr, high Nd isotopic ratios; but all sites, as well as zero-age sites, are not identical in these properties. North of the Hayes Fracture Zone, Pb isotopic ratios tend to be higher than to the south, but a range of values is observed; at the same time, both enriched and depleted material has been recovered north of the Hayes Fracture Zone. In this respect, the influence of "plumelike" mantle sources is observed. But, because of the complexity that has been reported (crossing patterns of extended Coryell-Masuda plots, more complex relationships between hygromagmaphile elements and isotopic ratio), it is not possible to deduce a clear picture along flow lines or along isochrons that could be related to a simple fixed hot spot at the Azores Triple Junction.

ACKNOWLEDGMENTS

We thank the crew, the drillers, and the scientific party of Leg 82 of the *Glomar Challenger*; all of them helped to make available this sample set from the Azores Triple Junction. We thank B. Weaver and H. McSween for comments and corrections. We are grateful to C. Ollivier for typing the manuscript.

REFERENCES

Allègre, C. J., Brévart, O., Dupré, B., and Minster, J. F., 1980. Isotopic and chemical effects produced in a continuously differentiating earth mantle. *Phil. Trans. R. Soc. London*, A297:447–477.

Aumento, F., Melson, W. G., et al., 1977. *Init. Repts. DSDP*, 37: Washington (U.S. Govt. Printing Office).

Anderson, R. N., Honnorez, J., Becker, K., et al., in press. *Init. Repts. DSDP*, 83: Washington (U.S. Govt. Printing Office).

Bertrand, H., Dostal, J., and Dupuy, C., 1982. Geochemistry of early mesozoic tholerites from Morocco. *Earth Planet. Sci. Lett.*, 58: 225–239.

Bougault, H., 1977. First transition series elements: fractional crystallization and partial melting. *In* Aumento, F., Melson, W. G., et al., *Init. Repts. DSDP*, 37: Washington (U.S. Govt. Printing Office), 539–546.

________, 1980. Contribution des éléments de transition à la compréhension de la génèse des basaltes océaniques. Analyse des éléments traces dans les roches par spectrométrie de fluorescence X [Thèse]. Université Paris VII, Paris.

Bougault, H., and Cambon, P., 1973. Dispersive X-ray fluorescence analysis on board oceanographic vessels. *Mar. Geol.*, 15:37–41.

Bougault, H., and Cambon, P., Corre, O., Joron, J. L., and Treuil, M., 1979. Evidence for variability of magmatic processes and upper mantle heterogeneity in the axial region of the Mid-Atlantic Ridge near 22° and 36°N. *Tectonophysics*, 55:11–34.

Bougault, H., Cambon, P., Joron, J. L., and Treuil, M., 1978. Trace elements: fractional crystallization and partial melting processes, heterogeneity of the upper mantle material. *In* Dmitriev, L., Heirtzler, J., et al., *Init. Repts. DSDP*, 46: Washington (U.S. Govt. Printing Office), 247–251.

Bougault, H., Joron, J. L., and Treuil, M., 1979. Alteration, fractional crystallization, partial melting, mantle properties from trace elements in basalts recovered in the North Atlantic. *In* Talwani, M., Harrison, C. G., and Hayes, D. E. (Eds.), *Deep Drilling Results in the Atlantic Ocean: Ocean Crust*: Washington (Am. Geophys. Union), Maurice Ewing Series, 2:352–368.

Bougault, H., and Treuil, M., 1980. Mid-Atlantic Ridge: zero age geochemical variations between Azores and 22°N. *Nature*, 286(5770): 209–212.

Bougault, H., Treuil, M., and Joron, J. L., 1978. Trace elements in basalts from 23°N and 36°N in the Atlantic Ocean: fractional crystallization, partial melting, and heterogeneity of the upper mantle. In Melson, W. G., Rabinowitz, P. D., et al., *Init. Repts. DSDP*, 45: Washington (U.S. Govt. Printing Office), 493–506.

Briqueu, L., Bougault, H., and Joron, J. L., in press. Several geochemical characteristics common to magmatisms associated with convergence zones: the Ta-Nb anomaly; petrogenetic implications. *Earth Planet. Sci. Lett.*

Bryan, W. B., and Moore, J. G., 1977. Compositional variations of young basalts in the Mid-Atlantic Ridge rift valley near lat. 36°49′N. *Geol. Soc. Am. Bull.*, 88:556–570.

Bryan, W. B., Thompson, G., and Ludden, J. N., 1981. Compositional variation in Normal MORB from 22°–25°N Mid-Atlantic Ridge and Kane Fracture Zone. *J. Geophys. Res.*, 86(B12): 11815–11836.

Bryan, W. B., Thompson, G., and Michael, P. J., 1979. Compositional variation in a steady state zoned magma chamber: Mid-Atlantic Ridge at 36°50′N. *Tectonophysics*, 55:63–85.

Cambon, P., Joron, J. L., Bougault, H., and Treuil, M., 1980. Emperor Seamounts: trace elements in transitional tholeiites, alkali basalts and Hawaiites—mantle homogeneity or heterogeneity and magmatic processes. *In* Jackson, E. D., Koizumi, I., et al., *Init. Repts. DSDP*, 55: Washington (U.S. Govt. Printing Office), 585–597.

Cambon, P., Bougault, H., Joron, J. L., and Treuil, M., 1983. Basalts from the East Pacific Rise: an example of typical oceanic crust depleted in hygromagmaphile elements. *In* Lewis, B. T. R., Robinson, P., et al., *Init. Repts. DSDP*, 65: Washington (U.S. Govt. Printing Office), 623–634.

Cameron, M., and Papike, J. J., 1981. Structural and chemical variations in clinopyroxenes. *Am. Mineral.*, 66:1–50.

Cande, S. C., Bougault, H., Hill, L., Morgan, W. J., and Schouten, H., 1983. North Atlantic hot spot tracks and the pattern of enriched or depleted basalts in Leg 82 drill holes. *EOS, Trans. Am. Geophys. Union*, 64(18):345. (Abstract)

Cohen, R. S., and O'Nions, R. K., 1982. Identification of recycled continental material in the mantle from Sr, Nd and Pb isotope investigations. *Earth Planet. Sci. Lett.*, 61:73–84.

Coryell, C. D., Chase, J. W., and Winchester, J. W., 1963. A procedure for geochemical interpretation of terrestrial rare earth abundance patterns. *J. Geophys. Res.*, 68:559.

Duncan, R. A., and Green, D. H., 1980. Role of multi-stage melting in the formation of the ocean crust. *Geology*, 8:22–26.

Dupré, B., and Allègre, C. J., 1980. Pb-Sr-Nd isotopic correlation and the chemistry of the North Atlantic Mantle. *Nature*, 286(57[illegible]): 17–22.

Dupuy, C., Dostal, J., Marcelot, G., Bougault, H., Joron, J. L., and Treuil, M., 1982. Geochemistry of basalts from central and southern New Hebrides arc: implication for their source rock composition. *Earth Planet. Sci. Lett.*, 60:207–225.

El Azzouzi, M., Bougault, H., Maury, R., and Villemant, B., 1982. Application du diagramme de Coryell-Masuda "élargi" à l'étude du fractionnement du titane et du vanadium dans la série alcaline de la chaîne des Puys. *C. R. Acad. Sci., Ser. II*, 295:1117–1120.

Engel, A. E. J., Engel, C. G., and Havens, R. G., 1965. Chemical characteristics of oceanic basalts and the upper mantle. *Geol. Soc. Am. Bull.*, 76:719–734.

Erlank, A. J., and Kable, E. J. D., 1976. The significance of incompatible elements in Mid-Atlantic Ridge basalts from 45°N with particular reference to Zr/Nb. *Contrib. Mineral. Petrol.*, 54:281.

Etoubleau, J., Corre, O., Joron, J. L., Bougault, H., and Treuil, M., 1983. Costa Rica Rift: variable depleted basalts in the same hole. *In* Cann, J. R., Langseth, M. G., Honnorez, J., Von Herzen, R. P., White, S. M., et al., *Init. Repts. DSDP*, 69: Washington (U.S. Govt. Printing Office), 765–773.

Flower, M. F. J., and Robinson, P. T., 1979. Evolution of the "FAMOUS" ocean ridge segment: evidence from submarine and deep sea drilling investigations. *In* Talwani, M., Harrison, C. G., and Hayes, D. E. (Eds.), *Deep Drilling Results in the Atlantic Ocean: Ocean Crust*: Washington (Am. Geophys. Union), Maurice Ewing Series, 2:314–330.

Frey, F. A., Bryan, W. B., and Thompson, G., 1974. Atlantic Ocean floor: geochemistry and petrology basalts from Legs 2 and 3 of the Deep Sea Drilling Project. *J. Geophys. Res.*, 79:5507–5527.

Frey, F. A., and Haskin, L. A., 1964. Rare earths in oceanic basalts. *J. Geophys. Res.* 69:775–780.

Frey, F. A., Haskin, M. A., Poetz, J. A., and Haskin, L. A., 1968. Rare-earth abundances in some basic rocks. *J. Geophys. Res.*, 73: 6085–6098.

Gast, P. W., 1968. Trace element fractionation and the origin of tholeiitic and alkaline magma types. *Geochim. Cosmochim. Acta*, 32: 1057–1086.

Gast, P. W., Tilton, G. R., and Hedge, C., 1964. Isotopic composition of lead and strontium from Ascension and Gough Islands *Science*, 145:1181.

Hart, S. R., Schilling, J. G., and Poweil, J. L., 1973. Basalts from Iceland and along the Reykjanes Ridge: Sr isotope geochemistry. *Nature*, 246:104.

Hawkins, S. J. W., 1977. Petrologic and geochemical characteristics of marginal basin basalts. *In* Talwani, M., and Pitman, W., III (Eds.), *Island Arcs, Deep-Sea Trenches and Back-Arc Basins*: Washington (Am. Geophys. Union), Maurice Ewing Ser., 1:355–366.

Jaffrezic, H., Joron, J. L., and Treuil, M., 1977. Trace element determination in rock powder. A study of the precision for a given analytical procedure: instrumental epithermal neutron activation. *J. Radioanal. Chem.*, 39:185–188.

Joron, J. L., Bollinger, C., Quisefit, J. P., Bougault, H., and Treuil, M., 1979. Trace elements in Cretaceous basalts at 25°N in the Atlantic Ocean: alteration, mantle compositions, and magmatic processes. *In* Donnelly, T., Francheteau, J., Bryan, W., Robinson, P., Flower, M., Salisbury, M., et al., *Init. Repts. DSDP*, 51,52,53, Pt. 2: Washington (U.S. Govt. Printing Office), 1087–1098.

Langmuir, C. H., Bender, J. F., Bence, A. E., Hanson, G. N., and Taylor, S. R., 1977. Petrogenesis of basalts from the "FAMOUS" area: Mid-Atlantic Ridge. *Earth Planet. Sci. Lett.*, 36:133–156.

Le Douaran, S., and Francheteau, J., 1981. Axial depth anomalies from 10 to 50° north along the Mid-Atlantic Ridge: correlation with other mantle properties. *Earth Planet. Sci. Lett.*, 54:29–47.

Leterrier, J., Maury, R., Thonon, P., Girard, D., and Marchal, M., 1982. Clinopyroxene composition as a method of identification of the magmatic affinities of paleo-volcanic series. *Earth Planet. Sci. Lett.*, 59:139–154.

Machado, N., Ludden, J. N., Brooks, C., and Thompson, G., 1982. Fine scale isotopic heterogeneity in the Sub-Atlantic Mantle. *Nature*, 295:222.

Masuda, A., 1962. Regularities in variation of relative abundances of lanthanide elements and an attempt to analyze separation-index patterns of some minerals. *J. Earth. Sci. Nagoya Univ.*, 10:173–187.

Morgan, W. J., 1971. Convection plumes in the lower mantle. *Nature*, 230:42–43.

O'Nions, R. K., Hamilton, P. J., and Evensen, N. M., 1977. Variation in ^{143}Nd/^{144}Nd and ^{87}Sr/^{86}Sr ratios in oceanic basalts. *Earth Planet. Sci. Lett.*, 34:13–22.

Pearce, J. A., and Cann, J. R., 1971. Ophiolite origin investigated by discriminant analysis using Ti, Zr, and Y. *Earth Planet. Sci. Lett.*, 12:339–349.

Rhodes, J. M., Dungan, M. A., Blanchard, D. P., and Long, P. E., 1979. Magma mixing at mid-ocean ridges: evidence from basalts drilled near 22°N on the Mid-Atlantic Ridge. *Tectonophysics*, 55: 35–61.

Richard, P., Skimizu, N., and Allègre, C. J., 1976. ^{143}Nd/^{146}Nd, a natural tracer: an application to oceanic basalts. *Earth Planet. Sci. Lett.*, 31:269–278.

Ringwood, A. E., 1955. The principles governing trace element behaviour during magmatic crystallization. Part II: The role of complex formation. *Geochim. Cosmochim. Acta*, 7:242–254.

Schilling, J. G., 1971. Sea-floor evolution: rare earth evidence. *Phil. Trans. R. Soc. London. Ser. A.*, 268:663.

———, 1973. Iceland mantle plumes: Geochemical evidence along Reykjanes Ridge. *Nature*, 242:565–571.

———, 1975. Azores mantle blob: rare earth evidence. *Earth Planet. Sci. Lett.*, 25:102–115.

Schweitzer, E. L., Papike, J. J., and Bence, E. A., 1979. Statistical analysis of clinopyroxenes from deep-sea basalts. *Am. Mineral.*, 64:501–513.

Shima, M., 1979. The abundances of titanium, zirconium and hafnium in stony meteorites. *Geochim. Cosmochim. Acta*, 43:353–362.

Stormer, J. C., 1983. Calcium zoning in olivine and its relationships to silica activity and pressure. *Geochim. Cosmochim. Acta*, 37: 1315–1821.

Sun, S. S., 1973. Lead isotope studies of young volcanic rocks from oceanic islands, mid-ocean ridges and island areas [unpublished Ph.D. thesis]. Columbia University, New York.

Sun, S. S., and Hanson, G. N., 1975. Origin of Ross Island basanitoids and mutations upon the heterogeneity of mantle sources for alkali basalts and nephelinites. *Contrib. Mineral. Petrol.*, 52:77–106.

Sun, S. S., Nesbitt, R. W., and Sharaskin, A. Y., 1979. Geochemical characteristics of mid-ocean ridge basalts. *Earth Planet. Sci. Lett.*, 44(1):119–138.

Sun, S. S., Tatsumoto, M., and Schilling, J. G., 1975. Mantle mixing along the Reykjanes Ridge axis: lead isotopic evidence. *Science*, 190:143–147.

Tarney, J., Wood, D. A., Saunders, A. D., Cann, J. R., and Varet, J., 1980. Nature of mantle heterogeneity in the North Atlantic: evidence from deep-sea drilling. *Phil. Trans. R. Soc. London*, A297: 179–202.

Tatsumoto, M., Hedge, C. E., and Engel, A. E. J., 1965. Potassium, rubidium, strontium, thorium, uranium and the ratio of strontium-87 to strontium-86 in oceanic tholeiitic basalt. *Science*, 150: 886–888.

Treuil, M., 1973. Critères pétrologiques, géochimiques et structuraux de la génèse et de la différentiation des magmas basaltiques: exemple de l'Afar [Thèse Université d'Orléans]. Orléans, France.

Treuil, M., Joron, J. L., Jaffrezic, H., Villemant, B., and Calas, G., 1979. Géochimie des éléments hygromagmaphiles, coefficients de partage minéraux/liquide et propriétés structurales de ces éléments dans les liquides magmatiques. *Bull. Mineral.*, 102:402–409.

Tual, E., Jahn, B. M., and Bougault, H., 1983. R.E.E. Geochemistry of basalts from DSDP Leg 83: Hole 504B. *Terra Cognita*, 3(213): 145.

White, W. M., and Schilling, J. G., 1978. The nature and origin of geochemical variation in Mid-Atlantic Ridge basalts from the Central North Atlantic. *Geochim. Cosmochim. Acta*, 42:1501–1516.

White, W. M., Schilling, J. G., and Hart, S. R., 1976. Evidence for the Azores mantle plume from strontium isotope geochemistry of the Central North Atlantic. *Nature*, 263:659–663.

Wilson, J. T., 1963. Evidence from Islands on spreading of ocean floors. *Nature*, 197:536.

Wood, D. A., Tarney, J., Varet, J., Saunders, A. A., Bougault, H., Joron, J. L., Treuil, M., and Cann, J., 1979. Geochemistry of basalts drilled in the North Atlantic by IPOD Leg 49: implications for mantle heterogeneity. *Earth Planet. Sci. Lett.*, 42:77–97.

Wood, D. A., Varet, J., Bougault, H., Corre, O., Joron, J. L., Treuil, M., Bizouard, H., Norry, M. J., Hawkesworth, C. J., and Roddick, J. C., 1979. The petrology, geochemistry and mineralogy of North Atlantic basalts: a discussion based on IPOD Leg 49. In Luyendyk, B. P., Cann, J. R., et al., *Init. Repts. DSDP*, 49: Washington (U.S. Govt. Printing Office), 597–656.

Date of Initial Receipt: 1 August 1983
Date of Acceptance: 22 December 1983

APPENDIX A

On-board and Onshore Trace Element Data (in ppm), MAPCO Cruise (Bougault and Treuil, 1980)

Dredge (latitude & longitude) Group number	N	Sc NAA	Ti XRF	V XRF	Cr XRF	Mn XRF	Fe XRF	Co XRF	Ni XRF	Zn XRF	Rb XRF	Sr XRF	Y XRF	Zr XRF	Nb XRF	Cs NAA	Ba NAA	La NAA	Eu NAA	Tb NAA	Hf NAA	Ta NAA	Th NAA	U NAA
Station CH97																								
DR02 (39°47′N 29°39′W)																								
101	2	34.7	7020	275	448	1239	72030	43	136	70	7.7	137	26	76	13.8	0.09	90	7.4	0.88	0.5	1.92	0.83	0.87	0.28
304	2	33.4	6720	252	415	1239	70350	42	128	70	6	149	24	73	14.0	0.09	88	7.3	1.06	0.52	1.87	0.81	0.87	0.26
401	1	34.6	8700	292	316	1316	73290	38	82	79	9.6	183	30	111	15.	0.10	105	9.9	1.31	0.63	2.54	1.04	1.12	0.39
DR03 (39°06′N 20°54′W)																								
101	1	29.5	12060	248	507		77980	59	232	106	3.0	365	31	160	29.0	0.03	139	19	1.72	0.77	3.72	1.80	2.06	2.2
DR05 (38°42′N 29°57′W)																								
1..[a]	3	35	11460	250	356	1162	66780	37	101	68	15	397	27	155	28	0.1	200	18.3	1.80	0.66	3.52	1.82	1.95	0.6
2..	4	36.3	8100	241	900	1162	64890	40	166	62	11	241	26	104	16	0.07	110	9.9	1.26	0.52	2.23	1.03	1.07	0.3
3..	8	38	6840	225	1600	1084	62020	48	330	57	8.5	192	21	86	13	0.07	92	7.5	1.03	0.45	1.91	0.80	0.75	0.24
DR06 (38°31′N 30°18′W)																								
1..	6	35	11100	350	25	1500	85000	42	24	88	16.5	260	32	135	31	0.18	220	19.5	1.90	0.85	3.45	2.10	2.30	0.67
Station CH98																								
DR02 (35°11′N 36°14′W)																								
1..	2	34.9	7400	255	322	1316	71630	41	66	67	5.5	155	26	75	12	0.15	70	7.7	1.13	0.63	2.21	0.87	0.91	0.30
201	1	36.6	8220	305	233	1626	82180	45	86	82	0.5	110	33	74	8.5		25	5.4	1.13	0.68	2.17	0.53	0.50	0.12
DR03 (33°44′N 37°40′W)																								
1..	2	30.1	4770	222	568	1084	58300	39	140	58	1.8	95	23	46	6	0.02	16	3.1	0.74	0.44	1.41	0.76	0.39	0.21
201	1	27.2	5220	192	1102	1162	65170	49	337	59	2	102	24	57	5		13	3.7	0.70	0.45	1.45	0.35	0.41	0.18
4..	2	29.4	5850	226	880	1200	69000	49	300	65	3	92	25	61	6		38	3.2	0.75	0.48	1.50	0.36	0.41	0.21
DR04 (33°30′N 39°05′W)																								
1..		35.2	6240	235	246	1300	69000	40	80	65	1.5	99	28	63	1.5			1.45	1.00	0.6	1.62	0.09	0.07	
2..	4																							
DR05 (33°02′N 39°20′W)																								
101	1	37.3	8100	274	427	1394	79240	52	171	80	6.2	93	35	86	1			2.55	1.27	0.97	2.36	0.10	0.07	
DR06 (32°17′N 40°21′W)																								
101	1		8880	294	282	1471	82530	46	121	83	1	87	37	91	2									
DR07 (32°17′N 40°11′W)																								
1..	4	35.5	8000	300	350	1400	78000	46	133	80	1	93	34	90	2			2.3	1.04	0.74	2.25	0.12	0.1	

DR08 (31°54′N 40°58′W)																							
101/103	2	35.7	10260	330	186	1600	88000	46	90	96	3.1	133	45	134	12	50	9.8	1.64	0.97	3.33	0.76	1.23	0.36
105/501	2	37.5	10560	350	150	1626	88500	46	66	98	2.7	139	46	134	12.3	55	11.1	1.62	1.00	3.55	0.80	1.29	0.30
102	1	32.5	8580	262	388	1394	76300	39	102	75	2.6	111	38	111	9.5	31	6.6	1.30	0.89	2.86	0.49	0.79	
2..	2	36.4	8340	293	321	1394	80640	47	123	81	0.1	81	38	90	2		1.9	1.24	0.79	2.48	0.11	0.1	
DR09 (31°28′N 40°57′W)																							
101/103	2		8460	267	275	1471	80570	47	105	81	nd	91	36	87	2		2.36	1.09	0.79	2.30	0.11	0.07	
201	1	35.1	6780	261	325	1394	64620	47	156	68	nd	89	30	69	1		1.73	0.95	0.62	1.81	0.11	0.07	
DR10 (31°04′N 41°25′W)																							
101	1	35.5	10080	310	336	1471	80850	46	148	84	1.3	110	42	113	3.5		3.24	1.41	0.89	3.07	0.19	0.18	
2..	2	33.7	7620	272	343	1220	72170	41	111	75	1.5	101	32	77	1.5		2.17	1.04	0.69	2.11	0.11	0.08	
3..	2	30.5	6960	257	570	1239	71470	46	218	70	1.3	75	31	71	1.5		1.81	0.97	0.63	1.78	0.10	0.07	
DR11 (30°41′N 41°49′W)																							
1..,3..,4..,7		35	8660	310	400	400	1394	46	144	81	1.1	92	36	92	1.5		2.6	1.25	0.80	2.55	0.12	0.08	
DR12 (30°10′N 41°55′W)																							
103/204	2	36	9600	310	289	1471	82000	45	110	89	0.7	92	41	103	2.5		2.5	1.4	0.86	2.69	0.14	0.12	
DR13 (29°56′N 42°46′W)																							
204/301	2	38	8940	268	330	1394	77700	41	80	73	2.5	122	35	110	3		2.8	1.4	0.83	2.84	0.22	0.15	
DR14 (29°17′N 43°05′W)																							
201	1	37	8820	310	277	1394	77070	43	94	74	1.8	111	34	93	2.7		2.15	1.32	0.81	2.62	0.21	0.15	
304	1	36	7860	300	348	1394	72380	43	85	73	1.9	105	32	85	1.5		2.32	1.2	0.67	2.16	0.12	0.12	
103	1	33.5	8700	281	310	1394	76020	41	121	74	1.8	110	35	88	2		1.65	1.19	0.80	2.41	0.14	0.10	
DR15 (27°46′N 44°05′W)																							
101	1	32	7200	241	458	1316	70000	46	199	64	0.4	107	30	79	1.8		2.28	0.99	0.68	2.12	0.10	0.09	
501	1	34.4	6900	269	385	1239	69860	41	141	66	1.4	111	29	70	1.8		2.29	0.93	0.63	1.86	0.16	0.12	
DR16 (25°16′N 45°20′W)																							
1..	2	32.7	8300	263	310	1300	70000	38	108	71	2.0	128	33	100	3		2.6	1.3	0.72	2.42	0.17	0.13	
201	1	37.6	9360			1316	75250	39	80	75	1.2	119	39	112	3.5		2.8	1.33	0.85	2.87	0.19	0.14	
202	1	34.5	7320			1239	64750		103	65	2.7	124	30	92	5		2.7	1.19	0.65	2.23	0.29	0.26	
DR17 (24°28′N 46°15′W)																							
201	1	39	7260	196	291	1162	59010	35	89	55	3.1	167	31	99	2.6		2.65	1.11	0.63	2.18	0.19	0.15	
301	1	36.7	10260	300	218	1394	76090	39	77	72	1.	136	38	125	3.5		3.9	1.55	0.86	3.00	0.24	0.18	
401	1	35.4	9000	285	291	1316	70350	40	87	66	1.7	138	34	110	3.0		3.0	1.42	0.75	2.67	0.21	0.14	

Note: N = the number of samples analyzed in each group; NAA = neutron activation analysis; XRF = X-ray fluorescence; ellipsis points (e.g., 1...) = ?

[a] For each dredge, the samples were divided into groups; each group is identified by the first digit (2..), and the two other digits are reserved for full sample identification (i.e., 201, 304). If several analyzed samples reveal the group to be homogeneous, only the first digit is used.

APPENDIX B

Ratios of Hygromagmaphile Element Concentrations Normalized to Chondrites between the Latitudes 40°N to 10°N[a]

Cruises	Station	Sample number	Latitude (all north)	Longitude (all west)	Depth	$[La/Sm]_{ch}$ (Schilling, 1975)	$[La/Ti]_{ch}$	$[Ta/Hf]_{ch}$ = $[Nb/Zr]_{ch}$	$[La/Ta]_{ch}$
MAPCO	CH97 DR02	101	39°46.8′	29°38.7′	1800		1.56	1.78	0.89
MAPCO	CH97 DR02	304	39°46.8′	29°38.7′	1800		1.61	1.79	0.90
MAPCO	CH97 DR02	401	39°46.8′	29°38.7′	1800		1.69	1.69	0.95
TR 89[b]	30D	2-3	39°37.9′	29°44.4′	1950–2100	2.5			
TR 89[b]	30D	5	39°37.9′	29°44.4′	1950–2100	2.5			
TR 89[b]	30D	10B	39°37.9′	29°44.4′	1950–2100	1.8			
TR 89[b]	31D	1	39°37.6′	29°42.3′	1700–1800	3.1			
TR 89[b]	31D	3	39°37.6′	29°42.3′	1700–1800	2.9			
TR 89[b]	31D	5	39°37.6′	29°42.3′	1700–1800	1.9			
MAPCO	CH97 DR03	101	39°06′	29°54′	1400		2.34	2.00	1.06
MAPCO	CH97 DR05	1..[c]	38.42′	29°57′	920		2.37	2.13	1.01
MAPCO	CH97 DR05	2..	38.42′	29°57′			1.81	1.91	0.96
MAPCO	CH97 DR05	3..	38.42′	29°57′			1.63	1.73	0.94
GIBRACO	G20	01	38.36.0′	30.42′	1152–1244		1.06	1.26	0.91
GIBRACO	G21	01	38.35.7′	30.40′	914			1.61	
MAPCO	CH97 DR06	1..	38.31′	30.18′	2200		2.61	2.51	0.93
TR 89	21D	1	38°26′	30°21.4′	2700–2850	2.4			
TR 89	21D	2	38°26′	30°21.4′	2700–2850	2.3			
TR 89	21D	3	38°26′	30°21.4′	2700–2850	2.3			
GIBRACO	G22	04	38°25.4′	29°59.6′	1350		2.48	2.44	0.96
TR 89	22D	1	38°25.3′	38°27′	1750–1850	2.5			
TR 89	22D	4	38°25.3′	38°27′	1750–1850	1.9			
TR 89	22D	5	38°25.3′	38°27′	1750–1850	1.8			
GIBRACO	G17	01	37°55.2′	31.06.1′	2138–2213		1.69	1.92	0.86
GIBRACO	G17	02	37°55.2′	31.06.1′	2138–2213		1.70	1.69	
GIBRACO	G17	03	37°55.2′	31.06.1′	2138–2213			1.85	
TR 122	5D	2	37.43.6′	31°28.2′	1630–1670	2			
TR 122	5D	4	37.43.6′	31°28.2′	1630–1670	2.1			
TR 122	5D	5	37.43.6′	31°28.2′	1630–1670	2			
GIBRACO	G19	01	37°43.2′	30.51.3′	1728–1350		1.62	1.41–1.28	1.01
GIBRACO	G19	04	37°43.2′	30.51.3′	1728–1350		1.52	1.43–1.22	0.96
FAMOUS area 1[d]			36°56′	33°04′	2100–2800		1.01	1.14	1.01
			36°58′	33°05′	2100–2800		1.48	1.50	1.01
			36°56′	33°09′	~3000		0.93	1.03	1.00
			36°57′	33°12′	~3000		1.88	1.76	1.00
			36°50′	33°14′			1.22	1.24	1.00
			36°52′	33°17′			1.50	1.45	1.00
TR 119	4D	1B	36°50.7′	33°13.7′	2275–2475	1.4			
TR 119	4D	3A	36°50.7′	33°13.7′	2275–2475	2			
TR 119	4D	4	36°50.7′	33°13.7′	2275–2475	1.8			
A II 73	18	6-1	36°46.3′	33°18.1′	2561	1.4			
A II 73	14	4-17	36°45.6′	33°17.3′	2448	1.4			
A II 73	16	5-2	36°43.2′	33°17.5′	2598	1.4			
A II 73	16	5-5	36°43.2′	33°17.5′	2598	1.4			
A II 73	10	2-19	36°43′	33°16′	2300	1.5			
A II 73	50	13-6	36°29′	33°38.7′	2561	1.6			
TR 119	6D	2B	35°50.2′	34°10.8′	2400–2500	1.4			
TR 119	6D	3A	35°50.2′	34°10.8′	2400–2500	1.4			
TR 119	7D	1	35°20′	34°54′	2100–2400	3.4			
TR 119	7D	5	35°20′	34°54′	2100–2400	3.6			
TR 119	7D	10	35°20′	34°54′	2100–2400	3.5			
MAPCO	CH98 DR02	1..	35.11′	36.14′	2940–3320		1.54	1.63	0.89
MAPCO	CH98 DR02	201	35.11′	36.14′	2940–3320		0.97	1.01	1.02
Y-30	RD6	P1	35°09′	35°43′	2020	1.1			
Y-30	RD8	P1	35°09′	35°44′	2135	1.7			
Y-30	RD8	P2	35°09′	35°44′	2135	1.1			
Y-30	RD7	P3	35°08′	35°44′	2130	1.2			
Y-30	RD7	P10	35°08′	35°44′	2130	1.2			
Vema	CH77 DR02	1	34°56.9′	36°24.7′	2148–2338		0.79	0.81	1.00
Vema	CH77 DR02	2	34°56.9′	36°24.7′	2148–2338		1.28	1.46	0.90
Vema	CH77 DR02	3	34°56.9′	36°24.7′	2148–2338				
TR 119	8D	1	34°56.3′	36°36.7′	1720–1780	2.3			
TR 119	8D	5	34°56.3′	36°36.7′	1720–1780	2.4			
TR 123	1D	5A	34°13.9′	37°07.6′	3100	0.95			
TR 123	1D	6	34°13.9′	37°07.6′	3100	0.88			
TR 123	1D	7	34°13.9′	37°07.6′	3100	0.71			
TR 123	1D	8F	34°13.9′	37°07.6′	3100	0.66			
MAPCO	CH98 DR03	1..	33.44′	37°40′	3340–3580		0.96	1.05	0.86
MAPCO	CH98 DR03	201	33.44′	37°40′	3340–3580		1.05	1.00	1.06
MAPCO	CH98 DR03	4..	33.44′	37°40′	3340–3580		0.81	0.99	0.89
MAPCO	CH98 DR04	1..	33°30.0′	39°05′	2240–2545		0.34	0.23	1.61
MAPCO	CH98 DR04	2..	33°30.0′	39°05′	2240–2545				
TR 123	4D	5	33°22.2′	39°04.8′	1950	0.35			

Appendix B. (Continued).

Cruises	Station	Sample number	Latitude (all north)	Longitude (all west)	Depth	$[La/Sm]_{ch}$ (Schilling, 1975)	$[La/Ti]_{ch}$	$[Ta/Hf]_{ch} = [Nb/Zr]_{ch}$	$[La/Ta]_{ch}$
TR 123	4D	7	33°22.2′	39°04.8′	1950	0.24			
TR 123	4D	9	33°22.2′	39°04.8′	1950	0.32			
MAPCO	CH98 DR05	101	33°02′	39°20′	2480–2800		0.47	0.17	2.55
TR 123	5D	1	32°37.4′	39°52.1′	2700	0.45			
TR 123	5D	2	32°37.4′	39°52.1′	2700	0.55			
TR 123	5D	3	32°37.4′	39°52.1′	2700	0.53			
MAPCO	CH98 DR06	101	32°17′	40°21′	2280–2320			0.21[e]	
MAPCO	CH98 DR07	1..	33°17′	40°11′	3000–3380		0.43	0.22	1.92
MAPCO	CH98 DR08	101	31°54′	40°58′	3100–3300		1.42	0.94	1.29
MAPCO	CH98 DR08	105	31°54′	40°58′	3100–3300		1.56	0.93	1.39
MAPCO	CH98 DR08	102	31°54′	40°58′	3100–3300		1.14	0.71	1.35
MAPCO	CH98 DR08	2..	31°54′	40°58′	3100–3300		0.34	0.18	1.73
A 150	RD	8	31°49′	42°25′	3700	0.59			
MAPCO	CH98 DR09	101	31°28′	48°57′	3000		0.41	0.2	2.15
MAPCO	CH98 DR09	201	31°28′	48°57′	3000		0.38	0.25	1.57
MAPCO	CH98 DR10	101	31°04′	41°25′	3100		0.48	0.26	1.71
MAPCO	CH98 DR10	2..	31°04′	41°25′	3100		0.42	0.22	1.97
MAPCO	CH98 DR10	3..	31°04′	41°25′	3100		0.39	0.23	1.81
MAPCO	CH98 DR11	1..	30°41′	41°49′	3500–3640		0.45	0.19	2.17
MAPCO	CH98 DR12	103	30°10′	41°55′	4130–4230		0.39	0.21	1.79
A 150	RD	20	30°04′	42°16′	4144	0.45			
A 150	RD	7	30°01′	42°04′	4280	0.58			
MAPCO	CH98 DR13	204	29°56′	42°46′	3300–3780		0.46	0.32	1.27
Vema	CH77 DR03	104	29°37.3′	42°49.7′	3210–3300		0.51	0.35	1.36
Vema	CH77 DR03	205	29°37.3′	42°49.7′	3210–3300		0.57	0.86	0.76
MAPCO	CH98 DR14	201	29°16′	43°05′	2300–2500		0.36	0.33	1.02
MAPCO	CH98 DR14	304	29°16′	43°05′	2300–2500		0.44	0.23	1.93
MAPCO	CH98 DR14	103	29°16′	43°05′	2300–2500		0.28	0.24	1.18
MAPCO	CH98 DR15	101	27°46′	44°05′	3340–3840		0.47	0.19	2.28
MAPCO	CH98 DR15	501	27°46′	44°05′	3340–3840		0.49	0.36	1.43
MAPCO	CH98 DR16	1..	25°16′	45°20′	2760–3900		0.46	0.29	1.53
MAPCO	CH98 DR16	201	25°16′	45°20′	2760–3900		0.44	0.27	1.47
MAPCO	CH98 DR16	202	25°16′	45°20′	2760–3900		0.55	0.54	0.93
MAPCO	CH98 DR17	201	24°28′	46°15′	4200–4500		0.54	0.36	1.39
MAPCO	CH98 DR17	301	24°28′	46°15′	4200–4500		0.56	0.33	1.63
MAPCO	CH98 DR17	401	24°28′	46°15′	4200–4500		0.49	0.32	1.43
Vema	CH77 DR04	170	23°42′	45°28′	4200		0.47	0.25	1.83
Vema	CH77 DR04	105	23°42′	45°28′	4200		0.55	0.21	2.33
Vema	CH77 DR05	401	23°25′	44°59′	4416		0.48	0.20	2.17
Vema	CH77 DR05	107	23°25′	44°59′	4416		0.58	0.26	1.87
Vema	CH77 DR06	201	14°07′	45°00′	2954		1.5	1.79	0.88
Vema	CH77 DR06	157	14°07′	45°00′	2954		1.85	2.02	0.89
Vema	CH77 DR08	26	10°37′	40°50′	4339		0.5	0.22	2.09
Vema	CH77 DR08	46	10°37′	40°50′	4339		0.58	0.22	2.13

[a] Data from Schilling (1975) and Bougalt (1980).

[b] *TR* represents the ship *Trident*.

[c] Ellipsis points (e.g., 1..) indicate a homogeneous group. (See note a, Appendix A.)

[d] No station or sample numbers given for FAMOUS area 1. Measurements indicate the ranges of variation within the given latitude and longitude.

[e] $(Nb/Zr)_{ch}$.

APPENDIX C

Average Concentrations (in ppm) and Standard Deviations for Each Chemical Group Recovered on DSDP Leg 82

Chemical group	N	Sc NAA	Ti XRF	V XRF	Cr XRF	Mn XRF	Fe XRF	Co XRF	Co NAA	Ni XRF	Ni NAA	Zn XRF	Rb XRF	Rb NAA	Sr XRF	Y XRF	Zr XRF	Nb XRF	Cs NAA	Ba NAA	La NAA	Eu NAA	Tb NAA	Hf NAA	Ta NAA	Th NAA	U NAA
Hole 556	●																										
I	2	38.6	6300	277	264	1239	62,475	41	46	116	116	67	3.2	2.2	104	28.2	62.5	0.8	0.10	21	1.8	0.94	0.58	1.77	0.1	0.09	06
II	16	37.0	8640	280	246	1335	76,085	39.9	42.7	75.4	80.2	74.9	4.7	5.3	100	38.9	94	2.0	0.23	20	2.6	1.21	0.79	2.53	0.14	0.13	0.04
		0.8	316	10	12	96	2180	1.9	1.8	6.8	7.7	4.3	2.3	1.9	2.5	1.6	6	0.7	0.19	5	0.2	0.06	0.04	0.16	0.01	0.02	0.01
III	11	37.8	5693	249	262	1238	64,500	38.9	43.8	93	93.7	58.6	4.6	3.8	101	26.2	57	1.3	0.18	15	1.5	0.89	0.53	1.50	0.08	0.08	0.08
		1.7	547	14	105	77	3970	3.7	4.5	13	12	4	0.7	1.1	2.3	2.3	3	0.7	0.07	6	0.2	0.07	0.04	0.14	0.02	0.02	0.03
IV	2	41.0	8160	326	48	1277	67,095	48	52	74	72	87	4.7	4.7	113	38.4	80	2.2	0.15	30	2.4	1.25	0.76	2.35	0.13	0.11	
V	2	32.5	1800	163	70	1000	45,600	31	35	95	109	28	0.3		90	10	11		0.02		0.3	0.41	0.12	0.19		0.02	
Hole 557	■																										
H1 CC	1	33.7	19,560	313	24	1394	107,380	42	43.3	25	28	128	11.3	10.7	344	49	219	43	0.05	161	27.2	2.64	1.16	5.2	2.83	2.69	0.9
I	3	38.1	20,960	432	36	1600	114,260	49	50	43	40	100	9.7	10.0	309	48	220	30.0	0.07	122	20.3	2.67	1.22	5.62	2.15	1.96	0.72
		0.2	124	23	5	160	2760	1	1	8	1	5	0.6	1.1	8	1	1	0.2	0.01	9	0.1	0.02	0.04	0.06	0.01	0.10	0.04
Hole 558	◆																										
I	1	32.2	7260	207	490	1239	75,740	47	50	259	287	73	3.6	1.9	128	26.6	83	8.6	0.06	40	5.7	1.03	0.56	1.95	0.57	0.53	0.15
II	3	37.6	6660	255	369	1188	69,930	44	46.8	141	144	73	3.9	3.4	92	29.3	66	3.2	0.19	10	2.5	0.99	0.57	1.81	0.16	0.16	0.07
		0.6	60	2	9	44	3620	1	1.6	10	13	1	0.7	0.7	4	0.5	3	0.3	0.10		0.2	0.04	0.02	0.05	0.01	0.01	0.01
III A	3	34.5	8362	277	342	1171	71,030	42.4	44.7	156	159	76	6.9	6.7	172	28.7	92	15.6	0.27	52	9.7	1.19	0.62	2.31	0.98	0.95	0.33
		0.5	71	4	6	96	1240	2.0	1.7	8	13	1	1.9	2.3	3	0.7	4	0.9	0.16	20	0.2	0.03	0.01	0.08	0.01	0.03	0.04
III B	5	34.5	7788	272	368	1084	68,796	42.8	43.9	156	155	73	5.2	5.2	180	26.0	81	13.6	0.19	36	8.9	1.11	0.56	2.09	0.89	0.88	0.23
		0.6	149	13	11	55	1858	2.3	1.5	7	10	3	1.1	1.8	5	0.9	2	0.6	0.10	13	0.2	0.03	0.01	0.04	0.02	0.04	0.05
IV	5	35.3	7236	267	365	1208	70,546	43.4	45.8	177	182	72	5.9	5.6	144	27.3	80	10.5	0.23	37	6.9	1.05	0.58	2.07	0.67	0.72	0.20
		0.5	202	13	14	42	1219	2.4	1.3	16	12	2	0.6	0.6	4	1.7	9	1.2	0.09	20	0.1	0.07	0.03	0.06	0.06	0.13	0.03
V	6	34.3	5700	224	447	1239	70,280	48.3	50.5	217	222	65	4.6	3.9	115	22.5	61	7.2	0.27	18	5.0	0.84	0.45	1.48	0.48	0.45	0.13
		1.0	147	14	14	69	1250	2.1	1.8	15	17	8	0.2	0.5	3	0.5	3	0.7	0.05	5	0.3	0.04	0.01	0.08	0.02	0.03	0.03
558-41-2, 143-146		35.9	5460	194	444	1239	74,060	50	52.8	219	235	61	3.2	2.3	107	22.7	51	2.0	0.22		1.7	0.77	0.46	1.30	0.14	0.12	0.05
Hole 559	◇																										
I	26	38.6	9093	317	272	1269	80,435	43	42.7	115	112.9	90	8.4	7.4	174	35.2	104	16.2	0.38	44	9.4	1.29	0.72	2.69	1.02	1.02	0.36
		2.8	400	43	16	183	5000	5	4.4	19	18.5	19	2.5	2.5	13	3.3	5	1.0	0.20	17	1.0	0.08	0.05	0.17	0.05	0.08	0.15
Hole 560	○																										
540-2-1, 93-96		5.9	7140	268	387	852	45,080	124	144	296	288	82	1.2	1.1	121	29.2	73	6.2	0.02	22	3.7	1.02	0.6	1.91	0.38	0.38	0.08
Hole 561	○																										
I	2	34.6	7140	265	406	1162	69,440	46.5	48.5	199	195	69	4.2	4.8		30.4	98	22.1	0.05	50	12.4	1.26	0.65	2.49	1.39	1.56	0.38
II	6	40.6	7980	352	228	1380	77,812	50.3	52.6	152	146	88	5.9	5.7	9.2	38.4	75	2.9	0.20	10	2.5	1.20	0.77	2.18	0.18	0.20	0.08
		0.6	161	6	7	58	1651	4.5	5.8	37	39	3	4.3	5.5	4	0.6	3	0.9	0.20	3	0.1	0.05	0.02	0.06	0.01	0.02	0.03
Hole 562	▽																										
I	19	40.0	9258	326	229	1394	81,432	42.7	44.6	93.5	93.8	80	4.0	3.9	101	41.2	94	2.9	0.20	10	2.9	1.30	0.84	2.60	0.19	0.17	0.07
		1.3	188	12	7	63	2172	1.5	1.5	6.7	6.5	4	2.9	2.9	6	1.2	3	0.6	0.23	4	0.2	0.09	0.02	0.06	0.02	0.03	0.05
II	5	34.9	6816	291	239	1177	69,510	40.6	42.7	96.6	96.2	68	3.8	3.6	97	30.8	68	2.5	0.18	11	2.2	0.99	0.65	1.85	0.16	0.13	0.05
		1.1	156	10	16	100	1383	1.5	1.4	7.4	6.3	4	1.7	1.5	9	0.8	2	0.7	0.13	5	0.1	0.04	0.06	0.06	0.01	0.01	0.01
II′	2	37.5	7470	337	263	1355	78,715	44	45	101	93	79	10.1	9.6	101	33.0	75	3.3	0.46	15	2.6	1.09	0.68	2.05	0.18	0.15	0.08
Hole 563	▲																										
I	4	41.1	5940	329	316	1277	74,970	41.7	44.0	99.5	100.5	68	8.3	8.5	85	27.5	55	1.6	0.28		1.8	0.90	0.56	1.54	0.12	0.13	0.09
		1.0	235	14	12	77	2809	0.5	2.0	7.9	9.0	3	2.4	1.7	2	0.6	2	0.6	0.08		0.2	0.06	0.01	0.07	0.01	0.02	—
II	6	39.7	5790	317	301	1227	67,246	43.3	47.1	119.2	116.7	66	3.1	2.6	84	27.3	53	1.7	0.11		1.7	0.88	0.54	1.51	0.12	0.11	0.08
		0.6	73	3	7	30	1560	2.7	3.8	14.2	13.7	3	1.4	1.8	1	0.4	3	0.6	0.05		0.2	0.03	0.02	0.04	0.01	0.01	—
Hole 564	△																										
I	26	40.9	8610	394	247	1358	82,790	46.8	47.0	116.3	114.9	83	5.4	4.9	105	39.3	92	4.6	0.28	17	3.7	1.25	0.79	2.52	0.30	0.29	0.09
		0.8	149	26	16	63	3104	3.0	3.8	14.1	13.8	4	2.0	2.0	4	1.3	4	1.0	0.15	7	0.3	0.06	0.03	0.11	0.04	0.06	0.04

Note: N = the number of samples for each analysis; NAA = neutron activation analysis; XRF = X-ray fluorescence; symbols in the N column correspond to symbols on Figures 14-19. Standard deviation is presented on the second line of many analyses. It corresponds to a single determination, the precision of the concentration for a chemical group should be estimated by dividing the above standard deviation by $\sqrt{N}$. Chemical Unit II was divided into two subunits (II and II′).

24. RARE-EARTH ELEMENTS, $^{87}Sr/^{86}Sr$, AND $^{143}Nd/^{144}Nd$ MANTLE SOURCE VARIATIONS[1]

M. L. Rideout and J.-G. Schilling, Graduate School of Oceanography, University of Rhode Island[2]

ABSTRACT

We report 48 analyses of rare-earth elements (REE) and 15 $^{143}Nd/^{144}Nd$ and $^{87}Sr/^{86}Sr$ analyses for basalts from the eight holes drilled during Leg 82. Discrete and distinct REE patterns and $^{143}Nd/^{144}Nd$ ratios characterize the eight holes, with little variation observed downhole except in Holes 561 and 558, thus suggesting dominantly long-term temporal and large-scale spatial variations in the mantle source of these basalts beneath the Mid-Atlantic Ridge over the last 35 Ma of its spreading activity. There is a good inverse correlation between $^{143}Nd/^{144}Nd$ and $(La/Sm)_{EF}$ with one exception in Hole 558 (approximately 35 Ma), the latter suggesting a recent (35 Ma) light REE depletion event, perhaps caused by dynamic or fractional melting. Short-term temporal and small-scale spatial mantle source variability is also evident in Hole 561 (approximately 18 Ma), which has rapid fluctuations in REE patterns and $^{143}Nd/^{144}Nd$ ratios (suggesting rapid transfer of magma from the time of melting) and is evidence contrary to the presence of a well-mixed magma chamber at this particular site and time.

The mantle source variations noted can be interpreted within two extreme models. The first model invokes a convecting mantle depleted in large ion lithophile elements (LILE) and containing lumps (or veins) of LILE-enriched material of various shapes and sizes, passively and randomly distributed throughout. A second more restrictive model considers the interaction of fixed mantle plumes and the LILE-depleted asthenosphere flowing towards a migrating Mid-Atlantic Ridge (MAR) axis. With the exception of Hole 558 and the uncertainties of reconstructions of absolute plate movements in the region, the observed variations can be explained by two hot spots; the nearly ridge-centered Azores hot spot (plume) and another hot spot located beneath the African plate that may be affecting the source of basalts currently erupting at the MAR axis at 35°N and which, in the past, would have produced the New England chain of seamounts on the North American plate and (later) the Atlantis-Great Meteor chain on the African plate.

Basalts erupted south of the Hayes Fracture Zone have not been affected by either of these two hot spots over the last 35 Ma and appear to have been continuously derived from the LILE-depleted source. Subaxial flow downridge from the Azores plume appears to have started 9 Ma, on the basis of the southward converging V-shaped time-transgressive ridges branching from the Pico and Corves Island, or not earlier than 16 Ma, on the basis of the geochemical results. Variations within Hole 558 remains unexplained by the latter model, unless we hypothesize a third hot spot.

INTRODUCTION

DSDP Leg 82 was designed to examine in detail the spatial and the temporal extent of mantle heterogeneities in the central North Atlantic, near the topographic high of the Azores Platform. Shallow volcanic platforms, such as this one, are characterized by high $^{87}Sr/^{86}Sr$ (low $^{143}Nd/^{144}Nd$) and Pb isotope ratios and enriched in the light rare-earth elements (LREE) relative to the heavy rare-earth elements (HREE). They are significant because they are derived from a different mantle source than the source from which mid-ocean ridge basalt (MORB) depleted in the large ion lithophile elements (LILE) originates. On the basis of known geochemical variations along the present Mid-Atlantic Ridge (MAR) axis (Schilling, 1975; White and Schilling, 1978; Bougault and Treuil, 1980) and temporal variations along the FAMOUS flow line from Leg 37 (Schilling et al., 1977; Aumento and Melson, 1977), nine holes were drilled during Leg 82, eight of which yielded basalts suitable for this study (Fig. 1).

The arrangement of holes, complemented with data from DSDP Leg 37 and from dredge samples along the present MAR axis, forms a coarse grid from which one may study (1) spatial variation along three isochrons (approximately 35 Ma, 18 Ma, from drilled basalt, and zero age from dredge sampling) and (2) temporal variations along four flow lines (Azores Platform, FAMOUS, 35°N, and south of the Hayes Fracture Zone, Fig. 1).

The important questions for which Leg 82 may provide answers are:

1. When and how did the large scale (>800 km) geochemical gradient currently observed along the present MAR axis develop?
2. Was the Hayes Fracture Zone always a boundary between the enriched Azores mantle domain, rich in LILE and radiogenic Sr and Pb (low Nd), and the depleted MORB source?
3. Is the spike-like anomaly superimposed on the large-scale geochemical gradient and currently present on the MAR axis at 35°N accidental or permanent feature that may be related to the activity of a hot spot other than the Azores?

In order to address these questions, we report 48 rare-earth analyses and 15 isotopes ratio analyses of Sr and Nd on basalts from Leg 82.

ANALYTICAL PROCEDURES

The samples were selected on board with the following considerations to ensure that the sampling was:

1. representative of a chemical group, as defined by core logging and available on-board incompatible and major element data;

---

[1] Bougault, H., Cande, S. C., et al., *Init. Repts. DSDP*, 82: Washington (U.S. Govt. Printing Office).

[2] Addresses: (Rideout, present address) Rice University, Department of Geology, Weiss School of Natural Sciences, Post Office Box 1892, Houston, Texas 77251; (Schilling) Graduate School of Oceanography, University of Rhode Island, Narragansett Bay Campus, Kingston, Rhode Island 02882.

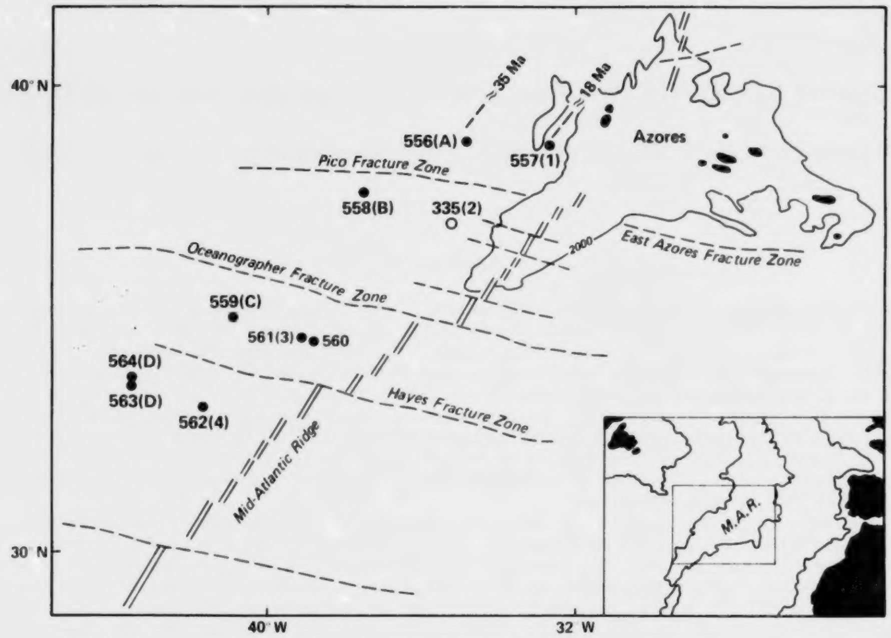

Figure 1. Map of the DSDP Leg 82 study area. Hole 335 (Leg 37), included for comparison, although it is dated at approximately 16.5 Ma. Sites along the approximately 18 Ma magnetic anomaly are represented in further diagrams by numerals, and sites along the approximately 35 Ma magnetic anomaly are represented by letters.

2. from the freshest section available, as determined by hand inspection and available geochemical and petrologic data from adjacent samples analyzed by X-ray fluorescence (XRF); and

3. frequent enough to represent adequately any chemical variations that may be present beyond what was suspected from the onboard XRF survey.

A special effort was made to take samples adjacent to XRF samples analyzed on board, wherever possible. Hand and petrologic descriptions of the basalt flows from which the samples were taken are found in the core descriptions for each site, referred to using DSDP nomenclature and numbering system.

All basalt samples were carefully broken down into small fragments; the fragments were selected to avoid calcite veinlets and alteration patches, and freshest fragments were ground into a fine powder in an agate mortar. Using approximately 0.5 g of sample powder, we analyzed 48 samples by instrumental neutron activation analysis (INNA), using essentially the same technique previously described by Schilling and Ridley (1975), slightly modified.

After INAA was completed, 15 samples were chosen for additional isotope work, based on the REE pattern identification from the concentration data. At least one sample per hole was measured, plus additional samples from Holes 558 and 561 that contained basalts with multiple REE signatures within a continuous series of basalt flows (see site chapters, Sites 558 and 561, this volume). Using approximately 0.3 g of sample powder, $^{87}Sr/^{86}Sr$ and $^{143}Nd/^{144}Nd$ isotopic ratios were determined from the same unspiked aliquot of sample. Detailed procedures for the isotopic methods used in this laboratory are described in detail in Rideout (1983) and are available on request from the authors. For $^{87}Sr/^{86}Sr$, the methods are essentially those of Hart and Brooks (1974), slightly modified to improve the separation of Ba from the rare-earth elements. Nd is then isolated from the rare-earth fraction and subsequently analyzed. Samples were run on triple filaments (Re-metal center, Ta-metal side ribbons) on a 2 VG Micro-Mass 30B mass spectrometer, with approximately 60–80 ratios collected from $^{87}Sr/^{86}Sr$ and 100–150 ratios collected for $^{143}Nd/^{144}Nd$ as a statistically representative data summation. $^{87}Sr/^{86}Sr$ data are normalized to the E & A standard of 0.70800 and $^{143}Nd/^{144}Nd$ to a BCR-1 value of 0.512650 (see Table 2 caption). The cumulative average in this laboratory for the E & A standard is 0.708031 ± 20 (2 s.d., n = 27) and the BCR-1 standard is 0.512569 ± 8 (2 s.d., n = 12), where n is the number of analyses reported and s.d. is the standard deviation.

RESULTS

Rare-Earth Abundances: Spatial and Temporal Variations

The results of the 48 rare-earth analyses are presented in Table 1; the data are arranged by site and increasing absolute depth.

Figure 2 is a composite of the rare-earth results, plotted relative to chondrites. The patterns are grouped by hole, and the holes are arranged geographically to be similar to Figure 1. Thus, interhole variations along a vertical column represents spatial variations along the ridge axis at a particular time (approximately 35 Ma, 18 Ma, and zero age), and interhole variation along a horizontal row illustrates the temporal variation at a given point on the ridge (or temporal variation along a flow line from the spreading ridge axis). The REE patterns suggest the existence of discrete chemical groups among the holes, and in two cases within a single hole (Holes 558 and 561). Thus, in general, each site is characterized by a unique type of REE pattern (i.e., depleted, enriched, or intermediate), with only slight second-order relative concentration variations downhole. This can be interpreted as reflecting long-term (temporal) and large-scale (spatial) variations at the Mid-Atlantic Ridge axis at approximately 18 and 35 Ma. As for the two exceptions noted, Hole 561 contains multiple REE patterns, strongly enriched in LREE at the top of the hole, and suddenly changing to strongly depleted in

Table 1. Rare-earth element analyses of DSDP Leg 82 basalts.

Hole-Core-Section (piece number)	La	Ce	Nd	Sm	Eu	Tb	Dy	Yb	Lu	$(La/Sm)_{EF}$
556-2-1 (6B)	1.7	6.6	5.7	2.37	0.90	0.62	5.0	2.43	0.344	0.51
556-3-1 (8B)	2.8	9.5	8.1	3.64	1.28	0.77	6.6	3.64	0.499	0.55
556-4-5 (3C)	3.1	11.2	8.9	3.70	1.31	0.87	5.9	3.75	0.533	0.58
556-6-2 (2A)	2.2	9.4	7.8	3.05	1.14	0.86	5.5	3.28	0.498	0.52
556-9-2 (3c)	1.9	5.2	4.9	2.33	0.90	0.54	4.1	2.49	0.328	0.58
556-11-1 (16)	2.4	7.9	7.4	3.12	1.19	0.69	4.7	3.14	0.445	0.53
556-12-3 (5B)	1.3	4.7	4.9	1.78	0.81	0.50	3.5	2.02	0.299	0.52
556-16-2 (15)	2.5	7.9	8.1	3.01	1.18	0.72		3.39	0.493	0.59
557-111, CC	25.5	61.7	32.0	7.58	2.61	1.37	7.6	3.95	0.499	2.36
557-1-1 (10)	18.7	43.3	25.7	7.29	2.39	1.54	8.1	3.39	0.463	1.79
558-27-3 (11B)	5.9	15.8	8.8	2.79	1.03	0.62	3.7	2.23	0.301	1.47
558-28-1 (2)	5.9	14.3	9.2	2.79	1.12	0.53	3.6	2.30	0.318	1.49
558-28-2 (16)	2.4	7.8	6.0	2.54	0.92	0.59	5.0	2.60	0.354	0.66
558-30-2 (11)	10.0	22.6	13.0	3.42	1.23	0.65		2.43	0.409	2.06
558-33-1 (4)	8.6	20.8	11.8	3.07	1.17	0.58		2.17	0.326	1.97
558-33-2 (9)	8.5	19.7	10.0	2.94	1.02	0.48	3.9	2.13	0.291	2.03
558-36-3 (3A)	7.6	19.0	11.0	2.97	1.12	0.61		2.64	0.370	1.79
558-38-1 (14)	4.8	12.2	6.9	2.11	0.82	0.51	2.8	2.13	0.276	1.59
558-39-2 (3A)	4.9	11.4	7.5	2.24	0.84	0.59	3.5	2.02	0.291	1.54
559-1-4 (2)	9.6	22.0	12.3	3.63	1.33	0.85		3.22	0.441	1.85
559-6-1 (5)	8.4	21.6	11.7	3.10	1.13	0.74		2.73	0.398	1.89
559-8-3 (3)	8.8	20.0	11.3	3.39	1.29	0.68		3.11	0.472	1.81
561-111, CC	12.7	26.4	12.7	3.60	1.25	0.72	4.4	2.54	0.332	2.46
561-1-1 (2C)	11.1	23.9	11.6	3.13	1.16	0.70		2.21	0.343	2.48
561-1-1 (9A)	2.7	8.2	8.0	3.14	1.14	0.75	5.7	3.62	0.495	0.60
561-1-2 (2C)	2.6	7.8	7.7	2.94	1.24	0.88		3.57	0.504	0.62
561-2-1 (3B)	2.7	7.7	5.9	3.01	1.11	0.73	5.8	3.47	0.505	0.63
561-2-2 (2A)	2.3	8.6	7.1	3.07	1.16	0.75	5.5	3.24	0.536	0.52
561-2-3 (10A)	2.4	9.4	7.5	3.01	1.19	0.87	5.5	3.52	0.554	0.56
561-3-1 (9J)	2.3	8.4	8.2	3.06	1.18	0.89	5.7	3.47	0.509	0.54
561-3-2 (4A)	2.4	9.4	8.7	3.05	1.18	0.88	5.1	3.54	0.466	0.55
562-2-2 (1)	2.7	9.5	8.6	3.36	1.31	0.83		3.78	0.544	0.57
562-4-1 (3E)	2.9	9.1	8.5	3.54	1.28	0.80	6.9	3.61	0.516	0.57
562-7-1 (4B)	2.6	7.6	6.1	2.73	0.98	0.85		3.14	0.419	0.67
562-8-1 (2)	2.4	7.7	6.0	2.76	1.09	0.66	5.3	2.95	0.412	0.61
562-9-1 (3B)	2.6	7.5	6.3	2.53	1.06	0.72		2.87	0.442	0.71
562-10-3 (1A)	2.4	8.0	7.8	2.72	1.02	0.64	5.0	2.94	0.418	0.63
563-23-1 (2A)	1.8	6.3	5.4	2.18	0.89	0.59	4.5	2.70	0.411	0.59
563-24-2 (3A)	1.8	5.8	4.9	2.13	0.89	0.48		2.69	0.387	0.60
563-24-3 (7F)	1.6	5.8	5.3	2.14	0.83	0.56	4.6	2.56	0.335	0.54
563-25-2 (2D)	1.9	5.6	5.8	2.13	0.91	0.66	4.5	2.59	0.369	0.63
564-1-1 (2B)	3.7	11.7	10.5	3.37	1.31	0.98	5.9	3.86	0.524	0.78
564-3-4 (2)	3.5	10.3	8.8	3.24	1.31	0.84		3.57	0.505	0.76
564-5-2 (4B)	3.8	10.0	9.2	3.44	1.07	1.00	5.6	3.59	0.494	0.77
564-6-4 (2K)	3.8	9.7	8.8	3.32	1.22	0.78	5.8	3.29	0.484	0.80
564-7-2 (6B)	4.2	11.8	9.7	3.36	1.25	0.85		3.63	0.525	0.87
564-8-1 (4F)	4.2	13.2	11.2	3.47	1.34	1.00	5.7	3.68	0.549	0.84
564-9-2 (9B)	4.2	11.1	9.6	3.44	1.32	0.95		3.77	0.522	0.86

Note: All concentrations are reported in ppm. Analyses performed by instrumental neutron activation analysis, using essentially the method of Schilling and Ridley, 1975. $(La/Sm)_{EF}$ is the La/Sm ratio normalized to chondrites. Chondrite values used for calculating enrichment factors (EF) are given in Schilling et al. (1977; 1983). For typical errors, see Schilling and Ridley, 1975.

LREE at a point downhole. No intermediate between these extremes is observed, implying that no mixing has occurred between the two "end-members." Hole 558 contains dominantly LREE-enriched patterns, but with one horizon of LREE-depleted material. In both cases, the patterns cross near the middle of the REE series.

Whereas the uniformity within a single drilled hole is interpreted as reflecting a lack of short-term geochemical variation for the interval sampled, the exceptions noted at Sites 558 and 561 would suggest the converse situation exists along the Mid-Atlantic Ridge at the time of emplacement of the ocean basalt crust at these two sites.

Figure 2 also readily demonstrates that the spatial variations observed along the ridge at approximately 0, 18, and 35 Ma are not identical to one another. Particularly with respect to the Azores hot spot, the geochemical gradient observed along the D Ma ridge axis is not present at 18 and 35 Ma, and thus must have developed later than 18 Ma or was far more complex in the past.

Temporal variations at a given point (i.e. along a flow line) are variable from one flow line to another. South

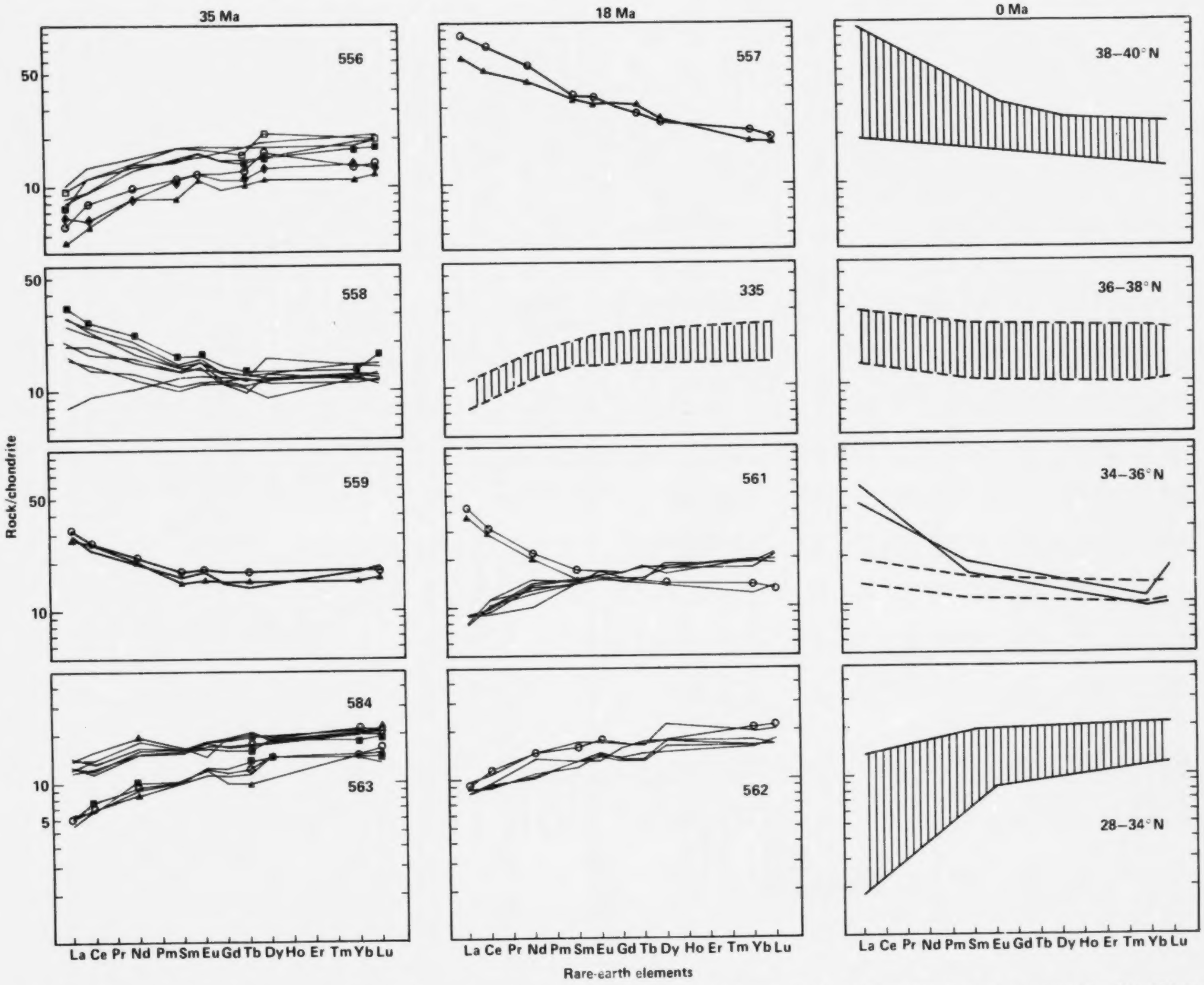

Figure 2. Composition of rare-earth abundances relative to chondrites as a function of atomic number. Data for age zero is from Schilling et al. (1983) and for Hole 335, Leg 37, from Schilling et al. (1977), O'Nions et al. (1977), and Aumento et al. (1977). Holes are grouped by isochron (columns) and spreading flow lines (rows) for direct comparison.

of the Hayes Fracture Zone, all material is uniformly depleted throughout the 35 Ma time range sampled. At the latitude of the Azores flow line, the enriched Azores anomaly was not present 35 Ma ago (Hole 556) but was present 18 Ma ago (Hole 557). Therefore, the LREE enriched anomaly must have begun at a time, *t*, so that 35 < *t* < 18 Ma. Along the FAMOUS flow line, Schilling et al. (1977) suggested a progressive increase in LREE enrichment, from the LREE-depleted basalts at Hole 335, Leg 37 (approximately 16.5 Ma) to progressively more LREE enrichment patterns in Hole 332 (3.5 Ma) (Aumento, Melson, et al., 1977) and, at the present, in the FAMOUS region. Thus, the gradient generated by the Azores hot spot did not exist at 16.5 Ma or did not extend that far down the ridge and must have developed at a time between 16.5 and 3.5 Ma (Holes 335 and 332). Extension of this flow to 35 Ma (Hole 558) suggests either (1) a reversal of this trend between 35 and 18 Ma, if the most abundant LREE-enriched basalts from this hole are considered, or (2) no variation at all, if the only LREE-depleted basalt is taken at face value. Finally, near the approximate latitude of the 35°N anomaly flow line, the evidence suggests that the present-day anomaly persisted during the last 35 Ma and that local variations within a single hole or within the 35°N anomaly existed for at least the last 18 Ma. The variability in REE patterns increases from the fairly uniform in Hole 559, to the complex and rapidly fluctuating in Hole 561, and to the spike seen at 35°N on the present MAR axis (and superimposed on the general trend seen at the zero-age MAR axis).

Comparison of REE Data with Shipboard XRF Incompatible Trace Element Data

It is of geochemical interest and importance to compare the incompatibility trace element data obtained on board by XRF, used in constructing the extended Coryell-Masuda diagram (Coryell et al., 1963), and the REE results obtained by instrumental neutron activation analysis (INAA) from this study. Remembering that the XRF data and INAA are not obtained from exactly the same sample, La vs. Nb (Fig. 3A) shows a remarkable nearly one to one correlation for these two highly incompatible elements, despite the analytical problems that exist in measuring Nb at the low concentrations found in ocean basalts (Etoubleau et al., this vol.) The correlation exists for all samples, hence all holes, analyzed from Leg 82. Sm vs. Zr (Fig. 3B), representing two somewhat less incompatible elements, also shows a nearly one to one correlation. In summary the XRF and INAA results corroborate that the trace elements (specifically Nb, Zr, Ti, Y, and V) behave similarly to the rare-earths (e.g., La, Sm, Eu, Tb, and Lu) and can be used as analogs to compare other chemical parameters and mantle source domains. Their relative enrichment signatures (constructed with the trace element data) can be used as geochemical tracers for ocean areas, as is usually done with the rare-earth elements.

Downhole Variations

To examine the chemical groups and trends identified on board by XRF further, a comparison of the major elements from XRF and $(La/Sm)_{EF}$ from INAA is plotted versus depth in Figure 4. In general, Mg-number inversely correlates with Ti. In contrast, no systematic variation is observed between the $(La/Sm)_{EF}$ and Mg-number, suggesting a lack of a correlation between Mg-number and relative rare-earth patterns in these holes. The inverse correlation between incompatible element content and Mg-number has been interpreted as usually reflecting a lack of a chemical imprint caused by low-pressure crystallization (e.g., Bryan and Moore, 1977). Such an event would not affect and be recorded in the relative rare-earth enrichment patterns (Schilling, 1971). Either variable degrees of partial melting of a homogeneous mantle reservoir or variable mantle sources are necessary to explain the observed $(La/Sm)_{EF}$ variations.

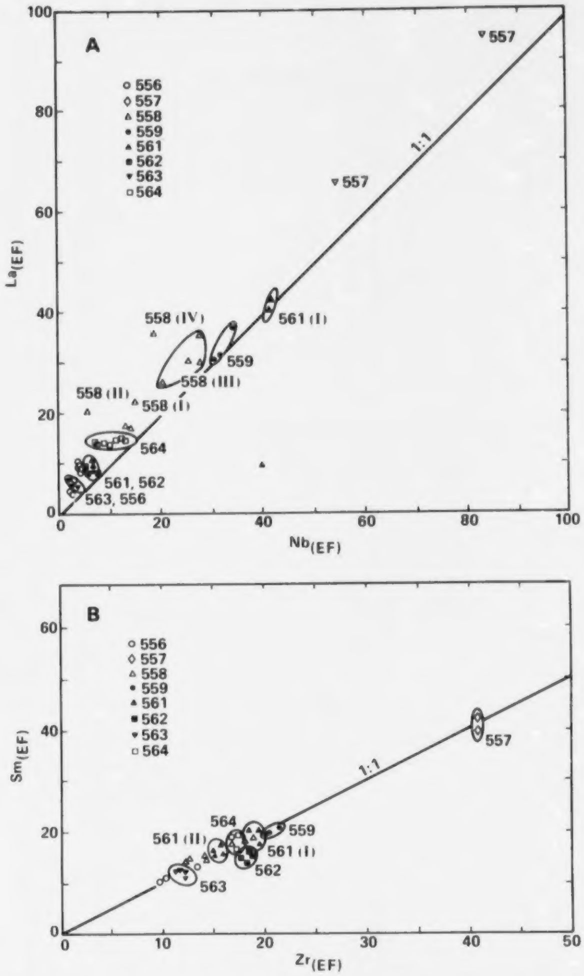

Figure 3. A. La versus Nb. All data are given in ppm. Roman numerals indicate chemical group (if more than one group was identified for the hole). Nd data are from site chapters, all sites except 560 (this volume), and La data, this report. Nb and La data are for sample horizons nearest to each other but not from identical samples. For further details of comparison see Rideout (1983). B. Sm versus Zr. All data are given in ppm. Zr data are from site chapters, all sites except 560 (this volume). Sm data are reported in Table 1.

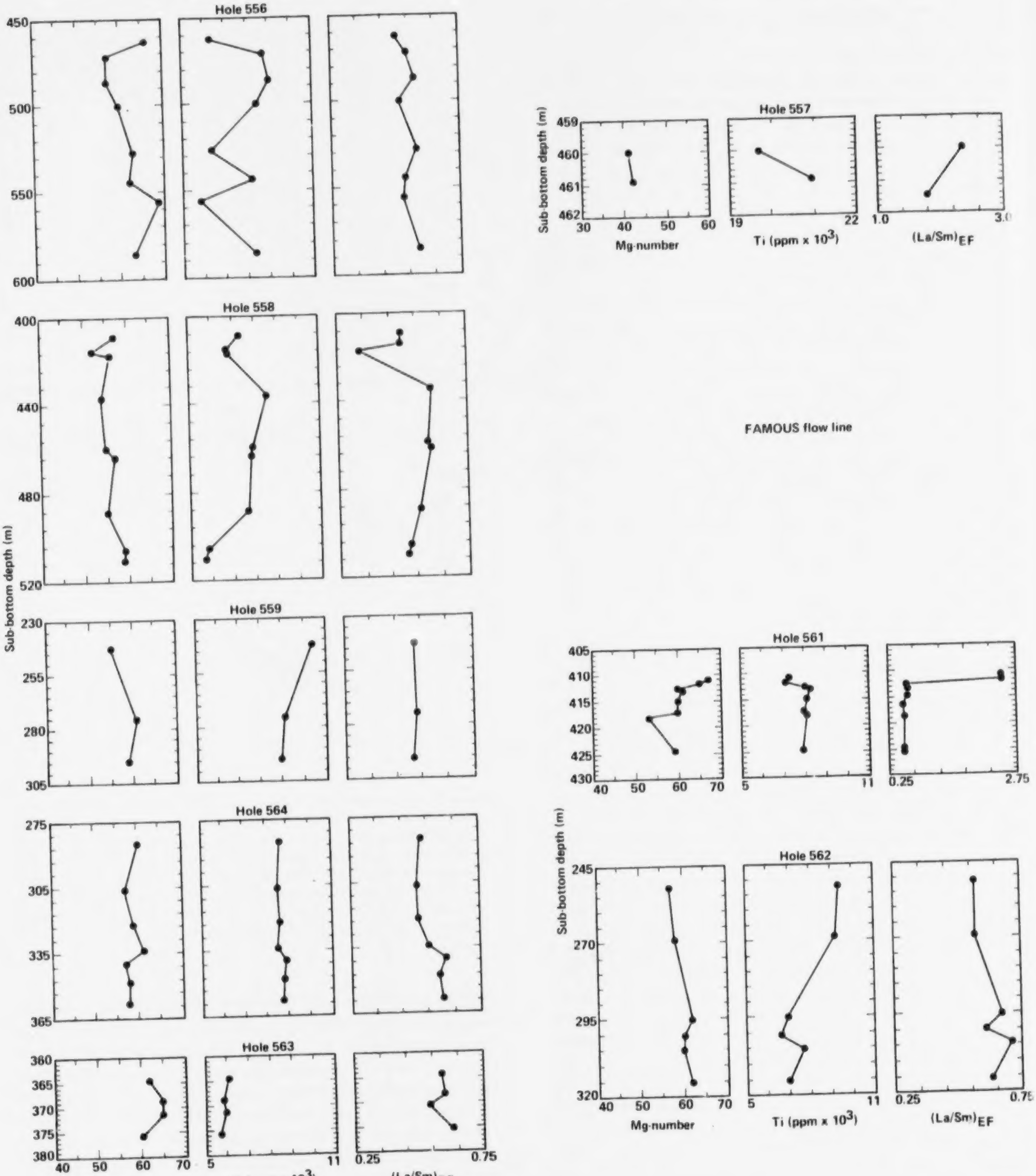

Figure 4. Mg-number, Ti, and $(La/Sm)_{EF}$ versus depth along cores. Mg-number and Ti major element data are from the on-board X-ray fluorescenc analyses, from site chapter, all sites except 560 (this volume). $(La/Sm)_{EF}$ instrumental neutron activation data are from Table 1. For details o comparison, see Rideout (1983).

$^{143}Nd/^{144}Nd$ and $^{87}Sr/^{86}Sr$ Variations

The 15 samples selected for $^{143}Nd/^{144}Nd$ and $^{87}Sr/^{86}Sr$ isotope analyses represent at least 1 sample per hole for holes that have uniform REE patterns; 5 samples from Hole 558 and 2 samples from Hole 561 were analyzed in order to cover the range of depleted and light REE-enriched patterns present in these two holes. The $^{87}Sr/^{86}Sr$ and $^{143}Nd/^{144}Nd$ isotope ratio results obtained are listed in Table 2. Leaching experiments were conducted on a few selected samples (566-16-2, [Piece 15]; 558-38-1 [Piece 14]; 559-6-1 [Piece 5]; 561-1-1 [Piece 2C]) following the method of O'Nions and Pankhurst, (1976). These data are also shown in Table 2.

With one exception (558-28-2, Piece 16), $^{143}Nd/^{144}Nd$ versus $(La/Sm)_{EF}$ (Fig. 5A) demonstrates that a good inverse correlation exists within and among holes, forming an inverse correlation between LREE fractionation patterns and $^{143}Nd/^{144}Nd$ isotope ratio signatures. An example illustrating the correlation within a single hole is shown in Figure 6A (Hole 561) and among holes by comparing Figures 6A and 6B (Holes 561 and 558). This correlation agrees well throughout the 18 and 35 Ma time periods, with the cited exceptions of Sites 558 and 561 (which will be discussed later).

In addition to the exception noted in Figure 5A, the $^{143}Nd/^{144}Nd$ versus $(La/Sm)_{EF}$ correlation suggests that the spatial and temporal variations observed in the REE patterns must also be derived from mantle sources because the $^{143}Nd/^{144}Nd$ ratio is not likely to be affected by equilibrium partial melting or subsequent fractional crystallization involved in the generation and evolution of these basalts. Thus, the simplest explanation for the dispersion of the REE patterns and Nd isotopic ratios would be tapping of a heterogeneous mantle source.

Table 2. DSDP Leg 82: $^{87}Sr/^{86}Sr$ and $^{143}Nd/^{144}Nd$ isotope ratios.

Core-Section, Piece	Sub-bottom depth (m)	$^{87}Sr/^{86}Sr$ ± 2 SE	$^{87}Sr/^{86}Sr$ ± 2 SE (leached)	$^{143}Nd/^{144}Nd$ ± 2 SE	Sm/Nd
556-6-2, 2A	499.70	0.703156 28		0.513195 22	0.391
556-16-2, 15	586.36	0.703290 26	0.702855 28	0.513156 18	0.372
557-H1, CC	(1.74)	0.704141 30		0.512979 20	0.237
557-1-1, 10	461.45	0.703851 20		0.512952 20	0.284
558-27-3, 11B	409.17	0.703392 22		0.512999 20	0.317
558-28-1, 2	414.59	0.703251 22		0.512967 20	0.303
558-28-2, 16	417.31	0.703591 26		0.513025 18	0.423
558-33-1, 4	459.78	0.703378 24		0.512897 20	0.260
558-38-1, 14	505.59	0.703724 34	0.703210 44	0.512976 22	0.306
559-6-1, 5	274.93	0.703008 30	0.702985 26	0.513048 16	0.265
561-1-1, 2C	412.01	0.704028 32	0.703479 24	0.512940 22	0.284
561-2-3, 10A	418.62	0.703430 24		0.513102 22	0.401
562-7-1, 4B	295.32	0.703169 24		0.513139 20	0.448
563-24-3, 7F	370.75	0.703101 24		0.513137 14	0.404
564-5-2, 4B	322.53	0.702729 24		0.513127 20	0.374

Note: $^{87}Sr/^{86}Sr$ isotope ratio results are normalized to an E & A value of 0.70800 and $^{143}Nd/^{144}Nd$ isotope ratio results are normalized to a BCR-1 value of 0.512650. For error in Sm/Nd, see Schilling and Ridley, 1975. SE is standard error.

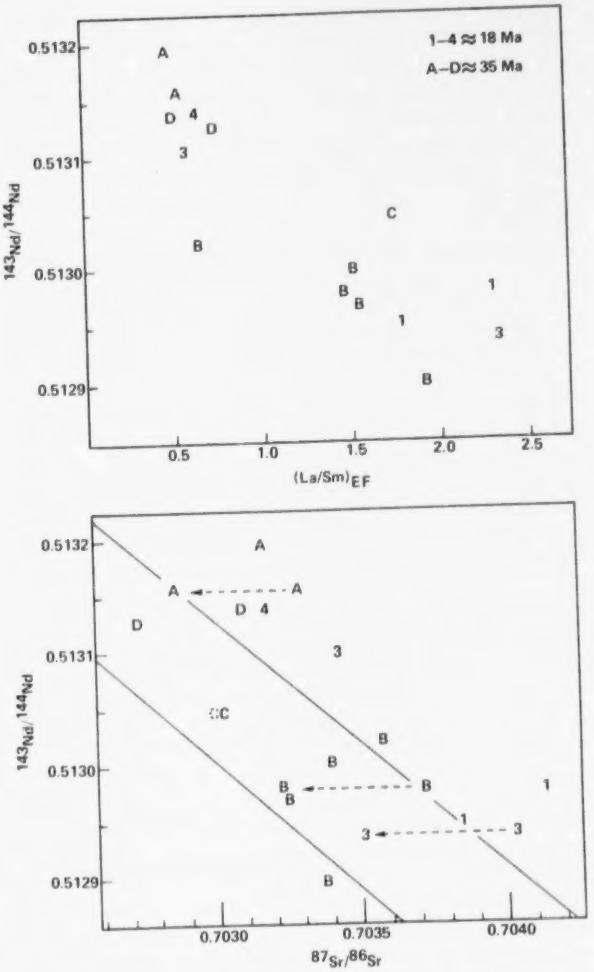

Figure 5. Top figure: $^{143}Nd/^{144}Nd$ versus $(La/Sm)_{EF}$. Bottom figure: $^{143}Nd/^{144}Nd$ versus $^{87}Sr/^{86}Sr$. $^{87}Sr/^{86}Sr$ results from leached residues are indicated by dashed lines.

It should be noted that the isotope ratios shown in Figure 5A and 5B are uncorrected for age. However, the age correction does not significantly affect the $^{143}Nd/^{144}Nd$ versus $(La/Sm)_{EF}$ correlation, but only slightly alters the slope of the correlation line. The correction would range between 2 to 4 × 10^{-5} for the 18 Ma isochron and 4 to 6 × 10^{-5} for the 35 Ma isochron, for the LREE-enriched and LREE-depleted patterns, respectively.

Overall, the data presented in Figure 5 are broadly consistent with binary mixing, although it could be argued that the data cluster into two groups within this diagram, suggesting a lack of mixing. We suggest that these two clusters are an artifact of the sampling density, as the gap seen in the $(La/Sm)_{EF}$ versus $^{143}Nd/^{144}Nd$ and $^{143}Nd/^{144}Nd$ versus $^{87}Sr/^{86}Sr$ space also corresponds to a gap in sampling between holes on the FAMOUS flow line and the 35°N flow line (Fig. 1). The distance

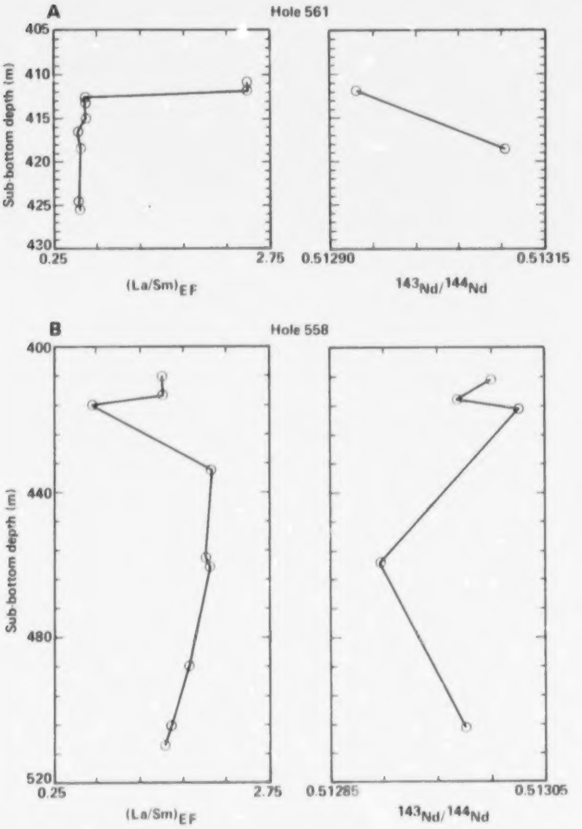

Figure 6. $(\mathrm{La/Sm})_{\mathrm{EF}}$ and $^{143}\mathrm{Nd}/^{144}\mathrm{Nd}$ versus depth for Holes 558 and 561.

between these two flow lines is on the order of 390 km, as compared to ~100 km between the Azores and FAMOUS flow line and ~100 km between the flow line 35°N and the flow line south of the Hayes Fracture Zone. It is important to note that the samples analyzed in this study, therefore, are from widely separated sites and are irregularly spaced. The gap observed in Figure 5 could possibly be closed if the holes were closer together and the density of sampling was more homogeneous.

$^{143}\mathrm{Nd}/^{144}\mathrm{Nd}$ versus $^{87}\mathrm{Sr}/^{86}\mathrm{Sr}$ (Fig. 5B) also shows an inverse correlation, but with significantly greater scatter. In general, the data fall within the so-called mantle array (using boundary lines that are two sigma deviations from a linear best fit to average ocean basalt values (Waggoner, in prep.)[3]. The scatter is predominantly to the right of the array and seems to have been caused by seawater alteration, which enhances the $^{87}\mathrm{Sr}/^{86}\mathrm{Sr}$ ratios of the basalts, whereas the $^{143}\mathrm{Nd}/^{144}\mathrm{Nd}$ ratios remain essentially unaffected (O'Nions and Pankhurst, 1976). Leaching experiments were conducted on samples suspected of having various degrees of $^{87}\mathrm{Sr}/^{86}\mathrm{Sr}$ enhancement from seawater alteration (including a sample that appeared not to have been so affected) to check the leaching technique and assumptions. Results of these experiments are presented in Table 2 and are indicated by the dashed lines in Figure 5. Samples displaced to the left are observed to plot closer or on the trend of the mantle array upon leaching, whereas one sample (symbol C) that plotted on the mantle array trend was not affected by the leaching, thus confirming seawater alteration. However, this presents an uncertainty in the $^{87}\mathrm{Sr}/^{86}\mathrm{Sr}$ data, so care must be taken to use the corrected $^{87}\mathrm{Sr}/^{86}\mathrm{Sr}$ data, within or contiguous to the mantle arra for later comparison.

In order to compare the rare-earth and isotope rati effects in time and space, $(\mathrm{La/Sm})_{\mathrm{EF}}$, $^{143}\mathrm{Nd}/^{144}\mathrm{Nd}$, an $^{87}\mathrm{Sr}/^{86}\mathrm{Sr}$ are shown plotted against latitude in Figure 7 The dashed envelopes shown in the $(\mathrm{La/Sm})_{\mathrm{EF}}$ and $^{87}\mathrm{Sr}/^{86}\mathrm{Sr}$ are the data for the zero-age Mid-Atlantic Ridg

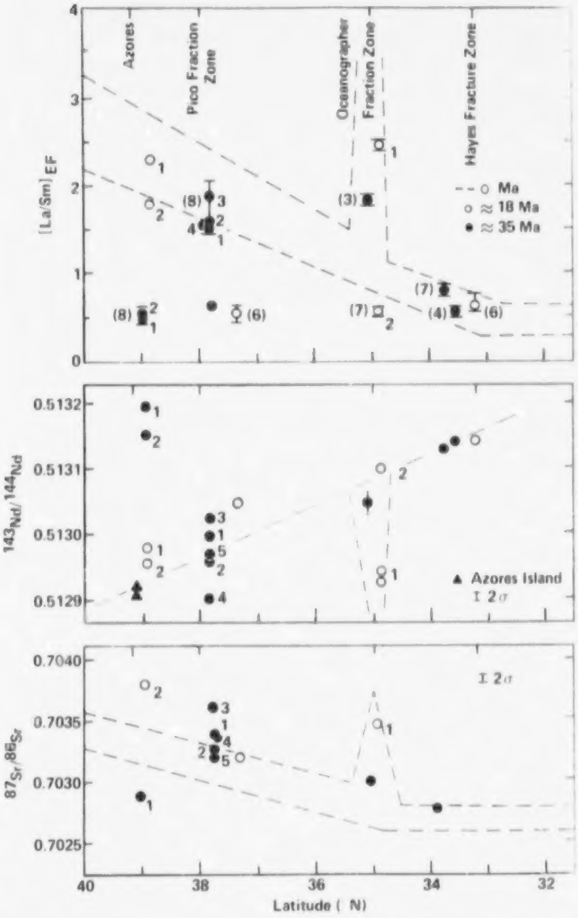

Figure 7. $(\mathrm{La/Sm})_{\mathrm{EF}}$, $^{143}\mathrm{Nd}/^{144}\mathrm{Nd}$, and $^{87}\mathrm{Sr}/^{86}\mathrm{Sr}$ results plotted versus latitude. Dashed lines for the zero-age variation are taken fo REE from Schilling (1975) and for $^{87}\mathrm{Sr}/^{86}\mathrm{Sr}$ from White and Schilling (1978); $^{143}\mathrm{Nd}/^{144}\mathrm{Nd}$ line is inferred from $^{87}\mathrm{Sr}/^{86}\mathrm{Sr}$ data an the mantle array relationship for ocean basalts. Open circles ar for 18 Ma and closed circles are for 35 Ma isochrons. $^{87}\mathrm{Sr}/^{86}\mathrm{Sr}$ data plotted are results that fall within or adjacent to the $^{143}\mathrm{Nd}/^{144}\mathrm{Nd}$ versus $^{87}\mathrm{Sr}/^{86}\mathrm{Sr}$ mantle array (Fig. 6B) and the leached samples.

---

[3] Waggoner, D. G. [Ph.D. dissert.] University of Rhode Island, Kingston.

(Schilling et al., 1983; White and Schilling, 1978). The dashed line on the $^{143}Nd/^{144}Nd$ diagram is an estimate of where the zero-age data would be, based on what data are now available and the correlation of $^{143}Nd/^{144}Nd$ to $^{87}Sr/^{86}Sr$ generally observed in mid-ocean ridge basalts and Figure 5.

The data are observed to generally follow the present day Mid-Atlantic Ridge trends (as indicated by the dashed lines) with the exceptions previously noted, namely Holes 556 (35 Ma, Azores Platform flow line) and 335 (16 Ma, FAMOUS flow line), both of which are uniformly LREE depleted, and a single horizon in Hole 558, which is also depleted in LREE but has a low $^{143}Nd/^{144}Nd$ ratio comparable to the basalts with LREE-enriched patterns that dominate this hole.

Thus, it would seem that a tendency for the development of a chemical gradient already existed in the past, with the exceptions noted above and below. In particular, the Nd isotope data in Figure 7 suggest that:

1. Anomalous Azores mantle enrichments were never present south of the Hayes Fracture Zone, thus, providing further evidence that the source of the depleted MORBs that occur worldwide is to a first order uniform or well mixed.

2. The enriched Azores mantle anomaly apparently was not present 35 Ma ago, as seen in the depleted LREE signature of Hole 556, and must appeared between 35 and 18 Ma to generate the enriched LREE patterns seen at Hole 557.

3. The gradient resulting from the enriched Azores mantle anomaly, 16.5 Ma ago, if at all present, did not extend down to the latitude of the FAMOUS flow line, as seen in the depleted LREE signature of Hole 335, Leg 37; rather, it began some time after, as seen by the increasing degree of LREE enrichment from Hole 332 (approximately 16 Ma) to the zero-age MAR axis.

4. The 35°N mantle anomaly has persisted for the last 35 Ma and influenced the eruptive products at the Mid-Atlantic Ridge axis at this latitude and time period and, thus, the corresponding flow lines as well. The large local variations (irregular mixing?) along this flow line seem to have appeared only 18 Ma ago.

5. Points 1–4 illustrate the presence of long-term, large-scale source variations in this region, whereas Hole 561 reflects short-term source variations.

6. A special explanation is necessary for Hole 558, which is anomalous in two ways: (1) we have noted that the inverse correlation between $^{143}Nd/^{144}Nd$ versus $(La/Sm)_{EF}$ breaks down for the only lava horizon from this hole that has a LREE-depleted pattern (i.e., 5587-28-2 [Piece 16]); and (2) the LREE-enriched patterns with low $^{143}Nd/^{144}Nd$ from Hole 558 cannot be related to the Azores hot spot anomaly, because the Azores anomaly does not appear to be present at 35 Ma along the Azores flow line.

We will now briefly discuss the anomaly in this hole. Sample 558-28-2 (Piece 16) is the only sample found in Hole 558 with a horizon characterized by a depleted LREE pattern (Fig. 2). It has a low $^{143}Nd/^{144}Nd$ for such a depleted pattern, falling in the upper part of the range of basalts with enriched LREE patterns from the same hole and other holes from Leg 82.

The discrepancy may suggest LREE depletion must be relatively recent, so that radiogenic ^{143}Nd had not had time to accumulate (Fig. 5B). Figures 4 and 5B show that this horizon is also systematically lower in Mg-number, Ti, and $(La/Sm)_{EF}$ relative to the chemical horizons above it or below it. Fractional melting with some garnet in the residue (Wood, 1979; 1981; Zindler et al., 1979) or dynamic melting (Langmuir et al., 1977) could be suggested to explain the presence of this anomalous chemical horizon and the crossing of the rare -earth patterns in the HREE within this hole. Such short-term fluctuations between sources within a single hole implies the absence of a well-mixed magma chamber or a wide zone of melting where interstitial melt droplets coalesce and mix. A rapid transfer of magma from the time of melting to the time of eruption is also implied.

Finally, $^{143}Nd/^{144}Nd$ versus Sm/Nd (Fig. 8) further demonstrates that the depleted sample also has an anomalously high $^{143}Nd/^{144}Nd$ for its Sm/Nd value plotted relative to the other LREE-enriched samples from this hole. An isochron line drawn through the four enriched samples yields a slope with an age of approximately 437 Ma (Fig. 8A). This can be further evaluated by Figures 8B and 8C, which include the data from Holes 558 and 561, and all the holes, respectively. Indeed, with the exception of the depleted sample from Hole 558 (558-28-2 [Piece 16]), the samples fall along broad linear correlation trends, corresponding respectively to ages of 362 Ma (Fig. 8B) and 310 Ma (Fig. 8C) if interpreted as isochrons (Table 3). Interestingly enough, the estimated ages fall in the range dating the earliest time (model age) that the enriched Azores source and the depleted MORB source could have been produced from a common source, based on the $^{87}Sr/^{86}Sr$ and Rb/Sr ratios of dredged basalts along the present MAR axis (White and Schilling, 1978). However, it is also possible that the line represents variable mixing between an enriched mantle component and depleted asthenospheric material. These two alternative models can be combined by assuming that the mixing event responsible for the large spectrum of variations observed between these two extreme mantle domains occurred subsequently.

INTERPRETATION AND DISCUSSION

In the previous discussion, fractional crystallization and partial melting have been eliminated as the primary causes of the temporal and spatial variations in REE patterns and $^{143}Nd/^{144}Nd$ isotopic variations seen in the Leg 82 study area. Dynamic melting may explain the complex geochemical patterns observed at Hole 558. Otherwise, the geochemical variations must reflect mantle heterogeneities and their possible dynamic interaction. Interpretation of the results in terms of mantle dynamics may be accomplished by considering two extreme models:

1. A veined or lumpy mantle that contains a random distribution of enriched domains of variable size and shape, all passively embedded in a LILE-depleted convecting upper mantle (e.g., Davies, 1981; Richter and Ribe, 1979); or

2. A mantle dominated by the interaction and mixing of buoyant, independently rising, LILE-enriched blobs

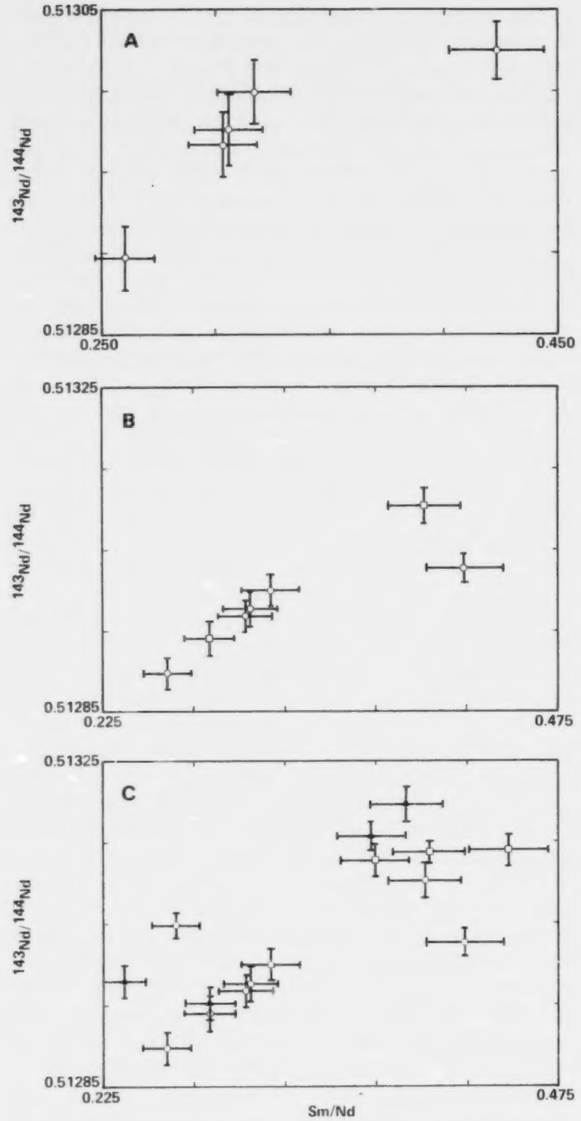

Figure 8. ^{143}Nd/^{144}Nd versus Sm/Nd using data population from A. Hole 558 only. B. Holes 558 and 561 combined (circles are for 558, squares for 561). C. The eight holes studied from Leg 82 (circles for Holes 558, 559, and 561, along the FAMOUS and 35°N flow lines; triangles for Holes 556 and 557, along the Azores flow line; squares for Holes 562, 563, and 564, south of the Hayes Fracture Zone).

(plume) with LILE-depleted asthenospheric material—a model formulated within the framework of fixed hot spots (or mantle plume) and migrating spreading ridges (Morgan 1971; 1981).

Model One: Random Distribution of Enriched Material within the Mantle

The first model could explain many of the geochemical observations for this region. Long-term and large-scale variations, seen along flow lines and along the ridge axis, could be a result of sampling of larger enriched bodies. Within these small bodies, small scale variations could be attributable to smaller bodies (with their own geochemical signature) lying within the domain of the larger bodies. Short-term and small-scale variations could be the result of (many) smaller bodies or many such bodies overlapping and mixing with each other and the depleted asthenospheric material in which they are embedded. Corrective stirring of the original anomaly of whatever size would result in a random and variable distribution of the original anomaly, depleted asthenosphere, and the products of mixing between the anomalies and the depleted asthenosphere (Richter and Ribe, 1979).

Table 3. ^{143}Nd/^{144}Nd versus Sm/Nd age calculations.

Coefficient or variable	Figure 8A	Figure 8B	Figure 8C
y_o	0.512446	0.512534	0.512639
m	2.86×10^{-3}	2.37×10^{-3}	2.03×10^{-3}
C	0.998	0.995	0.846
t	437×10^6	362×10^6	310×10^6

Note: Calculations use the radiogenic equation, $^{143}\mathrm{Nd}/^{144}\mathrm{Nd} = (^{143}\mathrm{Nd}/^{144}\mathrm{Nd})_o + (^{147}\mathrm{Sm}/^{144}\mathrm{Nd})(e^{\lambda t} - 1)$ and solving in the form, $y = mx + b$.

^{147}Sm/^{144}Nd values approximated from instrumental neutron activation analysis data by $^{147}\mathrm{Sm}/^{144}\mathrm{Nd} - \mathrm{Sm}/\mathrm{Nd} \times 0.6049$.

The slope, m, is obtained from regression of the data given in Tables 1 and 2 and summarized in Table 2. Correlation coefficients, C, are solved for dependent variables. Ages are obtained by substituting slope (m) and decay constant $\lambda = 6.54 \times 10^{-12}$ into $t = (1/\lambda) \ln (m + 1)$.

Thus, the first model can explain just about anything observed in the Leg 82 results, because the model is essentially unconstrained, but it can not explain everything well. This random model would require a special explanation to account for the zero-age observations (i.e., the regular gradient observed along the Mid-Atlantic Ridge axis as previously noted). We are unaware of any such explanation.

Model Two: Mantle Plume—Migrating Ridge Interactions

Morgan (1978) and Schilling and co-workers (1983) have shown that the mode of interaction of the LILE-enriched plume and the LILE-depleted asthenospheric material is a function of the relative distance from the ridge to the hot spot. The hot spot is defined as a source of the material, and the migrating spreading ridge acts as a sink for the material (see Vogt, 1976).

Three phases of such hot spot-lithosphere interactions can conveniently be described for the sake of discussion, namely, (1) a ridge-centered hot spot, (2) a near-ridge hot spot, once over the ridge but the ridge has since migrated, and (3) a purely intraplate hot spot.

In the central North Atlantic, Schilling (1973; 1975) and Schilling et al. (1983) have shown that the gradient south of Iceland and the Azores are a result of ridge-centered hot spot-spreading ridge interaction. In this case Schilling and Noe-Nygaard (1974) have suggested that when the flux of plume material is in excess of what is needed by the above spreading ridge, the excess is assimilated in two ways, (1) by building up a thicker crust (e.g., Iceland), and (2) by laterally flowing along the ridge axis, where the enriched plume material is progressively mixed with LILE-depleted asthenospheric material until there is no more left and a large-scale chemical gradient is observed in Layer 2A. The same process is envisioned south of the Azores Platform where a chemical and topographic gradient is observed down along the MAR axis up to the Hayes Fracture Zone (Schilling, 1975; White and Schilling 1978; Bougault and Treuil, 1980). In this case, local uniformity is observed along the gradient, such as in the FAMOUS region (White and Bryan, 1977; White, 1979; Dupre et al., 1981).

As the ridge moves away from the hot spot and the distance between the hot spot and ridge increases, a channel is established between the ridge (sink) and the hot spot (source), e.g., the Galapagos (Morgan, 1978; Schilling et al., 1983; Verma et al., 1983). The chemical gradient seen at the spreading ridge contracts finally to a point source, characterized as a spike of enriched anomalous material as the sub-ridge axial flow decreases and finally stops. Schilling et al. (1983, 1985) have also suggested that the sublithospheric flow from the hot spot to the ridge decreases also as the distance to the ridge increases, resulting in poor mixing and large variability in the geochemistry within that single anomalous data spike. Finally, the distance increases so much that the channel cannot connect to the ridge any longer and the hot spot becomes intraplate (e.g., Hawaii). There is no further direct interaction between the hot spot and the material normally feeding the spreading ridge.

Thus, the degree of variability observed in the product of mixing between the enriched and depleted material increases as the hot spot moves farther away from the ridge itself.

Two types of hot spots have been identified from kinematic studies in the central North Atlantic: (1) the Azores hot spot, which is believed to have become ridge centered only recently (i.e., when migrating Mid-Atlantic Ridge approached the hot spot and became ridge centered, approximately 20 Ma [Morgan 1981]), and (2) the so-called New England hot spot, which was intraplate beneath the North American plate from ~140 Ma to > ~80 Ma, intersected the ridge ~80 to 60 Ma ago, and since then has been overlain by the African plate (Morgan, 1981; Duncan, 1983; see Figure 9).

Within this model, the results from Legs 82 and 37 can be interpreted in the following way: (1) Holes 556 and 557 (Leg 82); Holes 335, 332A, and 332B (Leg 37); and the FAMOUS region provide evidence for the appearance of the Azores plume (blob) between 35 and 18 Ma and the progressive positioning of the Mid-Atlantic Ridge over it; and in contrast, (2) Holes 559 and 561 (Leg 82) along the approximate 35°N flow line reflect the migration of the Mid-Atlantic Ridge axis away from the New England hot spot over the past 35 Ma. The connection between the hot spot and the ridge need not have followed the most direct (shortest) and simplest route possible as the ridge migrated. Hole 558 is the on-

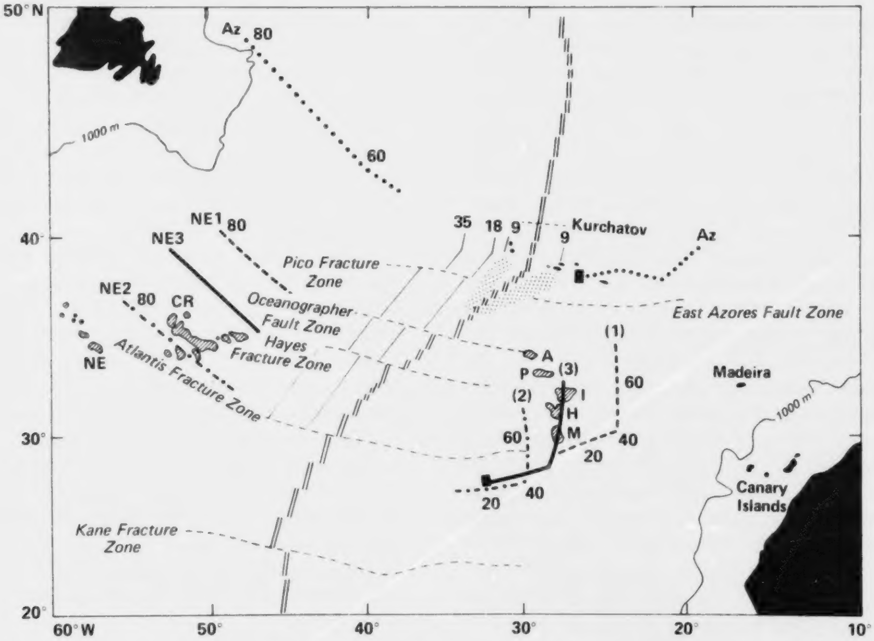

Figure 9. Tracks of the Azores (Az) and New England hot spots based on the following reconstructions: NE1 from Morgan (1981), Azores and NE2 from Duncan (1982), and NE3 from Duncan (1983). Stippled areas represent V-shaped time-transgressive ridges based on 1000-m contour lines, compiled from Olivet (1982), Vogt and Tucholke (1979), and Saemundsson (1984). Map modified from Cande et al. (1983). Symbols for seamounts are A: Atlantis, P: Platon, I: Irving-Cruiser, H: Hyer, M: Great Meteor, NE: New England, and CR: Corner Rise.

ly hole that is not explained by either of these models and requires additional discussion.

We now elaborate further on these two interpretations within the context of this model.

Azores hot spot. South of the Hayes Fracture Zone, all the material at Holes 562, 563, and 564, representing 18 and 35 Ma respectively (Fig. 1), is depleted. This agrees with the depleted signature for material seen at the present day Mid-Atlantic Ridge, suggesting that the Azores mantle anomaly never extended beyond the Hayes Fracture Zone during the last 35 Ma. It may be possible that the Hayes Fracture Zone is a physical barrier to flow of material from the Azores hot spot southward along the MAR; however, if this is so, it has assumed this function only recently.

Along the flow line at the latitude of the Azores anomaly, Hole 556 (approximately 35 Ma) is depleted. Thus, at 35 Ma, there is no evidence of a hot spot mantle plume (blob) at the latitude of the Azores. However, Hole 557 (approximately 18 Ma) is enriched. Hole 557 is interpreted as related to the ridge-centered Azores hot spot, known to be producing enriched material at the zero-age Mid-Atlantic Ridge. Therefore, one can postulate that the Azores hot spot blob rose through the lithosphere and began and/or manifested itself at some time between 35 and 18 Ma (i.e., between the time range sampled at Holes 556 and 557). Note, however, that only 1.5 m of actual core was retrieved from Hole 557.

Variation along the flow line of the FAMOUS region, (Holes 335, 332A, and 332B, Leg 37, and FAMOUS) suggest that subridge axial flow from the Azores plume had not reached the latitude of the FAMOUS flow line at 16 Ma (if Hole 559 is excluded). Subsequent mixing of the enriched Azores mantle plume with the depleted asthenosphere resulted in mixing products progressively enriched from 16.5 Ma to present. This interpretation is independently supported by the time transgressive V-shaped ridge branching from Flores and Pico (approximately 9 Ma) and meeting the MAR axis around 36°N, as shown in Figure 9. This is also shown in the topographic map of Olivet et al. (1982) and is discussed by Vogt et al. (unpublished paper[4]) and by Saemundsson (in press). Furthermore, Morgan (1981), in a kinematic reconstruction of plate motions relative to the fixed hot spot reference frame in the Atlantic, suggests that the Azores hot spot appears at the Earth's surface on the Eurasian plate only 20 Ma ago and since has been progressively approached by the Mid-Atlantic Ridge axis, which in this fixed reference frame has been migrating southwestward, leaving its trail on the Eurasian plate only (Fig. 9). This other independent evidence is broadly consistent with the isotope data, because the kinematics suggest that the Azores hot spot would become ridge centered only later than 20 Ma, as the plume-like isotope signature is apparent on the ridge axis for the first time only 18 Ma ago (Hole 557). However, our interpretation would be inconsistent with Duncan's reconstruction, which assumes that the Azores hot spot was continuously active for the last 80 Ma as reflected by the Newfoundland-Labrador Ridge (Fig. 9). Therefore, the LILE-depleted source present 35 Ma ago (Hole 556) would not be explained.

New England hot spot. A deviation from the uniform transitional REE patterns seen at the zero-age MAR axis is observed at ~35°N, expressed as a spike of LREE-enriched material above the uniform, slightly light REE-enriched patterns of the transitional ridge. The 35°N geochemical anomaly, represented by the enriched plume-like material, is superimposed over the large-scale gradient along the present-day MAR axis and is also observed on the 35 and 18 Ma isochrons, Holes 559 and 561, respectively. Thus, the anomaly seems to have persisted over the last 35 Ma. Large variability of source derivation is seen within this spike only since 18 Ma (Hole 561 and the present ridge axis). Only typically enriched or depleted mantle sources are observed in Hole 561, but intermediate types are also observed in the present day 35°N anomaly. We have indicated that this seems to be representative and characteristic of near-ridge hot spots (e.g., Schilling et al., 1983). Thus, these geochemical anomalies are interpreted as being related to a near-ridge hot spot. The question remaining is—which hot spot?

Kinematic reconstructions of plate motion relative to the reference frame of fixed hot spots have been studied in the North Atlantic by Morgan (1981), Duncan (1981, 1982, 1983), Olivet et al. (1982), and Burke et al. (1973). Reproduction of the trace left by the New England and Azores hot spots is shown in Figure 9, for the reconstructions of Morgan (1981) and Duncan (1982, 1983) and modified from the work of Cande (this vol.). It appears that the New England hot spot, represented by the New England Seamounts on the west flank of the MAR and the Great Meteor-Atlantis Seamount trail on the east side of the MAR, brackets the 35°N anomaly revealed along the 35°N flow line. Thus, within the uncertainty of plate reconstructions, the 35°N anomaly trace over the past 35 Ma could be the result of the activity of the New England hot spot. The present location of this hot spot is also uncertain. Burke et al. (1973), calling this the Colorado hot spot, placed it just north of the Oceanographer Fracture Zone at 34°N, 37.5°W. Morgan (1981) gave the present hot spot coordinates within his model as 22°N, 29°W, (or 29°N, 30°W for a more recent construction involving the Cruiser-Great Meteor Seamounts as a track on the African plate). Duncan (1982), using age determinations and correcting for the relative and absolute motion of North America and Africa, gave the present position of the New England Seamount hot spot at 27°N, 35°W. We conclude that, within these uncertainties, it is reasonable to assume that the 35°N hot spot regime reflects the New England plume activity and flow towards the migrating MAR over the last 35 Ma.

Hole 558. Hole 558 (approximately 35 Ma), on the latitude of the FAMOUS flow line, is not only the most complex of all the holes sampled but is the most difficult to explain by any model. Hole 558 is predominantly LREE enriched, with the exception of 558-28-2 (Piece 16), a LREE-depleted sample discussed earlier (which probably is related to recent fractional melting). Within the framework of the plume model, the enriched material seen in this hole cannot be simply explained by subridge axial flow from the Azores plume, because the evidence presented here indicates that the plume had not reached the surface 35 Ma ago. The hole is also quite far from the New England plume, which suggests a northward subridge axial flow from this plume 35 Ma ago. In any case, plate reconstructions indicate that the migrating MAR axis was centered over this hot spot in the period of 80–60 Ma, not 35 Ma.

---

[4] Vogt, P. R., Egloff, J., Johnson, G. L., and Perry, R. K., 1979. The Faial-Flores time-transgressive ridges: evidence for southward asthenospheric flow from the Azores mantle plume?

We conclude that the enriched nature of the source of basalts from Hole 558 remains unexplained within the framework of the plume-migrating MAR axis model, whether the New England or the Azores hot spot plumes are considered. However, it must also be realized that the Corner Seamounts do not fit the New England hot spot trace as proposed in the reconstructions of Morgan (1981) or Duncan (1983). Could it be that the Hole 558 enriched mantle source anomaly is related to the activity of the Corner Seamounts (McGregor and Krause, 1972)? Clearly, to test this possibility we would need better sampling as well as more accurate plate reconstructions.

CONCLUSIONS

The isotopic and REE data in basalts obtained from the eight holes drilled during Leg 82 reflect large-scale, long-term as well as smaller scale, short-term time variations of mantle sources present beneath the MAR over the last 35 Ma of its spreading activity. These variations can be fully explained by a mantle model in which the mantle is veined or lumpy and contains a random distribution of enriched domains of variable size and shape, all passively embedded in the LILE-depleted convecting upper mantle, as proposed by Davies (1981) and Richter and Ribe (1979).

With one notable exception (Hole 558), the variations can also be explained within the more restrictive model that hypothesizes interaction and mixing of buoyant, independently rising, LILE-enriched blobs (plumes) with LILE-depleted asthenospheric material—a model formulated within the framework of fixed hot spots (plumes) and a migrating, spreading MAR axis. The variations observed within this model framework require that at least two hot spots—the Azores and the New England hot spots—be considered. The variation along the 35°N flow line (Holes 559 and 561) reflect the flow and mixing over the last 35 Ma of the New England plume toward the migrating MAR axis and poor mixing conditions over the last 18 Ma. On the other hand, variations within Holes 556 and 557 and from Leg 37 suggest that the Azores plume did not leave its imprint along the migrating MAR before 18 Ma ago, and flow along the ridge occurred only later. These inferences are consistent with (1) plate reconstructions within the framework of fixed hot spots, which suggest that the Azores plume appeared on the Earth's surface only 20 Ma ago and which provide a trace of the New England hot spot whose uncertainties bracket the anomalous 35°N flow line, and (2) the V-shaped time-transgressive ridge converging southward towards the MAR from Flores and Pico, which suggests that a subaxial flow downridge started around 9 Ma ago.

It is conceivable, but not proven, that the enriched source of basalt for Hole 558, which cannot readily be explained by either of the two plume models, may be related to the activity of the Corner Seamounts (McGregor and Krause, 1972), which could (possibly) represent a third plume.

Finally, the short-term fluctuation observed between sources in Hole 561 implies rapid transfer of magma from the time of melting until eruption and provides evidence contrary to (1) the presence of a well-mixed magma chamber or (2) a wide zone of melting where magma droplets coalesce and mix at this particular location and time. Intense fracturing extending to the zone where melts are found could conceivably explain this particular situation.

ACKNOWLEDGMENTS

We thank F. DiMeglio and his staff for neutron activations and facilities at the Rhode Island Nuclear Science Center. This work was partly supported by NSF under Grants OCE 8200137 and OCE 8208014.

REFERENCES

Aumento, F., Melson, W. G., et al., 1977. *Init. Repts. DSDP*, 37: Washington (U.S. Govt. Printing Office).

Bougault, H., and Treuil, M., 1980. Mid-Atlantic Ridge: zero-age geochemical variations between the Azores and 22°N. *Nature*, 286:209–212.

Bryan, W. B., and Moore, J. G., 1977. Compositional variation of young basalts in the Mid-Atlantic Ridge rift valley near 36–46°N. *Geol. Soc. Am. Bull.*, 88:556–570.

Burke, K., Kidd, W. S. F., and Wilson, J. T., 1973. Relative and latitudinal motion of Atlantic hot spots. *Nature*, 245:133–137.

Cande, S. C., Bougault, H., Hill, L., Morgan, W. J., and Schouten, H., 1983. North Atlantic hot spot tracks and the pattern of enriched or depleted basalts in Leg 82 drill holes. *EOS, Trans. Am. Geophys. Union*, 64(18):345. (Abstract)

Coryell, C. D., Chase, J. W., and Winchester, J. W., 1963. A procedure for geochemical interpretation of terrestial rare-earth abundance patterns. *J. Geophys. Res.*, 68:559–566.

Davies, G. F., 1981. Earth's neodymium budget and structure and evolution of the mantle. *Nature*, 290:208–213.

Duncan, R, A., 1981. Hotspots in the southern oceans—an absolute frame of reference for the motion for of Gondwana continents. *Tectonophysics*, 74:29–42.

________, 1982. The New England Seamounts and the absolute motion of North America since mid-Cretaceous time. *EOS, Trans. Am. Geophys. Union*, 63:1103–1104.

________, 1983. The position of the North Atlantic spreading ridges in the hotspot reference frame, Cretaceous to Present. *EOS, Trans. Am, Geophys. Union*, 64:345.

Dupre, B., Lambret, B., Rousseau, D., and Allegre, C. J., 1981. Limitations on the scale of mantle heterogeneities under oceanic ridges. *Nature*, 294:552–554.

Hart, S. R., and Brooks, C., 1974. Clinopyroxene matrix partitioning of K, Rb, Cs, Sr, and Ba. *Geochim. Cosmochim. Acta*, 38: 1799–1803.

Langmuir, C. H., Bender, J. F., Bence, A. E., Hanson, G. N., and Taylor, S. R., 1977. Petrogenesis of basalts from the FAMOUS area: Mid-Atlantic Ridge. *Earth Planet. Sci. Lett.*, 36:133–156.

McGregor, B. A., and Krause, D. C., 1972. Evolution of the seafloor in the Corner Seamounts area. *J. Geophys. Res.*, 77:2525–2534.

Morgan, W. J., 1971. Convection plumes in the lower mantle. *Nature*, 230:42–43.

________, 1978. Rodriquez, Darwin, Amsterdam,..., A second type of hotspot island. *J. Geophys. Res.*, 83:5355–5360.

________, 1981. Hotspot tracks and the opening of the Atlantic and Indian Oceans. *In* Emiliani, C. (Ed.), *The Sea* (Vol. 7): New York (J. Wiley and Sons), 443–487.

Olivet, J. L., Bonnin, J., Beuzart, P., and Auzende, J. M., 1982. Cinematique des plaques et paleogeographie: une revue. *Bull. Soc. Geol. Fr.*, 7:?.

O'Nions, R. K., Hamilton, P. J., and Evensen, N. M., 1977. Variations in ^{143}Nd/^{144}Nd and ^{87}Sr/^{86}Sr ratios in oceanic basalts. *Earth Planet. Sci. Lett.*, 34:13–22.

O'Nions, R. K., and Pankhurst, R. J., 1976. Sr-isotopes and rare-earth element geochemistry of Deep Sea Drilling Project Leg 37 basalts. *Earth Planet. Sci. Lett.*, 31:255–261.

Richter, F. M., and Ribe, N. M., 1979. On the importance of advection in determining the local isotopic composition of the mantle. *Earth Planet, Sci. Lett.*, 43:212–222.

Rideout, M. L., 1983. DSDP Leg 82: spatial and temporal variations in the central North Atlantic [M. S. Thesis]. University of Rhode Island, Kingston.

Saemundsson, K., in press. Subaerial volcanism in the western North Atlantic. *The Decade of North American Geology (DNAG) Synthesis*, (Vol. 1: The Western Atlantic Region): Washington (Geol. Soc. Am.), DNAG Special Publications.

Schilling, J.-G., 1971. Sea-floor evolution: rare-earth evidence. *Phil. Trans. R. Soc. London., Ser. A*, 268:663–706.

________, 1973. Icelandic mantle plume: geochemical study of Reykjanes Ridge. *Nature*, 242:265–273.

________, 1975. Azores mantle blob: rare-earth evidence. *Earth Planet. Sci. Lett.*, 25:103–115.

Schilling, J.-G., Kingsley, R., and Bergeron, M., 1977. Rare earth abundances in DSDP Sites 332, 334, and 335, and inferences on the Azores mantle blob activity with time. *In* Aumento, F., Melson, W. G., et al., *Init. Repts. DSDP*, 37: Washington (U.S. Govt. Printing Office), 591–597.

Schilling, J.-G., and Noe-Nygaard, A., 1974. Faeroe-Iceland plume: rare-earth evidence. *Earth Planet. Sci. Lett.*, 24:1–14.

Schilling, J.-G., and Ridley, W. I., 1975. Volcanic rocks from DSDP Leg 29: petrography and rare-earth abundances. *In* Kennett, J. P., Houtz, R. E., et al., *Init. Repts. DSDP*, 29: Washington (U.S. Govt. Printing Office), 1103–1107.

Schilling, J.-G., Thompson, G., Kingsley, R., and Humphries, S., 1985. Hotspot-migrating ridge interactions in the South Atlantic. *Nature*, 313:187–191.

Schilling, J.-G., Zajac, M., Evans, R., Johnston, T., White, W., Devine, J. D., and Kingsley, R., 1983. Petrological and geochemical variations along the Mid-Atlantic Ridge from 29°N to 73°N. *Am. J. Sci.*, 283:510–586.

Verma, S. P., Schilling, J.-G., and Waggoner, D. G., 1983. Neodymium isotopic evidence for Galapagos hotspot-spreading centre system evolution. *Nature*, 306:654–657.

Vogt, P. R., 1976. Plumes, sub-axial pipe flow, and topography along the mid-oceanic ridge. *Earth Planet. Sci. Lett.*, 29:309–325.

Vogt, P. R., and Tucholke, B. E., 1979. The New England Seamounts: testing origins. *In* Tucholke, B. E., Vogt, P. R., et al., *Init. Repts. DSDP*, 43: Washington (U.S. Govt. Printing Office), 847–856.

White, W. M., 1979. Geochemistry of basalts from the FAMOUS area: re-examination. *Carnegie Inst. Washington Year Book*, [illegible]: 325–331.

White, W. M., Bryan, W. B., 1977. Sr-isotope, K, Rb, Cs, Sr, Ba, and rare-earth geochemistry of basalts from the FAMOUS area. *Geol. Soc. Am. Bull.*, 88:571–576.

White, W. M., and Schilling, J.-G., 1978. The nature and origin of geochemical variation in Mid-Atlantic Ridge basalts from the central North Atlantic. *Geochim. Cosmochim. Acta*, 42:1501–1516.

Wood, D. A., 1979. Dynamic partial melting: its application to the petrogenesis of basalts erupted in Iceland, the Faeroe Island, the Isle of Skye (Scotland), and the Troodos Massif (Cyprus). *Geochim. Cosmochim. Acta*, 43:1031–1046.

________, 1981. Partial melting models for the petrogenesis of Reykjanes Peninsula basalts, Iceland: implications for the use of trace elements as strontium and neodymium isotope ratios to record in homogeneities in the upper mantle. *Earth Planet. Sci. Lett.*, 52: 183–190.

Zindler, A., Hart, S. R., and Jakobsson, S. P., 1979. Nd and Sr isotope ratios and rare-earth element abundances in Reykjanes Peninsula basalts: evidence for mantle heterogeneity beneath Iceland. *Earth Planet. Sci. Lett.*, 45:249–262.

Date of Initial Receipt: 25 August 1983
Date of Acceptance: 4 April 1984

25. LEAD ISOTOPIC VARIATIONS IN OLD OCEAN CRUST NEAR THE AZORES[1]

B. Dupré and C. Göpel, Institut de Physique du Globe
and
H. Bougault, Institut Francais pour la Recherche et l'Exploitation de la Mer[2]

ABSTRACT

The aim of DSDP Leg 82 was to decipher the temporal and spatial evolution of Azores Plume. The Pb-isotopic results of this leg are rather complex, and can be summarized as follows:

1. At a given site (561, 558), variations of Pb isotopic compositions are generally accompanied by major changes in trace-element ratios, indicating significant heterogeneity of the source region. There is a correlation between Pb isotopes and trace elements.
2. In contrast, if all the data (i.e., all studied sites) of Leg 82 are considered together, no correlation can be discerned between Pb isotopes and trace elements. Site 556, especially, shows abnormal behavior.
3. Leg 82 samples not only cover the entire range of Pb isotopic composition previously established for the Atlantic Ocean, but extend this field to more radiogenic values.
4. The data are compatible with the hot-spot model proposed by Schilling (1975), if one considers that the Azores Plume itself is isotopically heterogeneous, and that it has been progressively contaminated to various degrees by upper mantle material.

INTRODUCTION

The region between 33 and 38°N in Atlantic Ocean was chosen for DSDP Leg 82 because it allows investigation of several geochemical problems in a relatively small area (Fig. 1). Studies on dredged samples from this area, analyzing trace elements (Wood et al., 1979; Bougault and Treuil, 1980; Schilling et al., 1980) and Sr, He, and Pb isotopes (White et al., 1976; White and Schilling, 1978; O'Nions et al., 1977; Kurz et al., 1982; Sun et al., 1975; Dupré and Allègre, 1980), have already shown the existence of important geochemical variations in this section of the ridge crest.

One aim of our study was to determine if these geochemical variations are related to the "Azores Plume" and to determine the exact geographical and temporal extension of this plume with new trace-element results and Pb isotopic data obtained on the same samples.

Samples from five sites (556, 558, 561, 562, 564) were selected for Pb isotopic analyses on the basis of trace-element data. Major elements as well as magmatophile elements (Nb, Zr, Ti, Y, Zr) were analyzed on board with an XRF (X-ray fluorescence) unit (Etoubleau et al., this volume). These latter elements have geochemical characteristics comparable to rare-earth elements (REE) (Bougault et al., this volume; Bougault, 1980; Erlank and Kable, 1976). In an "extended REE diagram," Nb is located between La and Ce, Zr between Nd and Sm. Thus, the Nb/Zr ratio is comparable to the La/Sm ratio and indicates whether the source region is enriched or depleted in light rare-earth elements (LREE). An Nb/Zr ratio smaller than the chondritic ratio (~0.1) (Bougault et al., this volume), indicates a depleted source, a larger ratio indicates an enriched mantle.

South of the Hayes Fracture Zone, basalts are found with characteristics of trace-element depletion. To the north of this fracture, samples are more enriched. During Leg 82, however, two sites (558 and 561) yielded rather complex patterns, in which basalts show depleted, flat, and enriched trace-element characteristics (site chapters, Sites 558 and 561, this volume; Bougault et al., this volume).

Combining trace-element data and isotopic data on the samples is necessary. The variations of magmatophile elements depend on two parameters—the chemical nature of the source region and the partial melting/fractional crystallization histories—but isotope data for the same samples allow us to characterize the nature of the source region and show whether it was homogeneous or heterogeneous.

Before using the Pb results, it is necessary to test whether alteration processes modified the isotopic composition of this relatively old ocean crust (14-37 Ma). Bulk samples and glass samples were compared, and leaching was performed.

ANALYTICAL TECHNIQUES

A lot of fresh aphyric glassy basalts were found during Leg 82. The glasses for analysis were handpicked under a binocular microscope.

The chemical procedure for Pb separation has been published by Manhes et al. (1978). Before dissolution, samples were leached one hour in warm 6N HCl. In three cases, Pb isotopic composition and Pb concentration were measured also in the leachates (Table 1).

Some of the samples were analyzed in Paris with a conventional mass spectrometer (Thompson THN 206), and the others were measured in Mainz with a multicollector on the Varian MAT system (Todt et al., 1983). Mass discrimination was controlled by repeated analyses of NBS Pb-standard SRM 981. Small samples (i.e., leachates) were measured with an electron multiplier.

---

[1] Bougault, H., Cande, S. C., et al., *Init. Repts. DSDP*, 82: Washington (U.S. Govt. Printing Office).

[2] Addresses: (Dupré and Gopel) Institut de Physique du Globe, Laboratoire de Géochemie and Cosmochimie, Tour 14-24, 4, Place Jussieu, 75230 Paris Cedex 05, France; (Bougault) IFREMER (formerly CNEXO), Centre de Brest, B. P. 337, 29273 Brest Cedex, France.

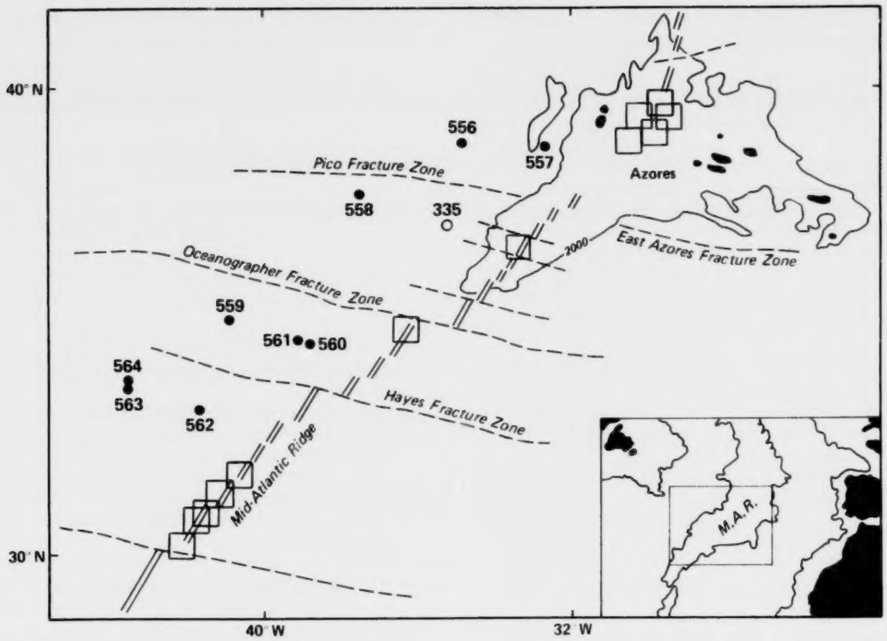

Figure 1. Sketch map of North Atlantic Ocean showing sites (circles) drilled during DSDP Leg 82. Squares represent samples dredged on the ridge crest during former cruises. Site 335 is added for reference only.

RESULTS

Pb isotopic compositions of the Leg 82 samples are listed in Table 1 and graphically presented in Figure 2. The observed variations of Pb isotopic composition in these samples are not only nearly equal to the entire range reported for Atlantic Ocean basalts (Church and Tatsumoto, 1975; Cohen and O'Nions 1982; Cohen et al., 1980; Dupré and Allègre, 1980; Dupré et al., 1981; Ito et al., 1982; Sun, 1980; Tatsumoto, 1978), but show even more radiogenic values, with $^{206}Pb/^{204}Pb$ ratios up to 20.26. Isotopic heterogeneity is found not only between the different sites of Leg 82, but also within a given site.

Table 1. Lead isotopic composition and Pb-concentration analyses of Leg 82 samples.

Hole-Core-Section, interval in cm (piece number)	$^{206}Pb/^{204}Pb$	$^{207}Pb/^{204}Pb$	$^{208}Pb/^{204}Pb$	Pb (ppb)
558-28-2, 75-79*	19.621	15.599	39.169	264
Leachate	19.606	15.613	39.149	31
558-27-3, 105-108*	19.676	15.619	39.405	424
558-39-3, 121-124	19.676	15.622	39.164	436
558-3-33, 133-136	20.048	15.633	39.504	
558-31-2, 39-41	20.253	15.634	39.625	
558-33-2, 22-25*	20.257	15.636	39.655	
558-30-2, 78-82	20.249	15.632	39.616	
561-2-3, 48-62*	18.758	15.521	38.308	267
Leachate	18.844	15.540	38.368	30
561-1-1, 24-27	19.530	15.583	39.284	535
Leachate	19.547	15.601	39.251	72
561-1-1, 128-133	18.837	15.536	38.334	134
561-1-2, 19-21	18.827	15.530	38.356	92
556-6-2, 21-23*	19.395	15.569	38.685	439
556-4-4, 71-74*	19.377	15.580	38.276	423
556-4-2, 45-44*	19.562	15.583	38.721	416
556-4-2, 102*	19.444	15.576	38.710	424
556-5-5, 72-74*	19.423	15.576	38.700	453
564-2-2, 90-92*	18.399	15.498	37.833	267
562-1-2, 142-145	18.256	15.474	37.708	
562-4-41, 60-62*	18.360	15.488	37.837	

Note: Asterisks indicate glass samples.

These heterogeneities cannot be due to alteration effects, because the results were obtained on unaltered glasses. Moreover, no difference can be observed between glass and basalt results for the same section of the core (Table 1). The isotopic heterogeneities cannot have been created by *in situ* decay of U since the creation of this ocean crust (37 Ma at most): $^{207}Pb/^{204}Pb$ variations are indeed too large to be explained by *in situ* U decay.

Variation of Isotopic Composition at Each Site

Site 561

Samples from Site 561 show the widest range of Pb isotopic composition and trace-element concentrations. These variations can be compared against those previously reported for the FAMOUS area (Dupré et al., 1981), where the $^{206}Pb/^{204}Pb$, $^{207}Pb/^{204}Pb$, and $^{208}Pb/^{204}Pb$ ratios displayed variations of 0.3, 0.05, and 0.25 respectively—much smaller than those for Site 561 alone (0.8, 0.06, and 1). Sample 561-1-1, 24-27 cm, with the most radiogenic Pb isotopic composition, exhibits also the highest Nb/Zr ratio and the highest Pb concentration (535 ppb). Within analytical error, no difference in Pb isotopic composition was found between the HCl-leachate of this sample and the final residue; in another glass sample (561-2-3, 48-62 cm), the $^{206}Pb/^{204}Pb$ ratio showed

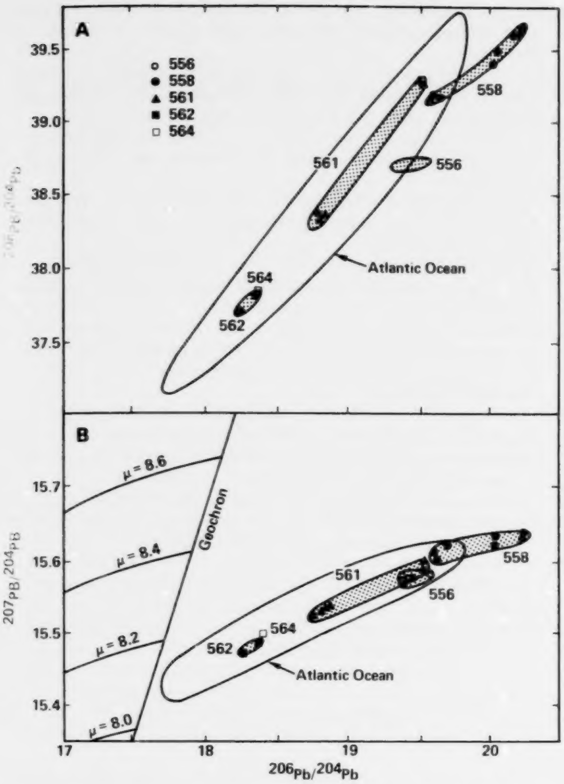

Figure 2. $^{208}Pb/^{204}Pb$ versus $^{206}Pb/^{204}Pb$ (A) and $^{207}Pb/^{204}Pb$ versus $^{206}Pb/^{204}Pb$ (B). Diagrams show the spread in Pb isotopic compositions of Leg 82 samples in relation to the field of Atlantic Ocean ridge basalts. Variation at a given site is indicated by stippled areas. (Data from Church and Tatsumoto, 1975; Cohen and O'Nions, 1982; Cohen et al., 1980; Dupré and Allègre, 1980; Dupré et al., 1981; Ito et al., 1982; Sun, 1980; Tatsumoto, 1978.)

only a slight difference between the leachate and the residue. Similar observations were published by Cohen and O'Nions (1982).

Site 558 (Hole 558)

Results for Site 558 are more difficult to interpret. Glass samples and bulk rock show rather evolved Pb isotopic compositions and extend the domain of the Atlantic Ocean basalts in the $^{206}Pb/^{204}Pb$, $^{207}Pb/^{204}Pb$, and $^{208}Pb/^{204}Pb$ diagrams (Fig. 2A and 2B).

Variations of the $^{206}Pb/^{204}Pb$, $^{207}Pb/^{204}Pb$, and $^{208}Pb/^{204}Pb$ ratios at this site are 0.6, 0.04, and 0.5, respectively—nearly double the variation found in the FAMOUS area.

At Site 558, no perfect correlation is evident between trace elements and isotopes; samples with nearly identical Nb/Zr ratios show quite different isotopic compositions.

Site 556

Samples from Site 556 show the smallest spread in Pb isotopic compositions. At this site, the variation is comparable to that found in the FAMOUS area. Although the trace-element ratios indicate that these samples are representative of depleted ocean basalts, Pb isotopic compositions are more evolved, $^{206}Pb/^{204}Pb$ ratios are higher than 19.0, and $^{207}Pb/^{204}Pb$ ratios range up to 15.58.

Sites 562 and 564

Three samples were analyzed from sites located south of the Hayes Fracture Zone (Sites 562 and 564). They show low Nb/Zr ratios, and yield rather nonradiogenic Pb isotopic compositions

Summary of Intrasite Isotopic Variation

The regular variations of Pb and Sr isotopes along the ridge crest of the Atlantic Ocean (Dupré et al., 1981; Sun et al., 1975; White et al., 1976, and the results of local studies (Dupré et al., 1981; White and Bryan, 1977; Langmuir et al., 1977), seemed to indicate a relatively good homogeneity of the mantle source at a relatively small scale (10 km). The Leg 82 results show that this is not always accurate; Leg 82 samples reveal important variations in Pb-isotope composition at a scale of tens of meters at a given site (Sites 558 and 561). A comparable spread of Pb isotopic compositions was found within a dredge south of the Hayes Fracture Zone by Hamelin et al. (1984).

That these isotopic heterogeneities at Leg 82 sites are generally accompanied by major changes in trace-element ratios can only be interpreted in terms of heterogeneity of the mantle source. Such isotopic variations cannot be created by partial melting or fractional crystallization processes.

Variations between the Leg 82 Holes

Despite the wide spread of Pb isotopic compositions at a given site, each site reveals specific features. The most important finding is the geochemical difference between samples drilled north and south of the Hayes Fracture Zone. All samples cored north of this zone exhibit $^{206}Pb/^{204}Pb$ ratios greater than 18.6, whereas samples taken farther to the south are less radiogenic. This is compatible with results of trace-element studies on the ridge crest nearby (Bougault and Treuil, 1980; Wood et al., 1979).

Although a correlation exists between trace elements and isotopes at a given site, this correlation no longer holds in a comparison of all sites of Leg 82. This also contrasts with the general trend found for this portion of the Atlantic Ocean (Fig. 3). Samples from Site 556, especially, show abnormal behavior; their trace-element characteristics are typical of depleted basalts, whereas the Pb isotopes are rather evolved. This apparent discrepancy is important, because the Pb isotopic composition shows the influence of the "Azores Plume" 34 Ma ago, which is not shown by trace elements.

Our data do not give a unique explanation for this decoupling between Pb isotopes and trace elements; it may be due to secondary processes (two melting episodes, etc.), which mainly affected the trace elements. It may also be the result of a complex mixing process with the "Azores Plume" in an early stage.

No simple relationship between age and distance to the upwelling Azores can be observed. Along the ridge

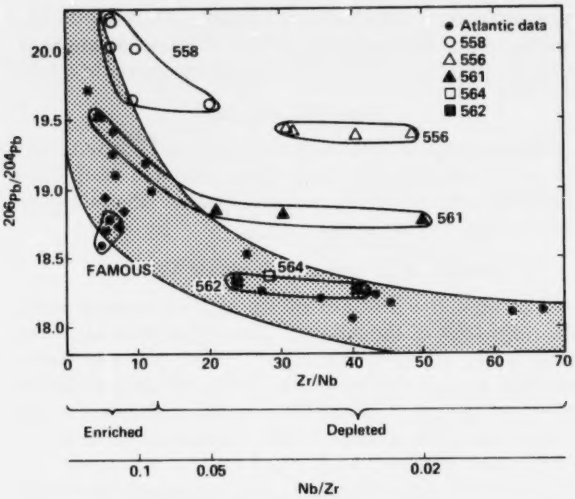

Figure 3. Plot of $^{206}Pb/^{204}Pb$ versus Nb/Zr ratio of Leg 82 samples. The trend of Atlantic Ocean ridge basalts is indicated by shading. Data sources are Bougault et al. (this volume); Bougault, 1980; Dupré et al., 1981; Dupré and Allègre, 1980; Hamelin et al., 1984.

crest between 30°N and the Azores, two isotopic "highs" were found (White and Schilling, 1978; White et al., 1976).

The Pb isotopic data of Leg 82 may be interpreted according to the model proposed by Schilling (1975) (mixing of a plume with upper mantle material), if one considers that the Azores Plume is heterogeneous. The complex characteristics of this plume were shown by Dupré et al. (1982). This may also explain the dispersion of the Pb isotopic compositions in the $^{208}Pb/^{204}Pb$ diagram for the samples of Leg 82 (Fig. 2B).

The Pb isotopic compositions of the samples from Site 558 are not only more evolved than all other samples from the Atlantic Ocean, but they are even more radiogenic than the alkali basalts from the Azores. This could indicate a mixing process between two sources, one of which (Azores) was less "contaminated" by upper mantle materials 34 Ma ago.

ACKNOWLEDGMENTS

This study was supported by Action Thematique Programmée. Ocean No. 39-82. We thank S. Hart and J.-G. Schilling for their critical reviews of the manuscript. IPG Contribution Number 711.

REFERENCES

Bougault, H., 1980. Contribution des éléments de transition à la compréhension de la genèse des basaltes océaniques. Analyse des éléments traces par spectrométrie de fluorescence X [Thèse]. Université Paris VII, Paris.

Bougault, H., and Treuil, M., 1980. Mid-Atlantic Ridge: Zero age geochemical variation between Azores and 22°N. *Nature*, 286:209-212.

Church, S. F., and Tatsumoto, M., 1975. Lead isotope relations in oceanic ridge basalts from the Juan de Fuca-Gorda Ridge area. N. E. Pacific Ocean. *Contrib. Mineral. Petrol.*, 53:253-279.

Cohen, R. S., Evensen, N. M., Hamilton, P. J., and O'Nions, R. K., 1980. U-Pb, Sm-Nd and Rb-Sr systematics of mid-ocean ridge basalt glasses. *Nature*, 283:149-153.

Cohen, R. S., O'Nions, R. K., 1982. The lead, neodymium, and strontium isotopic structure of ocean ridge basalts. *J. Petrol.*, 23: 299-324.

Dupré, B., and Allègre, C. J., 1980. Pb-Sr-Nd isotopic correlation and the chemistry of the North Atlantic mantle. *Nature*, 286: 17-22.

Dupré, B., Lambret, B., and Allègre, C. J., 1982. Isotopic variations within a single oceanic island: The Terceira case. *Nature*, 29 620-622.

Dupré, B., Lambret, B., Rousseau, D., and Allègre, C. J., 1981. Limitations on the scale of mantle heterogeneities under oceanic ridges. *Nature*, 294:552-554.

Erlank, A. J., and Kable, E. J. D., 1976. The significance of incompatible elements in Mid-Atlantic Ridge basalts from 45°N, with pa ticular reference to Zr/Nb. *Contrib. Mineral. Petrol.*, 54:281-29

Hamelin, B., Dupré, B., and Allègre, C. J., 1984. Lead-strontiu isotopic variations along the East Pacific Rise and the Mid-Atla tic Ridge. A comparative study. *Earth Planet. Sci. Lett.*, 6 340-350.

Ito, E., Göpel, C., White, W. M., Jochum, K. P., Seufert, H., Vo hage, H., and Hofmann, A., 1982. Inferences on the compositio and evolution of the source of MORB. *Fifth Conf. Geochronol Cosmochronol. Isotope Geol.* (Nikko), pp. 166-167.

Kurz, M. D., Jenkins, W. J., Schilling, J. G., and Hart, S. R., 198 Helium isotopic variations in the mantle beneath the central North Atlantic Ocean. *Earth Planet. Sci. Lett.*, 58:1-14.

Langmuir, C. H., Bender, J. F., Bence, A. E., and Hanson, G. M., 1977. Petrogenesis of basalts from the FAMOUS area: Mid-Atlantic Ridge. *Earth Planet. Sci. Lett.*, 36:133-156.

Manhes, G., Minster, J. F., and Allègre, C. J., 1978. Comparative U-Th-Pb and Rb-Sr study of the Saint Séverin amphoterite: Consequence for early solar system chronology. *Earth Planet. Sci. Lett.*, 36:133-156.

O'Nions, R. K., Hamilton, P., and Evensen, N., 1977. Variations in $^{143}Nd/^{144}Nd$ and $^{87}Sr/^{86}Sr$ ratios in oceanic basalts. *Earth Planet. Sci. Lett.*, 34:13-22.

Schilling, J. G., 1975. Azores mantle blob: rare earth evidence. *Earth Planet. Sci. Lett.*, 25:103-115.

Schilling, J. G., Bergeron, M. B., and Evans, R., 1980. Halogens in the mantle beneath the North Atlantic. *Phil. Trans. R. Soc. London, Ser.A*, 297:11.

Sun, S. S., 1980. Lead isotopic study of young volcanic rocks from mid-ocean ridges, ocean islands and island arcs. *Phil. Trans. R. Soc. London, Ser.A*, 297:409-445.

Sun, S. S., Tatsumoto, M., and Schilling J. G., 1975. Mantle plume mixing along the Reykjanes axis: lead isotopic evidence. *Science*, 190:143-147.

Tatsumoto, M., 1978. Isotopic composition of lead in oceanic basalt and its implication to mantle evolution. *Earth Planet. Sci. Lett.*, 38:63-87.

Todt, W., Dupré, B., and Hofmann, A. W., 1983. Pb isotope measurements using a multicollector: application to standards and basalts. *E.U.G. 2nd, Terra Cognita*, 3:140.

White, W. M., and Bryan, W. B., 1977. Sr-isotope, K, Rb, Cs, Sr, Ba and rare-earth geochemistry of basalts from the FAMOUS area. *Geol. Soc. Am. Bull.*, 88:571-576.

White, W. M., and Schilling, J. G., 1978. The nature and origin of geochemical variations in Mid-Atlantic Ridge basalts from the central North Atlantic. *Geochim. Cosmochim. Acta*, 42:1501-1516

White, W. M., Schilling, J. G., and Hart, S. R., 1976. Evidence for the Azores Mantle Plume from strontium isotope geochemistry of the central North Atlantic. *Nature*, 263:659-663.

Wood, D. A., Tarney, J., Varet, J., Saunders, A. W., Bougault, H Joron, J. L., Treuil, M., and Cann, J. R., Geochemistry of basal drilled in the North Atlantic by IPOD Leg 49: implications f mantle heterogeneity. *Earth Planet. Sci. Lett.*, 42:77-97.

Date of Initial Receipt: 17 August 1983
Date of Acceptance: 28 November 1983

26. ISOTOPIC AND TRACE ELEMENT COMPOSITION OF BASALTS FROM SITES 556–559 AND 561–564: CONSTRAINTS ON SOME PROCESSES AFFECTING THEIR COMPOSITION[1]

G. A. Jenner, Max-Planck-Institut fur Chemie,
J. Hertogen, Katholieke Universiteit,
and
Th. Sachtleben and H.-U. Schmincke, Ruhruniversität[2]

ABSTRACT

Sr and Nd isotopic composition of 23 basalts from Sites 556–559 and 561–564. are reported. The $^{87}Sr/^{86}Sr$ ratios in fresh glasses and leached whole rocks range from 0.7025 to 0.7034 and are negatively correlated with the initial $^{143}Nd/^{144}Nd$ compositions, which range from 0.51315 to 0.51289. The Sr and Nd isotopic compositions (in glasses or leached samples) lie within the fields of mid-ocean ridge basalts (MORB) and ocean island basalts (OIB) from the Azores on the Nd-Sr mantle array/fan plot.

In general, there is a correlation between the trace element characteristics and the $^{143}Nd/^{144}Nd$ composition (i.e., samples with $Hf/Ta > 7$ and $(Ce/Sm)_N < 1$ [normal-MORB] have initial $^{143}Nd/^{144}Nd > 0.51307$, whereas samples with $Hf/Ta < 7$ and $(Ce/Sm)_N > 1$ (enriched-MORB) have initial $^{143}Nd/^{144}Nd$ compositions < 0.51300). A significant deviation from this general rule is found in Hole 558, where the N-MORB can have, within experimental limits, identical isotopic compositions to those found in associated E-MORB.

The plume-depleted asthenosphere mixing hypothesis of Schilling (1975), White and Schilling (1978) and Schilling et al. (1977) provides a framework within which the present data can be evaluated. Given the distribution and possible origins of the chemical and isotopic heterogeneity observed in Leg 82 basalts, and some other basalts in the area, it would appear that the Schilling et al. model is not entirely satisfactory. In particular, it can be shown that trace element data may incorrectly estimate the plume component and more localized mantle heterogeneity (both chemical and isotopic) may be important.

INTRODUCTION

The origin of chemical and isotopic heterogeneity in the oceanic mantle is a subject of continuing debate (see, for example, White and Hofmann, 1982; Wood, 1979a; Schilling, 1973). One particular point of contention is whether the origin of the heterogeneity is related to a random distribution of distinct sources—the veined-mantle and/or plum-pudding models (Wood, 1979b; Davies, 1981)—or if the large part of the heterogeneity is related to the presence of mantle plumes (Schilling, 1975; White and Schilling, 1978).

The origin of the geochemical characteristics and their distribution in basalts erupted on the Mid-Atlantic Ridge (MAR) between 30 and 40°N has been explained by Schilling (1975) and White and Schilling (1978) as a result of mixing between an Azores mantle plume/blob (AMP/B) and a depleted low-velocity layer (DLVL). Briefly, the major features of their model can be summarized as follows: (1) presently, there is a major mantle plume centered at 39°N (the Azores mantle plume) and possibly a minor plume at 35°N (the Oceanographer mantle plume); (2) the plume source(s) are characterized by higher abundances of K, Ba, Sr, Cs, and light rare earth elements (LREE) and are enriched in the radiogenic Sr, Nd, and Pb isotopes (White et al., 1976; Hawkesworth et al., 1979; Sun, 1980); (3) mixing of the end-member sources depends on a number of factors, including spreading rate and plume flux (the rate of which can vary considerably and can also be episodic). In support of their model, White (1977) and White and Schilling (1978) have shown that, at least qualitatively, the distribution patterns of Sr isotopic composition, REE, and LIL (large ion lithophile) elements are consistent with a binary mixing model. The authors have also summarized supportive geophysical and morphologic features.

In addition to ascribing the origin of the zero-age geochemical features of MAR basalts to AMP/B-DLVL mixing, Schilling et al. (1977) have extended the model to include older basalts. Based on variations in $(La/Sm)_N$ ratios in basalts from Site 335 (Leg 37, 16 Ma), Site 332 (Leg 37, 3 Ma) (both from Aumento, Melson, et al., 1977), and FAMOUS (zero-age) (Schilling et al., 1977) suggested that the contribution from the AMP/B increases from (approximately) 0% at Site 335 to 30% at Site 332 and to 45% at the FAMOUS site.

At least one aim of the Leg 82 program was to determine if the geochemistry of basalts erupted over the last 35 Ma between 30 and 40°N is related to the presence of the Azores mantle plume. In order to evaluate the hypotheses of Schilling and his co-workers and to determine the origins of the heterogeneity in Leg 82 basalts, we have studied a number of basalts from Leg 82, using a wide variety of analytical techniques and approaches (see Sachtleben et al., in preparation[3]; Hertogen et al.,

---

[1] Bougault, H., Cande, S. C., et al., *Init. Repts. DSDP*, 82: Washington (U.S. Govt. Printing Office).

[2] Addresses: (Jenner, present address) Department of Earth Sciences, Memorial University of Newfoundland, St. John's, Newfoundland A1B 3X5 Canada; (Hertogen) Katholieke Universiteit, Leuven Celestijnenlaan 200C, B3030 Heverlee, Belgium; (Sachtleben and Schmincke) Ruhruniversität, D-4630 Bochum, Federal Republic of Germany.

[3] Sachtleben, Th., Schmincke, H.-U., Hertogen, J., and Jenner, G. A., in preparation. Petrology and geochemistry of Leg 82 basalts.

Table 1. Sr and Nd isotopic compositions of basalts from Leg 82.

Sample no.	1	2	3	4	5	6	7	8	9	10	11
Hole-Core-Section	556-3-2	556-4-2	556-4-2	556-5-5	556-8-2	557-1-1	558-27-3	558-28-3	558-30-2	558-31-2	558-32-1
Interval or depth in section in cm (Piece no.)	19-21 (2)	44-45 (1e)	102 (2e)	72-74 (5)	27-29 (2b)	105-108 (13)	69-72 (7)	118-120 (15)	78-82 (7)	39-41 (36)	123-125 (8b)
Specimen type[a]	WR	GL	GL	GL	WR	WR	WR	WR	WRL	GL	WR
Ratio											
$^{87}Sr/^{86}Sr$	0.70315 ± 2		0.70284 ± 3 0.70280 ± 3	0.70283 ± 3	0.70319 ± 3	0.70389 ± 2	0.70358 ± 2	0.70359 ± 2	0.70335 ± 2	0.70332 ± 3	0.70367 ± 2
$^{143}Nd/^{144}Nd^b$	0.513126 ± 16	0.513118 ± 15	0.513087 ± 21	0.513139 ± 15	0.513142 ± 20	0.513016 ± 18	0.512981 ± 18	0.513006 ± 20	0.512947 ± 22	0.512936 ± 14	0.512921 ±
$^{147}Sm/^{144}Nd^c$	0.222	0.222	0.222	0.224	0.228	0.151	0.177	0.207	0.157	0.157	0.150
$^{143}Nd/^{144}Nd^d$	0.513075	0.513067	0.513036	0.513088	0.513090	0.512998	0.512940	0.512959	0.512911	0.512900	0.512887

Note: Data are reported relative to values of $^{87}Sr/^{86}Sr = 0.70800$ for the E + A standard and $^{143}Nd/^{144}Nd = 0.51264$ for the BCR-1 standard (using $^{146}Nd/^{144}Nd = 0.7219$). Errors quoted are 2 s.e.m. based on within statistics.

[a] WR = whole rock; WRL = whole rock, leached; GL = glass.

[b] Measured ratio.

[c] Calculated from Sm and Nd concentrations on same samples.

[d] Calculated initial ratio using: (1) ages of 17 Ma for Holes 557, 561, and 562; 35 Ma for Holes 556, 558, 559, 563, and 564; (2) $\lambda_{Sm} = 6.54 \times 10^{-12}\ y^{-1}$.

this volume; Dupré et al., this volume). In this paper, we report Sr and Nd isotopic compositions on 23 samples and REE abundances in 10 samples. The samples were selected to represent the spatial and temporal, as well as geochemical, characteristics of Leg 82 basalts. Discussion of the data is broadly divided into two sections: one concerned with in-site variation, and the second concerned with how the data can be useful in delineating the origin of the heterogeneity.

The correlations between trace, Sr, and Nd isotopic composition and Pb isotopic composition are also briefly discussed. This aspect of the paper comes from joint work with B. Dupré at Mainz, in which 10 samples were analyzed for Sr, Nd, and Pb isotopic composition and REE abundances. For a more complete discussion of Pb techniques and results, see Dupré et al. (this volume).

METHODS

Conventional chemical techniques were used for the separation of Sr, Nd, and REE (see White and Patchett [1984] for details). Details of the blanks and mass spectrometry are also given in White and Patchett (1984). In this study, more specifically measured blanks are Sm < 50 pg; Nd < 180 pg; and Sr < 200 pg. Nd isotopic compositions were determined using double-filament, single-collector, and conventional-massspectrometric methods. Sr isotopic compositions were determined using a double-collector system installed on a Finnigan MAT 261 mass spectrometer. Errors reported for isotopic composition (Table 1) are two standard errors of the mean based on within-run statistics. This statistic slightly underestimates reproducibility.

The 10 samples for which REE data are reported (Table 2) were also analyzed for Pb isotopic composition. The procedure used for dissolution of these samples differed from that used on the other 13 samples. In particular, these samples had a 1-hour leach in warm 6N HCl, followed by Pb separation. The residue after Pb extraction was treated with $HClO_4$, HF, HCl, and the solution was split for isotope dilution (REE) and isotope composition analysis.

RESULTS

Sr and Nd isotopic compositions are reported in Table 1. Nd isotopic compositions have been corrected for age using the criteria given in Table 1. Sm/Nd ratios for samples 2, 3, 4, 9, 10, 12, 13, 17, 18, and 23 (see Table 1 for DSDP designations) are based on the isotope dilution REE measurements reported in Table 2; those for other samples are from the instrumental neutron activation data reported by Hertogen et al. (this volume). Values for CHUR (chondritic uniform reservoir) used in the ϵ $Nd_{(T)}$ calculations are based on a present-day value for $(^{143}Nd/^{144}Nd)_{CHUR} = 0.51264$ and $(^{147}Sm/^{144}Nd)_{CHUR} = 0.1966$. A summary of important trace element and isotopic data is given in Table 3. Chemical groups given in Table 3 refer to those assigned by the shipboard scientists. These groups do not conform to the subdivision into N (normal)-MORB and E (enriched)-MORB often used. For the purposes of this paper, N-MORB has Hf/Ta > 7, Zr/Nb > 13, and $(Ce/Sm)_N < 1$; E-MORB has Hf/Ta < 7, Zr/Nb < 13, and $(Ce/Sm)_N > 1$. This nomenclature is similar to that used by Wood et al. (1979), Sun et al. (1979), and many others.

Hole 556. All the samples analyzed are N-MORB; however, they come from two different shipboard-designated chemical groups. Within the limits of analytical error, all these basalts may be considered to have come from a source that is approximately uniform isotopically (see Table 3). The variation in Nd isotopic composition (ϵ $Nd_{(T)} = 8.6$ to 9.7) may indicate some heterogeneity, but further study is necessary for confirmation.

Hole 557. Only one sample was analyzed for isotopic composition. This sample is an E-MORB with an ϵ $Nd_{(T)}$ value of 7.4.

Hole 558. Eight samples were analyzed from this location. These basalts can show marked heterogeneity in trace and isotopic characteristics; however, the degree of correlation between the two types of heterogeneity is variable. The following points are notable: (1) Sample 8 (558-28-3, 118–120 cm), with N-MORB characteristics, compared to Sample 7 (558-27-3, 69–72 cm), an E-MORB, has essentially indistinguishable Nd (and Pb) isotopic composition; (2) Samples 8 and 13 (558-33-3, 133–136 cm) have N-MORB characteristics and identical Nd isotopic composition; however, they are different with respect to $^{206}Pb/^{204}Pb$ and $^{208}Pb/^{204}Pb$ composition; (3) Sample 8 versus Sample 12 (558-33-2, 22–25 cm) (N-MORB versus E-MORB) shows trace element heterogeneity accompanied by both Nd and Pb isotopic heterogeneity; (4) the $^{143}Nd/^{144}Nd$ isotopic compositions are positively correlated with $^{147}Sm/^{144}Nd$ (i.e., the data define an isochron/mixichron with an "age" of 224 ± 51 Ma).

Hole 559. The single sample selected from this site is an E-MORB with ϵ $Nd_{(T)}$ of 7.5.

Hole 561. Four samples were selected; the uppermost one is an E-MORB with ϵ $Nd_{(T)}$ of 6.9, whereas the other samples are N-MORB with ϵ $Nd_{(T)}$ ~ 9. In compari-

Table 1. (Continued).

12 558-33-2 22-25 (29) GL	13 558-33-3 133-136 (3) WRL	14 558-40-1 92-94 (8a) WR	15 559-8-1 127-129 (5c) WR	16 561-1-1 33-38 (2a) WR	17 561-1-1 128-133 WRL	18 561-1-2 19-21 WRL	19 561-3-2 41-53 (3c) WR	20 562-8-2 6-9 (1) WR	21 563-25-1 19-22 (1c) WR	22 564-1-2 21-25 (3a) WR	23 564-2-2 90-92 (5c) GL
0.70333 ± 2	0.70334 ± 2	0.70399 ± 2 0.70395 ± 3	0.70331 ± 2	0.70394 ± 2	0.70319 ± 3	0.70293 ± 2	0.70398 ± 2	0.70355 ± 2	0.70307 ± 3	0.70227 ± 2	0.70254 ± 3
0.512942 ± 23	0.513000 ± 21	0.512974 ± 16	0.513018 ± 15	0.512988 ± 21	0.513094 ± 21	0.513120 ± 25	0.513096 ± 20	0.513145 ± 36 0.513143 ± 17	0.513227 ± 17	0.513199 ± 32	0.513184 ± 15
0.157	0.194	0.190	0.176	0.153	0.268	0.276	0.230	0.213	0.236	0.232	0.216
0.512906	0.512956	0.512931	0.512978	0.512971	0.513064	0.513089	0.513070	0.513118	0.513173	0.513146	0.513135

Table 2. Isotope dilution, rare earth element abundances (in ppm).

Sample number Hole	2 556	3 556	4 556	9 558	10 558	12 558	13 558	17 561	18 561	23 564
Element										
Ce	6.62	7.13	6.90	23.00	22.90	18.70	7.45	3.33	3.25	8.70
Nd	6.62	7.18	6.98	13.60	13.60	11.10	5.98	4.10	4.40	7.87
Sm	2.42	2.63	2.58	3.53	3.51	2.86	1.92	1.81	2.00	2.80
Eu	0.86	0.94	0.94	1.21	1.20	1.00	0.94	0.85	0.94	1.04
Gd		3.74	3.69	4.00	3.98	2.91	2.57	2.92	3.28	3.84
Dy	4.26	4.61	4.54	4.52	4.47	3.55	2.91	3.88	4.27	5.00
Er	2.76	2.98	2.93	2.76	2.75	2.25	1.73	2.53	2.80	3.18
Yb	2.59	2.81	2.76	2.53	2.53	2.05	1.59	2.45	2.68	3.07
Lu	0.36	0.41	0.40	0.37	0.37	0.30	0.23	0.37	0.40	

Note: For DSDP designations of sample numbers, see Table 1. Errors are approximately 2-3% for Ce, Nd, Sm, Eu, Er, Yb, and Lu, and 4-6% for Gd and Dy.

Table 3. Shipboard chemical group; selected trace element and isotopic compositions for analyzed samples.

Hole and sample number	Shipboard chemical group	Hf/Ta	$(Ce/Sm)_N$	$^{87}Sr/^{86}Sr$	$\epsilon Nd_{(T)}$	$^{206}Pb/^{204}Pb$
Hole 556						
1	II	18.2	0.6		9.4	
2	II		0.6		9.2	19.56
3	II		0.6	0.70282	8.6	19.44
4	II		0.6	0.70283	9.6	19.42
5	III	19.5	0.5		9.7	
Hole 557						
6	I	2.5	1.4		7.4	
Hole 558						
7	I	3.5	1.1		6.7	(19.68)
8	II	11.3	0.7		7.1	(19.62)
9	IIIA		1.3	0.70335	6.2	20.25
10	IIIA		1.3	0.70332	6.0	20.26
11	IIIA	2.3	1.4		5.7	
12	IIIB		1.3	0.70333	6.1	20.26
13	IIIB		0.8	0.70334	7.0	20.05
14	V	3	1.2		6.6	
Hole 559						
15	I	2.6	1.2		7.5	
Hole 561						
16	I	1.7	1.6		6.9	(19.53)
17	II		0.3	0.70319	8.7	18.84
18	II		0.3	0.70293	9.2	18.83
19	II	13.2	0.6		8.8	
Hole 562						
20	II	11.4	0.6		9.8	
Hole 563						
21	II	12.8	0.6		11.3	
Hole 564						
22	I	13.4	0.5		10.8	
23	I		0.6	0.70254	10.5	18.40

Note: For DSDP sample designations, see Table 1. Hf/Ta ratios from Hertogen et al. (this volume). $(Ce/Sm)_N$ values are normalized to chondritic abundances. $^{87}Sr/^{86}Sr$ ratios are for glasses or leached whole rocks. $^{206}Pb/^{204}Pb$ values are from Dupré et al. (this volume). Values in parentheses indicate that the values are from the same unit, but not from the same sample.

son to Hole 558 basalts, the change in isotope characteristics between E-MORB and N-MORB are much more notable.

Holes 562, 563, and 564. All of the basalts analyzed are N-MORB. The initial $^{143}Nd/^{144}Nd$ ratios are generally higher than those for the other N-MORB samples studied here, but they are more consistent with those suggested as characterizing the N-MORB source region (White and Hofmann, 1982).

DISCUSSION

Isotopic Variability

Figure 1 shows the variation in the Nd and Sr isotopic composition of Leg 82 basalts. The results include data from fresh glasses, leached whole rocks, and whole rocks. Almost all the samples are olivine-hypersthene normative tholeiites and were selected as among the freshest samples available. No leached-unleached whole-rock pairs were tested; however, it appears that at least seven of the whole rocks have undergone significant alteration in Sr isotopic composition because of seawater/basalt interaction. Because of the uncertainty involved in using the whole-rock $^{87}Sr/^{86}Sr$ ratios, only $^{87}Sr/^{86}Sr$ data from the glasses and leached whole rocks are used to describe source characteristics.

The range of variation observed in Nd and Sr isotopic composition in Leg 82 basalts is quite large (spanning 5 ϵ Nd units). The pattern shown is consistent with previous studies on MORB; however, although all Leg 82 basalts would be considered MORB, they overlap in composition with the Azores Islands basalts. It is also somewhat surprising that in spite of having N-MORB with depleted to very depleted trace element abundances and patterns (see Hertogen et al., this volume), many of the N-MORB recovered during Leg 82 have initial $^{143}Nd/^{144}Nd$ less than that of the mean N-MORB reservoir (taken to be 0.51315 for zero-age basalts) (Jenner et al., in press).

Variation in $^{87}Sr/^{86}Sr$ is correlated with $^{206}Pb/^{204}Pb$ (Fig. 2) in a similar manner as observed in other MORB.

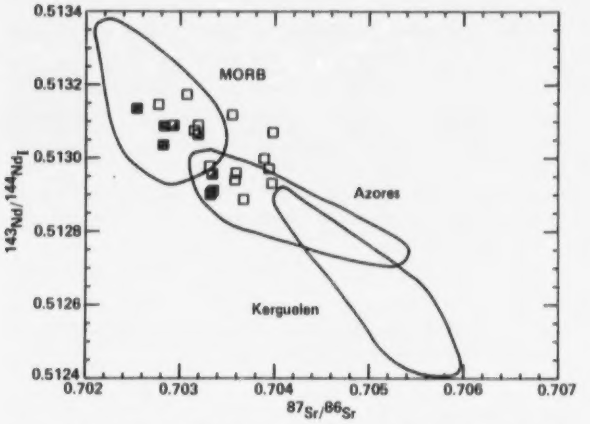

Figure 1. Initial $^{143}Nd/^{144}Nd$ versus $^{87}Sr/^{86}Sr$ for Leg 82 basalts. Solid squares = glasses; half-filled squares = leached whole-rock samples; open squares = whole-rock powders (no leach). Comparison fields from published literature and unpublished data from Max-Planck-Institute. MORB = Mid-ocean ridge basalts.

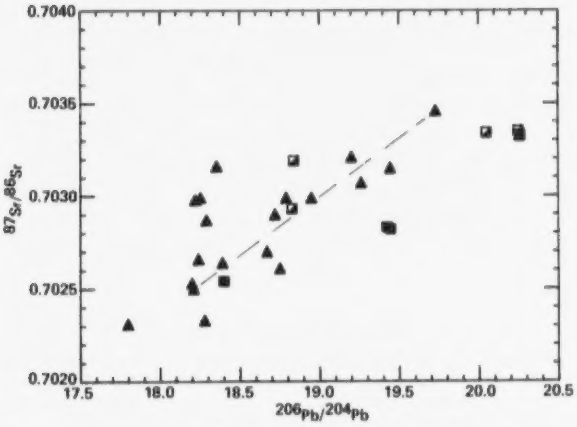

Figure 2. Comparison of $^{87}Sr/^{86}Sr$ versus $^{206}Pb/^{204}Pb$ for Leg 82 basalts and MORB. Triangles = data from Cohen and O'Nions (1982) and Dupré and Allegre (1980); dashed line shows trend from Mid-Atlantic Ridge (MAR) basalts (zero age); solid squares = glasses, Leg 82; half-filled squares = leached whole rocks. (Pb isotopic data for Leg 82 from Dupré et al., this volume.)

Note that the range of variation shown in Leg 82 is equivalent to, if not greater than, that previously observed in MORB. The dashed line in Figure 2 indicates the trend shown by MAR MORB. Compared to that MAR "trend," the Leg 82 basalts show some significant deviations at Sites 556 and 558. At these two sites, there is a markedly more radiogenic Pb isotopic composition for a given Sr isotopic composition. Pb isotopic composition in these sites is also anomalous with respect to the trace element characteristics of the sites (see Dupré et al., this volume).

Trace Element and Isotope Tests for Binary Mixing

As outlined in the introduction, Schilling and his coworkers (Schilling 1975, and White and Schilling, 1978) have developed a series of hypotheses relating variations in chemical characteristics to mixing between AMP/B and DLVL. As a first approximation, these authors have considered the mixing to be binary and also assumed that trace element ratios can be used to indicate the relative amount of components present. Accepting these conditions, one would hope to find a consistent (predictable) relationship between trace element and isotopic variation. To evaluate this possibility we have tested for mixing using trace elements and trace-element-isotope pairs. Because of our wider data base for initial Nd isotopic composition, only this isotopic system is considered here. Dupré et al. (this volume) discuss qualitatively the results for Pb isotopes versus trace elements.

Initial tests for a binary mixing relationship were made using variations in La/Ce versus Tb/Yb. These elements and ratios were selected for the following reasons: (1) an extensive base of good data was available (see Hertogen et al., this volume); (2) both ratios were thought to be reasonably free of fractional crystallization effects and thus to reflect source characteristics; (3) the ratio pairs were sufficiently different so as to minimize the introduction of artificially good mixing fits given element similarities. The variation in La/Ce versus Tb/Yb is shown in Figure 3. The mixing curve illustrated was calculated for E-MORB and N-MORB samples analyzed by Hertogen et al. (this volume). The scatter about this curve is similar to that found in earlier studies by Schilling (1975) and White and Schilling (1978).

It is easier to evaluate the mixing hypothesis using the reciprocal plot (Langmuir et al., 1978) of La/Ce versus Yb/Ce. In this plot a straight line should be formed with the data in the same relative order. For the data illustrated (Fig. 4), it is possible to calculate a linear least-squares regression line with $r^2 = 0.87$. This result essentially confirms the results of previous studies and would

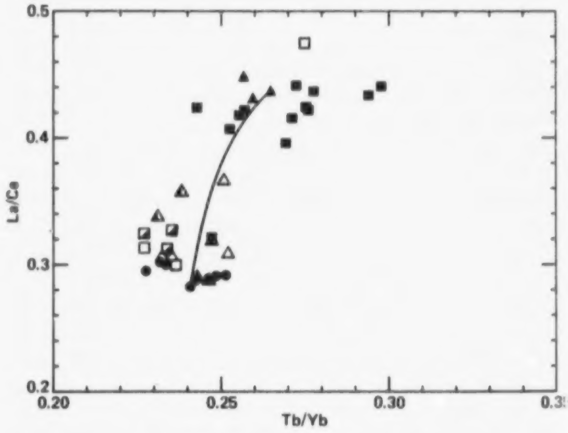

Figure 3. La/Ce versus Tb/Yb for Leg 82 basalts. Open symbols = 1 Ma (Hole 558 = square; Hole 562 = triangle). Closed symbols = 35 Ma (Hole 556 = circles; Hole 558 = square; Hole 559 = triangle). Half-filled symbols = 35 Ma (Hole 563 = square; Hole 56 = triangle). Solid line is calculated mixing curve between sample from Sections 556-2-5 and 559-8-1 (see Hertogen et al., this volume).

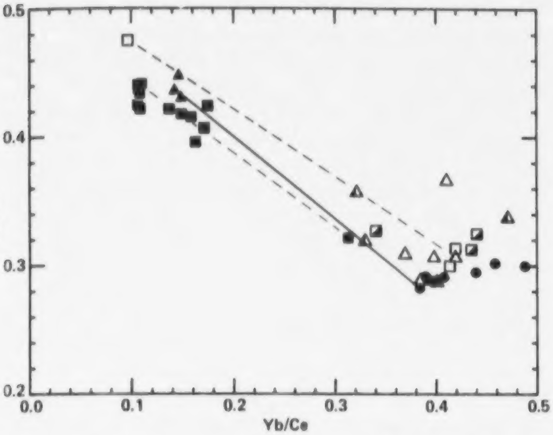

Figure 4. Reciprocal plot of La/Ce versus Yb/Ce for Leg 82 basalts. Mixing line for samples from Sections 556-2-5 to 559-8-1 shown in solid line. Dashed lines are sketched-in possible mixing lines for variations observed at Sites 561 and 558. Symbols same as Figure 3.

model. However, it is informative to consider the data in more detail. Figure 4 shows a calculated mixing line for mixing between the same basalt pair used in Figure 3. Also illustrated are two other possible mixing lines (note: dashed lines drawn between samples from same sites). It is possible then that the trends shown in Figures 3 and 4 illustrate mixing between different sets of binary end-members.

The relationship between Nd isotopic composition and trace elements is illustrated in Figure 5. $\epsilon\mathrm{Nd}_{(T)}$ was chosen to illustrate the Nd isotopic variation so as to remove age differences, minimize effects caused by differential evolution of N-MORB and less-depleted reservoirs over the last 35 Ma, and facilitate easier discussion of the Nd isotopic composition. The Ce/Sm ratio is used to illustrate the trace element variation because of the poor trace element data base for the 10 samples jointly analyzed for Pb isotopic composition. The mixing curve shown was calculated for mixing between Samples 563-25-1 (an N-MORB from this study) and Faial 33 (an Azores Island basalt). Faial 33 was recommended by W. White, and if binary mixing is applicable, then it is a reasonable representation of the Azores Islands. However, this is not strictly true because isotopic heterogeneity in the Azores seems unlikely to be explained by simple binary mixing (Hawkesworth et al., 1979; Dupré et al., 1982; White, pers. comm., 1983).

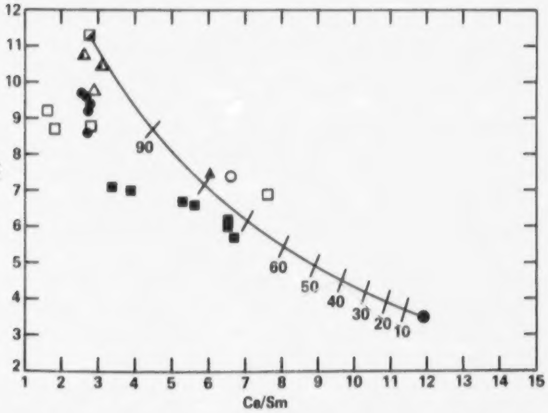

Figure 5. $\epsilon\mathrm{Nd}_{(T)}$ versus Ce/Sm for Leg 82 basalts. Symbols same as Figure 3, except that the large solid circle = Faial 33 (Azores) and open circle = Hole 557. Mixing curve is calculated for mixture of 563-25-1 and Faial 33. Labeled tick marks indicate percentage of N-MORB (563) end-member present. Trace and isotopic data for Faial 33 from White and Hofmann (1982) and White et al. (1979).

In general, the correlation observed between $\epsilon\mathrm{Nd}_{(T)}$ and Ce/Sm is the expected correlation for a mixing relationship between AMP/B and DLVL (i.e., E-MORB are characterized by lower $\epsilon\mathrm{Nd}_{(T)}$ values than N-MORB). The correlation is not as well developed as that required by a binary mixing model. Two points are worth noting (see also Table 3 and Fig. 5): (1) the basalts most depleted in trace element (Hole 556) do not have the highest $\epsilon\mathrm{Nd}_{(T)}$ values; and (2) in Hole 558 it is possible to find N-MORB and E-MORB with identical (within error) Nd isotopic compositions (see Results, Hole 558). As in the trace element mixing plots, it is easy to visualize a set of possible mixing curves as illustrated in Figure 5.

To more carefully evaluate the relationship between Nd isotopic composition and trace element characteristics, and its significance for AMP/B-DLVL mixing, we have considered our data plus that from the literature for a possible mantle flow line between the FAMOUS site and Hole 558 (Leg 82). The Hole 558-FAMOUS flow line may be considered to be defined by or sampled by the following points: Hole 558 (Leg 82), 35 Ma; Hole 335 (Leg 37) 16 Ma; Hole 332 (Leg 37), 3 Ma; and FAMOUS, zero-age. Data sources are: this study; White, 1979; Schilling et al., 1977; Cohen and O'Nions, 1982; O'Nions et al., 1977.

Schilling et al. (1977) had suggested on the basis of REE data that the AMP/B contribution increased from 0% at Hole 335 to 30% at Hole 332 and to 45% in FAMOUS. Considered scatter was observed in the trace element characteristics at these sites (Schilling et al., 1977), but nonetheless a significant temporal variation seemed to exist. In contrast to the findings of Schilling et al. (1977), we would suggest the following (see Fig. 6):

1. Based on $\epsilon\mathrm{Nd}_{(T)}$, the plume component in Hole 335, Hole 332, and the FAMOUS site can be considered to be constant at (for this specific model) ~8%.
2. REE data are not a good indication of plume component and give a range of 7-20% plume component.
3. Hole 558 would have the highest plume component. Therefore, if this is due to an AMP/B influence, then there was a marked decrease in intensity between 35 and 16 Ma followed by a relative constancy of plume effect. The effect on Hole 558 is greater than that at Hole 556, although the latter would probably have been closer to the AMP/B source at 35 Ma.
4. Within Hole 558 there are basalts that appear to have trace elements and isotopic composition characteristics correlated, whereas others show marked trace element changes with no marked Nd isotopic variability.

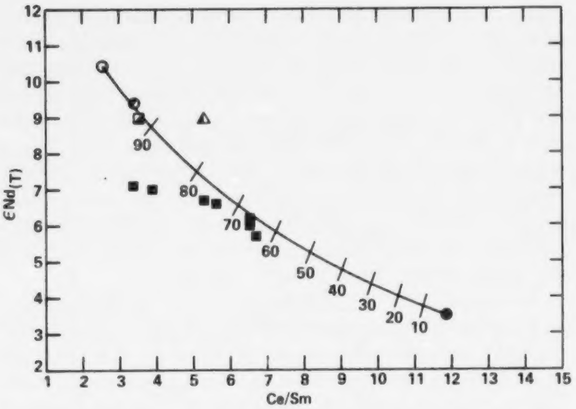

Figure 6. $\epsilon Nd_{(T)}$ versus Ce/Sm for possible Azores-Hole 558 flow line. Mixing line calculated for mixture of representative N-MORB reservoir basalt ($\epsilon Nd_{(T)}$ = 10.5) (large open circle) and Faial 33 (Azores) (large solid circle). Solid square = Hole 558 samples; half-filled squares = FAMOUS samples; half-filled triangle = Site 332 samples; half-filled circle = Site 335 samples.

SUMMARY AND CONCLUSIONS

The results presented here demonstrate that, in general, there is a correlation observed between isotopic and trace element characteristics in Leg 82 basalts. Those Leg 82 basalts classified as E-MORB have initial $^{143}Nd/^{144}Nd$ ratios < 0.51300, whereas, those basalts classified as N-MORB have initial $^{143}Nd/^{144}Nd$ ratios > 0.51307. A significant deviation from this general rule exists at Hole 558, where basalts defined as N-MORB by trace element characteristics have Nd isotopic characteristics of E-MORBs.

The degree of correlation observed between trace element and Nd isotopic composition is not as well developed as would be predicted by a unique binary AMP/B-DLVL mixing model. Rather it seems likely that there are more localized sets of end-members involved in mixing relationships. It is also clear that trace elements alone are not a reliable indicator of the proportion of components in mixing relationships. This study confirms earlier results, based on work on Leg 37 samples and FAMOUS samples (cf., Blanchard et al. 1976; White, 1979; and Langmuir et al., 1977), that trace elements can be separated from isotopic characteristics and reflect complex processes occurring just before or during mixing/partial melting of the source.

The nature of the processes that lead to significant trace element fractionation without accompanying isotopic changes are not well defined. One possibility discussed for the FAMOUS basalts is the concept of dynamic melting; this model is discussed fully in the paper by Langmuir et al. (1977) and provides an explanation for variations in REE patterns where the samples retain similar ratios of K/Ba, K/Rb, Rb/Sr, and Zr/Nb. This model would not appear to explain the severe trace element fractionation seen in Hole 558, where the changes in REE pattern are also accompanied by significant fractionation of Zr(Hf) and Nb(Ta). With the presently available limits on distribution coefficients for Zr and Nb, it would appear that no plausible simple partial melting model can explain the variation observed in Hole 558 (cf., Le Roex et al., 1981). Veining of the mantle within < 200 Ma before eruption of the Hole 558 basalts with a nephelinitic melt (cf., Wood, 1979b and Green, 1971) may be a partial solution, because mixes between these types of melts and DLVL sources can generate the right style of geochemical signature. The problem with Hole 558 is that it would appear to have had a reasonable chance of having E-MORB characteristics ($\epsilon Nd_{(T)}$ = 5 to 7), thus the problem is to generate the N-MORB characteristics. One possibility is that at some stage (<200 Ma before eruption) there was a local redistribution of elements caused by incipient partial melting, in which there was a volatile phase present in sufficient quantity to fractionate the trace elements in a more complex manner than that resulting from simple batch melting. In contrast to the "normal" veining episode, this melting/veining episode must generate a depleted trace element signature on top of an enriched isotope signature. The Pb isotopic variation observed in Hole 558 basalts suggests a possible redistribution event involving a fluid phase (melt + volatiles). If this recent fluid had a high μ value ($\mu = {}^{238}U/^{204}Pb$), it could help explain the relatively constant $^{207}Pb/^{204}Pb$ ratios and variable $^{208}Pb/^{204}Pb$ and $^{206}Pb/^{204}Pb$ ratios observed in Hole 558 basalts (Dupré et al., this volume).

The observations that simple binary mixing is not strictly applicable to Leg 82 basalts, and that trace elements are not a reliable indicator of mixing components necessitate a revision of the hypotheses proposed by Schilling and his co-workers (Schilling, 1975; and White and Schilling, 1978). The distribution of the observed heterogeneities also do not fit any simple AMP/B-DLVL mixing model. If initial $^{143}Nd/^{144}Nd$ ratios < 0.51305 are taken as evidence for a significant plume component in the source, then we would conclude that there was a plume input at the following: Sites 558 and 559 at 35 Ma; Sites 557 and 561 at 17 Ma; and the Azores at 0–10 Ma. The origin of this plume input at Sites 559 and 561 might be attributed to the Oceanographer plume of White and Schilling (1978). In fact, the data presented in this study may favor the plume explanation for the heterogeneity observed on the MAR in the vicinity of the Oceanographer Fracture Zone rather than the alternative explanations offered by these authors. However, the presence of a "plume" over the last 35 Ma in this area can only be inferred on geochemical grounds and lacks supporting bathymetric evidence. The Azores mantle plume may be the explanation for the characteristic geochemical and isotopic character ("plume input") at Site 557. However, it is difficult to attribute the plume input at Site 558 to the Azores mantle plume, as noted earlier in this paper. It is certainly possible to come up with AMP/B-DLVL explanations for the data. The plume hypothesis has become quite flexible with disconnected blobs, fluctuating intensity, and possibly "plume heterogeneity." At this stage the plume model becomes untestable and potentially unique to one area. We prefer to consider a model in which localized heterogeneity of not necessarily confirm or disprove the binary mixing both recent (e.g., Wood, 1979b; Green, 1971) and long-term (> 10^9 Ma) origin (e.g. Davies, 1981) plays a role. This type of heterogeneity may be superimposed upon regional heterogeneity generated by "plume mixing."

Resolution of the relative roles to be played by long-lived local heterogeneity, recent heterogeneity caused by complex partial melting, and regional plume-DLVL mixing is beyond the scope of this paper. We note only that the distribution and nature of the heterogeneities observed in the Azores area require a reevaluation of the hypotheses proposed by Schilling and his co-workers (Schilling, 1975; White and Schilling, 1978; Schilling et al., 1977).

ACKNOWLEDGMENTS

We are grateful N. T. Arndt, M. Flower, J. M. Rhodes, and W. M. White for their reviews. The first author also wishes to thank "Wild Bill" for his generous help in assisting with the computing, analytical, and scientific problems encountered during this study. We also appreciate the stimulating discussions with B. Dupré, C. Chauvel, and F. Albarede.

REFERENCES

Aumento, F., Melson, W., et al., 1977. *Init. Repts. DSDP*, 37: Washington (U.S. Govt. Printing Office).

Blanchard D. P., Rhodes, J. M., Dungan, M. A., Rodgers, K. V., Donaldson, C. H., Brannon, J. C., Jacobs, J. W., and Gibson, E. K., 1976. The chemistry and petrology of basalt from Leg 37 of the Deep Sea Drilling Project. *J. Geophys. Res.* 81:4231-4246.

Cohen, R. S., and O'Nions, R. K., 1982. The lead, neodymium and strontium isotopic structure of ocean ridge basalts. *J. Petrol.* 23: 299-324.

Davies, G. F., 1981. The earth's neodymium budget and structure and evolution of the mantle. *Nature*, 290:208-213.

Dupré, B., and Allegre, C. J., 1980. Pb-Sr-Nd isotopic correlation and the chemistry of the North Atlantic mantle. *Nature*, 286:17-22.

Dupré, B., Lambert, B., and Allegre, C. J., 1982. Isotopic variations within a single oceanic island: the Terceira case. *Nature*, 299: 620-622.

Green, D. H., 1971. Composition of basaltic magmas as indicators of conditions of origin: application to oceanic volcanism. *Phil. Trans. R. Soc. London, Ser. A*, 268:707-725.

Hawkesworth, C. J., Norry, M. J., Roddick, J. C., and Vollmer, R., 1979. ^{143}Nd/^{144}Nd and ^{87}Sr/^{86}Sr ratios from the Azores and their significance in LIL-element enriched mantle. *Nature*, 280:28-31.

Jenner, G. A., Dupré, B., Goepel, C., and Hertogen, J., in press. Trace, rare earth and radiogenic isotope composition of Leg 82 basalts: constraints on processes affecting the composition of oceanic crust. *J. Geodynamics*.

Langmuir, C. H., Bender, J. F., Bence, A. E., Hanson, G. N., and Taylor, S. R., 1977. Petrogenesis of basalts from the FAMOUS area: Mid-Atlantic Ridge. *Earth Planet. Sci. Lett.*, 36:133-156.

Langmuir, C. H., Vocke, R. D., and Hanson, G. N., 1978. A general mixing equation: applied to the petrogenesis of basalts from Iceland and the Reykjanes Ridge. *Earth Planet. Sci. Lett.*, 37:380-392.

Le Roex, A. P, Erlank, A. J., and Needham, H. D., 1981. Geochemical and mineralogical evidence for the occurrence of at least three distinct magma types in the "FAMOUS" region. *Contrib. Mineral. Petrol.*, 77:24-37.

O'Nions, R. K., Hamilton, P. J., and Evenson, N. M., 1977. Variations in ^{143}Nd/^{144}Nd and ^{87}Sr/^{86}Sr ratios in oceanic basalts. *Earth Planet. Sci. Lett.*, 34:13-22.

Schilling, J.-G., 1973. Iceland mantle plume: geochemical study of Reykjanes Ridge. *Nature*, 242:565-571.

________, 1975. Azores mantle blob: rare earth evidence. *Earth Planet. Sci. Lett.*, 25:103-115.

Schilling, J.-G., Kingsley, R., and Bergeron, M., 1977. Rare earth abundances in DSDP Sites 332, 334, and 335, and inferences on the Azores Mantle Blob activity with time. *In* Aumento, F., Melson, W. G., et al., *Init. Repts. DSDP*, 37: Washington (U.S. Govt. Printing Office), 591-597.

Sun, S. S., 1980. Lead isotopic study of young volcanic rocks from mid-ocean ridges, ocean islands and island arcs. *Phil. Trans. R. Soc. London, Ser. A*, 297:409-445.

Sun, S. S., Nesbitt, R. W., and Sharaskin, A. Y., 1979. Geochemical characteristics of mid-ocean ridge basalts. *Earth Planet. Sci. Lett.*, 44:119-138.

White, W. M., 1977. Geochemistry of igneous rocks from the Central North Atlantic: the Azores and the Mid-Atlantic Ridge [Ph.D. dissert.]. University of Rhode Island, Kingston.

________, 1979. Geochemistry of basalts from the FAMOUS area: a reexamination. *Carnegie Inst. Washington Year Book*, 78:325-331.

White, W. M., and Hofmann, A. W., 1982. Sr and Nd isotope geochemistry of oceanic basalts and mantle evolution. *Nature*, 296: 821-825.

White, W. M., and Patchett, J., 1984. Hf-Nd-Sr isotopes and incompatible element abundances in island arcs: implications for magma origins and crust-mantle evolution. *Earth Planet. Sci. Lett.*, 67: 167-185.

White, W. M., and Schilling, J.-G., 1978. The nature and origin of geochemical variation in Mid-Atlantic Ridge basalts from the Central North Atlantic. *Geochim. Cosmochim. Acta*, 42: 1501-1516.

White, W. M., Schilling, J.-G., and Hart, S. R., 1976. Evidence for the Azores mantle plume from strontium isotope geochemistry of Central North Atlantic. *Nature*, 263:659-663.

White, W., Tapia, M. D. M., and Schilling, J.-G., 1979. The petrology and geochemistry of the Azores Islands. *Contrib. Mineral. Petrol.*, 69:201-213.

Wood, D. A., 1979a. Dynamic partial melting: its application to the petrogenesis of basalts erupted in Iceland, the Faeroe Islands, the Isle of Skye (Scotland) and the Troodos Massif (Cyprus). *Geochim. Cosmochim. Acta*, 43:1031-1046.

________, 1979b. A variably veined suboceanic upper mantle-genetic significance for mid-ocean ridge basalts from geochemical evidence. *Geology*, 7:499-503.

Wood, D. A., Joron, J. L., and Treuil, M., 1979. A re-appraisal of the use of trace elements to classify and discriminate between magma series erupted in different tectonic settings. *Earth Planet. Sci. Lett.*, 45:326-336.

Date of Initial Receipt: 21 April 1983
Date of Acceptance: 28 November 1983

27. ABYSSAL GLASSES, PETROLOGIC MAPPING OF THE OCEANIC FLOOR AND "GEOCHEMICAL LEG" 82[1]

L. V. Dmitriev, A. V. Sobolev, N. M. Suschevskaya, and S. A. Zapunny, Vernadsky Institute of Geochemistry, U.S.S.R. Academy of Sciences[2]

ABSTRACT

The compositions of abyssal glasses obtained on Leg 82 of the *Glomar Challenger* and the MAPCO cruise of *Jean Charcot* have been investigated. Two main compositional groups of Atlantic glasses (A_1 and A_2) that are separated in space and time were identified. The distribution of these groups in the studied area allowed mapping of the transition zone from A_1 to A_2 between 30-35°N MAR. We infer that the compositional groups of abyssal glasses of the Atlantic and other oceans reflect the depth of separation of primary melts from the oceanic mantle. Specifically, the primary melt of Group A_1 separates from the mantle at a depth of 30-60 km (spinel-peridotite facies) and those for Group A_2 from a depth of 15-30 km (plagioclase-peridotite facies). Modifications of dynamic models of the ocean lithosphere are discussed.

INTRODUCTION

Layer 2—the volcanic layer—of the ocean crust was originally thought to be homogeneous. This view led to fairly simplified geologic and geophysical models of the ocean lithosphere and gave little reason for deep-sea basement drilling on the flanks of mid-ocean ridges or in abyssal planes. With more data, it became clear that ocean basalts are fairly diverse in composition and form (e.g., pillow flows, sheet flows, etc.). The data on their regional variations appeared to be most interesting, as first noted by Shido and Mijashiro (1973), who showed that the area of the Mid-Atlantic Ridge at 36°N reflected a rather sharp change in tholeiite compositions to the north and to the south.

The existence of this boundary required explanation. Therefore, a number of expeditions were undertaken between 1974 and 1979, including the work on FAMOUS project, Leg 37 of *Glomar Challenger* (Aumento, Melson, et al., 1977), the MAPCO cruise of *Jean Charcot* (Bougault and Treuil, 1980), and DSDP Leg 82. This study focuses on Leg 82 samples provided by the Deep Sea Drilling Project and on MAPCO samples provided by Henri Bougault.

PETROCHEMICAL CRITERION OF CLASSIFICATION

The compositional variation of basalts obtained at one site (i.e., from one drill hole) most probably reflects the origin of the magma as well as its pre-eruption cooling history, which may include crystal fractionation. In some cases, it is difficult to discriminate between these two processes when only bulk rock analyses are available. The composition of glass in pillow rinds yields liquid compositions directly, unmodified by the often irregular abundances of phenocrysts. Interpretations of the analyses of numerous such glasses (Melson et al., 1977) and our data have been published in a number of papers (Dmitriev et al., 1978; 1979a, b; 1980). The highlights of these interpretations follow below.

There are at least two main groups of abyssal glasses. They are simply identified with the help of an eight-component discriminant function (D):

$$D = 16.53\ Na_2O + 16.19\ TiO_2 + 3.114\ SiO_2 + 2.93\ MgO + 1.45\ CaO + 0.92\ Al_2O_3 - 32.94\ K_2O - 1.46\ FeO$$

D_0 value = 258.09 (Sushevskaya et al., 1983).

The standard error of D calculated from the data on the accuracy of microprobe analyses is ±3.0. A histogram of D is in Figure 1 where the area of uncertainty related to the analytical error is also plotted.

The variations within each group may result from the differences in the composition of primary melts, the degree of their differentiation, and magma mixing. All these processes influence the D value. Without going deeper

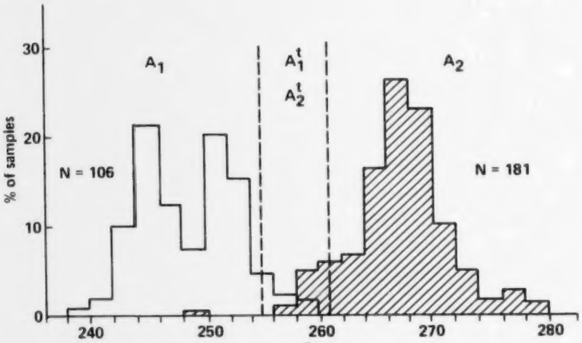

Figure 1. Histogram of the discriminant function D (an eight-component discriminant; see text) for the Atlantic. Uncertainty limit is between the dotted lines (see text). N is the number of analyses.

---

[1] Bougault, H., Cande, S. C., et al., *Init. Repts. DSDP*, 82: Washington (U.S. Govt. Printing Office).

[2] Address: Vernadsky Institute of Geochemistry, U.S.S.R. Academy of Sciences, Moscow, U.S.S.R.

into the problem of D dependence on these processes, we shall only note that its values are used in the present work as a general classification feature.

Figure 2 is a schematic map of the Atlantic Ocean showing the distribution of the two groups of glass compositions. The map uses data from the catalog by Melson et al. (1977) and our data published before 1980. Data from Leg 7 of *Prof. Shtokman* (20–30°S MAR, 1982) (Dmitriev, Charin, et al.; in press) were also used. The region of Leg 82 and the MAPCO cruise is outlined. One of the groups (solid circles, Fig. 2) is located along the ridge axis, terminates at 36°N, and continues southward to 35°S. The other group has a wider regional distribution, occurring not only on the northern section of the Mid-Atlantic Ridge but on the ridge flanks and abyssal plains as well. These compositions are referred to as Group I (A_1) or as "peripheral" types. The other compositions, located along the ridge axis, are referred to as Group 2 (A_2), or as "central" types.

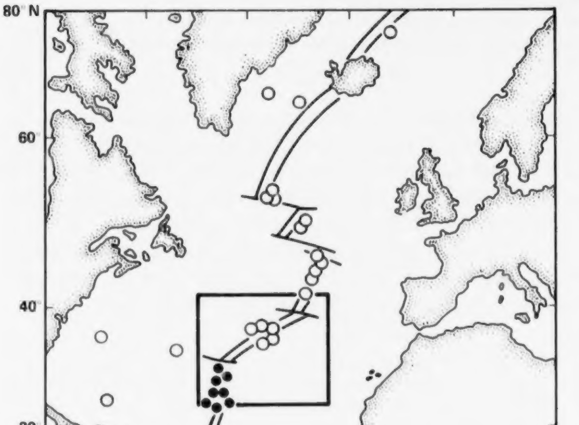

Figure 2. Schematic map of the Atlantic. Open circles = A_1, abyssal glass composition; closed circles = A_2, abyssal glass composition. Described area lies within center box.

Figure 3 shows D values plotted against latitude, quantitatively distinguishes the boundary between compositions of A_1 and A_2 in the north, and outlines this boundary in the south.

Basalts containing the glasses of the two groups also differ in petrographic and mineralogic features as well as in the concentration of some trace elements. A_1 basalts are frequently strongly differentiated, have phenocrysts with more basic compositions (Fig. 4), and are relatively enriched by the siderophile trace elements. A_2 basalts are often less differentiated, aphyric or sparsely phyric rocks; they have a less basic phenocryst composition; and they are relatively enriched in some cases by the lithophile trace elements.

MID-ATLANTIC RIDGE (25–40°N)

A great deal of detailed data are available for the region. In this paper, we confine our interpretations to the shipboard data from Leg 82 and the data from the MAPCO cruise (Bougault and Treuil, 1980). These data are summarized in Table 1.

These data, as well as previously available data, show that basalts at 25–40°N have features of typical ocean tholeiites. The examined samples are glassy fragments of pillow lava rinds. They include rocks with the phenocryst assemblage plagioclase + olivine. Some of them contain large plagioclase phenocrysts of up to 1 cm across. There are also conglomeroporphyritic rocks as well as sparsely phyric, plagioclase-phyric, and aphyric basalts.

Clinopyroxene phenocrysts are rare, although Bougault et al. (1980) describe basalt rich in clinopyroxene phenocrysts. This paper deals only with the chemical analyses of the glassy rinds. The compositions of glasses were determined with the HMA5 and JXA-5A electron microprobes (Japan) using an acceleration voltage of 15 kV, beam current I = 40–60 10^{-9} amps, and a beam diameter of 5–10 microns. Analytical procedure includes intensity accumulation at 4–5 spots with 10 s counting time for each grain. To prevent Na and K leaks under the beam, the samples were moved slowly during analysis. Reference samples were natural basalt glass USNM 111240/52 (VG-2) for Si, Al, Ti, Fe, Mg, Ca, and Na (kindly supplied by E. Jarosewish), described in Jarosewish et al. (1979), and pure synthetic orthoclase for K. All data were corrected for matrix effects by the Bence and Albee method (1968) and the results are shown in Table 2.

Figure 5 is a schematic map of Leg 82 and of the MAPCO cruise in which the dots shown by different signs show the compositions identified by D value. The figure also shows data from previous investigations (Leg 37 *Glomar Challenger* [Aumento, Melson, et al., 197] the FAMOUS project, and data from other expeditions, see Melson et al., 1977). It can be seen that compositions definitely belonging in Group A_1 occur in Holes 563, 564, 558, and 559 of Leg 82, in Site 97 of the MAPCO cruise, and at other sites mentioned by Bou-

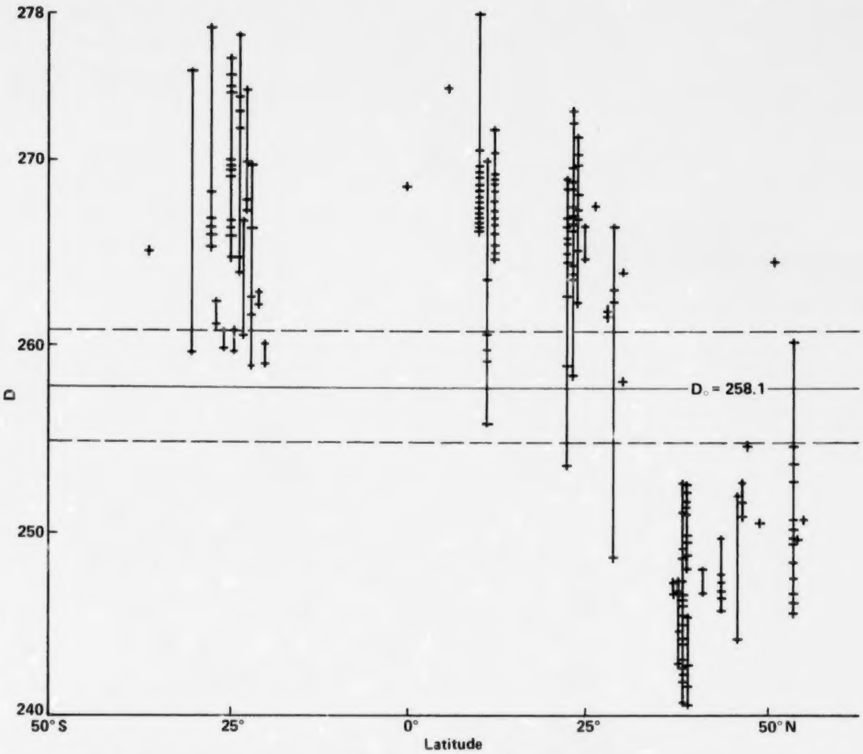

Figure 3. D-variation as the function of MAR latitude. Limits are uncertain between the dashed lines. D is an eight-component discriminant (see text).

gault and Treuil (1980). Compositions belonging in Group A_2 occur at Sites 98-11 and 98-15 of the MAPCO cruise and at all rift valley sites south of 30°N discussed by Melson et al. (1977). At the other sites, the distribution of compositions is less clear-cut. At these sites, the D value is close to D_0 (258.09). These compositions are intermediate between A_1 and A_2 and are transitional (t) from A_1 to A_2 and from A_2 to A_1, respectively. They are arbitrarily referred to as A_1^t and A_2^t. In Hole 556, the lower horizon is represented by A_1 and the upper horizon by A_1^t; in Hole 562, the lower is A_1, and the upper is A_2^t; and in Hole 561, the lower is A_2^t, and the upper is A_2. In all these sites the transition from A_1 to A_2 with decreasing age is evident. The transitional compositions A_1^t are found at MAPCO Sites 98-08 and 98-14 and the A_2^t compositions at MAPCO Sites 98-07, 98-09, and 98-12. The possible transition zone between both compositional groups is shaded in Figure 5. Its location at the astern ridge flank is arbitrarily based on the idea of symmetric structure.

DISCUSSION

The data reviewed here lead to the conclusion that there are at east two main types of composition of tholeiites that appear to be regularly distributed. How is this explained?

One of the possible explanations is based mainly on trace element data. These reveal lateral heterogeneity of the mantle source of melts and different degrees of its partial melting. Bougault (Bougault et al., 1978; Bougault and Treuil, 1980) develops this approach in his papers using the data on concentration of the lithophile elements. Papers by Flower (1980; 1981) describes relationships between the spreading rate of mid-ocean ridges and basalt compositions.

Natland (1980) and Natland and Melson (1980) have argued perceptively that evidence from the chemistries of natural glasses, trace element studies, experimental petrology, and geodynamic reconstructions of magmatism at the East Pacific Rise, the Siqueiros Fracture Zone, and the Galapagos spreading center support the lateral diversity of melts formed within the upper mantle.

Papers by O'Hara (1968), Jaques and Green (1980), and Stolper (1980) suggest that differentiation of primary picrite melts could produce the entire spectrum of major and minor element compositions of ocean tholeiites. Presnall et al. (1979) and Fujii and Bougault (1983) have shown experimentally that primary high magnesian tholeiite melts can form in the transitional zone between plagioclase and spinel lherzolite. These experimental studies would be consistent with a single primary melt, but do not explain the two stable separate compositional groups observed here.

In our models, we take into account the possible influence of mantle heterogeneity on trace element concentrations and on possible connections with spreading rate. However, we assume that the mantle is fairly homogeneous for the major elements.

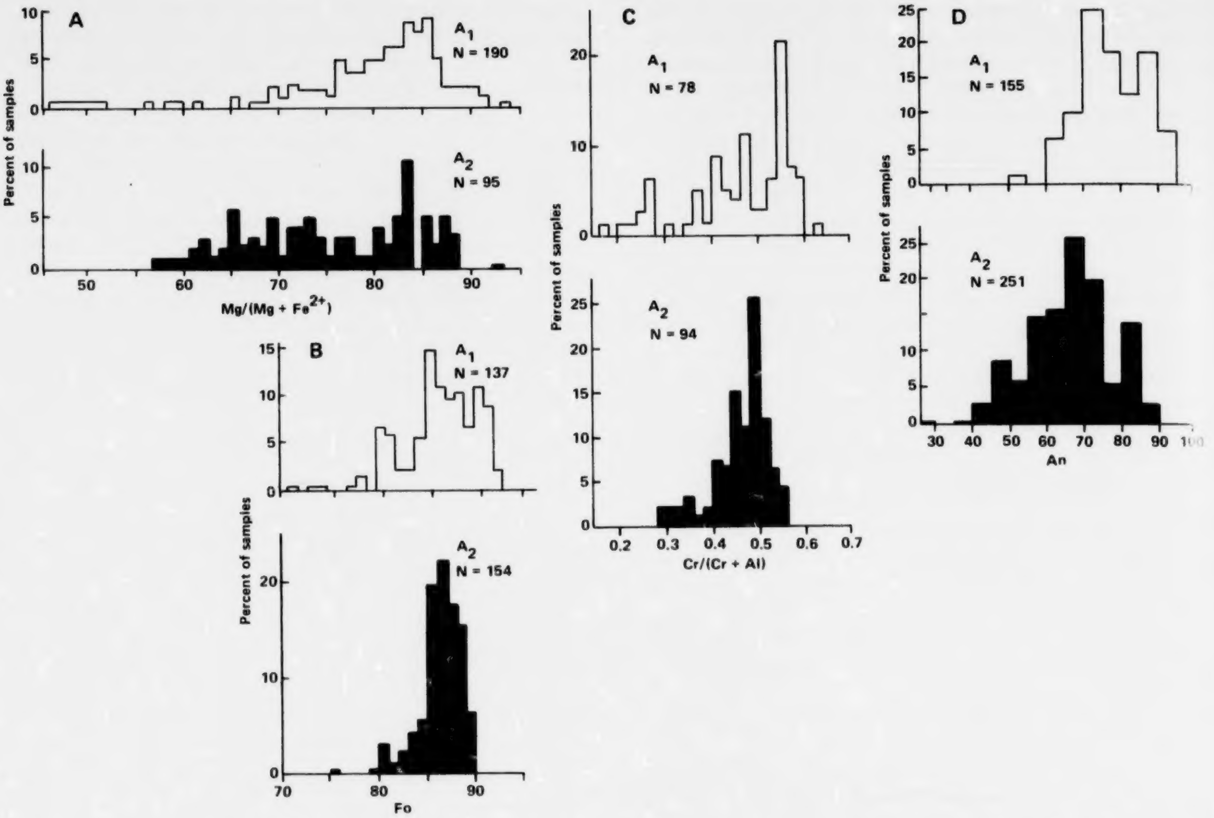

Figure 4. The compositions of major minerals from mid-ocean ridge basalts. A. Mg-values of clinopyroxene. B. Fo contents of olivine. C. Cr/(Cr + Al) values of spinel. D. An contents of plagioclase. N is the number of samples. Data from Ayuso et al. (1976); Baragar et al. (1977); Bonatti et al. (1977); Bryan et al. (1977); Bollinger and Semet (1980); Dick and Bryan (1978); Dickey et al. (1977); Donaldson and Brown (1977); Dungan et al. (1978); Fisk and Bence (1970); Flower et al. (1977a, b; 1978); Fujii and Fujioka (1979); Genkin et al. (1980); Graham et al. (1979); Hekinian et al. (1976); Hodges and Papike (1977); Sato et al. (1978); Sigurdsson and Schilling (1976); Sinton and Byerly (1980); Templeman (1979); and Wood et al. (1979).

Glass compositions of both groups give parallel trends in plagioclase-olivine-clinopyroxene projections (Fig. 6A). We suggest that the reason for this is the existence of two primitive initial melts with different compositions. These initial higher temperature liquids in Group A$_1$ contain olivine (Fo$_{91.5}$) and chromian spinel, and in Group A$_2$, contain olivine (Fo$_{90}$), plagioclase (An$_{89}$), and chromian spinel. Experimental homogenization of the melt inclusions established that the temperature of crystallization of phenocrysts in Group A$_1$ is noticeably higher than for phenocrysts in Group A$_2$, 1290°C and 1240°C, respectively.

The Fe^{3+}/Fe^{2+} ratio in some glass samples from both groups was determined by Mössbauer spectroscopy (Dmitriev et al., in press). We found that crystallization redox conditions of the two groups differed. Group A$_1$ melts crystallized under conditions close to quartz-fayalite-magnetite buffer, and those of Group A$_2$, close to the Ni-NiO buffer (Dmitriev, Melson, et al., in press).

The origins of the possible primary melts for the two groups was modeled by back calculation of their fractional crystallization. The calculation was performed by a computer program using steplike "dissolution" of equilibrium crystalline phases in a melt of varied composition (one step 0.1% mol.). The composition of such crystals were calculated using the equilibrium crystal-melt equations from Roeder and Emslie (1970) and Drake (1976) and the concept of highest equilibrium temperature (Nathan and Wankirk, 1978; Ariskin and Frenkel, 1982). At the end of eachs step the equilibrium parameters (the current compositions of melt, equilibrium crystal, temperature and Fe^{+3}/Fe^{+2} ratio) were recalculated. This procedure was repeated until the melt is in equilibrium with the highest temperature mineral assemblag known from petrography; Fo$_{91.5}$, for type A$_1$, and Fo$_{90}$ + An$_{89.0}$, for type A$_2$.

The specification of a back fractionation cotectic mod consists of subsequent "dissolution" of both plagioclas and olivine depending on their equilibrium temperatur (the phase with the lower equilibrium temperature wa "dissolved"). The chromian spinel, a well-known member of the most primitive liquids of both types, was no taken into account because of its negligible influence o the melt composition, given its extremely low concentra

Table 1. General description of samples.

Our sample number	Hole-Core-Section (interval in cm) (piece number)	Location		Age (Ma)	Brief petrograhy of basalt related to glasses
		Latitude (all north)	Longitude (all west)		
1	556-4-6, 41–44 (IE)	38°56.38′	34°41.12′	34	Sparsely Pl (Ol)-phyric
2	556-8-3, 56–58 (3C)	38°56.38′	34°41.12′	34	Pl-Ol-(Cpx) phyric. phenocrysts, 10–15%
3	558-33-1, 33–34 (5)	37°46.2′	37°20.61′	34–37	Aphyric
4	558-35-2, 84–85 (5A)				Aphyric
5	558-37-1, 75–76 (7A)				Sparsely Ol-phyric. Mt in glass
6	558-39-1, 25–26 (3)				Aphyric
7	559-5-2, 11–13 (2)	35°07.45′	40°55.00′	15–17	Sparsely Pl-Ol-phyric; phenocrysts, 0.5%
8	559-8-2, 102–103 (6)	35°07.45′	40°55.00′	15–17	Aphyric
9	561-2-1, 92–93 (5B)	34°47.10′	39°01.70′	14–17	Sparsely Pl-Ol-phyric; phenocrysts, 2–5%
10	561-3-1, 40–41 (5B)	34°47.10′	39°01.70′	14–17	Aphyric
11	562-1-2, 140–142 (8)	33°08.49′	41°40.76′	15–17	Aphyric
12	562-6-4, 45–46 (2B)	33°08.49′	41°40.76′	15–17	Sparsely Pl-phyric
13	563-24-1, 108–109 (7B)	33°38.53′	43°46.04′	34–37	Aphyric
14	563-25-2, 132–134 (4A)	33°38.53′	43°46.04′	34–37	Pl-phyric
15	564-3-2, 50–51 (4)	33°44.36′	43°46.03′	34–37	Sparsely Pl-Ol-phyric; phenocrysts, 1%
16	564-1-2, 99–100 (6C)				Aphyric
17	564-8-1, 2–3 (5–1)				Aphyric
18	564-9-3, 26–27 (2B)				Aphyric
19	Ch-97-02-101	39°06′	29°45′	"zero age"	Aphyric
20	Ch-98-07-G3	32°17′	40°11′		Aphyric
21	Ch-98-08	31°54′	40°58′		Sparsely Pl (Cpx) phyric
22	Ch-98-09-G3	31°28′	40°57′		Aphyric
23	Ch-98-11-G4	30°41′	41°49′		Sparsely Ol-phyric
24	Ch-98-12-G3	30°10′	41°55′		Aphyric
25	Ch-98-14-L02	29°17′	43°05′		Pl-phyric
26	Ch-98-15	27°46′	44°05′		Aphyric
27	Ch-98-15-101	27°46′	44°05′		Aphyric

Note: Pl = plagioclase; Ol = olivine; Cpx = clinopyroxene; Mt = magnetite. Ch numbers are sample numbers from MAPCO cruise of *Jean Charcot* (Bougault and Treuil, 1980).

tion. Compositions of the most magnesian glasses of the two groups were selected as initial compositions for the calculations.

Group A_1 melt is a high-magnesian olivine tholeiite, almost picrite, whereas Group A_2 melt is a high-alumina tholeiite. These compositions correspond to the homogenized melt inclusions in the highest-temperature phase (Table 3). Both primary melts are highly magnesian and are in equilibrium with olivine $Fo_{90-91.5}$, which is similar to the olivine in ocean harzburgite (Prinz et al., 1976). Thus, both compositions correspond to the model of ocean tholeiite formation: primary lherzolite = tholeiite melt + residual harzburgite (Dmitriev, 1969).

The trends (Fig. 6B) correspond to the experimental crystallization differentiation of tholeiites of different compositions under dry conditions at a pressure of 1 atmosphere (Bender et al., 1978; Zapunny et al., 1983). This model is consistent with fractionation in intermediate magma chambers at a comparatively shallow depth beneath the ocean floor prior to eruption.

What processes have generated the two postulated primary melts? Five different models can be suggested: (1) derivation of one melt from the other by crystal fractionation; (2) different abundances of volatiles during partial melting of an otherwise uniform mantle; (3) different degrees of partial melting of a uniform mantle at a constant depth; (4) different compositions of mantle material; and (5) different depths of melt separation from a uniform mantle.

1. Simple calculations show that fractionation of olivine, orthopyroxene, clinopyroxene, garnet, spinel, and plagioclase separately or in any combination from the more magnesian melt A_1 cannot produce A_2 melts. The main limitation is the similar Mg-number of both compositions.

2. The extremely low water contents of both the glass groups (Delaney et al., 1978) and the melt inclusions of phenocrysts prohibit Model 2. The high temperature of melt inclusion homogenization also points to extremely low water contents.

3. and 4. Figure 7, based on the data of experimental melting of dry lherzolite (pyrolite) (Jaques and Green, 1980) and using data from the model of two primary melts (Table 3) developed by Sobolev et al. (in press), shows that neither different degrees of mantle melting (Model 3) nor differences in mantle composition can account for the differences in composition of melts A_1 and A_2.

5. It is clearly shown (Fig. 7) that composition A_1 is in equilibrium with lherzolitic mantle at a pressure of around 10 kbar (spinel–peridotite depth facies) and that composition A_2 is in equilibrium with the same mantle at a pressure of 6–9 kbar (plagioclase depth facies). Figure 7 also indicates that A_1 composition can form at 15–20% of mantle partial melting and A_2 composition at 15%. These values are close to what we find from the partial melting reaction: ocean lherzolite (Dmitriev et al., 1972) = ocean harzburgite (Dmitriev et al., 1972) + melt A_1 (or A_2). This model gives 15% for the degree of partial melting for melt A_1 and 13% for melt A_2. Thus, Model 5 seems most plausible. In other words, the difference in the composition of the postulated primary melts A_1 and A_2 is affected by the melting depth of a homogeneous mantle with regard to major elements

Table 2. Electron microprobe analyses for abyssal glasses.

Our sample number	1	2	3	4	5	6	7	8	9	10	11	12	13
Hole	556		558				559		561		562		563
Core-Section (interval in cm) (piece number)	4-6, 41–44 (1E)	8-3, 56–58 (3C)	33-1, 33–34 (5)	35, 84–85 (3-5A)	37-1, 75–6 (3–7)	39-1, 25–26 (3)	5-2, 11–135 (2)	8-2, 102–103 (5–6)	2-1, 92–93 (5–5B)	3-1, 40–41 (5–5B)	1-2, 140–142 (5–8)	6-4, 45–46 (5–2B)	24-1, 108–109 (7B)
Number of analyses	3	3	3	2	1	1	1	2	4	5	6	4	2
SiO_2	51.30 (0.5)	50.71 (0.2)	50.94 (0.34)	51.82 (0.28)	50.60	50.71	51.15	50.29 (0.21)	51.38 (0.18)	51.27 (0.38)	50.77 (0.39)	51.09 (0.65)	50.96
TiO_2	1.72 (0.11)	0.98 (0.02)	1.39 (0.07)	1.28 (0.01)	1.63	1.63	1.52	1.49 (0.01)	1.64 (0.14)	1.5 (0.1)	1.64 (0.06)	1.29 (0.03)	1.14
Al_2O_3	14.47 (0.13)	15.41 (0.12)	15.55 (0.09)	15.09 (0.23)	15.38	15.19	14.90	15.17 (0.24)	15.12 (0.09)	14.76 (0.23)	14.73 (0.66)	15.34 (0.26)	15.15
FeO	10.75 (0.13)	8.68 (0.01)	8.61 (0.22)	9.27 (0.06)	10.23	10.49	11.64	10.09 (0.33)	11.22 (0.28)	11.27 (0.39)	10.85 (0.31)	10.15 (0.2)	10.63
MgO	6.58 (0.03)	7.73 (0.05)	8.06 (0.22)	8.79 (0.02)	7.76	7.35	6.91	7.49 (0.12)	7.3 (0.28)	7.18 (0.38)	7.28 (0.17)	7.72 (0.36)	7.18
CaO	11.35 (0.14)	13.04 (0.05)	11.95 (0.19)	11.78 (0.02)	11.41	10.99	11.62	11.27 (0.06)	11.52 (0.12)	11.65 (0.24)	11.65 (0.18)	12.15 (0.29)	12.47
Na_2O	2.55 (0.12)	2.64 (0.07)	2.45 (0.07)	2.14 (0.07)	2.57	2.56	2.36	2.53 (0.03)	2.54 (0.03)	2.60 (0.06)	2.6 (0.08)	2.31 (0.12)	2.23
K_2O	0.18 (0.02)	0.17 (0.0)	0.32 (0.0)	0.31 (0.06)	0.32	0.31	0.08	0.36 (0.01)	0.09 (0.01)	0.09 (0.02)	0.09 (0.02)	0.12 (0.03)	0.07
Total	98.90 (0.67)	99.36 (0.31)	99.27 (0.37)	100.48 (0.44)	99.90	99.23	100.18	98.69 (0.61)	100.81 (0.54)	100.32 (0.5)	99.61 (1.01)	100.17 (0.27)	99.83
D	257.1 (1.7)	254.5 (1.3)	253.8 (2.5)	250.3 (3.7)	254.4	252.5	254.1	248.2 (0.8)	261.1 (2.0)	259.0 (1.8)	260.2 (2.1)	253.8 (2.5)	249.4

Note: Results for DSDP holes are given in averages, with standard deviations; D refers to an 8-component discriminant (see text for discussion). Ch numbers are from MAPCO cruise of *Jean Charcot* (Bougault and Tre 1980).

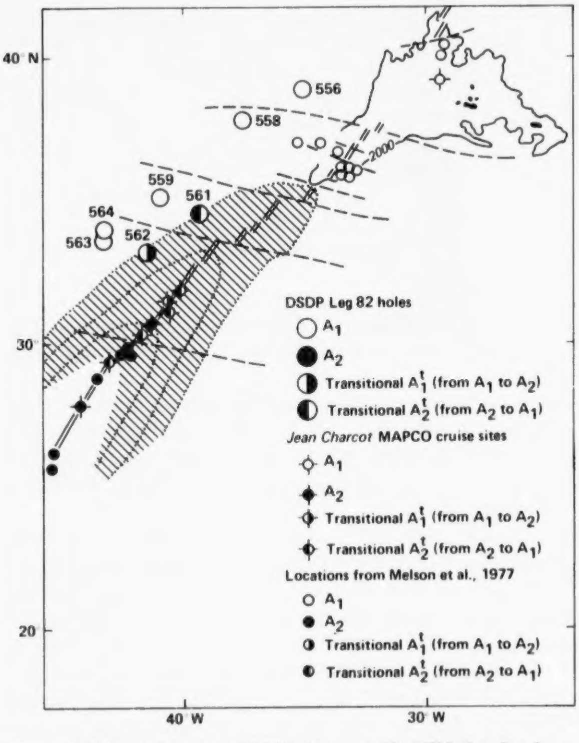
40 N
30
20
40 W
30 W
556
558
559
561
564
563
562
2000
DSDP Leg 82 holes
A_1
A_2
Transitional A_1^t (from A_1 to A_2)
Transitional A_2^t (from A_2 to A_1)
Jean Charcot MAPCO cruise sites
A_1
A_2
Transitional A_1^t (from A_1 to A_2)
Transitional A_2^t (from A_2 to A_1)
Locations from Melson et al., 1977
A_1
A_2
Transitional A_1^t (from A_1 to A_2)
Transitional A_2^t (from A_2 to A_1)

Figure 5. Schematic map of MAR between 25–40°N showing locations of glass compositional groups. The dashed area corresponds to the transitional zone between A_1 and A_2.

under dry conditions and at a similar degree of partial melting.

This model offers an explanation for the heterogeneity of basalts with regard to trace elements. Vertical trace element compositional heterogeneity of the mantle resulting from diapirism is suggested. Diapirism—the rise of plastic, partially melted mantle—should be accompanied by solid phase transitions of garnet-peridotite, then spinel-peridotite, and finally, plagioclase-peridotite assemblages. During these transformations, the redistribution of trace elements between phases will take place and their concentration may change at different depth levels, especially in the presence of ascending melt and fluid flow. The trace element enrichments of a primary tholeiite melt derived from the mantle at different depths and from different phase assemblages subjected to partial melting will also differ. Such an explanation has a number of advantages; above all, it does not require primary lateral heterogeneity of the mantle. Should primary lateral heterogeneity exist, it would still require special explanation. In the suggested model, the degree of mantle melting in both groups is low (about 15%), which is in good agreement with the calculations of optimal physical conditions for the separation of melt from the solid mantle (Arndt, 1976). Our model also seems to account more realistically for the occurrence of both melt groups in the same boundary area provided that their eruption is separated in time (i.e., in one drill hole). In such cases, repeated changes in the depth of melt separation from mantle and the mixing of both melt groups in an intermediate chamber may occur.

In summary, magmato-tectonic conditions along the MAR have been changing. For the last 15–17 Ma, for example, the process of melt separation southward of 36°N has risen from the depth of spinel–peridotite facies (30–60 km) to the level of plagioclase–peridotite facies (15–30 km). Between 35 and 30°N, the ascent appears to have been gradual, possibly with repeated changes in the depth of melt separation. To the south of 30°N during the same period of time, the depth of melt separation remained the same and corresponds to the plagioclase–peridotite mantle facies.

The regional difference in the composition and the dynamics of the lithosphere on each side of the Azores-Gibraltar Triple Junction is also probably connected to the change in the depth of melt separation beneath the spreading center. Lukashevich et al. (1982) found a change in the values of the free air gravity anomaly from 50 to 20 mGal between 35 and 30°N. The change of ridge morphology within the same latitude range Sclater et al., 1975; Lukashevich et al., 1982) as well as the data outlined here on the proposed difference in the depth of melt generation in the Atlantic lithosphere also favor this possible connection (Marillier and Mueller, 1982).

It is probable that a similar change in the geotectonic regime postulated for the Atlantic lithosphere also took

Table 2. (Continued).

14	15	16	17	18	19	20	21	22	23	24	25	26	27
563	564												
25-2, 132–134 (4A)	3-2, 50–51 (4)	7-2, 99–100 (6C)	8-1, 2-3 (5-1)	9-3, 26–27 (2B)	Ch97-02-101	Ch98-07	Ch98-08	Ch98-09	Ch98-11	Ch98-12	Ch98-14	Ch98-15	Ch98-15-101
3	2	2	1		1	1	1	1	1	1	1	1	1
50.98 (0.23)	51.09 (0.75)	51.52 (0.43)	51.0 (0.19)	51.3	50.99	50.86	50.58	50.39	50.81	51.22	50.09	50.65	50.21
1.15 (0.06)	1.48 (0.03)	1.53 (0.0)	1.52 (0.0)	1.59	1.16	1.38	1.66	1.45	1.45	1.44	1.60	1.39	1.29
15.04 (0.18)	14.87 (0.21)	14.83 (0.11)	15.03 (0.06)	15.20	15.32	15.23	14.35	15.20	14.92	14.88	15.45	15.43	16.10
10.30 (0.54)	11.06 (0.07)	11.52 (0.03)	11.62 (0.03)	11.65	9.01	10.27	11.41	10.40	9.82	10.21	10.30	9.39	9.18
7.60 (0.15)	6.99 (0.04)	6.95 (0.07)	6.92 (0.007)	7.04	7.59	7.77	7.25	7.49	9.44	8.54	7.37	8.15	8.27
12.74 (0.06)	11.53 (0.09)	11.46 (0.007)	11.33 (0.07)	11.37	12.02	11.41	11.04	11.52	11.00	11.31	11.26	11.53	11.78
2.18 (0.02)	2.45 (0.07)	2.30 (0.01)	2.38 (0.03)	2.33	2.02	2.55	2.60	2.60	2.33	2.45	2.49	2.59	2.64
0.07 (0.02)	0.15 (0.03)	0.14 (0.007)	0.15 (0.07)	0.15	0.12	0.08	0.12	0.08	0.07	0.08	0.08	0.09	0.09
100.06 (0.7)	99.62 (1.02)	100.25 (0.36)	99.95 (0.19)	100.63	98.23	99.55	99.01	99.13	99.84	100.13	98.64	99.22	99.56
250.6 (0.8)	253.4 (2.9)	252.6 (1.2)	251.4 (1.6)	253.2	247.61	258.56	257.20	258.18	260.91	260.88	257.9	261.16	260.63

Table 3. The compositions of primary melts for Atlantic tholeiites.

Group	A_1			A_2		
Analysis number	1	2	3	4	5	6
SiO_2	49.5	48.8	49.0	50.6	49.7	50.7
TiO_2	0.6	0.5	0.6	1.2	0.9	0.8
Al_2O_3	16.7	15.1	15.0	16.3	18.0	17.2
Fe_2O_3[a]	1.0	0.8		1.7	1.3	
FeO	7.4	7.7	7.6	7.3	6.3	7.9
MgO	10.2	13.9	13.0	8.5	9.5	9.0
CaO	12.8	11.6	12.3	12.0	11.9	12.3
Na_2O	1.7	1.5	1.6	2.4	2.3	2.4
K_2O	0.05	0.05	0.06	0.05	0.04	0.05
Total	99.95	99.95	99.16	100.05	99.94	100.35
$Mg/Mg + Fe^{2+}$	0.711	0.763	0.753	0.675	0.729	0.670
T_{calc} °C[b]	1242	1308		1202	1218	
Phase calc[b]	Ol (89.1)	Ol (91.5)		Ol (87.4) Pl (75.4)	Ol (90.0) Pl (78.5)	
T_{hom} °exp[c]			1290			1240
Phase host[c]			Ol (91.0)			Pl (88.6)
X	0	Ol 10.5		0	Ol 7.5 Pl 17.1	

Note: Analyses 1 and 4 are averages for the most magnesian glasses of Groups A_1 and A_2 from Dmitriev et al. (1979); Analyses 2 and 5 are calculated primary melts for Groups A_1 and A_2; Analysis 3 is composition of experimentally homogenized highest temperature for Group A_1 melt inclusion in olivine from Sample 332B-35-1, 130 cm, DSDP Leg 37; Analysis 6 is the average for six experimentally homogenized highest temperature for Group A_2 inclusions in plagioclase from Sample 21-2B, Vema Fracture Zone, Atlantic Ocean.

[a] Separation of Fe was calculated using the data of Sack et al. (1980) and oxygen fugacities corresponding to buffers QFM (for Group A_1) and Ni-NiO (for Group A_2).

[b] Composition of equilibrium liquidus phases Fo-content for olivines (Ol) and An-content for plagioclases (Pl) and temperatures calculated using the data of Drake (1976) and Roeder and Emslie (1970).

[c] Temperature of homogenization of primary melt inclusions and compositions of their host minerals. For an elaboration on this method, see Roedder (1979).

X = Calculated mole-fraction of crystals to be added to initial compositions 1 or 4 to construct primary melt compositions 2 or 5.

place in the South Atlantic at 35°S at the junction of the Rio Grande and Walvis ridges, with this junction serving as a magmatic-tectonic barrier. Analogous data on other oceans are useful for comparisons with our Atlantic model. We found magma (A_1 and A_2) groups, simply discriminated by D (Suschevskaya et al., 1983), are also recognizable in the Indian and Pacific oceans. Their distribution in space and time appears to follow the same patterns. It was also pointed out by Sushevskaya et al. (1984) that the basalts of the Red Sea and the Aden Gulf belong to the differentiation products of Group A_1 melts, whereas A_2 basalts occur only along the axis of the Carlsberg Ridge. Also, during formation of the Philippine Sea, the transition from the earlier to the later stages of tholeiite magmatism (i.e., from the West Philippine Basin to the Mariana Trough and to the Shikoku Basin; Zakariadze et al., 1980; Nesterenko and Sushevskaya, 1981) was accompanied by the gradual change of compositions from A_1 to A_2.

Hence, it looks as if earlier stages of ocean opening are characterized by melt separation from mantle at the depth of the spinel–peridotite facies. The ascent of mantle melting to the level of plagioclase–peridotite facies takes place during a later stage of crustal evolution. These are consistent with depth of melting as the main controlling factor in the composition of ocean tholeiites for

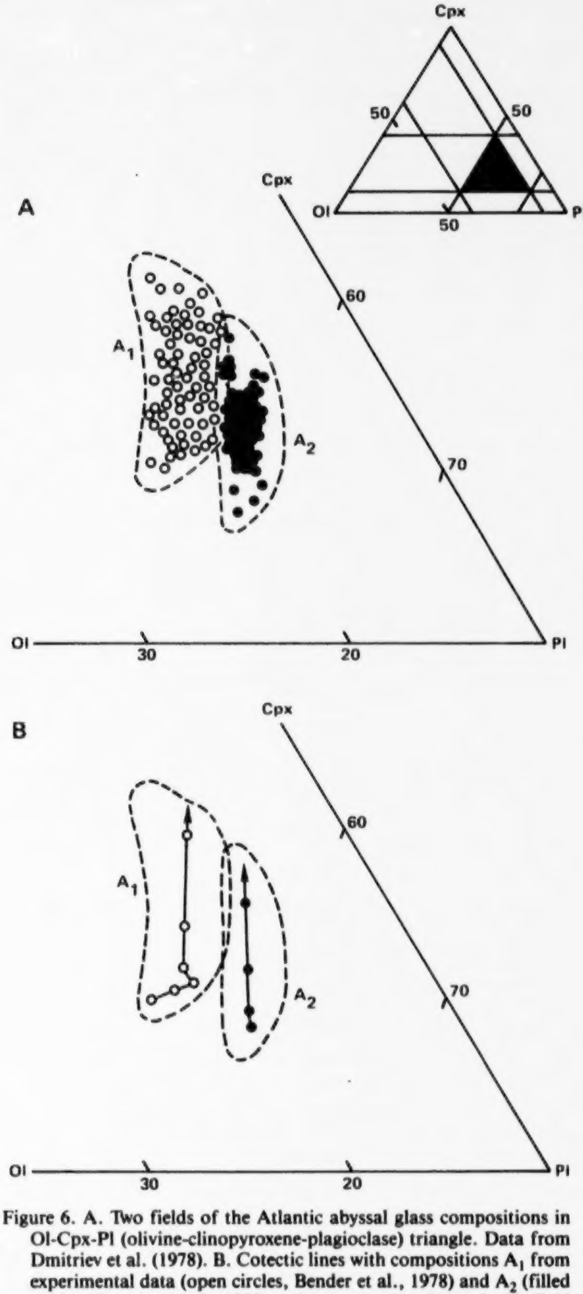

Figure 6. A. Two fields of the Atlantic abyssal glass compositions in Ol-Cpx-Pl (olivine-clinopyroxene-plagioclase) triangle. Data from Dmitriev et al. (1978). B. Cotectic lines with compositions A_1 from experimental data (open circles, Bender et al., 1978) and A_2 (filled circles, Zapunny et al., 1983) at 1 atm pressure. Arrow inside field A_1 shows temperature decrease from 1263 to 1190°C. Arrow in field A_2 shows a decrease from 1244 to 1185°C.

major, and possible trace, elements from a fairly homogeneous mantle composition in all oceans at the same depth level.

ACKNOWLEDGMENTS

The authors express their appreciation to Dr. M. N. A. Peterson, DSDP Project Manager, for his assistance. The authors are also grateful to H. Bougault for the samples and data that he provided and to W. Melson for his assistance in improving the presentation.

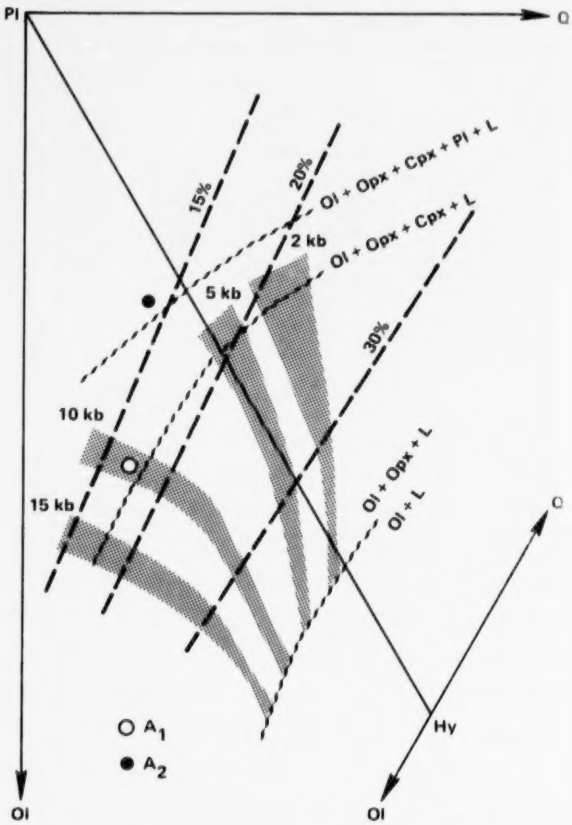

Figure 7. The relationship between melt composition (screened areas), degree of melting (%), pressure (kb), and phase equilibrium boundaries for dry lherzolite (pyrolite) after Jaques and Green (1980). Primary melt compositions: A_1, A_2 (see Table 3). Pl = plagioclase; Ol = olivine; Opx = orthopyroxene; Q = quartz, L = melt, Hy = hyperstene, cpx = clinopyroxene.

REFERENCES

Ariskin, A. A., and Frenkel, M. Y., 1982. Computer simulation of fractional crystallization of mafic silicate melts. *Geochemica*, 3: 338–356.

Arndt, T., 1976. The separation of magmas from partial molten peridotite. *Carnegie Inst. Washington, Year Book*, 76:424–428.

Aumento, F., Melson, W., et al., 1977. *Init. Repts. DSDP*, 37: Washington (U.S. Govt. Printing Office).

Ayuso, R. A., Bence, A. E., and Taylor, S. R., 1976. Upper Jurassi tholeiitic basalts from DSDP Leg 11. *J. Geophys. Res.*, 81(23): 4305–4323.

Baragar, W., Plant, A. G., Pringle, G., and Shan, M., 1977. Petrolog and alteration of selected units of Mid-Atlantic Ridge basalts, sampled from Sites 332 and 335 DSDP. *Can. J. Earth Sci.*, 14(4[2]) 837–874.

Bence, A. E., and Albee, A. L., 1968. Empirical correction factors fo the electron microanalysis of silicates and oxides. *J. Geol.*, 7 382–403.

Bender, J., Hodges, E., and Bence, A., 1978. Petrogenesis of basalt from the project FAMOUS area: experimental study from 0 to 1 kbars. *Earth Planet. Sci. Lett.*, 41(2):277–302.

Bollinger, C., and Semet, M., 1980. Chemical zonation of plagioclas phenocrysts from Leg 51, 52, and 53 basalts. *In* Donnelly, T. Francheteau, J., Byran, W., Robinson, P., Fower, M., Salisbury M., et al., *Init. Repts. DSDP*, 51, 52, 53, Pt. 2: Washington (U.S Govt. Printing Office), 1055–1061.

Bonatti, E., Hartman, K., Innocenti, F., and Kay, R., 1977. Basalt drilled at the Vema Fracture Zone, DSDP Leg 39. *In* Perch-Nielson, K., Supko, P. R., et al., *Init. Repts. DSDP*, 39: Washington (U.S. Govt. Printing Office), 507–511.

Bougault, H., Cambon, P., Joron, L., and Treuil, M., 1978. Trace elements: fractional crystallization and partial melting processes, heterogeneity of upper mantle material. *In* Dmitriev, L., Heirtzler, J., et al., *Init. Repts. DSDP*, 46: Washington (U.S. Govt. Printing Office), 247–251.

Bougault, H., and Treuil, M., 1980. Mid-Atlantic Ridge: zero-age geochemical variations between Azores and 22°N. *Nature*, 286(5770): 209–212.

Bryan, W. B., Thompson, G., Frey, F. A., Dickey, J. S., J., and Roy, S., 1977. Petrology and geochemistry of basement rocks recovered on Leg 37, DSDP *In* Aumento, F., Melson, W., et al., *Init. Repts. DSDP*, 37: Washington (U.S. Govt. Printing Office), 695–703.

Delaney, L., Muenow, D., and Graham, D., 1978. Abundance and distribution of water, carbon, and sulphur in the glassy rims of submarine pillow basalts. *Geochim. Cosmochim. Acta*, 42:581–594.

Dick, J. B. H., and Bryan, W. B., 1978. Variation of basalt phenocryst mineralogy and rock compositions in DSDP Hole 396B. *In* Dmitriev, L., Heirtzler, J. et al., *Init. Repts. DSDP*, 46: Washington (U.S. Govt. Printing Office), 215–225.

Dickey, J. S., Frey, J. F. A., Hart, S. R., and Watson, D., 1977. Geochemistry and petrology of dredged basalts from Bounvet Triple Junction, South Atlantic. *Geochim. Cosmochim. Acta*, 41: 1105–1118.

Donaldson, C. H., and Brown, R. W., 1977. Refractory megacrysts and magnesium-rich melt inclusions within oceanic tholeiites: indicators of magma mixing and parental magma composition. *Earth Planet. Sci. Lett.*, 37:81–92.

Dmitriev, L. V., 1969. Origin of the ultrabasic rocks in the rift zones of the Indian Ocean Ridge. *Geokhimiya*, 10:1179–1187. (English translation in *Geochem. Intern.*, 6(5):923–931.)

Dmitriev, L. V., Charin, G. S., Suschevskaya, N. M., and Zapunny, S. A., in press. South Atlantic basalts from data of the 7th cruise R/V *Professor Shtokman. Geokhimiya.*

Dmitriev, L. V., Melson, W. G., Sobolev, A. V., Ukhanov, A. V., and Malysheva, T. V., in press. Oxygen, fugacity for abyssal tholeiitic magmatism from studying of the cooling glasses. *Earth Planet. Sci. Lett.*

Dmitriev, L. V., Sobolev, A. V., and Suschevskaya, N. M. 1978. The primary melt of oceanic tholeiites and the composition of the oceanic upper mantle. *Dokl. Acad. Sci. USSR, Earth Sci. Sect.* (Engl. Transl.), 240(1):177–180.

———, 1979a. The conditions of the primary oceanic tholeiite melts and variability of their composition. *Geokhimiya*, 2:163–177.

———, 1979b. The primary basalt melt of the oceanic tholeiites and the upper mantle composition. *In* Talwani, M., Harrison, C. G., and Hayes, D. E. (Eds.), *Deep Sea Drilling Results in the Atlantic Ocean: Ocean Crust:* Washington, (Am. Geophys. Union), Maurice Ewing Series, 2:302–313.

———, 1980. Atlantic tholeiites petrology and geochemistry. *26th Int. Geol. Congr. Dokladi sovetskikh geologov Moskva*, pp. 32–42.

Dmitriev, L. V., Ukhanov, A. V., and Sharaskin, A. Y., 1972. Composition of the upper mantle. *Geokhimiya*, 10:1155–1167 (English translation in *Geochem. Intern.*, 9(5):781–792.)

Drake, M. J., 1976. Plagioclase-melt equilibrilea. *Geochim. Cosmochim. Acta*, 40:457–465.

Dungan, M. A., Rhodes, J. M., Long, P. E., Blanchard, D. P., Brannon, J. C., and Rodgers, K. V., 1978. Petrology and geochemistry of basalts from Site 396, Legs 45 and 46 of the Deep Sea Drilling Project. *In* Dmitriev, L. V., Heirtzler, J., et al., *Init. Repts. DSDP*, 46: Washington (U.S. Govt. Printing Office), 89–113.

Fisk, M. R., and Bence, A. E., 1980. Experimental crystallization of chrome spinel in FAMOUS basalt 537-1-1. *Earth Planet. Sci. Lett.*, 48:111–123.

Flower, M. F. J., 1980. Accumulation of calcic plagioclase in ocean-ridge tholeiite: an indication of spreading rate? *Nature*, 287: 530–532.

———, 1981. Thermal and kinematic control on ocean-ridge magma fractionation: contrasts between Atlantic and Pacific spreading axes. *J. Geol. Soc. London*, 138:695–712.

Flower, M. F., J., Ohnmacht, W., Schmincke, H. U., Gibson, I. L., Robinson, P. T., and Parker, R., 1978. Petrology and geochemistry of basalts from Hole 396B Leg 46. *In* Dmitriev, L., Heirtzler, J., et al., *Init. Repts. DSDP*, 46: Washington (U.S. Govt. Printing Office), 179–213.

Flower, M. F. J., Robinson, P. T., Schmincke, H. U., and Ohnmacht, W., 1977a. Magma fractionation systems beneath the Mid-Atlantic Ridge at 36–37°N. *Contrib. Mineral. Petrol.*, 64:167–195.

———, 1977b. Petrology and geochemistry of igneous rocks, DSDP Leg 37. *In* Aumento, F., Melson, W. G., et al., *Init. Repts. DSDP*, 37: Washington (U.S. Govt. Printing Office), 658–679.

Fujii, T., and Bougault, H., 1983. Melting relations of a magnesian abyssal tholeiite and the origin of MORB's. *Earth Planet. Sci. Lett.*, 62:283–295.

Fujii, T., and Fujioka, K., 1979. Petrology of dolerites, Hole 395A. *In* Melson, W. G., Rabinowitz, P. D., et al., *Init. Repts. DSDP*, 45: Washington (U.S. Govt. Printing Office), 519–528.

Genkin, A. D., Laputina, I. P., and Pertsev, N. N., 1980. Opaque minerals in basalts from Holes 417D and 418A. *In* Donnelly, T., Francheteau, J., Bryan, W., Robinson, P., Flower, M., Salisbury, M., et al., *Init. Repts. DSDP*, 51, 52, 53 Pt. 2: Washington (U.S. Govt. Printing Office), 1431–1450.

Graham, A. L., Symes, R. F., Bevan, J. C., and Din, V. K., 1979. Chromium-bearing spinels in some rocks of Leg 45: phase chemistry, zoning and relation to host basalt chemistry. *In* Melson, W. G., Rabinowitz, P. D., et al., *Init. Repts. DSDP*, 45: Washington (U.S. Govt. Printing Office), 581–586.

Hekinian, R., Moore, J. G., and Bryan, W. B., 1976. Volcanic rocks and processes of the Mid-Atlantic Ridge rift valley near 36°49′N. *Contrib. Miner. Petrol.*, 58:83–110.

Hodges, F. N., and Papike, J. J., 1977. Petrology of basalts, gabbros and peridotites from DSDP Leg 37. *In* Aumento, F., Melson, W. G., et al., *Init. Repts. DSDP*, 37: Washington (U.S. Govt. Printing Office), 711–723.

Jaques, A. L., and Green, D. H., 1980. Anhydrous melting of peridotite at 0–15 kb pressure and the genesis of tholeiitic basalts. *Contrib. Mineral. Petrol.*, 73:287–310.

Jarosewich, E., Nelen, J. A., and Norberg, J. A., 1979. Electron microprobe reference samples for mineral analyses. *Smithsonian Contrib. Earth Sci.*, 22:68–72.

Lukashevich, I. P., Pristavakina, E. I., and Sorochtin, O. G., 1982. The role of the dynamic and static factors in the formation of bottom relief in northern part of the Mid-Atlantic Ridge. *Okeanologia*, XXII(5):781–788.

Marillier, F., and Mueller, S., 1982. Structure of the upper mantle in the Northeastern Atlantic close to the Azores-Gibraltar Ridge from surface-wave and body-wave observations. *Tectonophysics*, 90: 195–213.

Melson, W. G., Byerly, G. R., Nelen, J. A., O'Hearn, T., Wright, T. L., and Vallier, T., 1977. A catalog of the major element chemistry of abyssal volcanic glasses. *In* Miner. Sci. Invest., 1974–1975, *Smithson. Contrib. Earth Sci.*, 19:31–60.

Nathan, H. D., and Wankirk, S. K., 1978. A model of magmatic crystallization. *J. Petrol.*, 19(1):79.

Natland, J. H., 1980. Effect of axial magma chambers beneath spreading centers on the compositions of basaltic rocks. *In* Rosendahl, B. R., Hekinian, R., et al., *Init. Repts. DSDP*, 54: Washington (U.S. Govt. Printing Office), 833–850.

Natland, J. H., and Melson, W. G., 1980. Compositions of basaltic glasses from the East Pacific Rise and Siqueiros Fracture Zone, near 9°N. *In* Rosendahl, B. R., Hekinian, R., et al., *Init. Repts. DSDP*, 54: Washington (U.S. Govt. Printing Office), 705–723.

Nesterenko, G. V., and Suschevskaya, N. M., 1981. Basaltic glasses of site N 442B (Philippine Sea). *Geokhimiya*, 9:1380–1385.

O'Hara, M. J., 1968. Are ocean floor basalts primary magma? *Nature*, 220:683–686.

Presnall, D. C., Dixon, J. R., O'Donnell, T. H., and Dixon, S. A., 1979. Generation of mid-ocean ridge tholeiites. *J. Petrol.*, 20(Pt. 1):3–35.

Prinz, M., Keil, K., Green, J. A., Reid, A. M., Bonatti, E., and Honnorez, J., 1976. Ultramafic and mafic dredge samples from equatorial Mid-Atlantic Ridge and fracture zone. *J. Geophys. Res.*, 81(23):4087–4103.

Roedder, E., 1979. Origin and significance of magmatic inclusions. *Bull. Mineral.*, 102:487–510.

Roeder, P. L., and Emslie, R. P., 1970. Olivine-liquid equilibrium. *Contrib. Mineral. Petrol.*, 29:274–289.

Sack, R. O., Carmichael, J. S. E., Rivers, M., and Chiorso, M. S., 1980. Ferric-ferrous equilibria in natural silicate liquids at 1 bar. *Contrib. Miner. Petrol.*, 75:369–376.

Sato, H., Aoki, K., Okamoto, K., and Fujita, B., 1978. Petrology and chemistry of basaltic rocks from Hole 396B, IPOD/DSDP Leg 46. *In* Dmitriev, L., Heirtzler, J., et al., *Init. Repts. DSDP*, 46: Washington (U.S. Govt. Printing Office), 115–141.

Sclater, J., Lawyer, L., and Parssons, B., 1975. Comparison of long-wave length residual elevation and free air gravity anomalies in North Atlantic and possible implications for the thickness of lithospheric plate. *J. Geophys. Res.*, 80:1031–1052.

Shido, F., and Mijashiro, A., 1973. compositional difference between abyssal tholeiites from North and South of the Azores on the Mid-Atlantic Ridge. *Nature*, 245(143):58–60.

Sigurdsson, H., and Schilling, J.-G., 1976. Spinels in the Mid-Atlantic Ridge basalts: chemistry and occurrence. *Earth Planet. Sci. Lett.*, 29:7–20.

Sinton, J. M., and Byerly, G. R., 1980. Mineral compositions and crystallization trends in Deep Sea Drilling Project Holes 417D and 418A. *In* Donnelly, T., Francheteau, J., Bryan, W., Robinson, P., Flower, M., Salisbury, M., et al., *Init. Repts. DSDP*, 51, 52, 53, Pt. 2: Washington (U.S. Govt. Printing Office), 1039–1054.

Sobolev, A. V., Dmitriev, L. V., and Suschevskaya, N. M., in press. The compositions and generation conditions of primary melts for tholeiitic magmatism of Atlantic ocean. *Geokhimiya*.

Stolper, E., 1980. Phase diagram for mid-ocean ridge basalts: preliminary results and implications for petrogenesis. *Contrib. Mineral. Petrol.*, 74:13–27.

Suschevskaya, N. M., 1982. Primary melt of the oceanic tholeiite and variability of basalts from the second seismic layer of Atlantic [Ph.D. dissert.]. Vernadsky Institute of Geochemistry and Analytical Chemistry, Moscow.

Suschevskaya, N. M., Dmitriev, L. V., Almuhamedov, A. I., Kolesov, G. M., and Sherbovsky, E., 1984. Origin and geochemical Red Sea tholeiitic melts. *Geokhimiya*, 8:1202–1208.

Suschevskaya, N. M., Dmitriev, L. V., and Sobolev, A. V., 1983. Petrochemical criterion for quenched abyssal glasses classification *Dokl. Acad. Sci. USSR, Earth Sci. Sect.* (Engl. Transl.), 268(6): 1475–1477.

Templeman, J. A., 1979. Chromian spinels in Leg 49 basalts: a preliminary chemical study. *In* Luyendyk, B. P., Cann, J. R., et al. *Init. Repts. DSDP*, 49: Washington (U.S. Govt. Printing Office) 745–747.

Wood, D. A., Varet, J., Bougault, H., Corre, O., Joron, J. L., Treuil M., Bizouard, H., Norry, M. J., Hawkesworth, C. J., and Roddick, J. C., 1979. The petrology, geochemistry, and mineralogy of North Atlantic basalts: a discussion based on IPOD Leg 49. *In* Luyendyk, B. P., Cann, J. R., et al., *Init. Repts. DSDP*, 49: Washington (U.S. Govt. Printing Office), 597–655.

Zakariadze, G. S., Dmitriev, L. V., Sobolev, A. V., Suschevskaya, N. M., 1980. Petrology of basalts of Holes 447A, 449, and 450, South Philippine Sea Transect, Deep Sea Drilling Project Leg 59. *In* Kroenke, L., Scott, R., et al., *Init. Repts. DSDP*, 59: Washington (U.S. Govt. Printing Office), 669–680.

Zapunny, S. A., Sobolev, A. V., Kadik, A. A., and Dmitriev, L. V., 1983. Crystallization of the basalts from Atlantic Ocean: experimental study at 1 atm under control oxygen fugacity. *IX Conf. Geochemistry Magmatic Rocks*, pp. 20–21.

Date of Initial Receipt: 5 May 1983
Date of Acceptance: 21 December 1983

28. THE SULFUR CONTENT AND ISOTOPIC COMPOSITION IN BASALTS FROM HOLES 558, 559, 562, AND 564[1]

Hans-W. Hubberten and Harald Puchelt, Institut für Petrographie und Geochemie der Universität
Technische Hochschule Karlsruhe[2]

ABSTRACT

The sulfur contents of 21 basalt samples from four DSDP Leg 82 holes were determined and the isotopic compositions of sulfur were measured on 15 of them. Most of the basalts are altered and have sulfur contents of about 100 ppm. Isotopic ratios for sulfate and total sulfur range from +0.7 to +10.5‰, indicating almost complete leaching of the igneous sulfide in low-sulfur samples by alteration.

Total sulfur content of some samples ranges between 960 and 1170 ppm, somewhat higher than expected for tholeiitic basalts. The isotope ratios of total sulfur in these samples are slightly shifted to values heavier than the generally assumed mantle ratio of zero, and this shift is thought to result from a secondary source of sulfur.

INTRODUCTION

Numerous investigations of the sulfur contents and sulfur isotopic compositions of ocean basalts have enlarged our understanding of the behavior of this element and its isotopes during the formation and alteration of ocean crust (Moore and Fabbi, 1971; Kanehira et al., 1973; Grinenko et al., 1975; Sakai et al., 1978; Puchelt and Hubberten, 1980; Hubberten and Puchelt, 1980; Sakai et al., 1982; Hubberten, 1983a; Hubberten, 1983b).

Basalt melts commonly erupt in a sulfur-saturated or nearly saturated stage (Mathez, 1976); the degassing of sulfur is inhibited by water pressure at depths exceeding 500 m (Moore and Fabbi, 1971; Sakai et al., 1982). The concentration of primary sulfur in rocks formed from such a melt varies between 800 and 1700 ppm, depending mainly on the iron content of the melt (Mathez, 1976; Czamanske and Moore, 1977; Erzinger, 1981; Hubberten, 1983b). This sulfur should reflect the isotopic composition of the mantle; that is, it should display $\delta^{34}S$ values around zero (Kanehira et al., 1973; Puchelt and Hubberten, 1980). Deviations from the zero value in the isotopic composition of the primary sulfur have been observed by Schneider (1970) for terrestrial basalts with different degrees of fractionation. Similar observations have not so far been made for ocean tholeiites. Several investigators have described a rather strong variation in the isotopic composition of sulfur in altered basalts, caused by interaction with cold seawater or hydrothermal solutions (Field et al., 1976; Krouse et al., 1977; Hubberten, 1983a; Alt et al., 1983).

The rocks retrieved during DSDP Leg 82 southwest of the Azores Platform in the central Atlantic are mostly aphyric to plagioclase-phyric pillow basalts showing a wide compositional variability (Sachtleben and Schmincke, 1982; Puchelt, this volume). Our study is based on 21 samples from four of the holes (558, 559, 562, 564) cored during Leg 82. With respect to chemical and petrographic parameters, almost all samples were altered in greater or lesser degree, and did not allow determination of the isotopic composition of primary sulfur (cf. Puchelt, this volume). The amount of sample in most cases was too small to determine the three possible sulfur phases (total S, sulfide-S, sulfate-S). The samples used for these investigations are all dense plagioclase-phyric or aphyric fine-grained basalts. Neither basalt glass nor serpentinite (Hole 558) was available for these analyses.

ANALYTICAL PROCEDURE

The samples were cleaned with distilled water, crushed, and pulverized (<200 mesh) for analysis. The total sulfur content was determined by combustion in oxygen, using the Leybold Heraeus Carbon Sulphur Analyzer 302. The total error of the determinations is less than ±15%. Sulfur-isotope determinations were made according to the method described by Puchelt and Hubberten (1980). In this procedure the igneous sulfides are first decomposed by treatment with hydrochloric acid, yielding the sulfide-S fraction. In a second step, the remaining S in the sample (sulfate-S fraction) is extracted with a reducing-acid mixture (Thode et al., 1961). Another split of the sample is directly decomposed with the reducing-acid mixture to obtain the total sulfur concentration. In each step, the sulfur is expelled as H_2S, which is then precipitated as CdS. This compound is oxidized to form the measuring gas SO_2 for mass spectrometry (cf. Ricke, 1964). Isotope ratios were measured on a VG-Micromass 1202 S mass spectrometer. The total error (preparation and measurement) of these determinations is less than ±0.2‰ for samples of normal size, but it can reach ±1‰ for undersized samples. The results are given in the usual δ-notation with respect to the Cañon Diablo standard.

RESULTS AND DISCUSSION

Sulfur Content

As can be seen from Table 1 and Figure 1, most of the samples have total sulfur contents close to 100 ppm; seven others range between 960 and 1170 ppm. The lower sulfur concentrations may result from two main processes: (1) relative to the rim, the interior of the pillow is depleted in sulfur, which may have escaped along cool-

---

[1] Bougault, H., Cande, S. C., et al., *Init. Repts. DSDP*, 82: Washington (U.S. Govt. Printing Office).

[2] Addresses: (Hubberten, present address) Universidad Autonoma de Nuevo León, Instituto de Geologia, Apartado Postal 104, 67700 Linares, Nuevo León, Mexico; (Puchelt) Institut für Petrographie und Geochemie der Universität Technische Hochschule Karlsruhe, D-7500 Karlsruhe, Federal Republic of Germany.

Table 1. Sulfur content and sulfur-isotope ratios for Leg 82 basalts.

Karlsruhe lab. number	Sample (interval in cm)	S-content (ppm)	$\delta^{34}S$ (‰) Total sulfur	Sulfide-S	Sulfate-S
086 01	558-27-3, 46-48	100	+3.1		
086 02	558-28-2, 6-8	100			
086 03	558-29-2, 6-8	1020	+2.6		+6.3
086 04	558-34-1, 113-115	100			
086 05	558-36-3, 44-46	160	+7.6		
086 06	559-1-1, 134-136	100			
086 07	559-1-4, 40-42	1000	+0.7		
086 08	559-6-2, 17-20	100			
086 09	559-7-1, 143-146	100	+8.7		
086 10	559-7-3, 15-17	100	+7.4		
086 11	562-2-5, 65-67	1090	+3.0		+7.8
086 12	562-4-2, 4-7	1160	+2.4	+1.6	
086 13	562-7-2, 7-10	120	+9.1		
086 14	562-8-1, 127-129	140	+9.5		
086 15	564-H1,CC (11)	120	+8.6		
086 16	564-1-1, 122-124	100	+7.4		
086 17	564-2-3, 110-114	150	+9.5		
086 18	564-5-2, 111-114	960			
086 19	564-7-2, 136-138	1170	+3.2		+7.1
086 20	564-9-1, 72-74	100	+10.5		
086 21	564-9-3, 76-79	1010			

Note: Blanks indicate that samples were too altered for determination of $\delta^{34}S$ and/or that the samples were too small for determining the three sulfur phases.

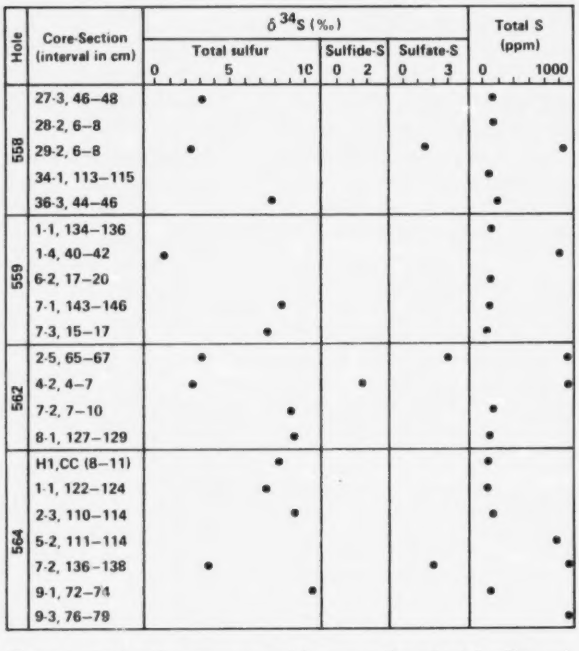

Figure 1. Total sulfur contents and isotope ratios of total sulfur, sulfide-sulfur, and sulfate-sulfur for DSDP Leg 82 basalt samples.

ing fractures (Moore and Fabbi, 1971; Hubberten, 1983b); or (2) during the low-temperature oxidative alteration of basalts, the igneous sulfides may have been completely oxidized to SO_4^{2-}, which would probably have been removed from the rock (cf. Andrews, 1979). Because the depletion of sulfur in most samples is too high, the first process seems to be less important. In addition, chemical evidence favors the second process. Alteration-sensitive components such as K, Tl, and the water content show a clear relation to the sulfur content (cf. Hubberten, 1983a). Higher concentrations of these components

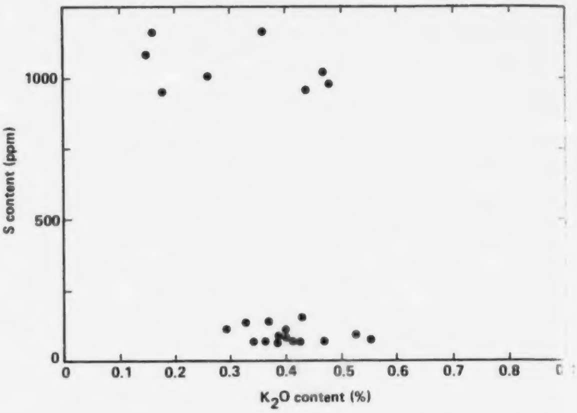

Figure 2. Total sulfur content versus K_2O content for Leg 82 basalts

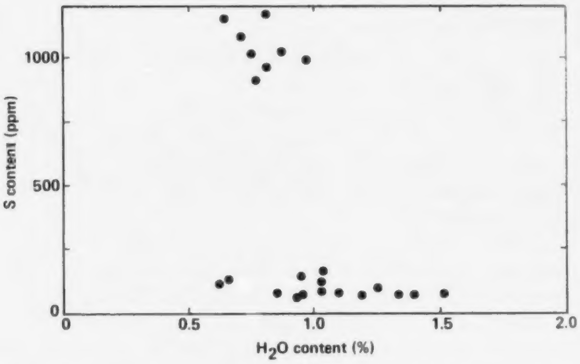

Figure 3. Total sulfur content versus H_2O content for Leg 82 basalts.

are mostly correlated with low sulfur contents (Figs. 2 and 3).

From these arguments it seems evident that the strong decrease in the sulfur content resulted from oxidative alteration of the igneous sulfides. Variations occurring because of sample locations at different distances from the pillow rim are overprinted by the larger effect of alteration. The relatively low iron contents of the investigated samples suggest, however, that sulfur was added during alteration or from a hydrothermal source. The rather high K_2O and H_2O contents of these samples classify them as altered and support this suggestion (Figs. 2 and 3).

Sulfur Isotopes

The isotope values of the total sulfur in the investigated basalts are obviously split into two groups (see Fig. 1 and Table 1). In one group $\delta^{34}S$ (total sulfur) ranges between +7.4 and +10.5‰, and this corresponds to samples with low sulfur content. In the other group, $\delta^{34}S$ is closer to zero (+0.7 to +3.2‰), and this group includes (with one exception: our sample no. 086 01) only samples with higher sulfur content.

According to numerous investigators, the isotopic composition of primary mantle sulfur is assumed to be close to the meteoritic value, that is, the zero point of the δ-scale (Kanehira et al., 1973; Grinenko et al., 1975; Sakai et al., 1978; Puchelt and Hubberten, 1980; Hubberten and Puchelt, 1980; Sakai et al., 1982; Hubberten, 1983a; Hubberten, 1983b). Most published investigations of sulfur isotopes in ocean basalts have demonstrated, until now, only small variations around this zero value (−0.5 to +1.5‰). Neither systematic variations related to the degree of fractionation of a rock nor an isotopic inhomogeneity of sulfur in the upper mantle could be detected. It is therefore assumed that the large deviations from zero determined in the Leg 82 basalts do not reflect variations in the primary isotopic composition, but probably result from secondary processes during alteration of the rocks.

During low-temperature alteration of basalts by seawater, the igneous sulfides are dissolved (Andrews, 1979), and the resulting SO_4^{2-} will be removed from the rock. Sulfur occurs in ocean tholeiites mainly as sulfides (pyrrhotite, chalcopyrite, and other sulfides of the Fe-Cu-(Ni)-S system), but variable amounts of primary sulfate have been mentioned (Ricke, 1960; Schneider, 1970; Sakai et al., 1978; Puchelt and Hubberten, 1980; Sakai et al., 1982). The results of the last two groups of authors showed that between 5 and 35% of the total sulfur in basalts may exist in the form of sulfate. With isotopic equilibrium between sulfide and sulfate in a basalt melt, the sulfate form of sulfur is always enriched in the heavier isotope ^{34}S (Sakai, 1968). Sakai et al. (1982) demonstrated in their investigation of basalts from Kilauea Volcano, Hawaii, that the sulfate in these rocks is 7.5 ± 1.5‰ heavier than the coexisting sulfide. Assuming a δ^{34}S value of zero for the sulfide sulfur in the Leg 82 basalts, and a fractionation between sulfide and sulfate similar to that observed by Sakai et al. (1982), the sulfate values for our samples should range between +6 and +9‰, which coincides rather well with the range of δ^{34}S (total sulfur) (+7.4 to 10.5‰) determined for the samples having low sulfur contents. (One of the low sulfur samples, however, plots slightly outside this range [+3.1‰].) If the unaltered sulfur content of the Leg 82 basalts ranges around 800 ppm as a typical value for rocks of this composition (cf. Moore and Fabbi, 1971; Hubberten, 1983b), a sulfate fraction of somewhat more or less than 10‰ could be reflected in the total sulfur content of the low-sulfur samples (from less than 100 to 160 ppm S). From this we assume that the determined δ^{34}S values of the total sulfur represent the isotopic composition of the primary sulfate not leached during alteration of the rocks. The three determined isotope ratios for sulfate-S fit perfectly in this range, and thus support our assumption. The slight shift toward heavier total-sulfur δ^{34}S values (+9.1 to +10.5‰) of four low-sulfur samples was probably caused by the addition of small amounts of seawater-derived sulfate ($\delta^{34}S = +20$‰) or by a somewhat lower solidification temperature of these basalts.

Only one of the high-sulfur samples shows a total-sulfur δ^{34}S value (+0.7‰) similar to the assumed mantle value. This sample represents the freshest basalt of this study. The others are enriched in ^{34}S to various degrees, and attain values of up to +3.2‰. If we considered these values to be the typical isotopic compositions of sulfur in unaltered basalts in the area, we should attribute them either to a slightly ^{34}S-enriched mantle source in this region of the Atlantic or to minor isotopic fractionation during the evolution of these rocks. But except for the one sample with a normal sulfur-isotope ratio, all the high-sulfur samples are altered, so we have to consider the effects of a possible secondary sulfur source. During alteration under oxic conditions, the primary sulfides are normally dissolved and the sulfate-S is removed from the system (see foregoing discussion). An addition of sulfur, as observed in the high-sulfur samples, may be caused by hydrothermal solutions precipitating epigenetic pyrite or by addition of seawater-derived sulfate ($\delta^{34}S = +20$‰). Because of the relatively minor enrichment of ^{34}S in the high-sulfur basalts, we assume that these samples have been altered by hydrothermal solutions, which normally are slightly enriched in ^{34}S when compared to primary magmatic sulfur (~0‰, Hubberten, 1983b). The addition of seawater sulfate would result in a higher enrichment of ^{34}S in the Leg 82 samples.

ACKNOWLEDGMENTS

This investigation was supported by a grant from the Deutsche Forschungsgemeinschaft, Bonn. Mrs. E. Weiher assisted in preparing the samples for isotope measurements.

REFERENCES

Alt, J. C., Honnorez, J., Hubberten, H. W., and Saltzmann, E., 1983. Occurrence and origin of anhydrite from DSDP Leg 70 Hole 504B, Costa Rica Rift. *In* Cann, J. R., Langseth, M. G., Honnorez, J., Von Herzen, R. P., White, S. M., et al., *Init. Repts. DSDP*, 69: Washington (U.S. Govt. Printing Office), 547-550.

Andrews, A. J., 1979. On the effect of low temperature seawater-basalt interaction on the distribution of sulfur in oceanic crust, Layer 2. *Earth Planet. Sci. Lett.*, 46:68-80.

Czamanske, G. K., and Moore, J. G., 1977. Composition and phase chemistry of sulfide globules in basalts from the Mid-Atlantic Ridge rift valley near 37°N lat. *Geol. Soc. Am. Bull.*, 88:587-599.

Erzinger, J., 1981. Zur Geochemie von Selen und Thallium in magmatischen Gesteinen—mit einem Beitrag zur Analytik von Selen in geochemischen Matrizes [dissertation]. University of Karlsruhe, Karlsruhe.

Field, C. W., Dymond, J. R., Heath, G. R., Corliss, J. B., and Dasch, E. J., 1976. Sulfur isotope reconnaissance of epigenetic pyrite in ocean-floor basalts, Leg 34 and elsewhere. *In* Yeats, R. S., Hart, S. R., et al., *Init. Repts. DSDP*, 34: Washington (U.S. Govt. Printing Office), 381-384.

Grinenko, V. A., Dmitriev, L. V., Migdisov, A. A., Sharas'kin, A. Y., 1975. Sulfur contents and isotope compositions for igneous and metamorphic rocks from mid-ocean ridges. *Geochem. Intern.*, 12: 132-137.

Hubberten, H. W., 1983a. Sulfur content and sulfur isotopes of basalts from the Costa Rica Rift (Hole 504B, DSDP Legs 69 and 70). *In* Cann, J. R., Langseth, M. G., Honnorez, J., Von Herzen, R. P., White, S. M., et al., *Init. Repts. DSDP*, 69: Washington (U.S. Govt. Printing Office), 629-635.

————, 1983b. Sulfur and sulfur isotope content of basalts from the Galapagos Rift (Legs 54 and 70). *In* Honnorez, J., Von Herzen, R. P., et al., *Init. Repts. DSDP*, 70: Washington (U.S. Govt. Printing Office), 419-422.

Hubberten, H. W., and Puchelt, H., 1980. Zur Schwefelisotopengeochemie basaltischer Gesteine. *Zentr. Inst. Isotope. Mitt. Leipzig*, 30:80-90.

Kanehira, K., Yui, S., Sakai, H., and Sasaki, A., 1973. Sulphide globules and sulphur isotope ratios in the abyssal tholeiite from the Mid-Atlantic Ridge near 30°N lat. *Geochem. J.*, 7:89-96.

Krouse, H. R., Brown, H. M., and Farquharson, R. B., 1977. Sulfur isotopic composition in DSDP Leg 37 cores, *Can. J. Earth Sci.*, 14:787–793.

Mathez, E. A., 1976. Sulfur solubility and magmatic sulfides in submarine basalt glass. *J. Geophys. Res.*, 81:4269–4276.

Moore, J. G., and Fabbi, B. P., 1971. An estimate of the juvenile sulfur content of basalts. *Contrib. Mineral. Petrol.*, 33:118–127.

Puchelt, H., and Hubberten, H. W., 1980. Preliminary results of sulfur isotope investigations on Deep Sea Drilling Project cores from Legs 52 and 53. *In* Donnelly, T., Francheteau, B., Bryan, W., Robinson, P., Flower, M., Salisbury, M., et al., *Init. Repts. DSDP*, 51, 52, 53, Pt. 2: Washington (U.S. Govt. Printing Office), 1145–1148.

Ricke, W., 1960. Ein Beitrag zur Geochemie des Schwefels. *Geochim. Cosmochim. Acta*, 21:35–80.

________, 1964. Präparation von Schwefeldioxid zur massenspektrometrischen Bestimmung des Schwefel-Isotopen-Verhältnisses $^{32}S/^{34}S$ in natürlichen Schwefelverbindungen. *Z. Anal. Chem.*, 199: 401–413.

Sachtleben, T., and Schmincke, H. U., 1982. Geochemie atlantischer Ozeanbodenbasalte, DSDP, Leg 82. *Fortschr. Min. Beih.*, 1(60): 182–183.

Sakai, H., 1968. Isotopic properties of sulfur compounds in hydrothermal processes. *Geochem. J.*, 3:29–49.

Sakai, H., Casadevall, T. J., and Moore, J. G., 1982. Chemistry and isotope ratios of sulfur in basalts and volcanic gases at Kilauea Volcano, Hawaii. *Geochim. Cosmochim. Acta*, 46:729–738.

Sakai, H., Ueda, A., and Field, C. W., 1978. $\delta^{34}S$ and concentration of sulfide and sulfate sulfurs in some ocean-floor basalts and serpentinites. *In* Zartman, R. E. (Ed.), *Short Papers of the Fourth Internat. Conf. Geochronol. Cosmochronol. and Isotope Geol.* U.S Geol. Surv. Open-File Rept., 78-701:372–374.

Schneider, A., 1970. The sulfur isotope composition of basaltic rocks *Contrib. Mineral. Petrol.*, 25:95–124.

Thode, H. G., Monster, J., and Dunford, H. B., 1961. Sulfur isotope geochemistry. *Geochim. Cosmochim. Acta*, 25:159–174.

Date of Initial Receipt: 28 July 1983
Date of Acceptance: 6 April 1984

29. PETROLOGY OF ULTRAMAFIC ROCKS FROM SITES 556, 558, AND 560 IN THE NORTH ATLANTIC[1]

Peter J. Michael, Department of Mineral Sciences, Smithsonian Institution
and
Enrico Bonatti, Lamont-Doherty Geological Observatory, Columbia University[2]

ABSTRACT

Strongly serpentinized peridotites occur at shallow crustal levels at DSDP Sites 556 (35-Ma-old crust), 558 (35-Ma-old crust), and 560 (12-Ma-old crust) in the North Atlantic. Primary peridotite silicate minerals are preserved only at Sites 556 and 558, but all three sites have primary spinel preserved. The serpentinites at all three sites were probably spinel harzburgite tectonites, with little or no clinopyroxene.

For orthopyroxene from Site 556, Mg/(Mg + Fe) ratios average 0.904, and Al_2O_3 contents are about 2.0–3.3 wt.%. Compositions of pyroxene-derived bastites from Sites 558 and 560 suggest that the original pyroxenes were probably low-alumina orthopyroxene. Spinels from all three sites have low Fe^{3+} and TiO_2. Spinels from Sites 556 and 560 have high Cr/(Cr + Al) (0.45–0.53). Those from Site 558 have Cr/(Cr + Al) values that are among the highest measured for any plagioclase-free oceanic peridotites (0.55–0.62).

Whole-rock chemistry, although affected by serpentinization, suggests that the peridotites had relatively low CaO, TiO_2, Al_2O_3, and Na_2O. Mineral and whole-rock chemistry and modal abundances suggest that Leg 82 peridotites are residua from partial melting, and that the extent of partial melting may have been greater in this region than farther south in the North Atlantic, or that the mantle was originally more depleted here.

INTRODUCTION

Serpentinized peridotites were recovered at DSDP Sites 556, 558, and 560 (Fig. 1). Site 556 was drilled in 35-Ma-old crust on a flow line away from the Azores Triple Junction. Peridotites were recovered underneath 461 m of sediments and 96 m of basalts. A cemented gabbro breccia directly overlies the serpentinized peridotites, which are interlayered with cemented serpentinite breccias, gabbros, and cemented gabbro breccias from 561–575 m subsurface. Gabbros and cemented gabbro breccias are present from 575 m to the hole bottom at 639 m, with two narrow serpentinite horizons at about 620 m.

Site 558 was drilled in 35-Ma-old crust on a flow line from the FAMOUS area. Serpentinized peridotites were recovered from 533 m depth to the hole bottom at 563 m. There are several serpentinite horizons with subtle color and textural differences. They are separated from each other by uncemented serpentinite breccias.

DSDP Site 560 was drilled in 12-Ma-old crust, midway between the Oceanographer and Hayes fracture zones. Serpentinized peridotite was encountered directly under 373 m of sediments. Two serpentinite horizons, at 373 m and at about 400 m depth are separated by gabbros and gabbro breccias.

PETROGRAPHY

About ten standard 20 × 30-mm thin sections from Sites 556 and 558 and five from Site 560 were examined. Serpentinites from all three sites had peridotite protoliths. Only those from Site 556 have primary silicates preserved, and even these samples contain no olivine. Primary spinel is preserved in serpentinites from all three sites, however.

Peridotites from the three sites exhibit the pseudomorphic texture that is typical of many oceanic peridotites (Pritchard, 1979). The rock is composed predominantly of mesh-textured serpentine and magnetite. In plane polarized light, the color or tint of the mesh-textured serpentine may vary from clear to light green or brown, and the sharpness of the magnetite framework is also variable. The mesh is the alteration product of olivine, which is generally the least stable phase during serpentinization. Within the mesh matrix are large (up to 10 mm) bastites or serpentinized pyroxene porphyroclast relics, which preserve the shape and fine details of the internal structure of the pyroxene, including kink-banding and exsolution lamellae.

It is difficult to discern the difference between orthopyroxene bastite and clinopyroxene bastite, or to reconstruct the original modes of the samples. Samples from Site 556 have islands of orthopyroxene preserved within the bastites. Small blebs of clinopyroxene, exsolved from the orthopyroxene in these samples, suggest that clinopyroxene was more resistant than orthopyroxene to serpentinization. The lack of clinopyroxene porphyroclasts is therefore a primary feature of the peridotite from Site 556. Sites 558 and 560 required a less direct approach for modal reconstruction. Petrographic and microprobe analysis of partly serpentinized peridotites from other locations (the Owen Fracture Zone), in which clinopyroxene and orthopyroxene porphyroclasts and their enclosing bastites are preserved, suggests that clinopyroxene bastite often has a different appearance than orthopyroxene bastite. For example, relict exsolution lamellae

---

[1] Bougault, H., Cande, S. C., et al., *Init Repts. DSDP*, 82: Washington (U.S. Govt. Printing Office).

[2] Addresses: (Michael, present address) Department of Geological Science, University of British Columbia, 6339 Storrs Rd., Vancouver V6T 2B4, British Columbia; (Bonatti) Lamont-Doherty Geological Observatory of Columbia University, Palisades, New York 10964.

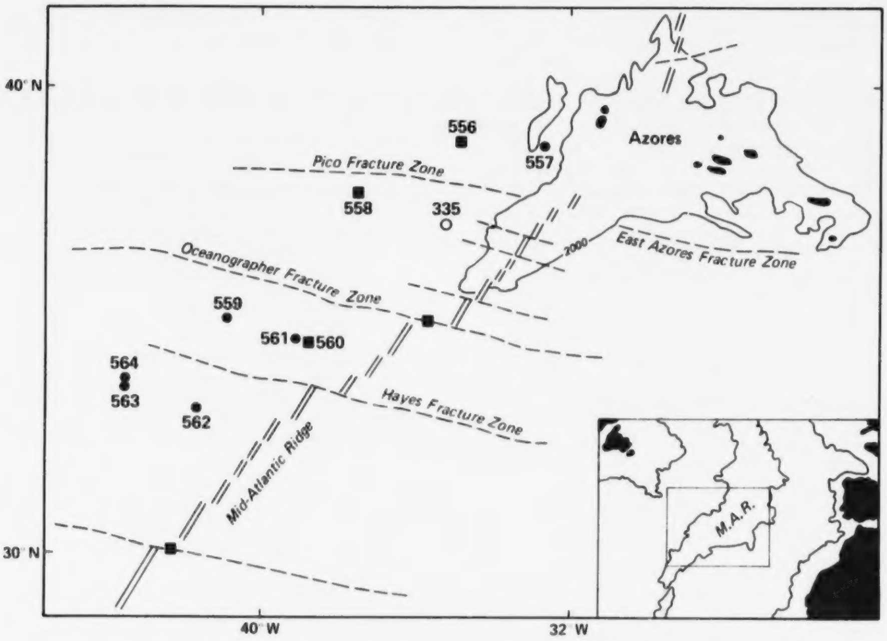

Figure 1. Locations of peridotite recoveries (solid squares), DSDP Leg 82, and surrounding region.

often "die out" toward the edges of clinopyroxene bastites. Clinopyroxene porphyroclasts generally have higher Cr contents than coexisting orthopyroxene porphyroclasts, and Cr concentrations and concentration differences are reflected in the bastites as well (Bonatti et al., in preparation[3]). With these observations in mind, we examined the bastites from Sites 558 and 560, and approximately 20 bastites from two sections of each site were analyzed for Cr content. The observations suggest that little or no porphyroclastic clinopyroxene was present in peridotites from Sites 558 and 560. Thus, even though the silicates have been completely serpentinized, it is possible to infer original peridotite modes and textures (Table 1). The reconstructions suggest that the samples were originally spinel harzburgite tectonites.

Spinel is preserved in all of the serpentinized peridotites. It is generally brick-red, with a varied habit, shape and association and is often contained within or near orthopyroxene or orthopyroxene bastite. In this association, spinel forms as long, curved grains (up to 8 mm) with xenomorphic texture around orthopyroxene; as symplectic textured clusters of small grains (0.1–0.5 mm); and as small grains near orthopyroxene. Similar associations of spinel with orthopyroxene in peridotites have been described by other authors (Hamlyn and Bonatti, 1980; Smith, 1977) and ascribed to the reaction: olivine + garnet → spinel + pyroxene. Spinel also occurs within the olivine-derived mesh-textured serpentine, as rounded or rectangular porphyroclasts (0.3–3 mm) or as tiny (0.1–0.3 mm) disrupted grains scattered throughout a larger (~1 cm) region.

Table 1. Modal abundance estimates (reconstructed).

Location	Olivine	Orthopyroxene	Clinopyroxene	Spinel	Number of samples
Site 556 (~39°N)	83	16	0.5	1	7
Site 558 (~37°N)	77	22	0	0.6	11
Site 560 (~34°N)	78	22	0	0.2	4
Oceanographer F.Z. (35°N)	80	19	0.1	0.5	27
Atlantis F.Z. (30°N)	65	30	5	1	11
Kane F.Z. (24°N)	64	33	1	1.5	7
Site 395 (23°N)	59	32	6	3	[a]

Note: Modal estimates largely from pseudo morphic-textured serpentinites. 400 points were counted for each sample (a standard 20 × 30-mm thin section). Data sources are the same as in Figure 2. F.Z. = Fracture Zone.

[a] Data from Sinton, 1979.

Opaque spinel is present in three associations: (1) with clinopyroxene and plagioclase (An_{65}), a probable gabbroic inclusion; (2) as an alteration product along the edges and cracks in red spinel; and (3) as complete grains, possibly also as a reaction product.

Veins of calciferous and noncalciferous amphiboles are variably present in the peridotites. Where they cut the rock, the nearby pyroxenes have been transformed into predominant amphibole and lesser serpentine. This may represent an earlier, high-temperature hydration of the original peridotite, and the amphibole may be more resistant to serpentinization than the primary, anhydrous silicates.

MINERAL CHEMISTRY

Mineral compositions were obtained with an automated, three-channel ARL-EMX microprobe at Lamont-Doherty Geological Observatory, using a 15-kV accelerating voltage, and a 0.15 μA beam current. Data were reduced online using a Bence-Albee procedure and reference to a suite of natural and synthetic mineral standards. For spinel analyses, a narrow (3–5 μm) beam was used. Fe^{2+} and Fe^{3+} were calculated assuming stoichiometry. A broad (70 μm) microbeam was used to obtain a more representative analysis of the heterogeneous orthopyroxenes and bastites. The mineral compositions presented in Tables 2-4 are based on averages of more than four spot analyses in each of two separate grains.

---

[3] Bonatti, E., Morandi, N., Brueckner, H., and Michael, P. J., Progressive serpentinization of mantle-derived ultramafic rocks from the Owen Fracture Zone.

Orthopyroxene. Site 556 peridotites have orthopyroxenes with high and variable Mg/(Mg + Fe) ratios, averaging 0.904 (Table 2). These ratios are slightly higher than those of pyroxenes from the Vema Fracture Zone (Hamlyn, unpublished data, 1982) and DSDP Site 395 (Sinton, 1979), but similar to those from the Kane and Atlantis fracture zones. The ratios are lower than orthopyroxenes from the Oceanographer Fracture Zone (Fig. 2).

Orthopyroxene alumina contents are quite low, averaging only 2.8% (Table 2). Site 556 orthopyroxenes contain less alumina than orthopyroxenes from most other oceanic peridotites, a feature shared by some other North Atlantic peridotites (Fig. 3). Site 556 orthopyroxenes approach the compositions of pyroxenes from some alpine peridotites, which are probably more depleted than oceanic peridotites (Dick, 1975). Chrome concentrations are quite high, about 1%, and Cr/(Cr + Al) is about 0.16-0.19; higher than other oceanic peridotites because of the low alumina. Orthopyroxene has about 3-5 mole% wollastonite component, which is similar to orthopyroxene of other oceanic peridotites. Measurement of this quantity is difficult because of the large-scale heterogeneity caused by exsolution.

Bastites of serpentinites from Sites 558 and 560 have very low alumina concentrations, about 1.2-2%. Preliminary work (Bonatti et al., in preparation) suggests that bastite's alumina content reflects to some degree the alumina content of the original pyroxene from which it derives, and that Al has limited mobility during the serpentinization process. Thus, orthopyroxenes from Sites 558 and 560 may have also had low alumina.

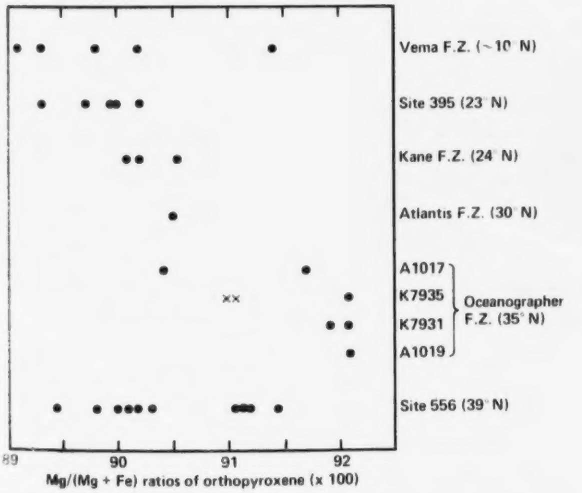

Figure 2. Mg/(Mg + Fe) ratios of orthopyroxenes from Sites 395 and 556, and other North Atlantic and equatorial Atlantic sites. F. Z. = Fracture Zone. Data sources are: Vema Fracture Zone, Hamlyn and Bonatti, unpublished data; Site 395, Sinton (1979); Kane, Atlantis, and Oceanographer fracture zones, Michael and Bonatti, unpublished data. x's are coexisting olivines.

Clinopyroxene. In serpentinized peridotites from Site 556, clinopyroxene occurs mostly as tiny (0.1-0.5 mm) blebs included within or spatially associated with much larger orthopyroxenes or orthopyroxene bastites. These are most likely exsolution products from the orthopyroxene. In one sample (556-13-1, 6-8 cm), a large primary clinopyroxene grain is associated with plagioclase ~An_{65}, and high-Ti spinel. This assemblage might be an inclusion from the surrounding gabbros, since the interval is adjacent to a gabbro breccia.

Exsolved clinopyroxene has high Mg/(Mg + Fe) ratios (0.907-0.921) and low alumina contents (2.30-4.48 wt.%) (Table 3). TiO_2 and Na_2O are positively correlated and quite variable. Chrome contents (about 1%) are lower than those observed from nonexsolved clinopyroxenes from other oceanic peridotites (Sinton, 1979).

Spinel. Spinels have variable and high Cr concentrations and very low Ti and Fe^{3+} (calculated assuming stoichiometry; Table 4). Spinels from Site 558 are among the most chromium-rich spinels measured for any oceanic peridotites (Cr/[Cr + Al] ~ 0.58), and spinels from Site 556 and 560 are only slightly less chromium rich (Fig. 4).

Opaque spinel, which is associated with plagioclase and clinopyroxene, has high TiO_2 (up to 3 wt.%) and Fe^{3+} and is more similar to spinel, which is in equilibrium at low pressure in basalts (Sigurdsson and Schilling, 1976). Opaque spinel that invades cracks and margins of brick red spinel approaches pure magnetite in composition. The third association of opaque spinel, as discrete grains, is slightly more iron-rich than coexisting brick-red spinel in a similar association, and underscores the fact that spinel compositions vary within individual grains and between grains within thin section. The significance of the variation is not clear, but has been ascribed (Hamlyn and Bonatti, 1980) to subsolidus reequilibration by the reaction: orthopyroxene + clinopyroxene + Al-spinel → olivine + plagioclase + Cr-spinel. Recently, Ozawa (1983b) noted that intergrain and intragrain variations in spinel chemistry arose from incomplete reequilibration of spinel with surrounding pyroxenes and olivine. Spinel compositional variation can also arise from the serpentinization reaction (Hoffman and Walker, 1978). Thus, the spinel compositional variation that is observed between different drilling sites or fracture zones may reflect the variation of the original peridotite protolith, or possibly later reactions.

WHOLE-ROCK MAJOR ELEMENT CHEMISTRY

Major element compositions were determined by standard X-ray fluorescence (XRF) methods, using a Siemens SRS-1 spectrometer and employing the sample preparation procedures of Harvey and others (1973). The results are shown in Table 5. Evaluation of these data must take into account that the samples are highly serpentinized, and that serpentinization, in addition to increasing the water content of the rock, may involve some elemental exchange.

The relatively high CaO and LOI in Samples 556-14-1, 61-65 cm and 558-41-3, 111-116 cm are due to

Table 2. Selected microprobe analyses of orthopyroxene from Hole 556 peridotites.

Core-Section (interval in cm)	13-1 60–75	13-1 6–8	13-1 6–8	14-1 61–63	14-1 110–111	14-1 116–118	14-2 79–82	14-2 115–121	14-2 115–121
Major elements (wt.%)									
SiO_2	55.46	56.42	55.57	55.08	55.63	55.34	54.81	55.74	54.94
TiO_2	0.00	0.03	0.19	0.01	0.03	0.00	0.01	0.00	0.00
Al_2O_3	2.75	2.83	2.19	2.83	2.64	2.90	3.30	2.66	2.83
Cr_2O_3	0.91	1.00	0.65	0.87	0.90	0.95	0.85	0.70	0.85
FeO	5.55	5.70	7.06	5.53	6.71	6.59	6.44	6.47	6.39
MnO	0.13	0.15	0.19	0.16	0.14	0.16	0.14	0.14	0.16
NiO	0.02	0.02	0.08	0.13	0.01	0.11	0.03	0.05	0.09
MgO	32.03	32.04	33.04	32.86	31.97	32.56	32.46	33.30	32.62
CaO	2.60	2.80	1.88	2.93	2.33	2.13	2.45	1.64	2.38
Total	99.45	100.99	100.85	100.40	100.36	100.74	100.49	100.70	100.26
Cations on the basis of 6 oxygens									
Si	1.933	1.943	1.922	1.908	1.930	1.914	1.901	1.922	1.910
Ti	0.000	0.001	0.005	0.000	0.001	0.000	0.000	0.000	0.000
Al	0.113	0.114	0.089	0.116	0.108	0.118	0.135	0.108	0.116
Cr	0.025	0.027	0.018	0.024	0.025	0.026	0.023	0.019	0.023
Fe*	0.162	0.163	0.204	0.160	0.195	0.191	0.187	0.187	0.186
Mn	0.004	0.004	0.006	0.005	0.004	0.005	0.004	0.004	0.005
Ni	0.001	0.001	0.002	0.004	0.000	0.003	0.001	0.001	0.003
Mg	1.664	1.630	1.703	1.697	1.653	1.678	1.678	1.712	1.690
Ca	0.097	0.102	0.070	0.109	0.087	0.079	0.091	0.061	0.089
Total	3.999	3.985	4.019	4.023	4.003	4.014	4.020	4.014	4.022
Mg/(Mg + Fe)	0.91	0.909	0.893	0.914	0.894	0.898	0.900	0.902	0.901
En	86.54	86.01	86.15	86.32	85.46	86.16	85.79	87.38	86.03
Fs	8.41	8.59	10.33	8.15	10.06	9.78	9.55	9.53	9.46
Wo	5.05	5.40	3.52	5.53	4.48	4.05	4.65	3.09	4.51

Note: All iron (Fe*) is assumed to be Fe^{2+}.

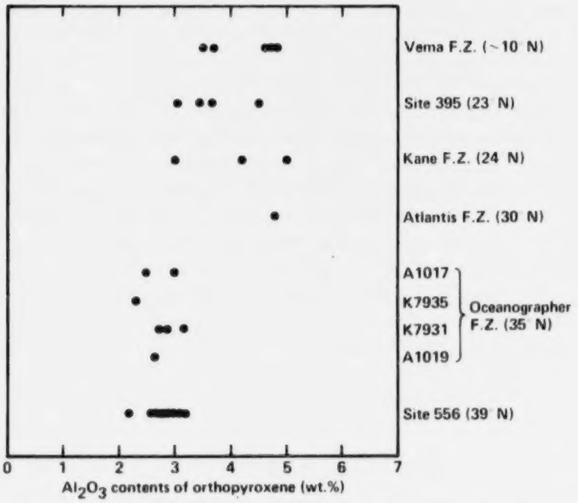

Figure 3. Al_2O_3 contents of orthopyroxenes from Sites 395 and 556, and other North Atlantic and equatorial Atlantic sites. F. Z. = Fracture Zone. Data sources are the same as Figure 2.

carbonate veins in the sample. Thus, in these two samples loss on ignition (LOI) must include significant quantities of carbonate-derived CO_2. If the data are recalculated on a LOI-free basis, the Al_2O_3 content of all samples, which should not be greatly affected by serpentinization, appears to be low compared to other oceanic serpentinites, paralleling the low Al content of orthopyroxenes, clinopyroxenes, and bastites. CaO, K_2O, and Na_2O are also rather low, but these elements, particularly CaO, are probably affected by serpentinization.

DISCUSSION

The following points can be drawn from the study of the ultramafic rocks recovered during DSDP Leg 82.

1. The rocks appear to be spinel harzburgites and to have undergone intense serpentinization. Their relict textures and the chemistry of relict pyroxene and spinel suggest they are tectonites of upper mantle derivation.

2. Pyroxenes have low Al content, which might be related to greater extent of melting compared to other analyzed oceanic ultramafics (Mysen and Kirshiro, 1977; Jaques and Green, 1980). Relatively high Mg/(Mg + Fe) and low Na contents both of pyroxenes and of whole rock suggest that we are dealing with residual material, depleted of a basaltic fraction.

3. Spinels are in general rich in Cr, but their composition is variable in these rocks, suggesting that their equilibrium with surrounding pyroxenes and olivine was incomplete. Although spinel composition may be related to the serpentinization process, its correlation with modal abundance of pyroxene suggests that it is primarily a function of the peridotite protolith composition.

4. Ultramafic rocks from DSDP Sites 556, 558, and 560, recovered in crust 35 Ma old (556 and 558) and 12 Ma old (560), are rather similar to those from Site 395, recovered in crust about 7 Ma old, though the latter con-

Table 3. Selected microprobe analyses of clinopyroxene from Hole 556 peridotites.

Core-Section (interval in cm)	13-1 60–75	13-1 6–8	14-1 110–111	14-1 116–118	14-2 115–121
Major elements (wt.%)					
SiO_2	52.57	53.16	53.44	51.87	53.60
TiO_2	0.01	0.78	0.73	0.14	0.03
Al_2O_3	4.48	2.30	2.96	3.72	3.05
Cr_2O_3	1.21	0.11	1.06	1.46	1.15
FeO	2.62	3.22	2.76	2.67	2.63
MnO	0.08	0.11	0.07	0.13	0.11
NiO	0.00	0.05	0.00	0.07	0.03
MgO	17.00	17.92	17.66	16.97	17.26
CaO	22.98	22.29	21.59	22.57	22.92
Na_2O	0.04	0.31	0.42	0.38	0.23
Total	100.99	100.25	100.69	99.98	101.01
Cations on the basis of 6 oxygens					
Si	1.891	1.928	1.923	1.892	1.928
Ti	0.000	0.021	0.020	0.004	0.001
Al	0.190	0.098	0.126	0.160	0.129
Cr	0.034	0.003	0.030	0.042	0.033
Fe*	0.079	0.098	0.083	0.081	0.079
Mn	0.002	0.003	0.002	0.004	0.003
Ni	0.000	0.001	0.000	0.002	0.001
Mg	0.912	0.969	0.947	0.923	0.925
Ca	0.886	0.866	0.833	0.882	0.883
Na	0.003	0.022	0.029	0.027	0.016
Total	3.997	4.011	3.994	4.017	3.998
Mg/(Mg + Fe)	0.920	0.908	0.919	0.919	0.921
En	48.59	50.13	50.85	48.92	49.02
Fs	4.20	5.05	4.46	4.32	4.19
Wo	47.21	44.82	44.69	46.77	46.79

Note: All except 13-1, 6–8 cm are exsolution blebs from much larger orthopyroxene. All iron (Fe*) is assumed to be Fe^{2+}

sist of lherzolite in addition to harzburgite (Sinton, 1979; Arai and Fujii, 1979) and seem to be less refractory than the Leg 82 samples.

5. The recoveries of ultramafic rocks at relatively shallow levels in the crust away from transform zones confirms earlier suggestions that mantle-derived ultramafic bodies are an important component of slow spreading, Atlantic-type crust. The complex stratigraphy at Holes 556, 558, and 560 suggests a major role of faulting in the shallow emplacement of ultramafics in the crust, as proposed by Bonatti (1976) and Francis (1981). The observation that peridotite tectonites are sandwiched between gabbro layers suggests that only the topmost layer of peridotites is being sampled.

6. Comparison of ultramafics from non–fracture-zone Sites 556, 558, and 560 with ultramafics recovered from nearby fracture zones (i.e., Oceanographer Fracture Zone at 35°N, see Fig. 1) suggests that fracture zones contain some ultramafic rocks that are slightly less refractory than ultramafic rocks recovered in nearby non-fracture-zone crust. This observation is supported by studies at DSDP Site 395 and the Kane Fracture Zone at about 24° (Michael and Bonatti, in preparation[4]). It is possible that the upper mantle associated with fracture zones may have undergone less extensive melting than nearby upper mantle material (Michael and Bonatti, in preparation). Similarly, comparison between Leg 82 and Oceanographer Fracture Zone ultramafics with ultramafics from farther south in the Atlantic (see, for instance, Fig. 4),

Table 4. Selected microprobe analyses of nonopaque spinels from peridotites of Sites 556, 558, and 560.

Hole	556				558				560	
Core-Section (interval in cm)	13-1 1–3	14-1 116–118	14-2 78–84	14-2 114–122	42-1 49–51	42-1 122–129	43-1 43–47	44-1 4–7	4-1 60–65	5-1 81–84
Major elements (wt.%)										
TiO_2	0.30	0.00	0.12	0.00	0.11	0.00	0.24	0.00	0.02	0.00
Cr_2O_3	41.64	37.11	38.46	36.90	45.33	45.01	45.51	46.61	40.46	40.11
Al_2O_3	25.31	29.66	28.43	31.05	22.20	25.41	22.80	22.38	28.75	29.96
Fe_2O_3	3.63	3.30	2.98	1.65	3.30	1.43	2.20	2.09	2.15	1.02
FeO	14.55	15.32	16.73	15.43	17.08	14.97	17.29	15.99	14.38	14.22
MnO	0.21	0.33	0.29	0.27	0.38	0.34	0.34	0.33	0.27	0.25
MgO	13.95	13.63	12.60	13.99	11.75	13.68	11.91	12.86	14.32	14.89
Total	99.59	99.35	99.61	99.29	100.15	100.84	100.29	100.26	100.35	100.45
Cations on the basis of 4 oxygens										
Ti	0.007	0.000	0.003	0.000	0.003	0.000	0.006	0.000	0.000	0.000
Cr	0.998	0.879	0.918	0.867	1.111	1.069	1.110	1.136	0.949	0.933
Al	0.904	1.047	1.013	1.087	0.811	0.900	0.829	0.810	1.005	1.039
Fe^{3+}	0.083	0.074	0.068	0.037	0.077	0.032	0.051	0.048	0.048	0.023
Fe^{2+}	0.369	0.384	0.423	0.384	0.443	0.376	0.446	0.411	0.357	0.350
Mn	0.005	0.008	0.007	0.007	0.010	0.009	0.009	0.009	0.007	0.006
Mg	0.630	0.608	0.567	0.620	0.543	0.613	0.548	0.589	0.633	0.653
$\frac{Cr}{Cr+Al}$	0.525	0.456	0.475	0.444	0.578	0.543	0.572	0.584	0.486	0.473
$\frac{Mg}{Mg+Fe^{2+}}$	0.630	0.613	0.573	0.618	0.551	0.620	0.551	0.589	0.639	0.651

Note: Fe^{2+} and Fe^{3+} calculated assuming stoichiometry.

---

[4] Michael, P. J., and Bonatti, E., Regional and tectonic variations of oceanic ultramafic rocks from the North Atlantic.

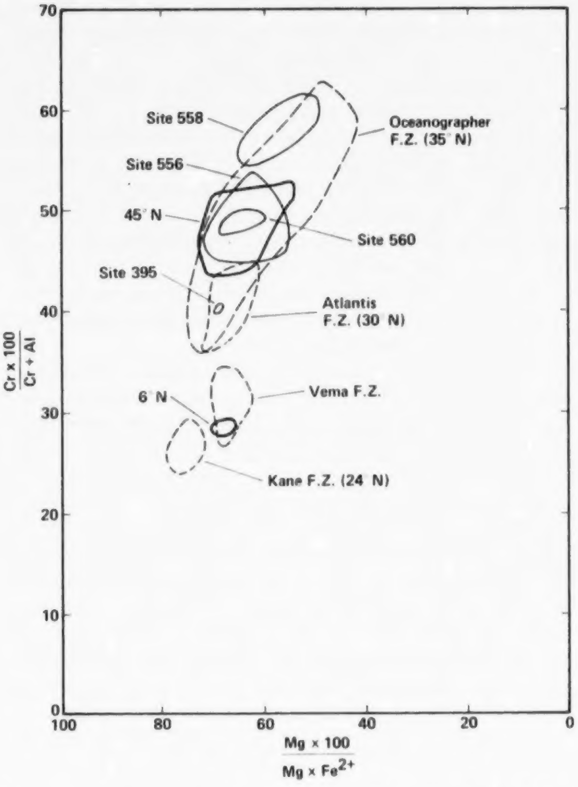

Figure 4. Spinel compositional variation in oceanic mantle-derived peridotites. Data sources are the same as Figure 2, plus 6°N, Michael and Bonatti, unpublished data; 45°N, Aumento and Loubat, 1971. F. Z. = Fracture Zone.

Table 5. Whole-rock major element chemistry of serpentinized peridotites from Holes 556, 558, and 560.

Hole	556			558		560		
Core-Section (interval in cm)[a]	13-1 64-68	14-1 61-65	14-2 78-84	41-3 111-116	42-1 57-59	4-1 60-65[b]	4-1 60-65[b]	5-1 101-105
Major elements (wt.%)								
SiO_2	39.89	37.10	40.56	37.72	38.12	39.21	39.30	39.58
TiO_2	0.02	0.02	0.05	0.02	0.02	0.02	0.02	0.02
Al_2O_3	0.82	0.75	1.34	0.77	0.72	0.84	0.87	0.71
Fe_2O_3[c]	8.09	7.61	9.12	6.67	7.29	6.61	6.78	7.09
MnO	0.10	0.10	0.14	0.07	0.11	0.08	0.08	0.07
MgO	37.34	34.37	35.56	37.39	39.53	39.06	39.27	39.73
CaO	0.32	4.00	0.38	2.01	0.08	0.01	0.01	0.00
Na_2O	0.15	0.07	0.19	0.12	0.15	0.09	0.06	0.06
K_2O	0.00	0.00	0.01	0.00	0.00	0.00	0.00	0.00
LOI[d]	12.91	15.70	13.26	16.07	13.03	12.86	12.86	13.37
Total	99.64	99.72	100.61	100.84	99.05	98.78	99.25	100.63

Note: Precision and accuracy are ± 2% for elements over 5% concentration, ± 5% for elements 1-5% concentration, and ± 50% or more for elements less than 0.5% (Na_2O, TiO_2, CaO, MnO, and K_2O).

[a] Each sample represents ~25 cm^3 of material.

[b] Replicate analyses of powder splits from the same sample; indicates reproducibility.

[c] Assumes all iron as Fe^{3+}.

[d] Volatile loss on ignition between 110 and 1050°C; includes H_2O and CO_2.

suggests systematic regional differences in upper mantle mineral chemistry and modes. The differences between the peridotite protoliths may be related either to greater degree of partial melting in the northernmost region or to preexisting heterogeneities in the mantle, as further discussed elsewhere (Michael and Bonatti, 1983; Dick and Bryan, 1983; Michael and Bonatti, in preparation).

NOTE ADDED IN PROOF

Subsequent sampling of peridotites from Hole 560 revealed th presence of primary orthopyroxene porphyroclasts averaging 2.8 Al_2O_3 and 91.1 Mg/(Mg + Fe) × 100.

ACKNOWLEDGMENTS

This research was supported by NSF Grant OCE 80-25252 and ON Contract N000-80-0098T. Contribution No. 3572 from Lamont-Do erty Geological Observatory.

REFERENCES

Arai, S., and Fujii, T., 1979. Petrology of ultramafic rocks from S 395. *In* Melson, W. G., Rabinowitz, P. D., et al., *Init. Repts. DSD* 45: Washington (U.S. Govt. Printing Office), 587–593.

Aumento, F., and Loubat, H., 1971. The Mid-Atlantic Ridge ne 45°N. XVI. Serpentinized ultramafic intrusions. *Can., J. Ea Sci.*, 8:631–663.

Bonatti, E., 1976. Serpentinite protrusions in the oceanic crust. *Ear Planet. Sci. Lett.*, 32:107–113.

Dick, H. J. B., 1975. Alpine peridotites and the oceanic lithosphere, comparison. *EOS, Trans. Am. Geophys. Union*, 56:1077.

Dick, H. J. B., and Bryan, W. B., 1983. Contrasting abyssal basalt liquidus trends and regional variations in the composition of abyssal peridotites. *EOS, Trans. Am. Geophys. Union*, 64:310.

Francis, T. J., 1981. Serpentinization faults and their role in the tectonics of slow-spreading ridges. *J. Geophys. Res.*, 86:11616–11622.

Hamlyn, P. R., and Bonatti, E., 1980. Petrology of mantle-derived ultramafics from the Owen Fracture Zone, Northwest Indian Ocean: implications for the nature of the oceanic upper mantle. *Earth Planet. Sci. Lett.*, 48:65–79.

Harvey, P. K., Taylor, D. M., and Hendry, R. D., and Bancroft, F., 1973. An accurate fusion method for the analysis of rocks and chemically related materials by X-ray fluorescence spectrometry. *X-ray Spectrom.*, 2:33–44.

Hoffman, M. A., and Walker, D., 1978. Textural and chemical variations of olivine and chrome spinel in the East Dover ultramafic bodies, south-central Vermont. *Geol. Soc. Am. Bull.*, 89:699–710.

Jaques, A. L., and Green, D. H., 1980. Anhydrous melting of peridotite at 0–15 Kb pressure and the genesis of tholeiitic basalts. *Contrib. Mineral. Petrol.* 73:287–310.

Michael, P. J., and Bonatti, E., 1983. Peridotites from DSDP Leg 82 and Oceanographer F. Z. *EOS, Trans. Am. Geophys. Union*, 64:345.

Mysen, B. O., and Kushiro, I., 1977. Compositional variations of coexisting phases with degree of melting of peridotite in the upper mantle. *Am. Mineral.*, 62:843–865.

Ozawa, K., 1983. Evaluation of olivine-spinel geothermometry as an indicator of thermal history for peridotites, *Contrib. Mineral. Petrol.*, 82:52–65.

Pritchard, H. M., 1979. A petrographic study of the process of serpentinisation in ophiolites and the ocean crust. *Contrib. Minera Petrol.*, 68:231–241.

Sigurdsson, H., and Schilling, J. G., 1976. Spinels in Mid-Atlant Ridge basalts: chemistry and occurrence. *Earth Planet. Sci. Lett*, 29:7–20.

Sinton, J. M., 1979. Petrology of (alpine-type) peridotites from Si 395. *In* Melson, W. G., Rabinowitz, P. D., et al., *Init. Repts. DSD* 45: Washington (U.S. Govt. Printing Office), 595–601.

Smith, D., 1977. The origin and interpretation of spinel-pyroxene cluste in peridotite, *J. Geol.*, 85:476–482.

Date of Initial Receipt: 12 August 1983
Date of Acceptance: 19 August 1983

PART V: SEDIMENTOLOGY AND PALEONTOLOGY

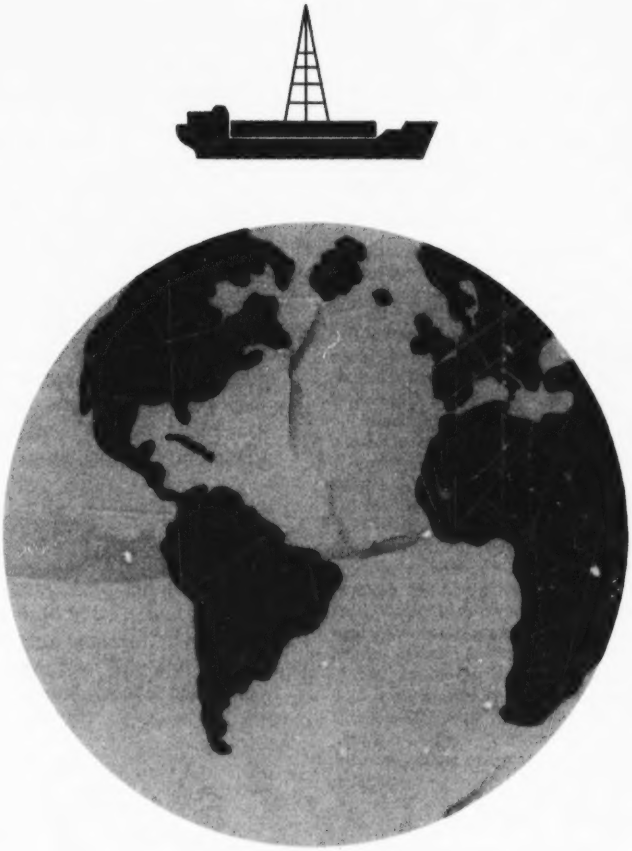

30. X-RAY MINERALOGY OF SITES 558 AND 563[1]

C. Latouche and N. Maillet, Institut de Géologie du Bassin d'Aquitaine, Université de Bordeaux I[2]

ABSTRACT

Downhole bulk-sample and clay-mineral analytical results for Sites 558 and 563 are presented in this chapter. These results show a Tertiary climatic and hydrologic evolution similar to that at other DSDP drill sites in the northeastern Atlantic Ocean (Sites 398, 403–406, 548–550, 552–555). The sediments recovered at both sites are primarily calcareous and chalky oozes characterized by >90% carbonate and minor quartz and plagioclase feldspar. Clay minerals smectite, kaolinite, illite, and chlorite are present throughout the cores; upsection, illite increases at the expense of smectite. The clay mineralogy suggests climatic cooling and increased ocean circulation during the Miocene. Intervals rich in very fine grained (<2 μm) quartz suggest times of increased eolian input. This could have resulted from development, during Oligocene and late Miocene time, of an arid, desertlike sediment provenance that lasted until the present day.

INTRODUCTION

Analysis of the Leg 82 sediments, collected on the western side of the Mid-Atlantic Ridge, south of the Azores, served to find out more about the North Atlantic Tertiary environments (climate, hydrology), which were directly implicated in the evolution of the sedimentation pattern. We chose to investigate Site 558 (near the Pico Fracture Zone) and Site 563 (south of the Hayes Fracture Zone) (Fig. 1) because the Tertiary sediments recovered at these sites were complete; very little Tertiary sediment was found at the other sites. Tertiary sediments from this region consist mainly of calcareous and chalky oozes.

X-ray diffraction was used in the mineralogic analysis of 65 samples recovered during Leg 82. The distribution of samples is as follows. Site 558: 43 samples (lower Oligocene to upper Miocene from Hole 558 and upper Miocene to Pleistocene from Hole 558A). Site 563: 22 lower Oligocene to upper Miocene samples. Two other samples were also analyzed, one from Site 560 (upper Miocene) and the other from Site 564 (middle Miocene–lower Oligocene).

METHODS

A Philips diffractometer was used, and operating conditions were as follows: nickel-filtered copper $K\alpha$ radiation at 40 kV, 20 mA.

Total Sediments

Total sediments were analyzed according to the powder diffractogram method; that is, sediments were dried, crushed, and, after being put in powder on a support, X-rayed. To determine the minerals involved, we used their characteristic peaks (Torre de Assunçâo and Garrido, 1953): quartz at 3.35 Å; plagioclase feldspar between 3.20 and 3.15 Å, calcite at 3.03 Å, and dolomite at 2.883 Å.

Semiquantitative concentrations of minerals: The peak height characterizing each mineral was transcribed on a standard curve, and mineral concentrations were evaluated. Calibration was based on four synthetic reference standards, formed of variable weight mixtures of quartz, feldspar, calcite, and dolomite. Clay quantity, occurrence of heavy minerals, and content of amorphous components were not taken into consideration.

Clay Fraction (<2 μm)

Total sediments were dispersed in deionized water, using mechanical agitation. Samples with high carbonate contents were first treated with N/10 HCl. After several (2–3) washings in deionized water, <2 μm subfractions were separated by gravity settling. After the <2 μm portion of the suspension was centrifuged, the resulting thick paste was spread across 3 slides, as follows: slide one was scanned untreated; slide two was saturated with ethylene glycol; slide three was heated at 550°C for an hour.

Minerals were identified on the basis of their typical reactions to classical treatment (Brown, 1961; Thorez, 1975). Percentages of the different minerals were estimated from the glycolated samples. The heights of the 001 peaks were used to determine smectite (17 Å), illite (10 Å), and kaolinite and chlorite (7.1 Å). Chlorite was distinguished from kaolinite on the basis of the difference between their reflections: 002 for kaolinite (3.57 Å) and 004 for chlorite (3.55 Å). Results are given in percentage values; these percentages are evaluated only with regard to the crystallized clay minerals in the <2 μm fraction. In this fraction several minerals such as zeolite and quartz were observed. The heulandite group in zeolites was identified (7.90 and 8.90 Å). After heating, a distinction was drawn between heulandite and clinoptilolite. Quartz, within the fine-grained fraction, was identified at 4.24 Å. The 3.35-Å peak, usually used to determine quartz, was superimposed on the illite 003 peak. The 4.24-Å peak—measured in millimeters—was used not to quantify quartz accurately, but to give it a relative value. All mineralogic analyses were carried out under the same operating conditions.

RESULTS

The major mineralogic characteristic at all sites studied is the dominance of carbonates (calcite) and the poor representation of coarse detrital elements such as quartz and feldspars within total sediments. Clay minerals are represented mainly by smectites within the Oligocene and upper Miocene. They are rich in illite at the base of the Miocene and in the Pliocene and Pleistocene. Quartz is often linked to this clayey fraction.

Site 558

The sediments studied are upper Oligocene and lower, middle, and upper Miocene (Hole 558) and upper Miocene, Pliocene, and Pleistocene (Hole 558A). Our results are given in Table 1 and Figure 2.

---

[1] Bougault, H., Cande, S. C., et al., *Init. Repts. DSDP*, 82: Washington (U.S. Govt. Printing Office).

[2] Address: Institut de Géologie du Bassin d'Aquitaine, Université de Bordeaux I, 351 Cours de la Libération, 33405 Talence Cedex, France.

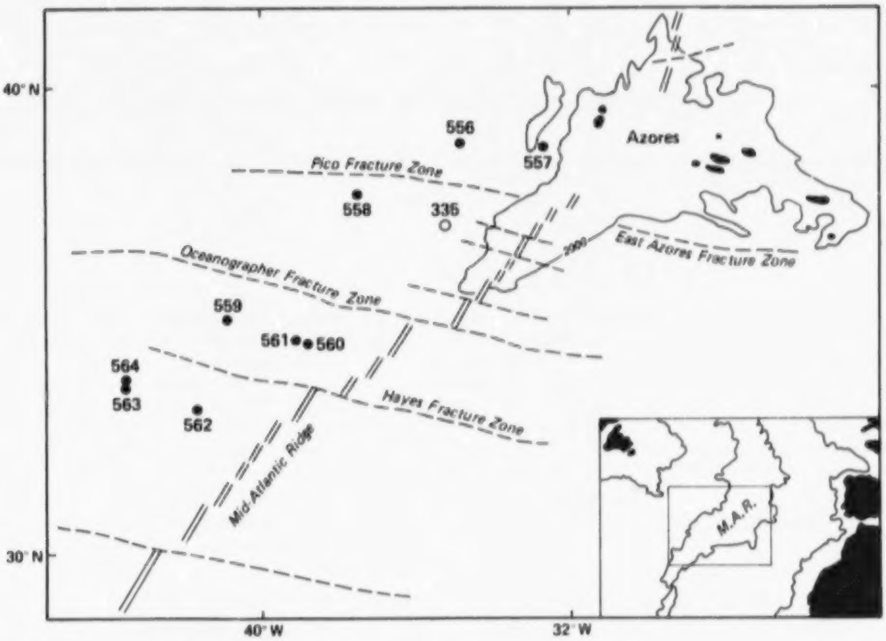

Figure 1. Locations of Leg 82 drill sites.

Upper Oligocene and undifferentiated Oligocene/Miocene (558-27-1, 51–55 cm to 558-17-1, 110–115 cm; nannofossil ooze). Sediment is carbonate, always calcite except at the base of the lower Oligocene, where dolomite was noted. Quartz is absent or present in trace amounts and plagioclase feldspars are rare (~3%). Clay minerals are represented mainly by abundant smectites (57–76%), illites (11–23%), kaolinites (7–13%), and chlorites (4–9%). Traces of zeolite (heulandite) are associated with the clay fraction.

Lower and middle Miocene (558-16-3, 110–115 cm to 558-12-1, 110–115 cm; nannofossil ooze). Sediment is dominantly carbonate (calcite), quartz is absent or present in trace amounts, and plagioclase feldspars are present (3–4%). Clay minerals are very rich in smectites (74–100%); illites, kaolinites, and chlorites are less common than in the underlying Oligocene/lower Miocene section. Zeolites (heulandite and clinoptilolite) are present in the clay fraction. Quartz decreases (in relative abundance) in the same fraction.

Middle and upper Miocene (558-11-1, 110–115 cm to 558-1-2, 120–125 cm; nannofossil ooze). Sediment is very rich in carbonates (calcite). In bulk samples, quartz is scarce and plagioclase feldspars are present (2–3%). Clay minerals are represented mainly by smectites (49–89%) and illites (6–28%); kaolinites occur in more dominant proportions (5–20%) than chlorite (trace to 7%). In this fine-grained fraction, quartz increases toward the top of the Miocene.

Upper Miocene, Pliocene, and Pleistocene (558A-1-1, 59–62 cm to 558A-16-1, 110–115 cm; nannofossil ooze). The carbonate content decreases slightly at the top of the Hole 558A. Quartz is present in traces, and plagioclase feldspars are present (3%). The composition of clay minerals varies. In Samples 558A-16-1, 110–115 cm to 558A-14-5, 110–115 cm (upper Miocene), clay minerals are dominated by illites (33–46%). In Samples 558A-13-1, 110–113 cm to 558A-9-2, 110–114 cm (Miocene, Pliocene), smectites constitute the most important component (41–55%). In Samples 558A-8-2, 120–123 cm to 558A-1-1, 59–62 cm (Pliocene, Pleistocene), the main clay mineral is illite (32–51%), and kaolinite and chlorite are well represented. Quartz is abundant in this clay fraction.

Site 563

The major mineralogic characteristics are the dominance of carbonates (calcite), the extreme paucity of plagioclase, and the scarcity of quartz. The clay fraction is rich in smectites from the base to the top of the sediment studied. Illite, kaolinite, and chlorite are well represented. Traces of zeolite (heulandite) are associated with the clay fraction in the Oligocene and middle-lower Miocene sediments. In this fine-grained fraction, quartz increases toward the top of the core (563-1-1, 110–115 cm).

Our results for Site 563 are given in Table 2 and Figure 3.

Site 560

This site is between the Oceanographer and Hayes fracture zones. The sample studied is upper Miocene (560-1-1, 28–30 cm; nannofossil ooze). The major characteristics are the dominance of carbonates (calcite), the presence of very few feldspars, and traces of quartz. Clay minerals are represented mainly by smectites (58%), accompanied by some illites (29%), kaolinites (20%), and chlorites (13%). Quartz is abundant in the clay fraction.

Table 1. X-ray diffractometry mineralogic analyses (%), Site 558 (Holes 558 and 558A).

	Bulk sample				<2 μm fraction					
Hole-Core-Section (interval in cm)	Calcite	Dolomite	Quartz	Plagioclase feldspars	Smectite	Illite	Kaolinite	Chlorite	Presence or absence of zeolite	Quartz (4.24 Å) (height in mm)
558A-1-1, 59-62	83		1	3	16	46	19	19		14
558A-2-1, 110-114	71		2	3	25	40	21	14		15
558A-2-4, 56-59	88		1	3	40	32	14	14		23
558A-3-1, 110-115	80		2	3	22	41	13	24		26
558A-4-1, 110-115	88		1	3	13	51	18	18		28
558A-5-1, 110-115	86		1	3	23	43	23	11		30
558A-6-2, 120-123	83		1	3	21	45	17	17		26
558A-8-2, 120-123	80		1	3	34	33	19	14		35
558A-9-2, 110-114	91		Tr	3	43	28	15	15		24
558A-10-1, 110-115	95		Tr	3	44	32	12	12		20
558A-11-1, 110-115	93		Tr	3	41	33	13	13		12
558A-12-1, 110-115	94		Tr	3	51	25	16	8		30
558A-13-1, 110-113	94			3	55	23	11	11		17
558A-14-5, 110-113	92		1	3	19	46	22	13		29
558A-15-1, 110-115	89		1	3	16	52	16	16		21
558A-16-1, 110-115	92		1	2	33	33	17	17		30
558-1-2, 120-125	91			2	49	28	19	4		16
558-2-1, 50-56	91			2	53	23	20	4		16
558-3-1, 110-115	91			2	60	19	14	7		6
558-4-1, 110-115	91			2	66	19	15			12
558-5-1, 110-116	90		Tr	2	69	17	17	Tr		Tr
558-6-1, 110-115	90		Tr	2	89	6	5	Tr		Tr
558-7-1, 70-76	91			2	55	27	18	Tr		Tr
558-8-1, 110-115	91			2	67	15	18	Tr		Tr
558-9-2, 110-115	91			3	62	24	14	Tr		10
558-10-1, 110-115	93			3	63	19	14	4		8
558-11-1, 110-115	90		Tr	3	64	16	16	4		15
558-12-1, 110-111	94		Tr	4	100		Tr			Tr
558-13-1, 110-115	91		Tr	4	82	9	9		H	Tr
558-14-1, 110-115	91		Tr	3	81	8	11			
558-15-1, 98-104	91			3	82	10	8		C	15
558-15-6, 23-28	88		Tr	3	74	13	9	4	C	15
558-16-3, 110-115	91			3	75	14	8	3	H	8
558-17-1, 110-115	91			3	76	11	9	4	H	6
558-18-1, 110-115	93		Tr	3	69	14	12	5	H	17
558-19-1, 110-114	91		Tr	3	65	16	12	7	H	10
558-20-1, 110-115	91		Tr	3	66	19	9	6	H	12
558-21-1, 110-115	91		1	3	62	20	10	8	H	10
558-22-1, 110-115	93		Tr	3	57	21	13	9		18
558-24-1, 84-89	88		Tr	3	58	20	14	8	H	17
558-25-1, 68-74	91		Tr	3	74	13	8	5		7
558-26-1, 110-115	81	Tr		3	61	23	10	6		4
558-27-1, 51-55	56	32		1	71	15	7	7		Tr

Note: H = heulandite; C = clinoptilolite; Tr = trace.

Site 564

This site is on the west flank of the Mid-Atlantic Ridge, south of the Hayes Fracture Zone. The sample studied (564-H1-7, 43–47 cm; nannofossil ooze) is undifferentiated lower Oligocene–middle Miocene. Carbonates predominate (calcite); quartz (3%) and plagioclase feldspars (3%) are present. Clay minerals are dominated by smectites (68%), accompanied by illites (16%) and kaolinites and chlorites (8% each).

SYNTHESIS AND DISCUSSION

The overall evolution of clay-mineral assemblages throughout the Tertiary and Quaternary shows very similar trends to the sediment evolution at sites previously studied in the North Atlantic: Leg 47B (Chamley et al., 1979), Leg 48 (Latouche and Maillet, 1979), Leg 78 (Latouche and Maillet, in press), Leg 80 (Chennaux et al., in press), and Leg 81 (Latouche and Maillet, in press). There exist, however, differences attributable mainly to the geographic and climatic environment.

Interpretation of the mineral assemblages recovered during Leg 82 was based on previous publications, the majority of which suggest that marine clays are of detrital origin. Particular attention was given to the work by Millot (1964), Yeroschev-Shak (1964), Griffin et al. (1968), Paquet (1969), Tardy (1969), Latouche (1975), Courtois and Chamley (1978), Chamley (1979), Latouche and Maillet (1982), Sarnthein and Erlenkeuser (1982), and Grousset et al. (1983). All these authors assume that the kaolinites and smectites are derived from humid tropical regions and that smectite genesis is favored by the presence of basic volcanic parent-rock. Illites and chlorites are thought to be located generally within intermediate- and high-latitude zones and/or to originate from acid rock dismantling. Illites and chlorites also occur in desert zones, and evidence of their inputs within a marine environment was attributed to atmospheric circulation.

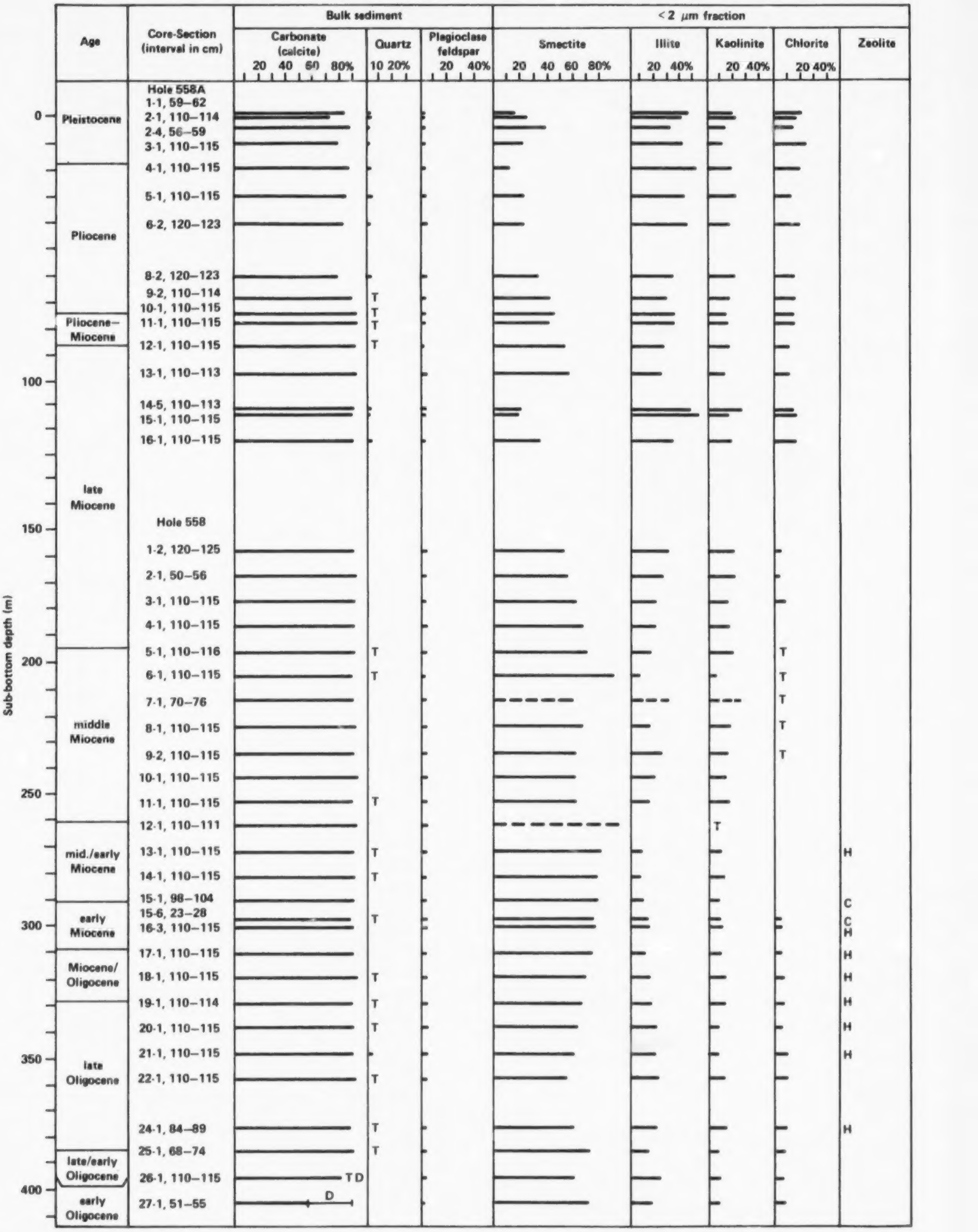

Figure 2. Mineralogic log, Site 558 (Holes 558 and 558A). D = dolomite, T = trace, C = clinoptilolite, H = heulandite. Dashed lines indicate very poorly crystallized. The following age ranges are undifferentiated: Pliocene-Miocene, middle/early Miocene, Miocene/Oligocene, and late/early Oligocene.

Table 2. X-ray diffractometry mineralogic analyses (%), Site 563 (Hole 563).

	Bulk sample				< 2μm fraction					
Core-Section (interval in cm)	Calcite	Dolomite	Quartz	Plagioclase feldspars	Smectite	Illite	Kaolinite	Chlorite	Presence or absence of zeolite	Quartz (4.24 Å) (height in mm)
1-1, 110–115	92		Tr	3	45	31	12	12		23
2-1, 110–115	94		Tr	3	71	16	8	5		28
3-1, 110–114	92		Tr	3	52	26	11	11		18
4-1, 110–114	96		Tr	Tr	50	28	13	9		8
5-1, 110–114	94			3	62	20	12	6		19
6-1, 110–114	97			Tr	54	21	15	10		19
7-1, 110–114	96		Tr	Tr	67	21	8	4		12
8-1, 110–114	97			Tr	70	15	9	6		Tr
9-1, 110–114	96		Tr	Tr	59	20	16	5		15
10-1, 120–125	91		Tr	2	62	16	13	9	H	20
11-1, 120–124	94		Tr	Tr	70	12	12	6		10
12-1, 127–132	94			Tr	63	17	13	7	H	14
13-2, 110–112	94			Tr	63	19	11	7	H	15
14-2, 124–128	96			Tr	67	15	18		H	20
15-1, 110–114	96			Tr	79	11	5	5		4
16-1, 110–114	96			Tr	64	21	8	7		10
17-1, 110–114	94			Tr	70	16	7	7	H	4
19-1, 108–112	91		Tr	Tr	51	18	31	Tr		8
20-1, 70–74	94			Tr	60	20	12	8		10
21-2, 107–111	96			Tr	68	18	11	3		8
22-1, 74–78	91	Tr		Tr	84	8	4	4		6

Note: H = heulandite; Tr = trace.

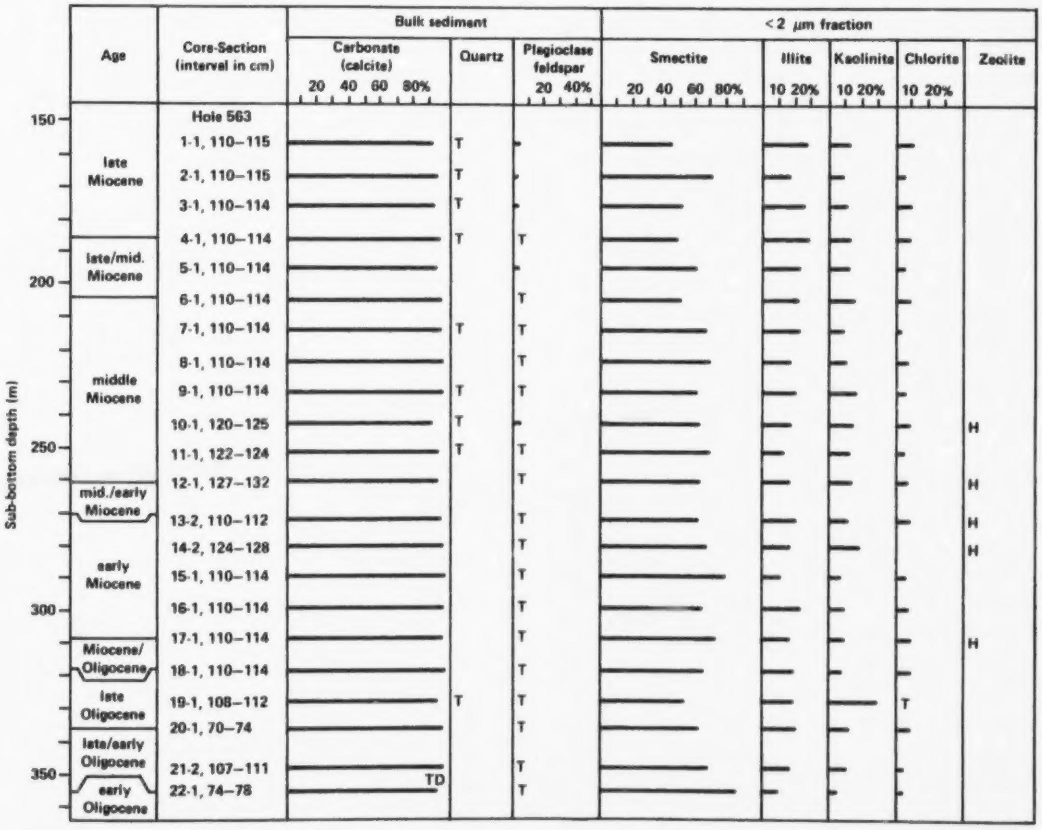

Figure 3. Mineralogic log, Site 563. D = dolomite, T = trace, and H = heulandite. The following age ranges are undifferentiated: late/middle Miocene; middle/early Miocene; Miocene/Oligocene; and late/early Oligocene.

Common General Evolution in the North Atlantic

In the North Atlantic, the major characteristic of this evolution, during the Cenozoic, was the smectite-group decrease and, from the middle late Miocene to the Quaternary (Fig. 2), the illite increase. Latouche and Maillet (1979, 1980) explained the occurrence of illites and chlorites by a northern water circulation that took form in the second half of the Tertiary. Although using different analytical methods, Vergnaud Grazzini et al. (1978) and Roberts and Montadert (1979) certified the same water circulation source. In the equatorial region studied herein, illite and chlorite contents tended to increase during the Miocene. This increase coincided with that in the North (Latouche and Maillet, 1979,1980), and can similarly be linked to north-south water circulations, as well as to climatic alterations already known. This mineralogic change, observed in the sediment record throughout the Atlantic, is somewhat different in this region because of the geographic location (low latitudes).

Regional Characteristics

The constant occurrence of smectite, illite, kaolinite, and chlorite in the examined sediments from all sites suggests varied input origins and, consequently, water circulation courses (initiated at the beginning of the Tertiary) enabling communication of the zone studied with regions at different latitudes. Further, the constant occurrence of illite and chlorite suggests the existence of other than northern input origins. This suggestion is enforced by the presence of very fine grained quartz, which presents two maxima (Fig. 4), one in the upper Oligocene and the other from the upper Miocene to the Pleistocene. This vertical distribution coincides fairly well with the illite variations observed mainly from the upper Miocene to the Quaternary. Just like clay minerals (Turekian, 1965; Gillette, 1974, 1981; Blifford and Gillette, 1971; Gillette and Walker, 1977), quartz associated with the fine-grained fraction is often considered to be the result of eolian phenomena. Consequently, the relative abundances of these mineral assemblages (quartz, illite, chlorite) could add to the information on climatic modifications, as in the example given by Janecek and Rea (in press) for the Pacific during the Cenozoic. This assemblage could also indicate, in this part of the Atlantic, dry and continental desert periods. In accordance with the assumptions of Janecek and Rea, there existed two dry periods: a less humid period in the late Oligocene (quartz abundant in Holes 558 and 558A) and a distinctly arid period in the Miocene and accentuated in the Pliocene and Pleistocene (quartz, illite, and chlorite are abundant).

ACKNOWLEDGMENTS

Special thanks are extended to H. Bougault for providing the samples analyzed. The manuscript has benefited from critical reviews by G. Chennaux and A. Desprairies. This investigation has been funded by the Action Thematique Programmée, Géologie et Géophysique des Océans.

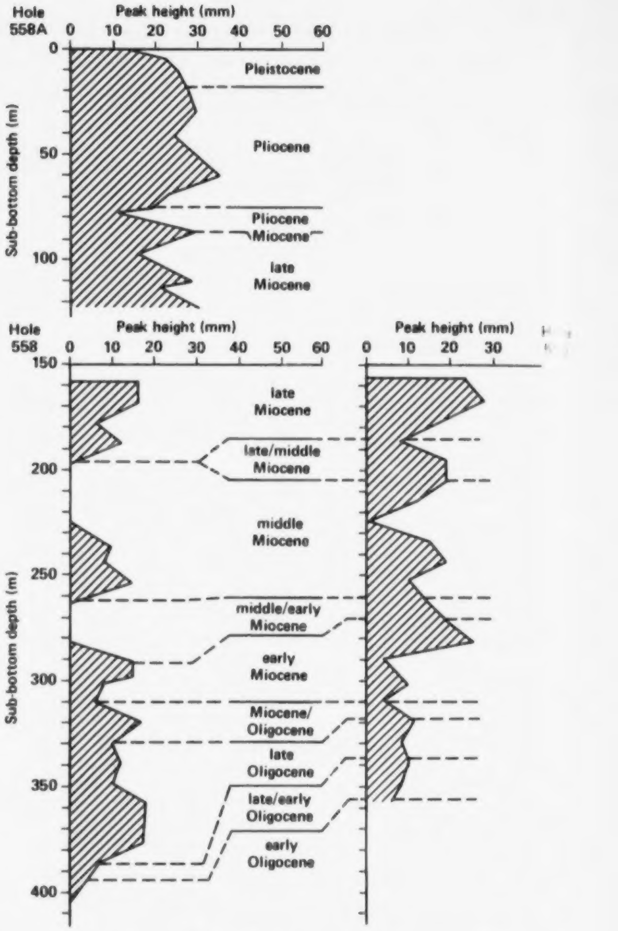

Figure 4. Quartz-associated with fine-grained (<2 μm) fraction. Identical analysis conditions were applied to all samples. (Peak at 4.24 A.)

REFERENCES

Blifford, I. H. J., and Gillette, D. A., 1971. Applications of the log normal frequency distribution of the chemical composition and size distribution of naturally occurring atmospheric aerosols. *Water, Air, Soil Pollution*, 1:106–114.

Brown, G., 1961. *The X-ray Identification and Crystal Structures of Clay Minerals:* London (Mineralogical Society).

Chamley, H., 1979. North Atlantic clay sedimentation and paleoenv ronment since the late Jurassic. *In* Talwani, M., and Ryan, W. F. (Eds.), *Deep Drilling Results in the Atlantic Ocean: Continent Margins and Paleoenvironments:* Washington (Am. Geophys. U ion), pp. 342-361.

Chamley, H., Debrabant, P., Foulon, J., Giroud d'Argoud, G., L touche, C., Maillet, N., Maillot, H., and Sommer, F., 1979. Mi eralogy and Geochemistry of Cretaceous and Cenozoic Atlan sediments off the Iberian Peninsula (Site 398, D.S.D.P. Leg 47 *In* Sibuet, J.-C., Ryan W. B. F., et al., *Init. Repts. DSDP*, 47, 2: Washington (U.S. Govt. Printing Office), 429–449.

Chennaux, G., Esquevin, J., Jourdan, A., Latouche, C., and Maill N., in press. X-ray mineralogy and mineral geochemistry of Cen zoic strata (Leg 80). *In* Graciansky, P. C., de Poag, C. W., et a *Init. Repts. DSDP*, 80: Washington (U.S. Govt. Printing Offic

Courtois, C., and Chamley, H., 1978. Terres rares et minéraux ar leux dans le Cretacé et le Cénozoique de la marge atlantique o entale. *C. R. Hebd. Seances Acad. Sci.* (Paris), t. 286, Ser. D: 671–674.

Gillette, D. A., 1974. On the production of soil wind erosion aerosols having the potential for long range transport. *J. Rech. Atmospheriques*, 8:735–744.

______, 1981. Production of dust that may be carried great distances. *In* Péwé, T. L. (Ed.), *Desert Dust: Origin, Characteristics and Effect on Man*. Spec. Pap. Geol. Soc. Am., 186:11–26.

llette, D. A., and Walker, T., 1977. Characteristics of airborne particles produced by wind erosion of sandy soil, high plains of west Texas. *Soil Sci.*, 123:94–110.

ffin, J. J., Wondom, H., and Goldberg, E. D., 1968. The distribution of clay minerals in the world ocean. *Deep-Sea Res.* (Oxford), 15:433–459.

usset, F., Latouche, C., and Maillet, N., 1983. Clay minerals as indicators of wind and current contribution to postglacial sedimentation on the Azores-Iceland Ridge. *Clay Miner.*, 18:65–75.

ecek, T. R., and Rea, D. K., in press. Eolian deposition in the northeast Pacific Ocean: Cenozoic history of atmospheric circulation. *Geol. Soc. Am. Bull.*

ouche, C., 1975. Les minéraux argileux des sédiments actuels de l'Atlantique nord-oriental et du sud de la Mer de Norvège. *Proc. Internat. Clay Conf.* (Mexico, July 16–23): Wilmette, Illinois (Applied Publ. Ltd.), pp. 45–54.

Latouche, C., and Maillet, N., 1979. X-ray mineralogy studies, Leg 48, Rockall Region (Sites 403, 404, 405 and 406). *In* Montadert, L., Roberts, D. G., et al., *Init. Repts. DSDP*, 48: Washington (U.S. Govt. Printing Office), 665–676.

______, 1980. Minéraux argileux et évolution des environnements sédimentaires du domaine atlantique nord-oriental durant le Paleogène. *Bull. Soc. Geol. Fr.*, 22(5):757–761.

______, 1982. Essai sur l'utilisation des argiles comme temoins des climats néogènes dans la province atlantique nord-orientale. *Bull. Soc. Geol. Fr.*, 24(3):482–496.

______, in press. X-ray mineralogy study of Tertiary deposits, Leg 81 (Sites 552, 553, 554, and 555). *In* Roberts, D. G., Schnitker, D., et al., *Init. Repts. DSDP*, 81: Washington (U.S. Govt. Printing Office).

Millot, G., 1964. *Géologie des Argiles:* Paris (Masson et Cie), p. 499.

Paquet, H., 1969. Evolution géochimique des minéraux argileux dans les altérations et les sols des climats méditerranéens et tropicaux à saisons contrastées. *Mem. Serv. Carte Geol. Alsace Lorraine*, 30: 1–212.

Roberts, D. G., and Montadert, L., 1979. Margin paleoenvironments of the northeast Atlantic. *In* Montadert, L., Roberts, D. G., et al., *Init. Repts. DSDP*, 48: Washington (U.S. Govt. Printing Office), 1099–1118.

Sarnthein, M., and Erlenkeuser, H., 1982. Termination I: the response of continental climate in the subtropics as recorded in deep-sea sediments. Actes Colloque Internat. C.N.R.S. (Bordeaux, Sept. 1981), *Bull. Inst. Geol. Bassin d'Aquitaine* (Bordeaux), 31:393–497.

Tardy, Y., 1969. Géochimie des altérations. Etudes des arènes et des eaux de quelques massifs cristallins d'Europe et d'Afrique. *Mem. Serv. Carte Geol. Alsace Lorraine* (Strasbourg), 31:1–199.

Thorez, J., 1975. *Phyllosilicates and Clay Minerals. A Laboratory Handbook for Their X-ray Diffraction Analysis*: Dison (G. Le Lotte).

Torre de Assunção, C., and Garrido, J., 1953. Tables pour la détermination des minéraux au moyen des rayons X. *Bull. Musee Lab. Mineral. Geol. Fac. Sci. Lisbonne*, Ser. 6, no. 20–21.

Turekian, K., 1965. Some aspects of the geochemistry of marine sediments. *In* Riley, J. P., and Skirrow, G. (Eds.), *Chemical Oceanography*, Vol. 2: London (Academic Press), 81–126.

Vergnaud Grazzini, C., Pierre, C., and Létolle, R., 1978. Paleoenvironment of the northeast Atlantic during the Cenozoic: oxygen and carbon isotope analyses at DSDP Sites 398, 400A and 401. *Oceanol. Acta*, 1(3):381–390.

Yeroschev-Shak, V. A., 1964. Clay minerals of the Atlantic Ocean. *Soviet Oceanogr.* (Moscow/Washington), 30-2:90–106.

Date of Initial Receipt: 2 December 1983
Date of Acceptance: 20 April 1984

31. INTERSTITIAL WATER STUDIES, CENTRAL NORTH ATLANTIC[1]

Joris M. Gieskes, Kirk Johnston, and Marcus Boehm, Scripps Institution of Oceanography,
University of California at San Diego[2]

ABSTRACT

Interstitial waters were collected at only two sites during Leg 82, Sites 558 and 563. Only very small changes in dissolved calcium and magnesium occur, presumably resulting from reactions in the underlying basement basalts. Dissolved strontium profiles indicate maxima, which can be understood in terms of carbonate recrystallization processes. Data on Sr/Ca in carbonates cannot be used to estimate the extent of recrystallization that has occurred in these sediments.

INTRODUCTION

During Leg 82 interstitial waters were obtained at two drill sites—Holes 558 and 563 (Fig. 1). Shipboard analyses showed only very small changes in dissolved calcium and magnesium, but in such a situation the study of carbonate diagenesis may be of great interest. Matter et al. (1975) have shown that in carbonate sediments of the Shatsky Rise, where calcium and magnesium changes are also negligible, carbonate recrystallization reactions lead to the decrease in the Sr/Ca ratio of carbonate and to an increase in the Mg/Ca ratio. Baker et al. (1982), using experimentally determined distribution coefficients for strontium in carbonates, were able to predict these variations quite well. Similar observations were made by Elderfield et al. (1982) for carbonate sediments on the Ontong Java Plateau (DSDP Sites 288 and 289). In the present paper we present more extensive analyses of the interstitial water samples obtained during Leg 82 as well as some analysis of the solid carbonate chemistry.

MATERIALS AND METHODS

Interstitial water samples were obtained at Sites 558 and 563 using the routine shipboard sampling program, i.e., sampling at 50-m depth intervals at minimum.

Shipboard analyses included salinity, pH, alkalinity, calcium, magnesium, and chloride content (Table 1). The acidified samples (alkalinity samples) were analyzed in our shore laboratory for dissolved silica, strontium, lithium, potassium, ammonia, and sulfate. Methods used have been discussed by Gieskes (1974), Gieskes and Lawrence (1976), and Gieskes et al. (1982).

Carbonate analyses (Table 2) were performed on whole sediment samples. These samples were dried at 105–110°C, powdered, and then 2 g were dissolved in acetic acid-sodium acetate buffer at pH ~5.5. Calcium analyses were carried out by titration (Gieskes, 1974), and magnesium and strontium were determined by means of atomic absorption techniques. Sea salt corrections were made by a separate chloride determination via a polarographic technique.

RESULTS AND DISCUSSION

Interstitial Waters

Hole 558 (Fig. 2).

Sediment accumulation rates in the upper 250–300 m averaged ~17 m/Ma. At these relatively low accumulation rates sulfate depletions, as a result of sulfate reduction processes, are often minor. This explains the small downcore decrease in sulfate (Table 1).

Of interest are the calcium and magnesium concentration gradients. The gradients are very small but discernible. In Figure 2 the calcium and magnesium data indicate a generally good linear correlation with $\Delta Ca/\Delta Mg = -1.25$. Just above basement, in a dolomitic chalk layer, an apparent reversal occurs in the gradients of calcium and magnesium. In our opinion, this represents a sample contaminated with seawater—additional reversals are observed for sulfate, strontium, and lithium. The latter two profiles, however, are not very reliable indicators of contamination, because maxima in the concentrations of these constituents are quite common at many other DSDP sites. Nonetheless, we are tempted to reject the bottom sample, and this would bring the albeit small increases in calcium and decreases in magnesium in accord with the general observation that in open-ocean sediments these gradients are caused by reactions in the basalts (McDuff, 1981; Gieskes and Lawrence, 1981; Gieskes, 1983).

Dissolved strontium shows a distinct maximum at ~325 m (i.e., at the top of the zone of chalk formation). This can be attributed to the process of calcium carbonate recrystallization (Baker et al., 1981; Elderfield et al., 1982). Dissolved lithium shows only very slight increases and deserves no further comment. Downhole changes in potassium are within the limits of error, and thus no significant sink for this element exists either in the basalts or in the sediments at Site 558. Dissolved sili-

---

[1] Bougault, H., Cande, S. C., et al., *Init. Repts. DSDP*, 82: Washington (U.S. Govt. Printing Office).

[2] Address: Scripps Institution of Oceanography, University of California at San Diego, La Jolla, California, 92093.

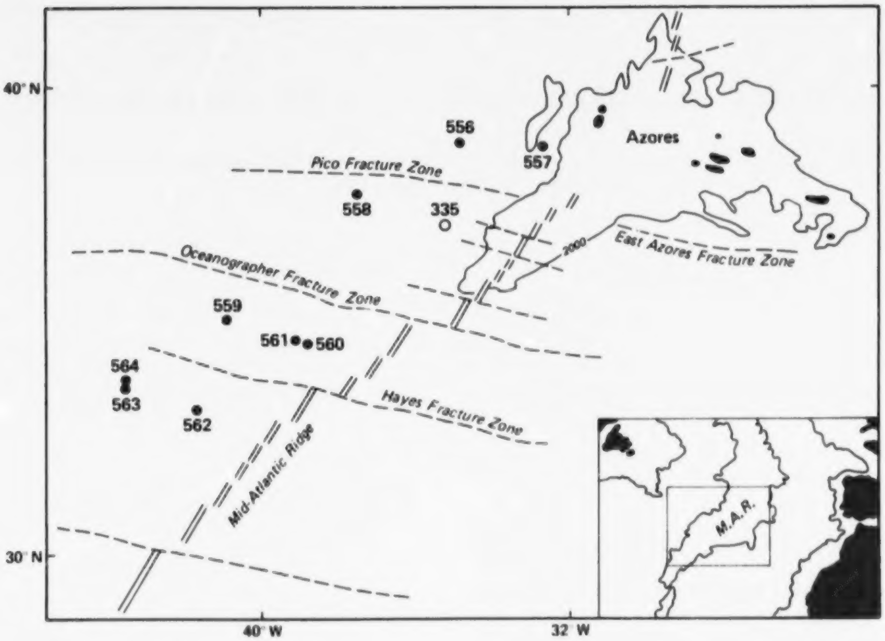

Figure 1. Map of study area, Leg 82.

Table 1. Interstitial water chemistry, Leg 82.

Hole	Core-Section (interval in cm)	Sub-bottom depth (m)	pH	Alkalinity (meq/dm^3)	Salinity (g/kg)	Ca (mM)	Mg (mM)	Cl (g/kg)	Sr (μM)	Li (μM)	K (mM)	SO_4 (mM)	NH_4 (μM)	Si (μM)
558	1-6, 144–150	168	7.36	2.99	37.6	11.0	50.7	19.48	323	41.7	11.5	25.8	0	187
	6-6, 140–150	215	7.43	3.50	36.4	12.1	50.0	19.41	356	42.0	11.0		0	603
	8-3, 110–120	230	7.42	4.79	35.3	12.6	50.1	19.58	374	37.4	10.8	26.9	16.0	951
	13-5, 144–150	280	7.31	3.92	36.8	13.4	50.2	19.62	400	36.9	10.4		0	790
	18-4, 110–120	325	7.34	4.03	35.3	14.1	48.3		411	42.2	10.6	26.6	0	247
	23-6, 140–150	377	7.39	3.27	35.3	15.2	47.8	19.04	305	47.1	10.2		0	219
	27-1, 140–150	407	7.13	3.00	36.2	12.1	53.3	19.31	104	31.3	9.8	28.1	0	62
558A	1-7, 12–19	10	7.43	3.47	35.1	10.7	52.2	19.55	120	31.4	11.5	27.1	0	419
	7-4, 144–150	56	7.44	3.19	36.3	10.7	51.4	19.62	256	41.8	11.8		0	219
	12-3, 143–150	82	7.42	3.20	36.1	11.0	51.1	19.65	282	36.6	10.5	26.4	15.7	157
563	1-2, 140–150	162	7.43	2.63	36.2	11.6	54.9	19.51	416	67.6	11.2	29.6	0	42
	6-5, 140–150	212	7.47	2.54	35.7	11.6	53.3	19.71	406	62.4	10.8		291.2	156
	11-4, 140–150	260	7.52	2.77	36.4	12.0	50.6	19.61	417	67.8	10.5	25.3	146.0	235
	16-6, 140–150	308	7.48	2.62	35.8	12.5	50.7	19.54	416	67.7	10.2		114.5	203
	21-6, 140–150	355	7.51	2.40	35.5	12.4	49.4	19.31	270	16.7	10.1	25.2	0	202

Table 2. Carbonate chemistry, Site 558.

Core-Section	$CaCO_3$ (%)	Mg/Ca (× 10^{-4})	Sr/Ca (× 10^{-4})
Hole 558			
1-6	93	20.4	16.3
6-6	89	8.4	19.5
8-3	94	12.2	17.2
13-5	89	19.5	16.2
18-4	89	32.5	15.0
23-6	87	33.7	15.3
27-1	53.5	89.4	14.2
Hole 558A			
2-7	89	9.4	19.2
7-4	88	28.5	18.3
12-3	93	28.5	17.5

ca indicates the presence of biogenic silica at the base of Unit I as well as in the upper sediment layers.

Hole 563 (Fig. 3)

This site is characterized by relatively low sedimentation rates. Unfortunately, the upper 150 m were not sampled. Again, dissolved sulfate decreases slightly downhole.

The calcium increase with depth and the magnesiu decrease with depth are barely significant. On the othe hand, dissolved strontium and lithium do show maxima. The former is related to the process of carbonate recrystallization—the ooze/chalk boundary is at the bas of Unit I. The increase in lithium may be related t this process or to the release by biogenic silica (Gieskes 1981), which appears enhanced in Unit II (cf., dissolve silica profile).

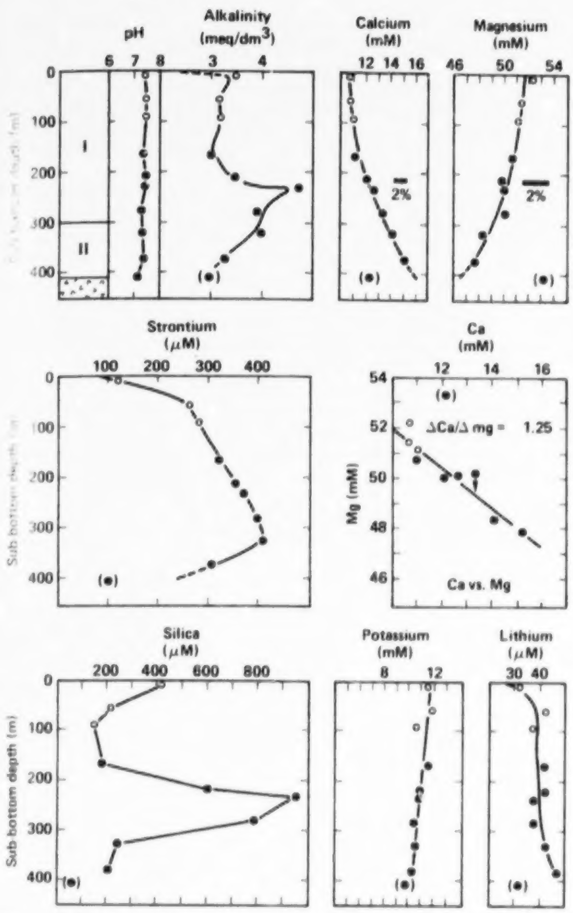

Figure 2. Interstitial water chemistry, Site 558. Lithology: I. Nannofossil ooze/chalk; siliceous nannofossil-foraminiferal ooze; foraminiferal-nannofossil ooze. II. Marly nannofossil chalk/limestone; dolomitic nannofossil chalk/limestone at base. Closed symbols, Hole 558; open symbols, Hole 558A.

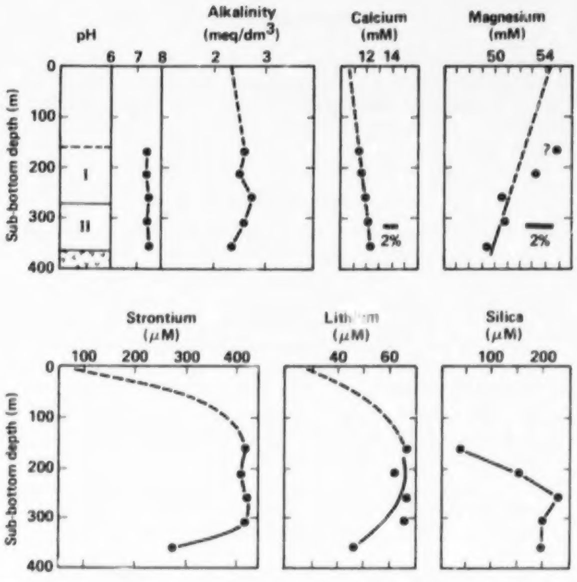

Figure 3. Interstitial water chemistry, Site 563. Lithology: I. Foraminiferal nannofossil ooze/chalk; nannofossil ooze. II. Chalks, dolomitic at base.

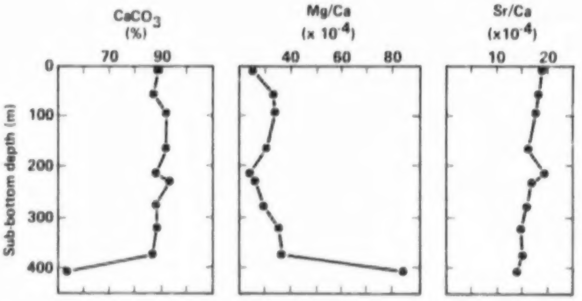

Figure 4. Carbonate chemistry, Hole 558A: CaCO$_3$ (%) and Mg/Ca and Sr/Ca (atomic ratios).

Carbonate Chemistry

Hole 558 (Fig. 4)

Carbonate contents in this site are relatively constant roughout at ~90%, with the exception of the basal diments.

Mg/Ca ratios are variable, but the lowermost sample able 2) shows a rather high ratio. Recent experience s indicated, however, that exchangeable Mg^{++} at low CO$_3$ contents or the dissolution of magnesium-rich ays may lead to erroneously high Mg/Ca ratios estiated by the present methodology. For these reasons g/Ca ratios reported here must be considered to be eliminary in nature.

Sr/Ca ratios are much less affected because interstial water concentrations and exchangeable Sr^{++} are ery low compared to the contents in the carbonates. he data in Figure 4 demonstrate a gradual decrease in r/Ca, which can be understood in terms of carbonate crystallization (Baker et al., 1982). The ratio decreases o about 14 × 10^{-4}. At the dissolved Sr^{++} maximum, where the rate of crystallization is presumably at a maximum, one calculates a theoretical Sr/Ca ratio of (13 ± 1) × 10^{-4} (i.e., close to the observed values). These data support the general contention that, at the level of the strontium maximum, carbonate recrystallization has been completed to large extent (Baker et al., 1982).

CONCLUSIONS

Interstitial waters sampled at Sites 558 and 563 indicate very small changes in calcium and magnesium with depth. The increase in calcium and decrease in magnesium are probably due to reactions taking place in the underlying basalts.

Carbonate recrystallization reactions are indicated by the occurrence of a strontium maximum near the ooze/chalk boundary. Increases in lithium may be associated with this process, but may also result from the release of biogenic silica.

ACKNOWLEDGMENTS

This research was supported by NSF grant OCE-80-23966 and OCE-82-18539. We thank the shipboard chemist, Mr. Don Marsee, for his diligent analyses in the laboratory of the *Glomar Challenger*. We thank Russ McDuff and Paul Baker for their reviews of this manuscript.

REFERENCES

Baker, P. A., Gieskes, J. M., and Elderfield, H., 1982. Diagenesis of carbonates in deep sea sediments: evidence from Sr/Ca ratios and interstitial Sr^{2+} data. *J. Sediment. Petrol.*, 52:71–82.

Elderfield, H., Gieskes, J. M., Baker, P. A., Oldfield, R. K., Hawkesworth, C. J., and Miller, R., 1982. $^{87}Sr/^{86}Sr$ and $^{18}O/^{16}O$ ratios, interstitial water chemistry and diagenesis in deep-sea carbonate sediments of the Ontong-Java Plateau. *Geochim. Cosmochim. Acta*, 46:2259–2268.

Gieskes, J. M., 1974. Interstitial water studies, Leg 25. *In* Simpson, E. S. W., Schlich, R., et al., *Init. Repts. DSDP*, 25: Washington (U.S. Govt. Printing Office), 361–394.

________, 1981. Deep sea drilling interstitial water studies: implications for chemical alteration of the oceanic crust, Layers I and II. *Spec. Publ., Soc. Econ. Paleontol. Mineral.*, 32:149–167.

________, 1983. The chemistry of interstitial waters of deep sea sediments: interpretation of deep sea drilling data. *In* Riley, J. P., and Chester, R. (Eds.), *Chemical Oceanography*, 8:221–269.

Gieskes, J. M., Elderfield, H., Lawrence, J. R., Johnson, J., Meyers, B., and Campbell, A., 1982. Geochemistry of interstitial waters and sediments, Leg 64, Gulf of California. *In* Curray, J. R., Moore, D. G., et al., *Init. Repts. DSDP*, 64, Pt. 2: Washington (U.S. Govt. Printing Office), 675–694.

Gieskes, J. M., and Lawrence, J. R., 1976. Interstitial water studies, Leg 35. *In* Hollister, C. D., Craddock, C., et al., *Init. Repts. DSDP*, 35: Washington (U.S. Govt. Printing Office), 407–424

________, 1981. Alteration of volcanic matter in deep sea sediments: evidence from the chemical composition of interstitial waters from deep sea drilling cores. *Geochim. Cosmochim. Acta*, 45:1687–1703.

McDuff, R. E., 1981. Major cation gradients in DSDP interstitial waters: the role of diffusive exchange between seawater and upper oceanic crust. *Geochim. Cosmochim. Acta*, 45:1705–1713.

Matter, A., Douglas, R. G., and Perch-Nielsen, K., 1975. Fossil preservation, geochemistry, and diagenesis, of pelagic carbonates from Shatsky Rise, northwest Pacific. *In* Larson, R. L., Moberly, R., et al., *Init. Repts. DSDP*, 32: Washington (U.S. Govt. Printing Office), 891–921.

Date of Initial Receipt: 26 July 1983
Date of Acceptance: 15 December 1983

32. CROSS-LAMINATED AND GRADED INTERPILLOW LIMESTONES, SITE 562[1]

Leslie A. Reynolds and Brad K. Linsley, Department of Geology, University of South Carolina[2]

ABSTRACT

Interpillow limestones were recovered from numerous cores of Leg 82. Limestones from Core 562-1, south of the Hayes Fracture Zone, display small-scale cross laminations composed of planktonic foraminiferal tests alternating with micrite. In nonlaminated portions of the limestones, graded bedding is evident. Foraminiferal species identified from thin sections date the limestones of Core 562-1 as early middle Miocene, approximately 16 Ma. This age corresponds with that determined for the lowermost sediments recovered at Site 562, which lie within 9 m of the interpillow limestones. The presence of undisturbed structures in the upper limestones may be the result of sediment void-infilling between pillow basalts, as opposed to a post-depositional intrusion of basalts into the carbonate sediments. Thus, the basalts have a minimum age of 16 Ma.

INTRODUCTION

The interaction of pelagic limestones and igneous rocks has been discussed in detail by Garrison (1974) who suggests that interpillow limestones were in fact recrystallized carbonate oozes and not inorganic precipitates. McKenzie and Kelts (1980) reported on the occurrence of interpillow limestones from Site 417D, Leg 51, and observed the progressive recrystallization of pelagic oozes. They concluded that basalt flows plunging into ponded carbonate oozes were responsible for the formation of these interpillow limestones. Limestones with high degrees of alteration were used in both studies.

The interpillow limestones recovered from Site 562 are distinct in that pelagic ooze preservation ranges from well-preserved, graded cross laminations to total recrystallization. The purpose of this study is to date the basalt flow biostratigraphically and discuss possible origins for interpillow limestone formation at Site 562.

OCCURRENCE OF INTERPILLOW LIMESTONES AT SITE 562

Cores 562-1 to 562-9 contain several scattered interpillow limestones, the largest of which is 4.0 cm in length. The limestones are found both welded to pillows of plagioclase phyric basalts and as individual clasts. Cross-laminated, foraminifer-rich limestones occur only in Core 1, the upper part of which lies within 9 m of the sediment/basalt interface. Structureless limestones containing few foraminifers occur in Core 2 and are typical of those observed in deeper cores. In this study we focus on the Core 1 and Core 2 limestones that are representative of the entire interpillow limestone suite recovered at Site 562. The locations of these limestones and a description of their structural preservation are listed in Table 1.

Table 1. Interpillow limestone locations, Hole 562.

Core-Section, Interval in cm (Piece number)	Sub-bottom depth (m)	Description
1-1, 31-32 (2A)	241.32	Homogeneous foraminifer-pellet grainstones
1-2, 17-19 (2A)	242.68	
1-2, 96-99 (5A)	243.47	
1-2, 130-131 (7)	243.81	
1-3, 108-110 (5A)	245.09	Cross-laminated foraminifer-pellet grainstones
1-3, 112-115 (5B)	245.14	
1-4, 1-4 (1)	245.53	
2-2, 20-22 (4)	251.71	Structureless limestones found in contact with basalt pillows
2-2, 43-44 (6)	251.93	
2-2, 78-80 (8D)	252.29	
2-2, 103-105 (11)	252.54	
2-3, 84-86 (4F)	253.85	

DESCRIPTION

The interpillow limestones found in Cores 1 and 2 are classified into three general groups based on their petrographic textures. The presence or absence of sedimentary structures and evidence of contact with cooling volcanogenic basalts are the main criteria for categorization. All samples examined have been classified as grainstones.

Cross-laminated, foraminifer-rich grainstones are found exclusively in Core 1 (Plate 1, Fig. 1). Three samples display alternating micrite and foraminifer-pellet laminations, range in color from white to buff, and have been replaced by sparry calcite cements. The cross laminations generally pinch out and may be truncated.

Foraminifer-pellet grainstones lacking cross laminations are also found in Core 1. Their bulk composition and color are similar in character to cross-laminated samples, although biogenic debris is more evenly dispersed. Calcite spar cements are dominant, and replacement of biogenic calcium carbonate and pore space is nearly complete.

The remaining limestones are structureless and in contact with basalt pillows. These grainstones are a darker yellow-buff, distinguishing them from the first two groups. Banded basalt and glass fragments are abundant.

---

[1] Bougault, H., Cande, S. C., et al., *Init. Repts. DSDP*, 82: Washington (U.S. Govt. Printing Office).

[2] Address: Department of Geology, University of South Carolina, Columbia, South Carolina 29208.

PLANKTONIC FORAMINIFERAL AGE DETERMINATIONS

We place the Core 1 interpillow limestones within the planktonic foraminiferal zone, lower N9 (Blow, 1969), based on the presence of *Globigerinoides sicanus* (Plate 1, Fig. 2), *Orbulina bilobata* (Plate 1, Fig. 3), and *Orbulina suturalis* (Plate 1, Fig. 4), suggesting a maximum early middle Miocene age, approximately 16 Ma, for the sediments (Ryan et al., 1974). *Globigerinoides trilobus, Globigerinoides immaturus, Globoquadrina venezuelana*, and *Globorotalia scitula* were also identified, supporting a 16 Ma age.

Core 2 limestones contain fewer and smaller foraminifers than Core 1 limestones. The presence of *Globigerinoides sicanus* and the apparent absence of *O. bilobata* and *O. suturalis* may indicate a late early Miocene age for these older sediments.

DISCUSSION

According to Garrison (1974), interpillow limestones that exhibit cross laminations are the result of sediment infiltration into pre-existing pillow basalt voids. Pelagic sediments accumulate over basalt flows and occasionally spill into the voids as small graded turbidites. In contrast, basalt flows that intrude pre-existing sediments destroy sedimentary structures. The presence of cross-laminated graded limestones in Core 562-1 indicates the infiltration mode by redeposition (Garrison, 1974). Garrison also noted that fragmental volcanic debris is a common product of post-pillow or syn-pillow formation and submarine erosion. Both the absence of volcanic debris in Core 562-1, and the correlative ages of sediments above and below the sediment/basalt interface suggest that little submarine erosion occurred at this site immediately after the last volcanic episode. The presence of randomly oriented fecal pellets in Core 1 also indicates a low-energy submarine environment.

Basalt flows below Core 1 may have intruded pre-existing sediments of the late early Miocene. The spar cements in Core 2 limestones are partly neomorphic, the result of pore-water cementation and heat-induced recrystallization (McKenzie and Kelts, 1980). In addition, a distinct sediment zone adjacent to pillow margins, approximately 1 cm thick, appears to be recrystallized (Plate 1, Fig. 5). The overall textural appearance of Core 2 limestones differs from the cross-laminated limestones of Core 1 (Plate 1, Fig. 6).

Core 1 and 2 limestones lack evidence of compaction, indicating that lithification and subsequent pore infilling was accomplished by early marine carbonate cements. Lower middle Miocene foraminiferal sediments are unlithified immediately above the uppermost basalts.

In conclusion, the analysis of Site 562 interpillow limestones has led to a minimum age placement of 16 Ma of the last volcanic episode in this region. The presence of several cross-laminated and graded limestones containing key index fossil foraminifers and the absence of volcanic debris derived from submarine erosion support this age placement.

ACKNOWLEDGMENTS

We wish to thank Drs. Dorothy Echols, Robert Thunell, and Michael Arthur for their assistance and helpful comments. We are also most grateful to Ric Pantonial for photographic work and to Eric Tappa for his assistance and helpful comments.

REFERENCES

Blow, W. H., 1969. Late middle Eocene to Recent planktonic foraminiferal biostratigraphy. *In* Brönniman, P., and Renz, H. H. (Eds.), *Proc. First Int. Conf. Plankt. Microfossils:* Leiden (E. J. Brill), 1: 199–421.

Garrison, R. E., 1974. Radiolarian cherts, pelagic limestones and igneous rocks in eugeosynclinal assemblages. *Spec. Publ. Int. Assoc. Sedimentol.*, 1:367–399.

McKenzie, J. A., and Kelts, K. R., 1980. A study of interpillow limestones from the *M*-Zero anomaly, Deep Sea Drilling Project, Leg 51, Hole 417D. *In* Donnelly, T., Francheteau, J., Bryan, W., Robinson, P., Flower, M., Salisbury, M., et al., *Init. Repts. DSDP*, 51, 52, 53, Pt. 2: Washington (U.S. Govt. Printing Office), 753–766.

Ryan, W. B. F., Cita, M. B., Rawson, M. D., Burkle, L. H., and Saito, T., 1974. A paleomagnetic assignment of Neogene stage boundaries and the development of isochronous datum planes between the Mediterranean, the Pacific, and Indian oceans in order to investigate the response of the world ocean to the Mediterranean "Salinity Crisis." *Riv. Ital. Paleontol.*, 80(4):631–688.

Date of Initial Receipt: 16 May 1983
Date of Acceptance: 1 May 1984

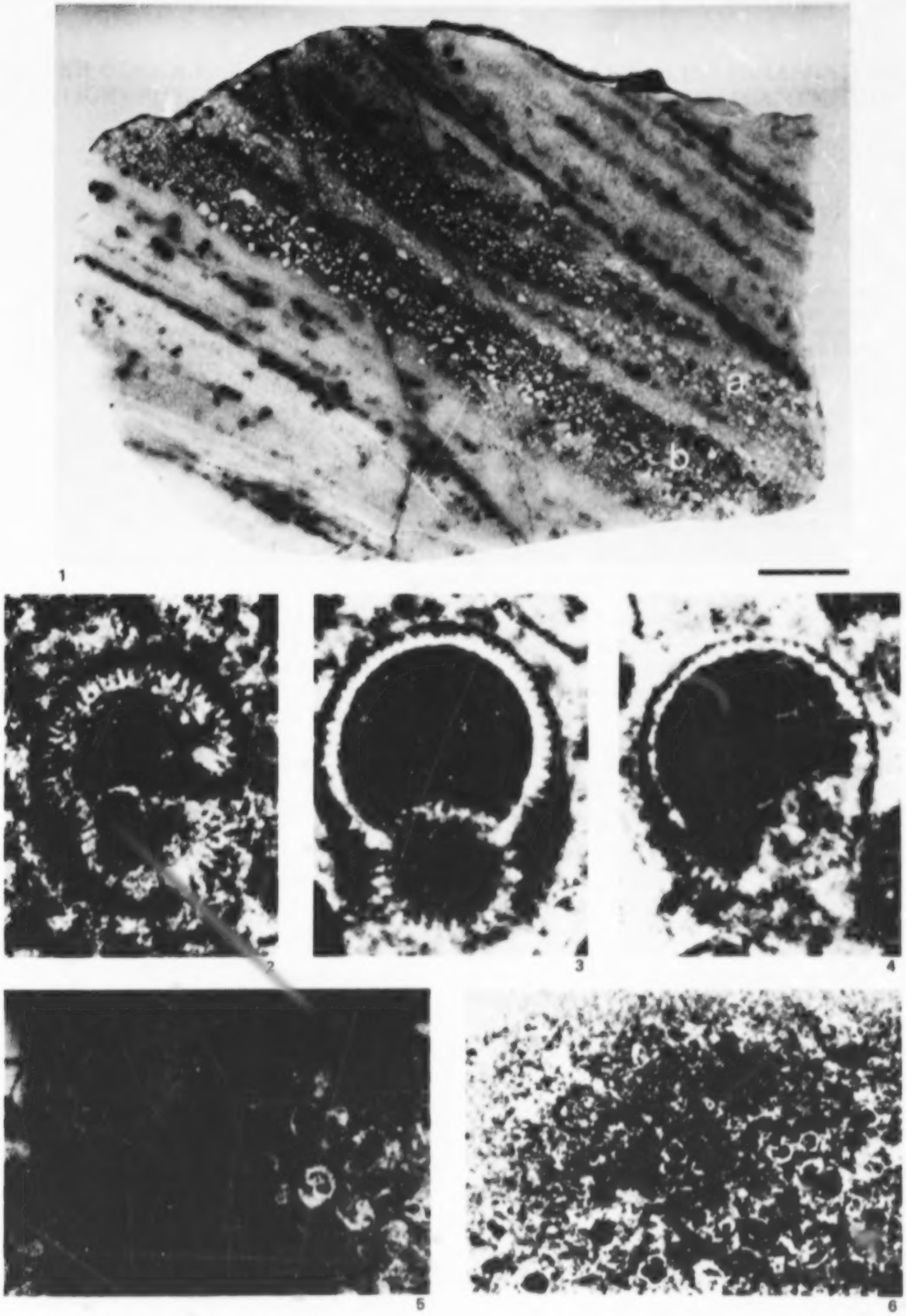

Plate 1. **1, 3, 4, 6.** Sample 562-1-3, 108–110 cm (piece 5A), (1) Cross-laminated (A) and graded (B) interpillow limestone; note truncation of cross-laminations; scale bar = 0.5 cm, (3) *Orbulina bilobata* thin section view, × 110, (4) *Orbulina suturalis* thin-section view, × 110, (6) Cross-lamination boundary between micrite and foraminifer-rich laminations. **2.** Sample 562-1-3, 112–115 cm (piece 5B), *Globigerinoides sicanus*, thin-section view, × 110. **5.** Contact of pillow basalt glass with calcareous sediments; note neomorphic region (McKenzie and Kelts, 1980), × 80.

33. LOWER OLIGOCENE THROUGH PLEISTOCENE PLANKTONIC FORAMINIFERAL BIOSTRATIGRAPHY, NORTH ATLANTIC SITES 558 AND 563 (MID-ATLANTIC RIDGE)[1]

Dorothy J. Echols, Department of Earth and Planetary Sciences, Washington University[2]

ABSTRACT

A preliminary biostratigraphic zonation of Site 558 (Holes 558 and 558A), lower Oligocene through Pleistocene, and Site 563, lower Oligocene through upper-middle Miocene, drilled on the west flank of the Mid-Atlantic Ridge is discussed. At Site 558 two holes were drilled by a combination of piston and rotary coring through a stratigraphic sequence from Oligocene through Pleistocene. Except for a gap of approximately 26 m in the upper-middle Miocene where Holes 558 and 558A do not overlap, the Cenozoic section recovered is the most complete and best preserved stratigraphic succession from this part of the Atlantic.

At Site 563 one hole was drilled. Sediments were washed down to 156.5 m and then rotary cored to basement . The lower Oligocene through upper-middle Miocene sediments recovered are similar to those drilled at Site 558 both in lithology and fauna.

The biostratigraphic succession at both sites is relatively undisturbed; no major gaps or reworking were noted and sedimentation accumulation rates are similar.

Notably *Bolboforma*, a tiny spherical calcareous *incertae sedis* (algae?), was recovered at both sites at the same stratigraphic horizon in the Miocene. This form may have potential as a regional marker in deep-sea sediments.

INTRODUCTION

Sites 556 through 564 (ten holes) were drilled during Leg 82 in an area on the west flank of the Mid-Atlantic Ridge and southwest of the Azores Platform (Fig. 1). The primary objectives of drilling in this area were to sample ocean crust in order to study mantle heterogeneity. The paleontologic objectives were to confirm basement ages and to recover a complete section of Cenozoic pelagic sediments from this part of the Atlantic and, if possible, establish a biostratigraphic zonation and reference section.

The biostratigraphic objectives were achieved; a nearly complete section of the lower Oligocene through Pleistocene was recovered through a combination of hydraulic piston coring and rotary coring in two holes at Site 558 (Fig. 2).

Before this cruise, study of the sedimentation, stratigraphy, paleoenvironment, and geologic history of the area between 20–40°N in the mid-Atlantic was limited and based on spot cores and partial sections. On Leg 2 (Blow, 1970), spot cores of the Cretaceous to Pleistocene were taken at Sites 10 and 11. On Leg 37 (Miles, 1977), Sites 334, upper Miocene calcareous pelagic ooze and chalk were cored and, at Site 335, spot cores were taken through 450 m of Pleistocene through middle Miocene sediments. On Leg 49 (Poore, 1978), at Sites 411, 412, and 413, only Quaternary sediments were recovered (no coring was done at Site 414).

In order to fill the gap in sampling and to provide data for study of the Cenozoic history and paleoenvironment of the area, it was decided that continuous coring should be done at as many sites as possible during Leg 82.

Of the nine sites drilled, Sites 558 and 563, located close to Anomaly 13, were chosen for continuous coring. Sediments recovered at these sites are lower Oligocene to Pleistocene and indicate that during this interval the sites were above the calcite compensation depth (CCD).

Site 558 is located at 37°46.2′N latitude and 37° 20.61′W longitude near the Pico Fracture Zone between Anomalies 13 and 15 on the flank of a basement high in water depth of 3754 m. Holes 558 and 558A were drilled at this site. Hole 558 was washed down to a depth of 158 m and sediments were continuously cored to a total penetration above basement of 408 m. After the first hole was successfully logged, Hole 558A was piston cored to a depth of 132 m, when mechanical problems in the inner core barrel forced termination before biostratigraphic overlap was accomplished. This gap of 26.5 m represents approximately 2 to 4 Ma of sedimentation (See Fig. 2 which shows the cored intervals, the foraminiferal planktonic zonation of the two holes, and the biostratigraphic gap at Site 558. It also shows for comparison the cored interval and zonation of Hole 563).

At Site 563 (latitude 33°38.53′N; longitude 43° 46.04′W; water depth, 3786 m), one hole was drilled on Anomaly 13 on the west flank of the Mid-Atlantic Ridge about 60 miles south of the Hayes Fracture Zone (Fig. 1). Sediments were washed down to 156.5 m and then 22 rotary sediment cores were taken to basement at 364 m. Sediment for the study of foraminifers was not obtained from Core 563-23, which reached basement.

The hydraulic piston coring program scheduled for this site to retrieve the younger section from 0–156.5 m had to be cancelled when the bit and core barrel were lost in the hole during the cutting of the third basalt core.

---

[1] Bougault, H., Cande, S. C., et al., *Init. Repts. DSDP*, 82: Washington (U.S. Govt. Printing Office)

[2] Present address: Curtis and Echols, Geological Consultants, 800 Anderson, Houston, Texas 77401.

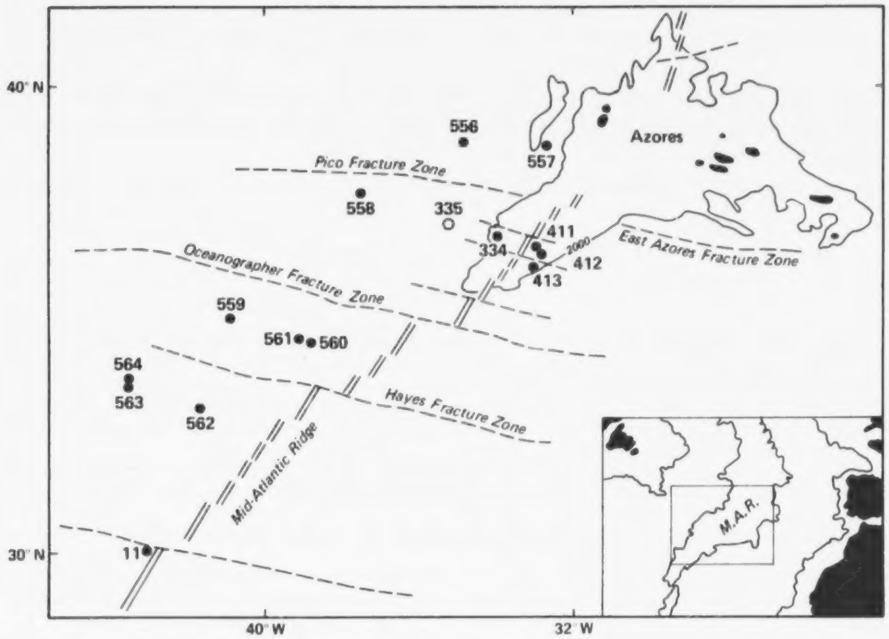

Figure 1. Location of Leg 82 sites and previously drilled Sites 11, 334, 335, 411, 412, and 413.

The sediments recovered at this site are lower Oligocene to late Miocene. The entire section comprises calcareous pelagic ooze. Two sediment units similar to Site 558 can be recognized and their boundary occurs roughly at the same age as Site 558 (Fig. 2).

The purpose of this chapter is to present a preliminary biostratigraphic zonation of the cores recovered at this two sites. At all other sites drilled on Leg 82, holes were washed down and only an occasional rotary core was taken. Brief descriptions of these holes are given in the site reports under Sedimentology and Biostratigraphy (this volume).

Figure 7 in the Explanatory Notes chapter (this volume) shows the biostratigraphic zonation used for all site chapters. The nannofossil and foraminiferal zonation are placed within a numerical time scale correlated with magnetostratigraphy and European stages.

BIOSTRATIGRAPHY

The planktonic foraminiferal zonation incorporates schemes developed by Bolli (1957); Blow (1969); Berggren (1972, 1978); Berggren and Amdurer (1973); Berggren and Van Couvering (1974, 1978); Hardenbol and Berggren (1978); Poore (1978); Postuma (1971); Salvatorini and Cita (1979); Stainforth et al. (1975); and Stainforth and Lamb (1981). Appendix A lists the cores from Holes 558A and 558 and Appendix B lists the cores from Holes 563 allotted for foraminiferal studies. Sample intervals in centimeters, depth below sea floor in meters, meters recovered, age, and planktonic zones are tabulated.

Figure 3 shows a plot of the distribution of selected planktonic foraminifers in Holes 558 and 558A. For comparison, Table 1 shows significant events in Holes 558 and 563.

The biozones recorded from Hole 558, Core 558-1 through 558-27-2 (158–406.95 m); Hole 558A, Core 558A-1 through 558A-16-6 (0–130.13 m); and Hole 563, Core 563-1 through 563-22-4 (156.50–360.04 m) are briefly discussed here from bottom to top.

Oligocene (basement)

Basalt was reached in 558-27-2 (408 m) and 563-23-3 (364 m). Washed residues of the last sediment retrieved in 558-27-2 (approximately 406 m) contains dolomite rhombs, rare fragments of foraminiferal shells, manganese nodules, and a few fish teeth. A small piece of limestone at the top of Core 563-23 was the last sediment retrieved from that hole.

At these sites, immediately after the formation of new ocean crust (early Oligocene), open ocean pelagic sedimentation began; it continues at present. The Oligocene zonal scheme (Fig. 4) is modified from Stainforth and Lamb (1981).

Pseudohastigerina micra Zone (P18)

Lower Oligocene sediments recovered at Cores 558-26 and 558-25, and Sections 563-22-5 through 563-22-7 contain abundant *P. micra*, a fair number of *Chiloguembelina*, and typical lower Oligocene globigerinids: *Globigerina venezuelana, G. tripartita, G. ampliapertura, G. angiporoides,* and *G. praebulloides*. The foraminifers show considerable fragmentation and/or dissolution because of proximity to underlying basalt. Dolomite crystals are abundant and the rhombs can be seen growing in and on the tests (Plate 1, Figs. 1–3).

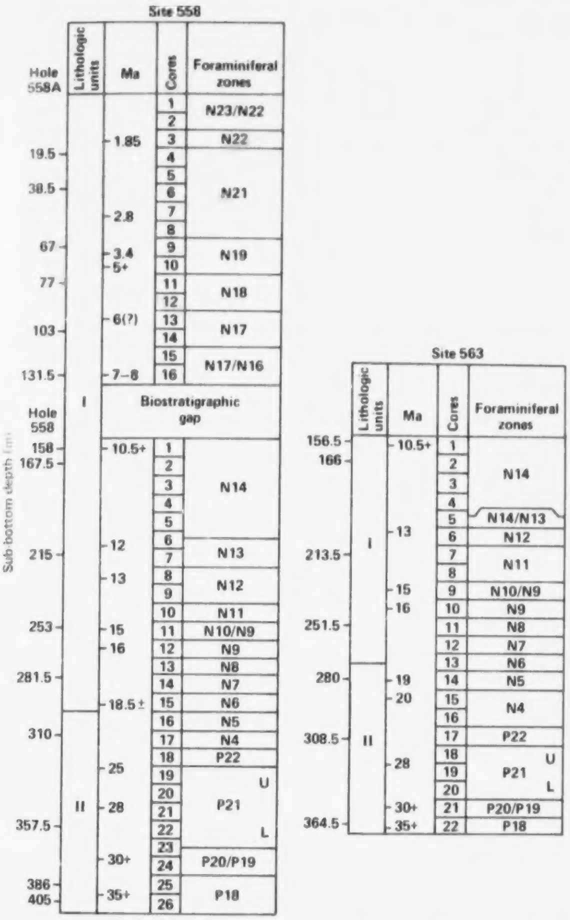

Figure 2. Planktonic foraminiferal zonation at Sites 558 (Holes 558 and 558A) and 563 (Hole 563) showing biostratigraphic gap and the two lithologic units recognized at the sites.

Globigerina ampliapertura Zone (P20/P19)

Cores 558-24 and 563-21 are assigned to the *G. ampliapertura* zone. This zone is defined as the interval from the first evolutionary appearance of *G. selli* to the level of the first occurrence of *G. angulisuturalis* (Blow, 1969; Postuma, 1971; Blow, 1979, Stainforth and Lamb, 1981). The extinction of *G. ampliapertura* occurs shortly after this horizon (Blow, 1969; Stainforth et al., 1975; Stainforth and Lamb, 1981).

The samples studied here are characterized by abundant tiny globigerinids, *Chiloguembelina,* and a continuation of the fauna found in the older sediments, but *Pseudohastigerina micra* becomes extinct. The foraminifers still reflect some destruction because of dissolution and dolomite recrystallization.

Globorotalia opima opima Zone (P21)

Cores 558-23, 558-22, 563-20, and 563-19 are assigned to the lower part of the *G. opima opima* zone. This entire zone has been defined by the first appearance of *Globigerina angulisuturalis* (Blow, 1969; Stainforth and Lamb, 1981; Beckmann et al., 1981) and by the extinction of the nominate subspecies at the upper boundary (Blow, 1969). A secondary datum may be the extinction of *Chiloguembelina cubensis* that occurs in the middle part of the zone and may mark the lower-upper Oligocene boundary. It has been suggested that because of the abrupt extinction of this species within the *G. opima opima* zone, this interval could be subdivided (Berggren and Amdurer, 1973) into a lower P21a unit and an upper P21b unit, designating the lower part the *C. cubensis* zone. In the present study the datum is readily recognized. The last occurrence of *C. cubensis* is in Sections 558-22-1 and 563-19-1, which marks the subzone boundary and the boundary between the lower and upper Oligocene.

Samples 558-21 through 558-19 and 563-18 are assigned to the upper part (P21b) of the *G. opima opima* zone. These samples contain, in addition to abundant tiny globigerinitas, very large forms such as *Catapsydrax, Globigerina tripartita, G. venezuelana,* and *G. gortanii.*

Globigerina ciperoensis Zone (P22)

Cores 558-18 and 563-17 are assigned to the *G. ciperoensis* zone. The base of this upper Oligocene zone is defined as the level of extinction of *Globorotalia opima opima* (Blow, 1969; Stainforth et al., 1975). The uppermost boundary and the corresponding base of the next younger (N4) zone is in some dispute. This limit has been defined variously on the first evolutionary appearance of *Globigerinoides primordius* (= *Globigerinoides* datum) (Blow, 1969), the level at which various species of *Globigerinoides* start to diversify (Stainforth et al., 1975; Beckmann et al., 1981), and the first appearance of *Globorotalia kugleri* (Bolli, 1957, 1966; Postuma, 1971; Stainforth and Lamb, 1981). Much of the confusion in determining the uppermost limits of this zone has been the result of attempts to use the *Globigerinoides* datum to define the Oligocene/Miocene (Paleogene/Neogene) boundary, a datum shown to be unreliable in many instances (Lamb and Stainforth, 1976; Stainforth and Lamb, 1981; Becker 1982, Srinivasen and Kennett, 1983). The first appearance of various forms of the genus *Globigerinoides* vary considerably in the geologic record depending upon environmental conditions (Lamb and Stainforth, 1976; Stainforth and Lamb, 1981). In some instances species of *G. trilobus* and *G. immaturus* are known to occur near the base of the *Globigerina ciperoensis* zone on the Atlantic continental slope, Florida Shelf, and in the Gulf of Mexico (Lamb and Stainforth, 1976; Stainforth and Lamb, 1981; Becker, 1982). Other evidence from around the world (Jenkins, 1960; Caralp et al., 1965; Srinivasen and Kennett, 1983) indicate that this depressed occurrence is not a local phenomenon. It therefore seems appropriate to revert to Bolli (1957; 1966) and his original recommendation and define the top of the *Globigerina ciperoensis* zone by the first appearance of *Globorotalia kugleri* (see Fig. 4). Species found within this zone include *Globigerina ciperoensis, G. tripartita, G. venezuelana, G. praebulloides, G. angulisuturalis,* and *Globorotalia siakensis.*

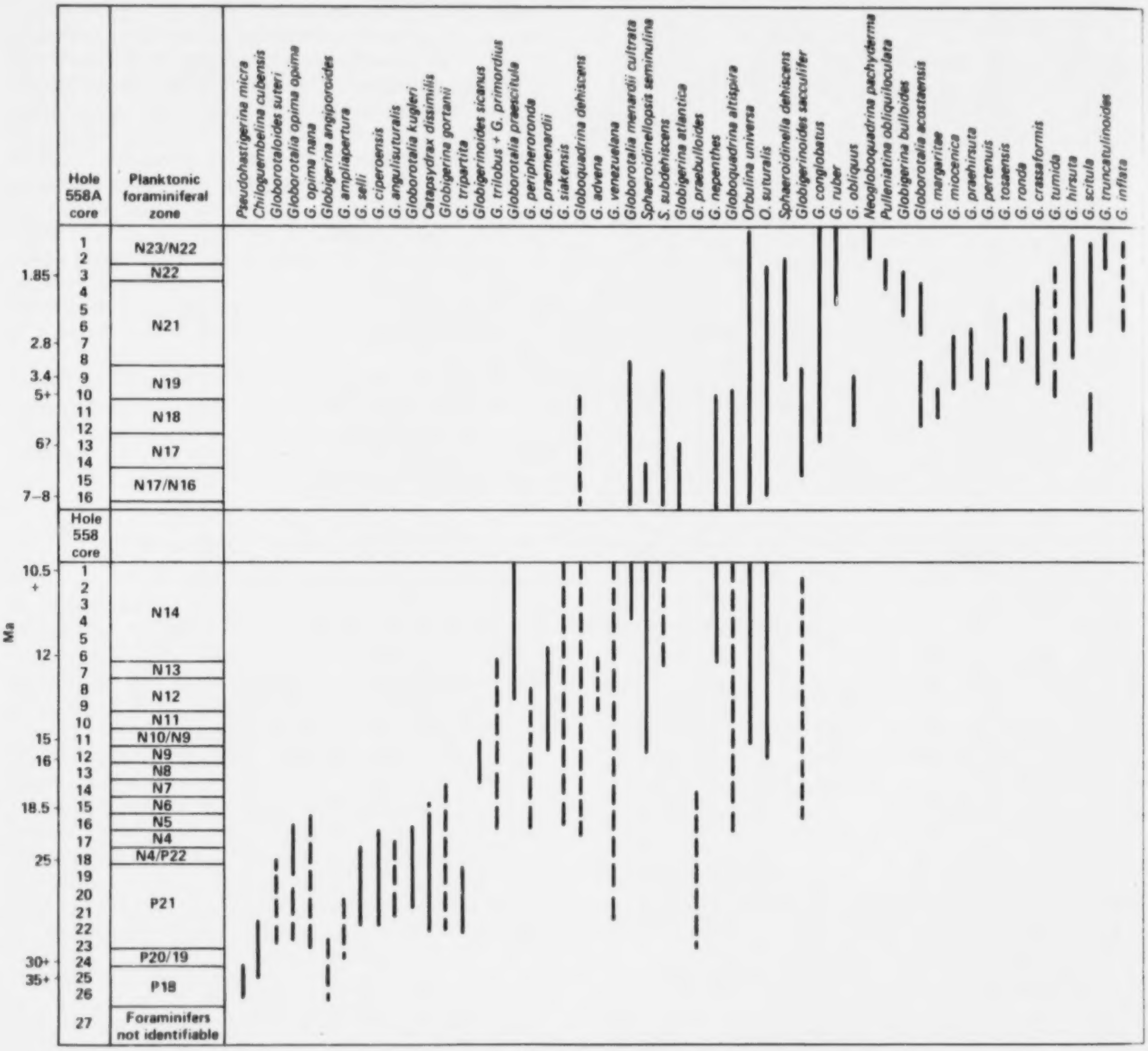

Figure 3. Range of selected Oligocene through Pleistocene planktonic foraminifers; Site 558, Holes 558 and 558A.

Oligocene/Miocene

Globorotalia kugleri Zone (N4)

In the framework we are using, N4 (the *G. kugleri* zone) straddles the Oligocene/Miocene boundary (see Fig. 4). Cores 558-17, 563-16, and 563-15 are assigned to this interval. The zone is described as the range of *G. kugleri* from its first appearance at the base (Stainforth and Lamb, 1981) to its disappearance in the lowermost Miocene (Bolli, 1957; 1966; Stainforth et al., 1975; Stainforth and Lamb, 1981).

Srinivasen and Kennett (1981; 1983) subdivided zone N4 into lower N4A and upper N4B units using the first evolutionary appearance of *Globoquadrina dehiscens* (a dissolution-resistant form of wide latitudinal range) as the base of N4B, which they also consider to coincid with the Oligocene/Miocene boundary. Their definitio of the two subzones of N4 are as follows:

1. Zone N4A *Globigerinoides primordius/Globoro talia kugleri*, concurrent range zone of Blow (1969). A uppermost Oligocene assignment is given to the interv from the first evolutionary appearance of *Globigerino des primordius* to the first evolutionary appearance *Globoquadrina dehiscens*.
2. Zone N4B *Globoquadrina dehiscens/Globorot lia kugleri*, concurrent range zone proposed. A low Miocene assignment is given to the interval from th first evolutionary appearance of *Globoquadrina dehi cens* to the last appearance of *Globorotalia kugleri*.

The base of N4B, therefore, marks the Oligocene Miocene boundary.

Table 1. First appearance datum (FAD) and last appearance datum (LAD) of a few significant species, Holes 558 and 563.

Hole 558 Core	Boundaries FAD/LAD	Sub-bottom depth (m)	Ma	Hole 563 Core	Boundaries FAD/LAD	Sub-bottom depth (m)	Ma
1				1			
2				2			
3				3			
4				4			
5		196.00		5	FAD *G. nepenthes*	194.50	
6	FAD *Globigerina nepenthes*	205.50		6	LAD *G. peripheroronda*	204.00	
7	FAD *Sphaeroidinellopsis subdehiscens*		12–13	7		213.50	
8	LAD *Globorotalia peripheroronda*			8			
9		234.00		9			
10		243.50		10	*Orbulina*	242.00	15–16
11				11			
12	*Orbulina*	262.50	15–16	12	FAD *G. sicanus*		
13				13	LAD *C. dissimilis*	270.50	18 +
14	FAD *Globigerinoides sicanus*			14			
15	LAD *Catapsydrax dissimilis*	291.00	18 +	15			22–25
16			22–25	16	FAD *G. dehiscens*		
17	FAD *Globoquadrina dehiscens*			17			
18				18			
19				19	LAD *C. cubensis*	327.50	28–30
20				20			
21				21	LAD *P. micra*	346.50	30 +
22	LAC *Chiloguembelina cubensis*	357.50	28–30	22			
23							
24	LAD *Pseudohastigerina micra*		30 +				
25							
26			35 +				

The first appearance of *Globoquadrina dehiscens* as an important planktonic event and a valuable datum for placement of the Oligocene/Miocene boundary was previously recognized by Jenkins (1965; 1971) who used it in New Zealand sequences as the base of the Miocene and by Berggren and Amdurer (1973) who used it in North Atlantic sequences as approximating the Oligocene/Miocene boundary. In lower Miocene sections in the equatorial Pacific, Keller (1980; 1981a, b) recognized the evolutionary first appearance of *G. dehiscens* as an isochronous event occurring at about 22.2 Ma, which is later than the first appearance of *Globigerinoides*.

In the present study, *Globoquadrina dehiscens* makes its first appearance in Samples 558-17 and 563-16. Within the *Globorotalia kugleri* N4 Zone, diminutive globigerinids become a predominant element of the fauna, and *Globoquadrina altispira* and *Globigerinoides primordius* makes their first appearances.

Miocene

Globoquadrina dehiscens Zone (N5)

The base of this zone is placed at the level of extinction of *Globorotalia kugleri* and the top is defined by the first appearance of *Globigerinatella insueta* (Blow, 1969). Cores 558-16 and 563-14 are assigned to this interval. These samples are characterized by abundant planktonic species and large and diverse benthic species; the fauna comprises abundant large and small globigerinids, abundant *Globigerinoides, Globoquadrina,* and *Catapsydrax.*

Globigerinatella insueta/Catapsydrax dissimilis Zone (N6)

The base of this zone is placed at the first appearance of *G. insueta* and the top defined by the extinction level of *C. dissimilis*. Cores 558-15 and 563-13 may belong in this interval.

Globigerinatella insueta–Globigerinoides quadrilobatus trilobus Zone (N7)

The base of the zone is placed at the horizon immediately above the extinction of *Catapsydrax dissimilis* and the upper boundary at the first appearance of *Globigerinoides sicanus*. Although tentative at this time, Cores 558-14 and 563-12 are assigned to this interval. The fauna is characterized by very abundant *Globoquadrina dehiscens,* very large globigerinids, and absence of *C. dissimilis*.

Globigerinoides sicanus–Globigerinatella insueta Zone (N8)

The base of N8 is marked by the first evolutionary appearance of *Globigerinoides sicanus* and the upper boundary by the first appearance of *Orbulina suturalis* (*Orbulina* datum). Cores 558-13 and 563-11 are assigned to this zone. The planktonic fauna is common but somewhat fragmented, preservation is moderate. Conspicu-

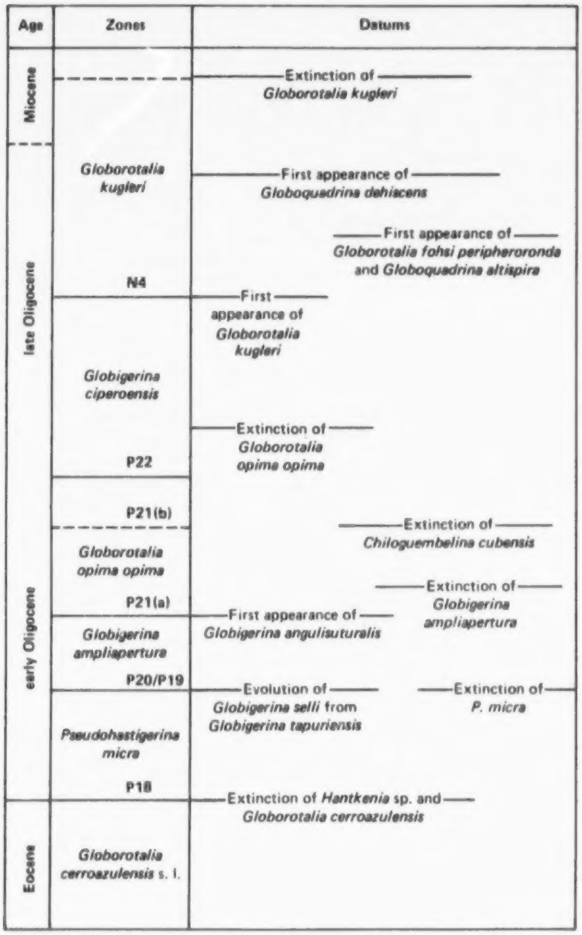
Age
Zones
Datums
Miocene
late Oligocene
early Oligocene
Eocene
Globorotalia kugleri
N4
Globigerina ciperoensis
P22
P21(b)
Globorotalia opima opima
P21(a)
Globigerina ampliapertura
P20/P19
Pseudohastigerina micra
P18
Globorotalia cerroazulensis s. l.
Extinction of Globorotalia kugleri
First appearance of Globoquadrina dehiscens
First appearance of Globorotalia fohsi peripheroronda and Globoquadrina altispira
First appearance of Globorotalia kugleri
Extinction of Globorotalia opima opima
Extinction of Chiloguembelina cubensis
Extinction of Globigerina ampliapertura
First appearance of Globigerina angulisuturalis
Evolution of Globigerina selli from Globigerina tapuriensis
Extinction of P. micra
Extinction of Hantkenia sp. and Globorotalia cerroazulensis

Figure 4. Oligocene zonation modified from Stainforth and Lamb (1981).

ous elements are *G. sicanus.*, *G. trilobus*, *Globoquadrina dehiscens*, *Globorotalia scitula*, and *Sphaeroidinellopsis seminulina*. The siliceous element (i.e., radiolarians and sponge spicules) is quite common.

Orbulina suturalis–Globorotalia peripheroronda Zone (N9)

The first appearance of *Orbulina suturalis* coincides with the lower boundary of this zone and the upper boundary with the first appearance of *G. peripheroacuta*. The top of Zone N9 virtually coincides with the first appearance and evolution of *G. praemenardii praemenardii* from its ancestor *G. praemenardii archeomenardii*. *Orbulina* first appears in Samples 558-12,CC and 563-10,CC, marking the base of the zone at approximately 266 and 247 m, respectively. The fauna is characterized by abundant but somewhat fractured planktonics.

Globorotalia peripheroacuta Zone (N10)

The base of this zone is placed at the horizon of the first evolutionary appearance of *G. peripheroacuta* (evolving from its ancestor *G. peripheroronda*) and the upper boundary at the first appearance of *G. praefohsi*. Cores 558-11 and 563-9 may belong within this zone, but at the present time the zone has not been positively identified in the section studied. These cores are therefore tentatively referred to N9/N10.

Globorotalia praefohsi Zone (N11)

This middle Miocene zone is defined at the base b the first appearance of *G. praefohsi* (evolving from i ancestor *G. peripheroacuta)* and at the top by the fir appearance of *G. fohsi*.

In temperate regions large carinate end forms of th *G. fohsi* lineage are frequently not well developed, an at the sites discussed here this seems to be the case. Ther is also some evidence that the local distribution of th *G. fohsi* series is subject to ecologic control. Within th interval, a highly evolved form of *G. praemenardii* wit limbated spiral and intracameral sutures in the penult mate whorl is recorded (Salvatorini and Cita, 1979).

Cores 558-10, 563-8, and 563-7 are tentatively assigne to N11.

Globorotalia fohsi Zone (N12)

The first appearance of *G. fohsi* s.s. defines the base of this zone and the first occurrence of *Sphaeroidinellopsis subdehiscens* marks the upper boundary. The interval is characterized by *G. siakensis*, *G. praemenardii*, *G. peripheroronda*, *G. praescitula*, *Orbulina universa*, and *O. suturalis*. Cores 558-9, 558-8, and 563-6 may be assigned to this zone. Although the *G. fohsi* lineage is not well developed in the area, *G. peripheroronda* is fairly common. The last occurrence of this form was recognized in samples within the N12 Zone.

Sphaeroidinellopsis subdehiscens–Globigerina druryi Zone (N13)

This zone is defined at the base by the first appearance of *S. subdehiscens*, and the upper limit or top of zone is defined by the first appearance of *Globigerina nepenthes*. Core 558-7 belongs in this interval.

Globigerina nepenthes–Globorotalia siakensis Zone (N14)

This zone is recognized by the first appearance of *Globigerina nepenthes* at the base and by the last appearance of *Globorotalia siakensis* at the upper boundary. The zone is therefore characterized by the concurrence of *Globigerina nepenthes* and *Globorotalia siakensis*. The first occurrence of *Globigerina nepenthes* (or the boundary of N13/N4) was recognized in Samples 558 6,CC and 563-5,CC. In these samples, a few typicall well developed specimens are present. These cores ar assigned to Zones N13/N14. Cores 558-6 (215–205.5 m and 563-5 (204–195 m) are particularly interesting because they contain the calcareous (algae?) *Bolboforma* (Echols, this volume) that seems to be restricted to thi short interval. These spherical to flattened spherical calcareous bodies found in the fine fractions have tiny apertures at the end of neck-like projections and are ornamented with spiral ridges and/or spines. They are referred to the *incertae sedis* (algae?) *Bolboforma* and described as cysts or reproductive bodies of an (as yet unknown) Miocene algae. They may be regional markers and possibly climatic indicators in deep-sea sediments.

Core 558-5 to Sample 558-1-1, 37–40 cm approximately 205–158 m sub-bottom) and Core 563-4 to Sample 563-1-1, 62–64 cm (approximately 195–157 m sub-bottom) are considered characteristic of Zone N14. The fauna includes abundant *Globorotalia menardii* complex, *Globigerina nepenthes,* common *Sphaeroidinellopsis seminulina* and *S. subdehiscens, Globoquadrina dehiscens, G. altispira,* and *Orbulina.*

Globorotalia acostaensis–G. merotumida Zone (N16)

The base of this zone defined by the first appearance of *G. acostaensis,* and the top limit is defined just below the first appearance of *G. plesiotumida. G. merotumida* appears in the zone just above the base.

Globorotalia plesiotumida Zone (N17)

The base of the zone coincides with the first appearance of *G. plesiotumida,* and the top is placed just below the first evolutionary appearance of *G. tumida.*

Cores 558A-16 and 558A-15 are assigned to either the middle of uppermost N16 or lowest N17. Cores 558A-14 and 558A-13 are assigned to N17.

Miocene/Pliocene

Globorotalia tumida–Sphaeroidinella subdehiscens paenedehiscens Zone (N18)

This zone is defined at the base by the appearance of *G. tumida,* and the top is defined just below the first evolutionary appearance of *Sphaeroidinella dehiscens.* Core 558A-12 is assigned to the lower part of Zone N18 and Core 558A-11 to the upper part of the interval.

Typical keeled sinestral *Globorotalia margaritae* were first observed in Core 558A-12.

Pliocene

Sphaeroidinella dehiscens–Globoquadrina altispira Zone (N19)

The base of Zone N19 is marked by the first evolutionary appearance of *S. dehiscens* from its immediate ancestor *Sphaeroidinellopsis subdehiscens paenedehiscens.* The top is the horizon immediately below the first evolutionary appearance of *Globorotalia acostaensis pseudopima* (Blow, 1969).

Cores 558A-10 and 558A-9 are assigned to this interval. The last occurrence of *Globigerina nepenthes* was noted in Core 558A-10 and *Globorotalia margaritae* last appears in Core 558A-9.

Globorotalia tosaensis tenuitheca Zone (N21)

The base of the zone is placed at the horizon of the first evolutionary appearance of *G. tosaensis tenuitheca* and the top is placed immediately below the first appearance of *G. truncatulinoides* (Blow, 1969).

The interval from Core 558A-8 through Section 558A-3-5 is assigned to this zone. The fauna is diverse and is characterized by *G. tosaensis, G. crassaformis, G. praehirsuta, G. miocenica, G. pertenuis, Sphaeroidinella dehiscens, Globigerinoides conglobatus,* and *G. sacculifer.*

Pleistocene

Globorotalia truncatulinoides Zone (N22)

The base of this zone is placed at the first appearance of *G. truncatulinoides,* which evolved from *G. tosaensis.* The zone is recognized and differentiated from the older N21 Zone by the angular and carinate *G. truncatulinoides,* even though the more rounded, nonkeeled *G. tosaensis* may persist into the zone.

Sections 558A-3-1, 558A-3-2, 558A-3-3, and 558A-3-4 contain specimens of the intermediate forms of the *G. tosaensis–G. truncatulinoides* sequence and are representative of this transitional zone close to the Pliocene/Pleistocene boundary.

Cores 558A-2 and 558A-1 are late Pleistocene upper N22 and contain a well-preserved modern fauna with abundant *Globorotalia truncatulinoides* and *G. inflata;* and *G. scitula, Globigerina bulloides, Globigerinoides ruber, G. obliquus, Neogloboquadrina pachyderma, N. dutertrei, Sphaeroidinella dehiscens.* and *Orbulina.* Benthic foraminifers, ostracodes, and abundant diverse radiolarians are well preserved.

SUMMARY

At Site 558 (Holes 558 and 558A), a nearly complete and continuous sequence of lower Oligocene through Pleistocene sediments was recovered. At Site 563, a section of lower Oligocene to upper middle Miocene very similar in both fauna and lithology to Hole 558 was retrieved. This stratigraphic succession is an excellent reference section and the most complete succession for this part of the Atlantic.

Figure 5 is a chart showing the correlation of the foraminiferal zones encountered on Leg 82 (Holes 558, 558A, and 563), together with Hole 334 drilled on Leg 37. The section of lower-upper Miocene retrieved in Hole 334 approximates the time intervals missing from sections cored on Leg 82. Therefore, we have a more complete sedimentary section than has previously been recovered from the Cenozoic of the Mid-Atlantic between 20–40°N latitude.

Preservation is good except for lower Oligocene faunas immediately overlying the basalt, which show destruction because of dolomite crystallization and fragmentation and/or dissolution in the middle and upper Miocene that may have been climatically induced.

Bolboforma, a Miocene algae (?), is present at both sites at approximately the same horizon, suggesting that it may be a useful marker.

REFERENCES

Becker, R. C., 1982. Oligocene foraminiferal zonation of a well in the Main Pass Area (Gulf of Mexico). [M. A. thesis] Washington University, St. Louis, Mo.

Beckmann, J. P., Bolli, H. M., Perch-Nielson, K., Proto Decima, F., Saunders, J. B., and Toumarkine, M., 1981. Major calcareous nannofossil and foraminiferal events between the middle Eocene and early Miocene. *Palaeogeogr., Palaeoclimatol., Palaeoecol.,* 36(3/4): 155–190.

Berggren, W. A., 1972. Cenozoic biostratigraphy and paleobiogeography of the North Atlantic. *In* Laughton, A. S., Berggren, W. A., et al. *Init. Repts. DSDP*, 12: Washington (U.S. Govt. Printing Office), 965-1001.

________, 1978. Recent advances in Cenozoic planktonic foraminiferal biostratigraphy, biochronology, and biogeography: Atlantic Ocean. *Micropaleontology*, 24:337-370.

Berggren, W. A., and Amdurer, M., 1973. Late Paleogene (Oligocene) and Neogene planktonic foraminiferal biostratigraphy of the Atlantic Ocean (Lat. 30 N to Lat. 30 S). *Rev. Ital. Paleontol. Strat.* 79:337-391.

Berggren, W. A., and Van Couvering, J. A., 1974. The late Neogene biostratigraphy, geochronology and paleoclimatology and the last 15 million years in marine and continental sequences. *Palaeogeogr., Palaeoclimatol. Palaeoecol.* 16(1/2):1-216.

________, 1978. Biochronology. *In* Cohee, G. V., Glaessner, M, F., and Hedberg, H. D. (Eds.), *The Geologic Time Scale*: Tulsa, Oklahoma (Am. Assoc. Pet. Geol.), Studies in Geology, 6:39-55.

Blow, W. H., 1969. Late middle Eocene to recent planktonic foraminiferal biostratigraphy. *In* Brönnimann, P., and Renz, H. H., (Eds.), *Proc. First Int. Conf. Plank. Microfossils:* Leiden (E. J. Brill), 1: 199-422.

________, 1970. Deep Sea Drilling Project, Leg 2, Foraminifera from selected samples. *In* Peterson, M. N. A., Edgar, N. T., et al., *Init. Repts. DSDP*, 2: Washington (U.S. Govt. Printing Office), 357-365.

________, 1979. The Cainozoic Foraminifera, 3 vol., Leiden, (E. J. Brill).

Bolli, H. H., 1957. Planktonic foraminifera from the Oligocene-Miocene Cipero and Lengua Formations of Trinidad, B. W. I. *U.S. Nat. Mus. Bull.*, 215:97-123.

________, 1966. Zonation of Cretaceous to Pliocene marine sediments based on planktonic foraminifera. *Bol. Inf. Asoc. Venez. Geol. Min. Pet.*, 9:3-32.

Caralp, M., Valenton, S., and Vigneaux, M., 1965. Les Foraminiferes pelagiques du tertiare terminal sub-aquitain. *C. R. Hebd. Seances Acad. Sci.*, 261(17):3431-3434.

Hardenbol, J., and Berggren, W. A., 1978. A new Paleogene numerical time scale. *In* Cohee, G. V., Glaessner, M. F., and Hedberg, H. D. (Eds.), *The Geologic Time Scale:* Tulsa, Oklahoma (Am. Assoc. Pet. Geol, Studies in Geology, 6:213-234.

Jenkins, D. G., 1960. Planktonic foraminifera from the Lake Entrance oil shaft, Victoria, Australia. *Micropaleontology*, 6:345-371.

________, 1965. The origin of the species *Globigerinoides trilobus* (Reuss) in New Zealand. *Contrib. Cushman Found. Foraminiferal Res.* 16 (3):116-120.

________, 1971. New Zealand Conozoic planktonic foraminifera. *N. Z. Geol. Surv. Paleontol. Bull.* 42:1-278.

Keller, G., 1980. Early to middle Miocene planktonic foraminiferal datum levels of the equatorial and subtropical Pacific. *Micropaleontology*, 26(4):372-391.

________, 1981a. Planktonic foraminiferal faunas of the equatorial Pacific suggest early Miocene origin of the present oceanic circulation. *Mar. Micropaleontol.*, 6:269-295.

________, 1981b. Miocene biochronology and paleoceanography of the North Pacific *Mar. Micropaleontol.*, 6(5/6) (Spec. Is., Cenozoic Paleoceanogr.):535-551.

Lamb, J. L., and Stainforth, R. M., 1976. Unreliability of *Globigerinoides* datum. *Am. Assoc. Pet. Geol. Bull.*, 60(9):1564-1569.

Miles, G. A., 1977. Planktonic Foraminifera from Leg 37 of the Deep Sea Drilling Project. *In* Aumento, F., Melson, W. G., et al., *Init. Repts. DSDP*, 37: Washington (U.S. Govt. Printing Office), 929-961.

Poore, R. Z., 1978. Oligocene through Quaternary planktonic foraminiferal biostratigraphy of the North Atlantic: DSDP Leg 49. *In* Luyendyk, B. P., Cann, J. R., et al., *Init. Repts. DSDP*, 49: Washington (U.S. Govt. Printing Office), 447-517.

Postuma, J. A., 1971. *Manual of Planktonic Foraminifera:* Amsterdam (Elsevier).

Salvatorini, G., and Cita, M. B., 1979. Miocene foraminiferal stratigraphy, DSDP Site 397 (Cape Bojador, North Atlantic). *In* von Rad, U., Ryan, W. B. F., et al., *Init. Repts. DSDP*, 47, Pt. 1: Washington (U.S. Govt. Printing Office), 317-373.

Srinivasen, M. S., and Kennett, J. P., 1981. Neogene planktonic foraminiferal biostratigraphy and evolution: Equatorial to Subantarctic, South Pacific. *Mar. Micropaleontol.* 6(5/6):499-533.

________, 1983. The Oligocene-Miocene boundary in the South Pacific. *Geol. Soc. Am. Bull.*, 94(6):798-812.

Stainforth, R. M., and Lamb, J. L., 1981. An evaluation of planktonic foraminiferal zonation of the Oligocene. *Univ. Kans. Paleontol. Contrib.*, Paper 104.

Stainforth, R, M., Lamb, J. L., Luterbacher, H., Beard, J. H., and Jeffords, R. M., 1975. Cenozoic planktonic foraminiferal zonation and characteristics of index forms. *Univ. Kans. Paleontol. Contrib.*, Paper 62.

Date of Initial Receipt: 21 April 1983
Date of Acceptance: 19 January 1984

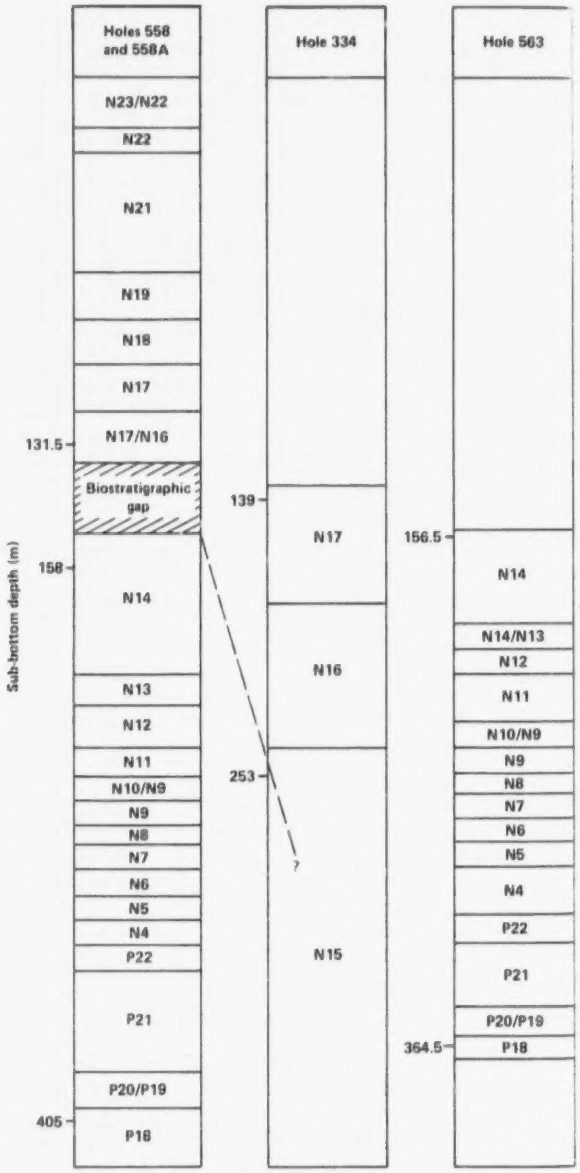

Figure 5. Correlation of the foraminiferal zones encountered on Leg 82, Holes 558, 558A, and 563, with Hole 334 drilled on Leg 37 (Aumento, Melson, et al.). The section of early-late Miocene retrieved in Hole 334 approximates the time intervals missing from sections cored on Leg 82.

APPENDIX A
Foraminifers from Site 558, Holes 558A and 558

Core-Section (interval in cm)	Depth below seafloor (m)	Meters recovered	Age	Ma	Planktonic zone
Hole 558A					
1-1, 45-46	0.0		Pleistocene (late)		N23/N22
1, CC		0.47			
2-1, 62-64	0.50		Pleistocene (late)		N23/N22
2-2, 62-64					
2-3, 62-64					
2-4, 62-64					
2-5, 62-64					
2-6, 62-64					
2, CC		9.36			
3-1, 62-64	10.0		Pleistocene (early)		N22
3-2, 62-64					
3-3, 62-64					
3-4, 66-68				1.85	
3-5, 62-64			Pliocene (late)		N21
3-6, 62-64					
3, CC		9.51			
4-1, 62-64	19.50		Pliocene (late)		N21
4-2, 62-64					
4-3, 62-64					
4-4, 62-64					
4-5, 62-64					
4-6, 62-64					
4, CC		9.32			
5-1, 62-64	29.00		Pliocene (late)		N21
5-6, 62-64					
5, CC		9.71			
6-2, 70-73	38.50		Pliocene (late)		N21
6-3, 70-73					
6-4, 70-73					
6-5, 70-73					
6-6, 70-73					
6, CC		9.70			
7-1, 90-93	48.00		Pliocene	2.8	N21
7-2, 90-93					
7-3, 90-93					
7-4, 90-93					
7-5, 90-93					
7, CC		8.22			
8-1, 90-93	57.50		Pliocene		N21
8-2, 90-93					
8-3, 90-93					
8-4, 90-93					
8-5, 90-93					
8, CC		7.78			
9-1, 128-129	67.00		Pliocene (early)	3.4	N19
9-2, 70-71					
9-3, 70-71					
9, CC		4.76			
10-1, 62,64	74.00		Pliocene		N19
10-2, 62-64					
10, CC		3.24			
11-1, 62-64	77.00		Pliocene	5 ±	N18
11-2, 62-64					
11-3, 62-64					
11-4, 62-64			Miocene		
11-5, 62-64					
11-7, 22-24					
11, CC		9.63			
12-1, 62-64	86.50		Miocene (late)		N18
12-2, 62-64					
12-3, 62-64					
12-4, 62-64					
12-5, 62-64					
12-6, 24-26					
12, CC		8.47			
13-1, 62-64	96.00		Miocene (late)	6?	N17
13-2, 62-64					
13-3, 62-64					
13-4, 62-64					
13-5, 62-64					
13, CC		6.98			
14-1, 87-89	103.00		Miocene (late)		N17
14-2, 62-64					
14-3, 62-64					
14-4, 62-64					
14-5, 62-64					
14-7, 42-44					
14, CC		9.65			
15-1, 62-64	112.50		Miocene (late)		N17/N16
15-2, 62-64					
15-3, 62-64					
15-4, 62-64					
15-6, 22-24					
15, CC		8.11			
16-1, 62-64	122.00		Miocene (late)	7/8	N17 (earliest) or N16 (latest)
16-2, 62-64					
16-3, 62-64					

Appendix A. (Continued).

Core-Section (interval in cm)	Depth below seafloor (m)	Meters recovered	Age	Ma	Planktonic zone
Hole 558A (Cont.)					
16-4, 62-64					
16-5, 62-64					
16-6, 62-64					
16, CC		8.78			
Hole 558					
1-1, 37-40	158.00		Miocene (late-middle)	10.5/12	N14
1-2, 37-40					
1-3, 37-40					
1-4, 37-40					
1-5, 37-40					
1-6, 37-40					
1-7, 45-47					
1, CC		9.15			
2-1, 110-113	167.50		Miocene (late-middle)		N14
2-2, 110-113					
2-3, 110-113					
2-4, 110-113					
2-5, 110-113					
2-6, 33-35					
2, CC		8.78			
3-1, 61-64	177.00		Miocene (late-middle)		N14
3-2, 61-64					
3-3, 61-64					
3-4, 61-64					
3-5, 61-64					
3-6, 61-64					
3, CC		9.48			
4-1, 61-64	186.50		Miocene (late-middle)		N14
4-2, 61-64					
4-3, 61-64					
4-4, 61-64					
4-5, 61-64					
4-6, 61-64					
4, CC		9.65			
5-1, 61-64	196.00		Miocene (late-middle)		N14
5-2, 61-64					
5-3, 61-64					
5-4, 61-64					
5-5, 61-64					
5-6, 62-64					
5, CC		9.40			
6-1, 61-64	205.50		Miocene (late-middle)		N14/N13
6-2, 61-64					
6-3, 61-64					
6-4, 61-64					
6-5, 61-64					
6-6, 61-64					
6, CC		9.05			
7-1, 32-35	215.00		Miocene (middle)	12/13	N13
7, CC		0.89			
8-1, 62-65	224.50		Miocene (middle)		N12
8-2, 62-65					
8-3, 62-65					
8-4, 62-65					
8, CC		5.65			
9-2, 62-65	234.00		Miocene (middle)	13/14	N12
9, CC		3.28			
10-1, 61-64	243.50		Miocene (middle)	14/15	N11
10, CC		1.54			
11-1, 62-64	253.00		Miocene (middle)	15/16	N10
11-2, 62-64					N9
11, CC		2.74			
12-1, 62-64	262.50		Miocene (middle)		N9
12-2, 62-64					
12-3, 42-44					
12-4, 62-64					
12, CC		7.05			
13-1, 62-64	272.00		Miocene (early-middle)		N8
13-2, 62-64					
13-3, 62-64					
13-4, 62-64					
13-5, 62-64					
13, CC		9.00			
14-1, 62-64	281.50		Miocene (late-early)	16/18	N7
14-2, 62-64					
14-3, 62-64					
14-4, 62-64					
14-5, 62-64					
14-6, 62-64					
14, CC		9.39			
15-1, 55-57	291.00		Miocene (early)	18.5 ±	N6
15-2, 62-64					
15-3, 62-64					

Appendix A. (Continued).

Core-Section (interval in cm)	Depth below seafloor (m)	Meters recovered	Age	Ma	Planktonic zone
Hole 558 (Cont.)					
15-4, 62-64					
15-5, 80-82					
15-6, 80-82					
15, CC		9.09			
16-1, 62-64	300.50		Miocene (early)	19/20	N5
16-2, 62-64					
16-3, 62-64					
16-4, 62-64					
16-5, 62-64					
16-6, 62-64					
16, CC		9.70			
17-1, 58-60	310.00		Miocene/Oligocene	22/25	N4
17-2, 62-64					
17-3, 62-64					
17-4, 62-64					
17-5, 62-64					
17, CC		7.43			
18-1, 62-64	319.50		Oligocene (late)	24+/26+	P22
18-2, 62-64					
18-3, 62-64					
18-4, 62-64					
18-5, 62-64					
18, CC		6.86			
19-1, 58-60	329.00		Oligocene (late)		P21 (upper)
19-2, 58-60					
19-3, 58-60					
19-4, 58-60					
19-5, 58-60					
19, CC		7.60			
20-1, 62-64	338.50		Oligocene (late)		P21 (upper)
20-2, 62-64					
20-3, 62-64					
20-4, 62-64					
20-5, 22-24					
20, CC		6.47			
21-1, 62-64	348.00		Oligocene (late)	26/28	P21 (upper)
21-2, 62-64					
21-3, 22-24					
21, CC		3.64			
22-1, 62-64	357.50		Oligocene (early)	28/30	P21 (lower)
22-2, 62-64					
22-3, 62-64					
22-4, 62-64					
22, CC		5.42			
23-1, 32-34	367.00		Oligocene		P21 (lower)
23-2, 32-34					
23-3, 32-32					
23-4, 32-34					
23-5, 32-34					
23-6, 32-34					
23, CC		9.36			
24-1, 42-45	376.50		Oligocene (early)	30+	P20/P19
24-2, 42-45					
24-3, 42-45					
24-4, 42-45					
24, CC		5.98			
25-1, 99-101	386.00		Oligocene (early)	35+	P18
25-2 99-101					
25-3, 99-101					
25-4, 99-101					
25-5, 99-101					
25-6, 122-124					
25, CC		8.97			
26-1, 18-20	395.50		Oligocene (early)		P18
26-2, 18-20					
26-3, 18-20					
26-4, 18-20					
26-5, 18-20					
26, CC		6.94			
27-1, 37-39	405.0		Oligocene (early)		
27-2, 44-46					
27, CC		3.78			

APPENDIX B
Foraminifers from Site 563, Hole 563

Core-Section (interval in cm)	Depth below seafloor (m)	Meters recovered	Age	Ma	Planktonic zone
1-1, 62-64	156.50		Miocene (late-middle)	10.5 +	N14
1-2, 62-64					
1-3, 62-64					
1, CC		4.52			
2-1, 62-64	166.00		Miocene (late-middle)		N14
2-2, 62-64					
2-3, 62-64					
2-5, 62-64					
2-6, 62-64					
2-7, 22-24					
2, CC		9.62			
3-1, 62-64	175.50		Miocene (late-middle)		N14
3-2, 62-64					
3-3, 62-64					
3-4, 62-64					
3-5, 62-64					
3-6, 62-64					
3, CC		9.02			
4-1, 62-64	185.00		Miocene (late-middle)		N14
4-2, 62-64					
4-3, 62-64					
4-4, 12-14					
4, CC		5.01			
5-1, 62-64	194.50		Miocene (late-middle)		N14/N13
5-4, 62-64					
5-5, 62-64					
5-6, 63-64					
5-7, 19-21					
5, CC		9.70			
6-1, 62-64	204.00		Miocene (middle)	13/14	N12
6-2, 62-64					
6-3, 62-64					
6-4, 62-64					
6-5, 62-64					
6-6, 62-64					
6-7, 22-24					
6, CC		9.51			
7-1, 62-64	213.50		Miocene (middle)	14/15	N11
7-2, 62-64					
7-3, 62-64					
7-4, 62-64					
7-5, 62-64					
7-6, 62-64					
7-7, 22-24					
7, CC		9.63			
8-1, 62-64	223.00		Miocene (middle)		N11
8-2, 62-64					
8-3, 62-64					
8-4, 62-64					
8-5, 62-64					
8-6, 62-64					
8, CC		9.31			
9-1, 50-52	232.50		Miocene (middle)	15/16	N10/N9
9-2, 50-52					
9-3, 50-52					
9-4, 50-52					
9-5, 50-52					
9-6, 50-52					
9, CC		9.58			
10-1, 45-47	242.00		Miocene (middle)		N9
10-2, 45-47					
10-3, 45-47					
10-4, 45-47					
10-5, 45-47					
10-6, 45-47					
10, CC		9.63			
11-1, 62-64	251.00		Miocene (early-middle)	16+	N8
11-2, 62-64					
11-3, 62-64					
11-4, 62-64					
11, CC		6.31			
12-1, 52-54	261.50		Miocene (late-early)	16/18	N7
12-2, 52-54					
12-3, 52-54					
12-4, 52-54					
12-5, 52-54					
12-6, 59-61					
12, CC		9.50			
13-1, 129-131	270.50		Miocene (early)	18.5 +	N6
13-2, 62-64					
13-3, 62-64					
13-4, 62-64					
13-5, 62-64					
13, CC		7.47			
14-1, 82-84	280.00		Miocene (early)	19/20	N5
14-2, 63-65					
14-3, 59-61					
14-4, 10-12					
14-5, 135-137					

Appendix B. (Continued).

Core-Section (interval in cm)	Depth below seafloor (m)	Meters recovered	Age	Ma	Planktonic zone
14-6, 110-112					
14-7, 27-29					
14, CC		9.50			
15-1, 40-42	289.50		Miocene (early)	22.5 +	N4 (upper)
15-2, 40-42					
15-3, 40-42					
15-4, 40-42					
15-5, 40-42					
15-6, 66-68					
15-7, 32-34					
15, CC		9.48			
16-1, 54-56	299.00		Miocene early Oligocene (late)		N4 (lower)
16-2, 54-56					
16-3, 54-56					
16-4, 54-56					
16-5, 54-56					
16-6, 57-59					
16-7, 37-39					
16, CC		9.60			
17-1, 72-74	308.50		Oligocene (late)	24+ / 26+	P22/P21
17-2, 72-74					
17-3, 76-78					
17-4, 79-81					
17-5, 72-74					
17-6, 34-36					
17-7, 34-36					
17, CC		9.56			
18-1, 72-74	318.00		Oligocene (late)		P21 (upper)
18-2, 72-74					
18-3, 72-74					
18-4, 72-74					
18-5, 40-42					
18, CC		6.85			
19-1, 68-70	327.50		Oligocene	28 / 30	P21 (lower)
19-2, 34-38					
19-3, 34-38					
19, CC		3.66			
20-1, 62-64	337.00		Oligocene		P21 (lower)
20-2, 62-64					
20-3, 98-100					
20-4, 69-71					
20-5, 19-21					
20-6, 8-10					
20-7, 27-29					
20, CC		9.66			
21-1, 83-85	346.50		Oligocene	30 +	P20/P19
21-2, 83-85					
21-3, 83-85					
21-4, 83-85					
21-5, 92-94					
21-6, 92-94					
21-7, 18-20					
21, CC		9.63			
22-1, 52-54	355.50		Oligocene (early)	35 +	P18
22-2, 52-54					
22-3, 52-54					
22-4, 3-5					
22, CC		4.79			

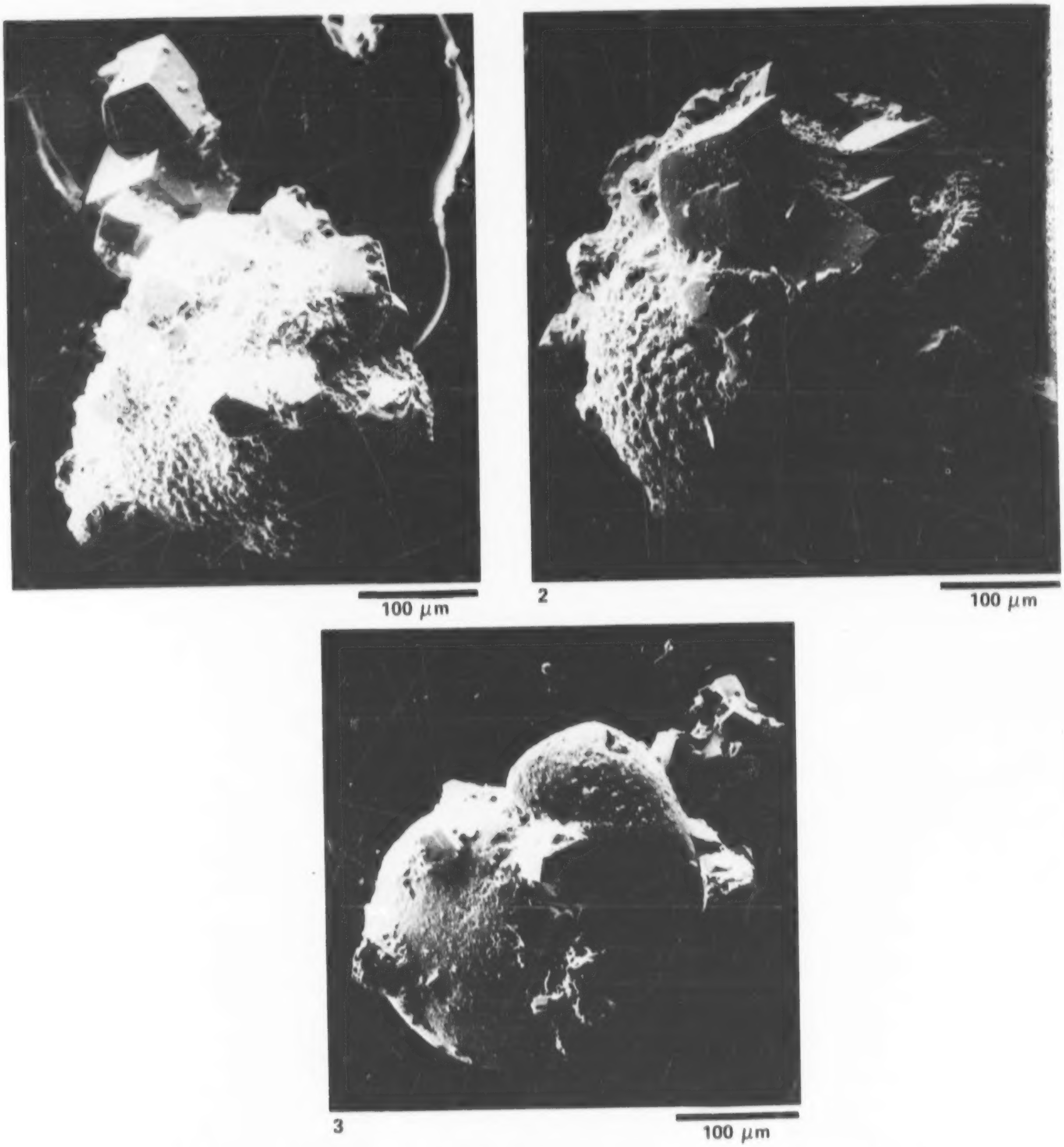
100 μm
2
100 μm
3
100 μm

Plate 1. Oligocene foraminifers. 1, 2. Dolomite crystals growing in and on planktonic foraminifers. 3. Dolomite crystals growing on benthic foraminifer.

34. CALCAREOUS NANNOFOSSILS OF DEEP SEA DRILLING PROJECT SITES 558 AND 563, NORTH ATLANTIC OCEAN: BIOSTRATIGRAPHY AND THE DISTRIBUTION OF OLIGOCENE BRAARUDOSPHAERIDS[1]

Mary E. Parker, Murlene Clark, and Sherwood W. Wise, Jr., Department of Geology, Florida State University[2]

ABSTRACT

Deep Sea Drilling Project Sites 558 and 563, located on the west flank of the Mid-Atlantic Ridge between 33 and 37°N latitude, yielded lower Oligocene through Pleistocene nannofossil-bearing sediments. A detailed study of the abundance, preservation, and biostratigraphic distribution of calcareous nannofossils at Sites 558 and 563 shows that preservation ranges from moderate to good and nannofossil assemblages are reasonably diverse. These long, continuously cored sections add substantially to the record of Tertiary nannofossiliferous sediments recovered in the North Atlantic. A hiatus of early Pliocene age is noted in Hole 558A, where the nannofossil Subzones CN10b, CN10c, and CN11a are missing. An increase in the relative abundance of triradiate forms of *Discoaster brouweri* proved useful in determining the LAD (last appearance datum) of *D. brouweri* in the presence of considerable reworking.

A significant occurrence of abundant braarudosphaerids, along with holococcoliths, was noted in the lower Oligocene section at Hole 563, but not at Hole 558, 400 km to the north, an indication that a provincial nannofossil boundary separates the two sites. This first report of abundant Oligocene braarudosphaerids from the central North Atlantic Ocean suggests that they should be pervasive in Northern Hemisphere mid-latitude and subtropical lower Oligocene sediments deposited above 2700 m. Together with Southern Hemisphere occurrences, this North Atlantic occurrence of braarudosphaerids may indicate a bipolar distribution in the maximum abundance of Oligocene *Braarudosphaera*.

INTRODUCTION

The purpose of this study is to describe the abundance, preservation, and biostratigraphic distribution of calcareous nannofossils at Sites 558 and 563. Any ecological differences expressed in the assemblages at each of these sites would also be of interest. The two sites (Fig. 1) are separated by 4° of latitude (about 400 km). Both were drilled on magnetic Anomaly 13, of early Oligocene age (site chapters, Sites 558 and 563, this volume). The oldest sediment, therefore, would have been deposited at or near the crest of the Mid-Atlantic Ridge at this time.

Although the Azores Triple Junction area has been studied extensively, few sedimentary sections have been continuously cored in that region. DSDP Leg 82 recovered the most complete section of Cenozoic pelagic sediments to date in the North Atlantic. Previous studies in the area have concentrated on crustal structure and geochemistry and include DSDP Legs 2, 37, and 49 (Peterson, Edgar, et al., 1970; Aumento, Melson, et al., 1977; Luyendyk, Cann, et al., 1979).

Both Sites 558 and 563 were cored down to basement. For this reason, the detailed discussions of the calcareous nannofossil biostratigraphy for each site begin at the base of each hole and then progress stratigraphically upward.

METHODS

One sample from each core section from Holes 558, 558A, and 563 was studied. Smear slides of all samples were made directly from raw sediment, according to the standard preparation technique, and were then examined on the light microscope. Calcareous nannofossils were abundant on all slides.

Smear slides were examined at a magnification of 1000× and the abundances of individual nannofossil species were tabulated on the range charts using the method proposed by Hay (1970). Estimates of the relative abundances of individual species in a given sample were made according to the following criteria:

H = highly abundant—101 to 1000 specimens per field of view at 1000×;
V = very abundant—11 to 100 specimens per field of view at 1000×;
A = abundant—1 to 10 specimens per field of view at 1000×;
C = common—1 specimen per 2 to 10 fields of view at 1000×;
F = few—1 specimen per 11 to 100 fields of view at 1000×; and
R = rare—1 specimen per 101 to 1000 fields of view at 1000×.

The abundances of reworked taxa and downhole contaminants are represented by lower-case letters.

A qualitative analysis of the state of preservation of the calcareous nannofossils found within each sample was made using the following criteria:

G = good—specimens exhibit little or no dissolution and/or overgrowth;
M-G = moderate to good—specimens exhibit slight to moderate dissolution and/or overgrowth, identification of some species is impaired;
M = moderate—specimens exhibit moderate dissolution and/or overgrowth, identification is impaired at the specific level; and
P = poor—specimens exhibit extreme dissolution and/or overgrowth.

These categories were determined based upon the "average" state of preservation of the calcareous nannofossils examined on the smear slides. There is generally considerable variation in the state of preservation of individual specimens observed in any given sample. Preservation ranged from moderate to good throughout the Leg 82 cored sedimentary sections.

Samples were prepared for scanning electron microscopy using procedures outlined by Wise and Kelts (1972). The samples were examined on a Cambridge Stereoscan S4-10 scanning electron microscope.

Species considered in this report are listed alphabetically by species epithets in the Appendix. Most of the bibliographic references for these taxa are presented in Loeblich and Tappan (1966; 1968; 1969; 1970a;

---

[1] Bougault, H., Cande, S. C., et al., *Init. Repts. DSDP*, 82: Washington (U.S. Govt. Printing Office).

[2] Addresses: (Parker, Wise) Department of Geology, Florida State University, Tallahassee, Fl 32306; (Clark, present address) Department of Geology and Geography, University of South Alabama, Mobile, Alabama 36688.

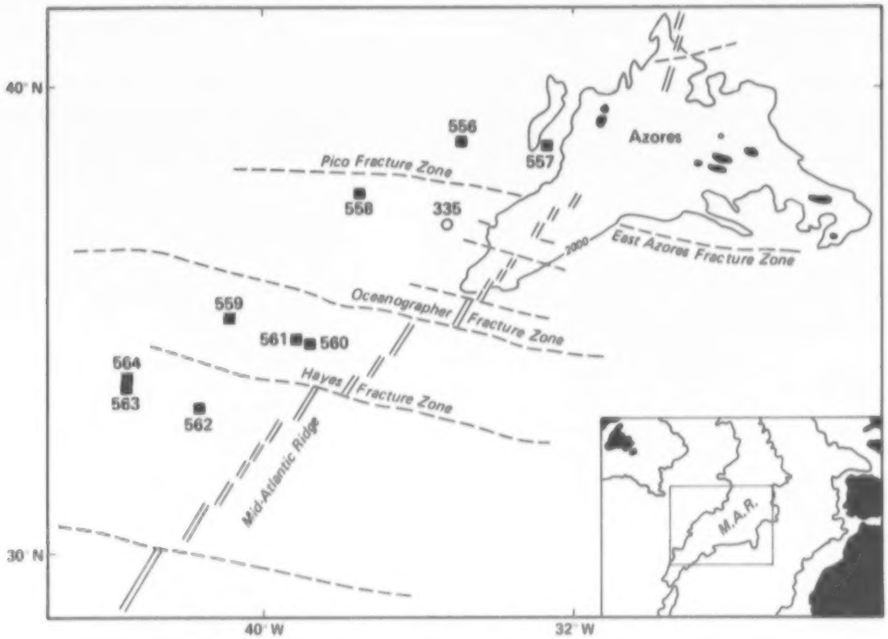

Figure 1. Location map for Deep Sea Drilling Project Leg 82 sites.

1970b; 1971; 1973) and in van Heck (1979a; 1979b; 1980a; 1980b; 1981a; 1981b; 1982a; 1982b; 1983a; 1983b). Any references not included in the above are listed in the references of this paper.

BIOSTRATIGRAPHIC ZONATION

Two published zonation schemes were used in this paper. For the Oligocene through Pliocene sections, Okada and Bukry's (1980) zonation was used; Gartner's (1977) zonation was used for the Pleistocene. This combination of zonations (Fig. 2) provides the highest degree of biostratigraphic resolution. Because both zonations use the last occurrence of *Discoaster brouweri* to date the Pliocene/Pleistocene boundary, the zonation scheme used in this paper is continuous. To avoid confusion, one should note that *Calcidiscus* (or *Cyclococcolithina) macintyrei* is used as a zone name by Gartner (1977), but as a subzone name for a different stratigraphic interval by Okada and Bukry (1980).

In some cases, preservation, scarcity of markers, and reworking problems limited the biostratigraphic resolution, and some zones and/or subzones could not be reliably discriminated. Dashed zonal and/or subzonal boundaries on the range charts indicate problems in discerning these boundaries. Reasons for the uncertainty about the position of such boundaries are outlined in detail in the discussions of the various sites. A synopsis of the calcareous nannofossil biostratigraphy for Sites 558 and 563 is presented in Figures 3 and 4.

A close comparison of the zonal assignments given in this chapter and those given in the site summaries for this volume will reveal some discrepancies. The site reports were compiled several months following the cruise and were based primarily on the examination of core-catcher samples. Because of the publication schedule established for this volume, there was no opportunity to modify that preliminary work after the more detailed examinations of the core sections were carried out.

SITE 558

(37°46.02′N; 37°20.61′W; water depth = 3766 m)

Site 558 was drilled about 48.3 km (30 mi.) south of the Pico Fracture Zone (Fig. 1) on the west flank of the Mid-Atlantic Ridge. Two holes were drilled in an attempt to recover a complete sedimentary section at this site. Unfortunately, the piston coring of the second hole had to be halted because of drilling problems before complete overlap of the sedimentary section was achieved. This left a 26 m stratigraphic gap between Holes 558 and 558A. However, this site does provide a nearly complete stratigraphic section from the lower Oligocene through the upper Pleistocene. It represents the first continuously cored section of lower Oligocene through Pleistocene calcareous pelagic sediments from the North Atlantic.

Hole 558

Hole 558 (Table 1) was washed down to a depth of 158 m and then continuously rotary cored for 250 m to basement. The lower Oligocene to upper Miocene sediments recovered contain abundant calcareous nannofossils. Preservation ranges from moderate to moderate-good.

Samples 558-27-2, 42–44 cm through 558-25,CC are assigned to the lower Oligocene *Helicosphaera reticulata* Zone (CP16). Preservation throughout this zone is moderate, with substantial overgrowth and dissolution noted

Age	Zone		Subzone		Datum
late Pleistocene	*Emiliania huxleyi* acme				FAD *E. huxleyi* acme
	Emiliania huxleyi				FAD *E. huxleyi*
	Gephyrocapsa oceanica				LAD *P. lacunosa*
early Pleistocene	*Pseudoemiliania lacunosa*				highest level of dominantly small *Gephyrocapsa*
	small *Gephyrocapsa*				LAD *H. sellii*
	Helicosphaera sellii				LAD *C. macintyrei*
	Calcidiscus macintyrei				LAD *D. brouweri*
late Pliocene	CN12	*Discoaster brouweri*	CN12d	*Calcidiscus macintyrei*	LAD *D. pentaradiatus*
			CN12c	*Discoaster pentaradiatus*	LAD *D. surculus*
			CN12b	*Discoaster surculus*	LAD *D. tamalis*
			CN12a	*Discoaster tamalis*	LAD *R. pseudoumbilica* or LAD *Sphenolithus* spp.
early Pliocene	CN11	*Reticulofenestra pseudoumbilica*	CN11b	*Discoaster asymmetricus*	FAD *D. asymmetricus* acme
			CN11a	*Sphenolithus neoabies*	LAD *A. primus* or LAD *A. tricorniculatus*
	CN10	*Amaurolithus tricorniculatus*	CN10c	*Ceratolithus rugosus*	FAD *C. rugosus* or LAD *C. acutus*
			CN10b	*Ceratolithus acutus*	FAD *C. acutus* or LAD *T. rugosus*
late Miocene			CN10a	*Triquetrorhabdulus rugosus*	LAD *D. quinqueramus*
	CN9	*Discoaster quinqueramus*	CN9b	*Amaurolithus primus*	FAD *A. primus*
			CN9a	*Discoaster berggrenii*	FAD *D. berggrenii* or FAD *D. surculus*
	CN8	*Discoaster neohamatus*	CN8b	*Discoaster neorectus*	FAD *D. neorectus* or FAD *D. loeblichii*
			CN8a	*Discoaster bellus*	LAD *D. hamatus*
	CN7	*Discoaster hamatus*	CN7b	*Catinaster calyculus*	FAD *C. calyculus*
middle Miocene			CN7a	*Helicosphaera carteri*	FAD *D. hamatus*
	CN6	*Catinaster coalitus*			FAD *C. coalitus*
	CN5	*Discoaster exilis*	CN5b	*Discoaster kugleri*	FAD *D. kugleri*
			CN5a	*Coccolithus miopelagicus*	LAD *S. heteromorphus*
	CN4	*Sphenolithus heteromorphus*			LAD *H. ampliaperta* or LAD *D. deflandrei* acme
early Miocene	CN3	*Helicosphaera ampliaperta*			FAD *S. heteromorphus* or LAD *S. belemnos*
	CN2	*Sphenolithus belemnos*			FAD *S. belemnos*
	CN1	*Triquetrorhabdulus carinatus*	CN1c	*Discoaster druggii*	FAD *D. druggii*
			CN1b	*Discoaster deflandrei*	LAD *C. abisectus* acme
late Oligocene			CN1a	*Cyclicargolithus abisectus*	LAD *S. ciperoensis* or LAD *D. bisectus*
	CP19	*Sphenolithus ciperoensis*	CP19b	*Dictyococcites bisectus*	LAD *S. distentus*
			CP19a	*Cyclicargolithus floridanus*	FAD *S. ciperoensis*
	CP18	*Sphenolithus distentus*			FAD *S. distentus*
early Oligocene	CP17	*Sphenolithus predistentus*			LAD *R. umbilica* or LAD *R. hillae*
	CP16	*Helicosphaera reticulata*	CP16c	*Reticulofenestra hillae*	LAD *C. formosus*
			CP16b	*Coccolithus formosus*	LAD *C. subdistichus* acme
			CP16a	*Coccolithus subdistichus*	LAD *D. barbadiensis* or LAD *D. saipanensis*

Figure 2. Zonation scheme used in this paper: adopted from Gartner (1977); Okada and Bukry (1980); with markers originally defined in Bukry (1973b; 1975). FAD = first appearance datum; LAD = last appearance datum.

Age	Zone or subzone	Hole 558A	Hole 558	Hole 563
Pleistocene	*E. huxleyi*	1-1/2-4	Washed	Washed
	G. oceanica	2-5/2,CC		
	P. lacunosa/	3-1/6-1		
	small *Gephyrocapsa*			
	H. sellii	6-2/7-1		
	C. macintyrei/	7-2/8-1		
Pliocene	CN12d *C. macintyrei*			
	CN12c *D. pentaradiatus*/	8-2/9-1		
	CN12b *D. surculus*			
	CN12a *D. tamalis*	9-2/9-3		
	CN11b *D. asymmetricus*	9-4/9,CC		
	CN11a *S. neoabies*	Hiatus		
	CN10c *C. rugosus*			
	CN10b *C. acutus*			
Miocene	CN10a *T. rugosus*	9,CC/12-4		
	CN9b *A. primus*	12-5/15,CC		
	CN9a *D. berggrenii*	16-1/16,CC		
	CN8b *D. neorectus*	Uncored		
	CN8a *D. bellus*		1-1/2-5	1-1/2-5
	CN7 *D. hamatus*		2-6/4-5	2-6/3,CC
	CN6/CN7 *C. coalitus*/*D. hamatus*		4-6/4,CC	
	CN6 *C. coalitus*		5-1	4-1
	CN5b *D. kugleri*/		5-2/12-1	4-2/8,CC
	CN5a *C. miopelagicus*			
	CN4 *S. heteromorphus*/		12-2/16-4	9-1/12,CC
	CN3 *H. amplificus*			
	CN2 *S. belemnos*		16-5/17-1	13-1/14,CC
	CN1c *D. druggii*		17-2/18-2	15-1/15-5
	CN1b *D. deflandrei*		18-3/19-3	15-6/15-7
Oligocene	CN1a *C. abisectus*			15,CC/16-5
	CP19b *D. bisectus*		19-4/21,CC	16-6/18,CC
	CP19a *C. floridanus*		22-1/22,CC	
	CP18 *S. distentus*		23-1/24-1	19-1/19,CC
	CP17 *S. predistentus*		24-2/25-6	20-1/21-7
	CP16c *R. hillae*		25,CC/26-2	21,CC/22-1
	CP16b *C. formosus*		26-3/27-2	22-2/22,CC

Figure 3. Zonal and geologic age assignments for cores from Sites 558 and 563, based on calcareous nannofossil assemblages. The highest and lowest sections are listed with a slash between them.

in the nannofossil assemblages. The discoasters present, *D. deflandrei* and *D. tanii*, are quite heavily overgrown, whereas the placoliths show the effects of dissolution.

No acme of *Coccolithus subdistichus* (included in *Clausicoccus fenestratus*) is present at the base of Hole 558, indicating that the lowermost sediment core belongs to the *C. formosus* Subzone (CP16b). However, because acmes can be environmentally controlled, the assignment of 558-27-2, 42–44 cm through 558-26-3, 16–18 cm to this subzone is tentative, and this Oligocene assemblage may actually be slightly older. It should also be noted that because of overgrowth, perforation counts could not be made for the central area of specimens of *Clausicoccus*, so the various species of that genus could not be distinguished. In this study, therefore, all forms are categorized under *C. fenestratus*. *Coccolithus formosus* is generally abundant in the above interval. *Coccolithus pelagicus, Cyclicargolithus floridanus, Discoaster deflandrei, Reticulofenestra bisecta, R. umbilica, Sphenolithus moriformis*, and *Zygrhablithus bijugatus* are abundant to very abundant, whereas *Bramletteius serraculoides* and *Isthmolithus recurvus* are common.

The holococcolith *Lanternithus minutus* is common to abundant from 558-26-4, 16–18 cm through 558-25-3,

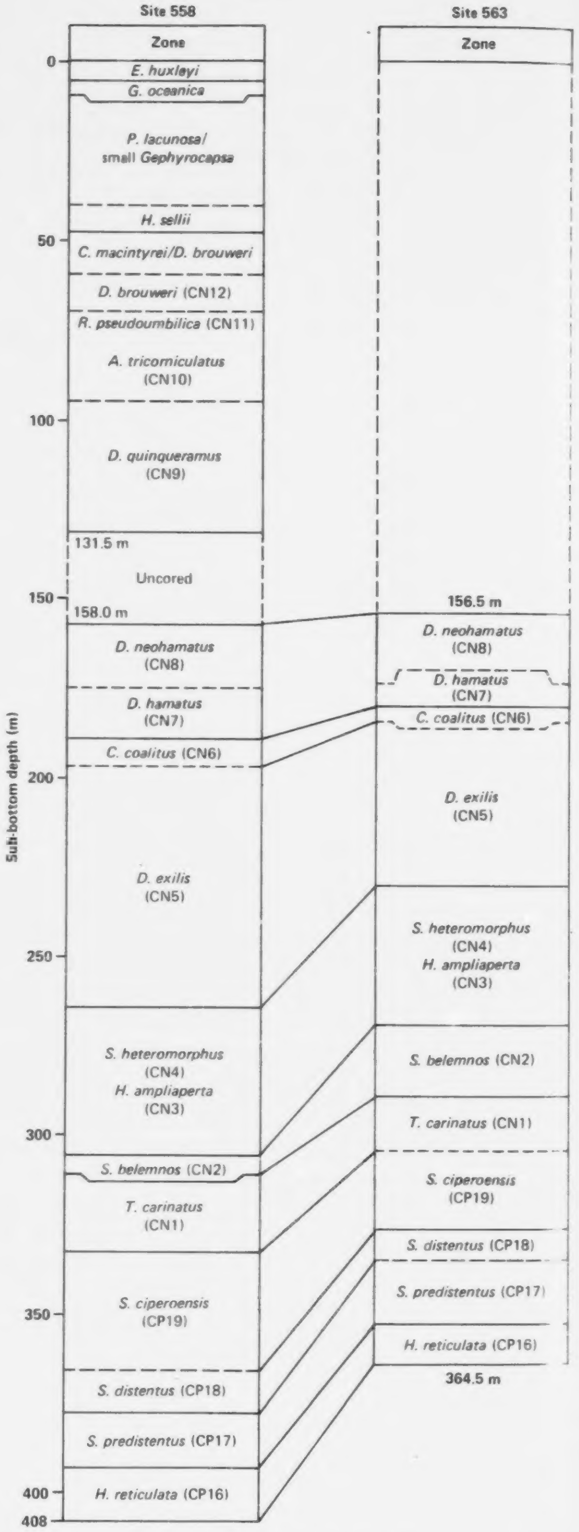
Site 558
Site 563
Zone
Zone
E. huxleyi
G. oceanica
P. lacunosa/ small Gephyrocapsa
H. sellii
C. macintyrei/D. brouweri
D. brouweri (CN12)
R. pseudoumbilica (CN11)
A. tricorniculatus (CN10)
D. quinqueramus (CN9)
131.5 m
Uncored
158.0 m
D. neohamatus (CN8)
D. hamatus (CN7)
C. coalitus (CN6)
D. exilis (CN5)
S. heteromorphus (CN4) H. ampliaperta (CN3)
S. belemnos (CN2)
T. carinatus (CN1)
S. ciperoensis (CP19)
S. distentus (CP18)
S. predistentus (CP17)
H. reticulata (CP16)
156.5 m
364.5 m
Sub-bottom depth (m)
0
50
100
150
200
250
300
350
400
408

Figure 4. Zonal correlations for Sites 558 and 563.

READEX FICHE best copy available

Table 1A. Distribution of calcareous nannofossils in Hole 558.

	Hole 558																																		
Age	Zone	Core-Section (interval in cm)	Abundance	Preservation	*Calcidiscus leptoporus / C. macintyrei*	*Catinaster calyculus*	*C. coalitus*	*C. miopelagicus*	*C. pelagicus*	*Coronocyclus nitescens*	*Cyclicargolithus floridanus*	*Discoaster aulakos*	*D. bellus*	*D. bollii*	*D. braarudii*	*D. brouweri*	*D. challengeri*	*D. deflandrei*	*D. exilis*	*D. hamatus*	*D. kugleri*	*D. moorei*	*D. neohamatus*	*D. pentaradiatus*	*D. prepentaradiatus*	*D.* sp. cf. *D. bolli*	*D. variabilis*	*Helicosphaera* spp.	*Minylitha convallis*	*Pontosphaera ovata / P. segmenta*	*Reticulofenestra pseudoumbilica*	small reticulofenestrids	*Sphenolithus heteromorphus*	*S. moriformis* plexus	*Triquetrorhabdulus rugosus*
Miocene	*Discoaster neohamatus* Zone (CN8) *Discoaster bellus* Subzone (CN8a)	1-1, 40–41	A	M-G	V				V				F		A	A							C	C	A		A	A	A		A	V		A	A
		1-2, 40–41	A	M-G	A				V						A	A							C	C	C		A	A	A		A	V		A	C
		1-3, 40–41	A	M-G	A				V				F		V	A				R			C	C	F		A	A	A		A	V		A	C
		1-4, 40–41	A	M-G	V				V				F		V	A							C	C	F		A	A	A		A	V		A	C
		1-5, 40–41	A	M-G	A				V				F		V	C							C	F	F		A	A	A		A	V		A	C
		1-6, 40–41	A	M-G	V				V				F		V	C							C	F	F		A	A	A		A	V		A	A
		1-7, 48–49	A	M-G	A				V				F	F	V	C				R			C	F	F		A	C	A	R	V	V		A	C
		1,CC	A	M-G	A				V				C	F	A	F							A	C	F		A	C	A		V	V		A	C
		2-1, 113–114	A	M-G	A				V				A	F	A	F							A	F	F		A	A	A		A	V		A	A
		2-2, 113–114	A	M-G	V				V				A	F	A								C	C	F		A	C	A		A	V		A	A
		2-3, 113–114	A	M-G	V				V				A	F	A								C	F	C		A	A	A		C	V		A	C
		2-4, 113–114	A	M-G	V				V				A	F	A								A	F	F		A	C	A	R	A	V		A	A
		2-5, 113–114	A	M-G	V				V				A	F	A								A	F	F		A	C	A		A	V		A	C
	Discoaster hamatus (CN7)	2-6, 35–36	A	M-G	V	F			V				A	F	A								A	F	F		A	A	C		A	V		A	C
		2,CC	A	M-G	V	F			A				A	F	A								C		F		A	C	C		A	V		A	C
		3-1, 60–61	A	M-G	V	C			A				A		A		F			C			F				A	F	F		A	V		C	C
		3-2, 60–61	A	M-G	V	C			A				A		A					C			F				A	C		R	A	V		A	C
		3-3, 60–61	A	M-G	V	C			A				C		C		F			F			F				A				V	V		A	A
		3-4, 60–61	A	M-G	V	C			A				C		C					F							A				A	V		C	C
		3-5, 60–61	A	M-G	V	C			A				C		F		F			F							A	C			A	V		C	C
		3-6, 60–61	A	M-G	V	C			A				C		F					F							A	C			A	V		C	A
		3,CC	A	M-G	V	C			A				C		C					F							A	C			A	V		A	C
		4-1, 60–61	A	M-G	V	C			A				F		F					F							A	F			A	V		F	C
		4-2, 60–61	A	M-G	V	C	F		A				C		F		F			F							A	F			A	V			C
		4-3, 60–62	A	M-G	V	C	F		A				F		F					R							A	C			A	V		C	A
		4-4, 60–61	A	M-G	V	C	F		A				F		F		F			R							A	A		R	A	V		A	C
		4-5, 60–61	A	M-G	V	F	C		A				R		F		F			R							A	C			C	V		C	C
	Catinaster coalithus/ Discoaster hamatus (CN6/CN7)	4-6, 60–61	A	M-G	V		C		A				F		F		F			?							A	F			A	V		C	C
		4-7, 16–18	A	M	A		F		A				F														A	C			A	V		C	C
		4,CC	A	M	A		F		A				F				F			?		F					A	A			A	V		C	C
	Catinaster coalitus (CN6)	5-1, 60–61	A	M	V		C		V								F					F					A				A	V		F	C
	Discoaster exilis (CN5) Discoaster kugleri (CN5b)	5-2, 60–61	A	M	A				A								F					F					A				A	V		C	A
		5-3, 60–61	A	M	V				A								F										A				A	V		C	A
		5-4, 60–61	A	M	A				V								F					F					A				A	V		C	A
		5-5, 60–61	A	M	A		r		A										F			F					A	F			A	V		C	A
		5-6, 60–61	A	M	A				V										F			F					A				A	V		C	A
		5,CC	A	M	A				V								F		R			F					A	F			A	V		C	A
		6-1, 60–61	A	M	V			A	V								F		C								A				A	V		F	A
		6-2, 60–61	A	M	A			A	A										C			F					A				C	V		F	C
		6-3, 60–61	A	M	A			A	A									F	A			F					A				C	V		F	A
		6-4, 60–61	A	M	A			A	A										C			F					A	F			C	V		C	A
		6-5, 60-61	A	M	A			A	A										C			F					A				A	V		F	C
		6-6, 60–61	A	M	A			A	A										C			F					A				A	V		F	C
		6,CC	A	M	A			C	A										A			C					A	F			A	V		C	C
		7-1, 13–15	A	M	A			C	V										A		C	F					A	F			A	V		C	C
		7,CC	A	M	A			C	V										A		C						A	C			V	V		A	A
	Coccolithus miopelagicus (CN5a)	8-1, 60–63	A	M	A			A	V		C								A								A	F			A	V		C	A
		8-2, 60–63	A	M	A			A	V		A								A								A				A	V		C	A
		8-3, 60–63	A	M	A			A	V		C								A								A	C			A	V		C	A
		8-4, 60–63	A	M	A			A	V		C							F	A								A	C			A	V		C	A
		8,CC	A	M	A			A	V		C								A								A	A			A	V		A	A
		9-1, 14–16	A	M	A			A	V		F							F	A								A	A			A	V		A	C
		9-2, 60–63	A	M	A			A	V	F	F								A			F					A				A	V		C	A
		9,CC	A	M	A			A	V		F								A			F					A	F			A	V		C	A
		10-1, 59–60	A	M	A			A	V		F								A								A	A			C	V		C	C
		10,CC	A	M	A			A	V		C								A								A	A				V		C	R
		11-1, 60–63	A	M	A			A	V		C								A			C					A	A				V		A	F
		11-2, 60–63	A	M	A			A	V		C								A			F					C					V		C	F
		11,CC	A	M	C			A	V		C								A								A	F				V		C	
		12-1, 60–62	A	M	A			A	V		C								A								A	A				V		C	
	Helicosphaera ampliaperta/ Sphenolithus heteromorphus (CN3/CN4)	12-2, 60–62	A	M	C			A	V		C								A								A	C				A	C	C	
		12-3, 40–42	A	M	A			C	V		C								A							R	A	F				A	A	C	
		12-4, 60–62	A	M	C			A	V		C								A			F				R	A	C				A	A	C	
		12-5, 8–10	A	M	A			A	V		C							F	A							F	A	F				V	A	C	
		12,CC	A	M	C			A	V		A								A							F	A	F				V	A	C	
		13-1, 60–62	A	M	C			A	V	F	A							F	A							F	A	C				A	A	A	
		13-2, 60–62	A	M	C			A	V	F	A								A							C	V	A				A	A	C	
		13-3, 60–62	A	M	A			F	V		A								A								V	A				V	A	C	
		13-4, 60–62	A	M	C			C	V		A							F	A								V	C				V	C	A	
		13-5, 60–62	A	M	C			C	V		A							F	F								A					F	A	A	
		13,CC	A	M	C			C	V		F								A								V	A		F		V	A	F	
		14-1, 60–62	A	M	C			C	V	F	C							F	A			F					V	A				A	A	C	
		14-2, 60–62	A	M	A			C	V	F	A							F	A								V	C				A	A	C	
		14-3, 60–62	A	M	A			A	V	F	V							F	A								A	A				C	A	A	
		14-4, 60–62	A	M	C			C	V		V							F	A								A	C				C	A	A	
		14-5, 60–62	A	M	C			C	V	F	V	F						F	A								A	F				A	A	C	
		14-6, 60–62	A	M	A			C	V		V	A						A	C								A	A				A	A	A	
		14,CC	A	M	A			C	V		C	A						A	F								A	A				V	A	A	

Table 1B. Distribution of calcareous nannofossils in Hole 558.

Hole 558				Abundance	Preservation	Braarudosphaerid fragments?	*Bramletteius serraculoides*	*Calcidiscus leptoporus/C. macintyrei*	*Chiasmolithus altus*	*Clausicoccus fenestratus*	*Coccolithus eopelagicus*	*C. formosus*	*C. miopelagicus*	*C. pelagicus*	*Coronocyclus nitescens*
Age	Zone	Subzone	Core-Section (interval in cm)												
Miocene	*Helicosphaera ampliaperta/ Sphenolithus heteromorphus* (CN3 and CN4)		15-1, 53–55	A	M			A						V	
			15-2, 6–8	A	M			A						V	
			15-3, 60–62	A	M			A					F	V	
			15-4, 60–62	A	M			A						V	F
			15-5, 78–80	A	M			C						A	
			15-6, 78–80	A	M			C						V	
			15,CC	A	M			C						V	F
			16-1, 60–62	A	M			F						V	C
			16-2, 60–62	A	M									V	C
			16-3, 60–62	A	M			F						V	A
			16-4, 60–62	A	M			F						V	A
	Sphenolithus belemnos (CN2)		16-5, 60–62	A	M			C						V	A
			16-6, 60–62	A	M			F						V	C
			16,CC	A	M			F						V	A
			17-1, 56–58	A	M			F						V	A
	Triquetro-rhabdulus carinatus (CN1)	*Discoaster druggii* (CN1c)	17-2, 60–62	A	M									V	A
			17-3, 60–62	A	M								F	V	C
			17-4, 60–62	A	M								C	A	C
			17,CC	A	M								A	V	C
			18-1, 60–62	A	M								A	V	C
			18-2, 60–62	A	M								A	V	F
		Cyclicargolithus abisectus/ Discoaster deflandrei (CN1a/CN1b)	18-3, 60–62	A	M								A	V	C
			18-4, 60–62	A	M								A	A	C
			18,CC	A	M					F			C	V	C
Oligocene			19-1, 60–62	A	M								C	V	C
			19-2, 60–62	A	M					A			F	V	A
			19-3, 60–62	A	M					C			A	V	C
	Sphenolithus ciperoensis (CP19)	*Dictyococcites bisectus* (CP19b)	19-4, 60–62	A	M					F			C	V	C
			19-5, 60–62	A	M					F				V	C
			19,CC	A	M									V	
			20-1, 60–62	A	M					C				V	C
			20-2, 60–62	A	M					C			C	V	F
			20-3, 60–62	A	M					C			C	V	C
			20-4, 60–62	A	M					F	C			V	C
			20-5, 20–22	A	M					F	C			V	C
			20,CC	A	M					F	A			V	R
			21-1, 60–62	A	M					F	C			V	F
			21-2, 60–62	A	M					F	C			V	R
			21-3, 20–22	A	M				F	C	C			V	C
			21,CC	A	M					F	A			V	C
		Cyclicargolithus floridanus (CP19a)	22-1, 60–62	A	M					F	A			V	C
			22-2, 60–62	A	M					F	C			V	C
			22-3, 60–62	A	M					F	C			V	F
			22-4, 60–62	A	M				R	F	A			V	C
			22,CC	A	M						A			V	C
	Sphenolithus distentus (CP18)		23-1, 30–32	A	M				F	F	A			V	C
			23-2, 30–32	A	M					C	A			V	C
			23-3, 30–32	A	M					F	A			V	C
			23-4, 30–32	A	M				C	F	A			V	F
			23-5, 30–32	A	M				R	F	C			V	C
			23-6, 30–32	A	M						C			V	C
			23,CC	A	M						A			V	C
			24-1, 40–42	A	M						A			V	F
	Sphenolithus predistentus (CP17)		24-2, 40–42	A	M				A	R	A			V	C
			24-3, 40–42	A	M				C	F	A			A	F
			24-4, 40–42	A	M					F	A			V	C
			24,CC	A	M				F	F	C			V	F
			25-1, 97–99	A	M				C	F	C			V	C
			25-2, 97–99	A	M				C	C	A			V	C
			25-3, 97–99	A	M					F	C			V	C
			25-4, 97–99	A	M				C	F	A			V	C
			25-5, 97–99	A	M					F	A			V	F
			25-6, 120–122	A	M				C	F	C			V	
	Helico-sphaera reticulata (CP16)	*Reticulofenestra hillae* (CP16c)	25,CC	A	M				F	R	A			V	
			26-1, 16–18	A	M				F	C	A			V	F
			26-2, 16–18	A	M	R	R		C	A	C			V	
		Coccolithus formosus (CP16b) ?	26-3, 16–18	A	M	F	C		F	A	A	C		V	
			26-4, 16–18	A	M	F	C			C	A	A		A	
			26-5, 16–18	A	M	F	C			F	C	A		A	
			26,CC	A	M	F	C				C	A		A	F
			27-1, 35–37	A	M	F	C				C	A		A	
			27-2, 42–44	A	M	F	C		F		C	A		V	

Table 1B. (Continued).

Cyclicargolithus abisectus	*C. floridanus*	*Discoaster aulakos*	*D. deflandrei*	*D. druggii*	*D. exilis*	*D. tani/D.* sp. cf. *D. tani*	*D. variabilis*	*Helicosphaera* spp.	*Isthmolithus recurvus*	*Lanternithus minutus*	*Lepidodiscus larvalis*	*Pontosphaera ovata/P. segmenta*	*Reticulofenestra bisecta*	*R. hillae*	*R. lockeri*	*R. umbilica*	Small reticulofenestrids	*Sphenolithus belemnos*	*S. ciperoensis*	*S. conicus*	*S. distentus*	*S. heteromorphus*	*S. moriformis* plexus	*S. predistentus*	*S. pseudoradians*	*Triquetrorhabdulus carinatus*	*T. milowii*	*Zygrhabdithus bijugatus*
	V	A	A		F		A	A									A					A	A				F	
	V	A	A		F		A	A									C					A	A				F	
	V	A	A		F		A	F														V	V				C	
	V	A	A				F	F														V	V				F	
	V	A	V																			A	A				F	
	V	A	V																			A	A				F	
	V	A	V																			A	V				F	
	V	A	V					F														A	V				F	
	V	A	V																			A	A				C	
F	V	F	V					C														A	A				C	
F	V		V																			C	V				A	
F	V		V															A					A			F	A	
F	V		V					F										A					A			A	C	
C	V		V															A					A			F	C	
C	V		V	F														A					A			C	C	
A	V		V	C																			A			F		
A	V		V	C		F						F											V			F		
C	V		V	C																			A			C		
A	V		V	F																			V			A		F
A	V		V	C		F																	V			A		F
A	V		V	C		F																	V			A		
C	V		V			R		F															A			A		F
A	V		V			F		F				F	R										V			A		
A	V		V			F							F										V			A		
A	V		V			F		F					C							C			V			A		
V	V		V			F		F				F	R							A			V			A		A
A	V		V			F		F					R							F			V			A		A
C	V		V			F						F	C						C	F			V			A		A
A	V		V			F						F	C						A				V			A		A
V	V		V			F						F	A						C				V			A		A
A	V		V			F		F				F	A						A				V			A		A
A	V		V			F		C				F	A						A				V			A		A
V	V		V			F							A						A				V			A		A
A	V		V			F						F	A						A				V			A		C
A	V		V					R				F	A						A				V			A		C
A	V		V			F						F	A						A				V			C		A
A	V		V			F						F	A						A				V			A		A
V	V		V			C							A						A				V			A		A
A	V		V			F						F	A						A				V			A		A
A	V		V			R						F	A						C				V			A		A
V	V		A			F		F				C	A						R		C		V	A		C		A
V	V		V			C						F	A						F		C		V	A		C		A
V	V		V			C						F	A						R		F		V	C		F		A
V	V		A			C						F	A						F		A		V	C		F		A
A	V		A			C							A		F				F		A		V	A	F	F		A
A	V		A			F						F	A		F						A		V	F		F		A
V	V		A			C		R				F	A		F						A		V	F	F	F		A
C	V		A			C		C				F	A		F						A		V	F	F	F		V
C	V		A			C		F			F	F	A								A		V	C				A
C	V		A			C		F				C	A		F						A		V	A	F			A
C	V		A			C		A				R	A		F						A		V	A	F			V
C	V		A			C		C					A								C		V	A	F			A
C	V		A			A		A					A								C		V	A				A
C	V		A			A		A			F	R	A										V	A	F			A
C	V		A			A		C					A										V	A	F			A
C	V		A			A		A					A										V	A	C			A
C	V		A			A		C				R	A										V	A				A
C	V		C			C		C			F		A										V	A	F			V
C	V		A			A		C			C		A										V	A				A
A	V		A			A		C		C	C	C	A										A	A	F			A
A	V		A			C		C		C	C		A										V	A				A
C	V		A			A		F		C			A										V	A	F			V
C	V		A			A		F	F	A			A										A	A	F			V
C	V		A			A		F	C	A			A			R							A	A	F			A
C	V		A			A		A	C	A	F		A	F		C							V	A				V
F	V		A			A		C		A	C	R	A	F		C							V	C	F			V
	V		A			C			R	C			A	C		A							A	F				V
	V		A			C			C	C			A	C		A							A	R	F			A
	V		A			A			C				A	A		A							A		C			A
	V		A			A			C				A	A		A							A					A
	V		A			A			A				A	A		A							A					A
	V		V			A			A				A	A		A							V					A

97–99 cm, but is heavily overgrown. A couple of very rare intact specimens of the genus *Braarudosphaera* were found in a sediment sample taken at the sediment/basalt contact. Calcite particles that may be from braarudosphaerid pentaliths were observed in the next few sections. However, because of the moderate preservation and the rarity of these particles, their identification must remain tentative.

Samples 558-26-2, 16–18 cm through 558-25,CC are placed in the *Reticulofenestra hillae* Subzone (CP16c). *Reticulofenestra umbilica* is common in 558-26-2, 16–18 cm and 558-26-1, 16–18 cm, but rare in Sample 558-25,CC.

The holococcoliths *L. minutus* and *Z. bijugatus* occur abundantly in the *R. hillae* Subzone (CP16c). *Clausicoccus fenestratus* is generally common. *Cyclicargolithus abisectus* and *Leptodiscus larvalis* first appear in this subzone.

Because the lower size limit of *C. abisectus* was not set unequivocally by the author of the species or by any subsequent investigator, it is important to state the size criterion used here for distinguishing this taxon from *C. floridanus*. Based on measurements of the holotype, in our opinion, specimens must be 9 μm or larger to be considered *C. abisectus*.

Samples 558-25-6, 120–122 cm through 558-24-2, 40–42 cm are assigned to the *Sphenolithus predistentus* Zone (CP17). *Sphenolithus predistentus* occurs abundantly throughout this zone. Both *I. recurvus* and *L. minutus* have their last appearances within the *S. predistentus* Zone (CP17). Few to common occurrences of *Coronocyclus nitescens* are noted in this interval.

Samples 558-24-1, 40–42 cm through 558-23-1, 30–32 cm are placed in the middle Oligocene *Sphenolithus distentus* Zone (CP18). Preservation of the assemblages within this zone is moderate. *Sphenolithus distentus* is common to abundant throughout this interval. Specimens of *Triquetrorhabdulus carinatus*, although few in number, first appear in this zone. *Zygrhablithus bijugatus* remains abundant to very abundant.

Samples 558-22,CC through 558-19-4, 60–62 cm are assigned to the upper Oligocene *Sphenolithus ciperoensis* Zone (CP19). The lower zonal boundary is questionable due to the rare occurrences of *S. ciperoensis*, the zonal marker, throughout Core 558-22. *Sphenolithus ciperoensis*, being both small in size (4–6 μm) and rare in these samples, could easily be missed during smear-slide examination. Alternatively, some might consider its presence in such small numbers to be the result of downhole contamination. Preservation is moderate throughout this zone.

The *Cyclicargolithus floridanus* Subzone (CP19a) is recognized in 558-22,CC through 558-22-1, 60–62 cm. *Sphenolithus distentus* and *S. predistentus* are common to abundant, but *S. ciperoensis* is generally rare. Specimens of *T. carinatus* are few to common in this interval.

Samples 558-21,CC through 558-19-4, 60–62 cm are placed in the *Dictyococcites bisectus* Subzone (CP19b). *Sphenolithus ciperoensis* is generally abundant throughout this subzone, as are *T. carinatus* and *Z. bijugatus*.

Although the last occurrence of *Sphenolithus ciperoensis*, the principal upper zonal marker for the *S. ciperoensis* Zone (CP19), is found in Section 558-19-4, *Reticulofenestra bisecta*, used as a secondary marker by Bukry (1973b; 1975), persists in small numbers through 558-18-4, 60–62 cm. Roth et al. (1971) noted that *R. bisecta* has its last occurrence below the LAD (last appearance datum) of *S. ciperoensis*. Bukry (1973b) commented that the disappearance of *R. bisecta* near the LAD of *S. ciperoensis* at the top of the *S. ciperoensis* Zone (CP19) could be used as a guide for recognizing the top of this zone in high latitudes where *S. ciperoensis* may not be a useful marker. In this North Atlantic section, there could be several reasons for the occurrence of *R. bisecta* above the last occurrence of *S. ciperoensis*. One possibility is that the LAD of *R. bisecta* actually occurs somewhat higher than the LAD of *S. ciperoensis*. A second possibility is that the higher occurrences of *R. bisecta* represent reworking of this taxon. A third possibility is that *S. ciperoensis* may be absent or too rare to be a useful marker due to latitudinal considerations. This, however, seems unlikely because *S. ciperoensis* is common to abundant in many samples in this stratigraphic section. Therefore, we consider the occurrence of *S. ciperoensis* to be a reliable datum and attribute the high occurrences of *R. bisecta* to one of the first two possibilities discussed above.

Preservation is moderate in the *Triquetrorhabdulus carinatus* Zone (CN1), which spans the Oligocene/Miocene boundary. Samples 558-19-3, 60–62 cm through 558-17-2, 60–62 cm are assigned to this zone. The *Cyclicargolithus abisectus* Subzone (CN1a) cannot be recognized in this section because *C. abisectus* occurs abundantly throughout the entire *T. carinatus* Zone. Obviously, the *Discoaster deflandrei* Subzone (CN1b) cannot be differentiated from the lower subzone because of the continued abundance of *C. abisectus*. Samples 558-19-3, 60–62 cm through 558-18-3, 60–62 cm are placed in the combined *C. abisectus/D. deflandrei* Subzones (CN1a and CN1b) based on the absence of *S. ciperoensis* and of *D. druggii*.

Many discoasters may resemble *D. druggii*, especially when the preservation is poor. Large 6-rayed discoasters with bluntly rounded tips and broad central areas occur commonly and consistently in this section. These discoasters average about 20 μm in diameter and are presumed to be *D. druggii*. However, because of overgrowth, absolute identification of these discoasters as *D. druggii* is impossible. Therefore, the *D. druggii* Subzone (CN1c) of the *T. carinatus* Zone is tentatively recognized in 558-18-2, 60–62 cm through 558-17-2, 60–62 cm.

Occurrences of discoasters resembling *D. tanii*, designated *D.* sp. cf. *D. tanii*, are found as high as 558-17-3, 60–62 cm, within the *T. carinatus* Zone. In addition, *Clausicoccus fenestratus* ranges unusually high in this North Atlantic section. The last occurrence of *Clausicoccus fenestratus* is in the *T. carinatus* Zone (CN1) in Sample 558-18,CC. Specimens of *C. fenestratus* are few in number in this sample, but *C. fenestratus* occurs abundantly in 558-19-2, 60–62 cm. Roth (1970, p. 841) also recorded a long range for *C. fenestratus* in Trinidad, noting that it ranged through the *S. ciperoensis-T. carinatus* Zone (perhaps reworked). On the Falkland Plateau, Wise (1983) noted the abrupt disappearance of *C. fenestratus* s.l. in the lower Oligocene below the *Reticulofenestra umbilica* datum.

Samples 558-17-1, 56–58 cm through 558-16-5, 60–62 cm are assigned to the lower Miocene *S. belemnos* Zone (CN2). *S. belemnos* occurs abundantly throughout this interval. *Triquetrorhabdulus milowii* is common to abundant, but quite overgrown, as preservation is moderate in this zone.

Martini (1971) used the last occurrence of *Triquetrorhabdulus carinatus* as a zonal marker. According to Martini's zonation, the NN3 Zone, defined as the interval from the last occurrence of *T. carinatus* to the last occurrence of *S. belemnos*, would be absent in this section, because the last appearance of both *T. carinatus* and *S. belemnos* is in 558-16-5, 60–62 cm. Therefore, if Martini's (1971) zonation were followed here, a lower Miocene hiatus would be present. However, we do not consider *T. carinatus* a particularly reliable marker and do not specifically designate a hiatus at this point. Preservation is moderate, and *T. carinatus* is both broken and heavily overgrown and thus difficult to positively identify (see additional comments on this interval in the Hole 563 discussion).

Preservation of nannofossil assemblages is moderate in the lower to lower middle Miocene of Hole 558. *Helicosphaera ampliaperta*, if present, is very rare and difficult to identify. There are several placolith rims present in the various samples, but we could not positively identify any specimens of *H. ampliaperta*. Because we did not observe *Helicosphaera ampliaperta*, it is difficult to differentiate the *H. ampliaperta* Zone (CN3) from the overlying *S. heteromorphus* Zone (CN4). Alternative markers are discussed below but are considered generally unreliable in this North Atlantic section. Consequently, the *H. ampliaperta* Zone (CN3) is not separated from the *S. heteromorphus* Zone (CN4) in this study. Samples 558-16-4, 60–62 cm through 558-12-2, 60–62 cm are assigned to the combined *H. ampliaperta/S. heteromorphus* Zones (CN3 and CN4). *Sphenolithus heteromorphus* is generally abundant throughout this interval.

Various criteria have been used by different workers to separate the *H. ampliaperta* and *S. heteromorphus* Zones when *H. ampliaperta* is not present. Bukry (1973b), working in the low latitudes, used the end of the *D. deflandrei* acme. He noted that this datum occurs at the top of the *H. ampliaperta* Zone and is distinctive in low latitude areas. However, the use of an acme to define a zonal boundary is not generally desirable, because the end of an acme may vary from place to place for a variety of reasons. Site 558 is not considered a low latitude DSDP site, and it is highly questionable whether the end of the *D. deflandrei* acme in 558-14-5, 60–62 cm coincides with the top of the *H. ampliaperta* Zone.

In the Site 558 chapter (this volume), the first appearance of long-armed discoasters was used to separate the *H. ampliaperta* (CN3) and *S. heteromorphus* (CN4) Zones. *Discoaster variabilis*, the first long-armed discoaster to appear in the column, first occurs in 558-15-4, 60–62 cm. *Discoaster variabilis* is few in number in this sample and abundant in higher samples.

Jiang and Gartner (1984) noted that, in the absence of *H. ampliaperta*, the first common occurrence of *Discoaster variabilis* can be used to subdivide the *H. ampliaperta* and *S. heteromorphus* Zones. On their range charts, Jiang and Gartner used the first appearance of *D. variabilis* even if numbers were few instead of common. *Discoaster deflandrei* was often common both above and below this level. To indicate uncertainty, Jiang and Gartner dashed the zonal boundary.

It is apparent that the positioning of any boundary between the *H. ampliaperta* and *S. heteromorphus* Zones in this section would be highly subjective. There is a difference of approximately one entire core between the boundary determined by the use of the end of the *D. deflandrei* acme and that determined by the use of the first appearance of long-armed discoasters. A shift in dominance among the discoasters from *D. deflandrei* to long-armed discoasters such as *D. variabilis* and *D. exilis* has also been used to separate these zones. This change may occur at yet another level. In this section, *D. exilis* has its first occurrence and *D. variabilis* becomes abundant in 558-15-3, before the end of the *D. deflandrei* acme in 558-14-5. In summary, we choose not to separate the *H. ampliaperta* Zone (CN3) from the *S. heteromorphus* Zone (CN4) in this study, because we did not observe *H. ampliaperta* and because a reliable alternate marker is lacking in this North Atlantic section.

Heavily overgrown 6-rayed discoasters with large central areas (6–8 μm) and large stellate stems, denoted as *D.* sp. cf. *D. bollii* on the range chart, occur commonly in 558-13-1, 60–62 cm and rarely in several overlying sections. These discoasters lack the tapered rays and bifurcated tips characteristic of *D. bollii*. Their occurrence in the *H. ampliaperta/S. heteromorphus* zones is stratigraphically lower than the occurrence of *D. bollii*.

Samples 558-12-1, 60–61 cm through 558-5-2, 60–62 cm are assigned to the middle Miocene *Discoaster exilis* Zone (CN5). *Discoaster kugleri*, the first appearance of which is used to subdivide this zone, occurs commonly in two samples in this interval, 558-7-1, 13–15 cm and 558-7,CC. Core recovery was very poor in Core 558-7; only 9% of the interval was recovered. Except for this species, there are no other significant first occurrences to serve as alternate markers. The last occurrence of *Cyclicargolithus floridanus* was used by Bukry (1975) as an auxiliary marker. However, *C. floridanus* has been found to occur commonly in the *D. kugleri* Subzone (CN5b) in some areas (Roth and Thierstein, 1972). In the present study, the last occurrence of *C. floridanus* is in 558-8-1, 60–63 cm and may be stratigraphically useful. Therefore, Samples 558-12-1, 60–62 cm through 558-8-1, 60–63 cm are assigned to the *Coccolithus miopelagicus* Subzone (CN5a). The upper subzonal boundary is dashed because preservation is moderate, and, although rare specimens of *D. kugleri* may be present below 558-7,CC, they would be difficult to identify. Samples 558-7,CC through 558-5-2, 60–62 cm are assigned to the *Discoaster kugleri* Subzone (CN5b).

Sample 558-5-1, 60–61 cm is placed in the *Catinaster coalitus* Zone (CN6). *Catinaster coalitus* is common and preservation is moderate-good in this sample. The lower zonal boundary is dashed due to moderate preservation below Section 558-5-1 and difficulty in identifying *Catinaster coalitus*. In Sample 558-5-5, 60–61 cm, a couple of rare specimens of *C. coalitus* were found. In other samples, small (4–8 μm), irregular, and generally circular particles of calcite are present that could be very heavily overgrown specimens of *C. coalitus*. Small discoasters of similar size are also present within this interval. Mobile mounts were made in an attempt to determine the presence of *C. coalitus*, but overgrowth was so extreme that positive identification was impossible. Therefore, the presence of rare *C. coalitus* in Section 558-5-5 may be the result of downhole contamination or may indicate extension of the *C. coalitus* Zone (CN6) downsection to at least this level, if not lower. In summary, it is likely that *C. coalitus* is present below 558-5-1, 60–61 cm, but preservation prohibits the placement of a definite lower zonal boundary.

Samples 558-4,CC through 558-4-6, 60–61 cm are placed in the *Catinaster coalitus* (CN6)/*Discoaster hamatus* (CN7) zones. Preservation ranges from moderate to moderate-good. *Catinaster coalitus* is few to common. *Discoaster bellus* first appears in 558-4,CC and is few in number throughout this interval. In addition, 5-rayed 14–16 μm discoasters which may be *D. hamatus* are few to rare and are denoted by a question mark on the range chart. These discoasters usually have broken arms and no larger specimens are present, so we can only tentatively identify these specimens as *D. hamatus*. Jiang and Gartner (1984) noted the first appearance of *D. bellus* and *D. hamatus* within the same sample in their South Atlantic study. If the first *D. bellus* can be used as an indicator of the base of the *D. hamatus* Zone (CN7), then CN7 would begin in 558-4,CC.

Samples 558-4-5, 60–61 cm through 558-2-6, 35–36 cm are assigned to the *Discoaster hamatus* Zone (CN7). Preservation is moderate-good throughout this interval. In Sections 558-4-5 through 558-4-3, specimens of *D. hamatus* are rare and small (14–16 μm; the species was originally described as 16–25 μm in diameter by Martini and Bramlette, 1963) and often have broken arms. Therefore, it is difficult to positively identify *D. hamatus* in this part of the zone. *Catinaster calyculus*, however, is easily identified and its presence indicates that these samples are in the *D. hamatus* Zone (CN7). *Catinaster calyculus* is generally common throughout the *D. hamatus* Zone of this hole. In 558-4-2, 60–61 cm, specimens of *D. hamatus* range up to 22–24 μm in diameter. *Discoaster hamatus* is few to common from Section 558-4-2 through 558-2,CC. The upper zonal boundary is dashed because in 558-2-6, 35–36 cm, specimens of *D. hamatus* are 14–16 μm, rare, broken, and difficult to positively identify. *Catinaster calyculus*, however, is still present. Because 558-2-6, 35–36 cm is the last sample in which *C. calyculus* is found, the *D. hamatus* Zone should not extend above this level. The zonal boundary could be slightly lower, because *C. calyculus* may range into the *Discoaster bellus* Subzone (CN8a) of the *Discoaster neohamatus* Zone (CN8). It is interesting to note that many specimens attributed here to *D. bellus* have rays that are somewhat curved at the ends, similar to those of *D. brouweri*.

Samples 558-2-5, 113–114 cm through 558-1-1, 40–41 cm are placed in the *Discoaster bellus* (CN8a) Subzone of the *Discoaster neohamatus* Zone (CN8), based in part on the presence of abundant *Discoaster prepentaradiatus* at the top of the interval. Preservation is moderate-good.

Hole 558A

Hole 558A (Table 2) was hydraulically piston cored to a total depth of 132 m when mechanical problems in the inner core barrel forced termination prior to biostratigraphic overlap. Upper Miocene to upper Pleistocene sediments were recovered from this interval. The calcareous nannofossils are abundant and preservation is generally good. A minor hiatus is detected at the Miocene/Pliocene boundary.

Samples 558A-16,CC through 558A-12-5, 60–62 cm are assigned to the upper Miocene *Discoaster quinqueramus* Zone (CN9). Core 558A-16 is placed in the *Discoaster berggrenii* Subzone (CN9a). At the base of this subzone, *D. loeblichii* and *D. berggrenii* co-occur. Although this co-occurrence was not noted by Bukry (1973b), Proto-Decima et al. (1978) and Mazzei et al. (1979) noted the co-occurrence of these discoasters in their sections. Based on the presence of *Amaurolithus primus* and of *D. quinqueramus*, 558A-15,CC through 558A-12-5, 60–62 cm are assigned to the *A. primus* Subzone (CN9b) of the *D. quinqueramus* Zone.

Samples 558A-12-4, 60–62 cm through 558A-9,CC (14–16 cm) are assigned to the *Triquetrorhabdulus rugosus* Subzone (CN10a) of the *Amaurolithus tricorniculatus* Zone (CN10). Few to common occurrences of *T. rugosus* are found in this interval. *Reticulofenestra pseudoumbilica* is very abundant. Numbers of sphenoliths vary from rare to abundant in this interval.

In 558A-9,CC a color change marks the position of a lower Pliocene hiatus. Sample 558A-9,CC (9–11 cm) contains abundant *R. pseudoumbilica*, common *Discoaster tamalis* and *Discoaster asymmetricus*, and few *Sphenolithus* spp. It is placed in the *D. asymmetricus* Subzone (CN11b) of the *R. pseudoumbilica* Zone (CN11). Subzone CN10b, CN10c, and CN11a of the lower Pliocene are absent.

Samples 558A-9,CC (9–11 cm) and 558A-9-4, 6–8 cm are assigned to the *D. asymmetricus* Subzone (CN11b). In 558A-9-4, 6–8 cm, *Reticulofenestra pseudoumbilica* is common and sphenoliths are few; this is the last consistent occurrence of both marker species. The upper boundary is uncertain due to reworking of *R. pseudoumbilica* and sphenoliths for a considerable distance upsection.

Samples 558A-9-3, 69–70 cm and 558A-9-2, 60–70 cm are placed in the *Discoaster tamalis* Subzone (CN12a) of the *Discoaster brouweri* Zone (CN12). *Calcidiscus macintyrei, D. brouweri, D. pentaradiatus, D. surculus, Gephyrocapsa caribbeanica, Helicosphaera carteri*, and *Pseudoemiliania lacunosa* are abundant in these samples.

Discoaster tamalis is abundant in 558A-9-3, 69–70 cm and few in number in 558A-9-2, 69–70 cm. The upper subzonal boundary is questionable due to reworking of *D. tamalis*. However, in higher samples *D. tamalis* is always rare and occurs sporadically.

Samples 558A-9-1, 127–128 cm through 558A-8-2, 70–71 cm are assigned to the combined *Discoaster surculus* (CN12b) and *Discoaster pentaradiatus* (CN12c) Subzones of the *D. brouweri* Zone (CN12) based on the absence of *D. tamalis* and the presence of both *D. surculus* and *D. pentaradiatus*. *Discoaster surculus* and *D. pentaradiatus* are common to abundant in lower samples of this interval. In 558A-8-2, 70–71 cm, only a few specimens of *D. pentaradiatus* are present, and *D. surculus* is rare. The upper boundary is uncertain due to reworking of both *D. surculus* and *D. pentaradiatus* throughout the remainder of the section.

Samples 558A-8-1, 70–71 cm through 558A-7-4, 70–71 cm are placed in the *Calcidiscus macintyrei* Subzone (CN12d) of Bukry's *Discoaster brouweri* Zone (CN12). It is uncertain whether Sections 558A-7-3 and 558A-7-2 are in the *C. macintyrei* Subzone or Gartner's *C. macintyrei* Zone. In Section 558A-7-4, triradiate forms of *D. brouweri* are common; triradiate forms are rare below this section and few in 558A-7-3. An increased abundance of triradiate *D. brouweri* may be used to indicate proximity to the LAD (last appearance datum) of *D. brouweri* (see Discussion and Conclusions section). The last appearance of *C. macintyrei* is in 558A-7-2, 70–71 cm, which also contains abundant 3-rayed and 6-rayed forms of *D. brouweri*. Above this sample, no 3-rayed forms of *D. brouweri* are found. The 6-rayed forms of *D. brouweri* drop in numbers to few or rare above 558A-7-2, 70–71 cm and are considered to be reworked. A short hiatus may be present with the *C. macintyrei* Zone of Gartner (1977) absent.

Samples 558A-7-1, 70–71 cm through 558A-6-2, 60–62 cm are assigned to Gartner's (1977) *Helicosphaera sellii* Zone. *Helicosphaera sellii* is few to common in this interval. The upper zonal boundary is questionable due to reworking of *H. sellii* in overlying cores. *Gephyrocapsa oceanica* occurs abundantly in this zone. Reworked discoasters in this interval include *D. brouweri* (6-rayed), *D. deflandrei, D. pentaradiatus, D. surculus*, and *D. variabilis*. *Discoaster brouweri* is found in every sample, but it is generally rare. Other reworked species occur sporadically.

Samples 558A-6-1, 52–54 cm through 558A-3-1, 60–62 cm are placed in the combined small *Gephyrocapsa* and *Pseudoemiliania lacunosa* Zones based on the absence of *H. sellii* and the presence of *P. lacunosa*. The abundances of small gephyrocapsids are very consistent throughout this section, so Gartner's (1977) small *Gephyrocapsa* Zone cannot be distinguished. *Pseudoemiliania lacunosa* is abundant to very abundant. Reworked species in this interval include *D. asymmetricus, D. brouweri* (6-rayed), *D. deflandrei, D. pentaradiatus, D. surculus, D. tamalis, D. variabilis*, and *H. sellii*.

Samples 558A-2,CC through 558A-2-5, 60–62 cm are assigned to the *Gephyrocapsa oceanica* Zone. *Calcidiscus leptoporus, Coccolithus pelagicus, Gephyrocapsa caribbeanica, G. oceanica, H. carteri*, and the small gephyrocapsids dominate the assemblages of this zone. There is considerable reworking in this interval, especially of discoasters.

Samples 558A-2-4, 60–62 cm through 558A-1-1, 44–45 cm are placed in the *Emiliania huxleyi* Zone based on the presence of *E. huxleyi* and confirmed by scanning electron microscopy. Reworked discoasters in this interval include *D. deflandrei, D. pentaradiatus, D. surculus*, and *D. variabilis*.

It is interesting to note that the interval of conspicuous reworking, which extends from the *Discoaster surculus* Zone to the present, coincides closely with the time of Northern Hemisphere glaciations as defined by Backman (1979) and Prell (1982). That being the case, this reworking probably reflects increased bottom current velocities associated with those glaciations.

SITE 563
(33°38.53′N; 43°46.04′W; water depth = 3796 m)

Site 563 is located on the west flank of the Mid-Atlantic Ridge about 96.5 km (60 mi.) south of the Hayes Fracture Zone (Fig. 1). Sediments recovered from the one hole drilled at this site consisted of calcareous pelagic ooze.

Hole 563

Hole 563 (Table 3) was washed down to 156.5 m before rotary coring was begun. The stratigraphic position of Core 563-1 was very close to that of Core 1 in Hole 558 (early late Miocene in age). The sedimentary section was then continuously cored from 156.5 m down to lower Oligocene basement at a depth of 364.5 m. A section very similar to that in Hole 558 was recovered and yielded calcareous nannofossils ranging from early Oligocene to early late Miocene in age.

All major nannofossil zones Okada and Bukry (1980) for this part of the geologic column are recognized, and no hiatuses in the cored section are apparent. Calcareous nannofossils are abundant and preservation is moderate throughout this hole.

The interval from 563-22,CC through 563-21,CC is assigned to the lower Oligocene *Helicosphaera reticulata* Zone (CP16). The most unusual aspect of this assemblage is the presence of abundant braarudosphaerids along with the holococcoliths *Lanternithus minutus, Peritrachelina joidesa*, and *Zygrhablithus bijugatus* (Fig. 5). This is the first report of abundant braarudosphaerids from the central North Atlantic. They occur as whole pentaliths and as disaggregated segments and persist upsection through Core 563-20. Their association with holococcoliths may have some depth connotation (see discussion and conclusions section).

Gartner and Bukry (1969) provide an excellent summary of Tertiary holococcoliths, with descriptions and light and transmission electron microscope illustrations of well-preserved specimens of many holococcoliths. The holococcoliths present in Hole 563 are not pristine but have undergone considerable diagenetic alteration and are heavily overgrown, thereby making identification difficult. Specimens of *Z. bijugatus* separate readily along

Table 2A. Distribution of calcareous nannofossils in Hole 558A.

	Hole 558A			Abundance	Preservation	*Calcidiscus leptoporus*	*C. macintyrei*	*Ceratolithus cristatus*	*C. rugosus*	*C. telesmus*	*Coccolithus pelagicus*	*Crenalithus doronicoides*	*Discoaster asymmetricus*	*D. berggrenii*	*D. brouweri* (3-rayed)	*D. brouweri* (6-rayed)	*D. deflandrei*	*D. pentaradiatus* (5-rayed)
Age	Zone	Subzone	Core-Section (interval in cm)															
Pleisto-cene	*Emiliania huxleyi* Zone		1-1, 44–45	A	G	V		F			A							r
			1,CC	A	G	V		F		R	A						r	
			2-1, 60–62	A	G	V		F		R	A							
			2-2, 60–62	A	G	V		F			A							
			2-3, 60–62	A	G	V		F		R	A							
			2-4, 60–62	A	G	V		F		R	A						r	r
	Gephyrocapsa oceanica Zone		2-5, 60–62	A	G	V		R			A		r			f		r
			2-6, 60–62	A	G	V		R			A					f		r
			2,CC	A	G	V		R			C							
	Pseudoemiliania lacunosa/ small *Gephyrocapsa* zones		3-1, 60–62	A	G	A					F	A				r		r
			3-2, 60–62	A	G	V		F			R	C						
			3-3, 60–62	A	G	V					F	F						
			3-4, 64–66	A	G	V					R	A						
			3-5, 60–62	A	G	V						V						r
			3-6, 60–62	A	G	V						V						
			3,CC	A	G	V					C	V						
			4-1, 60–62	A	G	V						V						
			4-2, 60–62	A	G	V						V				f		
			4-3, 60–62	A	G	V						V	r					r
			4-4, 60–62	A	G	V					C	A						
			4-5, 60–62	A	G	V					A	A						r
			4-6, 60–62	A	G	V					C	A						
			4,CC	A	G	V		R			C	V				r		
			5-1, 60–62	A	G	V	r				F	V						
			5-2, 60–62	A	G	V					A	A						
			5-3, 60–62	A	G	V					A	C						
			5-4, 60–62	A	G	V					C	C				f	r	f
			5-5, 60–62	A	G	V		R			A	C						
			5-6, 60–62	A	G	V					C	A						
			5,CC	A	G	V					F	A					r	
			6-1, 52–54	A	G	V						V		r				
	Helicosphaera sellii Zone		6-2, 60–62	A	G	V					C	A				f		
			6-3, 60–62	A	G	V					A	V				r	r	r
			6-4, 60–62	A	G	V					A	V				r		r
			6-5, 60–62	A	G	V					A	A				r		r
			6-6, 60–62	A	G	V					A	A				r		r
			6,CC	A	G	V		R			A	A				r		
			7-1, 70–71	A	G	V		R			C	C				r		r
	Calcidiscus macintyrei Zone		7-2, 70–71	A	G	V	A				A	A			A	A		r
			7-3, 70–71	A	G	V	A	R			A	V	r		F	C		r
Pliocene	*Discoaster brouweri* (CN12)	*C. macintyrei* Subzone (CN12d)	7-4, 70–71	A	G	V	A	R			A	V			C	A		r
			7-5, 70–71	A	G	A	A				A	V	r		R	A	r	
			7,CC	A	G	V	A	R			A	V			R	A		r
			8-1, 70–71	A	G	V	A	R			A	V			R	A		r
		Discoaster pentaradiatus/ *D. surculus* (CN12b/CN12c)	8-2, 70–71	A	G	V	A				A	V			R	C		F
			8-3, 70–71	A	G	V	A				V	V				A		A
			8-4, 70–71	A	G	V	A		R		A	V			R	A		A
			8-5, 70–71	A	G	V	A		R		V	V			R	A		A
			8,CC	A	G	V	A		F		V	V				A		A
			9-1, 127–128	A	G	V	A	R	F		V	V			R	A		C
		Discoaster tamalis (CN12a)	9-2, 69–70	A	G	A	A	R	F		V	V	C			A		A
			9-3, 69–70	A	G	V	A				A	V	C			A		A
	Reticulofenestra pseudoumbilica (CN11)	*Discoaster asymmetricus* (CN11b)	9-4, 6–8	A	G	V	A		R		V	V	C			A		A
			9,CC (9–11)	A	G	V	A				V	V	C		R	A		A

lower Pliocene hiatus

Table 2A. (Continued).

D. surculus	*D. tamalis*	*D. variabilis*	*Emiliania huxleyi*	*Gephyrocapsa caribbeanica*	*G. oceanica*	Small gephyrocapsids	*Helicosphaera carteri*	*H. sellii*	*Oolithotus antillarum*	*Pontosphaera* spp.	*Pseudoemiliania lacunosa*	*Reticulofenestra bisecta*	*R. pseudoumbilica*	*R. umbilica*	*Rhabdosphaera clavigera*	*R. procera*	*Scapholithus fossilis*	*Scyphosphaera apsteinii*	*S. conica*	*S. globulata*	*S. intermedia*	*S. kamptneri*	*S. lagena*	*S. pulcherrima*	*S. recurvata*	*S. rottiensis*	*S. tubifera*	*Sphenolithus abies/S. neoabies*	*Syracosphaera histrica*	*Umbilicosphaera cricota*	*U. mirabilis*
		f	V	V	V	V	A	r		C					C	C	F											r	C	R	F
			V	V	V	V	A			C					C	C	F												F		F
r		f	V	V	V	V	A			C			r		C	C	F												C	R	F
		f	V	V	V	H	A			C					C	C	R												C		F
		r	V	V	V	H	A			C					C	C													C		F
		f	A	V	V	H	A			C					C	C													C		F
		f		H	V	H	A			F					C	C	F											r	F	F	F
				H	V	H	A	c		F					C	C	R												F	R	F
				H	V	H	A	c		F					C	C													F	R	F
		f		A	A	H	A		F	A	V				C	C													F	R	F
r				A	A	H	A			C	V				C	C													F	R	
				V	A	H	A		F	A	V	r	r		C	C		R											F	F	F
				A	A	H	A		F	A	V				C	C													F	R	R
		r		C	C	H	A		R	A	A		r		C	C													C		R
				C	C	H	A		R	A	A				C	C													C	R	F
				A	A	H	A	r		C	A				C	C													C		R
				C	C	H	A		R	A	A				C	C	F												C	F	F
		r		C	F	H	A		F	A	A				C	C	F												C		R
				F	F	H	A		R	C	A				C	C													F		R
r				F	A	H	A		R	C	V				C	C													F		R
		r		C	A	H	A	r		C	V		r		C	C													F	R	
				A	V	H	A	f		A	V				C	C													F	R	R
		r		V	A	H	A	f	F	A	A				C	C		R					R	R					C	R	F
	r			V	A	H	A	r		A	A				C	C		R							R				C	R	F
		r		V	A	H	A	f	R	A	A				C	C								F	R				C	R	F
				V	A	H	A			C	A				C	C							R	F	F				C		F
		f		V	A	H	A		F	A	A				C	C	F	R					R	F					C		R
				V	A	H	A	r		A	A				C	C													C	R	
				V	C	H	A			A	A				C	C							R		R				C	R	R
				V	C	H	A			A	A				C	C		R					R	R	R				C	R	R
				A	C	H	A		F	A	C				C	C		F	R						R				C	R	R
		r		V	A	H	A	F		A	A				C	C		F	R	R	R				F				C	R	F
r		r		V	A	H	A	F	R	A	A			r	C	C		F	R	R	F		R		R				C	R	R
				V	A	H	A	C		A	A				F	F					F			R					C	R	F
		f		V	A	V	A	C	R	A	C				F	F				F				R	F				C	R	F
				V	A	V	A	F		A	A				F	F				F				R					C	F	F
				V	A	A	A	F		A	A				C	C							R						C	F	F
				V	A	A	A	F		A	A				F	F		F			F		R	F	R				F	F	F
r	r	f		V	C	C	A	A		A	A				C	C		F		R	F		R	F					C		R
		f		A	F		A	A		A	A				C	C		F		F				F	R				C	R	F
c		f		A	F		A	C	R	A	A				C	C	F	F		F				F	F				C		F
		f		A	F		A	A		A	C				C	C	R	F			F		R	F					C	R	F
		f		C			A	A		A	A				C	C	R	R		R		R		F	R				A	F	F
		f		C			A	C	F	C	A				C	C	R	R			R		F	F		R		r	A		R
R	r	f		C			A	F	R	C	A				C	C			F		F				F	R	R		C		R
C	r	f		C			A	C		C	A				C	C		F			F			F	F				A		
A	r			A			A	F		C	A				F	F		F		F	F								A	R	F
A		r		A			A	F		C	A				F	F	F	F		F	R				R				A	R	R
A	r			A			A	F		C	A				F	F		F	F		F			F			R		A	F	F
A				A			A	C		F	A				F	F		F		R	F	R							A	R	R
A	F			A			A	C		C	A				F	F		R	R		F		F	F					C	F	R
A	A			A			A	C		C	A		r		R	R		F			F								C	R	F
A	A			C			A	C		C	C		C		F	F	F	R	R				F	F			R	F	C	R	R
A	C						A	F		C	A		A		F	F											R	F	C	R	F

lower Pliocene hiatus

Table 2B. Distribution of calcareous nannofossils in Hole 558A.

		Hole 558A				*Amaurolithus amplificus*	*A. delicatus*	*A. primus*	*Calcidiscus leptoporus/C. macintyrei*	*Coccolithus pelagicus*	*Coronocyclus nitescens*	*Discoaster berggrenii*	*D. brouweri* (3-rayed)	*D. brouweri* (6-rayed)	*D. intercalcaris*	*D. loeblichii*	*D. pentaradiatus*	*D. quinqueramus*	*D. surculus*	*D. variabilis*	*Helicosphaera carteri*	*Minylitha convallis*	*Pontosphaera* spp.	*Reticulofenestra pseudoumbilica*	Small reticulofenestrids	*Scyphosphaera apsteinii*	*S. globulata*	*S. intermedia*	*S. lagena*	*S. pulcherrima*	*S. recurvata*	*Sphenolithus abies/S. neoabies*	*Triquetrorhabdulus rugosus*
Age	Zone	Subzone	Core-Section (interval in cm)	Abundance	Preservation																												
Miocene	*Amaurolithus tricorniculatus* (CN10)	*Triquetrorhabdulus rugosus* (CN10a)	9,CC 14-16	A	G		C	F	A	A			R	C	F		F		C	A	A		F	V	V	F		F	F	F	F	C	C
			10-1, 60-62	A	G			F	A	A			R	C	F		F		F	A	A			V	V							C	C
			10-2, 60-62	A	G		F	R	A	A				C	F		C		F	A	A			V	V							C	C
			10,CC	A	G	R	C	R	A	A				A	F		C		F	A	A		F	V	V							R	C
			11-1, 60-62	A	G		F		A	A				A	C		C			A	A			V	V							F	C
			11-2, 60-62	A	G		F	F	A	A				C	F		C			A	A		F	V	V							F	C
			11-3, 60-62	A	G		F	F	A	A				F	F		C		F	A	A		F	V	V		F			F		F	C
			11-4, 60-62	A	G			F	A	A				F	F		C			A	C			V	V							C	C
			11-5, 60-62	A	G		F	F	A	A				C	C		C			A	A		F	V	V							A	C
			11-6, 60-62	A	G		F	F	A	A				F	C		C			A	A			V	V					F		A	C
			11-7, 60-62	A	G		F	F	A	A				C	C		C			A	C			V	V							A	C
			11,CC	A	G		F		A	A				C	C		C			A	C		R	V	V							C	C
			12-1, 60-62	A	G		F		A	A				C	C		F			A	F			V	V							F	C
			12-2, 60-62	A	G		F		A	A				C	C		F			A	C			V	V							F	F
			12-3, 60-62	A	G	R		F	A	A				C	C		C			A	C			V	V							F	F
			12-4, 60-62	A	G	R	F	F	A	A				C	C		C			A	A			V	V							F	
	Discoaster quinqueramus (CN9)	*Amaurolithus primus* (CN9b)	12-5, 60-62	A	G		F		A	A				A	C		C	F		A	C			V	V							F	C
			12-6, 20-22	A	G				A	A				A	C		C	F		A	C			V	V							C	
			12,CC	A	G	F	F		A	A				C	A		C	C	F	A	C		R	V	V							C	C
			13-1, 60-62	A	G		F		A	A				C	A		F	A		A	C			V	V							R	
			13-2, 60-62	A	G			F	A	A				C	C		C	A		A	C			V	V							F	
			13-3, 60-62	A	G	F	F	F	A	A				C	A		A	A		A	C		R	V	V							C	F
			13-4, 60-62	A	G		F	F	A	V				C	A		F	A		A	A		R	V	V							C	F
			13-5, 60-62	A	G		F	F	A	V				A	C		F	A		A	A		R	V	V							C	F
			13,CC	A	G		C	F	A	V	C			A	A		C	A		A	A			V	V							F	F
			14-1, 60-62	A	G		C	F	A	A				C	A		C	A		A	C			V	V							F	C
			14-2, 60-62	A	G		C	F	A	V				C	A		F	A		A	C			V	V							R	F
			14-3, 60-62	A	G		F	F	A	V				C	C		F	C		A	C			A	V							F	
			14-4, 60-62	A	G	F	F	F	A	V	C			C	C		C	C		A	A		R	A	V					R		C	F
			14-5, 60-62	A	G	F		F	A	V	F			C	C		C	C		A	C		R	A	V							F	F
			14-6, 60-62	A	G	R	F	F	A	V	F			C	C		F	C		A	C			C	V								
			14-7, 40-42	A	G	F		F	A	V	F			C	C		F	C		A	F			C	V							F	
			14,CC	A	G			F	A	V	R			A	C		C	A	F	A	A			C	V								
			15-1, 60-62	A	G			F	A	V	F			A	A		F	A	F	A	C			C	V								
			15-2, 60-62	A	G			F	A	V	F	F		A	C		F	A	F	A	F			C	V							F	
			15-3, 60-62	A	G			F	A	V		R		A	C		C	A		A	C		R	C	V							C	R
			15-4, 60-62	A	G		C	C	A	V		F		A	C		F	A	C	A	C			F	V							C	C
			15-5, 60-62	A	G			F	A	V		C		C	C		C	A	F	A	C			F	V							F	C
			15-6, 20-22	A	G			F	A	V		C		C	C		C	A	C	A	C			F	V							F	A
			15,CC	A	G			F	A	V	F	C		C	C		C	A	F	A	C			C	V							C	A
		Discoaster berggrenii (CN9a)	16-1, 60-62	A	G				A	V		F		C	C		F	A		A	C			F	V							F	C
			16-2, 60-62	A	G				A	V	F	C		A	F		F	C	F	A	C			F	V							C	C
			16-3, 60-62	A	G				A	V		C		A	F		C	F	F	A	A			C	V							F	A
			16-4, 60-62	A	G				A	V		A		A	C		F	F	F	A	A	F	R	A	V							C	C
			16-5, 60-62	A	G				A	V		A		A	C	F	C	F	F	A	A	C		F	V							F	F
			16-6, 60-62	A	G				A	V		A		A	C	C	A	F	F	A	A	A	R	F	V							A	C
			16,CC	A	G				A	V		A		A	F	A	C		F	A	A	C		F	V							C	A

a plane passing through the middle of the holococcolith, so that two similar halves are formed (Gartner, 1967). These separated halves occur abundantly in this stratigraphic section. They are often broken and/or overgrown. *Lanternithus minutus* occurs abundantly in the *H. reticulata* Zone (CP16) and *Z. bijugatus* is abundant to very abundant. Because of their abundance, a few less heavily overgrown specimens can be found, and these confirm the identification of the more overgrown specimens. In addition, comparisons were made with other deep sea cores with similar holococcolith occurrences and in a similar state of preservation.

Bukry and Bramlette (1968) illustrated heavily calcified specimens of *P. joidesa* from JOIDES Blake Plateau cores that are very similar to specimens found in our North Atlantic section. They noted that rare, less calcified specimens indicate the identity of those heavily overgrown specimens. In Hole 563, specimens identified as *P. joidesa* are few to rare, occur sporadically, and are heavily overgrown. Consequently, identification of *P. joidesa* in this section is tentative. Broken and heavily overgrown fragments of discoasters may appear very similar to heavily overgrown specimens of *P. joidesa* and could be mistaken as such.

Samples 563-22,CC through 563-22-2, 52–54 cm are assigned to the *Coccolithus formosus* Subzone (CP16b) of the *Helicosphaera reticulata* Zone. *Clausicoccus fenestratus* occurs abundantly through 563-22-2, 52–54 cm, where the last *C. formosus* is found. This taxon, therefore, cannot be used to separate the *C. formosus* Subzone (CP16b) from the underlying subzone. Consequently, the lowermost samples in this hole may belong in the

Table 3A. Distribution of calcareous nannofossils in Hole 563.

	Hole 563		Abundance	Preservation	*Calcidiscus leptoporus/C. macintyrei*	*Catinaster calyculus*	*C. coalitus*	*Coccolithus pelagicus*	*Coronocyclus nitescens*	*Cyclicargolithus floridanus*	*Discoaster bellus*	*D. bollii*	*D. braarudii*	*D. brouweri*	*D. deflandrei*	*D. exilis*	*D. hamatus*	*D. kugleri*	*D. moorei*	*D. neohamatus*	*D. pentaradiatus*	*D. prepentaradiatus*	*D. variabilis*	*Helicosphaera* spp.	*Minylitha convallis*	*Pontosphaera ovata/P. segmenta*	*Reticulofenestra pseudoumbilica*	Small reticulofenestrids	*Sphenolithus heteromorphus*	*S. moriformis* plexus	*Triquetrorhabdulus carinatus*	*T. rugosus*
Age	Zone	Core-Section (interval in cm)																														
Miocene	*Discoaster neohamatus* Zone (CN8) *Discoaster bellus* Subzone (CN8a)	1-1, 60-62	A	M	A			V			R		A	A						C	C		V	A	A		F	C		A		F
		1-2, 60-62	A	M	A			V			F		A	A						A	F		V	A	A		C	C		A		F
		1-3, 60-62	A	M	A			A			C		A	A						A	F	F	A	C	A		C	A		C		F
		1,CC	A	M	A			V			A		A	A						A	F	F	V	A	A	R	R	F		V		F
		2-1, 60-62	A	M	A			V			A	F	A	A						A	F	F	V		A		A	A		A		F
		2-2, 60-62	A	M	A			A			A	F	C	A		F				A	F	C	V	C	A		A	V		A		F
		2-3, 60-62	A	M	A			A			A	F	C	C		C				A	F	F	V		A		A	V		A		C
		2-4, 60-62	A	M	V	F		A			A	F	C	F		C				A		F	V		C		A	V		A		C
		2-5, 60-62	A	M	V	F		A			A	F	F			C				F			V		C		A	V		C		C
	Discoaster hamatus (CN7)	2-6, 60-62	A	M	V	C		A			A	F	F			A	F			C			V		F		A	V		A		C
		2-7, 60-62	A	M	V	C		A			A		F			A	C			F			V				A	V		A		C
		2,CC	A	M	V	C		A			A		F			A	C						V				A	V		C		C
		3-1, 60-62	A	M	V	A		A			A					A	C						V				A	V		C		C
		3-2, 60-62	A	M	V	A		A			C		R			A	F						A				V	V		A		C
		3-3, 60-62	A	M	V	C	F	A			C		F			A	C		R				A	F			A	V		A		C
		3-4, 60-62	A	M	A	C	C	A			C		R			C	F		F				A				A	V		A		A
		3-5, 60-62	A	M	A	C	C	A			C					A	F		F				A				A	V		A		C
		3-6, 60-62	A	M	A	C	C	V			C					A	F		F				A	F		R	A	V		A		C
		3,CC	A	M	A	C	C	V			C					A	F		F				V	R			A	V		A		C
	Catinaster coalitus Zone (CN6)	4-1, 60-62	A	M	A		F	V								A			F				V				A	V		A		C
	Discoaster exilis (CN5)	4-2, 60-62	A	M	A			V								A			R				V				A	V		C		A
		4-3, 60-62	A	M	A			V								A			F				V				A	V		A		A
		4-4, 10-12	A	M	A			V								A			R				V	R			A	V		A		A
		4,CC	A	M	A			V								A			C				V				A	V		C		A
		5-1, 60-62	A	M	A			V								A			C				V				A	V		C		A
		5-2, 60-62	A	M	A			V								A			C				V				A	V		C		A
		5-3, 60-60	A	M	A			V								A			C				V				A	V		C		A
		5-4, 60-62	A	M	A			V								A			C				V				A	V		C		A
		5-5, 60-62	A	M	A			V								A			C				V				A	V		A		A
		5-6, 60-62	A	M	A			V								A			C				V	C			V	V		A		A
		5-7, 17-19	A	M	A			V								A		R	F				V	A			A	V		A		A
		5,CC	A	M	A			V								A		A	F				V	A			A	V		A		A
		6-1, 60-62	A	M	A			V								A							V	C			A	V		A		A
		6-2, 60-62	A	M	A			V		R						A			R				V	A		R	A	V		A		A
		6-3, 60-62	A	M	A			V		F						A							V	C			A	V		A		A
		6-4, 60-62	A	M	A			V		F						A			R				V	R		R	A	V		A		A
		6-5, 60-62	A	M	A			V		F						A							V	R		R	A	V		C		A
		6-6, 60-62	A	M	A			V		F						A							V				A	V		C		A
		6-7, 20-22	A	M	A			A		R						A		R					V	R			A	V		C		A
		6,CC	A	M	A			A		F						A		R	R				V	F			V	V		A		A
		7-1, 60-62	A	M	A			A		F						A		R	F				V	F			V	V		A		A
		7-2, 60-62	A	M	A			A		F						A		R					V	A			V	V		A		A
		7-3, 60-62	A	M	A			A		F						A			R				V	A			V	V		A		A
		7-4, 60-62	A	M	A			A		F						A			R				V	A			V	V		A		A
		7-5, 60-62	A	M	A			A	F	F						A			R				V	A			V	V		C		A
		7-6, 60-62	A	M	A			A		R					R	A			R				V	F			V	V		C		A
		7-7, 20-22	A	M	A			A	F	R					R	A							V	A			V	V		C		A
		7,CC	A	M	A			V		C					R	A							V	A		R	A	V		C		A
		8-1, 60-61	A	M	A			V		F					C	A			F				V	A			C	V		C		A
		8-2, 60-62	A	M	A			V		F						A							V	A		R	C	V		C		A
		8-3, 60-62	A	M	A			V		F					R	C			F				V	A			C	V		C		A
		8-4, 60-62	A	M	A			V		C						C			R				V	C			C	V		C		A
		8-5, 60-62	A	M	A			V		C						F							A	A			C	V		C		A
		8-6, 60-62	A	M	A			V		C						F							V	A			C	V		C		
		8,CC	A	M	A			V	A	R					R	F			F				V	A		R	A	V		A		
	Helicosphaera ampliaperta/ Sphenolithus heteromorphus (CN3/CN4)	9-1, 60-62	A	M	A			V	F	A					R	F			F				V	F			A	V	C	A		
		9-2, 60-62	A	M	C			V		A					F	F			F				V	C			C	V	A	A		
		9-3, 60-62	A	M	C			V		A					F	F			F				V				F	V	A	A		
		9-4, 60-62	A	M	C			V		A					F	C			R				V	C			F	V	A	C		
		9-5, 60-62	A	M	C			V	R	V					F	C			F				V	R				A	A	A		
		9-6, 60-62	A	M	C			V		V					C	C			F				V					A	A	C		
		9,CC	A	M	A			V		V					A	F			F				A	A				C	V	C		
		10-1, 40-42	A	M	C			V		V					A	F			A				A	C					A	A		
		10-2, 40-42	A	M	A			V	A	V					A				C				A	A					V	A		
		10-3, 40-42	A	M	C			V	F	V					V				C				C	F		R			A	A		
		10-4, 40-42	A	M	A			V	R	V					V				F				F	R					A	A		
		10-5, 40-42	A	M	C			V	F	V					A				C				A	C					A	A		
		10-6, 40-42	A	M	C			V	R	V					A				C				V	C		R			A	C		
		10,CC	A	M	C			V		V					V				C				F						A	A		
		11-1, 59-60	A	M	A			V		V					V				C				F	C					V	A		
		11-2, 60-62	A	M	A			V	F	V					V				F				F	C					V	A		
		11-3, 60-62	A	M	C			V	F	V					V				C				F	F					V	A		
		11-4, 60-62	A	M	C			V	R	V					V				C					C					V	V		
		11-5, 23-25	A	M	C			V		V					V				R										V	V		
		11,CC	A	M	C			V		V					V				F					F					V	V	R	

Table 3B. Distribution of calcareous nannofossils in Hole 563.

Age	Hole 563			Abundance	Preservation	Braarudosphaera bigelowii/B. rosa	Braarudosphaerid fragments	Bramletteius serraculoides	Chasmolithus altus	Clausicoccus fenestratus	Coccolithus eopelagicus	C. formosus	C. miopelagicus	C. pelagicus	Coronocyclus nitescens	Cyclicargolithus abisectus	C. floridanus	Discoaster deflandrei	D. druggii	D. moorei	D. pentaradiatus	D. tanii	D. variabilis	Helicosphaera spp.	Isthmolithus recurvus	Lanternithus minutus	Leptodiscus larvalis	Micrantholithus flos	Peritrachelina joidesa	Pontosphaera ovata/P. segmenta	Reticulofenestra bisecta	R. hillae	R. umbilica	Sphenolithus belemnos	S. capricornutus	S. ciperoensis	S. conicus	S. delphix	S. distentus	S. heteromorphus	Long-sp .ed bifurcated S. conicus	S. moriformis plexus	S. predistentus	S. pseudoradians	Triquetrorhabdulus carinatus	Zygrhablithus bijugatus
	Zone	Subzone	Core-Section (interval in cm)																																											
Miocene	*Helicosphaera ampliaperta/ Spenolithus heteromorphus* (CN3 and CN4)		12-1, 50-52	A	M									V	C		V	V		F										R										V		A			R	
			12-2, 50-52	A	M									V	A		V	V		C											r									V		A			R	
			12-3, 50-52	A	M									V	A		V	V		F				R																V		V			F	
			12-4, 50-52	A	M									V	A		V	V		F				F																V		V			F	
			12-5, 50-52	A	M									V	A		V	V		F				F						R										V		V			F	
			12-6, 57-59	A	M									V	A		V	V		F				F																A		V			F	
			12,CC	A	M									V	A		V	V		C				F						R	r			F						F		V			F	
	Sphenolithus belemnos (CN2)		13-1, 127-129	A	M									V	F		V	V		F														C								V			R	
			13-2, 60-62	A	M									V	C		V	V		C														A								V			R	
			13-3, 60-62	A	M									V	R		V	V		C														F								V			F	
			13-4, 60-62	A	M									V	A		V	V		C														C								V			F	
			13-5, 60-62	A	M									V	R		V	V		A														F								V			F	
			13,CC	A	M									V	C		V	V		C														F						r		A			F	
			14-1, 80-82	A	M									V	F		V	V		F										R				A								V			F	
			14-2, 61-63	A	M									V	A		V	V		F										R				A								V			F	
			14-3, 57-59	A	M									V	A		V	V		R										R				A								V			C	
			14-4, 8-10	A	M									A	F		V	V		F														F								V			R	
			14-5, 133-135	A	M									V	F		V	V		C										R				C								V			R	
			14-6, 108-110	A	M									V	C		V	V		F														A								V			R	
			14-7, 25-27	A	M									V	C		V	V		R														A								V			C	
			14,CC	A	M									V	A		V	V		R														C								V			F	
	Triquetrorhabdulus carinatus (CN1)	*Discoaster druggii* (CN1c)	15-1, 38-40	A	M								A	A	A	F	V	V	C		f		f							R										r	F	A			F	
			15-2, 38-40	A	M								C	A	A	F	V	V	F																							A			F	
			15-3, 38-40	A	M								F	A	A	F	V	V	R																							A			C	
			15-4, 38-40	A	M								A	V	A	C	V	V	F					R													F					V			A	
			15-5, 38-40	A	M								A	A	C	C	V	V	F																		F					V			C	
		Discoaster deflandrei (CN1b)	15-6, 64-66	A	M								A	V	C	C	V	V																			C					V			A	
			15-7, 30-32	A	M				R				A	A	C	C	V	V						R						R							C					V			A	
		Cyclicargolithus abisectus (CN1a)	15,CC	A	M								A	A	A	A	V	V												R							A					V			A	
			16-1, 52-54	A	M				F				A	A	A	A	V	V						R						R							C					V			A	
			16-2, 52-54	A	M								A	A	C	A	V	V						R													C					V			C	
			16-3, 52-54	A	M								F	A	C	A	V	V													R				C		A	C				V			C	F
			16-4, 52-54	A	M								F	A	C	A	V	V												R	R				A		A	A				V			A	A
			16-5, 52-54	A	M								C	V	A	A	V	V						R						R	R						A					V			A	C

Oligocene	*Sphenolithus ciperoensis* (CP19)		16-6, 55-57	A	M									V	A	A	V	V								R	R			R	C		V			R	C
			16,CC	A	M					F				V	A	A	V	V		R						R	R			F	C		V			A	A
			17-1, 70-72	A	M					R				V	F	A	V	V		R							R			C	F		V			C	A
			17-2, 70-72	A	M					R				V	R	C	V	V		R						R	F			C	F		V			R	C
			17-3, 74-76	A	M					C				V	F	A	V	V		R						R	C			A	F		V			F	A
			17-4, 77-79	A	M					C	R		R	V	F	A	V	V		F						F	A			A			V			F	A
			17-5, 70-72	A	M					F				V	F	A	V	V		R						R	C			A			V			C	A
			17-6, 32-34	A	M					R	R			V	F	A	V	V		F						R	A			A			V			R	C
			17-7, 32-34	A	M					R	C			V	F	A	V	V		R						R	A			A			V			C	A
			17,CC	A	M					R	C			V	F	A	V	V								F	A			A			V			C	A
			18-1, 69-71	A	M					R	C			V	F	A	V	V		R						R	A			A			V			C	A
			18-2, 69-71	A	M					R	C			V	F	A	V	V		R						R	C			A			V			C	A
			18-3, 69-71	A	M				R		C			V	F	A	V	V		R						R	A			A			V			C	A
			18-4, 69-71	A	M						C			V	R	A	V	V		R						F	A			A			V			F	A
			18-5, 38-40	A	M					R	C			V	F	A	V	V								R	A			A		F	V			F	A
			18,CC	A	M					R	C			A	R	C	V	V								R	A			A		F	V	R		C	A
	Sphenolithus distentus (CP18)		19-1, 66-68	A	M				F		C			A	R	C	V	A	C		C						A					F	A	A	F	F	A
			19-2, 32-34	A	M				F	R	C			A	C	C	V	A	A		C						A					C	A	A	F	F	A
			19-3, 32-34	A	M						C			V	F	A	V	A	A		R						V					R	A	A	C	R	A
			19,CC	A	M					R	C			V	F	A	V	A	A		F						V					R	A	A	C	R	A
	Sphenolithus predistentus (CP17)		20-1, 60-62	A	M		F		R	R	F			V		A	V	A	A			R					V						A	A			A
			20-2, 60-62	A	M	R	A				C			V	R	A	V	A	A			R					A						A	A			A
			20-3, 96-98	A	M	F	A			R	F			V		A	V	A	A	F							C						A	A			A
			20-4, 67-69	A	M		C		R	R	F			V	R	A	V	A	A	R							C						A	A	R		A
			20-5, 17-19	A	M	A	A			R	F			V	R	A	V	A	A	F			R				C						A	A	F		A
			20-6, 16-18	A	M	A	A			R	F			V	R	A	V	A	A	R				R			A					r	A	A			A
			20-7, 25-27	A	M	A	A			R	F			V		A	V	A	C	F			R				A						A	A			A
			20,CC	A	M	A	A		F		F			V	R	A	V	V	A	C		F	C				A						A	A	C		V
			21-1, 80-82	A	M	A	A			R	C			V		A	V	A	A	R		A	F				V						A	A	R		A
			21-2, 80-82	A	M	A	A				C			A	R	A	V	A	A	R		C	F	R			A					r	A	A	F		A
			21-3, 80-82	A	M	A	A			F	A			V		A	V	A	A	R		A	R				A					r	A	A	F		A
			21-4, 80-82	A	M	A	A			F	C			V		A	V	A	A	R		A	R				A					r	A	A	A		A
			21-5, 91-93	A	M	A	A		R		A			V	R	A	V	A	A			A	R	R			A					r	A	A	A		A
			21-6, 91-93	A	M	A	A		R		C			V	R	A	V	A	A	R		C	R		F		A						A	A	C		V
			21-7, 17-19	A	M	A	A	R	R		A			V		A	V	A	A	R		A	R				A						A	A	R		V
	Helicosphaera reticulata (CP16)	*Reticulofenestra hillae* (CP16c)	21,CC	A	M	A	A	A	R	C	C			V		A	V	A	C			A		R	F		A	R	C				A	A	F		V
			22-1, 50-52	A	M	A	A	A		C	C			V		A	V	A	C	C		A	F				A	R	C				A	A	R		V
		Coccolithus formosus (CP16b) ?	22-2, 52-54	A	M	A	A	C	F	A	C	C		V	R	A	V	A	A	F	F	A		R	R		A	C	A				A	A	C		V
			22-3, 52-54	A	M	C	A	C	R	A	C	A		V		A	V	A	C	C	F	A					A	C	A				A	A	C		A
			22-4, 1-3	A	M	C	A	C		A	C	A		V		A	V	A	C	F	F	A					A	C	F				A	C	F		A
			22,CC	A	M	F	A	A	R	A	C	C		V	R	A	V	A	C	R	C	A			R		A	C	F				A	C	C		V

Nannofossil species	Hole 558	Hole 563
Peritrachelina joidesa	None	21-6; 21,CC 22-2; 22,CC
Lanternithus minutus	25-3/26-4	20-1, 20-2 20,CC/22,CC
Braarudosphaera bigelowii/ B. rosa	None	20-2, 20-3 20-5/22,CC
Zygrhablithus bijugatus	17-1, 17-2 17,CC; 18-3 19-2/27-2	16-3/22,CC

Figure 5. Occurrences of braarudosphaerids and holococcoliths in Holes 558 and 563. The highest and lowest sections are listed with a slash between them; single section occurrences are separated by a comma.

underlying *C. subdistichus* Subzone (CP16a). Samples 563-22-1, 50–52 cm and 563-21,CC lack *C. formosus* but do contain common *R. umbilica* and are placed in the *Reticulofenestra hillae* Subzone (CP16c).

It is difficult to distinguish the *Sphenolithus predistentus* Zone (CP17) from the *Sphenolithus distentus* Zone (CP18) in Hole 563 because of the rare and inconsistent occurrence of *S. distentus*. Rare specimens of *S. distentus* are found as low as Section 563-21-5. *Sphenolithus distentus* is never abundant and is common only in 563-19-2, 32–34 cm.

Bybell (1982) reported the first appearance of *S. distentus* in the *H. reticulata* Zone in Alabama, where it occurs with *C. formosus* and *R. umbilica*. She noted that Perch-Nielsen also found a co-occurrence of *R. umbilica* and *S. distentus* in Barbados.

Samples 563-21-7, 17–19 cm through 563-20-1, 60–62 cm are placed in the *S. predistentus* Zone (CP17). Rare occurrences of *S. distentus* in this interval are considered to be the result of downhole contamination. Braarudosphaerids are abundant throughout most of this interval, but they do decrease in numbers by 563-20-4, 67–69 cm. Sample 563-20-1, 60–62 cm contains no intact braarudosphaerids and only a few disaggregated segments. *Peritrachelina joidesa* is found only in 563-21-6, 91–93 cm and the last abundant occurrence of *L. minutus* is in 563-21-1, 80–82 cm. Core 563-19 is placed in the *S. distentus* Zone (CP18) based on the consistent occurrence of *S. distentus* and the absence of *Sphenolithus ciperoensis*.

Samples 563-18,CC through 563-16-6, 55–57 cm are assigned to the upper Oligocene *Sphenolithus ciperoensis* Zone (CP19) based on the presence of *S. ciperoensis*. Bukry (1975) used the last occurrence of *S. distentus* to subdivide this zone. However, because of the inconsistency in the occurrence of *S. distentus* in this section, this zone is not subdivided. *Sphenolithus ciperoensis* is abundant throughout most of this zone. In Section 563-16-6, however, *S. ciperoensis* is rare. Being both small in size (4–6 μm) and rare, *S. ciperoensis* could easily be missed during smear-slide examination, so the upper zonal boundary is uncertain. *Reticulofenestra bisecta*, used by Bukry (1973b; 1975) as an auxiliary marker, is rare from 563-17-1, through 563-16-6. Very rare specimens of *R. bisecta* are noted through 563-16-3. As in Hole 558, *C. fenestratus* has a long range in Hole 563, with its last occurrence in 563-16,CC near the top of the *S. ciperoensis* Zone (CP19).

The *Triquetrorhabdulus carinatus* Zone (CN1) spans the Oligocene/Miocene boundary and is recognized in 563-16-5, 52–54 cm through 563-15-1, 38–40 cm. Sphenoliths present in this zone include *S. capricornutus*, *S. conicus*, and *S. delphix*.

The *Cyclicargolithus abisectus* Subzone (CN1a) of the *T. carinatus* Zone is separated from the overlying subzone by the termination of the *C. abisectus* acme (Bukry, 1973b). In Hole 558, this acme could not be used to subdivide the *T. carinatus* Zone. In Hole 563, however, the end of the *C. abisectus* acme appears to be stratigraphically useful, and 563-16-5, 52–54 cm through 563-15,CC are placed in the *C. abisectus* Subzone (CN1a). However, the reliability of this acme is still questionable, so the position of the upper subzonal boundary is uncertain and represented by a dashed line on the range chart.

Many discoasters may resemble *D. druggii*, especially when specimens are strongly overgrown as is the case here. Consequently, the boundary between the *D. deflandrei* (CN1b) and *D. druggii* (CN1c) Subzones is tentative in this section. Samples 563-15-7, 30–32 cm and 563-15-6, 64–66 cm are assigned to the *D. deflandrei* Subzone (CN1b). Samples 563-15-5, 38–40 cm through 563-15-1, 38–40 cm are placed in the *D. druggii* Subzone (CN1c).

Cores 563-13 and 563-14 are assigned to the lower Miocene *Sphenolithus belemnos* Zone (CN2). *Sphenolithus belemnos* and *S. heteromorphus* co-occur in Sample 563-12,CC. Bukry (1973b) noted the co-occurrence of these two species at DSDP Site 140 and stated that the first occurrence of the more cosmopolitan *S. heteromorphus* is considered the principal marker. Consequently, we use the first occurrence of *S. heteromorphus* instead of the last occurrence of *S. belemnos* to separate the *S. belemnos* Zone (CN2) from the overlying zone.

Both *S. belemnos* and *S. heteromorphus* are few in number in 563-12,CC and could represent a natural overlap. Alternatively, the co-occurrence of *S. belemnos* and *S. heteromorphus* in 563-12,CC could be the result of reworking or downhole contamination of the core-catcher. As pointed out by M. P. Aubry (personal communication, 1984), if one were to use Martini's (1971) zonation, a lower Miocene hiatus would be present between 563-12,CC and 563-13-1. As discussed for Hole 558, we do not consider *T. carinatus* a very reliable marker in this moderately preserved section where *T. carinatus* is quite heavily overgrown and difficult to identify. Heavily overgrown 14–20 μm rods, here attributed to *T. carinatus*, occur in small numbers through 563-11,CC. Therefore, we do not specifically delineate a lower Miocene hiatus. M. P. Aubry and K. G. Miller (personal communication, 1984), however, have informed us that they have additional evidence in the way of planktonic foraminiferal and magnetostratigraphic data that would allow them to place a hiatus between 563-12,CC and 563-13-1. They would then attribute the co-occurrence of *S. delemnos* and *S. heteromorphus* to reworking at the unconformity.

As was the case at Site 558, the *H. ampliaperta* (CN3) and *S. heteromorphus* (CN4) Zones are combined because we did not observe *H. ampliaperta*. Cores 563-9 through 563-12 are assigned to this interval. *Sphenolithus heteromorphus* is generally abundant to very abundant.

Discoaster variabilis first appears in 563-11-3, 60–62 cm and is very abundant by 563-10-6, 40–42 cm; *Discoaster deflandrei* is abundant in this sample. The end of the *D. deflandrei* acme is in 563-9-6, 60–62 cm. Therefore, as in Hole 558, different boundaries are obtained by the use of the first appearance of long-armed discoasters, the change in dominance among discoasters from *D. deflandrei* to long-armed discoasters, and the end of the *D. deflandrei* acme. In addition, discoaster abundances fluctuate considerably in Hole 563. Consequently, alternate datums are considered unreliable in this stratigraphic section.

The middle Miocene *Discoaster exilis* Zone (CN5) is recognized from 563-8,CC through 563-4-2, 60–62 cm. *Discoaster kugleri*, used by Bukry (1973b) to subdivide this zone, is abundant in 563-5,CC, but it occurs rarely and sporadically throughout the remainder of the zone. The last occurrence of *Cyclicargolithus floridanus*, used by Bukry (1975) as an auxiliary datum, is in 563-6-2, 60–62 cm. The last common occurrence of *C. floridanus* is in 563-7,CC. Because of the inconsistent and generally rare occurrence of *D. kugleri*, the principal datum, as well as the low abundance of *C. floridanus* throughout most of this zone, the *Discoaster exilis* Zone (CN5) is not subdivided.

Sample 563-4-1, 60–62 cm is placed in the *Catinaster coalitus* Zone (CN6). Preservation is moderate and *C. coalitus* is difficult to identify. Therefore, as in Hole 558, the lower zonal boundary is uncertain and dashed on the range chart.

Samples 563-3,CC through 563-2-6, 60–62 cm are assigned to the *Discoaster hamatus* Zone (CN7). Bukry's (1975) subdivision of this zone, based on the first evolutionary appearance of *C. calyculus*, cannot be used in this section because 563-3,CC contains both the first *Catinaster calyculus* and the first *D. hamatus*. *Catinaster calyculus* is common to abundant and *D. hamatus* is few to common throughout this interval. The first *Discoaster bellus* is found in the same sample as the first *D. hamatus*.

Samples 563-2-5, 60–62 cm through 563-1-1, 60–62 cm are placed in the *Discoaster bellus* Subzone (CN8a) of the *Discoaster neohamatus* Zone (CN8). *Discoaster neohamatus* is generally abundant throughout this interval. Some specimens of *D. neohamatus* are 24 μm in diameter and have sharply bent rays.

DISCUSSION AND CONCLUSIONS

Occurrence of Oligocene *Braarudosphaera* and Holococcoliths on the Mid-Atlantic Ridge

The discovery of lower to mid-Oligocene *Braarudosphaera*-rich nannofossil chalk at the Mid-Atlantic Ridge (Site 563) was unexpected. This is the first report of such an assemblage from the mid-ocean environment of the North Atlantic, and it extends the known geographic occurrence of this flora considerably. Before considering the significance and implications of this finding, previous reports of Cenozoic braarudosphaerid-rich sediments will be reviewed briefly along with hypotheses concerning their origin.

It should be noted at the outset that the first discoveries of mid-ocean braarudosphaerid chalks (in the Oligocene of the South Atlantic; Maxwell, Von Herzen, et al., 1970) preceded the refinement of the calcareous nannofossil biostratigraphic zonal schemes used today, and that the nomenclature and occurrence datums of the two currently most widely used zonal schemes, those of Martini (1971) and Okada and Bukry (1980), differ in several respects in the critical upper Eocene-Oligocene interval. Before proceeding with literature review, therefore, it is important to note these differences so the reader will not become hopelessly confused when comparing the age determinations as given by various authors cited in the literature summarized here.

All current Oligocene coccolith zonal schemes are based on the zone boundaries outlined in a table by Bramlette and Wilcoxon (1967, table 2). Unique datum levels were not specified by these authors, so a choice was left to subsequent workers as to which of several possible first or last occurrence datums would be used to define each zone. Percival (in Maxwell, Von Herzen, et al., 1970), Martini (1971), and Bukry (1973a; 1973b) each chose slightly different criteria for their adopted zonations. The Martini and Bukry schemes are compared in Figure 6, following the correlations indicated by Okada and Bukry (1980).

The important discrepancies to note in Figure 6 are (1) Martini (1971) subdivided Oligocene time into three subunits (early, middle, and late) whereas Okada and Bukry (1980) delineated two (early and late). The position of the latter boundary does not always appear in the literature at the same place relative to the Bukry zonal scheme (compare Okada and Bukry, 1980 with Haq, 1984, and Berggren et al., in press). (2) Martini (1971) and Okada and Bukry (1980) each number code their zone names, but with a different set of numbers for corresponding zones. (3) The two zonal schemes both use zonal names adopted from Bramlette and Wilcoxon (1967), but sometimes the same name applies to different intervals. For example, the *Sphenolithus distentus* Zone of Okada and Bukry (1980) corresponds to the upper portion of the *Sphenolithus predistentus* Zone of Martini (1971).

The upshot of this is that care must be taken to match zonal names and designations such as "early" and "late" used in the literature to the appropriate zonal scheme.

Age			Zone name (from Martini, 1971)		Zone and subzone names (from Okada and Bukry, 1980)		
	NP	CP					
Oligocene	late	late	*Triquetrorhabdulus carinatus*	NN 1	CN 1a	*Triquetrorhabdulus carinatus*	*Cyclicargolithus abisectus*
			Sphenolithus ciperoensis	NP 25	CP 19b	*Sphenolithus ciperoensis*	*Dictyococcites bisectus*
	middle		*Sphenolithus distentus*	NP 24	CP 19a		*Cyclicargolithus floridanus*
			Sphenolithus predistentus	NP 23	CP 18	*Sphenolithus distentus*	
		early			CP 17	*Sphenolithus predistentus*	
	early		*Helicosphaera reticulata*	NP 22	CP 16c	*Helicosphaera reticulata*	*Reticulofenestra hillae*
			Ericsonia subdisticha	NP 21	CP 16 a,b		*Coccolithus formosus/* *Coccolithus subdistichus*
Eocene	late		*Sphenolithus radians*	NP 20	CP 15b	*Discoaster barbadiensis*	*Isthmolithus recurvus*
			Isthmolithus recurvus	NP 19			
			Chiasmolithus oamaruensis	NP 18	CP 15a		*Chiasmolithus oamaruensis*

Figure 6. Comparison of the Martini (1971) upper Eocene-Oligocene zonation with that of Bukry, using correlations indicated by Okada and Bukry (1980).

In Figures 7 and 8 (backpocket), we have sought to compare the geographic occurrences of mid-Tertiary *Braarudosphaera* oozes, chalks, and *Braarudosphaera*/holococcolith associations cited in the literature for the Atlantic and Gulf of Mexico against the current Martini and Bukry calcareous nannofossil zonal schemes. The zonations are not correlated against linear time, although such a correlation could be made using the scheme of Berggren et al. (in press). With this explanation in mind, we can now return to our discussion.

A plot by Bukry (1970, fig. 1) of the distribution of *Braarudosphaera* holococcoliths based on early DSDP drilling in the North Atlantic indicated that these taxa were generally limited by ecological preference to near-shore pelagic environments. Discoveries of regionally restricted Tertiary braarudosphaerid-rich oozes and chalks in open ocean settings elsewhere in the world, therefore, have aroused considerable interest and speculation on the reasons for such occurrences. Attention has centered principally on Pliocene *Braarudosphaera* chalks from the western Pacific (Sites 236, 237, and 238; Roth, 1974), and on the Oligocene chalks and oozes encountered by several DSDP legs in the mid-latitudes of the South Atlantic (Legs 3, 39, 40, 73, and 74; Maxwell, Von Herzen, et al., 1970; Wise and Kelts, 1972; Supko, Perch-Nielsen, et al., 1978; Bolli, Ryan, et al., 1978; Noël and Melguen, 1978; Bukry, 1978a; LaBrecque et al., 1983; Hsü, LaBrecque, et al., 1984; Moore, Rabinowitz, et al., 1984).

Recently, additional note has been taken of the occurrence of *Braarudosphaera*/holococcolith associations of early Oligocene age in the Gulf of Mexico (Leg 77; Lang and Watkins, 1984). Another isolated occurrence of *Braarudosphaera* chalks has been reported by Bukry (1978a) at Oceanographer Canyon (*Alvin*-2698) in the western North Atlantic.

Danian and South Atlantic Mid-Oligocene Occurrences

A variety of hypotheses have been proposed to account for the occurrence of abundant braarudosphaerids over specific intervals of the Cenozoic record and at isolated localities in the world. Most of these center around the observation that modern *Braarudosphaera* are found most commonly in neritic environments along the margins of continents (Gran and Braarud, 193 ; Smayda, 1966; Lefort, 1973), although they have been reported, usually in small numbers, from the open ocean as well (Gaarder, 1954; Hulbert, 1962; Hulbert and Rodman, 1963). A possible link to a benthic phase in the life cycle of the organism has also been suggested (Bybell and Gartner, 1972), although the inability to achieve long-term cultures of the modern organism (Lefort, 1972; Bukry, 1978a) has prevented documentation of its life cycle. The apparent correlation of the organism with a neritic habitat led to early suggestions that the mid-Oligocene accumulations in the South Atlantic, which consist of up to 98% *Braarudosphaera*, may have been displaced from shallower depths, a notion that was soon discarded as the aerial distribution and sedimentological characteristics of the deposits became better understood (see discussion by Wise and Kelts, 1972). Instead, enhanced productivity due to peculiar oceanographic conditions, the nature of which is unknown, is generally assumed to have been the direct cause for the anomalous accumulations. As *Braarudosphaera* is ranked as one of the most dissolution susceptible nannofossil genera (Bukry, 1970), their absence in deep sea sediments except during times of enhanced productivity (which would lower the calcium compensation depth for that organism) is generally attributed to dissolution (Wise and Kelts, 1972).

The traditional problem, therefore, has been to explain enhanced productivity, and for this, the various geological occurrences need to be considered separately. An extreme case is the blooms that occurred during the earliest Danian when *Braarudosphaera* served as an opportunistic "disaster form" that filled, where permitted, the vacant niches of an ocean nearly devoid of competing coccolithophorid species (Fischer and Arthur, 1977). These blooms have been noted in some but not all of the Cretaceous/Tertiary boundary sections on which detailed coccolith studies have been conducted (Perch-Nielsen et al., 1982), and it is not yet clear just what climatic or paleoenvironmental factors controlled their occurrences.

A second extreme case is the mid-Oligocene occurrences of the South Atlantic that lie in a relatively narrow band between 15 and 35°S (Figs. 7–10). In that band, *Braarudosphaera* constitute up to 90–98% of the sediment and occur in beds up to a meter or more in thick-

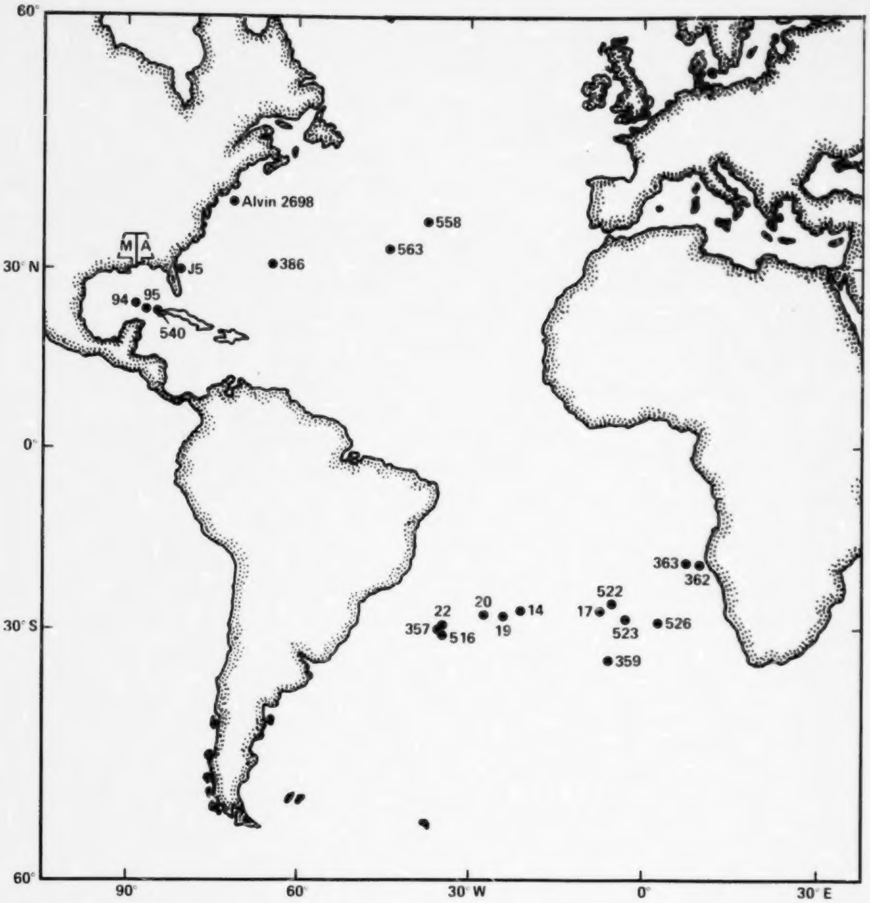

Figure 7. Location map for DSDP and other ocean or land outcrop sites at which braarudosphaerid ooze/chalk or braarudosphaerid/holococcolith associations have been reported from the upper Eocene-Oligocene. M = Mississippi; A = Alabama.

ness (Maxwell, Von Herzen, et al., 1970; Bolli, Ryan, et al., 1978). At Site 362, the occurrences are cyclical with as many as 34 *Braarudosphaera* chalk beds recorded in the section (Bukry, 1978a). Observing that the greatest modern concentrations of *Braarudosphaera* are found in the areas of reduced ocean salinities (high coastal runoff or upwelled water), Bukry (1978a) sought some mechanism that would have produced a short term lowering of near-surface water salinities, such as abnormally high regional rainfall (Bukry, 1974) or periodic influxes of glacial meltwaters from the Oligocene polar ice cap (personal communication from K. J. Hsü to D. Bukry, 1978). Similarly, Bolli, Ryan, et al. (1978) postulated high freshwater influx from the Orange River during the Oligocene, coupled with upwelling of nutrient-rich intermediate or deep low-salinity water to explain *Braarudosphaera* oozes in the Cape Basin. Considering the wide distribution of the deposits across the South Atlantic, Berger (1979) hypothesized that the blooms may represent mid-ocean upwelling.

In a recent discussion of the South Atlantic occurrences, LaBrecque et al. (1983) determined that the most prominent *Braarudosphaera* chalk layer at Sites 522 and 523 was deposited within the Oligocene magnetostratigraphic interval C10.18R to C10.35R (NP23 of Martini, 1971) with a second, although minor, occurrence in the lower Oligocene at C12.63R (NP22) of Hole 522B. They noted that the first zone correlates with an abrupt decrease in the eustatic sea level curve of Vail et al. (1977) and falls within the time of the opening of Drake Passage postulated by LaBrecque and Rabinowitz (1977) (early to mid-Oligocene magnetic Anomaly 10–13 time as opposed to the late Oligocene magnetic Anomaly 8 time as proposed by Barker and Burrell, 1977). LaBrecque et al. (1983) then concluded that the opening of Drake Passage and subsequent atmospheric instabilities because of the initiation of circum-Antarctic winds and strong latitudinal temperature gradients could have caused enhanced circulation within the South Atlantic and, consequently, the mid-ocean upwelling postulated by Berger (1979).

Regardless of whether a connection with the opening of Drake Passage can be firmly established, the hypothesis of mid-ocean upwelling is an attractive one. Braaru-

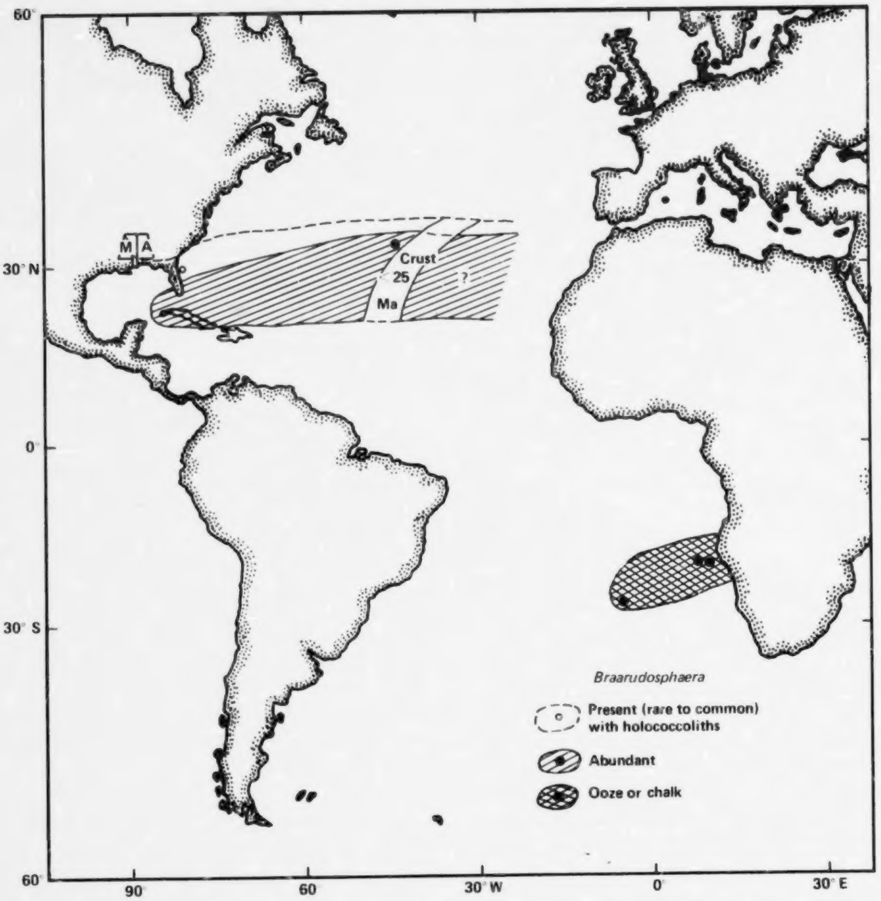

Figure 9. Map of reported *Braarudosphaera* oozes, chalks, and *Braarudosphaera*/holococcolith associations during NP22 (CP16c) time.

dosphaerid blooms first appeared off Africa during NP22 time (Figs. 8 [backpocket] and 9), extended across the South Atlantic to the Rio Grande Rise during NP23 (Figs. 8 [backpocket] and 10), and then continued to persist off Africa (DSDP Sites 262 and 263) during NP24. The persistence of the blooms at the two sites just off Africa could be attributed to upwelling associated with a northward flowing surface current whose velocity had increased, as suggested by LaBrecque et al. (1983), and/or whose flow had been perturbed by submarine features along the eastern Walvis Ridge, which would have been shallower than today.

The expansion of upwelling conditions across the entire South Atlantic over deep as well as shallow sites during NP23, however, would have required more than a local perturbation, but rather some form of large-scale divergence. In addition, the quality of the upwelled water should have been such that calcareous phytoplankton were favored over siliceous forms, and predominantly one taxon (*Braarudosphaera*) at that. Modern analogs for such a phenomenon, of course, are hard to find. Recently, however, special oceanographic conditions creating a modern day divergence and mid-ocean upwelling at comparable latitudes (30–31°S) in the South Pacific have been documented by deep sea drilling off New Zealand (Leg 90, Kennett, von der Borch, et al., 1983). Upwelling along the poorly known Subtropical Divergence (Tasman Front) has apparently resulted in enhanced productivity of calcareous nannoplankton rather than of siliceous organisms throughout the Neogene. No abnormal species diversity, however, was reported. Therefore, the analogy with braarudosphaerid blooms in the Oligocene of the South Atlantic breaks down at that point. However, exceptionally low (or high?) surface salinities in the South Atlantic Oligocene, as often suggested, could have served as a filter by which production of *Braarudosphaera* was enhanced at the expense of other coccolith taxa.

Other Oligocene Occurrences

The pattern of occurrence of *Braarudosphaera* elsewhere during the early to mid-Oligocene may have been somewhat less unusual than either of the two more extreme situations discussed above. These other Oligocene occurrences seem to be a continuation of a pattern tha developed during the late Eocene or before. The association of *Braarudosphaera* (and the closely related gen

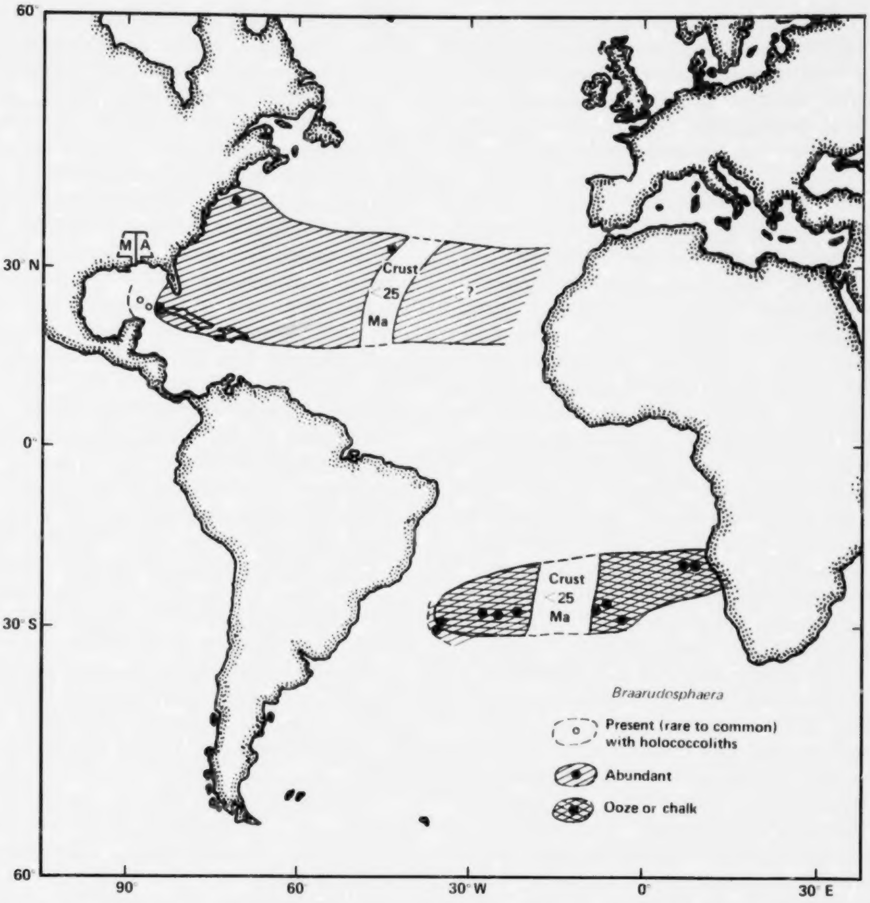

Figure 10. Map of reported *Braarudosphaera* oozes, chalks, and *Braarudosphaera*/holococcolith associations during NP23 (CP17/18) time.

era *Micrantholithus* and *Pemma*) with the holococcoliths *Lanternithus minutus, Peritrachelina joidesa*, and *Zygrhablithus bijugatus*[3], among others, has been noted for low to mid-latitude nearshore shelf to bathyal paleoenvironments of the upper Eocene at a number of localities (Fig. 8). In many instances, particularly in and around the Gulf of Mexico, these occurrences continue with little change into the lower Oligocene. These upper Eocene to lower and mid-Oligocene examples differ from the mid-Oligocene occurrences of the South Atlantic in that the braarudosphaerids never reach the overwhelming numbers (90 to 98%) reported for the latter. Instead percentages of whole and fragmented braarudosphaerid particles of up to 5 to 10% of the total sediment are more the norm for the peak Oligocene occurrences in the Northern Hemisphere.

An interesting comparison for the Leg 82 mid-ocean accumulations is provided by those recently reported from Site 540 in the southeastern Gulf of Mexico (lat. 23°N, long. 84°W; Lang and Watkins, 1984). This site, just over 100 km north of Cuba, lies at bathyal depths in 2926 m of water. Although the tectonic history of the site is not well known, there is no independent evidence to suggest that it was significantly shallower in the Oligocene than today. Lang and Watkins (1984) noted that the occurrence of braarudosphaerids in Sections 540-22-1 to 540-28-2 spans the upper Eocene to lower-middle Oligocene. Their numbers fluctuate between common and abundant throughout the interval, but they are only few to rare in the sections above and below. The holococcoliths *Peritrachelina joidesa, Lanternithus minutus*,and *Zygrhablithus bijugatus* are also present and their abundances seem to parallel those of the braarudosphaerids, particularly in the case of *Peritrachelina joidesa*. Lang and Watkins (1984) considered three possible mechanisms for the anomalous accumulation of the assemblages: (1) shallowing of the seaway, (2) selective dissolution of other nannofossil species, and (3) an increase in their productivity. They considered the first two possibilities unlikely, concluding, as have many previous workers, that the cause of the accumulations and the fluctuations in their abundances reflect changes in productivity, the causes for which are obscure. They noted that in modern environments *Braarudosphaera* can tolerate both decreased (Roth, 1974) and elevated (Martini, 1967) salinities better than most other species, and that either of these extremes or a fluctuating salinity could have enhanced their productivity at Site 540.

---

[3] *Z. bijugatus* is not plotted in Figure 8 (backpocket) because this most ubiquitous of the holococcolith species occurs in abundance at all but the deepest ocean sites.

Occurrences at Site 563

The most striking aspect of the mid-ocean occurrence of abundant braarudosphaerids at the North Atlantic Leg 82 site, Site 563, is that it falls within the mid-latitudes. Together with other known occurrences closer to the margins of the North American continent or near the island of Bermuda, they form a mirror image of the mid-latitude occurrences of the South Atlantic (roughly bracketed today between 15 and 40°S). Their absence at intervening sites in the Caribbean and the equatorial Atlantic produces an apparent bipolar distribution (Figs. 9 and 10) that suggests some type of zonal climatic control for this pattern. Bipolar distribution patterns for certain species are not uncommon among coccolith assemblages (McIntyre and Bé, 1967; Thierstein, 1981), however, and only denote a general ecological preference based on temperature. Beyond that correlation, the specific accumulations of braarudosphaerids and holococcoliths in the Atlantic require more detailed analysis and alternative explanations can be considered as well.

Among the Leg 82 sites, braarudosphaerids are present essentially only at Site 563. As sediments of apparently the same age were cored at both Sites 563 and 558, several mechanisms can be considered that might explain their essential absence at the northern site, namely: (1) erosion or nondeposition of braarudosphaerid bearing sediments at Site 558; (2) different Oligocene paleodepths (i.e., Site 563 was shallower than Site 558); (3) presence of some emergent land mass or island fostering the accumulation of neritic species near Site 563 but not near Site 558; and (4) ecologic exclusion based on temperature as discussed above.

The first possibility, that the braarudosphaerid interval at the northern site is missing due to erosion or nondeposition, seems unlikely because (1) no hiatuses were noted in the lower Oligocene section at Site 558, and (2) the Oligocene coccolith zones (CP16 and CP17) are of nearly equal thickness at both sites (Fig. 4).

The second possibility presupposes some major difference in paleobathymetry of the two sites that would cause the basement underlying Site 563 to form or remain at a shallower water depth during the early to mid-Oligocene. This, in turn, would enhance the chances that the relatively soluble braarudosphaerids would be preserved at the "shallower" site whereas they could have been destroyed by dissolution at the "deeper" site. This possibility is further suggested by the fact that the two sites are quite some distance apart (400 km) and are separated by two well-defined fracture zones (Fig. 1). The topography along mid-ocean ridges today is not uniform (Sclater et al., 1971), and it would be rather coincidental if the sites did actually lie at the same approximate water depth when the ocean crust beneath them was first generated. In addition, the crust on opposite sides of fracture zones often lies at different bathymetries, thus the two sites could conceivably have experienced somewhat different spreading histories resulting in different bathymetries during the course of seafloor spreading.

A simple way to evaluate the possibility of different bathymetric histories is to note the present depths of the Oligocene strata overlying basement today. At Site 558, the basal Oligocene stratum lies at 4175 m below the sea surface, whereas at Site 563 it lies at 4160.5 m. These values are surprisingly close to one another and would represent a remarkable coincidence if the two sites had experienced significantly different bathymetric histories. It would mean that the crust at Site 563 would have been at a significantly higher elevation during the early Oligocene, but subsequently it would have to have subsided much more rapidly to reach a present day depth only slightly shallower than that at Site 558. This seems highly unlikely.

The possibility that the deposition of braarudosphaerids at Site 563 was influenced by an emergent land mass or a nearby set of islands requires an examination of the ocean bathymetry not just around that site but along the conjugate magnetic anomaly on the opposite side of the Mid-Atlantic Ridge as well. The only obvious feature, in addition to the present day Azores, is a set of small seamounts just south of the Azores. These, however, would backtrack closer to Site 558 than to Site 563. Hence their possible influence on Site 563 can be eliminated.

The last possibility considered, that of ecologic exclusion based on temperature, assumes that the latitudinal distance of about 4° separating the two sites is significant. Whereas this may seem a trivial distance at first glance, it may well be important considering that the northern site, Site 558, lies close to the northern limit at which abundant Oligocene braarudopshaerids have been reported along the North American continental margin (Oceanographer Canyon; Bukry, 1978a). Because of other factors such as local warm surface currents (perhaps some type of proto-Gulf Stream), upwelling conditions, or differences in bathymetry, the northern limits of the distribution of abundant *Braarudosphaera* in the open ocean may have been somewhat less than along the continental margin at this time. In contrast to the braarudosphaerids, it is interesting to note that the holococcoliths were generally well represented at both sites, indicating that their abundance was not as restricted by temperature as were the braarudosphaerids. The only exception is *Peritrachelina joidesa* which occurred infrequently at the southern site and was not detected at all at the northern one (Fig. 5).

Taking all of the above into consideration, we believe the last possibility considered, that of ecologic (temperature) exclusion, to be the most probable explanation for the abundant accumulations of braarudosphaerids at Site 563 and their virtual absence at Site 558. In retrospect, it is regrettable that basal Oligocene sediments could not have been cored at the other sites drilled by Leg 82 on or near magnetic Anomaly 13 (Sites 556, 559, and 564). This would have provided far better evidence of the bathymetric histories of the various sites as well as more accurate information on the distribution of braarudosphaerids in the region.

The occurrence of braarudosphaerids and the holococcoliths in question on the Mid-Atlantic Ridge, however, provides one rather important parameter concerning their distribution. It provides a minimum depth above which one can reasonably except the forms to be preserved in sediment deposited within the geographic range of the organisms during the late Eocene-Oligocene. Assuming an average elevation of newly formed crust to be 2700 m (Sclater et al., 1971), one can accept that depth or one slightly greater as a working value for this parameter.

Although braarudosphaerids are common at Site 563, as noted previously, they never reach the overwhelming abundant proportions seen in the mid-Oligocene of the South Atlantic. Instead, their numbers are more in line with those deposited in localities closer to the continental margins during the late Eocene and early to mid-Oligocene. It is reasonable, therefore, to assume that rather extraordinary and different conditions caused the anomalous occurrences in the mid-Oligocene South Atlantic as opposed to elsewhere in the world. Oligocene occurrences elsewhere are more pervasive on a global scale and may be the norm for the upper Eocene-lower Oligocene within their range of distribution, limited otherwise by paleo-water depth (generally near or above 3000 m) and nutrient supply. Although a rough bipolar temperate-subtropical distribution marking their maximum abundance seems to be emerging (Figs. 9 and 10), the data are still sketchy and not totally convincing. Each Oligocene drill site and land section locality still needs to be analyzed in detail with respect to paleobathymetry and the presence of other coccolith species before a total picture can be drawn. On the other hand, the broader question of the reason for the generally high occurrence of braarudosphaerids during the late Eocene to mid-Oligocene in both nearshore and open ocean environments, from which the living stock for the extraordinary blooms of the South Atlantic mid-Oligocene was derived, is a broader question that is not addressed here. The fact that abundant open ocean occurrences were confined largely to the Eocene-Oligocene interval suggests the existence of peculiar paleo-oceanographic/paleoclimatic conditions not in existence before or since. Interestingly, this time interval was a critical transitional period in the evolution of Cenozoic climates, one in which global climates were deteriorating and in which the psychrosphere developed (Kennett, 1978).

PLIOCENE/PLEISTOCENE BOUNDARY STRATIGRAPHY

Takayama (1970) observed frequent 3-rayed forms of *D. brouweri* near the Pliocene/Pleistocene boundary in his study of the Le Castella section in Italy. Haq et al. (1977) noted the presence of reworked discoasters of early and late Tertiary age throughout the Pliocene/Pleistocene boundary stratotype section at Le Castella. They used an increase in the relative abundance of the 3-rayed variety of *D. brouweri* as an indicator of the LAD (last appearance datum) of *D. brouweri*. Above this level, Haq et al. (1977) found that *D. brouweri* (6-rayed) decreased abruptly in abundance. Backman et al. (1983) also used an increase in the relative abundance of triradiate forms as an indicator of the position of the Pliocene/Pleistocene boundary in their work on the Vrica section of Italy.

Rio (1982) reported the simultaneous extinction of the two varieties of *D. brouweri* from Sites 125 and 132 in the Mediterranean, Site 502 in the Caribbean, and from the Capo Rosella section of Sicily. Backman and Shackleton (1983) applied quantitative methods in order to improve the biostratigraphic resolution of Pliocene and early Pleistocene calcareous nannofossil extinction events in sediments from low and middle latitudes of the Pacific, Atlantic, and Indian oceans. In Pacific, Atlantic, and Indian ocean cores, regardless of latitudinal position of the cores, they found that the triradiate form of *D. brouweri* increases in proportion relative to the 6-rayed form between the Olduvai and the Gauss, shortly before their simultaneous extinction.

Backman and Shackleton (1983) concluded that this increase is a global phenomenon and a valuable guide for proximity to the extinction level of the species. The proportion of the triradiate form of *D. brouweri* showed no prominent peak other than that near the end of its range. The duration of the interval during which the triradiate form is relatively abundant was estimated by Backman and Shackleton (1983) to be between 0.10 and 0.15 Ma. Therefore, even in sections having considerable reworking, this triradiate signal may be biostratigraphically useful, because there is no older potential source from which the 3-rayed forms of *D. brouweri* may be reworked in sufficient numbers to imitate this peak.

In summary, the quantitative work of Backman and Shackleton (1983) established two biostratigraphically important relationships between the 6-rayed and 3-rayed forms of *D. brouweri*. First, the two forms have simultaneous extinctions. Secondly, the proportion of 3-rayed *D. brouweri* increases relative to 6-rayed forms of *D. brouweri* from values less than 10% to values in excess of 20% shortly before their joint extinction.

These relationships may be applied to the section at Hole 558A, which shows substantial reworking. The LAD of *D. brouweri* and the position of the Pliocene/Pleistocene boundary thus determined would be at the top of 558A-7-2, 70–71 cm. This sample contains abundant 3-rayed and 6-rayed *D. brouweri*, and above this sample 6-rayed forms of *D. brouweri* are few to rare and 3-rayed forms are absent. This section is problematic in that this sample also marks the final appearance of *Calcidiscus macintyrei*. Backman and Shackleton (1983) concluded that the extinction of *C. macintyrei* represents a reliable global datum event that should occur at approximately 1.45 Ma, above the LAD of *D. brouweri*.

One possible explanation for the nannofossil occurrences observed in Hole 558A is that a short hiatus is present and the *C. macintyrei* Zone of Gartner (1977) is absent. A length of 0.14 Ma was given by Gartner (1977) for the duration of the *C. macintyrei* Zone. The existence of such a short hiatus would be difficult to prove, however. In 558A-7-4, 70–71 cm, triradiate forms of *D. brouweri* are common; triradiate forms are rare in lower samples. Although samples above 558A-7-4 contain common to abundant *D. brouweri*, the *C. macintyrei* Zone, if present, may begin in Section 558A-7-3. Therefore, zonal boundaries are uncertain, and although the most probable position for the Pliocene/Pleistocene boundary is above 558A-7-2 with the presence of a hiatus likely, no hiatus is delineated on the range chart. More closely spaced samples through this interval were not available for this study, but such sampling might well resolve the problem.

Although the exact position of the Pliocene/Pleistocene boundary is questionable in Hole 558A, the increased abundance of triradiate forms of *D. brouweri* provides a valuable signal for proximity to that boundary, particularly in view of the reworking of *D. brouweri* in the section.

SUMMARY

A detailed study of the abundance, preservation, and biostratigraphic distribution of calcareous nannofossils at Sites 558 and 563 shows that only one hiatus (early Pliocene) is present in these sections. Subzones CN10b, CN10c, and CN1a are missing. In the uppermost Pliocene of Hole 558A, a peak in the relative abundance of 3-rayed *Discoaster brouweri*, followed by the absence of 3-rayed forms in overlying sections, provides a useful guide for the placement of the Pliocene/Pleistocene boundary where the extinction of 6-rayed *D. brouweri* has been obscured by reworking.

The most unexpected element of the nannofossil assemblages was the presence in Cores 563-20 through 563-22 of abundant braarudosphaerids, along with the holococcoliths *Lanternithus minutus, Peritrachelina joidesa*, and *Zygrhablithus bijugatus*. This is the first report of abundant lower Oligocene braarudosphaerids and this suite of holococcoliths from the central North Atlantic. Braarudosphaerids are absent in Hole 558, located approximately 400 km to the north. The sediments of the two holes are of the same age and were deposited at similar water depths. The absence of braarudosphaerids in Hole 558 is attributed to the crossing of a latitudinal (temperature dependent) provincial nannofossil boundary.

ACKNOWLEDGMENTS

This paper was derived from a master's thesis (Parker, 1984) submitted to the Department of Geology, Florida State University.

We thank William I. Miller III for his skillful operation of the SEM, Kim Riddle for the printing of the micrographs, Dennis Cassidy for the use of the Antarctic core facilities, and Sharon Reeves and Jill Arnold for typing the manuscript. We thank David K. Watkins and James A. Bergen (both at FSU) for their critical reviews of the manuscript and invaluable assistance throughout the research phase. The penultimate draft was critically reviewed by Marie-Pierre Aubry (Woods Hole Oceanographic Institution), Kenneth G. Miller (Lamont-Doherty Geologic Observatory), and Jay Bowdler (Union Oil Company of California, Houston). Dr. Aubry, who had examined some of the sections, made many helpful comments and suggested alternative means for zoning the sequences. Laboratory facilities for this research were supported by NSF grants DPP 8020382 and EAR 8025489.

REFERENCES

Aumento, F., Melson, W. G., et al., 1977. *Init. Repts. DSDP*, 37: Washington (U.S. Govt. Printing Office).

Backman, J., 1979. Pliocene biostratigraphy of DSDP Sites 111 and 116 from the North Atlantic Ocean and the age of Northern Hemisphere glaciation. *Stockholm Contrib. Geol.*, 32:115–137.

Backman, J., and Shackleton, N. J., 1983. Quantitative biochronology of Pliocene and early Pleistocene calcareous nannofossils from the Atlantic, Indian and Pacific oceans. *Mar. Micropaleontol.*, 8 141–170.

Backman, J., Shackleton, N. J., and Tauxe, L., 1983. The Pliocene Pleistocene at the Vrica section: quantitative nannofossil correlation to the deep sea. *Nature*, 304:156–158.

Barker, P. F., and Burrell, J., 1977. The opening of Drake Passage *Mar. Geol.*, 25:25–34.

Barker, P. F., Carlson, R. L., Johnson, D. A., et al., 1983. *Init. Repts DSDP*, 72: Washington (U.S. Govt. Printing Office).

Berger, W. H., 1979. Impact of deep drilling on paleoceanography. *I* Talwani, M., Hay, W. W., and Ryan, W.B.F. (Eds.), *Deep Drillin Results in the Atlantic Ocean: Continental Margins and Paleoenvironment*: Washington (Amer. Geophys. Union), Maurice Ewing Series 3:297–314.

Berggren, W. A., Kent, D. V., Flynn, J. J., and Van Couvering, J. A. in press. Cenozoic geochronology. *Geology*.

Bolli, H. M., Ryan, W. B. F., et al., 1978. *Init. Repts. DSDP*, 40: Washington (U.S. Govt. Printing Office).

Bramlette, M. N., and Wilcoxon, J. A., 1967. Middle Tertiary calcareous nannoplankton of the Cipero Section, Trinidad, W. I. *Tulane Stud. Geol.*, 5:93–131.

Bukry, D., 1970. Coccolith age determinations, Leg 2, Deep Sea Drilling Project. *In* Peterson, M. N. A., Edgar, N. T., et al., *Init. Repts. DSDP*, 2: Washington (U.S. Govt. Printing Office), 349–355.

________, 1973a. Coccolith stratigraphy, Leg 10, Deep Sea Drilling Project. *In* Worzel, J. L., Bryant, W., et al., *Init. Repts. DSDP*, 10: Washington (U.S. Govt. Printing Office), 385–406.

________, 1973b. Low-latitude coccolith biostratigraphic zonation. *In* Edgar, N. T., Saunders. J. B., et al., *Init. Repts. DSDP*, 15: Washington (U.S. Govt. Printing Office), 685–703.

________, 1974. Coccoliths as paleosalinity indicators—evidence from Black Sea. *Am. Assoc. Pet. Geol. Mem.*, 20:353–363.

________, 1975. Coccolith and silicoflagellate stratigraphy, northwestern Pacific Ocean, Deep Sea Drilling Project, Leg 32. *In* Larson, R. L., Moberly, R., et al., *Init. Repts. DSDP*, 32: Washington (U.S. Govt. Printing Office), 677–692.

________, 1977. Coccolith and silicoflagellate stratigraphy, South Atlantic Ocean, Deep Sea Drilling Project Leg 39. *In* Supko, P. R., Perch-Nielsen, K., et al., *Init. Repts. DSDP*, 39: Washington (U.S. Govt. Printing Office), 825–839.

________, 1978a. Cenozoic silicoflagellate and coccolith stratigraphy, southeastern Atlantic Ocean, Deep Sea Drilling Project Leg 40. *In* Bolli, H. M., Ryan, W. B. F., et al., *Init. Repts. DSDP*, 40: Washington (U.S. Govt. Printing Office), 635–649.

________, 1978b. Cenozoic silicoflagellate and coccolith stratigraphy, northwestern Atlantic Ocean, Deep Sea Drilling Project, Leg 43. *In* Benson, W. E., Sheridan, R. E., et al., *Init. Repts. DSDP*, 44 Washington (U.S. Govt. Printing Office), 775–805.

Bukry, D., and Bramlette, M. N., 1968. Stratigraphic significance o two genera of Tertiary calcareous nannofossils. *Tulane Stud. Geol.* 6:149–155.

Bybell, L. M., 1982. Late Eocene to early Oligocene calcareous nannofossils in Alabama and Mississippi. *Gulf Coast Assoc. Geo Soc. Trans.*, 32:295–302.

Bybell, L. M., and Gartner, S., 1972. Provincialism among mid-Eocene calcareous nannofossils. *Micropaleontology*, 18:319–336.

Fischer, A. G., and Arthur, M. A., 1977. Secular variations in the pelagic realm. *In* Cook, H. E., and Enos, P. (Eds.), *Deep-Water Carbonate Environments*, Soc. Econ. Paleontol. Mineral. Spec. Publ. 25:19–50.

Gaarder, K. R., 1954. Coccolithineae, Silicoflagellatae, Ptenospermataceae and other forms from the *Michael Sars* North Atlantic Dee

Sea Expedition, 1910. *Rep. Sci. Results Michael Sars North Atlantic Deep-Sea Exped.*, 2:3-20.

Gartner, S., 1967. Probable origin of an enigmatic calcareous nannofossil. *Micropaleontology*, 13:513.

_______, 1977. Calcareous nannofossil biostratigraphy and revised zonation of the Pleistocene. *Mar. Micropaleontol.*, 2:1-25.

Gartner, S., and Bukry, D., 1969. Tertiary holococcoliths. *J. Paleontol.*, 43:1213-1221.

Gran, H. H., and Braarud, T., 1935. A qualitative study of the phytoplankton in the Bay of Fundy and the Gulf of Maine. *J. Biol. Board Can.*, 1:279-467.

Haq, B. U., 1984. Jurassic to Recent nannofossil biochronology: an up date. *In* Haq, B. U. (Ed.), *Nannofossil Biostratigraphy*: Stroudsberg, Pennsylvania (Hutchinson Ross Publishing Co.), Benchmark Papers, Geology, 78:358-378.

Haq, B. U., Berggren, W. A., and Van Couvering, J. A., 1977. Corrected age of the Pliocene/Pleistocene boundary. *Nature*, 269: 483-488.

Hay, W. W., 1970. Calcareous nannofossils from cores recovered on Leg 4. *In* Bader, R. G., Gerard, R. D., et al., *Init. Repts. DSDP*, 4: Washington (U.S. Govt. Printing Office), 455-501.

Hsü, K. J., LaBrecque, J. L., et al., 1984. *Init. Repts. DSDP*, 73: Washington (U.S. Govt. Printing Office).

Hulbert, E. M., 1962. Phytoplankton in the southwestern Sargasso Sea and north equatorial current, February 1961. *Limnol. Oceanogr.*, 7:307-315.

Hulbert, E. M., and Rodman, J., 1963. Distribution of phytoplankton with respect to salinity between the coast of southern New England and Bermuda. *Limnol. Oceanogr.*, 8:263-269.

Jiang, M. -J., and Gartner, S., 1984. Neogene and Quaternary calcareous nannofossil biostratigraphy of the Walvis Ridge. *In* Moore, T. C., Jr., Rabinowitz, P. D., et al., *Init. Repts. DSDP*, 74: Washington (U.S. Govt. Printing Office), 561-595.

Kennett, J. P., 1978. The development of planktonic biogeography in the Southern Ocean during the Cenozoic. *Mar. Micropaleontol.*, 3:301-345.

Kennett, J. P., von der Borch, C. C., and Scientific Party, 1983. Leg 90 makes latitudinal traverse. *Geotimes*, 28:16-19.

LaBrecque, J. L., Hsü, K. J., Carman, M. F., Jr., Karpoff, A. M., McKenzie, J. A., Percival, S. F., Jr., Petersen, N. P., Pisciotto, K. A., Schreiber, E., Tauxe, L, Tucker, P., Weissert, H. J., and Wright, R., 1983. DSDP Leg 73: contributions to Paleogene stratigraphy in nomenclature, chronology and sedimentation rates. *Palaeogeogr., Palaeoclimatol., Palaeoecol.*, 42:91-125.

LaBrecque, J. L., and Rabinowitz, P. D., 1977. Magnetic anomalies bordering the continental margin of Argentina. *Am. Assoc. Pet. Geol.*, Spec. Map Ser., Tulsa, Oklahoma.

Lang, T. H., and Watkins, D. K., 1984. Cenozoic calcareous nannofossils from DSDP Leg 77: biostratigraphy and delineation of hiatuses. *In* Buffler, R. T., Schlager, W., et al., *Init. Repts. DSDP*, 77: Washington (U.S. Govt. Printing Office), 629-648.

Lefort, F., 1972. Quelques caractères morphologiques de deux specés actuelles de *Braarudosphaera* (Chrysophycées, Coccolithophoracées). *Botaniste*, 55:81-93.

_______, 1973. Étude de quelques Coccolithophoracées marins appartenaut aux genres *Hymenomonas, Ochrosphaera, Braarudosphaera* [Thése de 3$^{\text{éme}}$ cycle]. Université Rennes, Rennes, France.

Loeblich, A. R., Jr., and Tappan, H., 1966. Annotated index and bibliography of the calcareous nannoplankton. *Phycologia*, 5:81-216.

_______, 1968. Annotated index and bibliography of the calcareous nannoplankton III. *J. Paleontol.*, 42:584-598.

_______, 1969. Annotated index and bibliography of the calcareous nannoplankton III. *J. Paleontol.*, 43:568-588.

_______, 1970a. Annotated index and bibliography of the calcareous nannoplankton IV. *J. Paleontol.*, 44:558-574.

_______, 1970b. Annotated index and bibliography of the calcareous nannoplankton VI. *Phycologia*, 9:157-174.

_______, 1971. Annotated index and bibliography of the calcareous nannoplankton VI. *Phycologia*, 10:315-339.

_______, 1973. Annotated index and bibliography of the calcareous nannoplankton VII. *J. Paleontol.*, 47:715-759.

Luyendyk, B. P., Cann, J. R., et al., 1979. *Init. Repts. DSDP*, 49: Washington (U.S. Govt. Printing Office).

McIntyre, A., and Bé, A. W. H., 1967. Modern Coccolithophoridae of the Atlantic Ocean—I, placoliths and cyrtoliths. *Deep-Sea Res.*, 14:561-597.

Manivit, H., 1984. Paleogene and Upper Cretaceous calcareous nannofossils from Deep Sea Drilling Project Leg 74. *In* Moore, T. C., Jr., Rabinowitz, P. D., et al., *Init. Repts. DSDP*, 74: Washington (U.S. Govt. Printing Office), 475-499.

Martini, E., 1967. Nannoplankton und Umlagerungsershceinungen in Persischen Golf und in nordlichen Arabischen Meer. *N. Jb. Geol. Palaont. Mh.*, 10:579-607.

_______, 1971. Standard Tertiary and Quaternary calcareous nannoplankton zonation. *In* Farinacci, A. (Ed.), Proc. II Plankt. Conf. Roma: Rome (Edizioni Tecnoscienza), 2:739-785.

Martini, E., and Bramlette, M. N., 1963. Calcareous nannoplankton from the experimental Mohole Drilling. *J. Paleontol.*, 37:845-856.

Maxwell, A. E., Von Herzen, R. P., et al., 1970. *Init. Repts. DSDP*, 3: Washington (U.S. Govt. Printing Office).

Mazzei, R., Raffi, I., Rio, D., Hamilton, N., and Cita, M. B., 1979. Calibration of late Neogene calcareous plankton datum planes with the paleomagnetic record of Site 397 and correlation with Moroccan and Mediterranean sections. *In* von Rad, U., Ryan, W. B. F., et al., *Init. Repts. DSDP*, 47, Pt. 1: Washington (U.S. Govt. Printing Office), 375-389.

Moore, T. C., Jr., Rabinowitz, P. D., et al., 1984. *Init. Repts. DSDP*, 74: Washington (U.S. Govt. Printing Office).

Noël, D., and Melguen, M., 1978. Nannofacies of Cape Basin and Walvis Ridge sediments, Lower Cretaceous to Pliocene (Leg 40). *In* Bolli, H. M., Ryan, W. B. F., et al., *Init. Repts. DSDP.*, 40: Washington (U.S. Govt. Printing Office), 487-524.

Okada, H., and Bukry, D., 1980. Supplementary modification and introduction of code numbers to the "Low-latitude coccolith biostratigraphic zonation" (Bukry, 1973; 1975). *Mar. Micropaleontol.*, 5:321-325.

Parker, M. E., 1984. Calcareous nannofossil biostratigraphy of Deep Sea Drilling Project Leg 82 Sites 558 and 563, North Atlantic Ocean in the vicinity of the Azores [M. S. thesis]. Florida State University, Tallahassee, Florida.

Perch-Nielsen, K., 1977. Albian to Pleistocene calcareous nannofossils from the western South Atlantic, DSDP Leg 39. *In* Supko, P. R., Perch-Nielsen, K., et al., *Init. Repts. DSDP*, 39: Washington (U.S. Govt. Printing Office), 699-823.

Perch-Nielsen, K., McKenzie, J., and He, Q., 1982. Biostratigraphy and isotope stratigraphy and the "catastrophic" extinction of calcareous nannoplankton at the Cretaceous/Tertiary boundary. *In* Silver, L. T., and Schultz, P. H. (Eds.), *Geological Implications of Impacts of Large Asteroids and Comets on the Earth*. Geol. Soc. Am. Spec. Pap. No. 190, pp. 353-371.

Peterson, M. N. A., Edgar, N. T., et al., 1970. *Init. Repts. DSDP*, 2: Washington (U.S. Govt. Printing Office).

Prell, W. L., 1982. Oxygen and carbon isotope stratigraphy for the Quaternary of Hole 502B: evidence for two modes of isotopic variability. *In* Prell, W. L., Gardner, J. V., et al., *Init. Repts. DSDP*, 68: Washington (U.S. Govt. Printing Office), 455-464.

Proto Decima, F., Medizza, F., and Todesco, L., 1978. Southeastern Atlantic Leg 40 calcareous nannofossils. *In* Bolli, H. M., Ryan, W. B. F., et al., *Init. Repts. DSDP*, 40: Washington (U.S. Govt. Printing Office), 571-634.

Rio, D., 1982. The fossil distribution of coccolithophore genus *Gephyrocapsa* Kamptner and related Plio-Pleistocene chronostratigraphic problems. *In* Prell, W. L., Gardner, J. V., et al., *Init. Repts. DSDP*, 68: Washington (U.S. Govt. Printing Office), 325-343.

Roth, P. H., 1970. Oligocene calcareous nannoplankton biostratigraphy. *Eclogae. Geol. Helv.*, 63:799-881.

_______, 1974. Calcareous nannofossils from the northwestern Indian Ocean, Leg 24, Deep Sea Drilling Project. *In* Fischer, R. L., Bunce, E. T., et al., *Init. Repts. DSDP*, 24: Washington (U.S. Govt. Printing Office), 969-994.

Roth, P. H., Baumann, P., and Bertolino, V., 1971. Late Eocene-Oligocene calcareous nannoplankton from central and northern Italy. *In* Farinacci, H. (Ed.), *Proc. II Plankt. Conf. Roma*: Rome (Edizioni Tecnoscienza), 2:1069-1097.

Roth, P. H., and Thierstein, H. R., 1972. Calcareous nannoplankton: Leg 14 of the Deep Sea Drilling Project. *In* Hayes, D. E., Pimm,

A. C., et al., *Init. Repts. DSDP*, 14: Washington (U.S. Govt. Printing Office), 421–485.

Sclater, G., Anderson, R. N., and Bell, M. L., 1971. Elevation of ridges and evolution of the central eastern Pacific. *J. Geophys. Res.*, 76:7888–7915.

Siesser, W. G., 1983. Paleogene calcareous nannoplankton biostratigraphy: Mississippi, Alabama, and Tennessee. *Miss. Dept. Nat. Res. Bull.*, 125:1–61.

Smayda, T. J., 1966. A quantitative analysis of the ecological conditions and the phytoplankton dynamics at 8°45′N, 79°23′W from November 1954 to May 1957. *Inter.-Am. Tropical Tuna Comm. Bull.*, II:353–612.

Supko, P. R., Perch-Nielsen, K., et al., 1978. *Init. Repts. DSDP*, 39: Washington (U.S. Govt. Printing Office).

Takayama, T., 1970. The Pliocene-Pleistocene boundary in the Lamont Core, V21-98 and at Le Castella, Southern Italy. *J. Mar. Geol.*, 6:70–77.

Thierstein, H. R., 1981. Late Cretaceous nannoplankton and the change at the Cretaceous-Tertiary boundary. *In* Warme, J. E., and Winterer, E. L. (Eds.), *The Deep Sea Drilling Project: A Decade of Progress*. Soc. Econ. Paleontol. Mineral. Spec. Publ., 32: 355–394.

Thierstein, H. R., and Okada, H., 1979. The Cretaceous/Tertiary boundary event in the North Atlantic. *In* Tucholke, B. E., Vogt, P. R., et al., *Init. Repts. DSDP*, 43: Washington (U.S. Govt. Printing Office), 601–616.

Vail, P. R., Mitchem, R. M., Jr., and Thompson, S., 1977. Seismic stratigraphy and global changes of sea level, part 3: relative changes of sea level from coastal onlap. *Am. Assoc. Pet. Geol. Bull.*, 26: 63–98.

van Heck, S. E., 1979a. Bibliography and taxa of calcareous nannoplankton. *Int. Nannoplankton Assoc. Newslett* , 1:AB1-5, A1-12, B1-27.

________, 1979b. Bibliography and taxa of calcareous nannoplankton. *Int. Nannoplankton Assoc. Newslett.*, 1:AB VI, A13-28, B28-42.

________, 1980a. Bibliography and taxa of calcareous nannoplankton. *Int. Nannoplankton Assoc. Newslett.*, 2:5–34.

________, 1980b. Bibliography and taxa of calcareous nannoplankton. *Int. Nannoplankton Assoc. Newslett.*, 2:43–81.

________, 1981a. Bibliography and taxa of calcareous nannoplankton. *Int. Nannoplankton Assoc. Newslett.*, 3:4–41.

________, 1981b. Bibliography and taxa of calcareous nannoplankton. *Int. Nannoplankton Assoc. Newslett.*, 3:51–86.

________, 1982a. Bibliography and taxa of calcareous nannoplankton. *Int. Nannoplankton Assoc. Newslett.*, 4:7–50.

________, 1982b. Bibliography and taxa of calcareous nannoplankton. *Int. Nannoplankton Assoc. Newslett.*, 4:65–96.

________, 1983a. Bibliography and taxa of calcareous nannoplankton. *Int. Nannoplankton Assoc. Newslett.*, 5:4–13.

________, 1983b. Bibliography and taxa of calcareous nannoplankton. *Int. Nannoplankton Assoc. Newslett.*, 5:29–47.

Wise, S. W., Jr., 1983. Mesozoic and Cenozoic calcareous nannofossils recovered by Deep Sea Drilling Project Leg 71 in the Falkland Plateau region, southwest Atlantic Ocean. *In* Ludwig, W. J., Krasheninnikov, V. A., et al., *Init. Repts. DSDP*, 71: Washington (U.S. Govt. Printing Office), 481–550.

Wise, S. W., and Kelts, K. R., 1972. Inferred diagenetic history of a weakly silicified deep sea chalk. *Gulf Coast Assoc. Geol. Soc. Trans.*, 22:177–203.

Date of Initial Receipt: 21 October 1983
Date of Acceptance: 1 June 1984

APPENDIX

Calcareous Nannofossils Considered in this Chapter in Alphabetical Order by Species Epithets

Sphenolithus abies Deflandre, 1953
Cyclicargolithus abisectus (Müller) Wise, 1973
Chiasmolithus altus Bukry and Percival, 1967
Amaurolithus amplificus (Bukry and Percival) Gartner and Bukry, 1975
Oolithotus antillarum (Cohen) Reinhardt, 1968
Scyphosphaera apsteinii Lohmann, 1902
Discoaster asymmetricus Gartner, 1969
Discoaster aulakos Gartner, 1967
Sphenolithus belemnos Bramlette and Wilcoxon, 1967
Discoaster bellus Bukry and Percival, 1971
Discoaster berggrenii Bukry, 1971
Braarudosphaera bigelowii (Gran and Braarud) Deflandre, 1947
Zygrhablithus bijugatus (Deflandre) Deflandre, 1959
Reticulofenestra bisecta (Hay, Mohler and Wade) Roth, 1970
Discoaster bollii Martini and Bramlette, 1963
Discoaster braarudii Bukry, 1971
Discoaster brouweri Tan Sin Hok, 1927
Catinaster calyculus Martini and Bramlette, 1963
Sphenolithus capricornutus Bukry and Percival, 1971
Gephyrocapsa caribbeanica Boudreaux and Hay, 1967
Triquetrorhabdulus carinatus Martini, 1965
Helicosphaera carteri (Wallich) Kamptner, 1954
Discoaster challengeri Bramlette and Riedel, 1954
Sphenolithus ciperoensis Bramlette and Wilcoxon, 1967
Rhabdosphaera clavigera Murray and Blackman, 1898
Catinaster coalitus Martini and Bramlette, 1963
Scyphosphaera conica Kamptner, 1955
Sphenolithus conicus Bukry, 1971
Minylitha convallis Bukry, 1973
Umbilicosphaera cricota (Gartner) Cohen and Reinhardt, 1968
Ceratolithus cristatus Kamptner, 1950
Discoaster deflandrei Bramlette and Riedel, 1954
Amaurolithus delicatus Gartner and Bukry, 1975
Sphenolithus delphix Bukry, 1973
Sphenolithus distentus (Martini) Bramlette and Wilcoxon, 1967
Crenalithus doronicoides (Black and Barnes) Roth, 1973
Discoaster druggii Bramlette and Wilcoxon, 1967
Coccolithus eopelagicus (Bramlette and Riedel) Bramlette and Sullivan, 1961
Discoaster exilis Martini and Bramlette, 1963
Clausicoccus fenestratus (Deflandre and Fert) Prins, 1979
Cyclicargolithus floridanus (Roth and Hay) Bukry, 1971
Micrantholithus flos Deflandre, 1950
Coccolithus formosus (Kamptner) Wise, 1973
Scapholithus fossilis Deflandre, 1954
Scyphosphaera globulata Bukry and Percival, 1971
Discoaster hamatus Martini and Bramlette, 1963
Sphenolithus heteromorphus Deflandre, 1953
Reticulofenestra hillae Bukry and Percival, 1971
Syracosphaera histrica Kamptner, 1941
Emiliania huxleyi (Lohmann) Hay and Mohler, 1967
Discoaster intercalcaris Bukry, 1971
Scyphosphaera intermedia Deflandre, 1942
Peritrachelina joidesa Bukry and Bramlette, 1969
Scyphosphaera kamptneri Müller, 1974
Discoaster kugleri Martini and Bramlette, 1963
Pseudoemiliania lacunosa (Kamptner) Gartner, 1969
Scyphosphaera lagena Kamptner, 1955
Leptodiscus larvalis Bukry and Bramlette, 1969
Calcidiscus leptoporus (Murray and Blackman) Loeblich and Tappan, 1978
Reticulofenestra lockeri Müller, 1970
Discoaster loeblichii Bukry, 1971
Calcidiscus macintyrei (Bukry and Bramlette) Loeblich and Tappan, 1978
Triquetrorhabdulus milowii Bukry, 1971
Lanternithus minutus Stradner, 1962
Coccolithus miopelagicus Bukry, 1971
Umbilicosphaera mirabilis Lohmann, 1902
Discoaster moorei Bukry, 1971
Sphenolithus moriformis (Brönnimann and Stradner) Bramlette and Wilcoxon, 1967
Sphenolithus neoabies Bukry and Bramlette, 1969
Discoaster neohamatus Bukry and Bramlette, 1969
Coronocyclus nitescens (Kamptner) Bramlette and Wilcoxon, 1967
Gephyrocapsa oceanica Kamptner, 1943
Pontosphaera ovata (Levin and Joerger) Proto-Decima, Medizza and Todesco, 1978
Coccolithus pelagicus (Wallich) Schiller, 1930
Discoaster pentaradiatus Tan Sin Hok, 1927
Sphenolithus predistentus Bramlette and Wilcoxon, 1967

Amaurolithus primus (Bukry and Percival) Gartner and Bukry, 1975
Rhabdosphaera procera (Martini) Jafar, 1975
Sphenolithus pseudoradians Bramlette and Wilcoxon, 1967
Reticulofenestra pseudoumbilica (Gartner) Gartner, 1969
Scyphosphaera pulcherrima Deflandre, 1942
Discoaster quinqueramus Gartner, 1969
Scyphosphaera recurvata Deflandre, 1942
Isthmolithus recurvus Deflandre in Deflandre and Fert, 1954
Braarudosphaera rosa Levin and Joerger, 1967
Scyphosphaera rottiensis Jafar, 1975
Ceratolithus rugosus Bukry and Bramlette, 1968
Triquetrorhabdulus rugosus Bramlette and Wilcoxon, 1967
Pontosphaera segmenta (Bukry and Bramlette) Jafar and Martini, 1975
Helicosphaera sellii (Bukry and Bramlette) Jafar and Martini, 1975
Bramletteius serraculoides Gartner, 1969
Discoaster surculus Martini and Bramlette, 1963
Discoaster tamalis Kamptner, 1967
Discoaster tanii Bramlette and Riedel, 1954
Ceratolithus telesmus Norris, 1965
Scyphosphaera tubifera Kamptner, 1955
Reticulofenestra umbilica (Levin) Martini and Ritzkowski, 1968
Discoaster variabilis Martini and Bramlette, 1963

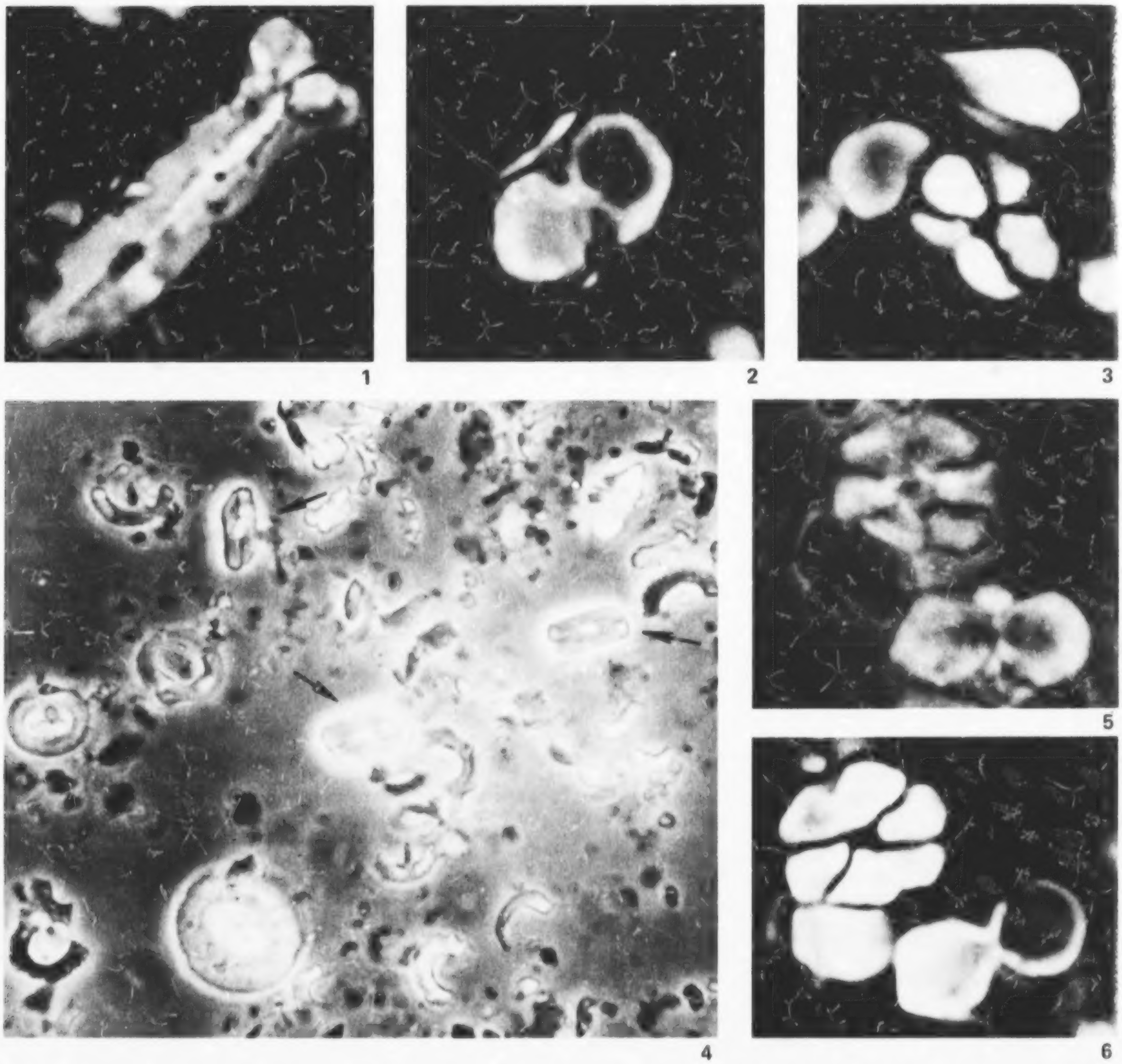

Plate 1. Lower Oligocene. **1–2.** *Zygrhablithus bijugatus* (Deflandre) Deflandre, cross-polarized light, Sample 558-26-1, 16–18 cm. (1) side vie × 4400. (2) plane view, × 6000. **3.** *Lanternithus minutus* Stradner, cross-polarized light, × 6000, Sample 558-26-1, 16–18 cm. **4.** Three spec mens of *Isthmolithus recurvus* Deflandre (see arrows), showing the overgrowth and general state of preservation in the basal Oligocene sectio phase contrast light, × 1600, Sample 558-27-2, 42–44 cm. **5–6.** *Lanternithus minutus* Stradner (top specimen) and *Zygrhablithus bijugat* (Deflandre) Deflandre (bottom specimen), plan view, × 6000, Sample 563-22-2, 52–54 cm. (5) phase contrast light, (6) cross-polarized light.

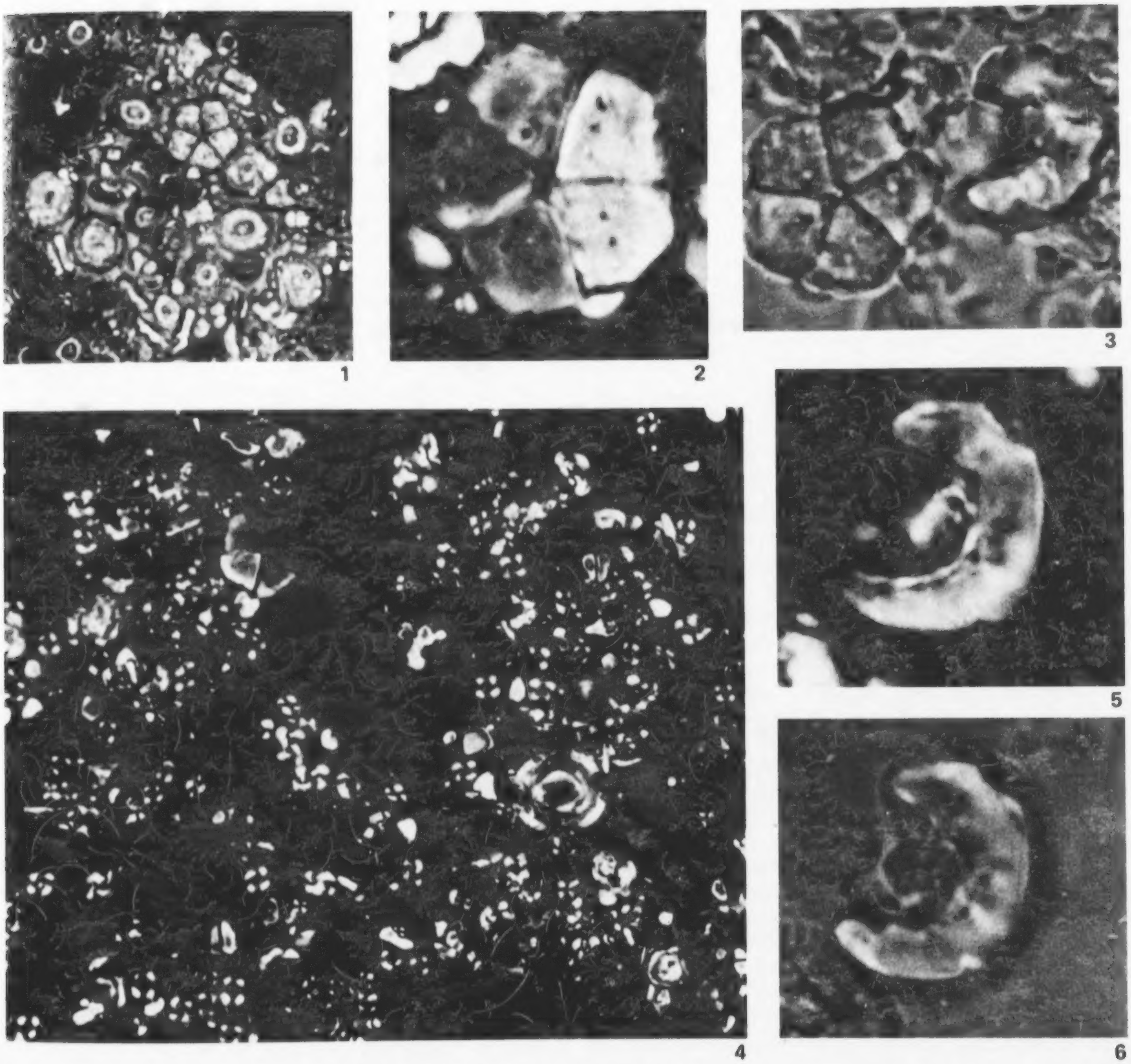

Plate 2. Lower Oligocene. **1.** Calcareous nannofossil assemblage with braarudosphaerids comprising approximately 5% of the assemblage, as in Fig. 4; phase contrast light, × 800, Sample 563-20-6, 16–18 cm. **2–3.** Intact braarudosphaerid, Sample 563-21,CC. (2) cross-polarized light, × 3600, (3) with overgrown *Peritrachelina joidesa* Bukry and Bramlette (right specimen), transmitted light, × 2500. **4.** Calcareous nannofossil assemblage, cross-polarized light, × 800, Sample 563-22-1, 50–52 cm. **5–6.** *Peritrachelina joidesa* Bukry and Bramlette, × 3600, Sample 563-21,CC. (5) cross-polarized light, (6) transmitted light.

35. MID-ATLANTIC RIDGE COCCOLITH AND SILICOFLAGELLATE BIOSTRATIGRAPHY, DEEP SEA DRILLING PROJECT SITES 558 AND 563[1]

David Bukry, United States Geological Survey and Scripps Institution of Oceanography[2]

ABSTRACT

Low-latitude coccolith zonation can be used for biostratigraphy at Mid-Atlantic Ridge sites DSDP 558 (lat. 38°N) and DSDP 563 (lat. 34°N). The low-latitude zonal sequence from lower Oligocene to Holocene is interrupted by cool-water assemblages in upper middle Miocene and by hiatuses that removed the lower Pliocene and part of the upper Pliocene. A gap in the range of zonal guide fossil *Discoaster druggii* in the lower Miocene, also identified in other ocean basins, occurs at both DSDP 558 and 563. Coccoliths are abundant and moderately overgrown at both sites. Pentaliths occur in the Oligocene at DSDP 563 but are missing at DSDP 558, probably the result of diagenesis. New taxa of coccoliths identified include *Cyclolithella*? *neoaprica* Bukry, n. sp., and *Sphenolithus calyculus* Bukry, n. sp.

Silicoflagellates are limited to the upper Quaternary at DSDP 558 with warm-water assemblages of the *Dictyocha aculeata* Zone and possibly the upper *Mesocena quadrangula* Zone, as indicated by the presence of *Dictyocha lingii*. A new silicoflagellate species, *Distephanus floridus* Bukry, n. sp., is described.

INTRODUCTION

Leg 82 of the Deep Sea Drilling Project cored nine sites in a small area on the west flank of the Mid-Atlantic Ridge, west and southwest of the Azores Triple Junction. Although the primary goal of Leg 82 was to study trace element geochemistry of different types of basalt, several long sedimentary reference sections were also cored at Sites DSDP 558 and DSDP 563. Coccoliths are especially abundant but moderately to thickly overgrown throughout and silicoflagellates are common only in the uppermost cores of DSDP 558. Biostratigraphic assignment for 200 samples from four sites of Leg 82 is based on Okada and Bukry (1980) for coccoliths and Bukry (1981a) for silicoflagellates. The coccolith zonal assignments of the cores are summarized (Table 1) and discussed. The mid-ocean assemblages of DSDP 558 are contrasted to those of DSDP 369, a site of coastal upwelling off northwestern Africa. The short upper Pleistocene silicoflagellate-bearing section of DSDP 558 is compared to other coeval assemblages from the Atlantic and Pacific. Two new species of coccoliths and one new silicoflagellate are described and illustrated.

Coccolith interpretations are based on light-microscope examination of smear-slide preparations, whereas silicoflagellate assemblages are enumerated from slides of acid-residue preparations.

BIOSTRATIGRAPHY

Site 558 (lat. 37°46.2′N, long. 37°20.61′W; water depth, 3754 m)

Site DSDP 558 is located on the west flank of the Mid-Atlantic Ridge about 50 km south of the Pico Fracture Zone, on the magnetically reversed interval between Anomalies 12 and 13 (approximately 35 Ma). The 408-m sedimentary section contains abundant coccoliths ranging from lower Oligocene (CP16b) to upper Quaternary (CN14/CN15). The lower Pliocene to uppermost Miocene interval is missing, or condensed and unrecovered, between upper Pliocene Subzone CN12a in Sample 558A-9-3, 90–91 cm and upper Miocene Subzone CN9b in Sample 558A-10-1, 90–91 cm.

First, Site 558 was rotary cored continuously from 158 to 415 m through the sedimentary section to basalt. This was followed by hydraulic piston coring to recover the complete upper sedimentary section from 0 to 132 m in Hole 558A. Coccolith biostratigraphy suggests a slight gap between the two holes in the interval of the upper Miocene *Discoaster neorectus* Subzone (CN8b).

The deepest sediment available from Sample 558-27-1, 90–91 cm (406 m) contains a typical lower Oligocene assemblage of the *Coccolithus formosus* Subzone (CP16b) including: *Coccolithus eopelagicus, C. formosus, Dictyococcites bisectus, Discoaster tanii, Helicosphaera compacta, Isthmolithus recurvus, Reticulofenestra umbilica, Sphenolithus predistentus, S. pseudoradians*, and *Zygrhablithus bijugatus. C. formosus* extends up to Sample 558-26-3, 81–82 cm (399 m) but is missing in the next higher Sample 558-26-1, 81–82 cm (396 m), which is assigned to the *Sphenolithus predistentus* Zone (CP17) because of the absence of *R. umbilica* and *R. hillae*, except for two reworked fragments. Therefore, the *Reticulofenestra hillae* Subzone is brief, if present, in the upper part of Core 558-26. *Sphenolithus distentus* occurs in Core 558-24 without *S. ciperoensis*, indicating the *Sphenolithus distentus* Zone (CP18). *Cyclicargolithus floridanus* is very abundant in both CP17 and CP18. The first *S. ciperoensis, Discolithina segmenta*, and *Cyclicargolithus abisectus* occur in Sample 558-23-5, 90–91 cm (374 m), where *Discoaster deflandrei* is the sole discoaster following the disappearance of *D. tanii* and then *D. nodifer* in Zone CP18. A conjunction of *S. cipero-*

---

[1] Bougault, H., Cande, S. C., et al., *Init. Repts. DSDP*, 82: Washington (U.S. Govt. Printing Office).

[2] Address: United States Geological Survey (A-015), Scripps Institution of Oceanography, La Jolla, California 92093.

Table 1. Cenozoic coccolith zonation of core samples from Leg 82 holes.

Age	Zone		Subzone		558	558A	563	560	564
Quaternary	CN15	*Emiliania huxleyi*				1-1/2-1			
	CN14	*Gephyrocapsa oceanica*	CN14b	*Ceratolithus cristatus*		2-3/2-5			
			CN14a	*Emiliania ovata*		3-1/5-1			
	CN13	*Crenalithus doronicoides*	CN13b	*Gephyrocapsa caribbeanica*		5-3/7-1			
			CN13a	*Emiliania annula*					
Pliocene	CN12	*Discoaster brouweri*	CN12d	*Discoaster triradiatus*		7-3/7-5			
			CN12c	*Discoaster pentaradiatus*					
			CN12b	*Discoaster surculus*		8-1/9-1			
			CN12a	*Discoaster tamalis*		9-3			
	CN11	*Reticulofenestra pseudoumbilica*	CN11b	*Discoaster asymmetricus*					
			CN11a	*Sphenolithus neoabies*					
	CN10	*Amaurolithus tricorniculatus*	CN10d	*Amaurolithus delicatus*					
			CN10c	*Ceratolithus rugosus*					
			CN10b	*Ceratolithus acutus*					
Miocene			CN10a	*Triquetrorhabdulus rugosus*					
	CN9	*Discoaster quinqueramus*	CN9b	*Amaurolithus primus*		10-1/15-3			
			CN9a	*Discoaster berggrenii*		15-5/16-5			
	CN8	*Discoaster neohamatus*	CN8b	*Discoaster neorectus*					
			CN8a	*Discoaster bellus*	1-1/2-5		1-1/2-5		
	CN7	*Discoaster hamatus*	CN7b	*Catinaster calyculus*	3-1/3-5		2-7/3-5		
			CN7a	*Helicosphaera carteri*	4-1				
	CN6	*Catinaster coalitus*			4-3/6-5		4-1		
	CN5	*Discoaster exilis*	CN5b	*Discoaster kugleri*	7-1		4-3/6-1		
			CN5a	*Coccolithus miopelagicus*	8-1/12-3		6-3/8-5		
	CN4	*Sphenolithus heteromorphus*			13-1/15-3 15-5		9-1/11-3	1-1	
	CN3	*Helicosphaera ampliaperta*			16-1/16-3		12-1/13-1		
	CN2	*Sphenolithus belemnos*			16-5/17-1		13-2/14-6		
	CN1	*Triquetrorhabdulus carinatus*	CN1c	*Discoaster druggii*	17-2/18-2		14-7/15-5		
			CN1b	*Discoaster deflandrei*	18-3/19-1		15-6/16-1		
Oligocene			CN1a	*Cyclicargolithus abisectus*	19-3		16-3/16-5		
	CP19	*Sphenolithus ciperoensis*	CP19b	*Dictyococcites bisectus*	19-5/21-3		16-7/18-5		
			CP19a	*Cyclicargolithus floridanus*	22-1/23-5				
	CP18	*Sphenolithus distentus*			24-1/24-3		19-1		H1-6
	CP17	*Sphenolithus predistentus*			25-1/26-1		19-3/21-7		
	CP16	*Helicosphaera reticulata*	CP16c	*Reticulofenestra hillae*			22-1		H1-7
			CP16b	*Coccolithus formosus*	26-3/27-1		22-3		
			CP16a	*Coccolithus subdistichus*					
Eocene	CP15	*Discoaster barbadiensis*	CP15b	*Isthmolithus recurvus*					
			CP15a	*Chiasmolithus oamaruensis*					
	CP14	*Reticulofenestra umbilica*	CP14b	*Discoaster saipanensis*					
			CP14a	*Discoaster bifax*					
	CP13	*Nannotetrina quadrata*	CP13c	*Coccolithus staurion*					
			CP13b	*Chiasmolithus gigas*					
			CP13a	*Discoaster strictus*					
	CP12	*Discoaster sublodoensis*	CP12b	*Rhabdosphaera inflata*					
			CP12a	*Discoasteroides kuepperi*					
	CP11	*Discoaster lodoensis*							
	CP10	*Tribrachiatus orthostylus*							
	CP9	*Discoaster diastypus*	CP9b	*Discoaster binodosus*					
			CP9a	*Tribrachiatus contortus*					
Paleocene	CP8	*Discoaster multiradiatus*	CP8b	*Campylosphaera eodela*					
			CP8a	*Chiasmolithus bidens*					
	CP7	*Discoaster nobilis*							
	CP6	*Discoaster mohleri*							
	CP5	*Heliolithus kleinpellii*							
	CP4	*Fasciculithus tympaniformis*							
	CP3	*Ellipsolithus macellus*							
	CP2	*Chiasmolithus danicus*							
	CP1	*Zygodiscus sigmoides*	CP1b	*Cruciplacolithus tenuis*					
			CP1a	*Cruciplacolithus primus*					

Note: The numbers assigned to zonal intervals are core and section numbers of samples examined. Where a zone or subzone is represented in samples from two or more core sections, the highest and lowest are given, separated by a slash. The name of Subzone CN12d (Okada and Bukry, 1980) is renamed the *Discoaster triradiatus* Subzone to avoid duplication of names with the *Calcidiscus macintyrei* Zone of Gartner (1977).

ensis with *S. distentus* signifies the upper Oligocene *Cyclicargolithus floridanus* Subzone (CP19a) in samples from Core 558-23 and lower Core 558-22. The uppermost sample of Core 558-22 is assigned to CP19a, but *S. ciperoensis*, which occurs above and below, was not identified there.

Assemblages from upper Oligocene and lower Miocene Zones CP19 and CN1 are characterized by abundant *Cyclicargolithus floridanus, Discoaster deflandrei*, and *Sphenolithus. Triquetrorhabdulus carinatus* occurs first in Subzone CP19b, Sample 558-20-1, 90–91 cm (339 m), but is not common below Core 558-18. Sparse *Sphenolithus delphix* and *S. capricornutus* occur in lower Core 558-18, below the first occurrence of *Discoaster druggii* in Sample 558-18-2, 89–90 cm (322 m). The lowest *Calcidiscus leptoporus* occurs in Sample 558-18-5, 40–41 cm (326 m), but *Helicosphaera carteri* (another auxiliary guide to basal Miocene assemblages) is not present. Minor reworking of *Dictyococcites bisectus* occurs in Sample 558-19-1, 90–91 cm (330 m) and Sample 558-18-5, 40–41 cm (326 m).

Discoaster druggii is sparse in Cores 558-17 and 558-18 at Site DSDP 558. A gap in the range of *D. druggii* occurs midway through the *Discoaster druggii* Subzone (CN1c) in Samples 558-17-4, 90–91 cm (315 m) and 558-17-5, 90–91 cm (317 m), dividing *D. druggii* occurrences into a lower and an upper range (Table 2). This two-part range for *D. druggii* has been previously demonstrated at DSDP sites in the Atlantic and Pacific (Bukry, 1976). The gap could record a minor global climatic pulse affecting plankton ecology. Barron and Keller (1982) also suggest a widespread sedimentary hiatus (NH 1a) at about this time. There is a slight reduction in coccolith diversity in the assemblages of the *D. druggii* Subzone gap at DSDP 558 and nearby DSDP 563.

The appearance of *Sphenolithus belemnos* s. str. (with a narrow, tall basal cycle and single apical spine) marks the base of the *Sphenolithus belemnos* Zone (CN2) in Sample 558-17-1, 90–91 cm (311 m). Zone CN2 is brief at Site DSDP 558, because *S. heteromorphus*, the guide to the top of the zone, is present in Sample 558-16-3, 90–91 cm (304 m) just 7 m higher. This may be evidence for hiatus NH 1b of Barron and Keller (1982) that is associated with a shortened or missing *S. belemnos* Zone. Aside from the abrupt change in sphenoliths from *S. dissimilis* and *S. belemnos* to *S. heteromorphus* (regular and small), the assemblages in Sections 558-16-3 and 558-16-5 are very similar.

The lower boundary of the *Sphenolithus heteromorphus* Zone (CN4) is in Sample 558-15-3, 90–91 cm (295 m), if the criterion of the appearance of *Calcidiscus macintyrei* is used. But just below, in Sample 558-15-5, 90–91 cm (298 m), a substantial abundance of long-rayed discoasters could provide a secondary marker for the base of Zone CN4, as applied in the tropical Pacific (Bukry, 1971). Because of some uncertainty for the higher latitude situation of Site DSDP 558, the assemblage in Sample 558-15-3, 90–91 cm is shown straddling the boundary (Table 1). Assemblages of Zone CN4, such as that in Sample 558-15-1, 90–91 cm (292 m) with *Calcidiscus macintyrei* (elliptic tube), *Coccolithus miopelagicus, C. pelagicus, Cyclicargolithus floridanus, Discoaster deflandrei, D. variabilis* s. ampl., *Helicosphaera granulata*, and *Sphenolithus heteromorphus* are augmented, in higher assemblages, by the addition of *Discoaster exilis* and *D. signus. D. signus*, which can serve as an ecostratigraphic guide for slightly warmer assemblages (Bukry, 1981b), is identified in Cores 558-12 and 558-13 with abundant *Coccolithus* spp. At nearby Site DSDP 563 it occurs in Cores 563-8 and 563-9, in the same stratigraphic interval bracketing the top of the *S. heteromorphus* Zone (CN4) and the bottom of the *Discoaster exilis* Zone (CN5). Higher assemblages show increasing abundances of *Reticulofenestra* placoliths and fewer discoasters, which suggest a middle middle Miocene cooling. Distinctly temperate conditions are shown in Sample 558-6-5, 90–91 cm (212 m) by a lack of short-ranged marker species and the dominance of low-diversity cool-water assemblages characterized by *Discoaster variabilis* and by *Reticulofenestra* spp. (with closed and open central areas) upward through Core 558-4. These assemblages correlate to the coeval temperate *Discoaster variabilis* Zone of the Pacific Coast (Bukry, 1973a; 1981b; Crouch and Bukry, 1979). Only in the late middle Miocene or early late Miocene *Catinaster calyculus* Subzone of Sample 558-3-5, 90–91 cm (184 m) did typical low-latitude taxa become re-established at Site 558. The cool-water middle Miocene assemblages at DSDP 558 correspond to Neogene hiatus NH 4 of Barron and Keller (1982). This supports their principle that widespread Neogene hiatuses represent cool-water events.

Coccolith assemblages in seven samples between Samples 558-4-3, 90–91 cm (190 m) and 558-6-5, 90–91 cm (212 m) are above the range of *Cyclicargolithus floridanus* and lack low-latitude guide species *Discoaster kugleri* and *Catinaster coalitus*, which define zonal units CN5b and CN6. *Coccolithus miopelagicus*, which is extinct or sparse above the *Catinaster coalitus* Zone (CN6), occurs only in Core 558-6. Therefore, Cores 558-4 and 558-5 may be equivalent to the *Discoaster hamatus* Zone (CN7) of low-latitude sites.

Cores 558-3 and 558-4 have especially abundant *Calcidiscus macintyrei*. Warm-water discoasters become more abundant from the top of Core 558-4, with *Discoaster neohamatus*, to Core 558-3, which contains the sparse *Catinaster calyculus* and *Discoaster hamatus* that define the *Catinaster calyculus* Subzone (CN7b).

The overlying upper Miocene *Discoaster bellus* Subzone (CN8a) is characterized at Site DSDP 558 by *Discoaster bellus, D. challengeri, D. neohamatus, D. prepentaradiatus*, and *D. variabilis* in the lower part of the subzone in Core 558-2. However, higher Core 558-1 has the lowest occurrence surface (LOS) of *D. pentaradiatus, D. brouweri* s. ampl. is more common, and *D. challengeri* is much rarer. Together with sparse specimens of *Discoaster blackstockae* and *D. quadramus* in Sample 558-1-3, 34–35 cm (160 m), this suggests a warming trend upward through the upper part of the subzone. There are no specimens of older *D. calcaris* or *D. hamatus* nor of younger *D. loeblichii* and *D. neorectus* in Cores 558-1 or 558-2. Other typical species for CN8a at DSDP 558, and elsewhere, include *Helicosphaera granulata,*

Table 2. Occurrence checklist of selected lower Miocene coccoliths at Mid-Atlantic Ridge Sites DSDP 558 and 563 to illustrate the species matrix in the vicinity of the *Discoaster druggii* Subzone (CN1c) and *Sphenolithus belemnos* Zone (CN2).

Coccolith zone or subzone	Core-Section (interval in cm)	Sub-bottom depth (m)	*Calcidiscus leptoporus*	*Coccolithus miopelagicus*	*C. pelagicus*	*Coronocyclus nitescens*	*Cyclicargolithus floridanus*	*C.* sp. cf. *C. floridanus* (large)	*Discoaster calculosus*	*D. deflandrei*	*D.* sp. cf. *D. deflandrei* (5-, 7-rayed)	*D. druggii*	*D.* sp. (4-rayed)	*Discolithina segmenta*	*Helicosphaera euphratis*	*Orthorhabdus serratus*	*Pyrocyclus orangensis*	*Reticulofenestra* sp.	*Sphenolithus belemnos*	*S. calyculus*	*S. capricornutus*	*S. conicus*	*S. delphix*	*S. dissimilis*	*S. dissimilis* (late, elongate form)	*S. heteromorphus*	*S. moriformis* (small)	*Triquetrorhabdulus carinatus*	*T. milowii*
DSDP 563																													
CN3	12-5, 94–95	268		X	X	X	X			X								X								X	X		X
	13-1, 90–91	271				X	X		X	X		X						X	X							X			
CN2	13-2, 90–91	273		X	X	X	X	X		X									X					X	X			X	
	13-3, 84–85	274		X	X	X	X	X		X	X	X			X	X		X	X						X		X		
	13-4, 90–91	276		X		X	X		X	X		X												X	X			X	
	13-5, 89–90	277		X	X	X	X			X														X			X		
	14-1, 90–91	281		X	X	X	X			X									X						X		X		
	14-2, 90–91	282	X	X	X	X	X	X		X	X														X		X	X	X
	14-3, 42–44	283			X	X	X	X		X	X								X								X	X	
	14-4, 24–25	285			X	X	X	X		X	X		X						X			X			X		X	X	X
	14-5, 139–140	287			X	X	X	X		X							X		X								X		
	14-6, 90–91	288					X	X		X	X	X							X						X		X		X
CN1c	14-7, 35–37	289		X	X	X	X			X				X										X	X		X	X	X
	15-1, 90–91	290		X			X			X		X												X					X
	15-2, 90–91	292		X		X	X			X		X												X			X	X	X
	15-3, 94–95	293		X		X	X			X		⁓												X	X			X	
	15-4, 90–91	295		X			X	X		X		X												X	X		X	X	X
	15-5, 88–89	296		X	X	X	X			X		X													X			X	X
CN1b	15-6, 90–91	298		X	X	X	X			X				X				X						X				X	
	15-7, 29–30	299		X	X	X	X			X														X			X		X
DSDP 558																													
CN3	16-1, 90–91	301	X	X	X	X	X			X								X						X		X			
	16-3, 90–91	304		X		X	X			X								X								X	X		
CN2	16-5, 90–91	307		X	X	X	X			X								X	X					X	X				X
	17-1, 90–91	311			X	X	X			X		X							X						X				X
CN1c	17-2, 89–90	312	X		X	X	X		X	X		X				X								X	X				
	17-3, 90–91	314		X	X	X	X		X	X		X												X	X		X		
	17-4, 90–91	315		X	X	X	X			X		⁓			X									X					X
	18-1, 40–41	320		X	X		X	X		X		X												X				X	
	18-2, 89–90	322		X	X	X	X	X		X		X			X			X						X			X	X	X
CN1b	18-3, 90–91	323		X	X	X	X			X														X			X	X	X
	18-4, 90–91	325	X	X	X	X	X	X		X											X	X		X			X	X	X
	18-5, 40–41	326	X	X		X	X	X		X				X	X			X		X	X		X	X			X	X	
	19-1, 90–91	330		X	X	X	X	X		X				X			X			X		X	X				X	X	

Note: The gap shown (⁓) in the range of *Discoaster druggii* has been noted in DSDP sections from other ocean basins.

Minylitha convallis, and *Triquetrorhabdulus rugosus*. Some warm-water taxa, such as *Discoaster blackstockae*, *D. brouweri* s. ampl., *D. quadramus*, and *Discolithina* sp., are recorded only in the upper part of Core 558-1. Overgrowth and etching are only slight. Typical placoliths in the subzone include *Calcidiscus leptoporus, C. macintyrei, C. rotula, Coccolithus pelagicus, Reticulofenestra pseudoumbilica* (closed and open centers), and *R*. spp. (small and medium).

The highest sample from the first hole at DSDP 558, Sample 558-1-1, 34–35 cm (158 m), contains an assemblage that appears to be well within Subzone CN8a and not near the boundary with the overlying Subzone CN8b. Coring of a second hole (558A) at this site from the seafloor to 132 m failed to sample Subzone CN8b or uppe Subzone CN8a because of the 36-m coring gap between the sections at Holes 558 and 558A.

The continuation of this section in the bottom o Hole 558A is in a distinctly higher assemblage assigned to the *Discoaster berggrenii* Subzone (CN9a). *Discoaster berggrenii, D. loeblichii*, and *D. surculus* determine the higher correlation for basal Sample 558A-16-5, 90–91 cm (129 m). Older taxa such as *Discoaster neohamatus, D. neorectus*, and *Minylitha convallis* persist. Warm conditions may be suggested by the high discoaster diversity and abundance of *Coccolithus pelagicus* relative to *Reticulofenestra pseudoumbilica* (Bukry, 1981c). A similar warming in the North Atlantic at about 8 Ma was recorded by Haq (1980), but without the *Coccolithus* abundance relative to *Reticulofenestra*. The first *Discoaster quinqueramus* occurs above in Sample 558A-16-3, 90–91 cm (126 m) and older *Discoaster neohamatus* Zone discoasters disappear shortly above this level.

Amaurolithus primus is missing from Sample 558A-15-5, 90–91 cm (119 m) but is present in Sample 558A-15-3, 90–91 cm (116 m), indicating that the base of the *Amaurolithus primus* Subzone (CN9b) occurs in the lower part of Core 558A-15. As is typical at other DSDP sites, *A. amplificus* appears just above, in Sample 558A-15-1, 90–91 cm (113 m). A thick section of Subzone CN9b extends through Sample 558A-10-1, 90–91 cm (75 m) yielding a sediment accumulation rate exceeding 29 m/Ma (= 41 m/1.4 Ma). This relation in Hole 558A is consistent with high sedimentation rates within the *A. primus* Subzone in the Indian Ocean (Vincent et al., 1980), Pacific Ocean (Keller, 1980; Keller and Barron, 1981), and Atlantic Ocean (Baldauf, in press).

Subzone CN9b assemblages range as high as Sample 558A-10-1, 90–91 cm (75 m) where *A. primus*, *A. tricorniculatus*, and *Triquetrorhabdulus rugosus* occur with *D. quinqueramus*, *D. surculus*, *D. tridenus*, and *D. variabilis*. Within the substantial thickness of Subzone CN9b (41 m), the absence of *Sphenolithus* and *Triquetrorhabdulus* and an increased abundance of *Reticulofenestra* suggest a cooling event in the interval of Samples 558A-14-2, 90–91 cm (105 m), 558A-13-3, 90–91 cm (100 m), and 558A-12-5, 90–91 cm (93 m), through the middle of the zone.

Just above Core 558A-10, a 7-m coring attempt for Core 558A-9 retrieved only 4.8 m. The missing 2.2 m (a void at the base of the core) represent 2.6 Ma between upper Miocene Subzone CN9b at 75 m and upper Pliocene Subzone CN12a at 71 m in Sample 558A-9-3, 90–91 cm (71 m). A hiatus that eliminated lower Pliocene sediment at this site appears to be the likely cause of the temporal gap between Cores 558A-9 and 558A-10; there is no change in the character of the pelagic foraminifer-rich and coccolith-rich sediment that would have occurred if sedimentary rates had slowed drastically.

The upper Pliocene assemblage of Sample 558A-9-3, 90–91 cm (71 m) contains a typical array including *Calcidiscus macintyrei*, *Ceratolithus rugosus*, *Crenalithus doronicoides*, *Coccolithus pelagicus*, *Discoaster asymmetricus*, *D. brouweri*, *D. pentaradiatus*, *D. surculus*, *D. tamalis*, *Helicosphaera sellii*, and *Rhabdosphaera clavigera*, but no *Reticulofenestra pseudoumbilica*. Overlying sediment, in Sample 558A-9-1, 133–134 cm (68 m), contains the next higher *Discoaster surculus* Subzone (CN12b) with a similar assemblage, but also including *Ceratolithus separatus*. The absence of discoasters *D. asymmetricus* and *D. tamalis* distinguish the two samples from Core 558A-9 as belonging to different subzones. *C. separatus*, with a saddle-shaped arch, was originally defined at Mid-Atlantic Ridge Site DSDP 396 in the Pliocene (Bukry, 1978a) in mixed-age assemblages. The occurrence at DSDP 558A confirms the upper Pliocene assignment for *C. separatus* that was inferred at DSDP 396. This new occurrence also extends the latitudinal range for the species 15° northward from latitude 23°N at DSDP 396 to latitude 38°N at DSDP 558.

The *Discoaster surculus* Subzone (CN12b) occurs through Core 558A-8, but *D. surculus* is very sparse in Sample 558A-8-1, 100–101 cm (59 m), suggesting that the short *Discoaster pentaradiatus* Subzone (CN12c) may occur in the unsampled upper part of Section 558A-8-1. *Discoaster* assemblages in Core 7 are reduced to only *D. brouweri* in Sample 558A-7-5, 100–101 cm (55 m) and *D. brouweri* and *D. triradiatus* in Sample 558A-7-3, 100–101 cm (52 m). Both samples belong to the uppermost Pliocene *Discoaster triradiatus* Subzone (CN12d) and are diverse and well-preserved with *Ceratolithus*, *Discolithina*, *Helicosphaera*, *Rhabdosphaera*, *Scyphosphaera*, and *Syracosphaera*, in addition to the typical array of placoliths.

Lower Pleistocene assemblages in Cores 558A-5 to 558A-7 are typified by abundant *Coccolithus pelagicus*, *Crenalithus productellus*, common *Discolithina japonica*, *Helicosphaera carteri*, and sparser, but continuously present, *Gephyrocapsa caribbeanica* and *Scyphosphaera*. The last continuous *Calcidiscus macintyrei*, in Sample 558A-7-1, 100–101 cm (49 m), has been dated at 1.51 Ma (Gartner, 1977) and occurs in the *Gephyrocapsa caribbeanica* Subzone (CN13b). *Helicosphaera sellii*, which disappeared about 1.22 Ma (Gartner, 1977), occurs as high as Sample 558A-5-1, 90–91 cm (30 m) and *Gephyrocapsa oceanica* first occurs just above in Sample 558A-4-5, 90–91 cm (26 m), marking the base of the *Gephyrocapsa oceanica* Zone (CN14). *Ceratolithus* is missing in most Quaternary assemblages of DSDP 558A; sparse occurrences are noted only in Samples 558A-1-1, 53–54 cm (1 m) and 558A-2-5, 90–91 cm (7 m). Previous coring along the Mid-Atlantic Ridge showed *Ceratolithus* to be sparse and sporadic north of latitude 35°N (Bukry, 1977).

The small placolith ooze of the middle Quaternary, about 0.9–1.2 Ma (Gartner, 1977), occurs in Sample 558A-3-3, 90–91 cm (14 m). The conjunction of this coccolith assemblage with the *Mesocena quadrangula* acme (silicoflagellate) at lower latitudes (DSDP Leg 54; Bukry, 1980) suggests it should correlate to a general cooling (Bukry, 1983). The last *Emiliania annula* dated at about 0.46 Ma (Thierstein et al., 1977) occurs in Sample 558A-3-1, 90–91 cm (11 m).

Reworking through the Quaternary is minor, and slight etching occurs in the well-preserved assemblages. Fluctuations in species dominance suggest that the Quaternary section at DSDP 558A should provide a good reference for paleoclimatic studies.

Site 560 (lat. 34°43.33′N, long. 38°50.56′W; water depth, 3443 m)

Site 560 is located on the west side of the Mid-Atlantic Ridge between the Oceanographer and Hayes fracture zones, on Magnetic Anomaly 5D. The sedimentary section from 0 to 373 m was washed instead of cored, in order to allow coring time to sample the igneous basement rocks. The single coccolith sample studied is from Core 560-1 and contains a lower middle Miocene *Sphe-*

nolithus heteromorphus Zone (CN4) assemblage of coccoliths. Sample DSDP 560-1-1, 48–49 cm (373 m) contains guide species *Calcidiscus macintyrei* and *S. heteromorphus,* in addition to *Coccolithus pelagicus, C. miopelagicus, Cyclicargolithus floridanus, Discoaster deflandrei, D. exilis, D. variabilis,* and *Helicosphaera granulata.* The coccoliths in this basal assemblage are slightly older and less etched than those recovered at the base of the sediment section at Site DSDP 396 (CN5a) to the south. The basal assemblage at nearby Site DSDP 335 is younger still (CN5b) and better preserved (Bukry, 1977; 1978a).

Site 563 (lat. 33°38.53′N, long. 43°46.04′W; water depth, 3786 m)

Site DSDP 563 is located on the west side of the Mid-Atlantic Ridge about 100 km south of the Hayes Fracture Zone on Magnetic Anomaly 13 (approximately 37 Ma). The upper sedimentary section was not cored. Continuous coring for Cores 563-1 to 563-22, between 157 and 365 m, recovered a coccolith zonal sequence from upper Miocene Subzone CN8a to lower Oligocene Subzone CP16b above basalt. Coccoliths are abundant but moderately to thickly overgrown throughout.

Lower Oligocene assemblages from Cores 563-20 to 563-22 (337 to 365 m) are characterized by shallow-water taxa such as *Braarudosphaera, Bramletteius, Peritrachelina, Vermiculithina, Zygrhablithus,* and even rare *Micrantholithus.* The CP16b, CP16c, and CP17 biostratigraphic units are identified by primary boundary species *Coccolithus formosus* and *Reticulofenestra hillae.* The upper Zone CP17 assemblages in Samples 563-20-1, 50–51 cm (338 m) and 563-19-3, 38–39 cm (331 m) lack all shallow indicators except *Zygrhablithus.* The upper Oligocene *Sphenolithus distentus* Zone is abbreviated, occurring only in Sample 563-19-1, 62–63 cm (328 m). The upper Oligocene *Sphenolithus ciperoensis* Zone, *Dictyococcites bisectus* Subzone (CP19b), occurs just above in Sample 563-18-5, 63–64 cm (325 m) and upwards to Sample 563-16-7, 31–32 cm (308 m), as identified by *Sphenolithus ciperoensis* with *Cyclicargolithus abisectus* and *Triquetrorhabdulus* spp. The *Braarudosphaera*-rich beds, which characterized the *S. distentus* Zone CP18 in the South Atlantic, do not occur at Site 563 and the CP19a Subzone and part of Zone CP18 may be missing at Site 563.

There is no clear occurrence of the *Cyclicargolithus abisectus* Subzone (CN1a) in Core 563-16 (299 to 309 m) at Site 563, owing to the scarcity of *C. abisectus.* The top of Core 563-16 and the base of Core 563-17 are assigned to *Discoaster deflandrei* Subzone (CN1b) because of the typical low diversity and great abundances of *Cyclicargolithus floridanus, Discoaster deflandrei,* and *Sphenolithus moriformis.*

Sample 563-15-5, 88–89 cm (296 m) contains the lower LOS of *Discoaster druggii,* which defines the base of Subzone CN1c. A discontinuity in the occurrence of *D. druggii* is noted in Sample 563-15-3, 94–95 cm (293 m) before the appearances of *Sphenolithus belemnos* and *S. heteromorphus.* At Site DSDP 558, this same gap and biostratigraphic sequence is recorded (Table 2). The gap in the range of *D. druggii* appears to be a general feature of the lower Miocene, being previously recorded at Sites DSDP 18, 238, 289, and 317 (Bukry, 1976). However, it might produce miscorrelation because *D. druggii* is needed to identify Subzone CN1c. The last common *D. druggii* coincides with the first *Sphenolithus belemnos,* and the first consistent large *C. floridanus* and five-rayed *Discoaster deflandrei* in Sample DSDP 563-14-6, 90–91 cm (288 m), suggesting an ecologic and sedimentary discontinuity from the underlying Sample 563-14-7, 35–37 cm (289 m). However, there is no obvious change in the sediment type between these samples. The large specimens of *C. floridanus* can be distinguished from *C. abisectus* by the pseudo-extinction gyres across the central area in cross-polarized light. Specimens of *D. druggii* in lower Core 563-13 are full-sized, but very sparse; at the top of Core 563-13 they are smaller.

A mixture of upper and lower Miocene assemblages occurs in Sample 563-13-1, 90–91 cm (271 m). The upper Miocene *Amaurolithus primus* Subzone (CN9b) is represented by *Amaurolithus primus, A. delicatus, Discoaster brouweri, D. pentaradiatus, D. quinqueramus, D. surculus,* and *D. variabilis,* whereas a lower Miocene contingent is characterized by *Discoaster calculosus, D. deflandrei, D. druggii, Sphenolithus belemnos,* and *S. heteromorphus.* There is no upper Miocene mixed with the *Helicosphaera ampliaperta* Zone (CN3) above in Core 563-12, so the Core 563-13 mixture is likely to be a downhole contamination from slightly above the 157-m level where coring was begun for this hole (compare nearby Hole DSDP 558A for the presence of CN9b in this area). Warm-water conditions for Zone CN3 are shown by the abundance of *D. deflandrei* and *S. heteromorphus,* with sparse *Hayaster perplexus* (Sample 563-12-3, 87–88 cm [265 m]).

The LOS of *Calcidiscus macintyrei* in Sample 563-11-3, 90–91 cm (255 m) and the diminished abundance of *Discoaster deflandrei,* in favor of longer-rayed discoasters, in Sample 563-11-1, 90–91 cm (252 m) characterize the base of the *Sphenolithus heteromorphus* Zone (CN4). Warm-water *Discoaster signus* occurs in several samples through the Zone CN4, but warm-water guides for higher zones are rare (*Catinaster coalitus*) or missing (*Discoaster kugleri*).

In the *Discoaster hamatus* Zone (CN7), *Discoaster bellus* and *D. calcaris* occur with *D. hamatus,* but warm-water *D. neohamatus* is missing. However, *D. neohamatus* is prominent in Sample 563-2-5, 90–91 cm (173 m) in the lower *Discoaster neohamatus* Zone (CN8) and upward to the top of the section with some variation. It is especially abundant in Sample 563-1-3, 90–91 cm (160 m), where *Minylitha convallis* is also abundant. Among the placoliths, *Calcidiscus macintyrei* and *Reticulofenestra pseudoumbilica* (closed-center and open-center forms of the same size) are abundant in Zone CN8. The coeval assemblage in Zone CN8 at nearby Site DSDP 558 shows the same species array and diversity.

Site 564 (lat. 33°44.36′N, long. 43°46.03′W; water depth, 3820 m)

Site DSDP 564 is located on the west side of the Mid-Atlantic Ridge about 100 km south of the Hayes Fracture Zone on Magnetic Anomaly 13 (approximately

36 Ma). Site 564 is only 10 km north of Site 563. Sediments were largely bypassed in the coring program, which was designed to test geochemical and geothermal properties of the igneous basement rocks.

One sediment core, just above basalt, contains upper Oligocene *Sphenolithus distentus* Zone (CP18) in Sample DSDP 564-H1-6, 134–135 cm (composite 0 to 284 m) and lower Oligocene *Reticulofenestra hillae* Subzone (CP16c) in Sample DSDP 564-H1-7, 42–43 cm (composite 0 to 284 m). Shallow-water taxa are prominent in Section 564-H1-7, including *Angulolithina arca, Braarudosphaera* spp., *Bramletteius serraculoides, Peritrachelina joidesa* s. ampl., and *Zygrhablithus bijugatus.* This is an ecologic facies similar to that recovered at JOIDES drill sites on the Blake Plateau (Bukry, 1970; Gartner, 1971). The CP18 assemblage of Section 564-H1-6 has abundant *Z. bijugatus* but lacks pentaliths and *Peritrachelina*. Therefore, the coeval (CP18) Oligocene *Braarudosphaera* bloom of the South Atlantic (Bukry, 1978b; 1981c) probably did not extend as far north as DSDP 564.

OLIGOCENE AND MIOCENE COCCOLITH CORRELATION, SITES 558 AND 369

Obtaining a mid-latitude Mid-Atlantic Ridge reference section for Oligocene calcareous microfossils on Leg 82 was one goal of the JOIDES Stratigraphic Correlations Panel (R. Z. Poore, written communication, 1981) because previous drilling had failed to recover this interval for biostratigraphic and biogeographic studies. Although the Oligocene reference site had been planned for Leg 49, hurricanes and mechanical delays prevented such coring. On Leg 82 both Holes DSDP 558 and 563 recovered nearly complete calcareous sections from lower Oligocene to upper Miocene for the Mid-Atlantic Ridge. Coccolith floras are abundant, moderately diverse, and well-preserved, with slight to moderate overgrowth.

Previous North Atlantic drilling on Legs 1, 2, 4, 11, 12, 39, 41, 43, 47, and 48 recovered partial Oligocene sections or nearly complete sections that were in coastal areas or at high or low latitudes. Therefore, the Oligocene floras for DSDP 558 and 563 provide new data on Mid-Atlantic correlations for mid-latitude.

The primary contrasts between high-latitude North Atlantic Oligocene floras from DSDP 112 and 116 of Leg 12 and low-latitude floras from DSDP 354 (Leg 39) are in diversity and abundance (Laughton, A. S., Berggren, W. A., et al., 1972; Supko, P. R., Perch-Nielsen, K., et al., 1977). High-latitude floras lack, or have only sparse, *Discoaster, Helicosphaera*, and *Sphenolithus;* placoliths predominate. Nevertheless, many different species of *Helicosphaera* and *Sphenolithus* occur through the low-latitude Oligocene sections.

DSDP 369 is a mid-latitude Oligocene reference (lat. 27°N) that is located in a coastal upwelling zone off northwestern Africa, as indicated by the rich silicoflagellate assemblages through the Oligocene (Bukry, 1978c). For this reason, it provides a contrast in fertility to the more oligotrophic Site DSDP 558 on the Mid-Atlantic Ridge (lat. 37°N). In Lower Oligocene Subzone CP16b, both sites contain sparse *Isthmolithus recurvus* and *Chiasmolithus*, indicating somewhat temperate conditions.

The flora of blue-water Site DSDP 558 is distinguished by the presence of *Sphenolithus moriformis, S. pseudoradians*, and *Zygrhablithus bijugatus* and the absence or scarceness of *Discolithina, Helicosphaera*, and *Rhabdosphaera.* The reverse is true for the coastal, presumably more turbid, waters at Site DSDP 369. Neither site contains pentaliths. Comparison between these two floras suggests that Oligocene *Helicosphaera, Rhabdosphaera*, and *Discolithina* preferred hemipelagic conditions. Etching of specimens is somewhat more intense at DSDP 369, presumably the result of acidity associated with biogenic opal. This comparison also suggests a blue-water preference for *Sphenolithus.*

In the upper Oligocene Zones CP18 and CP19, the flora at DSDP 558 is distinguished from the coastal flora at DSDP 369A by more abundant *Sphenolithus* and much rarer *Helicosphaera.* Another striking difference is the high abundance of tiny placoliths and relatively small numbers of *Cyclicargolithus floridanus* at DSDP 369A. Genus *Discoaster* is slightly more abundant at blue-water Site DSDP 558, but overall coccolith diversity is lower, especially in the lack of *Helicosphaera* and *Discolithina* species, which occur at the shallow Hole DSDP 369A, even though the assemblage is more etched at DSDP 369A. Complete remobilization of tiny placoliths, *Discolithina*, and *Helicosphaera* into solution and subsequent redeposition as secondary calcite overgrowths on the remaining DSDP 558A specimens could account for some of the observed differences. But such a solution effect would not account for the greater abundance of *Cyclicargolithus floridanus* and *Sphenolithus* at DSDP 558, which probably does suggest open-marine preference of these taxa for this interval.

The contrast in coccolith floras between DSDP 558 and DSDP 369A is less noticeable in the middle Miocene *Discoaster exilis* Zone (CN5) where the dominant placoliths and discoasters and other taxa are the same. The chief differences are in the greater abundance of *Discolithina* and *Helicosphaera* at DSDP 369A. This is probably an ecologic difference, because the species arrays and preservation are otherwise very similar. The continued restriction of *Discolithina* and *Helicosphaera* in the Oligocene and Miocene limits their biostratigraphic utility for correlation between ocean and coastal-water regimes.

Floras of the upper middle Miocene *Catinaster calyculus* Subzone (CN7b) are similar in character at DSDP 558 and 369A, but different for the upper Miocene *Discoaster bellus* Subzone (CN8a). The Subzone CN8a flora of DSDP Sample 558-2-3, 90–91 cm is characterized by abundant *Calcidiscus macintyrei*, abundant *Reticulofenestra* (large and medium), no tiny placoliths, and only rare *Helicosphaera.* The reverse is true at DSDP Sample 369A-3-3, 70–71 cm, which contains abundant *Helicosphaera* and tiny placoliths. *Discoaster* and *Sphenolithus* arrays are similar and permit correlation. But environmental distinction is shown by the differences in placolith abundances. The predominance of *C. macintyrei* and *Reticulofenestra* species with closed centers probably indicates cooler conditions at DSDP 558A, as indicated by the abundance of such *Reticulofenestra* at high latitude.

The highest correlation for the upper Miocene *Discoaster berggrenii* Subzone (CN9a) between Sample 558A-16-5, 90–91 cm (129 m) and Sample 369-1-3, 70–71 cm (3 m) is based on key species such as *Discoaster berggrenii, D. loeblichii*, and *D. neorectus*. Distinct differences in the species array between the two locations include the predominant placoliths, *Coccolithus pelagicus* and small *Crenalithus taganus*. At Hole DSDP 558A, *Coccolithus pelagicus* predominates over *Crenalithus taganus* 72 to 28 for a count of 100, whereas at Hole DSDP 369 the reverse prevails with *C. taganus* outnumbering *Coccolithus pelagicus* by 64 to 36 for a count of 100. *Reticulofenestra pseudoumbilica* is sparse at both sites, but *Calcidiscus macintyrei* is more common at open-ocean Hole 558A. The Oligocene distinctions between these two sites are recalled by the greater abundance of genera *Discolithina, Helicosphaera*, and *Rhabdosphaera* at coastal DSDP 369. The fewer specimens of *Helicosphaera* of Hole 558A are also clearly more incised and etched away by dissolution than the excellently preserved specimens at DSDP 369. Again, preservation in clayey nannofossil marl (carbonate = 60%) from the continental slope deposit of DSDP 369 is superior to the mid-ocean preservation in a nannofossil ooze (carbonate = 87%) for coccolith taxa that are solution prone. Therefore, the potential for continued refinements in correlation accuracy for nearshore ocean deposits is high because of original diversity and better preservation in hemipelagic sediment (Gartner and Bukry, 1969).

The somewhat larger abundance of *Sphenolithus* at Site DSDP 369 suggests that the warm-water preference of the genus became more important than the open-ocean preference. Overlapping factors, such as preservation, temperature, and turbidity, can be distinguished by quantitative comparison between ocean sites representing different regional settings (see the data set initiated by Haq, 1980). Detailed quantitative studies comparing selected sites such as DSDP 558 can clarify controls on fossil coccolith distribution.

OLIGOCENE PENTALITH FACIES AND MID-ATLANTIC DIAGENESIS

The South Atlantic regional *Braarudosphaera* Chalk Province (Bukry, 1978b; 1981c) of the upper Oligocene *Sphenolithus distentus* Zone (CP18) is not represented at DSDP Leg 82 sites. Unlike the *Sphenolithus distentus* Zone chalks predominated by *Braarudosphaera*, the coeval sediment in Cores DSDP 558-24, DSDP 563-19, and DSDP 564-H1 lack *Braarudosphaera*, limiting the northward extent of the *Braarudosphaera* Chalk Province in mid-ocean waters.

Lower in the Oligocene, in the *Helicosphaera reticulata* Zone (CP16) and *Sphenolithus predistentus* Zone (CP17), assemblages are not predominated by pentaliths, but Cores 568-20 to 563-22 at DSDP 563 and Core 564-H1 at DSDP 564 contain sparse to common pentaliths. This is typical of shallow-marine settings in more coastal areas at this time (Bukry, 1970; Bukry et al., 1971). Because there is no sedimentary evidence for a nearby landmass, the crustal block of DSDP 563 and 564 might have been shallower during the early Oligocene than that containing DSDP 558, north of the Hayes and Oceanographer fracture zones. The general state of preservation and overgrowth of coccoliths at DSDP 558, 563, and 564 is very similar, so post-depositional diagenetic differentiation of the assemblages to eliminate pentaliths at DSDP 558 could seem unlikely, except for the greater abundance of carbonate rhombs (dolomitic) and clay in the sediment of DSDP 558. A replacement of pentaliths by rhombs could be a fairly direct diagenetic exchange, fostered by pentalith dissolution susceptibility and by higher heat flow and pore-water circulation at DSDP 558. The alternative explanation of different ocean-current or water-mass conditions persisting over the sites in a non-oscillatory mode in such a small area for so long is unlikely; however, there are more cool-water *Chiasmolithus* at DSDP 558.

Although topographic or oceanographic changes are possible, the partition of pentaliths between DSDP 558 and DSDP 563 and 564 is attributed mainly to the effects of differing diagenesis on different crustal blocks.

SILICOFLAGELLATE CORRELATION FOR DSDP 558A

Upper Pleistocene silicoflagellates in Cores 558A-2 and 558A-3 (Table 3) have been compared to coeval assemblages of the *Dictyocha aculeata* Zone (Bukry, 1981a) from other DSDP sites in the Atlantic at DSDP 410 (45°N), 334 (37°N), 412 (36°N), 397 (27°N), 358 (38°S), 328 (38°S), and 331 (50°S), and in the eastern Pacific at 425 (1°N) and 427 (8°N). Total diversity is lowest (three taxa) at high latitude; *Dictyocha aculeata, D. stapedia stapedia*, and *Distephanus speculum speculum* are the most cosmopolitan.

A comparison of the sequence of events between silicoflagellate and coccolith species shows a tendency for the extinction of *Dictyocha lingii* just before the *D. aculeata* Zone and for an acme of *D. stapedia aspinosa* at a later time, during deposition of *D. aculeata* Zone sediment. The *D. lingii* and *D. stapedia aspinosa* sequence occurs at DSDP 558A, 412, and 397 in the Atlantic and is indicated for DSDP 425 in the Pacific by the acme of *D. stapedia aspinosa* within the zone. At all four sites the *D. stapedia aspinosa* acme is associated with the *Ceratolithus cristatus* Subzone of coccoliths. The top of *D. lingii* is associated with the *Emiliania ovata* Subzone of coccoliths at DSDP 412 and 558A, but not at DSDP 397, where it occurs in the uppermost *Gephyrocapsa caribbeanica* Subzone of coccoliths.

Although *D. lingii* may be used as a secondary guide fossil for the *Mesocena quadrangula* Zone (Dumitrică, 1973; Bukry, 1979), it disappeared slightly before *Mesocena quadrangula* at DSDP 397. Therefore, the presence of *D. lingii* in Sample 558A-3-3, 90–91 cm (14 m) at a location near the northern range limit for *M. quadrangula* (Bukry, 1977) suggests that this sample might well belong to the upper *M. quadrangula* Zone, even without the primary guide species. Association with the coccolith *E. ovata* Zone supports such a correlation.

Sample 558A-2-3, 90–91 cm (4 m) contains a low-diversity assemblage, limited by dissolution because near-

Table 3. Occurrence (in %) of Pleistocene silicoflagellate taxa at DSDP 558A.

Zone	*Dictyocha aculeata*				*D. aculeata* or *M. quadrangula*	—
Sub-bottom depth (m)	1	4	7	11	14	17
Hole-Core-Section (interval in cm)	558A-2-1 90–91	558A-2-3 90–91	558A-2-5 90–91	558A-3-1 90–91	558A-3-3 90–91	558A-3-5 90–91
Dictyocha aculeata	26	28	21		23	
D. sp. cf. *D. aculeata*	1	3	4	X		
D. calida calida			1	X	2	
D. calida ampliata			2	X	1	
D. lingii					3	
D. perlaevis perlaevis				X	6	
D. stapedia aspinosa	5		52		1	
D. stapedia stapedia	66	64	11		41	
D. subaculeata			1		8	
D. spp.	2	4	4		5	
Distephanus floridus			1			
D. speculum f. *coronata*			<1			
D. speculum minutus (coronatid)			1			
D. speculum speculum	<1		3		9	
Total specimens	300	200	300	4	300	0
Relative paleotemperature value (Ts)	100	100	96	—	90	—

Note: Relative paleotemperature values calculated according to Bukry (1981d). X = occurrence too sparse for meaningful percent.

ly all of the silicoflagellates are ghostly thin and fragments of the large diatom *Ethmodiscus rex* are more common (Mikkelsen, 1977) than elsewhere in Cores 558A-2 and 558A-3. The generally small size of *Dictyocha stapedia stapedia* at DSDP 558A is typical for the *Dictyocha aculeata* Zone.

Samples from DSDP 558A that were processed in acid for silicoflagellates but found to be barren include: 558A-1-1, 53–54 cm (1 m); 558A-3-5, 90–91 cm (17 m); 558A-4-1, 90–91 cm (20 m); 558A-4-3, 90–91 cm (24 m); 558A-4-5, 90–91 cm (26 m); 558A-5-1, 90–91 cm (30 m); 558A-5-3, 90–91 cm (33 m); 558A-6-2, 90–91 cm (41 m); 558A-7-3, 100–101 cm (52 m); and 558A-9-1, 133–134 cm (68 m).

CONCLUSION

The great abundance of coccoliths in the Oligocene-Miocene interval of DSDP 558 and 563, and the nearly omplete sequence between Zones CP16 and CN8 at oth sites provides the first middle Tertiary biostrati-raphic reference for the northern Mid-Atlantic region. lthough overgrowth of specimens is typically moder-te, diversity is sufficiently high to permit detailed stud-es of the assemblages. This initial study has shown a ignificant thinning or removal of sediment in higher in-ervals. No lower Pliocene sediment was identified in he samples studied, reminiscent of the spotty occur-ence of this interval for the nearby sites of DSDP Leg 7 (Bukry, 1977). Minor gaps in the upper Pliocene are lso indicated for Hole DSDP 558A.

The dual sections for the Oligocene-Miocene at DSDP 58 and 563 contain most of the low-latitude zonal boundary species, such as *Sphenolithus ciperoensis*. But a coolwater event is indicated at both sites for the upper middle Miocene upper *Discoaster exilis* Zone to lower *Discoaster hamatus* Zone, also correlated with Neogene hiatus NH 4 (Barron and Keller, 1982). The predominance of cosmopolitan species such as *Discoaster variabilis* and *Reticulofenestra pseudoumbilica* in that interval is more typical of the temperate-water *Discoaster variabilis* Zone. This contrasts with the warm-water conditions suggested by the presence of *Discoaster signus* at the upper *Sphenolithus heteromorphus* to the lower *Discoaster exilis* Zone boundary interval. The lower Miocene gap in the range of zonal guide *Discoaster druggii* can be identified and correlated at both DSDP 558 and 563. The Oligocene assemblages at these sites are very similar except for the presence of pentaliths at DSDP 563, attributed to more intense diagenesis at DSDP 558. The greater abundance of dolomitic rhombs at DSDP 558 may represent remobilized carbonate from formerly present pentaliths.

Silicoflagellates are present only in a short interval of the upper Quaternary at DSDP 558A. Although most of the section belongs to a warm-water facies of the *Dictyocha aculeata* Zone, the lowermost sample, containing *Dictyocha lingii*, may be equivalent to the underlying *Mesocena quadrangula* Zone of low latitude. The age of 0.70 to 0.89 Ma (Saito and Burckle, 1977) for the top of that zone would be within the range of the associated coccolith upper *Emiliana ovata* Subzone (CN14a) in DSDP Sample 558A-3-3, 90–91 cm (14 m).

SYSTEMATIC PALEONTOLOGY OF NEW TAXA

Silicoflagellates

Genus DISTEPHANUS Stöhr, 1880

Distephanus floridus Bukry, n. sp.
(Plate 1, Figs. 1–4)

not *Dictyocha octonaria* Ehrenberg, 1844, p. 186, 201. Figured by Lemmermann, 1901, pl. 11, fig. 18, as *Distephanus speculum* var. *octonarius* (Ehrenb.) Joerg.

not *Distephanus octonarius*, Hovasse, 1932, p. 455, figs. 3a–3c, fig. 4a. [Too elongate with thin apical ring.]

not *Distephanus octonarius* (Ehr.) Deflandre, 1932, p. 503, figs. 7–12. [Too axially elongate with elliptic apical rings.]

?*Dictyocha octonaria* Ehr., Deflandre, 1950 (in part), fig. 29? (not elongate figs. 30–41).

not *Distephanus octonarius* var. *polyactis* (Jörg.) Glezer, 1966, p. 273, pl. 21, figs. 7–8, and text fig. 21 (3). [Mistaken citation for *Distephanus octonarius* (Ehrenberg) var. *polyactis* (Ehrenberg) Jørgensen.]

Distephanus octonarius Deflandre, Ling, 1973, p. 752, pl. 2, figs. 5, 6. [Invalid basionym.]

Distephanus polyactis (Ehrenberg), Bukry, 1973b (in part), p. 864, pl. 1, figs. 9, 10.

Distephanus octonarius Deflandre, Ling, 1977, p. 207, pl. 2, fig. 11. [Invalid basionym.]

Description. *Distephanus floridus* has an eight- (rarely seven- or nine-) spined, regular, polygonal basal ring with equant axes. The spines are moderate to long and essentially coequal. Basal pikes may be present. The apical ring, like the basal ring, is polygonal and symmetric with no distinct elongation. Because of the large diameter of the apical ring and normal tube width, the ring appears continguous to the basal ring, seen in plan view.

Remarks. *Distephanus floridus* is distinguished from *Distephanus polyactis* (Ehrenberg) by more polygonal apical ring, slightly longer spines, consistent octagonal format, and a smaller size. Part of the distinction for *Distephanus floridus* involves establishing what the names *Distephanus octonarius* (Ehrenberg) and *Octactis pulchra* Schiller represent. I accept the Loeblich et al. (1968) validation for *D. octonarius* (Ehrenberg), which includes Lemmermann's (1901) illustration as the first figured specimen. The small and circular apical ring and short spines of *D. octonarius* (Ehrenberg) clearly distinguish it from *D. floridus*. *Octactis pulchra* Schiller has a delicate apical structure, axial elongation of the basal ring, and no basal pikes (see Poelchau, 1976). All these distinguish it from *D. floridus*.

Distephanus floridus may have been recorded as *Dictyocha octonaria* Ehrenberg in the past because of confusion over the nature of that species. The type specimen (see Loeblich et al., 1968), from the Holocene, has very short spines and a small, circular apical ring that can be easily distinguished from *Distephanus floridus*, which has moderate to long spines and a very large apical ring that is circular to polygonal. Deflandre (1950) illustrated a wide variety of modern octagonal specimens, all of which he considered variations of *Dictyocha octonaria*, but none of which has the short spines and small apical ring of the type specimen. Ling (1973; 1977), apparently influenced by Deflandre's species concept, illustrated specimens of *D. floridus* as *Distephanus octonarius* Deflandre. As a basionym, Ling (1973) cites Deflandre, 1932, p. 503, but Deflandre (1932, p. 503) repeatedly cites "*Distephanus octonarius* (Ehr.) Defl." with varieties and synonyms. Therefore Deflandre (1932) never claimed authorship for the name *octonarius*, as indicated in Ling (1973; 1977). As to the varietal names of Glezer (1966) discussed by Ling (1977), her specimen of *Distephanus octonarius* (Ehr.) Defl. var. *polyactis* (Jörg.) Glezer has nine short spines and a circular basal ring that distinguish it from *D. floridus*, which has a polygonal, basically eight-sided base and moderate to long spines. *D. octonarius* (Ehr.) Defl. var. *cyrtoides* (Haeck.) Glezer is irregular and typologically unrelated to *D. floridus*. The broad species group concept of Deflandre (1932) and Glezer (1966) seem less reproducible for purposes of biostratigraphic zonation than the typologic species concept of *D. floridus*.

The species *Dictyocha octonaria* Ehr. with the original figure by Lemmermann (1901) has been accepted as valid by Loeblich et al. (1968). There is no *Distephanus octonarius* Defl. The new species can be clearly distinguished from *Distephanus octonarius* (Ehr.) Defl. One of the wide-ringed specimens that Deflandre (1932) erroneously attributed to *D. octonarius* (Ehr.) Defl. may be assignable to the new species *D. floridus*. Ling's (1973; 1977) illustrations referred to *D. octonarius* Defl. belong to *D. floridus*.

Finally, *Distephanus speculum* var. *octonarius* f. *polyactis* (Ehrenberg) Jørgensen is a valid transfer of *Dictyocha polyactis* Ehrenberg, according to Loeblich et al. (1968). Its uncorrected citation in Ling (1973) as *Distephanus octonarius* var. *polyactis* (Jørgensen) Glezer, attributed to Jousé, could be confusing because this misauthored variety was equated to misauthored *Distephanus octonarius* Deflandre in Ling (1973).

Occurrence. *Distephanus floridus*, previously reported as various taxa including *Distephanus octonarius* and *D. polyactis*, is characteristic of Quaternary assemblages at middle and high latitudes at such sites as DSDP 310, 191, 184, and 173 in the North Pacific. It is missing from low-latitude coeval strata at such sites as DSDP 504, 425, 420, 321, and 157. The highest occurrence surface (HOS) of *D. floridus* is used as the top for the *Distephanus floridus* Zone (née *Distephanus octonarius* Zone) by Ling (1973), an interval in the mid-Quaternary of the North Pacific.

Size. Maximum internal diameter, 16 to 25 μm (holotype 18 μm).

Holotype. USNM 365401 (Pl. 1, Fig. 1).

Isotypes. USNM 365402 and 365403.

Type locality. North Atlantic, Mid-Atlantic Ridge, DSDP Sample 558-2-5, 90–91 cm (174 m).

Coccoliths

Genus CYCLOLITHELLA Loeblich and Tappan, 1963

Cyclolithella? *neoaprica* Bukry, n. sp.

(Plate 1, Figs. 6–12)

Description. *Cyclolithella*? *neoaprica* has a medium-sized, circular basal shield and an elevated tube cycle. Both the basal and tube cycle have sinistrally inclined crystallites in apical view. The periphery of each cycle is serrate. The tube opening occupies about a third the diameter of the basal shield and the outer tube wall occupies about half that diameter. The basal shield is composed of 25 to 35 crystallites and the tube cycle of 18 to 22 crystallites, both structures are bright in cross-polarized light. Crystallites in the low-relief basal shield are more distinct in cross-polarized light.

Remarks. *Cyclolithella*? *neoaprica* is distinguished from *Cyclolithella aprica* by a thicker and taller tube cycle and a much smaller central tube opening. Viewed with a single polarizer, the tube cycle of *C*.? *neoaprica* shows much higher optic relief than the basal shield, aiding identification among other circular coccoliths, such as *Coccolithus formosus*. *Cyclolithella aprica* was originally described from the middle Eocene of the Pacific (Roth, 1973).

Occurrence. *Cyclolithella*? *neoaprica* occurs in the lower Oligocene *Coccolithus formosus* Subzone (CP16b) of DSDP 558, Core 558-27 and lower Core 558-26, from the North Atlantic. It is meager in Core 558-27 and very sparse in Core 558-26.

Size. Maximum diameter, 7 to 11 μm (holotype 8 μm).

Holotype. USNM 365404 (Plate 1, Figs. 6, 7).

Isotypes. USNM 365405 and 365406.

Type locality. North Atlantic, Mid-Atlantic Ridge, DSDP Sample 558-27-1, 90–91 cm (406 m).

Genus SPHENOLITHUS Deflandre, 1952

Sphenolithus calyculus Bukry, n. sp.

(Plate 1, Figs. 13–19)

Description. *Sphenolithus calyculus* is slender with an apical spine equal to or taller than the height of the multispined base. The distinctive characters seen in cross-polarized light include the multispined base acting as four segments. With the major axis aligned to a polarization direction, the upper two segments are as large as the lower two and the upper two form a calyx for the apical spine, which is dark at this orientation. With the major axis aligned at 45° to the polarization direction, an X-shaped pattern occurs in the base and the apical spine is bright and continuous with the base.

Remarks. As indicated by the cross-polarized light image of the base, *Sphenolithus calyculus* is distinguished from *S. belemnos* by the much greater relative area occupied by the upper two segments, from *S. ciperoensis* by the crossing instead of separated pseudoextinction lines at 45° orientation, and from *S. conicus* by the longer and narrower apical spine and small size. The two upper segments of *S. calyculus* are equal to or larger than the basal segments, distinguishing it from *S. heteromorphus* and *S. belemnos*. The top of these upper segments is angled, forming a calyx to the base of the apical spine that may appear to extend a little beyond the spine outline in cross-polarized light. Previous references to upper Oligocene or lowermost Miocene *S. belemnos* or *S. heteromorphus* may have been based on specimens of *S. calyculus*.

Occurrence. *Sphenolithus calyculus* is sparse to meager in upper Core 558-19 and lower Core 558-18 at DSDP 558 in samples assigned to the basal Miocene *Discoaster deflandrei* Subzone (CN1b). Larger specimens occur in Core 558-18.

Size. Maximum height, 5 to 9 µm (holotype 5 µm).

Holotype. USNM 365407 (Plate 1, Figs. 13-15).

Isotypes. USNM 365408 and 365409.

Type locality. North Atlantic, Mid-Atlantic Ridge, DSDP Sample 558-19-1, 90-91 cm (330 m).

COCCOLITH TAXA CITED IN THIS REPORT

Amaurolithus amplificus (Bukry and Percival)
A. delicatus Gartner and Bukry
A. primus (Bukry and Percival)
Bramletteius serraculoides Gartner
Calcidiscus macintyrei (Bukry and Bramlette)
C. leptoporus (Murray and Blackman)
Catinaster calyculus Martini and Bramlette
C. coalitus Martini and Bramlette
Ceratolithus rugosus Bukry and Bramlette
C. separatus Bukry
Coccolithus eopelagicus (Bramlette and Riedel)
C. formosus (Kamptner)
C. miopelagicus Bukry
C. pelagicus (Wallich)
Coronocyclus nitescens (Kamptner)
Crenalithus doronicoides Black and Barnes
C. productellus Bukry
C. taganus (Fonseca)
Cyclicargolithus abisectus (Müller)
C. floridanus (Roth and Hay)
Dictyococcites bisectus (Hay, Mohler, and Wade)
Discoaster asymmetricus Gartner
D. bellus Bukry and Percival
D. berggrenii Bukry
D. blackstockae Bukry
D. brouweri Tan
D. calcaris Gartner
D. calculosus Bukry
D. challengeri Bramlette and Riedel
D. deflandrei Bramlette and Riedel
D. druggii Bramlette and Wilcoxon
D. exilis Martini and Bramlette
D. hamatus Martini and Bramlette
D. kugleri Martini and Bramlette
D. loeblichii Bukry
D. neohamatus Bukry and Bramlette
D. neorectus Bukry
D. nodifer (Bramlette and Riedel)
D. pentaradiatus Tan
D. prepentaradiatus Bukry and Percival
D. quadramus Bukry
D. quinqueramus Gartner
D. signus Bukry
D. surculus Martini and Bramlette
D. tamalis Kamptner
D. tanii Bramlette and Riedel
D. triradiatus Kamptner
D. variabilis Martini and Bramlette
Discolithina segmenta Bukry and Percival
Emiliania annula (Cohen)
Hayaster perplexus (Bramlette and Riedel)
Helicosphaera compacta Bramlette and Wilcoxon
H. euphratis Haq
H. granulata (Bukry)
H. sellii (Bukry and Bramlette)
Isthmolithus recurvus Deflandre
Minylitha convallis Bukry
Orthorhabdus serratus Bramlette and Wilcoxon
Peritrachelina joidesa Bukry and Bramlette
Pyrocyclus orangensis (Bukry)
Reticulofenestra hillae Bukry and Percival
R. pseudoumbilica (Gartner)
R. umbilica (Levin)
Rhabdosphaera clavigera (Murray and Blackman)
Sphenolithus belemnos Bramlette and Wilcoxon
S. capricornutus Bukry
S. ciperoensis Bramlette and Wilcoxon
S. conicus Bukry
S. delphix Bukry
S. dissimilis Bukry and Bramlette
S. distentus (Martini)
S. heteromorphus Deflandre
S. moriformis (Brönnimann and Stradner)
S. predistentus Bramlette and Wilcoxon
S. pseudoradians Bramlette and Wilcoxon
Triquetrorhabdulus carinatus Martini
T. milowii Bukry
Zygrhablithus bijugatus Deflandre

SILICOFLAGELLATE TAXA CITED IN THIS REPORT

Dictyocha aculeata (Lemmermann)
D. calida ampliata Bukry
D. calida calida Poelchau
D. lingii Dumitrică
D. perlaevis perlaevis Frenguelli
D. stapedia aspinosa Bukry
D. stapedia stapedia Haeckel
D. subaculeata (Bukry)
Distephanus speculum f. *coronata* Schulz
D. speculum minutus Bachmann emend. Bukry
Mesocena quadrangula Ehrenberg ex Haeckel

DIATOM TAXON CITED IN THIS REPORT

Ethmodiscus rex (Rattray)

ACKNOWLEDGMENTS

I thank Gerta Keller and John A. Barron, U.S. Geological Survey, for helpful reviews of this paper. Slides were prepared by Diane L. Lander, U.S. Geological Survey, and additional samples for an investigation of lower Miocene species ranges were supplied by Amy Altman, Deep Sea Drilling Project. I also thank Paula Worstell, Deep Sea Drilling Project, and Richard Z. Poore, U.S. Geological Survey, for their assistance in obtaining the valuable stratigraphic reference sections at DSDP 558 and DSDP 563. The manuscript was ably typed and proofed by Dorothy L. Blackstock, U.S. Geological Survey.

REFERENCES

Baldauf, J. G., in press. Cenozoic diatom biostratigraphy and paleoceanography of the Rockall Plateau Region, North Atlantic, Deep Sea Drilling Project Leg 81. *In* Roberts, D. G., Schnitker, D., et al., *Init. Repts. DSDP*, 81: Washington (U.S. Govt. Printing Office).

Barron, J. A., and Keller, G., 1982. Widespread Miocene deep-sea hiatuses: coincidence with periods of global cooling. *Geology*, 10: 577-581.

Bukry, D., 1970. Coccolith age determinations Leg 2, Deep Sea Drilling Project. *In* Peterson, M. N. A., Edgar, N. T., et al., *Init. Repts. DSDP*, 2: Washington (U.S. Govt. Printing Office), 349-355.

________, 1971. Coccolith stratigraphy Leg 7, Deep Sea Drilling Project. *In* Winterer, E. L., Riedel, W. R., et al., *Init. Repts. DSDP*, 7, Pt. 2: Washington (U.S. Govt. Printing Office), 1513-1528.

________, 1973a. Coccolith and silicoflagellate stratigraphy, Deep Sea Drilling Project Leg 18, eastern North Pacific. *In* Kulm, L. D., von Huene, R., et al., *Init. Repts. DSDP*, 18: Washington (U.S. Govt. Printing Office), 817-831.

________, 1973b. Coccoliths and silicoflagellates from Deep Sea Drilling Project Leg 19, North Pacific Ocean and Bering Sea. *In* Creager, J. S., Scholl, D. W., et al., *Init. Repts. DSDP*, 19: Washington (U.S. Govt. Printing Office), 857-867.

________, 1976. Coccolith stratigraphy of Manihiki Plateau, central Pacific, Deep Sea Drilling Project Site 317. *In* Schlanger, S. O., Jackson, E. D., et al., *Init. Repts. DSDP*, 33: Washington (U.S. Govt. Printing Office), 493-501.

________, 1977. Coccolith and silicoflagellate stratigraphy, central North Atlantic Ocean, Deep Sea Drilling Project Leg 37. *In* Aumento, F., Melson, W. G., et al., *Init. Repts. DSDP*, 37: Washington (U.S. Govt. Printing Office), 917-927.

________, 1978a. Neogene coccolith stratigraphy, Mid-Atlantic Ridge, Deep Sea Drilling Project, Leg 45. *In* Melson, W. G., Rabinowitz,

P. D., et al., *Init. Repts. DSDP*, 45: Washington (U.S. Govt. Printing Office), 307-317.

________, 1978b. Cenozoic silicoflagellate and coccolith stratigraphy, southeastern Atlantic Ocean, Deep Sea Drilling Project Leg 40. *In* Bolli, H. M., Ryan, W. B. F., et al., *Init. Repts. DSDP*, 40: Washington (U.S. Govt. Printing Office), 635-649.

________, 1978c. Cenozoic coccolith and silicoflagellate stratigraphy, offshore northwest Africa, Deep Sea Drilling Project Leg 41. *In* Lancelot, Y., Seibold, E., et al., *Init. Repts. DSDP*, 41: Washington (U.S. Govt. Printing Office), 689-707.

________, 1979. Comments on opal phytoliths and stratigraphy of Neogene silicoflagellates and coccoliths at Deep Sea Drilling Project Site 397 off northwest Africa. *In* Luyendyk, B. P., Cann, J. R., et al., *Init. Repts. DSDP*, 49: Washington (U.S. Govt. Printing Office), 977-1009.

________, 1980. Silicoflagellate biostratigraphy and paleoecology in the eastern equatorial Pacific, Deep Sea Drilling Project Leg 54. *In* Rosendahl, B. R., Hekinian, R., et al., *Init. Repts. DSDP*, 54: Washington (U.S. Govt. Printing Office), 545-573.

________, 1981a. Synthesis of silicoflagellate stratigraphy for Maestrichtian to Quaternary marine sediment. *Spec. Publ.—Soc. Econ. Paleontol. Mineral.*, 32:433-444.

________, 1981b. Pacific Coast coccolith stratigraphy between Point Conception and Cabo Corrientes, Deep Sea Drilling Project Leg 63. *In* Yeats, R. S., Haq, B. U., et al., *Init. Repts. DSDP*, 63: Washington (U.S. Govt. Printing Office), 445-471.

________, 1981c. Cenozoic coccoliths from the Deep Sea Drilling Project. *Spec. Publ.—Soc. Econ. Paleontol. Mineral.*, 32:335-353.

________, 1981d. Silicoflagellate stratigraphy of offshore California and Baja California, Deep Sea Drilling Project Leg 63. *In* Yeats, R. S., Haq, B. U., et al., *Init. Repts. DSDP*, 63: Washington (U.S. Govt. Printing Office), 539-557.

________, 1983. Upper Cenozoic silicoflagellates from offshore Ecuador, Deep Sea Drilling Project Site 504. *In* Cann, J. R., Langseth, M. G., Honnorez, J., Von Herzen, R. P., White, S. M., et al., *Init. Repts. DSDP*, 69: Washington (U.S. Govt. Printing Office), 321-342.

Bukry, D., Douglas, R. G., Kling, S. A., and Krasheninnikov, V., 1971. Planktonic microfossil biostratigraphy of the northwestern Pacific area. *In* Fischer, A. F., Heezen, B. C., et al., *Init. Repts. DSDP*, 6: Washington (U.S. Govt. Printing Office), 1253-1300.

Crouch, J. K., and Bukry, D., 1979. Comparison of Miocene provincial foraminiferal stages to coccolith zones in the California Continental Borderland. *Geology*, 7:211-215.

Deflandre, G., 1932. Sur la systématique des silicoflagellés. *Bull. Soc. Bot. Fr.*, 79:494-506.

________, 1950. Contribution a l'étude des silicoflagellidés actuels et fossiles. *Microscopie*, 2:72-108, 117-142, and 191-210.

Dumitrică, P., 1973. Cretaceous and Quaternary radiolaria in deep sea sediments from the northwest [sic northeast] Atlantic Ocean and Mediterranean Sea. *In* Ryan, W. B. F., Hsü, K. J., et al., *Init. Repts. DSDP*, 13, Pt. 2: Washington (U.S. Govt. Printing Office), 829-901.

Ehrenberg, C. G., 1844. Resultate seiner Untersuchungen der ihm von der Südpolreise des Capitain Ross, sc wie von den Herren Schayer und Darwin zugekommenen Materialien über das Verhalten des kleinsten Lebens in den Oceanen und den grössten bisher zugängiichen Tiefen des Weltmeers vor. *Abh. K. Preuss. Akad. Wiss. Berlin Ber.*, Jahrg. 1844:182-207.

Gartner, S., Jr., 1971. Calcareous nannofossils from the Joides Blake Plateau cores and revision of Paleogene nannofossil zonation. *Tulane Stud. Geol. Paleontol.*, 8:101-121.

________, 1977. Calcareous nannofossil biostratigraphy and revised zonation of the Pleistocene. *Mar. Micropaleontol.*, 2:1-25.

Gartner, S., Jr., and Bukry, D., 1969. Tertiary holococcoliths, *J. Paleontol.*, 43:1213-1221.

Glezer, Z. I., 1966. Silicoflagellatophyceae. *In* Gollerbakh, M. M., (Ed.), *Cryptogamic Plants of the U.S.S.R.* (Vol. 7): *Akad. Nauk SSSR, V. A. Komarova Bot. Inst.* (Moskva-Leningrad) (Translated from Russian by Israel Program for Scientific Translations Ltd., Jerusalem, 1970)

Haq, B. U., 1980. Miocene biogeographic history of calcareous nannoplankton and paleoceanography of the Atlantic Ocean. *Micropaleontology*, 26:414-443.

Hovasse, R., 1932. Contribution a l'étude des silicoflagellés. Multiplication, variabilité, hérédité, affinités. *Bull. Biol. Fr. Belg.*, 66: 447-501.

Keller, G., 1980. Middle to late Miocene planktonic foraminiferal datum levels and paleoceanography of the North and southeastern Pacific Ocean. *Mar. Micropaleontol.*, 5:249-281.

Keller, G., and Barron, J. A., 1981. Integrated planktic foraminiferal and diatom biochronology for the northeast Pacific and the Monterey Formation. *In* Garrison, R. E., Douglas, R. G., Pisciotto, K. E., Isaacs, C. M., and Ingle, J. C. (Eds.), The Monterey formation and related siliceous rocks of California. *Spec. Publ.—Soc. Econ. Paleontol. Mineral. Pacific Sec.*, 43-54.

Laughton, A. S., Berggren, W. A., et al., 1972. *Init. Repts. DSDP*, 12: Washington (U.S. Govt. Printing Office).

Lemmermann, E., 1901. Silicoflagellatae. *Dtsch. Bot. Ges. Ber.*, 19: 247-271.

Ling, H. Y., 1973. Silicoflagellates and ebridians from Leg 19. *In* Creager, J. S., Scholl, D. W., et al., *Init. Repts. DSDP*, 19: Washington (U.S. Govt. Printing Office), 751-775.

________, 1977. Late Cenozoic silicoflagellates and ebridians from the eastern North Pacific region. *Proc. First Int. Cong. Pacific Neogene Stratigraphy,* Tokyo, pp. 205-233.

Loeblich, A. R., III, Loeblich, L. A., Tappan, H., and Loeblich, A. R., Jr., 1968. Annotated index of fossil and recent silicoflagellates and ebridians with descriptions and illustrations of validly proposed taxa. *Geol. Soc. Am. Mem.*, 106:1-319.

Mikkelsen, N., 1977. On the origin of *Ethmodiscus* ooze. *Mar. Micropaleontol.*, 2:35-46.

Okada, H., and Bukry, D., 1980. Supplementary modification and introduction of code numbers to the low-latitude coccolith biostratigraphic zonation (Bukry, 1973; 1975). *Mar. Micropaleontol.*, 5: 321-325.

Poelchau, H. S., 1976. Distribution of Holocene silicoflagellates in North Pacific sediments. *Micropaleontology*, 22:164-193.

Roth, P. H., 1973. Calcareous nannofossils—Leg 17, Deep Sea Drilling Project. *In* Winterer, E. L., Ewing, J. I., et al., *Init. Repts. DSDP*, 17: Washington (U.S. Govt. Printing Office), 675-795.

Saito, T., and Burckle, L. H., 1977. Occurrence of silicoflagellate *Mesocena elliptica*. *J. Geol. Soc. Jpn.*, 83:181-186.

Supko, P. R., Perch-Nielsen, K., et al., 1977. *Init. Repts. DSDP*, 39: Washington (U.S. Govt. Printing Office).

Thierstein, H. R., Geitzenauer, K. R., Molfino, B., and Shackleton, N. J., 1977. Global synchroneity of late Quaternary coccolith datum levels: validation by oxygen isotopes. *Geology*, 5:400-404.

Vincent, E., Killingley, J. S., and Berger, W. H., 1980. The Magnetic Epoch-6 carbon shift: a change in the ocean's $^{13}C/^{12}C$ ratio 6.2 million years ago. *Mar. Micropaleontol.*, 5:185-203.

Date of Initial Receipt: 7 June 1983
Date of Acceptance: 14 May 1984

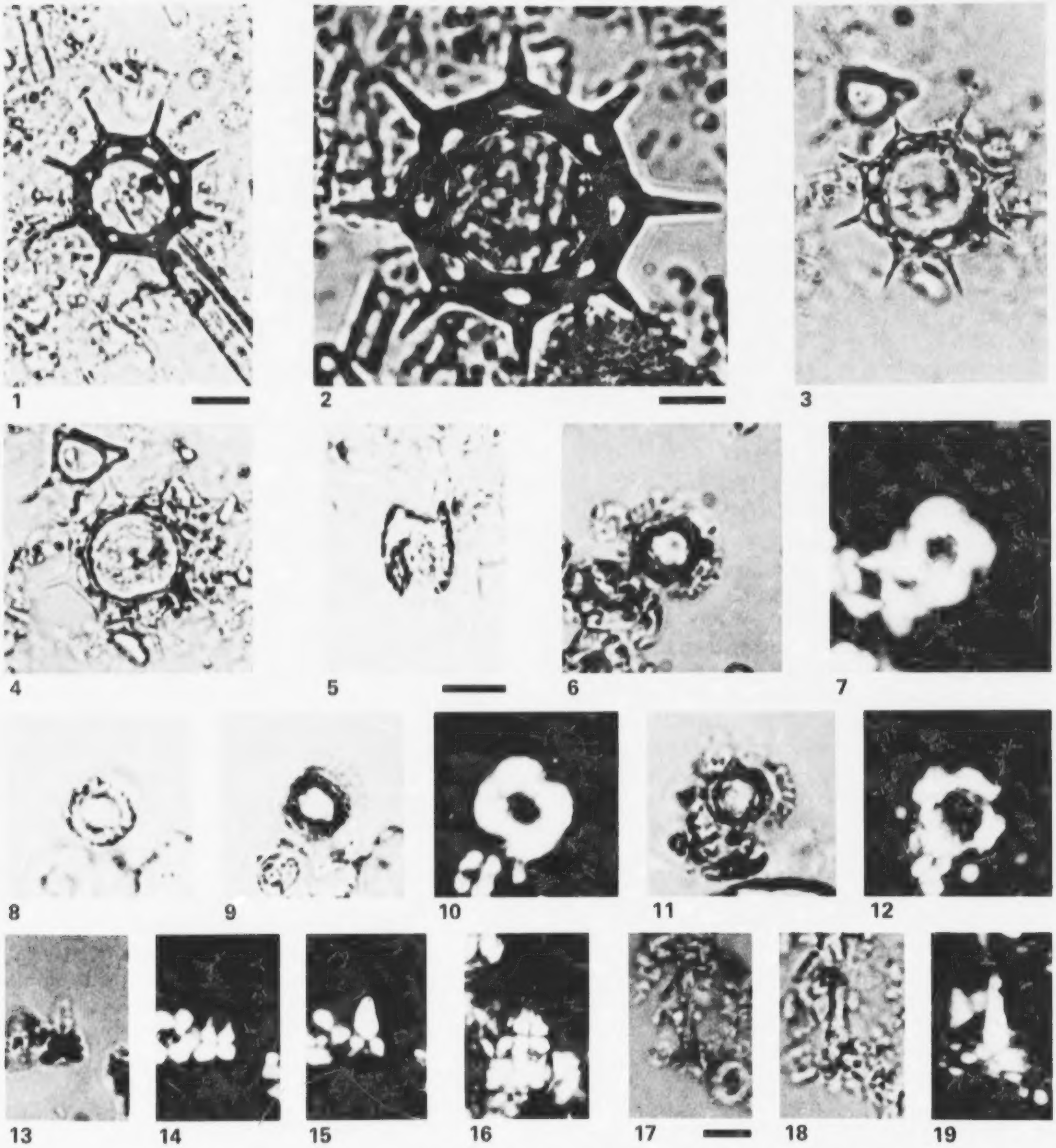

Plate 1. Cenozoic coccoliths and silicoflagellates from Sites DSDP 563, 558, and 190. Figures 1, 3, 4 magnified 900×, scale bar equals 10 μm. Figures 2, 5–16, 18, 19 magnified 1900×, scale bar equals 5 μm. Figure 17 magnified 1500×, scale bar equals 10 μm. **1–4.** ***Distephanus floridus*** Bukry, n. sp. (1) Holotype, USNM 365401, Sample 558A-2-5, 90–91 cm. (2) USNM 365402, Sample 190-4-1, 70–71 cm. (3, 4) USNM 365403, high and low focus, Sample 558A-2-5, 90–91 cm. **5.** ***Ceratolithus separatus*** Bukry, Sample 558A-9-1, 133–134. **6–12.** ***Cyclolithella? neoaprica*** Bukry, n. sp. All specimens from Sample 558-27-1, 90–91 cm. (6, 7) USNM 365405, single-polarized (SP) and cross-polarized (XP) views. (8–10) Holotype, USNM 365404, SP high focus on tube cycle, SP low focus on shield, and XP; smaller *Coccolithus pelagicus* (Wallich) s. ampl. at left. (11, 12) USNM 365406, SP and XP. **13–19.** ***Sphenolithus calyculus*** Bukry, n. sp. (13–15) Holotype, USNM 365407, Sample 558-19-1, 90–91 cm, SP (0°), XP (0°), XP (45°); *Cyclicargolithus floridanus* (Roth et Hay) at left. (16) USNM 365408, Sample 558-19-1, 90–91 cm, XP (0°). (17–19) USNM 365409, Sample 558-18-5, 40–41 cm, SP (45°), SP (0°), XP (45°).

36. *"BOLBOFORMA"*: A MIOCENE ALGAE(?) OF POSSIBLE BIOSTRATIGRAPHIC AND PALEOCLIMATIC VALUE[1]

Dorothy J. Echols, Department of Earth and Planetary Sciences, Washington University[2]

INTRODUCTION

Site 558 was drilled between Anomalies 13 and 15 atitude 37°46.2′N; longitude 37°20.61′W) at a water epth of 3754 m, and Site 563 was drilled on Anomaly 3 (latitude 33°38.53N; longitude 43°46.04′W) at a waer depth of 3786 m. At both sites lower Oligocene to Pleistocene sediments were recovered. In samples from Hole 558 (at approximately 205–214 m) and from Hole 563 (at approximately 195–205 m), the identified planktonic foraminifers indicate foraminiferal Zone N14 (middle Miocene). Within these intervals, tiny (65 to 180 μm) calcareous spheres, individuals of the fossil group called *Bolboforma,* are fairly common to abundant. *Bolboforma* was originally described by von Daniels and Spiegler (1974) as a genus of *incertae sedis* (possibly a Protozoa) from uppermost Oligocene and Miocene deposits of northwestern Germany. In 1976, these little organic bodies were first recorded and described from deep-sea sediments recovered on DSDP Leg 35 by Rögl and Hochuli (1976), who referred them to calcareous algae. Since then, they have been recorded from deep-sea sediments recovered on DSDP Leg 48 by Auffret and Pastouret (1979) and Murray (1979) and on DSDP Leg 80 by Müller et al. (in press). In all cases they seem to be confined to the Miocene in the deep-sea material and, when present, apparently occur in abundance.

It has been suggested (Rögl and Hochuli, 1976; Murray 1979) that this fossil group might be a worldwide biostratigraphic indicator in deep-sea sediments. It may also be of some value in climatic interpretations because intervals characterized by dissolution and probably associated with cooler waters are dominated numerically by *Bolboforma* (Müller et al., in press).

LITHOLOGY AND FAUNAL ASSOCIATION

At both Sites 558 and 563, samples in which *Bolboforma* are found are white to off-white, nannofossil-foraminiferal chalky and marly oozes. Planktonic foraminifers are fairly common to abundant but show some fragmentation and/or dissolution and some crystalline overgrowth on the globorotalid forms. Benthic foraminifers, ostracodes, fish teeth, sponge spicules, and radiolarians are also present and range in abundance from few to fairly common. The faunal association of planktonic foraminifers indicate that these samples belong in the *Globigerina nepenthes-Globorotalia siakensis* N14 Zone. This zone is recognized by the first occurrence of *Globigerina nepenthes* at the base and the last occurrence of *Globorotalia siakensis* at the upper boundary. The first appearance datum (FAD) of *Globigerina nepenthes* is recognized in Samples 558-6,CC and 563-5,CC. This gives us a numeric age of approximately 12 + Ma and places the samples near the boundary of planktonic foraminiferal Zone N13/N14 and nannofossil Zones CN7b/CN7a (upper NN9).

SYSTEMATIC CONSIDERATIONS AND PREVIOUS OCCURRENCES

As noted earlier, *Bolboforma* was first described from upper Oligocene and Miocene sediments in northwestern Germany by von Daniels and Spiegler (1974), who thought that the forms belonged to a fossil group of test-forming protozoans. Although they also noted that in previously published accounts this form had been described as the foraminifer *Lagena,* they discuss in some detail the affinities of *Bolboforma* to the testacea, tintinnina, and the calcareous algae. The eleven new species (*B. metzmacher, B. clodiusi, B. laevis, B. reticulata, B. aculeata, B. armata, B. intermedia , B. rotunda, B. spinosa, B. spiralis, and B. irregularis)* that they describe have distinct stratigraphic ranges and show definite changes in faunal assemblages and abundances in the lower Miocene Vierlande and Hemmoor stages of northwestern Germany.

In 1976, Rögl and Hochuli found these calcareous bodies in lower Miocene sediments drilled in the Antarctic during Leg 35 at Site 325 on the continental rise of the Bellingshausen Sea (65°02.79′S; 73°40.40′W). Based on the accompanying foraminiferal fauna, they assigned the sediments to Zones N6/N7, (lower Miocene to upper Burdigalian). Rögl and Hochuli, after a comparative study of the test and wall structure of *Bolboforma* with various encysting stages of protozoans and algae, concluded that the most advisable classification would be in an "hitherto unknown" group of the planktonic algae Chrysomondales to which the Coccolithineae also belong. At Site 325 they recorded four of the species described by von Daniels and Spiegler (*B. clodiusi, B. spinosa, B. laevis*, and *B.* cf. *rotunda)* and one *B.* sp., possibly abnormal, form (Rögl and Hochuli, 1976, Plates 1 and 2). They conclude that this fauna from the lower Miocene of the Antarctic area is stratigraphically transitional in composition of species and variety of forms to the material described by von Daniels and Spiegler from northwestern Germany.

---

[1] Bougault, H., Cande, S. C., et al., *Init. Repts. DSDP,* 82: Washington (U.S. Govt. Printing Office).

[2] Present address: Curtis and Echols, Geological Consultants, 800 Anderson, Houston, Texas 77401.

In 1979, on DSDP Leg 48, Murray recognized six species, *B. aculeata, B. clodiusi, B. intermedia, B. laevis, B. metzmacheri,* and *B. spiralis* from Sites 403, 404, and 406, drilled on the margin of Rockall Plateau. He noted that the occurrence of the genus at these sites is mainly in Zone N17, possibly ranging from N16–N18. On the same leg, at Site 400 (Hole 400A) Auffret and Pastouret (1979) also noted the occurrence of abundant algae cysts (Rögl and Hochuli, 1976) in Cores 400A-20–400A-36, which are assigned to the middle and upper Miocene. They also noted high dissolution rates in their samples within this interval.

On Leg 80 at Site 550 (48°30.91′N; 13° 26.37′W), Müller et al. (in press) found *Bolboforma* (but did not speciate the genus) in cores of middle and late Miocene age, Zone N16. He called them reproductive bodies (?) of an unknown algae and noted that they differed from calcispheres in shape and possession of spines.

BOLBOFORMA FROM LEG 82 AND CORRELATION WITH OTHER AREAS

The most recent discovery of *Bolboforma* is recorded here from middle Miocene sediments recovered on DSDP Leg 82, North Atlantic. *Bolboforma* is present at Site 558 in Samples 558-5,CC; 558-6-1, 61–64 cm; 558-6-2, 61–64 cm; 558-6-3, 61–64; 558-6-5, 61–64 cm; 558-6-6, 61–64 cm; and at Site 563 in Samples 563-5-2, 62–64 cm; 563-5-3, 62–64 cm; 563-5-4, 62–64 cm; 563-5-6, 62–64 cm; and 563-5-7, 19–21 cm in sediments assigned to the lower part of planktonic foraminiferal Zone N14. Four species (*B. clodiusi, B. spinosa, B. rotunda,* and *B. spiralis*) have been identified, and these are fairly common to abundant in the investigated samples.

At Site 558, Samples 558-5,CC, the common form is somewhat flattened and ornamented with spiral ridges in a petal-like arrangement. There are no prominent spines. A rounded aperture at the end of a projecting neck is obvious (Plate 1, Figs. 1, 2). This species is referred to *B. spiralis* and was originally recorded by von Daniels and Spiegler (1974) from the upper Oligocene-lower Miocene of northwestern Germany. This form was also observed in samples from the Palmer Ridge by L. Molinsky (personal communication to Rögl and Hochuli, 1976) and in samples from DSDP sites from the North Atlantic and the Bay of Biscay (Leg 12) (Molinsky, unpublished data, see Rögl and Hochuli, 1976).

Murray (1979, p. 420) also recognized *B. spiralis* in upper Miocene (planktonic foraminiferal Zone N17) sediments recovered from Hole 406 (DSDP Leg 48) located in the southern margin of the Rockall Plateau (Murray, 1979).

In samples from Core 558-6, two species occur. *B. spinosa,* which has a well-rounded test and is covered with either short sharp or blunted rounded spines (Plate 1, Figs. 3, 4; Plate 2, Fig. 1), and *B. rotunda,* which is a globular intermediate form in which spines are either worn away or not developed. (Plate 2, Fig. 2). Both *B. spinosa* and *B. rotunda,* originally described from the upper Oligocene and lower Miocene of northwestern Germany, are also described by Rögl and Hochuli (1976) from the lower Miocene of the Antarctic, DSDP Site 325.

At Site 563 in Core 563-5, the flattened onion-shaped form *B. clodiusi* is present. The surface of this species is ornamented with ridges from which rounded to angular short, stout spines project (Plate 2, Figs. 2, 4) and a short neck of variable shape bordered by an apertural lip is conspicuous. *B. clodiusi,* originally described by von Daniels and Spiegler (1974) from middle to uppe Miocene, has also been described by Rögl and Hochul (1976) from the Antarctic lower Miocene (N6-N7 zones and by Murray (1979) from upper Miocene (N16-N18 sediments from the Rockall Plateau.

SUMMARY AND CONCLUSION

Eight of the species originally described by von Daniels and Spiegler (1974) from northwestern Germany have been identified by later authors in deep sea sediments Of the four species identified in the present report from the North Atlantic (*B. clodiusi, B. rotunda, B. spinosa,* and *B. spiralis*), two (*B. rotunda* and *B. spinosa*) have also been recorded from the Antarctic, one *B. spiralis* is also recorded from other parts of the North Atlantic (Rockall Plateau) and the Bay of Biscay, and one *B. clodiusi* has been described from the Rockall Plateau and the Antarctic.

Figure 1 shows the stratigraphic position of the reported occurrences of the genus *Bolboforma.* The presence of *Bolboforma* on Leg 12 1972, personal communication to Rögl and Hochuli (1976) by L. Molinsky, is not documented in Volume 12 of the *Initial Reports of the Deep Sea Drilling Project* and the stratigraphic range of the genus in those samples is not given, therefore this report cannot be referenced in Figure 1.

In the present study the genus has only been found in the middle Miocene, but it is possible that more complete sample coverage will extend this range. The species recognized are distinctive and with the aid of the scanning electron microscope, fairly easily identified, so it seems likely that *Bolboforma* will be a useful guide to the Miocene and that its species may eventually be zoned.

Figure 2 shows the geographic locations from which the genus is reported and illustrates its wide distribution. During the time *Bolboforma* flourished, reported occurrences indicate the environment of deposition was deep, moderate to lower, bathyal waters. The intervals are also characterized by varing degrees of dissolution and contain faunas generally associated with cooler waters.

Bolboforma was probably a planktonic algae that may have bloomed and prevailed during incursions of colder waters.

ACKNOWLEDGMENTS

The author wishes to express gratitude to Dan Kremser for takin the SEM photographs and to Kris Henrick, Washington University, Department of Earth and Planetary Sciences, for typing the manuscript

REFERENCES

Auffret, G. A., and Pastouret, L., 1979. Upper cretaceous to Quaternary sedimentary processes in the Bay of Biscay from textural mineralogical, and coarse fraction studies. *In* Montadert, L., Roberts, D. G., et al., *Init. Repts. DSDP*, 48: Washington (U.S. Govt. Printing Office), 791-829.

Müller, C., Spiegler, D., and Pastouret, L., in press. The genus *Bolboforma* Daniels and Spiegler in the Oligocene and Miocene Sediments of the North Atlantic and Northern Europe. *In* Graciansky, P. C. de, Poag, C. W., et al., *Init. Repts. DSDP*, 80: Washington (U.S. Govt. Printing Office).

Murray, J. W., 1979. Cenozoic biostratigraphy and paleoecology of Site 403 and 406 based on the foraminifers. *In* Montadert, L., Roberts, D. G., et al., *Init. Repts. DSDP*, 48: Washington (U.S. Govt. Printing Office), 415-430.

Rögl, R., and Hochuli, P., 1976. The occurrence of *Bolboforma*, a probable algal cyst, in the Antarctic Miocene of DSDP Leg 35. *In* Hollister, C. D., Craddock, C., et al., *Init. Repts. DSDP*, 35: Washington (U.S. Govt. Printing Office), 713-719.

von Daniels, C. H., and Spiegler, D., 1974. *Bolboforma* n. gen. (Protozoa?) eine neue stratigraphisch wichtige Gattung aus dem Oligozän/Miozän Nordwestdeutschlands. *Palaontol. Z.*, 48:57-76.

Date of Initial Receipt: 21 April 1983
Date of Acceptance: 20 January 1984

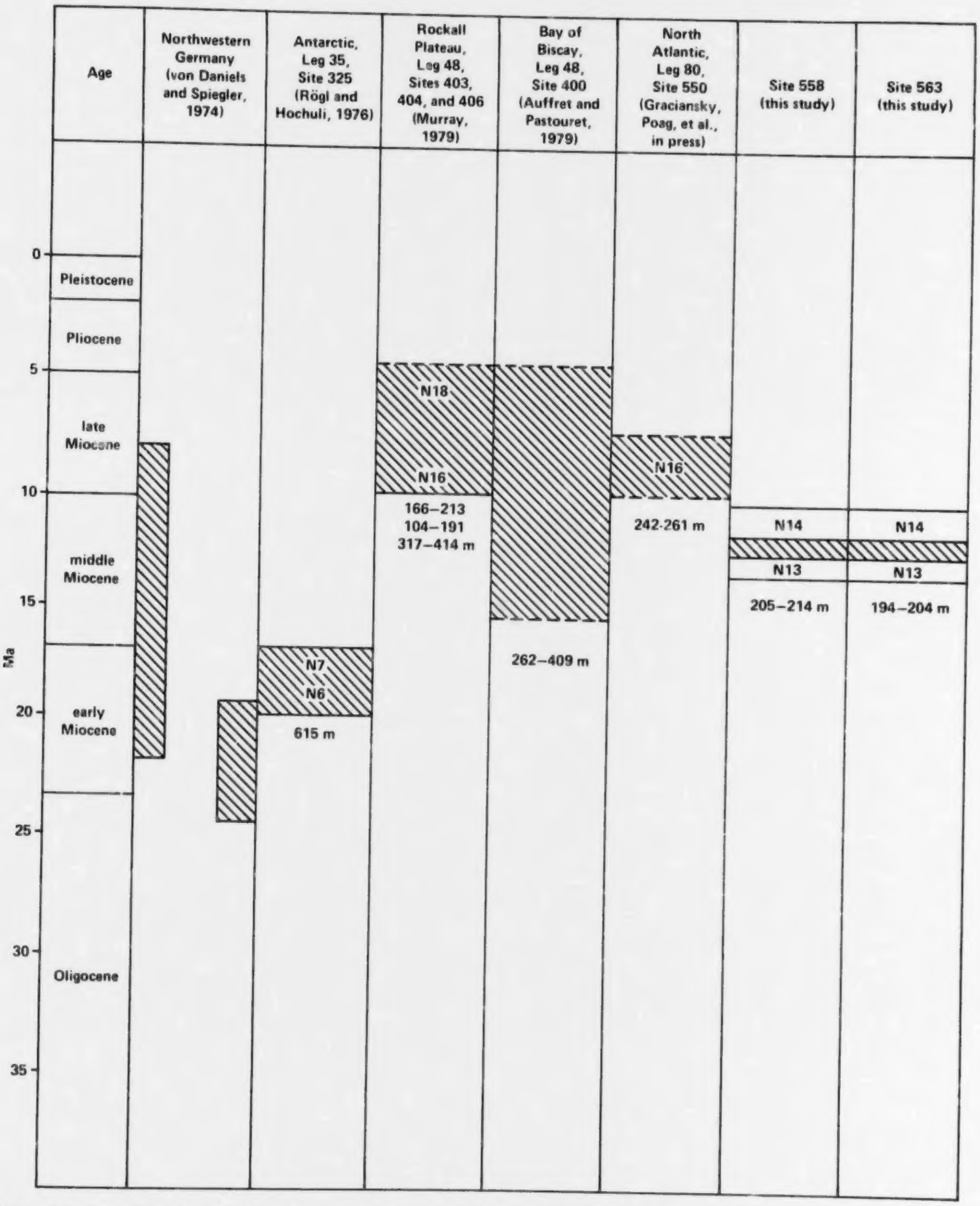

Figure 1. Stratigraphic distribution of *Bolboforma* recorded in the literature. Sub-bottom depths or depth intervals of *Bolboforma* occurrences are given in meters.

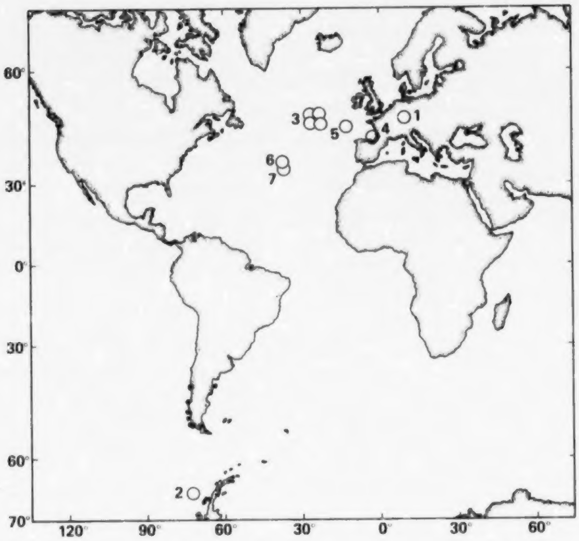
60°
30°
0°
30°
60°
70°
120°
90°
60°
30°
0°
30°
60°
1
2
3
4
5
6
7

Figure 2. Known occurrences of *Bolboforma*. Numbers indicate the source of data, as follows: (1) Northwestern Germany (von Daniels and Spiegler, 1974); (2) Antarctic (Rögl and Hochuli, 1976); (3) Rockall Plateau (Murray, 1979); (4) Bay of Biscay (Auffret and Pastouret); (5) North Atlantic (Graciansky and Poag, in press); and (6) Site 558 and (7) Site 563 (this study).

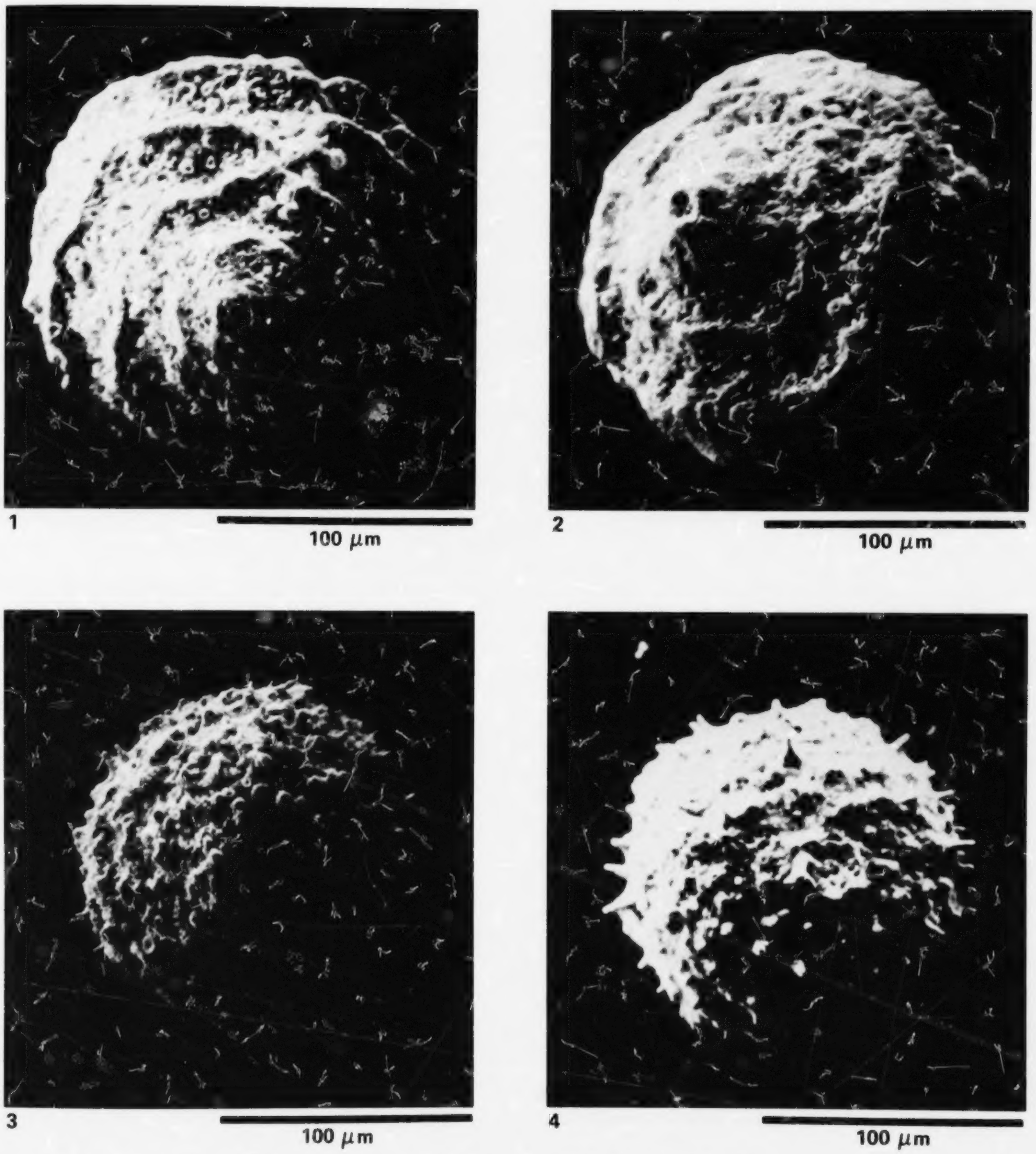
1
100 μm
2
100 μm
3
100 μm
4
100 μm

Plate 1. **1, 2.** *Bolboforma spiralis* ×400; Section 558-6-6. **3, 4.** *B. spinosa* ×400; Sample 558-5, CC.

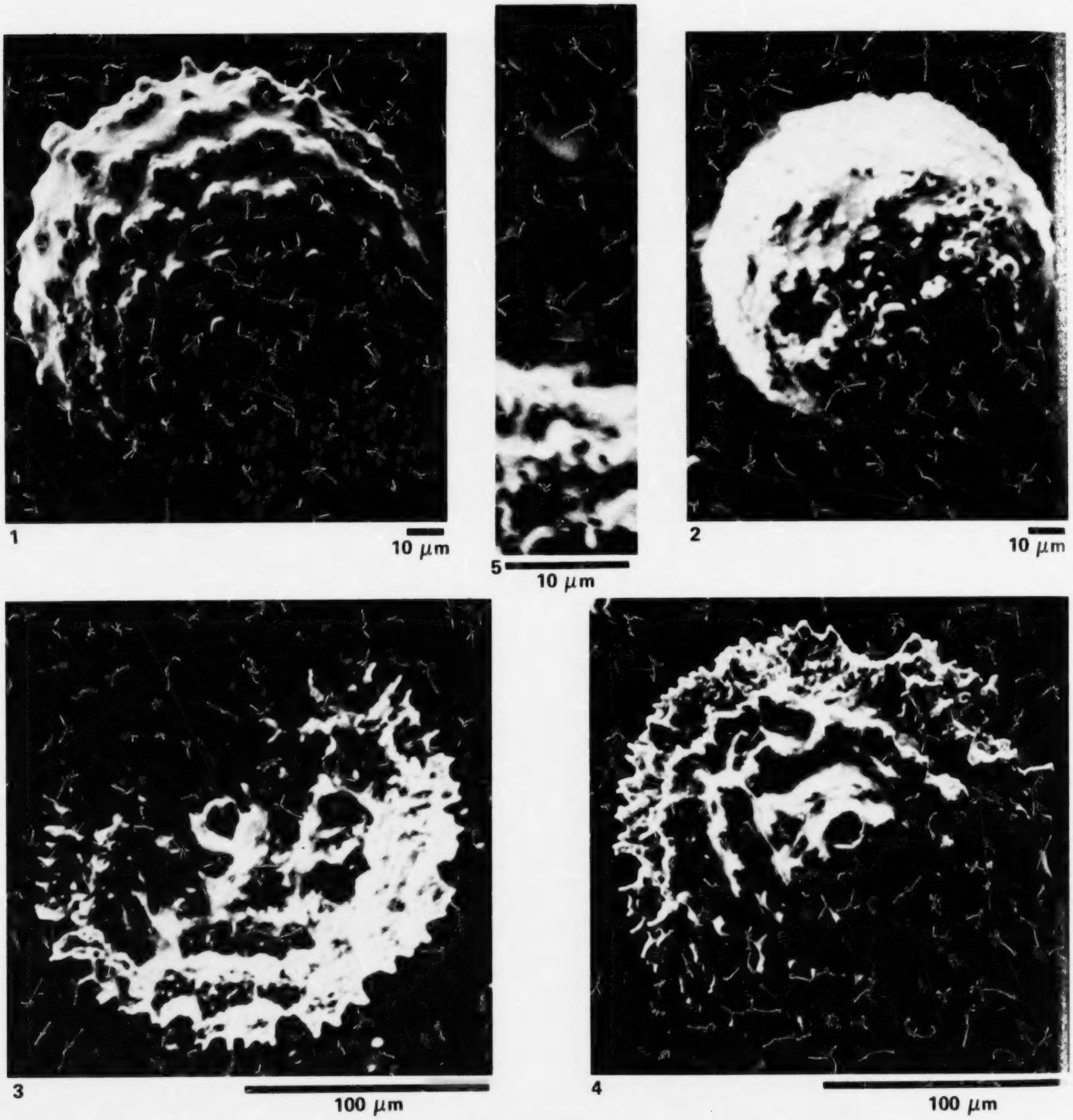
1
10 μm
5
10 μm
2
10 μm
3
100 μm
4
100 μm

Plate 2. Section 558-6-6 (unless indicated otherwise). **1.** *Bolboforma spinosa* ×600. **2.** *B. rotunda* ×600; Section 563-5-6. **3, 4.** *B. clodius* ×400. **5.** Coccolith slurry ×2000.

37. OLIGOCENE BENTHIC FORAMINIFERS FROM NORTH ATLANTIC SITES: BENTHIC FORAMINIFERS AS WATER-MASS INDEXES IN THE NORTH AND SOUTH ATLANTIC[1]

Anne Boersma[2]

ABSTRACT

Comparison of Oligocene benthic foraminiferal faunas from DSDP Sites 558, 563, 549, and 366 in the North Atlantic demonstrates, in the two deeper, less well preserved sections at Sites 558 and 563, lower diversity and lower abundance of benthic taxa, smaller sized individuals, and lower percentages of rectilinear species than in the shallower Sites 549 and 366, both of which underlie upwellings through parts of the Oligocene.

In Paleogene deep-water sections (1500–3000 m paleodepths), an increase in the rectilinear:rotaloid ratio and the presence of miliolids correlate with improvement in sample preservation and an apparent decrease in carbonate dissolution. Solution-resistant species in this depth range are *Globocassidulina subglobosa, Stilosmella abyssorum*, and *Cibicidoides* cf. *ungerianus;* they become strongly dominant in the North Atlantic at abyssal depths, in moderately dissolved samples from which the coarse planktonic foraminiferal carbonate has been largely dissolved.

Taxa typical of the Indo-Pacific region, such as *Laticarinina altocamerata, Cibicidoides verrucosus*, and *Heronallenia*, appeared in deep-water sections in Zone-P21 time, concurrent with a slight drop in bottom-water temperatures. *Rectuvigerina postprandia*, another Indo-Pacific species, was confined to intermediate water depths of less than approximately 1200 m. It migrated to the South Atlantic in Zone-P20 time and, along with other faunal changes, may signal the appearance of a new intermediate-water type.

Examination of faunas across the Eocene/Oligocene boundary and through the Oligocene from 12 North and South Atlantic locations has indicated that the distribution of *Nuttallides umbonifera* can be used to trace the pathways and depth-migration of newly-derived deep-water masses through the Atlantic. After the Eocene/Oligocene boundary event, the variations in the geographic occurrences of *N. umbonifera* from several deep-water and bottom-water depth sites parallel the stable isotopic records of bottom-water characteristics, thus reflecting the incursion of cooled bottom waters, which aged from south to north.

At one South Atlantic site (1000 m paleodepth), the brief but significant appearance of *N. umbonifera* is interpreted to reflect the influx of a new intermediate-water mass that entered the Atlantic during Zone-P20 time (about 32–33 Ma ago), coincident with the establishment of a circum-Antarctic surface circulation.

Faunas at all sites markedly changed their generic and intrageneric contents between the early and late Oligocene. The first appearances of several characteristic Neogene species through the upper Oligocene Zones P21–P22 are hypothesized to reflect the diachronous evolution of essentially "Neogene" water-mass stratification in the North and South Atlantic.

INTRODUCTION

Census of Oligocene benthic foraminiferal faunas at 12 Atlantic Ocean sites demonstrates their utility as tracers of bottom-water characteristics and circulation during the pronounced climatic shifts of the Oligocene. Coverage of North Atlantic benthic faunas in this study included two deep DSDP sites, 558 and 563, drilled near 3700 m in the central North Atlantic (Fig. 1), which were compared with (1) eastern North Atlantic deep-water faunas from the Bay of Biscay (DSDP Sites 549 and 550; *Vema* Core V27-134; (2) equatorial northeastern Atlantic deep-water faunas from DSDP Site 366 on the African margin; and (3) benthic faunas from six southern Atlantic sites representing a paleodepth range from 00 to nearly 4000 m (see Table 1).

This geographic coverage provided an overall picture of typical North Atlantic deeper-water benthic species from well-preserved calcareous sequences at a wide variety of locations and depths. The specific purposes of obtaining this coverage were (1) to identify possible deep-water index species for the North or South Atlantic by comparison of faunas from deep-water sites in both ocean areas; (2) to determine whether such index species migrated through depth or latitude during the major climatic shifts of the Oligocene; and (3) to determine whether changing benthic distribution patterns could be employed to describe deep-water circulation in the North Atlantic during the Oligocene.

METHODS

Biostratigraphy

Subdivision of low-latitude Site 366 was based on the criteria of Hardenbol and Berggren (1978). At middle-latitude sites, however, low-latitude criteria cannot necessarily be applied, owing to dissolution and/or the latitudinal effect on distributions of species. A composite of biostratigraphic criteria used to determine equivalency to the low-latitude zones in shown in Table 2.

Benthic Census

A minimum of one sample per core from each site was processed on a >63-μm sieve. All benthic foraminifers in 0.5 g of the >63-μm fraction were picked and identified, and all data were determined from this 0.5-g aliquot. Samples showing extreme carbonate dissolution were not included in this study.

PALEOGENE GEOGRAPHIC AND/OR WATER MASS PROPERTY INDEXES

Rey's 1954 study was one of the first to depict Paleogene geographic index species. Following the hypothesis

---

[1] Bougault, H., Cande, S. C., et al., *Init. Repts. DSDP*, 82: Washington (U.S. Govt. Printing Office).

[2] Address: Microclimates, Box 404, Rural Route 1, Stony Point, New York 10980.

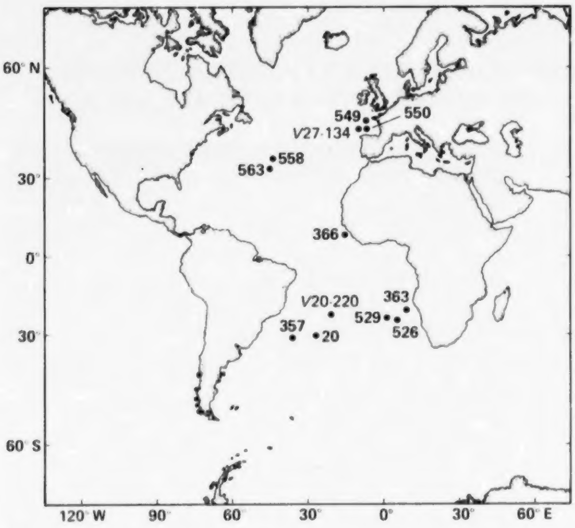

Figure 1. Location map of the 12 sites included in this study: base map redrawn from Tjalsma and Lohman (1983).

Table 1. Locations and water depths of drill sites described in this study.

Site	Latitude	Longitude	Depth (m)	Location
558	37°2′N	37°61′W	3754	Pico Fracture Zone
563	33°53′N	43°4′W	3786	Mid-Atlantic Ridge
549	49°5′N	13°5′W	2515	Bay of Biscay
*V*27-134[a]	48°00′N	12°6′W	3350	Bay of Biscay
550	48°3′N	13°26′W	4420	Bay of Biscay
366	4°40′N	19°51′W	2853	African margin
363	19°38′S	9°2′E	2248	Angola margin
*V*20-220[a]	28°30′S	30°03′W	4043	Brazil Basin
20	28°31′S	26°50′W	4506	Hunter Channel
357	30°00′S	35°33′W	2086	Rio Grande Rise
529	28°55′S	2°46′E	3035	Walvis Ridge
526	30°7′S	3°8′E	1054	Walvis Ridge

[a] *Vema* core numbers.

Table 2. Biostratigraphic criteria used to assign ages to middle-latitude sites.

Low-latitude zone	Middle-latitude criteria indicating equivalent age
P18–19	Loss of typical Eocene genera, presence of *Globoquadrina tapuriensis*, *"Turborotalia" pseudoampliapertura*, and *Pseudohastigerina* sp. without *Globoquadrina sellii*
upper P18–P19	Presence of *G. tapuriensis*, *"T." pseudoampliapertura*, *Pseudohastigerina* spp., and *G. sellii*
P20	Loss of *Pseudohastigerina* spp., presence of *"T." pseudoampliapertura*, and appearance of the 4–5-chambered globorotaliid-form species such as *"Turborotalia" siakensis*
P21a	Loss of *"T." pseudoampliapertura*, increase in large globoquadrinids, presence of *Chiloguembelina* spp.
P21b	Loss of *Chiloguembelina* spp., floods of *Globigerina praebulloides* in fine fraction
P22	Increase of large globoquadrinids, occasional presence of *Globigerina angulisturalis* and/or *Globigerina ciperoensis* in well-preserved faunas, presence of *"Turborotalia" birnagae* and/or *"Turborotalia" pseudokugleri* and the predecessor of *Globoquadrina dehiscens*

of Bettenstaedt and Wicher (1955) that there were strong similarities between Cretaceous benthic faunas throughout the world ocean, Rey compared the benthic foraminiferal faunas from several Paleogene Caribbean and Mexican localities with coeval faunas from North Africa, documenting their marked similarities. In addition, he identified several species that are dissimilar on the two sides of the Atlantic; these represented some of the first paleogeographic index species of the Paleogene.

Using similar reasoning, Berggren and Aubert (1975) distinguished Paleocene–Eocene shallower "Midway" faunas from deeper-water "Velasco" faunas, and plotted their distributions worldwide, thus further documenting the cosmopolitan distributions of many Paleogene species. "Velasco" faunas have since been charted elsewhere, for example by Schnitker (1979) in the Bay of Biscay and by Tjalsma and Lohmann (1983) at many Atlantic DSDP sites. Berggren and Aubert (1975) and Gradstein and Berggren (1981) continued to divide Atlantic Paleogene calcareous and agglutinated faunas into index assemblages named after analogous faunas from the older literature—for example, the "Barbados" fauna of Beckman (1953), the *Cibicidoides mexicanus* fauna first described by Nuttall (1932), and the *Rhabdammina* faunas known from the central European flysch basins (Brouwer, 1965).

Using the ideas of Streeter (1973), Schnitker (1974), and Bremer and Lohman (1982), among others, on the distributions of Pleistocene benthic taxa in the Atlantic, a few researchers have tried to relate distributions of Atlantic benthic foraminifers to Paleogene climatic changes and inferred water-mass characteristics. Tjalsma and Lohman (1983) used multivariate analyses to depict benthic faunal factors that could be related to changes in the oxygen-isotopic record of climate and bottom paleotemperatures. Although they reported no relationship between benthic foraminifers and the isotopically estimated paleotemperatures of the deep ocean, their data did indicate major biogeographic differentiation of benthic foraminifers in the middle Eocene at the time of the initial reduction in bottom-water temperatures (Savin, 1977; Boersma and Shackleton, 1977). Their data also suggested that a *Nuttallides* biofacies migrated to shallower depths during the warmest, most climatically equable phase of the Paleogene from the late Paleocene into the early Eocene. They concluded that in such regimes ocean circulation slows down, the lysocline migrates to shallower depths, and the presence of the *Nuttallides* biofacies reflects the migration of these more corrosive waters to shallower depths.

Schnitker (1979) demonstrated the depth migration of the bathyal benthic genus *Osangularia* into the abyssal regions of the Bay of Biscay during the bottom-temperature drop at Eocene/Oligocene boundary time. Miller (1982) attempted to relate changes in the *Nuttallides umbonifera* percentages to the carbon-isotope record at the bottom. He suggested that an acme of *N. umbonifera* in the middle Oligocene correlated with increased age and corrosiveness of bottom waters.

Boersma and Shackleton (1977) and Boersma (1977) attempted to relate increased spinosity of several Oligocene rectilinear benthic foraminifers from the Rio Grande Rise (South Atlantic) to the late Oligocene reduction in bottom-water temperatures. Boersma (1984b) demonstrated a consistent relationship between uvigerinid indexes and bottom depth in the upper bathyal zone on the Walvis Ridge. Alterations in the uvigerinid faunas, species diversity, and the rectilinear:rotaloid ratio were related to the late Oligocene decrease in bottom-water temperatures.

By analogy with the research on Pleistocene and modern benthic foraminifers, several index groups are proposed for the Paleogene. Uvigerinids are thought to characterize glacial-age, productive water masses; they are also most common in areas of high production of organic matter at the surface (Lutze, 1978) and in zones of high content of organic matter in clay along the continental margins. Several species of *Rectuvigerina* are limited to intermediate and shallower waters. *N. umbonifera* occupies corrosive, oxygen-rich, and generally cooled waters, and its abundance, along with that of other epistomellids, may be correlated with the presence of a type of Antarctic-derived bottom water. Miliolids, in part because of their high magnesium contents, are thought to be particularly susceptible to solution, and hence presumably avoid areas of colder, more corrosive bottom water. *Planulina-Cibicidoides-Cibicides* faunas are known to have predominated in the less productive, warmer, interglacial waters when uvigerinids became scarce, and may have alternated in abundance with uvigerinds during the Paleogene. Rectilinear benthic foraminifers, like those with large pores, are generally more susceptible to solution than rotaloid forms and therefore are not likely to occur in high percentages in corrosive bottom waters (Woodruff, 1979).

Because all these groups were present in the later Paleogene of the Atlantic, their distributions and/or histories may be relatable to the climatic and temperature records of that time.

BENTHIC FORAMINIFERAL FAUNAS

Site 558 (Hole 558)

Hole 558 was drilled at 37°2′N, 37°61′W (Fig. 1), at a water depth of 3754 m, near the Pico Fracture Zone of the Mid-Atlantic Ridge (Table 1). Oligocene calcareous sediments were recovered in Cores 27–18; benthic foraminifers from these cores are listed in Figure 2.

Sediments throughout the sections from Hole 558 are moderately well preserved, except in the lower two cores (27 and 26), which show evidence of strong alteration caused by contact with basement. Fossils appear dolomitized, fragmented, and cemented into lumps. Preservation deteriorates again above Core 21 (Zones P21–P22), where dissolution has removed large amounts of planktonic and benthic tests from the coarse fraction (>250 μm) and caused erosion and fragmentation of a large number of the remaining benthic tests. Most faunas from these cores are considered to be dissolution residues and therefore nonrepresentative of true upper Oligocene benthic diversity (species richness) in this area.

In most samples, the abundance of benthic tests per 0.5 g of sediment, called the benthic number (BN), is considered to reflect sediment dissolution rather than initial production and/or sediment accumulation rates. An occasional sample from Zone P22, however, shows improvement in preservation, so that even the solution-susceptible species *Globigerina angulisuturalis* is found. In these samples, true benthic diversity is assumed.

In the best-preserved samples, the rectilinear genera, especially *Stilostomella* and *Pleurostomella*, predominate. Cibicidids and anomalinids are the most abundant rotaloid groups of the lower Oligocene; in the upper Oligocene, the cibicidids are the most abundant.

The most consistently occurring species include *Oridorsalis umbonatus, Globocassidulina subglobosa, Stilostomella abyssorum*, and *Cibicidoides* cf. *ungerianus*. Since they occur in even the most dissolved samples, they may be considered dissolution-resistant forms. *Uvigerina pygmaea* and *Pleurostomella alternans* occur consistently, but only in the upper Oligocene, whereas *S. subspinosa* and *Anomalinoides* cf. *spissiformis* occur commonly only in the lower Oligocene section. The most common cibicidid is *Cibicidoides havanensis*.

Within genera, also, different species predominate in the lower and the upper Oligocene parts of the section. Among the uvigerinids, *U. spinicostata* in the lower Oligocene is replaced in importance by *U. pygmaea* in the upper Oligocene. The typical lower Oligocene cibicidids, *Heterolepa grimsdalei* and *Cibicides laurisae*, are replaced by *Cibicidoides haitiensis* and *H. kullenbergi* in the upper Oligocene. The lower Oligocene buliminid, *Bulimina semicostata*, has no upper Oligocene counterpart.

At least two species originally identified in New Zealand faunas by Finlay (1939) occur at Site 558. *Anomalinoides orbiculus* (Stache), an anomalinid with an ornamented umbilicus, was found in Section 558-25-5 (lower Oligocene). This species originated in the late Eocene in the New Zealand area. One specimen of *Laticarinina altocamerata* Chapman and Parr, a late Eocene to Pliocene form from New Zealand and the southwestern Pacific, occurred in Section 558-18-1 (uppermost Oligocene).

The influx of several new species in Zones P21b–P22 caused the faunas to assume a more Neogene character. These species include *Pullenia quinqueloba, U. pygmaea, H. kullenbergi, Textularia* sp. A, *Alabamina haitiensis*, and *Trifarina bradyi*.

Site 563

Site 563 is situated on the Mid-Atlantic Ridge (Fig. 1) at a depth of 3786 m (Table 1). Oligocene calcareous sediments were recovered in Cores 22 to 17; benthic foraminifers from these cores are listed in Figure 3. Although this section includes species from all Oligocene planktonic foraminiferal zones, the shortness of the zones suggests numerous erosional hiatuses and/or removal of large amounts of sediment by dissolution.

Preservation of the sediments at Site 563 is only moderately good to fair, and most faunas are less well preserved than their age equivalents at Site 558. Unlike sed-

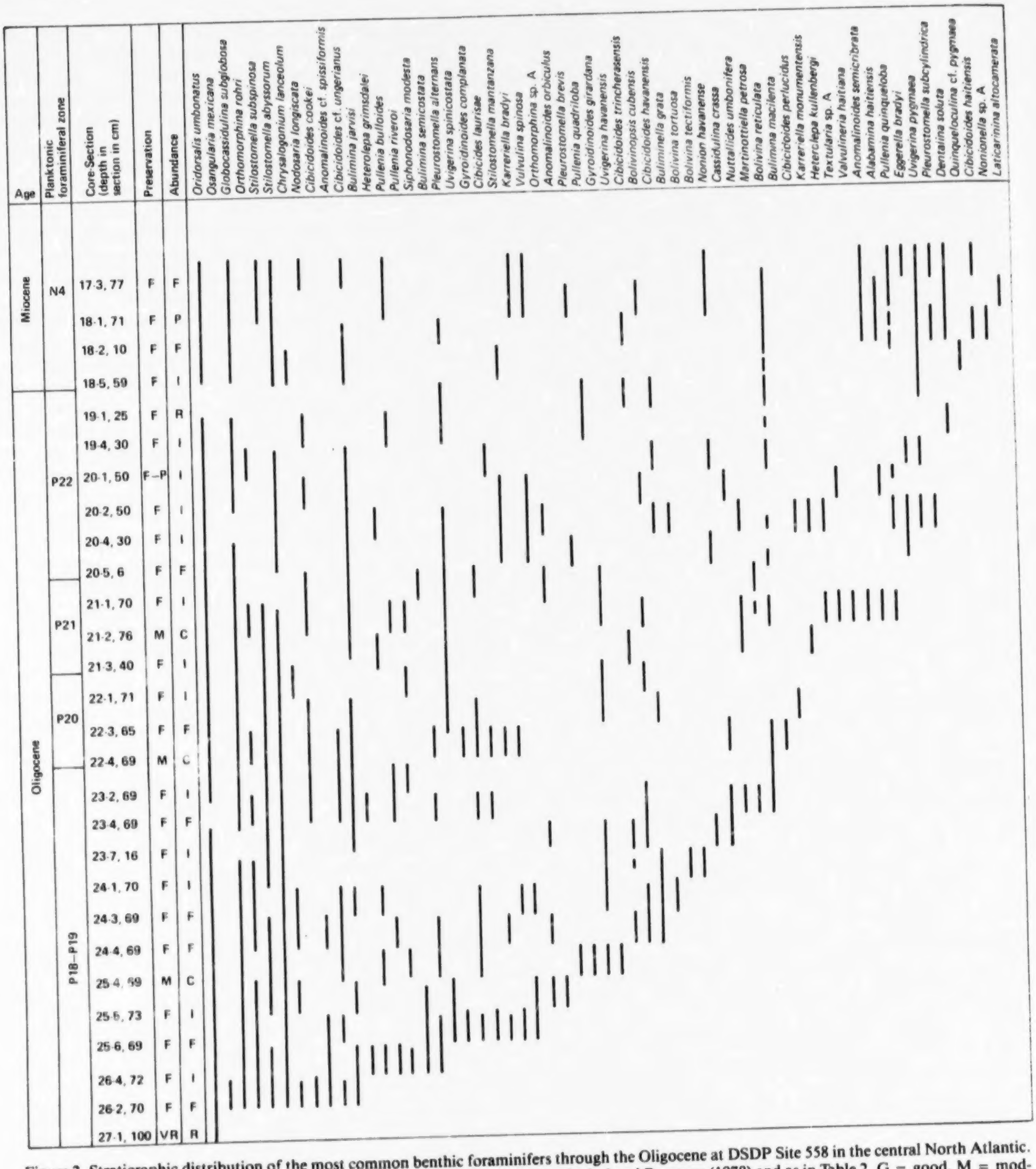

Figure 2. Stratigraphic distribution of the most common benthic foraminifers through the Oligocene at DSDP Site 558 in the central North Atlantic. Zonal assignments for Figures 2–5 and 9–10 according to the criteria of Hardenbol and Berggren (1978) and as in Table 2. G = good, M = moderate, P = poor; A = abundant, C = common; F = frequent; I = infrequent; V = very.

iments in the lower cores from Site 558, the sediments here show no evidence of contact with basement. As at Site 558, dissolution removal of large-fraction foraminifers increases markedly in upper Oligocene Zones P21b–P22; benthic faunas in Cores 19 to 17 are all considered dissolution residues.

The mediocre state of preservation of most of these sediments makes it difficult to assess benthic faunal patterns. No upper Oligocene fauna is considered representative of actual benthic production or diversity in this area of the Atlantic. As at Site 558, in the best-preserved samples rectilinear genera predominate over the rotaloids,

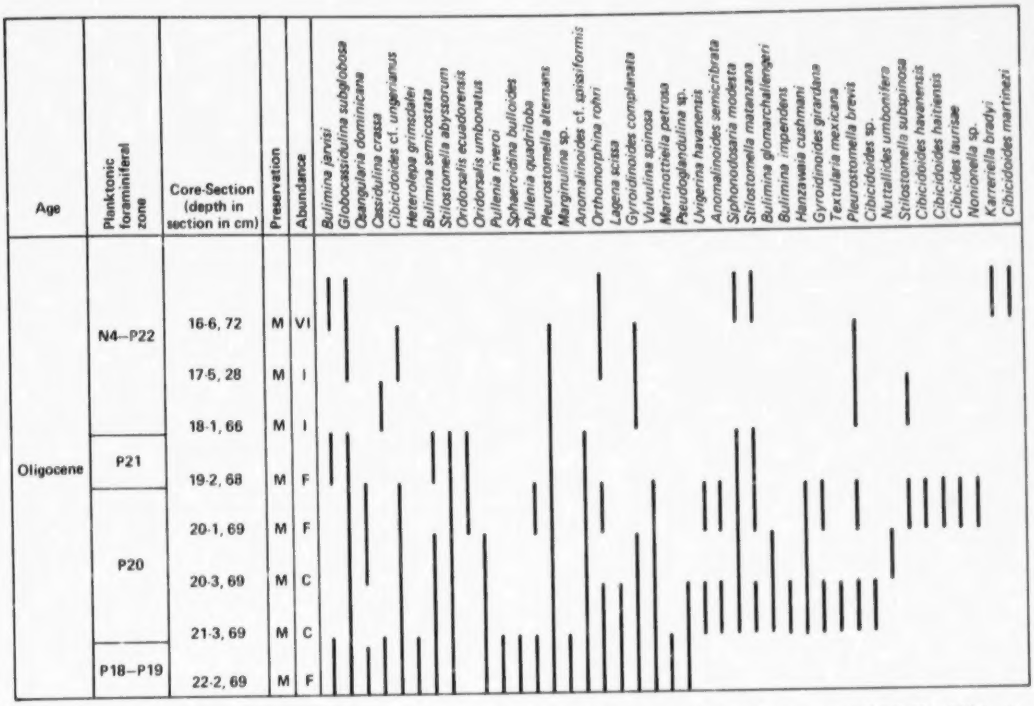

Figure 3. Stratigraphic distribution of the most common benthic foraminifers through the Oligocene at DSDP Site 563 in the central North Atlantic. Abbreviations and zonal assignments as in Figure 2.

and the cibicidids are the most common rotaloid forms. In such dissolution-depleted faunas, however, even the generic composition may not be representative of the original populations.

In the lower Oligocene, the most consistently occurring species are *Globocassidulina subglobosa, Cibicidoides* cf. *ungerianus*, and *Pleurostomella alternans*. The most abundant species, however, include *Oridorsalis umbonatus, Hanzawaia cushmani*, and *Bulimina semicostata*. As at Site 558, the most common buliminid is *B. semicostata*, and the most frequently encountered cibicidid is *C.* cf. *ungerianus*. In contrast with Site 558, the common lower Oligocene uvigerinid here is the nonspinose *Uvigerina havanensis*.

Site 549 (Hole 549A)

Hole 549A was drilled on DSDP Leg 80 in the Bay of Biscay (Fig. 1) at a water depth of 2515 m (Table 1). Oligocene calcareous–siliceous sediments were recovered in Cores 6–13; the ranges of benthic species in these cores are shown in Figure 4. The section at this site includes at least two hiatuses in the lower Oligocene and may be missing part of Zone P21 as well. In view of the siliceous contribution to the sediments, the section seems unusually short and the sediment accumulation rates too low, particularly in the upper Oligocene, where sediment accumulation increased in other oceanic areas.

Preservation at Site 549 is good in the lower Oligocene but only moderately good in the upper Oligocene. The sediments of the washed residues described here (all >63 μm) are nearly 99% carbonate; the 1% of siliceous material consists primarily of broken radiolarians. The amount of siliceous fossils decreases in upper Oligocene Cores 9 to 6, in which there has also been increased dissolution removal of large-fraction (>250 μm) foraminifers; preservation is only moderately good throughout the upper Oligocene section.

Sixty-three species of benthic foraminifers were identified from the Oligocene section at Site 549. Maximum diversity in a well-preserved lower Oligocene sample (549A-11-4, 110 cm) was 33 species. By contrast, upper Oligocene moderately well preserved samples contained only 16 to 18 species.

Individual calcareous specimens in these samples were noticeably larger than at the two previously described North Atlantic sites. Agglutinated individuals were also large, and frequently their grains were pyritized.

The most consistently occurring species were *Oridorsalis umbonatus, Globosassidulina subglobosa, Hanzawaia cushmani, Cibicidoides* cf. *ungerianus, Stilostomella subspinosa*, and *Cibicides laurisae*. In some samples *Uvigerina spinicostata* and *Vulvulina spinosa* also became very abundant. Species common in upper, but not lower, Oligocene faunas include *Alabamina haitiensis, Cibicidoides havanensis*, and a large rugose cibicidid tentatively referred to the New Zealand form *C. verrucosus* (Finlay).

The most commonly occurring group is the cibicidids; *Cibicidoides haitiensis* is more common in the lower Oligocene, whereas *C. havanensis* is more typical in the upper Oligocene. At the top of the section (549A-6-5, 50 cm), *H. mexicana* occurs for the first time.

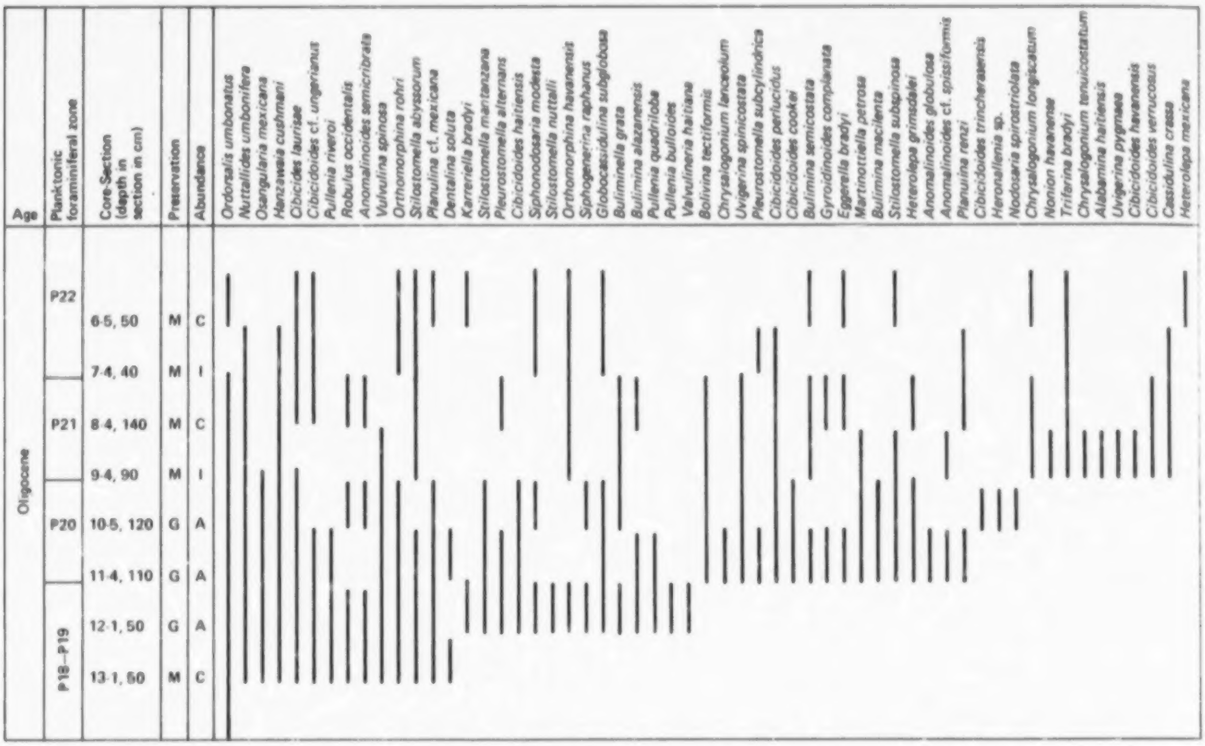

Figure 4. Stratigraphic distribution of the most common benthic foraminifers through the Oligocene at DSDP Site 549 (Hole 549A) in the Bay of Biscay. Abbreviations and zonal assignments as in Figure 2.

U. spinicostata, the uvigerinid typical of the lower Oligocene, becomes very abundant in the intermediate size fraction (149–250 μm) in Zone P20. In this interval there is a marked increase in siliceous fossils in the washed foraminiferal fraction.

Taxa found at Site 549, but not at the deeper, more westerly Sites 558 and 563, include *Robulus* ex. gr. *occidentalis*, large nodosariids such as *Nodosaria spirostriolata*, and large orthomorphinids such as *Orthomorphina havanensis*, Gavelinella aragonensis, *Anomalinoides globulosa*, and *Planulina renzi*.

Unusually large individuals of several species appeared in Zone P20 (Section 549A-10-5), accompanied by rare specimens of the genus *Heronallenia*. The first occurences of this genus outside the Indo-Pacific are considered synchronous worldwide (Aubert, pers. comm., 1974).

Site 366

Site 366, at 2853 m water depth on the continental slope of northwest Africa (Fig. 1, Table 1), was a locus of investigation on DSDP Leg 41. A long calcareous section with secondary amounts of siliceous fossils was recovered from Hole 366 (Cores 39 to 28) and from Hole 366A (Cores 10 to 6); faunas are listed in Figure 5. The top of Hole 366A overlaps in age (Zone P21) with the bottom of the section in Hole 366, so this long composite section appears nearly complete.

Sediments at Site 366 demonstrate variable degrees of induration, which Dean and Gardner (1978) have suggested represent Oligocene climatic cycles. Foraminiferal faunas in the more indurated samples are moderately well preserved; in one less indurated upper Oligocene sample (366-31-1, 8 cm), faunas are well preserved and very diverse. As as Site 549, the amount of the siliceous component in the washed residues decreases in upper Zone P21 and is minimal through the remainder of the Oligocene.

Faunas at this site closely resemble those described by Beckman (1953) from the Oligocene of Barbados. Of the 66 benthic species identified, the maximum diversity of 33 species occurs in Zone P22. As at Site 549, individual foraminifers at this site are large relative to those at Sites 558 and 563. Agglutinated foraminifers are pyritized.

The most consistently occurring species include *Oridorsalis umbonatus, Globocassidulina subglobosa, Stilostomella abyssorum, Cibicidoides haitiensis, S. subspinosa, Pullenia bulloides*, and *Bolivina tectiformis*.

Several genera are more diversified here than at any of the other sites. Eight species commonly attributed to *Cibicidoides* were identified. Uvigerinids, also more diverse, include *Uvigerina havanensis, U. spinicostata*, an elongate form called *U. longa*, and *U. pygmaea*. The several buliminids include *Bulimina consanguinea*, a taxon not found at any of the other North Atlantic sites but frequent in several deep-water sites in the South Atlantic (Boersma, 1984b).

Species found at Site 366, but not at other North Atlantic sites, are *Pleurostomella ecuadorana, Laticarinina bullbrooki, Siphonina pulchra*, and several miliolids.

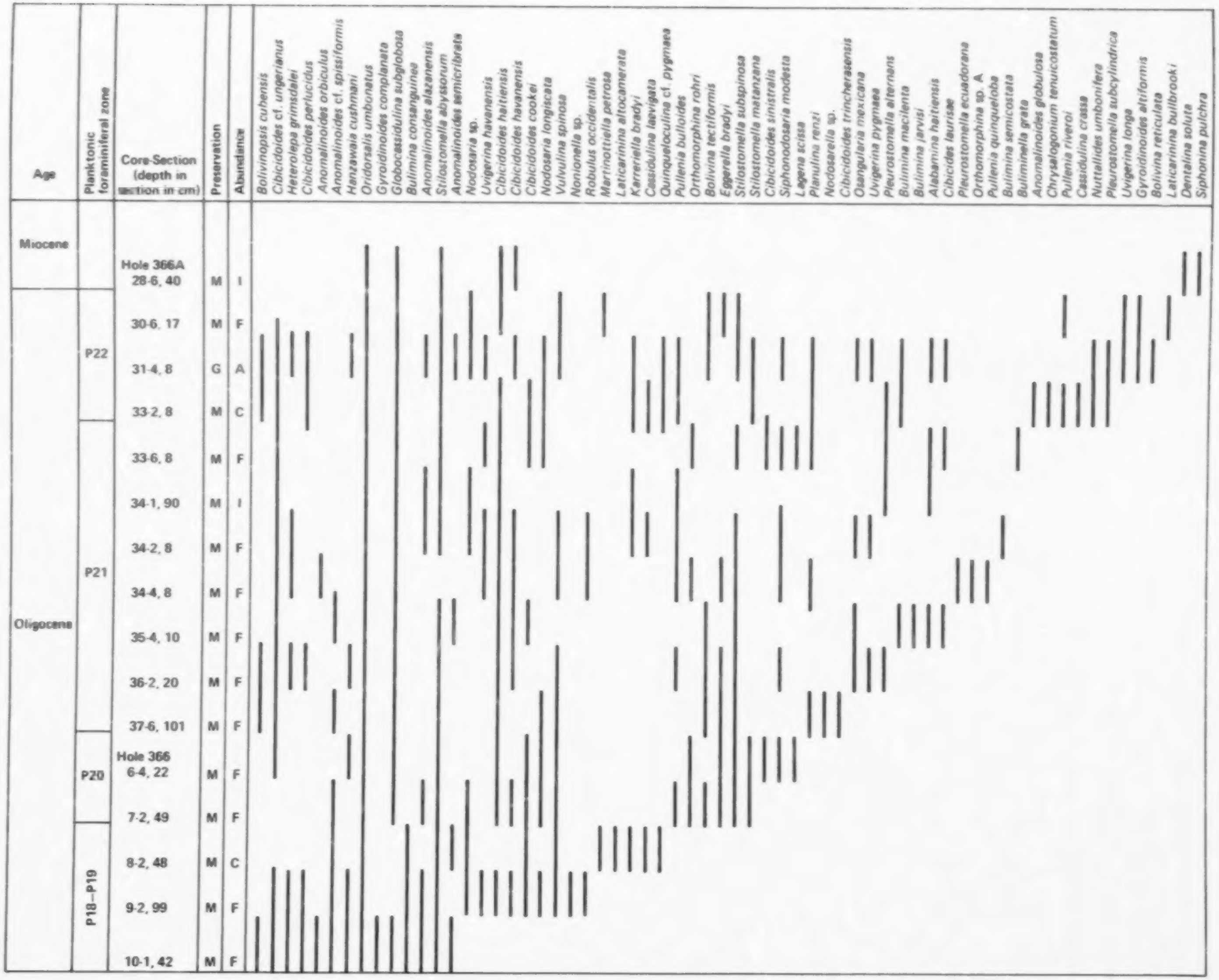

Figure 5. Stratigraphic distribution of the most common benthic foraminifers through the Oligocene at DSDP Site 366 (Holes 366 and 366A) in the equatorial North Atlantic. Abbreviations and zonal assignments as in Figure 2.

Bolivina tectiformis, Robulus spp., *Planulina renzi*, and *Anomalinoides globulosa* all occur at Sites 366 and 549, but not at the two deeper central North Atlantic sites.

Upper Oligocene faunas differ markedly from those below. *Bulimina semicostata* replaces *B. consanguinea* as the dominant buliminid. Other species that first occurred in the late Oligocene include *Pullenia quinqueloba, Alabamina haitiensis, Nuttallides umbonifera, U. pygmaea, U. longa*, and *Pleurostomella alternans*.

Distributional History of *Nuttallides umbonifera*

The distributional history of *Nuttallides umbonifera* is summarized in Figure 6 and Table 3 on the basis of its appearances and disappearances from the latest Eocene through the Oligocene at the 12 sites listed in Table 2. The first appearance of *N. umbonifera* at these sites, not considered here as the first evolutionary appearance (which Tjalsma and Lohman [1983] record in Zone P15), occurred at the time of the intensification of bottom and near-surface temperature decreases in the Atlantic Ocean during Zone-P16 time (around 37.5 Ma in Fig. 7). *N. umbonifera* occurred only in the western South Atlantic abyssal areas represented by *Vema* Core *V*20-220. There was, however, no eastern South Atlantic site of equivalent depth available to this study. I assume, nevertheless, that *N. umbonifera* initially adapted to and preferred the deepest, coldest areas of the South Atlantic Ocean. Tjalsma and Lohman (1983) also record *N. umbonifera* initially from DSDP Hole 20C, at a very deep central South Atlantic site.

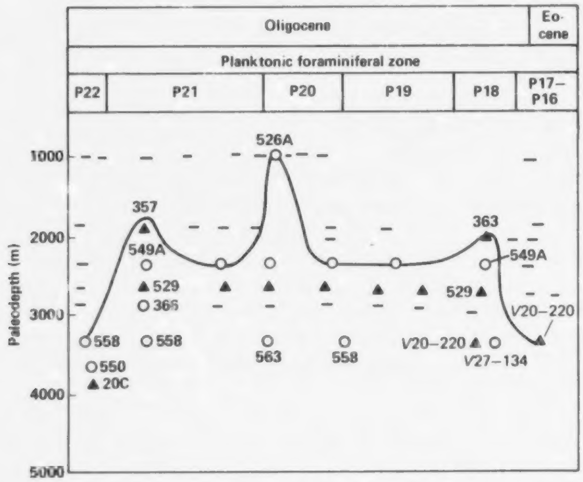

Figure 6. Schematic representation of the distribution of *Nuttallides umbonifera* through the latest Eocene and Oligocene in the Atlantic Ocean. Samples from the 12 sites listed in Table 1 were examined for this species; North Atlantic sites are indicated by open circles, South Atlantic sites by solid triangles. Samples examined for, but lacking, *N. umbonifera* are indicated by long dashes. Paleodepth estimates for the sites are taken from Supko, Perch-Nielsen, et al., 1977; Melguen, 1978; Moore, Rabinowitz, et al., 1984; and Boersma, 1984b. Sites 558, 563, and 549 are plotted slightly shallower than their actual drilling depths because their paleodepths are not presently available.

Table 3. Occurrence and abundance of *Nuttallides umbonifera* through the Oligocene and across the Eocene/Oligocene boundary in the North and South Atlantic.

Hole	Level[a]	Planktonic zone	Presence of *N. umbonifera*	*N. umbonifera* abundance
*V*20-220[b]	462	P16	X	3
526A	43,CC	P16	—	—
363	9-3, 117	P17	—	—
363	9-3, 67	P17	—	—
357	20-2, 40	P16	—	—
*V*27-134	260	P16	—	—
549A		P17	—	—
529	20-2, 120	P17	—	—
529	20-1, 120	P18–19	X	3
549A	13-9, 9	P18–19	X	1
366A	10-2, 42	P18–19	—	—
*V*27-134	180	P18–19	X	3
357	Cores 18 to 20	P18–19	—	—
*V*20-220	332	P18-19	X	3
558	23-4	P18-19	X	1
526A	Cores 41 to 37	P20	—	—
526A	Core 36	P20	X	4
563	20-3	P20	X	1
357	17-3	P21	X	1
366	33-2	P21	X	2
549A	8-4	P21	X	2
529	15-3	P21	X	3
558	21-3	P21	X	1
550	15,CC	P22	X	2
20C	2-1	P22	X	2
357	Cores 15 to 16	P22	—	—
549A	7-6	P22	—	—
366	30-6	P22	—	—
563	18-1	P22	—	—
558	19-4	P22	—	—
529	14-1	P22	X	2

Note: Since *N. umbonifera* made up $<1\%$ at all but Site 526, Core 526A-36, the table reflects its relative rarity at the various sites. 1 = very, very rare; 2 = very rare; 3 = rare; and 4 = 1% of the fauna picked from the >63 μm fraction. X indicates present; — indicates absent.

[a] Levels for *Vema* cores in cm. Levels at DSDP sites expressed as section-core, level in cm.

[b] *Vema* cores.

Just after the Eocene/Oligocene boundary event and following the isotopic event pictured in Figure 8, *N. umbonifera* migrated from the deep South Atlantic both upward into the 2000-m depth range in the South Atlantic and northward into the North Atlantic, where it occurred through approximately 2500 m depth. Sample refinement at Site 529 in the South Atlantic (Boersma, 1984a) indicates that *N. umbonifera* appeared some 20 cm above the level of the isotopic event; but an interval of strong dissolution bracketing the isotopic event may have erased part of the record of *N. umbonifera* there. Corliss (1981) also found an offset between faunal changes and the oxygen-isotopic event at the Eocene/Oligocene boundary.

Synchronous with the slight negative trend in oxygen isotopes in basal Zone P18–19 (shown on Figs. 7, 11B), *N. umbonifera* descends from the 2000-m depth range to levels below about 2500 m. The temporary disappearance of *N. umbonifera* from Site 529 at this time is accompanied by improved carbonate preservation and a pulse of miliolids (Fig. 9). The species is still more common in the South Atlantic than in the North Atlantic.

In basal Zone P18–19, shown on Figure 6, *N. umbonifera* descends from the 2000-m depth range to levels below about 2400–2500 m. The distribution of *N. umbonifera*, like the record of bottom temperatures, fluctuates only slightly through Zones P18–19 and into basal Zone P20. It appears, but is rare, during one interval in

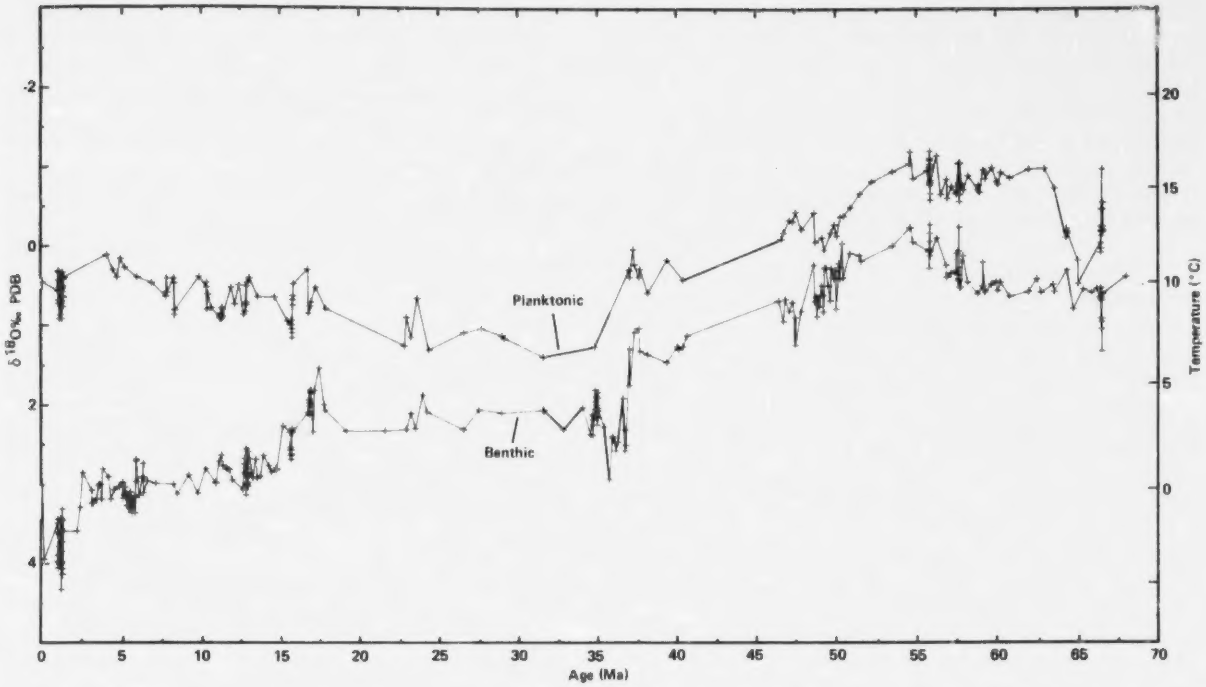

Figure 7. Oxygen isotope record in benthic and planktonic foraminifers, compiled from data for Sites 525, 526, and 529 on the Walvis Ridge (from Shackleton et al., 1984). Data are plotted on the time scale of Ness et al. (1980).

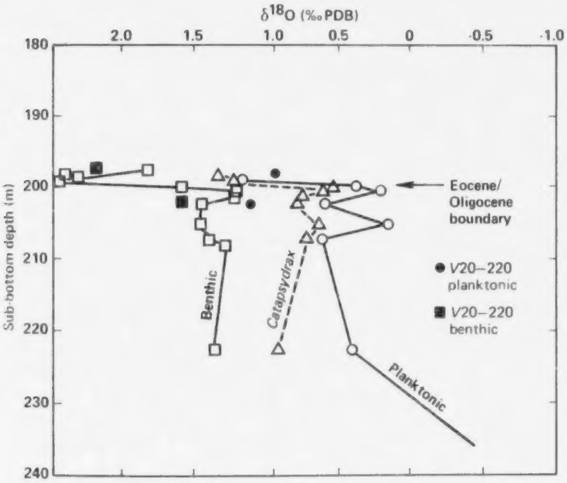

Figure 8. Oxygen-isotopic measurements across the Eocene/Oligocene boundary at DSDP Site 529 on the Walvis Ridge. The most negative value among the planktonic taxa measured was used to construct the planktonic curve. The most positive planktonic values were consistently registered by *Catapsydrax* spp. Benthic curves are composed of *Uvigerina* or *Bulimina* values and those for *Cibicidoides* spp. (from Shackleton et al., 1984).

Zone P18–19 at Site 558 (Fig. 2); the exact timing of this event is unclear, however, owing to uncertainties in the biostratigraphy. The species remains more common (though rare), and occurs more consistently, in the South Atlantic.

At most sites, *N. umbonifera* occurs with greater consistency beginning in Zone P20, although it is still very rare. For example, only two specimens were found in 0.5 g of sediment from Site 563. During Zone-P20 time it extended its depth range from near 3700 m to as shallow as 1000 m in the southeastern South Atlantic, and occupied most intermediate depths from 2000 to near 3700 m in both the North and the South Atlantic.

In one anomalous, brief instance, *N. umbonifera* ascended to nearly 900 m (Boersma, 1984b) at Site 526 on the Walvis Ridge (Fig. 10) during Zone-P20 time (about 32–33 Ma on Fig. 7). It constitutes up to 1% of the fauna, and is thus more abundant than at any other locality included in this study. Tjalsma (1983) does not, however, report finding this species in coeval Oligocene samples from Site 516, located at equivalent paleodepths on the Rio Grande Rise in the southwestern South Atlantic. Other faunal changes at this time at Site 526 (Figs. 10, 11A, Sample 526-37-3, 70 cm) include an increase in the ratio of rotaloid to rectilinear species, caused by a marked increase in large, fragmented robulinids; an increase in the benthic number from 249 to over 360 individuals; an increase in uvigerinids from more than 1% to over 8% of the picked fauna; a marked increase in pleurostomellids, in spinosity of buliminids, and in the ornamentation of several forms; and the first appearance of an Indo-Pacific morphotype, here called *Cibicidoides semiteres*. The overlying sample (526-37-2, 70 cm) contains the first incursion of several other Indo-Pacific morphotypes, including *Rectuvigerina postprandia*, a form characteristic of intermediate-depth ocean sites worldwide.

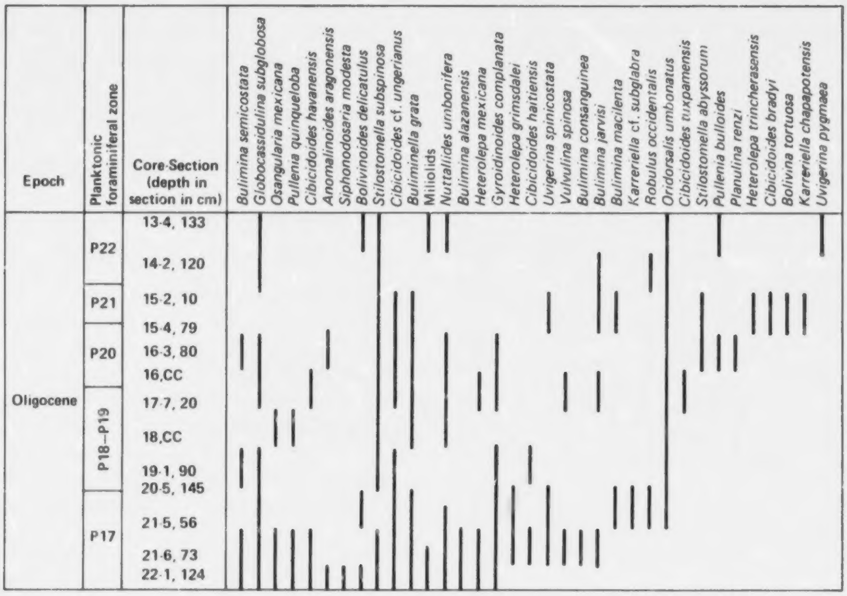

Figure 9. Stratigraphic distribution of the most common benthic foraminifers through the Oligocene at DSDP Site 529 on the Walvis Ridge.

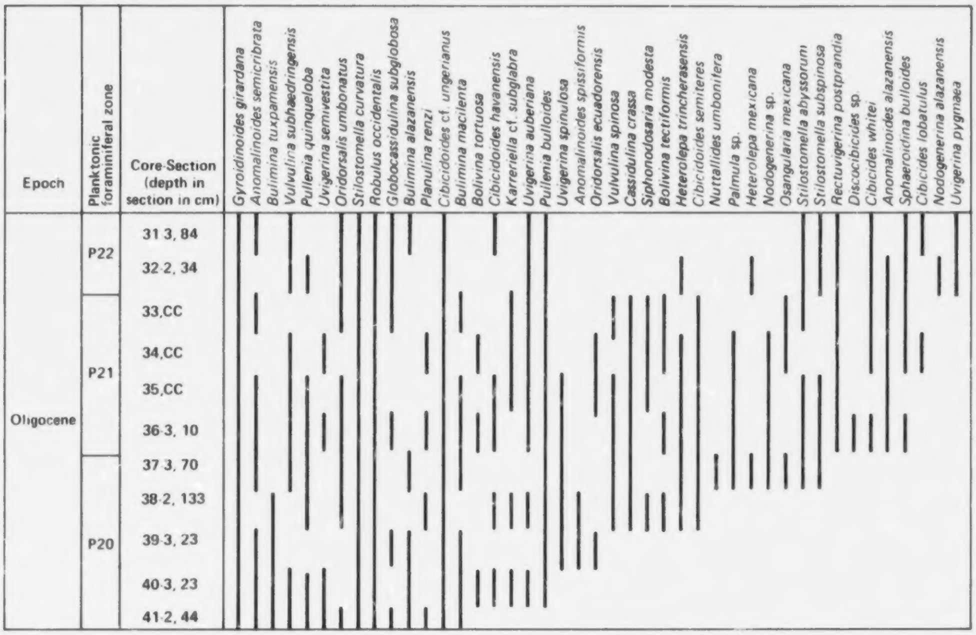

Figure 10. Stratigraphic distribution of the most common benthic foraminifers through the Oligocene at DSDP Site 526 (Hole 526A) on the Walvis Ridge.

Although sampling density is inadequate, the migration of the Indo-Pacific morphotypes, the indications of deteriorating carbonate preservation, and the increased abundance of uvigerinids all suggest the appearance of a different intermediate water impinging on the bottom at Site 526.

During Zone-P21b time, paralleling a slight positive trend in the bottom oxygen-isotope record (Fig. 7, about 26 Ma) which has been recorded also at DSDP Sites 357, 366, 526, and 529 (Boersma and Shackleton, 1977, 1978; Shackleton et al., 1984), *N. umbonifera* again ascended into the 2000-m depth range, just as it did after the Eocene/Oligocene boundary event. It spread, however, into a larger range of habitats, including Site 357 on the Rio Grande Rise and Site 366 on the North African margin, under a limited equatorial upwelling system. Again, it is more abundant in the South Atlantic than in the North Atlantic.

In conjunction with the negative trend in surface temperatures signaling the beginning of the late Oligocene-early Miocene warming, shown in Figure 7 at about 24-25 Ma, *N. umbonifera* disappeared from all but the deepest basins of the North and South Atlantic, where it occurred in nearly equal abundances.

To summarize: *N. umbonifera* appeared first in the late Eocene in the South Atlantic, where it resided only in abyssal areas. Immediately after the proposed Eocene/Oligocene boundary event and the increased carbonate dissolution at deep sites, *N. umbonifera* spread through the North and South Atlantic from abyssal depths to near 2500 m. It was more abundant and occurred more consistently in the South Atlantic, suggesting that it was occupying conditions closer to its preferred water type. *N. umbonifera* ascended into the 2000-m range both after the Eocene/Oligocene boundary event, during Zone-P20 time, (it occurs most consistently in Atlantic samples of Zone P20), and in Zone-P21b time, when (on the evidence of the oxygen-isotope record) cooling of bottom waters took place. This species occupied only abyssal areas in Zone-P16 time, during the gradual temperature drop preceding the Eocene/Oligocene boundary event, and again in Zone-P22 time, during the beginning phases of the late Oligocene to early Miocene warming. In this latter period, *N. umbonifera* occurred in nearly equal numbers at the North and South Atlantic sites and spread into areas of equatorial upwelling for the first time.

BENTHIC FORAMINIFERS AS POSSIBLE TRACERS OF BOTTOM-WATER MASS PROPERTIES

From studies of Quaternary benthic foraminifers, correlations have been suggested between the frequencies of benthic foraminiferal species and various properties of bottom-water masses. Properties of bottom or surface waters, which are reflected in the character of the sediment, are most likely to affect benthic foraminifers. It is thus feasible to seek similar relationships among Paleogene benthic foraminifers, particularly because several species already studied from the Pleistocene first occurred in the later Paleogene. Therefore, the data base of this study was expanded to include all Oligocene cores from the 12 sites listed in Table 1, in order to track faunal changes from both the South Atlantic and the North Atlantic, and to include the Eocene/Oligocene boundary as well. Benthic foraminiferal ranges from two additional sites, 529 and 526 on the Walvis Ridge, are shown in Figures 9 and 10.

In Quaternary studies, several forms have been related to carbonate saturation levels in bottom waters. Miliolids and *Nuttalides umbonifera* behave inversely with respect to carbonate saturation (Bremer and Lohman, 1982), whereas rectilinear species in general reflect less carbonate dissolution in ancient sediments (Woodruff, 1979). In the Paleogene of Sites 558 and 563, rectilinear benthic forms increase relative to rotaloid forms in the better-preserved samples. At Site 529, miliolids first appear in the better-preserved samples just above the dissolution interval marking the Eocene/Oligocene boundary. *N. umbonifera* first appears during this same dissolution interval. It is therefore possible that these forms may reflect the state of carbonate preservation in the Paleogene, as they appear to do in the Quaternary.

In other studies of Quaternary benthic foraminifers, *N. umbonifera* is considered an index of Antarctic Bottom Water (AABW) (Schnitker, 1974), a "new" cooled bottom-water type deriving from the Antarctic. Bremer and Lohman (1982) suggest, however, that *N. umbonifera* may be related primarily to carbonate saturation levels in waters such as AABW and may characterize other bottom waters similarly corrosive to carbonates. By analogy, *N. umbonifera* may be useful as a tracer for Antarctic-derived "new" and corrosive water masses in the Paleogene.

Evidence at the Eocene/Oligocene boundary for the initiation of a cooled, "new" water mass deriving from the Antarctic region includes (1) the concurrent increase in sediment erosion in the North Atlantic (Tucholke and Vogt, 1979); (2) increased clay entrainment in a new bottom-water current through the Argentine Basin (Supko, Perch-Nielsen, et al., 1977); (3) increased dissolution of carbonate in deep South Atlantic basins and its replacement by siliceous sediments (McCoy and Zimmerman, 1977); (4) a discrete dissolution interval across the Eocene/Oligocene boundary at deep South Atlantic sites such as Site 529 on the Walvis Ridge (Boersma, 1984b); and (5) a strong positive peak in oxygen isotopes at the bottom (Figure 8), which is now considered to represent both a decrease in bottom-water temperatures (Shackleton and Kennett, 1975; Keigwin, 1980; Vernaud Grazzini, et al., 1979) and a compositional effect resulting from the increased volume of Antarctic glacial mass (Mathews and Poore, 1980; Shackleton et al., 1984).

This evidence suggests the origination of a "new" and erosive, cooled bottom water deriving from the south, presumably from the Antarctic region, correlative with the glacial episode at the Eocene/Oligocene boundary. The idea that these cooled, Antarctic-derived waters would penetrate into the abyssal North Atlantic is corroborated by recent evidence on Atlantic equatorial fracture zones, which indicates that passage was possible through deep channels as early as the Eocene in both the Romanche and Vema fracture zones (Bonatti et al., 1977).

Support for a southern origin of this bottom water comes also from carbon-isotopic evidence. Carbon-isotopic patterns in the Recent Pacific Ocean (Kroopnick, 1974) indicate that benthic foraminiferal ^{13}C should be depleted in "older" water which has also become increasingly depleted in oxygen along its course (Broecker, 1974). Boersma and Shackleton (1978) demonstrated south-to-north depletion in benthic foraminifers throughout the South Atlantic during the time corresponding to Oligocene Zones P18–P19. Although there are isotopic disequilibrium effects and inter-ocean and intra-ocean

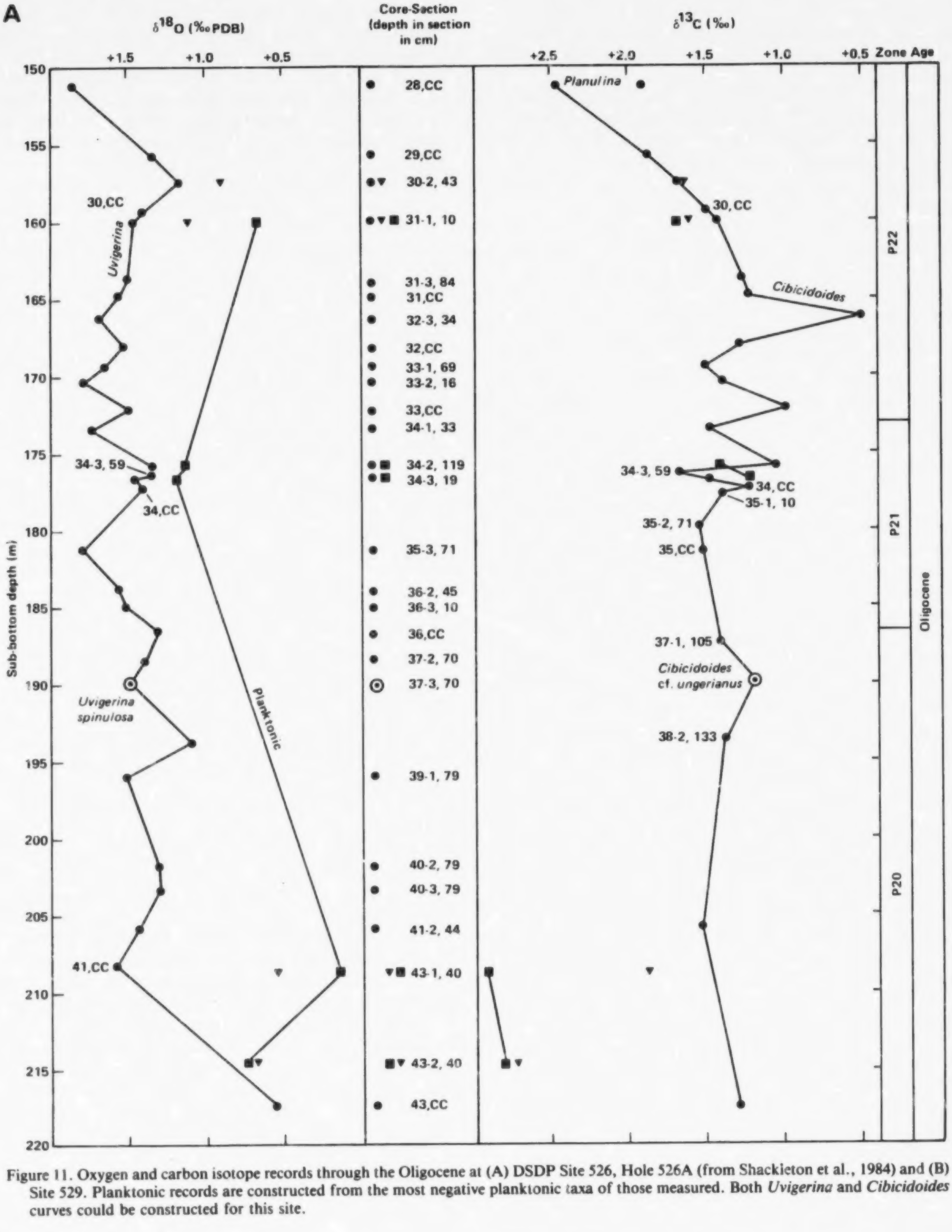

Figure 11. Oxygen and carbon isotope records through the Oligocene at (A) DSDP Site 526, Hole 526A (from Shackleton et al., 1984) and (B) Site 529. Planktonic records are constructed from the most negative planktonic taxa of those measured. Both *Uvigerina* and *Cibicidoides* curves could be constructed for this site.

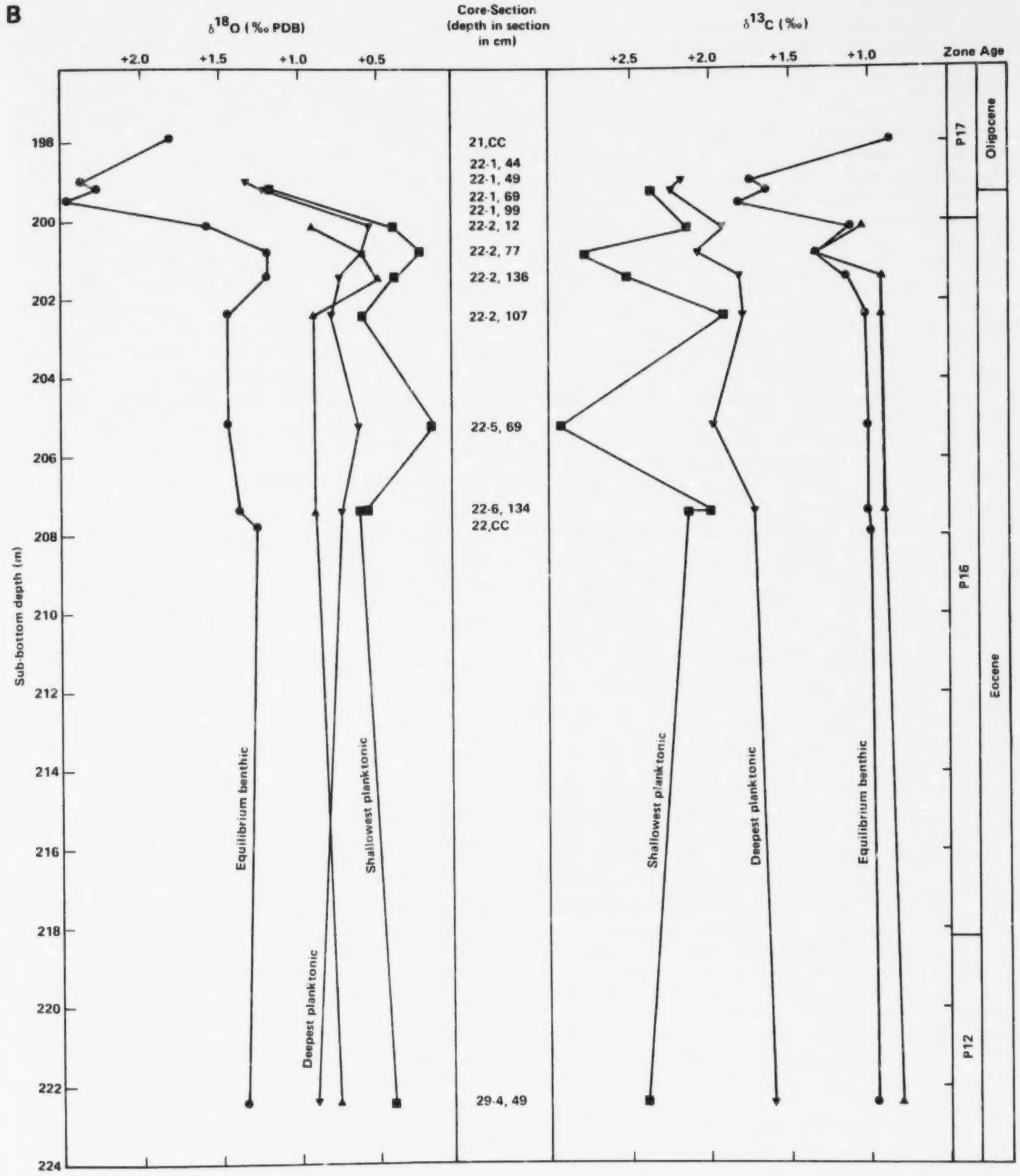

Figure 11. (Continued).

complexities in ^{13}C patterns, Table 4 demonstrates clear south-to-north depletion in ^{13}C beginning just above the Eocene/Oligocene boundary, but not below it. Although more synoptic data should be acquired, the data available at present corroborate a southern origin of the cooled mass of bottom waters after the Eocene/Oligocene boundary event.

If *N. umbonifera* can be used to trace cooled and corrosive bottom waters, one may wonder at its presence during Zone-P20 time at Site 526, with a paleodepth near 800 to 1000 m. As discussed in the preceding section, faunal changes suggest that during that time a different intermediate-water mass appeared, impinging on the bottom at Site 526. Faunal and isotopic evidence both suggest a southern source of this intermediate-water mass. The presence of Indo-Pacific benthic forms implies a connection to that region. Indo-Pacific species had migrated into the Mediterranean (Braga et al., 1975) and into intermediate-depth sites of the equatorial Atlantic, the Bay of Biscay (Schnitker, 1979), and the Gulf of Mexico during the middle Eocene. Several different deep-water species are reported from the Paleogene of DSDP Site 360 in the Cape Basin (Proto Decima and Bolli, 1978). They did not occur at intermediate-depth eastern South Atlantic sites, however, before Zone-P20 time. The additional fact that similar species are not recorded from the southwestern Atlantic intermediate-depth sites on the Falkland Plateau or Rio Grande Rise (Tjalsma, 1977; 1983) further suggests the derivation of these forms from the direction of the Indian Ocean.

Isotopic evidence from the South Atlantic has demonstrated a stronger connection between the Indian Ocean and the middle-latitude southeastern Atlantic than between the southeastern and southwestern Atlantic. Evidence for this connection includes a strong east-west middle-latitude paleotemperature gradient, which resulted from the strong influence of equatorially derived near-surface waters in the southwestern Atlantic (Boersma and Premoli Silva, 1983). Intermediate-depth bottom waters in the southeastern Atlantic were slightly cooler than in the southwestern Atlantic, though there was little overall temperature gradient through depth before the Eocene/Oligocene boundary event (Shackleton and Boersma, 1981). The paleotemperature data thus suggest circulation between the southeastern Atlantic and higher latitudes to the south and the southeast.

Unfortunately, isotopic data for Site 526 (Fig. 11) show no marked changes during Zone-P20 time correlative with the incursion of *N. umbonifera* into the 1000-m paleodepth range. In view of the faunal changes already discussed, it is clear that a change at the bottom had occurred. It is possible, therefore, that isotopic measurements at this site contain a diagenetic overprint. Shackleton et al. (1984) also suggest a problem with intermediate depth measurements, on the basis of anomalou comparative benthic oxygen-isotopic values.

Kennett et al. (1975), Kennett (1980), and Jenkin (1979), among others, have proposed initiation of a fully circum-Antarctic surface circulation by late Oligocene time. The exact timing of this event remains uncertain, but possibly the pulse of *N. umbonifera* at shallow depths in the South Atlantic reflects the northern influence of the initiation of a "new," more corrosive intermediate water of southern origin, generated by the progressive opening of the Indian Ocean to the Pacific before the establishment of a fully circum-Atlantic surface circulation.

Table 4. Carbon isotopic measurements ($\delta^{13}C$, ‰) on Atlantic Eocene–Oligocene benthic foraminifers.

V27-202 Cape Basin	529 Walvis Ridge	357 Rio Grande Rise	V20-220 Brazil Basin	94 Gulf of Mexico	548 Bay of Biscay	V27-134 Bay of Biscay
1.12	1.12	0.47	0.60	1.13	1.27	—
			Eocene			
			Oligocene			
1.30	1.95	—	1.73	—	0.74	0.45

Note: Data are from Shackleton et al. (1984) and from N. J. Shackleton, A. Boersma, unpublished data. All values are based on measurements of *Cibicidoides* sp. or are corrected to *Cibicidoides* according to the factors determined by Boersma and Shackleton (1977) and Shackleton et al. (1984). Samples are arranged from south to north. Eocene values are the uppermost Eocene measured at each site except Site 357, which is Zone P16 in age. Oligocene measurements are from the lowermost Oligocene at all sites.

The Evolution of Neogene Faunas and Water-Mass Structure

The appearance of several typically Neogene benthic foraminiferal species in the late Oligocene in the Atlantic Ocean changed the general aspect of both deep-water and intermediate-water benthic foraminiferal assemblages, giving them a more "Neogene character" for the first time. These species include *Uvigerina pygmaea, Rectuvigerina postprandia, Pullenia quinqueloba, Alabamina haitiensis, Trifarina bradyi, Eggerella bradyi, Heterolepa kullenbergi*, and an as yet unidentified species of *Textularia*, called *Textularia* sp. A. The first occurrences of four of these species from north to south in the Atlantic are shown in Figure 12.

All these species are recorded first from the South Atlantic. Except for *E. bradyi, T. bradyi*, and *R. postprandia*, all first occurred in the deeper-water Sites 366, 529, and 357 in the South Atlantic and equatorial Atlantic during Zone-P21b time, synchronously with the extinction of *Chiloguembelina* spp. At South Atlantic intermediate-depth Site 526, the major change in species occurred first in Zone-P20 time with the appearances of a characteristic southwestern Pacific/early Oligocene cibicidid–anomalinid fauna (Boersma, 1984b) (which was more typical of the late Oligocene and early Neogene in the southeastern Atlantic), of *Nuttallides umbonifera*, of the rectuvigerinids, and of several shallower-water forms such as *Nodogenerina* sp. and *Palmula* sp. (Fig. 10). Later in Zone-P21 time, several other of the characteristically Neogene species already listed first occurred at Site 526. Concurrently there was a sharp drop in specific diversity and in the overall abundance of benthic forms, paralleling an increase in sedimentation rate, which continued through the earliest Neogene at this site.

The appearances of these same taxa at deeper-water North Atlantic Sites 558, 563, and 549 were delayed until Zone-P21b–P22 time (Figs. 2–4), and accompanied

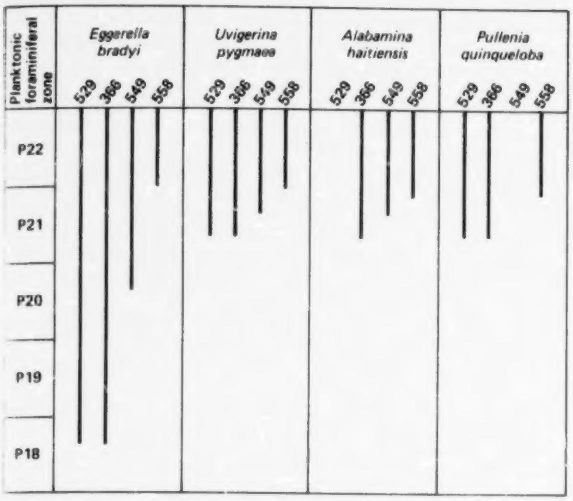

Figure 12. Stratigraphic distribution of four benthic species through the Oligocene at South Atlantic Site 529 on the Walvis Ridge, equatorial North Atlantic Site 366, Site 549 in the Bay of Biscay, and central North Atlantic Site 558. Data are summarized from Figures 2, 4, 5, and 9.

the retraction of *N. umbonifera* to deep ocean basins. Concurrently, a fauna containing *Heterolepa mexicana* first moved into the Bay of Biscay. Before this time, the *H. mexicana* fauna (called the *Cibicidoides mexicanus* fauna) is reported to have lived at bottom sites underlying the Norwegian Sea (Berggren and Schnitker, in press).

If benthic foraminiferal faunas reflect physicochemical water-mass properties as they affect the sediment/water interface and hence the sediment in the Paleogene as they appear to do in the Quaternary, then it can be stated that a more typically Neogene water-mass stratification occurred diachronously through depth and between the North and South Atlantic. Deeper sites developed a Neogene character slightly later than shallow- er areas, and the North Atlantic later than the South Atlantic.

CONCLUSIONS

Comparison of Oligocene North Atlantic faunas from ites 558, 563, 549, and 366 produced the following esults:

1. At the two deepest sites, 558 and 563, with drilling epths near 3700 m, individuals of most species are smal- er than at the two shallower sites, 549 and 366, both lo- ated in areas of moderate silica production. The per- entages of rectilinear species are less at the deeper Sites 58 and 563. Diversity, expressed as species richness, is lso lower at the two deeper sites, which, in addition, of- en show the effects of significant carbonate dissolution.

2. Dissolution-resistant taxa include *Globocassiduli- na subglobosa, Stilostomella abyssorum, Cibicidoides* f. *ungerianus*, and *Pleurostomella alternans*.

3. Criteria signaling decreased dissolution and possi- bly increased carbonate saturation levels include an in- crease in the rectilinear:rotaloid ratio and pulses of mili- olids.

4. A "Barbados" fauna occurs at equatorial Site 366 and developed to a lesser degree at Site 549 in the Bay of Biscay. Diversity is highest at Site 366, where intrageneric diversity is particularly high among the uvigerinids, cibicidids, anomalinids, nodosariids, and pleurostomellids. Robulinids are present, though not abundant, at Sites 549 and 366, but absent at the two deeper central Atlantic sites.

5. The New Zealand species *Laticarinina altocamerata, Anomalinoides semiteres*, and *Rectuvigerina postprandia*, and the Indo-Pacific genus *Heronallenia* all migrated into the Atlantic during Oligocene time.

6. Sites 558 and 563 contain only large spino-costate uvigerinids in the lower Oligocene. A peak of uvigerinids accompanies a pulse of radiolarians in Zone P20 in the Bay of Biscay. Uvigerinids were diverse, only for a short period during Zone-P22 time at equatorial Site 366; *U. pygmaea* is the only common form of the genus in the upper Oligocene at all sites.

Comparison of coeval North and South Atlantic faunas to identify water-mass or biogeographic index species, and to determine their relation to the reorganization of oceanic circulation during the climatic shifts of the Oligocene, provides a basis for proposing the following summary interpretations:

1. The distribution of *Nuttallides umbonifera* parallels in general the oxygen-isotopic record of paleotemperatures. When bottom temperature dropped, *N. umbonifera* spread more widely through the North and South Atlantic and migrated upslope to depths near 2000 m in the South Atlantic and 2500 m in the North Atlantic. During the apparent warming of near-surface temperatures at the end of the Oligocene, *N. umbonifera* was restricted to deepest basinal areas. This species was generally more abundant, and occurred more consistently, in the South Atlantic.

2. In the Oligocene the distribution of *N. umbonifera* from north to south and through the 2000–4000-m paleodepth range is an indicator of the pathway and distribution of "new" and/or cooled water-mass types, which aged from south to north thus demonstrating their southern origin.

3. The unusual occurrence and abundance of *N. umbonifera* near 900 m paleodepth on the Walvis Ridge at Site 526 during Zone-P20 time is interpreted to indicate the first influx of "new," surface-derived intermediate water, signaling the initiation of a circum-Antarctic circulation, which was fully developed in the late Oligocene. In this case the occurrence of *N. umbonifera* corresponds to the development of a "new" oxygenated, but not necessarily cooled, water type at the bottom.

4. The evolution of typically Neogene water-mass stratification in the North and South Atlantic is indicated by the appearances of typically Neogene benthic foraminiferal species through the latest Oligocene Zones P20–P22. The appearances of these species suggest that the South Atlantic was restructured first by the introduction of a new intermediate-water in Zone-P20 time, which was followed by a new deep-water type later in Zone-P21b time. The North Atlantic, however, apparently acquired a more typically Neogene water-mass stratifica-

tion in Zone-P22 time with the influx of deep waters possibly deriving from the Norwegian-Greenland Sea area.

ACKNOWLEDGMENTS

I would like to thank the scientists from DSDP Leg 82 for allowing me to study materials from their cruise. Thanks are also due to Dr. N. J. Shackleton for providing oxygen-isotopic and carbon-isotopic measurements on the foraminifers, and Drs. Leonard Tjalsma and Bill Sliter for critical review of the manuscript.

REFERENCES

Beckman, J. P., 1953. Die Foraminiferen der Oceanic Formation (Eocaen-Oligocaen) von Barbados, kl. Antillen. *Eclogae Geol. Helv.*, 46:301-412.

Berggren, W. A., and Aubert, J., 1975. Paleocene benthic foraminiferal biostratigraphy, paleobiogeography, and paleoecology of the Atlantic-Tethyan regions: Midway-type fauna. *Palaeogeogr., Palaeoclimatol., Palaeocol.*, 18:73-192.

Berggren, W. A., and Schnitker, D., 1983. Cenozoic marine environments in the North Atlantic and Norwegian-Greenland Sea. *In* Saxov, S. (Ed.), *Structure and Development of the Greenland-Scotland Ridge (NATO Adv. Res. Inst., Bressanne, Italy, 1981):* New York (Plenum Press), pp. 495-548.

Bettenstaedt, R. L., and Wicher, L., 1955. Stratigraphic correlation of Upper Cretaceous and Lower Cretaceous in the Tethys and Boreal by the aid of microfossils. *Proc. 4th World Pet. Congr.*, Sec. I/D, pap. 5:494-516.

Boersma, A., 1977. Eocene-Oligocene benthic Foraminifera—DSDP Leg 39 (South Atlantic). *In* Supko, P. R., Perch-Nielsen, K., et al., *Init. Repts. DSDP*, 39: Washington (U.S. Govt. Printing Office), 567-591.

________, 1984a. Cretaceous-Tertiary planktonic foraminifers from the southeastern Atlantic, Walvis Ridge Area, Deep Sea Drilling Project, Leg 74. *In* Moore, T. C., Jr., Rabinowitz, P. D., et al., *Init. Repts. DSDP*, 74: Washington (U.S. Govt. Printing Office), 501-524.

________, 1984b. Pliocene planktonic and benthic foraminifers from the southeastern Atlantic Angola Margin: Leg 75, Site 532, Deep Sea Drilling Project. *In* Hay, W. W., Sibuet, J.-C., et al., *Init. Repts. DSDP*, 75: Washington (U.S. Govt. Printing Office), 657-670.

Boersma, A., and Premoli Silva, I., 1983. Paleocene planktonic foraminiferal biogeography and the paleooceanography of the Atlantic Ocean. *Micropaleontology*, 29:355-381.

Boersma, A., Shackleton, N. J., 1977. Tertiary oxygen and carbon isotopic stratigraphy: Site 357 (mid-latitude South Atlantic). *In* Supko, P. R., Perch-Nielsen, K., et al., *Init. Repts. DSDP*, 39: Washington (U.S. Govt. Printing Office), 911-924.

________, 1978. Oxygen and carbon isotope record through the Oligocene, DSDP Site 366, equatorial Atlantic. *In* Lancelot, Y., Siebold, E., et al., *Init. Repts. DSDP*, 41: Washington (U.S. Govt. Printing Office), 957-962.

Bonatti, E., Sarntheim, M., Boersma, A., Gorini, M., and Honnorez, J., 1977. Crustal emersion and subsidence in the Romanche Fracture Zone, equatorial Atlantic. *Earth Planet. Sci. Lett.*, 35:369-383.

Braga, G., de Biase, R., Grunig, A., and Proto Decima, F., 1975. Foraminiferi bentonici del Paleocene ed Eocene della sezione di Possagno. *Schweiz. Palaontol.*, 97:85-111.

Bremer, M., and Lohman, G., 1982. Evidence for primary control of the distribution of certain Atlantic Ocean benthonic Foraminifera by degree of carbonate saturation. *Deep-Sea Res.*, 29:987-998.

Broecker, W., 1974. *Chemical Oceanography:* New York (Harcourt Brace Jovanovich).

Brouwer, J., 1965. Agglutinated foraminiferal faunas from some turbidite sequences. *I. Koninkl. Ned. Akad. Wetenschap. Proc.*, 68: 309-334.

Corliss, J., 1981. Deep-Sea benthonic foraminiferal faunal turnover near the Eocene/Oligocene boundary. *Mar. Micropaleontol.*, 6: 367-384.

Dean, W., Gardner, J., Jansa, L. F., Cêpek, P., and Seibold, E., 1978. Cyclic sedimentation along the continental margin of northwest Africa. *In* Lancelot, Y., Seibold, E., et al., *Init. Repts. DSDP*, 41: Washington (U.S. Govt. Printing Office), 965-991.

Finlay, H. J., 1939. New Zealand Foraminifera. Key species in stratigraphy, no. 3. *Trans. Proc. Roy. Soc. N. Z.*, 69:309-329.

Gradstein, F., and Berggren, W. A., 1981. Flysch-type agglutinated Foraminifera and the Maestrichtian to Paleogene history of the Labrador and north seas. *Mar. Micropaleontol.* 6:211-268.

Hardenbol, J., and Berggren, W. A., 1978. A new Paleogene numerical time scale. *Am. Assoc. Pet. Geol.*, Studies in Geology, 6 213-234.

Jenkins, D. G., 1979. *Guembelitria* aff. *stavensis* Bandy, a paleo oceanographic marker of the initiation of the circum-Antarcti current and the opening of the Drake Passage. *In* Bolli, H. M., Ryan, W. B. F., et al., *Init. Repts. DSDP*, Suppl. to Vols. 38, 39, 40 and 41, Pt. III: Washington (U.S. Govt. Printing Office), 687-695

Keigwin, L., 1980. Paleooceanographic change in the Pacific at th Eocene/Oligocene boundary. *Nature*, 287:722-725.

Kennett, J. P., 1980. Paleooceanographic and biogeographic evolutio of the Southern Ocean during the Cenozoic, and Cenozoic micro fossil datums. *Palaeogeogr., Palaeoclimatol., Palaeoecol.*, 31 123-152.

Kennett, J. P., and Shipboard Scientific Party, 1975. Antarctic glaciation and the development of the circum-Antarctic current. *In* Ke nett, J. P., Houtz, R. E., et al., *Init. Repts. DSDP*, 29: Washington (U.S. Govt. Printing Office), 1155-1170.

Kroopnick, P., 1974. Correlation between ^{13}C and CO_2 in surface waters and atmospheric CO_2. *Earth Planet. Sci. Lett.*, 22:397-403.

Lutze, G. F., 1978. Neogene benthonic Foraminifera from Site 369 Leg 41, Deep Sea Drilling Project. *In* Lancelot, Y., Seibold, E., e al., *Init. Repts. DSDP*, 41: Washington (U.S. Govt. Printing Office), 659-666.

McCoy, F., and Zimmerman, H., 1977. A history of sediment lithofacies in the South Atlantic Ocean. *In* Supko, P. R., Perch-Nielsen, K., et al., *Init. Repts. DSDP*, 39: Washington (U.S. Govt. Printing Office), 1047-1079.

Mathews, R., and Poore, R., 1980. Tertiary ^{18}O record and glacio-eustatic sea level fluctuations. *Geology*, 8:501-504.

Melguen, M., 1978. Facies evolution, carbonate sediments from eastern South Atlantic (DSDP Leg 40) since the early Cretaceous. *In* Bolli, H. M., Ryan, W. B. F., et al., *Init. Repts. DSDP*, 40: Washington (U.S. Govt. Printing Office), 981-1025.

Miller, K., 1982. Late Paleogene (Eocene to Oligocene) paleooceanography of the northern North Atlantic [unpublished Ph.D dissertation]. Woods Hole Oceanographic Inst.

Moore, T. C., Jr., Rabinowitz, P. D., et al., 1984. *Init. Repts. DSDP*, 74: Washington (U.S. Govt. Printing Office).

Ness, G., Levi, S., and Couch, R., 1980. Marine magnetic anomaly timescales for the Cenozoic and Cretaecous. *Rev. Geophys. Space Phys.*, 18:753-770.

Nuttall, W. L. F., 1932. Lower Oligocene Foraminifera from Mexico. *J. Paleontol.*, 6(1):3-35.

Proto Decima, F., and Bolli, H., 1978. Southeastern Atlantic Leg 40 Paleogene benthic Foraminifera. *In* Bolli, H. M., Ryan, W. B. F., et al., *Init. Repts. DSDP*, 40: Washington (U.S. Govt. Printing Office), 783-809.

Rey, M., 1954. Comparison des microfaunes du Nummulitique Nord Marocain et du Golfe du Mexique et de la Mer des Caraïbes. *Int Geol. Congr. Alger.*, pp. 39-60.

Savin, S., 1977. The history of the earth's surface temperature during the past 100 million years. *Annu. Rev. Earth Planet. Sci.*, 5 319-355.

Schnitker, D., 1974. Western Atlantic abyssal circulation during th past 120,000 years. *Nature*, 248:385-387.

________, 1979. Cenozoic deep water benthic Foraminifera, Bay o Biscay. *In* Montadert, L., Roberts, D. G., et al., *Init. Repts DSDP*, 48: Washington (U.S. Govt. Printing Office), 377-413.

Shackleton, N. J., and Boersma, A., 1981. The climate of the Eocen ocean. *J. Geol. Soc., London*, 138:153-157.

Shackleton, N. J., Hall, M. A., and Boersma, A., 1984. Oxygen an carbon isotope data from Leg 74 foraminifers. *In* Moore, T. C Jr., Rabinowitz, P. D., et al., *Init. Repts. DSDP*, 74: Washingto (U.S. Govt. Printing Office), 599-612.

Shackleton, N. J., and Kennett, J. P., 1975. Paleotemperature histor of the Cenozoic and the initiation of Antarctic glaciation: oxyge and carbon isotope analyses in DSDP Sites 277, 279 and 284. *I* Kennett, J. P., Houtz, R. E., et al., *Init. Repts. DSDP*, 29: Washington (U.S. Govt. Printing Office), 743-755.

Streeter, S., 1973. Bottom water and benthic Foraminifera in the North Atlantic: Glacial:interglacial contrasts. *Quat. Res.*, 3: 131–141.

Supko, P. R., Perch-Nielsen, K., et al., 1977. *Init. Repts. DSDP*, 39: Washington (U.S. Govt. Printing Office).

Tjalsma, R. C., 1977. Cenozoic Foraminifera from the South Atlantic, DSDP Leg 36. *In* Barker, P., Dalziel, I. W. D., et al., *Init. Repts. DSDP*, 36: Washington (U.S. Govt. Printing Office), 493–517.

_______, 1983. Eocene to Miocene benthic foraminifers from DSDP Site 516, Rio Grande Rise, South Atlantic. *In* Barker, P. F., Carlson, R. L., Johnson, D. A., et al., *Init. Repts. DSDP*, 72: Washington (U.S. Govt. Printing Office), 731–755.

Tjalsma, R. C., and Lohmann, G. P., 1983. Paleocene-Eocene bathyal and abyssal benthic Foraminifera from the Atlantic Ocean. *Micropaleontology Spec. Publ.* 4.

Tucholke, B., and Vogt, P., 1979. Western North Atlantic: sedimentary evolution and aspects of tectonic history. *In* Tucholke, B. E., Vogt, P. R., et al., *Init. Repts. DSDP*, 43: Washington (U.S. Govt. Printing Office), 791–826.

Vernaud Grazzini, C., Müller, C., Létolle, C. P., Peypouquet, J., 1979. Stable isotopes and Tertiary paleontological paleooceanography in the northeast Atlantic. *In* Montadert, L., Roberts, D. G., et al., *Init. Repts. DSDP*, 48: Washington (U.S. Govt. Printing Office), 475–491.

Woodruff, F., 1979. Deep sea benthic foraminiferal changes associated with the middle Miocene oxygen isotopic event, DSDP Site 289, equatorial Pacific [unpublished Ph.D. thesis]. Univ. of Southern California, Los Angeles, California.

Date of Initial Receipt: 1 August 1983
Date of Acceptance: 2 March 1984

38. CARBONATE AND COARSE FRACTION RECORDS OF THE PLEISTOCENE INTERVAL IN THE NORTH ATLANTIC, HYDRAULIC PISTON CORER HOLE 558A[1]

Gordon G. Start, Department of Geological Sciences, Brown University[2]

ABSTRACT

Carbonate and coarse fraction data from Hole 558A record variations in the carbonate system for the Pleistocene. The late Pleistocene carbonate record from Hole 558A can be correlated to Atlantic carbonate records with similar accumulation rates. The correlation between carbonate and coarse fraction record in Hole 558A does not remain constant. The early Pleistocene carbonate-coarse fraction correlation is opposite of the typical North Atlantic pattern, whereas late Pleistocene carbonate-coarse fraction correlation does not show consistent pattern. The different relationships between the carbonate and coarse fraction records suggests that the carbonate system in the North Atlantic changed between the early and late Pleistocene.

INTRODUCTION

Information about local and global ocean climate is provided by a variety of indexes from deep-sea sediments, such as oxygen isotopic values from foraminiferal tests (Emiliani, 1955); sediment composition (Arrhenius, 1952); and faunal abundances (Phleger et al., 1953). In late Pleistocene deep-sea sediments, the carbonate record has long been recognized as a monitor climatic change (Arrhenius, 1952; Ruddiman, 1971; Volat et al., 1980). However, the exact relationship between climate and carbonate systems varies between ocean basins (Volat et al., 1980). In late Pleistocene Atlantic sediments, low carbonate values correspond with glacial intervals and high carbonate values with interglacial intervals. This covariance is termed the "Atlantic-type" pattern. The Atlantic pattern also has high coarse fraction values during interglacials and low coarse fraction values during glacials (Broecker, 1971; Prell, 1978).

The oxygen isotope composition of foraminifers has been established as a measure of the climatic system to which other indexes are compared. The isotopic variations reflect changes in the amount of continental ice volume (Shackleton, 1967). In this paper, the oxygen isotope curve will be used as the measure of the variations in the climatic system.

Prell (1982) described two modes of variability in the $\delta^{18}O$ record for the Pleistocene. These two modes of variability span about equal periods of time and provide a simple division of the Pleistocene into two units: a late Pleistocene (0 to 0.8 Ma) and an early Pleistocene (0.8 Ma to the Pliocene/Pleistocene boundary). These informal units can be applied to the isotopic and other records of climatic variability.

Carbonate variations are not directly dependent on climate variations, but are linked to the climate system through a complex function of a large number of variables (Berger, 1976; Volat et al., 1980; Broecker and Peng, 1982). The majority of carbonate variance can, however, be expressed as a function of three primary factors: productivity, dissolution, and dilution. Upper Pleistocene North Atlantic carbonate values have been shown to be directly related to the noncarbonate (mostly terrigenous) component of the sediment (Ruddiman and McIntyre, 1976). Dissolution decreases the carbonate content and increases the fragmentation of foraminiferal tests resulting in lower coarse fraction values. Productivity affects the carbonate system by changing the input of carbonate material; however, increased productivity also increases dissolution of carbonate by increasing the amount of CO_2 in the water column.

Previous studies of long climate records have shown that the climatic system has different modes of variability (Shackleton and Opdyke, 1976; Berger, 1982; Prell, 1982). Other indexes dependent on climatic variations, including the carbonate system, should reflect these changes in variability, but the sense and the magnitude of the changes between modes are dependent on the links between climate and the recording index. These links between climate and the recording index may also change with time. Examination of long carbonate records should provide insights into the nature of the interrelationships between the climatic and carbonate systems and how they change.

Detailed carbonate records for the early Pleistocene are rare; most lack the resolution needed to define variations on the same scale as observed climatic variations. Hole 558A provides a record of the carbonate variations for the North Atlantic spanning the entire Pleistocene. Carbonate and coarse fraction curves for Hole 558A are presented in this report and compared to other carbonate and climatic records.

Hole 558A Record

Site 558 is located at approximately 37°N, 37°W on the west side of the Mid-Atlantic Ridge (Fig. 1). The water depth is 3750 m, well above the observed lysocline and carbonate compensation depths for the late Pleistocene North Atlantic. This site is near the southern bound-

---

[1] Bougault, H., Cande, S. C., et al., *Init. Repts. DSDP*, 82: Washington (U.S. Govt. Printing Office).

[2] Address: Department of Geological Sciences, Brown University, Providence, Rhode Island 02912-1846.

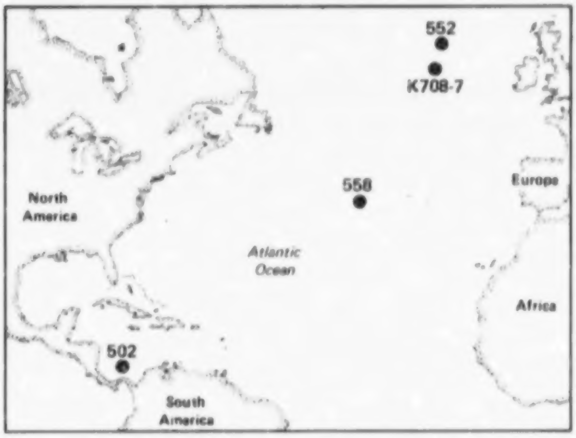

Figure 1. Map of the Atlantic Ocean, showing locations of Site K-7087 and of DSDP Sites 502, 552, and 558.

ary of major glacial to interglacial oceanographic fluctuations in the North Atlantic (CLIMAP, 1976; 1981).

Paleomagnetic data from Hole 558A show a complete upper Matuyama through Brunhes stratigraphy with well-defined reversals (M. J. Khan, pers. comm., 1983). The average accumulation rate for the upper 2-Ma section is 17 m/Ma. Accumulation rates vary between 11.3 m/Ma for the Olduvai Subchron to 19.2 m/Ma for the Brunhes chron (Table 1). The Jaramillo Subchron has an anomalously high accumulation rate of 48.6 m/Ma. Given these accumulation rates, we should be able to determine climatic variations identified in other deep-sea cores at Site 558.

Samples for carbonate and coarse fraction analyses were taken from the upper 34 m of Hole 558A. Sampling intervals generally were 10 cm resulting in an average sample spacing of 6 Ma.

METHODS

Coarse fraction determinations were made on all samples. A portion ~0.5 g) of sample was reserved for carbonate analysis; the remainder was dried at 50°C, weighed, and then soaked overnight in water to disaggregate the sample. The samples were wet sieved through a 150 μm sieve. Both coarse and fine fractions were retained; the coarse fractions were dried and weighed. Coarse fraction values are reported as the weight percent greater than 150 μm.

Wet sieving at 150 μm reduces the time required for sample preparation. Most faunal, isotopic, and dissolution studies work with a size fraction larger than 150 μm. For studies with large numbers of samples, the time saved can be significant.

Table 1. Accumulation rates calculated between magnetic reversals.

Magnetic boundary	Depth (m)	Age (Ma)	Accumulation rate (m/Ma)
Bruhnes/Matyuma	14.0	0.73	19.2
Top Jaramillo	16.2	0.91	12.2
Bottom Jaramillo	19.6	0.98	48.6
Top Olduvai	29.02	1.66	13.9
Bottom Olduvai	31.5	1.88	11.3

Note: The first column gives the lower boundary on the interval for the calculated accumulation rates. The magnetic reversals are from M. J. Khan (pers. comm., 1983).

Calcium carbonate analyses were made at Brown University using a differential-gasometric system similar in design to the vacuum-gasometric system described by Jones and Kaiteris (1983). In contrast to their system, the Brown system does not reference the resultant ga pressure after reaction to vacuum. The system measures the pressur difference between the carbonate bomb and the atmosphere.

The analytical system consists of two major components: (1) th sample chamber (carbonate bomb) and (2) the pressure manifold. Th sample chamber (Jones and Kaiteris, 1983, fig. 1), is a two-arm gla reaction vessel with a quick connector and a valve for releasing th CO_2 gas after reaction. The pressure manifold is composed of a quic connector, pressure gage, and relief valve.

Operation of the system can be summarized in four steps:

1. Raw samples (1/2 to 1 cm_3) are placed in an oven until dry. Th sample is ground to a fine powder in a morter and redried.

2. A weighed amount of the sample (0.1 to 0.2 g) is placed in th bottom of the reaction chamber; 3 ml of 42% phosphoric acid placed in the side arm.

3. After all samples are ready, the reaction vessel valves are clos and the acid is tipped onto the sample. The sample is agitated for 30 or until the reaction stops.

4. Thirty minutes after the sample is reacted the pressure is mea sured by the connection of each reaction chamber to the pressure man ifold. Temperatures are recorded at the time of pressure measur ments. Atmospheric pressures are observed during the reaction an measurement phase for changes that may affect the result.

In practice, an operator can perform 30 carbonate analyses in a 2.0-hr. period, beginning with dry, powdered samples. Consistency between operators and reaction chambers is checked by running 3 to 5 standards with each set of samples. Carbonate standard is 100% analytical grade carbonate.

Precision of the differential-gasometric method is greater than the carbonate variations in most deep-sea sediment cores. The mean difference between random duplicate determinations was 0.8% for 61 samples from Hole 558A.

RESULTS

The upper 34 m of Hole 558A record carbonate and coarse fraction variability spanning the last 2 Ma (Fig. 2, end-of-chapter Appendix). The carbonate values range between 65 and 95% with a mean value of 83% (σ = 6.5%). However, the pattern of carbonate variability is different for several sections of the record. Carbonate maxima and minima that correspond to isotopic Stages 3 through 12 are clearly defined in the upper 8 m of Hole 558A based on correlation to Holes 502 and 502B (Prell, 1982; Gardner, 1982) and Hole 552A (Shackleton and Hall, in press; Zimmerman et al., in press). During this interval, the carbonate record exhibits a characteristic Atlantic-type carbonate stratigraphy similar to carbonate records from Hole 552A and Core K708-7 (see Fig. 3). Core 558A-1 failed to recover the upper 0.5 m of sediment corresponding to the Holocene and last glacial maximum. Between 8 and 22 m, the record is characte ized by several broad carbonate maxima punctuated b two relatively sharp carbonate minima. Short-duratior low-amplitude variations are superimposed on the lon period cycles. Below 22 m, the relative duration an magnitude of major carbonate variations are similar t upper Pleistocene (0 to 8 m) section.

The record of coarse fraction has a mean value c 10% (σ = 3.8%); several patterns of variability occu within this record. The upper 6 m contains high-ampl tude, short-duration variations and higher average va ues when compared to the entire record. A pronounce low-coarse-fraction event occurs between 6 and 10 m co

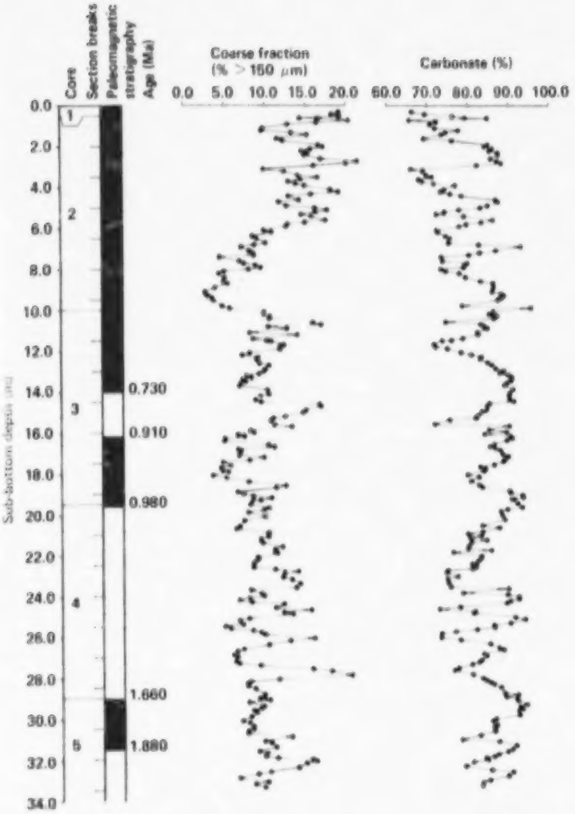

Figure 2. Coarse fraction and carbonate records from Hole 558A. Coarse fraction values are weight percent greater than 150 µm. Carbonate values are total weight percent carbonate. Magnetic time scale is from M. J. Khan (pers. comm., 1983). Magnetic ages are from Kent and Spariosu (1982). Hydraulic piston core numbers and section breaks are also shown. (See Table 1 for magnetic boundaries.)

responding approximately with Site 502 isotopic Stages 11 through 13 (Prell, 1982) (Fig. 3), that is not accompanied by a change in the carbonate record. Below 10 m, coarse fraction values display a complex pattern of variability. In particular, the section between 22 and 28 m displays high-amplitude variations similar to, but out of phase with, the carbonate record.

The data from the upper 18 m of Hole 558A show a poor correlation between the carbonate and coarse fraction records. Although the suggestion of an Atlantic-type correlation is present during short intervals (e.g., 3 to 3.5 m), the correlation over longer intervals is poor.

The lower Pleistocene section of Hole 558A (18 to 34 m) displays a clear negative correlation between carbonate and coarse fraction values ($r = -0.5$). This correlation is in contrast to the general positive correlation found in most upper Pleistocene North Atlantic sediments. The records of carbonate and coarse-fraction variability from Hole 558A may reflect the Pleistocene changes in the mode of climatic variability or may reflect changes in the response of the carbonate system to climatic fluctuations.

DISCUSSION

The carbonate record from Hole 558A is shown in Figure 3 with carbonate records from the Atlantic that have similar accumulation rates. Site 552 and Core K708-7 are North Atlantic carbonate records. The carbonate record from Site 502 (the Caribbean) is included for correlation with the $\delta^{18}O$ stratigraphy.

Correlation lines in Figure 2 are drawn between magnetic reversals and several major carbonate events. In each Pleistocene record, carbonate events of similar amplitude are present in both the lower and upper Pleistocene sections. In the upper Pleistocene (upper 14 m of Hole 558A), the general structure, as shown by the correlation lines, is similar. Detailed correlations between the North Atlantic carbonate records show higher amplitude and variance in Hole 552A and Core K708-7 records when compared to Hole 558A. The lower Pleistocene carbonate record from Hole 552 also has higher amplitude and variance. Sites 552 and K708-7 are approximately 20° north of Site 558 within a region influenced by fluctuations of the polar front (McIntyre et al., 1972; Ruddiman and McIntyre, 1976) and have a significant component of noncarbonate, ice rafted material resulting in an increased amplitude of the carbonate curve (Zimmerman et al., in press; Ruddiman and McIntyre, 1976). Site 558 is south of the maximum southern extent of the polar front during the last glacial maximum (CLIMAP, 1976, 1981; McIntyre et al., 1976) and thus less influenced by ice rafted material. Site 558 is also separated from major terrigenous sources by the Mid-Atlantic Ridge and the North American Basin. The accumulation rate for the lower Pleistocene of Hole 558A is lower than for the upper Pleistocene. The accumulation rate change in Hole 558A makes correlation to Holes 502B and 552A difficult; therefore, no carbonate correlation lines are drawn for the early Pleistocene.

The Pleistocene carbonate system presents a complex pattern of variability in Atlantic sediments. At Site 558, several modes of variability are present in both the carbonate and coarse fraction records. Whereas the entire lower Pleistocene does not have a single clear correlation, a significant interval (18 to 34 m) has an inverse correlation. Several factors may contribute individually to the change in correlation between carbonate and coarse fraction, such as sediment winnowing, carbonate dissolution and production, and noncarbonate dilution. Increased winnowing during low carbonate events can remove fine fraction material increasing the coarse fraction values and may account for the decreased accumulation rate in the lower Pleistocene. Increased dissolution could lead to lower carbonate values with a higher coarse fraction only if the effects of dissolution are more pronounced on the fine fraction component. Productivity changes and the resulting changes in dissolution could effectively increase the carbonate content, but also would increase carbonate dissolution. At periods of high carbonate dissolution, fragmentation of foraminiferal tests, which form nearly all the coarse fraction, would reduce the coarse fraction values. Thus, the carbonate and coarse fraction variations would be inversely related. Increased

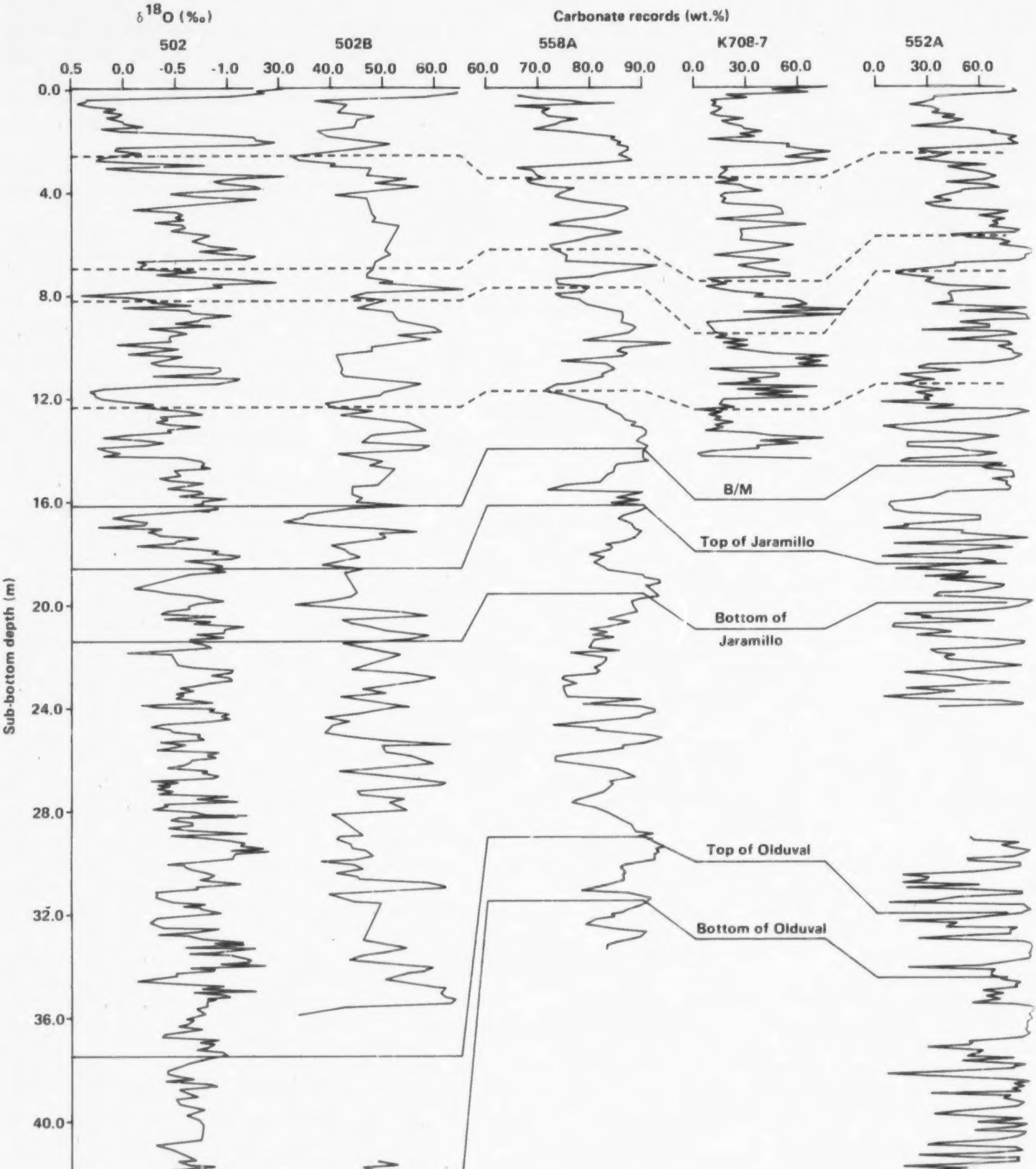

Figure 3. Correlation between $\delta^{18}O$ and carbonate records. Oxygen isotopic data (in ‰ versus PDB standard) are from Holes 502 and 502B (Prell 1982 plus additional data). Carbonate record from Caribbean Hole 502B is from Gardner (1982); piston core K-7087 record is a fine-fraction carbonate record from the North Atlantic (Ruddiman and McIntyre, 1976); North Atlantic Hole 552A carbonate data are from Zimmerman e al. (in press). Correlations are shown for magnetic (solid lines) and carbonate (dashed lines) events.

noncarbonate sedimentation could reduce the carbonate content, but should also reduce coarse fraction values (most of the noncarbonate material is in the fine fraction [Ruddiman and McIntyre, 1976]). Individually, these factors may contribute to the temporal variations in the carbonate system; however, the interrelationships between these factors must also be considered.

CONCLUSIONS

Examination of the carbonate and coarse fraction records from Site 558 and the correlation to other carbonate records reveals that:

1. Hole 558A contains records of carbonate and coarse fraction variations for the entire Pleistocene. Accumulation rates, however, may vary during the Pleistocene.
2. Carbonate and coarse fraction records display several modes of variability within the Pleistocene section. Among these modes are lower and upper Pleistocene sections containing high-amplitude variations.
3. The correlation between carbonate and coarse fraction records varies from low values in most of the upper Pleistocene (0 to 18 m) to a maximum of -0.5 for the lower Pleistocene (below 18 m). The lower Pleistocene correlation is the opposite of the upper Pleistocene correlation observed in other North Atlantic and Caribbean records.
4. Correlation between Atlantic carbonate records shows that the carbonate variability is higher in northern sites (Site 552 and K708-7) where ice-rafted material is an important noncarbonate component.

From these observations we infer that the North Atlantic has had several modes of sedimentation and preservation of carbonate material at Site 558 and that the response of the carbonate system to different modes is not the same for each component.

ACKNOWLEDGMENTS

I thank W. L. Prell and J. Imbrie for assistance during the preparation of this manuscript and B. Bellis for assistance in performing the carbonate determinations. This study was supported by National Science Foundation grant ATM-8018897 (SPECMAP).

REFERENCES

Arrhenius, G., 1952. Sediment cores from the East Pacific. *Fasc. I, Rep. Swed. Deep-Sea Exped.*, 5:6-227.

Berger, W. H., 1976. Biogenous deep sea sediments: production, preservation, and interpretation. *In* Riley, J. P., and Chester, R. (Eds.), *Chemical Oceanography*, (Vol. 5, 2nd ed.): London (Academic Press), pp. 265-388.

_______, 1982. Deep-sea stratigraphy: Cenozoic steps and the search for chemo-climatic feedback. *In* Einsele, G., and Seilacher, A. (Eds.), *Cyclic and Event Stratification:* Berlin (Springer), pp. 121-157.

Broecker, W. S., 1971. Calcite accumulation rates and glacial to interglacial changes in oceanic mixing. *In* Turekian, K. K. (Ed.), *The Late Cenozoic Glacial Ages:* New Haven (Yale), pp. 239-265.

Broecker, W. S., and Peng, T.-H., 1982. *Tracers in the Sea:* Palisades (Lamont-Doherty Geological Observatory).

CLIMAP, 1976. The surface of the ice-age Earth. *Sciences*, 191: 1131-1137.

_______, 1981. Seasonal reconstructions of the Earth's surface at the last glacial maximum. *In* McIntyre A., and Cline, R. (Eds.), *Map and Chart Series:* Boulder, Colorado (Geol. Soc. Am.), MC-36.

Emiliani, C., 1955. Pleistocene temperatures. *J. Geol.*, 63:538-578.

Gardner, J. V., 1982. High-resolution carbonate and Quaternary organic-carbon stratigraphies for the late Neogene and Quaternary from the western Caribbean and eastern equatorial Pacific. *In* Prell, W. L., Gardner, J. V., et al., *Init. Repts. DSDP*, 68: Washington (U.S. Govt. Printing Office), 347-364.

Jones, G. A., and Kaiteris, P., 1983. A vacuum-gasometric technique for rapid and precise analysis of calcium carbonate in sediments and soils. *J. Sediment. Petrol.*, 53:655-660.

Kent, D. V., Spariosu, D. J., 1982. Magnetostratigraphy of Caribbean Site 502 hydraulic piston cores. *In* Prell, W. A., Gardner, J. V., et al., *Init. Repts. DSDP*, 68: Washington (U.S. Govt. Printing Office), 419-433.

McIntyre, A., Kipp, N. G., Bé, A. W. H., Crowley, T., Kellogg, T., Gardner, J. V., Prell, W. L., and Ruddiman, W. F., 1976. Glacial North Atlantic 18,000 years ago: a CLIMAP reconstruction. *In* Cline, R. M., and Hays, J. D. (Eds.), *Investigation of the Late Quaternary Paleoceanography and Paleoclimatology:* Boulder, Colorado (Geol. Soc. Am.), Mem. 145:43-76.

McIntyre, A., Ruddiman, W. F., and Jantzen, R., 1972. Southward penetration of the North Atlantic Polar Front: faunal and floral evidence of large-scale surface water mass movement over the last 225,000 years. *Deep-Sea Res.*, 19:61-77.

Phelger, F. B., Parker, F. L., and Peirson, J. F., 1953. North Atlantic foraminifera. *Rept. Swed. Deep-Sea Exped. 1947-1948*, 7.

Prell, W. L., 1982. Oxygen and carbon isotope stratigraphy for the Quaternary of Hole 502B: evidence for two modes of isotopic variability. *In* Prell, W. L., Gardner, J. V., et al., *Init. Repts. DSDP*, 68: Washington (U.S. Govt. Printing Office), 455-464.

_______, 1978. Upper Quaternary sediments of the Columbia Basin: spacial and stratigraphic variations. *Geol. Soc. Am. Bull.*, 89: 1241-1255.

Ruddiman, W. F., 1971. Pleistocene sedimentation in the Equatorial Atlantic: stratigraphy and faunal paleoclimatology. *Geol. Soc. Am. Bull.*, 82:283-302.

Ruddiman, W. F., and McIntyre, A., 1976. Northwest Atlantic paleoclimatic changes over the past 600,000 years. *In* Cline, R. M., and Hays, J. D. (Eds.), *Investigation of the Late Quaternary Paleoceanography and Paleoclimatology:* Boulder, Colorado (Geol. Soc. Am.), Mem. 145:3-41.

Shackleton, N. J., 1967. Oxygen isotopes analyses and Pleistocene temperature re-assessed. *Nature*, 215:15-17.

Shackleton, N. J., and Hall, M. A., in press. Oxygen and carbon isotope stratigraphy of DSDP Site 552A: Plio-Pleistocene glacial history. *In* Roberts, D. G., Schnitker, D., et al., in press. *Init. Repts. DSDP*, 81: Washington (U.S. Govt. Printing Office).

Shackleton, N. J., and Opdyke, N. D., 1976. Oxygen-isotope and paleomagnetic stratigraphy of Pacific core V28-239 late Pliocene to latest Pleistocene. *In* Cline, R. M., and Hays, J. D. (Eds.), *Investigation of the Late Quaternary Paleoceanography and Paleoclimatology:* Boulder, Colorado (Geol. Soc. Am.), Mem. 145:449-464.

Volat, J.-L., Pastouret, L., and Vernaud-Graggini, C., 1980. Dissolution and carbonate fluctuations in Pleistocene deep-sea cores: a review. *Mar. Geol.*, 34:1-28.

Zimmerman, H. B., Shackleton, N. J., Backman, J., Kent, D. V., Baldauf, J. G., Kaltenback, A. J., and Morton, A. C., in press. History of Plio-Pleistocene climate in the northeastern Atlantic, Deep Sea Drilling Project Hole 552A. *In* Roberts, D. G., Schnitker, D., et al., *Init. Repts. DSDP*, 81: Washington (U.S. Govt. Printing Office).

Date of Initial Receipt: 8 November 1983
Date of Acceptance: 10 July 1984

APPENDIX

Sample Identification, Depth, Coarse Fraction, and Carbonate Values for Hole 558A

Core-Section (interval in cm)	Sub-bottom depth (m)	Carbonate (wt.%)	Coarse fraction (wt.%)
1-1, 29-31	0.30	66.27	19.12
1-1, 39-41	0.40	69.50	18.21
1-1, 49-51	0.50	76.25	19.19
1-1, 58-60	0.59	79.32	14.29
2-1, 9-11	0.60	84.81	16.55
2-1, 19-21	0.70	65.63	20.30
2-1, 29-31	0.08	72.30	16.39
2-1, 39-41	0.90	70.76	12.79
2-1, 58-60	1.09	71.98	9.76
2-1, 69-71	1.20	77.74	9.56
2-1, 80-82	1.31	74.54	13.25
2-1, 90-92	1.41	73.52	15.19
2-1, 108-110	1.59	69.20	11.48
2-1, 119-121	1.70	76.15	12.17
2-1, 139-140	1.90	84.90	16.56
2-1, 148-150	1.99	84.11	17.12
2-2, 9-11	2.10	85.98	15.62
2-2, 19-21	2.20	85.27	14.52
2-2, 29-31	2.30	87.40	15.28
2-2, 39-41	2.40	87.43	14.88
2-2, 58-60	2.59	85.59	16.87
2-2, 69-71	2.70	87.12	21.37
2-2, 80-82	2.81	88.17	20.02
2-2, 90-92	2.91	82.14	16.02
2-2, 109-111	3.10	65.96	9.80
2-2, 119-121	3.20	69.01	12.32
2-2, 138-140	3.39	69.80	14.04
2-2, 148-150	3.49	71.11	16.50
2-3, 9-11	3.60	67.92	14.39
2-3, 19-21	3.70	68.63	12.87
2-3, 30-32	3.81	71.63	13.77
2-3, 40-42	3.90	76.92	14.88
2-3, 58-60	4.09	74.16	18.05
2-3, 69-71	4.20	73.25	19.04
2-3, 80-82	4.31	75.60	15.68
2-3, 90-92	4.41	78.39	12.87
2-3, 109-111	4.60	86.80	14.19
2-3, 119-121	4.70	87.38	11.65
2-3, 138-140	4.89	84.74	12.60
2-3, 148-150	4.99	83.00	16.11
2-4, 9-11	5.10	77.78	17.64
2-4, 19-21	5.20	74.21	16.27
2-4, 29-31	5.30	72.17	14.41
2-4, 39-41	5.40	78.94	15.70
2-4, 58-60	5.59	86.11	17.45
2-4, 69-71	5.70	83.24	14.90
2-4, 79-81	5.80	79.54	12.77
2-4, 89-91	5.90	77.86	12.57
2-4, 109-111	6.10	72.25	9.80
2-4, 118-120	6.19	72.60	10.77
2-4, 138-140	6.39	74.52	8.42
2-4, 148-150	6.49	75.50	8.92
2-5, 20-22	6.71	75.18	10.03
2-5, 29-31	6.80	82.62	8.65
2-5, 39-41	6.90	92.93	7.03
2-5, 58-60	7.09	86.85	8.00
2-5, 69-70	7.19	82.82	8.43
2-5, 79-81	7.30	80.17	8.57
2-5, 89-91	7.40	73.37	4.38
2-5, 109-111	7.60	73.74	6.80
2-5, 119-121	7.70	79.73	7.34
2-5, 129-131	7.80	79.12	8.77
2-5, 139-141	7.90	78.83	9.40
2-5, 148-150	7.99	73.27	7.91
2-6, 9-11	8.10	74.43	4.92
2-6, 19-21	8.20	77.80	4.32
2-6, 39-41	8.40	79.33	5.01
2-6, 58-60	8.59	83.13	4.89
2-6, 69-70	8.69	86.16	5.38
2-6, 89-91	8.90	86.26	3.81
2-6, 109-111	9.10	85.90	2.60
2-6, 120-122	9.21	88.13	2.72
2-6, 129-131	9.30	88.75	2.97
2-6, 138-140	9.39	88.19	3.40

Appendix. (Continued).

Core-Section (interval in cm)	Sub-bottom depth (m)	Carbonate (wt.%)	Coarse fraction (wt.%)
2-7, 0-2	9.51	87.32	3.59
2-7, 29-31	9.80	78.56	4.71
2,CC (10-12)	9.91	95.43	5.61
3-1, 9-11	10.10	86.14	9.83
3-1, 19-21	10.20	85.14	9.73
3-1, 29-31	10.30	87.09	10.52
3-1, 39-41	10.40	86.24	10.42
3-1, 58-60	10.59	74.42	15.81
3-1, 69-71	10.70	83.10	16.83
3-1, 79-81	10.80	83.86	10.30
3-1, 89-91	10.90	84.68	12.60
3-1, 109-11	11.10	82.20	8.04
3-1, 119-121	11.20	82.45	13.90
3-1, 138-140	11.39	78.64	8.44
3-1, 148-150	11.49	75.86	10.15
3-2, 0-2	11.51	73.54	10.67
3-2, 19-21	11.70	71.47	12.25
3-2, 29-31	11.80	71.95	11.73
3-2, 39-41	11.90	74.88	11.79
3-2, 58-60	12.09	78.22	8.04
3-2, 69-71	12.20	80.68	7.11
3-2, 80-82	12.31	83.20	9.08
3-2, 89-91	12.40	82.93	8.89
3-2, 109-111	12.60	84.74	9.23
3-2, 119-121	12.70	85.80	10.41
3-2, 138-140	12.89	86.73	9.96
3-2, 148-150	12.99	88.76	9.76
3-3, 10-12	13.11	87.73	9.17
3-3, 19-21	13.20	89.88	7.64
3-3, 30-32	13.31	90.66	8.24
3-3, 39-41	13.40	90.62	7.17
3-3, 48-50	13.49	90.41	7.52
3-3, 58-60	13.59	89.43	6.93
3-3, 69-71	13.70	88.84	6.78
3-3, 89-91	13.90	90.96	10.19
3-3, 109-111	14.10	90.04	10.40
3-3, 119-121	14.20	90.02	9.32
3-3, 138-140	14.39	90.06	8.74
3-3, 148-150	14.49	91.13	9.43
3-4, 9-11	14.60	85.15	16.67
3-4, 19-21	14.70	84.62	16.80
3-4, 39-41	14.90	84.39	14.94
3-4, 49-51	15.00	83.24	14.65
3-4, 69-71	15.20	82.19	12.40
3-4, 78-80	15.29	81.74	10.95
3-4, 89-91	15.40	75.29	10.60
3-4, 109-111	15.60	71.68	11.04
3-4, 119-121	15.70	90.00	13.20
3-4, 138-140	15.89	85.00	8.11
3-4, 148-150	15.99	89.32	8.54
3-5, 9-11	16.10	83.93	6.55
3-5, 19-21	16.20	90.22	7.37
3-5, 29-31	16.30	90.69	4.95
3-5, 39-41	16.40	89.41	4.89
3-5, 58-60	16.59	86.25	10.32
3-5, 69-71	16.70	85.26	11.04
3-5, 79-81	16.80	86.56	6.58
3-5, 89-91	16.90	87.85	6.94
3-5, 109-111	17.10	88.43	6.69
3-5, 119-121	17.20	89.74	9.77
3-5, 133-135	17.34	88.96	7.99
3-5, 143-145	17.44	88.49	4.73
3-6, 9-11	17.60	86.25	5.69
3-6, 19-21	17.70	82.83	4.49
3-6, 29-31	17.80	84.14	4.63
3-6, 39-41	17.90	83.72	5.36
3-6, 58-60	18.09	79.71	3.48
3-6, 69-71	18.20	82.49	5.15
3-6, 89-91	18.40	80.52	7.86
3-6, 109-111	18.60	82.55	12.43
3-6, 119-121	18.70	83.24	11.27
3-6, 138-140	18.89	90.02	6.49
3-6, 148-150	18.99	90.32	7.19
3-7, 9-11	19.10	93.20	8.41

Appendix. (Continued).

Core-Section (interval in cm)	Sub-bottom depth (m)	Carbonate (wt.%)	Coarse fraction (wt.%)
3-7, 19-21	19.20	93.37	10.67
3-7, 30-32	19.31	91.08	9.34
3,CC (9-11)	19.30	90.54	8.40
4-1, 0-2	19.51	91.93	8.05
4-1, 19-21	19.70	93.11	10.34
4-1, 29-31	19.80	89.47	9.75
4-1, 39-41	19.90	87.82	7.78
4-1, 59-61	20.10	88.21	9.90
4-1, 79-81	20.30	88.93	7.31
4-1, 108-110	20.59	83.26	6.73
4-1, 119-121	20.70	87.51	6.32
4-1, 138-140	20.89	83.36	10.33
4-1, 148-150	20.99	79.70	10.23
4-2, 9-11	21.10	83.07	10.28
4-2, 19-21	21.20	80.25	9.34
4-2, 29-31	21.30	84.37	9.33
4-2, 39-41	21.40	80.58	9.55
4-2, 58-60	21.59	79.88	11.99
4-2, 69-71	21.70	79.64	11.07
4-2, 80-82	21.81	85.45	11.01
4-2, 89-91	21.90	76.07	11.34
4-2, 109-111	22.10	83.01	8.92
4-2, 119-121	22.20	82.86	9.02
4-2, 135-137	22.36	82.02	8.52
4-2, 147-149	22.48	80.60	8.37
4-3, 9-11	22.60	81.66	8.41
4-3, 19-21	22.70	80.84	11.06
4-3, 29-31	22.80	74.76	13.93
4-3, 39-41	22.90	74.35	12.20
4-3, 58-60	23.09	77.17	12.01
4-3, 69-71	23.20	74.63	13.12
4-3, 89-91	23.40	74.84	14.16
4-3, 109-111	23.60	75.40	13.69
4-3, 119-121	23.70	89.64	8.07
4-3, 138-140	23.89	78.40	9.41
4-3, 148-150	23.99	89.46	9.71
4-4, 9-11	24.10	92.26	7.88
4-4, 19-21	24.20	92.27	6.64
4-4, 29-31	24.30	90.10	8.17
4-4, 39-41	24.40	89.25	12.14
4-4, 58-60	24.59	77.68	11.11
4-4, 69-71	24.70	72.63	15.49
4-4, 80-82	24.81	81.35	12.08
4-4, 89-91	24.90	81.01	13.22
4-4, 109-111	25.10	91.32	7.84
4-4, 119-121	25.20	93.74	6.63
4-4, 138-140	25.39	90.13	7.09
4-4, 148-150	25.49	86.05	4.90
4-5, 9-11	25.60	86.22	5.54
4-5, 19-21	25.70	81.87	8.30
4-5, 29-31	25.80	76.63	9.32
4-5, 39-41	25.90	73.14	9.80
4-5, 58-60	26.09	73.02	15.88
4-5, 69-71	26.20	77.80	12.84
4-5, 89-91	26.40	85.09	10.23

Appendix. (Continued).

Core-Section (interval in cm)	Sub-bottom depth (m)	Carbonate (wt.%)	Coarse fraction (wt.%)
4-5, 109-111	26.60	87.32	7.15
4-5, 119-121	26.70	88.51	6.40
4-5, 138-140	26.89	83.54	5.95
4-5, 148-150	26.99	84.22	6.36
4-6, 19-21	27.20	82.95	6.18
4-6, 29-31	27.30	82.31	6.55
4-6, 39-41	27.40	80.63	9.21
4-6, 58-60	27.59	77.26	15.66
4-6, 69-71	27.70	76.24	17.97
4-6, 89-91	27.90	80.76	20.48
4-6, 109-111	28.10	83.27	11.48
4-6, 119-121	28.20	84.16	7.96
4-6, 129-131	28.30	85.15	7.62
4-6, 139-141	28.40	86.04	7.64
4-7, 4-6	28.55	87.72	8.55
4,CC (2-4)	28.83	88.55	9.68
4,CC (10-12)	28.91	91.94	9.68
4,CC (20-22)	29.01	89.02	9.05
5-1, 9-11	29.10	91.66	10.32
5-1, 19-21	29.20	91.84	7.77
5-1, 39-41	29.40	94.08	9.59
5-1, 48-50	29.49	92.41	9.27
5-1, 59-61	29.60	93.05	8.33
5-1, 69-71	29.70	91.11	8.73
5-1, 89-91	29.90	92.26	8.00
5-1, 109-111	30.10	86.45	6.94
5-1, 119-121	30.20	85.59	7.83
5-1, 138-140	30.39	86.65	8.30
5-1, 148-150	30.49	86.00	8.30
5-2, 9-11	30.60	86.21	7.68
5-2, 19-21	30.70	86.26	7.65
5-2, 39-41	30.90	82.55	13.02
5-2, 59-61	31.10	78.11	9.68
5-2, 69-71	31.20	87.19	10.50
5-2, 89-91	31.40	91.45	11.06
5-2, 109-111	31.60	90.39	8.97
5-2, 119-121	31.70	89.27	9.98
5-2, 133-135	31.84	87.05	9.72
5-2, 143-145	31.94	85.99	11.22
5-3, 0-2	32.01	83.89	15.53
5-3, 9-11	32.10	84.46	16.04
5-3, 19-21	32.20	80.91	14.78
5-3, 39-41	32.40	78.89	13.82
5-3, 59-61	32.60	85.33	10.36
5-3, 69-71	32.70	90.59	8.86
5-3, 89-91	32.90	89.41	6.60
5-3, 109-111	33.10	84.76	10.06
5-3, 119-121	33.20	83.14	8.52
5-3, 135-137	33.36	82.89	9.69

Note: Sub-bottom depths are expressed as depth to the middle of the sample interval as measured from the top of the section. Replicate carbon analyses were averaged. Coarse fraction values are wt.% greater than 150 μm.

PART VI: APPENDIX

APPENDIX. GEOCHEMICAL DATA FOR BASALTS[1]

H. Bougault, Institut Français pour la Recherche et l'Exploitation de la Mer, Centre de Brest,
and
D. Hawkins, Deep Sea Drilling Project, Scripps Institute of Oceanography[2]

The major-element and most of the trace-element data from the different laboratories that contributed to the study of samples recovered during Leg 82 are presented in the following tables. The different basalt groups, identified on the basis of their chemical properties (major and trace elements), were defined from the data available on board the *Glomar Challenger* as the cruise progressed (see site chapters, all sites, this volume). Most of the data obtained since the end of the cruise and presented in these tables confirm the classification that was proposed by the shipboard party (see site chapters, all sites, this volume). Nevertheless, special mention should be made about Site 564. The shipboard party proposed a single chemical group at this site but noticed significant variations down the hole, mainly in trace-element data. However, the range of variation was small compared to the precision of the measurements. These variations were confirmed by the onshore studies (see papers in Part IV of this volume, especially Brannon's paper, partly devoted to this topic).

Generally, the consistency between the major-element data from different laboratories is fairly good (except sometimes for Na_2O), because of the reliability of the analytical methods, mainly X-ray fluorescence. Although the consistency is also good for trace elements, some deviation is more common. The accuracy, at least for some of the trace elements, is lower than that of major elements because (1) the concentrations are sometimes closer to the limit of detection, and (2) the concentrations of many trace elements in the international standards are often not known with the precision necessary to permit discrimination between data for unknown samples analyzed by different laboratories. One example of shipboard determinations and derivation of proposed chemical groups is the discussion of Niobium analysis given by Etoubleau et al. (this volume). Niobium, although found in low concentrations in basalts, is a key "hygromagmaphile" trace element for deducing the "enriched" or "depleted" character of the different basalt units. The accuracy of the shipboard measurements of Nb has been verified by use of the constant Nb/Ta ratio in basalts (16) and by instrumental neutron activation analyses for Ta. The accuracy of the shipboard analyses for Nb is better than 1 ppm.

The reader of this appendix should examine the geochemical properties of the elements (e.g., alkali elements in respect to alteration processes) and should not rely on the concentration of a single element to decide that a certain part of a core could be an exception in a chemical unit (e.g., for the purpose of sampling).

We hope that this compilation of all data will be useful in observing variation in chemistry down the different holes and that it will help in selecting samples for future studies.

---

[1] Bougalt, H., Cande, S. C., et al., *Init. Repts. DSDP*, 82: Washington (U.S. Govt. Printing Office).

[2] Addresses: (Bougault) Institut Français pour la Recherche et l'Exploitation de la Mer (formerly Centre National pour l'Exploitation de Océans), Centre de Brest, B. P. 337, 29273 Brest Cedex, France; (Hawkins) Deep Sea Drilling Project, Scripps Institution of Oceanography, University of California at San Diego, La Jolla, California 92093.

Table 1. Major-element compositions (in wt.%) for basalts, Leg 82.

Sample	Depth (m)	Inv	Method	SiO_2	TiO_2	Al_2O_3	Fe_2O_3 (total)	FeO*	Fe_2O_3	FeO	MnO	M_gO	CaO	Na_2O	K_2O	P_2O_5	CO_2	H_2O+	Total	LOI	S
Hole 556																					
Chemical Group I																					
2-1, 74-76	462.25	DRA	XRF	50.55	1.05	15.63	9.54	8.58	-	-	0.15	7.58	12.52	2.01	0.35	0.12	-	-	99.50	-	-
2-1, 77-79	462.28	WEA	XRF	50.56	1.04	15.96	7.83	-	-	-	0.15	7.89	12.74	2.44	0.16	0.11	-	-	100.53	1.65	-
2-1, 78-82	462.30	BOG	XRF	50.57	1.04	16.06	8.65	-	-	-	0.16	7.50	13.00	2.58	0.16	0.11	-	-	100.52	0.69	-
2-1, 83-85	462.34	SHM	XRFWT	49.90	1.05	15.80	-	-	2.87	5.11	0.19	7.80	12.80	2.26	0.21	0.10	0.20	0.88	99.20	-	-
2-2, 132-135	464.34	WEA	XRF	50.02	1.02	15.65	8.44	-	-	-	0.15	8.04	12.42	2.49	0.17	0.12	-	-	100.26	1.74	-
2-2, 141-144	464.43	DRA	XRF	50.22	1.05	15.96	8.72	7.85	-	-	0.15	7.51	13.31	2.02	0.20	0.12	-	-	99.28	-	-
2-2, 145-149	464.47	BOG	XRF	50.15	1.06	15.85	9.20	-	-	-	0.16	7.86	13.00	2.58	0.17	0.12	-	-	100.93	0.78	-
Chemical Group II																					
2-4, 93-95	466.94	SHM	XRFWT	50.10	1.47	15.90	-	-	5.70	4.14	0.16	6.16	11.82	2.64	0.47	0.14	0.10	0.65	99.42	-	-
2-5, 5-7	467.56	SHM	XRFWT	48.80	1.44	15.90	-	-	5.22	4.98	0.16	6.18	11.86	2.57	0.40	0.14	0.05	1.43	99.16	-	-
2-5, 12-16	467.64	BOG	XRF	50.16	1.45	15.46	10.97	-	-	-	0.18	6.65	11.61	2.48	0.33	0.15	-	-	100.27	0.83	-
2-5, 26-28	467.77	DRA	XRF	50.04	1.49	16.05	10.91	9.82	-	-	0.17	6.64	11.72	2.83	0.31	0.15	-	-	100.31	-	-
2-6, 34-36	469.35	SHM	XRFWT	49.00	1.45	15.60	-	-	8.19	3.00	0.22	6.31	11.94	2.46	0.47	0.14	0.52	0.82	100.10	-	-
3-1, 36-38	471.37	SHM	XRFWT	50.00	1.49	16.20	-	-	5.76	4.42	0.16	6.33	11.83	2.66	0.37	0.14	0.07	0.79	100.25	-	-
3-1, 57-60	471.59	WEA	XRF	49.02	1.46	15.61	10.55	-	-	-	0.17	6.53	11.39	2.70	0.28	0.15	-	-	100.13	2.27	-
3-1, 60-70	471.65	BOG	XRF	49.89	1.44	15.44	10.94	-	-	-	0.17	6.43	11.59	2.86	0.27	0.15	-	-	100.23	1.05	-
3-2, 19-21	472.70	SHM	XRFWT	49.40	1.52	16.10	-	-	4.85	4.72	0.17	6.10	11.78	2.62	0.35	0.14	0.12	1.51	99.37	-	-
3-2, 49-51	473.00	WEA	XRF	49.66	1.41	15.76	10.37	-	-	-	0.18	6.84	11.34	2.65	0.28	0.14	-	-	100.18	1.55	-
3-2, 52-56	473.04	BOG	XRF	49.35	1.49	15.31	11.03	-	-	-	0.18	6.46	11.63	2.57	0.30	0.16	-	-	99.45	0.97	-
3-3, 66-69	474.68	DRA	XRF	50.03	1.41	15.46	11.42	10.28	-	-	0.18	6.92	11.74	2.58	0.37	0.16	-	-	100.27	-	-
3-3, 70-74	474.72	BOG	XRF	50.05	1.40	15.46	10.54	-	-	-	0.17	6.87	11.85	2.55	0.14	0.15	-	-	99.96	0.78	-
4-1, 25-27	480.26	SHM	XRFWT	50.30	1.46	15.80	-	-	4.09	5.58	0.17	6.98	11.65	2.52	0.22	0.13	0.05	0.59	99.50	-	-
4-2, 65-68	482.17	WEA	XRF	48.62	1.45	15.93	10.36	-	-	-	0.17	6.02	11.51	2.76	0.28	0.14	-	-	100.31	3.07	-
4-2, 77-84	482.31	BOG	XRF	49.26	1.50	15.11	10.99	-	-	-	0.19	6.60	11.59	2.76	0.20	0.15	-	-	99.20	0.85	-
4-2, 130-133	482.82	SHM	XRFWT	49.70	1.54	16.00	-	-	6.18	4.29	0.18	6.16	11.49	2.80	0.25	0.14	0.06	0.88	99.65	-	-
4-3, 21-23	483.22	SHM	XRFWT	51.00	1.56	16.20	-	-	4.29	5.35	0.18	6.15	11.64	2.62	0.25	0.15	0.07	0.73	100.17	-	-
4-3, 45-47	483.46	SHM	XRFWT	50.00	1.40	16.60	-	-	4.38	4.97	0.18	6.18	11.88	2.46	0.26	0.13	0.05	0.65	99.15	-	-
4-3, 132-136	484.34	BOG	XRF	49.82	1.51	14.93	10.77	-	-	-	0.20	6.49	11.65	2.81	0.09	0.16	-	-	99.52	1.09	-
4-5, 21-23	486.22	SHM	XRFWT	50.10	1.59	15.60	-	-	6.09	4.59	0.17	6.13	11.50	2.67	0.42	0.15	0.06	0.87	99.91	-	-
4-5, 31-33	486.32	BOG	XRF	49.80	1.50	15.37	11.12	-	-	-	0.18	6.61	11.52	2.61	0.18	0.15	-	-	99.71	0.67	-
4-6, 41-44	487.93	DT	PROBE	51.30	1.72	14.47	-	10.75	-	-	-	6.58	11.35	2.55	0.18	-	-	-	98.90	-	-
4-6, 61-63	488.12	BOG	XRF	49.71	1.51	15.20	11.34	-	-	-	0.17	6.55	11.46	2.69	0.40	0.18	-	-	100.28	1.07	-
5-1, 23-27	489.25	SHM	XRFWT	49.60	1.52	15.70	-	-	6.93	4.51	0.19	6.04	11.44	2.63	0.52	0.15	0.21	0.73	100.20	-	-
5-1, 73-75	489.74	BOG	XRF	50.11	1.49	15.59	10.73	-	-	-	0.17	6.03	11.64	2.71	0.36	0.16	-	-	100.19	1.20	-
5-1, 99-102	490.01	DRA	XRF	50.21	1.49	15.97	10.83	9.75	-	-	0.17	6.58	11.57	2.46	0.27	0.16	-	-	99.71	-	-
5-2, 65-73	491.19	BOG	XRF	49.59	1.41	15.29	11.04	-	-	-	0.18	7.11	11.68	2.59	0.29	0.14	-	-	100.28	0.96	-
5-3, 75-80	492.78	BOG	XRF	49.93	1.40	15.24	10.08	-	-	-	0.16	6.63	11.88	2.73	0.32	0.14	-	-	99.88	1.37	-
5-5, 145-150	496.48	BOG	XRF	50.01	1.39	14.85	11.33	-	-	-	0.17	6.93	11.60	2.44	0.07	0.14	-	-	99.83	0.90	-
6-1, 66-70	498.68	BOG	XRF	49.39	1.39	15.21	10.77	-	-	-	0.15	6.64	11.68	2.84	0.26	0.13	-	-	99.89	1.43	-
6-2, 14-17	499.66	SHM	XRFWT	49.40	1.36	15.70	-	-	6.37	3.99	0.16	6.47	11.94	2.61	0.36	0.13	0.33	0.88	99.66	-	-
6-2, 29-34	499.82	BOG	XRF	50.34	1.40	14.95	10.62	-	-	-	0.17	7.20	11.65	2.91	0.19	0.16	-	-	100.64	1.05	-
6-2, 53-56	500.05	SHM	XRFWT	49.40	1.44	15.80	-	-	5.67	4.81	0.19	6.18	12.15	2.68	0.42	0.16	0.68	0.55	100.09	-	-
6-3, 82-86	501.84	BOG	XRF	50.19	1.41	14.96	10.96	-	-	-	0.16	7.26	11.42	3.11	0.05	0.14	-	-	100.60	0.94	-
6-4, 115-120	503.68	WEA	XRF	49.73	1.37	15.26	10.75	-	-	-	0.16	7.20	11.35	2.67	0.10	0.13	-	-	100.26	1.54	-
6-4, 121-126	503.74	BOG	XRF	49.63	1.35	15.21	10.68	-	-	-	0.16	7.12	11.59	2.63	0.02	0.14	-	-	99.43	0.90	-
6-5, 64-67	504.66	DRA	XRF	50.69	1.39	16.33	9.75	8.77	-	-	0.17	6.84	11.80	3.09	0.14	0.14	-	-	100.34	-	-
6-5, 68-70	504.69	SHM	XRFWT	50.60	1.37	15.50	-	-	3.57	5.54	0.17	6.94	11.61	2.58	0.09	0.13	0.09	0.97	99.15	-	-
Chemical Group III																					
6-6, 44-48	505.96	BOG	XRF	49.25	1.01	15.55	9.56	-	-	-	0.16	7.72	13.33	2.31	0.16	0.09	-	-	100.52	1.28	-
6-6, 108-111	506.60	DRA	XRF	49.50	1.00	16.28	8.43	7.59	-	-	0.15	7.59	14.39	2.59	0.24	0.11	-	-	100.26	-	-
7-1, 85-87	507.86	SHM	XRFWT	47.60	0.97	15.40	-	-	3.83	4.01	0.14	6.74	14.90	2.25	0.27	0.08	2.23	0.36	98.77	-	-
7-1, 115-119	508.17	WEA	XRF	48.46	0.99	15.21	9.74	-	-	-	0.16	7.62	12.65	2.56	0.22	0.09	-	-	99.64	1.94	-
7-1, 123-126	508.25	BOG	XRF	49.88	1.00	15.46	9.55	-	-	-	0.17	7.67	12.64	2.28	0.14	0.10	-	-	100.24	1.35	-
7-1, 128-132	508.30	DRA	XRF	50.12	1.03	15.89	10.08	9.07	-	-	0.16	7.17	12.74	2.60	0.29	0.11	-	-	100.20	-	-
7-3, 12-15	510.14	BOG	XRF	49.93	1.00	15.54	9.90	-	-	-	0.16	7.25	12.55	2.52	0.15	0.11	-	-	100.37	1.26	-
7-3, 83-86	510.85	DRA	XRF	50.02	1.03	16.11	8.98	8.08	-	-	0.17	7.33	13.36	2.51	0.35	0.11	-	-	99.98	-	-
8-1, 107-111	517.09	BOG	XRF	49.06	0.85	15.21	9.14	-	-	-	0.15	7.27	13.77	2.01	0.36	0.11	-	-	99.82	1.89	-
8-1, 118-120	517.19	WEA	XRF	49.25	0.83	15.44	8.81	-	-	-	0.15	7.62	13.27	2.33	0.36	0.10	-	-	100.51	2.35	-
8-2, 13-16	517.65	DRA	XRF	50.37	0.88	15.85	8.33	7.50	-	-	0.14	7.87	14.25	2.38	0.27	0.11	-	-	100.44	-	-

8-2, 27-29	517.78	SHM	XRFWT	49.30	0.86	15.40	-	-	2.40	5.27	0.14	8.09	13.86	2.15	0.18	0.08	0.63	0.95	99.29	-	-
8-3, 56-58	519.57	DT	PROBE	50.71	0.98	15.41	-	8.68	-	-	-	7.73	13.04	2.64	0.17	-	-	-	99.36	-	-
8-4, 60-63	521.12	BOG	XRF	48.99	0.85	15.28	8.68	-	-	-	0.16	7.09	14.16	1.92	0.34	0.12	-	-	99.66	2.07	-
9-2, 82-84	527.33	BOG	XRF	49.97	1.04	15.16	9.41	-	-	-	0.17	7.04	13.27	2.40	0.24	0.12	-	-	99.93	1.11	-
9-2, 83-85	527.34	WEA	XRF	49.78	1.02	15.43	9.55	-	-	-	0.16	7.04	12.63	2.52	0.35	0.11	-	-	100.22	1.63	-
9-3, 106-108	529.07	SHM	XRFWT	50.90	1.06	15.30	-	-	3.88	4.34	0.16	7.90	12.66	2.51	0.22	0.09	0.22	0.43	99.71	-	-
9-4, 64-67	530.16	DRA	XRF	50.85	1.08	15.38	9.49	8.54	-	-	0.15	7.60	12.57	2.76	0.33	0.11	-	-	100.32	-	-
9-5, 64-68	531.66	BOG	XRF	50.60	1.05	14.76	9.59	-	-	-	0.17	7.66	12.39	2.41	0.22	0.09	-	-	100.16	1.22	-
10-1, 122-124	535.23	SHM	XRFWT	49.40	0.93	16.20	-	-	4.73	3.69	0.15	7.29	13.18	2.31	0.31	0.09	0.53	0.70	99.54	-	-
10-2, 130-133	536.82	WEA	XRF	47.95	0.77	17.09	8.08	-	-	-	0.15	7.15	13.73	2.41	0.21	0.08	-	-	99.63	2.01	-
10-2, 137-141	536.89	BOG	XRF	49.10	0.81	17.31	8.04	-	-	-	0.14	6.75	13.91	2.01	0.26	0.10	-	-	99.98	1.55	-
10-3, 63-66	537.65	DRA	XRF	49.71	0.83	17.79	7.55	6.79	-	-	0.12	7.19	14.16	2.54	0.25	0.10	-	-	100.24	-	-
10-4, 50-54	539.02	BOG	XRF	49.49	0.93	15.11	9.06	-	-	-	0.16	8.34	12.51	2.01	0.21	0.09	-	-	99.66	1.75	-
10-4, 72-75	539.24	DRA	XRF	50.26	0.99	16.38	8.72	7.85	-	-	0.15	7.09	13.53	2.33	0.38	0.12	-	-	99.94	-	-
Chemical Group IV																					
11-1, 105-115	544.10	BOG	XRF	51.23	1.36	15.05	9.62	-	-	-	0.19	6.98	11.49	2.99	0.12	0.15	-	-	100.35	1.17	-
11-1, 106-109	544.08	WEA	XRF	50.35	1.31	15.00	10.42	-	-	-	0.18	6.44	10.86	2.96	0.45	0.13	-	-	100.07	1.97	-
Chemical Group III																					
11-2, 121-124	545.73	DRA	XRF	50.41	1.02	15.49	9.19	8.27	-	-	0.16	7.57	13.38	2.26	0.38	0.10	-	-	99.96	-	-
12-1, 55-59	552.57	BOG	XRF	48.92	0.82	16.93	8.01	-	-	-	0.13	7.28	13.45	2.82	0.24	0.09	-	-	100.47	1.78	-
12-1, 68-72	552.70	WEA	XRF	49.01	0.84	16.44	8.44	-	-	-	0.15	8.18	12.39	2.31	0.20	0.08	-	-	100.32	2.28	-
12-3, 54-57	555.56	DRA	XRF	50.33	0.97	16.28	8.91	8.02	-	-	0.14	7.58	12.90	2.21	0.33	0.11	-	-	99.75	-	-
12-3, 78-80	555.79	SHM	XRFWT	49.30	0.93	15.80	-	-	4.01	4.28	0.15	7.99	12.81	2.07	0.23	0.08	0.04	1.39	99.11	-	-
12-3, 118-122	556.20	BOG	XRF	50.21	0.95	15.44	8.63	-	-	-	0.15	8.72	12.33	2.38	0.17	0.09	-	-	100.33	1.26	-
12-4, 27-30	556.78	DRA	XRF	50.46	0.99	16.00	9.11	8.20	-	-	0.15	7.26	12.88	2.30	0.53	0.11	-	-	99.78	-	-
Chemical Group V																					
13-1, 64-68	561.66	BT	XRF	39.89	0.02	0.82	8.09	-	-	-	0.10	37.34	0.32	0.15	0.00	-	-	-	99.64	12.92	-
14-1, 61-65	566.13	BT	XRF	37.10	0.02	0.75	7.61	-	-	-	0.10	34.37	4.00	0.07	0.00	-	-	-	99.72	15.70	-
14-2, 78-84	567.81	BT	XRF	40.56	0.05	1.34	9.12	-	-	-	0.14	35.56	0.38	0.19	0.01	-	-	-	100.61	13.26	-
15-3, 18-21	577.70	SHM	XRFWT	52.20	0.32	15.70	-	-	0.97	5.71	0.13	10.58	10.96	2.17	0.07	0.01	0.06	0.84	99.74	-	-
15-3, 33-35	577.84	BOG	XRF	52.24	0.32	15.90	7.13	-	-	-	0.14	10.11	11.79	2.40	0.00	0.03	-	-	100.57	0.51	-
15-3, 44-47	577.96	SHM	XRFWT	52.60	0.35	15.00	-	-	1.57	5.24	0.15	10.34	12.25	2.09	0.05	0.01	0.08	0.75	100.50	-	-
16-1, 14-18	583.66	WEA	XRF	52.10	0.26	18.14	5.73	-	-	-	0.11	8.89	11.92	2.62	0.07	0.02	-	-	100.57	0.71	-
16-1, 21-27	583.74	BOG	XRF	52.41	0.28	17.14	5.90	-	-	-	0.12	8.79	13.16	2.43	0.00	0.03	-	-	100.64	0.38	-
16-1, 29-32	583.81	SHM	XRFWT	52.70	0.23	17.30	-	-	0.91	4.71	0.13	8.73	11.01	2.58	0.06	0.02	0.11	0.63	99.15	-	-
Chemical Group III																					
16-2, 110-113	586.12	DRA	XRF	50.10	0.88	15.64	8.59	7.73	-	-	0.16	7.54	14.27	2.09	0.24	0.11	-	-	99.61	-	-
Chemical Group IV																					
16-2, 128-131	586.30	WEA	XRF	49.08	1.33	14.35	11.32	-	-	-	0.17	6.49	10.61	3.11	0.48	0.13	-	-	99.68	2.61	-
16-2, 131-133	586.32	SHM	XRFWT	50.50	1.38	14.70	-	-	4.43	6.28	0.17	6.57	10.74	3.07	0.46	0.13	0.10	0.65	99.14	-	-
16-2, 137-140	586.39	BOG	XRF	51.86	1.36	14.89	9.55	-	-	-	0.14	6.78	10.93	3.29	0.29	0.15	-	-	100.38	1.14	-
Hole 557																					
Chemical Group I																					
H1-CC, 21-23		BOG	XRF	48.75	3.26	13.35	15.34	-	-	-	0.18	4.69	9.46	3.27	0.61	0.46	-	-	99.90	0.53	-
1-1, 0-3	460.52	BOG	XRF	48.38	3.50	12.45	15.90	-	-	-	0.19	5.88	9.01	2.89	0.40	0.38	-	-	99.61	0.63	-
1-1, 25-28	460.77	BOG	XRF	47.89	3.51	12.27	16.68	-	-	-	0.20	5.58	9.66	2.55	0.46	0.40	-	-	99.88	0.68	-
1-1, 25-28	460.77	SHM	XRFWT	47.70	3.50	12.50	-	-	7.98	7.70	0.19	5.79	9.16	2.73	0.51	0.38	0.08	0.72	98.96	-	-
1-1, 38-41	460.90	WEA	XRF	47.18	3.42	12.73	16.10	-	-	-	0.21	5.04	9.79	2.82	0.55	0.33	-	-	100.45	2.28	-
1-1, 40-43	460.92	BOG	XRF	47.99	3.47	12.25	16.39	-	-	-	0.23	5.18	10.02	2.55	0.45	0.42	-	-	99.59	0.64	-
1-1, 50-53	461.02	DRA	XRF	47.87	3.67	12.73	16.51	14.86	-	-	0.22	5.01	10.00	2.66	0.52	0.41	-	-	99.59	-	-
1-1, 105-108	461.57	SHM	XRFWT	47.80	3.46	12.30	-	-	6.40	8.88	0.21	5.35	9.94	2.71	0.45	0.37	0.03	1.15	99.06	-	-
1-1, 144-147	461.96	WEA	XRF	46.40	3.43	12.38	17.17	-	-	-	0.20	5.11	9.85	2.85	0.48	0.34	-	-	99.66	2.45	-
Hole 558																					
Chemical Group I																					
27-3, 46-48	408.47	PUC	XRFWT	49.32	1.20	14.56	-	-	4.74	5.32	0.16	10.16	10.84	2.48	0.38	0.13	0.21	1.20	100.70	-	<0.01
27-3, 69-72	408.71	SHM	XRFWT	49.90	1.22	14.40	-	-	3.73	5.86	0.15	9.45	10.48	2.16	0.29	0.13	0.04	1.35	99.15	-	-
27-3, 74-77	408.76	BOG	XRF	50.23	1.21	13.98	10.82	-	-	-	0.16	9.78	10.46	1.89	0.18	0.14	-	-	99.72	0.87	-
27-3, 92-95	408.94	WEA	XRF	49.58	1.22	14.43	10.41	-	-	-	0.15	9.38	10.35	2.27	0.39	0.13	-	-	100.42	2.11	-
27-3, 112-114	409.13	DRA	XRF	50.60	1.25	14.64	10.32	9.29	-	-	0.15	9.53	10.62	2.21	0.26	0.15	-	-	99.72	-	-
27-3, 116-118	409.17	SHM	XRFWT	49.10	1.22	14.20	-	-	4.69	5.46	0.16	10.58	10.65	2.17	0.34	0.13	0.50	0.97	100.19	-	-

Table 1. (Continued).

Sample	Depth (m)	Inv	Method	SiO_2	TiO_2	Al_2O_3	Fe_2O_3 (total)	FeO*	Fe_2O_3	FeO	MnO	MgO	CaO	Na_2O	K_2O	P_2O_5	CO_2	H_2O+	Total	LOI	S
Hole 558 (Cont.)																					
Chemical Group II																					
28-1, 38-41	414.90	WEA	XRF	49.86	1.08	15.01	10.10	-	-	-	0.15	8.01	11.85	2.15	0.31	0.11	-	-	100.23	1.60	-
28-1, 46-47	414.97	SHM	PROBE	51.80	1.08	15.20	-	9.14	-	-	0.15	8.44	12.00	2.34	0.07	-	-	-	100.22	-	-
28-1, 55-58	415.07	DRA	XRF	51.09	1.16	15.82	8.80	7.92	-	-	0.16	8.26	12.40	2.15	0.17	0.12	-	-	100.14	-	-
28-1, 79-81	415.30	WEA	XRF	49.49	1.08	15.14	9.85	-	-	-	0.15	7.51	12.03	2.24	0.29	0.10	-	-	100.27	2.39	-
28-1, 91-94	415.43	BOG	XRF	50.46	1.11	15.00	10.12	-	-	-	0.15	7.44	12.16	1.76	0.21	0.12	-	-	99.50	0.97	-
28-2, 6-8	416.07	PUC	XRFWT	49.57	1.16	15.42	-	-	4.62	5.20	0.15	7.31	12.86	2.39	0.34	0.10	0.54	0.96	100.62	-	<0.01
28-2, 52-55	416.54	WEA	XRF	49.60	1.09	15.14	10.42	-	-	-	0.16	7.91	12.16	2.15	0.25	0.11	-	-	100.48	1.49	-
28-2, 80-83	416.82	SHM	XRFWT	50.00	1.12	15.00	-	-	4.80	5.36	0.17	7.87	11.69	2.01	0.35	0.09	0.08	0.45	98.97	-	-
28-2, 100-102	417.01	SHM	XRFWT	50.40	1.14	15.40	-	-	4.69	4.56	0.16	8.17	12.23	2.07	0.21	0.10	0.20	0.49	99.78	-	-
28-2, 121-125	417.23	BOG	XRF	50.67	1.12	15.05	9.42	-	-	-	0.16	8.17	12.16	1.70	0.11	0.13	-	-	99.34	0.65	-
28-3, 36-38	417.87	WEA	XRF	50.20	1.08	15.05	9.52	-	-	-	0.15	7.43	11.76	2.21	0.24	0.10	-	-	100.09	2.35	-
28-3, 60-64	418.12	BOG	XRF	50.07	1.10	14.87	10.43	-	-	-	0.15	7.27	12.05	1.82	0.21	0.10	-	-	99.16	1.09	-
28-3, 118-120	418.69	SHM	XRFWT	49.90	1.10	15.10	-	-	3.66	6.06	0.16	7.86	11.89	1.96	0.22	0.10	0.10	0.99	99.12	-	-
Chemical Group III																					
29-1, 63-65	424.14	SHM	XRFWT	50.80	1.42	14.70	-	-	2.10	7.54	0.17	8.79	11.10	2.21	0.33	0.19	0.08	0.60	100.02	-	-
29-1, 63-65	424.14	SHM	PROBE	51.80	1.06	15.02	-	9.07	-	-	0.19	8.57	11.11	2.41	0.32	-	-	-	99.54	-	-
29-1, 99-101	424.50	WEA	XRF	49.58	1.37	14.63	9.40	-	-	-	0.13	7.78	10.97	2.39	0.47	0.19	-	-	100.55	3.64	-
29-1, 120-125	424.73	BOG	XRF	51.23	1.40	14.49	9.94	-	-	-	0.14	7.54	11.21	2.01	0.42	0.19	-	-	100.37	1.80	-
29-2, 6-8	425.07	PUC	XRFWT	50.02	1.38	14.77	-	-	2.17	7.53	0.16	8.62	11.65	2.30	0.38	0.18	0.59	0.89	100.64	-	0.10
29-2, 110-113	426.12	SHM	XRFWT	49.80	1.40	14.50	-	-	2.72	6.92	0.17	8.63	11.16	2.17	0.36	0.18	0.21	0.79	99.03	-	-
29-3, 110-112	427.61	SHM	XRFWT	50.40	1.44	14.80	-	-	2.72	6.87	0.16	8.51	11.26	2.23	0.36	0.18	0.18	0.86	100.01	-	-
29-4, 71-76	428.74	BOG	XRF	50.01	1.39	14.58	10.19	-	-	-	0.15	7.94	11.33	1.95	0.38	0.21	-	-	99.83	1.70	-
29-4, 83-85	428.84	SHM	XRFWT	48.20	1.35	14.30	-	-	5.50	4.52	0.14	7.64	11.82	2.12	0.65	0.18	0.86	1.81	99.06	-	-
30-1, 60-64	433.12	BOG	XRF	50.24	1.39	14.32	10.46	-	-	-	0.18	8.65	11.29	1.85	0.26	0.18	-	-	98.94	0.12	-
30-1, 95-97	433.46	SHM	XRFWT	48.80	1.44	14.80	-	-	3.69	6.05	0.16	8.10	11.24	2.27	0.43	0.18	0.45	1.16	98.73	-	-
30-1, 115-118	433.67	DRA	XRF	50.32	1.45	15.16	10.46	9.41	-	-	0.15	8.17	11.58	2.30	0.46	0.21	-	-	100.27	-	-
30-3, 12-14	435.63	WEA	XRF	49.21	1.38	14.65	9.94	-	-	-	0.14	7.90	10.94	2.35	0.49	0.19	-	-	100.33	3.14	-
30-3, 94-96	436.45	SHM	XRFWT	49.90	1.44	14.80	-	-	4.77	4.43	0.15	7.95	11.11	2.36	0.44	0.19	0.07	1.16	98.73	-	-
30-3, 99-103	436.51	BOG	XRF	49.46	1.41	14.60	10.18	-	-	-	0.15	8.17	11.41	2.08	0.33	0.19	-	-	99.61	1.63	-
30-4, 2-4	437.03	SHM	XRFWT	50.40	1.42	14.50	-	-	4.03	5.69	0.16	8.83	11.28	2.28	0.31	0.18	0.39	0.63	100.10	-	-
30-4, 7-9	437.08	SHM	PROBE	51.20	1.39	14.84	-	8.99	-	-	0.14	8.99	11.11	2.51	0.31	-	-	-	99.08	-	-
30-4, 41-43	437.42	SHM	XRFWT	49.40	1.42	14.50	-	-	5.15	4.45	0.15	8.54	10.98	2.31	0.36	0.19	0.07	1.11	98.64	-	-
30-4, 55-59	437.57	BOG	XRF	50.83	1.40	14.56	9.92	-	-	-	0.14	7.67	11.33	1.99	0.23	0.20	-	-	99.71	1.44	-
31-1, 62-64	442.13	BOG	XRF	50.35	1.37	14.40	10.29	-	-	-	0.15	8.20	11.21	2.08	0.29	0.19	-	-	99.93	1.40	-
31-1, 79-82	442.31	SHM	XRFWT	48.90	1.34	14.20	-	-	4.85	4.78	0.14	8.27	11.36	2.17	0.45	0.18	0.61	1.81	99.09	-	-
31-1, 86-89	442.38	WEA	XRF	50.10	1.38	14.75	9.33	-	-	-	0.14	7.78	11.11	2.36	0.29	0.19	-	-	100.45	3.02	-
31-1, 118-120	442.69	SHM	XRFWT	50.20	1.41	14.50	-	-	2.28	7.31	0.17	8.73	11.06	2.18	0.33	0.18	0.14	0.68	99.18	-	-
31-1, 118-120	442.69	SHM	PROBE	51.70	1.42	14.91	-	9.12	-	-	0.17	8.67	11.18	2.57	0.32	-	-	-	100.07	-	-
31-2, 128-130	444.29	BOG	XRF	50.61	1.39	14.45	10.08	-	-	-	0.15	8.41	11.29	2.04	0.28	0.19	-	-	100.18	1.29	-
32-1, 41-44	450.93	SHM	XRFWT	50.80	1.43	14.70	-	-	2.08	7.51	0.17	8.87	11.07	2.29	0.31	0.19	0.08	0.63	100.09	-	-
32-1, 41-44	450.93	SHM	PROBE	51.90	1.37	14.93	-	9.04	-	-	0.14	8.66	11.07	2.60	0.31	-	-	-	99.98	-	-
32-1, 106-110	451.58	BOG	XRF	49.52	1.40	14.52	10.12	-	-	-	0.15	8.35	11.55	2.17	0.34	0.19	-	-	99.91	1.60	-
32-1, 115-117	451.66	WEA	XRF	48.41	1.38	14.78	9.74	-	-	-	0.14	7.85	11.30	2.35	0.39	0.20	-	-	100.14	3.60	-
32-1, 123-125	451.74	SHM	XRFWT	48.60	1.42	14.80	-	-	4.77	4.91	0.14	7.79	11.69	2.27	0.39	0.20	0.65	1.65	99.32	-	-
32-2, 57-59	452.58	SHM	XRFWT	49.80	1.30	14.70	-	-	2.22	6.78	0.16	9.13	11.40	2.08	0.32	0.17	0.17	0.68	98.88	-	-
32-2, 130-132	453.31	DRA	XRF	50.33	1.35	15.40	9.36	8.42	-	-	0.14	8.67	11.89	2.24	0.40	0.19	-	-	99.97	-	-
32-2, 145-147	453.46	SHM	XRFWT	49.00	1.33	14.90	-	-	5.43	4.05	0.14	8.39	11.45	2.24	0.48	0.17	0.11	0.99	98.65	-	-
32-3, 35-37	453.86	SHM	XRFWT	50.00	1.32	15.00	-	-	5.16	4.34	0.14	8.86	11.49	2.27	0.40	0.17	0.22	1.01	100.40	-	-
32-3, 38-40	453.89	WEA	XRF	48.36	1.26	14.82	9.52	-	-	-	0.14	8.73	11.33	2.32	0.32	0.18	-	-	100.54	3.56	-
32-3, 63-67	454.15	BOG	XRF	49.24	1.30	14.64	9.48	-	-	-	0.13	8.30	11.48	2.17	0.26	0.18	-	-	98.87	1.69	-
32-4, 73-75	455.74	DRA	XRF	50.42	1.30	14.86	9.83	8.85	-	-	0.17	8.97	11.63	2.13	0.31	0.17	-	-	99.80	-	-
32-4, 77-79	455.78	SHM	XRFWT	50.30	1.31	14.80	-	-	2.16	6.88	0.16	9.25	11.40	2.10	0.28	0.16	0.09	0.58	99.48	-	-
32-4, 111-113	456.12	SHM	XRFWT	49.60	1.34	15.00	-	-	5.46	3.64	0.15	8.52	11.64	2.29	0.33	0.16	0.21	1.13	99.44	-	-
32-5, 66-70	457.18	BOG	XRF	48.83	1.34	15.40	10.20	-	-	-	0.15	7.67	12.09	2.27	0.29	0.19	-	-	100.23	1.80	-
32-5, 88-90	457.39	WEA	XRF	49.08	1.27	14.86	9.46	-	-	-	0.14	8.56	11.24	2.26	0.41	0.17	-	-	100.32	2.87	-
32-5, 101-103	457.52	DRA	XRF	49.94	1.30	15.30	9.91	8.92	-	-	0.14	8.78	11.70	2.35	0.41	0.19	-	-	100.00	-	-
33-1, 33-34	459.84	DT	PROBE	50.94	1.39	15.55	-	8.61	-	-	-	8.06	11.95	2.45	0.32	-	-	-	99.27	-	-
33-1, 33-34	459.84	SHM	PROBE	51.70	1.28	15.37	-	8.64	-	-	0.10	8.55	11.68	2.44	0.29	-	-	-	100.08	-	-
33-1, 77-80	460.29	BOG	XRF	49.27	1.29	14.65	9.93	-	-	-	0.14	8.36	11.62	2.25	0.24	0.16	-	-	99.47	1.56	-

33-2, 71-73	461.72	SHM	XRFWT	48.80	1.30	15.30	-	-	5.55	3.70	0.13	7.84	11.67	2.20	0.41	0.16	0.15	1.94	99.10	-	-
33-2, 144-147	462.46	DRA	XRF	50.38	1.31	14.85	9.83	8.85	-	-	0.17	9.01	11.55	1.84	0.30	0.18	-	-	99.40	-	-
33-3, 7-9	462.58	SHM	XRFWT	50.40	1.28	14.70	-	-	1.52	7.38	0.16	9.02	11.35	2.11	0.28	0.16	0.10	0.60	99.04	-	-
33-3, 61-64	463.13	DRA	XRF	50.29	1.30	14.92	9.86	8.87	-	-	0.16	9.05	11.51	1.88	0.30	0.18	-	-	99.45	-	-
33-3, 89-91	463.40	SHM	XRFWT	49.40	1.33	15.10	-	-	5.60	3.48	0.14	8.59	11.92	2.23	0.34	0.16	0.33	1.06	99.64	-	-
33-3, 135-138	463.87	WEA	XRF	48.47	1.26	14.69	9.64	-	-	-	0.15	8.99	11.23	2.23	0.36	0.17	-	-	100.26	3.07	-
33-3, 139-141	463.90	DRA	XRF	49.93	1.31	15.34	9.72	8.75	-	-	0.15	8.70	11.74	2.36	0.38	0.18	-	-	99.81	-	-
33-3, 144-147	463.96	BOG	XRF	49.95	1.28	14.90	9.72	-	-	-	0.14	8.81	11.72	2.14	0.28	0.17	-	-	100.59	1.48	-
34-1, 30-32	468.81	SHM	XRFWT	49.80	1.26	15.00	-	-	2.67	6.08	0.14	8.91	11.23	2.03	0.25	0.16	0.06	1.52	99.08	-	-
34-1, 34-38	468.86	BOG	XRF	50.04	1.28	14.45	9.81	-	-	-	0.14	8.67	11.59	1.79	0.21	0.17	-	-	99.29	1.14	-
34-1, 63-65	469.14	WEA	XRF	48.39	1.26	15.12	9.40	-	-	-	0.13	7.68	11.61	2.36	0.36	0.17	-	-	100.36	3.88	-
34-1, 113-115	469.64	PUC	XRFWT	49.18	1.25	14.88	-	-	5.59	3.89	0.27	8.40	12.20	2.48	0.47	0.16	0.50	1.11	100.38	-	<0.01
Chemical Group IV																					
35-1, 46-47	477.97	SHM	PROBE	51.50	1.18	14.86	-	8.83	-	-	0.16	9.36	11.40	2.33	0.23	-	-	-	99.84	-	-
35-1, 120-122	478.71	WEA	XRF	49.13	1.18	14.56	9.65	-	-	-	0.15	9.16	11.31	2.17	0.33	0.14	-	-	100.18	2.40	-
35-1, 128-131	478.80	BOG	XRF	49.71	1.18	14.22	10.18	-	-	-	0.16	8.96	11.53	1.92	0.33	0.16	-	-	99.40	1.05	-
35-2, 2-4	479.03	SHM	XRFWT	50.70	1.24	14.80	-	-	2.89	6.73	0.17	9.42	11.49	2.04	0.25	0.14	0.09	0.44	100.44	-	-
35-2, 11-13	479.12	SHM	XRFWT	49.90	1.22	14.60	-	-	2.61	6.82	0.17	9.27	11.43	2.02	0.26	0.14	0.14	0.55	99.15	-	-
35-2, 64-65	479.65	SHM	PROBE	51.30	1.17	14.84	-	8.82	-	-	0.15	9.46	11.52	2.32	0.23	-	-	-	99.78	-	-
35-2, 84-85	479.85	DT	PROBE	51.82	1.28	15.09	-	9.27	-	-	-	8.79	11.78	2.14	0.31	-	-	-	100.48	-	-
35-2, 97-102	480.00	BOG	XRF	49.50	1.20	14.58	10.10	-	-	-	0.15	9.17	11.78	1.70	0.25	0.15	-	-	99.74	1.16	-
35-2, 112-114	480.13	WEA	XRF	48.50	1.20	14.88	10.02	-	-	-	0.16	8.30	11.71	2.26	0.35	0.16	-	-	100.52	2.98	-
35-3, 89-91	481.40	WEA	XRF	48.45	1.20	14.82	10.03	-	-	-	0.15	8.79	11.62	2.14	0.32	0.15	-	-	100.41	2.74	-
35-3, 100-103	481.52	BOG	XRF	49.76	1.17	14.24	9.88	-	-	-	0.15	9.32	11.50	1.89	0.30	0.13	-	-	99.32	0.98	-
35-3, 107-109	481.58	DRA	XRF	49.43	1.22	15.03	10.14	9.12	-	-	0.17	8.92	12.13	2.52	0.35	0.16	-	-	100.06	-	-
35-3, 110-113	481.62	SHM	XRFWT	49.50	1.19	14.80	-	-	3.39	5.63	0.15	9.05	11.56	2.09	0.35	0.14	0.27	1.76	99.84	-	-
35-4, 102-104	483.03	WEA	XRF	48.99	1.22	14.77	9.80	-	-	-	0.15	8.92	11.17	2.28	0.35	0.17	-	-	100.44	2.62	-
35-4, 106-108	483.07	SHM	XRFWT	49.60	1.22	14.90	-	-	4.35	5.35	0.16	8.91	11.67	2.11	0.36	0.14	0.13	1.53	100.45	-	-
36-1, 62-65	487.14	BOG	XRF	49.64	1.23	14.60	10.30	-	-	-	0.16	8.25	12.02	1.67	0.28	0.16	-	-	98.92	0.61	-
36-1, 74-78	487.26	DRA	XRF	49.22	1.31	15.54	10.43	9.30	-	-	0.18	7.82	12.26	2.28	0.41	0.20	-	-	99.63	-	-
36-1, 82-84	487.33	WEA	XRF	48.65	1.22	14.73	9.82	-	-	-	0.15	8.40	11.40	2.19	0.38	0.17	-	-	100.09	2.98	-
36-2, 100-102	489.01	WEA	XRF	49.04	1.23	14.92	9.66	-	-	-	0.15	8.48	11.23	2.30	0.39	0.17	-	-	100.51	2.94	-
36-2, 107-110	489.09	BOG	XRF	49.75	1.25	14.85	9.93	-	-	-	0.16	8.31	12.04	1.82	0.33	0.17	-	-	100.00	1.39	-
36-3, 17-19	489.68	SHM	XRFWT	48.60	1.32	15.50	-	-	7.19	2.90	0.16	7.25	12.16	2.30	0.38	0.18	0.44	1.11	99.49	-	-
36-3, 31-33	489.82	SHM	PROBE	52.00	1.23	15.26	-	8.84	-	-	0.13	8.78	11.22	2.48	0.27	-	-	-	100.18	-	-
36-3, 44-46	489.95	PUC	XRFWT	50.27	1.23	15.00	-	-	4.08	5.30	0.15	8.67	11.61	2.51	0.43	0.15	0.05	1.05	100.50	-	0.02
Chemical Group V																					
37-1, 75-76	496.26	DT	PROBE	50.60	1.63	15.38	-	10.23	-	-	-	7.76	11.41	2.57	0.32	-	-	-	99.90	-	-
37-1, 89-92	496.41	DRA	XRF	49.35	0.98	16.15	9.90	8.90	-	-	0.14	8.33	12.04	2.16	0.29	0.14	-	-	99.48	-	-
37-1, 137-141	496.89	BOG	XRF	48.75	0.93	15.22	10.03	-	-	-	0.15	10.10	11.85	1.49	0.21	0.09	-	-	99.69	0.87	-
37-1, 143-148	496.96	WEA	XRF	48.34	0.93	15.26	9.66	-	-	-	0.15	10.02	11.33	2.01	0.29	0.11	-	-	100.33	2.23	-
38-1, 34-36	504.85	SHM	XRFWT	50.10	0.98	15.50	-	-	2.50	6.76	0.16	10.29	11.53	1.97	0.18	0.11	0.10	0.37	100.55	-	-
38-1, 93-95	505.44	SHM	XRFWT	48.10	0.96	15.40	-	-	5.67	3.76	0.16	9.87	11.54	1.96	0.25	0.11	0.16	0.89	98.78	-	-
38-1, 97-99	505.48	DRA	XRF	49.12	0.95	15.70	9.87	8.88	-	-	0.17	10.80	11.71	2.09	0.22	0.13	-	-	100.76	-	-
38-1, 104-108	505.56	WEA	XRF	47.34	0.95	15.82	9.76	-	-	-	0.15	8.59	11.47	2.07	0.29	0.13	-	-	100.39	3.82	-
38-1, 126-130	505.78	BOG	XRF	48.23	0.95	15.14	9.90	-	-	-	0.16	9.89	11.87	2.04	0.15	0.11	-	-	99.65	1.21	-
38-2, 61-63	506.62	SHM	XRFWT	49.20	1.25	14.90	-	-	4.10	5.27	0.14	8.54	11.46	2.18	0.32	0.16	0.05	1.57	99.12	-	-
38-2, 84-88	506.86	BOG	XRF	48.89	0.98	15.71	10.35	-	-	-	0.16	8.01	12.18	2.30	0.20	0.13	-	-	100.84	1.93	-
38-2, 116-118	507.17	DRA	XRF	49.45	0.99	16.15	10.10	9.09	-	-	0.16	8.33	12.21	2.12	0.23	0.13	-	-	99.87	-	-
39-1, 20-22	509.21	SHM	XRFWT	49.40	1.01	16.10	-	-	4.47	4.34	0.16	8.47	11.84	2.22	0.23	0.11	0.10	1.12	99.55	-	-
39-1, 25-26	509.26	DT	PROBE	50.71	1.63	15.19	-	10.49	-	-	-	7.35	10.99	2.56	0.31	-	-	-	99.23	-	-
39-1, 55-57	509.56	WEA	XRF	48.19	0.96	15.85	9.32	-	-	-	0.16	8.44	11.67	2.14	0.24	0.12	-	-	100.28	3.19	-
39-1, 83-87	509.85	BOG	XRF	48.87	0.98	15.76	9.84	-	-	-	0.17	8.30	12.10	2.75	0.18	0.13	-	-	100.63	1.55	-
39-1, 111-113	510.12	DRA	XRF	48.89	1.02	16.61	10.48	9.43	-	-	0.17	7.54	12.92	2.32	0.30	0.14	-	-	100.38	-	-
39-2, 11-13	510.62	DRA	XRF	49.61	0.96	15.60	9.87	8.88	-	-	0.18	9.89	11.71	2.17	0.29	0.13	-	-	100.40	-	-
39-2, 35-38	510.87	BOG	XRF	49.24	0.93	15.11	10.10	-	-	-	0.17	9.99	11.74	2.06	0.22	0.12	-	-	100.74	1.06	-
39-2, 69-71	511.20	WEA	XRF	48.21	0.94	15.59	9.44	-	-	-	0.17	9.30	11.38	2.09	0.23	0.12	-	-	100.17	2.70	-
39-2, 112-113	511.63	SHM	PROBE	51.20	0.98	15.63	-	8.52	-	-	0.15	10.16	11.59	2.12	0.15	-	-	-	100.45	-	-
39-4, 98-100	514.49	WEA	XRF	47.96	0.94	15.57	9.66	-	-	-	0.15	8.47	11.90	2.14	0.25	0.12	-	-	100.31	3.15	-
39-4, 122-125	514.74	SHM	XRFWT	49.40	0.98	15.50	-	-	4.11	5.10	0.15	10.09	11.56	1.99	0.27	0.11	0.09	0.69	100.01	-	-
39-4, 131-135	514.83	BOG	XRF	48.53	0.93	14.80	10.02	-	-	-	0.15	9.86	11.69	1.87	0.20	0.11	-	-	99.05	0.89	-
40-1, 92-94	518.93	SHM	XRFWT	47.30	1.00	16.40	-	-	5.24	4.37	0.15	6.92	12.96	2.02	0.24	0.12	0.67	1.67	99.01	-	-
40-2, 7-9	519.58	SHM	XRFWT	46.90	1.45	15.90	-	-	6.13	2.91	0.14	6.86	13.16	2.11	0.76	0.28	0.94	0.88	98.40	-	-
41-2, 143-146	529.95	BOG	XRF	48.02	0.91	15.59	10.58	-	-	-	0.16	10.40	11.40	1.71	0.10	0.07	-	-	100.36	1.42	-
41-3, 111-116	531.14	BT	XRF	37.72	0.02	0.77	6.67	-	-	-	0.07	37.39	2.01	0.12	0.00	-	-	-	100.84	16.07	-
42-1, 57-59	536.58	BT	XRF	38.12	0.02	0.72	7.29	-	-	-	0.11	39.53	0.08	0.15	0.00	-	-	-	99.05	13.03	-

Table 1. (Continued).

Sample	Depth (m)	Inv	Method	SiO_2	TiO_2	Al_2O_3	Fe_2O_3 (total)	FeO*	Fe_2O_3	FeO	MnO	M_gO	CaO	Na_2O	K_2O	P_2O_5	CO_2	H_2O+	Total	LOI	S
Hole 559																					
Chemical Group I																					
H1-CC, 2-4	238.00	BOG	XRF	50.57	1.49	15.19	11.69	-	-	-	0.18	8.28	11.31	2.00	0.30	0.19	-	-	101.29	0.09	-
1-1, 25-29	238.27	SHM	XRFWT	50.10	1.50	15.00	-	-	2.36	7.80	0.18	8.28	11.18	2.38	0.33	0.19	0.17	0.68	100.15	-	-
1-1, 117-119	239.18	DRA	XRF	49.23	1.61	16.19	11.30	10.17	-	-	0.17	6.45	11.73	2.76	0.62	0.25	-	-	100.30	-	-
1-1, 120-123	239.22	BOG	XRF	49.13	1.54	15.52	11.83	-	-	-	0.15	6.82	11.55	2.28	0.48	0.23	-	-	101.33	1.80	-
1-1, 134-136	239.35	PUC	XRFWT	48.18	1.50	15.77	-	-	6.84	4.08	0.16	6.58	11.79	2.83	0.55	0.22	0.32	1.52	100.34	-	<0.01
1-2, 36-39	239.88	BOG	XRF	44.73	1.65	16.60	13.09	-	-	-	0.20	3.15	12.75	2.25	0.71	0.41	-	-	99.39	3.85	-
1-2, 52-56	240.04	SHM	XRFWT	48.90	1.48	15.40	-	-	5.44	4.19	0.13	7.30	11.39	2.42	0.42	0.18	0.11	1.73	99.05	-	-
1-2, 56-59	240.08	BOG	XRF	48.72	1.49	15.34	10.98	-	-	-	0.14	7.12	11.46	2.22	0.39	0.20	-	-	99.72	1.66	-
1-2, 118-120	240.69	WEA	XRF	46.40	1.46	15.36	10.98	-	-	-	0.15	6.50	11.38	2.68	0.48	0.23	-	-	100.23	4.61	-
1-3, 0-3	241.01	BOG	XRF	46.40	1.66	16.97	12.56	-	-	-	0.21	4.29	11.01	2.39	0.87	0.36	-	-	98.71	1.99	-
1-3, 44-47	241.46	BOG	XRF	45.28	1.55	16.09	11.94		-	-	0.16	3.85	13.72	2.25	0.62	0.28	-	-	98.78	3.04	-
1-3, 76-79	241.78	BOG	XRF	47.24	1.55	15.63	11.60	-	-	-	0.18	5.12	12.94	2.36	0.37	0.26	-	-	99.17	1.92	-
1-3, 129-132	242.31	BOG	XRF	46.97	1.66	16.59	12.54	-	-	-	0.23	3.83	12.71	2.30	0.49	0.28	-	-	99.49	1.99	-
1-3, 148-150	242.49	BOG	XRF	49.65	1.48	14.57	11.35	-	-	-	0.18	7.91	10.83	2.00	0.37	0.19	-	-	98.95	0.42	-
1-4, 20-22	242.71	BOG	XRF	48.33	1.72	15.45	12.95	-	-	-	0.18	6.91	8.78	2.94	0.96	0.16	-	-	99.67	1.29	-
1-4, 40-42	242.91	PUC	XRFWT	49.75	1.47	15.28	-	-	1.90	8.46	0.17	8.01	10.84	2.79	0.48	0.18	0.06	0.99	100.38	-	0.10
2-1, 1-3	247.02	BOG	XRF	49.12	1.52	15.37	10.88	-	-	-	0.14	6.82	11.69	2.17	0.37	0.20	-	-	99.91	1.63	-
2-2, 11-14	248.63	SHM	XRFWT	45.90	1.51	15.20	-	-	7.68	3.31	0.19	5.32	13.22	2.45	0.67	0.20	1.79	0.96	98.41	-	-
2-2, 18-20	248.69	WEA	XRF	47.30	1.46	15.48	10.77	-	-	-	0.16	7.16	12.14	2.49	0.42	0.20	-	-	100.51	2.93	-
2-2, 24-28	248.76	BOG	XRF	48.29	1.48	15.12	11.22	-	-	-	0.16	6.99	12.30	2.14	0.40	0.17	-	-	99.51	1.24	-
2-3, 75-79	250.77	BOG	XRF	49.00	1.45	14.67	11.59	-	-	-	0.17	7.43	11.59	2.16	0.48	0.18	-	-	100.33	1.61	-
2-3, 111-113	251.12	DRA	XRF	50.62	1.52	15.49	9.93	8.94	-	-	0.12	7.84	11.57	2.70	0.35	0.20	-	-	100.34	-	-
3-1, 13-14	256.14	BOG	XRF	50.28	1.48	15.00	11.23	-	-	-	0.18	7.80	10.90	2.34	0.40	0.18	-	-	99.93	0.14	-
3-1, 25-27	256.26	SHM	XRFWT	50.20	1.50	14.98	-	-	2.10	8.08	0.18	8.22	11.15	2.44	0.31	0.19	-	0.71	99.87	-	-
4-1, 118-121	257.70	WEA	XRF	47.59	1.45	14.82	10.34	-	-	-	0.13	7.37	11.14	2.65	0.38	0.19	-	-	100.35	4.29	-
4-1, 121-124	257.72	DRA	XRF	49.90	1.54	15.35	10.44	9.39	-	-	0.16	7.56	11.78	2.64	0.38	0.21	-	-	99.96	-	-
4-1, 125-129	257.77	BOG	XRF	49.47	1.49	15.06	10.83	-	-	-	0.14	7.23	11.43	2.28	0.33	0.21	-	-	100.22	1.75	-
4-2, 92-96	258.94	BOG	XRF	48.33	1.51	15.13	10.90	-	-	-	0.15	6.52	12.48	2.15	0.42	0.20	-	-	100.00	2.21	-
5-1, 36-38	265.37	SHM	XRFWT	49.00	1.53	15.30	-	-	6.58	3.78	0.15	7.27	11.35	2.59	0.39	0.18	0.19	1.20	99.48	-	-
5-1, 38-40	265.39	WEA	XRF	47.72	1.44	14.88	10.30	-	-	-	0.13	6.99	11.11	2.58	0.39	0.19	-	-	100.11	4.38	-
5-1, 45-48	265.47	BOG	XRF	48.74	1.46	14.72	10.86	-	-	-	0.14	7.31	11.25	2.17	0.35	0.19	-	-	98.90	1.71	-
5-1, 50-53	265.51	DRA	XRF	49.50	1.54	15.40	11.21	10.09	-	-	0.19	6.69	11.94	2.77	0.44	0.21	-	-	99.89	-	-
5-2, 11-13.5	266.62	DT	PROBE	51.15	1.52	14.90	-	11.64	-	-	-	6.91	11.62	2.36	0.08	-	-	-	100.18	-	-
5-2, 35-39	266.87	BOG	XRF	46.76	1.62	16.38	12.30	-	-	-	0.16	4.28	12.79	2.14	0.33	0.25	-	-	99.30	2.29	-
5-3, 25-29	268.27	BOG	XRF	47.47	1.54	15.60	11.80	-	-	-	0.15	4.97	12.85	2.32	0.43	0.22	-	-	99.92	2.57	-
6-2, 12-14	275.63	WEA	XRF	48.14	1.46	15.11	9.92	-	-	-	0.13	7.20	11.12	2.55	0.39	0.20	-	-	100.43	4.21	-
6-2, 14-16	275.65	DRA	XRF	49.67	1.54	15.39	10.59	9.53	-	-	0.15	7.28	11.69	2.39	0.44	0.20	-	-	99.35	-	-
6-2, 17-20	275.68	PUC	XRFWT	49.20	1.49	15.42	-	-	5.61	4.04	0.13	7.34	11.82	2.82	0.41	0.19	0.23	1.40	100.10	-	<0.01
6-2, 25-29	275.77	BOG	XRF	49.24	1.50	15.09	11.33	-	-	-	0.16	7.89	11.55	2.32	0.38	0.20	-	-	101.21	1.55	-
6-3, 27-31	277.20	BOG	XRF	49.14	1.44	14.61	10.67	-	-	-	0.14	7.45	11.27	2.18	0.37	0.19	-	-	99.18	1.72	-
7-1, 111-114	284.13	DRA	XRF	48.48	1.59	15.86	11.71	10.54	-	-	0.19	6.38	12.35	2.47	0.42	0.24	-	-	99.69	-	-
7-1, 137-140	284.39	BOG	XRF	48.72	1.46	14.53	11.11	-	-	-	0.17	7.32	11.33	2.08	0.41	0.19	-	-	99.24	1.92	-
7-1, 143-146	284.45	PUC	XRFWT	48.20	1.45	14.85	-	-	5.62	4.92	0.15	7.64	12.16	2.78	0.53	0.18	0.81	1.26	100.55	-	0.01
7-2, 1-3	284.52	SHM	XRFWT	49.20	1.52	15.00	-	-	5.80	4.57	0.16	7.79	11.17	2.46	0.49	0.19	0.16	0.99	99.49	-	-
7-2, 3-6	284.55	WEA	XRF	47.23	1.45	14.38	10.65	-	-	-	0.15	8.05	11.03	2.58	0.47	0.18	-	-	99.70	3.53	-
7-2, 143-146	285.95	BOG	XRF	48.86	1.49	14.89	11.02	-	-	-	0.16	7.37	11.42	2.11	0.34	0.19	-	-	99.47	1.62	-
7-3, 15-17	286.16	PUC	XRFWT	48.82	1.52	15.47	-	-	6.08	4.18	0.15	7.19	11.78	2.81	0.42	0.19	0.12	1.35	100.08	-	<0.01
7-3, 18-20	286.19	DRA	XRF	49.68	1.54	15.31	10.77	9.69	-	-	0.15	7.46	11.35	2.54	0.51	0.20	-	-	99.51	-	-
7-3, 103-106	287.05	DRA	XRF	49.97	1.52	14.97	10.80	9.72	-	-	0.16	7.52	11.24	2.59	0.39	0.21	-	-	99.38	-	-
7-3, 110-113	287.12	BOG	XRF	49.17	1.45	14.58	10.71	-	-	-	0.14	7.21	11.33	2.36	0.33	0.18	-	-	99.24	1.78	-
7-3, 114-117	287.16	SHM	XRFWT	49.10	1.49	15.00	-	-	6.44	3.59	0.19	7.33	11.14	2.60	0.42	0.18	0.09	1.08	98.69	-	-
8-1, 18-20	292.19	WEA	XRF	48.00	1.46	14.79	10.34	-	-	-	0.14	7.22	10.89	2.50	0.41	0.19	-	-	100.17	4.23	-
8-1, 48-51	292.50	BOG	XRF	49.38	1.47	14.85	10.48	-	-	-	0.14	7.27	11.41	2.14	0.30	0.18	-	-	99.30	1.68	-
8-1, 127-129	293.28	SHM	XRFWT	49.20	1.49	14.80	-	-	5.81	3.95	0.13	7.62	11.06	2.53	0.37	0.19	0.11	1.81	99.11	-	-
8-2, 102-103	294.53	DT	PROBE	50.29	1.49	15.17	-	10.09	-	-	-	7.49	11.27	2.53	0.36	-	-	-	98.69	-	-
8-3, 6-10	295.08	DRA	XRF	48.65	1.50	15.14	12.02	10.82	-	-	0.24	6.77	11.98	2.33	0.69	0.20	-	-	99.52	-	-
8-3, 19-21	295.20	BOG	XRF	49.05	1.46	14.53	11.30	-	-	-	0.15	7.32	11.23	2.35	0.40	0.20	-	-	99.81	1.82	-
Hole 560																					
2-1, 93-96	377.45	BOG	XRF	51.73	1.19	16.97	6.44	-	-	-	0.11	8.37	10.41	2.73	0.06	0.12	-	-	99.79	1.66	-

4-1, 60-65	399.13	BT	XRF	39.21	0.02	0.84	6.61	-	-	-	0.08	39.06	0.01	0.09	0.00	-	-	-	98.78	12.86	-
4-1, 60-65	399.13	BT	XRF	39.30	0.02	0.87	6.78	-	-	-	0.08	39.27	0.01	0.06	0.00	-	-	-	99.25	12.86	-
5-1, 101-105	404.53	BT	XRF	39.58	0.02	0.71	7.09	-	-	-	0.07	39.73	0.00	0.06	0.00	-	-	-	100.63	13.37	-
Hole 561																					
Chemical Group I																					
H1-CC, 1-5	411.50	SHM	XRFWT	48.80	1.21	15.20	-	-	6.24	3.72	0.16	7.29	12.26	2.38	0.44	0.21	0.36	1.02	99.28	-	-
H1-CC, 3-5	411.50	DRA	XRF	49.71	1.23	15.49	9.97	8.97	-	-	0.16	7.93	12.33	2.48	0.37	0.23	-	-	99.89	-	-
H1-CC, 9-13	411.50	WEA	XRF	48.53	1.16	15.13	9.47	-	-	-	0.15	8.18	11.72	2.36	0.37	0.22	-	-	100.08	2.79	-
H1-CC, 10-14	411.50	BOG	XRF	49.93	1.20	14.85	9.72	-	-	-	0.15	8.72	12.18	2.02	0.24	0.23	-	-	100.44	1.20	-
1-1, 4-9	411.57	DRA	XRF	49.75	1.21	15.26	9.87	8.88	-	-	0.15	8.18	12.10	2.51	0.36	0.23	-	-	99.62	-	-
1-1, 28-31	411.80	BOG	XRF	48.98	1.18	14.71	10.12	-	-	-	0.15	8.36	12.05	2.03	0.27	0.20	-	-	99.23	1.18	-
1-1, 28-31	411.80	JCB	INAA	-	-	-	-	9.02	-	-	-	-	-	2.37	-	-	-	-	-	-	-
1-1, 33-38	411.86	SHM	XRFWT	49.40	1.20	15.10	-	-	4.36	4.83	0.15	8.77	12.00	2.35	0.33	0.22	0.07	1.34	100.15	-	-
1-1, 44-47	411.96	WEA	XRF	48.30	1.16	14.84	9.67	-	-	-	0.15	9.05	11.76	2.30	0.35	0.22	-	-	100.43	2.63	-
Chemical Group II																					
1-1, 84-87	412.36	DRA	XRF	50.45	1.37	15.19	11.08	9.97	-	-	0.18	7.34	11.66	2.72	0.34	0.13	-	-	100.47	-	-
1-1, 119-122	412.71	JCB	INAA	-	-	-	-	10.15	-	-	-	-	-	2.40	-	-	-	-	-	-	-
1-1, 128-131	412.80	BOG	XRF	49.81	1.32	14.67	10.96	-	-	-	0.17	7.34	12.35	1.95	0.18	0.13	-	-	100.11	1.23	-
1-2, 3-6	413.05	JCB	INAA	-	-	-	-	9.90	-	-	-	-	-	2.34	-	-	-	-	-	-	-
1-2, 17-20	413.19	BOG	XRF	50.03	1.37	15.05	10.80	-	-	-	0.18	7.51	11.93	1.91	0.12	0.12	-	-	99.63	0.61	-
1-2, 22-24	413.23	WEA	XRF	48.76	1.34	14.91	10.93	-	-	-	0.18	8.02	11.49	2.41	0.15	0.11	-	-	99.83	1.53	-
1-2, 24-26	413.25	DRA	XRF	50.13	1.35	15.05	11.61	10.45	-	-	0.18	7.48	11.31	2.57	0.30	0.14	-	-	100.12	-	-
1-2, 36-38	413.37	JCB	INAA	-	-	-	-	11.21	-	-	-	-	-	2.45	-	-	-	-	-	-	-
2-1, 6-8	414.57	JCB	INAA	-	-	-	-	10.38	-	-	-	-	-	2.46	-	-	-	-	-	-	-
2-1, 52-55	415.04	BOG	XRF	49.81	1.34	14.48	11.40	-	-	-	0.18	7.59	11.81	1.96	0.12	0.13	-	-	99.56	0.74	-
2-1, 71-73	415.22	JCB	INAA	-	-	-	-	11.06	-	-	-	-	-	2.39	-	-	-	-	-	-	-
2-1, 78-80	415.29	JCB	INAA	-	-	-	-	10.00	-	-	-	-	-	2.42	-	-	-	-	-	-	-
2-1, 86-88	415.37	JCB	INAA	-	-	-	-	10.72	-	-	-	-	-	2.39	-	-	-	-	-	-	-
2-1, 92-93	415.43	DT	PROBE	51.38	1.64	15.12	-	11.22	-	-	-	7.30	11.52	2.54	0.09	-	-	-	100.81	-	-
2-1, 97-100	415.49	SHM	XRFWT	50.30	1.39	15.50	-	-	4.84	5.27	0.18	7.92	11.55	2.47	0.16	0.11	0.14	0.67	100.48	-	-
2-1, 100-103	415.52	DRA	XRF	50.25	1.33	14.96	11.82	10.64	-	-	0.18	7.08	11.42	2.58	0.54	0.13	-	-	100.28	-	-
2-1, 111-116	415.64	WEA	XRF	48.98	1.32	14.88	11.43	-	-	-	0.18	7.25	11.56	2.38	0.40	0.11	-	-	100.33	1.84	-
2-1, 143-146	415.95	SHM	XRFWT	49.50	1.38	14.80	-	-	3.94	6.73	0.18	7.68	11.24	2.25	0.22	0.12	0.08	1.06	99.21	-	-
2-2, 18-21	416.20	JCB	INAA	-	-	-	-	10.57	-	-	-	-	-	2.48	-	-	-	-	-	-	-
2-2, 25-28	416.27	JCB	INAA	-	-	-	-	10.45	-	-	-	-	-	2.48	-	-	-	-	-	-	-
2-2, 54-56	416.55	SHM	XRFWT	49.80	1.36	15.10	-	-	5.06	5.13	0.18	7.43	11.29	2.40	0.21	0.12	0.07	0.32	98.50	-	-
2-2, 61-63	416.62	JCB	INAA	-	-	-	-	10.12	-	-	-	-	-	2.43	-	-	-	-	-	-	-
2-2, 80-82	416.81	JCB	INAA	-	-	-	-	10.65	-	-	-	-	-	2.34	-	-	-	-	-	-	-
2-2, 82-84	416.83	DRA	XRF	49.99	1.35	15.28	10.94	9.84	-	-	0.20	7.85	11.66	2.55	0.28	0.13	-	-	100.23	-	-
2-2, 122-126	417.24	BOG	XRF	50.09	1.32	14.77	11.22	-	-	-	0.18	7.60	11.81	2.12	0.18	0.11	-	-	100.17	0.77	-
2-2, 138-141	417.40	SHM	XRFWT	49.20	1.33	14.90	-	-	3.52	5.83	0.18	7.50	12.33	2.23	0.14	0.11	0.80	0.97	99.02	-	-
2-3, 28-30	417.79	JCB	INAA	-	-	-	-	10.60	-	-	-	-	-	2.52	-	-	-	-	-	-	-
2-3, 52-54	418.03	JCB	INAA	-	-	-	-	8.91	-	-	-	-	-	2.55	-	-	-	-	-	-	-
2-3, 55-59	418.07	SHM	XRFWT	50.10	1.41	15.00	-	-	5.13	5.80	0.18	7.36	11.41	2.46	0.27	0.12	0.09	0.51	99.83	-	-
2-3, 71-73	418.22	BOG	XRF	50.21	1.34	14.20	13.26	-	-	-	0.19	6.72	11.34	2.20	0.49	0.12	-	-	100.56	0.49	-
2-3, 75-76	418.26	SHM	XRFWT	50.20	1.35	14.80	-	-	5.13	6.25	0.18	7.52	11.11	2.35	0.44	0.11	0.08	0.59	100.11	-	-
2-3, 124-127	418.76	SHM	XRFWT	49.60	1.33	14.60	-	-	5.27	5.78	0.18	7.14	11.26	2.27	0.45	0.11	0.30	0.66	98.94	-	-
2-3, 127-130	418.79	WEA	XRF	48.42	1.30	14.61	10.89	-	-	-	0.18	7.68	11.93	2.46	0.22	0.11	-	-	99.88	2.08	-
3-1, 9-13	423.61	DRA	XRF	50.11	1.34	14.88	11.89	10.70	-	-	0.18	7.22	11.49	2.59	0.50	0.13	-	-	100.33	-	-
3-1, 40-41	423.91	DT	PROBE	51.27	1.50	14.76	-	11.27	-	-	-	7.18	11.65	2.60	0.09	-	-	-	100.32	-	-
3-1, 76-79	424.28	DRA	XRF	50.09	1.39	15.10	11.39	10.25	-	-	0.17	7.44	11.69	2.53	0.29	0.13	-	-	100.22	-	-
3-1, 101-104	424.53	SHM	XRFWT	49.40	1.34	14.80	-	-	4.87	5.54	0.17	7.62	11.43	2.30	0.27	0.11	0.23	0.66	98.75	-	-
3-1, 114-118	424.66	BOG	XRF	49.03	1.29	14.36	11.20	-	-	-	0.17	7.07	12.52	2.48	0.27	0.12	-	-	100.24	1.73	-
3-1, 138-140	424.89	WEA	XRF	48.78	1.29	14.65	11.54	-	-	-	0.16	7.17	11.45	2.30	0.43	0.11	-	-	100.00	2.12	-
3-1, 140-142	424.91	JCB	INAA	-	-	-	-	10.40	-	-	-	-	-	2.43	-	-	-	-	-	-	-
3-2, 41-53	425.47	SHM	XRFWT	46.90	1.20	14.00	-	-	6.12	5.32	0.15	6.67	12.85	2.18	0.53	0.10	1.72	1.42	99.15	-	-
3-2, 56-60	425.58	JCB	INAA	-	-	-	-	9.01	-	-	-	-	-	2.34	-	-	-	-	-	-	-
3-2, 77-80	425.79	DRA	XRF	50.05	1.37	14.79	11.41	10.27	-	-	0.18	7.67	11.83	2.24	0.26	0.13	-	-	99.91	-	-
Hole 562																					
Chemical Group I																					
H1-CC, 5-8	241.00	SHM	XRFWT	48.80	1.59	15.60	-	-	6.23	5.23	0.17	6.15	11.49	2.55	0.35	0.14	0.11	0.62	99.01	-	-
H1-CC, 16-19	241.00	DRA	XRF	49.23	1.57	15.71	11.90	10.71	-	-	0.18	6.71	11.64	2.29	0.25	0.15	-	-	99.63	-	-
1-1, 57-60	241.59	SHM	XRFWT	50.60	1.60	14.91	-	-	1.66	9.33	0.20	7.81	11.45	2.57	0.08	0.13	0.09	0.27	100.97	-	-

Table 1. (Continued).

Sample	Depth (m)	Inv.	Method	SiO_2	TiO_2	Al_2O_3	Fe_2O_3 (total)	FeO^*	Fe_2O_3	FeO	MnO	M_gO	CaO	Na_2O	K_2O	P_2O_5	CO_2	H_2O+	Total	LOI	S
Hole 562 (Cont.)																					
Chemical Group I (Cont.)																					
1-1, 104-107	242.06	BOG	XRF	49.81	1.53	14.72	11.36	-	-	-	0.18	7.16	11.81	2.81	0.17	0.14	-	-	100.18	0.49	-
1-1, 110-112	242.11	SHM	XRFWT	49.30	1.50	15.10	-	-	4.79	5.87	0.16	6.80	11.53	2.33	0.37	0.13	0.13	1.32	99.31	-	-
1-2, 34-37	242.86	BOG	XRF	49.69	1.53	14.29	11.60	-	-	-	0.18	7.29	11.62	2.67	0.07	0.15	-	-	99.70	0.61	-
1-2, 82-84	243.33	WEA	XRF	49.77	1.62	15.58	9.92	-	-	-	0.17	6.16	12.34	2.72	0.29	0.15	-	-	99.59	0.87	-
1-2, 140-142	243.91	DT	PROBE	50.77	1.64	14.73	-	10.85	-	-	-	7.28	11.65	2.60	0.09	-	-	-	99.61	-	-
1-3, 92-95	244.93	BOG	XRF	49.19	1.50	14.79	11.66	-	-	-	0.18	7.61	11.74	2.47	0.20	0.14	-	-	100.05	0.57	-
2-1, 55-59	250.57	BOG	XRF	49.45	1.51	14.67	11.67	-	-	-	0.18	7.59	11.51	2.40	0.09	0.14	-	-	99.75	0.54	-
2-2, 54-59	252.07	BOG	XRF	48.74	1.55	14.72	11.82	-	-	-	0.18	6.95	11.76	2.27	0.33	0.14	-	-	99.38	0.92	-
2-3, 8-10	253.09	DRA	XRF	49.91	1.58	15.31	11.79	10.61	-	-	0.18	7.24	11.53	2.42	0.31	0.14	-	-	100.41	-	-
2-3, 61-65	253.63	BOG	XRF	50.20	1.56	14.48	11.70	-	-	-	0.18	7.35	11.48	2.17	0.17	0.14	-	-	99.83	0.40	-
2-4, 33-38	254.86	BOG	XRF	50.18	1.53	14.86	11.69	-	-	-	0.18	7.38	11.63	2.02	0.40	0.14	-	-	100.03	0.38	-
2-4, 68-70	255.19	SHM	XRFWT	49.80	1.55	15.20	-	-	3.80	6.52	0.18	7.02	11.41	2.39	0.18	0.14	0.08	0.50	98.81	-	-
2-4, 74-76	255.25	WEA	XRF	48.78	1.52	15.42	11.08	-	-	-	0.18	6.75	11.56	2.62	0.29	0.14	-	-	100.43	2.09	-
2-5, 65-67	256.66	PUC	XRFWT	50.20	1.54	15.25	-	-	3.84	6.82	0.17	6.93	11.94	2.92	0.15	0.13	0.10	0.73	100.72	-	0.11
2-5, 73-76	256.75	BOG	XRF	50.13	1.52	14.61	11.78	-	-	-	0.18	7.17	11.65	2.01	0.00	0.15	-	-	99.63	0.43	-
3-1, 46-48	259.47	JCB	INAA	-	-	-	-	10.10	-	-	-	-	-	2.51	-	-	-	-	-	-	-
3-1, 85-88	259.87	BOG	XRF	50.18	1.53	14.85	11.57	-	-	-	0.18	7.32	11.63	2.10	0.11	0.16	-	-	100.04	0.41	-
3-2, 141-143	261.92	WEA	XRF	49.42	1.51	15.51	11.09	-	-	-	0.17	7.08	11.46	2.44	0.20	0.14	-	-	100.32	1.30	-
3-3, 103-106	263.05	BOG	XRF	49.13	1.54	14.79	11.76	-	-	-	0.18	6.92	11.63	2.07	0.31	0.14	-	-	99.24	0.77	-
3-4, 120-123	264.72	BOG	XRF	49.62	1.55	14.84	10.95	-	-	-	0.17	6.77	11.74	2.17	0.02	0.14	-	-	98.88	0.91	-
4-1, 9-12	268.11	BOG	XRF	48.87	1.57	14.67	12.15	-	-	-	0.18	6.27	11.76	2.32	0.22	0.15	-	-	99.24	1.08	-
4-1, 14-16	268.15	JCB	INAA	-	-	-	-	10.89	-	-	-	-	-	2.71	-	-	-	-	-	-	-
4-1, 58-60	268.59	JCB	INAA	-	-	-	-	10.54	-	-	-	-	-	2.52	-	-	-	-	-	-	-
4-1, 75-77	268.76	DRA	XRF	49.83	1.60	15.21	11.75	10.57	-	-	0.19	7.41	11.42	2.55	0.13	0.17	-	-	100.26	-	-
4-1, 78-80	268.79	JCB	INAA	-	-	-	-	10.19	-	-	-	-	-	2.62	-	-	-	-	-	-	-
4-1, 91-93	268.92	SHM	XRFWT	49.00	1.51	15.20	-	-	3.76	6.74	0.16	7.46	11.65	2.44	0.09	0.13	0.08	0.52	98.70	-	-
4-2, 0-3	269.51	BOG	XRF	49.49	1.52	14.90	11.60	-	-	-	0.18	7.22	11.78	2.48	0.05	0.14	-	-	99.87	0.51	-
4-2, 4-7	269.56	PUC	XRFWT	49.64	1.51	15.32	-	-	2.51	8.20	0.17	7.46	11.75	2.61	0.16	0.14	0.07	0.65	100.19	-	0.12
4-2, 22-25	269.74	JCB	INAA	-	-	-	-	10.22	-	-	-	-	-	2.51	-	-	-	-	-	-	-
4-2, 45-47	269.96	WEA	XRF	49.64	1.49	15.63	10.71	-	-	-	0.17	6.69	11.49	2.49	0.22	0.14	-	-	100.18	1.51	-
4-3, 27-29	271.28	JCB	INAA	-	-	-	-	10.25	-	-	-	-	-	2.48	-	-	-	-	-	-	-
4-3, 64-67	271.66	JCB	INAA	-	-	-	-	10.69	-	-	-	-	-	2.54	-	-	-	-	-	-	-
4-3, 83-85	271.84	BOG	XRF	47.46	1.64	14.82	12.44	-	-	-	0.21	5.71	12.81	2.54	0.24	0.18	-	-	99.64	1.59	-
4-3, 86-88	271.87	JCB	INAA	-	-	-	-	10.88	-	-	-	-	-	2.69	-	-	-	-	-	-	-
4-4, 60-63	273.12	SHM	XRFWT	50.00	1.61	14.77	-	-	1.35	9.48	0.19	7.79	11.26	2.52	0.09	0.14	0.03	0.30	99.53	-	-
4-4, 100-103	273.51	BOG	XRF	49.20	1.55	15.03	11.46	-	-	-	0.17	6.42	11.63	2.07	0.32	0.15	-	-	98.68	0.68	-
4-4, 117-119	273.68	JCB	INAA	-	-	-	-	9.70	-	-	-	-	-	2.34	-	-	-	-	-	-	-
4-5, 26-28	274.27	JCB	INAA	-	-	-	-	10.02	-	-	-	-	-	2.50	-	-	-	-	-	-	-
5-1, 64-66	277.65	DRA	XRF	50.32	1.58	15.97	10.70	9.63	-	-	0.16	6.73	11.85	2.52	0.21	0.16	-	-	100.19	-	-
5-2, 76-79	279.28	BOG	XRF	49.93	1.58	14.93	11.32	-	-	-	0.17	7.17	11.70	2.18	0.13	0.15	-	-	99.72	0.46	-
5-2, 89-91	279.40	JCB	INAA	-	-	-	-	10.60	-	-	-	-	-	2.47	-	-	-	-	-	-	-
5-3, 9-11	280.10	JCB	INAA	-	-	-	-	10.34	-	-	-	-	-	2.56	-	-	-	-	-	-	-
5-3, 40-42	280.41	SHM	XRFWT	49.80	1.57	14.90	-	-	3.60	6.83	0.18	7.00	11.62	2.41	0.14	0.14	0.13	0.55	98.83	-	-
5-3, 58-60	280.59	JCB	INAA	-	-	-	-	10.22	-	-	-	-	-	2.47	-	-	-	-	-	-	-
5-3, 79-81	280.80	WEA	XRF	49.11	1.53	14.95	11.52	-	-	-	0.18	7.47	11.23	2.42	0.14	0.14	-	-	100.27	1.58	-
5-3, 104-107	281.06	BOG	XRF	49.57	1.55	14.97	11.55	-	-	-	0.18	7.17	11.71	1.88	0.10	0.15	-	-	99.47	0.64	-
5-4, 29-31	281.80	DRA	XRF	49.52	1.54	15.82	11.25	10.12	-	-	0.17	7.05	11.53	2.70	0.10	0.15	-	-	99.83	-	-
5-4, 106-108	282.57	JCB	INAA	-	-	-	-	10.05	-	-	-	-	-	2.64	-	-	-	-	-	-	-
5-4, 122-124	282.73	SHM	XRFWT	48.90	1.52	15.20	-	-	3.53	6.88	0.17	7.26	11.81	2.53	0.11	0.14	0.09	0.55	98.69	-	-
5-5, 69-71	283.70	JCB	INAA	-	-	-	-	10.28	-	-	-	-	-	2.50	-	-	-	-	-	-	-
5-5, 75-79	283.77	BOG	XRF	49.34	1.55	15.07	11.46	-	-	-	0.18	6.87	11.66	1.99	0.27	0.15	-	-	99.40	0.90	-
5-5, 95-97	283.96	JCB	INAA	-	-	-	-	10.33	-	-	-	-	-	2.52	-	-	-	-	-	-	-
6-3, 74-77	289.76	BOG	XRF	49.41	1.51	15.12	11.49	-	-	-	0.18	7.18	11.81	2.09	0.33	0.14	-	-	99.98	0.72	-
6-3, 120-123	290.22	SHM	XRFWT	50.10	1.56	15.10	-	-	4.68	5.66	0.17	6.83	11.58	2.38	0.30	0.14	0.06	1.14	99.74	-	-
6-3, 135-138	290.37	DRA	XRF	49.32	1.54	15.69	11.54	10.38	-	-	0.20	7.03	11.84	2.63	0.35	0.16	-	-	100.30	-	-
Chemical Group II																					
6-4, 1-5	290.53	SHM	XRFWT	48.30	1.18	16.90	-	-	3.56	5.93	0.17	6.85	12.68	2.20	0.14	0.11	0.28	0.35	98.66	-	-
6-4, 6-10	290.58	DRA	XRF	50.19	1.20	17.27	8.95	8.05	-	-	0.13	6.94	12.90	2.14	0.18	0.13	-	-	100.02	-	-
6-4, 18-21	290.70	WEA	XRF	48.08	1.07	17.64	9.34	-	-	-	0.14	6.62	12.54	2.12	0.28	0.11	-	-	100.52	2.58	-

6-4, 45-46	290.96	DT	PROBE	51.09	1.29	15.34	10.15	-	-	-	-	7.72	12.15	2.31	0.12	-	-	-	100.17	-	-
6-4, 74-78	291.26	BOG	XRF	48.28	1.15	16.41	9.65	-	-	-	0.15	6.65	13.43	1.77	0.16	0.12	-	-	99.11	1.34	-
7-1, 29-33	295.31	BOG	XRF	48.61	1.15	16.25	10.18	-	-	-	0.16	7.49	13.16	1.89	0.15	0.13	-	-	100.17	1.00	-
7-2, 7-10	296.59	PUC	XRFWT	48.93	1.23	15.42	-	-	4.18	5.51	0.16	7.51	13.22	2.41	0.29	0.11	0.84	0.64	100.45	-	0.01
7-2, 44-47	296.96	BOG	XRF	49.46	1.14	16.64	9.84	-	-	-	0.14	6.79	12.78	1.76	0.14	0.12	-	-	99.89	1.08	-
7-2, 56-58	297.07	DRA	XRF	49.98	1.20	16.22	10.34	9.30	-	-	0.16	7.19	12.31	2.01	0.22	0.12	-	-	99.75	-	-
7-2, 138-142	297.90	WEA	XRF	47.80	1.13	16.97	10.04	-	-	-	0.16	6.80	12.87	2.20	0.15	0.12	-	-	100.23	1.99	-
8-1, 35-38	300.37	SHM	XRFWT	46.90	1.14	16.70	-	-	5.21	4.19	0.17	5.89	13.88	2.26	0.38	0.11	1.72	0.75	99.33	-	-
8-1, 68-71	300.68	WEA	XRF	47.24	1.17	15.96	9.82	-	-	-	0.15	7.25	13.22	2.34	0.27	0.12	-	-	99.67	2.13	-
8-1, 95-98	300.97	BOG	XRF	48.94	1.09	16.67	9.99	-	-	-	0.17	6.61	12.96	2.06	0.24	0.11	-	-	100.18	1.34	-
8-1, 127-129	301.28	PUC	XRFWT	49.43	1.20	15.95	-	-	4.59	5.55	0.16	7.65	12.67	2.37	0.35	0.11	0.20	0.67	100.90	-	0.01
8-1, 132-134	301.33	DRA	XRF	49.67	1.25	16.38	9.89	8.90	-	-	0.16	7.28	12.63	2.17	0.21	0.13	-	-	99.79	-	-
8-1, 144-146	301.45	DRA	XRF	49.43	1.30	15.50	10.17	9.15	-	-	0.17	7.61	13.23	2.20	0.25	0.13	-	-	99.98	-	-
8-2, 6-9	301.58	SHM	XRFWT	48.80	1.19	15.80	-	-	4.14	5.01	0.17	6.76	12.96	2.18	0.30	0.11	0.77	0.94	99.16	-	-
8-2, 25-29	301.77	DRA	XRF	48.90	1.16	17.11	9.91	8.92	-	-	0.15	7.37	12.97	1.97	0.21	0.13	-	-	99.88	-	-
8-2, 26-29	301.78	BOG	XRF	48.93	1.22	14.92	11.55	-	-	-	0.18	6.94	12.31	2.09	0.38	0.13	-	-	99.98	1.33	-
8-2, 55-58	302.07	WEA	XRF	47.41	1.17	15.14	10.23	-	-	-	0.16	7.14	13.06	2.22	0.33	0.12	-	-	100.37	3.39	-
9-1, 21-24	304.22	SHM	XRFWT	48.60	1.16	16.50	-	-	4.73	4.76	0.16	7.20	12.33	2.17	0.26	0.10	0.06	0.68	98.73	-	-
9-1, 82-84	304.83	DRA	XRF	48.33	1.19	16.73	9.89	8.90	-	-	0.18	7.28	13.85	2.04	0.22	0.13	-	-	99.84	-	-
9-1, 140-142	305.41	BOG	XRF	50.02	1.27	15.03	10.94	-	-	-	0.17	7.43	12.32	1.86	0.38	0.16	-	-	100.25	0.67	-
9-1, 145-147	305.46	DRA	XRF	49.78	1.28	15.75	10.57	9.51	-	-	0.17	7.16	12.44	2.04	0.38	0.14	-	-	99.69	-	-
9-2, 81-83	306.32	WEA	XRF	48.18	1.12	16.36	9.84	-	-	-	0.16	7.50	12.48	2.23	0.24	0.11	-	-	100.07	1.85	-
10-1, 41-44	313.43	SHM	XRFWT	48.30	1.26	15.50	-	-	4.40	5.92	0.17	7.20	12.38	2.23	0.21	0.11	0.53	0.51	98.74	-	-
i0-1, 90-93	313.92	DRA	XRF	49.12	1.26	16.01	11.07	9.96	-	-	0.18	7.09	12.96	2.10	0.32	0.14	-	-	100.25	-	-
10-2, 86-88	315.37	WEA	XRF	45.47	1.00	16.08	10.09	-	-	-	0.15	6.18	14.41	2.06	0.41	0.11	-	-	100.44	4.48	-
10-2, 125-128	315.76	BOG	XRF	49.51	1.15	16.27	9.99	-	-	-	0.14	7.37	12.56	1.81	0.04	0.10	-	-	99.71	0.77	-
10-3, 52-55	316.54	DRA	XRF	49.72	1.29	15.38	10.60	9.54	-	-	0.17	7.82	12.45	2.02	0.26	0.13	-	-	99.84	-	-
11-1, 115-117	323.16	DRA	XRF	49.18	1.15	17.43	9.81	8.83	-	-	0.16	6.52	12.92	1.91	0.25	0.12	-	-	99.46	-	-
Hole 563																					
Chemical Group I																					
23-1, 22-25	364.74	BOG	XRF	49.64	1.01	15.25	10.43	-	-	-	0.17	7.66	13.40	1.61	0.22	0.10	-	-	99.95	0.46	-
23-1, 30-34	364.82	SHM	XRFWT	49.70	1.05	15.40	-	-	4.56	5.66	0.17	7.33	12.90	2.07	0.36	0.08	0.13	0.76	100.13	-	-
23-1, 104-106	365.55	WEA	XRF	48.50	0.93	16.23	9.81	-	-	-	0.16	6.98	13.59	2.06	0.30	0.08	-	-	100.58	1.94	-
23-1, 115-117	365.66	DRA	XRF	49.73	1.02	15.78	10.18	9.16	-	-	0.17	7.61	13.20	1.96	0.26	0.09	-	-	99.99	-	-
24-1, 22-25	366.74	DRA	XRF	49.47	0.97	16.40	10.26	9.20	-	-	0.15	7.47	13.07	1.88	0.32	0.10	-	-	100.11	-	-
24-1, 49-53	367.01	SHM	XRFWT	50.00	1.06	15.10	-	-	5.14	5.47	0.16	8.05	12.35	2.16	0.33	0.09	0.10	0.57	100.53	-	-
24-1, 57-60	367.09	DRA	XRF	49.26	1.05	15.76	9.98	8.98	-	-	0.15	8.04	12.94	1.97	0.26	0.10	-	-	99.52	-	-
24-1, 80-83	367.32	BOG	XRF	49.30	0.98	15.04	10.36	-	-	-	0.15	7.60	13.40	1.83	0.22	0.09	-	-	100.28	1.31	-
24-1, 108-109	367.59	DT	PROBE	50.96	1.15	15.15	-	10.63	-	-	-	7.18	12.47	2.23	0.07	-	-	-	99.83	-	-
24-1, 118-121	367.70	SHM	XRFWT	50.10	1.05	14.91	-	10.90	-	-	0.18	8.65	12.61	2.04	0.06	0.08	-	-	100.58	-	-
Chemical Group II																					
24-2, 88-91	368.90	BOG	XRF	49.51	0.96	15.73	9.48	-	-	-	0.15	7.87	13.46	1.77	0.07	0.08	-	-	99.96	0.88	-
Chemical Group I																					
24-2, 93-95	368.94	DRA	XRF	49.23	0.97	16.09	10.43	9.39	-	-	0.17	7.54	13.00	2.29	0.29	0.09	-	-	100.09	-	-
24-2, 103-106	369.05	SHM	XRFWT	48.50	0.98	15.90	-	-	4.42	5.24	0.17	7.28	12.81	2.10	0.31	0.09	0.53	0.43	98.73	-	-
24-2, 121-124	369.23	BOG	XRF	49.95	1.03	14.37	11.23	-	-	-	0.17	7.85	12.64	2.06	0.32	0.09	-	-	100.15	0.44	-
Chemical Group II																					
24-2, 123-127	369.25	DRA	XRF	49.98	1.05	15.40	9.89	8.90	-	-	0.16	8.03	13.01	2.21	0.25	0.09	-	-	100.06	-	-
24-4, 0-7	371.04	WEA	XRF	48.04	0.93	15.58	9.37	-	-	-	0.16	7.53	13.22	2.23	0.23	0.10	-	-	99.67	2.28	-
24-4, 2-5	371.04	SHM	XRFWT	48.90	0.98	15.50	-	-	4.55	4.60	0.15	7.53	13.09	2.08	0.25	0.08	0.53	0.58	98.79	-	-
24-4, 7-10	371.09	DRA	XRF	49.58	0.99	16.02	10.07	9.06	-	-	0.17	7.35	13.41	1.93	0.31	0.10	-	-	99.93	-	-
24-4, 38-41	371.40	BOG	XRF	49.54	0.98	15.15	9.67	-	-	-	0.16	7.96	13.13	1.65	0.09	0.09	-	-	99.49	1.07	-
25-1, 19-22	373.71	SHM	XRFWT	48.30	0.97	15.60	-	-	3.55	5.31	0.15	7.64	13.60	1.92	0.19	0.08	0.86	0.89	99.05	-	-
25-1, 36-38	373.87	DRA	XRF	49.79	0.98	16.37	9.72	8.75	-	-	0.16	7.80	12.97	2.20	0.20	0.09	-	-	100.27	-	-
25-1, 43-46	373.95	BOG	XRF	49.18	0.96	15.58	9.42	-	-	-	0.16	7.65	13.52	1.56	0.13	0.09	-	-	99.48	1.23	-
25-2, 21-24	375.23	SHM	XRFWT	49.60	1.43	15.00	-	-	4.39	6.29	0.17	7.56	11.99	2.24	0.26	0.14	0.13	0.74	99.94	-	-
25-2, 37-39	375.38	WEA	XRF	47.69	0.96	14.96	10.06	-	-	-	0.17	7.67	14.00	2.11	0.31	0.09	-	-	100.28	2.26	-
25-2, 39-41	375.40	BOG	XRF	48.94	0.96	15.24	9.39	-	-	-	0.16	7.77	14.07	1.59	0.12	0.09	-	-	99.78	1.45	-
25-2, 71-74	375.73	BOG	XRF	49.05	0.95	15.37	9.98	-	-	-	0.16	7.44	13.37	1.57	0.20	0.08	-	-	99.28	1.11	-
Chemical Group I																					
25-2, 79-81	375.80	BOG	XRF	49.02	0.94	15.10	10.82	-	-	-	0.17	7.27	13.20	1.44	0.33	0.08	-	-	99.69	1.32	-
Chemical Group II																					
25-2, 101-103	376.02	BOG	XRF	49.61	0.98	15.32	9.70	-	-	-	0.16	7.59	13.56	1.52	0.11	0.11	-		99.78	1.12	-

Table 1. (Continued).

Sample	Depth (m)	Inv.	Method	SiO_2	TiO_2	Al_2O_3	Fe_2O_3 (total)	FeO*	Fe_2O_3	FeO	MnO	MgO	CaO	Na_2O	K_2O	P_2O_5	CO_2	H_2O+	Total	LOI	S
Hole 563 (Cont.)																					
Chemical Group I																					
25-2, 115-117	376.16	DRA	XRF	49.96	1.01	15.85	10.35	9.51	-	-	0.17	7.55	13.06	2.20	0.27	0.11	-	-	100.53	-	-
Chemical Group II																					
25-2, 132-134	376.33	DT	PROBE	50.98	1.15	15.04	-	10.30	-	-	-	7.60	12.74	2.18	0.07	-	-	-	100.06	-	-
Hole 564																					
Chemical Group I																					
H1-CC, 8-11	284.00	PUC	XRFWT	48.47	1.42	15.35	-	-	6.08	5.31	0.17	6.53	12.70	2.46	0.40	0.14	0.37	1.04	100.44	-	0.01
H1-CC, 11-15	284.00	DRA	XRF	49.35	1.48	15.77	11.55	10.39	-	-	0.19	6.13	12.82	2.51	0.44	0.16	-	-	100.40	-	-
1-1, 108-111	285.10	BOG	XRF	49.97	1.41	14.53	10.94	-	-	-	0.16	7.09	11.97	1.76	0.27	0.17	-	-	99.28	1.01	-
1-1, 122-124	285.23	PUC	XRFWT	49.24	1.39	15.02	-	-	5.68	5.71	0.17	7.40	12.17	2.47	0.37	0.13	0.13	0.86	100.74	-	<0.01
1-1, 129-131	285.30	DRA	XRF	50.21	1.43	14.94	11.29	10.16	-	-	0.18	7.52	11.89	2.47	0.35	0.14	-	-	100.42	-	-
1-1, 140-143	285.42	BOG	XRF	50.50	1.43	14.45	10.99	-	-	-	0.17	7.22	12.03	1.89	0.34	0.15	-	-	99.71	0.54	-
1-2, 21-25	285.73	SHM	XRFWT	49.50	1.01	15.60	-	-	3.63	5.62	0.16	7.99	13.02	2.07	0.18	0.08	0.23	0.66	99.70	-	-
1-2, 38-40	285.89	SHM	XRFWT	49.40	1.42	14.60	-	-	5.19	5.65	0.18	7.53	11.66	2.16	0.36	0.14	0.17	0.46	98.96	-	-
1-2, 74-78	286.26	BOG	XRF	49.32	1.41	14.73	11.86	-	-	-	0.18	6.99	12.00	2.14	0.26	0.14	-	-	100.09	1.06	-
1-3, 38-40	287.39	DRA	XRF	49.86	1.40	14.71	11.58	10.42	-	-	0.17	7.59	11.63	2.76	0.36	0.15	-	-	100.22	-	-
1-3, 100-103	288.01	BOG	XRF	48.79	1.43	14.84	12.18	-	-	-	0.16	5.91	12.33	2.26	0.29	0.14	-	-	99.51	1.18	-
2-1, 53-55	293.54	BOG	XRF	48.31	1.45	15.12	12.37	-	-	-	0.18	6.07	12.34	2.08	0.19	0.15	-	-	99.28	1.02	-
2-1, 145-150	294.47	JCB	INAA	-	-	-	-	10.73	-	-	-	-	-	2.33	-	-	-	-	-	-	-
2-2, 1-4	294.53	JCB	INAA	-	-	-	-	10.73	-	-	-	-	-	2.38	-	-	-	-	-	-	-
2-2, 3-5	294.54	DRA	XRF	49.57	1.44	15.22	11.60	10.44	-	-	0.18	7.00	12.15	2.39	0.39	0.16	-	-	100.10	-	-
2-2, 15-22	294.68	JCB	INAA	-	-	-	-	10.67	-	-	-	-	-	2.36	-	-	-	-	-	-	-
2-2, 46-49	294.97	BOG	XRF	49.07	1.41	14.50	11.70	-	-	-	0.17	6.87	11.95	2.02	0.31	0.14	-	-	98.99	0.85	-
2-2, 65-67	295.16	JCB	INAA	-	-	-	-	10.82	-	-	-	-	-	2.42	-	-	-	-	-	-	-
2-2, 99-102	295.51	SHM	XRFWT	50.60	1.45	14.73	-	-	4.69	6.52	0.19	8.02	11.60	2.29	0.12	0.13	0.03	0.35	100.72	-	-
2-3, 18-20	296.19	DRA	XRF	50.58	1.47	15.17	10.11	9.10	-	-	0.17	7.77	12.05	2.26	0.20	0.15	-	-	99.93	-	-
2-3, 60-63	296.62	BOG	XRF	49.30	1.40	14.34	11.78	-	-	-	0.17	7.69	11.89	2.05	0.24	0.14	-	-	99.75	0.75	-
2-3, 110-114	297.12	PUC	XRFWT	49.45	1.41	14.88	-	-	5.41	5.57	0.16	7.29	12.07	2.57	0.37	0.13	0.23	0.97	100.51	-	0.02
3-1, 25-28	302.26	BOG	XRF	49.66	1.41	14.30	11.59	-	-	-	0.17	7.03	11.90	2.23	0.28	0.15	-	-	99.57	0.85	-
3-2, 5-8	303.57	WEA	XRF	47.90	1.41	14.88	11.97	-	-	-	0.18	6.70	11.82	2.32	0.35	0.14	-	-	100.38	2.71	-
3-2, 35-37	303.86	DRA	XRF	49.62	1.45	14.92	11.71	10.54	-	-	0.20	7.32	11.92	2.82	0.38	0.14	-	-	100.47	-	-
3-2, 50-51	304.01	DT	PROBE	51.09	1.48	14.87	-	11.06	-	-	-	6.99	11.53	2.45	0.15	-	-	-	99.62	-	-
3-2, 58-62	304.10	SHM	XRFWT	49.50	1.47	14.90	-	-	5.22	6.09	0.20	7.46	11.76	2.27	0.37	0.15	0.39	0.61	100.29	-	-
3-2, 58-62	304.10	SHM	XRFWT	50.20	1.44	14.59	-	-	1.40	9.39	0.19	7.91	11.57	2.30	0.12	0.14	0.04	0.35	99.64	-	-
3-2, 70-73	304.22	BOG	XRF	48.15	1.43	14.58	11.99	-	-	-	0.18	6.38	12.28	1.94	0.26	0.15	-	-	98.57	1.23	-
3-2, 127-129	304.78	JCB	INAA	-	-	-	-	10.46	-	-	-	-	-	2.30	-	-	-	-	-	-	-
3-3, 92-94	305.93	SHM	XRFWT	47.60	1.40	14.20	-	-	5.26	5.67	0.21	6.95	12.53	2.20	0.57	0.15	1.40	0.54	98.64	-	-
3-3, 138-141	306.39	BOG	XRF	50.28	1.41	14.35	11.58	-	-	-	0.16	6.79	11.77	1.84	0.15	0.14	-	-	99.20	0.73	-
4-1, 61-64	311.63	BOG	XRF	49.78	1.40	14.16	11.49	-	-	-	0.17	7.49	11.72	1.84	0.26	0.15	-	-	99.17	0.71	-
4-2, 37-41	312.89	DRA	XRF	49.87	1.46	14.89	11.92	10.73	-	-	0.20	7.32	11.76	2.31	0.36	0.15	-	-	100.26	-	-
4-2, 49-51	313.00	JCB	INAA	-	-	-	-	10.66	-	-	-	-	-	2.30	-	-	-	-	-	-	-
4-2, 68-72	313.20	SHM	XRFWT	50.30	1.46	14.60	-	-	1.83	9.11	0.19	8.02	11.54	2.33	0.13	0.14	0.08	0.37	100.10	-	-
4-2, 102-106	313.54	BOG	XRF	49.23	1.42	14.48	11.71	-	-	-	0.18	7.08	11.83	2.34	0.28	0.15	-	-	99.58	0.88	-
4-4, 86-89	316.38	BOG	XRF	49.93	1.42	14.41	11.69	-	-	-	0.17	7.01	11.72	2.03	0.34	0.15	-	-	99.67	0.80	-
4-4, 140-142	316.91	DRA	XRF	49.88	1.45	14.76	11.82	10.64	-	-	0.16	7.54	11.52	2.56	0.36	0.17	-	-	100.22	-	-
5-1, 17-19	320.18	BOG	XRF	48.84	1.46	14.86	11.98	-	-	-	0.18	6.36	12.06	2.42	0.25	0.15	-	-	99.42	0.86	-
5-1, 30-33	320.32	SHM	XRFWT	50.30	1.47	14.59	-	-	1.63	9.31	0.19	8.03	11.36	2.27	0.13	0.14	0.08	0.34	99.84	-	-
5-2, 26-28	321.77	JCB	INAA	-	-	-	-	10.26	-	-	-	-	-	2.31	-	-	-	-	-	-	-
5-2, 89-91	322.40	DRA	XRF	50.39	1.46	14.69	11.82	11.13	-	-	0.17	7.48	11.52	2.48	0.19	0.16	-	-	100.34	-	-
5-2, 96-100	322.48	BOG	XRF	50.29	1.43	14.33	11.76	-	-	-	0.18	7.50	11.70	2.05	0.13	0.16	-	-	100.28	0.75	-
5-2, 111-114	322.63	PUC	XRFWT	49.81	1.41	14.59	-	-	3.79	7.45	0.18	7.86	11.71	2.46	0.18	0.14	0.08	0.82	100.48	-	0.10
5-2, 115-118	322.67	WEA	XRF	49.42	1.41	14.38	11.73	-	-	-	0.18	7.76	11.28	2.26	0.20	0.14	-	-	100.05	1.29	-
5-3, 119-122	324.21	BOG	XRF	50.15	1.44	14.39	10.97	-	-	-	0.19	7.76	11.77	1.95	0.20	0.15	-	-	99.55	0.58	-
5-4, 24-27	324.76	DRA	XRF	49.44	1.51	14.99	12.37	10.67	-	-	0.19	6.78	11.76	2.58	0.40	0.17	-	-	100.19	-	-
6-1, 15-18	329.17	DRA	XRF	50.54	1.48	14.64	11.86	10.67	-	-	0.17	7.24	11.42	2.12	0.19	0.16	-	-	99.83	-	-
6-1, 26-28	329.27	WEA	XRF	49.76	1.46	14.67	11.27	-	-	-	0.17	7.27	11.32	2.35	0.20	0.15	-	-	100.29	1.67	-
6-1, 33-36	329.35	BOG	XRF	50.06	1.44	14.24	12.04	-	-	-	0.17	7.51	11.66	1.99	0.06	0.15	-	-	99.86	0.54	-
6-3, 63-66	332.65	BOG	XRF	49.31	1.44	14.10	12.06	-	-	-	0.18	7.34	11.40	1.96	0.37	0.14	-	-	99.30	1.00	-
6-3, 141-143	333.42	JCB	INAA	-	-	-	-	10.98	-	-	-	-	-	2.34	-	-	-	-	-	-	-

6-4, 15-17	333.66	JCB	INAA	-	-	-	-	10.33	-	-	-	-	-	2.36	-	-	-	-	-	-	-
6-4, 38-40	333.89	JCB	INAA	-	-	-	-	10.41	-	-	-	-	-	2.32	-	-	-	-	-	-	-
6-4, 44-47	333.96	BOG	XRF	49.19	1.41	14.14	11.79	-	-	-	0.18	8.19	11.45	1.74	0.18	0.15	-	-	99.16	0.74	-
6-4, 48-52	334.00	DRA	XRF	49.42	1.44	14.38	12.31	11.08	-	-	0.19	8.43	11.28	2.05	0.24	0.16	-	-	99.92	-	-
6-4, 54-57	334.06	WEA	XRF	49.48	1.43	14.48	11.81	-	-	-	0.18	7.62	11.25	2.36	0.22	0.15	-	-	100.46	1.48	-
6-4, 71-74	334.23	SHM	XRFWT	48.90	1.39	14.70	-	-	4.53	6.32	0.17	8.24	11.06	2.09	0.25	0.13	0.07	1.22	99.03	-	-
6-4, 139-142	334.91	JCB	INAA	-	-	-	-	10.75	-	-	-	-	-	2.41	-	-	-	-	-	-	-
6-4, 144-147	334.96	SHM	XRFWT	50.10	1.50	14.30	-	-	4.47	6.59	0.18	7.59	11.42	2.31	0.12	0.14	0.09	0.72	99.54	-	-
6-5, 22-24	335.23	JCB	INAA	-	-	-	-	10.44	-	-	-	-	-	2.31	-	-	-	-	-	-	-
6-5, 32-34	335.33	DRA	XRF	50.17	1.50	14.64	11.95	10.75	-	-	0.18	7.48	11.53	2.08	0.33	0.17	-	-	100.03	-	-
6-5, 43-46	335.45	BOG	XRF	50.20	1.48	14.28	11.46	-	-	-	0.18	7.14	11.64	1.86	0.22	0.15	-	-	99.42	0.81	-
6-5, 58-61	335.60	JCB	INAA	-	-	-	-	10.77	-	-	-	-	-	2.34	-	-	-	-	-	-	-
7-1, 12-15	338.14	DRA	XRF	49.77	1.49	14.50	11.96	10.76	-	-	0.17	7.42	11.45	2.10	0.41	0.16	-	-	99.42	-	-
7-2, 20-23	339.72	BOG	XRF	49.14	1.48	14.27	12.19	-	-	-	0.18	7.08	11.63	1.80	0.31	0.16	-	-	99.22	0.98	-
7-2, 38-41	339.90	SHM	XRFWT	49.80	1.48	14.35	-	-	1.58	9.39	0.19	8.06	11.19	2.28	0.14	0.14	0.05	0.41	99.06	-	-
7-2, 99-100	340.50	DT	PROBE	51.52	1.53	14.83	-	11.52	-	-	-	6.95	11.46	2.30	0.14	-	-	-	100.25	-	-
7-2, 136-138	340.87	PUC	XRFWT	49.37	1.20	15.97	-	-	2.88	7.04	0.16	7.48	12.60	2.52	0.36	0.11	0.05	0.82	100.56	-	0.12
7-3, 13-15	341.14	DRA	XRF	50.63	1.52	14.73	11.56	10.40	-	-	0.18	6.99	11.67	2.15	0.23	0.16	-	-	99.82	-	-
7-3, 58-61	341.60	BOG	XRF	49.84	1.46	13.93	12.02	-	-	-	0.18	7.56	11.52	1.76	0.18	0.15	-	-	99.33	0.73	-
7-3, 60-63	341.62	WEA	XRF	49.47	1.44	14.41	11.60	-	-	-	0.17	7.56	11.19	2.38	0.22	0.15	-	-	100.23	1.64	-
8-1, 3-5	347.04	DT	PROBE	51.00	1.52	15.03	-	11.62	-	-	-	6.92	11.33	2.38	0.15	-	-	-	99.95	-	-
8-1, 10-14	347.12	JCB	INAA	-	-	-	-	11.30	-	-	-	-	-	2.51	-	-	-	-	-	-	-
8-1, 25-27	347.26	JCB	INAA	-	-	-	-	10.88	-	-	-	-	-	2.40	-	-	-	-	-	-	-
8-1, 44-47	347.46	JCB	INAA	-	-	-	-	11.46	-	-	-	-	-	2.48	-	-	-	-	-	-	-
8-1, 76-79	347.78	JCB	INAA	-	-	-	-	11.74	-	-	-	-	-	2.54	-	-	-	-	-	-	-
8-2, 0-3	348.52	BOG	XRF	49.71	1.46	14.12	12.11	-	-	-	0.17	7.32	11.50	1.87	0.35	0.13	-	-	99.56	0.82	-
8-2, 7-10	348.59	DRA	XRF	49.87	1.48	14.56	11.90	10.71	-	-	0.17	7.54	11.40	2.22	0.42	0.16	-	-	99.73	-	-
8-2, 22-25	348.74	JCB	INAA	-	-	-	-	11.14	-	-	-	-	-	2.42	-	-	-	-	-	-	-
8-2, 75-77	349.26	BOG	XRF	48.07	1.48	14.76	12.76	-	-	-	0.18	5.87	11.84	1.92	0.24	0.17	-	-	98.50	1.21	-
9-1, 1-4	356.03	SHM	XRFWT	46.60	1.44	14.40	-	-	7.03	4.91	0.17	5.57	13.25	2.46	0.56	0.16	1.96	1.25	99.74	-	-
9-1, 18-20	356.19	DRA	XRF	47.24	1.52	15.16	13.07	11.76	-	-	0.19	5.20	13.83	2.26	0.62	0.21	-	-	99.31	-	-
9-1, 43-45	356.44	BOG	XRF	48.71	1.45	14.44	12.46	-	-	-	0.18	6.51	11.82	1.87	0.31	0.15	-	-	99.07	1.17	-
9-1, 72-74	356.73	PUC	XRFWT	49.12	1.47	15.05	-	-	6.53	5.34	0.16	6.88	11.52	2.86	0.40	0.15	0.35	1.05	100.88	-	0.01
9-1, 140-143	357.42	DRA	XRF	49.11	1.53	15.08	12.01	10.81	-	-	0.18	6.86	11.76	2.66	0.36	0.17	-	-	99.73	-	-
9-2, 128-130	358.79	DRA	XRF	48.99	1.58	15.04	12.53	11.28	-	-	0.18	6.70	11.86	2.28	0.35	0.17	-	-	99.67	-	-
9-2, 142-144	358.93	JCB	INAA	-	-	-	-	10.84	-	-	-	-	-	2.38	-	-	-	-	-	-	-
9-3, 25-28	359.27	SHM	XRFWT	49.80	1.50	14.32	-	-	2.02	9.07	0.19	8.03	11.15	2.27	0.14	0.15	0.07	0.63	99.34	-	-
9-3, 26-27	359.27	DT	PROBE	51.30	1.59	15.20	-	11.65	-	-	-	7.04	11.37	2.33	0.15	-	-	-	100.63	-	-
9-3, 68-71	359.70	DRA	XRF	49.34	1.55	14.96	12.56	11.30	-	-	0.20	6.81	11.87	2.44	0.33	0.17	-	-	100.23	-	-
9-3, 72-75	359.74	BOG	XRF	49.48	1.45	13.97	12.18	-	-	-	0.19	7.36	11.43	1.72	0.16	0.15	-	-	98.64	0.55	-
9-3, 76-79	359.78	PUC	XRFWT	50.07	1.46	14.65	-	-	2.99	8.39	0.18	7.76	11.54	2.46	0.26	0.14	0.07	0.76	100.73	-	0.10

Note: Sample numbers are given in core-section, interval in cm. Depth is sub-bottom depth.

Investigator (Inv) codes are: BOG = H. Bougault, IFREMER (Chapter 23, this volumne); BT = E. Bonatti, Lamont-Doherty Geological Observatory of Columbia University (Chapter 29, this volume); DT = L.V. Dmitriev, Vernadsky Institute of Geochemistry, USSR Academy of Sciences (Chapter 27, this volume); DRA = N. Drake, Department of Geology, University of Massachusetts (Chapter 20, this volume); JCB = J.C. Brannon, Department of Earth and Planetary Sciences, Washington University in St. Louis (Chapter 21, this volume); PUC = H. Puchelt, Institut für Petrologie und Geochemie der Universität Karlsruhe; SHM = H.-U. Schmincke, Ruhr Universität Bochum, Mineralogisches Institut (chapter may be published in future DSDP volume); WEA = B.L. Weaver, Department of Geology, University of Leicester (present address: School of Geology and Geophysics, University of Oklahoma, Norman, Oklahoma 73019) (Chapter 19, this volume).

The methods codes are: XRF = X-ray fluorescence; INAA = instrumental neutron activation analysis; PROBE = electron microprobe; WT = classical wet chemical techniques.

LOI is loss on ignition.

APPENDIX

Table 2. Trace-element compositions (in ppm) for basalts, Leg 82.

Sample	Depth (m)	Inv	Method	Sc	V	Cr	Co	Ni	Cu	Zn	Ga	Rb	Sr	Y	Zr	Nb
Hole 556																
Chemical Group I																
2-1, 74-76	462.25	DRA	XF	-	241.0	311.0	-	95.0	-	77.0	15.7	7.1	105.0	23.4	62.0	2.3
2-1, 77-79	462.28	WEA	XF	-	267.0	326.0	-	140.0	-	74.0	16.0	2.0	112.0	26.0	62.0	1.6
2-1, 77-79	462.28	WEA	NA	-	-	-	-	-	-	-	-	-	-	-	-	-
2-1, 78-82	462.30	BOG	XFNA	38.2	276.0	268.0	40.0	116.0	-	69.0	-	3.5	108.0	28.2	59.0	0.8
2-1, 78-82	462.30	BOG	NA	-	-	-	45.5	119.0	-	-	-	1.7	-	-	-	-
2-1, 83-85	462.34	SHM	XF	-	-	328.0	45.0	121.0	92	75.0	-	-	114.0	23.0	63.0	-
2-2, 132-135	464.34	WEA	XF	-	268.0	336.0	-	153.0	-	72.0	16.0	2.0	107.0	26.0	61.0	1.7
2-2, 141-144	464.43	DRA	XF	-	238.0	277.0	-	178.0	-	75.0	15.2	2.4	104.0	23.9	64.0	2.3
2-2, 145-149	464.47	BOG	XFNA	39.1	278.0	261.0	42.0	117.0	-	65.0	-	2.9	101.0	28.3	66.0	0.9
2-2, 145-149	464.47	BOG	NA	-	-	-	46.1	114.0	-	-	-	2.7	-	-	-	-
Chemical Group II																
2-4, 93-95	466.94	SHM	XF	-	-	286.0	47.0	74.0	82	89.0	-	-	105.0	35.0	91.0	-
2-5, 5-7	467.56	SHM	XF	-	-	278.0	53.0	79.0	74	83.0	-	-	108.0	35.0	94.0	-
2-5, 12-16	467.64	BOG	XFNA	35.2	280.0	228.0	40.0	73.0	-	72.0	-	6.5	99.0	37.9	89.0	0.9
2-5, 12-16	467.64	BOG	NA	-	-	-	40.6	76.0	-	-	-	6.4	-	-	-	-
2-5, 26-28	467.77	DRA	XF	-	55.0	235.0	-	84.0	-	92.0	16.7	5.5	101.0	32.7	97.0	2.2
2-6, 34-36	469.35	SHM	XF	-	-	263.0	36.0	83.0	72	82.0	-	-	112.0	32.0	90.0	-
3-1, 36-38	471.37	SHM	XF	-	-	279.0	46.0	81.0	83	87.0	-	-	111.0	36.0	92.0	-
3-1, 57-60	471.59	WEA	XF	-	292.0	284.0	-	70.0	-	87.0	17.0	6.0	102.0	36.0	92.0	3.3
3-1, 60-70	471.65	BOG	XFNA	36.7	292.0	241.0	39.0	71.0	-	76.0	-	6.4	99.0	39.1	91.0	2.2
3-1, 60-70	471.65	BOG	NA	-	-	-	41.2	75.0	-	-	-	6.1	-	-	-	-
3-2, 19-21	472.70	SHM	XF	-	-	278.0	51.0	72.0	70	83.0	-	-	108.0	35.0	94.0	-
3-2, 49-51	473.00	WEA	XF	-	280.0	287.0	-	72.0	-	85.0	17.0	4.0	100.0	34.0	90.0	2.8
3-2, 52-56	473.04	BOG	XFNA	37.1	291.0	259.0	41.0	70.0	-	81.0	-	7.1	97.0	39.7	94.0	1.5
3-2, 52-56	473.04	BOG	NA	-	-	-	42.1	80.0	-	-	-	6.2	-	-	-	-
3-3, 66-69	474.68	DRA	XF	-	238.0	251.0	-	88.0	-	84.0	16.1	7.1	99.0	30.7	89.0	2.4
3-3, 70-74	474.72	BOG	XFNA	35.6	274.0	250.0	40.0	74.0	-	71.0	-	2.8	98.0	37.3	90.0	3.0
3-3, 70-74	474.72	BOG	NA	-	-	-	41.0	79.0	-	-	-	-	-	-	-	-
4-1, 25-27	480.26	SHM	XF	-	-	276.0	47.0	84.0	75	80.0	-	-	99.0	33.0	89.0	-
4-2, 65-68	482.17	WEA	XF	-	304.0	300.0	-	69.0	-	89.0	17.0	5.0	101.0	36.0	93.0	2.8
4-2, 77-84	482.31	BOG	XFNA	37.0	282.0	257.0	41.0	75.0	-	80.0	-	3.8	97.0	40.7	101.0	3.3
4-2, 77-84	482.31	BOG	NA	-	-	-	42.8	77.0	-	-	-	3.4	-	-	-	-
4-2, 130-133	482.82	SHM	XF	-	-	252.0	39.0	72.0	70	80.0	-	-	105.0	34.0	95.0	-
4-3, 21-23	483.22	SHM	XF	-	-	256.0	43.0	78.0	66	89.0	-	-	105.0	36.0	95.0	-
4-3, 45-47	483.46	SHM	XF	-	-	265.0	48.0	74.0	82	84.0	-	-	108.0	32.0	86.0	-
4-3, 132-136	484.34	BOG	XFNA	38.9	295.0	250.0	42.0	88.0	-	80.0	-	1.8	98.0	41.9	94.0	2.9
4-3, 132-136	484.34	BOG	NA	-	-	-	46.2	91.0	-	-	-	-	-	-	-	-
4-5, 21-23	486.22	SHM	XF	-	-	259.0	44.0	74.0	83	85.0	-	-	106.0	36.0	96.0	-
4-5, 31-33	486.32	BOG	XFNA	36.5	285.0	234.0	39.0	69.0	-	73.0	-	3.5	98.0	40.0	104.0	1.9
4-5, 31-33	486.32	BOG	NA	-	-	-	41.8	72.0	-	-	-	4.8	-	-	-	-
4-6, 61-63	488.12	BOG	XFNA	36.8	292.0	241.0	42.0	72.0	-	80.0	-	7.7	100.0	41.6	99.0	2.5
4-6, 61-63	488.12	BOG	NA	-	-	-	42.2	73.0	-	-	-	7.7	-	-	-	-
5-1, 23-27	489.25	SHM	XF	-	-	243.0	46.0	70.0	69	88.0	-	-	104.0	36.0	94.0	-
5-1, 73-75	489.74	BOG	XFNA	37.0	292.0	228.0	38.0	77.0	-	80.0	-	8.6	100.0	40.1	102.0	1.6
5-1, 73-75	489.74	BOG	NA	-	-	-	41.3	74.0	-	-	-	7.4	-	-	-	-
5-1, 99-102	490.01	DRA	XF	-	238.0	251.0	-	88.0	-	87.0	16.4	4.3	101.0	33.1	87.0	2.6
5-2, 65-73	491.19	BOG	XFNA	37.4	281.0	262.0	41.0	79.0	-	73.0	-	6.4	107.0	38.4	93.0	1.7
5-2, 65-73	491.19	BOG	NA	-	-	-	42.4	82.0	-	-	-	5.7	-	-	-	-
5-3, 75-80	492.78	BOG	XFNA	37.3	283.0	267.0	44.0	93.0	-	76.0	-	6.8	100.0	38.5	97.0	1.9
5-3, 75-80	492.78	BOG	NA	-	-	-	47.5	103.0	-	-	-	6.2	-	-	-	-
5-5, 145-150	496.48	BOG	XFNA	37.3	267.0	242.0	39.0	67.0	-	76.0	-	1.6	100.0	38.3	90.0	2.9
5-5, 145-150	496.48	BOG	NA	-	-	-	42.7	76.0	-	-	-	0.9	-	-	-	-
6-1, 66-70	498.68	BOG	XFNA	37.3	266.0	258.0	40.0	78.0	-	72.0	-	5.1	116.0	37.0	86.0	1.9
6-1, 66-70	498.68	BOG	NA	-	-	-	42.1	80.0	-	-	-	5.1	-	-	-	-
6-2, 14-17	499.66	SHM	XF	-	-	292.0	47.0	82.0	108	78.0	-	-	103.0	32.0	84.0	-
6-2, 29-34	499.82	BOG	XFNA	37.4	275.0	246.0	39.0	72.0	-	71.0	-	3.8	98.0	37.3	95.0	1.9
6-2, 29-34	499.82	BOG	NA	-	-	-	43.4	81.0	-	-	-	3.8	-	-	-	-
6-2, 53-56	500.05	SHM	XF	-	-	264.0	45.0	72.0	90	82.0	-	-	109.0	35.0	87.0	-
6-3, 82-86	501.84	BOG	XFNA	38.1	272.0	243.0	37.0	77.0	-	68.0	-	1.9	98.0	37.2	89.0	0.7
6-3, 82-86	501.84	BOG	NA	-	-	-	42.9	79.0	-	-	-	-	-	-	-	-
6-4, 115-120	503.68	WEA	XF	-	274.0	277.0	-	71.0	-	78.0	18.0	2.0	97.0	34.0	85.0	2.1
6-4, 115-120	503.68	WEA	NA	-	-	-	-	-	-	-	-	-	-	-	-	-
6-4, 121-126	503.74	BOG	XFNA	36.9	261.0	230.0	37.0	72.0	-	69.0	-	1.7	97.0	36.9	86.0	1.8
6-4, 121-126	503.74	BOG	NA	-	-	-	42.8	85.0	-	-	-	-	-	-	-	-
6-5, 64-67	504.66	DRA	XF	-	250.0	280.0	-	97.0	-	97.0	17.0	1.8	98.0	30.7	88.0	2.7
6-5, 68-70	504.69	SHM	XF	-	-	308.0	48.0	109.0	201	82.0	-	-	103.0	28.0	82.0	-
Chemical Group III																
6-6, 44-48	505.96	BOG	XFNA	37.0	246.0	336.0	36.0	101.0	-	60.0	-	4.0	99.0	27.0	58.0	2.1
6-6, 44-48	505.96	BOG	NA	-	-	-	41.5	85.0	-	-	-	3.2	-	-	-	-
6-6, 108-111	506.60	DRA	XF	-	215.0	366.0	-	145.0	-	73.0	14.7	2.3	101.0	22.6	56.0	2.2
7-1, 85-87	507.86	SHM	XF	-	-	337.0	41.0	128.0	87	64.0	-	-	106.0	24.0	58.0	-
7-1, 115-119	508.17	WEA	XF	-	239.0	379.0	-	92.0	-	71.0	16.0	4.0	103.0	25.0	55.0	1.5
7-1, 123-126	508.25	BOG	XFNA	37.7	236.0	318.0	39.0	101.0	-	57.0	-	3.6	104.0	26.9	56.0	0.1
7-1, 123-126	508.25	BOG	NA	-	-	-	45.7	103.0	-	-	-	2.9	-	-	-	-
7-1, 128-132	508.30	DRA	XF	-	208.0	331.0	-	91.0	-	68.0	15.4	6.3	99.0	22.2	58.0	1.2
7-3, 12-15	510.14	BOG	XFNA	37.8	232.0	307.0	40.0	95.0	-	54.0	-	3.7	102.0	27.7	57.0	1.0
7-3, 12-15	510.14	BOG	NA	-	-	-	44.3	95.0	-	-	-	2.2	-	-	-	-
7-3, 83-86	510.85	DRA	XF	-	218.0	373.0	-	81.0	-	74.0	15.0	4.1	97.0	23.3	56.0	2.0
8-1, 107-111	517.09	BOG	XFNA	38.1	253.0	257.0	37.0	73.0	-	54.0	-	5.4	99.0	24.6	49.0	1.1
8-1, 107-111	517.09	BOG	NA	-	-	-	40.1	78.0	-	-	-	4.8	-	-	-	-
8-1, 118-120	517.19	WEA	XF	-	260.0	298.0	-	96.0	-	68.0	14.0	6.0	99.0	22.0	48.0	1.6
8-2, 13-16	517.65	DRA	XF	-	221.0	284.0	-	106.0	-	68.0	14.0	3.2	99.0	20.4	46.0	2.1
8-2, 27-29	517.78	SHM	XF	-	-	295.0	45.0	136.0	101	70.0	-	-	98.0	18.0	51.0	-
8-4, 60-63	521.12	BOG	XFNA	38.5	252.0	242.0	36.0	95.0	-	56.0	-	5.3	102.0	24.7	52.0	0.6
8-4, 60-63	521.12	BOG	NA	-	-	-	40.3	97.0	-	-	-	5.6	-	-	-	-
9-2, 82-84	527.33	BOG	XFNA	41.0	270.0	94.0	45.0	90.0	-	66.0	-	4.9	101.0	28.6	60.0	2.1
9-2, 82-84	527.33	BOG	NA	-	-	-	51.4	96.0	-	-	-	4.5	-	-	-	-
9-2, 83-85	527.34	WEA	XF	-	286.0	127.0	-	68.0	-	73.0	17.0	6.0	102.0	26.0	59.0	2.4
9-3, 106-108	529.07	SHM	XF	-	-	125.0	48.0	91.0	97	71.0	-	-	103.0	28.0	63.0	-
9-4, 64-67	530.16	DRA	XF	-	253.2	93.8	-	73.3	-	80.1	15.2	10.7	99.3	24.3	60.4	1.9

Table 2. (Continued).

Cs	Ba	La	Ce	Nd	Sm	Eu	Gd	Tb	Ho	Tm	Yb	Lu	Hf	Ta	Th	U
-	-	-	-	-	-	-	-	-	-	-	-	-	-	-	-	-
-	30.0	2.00	6.0	7.0	-	-	-	-	-	-	-	-	-	-	-	-
-	-	1.84	6.5	6.9	2.59	0.98	3.66	0.71	-	0.43	2.77	0.45	1.80	0.09	0.14	-
0.09	28.5	1.75	3.6	-	-	0.93	-	0.58	-	-	-	-	1.83	0.10	0.10	0.07
-	-	-	-	-	-	-	-	-	-	-	-	-	-	-	-	-
-	58.0	-	-	-	-	-	-	-	-	-	-	-	-	-	-	-
-	29.0	2.00	5.0	7.0	-	-	-	-	-	-	-	-	-	-	-	-
-	-	-	-	-	-	-	-	-	-	-	-	-	-	-	-	-
0.10	15.0	1.87	4.5	-	-	0.96	-	0.57	-	-	-	-	1.70	0.10	0.08	0.04
-	-	-	-	-	-	-	-	-	-	-	-	-	-	-	-	-
-	56.0	-	-	-	-	-	-	-	-	-	-	-	-	-	-	-
-	63.0	-	-	-	-	-	-	-	-	-	-	-	-	-	-	-
0.44	18.0	3.20	-	-	-	1.18	-	0.79	-	-	-	-	2.52	0.15	0.14	-
-	-	-	-	-	-	-	-	-	-	-	-	-	-	-	-	-
-	-	-	-	-	-	-	-	-	-	-	-	-	-	-	-	-
-	99.0	-	-	-	-	-	-	-	-	-	-	-	-	-	-	-
-	32.0	-	-	-	-	-	-	-	-	-	-	-	-	-	-	-
-	24.0	2.00	8.0	9.0	-	-	-	-	-	-	-	-	-	-	-	-
0.42	6.5	2.74	7.6	-	-	1.24	-	0.78	-	-	-	-	2.54	0.16	0.13	0.05
-	-	-	-	-	-	-	-	-	-	-	-	-	-	-	-	-
-	69.0	-	-	-	-	-	-	-	-	-	-	-	-	-	-	-
-	24.0	3.00	9.0	9.0	-	-	-	-	-	-	-	-	-	-	-	-
0.45	-	2.64	9.5	-	-	1.33	-	0.82	-	-	-	-	2.74	0.15	0.16	0.05
-	-	-	-	-	-	-	-	-	-	-	-	-	-	-	-	-
-	-	-	-	-	-	-	-	-	-	-	-	-	-	-	-	-
0.05	-	2.56	9.6	-	-	1.19	-	0.74	-	-	-	-	2.39	0.13	0.12	-
-	-	-	-	-	-	-	-	-	-	-	-	-	-	-	-	-
-	52.0	-	-	-	-	-	-	-	-	-	-	-	-	-	-	-
-	15.0	3.00	8.0	9.0	-	-	-	-	-	-	-	-	-	-	-	-
0.18	20.9	2.66	9.8	-	-	1.24	-	0.83	-	-	-	-	2.66	0.15	0.16	-
-	-	-	-	-	-	-	-	-	-	-	-	-	-	-	-	-
-	50.0	-	-	-	-	-	-	-	-	-	-	-	-	-	-	-
-	50.0	-	-	-	-	-	-	-	-	-	-	-	-	-	-	-
-	48.0	-	-	-	-	-	-	-	-	-	-	-	-	-	-	-
0.04	24.0	2.65	8.4	-	-	1.31	-	0.84	-	-	-	-	2.78	0.15	0.13	0.05
-	-	-	-	-	-	-	-	-	-	-	-	-	-	-	-	-
-	53.0	-	-	-	-	-	-	-	-	-	-	-	-	-	-	-
0.09	21.0	2.95	7.5	-	-	1.23	-	0.81	-	-	-	-	2.63	0.16	0.14	-
-	-	-	-	-	-	-	-	-	-	-	-	-	-	-	-	-
0.60	16.0	3.04	10.9	-	-	1.28	-	0.83	-	-	-	-	2.76	0.16	0.13	0.07
-	-	-	-	-	-	-	-	-	-	-	-	-	-	-	-	-
-	59.0	-	-	-	-	-	-	-	-	-	-	-	-	-	-	-
0.35	8.5	2.72	9.4	-	-	1.20	-	0.82	-	-	-	-	2.74	0.15	0.12	-
-	-	-	-	-	-	-	-	-	-	-	-	-	-	-	-	-
-	-	-	-	-	-	-	-	-	-	-	-	-	-	-	-	-
0.34	24.0	2.44	9.4	-	-	1.21	-	0.76	-	-	-	-	2.43	0.14	0.11	0.04
-	-	-	-	-	-	-	-	-	-	-	-	-	-	-	-	-
0.44	18.0	2.37	8.1	-	-	1.16	-	0.82	-	-	-	-	2.36	0.13	0.11	0.03
-	-	-	-	-	-	-	-	-	-	-	-	-	-	-	-	-
0.03	28.2	2.27	9.2	-	-	1.19	-	0.79	-	-	-	-	2.42	0.13	0.13	-
-	-	-	-	-	-	-	-	-	-	-	-	-	-	-	-	-
0.24	17.2	2.42	9.3	-	-	1.16	-	0.76	-	-	-	-	2.33	0.13	0.10	-
-	-	-	-	-	-	-	-	-	-	-	-	-	-	-	-	-
-	50.0	-	-	-	-	-	-	-	-	-	-	-	-	-	-	-
0.07	18.0	1.90	9.5	-	-	1.14	-	0.77	-	-	-	-	2.38	0.14	0.14	-
-	-	-	-	-	-	-	-	-	-	-	-	-	-	-	-	-
-	47.0	-	-	-	-	-	-	-	-	-	-	-	-	-	-	-
0.03	3.0	2.60	6.9	-	-	1.16	-	0.77	-	-	-	-	2.42	0.13	0.11	0.03
-	-	-	-	-	-	-	-	-	-	-	-	-	-	-	-	-
-	25.0	3.00	8.0	9.0	-	-	-	-	-	-	-	-	-	-	-	-
-	-	2.44	8.4	8.6	3.25	1.20	4.75	0.86	-	0.54	3.68	0.57	2.44	0.10	0.16	-
0.03	11.0	2.33	8.9	-	-	1.16	-	0.73	-	-	-	-	2.42	0.13	0.13	-
-	-	-	-	-	-	-	-	-	-	-	-	-	-	-	-	-
-	-	-	-	-	-	-	-	-	-	-	-	-	-	-	-	-
-	44.0	-	-	-	-	-	-	-	-	-	-	-	-	-	-	-
0.15	-	1.63	5.3	-	-	0.85	-	0.54	-	-	-	-	1.62	0.07	0.06	0.04
-	-	-	-	-	-	-	-	-	-	-	-	-	-	-	-	-
-	-	-	-	-	-	-	-	-	-	-	-	-	-	-	-	-
-	41.0	-	-	-	-	-	-	-	-	-	-	-	-	-	-	-
-	16.0	2.00	6.0	6.0	-	-	-	-	-	-	-	-	-	-	-	-
0.21	9.1	1.40	4.5	-	-	0.95	-	0.55	-	-	-	-	1.60	0.08	0.10	-
-	-	-	-	-	-	-	-	-	-	-	-	-	-	-	-	-
0.21	9.0	1.56	5.9	-	-	0.91	-	0.54	-	-	-	-	1.53	0.07	0.06	-
-	-	-	-	-	-	-	-	-	-	-	-	-	-	-	-	-
0.12	23.0	1.33	3.9	-	-	0.83	-	0.48	-	-	-	-	1.29	0.07	0.06	0.14
-	-	-	-	-	-	-	-	-	-	-	-	-	-	-	-	-
-	27.0	2.00	5.0	6.0	-	-	-	-	-	-	-	-	-	-	-	-
-	-	-	-	-	-	-	-	-	-	-	-	-	-	-	-	-
-	44.0	-	-	-	-	-	-	-	-	-	-	-	-	-	-	-
0.10	21.0	1.22	5.0	-	-	0.82	-	0.47	-	-	-	-	1.34	0.06	0.05	0.04
-	-	-	-	-	-	-	-	-	-	-	-	-	-	-	-	-
0.12	16.1	1.85	5.2	-	-	0.99	-	0.58	-	-	-	-	1.67	0.10	0.09	0.06
-	-	-	-	-	-	-	-	-	-	-	-	-	-	-	-	-
-	18.0	2.00	5.0	7.0	-	-	-	-	-	-	-	-	-	-	-	-
-	47.0	-	-	-	-	-	-	-	-	-	-	-	-	-	-	-
-	-	-	-	-	-	-	-	-	-	-	-	-	-	-	-	-

Table 2. (Continued).

Sample	Depth (m)	Inv.	Method	Sc	V	Cr	Co	Ni	Cu	Zn	Ga	Rb	Sr	Y	Zr	Nb
Hole 556 (Cont.)																
Chemical Group III (Cont.)																
9-5, 64-68	531.66	BOG	XFNA	39.3	270.0	89.0	44.0	74.0	-	61.0	-	5.2	105.0	29.4	60.0	1.4
9-5, 64-68	531.66	BOG	NA	-	-	-	49.6	80.0	-	-	-	4.3	-	-	-	-
10-1, 122-124	535.23	SHM	XF	-	-	384.0	44.0	99.0	72	66.0	-	-	102.0	22.0	58.0	-
10-2, 130-133	536.82	WEA	XF	-	218.0	439.0	-	106.0	-	58.0	15.0	4.0	98.0	19.0	45.0	1.1
10-2, 137-141	536.89	BOG	XFNA	34.7	237.0	353.0	34.0	95.0	-	63.0	-	13.0	99.0	21.8	42.0	2.5
10-2, 137-141	536.89	BOG	NA	-	-	-	37.8	93.0	-	-	-	10.5	-	-	-	-
10-3, 63-66	537.65	DRA	XF	-	201.9	381.2	-	90.0	-	76.1	16.1	3.8	99.1	18.2	46.4	2.4
10-4, 50-54	539.02	BOG	XFNA	36.8	243.0	364.0	39.0	114.0	-	56.0	-	5.0	90.0	25.6	55.0	1.3
10-4, 50-54	539.02	BOG	NA	-	-	-	43.8	116.0	-	-	-	3.1	-	-	-	-
10-4, 72-75	539.24	DRA	XF	-	229.4	404.6	-	90.2	-	77.3	15.4	10.7	97.2	21.5	58.1	1.7
Chemical Group IV																
11-1, 105-115	544.10	BOG	XFNA	40.3	332.0	47.0	53.0	84.0	-	87.0	-	2.8	113.0	39.4	80.0	2.6
11-1, 105-115	544.10	BOG	NA	-	-	-	55.3	80.0	-	-	-	2.3	-	-	-	-
11-1, 106-109	544.08	WEA	XF	-	320.0	48.0	-	40.0	-	90.0	17.0	9.0	110.0	33.0	79.0	2.6
Chemical Group III																
11-2, 121-124	545.73	DRA	XF	-	228.0	239.6	-	73.0	-	69.0	15.5	9.4	103.6	23.0	56.0	1.2
12-1, 55-59	552.57	BOG	XFNA	36.0	243.0	314.0	36.0	102.0	-	51.0	-	5.0	98.0	22.1	51.0	1.5
12-1, 55-59	552.57	BOG	NA	-	-	-	41.6	108.0	-	-	-	5.0	-	-	-	-
12-1, 68-72	552.70	WEA	XF	-	225.0	400.0	-	97.0	-	60.0	15.0	3.0	95.0	21.0	49.0	1.6
12-3, 54-57	555.56	DRA	XF	-	222.9	387.7	-	91.6	-	71.0	14.7	5.7	95.7	21.8	55.6	1.0
12-3, 78-80	555.79	SHM	XF	-	-	420.0	46.0	112.0	221	70.0	-	-	95.0	20.0	57.0	-
12-3, 118-122	556.20	BOG	XFNA	36.3	240.0	356.0	40.0	143.0	-	54.0	-	3.8	92.0	25.4	55.0	0.7
12-3, 118-122	556.20	BOG	NA	-	-	-	46.2	145.0	-	-	-	2.5	-	-	-	-
12-4, 27-30	556.78	DRA	XF	-	224.7	395.4	-	91.2	-	65.4	15.0	14.4	94.1	21.3	58.2	1.5
Chemical Group V																
15-3, 18-21	577.70	SHM	XF	-	-	92.0	12.0	105.0	17	41.0	-	-	79.0	11.0	18.0	-
15-3, 33-35	577.84	BOG	XFNA	32.4	162.0	72.0	34.0	96.0	-	32.0	-	0.2	86.0	9.4	11.0	0.0
15-3, 33-35	577.84	BOG	NA	-	-	-	38.7	117.0	-	-	-	-	-	-	-	-
15-3, 44-47	577.96	SHM	XF	-	-	107.0	21.0	124.0	114	64.0	-	-	75.0	13.0	19.0	-
16-1, 14-18	583.66	WEA	XF	-	148.0	84.0	-	80.0	-	39.0	14.0	< 1.0	94.0	9.0	9.0	< 1.0
16-1, 21-27	583.74	BOG	XFNA	32.6	164.0	67.0	28.0	94.0	-	25.0	-	0.4	94.0	10.8	11.0	0.0
16-1, 21-27	583.74	BOG	NA	-	-	-	32.9	102.0	-	-	-	-	-	-	-	-
16-1, 29-32	583.81	SHM	XF	-	-	77.0	5.0	121.0	72	53.0	-	-	95.0	17.0	39.0	-
Chemical Group III																
16-2, 110-113	586.12	DRA	XF	-	231.5	291.6	-	135.7	-	69.4	14.3	2.8	98.5	20.1	50.4	1.6
Chemical Group IV																
16-2, 128-131	586.30	WEA	XF	-	306.0	47.0	-	41.0	-	84.0	19.0	8.0	114.0	32.0	79.0	1.9
16-2, 131-133	586.32	SHM	XF	-	-	78.0	52.0	55.0	70	84.0	-	-	120.0	31.0	82.0	-
16-2, 137-140	586.39	BOG	XFNA	41.8	321.0	49.0	44.0	65.0	-	87.0	-	4.3	114.0	37.4	81.0	1.9
16-2, 137-140	586.39	BOG	NA	-	-	-	48.2	64.0	-	-	-	4.4	-	-	-	-
Hole 557																
Chemical Group I																
H1-CC, 21-23		BOG	XFNA	33.7	313.0	24.0	42.0	25.0	-	128.0	-	11.3	344.0	49.0	219.0	42.9
H1-CC, 21-23		BOG	NA	-	-	-	44.3	28.0	-	-	-	10.7	-	-	-	-
1-1, 0-3	460.52	BOG	XFNA	38.2	415.0	41.0	51.0	45.0	-	101.0	-	9.0	311.0	46.9	219.0	30.2
1-1, 0-3	460.52	BOG	NA	-	-	-	50.0	39.0	-	-	-	11.3	-	-	-	-
1-1, 25-28	460.77	BOG	XFNA	37.9	459.0	37.0	49.0	50.0	-	94.0	-	10.0	315.0	48.7	222.0	29.9
1-1, 25-28	460.77	SHM	XF	-	-	69.0	70.0	46.0	147	122.0	-	-	289.0	41.0	198.0	-
1-1, 25-28	460.77	BOG	NA	-	-	-	50.1	41.0	-	-	-	9.3	-	-	-	-
1-1, 38-41	460.90	WEA	XF	-	384.0	32.0	-	36.0	-	131.0	23.0	14.0	298.0	44.0	225.0	30.0
1-1, 40-43	460.92	BOG	XFNA	38.1	422.0	31.0	48.0	34.0	-	105.0	-	10.1	300.0	48.9	220.0	29.9
1-1, 40-43	460.92	BOG	NA	-	-	-	50.9	39.0	-	-	-	9.5	-	-	-	-
1-1, 50-53	461.02	DRA	XF	-	300.0	18.7	-	38.3	-	113.3	22.6	10.8	299.0	41.0	216.2	26.2
1-1, 105-108	461.57	SHM	XF	-	-	70.0	64.0	51.0	197	107.0	-	-	277.0	37.0	196.0	-
1-1, 144-147	461.96	WEA	XF	-	384.0	30.0	-	37.0	-	130.0	24.0	10.0	304.0	44.0	218.0	28.0
1-1, 144-147	461.96	WEA	NA	-	-	-	-	-	-	-	-	-	-	-	-	-
Hole 558																
Chemical Group I																
27-3, 46-48	408.47	PUC	XFNAAA	34.2	-	430.0	48.8	250.0	83	81.0	15.0	6.9	138.0	26.0	91.0	-
27-3, 69-72	408.71	SHM	XF	-	-	503.0	57.0	275.0	86	76.0	-	-	136.0	20.0	74.0	-
27-3, 74-77	408.76	BOG	XFNA	32.2	207.0	490.0	47.0	259.0	-	73.0	-	3.6	128.0	26.6	83.0	8.6
27-3, 74-77	408.76	BOG	NA	-	-	-	50.3	287.0	-	-	-	1.9	-	-	-	-
27-3, 92-95	408.94	WEA	XF	-	239.0	544.0	-	265.0	-	84.0	16.0	7.0	137.0	24.0	75.0	7.8
27-3, 92-95	408.94	WEA	NA	-	-	-	-	-	-	-	-	-	-	-	-	-
27-3, 112-114	409.13	DRA	NA	34.1	-	-	-	-	-	-	-	-	-	-	-	-
27-3, 112-114	409.13	DRA	XF	-	195.6	509.7	-	277.4	-	83.0	15.7	3.6	128.9	22.2	75.9	8.6
27-3, 116-118	409.17	SHM	XF	-	-	467.0	63.0	290.0	80	76.0	-	-	131.0	24.0	75.0	-
Chemical Group II																
28-1, 38-41	414.90	WEA	XF	-	270.0	448.0	-	140.0	-	84.0	15.0	8.0	88.0	28.0	66.0	2.8
28-1, 55-58	415.07	DRA	NA	40.1	-	-	-	-	-	-	-	-	-	-	-	-
28-1, 55-58	415.07	DRA	XF	-	238.3	400.5	-	169.8	-	90.3	16.0	2.5	94.7	25.6	66.5	3.1
28-1, 79-81	415.30	WEA	XF	-	268.0	445.0	-	136.0	-	82.0	17.0	6.0	88.0	25.0	64.0	2.4
28-1, 91-94	415.43	BOG	XFNA	37.2	256.0	373.0	45.0	149.0	-	73.0	-	4.4	93.0	28.8	63.0	2.8
28-1, 91-94	415.43	BOG	NA	-	-	-	46.9	149.0	-	-	-	3.4	-	-	-	-
28-2, 6-8	416.07	PUC	XFNAAA	39.9	-	445.0	41.1	130.0	83	87.0	16.0	6.6	101.0	29.0	84.0	-
28-2, 52-55	416.54	WEA	XF	-	280.0	462.0	-	116.0	-	81.0	17.0	5.0	91.0	27.0	63.0	3.2
28-2, 80-83	416.82	SHM	XF	-	-	366.0	49.0	117.0	70	76.0	-	-	96.0	25.0	65.0	-
28-2, 100-102	417.01	SHM	XF	-	-	395.0	51.0	181.0	81	78.0	-	-	92.0	28.0	67.0	-
28-2, 121-125	417.23	BOG	XFNA	38.3	257.0	359.0	44.0	154.0	-	74.0	-	3.1	96.0	29.5	69.0	3.5
28-2, 121-125	417.23	BOG	NA	-	-	-	48.5	153.0	-	-	-	2.7	-	-	-	-
28-3, 36-38	417.87	WEA	XF	-	259.0	430.0	-	138.0	-	80.0	16.0	4.0	89.0	27.0	66.0	2.7
28-3, 36-38	417.87	WEA	NA	-	-	-	-	-	-	-	-	-	-	-	-	-
28-3, 60-64	418.12	BOG	XFNA	37.3	253.0	375.0	42.0	130.0	-	72.0	-	4.1	88.0	29.7	65.0	3.2
28-3, 60-64	418.12	BOG	NA	-	-	-	45.2	129.0	-	-	-	4.2	-	-	-	-
28-3, 118-120	418.69	SHM	XF	-	-	420.0	44.0	127.0	100	78.0	-	-	91.0	22.0	63.0	-

Table 2. (Continued).

Cs	Ba	La	Ce	Nd	Sm	Eu	Gd	Tb	Ho	Tm	Yb	Lu	Hf	Ta	Th	U
0.31	15.0	1.71	4.3	-	-	0.98	-	0.60	-	-	-	-	1.60	0.11	0.10	-
-	-	-	-	-	-	-	-	-	-	-	-	-	-	-	-	-
-	44.0	-	-	-	-	-	-	-	-	-	-	-	-	-	-	-
-	19.0	< 2.00	4.0	5.0	-	-	-	-	-	-	-	-	-	-	-	-
1.56	-	1.37	5.5	-	-	0.77	-	0.51	-	-	-	-	1.31	0.07	0.10	0.11
-	-	-	-	-	-	-	-	-	-	-	-	-	-	-	-	-
-	-	-	-	-	-	-	-	-	-	-	-	-	-	-	-	-
0.24	-	1.53	5.2	-	-	0.88	-	0.52	-	-	-	-	1.56	0.07	0.07	-
-	-	-	-	-	-	-	-	-	-	-	-	-	-	-	-	-
-	-	-	-	-	-	-	-	-	-	-	-	-	-	-	-	-
0.07	25.4	2.44	7.5	-	-	1.21	-	0.76	-	-	-	-	2.25	0.13	0.11	-
-	-	-	-	-	-	-	-	-	-	-	-	-	-	-	-	-
-	31.0	3.00	10.0	9.0	-	-	-	-	-	-	-	-	-	-	-	-
-	-	-	-	-	-	-	-	-	-	-	-	-	-	-	-	-
0.27	9.0	1.36	4.1	-	-	0.86	-	0.48	-	-	-	-	1.37	0.07	0.07	0.08
-	-	-	-	-	-	-	-	-	-	-	-	-	-	-	-	-
-	17.0	< 2.00	6.0	7.0	-	-	-	-	-	-	-	-	-	-	-	-
-	-	-	-	-	-	-	-	-	-	-	-	-	-	-	-	-
-	52.0	-	-	-	-	-	-	-	-	-	-	-	-	-	-	-
0.21	-	1.72	5.3	-	-	0.88	-	0.48	-	-	-	-	1.62	0.08	0.09	-
-	-	-	-	-	-	-	-	-	-	-	-	-	-	-	-	-
-	-	-	-	-	-	-	-	-	-	-	-	-	-	-	-	-
-	10.0	-	-	-	-	-	-	-	-	-	-	-	-	-	-	-
0.02	-	0.26	-	-	-	0.42	-	0.08	-	-	-	-	0.15	-	0.02	-
-	-	-	-	-	-	-	-	-	-	-	-	-	-	-	-	-
-	10.0	-	-	-	-	-	-	-	-	-	-	-	-	-	-	-
-	9.0	< 2.00	< 4.0	2.0	-	-	-	-	-	-	-	-	-	-	-	-
-	-	0.28	-	-	-	0.41	-	0.17	-	-	-	-	0.24	-	-	-
-	-	-	-	-	-	-	-	-	-	-	-	-	-	-	-	-
-	10.0	-	-	-	-	-	-	-	-	-	-	-	-	-	-	-
-	-	-	-	-	-	-	-	-	-	-	-	-	-	-	-	-
-	45.0	3.00	9.0	8.0	-	-	-	-	-	-	-	-	-	-	-	-
-	56.0	-	-	-	-	-	-	-	-	-	-	-	-	-	-	-
0.23	34.0	2.40	8.3	-	-	1.30	-	0.77	-	-	-	-	2.45	0.14	0.12	-
-	-	-	-	-	-	-	-	-	-	-	-	-	-	-	-	-
0.05	161.0	27.20	52.8	-	-	2.64	-	1.16	-	-	-	-	5.20	2.83	2.69	0.90
-	-	-	-	-	-	-	-	-	-	-	-	-	-	-	-	-
0.06	114.0	20.60	50.3	-	-	2.65	-	1.21	-	-	-	-	5.56	2.14	2.04	0.75
-	-	-	-	-	-	-	-	-	-	-	-	-	-	-	-	-
0.06	131.0	20.60	45.8	-	-	2.69	-	1.19	-	-	-	-	5.67	2.15	1.84	0.73
-	216.0	-	-	-	-	-	-	-	-	-	-	-	-	-	-	-
-	-	-	-	-	-	-	-	-	-	-	-	-	-	-	-	-
-	133.0	21.00	52.0	30.0	-	-	-	-	-	-	-	-	-	-	-	-
0.08	120.0	21.00	50.8	-	-	2.68	-	1.26	-	-	-	-	5.64	2.16	2.00	0.68
-	-	-	-	-	-	-	-	-	-	-	-	-	-	-	-	-
-	-	-	-	-	-	-	-	-	-	-	-	-	-	-	-	-
-	219.0	-	-	-	-	-	-	-	-	-	-	-	-	-	-	-
-	123.0	21.00	52.0	30.0	-	-	-	-	-	-	-	-	-	-	-	-
-	-	20.00	47.3	31.0	7.83	2.57	8.70	1.39	-	0.61	3.60	0.55	5.36	1.86	1.85	-
0.47	-	6.50	15.8	10.3	3.13	1.03	4.10	0.66	0.98	0.37	2.40	0.40	2.30	0.41	0.35	0.20
-	106.0	-	-	-	-	-	-	-	-	-	-	-	-	-	-	-
0.06	40.0	5.70	14.4	-	-	1.03	-	0.56	-	-	-	-	1.95	0.57	0.53	0.15
-	-	-	-	-	-	-	-	-	-	-	-	-	-	-	-	-
-	55.0	6.00	13.0	9.0	-	-	-	-	-	-	-	-	-	-	-	-
-	-	6.05	15.2	9.4	3.04	1.06	3.46	0.63	-	0.35	2.26	0.38	2.05	0.52	0.67	-
-	-	6.42	14.7	12.0	2.81	1.01	-	-	-	-	2.42	0.38	1.97	-	-	-
-	-	-	-	-	-	-	-	-	-	-	-	-	-	-	-	-
-	44.0	-	-	-	-	-	-	-	-	-	-	-	-	-	-	-
-	11.0	< 2.00	9.0	9.0	-	-	-	-	-	-	-	-	-	-	-	-
-	-	3.06	7.5	9.7	2.63	0.96	-	-	-	-	3.06	0.43	1.70	-	-	-
-	-	-	-	-	-	-	-	-	-	-	-	-	-	-	-	-
-	9.0	2.00	8.0	8.0	-	-	-	-	-	-	-	-	-	-	-	-
0.27	8.1	2.67	7.7	-	-	0.95	-	0.58	-	-	-	-	1.76	0.16	0.15	0.08
-	-	-	-	-	-	-	-	-	-	-	-	-	-	-	-	-
0.36	-	3.00	9.6	6.2	2.79	0.68	4.20	0.63	0.92	0.39	2.70	0.45	1.90	0.11	< .20	< .20
-	13.0	< 2.00	10.0	8.0	-	-	-	-	-	-	-	-	-	-	-	-
-	48.0	-	-	-	-	-	-	-	-	-	-	-	-	-	-	-
-	15.0	-	-	-	-	-	-	-	-	-	-	-	-	-	-	-
0.07	13.0	2.25	6.9	-	-	0.98	-	0.55	-	-	-	-	1.81	0.16	0.16	-
-	-	-	-	-	-	-	-	-	-	-	-	-	-	-	-	-
-	12.0	2.00	9.0	8.0	-	-	-	-	-	-	-	-	-	-	-	-
-	-	2.68	8.5	7.5	2.63	0.97	3.59	0.70	-	0.48	2.73	0.45	1.87	0.14	0.24	-
0.23	-	2.61	7.3	-	-	1.04	-	0.59	-	-	-	-	1.86	0.16	0.17	0.07
-	-	-	-	-	-	-	-	-	-	-	-	-	-	-	-	-
-	44.0	-	-	-	-	-	-	-	-	-	-	-	-	-	-	-

Table 2. (Continued).

Sample	Depth (m)	Inv	Method	Sc	V	Cr	Co	Ni	Cu	Zn	Ga	Rb	Sr	Y	Zr	Nb
Hole 558 (Cont.)																
Chemical Group III																
29-1, 63-65	424.14	SHM	XF	-	-	328.0	51.0	163.0	69	83.0	-	-	167.0	27.0	92.0	-
29-1, 99-101	424.50	WEA	XF	-	282.0	380.0	-	170.0	-	82.0	17.0	7.0	175.0	26.0	90.0	14.3
29-1, 120-125	424.73	BOG	XFNA	34.7	277.0	339.0	45.0	182.0	-	77.0	-	7.9	176.0	28.9	97.0	15.3
29-1, 120-125	424.73	BOG	NA	-	-	-	46.2	170.0	-	-	-	8.6	-	-	-	-
29-2, 6-8	425.07	PUC	XFNAAA	37.3	-	299.0	41.3	142.0	70	90.0	16.0	7.0	173.0	29.0	104.0	-
29-2, 110-113	426.12	SHM	XF	-	-	324.0	51.0	156.0	73	79.0	-	-	168.0	27.0	90.0	-
29-3, 110-112	427.61	SHM	XF	-	-	331.0	48.0	156.0	70	82.0	-	-	177.0	27.0	90.0	-
29-4, 71-76	428.74	BOG	XFNA	34.0	273.0	332.0	38.0	140.0	-	76.0	-	9.7	171.0	27.9	91.0	15.7
29-4, 71-76	428.74	BOG	NA	-	-	-	41.0	136.0	-	-	-	9.6	-	-	-	-
29-4, 83-85	428.84	SHM	XF	-	-	343.0	45.0	148.0	120	92.0	-	-	174.0	23.0	86.0	-
30-1, 60-64	433.12	BOG	XFNA	33.7	281.0	352.0	42.0	157.0	-	75.0		7.4	165.0	28.6	97.0	14.3
30-1, 60-64	433.12	BOG	NA	-	-	-	43.6	158.0	-	-	-	8.4	-	-	-	-
30-1, 95-97	433.46	SHM	XF	-	-	332.0	55.0	162.0	80	82.0	-	-	162.0	25.0	91.0	-
30-1, 115-118	433.67	DRA	XF	-	257.9	356.3	-	157.5	-	89.5	15.6	9.7	170.0	24.2	92.8	15.3
30-3, 12-14	435.63	WEA	XF	-	280.0	383.0	-	151.0	-	85.0	17.0	9.0	169.0	25.0	89.0	14.0
30-3, 94-96	436.45	SHM	XF	-	-	333.0	147.0	170.0	73	79.0	-	-	174.0	27.0	92.0	-
30-3, 99-103	436.51	BOG	XFNA	35.3	278.0	340.0	43.0	163.0	-	76.0	-	8.0	173.0	28.8	96.0	15.2
30-3, 99-103	436.51	BOG	NA	-	-	-	45.0	149.0	-	-	-	6.7	-	-	-	-
30-4, 2-4	437.03	SHM	XF	-	-	332.0	73.0	159.0	65	78.0	-	-	176.0	27.0	90.0	-
30-4, 41-43	437.42	SHM	XF	-	-	348.0	52.0	175.0	76	83.0	-	-	173.0	26.0	89.0	-
30-4, 55-59	437.57	BOG	XFNA	34.2	268.0	341.0	43.0	160.0	-	76.0	-	4.0	172.0	28.3	90.0	16.0
30-4, 55-59	437.57	BOG	NA	-	-	-	45.3	165.0	-	-	-	2.7	-	-	-	-
31-1, 62-64	442.13	BOG	XFNA	34.7	277.0	344.0	42.0	158.0	-	74.0	-	5.7	174.0	30.3	89.0	16.4
31-1, 62-64	442.13	BOG	NA	-	-	-	45.5	169.0	-	-	-	4.8	-	-	-	-
31-1, 79-82	442.31	SHM	XF	-	-	350.0	52.0	154.0	80	76.0	-	-	187.0	20.0	86.0	-
31-1, 86-89	442.38	WEA	XF	-	284.0	387.0	-	152.0	-	84.0	17.0	5.0	174.0	25.0	91.0	14.8
31-1, 86-89	442.38	WEA	NA	-	-	-	-	-	-	-	-	-	-	-	-	-
31-1, 118-120	442.69	SHM	XF	-	-	331.0	45.0	160.0	71	75.0	-	-	167.0	25.0	88.0	-
31-2, 128-130	444.29	BOG	XFNA	34.6	280.0	347.0	43.0	158.0	-	75.0	-	5.6	172.0	28.1	90.0	17.2
31-2, 128-130	444.29	BOG	NA	-	-	-	44.9	162.0	-	-	-	4.8	-	-	-	-
32-1, 41-44	450.93	SHM	XF	-	-	339.0	47.0	167.0	71	76.0	-	-	169.0	27.0	90.0	-
32-1, 106-110	451.58	BOG	XFNA	34.7	280.0	338.0	43.0	161.0	-	77.0	-	8.1	171.0	29.1	87.0	15.0
32-1, 106-110	451.58	BOG	NA	-	-	-	46.7	174.0	-	-	-	8.1	-	-	-	-
32-1, 115-117	451.66	WEA	XF	-	286.0	386.0	-	156.0	-	85.0	17.0	7.0	172.0	28.0	91.0	14.5
32-1, 123-125	451.74	SHM	XF	-	-	365.0	52.0	180.0	73	81.0	-	-	175.0	23.0	91.0	-
32-2, 57-59	452.58	SHM	XF	-	-	351.0	47.0	165.0	67	70.0	-	-	179.0	22.0	80.0	-
32-2, 130-132	453.31	DRA	XF	-	242.8	367.0	-	170.6	-	85.6	15.1	2.5	179.5	21.8	84.6	13.8
32-2, 145-147	453.46	SHM	XF	-	-	362.0	42.0	161.0	67	74.0	-	-	177.0	23.0	81.0	-
32-3, 35-37	453.86	SHM	XF	-	-	367.0	48.0	172.0	68	78.0	-	-	176.0	23.0	80.0	-
32-3, 38-40	453.89	WEA	XF	-	269.0	412.0	-	153.0	-	84.0	17.0	6.0	177.0	24.0	78.0	13.0
32-3, 63-67	454.15	BOG	XFNA	34.7	274.0	380.0	46.0	157.0	-	78.0	-	5.7	173.0	25.3	81.0	13.9
32-3, 63-67	454.15	BOG	NA	-	-	-	51.7	165.0	-	-	-	2.7	-	-	-	-
32-4, 73-75	455.74	DRA	XF	-	249.8	388.9	-	156.2	-	83.9	15.4	6.6	174.8	21.6	82.6	14.5
32-4, 77-79	455.78	SHM	XF	-	-	354.0	46.0	162.0	70	70.0	-	-	172.0	24.0	82.0	-
32-4, 111-113	456.12	SHM	XF	-	-	354.0	46.0	154.0	75	78.0	-	-	182.0	24.0	81.0	-
32-5, 66-70	457.18	BOG	XFNA	35.4	291.0	377.0	42.0	149.0	-	75.0	-	6.1	187.0	26.4	80.0	12.9
32-5, 66-70	457.18	BOG	NA	-	-	-	42.2	137.0	-	-	-	6.3	-	-	-	-
32-5, 88-90	457.39	WEA	XF	-	267.0	403.0	-	154.0	-	77.0	16.0	6.0	181.0	24.0	80.0	13.3
32-5, 101-103	457.52	DRA	XF	-	233.9	371.6	-	157.9	-	81.3	14.0	6.8	176.4	21.2	81.5	13.4
33-1, 77-80	460.29	BOG	XFNA	33.9	267.0	369.0	42.0	157.0	-	71.0	-	5.6	180.0	27.2	82.0	13.0
33-1, 77-80	460.29	BOG	NA	-	-	-	44.2	157.0	-	-	-	6.8	-	-	-	-
33-2, 71-73	461.72	SHM	XF	-	-	397.0	42.0	137.0	67	78.0	-	-	180.0	19.0	79.0	-
33-2, 144-147	462.46	DRA	NA	36.1	-	-	-	-	-	-	-	-	-	-	-	-
33-2, 144-147	462.46	DRA	XF	-	243.7	384.8	-	156.1	-	87.7	15.4	5.4	174.5	21.8	82.2	13.4
33-3, 7-9	462.58	SHM	XF	-	-	361.0	48.0	166.0	63	76.0	-	-	178.0	23.0	83.0	-
33-3, 61-64	463.13	DRA	XF	-	252.0	398.3	-	155.9	-	98.5	14.8	6.8	173.0	21.1	82.8	14.0
33-3, 89-91	463.40	SHM	XF	-	-	361.0	41.0	150.0	65	81.0	-	-	182.0	25.0	81.0	-
33-3, 135-138	463.87	WEA	XF	-	258.0	392.0	-	155.0	-	79.0	16.0	6.0	177.0	23.0	80.0	13.2
33-3, 139-141	463.90	DRA	XF	-	233.4	362.8	-	175.0	-	84.7	16.2	6.9	175.2	21.2	80.2	12.7
33-3, 144-147	463.96	BOG	XFNA	34.5	274.0	361.0	44.0	167.0	-	71.0	-	5.5	183.0	24.9	83.0	13.9
33-3, 144-147	463.96	BOG	NA	-	-	-	45.8	156.0	-	-	-	6.4	-	-	-	-
34-1, 30-32	468.81	SHM	XF	-	-	383.0	49.0	160.0	110	75.0	-	-	176.0	19.0	78.0	-
34-1, 34-38	468.86	BOG	XFNA	34.0	255.0	352.0	40.0	151.0	-	69.0	-	3.3	177.0	26.2	79.0	14.2
34-1, 34-38	468.86	BOG	NA	-	-	-	43.5	158.0	-	-	-	3.6	-	-	-	-
34-1, 63-65	469.14	WEA	XF	-	278.0	420.0	-	134.0	-	84.0	17.0	5.0	182.0	23.0	79.0	12.9
34-1, 113-115	469.64	PUC	XFNAAA	36.5	-	316.0	38.6	140.0	67	76.0	15.0	13.2	191.0	25.0	88.0	-
Chemical Group IV																
35-1, 120-122	478.71	WEA	XF	-	270.0	416.0	-	181.0	-	80.0	16.0	5.0	145.0	25.0	74.0	9.2
35-1, 120-122	478.71	WEA	NA	-	-	-	-	-	-	-	-	-	-	-	-	-
35-1, 128-131	478.80	BOG	XFNA	35.6	261.0	367.0	45.0	178.0	-	71.0	-	6.4	146.0	26.7	75.0	10.4
35-1, 128-131	478.80	BOG	NA	-	-	-	46.6	180.0	-	-	-	5.1	-	-	-	-
35-2, 2-4	479.03	SHM	XF	-	-	361.0	46.0	182.0	73	76.0	-	-	146.0	25.0	77.0	-
35-2, 11-13	479.12	SHM	XF	-	-	359.0	53.0	180.0	75	72.0	-	-	144.0	26.0	76.0	-
35-2, 97-102	480.00	BOG	XFNA	35.6	273.0	378.0	44.0	183.0	-	73.0	-	5.5	146.0	25.7	79.0	9.3
35-2, 97-102	480.00	BOG	NA	-	-	-	45.8	187.0	-	-	-	4.9	-	-	-	-
35-2, 112-114	480.13	WEA	XF	-	280.0	433.0	-	168.0	-	83.0	15.0	5.0	147.0	25.0	75.0	9.2
35-3, 89-91	481.40	WEA	XF	-	280.0	431.0	-	174.0	-	80.0	16.0	6.0	148.0	25.0	76.0	9.8
35-3, 100-103	481.52	BOG	XFNA	34.4	250.0	370.0	46.0	196.0	-	69.0	-	5.4	141.0	25.9	69.0	9.4
35-3, 100-103	481.52	BOG	NA	-	-	-	47.1	198.0	-	-	-	5.6	-	-	-	-
35-3, 107-109	481.58	DRA	XF	-	239.9	380.5	-	185.8	-	87.0	14.8	6.0	142.2	22.5	76.0	9.5
35-3, 110-113	481.62	SHM	XF	-	-	391.0	52.0	193.0	73	75.0	-	-	145.0	20.0	72.0	-
35-4, 102-104	483.03	WEA	XF	-	268.0	374.0	-	169.0	-	78.0	16.0	4.0	144.0	25.0	81.0	10.8
35-4, 106-108	483.07	SHM	XF	-	-	393.0	52.0	186.0	83	79.0	-	-	149.0	22.0	73.0	-
36-1, 62-65	487.14	BOG	XFNA	35.5	284.0	344.0	40.0	152.0	-	73.0	-	5.5	139.0	29.1	83.0	11.5
36-1, 62-65	487.14	BOG	NA	-	-	-	43.7	165.0	-	-	-	6.3	-	-	-	-
36-1, 74-78	487.26	DRA	XF	-	246.4	308.5	-	152.5	-	87.4	15.3	7.7	145.9	24.0	85.6	11.3
36-1, 82-84	487.33	WEA	XF	-	263.0	355.0	-	166.0	-	81.0	17.0	7.0	147.0	25.0	82.0	11.6
36-2, 100-102	489.01	WEA	XF	-	264.0	353.0	-	167.0	-	81.0	17.0	7.0	144.0	26.0	81.0	11.5
36-2, 107-110	489.09	BOG	XFNA	35.3	265.0	314.0	42.0	176.0	-	75.0	-	6.6	149.0	29.2	93.0	12.1
36-2, 107-110	489.09	BOG	NA	-	-	-	45.6	180.0	-	-	-	6.3	-	-	-	-
36-3, 17-19	489.68	SHM	XF	-	-	351.0	44.0	150.0	83	78.0	-	-	169.0	26.0	85.0	-

Table 2. (Continued).

Cs	Ba	La	Ce	Nd	Sm	Eu	Gd	Tb	Ho	Tm	Yb	Lu	Hf	Ta	Th	U
-	111.0	-	-	-	-	-	-	-	-	-	-	-	-	-	-	-
-	57.0	10.00	23.0	13.0	-	-	-	-	-	-	-	-	-	-	-	-
0.38	56.0	9.40	24.0	-	-	1.22	-	0.62	-	-	-	-	2.34	0.98	0.96	0.33
-	-	-	-	-	-	-	-	-	-	-	-	-	-	-	-	-
< .14	-	10.50	24.4	14.9	3.85	1.24	4.50	0.75	0.91	0.42	2.60	0.44	2.70	0.78	0.88	0.40
-	134.0	-	-	-	-	-	-	-	-	-	-	-	-	-	-	-
-	128.0	-	-	-	-	-	-	-	-	-	-	-	-	-	-	-
0.47	42.0	9.50	23.2	-	-	1.16	-	0.61	-	-	-	-	2.21	0.97	0.96	0.34
-	-	-	-	-	-	-	-	-	-	-	-	-	-	-	-	-
-	73.0	-	-	-	-	-	-	-	-	-	-	-	-	-	-	-
0.08	93.0	9.80	19.2	-	-	1.17	-	0.62	-	-	-	-	2.24	0.97	0.91	0.31
-	-	-	-	-	-	-	-	-	-	-	-	-	-	-	-	-
-	115.0	-	-	-	-	-	-	-	-	-	-	-	-	-	-	-
-	-	-	-	-	-	-	-	-	-	-	-	-	-	-	-	-
-	49.0	9.00	24.0	13.0	-	-	-	-	-	-	-	-	-	-	-	-
-	71.0	-	-	-	-	-	-	-	-	-	-	-	-	-	-	-
0.45	25.7	10.00	22.3	-	-	1.18	-	0.63	-	-	-	-	2.33	0.98	0.99	0.38
-	-	-	-	-	-	-	-	-	-	-	-	-	-	-	-	-
-	118.0	-	-	-	-	-	-	-	-	-	-	-	-	-	-	-
-	78.0	-	-	-	-	-	-	-	-	-	-	-	-	-	-	-
0.10	46.0	9.70	20.4	-	-	1.18	-	0.62	-	-	-	-	2.20	0.97	0.92	0.33
-	-	-	-	-	-	-	-	-	-	-	-	-	-	-	-	-
0.21	58.0	10.00	22.1	-	-	1.25	-	0.62	-	-	-	-	2.37	0.98	0.98	0.36
-	-	-	-	-	-	-	-	-	-	-	-	-	-	-	-	-
-	70.0	-	-	-	-	-	-	-	-	-	-	-	-	-	-	-
-	56.0	9.00	23.0	14.0	-	-	-	-	-	-	-	-	-	-	-	-
-	-	10.60	22.9	13.7	3.76	1.29	4.05	0.74	-	0.47	2.68	0.43	2.53	0.90	1.12	-
-	133.0	-	-	-	-	-	-	-	-	-	-	-	-	-	-	-
0.13	55.1	9.90	22.3	-	-	1.22	-	0.63	-	-	-	-	2.38	0.99	0.96	0.25
-	-	-	-	-	-	-	-	-	-	-	-	-	-	-	-	-
-	149.0	-	-	-	-	-	-	-	-	-	-	-	-	-	-	-
0.35	38.4	9.70	22.4	-	-	1.16	-	0.63	-	-	-	-	2.41	1.00	0.94	0.32
-	-	-	-	-	-	-	-	-	-	-	-	-	-	-	-	-
-	48.0	21.00	-	13.0	-	-	-	-	-	-	-	-	-	-	-	-
-	83.0	-	-	-	-	-	-	-	-	-	-	-	-	-	-	-
-	107.0	-	-	-	-	-	-	-	-	-	-	-	-	-	-	-
-	-	-	-	-	-	-	-	-	-	-	-	-	-	-	-	-
-	90.0	-	-	-	-	-	-	-	-	-	-	-	-	-	-	-
-	78.0	-	-	-	-	-	-	-	-	-	-	-	-	-	-	-
-	42.0	9.00	22.0	12.0	-	-	-	-	-	-	-	-	-	-	-	-
0.19	-	9.10	20.6	-	-	1.08	-	0.57	-	-	-	-	2.16	0.90	0.84	0.20
-	-	-	-	-	-	-	-	-	-	-	-	-	-	-	-	-
-	-	-	-	-	-	-	-	-	-	-	-	-	-	-	-	-
-	99.0	-	-	-	-	-	-	-	-	-	-	-	-	-	-	-
-	87.0	-	-	-	-	-	-	-	-	-	-	-	-	-	-	-
0.26	35.8	9.10	17.4	-	-	1.08	-	0.58	-	-	-	-	2.06	0.92	0.86	0.24
-	-	-	-	-	-	-	-	-	-	-	-	-	-	-	-	-
-	46.0	8.00	19.0	11.0	-	-	-	-	-	-	-	-	-	-	-	-
-	-	-	-	-	-	-	-	-	-	-	-	-	-	-	-	-
0.23	22.8	8.80	19.5	-	-	1.11	-	0.55	-	-	-	-	2.09	0.88	0.89	0.15
-	-	-	-	-	-	-	-	-	-	-	-	-	-	-	-	-
-	82.0	-	-	-	-	-	-	-	-	-	-	-	-	-	-	-
-	-	9.79	19.4	17.1	3.09	1.10	-	-	-	-	2.36	0.34	2.01	-	-	-
-	-	-	-	-	-	-	-	-	-	-	-	-	-	-	-	-
-	111.0	-	-	-	-	-	-	-	-	-	-	-	-	-	-	-
-	-	-	-	-	-	-	-	-	-	-	-	-	-	-	-	-
-	62.0	-	-	-	-	-	-	-	-	-	-	-	-	-	-	-
-	41.0	9.00	21.0	12.0	-	-	-	-	-	-	-	-	-	-	-	-
-	-	-	-	-	-	-	-	-	-	-	-	-	-	-	-	-
0.27	32.0	8.80	16.4	-	-	1.14	-	0.55	-	-	-	-	2.05	0.88	0.94	0.28
-	-	-	-	-	-	-	-	-	-	-	-	-	-	-	-	-
-	91.0	-	-	-	-	-	-	-	-	-	-	-	-	-	-	-
0.03	54.0	8.60	16.8	-	-	1.13	-	0.55	-	-	-	-	2.08	0.87	0.88	0.27
-	-	-	-	-	-	-	-	-	-	-	-	-	-	-	-	-
-	42.0	7.00	19.0	11.0	-	-	-	-	-	-	-	-	-	-	-	-
0.52	-	9.40	20.9	12.0	3.30	1.08	4.20	0.63	0.91	0.33	2.20	0.36	2.30	0.65	0.78	0.40
-	38.0	6.00	16.0	9.0	-	-	-	-	-	-	-	-	-	-	-	-
-	-	6.62	16.3	10.1	2.99	1.05	3.44	0.67	-	0.44	2.39	0.38	1.99	0.58	0.75	-
0.26	28.0	6.41	12.5	-	-	1.01	-	0.55	-	-	-	-	2.01	0.62	0.62	0.16
-	-	-	-	-	-	-	-	-	-	-	-	-	-	-	-	-
-	89.0	-	-	-	-	-	-	-	-	-	-	-	-	-	-	-
-	77.0	-	-	-	-	-	-	-	-	-	-	-	-	-	-	-
0.28	25.0	6.80	11.3	-	-	0.97	-	0.58	-	-	-	-	2.06	0.64	0.72	0.19
-	-	-	-	-	-	-	-	-	-	-	-	-	-	-	-	-
-	36.0	6.00	16.0	11.0	-	-	-	-	-	-	-	-	-	-	-	-
-	33.0	7.00	15.0	9.0	-	-	-	-	-	-	-	-	-	-	-	-
0.24	23.0	6.20	17.2	-	-	1.01	-	0.55	-	-	-	-	2.02	0.61	0.56	0.20
-	-	-	-	-	-	-	-	-	-	-	-	-	-	-	-	-
-	-	-	-	-	-	-	-	-	-	-	-	-	-	-	-	-
-	69.0	-	-	-	-	-	-	-	-	-	-	-	-	-	-	-
-	40.0	7.00	19.0	11.0	-	-	-	-	-	-	-	-	-	-	-	-
-	95.0	-	-	-	-	-	-	-	-	-	-	-	-	-	-	-
0.08	73.0	7.20	19.2	-	-	1.14	-	0.62	-	-	-	-	2.15	0.75	0.87	0.22
-	-	-	-	-	-	-	-	-	-	-	-	-	-	-	-	-
-	-	-	-	-	-	-	-	-	-	-	-	-	-	-	-	-
-	42.0	8.00	19.0	11.0	-	-	-	-	-	-	-	-	-	-	-	-
-	44.0	8.00	20.0	11.0	-	-	-	-	-	-	-	-	-	-	-	-
0.30	36.0	7.70	20.3	-	-	1.11	-	0.62	-	-	-	-	2.13	0.73	0.85	0.24
-	-	-	-	-	-	-	-	-	-	-	-	-	-	-	-	-
-	81.0	-	-	-	-	-	-	-	-	-	-	-	-	-	-	-

Table 2. (Continued).

Sample	Depth (m)	Ins	Method	Sc	V	Cr	Co	Ni	Cu	Zn	Ga	Rb	Sr	Y	Zr	Nb
Hole 558 (Cont.)																
Chemical Group IV (Cont.)																
36-3, 44-46	489.95	PUC	XFNAAA	38.7	-	300.0	42.0	155.0	78	84.0	16.0	6.8	151.0	28.0	96.0	
Chemical Group V																
37-1, 89-92	496.41	DRA	XF	-	197.6	458.4	-	208.3		78.6	14.7	7.0	111.2	18.5	55.4	7.6
37-1, 137-141	496.89	BOG	XFNA	34.0	243.0	449.0	49.0	231.0	-	62.0		5.0	113.0	22.2	58.0	6.4
37-1, 137-141	496.89	BOG	NA	-	-	-	51.5	237.0				3.6	-	-	-	-
37-1, 143-148	496.96	WEA	XF	-	221.0	488.0		218.0		73.0	14.0	6.0	111.0	20.0	57.0	7.2
38-1, 34-36	504.85	SHM	XF	-	-	431.0	54.0	228.0	85	66.0	-		111.0	21.0	60.0	-
38-1, 93-95	505.44	SHM	XF		-	429.0	47.0	223.0	89	65.0	-		113.0	21.0	58.0	
38-1, 97-99	505.48	DRA	NA	35.9												
38-1, 97-99	505.48	DRA	XF	-	190.5	449.4	-	230.1	-	73.1	15.2	3.7	108.2	18.5	54.8	7.2
38-1, 104-108	505.56	WEA	XF	-	230.0	509.0	-	223.0	-	73.0	15.0	7.0	112.0	21.0	57.0	7.3
38-1, 126-130	505.78	BOG	XFNA	33.5	222.0	450.0	49.0	239.0	-	62.0	-	4.5	113.0	22.1	65.0	7.8
38-1, 126-130	505.78	BOG	NA	-	-	-	50.9	245.0	-	-	-	4.0	-	-	-	-
38-2, 61-63	506.62	SHM	XF	-	-	362.0	49.0	155.0	77	79.0	-	-	145.0	23.0	80.0	-
38-2, 84-88	506.86	BOG	XFNA	35.5	235.0	462.0	52.0	204.0	-	81.0	-	4.6	117.0	22.7	56.0	8.4
38-2, 84-88	506.86	BOG	NA	-	-	-	53.1	200.0	-	-	-	3.8	-	-	-	-
38-2, 116-118	507.17	DRA	XF	-	211.5	481.5	-	219.6	-	82.6	14.3	3.9	114.1	19.2	57.3	7.8
39-1, 20-22	509.21	SHM	XF	-	-	447.0	47.0	193.0	92	69.0	-	-	131.0	22.0	62.0	-
39-1, 55-57	509.56	WEA	XF	-	234.0	513.0	-	203.0	-	75.0	16.0	4.0	113.0	21.0	61.0	7.7
39-1, 83-87	509.85	BOG	XFNA	35.7	223.0	460.0	47.0	202.0	-	65.0	-	4.4	115.0	23.3	62.0	6.9
39-1, 83-87	509.85	BOG	NA	-	-	-	50.5	208.0	-	-	-	3.1	-	-	-	-
39-1, 111-113	510.12	DRA	XF	-	224.4	476.6	-	184.9	-	88.7	15.4	4.9	116.2	19.2	57.9	7.7
39-2, 11-13	510.62	DRA	XF	-	191.6	441.5	-	213.6	-	72.3	14.3	5.0	109.1	18.2	55.7	7.4
39-2, 35-38	510.87	BOG	XFNA	33.1	218.0	431.0	47.0	216.0	-	61.0	-	4.8	112.0	22.6	61.0	6.9
39-2, 35-38	510.87	BOG	NA	-	-	-	48.3	219.0	-	-	-	4.2	-	-	-	-
39-2, 69-71	511.20	WEA	XF	-	228.0	514.0	-	216.0	-	73.0	16.0	3.0	110.0	22.0	60.0	7.4
39-2, 69-71	511.20	WEA	NA	-	-	-	-	-	-	-	-	-	-	-	-	-
39-4, 98-100	514.49	WEA	XF	-	227.0	505.0	-	202.0	-	74.0	15.0	3.0	121.0	21.0	59.0	7.6
39-4, 122-125	514.74	SHM	XF	-	-	422.0	48.0	229.0	86	67.0	-	-	127.0	22.0	59.0	-
39-4, 131-135	514.83	BOG	XFNA	34.1	204.0	430.0	46.0	211.0	-	61.0	-	4.3	121.0	22.0	62.0	7.1
39-4, 131-135	514.83	BOG	NA	-	-	-	48.6	221.0	-	-	-	4.5	-	-	-	-
40-1, 92-94	518.93	SHM	XF	-	-	490.0	55.0	149.0	98	75.0	-	-	129.0	18.0	59.0	-
40-2, 7-9	519.58	SHM	XF	-	-	475.0	33.0	156.0	70	83.0	-	-	160.0	23.0	91.0	-
41-2, 143-146	529.95	BOG	XFNA	35.9	194.0	444.0	50.0	219.0	-	61.0	-	3.2	107.0	22.7	51.0	2.0
41-2, 143-146	529.95	BOG	NA	-	-	-	52.8	235.0	-	-	-	2.3	-	-	-	-
Hole 559																
Chemical Group I																
H1-CC, 2-4	238.00	BOG	XFNA	37.5	318.0	281.0	43.0	130.0	-	79.0	-	8.1	162.0	35.5	102.0	14.8
H1-CC, 2-4	238.00	BOG	NA	-	-	-	44.2	132.0	-	-	-	8.3	-	-	-	-
1-1, 25-29	238.27	SHM	XF	-	-	276.0	45.0	134.0	73	84.0	-	-	160.0	29.0	97.0	-
1-1, 117-119	239.18	DRA	XF	-	291.9	263.8	-	103.9	-	176.0	13.3	9.9	167.9	31.6	108.4	15.5
1-1, 120-123	239.22	BOG	XFNA	38.6	317.0	254.0	45.0	80.0	-	147.0	-	8.2	172.0	35.9	105.0	17.5
1-1, 120-123	239.22	BOG	NA	-	-	-	42.1	74.0	-	-	-	7.9	-	-	-	-
1-1, 134-136	239.35	PUC	XFNAAA	42.7	-	243.0	46.4	77.0	89	164.0	20.0	7.5	177.0	34.0	114.0	-
1-2, 36-39	239.88	BOG	XFNA	42.8	409.0	280.0	48.0	108.0	-	112.0	-	12.4	215.0	41.4	111.0	17.1
1-2, 36-39	239.88	BOG	NA	-	-	-	45.6	105.0	-	-	-	11.7	-	-	-	-
1-2, 52-56	240.04	SHM	XF	-	-	296.0	57.0	99.0	87	99.0	-	-	170.0	26.0	98.0	-
1-2, 56-59	240.08	BOG	XFNA	38.3	305.0	269.0	42.0	101.0	-	101.0	-	6.9	166.0	35.3	104.0	15.2
1-2, 56-59	240.08	BOG	NA	-	-	-	42.5	93.0	-	-	-	6.0	-	-	-	-
1-2, 118-120	240.69	WEA	XF	-	328.0	299.0	-	90.0	-	118.0	18.0	8.0	171.0	31.0	102.0	14.5
1-3, 0-3	241.01	BOG	XFNA	43.4	341.0	289.0	45.0	109.0	-	126.0	-	6.6	181.0	38.2	108.0	15.7
1-3, 0-3	241.01	BOG	NA	-	-	-	51.3	102.0	-	-	-	10.0	-	-	-	-
1-3, 44-47	241.46	BOG	XFNA	40.5	374.0	266.0	35.0	112.0	-	89.0	-	6.9	199.0	37.5	108.0	17.3
1-3, 44-47	241.46	BOG	NA	-	-	-	34.0	103.0	-	-	-	4.4	-	-	-	-
1-3, 76-79	241.78	BOG	XFNA	39.1	404.0	268.0	52.0	96.0	-	106.0	-	12.2	200.0	45.4	110.0	17.4
1-3, 76-79	241.78	BOG	NA	-	-	-	46.2	100.0	-	-	-	6.7	-	-	-	-
1-3, 129-132	242.31	BOG	XFNA	41.6	404.0	299.0	58.0	103.0	-	102.0	-	6.6	187.0	39.8	108.0	14.9
1-3, 129-132	242.31	BOG	NA	-	-	-	58.8	106.0	-	-	-	5.2	-	-	-	-
1-3, 148-150	242.49	BOG	XFNA	37.4	301.0	289.0	44.0	127.0	-	86.0	-	9.1	157.0	33.2	101.0	16.0
1-3, 148-150	242.49	BOG	NA	-	-	-	44.9	129.0	-	-	-	8.1	-	-	-	-
1-4, 20-22	242.71	BOG	XFNA	40.9	243.0	307.0	47.0	118.0	-	115.0	-	16.7	172.0	29.2	119.0	18.4
1-4, 20-22	242.71	BOG	NA	-	-	-	43.8	114.0	-	-	-	15.2	-	-	-	-
1-4, 40-42	242.91	PUC	XFNAAA	40.4	-	230.0	42.1	117.0	79	101.0	16.0	8.4	168.0	32.0	117.0	-
2-1, 1-3	247.02	BOG	XFNA	40.2	304.0	271.0	41.0	93.0	-	110.0	-	7.1	172.0	34.7	102.0	16.9
2-1, 1-3	247.02	BOG	NA	-	-	-	44.1	94.0	-	-	-	6.9	-	-	-	-
2-2, 11-14	248.63	SHM	XF	-	-	279.0	48.0	111.0	76	81.0	-	-	182.0	32.0	101.0	-
2-2, 18-20	248.69	WEA	XF	-	306.0	306.0	-	127.0	-	88.0	18.0	7.0	173.0	31.0	103.0	14.7
2-2, 24-28	248.76	BOG	XFNA	38.6	248.0	263.0	42.0	126.0	-	77.0	-	7.5	173.0	32.0	105.0	16.1
2-2, 24-28	248.76	BOG	NA	-	-	-	44.1	128.0	-	-	-	7.4	-	-	-	-
2-3, 75-79	250.77	BOG	XFNA	37.7	288.0	259.0	46.0	124.0	-	75.0	-	11.9	169.0	34.0	106.0	16.6
2-3, 75-79	250.77	BOG	NA	-	-	-	45.6	117.0	-	-	-	10.5	-	-	-	-
2-3, 111-113	251.12	DRA	XF	-	246.5	254.7	-	211.2	-	90.4	15.7	5.9	162.5	27.1	105.4	14.4
3-1, 13-14	256.14	BOG	XFNA	38.0	301.0	287.0	43.0	129.0	-	80.0	-	9.8	157.0	32.1	100.0	16.5
3-1, 13-14	256.14	BOG	NA	-	-	-	45.1	135.0	-	-	-	8.2	-	-	-	-
3-1, 25-27	256.26	SHM	XF	-	-	274.0	52.0	-	-	-	-	-	-	-	-	-
4-1, 118-121	257.70	WEA	XF	-	291.0	290.0	-	130.0	-	86.0	18.0	7.0	164.0	31.0	101.0	14.6
4-1, 121-124	257.72	DRA	XF	-	266.8	267.3	-	142.0	-	98.3	15.8	5.2	162.8	28.3	107.0	15.0
4-1, 125-129	257.77	BOG	XFNA	38.8	300.0	270.0	42.0	141.0	-	79.0	-	6.5	168.0	34.3	106.0	16.0
4-1, 125-129	257.77	BOG	NA	-	-	-	41.8	135.0	-	-	-	5.8	-	-	-	-
4-2, 92-96	258.94	BOG	XFNA	39.1	302.0	255.0	40.0	121.0	-	82.0	-	9.4	176.0	36.3	109.0	16.7
4-2, 92-96	258.94	BOG	NA	-	-	-	41.1	118.0	-	-	-	8.9	-	-	-	-
5-1, 36-38	265.37	SHM	XF	-	-	283.0	45.0	121.0	76	80.0	-	-	168.0	33.0	100.0	-
5-1, 38-40	265.39	WEA	XF	-	298.0	295.0	-	121.0	-	85.0	17.0	7.0	168.0	30.0	100.0	14.1
5-1, 45-48	265.47	BOG	XFNA	37.6	283.0	266.0	38.0	119.0	-	77.0	-	6.2	169.0	34.5	97.0	15.5
5-1, 45-48	265.47	BOG	NA	-	-	-	40.7	117.0	-	-	-	7.8	-	-	-	-
5-1, 50-53	265.51	DRA	XF	-	276.9	260.9	-	126.9	-	102.7	16.0	6.5	166.6	28.0	105.7	15.2
5-2, 35-39	266.87	BOG	XFNA	42.3	369.0	300.0	33.0	77.0	-	78.0	-	5.5	181.0	36.5	106.0	16.7
5-2, 35-39	266.87	BOG	XFNA	-	-	-	33.4	80.0	-	-	-	4.4	-	-	-	-
5-3, 25-29	268.27	BOG	XFNA	39.6	352.0	284.0	31.0	94.0	-	77.0	-	8.9	185.0	37.6	115.0	17.6
5-3, 25-29	268.27	BOG	NA	-	-	-	31.2	96.0	-	-	-	6.6	-	-	-	-
6-2, 12-14	275.63	WEA	XF	-	301.0	306.0	-	161.0	-	85.0	17.0	7.0	169.0	31.0	102.0	14.9

Table 2. (Continued).

Cs	Ba	La	Ce	Nd	Sm	Eu	Gd	Tb	Ho	Tm	Yb	Lu	Hf	Ta	Th	U
0.44		8.30	19.5	11.9	3.10	1.09	4.60	0.70	0.98	0.34	2.60	0.43	2.50	0.55	0.59	0.40
0.35	15.0	4.80	13.4	-	-	0.81	-	0.45	-	-	-	-	1.44	0.49	0.47	0.12
-	23.0	5.00	13.0	9.0	-	-	-	-	-	-	-	-	-	-	-	-
-	85.0	-	-	-	-	-	-	-	-	-	-	-	-	-	-	-
-	18.0	-	-	-	-	-	-	-	-	-	-	-	-	-	-	-
-	-	5.33	13.0	10.7	2.12	0.79	-	-	-	-	2.12	0.34	1.50	-	-	-
-	18.0	5.00	12.0	8.0	-	-	-	-	-	-	-	-	-	-	-	-
0.24	14.0	5.40	11.7	-	-	0.79	-	0.45	-	-	-	-	1.49	0.47	0.47	0.11
-	70.0	-	-	-	-	-	-	-	-	-	-	-	-	-	-	-
0.24	-	5.20	14.3	-	-	0.86	-	0.46	-	-	-	-	1.63	0.50	0.42	0.19
-	39.0	-	-	-	-	-	-	-	-	-	-	-	-	-	-	-
-	22.0	4.00	12.0	8.0	-	-	-	-	-	-	-	-	-	-	-	-
0.21	-	5.30	11.9	-	-	0.86	-	0.47	-	-	-	-	1.48	0.51	0.45	0.15
0.31	26.0	4.67	8.8	-	-	0.89	-	0.43	-	-	-	-	1.47	0.46	0.43	0.10
-	21.0	4.00	13.0	8.0	-	-	-	-	-	-	-	-	-	-	-	-
-	-	5.24	12.7	8.3	2.53	0.87	2.69	0.57	-	0.30	2.12	0.32	1.57	0.44	0.56	
-	21.0	5.00	11.0	8.0	-	-	-	-	-	-	-	-	-	-	-	-
-	49.0	-	-	-	-	-	-	-	-	-	-	-	-	-	-	-
0.31	17.0	4.80	9.2	-	-	0.88	-	0.45	-	-	-	-	1.38	0.47	0.49	0.14
-	53.0	-	-	-	-	-	-	-	-	-	-	-	-	-	-	-
-	114.0	-	-	-	-	-	-	-	-	-	-	-	-	-	-	-
0.22	-	1.75	4.5	-	-	0.77	-	0.46	-	-	-	-	1.30	0.14	0.12	0.05
0.11	69.0	9.20	17.2	-	-	1.21	-	0.71	-	-	-	-	2.66	0.98	1.04	0.27
-	110.0	-	-	-	-	-	-	-	-	-	-	-	-	-	-	-
0.55	35.0	9.50	17.1	-	-	1.26	-	0.71	-	-	-	-	2.64	1.01	0.99	0.30
0.54	-	10.60	22.7	14.2	3.92	1.28	5.00	0.84	1.39	0.43	3.20	0.53	2.80	0.78	0.82	0.40
0.36	59.0	10.70	23.1	-	-	1.45	-	0.81	-	-	-	-	2.95	1.11	1.05	0.82
-	106.0	-	-	-	-	-	-	-	-	-	-	-	-	-	-	-
0.56	32.0	8.50	17.1	-	-	1.24	-	0.71	-	-	-	-	2.61	0.99	1.08	0.18
-	44.0	10.00	24.0	13.0	-	-	-	-	-	-	-	-	-	-	-	-
0.30	38.1	12.20	24.2	-	-	1.44	-	0.91	-	-	-	-	3.06	1.11	1.21	0.72
0.11	39.0	10.20	15.7	-	-	1.30	-	0.72	-	-	-	-	2.76	1.06	1.05	0.57
0.33	34.0	9.60	23.3	-	-	1.31	-	0.75	-	-	-	-	2.75	1.04	1.09	0.41
0.11	55.0	10.90	22.2	-	-	1.35	-	0.75	-	-	-	-	2.88	1.08	1.05	0.51
0.11	75.0	9.10	18.2	-	-	1.24	-	0.67	-	-	-	-	2.52	0.99	1.02	0.27
0.32	69.0	7.70	22.1	-	-	1.16	-	0.64	-	-	-	-	3.02	1.12	1.00	0.37
0.22	-	9.50	21.3	12.3	3.61	1.19	5.50	0.75	0.98	0.43	3.00	0.49	2.60	0.74	0.74	0.40
0.42	34.0	11.60	22.6	-	-	1.43	-	0.76	-	-	-	-	2.89	1.04	1.01	0.22
-	57.0	-	-	-	-	-	-	-	-	-	-	-	-	-	-	-
-	53.0	9.00	20.0	13.0	-	-	-	-	-	-	-	-	-	-	-	-
0.18	66.0	9.30	18.4	-	-	1.36	-	0.73	-	-	-	-	2.59	1.02	1.03	0.22
0.68	37.0	9.00	17.1	-	-	1.29	-	0.69	-	-	-	-	2.50	0.98	0.96	0.24
0.11	91.0	8.70	17.8	-	-	1.33	-	0.69	-	-	-	-	2.63	0.98	0.86	0.32
-	146.0	-	-	-	-	-	-	-	-	-	-	-	-	-	-	-
-	42.0	9.00	24.0	13.0	-	-	-	-	-	-	-	-	-	-	-	-
0.52	36.0	9.10	20.5	-	-	1.25	-	0.73	-	-	-	-	2.74	1.00	0.99	0.28
0.54	28.1	9.00	22.9	-	-	1.20	-	0.73	-	-	-	-	2.61	1.01	1.12	0.34
-	61.0	-	-	-	-	-	-	-	-	-	-	-	-	-	-	-
-	40.0	9.00	21.0	13.0	-	-	-	-	-	-	-	-	-	-	-	-
0.50	32.0	8.90	19.9	-	-	1.19	-	0.70	-	-	-	-	2.55	0.99	0.84	0.31
0.13	38.0	10.10	24.9	-	-	1.36	-	0.81	-	-	-	-	2.83	1.11	1.15	0.54
0.31	41.0	8.90	20.0	-	-	1.39	-	0.74	-	-	-	-	2.83	1.04	1.03	0.43
-	39.0	9.00	21.0	13.0	-	-	-	-	-	-	-	-	-	-	-	-

Table 2. (Continued).

Sample	Depth (m)	Inv	Method	Sc	V	Cr	Co	Ni	Cu	Zn	Ga	Rb	Sr	Y	Zr	Nb
Hole 559 (Cont.)																
Chemical Group I (Cont.)																
6-2, 14-16	275.65	DRA	XF	-	267.1	277.1	-	127.3	-	91.0	17.2	7.4	161.8	27.8	107.5	14.7
6-2, 17-20	275.68	PUC	XFNAAA	39.7	-	224.0	46.3	125.0	79	90.0	17.0	6.4	173.0	32.0	114.0	-
6-2, 25-29	275.77	BOG	XFNA	37.8	314.0	275.0	43.0	134.0	-	83.0	-	8.7	171.0	34.5	104.0	15.3
6-2, 25-29	275.77	BOG	NA	-	-	-	43.1	134.0	-	-	-	7.2	-	-	-	-
6-3, 27-31	277.29	BOG	XFNA	37.8	298.0	261.0	42.0	121.0	-	77.0	-	8.1	167.0	34.5	102.0	16.3
6-3, 27-31	277.29	BOG	NA	-	-	-	43.1	116.0	-	-	-	7.4	-	-	-	-
7-1, 111-114	284.13	DRA	XF	-	291.9	276.1	-	113.2	-	96.6	16.9	6.9	171.4	29.2	111.6	15.6
7-1, 137-140	284.39	BOG	XFNA	37.5	290.0	260.0	43.0	115.0	-	75.0	-	8.7	166.0	33.6	99.0	16.1
7-1, 137-140	284.39	BOG	NA	-	-	-	42.5	108.0	-	-	-	7.9	-	-	-	-
7-1, 143-146	284.45	PUC	XFNAAA	42.3	-	237.0	42.2	116.0	75	87.0	16.0	12.5	172.0	32.0	112.0	-
7-2, 1-3	284.52	SHM	XF	-	-	274.0	51.0	130.0	72	77.0	-	-	166.0	30.0	99.0	-
7-2, 3-6	284.55	WEA	XF	-	289.0	290.0	-	134.0	-	84.0	16.0	9.0	164.0	30.0	100.0	14.6
7-2, 143-146	285.95	BOG	XFNA	37.4	307.0	266.0	42.0	131.0	-	79.0	-	6.7	166.0	34.3	100.0	15.8
7-2, 143-146	285.95	BOG	NA	-	-	-	41.6	118.0	-	-	-	5.6	-	-	-	-
7-3, 15-17	286.16	PUC	XFNAAA	41.3	-	231.0	44.1	115.0	79	94.0	18.0	5.4	176.0	33.0	115.0	-
7-3, 18-20	286.19	DRA	XF	-	253.8	247.3	-	121.0	-	96.5	16.5	7.0	161.8	28.2	106.8	15.4
7-3, 103-106	287.05	DRA	XF	-	252.7	245.5	-	108.9	-	88.3	15.7	7.0	161.1	27.6	107.0	15.0
7-3, 110-113	287.12	BOG	XFNA	38.3	297.0	261.0	45.0	154.0	-	77.0	-	7.3	167.0	33.4	98.0	14.0
7-3, 110-113	287.12	BOG	NA	-	-	-	46.0	147.0	-	-	-	4.9	-	-	-	-
7-3, 114-117	287.16	SHM	XF	-	-	278.0	49.0	122.0	77	84.0	-	-	173.0	29.0	96.0	-
8-1, 18-20	292.19	WEA	XF	-	291.0	281.0	-	117.0	-	87.0	17.0	8.0	171.0	31.0	103.0	16.1
8-1, 48-51	292.50	BOG	XFNA	37.2	304.0	262.0	46.0	139.0	-	76.0	-	5.6	167.0	32.1	100.0	16.1
8-1, 48-51	292.50	BOG	NA	-	-	-	45.5	137.0	-	-	-	3.5	-	-	-	-
8-1, 127-129	293.28	SHM	XF	-	-	292.0	55.0	146.0	82	81.0	-	-	168.0	26.0	95.0	-
8-3, 6-10	295.08	DRA	XF	-	253.6	253.6	-	134.4	-	83.6	17.2	17.0	169.0	27.1	103.1	14.5
8-3, 19-21	295.20	BOG	XFNA	36.8	284.0	241.0	40.0	101.0	-	74.0	-	8.4	168.0	31.9	96.0	15.6
8-3, 19-21	295.20	BOG	NA	-	-	-	38.9	97.0	-	-	-	6.7	-	-	-	-
Hole 560																
2-1, 93-96	377.45	BOG	XFNA	5.9	268.0	387.0	124.0	296.0	-	82.0	-	1.2	121.0	29.2	73.0	6.2
2-1, 93-96	377.45	BOG	NA	-	-		144.0	288.0	-	-	-	1.1	-	-	-	-
Hole 561																
Chemical Group I																
H1-CC, 1-5	411.50	SHM	XF	-	-	412.0	50.0	169.0	83	75.0	-	-	229.0	26.0	95.0	-
H1-CC, 3-5	411.50	DRA	XF	-	240.0	416.0	-	166.0	-	85.0	15.6	5.4	216.0	25.5	102.0	21.9
H1-CC, 9-13	411.50	WEA	XF	-	258.0	445.0	-	191.0	-	81.0	16.0	7.0	221.0	27.0	97.0	21.0
H1-CC, 10-14	411.50	BOG	XFNA	34.9	263.0	406.0	47.0	213.0	-	70.0	-	4.6	225.0	30.4	100.0	22.4
H1-CC, 10-14	8.62	BOG	NA	-	-	-	50.2	206.0	-	-	-	4.7	-	-	-	-
1-1, 4-9	411.57	DRA	NA	36.9	-	-	-	-	-	-	-	-	-	-	-	-
1-1, 4-9	411.57	DRA	XF	-	236.0	413.0	-	186.0	-	93.0	14.8	5.5	215.0	25.5	100.0	21.6
1-1, 28-31	411.80	BOG	XFNA	34.4	267.0	407.0	46.0	185.0	-	69.0	-	5.0	457.0	30.4	96.0	21.8
1-1, 28-31	411.80	BOG	NA	-	-	-	47.0	185.0	-	-	-	3.7	-	-	-	-
1-1, 33-38	411.86	SHM	XF	-	-	431.0	53.0	199.0	79	78.0	-	-	215.0	25.0	96.0	-
1-1, 44-47	411.96	WEA	XF	-	264.0	459.0	-	197.0	-	77.0	17.0	5.0	636.0	27.0	96.0	21.0
1-1, 44-47	411.96	WEA	NA	-	-	-	-	-	-	-	-	-	-	-	-	-
Chemical Group II																
1-1, 84-87	412.36	DRA	XF	-	297.0	228.0	-	120.0	-	104.0	18.1	6.8	100.0	32.3	76.0	3.5
1-1, 128-131	412.80	BOG	XFNA	39.8	356.0	228.0	53.0	182.0	-	89.0	-	5.2	98.0	39.3	80.0	4.3
1-1, 128-131	412.80	BOG	NA	-	-	-	55.5	172.0	-	-	-	2.2	-	-	-	-
1-2, 17-20	413.19	BOG	XFNA	41.4	359.0	227.0	57.0	192.0	-	91.0	-	2.1	97.0	39.2	76.0	2.5
1-2, 17-20	413.19	BOG	NA	-	-	-	60.1	189.0	-	-	-	3.4	-	-	-	-
1-2, 22-24	413.23	WEA	XF	-	343.0	260.0	-	144.0	-	93.0	19.0	2.0	91.0	34.0	72.0	2.8
1-2, 22-24	413.23	WEA	NA	-	-	-	-	-	-	-	-	-	-	-	-	-
1-2, 24-26	413.25	DRA	XF	-	305.0	245.0	-	123.0	-	109.0	17.6	6.9	88.0	31.4	75.0	2.1
2-1, 52-55	415.04	BOG	XFNA	40.4	347.0	242.0	51.0	149.0	-	90.0	-	3.3	90.0	38.1	72.0	2.6
2-1, 52-55	415.04	BOG	NA	-	-	-	52.2	149.0	-	-	-	2.2	-	-	-	-
2-1, 97-100	415.49	SHM	XF	-	-	252.0	56.0	156.0	91	90.0	-	-	94.0	33.0	73.0	-
2-1, 100-103	415.52	DRA	XF	-	292.0	222.0	-	126.0	-	96.0	17.4	13.8	87.0	30.7	71.0	2.6
2-1, 111-116	415.64	WEA	XF	-	338.0	249.0	-	137.0	-	96.0	20.0	9.0	91.0	35.0	71.0	2.3
2-1, 143-146	415.95	SHM	XF	-	-	254.0	56.0	106.0	82	87.0	-	-	91.0	31.0	74.0	-
2-2, 54-56	416.55	SHM	XF	-	-	252.0	65.0	164.0	89	90.0	-	-	95.0	34.0	74.0	-
2-2, 61-63	416.62	JCB	NA	41.7	-	230.0	48.6	160.0	-	-	-	-	-	-	-	-
2-2, 80-82	416.81	JCB	NA	41.2	-	226.0	51.4	150.0	-	-	-	-	-	-	-	-
2-2, 82-84	416.83	DRA	NA	42.5	-	-	-	-	-	-	-	-	-	-	-	-
2-2, 82-84	416.83	DRA	XF	-	302.0	237.0	-	159.0	-	106.0	17.4	6.5	90.0	31.7	73.0	2.6
2-2, 122-126	417.24	BOG	XFNA	41.1	349.0	222.0	47.0	138.0	-	88.0	-	5.0	92.0	38.5	76.0	3.3
2-2, 122-126	417.24	BOG	NA	-	-	-	51.1	132.0	-	-	-	5.6	-	-	-	-
2-2, 138-141	417.40	SHM	XF	-	-	264.0	64.0	220.0	95	90.0	-	-	96.0	31.0	72.0	-
2-3, 28-30	417.79	JCB	NA	42.7	-	229.0	46.5	120.0	-	-	-	-	-	-	-	-
2-3, 52-54	418.03	JCB	NA	46.0	-	240.0	56.1	130.0	-	-	-	-	-	-	-	-
2-3, 55-59	418.07	SHM	XF	-	-	253.0	46.0	109.0	85	90.0	-	-	94.0	34.0	76.0	-
2-3, 71-73	418.22	BOG	XFNA	40.7	359.0	230.0	44.0	89.0	-	83.0	-	14.3	86.0	38.0	75.0	1.5
2-3, 71-73	418.22	BOG	NA	-	-	-	44.2	87.0	-	-	-	15.4	-	-	-	-
2-3, 75-76	418.26	SHM	XF	-	-	253.0	51.0	121.0	77	89.0	-	-	90.0	34.0	72.0	-
2-3, 124-127	418.76	SHM	XF	-	-	241.0	50.0	119.0	81	89.0	-	-	89.0	33.0	72.0	-
2-3, 127-130	418.79	WEA	XF	-	336.0	256.0	-	135.0	-	93.0	19.0	5.0	91.0	35.0	71.0	2.8
3-1, 9-13	423.61	DRA	XF	-	290.0	217.0	-	114.0	-	96.0	16.8	12.1	86.0	31.0	73.0	3.1
3-1, 76-79	424.28	DRA	XF	-	313.0	236.0	-	128.0	-	101.0	17.0	6.6	86.0	32.6	77.0	2.0
3-1, 101-104	424.53	SHM	XF	-	-	249.0	49.0	139.0	85	88.0	-	-	88.0	34.0	73.0	-
3-1, 114-118	424.66	BOG	XFNA	-	345.0	221.0	50.0	160.0	-	88.0	-	6.0	90.0	37.8	73.0	3.3
3-1, 138-140	424.89	WEA	XF	-	332.0	256.0	-	126.0	-	91.0	19.0	12.0	88.0	34.0	70.0	3.0
3-1, 140-142	424.91	JCB	NA	41.8	-	224.0	49.4	120.0	-	-	-	-	-	-	-	-
3-2, 41-53	425.47	SHM	XF	-	-	251.0	50.0	129.0	98	77.0	-	-	97.0	26.0	66.0	-
3-2, 56-60	425.58	JCB	NA	43.4	-	232.0	48.3	160.0	-	-	-	-	-	-	-	-
3-2, 77-80	425.79	DRA	XF	-	311.0	238.0	-	138.0	-	101.0	17.7	5.2	85.0	32.4	76.0	3.0
Hole 562																
Chemical Group I																
H1-CC, 5-8	241.00	SHM	XF	-	-	241.0	48.0	80.0	81	91.0	-	-	116.0	38.0	90.0	-

Table 2. (Continued).

Cs	Ba	La	Ce	Nd	Sm	Eu	Gd	Tb	Ho	Tm	Yb	Lu	Hf	Ta	Th	U
0.47	-	9.50	20.3	12.5	3.55	1.16	4.30	0.65	1.14	0.40	2.90	0.48	2.50	0.72	0.73	0.40
0.54	34.7	8.90	21.0	-	-	1.29	-	0.71	-	-	-	-	2.61	1.00	1.07	0.27
0.58	34.0	8.90	18.1	-	-	1.31	-	0.71	-	-	-	-	2.61	1.00	1.00	0.28
0.62	35.0	8.80	16.1	-	-	1.27	-	0.69	-	-	-	-	2.41	0.98	0.97	0.35
0.64	-	9.80	21.8	12.9	3.73	1.17	4.00	0.72	1.27	0.43	3.00	0.50	2.70	0.75	0.80	0.40
-	94.0	-	-	-	-	-	-	-	-	-	-	-	-	-	-	-
-	49.0	8.00	21.0	12.0	-	-	-	-	-	-	-	-	-	-	-	-
0.46	36.0	9.00	17.0	-	-	1.30	-	0.71	-	-	-	-	2.47	0.99	0.98	0.32
0.45	-	9.70	21.6	10.8	3.78	1.18	4.20	0.72	1.20	0.43	3.00	0.50	2.70	0.74	0.74	0.40
0.56	17.0	8.90	1.5	-	-	1.35	-	0.69	-	-	-	-	2.66	0.95	1.04	0.32
-	50.0	-	-	-	-	-	-	-	-	-	-	-	-	-	-	-
-	48.0	9.00	21.0	12.0	-	-	-	-	-	-	-	-	-	-	-	-
0.43	42.0	9.10	19.2	-	-	1.24	-	0.65	-	-	-	-	2.63	0.96	0.85	0.30
-	103.0	-	-	-	-	-	-	-	-	-	-	-	-	-	-	-
0.58	32.8	8.80	18.5	-	-	1.20	-	0.69	-	-	-	-	2.55	0.93	1.02	0.32
0.02	22.0	3.70	8.4	-	-	1.02	-	0.60	-	-	-	-	1.91	0.38	0.38	0.08
-	75.0	-	-	-	-	-	-	-	-	-	-	-	-	-	-	-
-	55.0	12.00	26.0	13.0	-	-	-	-	-	-	-	-	-	-	-	-
0.06	41.6	12.20	26.2	-	-	1.26	-	0.66	-	-	-	-	2.40	1.40	1.67	0.36
-	-	13.99	26.8	20.0	3.68	1.22	-	-	-	-	2.88	0.44	2.20	-	-	-
0.05	59.0	12.70	25.2	-	-	1.26	-	0.65	-	-	-	-	2.49	1.38	1.46	0.40
-	85.0	-	-	-	-	-	-	-	-	-	-	-	-	-	-	-
-	125.0	13.00	27.0	13.0	-	-	-	-	-	-	-	-	-	-	-	-
-	-	14.10	30.1	16.3	4.14	1.40	4.86	0.82	-	0.44	2.88	0.47	2.68	1.39	1.92	-
0.14	13.0	2.44	13.1	-	-	1.22	-	0.76	-	-	-	-	2.13	0.17	0.21	0.12
0.06	-	2.48	8.0	-	-	1.17	-	0.79	-	-	-	-	2.29	0.18	0.22	0.11
-	12.0	3.00	9.0	8.0	-	-	-	-	-	-	-	-	-	-	-	-
-	-	3.04	8.9	9.2	3.32	1.28	4.66	1.03	-	0.66	4.01	0.62	2.34	0.18	0.31	-
0.07	-	2.65	9.8	-	-	1.26	-	0.75	-	-	-	-	2.21	0.18	0.16	0.06
-	34.0	-	-	-	-	-	-	-	-	-	-	-	-	-	-	-
-	10.0	2.00	10.0	8.0	-	-	-	-	-	-	-	-	-	-	-	-
-	60.0	-	-	-	-	-	-	-	-	-	-	-	-	-	-	-
-	41.0	-	-	-	-	-	-	-	-	-	-	-	-	-	-	-
0.24	-	2.60	8.5	-	3.14	1.15	-	0.85	-	-	3.70	0.57	2.36	0.21	0.16	-
0.33	-	2.60	8.4	-	3.10	1.11	-	0.86	-	-	3.64	0.56	2.38	0.17	0.13	-
-	-	2.87	8.2	9.8	3.02	1.41	-	-	-	-	3.78	0.55	2.10	-	-	-
0.19	7.2	2.27	6.9	-	-	1.22	-	0.76	-	-	-	-	2.18	0.18	0.20	0.06
-	49.0	-	-	-	-	-	-	-	-	-	-	-	-	-	-	-
0.17	-	2.71	8.7	-	3.25	1.14	-	0.91	-	-	3.73	0.59	2.43	0.20	0.14	-
0.06	-	3.13	10.0	-	3.73	1.33	-	1.00	-	-	4.41	0.70	2.58	0.20	0.12	-
-	49.0	-	-	-	-	-	-	-	-	-	-	-	-	-	-	-
0.56	11.0	2.49	8.5	-	-	1.13	-	0.78	-	-	-	-	2.13	0.17	0.22	0.06
-	34.0	-	-	-	-	-	-	-	-	-	-	-	-	-	-	-
-	32.0	-	-	-	-	-	-	-	-	-	-	-	-	-	-	-
-	9.0	2.00	10.0	9.0	-	-	-	-	-	-	-	-	-	-	-	-
-	35.0	-	-	-	-	-	-	-	-	-	-	-	-	-	-	-
-	10.0	2.00	10.0	8.0	-	-	-	-	-	-	-	-	-	-	-	-
0.10	-	2.58	8.1	-	3.15	1.14	-	0.83	-	-	3.72	0.58	2.36	0.10	0.17	-
-	61.0	-	-	-	-	-	-	-	-	-	-	-	-	-	-	-
0.17	-	2.69	8.6	-	3.22	1.16	-	0.89	-	-	3.78	0.58	2.42	0.17	0.15	-
-	24.0	-	-	-	-	-	-	-	-	-	-	-	-	-	-	-

Table 2. (Continued).

Sample	Depth (m)	Inv.	Method	Sc	V	Cr	Co	Ni	Cu	Zn	Ga	Rb	Sr	Y	Zr	Nb
Hole 562 (Cont.)																
Chemical Group I (Cont.)																
H1-CC, 16-19	241.00	DRA	XF	-	313.8	241.8	-	109.2	-	103.9	17.5	2.6	105.0	36.1	96.5	3.1
1-1, 57-60	241.59	SHM	XF	-	-	260.0	61.0	94.0	84	88.0	-	-	97.0	36.0	90.0	-
1-1, 104-107	242.06	BOG	XFNA	41.0	321.0	233.0	43.0	91.0	-	83.0	-	1.9	106.0	40.8	91.0	2.9
1-1, 104-107	242.06	BOG	NA	-	-	-	45.9	95.0	-	-	-	2.6	-	-	-	-
1-1, 110-112	242.11	SHM	XF	-	-	256.0	49.0	100.0	90	84.0	-	-	114.0	31.0	86.0	-
1-2, 34-37	242.86	BOG	XFNA	40.2	311.0	224.0	44.0	93.0	-	79.0	-	0.8	99.0	41.6	94.0	2.3
1-2, 34-37	242.86	BOG	NA	-	-	-	45.1	93.0	-	-	-	-	-	-	-	-
1-2, 82-84	243.33	WEA	XF	-	359.0	275.0	-	138.0	-	107.0	19.0	6.0	107.0	40.0	98.0	3.0
1-3, 92-95	244.93	BOG	XFNA	38.8	328.0	235.0	43.0	96.0	-	84.0	-	4.2	103.0	40.8	94.0	2.1
1-3, 92-95	244.93	BOG	NA	-	-	-	44.5	98.0	-	-	-	4.3	-	-	-	-
2-1, 55-59	250.57	BOG	XFNA	39.7	319.0	222.0	43.0	91.0	-	77.0	-	2.3	94.0	40.4	92.0	2.2
2-1, 55-59	250.57	BOG	NA	-	-	-	44.1	91.0	-	-	-	2.0	-	-	-	-
2-2, 54-59	252.07	BOG	XFNA	39.8	328.0	235.0	43.0	98.0	-	84.0	-	8.9	97.0	41.7	95.0	3.0
2-2, 54-59	252.07	BOG	NA	-	-	-	44.0	92.0	-	-	-	9.4	-	-	-	-
2-3, 8-10	253.09	DRA	XF	-	298.9	236.5	-	107.6	-	95.6	17.3	5.6	96.6	35.1	97.3	3.9
2-3, 61-65	253.63	BOG	XFNA	39.7	326.0	235.0	43.0	102.0	-	82.0	-	2.1	94.0	41.6	101.0	3.1
2-3, 61-65	253.63	BOG	NA	-	-	-	45.9	102.0	-	-	-	1.6	-	-	-	-
2-4, 33-38	254.86	BOG	XFNA	39.5	322.0	230.0	43.0	99.0	-	75.0	-	1.8	95.0	40.6	96.0	3.5
2-4, 33-38	254.86	BOG	NA	-	-	-	44.5	94.0	-	-	-	1.3	-	-	-	-
2-4, 68-70	255.19	SHM	XF	-	-	240.0	48.0	99.0	81	83.0	-	-	107.0	35.0	90.0	-
2-4, 74-76	255.25	WEA	XF	-	319.0	248.0	-	96.0	-	88.0	16.0	5.0	100.0	36.0	89.0	2.9
2-5, 65-67	256.66	PUC	XFNAAA	43.4	-	209.0	44.6	83.0	87	96.0	19.0	< 2.0	106.0	39.0	114.0	-
2-5, 73-76	256.75	BOG	XFNA	43.5	317.0	220.0	42.0	91.0	-	86.0	-	0.8	92.0	41.6	96.0	2.9
2-5, 73-76	256.75	BOG	NA	-	-	-	44.6	93.0	-	-	-	0.7	-	-	-	-
3-1, 46-48	259.47	JCB	NA	40.8	-	235.0	42.1	120.0	-	-	-	-	-	-	-	-
3-1, 85-88	259.87	BOG	XFNA	39.8	330.0	233.0	42.0	94.0	-	80.0	-	2.3	113.0	41.6	91.0	2.6
3-1, 85-88	259.87	BOG	NA	-	-	-	45.2	98.0	-	-	-	-	-	-	-	-
3-2, 141-143	261.92	WEA	XF	-	316.0	249.0	-	90.0	-	89.0	16.0	4.0	98.0	36.0	92.0	2.9
3-3, 103-106	263.05	BOG	XFNA	38.6	327.0	236.0	41.0	88.0	-	80.0	-	8.7	103.0	40.4	95.0	3.7
3-3, 103-106	263.05	BOG	NA	-	-	-	41.3	87.0	-	-	-	7.3	-	-	-	-
3-4, 120-123	264.72	BOG	XFNA	40.2	322.0	231.0	43.0	94.0	-	82.0	-	0.8	99.0	40.9	92.0	2.2
3-4, 120-123	264.72	BOG	NA	-	-	-	45.7	96.0	-	-	-	1.1	-	-	-	-
4-1, 9-12	268.11	BOG	XFNA	40.4	330.0	216.0	40.0	77.0	-	77.0	-	4.5	110.0	41.9	98.0	2.5
4-1, 9-12	268.11	BOG	NA	-	-	-	42.3	74.0	-	-	-	4.2	-	-	-	-
4-1, 14-16	268.15	JCB	NA	42.0	-	240.0	42.8	30.0	-	-	-	-	-	-	-	-
4-1, 58-60	268.59	JCB	NA	41.6	-	239.0	42.1	100.0	-	-	-	-	-	-	-	-
4-1, 75-77	268.76	DRA	XF	-	284.1	211.1	-	106.0	-	90.1	17.8	1.9	94.4	35.0	92.4	3.8
4-1, 78-80	268.79	JCB	NA	42.3	-	245.0	43.5	110.0	-	-	-	-	-	-	-	-
4-1, 91-93	268.92	SHM	XF	-	-	242.0	51.0	104.0	72	86.0	-	-	105.0	35.0	88.0	-
4-2, 0-3	269.51	BOG	XFNA	41.0	316.0	229.0	39.0	80.0	-	71.0	-	1.7	98.0	40.4	90.0	3.4
4-2, 0-3	269.51	BOG	NA	-	-	-	43.9	88.0	-	-	-	1.1	-	-	-	-
4-2, 4-7	269.56	PUC	XFNAAA	40.1	-	206.0	37.4	82.0	82	93.0	19.0	< 2.0	107.0	38.0	113.0	-
4-2, 22-25	269.74	JCB	NA	39.8	-	234.0	41.5	120.0	-	-	-	-	-	-	-	-
4-2, 45-47	269.96	WEA	XF	-	307.0	230.0	-	103.0	-	89.0	18.0	4.0	100.0	36.0	91.0	3.0
4-3, 27-29	271.28	JCB	NA	39.1	-	231.0	41.6	150.0	-	-	-	-	-	-	-	-
4-3, 64-67	271.66	JCB	NA	40.2	-	237.0	41.6	110.0	-	-	-	-	-	-	-	-
4-3, 83-85	271.84	BOG	XFNA	43.0	368.0	224.0	46.0	91.0	-	82.0	-	9.3	112.0	45.1	100.0	2.0
4-3, 83-85	271.84	BOG	NA	-	-	-	48.6	88.0	-	-	-	9.0	-	-	-	-
4-3, 86-88	271.87	JCB	NA	42.1	-	239.0	38.8	100.0	-	-	-	-	-	-	-	-
4-4, 60-63	273.12	SHM	XF	-	-	249.0	58.0	104.0	74	89.0	-	-	101.0	38.0	94.0	-
4-4, 100-103	273.51	BOG	XFNA	39.2	316.0	237.0	44.0	102.0	-	80.0	-	6.4	101.0	42.0	96.0	4.1
4-4, 100-103	273.51	BOG	NA	-	-	-	44.5	101.0	-	-	-	5.4	-	-	-	-
4-4, 117-119	273.68	JCB	NA	37.7	-	226.0	39.7	110.0	-	-	-	-	-	-	-	-
4-5, 26-28	274.27	JCB	NA	40.1	-	241.0	42.2	100.0	-	-	-	-	-	-	-	-
5-1, 64-66	277.65	DRA	XF	-	286.7	235.4	-	119.5	-	95.8	17.3	2.3	99.5	34.9	96.4	3.4
5-2, 76-79	279.28	BOG	XFNA	39.5	342.0	224.0	44.0	101.0	-	85.0	-	2.3	96.0	41.5	96.0	3.3
5-2, 76-79	279.28	BOG	NA	-	-	-	44.3	99.0	-	-	-	1.5	-	-	-	-
5-2, 89-91	279.40	JCB	NA	40.3	-	243.0	42.4	100.0	-	-	-	-	-	-	-	-
5-3, 9-11	280.10	JCB	NA	40.5	-	240.0	42.7	110.0	-	-	-	-	-	-	-	-
5-3, 40-42	280.41	SHM	XF	-	-	245.0	46.0	96.0	84	87.0	-	-	99.0	36.0	90.0	-
5-3, 58-60	280.59	JCB	NA	39.2	-	234.0	41.0	100.0	-	-	-	-	-	-	-	-
5-3, 78-81	280.80	WEA	XF	-	311.0	236.0	-	90.0	-	87.0	18.0	2.0	100.0	36.0	92.0	3.1
5-3, 104-107	281.06	BOG	XFNA	39.3	319.0	214.0	42.0	94.0	-	73.0	-	2.7	97.0	40.3	94.0	2.2
5-3, 104-107	281.06	BOG	NA	-	-	-	44.3	101.0	-	-	-	-	-	-	-	-
5-4, 29-31	281.80	DRA	XF	-	274.0	215.3	-	105.1	-	86.6	17.1	1.2	102.1	34.4	93.4	3.2
5-4, 106-108	282.57	JCB	NA	40.1	-	238.0	41.8	70.0	-	-	-	-	-	-	-	-
5-4, 122-124	282.73	SHM	XF	-	-	237.0	46.0	99.0	83	80.0	-	-	104.0	38.0	91.0	-
5-5, 69-71	283.70	JCB	NA	40.2	-	238.0	42.1	70.0	-	-	-	-	-	-	-	-
5-5, 75-79	283.77	BOG	XFNA	38.5	320.0	227.0	43.0	95.0	-	78.0	-	6.8	100.0	40.1	96.0	4.1
5-5, 75-79	283.77	BOG	NA	-	-	-	43.6	96.0	-	-	-	5.5	-	-	-	-
5-5, 95-97	283.96	JCB	NA	39.2	-	237.0	41.3	90.0	-	-	-	-	-	-	-	-
6-3, 74-77	289.76	BOG	XFNA	38.5	334.0	242.0	43.0	100.0	-	82.0	-	7.1	102.0	39.7	87.0	2.9
6-3, 74-77	289.76	BOG	NA	-	-	-	44.6	96.0	-	-	-	6.4	-	-	-	-
6-3, 120-123	290.22	SHM	XF	-	-	271.0	55.0	122.0	91	85.0	-	-	111.0	32.0	89.0	-
6-3, 135-138	290.37	DRA	XF	-	286.1	246.6	-	109.2	-	106.2	17.9	6.7	103.6	32.9	93.0	3.1
Chemical Group II																
6-4, 1-5	290.53	SHM	XF	-	-	253.0	46.0	92.0	87	78.0	-	-	96.0	29.0	67.0	-
6-4, 6-10	290.58	DRA	XF	-	250.0	244.9	-	169.5	-	83.0	16.1	3.1	91.9	26.5	69.0	2.5
6-4, 18-21	290.70	WEA	XF	-	260.0	266.0	-	79.0	-	75.0	17.0	6.0	96.0	26.0	63.0	2.4
6-4, 74-78	291.26	BOG	XFNA	36.1	302.0	236.0	41.0	106.0	-	74.0	-	3.2	93.0	31.3	68.0	3.7
6-4, 74-78	291.26	BOG	NA	-	-	-	43.7	103.0	-	-	-	2.2	-	-	-	-
7-1, 29-33	295.31	BOG	XFNA	35.4	299.0	264.0	41.0	96.0	-	70.0	-	3.0	97.0	31.3	71.0	2.3
7-1, 29-33	295.31	BOG	NA	-	-	-	42.6	96.0	-	-	-	3.5	-	-	-	-
7-2, 7-10	296.59	PUC	XFNAAA	38.2	-	233.0	40.4	104.0	101	92.0	16.0	4.8	114.0	32.0	90.0	-
7-2, 44-47	296.96	BOG	XFNA	33.8	287.0	242.0	41.0	102.0	-	68.0	-	4.4	110.0	31.7	69.0	2.6
7-2, 44-47	296.96	BOG	NA	-	-	-	42.9	99.0	-	-	-	3.1	-	-	-	-
7-2, 56-58	297.07	DRA	XF	-	243.3	242.8	-	105.7	-	80.1	16.3	3.5	97.5	26.3	67.5	2.2
7-2, 138-142	297.90	WEA	XF	-	290.0	280.0	-	83.0	-	80.0	18.0	2.0	97.0	29.0	65.0	2.4
8-1, 35-38	300.37	SHM	XF	-	-	221.0	40.0	85.0	77	73.0	-	-	113.0	26.0	65.0	-
8-1, 68-71	300.70	WEA	XF	-	281.0	271.0	-	117.0	-	81.0	16.0	5.0	91.0	29.0	66.0	2.8
8-1, 95-98	300.97	BOG	XFNA	33.6	277.0	219.0	38.0	90.0	-	62.0	-	6.5	100.0	30.0	66.0	2.2

Table 2. (Continued).

Cs	Ba	La	Ce	Nd	Sm	Eu	Gd	Tb	Ho	Tm	Yb	Lu	Hf	Ta	Th	U
-	-	-	-	-	-	-	-	-	-	-	-	-	-	-	-	-
-	38.0	-	-	-	-	-	-	-	-	-	-	-	-	-	-	-
0.10	5.0	2.47	9.4	-	-	1.34	-	0.86	-	-	-	-	2.58	0.16	0.17	0.04
-	-	-	-	-	-	-	-	-	-	-	-	-	-	-	-	-
-	49.0	-	-	-	-	-	-	-	-	-	-	-	-	-	-	-
0.04	-	2.78	5.4	-	-	1.04	-	0.85	-	-	-	-	2.53	0.15	0.16	-
-	-	-	-	-	-	-	-	-	-	-	-	-	-	-	-	-
-	13.0	3.00	10.0	9.0	-	-	-	-	-	-	-	-	-	-	-	-
0.15	10.0	2.65	10.0	-	-	1.27	-	0.82	-	-	-	-	2.60	0.17	0.18	-
-	-	-	-	-	-	-	-	-	-	-	-	-	-	-	-	-
0.03	-	2.59	6.5	-	-	1.29	-	0.81	-	-	-	-	2.51	0.17	0.15	-
-	-	-	-	-	-	-	-	-	-	-	-	-	-	-	-	-
0.50	-	2.75	9.1	-	-	1.29	-	0.83	-	-	-	-	2.65	0.17	0.14	0.07
-	-	-	-	-	-	-	-	-	-	-	-	-	-	-	-	-
-	-	-	-	-	-	-	-	-	-	-	-	-	-	-	-	-
0.05	-	3.20	8.9	-	-	1.37	-	0.85	-	-	-	-	2.57	0.19	0.15	-
-	-	-	-	-	-	-	-	-	-	-	-	-	-	-	-	-
0.02	10.0	3.00	8.3	-	-	1.33	-	0.83	-	-	-	-	2.61	0.19	0.16	-
-	-	-	-	-	-	-	-	-	-	-	-	-	-	-	-	-
-	63.0	-	-	-	-	-	-	-	-	-	-	-	-	-	-	-
-	10.0	3.00	10.0	9.0	-	-	-	-	-	-	-	-	-	-	-	-
<.14	-	2.80	9.9	9.4	3.61	1.21	6.50	0.80	1.30	0.52	3.70	0.61	2.50	0.11	<.20	<.20
0.01	-	2.79	8.1	-	-	1.28	-	0.85	-	-	-	-	2.57	0.16	0.18	0.05
-	-	-	-	-	-	-	-	-	-	-	-	-	-	-	-	-
0.05	-	2.70	9.0	-	3.49	1.22	-	1.02	-	-	3.72	0.57	2.73	0.16	0.12	-
0.02	-	2.96	11.9	-	-	1.35	-	0.83	-	-	-	-	2.70	0.19	0.21	0.04
-	-	-	-	-	-	-	-	-	-	-	-	-	-	-	-	-
-	11.0	3.00	9.0	9.0	-	-	-	-	-	-	-	-	-	-	-	-
0.51	13.3	2.85	10.0	-	-	1.24	-	0.82	-	-	-	-	2.57	0.19	0.17	-
-	-	-	-	-	-	-	-	-	-	-	-	-	-	-	-	-
0.02	-	2.95	7.6	-	-	1.40	-	0.86	-	-	-	-	2.66	0.19	0.16	0.07
-	-	-	-	-	-	-	-	-	-	-	-	-	-	-	-	-
0.25	10.0	5.00	7.5	-	-	1.38	-	0.82	-	-	-	-	2.60	0.20	0.17	0.10
-	-	-	-	-	-	-	-	-	-	-	-	-	-	-	-	-
0.27	-	3.03	9.8	-	3.69	1.29	-	1.06	-	-	3.86	0.59	2.74	0.18	0.29	-
0.03	-	3.07	9.4	-	3.68	1.29	-	1.07	-	-	3.88	0.60	2.75	0.20	0.05	-
-	-	-	-	-	-	-	-	-	-	-	-	-	-	-	-	-
0.04	-	2.94	9.6	-	3.59	1.27	-	1.06	-	-	3.88	0.58	2.73	0.19	0.10	-
-	45.0	-	-	-	-	-	-	-	-	-	-	-	-	-	-	-
0.02	9.0	2.78	11.1	-	-	1.35	-	0.83	-	-	-	-	2.56	0.19	0.14	0.04
-	-	-	-	-	-	-	-	-	-	-	-	-	-	-	-	-
<.14	-	3.40	11.1	8.3	3.81	1.29	5.00	0.91	1.26	0.58	3.80	0.54	2.40	0.15	<.20	<.20
0.03	-	2.90	9.0	-	3.51	1.22	-	1.03	-	-	3.64	0.57	2.54	0.19	0.20	-
-	10.0	3.00	9.0	9.0	-	-	-	-	-	-	-	-	-	-	-	-
0.02	-	2.85	9.0	-	3.46	1.20	-	1.02	-	-	3.62	0.54	2.57	0.21	0.03	-
0.30	-	2.91	9.4	-	3.45	1.26	-	1.05	-	-	3.69	0.55	2.63	0.19	0.09	-
0.78	12.0	3.40	10.8	-	-	1.47	-	0.91	-	-	-	-	2.96	0.21	0.16	0.22
-	-	-	-	-	-	-	-	-	-	-	-	-	-	-	-	-
0.85	-	3.08	9.6	-	3.73	1.30	-	1.12	-	-	3.91	0.60	2.81	0.18	0.08	-
-	59.0	-	-	-	-	-	-	-	-	-	-	-	-	-	-	-
0.36	-	3.00	9.8	-	-	1.28	-	0.85	-	-	-	-	2.63	0.21	0.18	0.05
-	-	-	-	-	-	-	-	-	-	-	-	-	-	-	-	-
0.01	-	2.94	9.2	-	3.43	1.19	-	1.00	-	-	3.61	0.56	2.56	0.19	0.14	-
0.06	-	3.06	9.8	-	3.68	1.24	-	1.04	-	-	3.88	0.59	2.68	0.19	0.10	-
-	-	-	-	-	-	-	-	-	-	-	-	-	-	-	-	-
0.03	9.0	3.20	10.7	-	-	1.34	-	0.85	-	-	-	-	2.59	0.21	0.22	0.06
-	-	-	-	-	-	-	-	-	-	-	-	-	-	-	-	-
0.04	-	3.14	9.9	-	3.64	1.27	-	1.06	-	-	3.80	0.59	2.74	0.23	0.21	-
0.05	-	3.17	10.0	-	3.71	1.25	-	1.05	-	-	3.93	0.60	2.69	0.21	0.21	-
-	46.0	-	-	-	-	-	-	-	-	-	-	-	-	-	-	-
0.04	-	2.99	9.4	-	3.56	1.22	-	1.01	-	-	3.74	0.59	2.58	0.22	0.10	-
-	12.0	3.00	10.0	8.0	-	-	-	-	-	-	-	-	-	-	-	-
0.04	-	3.34	9.8	-	-	1.24	-	0.86	-	-	-	-	2.76	0.22	0.17	0.07
-	-	-	-	-	-	-	-	-	-	-	-	-	-	-	-	-
-	-	-	-	-	-	-	-	-	-	-	-	-	-	-	-	-
0.07	-	3.12	9.8	-	3.65	1.23	-	1.03	-	-	3.91	0.59	2.60	0.22	0.17	-
-	50.0	-	-	-	-	-	-	-	-	-	-	-	-	-	-	-
0.01	-	3.10	9.6	-	3.66	1.22	-	1.04	-	-	3.97	0.61	2.66	0.19	0.07	-
0.40	20.0	3.00	10.8	-	-	1.34	-	0.83	-	-	-	-	2.57	0.21	0.16	0.09
-	-	-	-	-	-	-	-	-	-	-	-	-	-	-	-	-
0.20	-	3.01	9.0	-	3.57	1.19	-	1.04	-	-	3.79	0.58	2.57	0.22	0.10	-
0.46	8.0	2.66	7.7	-	-	1.26	-	0.82	-	-	-	-	2.54	0.22	0.25	-
-	-	-	-	-	-	-	-	-	-	-	-	-	-	-	-	-
-	82.0	-	-	-	-	-	-	-	-	-	-	-	-	-	-	-
-	-	-	-	-	-	-	-	-	-	-	-	-	-	-	-	-
-	41.0	-	-	-	-	-	-	-	-	-	-	-	-	-	-	-
-	-	-	-	-	-	-	-	-	-	-	-	-	-	-	-	-
-	12.0	2.00	7.0	8.0	-	-	-	-	-	-	-	-	-	-	-	-
0.13	10.0	2.04	7.8	-	-	1.02	-	0.75	-	-	-	-	1.84	0.17	0.12	0.07
-	-	-	-	-	-	-	-	-	-	-	-	-	-	-	-	-
0.13	16.0	2.37	7.4	-	-	0.97	-	0.63	-	-	-	-	1.83	0.17	0.13	0.04
-	-	-	-	-	-	-	-	-	-	-	-	-	-	-	-	-
0.28	-	2.90	8.9	8.1	3.04	1.02	3.60	0.73	1.24	0.44	3.10	0.45	1.80	0.13	<.20	0.30
0.23	-	2.15	6.5	-	-	0.94	-	0.62	-	-	-	-	1.79	0.16	0.13	-
-	-	-	-	-	-	-	-	-	-	-	-	-	-	-	-	-
-	-	-	-	-	-	-	-	-	-	-	-	-	-	-	-	-
-	12.0	<2.00	6.0	8.0	-	-	-	-	-	-	-	-	-	-	-	-
-	29.0	-	-	-	-	-	-	-	-	-	-	-	-	-	-	-
-	7.0	2.00	7.0	8.0	-	-	-	-	-	-	-	-	-	-	-	-
0.38	7.0	2.10	6.7	-	-	0.98	-	0.61	-	-	-	-	1.83	0.16	0.13	0.06

READEX FICHE best copy available

Table 2. (Continued).

Sample	Depth (m)	Inv.	Method	Sc	V	Cr	Co	Ni	Cu	Zn	Ga	Rb	Sr	Y	Zr	Nb
Hole 562 (Cont.)																
Chemical Group II (Cont.)																
8-1, 95-98	300.97	BOG	NA	-	-	-	40.3	86.0	-	-	-	5.7	-	-	-	-
8-1, 127-129	301.28	PUC	XFNAAA	37.2	-	220.0	36.8	88.0	98	88.0	16.0	7.7	103.0	32.0	90.0	-
8-1, 132-134	301.33	DRA	XF	-	267.0	262.0	-	102.0	-	88.1	16.5	3.9	96.4	27.7	72.1	2.7
8-1, 144-146	301.45	DRA	XF	-	278.4	267.8	-	121.6	-	93.1	16.1	4.5	108.4	29.4	74.3	2.5
8-2, 6-9	301.58	SHM	XF	-	-	287.0	48.0	100.9	100	78.0	-	-	102.0	26.0	68.0	-
8-2, 25-29	301.77	DRA	XF	-	243.4	248.6	-	98.7	-	81.2	15.5	3.3	90.4	25.1	65.7	2.3
8-2, 26-29	301.78	BOG	XFNA	37.5	316.0	261.0	41.0	96.0	-	75.0	-	10.1	98.0	31.2	73.0	2.4
8-2, 26-29	301.78	BOG	NA	-	-	-	42.1	86.0	-	-	-	10.3	-	-	-	-
8-2, 55-58	302.07	WEA	XF	-	296.0	276.0	-	94.0	-	82.0	17.0	8.0	98.0	30.0	67.0	3.2
9-1, 21-24	304.22	SHM	XF	-	-	256.0	47.0	95.0	85	74.0	-	-	99.0	29.0	67.0	-
9-1, 82-84	304.83	DRA	XF	-	254.6	251.2	-	109.6	-	83.6	16.1	4.1	101.3	26.0	67.8	3.0
9-1, 140-142	305.41	BOG	XFNA	38.0	359.0	265.0	46.0	107.0	-	84.0	-	10.1	105.0	34.8	76.0	4.2
9-1, 140-142	305.41	BOG	NA	-	-	-	47.2	99.0	-	-	-	9.0	-	-	-	-
9-1, 145-147	305.46	DRA	XF	-	282.7	265.1	-	112.5	-	93.9	16.9	8.2	114.4	28.7	73.4	2.3
9-2, 81-83	306.32	WEA	XF	-	277.0	279.0	-	93.0	-	79.0	17.0	3.0	99.0	28.0	65.0	2.4
10-1, 41-44	313.43	SHM	XF	-	-	262.0	47.0	95.0	87	82.0	-	-	108.0	29.0	70.0	-
10-1, 90-93	313.92	DRA	XF	-	277.3	264.2	-	104.2	-	99.3	16.6	6.1	95.1	28.0	73.3	2.7
10-2, 86-88	315.37	WEA	XF	-	259.0	248.0	-	86.0	-	73.0	16.0	11.0	105.0	25.0	59.0	2.6
10-2, 125-128	315.76	BOG	XFNA	35.7	290.0	238.0	42.0	89.0	-	68.0	-	1.9	85.0	29.9	67.0	1.8
10-2, 125-128	315.76	BOG	NA	-	-	-	43.9	97.0	-	-	-	-	-	-	-	-
10-3, 52-55	316.54	DRA	XF	-	279.9	268.1	-	124.4	-	95.2	16.5	4.6	89.6	28.5	74.0	2.5
11-1, 115-117	323.16	DRA	XF	-	244.2	250.6	-	98.2	-	81.1	15.9	4.7	94.5	25.2	65.0	2.8
Hole 563																
Chemical Group I																
23-1, 22-25	364.74	BOG	XFNA	42.2	341.0	322.0	41.0	99.0	-	68.0	-	6.6	86.0	28.1	58.0	0.6
23-1, 22-25	364.74	BOG	NA	-	-	-	44.1	101.0	-	-	-	7.0	-	-	-	-
23-1, 30-34	364.82	SHM	XF	-	-	365.0	53.0	109.0	149	78.0	-	-	90.0	23.0	57.0	-
23-1, 104-106	365.55	WEA	XF	-	318.0	347.0	-	98.0	-	73.0	15.0	5.0	92.0	25.0	51.0	2.3
23-1, 115-117	365.66	DRA	XF	-	293.4	330.2	-	110.3	-	81.3	15.1	5.5	86.7	23.7	55.9	2.0
24-1, 22-25	366.74	DRA	NA	41.4	-	-	-	-	-	-	-	-	-	-	-	-
24-1, 22-25	366.74	DRA	XF	-	279.8	322.8	-	98.0	-	78.0	15.9	7.4	83.3	22.8	52.5	2.1
24-1, 49-53	367.01	SHM	XF	-	-	340.0	50.0	103.0	249	124.0	-	-	92.0	26.0	59.0	-
24-1, 57-60	367.09	DRA	XF	-	306.4	338.1	-	95.3	-	81.1	15.6	5.2	86.0	24.9	59.2	2.9
24-1, 80-83	367.32	BOG	XFNA	41.1	332.0	318.0	42.0	108.0	-	66.0	-	5.9	87.0	27.0	54.0	1.9
24-1, 80-83	367.32	BOG	NA	-	-	-	46.8	111.0	-	-	-	6.7	-	-	-	-
24-1, 118-121	367.70	SHM	XF	-	-	346.0	59.0	120.0	164	78.0	-	-	90.0	26.0	65.0	-
Chemical Group II																
24-2, 88-91	368.90	BOG	NA	-	-	-	53.1	139.0	-	-	-	0.8	-	-	-	-
24-2, 88-91	368.90	BOG	XFNA	40.3	319.0	305.0	48.0	145.0	-	66.0	-	2.5	84.0	27.4	55.0	2.5
Chemical Group I																
24-2, 93-95	368.94	DRA	XF	-	285.5	326.1	-	103.8	-	78.0	15.7	6.8	82.1	22.8	55.3	1.7
24-2, 103-106	369.05	SHM	XF	-	-	311.0	44.0	103.0	139	71.0	-	-	92.0	26.0	59.0	-
24-2, 121-124	369.23	BOG	XFNA	41.2	336.0	327.0	42.0	89.0	-	65.0	-	10.8	83.0	27.8	55.0	2.0
24-2, 121-124	369.23	BOG	NA	-	-	-	42.6	89.0	-	-	-	10.0	-	-	-	-
Chemical Group II																
24-2, 123-127	369.25	DRA	XF	-	310.7	350.9	-	106.9	-	96.2	15.4	5.0	82.5	25.1	60.2	2.6
24-4, 0-7	371.04	WEA	XF	-	315.0	344.0	-	114.0	-	74.0	16.0	5.0	86.0	25.0	53.0	1.6
24-4, 2-5	371.04	SHM	XF	-	-	339.0	48.0	112.0	156	72.0	-	-	90.0	26.0	58.0	-
24-4, 7-10	371.09	DRA	XF	-	286.1	318.7	-	106.0	-	78.9	14.9	6.8	82.3	22.9	54.7	2.5
24-4, 38-41	371.40	BOG	XF	40.3	321.0	300.0	43.0	110.0	-	63.0	-	3.0	86.0	27.8	52.0	1.7
24-4, 38-41	371.40	BOG	XF	-	-	-	46.6	106.0	-	-	-	1.9	-	-	-	-
25-1, 19-22	373.71	SHM	XF	-	-	346.0	43.0	120.0	156	75.0	-	-	92.0	21.0	55.0	-
25-1, 36-38	373.87	DRA	XF	-	272.9	322.6	-	106.9	-	77.8	15.4	2.5	82.6	21.6	54.5	2.2
25-1, 43-46	373.95	BOG	XFNA	39.6	315.0	291.0	41.0	117.0	-	72.0	-	3.0	82.0	27.2	52.0	1.8
25-1, 43-46	373.95	BOG	NA	-	-	-	45.2	115.0	-	-	-	3.3	-	-	-	-
25-2, 21-24	375.23	SHM	XF	-	-	293.0	59.0	138.0	170	85.0	-	-	108.0	31.0	87.0	-
25-2, 37-39	375.38	WEA	XF	-	316.0	352.0	-	102.0	-	76.0	16.0	7.0	87.0	25.0	52.0	2.4
25-2, 39-41	375.40	BOG	XFNA	39.1	315.0	312.0	45.0	125.0	-	64.0	-	1.9	85.0	26.9	60.0	2.0
25-2, 39-41	375.40	BOG	NA	-	-	-	49.9	125.0	-	-	-	1.3	-	-	-	-
25-2, 71-74	375.73	BOG	XFNA	39.0	314.0	296.0	41.0	112.0	-	63.0	-	5.8	84.0	26.7	50.0	0.6
25-2, 71-74	375.73	BOG	NA	-	-	-	45.2	114.0	-	-	-	5.9	-	-	-	-
Chemical Group I																
25-2, 79-81	375.80	BOG	XFNA	39.8	310.0	299.0	42.0	102.0	-	60.0	-	9.9	84.0	27.0	54.0	1.8
25-2, 79-81	375.80	BOG	NA	-	-	-	42.7	107.0	-	-	-	9.7	-	-	-	-
Chemical Group II																
25-2, 101-103	376.02	BOG	XFNA	39.8	317.0	300.0	42.0	106.0	-	67.0	-	2.7	84.0	27.8	52.0	1.5
25-2, 101-103	376.02	BOG	NA	-	-	-	42.5	101.0	-	-	-	2.5	-	-	-	-
Chemical Group I																
25-2, 115-117	376.16	DRA	XF	-	298.0	324.9	-	96.7	-	79.1	15.5	5.7	83.7	23.6	54.9	2.6
Hole 564																
Chemical Group I																
H1-CC, 8-11	284.00	PUC	XFNAAA	43.0	-	243.0	40.9	102.0	172	99.0	17.0	5.4	128.0	36.0	109.0	-
H1-CC, 11-15	284.00	DRA	XF	-	352.0	277.4	-	122.7	-	101.3	17.4	7.5	115.1	31.7	93.7	4.1
1-1, 28-31	284.30	JCB	NA	35.6	-	399.0	44.9	165.0	-	-	-	-	-	-	-	-
1-1, 108-111	285.10	BOG	XFNA	41.1	385.0	265.0	61.0	226.0	-	82.0	-	6.3	112.0	38.0	89.0	3.4
1-1, 108-111	285.10	BOG	NA	-	-	-	59.8	226.0	-	-	-	5.8	-	-	-	-
1-1, 119-122	285.21	JCB	NA	42.0	-	231.0	51.0	180.0	-	-	-	-	-	-	-	-
1-1, 122-124	285.23	PUC	XFNAAA	42.6	-	239.0	37.6	102.0	166	100.0	17.0	5.8	120.0	37.0	108.0	-
1-1, 129-131	285.30	DRA	XF	-	346.6	261.5	-	138.5	-	95.3	16.1	6.4	106.8	32.3	91.3	3.9
1-1, 140-143	285.42	BOG	XFNA	42.2	413.0	264.0	43.0	106.0	-	87.0	-	9.6	108.0	40.3	91.0	3.3
1-1, 140-143	285.42	BOG	NA	-	-	-	42.9	105.0	-	-	-	10.2	-	-	-	-
1-2, 3-6	285.55	JCB	NA	41.8	-	226.0	52.0	160.0	-	-	-	-	-	-	-	-
1-2, 21-25	285.73	SHM	XF	-	-	347.0	48.0	122.0	162	76.0	-	-	89.0	23.0	56.0	-
1-2, 36-38	285.87	JCB	NA	41.7	-	228.0	54.2	130.0	-	-	-	-	-	-	-	-
1-2, 38-40	285.89	SHM	XF	-	-	268.0	60.0	104.0	136	90.0	-	-	107.0	34.0	87.0	-
1-2, 74-78	286.26	BOG	XFNA	40.5	397.0	260.0	48.0	96.0	-	85.0	-	5.1	106.0	38.3	89.0	3.6
1-2, 74-78	286.26	BOG	NA	-	-	-	45.1	94.0	-	-	-	5.2	-	-	-	-

Table 2. (Continued).

Cs	Ba	La	Ce	Nd	Sm	Eu	Gd	Tb	Ho	Tm	Yb	Lu	Hf	Ta	Th	U
-	-	-	-	-	-	-	-	-	-	-	-	-	-	-	-	-
0.48	-	2.60	8.8	6.7	2.88	0.98	3.90	0.75	0.92	0.43	2.90	0.42	1.70	0.13	< .20	< .20
-	-	-	-	-	-	-	-	-	-	-	-	-	-	-	-	-
-	-	-	-	-	-	-	-	-	-	-	-	-	-	-	-	-
-	54.0	-	-	-	-	-	-	-	-	-	-	-	-	-	-	-
-	-	-	-	-	-	-	-	-	-	-	-	-	-	-	-	-
0.53	8.8	2.61	7.7	-	-	1.04	-	0.67	-	-	-	-	1.99	0.18	0.14	0.10
-	-	-	-	-	-	-	-	-	-	-	-	-	-	-	-	-
-	12.0	2.00	6.0	8.0	-	-	-	-	-	-	-	-	-	-	-	-
-	13.0	-	-	-	-	-	-	-	-	-	-	-	-	-	-	-
-	-	-	-	-	-	-	-	-	-	-	-	-	-	-	-	-
0.40	20.0	2.64	8.0	-	-	1.14	-	0.70	-	-	-	-	2.10	0.18	0.17	0.07
-	-	-	-	-	-	-	-	-	-	-	-	-	-	-	-	-
-	-	-	-	-	-	-	-	-	-	-	-	-	-	-	-	-
-	10.0	2.00	7.0	8.0	-	-	-	-	-	-	-	-	-	-	-	-
-	44.0	-	-	-	-	-	-	-	-	-	-	-	-	-	-	-
-	-	-	-	-	-	-	-	-	-	-	-	-	-	-	-	-
-	9.0	2.00	7.0	7.0	-	-	-	-	-	-	-	-	-	-	-	-
0.02	-	2.30	7.5	-	-	1.03	-	0.64	-	-	-	-	1.95	0.16	0.13	-
-	-	-	-	-	-	-	-	-	-	-	-	-	-	-	-	-
-	-	-	-	-	-	-	-	-	-	-	-	-	-	-	-	-
-	-	-	-	-	-	-	-	-	-	-	-	-	-	-	-	-
0.17	-	1.93	4.2	-	-	0.88	-	0.57	-	-	-	-	1.60	0.13	0.13	0.10
-	-	-	-	-	-	-	-	-	-	-	-	-	-	-	-	-
-	24.0	-	-	-	-	-	-	-	-	-	-	-	-	-	-	-
-	8.0	2.00	6.0	6.0	-	-	-	-	-	-	-	-	-	-	-	-
-	-	-	-	-	-	-	-	-	-	-	-	-	-	-	-	-
-	-	1.93	5.6	7.8	2.08	0.82	-	-	-	-	2.67	0.41	1.37	-	-	-
-	-	-	-	-	-	-	-	-	-	-	-	-	-	-	-	-
-	50.0	-	-	-	-	-	-	-	-	-	-	-	-	-	-	-
-	-	-	-	-	-	-	-	-	-	-	-	-	-	-	-	-
0.27	-	1.85	6.8	-	-	0.98	-	0.56	-	-	-	-	1.58	0.13	0.11	-
-	-	-	-	-	-	-	-	-	-	-	-	-	-	-	-	-
-	45.0	-	-	-	-	-	-	-	-	-	-	-	-	-	-	-
-	-	-	-	-	-	-	-	-	-	-	-	-	-	-	-	-
0.05	-	1.92	4.6	-	-	0.88	-	0.55	-	-	-	-	1.56	0.12	0.11	-
-	-	-	-	-	-	-	-	-	-	-	-	-	-	-	-	-
-	10.0	-	-	-	-	-	-	-	-	-	-	-	-	-	-	-
0.31	-	1.75	5.8	-	-	0.85	-	0.56	-	-	-	-	1.54	0.12	0.13	-
-	-	-	-	-	-	-	-	-	-	-	-	-	-	-	-	-
-	-	-	-	-	-	-	-	-	-	-	-	-	-	-	-	-
-	7.0	2.00	6.0	7.0	-	-	-	-	-	-	-	-	-	-	-	-
-	20.0	-	-	-	-	-	-	-	-	-	-	-	-	-	-	-
-	-	-	-	-	-	-	-	-	-	-	-	-	-	-	-	-
0.11	10.0	1.78	7.2	-	-	0.92	-	0.56	-	-	-	-	1.48	0.12	0.06	0.07
-	-	-	-	-	-	-	-	-	-	-	-	-	-	-	-	-
-	33.0	-	-	-	-	-	-	-	-	-	-	-	-	-	-	-
-	-	-	-	-	-	-	-	-	-	-	-	-	-	-	-	-
0.13	-	1.64	4.7	-	-	0.85	-	0.54	-	-	-	-	1.55	0.12	0.11	0.11
-	-	-	-	-	-	-	-	-	-	-	-	-	-	-	-	-
-	60.0	-	-	-	-	-	-	-	-	-	-	-	-	-	-	-
-	10.0	2.00	6.0	6.0	-	-	-	-	-	-	-	-	-	-	-	-
0.06	-	1.84	5.3	-	-	0.86	-	0.51	-	-	-	-	1.47	0.12	0.11	-
-	-	-	-	-	-	-	-	-	-	-	-	-	-	-	-	-
0.19	-	1.75	4.4	-	-	0.90	-	0.54	-	-	-	-	1.51	0.12	0.11	0.05
-	-	-	-	-	-	-	-	-	-	-	-	-	-	-	-	-
0.36	-	1.56	4.8	-	-	0.89	-	0.54	-	-	-	-	1.43	0.12	0.13	0.08
-	-	-	-	-	-	-	-	-	-	-	-	-	-	-	-	-
0.11	-	1.34	5.8	-	-	0.90	-	0.55	-	-	-	-	1.51	0.12	0.11	-
-	-	-	-	-	-	-	-	-	-	-	-	-	-	-	-	-
-	-	-	-	-	-	-	-	-	-	-	-	-	-	-	-	-
0.33	-	3.90	11.0	7.6	3.57	1.20	5.10	0.87	1.25	0.53	3.60	0.52	2.20	0.19	< 20	0.20
-	-	-	-	-	-	-	-	-	-	-	-	-	-	-	-	-
0.08	-	12.50	26.9	-	3.71	1.21	-	0.78	-	-	2.54	0.42	2.47	1.43	1.58	-
0.43	-	3.20	10.4	-	-	1.18	-	0.76	-	-	-	-	2.37	0.25	0.23	0.08
-	-	-	-	-	-	-	-	-	-	-	-	-	-	-	-	-
0.09	-	2.61	8.2	-	3.18	1.10	-	0.91	-	-	3.52	0.59	2.30	0.20	0.08	-
0.56	-	3.60	11.2	7.4	3.53	1.15	4.50	0.83	1.25	0.49	3.60	0.52	2.10	0.17	0.26	< 20
-	-	-	-	-	-	-	-	-	-	-	-	-	-	-	-	-
0.32	21.0	3.40	8.5	-	-	1.25	-	0.82	-	-	-	-	2.62	0.26	0.24	0.04
-	-	-	-	-	-	-	-	-	-	-	-	-	-	-	-	-
0.15	-	2.65	8.3	-	3.24	1.10	-	0.91	-	-	3.65	0.58	2.24	0.21	0.15	-
-	38.0	-	-	-	-	-	-	-	-	-	-	-	-	-	-	-
0.20	-	2.65	8.1	-	3.16	1.13	-	0.89	-	-	3.52	0.56	2.30	0.24	0.25	-
-	58.0	-	-	-	-	-	-	-	-	-	-	-	-	-	-	-
0.33	4.0	3.40	10.6	-	-	1.21	-	0.79	-	-	-	-	2.53	0.25	0.29	0.12
-	-	-	-	-	-	-	-	-	-	-	-	-	-	-	-	-

Table 2. (Continued).

Sample	Depth (m)	Inv.	Method	Sc	V	Cr	Co	Ni	Cu	Zn	Ga	Rb	Sr	Y	Zr	Nb
Hole 564 (Cont.)																
Chemical Group I (Cont.)																
1-3, 38-40	287.39	DRA	XF	-	339.1	258.2	-	112.8	-	94.2	16.4	6.0	101.8	31.8	90.9	4.4
1-3, 100-103	288.01	BOG	XFNA	41.4	403.0	276.0	41.0	95.0	-	86.0	-	5.7	104.0	38.8	92.0	4.0
1-3, 100-103	288.01	BOG	NA	-	-	-	38.0	88.0	-	-	-	4.2	-	-	-	-
2-1, 6-8	293.07	JCB	NA	42.1	-	235.0	49.1	180.0	-	-	-	-	-	-	-	-
2-1, 53-55	293.54	BOG	XFNA	41.8	426.0	277.0	41.0	94.0	-	84.0	-	2.6	107.0	37.2	90.0	3.4
2-1, 53-55	293.54	BOG	NA	-	-	-	38.9	99.0	-	-	-	2.6	-	-	-	-
2-1, 71-73	293.72	JCB	NA	40.7	-	222.0	44.8	130.0	-	-	-	-	-	-	-	-
2-1, 78-80	293.79	JCB	NA	40.9	-	228.0	48.0	140.0	-	-	-	-	-	-	-	-
2-1, 86-88	293.87	JCB	NA	41.3	-	228.0	42.8	110.0	-	-	-	-	-	-	-	-
2-1, 145-150	294.47	JCB	NA	42.4	-	259.0	43.1	70.0	-	-	-	-	-	-	-	-
2-2, 1-4	294.53	JCB	NA	42.8	-	267.0	41.0	110.0	-	-	-	-	-	-	-	-
2-2, 3-5	294.54	DRA	XF	-	348.9	258.3	-	121.1	-	101.4	17.2	5.8	103.6	32.3	92.4	4.7
2-2, 15-22	294.68	JCB	NA	42.1	-	262.0	43.7	120.0	-	-	-	-	-	-	-	-
2-2, 18-21	294.70	JCB	NA	42.4	-	226.0	49.2	110.0	-	-	-	-	-	-	-	-
2-2, 25-28	294.76	JCB	NA	42.0	-	223.0	48.7	130.0	-	-	-	-	-	-	-	-
2-2, 46-49	294.97	BOG	XFNA	41.8	378.0	269.0	51.0	127.0	-	84.0	-	6.1	102.0	37.3	88.0	3.2
2-2, 46-49	294.97	BOG	NA	-	-	-	48.8	124.0	-	-	-	5.2	-	-	-	-
2-2, 65-67	295.16	JCB	NA	42.2	-	245.0	34.8	110.0	-	-	-	-	-	-	-	-
2-2, 99-102	295.51	SHM	XF	-	-	271.0	63.0	113.0	147	79.0	-	-	102.0	33.0	89.0	-
2-3, 18-20	296.19	DRA	XF	-	339.1	242.0	-	154.4	-	98.1	18.0	2.7	108.1	33.7	94.3	3.9
2-3, 60-63	296.62	BOG	XFNA	41.7	380.0	244.0	46.0	125.0	-	78.0	-	5.9	106.0	37.5	94.0	4.3
2-3, 60-63	296.62	BOG	NA	-	-	-	48.5	115.0	-	-	-	5.3	-	-	-	-
2-3, 110-114	297.12	PUC	XFNAAA	42.2	-	227.0	40.6	114.0	165	98.0	17.0	7.5	117.0	36.0	110.0	-
3-1, 25-28	302.26	BOG	XFNA	39.7	372.0	253.0	46.0	108.0	-	79.0	-	6.9	105.0	38.6	89.0	2.8
3-1, 25-28	302.26	BOG	NA	-	-	-	44.8	108.0	-	-	-	6.5	-	-	-	-
3-2, 5-8	303.57	WEA	XF	-	396.0	267.0	-	104.0	-	95.0	18.0	6.0	109.0	36.0	89.0	4.7
3-2, 35-37	303.86	DRA	XF	-	349.2	256.1	-	104.5	-	110.1	17.2	6.3	105.5	32.8	95.4	5.0
3-2, 58-62	304.10	SHM	XF	-	-	265.0	61.0	113.0	144	85.0	-	-	102.0	34.0	88.0	-
3-2, 58-62	304.10	SHM	XF	-	-	258.0	52.0	116.0	153	90.0	-	-	117.0	34.0	87.0	-
3-2, 70-73	304.22	BOG	XFNA	41.8	396.0	265.0	45.0	103.0	-	85.0	-	6.3	106.0	39.1	88.0	3.9
3-2, 70-73	304.22	BOG	NA	-	-	-	46.2	110.0	-	-	-	5.4	-	-	-	-
3-2, 127-129	304.78	JCB	NA	42.0	-	255.0	46.6	130.0	-	-	-	-	-	-	-	-
3-3, 92-94	305.93	SHM	XF	-	-	235.0	56.0	123.0	122	84.0	-	-	115.0	36.0	87.0	-
3-3, 138-141	306.39	BOG	XFNA	40.0	377.0	247.0	45.0	112.0	-	77.0	-	3.5	107.0	38.3	92.0	4.6
3-3, 138-141	306.39	BOG	NA	-	-	-	46.2	111.0	-	-	-	3.3	-	-	-	-
4-1, 61-64	311.63	BOG	XFNA	40.4	376.0	247.0	47.0	128.0	-	77.0	-	5.2	106.0	37.9	85.0	5.6
4-1, 61-64	311.63	BOG	NA	-	-	-	47.9	126.0	-	-	-	5.5	-	-	-	-
4-2, 37-41	312.89	DRA	XF	-	340.8	233.6	-	104.1	-	95.2	16.6	5.8	103.0	32.5	92.8	4.6
4-2, 49-51	313.00	JCB	NA	41.6	-	248.0	43.4	120.0	-	-	-	-	-	-	-	-
4-2, 68-72	313.20	SHM	XF	-	-	258.0	61.0	120.0	153	83.0	-	-	101.0	34.0	89.0	-
4-2, 102-106	313.54	BOG	XFNA	41.0	394.0	258.0	45.0	104.0	-	89.0	-	6.9	106.0	39.3	89.0	3.9
4-2, 102-106	313.54	BOG	NA	-	-	-	46.4	105.0	-	-	-	5.9	-	-	-	-
4-4, 86-89	316.38	BOG	XFNA	40.3	345.0	249.0	47.0	125.0	-	82.0	-	7.0	104.0	40.5	86.0	4.6
4-4, 86-89	316.38	BOG	NA	-	-	-	46.3	122.0	-	-	-	6.7	-	-	-	-
4-4, 140-142	316.91	DRA	XF	-	338.4	240.9	-	117.8	-	98.2	16.4	7.2	99.9	32.2	92.9	4.9
5-1, 17-19	320.18	BOG	XFNA	41.6	405.0	243.0	48.0	95.0	-	85.0	-	6.5	105.0	39.3	90.0	5.4
5-1, 17-19	320.18	BOG	NA	-	-	-	48.8	92.0	-	-	-	5.8	-	-	-	-
5-1, 30-33	320.32	SHM	XF	-	-	256.0	62.0	123.0	146	87.0	-	-	108.0	35.0	91.0	-
5-2, 26-28	321.77	JCB	NA	42.0	-	247.0	48.0	160.0	-	-	-	-	-	-	-	-
5-2, 89-91	322.40	DRA	XF	-	339.1	238.6	-	117.5	-	107.5	17.2	2.6	99.5	32.7	95.5	4.2
5-2, 96-100	322.48	BOG	XFNA	40.6	383.0	234.0	47.0	120.0	-	79.0	-	2.8	98.0	39.0	95.0	4.8
5-2, 96-100	322.48	BOG	NA	-	-	-	47.2	120.0	-	-	-	1.6	-	-	-	-
5-2, 111-114	322.63	PUC	XFNAAA	40.4	-	206.0	39.5	108.0	154	95.0	18.0	2.1	119.0	36.0	110.0	-
5-2, 115-118	322.67	WEA	XF	-	380.0	254.0	-	118.0	-	89.0	17.0	3.0	102.0	36.0	90.0	4.7
5-3, 119-122	324.21	BOG	XFNA	40.8	424.0	237.0	51.0	148.0	-	85.0	-	3.8	118.0	39.8	97.0	4.5
5-3, 119-122	324.21	BOG	NA	-	-	-	54.1	139.0	-	-	-	3.4	-	-	-	-
5-4, 24-27	324.76	DRA	XF	-	360.3	240.9	-	113.7	-	102.1	17.2	7.0	105.6	33.6	98.1	5.2
6-1, 15-18	329.17	DRA	XF	-	335.2	221.4	-	118.6	-	91.8	16.6	2.3	100.9	33.4	94.6	5.4
6-1, 26-28	329.27	WEA	XF	-	387.0	249.0	-	114.0	-	91.0	19.0	4.0	102.0	36.0	93.0	3.7
6-1, 33-36	329.35	BOG	XFNA	39.8	392.0	237.0	46.0	114.0	-	80.0	-	1.0	101.0	40.5	97.0	5.6
6-1, 33-36	329.35	BOG	NA	-	-	-	46.0	116.0	-	-	-	2.1	-	-	-	-
6-3, 63-66	332.65	BOG	XFNA	40.4	388.0	230.0	45.0	117.0	-	81.0	-	7.9	102.0	39.3	87.0	5.5
6-3, 63-66	332.65	BOG	NA	-	-	-	46.1	112.0	-	-	-	7.6	-	-	-	-
6-3, 141-143	333.42	JCB	NA	42.6	-	244.0	43.5	70.0	-	-	-	-	-	-	-	-
6-4, 15-17	333.66	JCB	NA	41.6	-	240.0	43.8	130.0	-	-	-	-	-	-	-	-
6-4, 38-40	333.89	JCB	NA	41.8	-	235.0	44.5	115.0	-	-	-	-	-	-	-	-
6-4, 44-47	333.96	BOG	XFNA	39.9	383.0	232.0	47.0	129.0	-	77.0	-	3.7	99.0	38.0	93.0	4.5
6-4, 44-47	333.96	BOG	NA	-	-	-	48.2	137.0	-	-	-	3.1	-	-	-	-
6-4, 48-52	334.00	DRA	XF	-	325.9	214.1	-	144.2	-	92.2	16.4	4.9	104.8	31.9	93.6	4.5
6-4, 54-57	334.06	WEA	XF	-	376.0	241.0	-	121.0	-	88.0	19.0	4.0	103.0	35.0	92.0	4.5
6-4, 71-74	334.23	SHM	XF	-	-	269.0	54.0	153.0	140	86.0	-	-	101.0	31.0	88.0	-
6-4, 139-142	334.91	JCB	NA	42.6	-	242.0	44.8	130.0	-	-	-	-	-	-	-	-
6-4, 144-147	334.96	SHM	XF	-	-	260.0	49.0	121.0	141	88.0	-	-	105.0	34.0	90.0	-
6-5, 22-24	335.23	JCB	NA	42.2	-	239.0	45.1	120.0	-	-	-	-	-	-	-	-
6-5, 32-34	335.33	DRA	XF	-	340.2	222.3	-	123.0	-	94.3	17.0	5.7	101.2	33.0	96.6	4.9
6-5, 43-46	335.45	BOG	XFNA	41.9	385.0	239.0	49.0	135.0	-	89.0	-	5.0	103.0	39.6	98.0	6.0
6-5, 43-46	335.45	BOG	NA	-	-	-	51.7	138.0	-	-	-	2.5	-	-	-	-
6-5, 58-61	335.60	JCB	NA	41.5	-	235.0	44.3	120.0	-	-	-	-	-	-	-	-
7-1, 12-15	338.14	DRA	XF	-	349.4	236.2	-	119.8	-	98.4	17.2	7.2	103.6	33.3	97.3	5.2
7-2, 20-23	339.72	BOG	XFNA	41.5	398.0	252.0	47.0	121.0	-	87.0	-	6.7	104.0	41.2	98.0	5.4
7-2, 20-23	339.72	BOG	NA	-	-	-	47.9	129.0	-	-	-	4.8	-	-	-	-
7-2, 38-41	339.90	SHM	XF	-	-	251.0	60.0	128.0	128	88.0	-	-	105.0	35.0	91.0	-
7-2, 136-138	340.87	PUC	XFNAAA	41.3	-	211.0	40.4	110.0	152	99.0	16.0	< 2.0	113.0	37.0	114.0	-
7-3, 13-15	341.14	DRA	XF	-	346.7	235.3	-	121.0	-	96.7	17.1	2.6	102.1	34.2	99.1	5.6
7-3, 58-61	341.60	BOG	XFNA	39.8	378.0	237.0	47.0	119.0	-	84.0	-	3.7	108.0	41.1	96.0	5.5
7-3, 58-61	341.60	BOG	NA	-	-	-	46.5	117.0	-	-	-	3.8	-	-	-	-
7-3, 60-63	341.62	WEA	XF	-	382.0	252.0	-	119.0	-	92.0	18.0	3.0	107.0	36.0	92.0	4.6
8-1, 10-14	347.12	JCB	NA	43.0	-	220.0	45.2	140.0	-	-	-	-	-	-	-	-
8-1, 25-27	347.26	JCB	NA	42.7	-	239.0	44.5	110.0	-	-	-	-	-	-	-	-
8-1, 44-47	347.46	JCB	NA	43.2	-	240.0	43.5	130.0	-	-	-	-	-	-	-	-
8-1, 76-79	347.78	JCB	NA	44.6	-	243.0	31.5	70.0	-	-	-	-	-	-	-	-

Table 2. (Continued).

Cs	Ba	La	Ce	Nd	Sm	Eu	Gd	Tb	Ho	Tm	Yb	Lu	Hf	Ta	Th	U
-	-	-	-	-	-	-	-	-	-	-	-	-	-	-	-	-
0.25	26.1	3.10	10.2	-	-	1.18	-	0.79	-	-	-	-	2.48	0.26	0.25	0.17
-	-	-	-	-	-	-	-	-	-	-	-	-	-	-	-	-
0.10	-	2.65	8.5	-	3.20	1.12	-	0.93	-	-	3.50	0.57	2.23	0.18	0.17	-
0.04	12.0	3.50	11.5	-	-	1.24	-	0.81	-	-	-	-	2.49	0.28	0.33	0.13
-	-	-	-	-	-	-	-	-	-	-	-	-	-	-	-	-
0.18	-	2.49	7.8	-	3.04	1.09	-	0.87	-	-	3.38	0.55	2.25	0.16	0.21	-
0.12	-	2.59	8.4	-	3.08	1.06	-	0.84	-	-	3.46	0.57	2.18	0.18	0.11	-
0.35	-	2.54	8.1	-	3.05	1.10	-	0.86	-	-	3.45	0.56	2.22	0.09	0.19	-
0.14	-	3.38	10.1	-	3.35	1.15	-	0.93	-	-	3.58	0.57	2.45	0.22	0.20	-
0.36	-	3.45	10.0	-	3.39	1.20	-	0.90	-	-	3.63	0.58	2.69	0.28	0.22	-
-	-	-	-	-	-	-	-	-	-	-	-	-	-	-	-	-
0.30	-	3.34	10.1	-	3.31	1.18	-	0.94	-	-	3.59	0.57	2.48	0.28	0.19	-
0.08	-	2.64	8.1	-	3.22	1.14	-	0.88	-	-	3.79	0.57	2.45	0.22	0.11	-
0.10	-	2.62	8.3	-	3.20	1.16	-	0.91	-	-	3.73	0.57	2.41	0.20	0.16	-
0.38	14.2	3.54	9.8	-	-	1.22	-	0.77	-	-	-	-	2.45	0.26	0.24	0.14
-	-	-	-	-	-	-	-	-	-	-	-	-	-	-	-	-
0.12	-	3.51	10.5	-	3.33	1.19	-	0.93	-	-	3.58	0.57	2.46	0.37	0.20	-
-	29.0	-	-	-	-	-	-	-	-	-	-	-	-	-	-	-
-	-	-	-	-	-	-	-	-	-	-	-	-	-	-	-	-
0.39	13.0	3.40	9.9	-	-	1.30	-	0.78	-	-	-	-	2.52	0.26	0.26	-
-	-	-	-	-	-	-	-	-	-	-	-	-	-	-	-	-
0.60	-	3.80	11.2	8.9	3.47	1.16	4.50	0.84	1.28	0.52	3.60	0.52	2.10	0.19	0.30	< .20
0.48	-	3.30	11.2	-	-	1.18	-	0.75	-	-	-	-	2.38	0.28	0.24	0.07
-	-	-	-	-	-	-	-	-	-	-	-	-	-	-	-	-
-	16.0	4.00	10.0	9.0	-	-	-	-	-	-	-	-	-	-	-	-
-	-	-	-	-	-	-	-	-	-	-	-	-	-	-	-	-
-	66.0	-	-	-	-	-	-	-	-	-	-	-	-	-	-	-
-	36.0	-	-	-	-	-	-	-	-	-	-	-	-	-	-	-
0.30	-	3.68	11.6	-	-	1.31	-	0.79	-	-	-	-	2.46	0.28	0.24	0.16
-	-	-	-	-	-	-	-	-	-	-	-	-	-	-	-	-
0.46	-	3.49	10.6	-	3.33	1.19	-	0.90	-	-	3.64	0.56	2.58	0.33	0.20	-
-	55.0	-	-	-	-	-	-	-	-	-	-	-	-	-	-	-
0.20	10.0	3.61	7.6	-	-	1.21	-	0.74	-	-	-	-	2.43	0.27	0.25	0.07
-	-	-	-	-	-	-	-	-	-	-	-	-	-	-	-	-
0.27	22.0	3.40	7.8	-	-	1.22	-	0.77	-	-	-	-	2.35	0.28	0.25	0.05
-	-	-	-	-	-	-	-	-	-	-	-	-	-	-	-	-
-	-	-	-	-	-	-	-	-	-	-	-	-	-	-	-	-
0.35	-	3.48	10.5	-	3.30	1.19	-	0.97	-	-	3.60	0.56	2.56	0.32	0.22	-
-	47.0	-	-	-	-	-	-	-	-	-	-	-	-	-	-	-
0.48	16.0	3.25	8.1	-	-	1.26	-	0.79	-	-	-	-	2.52	0.29	0.30	0.09
-	-	-	-	-	-	-	-	-	-	-	-	-	-	-	-	-
0.52	-	3.60	10.8	-	-	1.24	-	0.78	-	-	-	-	2.52	0.29	0.28	0.05
-	-	-	-	-	-	-	-	-	-	-	-	-	-	-	-	-
-	-	-	-	-	-	-	-	-	-	-	-	-	-	-	-	-
0.30	9.7	3.73	11.4	-	-	1.21	-	0.81	-	-	-	-	2.60	0.31	0.34	-
-	-	-	-	-	-	-	-	-	-	-	-	-	-	-	-	-
-	50.0	-	-	-	-	-	-	-	-	-	-	-	-	-	-	-
0.37	-	3.75	10.8	-	3.41	1.20	-	0.97	-	-	3.72	0.58	2.73	0.34	0.25	-
-	-	-	-	-	-	-	-	-	-	-	-	-	-	-	-	-
0.05	13.2	3.71	12.0	-	-	1.29	-	0.80	-	-	-	-	2.47	0.29	0.35	0.15
-	-	-	-	-	-	-	-	-	-	-	-	-	-	-	-	-
< .14	-	3.70	10.5	8.3	3.42	1.13	4.20	0.82	1.17	0.45	3.40	0.50	2.10	0.20	0.28	< .20
-	18.0	4.00	12.0	10.0	-	-	-	-	-	-	-	-	-	-	-	-
0.20	35.0	4.10	10.4	-	-	1.18	-	0.77	-	-	-	-	2.45	0.30	0.17	0.10
-	-	-	-	-	-	-	-	-	-	-	-	-	-	-	-	-
-	-	-	-	-	-	-	-	-	-	-	-	-	-	-	-	-
-	-	-	-	-	-	-	-	-	-	-	-	-	-	-	-	-
-	23.0	5.00	10.0	9.0	-	-	-	-	-	-	-	-	-	-	-	-
0.04	13.0	3.80	10.4	-	-	1.25	-	0.77	-	-	-	-	2.53	0.31	0.29	0.11
-	-	-	-	-	-	-	-	-	-	-	-	-	-	-	-	-
0.48	12.0	3.50	9.2	-	-	1.32	-	0.78	-	-	-	-	2.47	0.32	0.31	0.02
-	-	-	-	-	-	-	-	-	-	-	-	-	-	-	-	-
0.27	-	3.89	11.2	-	3.47	1.22	-	0.99	-	-	3.72	0.58	2.66	0.37	0.23	-
0.31	-	3.93	11.1	-	3.46	1.20	-	0.95	-	-	3.64	0.58	2.67	0.37	0.25	-
0.31	-	3.89	11.1	-	3.45	1.21	-	0.96	-	-	3.67	0.58	2.65	0.38	0.26	-
0.15	17.2	3.76	9.1	-	-	1.19	-	0.78	-	-	-	-	2.46	0.30	0.27	0.07
-	-	-	-	-	-	-	-	-	-	-	-	-	-	-	-	-
-	-	-	-	-	-	-	-	-	-	-	-	-	-	-	-	-
-	22.0	4.00	12.0	10.0	-	-	-	-	-	-	-	-	-	-	-	-
-	32.0	-	-	-	-	-	-	-	-	-	-	-	-	-	-	-
0.05	-	3.84	11.1	-	3.44	1.21	-	0.98	-	-	3.63	0.58	2.84	0.36	0.26	-
-	41.0	-	-	-	-	-	-	-	-	-	-	-	-	-	-	-
0.08	-	3.95	11.0	-	3.49	1.21	-	0.99	-	-	3.60	0.58	2.78	0.32	0.30	-
-	-	-	-	-	-	-	-	-	-	-	-	-	-	-	-	-
0.23	27.6	4.25	11.9	-	-	1.35	-	0.83	-	-	-	-	2.63	0.33	0.30	0.08
-	-	-	-	-	-	-	-	-	-	-	-	-	-	-	-	-
0.44	-	4.00	11.2	-	3.45	1.20	-	0.99	-	-	3.57	0.58	2.73	0.33	0.26	-
-	-	-	-	-	-	-	-	-	-	-	-	-	-	-	-	-
0.39	-	4.10	11.6	-	-	1.36	-	0.81	-	-	-	-	2.77	0.35	0.34	0.11
-	-	-	-	-	-	-	-	-	-	-	-	-	-	-	-	-
-	65.0	-	-	-	-	-	-	-	-	-	-	-	-	-	-	-
0.93	-	4.30	11.9	8.3	3.64	1.16	4.20	0.87	1.18	0.50	3.60	0.50	2.20	0.25	0.38	0.30
-	-	-	-	-	-	-	-	-	-	-	-	-	-	-	-	-
0.13	17.0	3.80	12.2	-	-	1.20	-	0.78	-	-	-	-	2.61	0.33	0.30	0.09
-	-	-	-	-	-	-	-	-	-	-	-	-	-	-	-	-
-	24.0	5.00	12.0	10.0	-	-	-	-	-	-	-	-	-	-	-	-
0.16	-	4.42	11.5	-	3.58	1.27	-	1.06	-	-	3.79	0.59	2.83	0.37	0.34	-
0.43	-	4.11	11.9	-	3.54	1.25	-	1.03	-	-	3.75	0.58	2.81	0.39	0.33	-
0.37	-	4.26	12.1	-	3.65	1.29	-	1.03	-	-	3.76	0.60	2.87	0.36	0.31	-
0.08	-	4.49	12.5	-	3.82	1.32	-	1.05	-	-	3.93	0.64	2.91	0.38	0.32	-

Table 2. (Continued).

Sample	Depth (m)	Inv.	Method	Sc	V	Cr	Co	Ni	Cu	Zn	Ga	Rb	Sr	Y	Zr	Nb
Hole 564 (Cont.)																
Chemical Group I (Cont.)																
8-2, 0-3	348.52	BOG	XFNA	40.1	378.0	243.0	47.0	110.0	-	83.0	-	7.6	108.0	40.0	96.0	6.0
8-2, 0-3	348.52	BOG	NA	-	-	-	45.8	112.0	-	-	-	7.6	-	-	-	-
8-2, 7-10	348.59	DRA	XF	-	346.0	232.3	-	118.6	-	97.6	16.2	7.5	103.2	32.5	97.4	5.5
8-2, 22-25	348.74	JCB	NA	42.6	-	239.0	40.1	100.0	-	-	-	-	-	-	-	-
8-2, 75-77	349.26	BOG	XFNA	42.8	463.0	228.0	56.0	136.0	-	94.0	-	5.2	109.0	41.7	96.0	6.1
8-2, 75-77	349.26	BOG	NA	-	-	-	55.3	129.0	-	-	-	4.0	-	-	-	-
9-1, 1-4	356.03	SHM	XF	-	-	261.0	61.0	111.0	124	84.0	-	-	113.0	31.0	88.0	-
9-1, 18-20	356.19	DRA	XF	-	383.7	217.2	-	103.9	-	85.3	19.3	14.7	114.6	35.6	96.1	5.8
9-1, 43-45	356.44	BOG	XFNA	41.2	463.0	208.0	50.0	125.0	-	81.0	-	7.3	108.0	41.3	99.0	5.4
9-1, 43-45	356.44	BOG	NA	-	-	-	50.8	109.0	-	-	-	7.7	-	-	-	-
9-1, 72-74	356.73	PUC	XFNAAA	43.1	-	217.0	49.0	120.0	70	109.0	18.0	6.8	118.0	37.0	114.0	-
9-1, 140-143	357.42	DRA	XF	-	362.1	222.8	-	139.7	-	111.2	17.7	6.9	106.9	33.4	98.9	6.0
9-2, 128-130	358.79	DRA	XF	-	371.3	215.1	-	121.2	-	109.7	17.1	6.2	107.9	34.1	100.5	5.7
9-2, 142-144	358.93	JCB	NA	42.5	-	238.0	52.2	90.0	-	-	-	-	-	-	-	-
9-3, 25-28	359.27	SHM	XF	-	-	248.0	60.0	124.0	141	88.0	-	-	104.0	35.0	93.0	-
9-3, 68-71	359.70	DRA	XF	-	365.3	233.7	-	117.6	-	107.3	17.4	6.3	107.2	33.8	101.3	6.7
9-3, 72-75	359.74	BOG	XFNA	40.1	375.0	235.0	45.0	116.0	-	83.0	-	2.9	102.0	40.6	100.0	4.6
9-3, 72-75	359.74	BOG	NA	-	-	-	46.9	116.0	-	-	-	2.4	-	-	-	-
9-3, 76-79	359.78	PUC	XFNAAA	41.4	-	207.0	40.3	109.0	145	102.0	17.0	< 2.0	115.0	37.0	115.0	-

Note: Sample numbers are given in core-section, interval in cm. Depth is sub-bottom depth.

Investigator (Inv.) codes are: BOG = H. Bougault, IFREMER (Chapters 3 and 23, this volume); DRA = N. Drake, Department of Geology, University of Massachusetts (Chapter 20, this volume); JCB = J.C. Brannon, Department of Earth and Planetary Sciences, Washington University in St. Louis (Chapter 21, this volume); PUC = H. Puchelt, Institut für Petrologie und Geochemie der Universität Karlsruhe; SHM = H.-U. Schmincke, Ruhr Universität Bochum, Mineralogisches Institut (chapter may be published in future DSDP volume); WEA = B.L. Weaver, Department of Geology, University of Leicester (present address: School of Geology and Geophysics, University of Oklahoma, Norman, Oklahoma 73019) (Chapter 19, this volume).

The methods codes are: XF = X-ray fluorescence; NA = instrumental neutron activation analysis; XFNA = XF and NA; XFNAAA = XF and NA and atomic absorption. Bougault's (BOG) samples have been analyzed as follows: V, Cr, Zn, Sr, Y, Nb, and Zr by XF; Sc, Cs, Ba, La, Ce, Eu, Tb, Hf, Ta, Th, and U by Na. Co, Ni, and Rb by both XF and NA.

Table 2. (Continued).

Cs	Ba	La	Ce	Nd	Sm	Eu	Gd	Tb	Ho	Tm	Yb	Lu	Hf	Ta	Th	U
0.56	25.0	3.88	12.1	-	-	1.24	-	0.81	-	-	-	-	2.62	0.35	0.40	0.13
-	-	-	-	-	-	-	-	-	-	-	-	-	-	-	-	-
-	-	-	-	-	-	-	-	-	-	-	-	-	-	-	-	-
0.37	-	4.19	11.7	-	3.59	1.23	-	0.99	-	-	3.71	0.58	2.80	0.35	0.31	-
0.18	11.0	4.20	9.7	-	-	1.36	-	0.86	-	-	-	-	2.71	0.38	0.40	0.08
-	-	-	-	-	-	-	-	-	-	-	-	-	-	-	-	-
-	67.0	-	-	-	-	-	-	-	-	-	-	-	-	-	-	-
-	-	-	-	-	-	-	-	-	-	-	-	-	-	-	-	-
0.32	23.5	4.16	11.5	-	-	1.23	-	0.79	-	-	-	-	2.71	0.36	0.39	0.14
-	-	-	-	-	-	-	-	-	-	-	-	-	-	-	-	-
0.30	-	4.50	12.2	8.5	3.63	1.18	4.80	0.86	1.18	0.49	3.70	0.51	2.30	0.25	0.36	0.30
-	-	-	-	-	-	-	-	-	-	-	-	-	-	-	-	-
-	-	-	-	-	-	-	-	-	-	-	-	-	-	-	-	-
0.33	-	4.24	11.7	-	3.47	1.22	-	1.00	-	-	3.62	0.57	2.67	0.35	0.32	-
-	62.0	-	-	-	-	-	-	-	-	-	-	-	-	-	-	-
-	-	-	-	-	-	-	-	-	-	-	-	-	-	-	-	-
0.05	21.0	4.21	8.4	-	-	1.26	-	0.81	-	-	-	-	2.58	0.37	0.36	0.07
-	-	-	-	-	-	-	-	-	-	-	-	-	-	-	-	-
< .14	-	4.50	11.9	8.0	3.52	1.14	5.40	0.84	1.34	0.49	3.50	0.50	2.10	0.25	0.42	< .20

Drilling locations

Leg	Location	Sites
Phase 1 1968–1970		
1	North Atlantic	1–7
2	North Atlantic	8–12
3	South Atlantic	13–22
4	Central Atlantic	23–31
5	North Pacific	32–43
6	North Pacific	44–60
7	Central Pacific	61–67
8	Central Pacific	68–75
9	Central Pacific	76–84
Phase 2 1970–1972		
10	Gulf of Mexico	85–97
11	North Atlantic	98–108
Re-entry trials		109–110
12	North Atlantic	111–119
13	Mediterranean	120–134
14	Central Atlantic	135–144
15	Caribbean	146–154
16	Central Pacific	155–163
17	Central Pacific	164–171
18	North Pacific	172–182
19	North Pacific	183–193
20	North Pacific	194–202
21	Coral Sea	203–210
22	Indian Ocean	211–218
23	Arabian Sea	219–230
24	Indian Ocean	231–238
25	Indian Ocean	239–249
Phase 3 1972–1975		
26	Indian Ocean	250–258
27	Indian Ocean	259–263
28	Antarctic	264–274
29	Tasman Sea	275–284
30	South Pacific	285–289
31	North Pacific	290–302
32	North Pacific	303–313
33	North Pacific	314–318
34	South Pacific	319–321
35	South Pacific	322–325
36	South Atlantic	326–331
37	North Atlantic	332–335
38	Arctic	336–352
39	Atlantic	353–359
40	South Atlantic	360–365
41	South Atlantic	366–370
42A	Mediterranean	371–378
42B	Black Sea	379–381
43	North Atlantic	382–387
44	North Atlantic	388–392
44A	North Atlantic	393–394
IPOD I 1975–present		
45	North Atlantic	395–396
46	North Atlantic	396A–396B
47	North Atlantic	397–398
48	North Atlantic	399–406
49	North Atlantic	407–414
50	North Atlantic	415–416
51A	North Atlantic	417–417A
51B	North Atlantic	417B–417D
52	North Atlantic	417D–418A
53	North Atlantic	418A–418B
54	Central Pacific	419–429
55	North Pacific	430–433
56	North Pacific	434–437
57	North Pacific	438–441
58	North Pacific	442–446
59	North Pacific	447–451
60	North Pacific	452–461
61	Central Pacific	462
62	North Pacific	463–466
63	North Pacific	467–473
64	Gulf of California	474–481
65	Gulf of California	482–485
66	Central Pacific	486–493
67	Central Pacific	494–500
68	Central Pacific	502–503
69	Central Pacific	504–505, 501
70	Central Pacific	506–510, 504B
71	South Atlantic	511–514
72	South Atlantic	515–518
73	South Atlantic	519–524
74	South Atlantic	525–529
75	South Atlantic	530–532
76	North Atlantic	533–534
77	Caribbean	535–540
78	North Atlantic	541–543, 395A, B
79	North Atlantic	544–547
80	North Atlantic	548–551
81	North Atlantic	552–555
82	North Atlantic	556–564

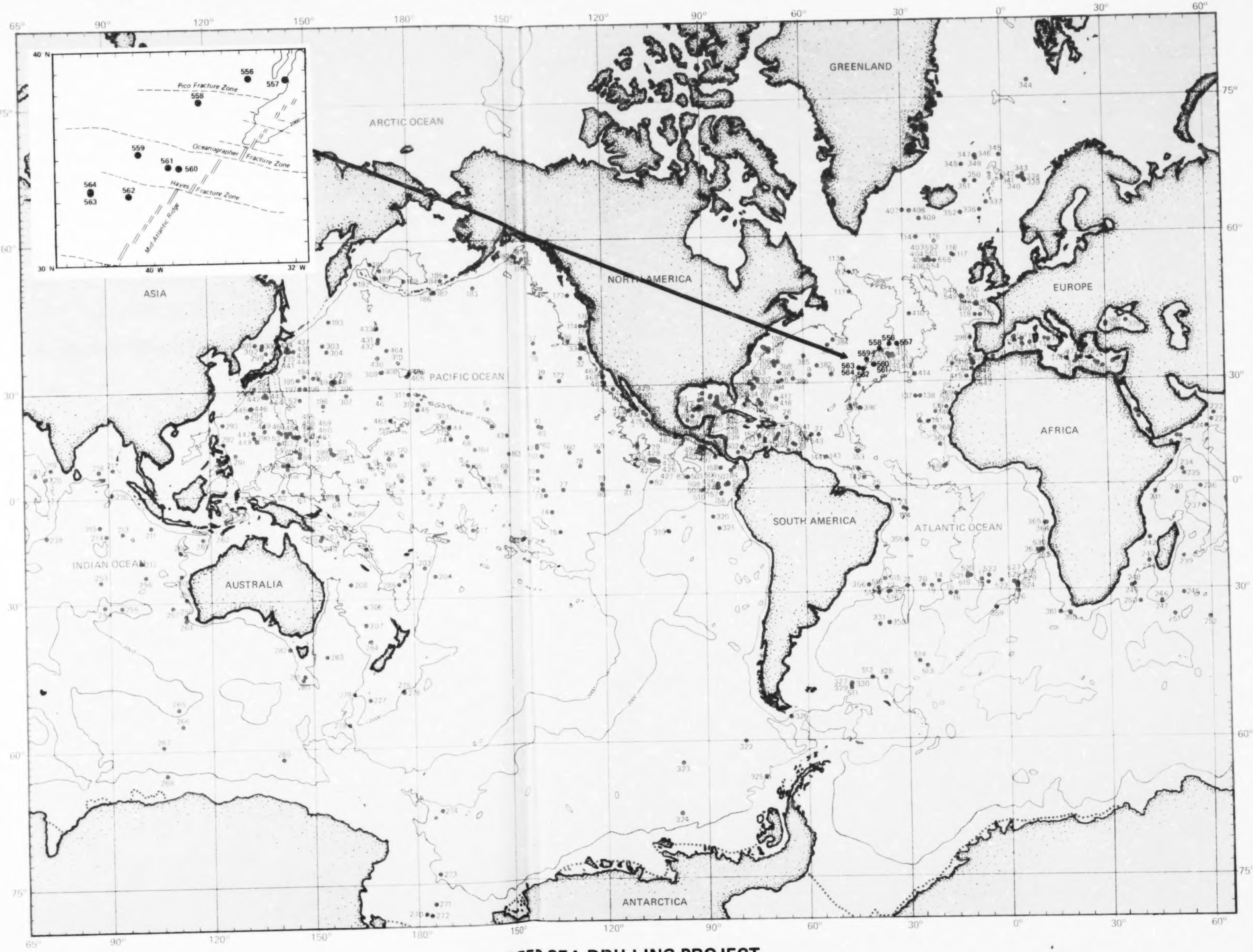
40 N
30 N
40 W
32 W
Pico Fracture Zone
Oceanographer Fracture Zone
Hayes Fracture Zone
Mid-Atlantic Ridge
556
557
558
559
560
561
562
563
564
ARCTIC OCEAN
GREENLAND
NORTH AMERICA
EUROPE
ASIA
PACIFIC OCEAN
AFRICA
SOUTH AMERICA
ATLANTIC OCEAN
INDIAN OCEAN
AUSTRALIA
ANTARCTICA
65°
90°
120°
150°
180°
60°
30°
0°
75°

DEEP SEA DRILLING PROJECT

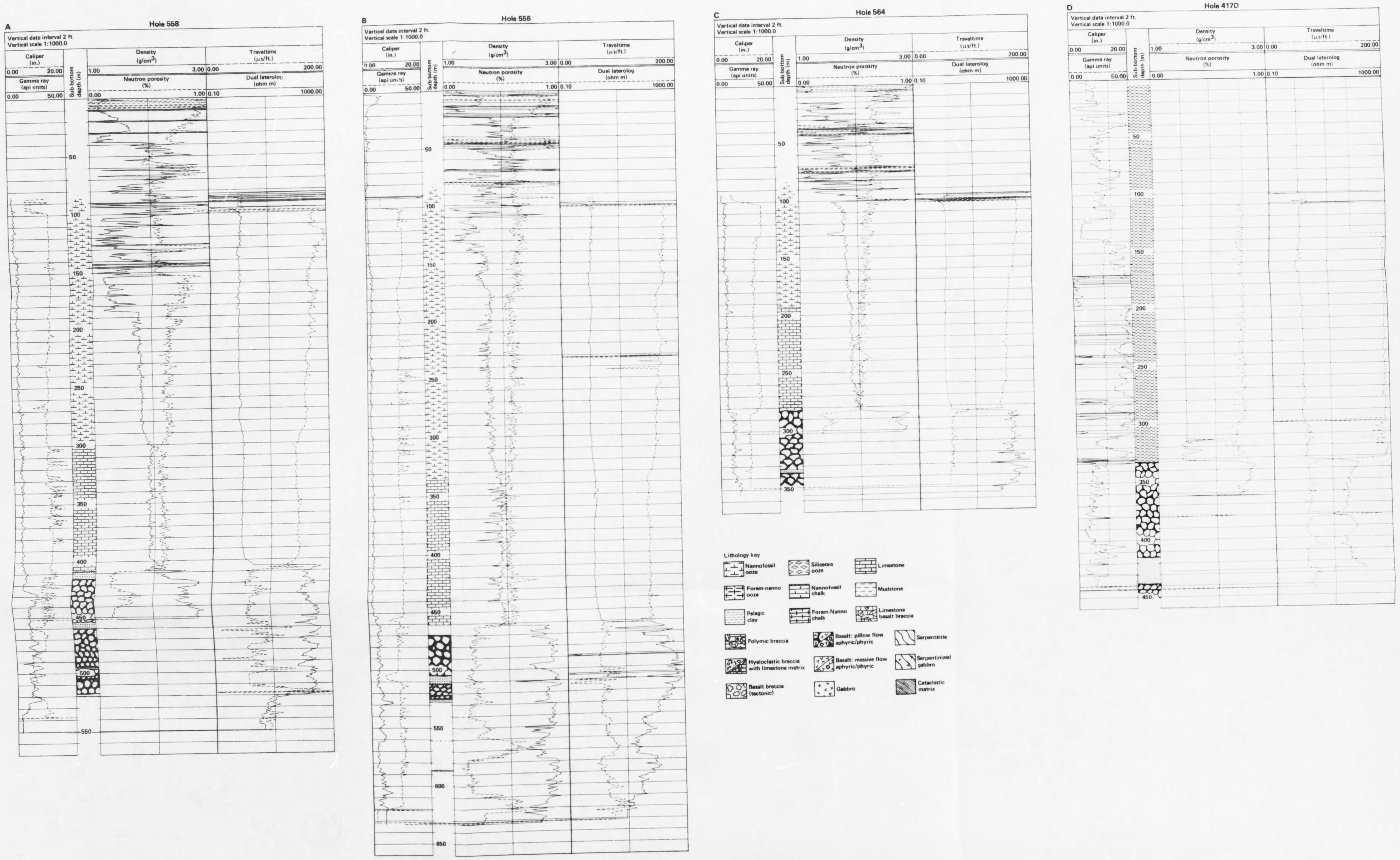

Volume 82: Chapter 14: Figure 4. Logged curves for Holes 558 (A), 556 (B), 564 (C), and 417D (D).

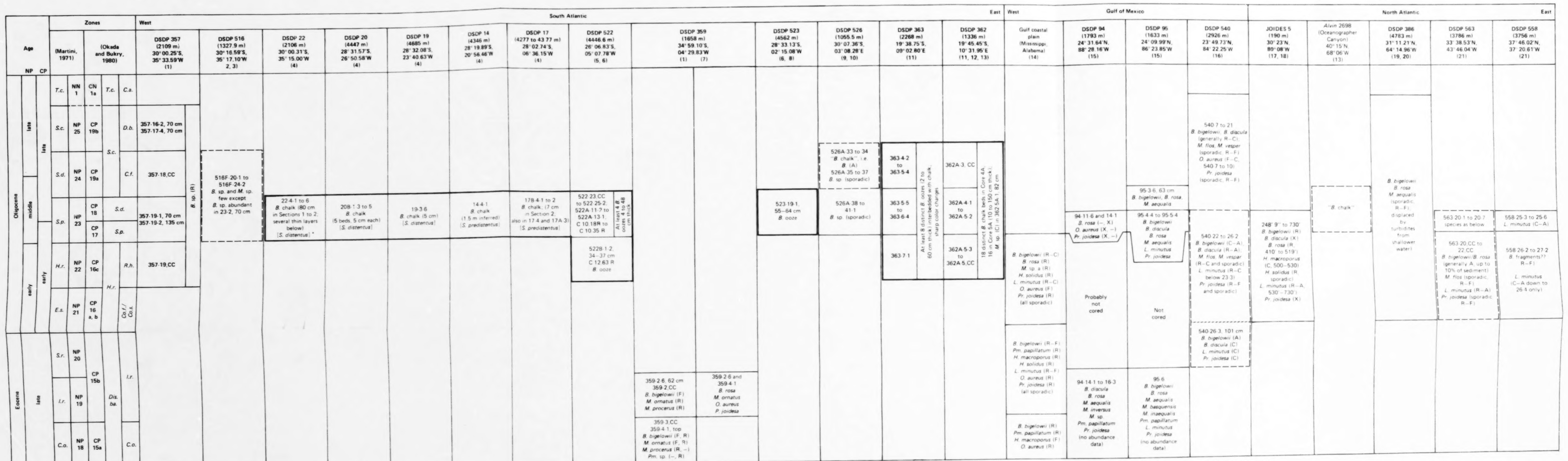
Age
NP
CP
Zones
(Martini, 1971)
(Okada and Bukry, 1980)
Oligocene
late
middle
early
Eocene
T.c.
NN 1
CN 1a
C.a.
S.c.
NP 25
CP 19b
D.b.
S.d.
NP 24
CP 19a
C.f.
S.p.
NP 23
CP 18
CP 17
H.r.
NP 22
CP 16c
R.h.
E.s.
NP 21
CP 16 a, b
Co.f./Co.s.
S.r.
NP 20
CP 15b
I.r.
NP 19
Dis. ba.
C.o.
NP 18
CP 15a
West
South Atlantic
East
DSDP 357 (2109 m) 30° 00.25'S, 35° 33.59'W (1)
357-16-2, 70 cm 357-17-4, 70 cm
357-18,CC
357-19-1, 70 cm 357-19-2, 135 cm
357-19,CC
B. sp. (R)
DSDP 516 (1327.9 m) 30° 16.59'S, 35° 17.10'W 2, 3)
516F-20-1 to 516F-24-2 B. sp. and M. sp. few except B. sp. abundant in 23-2, 70 cm
DSDP 22 (2106 m) 30° 00.31'S, 35° 15.00'W (4)
22-4-1 to 6 B. chalk (80 cm in Sections 1 to 2; several thin layers below) [S. distentus] *
DSDP 20 (4447 m) 28° 31.57'S, 26° 50.58'W (4)
20B-1-3 to 5 B. chalk (5 beds, 5 cm each) [S. distentus]
DSDP 19 (4685 m) 28° 32.08'S, 23° 40.63'W (4)
19-3-6 B. chalk (5 cm) [S. distentus]
DSDP 14 (4346 m) 28° 19.89'S, 20° 56.46'W (4)
14-4-1 B. chalk (1.5 m inferred) [S. predistentus]
DSDP 17 (4277 to 43 77 m) 28° 02.74'S, 06° 36.15'W (4)
17B-4-1 to 2 B. chalk; (7 cm in Section 2; also in 17-4 and 17A-3) [S. predistentus]
DSDP 522 (4446.6 m) 26° 06.83'S, 05° 07.78'W (5, 6)
522-23,CC to 522-25-2; 522A-11-2 to 522A-13-1; C 10.18R to C 10.35 R
At least 4 B. oozes 4 to 48 cm thick
522B-1-2, 34–37 cm C 12.63 R B. ooze
DSDP 359 (1658 m) 34° 59.10'S, 04° 29.83'W (1) (7)
359-2-6, 62 cm 359-2,CC B. bigelowii (F) M. ornatus (R) M. procerus (R)
359-3,CC 359-4-1, top B. bigelowii (F, R) M. ornatus (F, R) M. procerus (R, –) Pm. sp. (–, R)
359-2-6 and 359-4-1 B. rosa M. ornatus O. aureus P. joidesa
DSDP 523 (4562 m) 28° 33.13'S, 02° 15.08'W (6, 8)
523-19-1, 55–64 cm B. ooze
DSDP 526 (1055.5 m) 30° 07.36'S, 03° 08.28'E (9, 10)
526A-33 to 34 "B. chalk", i.e. B. (A) 526A-35 to 37 B. sp. (sporadic)
526A-38 to 41-1 B. sp. (sporadic)
DSDP 363 (2268 m) 19° 38.75'S, 09° 02.80'E (11)
363-4-2 to 363-5-4
363-5-5 to 363-6-4
363-7-1
At least 8 distinct B. oozes (2 to 60 cm thick) interbedded with chalk; sharp color changes
DSDP 362 (1336 m) 19° 45.45'S, 10° 31.95'E (11, 12, 13)
362A-3, CC
362A-4-1 to 362A-5-2
362A-5-3 to 362A-5,CC
18 distinct B. chalk beds in Core 4A, 16 in Core 5A (10 to 150 cm thick); M. sp. (C) in 362-5A-1, 82 cm
West
Gulf of Mexico
Gulf coastal plain (Mississippi, Alabama) (14)
B. bigelowii (R–C) B. rosa (R) M. sp. a (R) H. solidus (R) L. minutus (R–C) O. aureus (F) Pr. joidesa (R) (all sporadic)
B. bigelowii (R–F) Pm. papillatum (R) H. macroporus (R) H. solidus (R) L. minutus (R–F) O. aureus (R) Pr. joidesa (R) (all sporadic)
B. bigelowii (R) Pm. papillatum (R) H. macroporus (F) O. aureus (R)
DSDP 94 (1793 m) 24° 31.64'N, 88° 28.16'W (15)
94-11-6 and 14-1 B. rosa (–, X) O. aureus (X, –) Pr. joidesa (X, –)
Probably not cored
94-14-1 to 16-3 B. discula B. rosa M. aequalis M. inversus M. sp. Pm. papillatum Pr. joidesa (no abundance data)
DSDP 95 (1633 m) 24° 09.99'N, 86° 23.85'W (15)
95-3-6, 63 cm B. bigelowii, B. rosa, M. aequalis
95-4-4 to 95-5-4 B. bigelowii B. discula B. rosa M. aequalis L. minutus Pr. joidesa
Not cored
95-6 B. bigelowii B. rosa M. aequalis M. basquensis M. inaequalis Pm. papillatum L. minutus Pr. joidesa (no abundance data)
DSDP 540 (2926 m) 23° 49.73'N, 84° 22.25'W (16)
540-7 to 21 B. bigelowii, B. discula (generally R–C); M. flos, M. vesper (sporadic, R–F) O. aureus (F–C, 540-7 to 10) Pr. joidesa (sporadic, R–F)
540-22 to 26-2 B. bigelowii (C–A); B. discula (R–A); M. flos, M. vespar (R–C and sporadic) L. minutus (R–C below 23-3) Pr. joidesa (R–F and sporadic)
540-26-3, 101 cm B. bigelowii (A) B. discula (C) L. minutus (C) Pr. joidesa (C)
North Atlantic
East
JOIDES 5 (190 m) 30° 23'N, 80° 08'W (17, 18)
248' 9" to 730' B. bigelowii (R) B. discula (X) B. rosa (R, 410' to 519') H. macroporus (C, 500–530) H. solidus (R, sporadic) L. minutus (R–A, 530'–730') Pr. joidesa (X)
Alvin 2698 (Oceanographer Canyon) 40° 15'N, 68° 06'W (13)
"B. chalk"
DSDP 386 (4783 m) 31° 11.21'N, 64° 14.96'W (19, 20)
B. bigelowii B. rosa M. aequalis (sporadic, R–F), displaced by turbidites from shallower water)
DSDP 563 (3786 m) 33° 38.53'N, 43° 46.04'W (21)
563-20-1 to 20-7 species as below
563-20,CC to 22,CC B. bigelowii/B. rosa (generally A, up to 10% of sediment) M. flos (sporadic, R–F) L. minutus (R–A) Pr. joidesa (sporadic R–F)
DSDP 558 (3756 m) 37° 46.02'N, 37° 20.61'W (21)
558-25-3 to 25-6 L. minutus (C–A)
558-26-2 to 27-2 B. fragments?? R–F) L. minutus (C–A down to 26-4 only)

Volume 82: Chapter 34: Figure 8. Mid-Tertiary *Braarudosphaera* oozes, chalks, and *Braarudosphaera*/holococcolith associations. Abundances and taxonomic identifications of species are given as originally reported in the literature cited. Depths given are seafloor depths. C 10.18R to C 10.35R and C 10.35R magnetostratigraphic intervals.

*Zones originally assigned in (4) are indicated for Sites 14 to 22 in brackets.

T.c. = *Triquetrorhabdulus carinatus*
S.c. = *Sphenolithus ciperoensis*
S.d. = *Sphenolithus distentus*
S.p. = *Sphenolithus predistentus*
H.r. = *Helicosphaera reticulata*
E.s. = *Ericsonia subdisticha*
S.r. = *Sphenolithus radians*
I.r. = *Ismolithus recurvus*
C.o. = *Chiasmolithus oamaruensis*
C.a. = *Cyclicargolithus abisectus*
D.b. = *Dictyococcites bisectus*
C.f. = *Cyclicargolithus floridanus*
R.h. = *Reticulofenestra hillae*
Co. f. = *Coccolithus formosus*
Co. s. = *Coccolithus subdistichus*
Dis. ba. = *Discoaster barbadiensis*

Braarudosphaeraceae:

B. = *Braarudosphaera*
M. = *Micrantholithus*
Pm. = *Pemma*

Zygosphaeraceae (holococcoliths):

H. = *Holodiscolithus*
L. = *Lanternithus*
O. = *Orthozygus*
Pr. = *Peritrachelina*

Note: *Zygrhablithus* is not plotted.

(A) = Abundant
(C) = Common
(F) = Few
(R) = Rare
(–) = Absent
(X) = Present

(1) Perch-Nielsen (1977)
(2) Barker, Carlson, Johnson et al. (1983), p. 155–338.
(3) Wise, unpublished data
(4) Maxwell, Von Herzen, et al. (1970), p. 71–471.
(5) Hsü, LaBrecque, et al. (1984), p. 187–270.
(6) LaBrecque et al. (1983)
(7) Bukry (1977)
(8) Hsü, LaBrecque, et al. (1984), p. 271-321.
(9) Moore, Rabinowitz, et al. (1984), p. 161–235.
(10) Manivit (1984)
(11) Bolli, Ryan, et al. (1978), p. 183–356.
(12) Proto Decima et al. (1978)
(13) Bukry (1978a)
(14) Siesser (1983)
(15) Bukry (1973a)
(16) Lang and Watkins (1984)
(17) Bukry (1970)
(18) Roth (1970)
(19) Bukry (1978b)
(20) Thierstein and Okada (1979)
(21) this study

□ *B.* chalk or *B.* ooze

⬚ *B.* abundant